

21st Century COE Program
Evolution of Urban Earthquake Engineering

Fourth International Conference on Urban Earthquake Engineering



Center for Urban Earthquake Engineering
Tokyo Institute of Technology

Tokyo Tech
CUEE

21st Century COE Program
Evolution of Urban Earthquake Engineering

Fourth International Conference on Urban Earthquake Engineering

*Center for Urban Earthquake Engineering
Tokyo Institute of Technology*

Tokyo Tech
CUEE

Conference Papers

Keynote Lectures

Computational Simulation for Earthquake Engineering	1
<i>G. L. Fenves</i>	
Ground Motion Parameters for Loss Estimation.....	7
<i>A. Ansal and G. Tönük</i>	
Reconstruction after Catastrophe in Japan: Experience and Problems A Case Study of the 1995 Hanshin-Awaji Great Earthquake	15
<i>Y. Murosaki</i>	
Soil-Structure Interaction under Extreme Loading Conditions	19
<i>T. D. O'Rourke, J. E. Turner, S-S. Jeon, H. E. Stewart, Y. Wang and P. Shi</i>	
Parametric Structure-Specific Seismic Loss Estimation	45
<i>J. B. Mander, B. A. Bradley and R. P. Dhakal</i>	
Hurricane Katrina: Geosystems in Crisis.....	53
<i>T. D. O'Rourke and T. R. Briggs</i>	

Advanced Technology for Dynamic Response Analysis of Structures

High-Rise Reinforced Concrete Building Using Hydraulic Damper and High-Ductility Concrete and its Vibration Analysis.....	55
<i>K. Kawano, Y. Omika, Y. Yamamoto, M. Maruta and N. Koshika</i>	
Equilibration of Element with Multi-Deformation Components for Nonlinear Structural Analysis.....	63
<i>K. Li and X. Ye</i>	
Dynamic Analysis of High-Rise Building with Passive Dampers Using "Building 3D DYNA"	71
<i>M. Ishii and T. Kouno</i>	
Damage Behavior Simulation of RC Structure Subjected to Seismic Loads.....	79
<i>M. Mitsui, S. Sakai, S. Akiyama and K. Sato</i>	
Finite Element Simulation of Long-Period Ground Motions: The 1906 San Francisco Earthquake and Japanese Subduction-zone Earthquakes	85
<i>Y. Ikegami, K. Koketsu, T. Kimura and H. Miyake</i>	
Elastoplastic Beam Element with Consideration of Local Buckling Behavior	91
<i>K. Kaneko and S. Motoyui</i>	
Formulations and Applications for 3-D Nonlinear Analysis of Structures	99
<i>J.-H. Moon, J.-M. Kim, I.-H. Cho, H.-H Lee and D.-S. Shin</i>	
Analytical Simulation of Seismic Behaviour in Performance Based Engineering Using LS-DYNA.....	107
<i>M. Willford</i>	

Engineering Seismology

Strong Ground Motion Evaluation in the Tokyo Metropolitan Area: The 1923 Kanto Earthquake and Future Subduction-Zone Earthquakes.....	115
<i>K. Koketsu and H. Miyake</i>	
Long-Period Strong Ground Motions and Damage to Oil Storage Tanks due to the Mw8.0 2003 Tokachi-oki Earthquake.....	123
<i>K. Hatayama</i>	
Developing Constraints on Extreme Ground Motions Based on Foam Rubber Model.....	131
<i>Y. Uchiyama, M. D. Purvance, J. N. Brune, A. Anooshehpour and J. G. Anderson</i>	
Site Response in Taipei Urban Area from Dense Microtremor Survey.....	139
<i>K.-L. Wen, C.-M. Lin and C.-T. Chen</i>	
Overturning of Freestanding Objects with Application to Precariously Balanced Rocks.....	147
<i>M. D. Purvance, J. N. Brune, J. G. Anderson and N. A. Abrahamson</i>	
Input Motion Synthesis Considering the Information of the Response of Nonlinear Systems.....	155
<i>R. Honda and R. Yamashita</i>	
Simulation of the M _J 5.4 Earthquake with Use of the Empirical Green's Tensor Spatial Derivatives	163
<i>M. Ohori and Y. Hisada</i>	
A Study on Accuracy of Source Parameters Estimated by Waveform Inversion.....	171
<i>K. Motoki, H. Yamanaka and K. Seo</i>	
Three Dimensional Numerical Simulation of Seismic Response of Large-Scale Underground Infrastructure	177
<i>T. Yamada, T. Ichimura, N. Ohbo, Y. Yamaki, H. Itami and M. Hori</i>	
Development of a New Time-Domain Boundary Element Method in 3-D Elastodynamics for Seismic Analysis	185
<i>T. Saitoh, K. Kimoto and S. Hirose</i>	
Wave Propagation in 2D Anisotropic Layered Media Using Boundary Element Method.....	193
<i>A. Tan and S. Hirose</i>	
Using Stochastic Finite-Fault Modeling to Study the Site Effect in the Taipei Basin	199
<i>C.-T. Chen and K.-L. Wen</i>	
Evaluation of Site Amplifications at High Frequencies in the Taipei Basin.....	205
<i>M.-W. Huang, K.-L. Wen and J.-H. Wang</i>	
Parametric Study on Control of Waveforms Using All Pass Function	213
<i>K. Shirai and T. Ohmachi</i>	
Bi-Directional Structural Response under Near-Field Ground Motions	221
<i>A. Ruangrassamee, S. Siripala and P. Lukkunaprasit</i>	
A Model of Bedrock Structure for Hsinchu Basin, Taiwan Using Gravity Survey	227
<i>H. Morikawa, M. Komazawa, H.T. Chen, T. Shosaka and C. Takahasi</i>	
Some Examples Showing Very Vulnerable Condition in Earthquake Countries.....	231
<i>K. Seo</i>	

Bridge Structures

Strain-Based Verification Method for Seismic Design of Steel Bridge Structures	237
<i>H. Ge and T. Usami</i>	
Simulation Analysis on Collision Test Between Two Steel Bars	245
<i>Y. Kajita, T. Kitahara, Y. Nishimoto and H. Otsuka</i>	
Development of the New Restraining Devices for a Railway Bridge with Isolation Bearings	253
<i>A. Toyooka, H. Iemura, M. Ikeda, Y. Hishijima, S. Uno, M. Ikenaga and T. Harada</i>	
Fatigue Behavior of Defect-Containing Under-Matched Weld Joints under Plastic Strain	261
<i>A. Tanabe and X. Long</i>	
The Effect of Impulsive Ground Motion on the Residual Displacement	269
<i>G. Watanabe and K. Kawashima</i>	
Seismic Performance Evaluation of Existing Steel Bridge Frame Piers with Circular Column	277
<i>K. Kinoshita</i>	
Parametric Study for Shear Carrying Capacity of Externally Prestressed Concrete Members	285
<i>C. Sivaleepunth, J. Niwa and T. Miki</i>	
Seismic Performance of Horizontally Curved Bridges with and without Backfill Soil	293
<i>S. Nagata and I. G. Buckle</i>	

Passive Control and Base Isolation

Control Devices Incorporated with Shape Memory Alloy	301
<i>S. D. Xue and X. Y. Li</i>	
Recent Developments in Passive Control Technologies for Spatial Structures	313
<i>T. Takeuchi, S. D. Xue, S. Kato, T. Ogawa, M. Fujimoto and S. Nakazawa</i>	
Study of Lead Damper for Seismic Isolation System	321
<i>K. Morita and M. Takayama</i>	
Modal Coupling Effect of Mid-story Isolated Buildings	329
<i>M. Kobayashi and T. Koh</i>	
Time-History Analysis Model for Viscoelastic Damper under Long Duration Load	337
<i>D. Sato and K. Kasai</i>	
Seismic Performance Evaluation of Existing R/C Buildings with Hysteresis Dampers Based on Energy Balanced Response	345
<i>K. Fujii and H. Kitamura</i>	
Cumulative Damage of Damper in Elasto-Plastically Damped Buildings	353
<i>H. Ito and K. Kasai</i>	
Seismic Behavior and Performance of Buckling-Restrained Braced Frames	361
<i>L. Fahnestock, R. Sause and J. M. Ricles</i>	

Shaking Table Tests of Two-Story Wood Frames with Passive Control System	369
<i>K. Matsuda, K. Kasai, H. Sakata, Y. Ooki and A. Wada</i>	
Motion and Control Analysis of Structure under Earthquake Excitation	375
<i>C. Y. Wang, C. C. Chuang, S. H. Chen and R. Z. Wang</i>	
Seismic Testing of a Nonlinear Structure with a MR Damper	383
<i>T. Y. Lee, K. Kawashima and P. C. Chen</i>	
Pushover Analysis and Nonlinear Dynamic Analysis of a Three-Story Reinforced Concrete School Building.....	391
<i>H. T. Chen, R. Y. Chen and Y. M. Tien</i>	
Aluminum Shear Panels as Passive Energy Dissipation Devices for Steel Braced Frames.....	399
<i>D. C. Rai and D. Banerjee</i>	
Experiment of Composite Member Composed of Cedar-Glulam-Timber and Steel Plate Applied Friction Connector.....	407
<i>H. Sakata, T. Takeuchi, K. Matsuda and A. Tomimoto</i>	

Tsunami

Tsunami Load Determination for On-Shore Structures.....	415
<i>H. Yeh</i>	
Studies of Present, Past, and Future Tsunami Sources	423
<i>K. Satake</i>	
Vulnerability Estimation in Banda Aceh Using the Tsunami Numerical Model and the Post-Tsunami Survey Data	431
<i>S. Koshimura, T. Oie, H. Yanagisawa and F. Imamura</i>	
Preliminary Results of the Offshore Tsunami Observation by the Kuril Islands Earthquake of 15 November 2006	439
<i>H. Matsumoto, K. Kawaguchi and K. Asawaka</i>	
Effect of Tsunamis on the Gulf of Thailand.....	447
<i>A. Ruangrassamee and N. Saelem</i>	
Development of Numerical Tsunami Simulation Technique in Near Fault Area.....	453
<i>S. Inoue, G. Kubo and T. Ohmachi</i>	
Development of Tsunami Simulator with CIP/Multi-Moment Finite Volume Method	459
<i>R. Akoh, S. Ii and F. Xiao</i>	
Large Model Tests of Surge Front Tsunami Force	467
<i>T. Arikawa</i>	
A Scenario of Earthquake-Tsunami Disaster and a Policy of Measures for Road Networks.....	475
<i>S. Kataoka</i>	
Dynamic Impact of Tsunami Waterborne Massive Objects on Structures.....	483
<i>M. A. K. M. Madurapperuma, A. C. Wijeyewickrema and K. Shakya</i>	

Seismic Hazard Mitigation Planning and Human Behavior

Advanced Damage Detection for Hurricane Katrina: Integrating Remote Sensing and VIEWST TM Field Reconnaissance.....	491
<i>B. J. Adams, J. A. Womble and R. T. Eguchi</i>	
Building Damage Assessment after The 2006 Central Java Earthquake Using High-Resolution Satellite Images.....	511
<i>H. Miura, M. Matsuoka and F. Yamazaki</i>	
Damage Detection Technique Using Satellite SAR Imagery and its Application to Recent Earthquakes.....	519
<i>M. Matsuoka, F. Yamazaki, K. Horie and H. Ohkura</i>	
Study on Disaster Information Linkage between Fire Headquarters and Local Government -A Case Study for Landslide Disaster-	527
<i>T. Mizuta and K. Asano</i>	
What We Learn from Damages and Human Behavior in Condominium Buildings in The 2005 West Off Fukuoka Prefecture Earthquake.....	535
<i>H. Murakami, A. Kawano and K. Sakino</i>	
Seismic Risk Perception and Communication	541
<i>S. Fujii</i>	
Effectiveness of Floor Area Ratio System by Structures for the Reduction of Fire-Spreading Risk.....	553
<i>Y. Meshitsuka</i>	
Discrete Choice Analysis of Temporary Housing Choice After Urban Earthquake Disaster	561
<i>K. Sato, I. Nakabayashi and S. Midorikawa</i>	
Space-Time Distribution of Railroad Passengers for Disaster Prevention Planning	569
<i>T. Osaragi and I. Otani</i>	
Examination about Relations between Stiffness of Floor and Initial Inclination of Furniture at Earthquake: Fundamental Study on Establishment of Evaluation Method for Seismic Resistance of Floor Finishing System Part 3	577
<i>Y. Yokoyama, T. Yokoi and Y. Yoshida</i>	
An Attempt to Improve the Evacuation Drill with the Multi-Agent Simulation	583
<i>K. Hashimoto, T. Ohmachi and S. Inoue</i>	
Developing of Novel Room Relay Tool Using Real-Time Physics Simulation and Portable VR System for Preparedness of Earthquake Disaster	591
<i>J. Ryu and R. Ohno</i>	
Recovery Condition and Behavior of the Affected People -a Case of May 27 th , 2006 Central Java Earthquake-.....	599
<i>R. M. Syam and R. Ohno</i>	

Concrete Structures

Seismic Analysis of Underground Reinforced Concrete Structures and a New Challenge for Numerical Solution	607
<i>H.-W. Song, S.-H. Nam and S.-H. Jang</i>	
RC Pile Foundation-Soil Interaction Analysis Using 3-D Finite Element Method	625
<i>T. Maki, R. Tuladhar and H. Mutsuyoshi</i>	
Multi-Level Seismic Performance Assessment of a Damage-Protected Beam-Column Joint with Internal Lead Dampers.....	633
<i>K. M. Solberg, B. A. Bradley, J.B. Mander, R.P. Dhakal, G.W. Rodgers and J.G. Chase</i>	
Hysteretic Behavior of R/C Corner Joint with Headed Reinforcements	641
<i>S. -Y. Seo, S. -J. Yoon and G. -B. Choi</i>	
Lateral Force-Resisting Mechanism of Shear-Critical Reinforced Concrete Shear Wall Estimated from its Local Shear Forces.....	651
<i>Y. Sanada and T. Kabeyasawa</i>	
Ultimate Strength Equations for R/C Members Retrofitted by Circular Steel Tube.....	659
<i>Y. Sun and T. Fujinaga</i>	
Behavior of Reinforced Concrete Beams Strengthened with Composite Plates.....	667
<i>Y. C. Wang and K. Hsu</i>	
Structural Performance of RC Columns Subjected to Rebar Corrosion	675
<i>M. Iwanami, E. Kato and H. Yokota</i>	
Development of High Strength RC Flat Beam System and SRC Flat Beam System	683
<i>K. Nishimura, K. Takiguchi, H. Hotta, Y. Masui, Y. Tsuneki, Y. Koitabashi and N. Nakanishi</i>	
Mechanical Properties of Composite PC Bridges Using UFC Truss.....	691
<i>H. Murata, T. Miki and J. Niwa</i>	
Shear Strength of R/C Members Based on Plastic Theory Taking Account of Influence of Axial Force and Amount of Longitudinal Reinforcement.....	699
<i>H. Hotta and T. Harada</i>	
Bi-Axial Non-Linear Macroscopic Response Analysis of Slipping Type R/C Structure to Strong Earthquake Motion	707
<i>H. H. Nguyen, K. Nishimura and K. Takiguchi</i>	
Evaluation on Shear Mechanism of Corroded RC Beams by Lattice Model Analysis Considering Bond Deterioration	715
<i>T. Miki and J. Niwa</i>	
Seismic Pounding of Reinforced Concrete Buildings with Non-Equal Story Heights Considering Effects of Underlying Soil.....	723
<i>K. Shakya, A. C. Wijeyewickrema and M. Madurapperuma</i>	

Geotechnical Earthquake Engineering

Simulation of Cutting and Filling Ground in Niigata-ken Chuetsu Earthquake 2004	731
<i>K. Fukutake and A. Onoue</i>	
SAFETY -An Earthquake Disaster Mitigation Measure Considering Cost-Performance and Environmental Impact	739
<i>H. Hazarika</i>	
Evaluation of Seismic Stability of Foundations on Slope	745
<i>M. Okamura and Y. Sugano</i>	
Effects of Near Fault Strong Ground Motion on a Circular Tunnel	755
<i>A. Farahani, A. C. Wijeyewickrema and T. Ohmachi</i>	
Verification of Generalized Scaling Relations for Dynamic Centrifuge Experiments.....	763
<i>T. Tobita and S. Iai</i>	
Stress Reduction Factors in Simplified Liquefaction Susceptibility Analysis.....	771
<i>A. Ansal and G. Tönük</i>	
A Two Mobilized-Plane Model for Soil Liquefaction Analysis	779
<i>S. -S. Park, P. M. Byrne and D. Wijewickreme</i>	
A Unified Prediction for Liquefaction and Settlement of Saturated Sandy Ground.....	791
<i>R. Uzuoka, Y. Shimizu, A. Kamura, N. Sento and M. Kazama</i>	
Push-Over Analyses of Piles in Laterally Spreading Soil	799
<i>S. A. Ashford and T. Juirnarongrit</i>	
Analysis of Piles in Liquefying Soils	809
<i>M. Cubrinovski</i>	
Effects of Cyclic Loading on Mobilisation of Earth Pressure Acting on Pile Caps.....	817
<i>A. Takahashi, H. Sugita and S. Tanimoto</i>	
Fragility Curves for Lateral-Spreading Induced Damage to the Landing Road Bridge	825
<i>P. Kashighandi and S. J. Brandenberg</i>	
E-Defense Shaking Table Test of Model Ground with a Quay Wall on Liquefaction-Induced Lateral Spreading	833
<i>K. Tabata, M. Sato, K. Tokimatsu, H. Suzuki and H. Tokuyama</i>	
Seismic Stability of Rectangular Tunnels with Countermeasures	841
<i>J. Izawa, O. Kusakabe, H. Nagatani, T. Yamada and N. Ohbo</i>	
Soil-Pile-Structure Interaction during Multi-Dimensional Shaking through Physical Model Tests Using E-Defense Facility	849
<i>K. Tokimatsu, H. Suzuki, M. Sato and K. Tabata</i>	
Effects of Nonlinear Dynamic Properties of Surface Soils on Seismic Ground Motion and Building Damage in Ojiya during 2004 Mid Niigata Prefecture Earthquake.....	857
<i>K. Tokimatsu, T. Sekiguchi and H. Arai</i>	
Pullout Resistance of Anchor Bolts in Cemented Sand Subjected to Shear Strain.....	863
<i>J. Takemura, Y. Miyamoto and J. Izawa</i>	
A Series of Micro-Tremor Measurements at a Fill Dam Damaged by The 2004 Niigata-Chuetsu Earthquake.....	873
<i>T. Ohmachi, S. Inoue and S. Tomita</i>	

Steel Structures

Simulating Earthquake-Induced Fractures in Steel Structures: Models and Methods	881
<i>A. M. Kanvinde and G. G. Deierlein</i>	
Performance of Prefabricated Steel Stair Assemblies under Seismic and Gravity Loads	889
<i>C. Higgins</i>	
Earthquake Resistance Performance of Flexible-Stiff Mixed Structure for Effective Use of High-Strength Steel	897
<i>S.-H. Oh</i>	
Multiobjective Heuristic Approaches to Performance-Based Seismic Design	907
<i>M. Ohsaki, T. Kinoshita and P. Pan</i>	
Collapse Test of Steel Structural Model under High Gravity Force Field	915
<i>A. Wada, S. Yamada, M. Takazawa, M. Seki, H. Katsumata, S. Higuchi, H. Okuda and R. Okada</i>	
Cyclic Modeling of Bolted Connections for a Type of Pre-Fabricated Mezzanine Frames	923
<i>A. Sato and C. M. Uang</i>	
Evaluating Seismic Performance of Steel Reinforced Concrete Members	931
<i>H.-L. Hsu and J.-L. Juang</i>	
Experimental Simulation of Progressive Failure of Perimeter Frames in Framed-Tube Structures	939
<i>H. Tagawa, S. Sumitani, S. Yamada and A. Wada</i>	
Experimental Verification on Buckling-Restraint Design of Knee Brace Damper	945
<i>Y. Koetaka, Y. Byakuno and K. Inoue</i>	
A Beam Element for Approximate Analysis of Truss Beam Lateral Postbuckling Behavior ...	953
<i>S. Motoyui and S. Ogata</i>	
A Method for Evaluation of Elastic Buckling Strength of H Shaped Steel Member under Shear Bending	961
<i>T. Wang and K. Ikarashi</i>	

Education

Shake Table Competition to Stimulate Undergraduate Interest in Earthquake Engineering and Seismic Design	969
<i>S. A. Ashford, M. J. Gebman, S. J. Brandenberg and L. Cheng</i>	
A Practice of International Distance Lecture among Three Universities through the Internet	975
<i>H. Morikawa, A. Ruangrassamee and H.-T. Chen</i>	
Communication and Engineering Management for the Global Engineer	979
<i>K. Shankar and K. Tokimatsu</i>	

COMPUTATIONAL SIMULATION FOR EARTHQUAKE ENGINEERING

G.L. Fenves¹⁾

*1) Professor, Civil & Environmental Engineering, University of California, Berkeley, CA, U.S.A.
fenves@berkeley.edu*

Abstract: The goal of computational simulation for earthquake engineering is to estimate the behavior and performance of structural and geotechnical systems. Research on simulation models and algorithms is most effective when there is a flexible and extensible software framework for combining and exchanging software implementations. The Open System for Earthquake Engineering Simulation, OpenSees, is such a framework that has been developed and used extensively for modeling and analysis of soil-structure-foundation systems, and it has been extended for parallel processing and hybrid simulation as part of the Network for Earthquake Engineering Simulation.

1. INTRODUCTION

Computational simulation has revolutionized many fields of engineering, such aircraft design, crash worthiness of vehicles, and integrated circuit packaging, including micro-electromechanical systems. In bioengineering and medicine, computational simulation is used for understanding and design of surgical procedures and medical devices. The progress in the development and application of computational simulation in earthquake engineering has been good in the past decade, but not as rapid as in other engineering and science fields. In earthquake engineering research, simulation is used to improve understanding of structural and geotechnical systems, with the goal of improving the predictive ability to assess damage and performance up to collapse of a structure. Traditionally, fundamental understanding in structural and geotechnical engineering has been obtained by experimentation because computational models have not been realistic enough, and substantial research is necessary before simulation can provide highly realistic and verified estimates of performance. The second aspect of computational simulation is for engineering design. Nearly all design involves analysis, but at this time advanced computational simulation to include the nonlinear behavior and realistic failure modes of structures and soil systems is generally not employed in structural design. The two aspects of simulation, research and engineering design, should not be decoupled, because the research needs to drive the practice, but the practice needs to inform the research.

In the United States, the National Science Foundation's George E. Brown, Jr. Network for Earthquake Engineering Simulation (NEES) provides a singular opportunity to advance dramatically the knowledge needed for engineers to reduce the risk of catastrophic earthquakes. The physical simulation of systems in the laboratories at the NEES equipment sites provide unparalleled opportunities for researchers to investigate the behavior of components and systems. Nevertheless, experiments are also in fact a simulation because real systems have to be approximated in scale, boundary conditions, and loading. Even full-scale shake table testing often neglects effects such as soil structure interaction. Computational simulation is necessary, therefore, to understand system

behavior that cannot be determined experimentally. It involves creating a mathematical model of the structural system, solving the equations representing the physical behavior represented by the model, and interpreting the results within the assumptions of the model. Modern earthquake engineering research and professional practice cannot rely on only physical simulation or computational simulation alone. They are inextricably linked and closely dependent on each other for improving knowledge and practice, and ultimately the value of earthquake engineering for society (Fenves 2003).

The goal of this paper is to provide an overview of research and development on computational simulation for earthquake engineering underway at the Pacific Earthquake Engineering Research Center and more recently the Network for Earthquake Engineering Simulation.

2. OPEN SYSTEM FOR EARTHQUAKE ENGINEERING SIMULATION

To advance the state-of-the art in computational simulation for earthquake engineering and address the limitations of individual closed-source simulation software, the Pacific Earthquake Engineering Research (PEER) Center has had a major research thrust in simulation and information technology since the center began in 1997. A centerpiece of PEER's research on performance-based earthquake engineering has been the development of new technology for computational simulation of structural and geotechnical systems. PEER embarked on a new approach in earthquake engineering simulation by developing an open-source, object-oriented software framework named OpenSees, for Open System for Earthquake Engineering Simulation. OpenSees is not a "code" in the traditional sense, but rather it is a set of modules for creating a wide range of models and simulation procedures for structural and geotechnical systems. This is accomplished by providing software classes for many types of nonlinear elements (including beam-column, connection, plate, and continuum elements) and materials (uniaxial and multiaxial for structural materials and soils). A flexible approach for defining analysis methods provides robust solutions for highly nonlinear problems.

The overall organization of the modules in OpenSees is illustrated in Figure 1(b), which is contrasted with the architecture of type finite element software in Figure 1(a). Most traditional finite element software is fairly closed in terms of the algorithms, data structures, and model generation, with the exception of developers being able to add elements and materials in some cases. For such codes there is a defined application program interface (API) that is implemented as a function or subroutine call. OpenSees, in contrast, is a framework of interoperable components [Figure 1(b)] for creating models, elements, materials, constraints, solution procedures, solvers, and underlying compute technology. There are interfaces with databases and visualization software, all through API's. The framework is designed to be flexible and extensible to support different simulation applications built from the components. As outlined in a later section, the OpenSees software framework can be used to create other simulation applications, such as for high-performance parallel computing, hybrid simulation, or customized analysis packages for specific types of structures.

To achieve this flexibility, the OpenSees framework is designed and implemented using object-oriented principles. The object-oriented design underlying OpenSees was developed by McKenna (1997). Further research on software architectures for computational simulation in earthquake engineering was done by Scott (2004). Much of the OpenSees architecture is now expressed in terms of design patterns (Gamma et al. 1995). As an example, Figure 2(a) shows the high level classes for the data structures representing a simulation model using aggregation. One of the most flexible features of OpenSees is the ability to select an analysis procedure that is best for the problem, which is important for tracking structural behavior in the nonlinear range, which is illustrated in Figure 2(b). Static and dynamic analysis capabilities are available, along with various methods for representing constraints. The analysis procedures are developed to be robust and scalable to large

problem sizes (Filippou and Fenves 2004). Post-processing of response and state data is handled in OpenSees by defining recorders of response quantities of interest. The data from recorders can be placed in files or interfaced with database and visualization software.

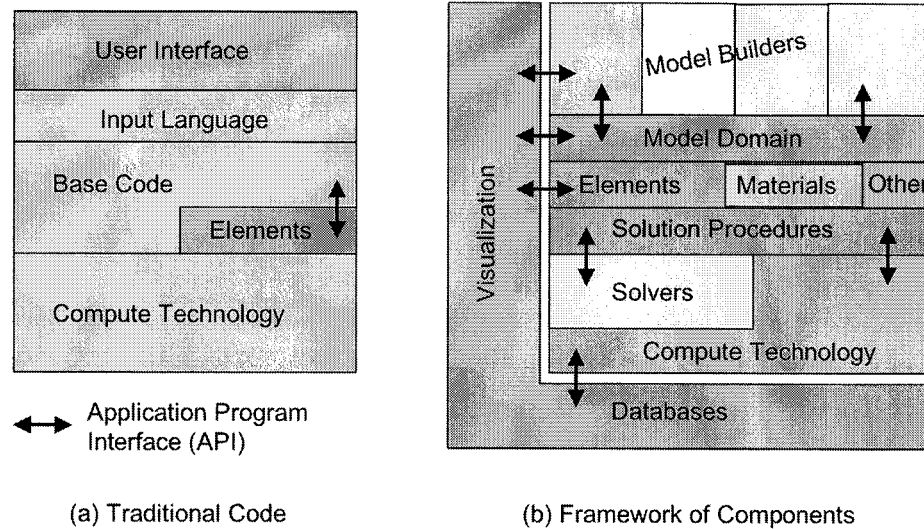


Figure 1 Overall Organization of (a) Traditional Finite Element Code and (b) OpenSees as a Framework of Interoperable Components

The current structural modeling capability includes a comprehensive hierarchy of beam-column elements continuum elements. The beam-column elements are used extensively for building and bridge structures. At the highest level, beam elements using displacement or force interpolation are available for linear and nonlinear problems in two and three dimensions. Large-displacement formulations are available to represent stability and P- Δ effects. Section behavior can be represented in terms of nonlinear relationships between stress resultants (moment, for example) or using a cross-section discretization. The cross-section discretization (e.g. fiber model) can be built up for a wide selection of uniaxial material models. A range of beam-column models is available using traditional displacement interpolation elements and the newer force-based elements (Spacone and Filippou 1995), including a useful element with plastic hinges that is objective for degrading and softening behavior (Scott and Fenves 2006). For continuum models, linear and nonlinear 2D and 3D elements are available, along with a robust plate element. Soil models and elements are available for geotechnical analysis applications.

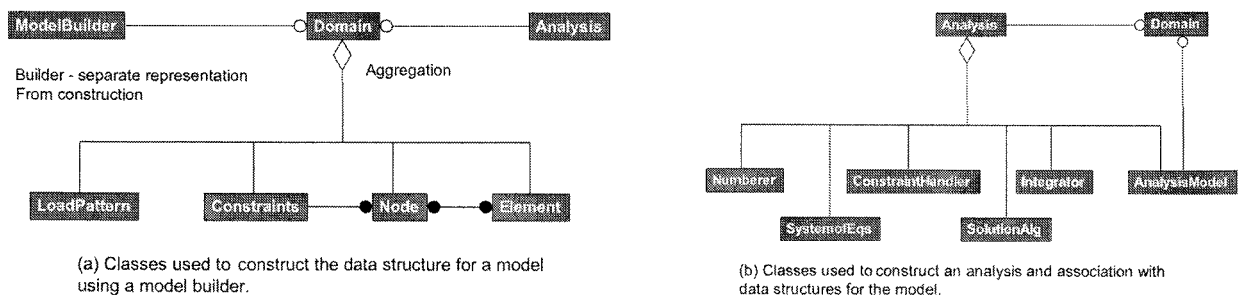


Figure 2 Class Diagrams for (a) Model and (b) Analysis in OpenSees Software Architecture

Following the object-oriented architecture of OpenSees, the software is implemented in C++. The APIs for all modules are specified through the class definitions. To meet the needs of most users, a general model builder has been developed that calls the classes to create objects for a specific problem. Users can control the modeling, analysis, and post-processing through a programmable scripting language, Tcl (Ousterhout 1994).

3. OPEN-SOURCE COMMUNITY FOR OPENSEES

OpenSees has been designed for exchange and interoperability to advance research in earthquake engineering simulation. Early on PEER made the decision that OpenSees should be open-source software in order to build a community of researchers, developers, and users (Fenves et al. 2004). Open-source means more than the source code is available freely. For open-source to be successful all members of the community need to have access to the source code including previous version, release versions, and development versions, and there needs to be protocol for tracking who in the community is working on what capability and a mechanism for accepting, validating, and checking in contributions to the software. Finally, there needs to be good documentation, education and training materials, and a community forum for exchanging information about the software for users and developers. This model has worked well in the information technology field, such as for system and application software like Linux, Apache, and MySQL, but it is the first time it has been attempted in the earthquake engineering field.

The OpenSees website (2006) provides these types of information and communication for the community. Figure 3 shows screen shots of the application program interface and the community forum. Currently, approximately 300 users are registered and about 40 individuals are developers who are working on or contributing software to OpenSees.

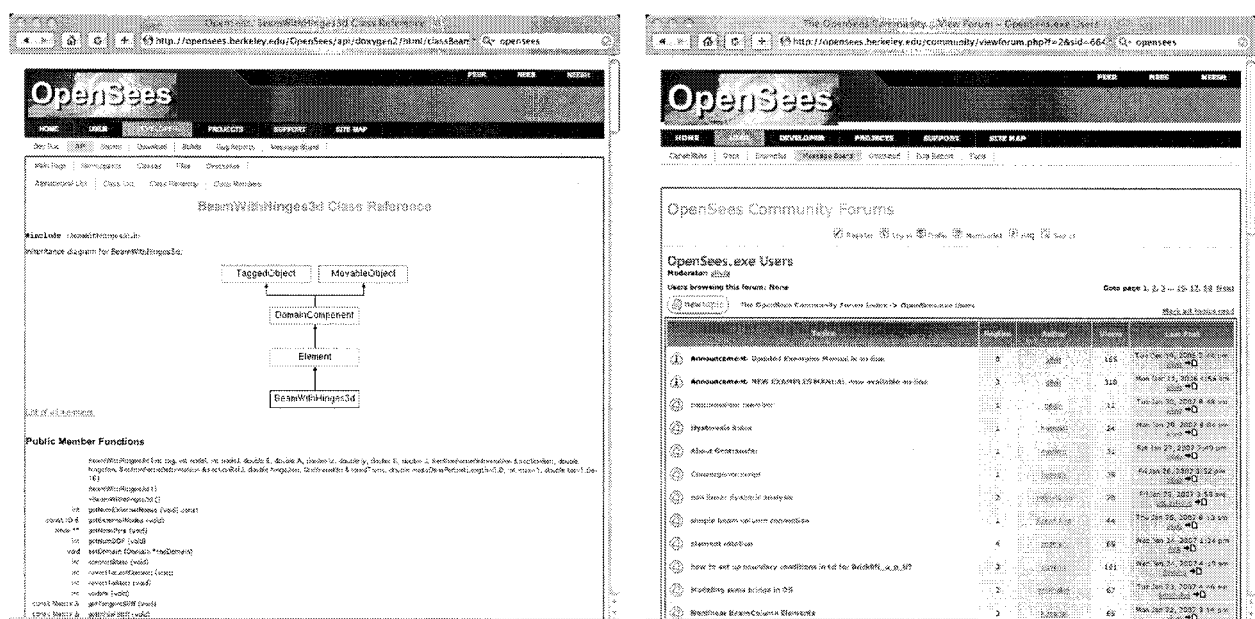


Figure 3 OpenSees (2006) Website Illustrating API and Community Forum for Exchanging Information About the Open-Source Software.

4. NEESit CAPABILITIES FOR SIMULATION USING OPENSEES

With the extensive development of simulation capabilities accomplished by PEER, NEES adopted OpenSees as a simulation tool under the NEES information technology program, NEESit. OpenSees provides NEES researchers a simulation tool for use in conducting research and a software platform for extending the modeling and simulation capability in a community-based open-source framework. To increase the impact of OpenSees for NEES research, three major efforts are underway to integrate the software into the NEESit systems.

The first is to develop interfaces between OpenSees and the NEESit data repository (NEEScentral). This will allow users to store, exchange, and archive models, analysis, and response data in the data repository, which is essential for collaborative research. The OpenSees data has metadata associated with it to support searching, visualization, and interpretation of the data. Ultimately, the user will be able to conduct an analysis and with one command upload all the data and metadata to the NEESit repository.

The second capability is to extend and optimize the parallel version of OpenSees to use the high-end computers available to NEESit at the San Diego Supercomputer Center and other parallel computers, such as clusters. As the model sizes increase the fidelity of the nonlinear models improve, parallel computing allows a drastic reduction in the execution times. For structural analysis, particularly dynamic analysis, domain decomposition is the most effective procedure because it allows implicit solution procedures (McKenna and Fenves 2000). In addition, recent work is demonstrating the effectiveness of explicit solution procedures for highly scalable parallel computation in OpenSees. The software also allows concurrent processing of multiple cases, such as for parameter studies, which is important in performance-based earthquake engineering applications that utilize statistics of response.

The third thrust is to integrate physical testing and computation simulation using hybrid-simulation. The same design principles for OpenSees have been applied to hybrid simulation, producing a flexible software environment for distributed testing and linking computational models with experiments (Takahashi and Fenves 2006). Recent applications of hybrid simulation have demonstrated the ability to represent structural collapse under earthquake loads using a standard reaction wall experimental setup (Schellenberg et al. 2006).

5. CONCLUSIONS

The Network for Earthquake Engineering Simulation was originally conceived as developing the data needed to eliminate testing and replace it with simulation for earthquake engineering research and practice. This is not likely, nor desirable, because of the large amount of information that needs to be discovered on how structural and geotechnical systems behave over time and under cyclic loading of earthquakes. However, NEES does present the opportunity and to improve the way research is done. There must be balanced support for computational simulation along with experimental research. It is in the interest of the earthquake engineering community to develop a strong research agenda and show breakthroughs in simulation to add justification for the NEES investment.

The current approach to simulation software in earthquake engineering results in “islands of software” is not tenable for major advances. Research should be coordinated using software standards and open-source software distribution. Open-source software has had enormous benefits

for innovation and rapid progress in other fields. NEES will help tremendously in this process because of the standards being developed for NEESit, both for experimental and computational simulation, along with supporting resources such as databases, visualization, and communication and control protocols. The momentum of this effort is gaining and it should be enhanced as a comprehensive simulation research program is developed within NEES.

The final comment is that advances in computational simulation for earthquake engineering will have transformative effects on engineering design, operations and maintenance of structures, and regional planning for disasters (natural and others). Robust simulation software will improve design and allow optimization, including design for target system reliability. Simulation will have a major effect on improving the operation and maintenance of systems. Finally, information from simulation of individual structures can be aggregated to understand inventories by an owner or region-wide by emergency management organizations.

Acknowledgements:

The support of the National Science Foundation through the Pacific Earthquake Engineering Research Center under grant no. EEC-9701568 is greatly appreciated, along with the many PEER faculty participants, students, and researchers who contributed to the development of OpenSees. Particular recognition is acknowledged for Dr. Frank McKenna, Prof. Michael H. Scott, Prof. Filip C. Filippou, Dr. Silvia Mazzoni, Dr. Jaesung Park, Prof. Stephen Mahin, and Prof. Boris Jeremic. The additional support of NEES with funding from NSF grant no. CMS-0402490 has allowed further integration of simulation methods in the NEES research enterprise. Particular thanks are due to Prof. Ahmed Elgamal, Dr. Lelli Van Den Eide, and Mr. Jon Lea of NEESit and NEES Inc.

References:

- Fenves, G.L. (2003), "A Vision for Computational Simulation in Earthquake Engineering", Community Workshop on Computational Simulation and Visualization Environment for the Network for Earthquake Engineering Simulation (NEES), Sponsored by the National Science Foundation, Roddis, K., editor, University of Kansas, Lawrence, KS.
- Fenves, G.L., McKenna, F., Scott, M.H., and Takahashi, Y. (2004), "An Object-oriented Software Environment for Collaborative network simulation," *Proceedings*, 13th World Conference on Earthquake Engineering, paper no. 1492, Vancouver, BC.
- Filippou, F.C., and Fenves, G.L. (2004), "Methods of Analysis for Earthquake-Resistant Design of Structures," *Earthquake Engineering: From Engineering Seismology to Performance-Based Engineering*, Borzogna, Y., and Bertero, V.V., eds., Ch. 6, CRC Press, Boca Raton, FL.
- Gamma, E., Helm, R., Johnson, R., Vlissides, J. (1995). *Design Patterns: Elements of Reusable Object-Oriented Software*, Addison-Wesley, New York, NY.
- McKenna, F. (1997), *Object-oriented Finite Element Programming : Frameworks for Analysis, Algorithms and Parallel computing*, Ph.D. Thesis, University of California, Berkeley, CA.
- McKenna, F., and Fenves, G.L. (2000), "An Object-Oriented Software Design for Parallel Structural Analysis," *Advanced Technology in Structural Engineering, Proceedings*, Structures Congress 2000, ASCE, Philadelphia, PA.
- OpenSees (2006), Open System for Earthquake Engineering Simulation, <http://opensees.berkeley.edu/>.
- Ousterhout, J.K. (1994), *Tcl and the Tk Toolkit*, Addison-Wesley, New York, NY.
- Schellenberg, A., Mahin, S., and Fenves, G.L. (2006). "Applications of an Experimental Software Framework for International Hybrid Simulation," *Proceedings*, 4th International Conference on Earthquake Engineering, Paper No. 261, Taipei, Taiwan.
- Scott, M.H. (2004), *Software Frameworks for the Computational Simulation of Structural Systems*, Ph.D. Thesis, University of California, Berkeley, CA.
- Scott, M.H., and Fenves, G.L. (2006), "Plastic Hinge Integration Methods for Force-Based Beam-Column Elements," *Journal of Structural Engineering*, Vol. 132, pp. 244-252.
- Spacone, E., and Filippou, F.C. (1996), "Mixed Formulation for Nonlinear Beam Finite Element," *Computers & Structures*, Vol. 58, pp. 71-83.
- Takahashi, Y., and Fenves, G.L. (2006), "Software Framework for Distributed Experimental-Computational Simulation of Structural Systems," *Earthquake Engineering & Structural Dynamics*, Vol. 35, pp. 267-281.

GROUND MOTION PARAMETERS FOR LOSS ESTIMATION

A. Ansal¹⁾ and G.Tönük²⁾

1) Professor, Kandilli Observatory and Earthquake Research Institute, Boğaziçi University, Istanbul, Turkey

2) Ph.D. Student, Kandilli Observatory and Earthquake Research Institute, Boğaziçi University, Istanbul, Turkey

ansal@boun.edu.tr, gokce.tonuk@boun.edu.tr

Abstract: Microzonation studies were carried out for five major municipalities located in highly seismic areas around the Marmara Sea in Turkey. The investigated municipalities were divided into cells by a grid system based on the availability of geological, geophysical and geotechnical data. Representative boreholes were assigned and site response analyses were conducted for each cell utilising an equivalent linear model. Three earthquake hazard compatible previously recorded acceleration records were used as outcrop motion scaled with respect to peak ground accelerations determined from probabilistic hazard analysis. Site specific ground motion data were calculated to be used for microzonation with respect to ground shaking intensity and for the assessment of the vulnerability of the building stock. The simpler option to calculate spectral accelerations for vulnerability assessment was to use NEHRP design spectra according to the NEHRP site classifications. The second option was to determine the NEHRP design spectra based on the average of the three acceleration response spectra calculated by site response analyses for each cell utilising a fitting algorithm giving the best outer envelop. The reliability and the accuracy of the results from both approaches are discussed and compared in terms of calculated spectral accelerations and building damage distributions.

1. INTRODUCTION

The adopted microzonation methodology was based on a grid system composed of cells and was implemented in three stages. In the first stage, the probabilistic seismic hazard analysis was conducted at the regional level to determine the earthquake characteristics for 475 years return period corresponding to 10% exceedance in 50 years. In the second stage, the representative soil profiles were determined for each cell based on the available borings and in-situ tests. The third stage involved site response analyses to obtain site specific earthquake characteristics on the ground surface.

Two options were considered for evaluating spectral accelerations on the ground surface to be used in the vulnerability assessment of the building stock. The first option was to use NEHRP site classification and NEHRP site amplification factors to determine short period (0.2s) and long period (1s) spectral accelerations. The second option is to use elastic acceleration response spectra obtained from site response analyses. The procedure proposed by Ansal et al. (2005a) was used to determine short period (0.2s) and long period (1s) spectral accelerations by fitting the best envelop NEHRP spectra to the average elastic acceleration response spectra obtained from site response analyses.

The building stock inventory (Aydınoglu & Polat, 2004) as well as the microzonation study conducted for Zeytinburnu Municipality (Ansal et al., 2005a; Kılıç et al., 2006) as a part of the Zeytinburnu Pilot Project within the scope of the Earthquake Master Plan for Istanbul (EMPI, 2003) with the basic purpose to produce input for urban planning, was utilised to evaluate the differences arising from both approaches in terms of building damage variations.

1.1 Seismic Hazard Analysis

A time-dependent regional (renewal) model taking into consideration the recent major earthquakes was used to estimate the seismic activity along the segmented linear source zones. The total hazard in the region was calculated as the summation of hazards computed from “background source activity” and “fault segmentation model” (Erdik et al., 2004, 2005). The results of the earthquake hazard analysis corresponding to 475 year return period were calculated for each cell in terms of peak ground and spectral accelerations at 0.2s and 1s to be used for microzonation and vulnerability assessment.

1.2 Site Classification

The investigated municipalities were divided into cells of 500m×500m or 250m×250m by a grid system depending on the availability of geological, geophysical and geotechnical data. Representative soil profiles for each cell where one or more borehole data were available were created by considering the most suitable borehole, and for the cells with no available borehole information, representative soil profiles were selected from the neighbouring cells by utilizing the available data. During this stage, interpolations between neighbouring boreholes were performed taking into consideration the surface geology.

The variations of shear wave velocities with depth were determined from SPT blow counts using empirical relationships proposed in the literature. Shear wave velocity profiles were established down to the engineering bedrock with estimated shear wave velocity of 760m/s. The calculated shear wave velocity profiles were compared with respect to measured or calculated shear wave velocity data obtained by in-situ seismic wave velocity measurements and modified when necessary. The site classification for each cell was established according to NEHRP (2001) as well as with respect to Turkish Earthquake Code (TEC, 1998).

1.3 Earthquake Input

Three real acceleration time histories compatible with the earthquake hazard assessment in terms of probable magnitude, distance and fault mechanism were selected as the input outcrop motion. The input acceleration time histories were scaled for each cell with respect to the peak accelerations obtained from earthquake hazard study since this approach was practical and gave consistent results as observed by Ansal et al., 2006a, and Durukal et al., 2006. The three scaled acceleration time histories for each cell were used as input motion for site response analyses by Shake91 (Idriss and Sun, 1992) and the average of the acceleration response spectra on the ground surface were determined for each cell to obtain the necessary parameters for microzonation. An effort was made to select acceleration time histories that are more compatible with the NEHRP spectra calculated in the earthquake hazard study for the area.

2. SEISMIC MICROZONATION WITH RESPECT TO GROUND MOTION

The ground-shaking microzonation map presents the estimated relative shaking intensity levels based on the combination of two parameters: The peak spectral accelerations (at 0.2s) calculated from Borchardt (1994) using equivalent shear wave velocities were adopted as one of the microzonation parameters and the second parameter adopted was the average spectral accelerations calculated between the 0.1s and 1s periods using the average acceleration spectra determined from the results of the three site response analyses conducted for each cell. The final microzonation map with respect to ground shaking intensity was obtained by the superimposition of maps with respect these two parameters. The approach was based on seismic microzonation studies conducted in Turkey during the last decade (Ansal et al. 2006b, 2005b, 2005a, 2004; Kılıç et al. 2006).

The proposed methodology for the microzonation maps involves the division of the area into three

zones (as A, B, and C) based on relative values of the parameters considered (Ansal et al., 2004). The site characterizations, as well as all the analyses performed, require various approximations and assumptions, thus it is recommended not to present the numerical values for any parameter since their relative values are more important than their absolute values. In all cases, the variations of the calculated parameters are considered separately and their frequency distributions were determined to calculate the 33 and 67 percentiles to define the boundaries between the three zones. The zone A shows the most favourable 33 percentile (i.e. low spectral accelerations), zone B shows the medium 34 percentile and zone C shows the most unsuitable 33 percentile (i.e. high spectral accelerations). However, if the difference between 33 and 67 percentiles was less than 30%, the area is divided into two zones using 50 percentile (median) as recommended by Ansal et al. (2004). The final zonation map is a superimposed map defined in terms of three relative zones independent of the absolute value of the ground shaking intensity as shown for Gemlik in Figure 1.

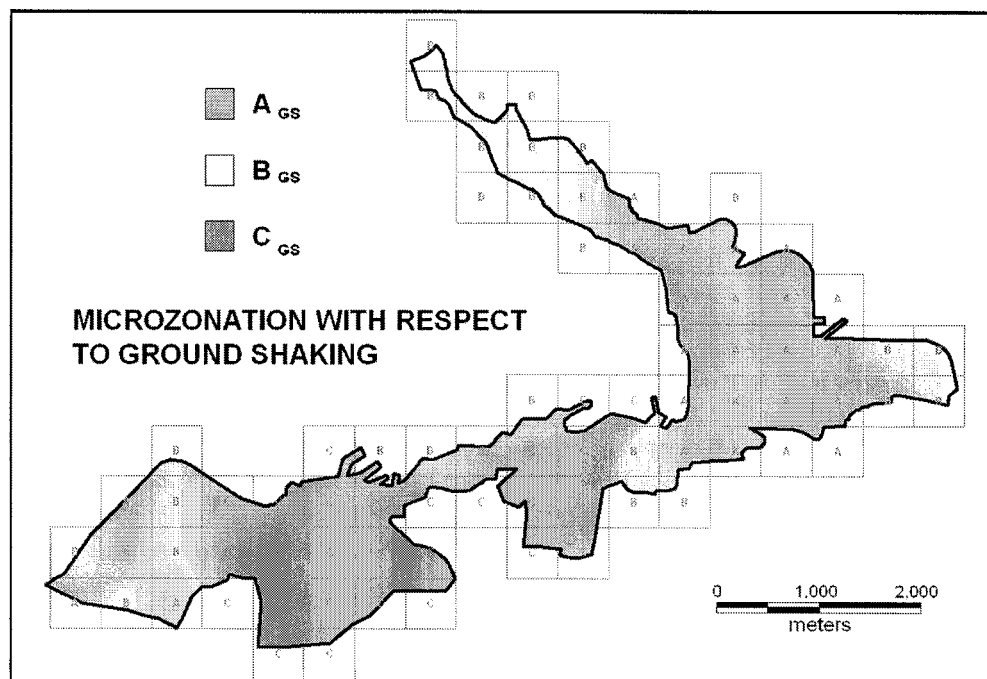


Figure 1 Microzonation with respect to ground shaking intensity

3. SPECTRAL ACCELERATIONS FOR VULNERABILITY ASSESSMENTS

The earthquake characteristics used in the assessment of the structural vulnerability may be calculated based on the conventional NEHRP procedure considering the microzonation map obtained in terms of NEHRP site classification. The spectral accelerations may also be calculated by site response analyses.

The average acceleration response spectra obtained for each cell from site response analyses were evaluated for determining the spectral accelerations for the short period (S_s) corresponding to 0.2s and for the long period (S_l) corresponding to 1s. An optimization algorithm was used to determine the best fit envelope to the calculated average acceleration response spectra (Ansal et al., 2005). All the requirements of the NEHRP spectra were adopted where the two independent variables in the developed optimization algorithm were (S_s) and (S_l). Some examples of the best fit envelopes obtained by this approach with respect to average acceleration response spectra are shown in Figure 2 in comparison with the three acceleration response spectra calculated for three selected PGA scaled input acceleration time histories (Ansal et al., 2005b).

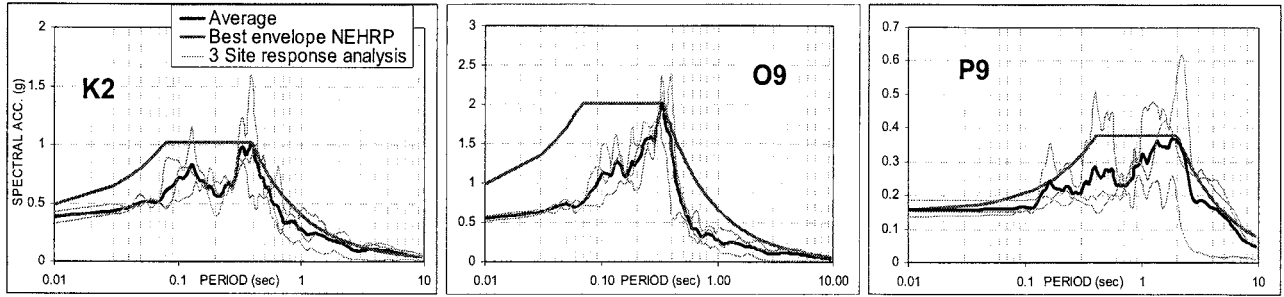


Figure 2 Some typical best envelop NEHRP spectra fitted to average acceleration response spectra and three acceleration response spectra calculated by site response analysis

The individual acceleration spectra obtained from the three site response analyses indicate some scatter among themselves but the average spectrum could be considered as the representative for all three spectra. The short and long period spectral, and peak ground accelerations determined by this procedure are mapped for each city. As an example, microzonation map with respect to spectral acceleration at $T=0.2$ s with increments of $0.3g$ determined for Bandırma city is shown in Figure 3.

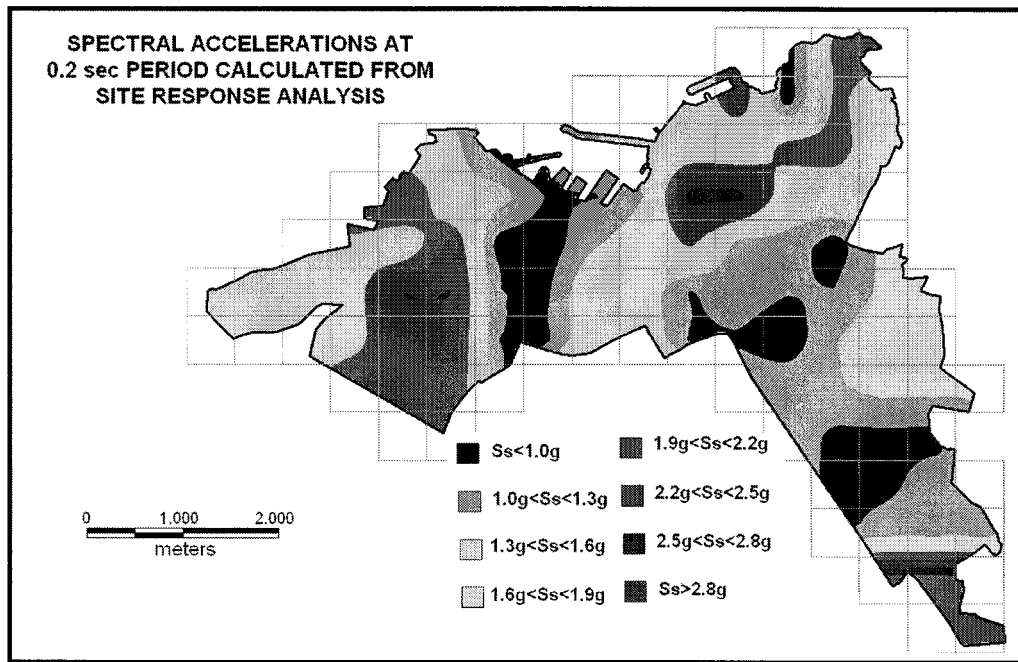


Figure 3 Variation of spectral acceleration at 0.2s determined by site response analysis for the city of Bandırma

The comparison between the spectral accelerations obtained from site response analyses using the best envelope fitting procedure with the values obtained by the NEHRP formulation are shown in Figure 4 for the five municipalities with respect to 871 cells. The values obtained by site response analyses show much larger range. The difference between the two approaches in the data range is much more significant in the case of short period spectral accelerations. This may be considered as an indication of more accurate determination of site effects. The narrow range of site amplifications calculated by the NEHRP procedure is due to the fact that shear wave velocity ranges used in the NEHRP site classes are defined within relatively large limits.

Most of the cells in the study areas were classified as NEHRP class C or D, as a result the spectral accelerations calculated on the ground surface based on the conventional formulation using NEHRP site related parameters F_a and F_v were same and the minor differences were due to the differences in the outcrop motion characteristics determined from the earthquake hazard study.

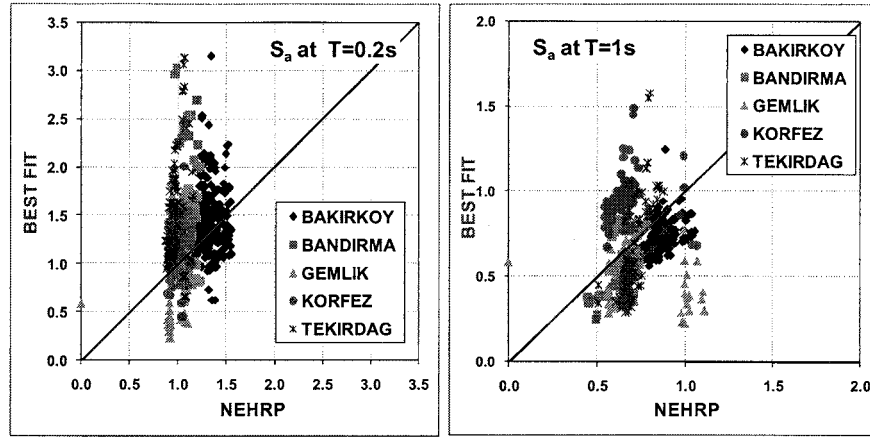


Figure 4 Correlation between spectral accelerations at 0.2s and 1s calculated by site response analyses and based on NEHRP approach for all five cities

The variability of the calculated parameters to be used for the vulnerability assessment of the building stock is important. Considering the variability taken into consideration by assigning different earthquake characteristics leading to different time history inputs for each cell and the differences in the soil profile, it appears logical to use the spectral acceleration values obtained from site response analysis for the vulnerability assessment. However, it is also possible to argue that the sophistication introduced during this process may not always give more correct or accurate results. In addition, the decision of using one of the spectral accelerations determined by best envelope approaches would play a very important role on the amplitude of the estimated vulnerability of the building stock.

At the present, one way to resolve these ambiguities is to rely on expert judgement and previously obtained damage data in similar earthquakes. However, the statistical evaluation of all the spectral accelerations obtained by both procedures may be useful in the decision process. Thus various relationships among different parameters obtained by site response analyses as well as by site characterisation were evaluated to understand the coherence among different parameters.

One of the correlations evaluated was the relationship between equivalent (average) shear wave velocity calculated for the top 30m and site amplification in terms of peak ground accelerations calculated by site response analyses. The vertical axis is the ratio of output peak ground acceleration calculated on the soil surface by site response analysis to the peak ground acceleration that was used to scale the input motion at the rock outcrop determined from the hazard study for NEHRP B/C boundary. The correlation coefficient can be considered significantly high ($R=0.627$) considering all the factors that may increase the scatter as shown in Figure 5(a).

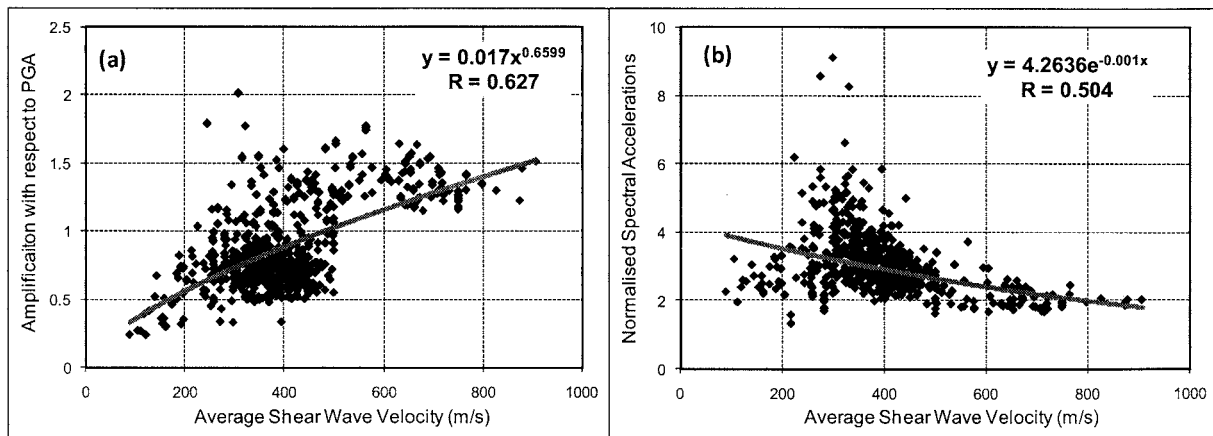


Figure 5 Correlation between PGA site amplification and PGA normalized spectral accelerations from the results of site response analyses with respect to the average (equivalent) shear wave velocity (Ansal et al., 2006b)

The second correlation studied was the relationship between the peak ordinate of the normalised spectra calculated as the ratio of the spectral accelerations of the envelope NEHRP spectra to the peak ground accelerations obtained from site response analyses on the ground surface. Again considering all the factors that may disperse such a correlation, the calculated correlation factor ($R=0.504$) may be considered meaningful as shown in Figure 5(b).

One possible and positive interpretation of these results could be towards supporting the reliability of the site response analyses and thus one may conclude that it may be recommendable to conduct site response analyses to determine spectral accelerations and PGA on the ground surface to be utilised in assessing the vulnerability of the building stock rather than using the NEHRP procedure which appears to be rather limited.

4 LOSS ESTIMATES FOR ZEYTINBURNU

The detailed building inventory data obtained from street surveys for approximately 16000 buildings were used to estimate the vulnerability for Zeytinburnu (Aydinoglu and Polat, 2004) based on vulnerability functions defined in terms of spectral displacements (BU-ARC, 2002). Building inventory was divided into three groups based on the construction type, number of stories and construction year (Erdik et al., 2003). All buildings were classified as Bijk where “i” shows the construction type as: (1) Reinforced concrete frame building, (2) Masonry building, (3) Reinforced concrete shear wall buildings, (4) Precast building. The number of stories (“j” dimension of the matrix) was defined as: (1) Low rise (1-4 stories, including basement), (2) Mid rise (5-8 stories, including basement), (3) High-rise (8 more stories, including basement). The construction date (“k” dimension of the matrix) was defined as: (1) Construction year: Pre-1979 (included) and (2) Construction year: Post-1980.

The damage levels in Zeytinburnu were evaluated separately for 13885 reinforced concrete frame buildings in the inventory taking into consideration the spectral accelerations calculated by site response analyses for the two input earthquake scenarios (1 set of PGA scaled real acceleration time histories, and 1 set of response spectra scaled simulated acceleration records compatible with the KOERI probabilistic earthquake hazard for $RP=475$ years) and using the spectral accelerations calculated based on NEHRP methodology.

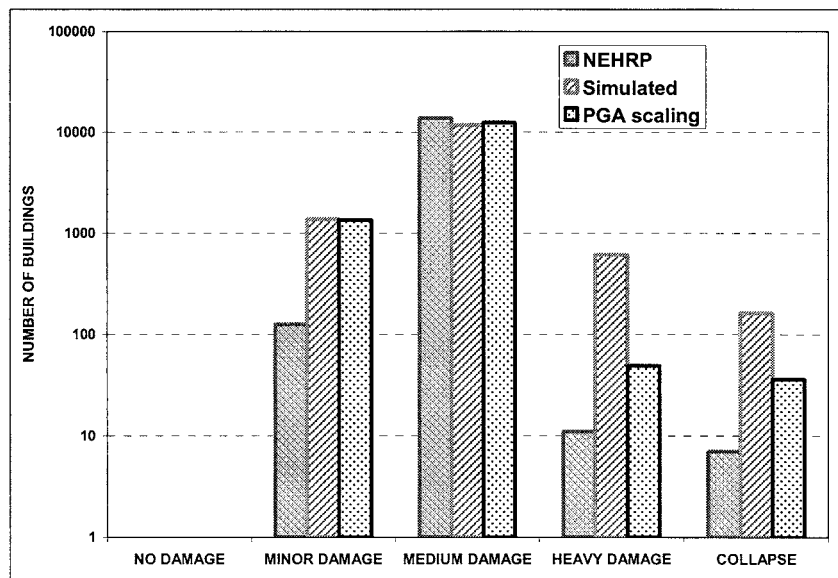


Figure 5 Variation of damage levels for RC buildings in Zeytinburnu taking into consideration the spectral accelerations calculated by site response analyses and the spectral accelerations calculated from NEHRP

Figure 6 shows the differences among the damage levels for the three alternatives. The vertical axis (number of buildings) is in logarithmic scale to show the difference among different levels of damage. The difference between heavy damage and collapsed buildings are very significant as much as ten fold when spectral accelerations were determined based on site response analysis using simulated or PGA scaled acceleration time histories in comparison to spectral accelerations calculated based on NEHRP. Since the number of damaged buildings especially in higher damage levels are important in assigning the priorities for retrofitting and for mitigation measures, the difference are important. Thus it is recommended to use site response analyses for microzonation as well as for vulnerability assessment.

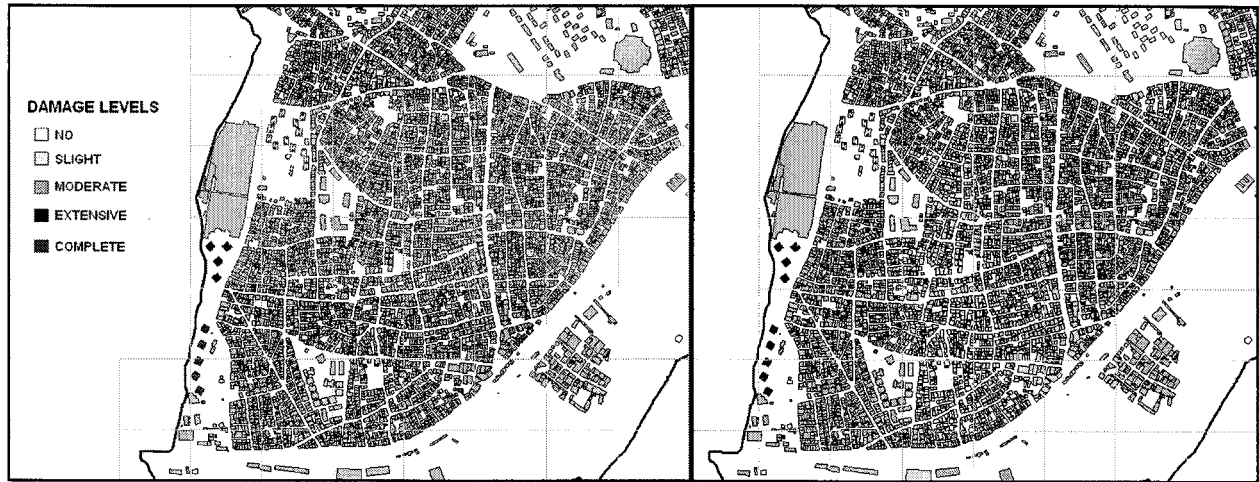


Figure 6 Damage level variation among reinforced concrete frame buildings taking into consideration the spectral accelerations calculated by site response analyses and the spectral accelerations calculated from NEHRP for Zeytinburnu

5. CONCLUSIONS

A detailed study was conducted to evaluate the microzonation maps for five municipalities in the Marmara Region based on the available geotechnical, geological and geophysical data. The results obtained from the earthquake hazard study by the Renewal model for a return period of 475 years were adopted to evaluate the site response characteristics to be used for microzonation and for the vulnerability assessment. The study areas were divided into cells of dimensions 250m×250m or 500m×500m. For each cell representative soil profiles were determined based on the detailed assessment of the available geotechnical data.

For the assessment of the vulnerability of the building stock, the average acceleration response spectra obtained for each cell from site response analyses were evaluated for determining the spectral accelerations for the short period corresponding to 0.2s and for the long period corresponding to 1s. An approach was adopted to determine the best fitting envelope to the calculated average acceleration response spectra. The results obtained are compared in terms of short period (0.2s) and long period (1s) spectral accelerations with the results obtained based on NEHRP site classes. It was observed that the spectral accelerations determined by fitting NEHRP spectrum to response spectrum obtained by site response analyses vary in much broader range. In most cases spectral accelerations obtained by the NEHRP procedure would yield values on the unsafe side compared to those determined by the site response analyses.

Also the results of loss estimates based on two procedures reveal that it appears possible to assume that it would be more reliable to perform site response analyses to determine spectral accelerations on the ground surface to be used as input to the vulnerability studies depending on the quality and accuracy of the building stock information.

Acknowledgements:

The Authors would like to acknowledge the significant contributions of Prof.M.Erdik, E.Durukal, M.Demircioglu, and K.Sesetyan during all microzonation projects conducted at Kandilli Observatory and Earthquake Research Institute and of the ABS team who worked very hard to supply the necessary input data and technical support to the authors in finalizing the microzonation studies within the context of the MEER project.

References:

- Ansal, A., Tönük, G., Demircioglu, M., Bayraklı, Y., Sesetyan, K., Erdik, M. (2006b), "Ground Motion Parameters for Vulnerability Assessment," *Proceedings of the First European Conference on Earthquake Engineering and Seismology*, Geneva, Switzerland, Paper Number: 1790.
- Ansal A, Durukal E, Tönük G (2006a) "Selection and Scaling of Real Acceleration Time Histories for Site Response Analyses". Proc. of ETC12 Workshop, Athens, Greece
- Ansal, A., Tonuk, G., Bayraklı, Y. (2005b), "Microzonation for Site Conditions for Bakırköy, Gemlik, Bandırma, Tekirdağ, Eskisehir and Körfez," *WB MEER Project -A3 Component, Microzonation and Hazard Vulnerability Studies For Disaster Mitigation in Pilot Municipalities*, Bogazici University, Kandilli Observatory and Earthquake Engineering Research Institute, Cengelköy, Istanbul.
- Ansal, A., Özyayın, K., Erdik, M., Yıldırım, M., Kılıç, H., Adatepe, S., Özener, P. T., Tonaroglu, M., Sesetyan, K., Demircioglu, M. (2005a) "Seismic Microzonation for Urban Planning and Vulnerability Assessment," *Proceedings of the International Symposium of Earthquake Engineering (ISEE2005)*, Geotechnical Session, Awaji Island, Japan.
- Ansal, A., Laue, J., Buchheister, J., Erdik, M., Springman, S. M., Studer, J., and Koksall, D. (2004), "Site Characterization and Site Amplification for a Seismic Microzonation Study in Turkey," *11th International Conference on Soil Dynamics and Earthquake Engineering and 3rd Earthquake Geotechnical Engineering*, 7-9 Jan. 2004, San Francisco.
- Aydinoglu, N. and Polat, Z. C. (2004), "First level evaluation and assessment of building earthquake performance, Report for the Istanbul Master Plan Zeytinburnu Pilot Project," Metropolitan Municipality of Istanbul, Planning and Construction Directorate (in Turkish)
- Borcherdt, R.D. (1994), "Estimates of Site Dependent Response Spectra for Design (Methodology and Justification)," *Earthquake Spectra*, **10**(4), 617-654.
- BSSC-Building Seismic Safety Council (2001), "NEHRP (National Earthquake Hazards Reduction Program) Recommended Provisions for Seismic Regulations for new buildings and other structures, 2000 Edition, Part 1: Provisions (FEMA 368)," Ch. 4, Washington, D.C.
- BU-ARC (2002), "Earthquake Risk Assessment for Istanbul Metropolitan Area, Project Report prepared by M. Erdik, M. N.Aydinoğlu, A.Barka, Ö.Yüzügüllü, B.Siyahi, E.Durukal, Y.Fahjan, H.Akman, G.Birgören, Y.Biro, M.Demircioğlu, C.Özbey and K.Şeşetyan (Bogazici University Publication)".
- Durukal, E., Ansal, A., and Tönük, G. (2006), "Effect of Ground Motion Scaling and Uncertainties in Site Characterisation on Site Response Analyses," *Proceedings of the 100th Anniversary Earthquake Conference Commemorating the 1906 San Francisco Earthquake*, San Francisco, USA.
- EMPI (2003) "Earthquake Master Plan for Istanbul," Bogaziçi University, Istanbul Technical University, Middle East Technical University, and Yıldız Technical University, Metropolitan Municipality of Istanbul, Planning and Construction Directorate Geotechnical and Earthquake Investigation Department, 569p
- Erdik, M., Demircioglu, M., and Sesetyan, and Durukal, E. (2005), "Assessment of earthquake hazard for Bakırköy, Gemlik, Bandırma, Tekirdağ and Körfez, WB MEER Project -A3 Component," *Microzonation and Hazard Vulnerability Studies For Disaster Mitigation in Pilot Municipalities*, Bogazici University, Kandilli Observatory and Earthquake Engineering Research Institute.
- Erdik M, Demircioglu M, Sesetyan K, Durukal E, Siyahi B (2004) Earthquake Hazard in Marmara Region. *Soil Dynamics and Earthquake Engineering* 24: 605-631.
- Erdik, M., Aydinoglu, N., Fahjan, Y., Sesetyan, K., Demircioglu, M., Siyahi, B., Durukal, E., Ozbey, C., Biro, Y., Akman, H. and Yuzugullu, O. (2003), "Earthquake Risk Assessment for Istanbul Metropolitan Area," *Earthquake Engineering and Engineering Vibration*, **2**(1), pp.1-25.
- Idriss, I. M. and Sun J. I. (1992), "Shake91, A Computer Program for Conducting Equivalent Linear Seismic Response Analysis of Horizontally Layered Soil Deposits Modified based on the original SHAKE program Published in December 1972 by Schnabel, Lysmer and Seed".
- Kılıç, H., Özener, P. T., Ansal, A., Yıldırım, M., Özyayın, K., Adatepe, S. (2006), "Microzonation of Zeytinburnu Region with respect to Soil Amplification: A Case Study," *Journal of Engineering Geology*, Elsevier, 86: 238-255
- Turkish Earthquake Code (1998), "Specification for Structures to be Built in Disaster Areas," Ministry of Public Works and Settlement, Government of Republic Turkey, English Translation, B.U. Kandilli Observatory and Earthquake Research Inst. <http://www.koeri.boun.edu.tr/depremmuh/>

RECONSTRUCTION AFTER CATASTROPHE IN JAPAN: EXPERIENCE AND PROBLEMS A CASE STUDY OF THE 1995 HANSHIN-AWAJI GREAT EARTHQUAKE

Y. Murosaki¹⁾

1) Director General, National Research Institute of Fire and Disaster, Japan

1. TARGET OF DISASTER RECONSTRUCTION

In case of massive disaster, the aim of reconstruction should be progression from the pre-disaster condition rather than restoration of the original condition. What would be the reasons to call for that kind of reconstruction? First, the reasons are because we need to learn from the disaster, and second, because we need to optimize the use of available resources for restoration. For learning from disaster experiences, the improvement of susceptible urban structures is unavoidable so that the same kinds of damage would not be repeated. For the utilization of resources, the desire would be to create a more ideal city by effectively using the massive resources and manpower that become available at a time of disaster reconstruction.

In advanced Western nations, such as the United States, disaster prevention is pursued in post-disaster reconstructions, and ideals of culture and economic life are materialized, as evident in the reconstruction after the 1874 great fire in Chicago and the 1906 San Francisco earthquake. These cities succeeded in rebuilding themselves so that they excelled in terms of both disaster prevention and ideal realization. In contrast, unfortunately, Japan has not been able not to rebuild post-disaster cities that excel in disaster-readiness or rebuild culturally or environmentally distinguished cities because restoration of the original state has been all it was able to do. Efforts have been made to create disaster-ready cities after the 1923 Great Kanto Earthquake and war damage of 1945, but the resultant reconstruction was not able to achieve the goal. The susceptibility of Japanese cities to fire was not improved, and the resultant construction was just the same as the pre-disaster state.

As we have seen, post-disaster reconstruction aims to construct a safe city and pursue a more ideal urban culture and infrastructure. However, we should not forget that there is an even more important goal of restoring the city functions of the disaster area and normalcy of disaster victims' lives. There cannot be disaster reconstruction if victims are sacrificed for other goals. In this paper, we shall examine, in light of these three reconstruction goals, the case and issues of reconstruction after the Hanshin-Awaji Great Earthquake that struck in 1995.

2. AN OVERVIEW OF RECONSTRUCTION AFTER THE HANSHIN-AWAJI GREAT EARTHQUAKE

Post-disaster reconstruction is multifaceted and is a chain reaction. Individual restoration and community restoration are intimately related. Similarly, material restoration and mental restoration are linked with each other. Restoration of homes, city, economy, culture, and natural environment also influence each other.

(1) Home reconstruction

After the earthquake, 50,000 emergency temporary homes were built in an approximately seven-month period, and 40,000 publicly operated permanent homes were built in an approximately five-year period. As far as quantity is concerned, a larger number of homes were secured in comparison with the number of homes before the earthquake. It is significant that a large number of government-operated homes were supplied for reconstruction. It should be noted here that in home reconstruction projects, handicap-accessible and collective houses were actively build and became popular.

However, several issues have arisen in the provision of public housing: first, eligibility for such housing was limited to low-income individuals and aged people; second, construction time was long; and third, the housing was built far from the disaster areas. As a result, not a small number of disaster victims were forced to move away from their earthquake struck residential areas, pay double mortgage and rent payments, and live in makeshift housing for a prolonged period of time.

(2) City Reconstruction

Approximately 80 urban reconstruction projects, such as the replanning of streets, urban redevelopment, and residential area improvement, among others, have been implemented mostly in the areas that suffered dimensionally from the earthquake. This is especially in the approximately 300 hectare area which sustained major damage that was designated as priority reconstruction communities. This area in turn resulted in street replanning in 12 communities and urban redevelopment projects in six communities.

In the communities where street planning and urban redevelopment projects have been implemented, roads, parks, and other infrastructure were further developed, which in turn contributed to rebuilding the communities into a safe urban environment. In addition, in the process of city reconstruction projects, more than 100 resident-operated Town Development Councils have been formed. The councils resulted in the construction of a new city development system in which community residents, development specialists, and non-profit organizations collaborate.

In contrast, a large number of problems have arisen. For example, many residents in a wide range of areas were unable to return to their original residential communities; the financial health of businesses was hurt as restoration was delayed; disparity between communities that had street replanning and other projects, and those which did not, widened.

(3) Economic Reconstruction

Economic reconstruction is the slowest of all restorations. Economic restoration in disaster struck communities was very slow due to the global slowing of the economy, in addition to earthquake damage. In fact, the unemployment rate in the communities was one of the worst in Japan. Another factor that made economic reconstruction difficult was that governmental measures for economic support in those communities were weaker in comparison with support for housing.

The government implemented hardware restoration measures such as construction of makeshift factories and stores, soft restoration measures such as financial support and loans, in addition to stimulation measures through restoration events. As a result, the economy in the disaster communities at the present moment, in terms of sales and output, has recovered 90 percent of what it had been before the earthquake.

However, it should be noted that recovery is slow in certain local industries, such as synthetic leather shoes, whose output reaches only about 60 percent of the pre-disaster time, and clay roof tiles, with only about 70 percent of pre-disaster output. In addition, the recovery of shopping streets and community markets is much slower than department stores and other large businesses, which have already recovered to the pre-disaster level. For example, the number of retail shops operating in disaster-struck communities at the present moment remains only a little more than 80 percent of the pre-earthquake period.

(4) Reconstruction of Culture

Cultural renewal and emotional uplifting were the goals of reconstructing cultural facilities, such as museums and cultural halls, as well as plays and concerts, for disaster area support.

However, we should note that in the process of restoration much of the original landscape and scenery, as well as historic culture, were lost. We must question ourselves for damaging scenery and culture as a result of prioritizing efficient reconstruction, and requiring earthquake-proof buildings.

3. RESTORATION OF NORMALCY IN VICTIMS' LIVES

The ultimate goal in disaster reconstruction is that all victims overcome their individual situations in regards to physical and mental well-being, and as a result, restore independent and creative lives. In order to realize this aim, restoration and maintenance of three basics of life – housing, jobs, and human relationships – are essential. For this reason, the goal of restoration of normalcy in life cannot be fulfilled unless homes are reconstructed, the economy is recovered, communities are restored, and further, culture is renewed.

Victims faced many difficulties after the Hanshin-Awaji Great Earthquake. It has been reported that in the reconstruction process, more than 50 percent of the victims had health problems, and over 20 percent of the workers in the disaster areas lost their jobs. This situation is because effective recovery support measures were lacking in each of the following areas: housing, economy, and community.

The lack of support measures for housing reconstruction was especially problematic. In Japan, financial support is in principle not extended to individual housing reconstruction due to the traditional idea that public tax money should not be used to help augment individual assets such as homes. However in reality, psychological stress creates a reduction of good health for people if there is no prospect of home reconstruction. As a result, a vicious cycle emerged; depopulation occurs when housing reconstruction takes too much time, which in turn causes a decline of communities. In Japan, deliberation of creating a system of financial support for housing reconstruction has started, based on this bitter experience.

It should be noted here that voluntary citizens' support activities, such as NPOs, helped ease the suffering of victims' lives during reconstruction. The fact that these volunteers played a large role in extending care as the third source after the government and community is highly significant.

4. INCREASING CITY DISASTER-READINESS

Large-scale disasters can be interpreted as nature's response or enlightenment against foolish human actions. For that reason, it is essential in reconstruction that we illuminate causes of disaster damage, and further, improve our response to the causes. In the Great Hanshin-Awaji Earthquake, three major issues have arisen in regards to disaster prevention: the lack of earthquake-proofness in wooden houses; the lack of fire-proofness in heavily populated areas; and the lack of readiness in social organizations. It is imperative that we make efforts to solve these issues in disaster reconstruction.

In regards to reconstruction after the earthquake, there has been progress in social organization readiness toward disasters, in the soft arena. However, in the hardware arena, there has been little improvement in the earthquake-readiness of wooden houses and fire-proofness of heavily populated areas. The long-time, ultimate disaster prevention goal for Japan is to build fire-proof, earthquake-ready cities, but that aim has not been achieved, except in certain communities where redevelopment projects were implemented. In most other disaster-struck communities, we allowed

restoration of urban areas that are heavily populated and have a concentration of wooden homes, as before the earthquake.

Construction of disaster-ready cities is difficult in Japan mostly because of the existence of obstacles in reconstruction legal system, reconstruction urban planning, and disaster-prevention consciousness. In regards to the system, due to the principle of not extending financial support for housing reconstruction beyond restoration of the original state, people become reluctant about improving disaster-readiness in homes and buildings. In terms of planning, due to the lack of debate on the building of a safe city, we fail to reach consensus about construction of the disaster-ready city in the chaotic post-disaster period. In regards to people's awareness, the Japanese people's traditional view of disasters has been that humans should not resist nature's forces. This in turn has resulted in the low-level concern about reforming urban structures in the hardware arena. Construction of safe cities in Japan is difficult unless these obstacles are removed.

5. CREATION OF AN IDEAL CITY

In disaster reconstruction, we should be actively working on a variety of issues faced by contemporary society, such as the earth's environment, social welfare, and city landscaping. Efforts to coexist with the natural environment, as well as attempts to solve other issues, lead to effective utilization of resources available for reconstruction. At the same time, these issues should be faced because they are indirectly linked with the improvement of city disaster-readiness. It is desirable to pursue ideal urban structure, in which security accompanies amenities, communities, and sustainability.

In the reconstruction after the Hanshin-Awaji Great Earthquake, proposals were made to build earth-friendly cities rich in water and plants, as well as the construction of health-conscious welfare cities that are friendly to the aged and the handicapped. Efforts have been made in order to materialize the goals that encourage the coexistence of humans and nature and diverse populations. However, their achievements of the pursuit of the ideals were limited. Overall, heavily populated urban communities have been rebuilt as in the pre-earthquake period, and little future-oriented, new urban structure has emerged. The criticism that reconstruction remained too primitive due to the hastiness to restore cities cannot be avoided.

6. TOWARD THE NEXT RECONSTRUCTION

The reconstruction of the Hanshin Awaji Great Earthquake has been significant in terms of the achievement of city function restoration and restoration of normalcy in people's lives in a relatively short period of time. In contrast, it left the issue of failure in creating disaster-ready, environmentally friendly cities. We have learned many lessons in the reconstruction. To conclude this paper, I would like to list three lessons:

First, it is important to hold reconstruction goals in common. Also important is that the debates be continued in regards to the ideal state of rebuilt post-disaster cities and to confirm consensus. If possible, it is desirable to deepen the debates before disasters strike.

Second, it is important to coordinate reconstruction issues. Specifically, a variety of reconstruction issues are linked with each other and coordinated, so that they can be comprehensively worked on. We should focus not only on support for hardware such as housing and vital infrastructure, but also economic and cultural support that would revitalize disaster-struck areas.

Third, it is important to develop disaster-readiness. It is imperative that organizations and systems for reconstruction be developed, as well as securing funds for the reconstruction and development of reconstruction manuals even before disasters strike.

SOIL-STRUCTURE INTERACTION UNDER EXTREME LOADING CONDITIONS

T. D. O'Rourke¹, J. E. Turner², S-S. Jeon³, H. E. Stewart⁴, Y. Wang⁵, and P. Shi⁵

ABSTRACT

Soil-structure interaction under extreme loading conditions includes performance during earthquakes, floods, landslides, large deformation induced by tunneling and deep excavations, and subsidence caused by severe dewatering or withdrawal of minerals and fluids during mining and oil production. Such loading conditions are becoming increasingly more important as technologies are developed to cope with natural hazards, human threats, and construction in congested urban environments. This paper examines extreme loading conditions with reference to earthquakes, which are used as an example of how extreme loading influences behavior at local and geographically distributed facilities. The paper covers performance from the component to the system-wide level to provide guidance in developing an integrated approach to the application of geotechnology over large, geographically distributed networks. The paper describes the effects of earthquake-induced ground deformation on underground facilities, and extends this treatment to the system-wide performance of the Los Angeles water supply during the 1994 Northridge earthquake. Large-scale experiments to evaluate soil-structure interaction under extreme loading conditions are described with reference to tests of abrupt ground rupture effects on urban gas pipelines. Large-scale tests and the development of design curves are described for the forces imposed on pipelines during ground failure.

INTRODUCTION

From a geotechnical perspective, extreme loading conditions are those that induce large plastic, irrecoverable deformation in soil. They are often associated with significant geometric changes in the soil mass, such as shear rupture, heave and void formation, and are accompanied by a peak, or maximum, interaction force imposed on embedded structures. Such loading takes soil well beyond the range of deformation related to the conventional design of civil structures. It applies to performance under unusual, extreme conditions. Such conditions include earthquakes, floods, landslides, large deformation induced by tunneling and deep excavations, and subsidence caused by severe dewatering or withdrawal of minerals and fluids during mining and oil production. Such loading conditions are becoming increasingly more important as technologies are developed to cope with natural hazards, human threats, and construction in congested urban environments.

Extreme loading conditions for soils are often accompanied by extreme loading conditions for structures. Examples include soil/structure interaction associated with pipelines subjected to fault rupture, piles affected by landslides, and soil failure imposed on underground facilities by explosions, flooding, and the collapse of voids. Such conditions induce large plastic, irrecoverable structural deformation that involves both material and geometric nonlinear behavior. Hence, analytical and experimental modeling

¹ Professor, Cornell University, Ithaca, NY 14853

² Engineer, Stephens Associates Consulting Engineers, LLC, Brentwood, NH 03833

³ Chief Researcher, Korea Highway Corporation, South Korea 445-812

⁴ Associate Professor, Cornell University, Ithaca, NY 14853

⁵ Graduate Research Assistant, Cornell University, Ithaca, NY 14853

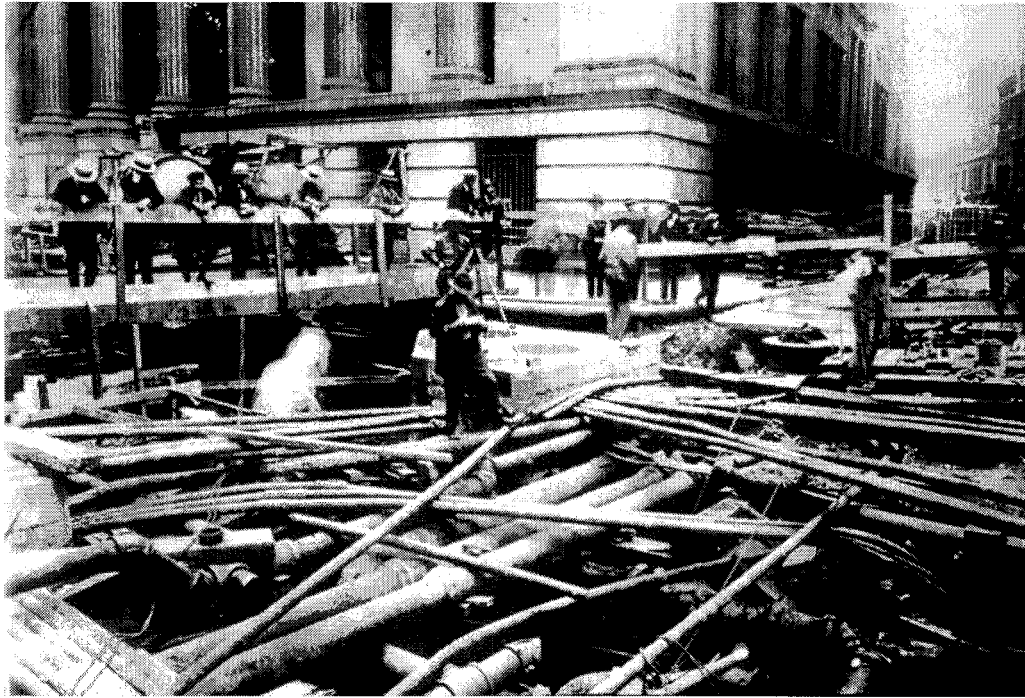


Fig. 1. Underground Infrastructure at Wall and Williams Streets in New York City, 1917

for soil-structure interaction under these conditions requires the coupled post-yield simulation of both soil and structural response. Such behavior generally poses significant challenges to our analytical capabilities, thus requiring large-scale experimental and case history data to improve the simulation process and validate the models.

Extreme loading conditions, especially those associated with natural hazards and severe human threats, may affect large systems of structures. Consider, for example, Figure 1, which is a photograph of the corner of Wall and Williams Sts. in New York City in 1917. The congestion shown in this photograph has not improved in the last 88 years, and is indicative of the situation in a multitude of cities worldwide. The photo illustrates at least two important features of the built environment. First, much of critical infrastructure is located underground, and its fate is intimately related to that of the surrounding ground. Second, the crowded nature of urban and suburban developments increases risk due to proximity. Damage to one facility, such as a cast iron water main, can rapidly cascade into damage in surrounding facilities, such as electric and telecommunication cables and gas mains, with system-wide consequences. Soil surrounding critical underground infrastructure is frequently both the perpetrator and mediator of loading that can affect the systemic performance of an entire city.

In this paper, soil-structure interaction under extreme loading conditions is examined with reference to earthquakes, which are used as an example of how extreme loading influences behavior at local and geographically distributed facilities. The paper begins with the effects of earthquake-induced ground deformation on underground facilities, and then expands this treatment to consider the system-wide performance of the Los Angeles water supply during the 1994 Northridge earthquake. Large-scale experiments to evaluate soil-structure interaction under extreme loading conditions are described with reference to tests of abrupt ground rupture effects on urban gas pipelines. Large-scale tests and the development of design curves are described for the forces imposed on pipelines during ground failure. The paper covers performance from the component to the system-wide level to provide guidance in developing an integrated approach to the application of geotechnology over large, geographically distributed networks.

GEOTECHNICAL EARTHQUAKE LOADING

Earthquakes cause transient ground deformation (TGD) and permanent ground deformation (PGD), both of which affect underground pipelines. TGD is the dynamic response of the ground, and PGD is the irrecoverable movement that persists after shaking has stopped. PGD often involves large displacements, such as those associated with surface fault rupture and landslides. TGD can cause soil cracks and fissures triggered by pulses of strong motion that develop localized shear and tensile strains exceeding the strength of surficial soils. In these cases, crack widths and offsets are primarily a reflection of surficial ground distortion and gravity effects, such as local slumping. They should not be mistaken as an expression of PGD generated by ground failure mechanisms of larger scale.

The principal causes of PGD have been summarized and discussed by O'Rourke (1998). They are faulting, tectonic uplift and subsidence, and liquefaction, landslides, and densification of loose granular deposits. Liquefaction is the transformation of saturated cohesionless soil into a liquefied state or condition of substantially reduced shear strength (Youd, 1973). Liquefaction-induced pipeline deformation can be caused by lateral spread, flow failure, local subsidence, post-liquefaction consolidation, buoyancy effects, and loss of bearing (Youd, 1973; O'Rourke, 1998). It is widely accepted that the most serious pipeline damage during earthquakes is caused by PGD. Furthermore, it is well recognized that liquefaction-induced PGD, especially lateral spread, is one of the most pervasive causes of earthquake-induced lifeline damage (Hamada and O'Rourke, 1992; O'Rourke and Hamada, 1992).

Ground displacement patterns associated with earthquakes depend on PGD source, soil type, depth of ground water, slope, earthquake intensity at a given site, and duration of strong ground shaking (O'Rourke, 1998). It is not possible to model with accuracy the soil displacement patterns at all potentially vulnerable locations. Nevertheless, it is possible to set upper bound estimates of deformation effects on buried lifelines by simplifying spatially distributed PGD as movement concentrated along planes of soil failure.

Various modes of pipeline distortion caused by PGD are illustrated in Fig. 2. Pipelines crossing a fault plane subjected to oblique slip are shown in Fig. 2a. Reverse and normal faults promote compression and tension, respectively. Strike slip may induce compression or tension, depending on the angle of intersection between the pipeline and fault. Fig. 2b shows a pipeline crossing a lateral spread or landslide perpendicular to the general direction of soil movement. In this orientation, the pipeline is subject to bending strains and extension. As shown in Fig. 2c, the pipeline will undergo bending and either tension or compression at the margins of the slide when the crossing occurs at an oblique angle. Fig. 2d shows a pipeline oriented parallel to the general direction of soil displacement. At the head of the zone of soil movement, the displacements resemble normal faulting; under these conditions, the pipeline will be subjected to both bending and tensile strains. At the toe of the slide, the displaced soil produces compressive strains in the pipeline.

Fig. 3 shows a compressive failure at a welded slip joint on the Granada Trunk Line, a 1,245-mm-diameter steel pipeline with 6.4-mm wall thickness that failed during the Northridge earthquake because of lateral ground movement triggered by liquefaction near the intersection of Balboa Boulevard and Rinaldi Street in the San Fernando Valley. The PGD pattern and pipeline failure mode associated with this site are similar to those depicted in Fig. 2d. Similar compressive failures were observed in trunk lines during the 1971 San Fernando earthquake and in the adjacent 1,727-mm-diameter (9.5-mm wall thickness) Rinaldi Trunk Line during the Northridge earthquake. Loss of both the Granada and Rinaldi Trunk Lines cut off water to tens of thousands of customers in the San Fernando Valley for several days.

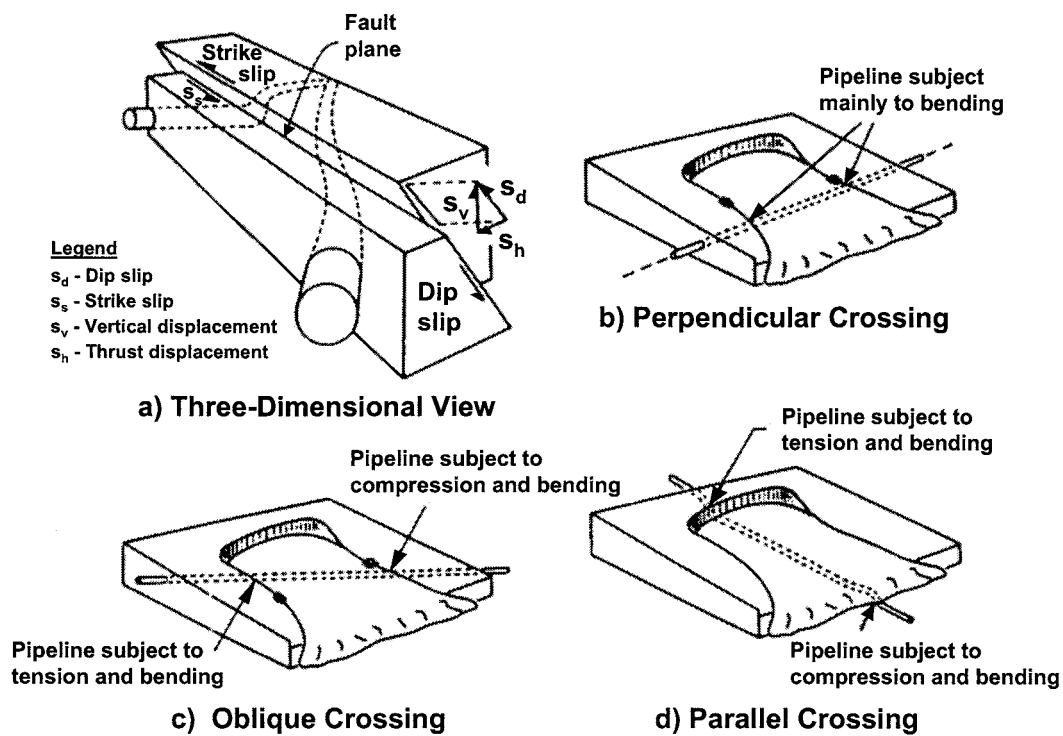


Fig. 2. Principal Modes of Soil-Pipeline Interaction Triggered by Earthquake-Induced PGD (O'Rourke, 1998)

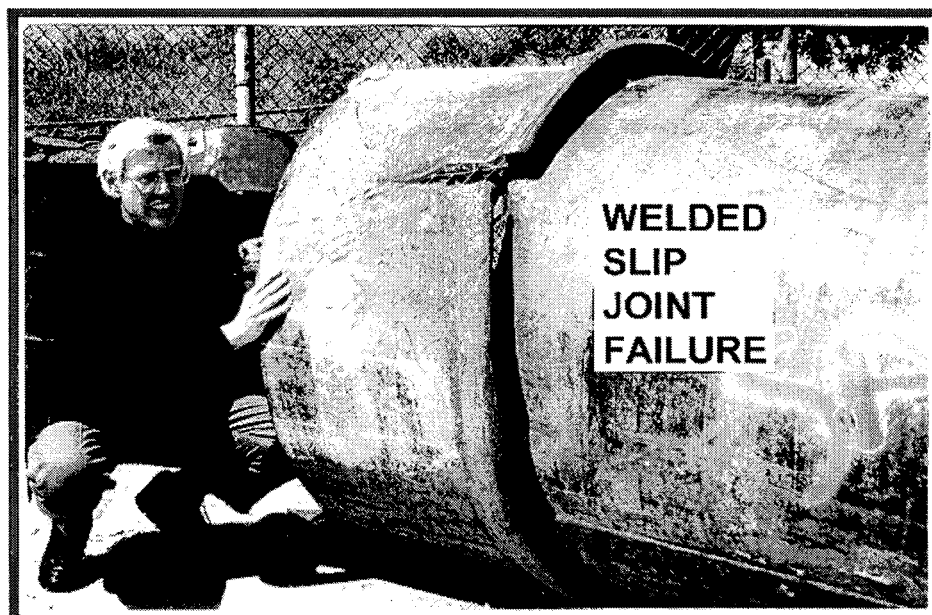


Fig. 3. Welded Slip Joint Failure of the Granada Trunk Line During the 1994 Northridge Earthquake (photo by Y. Shiba)

Various simplified models for soil-pipeline interaction have been developed to account for the effects of abrupt ground displacement illustrated in Fig. 2. (e.g., Newmark and Hall, 1975; Kennedy, et al., 1977; O'Rourke, et al., 1985; and O'Rourke and Liu, 1999). Moreover, various finite element codes (e.g., ABAQUS, ANSYS, and PIPLIN) are applied frequently to model PGD effects on the post-yield performance of line pipe. A hybrid model, representing line pipe as a combination of beam and shell elements, has been developed recently to analyze PGD effects on pipeline elbows (Yoshisaki, et al., 2001).

LIFELINE SYSTEM RESPONSE TO EARTHQUAKES

The 1994 Northridge earthquake caused the most extensive damage to a US water supply system since the 1906 San Francisco earthquake. Three major transmission systems, which provide over three-quarters of the water for the City of Los Angeles, were disrupted. Los Angeles Department of Water and Power (LADWP) and Metropolitan Water District (MWD) trunk lines (nominal pipe diameter ≥ 600 mm) were damaged at 74 locations, and the LADWP distribution pipeline (nominal pipe diameter < 600 mm) system was repaired at 1013 locations.

The earthquake-induced damage to water pipelines and the database developed to characterize this damage have been described elsewhere (O'Rourke, et al., 1998; O'Rourke, et al., 2001; Jeon and O'Rourke, 2005), and only the salient features of this work are summarized herein. GIS databases for repair locations, characteristics of damaged pipe, and lengths of trunk lines according to pipe composition and size were assembled with ARC/INFO software. Nearly 10,000 km of distribution lines and over 1,000 km of trunk lines were digitized.

Figure 4 shows the portion of the Los Angeles water supply system most seriously affected by the Northridge earthquake superimposed on the topography of Los Angeles. The figure was developed from the GIS database, and shows all water supply pipelines plotted with a geospatial precision of ± 10 m throughout the San Fernando Valley, Santa Monica Mountains, and Los Angeles Basin. The rectilinear system of pipelines is equivalent to a giant strain gage. Seismic intensity in the form of pipeline damage can be measured and visualized by plotting pipeline repair rates and identifying the areas where the largest concentrations of damage rate occur. The resulting areas reflect the highest seismic intensities as expressed by the disruption to underground piping.

To develop a properly calibrated strain gage, it is necessary to select a measurement grid with material having reasonably consistent properties and a damage threshold sensitive to the externally imposed loads being measured. Figure 5 presents charts showing the relative lengths of LADWP and MWD trunk and distribution lines, according to pipe composition. As shown by the pie chart, the most pervasive material in the LA distribution system is CI. The 7,800 km of CI pipelines have the broadest geographic coverage with sufficient density in all areas to qualify as an appropriate measurement grid. Moreover, CI is a brittle material subject to increased rates of damage at tensile strains on the order 250 to 500 $\mu\epsilon$. It is therefore sufficiently sensitive for monitoring variations in seismic disturbance.

Figure 6 presents a map of distribution pipeline repair locations and repair rate contours for cast iron (CI) pipeline damage. The repair rate contours were developed by dividing the map into 2 km x 2 km areas, determining the number of CI pipeline repairs in each area, and dividing the repairs by the distance of CI mains in that area. Contours then were drawn from the spatial distribution of repair rates, each of which was centered on its tributary area. A variety of grids were evaluated, and the 2 km x 2 km grid was found to provide a good representation of damage patterns for the map scale of the figure (Toprak, et al., 1999).

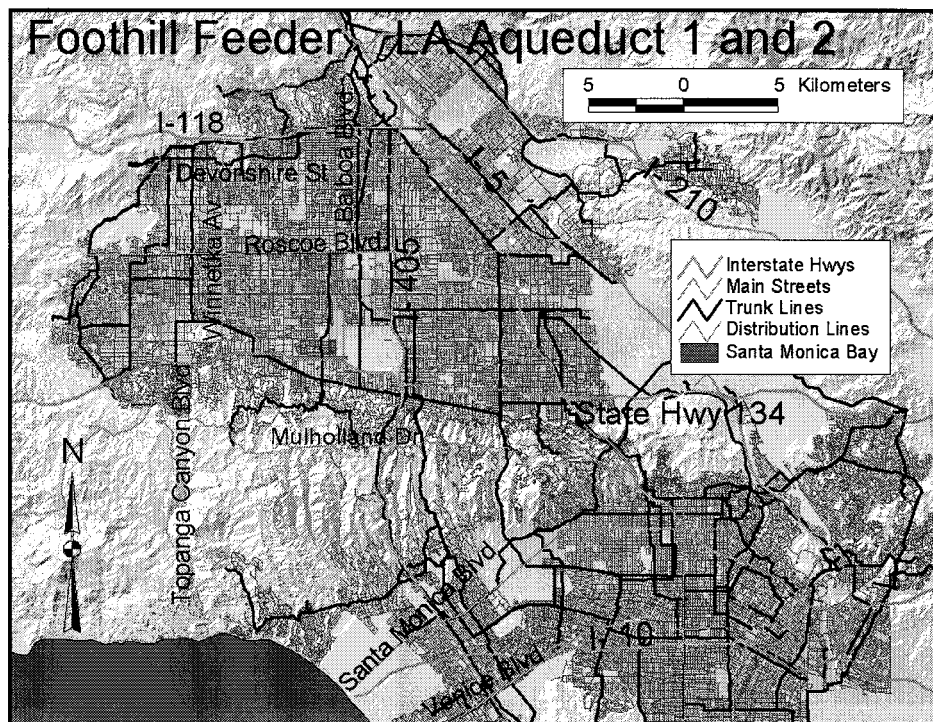


Fig. 4. Map of Los Angeles Water Supply System Affected by Northridge Earthquake (O'Rourke and Toprak, 1997)

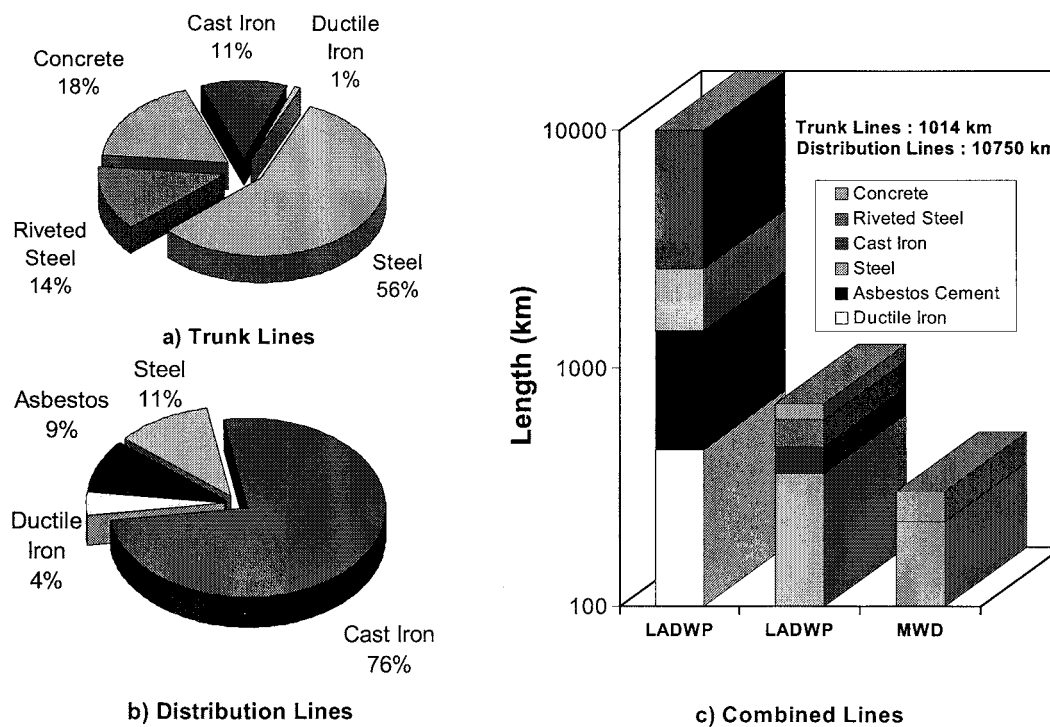


Fig. 5. Composition Statistics of Water Trunk and Distribution Lines in the City of Los Angeles (O'Rourke and Toprak, 1997)

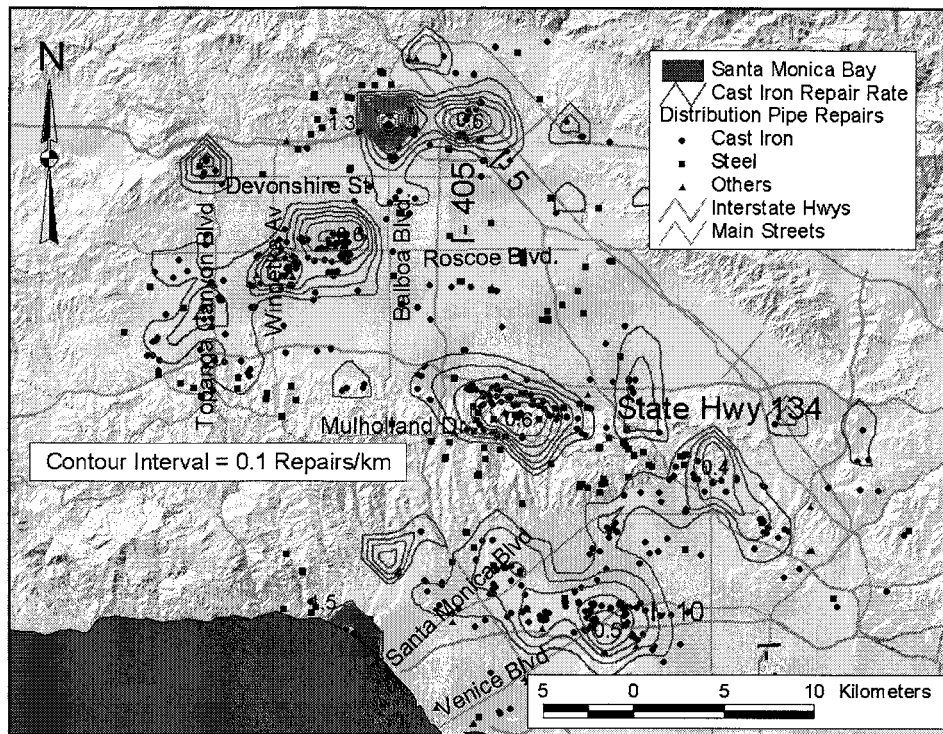


Fig. 6. Cast Iron Pipeline Repair Rate Contours for the Northridge Earthquake (O'Rourke and Toprak, 1997)

The zones of highest seismic intensity are shown by areas of concentrated contours. In each instance, areas of concentrated contours correspond to zones where the geotechnical conditions are prone either to ground failure or amplification of strong motion. Each zone of concentrated damage is labeled in Fig. 7 according to its principal geotechnical characteristics. In effect, therefore, Fig. 6 is a seismic hazard map for the Los Angeles region, calibrated according to pipeline damage during the Northridge earthquake.

Of special interest is the location of concentrated repair rate contours in the west central part of San Fernando Valley (designated in Fig. 7 as the area of soft clay deposits). This area was investigated by USGS researchers, who found it to be underlain by local deposits of soft, normally consolidated clay. Field vane shear tests disclosed clay with uncorrected, vane shear undrained strength, $S_{uvst} = 20\text{--}25$ kPa, at a depth of 5 m, just below the water table. USGS investigators concluded that the saturated sands underlying this site were not subjected to liquefaction during the Northridge earthquake. Newmark sliding block analyses reported by O'Rourke (1998) provide strong evidence that near source pulses of high acceleration were responsible for sliding and lurching on the soft, normally consolidated clay deposit. The results of GIS analysis and site investigations have important ramifications because they show a clear relationship between PGD, concentrated pipeline damage, and the presence of previously unknown deposits of normally consolidated clay.

The records from approximately 240 free field rock and soil stations were used to evaluate the patterns of pipeline damage with the spatial distribution of various seismic parameters. Fig. 8 shows the CI pipeline repair rate contours superimposed on peak ground velocity (PGV) zones, which were developed by interpolating the maximum horizontal velocities recorded at the strong motion stations. Using the GIS database, a pipeline repair rate was calculated for each PGV zone, and correlations were made between the repair rate and average PGV for each zone. As explained by O'Rourke (1998), similar correlations were investigated for pipeline damage relative to spatially distributed peak ground

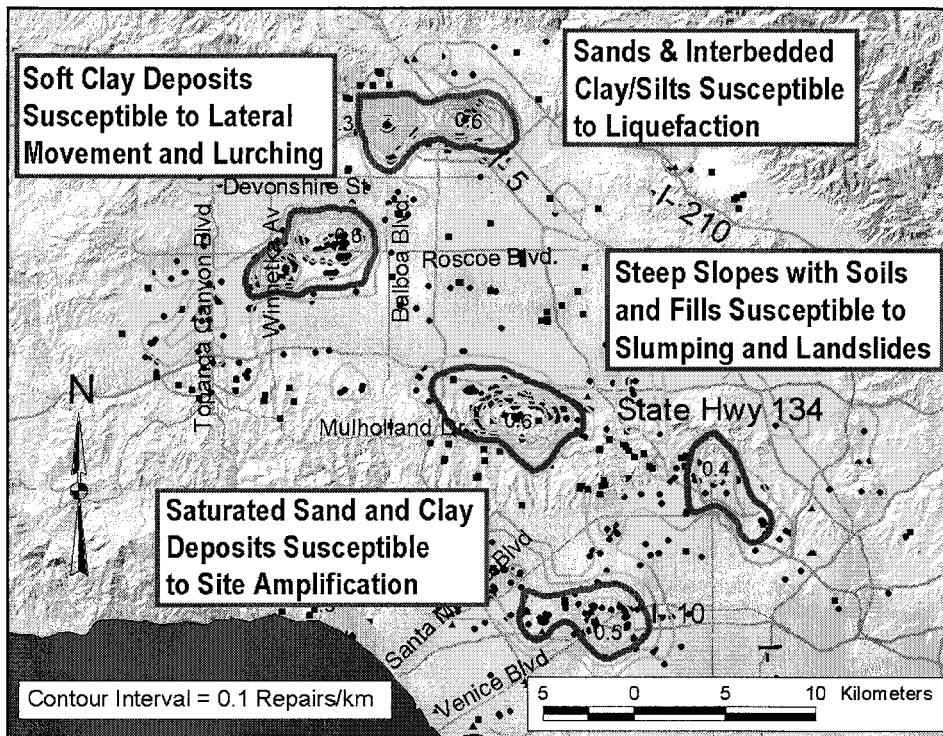


Fig. 7. Geotechnical Characteristics of the Areas of Concentrated Pipeline Damage After the Northridge Earthquake

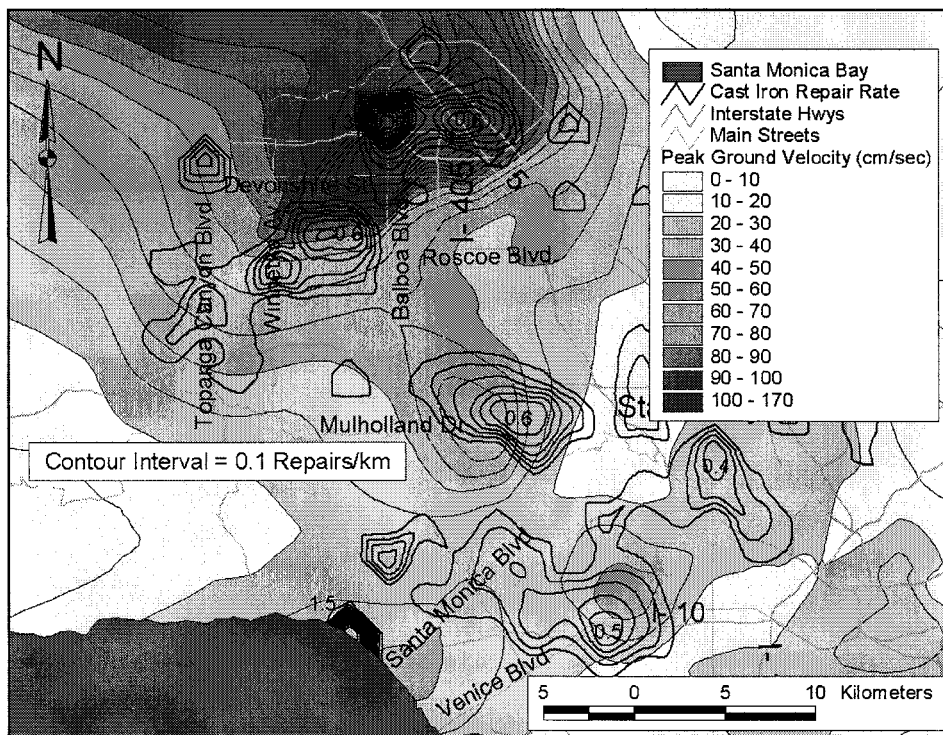


Fig. 8. Pipeline Repair Rate Contours Relative to Northridge Earthquake Peak Ground Velocity (O'Rourke and Toprak, 1997)

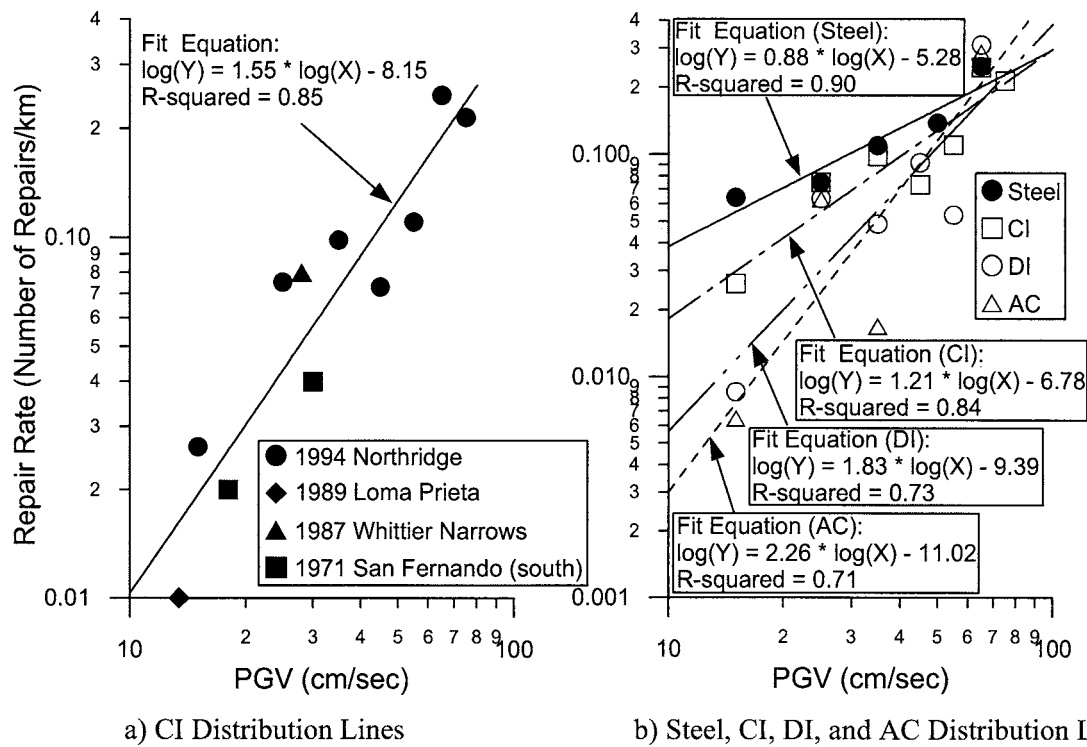


Fig. 9. Pipeline Repair Rate Correlation with PGV for Steel, CI, DI, and AC Distribution Lines

acceleration, spectral acceleration and velocity, Arias Intensity, Modified Mercalli Intensity (MMI), and other indices of seismic response. By correlating damage with various seismic parameters, regressions were developed between repair rate and measures of seismic intensity.

The most statistically significant correlations for both distribution and trunk line repair rates were found for PGV. Such correlations are important for loss estimation analyses that are employed to assess the potential damage during future earthquake and develop corrective measures and emergency response procedures to reduce the projected losses (e.g., Whitman, et al., 1997).

Fig. 9a presents the linear regression that was developed between CI pipeline repair rates and PGV on the basis of data from the Northridge and other U.S. earthquakes. Fig. 9b shows repair rate correlations for steel, CI, ductile iron (DI), and asbestos cement (AC) distribution lines. The regressions indicate that the highest rate of damage for a given PGV was experienced by steel pipelines. This result at first seems surprising because steel pipelines are substantially more ductile than CI and AC pipelines. Steel distribution pipelines in Los Angeles, however, are used to carry the highest water pressures and are subject to corrosion that has been shown to intensify their damage rates in previous earthquakes (Isenberg, 1979).

The regressions in Fig. 9 were developed after the data were screened for lengths of pipeline that represent approximately 1.5 to 2.5 % of the total length or population for each type of pipe affected by the earthquake (O'Rourke and Jeon, 1999). This procedure reduces the influence of local erratic effects that bias the data derived from small lengths of pipeline. The use of this filtering procedure leads to statistically significant trends, but with the resulting in regressions only applicable for $PGV \leq 75$ cm/s. For the Northridge earthquake, zones with PGV exceeding 75 cm/sec generally correspond to locations where PGD, from sources such as liquefaction and landsliding, was observed. Hence, this screening technique tends to remove damage associated with PGD, resulting in correlations relevant for TGD.

Of special interest is the work of Hamada and coworkers (Hamada, et al., 1986; Hamada and O'Rourke, 1992) in the use of stereo-pair air photos before and after an earthquake to perform photogrammetric analysis of large ground deformation. This process has had significant impact on the way engineers and geologists evaluate soil displacements by providing a global view of deformation that allows patterns of distortion to be quantified and related to geologic and topographic characteristics.

After the Northridge earthquake, pre- and post- earthquake air photo measurements in the Van Norman Complex were analyzed as part of collaborative research between U.S. and Japanese engineers (Sano, et al., 1999; O'Rourke, et al., 1998). Air photos taken before and after the earthquake were acquired by U.S. team members and analyzed through advanced photogrammetric techniques by Japanese team members. Ground movements from this initial set of measurements were corrected for tectonic deformation to yield movements caused principally by liquefaction and landslides.

The area near the intersection of Balboa Blvd. and Rinaldi St. has been identified as a location of liquefaction (Holzer, et al., 1999) where significant damage to gas transmission and water trunk lines was incurred. This location is the same area where the pipeline failure in Fig. 7 was observed. Ground strains were calculated in this area from the air photo measurements of horizontal displacement by superimposing regularly spaced grids with GIS software onto the maps of horizontal displacement and calculating the mean displacement for each grid. Grid dimensions of 100 m x 100 m were found to provide the best results (Sano, et al., 1999).

As illustrated in Fig. 10, ground strain contours, pipeline system, and repair locations were combined using GIS, after which repair rates corresponding to the areas delineated by a particular contour interval were calculated. Fig. 11 shows the repair rate contours for CI mains superimposed on the areal distribution of ground strains, identified by various shades and tones. In the study area, there were 34 repairs to CI water distribution mains and 2 for steel water distribution pipelines. There were 5 water trunk line repairs in the area. The repair rate contours were developed by dividing the map into 100 m x 100 m cells, determining the number of CI pipeline repairs in each cell, and dividing the repairs by the length of the distribution mains in that cell. The intervals of strain and repair rate contours are 0.001 (0.1%) and 5 repairs/km, respectively. The zones of high tensile (+) and compressive (-) strains coincide well with the locations of high repair rate.

In Fig. 12, the relationship between the absolute values of the ground strains and repair rates is presented graphically using linear regression. The repair rate in each ground strain range, 0-0.1, 0.1-0.3, and 0.3-0.5%, was calculated as explained previously. Ground strain contours, obtained by both air photo measurements and surface surveys, were used. The regression analysis shows that repair rates increase linearly with ground strain. In some instances, anomalously high repair rates were determined. Such values do not represent the actual distribution of damage, but are a consequence of locally high concentrations of repairs within a given cell. The occurrence of anomalously high values depends on the cell size and positioning of cells with respect to pipeline repair locations. It is important, therefore, to incorporate screening procedures to filter such erroneous types of data. For example, an investigation of the locally high data point in Fig. 12 showed that this repair rate was calculated for one particular positioning of the grid of GIS cells and not for others. As such, this locally high repair rate was not used in the regression analyses. A systematic investigation of cell size and positioning effects on GIS analytical results has been performed, and procedures for selecting an optimal cell sizes have been recommended (Toprak, et al., 1999).

Hamada and Wakamatsu (1996) showed a similar strong correlation between frequency of pipeline repairs and ground strains evaluated by air photo measurements after the 1995 Kobe earthquake. Seismic

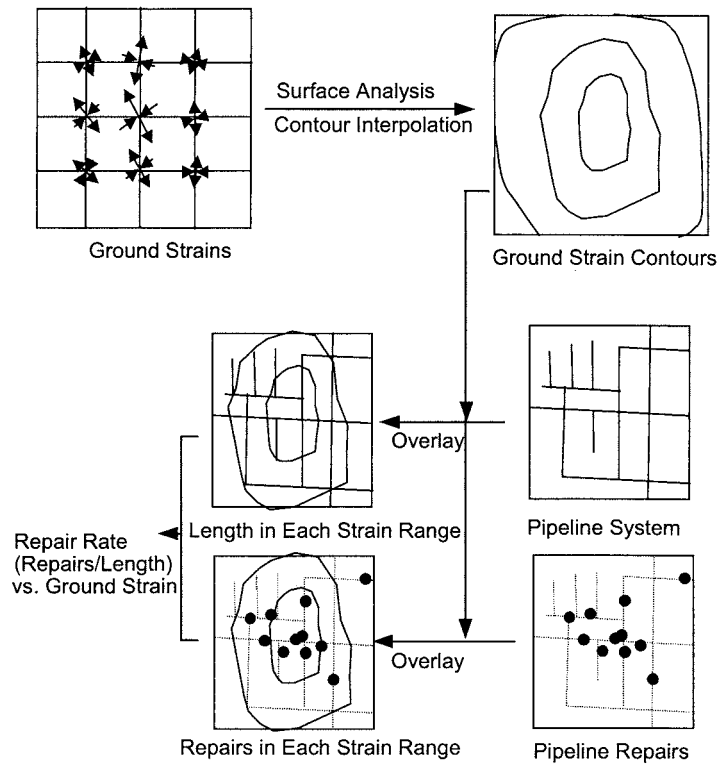


Fig. 10. Procedure for Calculating Repair Rate in Each Strain Range (O'Rourke et al., 1998)

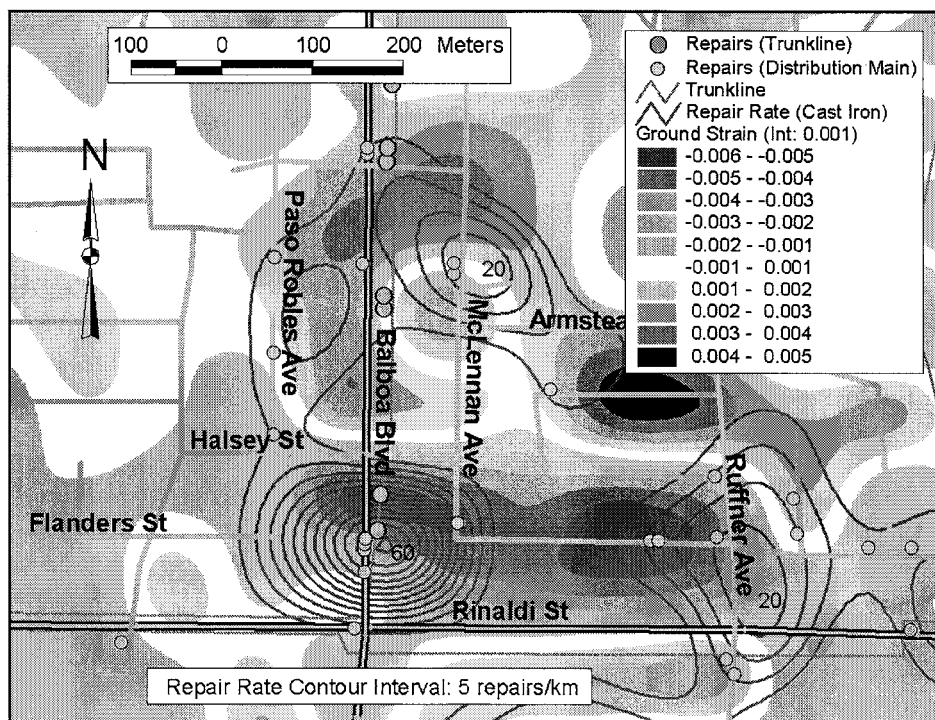


Fig. 11. Distributions of CI Repair Rate and Ground Strain (O'Rourke, et al., 1998)

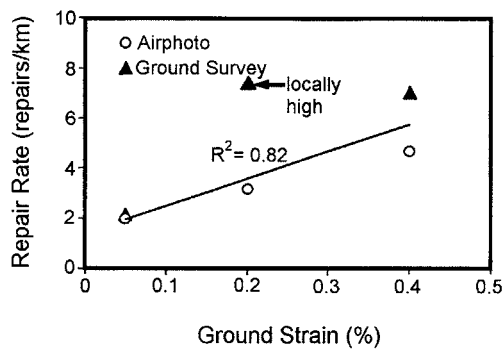


Fig. 12. Correlation Between Ground Strain and CI Repair Rate (O'Rourke, et al., 1998)

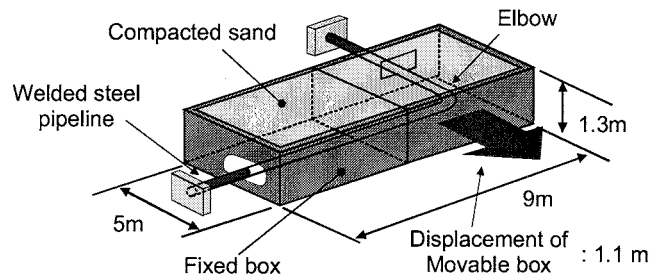


Fig. 13. Experimental Concept for PGD Effects on Buried Pipelines with Elbows

design codes for gas pipelines in Japan have been developed on the basis of acceptable strain levels (Japan Gas Association, 2000). These values, in turn, can be related to the anticipated levels of ground strain triggered by an earthquake.

LARGE-SCALE TESTS OF GROUND RUPTURE EFFECTS

A key component of modern research involving geotechnical engineering for extreme loading conditions has been testing at very large scale. Large scale experiments sponsored by NSF through MCEER at Cornell in conjunction with Tokyo Gas, Ltd. were performed to evaluate the effects of earthquake-induced ground rupture on welded steel pipelines with elbows. The experimental set-up involved the largest full-scale replication of PGD effects on pipelines ever performed in the laboratory.

Many pipelines must be constructed to change direction rapidly to avoid other underground facilities or to adjust to the shape of roads under which they are buried. In such cases the pipeline is installed with an elbow that can be fabricated for a change in direction from 90 to a few degrees. The response of pipeline elbows, deformed by adjacent ground rupture and subject to the constraining effects of surrounding soil, is a complex interaction problem. A comprehensive and reliable solution to this problem requires laboratory experiments on elbows to characterize their three-dimensional response to axial and flexural loading, an analytical model that embodies soil-structure interaction combined with three-dimensional elbow response, and full-scale experimental calibration and validation of the analytical model.

Fig. 13 illustrates the concept of the large-scale experiments. A steel pipeline with an elbow is installed under the actual soil, fabrication, and compaction procedures encountered in practice, and then subjected to lateral soil displacement. The scale of the experimental facility is chosen so that large soil movements are generated, inducing soil-pipeline interaction unaffected by the boundaries of the test facility in which the pipeline is buried. The ground deformation simulated by the experiment represents deformation conditions associated with lateral spread, landslides, and fault crossings, and therefore applies to many different geotechnical scenarios. In addition, the experimental data and analytical modeling products are of direct relevance for underground gas, water, petroleum, and electrical conduits.

Experiment Description and Results

A 100-mm-diameter pipeline with 4.1-mm wall thickness was used in the tests. It was composed of two straight pipes welded to a 90-degree elbow (E). The short section of straight pipe (D) was 5.4 m long, whereas the longest section was 9.3 m. Both ends of the pipeline were bolted to reaction walls. The elbows were composed of STPT 370 steel (Japanese Industrial Standard, JIS-G3456) with a specified minimum yield stress of 215 MPa and a minimum ultimate tensile strength of 370 MPa. The straight pipe

was composed of SGP steel (JIS-G3452) with a minimum ultimate tensile strength of 294 MPa. About 150 strain gauges were installed on the pipe to measure strain during the tests. Extensometers, load cells, and soil pressure meters were also deployed throughout the test setup. The pipeline was installed at a 0.9-m depth to top of pipe in each of three experiments. In each experiment soil was placed at a different water content and in situ density. The experiments were designed to induce opening-mode deformation of the elbow. They were conducted with nitrogen pressure of 0.1 MPa in the pipeline. Details of the tests and experimental results are provided by Yoshisaki, et al. (2001).

Approximately 60 metric tons of sand were moved from the storage bin into the test compartment for each experiment. The sand was obtained from a glacial-fluvial deposit, and contained approximately 2% by weight of fines. The water content of 0.5% for Test 1 is the hygroscopic water content, the lowest value possible without oven drying. Hence, the soil in Test 1 is dry sand, and is comparable to the dry sand used in previous soil-pipe interaction tests (Trautmann and O'Rourke, 1985). In contrast, Tests 2 and 3 were performed with sufficiently large water contents to investigate the effects of partial saturation. The grain size curve for the sand is shown in Fig. 14. The sand was placed and compacted in 150-mm lifts with strict controls on water content and in situ density, which are summarized in Table 1. The sand satisfied the standards for backfill specified by the Bureau of Construction of the Tokyo Metropolitan Government.

Fig. 15 shows the ground surface of the test compartment before and after an experiment. Surficial heaving and settlement can be seen in the area near the pipeline elbow and the abrupt displacement plane between the movable and fixed boxes after the test. In all cases, planes of soil slip and cracking reached the ground surface, but did not intersect the walls of the test compartment to any appreciable degree. One hundred and ten mm of surface settlement and 95 mm of surface heave were measured after the test. Fig. 16 shows an overhead view of the test compartment after soil excavation to the pipeline following Test 1. Leakage occurred at the connection between the elbow and the shorter straight pipe when the ground displacement was 0.78 m. Full circumferential rupture of the pipe occurred when the displacement was 0.94 m.

Analytical Model and Results

The pipeline was modeled with isotropic shell elements with reduced integration points. Average values of the actual thickness measured with an ultrasonic thickness meter were used for the elbow and straight pipes in the model. True stress-strain relationships from direct tension test data were approximated by multi-linear trends for the elbow and straight pipe. ABAQUS Version 5.8 was used as a solver for the analyses with geometric nonlinearity and large strain formulation. The von Mises criterion and associated flow rule were applied to the model. Since strains are in the same direction in strain space throughout the analyses, isotropic hardening was used in the model. An internal pressure of 0.1 MPa was also applied in the model. Soil-pipe interaction was modeled in accordance with Japan Gas Association guidelines (2000) and data presented by Trautmann and O'Rourke (1985).

Fig. 17 (a) compares the deformed pipeline shape of the analytical model with measured deformation of the experimental pipeline for Test 1. There is excellent agreement between the two, as well as close agreement between the analytical deformation and the overhead view of the deformed pipeline in Fig. 16. Fig. 17 (b) shows the measured and predicted strains under maximum ground deformation on both the compressive (extrados) and tensile (intrados) surfaces of flexure along the pipeline. Figs. 17 (c) and (d) show the measured and analytical strains around the pipe circumference in which the angular distance is measured from extrados to intrados of pipe, corresponding to 0 and 180°, respectively. In Fig. 17 (c), the data point with an upward arrow indicates the maximum strain measured when the gauge was disconnected during the experiment. Because the disconnection occurred before maximum deformation of the elbow, it is likely that the actual strain was larger than the value plotted. Overall, there is good agreement for both the magnitude and distribution of measured and analytical strains and deformation.

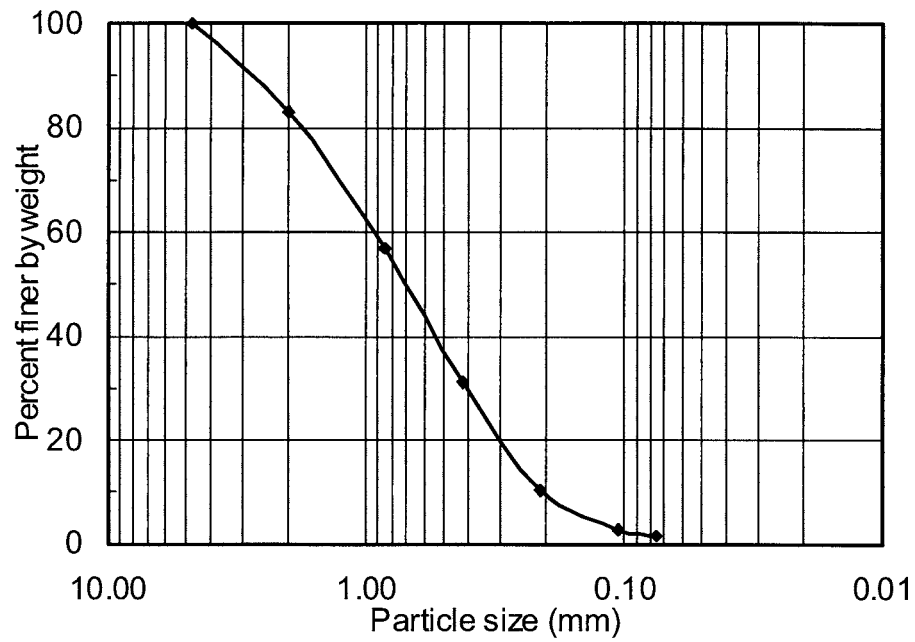


Fig. 14. Grain Size Distribution of Experimental Sand

Table 1 Properties of Experimental Sand

Parameters	Test 1	Test 2	Test 3
Water content, w (%)	0.5	3.1	3.4
Wet unit weight, γ_{wet} (kN/m^3)	18.4	17.0	16.7
Dry unit weight, γ_{dry} (kN/m^3)	18.3	16.6	16.2
Friction angle from slow triaxial compression tests (0.1%/min), $\phi_{TXC-0.1}$ (degree)	49	40	39
Friction angle from fast triaxial compression tests (5%/min), ϕ_{TXC-5} (degree)	51	43	42

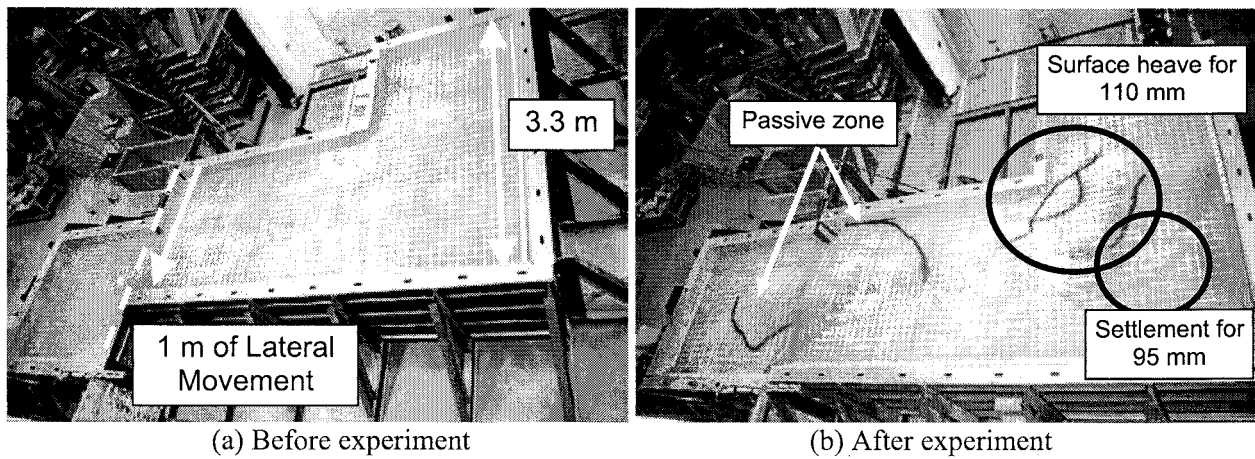


Fig. 15. Overhead View of Test Compartment Before and After the Experiment (Test 1)

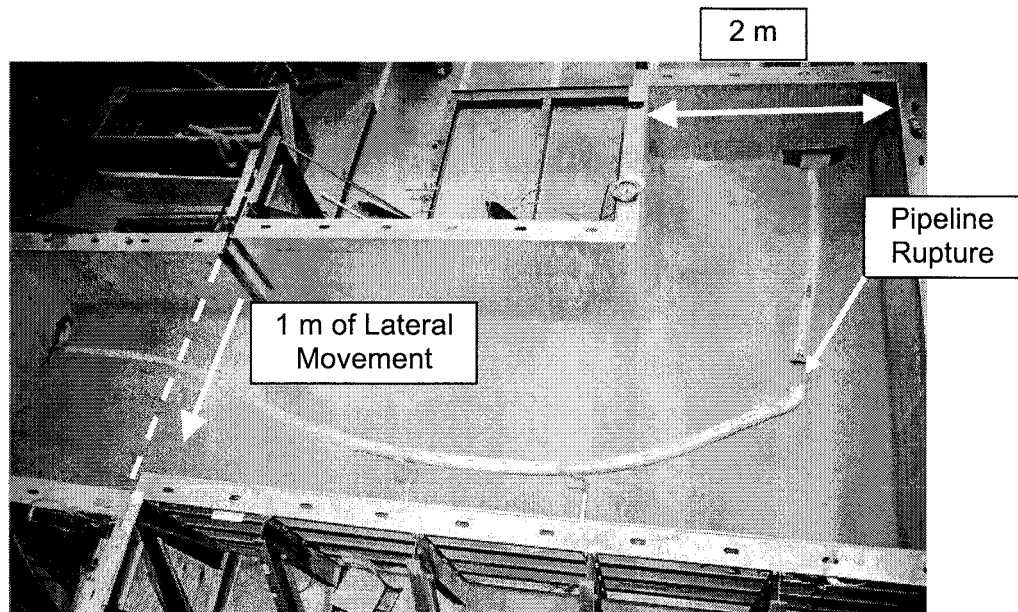
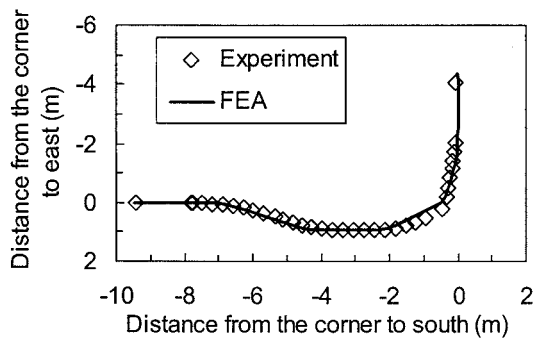
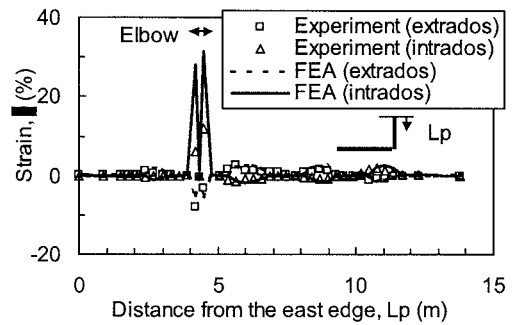


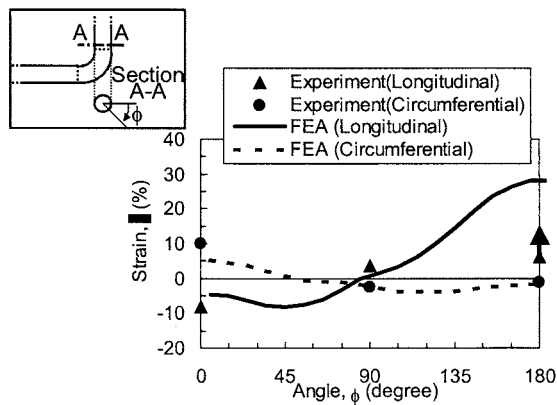
Fig. 16. Overhead View of Deformed Pipeline (Test 1)



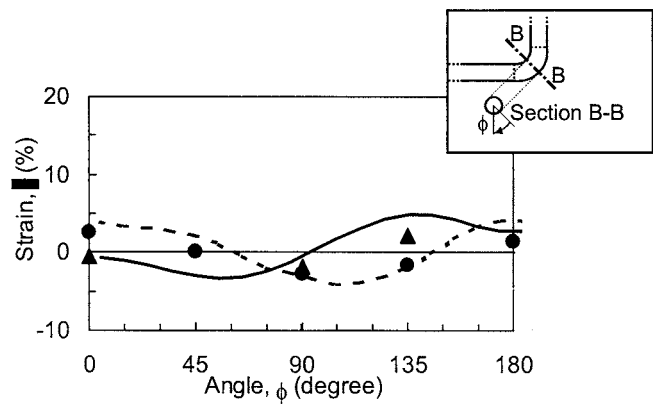
(a) Pipeline deformation after the test



(b) Distribution of axial strain in the longitudinal direction



(c) Strain distribution at Section A-A



(d) Strain distribution at Section B-B

Fig. 17. Comparison Between Analytical and Experimental Results

The soil deformation patterns adjacent to the pipeline were different for the dry and partially saturated sands. During PGD, the dry sand in Test 1 tended to flow around the experimental pipeline, filling the spaces behind it as relative horizontal movement of the pipe increased. In contrast, the partially saturated sand in Tests 2 and 3 possessed apparent cohesion because of surface tension generated by interstitial moisture among the sand particles. As a result, relative movement of the pipe generated rupture surfaces rather than flow in the adjacent soil.

The large-scale experiments had three principal results. First, they were used to improve and validate a hybrid finite element model, which combines beam and shell elements for the pipeline with nonlinear p-y formulations to simulate soil-structure interaction. This model is now used by Tokyo Gas to plan and design pipelines for extreme loading conditions. Second, the analytical model was used to show that increasing the wall thickness of pipe, which is welded to the elbow, by 1.5 mm results in strain reduction of approximately 200% for abrupt ground rupture of 2 m. Simple, relatively inexpensive adjustments in pipeline fabrication, therefore can lead to substantial improvements in performance. Third, the strains induced in the experimental pipeline were markedly higher for tests in partially saturated sand than for those in dry sand, even though most other variables were held constant.

SOIL-STRUCTURE INTERACTION DURING GROUND FAILURE

To explore the effects of partially saturated sand on the lateral force conveyed to buried conduits due to relative soil-pipe displacement, a series of additional tests were performed on pipe of similar size and composition. The tests were designed to be similar to those performed by Trautmann and coworkers (Trautmann and O'Rourke, 1985; Trautmann, et al., 1985), who established design charts from which p-y and q-z relationships can be developed for analyzing soil-structure interaction in response to lateral and vertical PGD.

These design charts were developed on the basis of experiments in dry sand. However, the great majority of pipelines in the field are embedded in partially saturated soils. Shear deformation of partially saturated sand mobilizes surface tension, or negative pore water pressure, which increases shear resistance relative to that in dry sand under comparable conditions of soil composition, in situ density, and loading. Moreover, the geometry of the failed soil mass for partially saturated sand is significantly different than the flow and displacement pattern of dry sand around buried pipelines.

The experimental facility was constructed to model the effects of relative horizontal displacement between soil and pipe under conditions that duplicate the actual scale, burial depth, and soil characteristics encountered in the field. Horizontal displacement was applied externally to a pipe section in a manner that allowed unrestricted vertical pipe movement as well as adjustments in pipe weight to replicate different contents such as gas, liquid fuel, and water. The application of force and displacement on the pipe was designed to duplicate soil-pipe interaction for conditions in which PGD is imposed on underground pipelines during surface faulting, landslides, and lateral spreads.

The experimental facility was designed to induce maximum lateral displacement of 152 mm, with burial depths to 20 diameters. The experimental facility was composed of a test compartment, pipe loading system, instrumentation and data acquisition system, and soil handling equipment. Figures 18 and 19 show plan and profile photographs, respectively, of the test compartment.

The test apparatus consisted of a box with interior dimensions 2.4 m × 1.2 m by 1.5 m deep. A special collar was fabricated to fit on top of the testing apparatus (not shown in the figure) that extended the depth of pipe burial to 2.3 m. The apparatus was filled with a false wall that was removed when deep embedment depths (pipe depth exceeding 10 times pipe diameter) were used. Lateral force and displacement were conveyed to the pipe through a special yoke that allowed for unrestricted vertical

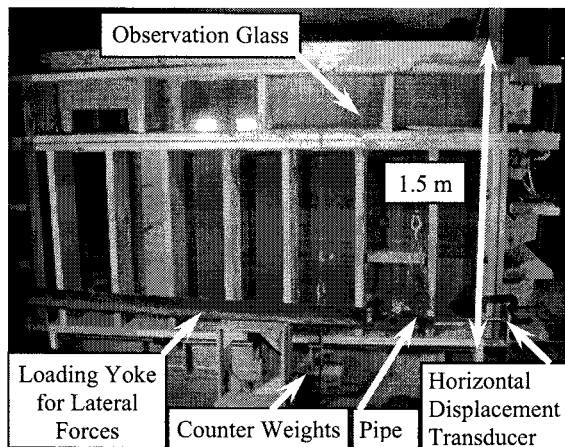


Fig. 18. Side View of Experimental Facility

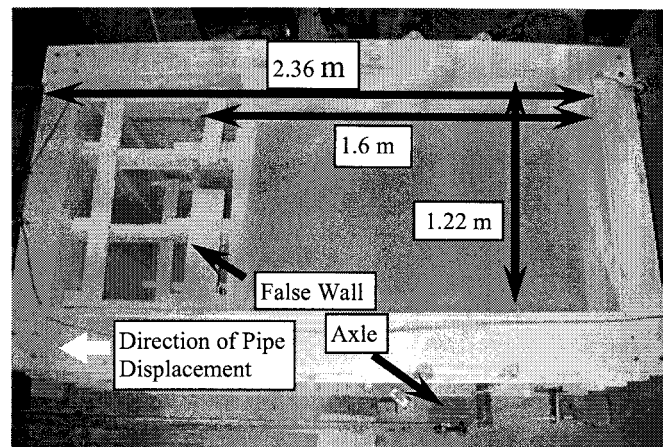


Fig. 19. Top View of Experimental Facility

movement as the pipe was displaced forward. Loads were applied by means of a hydraulic cylinder, and were measured with a calibrated load cell. A counterweight system was used to adjust the experimental pipe weight to be consistent with pipe weight in the field. Lateral and vertical pipe movements were measured with extensometers, and soil movements were measured by means of wooden dowels, embedded in the soil mass, which were visible through the glass sidewalls.

Sand similar to that used in the large-scale experiments with the pipeline-elbow assembly was placed in 150-mm lifts and compacted. The grain size distribution of the experimental sand was nearly identical to that in Fig. 14. Frequent in situ density and moisture content tests were performed. Dry unit weight and moisture content in the sand mass were controlled to within $\pm 2\%$ and $\pm 0.5\%$, respectively. The sand was placed dry and at moisture contents of approximately 4 and 8 %.

Direct shear tests were performed on samples of the experimental sand at nominal moisture contents of 0, 4 and 8%. The direct shear behavior of tests with 4 and 8% moisture contents were essentially identical, and therefore, these tests were combined into one dataset. The direct shear test results show a nearly linear relationship between friction angle and dry unit weight for moist sand $\gamma_d \leq 16.4 \text{ kN/m}^3$, and for dry sand $\gamma_d \leq 17.5 \text{ kN/m}^3$. For dry unit weights greater these values, the friction angle increases rapidly with increasing dry unit weight. To capture this nonlinearity, the data were fit with bi-linear trends as shown in Fig. 20. Turner (2004) has shown that the high compaction energy required for preparing dense (moist sand $\gamma_d \geq 16.4 \text{ kN/m}^3$, dry sand $\gamma_d \geq 17.5 \text{ kN/m}^3$) samples results in the wedging of smaller angular particles between the larger ones, locking the soil structure and increasing the friction angle.

Compared to the direct shear data for dry sand, the moist sand friction angles are about 3 to 5° higher at a given dry unit weight. For a given friction angle, the dry unit weight of moist sand is about 0.5 to 1 kN/m^3 lower than that of dry sand.

The dry unit weight of each large-scale test specimen was measured using the Selig density scoop (Selig and Ladd, 1973) with typically 90 or more measurements per test. For dry sand and sand with 4% moisture content and $\gamma_d \leq 16 \text{ kN/m}^3$, the dry scooped sample weight was calibrated to sand dry unit weight using the procedure described by Trautmann, et al. (1985). In this procedure, the operator applies downward force on the scoop while opening the handles to maintain contact between the scoop base plate and the soil surface, thereby consistently removing samples with a constant volume. For sand with 4% moisture at higher densities and sand with 8% moisture, the scoop tended to rise while closing the jaws due to dilatancy effects. Lifting of the scoop combined with greater variability in downward force applied by the operator resulted in smaller sample volumes and greater variability of the data.

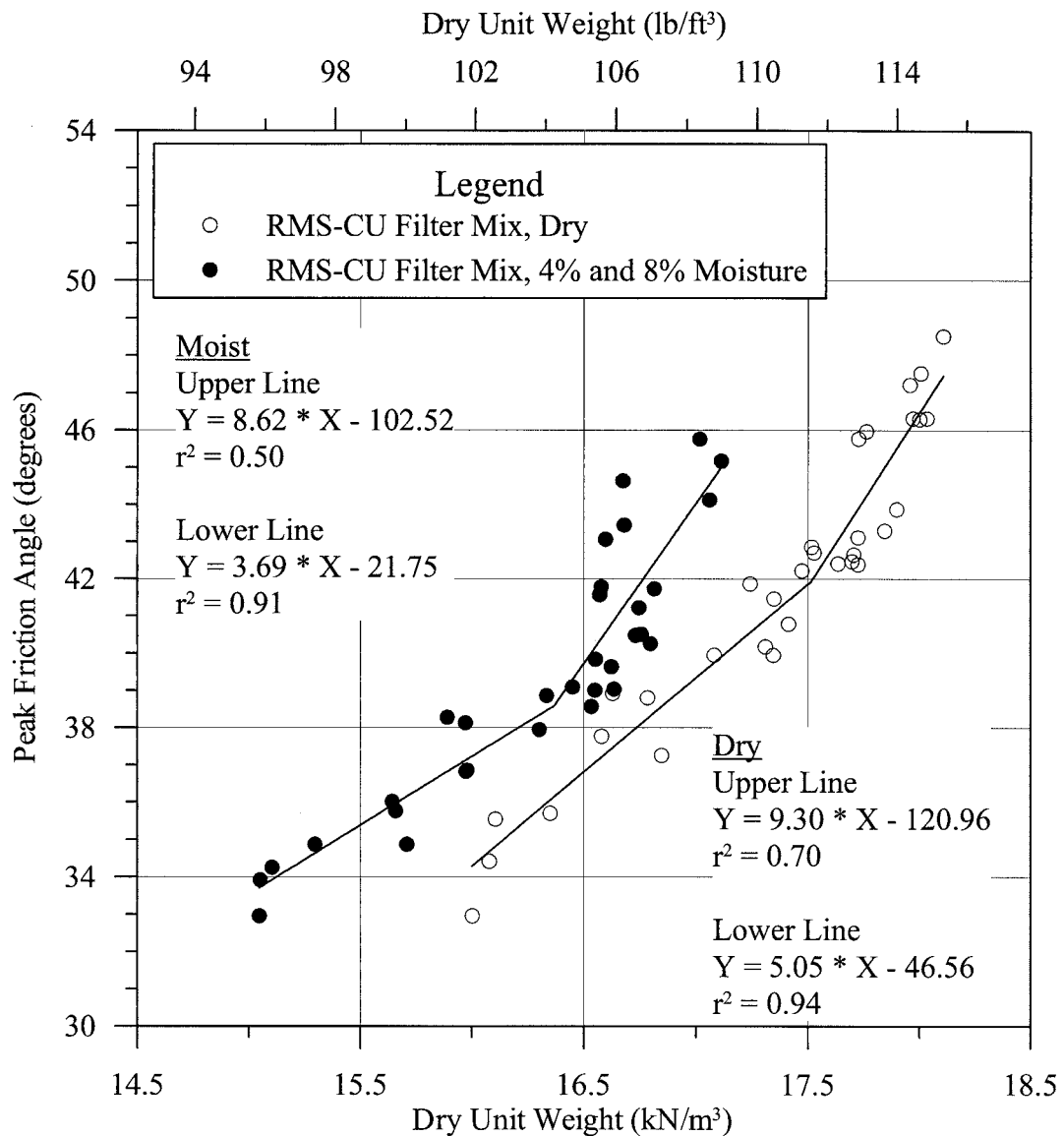


Fig. 20. Direct Shear Test Results for Dry and Moist Experimental Sand Shown with Bilinear Trends

An improved procedure was developed to minimize scoop movement and reduce operator variability in which lead blocks were stacked on the scoop base plate to provide a consistent reaction force. The weight of the lead blocks was varied proportionally to soil dry unit weight, as described by Turner (2004), to prevent the scoop from rising or punching into the soil while sampling. The calibration curves obtained for sand with 4 and 8% moisture contents using the new method, shown in Fig. 21, were nearly identical to the trend line obtained for dry sand, indicating that the new method limits scoop lifting and increases repeatability.

On the basis of previous field-scale experiments and an analytical model proposed by Ovesen (1964), Trautmann and O'Rourke (1983) developed a chart in which maximum dimensionless lateral force is plotted relative to dimensionless depth for various friction angles as determined with direct shear tests. These dimensionless charts were also published in a subsequent journal paper (Trautmann and O'Rourke, 1985) and the ASCE Guidelines for the Seismic Design of Oil and Gas Pipeline Systems (1984).

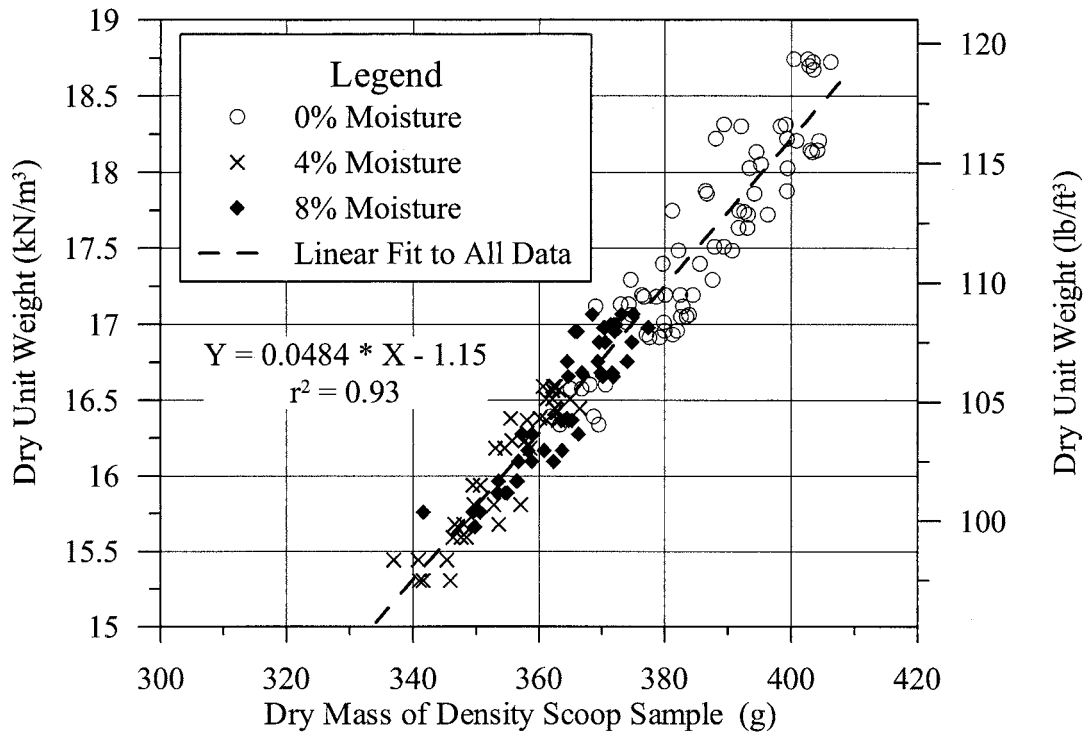


Fig. 21. Density Scoop Calibration Curves Developed Using New Procedure

Figure 22 shows select plots of dimensionless force vs. dimensionless displacement for tests on partially saturated sand with dry unit weights between 16.3 and 16.6 kN/m³ at ratios of depth to pipe centerline to external pipe diameter (H/D) of 6 and 8.5, respectively. The dimensionless force is the maximum measured lateral force, F , divided by the product of soil unit weight, γ , H , D , and length of pipe, L . This term provides a value that can be scaled to various depths, diameters, and soil conditions of practical interest. Table 2 summarizes information for each moist sand test shown in Fig. 22, including dry unit weight, water content, friction angle, and selected values of maximum dimensionless force, N_q . The characteristic displacement, Y'_f , corresponding to maximum force is shown for each curve with an arrowhead. The term Y' is the ratio of the horizontal displacement, Y , to D .

For comparison with the moist sand test results, the figures also show force-displacement curves for dry sand obtained from current tests and tests by Trautmann and O'Rourke (1983, 1985). The dry unit weight of the tests by Trautmann and O'Rourke (1983, 1985) was 16.4 kN/m³. The dry unit weights obtained during the dry sand tests by Turner (2004) were 16.7 and 16.9 kN/m³.

The force-displacement curves for moist sand tests reached a peak at relatively small displacement, typically at Y' between 0.1 and 0.2, and then decreased to a lower constant value at larger displacements, typically at Y' of 0.2 to 0.3. The maximum dimensionless force, N_q , for all moist sand tests and the corresponding dimensionless displacement, Y'_f , were selected at the initial peak in the curve. As shown in Fig. 22, force-displacement curves for dry sand with similar dry unit weight as the moist sand tests did not exhibit peak behavior. Maximum force was selected for these tests using a horizontal asymptote to the force-displacement curve, and Y'_f was selected using Hansen's (1963) 90% criterion as described by Fellenius (1980). To compare moist and dry sand test results at a second dry unit weight for H/D of 6, tests were also performed with dry unit weights of 15.7 and 15.8 kN/m³, respectively, as described by Turner (2004).

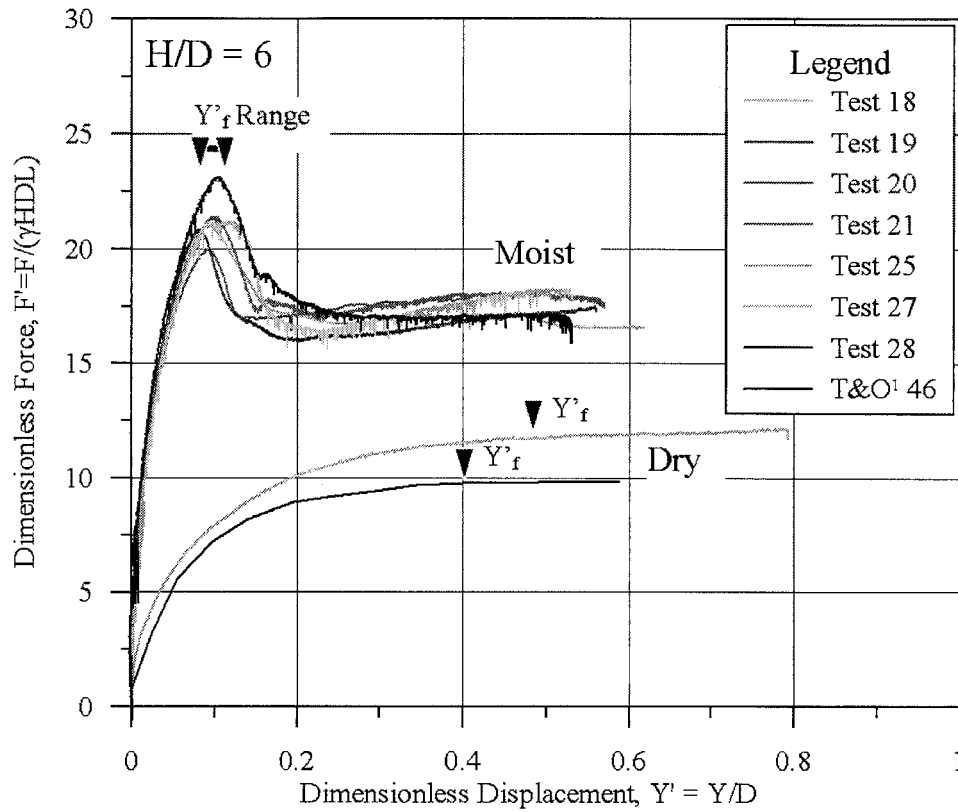










Fig. 22. Force-Displacement Curves for Tests with Dry Unit Weight of 16.3-16.7 kN/m³ and H/D = 6

Table 2. Summary Information for Tests with Dry Unit Weight of 16.3-16.7 kN/m³ and H/D=6

Line Symbol	Water Content (%)	Dry Unit Weight (kN/m ³)	Test No.	Friction Angle ²	N _q
	0	16.4	T&O ¹ 46	36	9.8
	0	16.7	25	37.1-37.8	12.2
	4.1	16.4	21	38.6-39.4	21.4
	4.2	16.4	20	38.6-39.5	20.9
	4.4	16.6	19	40.5-40.6	20.0
	4.6	16.4	18	38.6-39.4	21.0
	7.6	16.3	27	38.5-39.3	21.2
	7.8	16.4	28	38.5-39.3	23.2

¹ T&O = Test data from Trautmann & O'Rourke (1983)

² Friction angle range, in degrees, determined from exponential and bi-linear fits to direct shear data

The force-displacement curves shown in Fig. 22 illustrate several important features of soil-pipe interaction. First, the test results for sand with 4% moisture are nearly identical to the results for sand with 8% moisture, including maximum force, displacement at maximum force, and curve shape. Second, for similar dry unit weight, tests in moist sand experienced about twice the maximum force associated with tests in dry sand. Third, displacement at maximum force, Y'_f , was smaller for the moist sand tests compared to dry sand tests at the same density. Moreover, the initial curve slope, or stiffness, is greater for the moist sand test results. Also, for the same dry unit weight, the moist sand force-displacement curves reach a peak value and decrease, typical of dense, dilative dry sand, whereas the dry force-displacement curves approach a horizontal asymptote, typical of loose or medium dense dry sand.

Figure 23 summarizes values of maximum force vs. dimensionless depth, as determined from the experimental data. Test results for dry, medium dense sand from Trautmann and O'Rourke (1983, 1985) are also shown, and an interpretive curve is drawn through the moist test results and extrapolated to other H/D ratios. For H/D less than 6, this extrapolation was performed by multiplying the dry sand test results by the ratio of moist N_q to dry N_q determined at H/D of 6. For H/D greater than 8.5, the dry sand test data were multiplied by the ratio of moist N_q to dry N_q determined at H/D of 8.5. The interpretive curve between H/D of 6 and 8.5 was drawn as a line connecting the moist sand data points.

The force associated with partially saturated sand is approximately twice that generated under dry sand conditions. Direct shear test results show that increased shear resistance in partially saturated sand accounts only for about 30% of the increased lateral force relative to that for dry conditions. The principal cause of increased resistance can be explained with reference to Fig. 24, which shows the soil deformation patterns in dry and partially saturated sands. Dry sand deformation shows distinct zones of heave and subsidence, with continuous rotational movement between well-developed passive and active zones in front of and behind the pipe, respectively. In contrast partially saturated sand moves more like a coherent mass of soil that must be pushed forward and lifted by relative lateral movement of the pipe.

Figure 25 shows the maximum dimensionless force, N_q , vs. dimensionless depth, H_c/D , that are derived for partially saturated and dry sand tests, using the experimental data of Turner (2004) and Trautmann and O'Rourke (1985). Note that predicted curves for a friction angle of 30° are not shown in Fig. 25. Loose, dry sand consolidates during lateral loading, which, in effect, increases the friction angle and N_q values, and results in larger horizontal displacement to attain maximum load. Moist sand placed in the loose condition typically consists of a bulked, collapsible structure with inconsistent density, for which a uniform mass friction angle is not appropriate. Lateral loading of pipes in loose sand will result in collapse of the bulked structure and compaction of the sand, thereby increasing the dry unit weight and friction angle. With the available evidence from this and previous studies, a percent increase in N_q from dry to moist loose sand cannot be reliably predicted. Further experimental investigation is needed to confirm the force-displacement behavior of loose moist sand.

These experimental findings have important implications for lifeline design and construction. They confirm significantly increased lateral loads in partially saturated sand compared to those for dry sand that are currently used in practice (ASCE, 1984). The findings also illustrate the value of full-scale experiments, which were used to calibrate a general purpose analytical model, confirm higher reaction forces than predicted with current models, and point the way to a simple and effective means of reducing strain concentrations at elbows through moderate increases in the wall thickness of straight pipe sections adjoining the elbow.

In general, large-scale experiments play an essential role in discovering new mechanisms for soil and structural response, as well as key behavioral phenomena that were not previously appreciated. Such outcomes stimulate advances in modeling procedures.

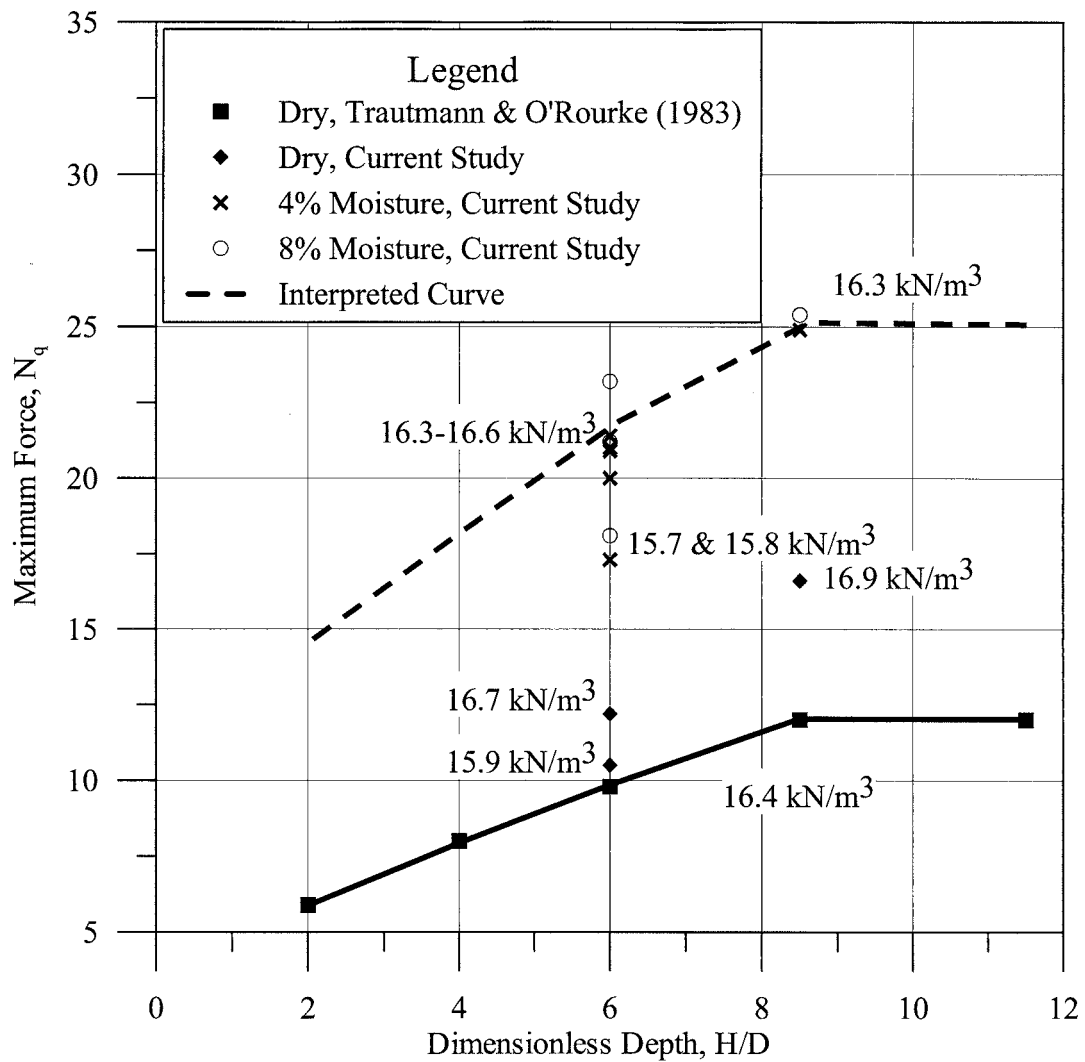


Fig. 23. Maximum Dimensionless Force vs. Dimensionless Depth for Varying Moisture Content, Dry Unit Weight As Shown.

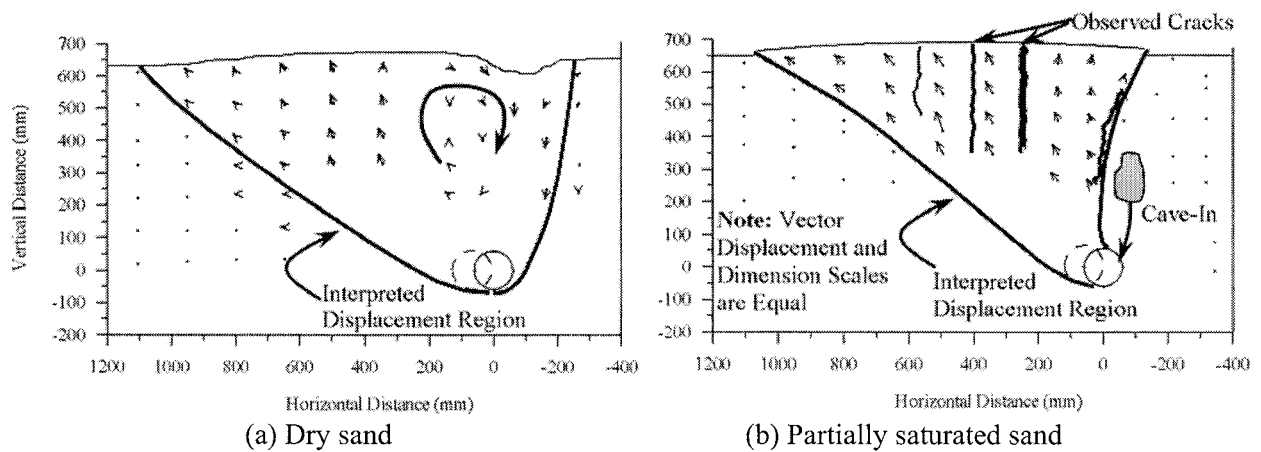


Fig. 24. Soil Displacement Patterns for Dry and Saturated Sand

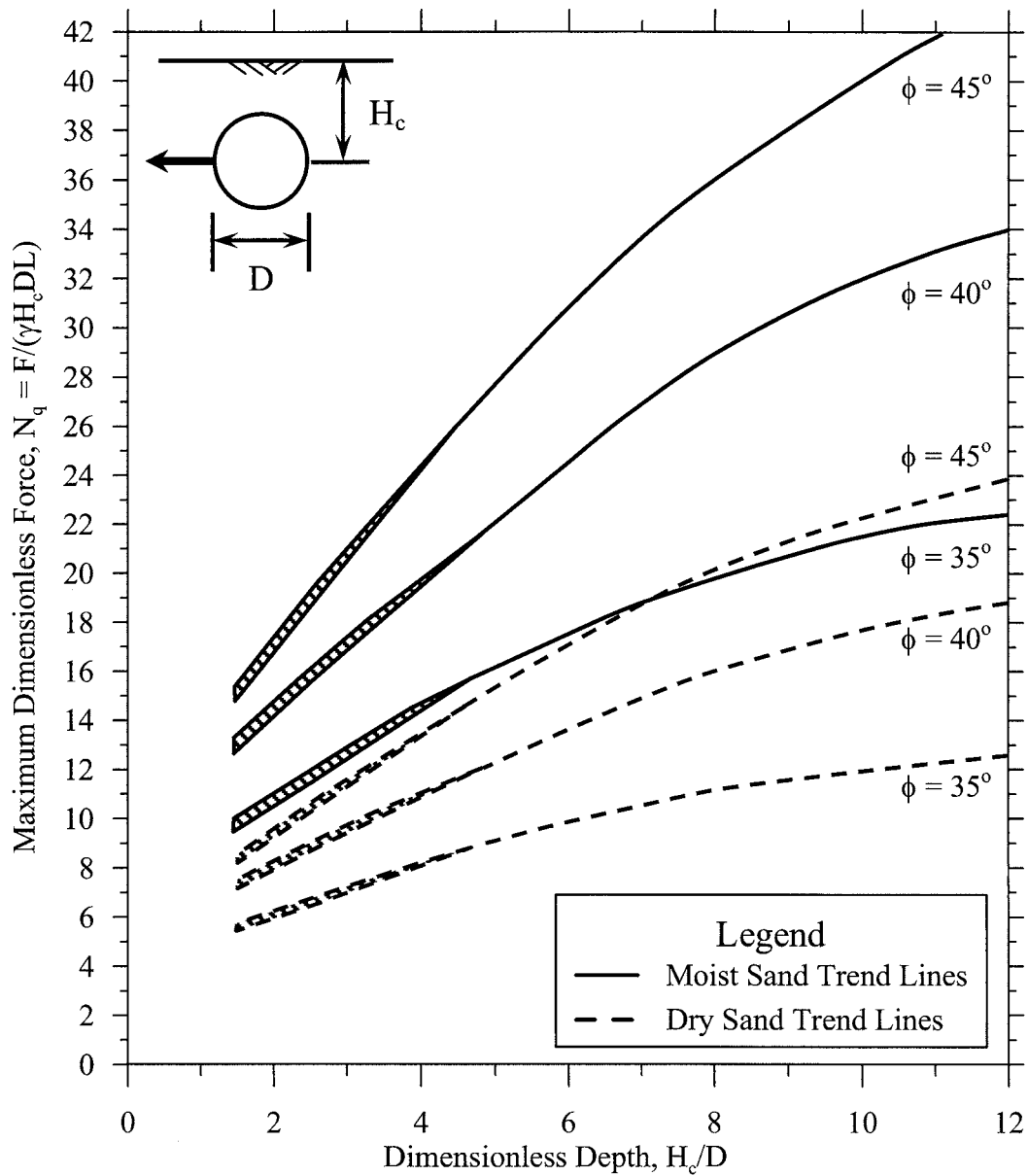


Fig. 25. N_q vs H_c/D For Horizontally Loaded Pipes in Dry and Moist Sand

Substantial emphasis is now being placed on the physical and numerical modeling of components with large and novel facilities, such as the George E. Brown, Jr. Network for Earthquake Engineering Simulation (NEES). This network is intended to unite a geographically dispersed system of equipment sites, users, modelers, and industrial partners through high performance Internet so that experiments at different sites can be coordinated, run, and numerically simulated at virtually the same time. Testing facilities for large displacement soil-structure interaction of lifeline components are being developed as part of NEES (Jones, et al., 2004). They provide a unique combination of large-scale and centrifuge modeling facilities. Large-scale testing duplicates pipe and soil behavior and the intricacies of soil-pipeline reactions. Centrifuge modeling provides an excellent complement, through which multi-g scaling is applied to extend the physical range of testing to larger prototype dimensions and rates of loading.

CONCLUDING REMARKS

Soil-structure interaction under extreme loading conditions includes performance during earthquakes, floods, landslides, large deformation induced by tunneling and deep excavations, and subsidence caused by severe dewatering or withdrawal of minerals and fluids during mining and oil production. Such loading conditions are becoming increasingly more important as technologies are developed to cope with natural hazards, human threats, and construction in congested urban environments.

This paper examines extreme loading conditions with reference to earthquakes, which are used as an example of how extreme loading influences behavior at local and geographically distributed facilities. The paper covers performance from the component to the system-wide level to provide guidance in developing an integrated approach to the application of geotechnology over large, geographically distributed networks. Specific topics covered include geotechnical earthquake loading, lifeline response to earthquakes, large-scale tests of ground rupture effects, and soil-structure interaction during ground failure.

Permanent ground deformation (PGD) is the most damaging consequence of an earthquake for underground facilities, including regional distribution networks for water and natural gas. The sources of PGD involve landslides, soil liquefaction, and surface faulting. The generic patterns of displacement for earthquake-triggered ground failure are similar to those for landslides, subsidence, and ground deformation associated with deep excavation, tunneling, and mining activities.

The systematic analysis of pipeline repair records after the 1994 Northridge earthquake show the locations of important seismic and geotechnical hazards and were used to identify zones of potential ground failure not recognized in previous explorations and risk assessments. Moreover, the systematic assessment of pipeline repairs with GIS resulted in regressions linking damage rates and various levels of strong motion. Such relationships are important for loss estimation studies of future earthquake impact to plan for and reduce the potential for seismic disruption.

Large-scale tests of pipeline response to abrupt ground rupture have resulted in analytical models that can simulate such behavior at critical locations, such as pipeline elbows, where local soil restraint and the three-dimensional distribution of deformation leads to increased risk of failure. Large-scale tests of soil-pipeline interaction performed at Cornell University helped show how increased pipe wall thickness near pipe-elbow welds can improve performance under extreme loading conditions by over 200%. They also showed that soil-structure interaction for partially saturated sand results in significantly greater concentration of pipeline strain than for dry sand. Full-scale tests of soil-structure interaction for buried pipelines subjected to large horizontal movements indicate that maximum lateral forces are approximately twice as high for large horizontal displacement in partially saturated sand as for dry sand. Design charts are developed on the basis of experimental results to predict maximum lateral load for different depths of burial, pipe diameters, and soil angle of shear resistance associated with partially saturated and dry sand.

ACKNOWLEDGEMENTS

Thanks are extended to the National Science Foundation, Multidisciplinary Center for Earthquake Engineering Research, Los Angeles Department of Water and Power, and Tokyo Gas Company, Ltd for their generous support of the work presented in this paper.

REFERENCES

- ASCE, (1984). *Guidelines for the Seismic Design of Oil and Gas Pipeline Systems*. Committee on Gas and Liquid Fuel Lifelines, American Society of Civil Engineers, Reston, Virginia.
- FELLENIUS, B.H., (1980). The Analysis of Results from Routine Pile Load Tests, *Ground Engineering*, Vol. 13, No. 6, September 1980, pp. 19-31.
- HAMADA, M. AND O'ROURKE, T. D. EDS., (1992). *Case Studies of Liquefaction and Lifeline Performance During Past Earthquakes*. National Center for Earthquake Engineering Research, State University of New York at Buffalo, Buffalo, NY, February 1992, Technical Report NCEER-92-0001.
- HAMADA, M. AND WAKAMATSU, K., (1996). *Liquefaction, Ground Deformation and Their Caused Damage to Structures*. The 1995 Hyogoken-Nanbu Earthquake – Investigation into Damage to Civil Engineering Structures, Committee of Earthquake Engineering, Japan Society of Civil Engineering, June 1996.
- HAMADA, M., YASUDA, S., ISOYAMA, R. AND EMOTO, K., (1986). *Study on Liquefaction Induced Permanent Ground Displacement*. Association for the Development of Earthquake Prediction, Tokyo, Japan, November 1986.
- HANSEN, J.B., (1963). discussion of "Hyperbolic Stress-Strain Response: Cohesive Soils," by R.L. Kondner, *Journal of the Soil Mechanics and Foundations Division*, ASCE, Vol. 89, No. SM4, July 1963, pp. 241-242.
- HOLZER, T. L., BENNETT, M. J., PONTI, D. J. AND TINSLEY III, J. C., (1999). Liquefaction and Soil Failure During 1994 Northridge Earthquake. *Journal of Geotechnical and Geoenvironmental Engineering*, ASCE, 1999, 125, No. 6, 438-452.
- ISENBERG, J., (1979). Role of Corrosion in Water Pipeline Performance in Three US Earthquakes. *Proceedings of the 2nd US National Conference on Earthquake Engineering*, Stanford, CA, August 1979, 683-692.
- JAPAN GAS ASSOCIATION, (2000). *Recommended Practices for Earthquake Resistant Design of Gas Pipelines*. Published in Earthquake Resistant Design Codes in Japan, Japan Society of Civil Engineering, Tokyo, Japan, January 2000.
- JEON, S-S. AND O'ROURKE, T.D., (2005). Northridge Earthquake Effects on Pipelines and Residential Buildings, *Bulletin of the Seismological Society of America*, BSSA, Vol. 95-1, Feb. 2005, pp. 1-25.
- JONES, S.L., KESNER, K.E., O'ROURKE, T.D., STEWART, H.E., ABDOUN, T., AND O'ROURKE, M.J., (2004). "Soil-Structure Interaction Facility for Lifeline Systems." *Proceedings of the 13th World Conference on Earthquake Engineering*, Vancouver, BC, Canada, Aug., 2004, Paper No. 1621.
- KENNEDY, R. P., CHOW, A. W. AND WILLIAMSON, R. A., (1977). Fault Movement Effects on Buried Oil Pipeline. *Journal of Transportation Engineering Division*, ASCE, 1977, 103, TE5, 617-633.
- NEWMARK, N. M. AND HALL W. J., (1975). Pipeline Design to Resist Large Fault Displacement. *US National Conference on Earthquake Engineering*, Ann Arbor, MI, 1975, Paper UILU-ENG-75-2011, 416-425.
- O'ROURKE, M. J. AND LIU, X., (1999). *Response of Buried Pipeline Subject to Earthquake Effects*. Multidisciplinary Center of Earthquake Engineering Research, State University of New York at Buffalo, Buffalo, NY, 1999, Monograph Series 3.
- O'ROURKE, T. D., (1998). An Overview of Geotechnical and Lifeline Earthquake Engineering. *Geotechnical Special Publication No. 75*, ASCE, Pakoulis, P., Yegian, M. and D. Holtz, Eds, Reston, VA, 1998, II, 1392-1426.

- O'ROURKE, T. D. AND GRIGORIU, M. D. AND KHATER, M. M., (1985). Seismic Response of Buried Pipes. *Pressure Vessel and Piping Technology – A Decade of Progress*, ASME, Sundarajan, C. Ed., 1985, 281-323.
- O'ROURKE, T. D. AND HAMADA, M. EDS., (1992). *Case Studies of Liquefaction and Lifeline Performance During Past Earthquakes*. National Center for Earthquake Engineering Research, State University of New York at Buffalo, Buffalo, NY, 1992, Technical Report NCEER-92-0002.
- O'ROURKE, T. D. AND JEON, S.-S., (1999). Factors Affecting the Earthquake Damage of Water Distribution Systems. *Proceedings of the 5th US Conference on Lifeline Earthquake Engineering*, Seattle, WA, ASCE, Reston, VA, August 1999, 379-388.
- O'ROURKE, T.D. AND TOPRAK, S., (1997). GIS Assessment of Water Supply Damage from the Northridge Earthquake. *Spatial Analysis in Soil Dynamics and Earthquake Engineering*, ASCE, Frost, D. Ed., 1997.
- O'ROURKE, T.D., STEWART, H.E., AND JEON, S-S., (2001). Geotechnical Aspects of Lifeline Engineering, *Proceeding of Institution of Civil Engineers Geotechnical Engineering*, 149, Issue 1, Jan. 2001, pp. 13-26.
- O'ROURKE, T.D., TOPRAK, S. AND SANO, Y., (1998). Factors Affecting Water Supply Damage Caused by the Northridge Earthquake. *Proceedings of the 6th US National Conference on Earthquake Engineering*, Seattle, WA, June 1998, 1-12.
- OVESEN, N.K., (1964). Anchor Slabs, Calculation Methods and Model Tests. *Bulletin 16*, Danish Geotechnical Institute, Copenhagen, 39 p
- SANO, Y., O'ROURKE, T. D. AND HAMADA, M., (1999). Geographic Information System (GIS) Evaluation of Northridge Earthquake Ground Deformation and Water Supply Damage. *Proceedings of the 5th US Conference on Lifeline Earthquake Engineering*, Seattle, WA, ASCE, Reston, VA, August 1999, 832-839.
- SELIG, E.T. AND LADD, R.S., (1973). Evaluation of Relative Density Measurements and Applications, *Evaluation of Relative Density and its Role in Geotechnical Projects Involving Cohesionless Soils*, STP 523, ASTM, Philadelphia, PA, pp. 487-504.
- TOPRAK, S., O'ROURKE, T. D. AND TUTUNCU, I., (1999). Geographic Information System (GIS) Characterization of Spatially-Distributed Lifeline Damage. *Proceedings of the 5th US Conference on Lifeline Earthquake Engineering*, Seattle, WA, ASCE, Reston, VA, August 1999, 110-119.
- TRAUTMANN, C.H., AND O'ROURKE, T.D., (1983). *Behavior of Pipe in Dry Sand Under Lateral and Uplift Loading*, *Geotechnical Engineering Report 83-7*, Cornell University, Ithaca, New York
- TRAUTMANN, C.H. AND O'ROURKE, T.D., (1985). Lateral Force-Displacement Response of Buried Pipe. *Journal of Geotechnical Engineering*, ASCE, Reston, VA, Vol. 111. No. 9, pp. 1068-1084.
- TRAUTMANN, C.H., O'ROURKE, T.D. and KULHAWY, F.H., (1985). Uplift Force-Displacement Response of Buried Pipe. *Journal of Geotechnical Engineering*, ASCE, Vol. 111, No. 9, 1985, pp.1061-1067.
- TURNER, J.E., (2004). *Lateral Force-displacement Behavior of Pipes in Partially Saturated Sand*, Master of Science Thesis, Cornell University, Ithaca, New York.
- WHITMAN, R. V., ANAGNOS T., KIRCHER, C. A., LAGORIO, H. J., LAWSON, R. S. AND SCHNEIDER, P., (1997). Development of a National Earthquake Loss Estimation Methodology. *Earthquake Spectra*, 1997, 13, No. 4, 643-661.
- YOSHISAKI, K., O'ROURKE, T. D. AND HAMADA, M. , (2001). Large Deformation Behavior of Buried Pipelines with Low-Angle Elbows Subjected to Permanent Ground Deformation. *Journal of Structural Mechanics and Earthquake Engineering*, JSME, No. 50, Vol. 4, April 2001, pp. 215-228.
- YOUD, T. L., (1973). *Liquefaction, Flow, and Associated Ground Failure*. US Department of the Interior, Washington, D.C., 1973, Geologic Survey Circular 688.

PARAMETRIC STRUCTURE-SPECIFIC SEISMIC LOSS ESTIMATION

J. B. Mander¹⁾, B. A. Bradley²⁾, and R. P. Dhakal³⁾

1) Professor, Department of Civil Engineering, University of Canterbury, New Zealand

2) Ph.D Candidate, Department of Civil Engineering, University of Canterbury, New Zealand

3) Senior Lecturer, Department of Civil Engineering, University of Canterbury, New Zealand

john.mander@canterbury.ac.nz, bab54@student.canterbury.ac.nz, rajesh.dhakal@canterbury.ac.nz.

Abstract: A loss estimation methodology is presented which provides several measures of seismic performance to decision-makers. The methodology is based on parametrically describing several key relationships between: (i) ground motion *intensity measure* (IM) and exceedance rate $v(IM)$; (ii) IM and *engineering demand parameter* (EDP); (iii) EDP and *damage states* (DS); and (iv) DS and economic loss (L). Both aleatoric and epistemic uncertainties are considered in each of the key relationships. A vector of EDPs is used and correlations between components are considered. The expected loss and standard deviation of loss as a function of the ground motion IM are obtained, allowing various percentile loss hazard curves to be computed. The distribution of Expected Annual Loss (EAL) is obtained for use in budgeting or assessing retrofit solutions. The methodology is applied to a case study of a typical bridge designed to New Zealand Standards.

1. INTRODUCTION

Performance Based Earthquake Engineering (PBEE) has emerged as a cornerstone of modern earthquake engineering as it attempts to capture the performance of structures over the full spectrum of structural behaviour, from initial elastic response through to global instability, when subjected to a range of ground motion excitations. Accurate quantification of seismic performance can be obtained by considering several key relationships, namely: (i) strong ground motion intensity vs. rate of exceedance; (ii) seismic intensity (demand) vs. structural response (capacity); (iii) structural response vs. structural damage; and (iv) structural damage vs. economic loss. Each of the aforementioned four relationships can be assessed separately and then integrated in various forms to provide useful information to key decision makers.

Loss estimation methodologies have emerged as a way of considering seismic vulnerability of a structure in terms of a monetary value, allowing easy comparison with non-engineering decision makers.

Recently, the Pacific Earthquake Engineering Research (PEER) centre has developed the so-called 'triple integral formula'. This formula, based on the total probability theorem allows the mean annual frequency of a decision variable (i.e. economic loss, or closure) to be obtained. While the triple integral formula provides a benchmark for many loss estimation applications it may be advantageous to consider different sequences of application in order to provide useful intermediate information, and also consider correlation between various components.

In this paper, a fully parametric method of structure-specific loss estimation, as opposed to regional loss estimation (HAZUS, 2003) is described, and then applied to a case study of a typical bridge structure designed to New Zealand Standards.

2. LOSS ESTIMATION METHODOLOGY

The loss estimation methodology is described first by considering each of the four key relationships separately and then how they are combined to provide useful information for decision makers.

2.1 Relation 1: Seismic intensity vs. rate of exceedance

In order to characterise the seismicity of a site a ground motion hazard plot is usually obtained via Probabilistic Seismic Hazard Analysis (PSHA). The hazard plot typically gives the rate of exceedance of a given ground motion parameter (herein referred to as *intensity measure*, IM). Bradley et al., (2007) developed a parametric relationship for the ground motion hazard curve considering uncertainty given in Equation 1:

$$\ln(v) = \ln(v_{asy}) + \left[\alpha \left\{ \ln \left(\frac{IM}{IM_{asy}} \right) \right\}^{-1} \right] + \varepsilon \quad (1)$$

where IM = ground motion *intensity measure* (e.g. PGA, S_A , S_d); v = rate of exceedance of IM; ε = lognormal random variable; v_{asy} , α , and IM_{asy} are parameters that are determined based on a curve fitting technique.

There are several sources of uncertainty in the seismic hazard model. These can be grouped into uncertainty associated with obtaining the data points (β_{RH}), and the additional uncertainty introduced by fitting the curves parametrically (β_{UH}). These are discussed elsewhere (Bradley et al., 2007). The two uncertainties can be combined to give the total uncertainty associated with the seismic hazard curve (Kennedy et al., 1980):

$$\beta_H = \sqrt{\beta_{UH}^2 + \beta_{RH}^2} \quad (2)$$

A comparison of the parametric fit given by Equation 1 and the raw data from the PSHA for a site in Wellington, New Zealand is given in Figure 1a.

2.2 Relation 2: Seismic intensity vs. structural response

Several methods (typically analytical) can be used to obtain the relationship between the IM and *engineering demand parameter* (EDP). A common method that has emerged is via Incremental Dynamic Analysis (IDA) (Vamvatsikos and Cornell, 2002). IDA involves carrying out non-linear dynamic time history analyses of a computational model of the structure subjected to ground motion records scaled to various levels of intensity, and monitoring a pre-determined EDP (e.g. interstorey drifts and/or floor accelerations). The resulting data from the IDA can then be used to define, probabilistically, a conditional IM-EDP relationship. The parametric form of this relationship used in this study is that derived by Jayaler (2002) which considers the separation of mutually exclusive and collectively exhaustive events of structural collapse and non-collapse, and is given in Equation 3.

$$P(EDP > edp | IM) = P(EDP > edp | IM, NC) [1 - P(C | IM)] + P(C | IM) \quad (3)$$

where $P(EDP > edp | IM, NC)$ = is the probability of exceeding an EDP of edp for a given IM and no collapse; $P(C | IM)$ = the probability of collapse given IM; $P(NC | IM)$ = the probability of no collapse given IM, note that $P(NC | IM) = 1 - P(C | IM)$. A comparison of IDA data and the parametric relationship given by Equation 3 is given in Figure 1b.

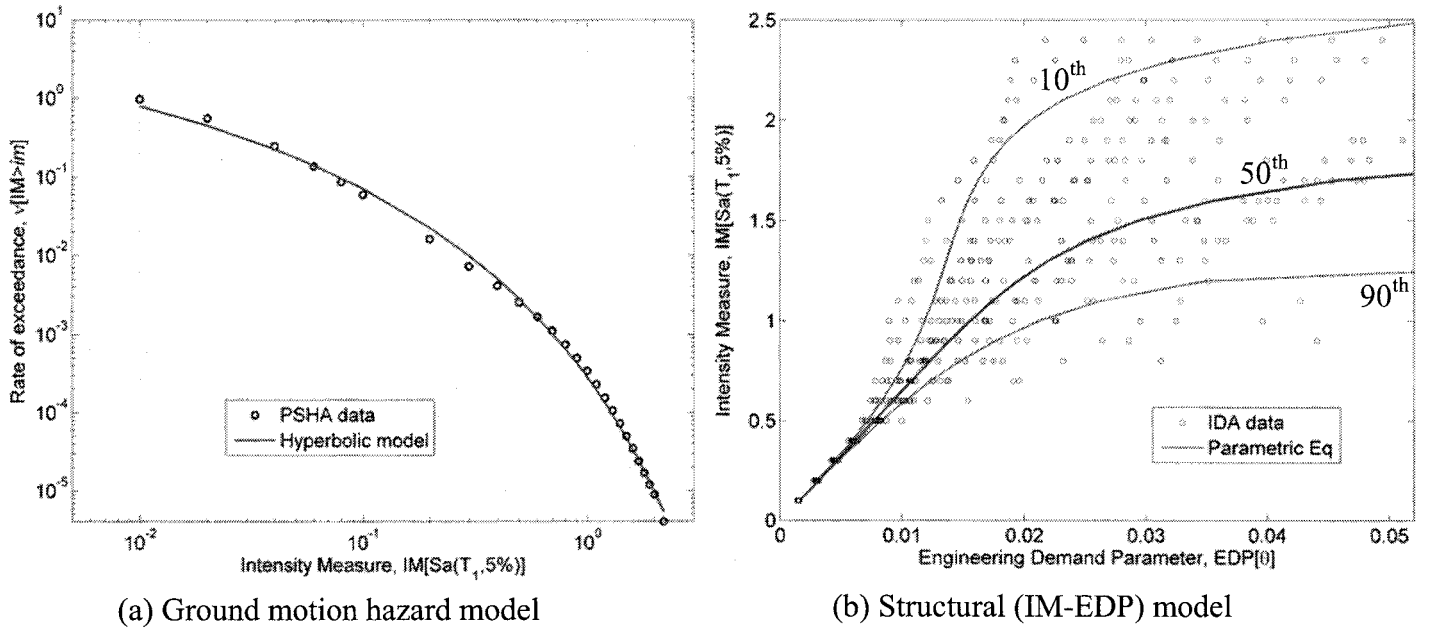


Figure 1: Hazard model and IDA curves

2.3 Relation 3: Structural response vs. structural damage

This relationship (as relationship 4) is typically assumed to be discrete (but still probabilistic) because discrete repairs are required on damage (i.e. a partition is either patched or not patched) which cost discrete amounts of money. The relation is based on the concept of *damage states* (DS), which define the damage to a specific component in a structure (e.g. concrete spalling, bar buckling etc.). The DS are defined with both an expected value (mean) and uncertainty (variance) such that each DS boundary is represented as a fragility curve.

2.4 Relation 4: structural damage vs. economic loss

Economic losses associated with damage to a structure can be both direct and indirect. Direct losses due to damage for example are the cost to repair/replace damaged components of the structure, while indirect costs can be death/injury to occupants and downtime of the services/companies that cannot inhabit/use the structure while it is under repair. These losses are typically also measured discretely and associated with the DS boundaries based on the structural response. Losses associated with DS are presented as an expected value and standard deviation of the normalised cost of the component.

2.5 Integration of key relationships

A brief description of the loss estimation methodology is presented below. A thorough discussion on a similar framework is presented elsewhere (Aslani, 2005).

The expected loss in a structure conditioned on the ground motion intensity measure can be expressed as the combination of the mutually exclusive and collectively exhaustive cases of collapse and non-collapse:

$$E[L|IM] = E[L|IM, NC]P(NC|IM) + E[L|C]P(C|IM) \quad (4)$$

where $E[L|IM, NC]$ = the expected loss for a given ground motion intensity, IM, given that collapse has not occurred; $E[L|C]$ = the expected loss given collapse. Note that $P(C|IM) = 1 - P(NC|IM)$, and can be obtained from the structural analysis (Figure 2a).

The expected loss in each component for a given EDP can be obtained as the summation of

the expected loss for each DS multiplied by the probability of exceeding the given DS. The expected loss in each component for a given IM can be obtained by convoluting the expected loss in each component for a given EDP with the differential of the conditional IM-EDP relation. The above sentences can be expressed mathematically as:

$$E[L|IM, NC] = \sum_{j=1}^{N_c} a_j \left[\int_0^{\infty} \left\{ \sum_{i=1}^{N_{ds}} E[L_j|NC, DS_i] P(DS_i|NC, EDP_j) \right\} dP(EDP_j|NC, IM) \right] \quad (5)$$

where a_j = cost of component j ; N_c = the number of components; N_{ds} = the number of damage states; $E[L_j|NC, DS_i]$ = the expected loss given DS_i ; $P(DS_i|NC, EDP_j)$ = the probability of being in DS_i given the EDP for component j ; and $dP(EDP_j|NC, IM)$ = the differential of the conditional EDP-IM relationship. The variance in the expected loss in each component conditional on the IM can be computed by:

$$\sigma_{[L_j|IM, NC]}^2 = E[L_j^2|IM, NC] - \{E[L_j|IM, NC]\}^2 \quad (6)$$

where $E[L_j^2|IM, NC]$ is computed in a similar fashion to $E[L_j|IM, NC]$. The variance for the entire structure given no collapse can then be calculated as:

$$\sigma_{[L|IM, NC]}^2 = \sum_{j=1:n} \sum_{j'=1:n} a_j a_{j'} \rho_{[L_j, L_{j'}|IM, NC]} \sigma_{[L_j|IM, NC]} \sigma_{[L_{j'}|IM, NC]} \quad (7)$$

where $\rho_{[L_j, L_{j'}|IM, NC]}$ = the correlation coefficient for losses in components j and j' .

The annual frequency of exceeding a certain level of economic loss, l_T (or loss hazard) in a structure can be computed as follows:

$$\nu(L_T > l_T) = \int P(L_T > l_T | IM) d\nu(IM) \quad (8)$$

where $P(L_T > l_T | IM)$ = the probability of exceeding l_T for a given level of ground motion, IM, and can be calculated from:

$$P(L_T > l_T | IM) = P(L_T > l_T | IM, NC) P(NC | IM) + P(L_T > l_T | C) P(C | IM) \quad (9)$$

where $P(L_T > l_T | IM, NC)$ = the probability of exceeding l_T for a given level of ground motion, IM, and no collapse. $P(L_T > l_T | IM, NC)$ is assumed to be normally distributed based on the central limit theorem (assuming loss, given no collapse, is not dominated by a few components), while $P(L_T > l_T | C)$ is lognormally distributed (Aslani, 2005).

3. APPLICATION TO BRIDGE STRUCTURES

In the following section the loss estimation methodology is used to assess the seismic performance of a typical bridge designed to New Zealand Standards (Standards New Zealand, 1995). The prototype bridge is a typical 'long' multi-span highway bridge on firm soil with five 40m longitudinal spans, 10m transverse width, and 7m circular piers. The structure has an estimated replacement cost of \$9M with a coefficient of variation of 0.31 (assumed lognormal distribution). Further design details and experimental modelling of the pier can be found elsewhere

(Mashiko, 2006; Solberg, 2007). The bridge was assumed to be located in the high seismicity region of Wellington, New Zealand. The fundamental period of the pier was 0.6 seconds.

Seismic hazard data for the site was obtained from Stirling et al. (2002). The IM selected was the spectral acceleration at the fundamental period of the structure, as it typically gives rise to low dispersion in the structural demand-response (IM-EDP) relationship (Shome and Cornell, 1999). From the hazard data, the parameters for Equation 1 were determined. A comparison of the data and the parametric fit are given in Figure 1. From the least squares regression β_{UH} was calculated to be 0.16. The uncertainty associated with the PSHA, β_{RH} is currently being investigated by the authors in conjunction with others, and was assumed to be equal to 0.2. Using Equation 2 therefore yields $\beta_H = 0.26$. A suite of ground motion records, previously used by Vamvatsikos and Cornell (2002) were adopted. These records, all of which were recorded on firm soil, have magnitude and direction ranges of 6.5-6.9 and 15.1-31.7 km, respectively.

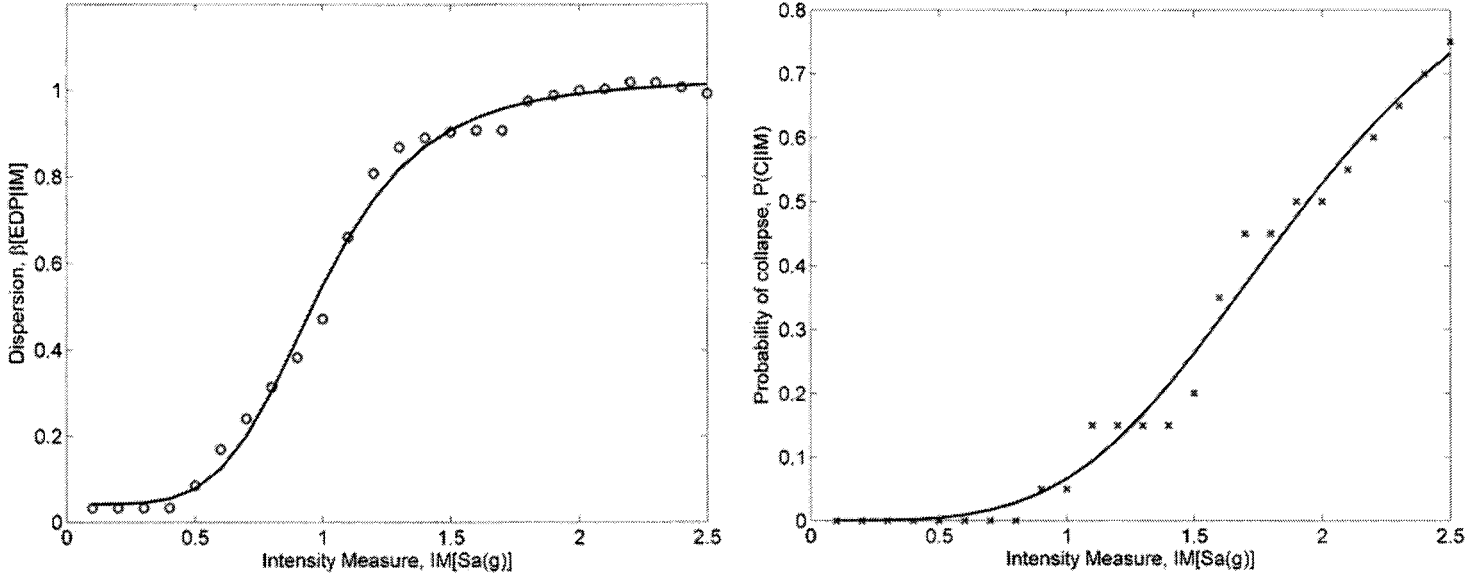
Using a finite element model of the bridge pier, IDA was used to provide the data to characterise the conditional IM-EDP relationship. The IDA was carried out using the spectral acceleration at the fundamental period of vibration as the intensity measure (IM), and the deck drift as the engineering demand parameter (EDP). The resulting IDA data from the structural analyses is presented in Figure 1b. The conditional IM-EDP relationship was then parameterised using Equation 2. $P(EDP > edp | IM, NC)$ was assumed to be lognormally distributed (Jalayer, 2002) with median $EDP = aIM^b$ and lognormal standard deviation (dispersion) β_{US} , where a and b parameters were determined by regression on the IDA data. The 10th, 50th and 90th percentile curves are shown in the figure. The bridge was deemed to collapse at a drift of 5.6% due to significant P- Δ effects from the superstructure. The epistemic uncertainty, β_{US} , due to the parametric fitting of the data was modeled using a hyperbolic tangent function of the form given in Equation 10.

$$\beta_{US} = \alpha_1 + \alpha_2 \tanh\{\alpha_3 IM\} \quad (10)$$

where α_1 - α_3 are constants determined from the regression on the data.

The variation of the collapse probability with IM was assumed to follow a lognormal distribution (Aslani, 2005). A comparison of the parametric fits for dispersion and collapse probability and the raw data points is given in Figure 2.

Loss modelling of the bridge considered structural damage only, as non-structural damage was considered to be relatively insignificant. Downtime of the structure in some instances (when the bridge is on main arterial routes) may be significant. Downtime was not considered hereafter, although it is being investigated in a separate study by the authors. As is typical for structural damage, the EDP selected was the drift angle of the bridge deck relative to the abutment, as it correlates well with the curvature demand in the plastic hinge zone at the base of the pier. Damage for non-collapse cases was assumed to only occur in the pier, hence only during collapse was the deck assumed to be damaged.



(a) β_{US} variation with IM

(b) $P_{collapse}$ variation with IM

Figure 2: Parametric fitting of the standard deviation and Probability of collapse

Table 1 presents the mean EDP values and *loss ratios* (LR) at the onset of each of the *damage states* (DS) as well as the associated standard deviations. The mean values are based on actual repair data from the Northridge and Loma Prieta earthquakes as given by Mander and Basoz (1999), while the standard deviations were determined indirectly, with reference to the coefficient of variations used by Aslani (2005) for reinforced concrete columns.

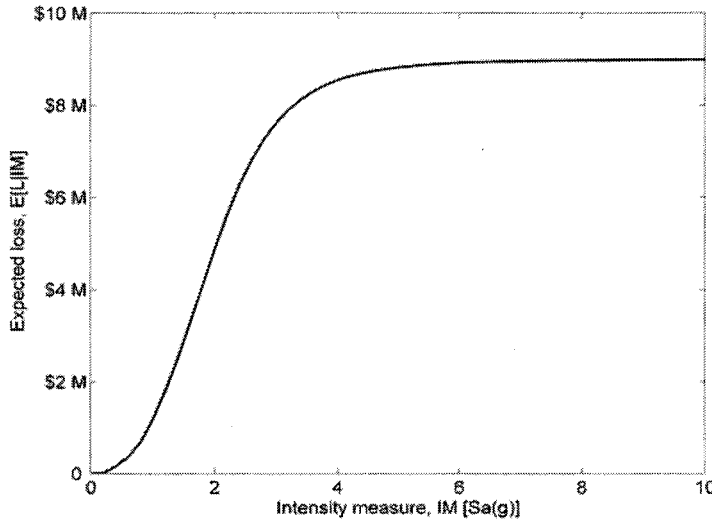
It was assumed that the direction of earthquake shaking was perpendicular to the longitudinal axis of the bridge, and it is also assumed that all piers are subjected to the same ground motion shaking in time (i.e. traveling wave effects are ignored). The correlation coefficients, $\rho_{[L_i, L_j]IM, NC}$ for the losses incurred at each of the piers can therefore be taken as unity. The correlation coefficients for when collapse occurs (i.e. requiring replacement of the structure), $\rho_{[CCI_i, CCI_j]}$, were also taken as one, with all of the bridge components being made primarily of concrete (Touran and Lerdwuthirong, 1997).

Table 1: Statistical parameters for the loss and damage functions in bridge piers

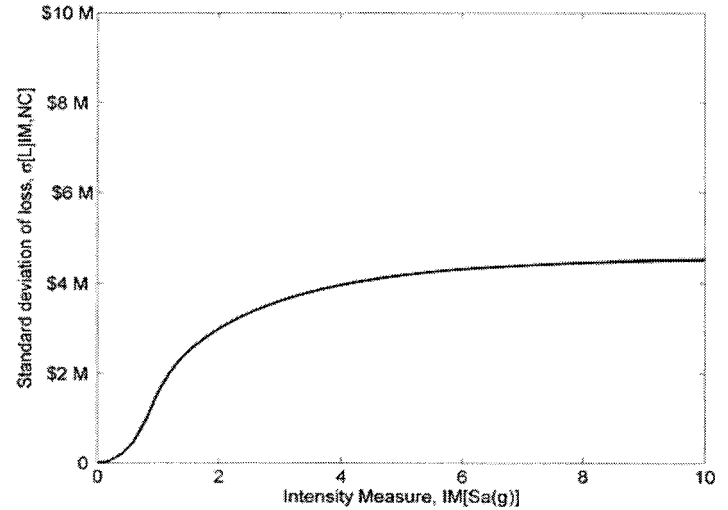
Damage State	\overline{EDP}	$\sigma_{ln EDP}$	$E[L_j DS_i]$	$\sigma[L_j DS_i]$	c.o.v.[$L_j DS_i$]
DS1: Yielding, cracking in hinge zone	0.0063	0.4	0.03	0.02	0.65
DS2: Spalling, bar buckling	0.016	0.45	0.08	0.05	0.65
DS3: Bar fracture/ significant strength degradation	0.046	0.6	0.25	0.18	0.7
DS4: Structural collapse	0.056	0.65	1.0	0.75	0.75

3.1 Loss estimation results

Equations 4 and 6 were computed to yield the expected loss and standard deviation in loss given no collapse as a function of the first mode spectral acceleration, which are plotted in Figure 3a and 3b, respectively. Note that the standard deviation given collapse is a constant (\$4.5 M). As would be expected, it can be seen that the expected loss increases with IM and similarly for the standard deviation. Hence, the loss estimation methodology takes into account the variation in dispersion with IM.



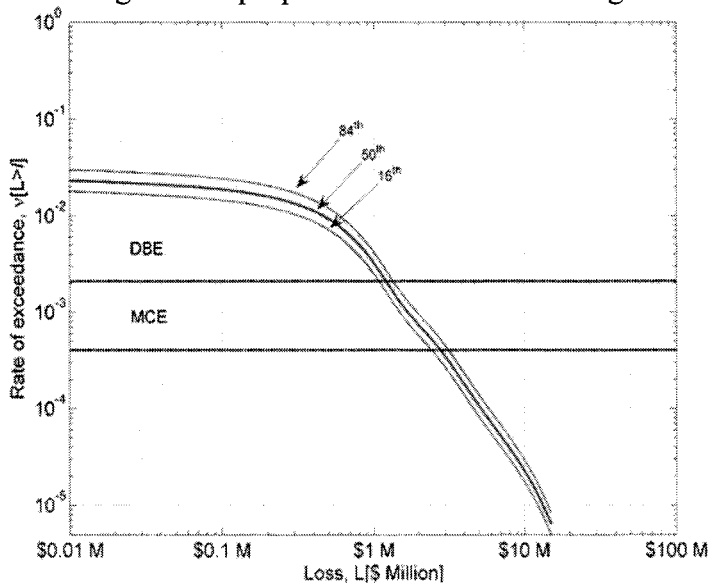
(a) Expected loss conditional on IM



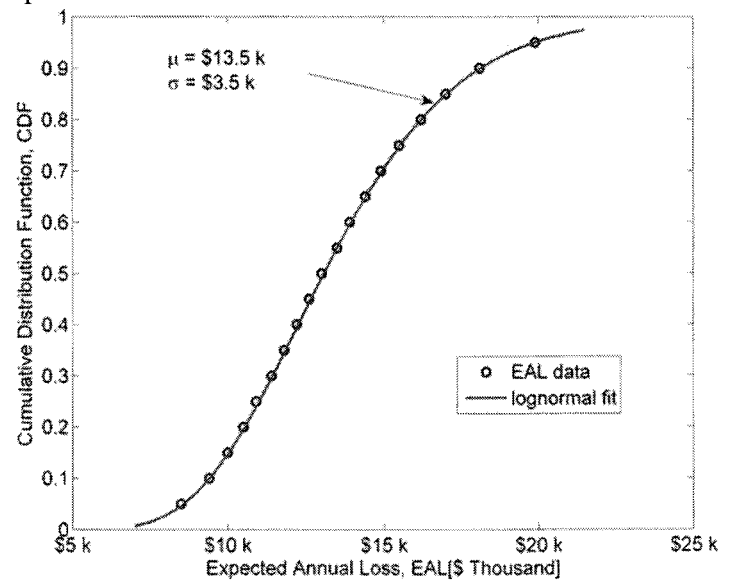
(b) Standard deviation of loss given no collapse

Figure 3 Expected losses and standard deviation conditional on IM

Equation 8 was then used to compute the loss hazard curves. As mentioned, uncertainty was also be incorporated into the seismic hazard model. By using the 16th, 50th, and 84th percentile seismic hazard curves (84th and 16th percentiles are \pm one standard deviation), the corresponding loss-hazard curves shown in Figures 4a are obtained. The loss hazard curves show the typical concave from below shape, and at the DBE and MCE occurrence rates (475 and 2475 year return periods, respectively) the median economic losses were approximately \$1.5 M and \$3.0 M, respectively. The change in slope of the hazard curves at approximately \$0.5 M is due to a significant proportion of losses occurring due to frequent events.



(a) Median and $\pm 1\sigma$ loss hazard curves



(b) Distribution of Expected Annual Loss (EAL)

Figure 4: loss hazard curves and EAL with uncertainty

The Expected Annual Loss (EAL) is a convenient measure of economic loss, as it incorporates a range of seismic scenarios, return rate and expected damage into a single dollar value. Such a value can be used for incorporation into company budgets, or for use in evaluating the benefits of different retrofitting strategies. From the loss hazard curves given in Figure 4a the EAL can be obtained by first converting the vertical axis to probability of exceedance by the

relationship: $P(L>I) = 1 - \exp[-v(L>I)]$ (Bradley et al., 2007), and then integrating the area below the resulting curve. When this is conducted for a range of loss hazard curves of different percentiles, then the data labeled as 'EAL data' in Figure 4b results. This data can be accurately approximated by a lognormal distribution (which for the case study structure has a mean of \$13.5 k and a standard deviation of \$3.5 k). The EAL can therefore be given with a certain level of confidence, i.e. it allows one to make a statement such as "one can be 95% confident that the expected annual loss will not exceed \$20 k". This distribution of EAL provides further information to decision makers, as opposed to just the mean EAL value. When considering EAL over several years a discount factor, λ (Wen et al., 2001) should be incorporated to account for the time value of money.

4. CONCLUSIONS

Based on the findings of this research the following conclusions can be drawn:

1. A fully parametric loss assessment method has been presented that provides various means of communicating seismic risk. The method incorporates uncertainty in all of the key relationships and considers correlations between components.
2. In particular, the method allows the Expected Annual Loss (EAL) to be given as a distribution, as opposed to a single value, providing EAL estimates with a certain level of confidence which is more insightful for decision makers.

References:

- Aslani H (2005). "Probabilistic Earthquake Loss Estimation and Loss Disaggregation in Buildings". *Ph.D. Thesis*, John A. Blume Earthquake Engineering Centre, Dept. of Civil and Environmental Engineering, Stanford University, Stanford, CA. 382 pages
- Bradley. BA, Dhakal, RP, Mander. JB, MacRae GA., 2007. "Improved Hazard Model for Performance Based Earthquake Engineering", *The New Zealand Society of Earthquake Engineering Conference*, Palmerston North, New Zealand
- HAZUS (2003), "Multi-hazard Loss Estimation Methodology, Earthquake Model" HAZUS-MH MR1 *Federal Emergency Management Agency (FEMA)*.
- Jalayer. F. (2003). "Direct Probabilistic Seismic Analysis: Implementing Non-linear Dynamic Assessments." *Ph.D Dissertation*, Department of Civil and Environmental Engineering, Stanford University.
- Kennedy R.P., Cornell C.A., Campbell R.D., Kaplan S., Perla H.F. (1980) "Probabilistic Seismic Safety Study of an Existing Nuclear Power Plant", *Nuclear Engineering and Design*; **59**(2): 315-338.
- Luco, N.; Cornell, C. A. (1998). "Seismic drift demands for two SMRF structures with brittle connections", *Structural Engineering World Wide*, Elsevier Science Ltd., Oxford, England, Paper T158-3.
- Mander JB and Basoz N. (1999). "Seismic fragility curve theory for highway bridges in transportation lifeline loss estimation". *Optimizing Post-Earthquake Lifeline System Reliability*, TCLEE Monograph No. 16. American Society of Civil Engineers: Reston, VA, USA; 31.40.
- Mashiko N. (2006). "Comparative performance of ductile and damage protected bridge piers subjected to bidirection earthquake attack". *Master of Engineering Thesis*. University of Canterbury, Christchurch, New Zealand.
- Shome, N., and Cornell, C. A., (1999). "Probabilistic seismic demand analysis of nonlinear structures". Report No. RMS-35, RMS Program, Stanford University, Stanford, CA.
- Solberg K.M. (2007). "Experimental and analytical investigations into the application of damage avoidance design". *Master of Engineering Thesis*. University of Canterbury, Christchurch, New Zealand.
- Standards New Zealand. NZS 3101: Part 1: (1995): "Concrete Structures Standard", *Standards New Zealand*, Wellington.
- Stirling M.W., McVerry G.H., Berryman K.R., (2002), "A New Seismic Hazard Model for New Zealand", *Bulletin of the Seismological Society of America*. **92**(5) pp 1878-1903.
- Touran A. and Lerdwuthirong S. (1997). "Rank correlations in simulating construction costs". *Journal of Construction Engineering and Management*, **188**(2), pp. 258-272
- Vamvatsikos D. & Cornell C.A. (2002). "Incremental Dynamic Analysis", *Earthquake Engineering and Structural Dynamics*. **31**: 491-514.
- Wen, Y.K., and Kamg, Y.J. (2001). "Minimum building life-cycle cost design criteria, I: Methodology" *ASCE Journal of Structural Engineering*, **127**(3), pp. 330-337.

HURRICANE KATRINA: GEOSYSTEMS IN CRISIS

Professor T.D. O'Rourke
Thomas R. Briggs Professor of Engineering
Cornell University

ABSTRACT

Hurricane Katrina was one of the greatest natural disasters of modern times. It literally changed U.S. policy from a post 911 focus on defense of critical infrastructure to the development of resilient communities. Professor O'Rourke will explore the concept of resilience in terms of civil infrastructure and its dependence on the geosystems that surround and underpin the City of New Orleans. He will discuss the dynamics of the Mississippi River, loss of wetlands, and increasing exposure to storm surge and river flooding that have influenced planning and politics for over two centuries in the Louisiana delta. He will describe the levee system that was constructed to protect New Orleans and the geotechnical conditions that affected its performance during Hurricane Katrina. He will discuss the technical reasons for failure of the levee system, including the mechanisms of failure where breaches occurred and the foundation characteristics and soil properties influencing failure. He will discuss the consequences of failure, with select descriptions of its influence on the energy infrastructure of New Orleans and Gulf of Mexico. He will describe current and planned improvements in the levee system, and will discuss prospects for the future.

Professor O'Rourke is a member of the US National Academy of Engineering and a Fellow of American Association for the Advancement of Science. He serves on the U.S. National Academies Committee on New Orleans Regional Hurricane Protection Projects, which was commissioned to review the investigations of the US Corps of Engineers and their future plans for levee improvements. He authored or co-authored over 300 technical publications, and has received numerous awards from professional and academic organizations. His research interests cover geotechnical engineering, earthquake engineering, underground construction technologies, engineering for large, geographically distributed systems, and geographic information technologies and database management.

HIGH-RISE REINFORCED CONCRETE BUILDING USING HYDRAULIC DAMPER AND HIGH-DUCTILITY CONCRETE AND ITS VIBRATION ANALYSIS

K. Kawano¹⁾, Y. Omika²⁾, Y. Yamamoto¹⁾, M. Maruta³⁾, and N. Koshika⁴⁾

1) Structural Engineering Group, A/E Design Division, Kajima Corporation, Japan

2) Senior Executive Officer, Kajima Corporation, Japan

3) Kajima Technical Research Institute, Japan

4) Kōbori Research Complex, Kajima Corporation, Japan

kawano-ken-ichi@kajima.com, omika@kajima.com, yamamoto-yukimasa@kajima.com,

maruta@kajima.com, koshika@kajima.com

Abstract: Herein was reported an overview mainly of the seismic response analysis for a high-rise RC seismic-control building employing, in the transverse direction, a flexural-control-type seismic-control system using an oil damper, and, in the longitudinal direction, ECC coupling beams that combine parallel shear walls.

1. INTRODUCTION

In recent years, for super high-rise reinforced concrete (RC) building structures, the use of tube frames and core wall (three-dimensional (3D) anti-seismic wall) frames has become widespread in Japan. These skeleton frames are “structures for concentrating seismic energy.” Here, since at the time of an earthquake, a huge stress works on a portion of the structural member, the design of that member must not only provide ultra-high yield strength, it must also have high energy absorption and high toughness characteristics.

The authors have developed, as shown in Fig. 1, a new skeleton frame configuration (flexural-deformation control-type seismic-control structure using an oil damper) for absorbing energy and controlling flexural deformation with top-portion super beams and oil damper (Omika et al. 2000). This skeleton frame configuration enables realization of a skeleton infill (SI housing) within a super high-rise residence such that there are no columns or beams within the living space. As a further development of this skeleton frame configuration, the authors have developed a novel skeleton frame configuration for absorbing energy with high-toughness coupling beams that provide connections between core walls. As shown in Fig. 2, a super high-rise RC residence has been realized having high anti-seismic characteristics together with superior living comfort, through the combination of an oil damper type in one direction with coupling beam type parallel shear walls in the other direction. Here, for the high-toughness coupling beams, engineered cementitious composites (ECC) are employed, as these show

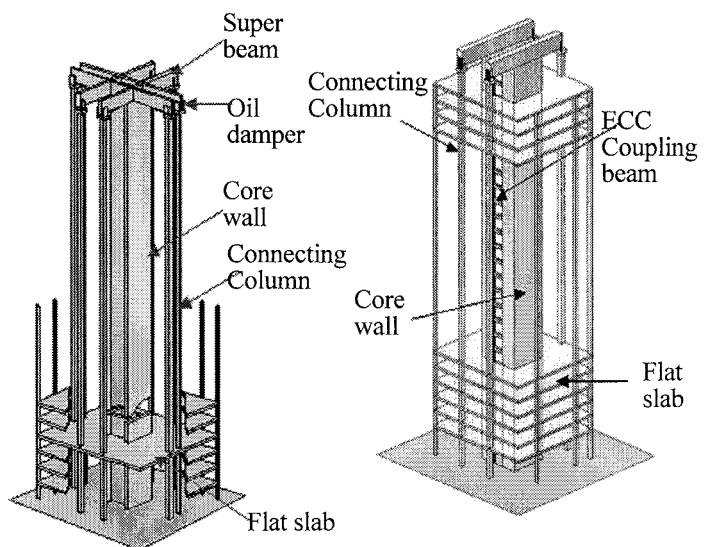


Fig.1 Super Frame Type Seismic Control Structure

Fig.2 New Combination Type Seismic Control Structure

superior tensile characteristics and, even when used for the short span, show sufficient energy absorption capabilities even for major deformations.

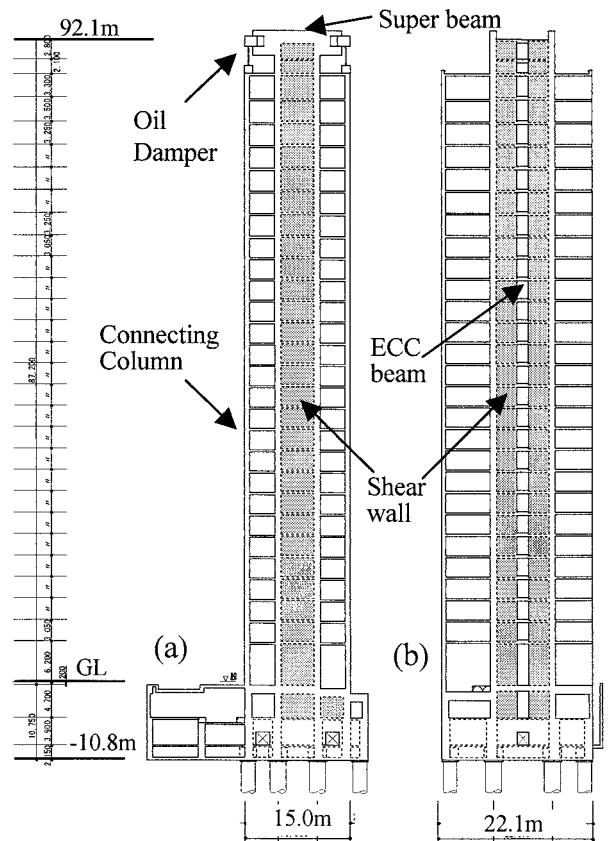
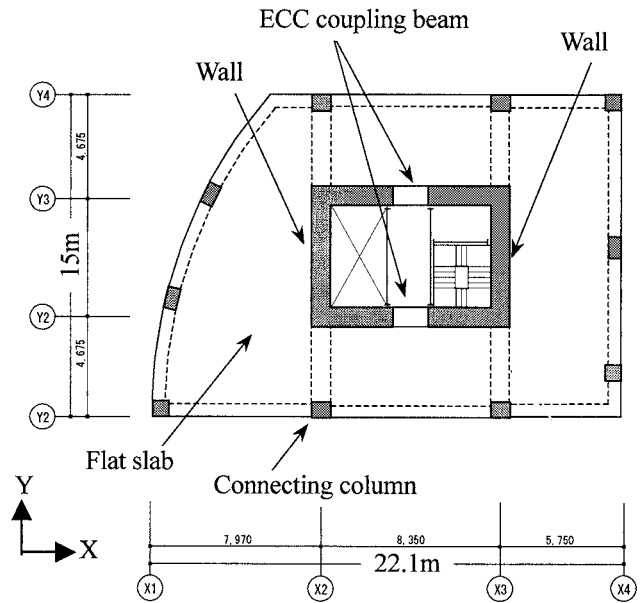
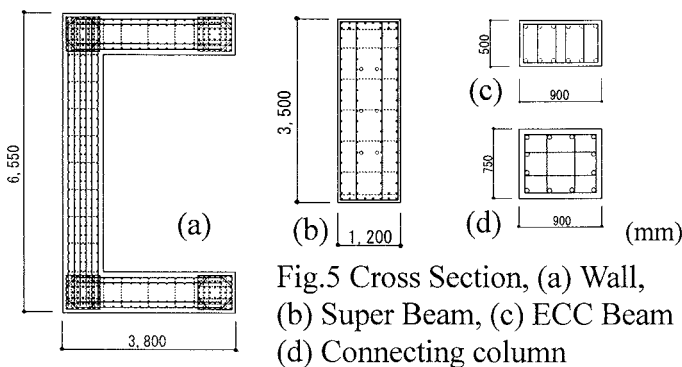
This report presents an overview of the RC super high-rise residence structure that combines two types of seismic control system, the oil dampers and coupling beams that combine the parallel shear wall.

2. STRUCTURAL CONFIGURATION OF THE HIGH-RISE RC SEISMIC-CONTROL BUILDING STRUCTURE

The subject building is a 27-floor building, constructed in Tokyo, that is a 93 m tall RC high-rise residence whose standard floor plan is shown in Fig. 3. At the outer periphery, 10 columns are arranged, and in the center, there is arranged a symmetrical configuration comprised of C-shaped core walls set in opposition to each other; here, the seismic force from any direction is mostly concentrated at the center core walls.

Fig. 4 shows the framing elevation for each direction. In the transverse (Y) direction, super beams are provided at the top portions of the core walls. An oil damper is provided between top portions of the outer periphery columns (connecting columns) and the apexes of the super beams; support of oil damper reactions is provided by a total of 4 connecting columns. The other columns are placed with the purpose of supporting the weight of each floor. In the longitudinal (X) direction, the parallel shear walls of the core are connected, at each floor, with ECC coupling beams. The ECC used here are materials having superior tensile capabilities compared with ordinary concrete, and are expected to have effects as dampers at times of deformation due to their large energy absorption capabilities.

Various elements of the cross sections of outer columns, and core walls, outer connecting columns, super beams, and coupling beams are shown in Table 1 and Fig. 5.



3. ECC CHARACTERISTICS (Maruta et al. 2005)

The ECC used in coupling beams of the parallel shear walls of X direction of the subject building are short-fiber (polyvinyl alcohol fibers) reinforced cement composite materials characterized by their showing strain-hardening tensile stress-strain and their evincing of high tensile straining, as well as, at times of tensile load, their evincing of crack breadth control capabilities, as multiple microscopic cracks occur at times of tensile load.

Fig. 6 shows, in schematic form, the strain-hardening tensile stress-strain curve obtained using ECC. In the same figure, at the initial period of tensile load, the ECC behaves elastically, and initial cracking occurs. At this time, the stress is 2.5 to 4 N/mm², while the strain is around 0.02%. From the time of this initial cracking on, due to the occurrence of numerous microscopic cracks, strain increases with the gradual increase in stress, and the behavior becomes analogous to that of the yield threshold of steel. Then, although at its ultimate point, the strain reaches several percentage points, here the occurrence of microscopic cracking comes to an end.

The crack breadth control capabilities that are the second characteristic of ECC are evinced in the portion from the initial cracking point of Fig. 6 to the ultimate point. Within this range, the increase of strain is induced by the increase in the number of cracks, and, as shown in Fig. 7, the width of individual microscopic cracks at the material level is held to a maximum of around 0.1 mm. Also, as shown in Fig. 8, even at multiple repeated loading at times of the major distortion of 2.5% (1/40 rad.), the decline of yield strength is extremely small, and no remarkable damage is seen; thus, the damage-reduction effects of ECC were confirmed.

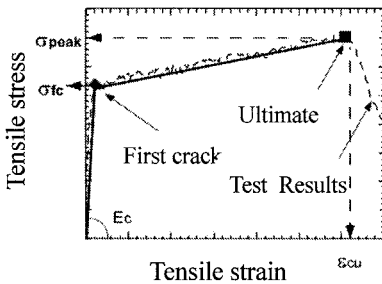


Fig.6 $\sigma - \varepsilon$ Curve of ECC

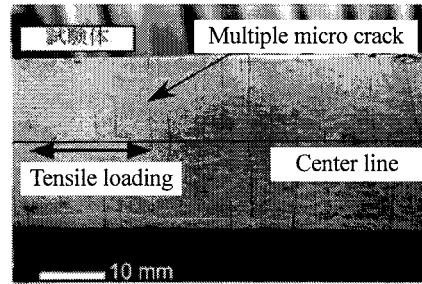


Fig.7 Crack Control Effect

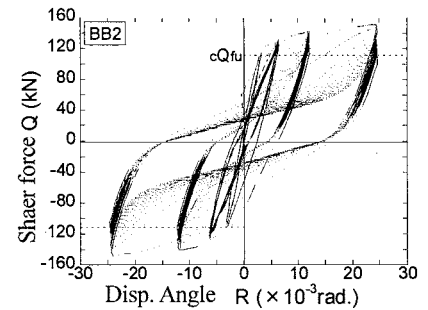


Fig.8 Q-R Curve of ECC Beam

4. ANALYTICAL MODEL

In the seismic response analysis, the below-listed procedures were followed, and analysis was performed with the setting of a 3D elasto-plasticity vibration model (Fig. 9).

1. The materials (walls, columns, coupling beams, top beams, and slabs) comprising the building were modeled as beam elements.
2. For the respective components modeled as beam elements, the elasto-plasticity characteristics noted below were considered.
 - Walls: bending and shear elasto-plasticity (tri-linear type), axial elasto-plasticity
 - Columns: bending elasto-plasticity (Tri-Linear type), shear elasticity, and for the columns equipped with the seismic control apparatus, axial elasto-plasticity
 - Coupling beams, top beams, slab-equivalence beams: bending elasto-plasticity (tri-linear type), shear elasticity
3. In this configuration, arranged is a seismic control device (oil damper) is installed between the top beams and column heads of perimeter columns. Here, the seismic control device is taken as a Maxwell-type model of dashpots, connected in series, having an equivalence spring and a damping

coefficient. The dashpots are given bi-linear type nonlinear characteristics.

4. For the tri-linear type skeleton curves regarding the bending and shear of the wall elements and the bending of columns and top beams, the degrading tri-linear type hysteresis rule of Fig. 10(a) (below, Muto loop) proposed by Dr. Muto was introduced. For the bending of slabs, an origin-oriented type hysteresis rule of fig. 10(b) was introduced. Also, for the coupling beams, to enable simulation of test results, given was a hysteresis rule having half each of the respective characteristics of a Muto loop and an origin-oriented type loop.

5. Within each floor, walls and columns were connected with a rigid floor; further, top beams and the seismic control device were attached.

6. The underground portion was taken as one rigid body, and the effects of piles and ground soil were considered with sway springs in the X and Y direction, and rocking springs within each respective vertical surface, introduced at the bottom edge of the foundation beams.

7. The design-use seismic ground motions were inputted via sway springs, seismic response analyses were performed for level 1 and level 2 seismic ground motions, and investigation was made of anti-seismic safety characteristics.

8. The analysis was done by a computer code developed by the Kajima Corporation.

This is a general-purpose nonlinear analysis program having 6 degrees of freedom at each nodal point, 3D beam nonlinear elements, nonlinear springs, and nonlinear dashpots. In this code, rigid element constraint characteristics, and all types of constraint characteristics are prepared. In an ordinary building analysis code, reduction is performed only for horizontals and rotations at the center of gravity of each floor; however, in the present program, since dashpot elements are attached vertically, analysis is performed with the vertical degrees of freedom remaining as they are at each node.

9. For damping of the building structure, a Rayleigh-type damping system is supposed. As for the damping constant, at the time of elasticity when the bottom of columns at first floor is fixed, damping factors of 0.03 are set respectively at the overall primary natural period (Y-direction primary) and overall sixth natural period (Y-direction secondary). The damping matrix is set proportionally to the initial rigidity matrix.

10. The ground spring used was an equivalence ground constant obtained via response analysis of the ground, and evaluation was performed considering burial effects and group pile effects. The analysis model considers buried portions of the underground portion as a mass-less and rigid

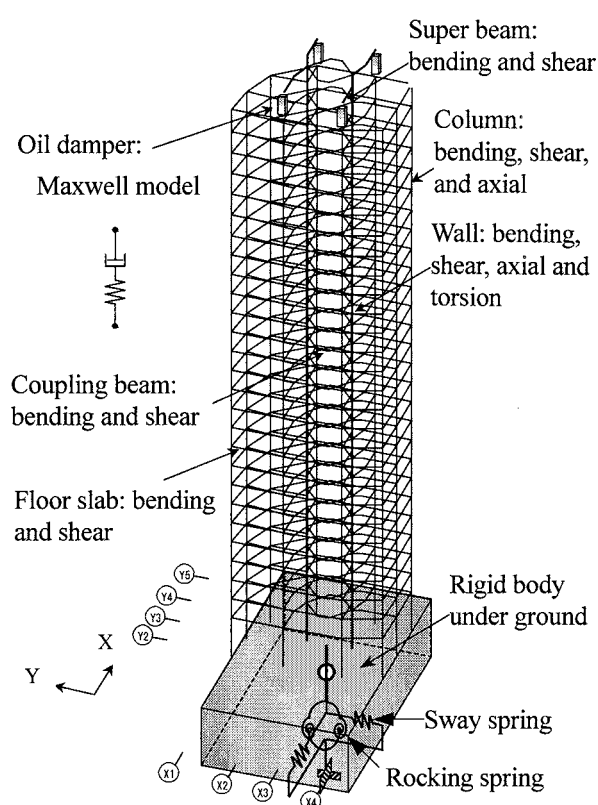


Fig.9 Analysis Model

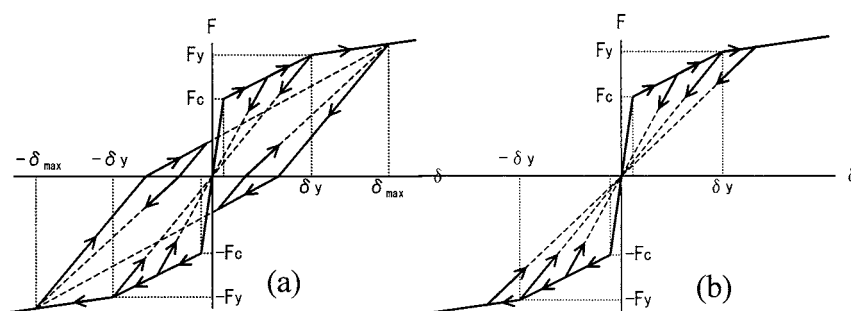


Fig.10 Hysteresis Loop, (a) Muto Loop, (b) Origin-oriented Loop

foundation, and this is a model with an added lateral dynamic spring at the buried portion side walls and a group pile dynamic spring at the bottom end of the foundation. An example of the ground spring characteristics is shown in Fig. 11.

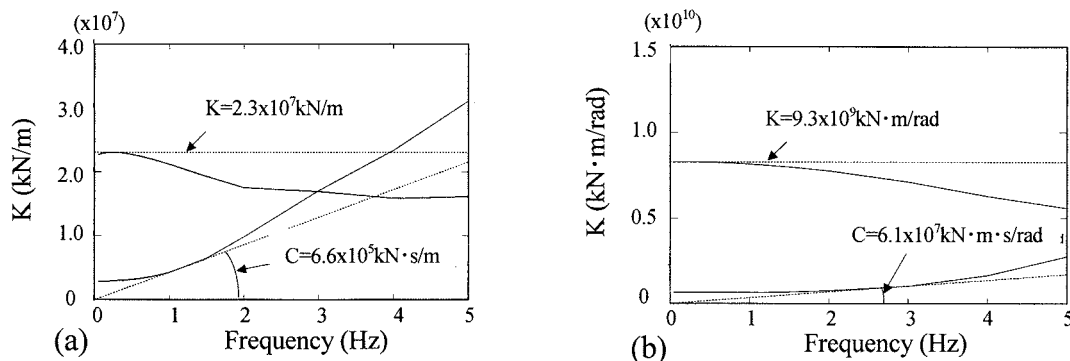


Fig.11 Sway and Rocking Spring, (a) Sway, (b) Rocking

5. SEISMIC RESPONSE ANALYSIS RESULTS

5.1 Input Earthquakes

Input earthquakes used in the seismic response analysis were of 2 levels: seismic ground motion of a magnitude that occurs rarely (Level 1), and seismic ground motion of a magnitude that occurs extremely rarely (Level 2); for each of these levels, actual waveforms of recorded ground motions in the past (recorded waves) and simulated earthquake waves were used.

As the seismic ground motion that occurs rarely, used were the waves whose maximum velocities are normalized to 0.25 m/s of the recorded waves, such as EL CENTRO 1940 (NS), TAFT 1952 (EW), and SENDAI038 1978 (EW). Also used were 3 waves (building code waves) that were simulated waves of different phases matched to the spectrum indicated in Japanese Building Code.

As the seismic ground motion that occurs extremely rarely, used were the waves whose maximum velocities are normalized to 0.50 m/s of the recorded waves of EL CENTRO 1940 (NS), TAFT 1952 (EW), and SENDAI038 1978 (EW), and 3 building code waves (BC wave-1, BC wave-2, BC wave-3).

5.2 Analysis Results

The natural vibration periods are shown in Table 1. Also, representative examples of seismic response analysis results are shown in Fig. 12.

Table 1 Natural Period						
Direction	X			Y		
Mode	1st	2nd	3rd	1st	2nd	3rd
Natural Period (s)	2.34	0.60	0.28	2.50	0.52	0.22

In regards to the response maximum inter-story drift angles for Level 2 seismic ground motion, at building code waves (RINKAI-92 phase) for both directions alike, at maximum, these were 1/113 in X direction, and 1/106 in Y direction; these were thus less than the criteria of inter-story drift angle of 1/100. It was also confirmed that, for flexure and shear responses of shear walls, respective ultimate strengths had a margin of 1.5 or higher. The maximum responses of rotation angle of edge portion of coupling beams were 1/41; it was thus confirmed that these were within the criteria of 1/30. The responses of the seismic control devices were confirmed, at a response maximum speed of 249 mm/sec, to be less than the tolerance value of 400 mm/sec, and the response maximum stroke was 43 mm, and thus less than the tolerance value of 100 mm.

Fig. 13 shows the energy absorption characteristics of each portion at the time of a Level 2 earthquake. In Y direction, the oil dampers bear 38.5%, and in X direction, the ECC coupling beams

bear 32.3%; it was thus understood that both of these make major contributions to reduction of building responses.

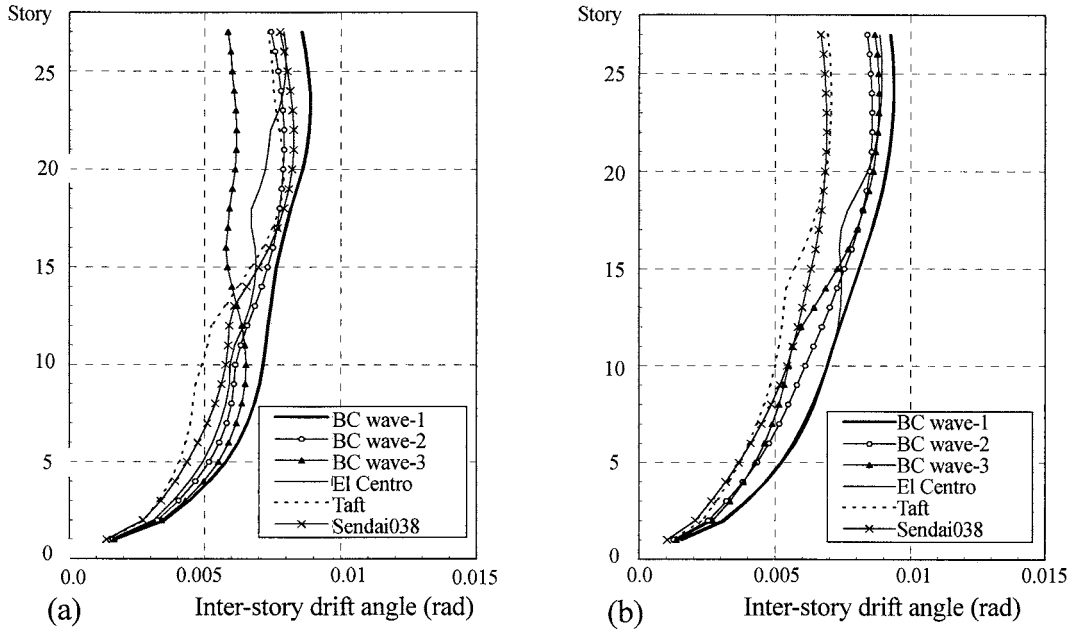


Fig.12 Maximum Inter-story Drift Angle, (a) X direction, (b) Y direction

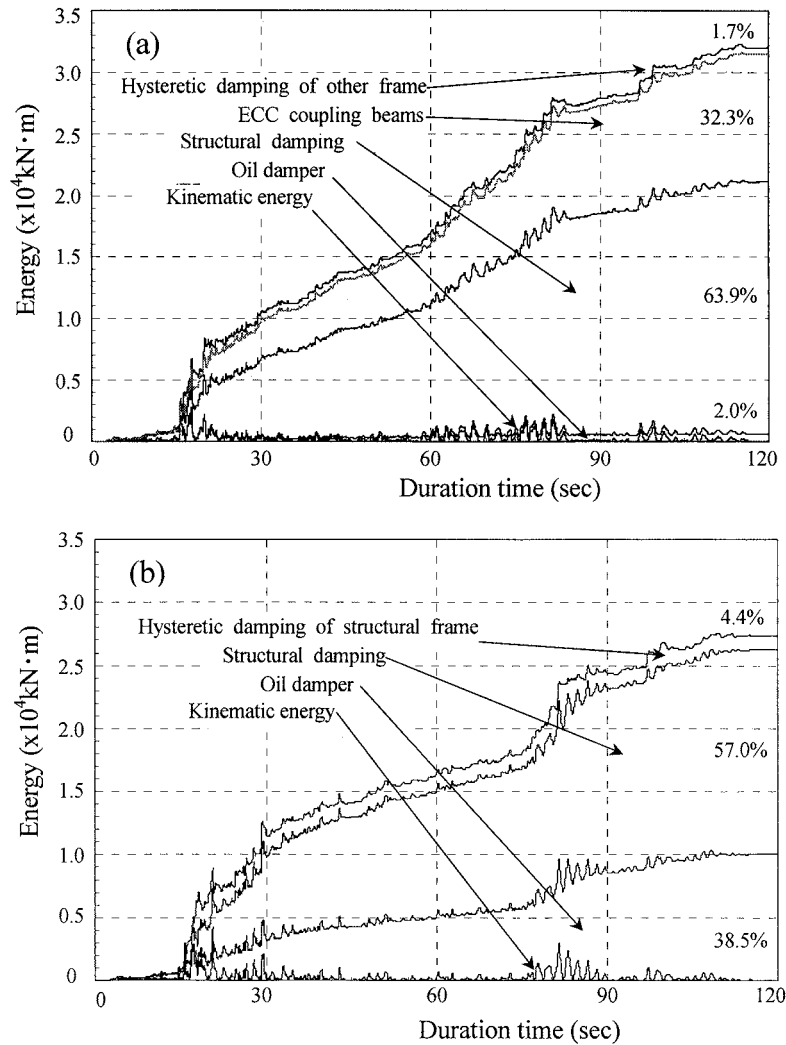


Fig.13 Energy Share Ratio of Each Element, (a) X direction, (b) Y direction

5.3 Dynamical Investigation of Piles

We performed seismic response analysis of piles with input motion of Level 2 Building Code waves, and investigated the anti-seismic safety characteristics of the pile bodies. In the analysis, as the pile stress at the time of an earthquake, consideration was made of pile stress due to inertia force from the upper portion of the structure, and pile stress due to ground vibration. The analysis model is shown in Fig. 14. As the analysis model, used was a lumped-mass model which collects the bending-shear elements of single piles for each different pile diameter of pile bodies, and in consideration of group pile effects at each mass point, we made this a model with added interaction springs. Used for the interaction spring were the equivalent S-wave velocity and the equivalent damping constant, and evaluation was performed using the 3-D thin layer element method. For the response analysis, the shear force waveform due to the inertia force of the upper portion of the structure was inputted at pile-head locations; in addition, inputted was the ground response waveform determined via a ground response analysis with the intervention of an interactive spring at each mass point of piles.

The analysis results confirmed that the pile flexural response values were within the ultimate flexural strengths, and that the pile shear response values were within the ultimate shear strengths.

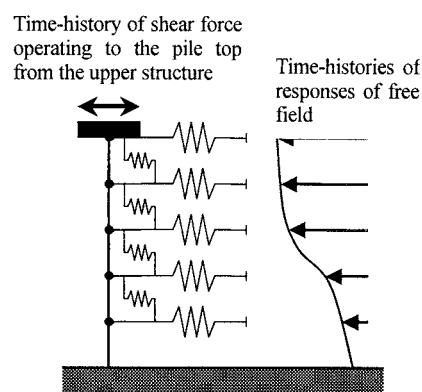


Fig.14 Soil-pile Analysis Model

6. SUMMARY

Herein was reported an overview mainly of the seismic response analysis for a high-rise RC seismic-control building employing, in Y direction, a flexural-control-type seismic-control system using an oil damper, and, in X direction, ECC coupling beam-type parallel anti-seismic walls.

The seismic response analysis that are based on the latest analysis technique show the control effectiveness of those seismic response control systems.

References:

- Omika, Y., Sugano T., Ohkawa J., Yoshimatsu T., Yamamoto Y., and Tsuji Y. (2000), "Seismic Design of a Super Frame Structural System with Passive Energy Dissipation Devices", *12th World Conference on Earthquake Engineering*
- Maruta, M., Kanda, T., Nagai, S., and Yamamoto, Y. (2005), "New High-rise RC Structure Using Pre-cast ECC Coupling Beam", *Concrete Journal*, Japan Concrete Institute, Vol. 43, No.11, pp.18-26

EQUILIBRATION OF ELEMENT WITH MULTI-DEFORMATION COMPONENTS FOR NONLINEAR STRUCTURAL ANALYSIS

Kangning LI¹⁾ and Xianguo Ye²⁾

1) *Principal, CANNY Structural Analysis, Vancouver, Canada*

2) *Professor, Hefei University of Technology, Hefei, Anhui, China*
Canny4NAS@shaw.ca, yexiang@mail.hf.ah.cn

Abstract: The element model used in nonlinear analysis of frame structure often consists of multiple deformation components. It results in element internal unbalance at the occurrence of stiffness degradation and overshooting. Treating the unbalance to maintain equilibrium and ensure the displacement compatible is key-importance for stable and reliable analysis results. This paper introduces the element model with multiple deformation components, and treats the element internal unbalance by applying equivalent load to the element of fixed-end. The load effect is then calculated and included in next time/load step to correct the unbalance. Applying the element model in nonlinear analysis of frame structure, the results show that the equilibrium among element internal forces and between the restoring force and external load is well-maintained and the analysis processing is stable and the results are reasonable.

1. INTRODUCTION

In frame structural nonlinear analysis it usually uses the element model consisting of multi-deformation components. The simplest case is two nonlinear springs in serial connection that forms an internal node between the springs, as shown in Figure 1. The well-used element model of beam and column is multi-deformation components of flexural and shear deformation, as well as axial tension/compression and torsion. Three-dimensional bending and axial tension/compression element in MS model (Lai 1985, Li 1993) is the case of complicated multi-component element. In some cases, e.g. the steel beam-column joint strengthened by side plate, the beam or column element may have relocated plastic hinge at an intended section away from the element-end, so it makes structural analysis have to adopt the element model with elastic zone at element-end. The Figure 2 illustrates the nonlinear flexural/shear element model with both elastic zone and elastic connection flexibility in rotational, transversal and axial deformations. Such element model is used in nonlinear structural analysis computer program — CANNY (Li 1993). The multi-component element model with any nonlinear component induces element internal unbalance at the occurrence of stiffness degradation and overshooting, e.g., the unbalanced spring force in the two-spring element (Figure 1), the unbalanced moment and shear force in beam/column element (Figure 2). Correcting the unbalances and maintaining equilibrium are key-importance for stable and reasonable results in nonlinear structural analysis using step-by-step technique. Iteration method is often employed to deal with unbalance but is great time-consuming in the analysis of huge building structures, and it still exists the problem of divergence due to the concrete material properties being non-continuous and multi-solutions (for multiple branches of crack, ascending and softening). While the method by applying equivalent load in next load/time step to correct the unbalances is

simple and fast and is adopted in the CANNY program. The element internal unbalance is treated by applying element internal load to relevant element components or at the element internal nodes to find out the load effect to all the element components (i.e., element internal force redistribution) and to the element-end relevant structural nodes (external equivalent load).

This paper introduces the element model dealing of multiple deformation components, and shows the method of solving element internal unbalances to maintain equilibrium and to meet compatible condition. Nonlinear structural analysis is performed to examine the equilibrium. Some past work (Li et al 1999) shows the reliability of using the nonlinear model in simulating building earthquake-responses.

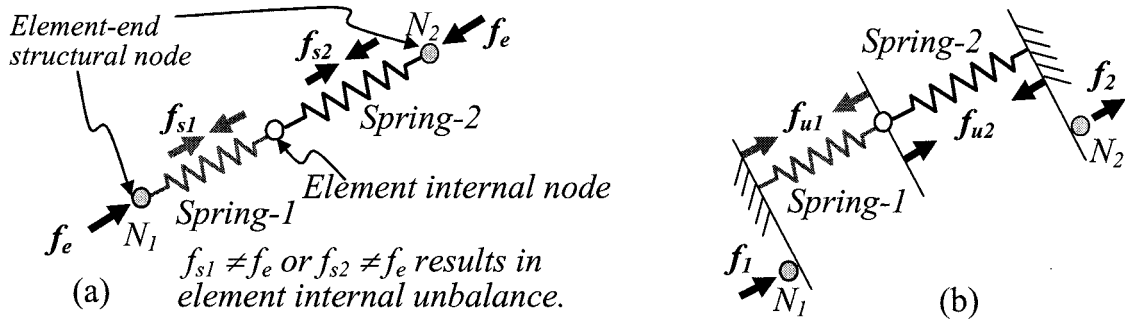
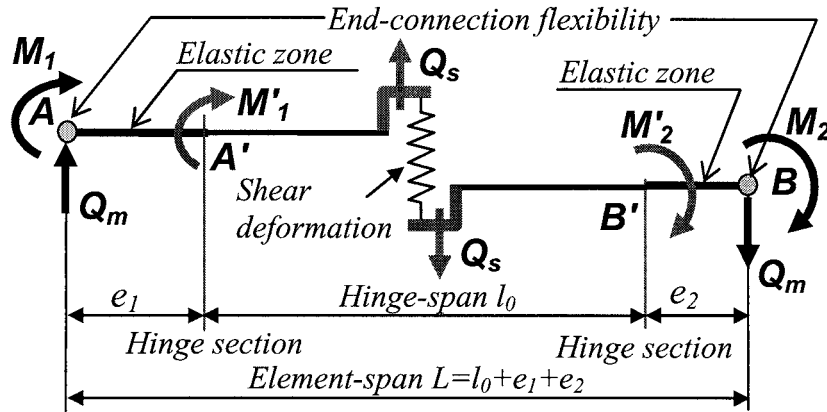


Figure 1: Multi-Component Element Model: (a) Serial-Connected Two-Spring Element, and (b) Applying Equivalent Load to the Element to Correct Unbalance



Existing internal unbalance if $Q_s \neq -(M_1 + M_2)/L$ or $M_1 \neq M'_1, M_2 \neq M'_2$
Figure 2: Multi-Component Element Model: Flexural-Shear Element with Elastic Zone

2. TREATING ELEMENT INTERNAL UNBALANCES

2.1 Serial-Connected Spring Element

Advanced earthquake resistant design adopts damper, isolator and many other kinds of vibration-control devices to main frame structure. The analysis dealing with the vibration control devices may have to use encapsulated element model that has two or more serial-connected springs with internal nodes. Figure 1 shows the simplest case of two serial-connected springs with one internal node. At the occurrence of overshooting (stiffness change) in any of the springs, the element internal unbalance is induced and is calculated as:

$$f_{u1} = f_e - f_{s1}, \quad f_{u2} = f_e - f_{s2} \quad (1)$$

Where f_e is the element force required for equilibrium; f_{s1}, f_{s2} are the restoring force and f_{u1}, f_{u2} the unbalanced force at spring 1 and spring 2, respectively. Figure 1 (b) shows the equivalent load applied to the element in fixed-end to bring it back in equilibrium meanwhile it keeps the displacement compatible to the element-end nodes. The fixed-end forces f_1, f_2 , which are the load effect at the element-end structural nodes to be included in next time/load step, are calculated as:

$$f_1 = -\frac{\delta_{s1}f_{u1} + \delta_{s2}f_{u2}}{\delta_{s1} + \delta_{s2}}, \quad f_2 = -f_1 \quad (2)$$

Where, δ_{s1} and δ_{s2} are the spring flexibility at current time step. The load effect to each spring is:

$$\text{Spring 1: } \tilde{f}_{s1} = f_1 + f_{u1}, \text{ Spring 2: } \tilde{f}_2 = -f_2 + f_{u2} \quad (3)$$

Where, the positive force is in compression and negative in tension to the element. Suppose the two springs have equal properties (symmetrical springs), that is $f_{s1} \equiv f_{s2}$, it results in $f_{u1} = f_{u2} = f_u, f_1 = -f_u, f_2 = f_u$, and the load effect to the springs becomes all zero. This means that the element becomes one-component element and the element unbalanced force can be treated directly by applying equivalent load at the element-end structural nodes.

2.2 Multi-component Flexural Element

The element model shown in Figure 2 represents line element in uniaxial bending. It is based on one-component beam model (Giberson 1969), and is added the shear spring for shear deformation. It may also include elastic zone and/or connection flexibility at the element-end. The elastic zone is resulted from relocated plastic hinge that is intended at any section within the element deformable span L (i.e., hinge span $l_0 < \text{element span } L$). The connection flexibility represents the element-end connection condition (semi-rigid connection), elastic or inelastic. Furthermore, the element model may include axial tension/compression and torsional deformation by adding one-component axial spring and torsional spring. These make the element model with multiple deformation components. It results in internal unbalance if any of the deformation components has nonlinear behavior.

The simple way to deal with the elastic zone is illustrated in Figure 3 (b), which replaces the elastic zone by rigid zone, and adds equivalent flexibilities at the hinge-section to represent the flexural deformation of the elastic zone. So that the flexural flexibility matrix of the element model (b) is built in the hinge-span l_0 between A'-B' and includes the flexibility of the elastic zone:

$$[\delta_f]_{A'-B'} = \begin{bmatrix} \frac{l_0}{3EI} + \delta'_{e1} & -\frac{l_0}{6EI} + \delta'_{e12} \\ -\frac{l_0}{6EI} + \delta'_{e12} & \frac{l_0}{3EI} + \delta'_{e2} \end{bmatrix} \quad (4)$$

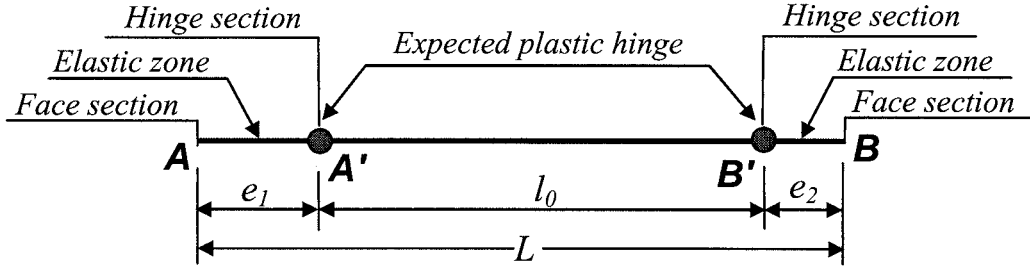
Where l_0 = element hinge-span; EI = element flexural stiffness; $\delta'_{e1}, \delta'_{e2}, \delta'_{e12}$ = flexural flexibility contributed by the elastic zone e_1 and e_2 . To make the equality between the element model (b) and the original element (a), the flexibility $\delta'_{e1}, \delta'_{e2}, \delta'_{e12}$ must be calculated as:

$$\delta'_{e1} = \frac{L}{3EI} \left[\frac{1 - 3\varepsilon_2(1 - \varepsilon_2)}{(1 - \varepsilon_1 - \varepsilon_2)^2} - (1 - \varepsilon_1 - \varepsilon_2) \right] \quad (5)$$

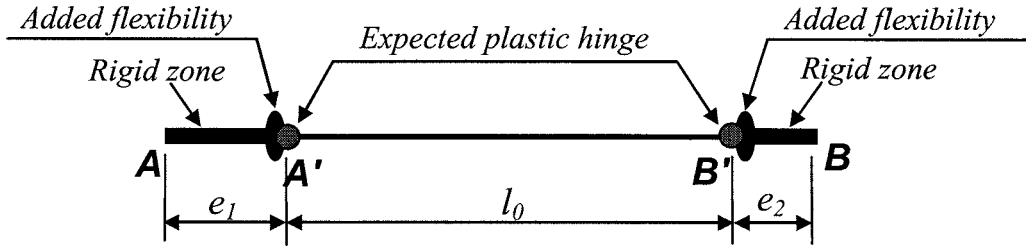
$$\delta'_{e2} = \frac{L}{3EI} \left[\frac{1 - 3\varepsilon_1(1 - \varepsilon_1)}{(1 - \varepsilon_1 - \varepsilon_2)^2} - (1 - \varepsilon_1 - \varepsilon_2) \right] \quad (6)$$

$$\delta'_{e12} = -\frac{L}{6EI} \left[\frac{1 - 3\varepsilon_1(1 - \varepsilon_2) - 3\varepsilon_2(1 - \varepsilon_1)}{(1 - \varepsilon_1 - \varepsilon_2)^2} - (1 - \varepsilon_1 - \varepsilon_2) \right] \quad (7)$$

Where, $\varepsilon_1, \varepsilon_2$ are the ratio of elastic zone to the element deformable span L , $\varepsilon_1 = e_1/L$, $\varepsilon_2 = e_2/L$. If the flexural element includes shear and axial deformation, the shear flexibility and axial flexibility can be simply calculated at the element span L . The equation (5) ~ (7) are also applicable to the element with pin-connection at one-end provided that the pin is located at the hinge section.



(a) Flexural Element with Relocated Hinge Section



(b) Analysis model for the element with elastic zone

Figure 3: Flexural Element with Elastic Zone beyond the Expected Plastic Hinge

As shown in Figure 2, the flexural and shear element has internal unbalance if $Q_s \neq -(M_1 + M_2)/L$ or $M_1 \neq M_1', M_2 \neq M_2'$, where Q_s = shear spring restoring force; M_1', M_2' = moment at hinge sections; M_1, M_2 = moment at element-end in equilibrium with external load. To solve the internal unbalance, equivalent load is applied to the element in fixed-end as shown in Figure 4, to cause additional load effect to relevant structural nodes at element-end, and to each deformation component of the element. The equivalent load M'_{u1}, M'_{u2}, Q_u , which have the positive direction shown in Figure 4, are calculated as following:

$$M'_{u1} = M_1 - M_1', \quad M'_{u2} = M_2 - M_2', \quad Q_u = -\frac{M_1 + M_2}{L} - Q_s \quad (8)$$

And the fixed-end forces are solved by flexibility method as following:

$$\begin{Bmatrix} m_1 \\ q_1 \end{Bmatrix} = \begin{bmatrix} 1 & -e_1 \\ 0 & 1 \end{bmatrix} \begin{Bmatrix} m_1' \\ q_1' \end{Bmatrix}, \quad \begin{Bmatrix} m_2 \\ q_2 \end{Bmatrix} = \begin{bmatrix} 1 & -e_2 \\ 0 & 1 \end{bmatrix} \begin{Bmatrix} m_2' \\ q_2' \end{Bmatrix} \quad (9)$$

$$\begin{Bmatrix} m_2' \\ q_2' \end{Bmatrix} = \frac{-([\Delta_{CA}] + [\Delta_{e1}] + [\Delta_p]) \begin{Bmatrix} M'_{u1} \\ M'_{u2} \end{Bmatrix} - \begin{bmatrix} 0 \\ L^2 \delta_s \end{bmatrix} Q_u}{[\delta_{CA}] + [\delta_{CB}] + [\delta_{e1}] + [\delta_{e2}] + [\delta_{fs}]}, \quad \begin{Bmatrix} m_1' \\ q_1' \end{Bmatrix} = \begin{bmatrix} -1 & -l_0 \\ 0 & 1 \end{bmatrix} \begin{Bmatrix} m_2' \\ q_2' \end{Bmatrix} \quad (10)$$

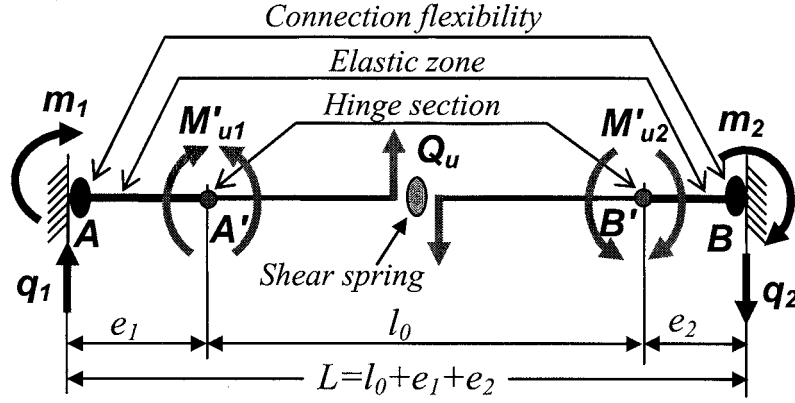
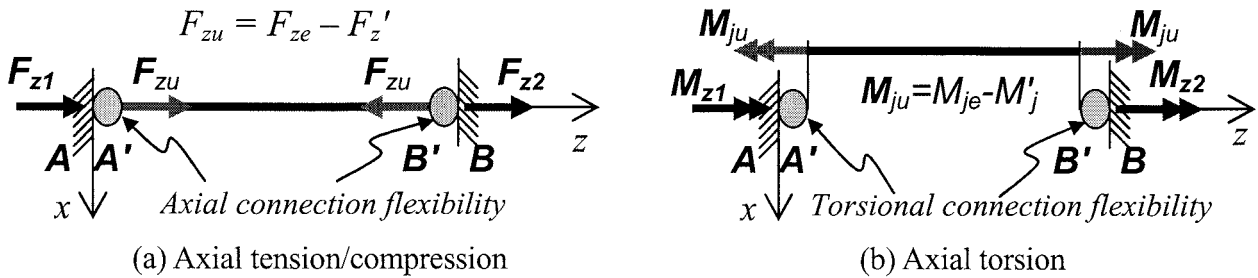


Figure 4: Equivalent Load and Fixed-End Forces to Solve Element Internal Unbalance

The matrices $[\Delta]$ and $[\delta]$ represent the deformation contribution of element components due to the equivalent load and the fixed-end forces, respectively. The matrix subscript "CA" and "CB" express the contribution of connection flexibility at element-end A and B; "e1" and "e2" of the elastic zone; "p" of plastic hinge; "fs" the contribution of flexural rotation and shear deformation. The item " $L^2 \delta_s$ " is the contribution of shear flexibility subjected to equivalent load Q_u . The fixed-end forces given by equation (9) become the external equivalent load acting at the element-end relevant nodes. $\{m'_1, m'_2\}$ and $\{q'_1, q'_2\}$ given by equation (10) are the load effect to the hinge section, and that to the shear spring is calculated as $q'_s = Q_u + q'_2$. These load effects are to be included in the element responses in next time/load step to bring the element forces back in equilibrium.

If the element has no elastic zone no connection flexibility, the equation (9) results in equal fixed-end forces at element-end and at hinge section. In this case, the moment unbalances M'_{u1}, M'_{u2} can be treated as external equivalent load directly applied at the element-end structural nodes, while the unbalance between the shear force and moment remains as element internal unbalance. If the element has pin-connection at one-end, usually considered at the hinge-section, e.g., at terminal-end hinge section, it makes $M'_{u2} = 0, m'_2 = 0$, while the rest components of the equivalent load and load effect can be calculated in the same way of equations (9), (10).

If the element model includes nonlinear axial deformation component and has axial connection flexibility at the element-end, then overshooting at the nonlinear axial component results in internal unbalanced axial force too. Assuming elastic connection flexibility at element-end, the equivalent load due to the internal axial unbalance is shown in Figure 5. The calculation for corresponding load effect under the equivalent load is simple and easy.



F_{ze}, M_{je} = element force required for equilibrium; F'_z, M'_j = element restoring force.

Figure 5: Equivalent Load and Fixed-End Force due to Element Unbalanced Axial Force

2.3 MS Element Model

The MS element is 3-dimensional element model used to represent the interaction among biaxial bending and axial tension/compression. It treats the sub-springs in force-displacement relation or stress-strain relation (fiber-model equivalent). In force-displacement relation, as shown in Figure 6, the element model includes two MS elements at element-end and a line element of elastic flexural and axial deformation, and has two internal nodes between the line element and the MS element. Note that the MS element has zero length and carries moment and axial force but not shear force. The line element may include one-component shear spring for uniaxial shear deformation, or multi-directional shear springs representing biaxial shear deformation. The element model may have elastic zone and connection flexibility at the element-end as well. It is always in need to treat element internal unbalances for the MS element model, and the equivalent load applied to the element in fixed-end is illustrated in Figure 6. The corresponding load effects can be calculated by flexibility method in same way of that mentioned in previous section 2.2.

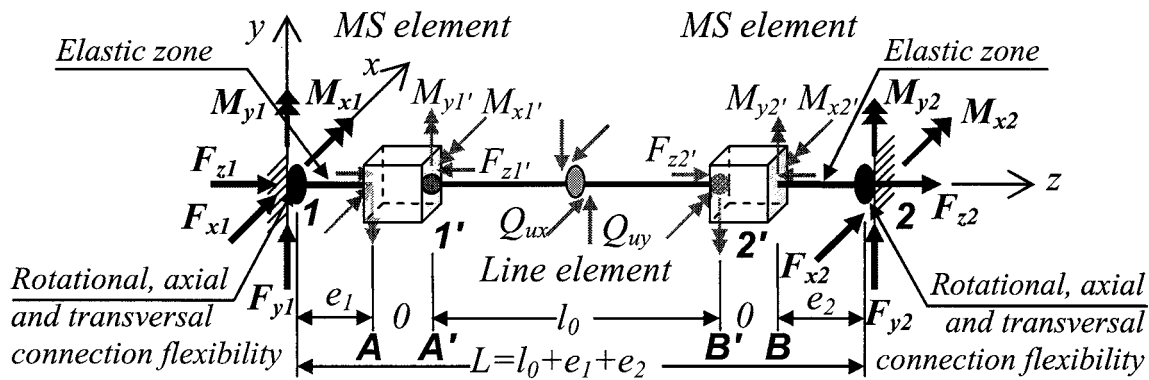


Figure 6: Equivalent Load and Fixed-End Forces of MS Element Model

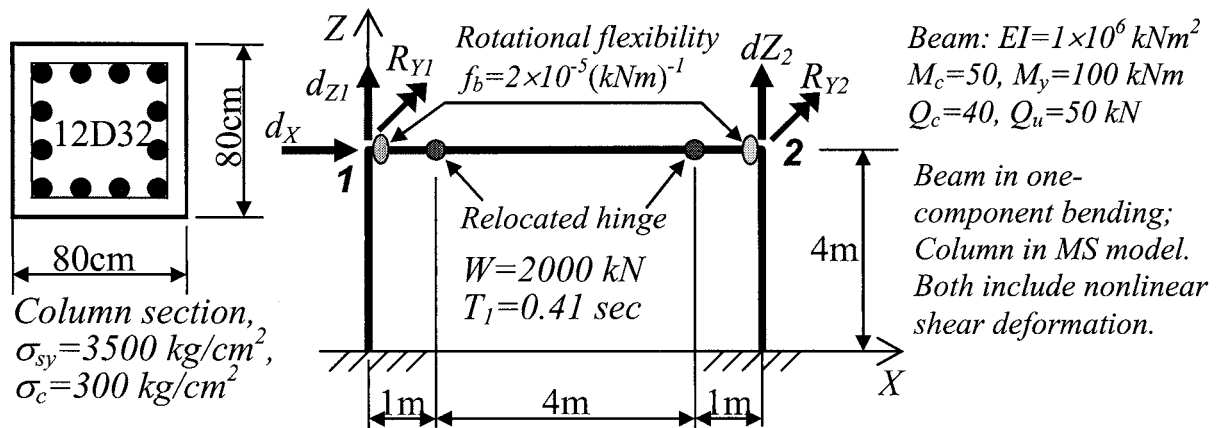


Figure 7: Portal Frame Used in Step-by-Step Analysis to Examine the Equilibrium

3. USING THE ELEMNET MODEL IN FRAME STRUCTURE ANALYSIS

3.1 Examining the Element Model in Step-by-Step Analysis

Step-by-step analyses in static pushover and dynamic response are performed using a portal frame model shown in Figure 7. The beam element is in one-component bending with shear deformation and with relocated plastic hinge to allow for elastic zone, and elastic rotational connection-flexibility at the element-end. The column is idealized in MS model with the sub-spring properties based on the concrete and steel material stress-strain relations. The stress-strain curve of

concrete material in use is assumed with softening branch down to zero strength at the strain of 5-times of that under maximum compression strength. Trilinear hysteresis model in Takada-rule is applied to all one-component nonlinear springs. The analysis results are shown in Figure 8 and 9, are used to examine the convergence and equilibrium. Both beam and column experienced flexural yielding and large plastic shear deformation, while the equilibrium between the moment and shear force is perfectly maintained that can be seen from the comparison of shear force Q_s against moment - $(M_1+M_2)/L$ in Figure 8 and 9, (b) and (c). Figure 8 (a) and 9 (a) show the unbalanced force at node, which reflects the equilibrium between restoring force and external load. The unbalance is corrected properly as noticeable unbalance only occurs at few load/time steps. It implies the analysis results stable and well-converged. From the results, the effectiveness and reliability of the method treating element internal unbalance are confirmed.

3.2 Reliability of Simulating Building Earthquake Response

An instrumented building, Holiday Inn located in Van Nuys, Southern California has observed earthquake response in records available for analysis study. The building is a seven-story RC frame structure with the records obtained during the North-Ridge Earthquake 1994. Details of the building and the earthquake record information can be found from the publications by Ventura et al 1995 and Rahmatian 1997. The calculated responses using CANNY program and comparing with recorded responses are done by Li et al 1999. The comparison shows satisfactory reliability in simulating the earthquake responses of real building structure.

4. CONCLUSIONS

The paper introduces the concept of multi-component element model for use in nonlinear analysis of frame structures, and the method of solving the element internal unbalances by applying equivalent load at the element in fixed-end to get load effect to be included in the next time/load step in analysis. The method ensures both equilibrium condition and displacement compatible condition. Applying the element model in step-by-step analysis of frame structure, it shows that equilibrium of the element among multi-components is well maintained, and that overshooting unbalance between restoring force and external load is corrected properly. Thus it results in stable and well-converged nonlinear analysis.

Acknowledgements:

The first author expresses thanks to Kozo System Inc., Japan for continuous support to the author's research and development of nonlinear structural analysis technologies and computer program.

References:

- M. F. Giberson, "Two Nonlinear Beams with Definitions of Ductility," *Journal of Structural Division, ASCE*, Vol.95, No.ST2, 1969, pp.137-157.
- S.-S. Lai, "Inelastic Analysis of Reinforced Concrete Space Frame under Biaxial Earthquake Motions," Ph.D. Thesis, University of Toronto, 1985.
- Kangning Li and Shunsuke Otani, "Multi-Spring Model for 3-Dimensional Analysis of RC Members", *Journal of Structural Engineering and Mechanics*, Vol.1, No.1, 1993, pp. 17-30.
- Kangning Li, "CANNY-C — A Computer Program for 3D Nonlinear Dynamic Analysis of Building Structures," *Research Report No.CE004, Department of Civil Engineering, National University of Singapore*, November, 1993.
- Ventura, C.E., Finn, W.D.L. and Schuster, N.D., "Seismic Response of Instrumented Structures During the 1994 Northridge, California Earthquake," *Canadian Journal of Civil Engineering*, 1995, Vol.22, pp316-337.
- Rahmatian, P., "Three-Dimensional Nonlinear Dynamic Seismic Behavior of a seven story reinforced Concrete Building," *thesis of master of applied science*, Dept. of Civil Eng., the University of British Columbia, 1997
- Kangning Li, Tetsuo Kubo and Carlos E. Ventura, "3-D Analysis of Building Model and Reliability of Simulated Structural Earthquake Responses," *Proceedings of International Seminar on New Seismic Design Methodologies for Tall Buildings*, Oct. 1999, Beijing, China, pp.34-41.

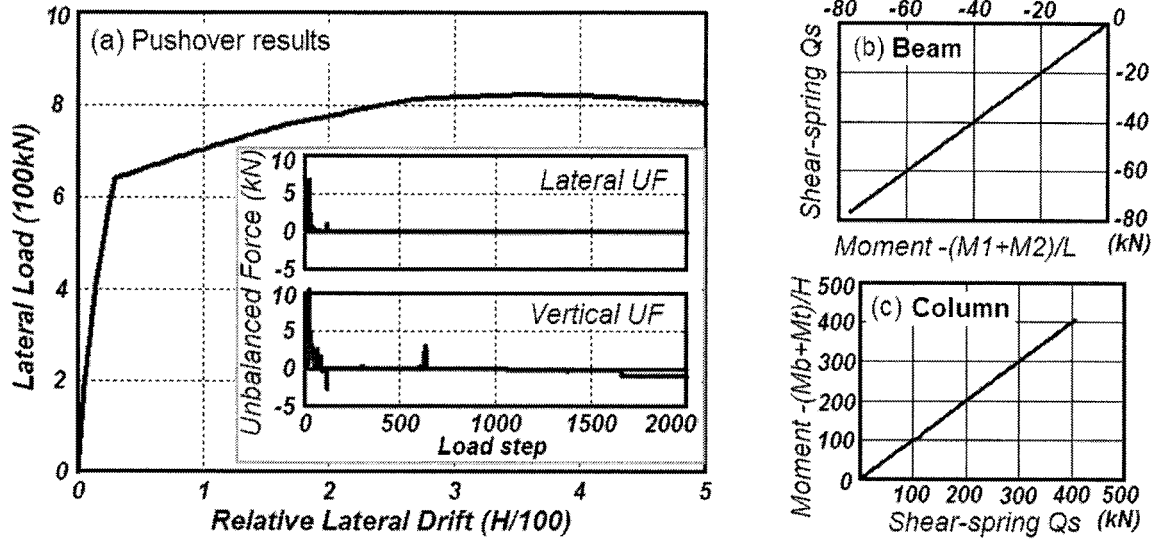
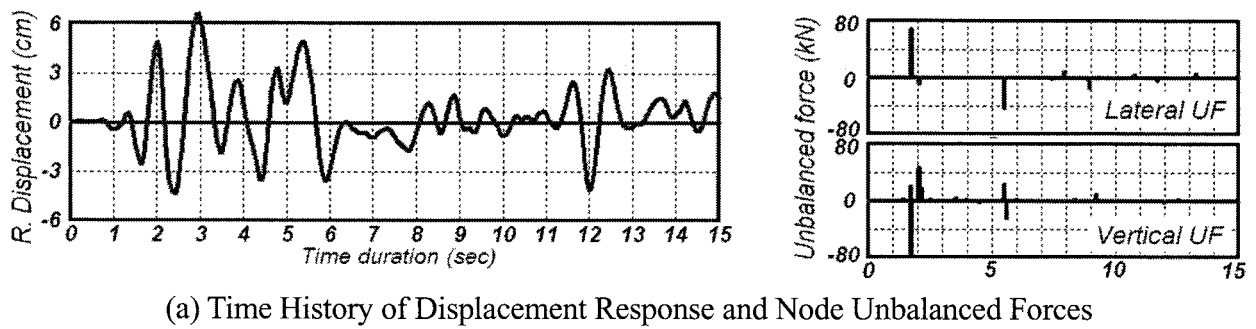
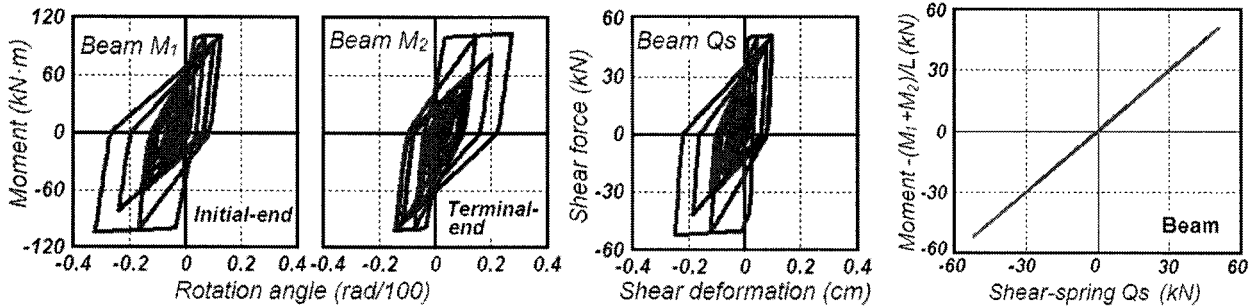


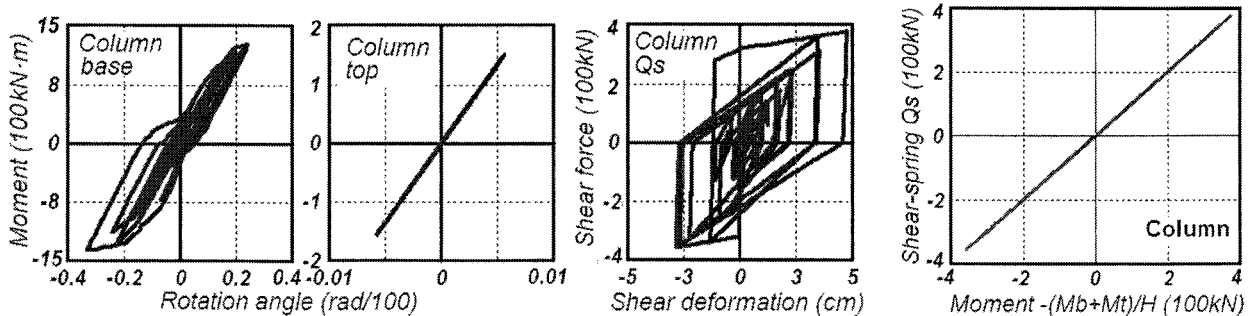
Figure 8: Pushover Results: (a) Load-Deflection Curve and Unbalanced Force at Node, (b) Beam Element Moment-Shear Force Equilibrium, and (c) Column MS element Equilibrium.



(a) Time History of Displacement Response and Node Unbalanced Forces



(b) Moment-Shear Force Hysteresis and Equilibrium of Beam Element



(c) Moment-Shear Force Hysteresis and Equilibrium of Column Element

Figure 9: Dynamic Response Results (Input: Original NS-Acceleration of 1940 El Centro Record)

DYNAMIC ANALYSIS OF HIGH-RISE BUILDING WITH PASSIVE DAMPERS USING "BUILDING 3D DYNA"

M. Ishii¹⁾, and T. Kouno¹⁾

*1) Struct. Eng. Dept., Nikken Sekkei Ltd., Japan
ishiim@nikken.co.jp, kounot@nikken.co.jp*

Abstract: We developed the total building structural calculation system "BUILDING3D", which deals with complex shaped buildings and checks safety of the input buildings by static analyses according to Japanese architectural standard. We also developed 3D nonlinear dynamic analysis system "BUILDING 3D DYNA", which considers the elast-plastic dynamic behavior of each member and carries out dynamic response analysis using the structural model passed down from "BUILDING 3D". In this report the dynamic analysis system is applied to a super high-rise building nearly 250 meters in height (the Toyota-Mainichi Building in Nagoya), which is installed with various types of passive dampers and connected to low-rise building using oil dampers.

1. INTRODUCTION

Seismic design is always the largest problem in structural design in Japan; in other words, the result of seismic design can control the quality of whole design. Recently designs of buildings are becoming more complicated due to the development of construction technology. In a sense, it owes to rapid progress of structural analysis technology and processing ability of computers to design various types of complex buildings with adequate seismic capacity.

In Japan, the total building structural calculation systems have been used for the structural design of normal buildings. The system executes many procedures (load calculations, stress calculations, check of member sections, etc.) according to the inputted information such as building shape, member sections, analytical conditions and load conditions, then the system checks the seismic capacity required by Japanese Law of the inputted building based on static analyses. The coverage of the systems used to be limited for simple shaped buildings, so complicated shape buildings used to be designed by using general structural calculation systems. Recently, almost all the total structural calculation systems deal with 3D member-to-member models and the coverage of the systems have been expanded.

In dynamic analysis, the buildings which have less eccentricity have been modeled as effective shear-bar models or effective flexible-bar models as shown in Fig.1(a). In cases of considering the effect of the eccentricity, as shown in Fig.1(b), the pseudo-space model have been applied in which each frame has been modeled as the effective shear-bar models or the effective flexible-bar models. However, these simplified models cannot simulate the behavior of such complicated buildings in detail. In order to grasp the accurate performance of those buildings, it is necessary to perform analysis using the 3D member-to-member model.

Since computers operating with an extensive memory and at high speed are now available, the

large number of calculations required for the 3D member-to-member dynamic analysis for large buildings can be handled practically.

The dynamic analysis system “BUILDING 3D DYNA” developed by NIKKEN SEKKEI Ltd. performs the time history analysis using structural model passed down from “BUILDING 3D”.

In this report the outline of “BUILDING 3D” and “BUILDING 3D DYNA” are introduced, and the dynamic analysis system is applied to a super high-rise building nearly 250 meters in height (the Toyota-Mainichi Building in Nagoya), which is installed with various types of passive dampers and connected to low-rise building using oil dampers.

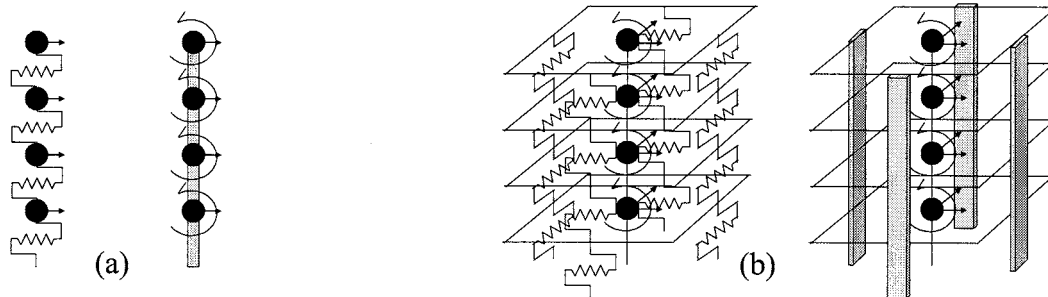


Figure 1 Analysis Models: (a) Simplified Model, and (b) Pseudo-Space Model

2. OUTLINE OF “BUILDING 3D” AND “BUILDING 3D DYNA”

2.1 Development Policy

The total building structural calculation system “BUILDING 3D”, developed by NIKKEN SEKKEI Ltd., can deal with not only simple shape buildings but also complicated shape building which consists of many complex coordinate groups or polar coordinates as shown in Fig.2. The developing concept of the system is that the coverage of the system never gives the limits of structural design.

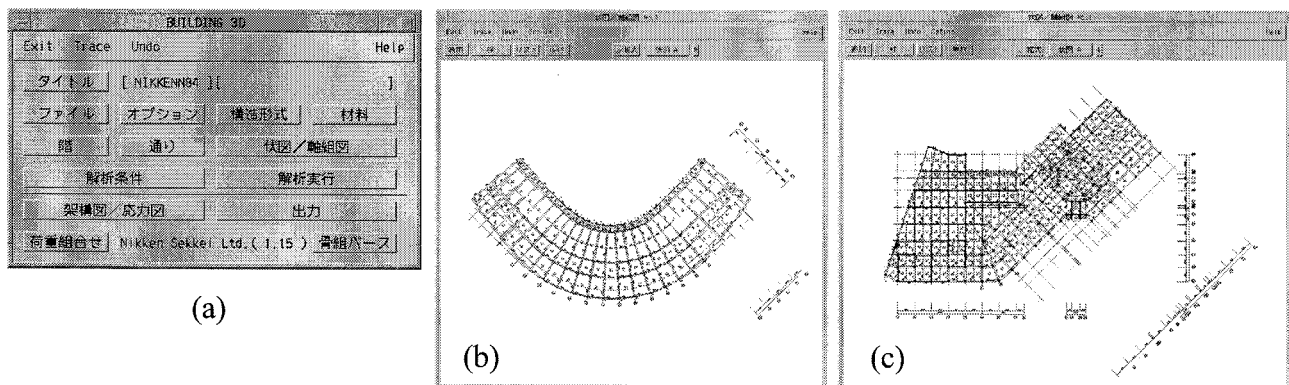


Figure 2 GUI Image of “BUILDING 3D”:

(a) Main Menu, (b) Using Polar Coordinates, and (c) Using Complex Grid Formations

2.2 Constitution of the System

“BUILDING 3D” is composed of the main program based on GUI for input and identification of building shape, and several sub-programs for processing the continuous calculations such as the conversion from building shape to analysis model, the forming of analysis model, the calculation of load conditions, the static analysis, the check of the section of the members, the post procedure of calculations, and the output of the calculation results. The intermediate files are used to connect the sub-programs. “BUILDING 3D DYNA” creates dynamic loads and performs the time history analysis by two sub-programs respectively using the analysis model created by “BUILDING 3D”.

2.3 Analysis Model

The analysis model is conformed according to the following points.

- The geometrical non-linearity is not considered according to the infinitesimal deformation theory. $P-\Delta$ effect is considerable.
- S, RC, SRC, and CFT sections are available.
- The beam elements, truss elements, and wall elements can be modeled as elasto-plastic elements, and slabs are modeled as elastic plane-stress elements.
- Rigid floor assumption is inputted by using dependent displacements described as linear combinations of other displacements.
- As is shown in Fig.3, the beam element is composed of rigid zones, elastic zones and a center zone. In the center zone, multispring (MS) model is adopted to describe the elasto-plastic interaction between axial force and biaxial bending moments at the ends of the center member, and multi-shear-spring (MSS) model is also used to express the elasto-plastic interaction of biaxial shear forces. To take the effect of long time loading into account, initial stresses can be considered at the end of the center zone. Column-girder panel elements can be inputted instead of elastic zones.
- In dynamic analysis, various types of non-linear passive dampers depending on their deformations and velocities, such as visco-elastic dampers, oil dampers and viscous dampers, are also available.

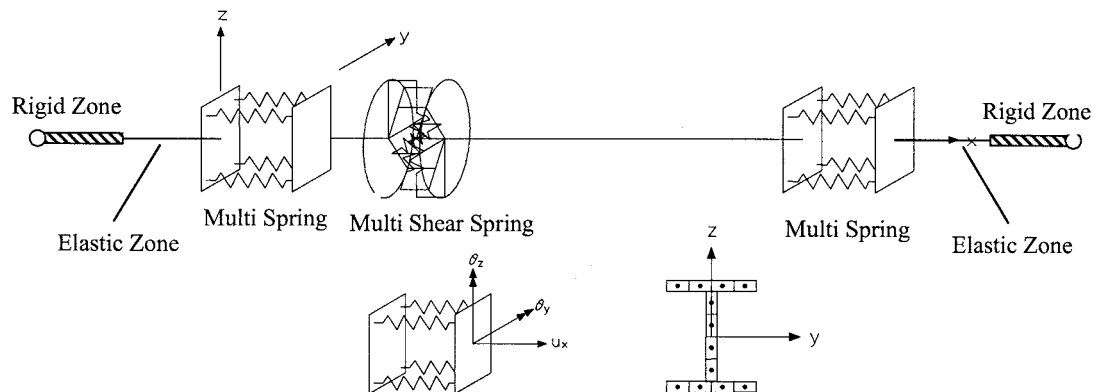


Figure 3 Beam Element

2.4 Features of static and dynamic analysis

In static analysis, applied forces on nodes and prescribed displacements of nodes are available for loading conditions, which can be changed during loading process. The total stiffness matrix is composed as a skyline matrix in order to reduce calculation time and save memory. The Newton-Raphson method is employed for nonlinear iterative procedure.

In dynamic analysis, dynamic external forces are added to degree of freedom with the mass as exciting forces. Thus earthquake forces and wind loads can be treated. Iterative procedure is not used, and residual force of previous step is added to the incremental load of the next step. As the solution method of the motion equations, either linear or average acceleration method is adopted.

3. DYNAMIC ANALYSIS EXAMPLE USING “BUILDING 3D DYNA”

3.1 Outline of the Building

The building is 247 meters high and 47 stories. The lower part is 50 meters high and 7 stories as shown in Photo 1, Figs. 4 and 5. The two parts are connected at the 7th floor level (33 meters high) with oil dampers. The floor plan of the upper part is about $53\text{m} \times 53\text{m}$ square, and the lower part is a trapezoidal shape. The north (upper) part is mainly for offices and the south (lower) part is for shops.

The underground which supports those two parts is 30 meters deep and 6 stories. The use of the basement is for parking area and machine rooms. The total floor area is about 200,000m². The structural outline is as follows. The upper part is composed of a perimeter rigid frame, continuous steel plate tubes and outrigger trusses with oil dampers. The lower part is made up of rigid frames and a continuous steel plate.

3.2 Design Policy on Expansion Joint

There are many examples of high-rise buildings with expanded lower parts. There are two structural solutions to this type of building. The first one is to connect the two parts rigidly, and the second is to separate each part with an expansion joint. In the former case, it is difficult to estimate the seismic loads because of the complex behavior. In the latter, we can estimate these loads more easily, however the displacement between the upper and lower parts becomes large, and we have to treat a difficult problem at the expansion joint.

In this example, we connect the lower part to the upper part with oil dampers. We have tried to improve the problem by this energy dissipation system. We have confirmed the effectiveness of this connected system through time history response analysis.



Photo 1 Building Perspective

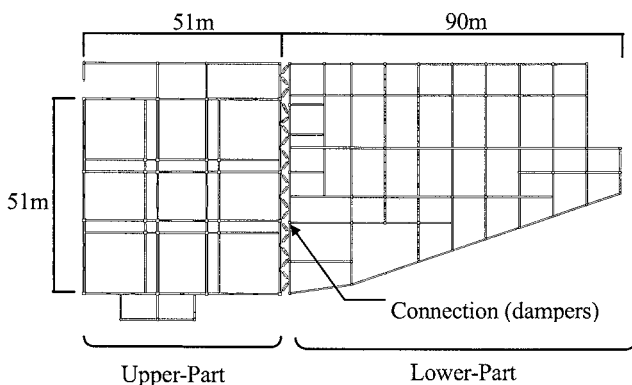


Figure 4 Main Structural Plan (7th Floor Level)

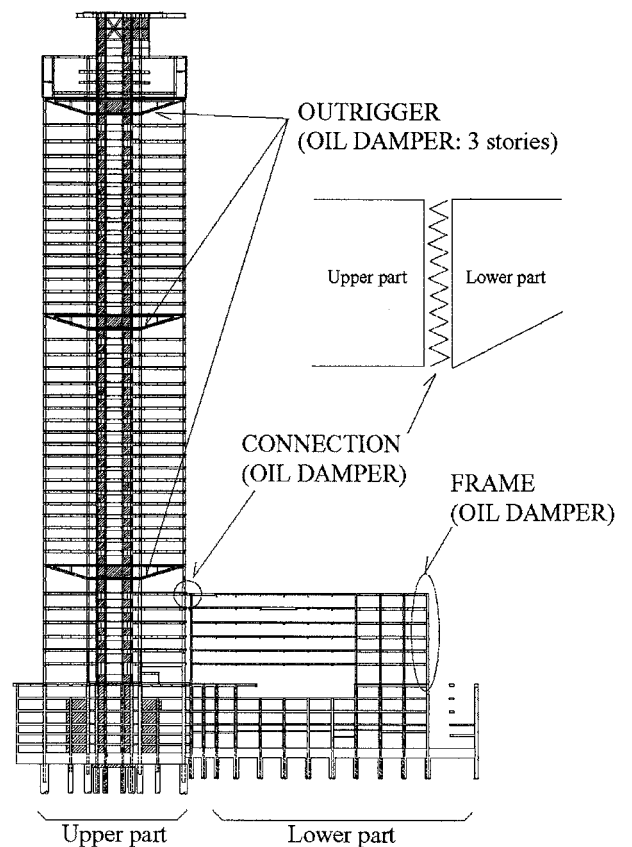


Figure 5 Structural Frame and Damper system

3.3 Analysis Model and Input Wave

As shown in Fig.6, all members are modeled as elastic elements in this study. Assuming that the slab on each floor is rigid excluding some areas without slab, the consistent mass is considered. Each mass has 3 degrees of freedom (2 directional displacements (X and Y), and rotation(Θ_z)) and has consistent mass and rotary inertia. According to this assumption, 45, 6, and 5 rigid floors are made for upper part, lower part and integrated underground part respectively. The joint displacements of the bottom floor (B6F) are fixed.

Table 1 and Fig.7 shows the specifications of each oil damper. Each damper is modeled as a elastic spring and nonlinear dashpot connected directly, with a Maxwell-type model. Three cases are performed as shown in Fig.8. The first is no oil damper case (Case1). The second is the case that the outrigger type and shear-link type dampers in the upper and lower part of the building are installed respectively (Case2). The third is the case that upper and lower parts of the buildings are connected with oil dampers in addition to the dampers in Case2 (Case3). Case3 is the result of the design. Weights and natural periods of Higher and lower parts are shown in Table 2

Fig.9 shows the velocity response spectrum of an input seismic wave for dynamic analysis. The input seismic wave is the artificial wave and is made by fitting to the response spectrum defined by Japanese building standards. The phase characteristic is HACHINOHE EW (1968 TOKACHI-OKI earthquake). To make structural damping matrix, the natural vibration modes related to the upper and lower part are selected, and the modal damping coefficient is given so as to being proportional damping to the stiffness for each part of the building ($\eta_1=2\%$). Dynamic analysis is performed only under the case of Y-direction input raising the level of its velocity response spectrum to 100 cm/s ($\eta=5\%$) in long period domain. The input wave lasts 120 seconds, analysis pitch is 0.01 seconds.

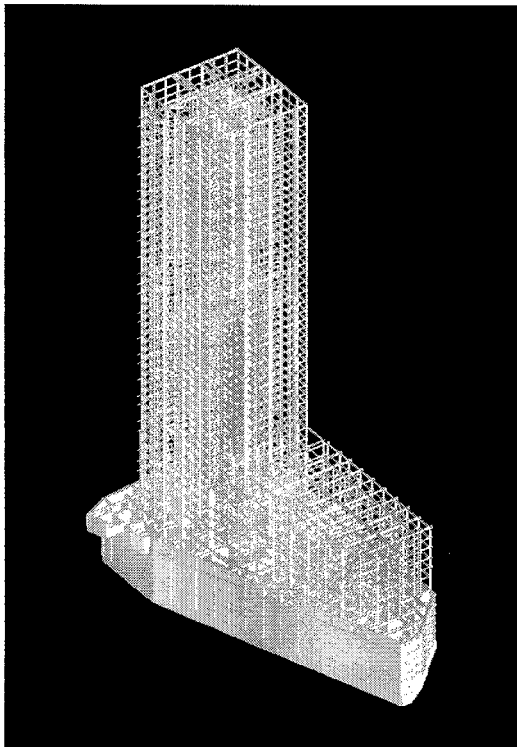


Figure 6 Model of Dynamic Analysis

Table 1 Damper Characteristics

	OUTRIGGER, FRAME	CONNECTION
Damping Force F_{max}	2000 kN	600 kN
Relief Load F_1	1600 kN	500 kN
1st damping coefficient C_1	750 kNs/cm	31 kNs/cm
2nd damping coefficient C_2	31 kNs/cm	0.54 kNs/cm
Limit of stroke δ	$\pm 100\text{mm}$	$\pm 600\text{mm}$

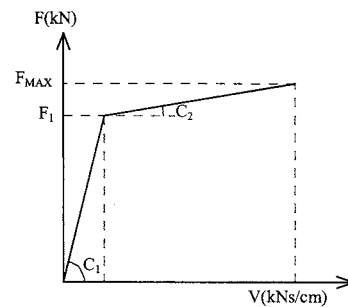


Figure 7 Force-Velocity Relation of Oil Dampers

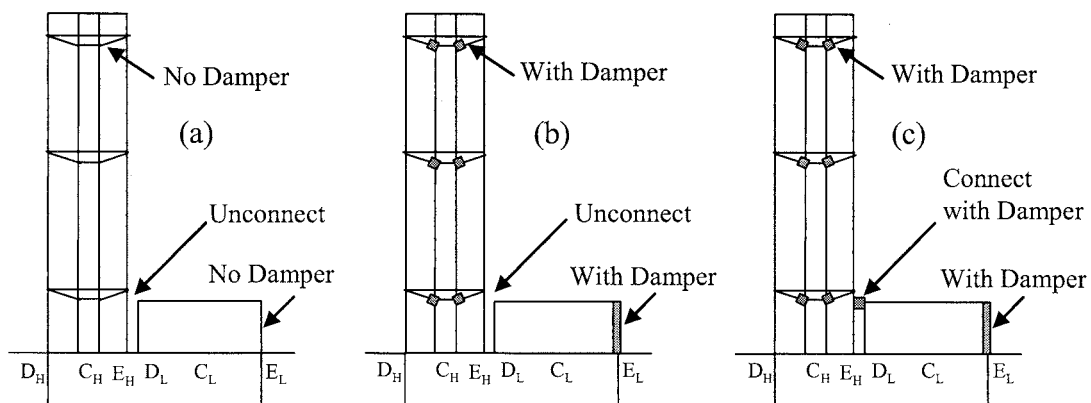


Figure 8 Model Cases : (a) Case1, (b) Case2 and (c) Case3

Table 2 Weight and Natural Period

	Upper	Lower
Weight	106000t	25000t
1st	5.9s (X)	1.4s (Y)
2nd	5.7s (Y)	1.3s (X)
3rd	4.5s (R)	1.2s (R)

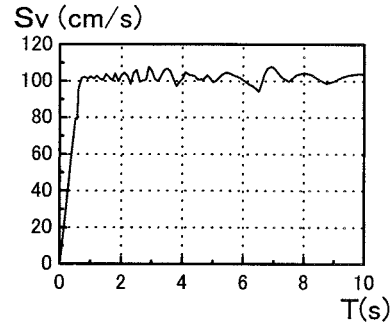


Figure 9 Velocity Response Spectrum of Input wave

3.4 Results of Dynamic analysis

We show the results under the case of Y-dir. input. Mainly, we study the displacement between higher part and lower part, with connection dampers and without. We show the points that we notice in this study (Fig.10).

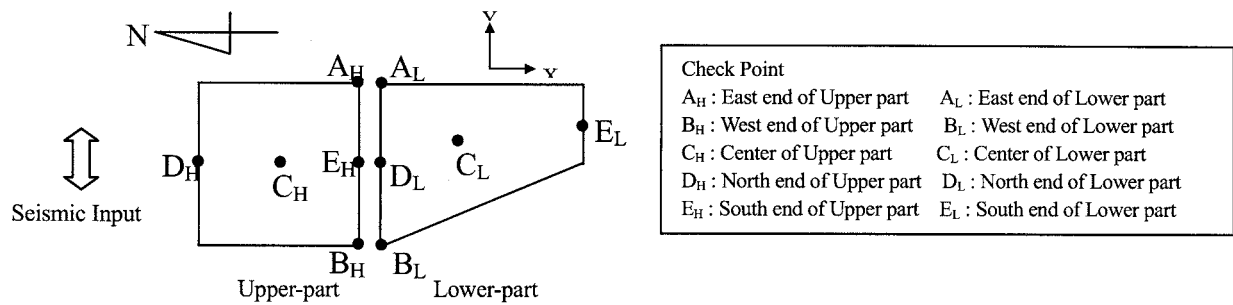


Figure 10 The check points of study

Fig.11 shows the maximum relative story drift angles of each part of the building. From the difference between case1 and case2, though the drift angles of the upper part are decreased to some extent owing to outrigger dampers, those of lower part at E_L are considerably decreased by dampers installed accompanied by eccentricity. The drift angles at D_L in Case2 are almost the same as in Case1.

Compared with the drift angles of the connected Case3 with the unconnected Case2, the drift angles at D_L are extremely decreased on the contrary in Case2, while the drift angles of the lower part at E_L and the upper part are almost the same as the unconnected Case2.

We also investigated the balance of the total input energy and percentage of energy absorbed by the dampers. Table 3 shows that the dampers absorbed about 30% of the total input energy in the connected case3. The connection dampers absorbed about 50% of the all dampers in the connected case3 as shown in Table 4.

We compare the displacement and rotation to the basement in the connected Case3 with the unconnected Case2 at the 7th floor level. Fig.12 shows the time history of relative displacement of Y-direction between the upper and lower part in the connection (A_H-A_L = B_H-B_L). The displacement is decreased and the maximum displacement in the connected Case3 is 12cm, and 40cm in the unconnected Case2. Fig.13 shows the time history of the rotations to the basement at the 7th floor of the upper and lower part. The lower part is decreased in the connected Case3.

In consequence of dynamic analyses, the effectiveness of the connecting system by oil dampers between the upper and lower part of the building is confirmed. Seismic performance on the lower part is extremely improved by means of the connecting damper system and the dampers installed within frames, and then no bad effects on the upper part take place.

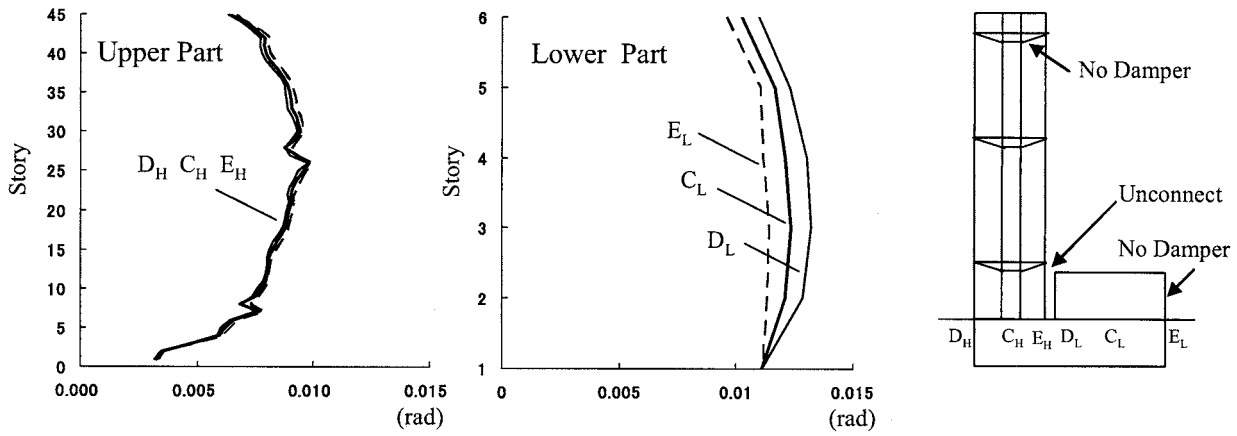


Figure 11 (a) The Maximum Story Drift Angles in Case1

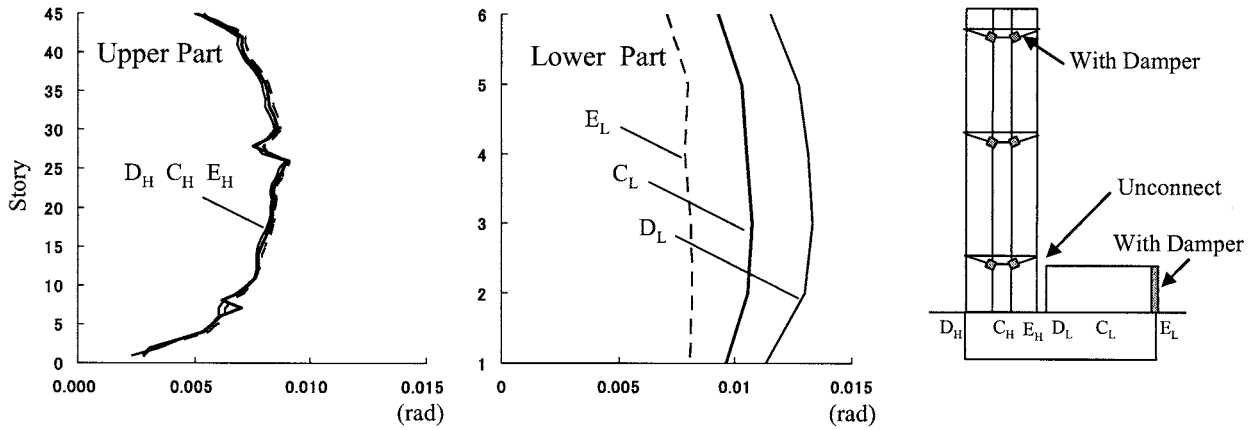


Figure 11 (b) The Maximum Story Drift Angles in Case2

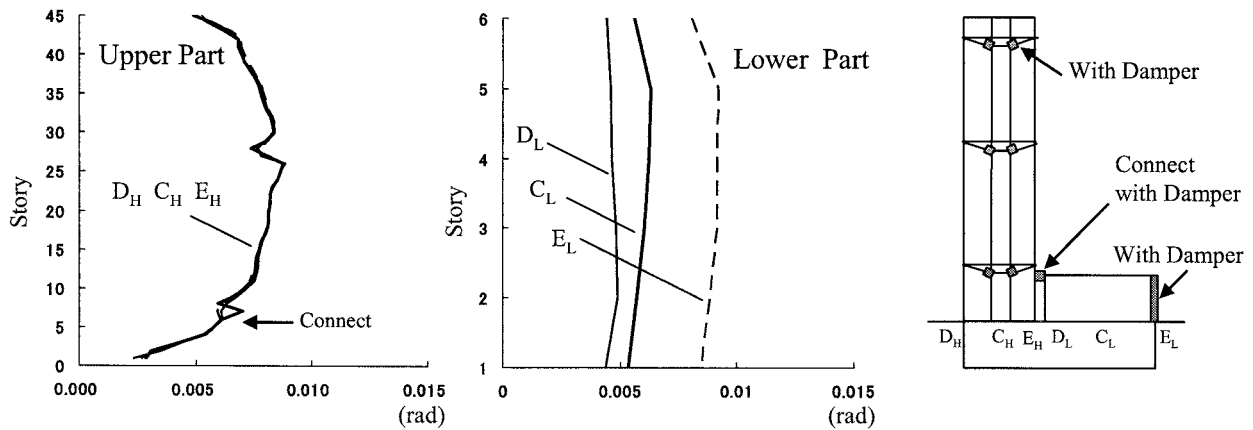


Figure 11 (c) The Maximum Story Drift Angles in Case3

Table 3 Energetic Response

Energy	Connected	Unconnected
	(kN·m)	(kN·m)
	(ratio)	(ratio)
Others	140200	169800
	72%	85%
Dampers	56700	30200
	28%	15%
Total Input	196900	200000
	100%	100%

Table 4 Energy of Each Damper

Energy	Connected	Unconnected
	(kN·m)	(kN·m)
	(ratio)	(ratio)
Outrigger	20800	20500
	37%	68%
Connection	26800	-
	47%	-
Lower	9000	9600
	16%	32%
Total of dampers	56600	30100
	100%	100%

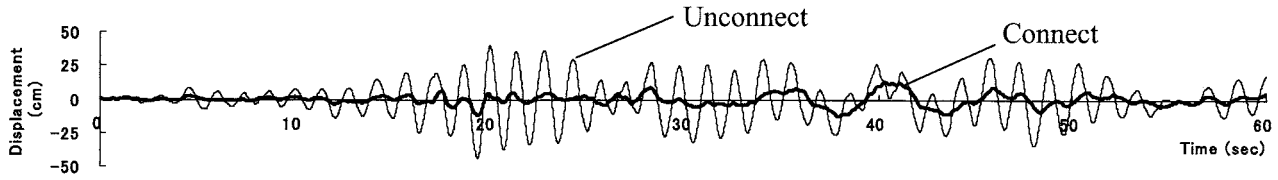


Figure 12 The Time History of Relative Displacements in the Y-direction (A_H-A_L , B_H-B_L)

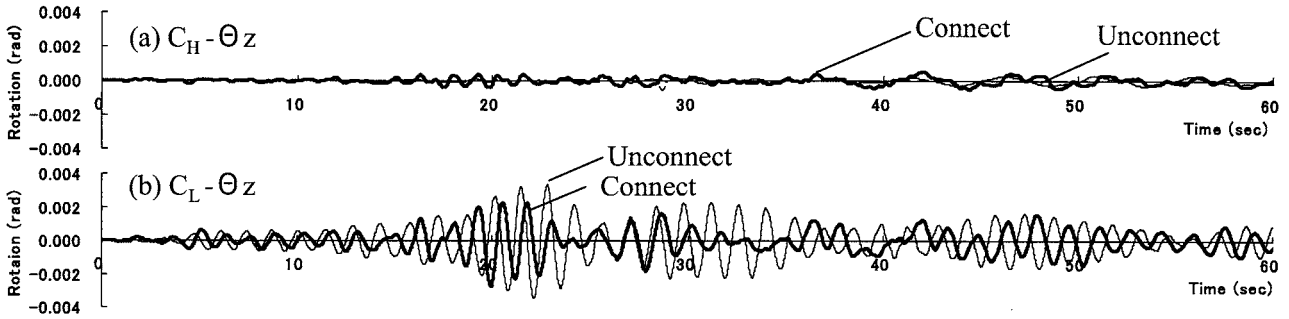


Figure 13 The Time History of Rotation, Θ_z : (a) C_H , and (b) C_L

4. CONCLUSION

The total building calculation system “BUILDING 3D” and its dynamic analysis sub-system “BUILDING 3D DYNA” are introduced through the dynamic analyses on the super high-rise building with passive oil dampers. In consequence of dynamic analyses, the effectiveness of the connecting system by oil dampers between the upper and lower part of the building is confirmed especially. Hereafter, we are willing to develop a better calculation system useful for structural design continuously.

DAMAGE BEHAVIOR SIMULATION OF RC STRUCTURE SUBJECTED TO SEISMIC LOADS

M. Mitsui¹⁾, S. Sakai¹⁾, S. Akiyama¹⁾ and K. Sato²⁾

1) Science and Engineering System Div., ITOCHU Techno-Solutions Corp., Japan

2) National Institutes for Earth Science and Disaster Prevention, Japan

masakazu.mitsui@ctc-g.co.jp shinkichi.sakai@ctc-g.co.jp

shinichi.akiyama@ctc-g.co.jp ksato@bosai.go.jp

Abstract: A numerical simulation system for the 3-D full scale earthquake testing facility (E-Defense) is developed. This system adopts the object-oriented framework for future prospect and expansibility. The first main purpose of this system which built in reinforced concrete material model proposed by Maekawa and Fukuura is to solve the precise damage and collapse behavior of reinforced concrete structure. In this paper, this system is verified whether it could simulate the dynamic behavior of an H-shaped reinforced concrete shear wall up to failure. As a result of the study, this analysis system is confirmed to be able to simulate the behavior of concrete structure more reliable than other usual systems.

1. INTRODUCTION

The 3-D full scale earthquake testing facility, E-defense was established in the National Institute for Earth Science and Disaster Prevention. E-defense was planned on the occasion of the Hanshin Awaji Great Earthquake to undertake unprecedented experiments in which actual buildings will be destroyed to observe the process, scale and causes of collapse under severe earthquakes. In order to use effectively various experimental results obtained in the E-Defense, development of the simulator which can reproduce these results in high performance is desired. We have developed a simulation system which can reproduce the behavior of reinforced concrete structure as a part of the simulator. In this paper, this system is verified whether it could simulate the dynamic behavior in earthquake resisting wall up to failure.

2. OUTLINE OF SIMULATION SYSTEM

Advantages on this system are given in following 3 points.

- 1) With the analysis module using implicit method and explicit method, it is possible to freely choose two modules in the midst of the calculation.
- 2) As a reinforced concrete material model, it has been equipped with the model proposed by Dr. Maekawa and Dr. Fukuura.
- 3) In order to ensure the performance of the simple expansion, this system adopts the object-oriented framework for future prospect and expansibility.

Fig.1 shows a reinforced concrete model proposed by Dr. Maekawa and Dr. Fukuura [1]. This model has been constructed by combining the constitutive law for concrete and that for reinforcing bars. The constitutive law adopted for the cracked concrete is composed of the Compression and tension model and the shear transfer model. By combining them with the reinforcing bar model, the present model for a reinforced concrete model has been constructed.

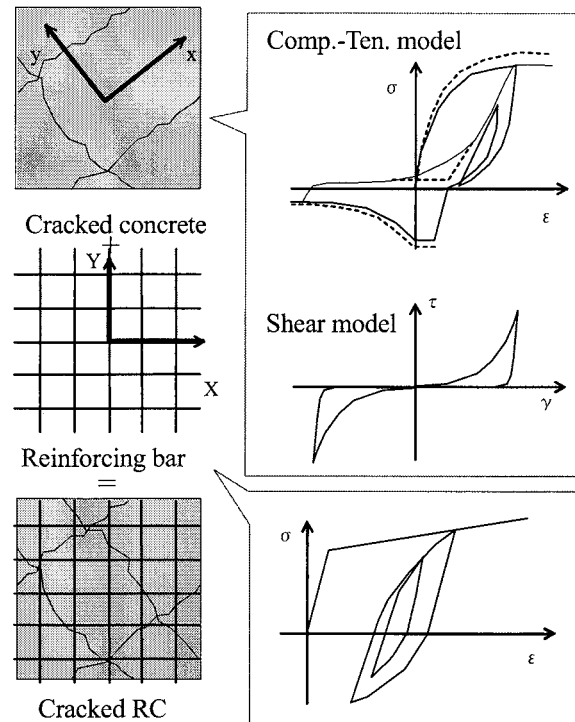


Fig. 1 A numerical reinforced concrete model

3. SIMULATION OF DYNAMIC TESTS

3.1 Outline of dynamic tests

The specimens of dynamic tests are corresponding to the reinforced concrete wall by Nuclear Power Engineering Corporation. The details of the specimen and the material properties are shown in Fig.2 and Table 1. Specimen is an H sectional wall with 1.22% of reinforcement ratio in web wall. The top of the walls has a top slab and additional lead weights. The input seismic waves of the experiment are shown at Table 2.

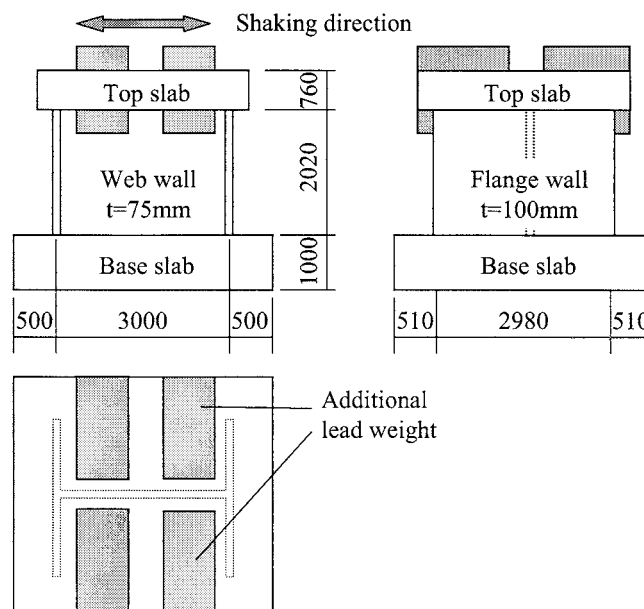


Fig. 2 The detail of specimen

Table 1 Material properties of specimen

Total weight of upper region (tf)	122.0
Compressive strength of concrete (MPa)	28.6
Tensile strength of concrete (MPa)	2.24
Elastic modulus of concrete (GPa)	22.9
Yield strength of rebar (MPa)	383
Elastic modulus of rebar (GPa)	184
Reinforcement ratio in flange, vertical, horizontal (%)	0.472, 0.457
Reinforcement ratio in web, both (%)	1.219

Table.2 Input vibration steps

Vibration step	Max acc. (gal)	Input target behavior
RUN-1	53	Elastic behavior
RUN-2	112	Shear crack initiation
RUN-3	325	3 times the RUN-2's behavior
RUN-4	577	Deformation angle of 2/1000 rad
RUN-5	1230	Ultimate behavior

3.2 Outline of simulation models

3-dimensional shell elements with a reinforced concrete model and solid elements with an elastic model were used to model the RC walls and other parts as shown Fig.3. The time integration method of dynamic analysis chose the Newmark- β method, and the coefficient β was set with 0.25. Using the rigidity proportional internal viscosity attenuation, the attenuation coefficient was determined from 1% for the first natural frequency. Generally, it is known that the stability of the nonlinear analysis is lacking by the localized damage of a part of concrete elements. In this system, the instability is avoided by two following methods. As a first, the analysis is carried out by the shorter interval time as the increment of the input acceleration is less than 15gal. As a second, the property of concrete elements was changed from nonlinear model to elastic model of the low rigidity on the way of calculation when principal shear strain remarkably increases.

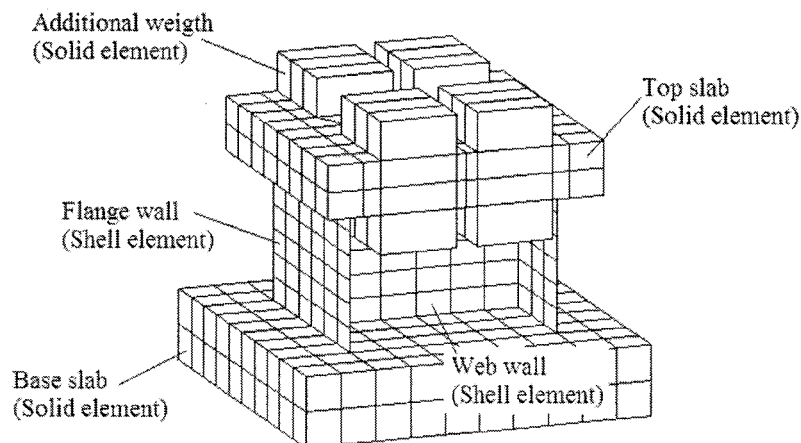


Fig.3 Simulation model

3.3 Analytical results

The relationships between internal force and horizontal displacement of the upper slab are shown in Fig.4. Horizontal response accelerations of the upper slab are shown in Fig.5. Horizontal response displacement of the upper slab is shown in Fig.6. The comparison between the experiment and the analysis on the development of cracking after RUN-4 and RUN-5 are shown in Fig.7.

In the experiment after the RUN-1, the crack in the walls was not generated and the response of specimen was elastic behavior. The analytical result showed elastic behavior as Fig.4(a) and Fig.5(a). After the RUN-3 and RUN-4 in the experiment, the shear crack is generated in the whole web wall, and the behavior offers the nonlinearity. The analytical results shows the nonlinear behavior, shear crack of a web wall and bending crack in two flange walls as shown in Fig.4, Fig.5 and Fig.7. The inner loops between internal force and horizontal displacement have swollen because the unbalance force in a step of calculation was accumulated in order to select the non-convergence method. After the RUN-5 in the experiment, a shear slip at the web wall was recognized at 4.0s and the period of the response is lengthened. In this analysis, it reaches the ultimate state at 4.0s due to the shear slip failure along cracks in the web wall as shown Fig.7.

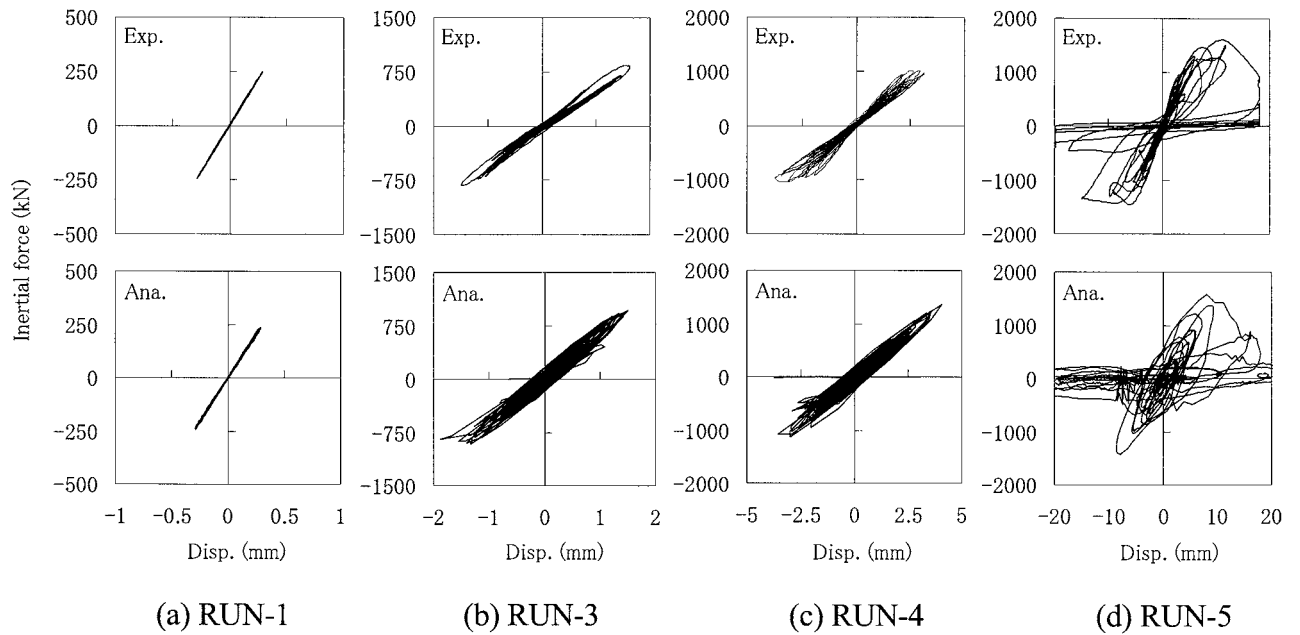


Fig.4 Relationship between inertial force and horizontal displacement of the upper slab

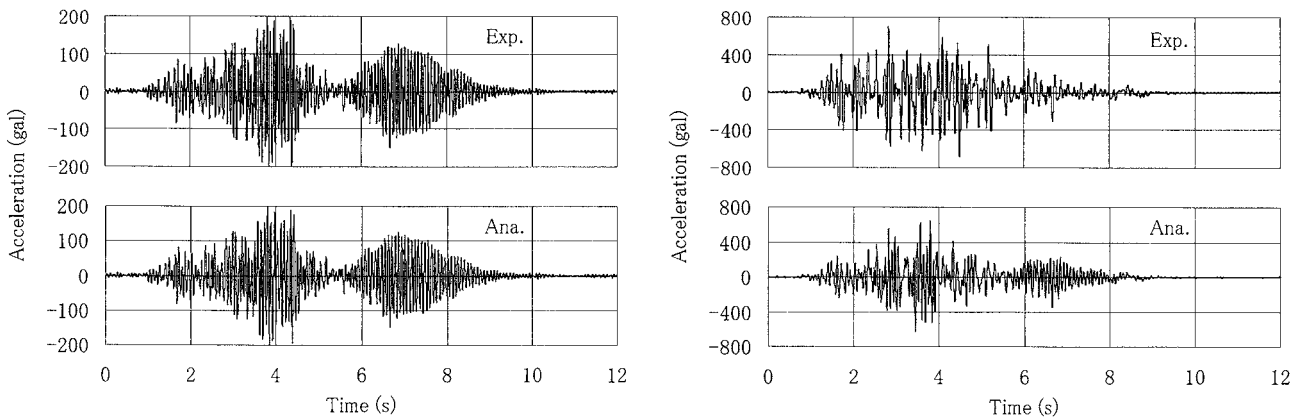
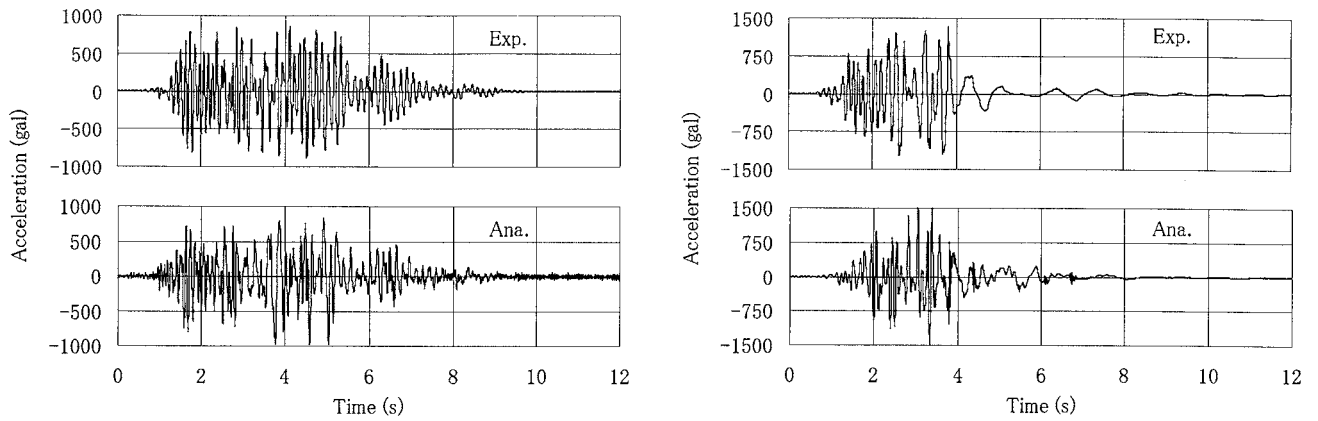


Fig.5 Horizontal response acceleration of the upper slab



(c) RUN-4

(d) RUN-5

Fig.5 Horizontal response acceleration of the upper slab

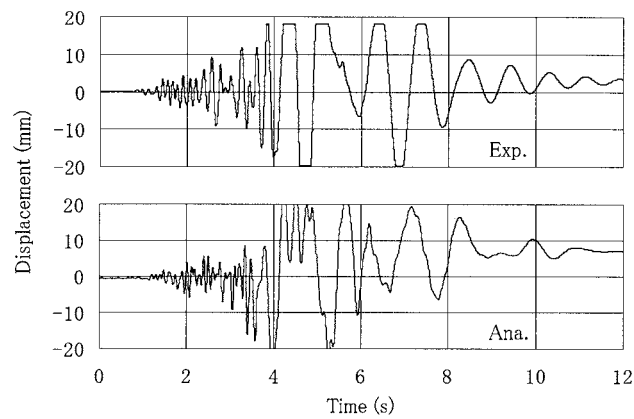
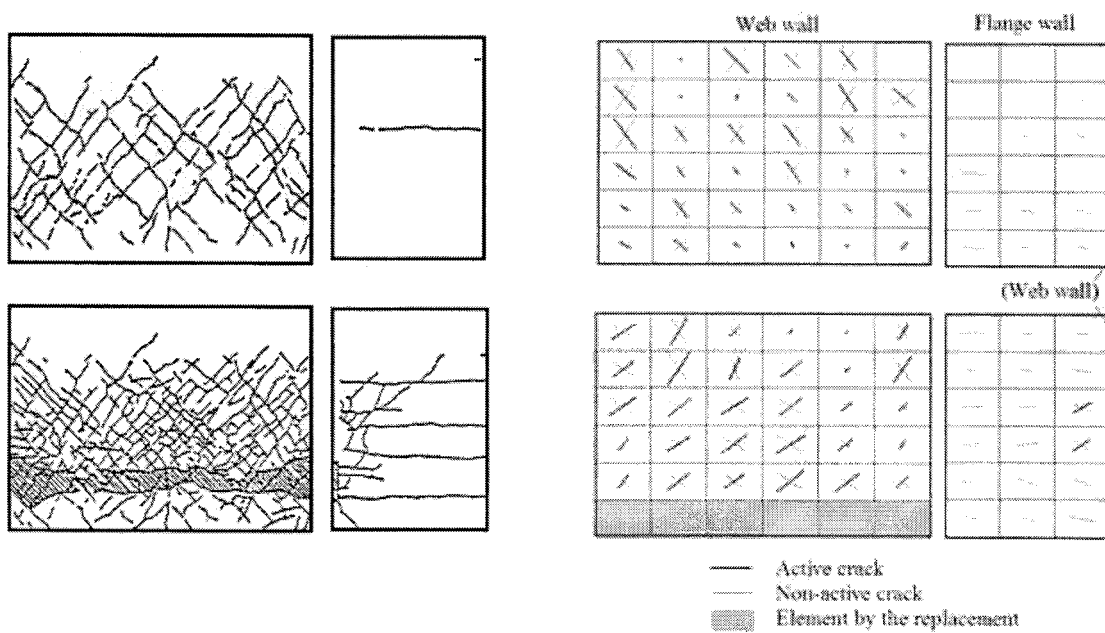


Fig.6 Horizontal response displacement of the upper slab (RUN-5)



(a) Experiment

(b) Analysis

Fig.7 Damage situation (top: after RUN-4, bottom: after RUN-5)

4. CONCLUSIONS

In this research, it was verified whether the behavior of the reinforced concrete structure object damaged in response to the earthquake would be reproducible with the developed simulation system. The verification was performed by carrying out simulation of the vibration test which used an H type shear wall specimen. As a result, the simulation system can be reproducing the experimental result to RUN-5 to which a web wall serves as ultimate failure from RUN-1 of a small response. In order to have the high performance in this system, it became clear that there are some points which must be improved in this system. These points are shown below; 1) An approach to carry over when the disproportionate force becomes large and 2) The failure criterion used for the component with which damage is progressing locally. From now on, we will solve those improving points, in order to increase the dependability of a this system.

Acknowledgements:

Nuclear Power Engineering Corporation, NUPEC provided with the experimental results and committees of the Japan Society for Computational Engineering and Science which obtained advice to this system is gratefully appreciated.

References:

- [1] Maekawa, K., Pimanmas, A. and Okamura, H. : Nonlinear Mechanics of Reinforced Concrete, 2003.

FINITE ELEMENT SIMULATION OF LONG-PERIOD GROUND MOTIONS : THE 1906 SAN FRANCISCO EARTHQUAKE AND JAPANESE SUBDUCTION-ZONE EARTHQUAKES.

Y. Ikegami¹⁾²⁾, K. Koketsu²⁾, T. Kimura²⁾ and H. Miyake²⁾

1) Science and Engineering Systems Div., ITOCHU Techno-Solutions Corp., Japan.

2) Earthquake Research Institute, University of Tokyo, Japan.

yasushi.ikegami@ctc-g.co.jp, koketsu@eri.u-tokyo.ac.jp, tkimura@eri.u-tokyo.ac.jp, hirooe@eri.u-tokyo.ac.jp

Abstract: Large earthquakes at shallow depths often excite long-period ground motions in distant sedimentary basins due to large-scale structures. For example, the 2003 Tokachi-oki, Japan, earthquake damaged oil tanks in the Yufutsu basin 250km away (Koketsu et al., 2005). Similar long-range effects were also observed during the 2004 off Kii-peninsula earthquake (Miyake and Koketsu, 2005). We simulated ground motions of these earthquakes using GeoWAVE which is FEM with a voxel mesh based on Koketsu et al. (2004). Besides, in order to examine whether the 1906 San Francisco earthquake excited long-period ground motions in the Los Angeles basin or not, we performed large-scale ground motion simulations in entire California region.

1. INTRODUCTION

The long-period component of seismic ground motion generated by earthquakes causes damage in near-fault regions through source effects such as the directivity effect of rupture propagation and the near-field term of body wave radiation. In addition, the long-period ground motions attenuate slowly with distance due to some path effects, and site effects amplify them in distant basins, so that they can carry destruction to a much greater range.

Large-scale structures such as tall buildings and big tanks can resonate with the long-period ground motions because their own natural periods are in the same frequency band. They can even be damaging in some circumstances; the worst example with over 20,000 fatalities in Mexico City at a distance of 400 km from the 1985 Michoacan earthquake. A further example was provided by the 2003 Tokachi-oki earthquake in Hokkaido, Japan. (Koketsu et al., 2005)

In this way, shallow & large events often excite long-period ground motions even in distant basins and damage large-scale structures with long natural periods, such as tall buildings and oil tanks. These damaging long-period ground motions are resulted from following three factors as Figure 1. First, shallow & large events generate long-period components of surface waves more than deep or small events. Second, on the path, velocity structures where attenuations of long-period waves are small existance, such as subducting slabs. Finally, these long-period ground motions enter the thick basins and amplified. We show the simulation results of 2003 Tokachi-oki earthquake and 2004 off Kii-peninsula earthquake in Japan.

Besides, we think a relationship between the 1906 S.F. EQ., Central Valley, and the L.A. area basins match to this situation. In order to examine whether the 1906 San Francisco earthquake and the Los Angeles (LA) basin are in such a case or not, we simulate long-period ground motions in almost the entire California caused by the earthquake using the FEM with a voxel mesh (Koketsu et al., 2004).

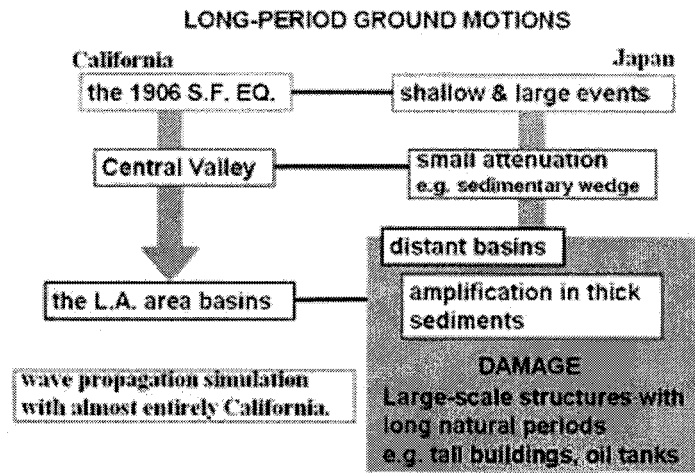


Figure 1. Motivation and Objective.

2. SIMULATIONS

2.1 2003 Tokachi-Oki earthquake (Mw:8.2)

We have simulated the 2003 Tokachi-Oki earthquake simulation to clarify the development of long-period ground motions in Yufutsu basins. The 3D velocity structure model is constructed the layers with V_s larger than 500m/s together with the surface and seabed topography (Geographical Survey Institute, 2004; Japan Oceanographic Data Center, 2004). The source model of the earthquake is constructed according to Koketsu et al 2004. Since we use a mesh intervals of 150m, the voxel FEM can compute seismic waves with periods larger than 3.0sec. The total elements number is about 350 million, which is calculated on PC cluster with 8CPUs.

The Figure 2 shows numerical results. The particle motions of Tomakomai(HKD129) is compared with observation. We can see the particle motions traces is good agreements with calculation and observations. The particle motion analysis helps identify the changing nature of the wave trains. The initial period part of the seismogram (50sec.~85sec.) consists primarily of S waves and surface Rayleigh waves, since the ground motion is polarized in the radial (east-west) direction. The second segment of long-period ground motion, indicated in purple, is polarized in the transverse direction with oval orbits (85sec. ~110sec.). This portion of the seismograms consists mainly of surface Love waves and some other waves associated with the 3D complexity of the basin structure. The maximum ground velocity of the surface waves on the north-south seismograms is 24.4 (cm/s). Finally, the third segment of long-period ground motion(110sec.~200sec.), This portion of the seismograms consists mainly of surface Love waves. Besides, Figure 2 shows the pattern of horizontal ground motion from the numerical simulations calculated by Koketsu et al., 2005. These results show the details of basins amplification which was same as our calculations. In order to see the developments of long-period ground motions by the basins structure effect, we compared with velocity response spectra of NS components at HDKH07 and HKD129. Therefore, we can see the strong excitation of long-period ground motion with period 7.4sec. in the Yufutsu basins.

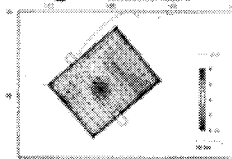
- many oil tanks were damaged.
- two of them caught fire.



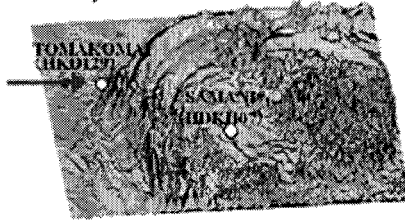
The 3D velocity structure model is constructed the layers with V_s larger than 500m/s together with the surface and seabed topography.



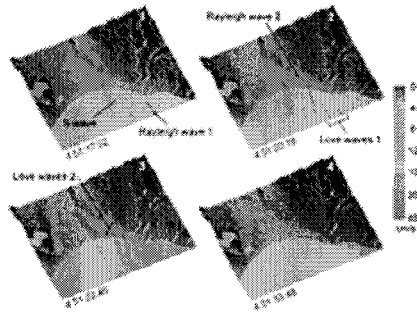
The source model is constructed according to Koketsu et al 2004.



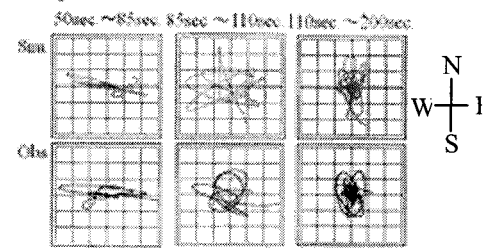
The distribution of ground velocity at 70 sec.



The snapshots of the distribution of simulated horizontal ground velocities around Yufutsu basin calculated by Koketsu et. al, 2005.



The particle motions of TOMAKOMAI compared with observation.



The simulated velocity waveform of TOMAKOMAI and amplification of velocity response spectra ($\ln=5\%$) in the Yufutsu basin.

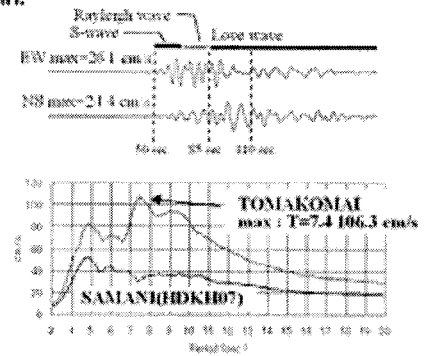


Figure 2. Results of 2003 Tokachi-Oki earthquake.

2.2 2004 off Kii-peninsula earthquak (Mw:7.5)

The 2004 off the Kii-peninsula earthquake excited long-period ground motions over a wide area of Honshu Island of Japan. These remarkable excitations were observed in the Osaka, Nobi, and Kanto basins as well as in the Omaezaki region. We simulate the development of long-period ground motions by passage effects. Since we use a mesh intervals of 450m, the voxel FEM can compute seismic waves with periods larger than 3.0 sec. The total elements number is about 200 million elements, which is calculated on PC cluster with 8 CPUs. Figure 3 shows the effect of sedimentary wedge, the wave propagation results are compared with sedimentary wedge exist or not. Also, comparing waveform at KIHO and KAWAZU. Consequently, we can see the sedimentary wedge has much effects to develop the later phases. Also, the propagation path of long-period ground motions are concentrated on the sedimentary wedge reaching to the Kanto basin. These effects lead to amplification of the long period ground motions in the Kanto basin.

The 3-D velocity structure model is constructed the layers with V_s larger than 1,590 m/s include sedimentary wedge.

The source model of the earthquake is constructed according to Wu et al. (2005).

The effect of sedimentary wedge, the snapshots and waveform at KIIHO and KAWAZU are compared with and without the sedimentary wedge.

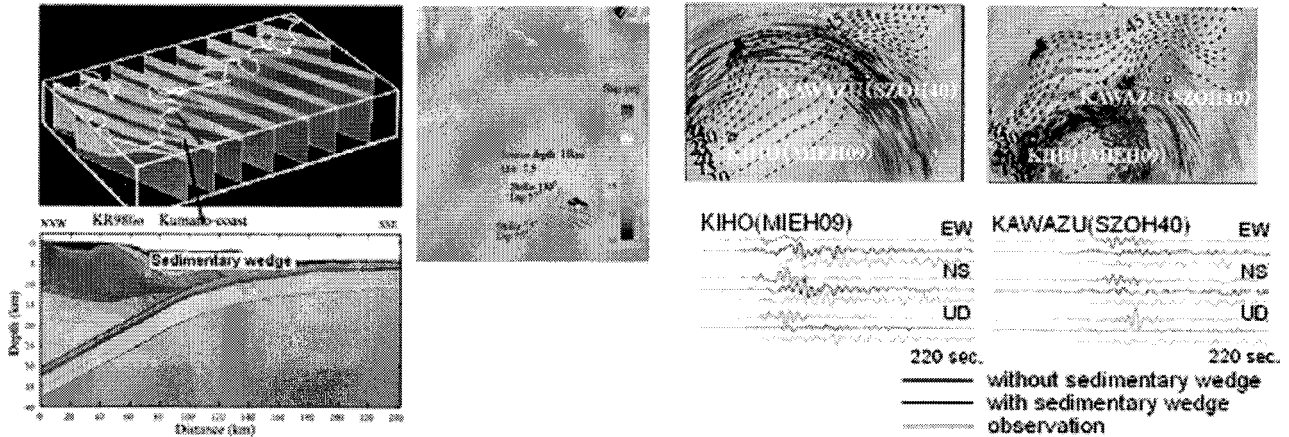


Figure 3. Results of 2004 off the Kii-peninsula earthquake.

2.3 1906 San Francisco earthquake (Mw:7.8)

The 1906 San Francisco earthquake was a major earthquake that struck San Francisco and the coast of northern California at 5:12am on Wednesday, April 18, 1906. The magnitude for the earthquake is Mw 7.8. The mainshock occurred 3 km offshore from the city. It ruptured along the San Andreas fault both northward and southward for a total length of 477 km. As shown in Figure 4 we constructed its source model according to Wald et al.(1993). The depth is assumed around 6 km. 3-D heterogeneous velocity structural model constructed based on the SCEC Unified Velocity Model for southern California and the USGS Bay Area Velocity Model for northern California. This model is constructed the layers with V_s larger than 500 m/s. This model is constructed from the free surface to the depth of 80 km include moho surfaces. Since we use a mesh with intervals of 200m, the voxel FEM can compute seismic waves with period larger than 4 sec. The total elements number is about 280 million elements, which is calculated on PC cluster of 4 nodes with 8 CPUs.

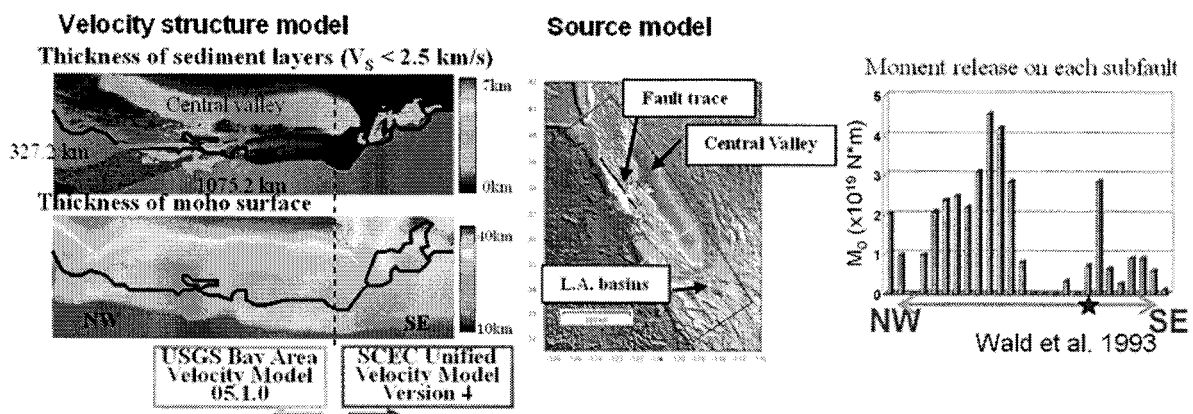


Figure 4 Velocity structure model and source model of 1906 San Francisco earthquake.

As shown in Figure 5 we can see the development of the long-period ground motions along the Central Valley and Los Angeles basin, but not so strong motion radiated to south region because of large asperities exist only north region of hypocenter. However, the particle motions show amplification of the long-period ground motions in the Los Angeles basin.

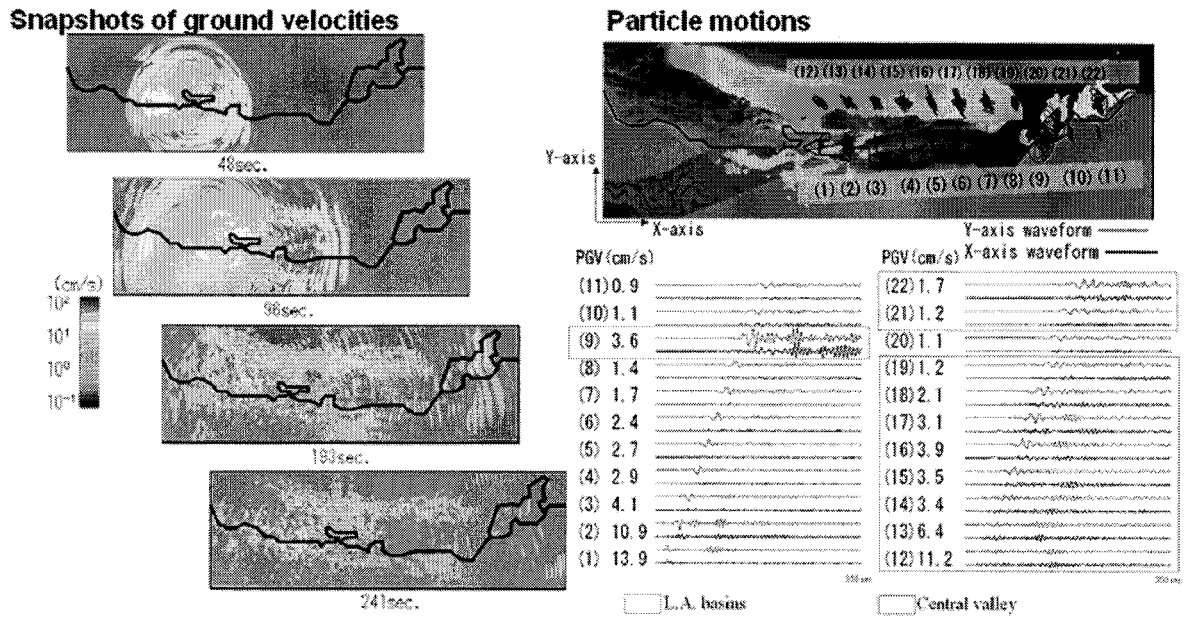


Figure 5 Development of the long-period ground motions along Central Valley and Los Angeles basin.

We show the numerical results for amplification of long-period ground motions in the Los Angeles basin as Figure 6. The maximum velocity response spectra of $T=7.0\text{sec.}$ ($h=5\%$) is 20cm/sec. in Oxnard. Also, we can see the velocity response spectra of $T=7\text{sec.}$ is most excited at Oxnard than outside basins. Ventura and Oxnard are located on the west side of the Los Angeles basin that has deep sediment layer. The distribution of velocity response spectra of $T=7\text{sec.}$ has similar distribution of thickness of sediment of Los Angeles basins.

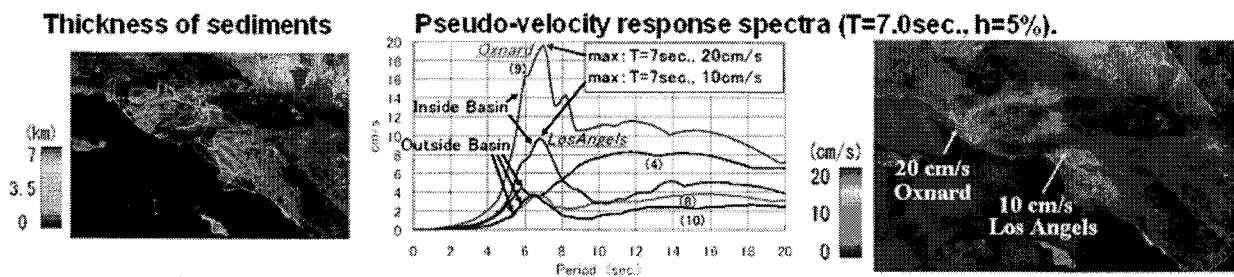


Figure 6 Amplification of the long-period ground motions in Los Angeles basin.

3. DISCUSSION AND CONCLUSIONS

As shown in Figure 7 we can see the two types of developed long period ground motions by the basin surface waves, either by the source or passage effect of the shallow and large offshore earthquake as pointed by Miyake and Koketsu (2005).

Concerning the 1906 San Francisco earthquake, the maximum velocity response of $T=7\text{sec.}$ was excited 20 cm/s at the Los Angel basin. But, these results are not so strong compared with the velocity response at Yufutsu basin during the 2003 Tokachi-Oki earthquake. We consider that weak rupture directivity effects towards the southern direction is one of reasons, because large asperities exist only north region of the hypocenter. If San Andreas fault ruptures towards the south with asperities, the Los Angels basin may be attacked by strong long-period ground motion as the 2003 Tokachi-Oki earthquake.

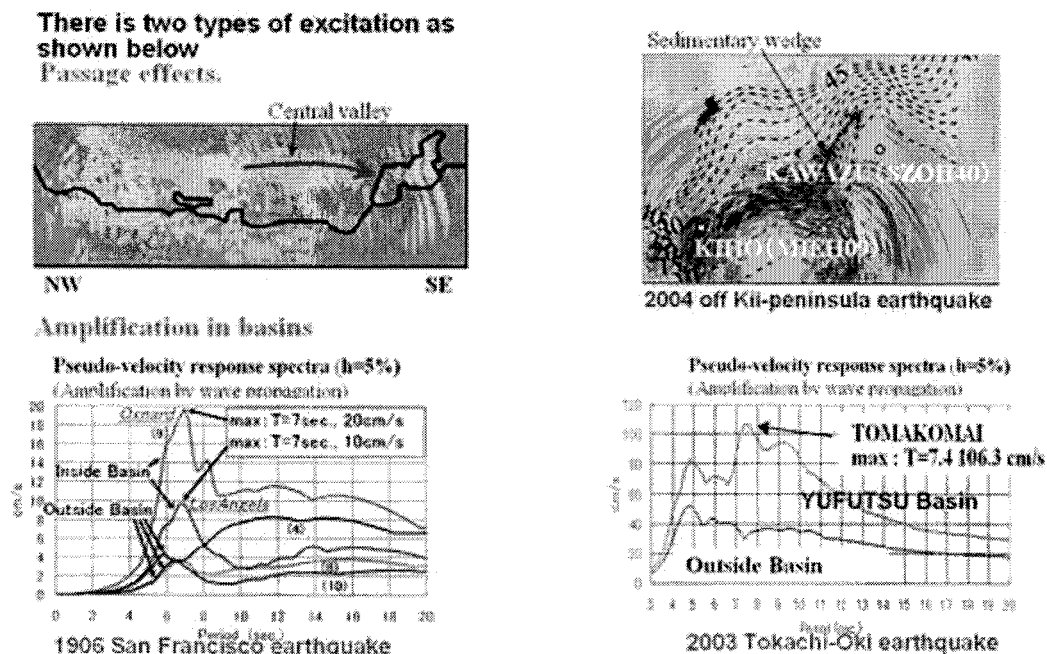


Figure 7 Comparison of the 1906 San Francisco earthquake and Japanese subduction-zone earthquake.

Acknowledgements:

We would like to thank JAMSTEC and NIED for providing 3-D structural model of 2004 off Kii-peninsula earthquake and 2003 Tokachi-Oki earthquake.

References:

- Boatwright, J. and Bundock, H., 2005, Modified Mercalli Intensity maps for the 1906 San Francisco earthquake plotted in ShakeMap format, *U.S. Geological Survey Open File Report* 2005-1135.
- Koketsu, K., Fujiwara, H. and Ikegami, Y., 2004, Finite-element simulation of seismic ground motion with a voxel mesh, *Pure Appl. Geophys.*, 161, 2463-2478.
- Koketsu, K., Hatayama, K., Furumura, T., Ikegami Y. and Akiyama, S., 2005, Damaging long-period ground motions from the 2003 Mw 8.3 Tokachi-oki, Japan, earthquake, *Seism. Res. Lett.*, 76, 67-73.
- Koketsu, K., Hikima, K., Miyazaki, S. Miyazaki and Ide, S., 2004, Joint inversion of strong motion and geodetic data for the source process of the 2003 Tokachi-oki, Hokkaido, earthquake, *Earth Planets Space*, 56, 329-334.
- Miyake, H. and Koketsu, K., 2005, Long-period ground motions from a large off-shore earthquake: The case of the 2004 off the Kii peninsula earthquake., Japan, *Earth Planets Space*, 57, 203-207.
- Wald, D. J., Kanamori, H. Helmberger, D.V. and Heaton, T. H., 2006, Source study of the 1906 San Francisco earthquake, *Bull. Seism. Soc. Am.*, 83, 981-1019.
- Wu, C., Koketsu, K. and Hikima, K., 2005, Rupture processes of the 2004 southeast off Kii-peninsula earthquakes inverted from far-field body waves and strong motion data, *Abstracts of the 2005 JEPS Joint Meeting*, 052-001.

ELASTOPLASTIC BEAM ELEMENT WITH CONSIDERATION OF LOCAL BUCKLING BEHAVIOR

K. Kaneko¹⁾ and S. Motoyui²⁾

1) Post-doctoral fellow of COE, Dept. of Built Environment, Tokyo Institute of Technology, Japan

*2) Assoc. Prof., Dept. of Built Environment, Tokyo Institute of Technology, Japan
kensaku@enveng.titech.ac.jp, motoyui@enveng.titech.ac.jp*

Abstract: This paper proposes the plasticity model which evaluates local inelastic behavior for beam-columns subjected to axial force and biaxial bending moment. In this paper, we present the beam element composed of fibers along axis of the element. First, the model describes the three dimensional plastic region represented by plastic regions with one dimensional expansion of plastic regions in each fiber. It is clarified how basic equations (the yield function, the plastic flow rule and the hardening rule should be formulated) in bilinear stress-strain relation. Finally, a convenient method to evaluate local buckling is mentioned and some numerical examples are shown to examine the validity of the proposed method.

1. INTRODUCTION

Recent development of numerical simulation methods for simulating collapse mechanism of structures are classified into these two following categories. The first one is for two or three dimensional elements such as solid and shell elements, which are specifically designed to show non-linear behavior of structures in a comprehensive manner. The second one is for one-dimensional element, which is widely used in frames, in which members are treated as one-dimensional element along their axis. Analytical methods using one-dimensional finite element such as beam elements is computationally efficient to know behavior of whole frames.

Analysis based on one-dimensional finite elements is surely accurate, the number of total degrees of freedom in the global stiffness matrix surge due to the element division. Moreover, it is difficult to characterize local buckling, which is crucial for degradation of the members. The one element methods which are categorized into the plastic hinge model or the multi-spring model are extensively employed not only in design fields but also research fields.

It is not clear how expansion of plastic regions influences member's behavior and how it should be treated in the plastic hinge model or the multi-spring model. These vague points should be clarified because maximum strengths of the structures can be overestimated without considering expansion of the plastic region^{1), 2)}. In this paper, we propose the beam element to account for expansion of plastic region. At this point, the yield criterion, the associated flow rule and the hardening rule in the form of nodal forces is derived from assuming ones in the form of stresses by using the same procedure the author have already showed for the two flange model⁷⁾. The proposed beam element is extended to assess flange local buckling behavior for H-shaped steel beams. The numerical simulations performed on the basis of the finite element method support the good predictive capabilities of the proposed model.

2. CONCEPT OF MACRO MODEL FOR BEAM ELEMENT

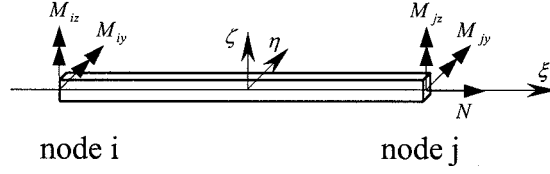


Fig. 1 Analysis model (simple beam)

The displacements in a beam are decomposed to rigid motion and relative displacements (deformation), which are assumed to be infinitesimal. We introduce co-ordinate system $(O-x, y, z)$ and $(O-\xi, \zeta, \eta)$ moving with the rigid motion of the beam. The geometric nonlinearity due to finite rotations is considered by the coordinate transformation. In this paper, the co-rotational beam element is formulated, which is based on the relative displacements.

Consider the beam element with the cross section area A , the moment of inertia around y, z axis I_y, I_z and the length of the element along its axis L . Let θ_{yi}, θ_{zi} be the nodal displacements around y, z axis at the node-i, θ_{yj}, θ_{zj} at the node-j and u the stretch of the element. Let the nodal forces be $\{N, M_{yi}, M_{zi}, M_{yj}, M_{zj}\}$ corresponding to the nodal displacements $\{u, \theta_{yi}, \theta_{zi}, \theta_{yj}, \theta_{zj}\}$. For torsion, the beam is assumed to behave elastically and the corresponding displacements are omitted for simplicity. Material is elastic plastic body with combined hardening (kinematic and isotropic), the yield function is based on von Mises criterion function and the plastic flow rule is the associative flow rule. The Helmholtz free energy function ψ , the yield function ϕ is expressed in the following form.

$$\psi = \frac{1}{2}E(\varepsilon - \varepsilon^p)^2 + \frac{1}{2}E^K \varepsilon^K^2 + \frac{1}{2}E^I \varepsilon^I{}^2, \quad \phi = \frac{|\sigma - \sigma^K|}{\sigma_Y} - \left(1 + \frac{\sigma^I}{\sigma_Y}\right) \leq 0 \quad (1a, b)$$

The basic equations in plasticity theory are derived from eq(1) as follows.

$$\text{(elastic constitutive equation)} \quad \sigma = E(\varepsilon - \varepsilon^p) \quad (2a)$$

$$\text{(plastic flow rule)} \quad \dot{\varepsilon}^p = \frac{\partial \phi}{\partial \sigma} \dot{\gamma}^p, \quad \dot{\varepsilon}^K = \frac{\partial \phi}{\partial \sigma^K} \dot{\gamma}^p, \quad \dot{\varepsilon}^I = \frac{\partial \phi}{\partial \sigma^I} \dot{\gamma}^p \quad (2b-d)$$

$$\text{(hardening rule)} \quad \dot{\sigma}^K = -E^K \dot{\varepsilon}^K, \quad \dot{\sigma}^I = -E^I \dot{\varepsilon}^I \quad (2e, f)$$

$$\text{(Kuhn-Tucker condition)} \quad \phi \leq 0, \quad \phi \dot{\gamma}^p = 0, \quad \dot{\gamma}^p \geq 0 \quad (2g, h)$$

where $\varepsilon, \varepsilon^p$ are the total and plastic strain; $\varepsilon^K, \varepsilon^I$ are the kinematic and isotropic hardening strain. $\sigma, \sigma^K, \sigma^I$ are the stress, the kinematic and isotropic stress respectively; σ_Y is the yield stress. E, E^K, E^I are the Young's modulus, the kinematic and isotropic hardening coefficient.

Total Helmholtz free energy for the beam is obtained by volume integral of eq(1).

$$\Psi = \int_X \int_A \psi(\xi, \eta, \zeta, \varepsilon, \varepsilon^p, \varepsilon^K, \varepsilon^I) dA d\xi \quad (3)$$

where $X = [-\frac{1}{2}, \frac{1}{2}]$. From the assumption of Bernoulli-Euler, the elastic constitutive equations expressed by the resultant stress are written as

$$N = EA \left(e - \frac{1}{A} \int_A \varepsilon^p dA \right), \quad M_y = EI_y \left(k_y - \frac{1}{I_y} \int_A B_z \zeta \varepsilon^p dA \right), \quad M_z = EI_z \left(k_z - \frac{1}{I_z} \int_A B_y \eta \varepsilon^p dA \right) \quad (4)$$

In the above form, the plastic components of the generalized strains should be defined as follows.

$$\mathbf{e}^p = \frac{1}{A} \int_A \boldsymbol{\varepsilon}^p(\eta, \zeta) dA, \quad k_y^p = \frac{1}{I_y} \int_A B_z \zeta \boldsymbol{\varepsilon}^p(\eta, \zeta) dA, \quad k_z^p = \frac{1}{I_z} \int_A B_y \eta \boldsymbol{\varepsilon}^p(\eta, \zeta) dA \quad (5)$$

Alternative form of Ψ is expressed by substituting eq(5) into eq.(3).

$$\Psi = W^e + H, \quad W^e = W^{e1} + W^{e2} \quad (6a, b)$$

$$W^{e1} = \int_x \frac{1}{2} (\mathbf{e} - \mathbf{e}^p)^T \mathbf{k}^e (\mathbf{e} - \mathbf{e}^p) L d\xi, \quad W^{e2} = \int_x \left(-\frac{1}{2} \mathbf{e}^{pT} \mathbf{k}^e \mathbf{e}^p + \frac{1}{2} E \int_A \boldsymbol{\varepsilon}^{p2} dA \right) L d\xi \quad (6c, d)$$

$$H = \int_x \left(\frac{1}{2} E^K \int_A \boldsymbol{\varepsilon}^{K2} dA + \frac{1}{2} E^I \int_A \boldsymbol{\varepsilon}^{I2} dA \right) L d\xi \quad (6e)$$

where the generalized strains $\mathbf{e}^T = \langle e \quad k_y \quad k_z \rangle$ and the resultant stress $\mathbf{s}^T = \langle N \quad M_y \quad M_z \rangle$. W^e is the total elastic stored energy. It should be noted that the additional component exists besides the elastic energy represented by the quadratic form in the exact form of the total elastic stored energy. W^{e2} represents the part of the elastic stored energy stored by statically indeterminate stresses.

3. ELASTOPLASTIC ANALYSIS OF BEAM

3.1 Analysis model

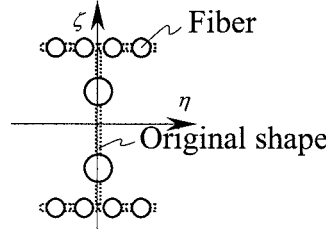


Fig. 2 Division of cross section (H-shaped)

Consider the idealized cross section composed of n fibers with area $A_{(r)}$ ($r=1,2,\dots,n$), in which the stresses are uniform. Let $\boldsymbol{\varepsilon}_{(r)} = \boldsymbol{\varepsilon}(\xi, \eta_{(r)}, \zeta_{(r)})$ be the strain of each fiber. The procedure presented in the foregoing section is extended to the assessment of the nodal forces. As shown in Fig. 2, consider the beam element with the idealized cross section mentioned previously. In this formulation, the plastic regions spread in the fiber one-dimensionally from the start point $\xi_{k(r)}^s$ to the end point $\xi_{k(r)}^e$, which prescribe the plastic regions $X_{i(r)}^p = [\xi_{i(r)}^s, \xi_{i(r)}^e]$ at the node-i and $X_{j(r)}^p = [\xi_{j(r)}^s, \xi_{j(r)}^e]$ at the node-j side. Let $\xi_{k(r)}^c$ be the center position of the plastic region and $L_{\xi_{k(r)}^p}$ the length of the plastic region, in which the subscripts k, r in $\xi_{k(r)}^c, \xi_{k(r)}^s, \xi_{k(r)}^e$ ($k=i, j, r=1, \dots, n$) denotes an index for node-i, j of the element and an index for each fiber, this manner evaluate the three-dimensional spread of plastic regions as shown in Fig. 3.

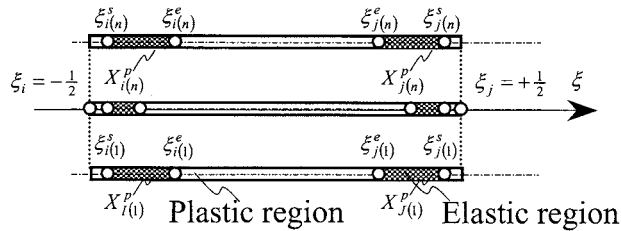


Fig. 3 Definition of plastic region(2D)

3.2 Plastic flow rule

Motivated by the plastic hinge method, the relative displacements in the element are split to the elastic component and the plastic component while the length of the plastic region is infinitesimal and plastic deformation is concentrated in the zero length. Let $\mathbf{f}^T = \langle N \quad M_{yi} \quad M_{zi} \quad M_{yj} \quad M_{zj} \rangle$ be

the nodal forces and the nodal displacements $\mathbf{u}^T = \langle u \ \theta_{yi} \ \theta_{zi} \ \theta_{yj} \ \theta_{zj} \rangle$. Assuming the relative displacement components are infinitesimal, resultant stress distribution $s(\xi)$ is expressed in the following manner.

$$\mathbf{s} = \mathbf{A}^T \mathbf{f}, \quad \mathbf{A}^T = \begin{bmatrix} 1 & 0 & 0 & 0 & 0 \\ 0 & -(\xi_i + \xi) & 0 & -(\xi_j + \xi) & 0 \\ 0 & 0 & -(\xi_i + \xi) & 0 & -(\xi_j + \xi) \end{bmatrix} \quad (7)$$

Then the elastic constitutive equation and the compatibility condition are derived.

$$\mathbf{f} = \mathbf{K}^e (\mathbf{u} - \mathbf{u}^p), \quad \mathbf{u}^p = \int_X \mathbf{A}(\xi) \mathbf{e}^p(\xi) L d\xi \quad (8)$$

It is understood that the plastic flow rule is determined by only the terms integrated in eq(42) and eq(43). Therefore, we define new plastic parameters.

$$\dot{\Lambda}_{k(r)}^p \equiv \int_{X_{k(r)}^p} \dot{\gamma}_{(r)}^p(\xi) A_{(r)} L d\xi, \quad \dot{\Lambda}_{k(r)}^\mu \equiv \int_{X_{k(r)}^p} (\xi_{k(r)}^s - \xi) \dot{\gamma}_{(r)}^p(\xi) A_{(r)} L d\xi \quad (9)$$

where $\dot{\Lambda}_{k(r)}^p, \dot{\Lambda}_{k(r)}^\mu$ are total amount of plastic dissipation rate and 1st moment of plastic dissipation rate at the k node in the r fiber respectively. The Kuhn-Tucker condition leads to the inequality $\dot{\Lambda}_{k(r)}^p \geq 0, \dot{\Lambda}_{k(r)}^\mu \leq 0$ and $\dot{\Lambda}_{k(r)}^\mu \geq 0$. The plastic flow rules for the nodal displacements are more simply expressed by substituting eq(5) into eq(2) and eq(8).

$$\dot{\mathbf{u}}^p = \sum_{k=1}^n \sum_{r=1}^n \mathbf{C}_{k(r)} \dot{\Lambda}_{k(r)}, \quad \dot{\mathbf{u}}_{k(r)}^K = -\mathbf{C}_{kk(r)} \dot{\Lambda}_{k(r)}, \quad \dot{\mathbf{u}}_{k(r)}^I = -\text{sgn} \sigma_{k(r)} \mathbf{C}_{kk(r)} \dot{\Lambda}_{k(r)} \quad (10)$$

The matrices $\mathbf{C}_{kl(r)}$ and $\mathbf{C}_{k(r)}$ are expressed as

$$\mathbf{C}_{kl(r)} = \begin{bmatrix} \delta_{kl} \frac{\partial \phi_{l(r)}}{\partial N} & 0 \\ \bar{\xi}_{kl(r)} \frac{\partial \phi_{l(r)}}{\partial M_y} & \frac{\partial \phi_{l(r)}}{\partial M_y} \\ \bar{\xi}_{kl(r)} \frac{\partial \phi_{l(r)}}{\partial M_z} & \frac{\partial \phi_{l(r)}}{\partial M_z} \end{bmatrix}, \quad \mathbf{C}_{k(r)} = \begin{bmatrix} \frac{\partial \phi_{k(r)}}{\partial N} & 0 \\ \bar{\xi}_{ik(r)} \frac{\partial \phi_{k(r)}}{\partial M_y} & \frac{\partial \phi_{k(r)}}{\partial M_y} \\ \bar{\xi}_{ik(r)} \frac{\partial \phi_{k(r)}}{\partial M_z} & \frac{\partial \phi_{k(r)}}{\partial M_z} \\ \bar{\xi}_{jk(r)} \frac{\partial \phi_{k(r)}}{\partial M_y} & \frac{\partial \phi_{k(r)}}{\partial M_y} \\ \bar{\xi}_{jk(r)} \frac{\partial \phi_{k(r)}}{\partial M_z} & \frac{\partial \phi_{k(r)}}{\partial M_z} \end{bmatrix}, \quad \mathbf{C}'_{kk(r)} = \mathbf{C}_{kk(r)} + \begin{bmatrix} 0 & 0 & \bar{\xi}_{kk} \frac{\partial \phi_{k(r)}}{\partial N} \\ 0 & 0 & 0 \\ 0 & 0 & 0 \end{bmatrix}$$

$$\mathbf{A}_{k(r)}^T = \langle \Lambda_{k(r)}^p \quad \Lambda_{k(r)}^\mu \rangle \quad \delta_{kl} : \text{Kronecker's delta} \quad (11a-d)$$

where $\phi_{k(r)}$ is a yield function in the r -th fiber at the node- k of the beam. It should be noted that plastic deformation influence on both of the nodal plastic rotations while it is neglected in the conventional plastic hinge model. As the plastic region spreads, this coupled effect would be larger.

3.3 Yield function and constraints

It is discussed to derive the constraint conditions including the yield criterions for this beam element. By analogy with the finite element method based on displacements, the generalized plastic may be expressed in the form.

$$\dot{\mathbf{e}}_{(r)}^K(\xi) = \mathbf{B}_{k(r)}^p(\xi) \dot{\mathbf{u}}_{k(r)}^K, \quad \dot{\mathbf{e}}_{(r)}^I(\xi) = \mathbf{B}_{k(r)}^p(\xi) \dot{\mathbf{u}}_{k(r)}^I, \quad \dot{\mathbf{e}}_{(r)}^p(\xi) = \hat{\mathbf{B}}_{k(r)}^p(\xi) \dot{\mathbf{u}}_{k(r)}^p \quad (\xi \in X_{k(r)}^p) \quad (12a-c)$$

$\mathbf{B}_{k(r)}^p, \hat{\mathbf{B}}_{k(r)}^p$ correspond to the strain-displacement matrix in the finite element method. $\mathbf{s}_{k(r)}^K, \mathbf{s}_{k(r)}^I$ represent the forces prescribing kinematic and isotropic hardening in the nodal force. The

hardening rules are expressed by taking derivative with respect to time in the following form.

$$\dot{\mathbf{s}}_{k(r)}^R = \sum_{s=1}^n \mathbf{k}_{k(rs)}^p \dot{\mathbf{u}}_{k(s)}^p, \quad \dot{\mathbf{s}}_{k(r)}^K = -\mathbf{k}_{k(r)}^K \dot{\mathbf{u}}_{k(r)}^K, \quad \dot{\mathbf{s}}_{k(r)}^I = -\mathbf{k}_{k(r)}^I \dot{\mathbf{u}}_{k(r)}^I \quad (13a-c)$$

in which

$$\mathbf{k}_{k(rs)}^p = \delta_{rs} \int_X \hat{\mathbf{B}}_{k(r)}^p{}^T \mathbf{k}_{k(s)}^p \hat{\mathbf{B}}_{k(s)}^p L d\xi - \int_{X_{(r)}^p \cap X_{(s)}^p} \hat{\mathbf{B}}_{k(r)}^p{}^T \mathbf{k}^e \hat{\mathbf{B}}_{k(s)}^p L d\xi \quad (14a)$$

$$\mathbf{k}_{k(r)}^K = \int_{X_{k(r)}^p} \mathbf{B}_{k(r)}^p{}^T(\xi) \mathbf{k}_{k(r)}^K \mathbf{B}_{k(r)}^p(\xi) L d\xi, \quad \mathbf{k}_{k(r)}^I = \frac{E^I}{E^K} \mathbf{k}_{k(r)}^K \quad (14b, c)$$

When the rate of plastic parameter vary linearly along the axis of the fiber in each plastic regions is assumed, the hardening matrices are expressed in the form of

$$\mathbf{k}_{k(r)}^K = \frac{E^K}{L(\frac{1}{2}\xi_{k(r)}^p)^3} \frac{A}{2A_{(r)}} \begin{bmatrix} A\left\{(\xi_k + \xi_{k(r)}^c)^2 + (\frac{1}{2}\xi_{k(r)}^p)^2\right\} & 3\frac{\bar{Z}_{y(r)}(\xi_k + \xi_{k(r)}^c)}{2\xi_{(r)}} & 3\frac{\bar{Z}_{z(r)}(\xi_k + \xi_{k(r)}^c)}{2\eta_{(r)}} \\ 3\frac{\bar{Z}_{y(r)}(\xi_k + \xi_{k(r)}^c)}{2\xi_{(r)}} & 3\frac{\bar{Z}_{y(r)}\bar{Z}_{y(r)}}{A(2\xi_{(r)})(2\xi_{(r)})} & 3\frac{\bar{Z}_{y(r)}\bar{Z}_{z(r)}}{A(2\xi_{(r)})(2\eta_{(r)})} \\ 3\frac{\bar{Z}_{z(r)}(\xi_k + \xi_{k(r)}^c)}{2\eta_{(r)}} & 3\frac{\bar{Z}_{z(r)}\bar{Z}_{y(r)}}{A(2\eta_{(r)})(2\xi_{(r)})} & 3\frac{\bar{Z}_{z(r)}\bar{Z}_{z(r)}}{A(2\eta_{(r)})(2\eta_{(r)})} \end{bmatrix} \quad (15a)$$

$$\mathbf{k}_{k(r)}^I = \frac{E^I}{E^K} \mathbf{k}_{k(r)}^K \quad (15b)$$

where

$$\bar{Z}_{y(r)} = \frac{Z_y Z_z^2 \xi_{(r)}^2}{Z_y^2 \eta_{(r)}^2 + Z_z^2 \xi_{(r)}^2}, \quad \bar{Z}_{z(r)} = \frac{Z_y^2 Z_z \eta_{(r)}^2}{Z_y^2 \eta_{(r)}^2 + Z_z^2 \xi_{(r)}^2} \quad (16a, b)$$

Note that proper small values should be added to the coordinate values to of the fiber which is zero to avoid to be divided by zero in case of $\eta_{(r)} = 0$ or $\xi_{(r)} = 0$. Considering the Kuhn-Tucker condition and the expression: $\dot{\mathbf{A}}_{k(r)} = \mathbf{I}_1 \cdot \dot{\mathbf{A}}_{k(r)} (\mathbf{I}_1^T = \langle 1 \ 0 \rangle)$, the constraint conditions are obtained during plastic loading.

$$\dot{\phi}_{k(r)} = \mathbf{C}_{k(r)}^T \dot{\mathbf{f}} - \mathbf{C}_{kk(r)}^T \dot{\mathbf{s}}_{k(r)}^R - \mathbf{C}_{kk(r)}^T (\dot{\mathbf{s}}_{k(r)}^K + \text{sgn} \sigma_{k(r)} \dot{\mathbf{s}}_{k(r)}^I) - \mathbf{I}_1 = \mathbf{0} \quad \text{for } \dot{\mathbf{A}}_{k(r)}^p > 0 \quad (17)$$

From the plastic loading condition: $\dot{\phi}_{k(r)} = \mathbf{0}$, the following simultaneous equation is given. Using this solution, we obtain the elasto-plastic stiffness matrix (tangent stiffness matrix) of the beam element.

$$\dot{\mathbf{f}} = \mathbf{K}^{ep} \dot{\mathbf{u}}, \quad \mathbf{K}^{ep} = \begin{cases} \mathbf{K}^e & \text{(elastic response)} \\ \mathbf{K}^e - \sum_{k,l \in \text{active}} \sum_{r,s \in \text{active}} (\mathbf{K}^e \mathbf{C}_{k(r)}) \mathbf{G}^{kl(rs)} (\mathbf{K}^e \mathbf{C}_{l(s)})^T & \text{(plastic response)} \end{cases} \quad (18a, b)$$

As the number of the loading reference point increase, time to calculate the nodal forces and the tangent stiffness matrix is expected to become longer. This advantage serves in dynamic analysis, in which the members is repeatedly plastic loading and elastic unloading.

4. ASSESSMENT OF LOCAL BUCKLING BEHAVIOR

In this chapter, the assessment of flange local buckling behavior for the H-shaped beam subjected an axial force and bending about the major axis is proposed in the limitation of elastic-perfectly plastic materials. In order to clarify the assessment of flange local buckling behavior, a mechanical model composed of fibers with rectangular shapes is proposed for plastic buckling behavior of the flange part. These fibers, which are constrained at the each end as shown

in Fig. 4, is assumed to deform laterally by a quantity ω as shown in Fig. 5. Although in the stress field of the flange plate, multi-axial stresses take place unlike bars, the proper change rule of ω is assumed to simulate the complex multi-axial stress field. Considering fully-plastic state holds in the direction of thickness after the plate yields and buckles, the $n - m$ correlation function at ultimate strength may be employed as the yield criterion in the form of

$$\phi = \frac{|n|}{n_y} + \kappa \frac{|m|}{m_p} - 1 \leq 0, \quad \kappa \geq 0 \quad (19)$$

in which n_y, m_p is the yield axial force and the fully plastic moment of the fiber. The plate with width b and thickness t is divided into the rectangle fibers with $b_{(r)}$ ($r = 1, 2, \dots, n$) width and t thickness. Basic equations are given by

$$(\text{Free energy}) \quad \psi_{(r)} = \left\{ \frac{1}{2} \frac{E a_{(r)}}{l^b/2} \left(\frac{\tilde{u}_{(r)}}{2} - \frac{\tilde{u}_{(r)}^p}{2} - \frac{\tilde{u}_{(r)}^b(\tilde{\theta}_{(r)})}{2} \right)^2 + \frac{1}{2} k_{(r)}^M (\tilde{\theta}_{(r)} - \tilde{\theta}_{(r)}^p)^2 \times 2 \right\} \times 2 \quad (20a)$$

$$(\text{Stiffness of rotary spring}) \quad k_{(r)}^M = \frac{6ED_{(r)}b_{(r)}}{l^b/2}, \quad a_{(r)} = b_{(r)}t, \quad D_{(r)} = \frac{t^3}{12(1-\nu^2)} \quad (20b-d)$$

$$(\text{stretch due to lateral displacement}) \quad \frac{\tilde{u}_{(r)}^b}{2} = -\frac{1}{2} \frac{l^b}{2} \tilde{\theta}_{(r)}^2 \quad (20e)$$

$$(\text{yield function}) \quad \phi_{(r)} = \text{sgn}(n_{(r)}) \frac{n_{(r)}}{n_{y(r)}} - \left(1 - \kappa_{(r)} \left| \frac{m_{(r)}}{m_{p(r)}} \right| \right) \leq 0, \quad \kappa_{(r)} > 0 \quad (20f)$$

$$(\text{elastic constitutive equation}) \quad n_{(r)} = \frac{E a_{(r)}}{l^b} (\tilde{u}_{(r)} - \tilde{u}_{(r)}^p), \quad m_{(r)} = k_{(r)}^M (\tilde{\theta}_{(r)} - \tilde{\theta}_{(r)}^p) \quad (20g, h)$$

$$(\text{plastic flow rule}) \quad \tilde{u}_{(r)}^p = \frac{\partial \phi_{(r)}}{\partial n_{(r)}} \dot{\lambda}_{(r)}^p, \quad \tilde{\theta}_{(r)}^p = \frac{1}{4} \frac{\partial \phi_{(r)}}{\partial m_{(r)}} \dot{\lambda}_{(r)}^p \quad (20i, j)$$

in which the subscript $k(r)$ signifies r fiber at k node. l_k^b is the buckling length (length of plastic region). $\omega_{k(1)}, \omega_{k(2)}$ are generalized displacements for local buckling models.

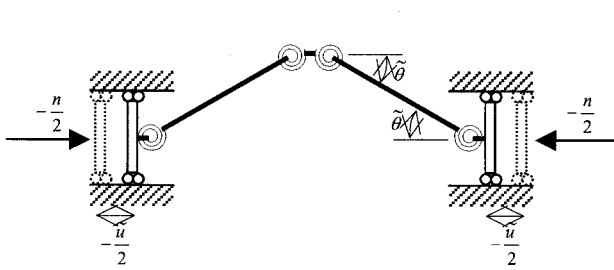


Fig. 4 Fiber involving lateral displacement (buckling model)

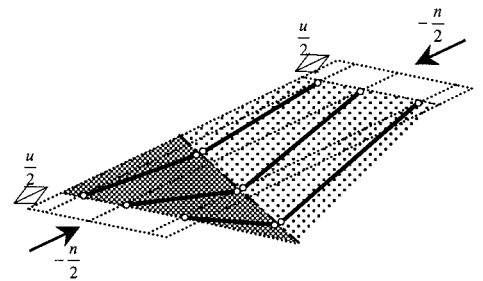


Fig. 5 Plate model

If the flanges buckle, the buckling flange and the corresponding web are deflected. Deflections in the flange are assumed to vary with coordinate η while a deflection in the web is assumed to be a cubic function.

$$\tilde{\theta}_{k(r)} = \begin{cases} |\eta_{(r)}| \omega_{k(1)} & (\text{lower flange}) \\ 0 & (\text{upper flange}) \\ \frac{B_z}{B_y} \left(\zeta_{(r)} - \frac{1}{2} \right)^2 \left(\zeta_{(r)} + \frac{1}{2} \right) \omega_{k(1)} & (\text{web}) \end{cases}, \quad \tilde{\theta}_{k(r)} = \begin{cases} 0 & (\text{lower flange}) \\ |\eta_{(r)}| \omega_{k(2)} & (\text{upper flange}) \\ -\frac{B_z}{B_y} \left(\zeta_{(r)} + \frac{1}{2} \right)^2 \left(\zeta_{(r)} - \frac{1}{2} \right) \omega_{k(2)} & (\text{web}) \end{cases} \quad (21a, b)$$

If both of the flange buckle, eq(21a) and eq(21b) are combined lineally.

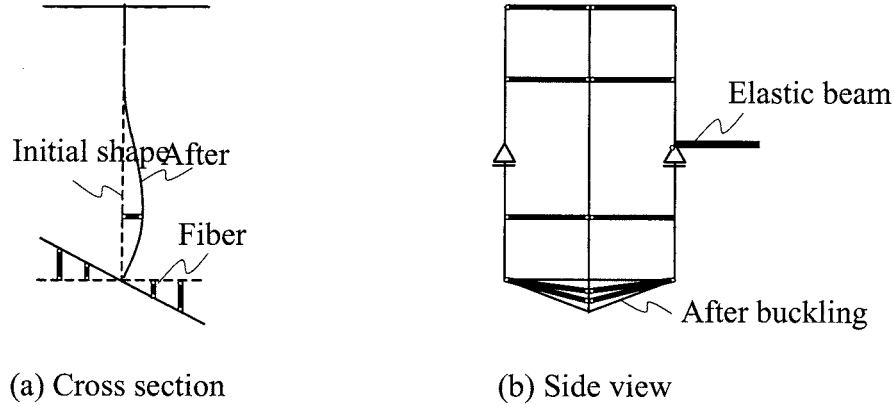


Fig. 6 Hinge model involving local buckling

In case of lower flange buckling, considering the plate with relatively small slenderness ratio, rotation rate $\dot{\omega}$ can be given in the form of

$$\dot{\omega} = -\frac{1}{\sigma_y \frac{1}{2} l^b \bar{\omega}} p \left(\frac{u}{u_{cr}}, \frac{l^b}{b} \right) \sum_{s \in active} \frac{d\tilde{\theta}_{(s)}}{d\omega} \frac{\partial \phi_{(s)}^{pb}}{\partial \tilde{\theta}_{(s)}} \dot{\lambda}_{(s)}^p \quad \text{for } |u^p| \geq u^{cr} (u^p \leq 0) \quad (22)$$

where p is a reduction factor identified through the results obtained by finite element analysis. The constraints involving local buckling are expressed in the following form.

$$\Phi_{k(r)}^{pb} = \left(1 + \chi_{k(r)} \tilde{\theta}_{k(r)} \right) \mathbf{d}_{k(r)}^T \mathbf{s}_{k(r)}^{eff} - 1 \leq 0, \quad \mathbf{s}_{k(r)}^{eff} = \mathbf{A}_k^T \mathbf{f} - \mathbf{s}_k^{p1} - \mathbf{s}_k^{p2} \quad (23a, b)$$

5. NUMERICAL EXAMPLE

The proposed model is used to predict the response of the finite element method. An analytical model is an H-shaped beam, which is stiffened at the middle of the axis to avoid lateral buckling. In the proposed model, the buckling length l_k^b is given by $l_k^b = B_y$. Displacements are applied at the i-node and $M=0$ holds at the j-node. Two numerical examples are carried out for the case of relatively large and low axial force. Fig.7, 8 shows numerical results, in which the plots signify the result obtained by the proposed model and the solid lines represent the finite element method. The numerical simulations performed on the basis of these data support the good predictive capabilities of the proposed model.

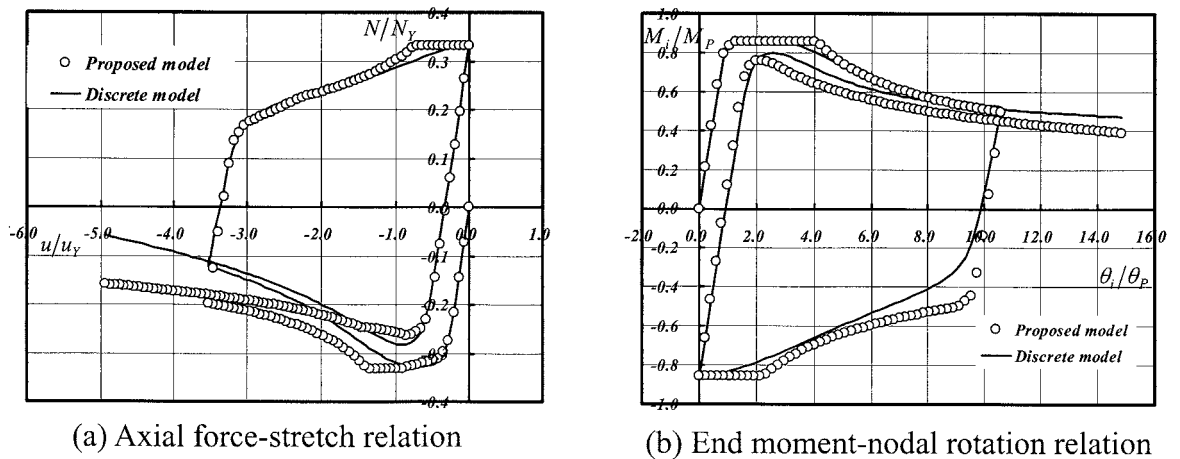
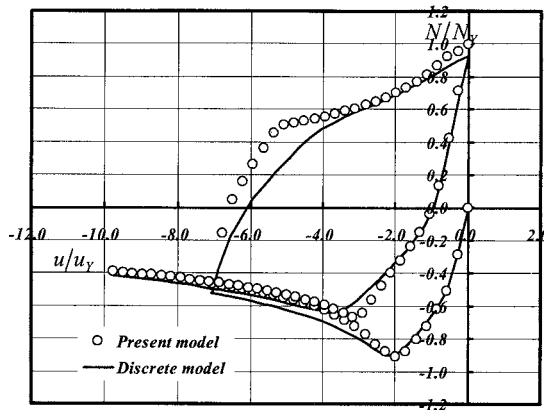
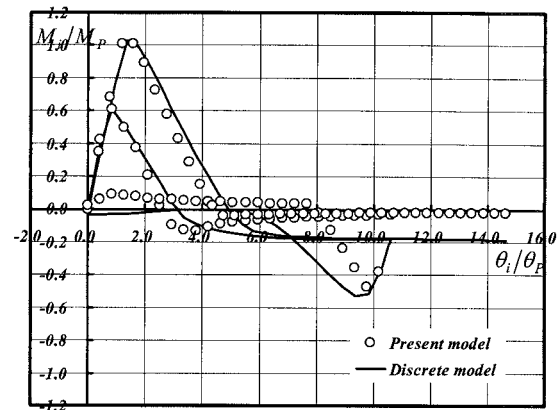


Fig. 7 Load-displacement curve



(a) Axial force-stretch relation



(b) End moment-nodal rotation relation

Fig. 8 Load-displacement curve

6. CONCLUSION

The plasticity model based on the co-rotational beam element, which is subjected to axial force and biaxial bending, with consideration of three-dimensional spread of plastic region has been developed in the limitation of bilinear stress-strain relationship. Furthermore, the beam element, based on the plasticity model, has been proposed in the limitation of elastic-perfectly plastic materials. We summarized the conclusion as follows.

- Both of the plastic rotations always occur due to the finite lengths of plastic regions during plastic loading.
- The method of additive decomposition for relative displacements in the beam leads to the hardening matrices involving the effect of spread of plastic regions for the beam element.
- The thermodynamics forces derived from the additional potential prescribes kinematic hardening. Non-active yield lines evolve as well as active yield lines. This complex behavior represents stress redistribution in a solid cross section.
- It is possible to simulate plastic buckling of plates by idealized plate model with one-dimensional fibers.

References

- 1) Takahiro O., Shojiro M., Kensaku K.: Truss element for H-shaped steel member involving elastoplastic buckling and local buckling behavior, Summaries of Technical Papers, Annual Meeting of AIJ, pp.391-392, 2005
- 2) W. McGuire: Spread of plasticity: Quasi-plastic-hinge approach, ASCE, Journal of Structural Eng., Vol. 120, No.8, pp.2451~2473, 1984
- 3) Ichiro I., Koji O.: A study on the plastic design of braced multi-story steel frames Part 2: On the overall static and dynamic behaviors of plastically designed multi-story braced frames, Journal of Structural and Construction Eng., No.268, pp.87~98, 1978
- 4) W.F. Chen and S.E. Kim: LRFD steel design using advanced analysis, CRC Press, Boca Raton, FL, 1997
- 5) S.I. Hilmy and J.F. Abel: Material and geometric nonlinear dynamic analysis of steel frames using computer graphics, Computer & Structures, Vol.21, No.4, pp.825~840, 1985
- 6) Shojiro M., Ki Y. B., Kensaku K.: A study on elasto-plastic beam element considered plastic hardening and plastic region size -In case of monotonic loading-, Journal of Structural and Construction Eng., No.563, pp.99~106, 2003
- 7) Shojiro M., Takahiro O.: Beam element for h-shaped steel member with local buckling, Journal of Structural and Construction Eng., No.582, pp.81~86, 2004

Formulations and Applications for 3-D Nonlinear Analysis of Structures

Jeong-Ho Moon¹⁾, Jong-Min Kim²⁾, In-Ho Cho³⁾, Hyung-Hoon Lee⁴⁾, Dae-Seock Shin⁵⁾

1) Director of research and Development, MIDASIT, Korea,

2) Section Engineer MIDASIT, Korea,

3) Intermediate Engineer, MIDASIT, Korea,

4) Vice Director, MIDASIT, Korea,

5) Group Manager, MIDASIT, Korea

(mnjh, jmkim, ihcho, leehh, dsshin) @midasit.com

Abstract: This paper presents mathematical formulations and applications for nonlinear static and dynamic analysis of structures. The analytical models for beam-columns are phenomenological hysteresis Model, plasticity model, and fiber model. The analytical models for walls are CRB model, MCPM model, fiber model, and FEA. Simple structures are analyzed with the models to show their characteristics. Then, a frame-wall structure subjected to three types of load pattern is evaluated by pushover analyses. An incremental nonlinear time-history analysis with El centro earthquake is conducted to show the differences of the results from pushover analyses.

1. INTRODUCTION

Recently the necessity for nonlinear analysis has increased due to the introduction of performance based seismic design approach. Unlike linear analysis, however, solution from nonlinear analysis is usually not unique ranging from exact to approximate. There are many theories, which fit to various analysis purposes and have merits and demerits. Many commercial softwares have been adopting different theories based on their development history and target users. Therefore it may not be possible to find softwares that can provide identical solution although their theories are the same. Furthermore, the complex theories may hinder practical engineers to use them without having troubles. It is thus very important to have operation and verification methods along with the correct knowledge of the characteristics of the given software. One of the efficient ways for execution of software and verification of solution is to select a simple example and to analyze it by software as well as by hand calculation. In other words the example should be selected as the one of which the analysts are sure about the correctness of results.

This paper explains the theories adopted in MIDAS/GEN and MIDAS/FEA and provides verification methods with simple examples. The products under MIDAS family are being developed for many years now hence most of popular theories till date are incorporated in the softwares to satisfy the prospective users with various needs. In addition to the verification examples, a prototype structure is chosen to explain the method of performance based seismic engineering.

2. NONLINEAR HINGE PROPERTIES

Analytical methods for a beam-column element can be classified into three groups as phenomenological hysteresis model, stress-resultant plasticity model, and fiber model.

Phenomenological hysteresis model is formulated for the direct application of the rules obtained from experiments. Compensating its theoretical simplicity, many rules have to be provided to the users so that they can simulate real physical behaviors. In addition, it is hard to represent the interaction effects such as axial force-moment (PM) or axial force-biaxial moments (PMM).

The stress-resultant plasticity model¹⁾ borrows the classical plasticity theory in the form of force-deformation relation. The yield or failure surfaces can be those such as PM or PMM interaction relations defined by design codes. With appropriate interaction relations, it can simulate PM or PMM behaviors. However, it cannot simulate complex behaviors, which would be seen from the experiments. Mathematically it is not possible to adopt complex surfaces.

Fiber model could be an alternative in order to overcome the defects of those two models. The cross section at an integration point is divided into many cells and a uniaxial stress-strain relation is assigned to each cell. The strain of a cell is computed from the cross sectional curvature, determined by Bernoulli's assumption. Although it is computationally expensive, PM or PMM interaction relations can be automatically taken into account regardless of cross sectional shapes.

Shear walls are commonly used in building structures to resist lateral forces. But the mathematical formulation is not simple due to its interacting behavior of shear-bending and its connectivity problem. The analytical models can be categorized into two groups, equivalent-column model and finite element model (FEM). The equivalent-column model can include column-rigid beam model (CRB model) and MCPM model²⁾. Although FEM can provide accurate solutions, the direct use of FEM is not practical. Thus FEM is usually chosen as a supplementary method in such a way to generate hysteresis rules or to define yield surfaces.

CRB model uses phenomenological hysteresis model, but MCPM model is a kind of fiber model. Both models are formulated with rigid links in order to be provided rotational degrees of freedom at four corners. Therefore hinge properties for CRB model are determined prior to the computation but those for MCPM model are not. This fact makes it difficult to model a wall with two or more CRB elements divided vertically. It could happen if a wall has T-shape. The flange of a T-shaped wall needs to be modeled with two elements. However, a correct solution cannot be obtained since one element has a set of its own axial and flexural strengths independent from the other. A correct solution could be obtained by MCPM model since hinge properties are being determined during the computation.

MIDAS/FEA, which is one of the MIDAS family programs, is formulated with a typical nonlinear finite element method. Thus it can be used for general purposes regardless of section shapes and openings in a wall. As mentioned previously, it could also be a tool for supplementary purposes.

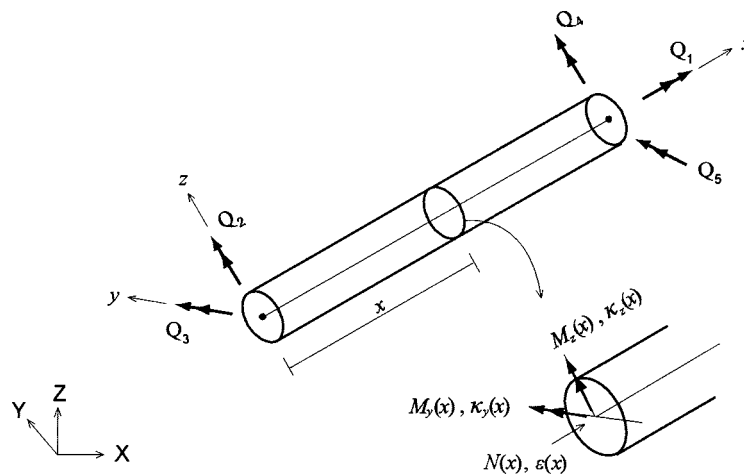


Figure 1 Generalized member forces and deformations of a beam-column element

3. Mathematical formulations

MIDAS/GEN provides various nonlinear elements for the modeling of trusses, beam-columns, and walls. In this paper, the formulation methods for beam-columns and walls are explained. Although there are many mathematical methods, the flexibility method³⁾ is selected because it uses exact interpolation functions for forces. Thus, it opens a possibility to model a member with a long element. The distribution of plastic hinge properties along an element is considered with lumped and distributed hinges. Lumped plasticity model uses moment-rotation relations and distributed plasticity model uses moment-curvature relations. Numerical integration for the distributed plasticity model is performed either by Gauss or by Newton-Conte methods. In addition to flexural hinges, shear and axial hinges could be used in the same way.

3.1 Formulation method

Generalized member forces and deformations of a beam-column element shown in Figure 1 are written as

$$\mathbf{Q} = \{N \quad M_{zi} \quad M_{yi} \quad M_{zj} \quad M_{yj}\}^T; \quad \mathbf{q} = \{\Delta \quad \theta_{zi} \quad \theta_{yi} \quad \theta_{zj} \quad \theta_{yj}\}^T \quad (1)$$

$$\mathbf{D}(x) = \{N(x) \quad M_z(x) \quad M_y(x)\}^T; \quad \mathbf{d}(x) = \{\epsilon_x(x) \quad \kappa_z(x) \quad \kappa_y(x)\}^T \quad (2)$$

The relation between member forces and section forces are expressed with the interpolation function matrix as shown in Eq. 3.

$$\Delta \mathbf{D}(x) = \mathbf{b}(x) \Delta \mathbf{Q} \quad (3)$$

$$\text{where } \mathbf{b}(x) = \begin{bmatrix} 1 & 0 & 0 & 0 & 0 \\ 0 & \xi - 1 & 0 & \xi & 0 \\ 0 & 0 & \xi - 1 & 0 & \xi \end{bmatrix}, \quad \xi = \frac{x}{L} \quad (4)$$

The relation of section forces and deformations is written with the flexibility matrix as in Eq. 5.

$$\Delta \mathbf{d}(x) = \mathbf{f}(x) \Delta \mathbf{D}(x) = \mathbf{f}(x) \mathbf{b}(x) \Delta \mathbf{Q} \quad (5)$$

The compatibility is enforced by an integration of section deformation along the element.

$$\Delta \mathbf{q} = \int_0^L \mathbf{b}(x)^T \Delta \mathbf{d}(x) dx = \int_0^L \mathbf{b}(x)^T \mathbf{f}(x) \mathbf{b}(x) dx \Delta \mathbf{Q} = \mathbf{F} \Delta \mathbf{Q} \quad (6)$$

Therefore, the element flexibility for generalized forces and deformations can be written as

$$\mathbf{F} = \int_0^L \mathbf{b}(x)^T \mathbf{f}(x) \mathbf{b}(x) dx \quad (7)$$

Phenomenological Hysteresis Model

In case of phenomenological hysteresis model, the flexibility matrix is obtained by inverting the section stiffness matrix.

$$\mathbf{f}(x) = \mathbf{k}^{-1}(x) \quad (8)$$

Phenomenological hysteresis models of MIDAS/GEN includes Kinematic hardening, Origin-Oriented, Peak-Oriented, Clough, Degrading Trilinear, Takeda, Takeda Trilinear, Modified Takeda, Modified Takeda Tetralinear, Normal Bilinear, Elastic Bilinear, Elastic Trilinear, Elastic Tetralinear, Slip Bilinear, Slip Bilinear/Tension, Slip Bilinear/Compression, Slip Trilinear, Slip Trilinear/Tension, and Slip Trilinear/Compression.

Plasticity Model

The plasticity model divides the flexibility matrix into elastic and plastic terms as in Eq. 9 and yield surfaces are differentiated to obtain the plastic deformations.

$$\mathbf{f}_t(x) = \mathbf{f}_e(x) + \mathbf{f}_p(x) \quad (9)$$

$$\text{where } \mathbf{f}_p(x) = \frac{\mathbf{g}\mathbf{g}^T}{\mathbf{g}^T \mathbf{K}_p \mathbf{g}} ; \quad \mathbf{g} = \left\{ \frac{\partial f}{\partial P} \quad \frac{\partial f}{\partial M_z} \quad \frac{\partial f}{\partial M_y} \right\}^T ; \quad \mathbf{K}_p = \text{diag}(K_{p,p} \quad K_{p,z} \quad K_{p,y}) \quad (10)$$

$$f = \left(\frac{M_y}{M_{y,\max}} \right)^\gamma + \left(\frac{P - P_{By}}{P_{\max} - P_{By}} \right)^\beta - 1; \quad f = \left(\frac{M_z}{M_{z,\max}} \right)^\gamma + \left(\frac{P - P_{Bz}}{P_{\max} - P_{Bz}} \right)^\beta - 1 \quad \text{for PM}$$

$$f = \left(\frac{|M_y|}{M_{y,\max}} \right)^\alpha + \left(\frac{|M_z|}{M_{z,\max}} \right)^\alpha - 1 \quad \text{for PMM} \quad (11)$$

Fiber Model

Fiber model makes the section stiffness matrix inverse to get the flexibility matrix.

$$\mathbf{f}(x) = \mathbf{k}^{-1}(x); \quad \mathbf{D}(x) = \int_{A(x)} \mathbf{L}^T(y, z) \boldsymbol{\sigma}(x, y, z) dA \quad (12)$$

$$\text{where } \mathbf{k}(x) = \int_{A(x)} \mathbf{L}^T(y, z) E(x, y, z) \mathbf{L}(y, z) dA = \int_{A(x)} E(x, y, z) \begin{bmatrix} 1 & z & -y \\ z & z^2 & -yz \\ -y & -yz & y^2 \end{bmatrix} dA \quad (13)$$

$$\mathbf{L}(y, z) = \{1 \quad z \quad -y\}; \quad \boldsymbol{\varepsilon}(x, y, z) = \mathbf{L}(y, z) \mathbf{d}(x) = \boldsymbol{\varepsilon}(x) + z\kappa_y(x) - y\kappa_z(x) \quad (14)$$

The material properties for the fiber model of MIDAS/GEN include model Kent & Park, Japan Concrete Specification, Japan Highway Specification, Nagoya Highway Cooperation, and Trilinear Concrete.

3.2 Wall Elements

Figure 2 and 3 show CRB model and MCPM model, respectively. As shown in the Figures, both models were developed mostly for the flexural behavior of walls. MCPM model, however, can take into account shear-bending interaction in a simple manner.

3.3 FEA

MIDAS/FEA is a nonlinear finite element analysis program for general purposes. Concrete is assumed as an orthotropic material with Total Strain Crack Model, which is exactly same as that of the TNO/DIANA⁴⁾. It includes fixed crack model and rotating crack model. Steel can be modeled with von Mises yield criteria.

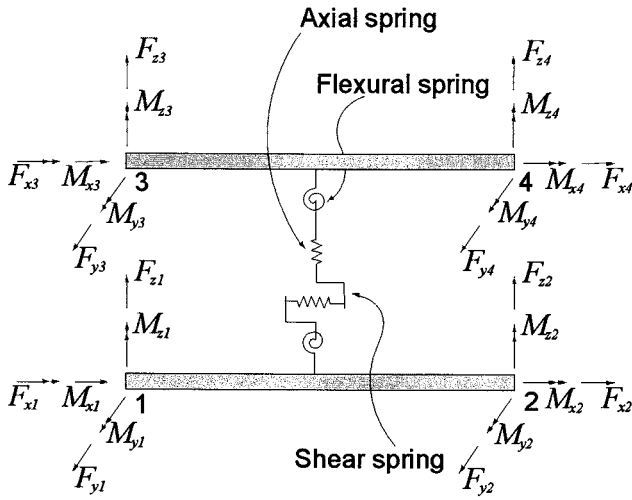


Figure 2 CRB Model

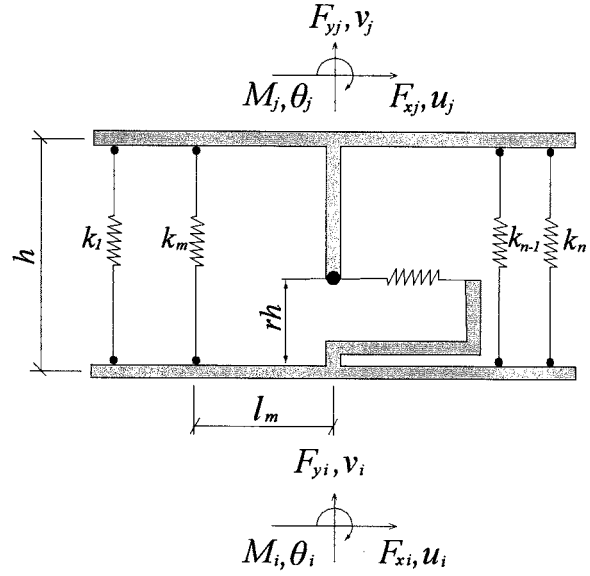


Figure 3 MCPM Model

4. Verification

4.1 PM and PMM Effects

As shown in Figure 4, a pin-ended steel frame 3m high and 6m long was designed with H-300x300x7.8595x14.898. The structure is subjected to a constant axial force of 500kN and an increasing lateral force on the top of each column. For PMM effects, the lateral forces were applied to both direction, x and y. PM yield surfaces for strong and weak axes are shown in Figure 5 and PMM yield surfaces are shown in Figure 6. Elastic-perfectly plastic behavior was assumed for members.

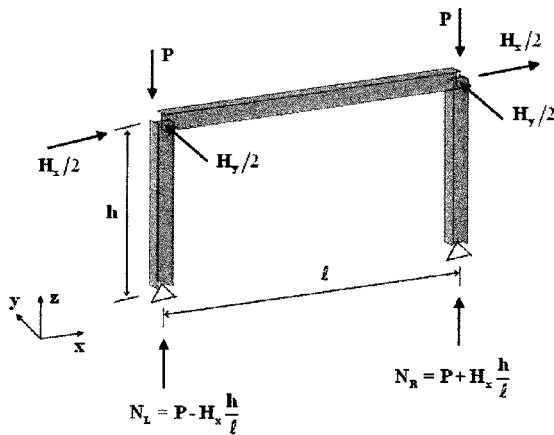


Figure 4 Frame structure for PM and PMM

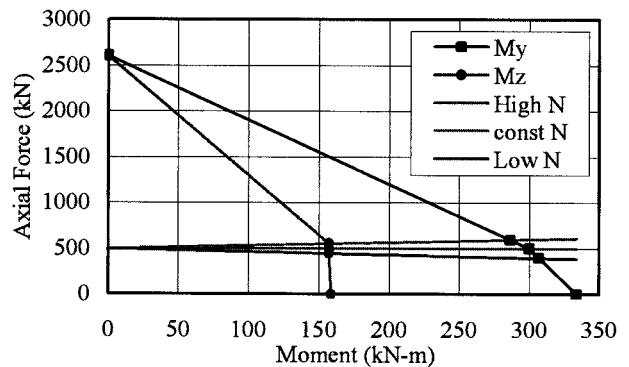


Figure 5 PM yield surfaces

The structure is analyzed for various cases; (a) no axial force and uniaxial moment, (b) constant axial force and uniaxial moment, (c) varying axial force and uniaxial moment, and (d) constant axial force and biaxial moments. In addition, the fiber model analysis for case (c), which is named as (e), was also carried out for comparison.

A relation of lateral displacement versus lateral force is shown in Figure 7. The lateral load capacity was the highest for case (a) and the lowest for case (d). The difference between case (b)

and (c) lie in the axial forces on column. Columns of case (b) are subject to constant axial force, but case (c) is subject to varying axial forces. Thus, the right-hand column of case (c) yields sooner, while the left-hand column yields later. After both columns of case (c) yield, the lateral load capacities of case (b) and case (c) become equal. Case (e) analysis with fiber model shows almost identical results as case (c) since it can take into account the PMM effects automatically.

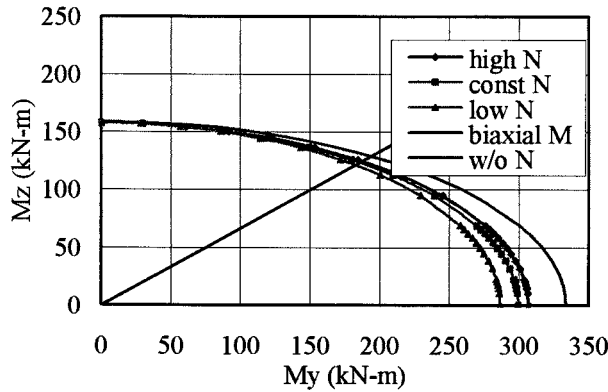


Figure 6 PMM yield surfaces

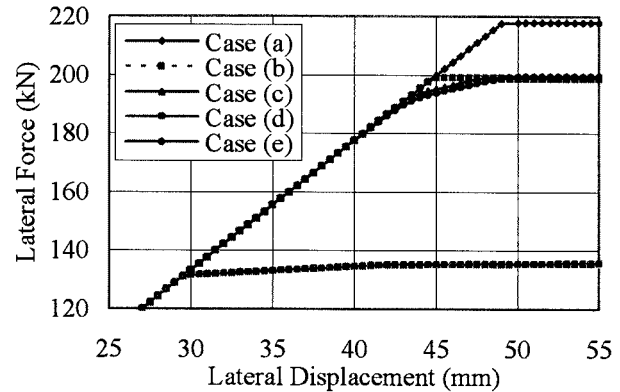


Figure 7 Analytical results of PM and PMM

4.2 Wall Analysis

A cantilever wall shown in Figure 8 was analyzed with various analytical methods which include CRB model, MCPM model, fiber model, and FEA model. The wall of 4.5m long, 3m high, and 250mm thick was modeled with one element for all methods. A two-element modeling with the CRB model was also used to illustrate an error that might occur due to the vertical division of a member.

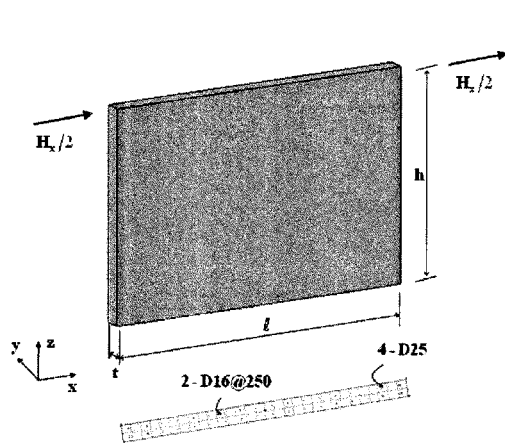


Figure 8 Cantilever wall

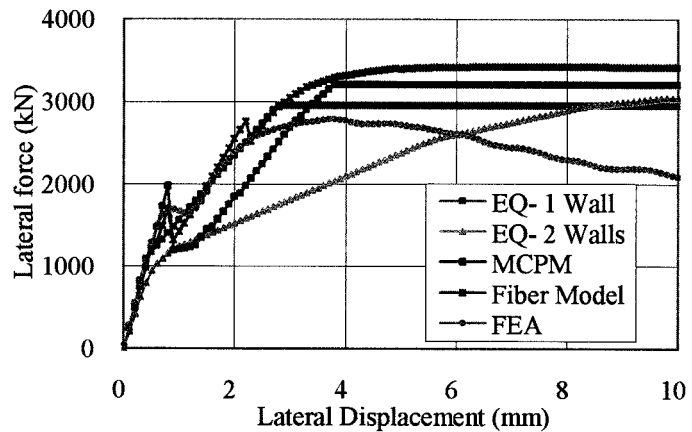


Figure 9 Analytical results of a wall

The compressive strength of concrete was 40MPa and the yield strength of reinforcing bars was 400MPa. The tensile strength of concrete was assumed to be one-tenth of the compressive strength for the cases of MCPM model, fiber model, and FEA model. The wall was reinforced with horizontal and vertical bars of 16mm diameter spaced at 250mm as well as four boundary vertical bars of 25mm diameter at each corner.

The predicted results with the models are plotted in Figure 9. FEA model showed the lowest load carrying capacity and a gradual degradation of strength after peak load. Fiber model revealed a behavior which is similar to FEA model up to near the peak load but showed higher capacity. MCPM model showed a sudden degradation of strength after cracking compared with others.

A trilinear moment-curvature relation was used for the CRB model, in which the stiffness after

cracking was assumed to be 8% of the elastic stiffness. The value was determined by comparing with the results of FEA model. CRB model forecasted analogous behavior to fiber and FEA models except for the peak strength. A significant difference, however, was found from CRB model with two elements.

4.3 Performance based Seismic Analysis

Static and dynamic nonlinear analyses were performed with a five-story building consisted of frames and shear walls as shown in Figure 10. Fixed-ended columns of 600mm x 600mm are spaced at 6m and beams of 600mm x 400mm are connected rigidly with the columns. Two shear walls of 100 thick and 2m long were provided to resist x-directional lateral forces. At each floor, a story diaphragm was used and a dead load of 10kN/m² was applied. Thus the summation of vertical loads is 1800kN (m=183.56g). Yield moments of beams, columns, and walls were 500kNm, 300kNm, and 1000kNm, respectively. No hardening behavior was assumed for the static nonlinear analysis (pushover analysis) as shown in Figure 11.

FEMA 356⁵⁾ or ATC 40⁶⁾ recommends to use at least two load patterns for the pushover analysis in order to take into account higher mode effects. The load patterns selected in this study were static load case, mode shape, and uniform acceleration. Eigen value analysis was carried out to find the governing mode shape in x-direction and the period obtained was 0.524 second at mode participation ratio Γ of 75.46%. The lateral loads were applied incrementally with the displacement control.

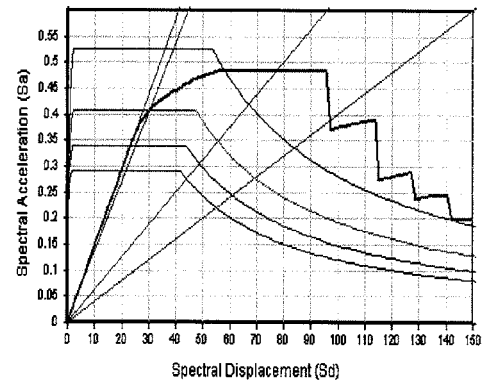
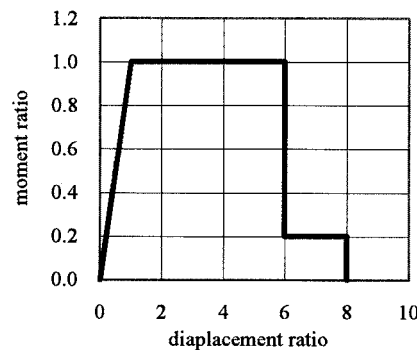
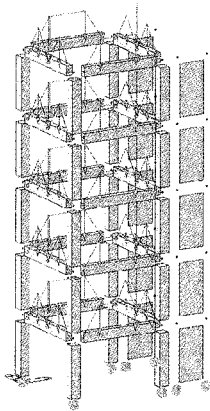


Figure 10 Frame-shear wall

Figure 11 Hinge property

Figure 12 Performance evaluation

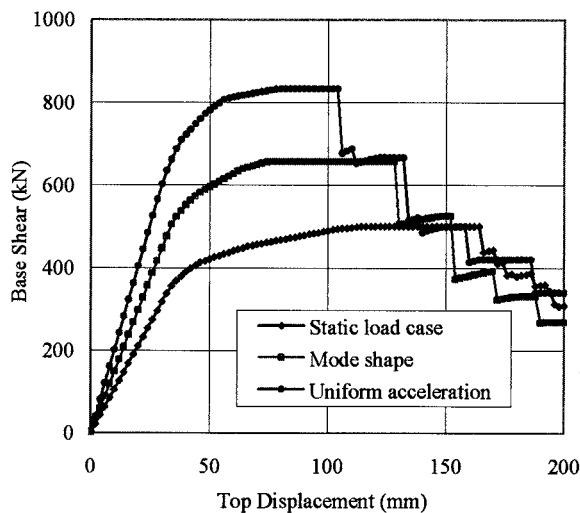


Figure 13 Base shear versus roof displacement

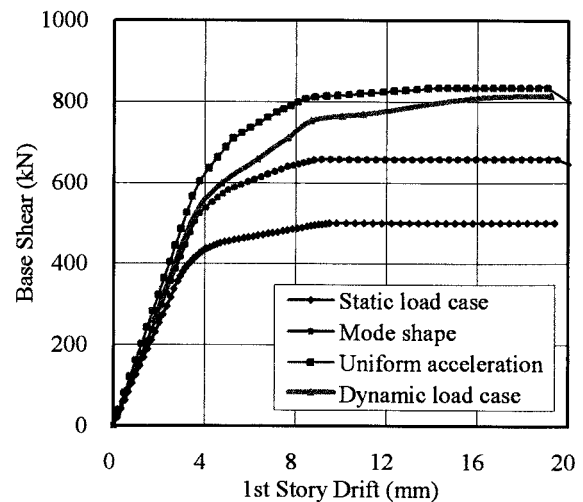


Figure 14 Base shear versus 1st story drift

The performance point for pushover analysis was computed from the load pattern of mode shape as shown in Figure 12. The figure shows that, at the performance point, the lateral displacement of roof level is 40.5mm at a base shear of 554.8kN and the effective period was 0.546 second. The spectral acceleration read from Figure 12 was 0.4085g. Thus the relation of those numbers will be as follows.

$$V = S_a g m \Gamma = 0.4085 \times 9.806 \times 183.56 \times 0.7546 = 554.8 \text{ kN}$$

Figure 13 shows a base shear versus roof displacement for each load pattern. It was found that the relation might be largely different depending on load patterns. The highest capacity was obtained by the uniform acceleration but the lowest capacity by the static load case.

A major drawback of pushover analysis lies in the fact that it cannot reflect the higher mode effects. Thus, an incremental time history analysis was performed with the same structure applying seismic forces incrementally. The structure was excited with the NS component of 1940 El centro earthquake varying scale factors from 0 to 2.0 (0.72g). The analytical results were expressed as a relation between first story drift and base shear. The relation was compared with the results of pushover analysis as shown in Figure 14. The time history analysis showed the structural behavior would lie somewhat in between the mode shape and the uniform acceleration analyses. This analytical result reveals that the pushover analysis cannot evaluate the nonlinear behavior accurately using only with one load pattern.

5. SUMMARY AND CONCLUSIONS

Various analytical models for beam-columns and walls implemented in MIDAS/GEN were introduced in this paper. PM and PMM effects were illustrated with a sample structure. The characteristics of wall models were compared from the analyses of a cantilever wall. The pushover and incremental time-history analyses were conducted with a frame-wall structure. The followings are summaries and conclusions obtained from this study.

1. PMM model and fiber model can accurately take into account the effects of axial force-moment or axial force-biaxial moment relations.
2. Each of nonlinear analysis models for walls has different characteristics and shows slightly different behavior. A careful selection, thus, is recommended to get proper solutions.
3. It is very unlikely that the pushover analysis with single load pattern can provide proper results because the effect of higher modes is not considered accurately.
4. Incremental method of nonlinear time-history analysis may be used as a possible tool to complement the drawback of pushover analysis.

REFERENCE

- 1) El-Tawil, Sherif, and Deierlein, G. G., "Nonlinear analysis of mixed steel-concrete frames. I: element formulation," *Journal of Structural Engineering*, Vol. 127, No. 6, June 2001.
- 2) Orakcal, Kutay and Wallace, J. W., and Conte, J. P., "Flexural Modeling of reinforced Concrete Walls-Model Attributes," *ACI Structural Journal*, Vol. 101, No. 5, Sept.-Oct. 2004.
- 3) Neuenhofer, Ansgar and Filippou, F. C., "Evaluation of Nonlinear Frame Finite-Element Models," *Journal of Structural Engineering*, Vol. 123, No. 7, July 1997.
- 4) TNO Building and Construction Research "DIANA User's manual – Material Library," Version 9.
- 5) Federal Emergency Management Agency, "Prestandard and Commentary for the Seismic Rehabilitation of Buildings," FEMA 356, Nov. 2000.
- 6) Applied Technology Council, "Seismic Evaluation and Retrofit of Concrete Building," Report No. SSC 96-01, Nov. 1996.

ANALYTICAL SIMULATION OF SEISMIC BEHAVIOUR IN PERFORMANCE BASED ENGINEERING USING LS-DYNA

Mr Michael Willford

Director, Advanced Technology and Research Group, Arup, London, UK

michael.willford@arup.com

Abstract: Performance based engineering is being adopted increasingly as a tool to manage seismic risks. This requires engineers to understand the dynamic behaviour of structures and soils in earthquakes in more detail than ever before, and this relies upon the use of nonlinear dynamic finite element simulation tools. This paper illustrates the use of LS-DYNA for this purpose in a number of diverse applications.

1. INTRODUCTION

In order to guard against unacceptable loss in an earthquake event the performance of buildings and facilities needs to be more reliably assessed at the design stage by the engineer. Increased computer power permits structures to be modelled in detail, and non-linear dynamic response simulations to be performed as part of the design process to predict a structures response to the required design earthquake motions. Such simulations allow the designer to understand the seismic performance of structures with greater detail and confidence than traditional code based design methods. The use of such tools enables the designer to assess the likely locations and degree of damage. Designs can thereby be improved.

These computer simulation techniques can be applied not only to the design of new structures, but also to the assessment (and retrofit design where necessary) of existing structures, which were often not designed to modern standards of safety and performance. This paper illustrates the use of LS-DYNA for the simulation of seismic response in the design of a number of projects performed by Arup over the past 15 years.

2. LS-DYNA FOR SEISMIC RESPONSE ANALYSIS

LS-DYNA is a non-linear finite element code of very high capability originating from Livermore Software Technology Corp. [LSTC], California. For many years it adopted exclusively the 'explicit' solution strategy, using very small time-steps and

involving no iteration or matrix inversion. In recent years an ‘implicit’ capability has been added, but the features available are much more restricted. The examples in this paper all utilised the explicit solver. The program calculates the non-linear response of general 3D systems to time-varying input functions and is capable of handling the most general class of seismic problem from first principles.

Arup has pioneered the use of LS-DYNA for seismic applications, and has contributed a number of additional features to the code to improve its capability in this field over the past 15 years. With appropriate material models, capable of representing degradation of stiffness and strength under cyclic action, this type of analysis can predict the location of damage and quantify effects such as the rotation of plastic hinges in framed structures, the non-linear response of concrete shear walls, and non-linear behaviour of soils.

3. SEISMIC ANALYSIS FEATURES IN LS-DYNA

LS-DYNA is widely used by industry to simulate short timescale highly non-linear events, and the program has been used extensively in the modelling of blast and impact response of structures and vehicles.

In order to meet the specific needs of seismic design, Arup, working in collaboration with LSTC have made a number of enhancements to LS-DYNA specifically for seismic response analysis. Some of these features are discussed below.

3.1 Lumped plasticity beam

In seismic response of building frames, the interaction of axial and flexural effects in elements can significantly affect the yield forces and plastic deformation. This applies particularly to columns (N-Mx-My interaction at hinges) and to braces which may suffer inelastic buckling. Although the ‘fibre’ beam element models existing in LS-DYNA can be used, this requires a fine discretisation and so they are computationally intensive.

Therefore an elastic beam element with plasticity lumped at the ends (‘plastic hinges’ was developed. The element takes account of the interaction between axial force and bi-axial bending on hinge formation, through a user-defined M-N yield surface, and axial and flexural plastic deformation follows the normality rule. Options exist to model the yield surfaces of steel and of reinforced concrete beam-columns and shear walls.

Post processing facilities permit the history of the element response to be plotted within the M-N interaction failure surface. This is particularly useful in assessing the performance of reinforced concrete elements since the axial force affects the permissible hinge rotation at any excursion to the failure surface. Figure 1 illustrates this feature.

3.2 Lumped plasticity brace

Inelastic buckling of compression members in a frame can be simulated by subdividing the member into a substantial number of beam elements of either the ‘fibre’ or ‘lumped plasticity’ type. This will give the classical “pinched” hysteresis loops exhibited by braces undergoing cyclic inelastic buckling. The observed degradation of tensile and compressive capacity under repeated cyclic loading of a steel brace can also be simulated in this way.

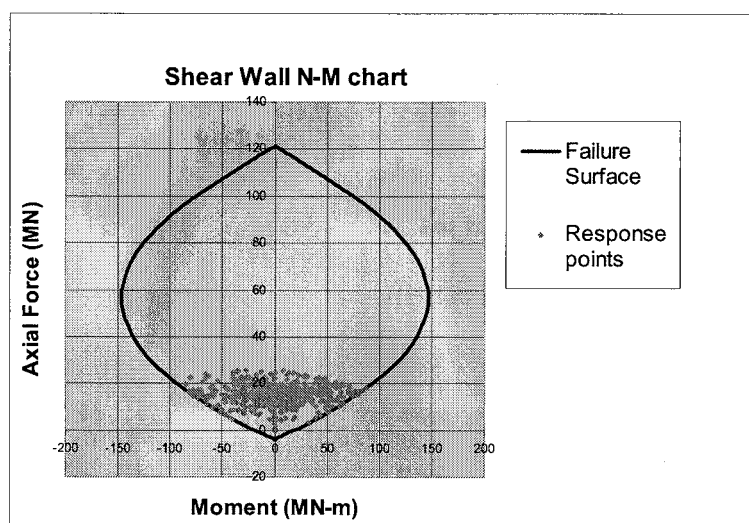


Figure 1 – Response history summary in M-N space for reinforced concrete column

However, to reduce model size and complexity, a further phenomenological beam model has been developed in which this behaviour is captured in a single element, and is intended primarily for seismic analysis of concentrically braced frames. Figure 2 illustrates typical behaviour characteristics.

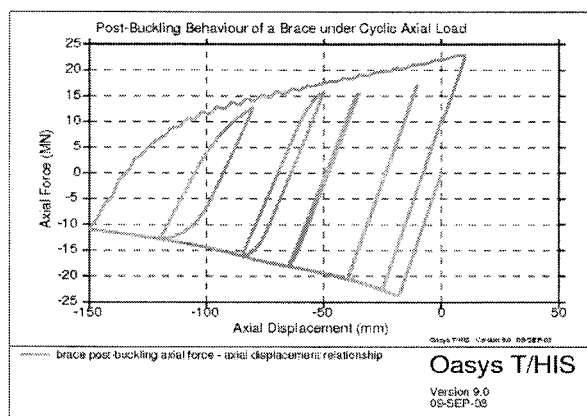


Figure 2 – Inelastic buckling element performance

3.3 Squat reinforced concrete shear wall element

A squat reinforced concrete shear wall model has been developed for use where shear failure governs. The observed behaviours of shear-critical walls have been captured in a special non-linear phenomenological spring element and 2-D plate element. The hysteresis rules are based on measured cyclical force-deflection behaviour for such walls following extensive examination of experimental research.

Figure 3 compares the results of an analytical simulation with a shake table test of a squat shear wall.

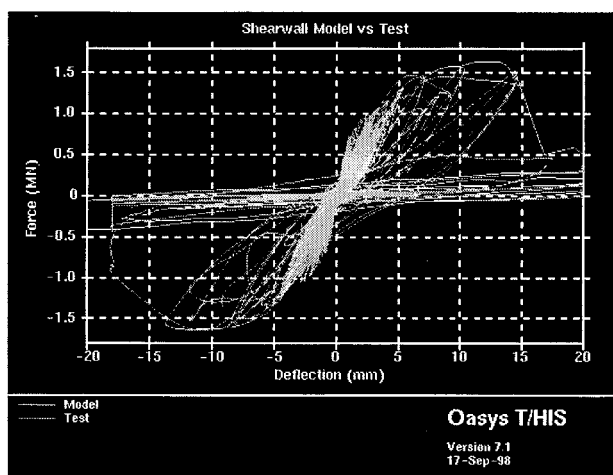


Figure 3 - Squat shear wall force-deflection simulation vs shake table test

This element can also be used for other phenomena requiring “pinched” hysteresis loops and degradation of stiffness and strength, such as reinforced concrete beam-column joints, and reinforced masonry walls.

3.4 Seismic isolation

Modern seismic design often incorporates seismic base isolation to reduce the forces, internal deformations and inelastic demands on the structure. Arup have developed a specific seismic isolator model that can model sliding (e.g. friction pendulum) and elastomeric seismic isolation bearings by applying bi-directional coupled plasticity theory.

3.5 Non-linear soil model

The behaviour of the soil beneath a structure can be very significant for the structure itself. The soil column above bedrock can modify the amplitude and frequency content of the seismic waves at the soil surface. Dynamic interaction between the structure and the soil on which it is founded is often significant. An enhanced dynamic soil material model, incorporating stress-strain hysteresis typical of cyclically loaded soils has been developed. Typical stress-strain behaviour in a soil-structure interaction analysis is shown in figure 4.

4. POST PROCESSING FEATURES

One of the principal purposes of non-linear seismic analysis is to identify the ductility demands on individual components of a structure, and then to check that the capacity for this deformation exists without brittle material fracture or unstable buckling. Facilities to extract this type of information in the form of force/deflection hysteresis diagrams and plastic hinge rotation diagrams are available using the programs Oasys D3PLOT and Oasys T/HIS developed by Arup. In addition D3PLOT

has facilities for animation of the deflection of a structure through an earthquake. It is possible to superimpose on this animation the variation of element force or plastic deformation indicated by changing colours during the event.

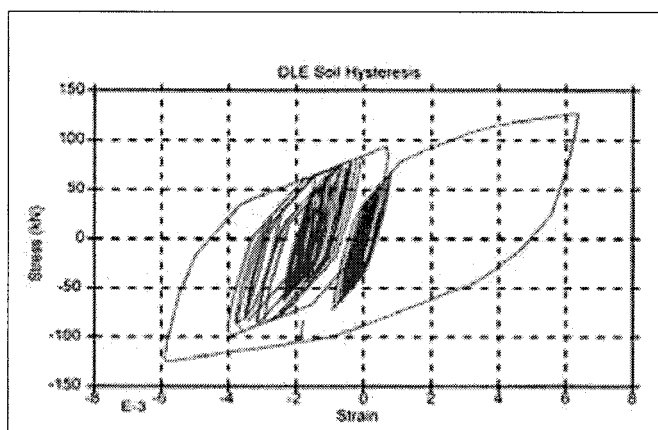


Figure 4 Non-linear hysteretic soil model

5. PROJECT EXAMPLES

This section highlights a small range of Arup projects in which performance based seismic engineering has been implemented using LS-DYNA.

5.1 Effect of basement on seismic motions for building design

It is common for major buildings to be constructed over extensive deep basements. When the basement is constructed through soft soil layers it can act as a 'box' which affects significantly the seismic motions experienced by the building constructed above. By modelling the foundation box together with surrounding soil down to a bedrock level a 3-D non-linear site response analysis can be performed in which the effect of the basement can be simulated. Figure 5 shows a 3-D analysis model for such a study, and the difference in the seismic response spectra at bedrock, soil free-field and at the top of the basement.

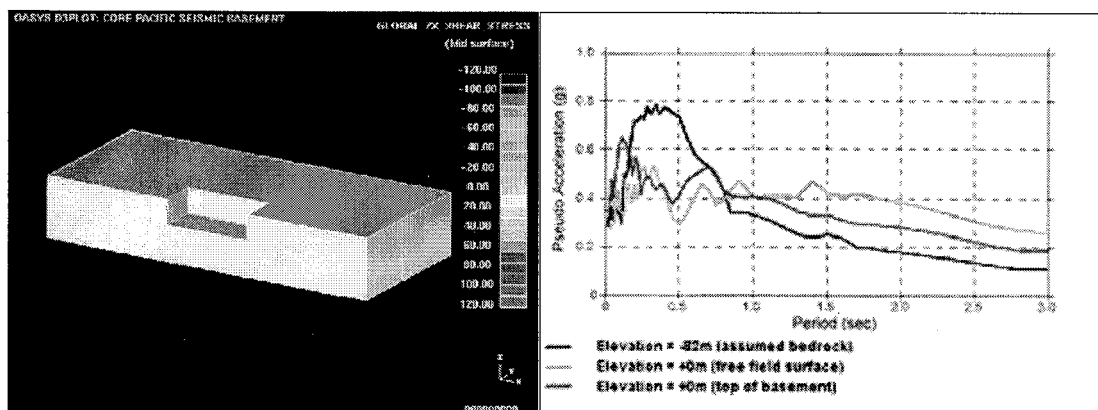


Figure 5 Non-linear site response analysis including basement structure

5.2 Maison Hermes, Tokyo

Renzo Piano's architectural concept for this iconic building in Tokyo dictated a very slender vierendeel seismic lateral resisting structure. Designing the lateral system in a conventional manner led to a high steel frame weight due to the large overturning moment resisted on a small lever arm. In addition, very high tension and compression foundation forces were generated.

An alternative concept, in which one of the two lines of columns was not tied down to the foundation, was explored using LS-DYNA. In this concept the 'stepping' column lifts off the foundation in extreme excursions of the seismic event. This concept proved very successful, leading to significant cost savings in the steel superstructure and in the foundations together with much improved seismic performance. A visco-elastic damper was introduced at the base of the uplifting column to reduce the degree of uplift. Features of the buildings and its analysis are shown in figure 6 and 7.

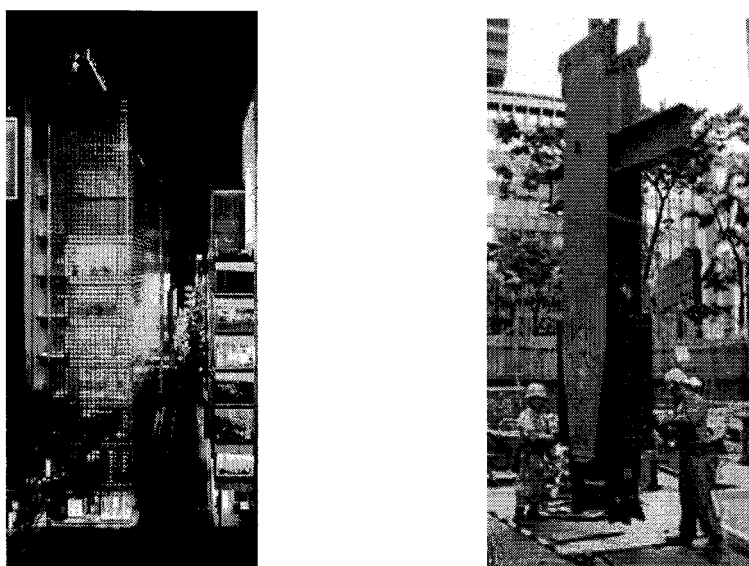


Figure 6 Maison Hermes Building, Tokyo and uplifting column base installation

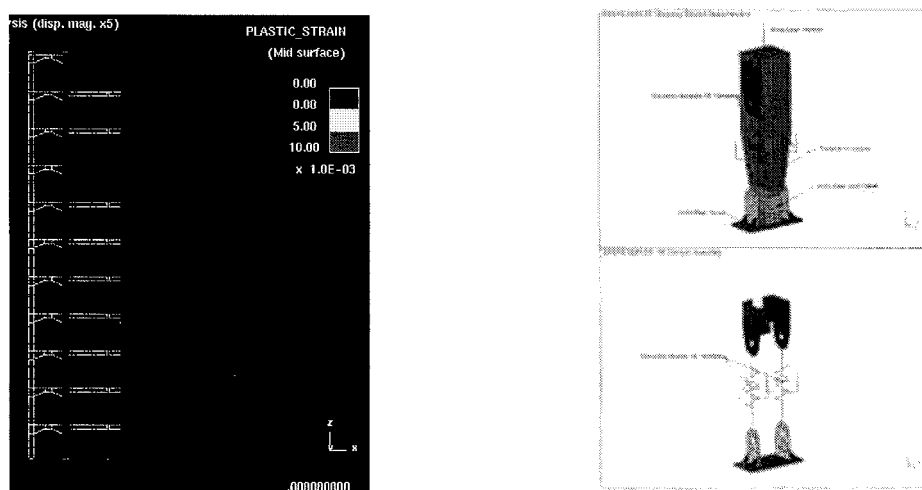


Figure 7 Seismic analysis of Maison Hermes building using LS-DYNA

5.3 Soil structure interaction analysis of LNG tank

Large double containment storage tanks are increasingly being used for natural gas (LNG) storage. In the project shown in

Figure 8 a detailed soil structure interaction analysis was able to properly capture the propagation of the seismic waves up from the bedrock through various soil layers and interact with the heavy piled foundation of the LNG tank. This analysis permitted the 'seismic isolation' effect of the soft upper soil layers to be taken account of in the tank design, which was of considerable commercial benefit.

Figure 9 shows a fully coupled fluid-structure analysis of a steel LNG tank able to capture the effect of elephant foot buckling at the tank base.

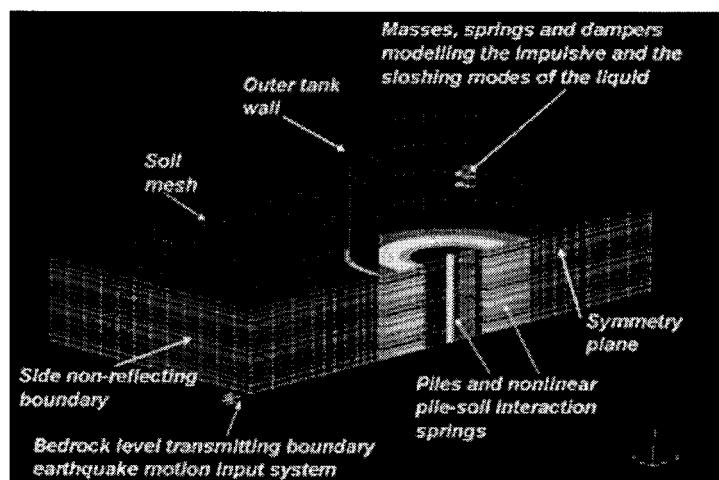


Figure 8 Global non-linear soil structure interaction of a large LNG tank

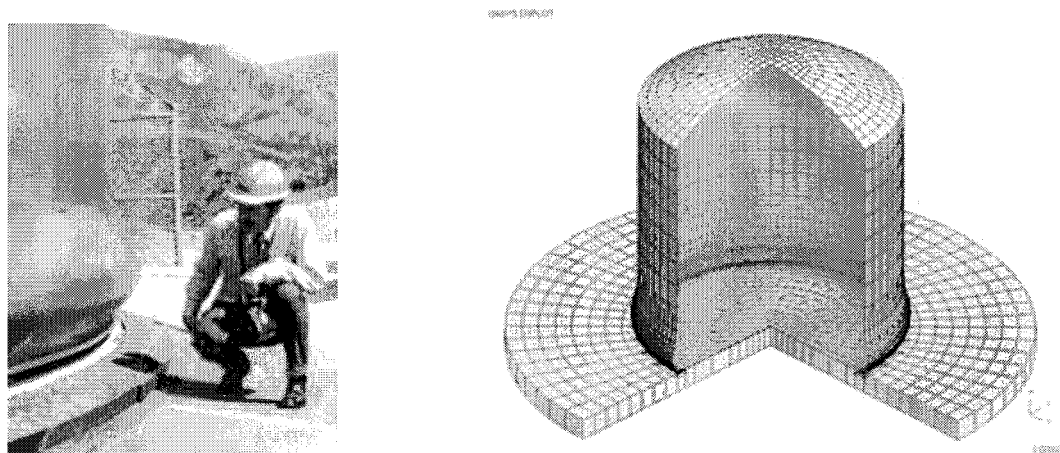


Figure 9 Simulation of 'elephant foot buckling' of an LNG tank in coupled fluid-structure analysis

5.4 Retrofit of Industrial Building

Arup undertook the retrofit design development of a 1950s riveted steel industrial structure. Typical construction details are illustrated in figure 10. The main members

were trusses composed of back-to back steel angle sections. Modern codes do not recognise this as a seismically resistant structural system, and performance based guidelines such as FEMA 356 did not have a category from which ductility capacities could be estimated.

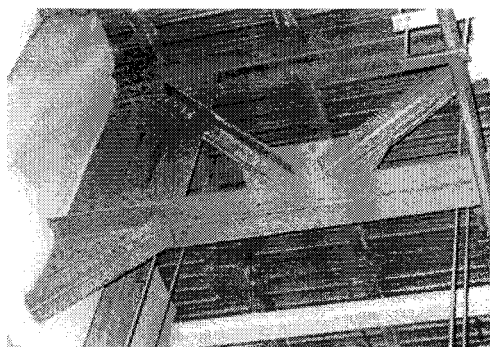


Figure 10 – Typical construction form

Therefore Arup set about establishing the component characteristics on a case by case basis using material tests on steel sections and rivets, and ‘virtual testing’ of typical assemblies using detailed models in LS-DYNA. The detailed computer models of the built up riveted steel sections were subjected to a cyclic loading regime as per FEMA 356 to derive ‘backbone’ resistance curves as shown in figure 11. These analyses were able to capture buckling, yielding and fracture of the steel members and the various forms of connection failure.

This virtual testing allowed Arup to determine component specific modification factors which were used in the global assessment and then for the retrofit design development of the structure.

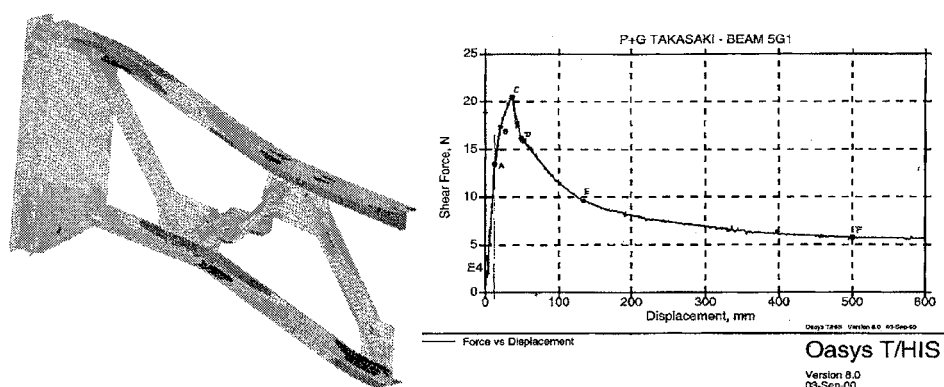


Figure 11 Typical ‘Virtual Test’ model and ‘backbone’ resistance curve

6 CONCLUSIONS

Advanced structural simulation for performance based earthquake engineering is of significant benefit in many situations. LS-DYNA is a highly capable analysis code suitable for this type of work.

STRONG GROUND MOTION EVALUATION IN THE TOKYO METROPOLITAN AREA: THE 1923 KANTO EARTHQUAKE AND FUTURE SUBDUCTION-ZONE EARTHQUAKES

K. Koketsu¹⁾ and H. Miyake²⁾

1) Professor, Earthquake Research Institute, University of Tokyo, Japan

*2) Research Associate, Earthquake Research Institute, University of Tokyo, Japan
koketsu@eri.u-tokyo.ac.jp, hiroe@eri.u-tokyo.ac.jp*

Abstract: We proposed a method of strong ground motion evaluation for subduction-zone earthquakes, carried out the strong ground motion evaluation in the Tokyo metropolitan area for subduction-zone earthquakes along the Sagami and Nankai troughs, and examined the validity of the method. For the 1923 Kanto earthquake, we also examined the source fault model and the velocity structure model in the Tokyo metropolitan area. For a hypothetical Tokyo metropolitan earthquake, we examined the effect of the shallow surface of the Philippine Sea plate, which was estimated from large-scale seismic reflection surveys, on the result of strong ground motion prediction. For a hypothetical Tokai earthquake, appropriate source parameters and wide-range velocity structure models extended to undersea parts, the crust and the plate enable us to carry out realistic broadband strong ground motion prediction. We confirmed that distinct long-period ground motions were excited in the Tokyo metropolitan area by a giant subduction-zone earthquake along the Nankai trough. Therefore, the deterministic simulation of long-period ground motion is essential for strong ground motion prediction of a subduction-zone earthquake.

1. EVALUATION METHOD OF STRONG GROUND MOTION

Various kinds of earthquakes such as active-fault earthquakes, plate-boundary earthquakes, and in-slab earthquakes are threatening the Tokyo metropolitan area (TMA). Among them, the kind of plate-boundary earthquakes is the greatest menace as they are generally larger with higher recurrence rates than the other kinds of earthquakes. Accordingly, the strong ground motion prediction for plate-boundary earthquakes is one of the most important issues for the TMA (Figure 1).

The Headquarters for Earthquake Research Promotion published the “National Seismic Hazard Maps for Japan” (NSHMJ) in 2005. The maps for specified earthquake sources in NSHMJ were constructed by computing time histories of broadband ground motions at the engineering basement surface. The earthquake source is represented by a characterized source model consisting of asperities and a background. Broadband ground motions for an active-fault earthquake are computed with the hybrid synthesis method (hybrid combination of theoretical long-period simulation and short-period statistical Green’s function method). However, those for a subduction-zone earthquake are computed only with the statistical Green’s function method, as large-scale computation is required and we have to construct a velocity model in a large land-sea region for the theoretical long-period simulation. Only the statistical Green’s function method was mainly used even in the strong ground motion prediction for subduction-zone earthquakes by the Central Council for Disaster Prevention.

Therefore, long-period ground motions from subduction-zone (plate-boundary) earthquakes have not yet been evaluated accurately in the TMA by using the theoretical simulation method, though the damage of oil storage tanks in Tomokomai due to long-period ground motions from the 2003

Tokachi-oki earthquake validated the necessity of their accurate simulation (Koketsu et al., 2005; Hatayama et al., 2004). Since a source model, a velocity structure model, and a computational scheme are the key components of the theoretical long-period simulation, we here upgrade the source and velocity structure models, and then evaluate long-period ground motions in the TMA for subduction-zone (plate-boundary) earthquakes. These will lead to the prediction of strong ground motions from subduction-zone (plate-boundary) earthquakes by the hybrid synthesis method.

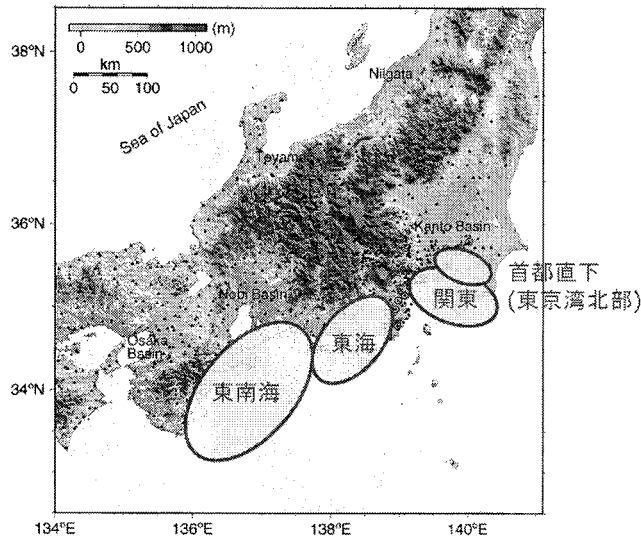


Figure 1. Subduction-zone earthquakes along the Sagami and Nankai troughs to be considered for the strong ground motion evaluation in the Tokyo metropolitan area. 首都直下, 関東, 東海, and 東南海 indicate the Tokyo metropolitan, Kanto, Tokai, and Tonankai earthquakes, respectively.

For constructing a source model used in strong ground motion prediction of a subduction-zone earthquake, the slip distributions obtained by waveform inversions can provide basic information. Murotani et al. (2005) and Miyake et al. (2006) compiled the results of waveform inversions for Japanese subduction-zone earthquakes, and extracted asperities from them. They then calculated regression relationships between rupture area or combined asperity area and seismic moment. These relationships are similar to those for crustal earthquakes, though the areas are a little (1.3 times) larger than those for crustal earthquakes with the same moment. However, there is a possibility that these asperities do not equally correspond to strong motion generation areas as for crustal earthquakes. Hata et al. (2006) examined this possibility and suggested that asperities almost correspond to strong motion generation areas if asperities are extracted from the result of a waveform inversion carried out with a minimum rupture area.

In addition, the asperity model has been studied extensively (e.g., Nagai et al., 2001; Okada et al., 2003; Yamanaka and Kikuchi, 2004; Wu and Koketsu, 2006), claiming that the same asperities are ruptured repeatedly and their combination is responsible for the magnitude of an earthquake. As shallow plate-boundary earthquakes have shorter recurrence intervals (100 – 200 years) than those of other subduction-zone earthquakes, we can know the shaking by a previous event for most of them. If this sort of plate-boundary earthquake repeats similar rupture, similar shaking should be repeated in a next event. Therefore, it is essential for strong ground motion prediction of a future plate-boundary earthquake to investigate the shaking by a past event in detail and examine its strong ground motions.

We here propose two procedures for source modeling of a subduction-zone earthquake as follows:

- (1) If we know the rupture process of a previous event, we take this process as a source model of a future event based on the hypothesis of repeated asperity rupture (Nagai et al., 2001). As the source time functions derived by waveform inversion for a large subduction-zone earthquake are often short of medium-period components, we introduce a pseudo-dynamic source model (Guatteri et al., 2004). (e.g., Kanto earthquake, Tonankai earthquake).
- (2) If we do not know the rupture process of a previous event, we take a characterized source model

(Irikura and Miyake, 2001; Miyake et al., 2003) based on the scaling of asperity size from the compilation of rupture process models. We empirically assume a stress drop of around 3 MPa and the ratio of a combined asperity and fault areas to be about 20% such that asperities appropriately correspond to strong motion generation areas. The characterized source model is constructed using these assumptions and the recipe of strong ground motion prediction (Irikura and Miyake, 2001; Irikura et al., 2003). (e.g., Tokyo metropolitan (Northern Tokyo Bay) earthquake, Tokai earthquake)

2. STRONG GROUND MOTION VALIDATION FOR THE KANTO EARTHQUAKE

The 1923 Kanto earthquake, which caused the great Kanto earthquake disaster, is a typical subduction-zone earthquake around the TMA. The fault plane of this earthquake is located on a shallow part of the Philippine Sea plate subducting from the Sagami trough. As the 1703 Genroku earthquake occurred in the combined region of the fault plane and a neighboring area in the east, the recurrence interval of the earthquake is about 220 years. It is only 82 years after the Kanto earthquake, so that the Earthquake Research Committee (ERC) (2005) obtained a 30-year probability as small as 0.065%. However, since the recurrence interval is not so long, a 50-year probability will reach 0.85%. We here perform strong ground motion validation for the 1923 Kanto earthquake in order to examine its source model and the velocity structure model in the TMA.

The large-scale seismic reflection surveys in 2002 and 2003 revealed the upper surface of the Philippine Sea plate to be shallower than the previous estimates (e.g., Ishida, 1992). Kobayashi and Koketsu (2005) carried out a rupture process inversion only with a fault plane at the previous depth, and so Sato et al. (2005) performed another inversion with a new fault plane on the shallow surface. We use the results of these inversions as source models for the 1923 Kanto earthquake (Figure 2). In the result for the new fault geometry, the second asperity in the east was relocated northward approaching the downtown Yokohama and Tokyo. Its depth was changed from 10 km to 15 km.

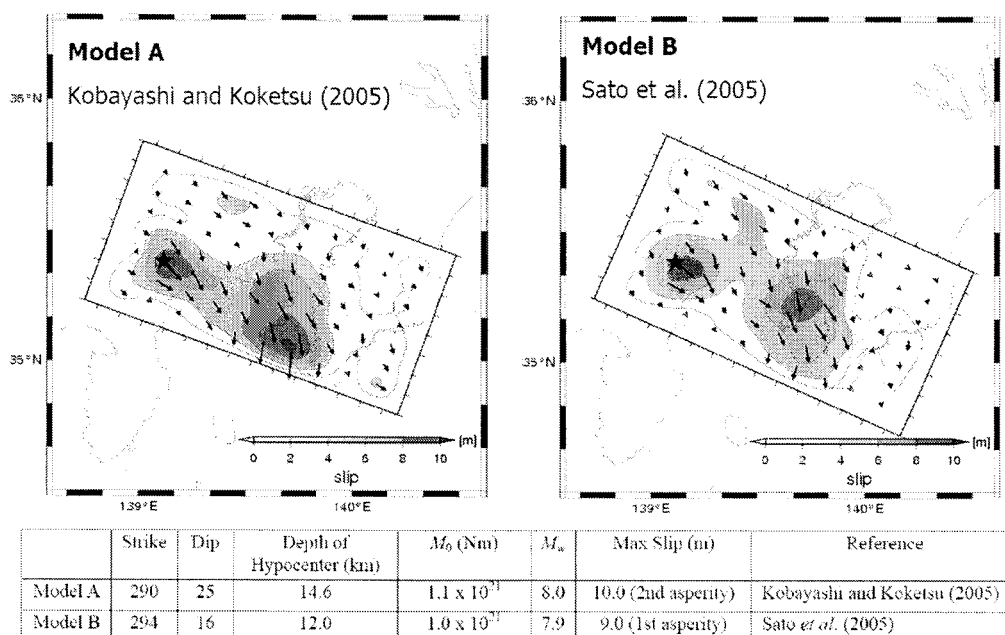


Figure 2. The results of the source process inversions with the fault models in the previous (left: Kobayashi and Koketsu, 2005) and new fault geometry (right: Sato et al., 2005).

For the velocity structure, we adopted the DaiDaiToku integrated model (Tanaka et al., 2005, 2006; Miyake et al., 2006; Table 1 and Figure 3), which was being constructed using exploration data. Figure 4 shows a cross section of the deep part of this model with three-dimensional extensions to the crust and the subducting Philippine Sea plate. We note that the shallow subsurface structure derived from

borehole data is already built in the DaiDaiToku integrated model.

	V_p (m/s)	V_s (m/s)	Density (kg/m^3)
Layer 1		350	
Layer 2		450	
Shimoso	1800	500	1850
Kazusa	2400	900	2080

Table 1. Property parameters in the DaiDaiToku integrated model in the Tokyo metropolitan area.

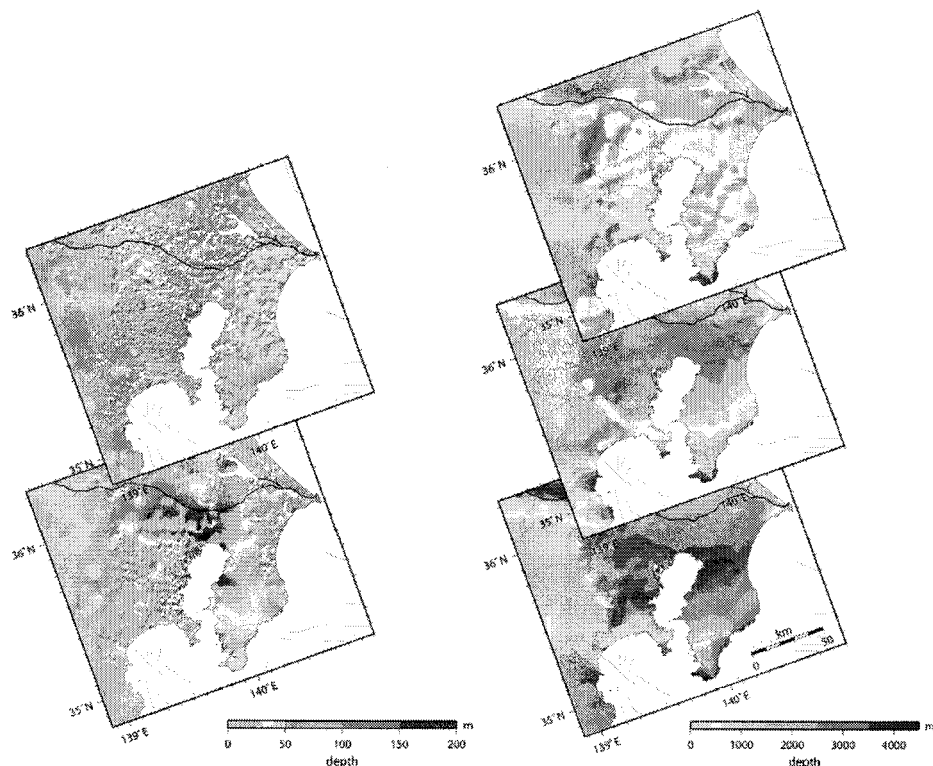
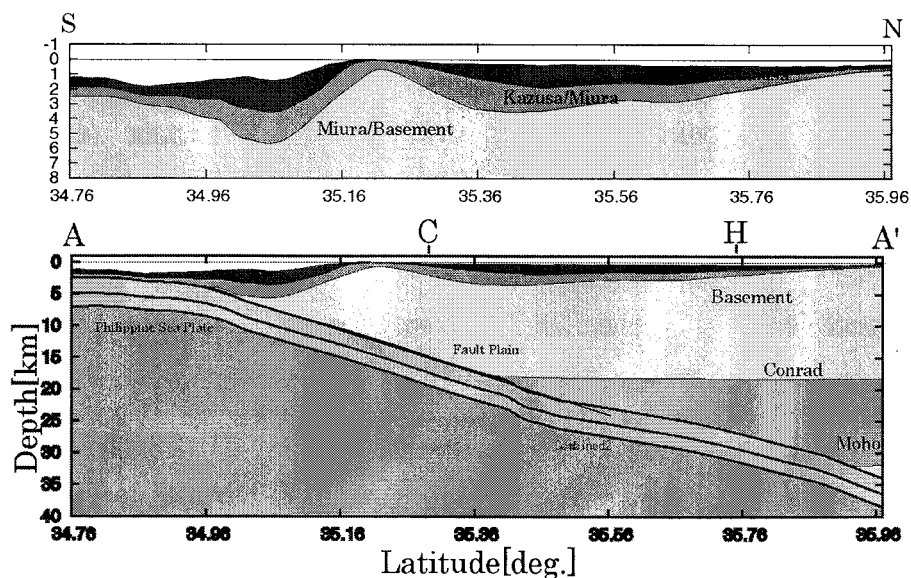


Figure 3. The DaiDaiToku integrated model for the velocity structure in the TMA. (Upper Left) Depth distribution of N values equal to 50. (Lower Left) Depth distribution of V_s equal to 500 m/s corresponding to the surface of the Shimoso layer. (Upper Right) Surface of the Kazusa layer. (Middle Right) Surface of the Miura layer. (Lower Right) Surface of the basement.

Figure 4. Cross section of the DaiDaiToku integrated model for the velocity structure in the TMA including three-dimensional extensions to the undersea parts, the crust, and the Philippine Sea plate (Tanaka et al., 2006).



For ground motions from a giant subduction-zone earthquake, it is pointed out that long-period ground motions effective on long and large structures can be threatening the TMA in addition to short-period ground motions relating to seismic intensities and damage to houses and ordinary structures. Therefore, it is preferable for this strong ground motion evaluation to compare synthetic seismograms with observed ground motions besides comparisons of attenuation relations and intensities distributions.

We carried out simulations of long-period ground motions using the result of the waveform

inversion as a source model, the DaiDaiToku integrated model as a velocity structure model, and the voxel finite element method (Koketsu et al., 2004) as a computational scheme. The obtained waveform well simulates the seismogram observed at Hongo, Tokyo during the 1923 Kanto earthquake. Figure 5 shows this agreement with the seismogram restored by Yokota et al. (1984). The original record was observed by an Imamura seismograph oriented N77°E at the Department of Seismology, the University of Tokyo in Hongo. The agreement in the time histories looks excellent, but the agreement in the response spectra is not so good at periods longer than 5 s, though good in a band from 2 s to 4s. In order to solve this problem, we have to revise the source and velocity structure models considering the excitation of surface waves.

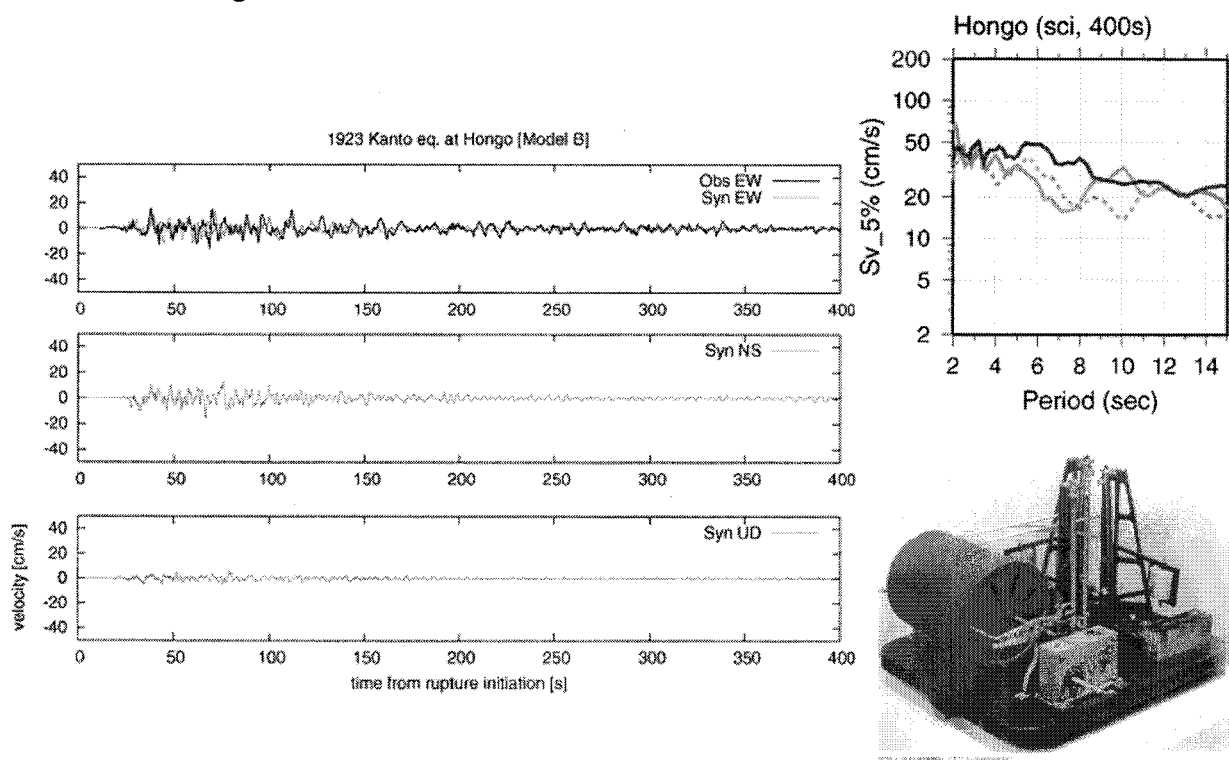


Figure 5. Comparison of the simulated (red) and observed seismograms (black) at Hongo, Tokyo. Only the east-west component was restored and the misplacement of the seismograph (rotated counterclockwise by 13°) was already taken into the simulations. The upper right panel shows velocity response spectra (red: observed east-west component, green solid: simulated east-west component, green dashed: simulated north-south component). The Imamura seismograph in the lower right panel obtained the observed record.

The short-period ground motions were computed with the statistical Green's function method and a pseudo-dynamic source model derived from the slip distribution of the inversion result. Their instrumental intensities at Hongo, Shinjuku and Yokohama are almost equal to or a little larger than the intensities estimated from the damage (Moroi and Takemura, 2002).

We computed long-period and short-period ground motions for the previous and new source models (Models A and B in Figure 2). The long-period ground motions of Model A are almost similar to those by Sato et al. (1999). The peak response spectra of the long-period ground motions for Model B are about halves of those for Model A, as the second asperity of Model B is located at a deeper part than that of Model A (Tanaka et al., 2005). In contrast, the short-period ground motions for Model B are a little larger than those for Model A, because the second asperity approached the TMA in Model B.

3. CONCLUSIONS

We proposed a method of strong ground motion evaluation for subduction-zone earthquakes using the information on the location and areas of asperities, which were greatly improved in recent years, and carried out the strong ground motion evaluation and prediction of subduction-zone earthquakes assumed along the Sagami or Nankai trough. We found that the modeling of an earthquake source has been improved, since the location and areas of asperities can be estimated not only by a source process inversion but also by exploration, analysis of seismicity, tomography and others.

We also proposed a method for the modeling of a velocity structure using the results of explorations and seismic records, and constructed the DaiDaiToku integrated model of the velocity structure beneath the TMA. We further improved this model by building in the shallow subsurface structure and three-dimensionally extending to the structures of the crust and Philippine Sea plate.

For the 1923 Kanto earthquake, the source and velocity structure models were reconstructed, as large-scale seismic reflection surveys provided us with the shallower estimate of the upper surface of the Philippine Sea plate than the previous depth. Since the eastern asperity approached Tokyo with a deeper depth, the excitation of long-period ground motions has been halved, and the short-period ground motions and seismic intensities have increased.

For the hypothetical Tokyo metropolitan earthquake, we carried out strong ground motion predictions with the deep and shallow source models on the previous and new geometry of the Philippine Sea plate, respectively. We confirmed that the strong ground motion for the shallow source model is a little larger than that for the deep source model. We also found the effects of the complex velocity structure in the TMA such as the reflection of surface waves at the western end of the Kanto basin and propagation of seismic wave along the northwestern corridor. This implies the importance of deterministic ground motion simulation.

For the hypothetical Tokai earthquake, we confirmed that a characterized source model and the hybrid synthesis method could work for broadband strong ground motion prediction if we could assume appropriate source parameters and a wide-range accurate velocity structure model three-dimensionally extended to undersea parts, the crust and Philippine Sea plate. We also confirmed the distinct excitation of long-period ground motion in the TMA by a giant subduction-zone earthquake along the Nankai trough. For a further improvement, we have to tune the velocity structure model and its details such as an accretionary prism, by using observed records of small- or medium-size earthquakes.

We constructed source and velocity structure models for subduction-zone earthquakes threatening the TMA and applied the method of strong ground motion prediction to them. We then confirmed the advancement of the strong ground motion prediction method, and in particular the usefulness of the deterministic method for evaluating long-period ground motions. As problems to be solved in a future, we should clarify the relation between asperities and strong motion generation areas on a plate boundary, and introduce heterogeneity based on a dynamic physics model into the source model. We should develop a method of efficiently tuning a velocity structure model with observed records and extend it to larger ranges.

Acknowledgements:

This study was supported by the DaiDaiToku project I from the Ministry of Education, Culture, Sport, Science, and Technology (MEXT).

References:

- Earthquake Research Committee (ERC) (2005), "National Seismic Hazard Maps for Japan", Separate Volume 1, 213pp. (in Japanese).
- Hata, N., Miyake, H. and Koketsu, K. (2006), "Strong motion generation area and asperity of subduction-zone earthquakes," *Abstracts of the Japan Geoscience Union Meeting 2006*, Paper No. S204-008.

- Hatayama, K., Zama, S., Nishi, H., Yamada, M., Hirokawa, M., Inoue, R. (2004), "Long-period strong ground motion and damage to oil storage tanks due to the 2003 Tokachi-oki earthquake," *Zisin*, **57**, 83-103 (in Japanese).
- Irikura, K. and Miyake, H. (2001), "Prediction of strong ground motions for scenario earthquakes, *J. Geography*, **110**, 849-875.
- Irikura, K., Miyake, H., Iwata, T., Kamae, K., Kawabe, K. and Dalguer L.A. (2003), "Recipe for predicting strong ground motion from future large earthquake," *Annals Disas. Prev. Res. Inst. Kyoto Univ.*, **46B**, 105-120 (in Japanese).
- Ishida, M. (1992), "Geometry and relative motion of the Philippine sea plate and Pacific plate beneath the Kanto-Tokai district, Japan," *J. Geophys. Res.*, **97**, 489-513.
- Miyake, H., Iwata, T. and Irikura, K. (2003), "Source characterization for broadband ground-motion simulation: Kinematic heterogeneous source model and strong motion generation area", *Bull. Seism. Soc. Am.*, **93**, 2531-2545.
- Kobayashi, R. and Koketsu, K. (2005), "Source process of the 1923 Kanto earthquake inferred from historical geodetic, teleseismic, and strong motion data," *Earth Planets Space*, **57**, 261-270.
- Koketsu, K., Fujiwara, H. and Ikegami, Y. (2004), "Finite-element simulation of seismic ground motion with a voxel mesh", *Pure Appl. Geophys.*, **161**, 2463-2478.
- Koketsu, K., Hatayama, K., Furumura, T., Ikegami, Y. and Akiyama, S. (2005), "Damaging long-period ground motions from the 2003 Mw 8.3 Tokachi-oki, Japan, earthquake," *Seismological Research Letters*, **76**(1), 67-73.
- Miyake, H., Koketsu, K., Furumura, T., Inagaki, Y., Masuda, T. and Midorikawa, S. (2006), "Integration of the shallow subsurface -structure model for strong ground motion prediction in the Tokyo metropolitan area," *Proc. 12th Jpn. Earthq. Eng. Symp.*, 214-217.
- Miyake, H., Murotani, S. and Koketsu, K. (2006), "Scaling of asperity size for plate-boundary earthquakes," *Chikyu Monthly*, extra issue No.55, 86-91 (in Japanese).
- Moroi, T. and Takemura, M. (2002), "Re-evaluation on the damage statistics of wooden houses for the 1923 Kanto earthquake and its seismic intensity distribution in and around southern Kanto district," *J. Jpn. Assoc. Earthq. Eng.*, **2**, 35-71 (in Japanese).
- Murotani, S., Miyake, H., Koketsu, K. (2005), "Source scaling of heterogeneous slip models for subduction-zone earthquakes," *Abstracts of the 2005 Japan Earth and Planetary Science Joint Meeting*, Paper No. S052-006.
- Nagai, R., Kikuchi, M. and Yamanaka, Y. (2001), "Comparative study on the source processes of recurrent large earthquakes in Sanriku-oki Region: the 1968 Tokachi-oki earthquake and the 1994 Sanriku-oki earthquake," *Zisin*, **54**, 281-298.
- Okada, T., Matsuzawa, T. and Hasegawa, A. (2003), "Comparison of source areas of M4.8 +/- 0.1 repeating earthquakes off Kamaishi, NE Japan: Are asperities persistent features?," *Earth Planet. Sci. Lett.*, **213**, 361-374.
- Sato, T., Graves, R.W., and Somerville, P.G. (1999), "Three-dimensional finite difference simulation of long-period strong motion in the Tokyo metropolitan area during the 1990 Odawara earthquake (MJ 5.1) and the great 1923 Kanto earthquake (Ms 8.2) in Japan," *Bull. Seism. Soc. Am.*, **89**, 579-607.
- Sato, H., Hirata, N., Koketsu, K., Okaya, D., Abe, S., Kobayashi, R., Matsubara, M., Iwasaki, T., Ito, T., Ikawa, T., Kawanaka, T., Kasahara, K. and Harder, S. (2005), "Earthquake source fault beneath Tokyo," *Science*, **309**, 462-464.
- Sato, H., Hirata, N., Koketsu, K., Okaya, D., Abe, S., Kobayashi, R., Matsubara, M., Iwasaki, T., Ito, T., Ikawa, T., Kawanaka, T., Kasahara, K. and Harder, S. (2005), "Earthquake source fault beneath Tokyo," *Science*, **309**, 462-464.
- Tanaka, Y., Koketsu, K., Miyake, H., Furumura, T., Sato, H., Hirata, N., Suzuki, H., Masuda, T. (2005), "The Daidaitoku community model of the velocity structure beneath the Tokyo metropolitan area (1)," 2005 Japan Earth and Planetary Science Joint Meeting, S079-P010.
- Tanaka, Y., Miyake, H., Koketsu, K., Furumura, T., Hayakawa, T., Baba, T., Suzuki, H. and Masuda, T. (2006), "The DaiDaiToku Integrated Model of the Velocity Structure beneath the Tokyo Metropolitan Area (2)," Japan Geoscience Union Meeting 2006, S116-P14.
- Yamanaka, Y. and Kikuchi, M. (2004), "Asperity map along the subduction zone in northeastern Japan inferred from regional seismic data," *J. Geophys. Res.*, **109**(B7), Art.No.B07307.
- Yokota, H., Kataoka, S., Tanaka, T. and Yoshizawa, S. (1989), "Estimation of long-period ground motion of the 1923 great Kanto earthquake," *J. Struct. Const. Eng. Trans. Arch. Inst. Jpn.*, 401, 35-45.
- Wu, C. and Koketsu, K. (2006), "Complicated repeating earthquakes on the convergent plate boundary: Rupture processes of the 1978 and 2005 Miyagi-ken oki earthquakes," *Report of the Grant-in-Aid for Special Purposes No. 178000022005*, 31-36.

LONG-PERIOD STRONG GROUND MOTIONS AND DAMAGE TO OIL STORAGE TANKS DUE TO THE MW8.0 2003 TOKACHI-OKI EARTHQUAKE

K. Hatayama¹⁾

*1) Senior Research Engineer, National Research Institute of Fire and Disaster, Japan
hatayama@fri.go.jp*

Abstract: The Mw8.0 2003 Tokachi-oki, Japan, earthquake generated large-amplitude long-period (several seconds to around 10 s) ground motions in the Yufutsu sedimentary basin, Hokkaido and the consequent large liquid sloshing in oil storage tanks caused severe damage such as fires and sinking of floating roofs to seven large tanks in the Tomamomai west port located in the basin. We present five lessons for predicting long-period strong ground motions and severe sloshing damage to oil storage tanks by reviewing the sloshing damage to the tanks in Tomakomai and analyzing the long-period strong ground motions observed in the Yufutsu basin.

1. INTRODUCTION

The 2003 Tokachi-oki earthquake of Mw8.0 (Japan Meteorological Agency, 2003) that occurred in the subduction zone southeast off Hokkaido, Japan, generated large-amplitude long-period ground motions with periods from several seconds to around 10 s in a few sedimentary basins in Hokkaido and these long-period strong ground motions excited the sloshing of liquid in large oil storage tanks and caused damage to many of them (Hatayama et al., 2004). The most severe damage occurred in floating-roof-type oil storage tanks of the refinery in the city of Tomakomai that occupies part of the Yufutsu sedimentary basin located in the southwestern part of Hokkaido. In the refinery, fire broke out from the top of two tanks and floating roofs sank into oil in six tanks. These severely damaged tanks had a natural period of the fundamental or the second mode of liquid sloshing between 5 and 12 s.

In and around the Yufutsu sedimentary basin, the strong ground motions from the 2003 Tokachi-oki earthquake were recorded at many sites by K-NET and KiK-net of the National Research Institute for Earth Science and Disaster Prevention and other strong-ground-motion seismograph networks in Japan. This dataset allows us to study the detailed features of shaking such as the spatial variation in amplitudes of long-period strong ground motions in the basin.

In this paper, we review the 2003 Tokachi-oki earthquake with respect to the sloshing damage to the oil storage tanks in the city of Tomakomai and the features of the long-period strong ground motions observed within the Yufutsu sedimentary basin to derive lessons in predicting long-period strong ground motions and severe sloshing damage to tanks.

2. DAMAGE TO OIL STORAGE TANKS

Table 1 lists oil storage tanks that suffered severe damage during the 2003 Tokachi-oki earthquake. All of these tanks stood in the refinery (R-Tomakomai in Figure 1) located in the Tomakomai west port. Two fires occurred at the tanks A and B. The one was the ring fire that lasted for about 7 hours (Photo 1), while the other was the open top fire (Photo 2) that lasted for about 44 hours. Photo 3 shows the two tanks C and D in which the floating roofs sank into the oil and the kerosene was exposed to the atmosphere. It is considered that the sinking occurred because the damage to the pontoons of the floating roofs by liquid sloshing led to loss of buoyancy of the floating roofs. Photo 3 also shows the naphtha tank B whose shell plate was deformed beyond recognition as a result of the 44-hour-lasting fire.

Table 1 also lists the observed maximum heights of sloshed oil and the calculated ones from the two horizontal components of the seismogram recorded in the refinery, together with the natural periods of the fundamental mode of sloshing (T_s) that are determined by the diameter of tank and the liquid height. The maximum height of sloshed oil usually means the maximum amplitude of sloshing round the inner wall of the shell plate of the tank. This table shows that the severely damaged tanks with a capacity of 30,000 or 40,000 m³ and 110,000 m³ suffered large sloshing with the maximum amplitude of about 3 m and about 1.3 m, respectively. The former tanks and the latter tanks had a natural period of the fundamental mode of sloshing of 7 to 8 s and about 12 s, respectively.

3. LESSONS FROM DAMAGE TO TANKS

3.1 Conditions for Severe Damage

Hatayama et al. (2004) found the conditions for which severe damage such as fires and sinking of floating roofs occurs, through checking the maximum heights of sloshed oil with the damage to the oil storage tanks. Since the maximum height of sloshed oil was not measured for all the tanks, they calculated it for all the large tanks in Tomakomai based on the seismograms obtained near the tank sites. For the tanks for which the maximum heights of sloshed oil were measured, the calculated heights

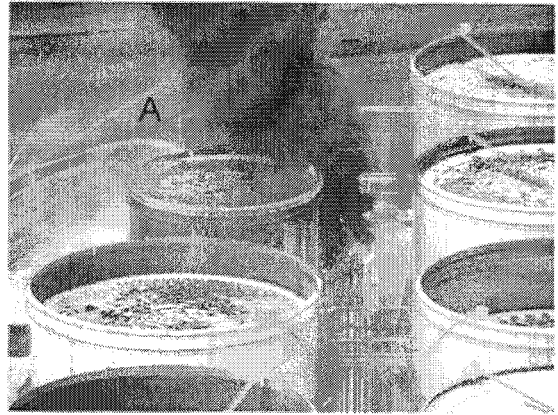


Photo 1. Ring fire at the crude oil tank A (Table 1) in the city of Tomakomai photographed by the Sapporo Fire Bureau. This fire lasted for about 7 hours.

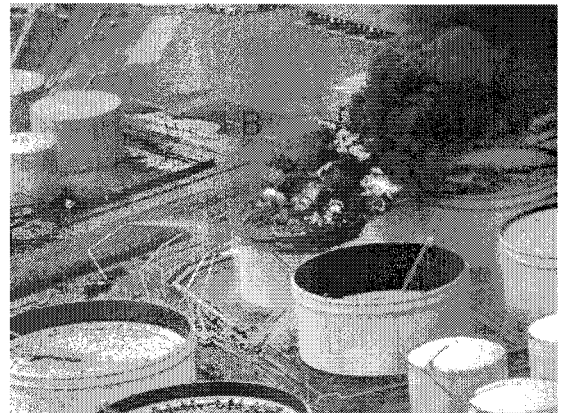


Photo 2. Open top fire at the naphtha tank B (Table 1) in the city of Tomakomai photographed by the Sapporo Fire Bureau. This fire lasted for about 44 hours.

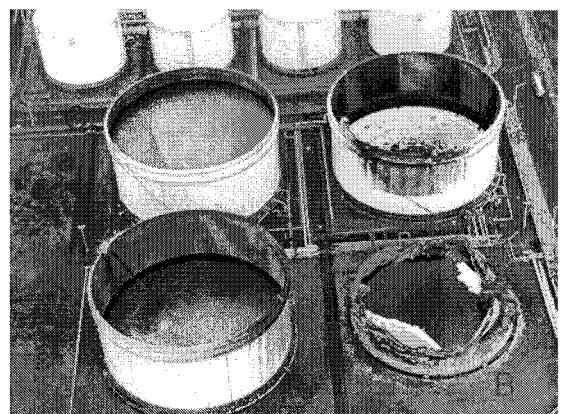


Photo 3. Floating roofs that sank in the two kerosene tanks C and D (Table 1) and deformed tank shell plate of the naphtha tank B after the long-lasting open top fire, photographed by the Sapporo Fire Bureau.

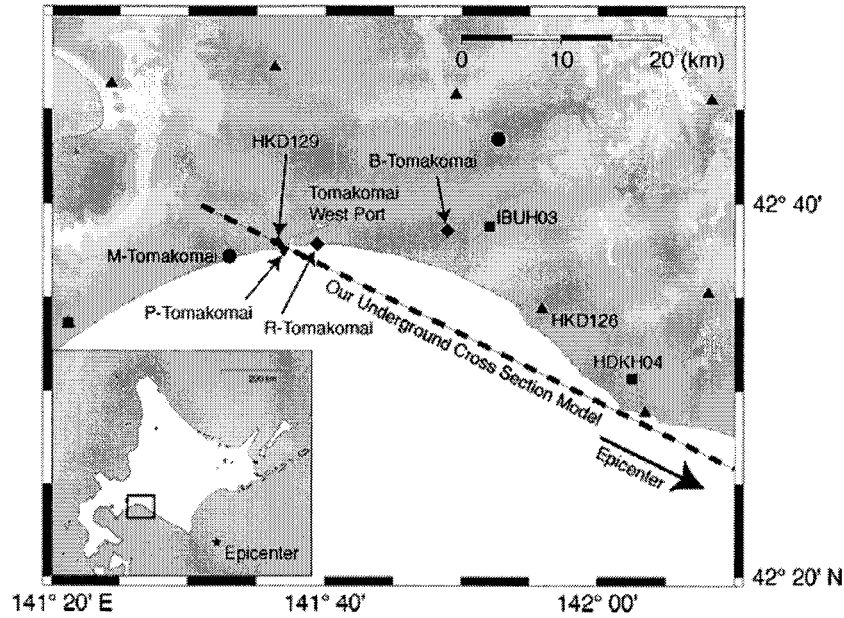


Figure 1. Strong-ground-motion observation stations in the Yufutsu basin. Along the broken line, our 2-D underground models were assumed for numerical simulations of wave propagation.

Table 1. Severely damaged floating-roof-type oil storage tanks in Tomakomai (after Hatayama et al., 2004).

Tank	Capacity (m ³)	Oil ¹⁾	Diameter (m)	Liquid Height ²⁾ (%)	Ts ³⁾ (s)	Wh (Obs.) ⁴⁾ (m)	Wh (Cal.) ⁵⁾ (m)	Damage ⁶⁾
A	32,778	CR	42.7	89	7.0	~3	2.9	R. Fire
B	32,779	N	42.7	77	7.1	-	2.9	Sink & O. Fire
C	43,872	K	49.4	91	7.6	>2.1	3.4	Sink
D	43,872	K	49.4	91	7.6	>2.1	3.4	Sink
E	43,872	S	49.4	64	8.1	-	2.9	Sink
F	109,900	CR	78.2	59	12.0	-	1.3	Sink
G	109,900	CR	78.2	58	12.1	~1.3	1.3	Sink

1) CR=Crude oil/N=Naphtha/K=Kerosene/S=Slop.

2) Percentage of liquid height during the earthquake to tank height.

3) Natural period of the fundamental mode of sloshing.

4) Observed maximum sloshing wave height.

5) Maximum height of sloshed oil calculated from the two horizontal components of the observed ground motion.

6) Sink=Sinking of floating roof/O. Fire=Open top fire/R. Fire=Ring fire.

agreed well with the observed ones. Figure 2 plots the calculated maximum heights of sloshed oil against Ts. The gray and black dots represent the tanks that suffered some sort of damage and the severe damage, respectively. These severely damaged tanks are listed in Table 1. This figure suggests that severe damage such as fires and sinking of floating roofs can occur if the sloshing amplitude is beyond around 3 m at the large tanks with Ts around 7 or 8 s. These natural periods correspond to a capacity of 30,000 or 40,000 m³ if the tank is full. This suggestion will be important as a condition to predict severe sloshing damage to tanks. Although some of the sloshing amplitudes are beyond 3 m in the tanks with Ts of around 5 s, they did not suffer the severe damage. This would be because the tanks of such size have structures hard to suffer the severe damage—their roofs are of cone or dome type. On the other hand, the tanks with Ts around 12 s suffered sinking of the floating roofs with the sloshing amplitude of only 1.3 m. We discuss the reason in the next subsection.

3.2 Effects of Higher Modes

The tanks that suffered sinking of the floating roofs with the sloshing amplitude of only 1.3 m are the tanks F and G (Table 1) with a capacity of about 110,000 m³. Figure 3 plots the liquid surface displacements for the tank F at a certain moment. These displacements were calculated based on the seismograms obtained near the tank site and the effects of the floating roof are omitted in this calculation. At this moment, the second mode of sloshing is predominant, although the fundamental model is also predominant at other moments. The higher modes may generate larger strain than the fundamental mode on the assumption that the floating roof follows the shape of the liquid surface. The higher modes do not contribute to the maximum heights of sloshed oil round the inner wall of the shell plate. These two things can explain the fact that the floating roofs of the tanks F and G were damaged even though the maximum heights of sloshed oil were not so large. We therefore consider that the higher modes can damage floating roofs of large tanks with a capacity of around 100,000 m³. For the

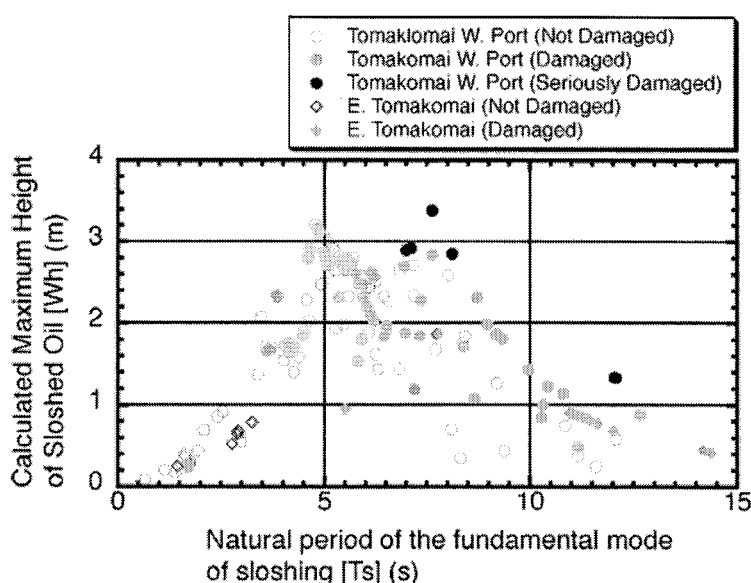


Figure 2. Calculated maximum heights of sloshed oil for large oil storage tanks in Tomakomai (after Hatayama et al., 2004). The calculation is made for the tanks in which the actual maximum heights were not measured as well as the tanks in which they were measured. The severely damaged tanks denoted by the black circles are listed in Table 1.

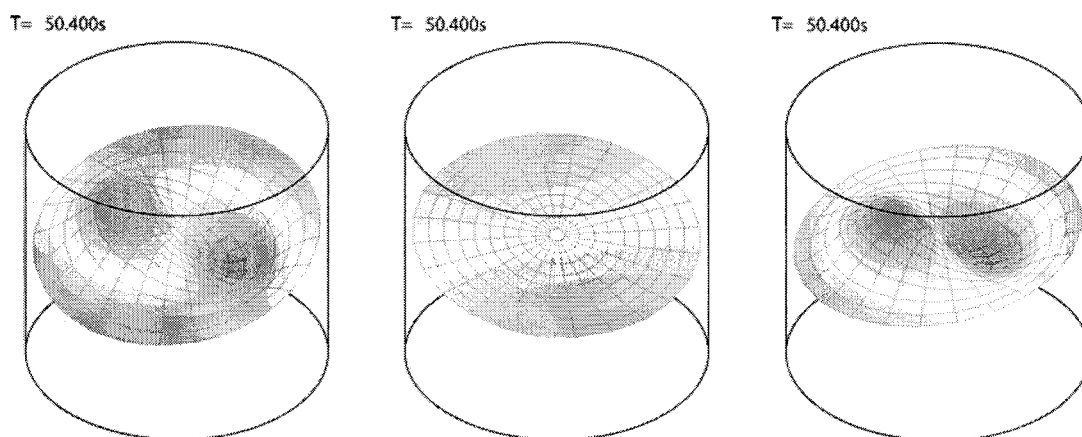


Figure 3. Liquid surface displacements calculated for Tank F listed in Table 1) of which floating roof sank into oil. This snapshot is from the moment when the second mode of sloshing is predominant. (Left) Sum of the fundamental, the second, and the third modes; (Middle) The fundamental mode only; (Right) The second mode only.

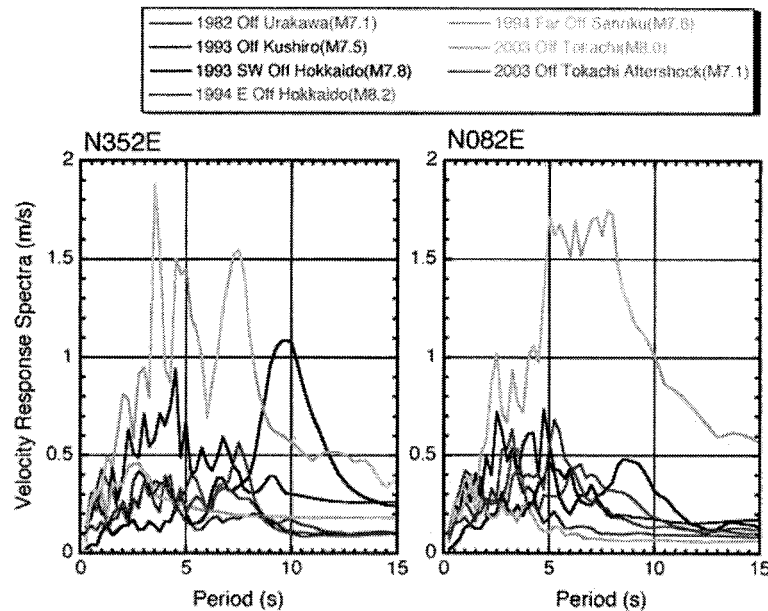


Figure 4. Velocity response spectra with adamping factor of 0.01 of the accelerograms recorded during the past large earthquakes at P-Tomakomai. (Left) N352E component; (Right) N082E component. The responses are calculated from the whole time histories.

tanks F and G, the natural period of the second mode was 5.6 s. The spectral amplitude of the ground motions observed near the tank site was larger at this period than at the natural period of the fundamental mode. It follows that the long-period strong ground motions should be predicted within a broad period range including not only the natural period of the fundamental mode of sloshing but also those of the higher modes in predicting sloshing damage to large tanks with a capacity of around 100,000 m³.

4. LESSONS FROM OBSERVED LONG-PERIOD STRONG GROUND MOTIONS

4.1 Earthquake-Dependent Predominant Periods

The station of P-Tomakomai (Figure 1) has been operated for about three decades by the Port and Airport Research Institute, Japan. Figure 4 shows the velocity response spectra with a damping factor (h) of 0.01 calculated from the P-Tomakomai seismograms of the large earthquakes after 1982. The velocity responses of the 2003 Tokachi-oki earthquake (orange line) are predominant at the periods from 5 to 8 s. Within this period range, the 2003 Tokachi-oki earthquake prevails over any other events in the velocity responses. However, the velocity responses of the 1993 Hokkaido Nansei-oki earthquake (black line) are predominant at the periods from 9 to 10 s. Within this period range, the N-S-component velocity responses are larger than those of the 2003 Tokachi-oki earthquake. This difference in the predominant periods means that the predominant periods of the long-period strong ground motions at the site of P-Tomakomai are not determined only by the underground structure in its vicinity and suggests the necessity of considering the source and the path effects as well as the site effects even in predicting only the predominant periods.

4.2 Significant Spatial Variations

Figure 5 shows the velocity response spectra ($h = 0.01$) calculated from the seismograms recorded at the strong-ground-motion stations (Figure 1) during the 2003 Tokachi-oki earthquake. The E-W-component spectra of the three stations (R-Tomakomai, P-Tomakomai, HKD129) in the Tomakomai west port area show high-level responses over 1.5 m/s in the period range of 4 to 8 s. On

the other hand, the velocity responses of M-Tomakomai and B-Tomakomai are much smaller compared with the port area at periods longer than 3 s. At a period of 7 s, for example, the E-W velocity response of R-Tomakomai (1.9 m/s) is almost double that of B-Tomakomai (0.9 m/s). It turns out that the amplitudes and the predominant periods of the observed long-period strong ground motions varied significantly within the basin, and the strongest long-period shaking was recorded around the Tomakomai west port area of all the sites in the basin.

Figure 6 implies more significant spatial variations in long-period strong ground motions. This figure displays the maximum heights of sloshed oil observed at the tanks in the oil storage base in the eastern part of Tomakomai (B-Tomakomai shown in Figure 1) during the 2003 Tokachi-oki

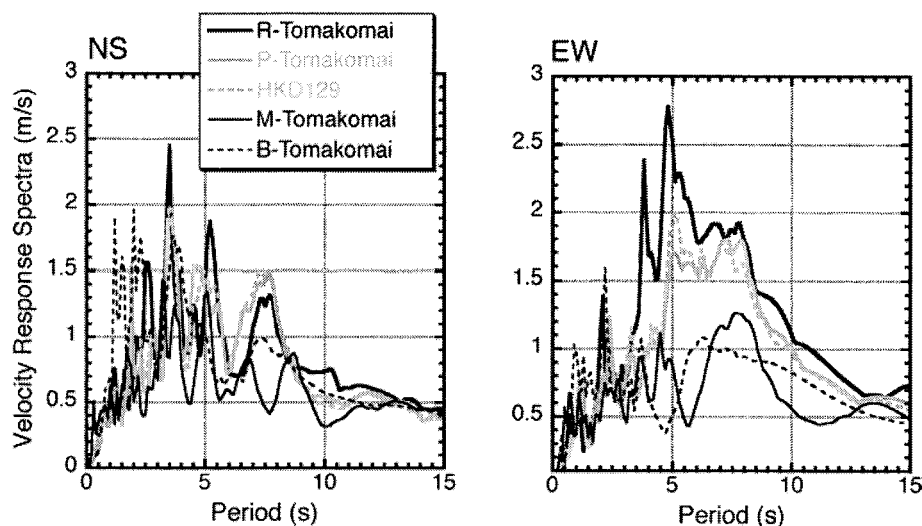


Figure 5. Velocity response spectra with a damping factor of 0.01 of the accelerograms recorded in the Yufutsu basin. (Left) N-S component; (Right) E-W component. The responses are calculated from the whole time histories.

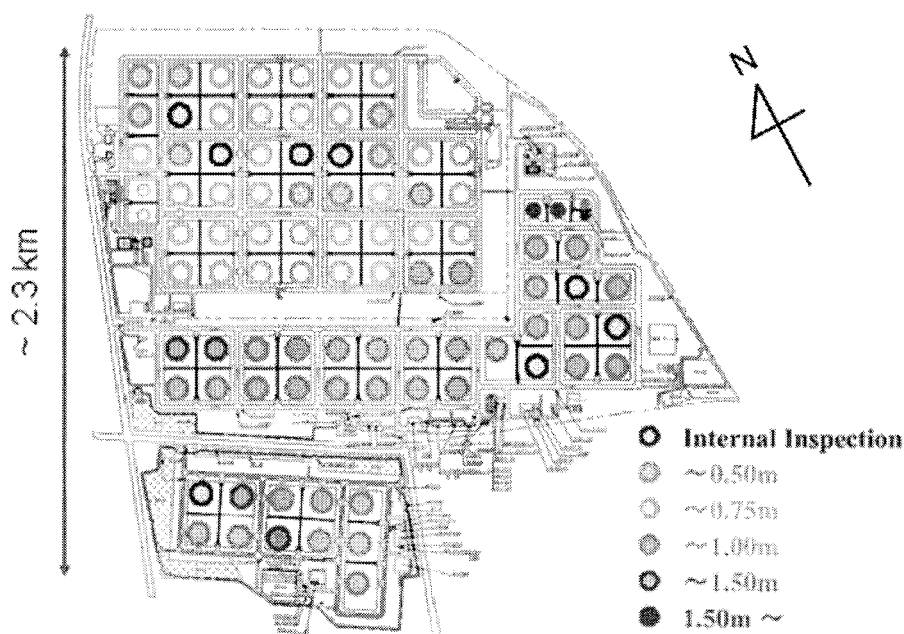


Figure 6. Maximum heights of sloshed oil observed at the tanks in the oil storage base in the eastern part of Tomakomai (B-Tomakomai shown in Figure 1) during the 2003 Tokachi-oki earthquake [after Kaita (2004)].

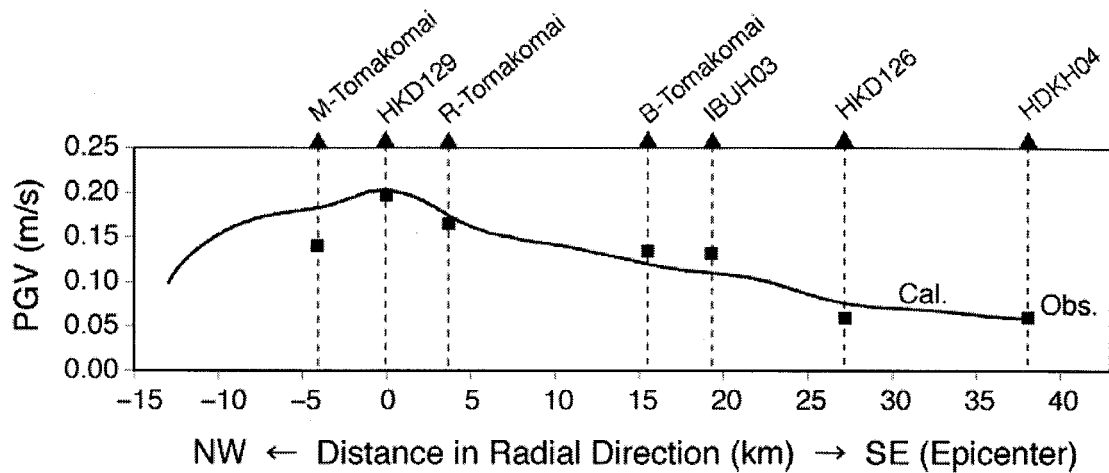


Figure 7. Peak ground velocities of the observed radial-component seismograms (squares) and the calculated ones (a thick line) by the 2-D numerical modeling for an assumed underground structure model of the Yufutsu basin. The period range is 6.5-15 s.

earthquake. The tank size ($\sim 110,000 \text{ m}^3$) and the liquid height ($\sim 21 \text{ m}$) are the same and accordingly the natural periods of sloshing are the same, but three different types of floating roofs are included. Larger sloshing was observed in the southern part of the base as compared with the northern part. This spatial variation in sloshing may possibly correspond to a spatial variation in the input long-period shaking, although it might be partly due to the difference in the type of the floating roof.

These observations indicate the possibility that the features of long-period strong ground motions can vary significantly within small distances of several kilometers and suggest the importance of pinpoint prediction of long-period strong ground motions.

4.3 Underground Structure Controlling Long-Period Strong Ground Motions

To study the reason why the strongest long-period shaking was observed around the Tomakomai west port, we simulated the seismic-wave propagation by 2-D modeling, assuming the underground structure model of the Yufutsu basin based on the data from the array measurements of microtremors conducted in the basin (Kanno et al., 2005). As a result, our calculated waveforms agreed very well with the observed ones. Figure 7 compares the PGVs of the observed and calculated traces within a period range of 6.5 to 15 s. This figure shows that the spatial variation of PGV in the Yufutsu basin is successfully reproduced by our simulation, except for some discrepancy at M-Tomakomai. It follows that our Yufutsu basin model can explain the spatial variation in amplitudes of the long-period strong ground motions observed there during the 2003 Tokachi-oki earthquake. The characteristics of the basin structure model assumed here are: (1) The depth of bedrock with an S-wave velocity over 3 km/s is about 4 km beneath the Tomakomai west port, whereas it increases to 6 km beneath the eastern part of Tomakomai, where the long-period shaking was weaker compared with the port area; (2) The low-velocity ($< 0.8 \text{ km/s}$) sedimentary layers deposited close to the ground surface are thickest in the port area. We therefore consider that the thickness of the near-surface ($< 1 \text{ km}$) soft sediments rather than the bedrock depth governed the spatial variation in amplitudes of the long-period (7 to 8 s) shaking in the basin during the 2003 Tokachi-oki earthquake. These findings suggest the importance of data of detailed structures of near-surface soft deposits as well as data of deep basin structures such as bedrock depth for accurate prediction of long-period strong ground motions in deep sedimentary basins.

5. CONCLUSIONS

We have presented five lessons for predicting long-period strong ground motions and severe sloshing damage to oil storage tanks, by reviewing the 2003 Tokachi-oki earthquake with respect to the sloshing damage to the oil storage tanks in the city of Tomakomai and by analyzing the long-period strong ground motions observed within the Yufutsu sedimentary basin.

The following two lessons have been derived from reviewing the sloshing damage to the tanks;

(1) Severe sloshing damage such as fires and sinking of floating roofs can occur if the maximum height of sloshed oil is beyond around 3 m at large floating-roof-type tanks whose capacity is over 30,000 m³;

(2) Not only the fundamental mode of sloshing but also the higher modes can cause damage to floating roofs of large tanks with a capacity of around 100,000 m³ and so long-period strong ground motions should be predicted within a broad period range including natural periods of higher modes as well as those of the fundamental mode.

The following three lessons have been derived from analyzing the observed long-period strong ground motions;

(3) Predominant periods of long-period strong ground motions can depend on earthquakes and so it is necessary to consider the source and the path effects as well as the site effects even in predicting only predominant periods at a certain site;

(4) Features of long-period strong ground motions can vary significantly within small distances of several kilometers in sedimentary basins and so the site specification is important in predicting long-period strong ground motions;

(5) It is important to consider detailed structures of soft deposits existing close to the ground surface as well as deep basin structures such as bedrock depth for accurate prediction of long-period strong ground motions in deep sedimentary basins.

Acknowledgements:

We used the strong-ground-motion data from K-NET and KiK-net of the National Research Institute for Earth Science and Disaster Prevention, Japan; the strong-motion observation stations in Japanese ports of the Port and Airport Research Institute, Japan; the Japan Meteorological Agency 95-type seismic intensity meters; the municipality seismic intensity meters; and the seismometers installed at the refinery and the oil storage base in Tomakomai. This study was partly supported by Grant-in-Aid for Scientific Research 16310125 from the Ministry of Education, Culture, Sports, Science and Technology, Japan.

References:

- Hatayama, K., Zama, S., Nishi, H., Yamada, M., Hirokawa, Y. and Inoue, R. (2004), "Long-period strong ground motion and damage to oil storage tanks due to the 2003 Tokachi-oki earthquake," *Zisin* (Journal of the Seismological Society of Japan) **57**, 83-103, in Japanese.
- Kaita, S. (2004), "The damage of the national oil storage bases by the 2003 Tokachi-oki earthquake," PVP-Vol. 490, Storage Tank Integrity and Materials Evaluation, ASME, 233-234.
- Kanno, T., Hatayama, K., Tsuno, S., Kudo, K., Maeda, T., Sasatani, T., Furumura, T. and Sakaue, M. (2005), "Estimation of deep underground structures in Yufutsu region by using array observations of microtremors," Programme and Abstracts of the 2005 Fall Meeting of the Seismological Society of Japan, p. 83, in Japanese.
- Koketsu, K., Hatayama, K., Furumura, T., Ikegami, Y. and Akiyama, S. (2005), "Damaging long-period ground motions from the 2003 Mw 8.3 Tokachi-oki, Japan, earthquake," *Seism. Res. Lett.*, **76**, 67-73.

DEVELOPING CONSTRAINTS ON EXTREME GROUND MOTIONS BASED ON FOAM RUBBER MODEL

Y. Uchiyama¹⁾, M. D. Purvance²⁾, J. N. Brune³⁾, A. Anooshehpour³⁾, and J.G. Anderson³⁾

1) Research Engineer, Technology Center, Taisei Corp., Japan

2) Post-Doctoral Fellow, Nevada Seismological Laboratory, University of Nevada, Reno, USA

3) Professor, Nevada Seismological Laboratory, University of Nevada, Reno, USA

*yasuo.uchiyama@sakura.taisei.co.jp, mdp@seismo.unr.edu, brune@seismo.unr.edu, rasool@seismo.unr.edu,
jga@seismo.unr.edu*

Abstract: Probabilistic seismic hazard analysis (PSHA) is based on statistical assumptions that are questionable when extended to very low probabilities. Some results of important PSHA studies are controversial due to prediction of what seem to be anomalously high hazards at long periods. The short historical database of instrumental recordings is not sufficient to determine the uncertainties in the statistics assumptions. To examine the potential to improve PSHA, we have studied the distribution of peak particle motions for 3708 identified events in the foam rubber model where loading conditions have been kept consistent between runs. The distributions of peak acceleration and peak velocity surprisingly show bi-modal distributions, with approximately log-normal distribution values for the most common types of events, and another peak at much higher but less frequent values.

1. INTRODUCTION

Probabilistic seismic hazard analysis (PSHA) is based on statistical assumptions that are questionable when extended to very low probabilities. For example, the computed mean hazard at Yucca Mountain, Nevada (the designated site of the United States high-level nuclear waste repository) predicts peak accelerations on hard rock of over 11 g and peak velocities of over 13 m/s for annual exceedance rates of 10^{-8} (Stepp et al., 2001). For comparison the largest observed peak acceleration is about 2-3 g, and the observed peak velocity is about 200-300 cm/s. We do not have accelerograph evidence to prove that the PSHA results are incorrect. The short historical database for instrumental recordings is not sufficient to determine the uncertainties in the statistical assumptions.

Brune (1996) found 10,000 year old precarious rocks near the San Andreas fault in Southern California that are not consistent with the national seismic hazard map at annual exceedance rates 4×10^{-4} (Frankel et al., 1996, 2002). These findings suggest that we should look for alternate methods to help understand the mechanisms that might lead to rare and extreme ground motions.

Brune (1973) first suggested that ruptures produced in foam rubber might provide valuable information regarding the dynamics of tectonic fault. Subsequent research has provided significant insight, the presence of dynamic slip pulses accompanied by fault normal separation (Brune et al., 1989; Anooshehpour and Brune, 1994), the lack of the frictional heat production during dynamic stick-slip events (Anooshehpour and Brune, 1994), dynamic geometric effects on strong ground motion (Brune and Anooshehpour, 1998, 1999a), and a means for better understanding of the physical parameters that control near field ground motions during earthquakes (Brune et al., 1993).

To examine the potential to improve PSHA, we are modeling strike-slip motion using foam rubber

in this study. We analyze the distributions of extreme peak particle motions and discuss the possibility of defining upper bounds on ground motions. These results were reported at the Annual Meeting of the Southern California Earthquake Center, 2006 (Purvance et al., 2006).

2. FOAM RUBBER MODEL

2.1 Rationale for Foam Rubber Modeling

Physical models of faulting, as distinct from some numerical or mathematical models, are guaranteed to obey static and dynamic mechanical laws and thus can be used to gain insight into possible physical processes involved. Of course, there are inherent problems of scaling laboratory models to the real Earth. Such models can nonetheless provide important insight and constraints on numerical and theoretical models.

Foam rubber is very flexible, that is, it has a low rigidity, so that it is easy to produce large strain and particle motions. Since foam rubber is lightweight, relatively large models can be constructed, enabling the scale of dynamic phenomena to be enlarged. This allows dynamic features to be more easily observed and recorded using relatively simple electronic devices, such as tiny accelerometers and position sensing devices. Foam-rubber models automatically assure that motions are physically realistic (no singularities or unreasonable specified slips). However, this does not guarantee that the motions will correspond to motions from actual earthquakes, since there are inherent difficulties scaling with any laboratory size model (rock or foam rubber) to large-scale Earth phenomena.

Some of the major limitations of foam-rubber modeling include the following:

1. Intrinsic Q is low (of the order 10) and cannot be controlled. This constrains the usefulness of foam rubber modeling to wave propagation distances which are not too large compared to the wavelengths involved. Thus it is most useful to gain insight into near-source phenomena. (An advantage of the low Q is that there is relatively little energy scattered back from the distant sides of the model, which could interfere with the dynamics.)

2. The fault surface friction conditions are difficult to control. The lattice of foam rubber vesicles produces extreme roughness on a small scale (of the order of a millimeter). The coefficient of friction is of the order of 10, whereas that for rocks is of the order of 0.5. Thus to produce fault slip, the strains must be very large, of the order of 10^{-2} , whereas in the Earth the corresponding strains may be as low as about 3×10^{-4} (stress drops are about 100 bars). As long as strains are approximately linear, the difference can be adjusted for. However, in both the foam rubber and the real Earth, the fault behaviors probably nonlinear on the fault trace, and there is no guarantee that the nonlinearities in the foam model correspond to those in the real Earth (similar concerns are common to kinematic models theoretical models, and rock and plastic analogs).

2.2 Description of Foam Rubber Model

The model consists of two large blocks of foam rubber ($1 \times 2 \times 2 \text{ m}^3$), one driven horizontally over the other by a hydraulic piston (Figure 1). The lower block is securely glued to a plywood sheet that is turn anchored to the concrete floor. The upper block and the attached rigid frame are supported by four steel pipes and are equipped with scaffolding jacks and guiding rollers at each corner. Normal force at the contact (fault) is provided by the weight of the upper block and is varied by lowering or raising the jacks. A hydraulic piston, placed between a concrete wall and the upper frame, pulls the upper block, creating the normal fault stress geometry.

As the upper block is forced to slide over the lower block, the strain in the blocks increases until the stress at the interface exceeds the frictional resistance and a stick-slip event occurs over the whole boundary. Successive events usually cause the same amount of average slip ($\sim 1 \text{ cm}$) between the blocks, but the pattern of slip can vary with the initiating at the different points and propagating in

different directions. If the driving displacement is steady, the events repeat more or less regularly until the upper block has slipped about 20 cm, corresponding to about 20 characteristics events with some additional smaller events. At this point, the hydraulic piston is fully extended, and one experiment run is complete. The stress is removed and the upper block lifted and moved back to the starting position for repeat of the procedure.

2.3 Instrumentation

Displacement at the foam surface is measured by a telescopic, two-axis, position-sensing detector, which is focused on a small LED embedded in the foam. The Dual Axis Super Linear Position Sensor (DLS10, manufactured by the United Detector Technology Sensor, Inc.) is a square of photovoltaic material, 1 cm on a side. The sensor locates the centroid of a light spot projected upon it and provides continuous output as the light spot moves from the null point to either direction along each of the two perpendicular axes. The output of the position-sensing detector depends on the location as well as the intensity of the bright spot. Therefore, it is necessary to calibrate detectors before and after each experimental run. The resolution of the DLS10 sensors is limited only by the intensity of the light source and the signal-resolving circuitry. In our experiments, the resolution is better than 0.01 cm.

Due to foam rubber's low density and high elasticity, particle acceleration in a stressed foam rubber model of earthquakes can exceed several hundred g. Slips of the order of 1 cm can take place in a few milliseconds, resulting in very large acceleration at high frequencies. In order to measure these accelerations, accelerometers with a high dynamic range and low mass (to minimize the mass loading effects) are needed. We have 64 ultra-light ENDEVCO Model 25A accelerometers (24 on the free surface and 38 on the fault plane). The model 25A accelerometers with a dynamic range of ± 1000 g. In order to further reduce the mass-loading effects, each accelerometer is mounted on a styrofoam disk, 3.8 cm in diameter, before inserting them in the foam; the 3-mm-thick styrofoam disk (with the same density as the foam rubber used in the model, but far more rigid) distributes the accelerometer's mass over a large area.

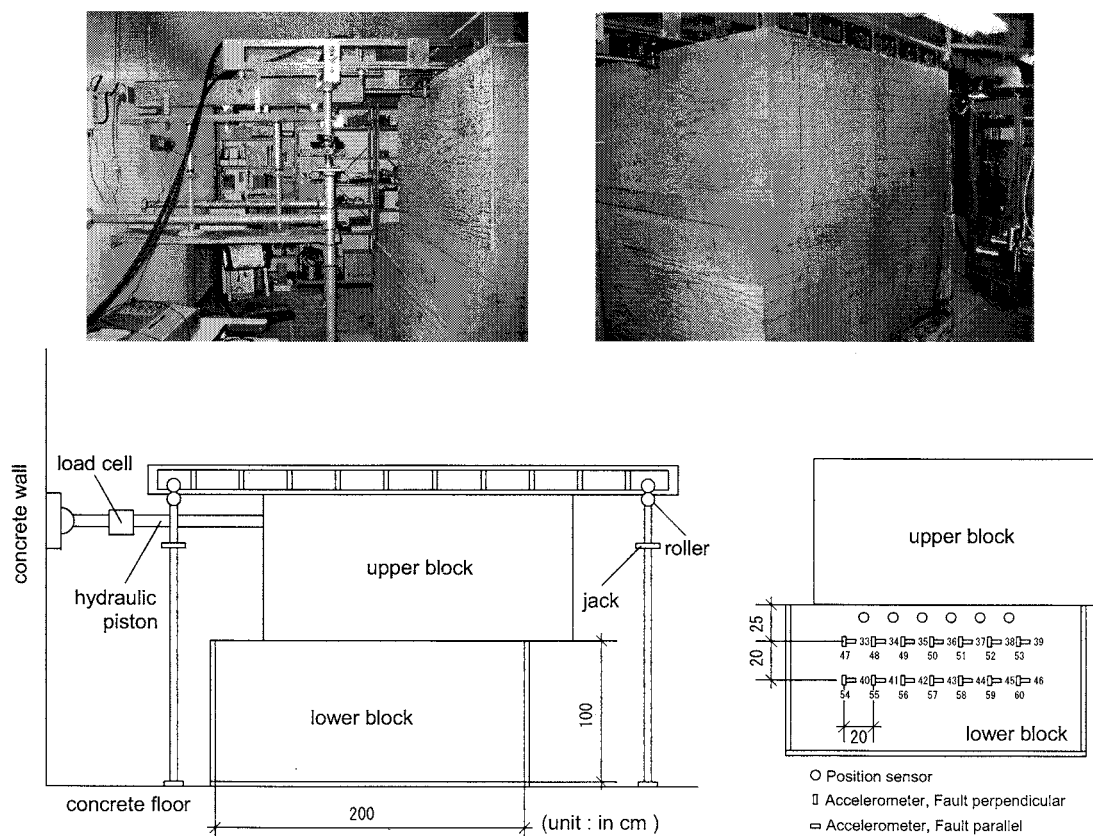


Figure 1. A diagrams of the foam rubber model of strike-slip faulting used in this study

3. ANALYSIS

3.1 Directivity Effects

In this study, we are modeling strike-slip motion (Figure 1). In order to obtain a sample of the rare, extreme particle motions, we have recorded over 3,000 foam-quakes. The waveforms are digitized 2500 samples per seconds and recorded on a PC with a data acquisition system. The initial stress conditions, the normal stress, and the forcing velocity have been controlled throughout the runs. Waveforms from each event have been visually inspected to ensure that the extreme values are not due to an instrument malfunction. The average stress drop and average displacement distributions in 1406 events are shown in Figure 2(a) and Figure 2(b), respectively. The small displacement events do not rupture the whole interface. This result suggests that the corresponding stress drops are underestimated since the total fault area has been assumed to rupture.

Figure 3 shows the plots of typical particle accelerations and velocities recorded at the first row of surface sensor. Numbers in Figure 3 correspond to the sensor number in Figure 1. In this figure, the distances from the hydraulic piston increase from bottom to top but the same fault distances (e.g., Boore-Joyner distance). Strong forward directivity is evident from increasing the amplitude of the particle motion at stations further from the nucleation position (left side of the model in Figure 1).

Figure 4 indicates PGA and PGV versus stress drop plots for sensors with increasing the distance from the hydraulic piston (from left to right), but same Boore and Joyner's fault distance. The variability of peak particle velocity increases with increasing the stress drop and the effects of forward directivity.

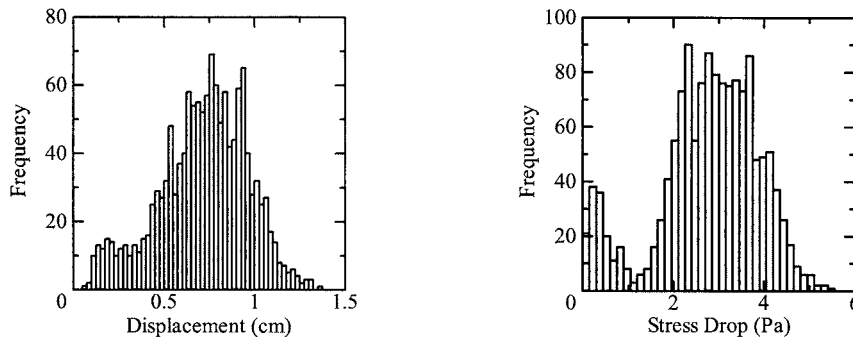


Figure 2. Average displacement and average stress drop distributions for a set of 1406 ruptures

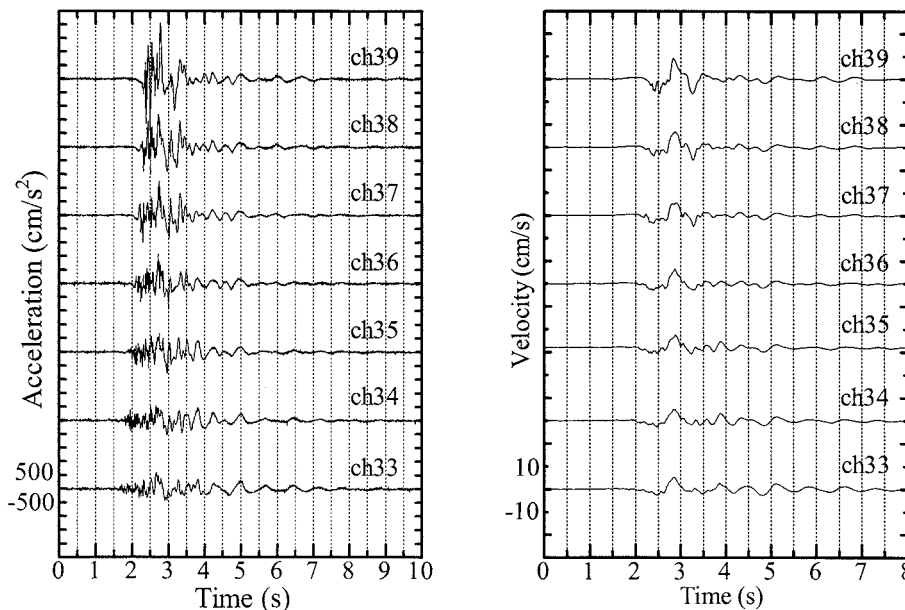


Figure 3. An example of acceleration and velocity records

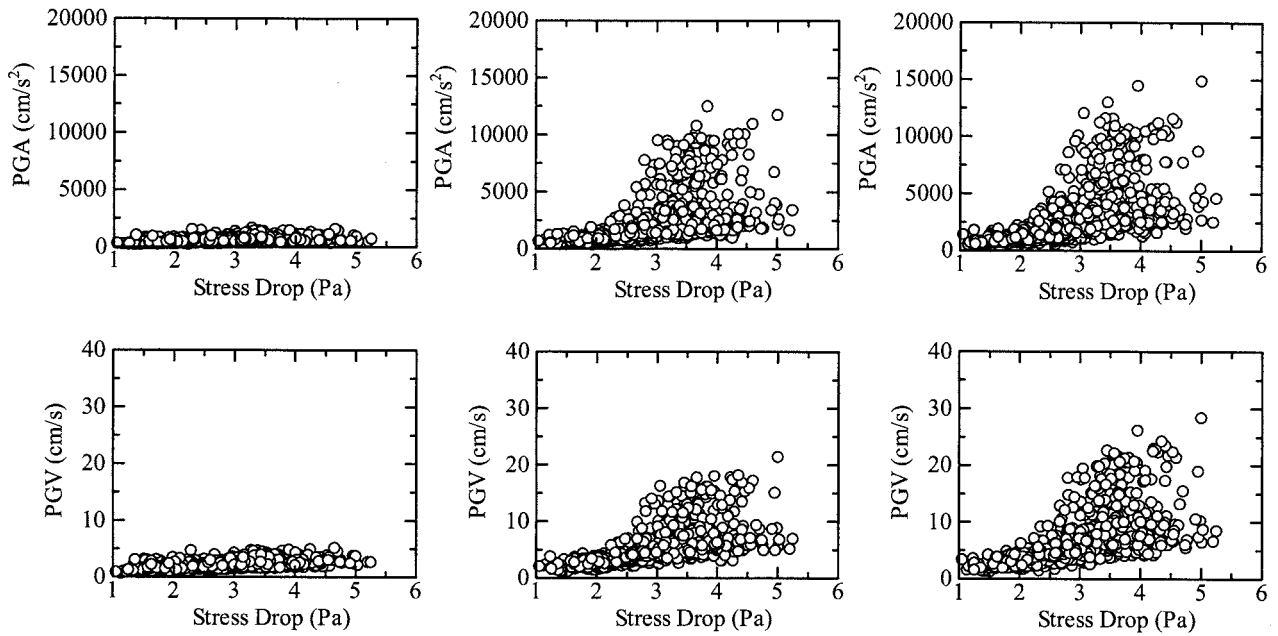


Figure 4. Fault parallel PGV versus stress drop

The largest PGV in the forward directivity direction are about a factor of 2 greater than those in the nucleation region. Apparently there are 2 distinct distributions of events, those lying in the main cloud of points and the extreme values due to forward directivity. Due to the high coefficient of friction, peak particle acceleration indicates very large values.

3.2 PGA and PGV distributions

The PGA and PGV distributions for the 7 sensors (first row sensors) and the total distributions are shown in Figure 5 and 6. The effects of forward directivity are clearly apparent in these figures. At high amplitudes, the total distributions decay more slowly than log-normal, suggesting bimodal distributions. To assess the ramifications of these extreme values when extrapolated to low probabilities, we have determined the best fitting log-normal distributions to the total PGA distributions without bias towards the heavy tails via obtaining the standard deviations from the full-width-half-maximum (FWHM) values. These main log-normal models are subtracted from the observed distributions, another log-normal distributions has been fit to the remaining extreme values. The means and standard deviations are given Table 1, while the distributions are shown in Figure 7. When extrapolated to low probabilities, the main and extreme log-normal distributions intersect.

Figure 8 shows the fault parallel and fault normal PGA, in comparison to a log-normal distribution (quantile-quantile plot). Most of data follow the log-normal distributions at least up to 2~3 standard deviation. But, the data does not follow the log-normal distributions more than 3 standard deviations.

In probabilistic seismic hazard analysis (PSHA), ground-motion prediction equations (attenuation relationships derived from strong motion data) define probabilistic distributions. For long return period, the PSHA estimates are driven by the tails of this distribution (Anderson and Brune, 1999). The variability of ground motions is characterized by the standard deviation of residuals about a median ground-motion prediction equation, which in general have found to conform to a Gaussian distribution. Typical standard deviation of a published attenuation relationships derived from strong motion data, given in \log_{10} units are the range of 0.2 to 0.3 (e.g., Fukushima and Tanaka, 1990; Abrahamson and Silva, 1997; Boore et al., 1997). These large standard deviation values have much effect on the PSHA results, especially at low probability. Should the main distribution be truncated based on these results, the PSHA estimates at low probabilities may be significantly smaller.

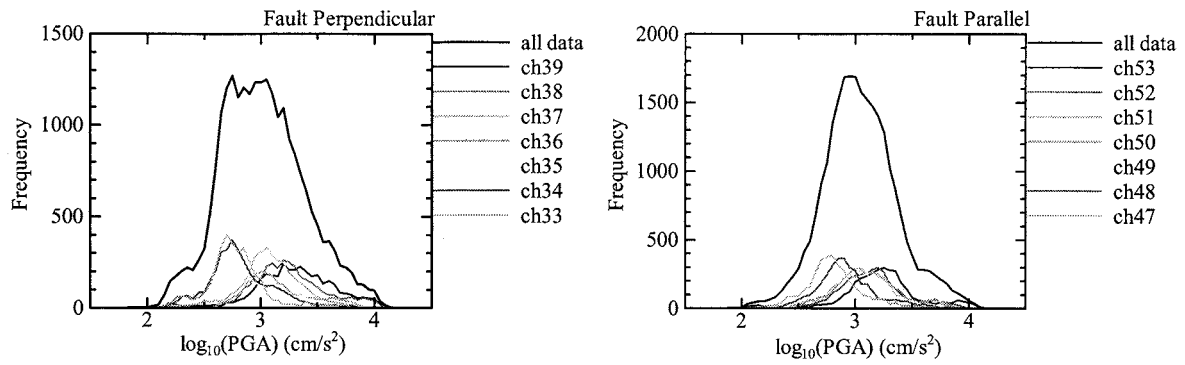


Figure 5. Fault perpendicular and fault parallel PGA distributions

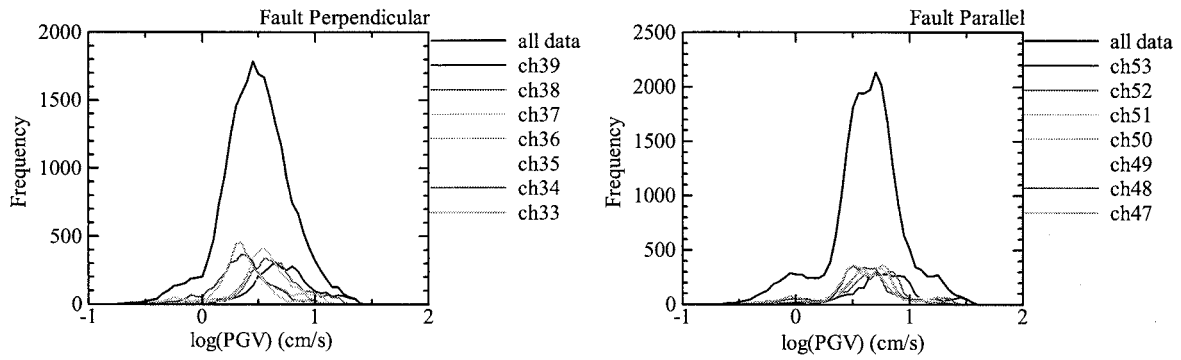


Figure 6. Fault perpendicular and fault parallel PGV distributions

Table 1. Means and standard deviation of log-normal distributions fit to PGA distributions

Fault Parallel				Fault Perpendicular			
Main		Extream		Main		Extream	
μ	σ	μ	σ	μ	σ	μ	σ
3.04	0.275	3.8	0.124	3.013	0.337	3.798	0.137

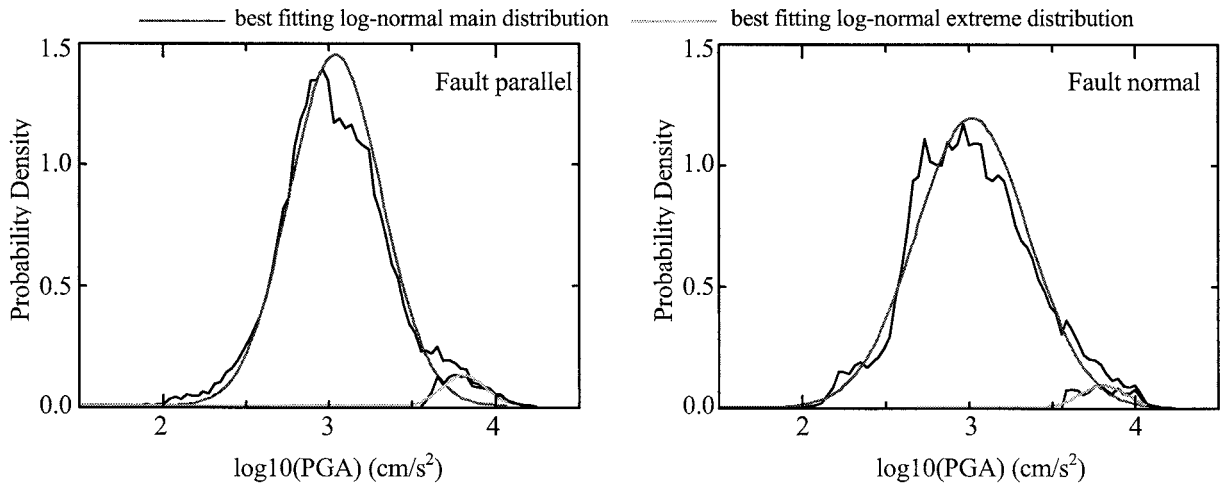


Figure 7. Fault parallel and fault normal probability density function of $\log_{10}(\text{PGA})$

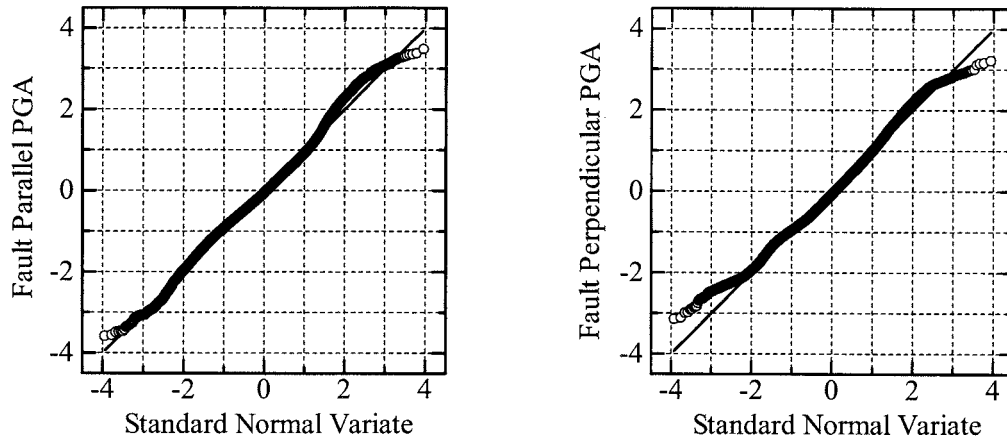


Figure 8. Q-Q plot of fault parallel and fault normal PGA

4. CONCLUSIONS

In this study, we have studied the distributions of peak particle motions for 3708 events in a foam rubber model of strike-slip faulting.

Strong forward directivity is evident from increasing the amplitude of the particle motions at stations further from nucleation position. Additionally, the variability of the peak amplitude indicates large values due to the forward directivity.

We also examined the distributions of the PGA and PGV. At high amplitude, the distributions decay more slowly than log-normal, suggesting the bimodal distribution. We have determined the best fitting log-normal distributions to the total PGA distributions without bias towards the heavy tails. These main log-normal models are subtracted from the observed distributions, another log-normal distributions has been fit to the remaining extreme values. When extrapolated to low probabilities, the main and extreme log-normal distributions intersect. In comparison to a log-normal distribution, most of data follow the log-normal distributions at least up to 2~3 standard deviation. But, the data does not follow the log-normal distributions more than 3 standard deviations.

For important engineering projects, such as nuclear power plants, probabilistic seismic hazard analysis (PSHA) is often employed to obtain the seismic-design load, in general, using long return period (Stepp et al., 2001; Bommer and Abrahamson, 2006). In PSHA, the ground motion is obtained from ground-motion prediction equation. These equations define probabilistic distributions, in general Gaussian distributions, of the ground motion parameter (e.g., peak acceleration, peak velocity, response spectra). For very long return period, the results of PSHA are driven by the untruncated tail of probabilistic distributions (Anderson and Brune, 1999). Brune (1999b) indicated that PSHA using ground-motion prediction equations with untruncated probabilistic distribution might overestimate ground motion with long return period based on precarious rocks in Mojave Desert, Southern California. Therefore, defining upper bounds on ground motion intensity and levels of truncation the distributions becomes very important issues in PSHA (Bommer et al., 2004; Bommer and Abrahamson, 2006). Although we have to do more experiment and analyze more data, this study can be expected to provide very useful insight into probabilistic seismic hazard analysis with very small annual frequencies exceedance.

References:

- Abrahamson, N.A. and Silva, W.J. (1997). "Empirical Response Spectral Attenuation Relations for Shallow Crustal Earthquakes," *Seismological Research Letter*, **68**(1), 94-127.
- Anderson, J.A. and Brune, J.N. (1999). "Probabilistic Seismic Hazard Assessment without the Ergodic Assumption,"

- Seismological Research Letter*, **70**(1), 19-28.
- Anooshehpour, A. and Brune, J.N. (1994). "Frictional Heat Generation and Seismic Radiation in a Foam Rubber Model of Earthquakes," *Pure and Applied Geophysics*, **142**(3/4), 735-747.
- Bommer, J.J., Abrahamson, N.A., Strasser, F.O., Pecker, A., Bard, P.-Y., Bungum, H., Cotton, F., Fah, D., Sabetta, F., Scherbaum, F. and Studer, J. (2004). "The Challenge of Defining Upper Bounds on Earthquake Ground Motions," *Seismological Research Letter*, **75**(1), 82-95.
- Bommer, J.J. and Abrahamson, N.A. (2006). "Why Do Modern Probabilistic Seismic-Hazard Analyses Often Lead to Increased Hazard Estimates?," *Bulletin of the Seismological Society of America*, **96**(6), 1967-1977.
- Boore, D.M., Joyner, W.B. and Fumal, T. E. (1997). "Equations for Estimating Horizontal Response Spectra and Peak Acceleration from Western North American Earthquakes: A Summary of Recent Work," *Seismological Research Letter*, **68**(1), 129-153.
- Brune, J.N. (1973), "Earthquake modeling by stick-slip along precut surfaces in stressed foam rubber," *Bulletin of the Seismological Society of America*, **63**(6), 2105-2119.
- Brune, J.N., Johnson, P.A. and Slater, C. (1989). "Constitutive relations for foam rubber stick-slip," *Seismological Research Letter*, **60**, 26.
- Brune, J.N., Brown, S., and Johnson, P.A. (1993). "Rupture mechanism and interface separation in foam rubber models of earthquakes: a possible solution to the heat flow paradox and the paradox of large overthrusts," *Tectonophysics*, **218**, 59-67.
- Brune, J.N. (1996), "Precariously Balanced Rocks and Ground Motion Maps for Southern California," *Bulletin of the Seismological Society of America*, **86**(1A), 43-54.
- Brune, J.N. and Anooshehpour, A. (1998), "A Physical Model of the Effects of a Shallow Weak Layer on Strong Ground Motion for Strike-Slip Ruptures," *Bulletin of the Seismological Society of America*, **88**(4), 1070-1078.
- Brune, J.N. and Anooshehpour, A. (1999a), "Dynamic Geometrical Effects on Strong Ground Motion in a Normal fault Model," *Journal Geophysical Research*, **104**(B1), 809-815.
- Brune, J.N. (1999b). "Precarious Rocks along the Mojave Section of the San Andreas Fault, California: Constrains on Ground Motion from Great Earthquakes," *Seismological Research Letter*, **70**(1), 29-33.
- Frankel, A., Mueller, C., Bernhard, T., Perkins, D., Leyendecker, E.V., Dickman, N., Hanson, S., and Hopper, M. (1996). "National Seismic Hazard Maps," U.S. Department of Interior, U.S. Geological Survey.
- Frankel, A., Peterson, M.D., Mueller, C.S., Haller, K.M., Wheeler, R.L., Leyendecker, Wesson, R.L., Harmsen, S.C., Cramer, C.H., Perkins, D.M., and Rukstales, K.S. (2002). "Documentation for the 2002 update of the National Seismic Hazard Maps," *U.S. Geological Survey Open-file Report*, 02-420.
- Fukushima, Y. and Tanaka, T. (1990). "A New Attenuation Relation for Peak Horizontal Acceleration of strong earthquake Motion in Japan," *Bulletin of the Seismological Society of America*, **80**(4), 757-779.
- Purvance, D.M., Uchiyama, Y., Anooshehpour, A., Brune, J.N., Anderson, J.G., Flint, J.A. and Hockensmith, N.C. (2006), "Extreme Particle Motion in a Foam Rubber Model of Spontaneous Ruptures: Analogous to Earthquake Ruptures," *Proceedings and Abstracts of the Southern California Earthquake Center 2006 Annual Meeting*.
- Stepp, J.C., Wong, I., Whitney, J., Quittmeyer, R., Abrahamson, N., Toro, G., Youngs, E., Coppersmith, K., Savy, J. and Sullivan, T. (2001) , "Probabilistic Seismic Hazard Analysis for Ground Motions and Fault Displacement at Yucca Mountain, Nevada," *Earthquake Spectra*, **17**(1), 113-151.

SITE RESPONSE IN TAIPEI URBAN AREA FROM DENSE MICROTREMOR SURVEY

Kuo-Liang Wen¹⁾, Che-Min Lin²⁾, Chun-Te Chen³⁾

1) Professor, Institute of Geophysics, National Central University, Taiwan

2) PhD Candidate, Inst. of Geophysics, National Central University, Taiwan

3) PhD Student, Inst. of Geophysics, National Central University, Taiwan

wenkl@earth.ncu.edu.tw, u2460323@cc.ncu.edu.tw, 93622008@cc.ncu.edu.tw

Abstract: Although Taipei basin already had a very dense observation network of strong motion accelerometers under the Taiwan Strong Motion Instrumental Program (TSMIP) which conducted by the Central Weather Bureau, a dense microtremor survey was done in the Taipei basin area by using large dynamic range digital recorder, because it can quickly yield the ground motion and spectral characteristics of the site. The variations of amplitude and predominant frequency throughout the basin are analyzed by using the horizontal-to-vertical spectral ratio method. The relationships between these variations and the geological structure of the Taipei basin are studied. The results from the microtremor survey consisted with that from the TSMIP earthquake records. Which shows the microtremor survey can serve as a rapid method for realizing the characteristics of the ground motion. The microtremor results can use as a reference in earthquake resistant design, microzonation, and ground motion prediction in the Taipei basin.

1. INTRODUCTION

Local amplification of strong ground motion by sedimentary deposits during an earthquake has been documented on a number of occasions. Many methods have been used to characterize the site amplification. The best approach is through direct observation of seismic ground motion, but such observations are limited to high seismicity areas and by high cost. The Taipei Basin is a triangle-shaped structure, with Shanchia, Kuantu, and Nankang at the southwestern, northwestern, and eastern corners (Figure 1). The Taiwan Strong Motion Instrumentation Program (TSMIP, Shin, 1993; Kuo *et al.*, 1995) was operated since 1991. There are many stations installed in the Taipei basin (Figure 2) and many data had been recorded which allows to study the site effects in the Taipei basin in detail (Wen *et al.*, 1995a; Wen and Peng, 1998).

The situations may not exist in many areas, where has very dense strong motion stations and high seismicity. In this study, we conducted dense microtremor surveys in the Taipei basin and calculated the site response from the horizontal-to-vertical spectral ratio. The results are compared with that from the TSMIP earthquake records for realizing the suitability of applying the microtremor survey in site effect analysis.

2. GEOLOGY OF THE TAIPEI BASIN

The Taipei Basin is a triangle-shaped structure, with Shanchia, Kuantu, and Nankang at the southwestern, northwestern, and eastern corners. The ground surface of the Taipei Basin is almost flat and tilting gently to the northwest. The total area of the Taipei Basin with an altitude below 20

meters is about 240 square kilometers. The Keelung River flows through it in an east-west direction and the Dahang Creek from the south through the basin center and then north-west to the ocean. Because the basin is filled with the unconsolidated sediments, the subsurface geology of the Taipei Basin can only be established by the information obtained from boring, electrical and seismic prospecting. Recently, the basement structure of the Taipei basin area has been explored by deep boring work undertaken by the Central Geological Survey and dense reflection seismic surveys conducted by the National Central University (Wang *et al.*, 1994a, 1994b; Hsieh *et al.*, 1994). The dotted contour lines in Figure 1 indicate the depth to the basement rock of the Taipei basin, from inner to outer each line shows the depth from 600 to 100 m, respectively.

The geological structure inside the basin has the Quaternary layers above the Tertiary base rock. The stratigraphic formations of the Quaternary layers are, in descending order, surface soil, the Sungshan Formation, the Chingmei Formation, and the Hsinchuang Formation. The Sungshan Formation is composed mainly of alternating beds of silty clay and silty sand, and covers almost the whole Taipei basin. The Chingmei Formation is a fan-shaped body of conglomerate deposits. The Hsinchuang Formation consists of bluish grey, clayey sand with some conglomerate beds (Wang and Lin, 1987). Recently, Teng *et al.* (1994) separated the Hsinchuang Formation into Wuku and Panchiao Formations. Wen *et al.* (1995b) calculated the V_p and V_s from surface to the depth of 350 meters through the travel time analysis of seismic waves by using the Wuku downhole records in the western part of Taipei basin. The average P- and S-wave velocity structures of the Taipei basin had been done by Wang *et al.* (1996) which was the results from the reflection seismic survey in the whole Taipei basin area.

3. MICROTREMOR SURVEY

The microtremor observation system which we used to do microtremor survey in the Taipei basin area is made by the Tokyo Sokushin. The model of the sensor is VSE-311C with the frequency response from 15 sec to 100 Hz within 3 dB. The recorder is SAMTAC-801B with 24 bits resolution.

We performed a very dense microtremor survey in the study area, including Taipei basin and nearby area. The distribution of the microtremor survey points is shown in Figure 3 of red triangle symbols. Totally, 500 survey points with average station interval of about 1 km. Each survey point measured 18 minutes with the sampling rate of 200 samples per second. In the downtown city, most microtremor measurements were done during the midnight to reduce artificial effects.

4. SITE EFFECTS ANALYSIS

4.1 Results From Microtremor Survey

Kagami *et al.* (1982; 1986) proposed that the ratio of the horizontal components of the velocity spectra at the sediment site to those at the rock site (soil-to-rock ratio) can be used as a measure of microseism ground motion amplification. This proposition assumes a common source and similar paths for sediment and bedrock sites. Nakamura (1989) proposed a hypothesis that microtremor site effects can be determined by simply evaluating spectral ratio of horizontal versus vertical components of motion observed at the same site (horizontal-to-vertical ratio, H/V ratio).

The measurements are done at each survey points in the Taipei basin area. Then, the horizontal-to-vertical spectral ratios are calculated at each station. From these spectral ratios, the values at each frequency can be selected at each site and drew the contours to show the basin effects at this frequency. Figure 4 shows the horizontal-to-vertical spectral ratio contours of the 0.2, 0.3, 0.5, 1, 2, and 3 Hz, respectively.

The results from the Nakamura's H/V ratio in the low frequency band (≤ 0.5 Hz) are concentrated in two areas, and these areas become larger from lower (0.2 Hz) to higher frequency (0.5 Hz). The responses in the north, east, and south edges are all show a contour high in the frequency band higher than 1 Hz.

4.2 Compare With the Results From TSMIP Network

Several earthquakes have been recorded by the TSMIP network since its installation. Wen and Peng (1998) used these events to study the site effects in the Taipei Basin area. In their study, the spectral ratios of the soft soil stations were calculated with respect to the TAP016 referent site which near the edge of the basin. Figure 5 shows the average spectral ratios at 2 and 0.5 sec of all events. From these figures, it is obvious that the waves at different frequencies have different amplifications in the Taipei Basin. The contours in Figures 4c and 5a are closely correlated with the geological structure of the top soil layer (Sungshan Formation, Figure 6), responses in these frequencies show that the variation can be a factor of about 3. But the contour high changed to near the basin edge in the Figures 4e and 5b of higher frequency responses, and the variation can be a factor of 7. The responses in the western part of the Taipei basin, which is the deepest area of the basin, show a contour high in the frequency lower than 1 Hz (4, 3, 2, and 1.5 sec). But it changes to a contour low area in the frequency higher than 1 Hz.

4.3 Dominant Frequency

From the horizontal-to-vertical spectral ratios of these dense microtremor measurement points, the dominant frequency at each survey point can be selected. Figure 7 shows the contour of the dominant frequency in the Taipei basin area. The two areas with dominant frequency lower than 0.8 Hz are consisted with the two contour high areas in Figures 4c and 5a. Whereas, the basin edge areas show the contour high in higher frequency band and the dominant frequencies at the basin edges also in higher frequency band.

The dominant frequency distribution can explain the site responses in the Taipei basin area. It also shows good correlation with the geology of Taipei basin. The previous two lower dominant frequency areas are very consist with the Sungshan Formation distribution. This shows that the results from the microtremor survey, include site response at different frequencies and dominant frequency distribution, can be used as a reference for microzonation work in Taipei basin area.

5. CONCLUSIONS AND DISCUSSIONS

From the analysis of the records of the dense Taipei strong motion observation network and the dense microtremor survey in the Taipei basin area, it is noted that the two thicker areas of the Sungshan Formation represented higher response at the lower frequency band of less than 1 Hz. From the analysis in this study, the authors therefore deduce that one single building code is not adequate for the whole basin area. Different areas have different local site responses. By comparison of the results from the earthquake records and the H/V ratio, the contour patterns are similar but the amplification factors in the higher frequency band (higher than 1 Hz) from the H/V ratio are lower than those from the earthquake records of two-station ratio.

From this study shows the microtremor survey can be used to study the basin response. The characteristics of the ground motions in the Taipei basin during earthquakes can be understood through the H/V ratios of the microtremor survey. The results of this study show that microtremor survey can serve as a rapid method for realizing the characteristics of the ground motion.

Acknowledgements:

This study was supported by the National Science Council under the Grant NSC94-2116-M-008-005 and NSC95-2745-M-008-003.

References

- Hsieh, C.H., Lin, C.M., and Hsieh, S.H. (1994), "Seismic and Well Logging Surveys in Taipei Basin," *Proc. Joint Symposium on Taiwan Quaternary (5) and on Investigation of Subsurface Geology/Engineering Environment of Taipei Basin*, 185-191.
- Kagami, H., Duke, C.M., Liang, G.C., and Ohta, Y. (1982), "Observation of 1- to 5-second Microtremors and Their Application to Earthquake Engineering. Part II. Evaluation of Site Effect Upon Seismic Wave Amplification Due to Extremely Deep Soil Deposits," *Bull. Seism. Soc. Am.*, **72**(3), 987-998.
- Kagami, H., Okada, S., Shiono, K., Oner, M., Dravinski, M., and Mal, A.K. (1986), "Observation of 1- to 5-second Microtremors and Their Application to Earthquake Engineering. Part III. A Two Dimensional Study of Site Effects in the San Fernando Valley," *Bull. Seism. Soc. Am.*, **76**(6), 1801-1812.
- Kuo, K.W., Shin, T.C., and Wen, K.L. (1995), "Taiwan Strong Motion Instrumentation Program (TSMIP) and Preliminary Analysis of Site Effects in Taipei Basin From Strong Motion Data, in Urban Disaster Mitigation: The Role of Engineering and Technology," Edited by F. Y. Cheng and M.-S. Sheu, Elsevier Science Ltd., 47-62.
- Nakamura, Y. (1989), "A Method for Dynamic Characteristics Estimation of Subsurface Using Microtremor on the Ground Surface," *Quarterly Report of Railway Tech. Res. Inst.*, **30**(1), 25-33.
- Shin, T.C. (1993), "Progress Summary of the Taiwan Strong Motion Instrumentation Program," *Proc. of the Symposium on Taiwan Strong Motion Instrumentation*.
- Teng, L.S., Wang, S.C., Chang, C.B., Hsu, C., Yuan, P.B., and Chen, P.Y. (1994), "Quaternary Strata Frame of the Taipei Basin," *Proc. Joint Symposium on Taiwan Quaternary (5) and on Investigation of Subsurface Geology/Engineering Environment of Taipei Basin*, 129-135.
- Wang Lee, C.M. and Lin, T.P. (1987), "The Geology and Land Subsidence of the Taipei Basin," *Memoir Geol. Soc. China*, **9** (Papers presented at the first SINO (Taiwan) - British Geological Conference on Geotechnical Engineering and Hazard Assessment in Neotectonic Terrains), 447-464.
- Wang, C.Y., Hsiao, W.C., and Sun, C.T. (1994a), "Reflection Seismic Stratigraphy in the Taipei Basin (I) - Northwestern Taipei," *J. Geol. Soc. China*, **37**(1), 69-95.
- Wang, C.Y., Tsai, Y.L., Ger, M.L., and Chang, H.C. (1994b), "Investigation of Tertiary Basement in Taipei Basin Using Shallow Reflection Seismics," *Proc. Joint Symposium on Taiwan Quaternary (5) and on Investigation of Subsurface Geology/Engineering Environment of Taipei Basin*, 169-175.
- Wang, C.Y., Lee, Y.H., and Chang, H.C. (1996), "P- and S-velocity Structures of the Taipei Basin," *Proc. Symp. on Taiwan Strong-Motion Instrumentation Program (II)*, Central Weather Bureau, 171-177.
- Wen, K.L. and Peng, H.Y. (1998), "Site Effect Analysis in the Taipei Basin: Results From TSMIP Network Data," *Terr. Atm. Oce.*, **9**, 691-704.
- Wen, K.L., Peng, H.Y., and Liu, L.F. (1995a), "Basin Effects Analysis From a Dense Strong Motion Observation Network," *Earthq. Eng. Struct. Dyn.*, **24**, 1069-1083.
- Wen, K.L., Fei, L.Y., Peng, H.Y., and Liu, C.C. (1995b), "Site Effect Analysis From the Records of the Wuku Downhole Array," *Terr. Atm. Oce.*, **6**(2), 285-298.

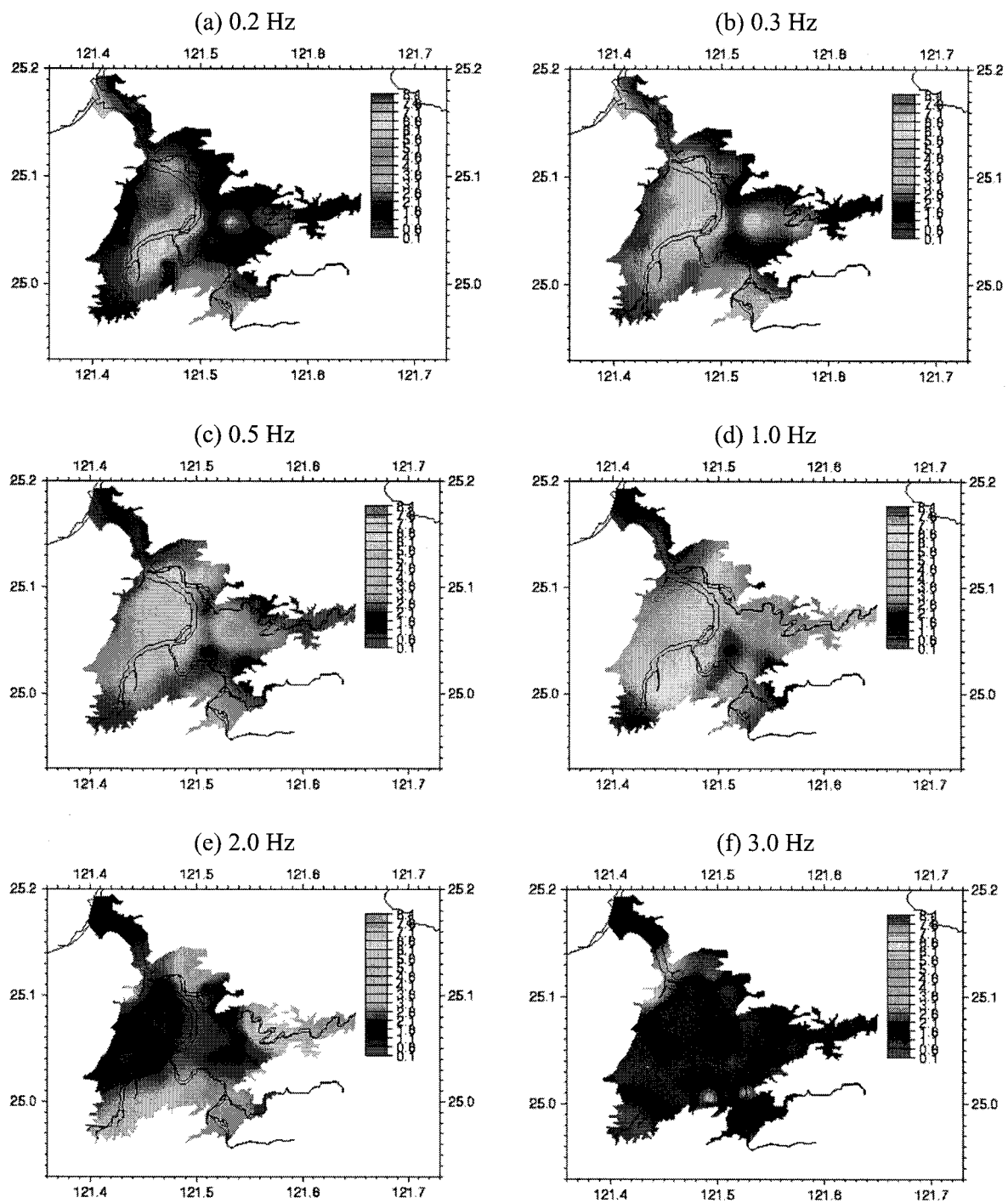


Figure 4 H/V spectral ratio contours at different frequencies.

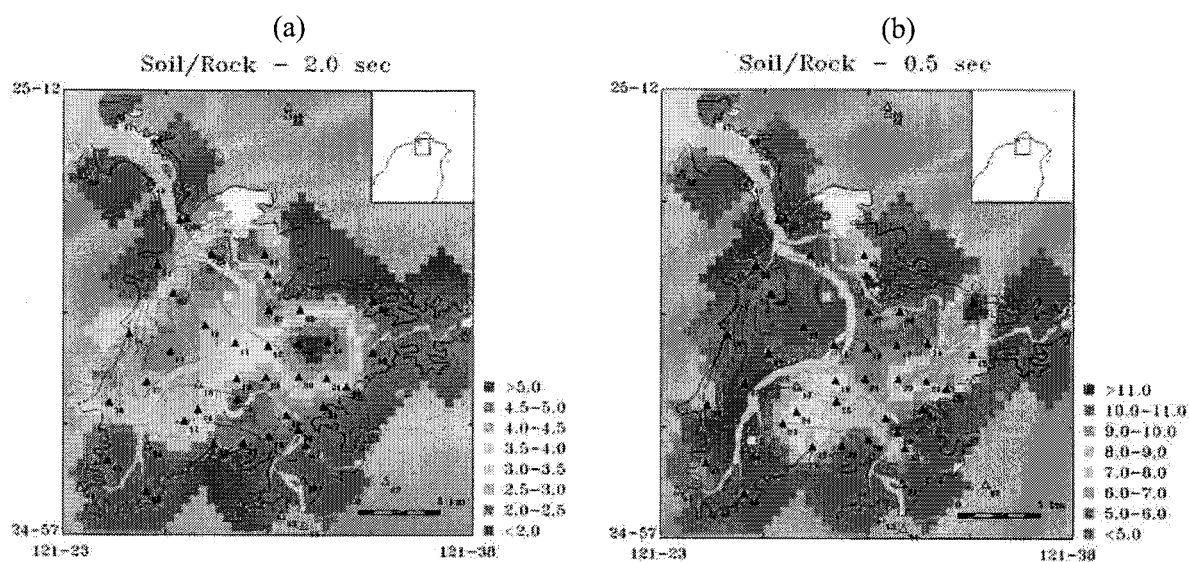


Figure 5 Spectral ratio contours at 2 and 0.5 seconds from the TSMIP earthquake records (redraw from Wen and Peng, 1998).

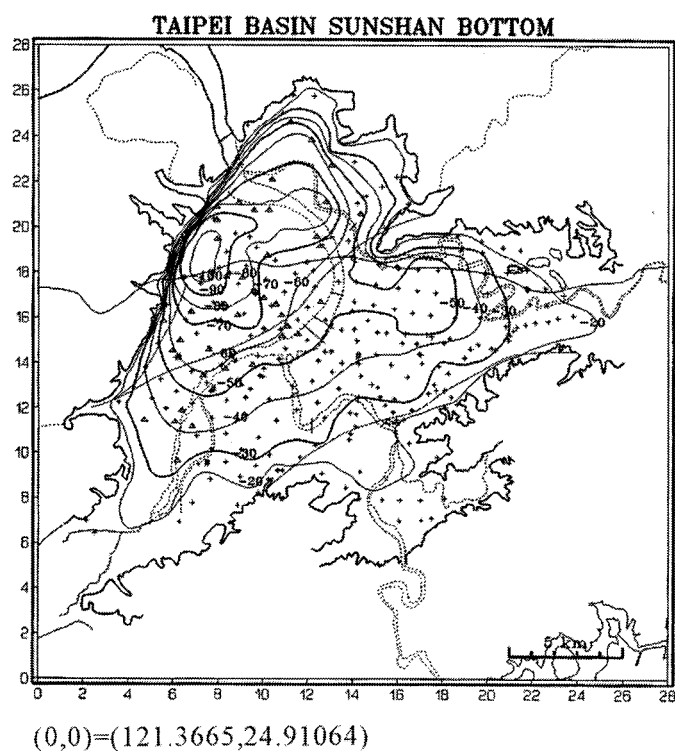


Figure 6 Depth to the bottom of the Sungshan Formation (Wang *et al.*, 1996).

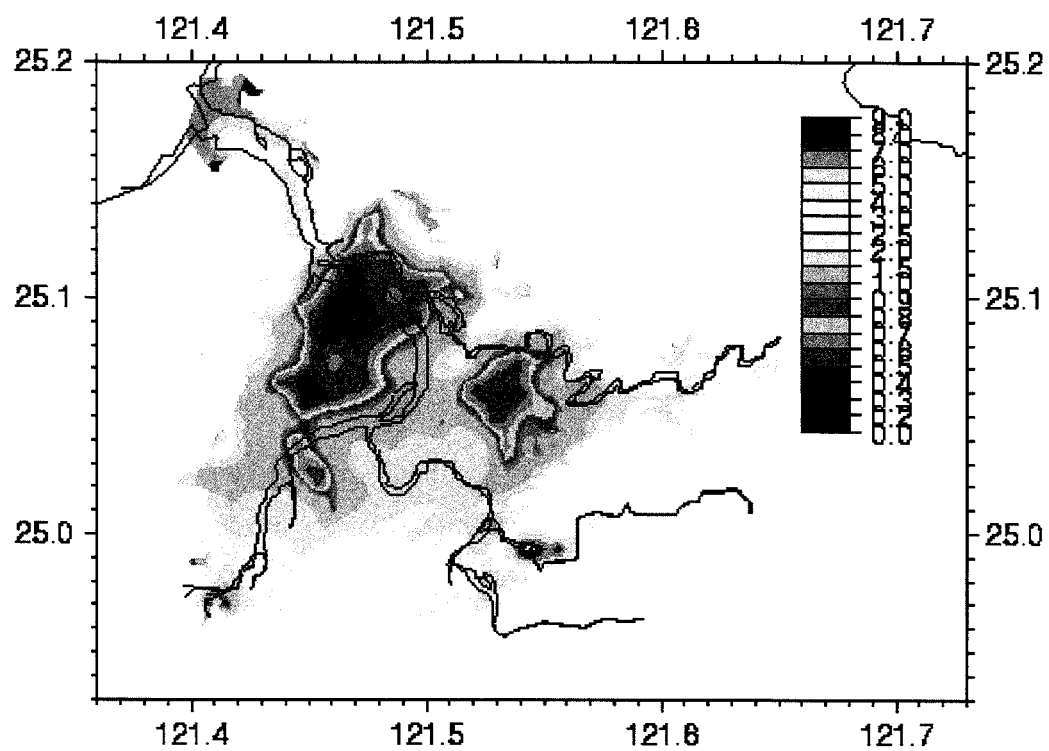


Figure 7 Dominant frequency contour in the Taipei basin area, result from the H/V ratio of dense microtremor survey.

OVERTURNING OF FREESTANDING OBJECTS WITH APPLICATION TO PRECARIOUSLY BALANCED ROCKS

M. D. Purvance¹⁾, J. N. Brune²⁾, J. G. Anderson²⁾, and N. A. Abrahamson³⁾

1) Postdoctoral Scholar, Dept. of Geophysics, University of Nevada, Reno, United States of America

2) Professor, Department of Geophysics, University of Nevada, Reno, United States of America

3) Engineering Seismologist, Pacific Gas and Electric Co., United States of America

mdp@seismo.unr.edu, brune@seismo.unr.edu, jga@seismo.unr.edu, naa3@earthlink.net

Abstract: The goal of this work is to quantitatively scrutinize seismic hazard estimates through constraints provided by freestanding objects. Previous investigations have shown that the overturning responses of freestanding blocks depend on their shapes and sizes along with both the lower-frequency (~0.5-1 Hz) and high-frequency (>10 Hz) ground motion amplitudes to which they are exposed. The current initiative utilizes these results to estimate the fragilities of precariously balanced rocks (e.g., freestanding corestones or boulders that are easily toppled) near to active faults in Southern California. A methodology is presented to convolve the precarious rock fragilities with seismic hazard estimates, providing estimates of the precarious rock overturning probabilities given their exposure ages. Probabilistic seismic hazard estimates similar to the 2002 USGS National Seismic Hazard Maps are found to be inconsistent with many of the precarious rocks. In addition, a methodology is demonstrated to weight the hazard models based on the precarious rock survival probabilities, yielding a physically constrained hazard estimate. On average weighted hazard values are reduced by 30% or more relative to the unweighted values.

1. INTRODUCTION

Policy decisions regarding the design specifications of civil structures are commonly based on probabilistic seismic hazard analyses (PSHA). In light of this fact, we contend that PSHA estimates warrant rational, quantitative examination. In particular, this work uses the fragilities of freestanding balanced rocks to investigate and constrain PSHA estimates. The rocking and overturning responses of freestanding objects have been studied for over a century. For example, Robert Mallet (1862) attempted to infer the ground motion intensity and directionality produced by the 1857 Neapolitan Earthquake via overturned and damaged manmade objects. Milne (1881), Perry (1881), Milne and Omori (1893), and Kirkpatrick (1927) all investigated the use of freestanding objects as seismoscopes. Contemporary initiatives generally utilize a momentum conserving formulation first derived by Kimura and Iida (1934). Housner (1963) independently derived this formulation and further developed approximate block overturning criteria. This work largely reinvigorated interest in rocking block dynamics and conditions leading to overturning.

Subsequent researcher has investigated the overturning responses of freestanding objects exposed to simplified excitations (e.g., Shi et al. 1996, Anooshehpour et al. 1999, Makris and Roussos 2000) and to stochastic ground motions (e.g., Dimentberg et al. 1993, Cai et al. 1995, Lin and Yim 1996). See Purvance (2005) for a thorough review. Yim et al. (1980) first demonstrated a probabilistic approach based on numerical solutions of the nonlinear, non-smooth governing equations. By cataloging the binary overturning responses (e.g., 0 for survival, 1 for overturning) of a set of

freestanding blocks exposed to an ensemble of realistic ground motions, Yim et al. (1980) developed a method to calculate the ensemble averaged overturning probability. Those authors demonstrated that the overturning probability increases with increasing high-frequency excitation amplitude, increasing block slenderness (height-to-width ratio), and with decreasing block size.

Purvance (2005), following the method of Yim et al. (1980), catalogued the overturning responses of both symmetric and asymmetric 2-D blocks (Figure 1). A suite of random vibration synthetics constructed by a modified version of the Boore (1983) method were utilized. Purvance (2005) determined relations for the high-frequency ground motion amplitude (*PGA*) associated with overturning at a specified probability in terms of the block geometrical parameters and the lower-frequency ground motion amplitude (either peak ground velocity *PGV*, 5% damped spectral acceleration at 1 second $S_a(1)$, or 5% damped spectral acceleration at 2 seconds $S_a(2)$) normalized by the *PGA*. Inversion of these relationships allows one to calculate the overturning probability given the amplitudes of the ground motions to which the objects are exposed, termed the fragility. This formulation has also been validated via shake table experiments (Purvance et al. submitted 2006). In addition, Purvance (2005) estimated prediction intervals about the median fragility models for use in assessing uncertainty in the fragility formulation. The current initiative applies this formulation to determine the consistency of precariously balanced rocks with the 2002 USGS seismic hazard estimates (Frankel et al. 2002) for sites in Southern California. A methodology is also presented to weight seismic hazard estimates via the precarious rock survival probabilities.

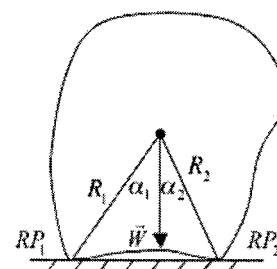


Figure 1 Freestanding block model where α_1 and α_2 are the angles between the vertical (\vec{W}) and the lines R_1 and R_2 . These lines connect the center of mass to the rocking points RP_1 and RP_2 . The slenderness of the i th side is given by $1/\tan(\alpha_i)$. See Purvance (2005) for additional details regarding the governing equations and fragility formulation.

2. PRECARIOUSLY BALANCED ROCKS

Brune et al. (2007) documents the development of the precariously balanced rock project. This program was conceived with observations of several easy to topple rocks on Yucca Mountain, Nevada, covered with rock varnish (Brune and Whitney 1992). The aptly named precariously balanced rocks are freestanding, balanced corestones sitting atop stone pedestals (see Figure 2). Field explorations have delineated precarious rocks in a number of tectonic environments, including near to major strike-slip faults (Brune 1999), asymmetrically distributed with fault distance on the footwall and hanging wall sides of thrust faults (Brune et al. 2004), close to trans-tensional strike-slip faults (Brune 2003), within a few hundred meters of the traces of normal faults on the footwall sides (Brune 2000), and equidistant (~15 km) between parallel strike-slip faults (Brune et al. 2006). Age dating campaigns have shown that a set of precarious rocks in southern Nevada and California have been exposed to ground motions for over 10,000 years (Bell et al. 1998), indicating their relevance to seismic hazard studies. The precarious rocks investigated are shown in Figure 2. These include rocks near the Mojave section of the San Andreas Fault (1-14), between the San Jacinto and Elsinore Faults (15-18), between the San Jacinto and San Andreas Faults (19-21), and near the Whitewolf Fault (22-24). In the analysis that follows, exposure times of 10,000 years are assumed ubiquitously with the exceptions of rocks 1-3 that are assumed to have been exposed for 2,000 years. Note that these assumed residence times may be significantly shorter than the actual precarious rock exposures ages; further age dating campaigns are currently in the planning stages.

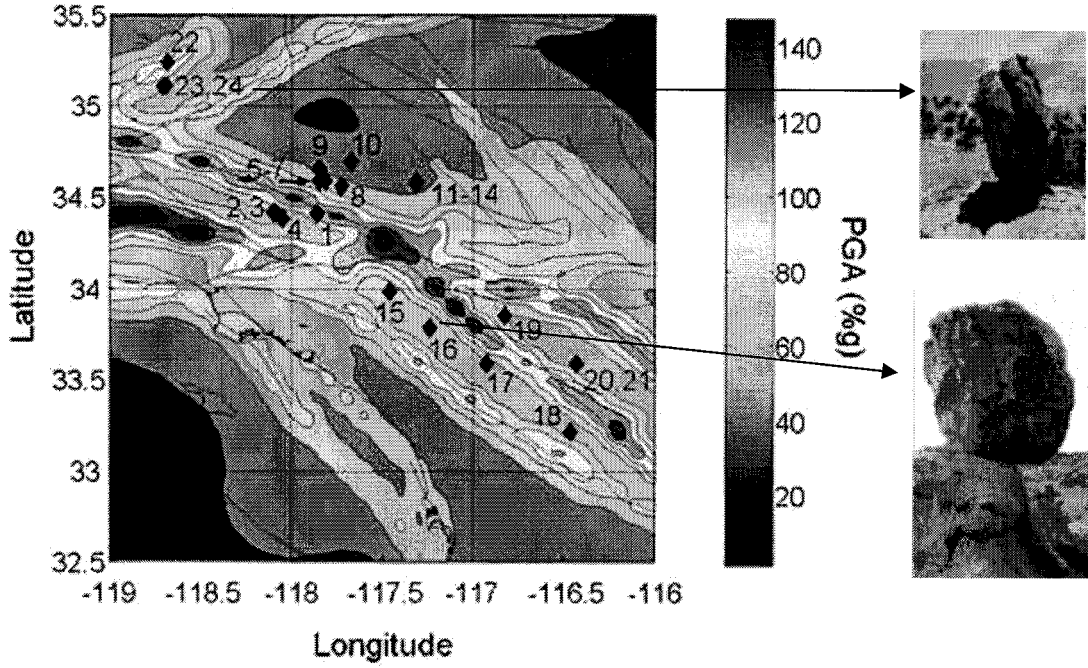


Figure 2 Precariously balanced rocks used in this study (black symbols) overlaid contours of *PGA* with a 2% probability of exceedence in 50 years taken from the 2002 USGS National Seismic Hazard Maps (Frankel et al. 2002). Numbers correspond to the rock identifiers used in subsequent figures.

3. METHODOLOGY

As mentioned above, the overturning probability of a freestanding object is related to the vector of ground motion intensity measures (*IMs*) *PGA* and either *PGV*, $S_a(1)$, or $S_a(2)$. Thus scalar PSHA estimates (Cornell 1968) must be extended to predict the simultaneous occurrence of multiple *IMs*, say IM_1 and IM_2 (e.g., *PGA* and $S_a(1)$). Bazzurro and Cornell (2002) developed the vector-valued PSHA or VPSHA method to accomplish this goal. Whereas the scalar PSHA method uses univariate lognormal probability density functions to describe the expected ground motions, the VPSHA method utilizes bivariate lognormal probability density functions. Suppose that there are $K = I \times J$ bins in $IM_1 \times IM_2$ space with $i = 1 \oplus I$ bins of IM_1 and $j = 1 \oplus J$ bins of IM_2 . Suppose also that the k th bin has boundaries $a_{k1} \leq IM_1 \leq b_{k1}$ and $a_{k2} \leq IM_2 \leq b_{k2}$. The VPSHA method provides the marginal ground motion occurrence rates within the K ground motion bins (Figure 3a). For instance, $RT\{IM_1, IM_2 \in k\}$ corresponds to the yearly rate that ground motions occur with intensities falling within bin k . The marginal occurrence rates are conventionally converted to exceedence rates, yielding a seismic hazard curve. Suppose that one is given the fragility, *OP*, of a freestanding object (Figure 3b). The rate of overturning due to ground motions with intensities falling within bin k is given by

$$OR\{IM_1, IM_2 \in k\} = RT\{IM_1, IM_2 \in k\} \times OP\{IM_1, IM_2 \in k\} \quad (1)$$

An example of a vector-valued overturning rate surface, *OR*, is shown in Figure 3c, the product of the vector-valued ground motion occurrence rates (Figure 3a) and the fragility (Figure 3b). Summing over the K ground motion bins yields the total overturning rate

$$OR = \sum_{k=1}^K OR\{IM_1, IM_2 \in k\} \quad (2)$$

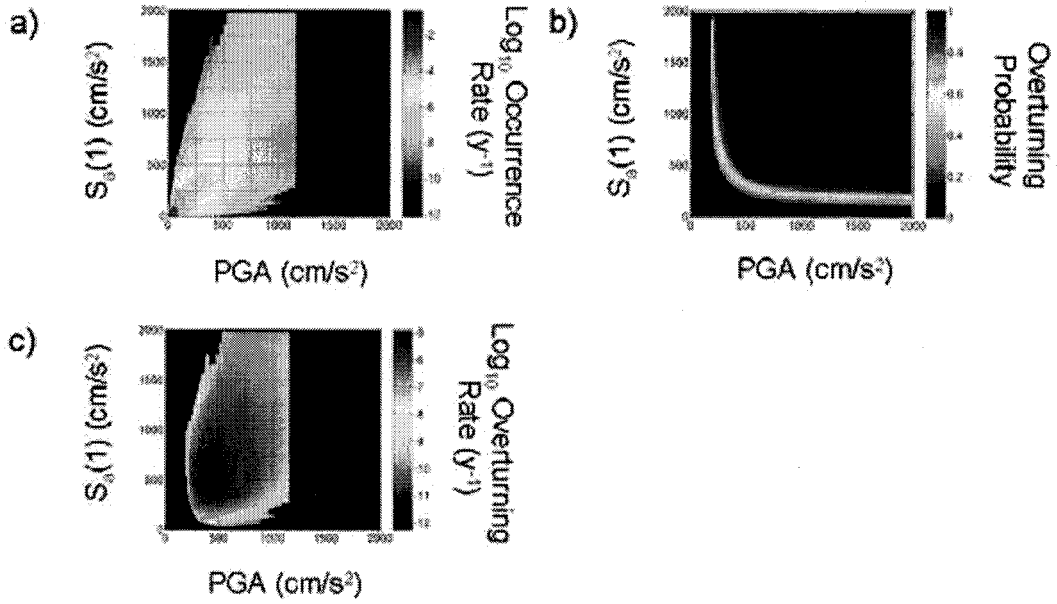


Figure 3 a) VPSHA model of the marginal ground motion occurrence rates, RT , where the ground motion prediction equation has been truncated at 3σ . b) Fragility estimate, OP , of a freestanding block based on the formulation of Purvance (2005). c) The product of the occurrence rates and the fragility estimate provides the overturning rates, OR .

Equation 2 gives the yearly rate that a freestanding object overturns when exposed to the set of all ground motions from all earthquakes. Assuming Poissonian ground motion recurrence and a time interval that the object has been exposed to ground shaking, T , one can estimate the overturning probability

$$OP_T = 1 - \exp(-\mathbf{OR} \times T) \quad (3)$$

The application of equation 3 provides the means to compare VPSHA models with the existences of precariously balanced rocks. Should OP_T be exceedingly high, it is likely that the VPSHA model is unrealistically high at the precarious rock site (Anderson and Brune 1999).

Now suppose that there is a discrete distribution of N VPSHA estimates, RT^1, RT^2, \dots, RT^N , that are equally likely. For instance, this distribution may account for the uncertainty in the VPSHA model. The product of the precarious rock fragility, OP , and the n th VPSHA estimate, RT^n , results in the total overturning rate \mathbf{OR}^n after summing over the total set of ground motion bins. Using equation 3, one can estimate the overturning probability, OP_T^n , for each of the N VPSHA models. This work aims to go beyond assessing the consistency of precariously balanced rocks with VPSHA estimates to constraining the VPSHA models via the precarious rock fragilities. In order to achieve this end, one can weight each VPSHA model according to its propensity to produce overturning. For instance, if VPSHA model A overturns the rock in question with 90% probability while VPSHA model B overturns the rock with 10% probability, the weights should reflect a higher level of consistency with VPSHA model B than A. This is accomplished by weighting the n th VPSHA model by the normalized survival probability

$$w^n = \frac{1 - OP_T^n}{\sum_{n=1}^N (1 - OP_T^n)} \quad (4)$$

where the sum is taken over the N VPSHA models. Normalization ensures that the sum of the weights is equal to 1. In this way, one can rationally define a set of weights accounting for the presence of precariously balanced rocks. These weights act bin-by-bin to define the weighted mean VPSHA model. Thus the weighted mean VPSHA occurrence rate within ground motion bin k is given by

$$RT\{IM_1, IM_2 \in k\} = \sum_{n=1}^N w^n \times RT^n\{IM_1, IM_2 \in k\} \quad (5)$$

Note that this formulation does not place any restrictions on the form of the individual VPSHA models. In other words, highly variable VPSHA models may be included in this analysis if desired. The weighting process is shown schematically in Figure 4 with a scalar PSHA model for clarity.

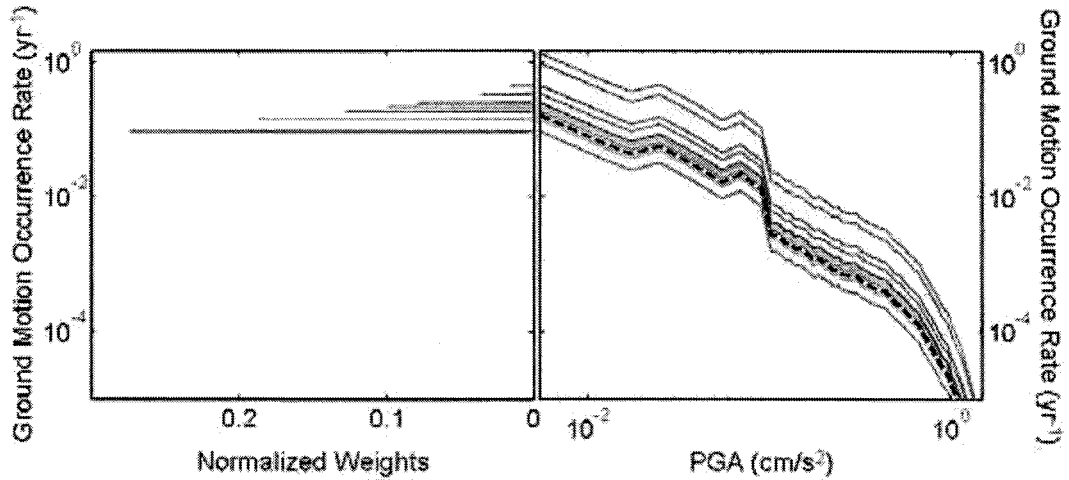


Figure 4 Application of the weighting scheme using a discrete distribution of scalar PSHA models (solid lines in the right panel). The associated weights are shown in the left panel as a function of the occurrence rates at small PGA . The dashed black line is the weighted mean ground motion occurrence rate model.

4. RESULTS

VPSHA models using the ground motion prediction equations of Abrahamson and Silva (1997), Boore et al. (1997), Sadigh et al. (1997), and Campbell and Bozorgnia (2003) have been calculated. Pullammanappallil et al. (2006) confirmed via Vs30s measurements that the precarious rock sites are generally near the site class B-C boundary. Thus the “hard rock” versions of the Abrahamson and Silva (1997) and Sadigh et al. (1997) models have been used along with the “firm rock” (Vs30 ~ 830 m/s) model of Campbell and Bozorgnia (2003). Vs30s, when known, have been used in the Boore et al. (1997) relations or have alternatively been set to 760 m/s. The marginal ground motion occurrence rates are averaged within each ground motion bin, consistent with the USGS scheme. The VPSHA calculations also use the USGS faulting input parameters. Note that unlike the 2002 USGS estimates, this analysis does not account for gridded seismicity nor background earthquakes.

Purvanco (2005) estimated prediction intervals around the median fragility models to assess uncertainty in the fragilities. In addition to the median fragility model, one can define the median + 1σ and median + 2σ fragility models which are increasingly less fragile (e.g., more difficult to topple). The range of the OP_T values using these alternate fragility models demonstrate the level of certainty in OP_T . Figure 5 presents OP_T values corresponding to the median, median + 1σ , and median + 2σ fragility models. 14 of the 24 median precarious rock fragility models overturn with greater than 95% probability during their presumed exposure times. In fact, 22 of the median precarious rock fragility models overturn with greater than 50% probability. 10 of the median + 1σ and 3 of the median + 2σ precarious rock fragility models overturn with greater than 95% probability over their presumed lifespans. These findings strongly suggest that the median VPSHA models are unrealistically high at many of the precarious rock sites.

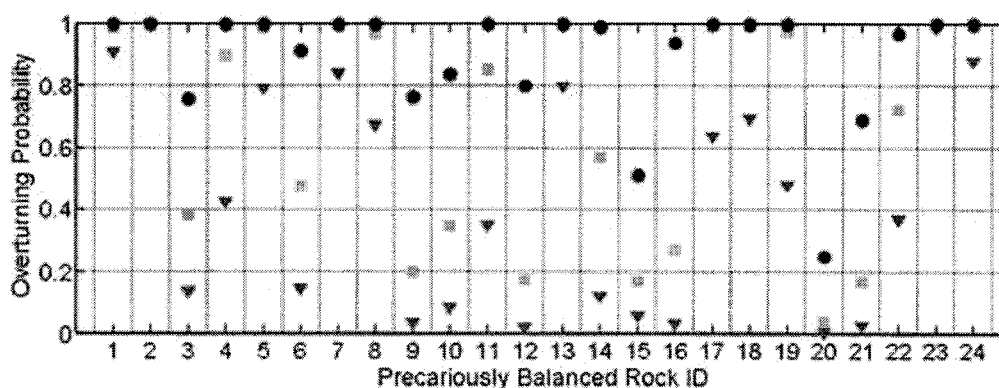


Figure 5 Overturning probabilities, OP_T , of the median (blue circles), median + 1σ (green squares), and median + 2σ (red triangles) precarious rock fragility models when exposed to the median VPSHA models. The VPSHA models and fragility estimates are in terms of PGA and $S_a(1)$.

The 2%, 5%, and 10% probability of exceedence (PE) in 50 year hazard values are used to assess the ramifications of the proposed weighting scheme. In particular, these hazard values have been calculated for both the weighted mean and unweighted median VPSHA models. In all cases the median precarious rock fragility models have been used. Figures 6a and 6b demonstrate the ratios of the weighted to unweighted hazard values for PGA and $S_a(1)$, respectively. Thus a hazard ratio close to 1 indicates little change in the weighted VPSHA model relative to the unweighted VPSHA model. This is the case for precarious rocks that are largely consistent with the VPSHA models (e.g., rocks 15, 20, and 21). The remaining 21 weighted hazard values are all reduced by at least 10% for both PGA and $S_a(1)$. Averaged over the whole data set, the 2%, 5%, and 10% PE in 50 year weighted PGA values are reduced by ~ 30%, 37%, and 42% relative to the unweighted hazard values. The weighted $S_a(1)$ values are reduced by ~ 36%, 42%, and 46% on average relative to the unweighted values. These constitute very significant reductions in the 2002 USGS hazard values for PGA and $S_a(1)$ at sites very close to active faults.

5. CONCLUSIONS

Though PSHA estimates are used frequently in specifying engineering design criteria, these models generally lack quantitative scrutiny of their applicability. This work proposes methodologies to both inspect hazard models for consistency with independent ground motion constraints and also to incorporate these constraints, yielding a hybrid hazard model. Precariously balanced rocks provide

just the long term constraints on the level of ground shaking to make these goals viable. The product of a precarious rock fragility model and a VPSHA occurrence rate model provides an estimate of the precarious rock overturning rate. The assumption of Poissonian ground motion recurrence produces the precarious rock overturning probability given the rock exposure time. The overturning probabilities are generally high for the set of rocks investigated, suggesting that the VPSHA models are unrealistically high. Weighting the VPSHA models is achieved by determining the precarious rock survival probabilities. The average reduction of the weighted hazard values relative to the unweighted values is greater than 30% for both PGA and $S_a(1)$. These reductions are significant in terms of design specifications of civil structures near to active faults. Future initiatives will focus on obtaining better age constraints on the precarious rocks, undertaking further field explorations, and refining the fragility models.

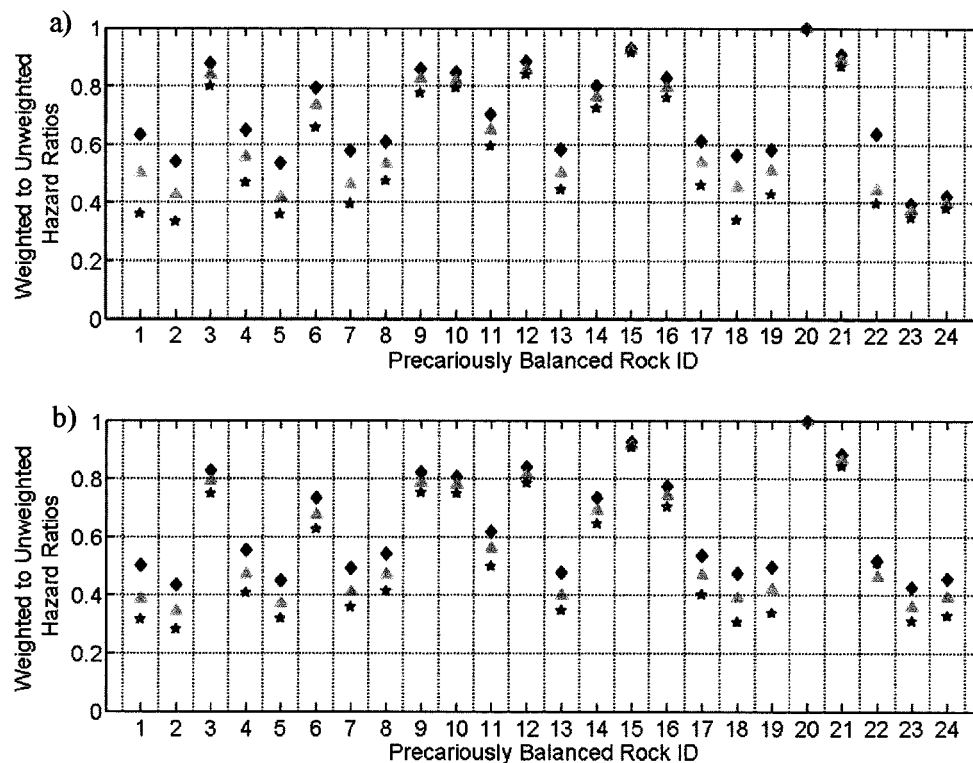


Figure 6 Ratios of the weighted to unweighted 2% (blue diamonds), 5% (green triangles), and 10% (red pentagrams) PE in 50 year hazard values for a) PGA and b) $S_a(1)$.

References:

- Abrahamson, N.A. and W.J. Silva (1997), "Empirical response spectral attenuation relations for shallow crustal earthquakes," *Seis. Res. Letts.*, **68**, 94-127.
- Anderson, J.G. and J.N. Brune (1999), "Methodology for using precarious rocks in Nevada to test seismic hazard models," *Bull. Seism. Soc. Am.*, **89**, 456-467.
- Anooshehpour, A., T. Heaton, B. Shi, and J. Brune (1999), "Estimates of the ground acceleration at Point Reyes Station during the 1906 San Francisco earthquake," *Bull. Seism. Soc. Am.*, **89**(4), 845-853.
- Bazzurro, P. and C.A. Cornell (2002), "Vector-valued probabilistic seismic hazard analysis (VPSHA)," in Proc. 7th U.S. National Conf. on Eq. Engrg., Boston, Massachusetts, 21-25 July 2002, Paper No. 61.
- Bell, J.W., J.N. Brune, T. Liu, M. Zreda, and J.C. Yount (1998), "Dating precariously balanced rocks in seismically active parts of California and Nevada," *Geology*, **26**(2), 495-498.
- Boore, D.M., W.B. Joyner, and T.E. Fumal (1997), "Equations for estimating horizontal response spectra and peak acceleration from western North American earthquakes: a summary of recent work," *Seism. Res. Letts.*, **68**, 128-153.

- Brune J. N. and J.W. Whitney (1992), "Precariously balanced rocks with rock varnish: paleoindicators of maximum ground acceleration?" *Seism. Res. Lett.*, **63**(1), 21.
- Brune, J.N. (1999), "Precarious rocks along the Mojave section of the San Andreas Fault, California: constraints on ground motion from great earthquakes," *Seism. Res. Lett.*, **70**(1), 29-33.
- Brune, J.N. (2000), "Precarious rock evidence for low ground shaking on the footwall of major normal faults," *Bull. Seism. Soc. Am.*, **90**(4), 1107-1112.
- Brune, J.N. (2003), "Precarious rock evidence for low near-source accelerations for transtensional strike-slip earthquakes," *Phys. Earth Plan. Int.*, **137**, 229-239.
- Brune, J.N., A. Anooshehpour, B. Shi, and Y. Zeng (2004), "Precarious rock and overturned transformer evidence for ground shaking in the Ms 7.7 Kern County earthquake: an analog for disastrous shaking from a major thrust fault in the Los Angeles basin," *Bull. Seism. Soc. Am.*, **74**(6), 1993-2003.
- Brune, J.N., A. Anooshehpour, and M.D. Purvance (2006), "Band of precariously balanced rocks between the Elsinore and San Jacinto, California, fault zones: Constraints on ground motion for large earthquakes," *Geology*, **34**, 137-140.
- Brune, J.N., M.D. Purvance, and A. Anooshehpour (2007), "Gauging earthquake hazards with precariously balanced rocks," *American Scientist*, **95**, 36-43.
- Cai, G., J. Yu, and Y. Lin (1995), "Toppling of rigid block under evolutionary random base excitations," *J. Eng. Mech.*, **121**(8), 924-929.
- Campbell, K.W. and Y. Bozorgnia (2003), "Updated near-source ground motion (attenuation) relations for the horizontal and vertical components of peak ground acceleration and acceleration response spectra," *Bull. Seism. Soc. Am.*, **93**, 314-331.
- Cornell, C.A. (1968), "Engineering seismic risk analysis," *Bull. Seism. Soc. Am.*, **58**(5), 1583-1606.
- Dimentberg, M., Y. Lin, and R. Zhang (1993), "Toppling of computer-type equipment under base excitation," *J. Eng. Mech.*, **119** (1), 145-160.
- Frankel, A., M.D. Petersen, C.S. Mueller, K.M. Haller, R.L. Wheeler, E.V. Leyendecker, R.L. Wesson, S.C. Harmsen, C.H. Cramer, D.M. Perkins, and K.S. Rukstales (2002), "Seismic hazard maps for the conterminous United States, Map C - Horizontal Peak Acceleration with 2% probability of exceedence in 50 years," *U.S. Geol. Surv. Open-File Rep. 02-420-C* (<http://eqhazmaps.usgs.gov/>).
- Housner, G.W. (1963), "The behavior of inverted pendulum structures during earthquakes," *Bull. Seism. Soc. Am.*, **53**(2), 403-417.
- Kimura, T.R. and K. Iida (1934), "On the rocking of rectangular columns (I)," *Zisin*, **6**(3), 125-149.
- Kirkpatrick, P. (1927), "Seismic measurements by the overthrow of columns," *Bull. Seism. Soc. Am.*, **17**(2), 95-109.
- Lin, H. and S. Yim (1996), "Deterministic and stochastic analyses of chaotic and overturning responses of a slender rocking object," *Nonlin. Dyn.*, **11**(1), 83-106.
- Makris, N. and Y.S. Roussos (2000), "Rocking response of rigid blocks under near-source ground motions," *Geotechnique*, **50**(3), 243-262.
- Mallet, R. (1862), "The Great Neopolitan Earthquake of 1857," London: Chapman and Hall.
- Milne, J. (1881), "Experiments in observational seismology," *Trans. Seism. Soc. Japan*, **3**, 12-64.
- Milne, J. and F. Omori (1893), "On the overturning and fracturing of brick and other columns by horizontally applied motion," *Seism. J. Japan*, **1**, 59-85.
- Perry, J. (1881), "Note on the rocking of a column," *Trans. Seism. Soc. Japan*, **3**, 103-106.
- Pullammanappallil, S., M.D. Purvance, J.N. Brune (2006), "Refraction microtremor (ReMi) results for Vs30 at precarious rock sites between the Elsinore and San Jacinto faults," *Proceedings 2006 Annual SCEC Meeting*, Palm Springs, Ca., September 10-13.
- Purvance, M.D. (2005), "Overturning of slender blocks: numerical investigation and application to precariously balanced rocks in southern California," *PhD Dissertation*, University of Nevada, Reno, Nevada.
- Purvance, M.D., A. Anooshehpour, and J.N. Brune (submitted 2006), "Overturning of freestanding blocks exposed to earthquake excitations," *Earthquake Engineering and Structural Dynamics*.
- Sadigh, K., C.Y. Chang, J. Egan, F. Makdisi, and R. Youngs (1997), "Attenuation relationships for shallow crustal earthquakes based on California strong motion data," *Seism. Res. Letts.*, **68**, 180-189.
- Shi, B., A. Anooshehpour, Y. Zeng, and J. Brune (1996), "Rocking and overturning of precariously balanced rocks by earthquakes," *Bull. Seism. Soc. Am.*, **85**(5), 1364-1371.
- Yim, C.S., A. Chopra, and J. Penzien (1980), "Rocking response of rigid blocks to earthquakes," *Eq. Eng. Strct. Dyn.*, **8**, 565-587.

INPUT MOTION SYNTHESIS CONSIDERING THE INFORMATION OF THE RESPONSE OF NONLINEAR SYSTEMS

Riki Honda¹⁾ and Ryuji Yamashita²⁾

1) Associate Professor, Department of Civil Engineering, University of Tokyo, Japan

2) Graduate Student, Department of Civil Engineering, University of Tokyo, Japan

rhonda@civil.t.u-tokyo.ac.jp, yamashita@ohrki.t.u-tokyo.ac.jp

Abstract: In the modern seismic design, consideration of a single input motion may not be sufficient because nonlinear dynamic behavior of structures are affected by indigenously uncertain factors. Consideration of all possible input motions, however, makes the design procedure unaffordable. This paper proposes to generate an input motion that is sufficiently large in terms of the response of nonlinear structural systems exposed to variety of possible input motions. Performance of the scheme is verified by a simple case treating the uncertainty of fault parameters in seismic wave synthesis.

1 INTRODUCTION

Seismic design should be conducted based on wide range of available informations. Various information such as the data of past earthquakes, strong motion records, surface ground conditions and deep ground structure provide useful information to the seismic design. However, different information leads to different input motions. Different sets of fault parameters naturally generate different ground motions.

Suppose a certain set of fault and structural parameters are assumed in the ground motion synthesis. If an earthquake happens in a different manner, or structures have different strength capacity, the actual behavior of structures can be totally different.

It should be also noticed that no factors related to the event of earthquake damage, including parameters of source faults, ground conditions, structural parameters are perfectly known. Therefore if all possible conditions are taken into consideration, cases to be considered will increase without limit and design procedure becomes costly, without actually improving the seismic performance of structures.

In the actual seismic design, to avoid such problems, a ground motion that is sufficiently "strong" (or affective to structures) has been used as an input motion. It is an efficient scheme when the seismic design is conducted based on a simple index such as PGA or peak response acceleration, which has been adopted for decades. In the recent trend of performance based design, however, design procedure requires nonlinear dynamic analyses to assure the performance, making the process complicated. Under such circumstances, simple index such as peak

response value is not necessarily the dominant factor. Even if a structure is designed based on the ground motion with large peak response acceleration, it is possible that the structure cannot resist some different (but possible) ground motions. It is not easy to pick up the “best” input motion, because dynamic behavior of nonlinear structures are complicated. It is even likely that such a wave does not exist, because a ground motion that damages a certain structure most may not be the toughest when some structural parameter are varied.

Due to above reasons, even if various information about the seismic source is available, it is not easy to find the most appropriate ground motion, especially for the performance based design with nonlinear behavior of structures.

Considering such background, we present a scheme to generate a input motion that can be used as an input motion. We select some indices that quantify the effect of the input motions to structures and synthesize an input motion that is large in terms of those indices.

Attention is also paid to the cost. Adoption of an excessively strong input motion would not make sense even if it is the largest among the possible input motion candidates, because that leads to the uneconomical increase of construction cost.

2 INPUT MOTION SYNTHESIS

2.1 Input motion for seismic design

Ground motion can be estimated by various manners such as numerical simulation, empirical relationship, etc. Different conditions lead to different ground motions and, in the existence of wide range of uncertainty in various conditions, the number of input motions to be considered increase without limit, making it impossible to use all possible ground motions in the seismic design.

We aim to generate a ground motion that allows us to design structures in a manner as we do when all ground motions are considered. Such input motion can be said to reflect all available information about various factors such as ground conditions and fault parameters including their uncertainty. No input motion, however, will satisfy that condition in a strict sense. As an alternative approach, we set up indices that are important for the evaluation of the strength of input motions, and generate a wave that is strong enough in terms of those indices.

Suppose we have m possible input motions. We consider a certain index r to evaluate the strength of input motions. Let us assume that the index is taken so that the larger value corresponds to the large input motion. Most indices which are used in the current earthquake engineering, such as response acceleration of a single degree of freedom (SDOF) system, can be adopted. Let \bar{r} denote the index value of the target input motion. Then it should satisfy

$$\bar{r} \geq \max_i \{r_i\} \quad (1)$$

where r_i denotes the index of i -th input motion.

We also assume structures have uncertainty in their parameters such as initial stiffness and yield strength. Let \mathbf{k} denote a set of structural parameters with uncertainty and \mathbf{K} the range of possible values of parameters in \mathbf{k} . Write response index as a function of structural parameters as $r(\mathbf{k})$. Then we have

$$\bar{r}(\mathbf{k}) \geq \max_i \{r_i(\mathbf{k})\} \quad \text{if } \mathbf{k} \in \mathbf{K}. \quad (2)$$

When more than one indices are considered, Eq (2) must hold for each of all indices.

Attention should be also paid to the cost. It is obvious that Eq (2) will be satisfied, if the target input motion is taken much larger than the candidate input motions. It leads to, however, redundant capacity against actual seismic load and uneconomical design. Therefore efforts should be made to minimize the margin of Eq (2).

2.2 Indices for Evaluation

Let us assume that indices to evaluate the strength of the input motions increase as the input motions become large. Note that the index does not have to be a strictly increasing function of amplitude of input motions. It is important that it exhibits good correlation with essential factors of input motion strength. Conventional indices such as PGA, response spectra values, SI-values, Seismic intensity, obviously satisfy the conditions.

In this paper, we use the peak response velocity and hysteretic energy of the nonlinear SDOF system. They are used to quantify the damage of the structure exposed to input motions (Park and Ang, 1985).

2.3 Searching Algorithm

The input motion was generated by modifying the input motion so that Eq.(2) is satisfied with small margin. This is achieved by updating the input motion step by step iteratively. In each updating step, $N = 341$ candidate input motions are generated by modifying the wavelet transform of the input motion. Discrete wavelet transform of the input motion $s(t)$ is denoted by $\hat{s}_{j,k}$ where j, k are indices associated with scale and time-shift, respectively. Complex wavelet function is used and $\hat{s}_{j,k}$ are complex variables. In generation of a candidate input motion, three adjacent wavelet coefficients $\hat{s}_{j,k}$'s are modified at a time. They are close next to each other in terms of time-shift and frequency scale. Two temporally consecutive wavelet coefficients are selected from one scale and another coefficient is from the neighboring lower scale so that its time shift is equal to the mean of the two wavelet coefficients from the higher scale. Each of the three wavelet coefficients are increased by a complex value s_r whose arguments (phases) is given randomly. Let us refer to the candidate waves as p_i , $i = 1, \dots, N$.

Among the generated candidates, the input motion that improved the performance most is adopted. The performance of the input motions can be evaluated by various manners. In this paper, we use an evaluation function described below.

In the computation, uncertainty of structural parameters is taken into consideration by Monte Carlo simulation, generating M structures by changing parameters. Each realizations are referred to by subscript j in the following.

Denote by r_j^* the right-hand side of Eq (2) of j -th structure, then r_j^* is a function of the input motion p_i . The index r_j of the j -th structure is also given as a function of p_i . Evaluation function to estimate the performance of the input motion p_i , $f(p_i)$ can be given as

$$f(p_i) = \sum_{j=1}^M \left\{ \frac{1}{M} d(r_j, r_j^*) - |\tilde{r}_j - r_j^*|/r_j^* \right\} \quad (3)$$

where r_j, r_j^* and \tilde{r} are function of p_i , but it is not explicitly written for simple expression, and d is an index function defined as

$$d(\tilde{r}_j, r_j^*) = \begin{cases} 1 & \text{if } \tilde{r}_j \geq r_j^* \\ 0 & \text{if } \tilde{r}_j < r_j^* \end{cases} \quad (4)$$

Table 1: Assumed Fault Parameters (Mean Values)

Fault size	Length = 31.8 [km], Width = 38 [km]
Epicenter (on the fault)	x = 31.8 [km], y = 19 [km]
S wave velocity	3.0 [km/s]
Fracture velocity	2.1 [km/s]

Table 2: Structural Parameters

Mass	1.0 [-]
Initial stiffness	0.75 ~ 1.25 [$\times 10^2 \text{ sec}^{-2}$]
(Natural Period)	0.56 ~ 0.73 [sec]
Stiffness ratio	0.2
Damping ratio	0.05

Index function d is used as a penalty to avoid over-amplification of the input motion.

3 NUMERICAL SIMULATIONS

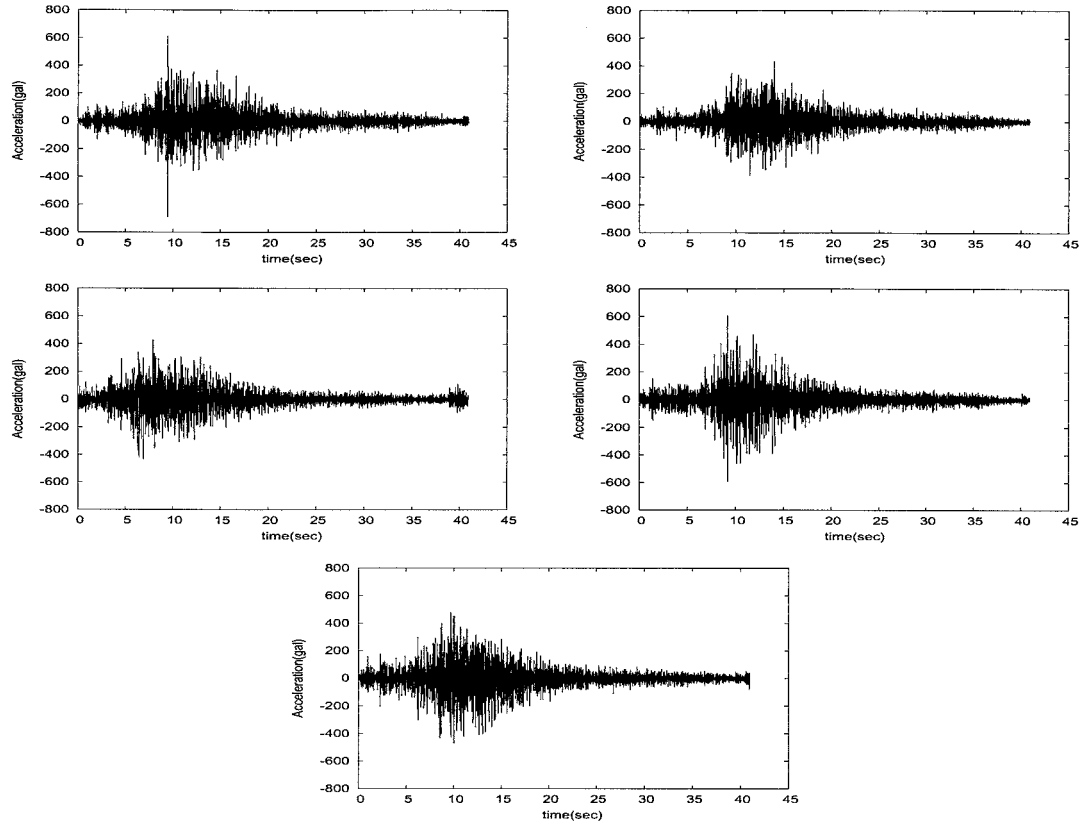
3.1 Simulation Conditions

To show the performance of the proposed scheme, we conducted a numerical simulation. The 2005 Miyagiken-Oki Earthquake (M 7.2) is adopted as a numerical example. Ground motion of the earthquake is generated by empirical Green's function method (Irikura, 1983) using aftershock records of the Miyagiken Oki Earthquake as small event records. Time histories of the synthesized ground motions, which have relatively large amplitude, are plotted in Fig-1. They exhibit difference in peak values and temporal variation of amplitudes, but the difference is not large enough to pick up one as the input motion for seismic design.

Fault parameters are listed in Table-1. In order to emulate the case that we have to face the uncertainty of the parameters, we give Gaussian noise to the shear wave velocity and fracture propagation velocity. Amplitude of the noise is set as the 5% of the mean value. Randomized parameters give different ground motion and in total 1,000 ground motions are generated. They are used as the set of possible input motions to be considered in this case.

As a structure model, SDOF system with a bi-linear stiffness model. Parameter values are listed in Table-2. Initial stiffness and yielding strength are supposed to have uncertainty and to be uniformly distributed in the range specified in Table-2. Number of realizations to be used in Eq.(3) is set as $M = 100$. The peak response velocity and total hysteretic energy of the nonlinear system are used as the indices to be considered in the evaluation function Eq.(3). Amplitude of increment, s_r , which is added to the wavelet coefficients, is set as 5% of the total power of the original wave.

We started the searching algorithm, using one of the ground motions generated by simulation as the initial ground motion. Its time history is shown at the bottom of Fig-1. It was adopted because it causes the largest hysteretic energy in the nonlinear dynamic analysis.



(This was used as the initial input motion)

Fig. 1: Input motions Synthesized by Empirical Green's Function Method

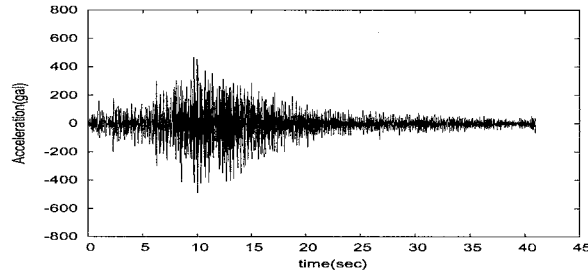


Fig. 2: Synthesized Input Motion

3.2 Computation Results

Fig-2 shows the time history of the generated input motion. For the purpose of comparison, we also make an input motion that satisfies the required condition by amplifying the original input motion with a constant amplification factor. Time history of the input motion plotted in Fig-3 indicates the amplitude is redundantly larger than that of the synthesized input motion (Fig-2).

The mean values of the increment ratio of nonlinear response values are compared in Table-3. In this comparison, 1,000 structures are generated, assuming uncertainty in two parameters: the initial stiffness and yielding displacement. Gaussian noise with the standard deviation of

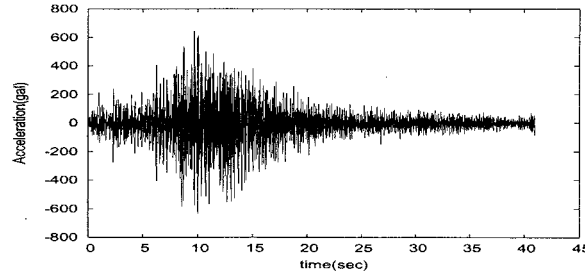


Fig. 3: Input motion generated by multiplying a constant so that it satisfies the required condition.

Table 3: Increase of Response Values

Resp. Val.	Synthesized	Constantly Amplified
Velocity	0.06	0.35
Displacement	0.07	0.18
Hysteretic Energy	0.26	0.76

10% of the mean value is added to each of the parameters. The response velocity of the synthesized motion is 6% larger than that of the original motion in average, while the constantly amplified motion claims 35% increase. Similarly, the constantly amplified input motion requires the larger increase in the response displacement and hysteretic energy.

The same can be observed in the distribution of the increment ratio of the peak response displacement and hysteretic energy are plotted in Fig-4. In the figure, red dots denote the ratio for the amplified input motion and the green the input motion synthesized by the presented scheme. The distribution of hysteretic energy shows that the synthesized input motion has smaller variation. It enables the satisfaction of condition without exceedingly amplifying the input motion. It should be noticed that the synthesized input motion satisfies the required condition Eq.(2).

The results indicate that the synthesized input motion enables efficient and economical seismic design, because it does not require redundantly seismic performance. It means that the synthesize input motion allows us to satisfy the with less increment of the cost.

Response values of nonlinear SDOF systems to the synthesized input motion are compared with those of the strong motion record of the main shock of Miyagiken Oki Earthquake (Fig-5). The comparison shows that those of the synthesized input motion exceeds those of the strong motion records, indicating the good performance of the proposed scheme.

4 CONCLUSION

This paper presents a scheme to produce an input ground motion for seismic design, considering the possible input motions generated by various methodologies, assuming uncertainty of many factors.

The “largest” input motion among possible ground motions has been used for the design purpose when plural input motions are available as candidates. However, response of nonlinear dynamic analysis varies widely depending on various factors and it is not easy to define the “largest.” To avert this problem, we use as indices, response values of nonlinear structures with

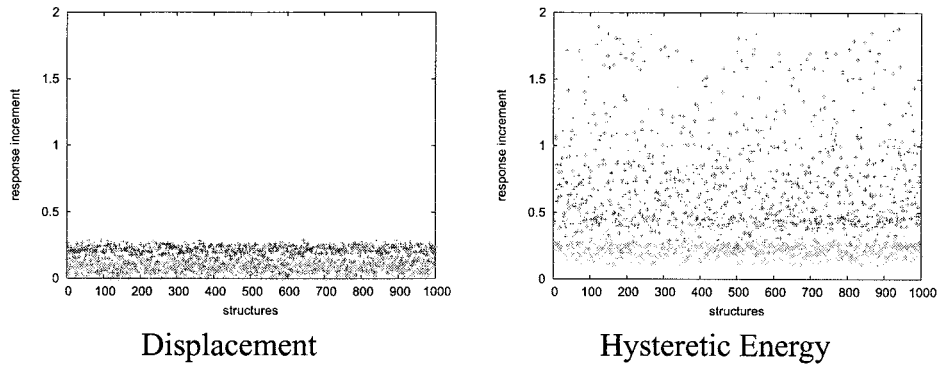


Fig. 4: Increase Ratio of Nonlinear Response Values

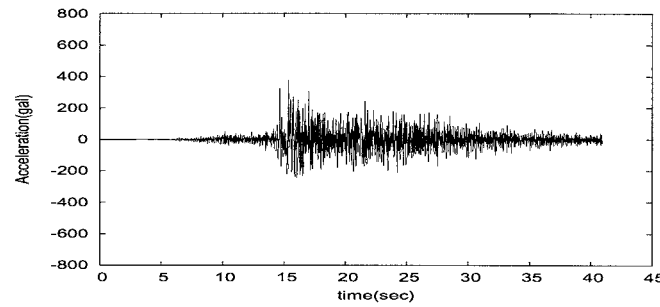


Fig. 5: Strong Motion Record (Ojika Station) of 2005 Miyagiken-Oki Earthquake

uncertain parameters. The input motion that is sufficiently large in terms of these indices are synthesized is generated by a step-by-step searching algorithm.

The performance of the proposed scheme is verified by numerical examples. Number of input motions are generated by empirical Green's function by changing values of some parameters. The proposed scheme is used to synthesize the input motion that reflects the uncertainty of parameters in empirical Green's function method. Comparison with the input motion made by multiplying a constant shows that the input motion by the proposed scheme enables rationally economical seismic design.

Currently we are working on the development of wave synthesis algorithm, which can generate more sophisticated input motions.

Acknowledgment

This research was partially supported by the Ministry of Education, Science, Sports and Culture, Grant-in-Aid for Young Scientists (A), 17686040, 2005–2007. We used ground motion records from Strong-Motion Seismograph Network (K-NET) of National Research Institute for Earth Science and Disaster Prevention. Our sincere appreciation is expressed.

References:

Housner G.W. (1975). Measure of severity of earthquake ground shaking *Proc. U.S. National Conf. Earthq. Engnrg.*, 25–33

- Park Y. J., Ang A. H. S. (1985). Mechanistic seismic damage model for reinforced concrete *Journal of Structural Engineering, ASCE*, vol.11, 4, 723–739
- Park Y. J., Ang A. H. S. (1985). Seismic damage analysis reinforced concrete buildings *Journal of Structural Engineering, ASCE*, vol. 11, 4, 740–757
- Williams, M. S. and Sexsmith, R. G. (1995), Seismic damage indices for concrete structures: A state-of-the-art review, *Earthquake Spectra*, Vol. 11, No. 2, 319–349
- Irikura, K.(1986). Prediction of strong acceleration motion using empirical Green's function, *Proc. 7th Japan Earthq. Eng. Symp.*, Tokyo, 151–156
- National Research Institute for Earth Science and Disaster Prevention, Kyoshin Net (K-NET)
<http://www.k-net.bosai.go.jp>

SIMULATION OF THE M_J5.4 EARTHQUAKE WITH USE OF THE EMPIRICAL GREEN'S TENSOR SPATIAL DERIVATIVES

M. Oori¹⁾ and Y. Hisada²⁾

1) Research Fellow, Center for the Urban Earthquake Engineering, Tokyo Institute of Technology, Japan

2) Professor, Department of Architecture, Kogakuin University, Tokyo, Japan

ohori@enveng.titech.ac.jp, hisada@cc.kogakuin.ac.jp

Abstract: Based on the empirical Green's tensor spatial derivatives (EGTD) estimated from data of 11 aftershocks (M_J3.5-4.7), we simulated the strong motion records for the mainshock (M_J5.4) of the 2001 Hyogo-Ken Hokubu, Japan earthquake. The targeted station is one of K-NET stations, HYG004, located at about 6-10 km in epicentral distance from the source region. To demonstrate the applicability of the EGTD method to simulation of the near-field strong motion, a direct comparison with the EGTD method and the empirical Green's function (EGF) method are carried out. We confirmed that a good agreement between the observed waveform and the calculated ones from two methods is satisfactory for the long duration as well as the amplitude level. In addition, the EGTD method gives a better matching with the data compared with the EGF method.

1. INTRODUCTION

Since a pioneering work by Hartzell (1979), the empirical Green's function (EGF) method has been recognized as one of the most practical techniques to predict the strong ground motion for large earthquakes. Basically, the use of this method is limited to the case when the focal mechanism of a small event is identical or similar to that of a targeted event. Also, to compensate the difference in the focal mechanisms approximately, radiation pattern basis corrections are often done. This correction induces another concern because correction coefficients sometimes become extraordinarily large and the prediction results fall into unstable solutions, especially when the targeted station is near the node in the radiation pattern for small events.

On the other hand, the empirical Green's tensor spatial derivative (EGTD) method (Plicka and Zahradnik, 1998), has potential to get over the difference of focal mechanisms between small events and a targeted one, and predict the ground motion for an event with an arbitrary focal mechanism. The EGTD elements are estimated from a kind of single-station and single-component inversion using waveform data for several small events whose focal mechanisms and source time functions are well determined. This technique is expected to provide considerably accurate and stable prediction results, but its application is found only in limited literatures (Ito et al., 2001; Ito, 2005, Oori and Hisada, 2006). Moreover, a direct comparison between the EGTD method and the EGF one still remains.

In this article, we present an example application of the EGTD method to simulation of the near-field strong motion records during the 2001 Hyogo-ken Hokubu, Japan earthquake (M_J5.4). A nearby station located at 6-10 km in epicentral distances is targeted. The EGTD is estimated based on the data from 11 aftershocks (M_J3.5-4.7) whose source parameters are re-evaluated by the two-step moment tensor inversion. The strong motion is simulated based on the EGTD method and compared with observed data and synthesized one from the EGF method.

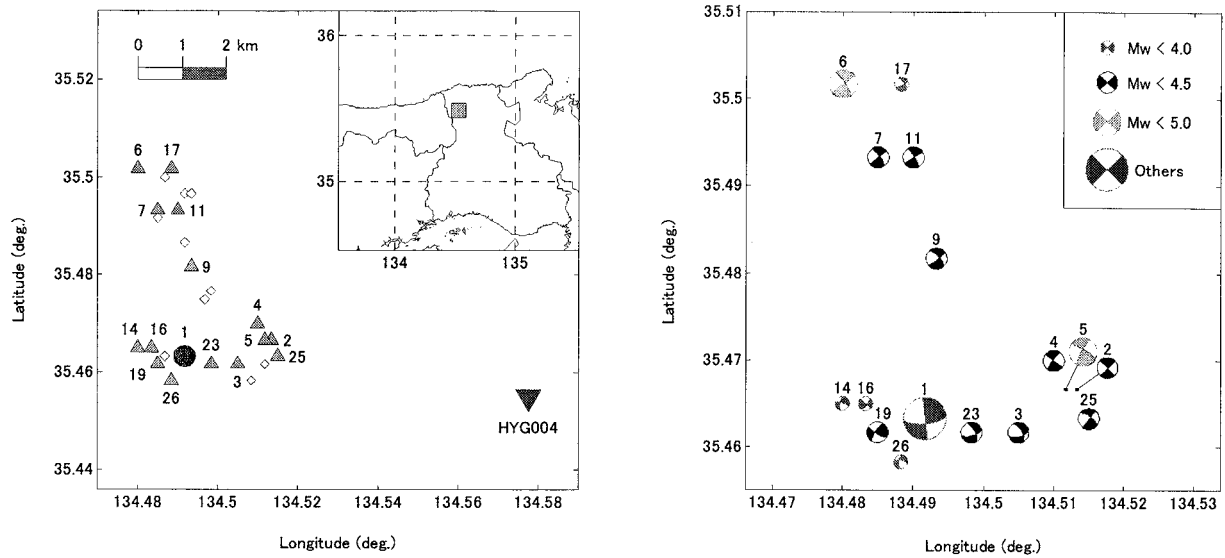


Figure 1. Maps showing locations of epicenters and the targeted station (left) and re-evaluated focal mechanisms for mainshock (Event 1) and aftershocks (Event 2-26) (right).

2. LOCATIONS OF EPICENTERS AND STATION

In Figure 1(left), we show epicenter locations of the mainshock ($M_j 5.4$) and 25 aftershocks ($M_j 3.1-4.7$) of the 2001 Hyogo-ken Hokubu earthquake and the target station, HYG004. The mainshock and 15 aftershocks of which data are recorded at HYG004 are indicated by solid circles and solid triangles, respectively. The other 10 aftershocks not used in present study are represented by open diamonds. One of the K-NET station, HYG004 was chosen as a target station because it was a rock site, located at the closest epicentral distance (6 to 10 km) from the fault zone whose range extended to 4 km in the east-west direction and to 6 km in north-south direction. The depth of sources is in a range of about 6-12 km. The station, HYG004 is shown by an upside-down solid triangle. The inset at top right in Figure 1 (left) shows the surrounding region with the target area enclosed by a solid rectangle.

3. RE-EVALUATION OF THE SOURCE MODELS

The observed acceleration records at HYG004 from a mainshock and 15 aftershocks ($M_j 3.5-4.7$) were integrated into the velocity waveform data with a bandpass-filter between 1 to 5 s. Prior to the EGTD inversion, we used the strong motion data from the mainshock and 15 aftershocks mentioned above to re-evaluate their source parameters by the following two-step single-station waveform inversion.

In the first step, we estimated the strike, dip, and rake of a double-couple point source by the grid search technique (Ohori, 2005). In calculation of the theoretical Green's function using a Fortran code (Hisada, 1995), the smoothed ramp function with a rise time of 0.32 s was used for the source time function. The underground structure we used is the same as the model used for the rupture process estimation of the 2000 Tottori-ken Seibu, Japan earthquake (Table 4 in Kuge, 2003). We inverted data of 5 s including the P-wave arrival and the S-wave main portion. The searching ranges of these parameters were set within 20 deg. from the solutions of the F-net. In addition, source depth was searched in a range of 6 to 12 km with an increment of 1 km.

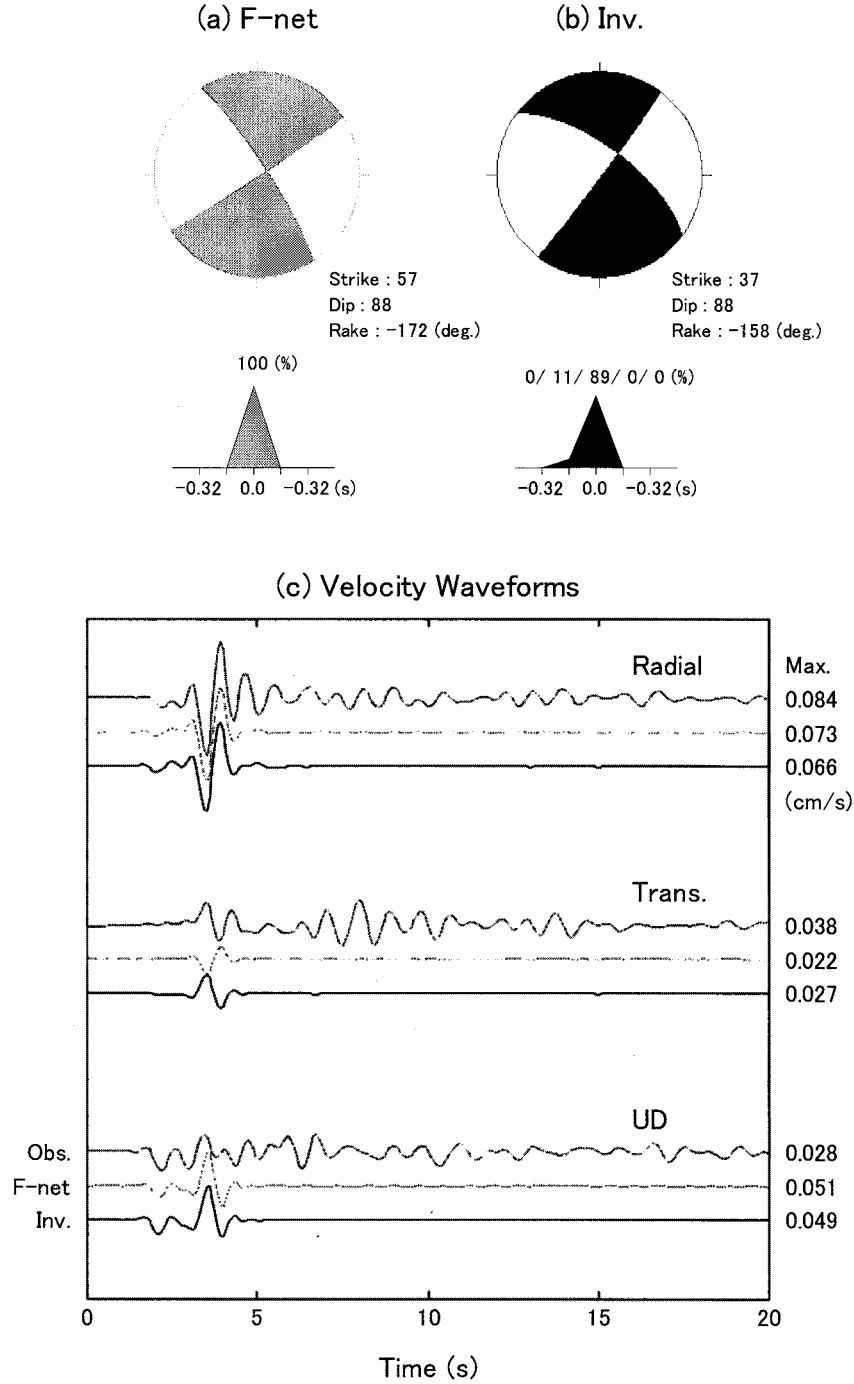


Figure 2. Source models and velocity waveforms for the mainshock.

In the second step, fixing the fault mechanism and source depth estimated above, we determined the seismic moments and the source time function. The seismic moments released by five sequential slips were estimated by the least-square method with non-negative constraints (Lawson and Hansen, 1970).

In Figure 1(right), we shows re-evaluated focal mechanisms of 16 events (the mainshock and 15 aftershocks) in this study. Note that the events 3, 17, 19, and 26 are excluded in the following EGTD inversion because of the discrepancy in waveform matching between the data and synthesis. As an example result of the moment tensor inversion, in Figure 2, we show source models for Event 25 and comparison of the observed and the synthesized velocity waveforms. In Figure 2, the source model (a)

is based on the focal mechanism from the F-net and combined with a single-slip source time function. Another source model (b) is based on the results derived from present study. In the lower panel (c), we compared the observed velocity waveforms (upper traces) with the synthesized ones (middle and lower traces). Absolute peak amplitudes are shown by numerals at the end of each trace. We can find that fitting between observed waveforms and synthesized ones are greatly improved by re-evaluation of the source model (Inv.) compared with the initial source model (F-net). For this event, the former source model successfully expressed the observed polarity of the initial S-wave portion in transverse component, although the latter one failed. In addition, the re-evaluated source model for the mainshock (Event 1) can be seen in Figure 6 (right).

4. METHOD OF THE EGTD INVERSION

4.1 Basical Equations

Ground motion displacement $u_i(x_o, t)$ ($i = x, y, z$) excited by a double-couple point source is theoretically expressed in a form of convolution with moment tensor elements $M_{pq}(x_s, \tau)$ ($p, q = x, y, z$) and the Green's tensor spatial derivative elements $G_{ip,q}(x_o, t | x_s, \tau)$ as follows,

$$u_i(x_o, t) = M_{pq}(x_s, \tau) * G_{ip,q}(x_o, t | x_s, \tau) \quad (1)$$

Hereafter, we abbreviate $u_i(x_o, t)$, $M_{pq}(x_s, \tau)$, and $G_{ip,q}(x_o, t | x_s, \tau)$ with u_i , M_{pq} and $G_{ip,q}$, respectively. Explicit expressions of M_{pq} can be found in many literatures (e.g. Aki and Richards, 1980). Considering symmetrical conditions ($M_{pq} = M_{qp}$) and no volume change [$M_{xx} = -(M_{yy} + M_{zz})$] in moment tensor elements, we can rewrite Equation (1) as

$$u_i = \sum_{j=1}^5 M_j * G_{ij} \quad (2)$$

where M_j ($j = 1, 2, \dots, 5$) and G_{ij} ($j = 1, 2, \dots, 5$) are defined in what follows, respectively.

$$\begin{cases} M_1 = M_{xy} \\ M_2 = M_{yy} \\ M_3 = M_{yz} \\ M_4 = M_{xz} \\ M_5 = M_{zz} \end{cases} \quad (3), \quad \begin{cases} G_{i1} = G_{ix,y} + G_{iy,x} \\ G_{i2} = G_{iy,y} - G_{ix,x} \\ G_{i3} = G_{iy,z} + G_{iz,y} \\ G_{i4} = G_{ix,z} + G_{iz,x} \\ G_{i5} = G_{iz,z} - G_{ix,x} \end{cases} \quad (4)$$

In the moment tensor inversion, given u_i and G_{ij} , M_j are the unknowns to be solved in a least square sense. Conversely, in the EGTD inversion, given u_i and M_j for targeted events, G_{ij} are the unknowns to be solved. Note that the EGTD inversion is carried out for each component and for each station.

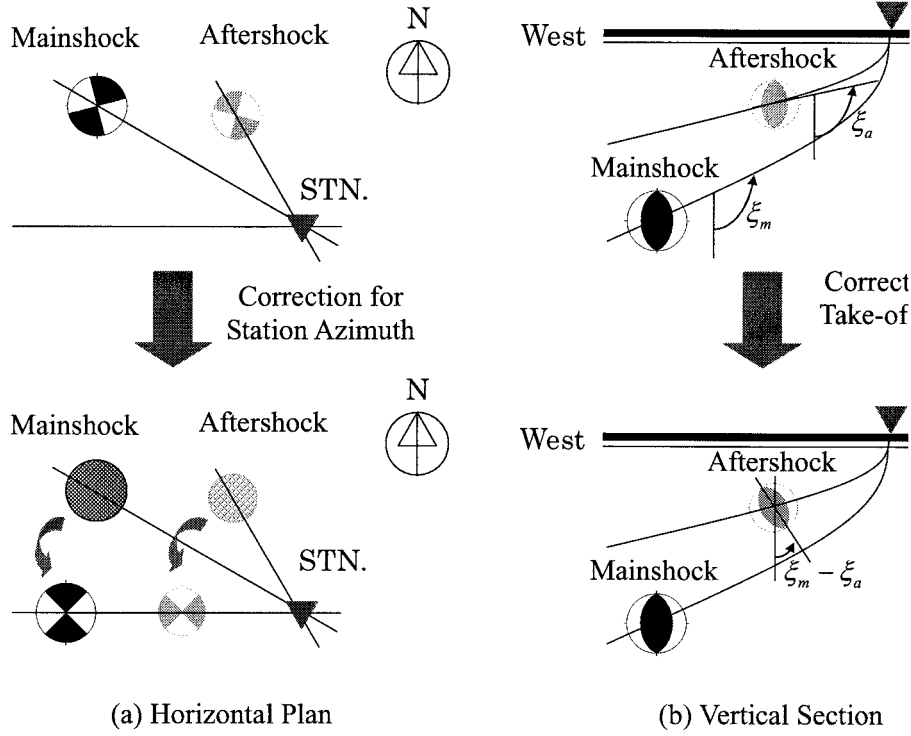


Figure 3. Horizontal and vertical rotations applied to the focal mechanisms.

4.2 Correction for the Focal Mechanisms

The differences of source locations between the mainshock and aftershocks are significant in the EGTD inversion. To compensate this discrepancy, we apply horizontal and vertical rotations of the focal mechanisms, referring to the literature (Ito et al., 2001, Ito, 2005). By the horizontal rotation in Figure 3(a), the station azimuths of both mainshock and aftershocks are set to 90 deg. measured from the north, so that the degree of freedom in the Green's tensor spatial derivatives is reduced to 3 ($G_{i1} = G_{i4} = 0$) in radial ($i = y$) and vertical ($i = z$) components and 2 ($G_{i2} = G_{i3} = G_{i5} = 0$) in transverse one ($i = x$). By the vertical rotation in Figure 3(b), the discrepancy in the take-off angles between the mainshock and aftershocks are corrected, following the horizontal rotation. In the right top panel of Figure 3, take-off angles for the mainshock and aftershocks are denoted by ξ_m and ξ_a , respectively. Note that the difference between take-off angles, $\xi_m - \xi_a$ is slightly exaggerated in right below panel of Figure 3 for the graphical purpose.

4.3 Correction to Waveform Data

To adjust the timing of waveform data among the mainshock and aftershocks, we give time shifting to data from aftershocks. Also, to remove the discrepancy in the source time function, we carried out deconvolution to data for aftershocks. In Figure 4, we show transverse-components as example corrected observed waveforms used in estimation of the empirical Green's tensor spatial derivatives. Each traces are corrected for the source time function to have a constant seismic moment ($1.0 \times 10^{15} \text{N} \cdot \text{m}$) and a single isosceles slip velocity function with rise time of 0.32 s. Absolute peak amplitudes are shown by numerals at the end of each trace. Note that the top trace for the mainshock (Event 1) is not included in the EGTD inversion

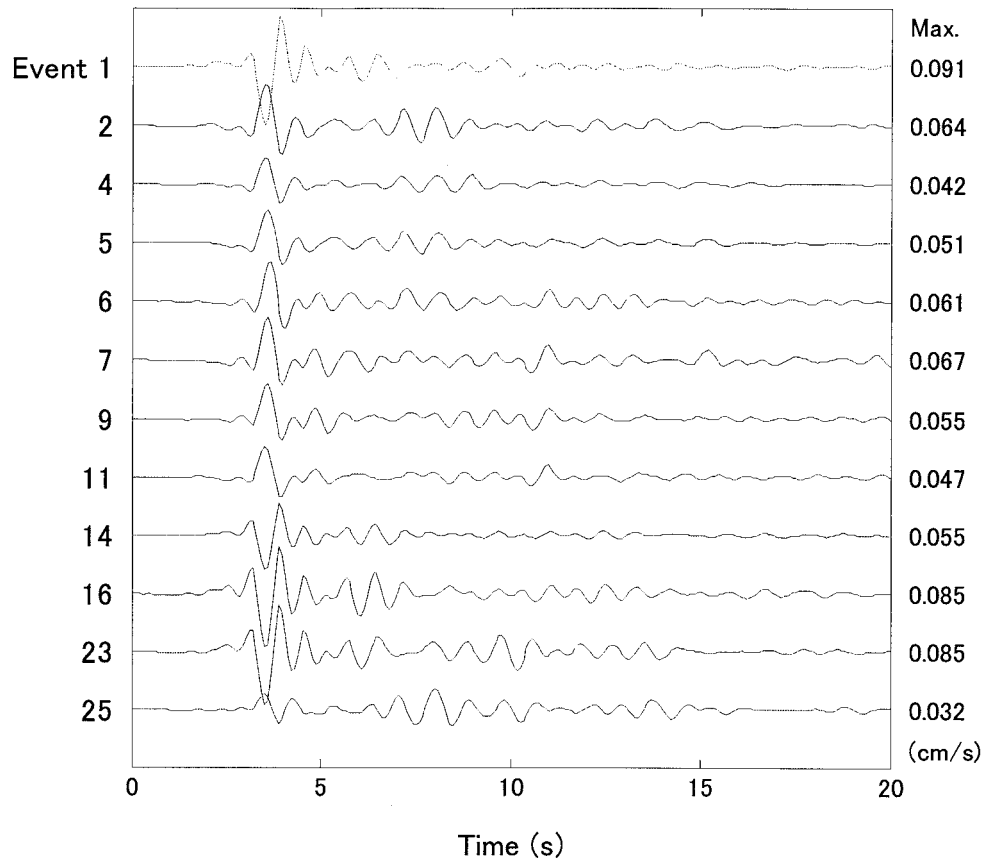


Figure 4. Transverse components of corrected observed waveforms.

5. ESTIMATION OF THE EGTD AND SIMULATION OF STRONG GROUND MOTION

In Figure 5, we show a comparison of the theoretical Green's tensor derivative elements (the top trace, Syn.), the empirical ones estimated from numerical experiments using synthesized waveforms for 11 aftershocks instead of recorded data (the second and the third traces, Test 1 and Test 2, respectively), and empirical ones using aftershock records (the fourth traces, Emp 2). The Green's tensor spatial derivative elements are defined by Equation (4). In Figure 5, absolute peak amplitude is shown by numerals at the end of each trace. The Green's tensor spatial elements are scaled with the seismic moment of $1.0 \times 10^{15} \text{ N} \cdot \text{m}$. The focal mechanisms are corrected by the horizontal rotations in Test 1, and by both the horizontal and vertical rotations in Test 2 and Emp 2. First, taking a look at the results of top three traces in Figure 5, we can observe that both numerically experimental results (Test 1 and Test 2) show a good agreement with theoretical one (Syn.) but Test 2 gives better fitting to the Syn. rather than Test 1. We, therefore, used the same analytical conditions in Emp 2 as those in Test 2. Comparing Emp 2 with Syn., we can find that the former reproduces well the latter's duration characteristics lasting long after the S-wave main portion.

In Figure 6, we show a comparison of the observed mainshock (Event 1) velocity waveforms (upper traces, Obs.), the synthesized ones based on the empirical EGTD (middle traces, EGTD) and the synthesized ones based on the empirical Green's function using data of the largest aftershock (Event 5) with radiation pattern basis corrections (lower traces, EGF). Synthesized waveforms are calculated based on the source model in the right panels of Figure 6, obtained in the present study. In Figure 6, absolute peak amplitude is shown by numerals at the end of each trace. We can find that a good agreement between the observed waveform and the calculated ones from two methods is

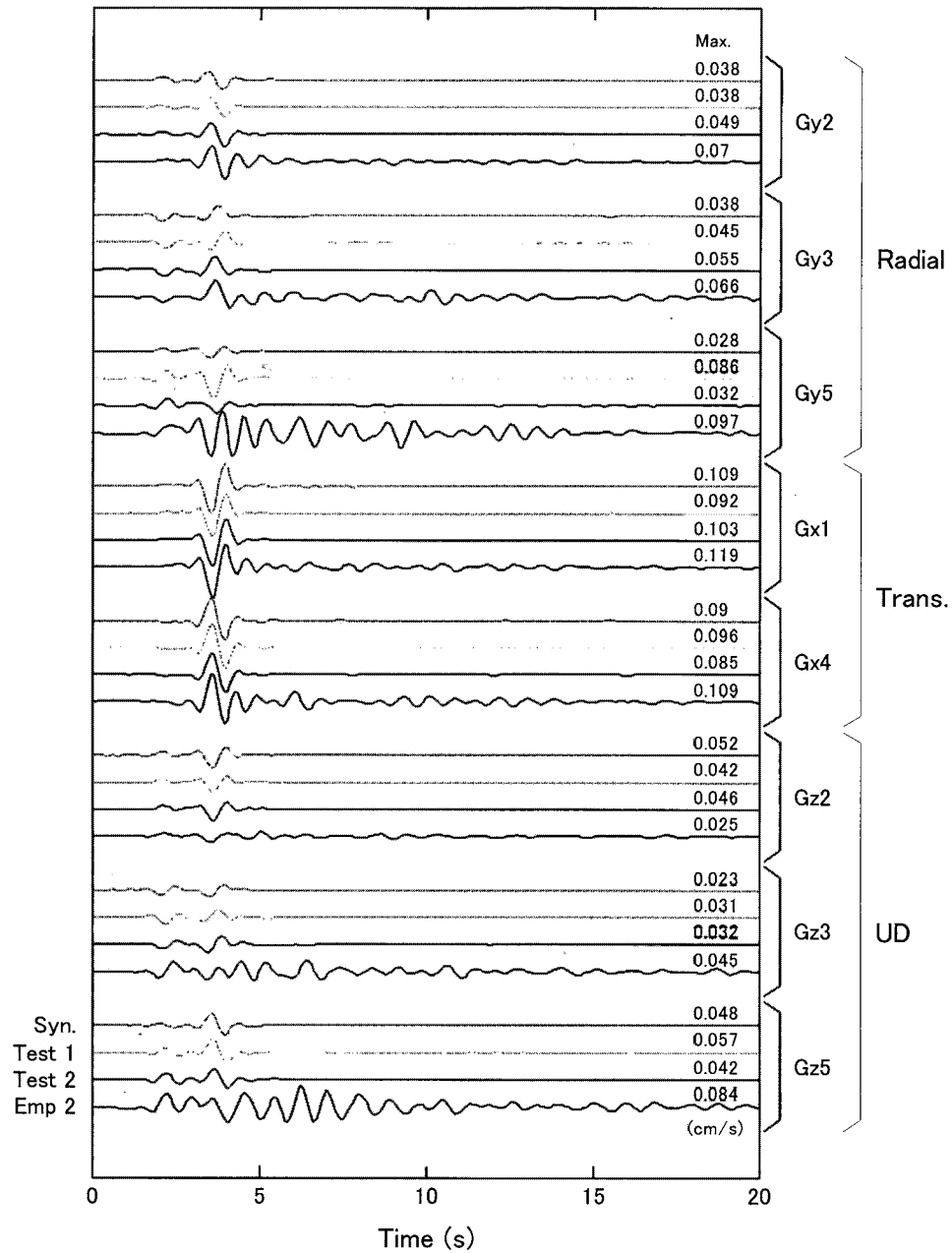


Figure 5. Theoretical and empirical Green's tensor spatial derivative elements.

satisfactory for the long duration as well as the amplitude level. Especially, the EGTD method gives a better matching with the data compared with the EGF method.

6. CONCLUSIONS

Through this study, we demonstrated the applicability of the EGTD method to simulate the near-field strong motion records. Successful simulation results for the 2001 Hyogo-ken Hokubu, Japan, earthquake ($M_j 5.4$) suggests that the EGTD method gives us stable and accurate solutions for the strong motion prediction.

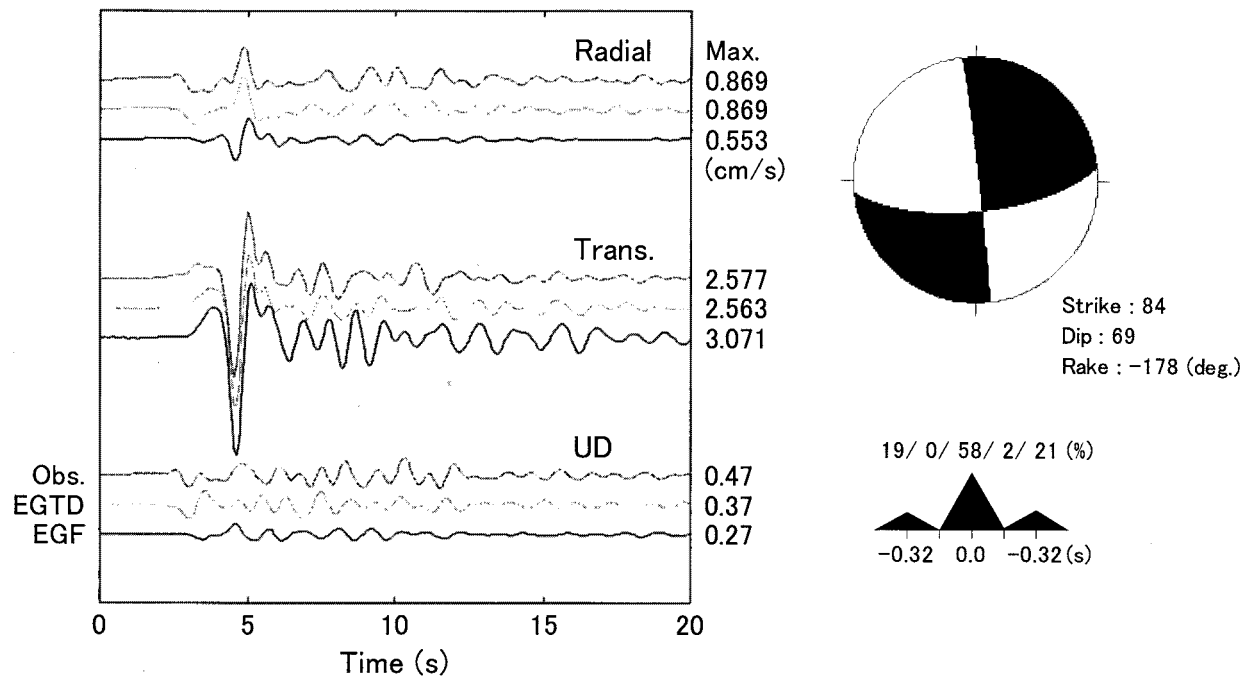


Figure 6. Observed and synthesized velocity waveforms for the mainshock (left), re-evaluated focal mechanisms for mainshock (right top), and slip velocity time function (right below).

Acknowledgements:

In this study, we used the strong motion data of the K-NET, operated by the National Research Institute for Earth Science and Disaster Prevention. Our sincere gratitude is given to whom it may concern.

References:

- Aki, K. and P. G. Richards (1980), "Quantitative seismology, theory and methods", W. H. Freeman, San Francisco, 932 pp.
- Kyoshin Network (K-NET) operated by National Research Institute for Earth Science and Disaster Prevention, <http://www.kyoshin.bosai.go.jp/>.
- Full Range Seismograph Network (F-net) operated by National Research Institute for Earth Science and Disaster Prevention, <http://www.fnet.bosai.go.jp/freesia/index.html>.
- Hartzell, S. H. (1978), "Earthquake aftershocks as Green's functions", *Geophys. Res. Lett.*, 5, 1-5.
- Hisada, Y. (1995), "An efficient method for computing Green's functions for a layered half-space with sources and receivers at close depths (Part 2)", *Bull. Seism. Soc. Am.*, 85, 1080-1093.
- Ito, Y., T. Okada, T. Matsuzawa, N. Umino, and A. Hasegawa (2001), "Estimation of stress tensor using aftershocks of 15 September 1998 M5.0 Sendai, NE Japan, earthquake", *Bull., Earthq. Res. Inst.*, 76, 51-59. (in Japanese)
- Ito, Y., 2005, "Mechanisms of aftershock generation", Report of the National Research Institute for Earth Science and Disaster Prevention, 68, 27-89. (in Japanese)
- Kuge, K. (2003), "Source modeling using strong-motion waveforms: towards automated determination of earthquake fault planes and moment-release distributions", *Bull. Seismol. Soc. Am.*, 93, 639-654.
- Lawson, C. L. and D. J. Hanson (1974), "Solving least squares problems", Prentice-Hall Inc., Englewood Cliffs, New Jersey, 337 pp.
- Ohori, M. (2005), "Source model estimation by waveform inversion using one- or two-station strong motion records, - A case from the 1990 Odawara earthquake (M_J5.1) -", *Zisin* 2, 57, 257-273. (in Japanese)
- Ohori, M. and Y. Hisada (2006), "Estimation of empirical Green's tensor spatial derivatives using aftershock of the 2001 Hyogo-ken Hokubu earthquake and simulation of mainshock (M_J5.1) strong motion", *Zisin* 2, 59, 133-146. (in Japanese)
- Plicka, V., and J. Zahradnik (1998), "Inverting seismograms of weak events for empirical Green's tensor derivatives", *Geophys. J. Int.*, 132, 471-478.

A STUDY ON ACCURACY OF SOURCE PARAMETERS ESTIMATED BY WAVEFORM INVERSION

K. Motoki¹⁾, H. Yamanaka²⁾, and K. Seo³⁾

1) Research Associate, Dept. of Built Environment, Tokyo Institute of Technology, Japan

2) Associate Professor, Dept. of Environmental Science and Technology, Tokyo Institute of Technology, Japan

3) Professor, Dept. of Built Environment, Tokyo Institute of Technology, Japan

kmoto@enveng.titech.ac.jp, yamanaka@depe.titech.ac.jp, seo@enveng.titech.ac.jp

Abstract: Strong motions near source regions highly depend on the heterogeneity of the source, and an appropriate procedure to distribute asperities is necessary. A number of source models have been already evaluated in recent a couple of decades since Hartzell and Heaton (1983). But their source models are too complicated to directly apply a model for an estimation of future earthquakes. The information compiled by Somerville et. al. (1999) are referred to make a source model as inner source parameters. Our developed waveform inversion to directly calculated characterized source model successfully reproduced observed waveforms. In this paper, we focused on the accuracy of source parameters estimated by this waveform inversion for the 1995 Kobe earthquake. Especially we take up the influency of the difference of the subsurface models to the locations of asperities for discussion.

1. INTRODUCTION

The heterogeneity of source process is very effective for an estimation of strong motions near the source regions or huge earthquakes. In order to obtain the heterogeneity, a number of studies have been made on detailed source processes for the past few decades since Hartzell and Heaton(1983) and Olson and Apsel(1982) developed waveform inversion techniques. The resultant source processes are regarded as one of the most appropriate models. The source models calculated for past earthquakes are used as basic materials to estimate for future earthquakes. The characterization suggested by Somerville et. al. (1999) were performed to simplify the already calculated source models, because of difficulty to convert them as it is. We developed an waveform inversion method to directly estimate characterized source models (Motoki et. al. (2006)).

In this paper, accuracy of source parameters estimated by our waveform inversion to discuss its applicable coverage, and validity. Despite most of the source models evaluated in previous research have been applied the method developed by Hartzell and Heaton (1983), the source models of the same earthquake have not been always similar even if under the similar model. Takemura(1998) discussed the differences and the commons among several source models for Kobe earthquake. It is well-known that some differences in source models are appeared due to difference the using data and modelization. There are few researches to discuss this difference in source models. The discussion of accuracy of source model has still remained difficulty, because the source model is affected by many input parameters and data set complicatedly. In order to simplify this issue, we take up the influency of the difference of the subsurface models to the location of asperities for discussion. We tried our developing method for Kobe earthquake, because the earthquake is the most devastating for recent 50 years, and lots of source models have been evaluated in previous researches.

2. METHOD

The source behavior in the inversion problem is parameterized to the moment rate tensor as a function of time and space. In this paper, we adopt an asperity model to evaluate source processes as shown in Fig.1. Before an inversion with GA, the Greens function need to be calculated to decrease calculation costs. We calculated synthetics with an interval of 1km, that is, dx and dy is set to 1km. The asperity model moving already set position. The unknown parameters are listed in Fig. 1. The asperities are uniformly behaved in each asperity, and each parameter is allocated to each asperity one by one. The source time function for each asperity is modeled to imitate dynamical source processes reported by Nakamura and Miyatake (2000) as shown in Fig.1, and T1 and T2 are 0.8 and 1.6 seconds respectively. The misfit function, $E(m)$ for the model, m , is calculated from

$$E(m) = \frac{1}{N} \sum \frac{|F_c - F_d|^2}{\sigma^2} \quad \sigma = \begin{cases} \sigma_c & (\sigma_c \leq \sigma_o) \\ \sigma_o & (\sigma_o < \sigma_c) \end{cases}$$

where F_c and f_o are a synthetic velocity and an observed velocity, and σ and N are standard deviation and the number of observed data, respectively. The standard deviation is changed depending on the amplitude of synthetic waveform in order to fit not only the phase but the amplitude. We adopt genetic algorithms (GA) as a heuristic method. The algorithms were developed to study artificial intelligence by Holland (1975). Yamanaka and Ishida (1996) successfully calculated the model underground velocity structure using GAs with phase velocity based on microtremor array exploration and we confirmed that GA is useful for this calculation. As Motoki et. al. (2006) mentioned, more than 2 asperities cannot be inverted at a time, because of huge calculation cost for GA. For more than 2 asperities, we invert asperities one by one as suggested. The population is set to 500 and the final generation is set to 500. Therefore, the total number of calculation counts to 250000. GA calculation were performed 10 times for each inversion, and an appropriate result is selected in the ten results.

3. DATA

We used strong ground motion records observed by Committee of Earthquake Observation and Research in the Kansai Area (CEORKA), Japan Meteorological Agency (JMA) and Osaka Gas and Railway Technical Research Institute for analysis and the locations of the stations are shown in Fig. 2. The distribution of stations is almost near the source region, because the characteristics of the seismic source include into the seismogram near the seismic source better than the surrounding stations. The seismograms recorded by accelerographs were numerically integrated to obtain the velocity waveforms. The resultant velocities are band-pass filtered between 0.1 and 1.0 Hz and sampled with an interval of 0.1s. In calculation of the Green's functions, frequency range

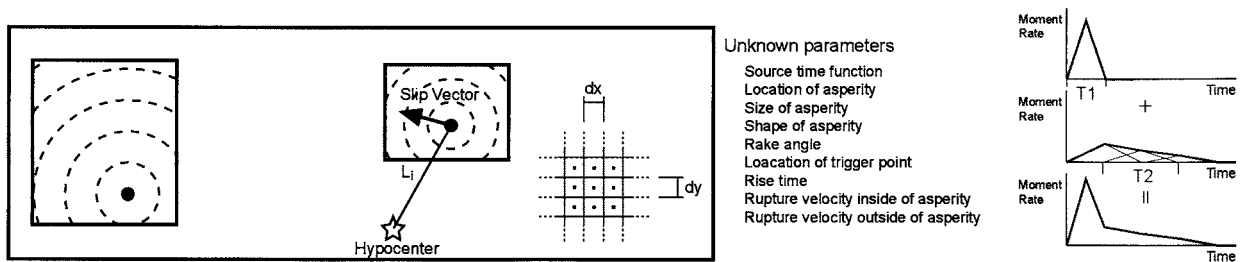


Figure 1 Schematic Image of characterized source model adopt in this study. The sources can move only on release point on which Green's function were calculated in advance.

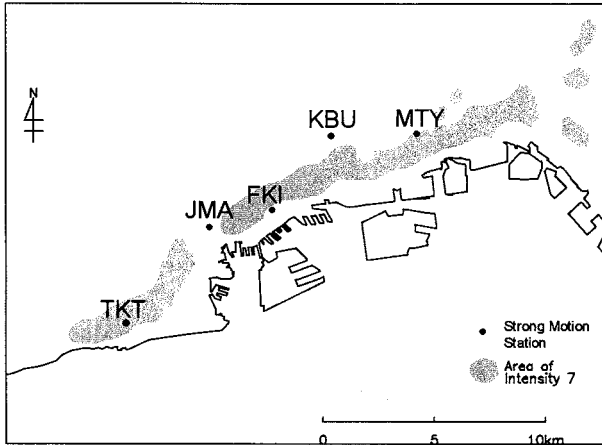


Figure 2 Distribution of observation stations.

TABLE 1 Velocity Structure Model

D(km)	Vp(km/s)	Vs(km/s)	p(g/cm ³)	Qp	Qs
d1	1.8	0.5	1.8	100	50
d2	1.9	0.6	1.9	100	50
d3	2.2	0.8	2.0	150	75
d4	2.5	1.0	2.1	150	75
2.0	5.5	3.2	2.6	300	150
22.0	6.0	3.46	2.7	500	250
32.0	6.6	3.81	3.0	800	400
∞	7.8	4.5	3.2	1000	500

Name	d1	d2	d3	d4
JMA	0.05	0.10	0.15	0.80
TKT	0.10	0.20	0.30	1.00
FKI	0.10	0.20	0.30	0.90
KBU	0.006	0.010	0.03	0.20
MTY	0.15	0.30	0.50	1.00

are used same to the observed data. We adopt the stratified velocity structure model shown in TABLE 1, which was based on refraction experiments (Aoki and Muramatsu(1974)) and reflection experiments. We use the reflectivity method extended by Kohketsu (1985) to calculate the Green's function. The geometry of the fault surface is set to same to the model of Yoshida et. al. (1996).

4. RESULTS AND DISCUSSION

A comparison of waveforms between observed and synthetic of an example solution for 3 asperity model is shown in Fig. 3. We inversed the source model at 2 cases. One is using structure model to be TABLE 1 and another is the different subsurface structure model in which the thickness of deposits to the seismic bedrock ($V_s=3.2\text{km/s}$) is extended to the 120% thickness shown in TABLE 1. Below the seismic bedrock, which means under 2km depth, the structure model is set same to model in TABLE 1. The solid lines, the broken lines and gray lines are indicated observed waveforms, synthetic waveforms using regular structure model and synthetic ones using thickened structure model, respectively. By and large, the synthetic waveforms successfully reproduce the main phases of observed ones, and it can be said that 3 asperity model can almost reproduce waveforms near the source region. But is recognized that there are some differences in synthetic waveforms evaluated using different structure model. The predominant period of synthetic waveforms using original structure model can be seen shorter than ones using thickened model, in spite of same rise time. The thickened models have surely longer periods and it can be considered that this difference appear on the waveforms.

The inversed source model by which synthetic waveforms in Fig. 3 calculated is shown in Fig. 4. small solid circles represent trigger points, and the rupture propagate from these points. The location of trigger points is calculated using GA together with other parameters. The location and the trigger points of asperity A and asperity B is similar to both model, but those of asperity C can be regarded as different. Their moment magnitude is also shown in Fig. 4. The magnitudes of all 3 asperities of original model is larger than those of thickened model. Total seismic moment is about twice. The difference of these models are only thickness of soils, it can be considered that frequency characteristics will be different but the amplification factor will not be changed so much because of same material of surface layer. The amplitudes of waveforms using original model is larger than those using thickened model as shown in Fig.3. It is inferred that the frequency response make difference in the amplitude.

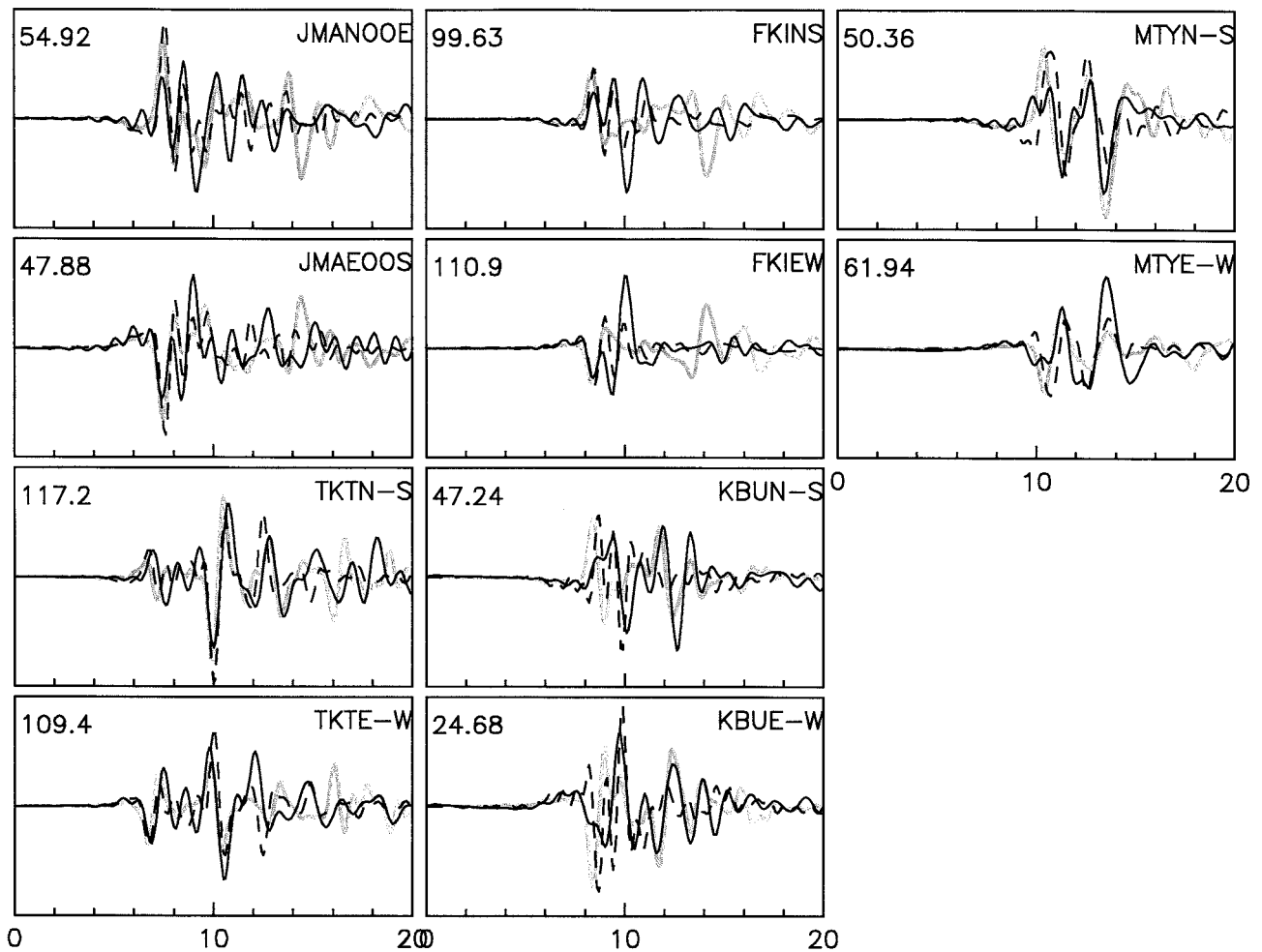
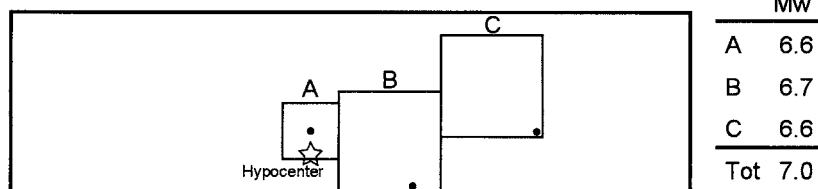


Figure 3 Comparison of observed and synthetic waveforms as an example of 3 asperity model. The solid lines, the broken lines and gray lines are indicated observed waveforms, synthetic waveforms using regular structure model and synthetic ones using thickened structure model, respectively.

Using structure model shown in Table 1



Using thickened structure model

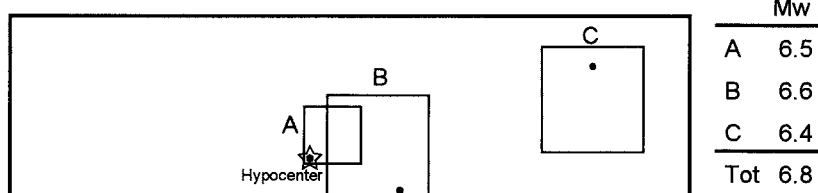


Figure 4 The inversed source model by which synthetic waveforms in Fig. 3 calculated. The hypocenter and the trigger point of asperities are indicated with star and solid small circles, respectively

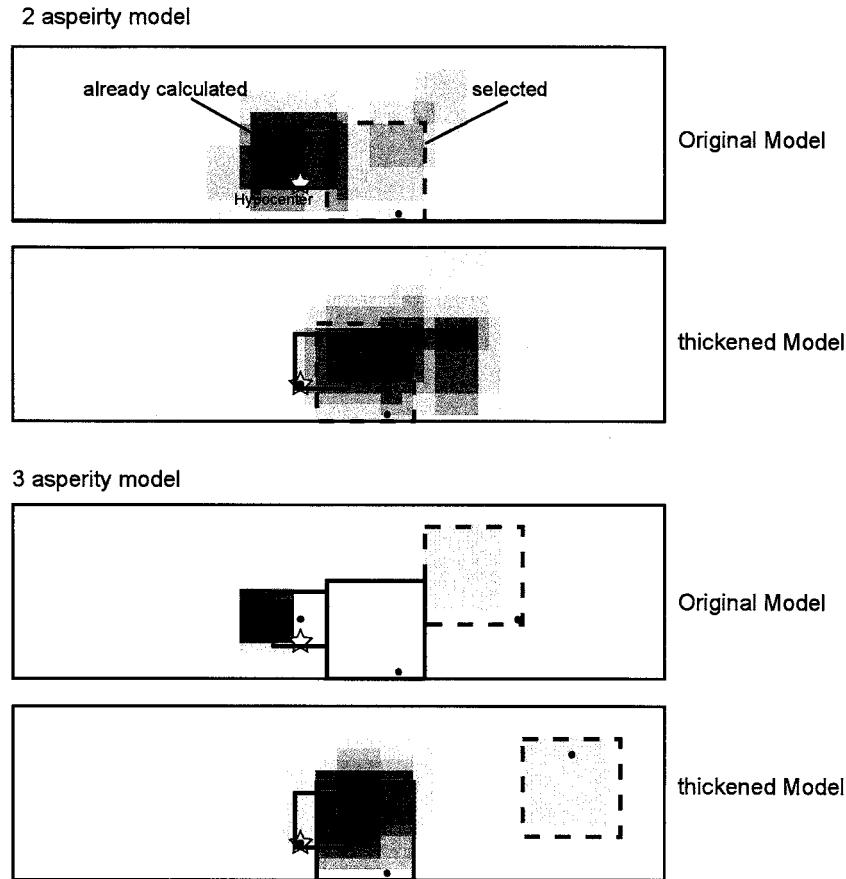


Figure 4 The processes calculating the asperities. The color of each asperity is light gray and the area overlaying asperities becomes dense.

The processes calculating the 2 and 3 asperity models are shown in Fig. 5. In all cases, GA calculation were performed 10 times and produced 10 result. The color of each asperity is light gray and the area overlaying asperities becomes dense. The more dense the color of area is, the more the solutions are on the area. Namely, the density shows the probability of the existence of an asperity. The first asperities of both models are similar location, but the locations of solutions are different from each other and the deviation of solutions on each asperity can be also recognized. For 3 asperity model, the difference become larger than that for 2 asperity model. The difference of thickness of soils changes travel time, therefore the location of solution is shifted. The averages of magnitude of solutions for 10 times are 6.99 and 6.81 using original and thickened model, respectively.

The analysis in this paper can be regarded as sensitivity test that the location and magnitude of asperities is affected by changing the subsurface structure. In addition, this paper took up 1 case in discussion and represents example of sensitivity from input to output. Other input data will be analyzed similarly. The different solutions derived have possibilities to be plausible, but they cannot be said true model. Consequently, the accuracy of source parameters cannot be discuss in a strictly sense. If the artificial waveforms can be imitated to observed motion by adding to noise, we can make the further discussion for accuracy of source model.

5. CONCLUSIONS

We investigated the accuracy of the new waveform inversion method using genetic algorithms

with changing subsurface structure model. It was confirmed that changing only 20 percents of thickness of subsurface structure affect the location and magnitude of asperities. We can show that an example of sensitivity from input to output. Other input data will be analyzed similarly and we will try other procedure to reveal the validity and the coverage of the inversion.

Acknowledgements:

We thank the Committee of Earthquake Observation and Research in the Kansai Area, the Japan Meteorological Agency, Osaka Gas and Railway Technical Research Institute for providing the strong motion data. The Research was partially supported by the Minisry of Education, Science, Sports and Culture-in-Aid for Young Scientists (B), 15760423, 2003-2005.

Reference:

- Aoki H. and I. Muramatsu, Crustal structure in the profile across Kinki and Shikoku, Japan, as derived from the Miboro and the Toyama explosions, *Zishin*, 27, 104-109, 1974 (in Japanese)
- Hartzell, S. H. and T. H. Heaton, Inversion of strong ground motion and teleseismic waveform data for the fault rupture history of the 1979 Imperial Valley, California, earthquake, *Bull. Seism. Soc. Am.*, 73 1553-1585, 1983.
- Holland, J. H., Adaptation in natural and artificial systems, University of Michigan press, Ann. Arbor, MI. 1975
- Koketsu K., The extended reflectivity method for synthetic near-field seismograms, *J. Phys. Earth*, 33,121-131, 1985
- Motoki, K., H. Yamanaka and K. Seo, A Trial Study on Waveform Inversion Directly for Characterised Source Models, the Proceedings of the 12th Japan Earthquake Engineering Synposium, 2006
- Nakamura, H. and T. Miyatake, An Approximate Expression of Slip Velocity Time Function for Simulation of Near-Field Strong Ground Motion, *ZISIN J. Seism. Soc. Japan*, Vol. 53, 1-9, 2000.
- Olson, A. H. and R. J. Apsel, Finite faults and inverse theory with applications to the 1979 Imperial Valley earthquake, *Bull. Seism. Soc. Am.*, 72, 1969-2001, 1982
- Somerville, P., K. Irikura, R. Graves, S. Sawada, D. Wald, N. Abrahamson, Y. Iwasaki, T. Kagawa, N. Smith and A. Kowada, Characterizing crustal earthquake slip models for the prediction of strong ground motion, *Seism. Res. Lett.*, 70, No.1, 59-80, 1999
- Takemura M., Review of source process studies for the 1995 Hyogo-ken-nanbu earthquake part. 1 results from waveform inversion, Programme and Abstracts The Seismological Society of Japan, A49, 1996 No.2, (in Japanese)
- Yamanaka H. and H. Ishida, Application of genetic algorithms to an inversion of surface-wave dispersion data, *Bull. Seism. Soc. Am.*, 86, 436-444, 1996
- Yoshida, Shingo, Kazuki Kohketsu, Bunichiro Shibazaki, Takeshi Sagiya, Teruyuki Kato, Yasuhiro Yoshida, Joint Inversion of Near- and Far-Field Waveforms and Geodetic Data for the Rupture Process of the 1995 Kobe Earthquake, *J. Phys. Earth*, Vol. 44, 437-454, 1996

THREE DIMENSIONAL NUMERICAL SIMULATION OF SEISMIC RESPONSE OF LARGE-SCALE UNDERGROUND INFRASTRUCTURE

T. Yamada¹⁾, T. Ichimura²⁾, N. Ohbo³⁾, Y. Yamaki⁴⁾, H. Itami⁵⁾, and M. Hori⁶⁾

1) Supervisory Research Engineer, Kajima Technical Research Institute, Kajima Corporation, Japan

Doctoral student, Department of Civil Engineering, Tokyo Institute of Technology, Japan

2) Associate Professor, Department of Civil Engineering, Tokyo Institute of Technology, Japan

3) Supervisory Research Engineer, Kajima Technical Research Institute, Kajima Corporation, Japan

4) Master student, Department of Civil Engineering, Tokyo Institute of Technology, Japan

5) Research Engineer, Kajima Technical Research Institute, Kajima Corporation, Japan

6) Professor, Earthquake Research Institute, University of Tokyo, Japan

takemine@kajima.com, ichimura@cv.titech.ac.jp, ohbo@kajima.com,

yamaki@e-society.cv.titech.ac.jp, itamihi@kajima.com, hori@eri.u-tokyo.ac.jp

Abstract: With an increasingly active use of underground spaces, large-scale complicate underground infrastructures overcrowd in the metropolitan area in Japan. Nevertheless, the seismic design basis of shield tunnel requires performing the seismic design independently in the direction of tunnel axis and its orthogonal direction in order to confirm the safety. Three-dimensional effects on the seismic response cannot be taken into consideration, so the safety during an earthquake is not sufficiently confirmed for such structures. In order to solve this problem, the authors have discussed three-dimensional behaviors of large-scale underground infrastructure by using dynamic FEM analysis with a detailed modeling of entire underground infrastructures. This paper describes the investigation cases and their findings of the large-scale complicate underground infrastructures, and shows the validity of this approach.

1. INTRODUCTION

The damage at Daikai Station during the Hyogo-ken Nanbu Earthquake (1995, Hyogo-ken, Japan) has provided an important issue in the seismic safety of underground infrastructures, as shown in the report by JSCE (1998). The underground infrastructures considered safe so far, suffered severe damage during the earthquake particularly, so that the metropolitan functions were paralyzed. After the event, it took long time to restore them. Through this experience, it was confirmed that not only the non-uniform structural section area but also the ground layers subject to sudden changes in spite of seismic design. The dynamic behaviors of such ground and structure are investigated using the dynamic analysis (Ohbo *et al.* 1992) and the earthquake observations (Ohbo *et al.* 2000). Nowadays, however, the three dimensional behaviors of the underground infrastructure have been sparsely understood and the seismic design has not yet been prepared to evaluate them.

“Special Measures Concerning the Public Use of the Deep Underground” enforced in April 2001 has enabled to use the deep underground space more effectively. In Tokyo Metropolitan area, construction plans of expressways or railways in such deep undergrounds are now in progress. Together with this, a seismic evaluation method of complicate underground infrastructures is now in discussion. The establishment of this evaluation method follows the need to secure safety and to confirm function against a severe earthquake; the major concerns are the joint parts of vertical shaft and shield tunnel, bifurcation, confluence and curved part into the expressway in the deep

underground layers.

Taking an advantage of the rapid progress of the information technology and the preparation of digital data (GIS, CAD, etc.) of the metropolitan areas, a newly developed earthquake disaster forecast and protection system called Integrated Earthquake Simulator (IES) is now available, as shown in the work by Ichimura *et al.* (2005a, 2005b). This achieves comprehensive forecast of possible earthquake disasters in the metropolitan areas by building the virtual city based on those digital data.

In addition to the ground infrastructures like public buildings and road and railway networks which include bridges, underground infrastructures are important public assets to sustain the metropolitan functions and to support its economical activities. The underground infrastructures in the metropolitan areas are becoming more complicated, larger and longer. Therefore, an accurate forecast of earthquake damage of the underground infrastructure becomes more important, and needs to evaluate three-dimensional behaviors of such complicate underground infrastructures.

The authors are studying accurate modeling of these underground infrastructures and examining the seismic safety performance concerning three-dimensional behaviors. The authors performed earthquake response analyses on some structures by using one method of IES, the macro-micro analysis as shown in the work by Ichimura *et al.* (2006). This paper describes major analysis results, and discusses the need full three-dimensional analysis to examine the seismic safety of large-scale underground infrastructure.

2. NECESSITY OF THREE DIMENSIONAL EARTHQUAKE RESPONSE ANALYSIS FOR UNDERGROUND INFRASTRUCTURE

There are many of the underground infrastructures which are complicated, enlarged and deeply embedded. A large number of the underground expressway networks were provided at the time of Tokyo Olympics in the 1960's. Moreover, Miyakezaka Junction opened in 1973 has intersections of three main line expressways; this is unusual in the world, because the bifurcation and confluence are in the underground. Tokyo Bay Aqua Line constructed in 1997 is a leading design application of the present seismic design of the tunnel. As for the subways, network lines were being constructed one after another starting with the Ginza Line constructed for the first time in Japan in 1927. These existing underground infrastructures cover a great part of the metropolitan area today. In addition, they are also large-scaled and deeply embedded.

Many underground infrastructure constructions are being made. For instance, the subway No. 13 connecting Shibuya and Ikebukuro stations is under construction. Regarding the expressways, Shinjuku Central Circular Route is under construction, and the construction for its extended expressway called Shinagawa Route will also start in the year 2007. Moreover, the construction of the outer expressways like Kannetsu, Chuo, and Tomei expressways, are scheduled.

These structures are widely and deeply located in the thick deposit layers which will have large amplification effect of ground motion. An earthquake response differs greatly depending on the type of the structure and the surrounding soil deposits. It is important to carefully state these influences in seismic evaluation. On the other hand, seismic design in the direction of the tunnel axis and its orthogonal direction may lead to less accurate evaluation of the seismic safety of an underground infrastructure. In the orthogonal direction, the seismic coefficient method or the equivalent linear method is used for two-dimensional sectional model. In the direction of the tunnel axis, the response displacement method with multi mass-spring model that reflects non-homogeneous properties of the soil structure is used. A seismic design is done respectively by using two earthquake motions of level 1 and level 2 scales. These seismic design methods, especially the response displacement method applied in the direction of tunnel axis, have unsolved problems such as the influences of the tunnel cross section size, the complex three dimensional geometrical structure, three dimensional ground structure, and etc.

To demonstrate these problems, the authors perform the evaluation of dynamic behaviors of the underground infrastructure by using a large-scale three-dimensional dynamic FEM analysis.

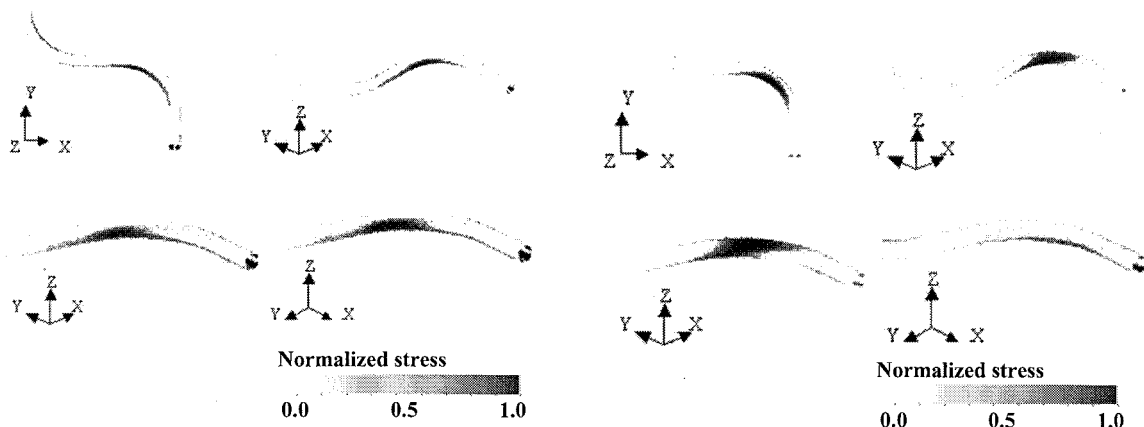
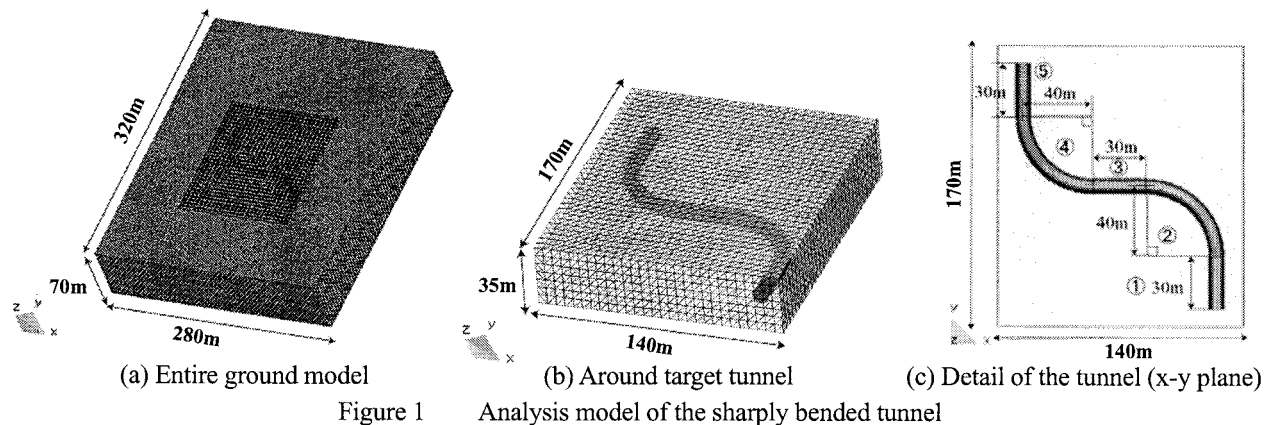
3. INVESTIGATION CASE OF AN UNDERGROUND INFRASTRUCTURE AND ITS USE

This paper introduces the investigation case of the three dimensional seismic behaviors of a large-scale underground infrastructure using a large-scale dynamic FEM analysis. The results obtained are shown in the following sections.

3.1 Behaviors of sharply bended part of tunnel

In order to clarify the dynamic behaviors of a curved tunnel, the large-scale three dimensional dynamic FEM analysis was performed for the model with the outer diameter of 8.8m, the thickness of 0.4m and the earth covering of 15.5m, as shown in Figure 1. To confirm the influence of the tunnel bending on the earthquake response, a curved tunnel was assumed to have a sharp bending with radius of curvature being 40m. For the tunnel body, the concrete strength is set to the standard design strength. For comparison, the analysis was made under the same condition for a straight tunnel with the same section connecting the same A-A' points. The ground was assumed to have a single horizontal layered soil structure. The soil properties were assumed to be the same as those around Tokyo. The details of the model are shown in the work by Yamada *et al.* 2004. The influence on the tunnel response of the different predominant period of input motion and the phase difference was clarified.

The distribution of the maximum von Mises stress for each case is shown in Figure 2. The stress concentrates around the curve part, thus increasing the sectional force compared with the straight tunnel on the same cross section. The phase angle difference and frequency of the input wave influence the force appearing in the tunnel.



3.2 Behaviors of the joint part of vertical shaft and shield tunnels

It is important to evaluate the safety of the joint part of the vertical shaft and the shield tunnel. In order to evaluate the behaviors of the joint part during an earthquake, an earthquake observation was made. The verification of observed earthquake motion was performed using three-dimensional analysis. A three-dimensional model made based on the observation of the vertical shaft and the shield tunnel. A large-scale three-dimensional dynamic FEM analysis was performed using the waves obtained from the earthquake observation. At the same time, the analysis method was verified using some observed earthquake motions. From the result of this analysis, three-dimensional behaviors which are not obtained from the earthquake observation become clear.

The section of the joint part and the locations of the seismometers are shown in Figure 3. Velocity seismometers were used in order to easily obtain displacement waves. The analysis model is shown in Figure 4. The details of the model are shown in the work by Itami *et al.* (2005). To clarify the influences on the response of the structure for different directions of the input motions, input waves are applied in the direction of tunnel axis and in its orthogonal.

An example of the results is shown in Figure 5. It was confirmed that the maximum displacement of the structure increased up to 1.1 times and the maximum stress, up to 1.2-1.3 times, in the axial direction and in the orthogonal direction. In case of the axial direction input motion, a large stress is generated at the top and bottom of the joint part because the shield tunnel restricts the deformation of the vertical shaft. In case of the orthogonal direction input motion, a large stress was generated on the right and left sides of the joint part in accordance with the shear deformation of the shield tunnel.

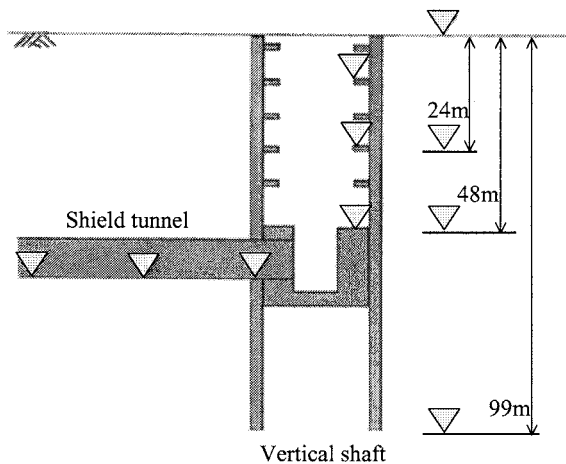


Figure 3 Earthquake observation points of the vertical shaft and the shield tunnels

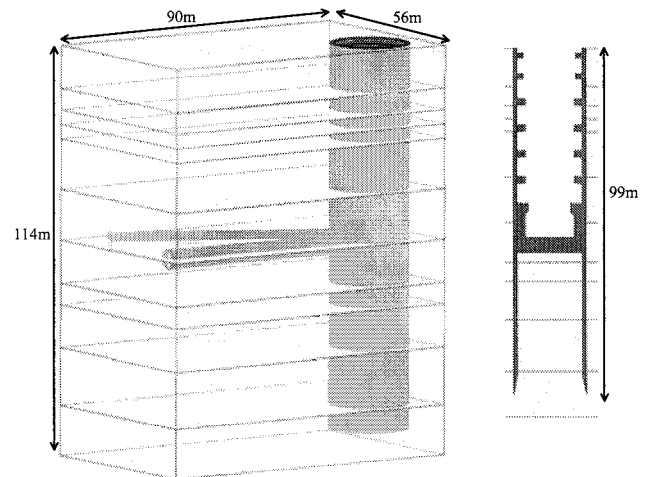


Figure 4 Analysis model of jointed part of the vertical shaft and the shield tunnels

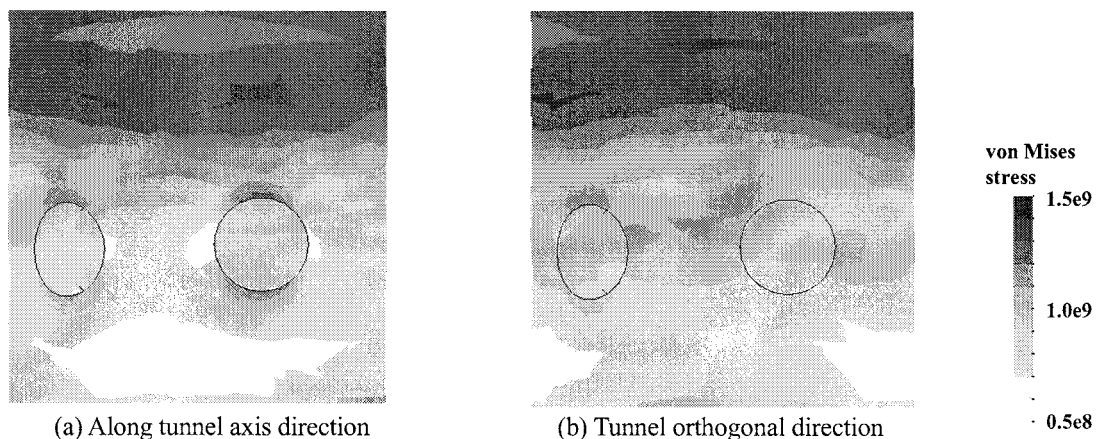


Figure 5 Stress distribution of the jointed part with vertical shaft

3.3 Behaviors of an underground infrastructure with side ramp

A model of a large-scale underground infrastructure, an underground expressway tunnel with side ramp tunnel, was made and its behaviors were studied during earthquake event. The model is a structure where the main tunnel with the outer diameter 13m connects with a ramp tunnel with the outer diameter 9m to access to the ground surface; see Figure 6. The infrastructure is composed of three parts; the main tunnel, the ramp tunnel and the joint part of the two tunnels. The ground structure is assumed to be three horizontal layer soil structures with the length of 550m, the width of 150m, and the depth of 50m. The depth between the top of the tunnel and the ground level is 20m. The inclination of the side ramp tunnel is assumed to be 6%. The analytical model considering the construction condition is made. The details of the model are shown by Ohbo *et al.* (2004) and Yamada *et al.* (2005). To examine the characteristics of the seismic response of this underground infrastructure, a large-scale dynamic FEM analysis was performed by inputting level 2 earthquake (Port Island wave with the maximum acceleration of 500Gal) in the direction of the tunnel axis and its orthogonal one.

A part of the analytical result is shown in Figure 7, which is the case of inputting the wave in the direction of the tunnel axis. The ramp tunnel is greatly deformed, and a big axial stress is generated. In the junction part, a non-negligible shear stress is generated in the side of section. Although the current seismic design of shield tunnel is considered in the direction of the tunnel axis and in its orthogonal direction independently, this result clarifies the need of three-dimensional analysis is necessary for seismic design of such complex parts of structures.

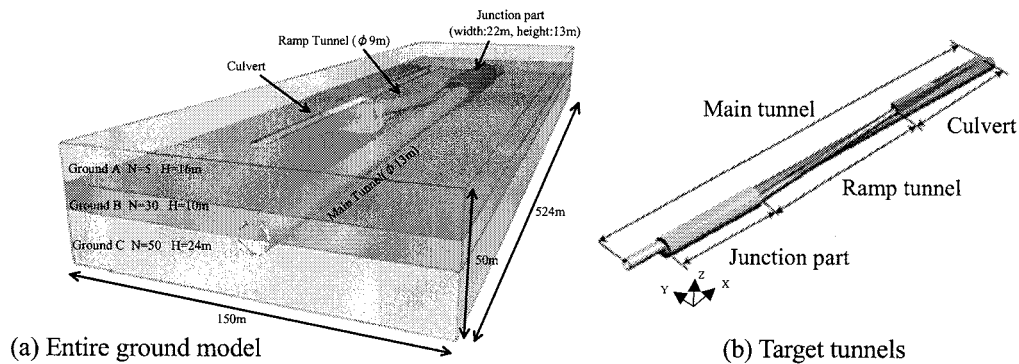


Figure 6 Analysis model of underground Expressway tunnels with a side ramp tunnel

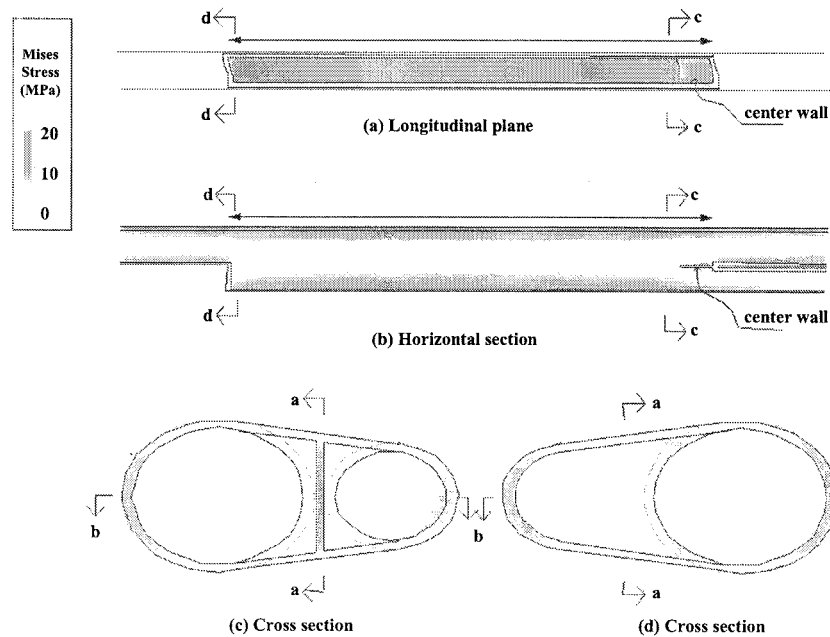


Figure 7 Deformation and Stress distribution of junction part of side ramp tunnels (input wave was in the direction of tunnel axis)

3.4 Behaviors of underground infrastructure with central ramp

To clarify the behaviors of an underground infrastructure with a central ramp during an earthquake, a large-scale three-dimensional analysis was performed. The model is an underground infrastructure with two main line tunnels running in parallel and a ramp tunnel to the ground surface between them, connecting with the confluence and bifurcation.

The tunnel structure was simplified as shown in Figure 8, in order to meet the main purpose of obtaining main characteristics of the tunnel behaviors during an earthquake. The main tunnel was modeled to be a steel segment of the circular cylinder with the even thickness; the outer diameter of 12.83m, the inner diameter of 11.77m and the thickness of 0.53m. The ramp tunnel and the confluence and bifurcation part were modeled to be as RC structure of the box shape. The inclination of the ramp tunnel was assumed to be the average value of the actual structure. The soil model was assumed to be two horizontal layered structures. The details of the model are shown by Dobashi *et al.* (2006). The input wave at the bottom of the model was calculated using SHAKE and applied in the direction of the tunnel axis and the orthogonal direction.

Figure 9 shows that the tunnel responses at the point of the displacement are enlarged when the input motion was applied in the orthogonal direction. This figure shows that the ramp tunnel in the upper layer has a tendency to shake sideways where the displacement becomes large. On the other hand, in the lower second layer where the displacement response was small, large deformation of the ramp tunnel are observed near the boundary. The relative displacement is relatively smaller near the boundary and the ground surface than in the middle of the first layer. Thus, it is clarified that the tunnel was twisted in the orthogonal direction towards the direction of the tunnel axis.

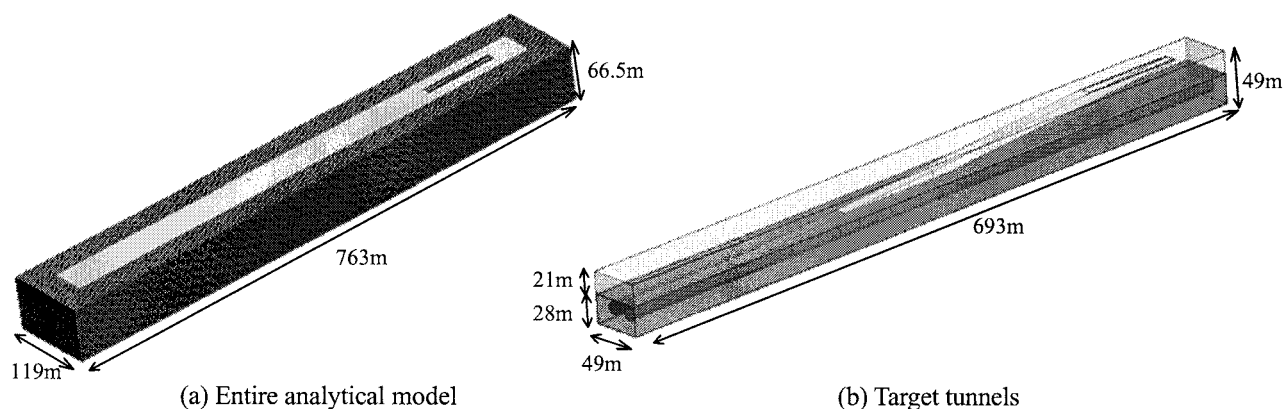


Figure 8 Analysis model of Underground expressway including two main tunnels with a center ramp tunnel including two main tunnels with a center ramp tunnel

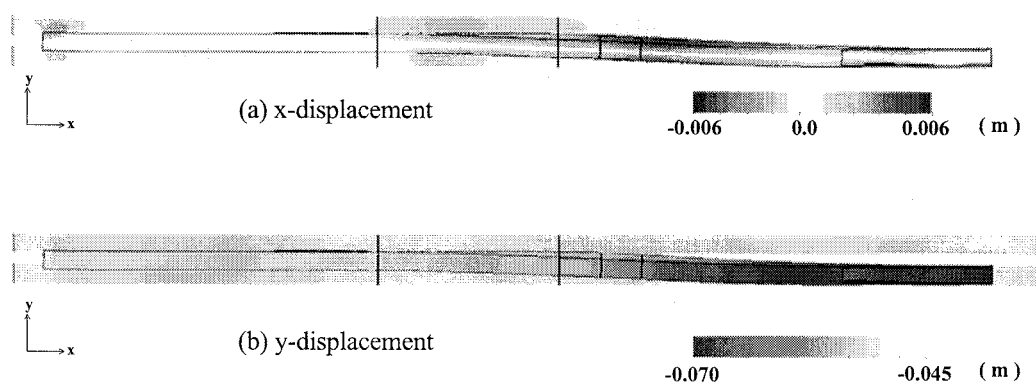


Figure 9 Deformation and displacement distribution of the tunnels

4. CONCLUSIONS

There will be an increasing need for the seismic evaluation of underground infrastructure. Three-dimensional effect is increasingly becoming necessary, as the underground infrastructure in the metropolitan areas tends to become more complex. It is shown that the dynamic three-dimensional analysis is a useful tool for the investigation of the three dimensional response.

As a future extension of this work, the authors expect to investigate three dimensional behavior of an underground infrastructure based on the practical design using the integrated earthquake simulator. The rational modeling and analysis of the underground infrastructures will be the future challenges of this work.

Acknowledgements:

The authors would like to express special thanks to Mr. Dobashi and Mr. Ochiai of Tokyo Metropolitan Expressway for their cooperation during this investigation.

References:

- JSCE (1998), "2 Tunnels and Underground Structures", Report on the Hanshin-Awaji Earthquake Disaster, Damage to Civil Engineering Structures (in Japanese), 1-105.
- Ohbo, N., Hayashi, K., Ueno, K. (1992), "Dynamic behavior of supper deep vertical shaft during earthquake", *10th World Conference on Earthquake Engineering*, 5031-5036.
- Ohbo, N., Furuya, T., Takamatu, K., Komaki, S. (2000), "SEISMIC BEHAVIOR OF SHIELD TUNNEL ACROSS ACTIVE FAULT", *12th World Conference on Earthquake Engineering*, Paper No.1888.
- Ichimura, T., Itami, H., Samo, T., Hori, M., and Ymaguchi, T. (2005a), "Construction of Digital City KOBE & A Basic Discussion on Application of IES approach to Earthquake Disaster Simulation", *Journal of Structural Engineering*, 513-520 (in Japanese).
- Ichimura T., Hori M., Terada K., Yamakawa T. (2005b), "On Integrated Earthquake Simulator Prototype: Combination of Numerical Simulation and Geographical Information System", *Structural Eng./Earthquake Eng.*, Vol.22, No.2, pp. 233-243, DOI: 10.2208/jscesee.22.233s.
- Ichimura T. and Hori M. (2006), "Macro-Micro Analysis Method for Wave Propagation in Stochastic Media", *Earthquake Engineering & Structural Dynamics*, Vol.35, pp 419-432, DOI: 10.1002/eqe.533.
- Yamada. T., Ichimura, T., Ohbo, N., Samo T., Ikeda K., and Hori M. (2004), "Seismic Response of Underground Complicated Structure by 3D FEM Analysis" (in Japanese), *Journal of Applied Mechanics*, JSCE, 909-916.
- Itami, H., Ichimura T., and Ohbo N. (2005), "Dynamic response of shaft jointed with shield tunnels by 3D FEM analysis" (in Japanese), *Proceeding of the 4th annual Meeting of Japan Association for Earthquake Engineering*, 484-485.
- Ohbo, N., Horikoshi, K., Yamada T., Tachibana K., and Akiba, H. (2004), "DYNAMIC BEHAVIOR OF A UNDERGROUND MOTOWAY JUNCTION DUE TO LARGE EARTHQUAKE", *13th World Conference on Earthquake Engineering*, Paper No.1215.
- Yamada, T., Ichimura, T., Ohbo, N., Samo, T., Ikeda, K., and Hori, M. (2005), "Seismic Response Behavior of Ramp Structure in the Tunnel and its Countermeasure" (in Japanese), *Journal of Structural Engineering*, **51A**, 561-568.
- Dobashi, H., Miyama, D., Ichimura, T., Hori M., Ohbo, N., Yamaki, Y., Moriguchi, M., and Yamada, T. (2006), "3D EARTQUAKE RESPONSE OF RAMP WAY TUNNEL AND UNDERGROUND JUNCTION", *Proceeding of the Symposium on Underground Space*, 183-188 (in Japanese).

DEVELOPMENT OF A NEW TIME-DOMAIN BOUNDARY ELEMENT METHOD IN 3-D ELASTODYNAMICS FOR SEISMIC ANALYSIS

T. Saitoh¹⁾, K. Kimoto²⁾, and S. Hirose³⁾

1) Course of Nuclear Power and Safety Energy Engineering, University of Fukui, Japan

*2) Research assistant, Dept of Mechanical and Environmental Informatics,
Tokyo Institute of Technology, Japan*

*3) Professor, Department of Mechanical and environmental informatics,
Tokyo Institute of Technology, Japan*

tsaito@taku.anc-d.fukui-u.ac.jp, kimoto@cv.titech.ac.jp, shirose@cv.titech.ac.jp

Abstract: This paper presents a new time-domain Boundary Element Method (BEM) using the Operational Quadrature Method (OQM) developed by Lubich (1988, 1994) for the 3-D seismic analysis. In this formulation, the convolution integral is numerically approximated by a quadrature formula, whose weight are computed by using the Laplace transform of the fundamental solution of conventional BEM and a linear multistep method. The new time-domain BEM formulation for 3-D elastodynamics is described after the OQM is reviewed. As numerical examples, 3-D scattering problems by spherical cavities are solved by the proposed method and the accuracy and computational efficiency of the proposed method are also discussed.

1. INTRODUCTION

Seismic motions produced by an earthquake propagate in ground as elastic waves and sometimes cause tremendous destruction of buildings and infrastructures. Therefore, the understanding of elastic waves can help not only predict ground motions by earthquake but also reduce seismic damages. Furthermore the analysis of elastic waves may play an important role in quantitative ultrasonic non-destructive testing of earthquake-damaged structures.

In general, Boundary Element Method (BEM) is known as a suitable numerical approach for elastic wave analysis in an infinite or half space domain because BEM can deal with an infinite region without any modification. Transient problems can usually be solved for unknown time-dependent quantities by a direct time-domain BEM with a time-stepping scheme. However, the use of direct time-domain BEM sometimes causes the instability of time-stepping solutions. To overcome this difficulty, in this paper, a new time-domain boundary element method in 3-D elastodynamics is developed for the seismic analysis.

In the formulation of the proposed method, the Operational Quadrature Method (OQM) developed by Lubich (1988, 1994) is applied to establish the stability behavior of the time-stepping scheme and the convolution integral is numerically approximated by quadrature formulas, whose weights are computed by using the Laplace transform of the fundamental solution and a linear multistep method. The computational complexity becomes $O(LM^2N)$ for the problem with M elements, N time steps, and L expansion terms. In recent years, several researchers have applied to the OQBEM to some engineering problems such as 2-D scalar wave problem (Abreu et al, 2003) and poroelastic problem (Schanz and Struckmeier, 2005).

In this paper, the basic concept of the OQM is presented, as well as its application to time-domain

boundary element method in 3-D elastodynamics. As numerical examples, 3-D scattering problems by spherical cavities subjected to a incident longitudinal waves are implemented by the proposed method and the accuracy and efficiency of the proposed method is confirmed to validate the proposed method.

2. OPERATIONAL QUADRATURE METHOD

In this section, the operational quadrature method (OQM) is briefly described. The Operational Quadrature Method (OQM), first proposed by Lubich (1988, 1994), approximates the convolution $f * g(t)$ by a discrete convolution using the Laplace transform of the time dependent function $f(t - \tau)$. In general, the convolution integral is defined as follows:

$$f * g(t) = \int_0^t f(t - \tau)g(\tau)d\tau \quad , \quad t \geq 0 \quad (1)$$

where $*$ denotes the convolution. The convolution integral defined by equation 1 is approximated by OQM as follows:

$$f * g(n\Delta t) \simeq \sum_j \omega_{n-j}(\Delta t)g(j\Delta t) \quad (2)$$

where the time t was divided into N equal steps Δt . Moreover, $\omega_j(\Delta t)$ denotes the quadrature weights which are determined by the coefficients of the following power series with complex variable z , namely

$$F\left(\frac{\delta(z)}{\Delta t}\right) = \sum_{n=0}^{\infty} \omega_n(\Delta t)z^n. \quad (3)$$

In equation 3, F is the Laplace transform of time dependent function f . The power series defined in equation 3 can be calculated by Cauchy's integral formula. Considering a polar coordinate transformation, the Cauchy's integral is approximated by a trapezoidal rule with L equal steps $2\pi/L$ as follows:

$$\omega_n(\Delta t) = \frac{1}{2\pi i} \int_{|z|=\rho_s} F\left(\frac{\delta(z)}{\Delta t}\right) z^{-n-1} dz \simeq \frac{\rho_s^{-n}}{L} \sum_{l=0}^{L-1} F\left(\frac{\delta(z_l)}{\Delta t}\right) e^{\frac{-2\pi i n l}{L}} \quad (4)$$

where $\delta(z)$ is the quotient of the generating polynomials of a linear multistep method and z_l is given by $z_l = \rho_s e^{2\pi i l/L}$. In addition, ρ_s is the radius of a circle in the domain of analyticity of F .

3. BEM FORMULATION FOR 3-D ELASTODYNAMICS IN TIME-DOMAIN

We consider the scattering problem of elastic waves in an exterior domain D as shown in Figure 1. When the incident wave u_i^{in} hits the boundary surface S of a scatterer \bar{D} , scattered waves are

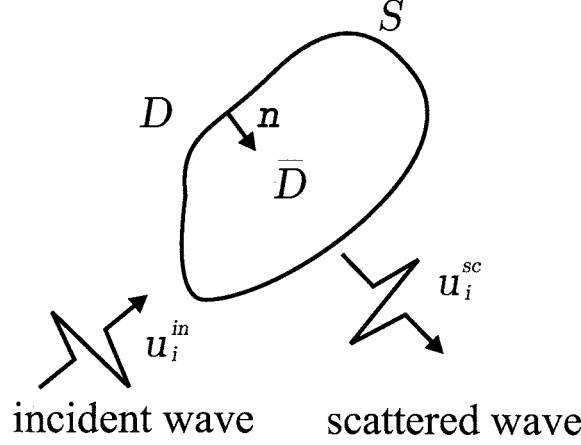


Figure 1 Scattering model of elastic waves

generated by the interaction with the scatterer \bar{D} . Assuming the zero initial conditions, i.e., $u_i(\mathbf{x}, t = 0) = 0$ and $\partial u_i(\mathbf{x}, t = 0)/\partial t = 0$, the displacement field u_i satisfies the governing equation and boundary conditions as follows:

$$\mu u_{i,jj}(\mathbf{x}, t) + (\lambda + \mu) u_{j,ij}(\mathbf{x}, t) + b_i(\mathbf{x}, t) = \rho \ddot{u}_i(\mathbf{x}, t) \quad \text{in } D \quad (5)$$

$$\mathbf{u}(\mathbf{x}, t) = \hat{\mathbf{u}}(\mathbf{x}, t) \quad \text{on } S_1, \quad \mathbf{t}(\mathbf{x}, t) = \hat{\mathbf{t}}(\mathbf{x}, t) \quad \text{on } S_2, \quad S_2 = S \setminus S_1 \quad (6)$$

where c_L and c_T are the velocity of P and S-waves defined by $c_L = \sqrt{\lambda + 2\mu/\rho}$ and $c_T = \sqrt{\mu/\rho}$ where ρ is the density and, λ and μ are the Lamé constants. Moreover, b_i shows the body force per unit volume and $(\ddot{\cdot})$ indicates the partial derivative with respect to time t . In equation 6, $\hat{\mathbf{u}}(\mathbf{x}, t)$ and $\hat{\mathbf{t}}(\mathbf{x}, t)$ are given boundary values. Assuming the body force to vanish and taking the limits from $\mathbf{x} \in D \rightarrow \mathbf{x} \in S$, the time-domain boundary integral equation for 3-D elastodynamics can be expressed by

$$\frac{1}{2} u_i(\mathbf{x}, t) = u_i^{\text{in}}(\mathbf{x}, t) + \int_S U_{ij}(\mathbf{x}, \mathbf{y}, t) * t_j(\mathbf{y}, t) dS_y - \int_S T_{ij}(\mathbf{x}, \mathbf{y}, t) * u_j(\mathbf{y}, t) dS_y \quad \text{for } \mathbf{x} \in S. \quad (7)$$

In equation 7, $U_{ij}(\mathbf{x}, \mathbf{y}, t)$ and $T_{ij}(\mathbf{x}, \mathbf{y}, t)$ denote the time-domain fundamental solution and its double layer kernel (Kobayashi, 2000) in 3-D elastodynamics, respectively, defined as follows:

$$U_{ij}(\mathbf{x}, \mathbf{y}, t) = \frac{t}{4\pi\rho} \left\{ \left(\frac{1}{r} \right)_{,ij} \left[H\left(t - \frac{r}{c_L}\right) - H\left(t - \frac{r}{c_T}\right) \right] - r_{,i} \left(\frac{1}{r} \right)_{,j} \right. \\ \left. \times \left[\frac{1}{c_L} \delta\left(t - \frac{r}{c_L}\right) - \frac{1}{c_T} \delta\left(t - \frac{r}{c_T}\right) + \frac{\delta_{ij}}{r^2 c_T} \delta\left(t - \frac{r}{c_T}\right) \right] \right\} \quad (8)$$

$$T_{ij}(\mathbf{x}, \mathbf{y}, t) = C_{jlnm} n_l(\mathbf{y}) \frac{\partial}{\partial y_n} U_{im}(\mathbf{x}, \mathbf{y}, t) \quad (9)$$

where r is given by $r = |\mathbf{x} - \mathbf{y}|$, $\delta(\cdot)$ is the Dirac delta function and C_{jlnm} are elastic constants

given by $C_{jlnm} = \rho\{(C_L^2 - 2c_T^2)\delta_{jl}\delta_{nm} + c_T^2(\delta_{jn}\delta_{lm} + \delta_{jm}\delta_{ln})\}$. Also, $n_l(\mathbf{y})$ is a unit normal vector to the surface S . Normally, equation 7 is discretized by using the appropriate interpolation functions for the unknown values and solved by a time-stepping algorithm (Hirose, 1988). However, there are mainly two disadvantages for the conventional time-domain BEM. One is an instability problem encountered in the time-stepping procedure. The other is the difficulty in solving problems such as viscoelastodynamics and poroelastodynamics where no time-domain fundamental solutions are available.

4. OQ-BEM FORMULATION FOR 3-D ELASTODYNAMICS IN TIME-DOMAIN

To overcome the disadvantage of the conventional time-domain BEM, the operational quadrature method (OQM) is introduced. In solving the system of the boundary integral equation 7 numerically, the unknown displacement \mathbf{u} and the traction \mathbf{t} are represented by using the approximation functions ϕ^I as follows:

$$u_i(\mathbf{x}, t) = \sum_I \phi^I(\mathbf{x}) u_i^I(t), \quad t_i(\mathbf{x}, t) = \sum_I \phi^I(\mathbf{x}) t_i^I(t) \quad (10)$$

where $u_i^I(t)$ and $t_i^I(t)$ are time dependent boundary values for the I-th basis. Substituting equation 10 into the convolution boundary integral equation 7 and yields the following equations

$$\begin{aligned} \frac{1}{2} \sum_I \phi^I(\mathbf{x}) u_i^I(n\Delta t) &= u_i^{in}(\mathbf{x}, n\Delta t) \\ &+ \sum_I \sum_{k=1}^n \left[A_{ij}^{n-k,I}(\mathbf{x}) t_i^I(k\Delta t) - B_{ij}^{n-k,I}(\mathbf{x}) u_i^I(k\Delta t) \right]. \end{aligned} \quad (11)$$

Applying equations 2 and 4 in the OQM to the convolution integrals in equation 7, the influence functions $A_{ij}^{m,I}$ and $B_{ij}^{m,I}$ can be obtained as follows:

$$A_{ij}^{m,I}(\mathbf{x}) = \frac{\rho_s^{-m}}{L} \sum_{l=0}^{L-1} \int_S \hat{U}_{ij}(\mathbf{x}, \mathbf{y}, s_l) \phi^I(\mathbf{y}) e^{\frac{-2\pi i m l}{L}} dS_y \quad (12)$$

$$B_{ij}^{m,I}(\mathbf{x}) = \frac{\rho_s^{-m}}{L} \sum_{l=0}^{L-1} \int_S \hat{T}_{ij}(\mathbf{x}, \mathbf{y}, s_l) \phi^I(\mathbf{y}) e^{\frac{-2\pi i m l}{L}} dS_y \quad (13)$$

where s_l is given by $s_l = \delta(z_l)/(c_\beta \Delta t)$ ($c_\beta = c_L$ or c_T). In addition, the parameter ρ_s has to be $\rho_s < 1$ and is taken as $\rho_s^L = \sqrt{\epsilon}$ where ϵ shows the assumed error in the computation of equations 12 and 13. To determine $\delta(z_l)$, we use the backward differential formula (BDF) of order two as follows:

$$\delta(z) = (1 - z) + \frac{(1 - z^2)}{2}. \quad (14)$$

Note that equations 12 and 13 are identical to the discrete Fourier transform. Therefore, the calculations of equation 4 can be evaluated by means of the FFT algorithm. Applying the Laplace transforms

$$F(s) = \int_0^\infty f(t)e^{-st}dt \quad (15)$$

to the time-domain fundamental solutions $U_{ij}(\mathbf{x}, \mathbf{y}, t)$ and $T_{ij}(\mathbf{x}, \mathbf{y}, t)$ defined by equations 8 and 9 yields the Laplace domain fundamental solutions $\hat{U}_{ij}(\mathbf{x}, \mathbf{y}, s)$ and $\hat{T}_{ij}(\mathbf{x}, \mathbf{y}, s)$ as follows:

$$\begin{aligned} \hat{U}_{ij}(\mathbf{x}, \mathbf{y}, s) = & \frac{1}{4\pi\rho} \left[\frac{3r_{,i}r_{,j} - \delta_{ij}}{r^3} \left\{ \frac{sr + c_L}{c_L s^2} e^{-\frac{sr}{c_L}} - \frac{sr + c_T}{c_T s^2} e^{-\frac{sr}{c_T}} \right\} \right. \\ & \left. + \frac{r_{,i}r_{,j}}{r} \left\{ \frac{e^{-\frac{sr}{c_L}}}{c_L^2} - \frac{e^{-\frac{sr}{c_T}}}{c_T^2} \right\} + \frac{\delta_{ij}}{rc_T^2} e^{-\frac{sr}{c_T}} \right] \end{aligned} \quad (16)$$

$$\hat{T}_{ij}(\mathbf{x}, \mathbf{y}, s) = \rho(c_L^2 - 2c_T^2)\hat{U}_{kj,k}(\mathbf{x}, \mathbf{y}, s)n_i(\mathbf{y}) + \rho c_T^2(\hat{U}_{ij,k}(\mathbf{x}, \mathbf{y}, s) + \hat{U}_{kj,i}(\mathbf{x}, \mathbf{y}, s))n_k(\mathbf{y}) \quad (17)$$

where s is the Laplace parameter. Construction of equation 11 for all nodes of the discretized boundary leads to the following matrix form:

$$\frac{1}{2}\mathbf{u}^n = \mathbf{u}^{in,n} + \sum_{k=1}^n \mathbf{A}^{n-k} \mathbf{t}^k - \sum_{k=1}^n \mathbf{B}^{n-k} \mathbf{u}^k. \quad (18)$$

In equation 18, n and k correspond to the discrete times $t_n = n\Delta t$ and $t_k = k\Delta t$, respectively. \mathbf{A} and \mathbf{B} are the coefficient matrices assembled from the element contributions, and \mathbf{u} and \mathbf{t} are the displacement vector and traction vector respectively. In general, gathering the terms with respect to the prescribed boundary values on the right-hand side and shifting the unknown boundary quantities and the corresponding columns of \mathbf{A} and \mathbf{B} to the left-hand side, the system of equations can be solved for the unknown values.

5. NUMERICAL EXAMPLES

The proposed method is now applied to analyze the transient behaviors of the spherical cavities with radius a . For all numerical calculations, the boundary conditions of the spherical cavities are supposed to be traction $\mathbf{t} = 0$ on S and the boundary of the spherical cavity was divided into 384 elements, which are discretized with the constant approximation. Also, the Poisson's ration is $\nu = 0.25$ and the time increment is $c_T \Delta t / a = 0.12$. In the calculations of equations 12, 13, the parameters L and ρ are taken as $L = 128$ and $\rho = 0.94746353$ which was given by assuming $\epsilon = 10^{-6}$, respectively.

5.1 Elastic wave scattering by a spherical cavity

As a first numerical example, elastic wave scattering problem by a spherical cavity subjected to an incident longitudinal wave is considered. The displacement component $u_i^{in}(\mathbf{x}, t)$ of the incident longitudinal wave and its corresponding stress component $\sigma_{ij}(\mathbf{x}, t)$ are given by

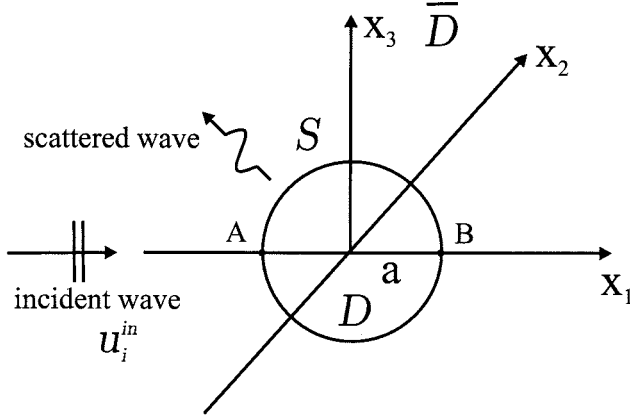


Figure 2 Elastic wave scattering model by a cavity subjected to the incident wave.

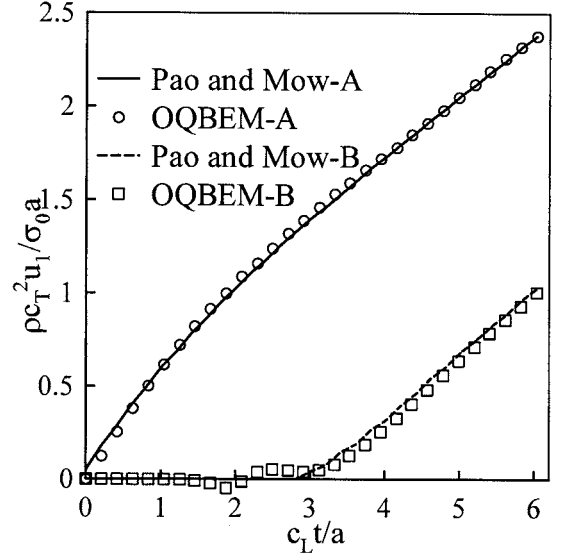


Figure 3 Displacement u_1 as a function of time at point A and B on the spherical cavity as shown in Figure 2.

$$u_i^{in}(\mathbf{x}, t) = \delta_{i1} \frac{\sigma_0}{\rho c_L^2} (c_L t - x_1 - a) H(c_L t - x_1 - a) \quad (19)$$

$$\sigma_{ij}^{in}(\mathbf{x}, t) = -\sigma_0 \{ (1 - 2\kappa) \delta_{ij} + 2\kappa \delta_{i1} \delta_{j1} \} H(c_L t - x_1 - a) \quad (20)$$

where κ is defined by $\kappa = (c_T/c_L)^2$ and σ_0 is the stress amplitude. Moreover, H is the step function. This problem has been analytically solved in the frequency domain by Pao and Mow (Pao and Mow, 1973). The transient solution can be obtained by superposing the results in the frequency domain with the aid of the fast Fourier transform.

Figure 3 shows the vertical displacements as a function of time at point A and B of the spherical cavity as shown in Figure 2. Numerical results by the proposed method are in good agreement with the analytical-numerical results of Pao and Mow. We can, however, see a small discrepancy in the early time solutions at the point B. This discrepancy is due to the fact that the mesh patterns of the elements of the cavity are not always consistent with the positions of the travelling wave fronts in early times.

5.2 Elastic wave scattering by two spherical cavities

Next, the scattering problem by two spherical cavities subjected to the incident wave given by equation 19 and 20 is considered as shown in Figure 4. The distance d between the centers of two cavities is $5a/2$. Figure 5 shows the displacements u_1 as a function of time at the points A, B, C, D, E and F on the spherical cavities in Figure 4. As a whole tendency, displacements u_1 at A, B, E and F steadily increase as time passes. These tendencies are almost the same as those at A, B in Figure 2. However, dynamic responses caused by the interaction of two cavities can be seen at the points C and D. The interaction phenomena can be found only in the local area between the two cavities.

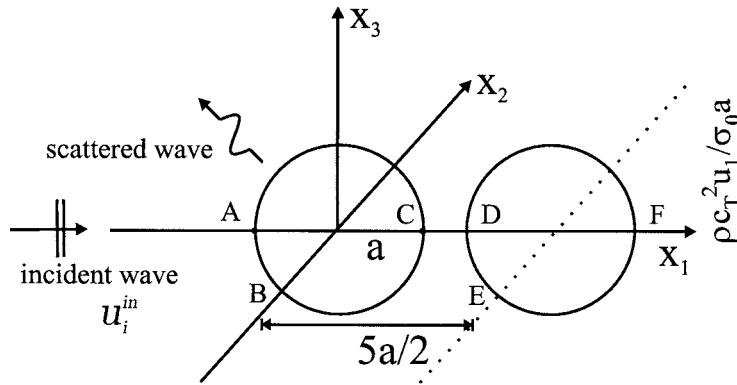


Figure 4 Elastic wave scattering model by two cavities subjected to the incident wave.

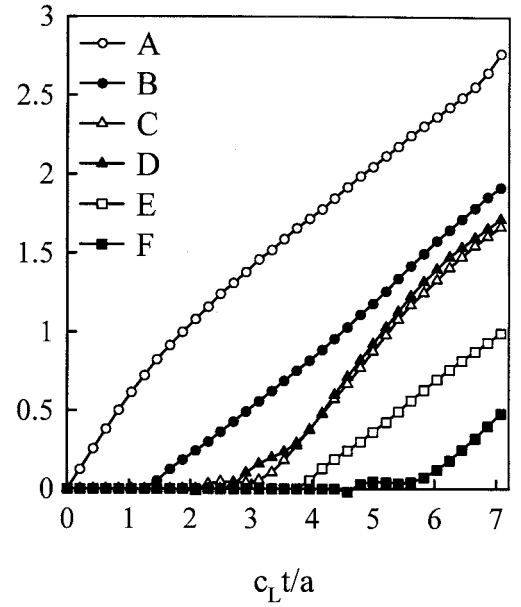


Figure 5 Displacement u_1 as a function of time at several point A, B, C, D, E and F on the spherical cavity as shown in Figure 4.

The OQBEM formulation is an elegant way of solving the wave propagation problem. This method (also a conventional time-domain BEM), however, needs much computational time and memory. In recent years, the Fast Multipole Method (FMM) (Greengard and Rokhlin, 1987) is attracting attention as a new method for solving large scale problems. For more realistic time-domain seismic and ultrasonic NDE simulation, it is one of the important keys to improve the computational efficiency by means of Fast Multipole Boundary Element Method (FMBEM) (Nishimura 2002, Saitoh and Hirose, 2002), which is the coupling of BEM and FMM.

6. CONCLUSIONS

In this paper, the new time-domain BEM formulation using OQM was developed for 3-D elastic wave propagation problems. The convolution integrals were discretized based on the OQM in time coordinate and fundamental solutions in Laplace domain were used for the calculations of influence functions. As numerical examples, scattering problems by spherical cavities were demonstrated. In near future, we will not only develop the new OQBEM using Fast Multipole Method (FMM) for 3-D Helmholtz problem, 3-D elastic and poroelastic problems but also apply the proposed method to the seismic analysis.

Acknowledgment:

This work is supported by Japan Society of the Promotion of Science.

References:

- Lubich, C. (1988), "Convolution quadrature and discretized operational calculus I", *Numer. Math.*, **52**, 129-145.
- Lubich, C. (1988), "Convolution quadrature and discretized operational calculus II", *Numer. Math.*, **52**, 413-425.
- Lubich, C. (1994), "On the multistep time discretization of linear initial boundary value problems and their boundary integral equations", *Numer. Math.*, **67**, 365-389.
- Abreu, A. I., Carrer, J. A. M. and Mansur, W. J. (2003), "Scalar wave propagation in 2D: a BEM formulation based on the operational quadrature method", *Engineering analysis with Boundary Elements*, **27**, 101-105.
- Schanz, M. and Struckmeier, V. (2005), "Wave propagation in a simplified modelled poroelastic continuum: Fundamental solutions and a time domain boundary element formulation", *Numer. Math.*, **64**, 1816-1839.
- Kobayashi, S. (2000), *Wave analysis and boundary element method*, Kyoto University Press (in Japanese).
- Hirose, S. (1991), "Boundary integral equation method for transient analysis of 3-D cavities and inclusions", *Engineering Analysis with Boundary Element Method*, **8**, 69-74.
- Pao, Y.-H. and Mow, C. C. (1973), "Diffraction of Elastic Waves and Dynamic Stress Concentrations", Crane and Russak, New York.
- Greengard, L. and Rokhlin, V. (1987), "A fast algorithm for particle simulations", *Journal of Computational Physics*, **73**, 325-348.
- Nishimura, N. (2002), "Fast multipole accelerated boundary integral equation methods", *Applied Mechanics Review*, **55-4**, 299-324.
- Saitoh, T. and Hirose, S. (2002), "Development of fast multipole boundary element method for large scale wave analysis", *Technical Report of Department of Civil Engineering, Tokyo Institute of Technology*, **65**, 109-122 (in Japanese).

WAVE PROPAGATION IN 2D ANISOTROPIC LAYERED MEDIA USING BOUNDARY ELEMENT METHOD

A. Tan¹⁾, and S. Hirose²⁾

1) *Postdoctoral Researcher, Center for Urban Earthquake Engineering, Tokyo Institute of Technology, Japan*

2) *Professor, Dept. of Mechanical and Environmental Informatics, Tokyo Institute of Technology, Japan*

tan.a.aa@m.titech.ac.jp, shirose@cv.titech.ac.jp

Abstract: This research work is to make a model for 2D Boundary element for layered anisotropic media. A two dimensional boundary element analysis for anisotropic solids is applied to a layered media with inclusion or crack. Based on the 2D boundary element analysis of anisotropic elastic solids, the material is divided into two regions along the interface and/or layer boundaries. Displacement boundary integral equations are used for each region/layer and the corresponding boundary conditions are applied to the interface/layer boundaries. Initially here, an interface crack is used to check the model and validate it to the isotropic solid. The crack part is considered traction free while the bonded interface is assumed to be perfectly bonded. The basic idea here is to assume that an interface is present along the cracked solid. Then the solution is compared to other crack analysis. Then further analysis will be done by applying earthquake effect or double couples- equivalent force from the far field.

1. INTRODUCTION

Soil and rock formations are mostly layered and modeling it as layered material should be done. The main purpose of this research is to model waves propagating in layered anisotropic solids. Simulations for the effect of seismic waves on underground or buried structures (i.e., buried pipes, Slabs, Footings) are quite important. The effects of these waves on the layered soil as well as on the structure are to be investigated. It should be noted that only the validation of the program was shown here and further analysis will be done. The aim of this paper is to analyze the interaction of the elastic wave or seismic waves on interfacial cracks and inclusions (inclusions can later be changed to an underground tunnel). In this research an interface or layered media is subjected to an incident elastic wave. The 2D boundary element analysis of anisotropic elastic solids of Tan *et al.* (2005) is used for this study. The joined media are assumed to be elastic half-spaces.

2. PROBLEM STATEMENT

Consider two homogeneous anisotropic linearly elastic media connected with an inclusion in the boundary between the layers as shown in Figure 1. The media are assumed to be two dimensional half spaces. An incident wave is propagated along the elastic media. Without body forces, the solids satisfy the equations of motion and Hooke's law given (see Zhang *et al.*,2002) by

$$\sigma_{i\beta,\beta}^{(m)} = \rho^{(m)} \ddot{u}_i^{(m)} \quad (1)$$

$$\sigma_{i\beta}^{(m)} = C_{i\beta k\lambda}^{(m)} u_{k,\lambda}^{(m)} \quad (2)$$

where $u_i^{(m)}$ denote the displacement components, $\sigma_{i\beta}^{(m)}$ are the stress components, $\rho^{(m)}$ denotes the mass density, $C_{i\beta k\lambda}^{(m)}$ are the components of the elasticity tensor, and “(m)” indicates either of the half-space (1) or (2).

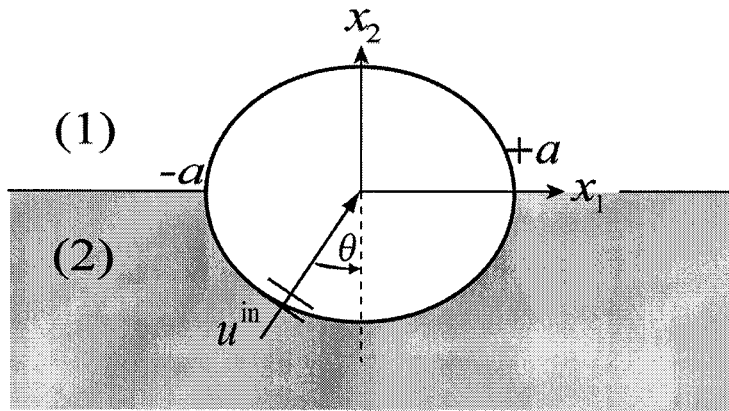


Figure.1 Inclusion in two anisotropic media

3. BOUNDARY ELEMENT METHOD

The boundary integral equations are written by using the Betti–Rayleigh reciprocal theorem. The equations for the upper region or region (1) are written as

$$\begin{aligned} & - \int_{S^{(1)}} h_{ik}^{(1)} [(x - y), e(x); t] * u_i^{(1)}(x, t) dx \\ & + \int_{S^{(1)}} g_{ik}^{(1)} [(x - y), e(x); t] * t_i^{(1)}(x, t) dx = \begin{cases} u_k^{(1)}(y, t) & y \in D^{(1)} \\ u_k^{(1)}(y, t)/2 & y \in S^{(1)} \\ 0 & \text{otherwise} \end{cases} \end{aligned} \quad (3)$$

The equations for the lower region or region (2) are written as

$$u_k^{in}(\mathbf{y}, t) - \int_{S^{(2)}} h_{ik}^{(2)}[(\mathbf{x} - \mathbf{y}), e(\mathbf{x}); t] * u_i^{(2)}(\mathbf{x}, t) d\mathbf{x} + \int_{S^{(2)}} g_{ik}^{(2)}[(\mathbf{x} - \mathbf{y}), e(\mathbf{x}); t] * t_i^{(2)}(\mathbf{x}, t) d\mathbf{x} = \begin{cases} u_k^{(2)}(\mathbf{y}, t) & \mathbf{y} \in \mathbf{D}^{(2)} \\ u_k^{(2)}(\mathbf{y}, t)/2 & \mathbf{y} \in \mathbf{S}^{(2)} \\ 0 & \text{otherwise} \end{cases} \quad (4)$$

The two sets of equations only differ in the presence of the incident wave displacements in the lower region (2). \mathbf{D} is for the domain and \mathbf{S} is for the surface, \mathbf{x} and \mathbf{y} are the source and observation points, respectively, $h_{ik}^{(m)}$ are the time-domain elastodynamic stress fundamental solutions defined by

$$h_{ik}^{(m)}[(\mathbf{x} - \mathbf{y}), e(\mathbf{x}); t] = C_{\alpha\beta}^{(m)} e_\alpha g_{jk,\beta}^{(m)}[(\mathbf{x} - \mathbf{y}); t], \quad (5)$$

and $g_{jk}^{(m)}$ represent the displacement fundamental solutions. “*” stands for Riemann convolution. For brevity, the time domain fundamental solutions for 2D anisotropic solids as derived by Wang *et al.* (1994) are given as follows,

$$g_{ij}^S(\mathbf{x}) = -\frac{1}{4\pi^2} \int_{|\mathbf{n}|=1} \sum_{l=1}^L \frac{P_{ij}^l}{\rho c_l^2} \log|\mathbf{n} \cdot \mathbf{x}| d\mathbf{n} \\ g_{ij}^R(\mathbf{x}, t) = \frac{H(t)}{4\pi^2} \int_{|\mathbf{n}|=1} \sum_{l=1}^L \frac{P_{ij}^l}{\rho c_l^2} \log|c_l t + \mathbf{n} \cdot \mathbf{x}| d\mathbf{n} \quad (6)$$

where $P_{ij}^l = E_{il} E_{jl}$,

$$\{\Gamma_{pi}(n_1, n_2) - \rho c_l \delta_{pi}\} E_{il} = 0, (l = 1, \dots, L), \quad (7)$$

superscripts R and S denotes static (singular) parts and the dynamic (regular) parts.

4. NUMERICAL RESULTS

For verification of results, an interface crack is being modeled in two joined infinite half-spaces, the interface is discretized up to a point where the waves will not affect the solution of the region of interest. Figure 2a shows the region of interest. In Figure 2b, the boundary conditions are shown along the interface. In the crack surfaces, the boundaries are assumed to be traction free and displaces with different deformation while the boundaries in the connected. The media are assumed to be in perfect contact.

To verify the BEM, consider first a crack of finite length $2a$ in an infinite, linearly elastic and isotropic solid with Poisson's ratio of $\nu = 0.25$ subject to an impact longitudinal wave loading described by:

$$u_i^{in} = U_L \begin{Bmatrix} \sin \theta \\ \cos \theta \end{Bmatrix} \left[c_L t - (x_1 + a) \sin \theta - x_2 \cos \theta \right] \times H \left[c_L t - (x_1 + a) \sin \theta - x_2 \cos \theta \right] \quad (8)$$

where U_L is the displacement amplitude of the incident L-wave, θ is the incident angle, $H[\cdot]$ is the Heaviside function, c_L is the longitudinal wave speed and, c_T is the transverse wave speed.

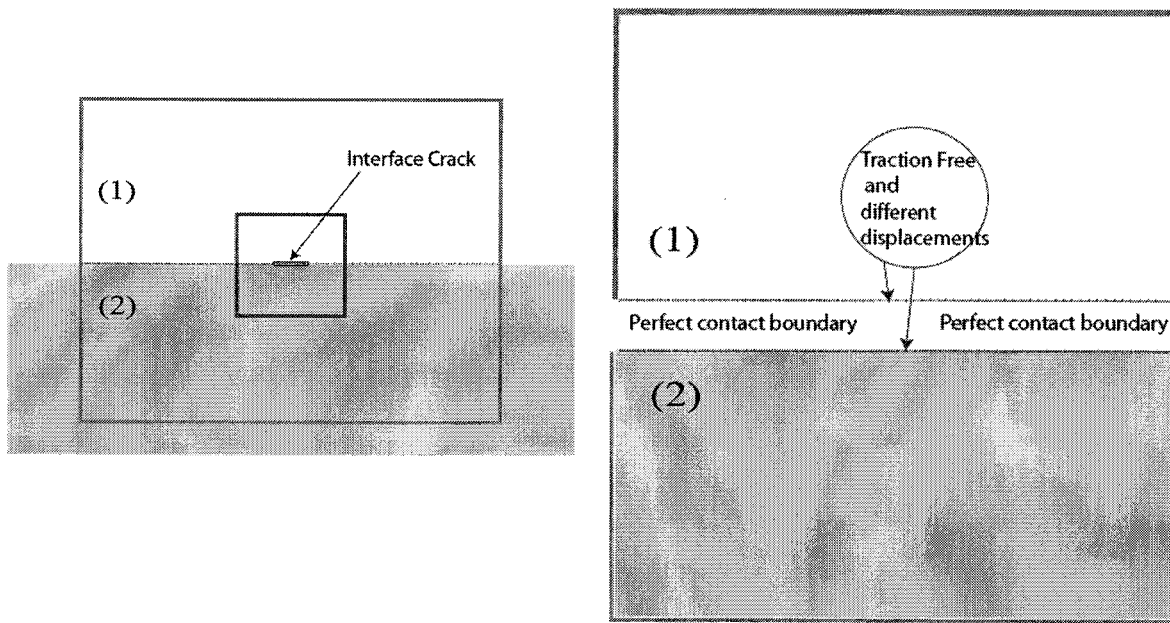


Figure 2: a. Model of the interface and the interface crack, b. Boundary conditions along the interface

The isotropic solid is modeled into two isotropic half-spaces divided along the crack line. Numerical calculations are carried out with a time step of $\Delta t = 0.1a/c_T$. Figure 3 shows the results for the calculated crack opening displacements (COD) Δu_2 at several time instants and compared to the traction BEM's results of Tan *et al.* (2005). The crack is discretized into 20 elements and the interface consists of 180 elements (-10 to 10 in the x direction). A good agreement between the different methods is achieved.

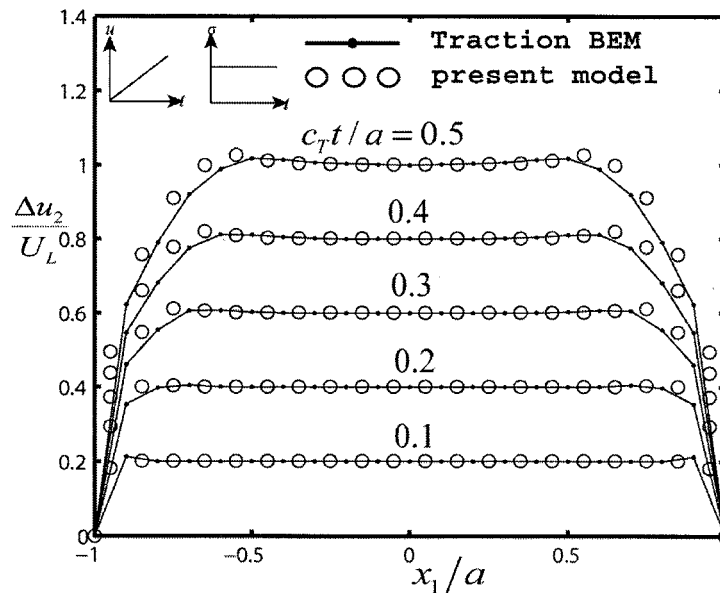


Figure.3 Results for isotropic-isotropic

Finally, consider the crack in the interface between a transversely isotropic solid (TVI) and isotropic (Iso) solid. For this purpose, a graphite epoxy composite is chosen as the transversely

isotropic solid with the elastic constants in GPa given by

$$\begin{bmatrix} C_{11} & C_{12} & C_{13} & C_{14} & C_{15} & C_{16} \\ & C_{22} & C_{23} & C_{24} & C_{25} & C_{26} \\ & & C_{33} & C_{34} & C_{35} & C_{36} \\ & & & C_{44} & C_{45} & C_{46} \\ & sym & & & C_{55} & C_{56} \\ & & & & & C_{66} \end{bmatrix} = \begin{bmatrix} 160.7 & 6.44 & 146.56 & 0 & 0 & 0 \\ & 13.92 & 6.44 & 0 & 0 & 0 \\ & & 160.70 & 0 & 0 & 0 \\ & & & 3.5 & 0 & 0 \\ & sym & & & 7.07 & 0 \\ & & & & & 3.5 \end{bmatrix} \quad (9)$$

Define Iso-TVI as two regions with an isotropic solid as region (1) and TVI as region(2) while TVI-Iso means TVI as region (1) and Iso as region (2). Region (2) is subjected to an incident wave field with a triangular pulse shape (shown in Figure 6) and described by

$$u_i^{in}(x,t) = (u_0/\delta) \begin{Bmatrix} \sin \theta \\ \cos \theta \end{Bmatrix} \left[p_j H(p_j) - 2(p_j - \delta) H(p_j - \delta) - (p_j - 2\delta) H(p_j - 2\delta) \right] \quad (10)$$

where $p_1 = t - c_1^{-1}(x_2 + a)$ and $p_2 = t - c_2^{-1}(x_2 + a)$, $\delta = 0.25a/c_1$ is the half the base of the triangular load, c_1 is the quasi-longitudinal speed, $c_2 = \sqrt{c_{66}/\rho}$ is the quasi-transverse speed and u_0 is the amplitude of the load.

Figure 4 shows the scattered wave fields in Iso-TVI interface. After the incident wave arrives and hits the crack, reflected waves propagate. Sideways wave scattering by the tips can also be clearly as it develops. It should be noted here that since the wave speeds between the two regions are different, the transverse waves travel in a faster direction in the TVI interface. The plotted values here are the absolute values of the displacement in x and y direction.

It should be noted here that the time-domain BEM applied here uses an explicit time-stepping scheme and thus is only conditionally stable. The time-step selected depends on the size of the elements and as a guarantee for stability, both should be selected where the smallest wave velocity should traverse one element length for each time step.

5. CONCLUSIONS

In summary, the 2D BEM for anisotropic solids was successfully implemented for an interface crack. The method was compared to previous solutions by assuming a finite crack in an infinite domain. Calculations for the wave fields of a region with two materials show interesting results and show the effect of the crack on the wave field. Results of this type are of great interest in understanding the scattered waves. Results here are plotted as functions of position and dimensionless time. Further simulations are to be done for 2D BEM for layered media and will include a body force equivalent to an earthquake load (i.e. double couples, or slip).

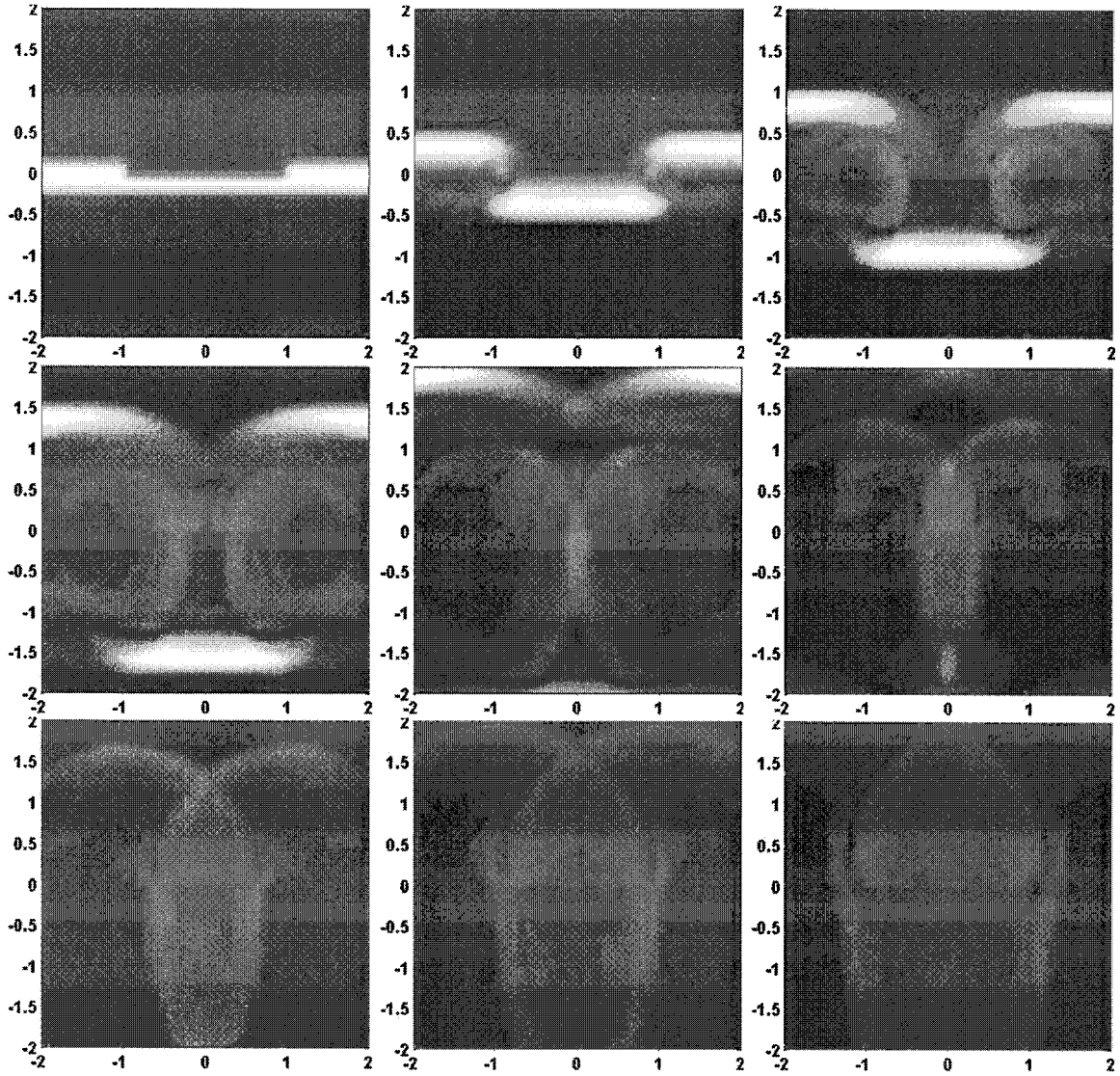


Figure. 4: Scattered wave field by an interface crack for a normal incidence of a plane

L-wave for Iso-TVI at times: $\sqrt{c_{66}/\rho} \, t/a = 0.1, 0.3, 0.6, 0.9, 1.2, 1.5, 1.8, 2.1, \text{ and } 2.4$.

Acknowledgements:

The authors acknowledge support from Japan Ministry of Education, Culture, Sport, Science, and Technology (MEXT) for establishing the Center for Urban Earthquake Engineering (CUEE) in Tokyo Institute of Technology.

References:

- Tan, A., Hirose, S., Zhang, Ch., and Wang, C.-Y. (2005), "A 2D Time-domain BEM for Transient Wave Scattering Analysis by a Crack in Anisotropic Solids," *Engineering Analysis with Boundary Elements*, **28**, 610-623.
- Zhang, Ch. and Zhu, H. (2002), "Transient Dynamic Analysis of an Antiplane Interface Crack in Anisotropic Solids," *Electronic Journal of Boundary Elements*, Vol. BETEQ2001, **2**, 179-186.
- Wang C-Y and Achenbach, JD. (1994), "Elastodynamic fundamental solutions for anisotropic solids," *Geophys J Int*, **118**, , 384-392.

USING STOCHASTIC FINITE-FAULT MODELING TO STUDY THE SITE EFFECT IN THE TAIPEI BASIN

Chun-Te Chen¹⁾, Kuo-Liang Wen²⁾

1) PhD Student, Institute of Geophysics, National Central University, Taiwan

2) Professor, Institute of Geophysics, National Central University, Taiwan
956402004@cc.ncu.edu.tw, wenkl@earth.ncu.edu.tw

Abstract: The method of the stochastic finite-fault modeling is used to analyze site effect in the Taipei basin. Local site effects are considered by soil/rock spectral ratios calculated as ratios between spectra of Chi-Chi earthquake record and finite-fault modeled for rock site. The dominant frequency and amplification is the indicator clearly shown that local site effect. The data records at 14 Site class B TAP stations are aimed the model calibration. Simulation and spectra ratio analysis indicate that TAP103 is an unusual rock site which is recorded large ground motions and may be caused by geography effect. In Taipei basin the Dominant frequency range from 0.5Hz to 1.5Hz, but in Xinyi and Shulin are about 2.0Hz, higher than other sites. The calibrated model is then used to simulate Chi-Chi earthquake ground motion on soil site with average transfer function that estimated by the spectra-ratio technique. The result shows that the H/V technique no absolute response the chi-chi earthquake amplification effect, reveal there are 2D-3D effects influence the site effects.

1. INTRODUCTION

A complete earthquake records should consider the source effect, path effect and site effect. In recent earthquakes, sit effect shown a basiliic part of these three effects, for instance, 1985 Michoacan earthquake and 1999 Chi-Chi earthquake. Anderson et al. (1996, p.1749) indicated that the top soft alluvium will acted the important role for site effects. For this reason, study the site effects is critical for mitigating damage during an earthquake.

Recent year, strong motion prediction is widely used in engineering analyses for the regions with less earthquake records data (Atkinson and Beresnev., 1998a; Sokolov et al., 2001). Stochastic finite-fault modeling is a popular tool of strong ground motion for large earthquake. In this study, the stochastic finite-fault method for simulating ground motions is applied to the records of the 1999 Chi-Chi earthquake around the Taipei basin.

We used the stochastic model dismissed the amplification to generate synthetic motions at the sites within the Taipei basin. The ratios of observed to predicted spectrum could be considered the amplification ratios. The amplification ratios reflected the local site response, and the results can use as a reference for the future seismic hazard mitigation.

2. METHOD

Stochastic modeling is a both point source and finite-fault implementation; it involves discretization of the fault plane into smaller subfaults, each of which is assigned a ω^2 Spectrum. The stochastic finite-fault method was incorporated in the fortran code FINSIM

(Beresnev and Atkinson., 1998b), all simulations in this article are carried out using the computer program.

The method consists of two steps; model validation is the first step. The stochastic finite-fault modeling is used to simulating the observed records of Chi-Chi earthquake at rock sites. Then compare the simulation and observation data, to see whether the model suitable this area or not and a satisfactory model with near-zero bias. The bias is defined as the logarithm of the ratio of the observed to simulated Fourier spectra, average over all rock sites. The calibrated model is used to simulating the ground motion at the soil sites; the mismatch could be called the amplification ratio. The second step applies the calibrated model to simulation of soil records with the empirical transfer function.

◆ Model validation

The locations of 14 rock stations used to validate the stochastic model are shown in Figure 1. Table 1 summarizes all the parameters used in this synthetic model.

The performance of our calibrated model is demonstrated in Figure 2, where we compare the observed and simulated Fourier spectra and acceleration time histories at all 14 rock sites. In most events, the fit of Fourier spectra and peak values of acceleration are well matched and satisfactory, but expect for the TAP103 station. In order to find the reason of the mismatch at the TAP103, we used the H/V spectrum analysis (Lermo *et al.*, 1993) to check the original observed data, the result also shown that the TAP103 has an eminent high-amplification, the peculiarity may be caused by effects of local topography or influence of nearby building.

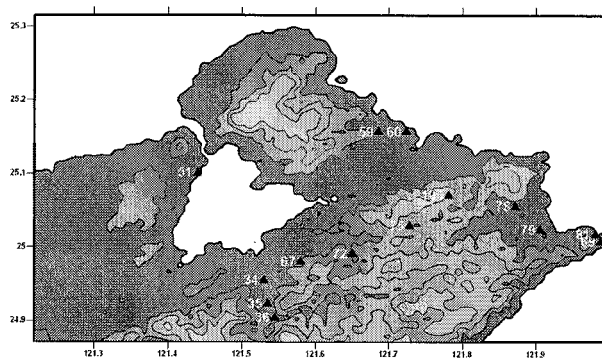


Figure 1. The locations of 14 rock stations.

The model bias for the rock stations, calculated as the logarithm (base 10) of the ratio of the observed to simulated Fourier spectra, average over 13 sites (we removed the peculiarity station -TAP103), is shown in Figure 3. The mean bias is within the ± 1 standard deviation limits of zero throughout almost the entire frequency range, indicating that the model is acceptable to simulating the observed records during the Chi-Chi earthquake in the Taipei basin.

◆ Calculation of main shock PGA at Soil Site

As the second step in this analysis, the calibrated model was combined with the empirical transfer function to simulate the spectra during the Chi-Chi earthquake at soil sites. We collect and analyze the TSMIP earthquake records for obtaining the empirical transfer function by using the spectra ratio method.

The number of soil stations (site class C, D, E) recorded the Chi-Chi main shock is 36. So, we applied the finite-fault code to the 36 sites for which we obtained transfer function. This was the only difference in the input parameters in soil site simulations compared with the calibrated model.

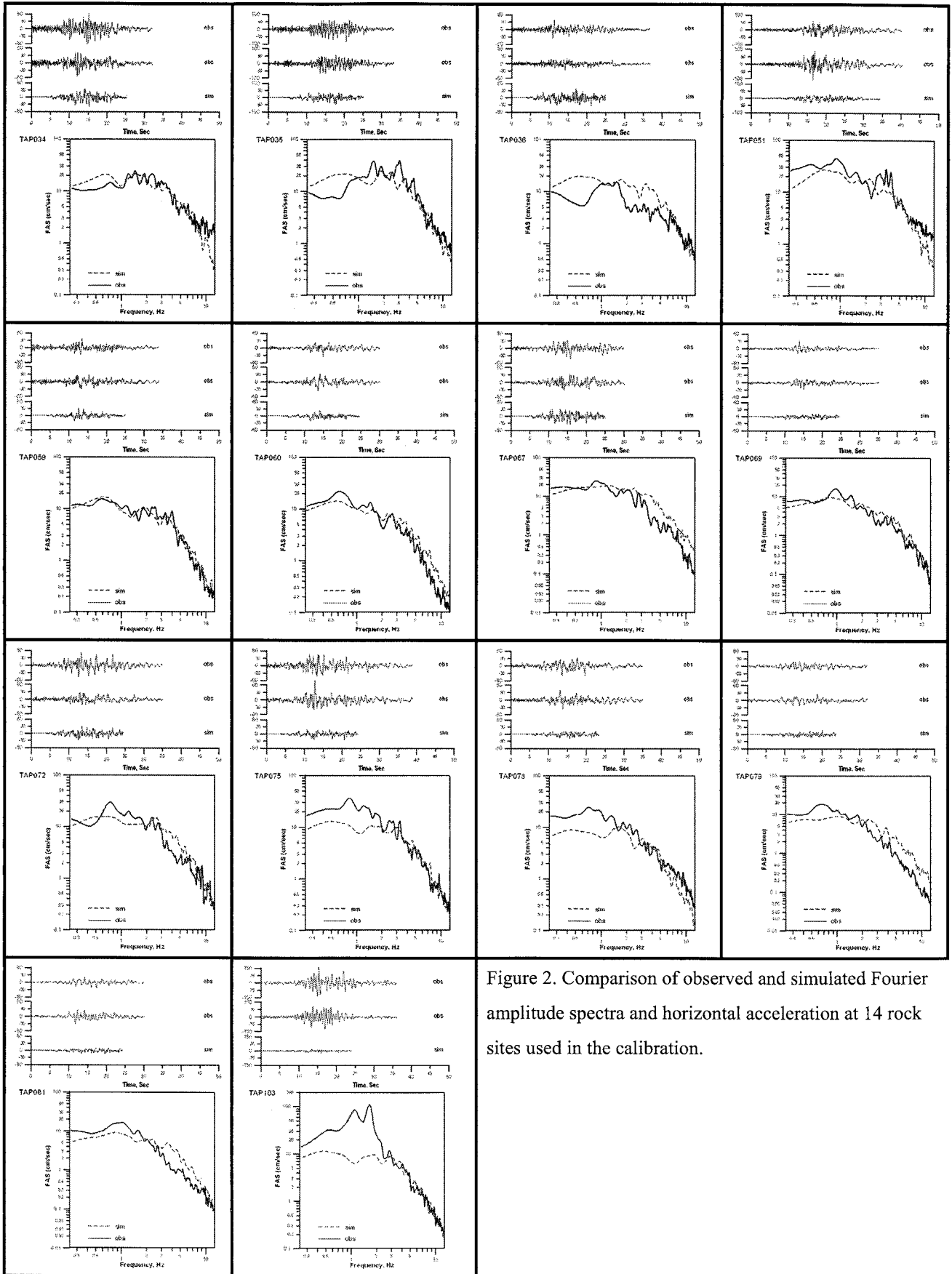


Figure 2. Comparison of observed and simulated Fourier amplitude spectra and horizontal acceleration at 14 rock sites used in the calibration.

Table 1
Modeling parameters

Parameter	value
Fault orientation (strike/dip)	5°/34° (Chang et al., 2000)
Fault dimensions along strike and dip (km)	110 by 40 (Ma et al., 2001)
Depth of the upper edge of the fault (km)	0
Magnitude(M_w)	7.6
Subfault dimensions (km)	11×10
Stress parameter D_r (bar)	50
Radiation-strength factor	1.0
Number of subsources summed	46
$Q(f)$	$117 \cdot f^{0.77}$ (Chen et al., 1989)
Geometric spreading	$1/R$ for $R < 50$ km (Sokolov, 2000)
	$1/R^0$ for $50 \text{ km} \leq R < 150$ km
	$1/R^{0.5}$ for $R \geq 150$ km
Windowing function	Cosine-tapered boxcar
Kappa (sec)	0.07
Crustal amplification	Sokolov(2004) Taiwan Generalizes B
Crustal shear-wave velocity (km/sec)	3.2
Rupture velocity (km/sec)	$0.8 \times (\text{shear-wave velocity})$
Crustal density (g/cm ³)	2.7

3. IDENTIFICATION OF SITE EFFECT

In this study, the spectra ratios are calculated with respect to the synthetic motion, but the number of the events recorded the main shock is not many, so the dominant frequencies found from the research may be biased. One of the useful methods of improving the disamenities is stacking more earthquakes. However, it is a fast and useful method to survey the site effect or predict the ground motion during an earthquake.

Figure 4 represents the contour of the dominant frequency in the Taipei basin from the observed/synthetic spectra ratios. The distribution of the dominant frequencies shows that the areas near the basin edge have a higher dominant frequency, but the center of basin have a low dominant frequency to 0.5 Hz. We also found that the contour of the dominant frequency seeming have a correlation with the basin depth (Figure 6), and the low dominant frequency usually occurs over the deepest part of the basin.

Top of the layer within Taipei basin is the Sungshan formation, some survey (Wen *et al.*, 1998) indicates the formation carry out the burden of the site effects at low frequency, and we also found the same result in the study. Figure 5 presents the contour of the observed/synthetic spectra ratios at 0.5Hz in the Taipei basin. It is very clearly shown that the high-amplification hot spots occur in two areas, the western and eastern part of Taipei basin. The areas are also the deepest parts of the Sungshan formation (Figure 7). We believe the cause of this amplification is thought to be the shock wave resonated within the soft layer.

The result of the PGA simulation is displayed in a residual map (Figure 8); the residual is defined by equation 1. We have a satisfactory prediction in the central of basin but there are three underestimates occurred in northern, eastern and southern part. These mismatches are

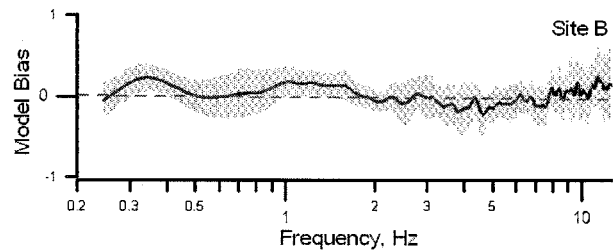


Figure 3. Bias of the calibrated model. Shallow correspond to ± 1 standard deviation of the data.

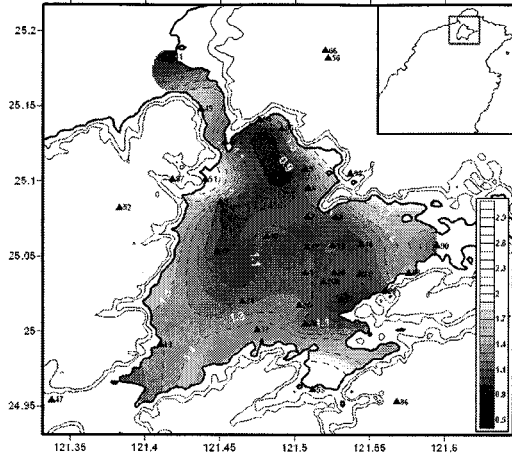


Figure 4. Contour of the dominant frequency in the Taipei basin from the observed/synthetic spectra ratios.

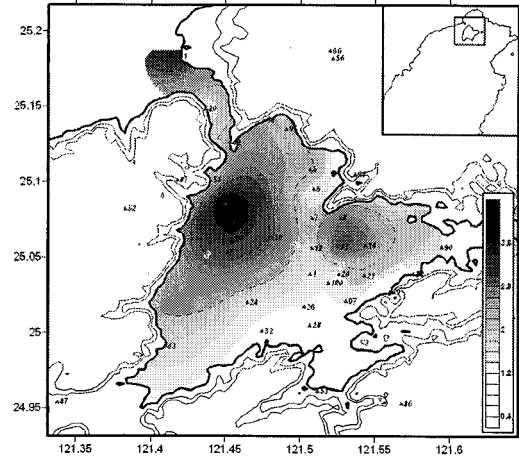


Figure 5. Contour of the observed/synthetic spectra ratios at 0.5Hz in the Taipei basin.

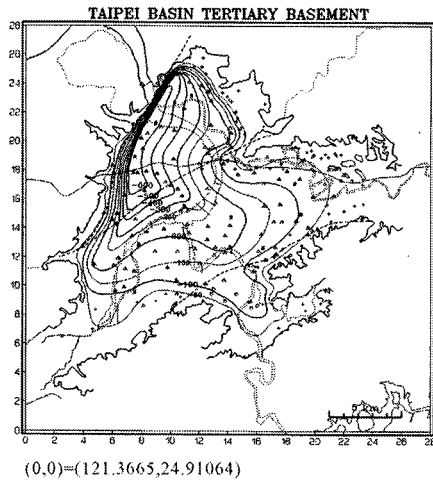


Figure 6. Contour map indicates the depth in meters to the bottom of basement in the Taipei basin (Wang *et al.*, 2004).

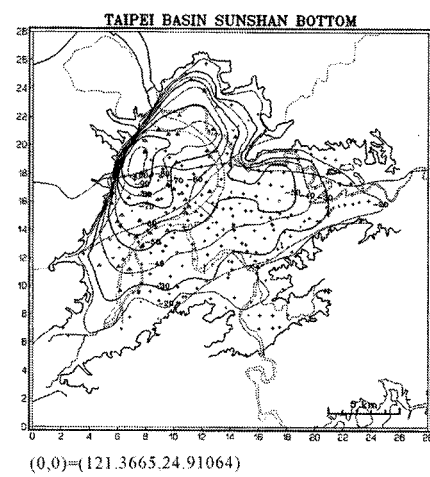


Figure 7. Contour map indicates the depth in meters to the bottom of Sungshan Formation in the Taipei basin (Wang *et al.*, 2004).

all appeared on the edge of basin; they may be caused by the alluvium thinning out gradually in these parts. It also indicates that the H/V technique may be work in the horizontal or flat layer adaptable, but not in the complex structure.

$$\text{Residual} = \frac{\text{Observed PGA} - \text{Simulated PGA}}{\text{Observed PGA}}$$

Equation 1.

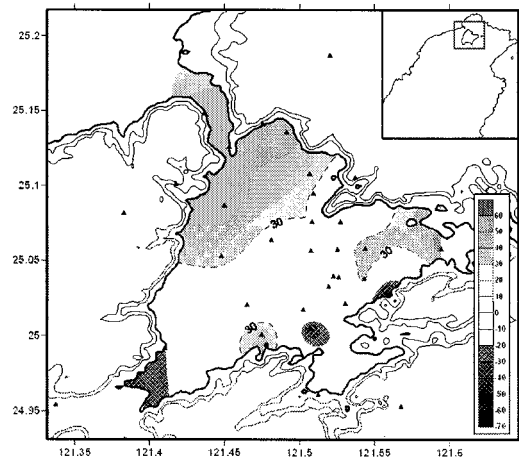


Figure 8. Residual map of the PGA simulation

4. DISCUSSION AND CONCLUSION

As a result of this study, we used the finite-fault stochastic model which has been calibrated on rock sites in order to make it effective to obtain the site effect and the ground motion prediction within the Taipei basin. Our principal findings and suggestions are summarized in the following:

1. The rock site station may be unusual records, we should to pay attention to collect the rock site data when the model validating.
2. Shunshan formation played an important role to control the site effect in the Taipei basin. In order to mitigate damage during earthquakes and supply for ground motion prediction, it is necessary to survey the layer more detail.
3. The distribution of the underestimates of ground motion prediction indicated that empirical transfer function may be unsuitable for the edge of the basin. On the other words, there is 2D or 3D effect influence the site effects in the Taipei basin.
4. Similar studies must ideally be done in order to develop more earthquakes site-specific transfer function to reject the indeterminacy. More accurate ground motion prediction can provide a good reference for the future seismic hazard mitigation.

Acknowledgements:

The earthquake data were provided from National Center for Research on Earthquake Engineering, ROC. This study is supported by National Science Council, ROC, under the grant no. NSC 94-2625-Z-008-012 · NSC-93-2625-Z-008-004.

References:

- Anderson, J.G., Lee, Y., Zeng, Y., and Day, S. (1996), "Control of strong motion by the upper 30 meters," *Bull. Seism. Soc. Am.* 86(6), 1749-1759.
- Beresnev, I. A. and G. M. Atkinson, (1998a), "Stochastic finite-fault modeling of ground motions from the 1994 Northridge, California, earthquake. I. Validation on rock sites," *Bull. Seism. Soc. Am.* 88, 1392-1401.
- Beresnev, I. A. and G. M. Atkinson, (1998b), "FINSIM—a fortran program for simulating stochastic acceleration time histories from finite fault," *Seism. Res. Lett.* 69, 27-32.
- Chang, G., Y. M. Wu, and T. C. Shin, (2000), "Relocating the 1999 Chi-Chi Earthquake, Taiwan," *TAO*. 11, 581–590.
- Chen, K. C., T. C. Shin, and J. H. Wang, (1989), "Estimates of coda Q in Taiwan," *Proc. Geol. Soc. China* 32, 339–353.
- Lermo, J. and F. J. Chavez-Garcia, (1993), "Site effect evaluation using spectral ratios with only one station," *Bull. Seism. Soc. Am.* 83, 1574-1594.
- Ma, K.F., J. Mori, S. J. Lee, and S. B. Yu, (2001), "Spatial and temporal distribution of slip for the 1999 Chi-Chi, Taiwan, earthquake," *Bull. Seism. Soc. Am.* 91, 1069–1087.
- Sokolov, V. Yu, (2000), "Spectral parameters of ground motion in different regions: comparison of empirical models," *Soil Dyn. Earthquake Eng.* 19, 173–181.
- Sokolov, V. Yu, C. H. Loh, and K.L. Wen, (2001), "Empirical models for site-and region-dependent ground-motion parameters in the Taipei Area: A Unified Approach," *Earthquake Spectra*. 17, 313-331.
- Sokolov, V. Yu, C. H. Loh, and K.L. Wen, (2004), "Evaluation of Generalized Site Response Functions for Typical Soil Classes (B, C, and D) in Taiwan," *Earthquake Spectra*. 20, 1279-1316.
- Wang, C.Y., (2004), "Subsurface Structures and P- and S- wave Velocities of the Taipei Basin, Taiwan," *Seismic Hazard Assessment in the Taipei Basin*, 3.
- Wen, K.L. and H.Y. Peng, (1998), "Site Effect Analysis in the Taipei Basin: Results from TSMIP Network Data," *TAO*, 9, 4, 691-704.

EVALUATION OF SITE AMPLIFICATIONS AT HIGH FREQUENCIES IN THE TAIPEI BASIN

M.-W. Huang¹⁾, K.-L. Wen²⁾, and J.-H. Wang³⁾

1) Assistant Researcher, National Science and Technology center for Disaster Reduction, Sindian, Taiwan

2) Professor, Institute of Geophysics, National Central University, Chungli, Taiwan

3) Researcher, Institute of Earth Sciences, Academia Sinica, Taipei, Taiwan

mwhuang@ncdr.nat.gov.tw, wenkl@earth.ncu.edu.tw, jhwang@earth.sinica.edu.tw

Abstract: The site amplifications as a function of frequency, at 18 free-field strong-motion stations in and near the Taipei Basin are evaluated from geotechnical data through the quarter-wavelength approximation provided by Boore and Joyner (1997). The V_{30} , which is the average of the S -wave velocities in the topmost 30 m, is a significant factor in classifying the sites. The evaluated results show that the site amplifications at all sites in study are larger than 1 and functions of frequency. Compared with the calculations based on the Haskell method, the quarter-wavelength approximation is almost an average and a good representation of the overall amplifications. It is noted that the site amplifications evaluated in this study can apply only to frequencies greater than about 1.5 Hz, which could affect the high buildings.

1. INTRODUCTION

The site effect affects the ground motions. The seismic waves are amplified while propagating through the low-shear-velocity and low-density layers. The amplification of seismic waves is usually a function of frequency, and stronger at a soil site than at a rock one. Numerous seismic stations are built on the soil sites, and, thus, it is necessary to eliminate the site effects. Conventionally, two ways are applied to evaluate the frequency-dependent site amplifications. The first way, which can only provide the relative amplification, is the comparison of the Fourier amplitude spectrum at a certain site to that at a reference one, which is located at a hard rock and specified with nearly flat response to the sub-surface media. However, it is actually not easy to locate a perfect reference site, and, thus, uncertainties are introduced. The second way, which gives the absolute amplification, is the division of the Fourier amplitude spectrum of recorded ground motions by that simulated based on a absolute-source-spectra model, which is assumed to have no site effects (cf. Malagnini et al. 2004). For this way, precise information of both the source spectra and the path effects underneath a study site is needed.

From surficial geology, Lee et al. (2001) classified 708 free-field strong-motion station sites in Taiwan into four categories, i.e. classes B, C, D, and E, following the criteria of the 1997 Uniform Building Code (UBC) provisions. Meanwhile, they also studied the response spectral shape in the period range 0–3 sec and the horizontal-to-vertical spectra ratios in the period range 0.03–3 sec. Their results show frequency-dependence of the site effect. However, the results can only be applied to engineering problems, yet not enough for scientific purposes. Based on the results obtained by Lee et al. (2001), Zhang (2004) evaluated the site amplification, with seismic-wave attenuation, in the frequency range 0.7–6 Hz. The latter two studies are both based on the site classification made by Lee et al. (2001). However, as mentioned below the re-classification for numerous station sites is needed as taking the well-logging data into account.

In the Taipei region, pre-1970 large distant earthquakes did not cause remarkable damages, while several post-1970 events did (cf. Wang, 1998). Observations show that the predominant frequencies of seismic waves in the Taipei Basin generated by distant earthquakes are 0.5–1.0 Hz (Chen, 2003). This would result in large damage on the buildings with 10–20 floors. Before 1970, there were buildings with only few floors, usually less than 4, and, thus, the damage was small. Since 1970 a large number of high-rises with 10–20 floors or more have been constructed, and, thus, the earthquake-induced damage increases, even though the quality of construction has been substantially upgraded. Meanwhile, the population has remarkably increased, a rapid transportation system has been in operation, and two nuclear power plants located in the vicinity of the area have been operated for a long time. Hence, much attention for seismic hazard mitigation must be paid in the area.

Wen et al. (1995a,b; 1998) studied the characteristics of site effects on strong ground motions in the Taipei Basin. They also simulated 3-second ground motions by using the boundary integral method. However, the site effect for the 3-second seismic waves is not enough for the purpose of mitigating seismic hazards. The thick recent deposits in the basin would enhance the strong ground motions, thus leading to great damage, even though earthquakes occur far away from the area. From a comparison of *S*-wave velocity model with the spatial distribution the PGA values averaged over 50 earthquakes, Wang et al. (2004) stated that larger PGA is associated with lower *S*-wave velocity. From the analyses of the strong ground motions generated from the March 31, 2002, Hualien, Taiwan, earthquake, which was about 150 km far away from the basin, Chen (2003) stressed that the seismic waves reflected from the Moho enlarged the accelerations at a small area in the eastern side of the basin.

In Taiwan, a project intended to exploring the shallow geological and seismic velocity structures near strong-motion station sites has been launched by the Central Weather Bureau (CWB) and conducted by the National Center for Research on Earthquake Engineering (NCREE) since 2000. Well-loggings are made near the station sites for measuring several seismic parameters, e.g., the density (ρ), the specific gravity, the *P*-wave velocity (V_p), and the *S*-wave (shear) velocity (V_s), at different depths. The seismic-wave velocities are measured using the technique of Suspension *P-S* Logging, developed by OYO Corporation of Japan. The boreholes are drilled down to, at least, 30-m depth. In the Taipei Metropolitan, there are 18 boreholes near the strong-motion stations, as shown in Fig. 1. From well-logging data of shear velocities and densities, an attempt is made to evaluate the absolute frequency-dependent site amplifications of shallow sediments at the 18 boreholes in the Taipei Basin using the method proposed by Boore and Joyner (1997). Also estimated are the averaged frequency-dependent site amplifications from the results of individual boreholes.

2. Geological Setting

The Taipei Basin is specified with sedimentary layers (CGS, 1999; Wang et al., 2004; Wang-Lee et al., 1987). In the basin, Quaternary sediments lie on a Tertiary basement. The Quaternary sediments are composed of three formations, i.e., the Sungshan, Chingmei, and Hsinchuang formations from top to bottom. Teng et al. (1994) divided the Hsinchuang formation into two, i.e., the Wuku and Banchiao formations. Fig. 1b shows the subsurface geological structures along Line AB depicted in the SE-NW direction in Fig. 1a. The topmost part of the Sungshan formation is a soft layer, which composes of unconsolidated sand, silt and clay with a thickness varying from 50 m in the southeast to 120 m in northwest. The lower part of the formation is dominated by silt. The Chingmei formation is full of gravels. The Hsinchuang formation is composed of sand and silt. From shallow reflection experiments and the borehole drilling results, Wang et al. (2004) concluded that the three layers of the Sungshan formation are specified with low V_s , i.e., 170, 230, and 340 m/s, respectively. The values of V_s in the Chingmei, Wuku, and Banchiao formations are, respectively, 450, 600, and, 880 m/s. The uncertainties of V_s are lower for the former formation than the latter two. The value of V_s of the Tertiary basement is about 1500 m/s.

3. Method

Joyner et al. (1981) first introduced the quarter-wavelength approximation method to evaluate the frequency-dependent site amplifications. At a particular frequency, the amplification is the squared root of the ratio of the seismic impedance (velocity times density) averaged over a depth, which corresponds to a quarter wavelength, to that at the depth of the source of seismic waves. Day (1996) made some theoretical justification for improving the calculation. The approximation is relatively insensitive to the discontinuities in seismic velocities beneath a site, and the method does not include both the nonlinear response due to the different input intensities of seismic wave amplitudes and the resonance due to subsurface topography.

The incident-plane waves through attenuation corrections are taken into account in the approximation. Boore and Joyner (1997) defined the amplification to be the ratio of the Fourier amplitude spectrum of the surface motion produced for un-attenuated incident plane waves to that recorded at the surface of a uniform half-space by the same incident waves. The amplification decreases with wavelength, therefore, approaches unity for very long-period waves. They denoted $S_H(z)$, $\beta(z)=z/S_H(z)$, and $\rho(z)$, respectively, to be the average S -wave travel time, the average velocity, and the average density. The average density is defined to be $S_H^{-1}(z) \cdot \Sigma(z_i \rho_i / \beta_i)$, where z_i , ρ_i , and β_i are the thickness, density, and S -wave velocity in the i -th layer in consideration). From the three quantities, they evaluate the frequency, i.e., $f(z)=1/[4S_H(z)]$, and the site amplification, i.e., $A[f(z)]=[\rho_s \beta_s / \rho(z) \beta(z)]^{1/2}$, where the subscript “s” represents the source area, associated with the layer thickness of z from which the seismic waves are incident to the sediments. The above-mentioned five quantities are all defined from the ground surface to depth z .

4. Borehole data

The localities of the 18 boreholes are shown in Fig. 1. The core samples of the 18 sites show that geological materials below them belong to the Sungshan formation, which is a soft layer and composes of unconsolidated sand, silt and clay. The depths of the 18 boreholes range from 31 to 56 m. The majority of the boreholes have a depth of 30 m. The depths of 2 boreholes, respectively, at a Class-D site and a Class-E one are greater than 40 m.

At each borehole, the $V_s(z)$ was measured every 0.5 m. The depth profiles of V_s at four borehole sites numbered as 71, 02, 09, and 01, respectively, for Class-B, C, D, and E site, are shown in Fig. 2b with a solid line. The total number of samples of shear-velocity loggings is 1126 and the measured values are in the range 93–1235 m/s. The ranges of measured shear velocities at the 18 boreholes are shown in Fig. 2b, where all sites are projected to Line AB in Fig. 1. Except for few sites, the velocity range is smaller inside than outside the Taipei Basin. Inside the basin, except for sites 09 and 22, the maximum velocity is less than 500 m/s. The maximum velocity is larger to the east than to the west of the basin. The US's criteria to classify sites (cf. Lee et al., 2001) are based on V_s : $V_s=760$ –1500 m/s, for Class-B, $V_s=360$ –760 m/s for Class-C, $V_s=180$ –360 m/s for Class-D, and $V_s<180$ m/s for Class-E. Based on the criteria, Lee et al. (2001) classified the 708 free-field strong-motion station sites in Taiwan from surficial geology. However, from the well-logging data, it is necessary to re-classify numerous sites in the Taipei Basin, and the classes of 13 station sites must be revised. Well-logging data show that among the 18 sites in Fig. 1, there is a Class-B site (denoted by a circle), 6 Class-C sites (denoted by squares), 10 Class-D sites (shown by triangles), and a Class-E site (depicted by a diamond). The Class-B and C stations sites are located at the mountains outside the Taipei Basin, while the Class-D and E ones inside the basin.

$\rho(z)$ was not measured regularly every 0.5 m and only done at one point in a certain geological layer. The total number of logging samples of $\rho(z)$ is 308 and the measured values are in the range 1.3–2.3 gm/cc. At some well-logging points, where the V_s was measured, yet lack of ρ , then the ρ value is taken from a nearby one, which belongs to the same geological layer as the former, is assigned. A complete well-logging profile including the two parameters can, thus, be constructed at each borehole site. Included also in Fig. 2a are the values of $\rho(z)$ (denoted by a solid circle) at four

borehole sites.

Fig. 3a shows that the $S_H(z)$ increases with depth z . There are four peculiar variations of $S_H(z)$ versus depth in Fig. 3b. Two of them are related to the Class-C sites with station codes 02 and 89, which are located at the mountains to the west and east, respectively, of the Taipei Basin. The values of $S_H(z)$ with depths less than 8 m at the two sites are larger than or equal to those at other Class-C ones and two Class-D ones coded by 54 and 90 (see Fig. 3b).

5. Amplifications from Borehole data

There are two steps for calculating the frequency-dependent site amplifications of shallow sediments in the Taipei Basin. On the first step, we evaluate the amplifications at each site. For this purpose, the values of β_s and ρ_s of the basement are needed. From the velocity model inferred by Wang et al. (2004), we take the average shear velocity, i.e., 1500 m/s, of the Tertiary basement to be β_s . There is no detailed density model right below the Taipei Basin due to limited gravity data. From the gravity survey in the Tatun Volcano Group (TVG), northern part of the Taipei Basin, Tzou and Yu (1987) inferred that from top to bottom there are three layers with different densities: 2.40 gm/cc in the range 0 to 400 m, 2.45 in the range 400 to 1600 m, and 2.55 below 1600 m. In the basin the thickness of sediments ranges from 100 m to 700 m; while outside the basin the sediments become thin. The 3-D velocity tomography (e.g., Ma et al., 1996) shows that the deeper structures below TVG and the basin are similar. Hence, we can take the density ($=2.45$ gm/cc) of the second layer to be ρ_s . From the well-logging V_s and ρ , we calculate the values of $A[f(z)]$ and $f(z)$. The plots of $A[f(z)]$ versus $f(z)$ are displayed in Fig. 4 with different symbols: solid circles, open squares, open triangles, and solid diamonds, respectively, for the Class-B, C, D, and E sites. The frequency ranges are different for the four classes of sites. The values of $V_{30}=30/S_H(30)$ (in m/s) controls the lower bound frequency, f_{30} , associated with a 30-m layer. The value of V_{30} is 832.5 m/s and 162.0 m/s, respectively, for the Class-B and E sites, and in the range of 375.7–661.1 m/s for the Class-C sites and 182.4–324.6 m/s for the Class-D ones. Therefore, the values of f_{30} are: 6.9 Hz for the Class-B site, 3.1–5.5 Hz for Class-C, 1.5–2.7 Hz for Class-D, and 1.3 Hz for Class-E. As taking the deepest borehole at each class taken into account, the value of f_{low} can reach 6.9 Hz for the Class-B site, 3.1 Hz for the Class-C ones, 1.1 Hz for the Class-D ones, and 1.0 Hz for the Class-E one. This can be seen in Fig. 4 that for the Class-C sites, except for few boreholes deeper than 30 m there are no data points for $f(z)<3$ Hz. Obviously, the plots can be divided into four groups according to the V_{30} value, which are associated, respectively, with the Class-B, C, D, and E sites from bottom to top. Of course, the plots of the unique Class-E site are inside the Class-D group.

On the second step, the average amplifications are calculated from those of individual sites at the same borehole depth. Of course, for a certain depth the frequencies at different sites vary in a small range due to unequal velocity profiles. The average frequency is taken to be the frequency related to such a depth. Since there is only one Class-B as well as Class-E site, therefore, it is not necessary to take the average for them. The data points of average amplification versus average frequency are displayed in Fig. 4: circles, squares, triangles, and diamonds, respectively, for the Class-B, C, D, and E sites. The solid symbols represent the average values. Included also in Fig. 4 are the error bars of both $A[f(z)]$ and f for the Class-C and D sites. At the Class-B site, $A[f(z)]$ first slightly decreases and then increases with increasing f from 7 to 50 Hz. The values of $A[f(z)]$ vary in a small range of from 1.5 to 1.6. At the Class-C sites, average $A[f(z)]$ first increases with f , and then almost becomes a constant of about 3.0 when average $f(z)>12$ Hz. However, the value of $A[f(z)]$ at $f=3.5$ Hz is larger than that at $f=4$ Hz. At the D sites, average $A[f(z)]$ first increases with f and suddenly drops to a smaller value at $f=2$ Hz, then increases with f again and finally almost becomes a constant of about 3.6 when $f>10$ Hz. When $f<10$ Hz, the increasing rate is much larger for the Class-C sites than for the Class-D ones. When $f>10$ Hz the data points for the Class-C and D sites are somewhat below the individual trend. This might be due to lower reliability of measured values at shallow depths. At the Class-E site, $A[f(z)]$ first increases and then decreases with increasing f . The values of $A[f(z)]$ vary from 3.0 to 3.8, with a peak at $f=2$ Hz.

The amplifications of the Class-E site approximately reach a value of 3.6 when $f > 7$ Hz. The turning frequency for the appearance of constant decreases from hard to soft rock sites. For the soft-rock sites, the turning frequency is smaller than 12 Hz and still in the frequency range of engineering interests. It is necessary to further investigate this problem.

6. Conclusion

From the quarter-wavelength approximation method by Boore and Joyner (1997), we evaluate the frequent-dependent site amplifications at 18 free-field strong-motion stations in the Taipei Metropolitan area from well-logging data. Results show that the site amplifications at all sites in study are larger than 1 and a function of frequency. At the Class-B site, $A[f(z)]$ first slightly decreases and then increases with increasing f , varying from 1.5 to 1.6. At the Class-C sites, average $A[f(z)]$ first increases with f , and then almost becomes a constant of about 3.0 when average $f(z) > 12$ Hz. At the D sites, average $A[f(z)]$ first increases with f and suddenly drops to a smaller value at $f = 2$ Hz, then increases with f again and finally almost becomes a constant of about 3.6 when $f > 10$ Hz. At the Class-E site, $A[f(z)]$ first increases and then decreases with increasing f , varying from 3.0 to 3.8, with a peak at $f = 2$ Hz. Compared with the Haskell method, the quarter-wavelength approximation is almost an average and a good representation of the overall amplifications. It is noted that the site amplifications evaluated in this study can apply only to frequencies greater than about 1.5 Hz.

References:

- Boore, D.M. and W.B. Joyner (1997), "Site amplifications for generic rock sites," *Bull. Seism. Soc. Am.*, 87, 327-341.
- CGS (Central Geological Survey) (1999), "Subsurface Geology and Engineering Environment of the Taipei Basin" (in Chinese), *Special Pub. 11, Central Geol. Survey, Ministry of Economic Affairs, ROC*, 406pp.
- Chen, K.C. (2003), "Strong ground motion and damage in the Taipei Basin from the Moho reflected seismic waves during the March 31, 2002, Hualien, Taiwan, earthquake," *Geophys. Res. Lett.* 30(11), doi:10.1029/2003GL017193.
- Day, S.M. (1996), "RMS response of a one-dimensional half space to SH," *Bull. Seism. Soc. Am.*, 86, 363-370.
- Haskell, N.A. (1960), "Crustal reflection of plane SH waves", *J. Geophys. Res.*, 65, 4147-4150, 1960.
- Joyner, W.B., R.E. Warrick, and T.E. Fumal (1981), "The effect of Quaternary alluvium on strong ground motion in the Coyote Lake, California, earthquake of 1979," *Bull. Seism. Soc. Am.* 71, 1333-1349.
- Lee, C.T., C.T. Cheng, C.W. Liao, and Y.B. Tsai (2001), "Site classification of Taiwan free-field strong-motion stations," *Bull. Seism. Soc. Am.* 91, 1283-1297.
- Ma, K.F., J.H. Wang, and D. Zhao (1996), "Three-dimensional seismic velocity structure of the crust and uppermost mantle beneath Taiwan," *J. Phys. Earth.* 44, 85-105.
- Malagnini, L. K., Mayeda, A. Akinci, P. L. Bragato (2004). "Estimating Absolute Site Effects," *Bull. Seism. Soc. Am.* 94, 576-590.
- Teng, L.S., S.C. Wang, C.B. Chang, C. Hsu, P.B. Yuan, and P.Y. Chen (1994), "Quaternary strata frame of the Taipei basin" (in Chinese), *Proc. Joint Symposium on Taiwan Quaternary (5) and on Investigation of Subsurface Geology/Engineering Environment of Taipei Basin*, 129-135.
- Tzou, Y.H. and G.K. Yu (1987), "Subsurface structure of the Tatun volcano group area inferred from the gravity data," *Bull. Geophys., Natl. Central Univ.*, 27/28, 45-60.
- Wang, C.Y., Y.H. Lee, M.L. Ger, and Y.L. Chen (2004), "Investigating subsurface structures and P- and S-wave velocities in the Taipei Basin," *Terr. Atmos. Ocean. Sci.* 14, 609-628.
- Wang, J.H. (1998), "Studies of earthquake seismology in Taiwan during the 1897-1996 period," *J. Geol. Soc. China*, 41, 291-336.
- Wang-Lee, C.M. and T.P. Lin (1987), "The geology and land subsidence of the Taipei Basin," *Memoir Geol. Soc. China*, 9, 447-464.
- Wen, K.L., L.Y. Fei, H.Y. Peng, and C.C. Liu (1995a), "Site effect analysis from the records of the Wuku downhole array," *Terr. Atmos. Ocean. Sci.* 6(2), 285-298.
- Wen, K.L., H.Y. Peng, L.F. Liu, and T.C. Shin (1995b), "Basin effects analysis from a dense strong motion observation network," *Earthquake Eng. Struct. Dyn.* 24(8), 1069-1083.
- Wen, K.L. and H.Y. Peng (1998), "Site effect analysis in the Taipei Basin: Results from TSMIP Network data," *Terr. Atmos. Ocean. Sci.* 9(4), 691-704.
- Zhang, F. (2004), "Site response and attenuation analysis using strong motion and short-period data," *Ph.D. Dissertation, Dept. Civil Struct. Environ. Eng., SUNY- Buffalo*, 278pp.

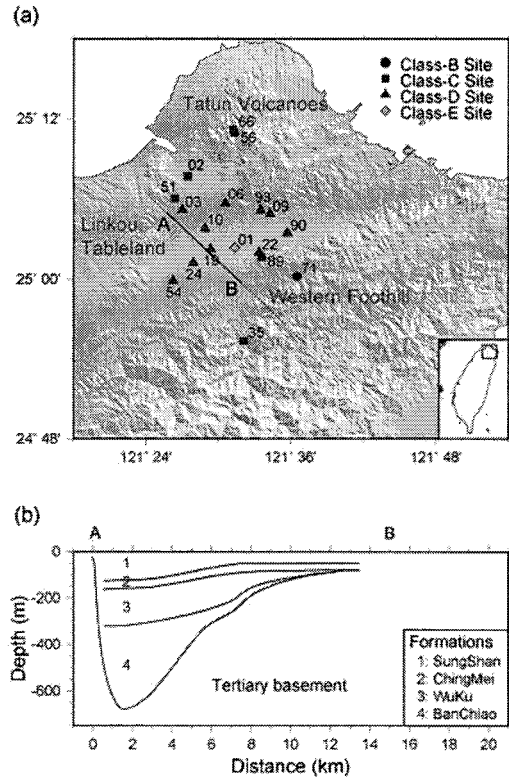


Figure 1. (a) A map to show the Taipei Basin and surrounding geological provinces. The station sites in use are displayed in circles, squares, triangles, and diamonds for the Class-B, C, D, and E sites, respectively; and (b) Subsurficial geological structures in the Taipei Basin (modified from Wang et al., 2004).

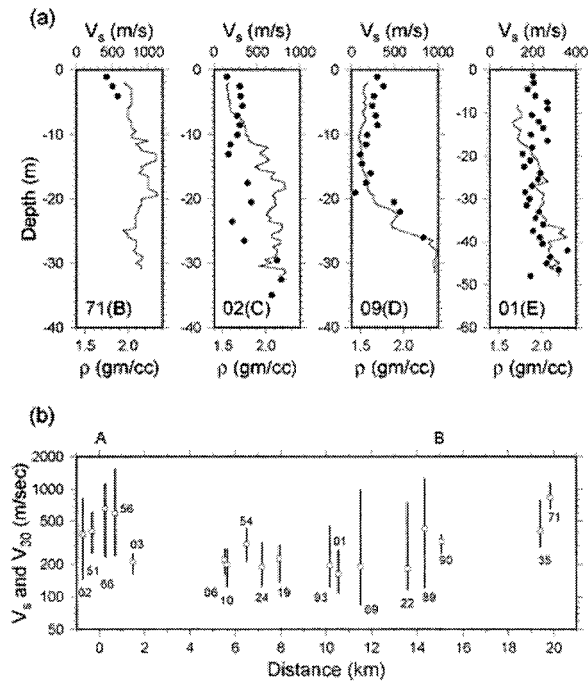


Figure 2. (a) Four examples of well-loggings of S -wave velocity (lines) and density (circles) varied with depth; and (b) the measured velocity range (in a vertical line segment) and V_{30} (in an open square) at each borehole site, whose station code is given in and locality is projected on Line AB shown in Figure 1a.

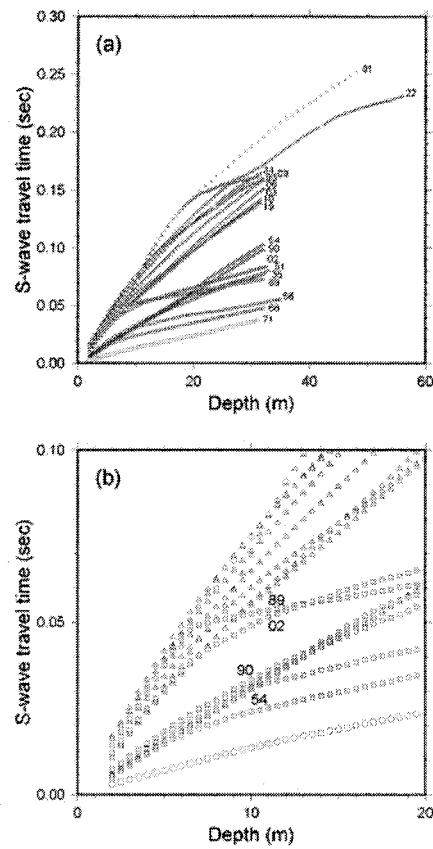


Figure 3. (a) S-wave travel time versus depth: gray, red, blue, and green for Class-B, C, D, and E sites, respectively. (b) Enlarged figure of dashed region in (a), symbols are same as (a).

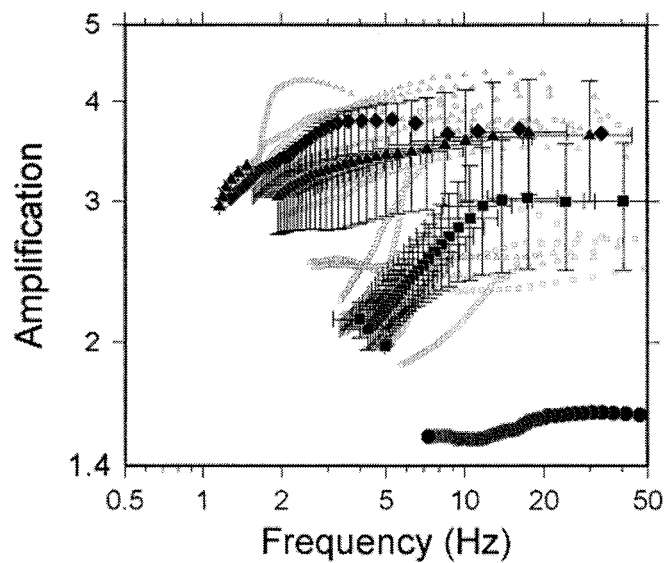


Figure 4. The plots of $A(f)$ versus f : circles, squares, triangles, and diamonds for Class-B, C, D, and E sites, respectively. (a) The average values, with error bars, from various boreholes at the same depth are displayed by solid symbols.

PARAMETRIC STUDY ON CONTROL OF WAVEFORMS USING ALL PASS FUNCTION

K. Shirai¹⁾ and T. Ohmachi²⁾

1) Graduate Student, Department of Built Environment, Tokyo Institute of Technology, Japan

2) Professor, Department of Built Environment, Tokyo Institute of Technology, Japan

kshirai@enveng.titech.ac.jp, ohmachi@enveng.titech.ac.jp

Abstract: The objective of this paper is how to control waveforms by means of all pass functions. Causal time functions such as earthquake records are factorized into minimum phase shift and all pass functions, which is called factorization. This concept is applied to impulse function to investigate effects of all pass phases when they are parametrically changed. With linear all pass phase shifts, waveforms of the response are unchanged but the rise time shifts appear. When it is assumed that non linearity is expressed as $-c \cdot \omega^n$, waveforms of the response show irregular attenuation and their maximum amplitudes are smaller than the original ones.

1. INTRODUCTION

To design input earthquake ground motions, response spectra are often used in frequency domain. When time histories are needed, we must set both Fourier amplitude and phase spectra. From past many studies, it has been clear what Fourier amplitude spectra of earthquake records inform, and how they have been theoretically formulated. However, as for Fourier phase spectra, those of the past records, for example the 1940 EL Centro, the 1952 Taft, the 1968 Hachinohe and so on, are used because it hasn't been clear what they inform and they haven't yet been formulated.

In signal analyses (e.g. Papoulis 1962, Papoulis 1977, Oppenheim and Schaffer 1989), it is known that causal time functions such as earthquake records are decomposed into minimum phase shift and all pass functions. On the minimum phase shift functions, their Fourier phase and amplitude spectra depend on each other. On the other hands, the all pass functions have only Fourier phase spectra and their group delay time shows arrival time of the signal.

Izumi et al. (1990) applied this theory to earthquake records and pointed out that the minimum phase shift function is a transfer function of the ground and the all pass function includes information of travel time of direct S-wave from source to station. Sato et al. (1999) formulated characteristics of source, pass and ground by means of the group delay time of the minimum phase shift function. Sato (2005) used the all pass function as a receiver function to estimate P-SP time. These studies showed that the all pass function seems to be linear and the group delay time expresses arrival time of direct S-wave from the source. However, the all pass function calculated from the earthquake records shows non linearity (Shirai and Ohmachi 2005) because the all pass function includes arrival times of not only direct S-wave but also direct P-wave, reflected and refracted body waves and surface waves. If the all pass function is theoretically formulated, Fourier phase spectra will be modeled because Fourier phase spectra of the minimum phase shift are determined from its Fourier phase in terms of Hilbert Transforms (Papoulis 1962, Papoulis 1977).

This paper describes a fundamental study on the response to impulse function when the all pass

function is parametrically changed.

2. CHARACTERISTICS OF MINIMUM PHASE SHIFT AND ALL PASS FUNCTIONS

2.1 De-convolution of a Causal Time Function

A time function is causal if it equals zero for negative time:

$$x(t) = 0 \quad \text{for} \quad t < 0 \quad (1)$$

A causal time function can be decomposed into two functions. One is the minimum phase shift function and another is the all pass function. A causal time function $x(t)$ is written by convolution of minimum phase shift $x_M(t)$ and all pass $x_A(t)$ as follows Eq.(2)

$$x(t) = x_M(t) * x_A(t) \quad (2)$$

Where the subscripts M and A denote minimum phase shift function and all pass function, respectively. The decomposition is often introduced as factorization of a causal time function in signal analysis (Papoulis 1977). $x_M(t)$ and $x_A(t)$ satisfy

$$x_M(t) = 0 \quad \text{for} \quad t < 0 \quad (3)$$

$$x_A(t) = 0 \quad \text{for} \quad t < 0 \quad (4)$$

In the meantime, Fourier transforms $F(\omega)$ is defined by

$$x(t) \Leftrightarrow F(\omega) = |F(\omega)| e^{i\phi(\omega)} \quad (5)$$

Where ω is angular frequency, the absolute $|F(\omega)|$ Fourier amplitude and $\phi(\omega)$ its phase.

When the Fourier transform is applied to Eq.(2), Eq.(6) will be obtained below:

$$F(\omega) = F_M(\omega) F_A(\omega) \quad (6)$$

Minimum phase shift and all pass functions have the Fourier amplitude and phase respectively as follows:

$$F_M(\omega) = |F_M(\omega)| e^{i\phi_M(\omega)} \quad (7)$$

$$F_A(\omega) = |F_A(\omega)| e^{i\phi_A(\omega)} \quad (8)$$

Here, the Fourier amplitude of all pass function is unity:

$$|F_A(\omega)| = 1 \quad (9)$$

The Fourier transform $F(\omega)$ of $x(t)$ shall be written by means of minimum phase shift and all pass functions:

$$F(\omega) = |F_M(\omega)| e^{i(\phi_M(\omega) + \phi_A(\omega))} \quad (10)$$

Therefore the Fourier amplitude $|F(\omega)|$ is equals to $|F_M(\omega)|$ and the Fourier phase of $x(t)$ is the sum of minimum phase shift and all pass phases.

$$|F(\omega)| = |F_M(\omega)| \quad (11)$$

$$\phi(\omega) = \phi_M(\omega) + \phi_A(\omega) \quad (12)$$

The Fourier amplitude and phase of minimum phase shift satisfy the equations:

$$\phi_M(\omega) = \frac{1}{\pi} \int_{-\infty}^{\infty} \frac{\log |F_M(y)|}{\omega - y} dy \quad (13)$$

$$\log |F_M(\omega)| = -\frac{1}{\pi} \int_{-\infty}^{\infty} \frac{\phi_M(y)}{\omega - y} dy \quad (14)$$

Eq.(13) and Eq.(14) are known as the Hilbert transforms .

This paper omits the method to calculate minimum phase shift and all pass functions because past studies (e.g. Izumi et al 1988, Katsukura et al. 1989) mentioned in detail.

2.2 Characteristic of Unit Impulse Function

Figure 1 represents unit impulse function which rises at 12 seconds and Fourier transform of the function. When this function is factorized into minimum phase shift and all pass functions in time domain, each time history is shown in Figure 2. In Figure 2, each time history show impulse but the

rise time and maximum amplitude are different from each other. As for minimum phase shift, impulse rises at 0 second and amplitude is same as the original impulse. As for all pass function, impulse rises at 12 seconds whose amplitude is 100 and rise time is same as the original impulse function.

Fourier transform of the minimum phase shift and all pass function are represented in Figure 3. Horizontal axis of the figures in frequency domain is plotted against angular frequency (rad/sec) in this paper. Fourier amplitude of the minimum phase shift function is unity and the phase is zero all over frequency. From now on, only all pass function is mentioned because Fourier amplitude and phase spectra of the minimum phase shift function satisfy Eq.(13) and (14), and they are dependent together.

Fourier amplitude of the all pass function in Figure 3 is unity, the phase of that is linear and its group delay, which is defined as $-d\phi(\omega)/d\omega$, is 12. This is rise time of impulse function in Figure 1. From this result, all pass function includes arrival time of the original impulse function, and Fourier phase of all pass function is expressed as,

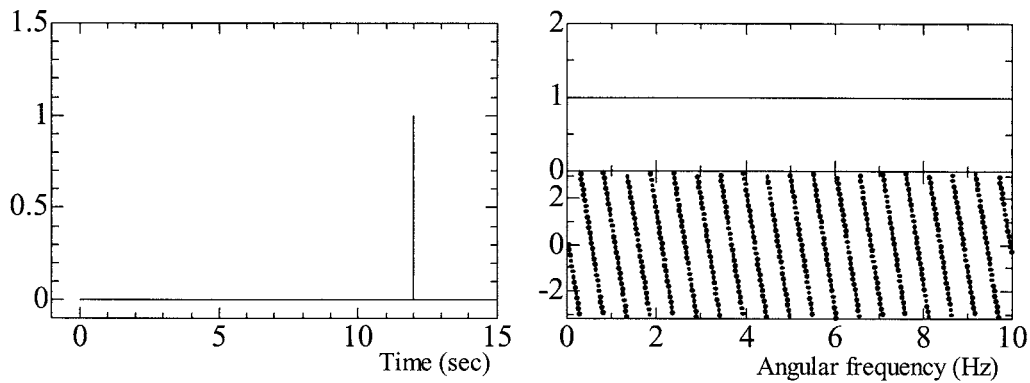


Figure1. Unit impulse function (Left) and Fourier amplitude and phase of that (Right).

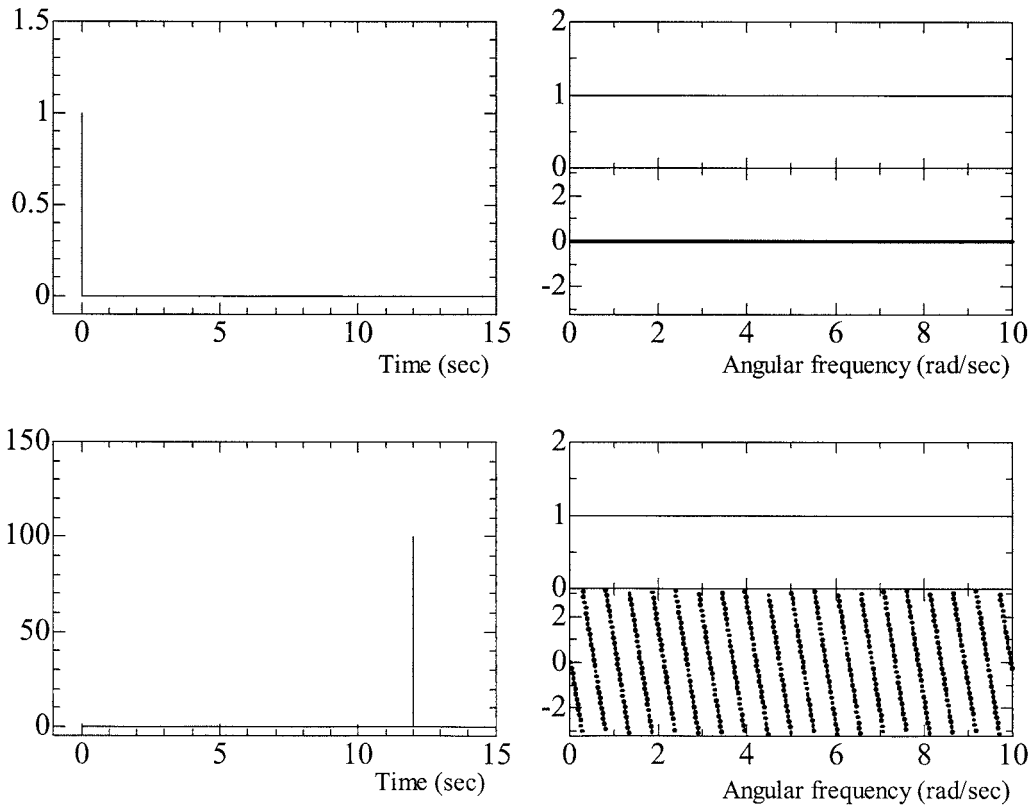


Figure 2. Time histories of minimum phase shift (Upper) and all pass functions.

Figure 3. Fourier transform of minimum phase shift (Upper) and all pass functions.

$$\phi_A(\omega) = -\tau \cdot \omega \quad (15)$$

In Eq.(15), τ means arrival time of the impulse.

3. EFFECT OF ALL PASS FUNCTION SHIFTS

3.1 Non-Linear Shifts of All Pass function

Firstly, non linearity is taken into consideration in linear phase of all pass function Eq.(15). Assumed that non linearity is expressed by a constant and a multiplier of angular frequency, a term of non linearity is written by

$$c \cdot \omega^n \quad (16)$$

All pass function of linear phase in Eq.(15) is written over again as follows:

$$\tilde{\phi}_A(\omega) = -\tau \cdot \omega - c \cdot \omega^n \quad (17)$$

Tilde means non linear phase of all pass function. Now, τ are fixed at 12 as same as the original impulse in Figure 1. As first numerical experiments, constant c is equal to 1, and multiplier n is changed from 0.0 to 2.0 at intervals of 0.1. Those time histories are illustrated in Figure 4. Except $n=0.0$ and 1.0, time histories are not impulse and they shows attenuation and envelopes appear. Moreover, when multiplier n is over 1.0, those time histories aren't similar to earthquake motions. This paper aims to model Fourier phase spectra of input earthquake ground motion, the following range of multiplier n is limited from 0 to 1.0.

Next, multiplier n is fixed at 0.5 intermediate values from 0 to 1.0 and constant c is changed from

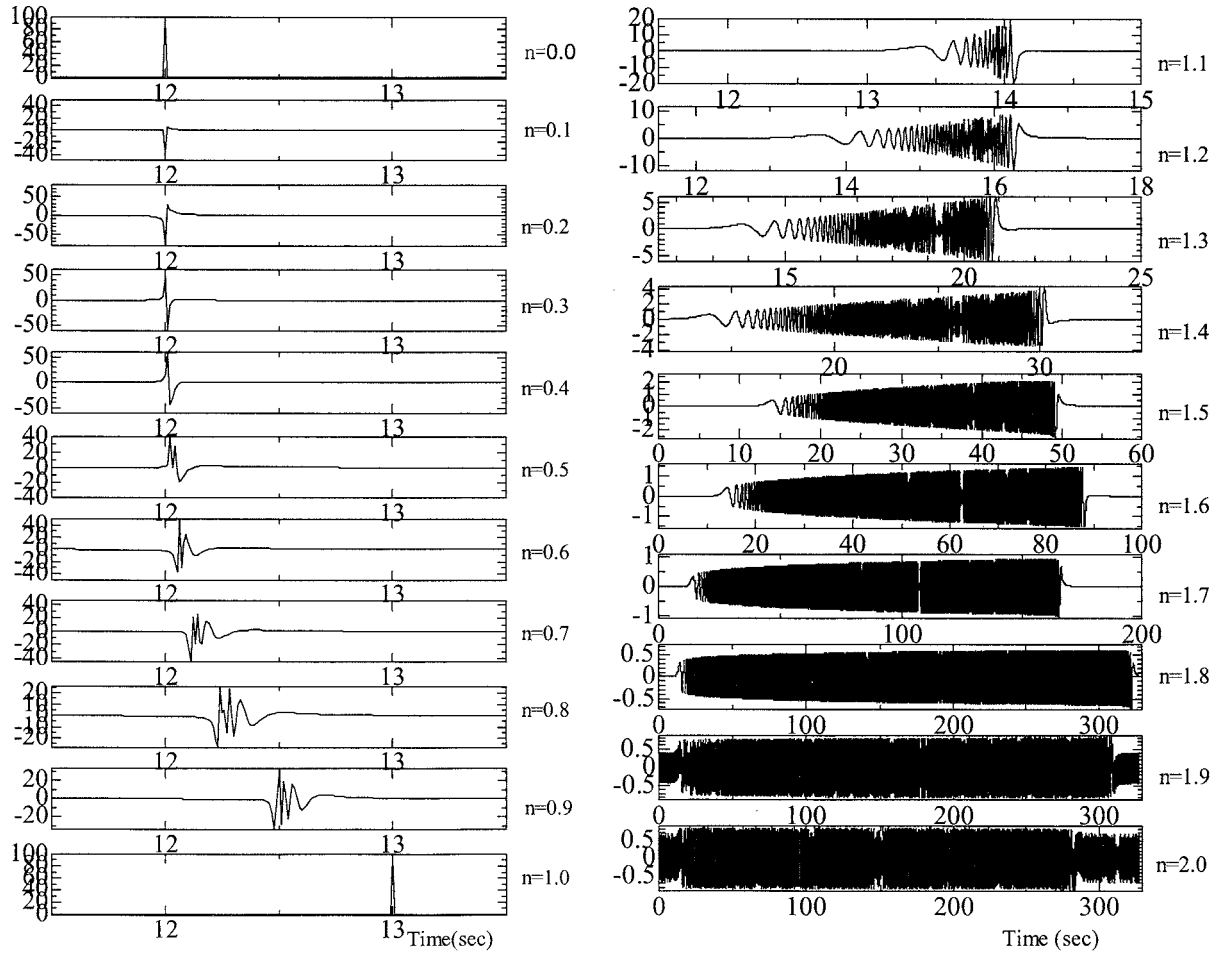


Figure 4. Time histories of all pass function whose constant c in term of non linearity is fixed at 1, and multiplier is parametrically changed.

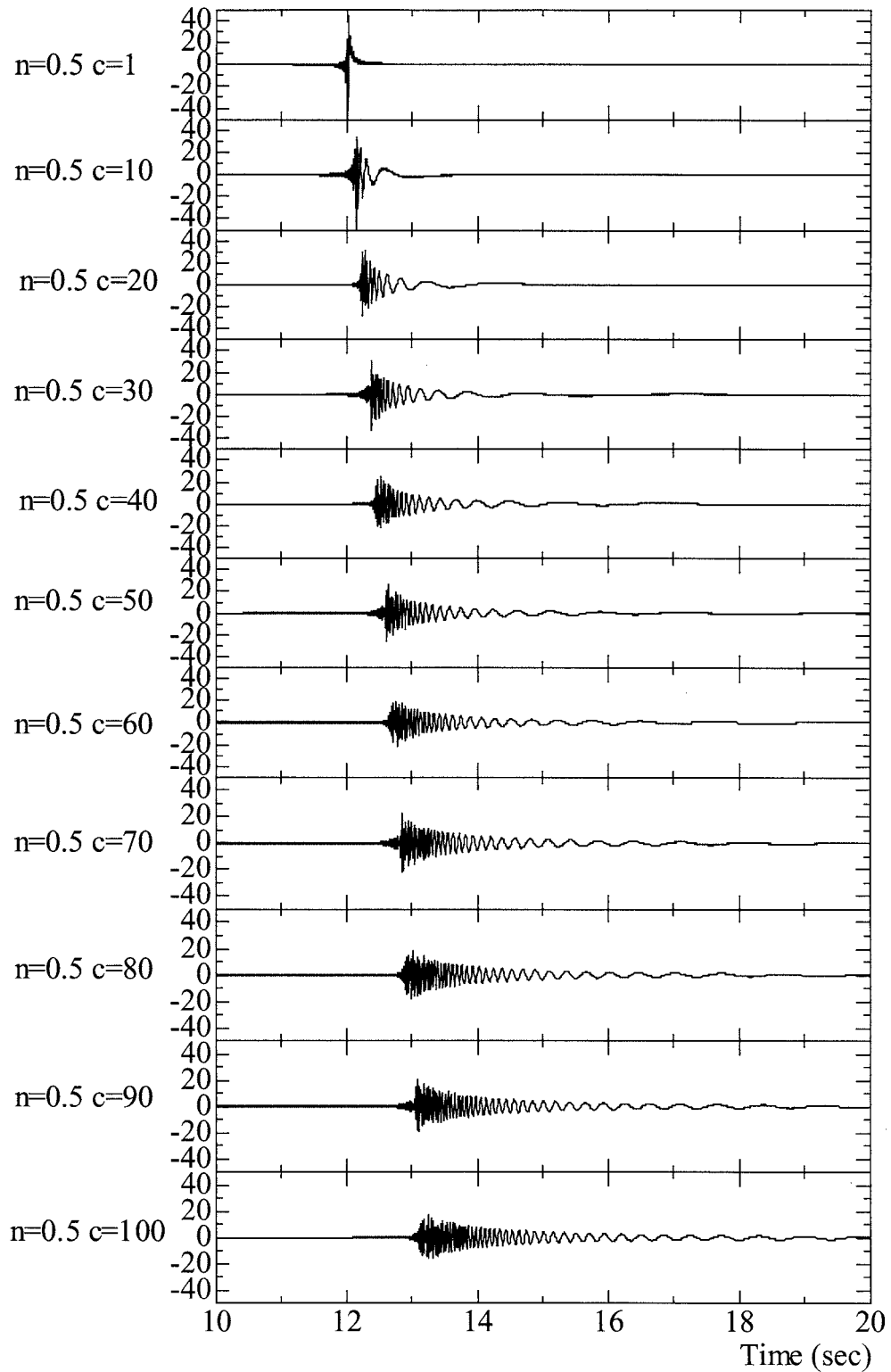


Figure 5. Time histories of all pass functions, whose multiplier is fixed at 0.5 and constant c in term of non linearity is parametrically changed.

1.0 to 100 at intervals of 10. It is shown in Figure 5. The duration of time histories becomes longer when constant c is larger but maximum amplitude of those become smaller. Moreover, long period waves arrive after short period waves, which are seen especially at $c=30, 40, 50$ and 60 in Figure 5.

3.2 Discussions

Finally, new findings by parametric study above mentioned are discussed. In Figure 2 and 3, time history of all pass function shows impulse at 12 seconds and the phase is linear and its group delay time is 12. It causes that linear phase in frequency domain is transformed into impulse function in time domain. Therefore,

$$1 \cdot e^{i\tau\omega} \Leftrightarrow \delta(t - \tau) \quad (18)$$

In Eq.(18), τ means delay time, δ means Heaviside step function and double arrow means Fourier transform. Amplitude of all pass function is 100 at 0.01 seconds.

In Figure 4 and 5, when term of non linearity is considered and multiplier n becomes larger, the original impulse is collapsed and the envelope appears and time duration is extended. Constant c is more effective on the duration and maximum amplitude of time history when c become larger.

In the Engineering seismology, it is well known that the time duration and the envelope cause by dispersion of seismic wave through heterogeneous ground (Sato and Fehler 1998). Moreover, quality factor Q value which expresses attenuation of ground is effective on dispersion of seismic wave. In the past studies, Q value is expressed as;

$$Q(\omega) = Q_0 \cdot \omega^n \quad (19)$$

As for Q value of S wave, Q_0 and n are approximated as (Fukushima 1993);

$$Q_0 \cong 31.6 \quad (20)$$

$$n \cong 0.77 \quad (21)$$

In this paper, n greater than 1.0 is excluded and fixed at 0.5 because the response of time history doesn't show attenuation like earthquake motions. 0.5 is a little smaller than Eq.(21) but is closely same. Furthermore, non linearity is effective on waveforms such as duration, envelope and attenuation. On trial, when Eq.(20) and (21) is subscribed for Eq.(17) and τ is at 12, the time history calculated by inverse Fourier transform is illustrated in Figure 6. The time history show long time duration and envelope such as input earthquake motions. From this result, term of non linearity is seemed to be related to quality factor Q . However, more studies on relationship between non linearity and Q value are needed as the future works.

In Figure 5 and 6, long period waves in time history arrive after short period waves. When multiplier n is greater than 0.0 and less than 1.0, Eq.(17) shows asymptotic curve in Figure 7. In lower

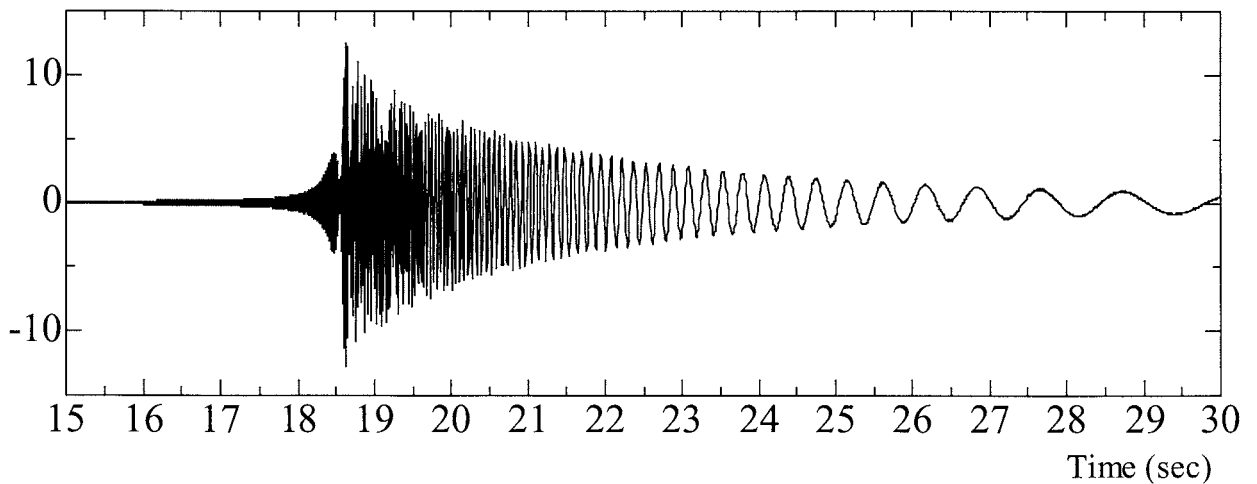


Figure 6. Time history of all pass function with $c=31.6$, $n=0.77$ and $\tau=12$ shows long time duration and envelope.

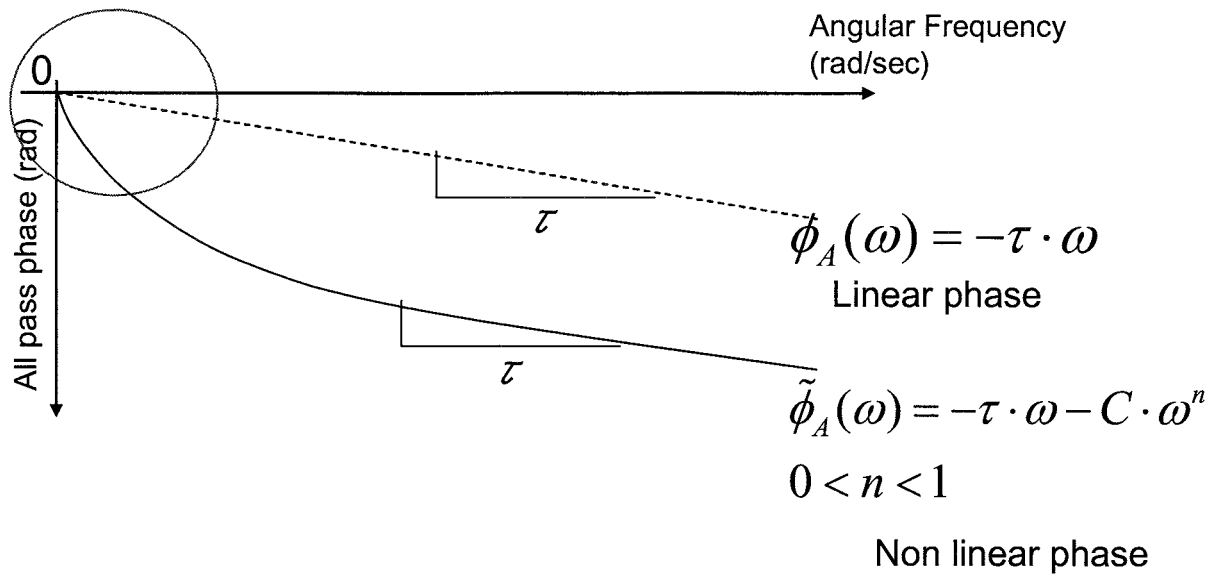


Figure 7. Eq.(17) shows asymptotic curve, whose group delay in lower frequency (in a circle) is greater than in higher frequency and the long period wave arrives after short one.

frequency, the group delay time is larger than that in higher frequency, then lower frequency waves, which is dominant to long period, arrive after higher frequency ones, which is dominant to short period. It is due to term of non linearity in Eq.(17).

4. CONCLUSIONS

Based on the concepts of the factorization and causality widely used in signal analyses, this paper has been focused on how to control waveforms by means of the all pass functions, with findings like the follows:

1. All pass functions of impulse functions are linear, and their group delay time gives a rise time of signals.
2. When the Fourier phase spectra of an all pass function is non linearly expressed as, $\tilde{\phi}_A(\omega) = -\tau \cdot \omega - c \cdot \omega^n$, the all pass function causes some changes in the original impulse function, such as decrease in the amplitude and increase in the duration.
3. When we use the multiplier n in the phase spectra $n > 1$, resulting waveforms of an original function is far from earthquake motions.
4. The larger the constant c in the phase spectra we use, the longer the duration of the original function becomes.
5. Interestingly, the multiplier n might be related to the quality factor Q of the ground.

References:

- Papoulis, A. (1962), "Fourier Integral and its Applications", McGraw-Hill.
- Papoulis, A. (1977), "Signal Analysis", McGraw-Hill.
- Oppenheim, A. V. and Schaffer, R. W. (1981). "Discrete-Time Signal Processing", Prentice-Hall.
- Izumi, M., Kurita, S., Endo, Y., Tobita, J. and Hanzawa, T. (1990), "Study on Causality of Transfer Functions and Components of Causal Transfer Functions in Systems of Seismic Wave Propagation in Soil", *Journal of Structural and Construction Engineering, Architectural Institute of Japan*, **412**, 31-41.
- Sato, T., Murono, Y. and Nishimura, A. (1999). "Modeling of phase characteristics of strong earthquake motion," Japan Society of Civil Engineers, *Journal of Structural and Earthquake Engineering*, **612/I-46**, 201-213.
- Sato, T. (2005), "Detection method of P-to-S converted Waves From Seismic Bedrock Using All-Pass function Deconvolved from Receiver Function," *Journal of Structural and Construction Engineering, Architectural Institute of*

Japan, **592**, 67-74.

- Shirai, K. and Ohmachi, T. (2005), "Correlation Between Horizontal and Vertical Components of Near-Field Strong Motions", *Proceedings of the 2nd International Conference on Urban Earthquake Engineering, Center for Urban Earthquake Engineering, Tokyo Institute of Technology*, 295-300.
- Izumi, M., Katsukura, H. and Ohno, S. (1988), "A Study on Deconvolution on Seismic Waves," *Journal of Structural and Construction Engineering, Architectural Institute of Japan*, **390**, pp27-33.
- Katsukura, H., Ohno, S. and Izumi, M. (1989), "Symmetrical FFT Technique and Its Applications to Earthquake Engineering", *Earthquake Engineering and Structural Dynamics*, **18**, 717-725.
- Sato, H. and Fehler, M. (1998), "Seismic Wave Propagation and Scattering in the Heterogeneous Earth," Springer-Verlag.
- Fukushima, Y. (1993). "Surface of Recent Studies on Attenuation Relation of Strong Ground Motion (Empirical Prediction Relation)." *Zishin Series 2, Seismological Society of Japan*, **46**, 315-328.

BI-DIRECTIONAL STRUCTURAL RESPONSE UNDER NEAR-FIELD GROUND MOTIONS

A. Ruangrassamee¹⁾, S. Siripala²⁾, and P. Lukkunaprasit³⁾

1) Assistant Professor, Department of Civil Engineering, Chulalongkorn University, Thailand

2) Structural Engineer, Black&Veatch (Thailand) Ltd., Thailand

*3) Professor, Department of Civil Engineering, Chulalongkorn University, Thailand
fcearr@eng.chula.ac.th, siripalas@bv.com, lpnitan@chula.ac.th*

Abstract: In seismic design of structures, excitations are usually considered separately in two perpendicular directions of structures. In fact, the two components of ground motions occur simultaneously. The directivity effects of near-field ground motions may cause the deviation from the conventional procedure in the codes. This paper clarifies the bi-directional response of structures subjected to bi-directional excitations from near-field earthquakes and proposes the response spectra called “response spectra with bi-directional excitation effects.” A simplified analytical model of a two-degree-of-freedom system is employed. In the development of the spectra, 30 horizontal near-field ground motion records from rock, stiff soil and soft soil sites are considered. The effect of directivity of ground motions is taken into account by applying strong motion records in all directions. The analytical results are presented in the form of the displacement ratio response spectrum defined as the radial displacement response spectrum normalized by a conventional displacement response spectrum. In addition, the direction response spectrum is also presented to identify the direction of the maximum radial displacement. The result shows that maximum radial displacement occurs in the angle with the highest spectrum intensity of the ground motion acting in the longer period axis. It is found that natural periods in two horizontal axes of the structure and the angle of a ground motion significantly affect the displacement ratio response spectra and the direction response spectra.

1. INTRODUCTION

It has been found from past studies that bridge columns under bi-directional excitations have less strength and ductility than those under uni-directional excitations (Olivia and Clough 1987, Zeris and Mahin 1991, and Wong et. al. 1993). In the current seismic design codes, excitations are considered separately in two perpendicular directions of structures and combined using a certain combination rule (AASHTO 2002). In fact, the two horizontal components of ground motions occur simultaneously and results in the damage to structures. The directivity effects of near-field ground motions may also cause the deviation from the conventional procedure in the codes. The effect of bi-directional excitation of structures with different natural periods in two orthogonal axes needs to be clarified for proper design. This paper clarifies the bi-directional response of structures subjected to bi-directional excitations from near-field earthquakes and proposes the response spectra called “response spectra with bi-directional excitation effects.”

2. ANALYTICAL MODEL AND PARAMETERS

A linear two-degree-of-freedom system is employed to investigate the bi-directional response of a bridge subjected to two horizontal components of ground motions. Figure 1 shows the idealized model.

The mass is subjected to the ground excitation in the x- and y- axes. The stiffness and damping in each direction are idealized as a linear spring and a viscous damper, respectively. The degrees of freedom are the translations in the x- and y-axes. Since the system is linear and uncoupled between both axes, dynamic properties of both axes can be expressed independently. The natural periods for x- and y- axes are defined as T_x and T_y , respectively. And the damping ratios are ξ_x and ξ_y for the x- and y- axes, respectively. The natural periods are varied from 0.05 s to 4 s to cover typical range of natural periods of bridges and the damping ratio is assumed as 0.05, typical for reinforced-concrete bridges.

The directivity effect is significant in near-fault ground shaking. To investigate the effect, 30 near-fault ground motion records are used in the analysis. The records are obtained from the stations located within 20 km from epicenters of earthquakes with magnitudes from 6.0 to 7.6. There are 10 records for three site conditions which are rock, stiff soil, and soft soil sites. The angle for applying the ground motion to the analytical model, θ , is varied from 0 to 360 degree with an interval of 5 degree. The angle reflects the fact that the ground motion may excite a structure at any direction with respect to the principle axes of the structure.

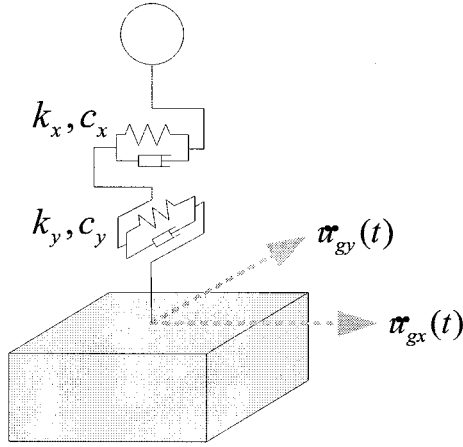


Figure 1 Idealized model for analysis

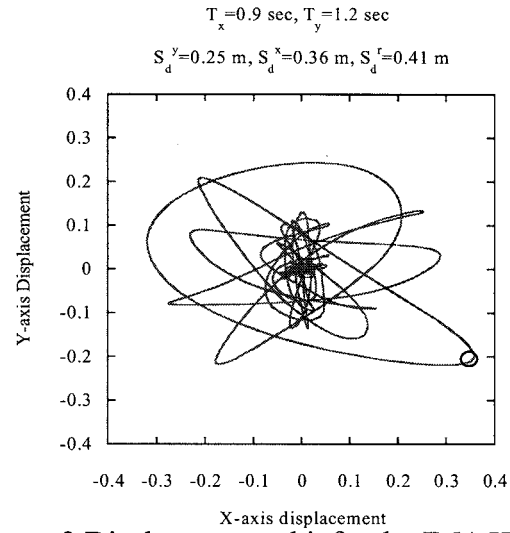


Figure 2 Displacement orbit for the JMA Kobe record

3. DEFINITION AND EXAMPLE OF PROPOSED RESPONSE SPECTRA

From Figure 1, the displacements in the x- and y- axes are expressed as $u_x(T_x, \theta, t)$ and $u_y(T_y, \theta, t)$, respectively. The radial displacement can be computed from

$$u_r(T_x, T_y, \theta, t) = \sqrt{(u_x(T_x, \theta, t))^2 + (u_y(T_y, \theta, t))^2} \quad (1)$$

Figure 2 shows the displacement orbit of a system with $T_x = 0.9$ s, $T_y = 1.2$ s, and $\theta = 0$ for the JMA Kobe record. The radial displacement is 0.41 m while the maximum displacements in the x- and y- axes are 0.36 m and 0.25 m, respectively. It is obvious that the radial displacement is larger than the displacements in the principle axes of the system. A radial displacement response spectrum can be obtained by determining the maximum radial displacement for various T_x , T_y , and θ . The radial displacement response spectrum is a function of T_x , T_y , and θ as follows

$$S_d^r(T_x, T_y, \theta) = \max_t |u_r(T_x, T_y, \theta, t)| \quad (2)$$

Figure 3 shows $S_d^r(T_x, T_y, \theta)$ for different angles. In the design, the angle of ground motion components is not predictable except at the location of known faults. It is conservative to consider any

possible angle. The radial response spectrum obtained from the maximum values for any angle should be used. It can be expressed as

$$\tilde{S}_d^r(T_x, T_y) = \max_{\theta} |S_d^r(T_x, T_y, \theta)| \quad (3)$$

Figure 4 shows $\tilde{S}_d^r(T_x, T_y)$ for the JMA Kobe record. The maximum value is about 0.5 m. The spectrum is symmetric about the line $T_x = T_y$. The conventional displacement response spectrum can be expressed as

$$\tilde{S}_d^x(T_x, T_y) = \max(S_d^x(T_x, \theta = 0), S_d^x(T_y, \theta = 0)) \quad (4)$$

where $S_d^x(T_x, \theta = 0)$ is the spectral displacement of the x-component ground motion for $\theta = 0$ and various T_x ; and $S_d^x(T_y, \theta = 0)$ is the spectral displacement of the x-component ground motion for $\theta = 0$ and various T_y . Figure 5 shows $\tilde{S}_d^x(T_x, T_y)$ for the JMA Kobe record. The ratio of Equation (3) to Equation (4) represents the amplification of the displacement when considering the bi-directional excitation. The displacement ratio response spectrum is expressed as

$$R(T_x, T_y) = \frac{\tilde{S}_d^r(T_x, T_y)}{\tilde{S}_d^x(T_x, T_y)} \quad (5)$$

The displacement ratio response spectrum is shown in Figure 6. The value is larger than one and increases as the difference between the natural periods increases. In addition to the radial displacement, it is equally important to know the direction where the maximum radial displacement occurs. The direction response spectrum is defined as

$$\tilde{\alpha}(T_x, T_y) = \alpha(T_x, T_y, \theta : \max S_d^r) \quad (6)$$

where

$$\alpha(T_x, T_y, \theta) = \tan^{-1} \left(\frac{u_y(T_y, \theta, t : \max |u^r|)}{u_x(T_x, \theta, t : \max |u^r|)} \right)$$

The direction is measured counter-clockwise from the x- axis. Figure 7 shows $\tilde{\alpha}(T_x, T_y)$ for the JMA Kobe record. When T_y is close to zero, meaning that the system is rigid in the y axis, the displacement inclines to the x axis (the direction is close to 0 degree.). When T_x is close to zero, meaning that the system is rigid in the x axis, the displacement inclines to the y axis (the direction is close to 90 degree.).

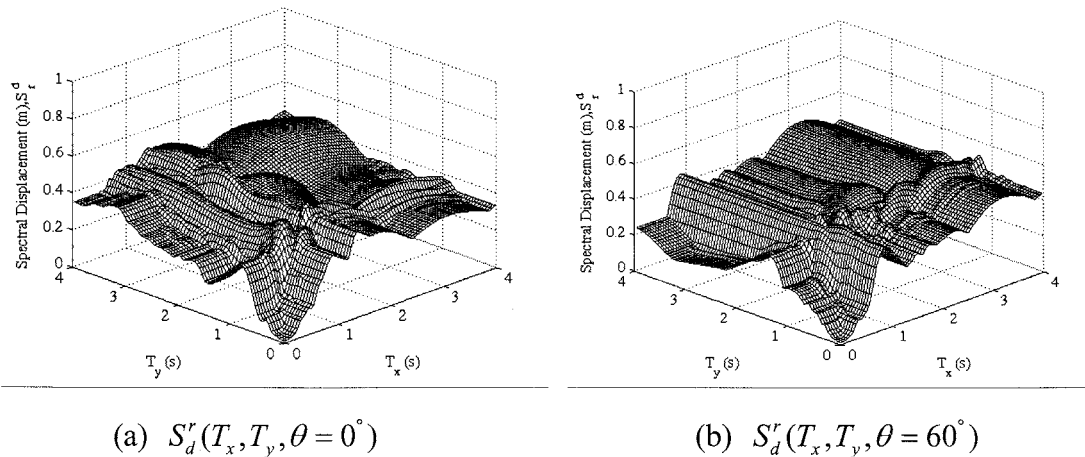


Figure 3 Radial displacement response spectra for the JMA Kobe record

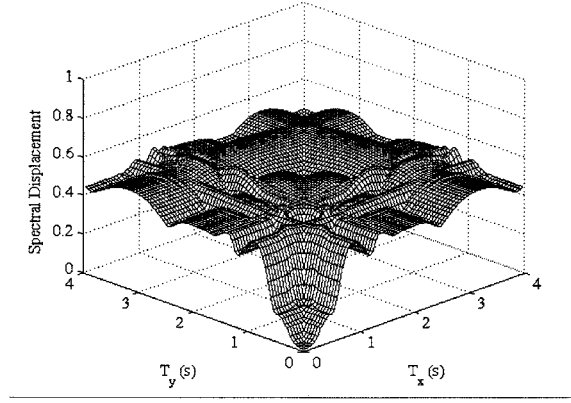


Figure 4 $S_d^y(T_x, T_y)$ for the JMA Kobe record

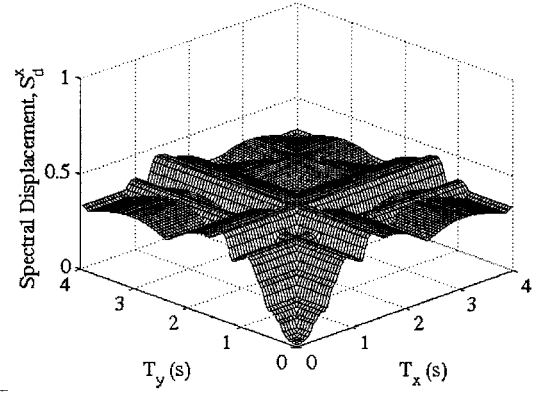


Figure 5 $S_d^x(T_x, T_y)$ for the JMA Kobe record

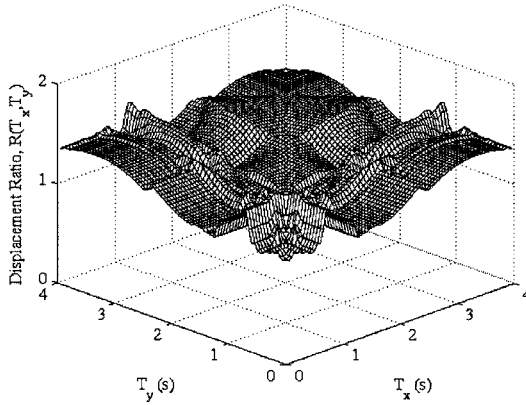


Figure 6 $R(T_x, T_y)$ for the JMA Kobe record

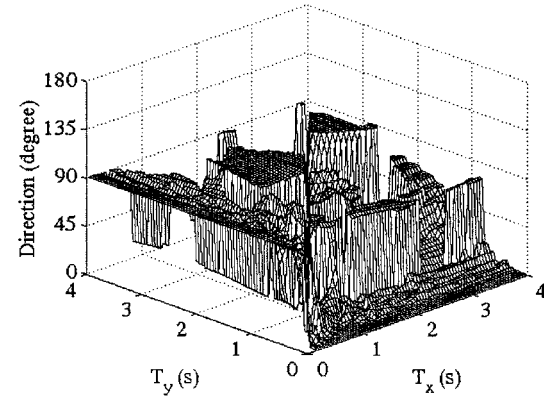


Figure 7 $\alpha(T_x, T_y)$ for the JMA Kobe record

4. CHARACTERISTICS OF RESPONSE SPECTRA

In order to explain the effects of parameters on the response spectra, it is important to define a parameter representing the amount of directivity inherited in a ground motion record. The displacement spectral intensity $I_d(\theta)$ is defined as

••

$$I_d(\theta) = \int_{T_1}^{T_2} S_d^x(T, \theta) dT \quad (7)$$

where $S_d^x(T, \theta)$ is the displacement response spectrum of the x component of a record. $I_d(\theta)$ is the area under a displacement response spectrum from a natural period of T_1 to a natural period of T_2 . Figure 8 is obtained from computing $S_d^x(T, \theta)$ at the angle θ of the maximum $I_d(\theta)$ divided by $S_d^x(T_x, \theta)$ at the angle perpendicular to that for all ground motions and averaging the values for three site conditions. Figure 8 presents the amount of directivity for different site conditions. It is seen that the ratio of the spectral displacement is large for rock sites and small for soft soil sites. Figure 9 shows the direction of the maximum displacement of systems with the same T_x and T_y . It is obvious that the displacement is biased to the same direction. It is found that the direction corresponds to the direction with the maximum displacement spectral intensity.

From a series of analyses, it is found that there is not consistent relationship among $R(T_x, T_y)$,

epicentral distance, and earthquake magnitudes. The mean plus standard deviation and mean $R(T_x, T_y)$ are developed as shown in Figure 10. It is clear that site conditions have a significant effect on $R(T_x, T_y)$ due to the directivity shown in Figure 8. The mean displacement ratio response spectra have values about 1.1-1.7 for rock sites, 1.1-1.6 for stiff soil sites and 1.1-1.4 for soft soil sites. And the value increases as the different between T_x and T_y increases. The mean $\phi(T_x, T_y)$ is also proposed to use with $R(T_x, T_y)$ for determining the maximum displacement in each axis.

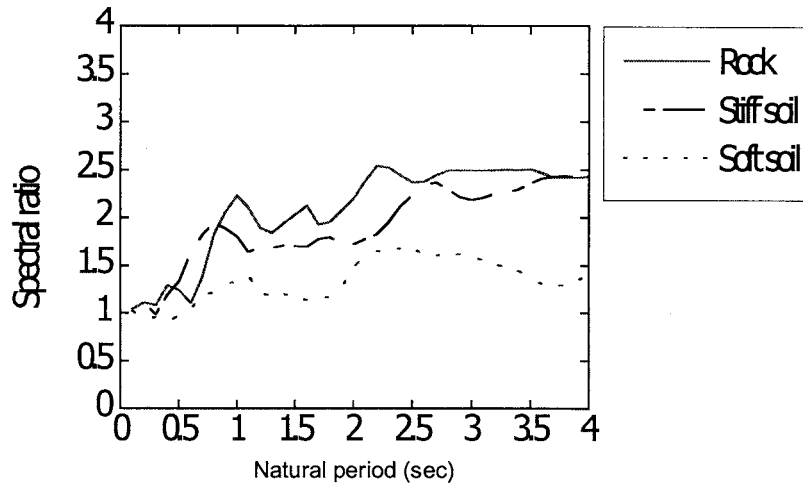
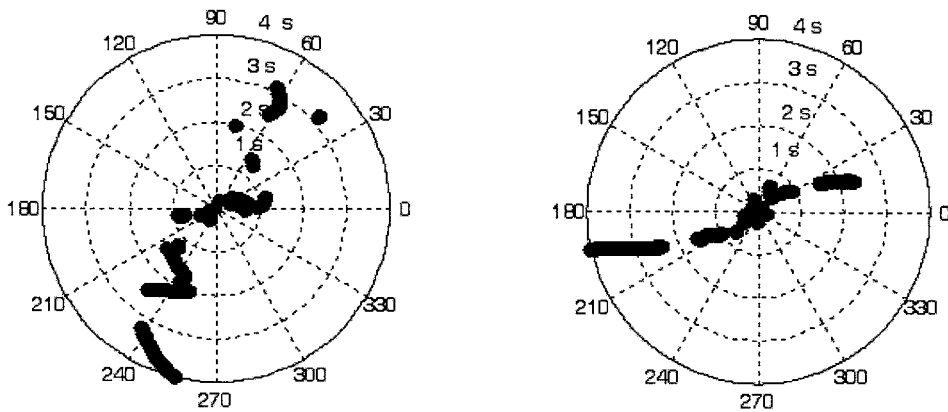


Figure 8 Average spectral ratios for various site conditions



(a) 1966 Parkfield, Temblor record

(b) 1971 San Fernando Pacoima Dam record

Figure 9 Direction of maximum radial displacements for $T_x = T_y$

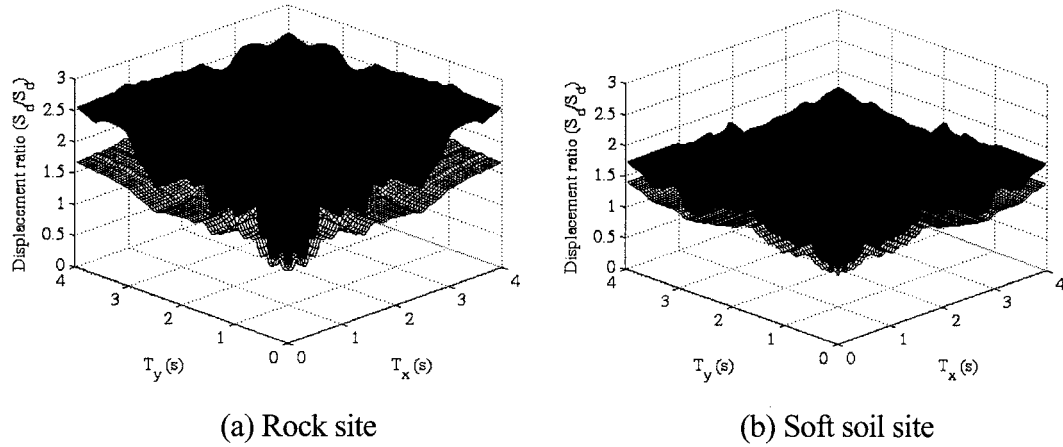


Figure 10 Mean plus standard deviation and mean $R(T_x, T_y)$

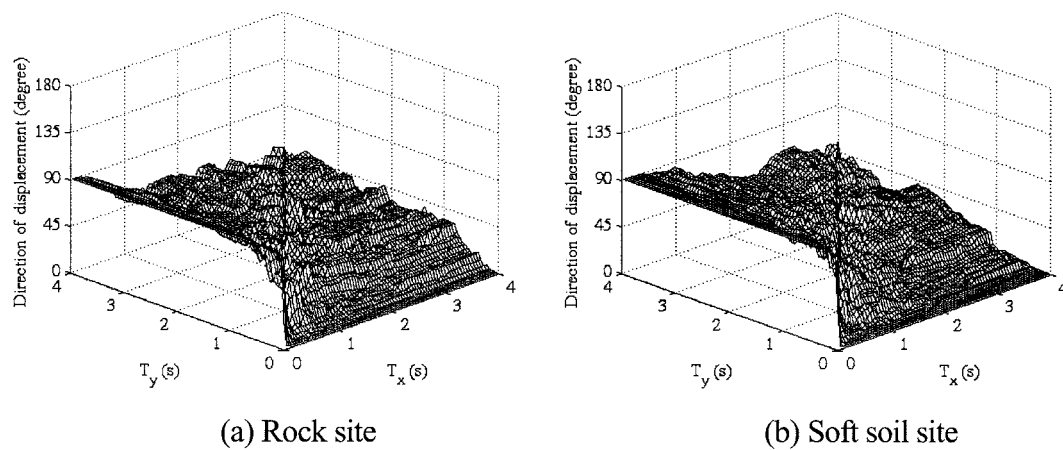


Figure 11 Mean $\alpha(T_x, T_y)$

5. CONCLUSIONS

In this research, the displacement response spectra with bi-directional excitation effects are proposed. The result shows that maximum radial displacement occurs in the angle with the highest spectrum intensity of the ground motion. It is found that natural periods in two horizontal axes of the structure and the angle of a ground motion significantly affect the displacement ratio response spectra and the direction response spectra. The maximum radial displacement tends to occur in the axis of a longer period. The mean displacement ratio response spectra have values about 1.1-1.7 for rock sites, 1.1-1.6 for stiff soil sites and 1.1-1.4 for soft soil sites. The amount is larger than the 30% rule used in current design codes.

References:

- American Association of State and Highway Transportation Officials (2002), "Standard Specifications for Highway Bridges," 17th Edition, AASHTO.
- Olivia, M. G. and Clough, R. W. (1987), "Biaxial Seismic Response of R/C Frames". *Journal of Structural Engineering*, American Society of Civil Engineers, **113**, 1264-1281.
- Wong, Y. L., Paulay, T., and Priestley, M. J. N. (1993), "Response of Circular Reinforced Concrete Columns to Multi-Directional Seismic Attack". *Structural Journal*, American Concrete Institute, **90**, 180-191.
- Zeris, C. A. and Mahin, S. A. (1991), "Behavior of Reinforced Concrete Structures Subjected to Biaxial Excitation". *Journal of Structural Engineering*, American Society of Civil Engineers, **117**, 2657-2673.

A MODEL OF BEDROCK STRUCTURE FOR HSINCHU BASIN, TAIWAN USING GRAVITY SURVEY

H. Morikawa¹⁾, M. Komazawa²⁾, H.T. Chen³⁾, T. Shosaka⁴⁾, and C. Takahasi⁵⁾

1) Associate Professor, Department of Built Environment, Tokyo Institute of Technology, Japan

2) Senior Researcher, Geological Survey of Japan, AIST, Japan

3) Associate Professor, Department of Civil Engineering, National Central University, Taiwan

*4) Undergraduate Student, Department of International Development Engineering,
Tokyo Institute of Technology, Japan*

*5) Graduate Student, Department of Built Environment, Tokyo Institute of Technology, Japan
morika@enveng.titech.ac.jp, komazawa-m@aist.go.jp, chenhtofpadau@seed.net.tw,*

shosaka@enveng.titech.ac.jp, tchika@enveng.titech.ac.jp

Abstract: To obtain the detailed model of the three-dimensional ground structure, the gravity survey is carried out around Hsinchu area, Taiwan. The observations at 393 sites have been carried out and the structure with some different scales are found from the Bouguer anomaly. The trend of the Bouguer anomaly is independent of the topography and some localized structures are observed.

1. INTRODUCTION

To estimate the earthquake ground motions, it is very important to know the ground structure, especially, deep and three-dimensional structure, because the ground motions excited by a large earthquake predominate components with long period which relates to the deep structure. For this purpose, we have many kinds of technique for the geological survey, though some of them may be costly. The microtremor and gravity survey are easy to conduct the survey and not so expensive techniques. Thus, for estimating the three-dimensional ground structure over a large area, these techniques are useful and provide good information without much cost. Especially, the gravity survey is suitable for the survey of very large area and can provide detailed configuration of bedrock, because of the easy operation by means of the automatic gravimeter and GPS (global positioning system).

The geological setting of Taiwan is really complicated because there is the boundary between the Eurasia and Philippine plates and we can find so many active faults in the Taiwan island. This means that the seismic activity is very high in Taiwan. Under this circumstance, we focus the target for gravity survey on Hsinchu city, where many industrial factories, especially for IT, computer, and semiconductor companies are located. Thus, we may say that Hsinchu area should be key for the Taiwanese economy.

From this, we can say that it is very important to know the ground structure and to estimate some strong ground motions in this area. As a first step to estimate earthquake ground motion for earthquake disaster mitigation, we will try to make a preliminary model of three-dimensional shape of the surface for the bedrock which is defined, hereafter, as hard rock with shear wave velocity of more than 3 km/s.

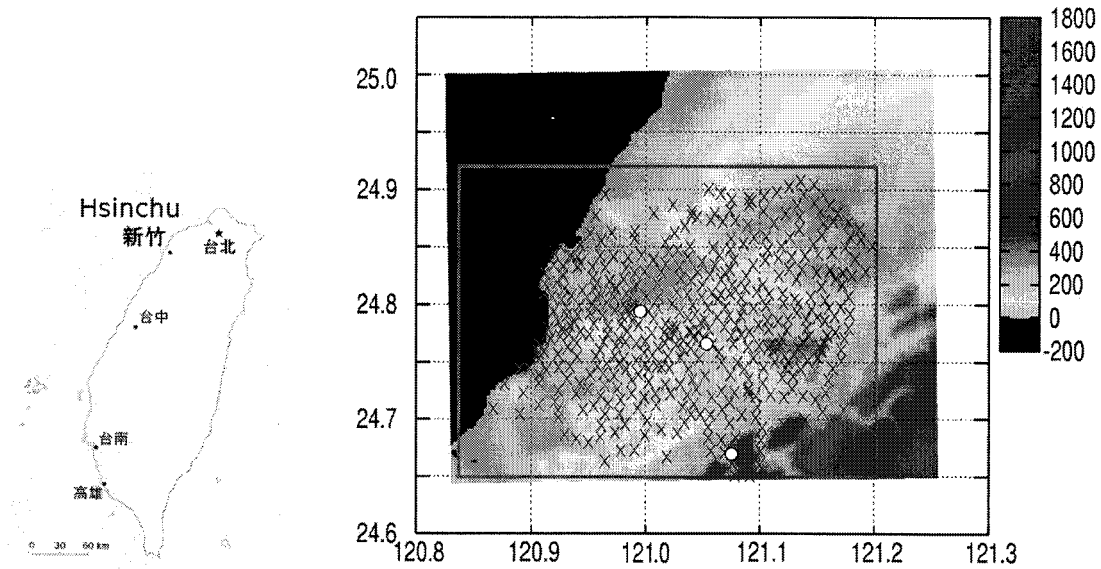


Figure 1 Observation sites of the gravity and the topography around Hsinchu city. The open circles (○) stand for control points to analyze the bedrock structure, cross symbols (×) for the observation sites. The large square indicates the observation area, where corresponds to the area of the following maps for Bouguer anomaly and gravity basement.



Figure 2 Observation system for the gravity. GPS receiver and its antenna on the tripod, and LaCoste & Romberg Gravimeter (Type G) below them.

2. OBSERVATIONS

To obtain the three-dimensional ground structure at Hsinchu city accurately, we carried out the measurements of gravity at its surrounding area, which includes many towns in Hsinchu County: $24^{\circ}39'N - 24^{\circ}55'N \times 120^{\circ}50'E - 121^{\circ}12'E$: that is, 33km NS \times 40km EW.

Firstly, we set a reference site with absolute gravity value in Hsinchu city through the comparison between our reference site and the official gravity base site. Then, using the reference site, we carried out the relative observations of gravity and the absolute values of the gravity were determined at each site. The data at 393 sites were obtained during 7th to 28th September, 2006. The location of the observation sites are shown Figure 1 over the topographical map.

For the observation, we use the Burris automatic gravity meter by ZLS Corporation and Type G Gravimeter by LaCoste & Romberg. To determine the position of the observation site accurately, the differential survey using the GPS (Global Positioning System) is performed. As a result, the error of the horizontal and vertical position is less than 1m. The observation system are shown in Figure 2.

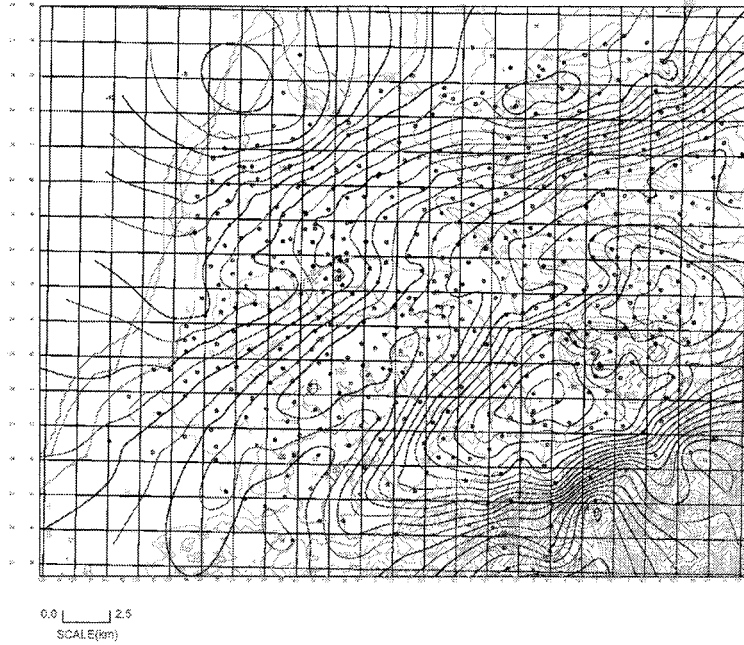


Figure 3 Bouguer anomaly map around Hsinchu area. For this analysis, gravity data at 453 sites, which includes 60 existent data, are used. In this figure, we used the following parameters: assumed density = 2.1 t/m³; contour interval = 1 mGal.

3. RESULTS AND DISCUSSION

We analyze our own data at 393 sites with the existent gravity data, which were obtained at 60 sites in this area. After some data correction such as corrections for height of the instrument, tide, drift, terrain, free-air, and Bouguer correction, the Bouguer anomaly can be obtained. For the Bouguer correction, we have to give a value of assumed density ρ . For this purpose, some methods are proposed such as the G-H relation method (Komazawa, 1988), and a method to check the correlation between the Bouguer anomaly map and topography. We apply the latter technique and determine ρ as 2.1 t/m³, which corresponds to the density of sediment.

The obtained Bouguer anomaly map is shown in Figure 3. From this figure, we can summarize the feature of the Bouguer anomaly as follows:

- The Bouguer anomaly in the target area is negative and the negative anomaly increases from north-west to south-east. This trend is independent of the topography of the hilly area.
- Around the south-eastern area of the Hsinchu city, minimum value of the Bouguer anomaly is found. This minimum value seems to correspond to the local minimum which is shown in the Bouguer anomaly map for whole Taiwan island.
- For most parts of south-eastern area, it is observed that the steep change in Bouguer anomaly corresponds to the topography. This suggests the existence of steep slope of the bedrock in this area.
- We may find some small scale structure like a dike in the southern area of Hsinchu city.

Furthermore, we estimate the 3-D gravity basement under the assumption that the ground consists of two layers and the sediment and basement are homogeneous with density of 2.1 and 2.4 t/m³, respectively.

To obtain a realistic model of gravity basement, we consider the follows: to remove the contribution for the Bouguer anomaly from the deep structure such as upper mantle and to constrain the depth to the bedrock using some other information. For the former, a band-pass filter is applied to the Bouguer anomaly. For the latter, we give some control points, that is, 3

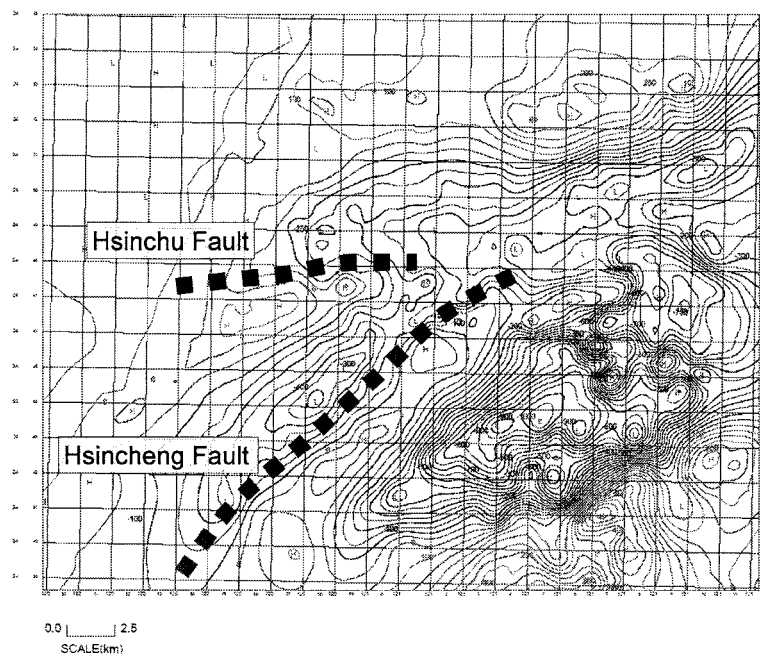


Figure 4 Depth to the gravity basement estimated from the Bouguer anomaly. To obtain this map, we assume a two layered medium: the one is bedrock with 2.4 t/m^3 and the other is sediment with 2.1 t/m^3 of density. It is observed that some remarkable structure corresponds to the known fault.

sites from deep boreholes which reach to the bedrock. The 3-D shape of the gravity basement, which is calculated by using a method proposed by Komazawa (1998), is shown in Figure 4.

Consequently, depth of the gravity basement reaches to about 1200 m in the south-eastern area and about 200m around the downtown of Hsinchu City. Furthermore, steep slopes of the gravity basement are observed around the southern area of Hsinchu City, whose location corresponds to the known fault; Hsinchu and Hsincheng faults.

4. CONCLUSIONS

We have carried out the gravity observation at 393 sites around Hsinchu area, Taiwan. Using this data, we estimated the Bouguer anomaly and gravity basement around this area. From this, we can say that the three-dimensional structure is very complicated: some different scales of structure are found.

Acknowledgments:

The authors wish to express their gratitude for the support of gravity data in Taiwan from Professor Cheinway Hwang of department of civil engineering, National Chiao Tung University, Taiwan and Ministry of Interior, Taiwan, Republic of China. Furthermore, we gratefully acknowledge helpful discussions and valuable comments with Profs. K.-L. Wen and H.-Y. Yen of Institute of Geophysics, National Central University, Taiwan, Republic of China. The following students of graduate school of civil engineering, National Central University, Taiwan are also gratefully acknowledged for their kind supports for the gravity observation in Hsinchu area: Mr. Dong-Ching Lin, Mr. Rey-Yung Chen, Mr. Jen-Jei Wu, Mr. Shan-Ming Hwang, and Mr. Wen-Shi Hwang.

References:

Komazawa, M. (1998) Gravity survey, *Handbook of Exploration Geophysics*, Vol.4, Society of Exploration Geophysicists of Japan.

SOME EXAMPLES SHOWING VERY VULNERABLE CONDITION IN EARTHQUAKE COUNTRIES

Kazuoh SEO

*Professor, Department of Built Environment, Tokyo Institute of Technology, Japan
seo@enveng.titech.ac.jp*

Abstract: When we visit some district after a natural disaster caused by earthquake, volcanic eruption or heavy rain, we wonder why people must live in such dangerous condition. In this report, some examples showing very vulnerable condition against natural disasters will be presented. Some of them could be seen in developing districts but some others in modern cities. It should be pointed out that some vulnerable condition against natural hazards could be made not only because of poor economy, but also because of lack of engineering sense.

1. INTRODUCTION

It is believed in general that we will learn much more lessons through a failure rather than a success. For this reason, it is very important to visit a damaged area just after a natural disaster and to have some kind of new findings in such failures. After that, we will make very careful evaluation to identify them, what are very useful even in the future, what are solved already, and what are not so important anymore. In the process of such integration among natural disasters in different types, in different countries, and in different ages, we will find some interesting lessons. Some of the lessons as new findings look quite similar among very different and distant districts. Some of examples will be presented in the following chapters.

2. TWELVE YEARS SINCE THE 1995 KOBE EARTHQUAKE

Twelve years have already passed since the 1995 Kobe earthquake. Every year on January 17, local governments in Hyogo prefecture hold some memorial events to keep the disaster in their mind. Such events are reported by mass communication with some comments. But after a while, maybe next day or after a couple of days, the related news goes away from newspapers as if nobody shows interest on it anymore. Have we finished learning from the 1995 Kobe earthquake? No we haven't. We need to learn the further lessons from the Kobe earthquake to make sure very vulnerable condition still remained around the damaged districts, and to transfer such knowledge to other districts where we may have similar disasters.

2.1 How to count the amount of casualties during the disaster?

Just after the earthquake, nobody could estimate the amount of casualties at all. According to TV news and/or newspapers, they have reported 22 deaths after 4 hours, and 203 total deaths after 6 hours from the earthquake. The reports continued as 1,407 deaths at midnight, 1,885 deaths next day

morning, 4,057 deaths after two days, 5,096 deaths after two weeks. Finally they estimated the total amount of direct deaths as 5,500, most of victims buried under collapsed houses and some others by big fires. Further more, the official number of total deaths was presented as 6,433 after one year from the earthquake. Additional 900 were regarded as indirect deaths (some of them are called as solitary deaths) caused by illnesses, alcohol dependencies and even suicides within five years in evacuation temporal houses those were completely closed after five years from the earthquake.



Photo 1 Temporal houses prepared after the 1995 Kobe earthquake.

It was so good that the government took such indirect victims into account as the first attempt. But one question remains why they stopped counting the number of victims after five years? Maybe we need a definition identifying indirect victims. Otherwise we are not sure how to count the amount of victims for individual disaster. And the number of indirect victims will increase year by year. According to recent newspaper, additional 400 and more deaths were confirmed after five to ten years from the 1995 earthquake in reconstructed houses. Such condition looks very uncertain and vulnerable, doesn't it?

2.2 How to evaluate the improvements of building structural engineering?

According to many technical reports after the 1995 Kobe earthquake (for example Tohdo, 1998), the revision of the Japanese Building Code in 1971 and in 1981 seems to have been very successful. The most of collapsed and heavily damaged buildings during the 1995 earthquake were constructed using the older building code. On the other hand, the buildings constructed with the newer code did not collapse so much in the 1995 earthquake. Such statistical results could be seen in Fig.1. We could not have enough time to discuss moderate and slight damage in detail because of amount of collapsed buildings and houses. Then in our general understanding, the revision of the building code in 1971 and in 1981 was confirmed very well through the damage characteristics of buildings.

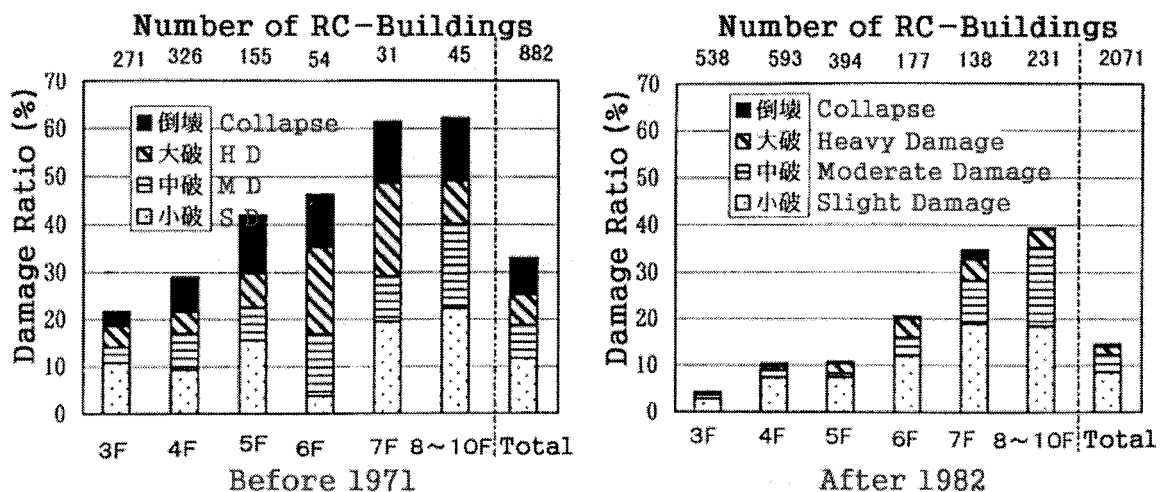


Fig.1 Quite different damage ratios of RC-buildings during the 1995 Kobe earthquake between constructions with the older building code (the left) and the newer code (the right). after Tohdo (1998)

Situation of the 2005 Fukuoka-Oki earthquake with M7 was quite different. At that time, most of damage was moderate and/or slight in building structures those were distributed in urban areas of the

modern city. The point in this case was that such damage could be seen mostly in non-engineering parts of the newer buildings within five years since the construction rather than the older ones. It means that the structural design of buildings became very critical. It can be explained also that modern cities have become more vulnerable than before. The problem in such non-engineering damage must be that even non-engineering failure is serious enough to kill residential people. It was just fortunate that the 2005 earthquake did not kill the people only because it took place in a Sunday morning.

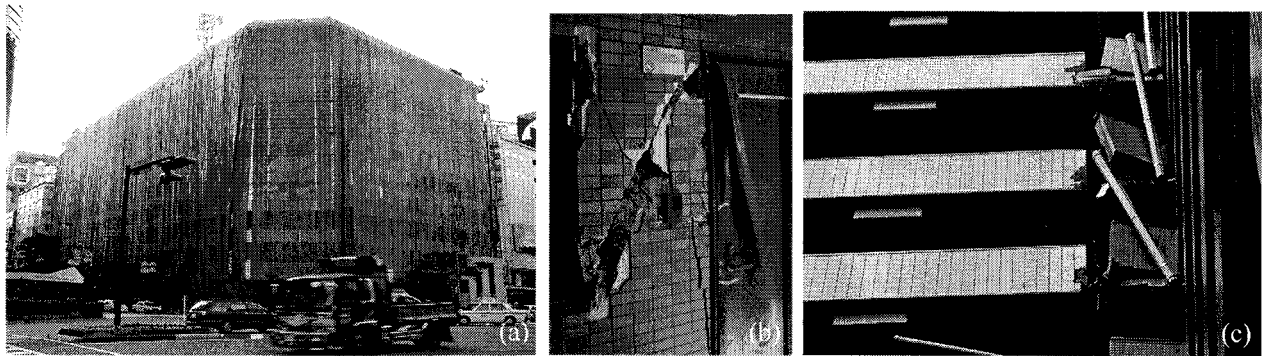


Photo 2 Non-engineering damage during the 2005 Fukuoka-Oki earthquake. Failure of window glasses (a), failure of entrance door by the neighboring non-engineering wall (b), and failure of expansion-joint (c).

2.3 How to maintain the policy about infrastructures such as railways and highways?

In the 1995 Kobe earthquake, very primitive failures were found mostly in public transportation facilities such as railways and highways. The authority revised the seismic code and made very quick reinforcement works. But it is questionable whether they have made very careful surveys to find true reasons of the failures or not. Because they have demolished the failures very quickly. The experience may be useful in similar cases with the 1995 earthquake, but it is uncertain that the experience in Kobe could be also effective in different type of earthquakes. Therefore vulnerable condition still remains in the future.



Photo 3 Highway structure collapsed during the 1995 Kobe earthquake. Photo before the earthquake (a), Just after the earthquake (b), and after 18 months from the earthquake (c).

3. SIMILAR CONDITION BETWEEN DIFFERENT DISTRICTS

When we visit some places affected by natural disasters, we often feel a kind of similar condition with some area where we have been there. The followings are some of such examples. It is fortunate if you feel some kind of similarity between two districts.

3.1 Caracas and Kobe

Caracas, the capital of Venezuela, is located in a deep sediments in a valley between mountains with more than 2,000 meters in altitude. As an active fault that can excite M7 earthquake exists at the foot of the northern mountain, Caracas city has the possibility to suffer a major earthquake. The area

shows very high seismicity, because the location is just on the border of very active Caribbean plate. At the same time, Caracas city showed a very quick development with full of tall and soft buildings, then it looks quite vulnerable in this coming major earthquake. Such condition looks quite similar with Kobe city before the 1995 earthquake. You can compare the scenes with the following pictures.

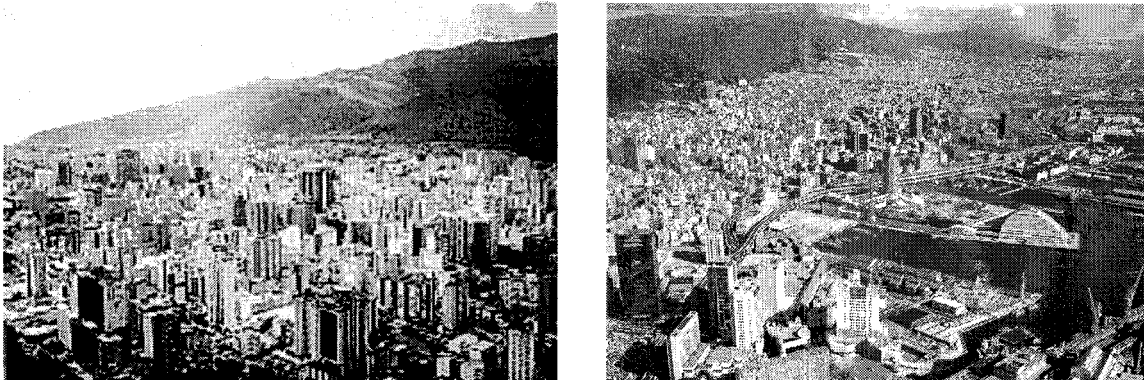


Photo 4 Similar condition between Caracas (the left) and Kobe (the right) because of existing very quick developments in city areas and having active faults those may trigger M7 earthquakes.

3.2 El Salvador and Kagoshima

El Salvador is a volcanic and seismic country located between Cocos plate in the Pacific Ocean and Caribbean plate. The most of the land is covered with volcanic ashes, they call it “tierra blanca (white soil)”, because volcanic activities are so often. Very thick volcanic sediments show erosion during rainy seasons and they make huge scale of slopes everywhere in the country. Heavy rain falls every year and earthquakes with the period of several ten years collapse such vulnerable slopes. Then microzonation studies for natural disasters seem very important. Such condition can be compared with the similar volcanic condition in Kagoshima, Kyusyu Island, Japan. Very similar sedimentation of volcanic ashes, they call it “Shirasu (the meaning is also white soil)”, is found around the Kagoshima Bay (the Aira Caldera of 20 thousands years ago). They collapse with some frequency around a hundred years, and a heavy rain or a major earthquake will trigger the collapse. In Kagoshima, they have a lot of experiences how to maintain such slopes. Therefore we are sure that some cooperation from Kagoshima to El Salvador may be possible in the future.

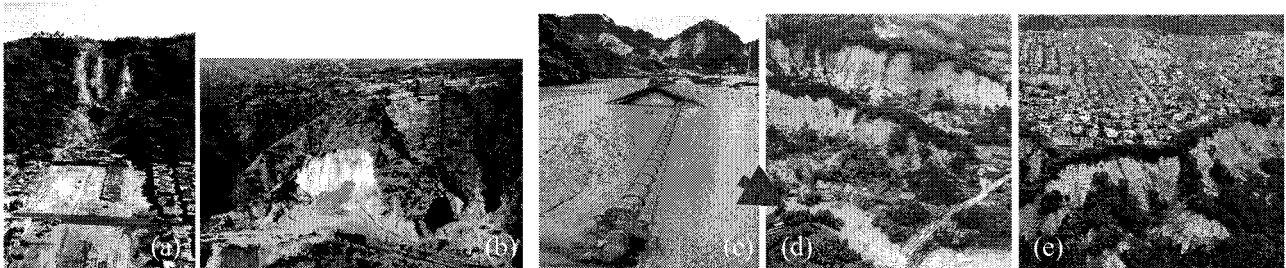


Photo 5 Similar condition between El Salvador and Kagoshima in terms of slope failures. Large scale slope failures due to the 2001 earthquake in El Salvador (a) and (b), and also slope failures due to heavy rain of 1993 in Kagoshima (c), (d) and (e).

3.3 Armenia and Cuba

What is the similarity between Armenia and Cuba? They look quite different and look to have no relation at all. For example, a similar condition between them is that they have been members of Soviet Union, and they expected too much on Soviet Union, not only in politics but also in economy, culture, science and engineering. Another similarity we can find in Armenia and Cuba could be very high seismicity. In fact, the 1988 Spitak earthquake in Armenia brought 25 thousand deaths in minimum, great number of damage in building structures and economic activities. Yerevan, the capital

of Armenia, was saved from the earthquake because of far distance, but the capital still remains in very vulnerable condition in future earthquakes. Cuba is also put in vulnerable condition since the collapse of Soviet Union in 1991. Santiago de Cuba, the former capital of Cuba, faces to have M7 earthquake, which may occur in the Caribbean trench. Building structures in Cuba are identified in two types. One was constructed by Spanish people and then after Americans painted in color. Another one was constructed by the technology of Soviet Union. Both of them look very vulnerable because there was no support to maintain such buildings after the collapse of Soviet Union. You will find vulnerable framed precast reinforced concrete (RPC) structures everywhere in Armenia and Cuba even now.

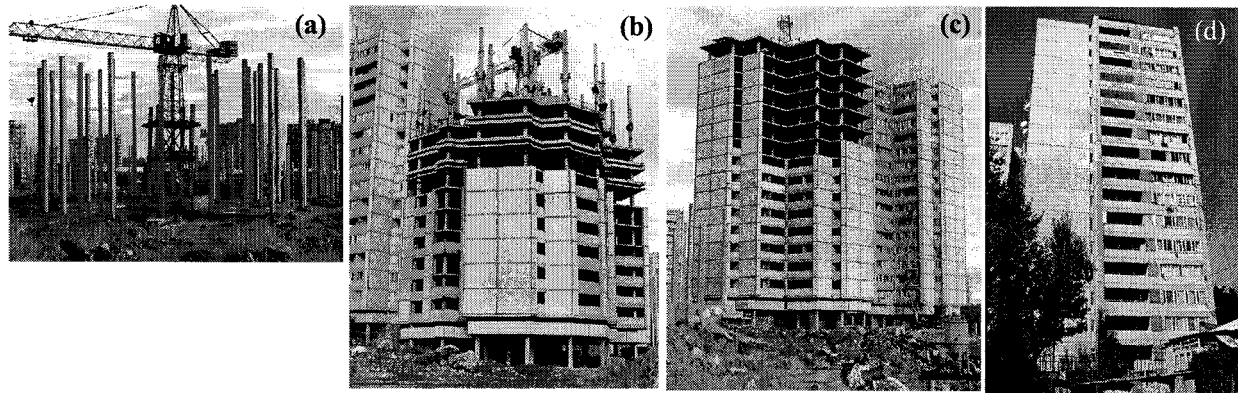


Photo 6 Construction of tall buildings with lift-slab method in Yerevan, Armenia, has kept stopping since 1991 (a). There is no wall on the ground level, and outer walls in upper floors are non-seismic (b), (c). Another RPC structure with 16 floors in Yerevan (d).

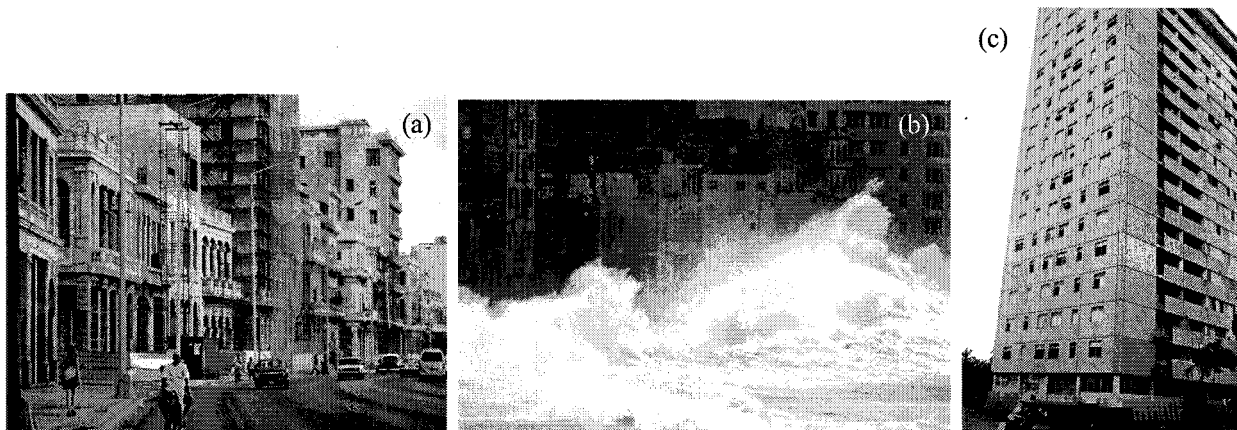


Photo 7 Weathered Spanish buildings in Havana, Cuba, (a), those were attacked by Hurricane Wilma in 2005 (b). Similar RPC structure with 18 floors in Santiago de Cuba (c).

4. VULNERABLE DEVELOPMENTS IN VERY HIGH SEISMICITY

One of the most popular structures in the world might be reinforced concrete framed building structure with non-engineering walls. We can find such building structures everywhere in the southern Europe and northern Africa along the Mediterranean Sea, and Latin American countries. Besides the vulnerability of structures themselves, the manner of development also seems quite vulnerable. We can see the most typical example in Granada city, Spain, but the similar developments have been taken into account everywhere in the world. In the first stage, a foot of a mountain with very comfortable condition has been developed. Then an area in the lower neighboring level could be developed. Finally in accordance with the increase of population, the central basin areas with soft and uncomfortable condition must be developed because they cannot choose any other places. After such developments, natural disasters like earthquakes, heavy rains or hurricanes will attack the districts. It is very sure the

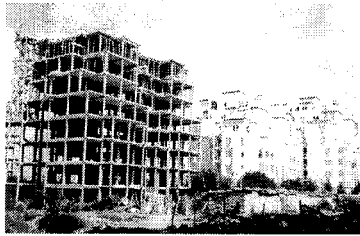


Photo 8 Very vulnerable RC framed structures with non-engineering walls in Morocco.



Photo 9 City developments in Granada, Spain. The first development by Moor people (a), secondary by Spanish people in the Middle Ages (b), and recent development toward the central basin (c).

heaviest damage will be found in the most vulnerable part of a city, where is the newly developed area.

A serious question is whether we have similar or related vulnerable condition in Japan as in earthquake countries or not? How can we say there is no problem in Japan? The author is hesitating to present very vulnerable examples those can be seen in Japanese modern urbanized areas in this report. Such examples may appear in our poster session.

5. CONCLUSIONS

When we visit some district after a natural disaster caused by earthquake, volcanic eruption or heavy rain, we wonder why people must live in such dangerous and vulnerable condition. In this report, some examples showing very vulnerable condition against natural disasters were presented. Some of them could be seen in developing districts but some others in modern cities. It should be pointed out that some vulnerable condition against natural hazards could be made not only because of poor economy, but also because of lack of engineering sense. The most of such cases will require huge amount of financial supports. But at any rate all we have to do now is to start finding such cases around us for more discussion how to solve the condition.

Acknowledgements:

The author acknowledges support from Japan Ministry of Education, Culture, Sport, Science, and Technology (MEXT) for establishing field surveys. The support has made possible this international joint research on seismic microzonation. The author would like to express his sincere appreciation for many colleagues in earthquake countries who are making good collaborations.

References:

- Minami-Nippon Shimbun (1993), "News Photographs on the Typhoons and Rain Disasters of 1993 Summer in Kagoshima," *Special Issue by Minami-Nippon Shimbun Co. Ltd.*
- Tohdo, M. (1998), "Structural Performance and Damage under Strong Motion Excitations during the 1995 Hyogo-Ken Nanbu Earthquake," *Proceedings of 26th Earthquake Ground Motion Symposium in the Architectural Institute of Japan*, 21-26. (in Japanese)
- Salazar, W. and Seo, K. (2003), "Earthquake Disasters of 13 January and 13 February 2001, El Salvador," *Seismological Research Letters, Seismological Society of America*, Vol.74, No.4, 420-439.
- Seo, K., Motoki, K., Kurita, K., Momii, T., Shigeta, T., and Niwa, N. (2004), "Several Subjects Still Remained Since the 1995 Kobe Earthquake," *Proceedings of the 1st International Conference on Urban Earthquake Engineering*, 263-270.
- Seo, K., Sasano, S., and Motoki, K. (2005), "Research Activities on Earthquake Disaster Mitigation in Armenia," *Proceedings of the 2nd International Conference on Urban Earthquake Engineering*, 279-285.
- Nishi-Nippon Shimbun (2005), "News Photographs on the Fukuoka-Oki Earthquake of 20 March, 2005," *Special Issue by Nishi-Nippon Shimbun Co. Ltd.*
- Seo, K., Motoki, K., and Eto, K. (2006), "Lessons Learned from Recent Earthquake Disasters – for Mega-Cities on Huge Sedimentary Basins –," *Proceedings of the 3rd International Conference on Urban Earthquake Engineering*, 593-600.
- Seo, K., Motoki, K., and Ueda, R. (2006), "Non-Structural Damage of Residential RC Buildings during the 2005 Fukuoka-Oki Earthquake as a Typical Urban Disaster," *Proceedings of the 12th Japan Symposium on Earthquake Engineering*, Paper No.0056 CD-ROM (in Japanese)

STRAIN-BASED VERIFICATION METHOD FOR SEISMIC DESIGN OF STEEL BRIDGE STRUCTURES

Hanbin Ge¹⁾ and Tsutomu Usami²⁾

1) Associate Professor, Department of Civil Engineering, Nagoya University, Nagoya 464-8603, Japan

2) Professor, Department of Civil Engineering, Meijo University, Nagoya, 468-8502, Japan

ge@civil.nagoya-u.ac.jp, usamit@ccmfs.meijo-u.ac.jp

ABSTRACT: A seismic performance evaluation procedure based on response strain from the dynamic analysis for steel structures is presented in this paper. In the proposed procedure, response time history of the average axial strain in some prescribed segments of members, where damage is expected to occur, is obtained from a seismic response time-history analysis with which local buckling is not considered, as utilized in the engineering design practice. The average axial strain along the compressive side plate of each critical segment is then compared with the corresponding ultimate strain over the excitation history. The ultimate strain of steel sections can be calculated from available ultimate strain formulas involved in the failure criteria proposed by authors for failure check caused by local buckling, since such damage occurs locally, but affects globally.

1. INTRODUCTION

After the 1995 Hyogoken-Nanbu earthquake, the revised Japanese design codes (JRA, 1996 and 2002), in which a two-level seismic design method has been proposed respectively for moderate (called Level-I) and extreme (called Level-II) ground motions, recommend that a structure like steel bridges, which is expected to exhibit a complicated seismic behavior in case of an earthquake, should be designed based on the results of a dynamic analysis. On the other hand, how about the seismic behavior of existing steel bridges when subjected to Level-II earthquakes, which were designed considering Level-I earthquake only, is a question remaining to be answered. Recently, acceptable performance under Level-II earthquakes for two objectives (i.e., safety of the whole structure and post-earthquake serviceability) has been established for steel bridges and can be expressed in Table 1, which is based on the strain demand control of some critical parts (Usami et al., 2006).

Although there are some researches available on analytical approaches and seismic behavior of civil engineering structures, studies in this field are still very few, and especially investigations of inelastic behavior of steel structures are very limited and insufficient, as well as a rational seismic performance evaluation procedure for design practice.

In this paper, a seismic performance evaluation procedure based on the response strain index is proposed for steel structures and examples of performance evaluation are shown.

2. PROPOSED SEISMIC PERFORMANCE VERIFICATION METHOD

In this section, a dynamic analysis based seismic performance evaluation procedure for steel structures is presented. In the proposed procedure, response time history of the average axial strain in some prescribed segments of members, where damage is expected to occur (hereafter called critical

Table 1: Acceptable performance of steel structures under Level-II earthquake

For safety check	$\varepsilon_a)_{\max} < \varepsilon_u$
For post-earthquake serviceability check	$\varepsilon_a)_{\max} < 2.0\varepsilon_y$ (to limit damage to a certain extent)

$\varepsilon_a)_{\max}$ = Maximum average axial strain along the compressive side plate of a critical segment, ε_u = Ultimate strain, and ε_y = Yield strain of the steel.

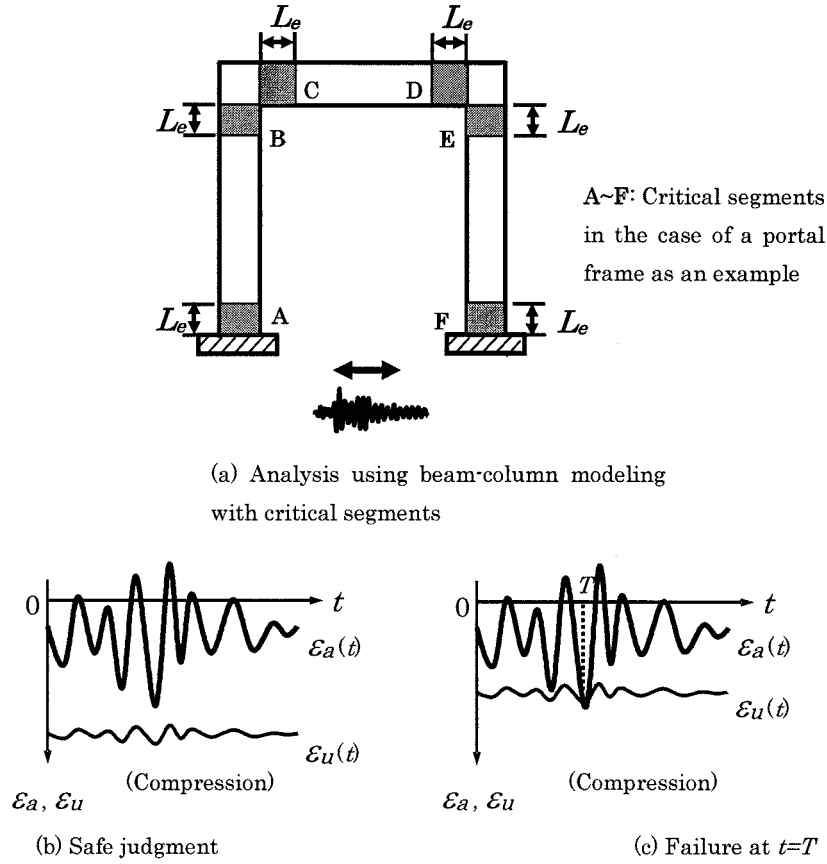
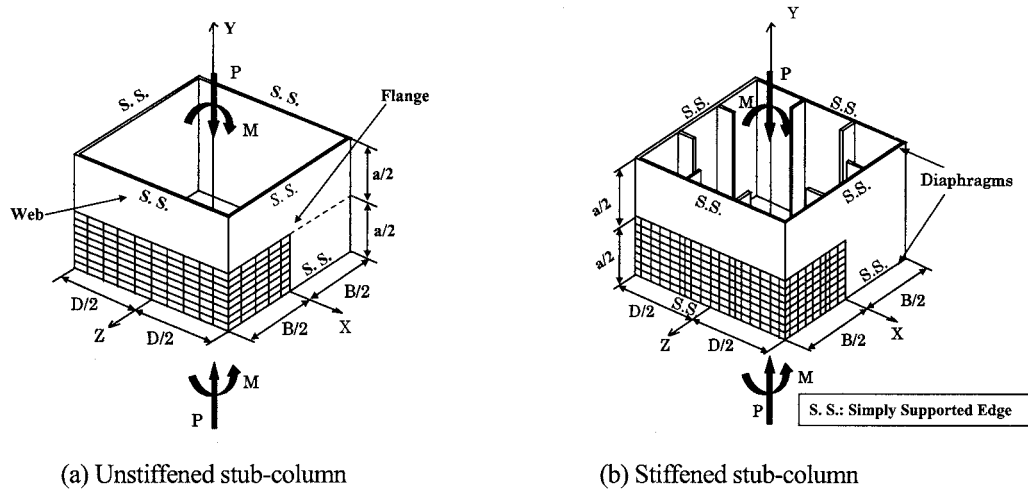


Figure 1 Concept of Proposed Strain-Based Seismic Evaluation Method

segment, and its length is defined as effective failure length which will be addressed in the following context), is obtained from a seismic response time-history analysis using beam-column elements with which local buckling is not considered. The average axial strain along the compressive side plate of each critical segment is then compared with the corresponding ultimate strain over the excitation history, as

$$\varepsilon_a)_{\max} \leq \varepsilon_u \quad (1)$$

in which $\varepsilon_a)_{\max}$ is the maximum average axial compressive strain along the compressed side plate (flange) within an effective length of a critical member. The ultimate strain ε_u of the compressed flange is from the empirical equations proposed based on extensive FEM investigations using shell elements on local buckling behavior of steel stub columns, expressed in terms of the governing parameters such as the axial force ratio and width-to-thickness ratio of the cross-section, as given in the next section. Then,



(a) Unstiffened stub-column (b) Stiffened stub-column
Figure 2 Box-Shaped Stub-Columns under Combined Compression and Bending

whether the structure exhibits sufficient seismic performance can be verified by comparing the maximum average strain demand, $\epsilon_{a,\max}$ from the dynamic analysis with the ultimate strain, ϵ_u . Once the ultimate state of any one of the critical segments is reached, local buckling of that location is thought to occur and the ultimate state of the whole structure is thought to be reached.

To conceptually explain such a dynamic seismic evaluation method, a portal frame is adopted for demonstration for simplicity, as shown in Figure 1. In this case, six segments with an effective failure length are critical locations possibly to fail under seismic excitation. Time history of the average axial strain is from the dynamic analysis, and the ultimate strain is given by the empirical formula. A graph together with the average strain demand and ultimate strain curves is plotted for performance evaluation.

It should be noted that the examination is performed only to compression side. The segment is judged as safe when the average strain time history is always smaller than the ultimate strain in quantity (i.e., the ultimate strain curve is always below the response strain curve). On the other hand, in the case that the response curve of the average strain intersects the ultimate strain curve at a certain time $t = T$, it is believed that the ultimate state of the segment is reached at that moment. For steel structures composed of relatively thin-walled sections in the civil engineering field, excessive inelastic deformation tends to intensify in the segment at a local part and causes local buckling of the member, as will make the local member fail during excitation and induce the failure of the whole structure. Thus, once the ultimate state at any one of the critical segments, which is judged according to the above procedure, is reached, the ultimate state of the whole structure system is thought to be reached. Certainly, in some cases the evaluation may be on a safety side, which is evidenced in the work by Morishita et al. (2002).

3. ULTIMATE STRAINS

The failure criterion is of great significance when using the proposed procedure. Local buckling of steel members always governs capacity of plated steel structures. Numerous experiments and FEM simulations have shown that the critical buckling of thin-walled steel members always appears in the compressive flange within an effective failure length, thus a failure criterion for box-section steel members based on this feature has been firstly proposed by Zheng et al. (2000). According to this criterion, the ultimate state is thought to be reached when the average strain over the effective failure length at a critical place reaches the ultimate strain given by the proposed ultimate strain formula. The effective failure length of L_e of a box-section member is assumed as $L_e = \min\{0.7B, L_d\}$, where B is the flange width and L_d is the distance between two adjacent diaphragms.

Zheng et al. (2000) studied the local buckling behavior of box-section stub columns as shown in Figure 2 and proposed empirical formulas of ultimate strain as follows.

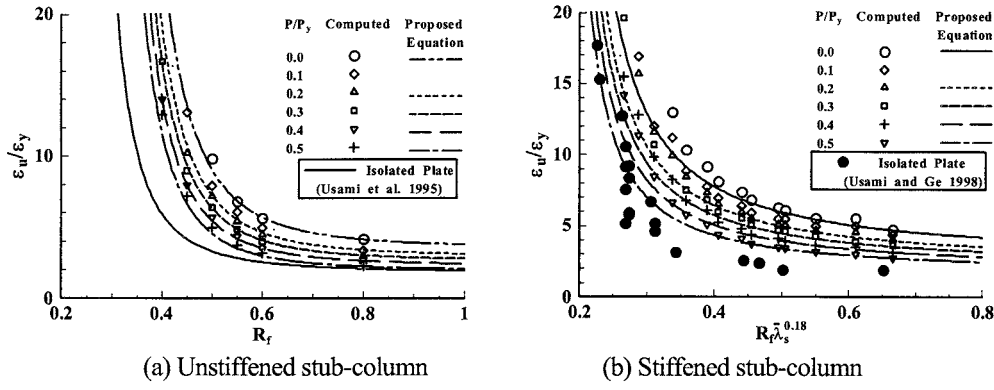


Figure 3 Ultimate Strains of Box-Shaped Stub-Columns

For unstiffened box sections:

$$\frac{\varepsilon_u}{\varepsilon_y} = \frac{0.108(1 - N/N_y)^{1.09}}{(R_f - 0.2)^{3.26}} + 3.58(1 - N/N_y)^{0.839} \leq 20.0, \quad \begin{matrix} 0.2 \leq R_f \leq 0.7 \\ 0.0 \leq N/N_y \leq 0.5 \end{matrix} \quad (2)$$

For stiffened box sections:

$$\frac{\varepsilon_u}{\varepsilon_y} = \frac{0.8(1 - N/N_y)^{0.94}}{(R_f \bar{\lambda}_s^{0.18} - 0.168)^{1.25}} + 2.78(1 - N/N_y)^{0.68} \leq 20.0, \quad \begin{matrix} 0.3 \leq R_f \leq 0.5 \\ \gamma/\gamma^* \geq 1.0 \\ 0.0 \leq N/N_y \leq 0.5 \end{matrix} \quad (3)$$

in which N = axial force; N_y = squash load; and R_f = flange width-thickness ratio parameter of the box section defined by

$$R_f = \frac{B}{t} \sqrt{\frac{12(1 - \nu^2)}{4n^2 \pi^2}} \sqrt{\frac{\sigma_y}{E}} \quad (4)$$

and $\bar{\lambda}_s$ = stiffener's slenderness ratio parameter, given by

$$\bar{\lambda}_s = \frac{1}{\sqrt{Q}} \frac{a}{r_s} \frac{1}{\pi} \sqrt{\frac{\sigma_y}{E}} \quad (5)$$

In equations (4) and (5), B and t denote the width and thickness of the flange plate, respectively; and n = number of subpanels divided by the longitudinal stiffeners (n = unity for unstiffened sections); a = stiffener's length (i.e., diaphragm spacing, L_d); r_s = radius of gyration of a T-shape cross section consisting of one longitudinal stiffener and the adjacent subpanel of width B/n ; and Q = local buckling strength of the subpanel plate, defined by

$$Q = \frac{1}{2R_f} \left[\beta - \sqrt{\beta^2 - 4R_f} \right] \leq 1.0 \quad (6)$$

$$\beta = 1.33R_f + 0.868 \quad (7)$$

The proposed formulas are plotted in Figure 3.

However, the above formulas are applicable for the axial force up to $0.5N_y$ only. Considering the fact that in steel arch bridges axial force demand may be very large, as shown in the previous dynamic analysis, Ge et al. (2003) made more FEM investigations to account for wider range of axial compression with an upper limit of N_y , and proposed a set of revised ultimate strain formulas, as shown below.

For unstiffened box sections:

$$\frac{\varepsilon_u}{\varepsilon_y} = \frac{0.24}{(R_f - 0.2)^{2.8} (1 + N/N_y)^{2.4}} + \frac{2.8}{(1 + N/N_y)^{0.6}} \leq 20.0, \quad \begin{matrix} 0.2 \leq R_f \leq 0.7 \\ 0.0 \leq N/N_y \leq 1.0 \end{matrix} \quad (8)$$

For stiffened box sections:

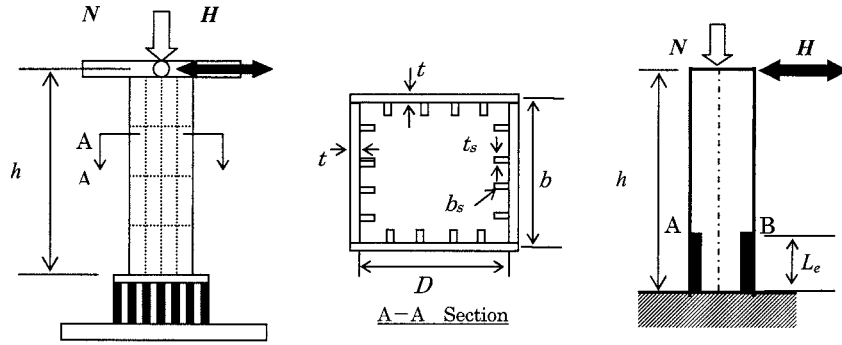
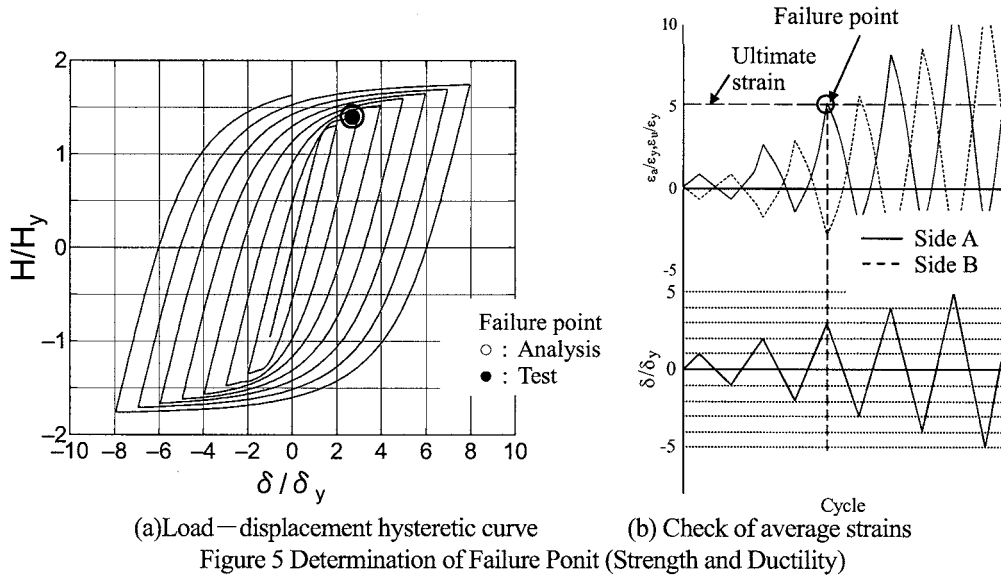


Figure 4 Cantilever-Type Steel Column



$$\frac{\epsilon_u}{\epsilon_y} = \frac{0.7}{\left(R_f \bar{\lambda}_s^{-0.18} - 0.18\right)^{1.3} (1 + N/N_y)^{2.2}} + \frac{3.2}{(1 + N/N_y)} \leq 20.0, \quad \gamma/\gamma^* \geq 1.0 \quad (9)$$

$$0.3 \leq R_f \leq 0.5$$

$$0.0 \leq N/N_y \leq 1.0$$

These new ultimate formulas are employed in the procedure herein. A summary of empirical equations obtained either from experiments or from analyses on various steel sections is available in two new books (Usami and Ge, 2006, Usami et al., 2006).

4. VALIDATION OF THE PROPOSED METHOD

In this section, the accuracy of the proposed method is evaluated by comparing the results with those of cyclic and nonlinear time-history tests. Due to the page limitation, only cantilever-typed steel column shown in Figure 4 is considered here, although this method has also been verified on framed structures (Morishita et al., 2002).

To compare with results of the cyclic tests, capacities such as ultimate strength and ductility of the box-shaped steel column are predicted using the proposed method. For this purpose, a cyclic pushover analysis using beam-column elements is carried out and the ultimate state is determined using ultimate strains of cross sections presented in the previous section. It is noted that in such a cyclic pushover analysis the average axial strain within an effective length of a critical member should be checked over two sides, as illustrated in Figure 5. Both the pushover analysis and time-history analysis are carried out by using the FEM program ABAQUS (2003).

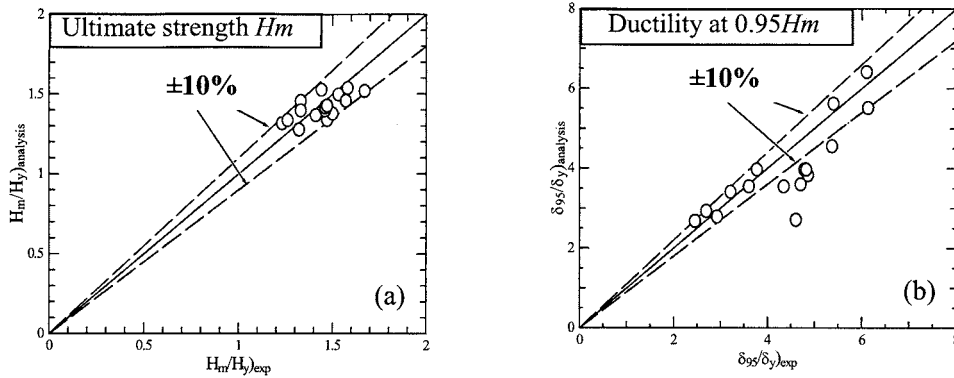


Figure 6 Verification of the Proposed Method with Cyclic Tests

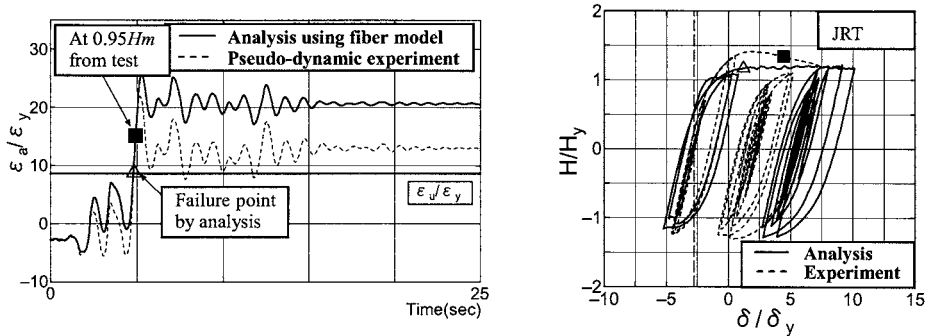


Figure 7 Verification of the Proposed Method with Pseudo-Dynamic Tests

Figure 6 shows comparisons of strength and ductility between the predicted and experimental results. Here, the ultimate strength stands for the maximum load, H_m , while the ductility is expressed by the lateral displacement, δ_{95} , corresponding to 95% of the maximum load after the peak point, instead of that corresponding to the maximum load, δ_m . As can be seen from the figure, the present method with the use of ultimate strain of the critical segments is of good accuracy in the prediction of the strength and ductility of steel structures.

Figure 7 gives comparisons of average strain time histories and load-displacement hysteretic response of a box-shaped steel column from the proposed method and pseudo-dynamic experiment. It can be observed that the maximum displacement response can be accurately predicted by the proposed method, but there is a significant difference in the residual displacement response. In the present method, the analysis employed is simple for practical use in the seismic design because the structure is modeled with the fiber model and the constitutive law of steel is classic material model such as a bilinear type of stress-strain relation combined with kinematic hardening rule. To accurately predict residual displacement, modeling with shell elements and use of advanced material models like the modified two-surface model (Shen et al., 1995) are needed. Another way is to use a correlation between the maximum displacement and residual displacement as proposed by Usami et al. (2001).

5. EVALUATION EXAMPLE: STEEL ARCH BRIDGE

Based on the afore-described procedure, an examination of a steel arch bridge shown in Figure 8 under the transverse excitation (JRT-EW-M) is performed monitoring the section at the side pier base where the response strain is the most significant. The average response strain, ε_a , along the effective length from the analysis of the original structure and the ultimate strain, ε_u , from the empirical formula are shown in Figure 9 (a). As seen from the figure, the average compressive strain of outside flange has reached the ultimate strain at nearly 3 second. Accordingly it can be judged that this arch bridge reaches

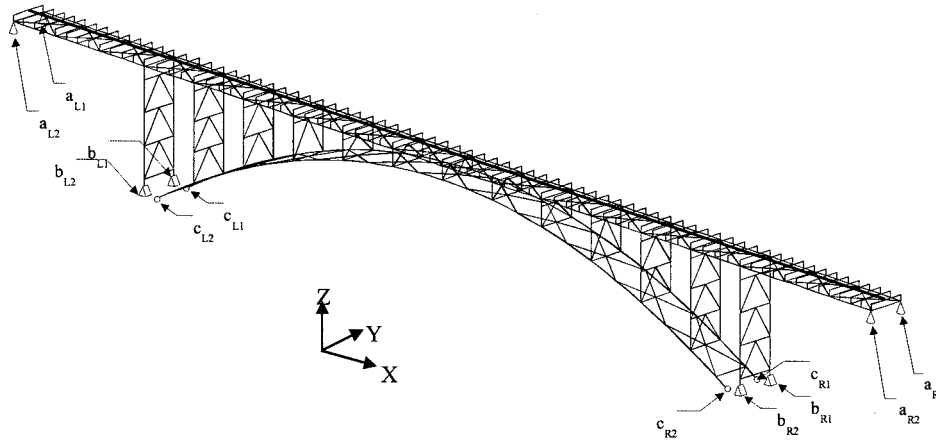


Figure 8 Steel Arch Bridge to be Evaluated

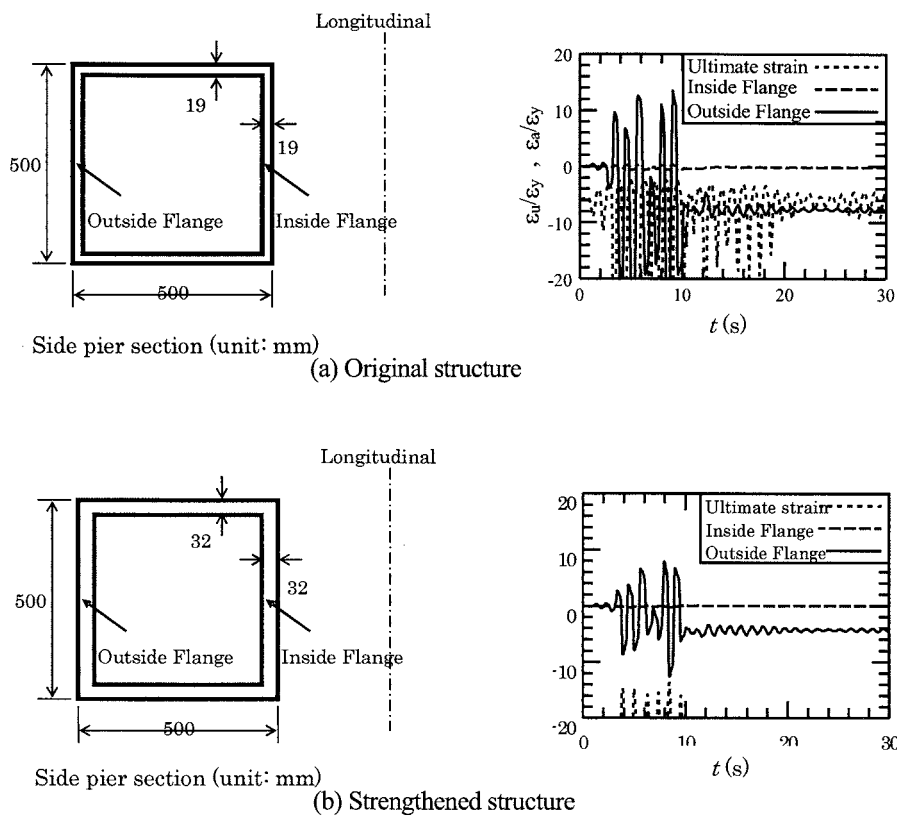


Figure 9 Performance Evaluation of Steel Arch Bridge using the Proposed Method

the ultimate state at this moment. The reason why the ultimate state was reached so quickly is that a very large axial compression demand appears in this segment while a low ductility capacity is provided by the segment, with a width-thickness ratio parameter R_f of 0.575. Side piers are weakest parts in this structure. For better seismic performance, thickness of the side pier section is modified from 19 mm to 32 mm, with a width-thickness ratio parameter R_f of 0.350. The structure is reevaluated under the transverse excitation and the result is shown in Figure 9 (b). In this case, the average strain response of the side pier section is greatly reduced while larger ultimate strain is provided by the thicker section. As a result, the structure is then safe when subjected to the ground motion since there is no intersection between the strain demand and ultimate strain curves.

Another point worthy to be noted in the evaluation is that the response strain of the inner side flange is significantly small compared with that of the outside flange. Supposing the bridge falls on a side with

the section, a compressive axial force will be applied to this section. Meanwhile, the direction of a bending moment comes from the inner side flange to the outside flange. As a result, the stress produced by the bending moment is in compression on the outside flange but in tension on the inside flange. Therefore, a fact that the compressive strain on the outside flange increased and the stress on the inner side flange was offset on the contrary results in a large difference of the strain responses on both sides.

6. CONCLUSIONS

A seismic performance evaluation procedure based on response strain from the dynamic analysis for steel bridge structures was presented. In the proposed procedure, the average axial strain along the compressive side plate of each critical segment is compared with the corresponding ultimate strain over the excitation history. The validity of the proposed method was shown by comparing the predicted results with cyclic and pseudo-dynamic experimental results. Furthermore, such a procedure was also applied to a complicated steel arch bridge. The results presented in this paper show that the proposed method can be easily used for practical seismic design of various steel structures.

References:

- Shen, C., Mamaghani, I. H. P., Mizuno, E., and Usami, T. (1995), "Cyclic Behavior of Structural Steels. II: Theory." *Journal of Engineering Mechanics, ASCE*, 121(11), 1165–1172.
- Japan Road Association (1996), "Specifications for Highway Bridges, Part V. Seismic Design", Tokyo, Japan.
- Zheng, Y., Usami, T. and Ge, H. B. (2000), "Ductility of Thin-walled Steel Box Stub-columns", *Journal of Structural Engineering, ASCE*, 126(11), 1304-1311.
- Usami, T, Zheng, Y. and Ge, H. B. (2001), "Seismic Design Method for Thin-walled Steel Frame Structures", *Journal of Structural Engineering, ASCE*, 127(2), 137-144.
- Japan Road Association (2002), "Specifications for Highway Bridges, Part V. Seismic Design", Tokyo, Japan.
- Morishita, K., Usami, T., Banno, T. and Kasai, A. (2002), "Application on Dynamic Verification Method for Seismic Design of Steel Bridge Piers", *Journal of Structural Mechanics and Earthquake Engineering, JSCE*, 710/I-60, 181-190.
- Ge, H. B., Kono, T. and Usami, T. (2003), "Failure Strain of Steel Segments Subjected to Combined Compression and Bending and Application to Dynamic Verification of Steel Arch Bridges", *Journal of Structural Engineering, JSCE*, 1479-1488.
- ABAQUS/Standard User's Manual, Version 6.3 (2003), Hibbitt, Karlsson & Sorensen, Inc., Pawtucket, R.I.
- Usami, T. and Ge, H.B. (2006), "Analysing the Strength and Ductility of Plated Structures", Chapter 10 in *Analysis and Design of Plated Structures* (Edit by N.E.Shanmugam and C.M.Wang), CRC.
- Usami, T. et al. (2006), "Seismic and Control Design of Steel Bridges", Edit by Japan Society of Steel Construction (JSSC), Gihodo-Shuppan.

SIMULATION ANALYSIS ON COLLISION TEST BETWEEN TWO STEEL BARS

Y Kajita¹⁾, T. Kitahara²⁾, Y. Nishimoto³⁾ and H. Otsuka⁴⁾

1) Associate Professor, Dept. of Civil and Structural Eng. Kyushu University, Fukuoka, Japan

2) Associate Professor, Dept. of Civil and Environmental Eng., Kanto-Gakuin University, Yokohama, Japan

3) Researcher, Research Development Group, Shibata Industrial Co. Ltd., Akashi, Japan

4) Professor, Dept. of Civil and Structural Eng. Kyushu University, Fukuoka, Japan

ykajita@doc.kyushu-u.ac.jp, kitahara@kanto-gakuin.ac.jp, Yasushi.Nishimoto@sbt.co.jp, otsuka@doc.kyushu-u.ac.jp

Abstract: We carried out a collision test between two steel solid bars in order to investigate the relationship between the maximum impact force and the collision velocity. In this paper, we conducted simulation analyses by using the 3-dimensional finite element method. From the simulation analyses, we can roughly estimate the maximum impact force and the stiffness of the natural rubber if the strain rate effect of the natural rubber can be set appropriately.

1. INTRODUCTION

After the 1995 Hyogoken-Nanbu Earthquake, bearings have been replaced by rubber bearings in order to improve earthquake resistance. When the rubber bearings are used, the inertial force of the superstructure subjected to the pier can be reduced so that the damage of the pier is lessened. However, the displacement response of the superstructure increases. Therefore, it is expected that frequency of the pounding phenomena will become large, e.g., the pounding girders and the collision between the superstructure and the abutment, etc., will increase.

When a girder collides with another girder, an abutment and a device which prevents a girder from falling off, the girder is subjected to the impulsive force. So, there is a possibility that the girder ends will be damaged. In the worst case, an emergency car cannot traverse the bridge shortly after a strong earthquake occurs because of the damage of the girder ends. Therefore, in order to reduce the impact force during a collision, the Japanese Specifications of Highway Bridges requires that shock absorbers, such as those made of rubber, be installed at the girder ends in addition to devices which prevent girders from falling off. However, the specification has no detail prescript regarding the thickness of shock absorbing rubbers because it has not clarified how much impact force is produced during a collision.

Several studies focusing on the collision problem have been carried out [Kubota et al., 1997, Sonoda et al., 2001, Murata et al., 2001]. In these papers, a mass collides with a concrete wall which is fitted with several kinds of shock absorbers, such as a natural rubber, a piece of synthetic resin, a sandbag etc. From the results of these researches, it was found that the shock absorber has a quantitative effect on the reduction of the impact force. However, to focus on the pounding girders, the method of these tests cannot replicate the circumstances of the pounding girders. Therefore, we develop the new test apparatus which can levitate two steel bars by using compressed

air. By using this test apparatus, two objects move freely into a horizontal direction without kinetic friction. The collision test between steel bars was carried out as the first step toward developing the design method of the shock absorber [Kitahara et al., 2005]. Seven kinds of the thickness of the natural rubber are prepared and seven kinds of the collision velocity are set. The maximum impact force by focusing on the difference of the collision velocity was summarized.

In this paper, the simulation analyses are carried out by using the general-purpose finite element method code, called LS-DYNA, which is specialized for dynamic structural crush analyses.

2. OUTLINE OF THE COLLISION TEST

2.1 Test Setup

Before the explanation of the simulation analysis, the outline of the collision test is explained. The test is carried out by using a horizontal hydraulic high-speed loading machine. This machine has a loading capacity of 1000 (kN) and a maximum loading speed of 3.0 (m/s). The collision test was carried out as follows: (i) two steel bars are set in a line on a guide rail with a length of 3000 (mm) as shown in Figure 1 and Photo 1. (ii) Two steel bars hover above the guide rail by using the compressed air. (iii) One steel bar rests above the guide rail and the horizontal hydraulic high-speed loading machine drives the other up to a certain velocity. (iv) The collision between girders is simulated in this way. The rectangular solid steel bar was 1000 (mm) long, 200 (mm) wide and 200 (mm) high, and its mass was 300 (kg). In this test, the specimen to which the initial velocity is applied is named the colliding specimen, and the specimen resting above the guide rail before the collision is named the collided specimen, respectively. When the specimen is moving, the sliding friction force slows the movement of the steel bars. In this test, however, the sliding friction force is reduced by using the compressed air. Therefore, the energy loss caused by the sliding friction force is suppressed during the collision.

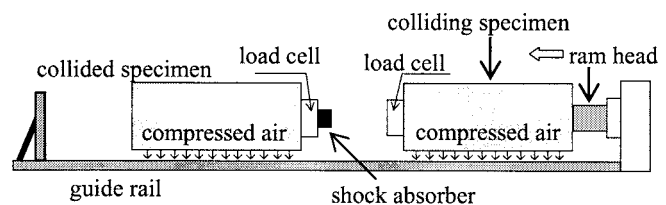


Figure 1 Test setup

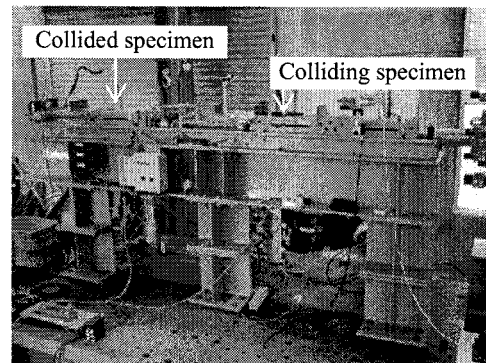


Photo 1 Overview of the test

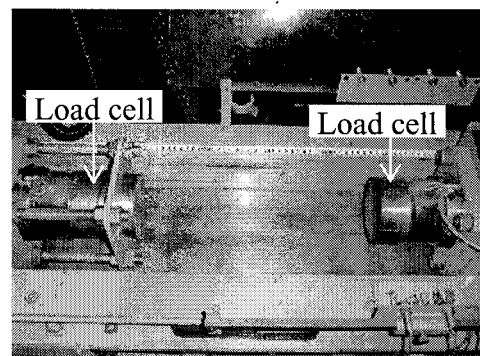


Photo 2 Load cell setup

2.2 Measuring system

As for a collision problem involving two bodies, there are three characteristic measures to be evaluated: the impact force, the law of conservation of momentum and the kinetic energy loss. In this study, in order to evaluate these measures, the impact force during the collision and the velocity before and after the collision are measured. In order to determine the velocity of the steel bars, the travelling distance of the colliding and collided specimens and the relative displacement between two specimens are measured by a laser displacement sensor. The method of least squares is applied in order to obtain the velocity of the specimen from the time history of movement. To be more precise, the velocity of the specimen is found by approximating the time-displacement

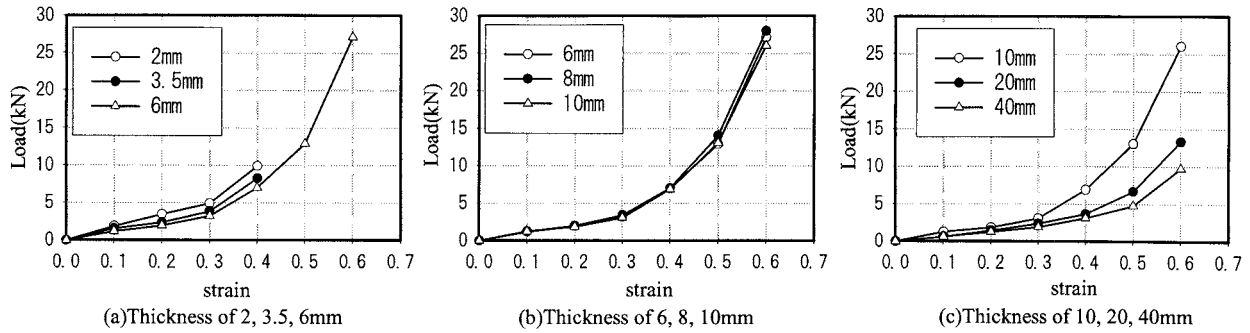


Figure 2 Load-strain curve of the shock absorbers

relationship with the linear expression with respect to time. The impact force working on the collision surface is measured by a load cell which is installed on the edge of the steel bar as shown in Photo 2. Two kinds of the load cell are prepared in this test. The load rating of two load cells is 500 (kN) and 3000 (kN), respectively. In the case that the shock absorber is installed, the one whose load rating is 500 (kN) is used. On the other hand, in the case that the shock absorber is not installed, the other one is used. The case where the shock absorber is installed, the sampling time of the measurement is set at 5.0×10^{-5} (sec). On the other hand, the case where the shock absorber isn't installed, that is set at 1.0×10^{-5} (sec).

2.3 Shape of shock absorbers

In this test, natural rubber is prepared as shock absorbers. The natural rubber has a degree of hardness of 50 (JIS K 6301). The shape of the natural rubber is a cuboid. The cross section of the rubber has 40 (mm) long, 40 (mm) wide. The thickness is 2, 3.5, 6, 8, 10, 20 and 40 (mm) respectively. So, the ratio of the pressed area to free surface area ranges from 0.2 to 4.0. We call this ratio as the shape factor. As mentioned before, there is no rule to determine the thickness of the shock absorbers. The bridge designer generally uses the shock absorbers whose shape factor is from 0.3 to 1.0. Therefore, the prepared natural rubber covers the range of the shape factor of the natural rubber which is installed in the real bridge.

2.4 Setting Velocity

According to the similarity law, the velocity of the scaled model is equivalent to that of the actual phenomenon because this test is not influenced by gravity [Emori et al., 2000]. K. Izuno and S. Takeno performed numerical analysis of an elevated bridge [Izuno and Takeno, 1999] and made clear that the response velocity of the superstructure is from about 0.5 (m/s) to 3.0 (m/s) during severe ground motion such as the 1995 Hyogoken-Nanbu Earthquake. Therefore, the initial velocity of the colliding specimen is set from 0.2 (m/s) to 1.0 (m/s) on 7 stages.

2.5 Material Properties of Natural Rubber

Before the collision test is carried out, the static compression test on the shock absorbers is carried out by using the 50kN compression test machine. The compression load is applied until the shock absorber is compressed to up to 60% of the original height in the case that the thickness of the natural rubber is more than 6 (mm). In the case that the thickness of the natural rubber is 2 (mm) and 3.5 (mm), the compression load is applied until the shock absorber is compressed to up to 40% of the original height. The load-deformation curves of the shock absorbers are shown in Figure 2. In Figure 2, the thinner the thickness of the natural rubber is, the smaller the stiffness of the natural rubber is. In the case that the thickness is 2.0, 3.5 (mm), the stiffness becomes large suddenly when the strain goes over 0.3. In the other cases, the stiffness becomes large suddenly when the strain exceeds 0.4.

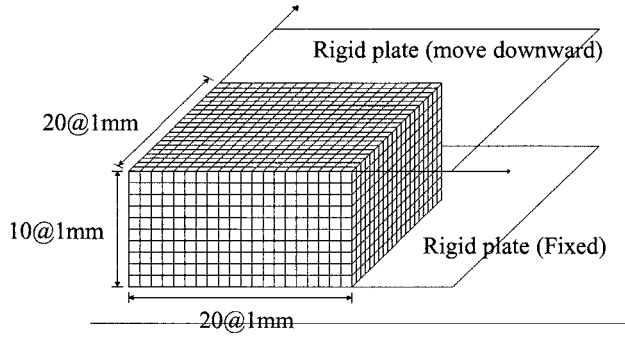


Figure 3 Finite element discretization

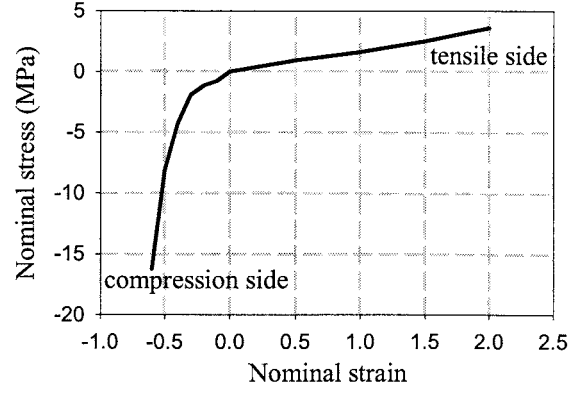


Figure 4: Stress-Strain curve of natural rubber

3. STATIC COMPRESSION ANALYSIS ON NATURAL RUBBER

3.1 Finite Element Modeling for the Static Compression Test

Previous to the simulation analysis for the collision test, we carried out the static compression analysis for the natural rubber by using the general-purpose finite element method code, called LS-DYNA, which is specialized for dynamic structural crush analysis. The case of the thickness of 10mm is only simulated. The finite element discretization of the analytical model is shown in Figure 3. The natural rubber is discretized by an 8-node solid element with a cube 1mm on a side. We sandwich the natural rubber between the rigid plates. One plate is fixed and the other plate is moved downward at the speed of 1 mm/sec. The number of the nodes and the elements are 4851 and 4000, respectively.

The constitutive law of the natural rubber is modeled as the Ogden's law as shown in Equation 1 [Ogden 1972].

$$W = \sum_{n=1}^2 \frac{\mu_n}{\alpha_n} (\lambda_1^{\alpha_n} + \lambda_2^{\alpha_n} + \lambda_3^{\alpha_n} - 3) \quad (1)$$

λ_i is the elongation ratio of i-direction. μ_n and α_n are material constants that are determined from the nominal stress-nominal strain curve of the natural rubber as shown in Figure 4. The curve in the tensile side is obtained from the uniaxial tensile test which is defined by the Japan Industrial Standards (JIS K 6301). The curve in the compression side is obtained from the uniaxial compression test as shown in Figure 2.

The LS-DYNA is capable of solving the contact problem as an option, based on the penalty method. The analytical procedure of the penalty method is as follows: the spring is set in the normal direction of the contact surface, the stiffness (k) of which is given by

$$k = \frac{\alpha K A^2}{V} \quad (2)$$

in which α is the penalty coefficient related to the friction coefficient on the contact surface (this value is input by the user and suggested to be 0.1 by the normal), K is the bulk modulus, A is the area of contact and V is the volume of the element in contact. In this analysis, α is set to be 10. If α is small, the rigid plate penetrate the natural rubber because natural rubber is much softer

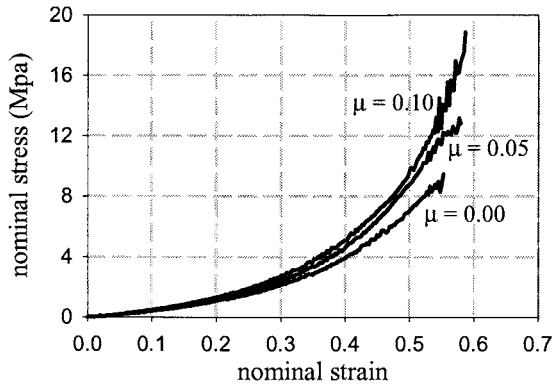


Figure 5 Stress-strain curve (Analytical results)

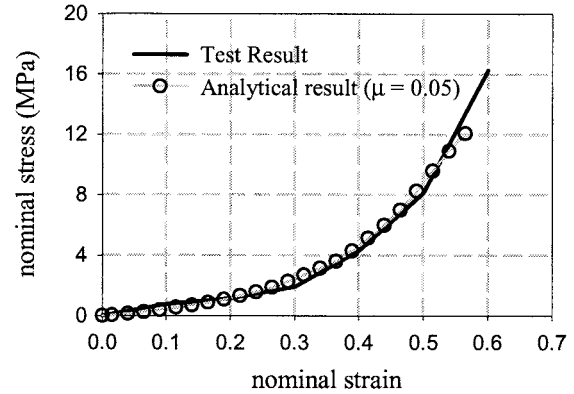


Figure 6 Comparison of the stress-strain curve

than major construction materials such as steel and concrete. The friction force between the rigid plate and the natural rubber is considered in this analysis.

3.2 Analytical Results and Discussions

Figure 5 shows the relationship between stress and strain. It can be found that the stiffness becomes larger with increasing the coefficient of the friction (μ). The analytical result agrees very well the test result in the case that the coefficient of the friction is 0.05 as shown in Figure 6. The calculation is terminated forcibly when the compressive strain reaches about 0.60. That is because the solid element changes an irregular shape. So, if we need the stress in the large compressive area, we should devise the analytical procedure.

4. SIMULATION ANALYSIS FOR THE COLLISION TEST

4.1 Finite Element Modeling for the Collision Test

The direction in which the specimen moves is defined as the y-axis direction and the vertical direction is defined as the z-axis direction. The finite element discretization of the analytical model is simplified by considering the structural symmetry to the x-y plane and y-z plane; in other words the quarter size is modeled. In addition, the specimen is fixed and not allowed to move in the z-axis direction. In the discretization of the steel bar, 8-node solid elements which have a size of 2.0*2.0*100 (mm) are used. On the other hand, the natural rubber is discretized by an 8-node solid element with a size of 2.0*2.0*1.0 (mm). The number of the nodes and the elements are 6691 and 5080, respectively.

The constitutive law of the natural rubber is modeled as the Ogden's law, as is the case with the static compression analysis. The steel bar is assumed to behave elastically. The time interval is determined by the LS-DYNA automatically to satisfy the Courant's condition, which is that the time interval should be shorter than the time necessary for the stress wave to pass through one element. In addition, no damping of the steel bar or the natural rubber is considered in this analysis.

It is found from the test results that the maximum compressive strain is larger than 0.60 when the collision velocity exceeds about 1.0 (m/s). From the result of the compression analysis, the calculation is terminated when the compressive stress reaches about 0.60. So, in this study, we conducted the analysis at only three cases, that is, the collision velocities of 0.34, 0.68 and 0.85 (m/s).

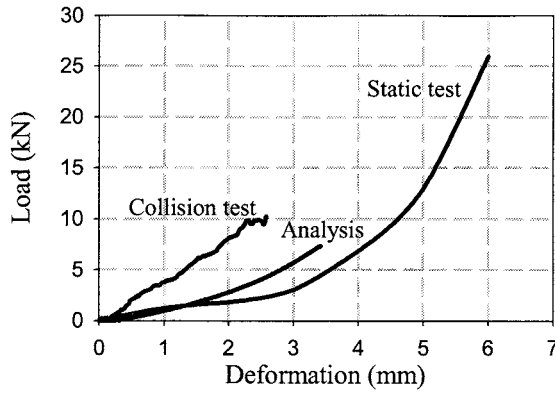


Figure 7 Load-Deformation curve ($v=0.34\text{m/s}$)

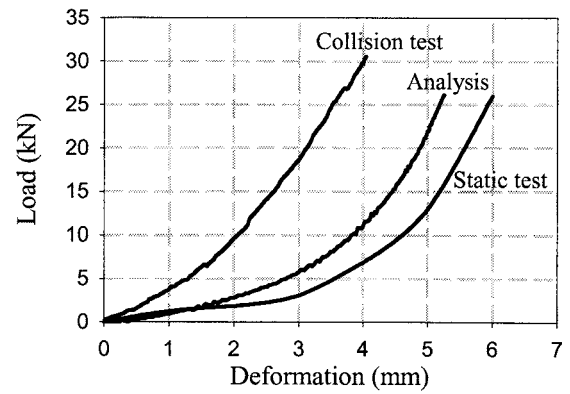


Figure 8 Load-Deformation curve ($v=0.68\text{m/s}$)

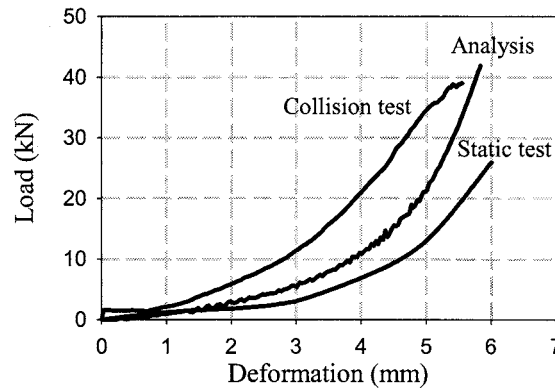


Figure 9 Load-Deformation curve ($v=0.85\text{m/s}$)

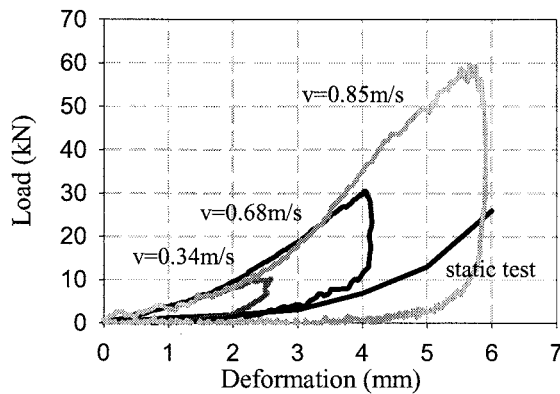


Figure 10 Load-Deformation curve
(thickness 10mm)

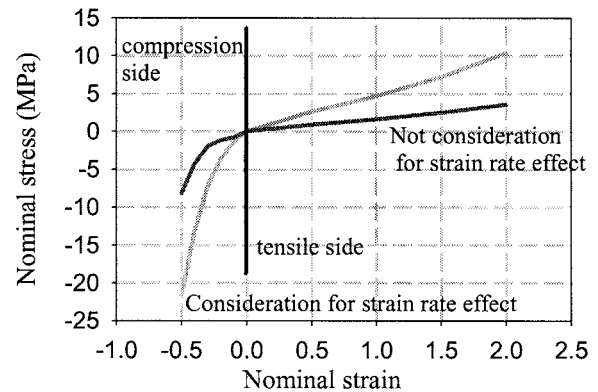


Figure 11 Stress-Strain curve

4.2 Analytical Results and Discussions

Figures 7-9 show the load-deformation curve of the natural rubber. In the case of the collision velocity of 0.85m/s , the calculation is terminated before two steel bars are separated. From these figures, it is found that the maximum impact force nearly matches the one obtained from the collision test. However, as far as the stiffness concerned, the analytical results hardly coincide with the test results. This is because it is thought that the strain rate effect of the natural rubber is not considered in this analysis.

Figure 10 shows the load-deformation curve of the natural rubber obtained from the collision test. It is found that the stiffness of the natural rubber doesn't change even if the collision velocity changes. But the collision test results are clearly different from the static compression test result.

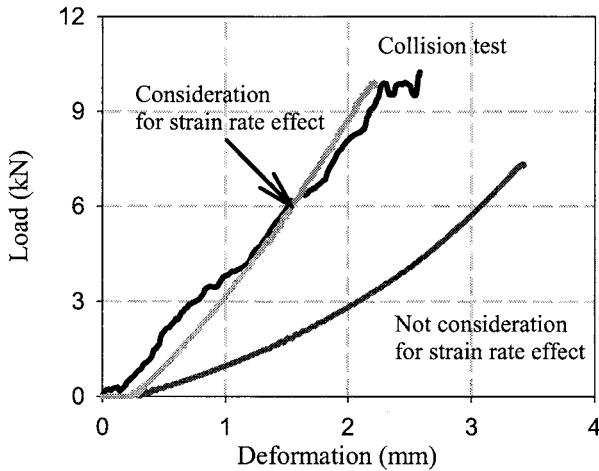


Figure 12 Load-Deformation curve ($v=0.34\text{m/s}$)

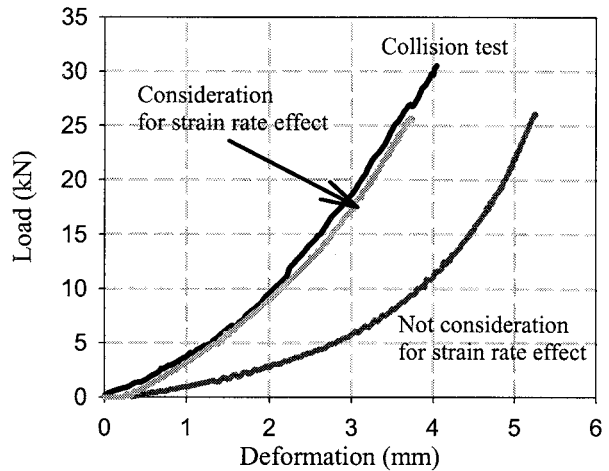


Figure 13 Load-Deformation curve ($v=0.68\text{m/s}$)

So, the stress-strain curve is redefined as shown in Figure 11. In the compression area, the stress-strain curve is used from the collision test result as shown in Figure 10. In the tensile area, the high speed tensile test has not been conducted. So, the increase ratio of the stiffness between the collision test and the static compression test is about 2.8. Therefore, the stress is set to be 2.8 times as the stress obtained from the static tensile test.

Figures 12 and 13 show the analytical result. It is found that maximum impact force is almost same whether or not the strain rate effect is considered. However, the stiffness is simulated well. Moreover, compared with the stiffness under unloading between the test result and the analytical result is different significantly. At the present time, the energy absorption isn't expressed in the analytical result.

5. CONCLUSIONS

In this paper, we carried out simulation analyses of the collision test by using the 3-dimensional finite element method. The conclusions and future research needs are described as follows:

- (1) From the static compression analysis, the calculation is terminated forcibly when the compressive strain becomes more than 0.60. At the present time, it is difficult to calculate the stress of the natural rubber precisely in the large compressive strain area.
- (2) From the simulation analysis for the collision test, the maximum force matches the one obtained from the test result approximately; however, as for the stiffness of the natural rubber, the analytical results don't coincide with the test results when the strain rate effect of the natural rubber isn't considered in this analysis.
- (3) Considered with the strain rate effect, the stiffness of the natural rubber is simulated well. But, In this analysis, the strain rate effect is set from the test data. So, it is important to grasp the strain rate effect of the natural rubber.

Acknowledgements:

The research was conducted under the support of Japan Society for the Promotion of Science, Grants-in-Aid for Scientific Research, Scientific Research(B)(Research No. 17360219). This support is gratefully acknowledged.

References:

- Emori, I., Saito, K., and Sekimoto, K. (2000). The Theory and Application of the Model Experiment (Third Edition), Gihodo, Tokyo, (in Japanese).
- Izuno, K., and Takeno, S. (1999). "Impact Velocity of Adjacent Members of Bridges during Earthquakes." *Proceedings of the 3rd Symposium on Ductility Design Method for Bridges*, 209-214 (in Japanese).
- Kitahara, T., Kajita, Y., Nishimoto, Y., and Katsuki, S. (2005). "Collision Test between Steel Bars with Shock Absorbing Rubber for Bridge Restrainer System using Frictionless Impact Testing Apparatus." *Proceedings of the First International Conference on Advances in Experimental Structural Engineering*, 901-907
- Kubota, K., Kanno, T., Kamihigashi, Y., and Ishida, H. (1997). "Collision Experiment and Earthquake Response Analysis of Aseismic Concrete Block with Shock Absorber." *Japan Highway Research Institute Report*, Vol.34, 98-104 (in Japanese).
- Murata, K., Takayama, T., Gotoh, T., Yamada, M., Ikoma, N., and Ukishima, T. (2001). "Seismic Retrofit Effect by a Bridge Restrainer with Energy Absorption" *Journal of Structural Mechanics and Earthquake Engineering, JSCE*, Japan, No.689, I-57, 275-288 (in Japanese).
- Ogden, R.W.(1972): *Proceedings of the Royal Society of London, Series A*, 326, 565
- Sonoda, Y., Nishimoto, Y., Ishikawa, N., and Hikosaka, H. (2001). "Fundamental Study on the Mitigating Effect of Rubber as a Shock Absorber." *Journal of Structural Mechanics and Earthquake Engineering, JSCE*, Japan, No.689, I-57, 215-224 (in Japanese).

DEVELOPMENT OF THE NEW RESTRAINING DEVICES FOR A RAILWAY BRIDGE WITH ISOLATION BEARINGS

A. Toyooka¹⁾, H. Iemura²⁾, M. Ikeda³⁾,
Y. Hishijima⁴⁾, S. Uno⁵⁾, M. Ikenaga⁶⁾, and T. Harada⁷⁾

1) Research Associate, Dept. of Urban Management, Kyoto University, Japan

2) Professor, Dept. of Urban Management, Kyoto University, Japan

3) Associate Chief Researcher, Railway Technical Research Institute, Japan

4) Executive Managing Director, Kawaguchi Metal Corp., Japan

5) Manager, Kawaguchi Metal Corp., Japan

6) Manager, Oiles Corp., Japan

7) Associate Manager, Nippon Chuzo Corp., Japan

toyo@catfish.kuciv.kyoto-u.ac.jp, iemura@catfish.kuciv.kyoto-u.ac.jp, manabu@rtri.or.jp,

hishijima@kawakinkk.co.jp, uno@kawakinkk.co.jp, ikenaga@oiles.co.jp, t_harada@nipponchuzo.co.jp

Abstract: In this research, the new restraining device applicable for a railway structure with isolation bearings is proposed. These devices were designed to attain the running safety of a train under small earthquake as well as the reduction of structural damage under extreme motion simultaneously. Three prototype devices were developed, and their fundamental characters were tested by a static loading test. It was then confirmed through the large-scale shaking table tests using girder model, rubber supports that these new restrainers could attain the desirable performances under both small and extreme motions.

1. INTRODUCTION

Railway systems have been regarded as one of the significant and indispensable infrastructures from the standpoint of rapid and mass transportation, and only a limited damage or residual displacement is permissible even under extreme earthquake for preventing derailment and rapid reconstruction. In order to attain such a high performance structure, base isolation design is one of the promising technologies, in which acceleration and displacement can be reduced by elongation of the natural period and supplemental damping.

On the contrary, securing the running safety of a train under the small but frequent (Level 1) earthquake is another important concern for designing a railway structures. For this purpose, a stiff side blocks is generally placed in transverse direction together with isolation support to prevent the distortion of the rail. However, such a restrainer might prevent the isolation from working effectively by tightly fixing the bearing even under extreme (Level 2) motion.

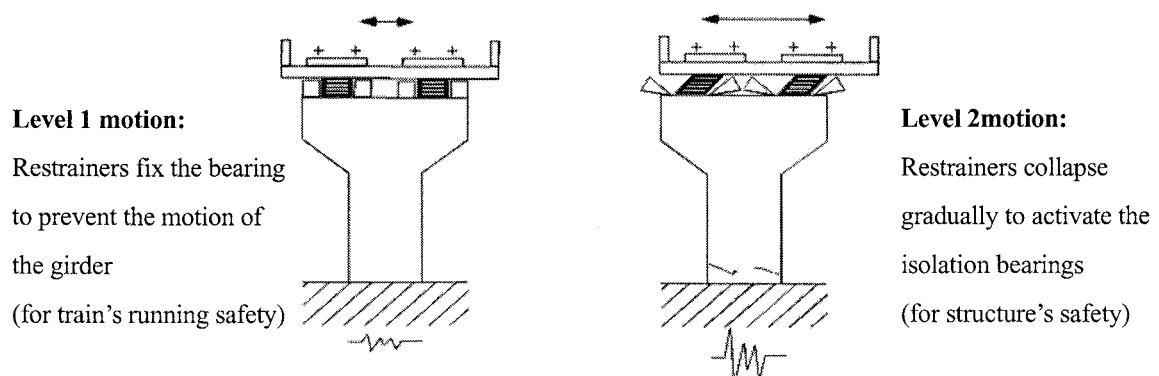


Figure 1 Concept of the newly developing restrainers used with isolation bearings

Taking such inconsistent demanding performances for a railway structure into account, it is necessary to develop a new device which restrains the motion of bearing only when the earthquake is considerably small. The device, however, should lose its restraining function to activate the isolation bearings when the extreme motion is induced to the structure (see Figure 1).

In this research, some different types of new restraining devices having such features were proposed for a railway structure with isolation bearings. The dynamic behaviors of the restrainers were clarified through the large-scale shaking table tests.

2. PERFORMANCE DEMANDS FOR A NEW RESTRAINER

It is desirable for a new restrainer used with an isolation supports of railway structures to secure running safety of trains under Level 1 motion and to suppress the structure's damage in a small extent under Level 2 motion simultaneously. For attaining the running safety, the restrainer should be stiff enough to restrain the distortion of railways in transverse direction. On the contrary, the restrainer should collapse under Level 2 motion so that the isolation supports work effectively to moderate the damage of the structure. Figure 2 shows the schematic diagram of the desirable performance of the restrainers as a comparison with a character of an isolation bearing. It should be noted that the restrainer should decrease its resisting force gradually under strong motion so that the large inertia force is not suddenly transmitted to the isolation supports. Having these performances, the bearing could alter its character from rigid to isolation in accordance with the strength of an earthquake.

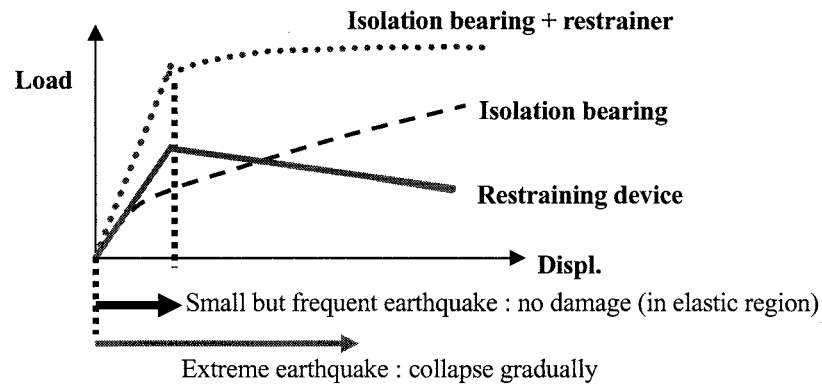


Figure 2 Schematic of the demanding performance of a new restrainer

3. DEVELOPED RESTRAINERS

Three different types of new restrainers (denote device type A, B, and C in the followings) that attain the necessary performance for a railway structure mentioned in the previous section were developed as shown in Figure 3. These devices are to be placed between a girder and a pier to work cooperatively with isolation bearings. Additionally, a gap between a girder and the restrainer should be needed so as not for the device to restrain the longitudinal motion of isolation bearings.

3.1 Device type A

The appearance of the device is similar to the ordinal restraining device, except the hinge placed at the bottom of the block (see Figure 3 (a)). If the large inertia force is applied to the triangle block, the hinge will be twisted and broken. The nonlinear behavior of the hinge causes the gradual decline of the resisting force. The maximum reaction force and corresponding displacement are controlled by a size of the hinge.

3.2 Device type B

As shown in Figure 3 (b), the device consists of a hinged block and steel plate on its back. The block supported by the back plate resists the inertia force under Level 1 motion. However, the plastic behavior of the hinge as well as plastic buckling of the plate gradually decreases the strength of the device if a large inertia force is applied to the block. The maximum resisting force depends on a section area of the plate and a size of the hinge.

3.3 Device type C

The device has three bolts (A and B in Figure 3(c)), one of which (B in Figure 3(c)) is placed on the slit. The inertia force is first transmitted to and accumulated by bolts A under Level 1 motion. However, the bolts A will be broken to transmit the inertia force to bolt B, if the load exceeds the strength of bolts A. The bolt B will then squeeze the slit in order to prevent the sudden decline of the resisting force due to the collapse of bolts A. The maximum resisting force and total force-displacement relation are controlled by the shear strength of bolts as well as the size of the slit.

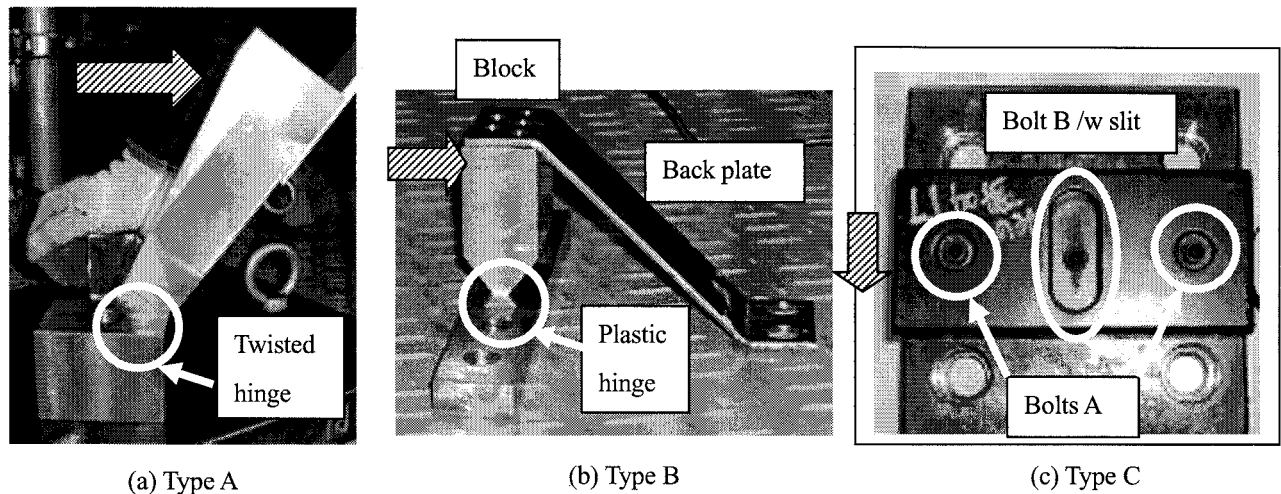


Figure 3 Schematics of the developed new restrainers

(Hatched arrow in the figure indicates the loading point and direction of the inertia force)

4. SHAKING TABLE TESTS

The prototype models of the proposed new restrainers were prepared, and the large-scale shaking table tests were performed in order to investigate the dynamic behaviors of these devices.

4.1 Specification of the shaking table

The large-scale shaking table facility in Disaster Prevention Research Institute of Kyoto University was used for the test. The shake table has a capability to drive the table (5.0 m×3.0 m) up to 1.0 G in acceleration and 150 kine in velocity with maximum specimen weight of 150 kN. The maximum strokes are 300 mm in longitudinal, 250 mm in transverse, and 200 mm in up-down directions.

4.2 Test setup

Figure 4 shows the schematic diagram of the test setup in case specimen Type A is assembled. The high damping rubber (HDR) supporting the RC slab was put on the shake table, and two restrainers were placed in the shaking direction. The specification of the HDR is shown in Table 1.

Table 1 Specifications of the HDR

Section property	230×230 mm	Shear module	0.4 N/mm ²
Total rubber height	6 mm×30 layers=180 mm	Equivalent stiffness (650%)	77.3 kN/m
Steel plates	2.3 mm×29	Equivalent damping (650%)	22.5 %

Additionally, the counterweight was mounted on the slab in order to adjust the natural frequency of the total test system to 1 sec. The total weight of the slab and the weight was approximately 100 kN. The inertia force of the slab was transmitted to the restrainers by the plates attached to the bottom of the slab. The gap between the plate and the restrainer was adjusted to 1.5 mm so as for the restrainer not to disturb the motion perpendicular to the shaking direction.

For data acquisition, the accelerometers and laser displacement sensors were placed on the slab and shake table. The reaction force of the isolation bearing was directly measured by the multi-directional load transducer placed between the bearing and the table shown in Figure 4. Since the inertia force of the slab was estimated by the given weight and measured accelerations, reaction force with regard to the restrainer can be obtained by subtracting that of isolation bearing from the total inertia force.

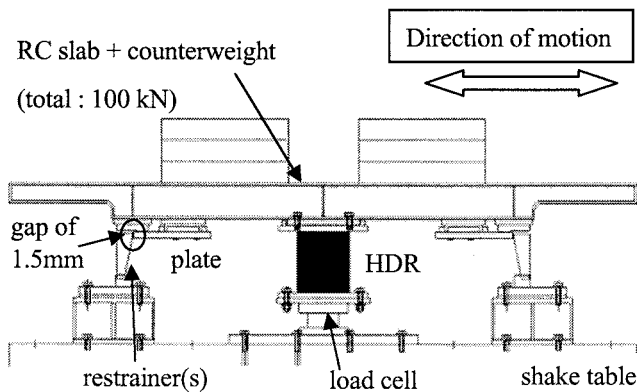


Figure 4 Overview of the test setup

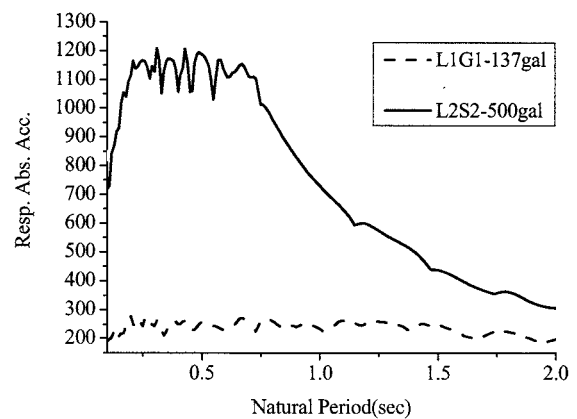


Figure 5 Absolute acceleration response spectra

4.3 Input motion for the shake table

The test specimen was excited in the longitudinal direction by the motions of the Level 1 and Level 2 spectrum II in the bedrock, designated in the seismic design code for railway structures in Japan. The Level 1 motion assumes the small but frequent earthquake, and the Level 2 spectrum II is the very rare strong inland earthquake. The Level 1 motion was used to check if the response of the restrainer is in an elastic region. On the contrary, the test setup was excited by the Level 2 motion to confirm the restrainer be gradually broken to activate the isolation bearing.

Maximum accelerations of Level 1 and Level 2 motions were adjusted to 137 gal and 500 gal respectively due to stroke limitation of the shake table. The linear absolute acceleration response spectra with a damping of 5 % with regard to these motions are shown in Figure 5. In the following discussion, Level 1 and Level 2 spectrum II motions are abbreviated to L1 and L2 respectively.

4.4 Specifications of the restrainers

The yielding force and its displacement should be properly determined to design a restrainer. A yielding displacement is determined as 5 mm, which corresponds to the regulation of maximum displacement in transverse direction under L1 motion to secure train's running safety. The yielding force is determined so that the response of the restrainer is in an elastic region under L1 motion and

exceeds the level in case of L2 motion.

It is estimated from Figure 5 that the demanding seismic intensity is at least 0.3 in order to keep the device response below the yielding level under L1 motion. Since the weight of the slab is 100 kN, the total resisting force due to the bearing and restrainer should be at least 30 kN ($=100 \times 0.3$) in this experiment. By subtracting the reaction force of the isolation bearing at the yielding displacement of 5 mm (approximately 5 kN) from the total requiring force, the minimum yielding force of 25 kN was determined for the restrainer.

Figure 6 shows the force versus displacement relations with regard to restrainers Type A, B and C obtained from the preliminary static loading tests. It is observed from these figures that all devices meet the minimum yield force and displacement demanded, apart from nonlinear behavior and maximum resisting force.

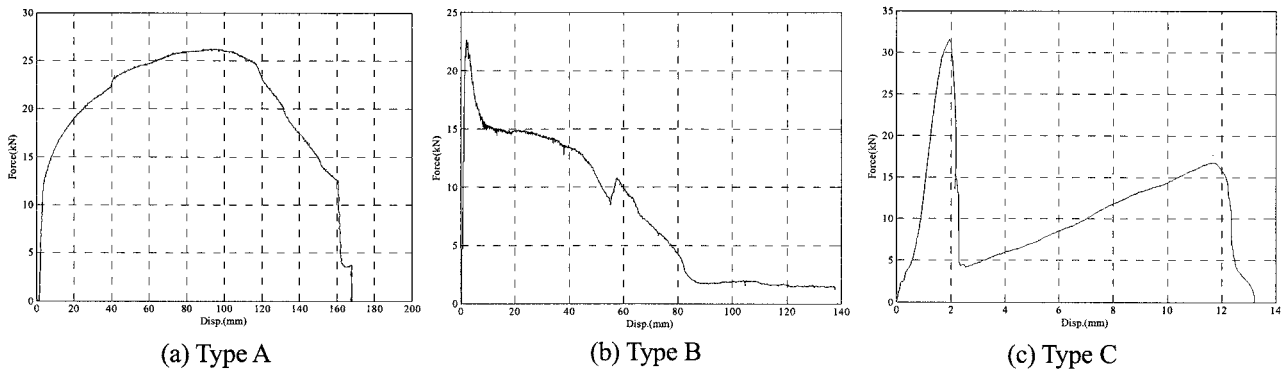


Figure 6 Load-displacement relations of devices via static loading tests

5. EXPERIMENTAL RESULTS AND DISCUSSIONS

5.1 Level 1 motion

The relative displacements of the slab with Type A, B, and C restrainers under L1 excitation as well as corresponding displacement versus reaction force relations are shown in Figures 7, 8, and 9 respectively. The response without the restrainer is also depicted for comparison. It is obvious from these figures that all the devices regulated the girder's displacement below 5 mm, corresponding to the yielding displacement of the device. It implies that the responses of all devices were in almost an elastic region without any severe damage. From these results, it is concluded that the proposed devices satisfied the required performance to secure running safety of a train.

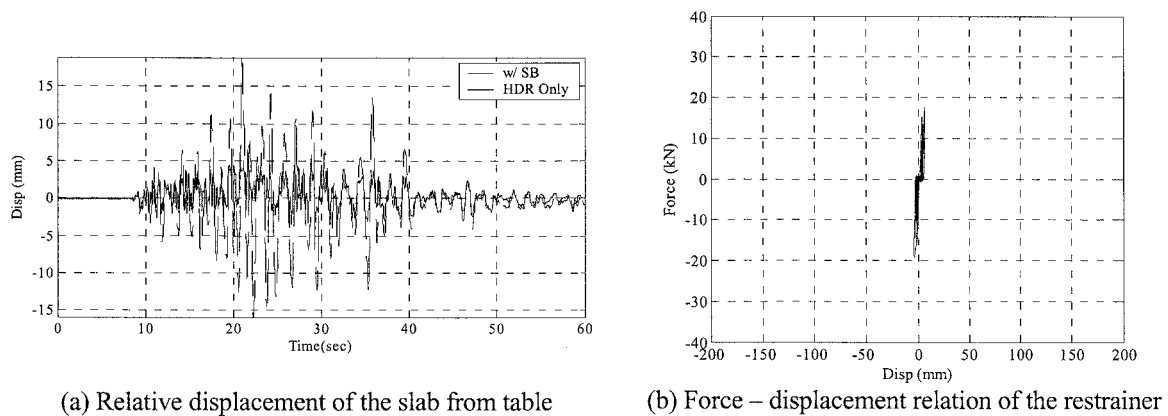


Figure 7 Dynamic behavior of the restrainer Type A under L1 motion

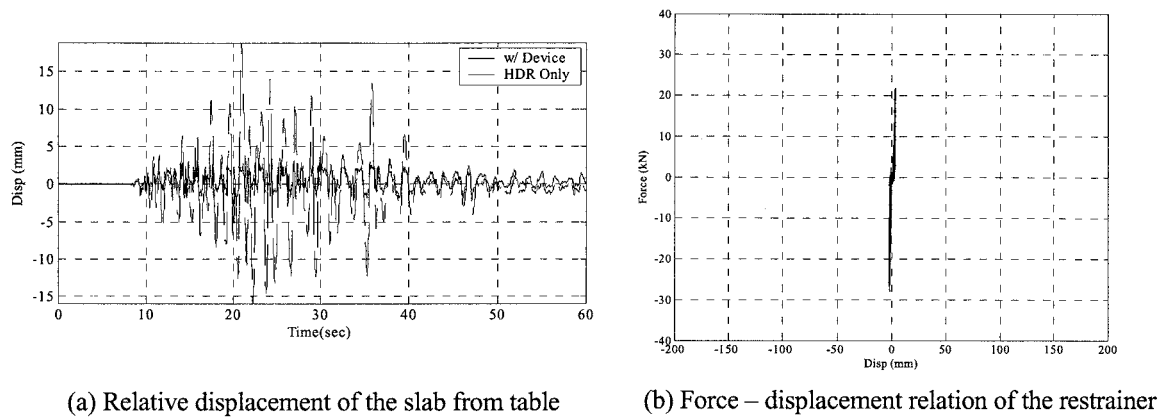


Figure 8 Dynamic behavior of the restrainer Type B under L1 motion

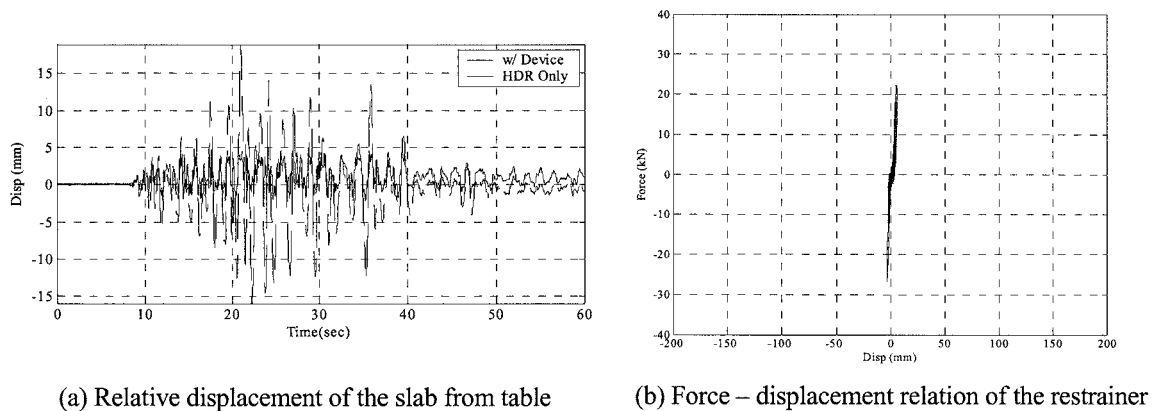


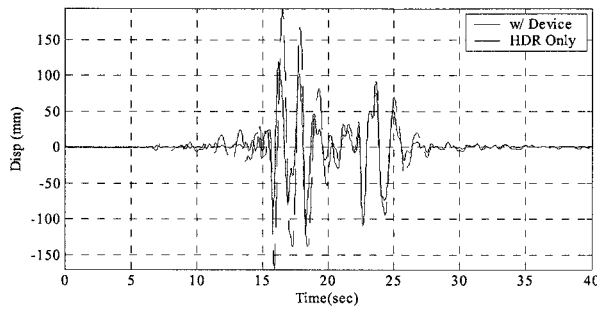
Figure 9 Dynamic behavior of the restrainer Type C under L1 motion

5.2 Level 2 motion

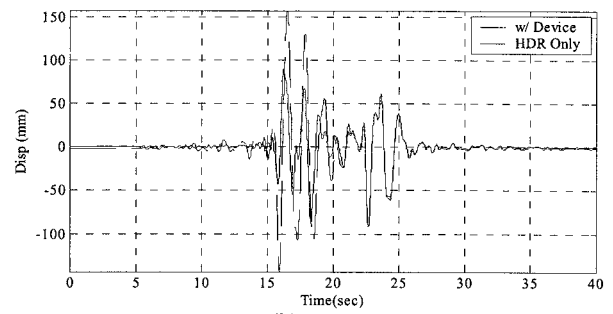
As with the L1 excitation, relative displacements of the slab Type A, B, and C restrainers under L2 excitation are shown in Figure 10. Figures 11(a), 12(a), and 13(a) present the displacement versus reaction force relation of Type A, B, and C restrainers. It is clarified from these figures that all the devices were broken after restraining the large deformation due to the first shock of the input motion. Particularly, Type A device could restrict the maximum relative displacement of the slab approximately 50 % compared to that without the device.

As for the nonlinear characters of devices, it is observed from the comparison of Figures 11(a), 12(a), and 13(a) with Figure 6 that hysteretic response of devices under dynamic excitation almost traced those of static loading tests. In case of Type A and B restrainers, however, maximum resisting forces obtained from dynamic loading tests slightly exceeded those in static conditions. The difference probably arose from the velocity-dependent damping, which does not take place in static conditions.

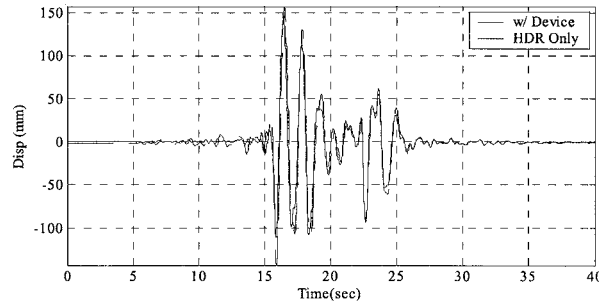
In addition, Figures 11(b), 12(b), and 13(b) show comparisons of the total inertia force versus relative slab displacement relations with and without restrainers. From these figures, it is confirmed that the reaction force of each device was gradually declined and the slab response asymptotically reached to that without the device. It consequently follows that the devices altered the character of the bearing from the fixing to the isolation support in accordance with the strength of the input motion. Moreover, the maximum total inertia forces that relate to the structural damage were not significantly increasing compared to that without the device. The results imply that proposed devices are readily be installed to the an existing structure which is designed only considering the behavior of the isolation devices, if parameters for the device is carefully chosen and its dynamic behavior is closely investigated.



(a) Type A

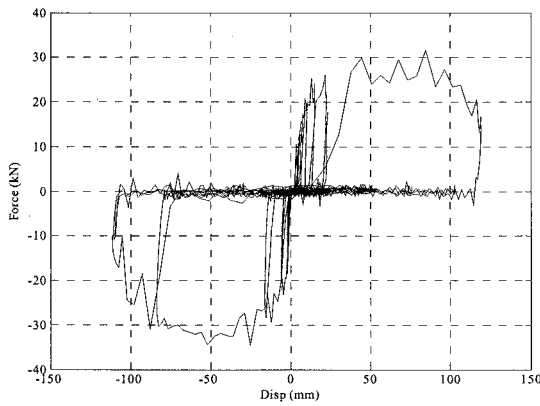


(b) Type B

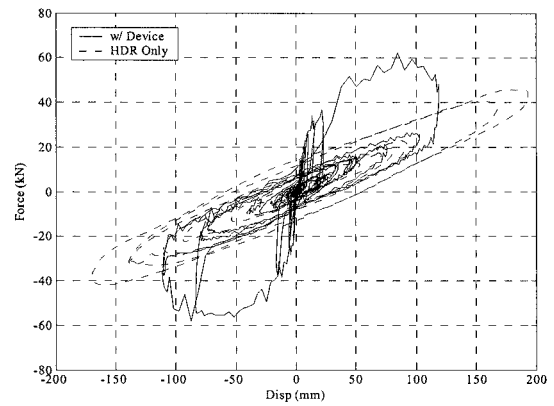


(c) Type C

Figure 10 Slab relative displacements from the table as a comparison w/o devices

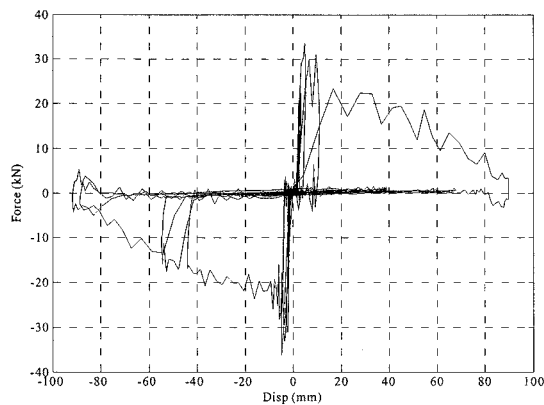


(a) Force – displacement relation of the restrainer

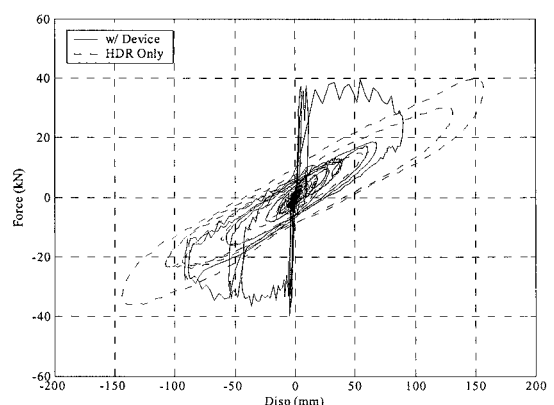


(b) Total inertia force – displacement relation

Figure 11 Dynamic behavior of the restrainer Type A under L2 motion



(a) Force – displacement relation of the restrainer



(b) Total inertia force – displacement relation

Figure 12 Dynamic behavior of the restrainer Type B under L2 motion

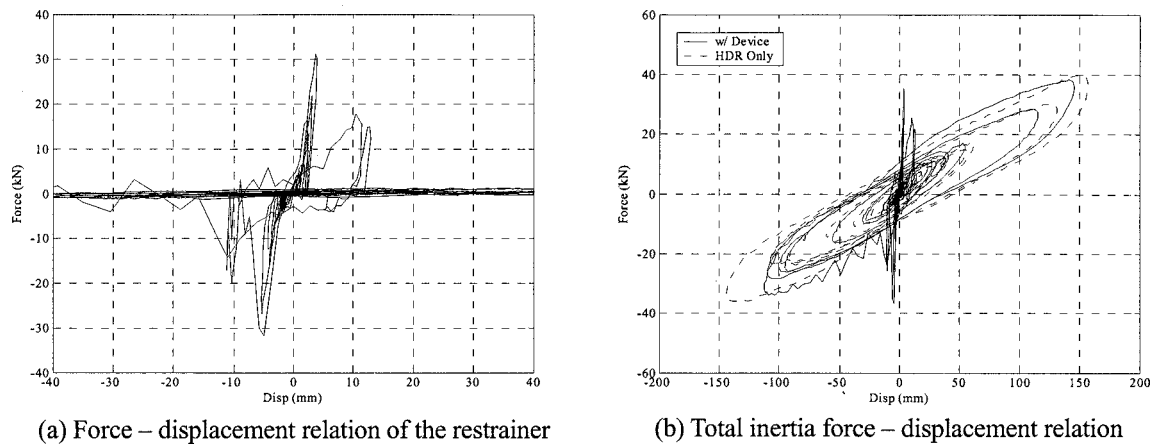


Figure 13 Dynamic behavior of the restrainer Type C under L2 motion

6. CONCLUDING REMARKS

In this paper, the new restraining device applicable for a railway structure with isolation bearings is proposed, by which the running safety of a train under small earthquake as well as the reduction of structural damage under extreme motion are secured simultaneously. The fundamental characters of three prototype devices were tested by a static loading test. The dynamic behaviors of these devices were then investigated through shaking table tests, on which the girder and rubber bearing were mounted. It was confirmed that the devices hold the motion of the isolation bearing without severe damage under excitations in a small level, while collapsed gradually to activate the isolation bearing under extreme motion.

Acknowledgements:

The dedication of Mr. Ichikawa (Engineering staff of Kyoto University), Mr. Nakanishi (Engineering staff of Kyoto University at the time of experiment), Nomura Jyuuki Ltd., and students of structural dynamics laboratory of Kyoto University for carrying out the shaking table tests is fully appreciated.

References:

- Ikeda, M., Toyooka, A., Iemura, H., Hishijima, Y., Uno, S., Ikenaga, M., and Harada, T. (2005), "Shaking Table Tests of the Damped Restrainers for a Isolated Railway Structures," Proc. of 8th Symposium on Ductility Based Seismic Design (in Japanese)
- Toyooka, A., Ikeda, M., Iemura, H., Murata, K., and Ichikawa, A. (2005), "Effect of the Rail Track on Dynamic Behavior of the Base-Isolated Railway Bridges," Proc. of the IABSE symposium on structures and extreme events
- Railway Technical Research Institute (1999), "Seismic Design Code for Railway Structures," Maruzen

FATIGUE BEHAVIOR OF DEFECT-CONTAINING UNDER-MATCHED WELD JOINTS UNDER PLASTIC STRAIN

Atsushi Tanabe¹ and Xiao Long²

1) Research Associate, Department of civil Engineering, Tokyo Institute of Technology

2) Graduate Student, Department of civil Engineering, Tokyo Institute of Technology
tanabe@cv.titech.ac.jp, -

Abstract: All of codes and specification request that the yield strength of the deposit metals should be higher than the yielding strength of base metals in order to prevent damage in weldment. However, under-matched welded joint, which is the joint that yield point of deposit metal is lower than that of base metal, can be used intentionally in order to improve weldability. In case of under-matched welded joint, deposit metal yield first when seismic force applied. And then strain will concentrates in the deposit metal. However, stress/strain triaxiality in the deposit metal increases tensile strength of the joint. On the other hand, such triaxiality may affect fatigue strength under cyclic plastic strain due to earthquakes, especially when welded defects exist in the deposit metal. This study aims to evaluated fatigue strength of defect-containing under-matched welded joints suffering cyclic loading due to earthquakes. FEA and cyclic loading tests of under-matched welded joint specimens with an artificial defect were carried out. As a result, crack initiation life of such joint was short because of high strain concentration due to triaxiality, and the effects of under-matching on crack initiation could be considered by FEA.

1. INTRODUCTION

In urban area, many steel structures are used due to land limitation because welding make possible to construct complex steel structures. However, welded joint can become weak point because welding quality may vary widely and weld defects may remain in the deposit metal. Therefore, damage of weld joint should be avoided during earthquakes. Thus, the yield strength of the deposit metals should be higher than the yielding strength of base metals in order to avoid damage in the deposit metal. However, this requirement can not always be satisfied because of following reasons. [1] Softer welding materials are used intentionally in order to improve weldability in case of high strength steel. [2] Actual yield strength of base metal can be significantly higher than the value in the provision for yield strength. In such cases, the weld joint becomes an under-matched welded joint.

When seismic force applies to under-matched welded joints, deposit metal yields first, then strain will be concentrate into the deposit metal. However, the deposit metal will be constrained by non-yielded base metals and stress triaxiality will be introduced (Henry et al. 1997, Hancock et al. 1993). Because of such triaxiality, under-matched welded joints had almost same tensile strength as usual welded joints, but it had a tendency of low elongation (Satoh and Toyoda 1971).

Besides under-matching, weld joints have risk to include weld defects such as blow-holes, slag-inclusions, cracks, etc., and these defects reduce fatigue strength (Miki et al. 2001). If defects exist in under-matched welded joints, fatigue strength under cyclic plastic strain may decrease

because of strain concentration due to both of defects and under-matching. Furthermore, there is the possibility of that stress concentration due to weld defect causes local yielding, even in service condition. In such case, high strain concentration may occur and it may affect fatigue strength.

Basically, as a significant parameter in the structural behavior elastic stress concentration factor mainly depends on the geometry and location of the embedded discontinuity. Figure 1 shows the conceptual diagram of stress/strain concentration factor development. In elastic region, strain concentration factor and stress concentration factor are same (K_t). When local stress reaches yield strength, stress concentration factor and strain concentration factor bifurcate. Strain concentration factor increases and stress concentration factor decreases. The happening of the bifurcation depends on the yield strength of material. In case of under-matched welded joints, the bifurcation initiates at lower nominal stress, which is shown as the dashed line in Figure 1. In this point of view, under-matched joint may have higher strain concentration factor. Thus the effect of weld defects on the strain-controlled fatigue behavior of under-matched joints must be evaluated.

Kyuba et al. (2001) carried out the cyclic loading test of specimens with and without 2mm diameter penetrated hole under three matching conditions. They pointed out that the small amount of under-matching had equivalent cyclic loading capacities with even/over-matched joints and that the weakest matching condition had extreme poor capacities. However, relationship between triaxiality and defects were still not so clear. Thus, the effect of triaxiality on local strain concentration and low-cycle fatigue behavior should be examined.

This study aims to grasp the fatigue behavior of defect-containing under-matched weld joints under cyclic plastic strain due to earthquake. FEM analyses and fatigue tests of under-matched welded joints with an artificial defect were carried out.

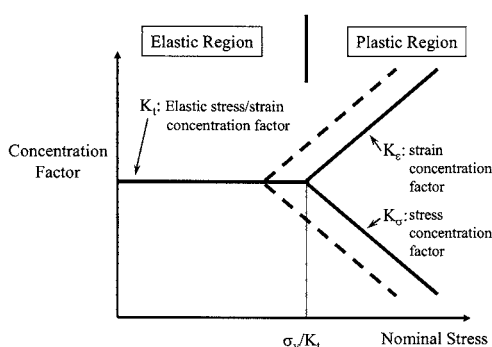


Figure 1 Stress/Strain Concentration Factor Development

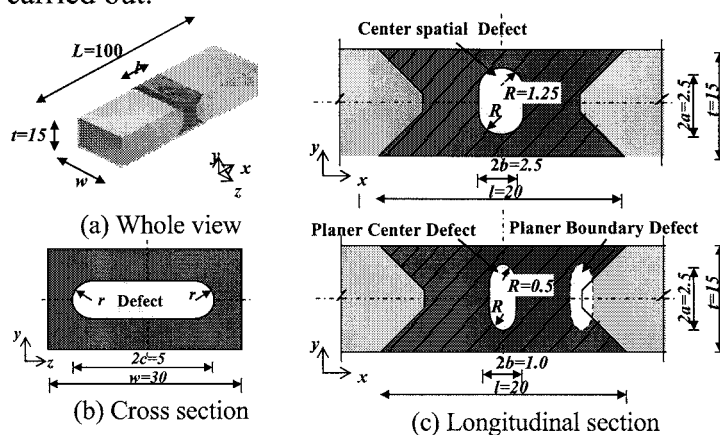


Figure 2 geometry and location of defect

2. FACTOR ON LOCAL STRAIN CONCENTRATION

In order to grasp the influence of location and geometry of embedded defects on local strain condition, parametric FEA was carried out. Parameters were under-matching ratio and defect type. Under-matching ratio of 0% (even match), 10% and 20% were considered. Three type defects were considered: boundary planar defect, center planar defect and center spatial defect. The boundary planar defect simulates incomplete penetration and lack of fusion. The center planar defect simulates weld crack. The center spatial defect simulates of brow-hole and slag inclusion. Detailed dimension of models is shown in Figure 2. Figure 3 shows the FEA models. Minimum mesh size was 0.1 mm. Symmetrical conditions were considered. The analysis code was ABAQUS (2003). Kinematic hardening was used as constitutive equation.

2.1 Analysis results

Figure 4 shows the distribution and peak value of maximum principal strain when nominal stress was 350MPa ($\approx 0.2\%$ nominal strain). The locations of peak strain were same for all models. Under-matching, location of defect, and geometry of defects did not affect peak location of maximum principal strain. Comparison of peak values of maximum principal strain showed that peak strain values of 10% under-matching models were about 1.13 times higher than the peak strain values of even-matching models. In case of 20% under-matching models, the peak strain values were about 1.2 times higher than that of even-matching models. Contrary to expectation, the defect location had almost no effect on strain distribution.

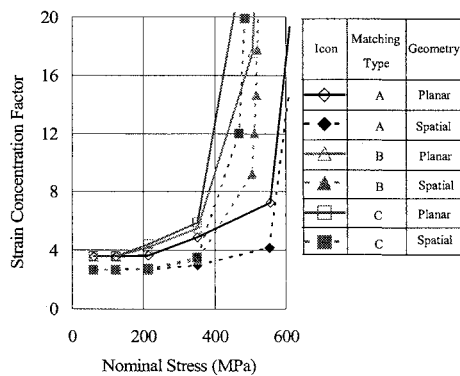
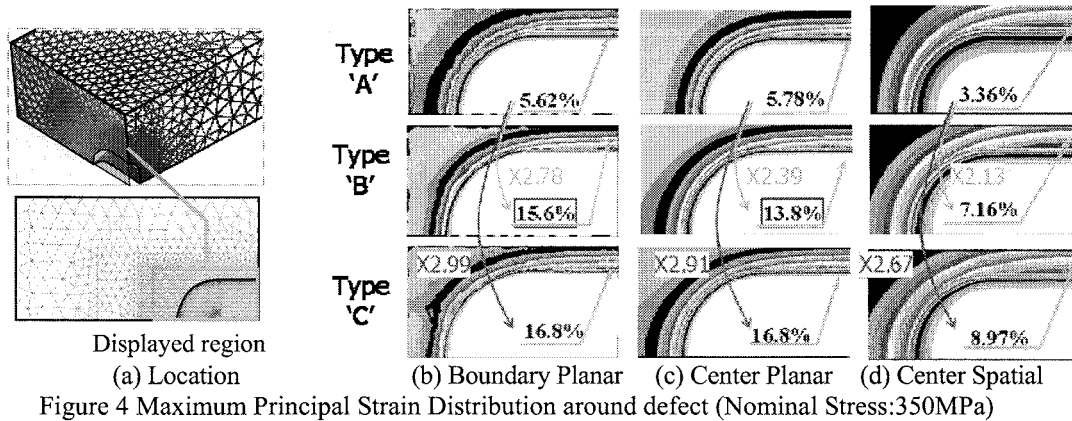
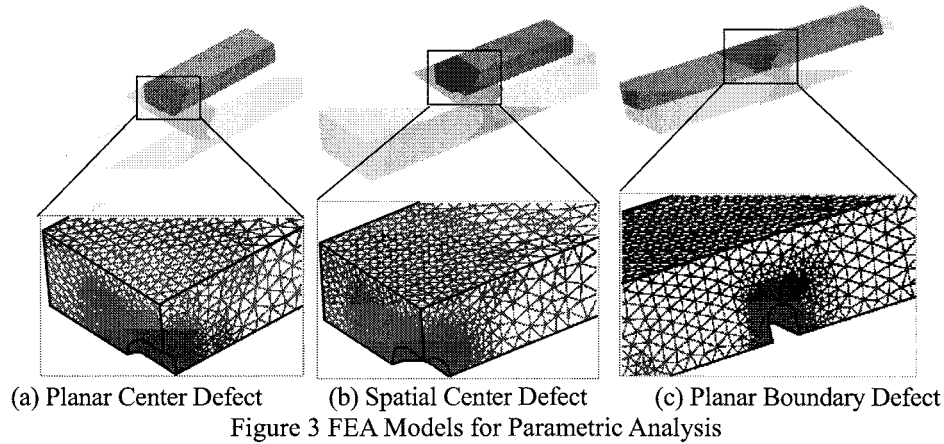


Figure 5 Development of Strain Concentration Factor vs. Defect Geometry (Center Defect)

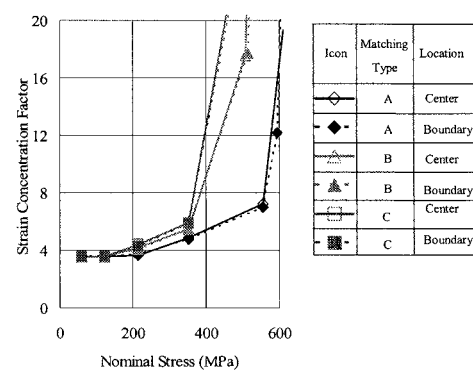


Figure 6 Development of Strain Concentration Factor vs. Defect Location (Planar Defect)

Bifurcation of the concentration factor curves (like what is shown in Figure 1) and local strain were considered at the point where highest local strain happens according to the result of analysis. Figure 5 shows the comparison of strain concentration factor development between planar defect

and spatial defect, and Figure 6 shows strain concentration development of center planar defect and boundary planar defect. Strain concentration factors were rapidly increased when nominal strain was close to yield strength of welded metal. Therefore, when nominal stress is close to yielding strength of deposit metal, under-matching ratio was most effective parameter.

Table 1 Mechanical property and welding condition

	Base metal	Welding material		
		Evenmatch	10% under-matching	20% under-matching
Material Name	BHS500	SF-60L	SF-60	YM-28S
Thickness (mm)	20	-	-	-
Yield Strength (MPa)	611	650	530	485
Tensile Strength (MPa)	691	640	605	540
Elongation (%)	36	24	26	33
Heat input (kJ/mm)	-	1.84	2.20	1.69

Table 2 Chemical Composition (mass% excluding [N]&[B], [N]&[B]: ppm)

	BHS500	SF-60L	SF-60	YM28-S
C	0.09	0.07	0.04	0.08
Si	0.29	0.38	0.5	0.35
Mn	1.57	1.38	1.53	0.85
P	0.014	0.017	0.009	0.011
S	0.003	0.01	0.004	0.005
Cu	0.01			
Ni	0.01	1.33	0.49	
Cr	0.02			
Mo	0.09			
Nb	0.02			
V	0.04			
P _{cm}	0.18			

3. FATIGUE TEST UNDER PLASTIC STRAIN

3.1 Specimens and Testing Condition

For under-matching conditions, even-matching (type 'A'), 10% under-matching (type 'B') and 20% under-matching (type 'C'), were considered. BHS500 was used as base metal, and three welding material were used: SF-60L, SF-60 and YM28-S. Table-1 and Table-2 show the mechanical properties and chemical composition, respectively.

Figure 7 shows the dimensions of specimen. Figure 8 shows the photo of macro-etched welding part. "X" groove shape was used. This specimen aimed to make high stress concentration at the tip of hole, where highest triaxiality occurs (Tanabe and Kato 2006). Thus, a half penetrated hole of $\phi 2.5$ was drilled into deposit metal. Reinforcements were removed and surfaces of the specimens were finished.

Figure 9 shows the test setup. The fatigue tests were carried out by controlling nominal strain of 100mm gauge length. Four nominal strain ranges from 0.25% to 0.6% were considered. The nominal strain was measured by two pi gauges which were installed on the both side of specimens. Table-3 shows the test cases. Total 11 specimens were tested.

3.2 Test Results

In order to identify crack initiation from the artificial defect, beach marking and ultrasonic testing (UT) were carried out.

Beach marking was carried out to specimens of 0.3% nominal strain range. Beach marks were successfully remained into two specimens. Figure 10 shows the fracture surface and beach marks of the 20% under match 0.3% nominal strain range specimen. This figure indicates that the location of crack initiation was the edge of hole but not the tip of the hole. Fracture surfaces of other specimens were also observed in order to identify crack initiation location. The crack initiation location of

other specimen were also the edge of the hole, except for type-'C' 0.6% nominal strain. Crack initiation location of type-C 0.6% nominal strain specimen was tip of the hole.

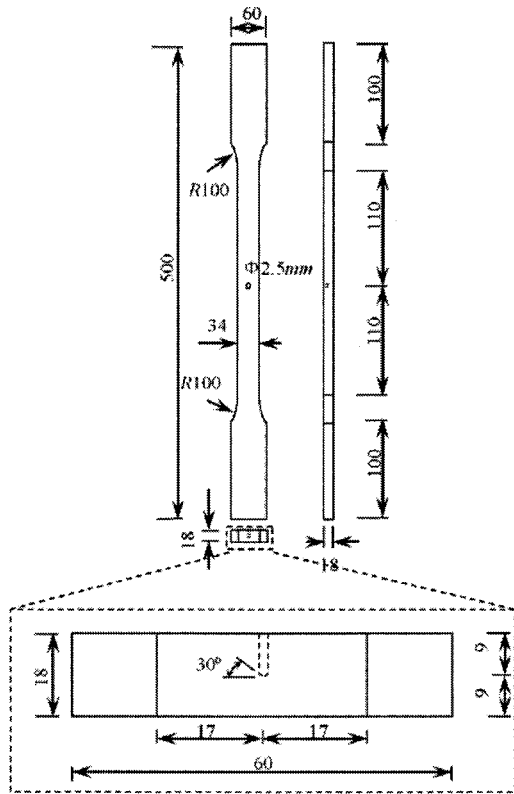
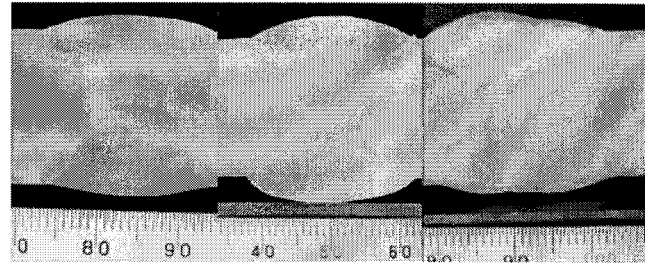


Figure 7 Dimensions of specimen



(a) Type 'A' (b) Type 'B' (c) Type 'C'
Figure 8 Macro-etched welding part

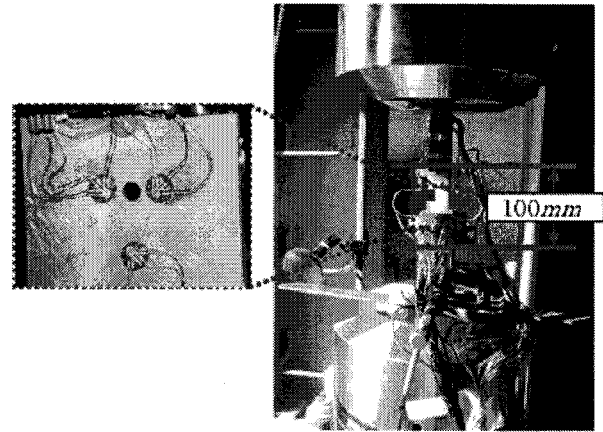


Figure 9 Test Setup

In this study, tandem array probe UT system and SAFT imaging (Rattanasuwannachart et al. 2005) were also used. Figure 11(a) shows the setup of UT test. UT was conducted from the back surface of the specimen for several cycles: basically every 50 cycles and every 10 cycles from beginning to 100 cycles. Figure 11(b) shows the visualized images around the artificial hole. A small red spot appeared in the image of 200 cycles (A in Figure 11(b)). The red spot located at the edge of the artificial hole. The red zone expanded with more loading cycles (B and C in Figure 11(b)). Comparison with beach marks indicates that the red zone represented the fatigue crack. Therefore, cycles detected by applying UT was used as crack initiation life N_c .

Table-4 shows the fatigue life N_f , crack initiation life N_c and propagation life $N_p (=N_f - N_c)$ of each specimen. In this study, 30% load drop was used as the definition of fatigue life (Kyuba et al. 2001). This table indicates that crack initiate very early; Under-matching strongly affected on the crack initiation life. The N_c of 20% under-matching specimen was less than 1/3 of the N_c of the even-matching specimen for any nominal strain range. Even in case of 10% under-matching, the N_c of 10% under-matching specimen was less than a half of the N_c of even-matching specimen for all nominal strain range. Thus, the crack initiation life of defect containing under-matching joint under plastic strain was short. Therefore, the most of fatigue life was propagation life, and this fact indicates that the fracture mechanics approach is suitable in order to evaluate the fatigue life of the defect containing under-matching joints under plastic strain.

4. CORRESPONDING FEM ANALYSES

In order to obtain triaxiality and local strain concentration status, corresponding non-linear elasto-plastic FEM analyses were carried out.

Type	Nominal strain range (%)			
	0.25	0.3	0.45	0.6
A(even)	-	✓	✓	✓
B(10% under)	✓	✓	✓	✓
C(20% under)	✓	✓	✓	✓

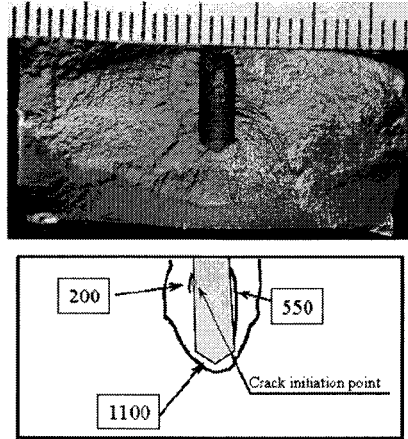
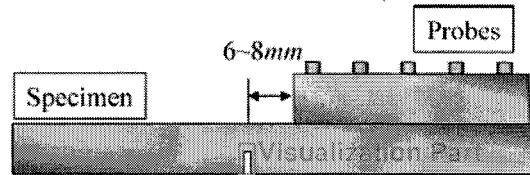


Figure 10 Fracture surface and Beach Marks (Type 'C' [20% under-matching], nominal strain range: 0.3%)

Nominal Strain Range (%) (Gauge Length: 100mm)	Type	N _f	N _c	N _p
0.25	B (10%)	7881	1700	6181
	C (20%)	6019	1400	4619
0.3	A (even)	4933	1300	3633
	B (10%)	3041	250	2791
	C (20%)	2193	200	1993
0.45	A (even)	1082	200	882
	B (10%)	467	90	377
	C (20%)	448	70	378
0.6	A (even)	405	80	325
	B (10%)	219	30	189
	C (20%)	169	10	159



(a) Layout of UT device

Cycle	0	100	200(N _c)	500	1100
UT result					

(b) Visualized image of UT results

Figure 11 Estimation of crack initiation life by using UT (Type 'C', nominal strain Range: 0.3%)

4.1 FEM model

Because of symmetric conditions, only one quarter model was extracted as analysis objective. The dimensions of the model are set the same as that of specimens. The displacement controlled length (gauge length) was also 100mm. Figure 12 shows the FEM model. In this study, ABAQUS (ABAQUS, Inc. 2003) was used as analysis code. Minimum mesh size was 0.1 mm. Second order tetrahedral solid element was used for this analysis. Kinematic hardening was used for the constitutive equations. Heat Affected Zone (HAZ) was ignored in this FEM model.

4.2 Analysis Results and Discussion

Figure 13 shows the maximum principal strain distribution of type B and C under 0.6%

nominal strain. The location of peak of the maximum principal strain range was the edge of the hole and close to the surface as shown in Figure 13(a) except in case of type C under 0.6% nominal strain. In case of type C under 0.6% nominal strain, the peak location was the tip of the hole as shown in Figure 13(b). These locations were the same locations of the fatigue crack initiation of the fatigue test specimens. Thus, it can be said that fatigue crack initiates from the peak point of maximum principal strain, and that the initiation point of fatigue crack could be estimated by FEA.

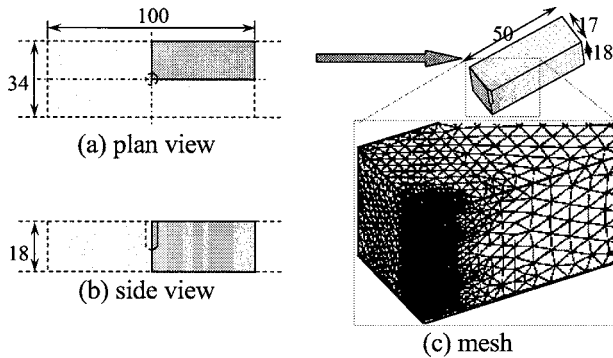


Figure 12 FEM Model

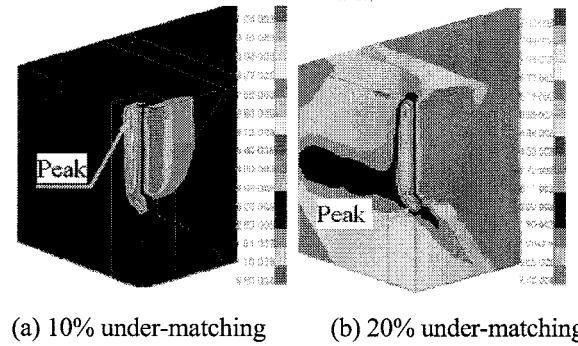


Figure 13 Maximum Principal Strain Range Distribution (nominal strain: 0.6%)

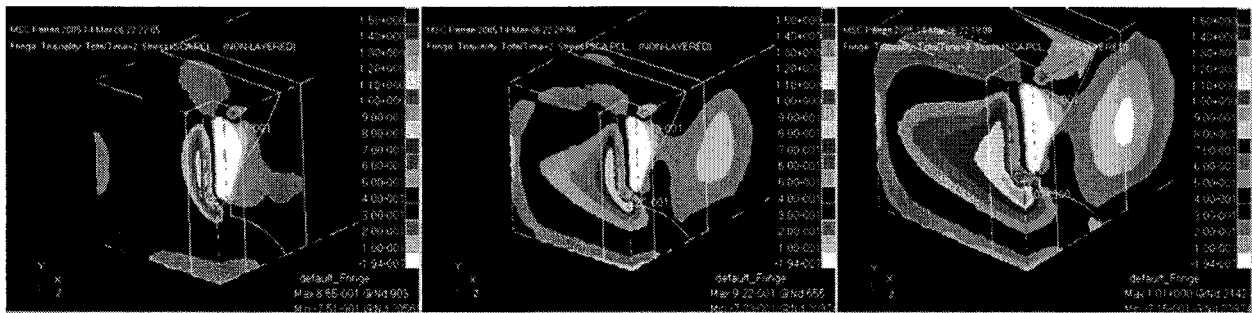


Figure 14 Distribution of Triaxiality, 0.6% nominal strain

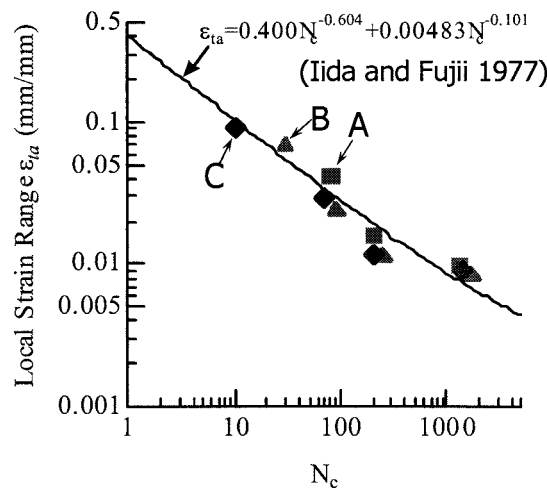


Figure 15 Local Plastic Strain Range vs. Crack Initiation Life (N_c)

Figure 14 shows the distribution of triaxiality when Nominal Strain is 0.6%. High triaxiality occurred around the tip of the artificial hole. Furthermore, 20% under-matching cases have high triaxiality at the tip of the half penetrated hole. Such high triaxiality might change the peak location of maximum principal strain.

Relationship between local plastic strain range $\Delta \epsilon_{pr}$ and N_c is shown in Figure 15. In this figure, $\Delta \epsilon_{pr}$ - N_c relationship by material tests (Iida and Fujii 1977) is also provided. The relationship

between N_c and local plastic strain range by FEA results had good agreement with the material's $\Delta\varepsilon_{pr} - N_c$ relationship. This fact means that defects and under-matching affect on local (plastic) strain concentration development only, and that the effects of defects and under-matching can be estimated by FEA.

5. CONCLUSIONS

In this study, several strength under-matched welded joint specimens with a center artificial defect were experimented and analyzed under various nominal strain ranges in order to evaluate seismic resistance of defect-containing under-matched joints. Following conclusions were made from this study.

- Crack initiation lives of defect containing under-matching welded joints under plastic strain are very short due to high strain concentration at the defect.
- Effects of under-matching and defects can be evaluated by using non-linear FEA, because relationship between local plastic strain range and crack initiation life agree with material's relationship.
- Under-matching had strong effects on local strain concentration development when nominal stress was close to yield strength of deposit metal.
- Crack initiation lives could be estimated by using tandem array probe UT system and special SAFT imaging.

References

- Satoh, K. and Toyoda, M. (1971) "Effect of Mechanical Heterogeneity on the Static Tensile Strength of Welded Joints" *Journal of the Japan Welding Society*, **40**(9), 885-900,
- Iida, K. and Fujii, E. (1977) "Low cycle fatigue strength of steels and welds in relation to static tensile properties" *IIW Doc. XIII-816-77*
- Hancock, J. W., Reiter, W. G. and Parks, D. M. (1993) "Constraint and toughness parameterized by T. Constraint Effects in Fracture" *ASTM STP1171*, American Society for Testing and Materials, 21-40
- Henry, B. S. and Luxmoore, A. R. (1997) "The stress triaxiality constraint and the Q-value as a ductile fracture parameter" *Engineering Fracture Mechanics*, **57**(4), 375-390
- Kyuba, H., Fukuda, Y. and Miki, C. (2001) "Cyclic Loading Capacity of Butt-Welded Joints with Various Matching Conditions" *IIW Doc. XIII-1886-01*
- Miki, C., Fahimuddin, F. and Anami, K. (2001) Fatigue Performance of Butt-Welded Joints Containing Various Embedded Defects. *Structural Engineering / Earthquake Engineering of JSCE*, **18**(1), 13s-28s
- ABAQUS, Inc. (2003) "ABAQUS Analysis User's Manual" Ver.6.4
- Rattanasuwannachart, N., Takahashi, K., Miki, C. and Hirose, S. (2005) "Development Of 3d Flaw Detection System With Multi-Channel Planar Array Probes And 3d Saft Algorithms", *Proc. of JSCE*, **787**, 33-45
- Tanabe, A. and Kato, M. (2006) "Ductility of Welded Joints with Weaker Welding Material" *Proc. of Third International Conference on Urban Earthquake Engineering*, Center for Urban Earthquake Engineering, Tokyo Institute of Technology, 449-456

THE EFFECT OF IMPULSIVE GROUND MOTION ON THE RESIDUAL DISPLACEMENT

Gakuho Watanabe¹⁾ and K. Kawashima²⁾

1) Research Associate, Department of Civil Engineering, Tokyo Institute of Technology, Japan

2) Professor, Department of Civil Engineering, Tokyo Institute of Technology, Japan

gakuho.w.aa@m.titech.ac.jp, kawashima.k.ae@m.titech.ac.jp

Abstract: Near-fault ground motion with prominent acceleration pulses resulted in the severe damage to the bridge structures. Such ground motions often exhibit special pulse-like characteristics and results in the permanent displacement to the structures after the earthquakes. This paper focuses on the effect of the near-fault ground motions with impulsive pulse on the residual displacement.

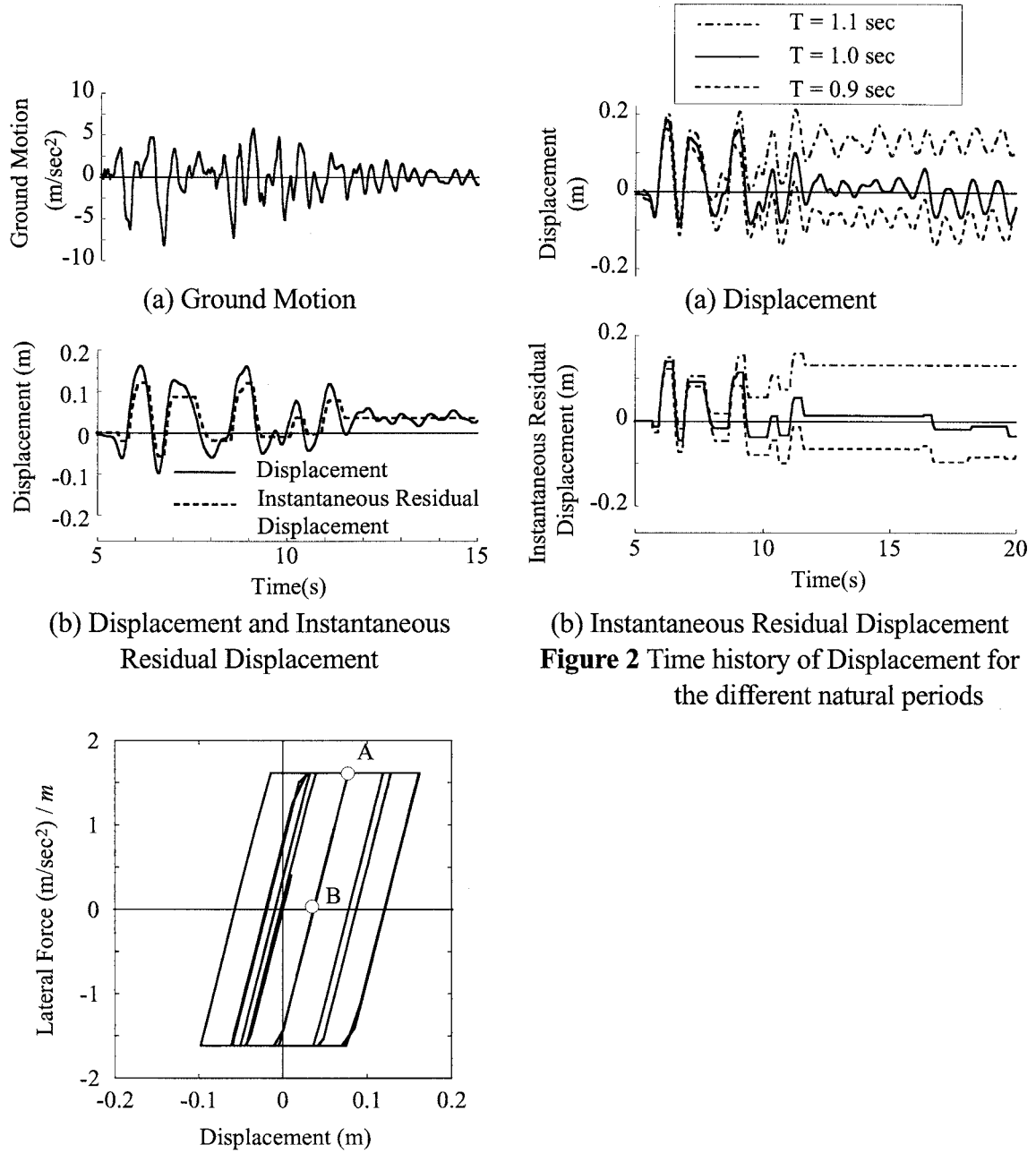
1. INTRODUCTION

Current seismic design of bridge structures requires high ductility capacity to ensure adequate seismic performance during strong excitations. A bridge structure subjected to a strong ground motion exhibits inelastic hysteretic behavior which may result in residual displacement. If such residual displacement is extensively large, such is the case reconstruction of the structure may be required. In the 1995 Kobe earthquake, wherein Route 3 of the Kobe Line of Hanshin Expressway suffered residual rotational deformation at the base larger than one degree. As a consequence, bridge columns had to be reconstructed following the earthquake. Thus, the post-earthquake residual displacement becomes a major concern. Since the residual displacement exhibit the large scattering depending on the natural period of the structure, nonlinear hysteresis and ground motions, a probabilistic approach is effective in evaluating the residual displacement. In this paper, evaluation of the residual displacement of bridge structures is undertaken.

Recently, the extensive failures of bridge structure due to the near-field ground motion have been reported. As the number of recorded near-field ground motions increases and the mechanism of its generation is known, the effect of near-field ground motions on the seismic demand of bridge structures becomes a major concern. There are, however, few discussions about the effect of recorded near-field ground motions on bridge responses. A special emphasis of this paper is then provided on the effect of near-field ground motions on the residual displacement of bridge structures.

2. RESIDUAL DISPLACEMENTS

Figure 1 shows the typical seismic response for 1995 Kobe earthquake which is computed by using the nonlinear SDOF model with elasto-perfectly plastic hysteresis, the natural period of 1.0 sec. The computed response shows the inelastic hysteretic response with the displacement ductility of 4, wherein the peak displacement is 0.18 m at 8.8 sec, and the residual displacement is 0.04 m at 15 sec. When the unloading occurs from the ordinary point A as shown in Figure 1 (c), the displacement at point B where the lateral force is equal to zero represents the instantaneous residual displacement $u_{r,inst}$. The instantaneous residual displacement $u_{r,inst}$ are also shown in Figure 1. The peak value represents the maximum possible residual displacement $u_{r,max}$.



(c) hysteresis relationship between Lateral Force vs. Lateral Displacement

Figure 1 Typical Seismic Response

Figure 2 shows the displacement response $u(t)$ and the instantaneous residual response $u_{r,inst}(t)$ of SDOF systems with the natural periods of 0.9, 1.0 and 1.1 sec. Since the natural periods of SDOF systems are close, those displacement responses exhibit the similar shapes of oscillation. Thus, the maximum displacements are the same level. On the other hand, the residual displacements u_r showed the difference after 8.8 sec depending on the natural periods.

Figure 3 shows the response spectra of the linear and nonlinear peak displacement, $S_{D,EL}$ and $S_{D,NL}$, the maximum possible residual displacement, $S_{r,max}$, and the residual displacement, S_r . Ruiz-Garzia and Miranda [2006] studies the ratio defined as:

$$C_r = \frac{u_r}{u_{EL,max}} = \frac{S_r}{S_{D,EL}} \quad (1)$$

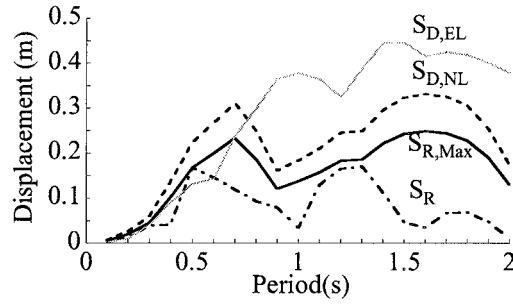


Figure 3 Maximum, Maximum Possible Residual Displacement and Residual Displacement spectra

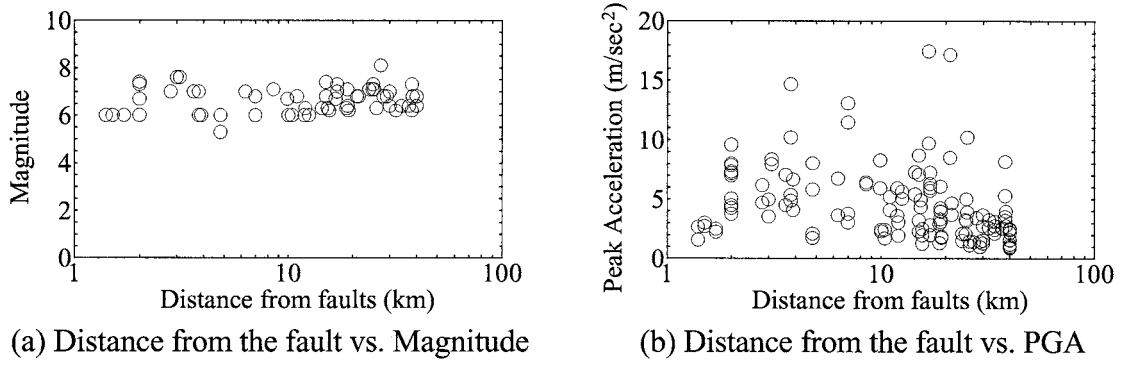


Figure 4 Data set of ground motion in the present study

For the design purpose, Kawashima et al. [1997] proposed the residual displacement ratio defined as:

$$\gamma_r = \frac{u_r}{u_{r,max}} = \frac{S_r}{S_{r,max}} \quad (2)$$

In the seismic code of JRA[1996], the residual displacement ratio is defined as 0.6 for mean value with second stiffness ratio of zero.

Data Set of Near Field Ground Motion Records

The present study is based on 150 recorded ground motions. These records are classified into two categories depending on the distances from the fault D_{CF} . Hence, 60 records for near-field ground motions ($D_{CF} < 10\text{km}$) and 90 for middle-field ground motions ($10\text{km} \leq D_{CF} < 40\text{km}$) are used, respectively. These records are non-uniformly distributed over the entire magnitude range from $M = 5.3$ to 8.1 and the peak ground acceleration range from 0.9 to 17.5 m/sec^2 as shown in Figure 4. The response spectra depending on the probability of non-exceedance are computed. The probability of non-exceedance $p_r(X)$ (D'Ambrisi and Mezzi 2005) is the probability that the estimators X does not exceed a certain value of b . It may be defined as:

$$p_r(X) = 1 - P(X \leq b) = 1 - \int_{-\infty}^b p(X) dX \quad (3)$$

where $p(X)$ is the probability of occurrence of the estimators.

Figure 5 shows the elastic seismic response spectra of acceleration and displacement depending on the non-exceedance probability depending on the distance from the fault D_{CF} . For both cases of $D_{CF} \leq 10\text{km}$ and $10\text{km} \leq D_{CF} < 40\text{km}$, the peak levels of acceleration response spectra with $p_r = 0.5$ and 0.9 are 7.5 m/sec^2 and 20 m/sec^2 , respectively. The acceleration response spectrum for $10\text{km} < D_{CF} \leq 40\text{km}$ has obvious peaks at 0.2 sec . On the other hand, the acceleration response

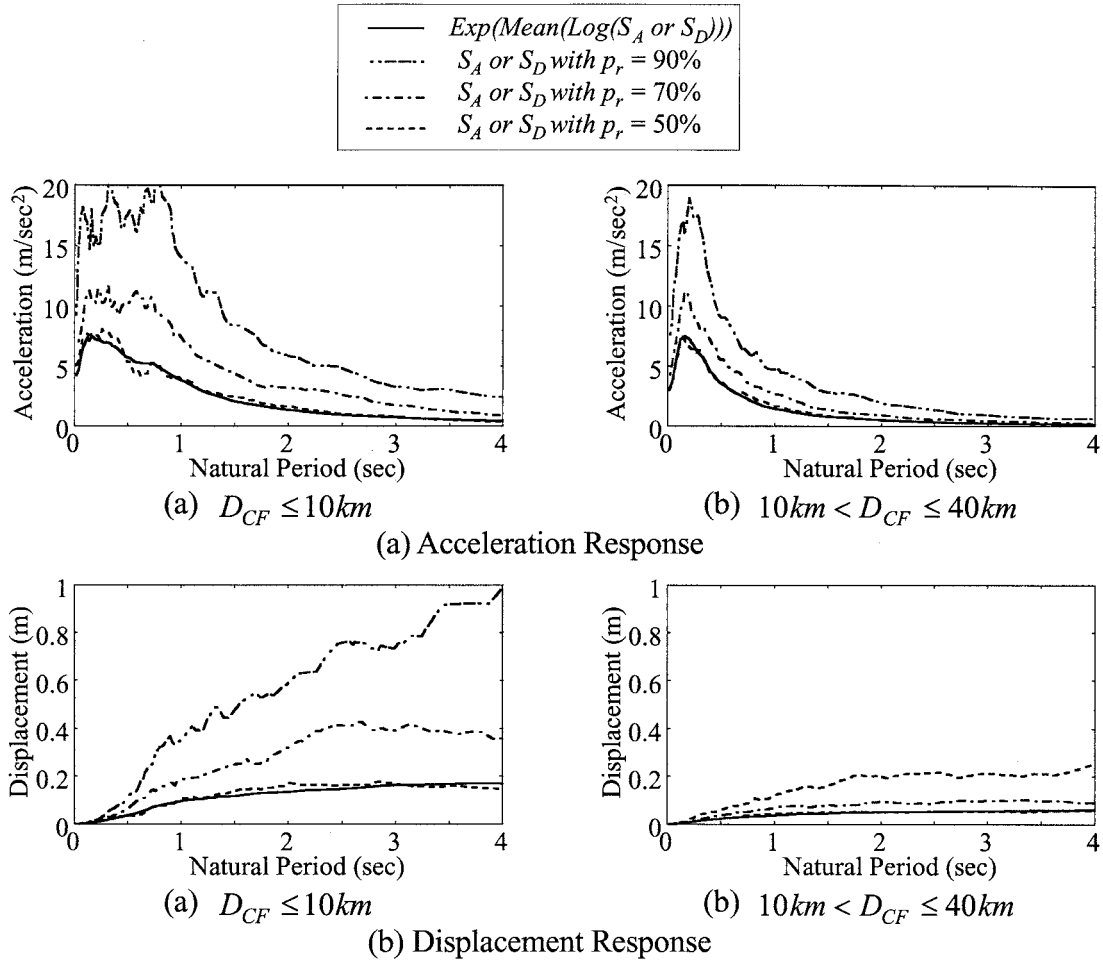


Figure 5 Response Spectra for each category of ground motions

spectrum for $D_{CF} \leq 10km$ is wide-band spectra. The acceleration response $S_{D, p_r=0.9}$ for $D_{CF} < 10km$ is equivalent to the elastic seismic force in the current seismic code of JRA (2002).

As shown in Figure 5(b), the elastic displacement response spectrum $S_{D, p_r=0.9}$ for $D_{CF} < 10km$ is 4 times larger than $S_{D, p_r=0.9}$ for $10km < D_{CF} \leq 40km$, since the acceleration spectra $S_A(D_{CF} \leq 10km)$ is wide-band spectra.

Since S_A and S_D spectra are log-normally distributed, the mean spectra of $LN(S_A)$ and $LN(S_D)$ are computed. $Exp(Mean(LN(S_A)))$ and $Exp(Mean(LN(S_D)))$ as shown in Figure 5 show the good correlation of $S_{A, p_r=0.5}$ and $S_{D, p_r=0.5}$.

3. MAXIMUM AND RESIDUAL DISPLACEMENT SPECTRA

Figure 6 shows the inelastic maximum displacement response spectra $S_{D, NL}$ and residual displacement response spectra S_R depending on the probability of non-exceedance p_r . The hysteresis type of SDOF system is assumed as elasto-perfectly plastic. Only the results for the target ductility of 4 ($\mu_T = 4$) are presented here, since the results for other target ductility factors exhibit similar characteristics. Since $S_{D, NL}$ and S_R spectra are log-normally distributed as same as S_D as shown in Figure 5, mean spectra of $LN(S_{D, NL})$ and $LN(S_R)$ are computed and $Exp(Mean(LN(S_{D, NL})))$ and $Exp(Mean(LN(S_R)))$ are also shown. $Exp(Mean(LN(S_{D, NL})))$ and $Exp(Mean(LN(S_R)))$ show the good correlation of $S_{D, NL, p_r=0.5}$ and $S_{R, p_r=0.5}$.

The normalized deviation $U_{D, NL}$ and U_R are shown in Figure 7. $U_{D, NL}$ and U_R are defined

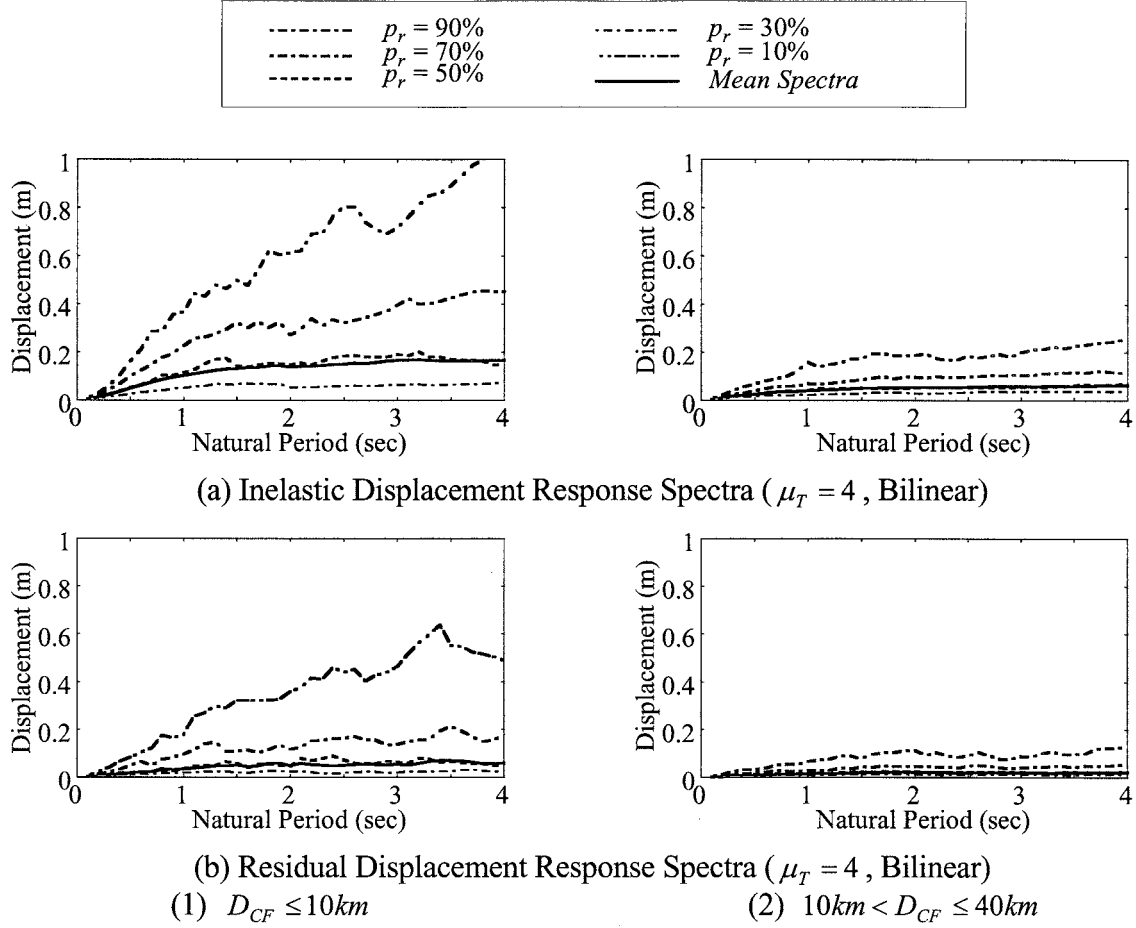


Figure 6 Response spectra depending on the probability of non-exceedance

as:

$$U_{D,NL} = \frac{LN(S_{D,NL}) - \mu(LN(S_{D,NL}))}{\sigma(LN(S_{D,NL}))} \quad (4)$$

$$U_R = \frac{LN(S_R) - \mu(LN(S_R))}{\sigma(LN(S_R))} \quad (5)$$

where $\mu(X)$ and $\sigma(X)$ are the mean and standard deviation of the statistical variable X .

$U_{D,NL}$ and U_R spectra depending on the probability of the non-exceedance p_r are roughly independent of natural period for any p_r . Figure 8 shows the probability density of normalized deviation of $LN(S_{D,NL})$ and $LN(S_R)$ for all natural periods. $LN(S_{D,NL})$ and $LN(S_R)$ exhibit the normal distribution.

4. MEAN RESIDUAL DISPLACEMENT RESPONSE SPECTRA FOR NEAR FIELD GROUND MOTIONS

Figure 9 shows the mean spectra of $LN(S_R)$ depending on the target displacement ductility μ_T of 2, 4, 6 and 8. As the natural period and the target ductility μ_T increase, mean spectra of $LN(S_R)$ increases. It can be observed, however, that the $\mu(LN(S_R))$ for the target ductility of 4, 6 and 8 are nearly same each other. On the other hand, $\mu(LN(S_R))$ for the target ductility of 2 is smaller than that for the other target ductility

To quantify the dependency of the mean spectra of $LN(S_R)$ on the natural period, the following

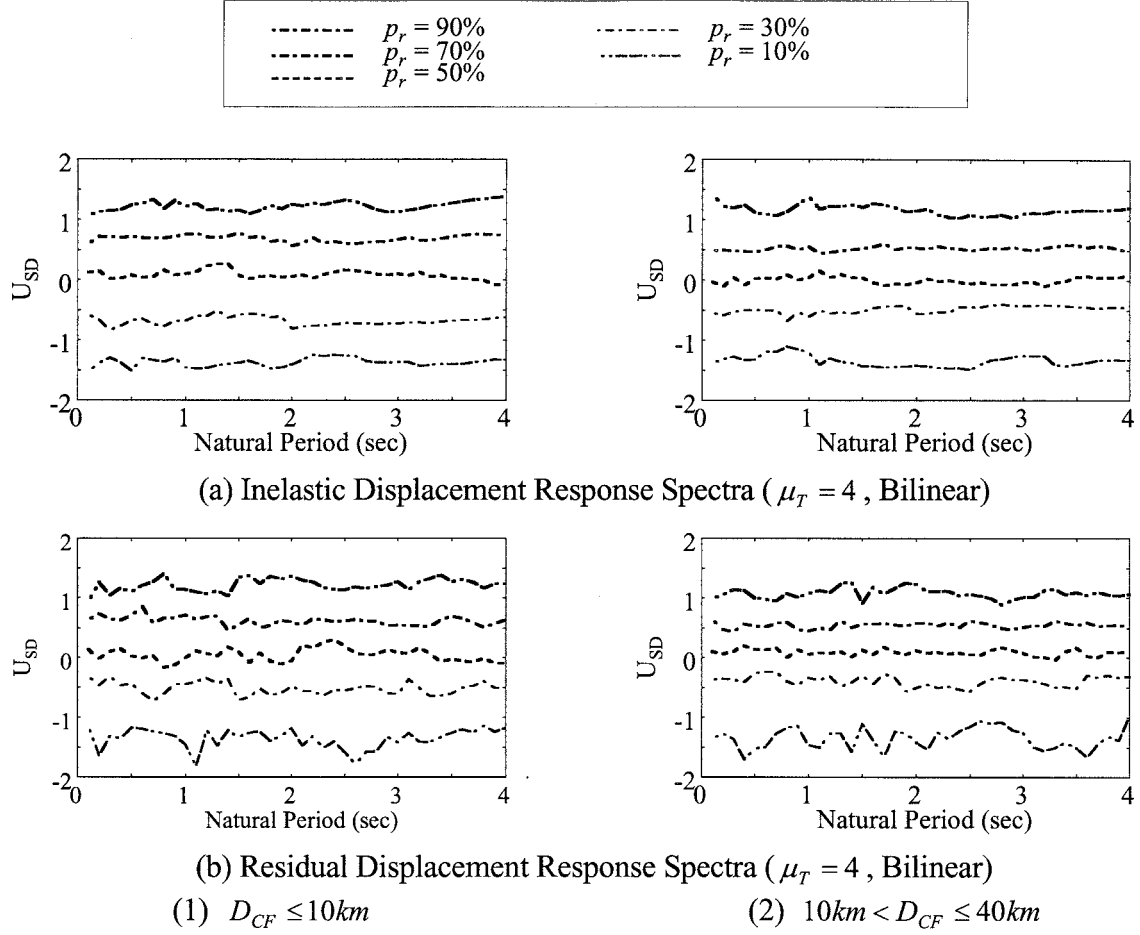


Figure 7 $U_{D,NL}$ and U_R spectra depending on the probability of the non-exceedance p_r

equation is proposed as:

$$\mu(LN(S_R)) = -\frac{a}{T^b} - c \quad (6)$$

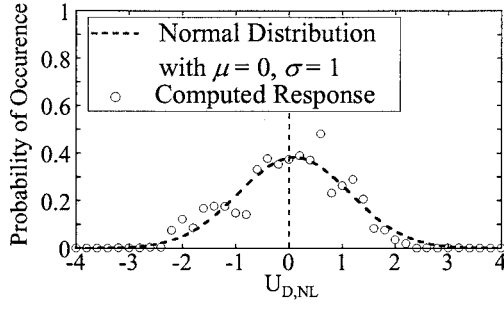
where T : the natural period, a , b , c : parameters which are obtained by the nonlinear regression analysis.

The parameters a , b to give good estimations are roughly determined as 1, 0.5, respectively. Depending on the distance from the faults, D_{CF} , for the target ductility of 4, 6 and 8, the parameter c is determined as 2.2 for $D_{CF} \leq 10km$ and 3.2 for $10km < D_{CF} \leq 40km$, respectively. The mean spectra computed by the proposed equation, Eq.(6) are also shown in Figure 9. For both cases of $D_{CF} \leq 10km$ and $10km < D_{CF} \leq 40km$, the proposed equations gives the good estimation.

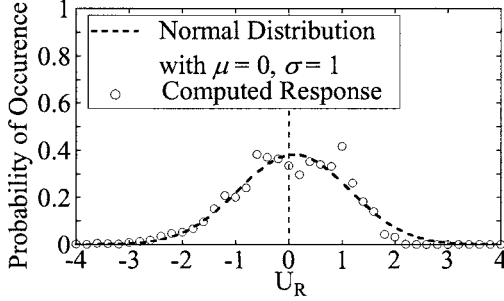
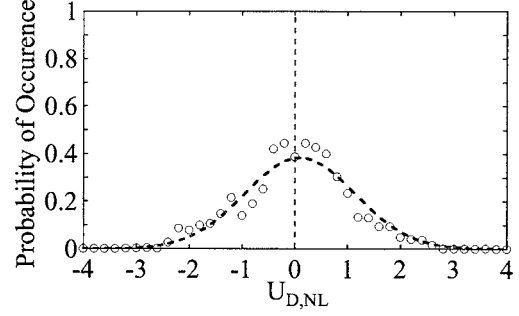
Figure 10 shows the standard deviation spectra of $LN(S_R)$, depending on the target displacement ductility μ_T of 2, 4, 6 and 8. Not depending on the distance D_{CF} , the standard deviation spectra $\sigma(LN(S_R))$ takes the value from the 1 to 2. As the natural period increase, the standard deviation, $\sigma(LN(S_R))$, increases. The difference of $\sigma(LN(S_R))$ due to the target ductility are, however, relatively small, since the standard deviation $\sigma(LN(S_R))$ exhibits the large scattering due to the natural period.

As same as $\mu(LN(S_R))$, the following equation is proposed to quantify the standard deviations of $LN(S_R)$ as:

$$\sigma(LN(S_R)) = -\frac{d}{T^e} - f \quad (7)$$

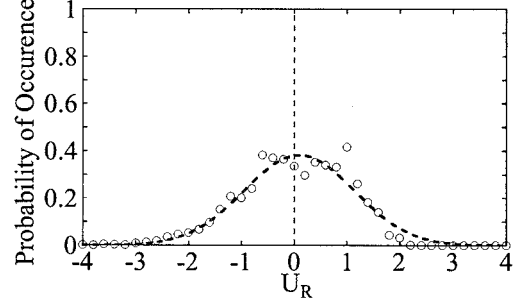


(a) Inelastic Displacement Response ($\mu_T = 4$, Bilinear)



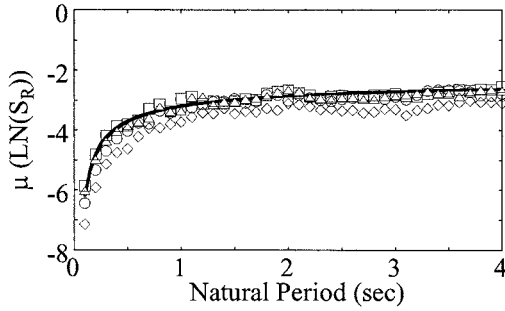
(b) Residual Displacement Response ($\mu_T = 4$, Bilinear)

(1) $D_{CF} \leq 10 \text{ km}$

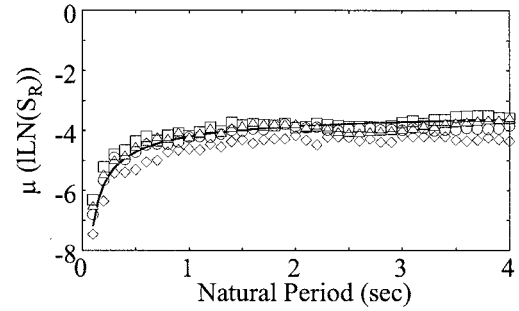


(2) $10 \text{ km} < D_{CF} \leq 40 \text{ km}$

Figure 8 Probability Density of Normalized Deviation of $LN(S_{D,NL})$ and $LN(S_R)$



(1) $D_{CF} \leq 10 \text{ km}$



(2) $10 \text{ km} < D_{CF} \leq 40 \text{ km}$

Figure 9 Mean Spectra of Residual Displacement in Log-Scale

where d , e , f are the parameters which are obtained by the nonlinear regression analysis as 0.2, 0.5 and 1.65.

In Figure 10, the estimation of $\sigma(LN(S_R))$ defined by the Eq. (7) are also shown, and it gives the good estimation.

From the mean and standard deviation of $LN(S_R)$, the residual displacement response can be estimated by the following equation $\tilde{S}_R(p_r, T)$:

$$\tilde{S}_R(p_r, T) = \text{Exp}(\mu(LN(S_R)) + f(p_r) \cdot \sigma(LN(S_R))) \quad (8)$$

where $f(p_r)$ is the inverse function that provides the probability dense of the standard normal distribution for the non-exceedance probability.

Figure 11 shows the comparison of the residual displacements, with the non-exceedance probability of 0.5 and 0.7, between computed responses as shown in Figure 6 and the residual displacements proposed by the Eq.(8). The proposed residual displacement response spectra provide good estimations for any probability of non-exceedance. The proposed residual displacement for

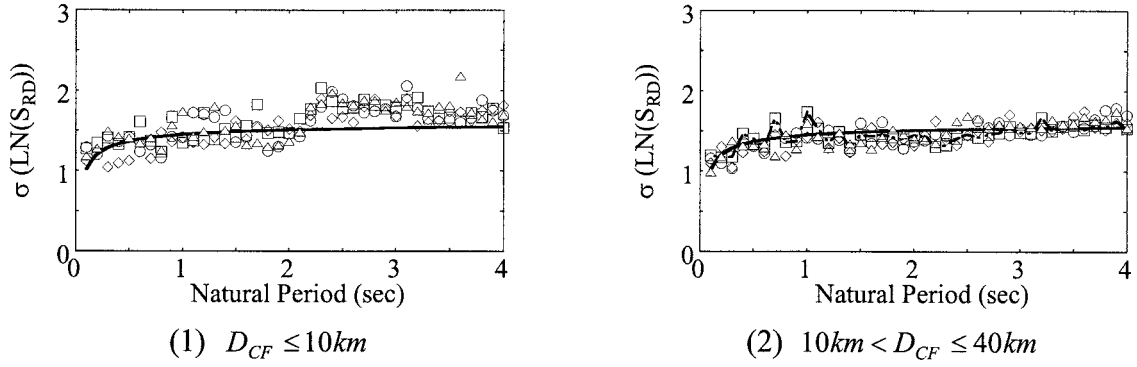


Figure 10 Standard Deviation Spectra of Residual Displacement in Log-Scale

$D_{CF} \leq 10km$ is 2.7 times larger than that for $10km < D_{CF} \leq 40km$. It can be found that the residual displacement clearly depends on the distance from the fault.

CONCLUSIONS

The main purpose of this paper was to evaluate the residual displacement subjected to near-field ground motions. For that purpose, the evaluation of probabilistic distribution of the residual displacement which occurs in the SDOF systems was conducted.

The residual displacement exhibits the log-normal distribution. Thus, the estimation of the residual displacement can be done by clarification of the mean and standard deviation of $LN(S_R)$. To quantify the mean and standard deviation of $LN(S_R)$, empirical models to estimate the mean and standard deviation of the $LN(S_R)$ were proposed depending on the distance from the fault. The near-fault ground motion for $D_{CF} \leq 10km$ gives larger mean residual displacement spectra. The scattering of the residual displacement is, however, independent of the distance from the fault D_{CF} .

The proposed equation of the residual displacement with the non-exceedance probability, $\tilde{S}_R(p_r, T)$, provides a good estimation of the residual displacement for the SDOF systems.

References:

- Ruiz-Garcia, J, and Miranda, E.(2006), "Residual Displacement Ratio", Earthquake Engineering and Structural Dynamics, Vo.35, pp. 315-336.
- Kawashima, K, MacRae, G. A., Hoshikuma, J., and Nagaya, K. (1998), "Residual displacement response spectra," Journal of Structural Engineering, ASCE, 124(5), 513-530.
- Japan Road association (2002), "Part V Seismic design, Design specifications of highway bridges," Maruzen, Tokyo, Japan.
- D'Ambrisi. A and Mezzi M.(2005) , "A probabilistic approach for estimating the seismic response of elasto-plastic SDOF systems", Earthquake engineering and structural dynamics, Vol. 34, pp. 1737-1753.

SEISMIC PERFORMANCE EVALUATION OF EXISTING STEEL BRIDGE FRAME PIERS WITH CIRCULAR COLUMN

K. Kinoshita

1) *Doctoral Student, Department of Civil Engineering, Tokyo Institute of Technology, Japan*
kinoshita@cv.titech.ac.jp

Abstract: Steel bridge frame piers with circular column have been adopted in metropolitan expressway. However, there are many piers that were designed for the past lower earthquake. In this research, in order to investigate the damage pattern and the effect of the seismic retrofitting work for the seismic resistance, pushover analyses were carried out. In addition, earthquake response analyses were conducted to evaluate seismic performance for level 2 earthquakes. Several frame piers were selected based on the actual survey results. As a result, the damage patterns were affected by the balance of the strength between the column, the beam and the beam-to-column connection and we attempted to classify them by using their balance. The effects of the placing concrete on 1-layer type and 2-layer types of frame piers were different. In addition, seismic performance was enough for level 2 earthquakes and they have high seismic resistance before applying the seismic retrofitting work.

1. INTRODUCTION

Steel bridge frame piers with circular column are often adopted to support ramp bridges and curved bridge because of the feature of same inertia for any directions. Seismic damage of them during the Great Hanshin Earthquake of 1995 has been reported (JSCE 1999). After the earthquake, the seismic design specification was revised to use large earthquakes, namely the level 2 earthquake. However, there are many frame piers that were designed for the past lower earthquake. Therefore, it is necessary to clarify the seismic performance for level 2 earthquakes.

According to the seismic damage patterns, the beam-to-column connections did not suffer severe damage. So, it may be caused due to the conservative design for the connections and it is necessary to consider it in evaluation.

Moreover, after the earthquake, seismic retrofitting works for the column of existing frame piers were carried out, such as placing concrete, installing additional longitudinal ribs (Imamura et al. 1999). However, the effects of seismic retrofitting works have not been examined, because their investigations were based on single type piers.

In this research, in order to investigate the damage patterns and the effects of the seismic retrofitting work for the seismic resistance, pushover analyses were conducted. In addition, earthquake response analyses were carried out to evaluate seismic performance for level 2 earthquakes.

2. THE DESIGN AND THE ACTUAL SURVEY

2.1 The design of the connection and circular column

Generally, the beam of the connection was designed for the consideration in the elastic design of the

local stress concentration by the shear-lag phenomenon (Okumura et al. 1968). Therefore, it has low possibility of occurring damage at the beam of the connection before the other members. For the circular column of the connection, the local stress concentration was not considered, but there is a limitation for radius-thickness ratio (R/t) as shown in Table 1. This limitation was for preventing the local buckling. There are the limitations for the column member and the connection, respectively.

The limitation for the column member was calculated by Eq. (1). The equation was formulated based on the elastic local buckling strength σ_B under a pure compression considering an imperfection. It was calculated by means of the allowable compression stress σ_a instead of σ_B with safety factor 3.

$$\frac{R}{t} = \frac{0.2E}{\sigma_B} \cdot \frac{1}{3} \quad (1)$$

where E is elastic-modulus. The reason of the safety factor 3 was explained as "The influence of the imperfection of pipe structures has not been grasped enough. Therefore, the safety factor of pipe structures was 3, although the safety factor 1.8 has been used for the buckling."

On the other hand, the limitation of the connection was determined based on experiments using large specimens (Okumura et al. 1968).

The limitation was revised in 1969. The limitation for SM50Y, SM53 was added and the limitation of the connection of every grade of steel was changed to $R/t \leq 40$.

Previous research noted that "The connection was the large thickness when it was determined by the limitation" (Hamajima et al. 1979). This is because it may cause the allowance for stress. For that reason, it has low possibility of occurring damage at the connection if it was determined by the limitation. Therefore, it is necessary to grasp whether actual connections were determined by the limitation or not.

2.2 Outline of the survey

In order to grasp whether actual connections were determined by limitation or not and the balance of strength between the connection and the column member, a survey of actual columns was carried out. 264 of actual steel bridge frame piers with circular columns, which were constructed from 1964 to 1993, were surveyed. Target column sections were the connections, the section under the connection and the column base. In this research, they were selected by referring the research experiment (PWRI 1999). According to this, main seismic damage occurred at the base and the column section under the connection.

The sections were determined by the stress verification for an allowable compression stress of using an effective length of an elastic buckling theory when the sections were not determined by the limitation. In this research, the sections determining by the stress verification and the limitation are called as stress sections and R/t sections, respectively.

2.3 Results of survey

Figure 1, 2, 3 shows the relationship between the column diameter and R/t . The limitation of each grade of steel was shown in each figure by a horizontal line. Figure 1 shows the section under the connection. Figure 2 shows the base. Figure 3 shows the connection. The connections applying the limitation of 1965 and 1969 were shown in Figure 3(a) and Figure 3(b), respectively. Figure 3(b) was not classified into each grade of steel. From Figure 1 to Figure 2, it was quite obvious that the great number of the sections was stress sections and also R/t was increased steadily with the increase of the

Table 1 The limitation of R/t

	Column member				Beam-to-column connection			
	SM41,SS41	SM50	SM50Y,SM53	SM58	SM41,SS41	SM50	SM50Y,SM53	SM58
Limitation at 1965	110	80	-	60	36	33	-	30
Limitation at 1969	110	80	70	60	40			

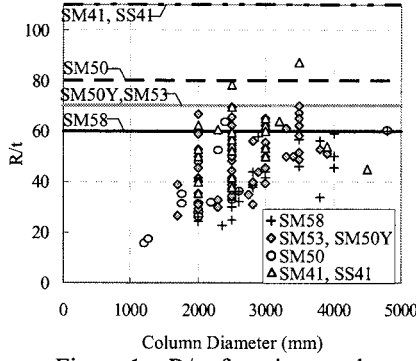


Figure 1 R/t of sections under beam-to-column connection

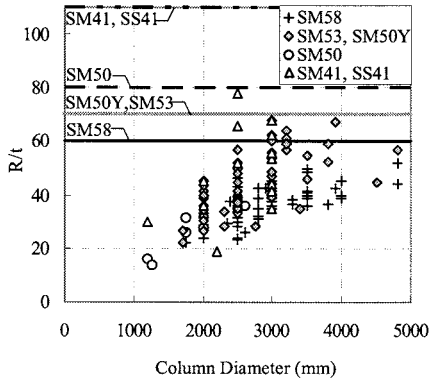
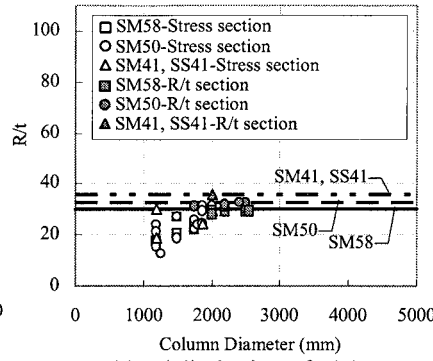
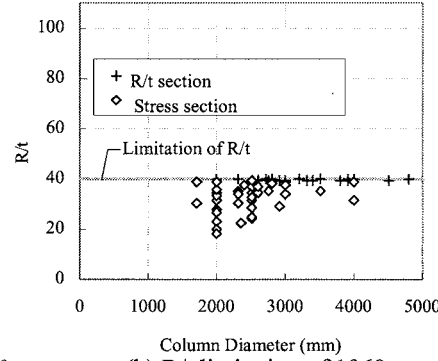


Figure 2 R/t of column bases

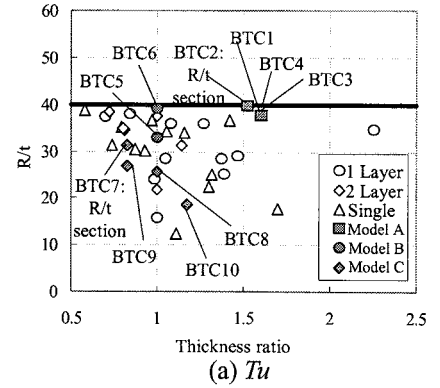


(a) R/t limitation of 1965

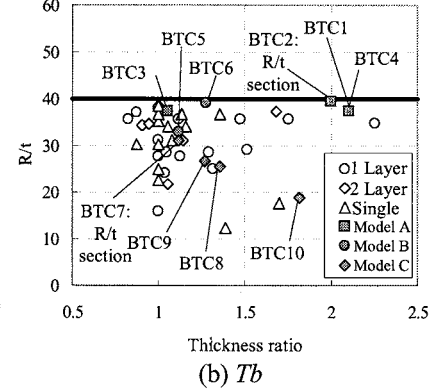


(b) R/t limitation of 1969

Figure 3 R/t of beam-to-column connections



(a) T_u



(b) T_b

Figure 4 Relationship of Thickness Ratio and R/t

column diameter. On the other hand, as shown in Figure 3(a), R/t sections were increased with exceeding 2000mm, and as shown in Figure 3(b), R/t sections were increased with exceeding 3000mm. Therefore, we found out that a great number of the base and the section under the connection were stress section and a number of the connections were R/t sections.

In addition, in order to investigate the balances of strength between the beam-to-column connections and the column member, thickness ratio was used. Figure 4 shows the thickness ratio of the connection and sections under the connection (T_u) or the connection and the base (T_b) in the horizontal axis and shows R/t in the vertical axis. Only frame piers, which are the base and the connection was stress section, was used for Figure 4.

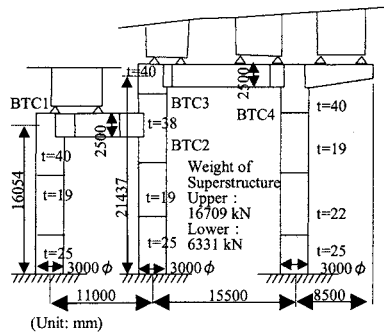
The increase of R/t indicated the increase of the possibility of the occurrence of the local buckling. Due to the limitation, R/t near 40 have a most high possibility of it. It can see that T_u and T_b are covering a wide range. Therefore, it is necessary to investigate as widely as possible in Figure 4.

2.4 Selected frame piers

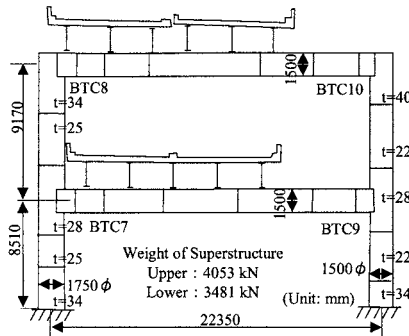
There are 3 the influential parameters for the seismic resistance. The one is stiffness ratio K . Second one is Thickness ratio T_u and T_b , and third one is R/t of the connection. K can be expressed as Eq. (2) (JRA 2002).

$$K = \frac{I_C / h}{I_B / L} \quad (2)$$

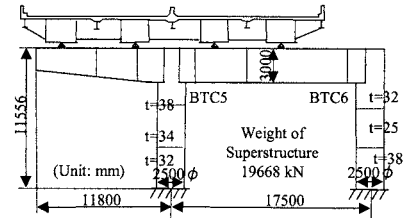
where I_C and I_B is the moment of inertia of the column and beam. h and L is the column height and the beam span. Basically, K can evaluate the balance of strength between the column and the beam. The increase of K indicated the increase of the strength of the column. Previous research of the actual survey said that K between 0.5 and 2.0 was recognized as general for frame piers (Nakai et al. 2002). The previous research experiment was based on this result (PWRI 1999). So, it is necessary to select several frame piers with K between 0.5 and 2.0.



(a) Model A

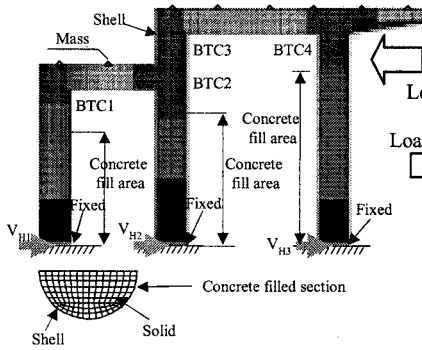


(b) Model B

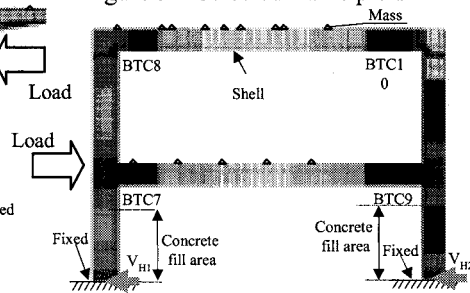


(c) Model C

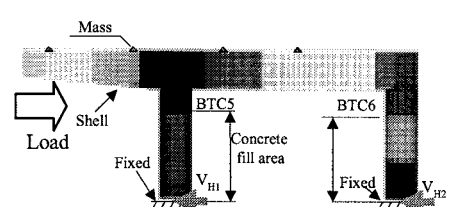
Figure 5 Selected frame piers



(a) Model A



(b) Model B



(c) Model C

Figure 6 FEM models

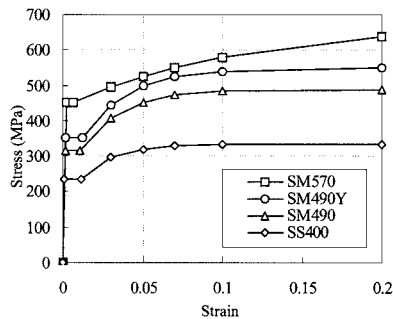


Figure 7 Stress-Strain Curve of Steel

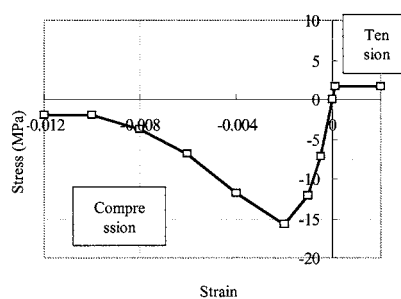


Figure 8 Stress-Strain Curve of Concrete

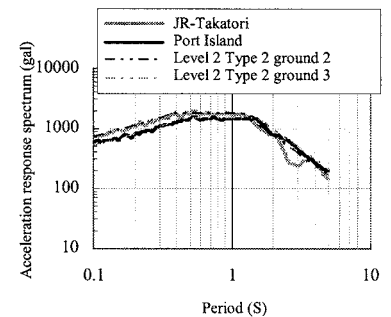


Figure 9 Acceleration response spectrum of earthquake waves

We selected the frame piers based on the both survey mentioned above. Selected frame piers were shown in Figure 5. Model A is 2-spanned type of the frame pier. K was 1.4. Model B is 1-layer type with a one side cantilever beam of the frame pier. K was 1.1. T_u , T_b and R/t of the connection of BTC5 were 1.1, 1.0 and 32.9, respectively. T_u , T_b and R/t of the column connection of BTC6 were 1.3, 1.0 and 39.1, respectively. Model C is 2-layer type of the frame pier. K of 1-layer was 1.6. K of 2-layer was 1.7. The connections of each selected frame piers were plotted in Figure 7.

3. FEM MODEL AND ANALYSIS

FEM models are shown in Figure 6. The existence of the placing concrete was considered to investigate the effects of the seismic retrofitting work. 6 FEM models were prepared. Model A with the concrete was called as A-N, and without the concrete was called as A-Con. The same way with Model A was applied to Model B and Model C.

Steel members were modeled by shell elements and concrete members were modeled by solid elements. Nodes of shell elements were combined with nodes of solid elements. The symmetry condition was used, and column bases were fixed. Mass elements were used to consider a weight of the superstructure. To consider the dead load of steel bridge frame piers and superstructures, gravity

was taken into account. Stress-Strain curves of the steel member and the concrete member used in FEM model were shown in Figure 7, 8, respectively. The kinematics hardening was used for steel members.

In order to investigate the effects of the influential parameter above and the seismic retrofitting for seismic resistance, Pushover analyses were conducted. An ultimate state was assumed at the maximum base shear to evaluate safely. In order to evaluate safely of the ultimate state of concrete member, a failure criterion for concrete member, shown in Eq (3), was utilized.

$$D_c = \frac{\varepsilon_{a,c}}{\varepsilon_{u,c}} \quad (3)$$

where D_c is the damage index of the concrete member, $\varepsilon_{a,c}$ is the compressive strain at the outer concrete, $\varepsilon_{u,c}$ is the failure strain of the concrete. The reason of the use the criterion was that the deterioration of the concrete could not be accurately reproduced in the analyses due to the inconsideration of a softening behavior of the concrete by tension cracks, a contact behavior between the steel member and concrete member and so on.

In addition, earthquake response analyses were carried out to evaluate seismic performance. Earthquake acceleration was applied as inertial forces. As great earthquakes, the East-West components of JR-Takatori and Port Island record wave, which waves have adjusted to a response acceleration spectrum of level 2 earthquakes, were used (Figure 9). Rayleigh-dumping was used.

4. PUSHOVER ANALYSIS RESULTS

4.1 Model A

Figure 10 shows the relationship between the base shear and a horizontal displacement at a column

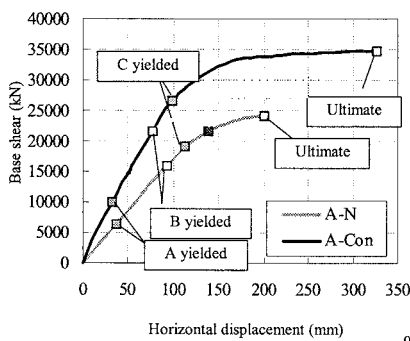


Figure 10 Base shear versus Horizontal displacement of Model A

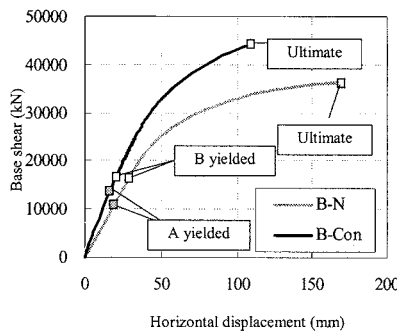


Figure 13 Base shear versus Horizontal displacement of Model B

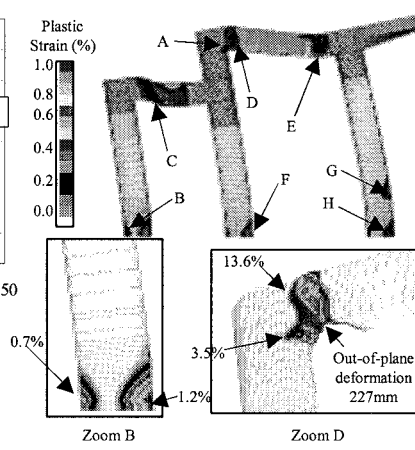


Figure 11 Ultimate State of A-N

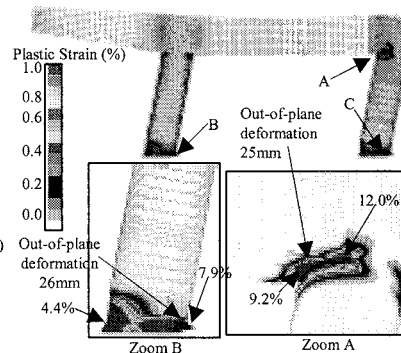


Figure 14 Ultimate State of B-N

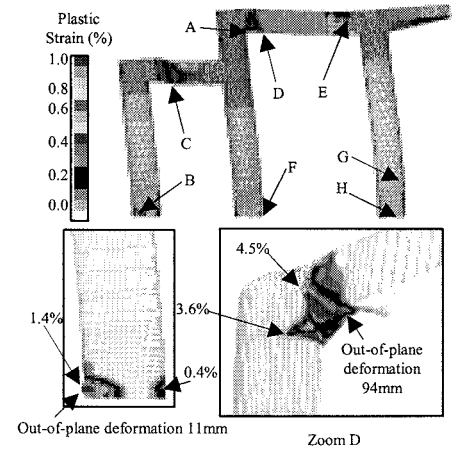


Figure 12 Ultimate State of A-Con

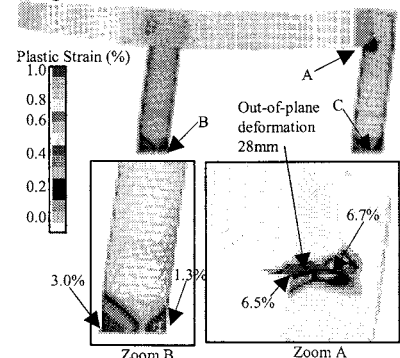


Figure 15 Ultimate State of B-Con

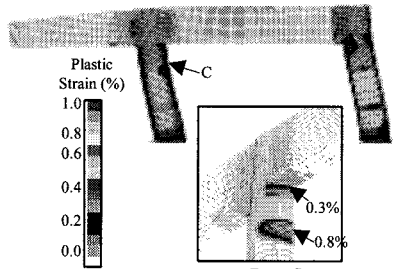


Figure 16 Ultimate State of opposite loading case of B-N

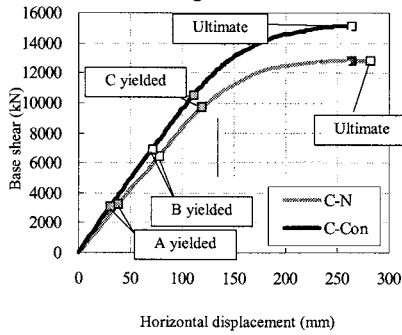


Figure 17 Base shear of Model C

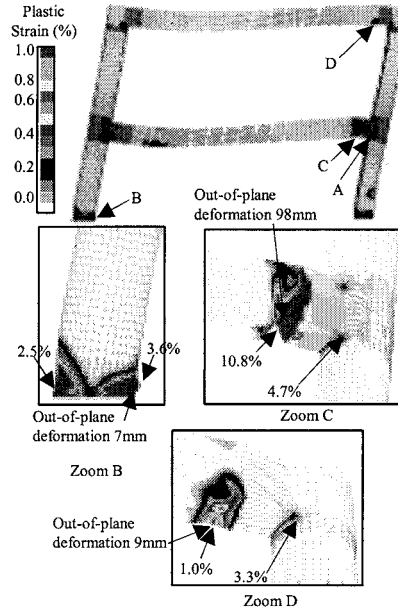


Figure 18 Ultimate State of C-N

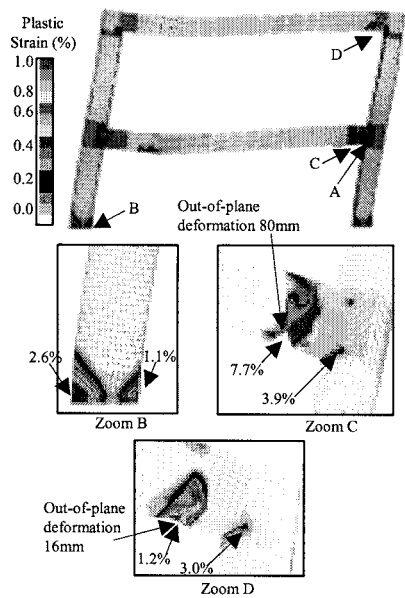


Figure 19 Ultimate State of C-Con

top. The loading direction was shown in Figure 6 by an arrow. In figure 10, the points when the yield occurred at each member were denoted by square marks. Yielded locations are shown in Figure 11. Figure 11, 12 shows the deformation and the plastic strain distribution at the ultimate state of A-N and A-Con for evaluating the damage modes of frame piers.

The main plastic deformation occurred at not only the base, but also the thickness changing point of the beam. This was because of the large thickness due to the consideration of the shear-lag phenomenon. Thus, it can be expected that the base and the beam suffer mainly damage when K is larger than 1.4.

Moreover, it can be seen that effects of the concrete were the improvement of the strength and ductility (Figure 10). Although the out-of-plane deformation and plastic strain of the beam of A-Con was lower than that of A-N by applying the concrete while the horizontal deformation of frame piers was the small range, the deformation and the strain of the beam of A-Con was much higher than that of A-N. On the other hand, the strain at the connection of both A-N and A-Con was approximately same. This meant the section force for connections was restricted by the occurrence of the plastic hinge at the thickness changing point of the beam.

4.2 Model B

Figure 13 shows the base shear versus the displacement at the column top. The deformation and strain distribution of B-N and B-Con are presented in the Figure 14, 15. In case of model B, the main plastic deformation occurred at not only the base, but also the connections of BTC6. On the other hand, with respect to the opposite direction load results of B-N, as shown in Figure 16, the plastic deformation occurred at the section under the connection before the connection of BTC5. Hence, it seemed that the base and the connection or the section under the connection suffer damage mainly when K is smaller than 1.1. Also, when R/t of the connection is over 33 and T_u is smaller than 1.3, the base and the connection suffers mainly damage. However, it was noted that this is dependent on R/t of the connection. The analysis results suggest that in case of R/t smaller than 30, the range of T_u was enabled wide until 1.0.

Moreover, although by applying the concrete, the strength was improved, the deformation and strain of the connection of B-Con was higher than that of B-N.

4.3 Model C

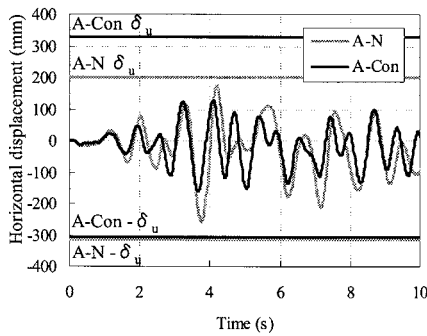
Pushover analysis results of Model C show in Figure 17 and Figure 18 and 19. The main plastic deformation occurred at not only the base, but also the thickness changing point of the both 1-layer and 2-layer beam. Hence, this result emphasized that when K is larger than 1.4, the base and the beam may suffer mainly damage.

On the other hand, although not only the strength was improved but also the plastic strain of the 1-layer beam and the connection of C-Con was lower than that of C-N, the out-of-plane deformation and strain of the 2-layer beam of C-Con was higher than that of C-N. The most likely reason for this behavior was the increase of the deformation due to the stiffening of the 1-layer. Therefore, the effect of the concrete may be relatively low.

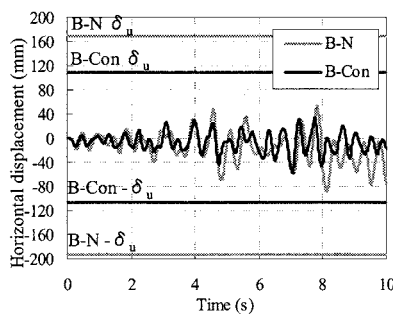
5. EARTHQUAKE RESPONSE ANALYSIS RESULTS

Figure 20, 21, 22 shows the time history of the horizontal displacement at the column top of each model. In those figures, in order to evaluate the seismic performance for the level 2 earthquakes, the displacements of the ultimate state (δu) obtained from pushover analyses were compared with the maximum response. The response of each model with the concrete was within δu . Furthermore, the response of B-N and C-N, without the concrete, did not exceed δu . Only the response of A-N during Port Island waves exceeded δu (at ① in Figure 20 (b)). Hence, those results mean seismic performance is enough for the level 2 earthquakes and they have high seismic resistance before applying the seismic retrofitting work.

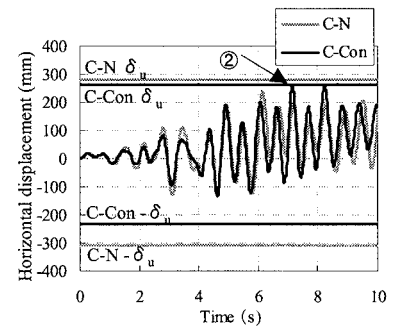
However, the maximum response during JR-Takatori wave of C-Con was near δu (at ② in Figure 22 (a)) and higher than that of C-N. Therefore, this result showed the possibility of the deterioration of seismic performance of 2 layer type by applying the placing concrete.



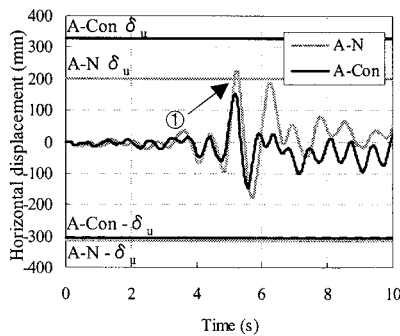
(a) JR-Takatori



(a) JR-Takatori

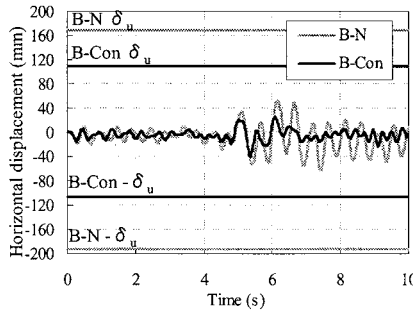


(a) JR-Takatori



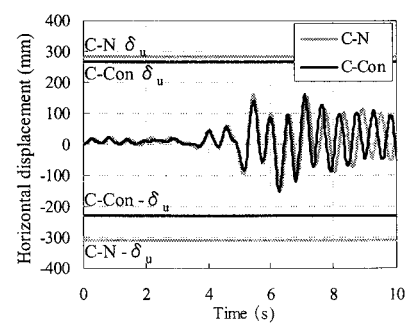
(b) Port Island

Figure 20 Response of Model A



(b) Port Island

Figure 21 Response of Model B



(b) Port Island

Figure 22 Response of Model C

6. CONCLUSIONS

The conclusions of this research can be summarized as follows.

1. When the stiffness ratio K of the existing frame piers is larger than 1.4, it is possible to suffer damage at the column base and the thickness changing points of the beam. When K is smaller than 1.1, it is possible to suffer damage at the column base and the beam-to-column connection or the column section under the beam-to-column connection.
2. When R/t of the connection is larger than 31 and Tu is smaller than 1.3, there is a possibility that the base and the connection suffer damage. In addition, when R/t is smaller than 31, Tu is smaller than 1.0.
3. From results of the actual survey, we found that a number of existing frame piers are that the column member suffer damage before the connection because of the large thickness determining by the limitation of R/t .
4. Seismic performance was enough for the level 2 earthquakes and they have high seismic resistance before applying the placing concrete.
5. The effects of the placing concrete on 1-layer type and 2-layer type of frame piers were different. In case of 2-layer type, there is a possibility of the deterioration of seismic performance by applying the placing concrete.

References:

- JSCE, Committee of Steel Structures. (1999) "Actual damage and analysis of steel structures during the Great Hanshin Earthquake"
- Imamura, K., and Takahashi, M. (1999) "Retrofitting of Existing Piers in Metropolitan Expressway", *Bridge and Foundation Engineering*, Vol. 33, 163-165.
- Okumura, T., and Ishizawa, S. (1968) "The design of knee joints for rigid steel frames with thin walled section", *Journal of Structural Mechanics and Earthquake Engineering*, Vol. 153, 1-18.
- Hamajima, R., and Okumura, T. (1979) "Stress concentration in rigid frame corner connection with circular tubular column", *Journal of Structural Mechanics and Earthquake Engineering*, Vol. 292, 29-40.
- PWRI (1999) "Summary of the Cooperation Research on the Seismic Limit State Design of Highway Bridge Piers"
- JRA (2002) "Design Specifications of Highway Bridges, Part II, Steel Bridge"
- Nakai, H, Kitada, T, Kawai, A, Miki, T and Yoshikawa, N (1982) "The survey of steel bridge frame piers", *Bridge and foundation Engineering*, June, 35-40.

PARAMETRIC STUDY FOR SHEAR CARRYING CAPACITY OF EXTERNALLY PRESTRESSED CONCRETE MEMBERS

C. Sivaleepunth¹⁾, J. Niwa²⁾ and T. Miki³⁾

1) *PhD. Candidate, Graduate School of Civil Engineering, Tokyo Institute of Technology, Japan*

2) *Professor, Department of Civil Engineering, Tokyo Institute of Technology, Japan*

3) *Assistant Professor, Department of Civil Engineering, Tokyo Institute of Technology, Japan*
chunyakom@cv.titech.ac.jp, jniwa@cv.titech.ac.jp, mikitomo@cv.titech.ac.jp

Abstract: The parametric study using FEM for concrete beams prestressed with external tendons have been performed to investigate the factors thought to influence on the shear mechanism of externally prestressed concrete beams. The effects of prestressing force and stirrup can be observed as important factors in the failure mechanism. A simplified truss model, having a small number of degrees of freedom, has been modified and proposed by adapting the formulation to predict the inclination of concentrated stress flow and the thickness of diagonal compression members for evaluating the shear carrying capacity of externally prestressed concrete beams. The predicted results show good agreement with the experimental results.

1. INTRODUCTION

By taking the advantages of prestressing force, the prestressed concrete members can be perfectly utilized to respond the requirements of high shear resistance and reduction of dead load to the substructures. When the earthquake occurred, it is necessary to confirm that the shear failure of prestressed concrete superstructures does not take place before the development of hinge in the columns as illustrated in Figure 1. Recently, externally prestressed concrete beams, in which the prestressing tendons are placed outside the concrete section and transfer the load to the concrete through end anchorages and deviators, have been recognized as an effective method for the modern construction of segmental box girder bridges and in the strengthening of existing structures. Their many advantages include the simplicity in constructions, aesthetic appeal and rapid construction. With the widely use of this type of structure, an examination of the design and analysis of such structures with high accuracy in prediction of shear carrying capacity is needed.

For evaluating the shear carrying capacity of slender prestressed concrete beams (shear span to effective depth ratio, a/d , is greater than or equal to 2.5.), which are found to fail in shear compressive mode of failure, most of recently methods, such as decompression moment method from JSCE (JSCE 2002), and consideration of resistance at flexural crack from M_{cr} method (Ito et al. 1994) are proposed based on the empirical equations without the comprehensive explanation and clarification of influence factors. On the other hand, Lertsamattiyakul (Lertsamattiyakul et al. 2004) conducted the parametric study by using the nonlinear finite element method (FEM) and proposed a simplified truss model in order to evaluate the shear carrying capacity of slender prestressed concrete beams without transverse reinforcement. The influential parameters, such as lower fiber stress, upper fiber stress, etc., were found to have a significant effect on the change of the inclination of concentrated stress flow, which is a key to solve the problem of shear compression failure mode. The model was found to be able to predict the several experimental results of beams prestressed with bonded prestressing bars very well.

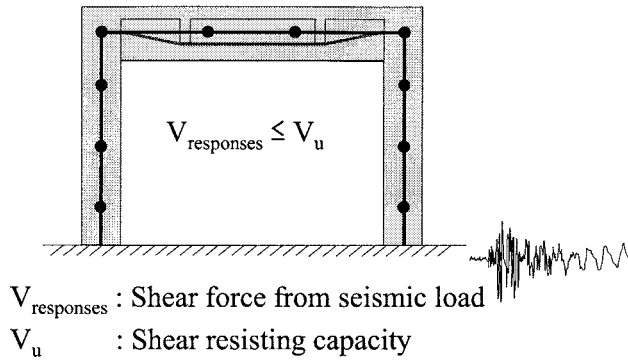


Figure 1 Seismic performance of externally prestressed concrete girder

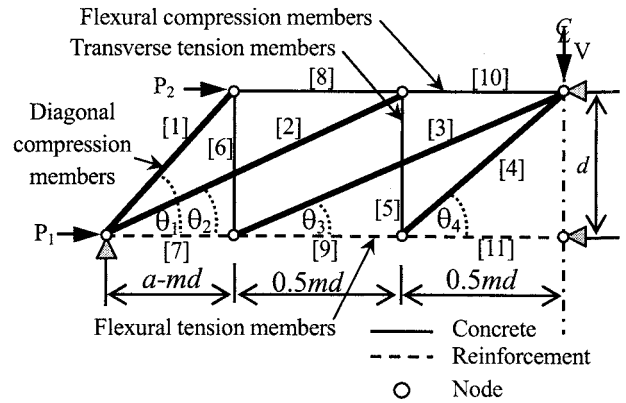


Figure 2 Schematic diagram of the simplified truss model (half of the beam)

However, the model does not extend to solve the shear problem of externally prestressed concrete beams with and without transverse reinforcement.

This study was therefore carried out to perform the parametric study using the nonlinear FEM concrete beams prestressed with external tendons in order to propose the simplified truss model using for externally prestressed concrete beams, which can clarify the significant parameters on the shear behavior and the shear compression failure mechanism of such beams. The tendency of stress flows obtained from the nonlinear FEM is summarized and applied to propose the prediction equations for the inclination of concentrated stress flow, and the thickness of diagonal compression members, which are used in the simplified truss model. The simplified truss model is modified and utilized to compare the shear carrying capacity and the failure patterns with the experimental results of externally prestressed concrete beams to confirm the applicability of the proposed model.

2. SIMPLIFIED TRUSS MODEL

The schematic diagram of the simplified truss model (half of the beam), which is adopted in this study due to the comprehensive explanation for the failure mechanism, for analyzing the shear carrying capacity of concrete beams prestressed with bonded prestressing bars without transverse reinforcement is illustrated in Figure 2. The model is based on the concept of stress flow inside the prestressed concrete beams. The model consists of 7 nodes and 11 elements for flexural compression members, transverse tension members, diagonal compression members and flexural tension members. The model is fixed in X-direction at both nodes along the center line and in Y-direction at the support.

However, the behavior of stress flow inside externally prestressed concrete beams may different with the concrete beams prestressed with bonded prestressing bars due to the unbonded of external tendon to concrete section and the uplift forces from the reaction of tendons at the location of deviators.

2.1 Parametric Study Using Finite Element Method

(1) Finite element method

The nonlinear FEM using DIANA system has been conducted to examine the shear failure mechanism of externally prestressed concrete beams with and without transverse reinforcement. Four node quadrilateral isoparametric plane stress elements in a two dimensional configuration were adopted for concrete as illustrated in Figure 3. Details of geometric properties of the analytical model are demonstrated in the figure. In Figure 3, the interface element used at the deviators and the end anchorages is also demonstrated. The friction between the tendons and the deviators is neglected. The stiffness in n-axis, D_n , is set to be zero before the external vertical load is applied and infinity after the external vertical load is introduced as shown in Figure 3. The stiffness in t-axis, D_t , is set to be

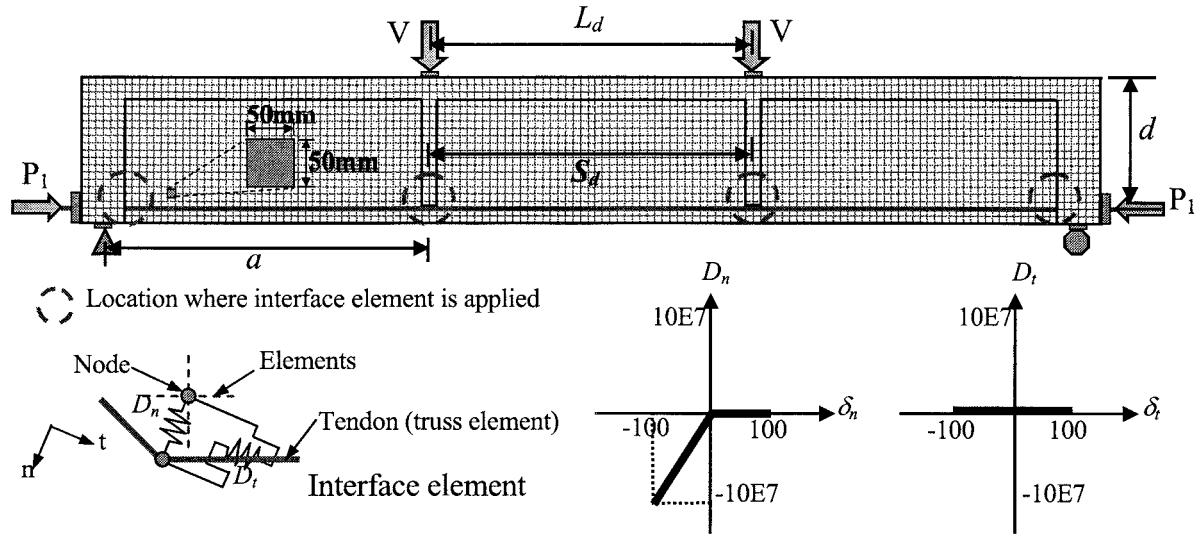


Figure 3 Finite element analytical model and interface element at deviator and end anchorage

zero due to the assumption of frictionless between the deviator and tendons.

In the analysis, the smeared crack model is adopted as the crack model to concrete elements. For the constitutive model, Thorenfeldt's model (Thorenfeldt et al. 1987) is applied in compression. After cracking, the tension softening model proposed by Hordijk (Hordijk 1991) is utilized as the concrete constitutive model under tension.

Two node truss elements are applied as the tendon elements. These truss elements are connected to the concrete only at the deviators and end anchorages by means of the interface element as shown in Figure 3. The reinforcement elements are modeled for internal bonded reinforcing bars to have the perfect bond with concrete. The bilinear elastoplastic model of steel is adopted for the longitudinal reinforcement and prestressing tendons.

(2) Parametric study

The parametric evaluation is performed with the investigation on ten significant parameters, which may affect the inclination of concentrated stress flow in externally prestressed concrete beams. The location of deviator, S_d/L , the upper extreme fiber stress, σ_u , the lower extreme fiber stress, σ_l , the compressive strength of concrete, f'_c , the shear span to effective depth ratio, a/d , the stirrup ratio, r , the effective depth, d , the flange width to web width ratio, b_f/b_w , internal bonded tensile reinforcement ratio, ρ_w and the bearing plate width are considered in this parametric study. The range of these parameters is selected such that it covers a practical range. The variables and the numbers of cases considered in the parametric study are tabulated in Table 1.

Due to the uplift force at the deviator, the location of deviator along the beam is considered in order to examine its influence on the inclination of stress flow by varying the deviator spacing-to-span ratio, S_d/L from 0 to 0.6. Since the compressive stress in concrete due to prestress is found to play an important role to shear carrying capacity of prestressed concrete beams, the upper extreme fiber stress, σ_u , and the lower extreme fiber stress, σ_l , are considered, and their values are changed in the range of -1.0N/mm^2 to -5.0N/mm^2 and 3.5N/mm^2 to 20.0N/mm^2 , respectively (tension < 0 , compression > 0). The values of a/d are changed from 2.5 to 4.5. The compressive strength of concrete, f'_c , varying from 30 to 70 N/mm^2 is used. The stirrup ratio is set to be the range of 0% to 0.36%. The effective depth, d , is in the range from 300mm to 900mm. The ratio of widths of flange and web, b_f/b_w , is changed from 1.0 to 3.0. The longitudinal reinforcement ratio, ρ_w , is varied from 0.5% to 5.0%.

(3) Evaluation of inclination of concentrated stress flow

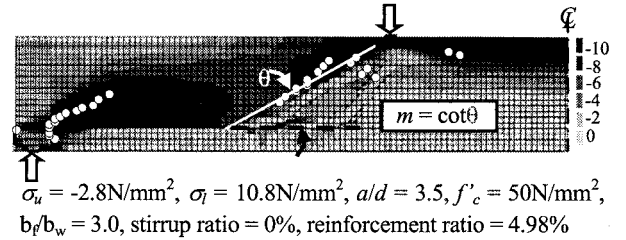
In order to apply the analytical results to propose the model, the tendency of inclination of critical stress flow is investigated. Based on the consideration of the minimum principal stress, σ_2 , at each Gauss's point at 90% of shear carrying capacity, the tendency of inclination of critical stress flow can

be found. Figure 4 demonstrates the marked location of the maximum absolute values of σ_2 of each horizontal level, $\sigma_{2i-\max}$, between the upper and lower bars at the failure side of the beam. By considering the location of $\sigma_{2i-\max}$ as the coordination in X-Y axes, (x_i, y_i) , the correlation coefficient is calculated from the equation as shown in the figure. This parameter expresses the agreement between the estimated equation and the selected data. A part of Gauss's points, which gives a high value of correlation coefficient (≥ 0.95), is chosen. The concentrated stress flow is evaluated in terms of m , where $m = \cot\theta$ and θ is an angle of the estimated inclination of the concentrated stress flow.

From the parametric study using nonlinear FEM, it can be noticed that the location of the deviator along the beam, deviator spacing-to-span ratio, S_d/L , has less significant to the value of m as illustrated in Figure 5. That means the uplift force that may occur at the deviator has less influence to the directions of the concentrated stress flow. As for example, the relationships between m and σ_1 with σ_u are summarized and approximated in Figure 6. The parameter σ_m , mentioned by Lertsamattiyakul (Lertsamattiyakul et al. 2005) as shown in Figure 6, is applied in this study in order to consider not only the influence of σ_1 , but also with the additional effect of σ_u on m . Moreover, the relationships between m , excluding the effect of prestressing forces, and the other significant factors, such as a/d , f'_c , stirrup ratio, b_f/b_w and d are also collected and summarized. The value of m is strongly influenced by σ_1 with an extra effect by σ_u . It is also noticed that the values of m become larger with the increase in values of a/d and f'_c , while the values of S_d/L , r , d and b_f/b_w have less significant effect on the value of m . The formulation to find the value of m for externally prestressed concrete beams can be written base on the simplicity as shown in Eq. (1).

Table 1 Summary of variables

Parameter	Range	No. of case
S_d/L	0 to 0.6	4
σ_u (N/mm ²)	-1.0 to -5.0	15
σ_l (N/mm ²)	3.5 to 20	15
a/d	2.5 to 4.5	3
f'_c (N/mm ²)	30 to 70	3
r (%)	0 to 0.36	3
d (mm)	300 to 900	3
b_f/b_w	1.0 to 3.0	4
ρ_w (%)	0.5 to 5.0	4
bearing plate width (mm)	100 to 200	3



$$\frac{1}{nS_xS_y} \sum_{i=1}^n (x_i - \bar{x})(y_i - \bar{y}) \geq 0.95$$

\bar{x} , \bar{y} : Mean of x and y
 n : Number of considered data
 S_x , S_y : Standard deviation of x and y

Figure 4 Evaluation of slope of concentrated stress flow in term of m

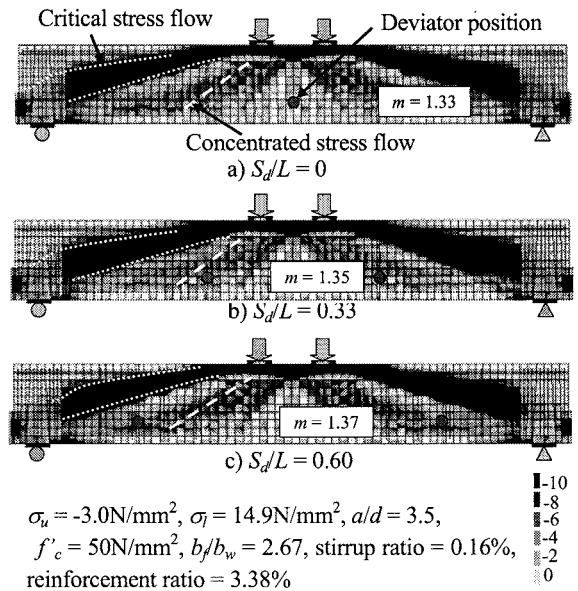


Figure 5 Contour figures of principal stress σ_2 varying S_d/L

$$m = 1.3 \left[\left(1 + 0.2 \frac{\sigma_u}{\sigma_u + \sigma_l} \right) \sigma_l \right]^{-\frac{2}{3}} \left(\frac{a}{d} \right)^{\frac{2}{5}} (f'_c)^{\frac{1}{3}} \quad (1)$$

(4) Cross sectional area of struts

In order to obtain the reasonable cross sectional area of diagonal compression members, nonlinear

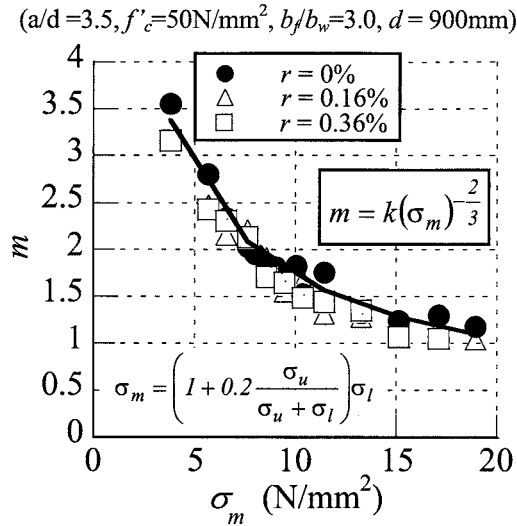


Figure 6 Relationships between m and σ_m

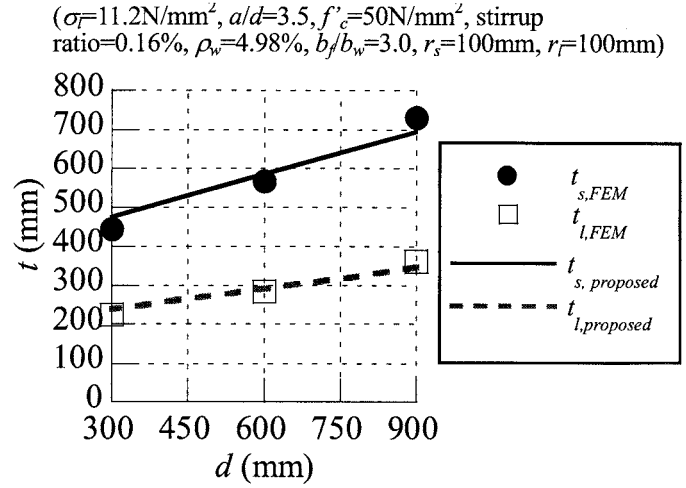


Figure 7 Influence of effective depth on thickness of strut member

FEM has been carried out by varying σ_l , a/d , f'_c , stirrup ratio, d , loading and support plates, b_f/b_w and longitudinal bonded tensile reinforcement ratio. At 90% of shear carrying capacity, the stresses in the vertical direction at each Gauss's points in each horizontal level, σ_{yi} , are considered. The ranges of $0.2d$ inner side of a beam from the top steel bar and the bottom prestressing tendon at the failure side of the beam are investigated. From the distributions of stress σ_{yi} in the vicinity areas to the loading plate and support, the horizontal thickness of stress flow, t , are assessed. The horizontal thickness of stress flow is determined as the horizontal width of the distribution, t_i , where the ratio of σ_{yi} and the maximum values in that horizontal level, $\sigma_{yi-\max}$ is equal to 0.3, which is considered to be not too high or too low to be affected by the disturbance. The average value of the t_i is determined as the horizontal thickness of the concentrated stress flow, t . The obtained horizontal thickness in the vicinity area of a loading point, t_l , and a support, t_s , with the variations of influential parameters are summarized and shown as the example in Figure 7. It is found that the value of t can be approximated in terms of width of the loading plate, r_l or support plate, r_s , the effective depth, d , the value of b_f/b_w , the longitudinal bonded tensile reinforcement ratio and stirrup ratio. The values of t_l and t_s can be estimated as Eqs. (2) and (3).

$$t_l = (r_l + 0.1d) \left(\frac{b_f}{b_w} \right)^{\frac{1}{5}} \left(1 + \sqrt{\frac{A_s}{b_w d}} \right) \left(1 + \left(\frac{A_{sv}}{b_w s} \right)^{\frac{1}{4}} \right) \quad (2)$$

$$t_s = 2(r_s + 0.1d) \left(\frac{b_f}{b_w} \right)^{\frac{1}{5}} \left(1 + \sqrt{\frac{A_s}{b_w d}} \right) \left(1 + \left(\frac{A_{sv}}{b_w s} \right)^{\frac{1}{4}} \right) \quad (3)$$

where, A_s is the cross sectional area of longitudinal bonded tensile reinforcement; A_{sv} is the cross sectional area of stirrup; s is the spacing of stirrups.

In the model, the members [1] – [2], and members [3] – [4] in Figure 2 are considered to be affected by support and loading plates, respectively. The cross sectional area of each strut member can be computed as the values of t_l or t_s multiplied with b_w and its inclination.

2.2 Evaluation of Shear Carrying Capacity

The evaluation process is summarized in Figure 8. In order to calculate the shear carrying capacity of externally prestressed concrete beams, the equivalent elastic analysis is applied. That is, after computing the value of m (Eq. (1)), each member force, F_i , caused by the externally applied shear force, V , can be determined by employing the Castigliano's second theorem, which is the theorem of minimum strain energy. The stiffness of concrete at the ultimate stage, where the strain at the maximum compressive strength, ϵ'_0 , is 0.002, as the secant modulus, E_{cu} , is applied for diagonal compression members. The initial elastic stiffness of concrete, E_c , is used to flexural compression members, which are considered to behave in the elastic range.

On the other hand, the resistance of each strut, R_i , can be calculated from f'_c incorporating the concrete softening parameter, η , the cross sectional area, A_i , and the inclination of each member (Eq. 1). Finally, the shear carrying capacity can be estimated by comparing the value of F_i with R_i , when one of struts becomes critical that is value of F_i/R_i become greatest and equal to 1.0.

4. ACCURACY OF EXISTING PREDICTION EQUATIONS AND PROPOSED METHOD

In this study, a total of 19 beams of experimental investigations for externally prestressed concrete beams with and without transverse reinforcement, conducted by Sivaleepunth et al. 2006 (4), Tan et al. 1998 (5), Kondo et al. 1994 (2), Mitamura et al. 2001 (2), Niitsu et al. 1999 (1) and Hosoda et al. 2002 (5) (the number in parentheses indicate the number of beams), was used to confirm the applicability of the proposed simplified truss model. The experimental results cover several factors, such as shear span to effective depth ratio, a/d , effective depth, d , compressive strength of concrete, f'_c , upper fiber stress in concrete, σ_u , lower fiber stress in concrete, σ_l , support plate width, r_s , loading plate width, r_l , internal bonded tensile reinforcement ratio, ρ_w , and stirrup ratio, r . Table 2 tabulates the details of these beams. The values of a/d vary from 2.5 to 3.6, and the values of d change in the range of 200mm to 500 mm. The range of f'_c is between 29.8 N/mm² and 59.5 N/mm². The values of σ_l vary from 5.7 N/mm² to 14.3 N/mm². The values of ρ_w and r change in the range of 0% to 4.58% and the range of 0% to 1.69%, respectively.

In calculation of the simplified truss model, four diagonal compression members are considered in order to find out the one which causes the shear compression mode of failure. The number of diagonal compression member shown in Figure 2.

The typical crack patterns from the experiments at the ultimate stage are utilized to compare with the critical members in the simplified truss model as illustrated in Figure 9. The bold dashed line represents the critical member of each case. From these comparison results, it is proven that the proposed model is applicable for predicting the failure pattern of externally prestressed concrete beams with and without transverse reinforcement, even if the high strength concrete, lightweight aggregate (Mitamura et al. 2001), or high prestressing force is applied to the beams.

Furthermore, the comparisons of shear carrying capacity for externally prestressed concrete beams between the experimental results and the calculated results from the decompression moment method recommended by JSCE (JSCE 2002), M_{cr} method (Ito et al.

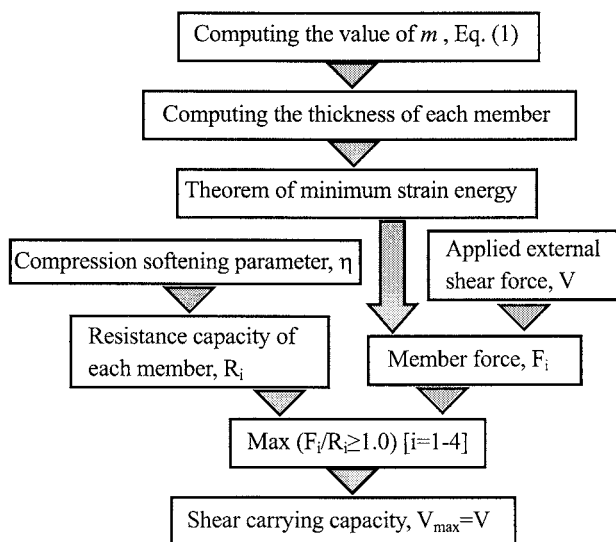


Figure 8 Calculating process

Table 3 Summary of experimental data used in verification of the proposed method

References	Beams	a/d	Effective depth, d (mm)	Compressive strength of concrete, f_c (N/mm ²)	Upper fiber stress, σ_u (N/mm ²)	Lower fiber stress, σ_l (N/mm ²)	r_t/r_s	Internal bonded tensile reinforcement ratio, ρ_w (%)	Stirrup ratio, r (%)	V_{EXP} (kN)			
Present study	ns7	3.5	400	53.6	-1.5	7.3	150/150	4.07	0	245.6			
	ns14			55.8	-2.9	14.3				287.4			
	s7			57.4	-1.5	7.3			0.21	280.3			
	s14			58.6	-2.9	14.3				330.3			
Tan ⁽¹⁰⁾	ST1	2.5	200	34.5	-0.3	9.1	100/100	1.81	1.22	194.0			
	ST2	29.9		156.0									
	ST2C	26.2		-0.2	9	151.2							
	ST2P	36.3		-0.3		165.4							
	ST2S	31.1		-0.2		0.46			148.4				
	Kondo ⁽¹¹⁾	no.2		3.6	250	38			-1.6	10.2	150/150	4.58	0.35
no.4		38	1.41			174.1							
Mitamura ⁽¹²⁾	no.2	3.6	250			59.5	-1.1	5.7	100/100	3.1	0	65.0	
	no.3					55.3	-2.4	11.1				109.5	
Niitsu ⁽¹³⁾	no.2					38.1	-2.2	10.6	150/150	0.68		1.69	120.0
Hosoda ⁽¹⁴⁾	case1					500	48.7	-1.9					7.3
	case2						49.8				163.0		
	case3						53.9				0	207.0	
	case4	46.2	0	170.0									
	case5	29.8	0.68	0	123.5								

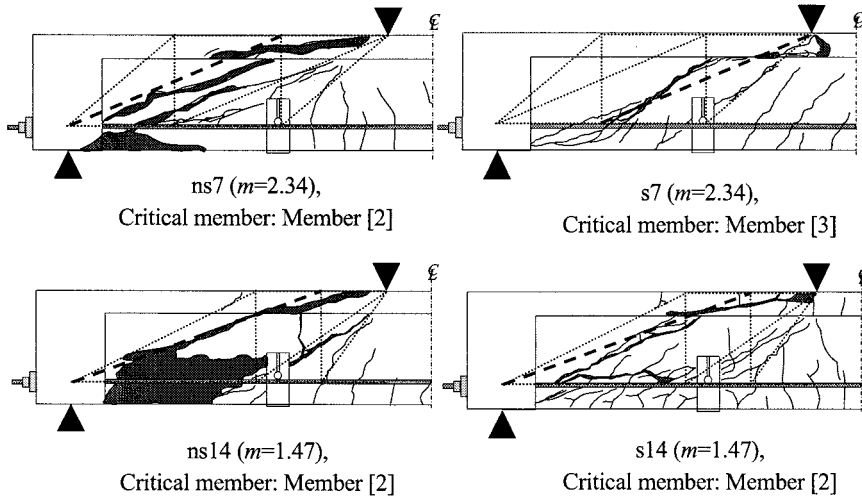


Figure 9 Critical members and crack patterns (Present study)

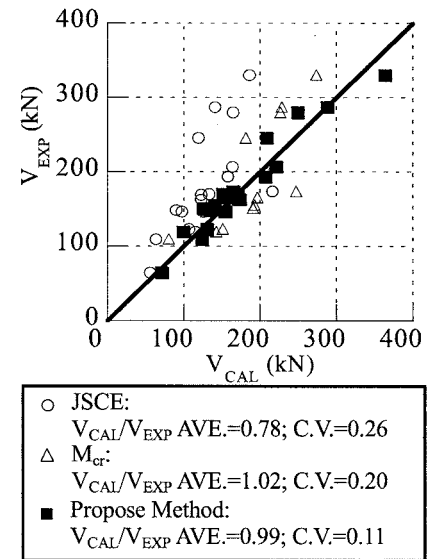


Figure 10 Validation of prediction equations

1994) and the proposed simplified truss model are performed and summarized in Figure 10. By comparing these three simplified methods, the proposed model yields the superior accuracy and reliability in prediction with an average value (AVE.) of V_{CAL}/V_{EXP} of 0.99 and a coefficient of variation (C.V.) of 0.11, while the AVE. of V_{CAL}/V_{EXP} and the C.V. of JSCE are 0.78 and 0.26, respectively. For M_{cr} method, its AVE. of V_{CAL}/V_{EXP} and its C.V. are 1.02 and 0.20, respectively. Therefore, it is proven that the proposed simplified truss model provides the well-predicted results compared with the experimental results in the variety of parameters.

5. CONCLUDING REMARKS

The parametric evaluation by applying the nonlinear FEM on the shear failure mechanism of externally prestressed concrete beams with and without transverse reinforcement were performed to

investigate the effects of prestressing force, shear span to effective depth ratio, compressive strength of concrete, effective depth, stirrup ratio and internal bonded tensile reinforcement ratio on the inclination of concentrated stress flow and the shear carrying capacity. The inclination of concentrated stress flow and the thickness of diagonal compression members assessing from the analysis results is computed by considering the influences of bearing plates, the effective depth, the ratio of widths of flange and web, the internal bonded tensile reinforcement ratio and the stirrup ratio. After computing the inclination of concentrated stress flow and the thickness of diagonal compression members, t , the shear carrying capacity can be predicted by comparing with the member force estimated by theorem of minimum strain energy. It is found that the simplified truss model, which is modified, provides a good correlation for predicting the shear carrying capacity of externally prestressed concrete beams. Moreover, the model can also satisfactorily predict the failure patterns matching with the actual failure for externally prestressed concrete beams.

Acknowledgements:

Sincere gratitude is expressed to Mr. Satoshi Tamura and Dr. Yuzuru Hamada, research engineers, Research and Development Center, DPS Bridge Works Co., Ltd., and Dr. Khac Diep Bui, postdoctoral researcher, Department of Civil Engineering, Tokyo Institute of Technology for their assistance in conducting the experiment. The authors also would like to express their gratitude to the COE program for providing financial support to accomplish this research.

References:

- Japan Society of Civil Engineers (JSCE) (2002), "Standard Specification for Concrete Structures," *Structural Performance Verification*.
- Ito, T., Yamaguchi, T. and Ikeda, S. (1994), "Flexural Shear Behavior of Precast Segmental PC Beam," *Proceedings of the JCI*, **16**(2), 967-972.
- Lertsamattiyakul, M., Niwa, J., Tamura, S., and Hamada, Y. (2005), "Simplified Truss Model for Shear Carrying Capacity Analysis of Non-rectangular Cross Sectional PC Slender Beams," *Proceeding of Second International Conference on Urban Earthquake Engineering (CUEE)*, 381-388.
- Thorenfeldt, E., Tomaszewicz, A. and Jensen, J.J. (1987), "Mechanical Properties of High-strength Concrete and Applications in Design," *Symposium Proceedings, Utilization of High-strength Concrete*, Norway.
- Hordijk, D.A. (1991), "Local Approach to Fatigue of Concrete," *PhD thesis*, Delft University of Technology.
- Sivaleepunth, C., Niwa, J. and Miki, T. (2005), "Applicability of Design Code and Simplified Truss Model for Shear Carrying Capacity of Externally Prestressed Concrete Beams," *Proceeding of Third International Conference on Urban Earthquake Engineering (CUEE)*, 713-720.
- Tan, K.H. and Ng, C.K. (1998), "Effect of Shear in Externally Prestressed Concrete Beams," *ACI Structural Journal*, **95**(2), 116-128.
- Kondo, E., Mutsuyoshi, H., Takahashi, H. and Sano, M. (1994), "Influence of External Prestressing Force on Shear Strength of PC Beams," *Proceeding of the JCI*, **16**(2), 1015-1020.
- Mitamura, H., Ikeda, K., Hishiki, Y. and Fukuda, I. (2001) "Experimental Study on Shear Strength of Externally Prestressed Concrete Beams using High Performance Lightweight Concrete," *Proceeding of the JCI*, **23**(3), 619-624.
- Niitsu, T., Mutsuyoshi, H., Sano, M., and Tonogawa, K. (1999) "Investigation on the Increase in Shear Strength due to External Prestressing," *Proceeding of the JCI*, **21**(3), 949-954.
- Hosoda, A., Kobayashi, K. and Kino, J. (2002) "Shear Properties of PC Segmental Beams Using External Cable Method," *Proceeding of the JCI*, **24**(2), 589-594.

SEISMIC PERFORMANCE OF HORIZONTALLY CURVED BRIDGES WITH AND WITHOUT BACKFILL SOIL

S. Nagata¹⁾, and I. G. Buckle²⁾

1) 21st Century COE Post-doctoral Researcher, Dept. of Civil Engineering, Tokyo Institute of Technology, Japan

2) Professor, Dept. of Civil and Environmental Engineering, University of Nevada, Reno, USA

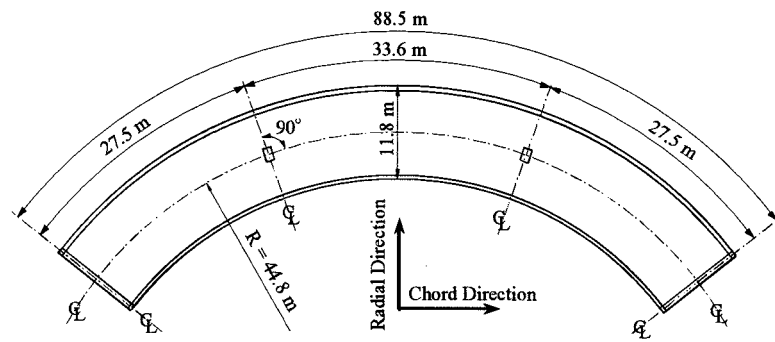
nagata.s.aa@m.titech.ac.jp, igbuckle@unr.edu

Abstract: This study focused on the effect of the reaction forces caused by the backfill soil behind the abutments on the seismic performance of a horizontally curved bridge. A series of nonlinear dynamic response analyses were conducted on a three-span continuous concrete curved bridge supported by two single column bents and two abutments. Unilateral earthquake excitation was imposed in chord or radial directions to the analytical model with and without backfill soil. Analysis under bilateral excitation was also performed to compare the results under the unilateral excitations. It was found that although the backfill forces reduce the overall displacement response of the bridge, the displacement response has a bias in the direction in which the deck moves away from the abutments. The bilateral excitation results in more significant damage of the columns than that estimated by the combined unilateral response.

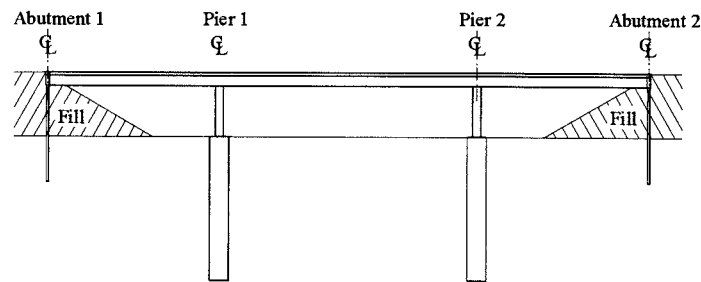
1. INTRODUCTION

Among many of the lessons learned from previous earthquakes, bridge irregularity is one of the most significant issues related to undesirable damage. Bridge irregularity exists in many different forms including variations of span, height and section properties, skew, curve, etc. During the 1971 San Fernando earthquake, a number of reinforced concrete bridges with irregularity suffer extensive damage. Based on this experience, extended attention has been given to the study of seismic effects on irregular bridges such as horizontally curved bridges. Williams and Godden (1979) conducted shake table tests to clarify dynamic response of curved bridges. They emphasized sensitivity of the seismic behavior of the long-span curved bridges to locations and properties of the joints. These results were analytically correlated by Kawashima and Penzien (1979). Otsuka *et al.* (1997) investigated the effect of various bearing conditions on the nonlinear dynamic behavior of a continuous curved viaduct system. Sextos *et al.* (2004) analytically evaluated the effect of the wave passage, the ground motion angle, and the ground motion characteristics on seismic response of a curved, twelve-span bridge constructed in northern Greece. By using the same bridge, application of the multi-mode pushover analysis was evaluated as a simple estimation method for seismic action of curved bridges (Paraskeva *et al.*, 2006).

The previous studies described above mainly focused on the effect of the complicated seismic action due to the curvature on the design of columns, bearings and joints. However, the knowledge for the curved bridge system is insufficient especially for the effect of the backfill soil reaction. The seismic performance of such a bridge is highly dependent on the manner in which the abutments behave. Due to the curve, the structure will experience different resistances depending on whether it is moving away from the backfill soil or into the backfill. In this study, seismic performance of curved bridge systems with and without backfill soil behind the abutments was analytically investigated.

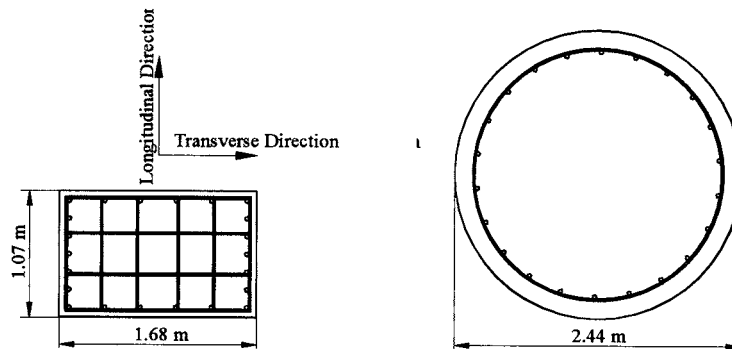


(a) Plan View



(b) Elevation View

Figure 1 Three-Span Continuous Curved Bridge supported on Single Columns and Abutments



(a) Column

(b) Pile Shaft

Figure 2 Cross-sections of Column and Pile Shaft

2. TARGET BRIDGE AND ANALYTICAL IDEALIZATION

2.1 Target Bridge

A curved bridge illustrated in the Seismic Design of Bridges Design Example No. 6 (FHWA, 1996) was used in this study as a target structure. Figure 1 provides configuration of the bridge. The structure is three-span, concrete box girder bridge supported by reinforced concrete single columns and abutments. The girder is constructed monolithically with the column bents as well as abutments. The columns and the abutments are founded on drilled shafts and steel pipe piles respectively. The bridge is located on a site underlain by a deep deposit of cohesionless material. The alignment of the roadway over the bridge is sharply curved, horizontally (104 degree), but there is no vertical curve.

The total span length of the deck is 88.5 m along the centerline and the curve radius is 48.8 m. The substructure elements are oriented at right angle to the bridge centerline at each substructure station. Figure 2 shows the cross-section of the column and the pile shaft. The column is 6.7 m tall and has a 1.07 m by 1.68 m square cross section. An 18.3 m long reinforced concrete pile shaft with a diameter of 2.4 m supports the column. The bridge is assumed to be built in the Northwestern United States in a seismic zone with an acceleration coefficient of 0.2 g . The bridge components are designed based on current seismic design specifications (AASHTO, 1993). In the design procedure the earthquake loading was considered in two orthogonal directions, which was taken along the chord between the two abutments and along a line perpendicular to the chord. These two directions are called hereinafter the chord direction and the radial direction respectively (see Figure 1).

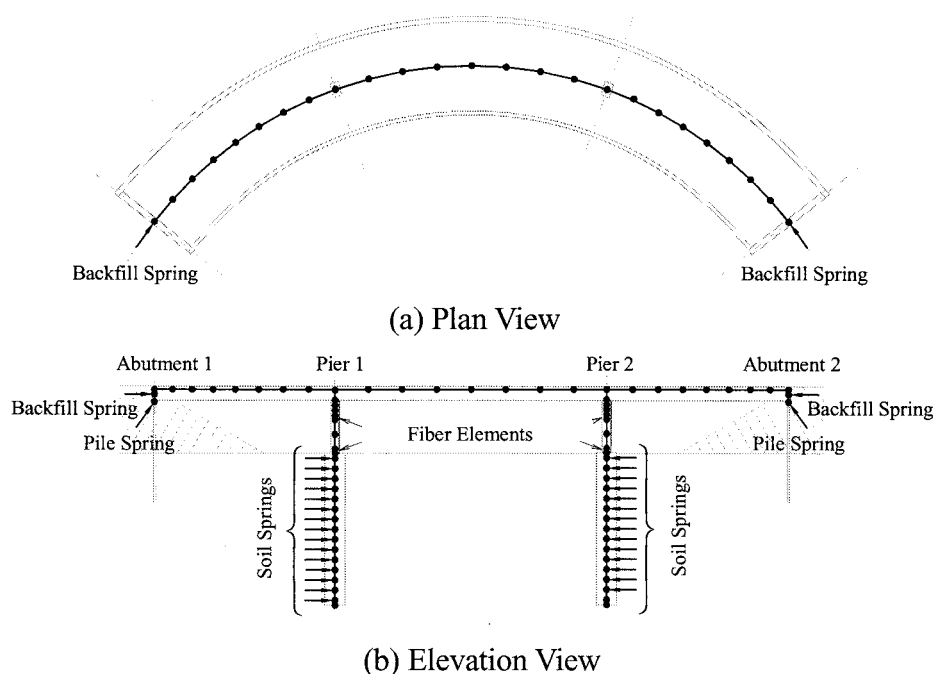


Figure 3 Analytical Idealization of the Target Bridge

2.2 Analytical Idealization

The structural analysis program OpenSees version 1.7.3 (Mazzoni *et al.*, 2006) was used for the analysis. The mathematical model used here is shown in Figure 3. This model includes a single line of beam elements with the cracked stiffness (a half of the gross section stiffness) for each of the superstructure and the substructures including the full length of the drilled shafts. The drilled shafts are restrained by sets of uniformly spaced elastic springs oriented in the two orthogonal directions. The abutments are supported by elastic springs which represent the resistance due to the steel pipe piles. To capture the nonlinear flexural behavior at the top and bottom of the columns, fiber elements are applied assuming that plastic hinge length is a half of the column width (along the weak axis of the section). Two version of the model are considered. The first model includes only the pipe pile resistance for the abutments, and is called the “without backfill model”. For the second model, which is called the “with backfill model,” the resistance due to the backfill soil behind the abutment is added to the pipe pile contribution. To represent backfill resistance, compression only spring was employed.

The fundamental natural periods for the without backfill model are 0.74 sec and 0.70 sec in the radial and chord directions respectively, while those for the with backfill model are 0.63 sec and 0.23 sec in the chord and the radial directions respectively. The backfill resistance significantly reduces the

natural period for the radial direction.

To simulate the significant nonlinear behavior of the bridge under extensive earthquake which exceeds the design level, JR Takatori records observed in 1995 Kobe, Japan, Earthquake are used as an input ground motion. The maximum accelerations in the NS and EW components are $0.64g$ and $0.67g$, respectively. By using this ground excitation, extensive damage is expected to the bridge because design level acceleration was assumed to be $0.2g$. In the following analysis, the NS component of Takatori ground motion will be first imposed in the chord direction to the without and with backfill model. Second, the EW component will be applied to the two models in the radial direction. Finally the NS and EW components will be simultaneously imposed to the two models in the chord and the radial directions, respectively.

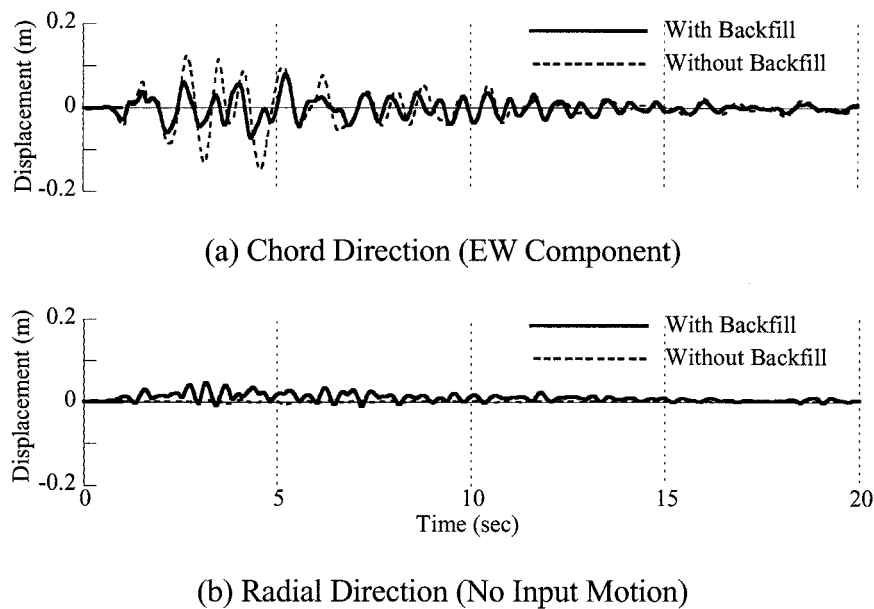


Figure 4 Displacement Response at Midspan of the Deck under Chord Excitation

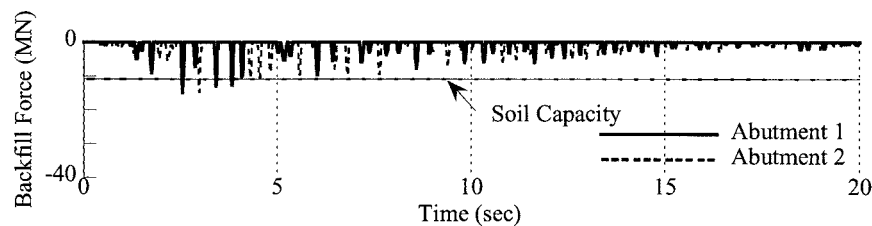


Figure 5 Reaction Force by the Backfill Soil under Chord Excitation

3. SEISMIC PERFORMANCE UNDER CHORD EXCITATION

Figure 4 presents the displacement response at the midspan of the deck for the with and without backfill model under the chord excitation. The reaction forces by the backfill soil behind the abutment for the with backfill model are shown in Figure 5. The resistant by the backfill soil resulted in reduction of the overall deck displacement. However, due to the curvature of the bridge, the reaction force by the backfill soil has the two components in the chord and radial directions, which results in the displacement response in the radial direction as shown in Figure 4(b). Table 1 shows the maximum shear forces, bending moments, and the curvature developed at the top and bottom of columns. In the

without backfill model, all values are more significant in the longitudinal direction than that in the transverse direction because bridge subjected to the chord direction. On the other hand, in the with backfill model, the significant shear force and bending moment developed not only in the longitudinal direction but also in the transverse direction, because the backfill force acts in the radial direction as well.

Table 1 Shear force, Bending Moment, and Curvature of the Pier 1 under Chord Excitation

Model type		Without backfill model		With backfill model	
Direction		Longitudinal	Transverse	Longitudinal	Transverse
Top of column	Shear force (MN)	2.62	0.870	1.930	1.908
	Moment (MN-m)	6.133	2.376	4.952	5.265
	Curvature (1/m)	0.0437	0.0051	0.0021	0.0008
Base of column	Shear force (MN)	2.692	0.892	1.954	1.955
	Moment (MN-m)	6.029	1.764	3.930	3.708
	Curvature (1/m)	0.0281	0.0029	0.0011	0.0004

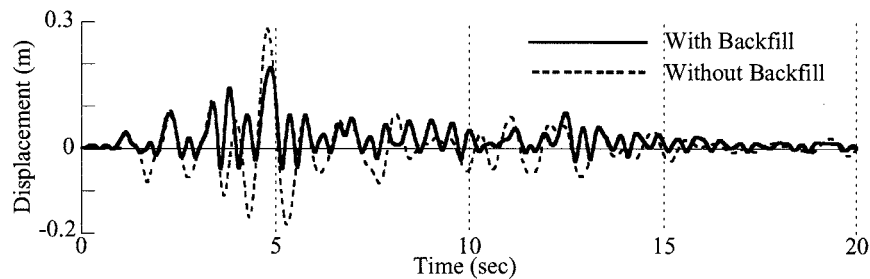


Figure 6 Displacement Response at Midspan of the Deck under Radial Excitation
(Radial Direction, NS Component)

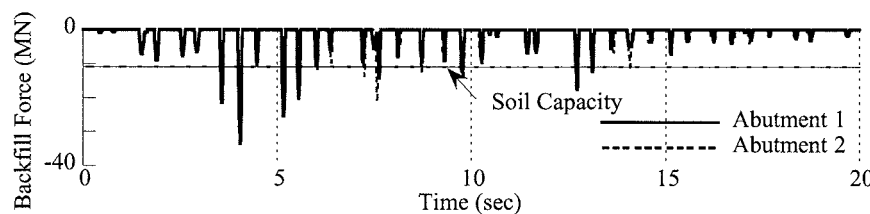


Figure 7 Reaction Force by the Backfill Soil under Radial Excitation

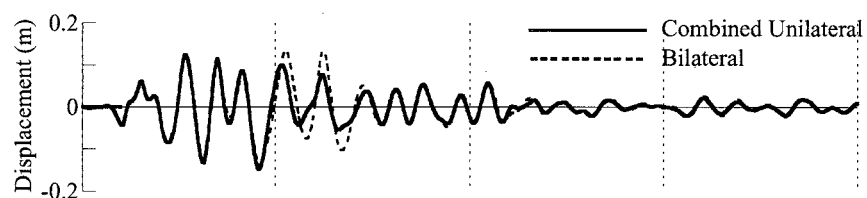
4. SEISMIC PERFORMANCE UNDER RADIAL EXCITATION

The displacement response at the midspan of the deck and the reaction force by the backfill soil under the radial excitation are shown in Figures 6 and 7. Only the displacement response in the radial direction is shown in Figure 6, because the structure is symmetric in this direction and no displacement response was developed in the chord direction. Similar to the results under the chord excitation, the displacement response was reduced due to the backfill forces. However, the backfill reaction is effective only when the deck moves into the abutment, the reduction of the displacement the negative side is more significant than the positive side. As a result the displacement response for

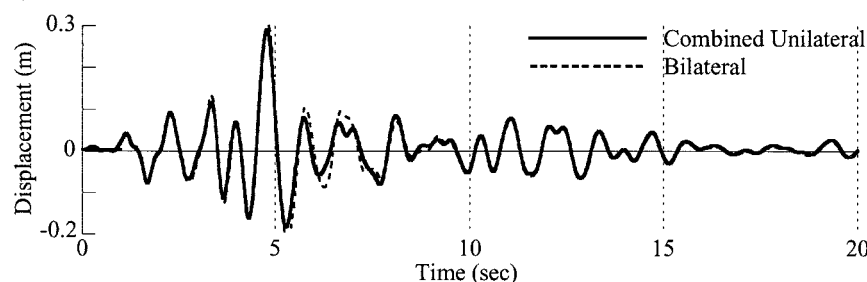
the with backfill model has a bias in the positive side which corresponding to the direction in which the deck moves away from the abutments. Table 2 shows the shear forces, the moment, and the curvatures of the column. Because the bridge was subjected to the radial earthquake all the values are more significant in the transverse direction. When the effect of the backfill soil is included, the column forces developed in the transverse direction become small compared with the case without backfill. This is because not only the columns but also backfill soil resists the inertia force of the deck in the radial direction.

Table 2 Shear Force , Bending Moment, and Curvature of the Pier 1 under Radial Excitation

Model type		Without backfill model		With backfill model	
Direction		Longitudinal	Transverse	Longitudinal	Transverse
Top of column	Shear force (MN)	1.305	3.025	1.407	2.831
	Moment (MN-m)	3.984	9.606	4.286	7.775
	Curvature (1/m)	0.0266	0.0323	0.0087	0.0128
Base of column	Shear force (MN)	1.288	3.117	1.433	2.891
	Moment (MN-m)	2.313	6.610	2.223	6.812
	Curvature (1/m)	0.0007	0.0008	0.0007	0.0009



(a) Chord Direction (EW Component)



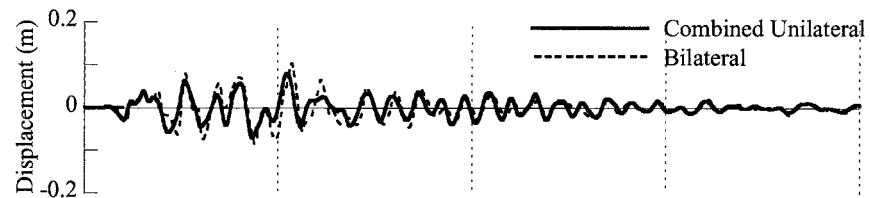
(b) Radial Direction (NS Component)

Figure 8 Comparison of Displacement Response of Deck between Unilateral and Bilateral Excitations (Without Backfill Model)

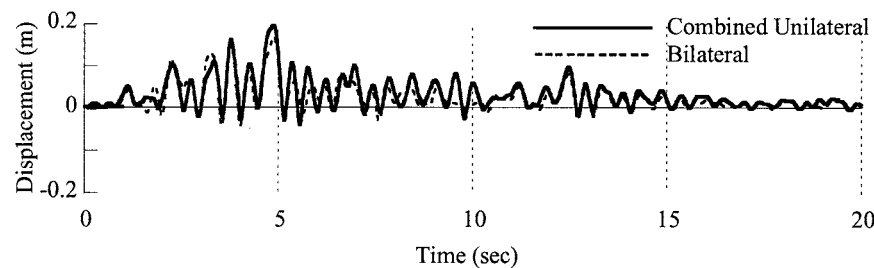
5. EFFECT OF BILATERAL EXCITATION

The displacement responses of the deck under the bilateral excitation are compared to the results of the unilateral cases described above as shown in Figures 8 and 9. Because under the unilateral excitation the response developed not only in the direction in which earthquake motion was applied but also in the other orthogonal direction, this effect is combined in the results of the unilateral response shown in Figures 8 and 9. Based on the comparison, the effect of the bilateral excitation on

the deck displacement seems not significant. However, the bilateral excitation results in more extensive damage at the columns than that estimated by the combined unilateral response. Because the column exhibit nonlinear flexural behavior, the maximum curvature of the combined unilateral response and the bilateral response are compared in Table 3, in order to evaluate the damage level of the column. Except for the top of the column in the transverse direction, the curvatures were larger in the bilateral response than those in the combined unilateral response for the both with and without backfill models.



(a) Chord Direction (EW Component)



(b) Radial Direction (NS Component)

Figure 9 Comparison of Displacement Response of Deck between Unilateral and Bilateral Excitations (With Backfill Model)

Table 3 Maximum Curvature for Combined Unilateral and Bilateral Response

Model type		Without backfill model		With backfill model	
Direction		Longitudinal	Transverse	Longitudinal	Transverse
Top of column	Combined Unilateral	0.0703	0.0374	0.0108	0.0136
	Bilateral	0.0854	0.0310	0.0304	0.0088
	Bilateral/Combined Unilateral	1.21	0.83	2.81	0.647
Base of column	Combined Unilateral	0.0288	0.0037	0.0018	0.0013
	Bilateral	0.0460	0.0093	0.0164	0.0021
	Bilateral/Combined Unilateral	2.02	2.51	9.11	1.62

6. CONCLUSIONS

To clarify effect of backfill soil on seismic performance of curved bridges, a series of dynamic response analyses were conducted. Based on the analytical results presented herein, the following conclusions may be deduced:

- 1) The resistant by the backfill soil resulted in reduction of the overall deck displacement under the chord excitation. However, because the reaction force by the backfill soil has the radial component, this results in the displacement response in the radial direction and increases the column forces in the transverse direction.

- 2) Similar to the results under the chord excitation, the displacement response is reduced due to the backfill forces under the radial direction. However, because the backfill reaction is effective only when the deck moves into the abutments, the displacement response has a bias in the direction in which the deck moves away from the abutments.
- 3) Although the effect of the bilateral excitation on the deck displacement is not significant, the bilateral excitation results in more extensive damage at the columns than that estimated by the combined unilateral response.

Acknowledgements:

This project was supported from Center for Urban Earthquake Engineering (CUEE) in Tokyo Institute of Technology. The opportunity for the first author to study abroad at University of Nevada, Reno was provided by Professor Kazuhiko Kawashima, Tokyo Institute of Technology. The authors express sincere appreciation for their invaluable supports.

References:

- American Association of State Highway and Transportation Officials (AASHTO), (1993), "*Standard Specifications for Highway Bridges-Division I-A*," Washington, DC.
- Federal Highway Administration (FHWA), (1996), "*Seismic Design of Bridges - Design Example No. 6 Tree-Span Continuous CIP Concrete Box Bridge*," Report No. FHWA-SA-97-011, McLean, VA, September.
- Kawashima, K., and Penzien, J. (1979), "Theoretical and Experimental Dynamic Behavior of a Curved Model Bridge Structure," *Earthquake Engineering and Structural Dynamics*, 7, 129-145.
- Mazzoni, S., McKenna, F., Scott, M., S., Gregory, L., Fenves, G., L., et al., (2006), "*Open System for Earthquake Engineering Simulation User Command-Language Manual*" Pacific Earthquake Engineering Research Center (PEER), University of California, Berkeley.
- Otsuka, H., Kanda, M., Suzuki, M., and Yoshizawa, T. (1997), "Dynamic Analysis of Sliding Behavior of Curved Bridge Superstructure caused by Horizontal Ground Motion," *J. of Structural Mechanics and Earthquake Engineering*, JSCE, 570 (I-40), 305-314 (in Japanese).
- Paraskeva, T.S., Kappos, A.J., and Sextos, A.G. (2006), "Extension of Modal Pushover Analysis to Seismic Assessment of Bridges," *Earthquake Engineering and Structure Dynamics*, 35(10), 1269-1293.
- Sextos, A., Kappos, A.J., and Mergos, P. (2004), "Effect of Soil-Structure Interaction and Spatial Variability of Ground Motion on Irregular Bridges: the Case of the Krystallopigi Bridge," *Proc. of 13th World Conference on Earthquake Engineering*, Paper No. 1156, Vancouver, Canada, August.
- Williams, S., and Godden, W. (1979), "Seismic Response of Long Curved Bridge Structures: Experimental Model Studies," *Earthquake Engineering and Structural Dynamics*, 7, 107-128.

CONTROL DEVICES INCORPORATED WITH SHAPE MEMORY ALLOY

S. D. Xue¹⁾ and X.Y. Li²⁾

1) Professor, The College of Architecture and Civil Engineering, Beijing University of Technology,
Beijing 100022, China

2) PhD Candidate, The College of Architecture and Civil Engineering, Beijing University of Technology,
Beijing 100022, China

sdxue@bjut.edu.cn; xiongy2006@126.com

Abstract: Shape Memory Alloy (SMA) is a type of material that shares several unique characteristics fit for control devices for vibration control applications. Based on material properties of shape memory alloy, four types of control devices incorporated with NiTi SMA wires are introduced in this paper, which involve three types of dampers (SMA damper, SMA-MR damper and SMA-Friction damper) and one kind of isolation bearing (SMA-rubber bearing). Mechanical models of these devices and their experimental verifications are presented. To investigate the control performance of the developed devices, SMA-MR damper and SMA-rubber bearing are applied to structures. The results show that the control devices can be effective.

1. INTRODUCTION

Over past few years, various types of control devices have been developed and successfully applied to tall buildings, high-rise structures, long span bridges, etc. (Kareem 1983, Zhang and Soong 1992, Constantinou *et al.* 1993, Tamura 1997, DesRoches 2000, Xue *et al.* 2002). Generally, control devices based on energy dissipation and seismic isolation are commonly used in practical applications. Previous studies have shown that mechanical damper is an effective control device for energy dissipation, and the seismic isolation can be realized by bearing.

Shape memory alloy (SMA) is a type of material that displays several unique characteristics over other damping materials, such as shape memory effects, high damping performance, highly reliable energy dissipation capacity, large strain behavior, excellent fatigue property and corrosion resistance ability, etc. (Graesser and Cozzarelli 1991, Soong and Dargush 1997, Dong *et al.* 2002). Such excellent functions come from the unique thermo-mechanical behaviors of SMA which are resulted from the internally twinned martensite phase transformation and its reverse transformation induced by temperature and stress.

Based on material properties of shape memory alloy, four types of control devices incorporated with NiTi SMA wires are introduced in this paper, which involve three types of dampers (SMA damper, SMA-MR damper and SMA-Friction damper) and one kind of isolation bearing (SMA-rubber bearing). Mechanical models of these devices and their experimental verifications are presented. To investigate the control performance of the developed devices, SMA-MR damper and SMA-rubber bearing are applied to structures. The results show that the control devices can be effective.

2. MATERIAL PROPERTIES OF SMA

In practical applications, two material properties of SMA are of interest: (1) superelastic behavior; (2) shape memory effect. Under superelastic state, the material will provide ideal hysteretic damping. One of the main differences between SMA and normal metals is that the SMA changes its elasticity and dissipates energy through the changes of crystalline phases. After full unloading, the material will return to its original undeformed geometry with zero residual strain. However, for conventional steel, the resulting hysteresis is due to a plastic deformation that leads to damages of the material. When incorporating shape memory alloy with control devices, the superelastic and energy dissipation capability of the material have important effects on the control ability of the device. So it is necessary to learn more about material properties through experiments. In our study, a type of SMA wire made of nitinol alloy (NiTi SMA) is selected to be tested. The nominal diameter of the wire is 1.00mm. In terms of the service temperature of the SMA wire used in civil engineering, the nature temperature, which is the austenite transformation finishing temperature, is determined at -5°C , so as to ensure most of the cases the material keep in austenite phase. All of the tests are carried out at the temperature of 20°C .

To investigate the superelastic capability of the wire, five limited strains ($\varepsilon=3\%$, 4% , 5% , 6% and 7%) are set initially to the cycle of loading and unloading, and the loading frequency is taken as 0.01Hz . Figure 1 shows the stress-strain curves of the wire with different limited strains. It is seen that the SMA wire shares excellent superelastic capability within the strain of 6% . The superelastic deformation of the SMA material is about 30 times larger than that of normal steel, which can only sustain strains of less than 0.2% under elastic stage.

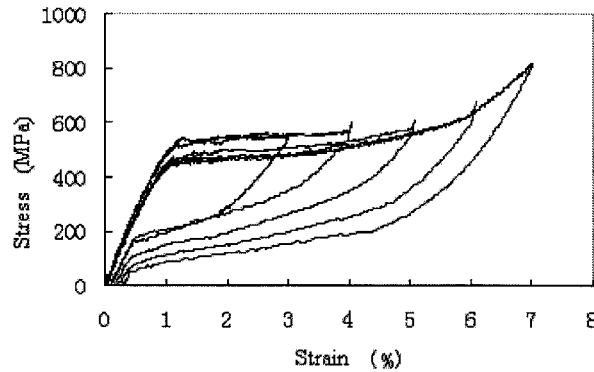
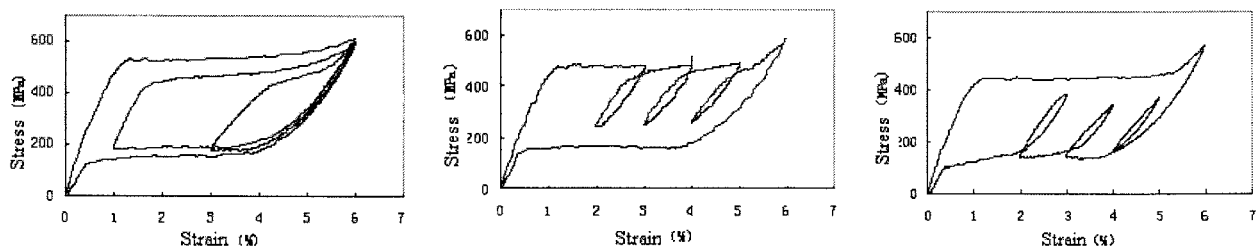


Figure 1 Testing Curves of Superelastic Capability for NiTi SMA wire (0.01Hz , 20°C)

Figure 2 presents the energy dissipation capability of the SMA wire with loading frequency of 0.02Hz . Three types of cycles of strains, $\varepsilon(\%)=0-6-1-6-3-6-5-6$, $\varepsilon(\%)=0-3-2-4-3-5-4-6-0$ and $\varepsilon(\%)=0-6-4-5-3-4-2-3-0$, are tested. It is apparent that NiTi SMA wires possess good function of energy absorbing.



(a) $\varepsilon(\%)=0-6-1-6-3-6-5-6$

(b) $\varepsilon(\%)=0-3-2-4-3-5-4-6-0$

(c) $\varepsilon(\%)=0-6-4-5-3-4-2-3-0$

Figure 2 Testing Curves of Cycle Loading for NiTi SMA wire (0.02Hz , 20°C)

3. CONTROL DEVICES

Based on material properties of SMA, some types of control devices incorporated with SMA wires have been developed by our research team, and their theoretical models have been established as well. In this paper, four types of control devices, i.e., SMA damper, SMA-MR damper, SMA-Friction damper, and SMA-rubber bearing, will be introduced.

3.1 SMA Damper

By utilizing the SMA hysteretic effect under superelasticity, an energy absorbing device---a new type of SMA damper is designed as shown in Figure 3. The damper is composed of four groups of SMA wires, where for each group of the SMA wire, one end of the wire is connected to a guiding shaft through clip block, while the other end is connected to an adjustable bolt. The SMA wires are pre-tensioned by adjustable bolt to prevent a relaxation of the wire. During working, when the guiding rod, which is connected to the guiding shaft, moves along the guiding conduit, the SMA wires will work interactively to dissipate energy through hysteretic damping.

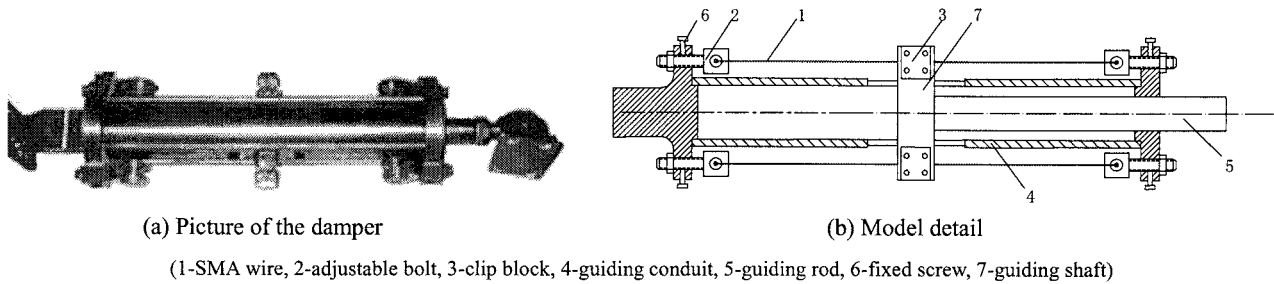


Figure 3 SMA Damper

A simplified theoretical model is developed for predicting F-Δ relations of the SMA damper, where F is the restoring force and Δ is displacement of the damper. According to material tests on NiTi SMA wire, the stress-strain relations for a single SMA wire in tension state can be approximately represented by Figure 4 and equation (1),

$$\sigma(\varepsilon) = \begin{cases} k_1 \varepsilon & (0 \rightarrow \varepsilon_{ms}, \varepsilon_{af} \rightarrow 0) \\ (k_1 - k_2) \varepsilon_{ms} + k_2 \varepsilon & (\varepsilon_{ms} \rightarrow \varepsilon_{mf}) \\ (k_1 - k_2)(\varepsilon_{ms} - \varepsilon_{mf}) + k_1 \varepsilon & (\varepsilon_{mf} \rightarrow \varepsilon_{as}) \\ (k_1 - k_2) \varepsilon_{af} + k_2 \varepsilon & (\varepsilon_{as} \rightarrow \varepsilon_{af}) \end{cases} \quad (1)$$

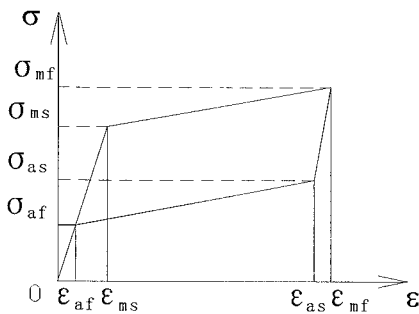


Figure 4 Simplified Stress-Strain Relation

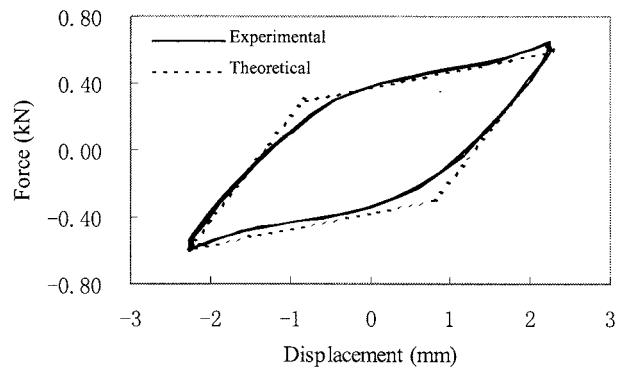


Figure 5 Comparison between Experimental and Theoretical Results

The F-Δ relation for the damper is then developed by

$$F = \sigma(\varepsilon_A)A_A - \sigma(\varepsilon_B)A_B \quad (2)$$

$$\varepsilon_A = \varepsilon_0 + \frac{\Delta}{L}; \quad \varepsilon_B = \varepsilon_0 - \frac{\Delta}{L} \quad (3)$$

where ε_A , A_A are, respectively, the strain and the cross-sectional area of the SMA wires on the left side of guiding shaft; ε_B , A_B are, respectively, the strain and the cross-sectional area of the SMA wires on the right side of guiding shaft; ε_0 is the pretension strain of the SMA wire; L is the length of SMA wire; k_1 , k_2 are, respectively, the first and the second slopes of the lines in Figure 4. The parameters in Figure 4 can be determined by material tests.

In order to verify the theoretical model, a series of performance tests of the damper were carried out. A good agreement was obtained between experimental and theoretical results (Figure 5). It is seen that the damper can provide good hysteretic damping.

3.2 SMA-MR Damper

SMA and Magnetorheological (MR) fluid are two kinds of smart materials commonly used in a few adaptive-passive vibration control applications. The well-known characteristic of MR is that its state can be transformed from freely flowing viscous fluid to semi-solid with controllable stiffness with the effect of magnetic field, furthermore, the transformation is reversal (Li *et al.* 2003). Based on the superelastic and shape memory property of SMA material and the feature of MR fluid, a SMA-MR composite damper is designed as shown in Figure 6. Figure 7 is the sketch drawing of SMA wire arranged for the damper. The cross section of the damper is presented in Figure 8. Table 1 offers the fundamental parameters of the damper.

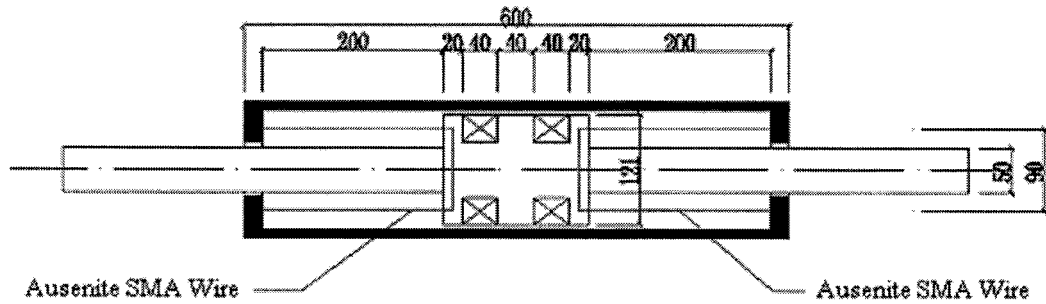


Figure 6 Model of the SMA-MR Damper

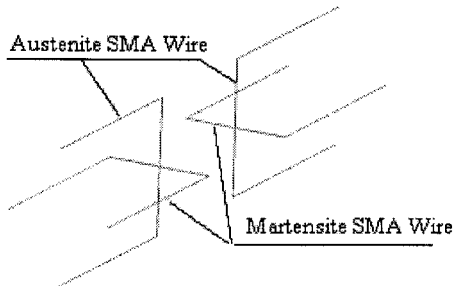


Figure 7 Arrangement of SMA Wires

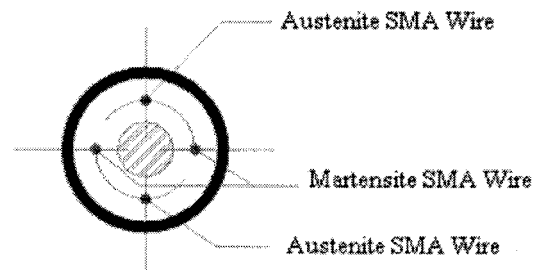


Figure 8 Section of the SMA-MR Damper

The creative intellectual device is combined with SMA and MR which can work together harmoniously. When the seismic excitation or vibration is weak, the input energy is absorbed by austenite SMA wires with their superelastic deformation, and the MR keeps fluid. With the

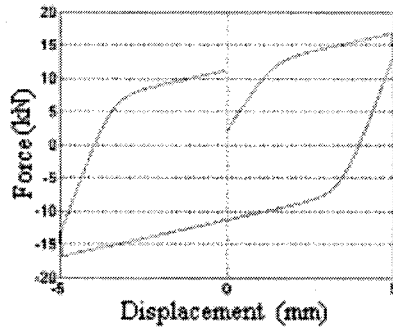
earthquake getting stronger, the martensite SMA wires are heated, and the hysteretic force is offered by the shape memory effect. Meanwhile, being MR set up an electric circuit, part of them transforms to solid, and more hysteretic force is accessible. The mechanical model of the damper can be described as

$$F = \begin{cases} F_{SMA1} + F_{MR} & |x| \leq \Delta \\ F_{SMA1} + F_{SMA2} + F'_{MR} & |x| > \Delta \end{cases} \quad (4)$$

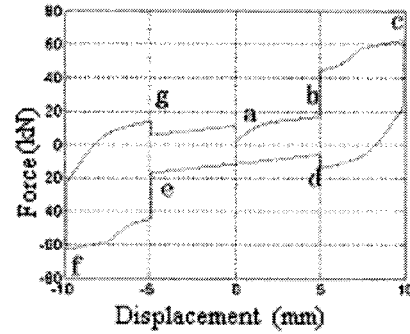
where F_{SMA1} and F_{SMA2} are the hysteretic forces from austenite SMA wire and heated martensite SMA wire, respectively; F_{MR} and F'_{MR} represent, respectively, the damping force from MR in flowing state ($I=0$, without current in the magnetic loops) and that from part of MR being solid ($I=2A$, with constant current in the magnetic loops). In which x is the displacement of piston rod, and Δ is a limited value, which can be assigned as $\Delta=0.02l_0$. Details about the developing and calculating of the hysteretic and damping forces can refer to the literature by Bian and Xue (2004).

Table 1 Fundamental Parameters of the SMA-MR Damper

Internal Diameter of the Damper (mm)	Gap (mm)	Diameter of the Pistol D (mm)	Diameter of Pistol Rod d (mm)	Effective Length of Pistol L (mm)	Initial Length of SMA Wire $2l_0$ (mm)
125	2	121	50	80	2×248



(a) $A=5$ mm



(b) $A=10$ mm

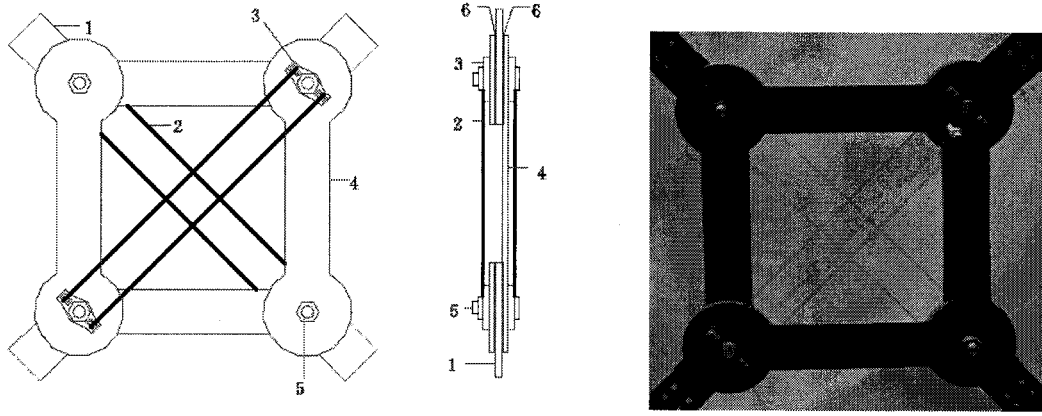
Figure 9 Hysteretic Loops of the SMA-MR Damper for Sinusoidal Loading with Amplitude of 5mm and 10mm

Figure 9 presents the hysteretic loops of the SMA-MR damper for sinusoidal excitation $x = A \sin(\omega t)$ with the loading amplitude A to be 5 mm and 10 mm, respectively. The SMA core is combined with 25 pieces of wires, and the diameter of each wire is 1mm. In addition, $\Delta = 0.02l_0 = 5\text{mm}$. In Figure 9(b), the line ab , de and ga represent the phase with only austenite SMA wire and MR in fluid ($I=0$, without current in the magnetic loops), and the line bcd and efg are the phase that the hysteretic force and the damping force are offered by austenite SMA wire, heated martensite SMA wire and MR with constant current in its magnetic loops. It is seen that the SMA-MR damper shares excellent capability of energy dissipation in any cases.

3.3 SMA-Friction Damper

Frictional energy dissipation is an efficient means for vibration control. However, the ability of energy absorbing for frictional device is limited. Based on the frictional mechanism and energy dissipation characteristic of SMA wire, a new type of SMA-friction damper, which is combined

SMA wire with frictional apparatus, is created. Figure 10 shows the components of the device and its realized model. When the loading on damper is less than the limitation for frictional sliding, the device keeps stable, and the damper corresponds to normal bracing system. Once the loading is over limitation to slide, the frictional apparatus starts to work. Meanwhile, the incorporated SMA wires work interactively to absorb the input energy.



(1-connecting element, 2- pre-tensioned SMA wire, 3-clamp, 4-connecting rod, 5- bolt, 6-frictional pad)

Figure 10 Model of the SMA-Friction Damper

The mathematical model of the damper is written as

$$F_d = F_f \text{sign}(\dot{x}) + F_{SMA} \quad (5)$$

where F_d is the total damping force of the damper; F_f and F_{SMA} represent, respectively, frictional force and hysteretic force contributed from frictional sliding and SMA wire; $\text{sign}(\cdot)$ is a signum function. Details for developing and calculating of F_f and F_{SMA} can refer to Xue *et al.* (2006).

To examine the control performance, a series of performance tests of the damper were carried out. A comparison between experimental and theoretical results is shown in Figure 11. It is seen that the damper can provide good hysteretic damping.

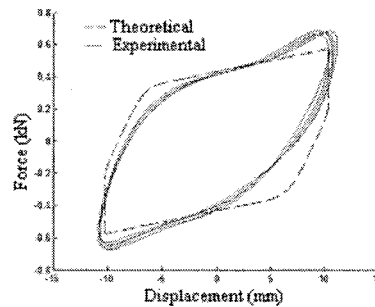


Figure 11 Comparison Between Experimental and Theoretical Results

3.4 SMA-Rubber Bearing

Laminated rubber pads have been successfully used as isolation bearings in many building structures. However, some problems occur in the application of rubber bearings, such as poor fatigue property, unreturnable deformation in strong ground motions, and rather low energy dissipation capacity, and so forth. To improve the vibration isolation performance, a new type of

SMA-rubber bearing is designed by combining shape memory alloy with ordinary rubber bearing. The detail of the SMA-rubber bearing can be seen in Figure 12. According to the design, two groups of SMA wires are used as the energy absorbing components and each group, which is through the ring of the regulating bolt along the diagonal line of the connecting plate 1, is fixed at the chuck along diagonal line of connecting plate 2. By screwing the regulating bolts, pre-tensions can be exerted to SMA wires before use.

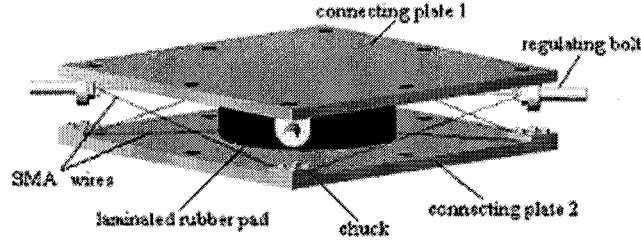


Figure 12 Detail of the SMA-Rubber Bearing

The mathematical model for the restoring force of the bearing can be represented by

$$F_{SRB}^t = K_r x + F_{SMA}(x, \dot{x}) \quad (6)$$

where K_r is the elastic stiffness of laminated rubber pads; F_{SMA} is the control force resulted from SMA wires; and x, \dot{x} represent, respectively, displacement and velocity of the bearing. A derivation for the control force of SMA wire can refer to Xue *et al.* (2005).

A series of performance tests were carried out for the new SMA-rubber bearing. Figure 13 shows a comparison between experimental and theoretical results.

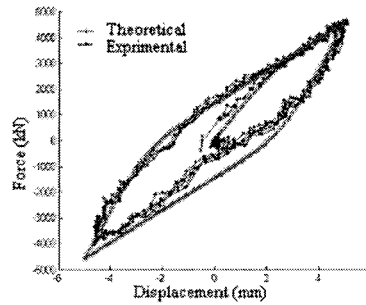


Figure 13 Comparison Between Experimental and Theoretical Results

4. APPLICATIONS

4.1 Control Performance of SMA-MR Damper for a Canopy Roof Structure

The developed SMA-MR damper is applied to a canopy roof to investigate its control effectiveness under seismic excitation (Figure 14). The roof structure is a double layer grid with a plan of 30m×30m and a thickness of 2m. The grid is composed of a series of 3m×3m square pyramids mounted orthogonally in plane. Steel tubes of Ø60×3.5mm are selected as the members of the grid. In order to reduce the response under dynamic load, two sets of SMA-MR dampers are installed as shown in Figure 14(a) and (b).

For structures with SMA-MR dampers installed, the governing equation for the controlled structural system can be written by

$$[M]\{\ddot{x}\} + [C]\{\dot{x}\} + [K]\{x\} = -[M]\{\ddot{x}_g\} - [H]\{F(t)\} \quad (7)$$

where $[M]$, $[C]$, $[K]$ are the mass, damping and stiffness matrices of the structure, respectively; $\{F(t)\}$ is the control force vector induced by SMA-MR damper; $[H]$ is an indication matrix representing the locations of the control force. The control effectiveness can be evaluated by the reduction factor defined by

$$\beta = \frac{R_{\max} - R_{\max}^c}{R_{\max}} \quad (8)$$

where R_{\max} is the maximum peak response value without control; and R_{\max}^c is the maximum peak response value with control.

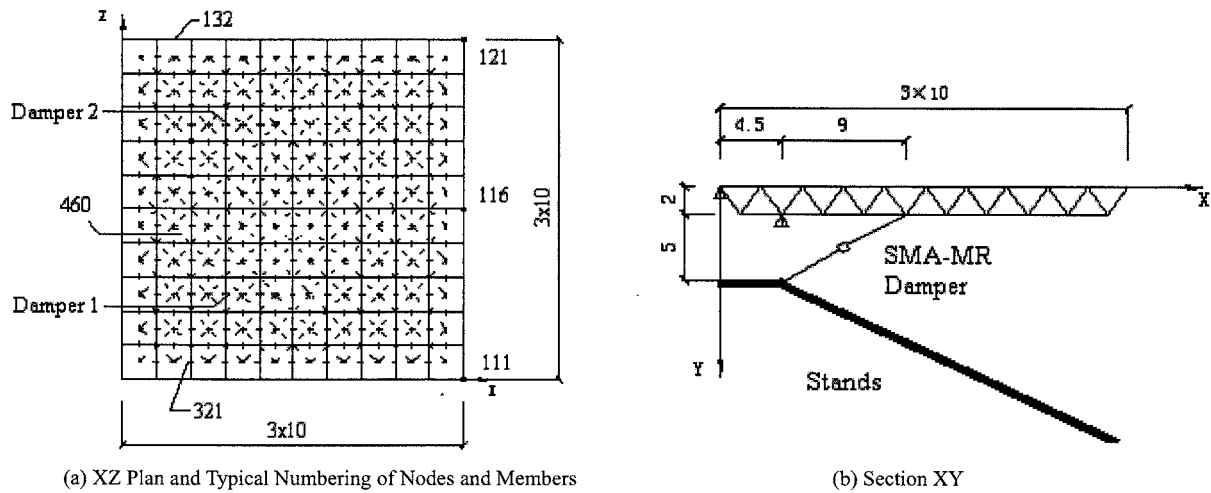


Figure 14 Model of the Canopy Roof with SMA-MR Dampers (Dimensions in m)

Seismic analyses are performed by inputting El-Centro earthquake waves with, respectively, 0.2g, 0.4g and 1.0g peak acceleration of ground motions, from which seismic responses for both nodal displacements and internal forces of members are obtained. Tables 2 and 3 show some of the results of control effectiveness for nodal displacements and internal forces of members, respectively. It is shown that the new type of SMA-MR damper is very effective to mitigate earthquake responses of the roof structure.

Table 2 Control Effectiveness for Nodal Displacements in Directions X, Y and Z

Peak Acceleration of Ground Motion	Nodal No.	X			Y			Z		
		Without Control (mm)	With Control (mm)	β	Without Control (mm)	With Control (mm)	β	Without Control (mm)	With Control (mm)	β
0.2g	111	1.4	1.1	21%	21.8	15.3	30%	2.7	2.7	0
	116	1.2	1.1	8%	21.5	15.7	27%	2.6	2.7	-4%
	121	1.5	1.4	7%	20.9	15.6	25%	2.7	2.7	0
0.4g	111	2.7	1.9	30%	43.5	22.9	47%	5.4	5.4	0
	116	2.4	1.7	29%	43.1	24.3	44%	5.3	5.3	0
	121	2.9	2.4	17%	41.7	25.1	40%	5.3	5.4	2%
1.0g	111	6.9	4.4	36%	108.8	61.0	44%	13.4	13.4	0
	116	6.1	4.2	31%	107.7	59.5	45%	13.2	13.2	0
	121	7.3	5.5	25%	104.4	56.9	45%	13.4	13.4	0

Table 3 Control Effectiveness for Axial Forces of Members

Peak Acceleration of Ground Motion	Member No.	Maximum Axial Forces (kN)		β
		Without Control	With Control	
0.2g	Top chord 132	14.1	12.0	15%
	Bottom chord 321	16.2	10.5	35%
	Web member 460	4.6	4.4	4%
0.4g	Top chord 132	28.1	21.4	24%
	Bottom chord 321	32.4	19.3	40%
	Web member 460	9.3	8.5	9%
1.0g	Top chord 132	70.4	49.1	30%
	Bottom chord 321	81.0	46.5	43%
	Web member 460	23.2	22.3	4%

4.2 Seismic Response Analysis of Lattice Shells Incorporating SMA-Rubber Bearing

Dynamic analysis of a single-layer spherical lattice shell is applied in this study to examine the effectiveness of the SMA-rubber bearing. The vertical view of the lattice shell is shown in Figure 15 where the symbol \odot is used to represent the seismic isolation bearing. The numbering of some joints and members is shown in Figure 16. The span of the shell structure is 35.5m, and the height to span ratio of the shell is 0.23. The main steel members (Q235) of the roof structure consist of the rib bars ($\phi 325 \times 8\text{mm}$), the ring bars ($\phi 323.9 \times 8\text{mm}$) and the diagonal bars ($\phi 325 \times 8\text{mm}$). The steel edge ring beam is chosen as HK500b. Two arrangement schemes of seismic isolation bearings are considered as shown in Figure 15.

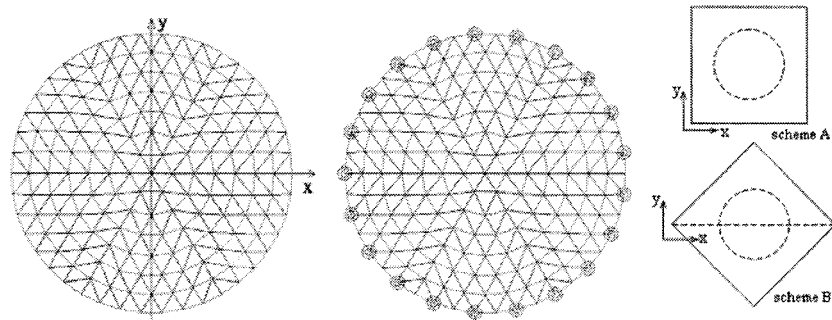


Figure 15 Vertical View of the Lattice Shell

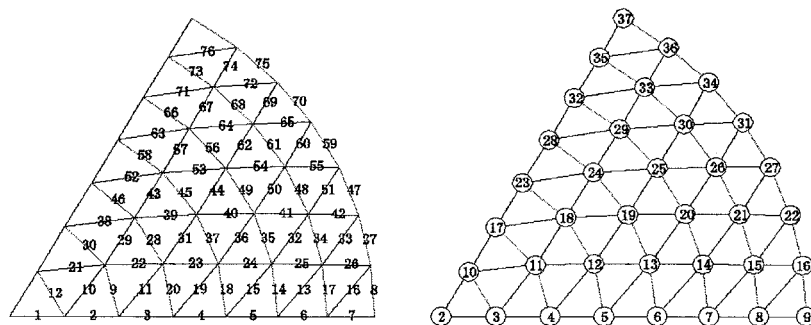


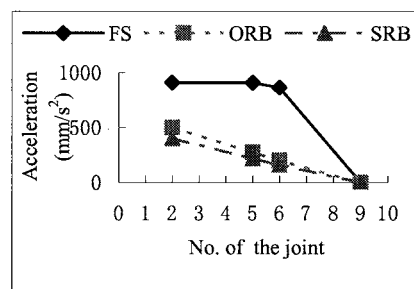
Figure 16 Numbering of Joints and Members

In present study, El-Centro earthquake record is adopted as earthquake excitation along the X-axial direction. The peak value acceleration of earthquake wave is scaled to 0.30g in the analysis.

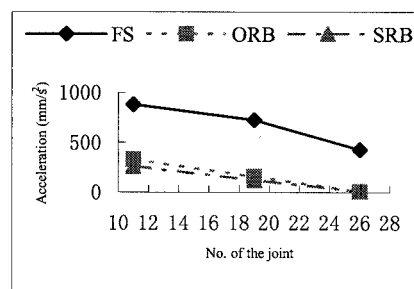
Cases of numerical simulations are indicated in Table 4. Some of the results are illustrated in Figures 17 to 19. It is shown that the seismically isolated lattice shell has smaller peak values in general and more even distributions of the maximum responses than the shell with fixed support. It is evident that SMA-rubber bearing behaves better isolation performance than ordinary rubber bearing. In addition, scheme B is a little bit superior to scheme A.

Table 4 Cases of Numerical Simulations

Earthquake wave	Peak value of scaled acceleration	Supporting conditions
El-Centro record (NS)	0.30g	Fixed support (FS)
		Ordinary rubber bearing (ORB)
		SMA-rubber bearing (SRB, Scheme A)
		SMA-rubber bearing (SRB, Scheme B)

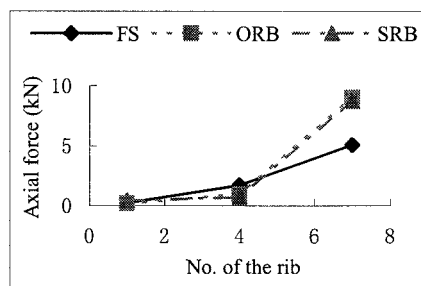


(a) 2→5→6→9

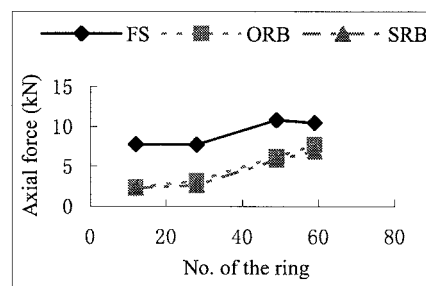


(b) 11→19→26

Figure 17 Peak Value of Acceleration in the X Direction (scheme A)

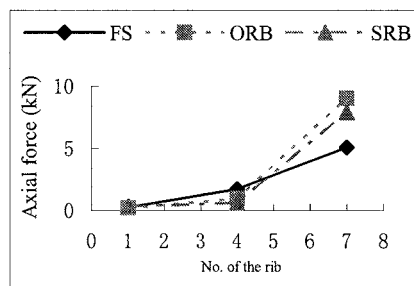


(a) 1→4→7

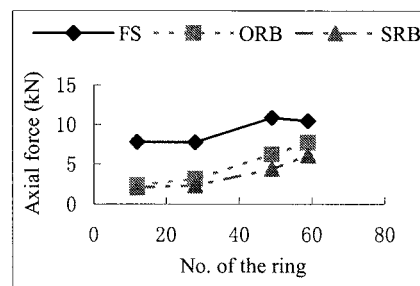


(b) 12→28→49→59

Figure 18 Peak Value of Axial Force (scheme A)



(a) 1→4→7



(b) 12→28→49→59

Figure 19 Peak Value of Axial Force (scheme B)

5. CONCLUSIONS

Based on material properties of NiTi SMA wire, the design of three types of dampers and one kind of isolation bearing incorporated with shape memory alloy are introduced. Mechanical models of the devices have been given. These models were verified by a series of experiments. Good agreement has been obtained between experimental and theoretical results. The studies indicate that the developed control devices can provide high hysteretic damping.

To investigate the performance of the developed devices, SMA-MR damper and SMA-rubber bearing are applied to structures. The potential use of the SMA-MR damper to a canopy roof shows that seismic responses of the structure can be effectively reduced. In comparison with ordinary fixed supports and rubber bearings, the SMA-rubber bearing provides superior performances. The seismic displacements, accelerations and dynamic internal forces of lattice shell structures can be effectively reduced by using SMA-rubber bearing.

The developed devices in this paper are of many distinguished advantages over other damping devices, such as stable performance, long service life, good durability, good energy dissipation capability, excellent fatigue and corrosion resistance property, etc. Therefore, they are very suitable for vibration control of structures.

Acknowledgements:

The authors gratefully acknowledge the support from the funding project for academic human resources development in institutions of higher learning under the jurisdiction of Beijing municipality. The research was also supported by the National Natural Science Foundation of China (50178006) and the Beijing Natural Science Foundation (8042008).

References:

- Bian, X.F. and Xue, S.D. (2004), "SMA-MR composite damper", *World Earthquake Engineering*, 20(2), 23-29.
- Constantinou, M.C., Symans, M.D., Tsopelas, P., and Taylor, D.P. (1993), "Fluid Viscous Dampers in Application of Seismic Energy Dissipation and Seismic Isolation", *Proc. ATC 17-1 on Seismic Isolation, Energy Dissipation, and Active Control*, 2, 581-591.
- DesRoches, R. (2000), "Shape Memory Alloy—Based Response Modification of Simply Supported Bridges", *Advances in Structural Dynamics*, J.M. Ko and Y.L. Xu (Eds.), Vol. I, 267-274.
- Dong, J.H., Xue, S.D., and Zhou, Q. (2002), "Applications of Shape Memory Alloy in Structural Vibration Control", *World Earthquake Engineering*, 18(3), 123-129.
- Graesser, E.J. and Cozzarelli, F.A. (1991), "Shape Memory Alloys as New Materials for Aseismic Isolation", *J. Engng. Mech., ASCE*, 117(11), 2590-2608.
- Kareem, A. (1983), "Mitigation of Wind Induced Motion of Tall Buildings", *J. Wind Engng. and Industrial Aerodyn.*, 11, 273-284.
- Li, Z.X., Wu, L.L., Xu, L.K., and Zhou, Y. (2003), "Structural Design of MR Damper and Experimental Study for Performance of Damping Force", *Earthquake Engineering and Engineering Vibration*, 23(1), 128-132.
- Skinner, R.I., Robinson, W.H., and McVerry, G.H. (1993), "An Introduction to Seismic Isolation", John Wiley and Sons.
- Soong, T.T. and Dargush, G.F. (1997), "Passive Energy Dissipation Systems in Structural Engineering", John Wiley & Sons.
- Tamura, Y. (1997), "Application of Damping Devices to Suppress Wind-Induced Responses of Buildings", *Proc. 2nd European & African Conf. on Wind Engng.*, 45-60.
- Xue, S.D., Ko, J.M., and Xu, Y.L. (2002), "Wind-Induced Vibration Control of Bridges using Liquid Column Damper", *Earthquake Engineering and Engineering Vibration*, English edition, 1(2), 271-280.
- Xue, S.D., Wang, L., and Zhuang, P. (2006), "Design and Performance Study of a SMA Incorporated Friction Damper", *World Earthquake Engineering*, 22(2), 1-6.
- Xue, S.D., Zhuang, P., and Li, B.S. (2005), "Seismic Isolation of Lattice Shells using a New Type of SMA-Rubber Bearings", *Proceedings of IASS Symposium 2005*, 353-358.
- Zhang, R.H. and Soong, T.T. (1992), "Seismic Design of Viscoelastic Dampers for Structural Applications", *J. Struct. Engng., ASCE*, 118 (5), 1375-1392.

RECENT DEVELOPMENTS IN PASSIVE CONTROL TECHNOLOGIES FOR SPATIAL STRUCTURES

T. Takeuchi¹⁾, S. D. Xue²⁾, S. Kato³⁾, T. Ogawa⁴⁾, M. Fujimoto⁵⁾, and S. Nakazawa⁶⁾

1) Associate Professor, Dept. of Arch. & Build. Eng., Tokyo Institute of Technology, Japan

2) Professor, College of Arch. And Civil Eng., Beijing University of Technology, China

3) Professor, Dept. of Arch. and Civil Eng., Toyohashi University of Technology, Japan

4) Professor, Dept. of Arch. and Build. Eng., Tokyo Institute of Technology, Japan

5) Professor, Dept. of Arch. and Build. Eng., Osaka City University, Japan

*6) Assistant professor, Dept. of Arch. and Civil Eng., Toyohashi University of Technology, Japan
ttoru@arch.titech.ac.jp, sdxue@bjut.edu.cn, kato@tutrp.tut.ac.jp, togawa@o.cc.titech.ac.jp,
fujimoto@arch.eng.osaka-cu.ac.jp, nakazawa@tutrp.tut.ac.jp*

Abstract: This paper presents several important advances in the application of passive control technology for metal spatial structures in several countries, and references to recently implemented projects in Japan, USA, China, and other countries have been provided. These structural systems are categorized and classified into truss, cable, and roof structures. Detailed projects have been described based on these categories, along with information on the type of devices and their performance.

1. INTRODUCTION

Recently several types of passive response control techniques have been practically implemented in buildings in seismic areas of Japan, USA, China, etc. Such trends affects the spatial structures, and application of various kinds of passive response control techniques to domes, truss structures, or cable structures have been increasing recently. This paper categorizes these recent developments in order to appropriately apply passive control technologies to metal spatial structures, and introduces the recently realized projects based on these categories in detail.

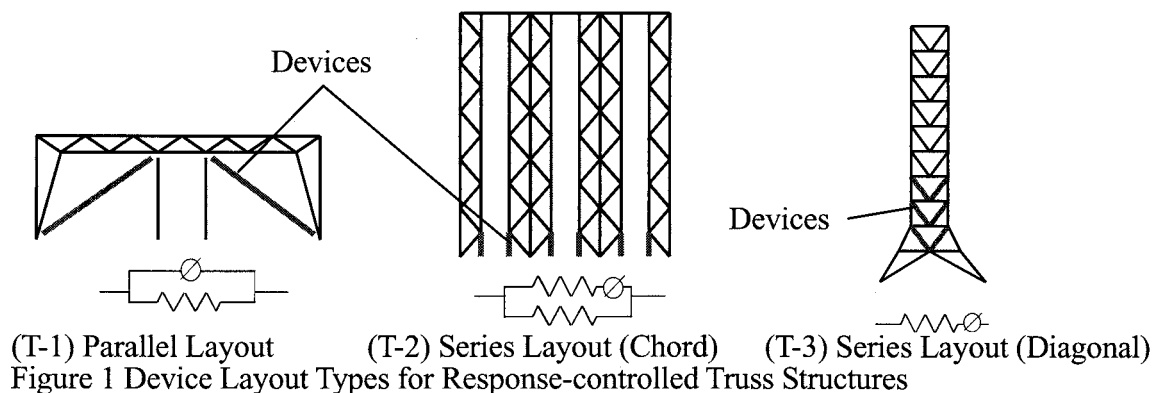
2. TYPES OF STRUCTURAL SYSTEM

2.1 Truss Structures

Truss structures are usually composed of slender axial members; their collapse mechanism is determined by their member buckling. Due to their less-ductile characteristics, truss frame structures usually have to be elastically designed against design loads. However, elastically designing truss structures against large-scale earthquakes is often uneconomic, inelegant in design, and involves the risk of fragile collapse in the events of seismic force exceeding the design criteria. Figure 1 shows an example of a response control concept for truss structures (Kato et. al. 2003, Takeuchi et.al.2003, Yamada et. al. 2005). By replacing the critical members with axial dampers as Buckling Restrained Braces (BRBs), not only is the seismic response reduced due to their energy dissipation effect but also the collapse mechanism of the truss structure can be determined by the yield of the dampers; further, the other truss members are prevented from buckling as a result of the force limiting function of the

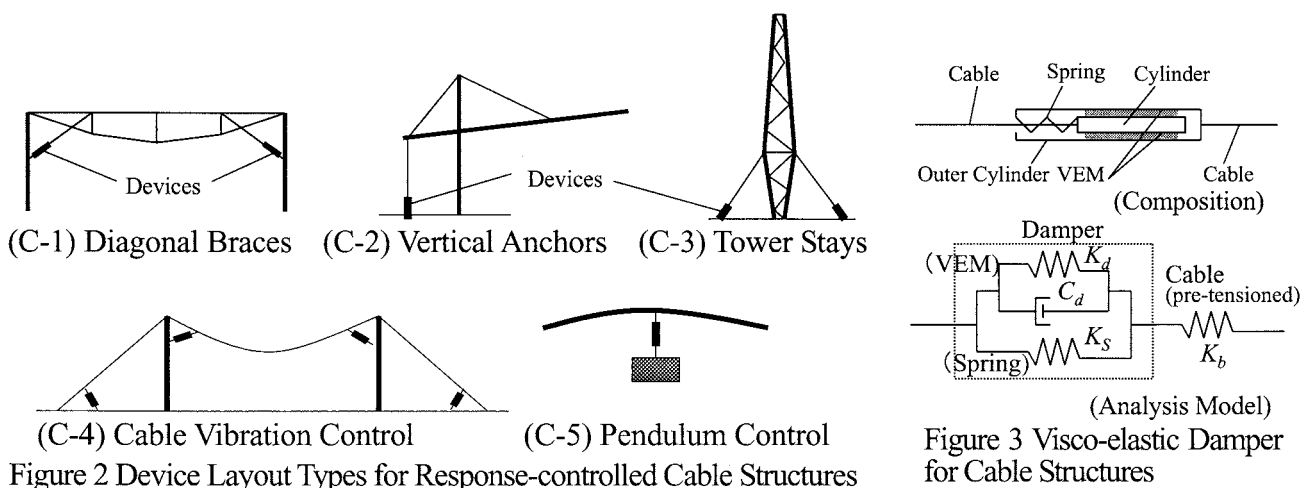
dampers. In Figure 1 (T-1), the devices are installed parallel to the main frame, while in (T-2), each chord member is replaced by a corresponding device in each truss column. (T-3) shows another layout for replacing the diagonal members. For arranging such devices in truss frames, the following method can be implemented in general design.

- 1) For truss structures with low stiffness, the energy dissipation members are installed such that they connect two points that are subjected to the largest relative displacement against the expected loads.
- 2) For truss structures with high stiffness, a push-over analysis is first conducted without evaluating member buckling and then the yielded members are replaced by energy dissipation members.



2.2 Cable Structures

For cable structures, the response control techniques can be classified into two types. In the first category, a device is installed parallel to a cable in order to reduce the vibration of the cable itself. In the other category, a series of devices is connected to a cable, and the cable is used together with the device as the energy dissipation member. The typical layouts are shown in Figure 2. Parallel layouts (C-4) are often used as cable stays of bridges, and viscous or visco-elastic materials are used in the energy dissipation devices. For the series layout (C-1, 2, 3), devices are often required to maintain the pre-tension forces introduced in the cable. However, viscous or visco-elastic materials exhibiting typical properties cannot maintain these pre-tension forces. Figure 3 shows one example that can be employed to solve this problem; here, viscous or visco-elastic materials are introduced in parallel with an elastic spring (Takeuchi et. al. 2001). The elastic spring maintains the pre-stressed forces, and it deforms when the axial force changes. Then, these viscous or visco-elastic materials absorb the energy along the given deflections. The same mechanism can be realized by using a parallel layout of soft cable and viscous dampers.



2.3 Roof Structures

The seismic responses of raised lattice domes or shells are known to amplify vertical vibrations even when subjected to a horizontal input. This acceleration can be roughly modeled as a combination of

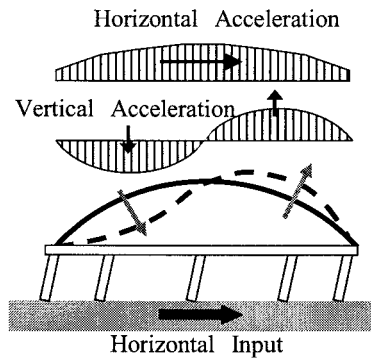


Figure 4 Seismic Response of Raised Roof Structures

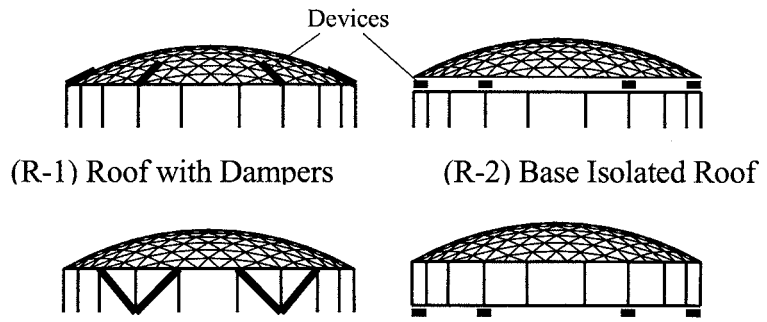


Figure 5 Device Layouts for Response-controlled Roof Structures

horizontal and vertical distributions, as shown in Figure 4 (Kato et. al. 2001, Takeuchi et.al.2005). These amplitudes are determined by a horizontal input from the supporting structures, and the response reduction of such oscillation is achieved by installing energy dissipation devices, as shown in Figure 5. In (R-1), the devices are installed against the in-plane vibration of the roofs; its performance is not necessarily effective in reducing the out-of-plane response. Such systems have been investigated in Kasai et. al. 2001, or Yigang et. al. 2001. (R-2) shows an intermediate base-isolated roof, which is effective in reducing both horizontal and vertical responses, and many practical examples of such roofs have been realized. Such systems have been studied in Uchikoshi et. al. 2001, or Matsui et. al. 2001. When compared with multistory buildings, the weight of the roof structures is light and the space necessary for device deformation is insufficient. Therefore, the natural period of the roof tends to be lesser than that of base-isolated multistory buildings. For isolation bearings, laminated rubber bearings are often used in Japan; further, a friction pendulum that can independently adjust its natural period with the weight of the roof is also commonly used in the USA and other countries. Pod-type friction bearings or a combination of such bearings with laminated rubber bearings have also been practically implemented in China; further effective bearing systems with dampers are currently under development by many researchers (Xue et. al. 2004). (R-3) shows a structure in which energy dissipating braces are distributed in the substructures; they are expected to produce the same effect as that by (R-2). These types of structures are widely used for stadiums or gymnasiums; many examples have also been realized. (R-4) shows a base-isolation system for an entire structure, which have been applied to multistory buildings with roofs such as airport terminals.

3. REALIZED STRUCTURES

3.1 Truss Structures

Safeco Field Stadium (USA) is an early example that employs a passive-controlled truss structure (Daniels et. al. 1999), as shown in Figure 6. This roof structure is realized in the form of a large movable truss frame in which the eight end chord members are replaced with 3600-kN fluid dampers. They are expected to absorb the vibration energy against the wind and seismic fluctuations and roof traveling. Based on the aforementioned description, this system can be categorized as (T-2) in Figure 1.

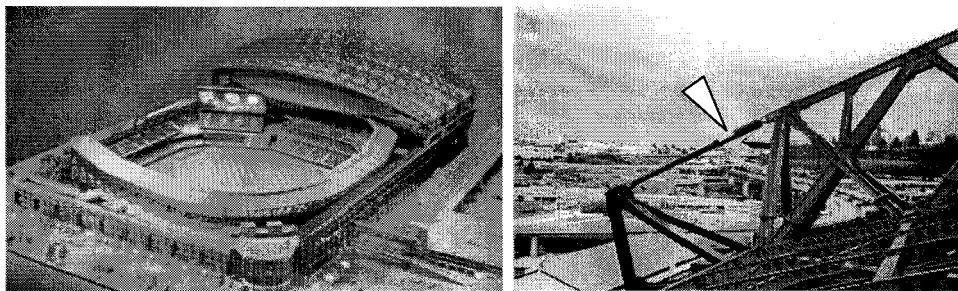


Figure 6 Safeco Field Stadium

Figure 7 shows a gymnasium for a high school in Japan (Takeuchi et. al.2005); it is an example of a truss structure using hysteretic dampers with a parallel layout, as indicated in Figure 3 (T-1). This structure comprises a system truss and has a span of 32m. Four BRBs are attached on both ends of the frame, which dissipate seismic energy due to earthquake motions in long-span directions. The BRB is employed as a buckling restrained element connected in series with tubular members (Figure 8) and it has yield strength of 180 kN. In its design, each truss member are maintained within an elastic range against a level-2 earthquake ($A_{max} = 500 \text{ cm/s}^2$). The response reduction ratio due to the dampers was estimated as 72-75% in story drift and by 27-30% in its base shear.

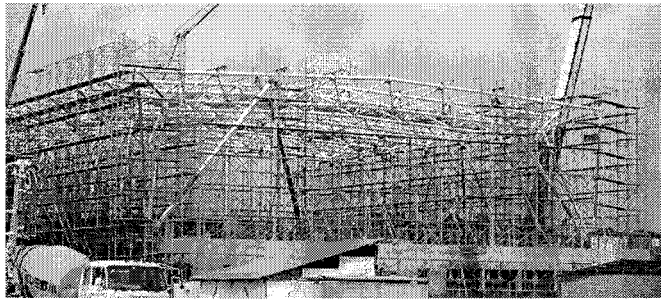


Figure 7 Soma High School Gymnasium

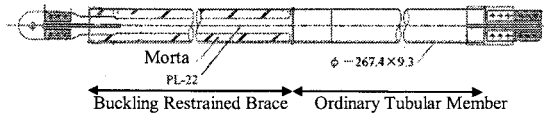
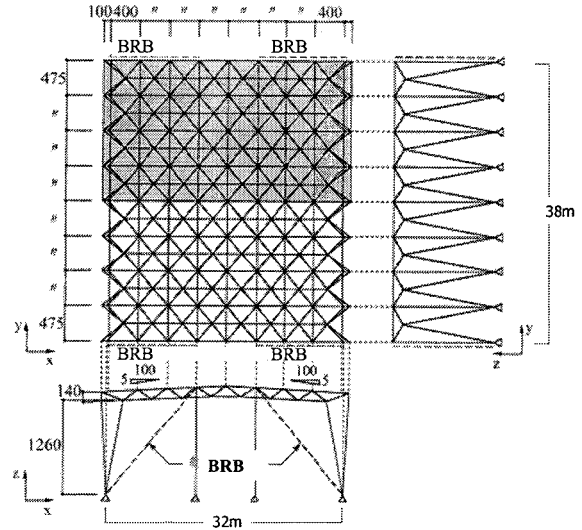


Figure 8 BRB connected with a CHS Member



The BRB system is also used to retrofit truss structures (Ookouchi et. al. 2005). Figure 9 shows a communication tower constructed in Japan during the 1970's. Such towers have been constructed on buildings, and they suffer from risks of collapsing during severe earthquakes as a results of amplification by the supporting buildings. Retrofit works were carried out by replacing the critical diagonals members with BRBs, as that in Figure 1 (T-3). Forty eight diagonal members were replaced for six layers; the retrofit works were completed by four workers in only six days. As a results of this retrofit, the maximum story drift is expected to be reduced to 50%, and buckling will be prevented in all members during the Tokai Earthquake expected in the near future.

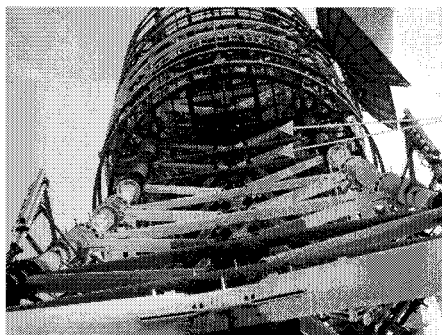
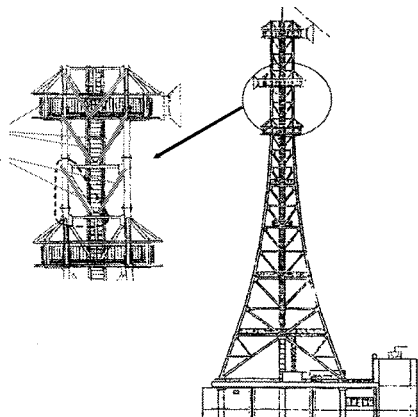


Figure 9 Communication Tower Retrofit

Critical Members
Replaced by BRBs

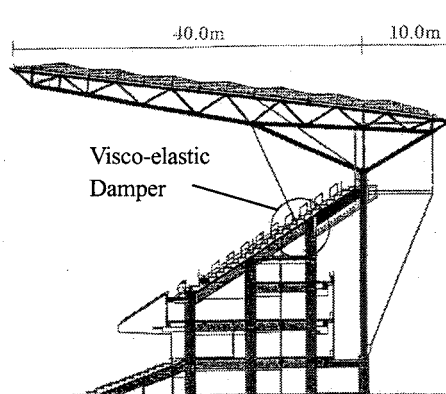


3.2 Cable Structures

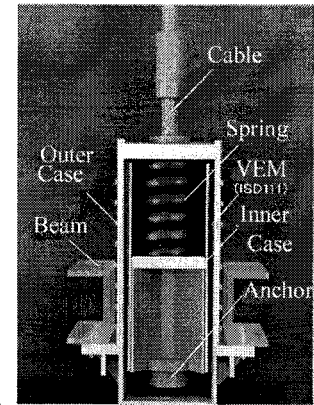
Figure.10 shows the Sizuoka football stadium "Ecopa" (Kaneda et. al. 2001). In this studium,the large cantilever roofs are supported by back-stay cables and front cables, and a visco-elastic damper with a paralell spring as in Figure 10(c) is inserted in each anchor of the front cables in order to reduce the vibration due to wind and earthquakes. A detailed site experiment was carried out after the completion of its construction. The time histories for one of the free vibrations without and with a damper are shown in Figure11 (a) and (b), respectively. Due to the dampers, the damping ratio was estimated to increase of from $\eta=1\%$ to $\eta=4\%$



(a) Stadium Roof

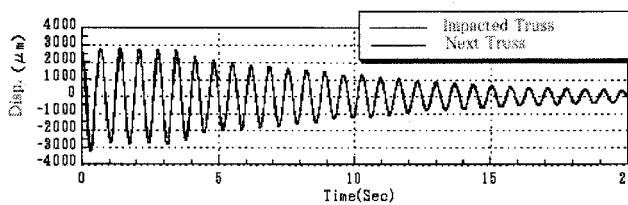


(b) Section of the Roof

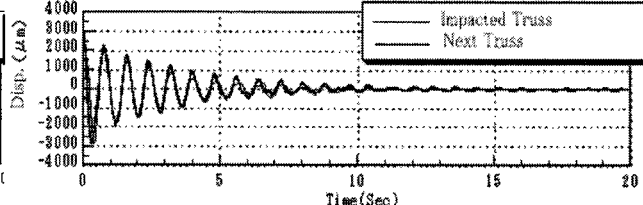


(c) Visco-elastic Damper

Figure 10 Sizuoka Football Stadium "Ecopa"



(a) Without Damper



(b) With Damper

Figure 11 Effect of VEM Damper

Figure.12 shows a cable-stayed telecommunication tower constructed in Osaka, Japan (Hayashi et. al. 2002). The building itself is base-isolated and the wind and seismic response of the tower are controlled by installing four pairs of rotational damping tubes (RDT) that were installed in parallel with the cables along with two TMDs with weight of 7.5 ton each. These units works as viscous dampers along with the spring and they can be categorized as (C-3) in Figure 2.

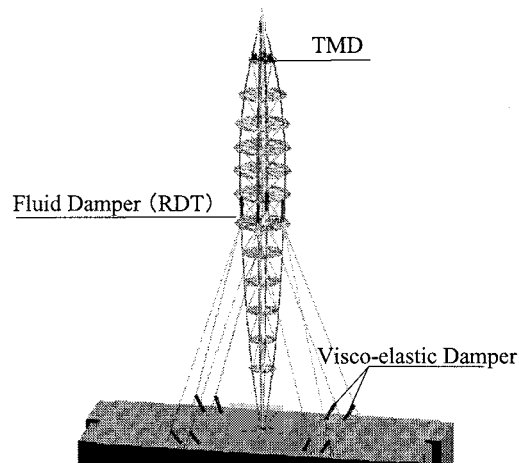
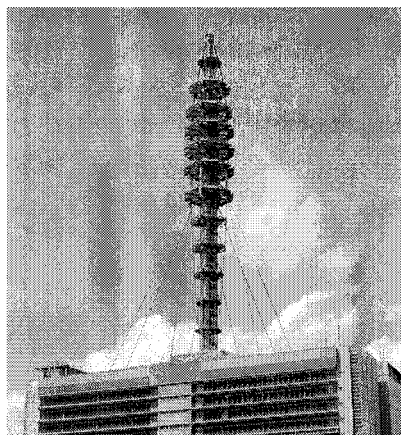


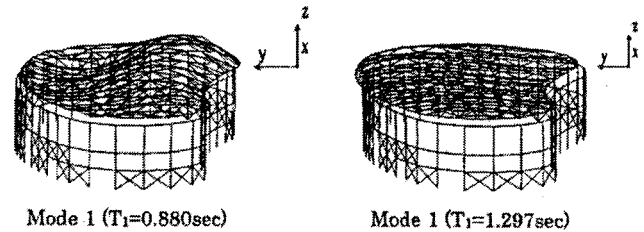
Figure 12 NTT DoCoMo Telecommunication Tower

3.3 Roof Structures

For roof structures, an isolated-type system, as shown in Figure 5 (R-2), has been practically implemented in many projects. In Japan, this system has been partially implemented in the Saitama Super Arena (Kobori et. al. 2001), Yamaguchi Kirara Dome (Hitomi et. al. 2001), and Kyoto Aqua Arena (Kaneda et. al. 2001). Laminated rubber bearings are used for supporting these roofs and a reduction in the seismic responses and thermal stresses are expected. Figure13 shows the interior view of the Kyoto Aqua Arena. Although the roof is relatively heavy due to the installation of solar panels on the roof, rubber bearings have been installed along with friction bearings and U-type steel dampers in order to maintain the sways within an allowable range. Figure.14 shows a result in which the out-of-plane vibration modes disappear as the result of the use of isolation bearings.



Figure 13 Kyoto Aqua Arena



(a) Fixed Roof

(b) Isolated Roof

Figure 14 Vibration Mode

On the contrary, a type of friction pendulum has been commonly used by US designers. Figure 15 shows the terminal roof of the Istanbul Ataturk International Airport supported by friction pendulum bearings (Constantinou et. al. 2000). This building suffered damage during the Izmit earthquake that struck in 1999 when it was just under construction; therefore isolation bearings were inserted under the roof structure. The natural period of the isolated roof is 3 sec. In the time history analyses, the maximum displacement of the roof was reported to be 190 mm against an expected earthquake within a deflection capacity of 260 mm.

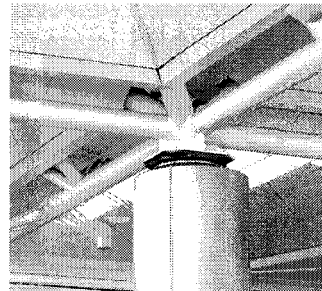
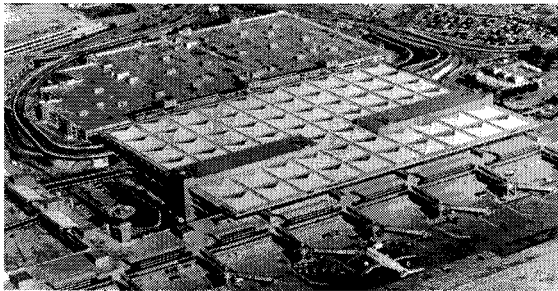


Figure 15 Istanbul Ataturk Airport Terminal Roof

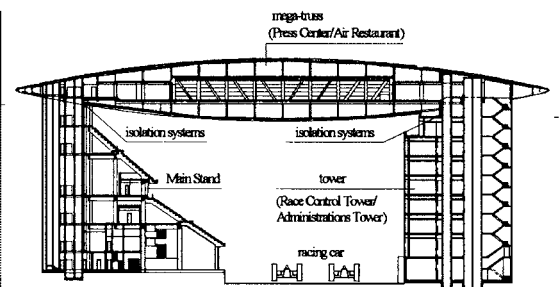


Figure 16 Shanghai International F1 Circuit Building

Remarkable developments have been observed in China with regard to isolated roofs. Figure 16 shows a 91-m-span structure of the Shanghai International F1 Circuit (Lu et. al. 2003). In the bearings used, four sets of 1340-mm-diameter pod-type friction bearings are combined with four sets of 650-mm-diameter laminated bearings in order to maintain the maximum deflection below 226mm against an earthquake with $A_{max} = 220 \text{ cm/s}^2$. The isolation assists in the reduction of thermal stresses at the roof support structures. For such isolation bearings, further developments toward new bearing systems are under investigation.

A system of dampers installed within the supporting substructures, as shown in Figure 5 (R-3), is also very common; this system has been implemented in the Toyota stadium in Nagoya, Japan. In this structure, the BRBs are used as dampers installed within the substructures.

Base-isolation systems for entire structures have also been realized in some projects. The terminal building of the San Francisco International Airport, for example, is supported by many sets of friction pendulums with a natural period of 3 sec. and a maximum deflection of 500 mm (Mokha et. al. 1999).

When compared with the above mentioned systems, only a few systems employing the structure shown in Figure 5 (R-1) has been implemented thus far. Figure 17 shows the Symokita Dome (Hosozawa et. al. 2005); here, BRBs are inserted into the roof as well as the supporting structure. The design is examined by means of time history analyses. Due to the roof damper, the reductions in the horizontal and vertical accelerations were reported as 17% and 1% respectively. This reduction is smaller than the effect of dampers provided in the supporting structure, 26% and 17% in the horizontal and vertical accelerations, respectively.

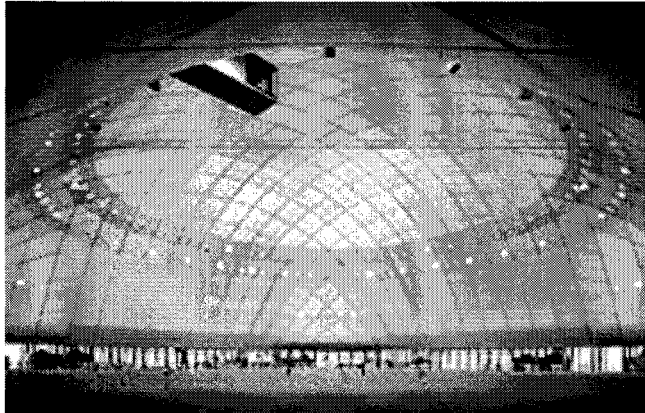
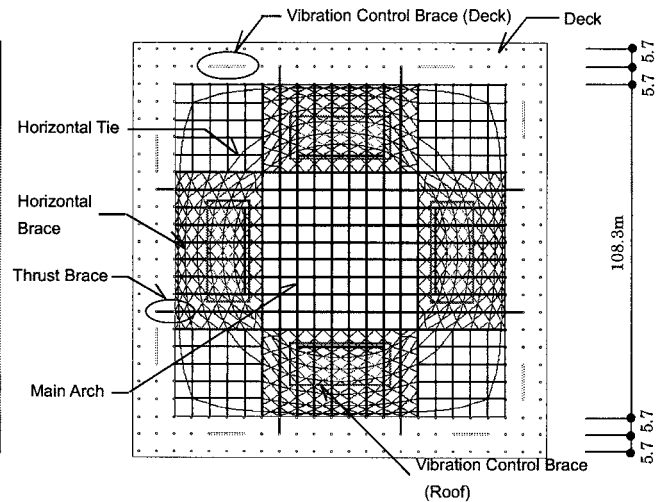


Figure 17 Shimokita Dome



The realized projects have been listed in Table 1. Although variations exist in the design criteria and used devices used, their structural systems can be roughly categorized into the proposed manner. From this table, it can be seen that the roof isolation system (R-2) has been implemented relatively often. Their natural periods range within 1 to 3 sec; not only seismic response reduction but also a release in the thermal stresses induced in the roofs are expected in many cases.

Table1 List of Realized Projects

Category	No.	Project Name	Site	Year	Type	Devices
Truss Structures	1	Safeco Field Stadium	Seattle, USA	1999	T-2	Fluid
	2	Soma High School Gymnasium	Tochigi, Japan	2003	T-1	BRB
	3	Communication Tower Retrofit	Aichi, Japan	2005	T-3	BRB
Cable Structures	4	Yoyogi Sports Gymnasium	Tokyo, Japan	1964	C-4	Fluid
	5	M-Wave	Nagano, Japan	1996	C-1	Fluid
	6	Sizuoka Football Stadium Ecopa	Sizuoka, Japan	2001	C-2	VEM
	7	DoCoMo Telecommunication Tower	Osaka, Japan	2003	C-3	Fluid
	8	Osaka Dome	Osaka, Japan	1997	C-5	VEM
Roof Structures	9	Saitama Super Arena	Saitama, Japan	2000	R-2	Laminated Rubber
	10	Yamaguchi Kirara Dome	Yamaguchi, Japan	2001	R-2	Laminated Rubber
	11	Kyoto Aqua Arena	Kyoto, Japan	2002	R-2	Laminated Rubber
	12	Ataturk Int. Airport Terminal	Istanbul, Turkey	2000	R-2	Friction Pendulum
	13	Seahawks Football Stadium	Seattle, USA	2002	R-2	Friction Pendulum
	14	Shanghai Int. F1 Circuit	Shanghai, China	2004	R-2	Pot-type Friction
	15	Toyota Stadium	Aichi, Japan	2001	R-3	BRB
	16	San Francisco Int. Airport Terminal	SF, USA	2000	R-4	Friction Pendulum
	17	Suqian City Gymnasium	Jyangu, China	2002	R-4	No Data
	18	Shimokita Dome	Aomori, Japan	2005	R-1	BRB

3. CONCLUSIVE REMARKS

Several applications of passive control technologies for metal spatial structures have been simultaneously investigated by studying projects realized in Japan, USA, China, and other countries. Their response control systems were categorized and classified into truss, cable, and roof structures. Several projects have been investigated in detail based on these categories. Although the design criteria and devices used vary according to the structures, their structural systems are generally found to confirm to the common categories. Such techniques are generalized to in order to reduce not only the seismic and wind responses but also the thermal stresses and other functions. The application areas of these structures are increasing, and further researches and practical developments in this engineering field are expected.

Acknowledgements:

This paper is organized from a part of the working reports of International Association of Shell and Spatial Structures, WG8, reported in IASS symposium 2006, Beijing.

References:

- S.Kato, F.Atumi, S.Shimaoka, S.Nakazawa, T.Ueki "Reduction of Structural Material and Increase of Seismic Performance Based on Additional Use of Hysteresis Dampers Applied to the Feet of Columns of Gable Trusses", *IASS Symposium 2003, Taipei*, pp108
- T.Takeuchi, K.Suzuki "Performance-Based Design for Truss Frame Structures using Energy Dissipation Devices", *Steel Structures in Seismic Area (STESSA) 2003, Naples*, pp55
- K.Yamada, K.Ishihara "Application of the Damage Control Design to an Arch", *IASS Symposium 2005, Bucharest*, pp407
- T.Takeuchi, K.Kaneda, M.Iwata, A.Wada, M.Saitoh "Vibration-Control Devices For Tension Structures Using Visco-elastic or Viscous Material with Spring", *IASS Symposium 2001, Nagoya*, TP121
- K.Kato, S.Nakazawa "Seismic Design Method to Reduce the Responses of Single Layer Reticular Domes by Means of Substructure under Severe Earthquake Motions", *IASS Symposium 2001, Nagoya*, TP077
- T.Takeuchi, T.Ogawa, C.Yamagata, T.Kumagai "Seismic Response Evaluation of Cylindrical Lattice Shell Roofs with Substructures using Amplification Factors", *IASS Symposium 2005, Bucharest*, pp.391
- K. Kasai, S. Motoyui, Y. Ooki "Viscoelastic Damper Modeling and its Application to Dynamic Analysis of Viscoelastically Damped Space Frames", *IASS Symposium 2001, Nagoya*, TP119
- Z. Yigang, R. Guangzi "A Practical Method on Seismic Response Controlled Double Layer Cylindrical Latticed Shell with Variable Stiffness Members", *IASS Symposium 2001, Nagoya*, TP122
- M. Uchukoshi, S. Kato, S. Nakazawa, T. Mukaiyama "How to Realize a Super Large Dome under Severest Earthquake? A Dome with Seismic Isolation System", *IASS Symposium 2001, Nagoya*, TP115
- T. Matsui, F. Qiao, Y. Moribe, E. Sugiyama, Y. Esaka "Response of Seismically Isolated Large Span Domes to Fluctuating Wind Loads", *IASS Symposium 2001, Nagoya*, TP120
- S. D.Xue, J.H Dong "A Model of Shape Memory Alloy Damper for Vibration Control of Spatial Structures", *IASS Symposium 2004, Montpellier*, pp126
- Daniels, Stephen H. "Let the Sun Shine In, Four 'long' years of work so roof can retract in minutes", *Engineering News Record, March 8, 1999*, pp.36-40
- T.Takeuchi, T.Ogawa, T.Suzuki, T.Kumagai, C.Yamagata "A Basic Study on Damage-Controlled Design Concept for Truss Frame Structures", *AIJ, J. of Struct. Eng., Vol.51B*, pp. 31-37, 2005.3 (in Japanese)
- Y.Ookouchi, T. Takeuchi, K. Suzuki, T. Marukawa, T. Ogawa, S. Kato "Experimental Studies of Tower Structures with Hysteretic Dampers", *IASS Symposium 2005, Bucharest*, pp.299
- K. Kaneda, M. Saitoh: Endeavors to Control the Vibration of Long Span Structures, *IASS Symposium 2001, Nagoya*, TP116
- M. Hayashi, I. Shibata, S. Umeda, H. Tadokoro, T.Tsuchiya, K. Sumimura, K. Saitou, T. Nakano "Engineering Seismic Isolated Building with Guyed Tower Part 1-3", *SEWC 2002, Yokohama*,
- T. Kabori, H. Harada, O. Hosozawa, M. Saito "The Structural Design and Work for the Saitama Super Arena", *IASS Symposium 2001, Nagoya*, TP171
- Y. Hitomi, K. Osawa, S. Nakagawa, M Saito "Structural Design of Yamaguchi Dome", *IASS Symposium 2001, Nagoya*, TP155
- M. Constantinou, A. S. Whittaker, E Velivasakis "Seismic Evaluation and Retrofit of the Ataturk International Airport Terminal Building", *Research Progress and Accomplishments: 2000-2001, MCEER Bulletin*.
- X. Lu, D. Wen, W. Shi, Z. Yang "Application of Passive Control Technology to Two Large Engineering Structures", *Passive Control Symposium 2004, Tokyo Institute of Technology*, pp47-61
- A. S. Mokha, P. L. Lee, X. Wang, P. Yu "Seismic Isolation Design of the New International Terminal at San Francisco International Airport", *Conference on Struct. Eng. In the 21st Century, 1999*, 95-98
- O.Hosozawa, T.Mizutani "Structural Design of Simokita Dome", *IASS Symposium 2005, Bucharest*, pp707

STUDY OF LEAD DAMPER FOR SEISMIC ISOLATION SYSTEM

K. Morita¹⁾ and M. Takayama²⁾

1) Research Assistant, Dept. of Architecture, Fukuoka University, Fukuoka, Japan

2) Professor, Dept. of Architecture, Fukuoka University, Fukuoka, Japan

keikomt@fukuoka-u.ac.jp, mineot@fukuoka-u.ac.jp

Abstract: The lead is used as an energy dissipation device of seismic isolation systems and vibration control systems because pure lead shows the characteristics of low stress yield, very high ductility, and large plastic deformation. The hysteretic behavior shows the shape, which is approximate to elasto-plastic restoring force characteristics, and this allows it to provide high damping performance. The U-shaped lead damper is one of hysteretic dampers for the seismic isolation system. This paper presents the results of response analysis of the seismic isolated building with the U-shaped lead damper. Two models are proposed, and are compared with a typical bi-linear model. The results of the analysis can be approximately explained using the theory of energy balance.

1. INTRODUCTION

Seismic isolation systems, in which buildings are separated from the ground motion during earthquakes, protect not only the structures but also humans and furniture, etc. inside the buildings against large earthquakes. In the majority of seismic isolation structures a seismic isolation interface is installed between the base-structure and the superstructure. The seismic isolation interface is basically composed of isolators and dampers as seismic isolation members. During an earthquake the restoring force characteristics of the isolators show linear behavior, and this enables them to stably support the weight of the building and accept large deformation. The dampers absorb the earthquake energy, thus allowing the movement to rapidly settle down after the earthquake.

Pure lead shows the characteristics of low stress yield, very high ductility, and large plastic deformation. The U-shape lead damper has same merits. Its yields in smaller deformation than the steel damper, and demonstrates damping performance from the small deformation.

To grasp the behavior of the building during an earthquake, numerical analysis is used. When a seismic isolation structure is designed, the restoring force characteristics of the hysteretic dampers, such as the lead dampers, are modeled as bi-linear. However, the restoring force loops of actual dampers are slightly different from the bi-linear modeling loop. Two models are proposed, and are compared with the bi-linear model.

2. ANALYSIS MODEL

2.1 Outline of structure

The seismic isolation structure is composed of superstructure and seismic isolation interface which installed isolators and dampers separately. The isolators support the vertical load, and seismic input energy is absorbed as elastic strain energy. The dampers absorb the seismic input energy as plasticity

energy or thermal energy, and decrease its response deformation. This structure model intends isolating only horizontal earthquake movement.

The superstructure is modeled as 1 mass system, by treating the structure as rigid. The outline of the analytical model is shown in figure 1. The weight W is 9,800tonf. It shows elastic linear characteristic as isolators and elasto-plastic characteristics as dampers. In case of seismic isolation structure being supported only by the isolators, stiffness of the isolators is shown with K_f . The primary stiffness of the damper is shown with K_1 , and secondary stiffness is shown with $K_2 \cong 0$. In the analysis, it puts two restoring force characteristics together as a model of the seismic isolation interface.

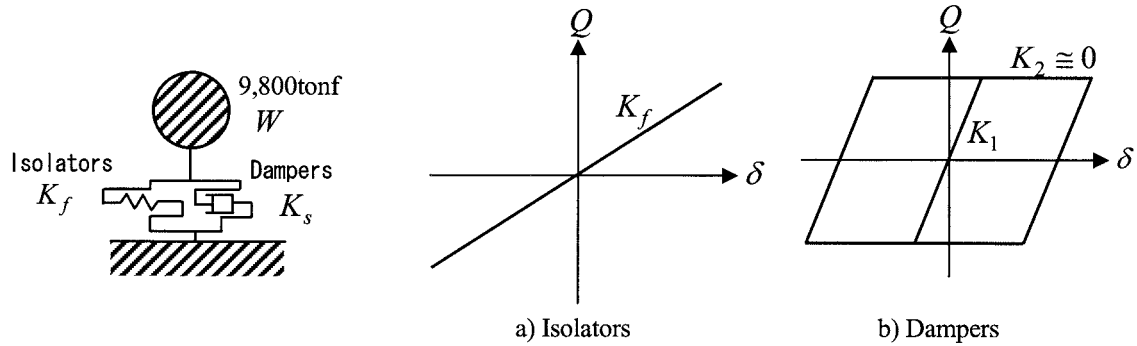


Figure 1 Outline of Analytical Model

2.2 Earthquakes for Analysis

5 earthquakes are used for the analysis, El Centro(NS) of Imperial valley earthquake (1940), Hachinohe(NS) of Tokachioki earthquake (1968), Sylmar(NS) of Northridge earthquake (1994), Takatori(NS) of Hogoken Nanbu earthquake (1995), and Taft(NS) of Kern county earthquake (1952). These are used by standardizing the maximum velocity in 11 types as 5, 10, 15, 20, 25, 40, 50, 75, 100, 125, 150kine.

2.3 Modeling of Isolator

The restoring force characteristics of the isolator decide fundamental and important characteristic. The restoring force characteristic of natural rubber bearings (Isolators) is linear, therefore the natural period of seismic isolation T_f is not dependent on the deformation of the isolators. It can be simply calculated in equation (1). The natural period of seismic isolation T_f is an important standard, which confirms seismic isolation performance.

$$T_f = 2\pi \sqrt{\frac{W}{g \cdot K_f}} \quad (1)$$

where, K_f : total stiffness of the isolators
 g : gravitational acceleration (980cm/cm²)
 W : total weight of superstructure

In this analysis, Stiffness of the isolator K_f is defined so that natural period of seismic isolation may become 2 sec, 3 sec and 4 sec. When T_f is 2 sec, 3 sec and 4 sec, then K_f is 98.70 N/mm, 43.86 N/mm and 24.67 N/mm.

2.4 Modeling of U-Shaped Lead Damper

The outline of the damper is shown at figure 2 and table 1. The U-shaped lead damper has been composed of flexible part, haunch and steel flange. When the flexible part transforms horizontally,

the energy of the earthquake is absorbed. The U180 type damper is used in the actual building, and it is modeled.

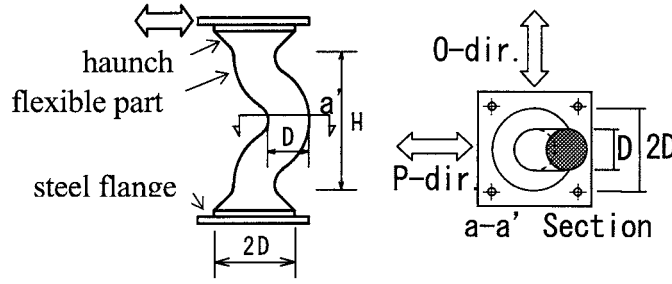


Figure 2 U-Shaped Lead Damper

Table 1 Outline of U-Shaped Lead Damper

	Diameter D (mm)	height H (mm)	Length L (mm)	L/H
U180	180	560	660	1.18

2.4.1 Outline of Hysteresis Loop of U-Shaped Lead Damper

The outline of the hysteresis loop of the lead damper is shown in figure 3. The arrow in the figure shows the deformation route. It is possible to divide the hysteresis loop of the U-type lead damper into small deformation region and large deformation region.

In the small deformation region, the hysteresis loop shows the shape that is approximate to rigid plasticity. The lead shows the low yield force first, and it increases the load value of the y-intercept of the hysteresis loop according to increase of deformation. Maximum value Q_e is shown on the load value of the y-intercept, after it reaches deformation δ_e . The load value of the y-intercept shows the almost same value, even if deformation increases further. Maximum value Q_e is defined as a yield force of the U-Shaped lead damper.

Amplitude region that exceeded δ_e is defined as a large deformation region. In this region, the hysteresis loop begins to show hardening by the effect of the axial deformation.

When the hysteresis loop is modeled, 3 types of stiffness are used, primary stiffness K_1 , post-yield stiffness K_2 and hardening stiffness K_3 . From the experiment results K_2 shows smaller value than K_1 . The hysteresis loop can be considered bi-linear of complete elasto-plastic loop. ($K_2 \cong 0$)

The load of the elastic limit of the lead shows smaller value of the load before processing than the load after processing. The yield force before the processing is shown in $\beta \cdot Q_e$, and it is shown in equation (2).

$$\beta \cdot Q_e = K_1 \cdot \delta_{y1} \quad (2)$$

$$Q_e = K_1 \cdot \delta_{y2} = K_1 \cdot \gamma_{y2} \cdot H \quad (3)$$

where, $\beta = 0.4145$, $\gamma_{y2} = 0.0085$ (The experimental value)

Q_e : yield force of the lead damper.

H : height of flexible part of the lead damper

δ_{y1} is defined as primary yield deformation, δ_{y2} is defined as yield deformation. Primary stiffness K_1 and yield force Q_e intersect at yield deformation δ_{y2} , K_1 and $\beta \cdot Q_e$ intersect at primary yield deformation δ_{y1} . Deformation δ_e is shown in equation (4).

$$\delta_e = \gamma_e \cdot H \quad (4)$$

where, $\gamma_e = 0.27$ (The experimental value)

In the large deformation region over deformation δ_e , the hysteresis loop begins to show hardening. It is shown in equation (5).

$$K_3 = \gamma_k \cdot K_1 \quad (5)$$

Where, $\gamma_k = 0.015$ (The experimental value)

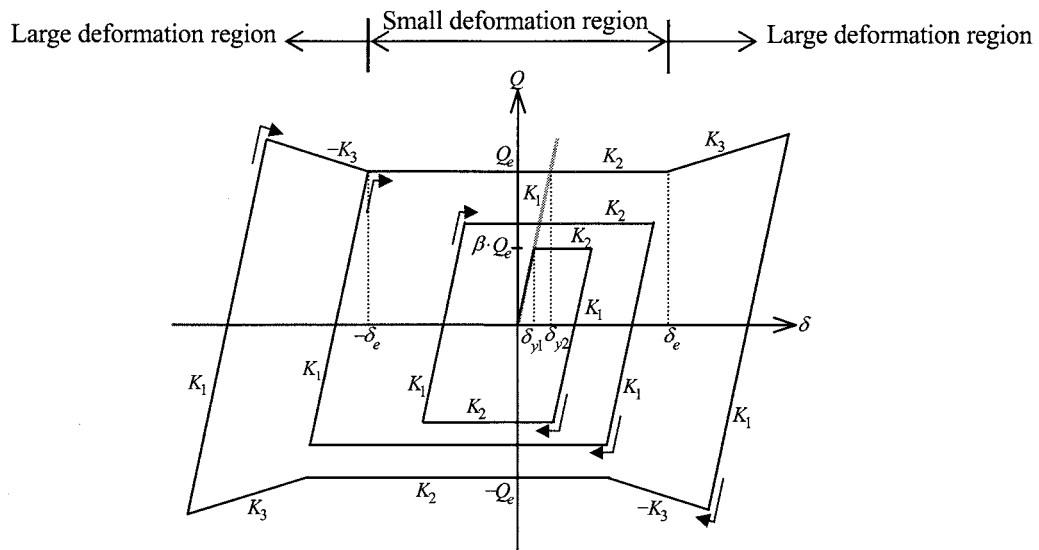


Figure 3 Outline of Hysteresis Loop of Lead Damper

Table 2 Parameters of Models

	α_s	K_1 (N/mm)	K_2 (N/mm)	K_3 (N/mm)	δ_{y1} (cm)	δ_{y2} (cm)	β	Q_e (kN)	δ_e (cm)
Simple bi-linear	0.02	408	0	0	0.48	0.48	1	1960	15
	0.03	604	0	0	0.48	0.48	1	2900	15
	0.04	817	0	0	0.48	0.48	1	3920	15
	0.06	1208	0	0	0.48	0.48	1	5800	15
	0.08	1633	0	0	0.48	0.48	1	7840	15
Type 1	0.02	408	0	0	0.2	0.48	0.4145	1960	15
	0.03	604	0	0	0.2	0.48	0.4145	2900	15
	0.04	817	0	0	0.2	0.48	0.4145	3920	15
	0.06	1208	0	0	0.2	0.48	0.4145	5800	15
	0.08	1633	0	0	0.2	0.48	0.4145	7840	15
Type 2	0.02	408	0	6.12	0.48	0.48	1	1960	15
	0.03	604	0	9.06	0.48	0.48	1	2900	15
	0.04	817	0	12.26	0.48	0.48	1	3920	15
	0.06	1208	0	18.12	0.48	0.48	1	5800	15
	0.08	1633	0	24.50	0.48	0.48	1	7840	15

2.4.2 Yield Shearing Force Coefficient

When the elasto-plastic damper is used, an additional parameter requires. The deformation of the seismic isolation interface is suppressed depend on volume of damping. This parameter is yield shearing force coefficient of lead damper α_s , and it is related to the mass M ($=W/g$) and the yield force of the lead damper Q_e using equation (6). And shearing force coefficient of the isolator α_f is related to the mass M and the maximum shearing force of the isolator $f Q_{\max}$ using equation (6). Therefore the shear force coefficient of the seismic isolation interface is showed in the sum of α_s

and α_f . The analyses in the case of $\alpha_s=2, 3, 4, 6, 8\%$ are carried out.

$$\alpha_s = \frac{Q_e}{M}, \quad \alpha_f = \frac{f Q_{\max}}{M} \quad (6)$$

2.4.3 Simple Bi-linear Model

The simple bi-linear model has the elasto-plastic characteristic, and shown using K_1 and K_2 (refer figure 3 and table 2). The yield deformation δ_{y2} is defined as 0.48cm using equation (3). In this model, hardening is not considered, even if the deformation exceeds δ_e .

2.4.4 Type 1 model (Model of Yield Force Depending on Magnitude of Amplitude)

The hysteretic behavior of the small deformation region is modeled. This model has the hysteretic behavior in which yield force increases with the increase in the amplitude, until the deformation becomes δ_e . The parameter is shown in figure 3 and table 2. The yield deformation δ_{y1} and δ_{y2} are defined as 0.2cm and 0.48cm using equation (2) and (3). The yield force until it reaches δ_e moves on the line which connects $\beta \cdot Q_e$ with Q_e at δ_e . In this model, hardening is not considered too, even if the deformation exceeds δ_e .

2.4.5 Type 2 model (Tri-linear Model)

The hysteretic behavior of the large deformation region is modeled. This model shows the same hysteretic behavior with the simple bi-linear model until the deformation reaches δ_e . The parameter is shown in figure 3 and table 2. The yield deformation δ_{y2} is defined as 0.48cm using equation (3). Hardening is considered in the hysteretic behavior, when the deformation exceeded δ_e . The hardening stiffness K_3 is defined as $0.015 \cdot K_1$ using equation (5).

3. PREDICTION OF RESPONSE DEFORMATION

It is possible to explain the effect of the difference of hysteresis loop of the damper on the response deformation using the energy theory approximately. Figure 4 shows the distribution of load Q_x of each damper model at deformation x . The load Q_x of the simple bi-linear model is fixed to Q_e . (Figure 4 a))

The load Q_x of the type 1 model is shown using equation (7). (Figure 4 b)) The load Q_x of the type 2 model is shown using equation (8). (Figure 4 c))

$$\text{Type 1 model} \quad Q_x = \beta \cdot Q_e + \frac{1-\beta}{\delta_e} Q_e \cdot x \quad (0 < x < \delta_e) \quad (7)$$

$$Q_x = Q_e \quad (x > \delta_e)$$

$$\text{Type 2 model} \quad Q_x = Q_e \quad (0 < x < \delta_e) \quad (8)$$

$$Q_x = Q_e + \frac{Q_e(x-\delta_e)}{\delta_e} \gamma \quad (x > \delta_e)$$

$$\text{where, } \gamma = \frac{\gamma_k \cdot \gamma_e}{\gamma_{y2}}$$

And figure 5 shows the hysteresis area ratio of each damper model at deformation x . A_0 is the hysteresis area of the simple bi-linear, and A is the area of each model.

Figure 5 a) is comparison between the simple bi-linear model and the type 1 model. When the deformation is δ_e , the hysteresis area ratio of the type 1 model to the simple bi-linear model is

0.707:1.0. It is estimated that the response deformation of the type 1 model increases further than the simple bi-linear model, because its energy absorption is smaller.

Figure 5 b) shows the ratio of the hysteresis area of the type 2 model. When the deformation is $2\delta_e$, the hysteresis area ratio of the type 2 model to the simple bi-linear model is 1.119:1.0. It is estimated that the response deformation of the type 2 model decreases than the simple bi-linear model.

4. RESULTS OF ANALYSIS

Figure 6 shows the restoring force characteristics of the seismic isolation interface by the response analysis. The hysteresis loop of the type 1 model shows that yield force increases with the increase in the amplitude until the deformation becomes $\delta_e=15\text{cm}$. That of the type 2 model shows hardening property, when the deformation exceeded $\delta_e=15\text{cm}$.

Figure 7 shows the relationship between the response deformation ratio of the seismic isolation interface and the response deformation of the simple bi-linear model. The response deformation ratio is defined as (the deformation of the type 1 model)/(the deformation of the simple bi-linear model) and (the deformation of the type 2 model)/(the deformation of the simple bi-linear model). The response ratio shows almost same tendency without dependency on natural period of seismic isolation. The response predicted deformation is shown in the figure by the gray line. The response prediction deformation is shown using equation (9) and (10).

$$\text{Type 1 model} \quad f(x) = \frac{x_0}{\beta + \frac{1-\beta}{2\delta_e}x_0} \quad (0 < x_0 < \delta_e) \quad (9)$$

$$f(x) = \frac{x_0}{1 - \frac{1-\beta}{2x_0}\delta_e} \quad (x_0 > \delta_e)$$

$$\text{Type 2 model} \quad f(x) = x_0 \quad (0 < x_0 < \delta_e) \quad (10)$$

$$f(x) = \frac{x_0}{1 + \frac{(x_0 - \delta_e)^2}{2\delta_e \cdot x_0} \gamma \cdot \kappa} \quad (x_0 > \delta_e)$$

where, x_0 : deformation of the simple bi-linear model
 κ : correcting factor

Figure 7 a) shows the relationship of the response deformation ratio of the type 1 model. The response deformation ratio decreases, as the deformation of the simple bi-linear model increases. The analytical results show almost same or smaller value than the prediction. When the deformation is δ_e , the response deformation ratio of the type 1 model to the simple bi-linear model is 1.41:1.0. The response deformation ratio approaches 1.0, when deformation exceeds $3\delta_e$.

Figure 7 b) shows the relationship of the response deformation ratio of the type 2 model. The response deformation ratio decreases, as the deformation of the simple bi-linear model increases. In this figure, predictive values are obtained using the correcting factor $\kappa=0.5$ and 1.0. The $\kappa=1.0$ means that all increased hysteresis area are evaluated, and $\kappa=0.5$ means that half of that are evaluated. In case of $2\delta_e$ and $\kappa=1.0$, the response deformation ratio of the type 2 model to the simple bi-linear model is 0.89:1.0. The predictive values show smaller value than the analytical results. If $\kappa=0.5$ is used, then the predictive value is almost equal to lower value of analytical result. The effect of hardening is excessively evaluated, if $\kappa=1.0$ is used.

5. CONCLUSIONS

In the design of seismic isolation structure, the restoring force characteristic of the damper is often modeled as the simple bi-linear. In the small deformation region the yield point depends on the magnitude of the amplitude, and in the large deformation region it shows hardening property. It is effective to use the model in proportion to the purpose properly. It is effective to use the type 1 model for the analysis of small response, such as during strong wind, etc. By considering the area of the hysteresis loop which was simplified, it is considered that the response deformation of the seismic isolation interface can be estimated within ensuring the safety.

References:

- Architectural Institute of Japan (2001), "Recommendation for the Design of Base Isolated Buildings"
- Ono, Y., and Kaneko, H. (2001), "Constitutive Rule of the Steel Damper and Source Code for the Analysis Programs," *Passive Control Symposium 2001*, 163-170.
- Morita, K., Takayama, M. (2003), "Experimental Study of Lead Damper for Seismic Isolation System, Hysteresis Model and Repetition Performance of Lead Damper," *Journal of Structural and Construction Engineering*, Architectural Institute Japan, (570), 53-60
- Morita, K., Takayama, M. (2004), "Response Analysis of Seismic Isolated building with Lead Dampers, On the effect of the difference of the hysteretic loop," *Journal of Structural and Construction Engineering*, Architectural Institute Japan, (580), 35-42
- Akiyama, H. (1999), "Earthquake-Resistant Design Method for buildings Based on Energy Balance"

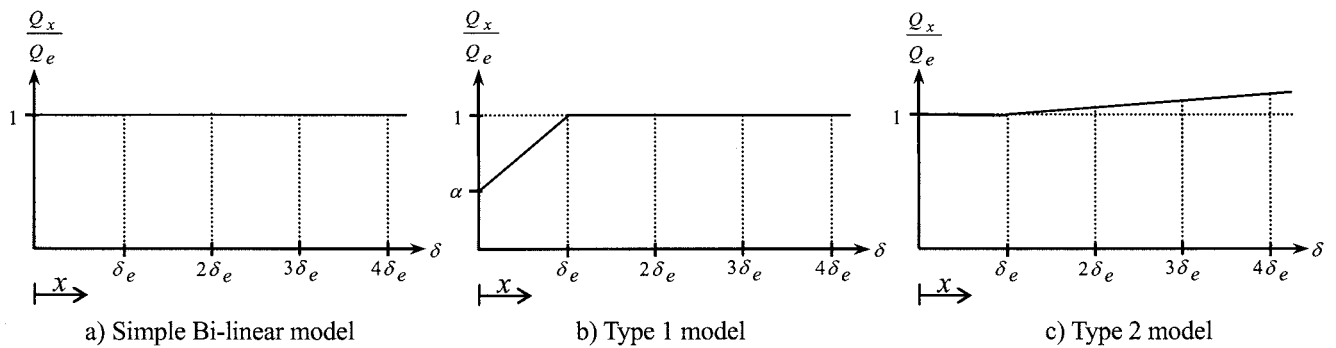


Figure 4 Distribution of Load Q_x of Each Damper Model at Deformation x

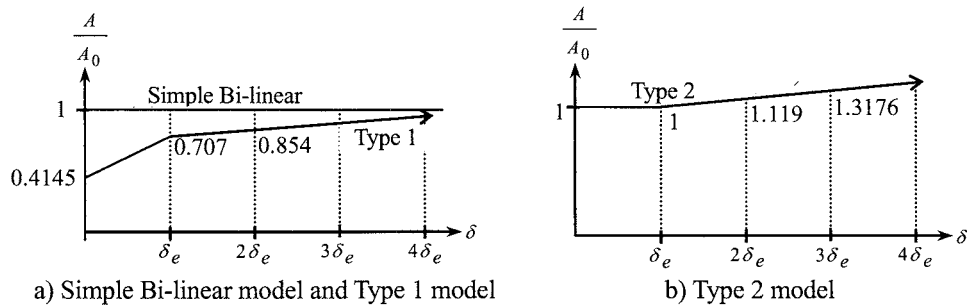


Figure 5 Hysteresis Area Ratio of Each Damper Model at Deformation x

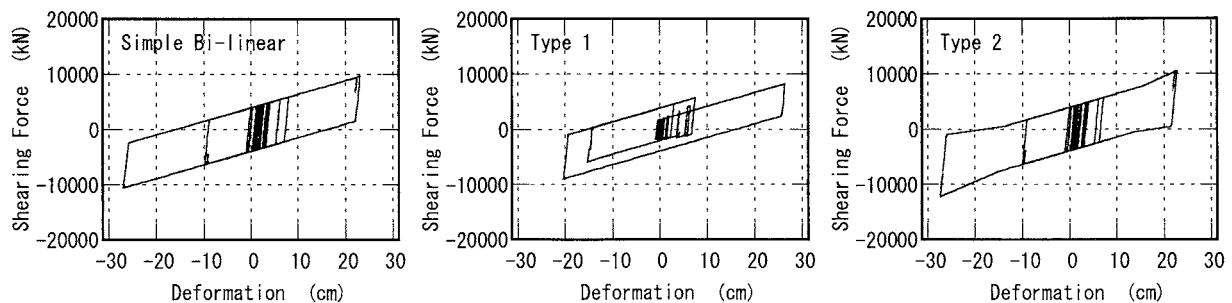


Figure 6 Restoring Force Characteristics ($T_f=2\text{sec}$, $\alpha_s=0.04$, Sylmar 75kine)

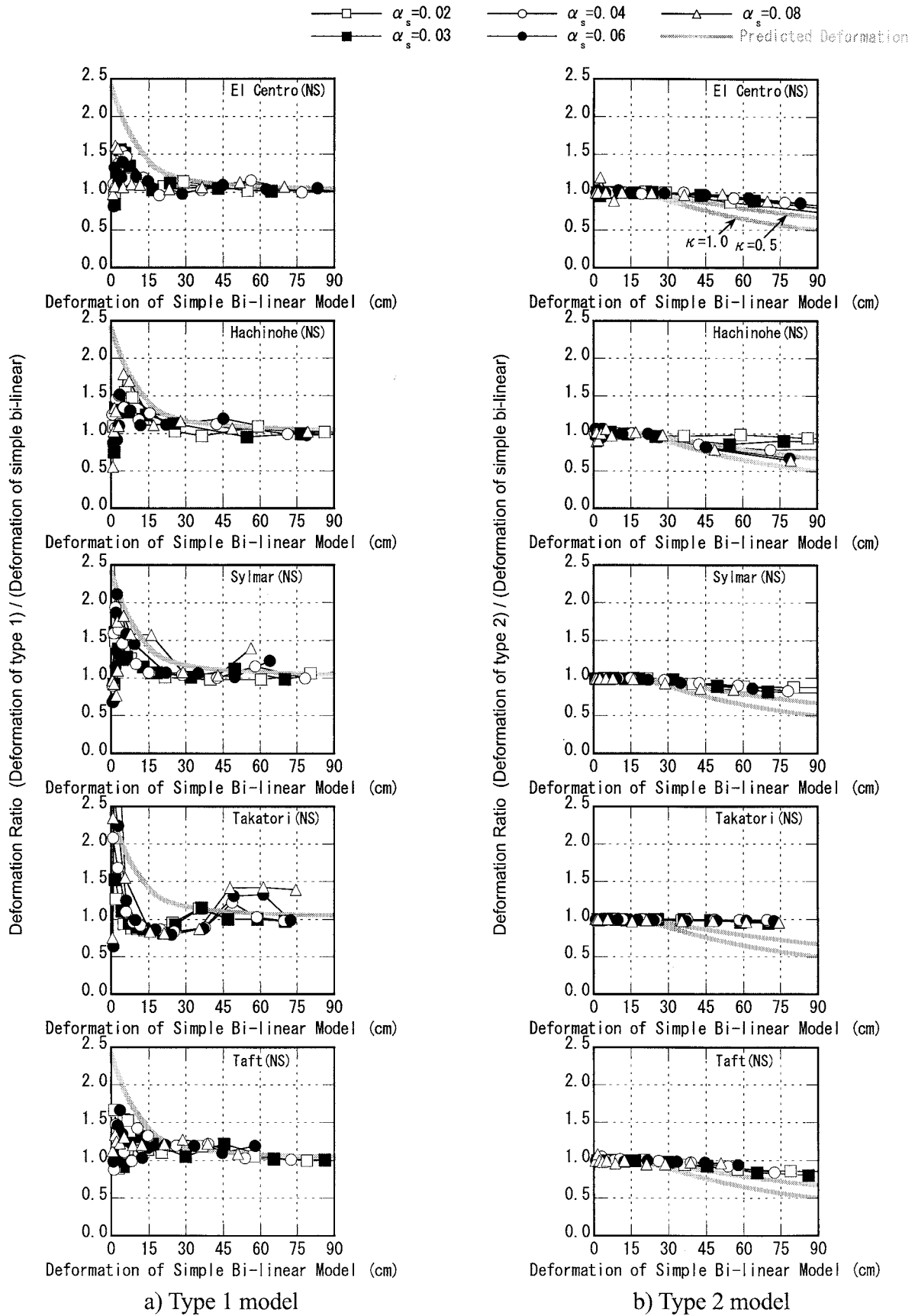


Figure 7 Response Deformation Ratio of Seismic Isolation Interface ($T_f = 3\text{sec}$)

MODAL COUPLING EFFECT OF MID-STORY ISOLATED BUILDINGS

M. Kobayashi¹⁾, and T. Koh²⁾

1) Lecturer, Department of Architecture, School of Science and Technology, Meiji University, Japan

2) Professor Emeritus, Meiji University, Japan

masahito@isc.meiji.ac.jp

Abstract: This paper describes vibration characteristics of Mid-story isolated buildings based on the calculation results by analyses of an eigenvalue analysis and frequency transfer functions. Especially, it is clarified that response amplification of the upper structure of the isolation story is caused by modal coupling effect between modes of vibration on the upper and lower structure. In this paper, the results obtained by the eigenvalue analysis and frequency transfer functions are as follows: 1) The modal coupling effect is caused by vibration modes on which the isolation story is not deformed, and 2) The modal coupling effect amplifies the earthquake response of the upper structure and decreases effect of seismic isolation, however the modal coupling effect does not influence inter-story drift of the isolation story.

1. INTRODUCTION

Since 1995-Hyogoken-Nanbu-Earthquake, seismic isolation has been esteemed for structural safety and maintaining of functional capacities. Mid-story isolated buildings have recently attracted attention for adaptability to diverse needs such as urban redevelopment projects and seismic retrofit in Japan (Murakami et al. 1999, Kuroda et al. 1997).

Seismic design and seismic performance evaluation of the mid-story isolated buildings are generally verified by a time history response analysis, because the mid-story isolation buildings have complex structure system consist of the upper and lower structure of the isolation story as shown in Fig.1. From the numerical analysis (Kobayashi et al. 2002), the authors have found that response amplification of the upper structure of the isolation story is caused by modal coupling effect between modes of vibration on the upper structure and on the lower structure.

In this paper, we describe how the modal coupling effect arise on the mid-story isolated buildings based on the calculation results by an eigenvalue analysis and frequency transfer functions.

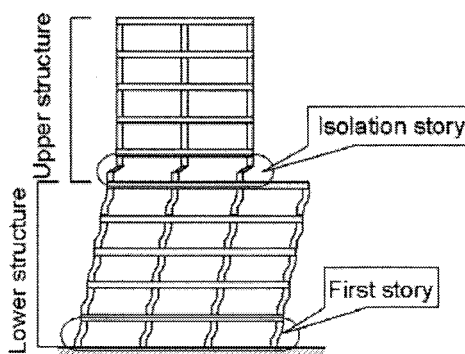


Figure 1 Mid-Story Isolated Building

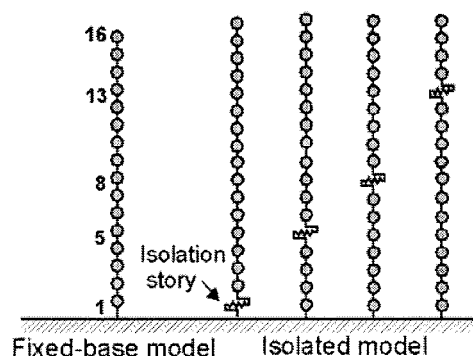


Figure 2 16-Story Shear Deformation Models

2. MODAL COUPLING EFFECT OF MID-STORY ISOLATED BUILDINGS

This section describes the modal coupling effect from analytical examples. 16-story shear deformation models are examined (Fixed-base model and Isolated model shown in Fig.2). On the Fixed-base model, mass for each story, which is uniformly given along height of the building, is 1,000 tons. i -th story stiffness, k_i is decided so that the building shows uniformly distributed inter-story drift under the static lateral force given by Japanese seismic code, and the 1st natural period is 1.0 second. The relationship between the resisting force and inter-story drift of each story is linear.

On the Isolated model, the position of the isolation story is set to the 1st, 5th, 8th and 13th story as shown in Fig.2. Mass and story stiffness are the same as the Fixed-base model excluding the isolation story. In the isolation story, the isolator and the damper have the resisting force Q – inter-story drift δ characteristics shown in Fig.3. k_f and k_s as lateral stiffness of the isolator and the damper are adjusted to 1/100 and 1/20 of the lateral stiffness of the same story of the Fixed-base model, respectively. Then, natural vibration period of the 1st, 5th, 8th and 13th story isolated model (with the upper and lower structure assumed to be rigid) are 3.4, 3.1, 2.9 and 2.5 second, respectively. The sQ_y as the yield strength of the damper is given as story shear coefficient α_s . The α_s of 1st, 5th, 8th and 13th story isolated model are set to 0.05, 0.055, 0.06 and 0.09, respectively, so that base shear coefficient is effectively reduced (Kobayashi and Koh et al. 2004). The initial structural damping is applied by stiffness-proportional damping in which the 1st mode damping factor is set to 0.02 on the upper structure and lower structure, respectively.

Analysis results are shown in Fig. 4, when an observed earthquake (El Centro NS, Max.Acc. was amplified to 510.7 cm/sec²) was input to four isolated models. In this figure, the acceleration response and the story shear coefficient of the upper structure on the 8th story isolation model are remarkably large compared with other models. This is called ‘Modal Coupling Effect’. We describe how the modal coupling effect arises on the mid-story isolated building in the next chapter.

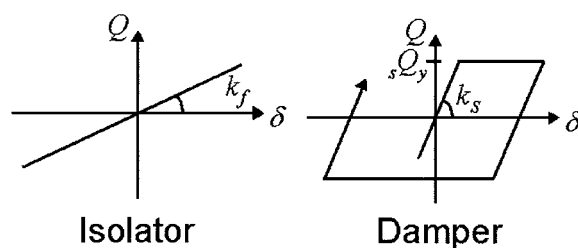


Figure 3 Force—Displacement Characteristics of Isolator and Damper

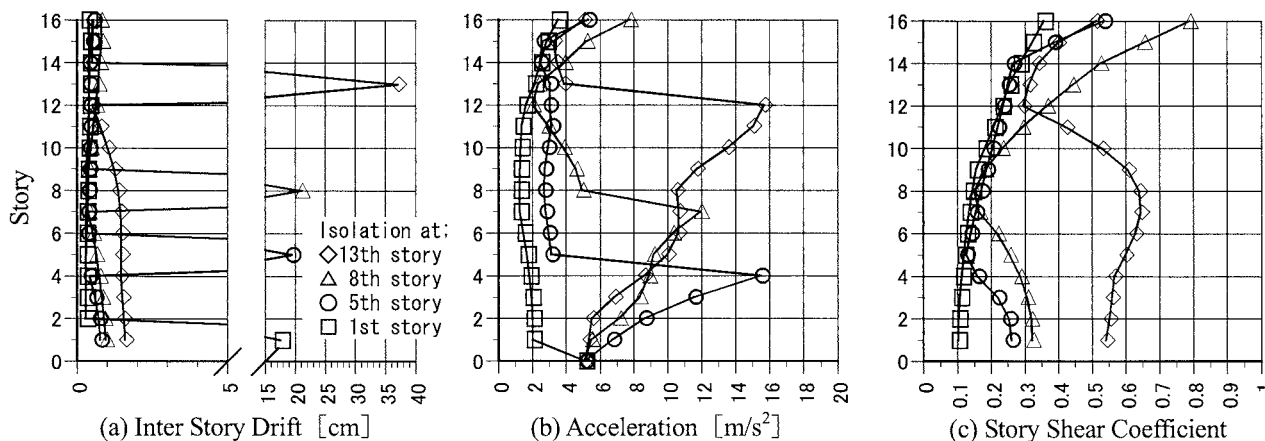


Figure 4 Maximum Response of Isolated Model

3. ANALYTICAL MODEL AND ANALYSIS METHOD

3.1 Analytical Model

Analytical Models shown in Fig.5 are 10-mass-system as the mid-story isolated building and two 5-mass-systems as the base isolation model and the lower structure model obtained dividing 10-mass-system. For the simplification of the analysis, the mass is uniformly given along height of the building. Story stiffness of the lower structure is decided so that the 1st natural period of the lower structure is 0.5 second (2Hz). And, lateral stiffness of the isolator is decided so that natural period (with the upper and lower structure assumed to be rigid) is 4.0 second (0.25 Hz). Story stiffness of the upper structure is made to change as the analytical parameter. Lateral stiffness of the upper and lower structure are assumed to be even distribution. The initial structural damping is applied by stiffness-proportional damping in which the 1st mode damping factor is set to 0.02 on the upper structure and the lower structure, respectively. The damping factor of isolation story is set to 0.2 to express the effect of the damper simply.

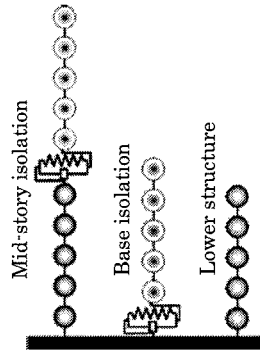


Figure 5 Analytical Model

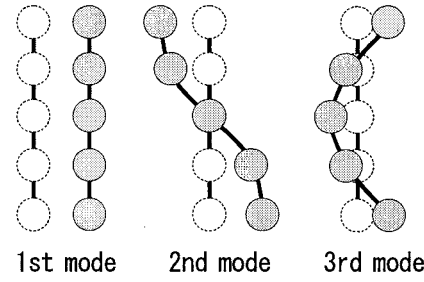


Figure 6 Free-Free Mode Shape Vector

3.2 Free-Free Mode of Vibration

Skinner (1993) has revealed the contribution of the higher mode to earthquake responses of base isolation buildings by sweeping the modal response with free-free mode shape vectors. In this study, the same method is applied to mid-story isolation buildings. When stiffness of the isolation story is zero, the mode shape vector \mathbf{u}_0 and the natural circular frequency ω_0 are as follows:

$$\mathbf{K}_0 \mathbf{u}_0 = \omega_0^2 \mathbf{M} \mathbf{u}_0 \quad (1)$$

Where \mathbf{K}_0 and \mathbf{M} are stiffness and mass matrix, respectively, as the stiffness of isolation story is zero. Two frequency equations obtained from Eq.(1) are as follows:

$$\det[\mathbf{K}_0 - \omega_{FF,u}^2 \mathbf{M}] = 0, \quad \det[\mathbf{K}_0 - \omega_l^2 \mathbf{M}] = 0 \quad (2a, b)$$

Where \mathbf{K}_0 and \mathbf{M} are stiffness and mass matrix of the upper structure, \mathbf{K}_l and \mathbf{M}_l are stiffness and mass matrix of the lower structure. The modal matrix \mathbf{U} is as follows:

$$\mathbf{U} = [\mathbf{u}_{0,s}] = \begin{bmatrix} \mathbf{u}_{FF,1} & \mathbf{u}_{FF,2} & \cdots & \mathbf{0} & \mathbf{0} & \cdots \\ \mathbf{0} & \mathbf{0} & \cdots & \mathbf{u}_1 & \mathbf{u}_2 & \cdots \end{bmatrix} \quad (3)$$

where $\mathbf{u}_{FF,i}$ is the i -th mode shape vector obtained from Eq.(2a) (i.e. the free-free mode shape vectors show in Fig.6) and \mathbf{u}_j is the j -th mode shape vector obtained from Eq.(2b). Here, the ratio

γ of the ${}_u\omega_{FF,2}$ (as the 2nd natural circular frequency of free-free mode) and the ${}_l\omega_1$ (as the 1st natural circular frequency of the lower structure) is defined as Eq.(4). This is the analytical parameter in this study.

$$\gamma = {}_u\omega_{FF,2} / {}_l\omega_1 \quad (4)$$

3.3 Eigenvalue Analysis

Since the mid-story isolation models are the non-classically damped system, the eigenvalue problem of Eq.(5) is solved to obtain the i -th modal parameters. \mathbf{M} , \mathbf{C} , \mathbf{K} and \mathbf{I} are mass, damping, stiffness and unit matrix, respectively.

$$\mathbf{A}\mathbf{u}_i = \lambda_i \mathbf{u}_i, \quad \mathbf{A} = \begin{bmatrix} \mathbf{0} & \mathbf{I} \\ -\mathbf{M}^{-1}\mathbf{K} & -\mathbf{M}^{-1}\mathbf{C} \end{bmatrix} \quad (5a, b)$$

where λ_i and \mathbf{u}_i are complex eigenvalue and eigenvector. The i -th natural frequency f_i and damping factor h_i are given by Eq.(6).

$$f_i = 2\pi|\lambda_i|, \quad h_i = -\text{Re}(\lambda_i)/|\lambda_i| \quad (6a, b)$$

3.4 Frequency Response Function

The $H_{y,j}(i\omega)$ as the frequency response function of the j -th story displacement under sinusoidal excitation $\ddot{y}_g = e^{i\omega t}$ is evaluated as follows:

$$\mathbf{H}_y(i\omega) = -(-\omega^2 \mathbf{M} + i\omega \mathbf{C} + \mathbf{K})^{-1} \mathbf{M} \mathbf{r}, \quad \mathbf{r} = [1 \quad 1 \quad \dots]^T \quad (7a, b)$$

$$\mathbf{H}_y(i\omega) = [H_{y,1}(i\omega) \quad H_{y,2}(i\omega) \quad \dots \quad H_{y,j}(i\omega) \quad \dots]^T \quad (8)$$

The $H_{A,j}(i\omega)$ as the frequency response function of the j -th story absolute acceleration, and $H_{r,j}(i\omega)$ as that of inter-story drift of the j -th story are evaluated by $H_{y,j}(i\omega)$ as follows:

$$H_{A,j}(i\omega) = 1 - \omega^2 H_{y,j}(i\omega) \quad (9)$$

$$H_{r,j}(i\omega) = H_{y,j}(i\omega) - H_{y,j-1}(i\omega), \quad H_{r,1}(i\omega) = H_{y,1}(i\omega) \quad (10a, b)$$

The σ_X as the root-mean-square (RMS) value of a random vibration response X to $S(\omega)$ as the power spectrum of ground acceleration is expressed by using a frequency response function $H_X(i\omega)$ as Eq.(11). When the power spectrum $S(\omega)$ is assumed to be white noise, the $\phi_{m,n}$ as RMS value ratio of random vibration responses m and n is evaluated by Eq.(12).

$$\sigma_X^2 = \int_0^\infty |H_X(i\omega)|^2 S(\omega) d\omega \quad (11)$$

$$\phi_{m,n} = \sigma_m / \sigma_n = \sqrt{\int_0^\infty |H_m(i\omega)|^2 d\omega / \int_0^\infty |H_n(i\omega)|^2 d\omega} \quad (12)$$

4. ANALYSIS RESULTS AND DISCUSSIONS

4.1 Natural Frequency and Modal Damping Factor

Fig.7 and Fig.8 show the relationship between the analytical parameter γ calculated by Eq.(4) and the natural frequency and the modal damping factor calculated by Eq.(6) on the mid-story isolation model show in Fig.5. Fig.7 shows that the 2nd and 3rd natural frequencies reach a close value near $\gamma = 1$. Moreover, Fig.8 shows that the 2nd and 3rd modal damping factors change greatly near $\gamma = 1$. The 2nd damping factor decreases rapidly, and the 3rd one increases.

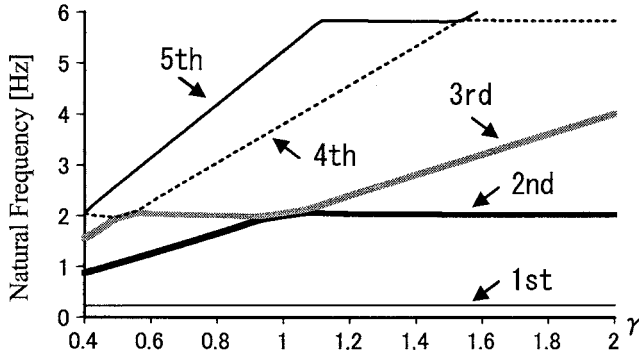


Figure 7 Relationship between γ and Natural Frequency

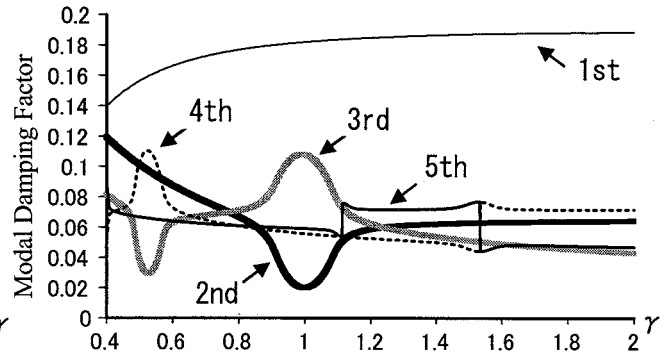


Figure 8 Relationship between γ and Modal Damping Factor

4.2 Mode of Vibration

Fig.9 shows the modal participation functions βu as classically mode vectors and the value of the natural frequency and modal damping factor calculated by Eq.(6). When $\gamma = 0.9$, the direction of the 2nd and 3rd modal participation functions of the upper structure are opposite, and these amplitude is almost equal. The inter story drift of the isolation story is large in the 3rd mode, and it is small in the 2nd mode. This tendency becomes the most remarkable at $\gamma = 1.0$. The 2nd and 3rd modal participation functions of the isolated upper structure become considerable amplitude. Moreover, the inter story drift of the isolation story is extremely small in the 2nd mode. According to these tendencies, the change of the modal damping factor show in Fig. 4 can be understood. When $\gamma = 1.0$, the 2nd modal damping factor becomes 2% given as structural damping, because high damping of the isolation story cannot be taken in the 2nd mode. On the other hand, the 3rd modal damping factor becomes 10.7%, because high damping of the isolation story can be efficiently taken in the 3rd mode. The 2nd mode at $\gamma = 1.0$ shown in Fig.9 has slight damping factor as 2% and considerable amplitude participation function on the isolated upper structure. Such a mode of vibration causes the modal coupling effect.

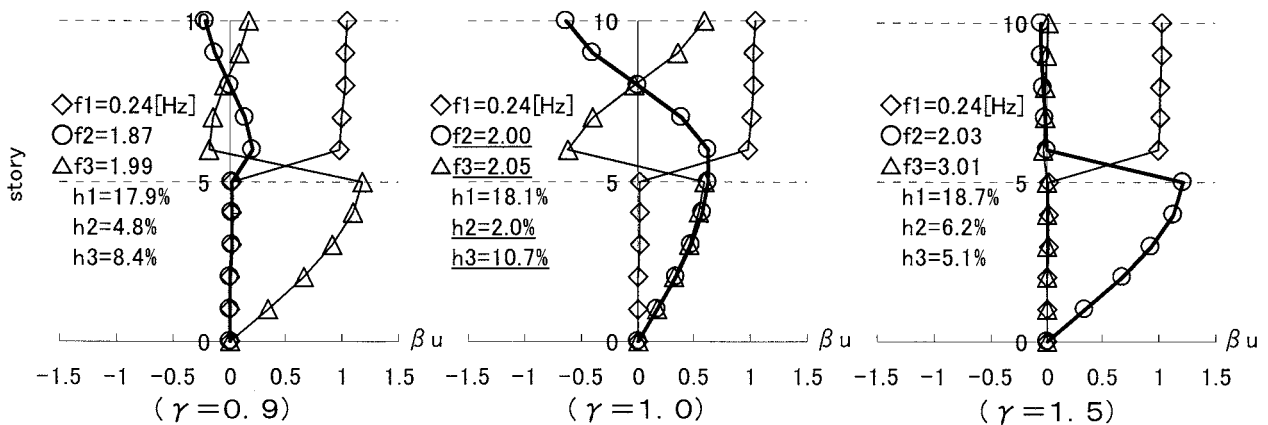


Figure 9 Modal Participation Function βu

4.3 Frequency Response Function and Random Vibration Response

In this section, it is shown how the characteristics of the modal parameter described in the previous section influence an earthquake response to white noise ground motion. Fig.10, Fig.11 and Fig.12 show the frequency response function of the 10th Story (building top) absolute acceleration calculated by Eq.(9), that of the 6th inter story (isolation story) drift and that of the 1st story calculated by Eq.(10), respectively. The Base isolation and the Lower structure model described in these figures are these in Fig.5. The frequency response functions of the 10th story absolute acceleration and the 6th inter story drift increase compared with the Base isolation near 2Hz as the 1st natural frequency of the Lower structure. This tendency becomes the most remarkable, when $\gamma = 1.0$ on the 10th story absolute acceleration shown in Fig. 10. On the other hand, the response of the 1st inter-story drift shown in fig.12 decreases compared with the response of the Lower structure model. This is called 'mass damper effect'. This response reduction when $\gamma = 1.0$ is smaller than when $\gamma = 1.5$. For this result, it is understood that the modal coupling effect influences not only the upper structure but also the lower structure.

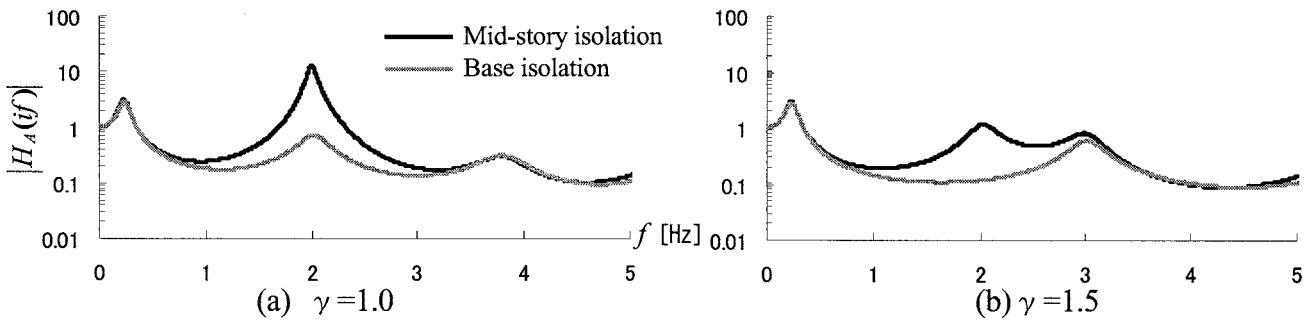


Figure 10 Frequency Response Function of 10 th Story Absolute Acceleration

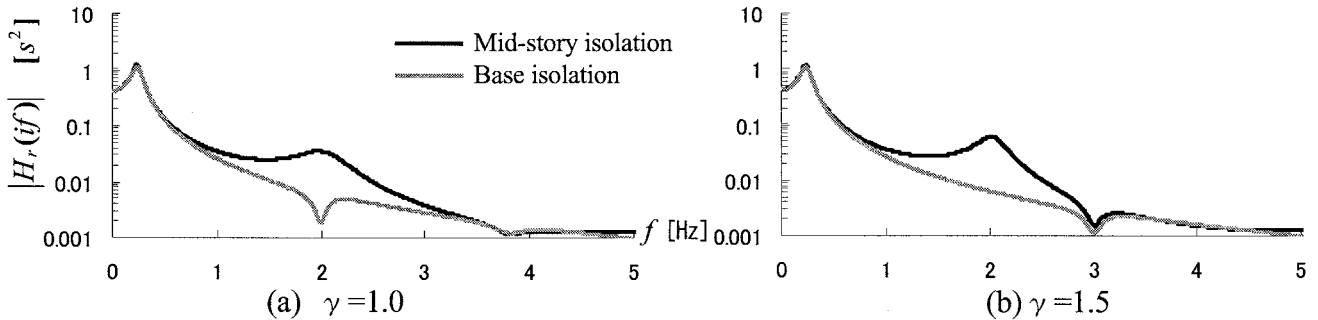


Figure 11 Frequency Response Function of 6th Inter Story Drift

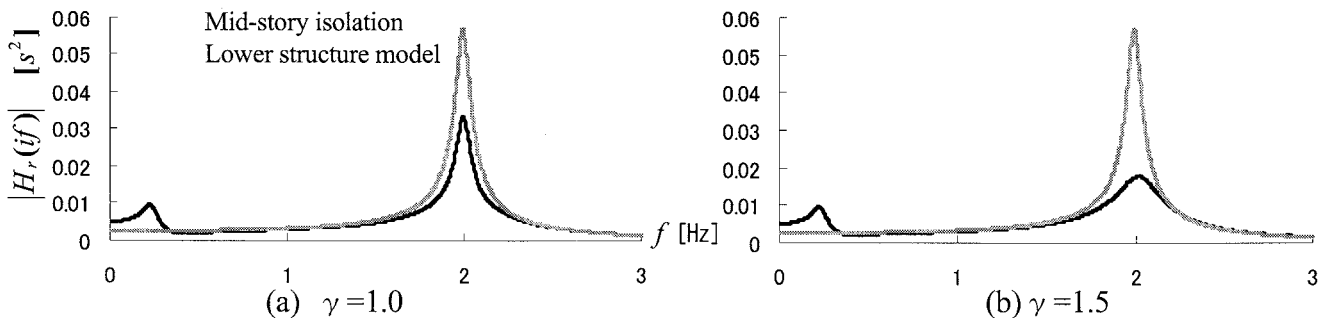


Figure 12 Frequency Response Function of 1st Inter Story Drift

The results of the RMS value ratio of the random vibration response calculated by Eq.(12) is shown in Fig.13. Fig.13(a) and (b) show the ratio of the response of the Mid-story isolation and the Base isolation. That is, it is response amplification to the Base isolation. And, Fig.13(c) shows the ratio of the response of the Mid-story isolation and the Lower structure model. That is, it is response reduction to the Lower structure model. The RMS value ratio shown in Fig.13(a) and (b) are greatly amplified by the modal coupling effect at $\gamma = 1.0$. However, the modal coupling effect does not influence the story drift of the isolation story. The RMS value ratio shown in Fig.13(c) is smaller than 1.0. That is, the inter-story drift of the Lower structure of the Mid-story isolation is smaller than that of the Lower structure model. However, when $\gamma = 1.0$, the RMS value ratio increase, and the response reduction becomes inefficient.

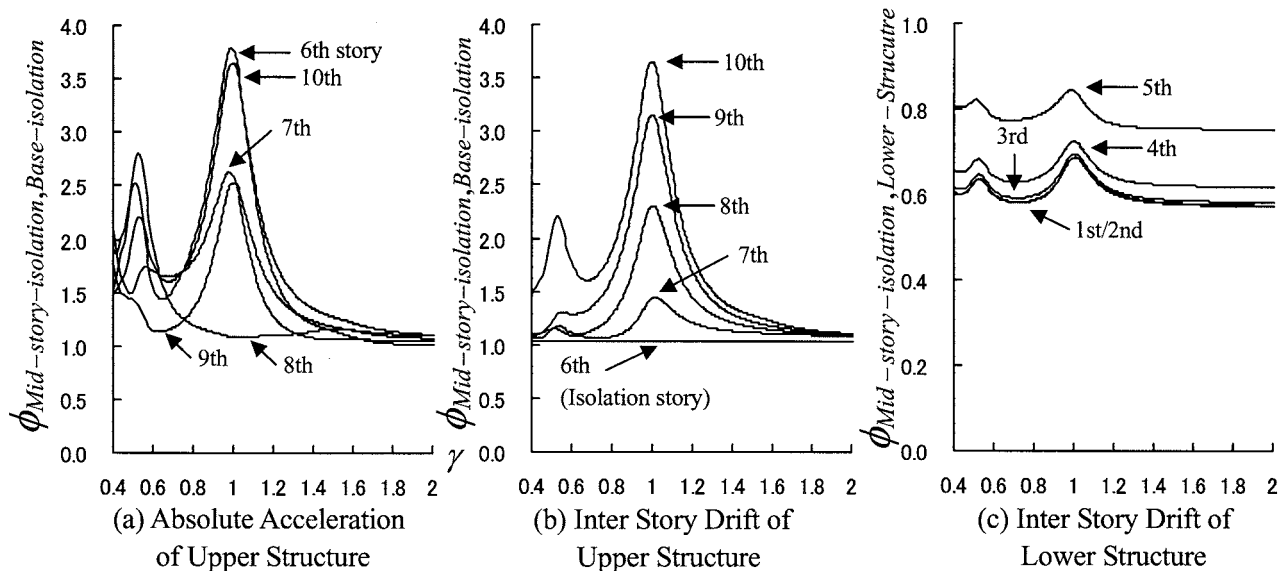


Figure 13 RMS Value Ratio of Random Vibration Response

5. CONCLUSIONS

This paper describes the vibration characteristics of mid-story isolation buildings based on the calculation results by the eigenvalue analysis and the frequency transfer functions. Especially, it is clarified that the response amplification of the upper structures of the isolation story is caused by the modal coupling effect. In this paper, the results obtained by the analytical study are as follows: 1) The modal coupling effect is caused by the vibration modes on which isolation story is not deformed. 2) The modal coupling effect does not influence the inter-story drift of isolation story, however it amplifies the earthquake response of the upper structure and decreases effect of seismic isolation.

References:

- Murakami, K., Kitamura, H., Ozaki, H. and Yamanashi, T. (1999), "Design of a Building with Seismic Isolation System at the Mid-story," *AIJ Journal of Technology and Design*, **7**, 51-56(in Japanese).
- Kuroda, M., Narita, I., Tanaka, S., Kawamura, S., Ogura, K. and Yajima, A. (1997), "Seismic Isolation Retrofit at Mid Story and Base-Planning and outline of works-," *AIJ Journal of Technology and Design*, **5**, 18-22(in Japanese).
- Kobayashi, M., Izawa, Y., Koh, T. (2002), "The Prediction Method of Earthquake Responses on Mid-story Isolated System Considering Modal Coupling Effect," *Journal of Structural and Construction engineering*, **572**, 73-80(in Japanese)
- Kobayashi, M., Koh, T. (2004), "Seismic Performance Evaluation of Mid-story Isolation Buildings", *JSSI 10th Anniversary Symposium on Performance of Response Controlled Buildings*, Yokohama Japan, CD-ROM S3-2, JSSI(Japan Society of Seismic Isolation)
- R.Ivan Skinner, William H.Robinson and Graeme H.McVerry, (1993), "An Introduction to Seismic Isolation", Wiley.

TIME-HISTORY ANALYSIS MODEL FOR VISCOELASTIC DAMPER UNDER LONG DURATION LOAD

D. Sato ¹⁾, and K. Kasai ²⁾

1) Researcher, Center of Urban Earthquake Engineering, Tokyo Institute of Technology, Japan

2) Professor, Structural Engineering Research Center, Tokyo Institute of Technology, Japan

daiki@enveng.titech.ac.jp, kasai@serc.titech.ac.jp

Abstract: Viscoelastic damper dissipates energy through shear deformation of the viscoelastic material, and this causes temperature rise and softening of the material. Under long duration load, therefore significant heat conduction and transfer can occur and control the temperature-rise effects. These and frequency sensitivities are considered in the analysis method proposed: The combines one-dimensional heat transfer analysis and viscoelastic constitutive rule using fractional time-derivatives of stress and strain, and it calculates step-by-step the force-deformation time histories of the damper.

In addition, this paper proposes a fast and sufficiently accurate algorithm for calculating fractional time-derivatives of stress and strain in the viscoelastic damper. The algorithm also has an advantage of requiring substantially smaller memory space. At every step, numerical integration using past stress and strain data is required, but the proposed algorithm needs only a small portion of such data: it selects and stores the data at much longer interval than the original algorithm.

1. INTRODUCTION

It has been recognized that viscoelastic (VE) dampers have significant advantage over other types of dampers in controlling responses of buildings against not only wind but also earthquake excitation. VE damper dissipates energy through shear deformation of the VE material, and making temperature rise and softening the material. Under long duration load, therefore, significant heat conduction and transfer can occur and control the temperature-rise effect.

Kasai et al (Kasai et al. 1993, 2001) proposed the nonlinear model of VE damper based on the fractional time-derivative with focus on the effect of temperature-rise. This model is called "Short duration model" in this study. However, this model dose not consider the heat conduction and heat transfer, which are still significant even in cases of short duration load such as earthquake.

In case of long duration load such as wind force, heat conduction and heat transfer effects must be considered. These effects and frequency sensitivities are considered in the analysis method proposed in this study. This method, which is called "Long duration model", combines one-dimensional heat transfer analysis and viscoelastic constitutive rule using fractional time-derivatives of stress and strain, and it calculates step-by-step the force-deformation time histories of the damper. The accuracies of both analysis methods are demonstrated by comparing with the results of experiments applying cyclic loading of long duration.

In addition, this paper proposes a fast and sufficiently accurate algorithm for calculating fractional time-derivatives of stress and strain in the viscoelastic damper. The algorithm also has an advantage of requiring substantially smaller memory space. At every step, numerical integration using past stress and strain data is required, but the proposed algorithm needs only a small portion of such data: it selects and stores the data at much longer interval than the original algorithm. Its numerical efficiency and accuracy are demonstrated through comparison with the original and precise algorithm.

2. LONG DURATION MODEL OF FRACTIONAL DERIVATIVE

2.1 Difference between Short Duration and Long Duration Model.

Figure 1 and 2 illustrate the distributions of temperature, stiffness, and strain along thickness (Z-) direction of the VE damper. Figure 1 depicts the case of the short duration loading like a typical earthquake (short duration model), and Figure 2 shows the case of the long duration loading such as long period earthquake or wind force (long duration model).

As shown as Figure 1, the short duration model considers only the effect of temperature-rise caused by dissipation of energy. Due to the small heat conductivity of the VE material, heat conduction from VE material to steel plate and heat transfer to air are very slow, compared with the short duration of the loading. Therefore, the distributions of temperature, strain and stress are considered to be uniform within the VE material, and such a model has been found sufficiently accurate when typical earthquake loading is considered (Kasai et al. 1993, 2001).

However, in case of the long duration loading, the distributions of temperature, strain and stress inside of VE material do not uniform because of the heat conduction and the heat transfer effects as shown as Figure 2. Thus, the analysis model of VE damper under the long duration loading must be considered not only the heat generation but also the heat conduction and the heat transfer. Therefore, the analysis model assumes that the heat generated inside the VE material moves toward the steel plates, and transmitted to the air through the steel plates. Accordingly, strain and temperature can be expressed as $\gamma(t, z)$ and $\theta(t, z)$, which is the function of time " t " and the thickness direction coordinate " z ".

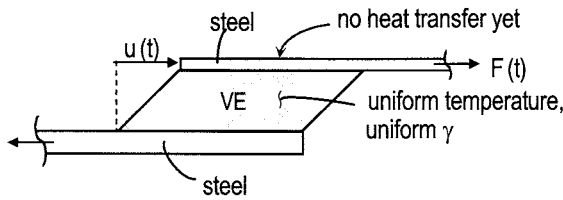


Figure 1 Short Duration Model

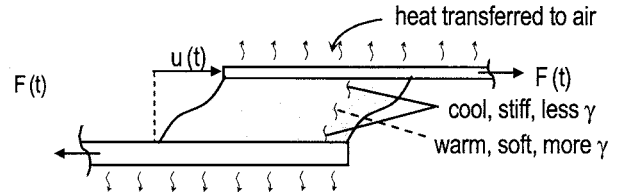


Figure 2 Long Duration Model

2.2 Algorithm of Long Duration Model

The nonlinear model of VE damper was proposed earlier by Kasai et al. (Kasai et al. 1993, 2001), and it called "Short duration model". This model does not consider the heat conduction and heat transfer, which are still reasonable in case of short duration load like a typical earthquake.

It is recognized that the temperature distribution inside the VE damper can be express by using one-dimensional (1D) heat problem (Kasai et al. 2006a). In this study, the time history analysis method of VE damper considering 1D heat transfer analysis is proposed, and it is called "long duration model". It combines 1D heat transfer analysis and viscoelastic constitutive rule using fractional time-derivatives of stress and strain, and it calculates step-by-step the force-deformation time histories of the damper.

Figure 3 shows the example that VE damper thickness is divided into 10 elements ($m = 10$; $m =$ total element number of the long duration model). Where, j is node number, and the nodes j_1 to j_2 are VE material, other nodes are steel part, and d_j is length of element j .

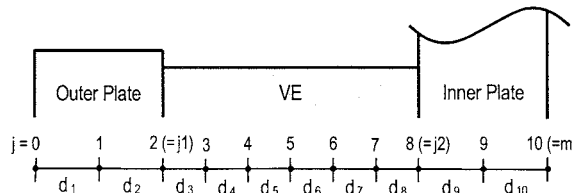


Figure 3 Example of element division for damper

When n^{th} step damper deformation $u_d^{(n)}$ is known, the compatibility equation between the damper deformation $u_d^{(n)}$ and shear strain $\gamma_j^{(n)}$ can be expressed by Eq. (1).

$$u_d^{(n)} = \frac{1}{2} \sum_{j=j_1}^{j_2} \zeta_j \gamma_j^{(n)} \quad (1)$$

here $\zeta_{j_1} = d_{j_1+1}$, $\zeta_{j_2} = d_{j_2}$ and $\zeta_j = d_j + d_{j+1}$ when $j_1 < j < j_2$.

Shear stress $\tau^{(n)}$ is assumed to be constant throughout the thickness of VE material based on equilibrium equation. However, since strain and temperature distribution are not uniform throughout the thickness of the VE material, therefore, the fractional derivative is written as in Eq. (2).

$$\tau^{(n)} + a_j D^\alpha \tau^{(n)} = G \left[\gamma_j^{(n)} + b_j D^\alpha \gamma_j^{(n)} \right] \quad (2)$$

Where, $D^\alpha (= d^\alpha/dt^\alpha)$ = the fractional derivative operator, α = order of the fractional derivative, a_j , b_j and G = parameter of the fractional derivative. a_j and b_j are depended on temperature θ_j , and these are expressed as follows;

$$a_j = a_{ref} \lambda_j^\alpha, \quad b_j = b_{ref} \lambda_j^\alpha, \quad \lambda_j = \exp \left[-p_1 (\theta_j - \theta_{ref}) / (p_2 + \theta_j - \theta_{ref}) \right] \quad (3a-c)$$

here, λ_j is called "shift factor", θ_{ref} = reference temperature, a_{ref} and b_{ref} = value of a and b at θ_{ref} respectively. The parameters of the fractional derivative for ISD 111 (3M Corp.) are; $G = 6.516$ N/cm², $\alpha = 0.609$, $a_{ref} = 0.015$, $b_{ref} = 21.157$, $\theta_{ref} = 0.2^\circ\text{C}$, $p_1 = 19.5$ and $p_2 = 80.2$.

Considering the step-by-step integration scheme, Eq. (2) is expressed as follows;

$$\tau^{(n)} + a_j \sum_{i=0}^N w^{(i)} \tau^{(n-i)} = G \left[\gamma_j^{(n)} + b_j \sum_{i=0}^N w^{(i)} \gamma_j^{(n-i)} \right] \quad (4)$$

where Δt = time step size, N = number of integration step, and N is decided as, which is considered until the 3rd frequency of building, $N = 1.5 T$ (Kasai et al. 2001). Here, T = natural frequency of the building. $w^{(i)}$ ($i = 0 \sim N$) = weight function are expressed as follows;

$$w^{(0)} = 1/\Gamma(2-\alpha)/(\Delta t)^\alpha, \quad w^{(i)} = w^{(0)} \left\{ (i-1)^{1-\alpha} - 2i^{1-\alpha} + (i+1)^{1-\alpha} \right\}, \quad (5a-c)$$

$$w^{(N)} = w^{(0)} \left\{ (N-1)^{1-\alpha} - N^{1-\alpha} + (1-\alpha)N^{-\alpha} \right\}$$

By rearranging and manipulating about Eq. (4), strain $\gamma_j^{(n)}$ can be written as in Eq. (6).

$$\gamma_j^{(n)} = \frac{\tau^{(n)} (1 + a_j w^{(0)}) + \tilde{A}_j - \tilde{B}_j}{G(1 + b_j w^{(0)})}, \quad \tilde{A}_j = a_j \sum_{i=1}^N w^{(i)} \tau^{(n-i)}, \quad \tilde{B}_j = G b_j \sum_{i=1}^N w^{(i)} \gamma_j^{(n-i)} \quad (6a-c)$$

Then, by substituting Eq. (6a) into Eq. (1), stress $\tau^{(n)}$ is expressed by Eq. (7).

$$\tau^{(n)} = \left\{ 2G u_d^{(n)} - \sum_{j=j_1}^{j_2} \frac{\zeta_j (\tilde{A}_j - \tilde{B}_j)}{1 + b_j w^{(0)}} \right\} / \sum_{j=j_1}^{j_2} \frac{\zeta_j (1 + a_j w^{(0)})}{1 + b_j w^{(0)}} \quad (7)$$

The damper force $F_d^{(n)}$ is calculated by Eq. (8).

$$F_d^{(n)} = \tau^{(n)} A_v \quad (8)$$

The temperature rise $\Delta\theta_j^{(n)}$ results from the energy dissipates for Δt at point j is expressed by Eq. (9).

$$\Delta\theta_j^{(n)} = \frac{1}{2} \left(\frac{\Delta\overline{W}_j}{s_j \rho_j} + \frac{\Delta\overline{W}_{j+1}}{s_{j+1} \rho_{j+1}} \right), \quad \Delta\overline{W}_j = (\tau^{(n)} + \tau^{(n-1)}) \left(\gamma_{j-1}^{(n)} - \gamma_{j-1}^{(n-1)} + \gamma_j^{(n)} - \gamma_j^{(n-1)} \right) / 4 \quad (9a,b)$$

where $\Delta\overline{W}_{j_1} = \Delta\overline{W}_{j_2+1} = 0$ because there are steel plate parts. In order to predict the $(n+1)^{\text{th}}$ step's temperature distribution of VE damper $\theta_j^{(n+1)}$, not only temperature rise from the energy dissipates $\Delta\theta_j^{(n)}$ but also temperature rise and/or fall results from the heat transfer and conduction $\bar{\theta}_j^{(n)}$ (Eq. (10)).

$$\theta_j^{(n+1)} = \Delta\theta_j^{(n)} + \bar{\theta}_j^{(n)}, \quad \bar{\theta}_j^{(n)} = \sum_{k=0}^m x_{jk} \theta_k^{(n)} + y_j \quad (10a,b)$$

where Eq. (10b) expresses the simplified 1D-heat transfer equation solution.

The heat-transfer coefficient, which is used in the long duration model analysis, are decided in order that the heat flow rate of the long duration model is same as 3D-FEM results (Kasai et al. 2006a). Thus, the inner plate side's heat-transfer coefficient $\alpha_{c,in}$ and the outer plate side's heat-transfer coefficient $\alpha_{c,out}$ are expressed as follows;

$$\alpha_{c,in} = Q_{in} / \{A_d (\theta_{in} - \theta_c)\}, \quad \alpha_{c,out} = Q_{out} / \{A_d (\theta_{out} - \theta_c)\} \quad (11a,b)$$

where, θ_c = ambient temperature, Q_{in} and Q_{out} = the heat flow rate at inner plate side and outer plate side obtained from 3D-FEM analysis results (Kasai et al. 2006a), respectively, θ_{in} and θ_{out} = the average temperature of surface at inner plate side and outer plate side obtained from 3D-FEM analysis results (Kasai et al. 2006a), respectively. Then $\alpha_{c,in} = 0.956 \text{ N/s/cm}^2\text{C}$, $\alpha_{c,out} = 0.524 \text{ N/s/cm}^2\text{C}$.

2.3 Test Specimen Description and Test Setup

A long duration loading test of individual VE damper has been carried out to investigate characteristic of VE damper under long duration loading and to validate the proposed analytical methods. Figure 4 shows the test specimen of VE damper. The damper is made from acrylic polymer VE material produced by 3M Corp., with brand name ISD 111. The two VE material laminations are bonded between outer steel plate and inner steel plate. The wide of VE lamination $B = 37.6 \text{ mm}$, the length $L = 50.8 \text{ mm}$ and the thickness of one VE lamination $d_v = 13.3 \text{ mm}$. The total area of two VE material laminations $A_v = 3,817 \text{ mm}^2$. The thickness of one steel plate $d_s = 4.8 \text{ mm}$.

The sinusoidal displacement having peak amplitude $u_{d,max} = 6.6 \text{ mm}$ (50% shear strain) and 3.0 seconds period is applied to the inner plate. The duration of sinusoidal wave is 3,000 seconds. After the excitation, decrease of damper temperature is monitored up to 5000 seconds. Ambient temperature θ_c is maintained at 24°C for 5,000 seconds.

As shown in Figure 4, the temperature of VE damper is measured at the four positions; (A) air side of outer steel plate, (B) 1/4 thickness of the VE lamination, (C) 1/2 thickness point of the VE lamination, and (D) center of inner steel plate.

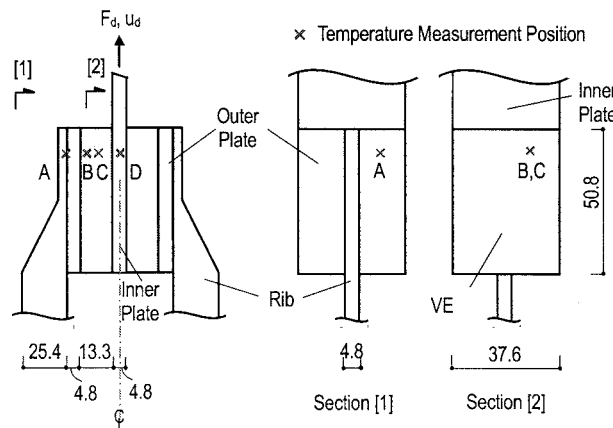


Figure 4 Test specimen & temperature measurement position (unit: mm)

2.4 Comparison between Test and Long Duration Model Results

Figure 5 shows the comparison of temperature between the test results and the analysis results which are calculated by the long duration model and by the short duration model (Kasai et al. 1993, 2001). As can be seen from the test results in Figure 5, it is recognized that the change of temperature is different depending upon the temperature measurement position A ~ D. In addition, Figure 5 shows that temperature rise becomes sluggish and temperature is constant at each measurement point after 1,000 seconds. In case of under the long duration loading such as in this study, because of effect of the heat conduction & transfer to the steel plates, temperature of VE damper attains the steady state at a certain time, and temperature does not continue to rise even if the VE damper is still vibrating. After 3,000 seconds when the vibration finished, temperature of each point rapidly decreases to 24 °C because the internal heat generation inside the VE materials has stopped.

The long duration model results agrees well with test result, however, the short duration model results fails prematurely because the short duration model can not consider the heat conduction & transfer.

Figure 6 shows damper hysteresis loop obtained from (a) test result, and calculated by (b) the long duration model, and (c) the short duration model, respectively.

Figure 7(a), (b), respectively, show the comparison of K'_d and K''_d between test (plot) and the long duration model (broken line) and the short duration model (solid line) analysis results. Obviously, K'_d and K''_d calculated by the long duration model are in good agreement with the test results. However, the results which are obtained from the short duration model calculation are significantly softened due to the overestimated temperature (See Figure 5).

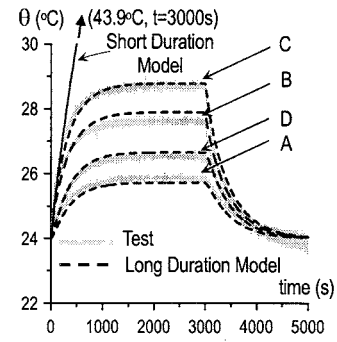


Figure 5 Comparison of temperature with test, long duration model and short duration model.

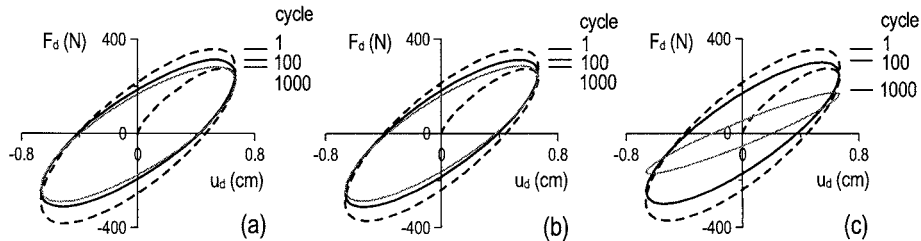


Figure 6 Comparison of loop: (a) Test, (b) Long duration model, (c) Short duration model

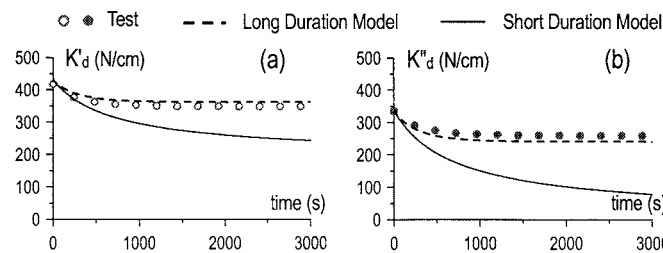


Figure 7 Comparison of K'_d , K''_d with test, long duration model and short duration model.

3. FAST ALGORITHM FOR FRACTIONAL DERIVATIVE

3.1 Concept of Fast Algorithm for Fractional Derivative

The numerical integration method of the fast algorithm for fractional derivative, which is proposed

in this study, is carried out at every time step Δt , therefore the integration points used in the integration are selected and stored every certain interval, which is so-called " skip interval L ". Thus, this method can reduce drastically not only the calculation time but also the memory space. Figure 8 depicts the concept of the fast algorithm for fractional derivative, using $L = 5$ for example.

Figure 8(a) shows $n \leq L$ case ($n = 3$). When $n = 3$, the stored data $y^{(0)}, y^{(1)}, y^{(2)}$ and this step's data $y^{(3)}$ are used by the integration of the fractional derivative $D^\alpha y^{(3)}$. Then the above operation continues and all the data are stored until $n = L$.

Figure 8(b) presents $L < n \leq 2L$ case ($n = 8$). When $n = 8$, the stored data $y^{(3)}$, which is data of L^{th} step before, and this step's data $y^{(8)}$ are only used by the integration of the fractional derivative $D^\alpha y^{(8)}$. Then the above operation continues until $n = 2L = 10$. Only $y^{(0)}, y^{(5)}, y^{(10)}$ are stored when 10^{th} step's calculation is done. After that, the data are stored every L steps.

Figure 8(c) shows $n > 2L$ case ($n = 13$). When $n = 13$, the data $y^{(3)}$ and $y^{(8)}$, which are calculated by the linear interpolation using the stored data $y^{(0)}, y^{(5)}, y^{(10)}$, respectively, and this step's data $y^{(13)}$ are only used by the integration of the fractional derivative $D^\alpha y^{(13)}$.

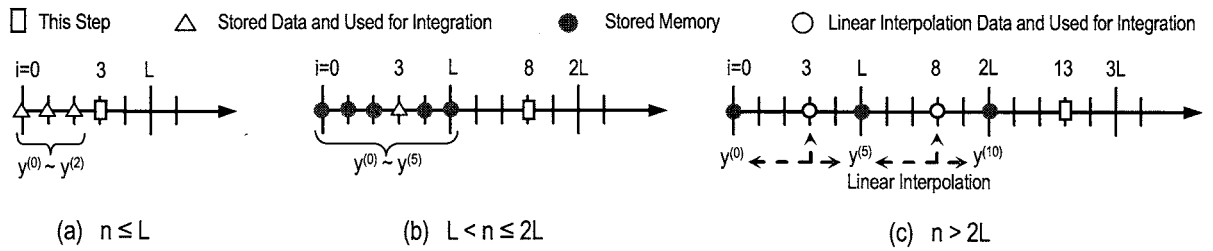


Figure 8 Concept of the fast algorithm of the fractional derivative ($L = 5$ for example)

The general formula of n^{th} step's integration of the fractional derivative $D^\alpha y^{(n)}$, as shown in Figure 9, can be expressed by Eq. (12).

$$D^\alpha y^{(n)} = w^{(0)} y^{(n)} + \{MQ + (L-M)Q'\} / L \quad (12)$$

where, $w^{(i)}$ ($i = 0 \sim N$) which is the weight function considering the skip interval L , and Q, Q' are calculated by Eq. (13), respectively.

$$w^{(i)} = w^{(i)} / L^\alpha, \quad Q = \sum_{i=1}^{N'} w^{(i)} y^{(n'L - iL + L)}, \quad Q' = \sum_{i=1}^{N'} w^{(i)} y^{(n'L - iL)} \quad (13a-c)$$

here,

$$n' = \text{integer}[(n-1)/L], \quad M = n - n'L, \quad N' = N/L = 1.5T/(L\Delta t) \quad (14a-c)$$

Q in Eq. (13b) is calculated every L steps only, thus, as the skip step L grows larger, the calculation time becomes shorter. In addition, Q' in Eq. (13c) is the same as Q which is calculated at L step before, so we do not need to calculate new Q' .

In case of $n \leq L$, $L = 1$ is substituted into Eq. (12), (13), (14a), (14b) and N' is replaced by n . In case of $L < n \leq 2L$, $N' = 1$ and $M = L$ are substituted into Eq. (12), (13b) respectively, and $n' = (n/L) - 1$ is used instead of Eq. (14a). In case of $2L < n < NL'$, N' is replaced by n' in Eq. (13a)

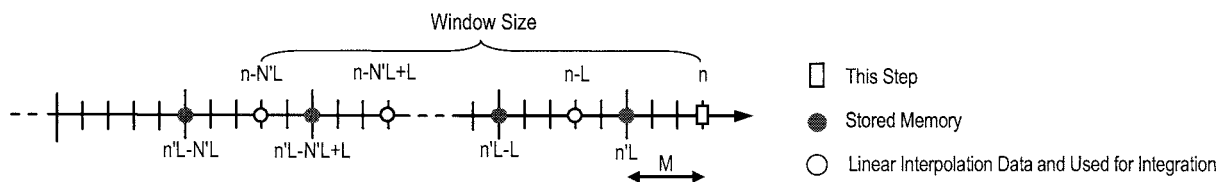


Figure 9 Concept of the fast algorithm of the fractional derivative at n^{th} step ($n > N'L$)

3.2 Application of Fast Algorithm to Long Duration Model

By using the fast algorithm of fractional derivative as shown in Eq. (12), the long duration model integration scheme, which is shown in Eq. (4), is written as in Eq. (15).

$$\tau^{(n)} + a_j \sum_{i=0}^{N'} w'^{(i)} \tau^{(n-iL)} = G \left[\gamma_j^{(n)} + b_j \sum_{i=0}^{N'} w'^{(i)} \gamma_j^{(n-iL)} \right] \quad (15)$$

where

$$\sum_{i=0}^{N'} w'^{(i)} \gamma_j^{(n-iL)} = w'^{(0)} \gamma_j^{(n)} + \{MR_j + (L-M)R'_j\}/L \quad (16a)$$

$$\sum_{i=0}^{N'} w'^{(i)} \tau^{(n-iL)} = w'^{(0)} \tau^{(n)} + \{MS + (L-M)S'\}/L \quad (16b)$$

here, R_j , R'_j , S , S' are respectively expressed as follows;

$$R_j = \sum_{i=1}^{N'} w'^{(i)} \gamma_j^{(n'L-iL+L)}, \quad R'_j = \sum_{i=1}^{N'} w'^{(i)} \gamma_j^{(n'L-iL)}, \quad S = \sum_{i=1}^{N'} w'^{(i)} \tau^{(n'L-iL+L)}, \quad S' = \sum_{i=1}^{N'} w'^{(i)} \tau^{(n'L-iL)} \quad (17a-c)$$

As mentioned above, R'_j and S' are the same as R_j and S which are respectively calculated at L step before, so we do not need to calculate new R'_j and S .

Then, by substituting Eq. (16), (17) into Eq. (15), strain $\gamma_j^{(n)}$ is expressed by Eq. (18).

$$\gamma_j^{(n)} = \frac{\tau^{(n)} (1 + a_j w'^{(0)}) + \tilde{A}_j - \tilde{B}_j}{G(1 + b_j w'^{(0)})} \quad (18)$$

where,

$$\tilde{A}_j = \frac{a_j \{MS + (L-M)S'\}}{L}, \quad \tilde{B}_j = \frac{Gb_j \{MR_j + (L-M)R'_j\}}{L} \quad (19a,b)$$

In addition, stress $\tau^{(n)}$ is calculated by Eq. (20).

$$\tau^{(n)} = \left\{ 2Gu_d^{(n)} - \sum_{j=j_1}^{j_2} \frac{\zeta_j (\tilde{A}_j - \tilde{B}_j)}{1 + b_j w'^{(0)}} \right\} / \sum_{j=j_1}^{j_2} \frac{\zeta_j (1 + a_j w'^{(0)})}{1 + b_j w'^{(0)}} \quad (20)$$

By substituting $\tau^{(n)}$, which is obtained from Eq. (20), into Eq. (18), strain at j $\gamma_j^{(n)}$ can be obtained.

3.3 Comparison between Original Algorithm and Fast Algorithm for Long Duration Model

The original algorithm, which is shown in chapter 2, and the fast algorithm are compared. In this section, the analytical condition of the original algorithm is $t/\Delta t = 1,000$, $N = 1,500$. On the other hand, the analytical condition of the fast algorithm is $t/\Delta t = 1,000$ and the skip step L is 1, 2, 10, 50, 100. Then, $N' = 150$ in the fast algorithm when $L = 10$.

Figure 10 shows only the 1st and 1,000th cycle's damper deformation u_d – force F_d hysteresis loop for comparing the original and the fast algorithm. The results obtained from the fast algorithm analysis are in good agreement with the original algorithm analysis results if the skip interval L is small than 10, however, as L grows larger, the accuracy of the fast algorithm results decreases.

Figure 11 shows the temperature time history at each measurement points of the VE damper (See Figure 4) which are calculated by the original algorithm and by the fast algorithm when $L = 10$ and 100. For $L = 10$, the temperature which is obtained from the fast algorithm analysis matches well with the original algorithm result; whereas, for $L = 100$, the temperature obtained by the fast algorithm analysis is smaller than the original results.

The comparison of $F_{d,max}$, $F_{d,min}$, energy, and the calculation time is shown in Table 1. When L

increases, for example $L=10$, the calculation time decreases drastically. However, even if L gets larger over $L=10$, such as $L=50$ or 100 , the calculation time is almost similar with the $L=10$ case. In addition, the accuracy of the fast algorithm in case of $L=50$ or 100 decreases drastically. Finally, these results lead us to the conclusion that the skip interval L should be decided as the number of integration have over 100 points per 1cycle, and $N' \geq 150$ in order to obtain the accurate calculation results.

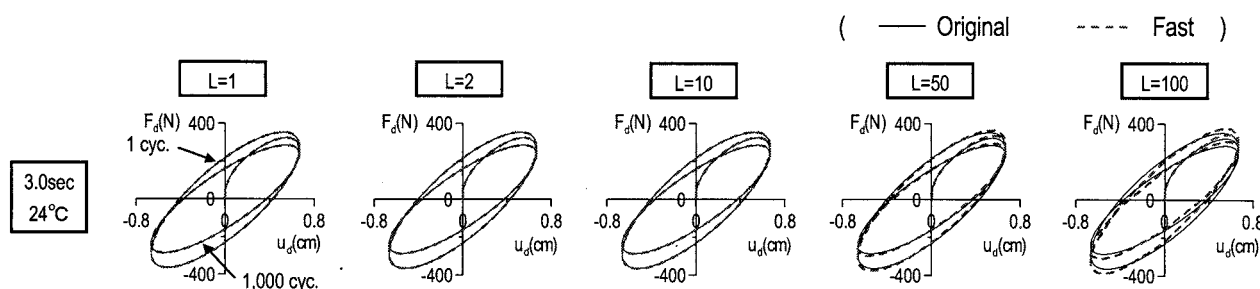


Figure 10 Comparison of the hysteresis loop with the original and the fast algorithm

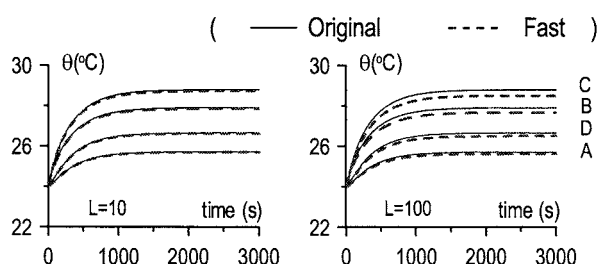


Figure 11 Comparison of temperature with the original and the fast algorithm

Table 1 Comparison with the original and the fast algorithm (Fast / Original)

	L=1	L=2	L=10	L=50	L=100
$F_{d,max}$	1.000	1.000	1.005	1.032	1.067
$F_{d,min}$	1.000	1.000	1.004	1.029	1.064
Energy	1.000	1.000	0.999	0.985	0.937
Cal. Time	1.035	0.323	0.139	0.132	0.131

4. CONCLUSIONS

This paper proposed the one-dimensional non-linear hysteretic model of VE damper considering heat conduction and heat transfer. Good accuracy of these analysis methods are demonstrated by comparing with the test results of experiments that used cyclic loading of long duration. This model can be used for design of the VE damper and / or the building having VE damper under the long duration force such as the wind force.

In addition, the fast and sufficiently accurate algorithm for calculating fractional time-derivatives of stress and strain in the viscoelastic damper is proposed, and this algorithm can reduce not only the calculation time but also the memory space.

References:

- Kasai, K., Munshi, J.A., Lai, M.-L., and Maison, B.F. (1993), "Viscoelastic Damper Hysteresis Model", Theory, Experiment, and Application ATC17-1 Seminar, Applied Technology Council, Vol1.2, pp.521-532, Mar.
- Kasai, K., Teramoto, M., Okuma, K., and Tokoro, K. (2001), "Constitutive Rule for Viscoelastic Materials Considering Temperature and Frequency Sensitivity (Part1: Linear Model with Temperature and Frequency Sensitivities)", *Journal of Structural and Construction Engineering (Transactions of AIJ)*, No. 543, pp. 77-86, May. (in Japanese)
- Kasai, K., Sato, D., Huang, Y. (2006a), "Analytical Methods for Viscoelastic Damper Considering Heat Generation, Conduction, and Transfer Duration Cyclic Load", *Journal of Structural and Construction Engineering (Transactions of AIJ)*, No. 599, pp. 61-69, Jan. (in Japanese)
- Kasai, K., Sato, D. (2006b), "Fast Algorithm for Fractional Derivative Constitutive Rule of Viscoelastic Damper", *Journal of Structural and Construction Engineering (Transactions of AIJ)*, No. 606, pp. 113-121, Aug. (in Japanese)

SEISMIC PERFORMANCE EVALUATION OF EXISTING R/C BUILDINGS WITH HYSTERESIS DAMPERS BASED ON ENERGY BALANCED RESPONSE

K. Fujii¹⁾, H. Kitamura²⁾

1) *Research Associate, Department of Architecture, Tokyo University of Science, Japan*

2) *Professor, Department of Architecture, Tokyo University of Science, Japan*

kfujii@rs.noda.tus.ac.jp, kita-h@rs.noda.tus.ac.jp

Abstract: It is well accepted that the existing R/C buildings with brittle members are vulnerable to earthquakes, and therefore the seismic rehabilitation of those buildings is important issue. In this paper, seismic performance of existing R/C buildings with hysteresis dampers is discussed based on energy response. The seismic upgrading ratio, which is equal to the structural seismic capacity index (Is-Index) of rehabilitated building divided by that of original building, is formulated based on energy balanced response. The nonlinear time-history analysis results shows the proposed equations can be satisfactorily estimated the seismic performance of existing R/C buildings with hysteresis dampers.

1. INTRODUCTION

It is well accepted that the existing R/C buildings with brittle members are vulnerable to earthquakes. Since the 1995 Hyogoken-nanbu Earthquake has caused serious damage in many existing R/C building designed before 1981, the seismic rehabilitation of those buildings is an important issue. The most common rehabilitation schemes employed for R/C buildings are the infill of new R/C wall and steel framed braces (Nakano 2004). However, the seismic rehabilitation scheme using energy dissipative dampers has been also studied for R/C buildings in recent years (ex. Lobo et al, 1993, Dolce et al, 2005).

The main point of the seismic rehabilitation scheme using energy dissipative dampers is to dissipate the most of seismic energy input by dampers to minimize cumulative damage of existing members and to reduce the floor acceleration and/or story drift. Therefore it is essential to discuss the seismic performance of such buildings with dampers based on the energy balanced response.

In this paper, seismic performance of existing R/C buildings with hysteresis dampers is discussed based on energy response. The seismic upgrading ratio, which is defined as the ratio of the structural seismic capacity index (Is-Index) of rehabilitated building to that of original building, is formulated based on energy balanced response.

2. FORMULATION OF SEISMIC PERFORMANCE OF R/C BUILDINGS WITH DAMPERS BASED ON ENERGY BALANCED RESPONSE

The seismic upgrading ratio of the building rehabilitated by energy dissipative dampers, α , is defined as equation (1).

$$\alpha = {}_R Is / {}_O Is \quad (1)$$

Where ${}_O I_s$ and ${}_R I_s$ are the seismic structural capacity index (I_s) of original/rehabilitated building. Since the I_s -index can be interpreted as the index related to the ground motion intensity which causes the response equal to the ultimate displacement of original/rehabilitated building, the ratio α can be considered as the ratio of the ground motion intensity. In this paper, the ground motion intensity is defined by energy spectrum (V_E Spectrum), and the ratio α is formulated base on energy balanced response (Akiyama, 1985, Akiyama, 1999).

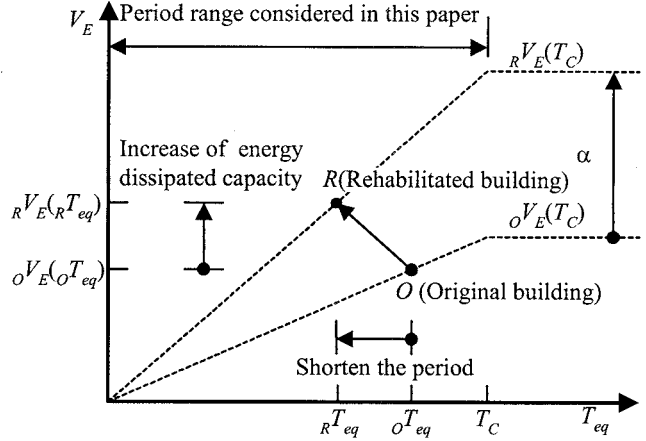


Figure 1 Idealized V_E Spectrum

Fig. 1 shows the idealized V_E spectrum.

Assuming the building considered in this study is within the short-period range and V_E is proportional to the natural period T , Eq. (1) can be rewritten as Eq. (2).

$$\alpha = \frac{{}_R I_s}{{}_O I_s} = \frac{{}_R V_E(T_C)}{{}_O V_E(T_C)} = \frac{{}_O T_{eq}}{R T_{eq}} \frac{{}_R V_E(R T_{eq})}{{}_O V_E(O T_{eq})} \quad (2)$$

Where ${}_O V_E(T)$ and ${}_R V_E(T)$ are V_E spectra of the ground motion which cause response displacement equal to the ultimate displacement of original/rehabilitated buildings at period T , T_C is the corner period (boundary period of the range where V_E is proportional to T and V_E is independent with T), ${}_O T_{eq}$ and ${}_R T_{eq}$ are the equivalent period of original/rehabilitated building. The equation of energy balance of original/rehabilitated buildings can be expressed as Eq. (3), assuming the mass of the building M remains unchanged due to rehabilitation.

$${}_O W + {}_O W_h = {}_O E_I = M {}_O Y_E({}_O T_{eq})^2 / 2, {}_R W + {}_R W_h = {}_R E_I = M {}_R Y_E({}_R T_{eq})^2 / 2 \quad (3)$$

Where ${}_O W$ and ${}_R W$ are the total strain energy (elastic strain energy + cumulative plastic strain energy) of original/rehabilitated building, ${}_O W_h$ and ${}_R W_h$ are the dissipated energy due to damping of existing members of original/rehabilitated building, and ${}_O E_I$ and ${}_R E_I$ are the input seismic energy. Assuming that ${}_R W_h$ is equal to ${}_O W_h$ for the simplicity, Eq. (4) can be obtained from Eq. (3).

$$\frac{{}_R V_E({}_R T_{eq})}{{}_O V_E({}_O T_{eq})} = \sqrt{1 + \frac{{}_R W - {}_O W}{{}_O W + {}_O W_h}} \quad (4)$$

Substituting Eq. (4) into Eq. (2), the seismic upgrading ratio of the building rehabilitated by energy dissipative dampers, α , can be expressed as Eq. (5).

$$\alpha = \frac{{}_R I_s}{{}_O I_s} = \frac{{}_O T_{eq}}{R T_{eq}} \sqrt{1 + \frac{{}_R W - {}_O W}{{}_O W + {}_O W_h}} \quad (5)$$

Eq. (5) is the seismic upgrading ratio of the building for the general case. In this chapter, the idealized single-degree-of-freedom (SDOF) model consists of existing brittle R/C members dominated by shear and hysteresis dampers is discussed as follows. Fig. 2 shows the idealized SDOF model. The equation of energy balance of SDOF model can be expressed as Eq. (6).

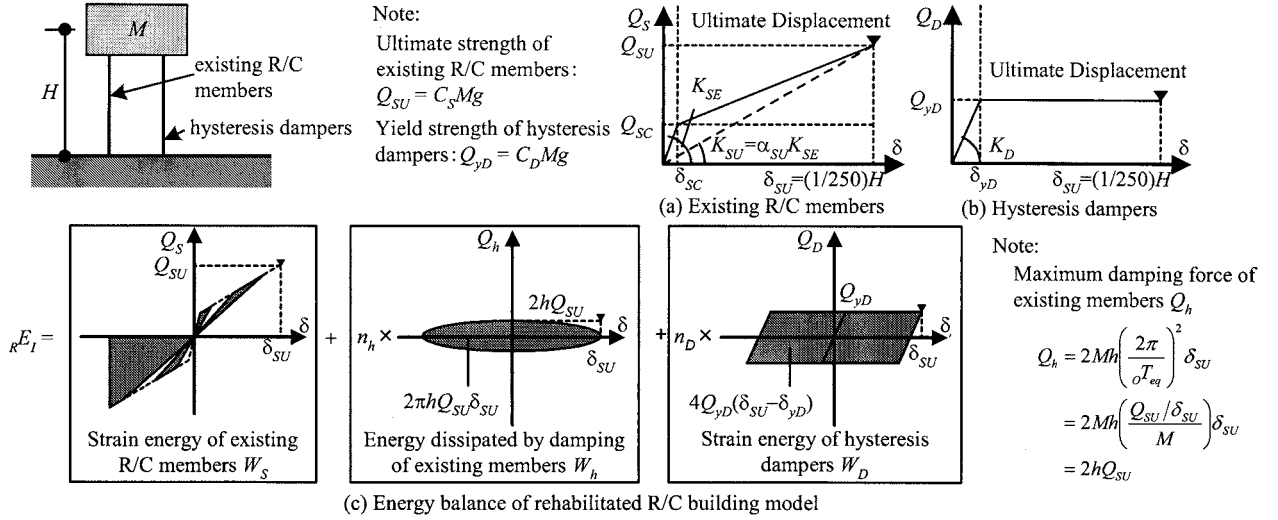


Figure 2 Energy Balanced Response of Idealized SDOF Model

$$W_S + W_h = {}_O E_I = M \gamma_E^2 ({}_O T_{eq})^2 / 2, W_S + W_D + W_h = {}_R E_I = M \gamma_E^2 ({}_R T_{eq})^2 / 2 \quad (6)$$

Where $W_S = W_{eS} + W_{pS}$: strain energy of existing R/C members dominated by shear (elastic strain energy W_{eS} + plastic strain energy W_{pS}), $W_D = W_{eD} + W_{pD}$: strain energy of hysteresis dampers (elastic strain energy W_{eD} + plastic strain energy W_{pD}), W_h : dissipated energy due to damping of existing members. Assuming that the hysteresis rule of existing members is the origin-oriented model (Shiga, 1976, Otani, 2002), W_S can be written as Eq. (7).

$$W_S = W_{eS} + W_{pS} = \frac{1}{2} \{ Q_{SC} \delta_{SC} + (Q_{SC} + Q_{SU}) (\delta_{SU} - \delta_{SC}) \} = \frac{1}{2} \gamma_S C_S Mg \delta_{SU} \quad (7)$$

$$\gamma_S = \{ 1 + (1 - \alpha_{SU}) (Q_{SC} / Q_{SU}) \} \quad (8)$$

Where $g (= 9.8 \text{ m/s}^2)$ is the gravity acceleration. The dissipated energy due to damping of existing members W_h can be written as Eq. (8), assuming n_h is the equivalent number of cycle for damping.

$$W_h = n_h \times 2\pi h Q_{SU} \delta_{SU} = n_h \times 2\pi h C_S Mg \delta_{SU} \quad (9)$$

Where h is the damping ratio of the existing R/C members and taken as 0.05. As shown by Akiyama (Akiyama, 1999), the equivalent number of cycle for damping n_h may be taken as 3 for elastic system. Therefore assuming that n_h can be taken as 3, Eq. (9) can be rewritten as Eq. (10).

$$W_h = 6\pi h C_S Mg \delta_{SU} \quad (10)$$

The strain energy of hysteresis dampers W_D can be approximated as shown in Eq. (11), assuming n_D is the equivalent number of cycle for hysteresis dampers and neglecting elastic strain energy W_{eD} .

$$W_D \approx W_{pD} = 4n_D \times Q_{yD} (\delta_{SU} - \delta_{yD}) = 4n_D \times C_D Mg \left(1 - \frac{\delta_{yD}}{\delta_{SU}} \right) \quad (11)$$

The equivalent period of original/rehabilitated model, ${}_O T_{eq}$ and ${}_R T_{eq}$, respectively, are assumed to be determined from the secant stiffness of ultimate displacement and expressed as Eq. (12).

$${}_oT_{eq} = 2\pi \sqrt{\frac{M}{Q_{SU}/\delta_{SU}}} = 2\pi \sqrt{\frac{\delta_{SU}}{C_S g}}, {}_RT_{eq} = 2\pi \sqrt{\frac{M}{(Q_{SU} + Q_{yD})/\delta_{SU}}} = 2\pi \sqrt{\frac{\delta_{SU}}{(C_S + C_D)g}} \quad (12)$$

Substituting Eqs. (7) to (10) into Eq. (6) and from Eq. (2), the seismic upgrading ratio of the building rehabilitated by energy dissipative dampers, α , for the idealized SDOF model consists of existing brittle R/C members and hysteresis dampers can be expressed as Eq. (13).

$$\alpha = \frac{{}_R I_s}{{}_o I_s} = \sqrt{1 + \frac{C_D}{C_S}} \sqrt{1 + \frac{C_D}{C_S} \frac{8n_D}{\gamma_S + 12\pi h} \left(1 - \frac{\delta_{yD}}{\delta_{SU}}\right)} \quad (13)$$

3. NUMERICAL ANALYSIS OF SDOF MODEL

3.1 Description of SDOF Model

The building model considered in this paper is as shown in Fig. 2: the mass M is assumed 1000ton, the height of the model, H , is assumed 3.75m and 11.25m, respectively. The ultimate strength of existing R/C members, Q_{SU} , is assumed $0.4 \times Mg$, and the crack strength of R/C members, Q_{SC} is one-third of Q_{SU} , and the ratio of the secant stiffness to the initial stiffness of existing R/C members, α_U is assumed 0.2. The ultimate displacement of existing R/C members, δ_{SU} , is assumed $(H/250)$. The initial periods of model are 0.174s and 0.301s, respectively

The parameters of the model are (1) ratio of the yield strength of hysteresis dampers to the ultimate strength of existing R/C members, and (2) yield displacement of hysteresis dampers. Firstly, the ratio of the yield strength of hysteresis dampers Q_{yD} to the ultimate strength of existing R/C members Q_{SU} , equals to C_D / C_S , is assumed 0.0 to 0.5 with an interval of 0.05. Secondly, the yield displacement of hysteresis dampers, δ_{yD} , is assumed $(H/500)$, $(H/750)$, $(H/1000)$, $(H/1250)$, and $(H/1500)$, respectively. Therefore, total $2 \times 11 \times 5 = 110$ models are investigated in this analysis.

3.2 Ground Motion Data

In this study, five of artificial ground motions are used. The first 60 seconds of the following records are used to determine phase angles of the ground motion: El Centro 1940 NS (referred to as ELC), Taft 1952 EW (TAF), Hachinohe 1968 EW (HAC), Tohoku University 1978 NS (TOH), and JMA Kobe 1995 NS (JKB). Target V_E spectrum with 10% of critical damping $V_E(T)$ is defined as Equation (14):

$$V_E(T) = \begin{cases} 1.784 \cdot T & \text{m/s} \quad T < 0.96\text{s} \\ 1.713 & T \geq 0.96\text{s} \end{cases} \quad (14)$$

Table 1 shows the list of artificial ground motion used in this study, and elastic V_E spectrum with 10% of critical damping and the elastic acceleration response spectrum S_A of artificial ground motions with 5% of critical damping are shown in Fig. 3. From Eq. (14), S_A of artificial ground motions with 5% of critical damping can be expressed as Eq. (15), and S_A expressed by Eq. (15) is also shown in Fig. 3(b).

$$S_A(T, 0.05) = \frac{1}{\sqrt{1 + 12 \times 0.05\pi}} V_E(T) = \begin{cases} 6.615 & \text{m/s}^2 \quad T < 0.96\text{s} \\ 6.350/T & T \geq 0.96\text{s} \end{cases} \quad (15)$$

Table 1 List of Artificial Ground Motions

Record ID	Artificial Ground Motion ID	Max. Acc. A_0 (m/s ²)	Max. Vel. V_0 (m/s)
ELC	Art-ELC	3.024	0.614
TAF	Art-TAF	2.935	0.591
HAC	Art-HAC	2.526	0.587
TOH	Art-TOH	2.777	0.779
JKB	Art-JKB	4.639	0.749

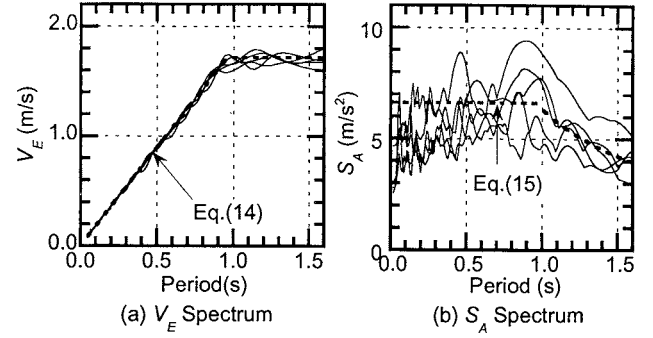


Figure 3 V_E Spectrum and S_A Spectrum of Artificial Ground Motions

3.3 Numerical Analysis Procedure

In this study, the damping is assumed proportional to the instant stiffness of existing R/C members and 5% of the critical damping. Newmark- β method ($\beta = 1/4$) is applied in numerical integrations. The time increment for numerical integration is 0.005 sec. The unbalanced force due to stiffness change is corrected at a next time step during analysis. The input ground motions are scaled for each model so that the maximum displacement reaches the ultimate displacement of existing R/C members.

3.4 Analysis Results

The equivalent number of cycles for hysteresis dampers, n_D , can be obtained by Eq. (16), based on the time-history analysis results.

$$n_D = \frac{W_D}{4Q_{yD}(\delta_{SU} - \delta_{yD})} \quad (16)$$

Fig. 4 shows the relation of the equivalent number of cycles for hysteresis dampers n_D and the ratio of yield strength of dampers to ultimate strength of existing R/C members (C_D/C_S). Akiyama (1999) has investigated about the system consisting of stiff elasto-plastic element (stiff element) and flexible elastic element (flexible element). He had concluded that the minimum value of n_D can be taken as 2 if the ratio $r_Q (= f_{Qmax}/s_{Qy})$, where f_{Qmax} : maximum restoring force of flexible element, s_{Qy} : the yield strength of stiff element) is larger than 1.0. Since the existing R/C members and the hysteresis dampers can be considered as flexible and stiff element, respectively, so the ratio (C_D/C_S) corresponds to ($1/r_Q$); therefore, the analysis cases investigated in this paper can be considered as r_Q is larger than 2. As shown in Fig. 4, n_D tends to decrease as (C_D/C_S) increases; in Fig. 4(a) ($\delta_{yD} = H/500$), n_D is lower than 1.0 in case of (C_D/C_S) < 0.2. Similar trends can be found in Fig. 4 (b) to (e), although the minimum of n_D tends to be larger as the yield displacement of hysteresis damper δ_{yD} becomes smaller. This implies that δ_{yD} should be smaller as possible

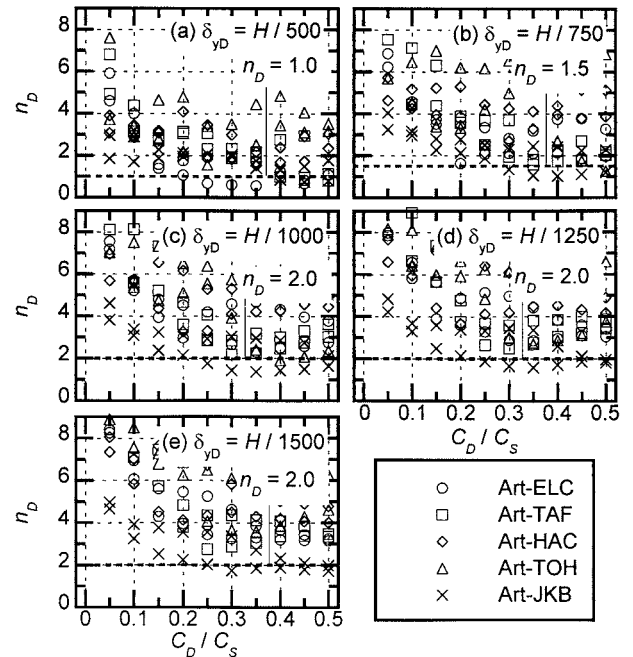


Figure 4 Relation of n_D and (C_D/C_S)

for the efficient seismic rehabilitation using hysteresis dampers.

Fig. 5 shows the relation n_D of and δ_{SU}/δ_{yD} . As shown in this figure, the minimum value of n_D can be expressed as Eq. (17) in case of $(C_D/C_S) \leq 0.5$.

$$n_D = \begin{cases} 0.5(\delta_{SU}/\delta_{yD}) & 2 \leq (\delta_{SU}/\delta_{yD}) \leq 4 \\ 2 & \delta_{SU}/\delta_{yD} \geq 4 \end{cases} \quad (17)$$

Fig. 6 shows the relation of the seismic upgrading ratio of the building rehabilitated by energy dissipative dampers, α , and the ratio of (C_D/C_S) . In this figure, the estimated results using Eqs. (13) and (17) are also shown. As shown in this figure, the estimation results from Eqs. (13) and (17) are conservative and approximated the lower bound of time-history analysis results.

4. APPLICATION TO EXISTING R/C BUILDING REHABILITATED BY ENERGY-DISSIPATIVE BRACES

In this chapter, the seismic upgrading ratio of the buildings rehabilitated by energy dissipative dampers discussed above is applied to the five-story R/C building rehabilitated by using hysteresis dampers.

Figs. 7 and 8 show the elevation of the building in longitudinal direction and the energy dissipative braces used as dampers for seismic rehabilitation (Ishii et al, 2006), respectively. This building was designed in 1970 as an apartment building; the design concrete strength was 21MPa, and SR295 and SR235 were used for the longitudinal and transverse reinforcement. Since the minimum I_s -index of the building obtained according to the second screening method (JBDPA, 2001) is 0.44 (2nd story) $< I_{s0} = 0.6$, the seismic rehabilitation is needed. Note that this building has enough seismic capacity in transverse direction (not shown in this paper).

The seismic rehabilitation scheme of this building is as shown in Fig. 7; the concept of seismic rehabilitation design is that the most of seismic energy input is dissipated by dampers located in the first and the second stories. Table 2 shows the rehabilitation design criteria, under seismic excitation scaled as the maximum velocity V_0 is 0.5m/s. Twenty-six buckling-restrained tube-in-tube energy dissipative braces using low-yield strength steel ($\sigma_y = 100\text{MPa}$) are installed as dampers in all stories

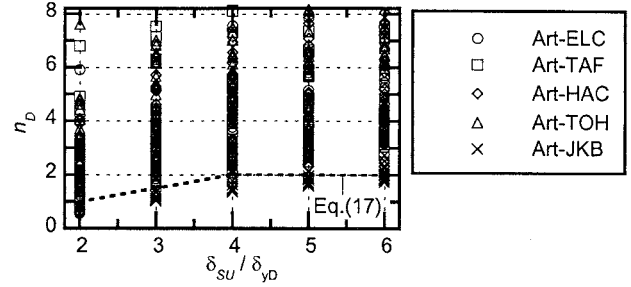


Figure 5 Relation of n_D and (C_D/C_S)

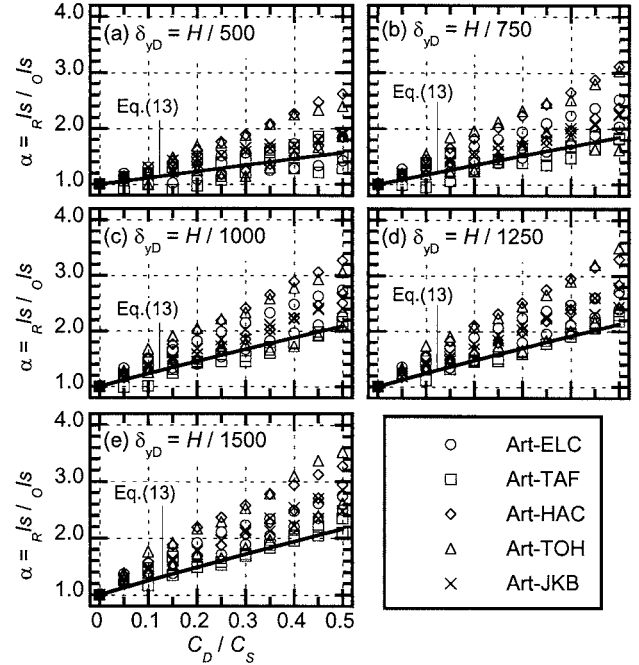


Figure 6 Relation of $\alpha (=R/I_s / O/I_s)$ and (C_D/C_S)

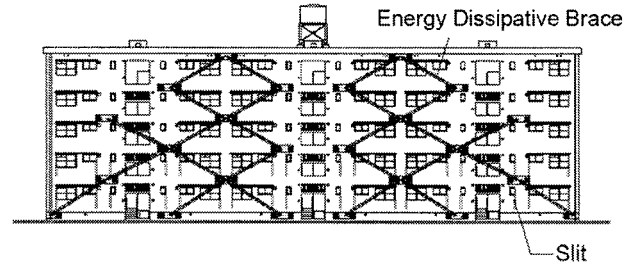


Figure 7 Elevation of Existing R/C building

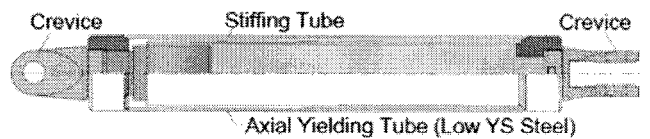


Figure 8 Energy Dissipative Braces

so that ultimate story shear coefficient in all stories are larger than 0.6. Slits are installed at all columns in the first and the second story of the frame shown in Fig. 7, to improve the drift capacity of those stories.

The seismic upgrading ratio is calculated from Eq. (5) based on pushover analysis. Fig. 9 shows the pushover curve of the original/rehabilitated buildings. The pushover analysis of original building was carried out until one of the existing members fails by shear as shown in Fig. 9(a). The equivalent period ${}_oT_{eq}$, the total strain energy ${}_oW$, and the dissipated energy due to damping of existing members ${}_oW_h$ were calculated from Eqs. (18) and (19), respectively.

$${}_oT_{eq} = 2\pi \sqrt{\sum_i (m_i \cdot {}_o d_{Ui}^2) / \sum_i ({}_o P_{Ui} \cdot {}_o d_{Ui})} \quad (18)$$

$${}_oW = \sum_i \int_0^{{}_o \delta_{Ui}} {}_o Q_i d {}_o \delta_i, {}_o W_h = 6\pi h \sum_i {}_o Q_{Ui} \cdot {}_o \delta_{Ui} \quad (19a, b)$$

Where ${}_o P_{Ui}$, ${}_o d_{Ui}$ are the horizontal force and displacement of i -th floor at ultimate step, when the one of the members fails by shear, m_i is floor mass, ${}_o Q_i$, ${}_o \delta_i$ are the story shear force and story drift of i -th story, respectively, and ${}_o Q_{Ui}$, ${}_o \delta_{Ui}$ are the story shear force and story drift of i -th story at ultimate step, respectively. The damping ratio h is assumed 0.05.

The pushover analysis of rehabilitated buildings were carried out until the drift at one of the stories reaches at drift capacity, as shown in Fig. 9(b). The equivalent period ${}_RT_{eq}$, the total strain energy ${}_RW$ were calculated from Eqs. (20), (21).

$${}_RT_{eq} = 2\pi \sqrt{\sum_i (m_i \cdot {}_R d_{Ui}^2) / \sum_i ({}_R P_{Ui} \cdot {}_R d_{Ui})}, {}_RW = {}_RW_F + {}_RW_D \quad (20a, b)$$

$${}_RW_F = \sum_i \int_0^{{}_R \delta_{Ui}} {}_R Q_{Fi} d {}_R \delta_i, {}_RW_D = 4n_D \sum_i {}_R Q_{yDi} \cdot ({}_R \delta_{Ui} - {}_R \delta_{yDi}) \quad (21a, b)$$

Where ${}_R P_{Ui}$, ${}_R d_{Ui}$ are the horizontal force and displacement of i -th floor at ultimate step, ${}_RW_F$ and ${}_RW_D$ are the strain energy of the existing R/C frames and dampers, respectively, ${}_R Q_{Fi}$, ${}_R \delta_i$ are the shear force of R/C frames and story drift of i -th story, respectively, and ${}_R \delta_{Ui}$ is the story drift of i -th story at ultimate step. The yield damper shear force and the story drift at yielding of dampers of i -th story, ${}_R Q_{yDi}$ and ${}_R \delta_{yDi}$ are determined by bi-linear idealization of damper shear force ${}_R Q_{Di}$ - story drift ${}_R \delta_{Di}$ relationship. The equivalent number of cycles for hysteresis dampers n_D is assumed 2.

From Eqs. (18) and (19), equivalent period ${}_oT_{eq}$, total strain energy ${}_oW$, and the dissipated energy due to damping of existing members ${}_oW_h$ are obtained as 0.427s, 109.4kNm and 148.7kNm, respectively, and from Eqs. (20) and (21), equivalent period ${}_RT_{eq}$, total strain energy ${}_RW$ are obtained as

Table 2 Rehabilitation Criteria

Story	Story Drift	Max. Ductility of existing R/C member	
		Flexure	Shear
5	< 1/800	< 1.0	< 1.0
3, 4	< 1/400		
2, 1	< 1/200	< 1.0 (Column)	
		< 2.0 (Beam)	

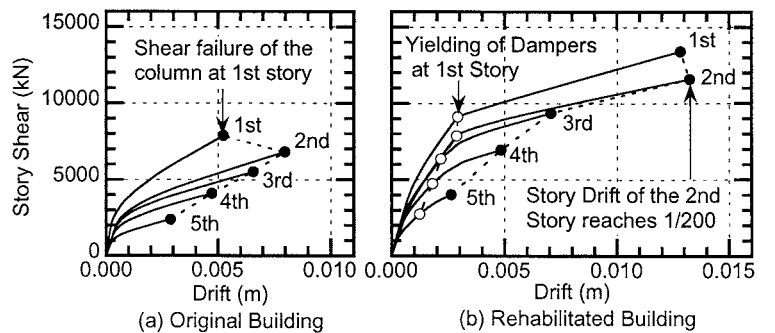


Figure 9 Pushover Curve of Original/Rehabilitated Buildings

0.415s and 1106kNm, respectively. Therefore, the seismic upgrading ratio of the building α is obtained from Eq. (5).

$$\alpha = \frac{R}{o} \frac{I_s}{I_s} = \frac{0.427}{0.415} \sqrt{1 + \frac{1106 - 109.4}{109.4 + 148.7}} = 2.27$$

Fig. 10 shows the maximum story drift of original/rehabilitated buildings obtained from nonlinear dynamic analysis; the input ground motions are ELC, HAC and TOH scaled as $V_0 = 0.5\text{m/s}$. As shown in this figure, the story drift of original building exceed the rehabilitation criteria; in case of TOH input, the drift at the 2nd story exceeds 1/50. For rehabilitated building, the story drift of all stories are within the rehabilitation criteria; no shear and flexural failure is occurred for all input ground motions.

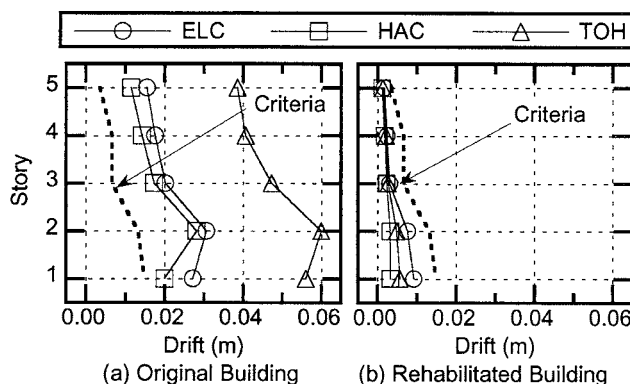


Figure 10 Maximum Story Drift of Original/Rehabilitated Building

5. CONCLUSIONS

In this paper, the seismic upgrading ratio, which is defined as the ratio of the structural seismic capacity index (I_s -Index) of rehabilitated building to that of original building, is formulated based on energy balanced response. The nonlinear dynamic analysis results show that those equations formulated in this paper provides the conservative estimation of the seismic upgrading ratio of buildings rehabilitated by hysteresis dampers.

Acknowledgements:

This paper is the part of the results of joint-research project by JFE Civil Engineering and Construction Corporation, JFE Steel Corporation and Tokyo University of Science entitled "Study on Seismic Rehabilitation for Existing R/C Building Using Energy Dissipative Braces". The drawings and materials of existing R/C apartment buildings were provided from Hyogo Prefecture Office. The authors would like to express their thanks to the people engaged in this research.

References:

- Nakano, Y. (2004), "Seismic Rehabilitation of School Buildings in Japan", *Journal of Japan Association for Earthquake Engineering*, Vol. 4, No. 3, 218-229.
- Lobo, R. F., Bracci, J. M., Shen K.L., Reinhorn, A. M., and Soong, T. T. (1993), "Inelastic Response of R/C Structures with Viscoelastic Braces", *Earthquake Spectra*, Vol. 9, No. 3, 419-446.
- Dolce, M., Cardone, D., Ponzo, F. C., and Valente, C. (2005), "Shaking Table Tests on Reinforced Concrete Frames without and with Passive Control Systems", *Earthquake Engineering and Structural Dynamics*, Vol. 34, 1687-1717.
- Akiyama, H. (1985), "Earthquake-Resistant Limit-State Design of Buildings", Second Edition, University of Tokyo Press
- Akiyama, H. (1999), "Earthquake-Resistant Design Method for Buildings Based on Energy Balance", Giho-do Shuppan, (in Japanese)
- Shiga, T. (1976), "Vibration of Structures", Structural Series, Vol. 2, Kyoritu Shuppan, (in Japanese)
- Otani, S. (2002), "Nonlinear Earthquake Response Analysis of Reinforced Concrete Buildings", Lecture Note, Department of Architecture, Graduate School of Engineering, University of Tokyo
- Ishii, T., Fujisawa, K., Shimizu, T., and Miyagawa, K. (2006), "Seismic Retrofitting for Existing R/C Buildings Using Buckling-Restrained Tube-in-Tube Energy Dissipative Braces", *JFE Technical Report*, No. 8, 63-70
- JBDPA/The Japan Building Disaster Prevention Association (2001), "Guideline for Seismic Capacity Evaluation of Existing Reinforced Concrete Building" (in Japanese)

CUMULATIVE DAMAGE OF DAMPER IN ELASTO-PLASTICALLY DAMPED BUILDINGS

H. Ito¹⁾ and K. Kasai²⁾

1) Post-Doctoral Research Fellow, Center for Urban Earthquake Engineering, Tokyo Institute of Technology, Japan

2) Professor, Structural Engineering Research Center, Tokyo Institute of Technology, Japan

ihiroshi@enveng.titech.ac.jp, kasai@serc.titech.ac.jp

Abstract: This paper discusses cumulative damage of elasto-plastic (EP) damper in multi-story building under earthquake ground motion. Cumulative plastic deformation of damper can be clearly expressed as a function of stiffness parameter, ductility demand, natural vibration period of structure and duration of earthquake ground motion, based on the seismic behavior of single-degree-of-freedom (SDOF) elasto-plastically damped structure. The proposed method converts it to the prediction for multiple-degree-of-freedom (MDOF) model of multi-story building, with a consideration for stiffness balance of damper to frame. The method is validated via numerous MDOF time history analyses of the designed passive control systems, covering wide ranges of building height, frame stiffness distribution, maximum ductility factor, and earthquake type.

1. INTRODUCTION

Passively-controlled building structures have become a common practice in Japan, taking full advantage of various energy dissipation devices developed recently. Especially, passively-controlled structure with elasto-plastic (EP) dampers, such as buckling-restrained brace, has gained widespread practical applications. The EP dampers substantially reduce building drifts and member forces by adding hysteretic damping and stiffness to the structure under earthquake ground motion. The performance of EP damper is closely related to its maximum deformation capacity of EP damper and cumulative plastic deformation capacity, but design method considering such an aspect has not been proposed to-date.

The objective of this paper is to propose a cumulative damage prediction method for elasto-plastic damper under earthquake ground motion, and to verify accuracy of the proposed method. The proposed method is based on the seismic behavior of single-degree-of-freedom (SDOF) elasto-plastically damped structure, cumulative plastic deformation of damper can be clearly expressed as a function of natural period of structure and duration of earthquake ground motion, which haven't been considered exactly by Akiyama et al (1999) and Ogawa et al (2002), as well as stiffness parameter and maximum ductility factor. Cumulative plastic deformation of damper tends to increase strongly with short period structure and long-duration earthquake, as well as with low-stiffness and low-yield-strength damper. The proposed method converts it to the prediction for multiple-degree-of-freedom (MDOF) model of multi-story building, with a consideration for distribution of stiffness balance of damper to frame. The method is validated via numerous MDOF time history analyses of the designed passive control systems, covering wide ranges of building height, frame stiffness distribution, maximum ductility factor, and earthquake type.

2. CUMULATIVE PLASTIC DEFORMATION OF SDOF SYSTEM WITH EP DAMPER

2.1 SDOF System with EP Damper

As shown in Figure 1, SDOF model of system with EP Damper consists of mass and two springs, which represent EP damper and frame, connected in a row to the mass. EP damper is modeled as elasto-perfectly-plastic with elastic stiffness K_d , yield deformation u_{dy} , yield strength F_{dy} ($=K_d \times u_{dy}$) and maximum ductility factor μ_d , whereas frame behaves linearly with elastic stiffness K_f (Figure 2(a),(b)). Thus, maximum displacement of system u is identical to the one of frame u_f , and one of damper u_d , moreover maximum ductility factor μ and yield deformation u_y of system are identical to those of damper μ_d , u_{dy} , respectively. Natural vibration period and damping ratio of frame are defined as T_f and h_0 . Elastic stiffness $K_f + K_d$ and natural vibration period T_0 of EP system are given by Eq. 1(a)-(c).

$$K_0 = K_f + K_d, \quad T_0 = \sqrt{p} \cdot T_f, \quad p = \frac{K_f}{K_f + K_d} \quad (1a-c)$$

where p = ratio of post-yield stiffness to elastic stiffness of system.

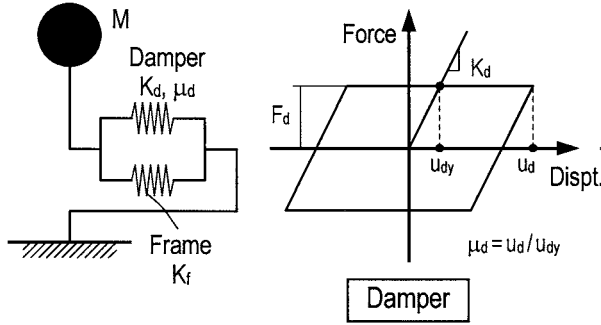


Figure 1 SDOF model of system with EP damper

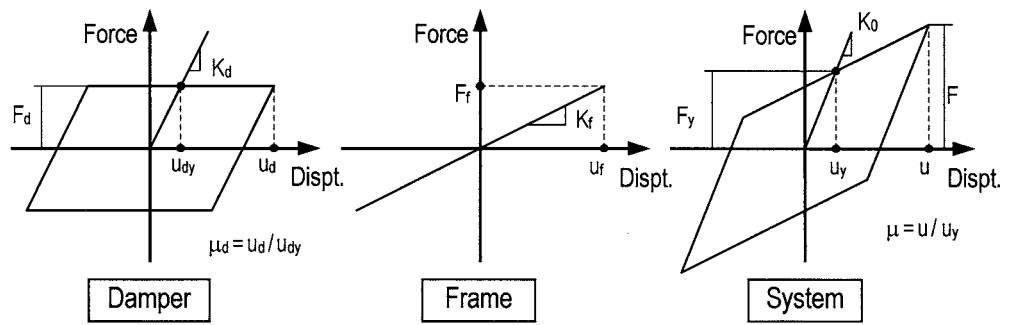


Figure 2 Hysteresis curve of damper, frame and system

Cumulative deformation ductility factor of damper η , which is an index of cumulative energy dissipation of damper, is defined as follows.

$$\eta = \sum \Delta \mu \quad (2)$$

where $\Delta \mu$ = deformation ductility factor in each half cycle (Figure 3).

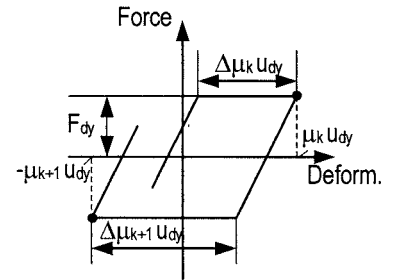


Figure 3 Deformation ductility factor of damper in each half cycle

2.2 Trends of Cumulative Plastic Deformation of SDOF System with EP Damper

This section discusses the trends of cumulative plastic deformation of SDOF system with EP damper. From statistical investigation on numerous analysis results of SDOF system with EP damper, cumulative plastic deformation of damper η tends to increase strongly with short period structure and long-duration earthquake, as well as with low-stiffness and low-yield-strength damper. It is found that this trend of η can be estimated by investigating complex effects of key factors such as post-yield stiffness ratio p , maximum ductility factor μ , natural vibration period T_0 and duration of earthquake ground motion t_d (Ito and Kasai, 2006). By considering the complex effects of p , μ , T_0 and t_d , the formula for prediction of cumulative deformation ductility factor η of damper is obtained as follows.

$$\eta = \frac{1 + \sqrt{p}}{3} \left[(1 + \sqrt{p})(\mu - 1)^2 + \frac{t_d}{T_0} \frac{0.3 T_0^{1/3} (\mu - 1)^{3/2} \exp(0.55 T_0^{1/4} p)}{1 - 0.18(1 - p) \ln(T_0)} \right] \quad (3)$$

Moreover, the formula for relationship between cumulative deformation ductility factor η and maximum ductility factor $(\mu - 1)$ of damper is also obtained by dividing Eq. 3 by $(\mu - 1)$.

$$\frac{\eta}{\mu - 1} = \frac{1 + \sqrt{p}}{3} \left[(1 + \sqrt{p})(\mu - 1) + \frac{t_d}{T_0} \frac{0.3 T_0^{1/3} (\mu - 1)^{1/2} \exp(0.55 T_0^{1/4} p)}{1 - 0.18(1 - p) \ln(T_0)} \right] \quad (4)$$

Figure 5 plots $\eta/(\mu - 1)$ against p for different $\mu = 2, 4, 8$ and 15 , $T_0 = 0.3, 1.0$ and 3.0 , and $t_d = 15, 30$ and 60 by Eq. 4. Eq. 4 can express trends of analysis results, which are the strongly increase η -value in case of short period structure and long-duration earthquake, as well as behavior of low-stiffness and low-yield-strength damper.

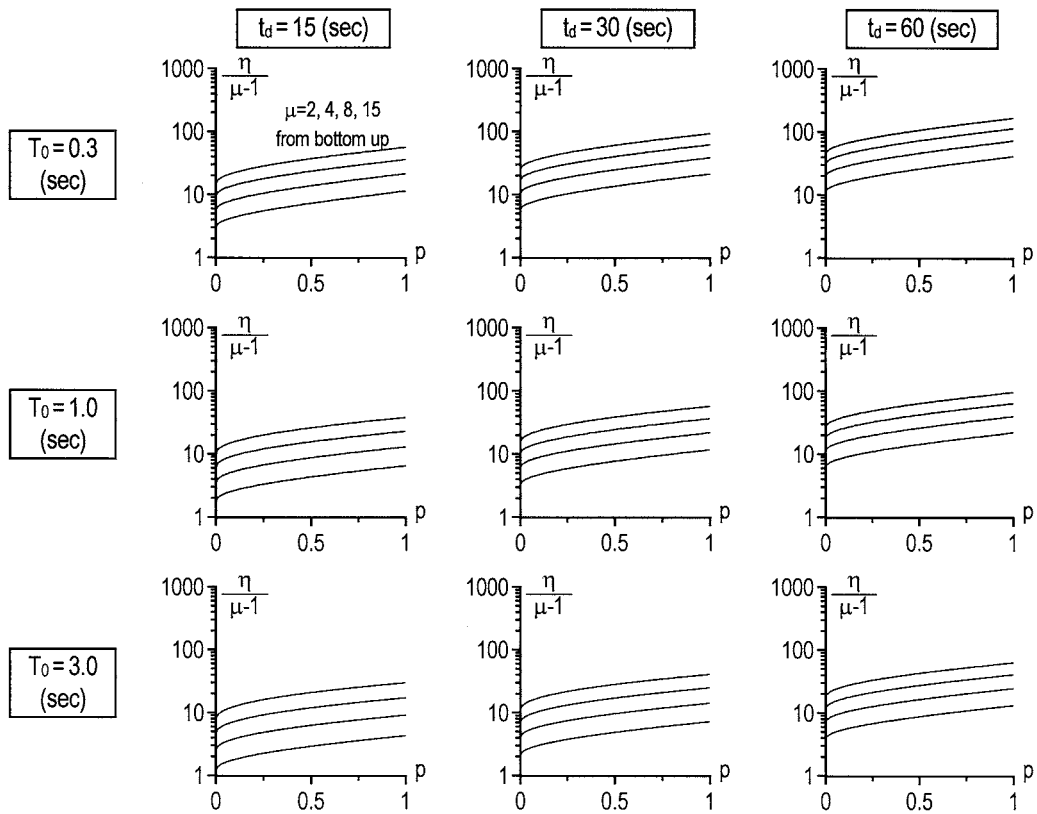


Figure 4 Relationship between $\eta/(\mu - 1)$ and p for different μ , T_0 and t_d by Eq. 4

3. CUMULATIVE PLASTIC DEFORMATION OF MDOF SYSTEM WITH EP DAMPER

3.1 Frame Models and Design Earthquake

In order to investigate cumulative plastic deformation of damper in multi-story elasto-plastically damped building structure, we will use MDOF shear-beam models created from the member-by-member frame models of 4, 10 and 20-story steel moment-resisting frames that were designed by JSSI (JSSI, 2005, and Kasai and Ito, 2005). In addition to the original frame horizontal stiffness distribution (JSSI-Type), three other types of distribution are considered for each of 4, 10 and 20-story buildings, by maintaining the mass distribution m_i , story height distribution h_i , and natural

vibration period T_f identical to those of the JSSI-Type. The three types are called as standard type (S-Type), soft upper story type (U-Type) and soft lower story type (L-Type). Figure 5 shows story stiffness distributions of 4 types of frame for 4, 10 and 20-story buildings; they are the normalized value of product of stiffness K_{fi} and story height h_i at i -th story to it of stiffness K_{f1} and story height h_1 at 1st story. The frame stiffness K_{fi} at i -th story of S-Type is designed such that story drift angle may distribute uniformly under the A_i lateral force distribution (BRI, 2004). In U-Type frame, story drift angle tends to be larger at upper stories, whereas in L-Type frame, story drift angle tends to be larger at lower stories. As mentioned above, story stiffness distributions of S, U and L-Type frame are obtained such that natural vibration period of them may be identical to JSSI-Type. Natural vibration period of frame T_f and the total building height H are shown in Table 1. The initial damping ratio of frame is $h_0 = 0.02$.

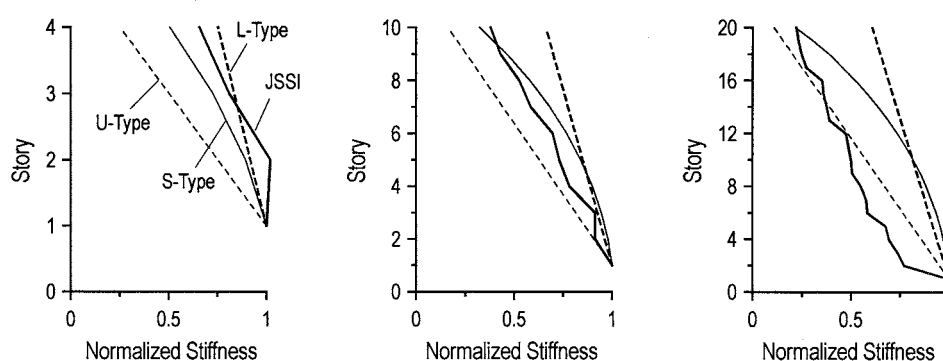


Figure 5 4 Types of story stiffness distributions of frames for various building heights

Table 1 Natural vibration period T_f and total height H of frame

	T_f (sec)	H (m)	T_f / H
4-story	0.640	18.0	0.036
10-story	2.012	42.0	0.048
20-story	3.704	82.0	0.045

6 artificial and 4 past earthquake ground motions for design are shown in Table 2. Design response spectrum and response spectra of 6 artificial earthquake ground motions (Table 2) for damping ratio $h = 0.02$, which are considered as extremely severe earthquake level, are shown in Figure 6. Pseudo velocity spectra S_{pv} of 6 artificial earthquake ground motions will be assumed to be period-independent in the range greater than 0.64 sec, pseudo acceleration spectra S_{pa} of 6 artificial earthquake ground motions will be also assumed to be period-independent in the range of shorter vibration period (0.16 - 0.64 sec). The values of duration t_d of those earthquake ground motions are also shown in Table 2. The duration of earthquake ground motion t_d is defined as cumulative duration, which is the time interval during which the central 90% of the contribution to the integral of the square of the acceleration takes place (Trifunac and Brady, 1975). As an example, Figure 7 shows definition of t_d and its value for El Centro NS ground motion.

Table 2 List of earthquake ground motions

Artificial Earthquake Ground Motions	Record Length (sec)	Duration t_d (sec)	Past Earthquake Ground Motions	Record Length (sec)	Duration t_d (sec)
BCJ-L2	120.0	65.3	El Centro NS	53.7	24.4
Hachinohe EW	60.0	49.2	Taft N111E	54.4	28.8
JMA Kobe NS	60.0	14.8	Hachinohe NS	51.0	28.4
Tohoku Univ. NS	60.0	30.4	JMA Kobe NS	30.1	8.1
El Centro NS	53.7	41.4			
Taft N111E	54.4	41.5			

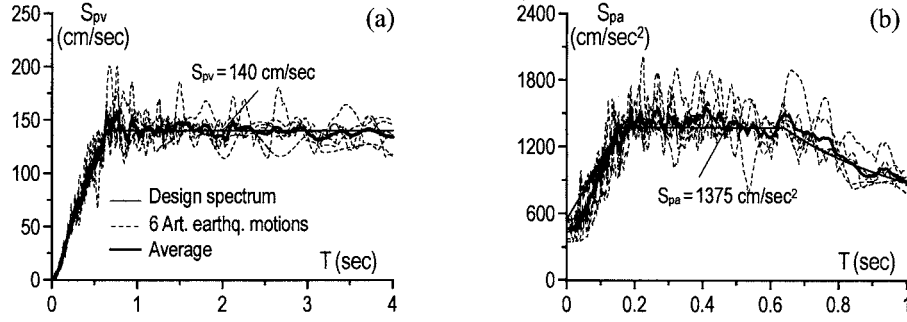


Figure 6 Response spectrum of 6 artificial earthquake ground motions ($h_0 = 0.02$)

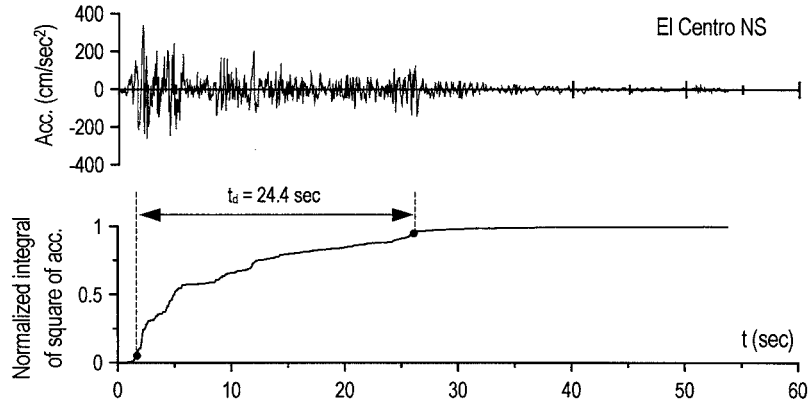


Figure 7 Definition of duration of earthquake ground motion t_d

3.2 Passive Control Design and Analysis Model

In order to investigate cumulative plastic deformation of damper in multi-story elasto-plastically damped building structure, time history analysis were carried out for 1440 ($=4 \times 3 \times 4 \times 3 \times 10$) MDOF systems with EP dampers designed: 4 types of frame which are JSSI, S, L and U-Type shown in Figure 5, 3 building heights which are 4, 10 and 20-story frame; 4 target ductility demands $\mu = 2, 4, 6$ and 8; 3 target drift angles $\theta = 1/200, 1/150$ and $1/125$ rad; and 6 artificial and 4 past earthquake ground motions shown in Table 2.

In passive control design for MDOF system with EP damper, damper stiffness K_{di} and damper yield strength F_{dyi} at i -th story are determined by the method to satisfy the target of maximum story drift angle and maximum ductility demand, and assure uniformly distributed maximum story drift angle and maximum ductility factor over the building height under the design earthquake ground motion considered (Kasai and Ito, 2005, 2006). Yield story drift angle $\theta_y (= \theta / \mu)$ of MDOF system is the same among all story levels. In design and analysis, each story of MDOF system with damper is considered as mass and two shear springs which show EP damper with elasto-perfectly-plastic behavior and frame with linear behavior in a row to the mass (Figure 8).

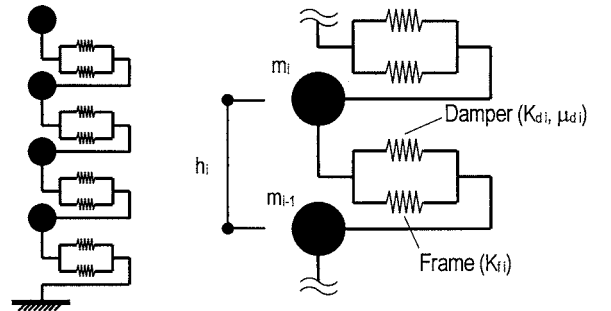


Figure 8 MDOF system with EP damper

3.3 Validation Study

Validation study for the proposed method is carried out using a wide range of MDOF models indicated in section 3.2 (1440 models in total), the accuracy of estimated cumulative plastic

deformation factor η_i of damper at i -th story is verified with time history analysis results.

In validation study for MDOF system with various post yield stiffness ratio $p_i (=K_{fi}/(K_{fi}+K_{di}))$ over the building height, cumulative plastic deformation factor obtained from analysis results at story level with higher p_i value tends to increase strongly and exceed the estimation by Eq. 4 considering complex effects of key factors such as p , μ , T_0 and t_d in SDOF system. Thus, by multiplying Eq. 4 by revised factor (p_i/p) considered such effect by p_i distribution of MDOF system, the formula for prediction of cumulative deformation ductility factor η_i of damper at i -th story is revised as follows.

$$\eta_i = \frac{1+\sqrt{p_i}}{3} \left[(1+\sqrt{p_i})(\mu_i-1)^2 + \frac{t_d}{T_0} \frac{0.3 T_0^{1/3} (\mu_i-1)^{3/2} \exp(0.55 T_0^{1/4} p_i)}{1-0.18(1-p_i)\ln(T_0)} \right] \frac{p_i}{p}$$

$$p = \frac{1}{1 + \sum_{i=1}^N K_{di} / \sum_{i=1}^N K_{fi}} \quad (5a,b)$$

where p = post stiffness ratio of equivalent SDOF system to which is converted MDOF system.

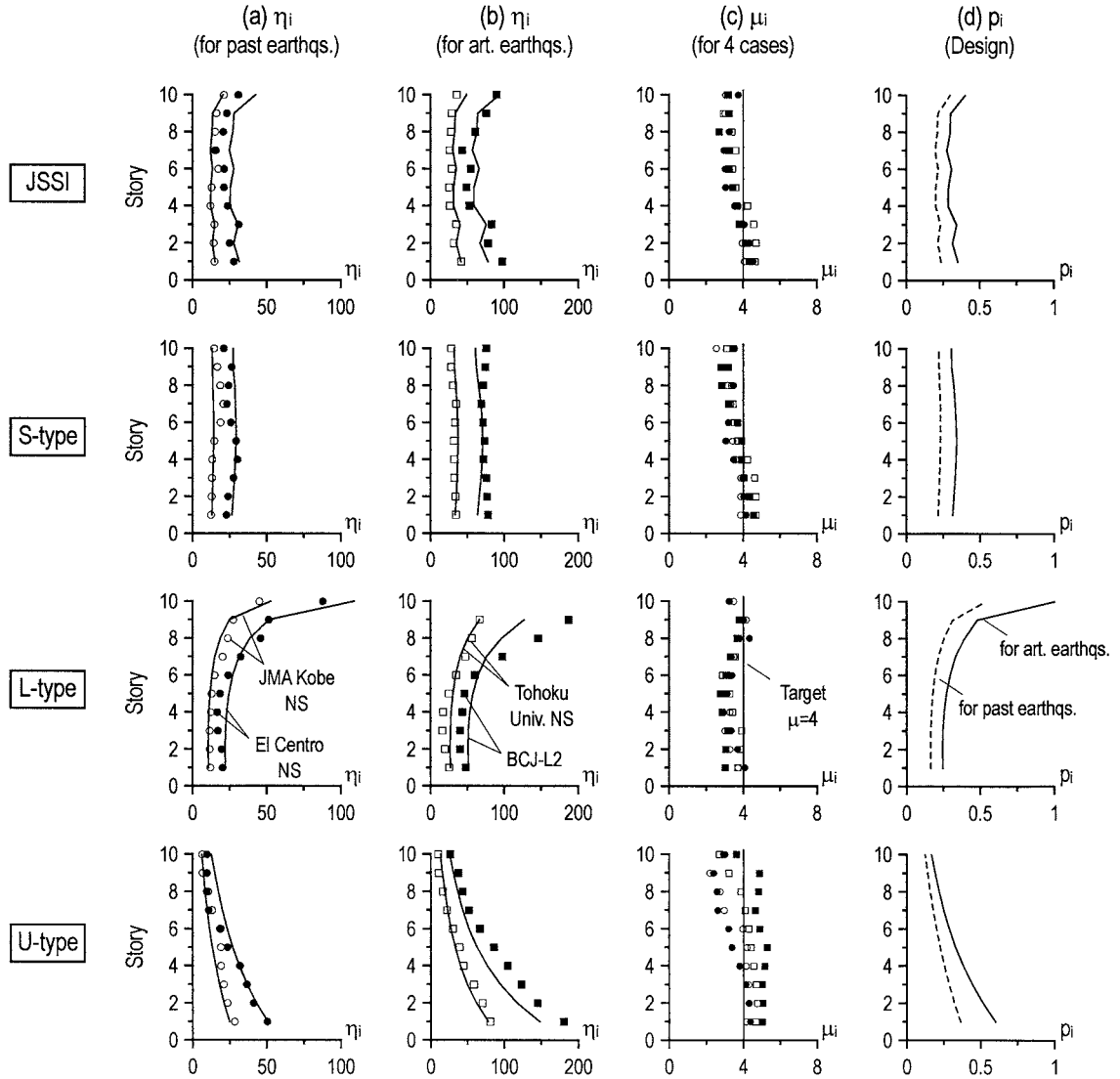


Figure 9 Comparison proposed method with analysis results
(10-story, $\theta = 1/150$ rad ($\theta_r = 1/600$ rad), $\mu = 4$, symbol : analysis, solid line : prediction (Eq. 5))

We will estimate the η_i -value of damper based on target ductility demand μ , because μ_i obtained from analysis results becomes nearly equal to μ by utilizing above mentioned response control method (Kasai and Ito, 2005, 2006). The cumulative plastic deformation factor of damper obtained from analysis results (symbol) under 4 ground motions (El Centro NS, JMA Kobe NS, BCJ-L2 and Tohoku Univ. NS) and prediction (solid line) by Eq. 5, in case of 4 types of 4, 10 and 20-story frame; $\theta=1/150$ rad; $\mu=4$, are shown in Figure 9(a),(b). The maximum ductility factor obtained from analysis results under 4 ground motions and post yield stiffness ratio of system $p_i (=K_{fi}/(K_{fi}+K_{di}))$ are also shown in Figure 9(c),(d). As you can see Figure 9(c), maximum ductility factor of analysis results fairly satisfy the design target due to inserting a sufficient amount of damper at each story regardless of frame stiffness distribution. In JSSI and S-Type MDOF system with almost uniform value of p_i over the building height, distributions of η_i -value obtained from analysis results tend to be also uniform over the building height. On the other hand, in L and U-Type MDOF system with various value of p_i over the building height, η_i -value obtained from analysis results tends to increase strongly at story level with higher p_i value. Such tendencies are predicted accurately by proposed method (Eq. 5) based on the behavior of SDOF system, regardless of variety of stiffness balance of damper to frame over the building height. Note that natural vibration period of system T_0 is 0.86 to 1.25 sec and post yield stiffness ratio of equivalent SDOF system p (Eq. 5(b)) is 0.2 to 0.37 in each case shown in Figure 9.

The η_i -value of damper estimated by the proposed method based on design target μ are plotted against the time history analysis results in Figure 10, where each data point corresponds to value at one story of one analysis case. Instead of calculating the median and standard deviation of η_i (prediction) / η_i (analysis), median a and standard deviation σ can equivalently be obtained by performing a one-parameter log-log linear least squares regression of η_i (prediction) on η_i (analysis). The regression model is expressed “ $\ln(\eta_i \text{ (prediction)}) = \ln(a) + \ln(\eta_i \text{ (analysis)}) + \ln(\varepsilon)$ ”, where a is incline of regression line and ε is the random error in η_i (prediction) given η_i (analysis) with median 1 and standard deviation σ . Median a and standard deviation σ for different story height and earthquake type are shown in Table 3. It can be seen that the proposed method gives good estimation in average, although we observe some scattering of its estimation. In order to give a reasonably conservative estimation for practice, η_i -value of damper estimated by Eq. 5 should be scaled by a conservative factor 1.75 as the sum of a and σ for all data points. Statistically, this conservative factor would give more than 93% confidence for the η_i to be greater the exact value obtained from time history analysis.

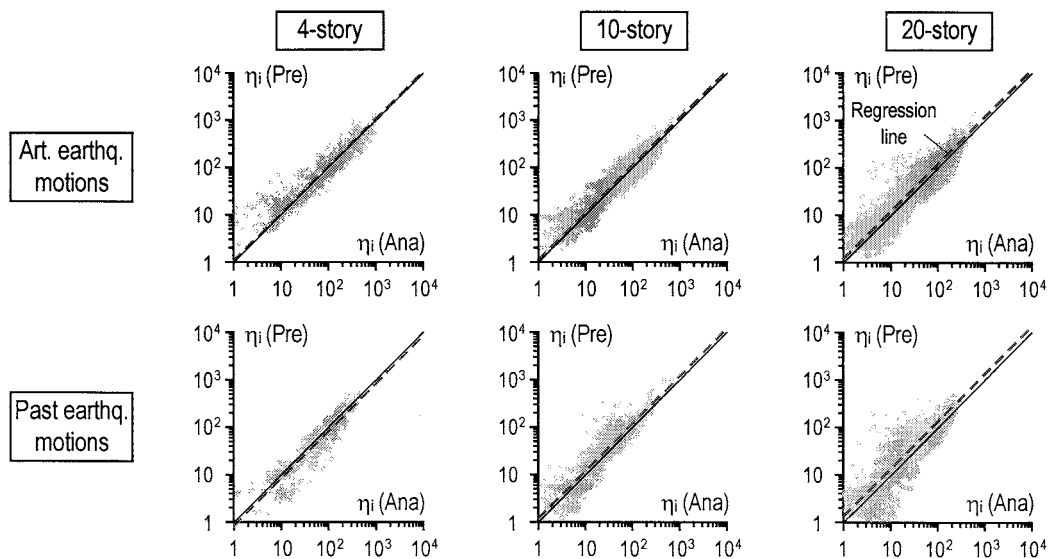


Figure 10 Comparison proposed method with analysis results of cumulative deformation ductility factor η_i (a : median, σ : standard deviation)

Table 3 Accuracy of proposed method in prediction of cumulative deformation ductility factor η_i (upper: median a , lower: standard deviation σ)

	4-story					10-story					20-story				
	Total	JSSI	S	L	U	Total	JSSI	S	L	U	Total	JSSI	S	L	U
Art. Earthq. Motions	1.089 (0.527)	1.010 (0.407)	0.955 (0.388)	1.174 (0.457)	1.294 (0.741)	1.141 (0.432)	1.191 (0.390)	1.119 (0.367)	1.288 (0.431)	0.990 (0.491)	1.200 (0.481)	1.241 (0.486)	1.210 (0.383)	1.430 (0.471)	0.971 (0.496)
Past Earthq. Motions	0.839 (0.527)	0.788 (0.435)	0.887 (0.430)	0.852 (0.468)	0.818 (0.725)	1.205 (0.480)	1.228 (0.457)	1.124 (0.395)	1.381 (0.580)	1.110 (0.443)	1.345 (0.721)	1.401 (0.694)	1.284 (0.595)	1.722 (0.875)	1.065 (0.610)

4. CONCLUSIONS

This study is aimed to develop the prediction method for cumulative plastic deformation of damper in multi-story elasto-plastically damped building. The proposed method is based on the behavior of SDOF system with EP damper subjected to earthquake ground motion, a rule to convert it to the prediction for MDOF model of multi-story building, with a consideration for distribution of stiffness balance of damper to frame, is also presented. The conclusions are as follows:

1. The prediction theory for cumulative plastic deformation of damper, by considering complex effects of stiffness parameter, maximum ductility factor, natural vibration period of structure and duration of earthquake ground motion gives good estimation in average, with some scattering of its estimation.
2. In MDOF system with various post yield stiffness ratio over the building height, cumulative plastic deformation factor at each story tends to depend strongly on the balance of post yield stiffness ratio over the building height. Cumulative plastic deformation factor at story level with higher post yield stiffness ratio extremely increases.

Acknowledgements:

This study is financially supported by the 21st Century COE program "Evolution of Urban Earthquake Engineering".

References:

- Building Research Institute (2004), "The Building Standard Law of Japan," Building Center of Japan (In Japanese)
- Ito, H. and Kasai, K. (2006), "Prediction For Cumulative Plastic Deformation of Damper In Elasto-Plastically Damped Structure," *Proceedings of 3rd International Conference on Urban Earthquake Engineering*, Center on Urban Earthquake Engineering, pp.497-504, Yokohama, JAPAN, March
- Ito, H. and Kasai, K. (2006), "Evaluation Method for Cumulative Plastic Deformation of Damper Based on Maximum Deformation of Elasto-Plastically Damped Structure," *Journal of Structural and Construction Engineering*, Transactions of Architectural Institute of Japan No.607, pp53-61, September (In Japanese)
- Ito, H. and Kasai, K. (2006), "Design of MDOF Passive Control System with Elasto-Plastic Damper," *Proceedings of 4th International Symposium on Steel Structures*, Korean Society of Steel Construction, pp.114-124, Seoul, KOREA, November
- Japan Society of Seismic Isolation (2005), "JSSI Manual for Design and Construction of Passively-Controlled Buildings 2nd Edition," (In Japanese)
- Kasai, K. and Ito, H. (2005), "Passive Control Design Method Based on Tuning of Stiffness, Yield Strength, and Ductility of Elast-Plastic Damper," *Journal of Structural and Construction Engineering*, Transactions of Architectural Institute of Japan No.595, pp45-55, September (In Japanese)
- Ogawa, K. and Hirano, T. (2002), "Ductility Demanded of Hysteretic Dampers," *Journal of Structural and Construction Engineering*, Transactions of Architectural Institute of Japan No.558, pp.197-204 (In Japanese)
- Takahashi, M. and Akiyama, H. (1999), "The Maximum Displacement and Energy Response of Multi-Story Frames under Earthquakes," *Journal of Structural and Construction Engineering*, Transactions of Architectural Institute of Japan No.515, pp.59-66 (In Japanese)
- Trifunac, M.D. and Brady, A.G. (1975), "A Study on Duration of Strong Earthquake Ground Motion," *Bulletin of the Seismological Society of America*, **65**(3), 581-626

SEISMIC BEHAVIOR AND PERFORMANCE OF BUCKLING-RESTRAINED BRACED FRAMES

L. Fahnestock¹⁾, R. Sause²⁾, and J. M. Ricles³⁾

1) Assistant Professor, Department of Civil and Environmental Engineering, University of Illinois at Urbana-Champaign

2) Joseph T. Stuart Professor, Department of Civil and Environmental Engineering, Lehigh University

3) Bruce G. Johnston Professor, Department of Civil and Environmental Engineering, Lehigh University
fhnstck@uiuc.edu, rs0c@lehigh.edu, jmr5@lehigh.edu

Abstract: In response to the recent attention that buckling-restrained braced frames (BRBFs) have received in the United States and the resulting need for knowledge about system behavior and performance, an integrated analytical and large-scale experimental research program on BRBFs was conducted at the ATLSS Center, Lehigh University. Nonlinear dynamic analyses were performed on a 4-story prototype BRBF using a suite of earthquake ground motion records scaled to two seismic input levels: the design basis earthquake (DBE) and the maximum considered earthquake (MCE). Good performance was observed at both seismic input levels and the analytical studies were used to plan the large-scale experimental program. Laboratory experiments were conducted using the pseudo-dynamic testing method to simulate seismic input of various levels, including the DBE and MCE. The test frame sustained significant drift demands with almost no damage. Story drifts of nearly 0.05 radians and buckling-restrained brace (BRB) maximum ductility demands of over 25 were observed during the MCE simulation. No stiffness or strength degradation was observed. Although residual drifts were large, the testing program demonstrated that the BRBF system can withstand significant seismic input and retain full lateral load-carrying capacity.

1. INTRODUCTION, BACKGROUND, AND PRIOR RESEARCH

Owing to the limited ductility and energy dissipation capacity of conventional concentrically braced frame (CBF) systems, significant research efforts have gone towards developing new CBF systems with stable hysteretic behavior, good ductility and large energy dissipation capacity. One such CBF system is the buckling-restrained braced frame (BRBF). A BRBF is a CBF with buckling-restrained braces (BRBs). A BRB has two basic components: a steel core element that carries the brace axial force, and a restraining exterior element that prevents the core from buckling in compression and allows it to yield in both tension and compression. Figure 1(a) illustrates a typical BRB configuration in which the steel core is confined within a concrete-filled steel tube (CFT). The core, which is tapered in the center to create a region of contained yielding, is debonded from the confining concrete and carries the axial force independent of the CFT. The excellent cyclic behavior exhibited by BRBs is illustrated in Figure 1(b).

BRBs were first developed in Japan nearly 30 years ago by Kimura et al. (1976). The BRB concept has become very popular in Japan, and since the first application in the mid-1980s, BRBs have been used in over 200 Japanese buildings (Sabelli and Aiken 2003). However, BRBs have been used in North America only recently. As the interest in using BRBFs in the United States has grown in the last several years, numerous research programs have been conducted (e.g. Sabelli 2001, Aiken et al. 2002, Merritt et al. 2003). Although the BRBF knowledge base has grown steadily, there has been a

need for studies of system-level behavior and performance. To address this research need, integrated analytical and large-scale experimental studies on BRBFs were conducted at the ATLSS Center, Lehigh University.

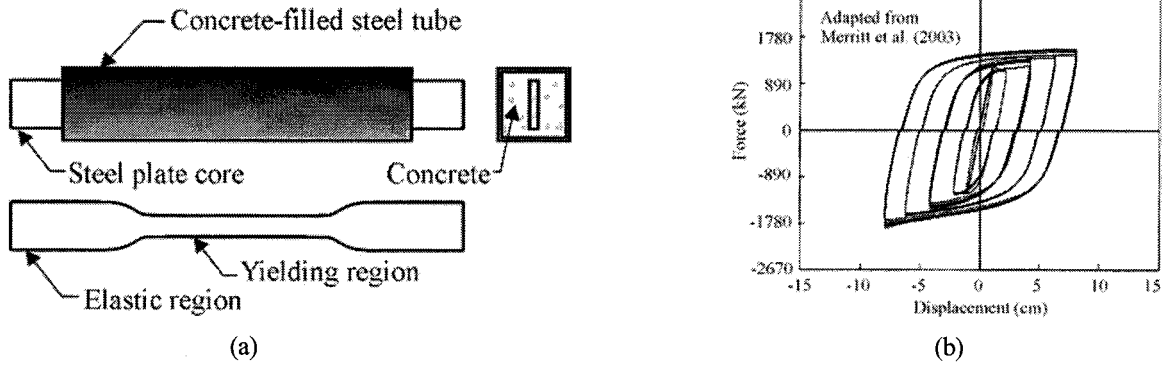


Figure 1 – Buckling-restrained brace: (a) schematic; (b) behavior (Merritt et al. 2003).

Since the first BRB tests conducted by Kimura et al. (1976), numerous researchers have tested isolated BRBs (e.g., Watanabe et al. 1988; Black et al. 2002; Usami et al. 2003; Merritt et al. 2003; Tsai et al. 2003b). These tests have demonstrated that BRBs are capable of withstanding large maximum ductility demands, μ_{\max} , and cumulative ductility demands, μ_c . These ductility demands are defined as:

$$\mu_{\max} = \frac{\Delta_{\max}}{\Delta_{by}} \quad (1)$$

$$\mu_c = \frac{\sum \Delta_{\text{plastic}}}{\Delta_{by}} \quad (2)$$

where Δ_{\max} = BRB maximum deformation, Δ_{by} = BRB yield deformation and Δ_{plastic} = BRB plastic deformation. μ_{\max} of 25 in compression (Usami et al. 2003) and over 48 in tension (Tsai et al. 2003b), and μ_c of 1600 (Merritt et al. 2003) have been sustained without BRB failure.

Although the excellent ductility capacity of isolated BRBs has been clearly established, the ability of BRBs to develop their full ductility capacity when installed in frames has not been verified. Large-scale tests of subassemblies and frames containing BRBs have consistently developed similar failure modes. These tests, conducted by Aiken et al. (2002), Tsai et al. (2003a, 2003b and 2006) and Roeder et al. (2006), demonstrated that stiff beam-column-brace connections attract large force and deformation demands, which can lead to undesirable failure modes. For BRBFs using stiff connections, reasonable performance has been observed for story drift up to 0.02 radians. However, gusset plate distortion and brace instability have typically been observed for story drift between 0.02 and 0.025 radians. The research presented in this paper examines global performance of BRBFs and focuses special attention on modified BRBF connection details that have improved performance and the ability to sustain large story drift.

2. PROTOTYPE BUILDING AND FRAME

The prototype building for the present study is an office building located on a stiff soil site in Los Angeles, California. BRBFs are the lateral-load-resisting system for the building. A one-bay prototype frame was extracted from the prototype building and used as the focus for the research program. The design procedure was based on the equivalent lateral force procedure in the International Building Code 2000 (ICC 2000) and the BRBF design guidelines in the AISC Seismic Provisions (2005). The

design coefficients, based on the guidelines given in the AISC Seismic Provisions, are the response modification coefficient, R , equal to eight, the system overstrength factor, Ω_0 , equal to two, and the deflection amplification factor, C_d , equal to 5.5.

The floor plan of the prototype building is shown in Figure 2(a). Lateral loads are resisted by a total of eight BRBFs, four in each direction. The prototype building is four stories tall and has one basement story. The prototype frame, shown in Figure 2(b), is defined to be one of the BRBFs from the prototype building. Both the floor and roof systems are assumed to act as rigid diaphragms that transfer the earthquake-induced inertial forces into the BRBFs. The beams and columns in the prototype frame are A992 steel wide-flange sections. The BRB core plates were designed with A36 steel, which has a nominal yield stress of 248 MPa. The actual yield stress of the plate used in the BRBs of the test frame was 317 MPa and this value was used in designing the prototype frame BRBs. The BRBs were designed for lateral forces only (neglecting gravity load effects). The BRB yield forces, P_y , were set equal to the design forces and the core areas were calculated based on the actual steel yield strength.

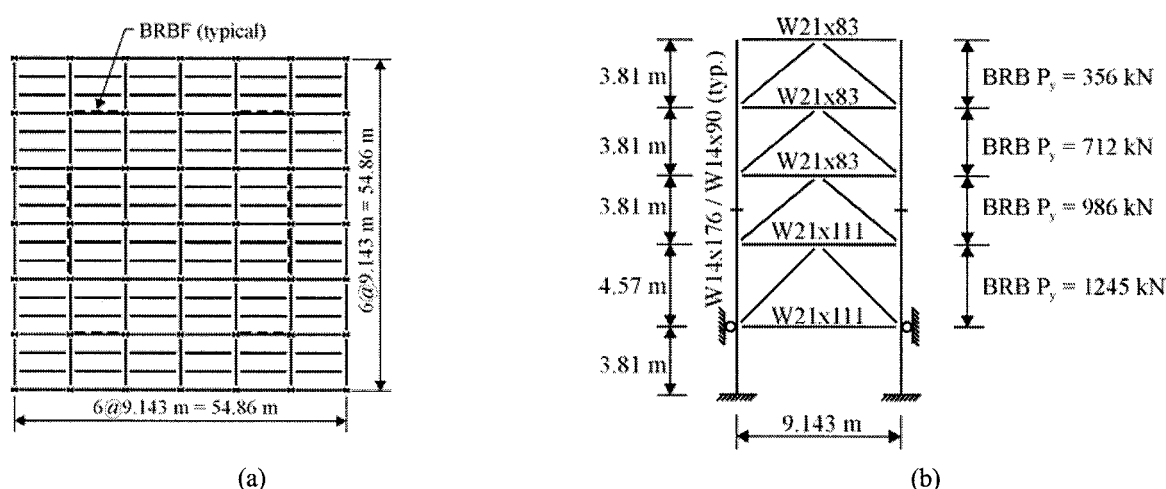


Figure 2 – Prototype: (a) building floor plan; (b) frame elevation.

3. NONLINEAR DYNAMIC ANALYSES

The computer program DRAIN-2DX (Prakash et al. 1993) was used to analyze the prototype frame. Fiber elements were used to model the beams and columns. The BRBs were modeled using inelastic truss elements, which included isotropic and kinematic hardening effects. The truss elements, with pinned ends, spanned between beam-column elements modeling the connection regions. Gravity loads were applied to the prototype frame and a lean-on column was included to model the second-order effects due to the building gravity loads. Floor masses were lumped at the nodes of the leaning column. Rayleigh damping was used with a viscous damping ratio of 2% assumed in the first and third modes. The natural ground motion records used in the present study were selected from the PEER Center strong motion database (PEER 2000) and the SAC database (SAC 1997). The scaling procedure was based on the recommendations of Somerville et al. (1997). Twelve ground motion records were scaled to the DBE seismic input level and fifteen ground motion records were scaled to the MCE seismic input level.

Performance objectives, which related the seismic input level to the expected seismic performance level, were established to evaluate the nonlinear dynamic analysis results. The NEHRP Recommended Provisions (FEMA 2003) define two seismic input levels, the design basis earthquake (DBE) and the maximum considered earthquake (MCE), and four seismic performance levels. For this study, the life safety (LS) and near collapse (NC) performance levels were chosen as the target performance levels

for the DBE and MCE, respectively. Table 1 lists some of the response limits that were used to evaluate performance of the prototype BRBF and individual BRBs. The broad performance goal underlying these objectives was to allow yielding in the BRBs and to minimize damage in other portions of the BRBF.

Table 1 – Performance objectives.

Response limits	Life safety performance level	Near collapse performance level
BRB core yielding	Yes	Yes
BRB core fracture	No	No
BRB maximum ductility demand	15	25
Maximum roof drift	0.015	0.03
Maximum story drift	0.02	0.04

Since the ground motion records were selected to represent earthquakes with a wide range of spectral characteristics, the analysis results are evaluated statistically. Table 2 provides a summary, in terms of the mean, μ , and the standard deviation, σ , of the peak BRB maximum ductility demand, story drift and roof drift under the DBE and MCE level ground motions. Comparison with the design criteria from Table 1 shows that the μ drifts are at or below the response limits, but the $\mu + \sigma$ drifts are above the response limits. The $\mu + \sigma$ response for BRB maximum ductility demand is below the response limits for both seismic input levels. Based on these response levels and the minimal structural damage observed in the frame, the performance objectives are met in terms of structural damage.

Table 2 – Response quantities from nonlinear dynamic analyses and experimental simulations.

Earthquake hazard level	Statistical quantity	Nonlinear dynamic analyses			Pseudo-dynamic simulations		
		Roof drift	Story drift	BRB maximum ductility demand	Roof drift	Story drift	BRB maximum ductility demand
FOE	Maximum	-	-	-	0.004	0.006	4.7
DBE	μ	0.015	0.020	11.1	-	-	-
	$\mu + \sigma$	0.019	0.025	14.0	-	-	-
	Maximum	0.024	0.029	16.9	0.021	0.030	15.8
MCE	μ	0.026	0.033	18.4	-	-	-
	$\mu + \sigma$	0.033	0.041	22.7	-	-	-
	Maximum	0.037	0.044	24.9	0.036	0.048	26.0
Aftershock	Maximum	-	-	-	0.015	0.021	10.1

4. EXPERIMENTAL PROGRAM

The test frame is related to the prototype frame through a scale factor, λ , equal to 0.6. Similitude between the prototype frame and the test frame was established by using the same materials and maintaining equal stresses. Thus, length dimensions are related by λ , and forces are related by λ^2 . The test frame BRB properties were scaled down from the prototype frame BRBs, leading to yield strengths of 445, 356, 267 and 133 kN for Stories 1 through 4, respectively. Wide-flange shapes for the test frame beams and columns were selected so that their section properties would be as close as possible to the scaled prototype frame section properties within the constraints of discrete member

sizes. The test frame beam and column sections are W12x40 and W8x67, respectively. Figure 3(a) shows a photograph of the test frame. For simplicity, the column splice was eliminated and the same beam size was used at all levels. The test frame member sizes are shown in Figure 3(b).

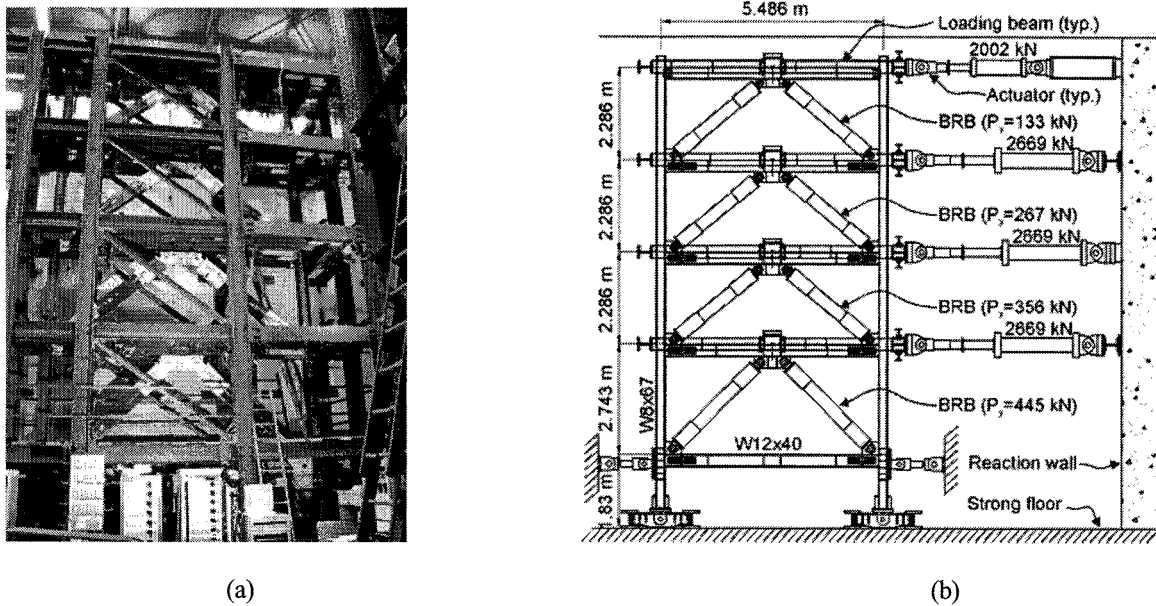


Figure 3 – Test frame: (a) photograph; (b) elevation.

In response to the connection problems observed in prior experimental research programs, special attention was given to the beam-column-brace connections. These connections were detailed to allow rotation while limiting flexural demands on the connection region. As illustrated in Figure 4(a), the brace-gusset connections were pinned connections and a bolted beam splice using double structural tees was introduced between the beam and the beam stub. The double structural tees effectively transfer axial force but provide minimal flexural resistance. Thus, the connection elements can be capacity-protected based on the BRB and double tee strengths.

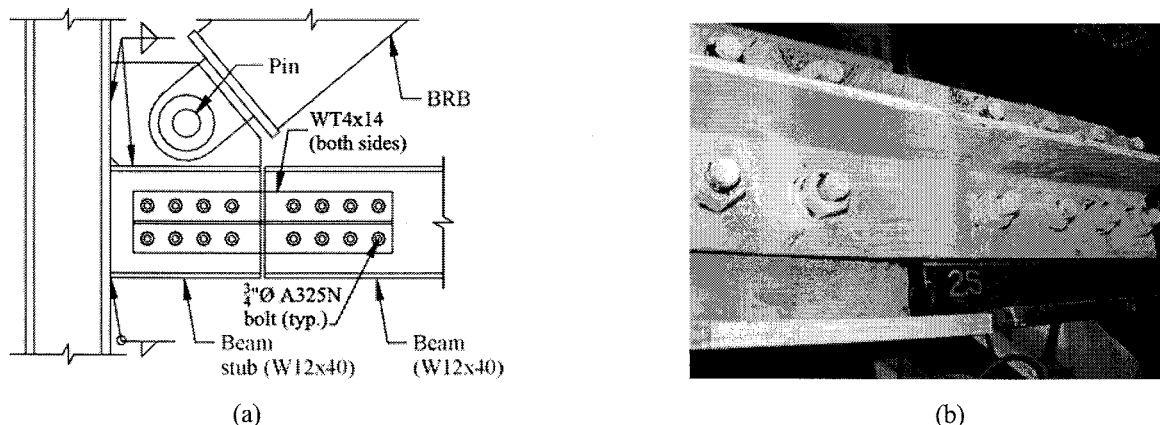


Figure 4 – Connection: (a) detail; (b) bolted beam splice after MCE simulation.

To evaluate the response of the test frame under seismic input, earthquake simulations were conducted using the pseudo-dynamic testing method (Mahin and Shing 1985). The explicit Newmark algorithm was used to solve the time-discretized equations of motion and a hybrid procedure was implemented to account for the second-order effects that were not included experimentally (Herrera 2005). Since acceleration was held constant between the prototype and test frames, the earthquake time scales were modified by $\lambda^{1/2}$. Four earthquake simulations were conducted: a frequently

occurring earthquake (FOE) simulation and DBE and MCE simulations followed by an additional simulation that investigated the ability of the test frame to withstand a large aftershock event (80% of the DBE). The Saticoy 180 record from the 1994 Northridge earthquake was scaled to the target spectra for the DBE and MCE hazard levels using an approach similar to the one recommended by Somerville et al. (1997). Since a frequently occurring earthquake (FOE) hazard level is not defined in design codes, a record designated to represent a 50% probability of being exceeded in 50 years for the Los Angeles site was selected from the SAC database (1971 San Fernando, Hollywood Storage).

A summary of the significant response quantities for all four earthquake simulations is presented in Table 2. These quantities are peak values for the entire frame. The FOE and DBE simulations were conducted without reaching significant limit states, other than BRB yielding. Under the FOE, minor localized yielding was observed in the connection double tees. During the DBE, the yielding spread slightly but was still localized. The BRB maximum ductility demand was around 5 for the FOE and 16 for the DBE. After the FOE, the test frame had only a small amount of residual drift, but the residual drift was significant after the DBE, over 0.01 radians at the roof.

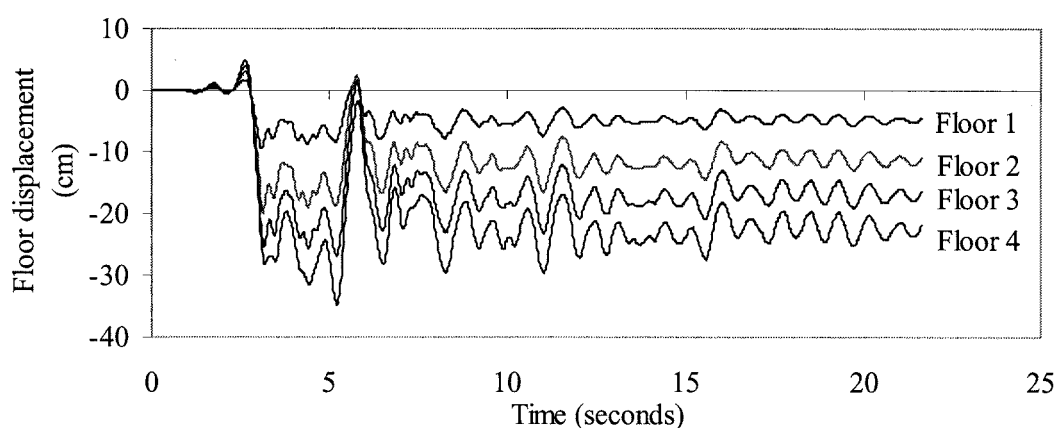


Figure 5 – Floor displacement histories for MCE simulation.

Since the MCE simulation was intended to represent an earthquake affecting an undamaged structure, the residual drift after the DBE was eliminated by straightening the test frame. The floor displacement histories in Figure 5 show that the test frame MCE response was significantly offset in the negative direction after the first large displacement peak. Under the MCE, maximum story drift was nearly 0.05 radians and BRB maximum ductility demand was over 25. Despite these exceptionally large demands, the test frame exhibited excellent performance. The only observed inelastic response was minor yielding in the connection regions, as shown in Figure 4(b), and yielding of the BRBs.

Figure 6 plots normalized BRB force-deformation response for the MCE simulation. As illustrated, no strength or stiffness deterioration occurred and the BRBs exhibited excellent ductility and energy dissipation capacity. Significant isotropic hardening developed throughout the earthquake simulations and the maximum BRB overstrength (P/P_y) was near 1.5 in tension and 1.75 in compression. The BRBs exhibited positive post-yield stiffness ranging from 1% to 5% of the initial elastic stiffness. The post-yield stiffness was typically greater in compression due to core confinement, but the effect of confinement was dependent upon the position on the force-deformation curve.

The connections performed well and accommodated the large drift demands without distress. Slip was observed in the bolted beam splices. Additional localized yielding was observed in the double tees. No distortion was visible in the gusset plates and the connection welds did not develop any cracks. The beam-column-brace connection details, which incorporated pinned BRB end connections and bolted beam splices, demonstrated the ability to withstand extreme story drift demands and to avoid the undesirable failure modes observed in previous BRBF experimental programs. Although the test

frame demonstrated the ability to withstand extreme demands without difficulty, appreciable residual drift remained after the DBE and MCE simulations, over 0.01 radians and 0.02 radians at the roof, respectively. These large residual drifts could prevent continued use of an actual building after an earthquake despite the fact that the BRBFs are capable of remaining in service.

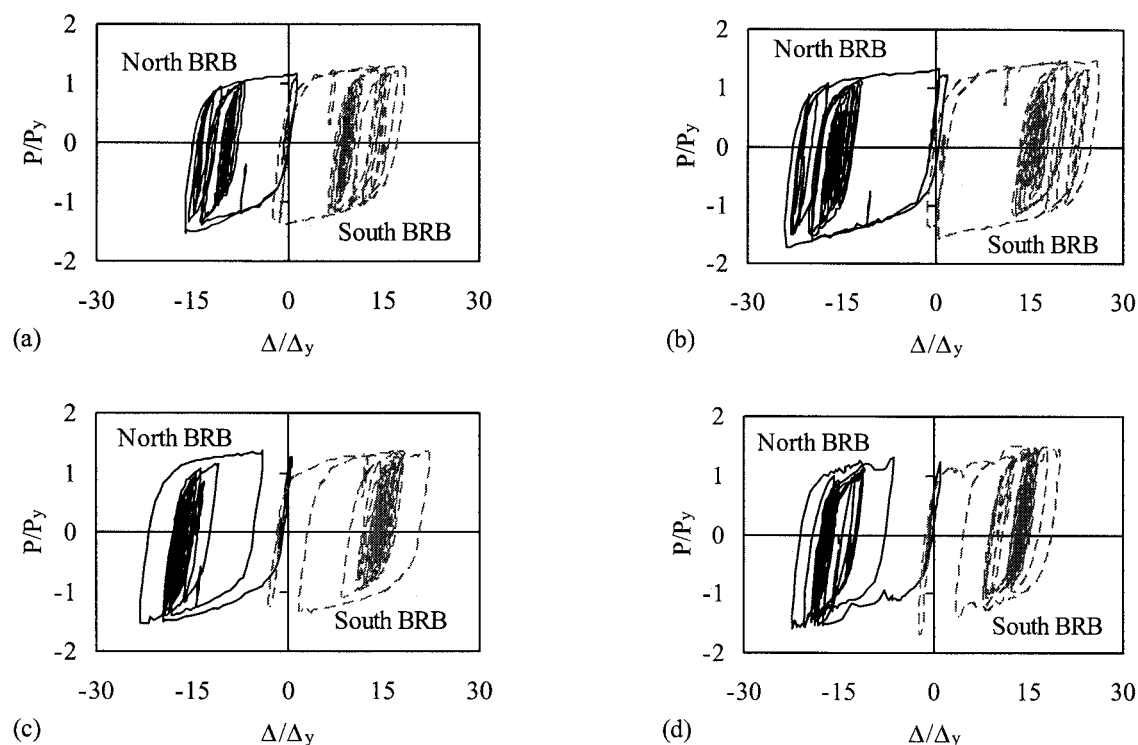


Figure 6 – Normalized BRB force-deformation for MCE simulation: (a) Story 1; (b) Story 2; (c) Story 3; (d) Story 4.

5. SUMMARY AND CONCLUSIONS

The analytical and large-scale experimental program described in this paper has established the range of seismic demands that can be expected in typical BRBFs. Experimental demands during pseudo-dynamic tests were greater than $\mu + \sigma$ demands from nonlinear dynamic analyses for both DBE and MCE levels. The experimental program demonstrated the ability of a well-detailed BRBF to undergo significant drift demands with almost no damage. No stiffness or strength degradation was observed. Connection details that minimized connection moment and allowed rotation exhibited excellent performance and sustained only minor yielding at very large story drifts. This result is particularly significant in view of the undesirable failure modes observed in previous BRBF experimental programs. Story drifts near 0.05 radians and BRB maximum ductility demands over 25 were observed in the MCE simulation. The large demands imposed on the test frame verify the significant maximum ductility capacity of BRBs. During the MCE simulation, five of the BRBs sustained maximum ductility demands ranging from 22 to 26. These results indicate that BRB ductility capacities in this range can realistically be achieved in properly designed and detailed BRBFs. Although residual drifts were large, over 0.02 radians at the roof after the MCE simulation, the test frame retained its full load-carrying capacity after significant seismic input. Properly detailed BRBFs are shown to withstand extreme seismic input and maintain their structural integrity. A full description of the research program summarized in this paper is provided by Fahnestock et al. (2006).

Acknowledgements:

Funding for this research was provided by the National Science Foundation (Award No. CMS-9905870) and the Pennsylvania Infrastructure Technology Alliance, funded by a grant from the Pennsylvania Department of Community and Economic Development. Financial support for the first author was provided in part by the AISC Klingelhofel Fellowship and the EERI/FEMA NEHRP Graduate Fellowship. The BRBs for the test frame were provided by Star Seismic, LLC and the test frame was fabricated by Samuel Grossi and Sons, Inc.

References:

- Aiken, I.D., Mahin, S.A., Uriz, P. (2002), "Large-Scale Testing of Buckling Restrained Braced Frames", *Proceedings, Japan Passive Control Symposium*, Tokyo Institute of Technology, Yokohama, Japan, December.
- AISC (2005), *Seismic Provisions for Structural Steel Buildings*, American Institute of Steel Construction.
- Black C.J., Makris N. and Aiken I.D. (2002), "Component Testing, Stability Analysis and Characterization of Buckling Restrained 'Unbonded' Braces," Technical Report PEER 2002/08, Pacific Earthquake Engineering Research Center, University of California at Berkeley, Berkeley, CA.
- FEMA (2003), NEHRP Recommended Provisions for Seismic Regulations for New Buildings and Other Structures, Part 1 - Provisions and Part 2 - Commentary, FEMA 450, Federal Emergency Management Agency, Washington, D.C.
- Fahnestock, L.A., Ricles, J.M. and Sause, R. (2006), "Analytical and Experimental Studies of Earthquake-Resistant Buckling-Restrained Braced Frame Systems," ATLSS Report 06-01, Lehigh University, Bethlehem, PA, Sept. 2006.
- Herrera, R. (2005). "Seismic Behavior of Concrete Filled Tube Column-Wide Flange Beam Frames," Ph.D. dissertation, Lehigh University, Bethlehem, PA.
- ICC (2000), *International Building Code*, International Code Council, Falls Church, VA.
- Kimura, Y., Takeda, Y., Yoshioka, K., Furuya, N. and Takemoto, Y. (1976), An Experimental Study on Braces Encased in Steel Tube and Mortar, *Proceedings of the AIJ Annual Meeting*, October 1976, pp. 1041-1042 (in Japanese).
- Mahin, S.A. and Shing, P.B. (1985), "Pseudodynamic Method for Seismic Testing," *Journal of Structural Engineering*, American Society of Civil Engineers, **111** (7): 1482-1503.
- Merritt, S., Uang, C.M. and Benzoni, G. (2003b), "Subassemblage Testing of Star Seismic Buckling-Restrained Braces," Structural Systems Research Project, Report No. TR-2003/04, University of California, San Diego.
- PEER (2000), "Pacific Earthquake Engineering Research Center Strong Motion Database," PEER Center, <http://peer.berkeley.edu/smcat/>
- Prakash V., Powell G.H., and Campbell S. (1993), "DRAIN-2DX Base Program Description and User Guide – Version 1.10," Report No. UCB/SEMM-93/17 and 18, Structural Engineering Mechanics and Materials, Department of Civil Engineering, University of California, Berkeley, CA.
- Roeder, C.W., Lehman, D.E. and Christopoulos, A. (2006), "Seismic Performance of Special Concentrically Braced Frames with Buckling Restrained Braces," *Proceedings, 8th U.S. National Conference on Earthquake Engineering*, Earthquake Engineering Research Institute, Oakland, CA, Paper No. 1503.
- Sabelli R. (2001), "Research on Improving the Design and Analysis of Earthquake-Resistant Steel Braced Frames," The 2000 NEHRP Professional Fellowship Report, Earthquake Engineering Research Institute, Oakland, CA.
- Sabelli R. and Aiken I. (2003), "Development of Building Code Provisions for Buckling-Restrained Braced Frames," *Behavior of Steel Structures in Seismic Areas, STESSA 2003*, Mazzolani, F. (ed.), Naples, Italy, June 9-12, pp. 813-818.
- SAC (1997), "Suites of Earthquake Ground Motions for Analysis of Steel Moment Frame Structures," http://quiver.eerc.berkeley.edu:8080/studies/system/ground_motions.html
- Somerville P., Smith N., Punyamurthula, S. and Sun J. (1997), "Development of Ground Motion Time Histories for Phase 2 of the FEMA/SAC Steel Project," SAC Background Document SAC/BD-97/04, SAC Joint Venture, Sacramento, CA.
- Tsai, K.C., Hsiao, B.C., Lai, J.W., Chen, C.H., Lin, M.L. and Weng, Y.T. (2003a), "Pseudo Dynamic Experimental Response of a Full Scale CFT/BRB Composite Frame," *Proceedings, Joint NCREE/JRC Workshop on International Collaboration on Earthquake Disaster Mitigation Research*, Taipei, Taiwan.
- Tsai K.C., Loh C.H., Hwang Y.C. and Weng C.S. (2003b), "Seismic Retrofit of Building Structures with Dampers in Taiwan," *Proceedings, Symposium of Seismic Retrofit of Buildings and Bridges with Base Isolation and Dampers*, Kyoto University, Kyoto, Japan.
- Tsai, K.C., Weng, Y.T., Wang, K.J., Tsai, C.Y. and Lai, J.W. (2006), "Bi-directional Sub-structural Pseudo-dynamic Tests of a Full-Scale 2-Story BRBF, Part 1: Seismic Design, Analytical and Experimental Performance Assessment," *Proceedings, 8th U.S. National Conference on Earthquake Engineering*, Earthquake Engineering Research Institute, Oakland, CA, Paper No. 1097.
- Usami T., Kasai A., and Kato M. (2003), "Behavior of Buckling-Restrained Brace Members," *Behavior of Steel Structures in Seismic Areas, Proceedings, STESSA 2003*, Mazzolani, F. (ed.), Naples, Italy, pp. 211-216.
- Watanabe A., Hitomi Y., Saeki E., Wada A., and Fujimoto M. (1988), "Properties of Brace Encased in Buckling-Restraining Concrete and Steel Tube," *Proc., 9th World Conference on Earthquake Engineering*, Tokyo-Kyoto, Japan.

SHAKING TABLE TESTS OF TWO-STORY WOOD FRAMES WITH PASSIVE CONTROL SYSTEM

K. Matsuda¹⁾, K. Kasai²⁾, H. Sakata³⁾, Y. Ooki⁴⁾, and A. Wada⁵⁾

1) Graduate Student, Department of Built Environment, Tokyo Institute of Technology, Japan

2) Professor, Structural Engineering Research Center, Tokyo Institute of Technology, Japan

3) Associate Professor, Structural Engineering Research Center, Tokyo Institute of Technology, Japan

4) Research Associate, Structural Engineering Research Center, Tokyo Institute of Technology, Japan

5) Professor, Integrated Institute, Tokyo Institute of Technology, Japan

matsuda@serc.titech.ac.jp, kasai@serc.titech.ac.jp, hsakata@serc.titech.ac.jp

ooki@serc.titech.ac.jp, wada@serc.titech.ac.jp

Abstract: In Japan there are 10 million inadequate wooden houses against building standard law and most of them are composed of conventional post-and-beam. Passive control schemes to mitigate their seismic damage are important. In order to reduce seismic response and damage of wooden houses effectively, a series of so-called shear-link-type passive control systems, which include both velocity- and deformation-dependent dampers were proposed. In this study, a number of shaking table tests of the full-scale two-story wooden frame specimens were carried out. The specimens are composed of conventional post-and-beam with structural plywood, or K-brace and damper for structural element. When the structure is subjected to seismic acceleration equivalent to the maximum 0.6g, the layer with only structural plywood behaved with slip hysteresis. The subsequent deformation increases against seismic acceleration equivalent to the maximum 0.2g. The deformation mode is sensitive to the ratio of layer's stiffness. The layer with only K-brace and viscoelastic damper exerts high energy absorbing-capacity from small to large amplitude. If the layer deforms to the maximum story drift angle of 1/45rad., the subsequent response changes little from the response in the previous cycles. Moreover, viscoelastic dampers absorb 80 percent of total energy absorbed by the whole layer.

1. INTRODUCTION

In Japan, it is not necessarily an exaggeration that the damage cost from earthquakes is almost determined by the damage induced into many wooden houses. In the Hanshin-Awaji (Kobe) Earthquake that occurred in 1995, the number of collapses or seriously damaged of wooden houses were approximately 250,000 (steel structure is 460, reinforced concrete structure is 600). It is said that approximately 10 million wooden houses are insufficient for earthquake resistant in Japan, and those houses need to be reinforced immediately. Moreover, to design new wooden houses to be resistant to earthquakes, it is important to investigate rational methods applying the passive control to wooden houses.

In order to mitigate the damage of wooden houses and seismic response, dynamic cyclic loading tests for wooden frames with passive controls¹⁾ and shaking table tests for one-story wooden frames that corresponded to mass for two-story were carried out²⁾. In this study, design and construction of two-story wooden frames with viscoelastic damper or friction damper or structural plywood were undertaken. The objective of this study is to figure out the dynamic behavior of these specimens by shaking table tests.

2. OUTLINE OF SHAKING TABLE TEST

2.1 Specimen Concept and Setup

Figure 1 illustrates the setup. The specimen (wooden frame) is composed of conventional post-and-beam and has a configuration of piled-up two cubes with 2730mm length on each side. The wooden frame has glulam spruce timber for the post (105 x 105mm), glulam red pine timber for the groundsill (105 x 105mm), glulam red pine timber for the beam (105 x 180mm), and structural plywood for the floor slabs (thickness of 28mm).

Seismic resistant frame is allocated in the center plane in the shaking direction. In the other planes the joints are almost pin-connected to limit the story shear force to be induced. The weight of the specimen is determined so that the two structural elements of the wall-strength-factor 2 have the resistance equivalent to the design lateral force for one story. Design lateral force for one story is obtained as a product of the weight of the specimen and the standard base shear coefficient ($= 0.2$). Here, the wall-strength-factor is defined as the value of the lateral force corresponding to the 1/120rad. story drift angle deformation of 1m structural element divided by 1.96kN (= shear force which 1m wall can resist). The mass ratio of the 2nd-story to the 1st-story, $\alpha (= m_2/m_1)$, is 0.9, assuming the heavy roof and house where the area of the 1st-story is equal to that of the 2nd-story. The weights over the structural element have an effect on the pull-out of the post of the structural element. Therefore, the weights over the structural element are determined so that permanent axial load of the post of structural element is approximately equal to the dead load of the post of real houses. In the plane orthogonal to the shaking direction, the wood braces are set up to prevent torsion.

2.2 Measurement and Vibration Scheme

Figure 2 illustrates the measurement. Laser displacement sensors on the measurement frame built in the shaking table were used to measure the relative displacement of the specimen to the shaking table, and story drifts u_1 , u_2 are calculated by using Equation 1. There are acceleration sensors at the specimen's groundsill, beams on the 1st-story and the 2nd-story, and the story lateral force, F_1 and F_2 , are calculated by using Equation 2. The calculation of the story lateral force is found to be correct since Equation 3 was verified by using the data of the shear-type load-cell arranged under the basement.

$$u_2 = d_2 - d_1 \quad u_1 = d_1 - d_0 \quad (1)$$

$$F_2 = m_2 \times a_2 \quad F_1 = F_2 + m_1 \times a_1 \quad (2)$$

$$F_1 + m_0 \times a_0 = \sum F_{load} \quad (3)$$

Vibration scheme is listed in Table 1. For all earthquakes, the coefficient of variation of the displacement response spectrum and the pseudo-acceleration response spectrum obtained from the

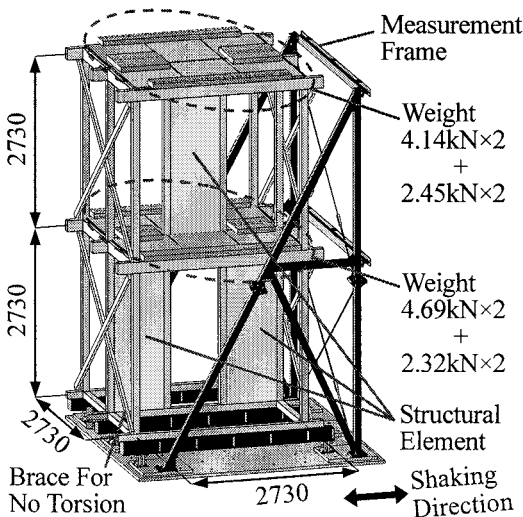


Figure 1 Setup

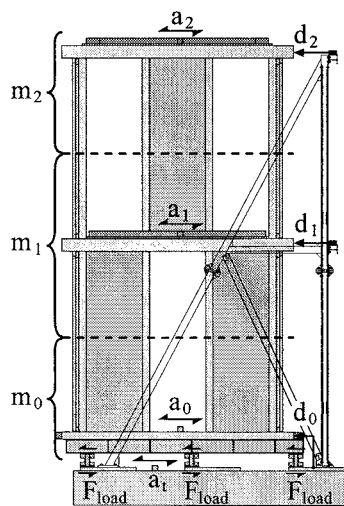


Figure 2 Measurement

Table 1 Vibration Scheme

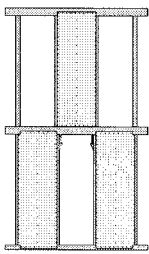
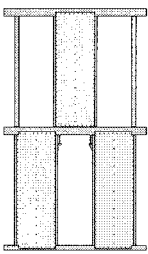
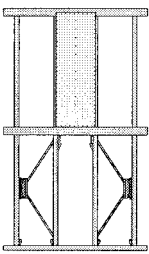
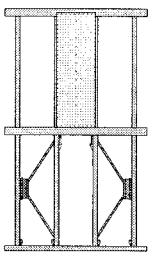
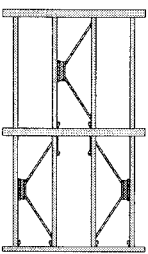
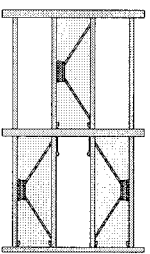
No.	Name	Maximum Acc.(g)
1	W1	0.1
2	Taft0.2g	0.2
3	W2	0.1
4	Kobe0.2g (1st)	0.2
5	W3	0.1
6	Kobe0.6g	0.6
7	W4	0.1
8	Kobe0.2g (2nd)	0.2
9	W5	0.1
Bolt The Joint Again		
10	W6	0.1
11	Kobe0.83g	0.83
12	W7	0.1

acceleration at the specimen's groundsill against target spectrum was checked to be within 5% for the natural period from 0.1 to 1.0 second. In addition, 2WP-1.6WP was not vibrated in Kobe0.83g because of the risk of collapse and 2VW-VW was vibrated in Kobe0.83g twice.

2.3 Parameter of Specimen

Specimen parameter is listed in Table 2. The effective-wall-length in Table 2 is represented by the product of the wall-strength-factor of structural element and the length. For structural plywood of the 2nd-story, the wall is represented by the value considering the strength-factor at the adjustment since stiffness and strength by the number of nails obtained by Murakami and Inayama's equations were changed³⁾. In addition, the letters of WP and W mean Plywood, K means K-Brace, V means Viscoelastic Damper, and F means Friction Damper.

Table 2 Parameter of Specimen

No.	1	2	3	4	5	6
Specimen						
Name	2WP-1.6WP	2WP-1.2WP	2FK-1.6WP	2VK-1.6WP	2VK-VK	2VW-VW
Kind	2 Wood Panel	Wood Panel	Wood Panel	Wood Panel	VE Damper	VK + 1.2WP
	1 Wood Panel	Wood Panel	Friction Damper	VE Damper	VE Damper	2VK + 2WP
Effective wall length	2 4.8×0.91m	3.6×0.91m	3.6×0.91m	3.6×0.91m	5.0×0.91m	8.6×0.91m
	1 3.0×1.82m	3.0×1.82m	6.0×1.82m	5.0×1.82m	5.0×1.82m	8.0×1.82m
$\beta = k_2/k_1$	0.58	0.55	0.39	0.77	0.48	0.44
1st Freq.	3.64	3.62	3.91	3.31	2.86	3.86

3. TEST RESULTS AND COMSIDERATION

3.1 Relationships Between Lateral Force and Displacement

Figure 3 illustrates the relationships between lateral force and displacement. The maximum displacement is listed in Table 3. Figure 4 illustrates how nails came off structural plywood.

1st and 2nd-Story Have Structural Plywood: When the specimens were initially subjected to seismic acceleration equivalent to the maximum 0.2g, the specimens behaved within the story drift angle of 1/240rad. However when the specimens were subjected to Kobe0.6g, the specimens behaved with pinched hysteresis having slippage after nails came off structural plywood. When the layer deformed to the maximum story drift angle of 1/40rad., it was observed that corner nails were slightly pulled out of plywood (Figure 4. (a)). The subsequent deformation increased against Kobe0.2g(2nd). In 2WP-1.6WP, the 1st-story was transformed more than the 2nd-story. However, in 2WP-1.2WP, the 2nd-story was transformed more than the 1st-story. Therefore, it is found that the deformation mode is sensitive to the ratio of the story stiffness.

1st-Story Has Passive Control, 2nd-Story Has Structural Plywood: Lateral force of the story with friction damper (1st-story of 2FK-1.6WP) plateaued since friction damper had a slide, and after Kobe0.6g the story had the residual story drift angle of approximately 1/120rad. since the story did not have any other stiffness. The hysteresis of the story with viscoelastic damper (1st-story of 2VK-1.6WP) formed the ellipsoid. When the specimen was subjected to Kobe0.6g, the story deformed to the maximum story drift angle of 1/80rad. However, it can be said that the damage of the story is little, since the deformation of story in Kobe0.2g(2nd) was almost equal to that in Kobe0.2g(1st). The story with structural plywood behaved with pinched hysteresis having slippage after nails slightly come off structural plywood (Figure 4.(c), (d))

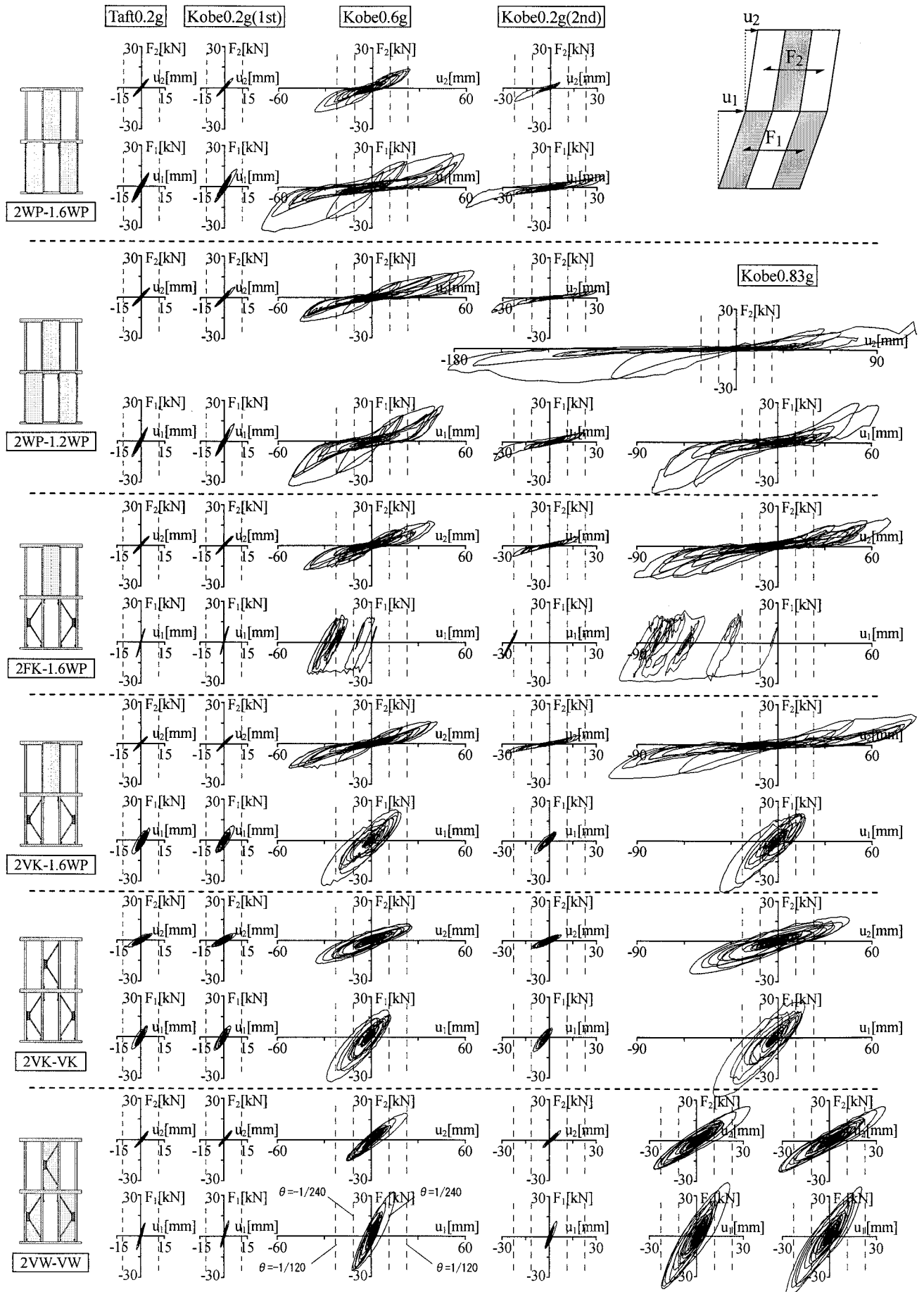


Figure 3 Relationships Between Lateral Force and Displacement

1st and 2nd-Story Have Passive Control: When 2VK-VK was subjected to Kobe0.6g, 2nd-story of 2VK-VK deformed to the maximum story drift angle of 1/75rad. Then, after the story of 2VW-VW –plywood was attached to 2VK-VK, it deformed to the maximum story drift angle of only 1/120rad. When 2VW-VW was subjected to Kobe0.83g, the deformation increased beyond the story drift angle of 1/120rad. However it is verified that structural plywood attached to the viscoelastic damper in parallel functioned effectively, since the deformation of the second Kobe0.83g increased a little beyond the first Kobe0.83g. There was especially no damage observed in appearance after the experiment.

Table 3 Maximum Displacement

Specimen	Story	Taft0.2g		Kobe0.2g(1st)		Kobe0.6g		Kobe0.2g(2nd)		Kobe0.83g	
		mm	rad.	mm	rad.	mm	rad.	mm	rad.	mm	rad.
2WP-1.6WP	2	5.2	525	5.5	496	36.9	74	22.7	120	-	
	1	6.1	448	8.0	341	70.4	39	53.1	51		
2WP-1.2WP	2	5.5	496	6.7	407	64.9	42	37.1	74	184.2	15
	1	5.8	471	6.4	427	53.2	51	35.2	78	80.3	34
2FK-1.6WP	2	5.2	525	6.0	455	43.4	63	23.4	117	91.9	30
	1	3.0	910	3.2	853	41.0	67	29.8	92	101.0	27
2VK-1.6WP	2	4.6	593	5.7	479	52.8	52	26.9	101	107.9	25
	1	5.7	479	6.6	414	32.0	85	9.5	287	37.3	73
2VK-VK	2	8.0	341	7.7	355	35.3	77	11.4	239	56.5	48
	1	5.7	479	6.1	448	28.6	95	10.3	265	41.5	66
2VW-VW	2	4.9	557	5.3	515	23.4	117	7.4	369	34.3	80
	1	3.0	910	3.3	827	15.7	174	5.0	546	22.3	122

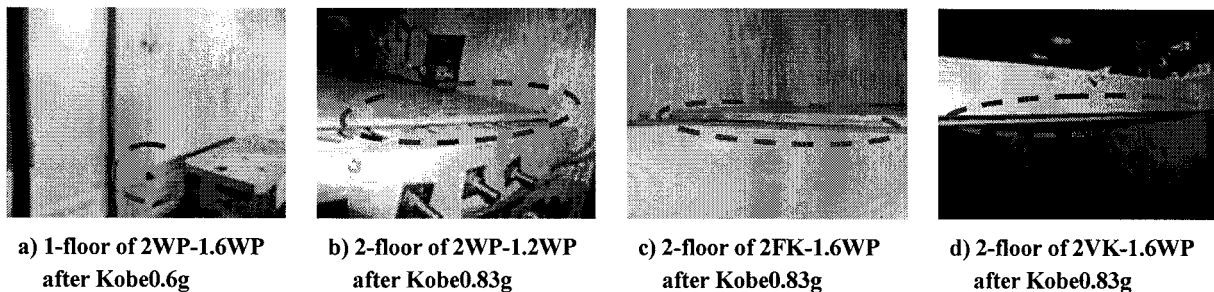


Figure 4 Nails Coming off Structural Plywood

3.2 Ratio of 2nd-Story to 1st-Story of Stiffness

Effective-wall-length and the ratio of the 2nd-story stiffness to the 1st-story stiffness, $\beta (= k_2/k_1)$, is listed in Table 4. In all specimens, effective-wall-length of the specimen exceeds the nominal effective-wall-length. For β from W1 in Table 1, there is little disparity between 2WP-1.6WP and 2WP-1.2WP in spite of the modulation of nails so that β of 2WP-1.6WP is 0.8 and β of 2WP-1.2WP is 0.6. This is because the effect of shear force of nails is small against the acceleration equivalent to 0.1g due to the integration of structural plywood and wooden frame by the friction of interface. This is clearly shown by the fact that there is large disparity between 2WP-1.6WP and 2WP-1.2WP for β

Table 4 Effective-Wall-Length and Ratio of 2nd-Story Stiffness to 1st-Story Stiffness

Specimen	Assumption	Effective Wall Length				from W1			from Taft0.2g		
		Assumption		Experiment							
	β	1st-story	2nd-story	1st-story	2nd-story	k1	k2	β	k1	k2	β
	-	[m]		[m]		[kN]		-	[kN]		-
2WP-1.6WP	0.80	6.0	4.8	11.1	8.3	2.80	1.62	0.58	1.95	1.35	0.69
2WP-1.2WP	0.60	6.0	3.6	12.6	7.6	2.83	1.56	0.55	2.10	1.19	0.56
2FK-1.6WP	0.60	8.0	4.8	11.8	8.4	3.80	1.48	0.39	3.62	1.24	0.34
2VK-1.6WP	0.48	10.0	4.8	16.9	7.7	1.70	1.30	0.77	1.55	1.11	0.72
2VK-VK	0.50	10.0	5.0	17.5	7.3	1.47	0.71	0.48	1.50	0.60	0.40
2VW-VW	0.54	16.0	8.6	23.7	11.5	3.23	1.41	0.44	3.35	1.34	0.40

from Taft0.2g. In case of the specimens that have the same type of structural elements in the 1st-story and 2nd-story, β obtained from the experiment is less than assumed β . This is because the pulling-bolt in the 1st-story uses the steel beam which intends the foundation for reaction force and pulling-bolt in the 2nd-story use the post of the 1st-story for reaction force.

3.3 Distribution of Energy

Figure 5 illustrates the distribution of energy. The horizontal axis shows the number of specimens (Table 3). In general, energy spectrum is proportional to the natural period in the short period range and this tendency is observed in this experiment too. 2FK-1.6WP, 2VW-VW with short natural period absorbed less energy than the other specimens. In the specimen with the friction damper, when the specimen is subjected to earthquake of 0.2g, the damper absorbs little energy because of no slide of damper, when the specimen is subjected to earthquake of 0.6g and 0.83g the damper absorbs 60% of the entire energy (No.3). In the specimen with the viscoelastic damper, the damper absorbs constant energy, and in 2VK-VK the damper absorbs 80% of the entire energy (No.5). It is clear that the damage of the wooded frame is a little because the damper absorbs most part of entire energy.

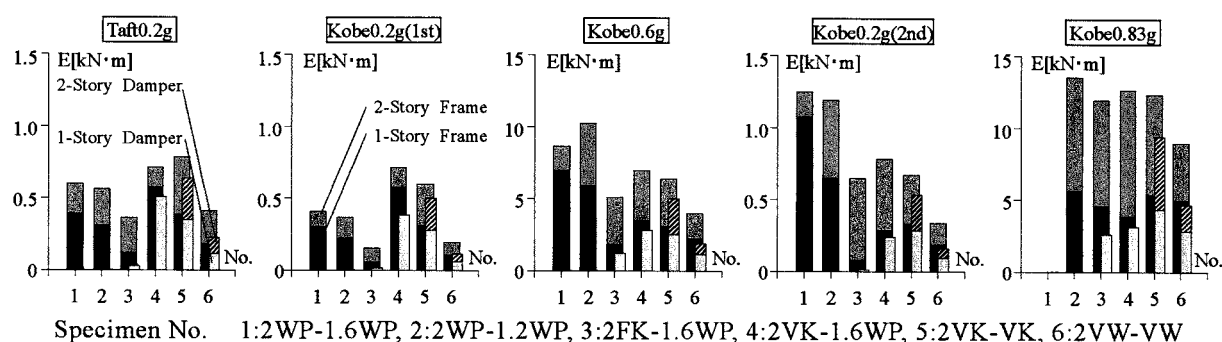


Figure 5 Distribution of energy

4. CONCLUSIONS

- When the structure is subjected to seismic acceleration equivalent to the maximum 0.6g, the layer with only structural plywood behaviors with pinched hysteresis having slippage after nails struck to plywood pull out. The subsequent deformation increases against seismic acceleration equivalent to the maximum 0.2g.
- The deformation mode is sensitive to the ratio of layer's stiffness.
- The layer with only K-brace and viscoelastic damper exerts high energy absorbing-capacity from small to large amplitude. If the layer deforms to the maximum story drift angle of $1/45$ rad., the subsequent response changes little from the response in the previous cycles. Moreover, viscoelastic dampers absorb 80 percent of total energy absorbed by the whole layer.

Acknowledgements:

This study is program supported by a grant from "Electric Power Development Co., Ltd". We would like to express our appreciation to the company.

References:

1. Kasai, K. and Sakata, H. and Wada, A. and Miyashita, T.: "Dynamic behavior of a wood frame with shear link passive control mechanism involving k-brace", *Journal of Structural and Construction Engineering*, No.598, 2005.12, pp.51-60
2. Kasai, K. and Sakata, H. and Wada, A. and Midorikawa, M. and Ooki, Y. and Nakagawa, T.: "Shaking table tests of wood frames with deformation-dependent dampers", *Journal of Structural and Construction Engineering*, No.594, 2005.8, pp.101-110
3. Murakami, M. and Inayama, M.: "Formulae to predict the elastic and plastic behavior of sheathed walls with any nailing arrangement pattern", *Journal of Structural and Construction Engineering*, No.519, 1999.5, pp.87-93

MOTION AND CONTROL ANALYSIS OF STRUCTURE UNDER EARTHQUAKE EXCITATION

C. Y. Wang¹⁾, C. C. Chuang²⁾, S. H. Chen³⁾ and R. Z. Wang⁴⁾

1) Professor, Department of Civil Engineering, National Central University, Taiwan

2) Associate Professor, Dept of Civil Engineering, Chuang-Yuan Christian University, Taiwan

3) Graduate Student, Department of Civil Engineering, National Central University, Taiwan

4) Assistant Research Fellow, National Center for Research on Earthquake Engineering, Taiwan

cywang@cc.ncu.edu.tw tchuang@cycu.edu.tw 9372011@gmail.com rzwang@ncree.org.tw

Abstract: In this paper, the explicit vector form intrinsic finite element (VFIFE) method is used to conduct the motion and control analysis of structure under earthquake excitation. This VFIFE method can do the motion analysis of structure with large deformation and rotation from continuous states to discontinuous states. Three dimensional frame elements of the VFIFE method are used to model the progressive failure of structure. Two dimensional frame elements of VFIFE are used to conduct the passive control analysis of structure under earthquake excitation.

1. INTRODUCTION

To prevent the immeasurable losses of human lives and social properties due to earthquakes, the seismic resistance evaluation and retrofitting of civil infrastructures becomes an important issue of many countries in the world. Besides experimental and theoretical study, the numerical simulation is another way to assist engineers to understand the nonlinear dynamic failure behavior of structure under the earthquake excitation. Large deformation, progressive failure and collapse are the most critical deformation states causing structure damage and the threatening to lives. However, the mechanical behaviors inherited in these failure modes are extremely complicated and some physical quantities are difficult to be measured in the test. Therefore, the numerical techniques for the motion and control analyses of a given structure system under earthquake loading are essential in the evaluation of the capability of seismic resistance.

Nonlinear analysis methods developed since last century are used to study the behavior of structures with material and geometrical nonlinearities (Argyris et al.1978, Elias 1986, Leu and Yang 1990, Leu and Yang 1991, Yang and Kuo1994). It is clear seen that the core idea of the nonlinear analysis of structure is how to clearly identify the rigid body component and the deformation component in the motion.

A new computational method so called the Vector Form Intrinsic Finite Element (VFIFE) is developed by Ting et al. (2004 a, b) to handle engineering problems with the following characters: (1) containing multiple deformable bodies and mutual interactions, (2) material non-linearity and discontinuity, (3) large deformation and arbitrary rigid body motions of deformable body. Since the conventional FEM based on variational method requires the total virtual work to be zero but does not require the balance of forces at nodes. These unbalanced residual forces will do some non-zero work

under virtual rigid body motion and cause the inaccuracy and un-convergence of the calculation results. The computation procedure and some concepts of this VFIFE method are similar to the FEM. But the major difference is that the VFIFE does not apply the variational principle on the stress expressed equilibrium equations in its formulation. Instead, VFIFE maintains the intrinsic nature of the finite element method and makes strong form of equilibrium at nodes, the connections of members. All the forces balanced at each node are obtained from the principle of virtual work and the associated deformations are satisfied with the compatibility condition of deformation. Instead of initial boundary value problems as treated by conventional finite element approaches, VFIFE treats the motion of structures or solids as an initial value problem only. In other words, the continuous bodies are represented by a set of particles as shown in Fig. 1. It is also different from those of the explicit finite element approaches which use the lumped mass techniques. The lumped mass technique is nothing but a solution procedure of explicit finite element under the mathematical framework. However, the mass points or particles in VFIFE have physical significance which is interpretable. The particulate nature of the VFIFE method allows it does not have to solve the matrix equations and can avoid dealing the mathematical difficulties in solving matrix equations with ill conditions.

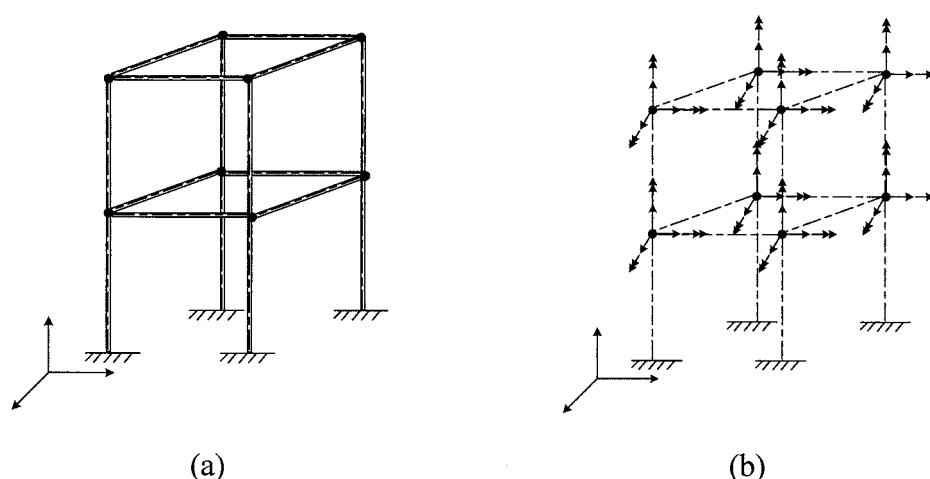


Figure 1 (a) A space frame structure, (b) Discrete particles modeling of a space frame structure system by the VFIFE method.

Recently, VFIFE method has been successfully applied to the nonlinear motion analysis of 2D frame (Wu et al. 2006) and the dynamic stability analysis of space truss structure (Wang et al. 2005, 2006). Wang et al. (2006b) have briefly introduced the formulation of the 3D frame element and applied to the collapse analysis of frame structure under earthquake analysis. Due to the outstanding characters of the VFIFE method, it is very easy to be applied to study the highly nonlinear dynamic behavior of a structure system from continuous to discontinuous states.

In this paper, the applications of frame element in VFIFE on the passive control of structure are presented.

2. FUNDAMENTALS OF THE FRAME ELEMENT IN VFIFE

The basic modeling assumptions for the VFIFE method for 3D frame structures are essentially the same as those in classical structural analysis. A frame is constructed by means of prismatic members and joints. Members are subjected to forces and moments as shown in Fig. 1(b). Joints have work equivalent masses and mass moment of inertias, and can be modeled as discrete rigid bodies. Motions of the joints can be described by the principles of virtual work or equations of motion for particles. Members have no mass, and are thus in static equilibrium. Therefore, the

structural configuration of a space frame structures can be described by the positions of a set of discrete rigid bodies as shown in Fig. 1(b).

The basic modeling assumptions of the 3D frame structure in VFIFE are:

- 1) Each joint and discrete rigid particle has three translational degrees of freedom and three rotational degrees of freedom.
- 2) The mass of each particle is not changed during the motion. However, the matrix of the mass moment of inertias is changed with the directions of the principal axes of the frame element.
- 3) The connection between frame elements can be rigid or hinge.
- 4) The equivalent internal forces and external forces applied on each particle are the summation of the internal force and external forces of the nodes of the elements connecting with the particle.
- 5) Each frame element satisfies the static equilibrium condition, while its internal forces are characterized by the nodes connected to the corresponding particles. The motion of each rigid body particle satisfies the Newton's second law and the Euler's equation.
- 6) The frame element is straight and prismatic and is made of linear elastic material.

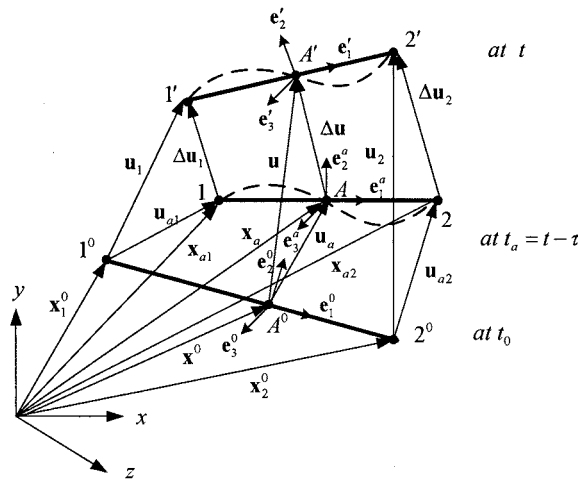


Figure 2 Nodal displacements and displacement increments of a frame element in the spatial-temporal space.

To effectively separate the rigid body displacements from the total displacement of a deformable body, VFIFE constructs a convected material frame to describe the deformation and internal forces of the frame component moving in the spatial-temporal space. The configuration of the frame element at time t_a is chosen as the material frame for the analysis. The displacement vector of the two nodes on the frame element at time t_a is defined as (u_{a1}, u_{a2}) and the time increment used in the analysis is defined as $\tau = t - t_a$. As shown in Fig. 2, the displacement vector of an arbitrary point A at time t_a is defined as u_a . The directional vectors of the principal axis of the cross section at time t_0 , t_a and t are denoted by (e_1^0, e_2^0, e_3^0) , (e_1^a, e_2^a, e_3^a) and (e_1', e_2', e_3') , respectively. The procedure of the construction of these principal directions is clearly explained in the paper for space truss element by the first author (Wang et al., 2006a). The detail of the calculation of internal forces applied on each mass particle can be seen in the paper by Wang et al. (2006b).

Since the VFIFE method uses the motion and relative displacements of particles to identify the internal forces among them. This feature allows users to easily apply the displacement control type excitation to the structure. In the seismic analysis, variations of the displacements and rotations of the element nodes connected to ground can be assigned according to the history of ground motion.

In the following sections, the methods of applying VFIFE on the passive control analysis are explained.

3. MODELLING OF THE PASSIVE CONTROL DEVICES BY THE VFIFE METHOD

The types of devices used in passive control of structures can be characterized by their material property as viscous damper, rubber bearing and by their internal mechanism as Tuned Mass Damper (TMD), Friction Pendulum Bearing (FPB). The modeling of some passive control devices are described as following:

3.1 Tuned Mass Damper (TMD)

Since the VFIFE can perform the motion analysis with large rigid body motion, the motion of tuned mass damper can be modeled by a truss member with a lumped mass at one end as shown in Fig. 3. The length of the pendulum, L , can be calculated according to the design frequency ω_d by the following equation.

$$L = g / \omega_d^2 \quad (1)$$

Where g is the gravity acceleration.

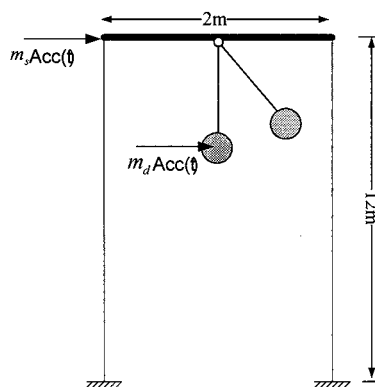


Fig. 3 A frame structure equipped with TMD.

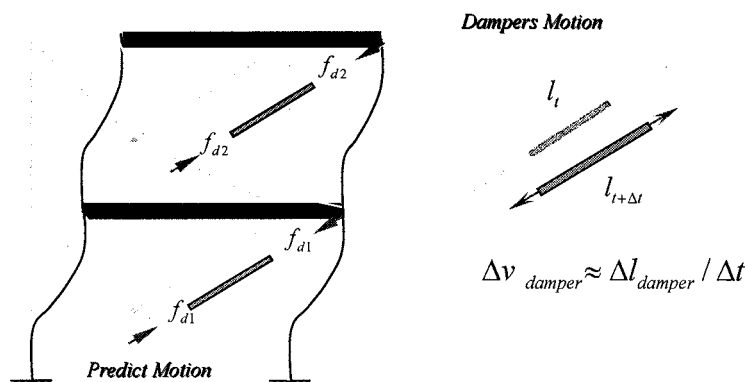


Fig. 4 Calculation of the control force provided by the viscous damper.

3.2 Viscous Damper

In the VFIFE method, as shown in Fig. 4, the control force f_d provided by the viscous damper is determined by the relative velocity between the two joint points of the damper by the following equation

$$f_d = C \left| \frac{\Delta L}{\Delta t} \right|^\alpha \text{sgn}\left(\frac{\Delta L}{\Delta t}\right) \quad (2)$$

Where the $\Delta L / \Delta t = v_D$ is the relative velocity of the two ends of the damper, C is the viscous coefficient of the damper, α is the nonlinearity parameter of the damper and the Δt is the time step used in the numerical analysis.

3.3 Friction Pendulum Bearing (FPB)

The friction pendulum bearing belongs to the sliding base isolation type device. As shown in Fig. 5, the contact analysis procedure is used to calculate the contact force between the sliding surface and the support of the bearing by the penalty method.

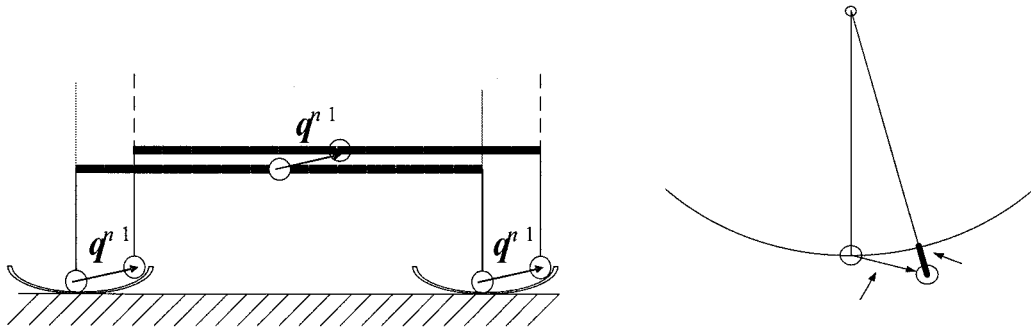


Fig. 5. Modeling of the Friction Pendulum Bearing

4. NUMERICAL EXAMPLE

Energy dissipation or damping system has been widely used in construction to dissipate much of the earthquake-induced energy in elements. Toggle-brace-dampers with various configurations have been used for the delivery of forces from the energy dissipation devices to the structural frame. Constantinou et al. (2001) investigated the “toggle-brace-damper” system and verified its ability to amplify the axial displacements of damper and the efficiency of energy dissipation through both cyclic loading tests and shaking table tests with a single degree of freedom steel model. Huang et al. (2005) conducted shaking table tests to investigate the seismic responses of a three-story steel model with and without linear viscous toggle-brace-dampers. In his research, a procedure for determining the relationship between the displacement magnification factor and the geometry of the toggle-brace mechanism is established to facilitate practical applications. For the structure with complex configuration, the design and testing of ability of damper system are difficult and costly. The numerical simulation can be an effective tool to assist the engineering analysis.

As shown in Fig. 6, the behaviors of frame structure with brace damper subjected to earthquake loading were investigated by the VFIFE method. The mass density of the column is $\rho = 0.01 \text{ kg/m}^3$,

Young's modulus $E = 288000 \text{ kN/m}^2$, mass moment of inertial $I = 1 \text{ m}^4$, cross sectional area $A = 1 \text{ m}^2$. Rigid beam of mass density $\rho = 50 \text{ kg/m}^3$ is used to simulate the floor. Both linear and nonlinear dampers were used to do the simulation. The parameters of the linear damper are $\alpha = 1.0$, $C = 191 \text{ kN/(m/sec)}$ and are $\alpha = 0.5$, $C = 1500(N - (\text{sec/mm})^\alpha)$ for the nonlinear damper. The length of the damper is 8.062 m with cross sectional area $A = 1 \text{ m}^2$ and has mass density $\rho = 0.01 \text{ kg/m}^3$. The length of the two brace is 4.123 m and 8.062 m , respectively. These braces have the same mass density $\rho = 0.01 \text{ kg/m}^3$ and the cross sectional area $A = 1 \text{ m}^2$.

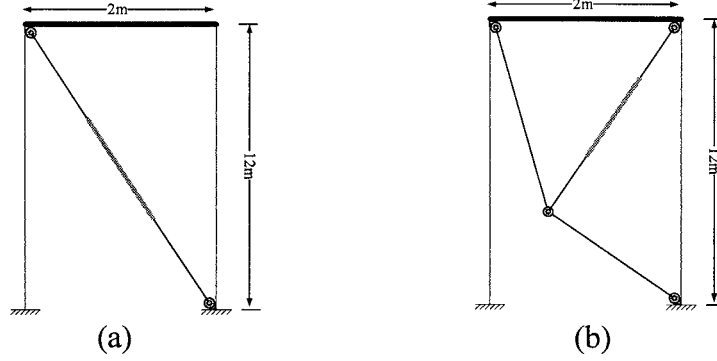


Fig. 6. Frame structure with brace damper subject to earthquake excitation: (a) diagonal brace-damper system; and (b) upper toggle brace damper system.

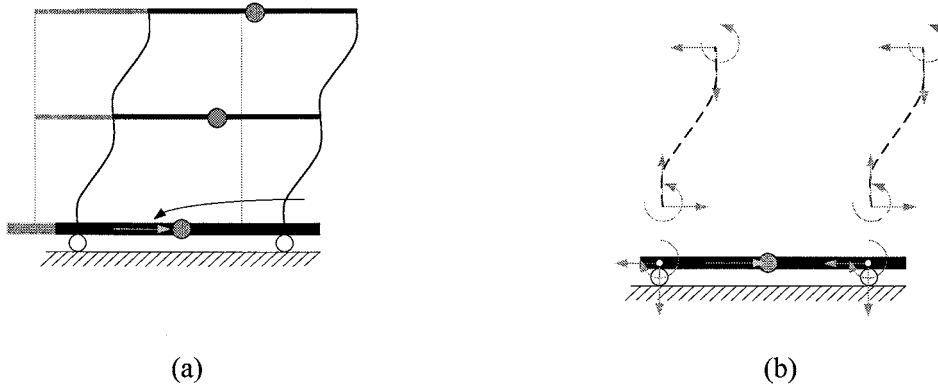


Fig. 7 Shaking table type loading based on the ground linear and angular accelerations

Two ways of loading deployment were used for the structure to subject El Centro earthquake. One is the pseudo dynamic loading conventionally used in the structural dynamic analysis and the other one is the shaking table type excitation. Since the VFIFE is very flexible to apply load and displacement control on the structure, a rigid plate is added into the process of simulation. An acceleration equivalent force is calculated by multiplying the mass of the rigid plate by the ground acceleration of the structure. The equation of motion of the rigid plate can be solved to ensure the acceleration of the plate is equivalent to the desired ground acceleration. The dynamic displacements of the points on the plate connected to the structure are used into the VFIFE analysis as the displacement boundary conditions (see Fig. 7). This technique can be used to simulate the dynamic behaviors of structure subjected ground motion with rotational degrees of freedom.

From the comparisons shown in Figs. 8-10, one can realize that the toggle-brace-damper can amplify the damper displacement and dissipate energy effectively compared with the diagonal brace damper. Besides, the shaking type loading excitation is accurate and rational. This newly proposed VFIFE

method is quite effective for engineers to conduct motion and control analyses of structures under various types of dynamic excitations.

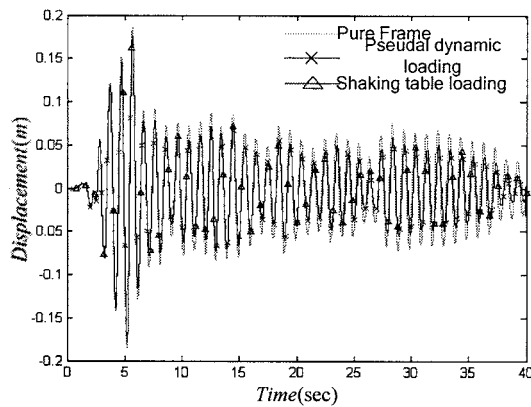


Fig. 7 Comparison of analytical responses of linear diagonal brace damper frame and pure frame subjected to pseudo dynamic and shaking table type loadings.

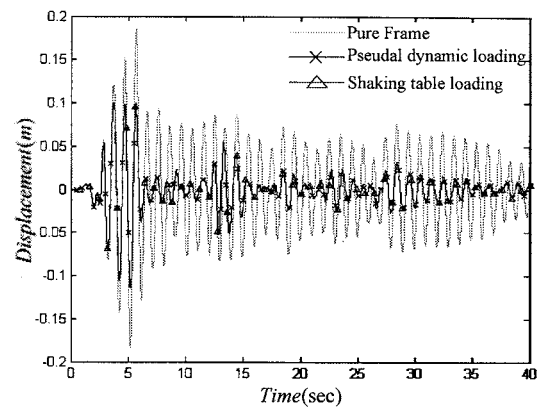


Fig. 8 Comparison of analytical responses of linear upper toggle-brace damper frame and pure frame subjected to pseudo dynamic and shaking table type loadings.

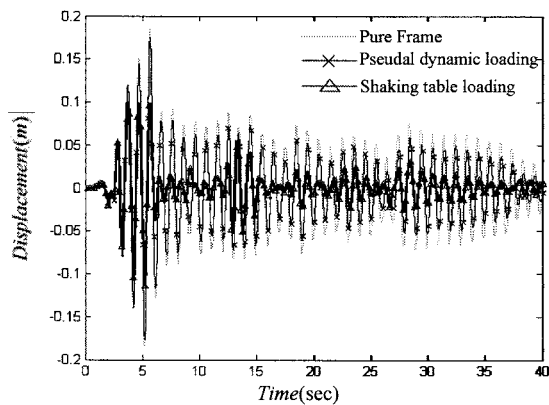


Fig. 9 Comparison of analytical responses of nonlinear diagonal brace damper frame and pure frame subjected to pseudo dynamic and shaking table type loadings.

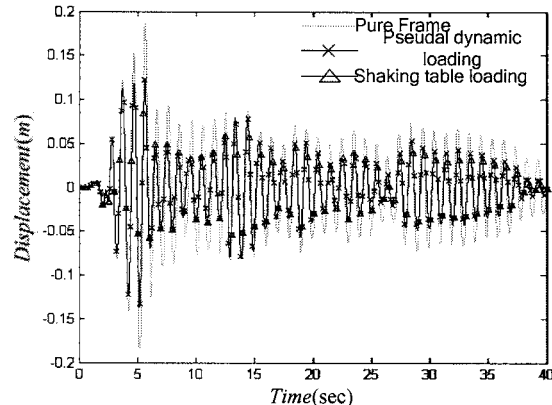


Fig. 10 Comparison of analytical responses of nonlinear upper toggle-brace damper frame and pure frame subjected to pseudo dynamic and shaking table type loadings.

5. CONCLUSIONS

A novel numerical method called the Vector Form Intrinsic Finite Element (VFIFE) method for the motion analysis of frame structure is presented. Numerical examples demonstrate that the VFIFE method can effectively conduct passive control analysis of structure under earthquake excitation. Due to some special features of VFIFE, it can conduct simulations of the hybrid control of structure with progressive failure and collapse. It is believed that the further development of VFIFE method can provide engineers as an effective and friendly tool to analyze very complicated engineering

problems.

Acknowledgements:

The authors acknowledge support from Japan Ministry of Education, Culture, Sport, Science, and Technology (MEXT) for establishing the Center for Urban Earthquake Engineering (CUEE) in Tokyo Institute of Technology. The support has made possible this international conference, as well as international joint research projects and exchange programs with foreign universities.

References:

- Argyris, J. H., Dunne, P. C., and Scharpf, D. W., (1978), "On large displacement-small strain analysis of structures with rotational degree of freedom," *Computer Methods in Applied Mechanics Engineering*, **14**, 401-451.
- Constantinou, M.C., Tsopelas, P., Hammel, W., and Sigaher, A.N.(2001), "Toggle-Brace-Damper Seismic Energy Dissipation Systems," *Journal of Structural Engineering*, Volume 127, No. 2, 105-112.
- Elias, Z. M., (1986), *Theory and Methods of Structural Analysis*, John Wiley & Sons, New York, N.Y.
- Huang, J.S., Y. N. Huang, and Y. H. Hung (2005), "Analytical and Experimental Study of Toggle-Brace-Damper Systems," *Journal of Structural Engineering*, ASCE, Vol. 131, No. 7, 1035-1043.
- Leu, L. J., Yang, Y. B., (1990), "Effects of rigid body and stretching on nonlinear analysis of trusses," *Journal of Structural Engineering*, ASCE, Vol. 116, No. 10, 2582-2598.
- Leu, L. J., and Yang, Y. B., (1991), "Post-buckling analysis of steel space trusses," *Journal of Structural Engineering*, ASCE, Vol. 117, No. 12, 3824-3828.
- Shih, C., Wang, Y. K., and Ting, E. C., (2004), "Fundamentals of a vector form intrinsic finite element: Part III. Convected material frame and examples," *Journal of Mechanics*, Vol. 20, No. 2, 133-143.
- Symans, M.D., Constantinou, M.C. (1999). "Semi-active control systems for seismic protection of structures: a state-of-the-art review," *Engineering Structure*, 21, 469-481.
- Ting, E. C., Shih, C., and Wang, Y. K., (2004a), "Fundamentals of a vector form intrinsic finite element: Part I. basic procedure and a plane frame element," *Journal of Mechanics*, Vol. 20, No. 2, 113-122.
- Ting, E. C., Shih, C., and Wang, Y. K., (2004b), "Fundamentals of a vector form intrinsic finite element: Part II. plane solid elements," *Journal of Mechanics*, Vol. 20, No. 2, 123-132.
- Wang, C. Y., Wang, R. Z., Wu, T. Y., Ting, E. C., and Kang, L. C., (2003), "Nonlinear Discontinuous Deformation Analysis of Structure," *Proceedings of the Sixth International Conference on Analysis of Discontinuous Deformation (ICADD-6)*, edited by Ming Lu, 79-91, A. A. Balkema Publishers.
- Wang, C. Y., Wang, R. Z., Kang, L. C., and Ting, E. C., (2004), "Elastic-Plastic Large Deformation Analysis of 2D Frame Structure," *Proceedings of the 21st International Union of Theoretical and Applied Mechanics*, IUTAM, August 15-21, Warsaw, Poland.
- Wang, C. Y., Wang, R. Z., Chuang, C. C., and Wu, T. Y., (2006), "Nonlinear Dynamic Analysis of Reticulated Space Truss Structure," *Journal of Mechanics*, Vol. 22, No. 3, 235-248.
- Wang, C. Y. and R. Z. Wang, (2006) "Numerical Simulation of the Progressive Failure and Collapse of Structure Under Seismic and Impact Loading," *Proceedings of the 4th International Conference on Earthquake Engineering*, October 12-13, 2006, Taipei, Taiwan.
- Wang, R. Z., Chuang, C. C., Wu, T. Y., and Wang, C. Y., (2005), "Vector form analysis of space truss structure in large elastic-plastic deformation," *Journal of the Chinese Institute of Civil Hydraulic Engineering*, Vol. 17, No. 4, 633-646 (in Chinese).
- Wang, R. Z., Kang, L. C., Wu, S. Y., Wang, C. Y., (2005), "Numerical Simulation of the Whipping Problem of High Pressure Piplin," *Chinese Society of Structural Engineering*, Vol. 20, No. 4, 120-143 (in Chinese).
- Wu, T. Y., Wang, R. Z., and Wang, C. Y., (2006), "Large deflection analysis of flexible planar frames," *Journal of the Chinese Institute of Engineers*, Vol. 29, No. 4, 593-606.
- Yang, Y. B., and Chiou, H. T., (1987b), "Rigid body motion test for nonlinear analysis with beam elements," *Journal of Structural Engineering*, ASCE, Vol. 113, No. 9, 1404-1419.
- Yang, Y. B., and Kuo, S. R., (1994), *Theory & Analysis of Nonlinear Framed Structures*, Prentice-Hall.

SEISMIC TESTING OF A NONLINEAR STRUCTURE WITH A MR DAMPER

T. Y. Lee¹⁾, K. Kawashima²⁾, and P. C. Chen³⁾

1) Assistant Professor, Department of Civil Engineering, National Central University, Taiwan

2) Professor, Department of Civil and Environmental Engineering, Tokyo Institute of Technology, Japan

3) Graduate Student, Department of Civil Engineering, National Central University, Taiwan

tylee@ncu.edu.tw, kawashima.k.ae@m.titech.ac.jp, 943202021@cc.ncu.edu.tw

Abstract: A series of shaking table tests by using a two-story shear-type structure model to mimic the dynamic behavior of an isolated bridge was conducted to demonstrate the performance of a semiactive control system. The semiactive control system by using a MR damper and based on the sliding mode control algorithm was successfully implemented and evaluated. Numerical simulations based on the results of the system identification and under ideal control situations were performed. Through the comparison between analytical and experimental time history results, the correlations for the control damping force and the response quantities are satisfactory. The MR damper is capable of tracing the control force demanded by the control algorithm. The results show that the semiactive control system based on the sliding mode control has outstanding performance. The semiactive control system provides a valuable control method for nonlinear structures.

1. INTRODUCTION

Although active control systems have been studied to mitigate the seismic response of a structure, they require extensive external power supply and their applicability is still the issue of concern. Semiactive control systems combine the major advantages of active control systems having versatility and adaptability and passive control systems having reliability. In particular, they require lower energy supply. Studies on semiactive control for linear structures have been performed by a number of researchers (e.g. Spencer and Nagarajaiah 2003). However few studies on semiactive control for nonlinear structures have been investigated (Lee and Kawashima 2006). Numerical simulation results indicate that semi-active control is capable of achieving comparable performance to active control for isolated bridges which exhibit nonlinear behavior under near-field ground motions. In this paper, shaking table experimental tests were performed to verify the effectiveness of semi-active control and show the practical implementation. A two-story shear-type structure model was designed to imitate the dynamic behavior of an isolated bridge. A magneto-rheological (MR) damper was installed on the second story to be the semi-active control device. The used control algorithm is sliding mode control method which has been showed to be particularly attractive for control of nonlinear structures. Two ground motions recorded in 1995 Kobe earthquake and 1999 Chi-Chi earthquake were used as the input excitations. Experimental data demonstrate that the semi-active control system based on the sliding mode control is quite effective for practical implementation on nonlinear structures.

2. EXPERIMENTAL SETUP AND SYSTEM IDENTIFICATION

Experimental evaluation of a semi-active control system with a MR damper was conducted on the shaking table at Department of Civil and Environmental Engineering, Tokyo Institute of Technology, Japan. A two-story shear-type structure model made of steel plates was designed to imitate the dynamic behavior of isolated bridges, as shown in Figure 1. The model did not represent a similitude-scaled replica of a full-scale structure. Rather, the structure model was designed as a small structural system. About 100 kg of mass was put on the top level to simulate the bridge deck weight. Most mass of the model is concentrated on the first and second floor levels. There are 85 kg and 200 kg on the first and second floors, respectively. In particular, since the column plates are replaceable, next nonlinear test can be continued using the same model by only changing the steel plates. A magneto-rheological (MR) damper with capacity of 2 kN, produced by Lord Corporation, USA, was installed on the second story as the semi-active control device. A load cell (capacity 2 kN) is set between the MR damper and the supporting bracket to measure the force generated by the damper. The acceleration and displacement responses of all floor levels were recorded during experimental testing by using accelerometers and LVDTs. However, only data from accelerometers are utilized for feedback. The displacements are recorded for reference only.

Prior to each nonlinear experimental test, the dynamic properties of the test modal were identified using white noise as input to the shaking table and free vibration. The first two natural frequencies are 9.2 and 31.0 rad/sec. The damping ratios for both modes are 0.4%.

In order to understand the behavior of the MR damper, the MR damper was excited by a servo-hydraulic actuator under harmonic excitations of 0.5 Hz, 1 Hz, and 2 Hz, with current varying from 0 mA to 1000 mA, as shown in Figure 2. The force-displacement behavior of the damper is shown in Figure 3. The MR damper model consisting of friction damping force and viscous damping force, which are functions of current, was constructed (Ruangrassamee and Kawashima 2001) as.

$$V_{MR}(t) = f_m(t) + c_m(t)\dot{x}_m(t) \quad (1)$$

where $V_{MR}(t)$ is the exerting damping force by the MR damper; f_m and c_m are assumed as the forms of

$$f_m(t) = f_{m1} + f_{m2}I(t); \quad c_m(t) = c_{m1} + c_{m2}I(t) \quad (2)$$

The friction damping force and viscous damping coefficient of the MR damper with respect to current are shown in Figure 4.

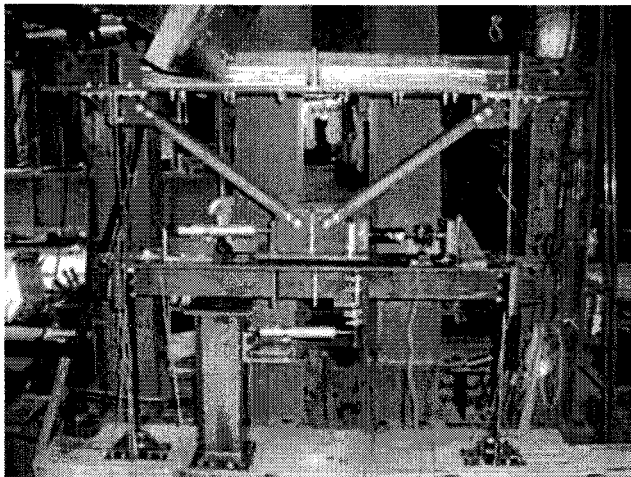


Figure 1 Two-story Shear-Type Test Structure

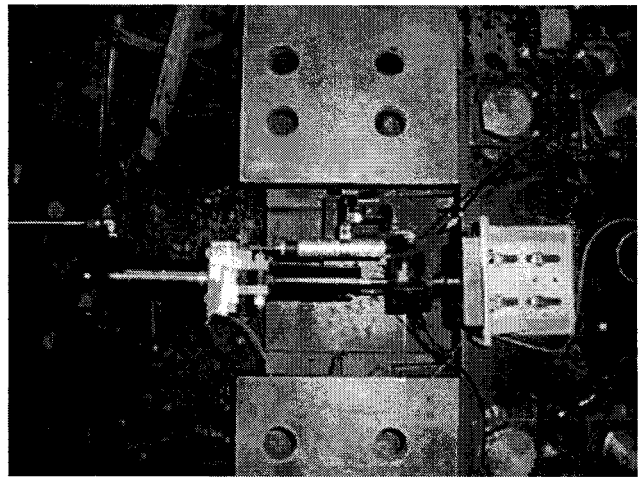


Figure 2 Test set-up for the MR damper

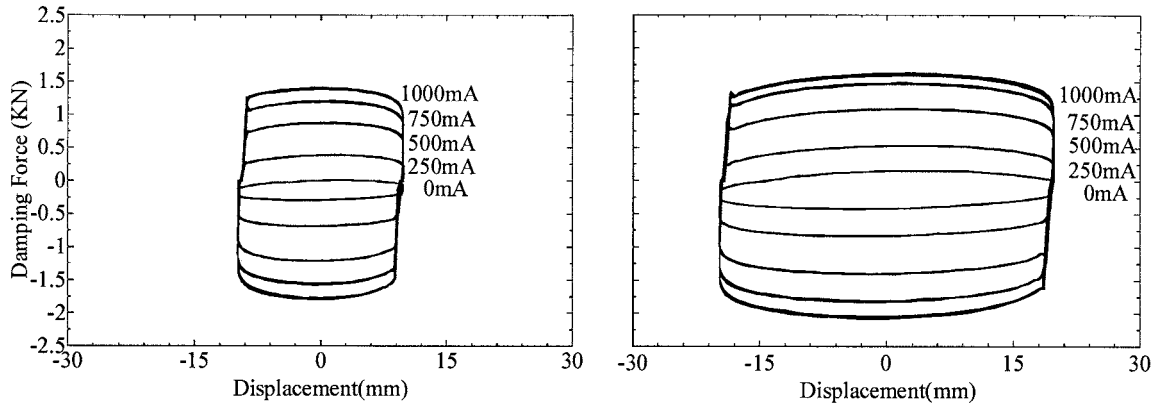


Figure 3 Force-Displacement Response of MR Damper

3. CONTROL ALGORITHM

Sliding mode control is used to command the MR damper. The method of sliding mode control is described briefly in the following. The equation of motion for a lump-mass nonlinear shear-type structure subjected to an earthquake acceleration \ddot{x}_g can be expressed as

$$\mathbf{M}\ddot{\mathbf{X}}(t) + \mathbf{C}\dot{\mathbf{X}}(t) + \mathbf{F}[\mathbf{X}(t)] = \mathbf{H}\mathbf{U}(t) + \boldsymbol{\eta}\ddot{x}_g(t) \quad (3)$$

in which $\mathbf{X}(t) = [x_1, x_2, \dots, x_n]^T$ is an n -vector with $x_j(t)$ being the displacement of the j th mass; \mathbf{M} and \mathbf{C} are $(n \times n)$ mass and damping matrices, respectively, where linear viscous damping is assumed for the bridge; $\mathbf{F}[\mathbf{X}(t)]$ is an n -vector denoting the nonlinear restoring force that is assumed to be a function of $\mathbf{X}(t)$; \mathbf{H} is a $(n \times r)$ matrix denoting the location of r controllers; and $\boldsymbol{\eta}$ is an n -vector denoting the influence of the earthquake excitation.

The nonlinear restoring force vector $\mathbf{F}[\mathbf{X}(t)]$ in Eq. (3) can be subdivided into two parts as

$$\mathbf{F}[\mathbf{X}(t)] = \mathbf{K}\mathbf{X}(t) + \hat{\mathbf{F}}[\mathbf{X}(t)] \quad (4)$$

in which \mathbf{K} is an $(n \times n)$ initial stiffness matrix; and $\hat{\mathbf{F}} = [f_1, f_2, \dots, f_n]^T$ is an n -vector representing the nonlinear force part of the restoring force as a function of $\mathbf{X}(t)$.

Substituting Eq. (4) into Eq. (3), the space-state motion equations can be arranged as

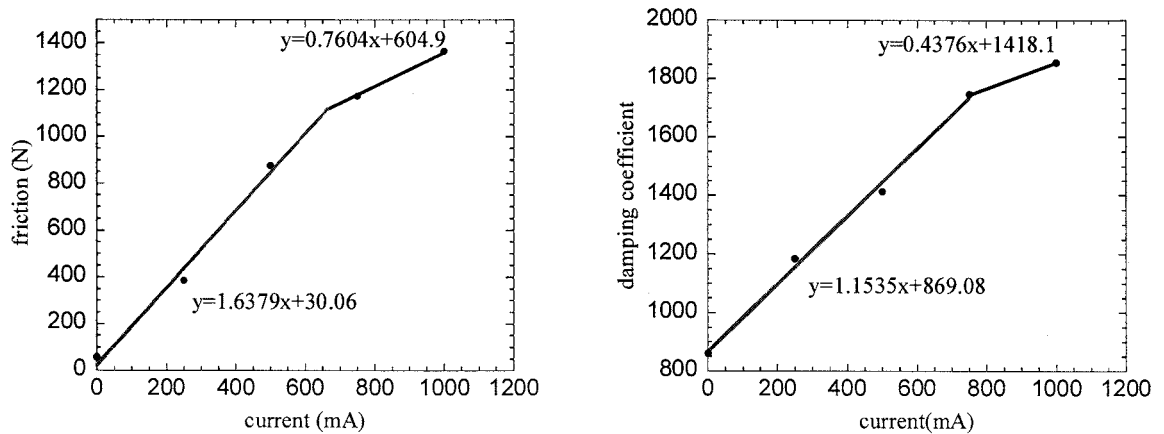


Figure 4 (a) Friction Damping Force and (b) Viscous Damping Coefficient of MR Damper Model

$$\dot{\mathbf{Z}}(t) = \mathbf{A}\mathbf{Z}(t) - \mathbf{f}(t) + \mathbf{B}\mathbf{U}(t) + \mathbf{E}(t) \quad (5)$$

where $\mathbf{Z}(t) = \begin{bmatrix} \mathbf{X}(t) & \dot{\mathbf{X}}(t) \end{bmatrix}^T$ is a $2n$ state vector and the other matrices are defined as follows:

$$\mathbf{A} = \begin{bmatrix} \mathbf{0} & \mathbf{I} \\ -\mathbf{M}^{-1}\mathbf{K} & -\mathbf{M}^{-1}\mathbf{C} \end{bmatrix}; \quad \mathbf{f}(t) = \begin{bmatrix} \mathbf{0} \\ \mathbf{M}^{-1}\hat{\mathbf{F}} \end{bmatrix}; \quad \mathbf{B} = \begin{bmatrix} \mathbf{0} \\ \mathbf{M}^{-1}\mathbf{H} \end{bmatrix}; \quad \mathbf{E}(t) = \begin{bmatrix} \mathbf{0} \\ \mathbf{M}^{-1}\boldsymbol{\eta} \end{bmatrix} \ddot{x}_g(t) \quad (6)$$

in which \mathbf{A} is a $(2n \times 2n)$ linear elastic system matrix; \mathbf{f} is a $2n$ nonlinear part force vector; \mathbf{B} is a $(2n \times r)$ control force location matrix, and \mathbf{E} is a $2n$ earthquake ground excitation vector.

In sliding mode control, the response trajectory is driven toward the sliding surface by the designed controller, where the motion on the sliding surface defined by $\mathbf{S} = \mathbf{0}$ is stable, and then it is maintained on the sliding surface. The sliding surface can be determined using the pole assignment method or the LQR method. To design the controller, Lyapunov function $\dot{V} = \mathbf{S}^T \dot{\mathbf{S}} \leq 0$ is considered to obtain a possible continuous controller as (Yang 1995)

$$\mathbf{U} = \mathbf{G} - \delta \boldsymbol{\lambda}^T \quad (7)$$

where

$$\mathbf{G} = -(\mathbf{P}\mathbf{B})^{-1} \mathbf{P}(\mathbf{A}\mathbf{Z} - \mathbf{f} + \mathbf{E}); \quad \boldsymbol{\lambda} = \mathbf{S}^T \mathbf{P}\mathbf{B} \quad (8)$$

, and both $\boldsymbol{\alpha}$ and δ are specified by designers.

Considering one step of time delay and rearranging the state motion equations by Eq. (5) as $\mathbf{A}\mathbf{Z}(t) - \mathbf{f}(t) + \mathbf{E}(t) = \dot{\mathbf{Z}}(t) + \mathbf{B}\mathbf{U}(t)$ and substituting it into $\mathbf{G}(t)$ in Eq. (8), one obtains an alternate equivalent controller to be

$$\mathbf{G}(t) = -(\mathbf{P}\mathbf{B})^{-1} \mathbf{P}[\dot{\mathbf{Z}}(t) + \mathbf{B}\mathbf{U}(t)] \quad (9)$$

The estimated control force by Eq. (7) can then be rewritten as

$$\mathbf{U}(t + \psi) = \mathbf{U}(t) - (\mathbf{P}\mathbf{B})^{-1} \mathbf{P}\dot{\mathbf{Z}}(t) - \delta \boldsymbol{\lambda}^T(t) \quad (10)$$

It is observed from Eq. (10) that the feedback information of $\mathbf{Z}(t)$ (displacement and velocity) and $\mathbf{f}(t)$ switches to $\dot{\mathbf{Z}}(t)$ (velocity and acceleration) and $\mathbf{U}(t)$ (current control force). It is noted that it is more practical to measure acceleration than displacement in implementation of structural control. However, only accelerations and velocities are needed for feedback. The velocity responses can be obtained using filters and integrators.

In semi-active control, the MR damper is expected to provide the demanded control force $\mathbf{U}(t)$ by Eq. (10). Equating the demanded control force by Eq. (10) and the exerting damping force from the MR damper by Eq. (1) yields the demanded current. The control force cannot be commanded directly but the current has to be regulated in the MR damper to achieve various damping force. The external energy required for such semi-active controls is generally much smaller than that required for the active control.

4. EXPERIMENTAL AND ANALYTICAL RESULTS

The structural system was tested using two near-field ground motions recorded at JMA Kobe Observatory in the 1995 Kobe, Japan earthquake and Sun-Moon Lake in the 1999 Chi-Chi, Taiwan earthquake. Due to the capacity of the shaking table, the maximum peak ground accelerations have to be scaled down to 45% and 30% of the JMA Kobe and Sun-Moon Lake ground motions, respectively. Before the tests under the maximum ground motions, which caused nonlinear structural responses, three linear tests were conducted using the ground accelerations scaled in magnitude by factors of 5%, 10% and 15%. Numerical simulations based on the results of the system identification and under ideal control situations were performed for comparison. Analytical and experimental time histories of the

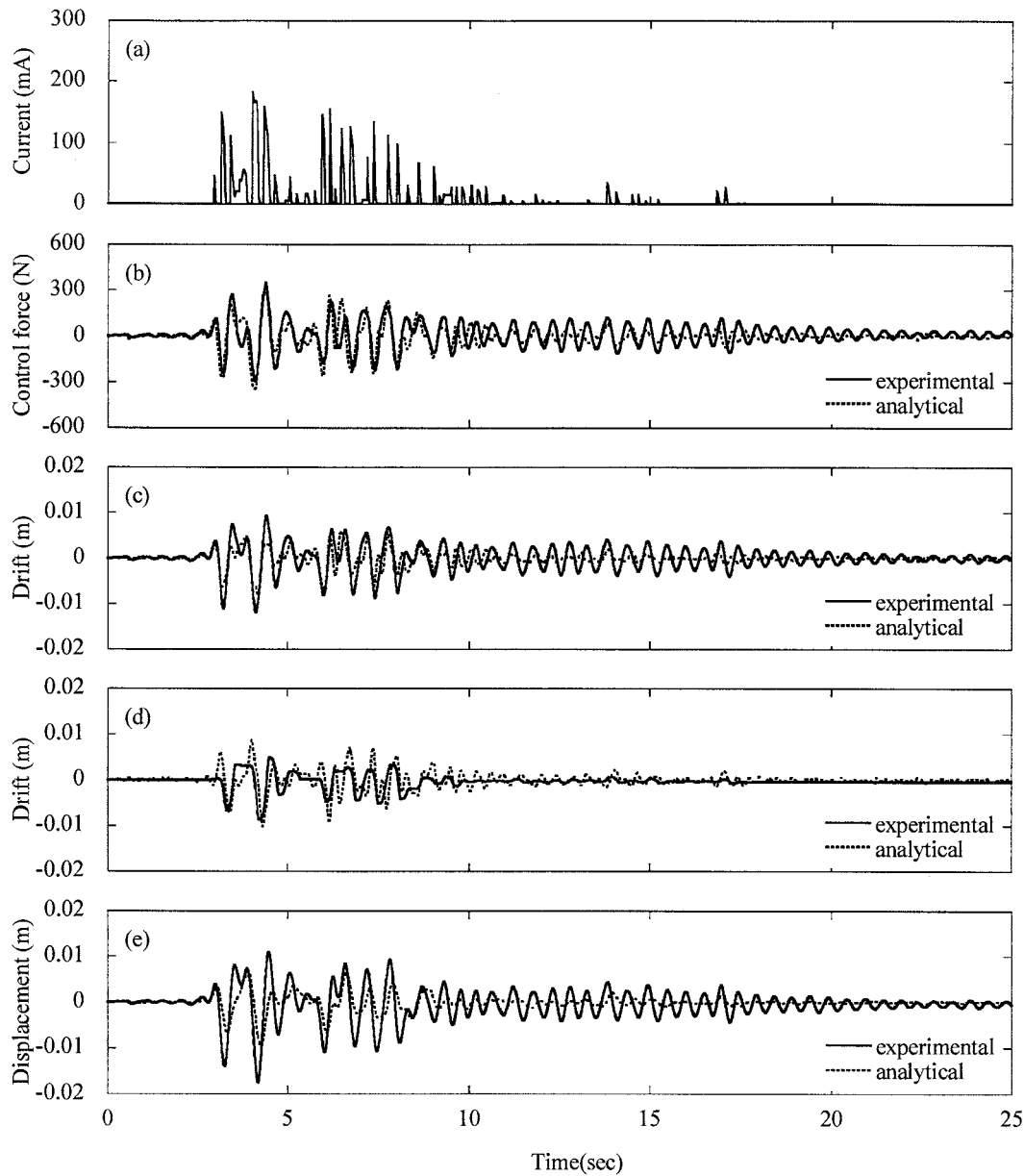


Figure 5 (a) Applied Current , Comparison of Experimental and Analytical Time Histories for (b) Control force, (c) the First Story Drift, (d) the Second Story Drift and (e) Displacement of the Second Floor under 15% JMA Kobe Ground Motion

control damping force, applied current, interstory drifts and the displacement at the top floor level under 15% of JMA Kobe ground motion are compared in Figure 5. The results show that the correlations for the control damping force and the response quantities are satisfactory. The MR damper traced the control force demanded by the control algorithm well.

Figure 6 shows the control damping force and the comparison of the interstory drifts and the displacement at the top floor level between uncontrolled system and semi-active controlled system under 45% of JMA Kobe ground motion. It is noted that the test structure underwent nonlinear behavior during testing. The results show that the displacement responses decrease drastically. The displacement of the second floor decreases from 92 mm to 46 mm. It is presented that the control performance of semi-active control based on the sliding mode control algorithm is quite impressive.

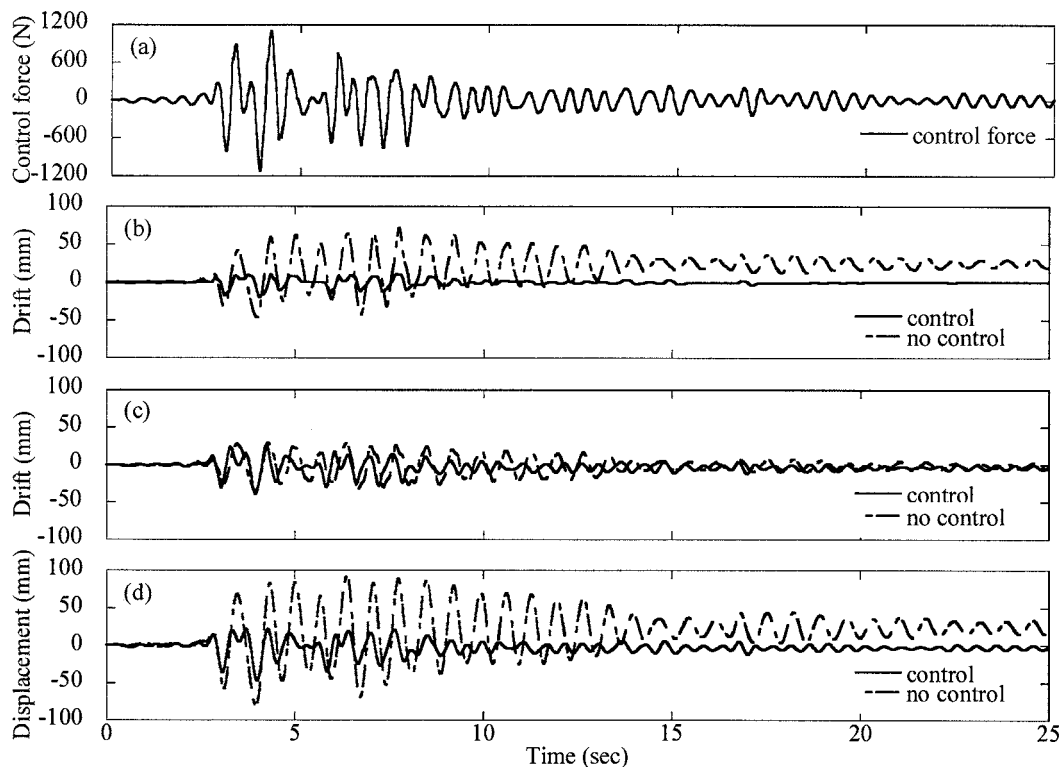


Figure 6 (a) Control Damping Force, Comparison for (b) the First Story Drift, (c) the Second Story Drift and (d) Displacement of the Second Floor under 45% JMA Kobe Ground Motion

5. CONCLUSIONS

A series of shaking table tests by using a two-story shear-type structure model has been conducted to demonstrate the performance of a semiactive control system. The semiactive control system by using a MR damper and based on the sliding mode control algorithm was successfully implemented and evaluated. Compared to the control methods based on feedback of displacements and velocities, the sliding mode control based on feedback of velocities and accelerations shows more practical application into real structures, because it is easier to measure acceleration than displacement during earthquakes. Through comparison between analytical and experimental results, the MR damper satisfactorily traced the demanded control force by the control algorithm and the response time histories agreed to each other well. In addition, the test modal exhibited nonlinear behavior under both uncontrolled system and controlled system to larger ground motions. Finally, since the results present that the semiactive control system has outstanding performance, the semiactive control system based on the sliding mode control provides a valuable control method for nonlinear structures.

Acknowledgements:

The writers acknowledge the assistance in the experimental tests from all members at Kawashima lab, Department of Civil and Environmental Engineering, Tokyo Institute of Technology, Japan.

References:

- Lee, T. Y. and Kawashima, K. (2006) "Effectiveness of Semi-active Control on a Seismic-Excited Isolated Bridge," 1st European Conference on Earthquake Engineering and Seismology, Geneva, Switzerland.
- Ruangrassamee A., and Kawashima, K. (2001), "Semi-Active Control of Bridges with Use of Magnetorheological Dampers," *Smart Materials and Structures*, **10**, 323-332.
- Spencer, B. F. and Nagarajaiah, S. (2003), "State of the Art of Structural Control," *Journal of Structural Engineering*, ASCE,

129(7), 845-856.

Yang, J. N., Wu, J. C., Agrawal, A. K. and Li, Z. (1994), "Sliding Mode Control for Seismic-Excited Linear and Nonlinear Civil Engineering Structures," Technical Report NCEER-94-17, National Center for Earthquake Engineering Research, Buffalo, N.Y.

Yang, J. N., Wu, J. C. and Agrawal, A. K. (1995), "Sliding Mode Control for Nonlinear and Hysteretic Structures," Journal of Engineering Mechanics, ASCE, 121(12), 1330-1339.

PUSHOVER ANALYSIS AND NONLINEAR DYNAMIC ANALYSIS OF A THREE-STORY REINFORCED CONCRETE SCHOOL BUILDING

H.T. Chen¹⁾, R.Y. Chen²⁾ and Y.M. Tien³⁾

1) Associate Professor, Department of Civil Engineering, National Central University, Taiwan

2) Graduate Student, Department of Civil Engineering, National Central University, Taiwan

*3) Professor, Department of Civil Engineering, National Central University, Taiwan
chenht@cc.ncu.edu.tw*

Abstract: The pushover analysis became popular in recent years due to its easy implementation. In this study a three-story reinforced concrete school building constructed in 1961 is adopted for comparing the results obtained by the pushover analysis and the nonlinear dynamic analysis. Although the pushover analysis predicts more plastic hinges over B-IO range than the nonlinear dynamic analysis, the plastic hinges over the ranges other than B-IO appear in the dynamic analysis. For the maximum story drift ratios, no clear trends can be observed. Although for some cases the maximum drift ratios predicted from the pushover analysis agree well with those obtained from the nonlinear dynamic analysis, for certain cases, the differences may be large. This indicates that the earthquake motions at the site of a building have to be used for the final check of design or strengthening strategy.

1. INTRODUCTION

A reliable and accurate estimation of the seismic deformation of a building is a critical issue in the practice of performance-based seismic engineering and in developing an appropriate measure to strengthen or to rehabilitate an existing building. To avoid the complicated and time-consuming nonlinear time-history analysis, a nonlinear static analysis called pushover method became popular in engineering community in recent years. Currently the procedures adopted by structural engineering profession to perform the pushover analysis are those described in ATC-40(1996), FEMA-273(1997), FEMA356 (2000) documents. Using such procedures, a building is subjected to monotonically increasing lateral force with an invariant height-wise distribution and the resulting displacement (e.g. the roof displacement of the building) is plotted against the load to generate a capacity or pushover curve. The maximum global displacement is then estimated using the spectral representation of ground motions as an intensity measure for earthquake shaking and the pushover curve. The resulting displacement is called a performance point (ATC-40, 1996), or a target displacement (FEMA-356, 2000) for the given ground motion intensity. With this displacement, the nonlinear static analysis is revisited to determine the building's member forces and deformations at this point. With the popularity of the pushover method, it is now included in the commercially available software such as SAP2000. The underlying assumptions and limitations of pushover method have been discussed by many researchers (Krawinkler and Seneviratna, 1998; Kim and D'Amore, 1999). The pushover method is limited in its ability to consider higher mode effects and possible redistribution of inertial forces in a structure due to yielding. On the other hand, many researchers have devoted to developing the improved methods for estimating the seismic demands in the past several years, and Chopra (2004) classified these procedures into three categories: probabilistic approach based on incremental dynamic analyses, nonlinear response history analysis and improved pushover analysis

procedures taking into account contributions of higher modes. However, it should be pointed out that the pushover method can lead to good estimates of seismic demands for low-rise and medium-rise buildings in which inelastic action is distributed throughout the height of the building (Krawinkler and Seneviratna, 1998).

In Taiwan, after 1999 ChiChi earthquake, the Ministry of Education appropriated funds to perform the seismic evaluations of school buildings. Despite the fact that the pushover method is popular in the US, it is not applied to such evaluations in Taiwan. With a call for using such a method, it is expected that in the future such a method will also be adopted in Taiwan. In this paper, a three-story reinforced concrete school building is used for performing pushover analysis following the procedures described in ATC-40 first and then its results will be examined by nonlinear dynamic analyses using the ground motions recorded at different sites.

2. MODELING AND ANALYSIS TECHNIQUE

In this study SAP2000 version 9 was used to perform both the pushover analysis and the dynamic time history analysis of the selected target building. The pushover analysis was preformed using the pushover procedures of ATC-40 included in the program. The nonlinear dynamic analysis of the building used the recorded ground motions of 1999 ChiChi earthquake as input motions. In the following, a brief description of the building is given first, followed by the explanation of nonlinear hinge assignment for members.

2.1 Description of Selected School Building

The school building used for seismic evaluation is a junior high school building located in Tainan city, which has been used for the study of seismic evaluation and strengthening previously (Hsu, 1994). It is a three-story reinforced concrete building and its plane views are shown in Figure 1. In the longitudinal direction (X direction), it has ten spans with span length of 5m and in the transverse direction (Y direction) it has three spans with total length of 11.4m. The floor height is 3.4m for each floor. In the analysis, the brick wall was replaced by an equivalent truss model (Zeng, 1994; Lin, 1995) which is assumed to resist axial force only.

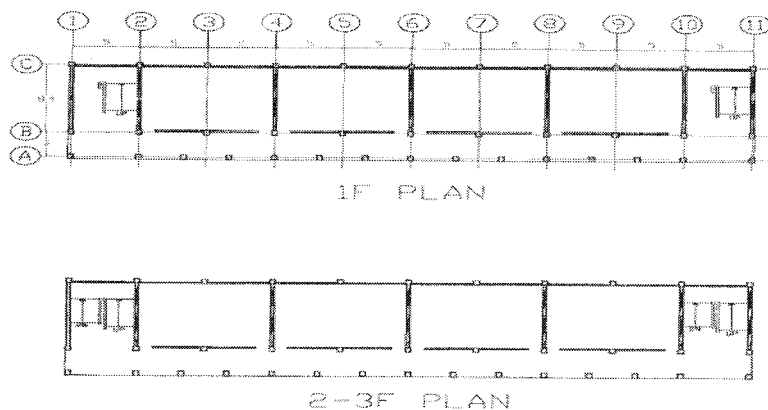


Figure 1 Plane view of selected school building

Since the building was constructed in 1961, the stiffness of each member was reduced according to the recommendation of ATC-40. For shear stiffness, an effective stiffness equal to 40% of area to resist shear was used, while a 50% of reduction in the gross section was considered to obtain the effective flexural stiffness. For columns, ATC-40 recommends that a reduction of 50% and 70% in stiffness be made for column in tension and in compression, respectively. However, considering that

under the action of earthquake, the column may be subjected to tension and compression alternatively; thus, in this study a 60% of reduction was adopted. As for the connection of beam and column, a reduction of 50% in the rigid zone was employed.

Based on these initial stiffnesses and designed loading, the natural frequencies of the first two modes of this building are 1.85 Hz and 2.71 Hz, respectively.

2.2 Nonlinear Hinge Assignment

To model the nonlinear behavior of any structural element, the concept of nonlinear hinge is adopted in ATC-40 which has the relation as shown in Figure 2. This figure will be used in the discussion of results. The values for the parameters a , b and c are provided for different conditions, where a and b are the indices for ductility and c is the residual capacity of the member. In ATC-40, between the points B and C, it is further divided into four intervals with internal points labeled as IO (immediate occupancy), LS (life safety) and SS (structural stability) to serve as the performance levels. These values are also provided for different conditions and will not affect the plastic behavior of the member. In this study three types of elements were used: beam, column and bracing to model brick wall and their nonlinear hinge assignments are described in the following.

For a beam element, since it was controlled by flexure, the M3 type nonlinear hinges were assigned at both ends of a beam. Because it was unclear about the layout of the transverse reinforcement, the suggested values for non-conforming details in ATC-40 were selected. Furthermore, due to the fact that the shear force may vary during loading, all the suggested values of a , b , c and different performance levels for non-conforming details were averaged for use. The yielding moment was determined by the program automatically.

For a column element, the P-M-M hinges were assigned at its two ends. The P-M-M hinge takes into account the interaction effect between the axial force and the flexural moment. Since it was unclear about the layout of the transverse reinforcement, the suggested values for non-conforming details in ATC-40 were selected. Furthermore, due to the fact that the axial force and the shear force may vary during loading, all the suggested values of a , b , c and different performance levels for non-conforming details were averaged for use.

For an axial element modeling the brick wall, it was assigned an axial plastic hinge at the middle of the element. Assuming that the shear failure of brick wall is brittle and does not possess any residual strength, the values of a , b , c and different performance level were taken as zero.

Shown in Table 1 are the values adopted for the analysis in this study.

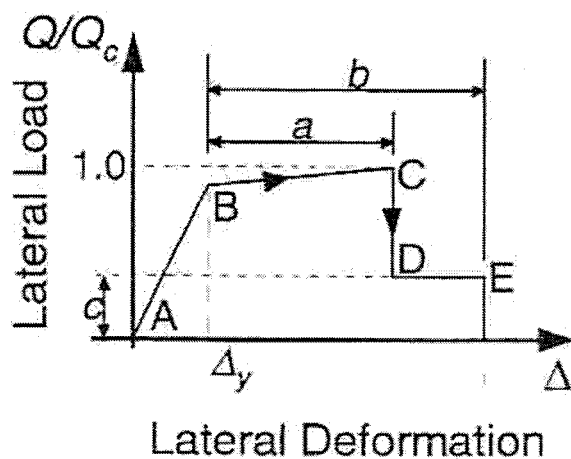


Figure 2 Behavior of nonlinear hinge in ATC-40

Table 1 Values of nonlinear hinge parameters used in the analysis

Element	Type	Location	Item	Point					Plastic Rotation/SF			SF
				A	B	C	D	E	IO	LS	SS	
Beam	M3	Two Ends	Moment/SF	0	1	1.1	0.2	0.2				M_y
			Rotation/SF	0	0	0.01125	0.01125	0.0175	0.0025	0.0075	0.01125	1
Column	PMM	Two Ends	Moment/SF	0	1	1.1	0.2	0.2				M_y
			Rotation/SF	0	0	0.005	0.005	0.00625	0.0025	0.0025	0.005	1
	V2	Middle	Force/SF	0	1	1	0	0				13367.8
			Displacement/SF	0	1	1	1	1	0	0	0	Δ_y
Brick Wall	P	Middle	Force/SF	0	1	0	0	0				10746
			Displacement/SF	0	1	1	1	1	0	0	0	0.4304

Note : in the last column

1. If SF is represented as M_y and Δ_y , it is determined by the program.

2. If SF is taken as 1, it is the suggested values in ATC-40.

3. If SF equals to value other than 1, it is obtained through analysis using the recommendation of codes or references..

2.3 Input Earthquake Motions

In this study the recorded ground motions of the 1999 ChiChi earthquake at three stations, denoted as NCU, CHY014 and CHY094, were used as input ground motions for performing the nonlinear dynamic analysis. These records were selected in such a way that they will have different predominant frequency ranges. The reason to do so is to examine how the predominant frequency of an earthquake will affect the predicted results of pushover analysis. Table 2 shows the peak ground accelerations and the predominant frequency range of all records. It can be seen that the natural frequency of first mode of the building lies in the range of the predominant frequency range of the CHY014 record.

Table 2 Peak ground accelerations and predominant frequency range of all records

Station	Location	Peak Ground Acceleration (gal)			Predominant Frequency(Hz)
		EW	NS	UD	
NCU	Jhongli, Taoyuan	53.45	99.46	29.26	0.2~1.5
CHY014	Dapu, Chiayi	224.16	228.07	94.1	1.5~2.0
CHY094	Lunbei, Yunlin	64.31	52.95	37.25	0.2~0.4

3. RESULTS AND DISCUSSIONS

Three peak ground accelerations were considered in this study: 0.1g, 0.15g and 0.2g, where g is the gravitational acceleration. For the pushover analysis, four pushes were taken, labeled as push+X, Push-X, Push+Y and Push-Y where positive and negative signs indicates the push were performed along positive and negative directions, respectively. The lateral load of the pushover analysis was in the form of equivalent lateral force. In the nonlinear dynamic analysis, at each station, the largest acceleration of three components of ground motion was normalized to the desired peak ground acceleration, while the same ratio was applied to the other two components. The duration of

earthquake motions of NCU, CHY014 and CHY094 was taken as 50 seconds, 75 seconds and 100 seconds, respectively.

Table 3 shows the number of plastic hinge from the pushover analysis. For PGA of 0.1g, only the pushover along the X direction predicts the plastic hinges over B-IO. For PGA of 0.15g, the pushover made along the X and Y directions causes plastic hinges over B-IO only. When PGA is 0.2g, the pushover along Y direction still causes the plastic hinge over B-IO only, while the plastic hinges over LS-SS and C-D are predicted for pushover along the X direction. In general, the number of plastic hinge increases with increasing PGA. For the pushover along Y direction, only the plastic hinges over B-IO are developed; this is due to the fact that there are many walls along this direction.

Table 3 Number of plastic hinges from pushover analyses

PGA	Case	No. of Plastic Hinge							
		B-IO	IO-LS	LS-SS	SS-C	C-D	D-E	>E	Total
0.1g	Push+X	12	0	0	0	0	0	0	12
	Push-X	21	0	0	0	0	0	0	21
	Push+Y	0	0	0	0	0	0	0	0
	Push-Y	0	0	0	0	0	0	0	0
0.15g	Push+X	69	0	0	0	0	0	0	69
	Push-X	44	0	0	0	0	0	0	44
	Push+Y	8	0	0	0	0	0	0	8
	Push-Y	4	0	0	0	0	0	0	4
0.20g	Push+X	88	0	12	0	1	0	0	101
	Push-X	65	0	31	0	0	0	0	96
	Push+Y	33	0	0	0	0	0	0	33
	Push-Y	27	0	0	0	0	0	0	27

Table 4 shows the number of plastic hinge from the nonlinear dynamic analysis. It should be pointed out that except the cases of NCU and CHY094 normalized to 0.1g, all the other dynamic analyses render nonconvergent results before the desired durations are reached and the exact durations used in each analysis are shown in the last column of the table. In fact, when the execution of the program stopped due to nonconvergence, the peak ground acceleration was not even reached. For PGA of 0.1g, no plastic hinge is developed for the case of NCU, while nonconvergent result is obtained for the case of CHY014. This may be due to the fact that the fundamental frequency of the building lies within the predominant frequency range of this ground motion record. Although the pushover analysis predicts more plastic hinges over B-IO than the nonlinear dynamic analysis, the plastic hinges over the range other than B-IO appear in the dynamic analysis. It should also be noted that for PGA of 0.2g, the solution can not converge earlier than for PGA of 0.15g and it may be the reason for having fewer numbers of plastic hinges over the C-D and D-E ranges.

Shown in Table 5 are the maximum floor drift ratios from the pushover and the dynamic analyses. No clear trend can be observed. Even for the same set of earthquake records normalized to different PGAs, the maximum drift ratios for the large PGA need not be necessarily larger than those for the smaller PGA. Although for some cases the drift ratios predicted from the pushover analysis agree well with those obtained from the nonlinear dynamic analysis, for certain cases, e.g. the drift ratio for Y direction of NCU at PGA of 0.2g, the difference may be 3 times. Although the fundamental frequency of the building lies within the predominant frequency range of CHY014, only in the X

direction the maximum drift ratios are larger than those predicted by the pushover analysis for PGA of 0.1g and 0.15g, while the trend is reversed for PGA of 0.2g. On the other hand, for the maximum drift ratios in the Y direction, the nonlinear dynamic analysis predicts smaller values than the pushover analysis; by examining the ground motion records, it is found that this may be due to the smaller motion in the Y direction.

Table 4 Number of plastic hinges from nonlinear dynamic analyses

PGA	Station	No. of Plastic Hinge								Duration (second)
		B-IO	IO-LS	LS-SS	SS-C	C-D	D-E	>E	Total	
0.1g	NCU	0	0	0	0	0	0	0	0	50
	CHY014	39	0	0	0	3	0	2	44	13.26
	CHY094	1	0	0	0	0	0	0	1	100
0.15g	NCU	4	0	1	0	1	0	1	7	20.72
	CHY014	39	0	0	0	12	5	1	57	12.78
	CHY094	40	0	0	1	4	0	0	45	23.72
0.2g	NCU	21	0	0	0	1	0	0	22	15.08
	CHY014	26	0	0	0	1	0	0	27	12.16
	CHY094	45	0	11	1	1	0	1	59	20.00

Table 5 Maximum floor drift ratios from pushover and dynamic analyses

PGA	Floor	Push +X	Push -X	Push +Y	Push -Y	NCU		CHY014		CHY094	
						X	Y	X	Y	X	Y
0.1g	1	0.0016	0.0018	0.0009	0.0009	0.0021	0.0009	0.0029	0.0008	0.0023	0.0011
	2	0.0029	0.0031	0.0014	0.0014	0.0031	0.0013	0.0043	0.0011	0.0034	0.0016
	3	0.0030	0.0033	0.0014	0.0014	0.0022	0.0008	0.0030	0.0007	0.0024	0.0010
0.15g	1	0.0021	0.0020	0.0012	0.0012	0.0012	0.0013	0.0033	0.0009	0.0025	0.0011
	2	0.0038	0.0035	0.0020	0.0020	0.0040	0.0015	0.0055	0.0013	0.0038	0.0016
	3	0.0047	0.0042	0.0019	0.0019	0.0022	0.0009	0.0049	0.0009	0.0026	0.0011
0.2g	1	0.0023	0.0023	0.0014	0.0017	0.0029	0.0007	0.0023	0.0012	0.0018	0.0015
	2	0.0044	0.0044	0.0024	0.0027	0.0044	0.0010	0.0034	0.0018	0.0046	0.0022
	3	0.0062	0.0064	0.0024	0.0029	0.0033	0.0007	0.0024	0.0012	0.0055	0.0014

4. CONCLUSIONS

In this study a three-story reinforced concrete school building constructed in 1961 is adopted for comparing the results obtained by the pushover analysis and the nonlinear dynamic analysis. Although the pushover analysis predicts more plastic hinges over B-IO range than the nonlinear dynamic analysis, the plastic hinges over the ranges other than B-IO appear in the dynamic analysis. For the maximum story drift ratios, no clear trends can be observed. Although for some cases the maximum drift ratios predicted from the pushover analysis agree well with those obtained from the nonlinear dynamic analysis, for certain cases, the differences may be large. This indicates that the earthquake motions at the site of a building have to be used for the final check of design or strengthening strategy.

References:

- ATC-40 (1996), "Seismic Evaluation and Retrofit of Concrete Buildings," Applied Technology Council, California.
- FEMA-273 (1997), "NEHRP Guidelines for the Seismic Rehabilitation of Buildings," Federal Emergency Management Agency, Washington DC.
- FEMA-356 (2000), "Prestandard and Commentary for the Seismic Rehabilitation of Buildings," Federal Emergency Management Agency, Washington DC.
- SAP2000, Version 9, Computers and Structures, Inc., California.
- Krawinkler, H, and Seneviratna, GDPK (1998), "Pros and Cons of a Pushover Analysis of Seismic Performance Evaluation," *Journal of Structural Engineering*, ASCE, 20, 452-464.
- Kim, B. and D'Amore, E. (1999), "Pushover Analysis Procedure in Earthquake Engineering," *Earthquake Spectra*, 13(2), 417-434.
- Chopra, A.K. (2004), "Estimating Seismic Demands for Performance-Based Engineering Design of Buildings," *Proceedings of 13th World Conference on Earthquake Engineering*, Paper No. 5007.
- Hsu, G.C. (1994), "Seismic Evaluation and Strengthening of Reinforced Concrete School Buildings," *Master Thesis*, Department of Architecture, National Cheng Kung University, Taiwan, Taiwan (in Chinese).
- Zeng, K.H. (1994), "Experimental Study on Mechanical Behavior of Brick Piers and Brick Walls," *Master Thesis*, Department of Architecture, National Cheng Kung University, Taiwan, Taiwan (in Chinese).
- Lin, C.W. (1995), "Aseismic Experiment and Equivalent Truss Analysis for Brick Walls with Boundary RC Frames," *Master Thesis*, Department of Architecture, National Cheng Kung University, Taiwan, Taiwan (in Chinese).

ALUMINUM SHEAR PANELS AS PASSIVE ENERGY DISSIPATION DEVICES FOR STEEL BRACED FRAMES

Durgesh C Rai¹⁾, and Dhritiman Banerjee²⁾

1) Associate Professor, Department of Civil Engineering, Indian Institute of Technology Kanpur, India

*2) Former Graduate Student, Department of Civil Engineering, Indian Institute of Technology Kanpur, India
dcrai@iitk.ac.in, dhritiman_b@rediffmail.com*

Abstract: Thicker panels of Aluminum can sustain large shearing strains in the excess of 20% resulting in significant amount of hysteresis energy dissipation per unit volume of the material. Aluminium shear-links sandwiched between the tops of the diagonal braces and floor beam of an Ordinary Concentric Braced Frame (OCBF), considerably improves its performance by dissipating energy through inelastic deformations in shear mode. To proportion such Shear-Link Braced Frame (SLBF) a simplified procedure is developed that addresses the interaction between the stiffness of the bare frame (braces) and the damping device (shear-link) along with the equivalent damping. For an equivalent SDOF representation for the first mode of the SLBF system, a set of response curves are developed to determine the stiffness parameters and ductility of the frame to achieve a certain level of performance. The SDOF theory is then extended to MDOF systems to determine the damper and brace stiffness at each level. The design technique is verified by nonlinear direct integration time history analysis in software SAP2000 for a 4-storey office building. The response of the MDOF-SLBF system was found quite similar to the predicted response.

1. INTRODUCTION

Passive energy dissipation systems have evolved as efficient structural control systems reducing energy dissipation demand on the primary structural members and minimising possible structural damage. Amongst the numerous Energy Dissipation Devices (EDDs) that are currently used for passive control, metallic dampers have been found to be quite effective. The underlying dissipative mechanism of all metallic dampers results from the inelastic deformation of the metal. In this context the shear yielding of I-shaped shear-links (Figure 1a.) of low yielding alloy metals such as aluminium have been found to be very ductile and large inelastic deformations are possible without tearing or buckling of the member. Such I-shaped aluminium shear-links sandwiched between the bottom of the floor beam and top of the diagonal braces finds a major application in the seismic up gradation of Chevron type Ordinary Concentric Braced Frames (OCBF). The upgraded system termed as Shear-Link Braced Frame (SLBF) resists lateral loads by deforming in shear mode through the deformations in the shear-link and brace (Figure 1b) [Rai and Wallace 1998].

Previous study has shown that the SLBF system should be designed for reduced base shear forces due to the hysteretic damping imparted by the yielding shear-link [Rai and Wallace 1998] and the reduction in frame elastic stiffness due to the shear-link and brace lateral stiffness acting in series. It should be noted that the SLBF system differs from conventional Moment Resisting Frames (MRFs) equipped with Elasto-plastic (EP) or Visco-elastic (VE) dampers in resisting seismic forces wherein the bending stiffness of the beams and columns interact with the stiffness of the EDDs [Kasai et al. 1998, Ito and Kasai 2006]. In this paper a method is proposed based on equivalent Single Degree of Freedom (SDOF) system idealization of a Multiple Degree of Freedom (MDOF) SLBF system deflecting in its fundamental mode with proper modification for the increased fundamental period due to the reduced stiffness and damping ratio due to yielding of the shear-link. The SDOF design is further extended to a MDOF-SLBF system with a consideration to arrange damper stiffness in order to

get uniform drift over the building height. The design method is validated by nonlinear direct integration time history analysis on a 4-storey office building for a suite of 14 strong motion records.

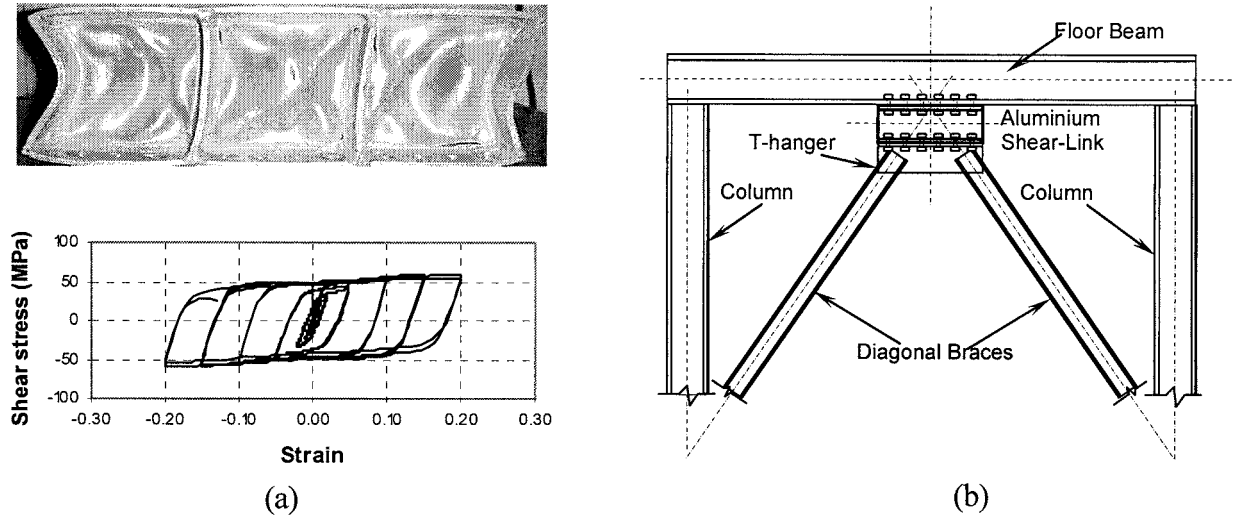


Figure 1 (a) Yielded Aluminum panel, its hysteretic response, and (b) arrangement of SLBF system

2. DESIGN OF SDOF-SLBF SYSTEM

The mass-stiffness-damper model of the condensed MDOF-SLBF system is shown in Figure 2 in which the brace is assumed to remain elastic. The SDOF-SLBF system has a bilinear load-deformation behaviour due to strain hardening in the aluminium shear-link after yielding, which is based on a series of ‘slow’ cyclic test results conducted on full scale models [Banerjee 2005]. The ratio of post elastic stiffness K_{d2} to elastic lateral stiffness K_{d1} of the shear-link defined as the parameter s and is found to be equal to 0.023. The shear strain in the link corresponding to the yield displacement is 0.015.

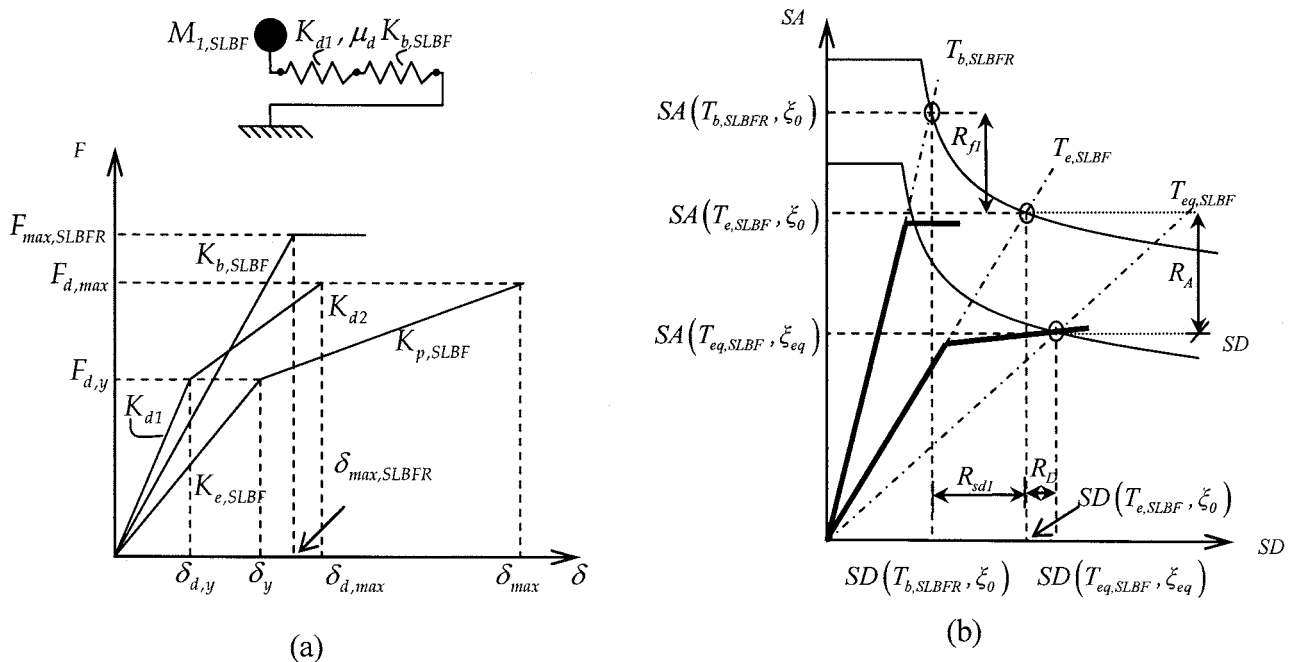


Figure 2 (a) Idealized bilinear load-deformation of SLBF system and (b) response reduction and modification arrangement of SLBF system

2.1 Effect of Increased Damping Ratio

The elastic response spectrum for a damping ratio ξ_{eq} can be taken as the product of the elastic response spectrum for initial damping ratio ξ_0 and damping reduction factor B . In this study B is taken as proposed by Ashour, (1987) with the value of α equal to 18:

$$B = \sqrt{0.05(1 - e^{-\alpha\xi}) / \xi(1 - e^{-\alpha 0.05})} \quad (1)$$

2.2 Equivalent Period And Equivalent Damping

The idealized bilinear SDOF-SLBF system, under a given earthquake ground motion the system develops a peak ductility demand μ at which the *equivalent stiffness* and *equivalent vibration period* of the system can be given as follows:

$$K_{eq,SLBF} = K_{e,SLBF} \{1 + p(\mu - 1)\} / \mu, \quad T_{eq,SLBF} = T_{e,SLBF} \sqrt{K_{e,SLBF} / K_{eq,SLBF}} \quad (2)$$

where p is the post elastic to elastic stiffness ratio of the system. The elastic stiffness of the system $K_{e,SLBF}$ is further expressed as follows

$$K_{e,SLBF} = K_{d1} K_{b,SLBF} / (K_{d1} + K_{b,SLBF}) = \{a / (1 + a)\} K_{b,SLBF} \quad (3)$$

where, a is the stiffness parameter defining the elastic stiffness of the shear-link as a ratio of the brace stiffness $K_{b,SLBF}$ in the system. The ductility demand μ on the system is a function of the ductility demand on the shear-link and is expressed as

$$\mu = 1 + (1 + as)(\mu_a - 1) / (1 + a) \quad (4)$$

The equivalent damping ratio of the system at ductility demand μ is evaluated by the expression given by Kasai *et al* (1998) as

$$\xi_{eq} = \xi_0 + (2 / \pi p \mu) \ln \left[\{1 + p(\mu - 1)\} / \mu^p \right] \quad (5)$$

2.3 Peak Response Prediction of SDOF-SLBF System

The SDOF-SLBF system is best effective when its fundamental period lies in the velocity critical region of the spectrum. The peak response of the SDOF-SLBF system (SD and SA) is determined as a ratio of the elastic response of the system A . The peak response SDOF-SLBF system is determined as a ratio of the elastic response of SLBF system assuming rigid shear-link, which is influenced by two factors: (1) The effect of increase in critical damping ratio from ξ_0 to ξ_{eq} generally reduces both SD and SA , and (2) the effect of vibration period increasing from $T_{b,SLBF}$ to $T_{eq,SLBF}$ generally reduces SA while increases SD . These effects can be represented by Displacement Enhancement Factor R_{sd} and Acceleration Reduction Factor R_f as defined below:

$$R_{sd} = B \times \sqrt{[(1 + a) / a] (1 / K_{e0})}; \quad R_f = B \times \sqrt{[a / (1 + a)] (K_{e0})}, \quad K_{e0} = \{1 + p(\mu - 1)\} / \mu \quad (6)$$

The elastic response of the SDOF-SLBF system is derived for $\mu = 1.0$ as follows:

$$R_{sd1} = \sqrt{(1 + a) / a} \quad R_{f1} = \sqrt{a / (1 + a)} \quad (7)$$

The inelastic response is therefore obtained by dividing the elastic responses SD and SA by Displacement Modification Factor, R_D and Response Reduction factor, R_A , respectively, as follows:

$$R_D = R_{sd1} / R_{sd2} = 1 / B \sqrt{K_{e0}}; \quad R_A = R_{f1} / R_{f2} = 1 / B \sqrt{1 / K_{e0}} \quad (8)$$

The response reduction and modification of the SDOF-SLBF system is explained by Figure 3. It is clear from the above set of equations that factors R_{f1} , R_{sd1} , R_{f2} and R_{sd2} are functions of stiffness

parameter a and μ . Since μ is a function of shear-link ductility μ_d [Equation (4)], a set of response curves is developed for R_{f1} , R_{sd1} , R_{f2} and R_{sd2} by varying the values of stiffness parameter a and μ_d . The response curves (Figure.4) are generated for different values of μ_d ranging from a minimum of 2 to a maximum of 10 corresponding to minimum and maximum shear-link strain of 3% and 15%, respectively. The value of parameter a is varied at different increments with minimum and maximum values being 0.1 and 6.0 respectively.

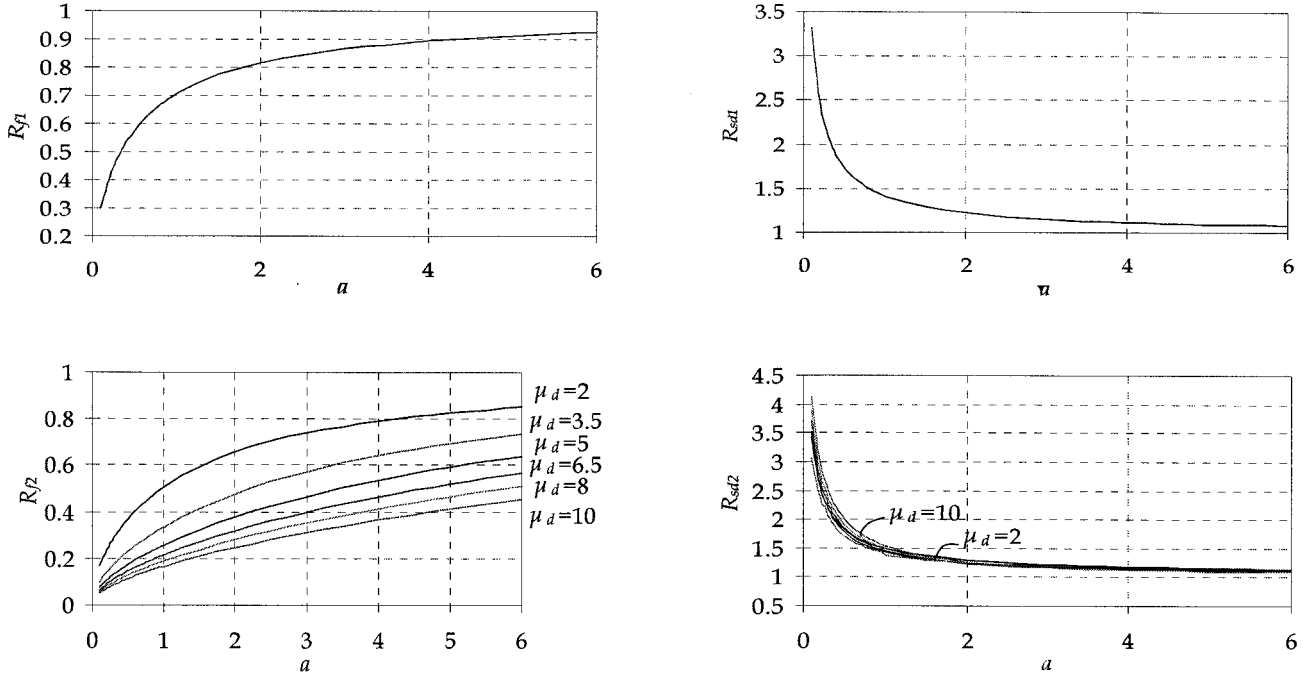


Figure 4: Response Curves: R_{f1} , R_{sd1} , R_{f2} , and R_{sd2}

3. DESIGN OF MDOF-SLBF SYSTEM

The designed SDOF-SLBF system is converted to a MDOF system deflecting in linear fundamental mode by equating the properties between the two systems with specific constraints as follow: (1) The magnitude of the equivalent damping ratio ξ_{eq} expressed as a ratio of energy dissipated by the shear-link per cycle to total system strain energy is equal for both SDOF and MDOF system, (2) Under elastic pushover force the drift distribution of the MDOF system is uniform and is equal to the SDOF system, and (3) Elastic vibration period for both systems is equal. Constraints (1) and (2) leads to following equation which is used to convert SDOF-SLBF system to a MDOF system :

$$\sum_{i=1}^n K_{p,i(SLBF)} / \sum_{i=1}^n K_{e,i(SLBF)} = K_{p(SLBF)} / K_{e(SLBF)} = p \quad (9)$$

Since storey drifts are equal, the ductility demand on each floor in the MDOF system is constant corresponding to a value of shear-link ductility demand in the SDOF system. Thus it can be concluded from Equation (4) that stiffness parameter a_i at each floor is a constant and is equal to stiffness parameter a of the SDOF system. The elastic response of the MDOF system in the fundamental mode is thus given by the elastic response of the SDOF-SLBF system and is given as

$$SA(T_{e,SLBF}, \xi_0) = SA(T_{b,SLBFR}, \xi_0) \times R_{f1}; \quad SD(T_{e,SLBF}, \xi_0) = SD(T_{b,SLBFR}, \xi_0) \times R_{sd1} \quad (10)$$

4. DESIGN LIMITS FOR SLBF SYSTEM

The choice of stiffness parameter a and shear-link ductility demand μ_d is governed by two limits related to SLBF behaviour. Firstly, the elastic period of SLBF system should lie in velocity critical zone of the design spectrum. This condition reduces to

$$R_{sd1}/R_{f1} \geq (T_s/T_{b,SLBFR})^2 \quad (11)$$

where T_s is period corresponding to transition zone of acceleration and velocity critical zones of the response spectrum. Secondly, the height of the shear-link is limited $h_i/12 \leq h_{d,i} \leq h_i/10$ (Rai and Wallace 1998), where h_i is the storey height and $h_{d,i}$ is the height of shear-link at i^{th} storey. Since the shear strain in the shear-link is given as $\gamma = \delta_d/h_d$, the displacement range for $\gamma = 0.015$ (yield strain of shear-link) within which link height is to be satisfied if

$$\left[\left\{ (0.00125nh_i) / (SD(T_{b,OCBF}, \xi_0) \Gamma_{1,SLBF}) \right\} \leq H_f \leq \left\{ (0.0015nh_i) / (SD(T_{b,OCBF}, \xi_0) \Gamma_{1,SLBF}) \right\} \right]; \quad (12)$$

$$H_f = R_{sd2} / \{ \mu(1+a) \}$$

where $\Gamma_{1,SLBF}$ is the first mode participation factor of SLBF and n is the number of storeys in the frame. Equations (11) and (12) are necessary conditions that require being satisfied for the design of SLBF system. The variation of the expressions R_{sd1}/R_{f1} and H_f for different values of stiffness parameter a and shear-link ductility μ_d are given by Figure 5.

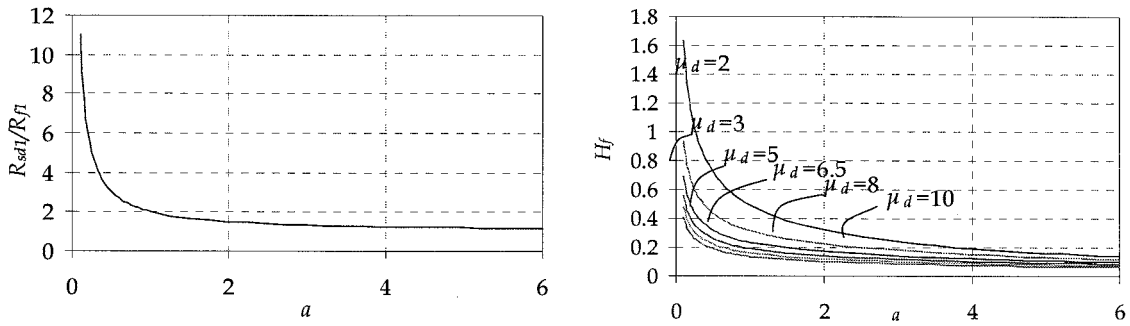


Figure 5: Variation of R_{sd1}/R_{f1} and H_f with a

5. SUMMARY OF MDOF-SLBF DESIGN

The design procedure for MDOF-SLBF system is summarized below.

1. Assume period of SLBF system with rigid link and obtain responses $SA(T_{b,SLBFR}, \xi_0)$ and $SD(T_{b,SLBFR}, \xi_0)$ from design response spectrum. Calculate fundamental mode mass and participation factor of SLBF assuming linear mode shape.
2. Read required stiffness parameter a and shear-link ductility μ_d satisfying Equations (11) and (12) from Figure 5. Steps (1) and (3) are repeated with different value of $T_{b,SLBFR} \geq T_s$ if no values of a and μ_d can be found that satisfies above equations.
3. Read R_{f1} , R_{sd1} , R_{f2} and R_{sd2} from Figure 4.
4. Evaluate base shear and roof displacement for the elastic response of SLBF as follows:

$$V_{e(SLBF)} = SA(T_{b,SLBFR}, \xi_0) \times R_{f1} \times M_{1,SLBF}; \quad \Delta_{e(SLBF)} = SD(T_{b,SLBFR}, \xi_0) \times R_{sd1} \times \Gamma_{1,SLBF} \quad (13)$$

5. Evaluate inelastic response as follows using R_D and R_A from Equation (8). The maximum design storey drifts and storey shears are evaluated corresponding to the following equation.

$$V_{D,(SLBF)} = V_{e,(SLBF)} / R_A, A_{(SLBF)} = A_{e,(SLBF)} / R_D \quad (14)$$

6. Determine ductility demand μ from Equation (4).
7. Determine yield shear force and drift at each storey as follows:

$$\delta_{y,i(SLBF)} = \delta_{max,i(SLBF)} / \mu, F_{y,i(SLBF)} = \delta_{max,i(SLBF)} / \mu \times K_{e,i(SLBF)} \quad (15)$$

$\delta_{max,i(SLBF)}$ is the maximum storey drift at i^{th} storey and $K_{e,i(SLBF)}$ is elastic storey stiffness at i^{th} storey.

8. Evaluate elastic lateral stiffness of shear-link and brace

$$K_{dl,i} = K_{e,i(SLBF)} (1 + a), K_{b,i(SLBF)} = K_{dl,i} K_{e,i(SLBF)} / (K_{dl,i} - K_{e,i(SLBF)}) \quad (16)$$

9. Determine horizontal web area of shear-link and brace by[Rai and Wallace 1998]

$$A_{w,i(SLBF)} = F_{y,i(SLBF)} / 0.75 \times \sigma_{0.2}, A_{b,i(SLBF)} = K_{b,i(SLBF)} L_{i,(SLBF)} / 2E \cos^2 \theta \quad (17)$$

10. Determine maximum forces and design drift

$$F_{max,i(SLBF)CP} = F_{y,i(SLBF)} + sK_{dl,i} \delta_{dy,i} (\mu_{d,max} - 1) \quad (18)$$

11. $\delta_{dy,i}$ is the yield displacement in the shear-link.

$$\delta_{max,i(SLBF)CP} = \delta_{y,i(SLBF)} \times \mu_{max} \quad (19)$$

μ_{max} is the frame ductility demand corresponding to $\mu_{d,max}$

12. Select brace sections having area given by Equation (14) such that its critical buckling load satisfies the following equation

$$P_{cr,i} > F_{max,i(SLBF)CP} / 2 \cos \theta \quad (20)$$

$F_{max,i(SLBF)CP}$ is the maximum force at i^{th} floor at CP state and θ is the inclination of the brace.

6. VALIDATION OF DESIGN METHOD

The verification of the proposed design method is done by nonlinear time history analysis of a 4-storey office building. The typical plan and elevation of the building is shown in Figure 6. The frames 1 and 6 resist the lateral forces along E-W direction. In the N-S direction two bracing frame systems provide seismic resistance. The SLBFs are placed symmetrically along the line C and D separated by two bay widths. The building has a dead load and live load of 1 kPa and 1.2 kPa, respectively, on the roof. The floors have a dead load and live load of 3.9 kPa. The building frame has a total seismic weight of 11445 kN. The building is assumed to be located on hard soil. The parameters S_{DI} and S_{DS} of the design response spectrum are taken as 0.4g and 1.0g, respectively.

The parameters adopted for designing the SLBF system and its salient properties are given in Table.1. The calculated values of the brace and damper stiffness as well as the respective sectional areas are shown in Figure 6. Nonlinear time history analysis of the designed building is done in general purpose structural analysis software SAP 2000 Version 10.0 [CSI 2005].

A suite of 14 strong motion records are selected such that the effect of near field as well as far field earthquakes is represented. The average PGA value of the selected motions is 0.44g. The selected ground motions are suitable scaled as per SEI/ASCE 7 (2002) criteria, with a scaling factor 1.09

(Figure 7). The results of the nonlinear direct integration time history analysis are represented by response envelopes of the normalized storey shear and the drift in Figure 8(a) and (b). The storey shears are normalized by the seismic weight. Table 2 shows that the average of the time history responses conforms to the values corresponding to the design limit states. The proposed design method gives quite accurate results for the studied case. The first mode response assumption made in the design seems to give rather uniform distribution of drift over the building height, for the studied case wherein higher mode contribution is not significant.

Table.1. Design parameters for SLBF

Property	α	μ_d	R_{f1}	R_{sd1}	R_{f2}	R_{sd2}	$T_{e,SLBF}$	μ at LS state	μ_{max} at CP state
Value	0.5	6.5	0.577	1.732	0.146	1.834	0.96s	4.71	7.07

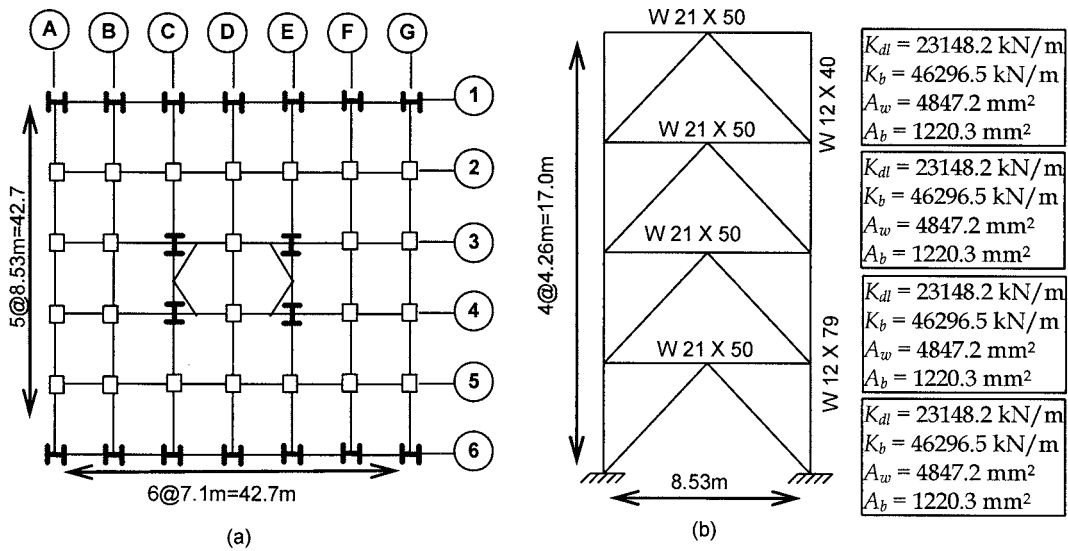


Figure 6 (a) Plan (b) Elevation of 4-Storey office Building

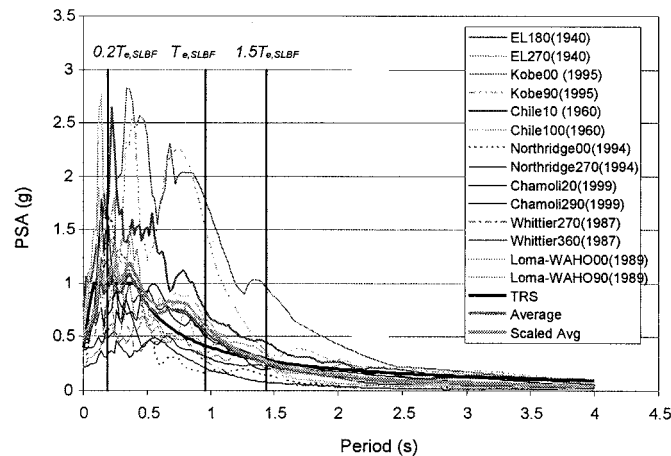


Figure 7: Scaling of response spectra of suite of motions

7. CONCLUSIONS

The present study is aimed at developing a simplified design method for shear-link braced frame systems taking into account the increased damping due to excellent energy dissipation for aluminum

shear panels and reduced stiffness of the overall SLBF system. The method is based on equivalent SDOF idealization of the MDOF-SLBF system deflecting in its fundamental mode. The interaction between the brace and shear-link stiffness along with the associated damping in the system is addressed through a set of response curves that modifies the design response spectrum and predicts the response of the SDOF system. A rule to convert the SDOF design to a MDOF system design including arrangement of damper stiffness is proposed. Results of time history analysis conformed to the proposed design. The first mode assumption to predict the MDOF response of the SLBF system is found quite satisfactory for a low-rise building.

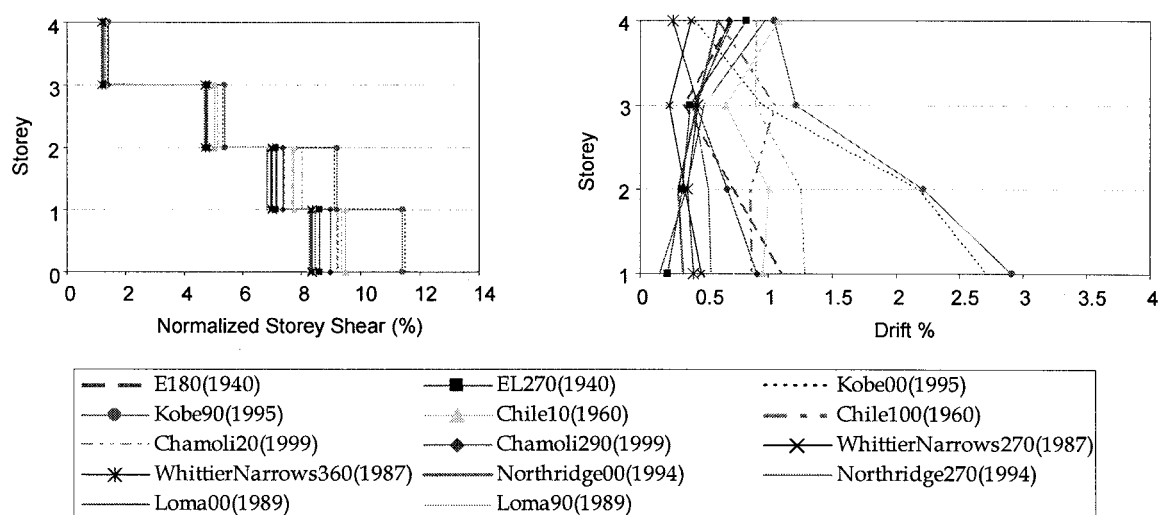


Figure 8: (a) Storey shear response envelope (b) storey drift response envelope

Table.2. Comparison of Maximum Storey Shear and story drifts with design

	Storey Shears (kN)				Story Drifts (%)			
	1	2	3	4	1	2	3	4
Average (Absolute Max)	1048.6	865.4	564.2	564.2	0.97	0.85	0.62	0.72
LS (Design)	1020.4	874.3	582.3	582.3	0.92			
CP(Design)	1093.3	936.8	623.9	623.9	1.38			

Acknowledgements:

The authors acknowledge support from Ministry of Human Resources Department of Gov. of India, New Delhi.

References:

- American Society of Civil Engineers (ASCE) (2002), "Minimum Design Loads for Buildings and other Structures," SEI/ASCE 7-02, Revision of ASCE 7-98, Reston, Virginia
- Ashour, S.A. (1987), "Elastic Seismic Response of Buildings with Supplemental Damping," *PhD Dissertation*, Department of Civil Engineering, University of Michigan, January.
- Banerjee, S. (2005), "Control of Out-of-Plane Deformation of Inelastically Buckling Aluminium Shear Panels," *MTech Thesis*, Dept. of Civil Engineering, Indian Institute of Technology Kanpur, Kanpur, India.
- CSI (2005), *SAP 2000* Version 10.0, Computers and Structures Inc., California.
- Ito, H. and Kasai, K. (2006), "Performance evaluation of SDOF Passive Control System with Elasto-Plastic Damper" *Proceedings of International Symposium on Steel Structures*.
- Kasai, K., Fu, Y., and Watanabe, A. (1998), "Passive Control Systems for Seismic Damage Mitigation," *Journal of Structural Engineering*, American Society of Civil Engineers, **124**(5), 501-512
- Rai, D.C. and Wallace, B.J. (1998), Aluminium Shear Link for Enhanced Seismic Resistance, *Journal of Earthquake Engineering and Structural Dynamics*, John Wiley, **27**, 315-342.

EXPERIMENT OF COMPOSITE MEMBER COMPOSED OF CEDAR-GLULAM-TIMBER AND STEEL PLATE APPLIED FRICTION CONNECTOR

H. Sakata¹⁾, T. Takeuchi²⁾, K. Matsuda³⁾, and A. Tomimoto⁴⁾

1) Associate Professor, Structural Engineering Research Center, Tokyo Institute of Technology, Japan

2) Associate Professor, Department of Architecture and Building Engineering, Tokyo Institute of Technology, Japan

3) Graduate Student, Department of Built Environment, Tokyo Institute of Technology, Japan

4) Nippon Steel Engineering Co., Ltd, Japan

hsakata@serc.titech.ac.jp, ttoru@arch.titech.ac.jp, matsuda@serc.titech.ac.jp, tomimoto.atsushi@eng.nsc.co.jp

Abstract: Massive amount of Japanese cedar trees planted in Japan in 1950's are recently ready to be cut for usage, and various techniques utilizing such domestic cedar are required. However, for cedar timber has less stiffness and strength than American pines, combination with steel to provide composite members will be one of the effective methods to expand the structural variations. In other times, a composite member that thin steel plate was sandwiched between two cedar-glulam-timbers using shear-ring connectors and bolts was developed. In case of shear-ring connector, matter of initial backlash and work to build up the composite member occurred. Improvement connectors of friction joint were developed. In this study, axial compression tests were conducted again to determine the compression characteristic using friction connectors and equations for estimating were proposed again. Friction connector has higher shear stiffness compared to shear-ring connector, and is able to cancel the initial backlash and built up easily. In case of friction connector, two glulam timbers strain 20% of axial force which composite member strains. It is possible to demonstrate their prediction capability against axial compression load with sufficient accuracy by estimating shear stiffness of friction connector appropriately.

1. INTRODUCTION

1.1 Background and Objective

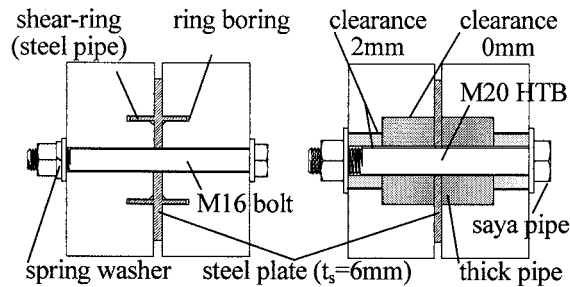
Massive amount of Japanese cedar trees planted in Japan in 1950's are recently ready to be cut for usage, and various techniques utilizing such domestic cedar are required. However, cedar timber has less stiffness and strength than American pines, combination with steel to provide composite members will be one of the effective methods to expand the structural variations. In other times, a composite member that thin steel plate was sandwiched between two cedar glulam timbers using shear-ring connectors (Figure 1(a)) and bolts were developed. Axial compression tests and bending tests were conducted to determine the compression and bending characteristics. Equations for estimating the strength and buckling mode were proposed, and their prediction capability with sufficient accuracy was demonstrated¹⁾.

In case of shear-ring connector, matter of initial backlash and work to build up the composite member occurred. So improvement connectors using friction joint and composite member using the joint were developed (Figure 1(b)). The objective of this study is to propose equations for estimating the members by shear tests of friction connector and axial compression tests.

1.2 Friction Connector

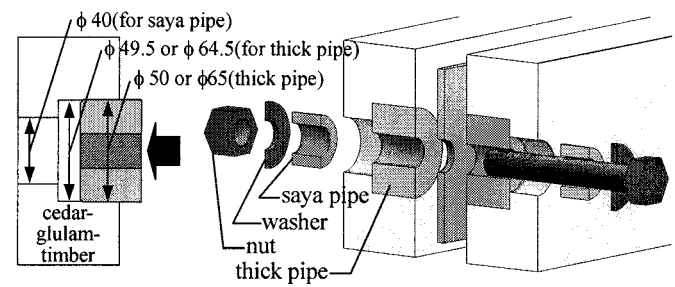
About the composition of friction connector, initially thick pipe is inserted to prior hole whose

diameter is 0.5mm smaller than thick pipe's that (Figure 2 (a)). Subsequently, the thick pipe is connected with the steel plate by friction force using M20 HTB as shown in Figure 2 (b). If thickness of the cedar-glulam-timber is larger than height of the thick pipe, saya pipe ($=\phi 38\text{mm}$, $t_s=8\text{mm}$) is used. There is 2mm clearance between saya pipe and prior hole for saya pipe because the diameter of prior hole for saya pipe is 40mm. Therefore shear force between steel plate and cedar-glulam-timber is attributed to bearing force between thick pipe and cedar-glulam-timber.



(a) shear-ring connector (b) friction connector

Figure 1 Detail of Two Connectors



(a) inserting thick pipe (b) composing after in setting

Figure 2 How to compose friction connector

2. SHEAR TESTS OF FRICTION CONNECTOR

2.1 Specimens and Material Property

The shear tests of friction connector were conducted to examine shear stiffness of friction connector. The parameters are thickness of glulam timber and shape of thick pipe. Four types of specimens were planed and quantity of specimens is twelve (three copies each). The specimens of connector tests were listed table 1, used material property is listed table 2. About names of specimens, h_w indicates thickness of the cedar-glulam-timber, ϕ and h indicate shape of thick pipe. " $h_w50\phi 50h50$, $h_w64\phi 50h50$, $h_w64\phi 65h38.5$ " were used in axial compression tests of composite member (chapter 3).

Table 1 Specimen of Connector Shear Tests

name	$h_w50\phi 50h50$	$h_w64\phi 50h50$	$h_w64\phi 65h38.5$	$h_w120\phi 50h75$	h_w : thickness of cedar-glulam-timber ϕ : diameter of thick pipe h : height of thick pipe b_w : width of cedar-glulam-timber t_s : thickness of steel plate b_s : width of steel plate
thick pipe	$\phi 50, h=50$			$\phi 50, h=75$	
(inside diameter 22mm)	$\phi \times h$	2500			3750
	h/ϕ	1.00	0.59	1.50	
saya pipe (thickness = 8mm)	-	diameter=38, height=14	diameter=38, height=25.5	diameter=38, height=45	
steel plate	$t_s=6, b_s=125$				
property	table 2 A		table 2 B	table 2 A	
cedar-glulam-timber	$h_w=50, b_w=150$	$h_w=64, b_w=150$		$h_w=120, b_w=150$	
property	table 2 A		table 2 B	table 2 A	(Unit:mm)

Table 2 Material Property

K i n d	Steel Plate (SM490)			Glulam-Timber (E65-F225)			
	Stretch	Yeild Stress	Tension Stress	Bending Young Coef.		Bending Stress	
	%	N/mm ²	N/mm ²	N/mm ²		N/mm ²	
				x-x	y-y	x-x	y-y
A	25.1	414	545	8100	-	40.2	-
B	22.9	392	544	8250	6700	51.2	47.3
							16.9
							12.5

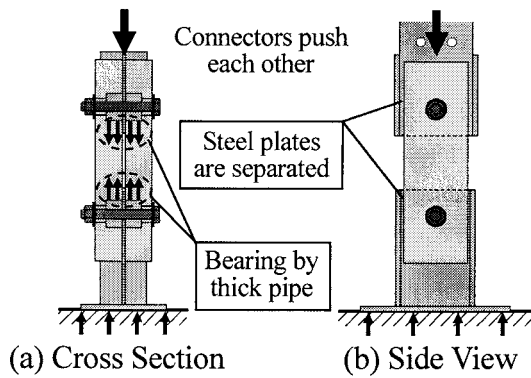


Figure 3 Setup of Shear Tests of Friction Connector

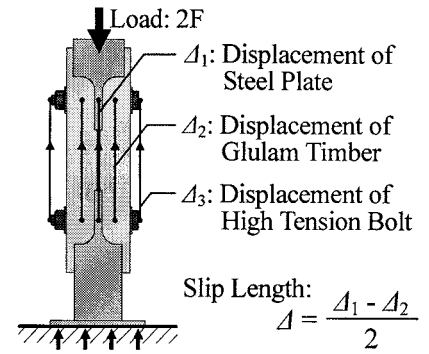
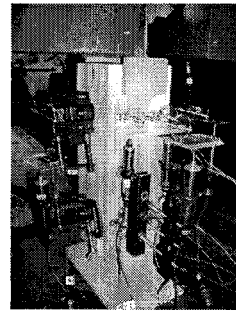


Figure 4 Measurement

2.2 Load and Measurement Method

Figure 3 illustrates setup of shear tests of friction connector. The load method was static monotonic compression that connectors push each other. The load velocity was 0.5mm/min. Figure 4 illustrates measurement. Δ_1 is displacement of steel plate, Δ_2 is displacement of glulam timber. And displacement of high tension bolts (HTB) is measured (Δ_3) to check that slip of frictional surface between steel plate and thick pipe is nothing on presumption that thick pipe and HTB are uninterrupted. Δ (slip per connector on one side) is defined as figure 4. There are strain gage on HTB and axial tension of HTB is measured. The shear tests started after stable axial tension of HTB is 200kN. F (force per connector on one side) is defined as a force that force acting on specimen divided by two.

2.3 Tests Results

The results of connector tests are listed table 3, and figure 5 illustrates relationship between force and slip length per one friction connector on one side. The value is average of the three copies. Slip of frictional surface between steel plate and thick pipe is little since Δ_1 and Δ_3 are approximately corresponding. The shear stiffness is a major factor in determining evaluation of composite member. So it compare shear stiffness each parameter as follows.

[Thickness of Glulam Timber, t]

When $h_w50\phi50h50$ and $h_w64\phi50h50$ are compared, the shear stiffness is almost equal value until the load arrives at 20kN. However shear stiffness of $h_w64\phi50h50$ is larger than that of $h_w50\phi50h50$ subsequently. Therefore, it is necessary that the thickness of glulam timber is larger than height of thick pipe to assure the effective shear stiffness of connector²⁾.

[Shape of Thick Pipe]

When $h_w64\phi65h38.5$ and $h_w64\phi50h50$ are compared, shear stiffness of $h_w64\phi50h50$ is larger than that of $h_w64\phi65h38.5$ in most loading area. On the other hand, when $h_w120\phi50h75$ and $h_w64\phi50h50$ are compared, shear stiffness of $h_w120\phi50h75$ almost equal that of $h_w64\phi50h50$ in spite of $h_w120\phi50h75$ has larger bearing area than $h_w64\phi50h50$. Since, in case of $h_w120\phi50h75$, effect of overturning moment of thick pipe become large. Hence, about the shape of thick pipe, $h_w50\phi50h50$ that aspect ratio equal 1 is suitable shape against shear stiffness.

Table 3 Result of Connector Shear Tests

Time	Shear Stiffness of a Connector (K_C) [kN/mm]					Maximum Strength of a Connector [kN]
	10kN	20kN	30kN	40kN	50kN	
$h_w50\phi50h50$	244	195	139	115	81	52.9
$h_w64\phi50h50$	219	213	188	173	146	64.0
$h_w64\phi65h38.5$	240	175	146	133	115	61.0
$h_w120\phi50h75$	275	212	186	167	148	84.7

(indicating per one friction connector on one side)

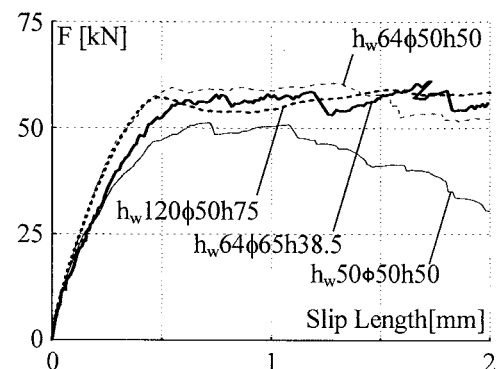


Figure 5 Relationship of Force and Slip Length

3. AXIAL COMPRESSION TESTS OF COMPOSITE MEMBER

3.1 Specimens

Specimens of axial compression of composite member using friction connector are listed table 4, figure 6 illustrates type of the specimens. About names of specimens, initial Roman number indicates number of connector, h_w indicates thickness of the cedar-glulam-timber, ϕ and h indicate shape of thick pipe. Used material property is listed king B of table 2. Cedar-glulam-timber for buckling stiffener is strength grade E65F225 and is composed of 10 pieces of 15mm thickness laminate. Strength grade of steel plate is SM490 and there is flange in edge area to increase local buckling load. The parameters of specimens are number of connector, thickness of glulam timber and shape of thick pipe. There are one III type that three connectors are set at even intervals, two IIIB type that three connectors are set at even intervals and two bolts are set at midspan, three IV type that four connectors are set at even intervals, hence the quantity of specimens is six. About glulam timber thickness, two type that P_{cri}/P_{ys} equal 0.58, 1.17 is made up. Figure 7 illustrates definitions of P_{ys} and P_{cri} . P_{ys} is yield strength of steel plate. P_{cri} is Euler buckling strength when two glulam timbers and steel plate are combined entirely.

3.2 Load and Measurement Method

The load method was static axial compression using dynamic actuator (figure 8). The load velocity was 0.01mm/sec. After maximum strength, when the strength fell below 80% of maximum strength,

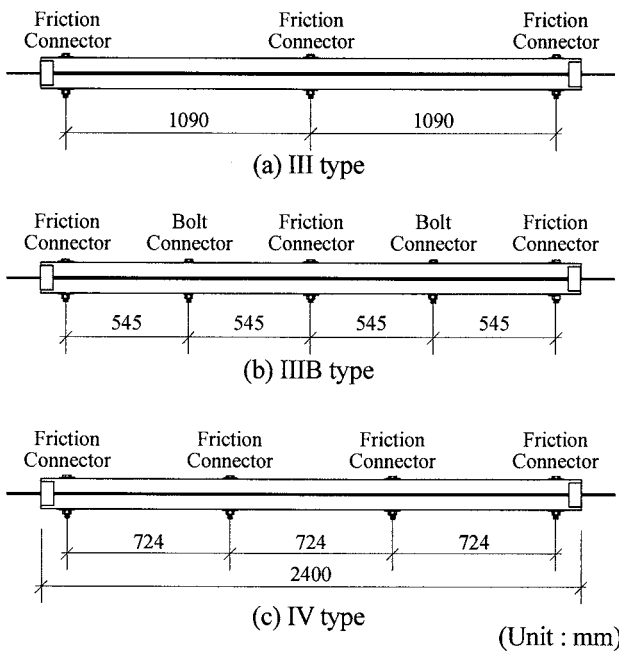


Figure 6 Specimens of Axial Compression Tests

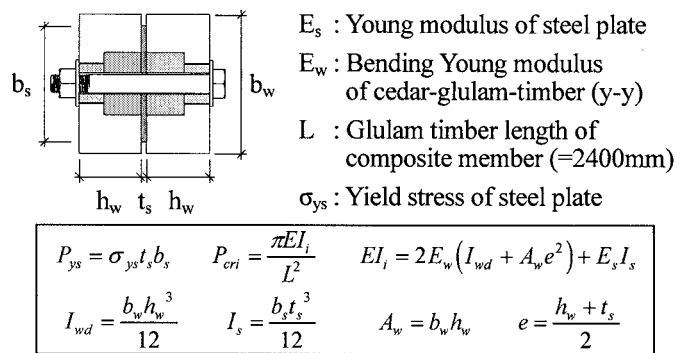


Figure 7 Definitions of P_{ys} and P_{cri}

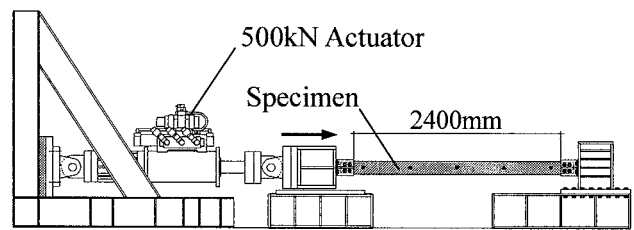


Figure 8 Setup

Table 4 Result of Axial Compression Tests

(Unit : mm)

No.	1	2	3	4	5	6
Name	IIIh _w 64φ65h38.5	IIIBh _w 64φ65h38.5	IIIBh _w 64φ50h50	IVh _w 64φ65h38.5	IVh _w 64φ50h50	IVh _w 50φ50h50
Steel Plate	t _s = 6, b _s = 125					
Cedar-Glulam-Timber	h _w = 64, b _w = 150					h _w =50,
Thick Pipe	φ65h38.5		φ50h50	φ65h38.5	φ50h50	
Saya Pipe	φ38h25.5		φ38h14	φ38h25.5	φ38h14	-
Number of Connector	3 (III type)	3+Bolt2 (IIIB type)		4 (IV type)		
P _{cr1} /P _{ys}	1.17					0.58

Roman number : Number of connector, h_w : Thickness of cedar-glulam-timber, ϕ : Diameter of thick pipe, h : Height of thick pipe
 b_w : Width of cedar-glulam-timber, t_s : Thickness of steel plate, b_s : Width of steel plate, Material Property is Table 2 B

the tests were stopped and load was excepted. Axial displacement and out-of-plane deformation were measured. There were strain gage on steel plate and glulam timber and axial force which was bore by each members was measured.

3.3 Tests Result

3.3.1 Relationships of Axial Load and Displacement

Result of axial compression tests of composite member is listed table 5, figure 9 illustrates relationships between axial force and displacement, figure 10 illustrates out-of-plane displacement and buckling aspect. To compare friction connector with shear-ring connector, the specimen of $P_{cri}/P_{ys} = 0.78$ using shear-ring connector is illustrated in figure 9 against specimens of $P_{cri}/P_{ys} = 0.58$ using friction connector. In the same way, the specimen of $P_{cri}/P_{ys} = 1.55$ using shear-ring connector is illustrated in figure 9 against of the specimens of $P_{cri}/P_{ys} = 1.17$ using friction connector.

Table 5 Result of Axial Compression Tests of Composite Member

Specimen's Name			IIIh _w 64φ65h38.5	IIIBh _w 64φ65h38.5	IIIBh _w 64φ50h50	IVh _w 64φ65h38.5	IVh _w 64φ50h50	IVh _w 50φ50h50
Experimental Result	Initial Stiffness	kN/mm	121	120	121	122	119	113
	Maximam Strength	kN	230	227	229	253	229	129
Buckling Mode			Total Buckling	Total Buckling	Total Buckling	Local Buckling	Local Buckling	Total Buckling
Calculation Result	Elastic Stiffness	kN/mm	130					
	Estimation	kN	232	236	252	252	267	128
	Johnson Equation	kN	266	266	261	264	258	258
	Yield Strength	kN	294					

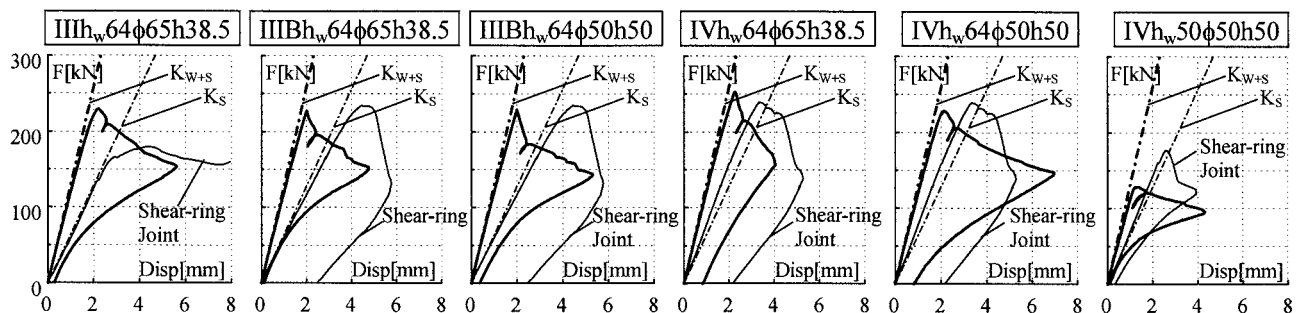


Figure 9 Relationships Between Axial Force and Displacement

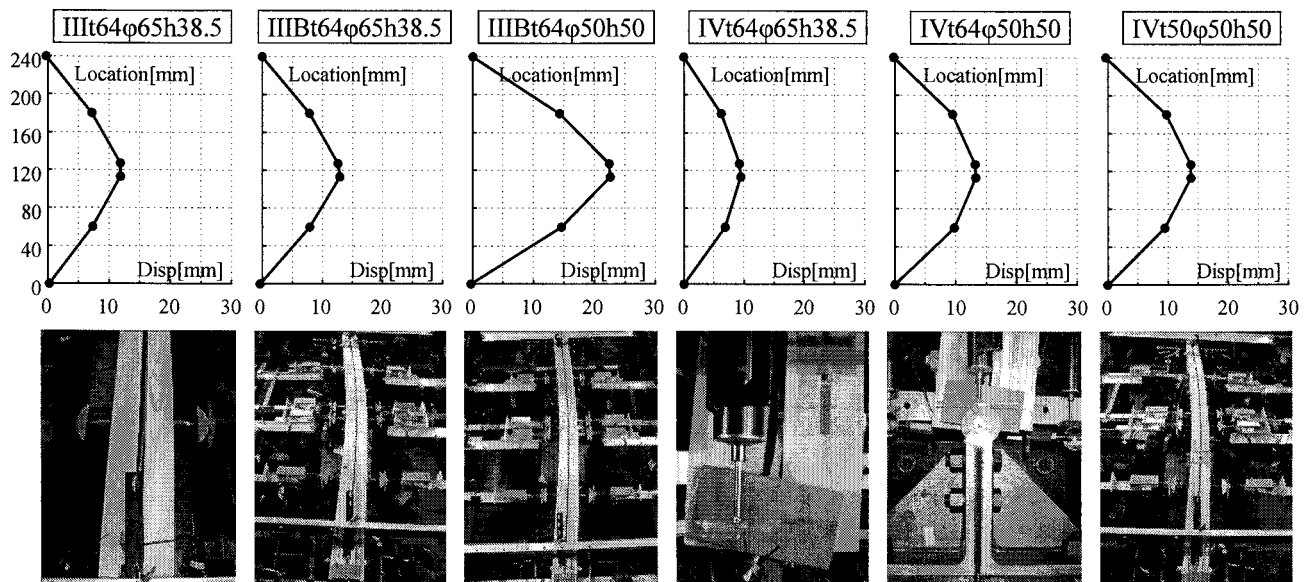


Figure 10 Out-of-Plane Displacement and Buckling Aspect

[Axial Stiffness]

Initial stiffness of specimen using shear-ring connector approximately equals elastic stiffness of steel plate (K_s). On the other hand, Initial stiffness of specimen using friction connector equals elastic stiffness of composite member when two glulam timbers and steel plate are combined entirely (K_{w+s}). Hence in case of friction connector there is little initial slip and friction connector has enough initial stiffness to judge that two glulam timbers and steel plate are combined entirely.

[Maximum Axial Strength and Buckling Aspect]

Maximum strength of specimen of $P_{cri}/P_{ys} = 1.17$ except for IV h_w64 φ65h38.5 approximately equaled. When the specimen using shear-ring connector is compared, the specimens of $P_{cri}/P_{ys}=1.17$ using friction connector equaled the specimen of $P_{cri}/P_{ys} = 1.55$ using shear-ring connector in maximum strength in spite of P_{cri}/P_{ys} was lower. Buckling aspects of III h_w64 φ65h38.5, IIIBh_w64 φ65h38.5, IIIBh_w64 φ50h50, and IVh_w50 φ50h50 were total buckling, and in IIIh_w64 φ65h38.5 there were high buckling mode of steel plate between connectors. On the other hand, buckling aspects of IVh_w64 φ50h50 and IVh_w64 φ65h38.5 were local buckling in edge area.

3.3.2 Distribution of Axial Load

Figure 11 illustrates composite member model, used spring modulus is listed table 6 and distribution of steel axial force which was derived from the model of figure 11 and strain gage value of tests is illustrated by figure 12. The steel axial force which is derived from strain gage value of tests considerably turns down in the edge part and it is approximately constant in the central part. The two glulam timbers strain 20% of axial force which composite member strains. When calculation and tests value are compared, their distribution shape correspond qualitatively each other. Hence, it is possible to estimate shear force of friction connector by this calculation method.

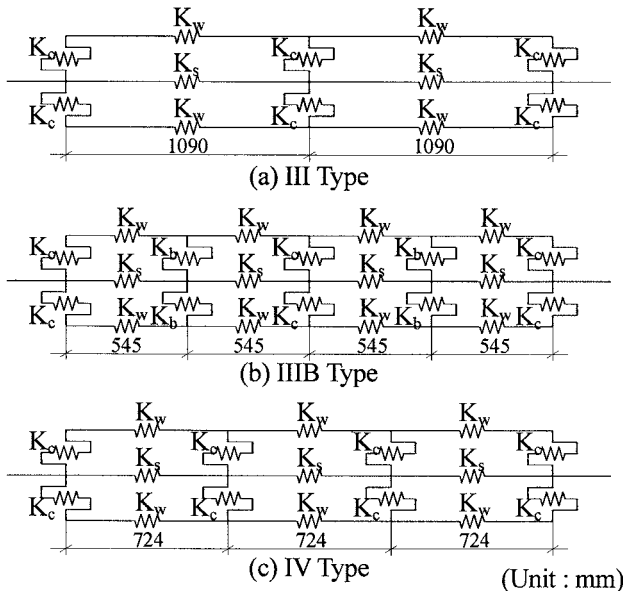


Figure 11 Model of Composite Member

Table 6. Spring Modulus

Specimen	K_c	K_w	K_s	K_b
	kN/mm			
IIIIt64φ65h38.5	132	73	141	-
IIIBt64φ65h38.5	132	145	282	9.8
IIIBt64φ50h50	173	145	282	9.8
IVt64φ65h38.5	132	109	212	-
IVt64φ50h50	173	109	212	-
IVt50φ50h50	115	109	212	-

K_c : Shear stiffness of friction connector from shear tests of friction connector when F equals 40kN

K_s : Elastic stiffness of steel plate from material property

K_w : Elastic stiffness of cedar-glulam-timber from material property

K_b : Shear stiffness of bolt connector from shear tests of bolt connector (Reference 1)

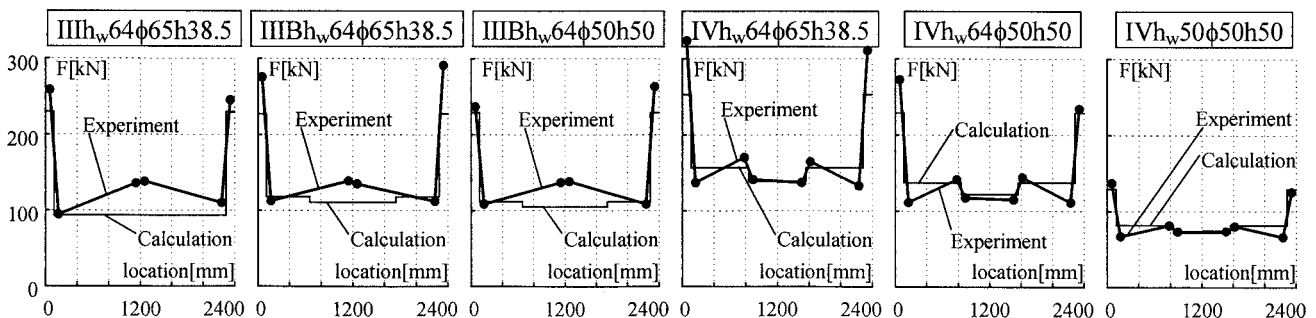


Figure 12 Distribution of Steel Axial Force

4. EQUATIONS FOR ESTIMATING

4.1 Concept of New Estimation Method

In case composite member using shear-ring connector, shear force at connector was not large and it was possible to judge that behavior of the connector is linear elasticity. Therefore, by using constant shear stiffness of connector, maximum strength of composite member using shear-ring was estimated as P_{TB} or P_{LB} whichever is smaller. P_{TB} is strength upon considering unity of glulam timber and steel plate for the case of total buckling. P_{LB} is strength for the case of local buckling at edge. The method to calculate P_{TB} and P_{LB} are illustrated figure 13 (Reference 1)).

However in case of composite member using friction connector, shear force of the connector becomes large because friction connector has more unity than shear-ring connector. It is necessary to consider P_{QC} which is axial load of composite member when shear force of friction connector becomes limit shear force, Q_{CL} . P_{QC} is calculated by changing shear stiffness of connector. The shear stiffness is calculated by using relationship between shear force and slip length in shear tests of friction connector. Designers can set any P_{QC} judging the relationship between force and slip length of friction connector (Figure 5) It is not necessary to consider limit shear force of bolt connector because friction connector approaches limit shear force earlier than bolt connector. In the new estimation method, the minimum value of P_{TB} , P_{LB} and P_{QC} is maximum axial strength of the composite member using friction connector.

In case of Total Buckling ¹⁾

$$P_{TB} = \frac{9.6EI_c}{L^2} \quad EI_c = \mu EI_d \quad EI_d = 2E_w I_{wd} + E_s I_s$$

$$\mu = \frac{L^2}{\left(1 - \frac{\beta e}{\alpha}\right)L^2 - \frac{8\beta}{\alpha^2}e \left(\cosh \frac{\sqrt{\alpha}L}{2} - \tanh \frac{\sqrt{\alpha}L}{2} \sinh \frac{\sqrt{\alpha}L}{2} - 1 \right)}$$

$$\alpha = K \left(\frac{1}{E_w A_w} + \frac{e^2}{2EI_d} \right) \quad \beta = \frac{Ke}{2EI_d} \quad K = \frac{(m-0.3)K_r + nK_b}{L}$$

(Refer to Figure 7.)

In case of Local Buckling ³⁾

$$P_{LB} = \sigma_{crj} t_s b_s \quad \sigma_{crj} = \left\{ 1 - 0.4(\lambda_s / \Lambda_s)^2 \right\} \sigma_{ys}$$

$$\lambda_s = \frac{L_{LB}}{i_s} \quad \Lambda_s = \sqrt{\frac{\pi E_s^2}{0.6 \sigma_{ys}}} \quad i_s = \sqrt{\frac{I_s}{A_s}} \quad A_s = b_s t_s$$

m : Number of friction connector
n : Number of bolt connector
 K_r : Shear stiffness of friction connector
 K_b : Shear stiffness of bolt connector
 i_s : Radius of gyration of steel plate
 λ_s : Slenderness ratio of steel plate
 Λ_s : Limit slenderness ratio of steel plate

	ϕ	L_{LB}
III type	65	77.5
IIIB type	50	85
IV type	65	81.5
	50	89

(Unit : mm)

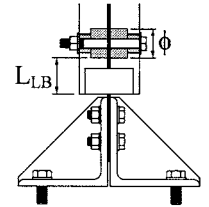
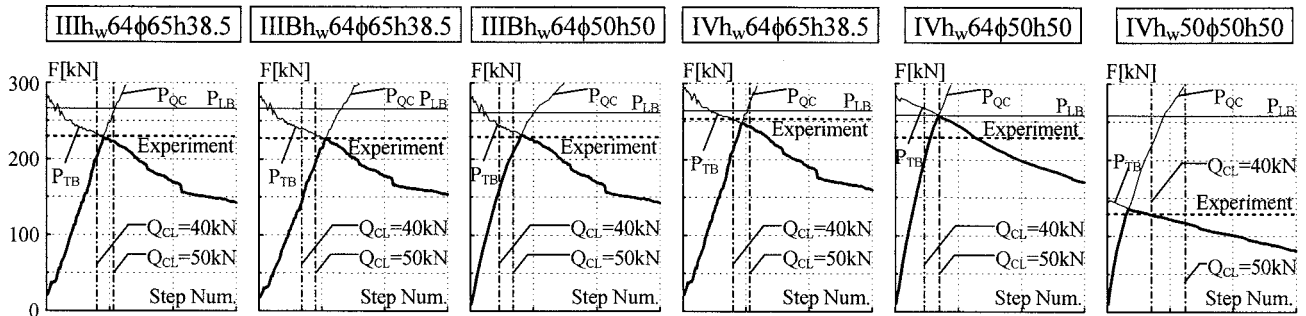


Figure 13 Calculation of Two Buckling Strength

4.2 Result of New Estimation Method

Figure 14 illustrates variation of P_{TB} , P_{LB} and P_{QC} . The horizontal axis represents step number in shear tests of friction connector (chapter 2). Shear stiffness of friction connector (K_C) is exchanged step by step. The broken line indicates the maximum axial strength, the chain line indicates the point for Q_{CL} to reach 40kN and 50kN. Judging between force and slip length of friction connector (Figure 5),



P_{TB} : Axial strength when total buckling occurs, P_{LB} : Axial strength when local buckling occurs
 P_{QC} : Axial strength when friction connector reaches limit shear force (Q_{CL})

Figure 14 Relationship Between P_{TB} , P_{LB} and P_{QC}

the skeleton curve behaves linear elasticity until force reaches 40kN. Therefore, in case of this detail, there is no backlash between thick pipe and cedar-glulam-timber by cyclic load if designer set that shear force of friction connector becomes 40kN or less.

When the axial load of the tests result and estimated value are compared, they approximately correspond each other. Therefore this new estimation method is useful against composite member using friction connector. Moreover it is possible to figure out visually relationship of three strengths and transition of buckling mode by these figures.

5. CONCLUSIONS

Shear tests of friction connector and axial compression tests of composite member were conducted. Major findings are:

- 1) Friction connector has higher shear stiffness compared to shear-ring connector, and is able to cancel the initial backlash and built up easily.
- 2) In case of friction connector, two glulam timbers strain 20% of axial force which composite member strains.
- 3) It is possible to demonstrate their prediction capability against axial compression load with sufficient accuracy by estimating shear stiffness of connector appropriately.

In addition, about the backlash between thick pipe and cedar-glulam-timber, there is a possibility that secular distortion of cedar-glulam-timber influences. It is considered that there is little possibility of the effect since the thick pipe is inserted to prior hole which is smaller than itself when the friction connector is composed. However detailed study is assumed the problem for the future.

References:

- 1) Horii, T. and Sakata, H. and Takeuchi, T. and Suzuki, T. and Nakamura, H.: "Experimental study on mechanical behavior of glulam timber steel composite member using shear-ring connector", *Journal of Structural and Construction Engineering*, No.584, 2004.10, pp.51-60
- 2) Suzuki, T. and Sakata, H. and Takeuchi, T. and Matsuoka, Y. and Nagayama, K. and Matsuda, K.: "Study on mechanical behavior of Glulam Timber-Steel composite member" *Summaries of Technical Papers of Annual Meeting*, Architectural Institute of Japan, C1, 2005, pp.277-278
- 3) *Recommendations for Stability Design of Steel Structures*, Architectural Institute of Japan, 1996

TSUNAMI LOAD DETERMINATION FOR ON-SHORE STRUCTURES

Harry Yeh

Professor, Department of Civil Engineering, Oregon State University, USA
harry@engr.orst.edu

Abstract: Tsunamis often cause structural damage by direct water forces as well as impact forces by water-born missiles. The available design guidelines for tsunami forces are reviewed and evaluated. Synthesizing technical information, a rational methodology is developed for the determination of design tsunami forces on buildings located in inshore areas where tsunami inundation maps are available. Although there are substantial uncertainties with respect to tsunami phenomena themselves, this simple methodology can be used for preliminary evaluation of tsunami forces.

1. INTRODUCTION

Very large tsunamis are rare and the forewarning is possible (even though the lead time can be short). Therefore, the primary mitigation tactic to date has been evacuation; most efforts in the US have focused on the development of effective warning system, inundation maps, and tsunami awareness (e.g., National Tsunami Hazard Mitigation Program, 2005). The strategy of warning and evacuation makes sense from the standpoint of saving human lives. However, it does not address the devastating damage to buildings and critical coastal infrastructures. Failure of critical infrastructures could create enormous economic setbacks. Furthermore, in some coastal areas, the strategy of evacuating people to a high ground may be impractical. People living on a spit or a small island with no high ground may not have sufficient time to reach a natural safe haven. Only possible way to minimize human casualties is to evacuate people to the upper floors of tsunami-resistant buildings. In this paper, we present a rational methodology to determine the design tsunami forces on a structure that is at an onshore location.

The existing design manuals provide guidelines for loads that would be expected on a structure in flood and wind wave situations: e.g., ASCE/SEI Standard 7-05 (ASCE, 2005) and the Federal Emergency Management Agency's Coastal Construction Manual (FEMA-CCM, 2005). Interestingly, most of the flood- and wave-loading estimates are based on a Dames & Moore study performed in 1980, which drew from prior work performed by Ocean Engineering Consultants, Inc. (Bretschneider, 1974). The Coastal Construction Manual refers to tsunami loads, indicating that the flood velocity is expected to be substantially higher than other forms of flooding. The City and County of Honolulu Building Code (CCH, 2000) provides specific guidance for structural design of buildings subject to tsunamis. The loading requirements are also based on the 1980 Dames & Moore study. In Japan, the Building Center of Japan (BCJ, 2004) provides an outline for design of tsunami refuge buildings; the design tsunami loads are evaluated based on a laboratory study by Asakura, et al. (2000).

Most of the existing guidelines consider the following loads: 1) hydrostatic force, 2) buoyant force, 3) hydrodynamic force, 4) surge force, 5) debris impact force, and 6) wave-breaking force.

Among these forces, wave-breaking force would be unlikely to affect onshore buildings. The term ‘wave breaking’ is defined here as a plunging-type breaker: the process of over-turning motion of the entire wave front. In general, when waves break in a plunging mode, a wave front becomes almost vertical before it overturns. If this almost vertical front face impacts directly on the wall, a very high pressure is generated in the extremely short duration. Evidently, such a wave-breaking process takes place offshore for tsunamis where the depth of water is finite. Once over-turning tip of wave touches down to the water in front of it, the wave becomes a broken wave. The broken wave can be considered as a “bore” for tsunami because of its very long wavelength. The subsequent runup onto the dry land is often termed “surge.” A highly turbulent tsunami tongue sweeps the land, and its initial impact creates the surge forces.

2. TSUNAMI LOAD ANALYSES

Hydrostatic force occurs when standing water encounters a structure. Hydrostatic force may not be relevant to a structure with a relatively short breadth, around which the water can quickly flow and fill in on all sides. Hydrostatic force is usually important for long structures such as sea walls and dikes, or for evaluation of an individual wall panel where the water level on one side differs substantially from the water level on the other side.

Buoyant force will act vertically through the centroid of the displaced volume of a structure subjected to partial or total submergence. Buoyant force is a concern for structures that have little resistance to upward forces (e.g. light wood frame buildings). Both hydrostatic and buoyant forces can be rationally determined once the design inundation depth is estimated; hence no further discussion will be made in this paper.

When water flows around a structure, hydrodynamic force is applied to the structure as a whole. Hydrodynamic force is induced by quasi-steady flows, and is a function of fluid density ρ , flow velocity u and structure geometry. It is often called the drag force. The design hydrodynamic force can be computed by

$$F_d = \frac{1}{2} \rho C_d B (h u^2)_{\max}, \quad (1)$$

where h is the flow depth at the location of interest when there is no flow obstruction (i.e. no structure); the combination $h u^2$ represents the momentum flux per unit mass per unit breadth; B is the breadth of the structure in the plane normal to the flow direction. FEMA-CCM (2005) recommends $C_d = 2.0$ for square or rectangular objects and 1.2 for cylindrical objects. At a given location, the maximum flow depth h_{\max} and maximum flow velocity u_{\max} may not occur at the same time: $(h u^2)_{\max} \neq h_{\max} u_{\max}^2$. The hydrodynamic force must be based on the maximum momentum flux, $(h u^2)_{\max}$, occurring at the site (but no structure) during the tsunami inundation.

In the area of coastal engineering, hydrodynamic forces are evaluated in combination of the drag force (1) and the inertial force. Because tsunami wave periods are very long, the inertial force is considered unimportant except at the impact of tsunami’s leading edge, which is called the surge force.

Surge force is caused by the leading edge of surge of water impinging on a structure. The CCH (2000) adopted the following equation (Dames & Moore, 1980) for surge force F_s per unit width:

$$F_s = 4.5 \rho g h^2, \quad (2)$$

where h is the surge height that is difficult to identify, as we discussed later. The surge-force computation by (2) would result in excessively overestimated values if the maximum inundation depth were used for the value of h : the estimation made by (2) implies that the surge force would be

9 times the hydrostatic force alone. Note that (2) was derived by summing the hydrostatic force and the change in linear momentum at the impingement of a surge front on a vertical wall; the surge impingement is treated as steady using the flow velocity of $u = 2\sqrt{gh}$. Evidently, the surging is highly transient and the validity of (2) is in question.

Interestingly, the design load identical to (2) is also suggested by the Building Center of Japan (BCJ, 2004) based on the experimental study by Asakura et al. (2000). However, (2) in BCJ is not a presentation of surge forces, but the maximum force on a two-dimensional vertical wall, i.e. a space behind the wall being dry all the time, and the incoming tsunami stops completely at the vertical wall. The parameter h in this case is the maximum wave elevation from the ground level when the wall is absent.

The flow velocity $u = 2\sqrt{gh}$ is identical to that of the velocity of the leading wave front advancing on a frictionless horizontal dry bed in the classic dam-break problem; the flow is generated by breaking a dam with the initially quiescent impoundment depth h (see e.g. Stoker, 1957). Note that the dam impoundment depth is hardly a good estimate for tsunami's flow depth. Tracing back to the origin from Dames & Moore (1980), we found that $u = 2\sqrt{gh}$ was suggested by Camfield (1980) who referred it to Keulegan (1950), who made 'that conjecture' based on the laboratory data. In Keulegan's conjecture, h is the thickness of the leading surge tip that is influenced by the bed friction: this is a type of boundary layer that saturates the entire flow depth at the tip as discussed in his analytic model by Whitham (1955). Note that, as we discuss the next, such a depth is small and difficult to be identified due to gradual increase in flow depth at the leading tongue of a tsunami surge.

Ramsden (1993) performed comprehensive experiments on surging forces. Laboratory data as shown in Fig. 1 show no initial impact force (surging force) in dry-bed surges, but an overshoot in force was observed in bores: note that there is a water (not dry) in front of the bore propagation. The maximum overshoot is approximately 1.5 times the subsequent hydrodynamic force, which is consistent with independent laboratory data obtained by Arnason (2005) as shown in Fig. 2. The lack of overshoot in dry-bed surge can be attributed to the relatively mild slope of the wave-front profile, while the impact momentum increases with the sudden slam of the steep front of bores (see, Fig. 1a). This demonstrates that the initial impingement of a 'dry-bed' surge is not important for the evaluation of tsunami forces. If the runup zone is flooded by an earlier tsunami runup, subsequent waves could impact structures with the formation of bores. For conservatism, we can estimate the design surge force by (1) using $C_d = 3.0$, which is 1.5 times the drag coefficient $C_d \approx 2.0$ for a square or rectangular shaped object.

The hydrodynamic and surge forces can be computed by (1). A problem is how to estimate the maximum value of $(hu^2)_{\max}$ in (1). In fact this is the reason why many existing force formulae are expressed with a function of depth only (but not flow velocity). Ideally, the maximum value of hu^2 should be obtained by running a detailed numerical simulation model (or acquiring the existing simulation data). It is however cautioned that the numerical model in the runup zone must be run with a very fine grid size (say, less than 10 m) to ensure adequate accuracy in the prediction of hu^2 . When suitable simulation model data are unavailable, the value $(hu^2)_{\max}$ can be roughly estimated using the equation given by Yeh (2006), who developed the envelope curve of hu^2 based on the exact analytic solution of the shallow-water wave theory. It must be noted that Yeh's analytic solution is for a uniform beach slope; therefore, some adjustments need to be made for a real situation. It is convenient to express Yeh's equation as a function of the ground elevation, instead of the horizontal location; the transforming his equation yields

$$\frac{(hu^2)_{\max}}{gR^2} = 0.125 - 0.235\frac{z}{R} + 0.11\left(\frac{z}{R}\right)^2, \quad (3)$$

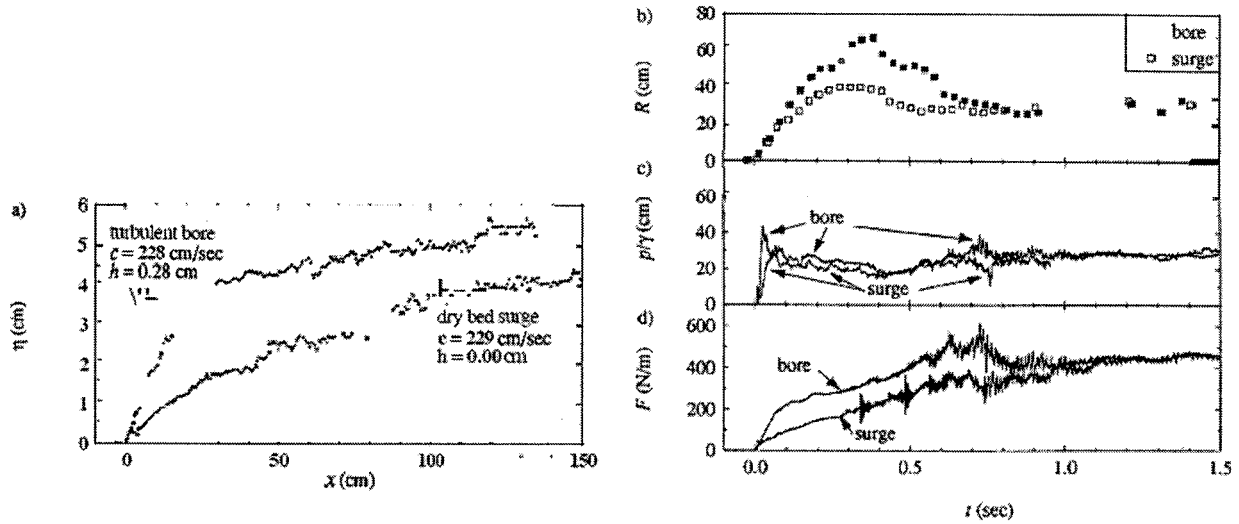


Figure 1. Comparison of the experimental (a) wave profile; (b) runup; (c) pressure head; and (d) force due to a strong turbulent bore and a dry bed surge with approximately the same celerity. (after Ramsden, 1993)

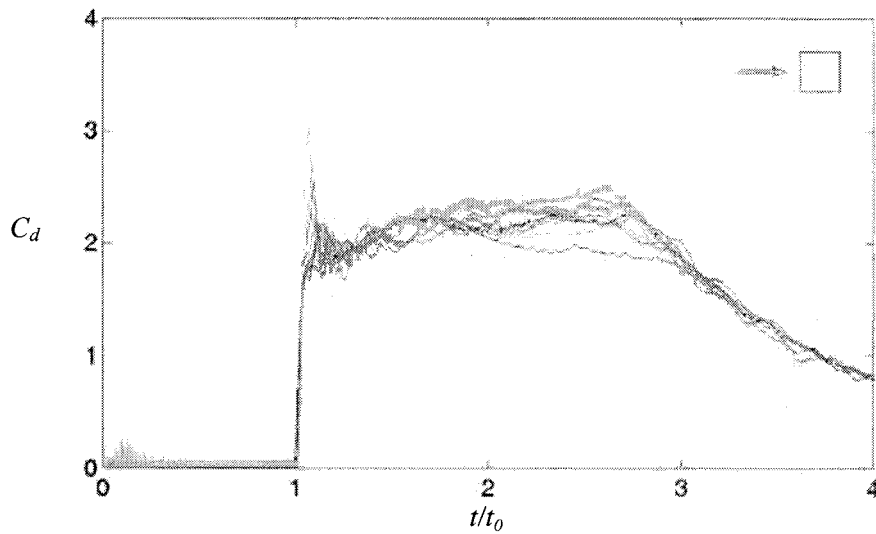


Figure 2. Laboratory data of temporal variations of exerted forces on a square column by various bore conditions. (after Arnason, 2005)

where R is the ground elevation at the maximum penetration of tsunami runup, measured from the initial shoreline, and z is the ground elevation of the location of interest. The values of R and z can be readily obtained if the tsunami inundation map is available. It must be re-emphasized that the formula is based on the condition of tsunami runup on a uniformly sloping beach with no lateral topographical variation; hence the computed value must be considered as a guide for further engineering evaluation and judgment.

Impact forces from waterborne missiles (e.g., floating driftwood, boats, shipping box containers, automobiles, buildings) can be a dominant cause of structure destruction. Unfortunately, it is difficult to estimate this force accurately. Most available models are based on the impulse-momentum concept, in which the impulse I of the resultant force F acting for an infinitesimal time t^* is equal to the change in linear momentum:

$$I = \int_0^{t^*} F dt = d(mu_b); \quad t^* \rightarrow 0, \quad (4)$$

where m is the mass of water-borne missile and u_b is the velocity of the missile. The existing manuals (ASCE, 2005; FEMA-CCM, 2005; CCH, 2000) contained similar equations that resulted in the following generalized expression for impact force F_I acting for a small but finite time Δt (not infinitesimal), and the average change in momentum are used as an approximation:

$$F_I = m \frac{du_b}{dt} = m \frac{u_b}{\Delta t}. \quad (5)$$

In (5), there is, however, significant uncertainty in evaluating the duration of impact Δt . The following are other available formulae for missile-impact force estimation.

Matsutomi (1999) investigated the impulse forces of wood logs. He performed two sets of experiments: one in a small water tank and the other for full-scale impact in air. The impact condition in the air may significantly differ from an actual waterborne case because of the absence of added-mass effect of water: prior to the impact, the waterborne missile is carried by the surrounding water flow and the momentum carried by the water itself must contribute to the impact force. Matsutomi compensated for the added-mass effect with the data obtained from his small-scale water tank experiments. Based on his regression analysis of the data, Matsutomi proposed the impact-force equation as

$$\frac{F_I}{\gamma_w D^2 L} = 1.6 C_M \left(\frac{u}{\sqrt{gD}} \right)^{1.2} \left(\frac{\sigma_f}{\gamma_w L} \right)^{0.4}, \quad (6)$$

where γ_w is the specific weight of the log, D and L are the diameter and the length of the log, respectively, C_M ($\approx 1.7 \sim 1.9$) is the added-mass coefficient, u is the velocity of the log at impact, and σ_f is the yield stress of the wood. In spite of a thorough study with a large amount of laboratory data, the derived form of (6) is inconvenient for practice due to its particular choice of the scaling parameters; it is only applicable to driftwood or logs. Ikeno et al. (2001; 2003) performed laboratory experiments similar to Matsutomi (1999) to examine the impact forces of the objects other than driftwood or logs, and suggest the empirical formula in the similar but different scaled form from (6): note that the experiments by Ikeno et al. were performed in a narrow 2-D flume, hence the incoming flow stopped completely at the vertical wall, which makes significant difference in the results.

Haehnel and Daly (2002) performed experiments using reduced-scale logs in steady flow in a small flume, and prototype logs in a large towing basin. It must be noted that, in the towing basin the water is stationary (i.e. no added-mass effect being taken into account), while in the actual tsunami condition moving water carries the missile. Haehnel and Daly analyzed the data based on the linear dynamic model with one degree of freedom. Since the collision occurs over a short duration, damping effects are neglected; hence the model can be formulated by:

$$m \ddot{x} + kx = 0, \quad (7)$$

where x is the summation of the compression of the building and the log during impact and rebound, and k is the effective constant stiffness associated with both the log and the building, and the dot denotes the time derivative. Solving (7) yields the maximum force:

$$F_I = \text{Max.} \langle kx \rangle = u \sqrt{km}. \quad (8)$$

Review of the previous work demonstrates the immaturity and uncertainty of our present understanding of missile-impact forces. As we stated, proper estimate of Δt is formidable for the impulse-momentum approach. Although (6) by Matsutomi is based on his substantial analyses of a large set of the laboratory data, the form of (6) is physically ambiguous because of the choice of the scaling parameters, is limited only to cylindrical shaped missiles (logs), and is inconvenient for the use in actual practice. The empirical equation by Ikeno et al. is based on their small-scale laboratory experiments with an impermeable wall; no flow passes beyond the structure. The value of effective constant stiffness k is difficult to evaluate for Haehnel and Daly's (8). In reality, k is not constant; it is likely a function of x during the impact. Hence, the linearized equation (7) may be inadequate. Since the added mass effect appears important at the impact, the results derived from the compromised experimental conditions may contain significant discrepancies. Even if the impact velocity u and the missile mass m were given, each formula would yield a different functional relation to predict the forces, which indicates complexity and uncertainty inherent in the problem.

In spite of the flaw for each model, until more comprehensive studies be made, we propose the constant stiffness approach (8) because of its simple-but-rational formulation. In addition, the functional relation of m and u to the force F_I is similar to Matsutomi's empirical equation (6). Considering that Matsutomi's empirical treatment was based on the impulse-momentum approach, the coincidental similarity with the constant-stiffness approach provides additional confidence in the formulation. Since the added-mass effect must be included, (8) should be modified as

$$F_I = C_M u_{\max} \sqrt{k m}, \quad (9)$$

with $C_M \approx 2$ for conservatism (note that Matsutomi (1999) found that $C_M \approx 1.7 \sim 1.9$ and Ikeno et al. (2001, 2003) used $C_M \approx 1.5 \sim 2.0$) and k must be determined based on the model missile ($k = 2.4 \times 10^6$ N/m was recommended for a log by Haehnel and Daly). Note that a proper estimate of k is the key. An additional advantage for the use of (9) is that the value of k is not as sensitive as Δt in the impulse-momentum approach: it can be shown that Δt are proportional to $\sqrt{1/k}$.

As we discussed earlier, for the prediction of flow velocities and depths at a site of interest for a given design tsunami, the best practice is to run a detailed numerical simulation model with a very fine grid size (say, less than 10 m) in the runup zone. The numerical simulation can provide the complete time history of flow velocity and depth at the site of interest.

Alternatively, just as we presented earlier for the value of $(hu^2)_{\max}$, the use of analytical solution can be considered to obtain the maximum velocity in order to compute (9). The available analytical solution is based on one-dimensional, nonlinear shallow-water-wave theory with a uniformly sloping beach. With those assumptions, Shen and Meyer (1963) provided the exact solution for the runup of an incident bore. The maximum fluid velocity occurs at the leading runup tip and their solution can be expressed as a function of the ground elevations z and R :

$$u_{\max} = \sqrt{2gR \left(1 - \frac{z}{R}\right)}, \quad (10)$$

Equation (10) indicates that the flow of the leading tip moves up the beach under gravity just like a particle: simple energy exchange between its kinetic and potential energies. Yeh (2006) demonstrated that (10) provides indeed the upper-limit envelope of the flow velocity for all incident tsunami forms. This flow velocity occurs at the leading tongue of the flow where the flow depth is nil. Hence, excessive overestimation of the impact load may result.

Based on the analysis by Shen and Meyer (1963), Peregrine and Williams (2001) provided the equations for temporal and spatial variations in flow velocity u and depth h for an incident bore runup onto a uniformly sloping beach. With slightly different scaling, Peregrine and Williams' formulae can be expressed as

$$\begin{cases} \eta = \frac{1}{36\tau^2} (2\sqrt{2}\tau - \tau^2 - 2\zeta)^2 \\ v = \frac{1}{3\tau} (\tau - \sqrt{2}\tau^2 + \sqrt{2}\zeta) \end{cases}, \quad (11)$$

where $\eta = h/R$, $v = \frac{u}{\sqrt{2gR}}$, $\tau = t \tan \alpha \sqrt{g/R}$, $\zeta = z/R$, in which t is the time ($t = 0$ when the bore passes at the initial shoreline), and z is the ground elevation of the location of interest, measured from the initial shoreline. For a given tsunami penetration, the incident-bore formation should yield the maximum flow velocity; gradual flooding of non-breaking tsunamis should result slower flow velocities. Therefore, (11) can be used to determine the maximum flow velocity at a given location for a given flow depth. Combining the two equations in (11) and eliminating τ yield Fig. 3. Each curve in the figure represents the dimensionless flow velocity v vs. the location ζ (in terms of its ground elevation z) for a given local flow depth h . This figure can be used to evaluate the maximum flow velocity u_{\max} that can carry a water-borne missile with a finite draft d , since draft of the debris must be smaller than the flow depth to make the debris afloat ($h \geq d$). The lower curve in Fig. 3 represents the maximum flow velocity at the maximum runup penetration of flow depth η . This curve can be considered as the lower limit of the maximum flow velocity with the depth η . Note that the results in Fig. 3 are for incident bores. Local inundation depths of other tsunami forms exceed that of a bore runup, and the maximum flow velocity is lower than the limit curve in Fig. 3. Hence when a water-borne missile has its draft that exceeds the flow depth of the bore runup, the design velocity u_{\max} can be estimated conservatively with the lower limit curve.

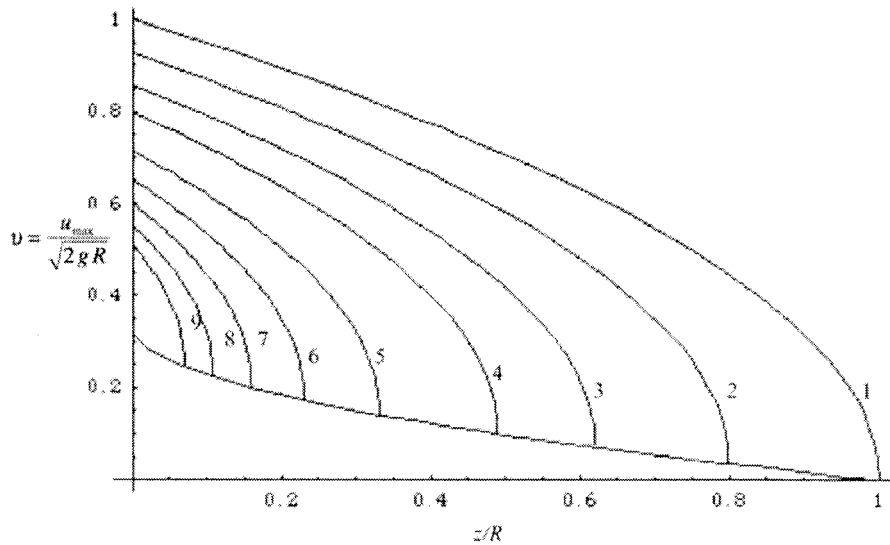


Figure 3. The maximum flow velocity of depth d at the ground elevation z , when the maximum runup elevation R . The curves from the outside toward the origin represent, respectively, 1) $\eta = h/R = 0$, 2) 0.0025, 3) 0.01, 4) 0.02, 5) 0.04, 6) 0.06, 7) 0.08, 8) 0.10, and 9) 0.12. Use the lower curve for the minimum flow velocity.

3. CONCLUSIONS

The existing methods to determine design tsunami forces are reviewed and evaluated. A rational methodology to determine the design tsunami loads on onshore structures with finite breadth is proposed: (1) and (9). The necessary parameters for the load computations by (1) and (9) can be estimated based on the analytic solutions, i.e. (3) and Fig. 3, when the tsunami inundation maps are available. Although some simplifications and assumptions must be imposed in the analytic solutions, the results should be useful to guide the further analyses.

Acknowledgements:

This work was supported by the National Tsunami Hazard Mitigation Program through Washington State Military Department, Federal Emergency Management Agency through Applied Technology Council, and by the US National Science Foundation (CMS-0245206).

References

- ASCE, 2005, *Minimum Design Loads for Buildings and Other Structures*, ASCE/SEI Standard 7-05, American Society of Civil Engineers, Reston, Virginia.
- Arnason, H. 2005. Interactions between and Incident Bore and a Free-Standing Coastal Structure, Ph.D. Thesis, University of Washington, Seattle, 172pp.
- 朝倉良介、岩瀬浩二、池谷毅、高尾誠、金戸俊道、藤井直樹、大森政則、2000. 護岸を越流した津波による波力に関する実験的研究：海岸工学論文集 第47巻 pp.911-915
- Bretschneider, C.L., 1974, *Development of Structural Standards in Flood and Tsunami Areas for the Island of Hawaii*, Ocean Engineering Consultants, Inc., Honolulu, Hawaii.
- Camfield, F. 1980. Tsunami Engineering, Coastal Engineering Research Center, US Army Corps of Engineers, Special Report (SR-6), 222 p.
- City and County of Honolulu Building Code (CCH), Department of Planning and Permitting of Honolulu Hawai'i. 2000.. Chapter 16 Article 11. July.
- Dames & Moore, 1980, *Design and Construction Standards for Residential Construction in Tsunami-Prone Areas in Hawaii*, prepared for the Federal Emergency Management Agency by Dames & Moore, Washington D.C
- FEMA-CCM 2000. *Coastal Construction Manual*. FEMA 55, Federal Emergency Management Agency.
- Haehnel, R.B., and Daly, S.F. 2002. Maximum impact force of woody debris on floodplain structures. Technical Report: ERDC/CRREL TR-02-2, US Army Corps of Engineers, 40 pp.
- Ikeno, M., Mori, N., and Tanaka, Y. 2001. Proceedings of Coastal Engineering, Japan Society of Civil Engineering, Vol. 48, 846-850. (Japanese)
- Ikeno, M. and Tanaka, Y. 2003. Proceedings of Coastal Engineering, Japan Society of Civil Engineering, Vol. 50, 721-725. (Japanese)
- Keulegan, G. H. 1950. Wave motion. (In: Engineering Hydraulics, H. Rouse Ed.) John Wiley & Son, Inc. New York, 711 – 768.
- Matsutomi, H. 1999. A practical formula for estimating impulsive force due to driftwoods and variation features of the impulsive force. Proceedings of the Japan Society of Civil Engineers, 621, 111-127. (Japanese)
- Okada, T., Sugano, T., Ishikawa, T., Ohgi, T., Takai, S., and Kamabe, C. 2005. Structure design method of buildings for tsunami resistance (proposed). English translation of The Building Letter, 2004.
- Peregrine, D.H. and Williams, S. M. 2001. Swash overtopping a truncated plane beach. J. Fluid Mech. 440, 391-399.
- Ramsden, J.D. 1993. Tsunamis: Forces on a vertical wall caused by long waves, bores, and surges on a dry bed. Report No. KH-R-54, W.M. Keck Laboratory, California Institute of Technology, Pasadena, Calif., 251 pp.
- Shen, M.C. and Meyer, R.E. 1963. Climb of a bore on a beach Part3. Run-up. J. Fluid Mech. 16, 113-125
- Stoker, J.J. 1957. Water waves. Interscience Publishers, Inc., New York, 567 pp.
- Whitham, G.B. 1955. The effects of hydraulic resistance in the dam-break problem. Proc. Roy. Soc. A. 227, 399-407.
- Yeh, H. 2006. Maximum fluid forces in the tsunami runup zone. J. Waterway, Port, Coastal, and Ocean Engineering, ASCE, 132, 496-500.

STUDIES OF PRESENT, PAST, AND FUTURE TSUNAMI SOURCES

K. Satake¹⁾

*1) Deputy Director, Active Fault Research Center, National Institute of Advanced Industrial Science and Technology, Japan
kenji.satake@aist.go.jp*

Abstract: Studies of tsunami sources, by forward and inverse modeling, are reviewed. Once the source is known, numerical simulation of tsunami generation and propagation can be used for tsunami warning for present tsunami and for hazard assessment for future tsunamis. The current tsunami warning system is based on seismological and sea-level measurements, as well as pre-made computer simulation results stored in database. The tsunami source of the 2004 Sumatra-Andaman earthquake was studied from instrumental sea-level data in the Indian Ocean. The largest slip on the fault, about 25 m, was estimated off Sumatra Island. Date and size of the 1700 Cascadia earthquake has been studied from geological data in North America and historical data in Japan. Tsunami deposits in Hokkaido revealed the unusual tsunamis in the 17th century. For future tsunamis, probability of earthquake occurrence and possible tsunami heights can be estimated. Tsunami hazard maps have been made for many coastal communities for tsunami hazard reduction.

1. INTRODUCTION

Tsunamis are generated by submarine earthquakes, volcanic eruptions or landslides. Such submarine geological processes produce water surface disturbance, which propagates toward coasts. Tsunami propagation in deep oceans is rather simple; the velocity depends only on water depth. Once initial condition, or the tsunami source, is known, the propagation and coastal behavior can be modeled by computer simulation. Such an approach is called forward modeling, and used for engineering and hazard assessment purposes (Fig. 1).

For geological studies on earthquake sources, on the contrary, we need to start from the observed tsunami data, by also using computer simulation to evaluate the propagation process, to estimate the tsunami source. Such an approach is called inverse modeling, and mainly used for earth sciences. As the observed tsunami data, in addition to instrumental data recorded on sea level measurements for modern tsunamis, historical or geological data are used to study past tsunamis.

In this paper, some examples of forward and inverse modeling for the studies of tsunami sources are reviewed. For the present tsunami, forward modeling based on seismological measurements are used for quantitative tsunami warning system. Inversion of instrumental tsunami data, waveforms recorded at tide gauge stations and sea surface heights measured by satellite altimeters, of the 2004 Sumatra-Andaman earthquake will be described. Inverse modeling for past tsunamis, the 1700 Cascadia earthquake and the 17th century Hokkaido earthquake, based on historical and geological data will be described. For future tsunami, we can make probabilistic estimates of earthquake occurrence and tsunami heights, and make hazard maps showing the possible inundation areas.

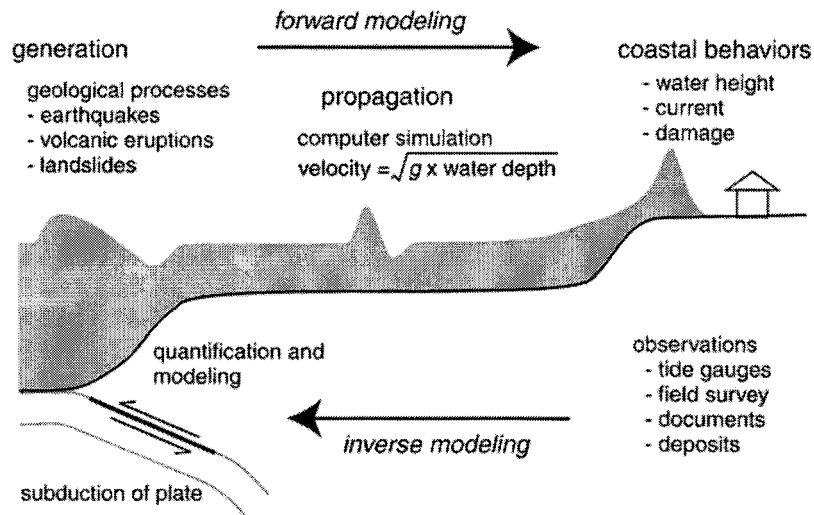


Figure 1 Forward and inverse modeling of tsunamis.

2. STUDY OF PRESENT TSUNAMIS

2.1 Tsunami Forward Modeling and Warning System

Generation and propagation of tsunami can be modeled numerically, if the initial condition and bathymetry along the propagation path are known. The equation of motion for shallow-water (long) waves and the equation of continuity can be solved by using finite-difference method. Digital bathymetry database for global oceans, ETOPO2, are compiled from satellite gravity data and bathymetry sounding (Smith and Sandwell 1997); these are accurate for deep oceans. As the initial condition, the seafloor deformation is computed from the fault parameters, such fault location, depth, geometry, size and the slip amounts (Okada 1985). These parameters can be estimated from seismological observations.

Japan Meteorological Agency (JMA) is responsible to issue tsunami warnings in Japan. Currently, six Regional Tsunami Warning Centers are under operation for 24 hours a day and seven days a week. JMA uses data from hundreds of seismic stations to detect tsunamigenic earthquakes, and data from sea level monitoring stations to confirm the tsunami generation. JMA has constantly improved the tsunami warning system. In the 1950s, it took about 20 minutes to issue tsunami warnings, but now it takes only 2 to 5 minutes after a large earthquake. To forecast the tsunami arrival times and heights, JMA introduced a numerical simulation technique in April 1999 (Tatehata 1997); tsunami generation and propagation for 100,000 different cases were calculated in advance, and the results have been stored as a database. When a large earthquake occurs, the most appropriate case for an actual location and a magnitude of the earthquake is retrieved from the database.

In the Pacific Ocean, three tsunami warning centers, Pacific Tsunami Warning Center in Hawaii, West Coast/Alaska Tsunami Warning Center in Alaska, and the Northwest Pacific Tsunami Advisory Center in Tokyo, monitor seismic activity and issue tsunami warning. All these centers share information and coordinate message content before issuing warning or advisory messagers. Because there are hours before tsunami arrival, it is very important to actually confirm the tsunami generation. For this purpose, sea level monitoring systems, located on coasts and offshore, are in operation. If tsunami is actually measured, the tsunami warning message can be updated. If no tsunami is detected, or when the generated tsunami becomes smaller after some time, the tsunami warning must be canceled.

At the time of December 26, 2004, tsunami generated from the Sumatra-Andaman earthquake (Mw 9.5), the Pacific Tsunami Warning Center issued the first information bulletin at 1:14 GMT, only

15 minutes after the earthquake. An earthquake was located off the west coast of northern Sumatra, but the magnitude was estimated as 8.0. The second bulletin was issued at 2:08 GMT, 69 minutes after the earthquake yet before the tsunami arrivals at Thai, Sri Lankan or Indian coast. The earthquake size was upgraded to 8.5 and a possibility of local tsunami was mentioned in the bulletin.

2.2 Inversion of Instrumental Data for the 2004 Sumatra-Andaman Tsunami

Seismological analyses of the Sumatra-Andaman earthquake indicate that the source region extended from off Sumatra through the Nicobar to Andaman Islands with the total length of 1,200 to 1,300 km and the total duration of rupture was about 500 s (Lay et al. 2005). The fault slip was the largest near off the northern Sumatra, followed by off Nicobar Islands (Ammon et al. 2005). Fault slip around Andaman Islands was estimated to be small from seismological analysis.

Analyses of satellite images indicate that the sea level changes were observed on Sumatra, Nicobar and Andaman Islands, suggesting that the source length was as long as 1,600 km (Meltzner et al. 2006; Tobita et al. 2006). Field investigations indicate that the largest subsidence was 3 m at Great Nicobar island, while the small islands west off Middle Andaman uplifted about 1.5 m (Malik and Murty 2005; Kayanne et al. 2007). Tide gauge record at Port Blair on South Andaman shows a slow subsidence with a duration of at least 15 minutes but possibly 40 minutes (Singh et al. 2006).

The tsunami source was estimated from tsunami arrival times as 600 – 700 km (Lay et al. 2005), but later revised to be ~ 900 km (Neetu et al. 2005) extending to the south of Andaman Islands. The satellite altimeter data supports longer, more than 1,000 km long, tsunami source (Fine et al. 2005; Hirata et al. 2006). The tide gauge data do not support tsunami source beneath Andaman Islands (Tanioka et al. 2006).

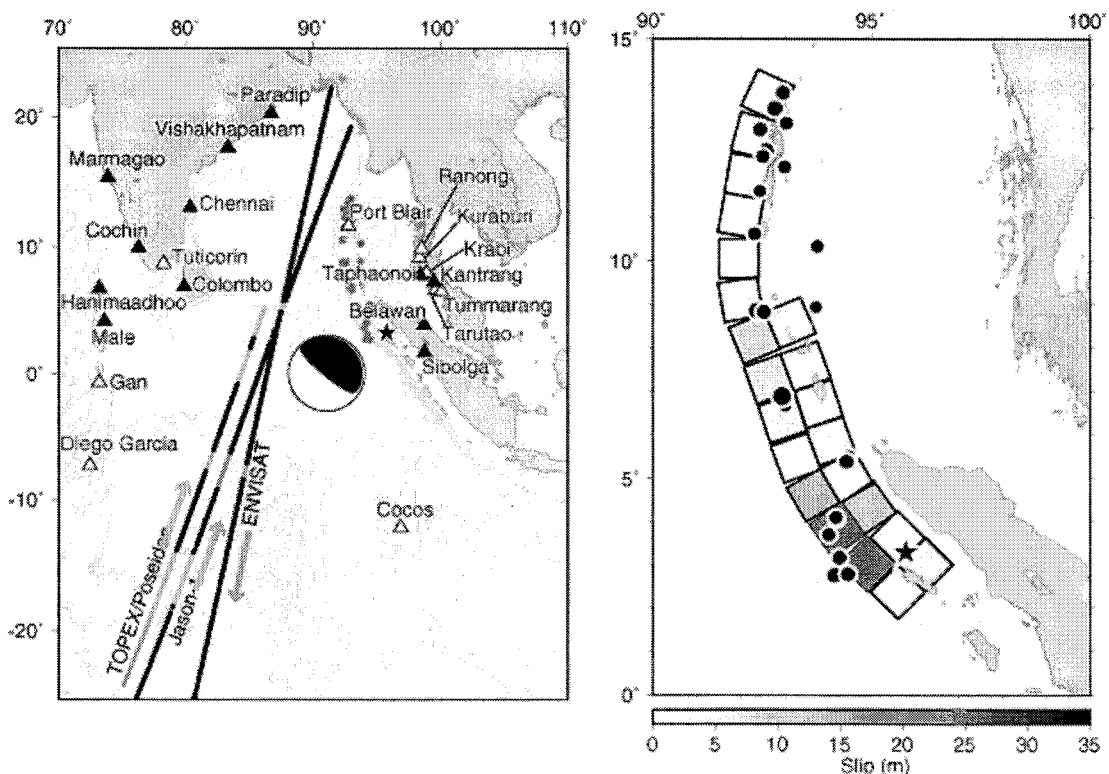


Figure 2 (left) Location of satellite path (solid lines) and tide gauge stations (triangle) used for the inversion. (right) Slip distribution on fault of the 2004 Sumatra-Andaman earthquake by joint inversion of satellite and tide gauge data. From Fujii and Satake (2007).

We used tsunami waveforms recorded at 12 tide gauge stations around the source and the sea surface heights measured by three satellites: Jason-1, TOPEX/Poseidon and Envisat (Fujii and Satake

2007). Tsunami propagation is numerically computed on realistic bathymetry; over 66,000 depth points were digitized from nautical charts and combined with the ETOPO2 data. Inversion of satellite data indicates that the tsunami source extended to the Andaman Islands with a total length of 1,400 km, but such a model produces much larger tsunami waveforms than observed at Indian tide gauge stations. Inversion of tide gauge records and the joint inversion indicate that the tsunami source was about 900 km long. The largest slip, about 13 to 25 m, was located off Sumatra Island and the second largest slip, up to 7 m, near the Nicobar Islands.

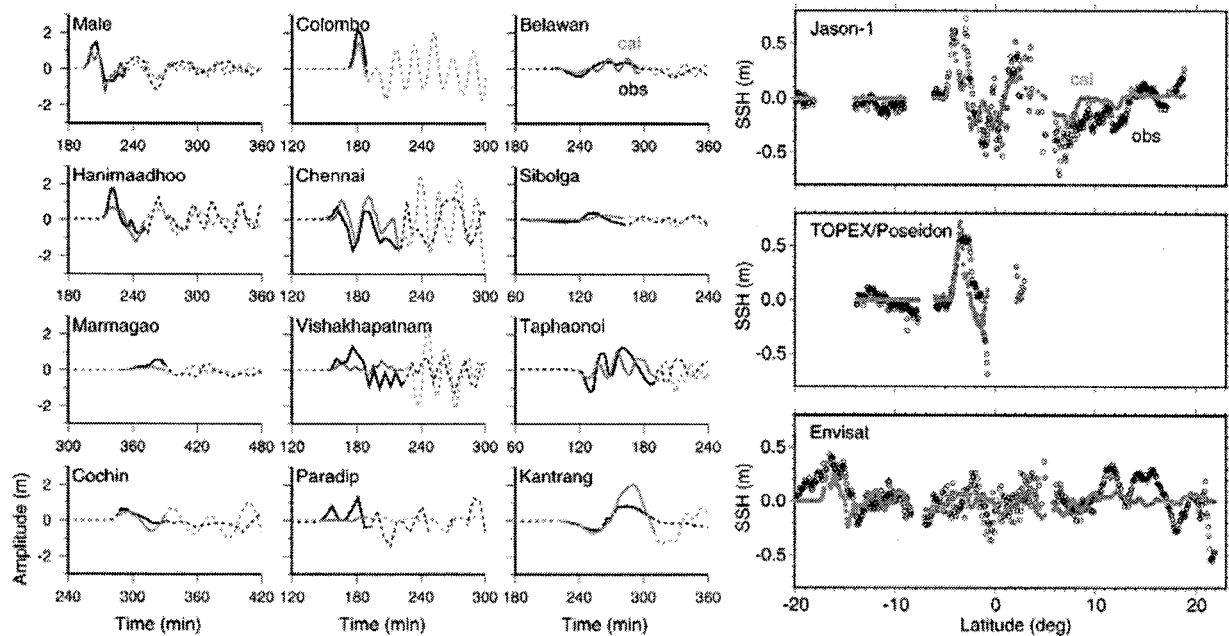


Figure 3 Comparison of the observed and computed instrumental data of the 2004 tsunami. (left) Tsunami waveforms recorded at tide gauge stations. (right) Sea surface heights along the satellite tracks. In both cases, the black symbols indicate the observed record and the gray symbols are computed from the estimated source model by inverse modeling (Figure 4). Dashed part was not used for the analysis. From Fujii and Satake (2007).

3. STUDY OF PAST TSUNAMIS

3.1 The 1700 Cascadia Earthquake

Geological and historical studies show the evidence of past earthquakes and tsunamis. Evidence of a great prehistoric earthquake that occurred along the Cascadia subduction zone, which extends 1,100 km along the Pacific coast of North America, has been recently found both near and far from the source (Atwater et al. 2005). Along the Pacific coast of North America, geological and tree-ring evidence indicates that coseismic subsidence took place about 300 years ago. In addition, tsunami deposits found throughout the Pacific Northwest indicate that this earthquake generated a sizable tsunami. In Japan, a widespread tsunami with heights of 1 – 5 m struck Honshu's Pacific coast, from which the tsunami origin is inferred about 9 p.m. Pacific Standard Time on 26 January, 1700. From comparisons of Japanese tsunami heights with simulated heights, the earthquake size was estimated to be $M_w = 8.7 - 9.2$, very similar to the 2004 Sumatra-Andman earthquake (Satake et al. 1996, 2003).

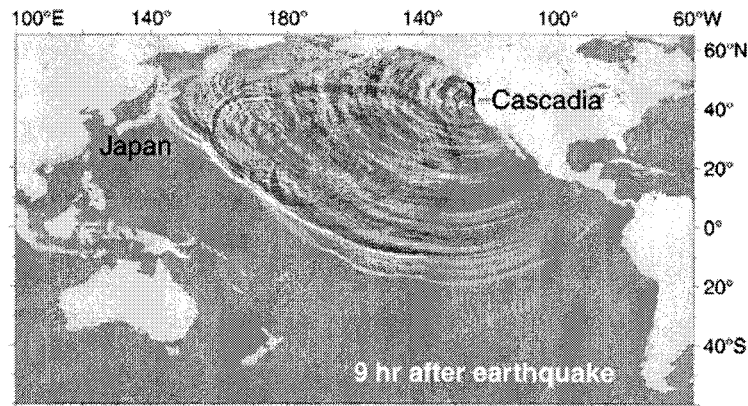


Figure 4 Snapshot of computed tsunami from the 1700 Cascadia earthquake.

3.2 The 17th Century Unusual Tsunami in Hokkaido

Tsunami deposits show that the southern Kuril trench repeatedly produced tsunamis larger than those recorded in the last few centuries in Japan. Along the southern Kuril trench (Fig. 5 *left*), where the Pacific plate subducts beneath Hokkaido, recurrence of great (M~8) earthquakes has been recorded; 1843 (M 8.0), 1952 (M 8.2) and 2003 (M 8.0) in Tokachi-oki and 1894 (M 7.9) and 1973 (M 7.4) in Nemuro-oki (Satake et al. 2005). Tsunami deposits from the past 7,000 years in eastern Hokkaido show that the southern Kuril trench repeatedly produced earthquakes and tsunamis larger than those recorded in the region's 200 years of written history (Nanayama et al. 2003). Deposits of prehistoric tsunamis underlie lowlands and lagoons along 200 km of eastern Hokkaido's Pacific coast. In Kiritappu (Fig. 5 *right*), prehistoric sand sheets extend as much as 3 km inland across a beach-ridge plain, where the 1952 tsunami penetrated only about 1 km from the coast. The time intervals between the extensive sand sheets average about 500 years, as inferred from volcanic ash layers. These outsized tsunamis, characterized by large inundation area and long recurrence interval, are best explained by earthquakes that rupture multiple segments, including Tokachi-oki and Nemuro-oki, of the Kuril subduction zone (Nanayama et al. 2003, Satake et al. 2005).

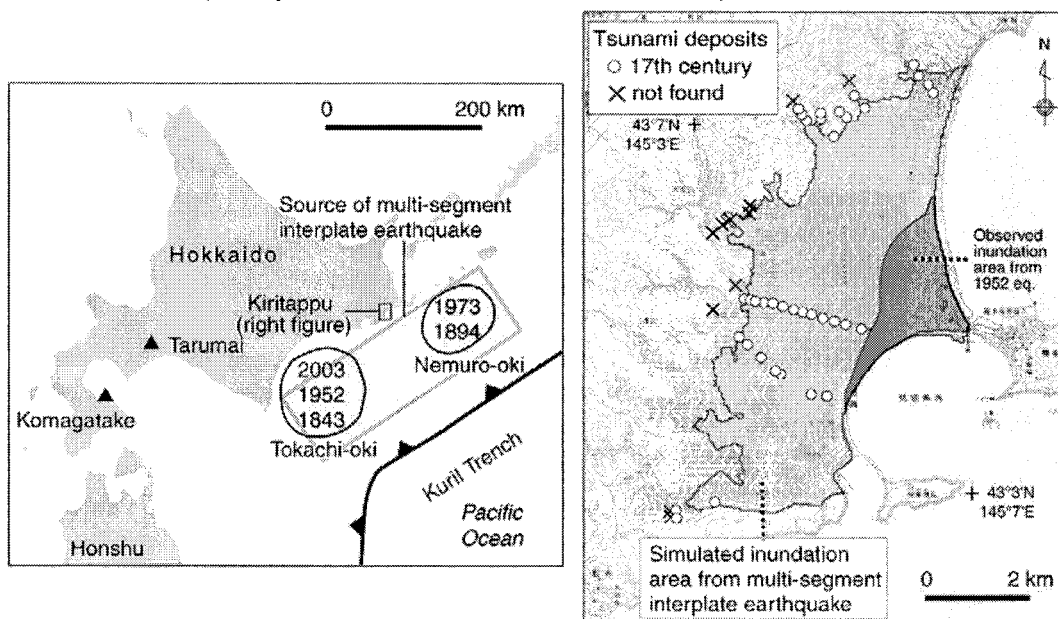


Figure 5 (*left*) Location of earthquake sources along the southwestern Kuril Trench off Hokkaido. (*right*) Distribution of 17th century tsunami deposits and inundation areas from the 1952 Tokachi-oki (surveyed) and 17th multi-segment earthquake (computed).

4. STUDY OF FUTURE TSUNAMIS

4.1 Probabilistic Tsunami Hazard Assessments

Great earthquakes repeat at plate boundaries more or less regularly. When the cyclic nature of past earthquakes is known, it can be used to calculate the probability of earthquake occurrence. The time interval between earthquakes can be modeled using a probability density function. The Brownian passage-time (BPT) distribution has been recently used, because it models steady tectonic loading plus Brownian perturbation (Matthews et al. 2002). The probability of next earthquake in the specific time window can be computed if the average recurrence period and the date of the most recent event, as well as aperiodicity parameter or variation coefficient, are known.

Probabilistic earthquake forecast had some success in Japan. In March 2003, the Japanese government made a long-term forecast for great ($M \sim 8$) earthquakes along the Kuril trench. The committee estimated that the probability in the next 30 years (starting March 2003) is 60 % in Tokachi-oki and 20–30 % in Nemuro-oki. This forecast was based on the mean inter-event time of great earthquakes for the southern Kuril region in the 19th and 20th centuries (<http://www.jishin.go.jp>). Six months later, on September 26, 2003, a great Tokachi-oki earthquake ($M 8.0$) actually occurred.

When the fault parameters of the characteristic tsunamigenic earthquake are known, tsunami heights can be estimated by numerical computations, and the probabilistic tsunami heights can be calculated. Such a probabilistic estimate of tsunami heights was made in 1980's for the Japanese coasts (Rikitake and Aida 1988). For the Pacific coast of central Japan where a large earthquake (Tokai earthquake) is expected, the probability of having 5 m tsunami for the period between 2000 and 2010 is as high as 41 %. For the Pacific coast of Hokkaido along the Kuril Trench, where the 2003 Tokachi-oki earthquake actually generated the tsunami, the probability of 2 m tsunami was estimated as 7–15 % and that of 5 m tsunami was 7 %. The actual tsunami heights in 2003 were up to 4 m, although the coastal runup heights and the tsunami source were different from those of the previous Tokachi-oki earthquake in 1952 (Satake et al. 2006).

Probabilistic models have been developed to estimate coastal tsunami heights from future earthquakes. Such methods have been widely used for seismic hazard (Probabilistic Seismic Hazard Analysis), but only recently applied to tsunamis. Power et al. (2007) developed a Probabilistic Tsunami Hazard Analysis (PTHA) method and applied it for estimating probabilistic tsunami heights from distant earthquakes. The end result is a map showing expected maximum tsunami heights in the next 500 years around New Zealand from earthquakes off South America.

A method for evaluating tsunami risk at nuclear power facilities in Japan is proposed by Yanagisawa et al. (2007). Their method is based on a parametric study, in which numerical simulations are repeated for element tsunamis with various fault parameters, and the element tsunami with the greatest influence is selected as the design tsunami. The design tsunami is further compared with the historical data to ensure that it produces tsunami heights larger than those historically recorded. Annaka et al. (2007) proposed a logic-tree approach for PTHA. Their end product is a hazard curve, a relationship between coastal tsunami heights and the probability of exceedance at a particular site. The hazard curve is obtained by integration over the aleatory uncertainties, whereas a large number of hazard curves are obtained for different branches of logic-trees representing epistemic uncertainty, such as tsunami sources, size and frequency of tsunamigenic earthquakes, standard errors of estimated tsunami heights.

4.2 Tsunami Hazard Maps

For an assumed tsunami source, numerical simulation of tsunami generation and propagation makes it possible to estimate inundation areas. The such simulation results can be published as tsunami hazard maps. For public use, safe places such as tsunami shelters to evacuate can be also shown in tsunami hazard maps. Tsunami hazard map help coastal communities prepare for tsunami hazards.

On the basis of tsunami hazard maps, evacuation plans can be established by responsible officials such

as civil defense officials. One of the lessons from the 2004 Asian tsunami is that not only coastal residents but also foreign tourists need to be informed on tsunami hazards. For the Hawaiian Islands, tsunami hazard maps are prepared for most of the occupied coasts and published in the local phone book which is available at every hotel room. The maps show, in addition to the inundation area and places to evacuate, evacuation instructions. For example, those in high-rise buildings are instructed to move vertically to the third or higher floors, rather than moving out of the area.

Tsunami hazard assessment has been carried out on the Japanese coasts. Numerical simulations were used to estimate the time and heights of tsunami and possible damage including casualties. For example, for the future Tonankai-Nankai earthquake off the western Japan, inundation of 40,000 houses and 2,200–8,600 casualties are estimated (<http://www.bousai.go.jp/jishin/chubou/>).

5. CONCLUSIONS

For tsunami studies, either based on numerical simulation or physical experiments, information on tsunami source is essential. However, little is known about the actual tsunami sources, due to lack of direct observation. For operational tsunami warning system, quick analysis of seismological data and confirmation of sea-level data are essential. For modern tsunamis, their sources can be studied by inversion of tsunami instrumental data. For past tsunamis, historical and geological data can be used to study the tsunami sources such as earthquakes. On the basis of past recurrence history, probabilistic forecast of future earthquake and tsunami can be made.

References:

- Ammon, C. J., Ji, C., Thio, H. K., Robinson, D., Ni, S. D., Hjorleifsdottir, V., Kanamori, H., Lay, T., Das, S., Helmberger, D., Ichinose, G., Polet, J. and Wald, D. (2005), "Rupture Process of the 2004 Sumatra-Andaman Earthquake," *Science*, **308**, 1133-1139.
- Annaka, T., Satake, K., Sakakiyama, T., Yanagisawa, K., and Shuto, N. (2007), "Logic-tree Approach for Probabilistic Tsunami Hazard Analysis and its Applications to the Japanese Coasts," *Pure and Applied Geophysics*, **164**, in press.
- Atwater B. F., Musumi-Rokkaku, S., Satake, K., Tsuji, Y., Ueda, K., and Yamaguchi, D. K. (2005), "The Orphan Tsunami of 1700," *U. S. G. S. Professional Paper*, **1707**, 133 pp.
- Fine, I. V., Rabinovich, A. B. and Thomson, R. E. (2005), "The Dual Source Region for the 2004 Sumatra Tsunami," *Geophysical Research Letters*, **32**, doi:10.1029/2005GL023521.
- Hirata, K., Satake, K., Tanioka, Y., Kuragano, T., Hasegawa, Y., Hayashi, Y. and Hamada, N. (2006), "The 2004 Indian Ocean Tsunami: Tsunami Source Model from Satellite Altimetry," *Earth, Planets and Space*, **58**, 195-201.
- Kayanne, H., Ikeda, Y., Echigo, T., Shishikura, M., Kamataki, T., Satake, K., Malik, J. N., Basir, S. R., Chakraborty, G. K. and Ghosh Roy, A. K. (2007), "Coseismic and Postseismic Creep in the Andaman Islands Associated with the 2004 Sumatra-Andaman Earthquake," *Geophysical Research Letters*, **34**, L01310, doi: 10.1029/2006GL028200.
- Lay, T., Kanamori, H., Ammon, C. J., Nettles, M., Ward, S. N., Aster, R. C., Beck, S. L., Bilek, S. L., Brudzinski, M. R., Butler, R., DeShon, H. R., Ekstrom, G., Satake, K., and Sipkin, S. (2005), "The Great Sumatra-Andaman Earthquake of 26 December 2004," *Science*, **308**, 1127-1133.
- Malik, J. N., and Murty, C. V. R. (2005), "Landscape Changes in Andaman and Nicobar Islands (India) due to Mw 9.3 Tsunamigenic Sumatra Earthquake of 26 December 2004," *Current Science*, **88**, 1384-1386.
- Matthews, M. V., Ellsworth, W. L., and Reasenberg, P. A. (2002), "A Brownian Model for Recurrent Earthquakes," *Bulletin of Seismological Society of America*, **92**, 2233-2250.
- Meltzner, A. J., Sieh, K., Abrams, M., Agnew, D. C., Hudnut, K. W., Avouac, J.-P. and Natawidjaja, D. H. (2006), "Uplift and Subsidence Associated with the Great Aceh-Andaman Earthquake of 2004," *Journal of Geophysical Research*, **111**, doi:10.1029/2005JB003891.
- Nanayama, F., Satake, K., Furukawa, R., Shimokawa, K., Atwater, B. F., Shigeno, K., and Yamaki, S. (2003), "Unusually Large Earthquakes Inferred from Tsunami Deposits along the Kuril Trench," *Nature*, **424**, 660-663.
- Neetu, S., Suresh, I., Shankar, R., Shankar, D., Shenoi, S. S. C., Shetye, S. R., Sundar, D., and Nagarajan, B. (2005), "Comment on 'The great Sumatra-Andaman Earthquake of 26 December 2004'," *Science*, **310**, 1431.
- Okada, Y. (1985), "Surface Deformation due to Shear and Tensile Faults in a Half-space," *Bulletin of Seismological Society of America*, **75**, 1135-1154.
- Power, P., Downes, G., and Stirling, M. (2007), "Estimation of Tsunami Hazard in New Zealand due to South American

- Earthquakes,” *Pure and Applied Geophysics*, **164**, in press.
- Rikitake, T. and Aida, I. (1988), “Tsunami Hazard Probability in Japan”, *Bulletin of Seismological Society of America*, **78**, 1268-1278.
- Satake, K., Shimazaki, K., Tsuji, Y., and Ueda, K. (1996), “Time and Size of a Giant Earthquake in Cascadia Inferred from Japanese Tsunami Records of January 1700,” *Nature*, **379**, 246-249.
- Satake, K., Wang, K., and Atwater, B. F. (2003), “Fault Slip and Seismic Moment of the 1700 Cascadia Earthquake Inferred from Japanese Tsunami Descriptions,” *Journal of Geophysical Research*, **108**, 2535, 10.1029/2003JB002521.
- Satake, K., Nanayama, F., Yamaki, S., Tanioka, Y., and Hirata, K. (2005), “Variability Among Tsunami Sources in the 17th-21st Centuries along the Southern Kuril Trench,” In: Satake K (ed.) *Tsunamis: Case Studies and Recent Developments*, Springer, 157-170.
- Satake, K., Hirata, K., Yamaki, S., and Tanioka, Y. (2006), “Re-estimation of Tsunami Source of the 1952 Tokachi-oki Earthquake,” *Earth, Planets and Space*, **58**, 535-542.
- Singh, S. K., Ortiz, M., Gupta, H. K., and Ramadass, D. G. A. (2006), “Slow Slip below Port Blair, Andaman During the Great Sumatra-Andaman Earthquake of 26 December, 2004,” *Geophysical Research Letters*, **33**, doi:10.1029/2005GL025025.
- Smith, W. H. F. and Sandwell, D.T. (1997), “Global Sea Floor Topography from Satellite Altimetry and Ship Depth Soundings”, *Science*, **277**, 1956-1962.
- Tanioka, Y., Yudhicara, Kususose, T., Kathiroli, S., Nishimura, Y., Iwasaki, S. I., and Satake, K. (2006). “Rupture Process of the 2004 Great Sumatra-Andaman Earthquake Estimated from Tsunami Waveforms,” *Earth, Planets and Space*, **58**, 203-209.
- Tatehata, H. (1997), “The New Tsunami Warning System of the Japan Meteorological Agency,” In: Hebenstreit G (ed.) *Perspectives on Tsunami Hazards Reduction*, Kluwer Academic Publishers, Dordrecht, 175-188.
- Tobita, M., Suito, H., Imakiire, T., Kato, M., Fujiwara, S. and Murakami, M. (2006), “Outline of Vertical Displacement of the 2004 and 2005 Sumatra Earthquakes Revealed by Satellite Radar Imagery,” *Earth, Planets and Space*, **58**, e1-e4.
- Yanagisawa, K., Imamura, F., Sakakiyama, T., Annaka, T., Takeda, T., and Shuto, N. (2007), “Tsunami Assessment for Risk Management at Nuclear Power Facilities in Japan,” *Pure and Applied Geophysics*. **164**, in press.

Vulnerability estimation in Banda Aceh using the tsunami numerical model and the post-tsunami survey data

**Shunichi KOSHIMURA¹⁾ Takayuki OIE²⁾, Hideaki YANAGISAWA²⁾
and Fumihiko IMAMURA³⁾**

1) Associate Professor, Disaster Control Research Center, Tohoku University, Japan

Email : koshimura@tsunami2.civil.tohoku.ac.jp

2) Graduate Student, School of Engineering, Tohoku University, Japan

3) Professor, Disaster Control Research Center, Tohoku University, Japan

Abstract: Focusing on the city of Banda Aceh, Indonesia, which was significantly damaged by the 2004 Indian Ocean tsunami disaster, the authors developed a method to assess the vulnerability against tsunami disaster. Throughout the estimation using the high resolution numerical model of tsunami inundation and the post-tsunami survey data from damaged city, we found that the number of destroyed structures and the fatality rate due to tsunami are significantly increase for 2 or 3 m as local tsunami inundation depth.

1. INTRODUCTION

The 2004 Indian Ocean tsunami disaster attacked the city of Banda Aceh, Indonesia, and resulted more than 70,000 of casualties corresponding to 27 % of population before disaster and more than 12,000 of house damage¹⁾. The estimated extent of tsunami inundation zone reached 6.32 km² within the densely populated area of the city²⁾.

The present study aims to understand the vulnerability against the tsunami disaster, by using the numerical model of tsunami propagation and run-up, and GIS analysis with post-tsunami survey data in terms of casualties and structural damage. The post-tsunami survey data were obtained by an effort of JICA (Japan International Cooperation Agency) mission of the study on the urgent rehabilitation and reconstruction support program for Aceh province and affected areas in north Sumatra. The tsunami numerical model results in terms of the extent of inundation zone and local flow depth distribution within the city of Banda Aceh are combined with the survey data to develop the inundation depth-damage diagram by using GIS analysis.

2. NUMERICAL MODEL FOR TSUNAMI INUNDATION

We performed the numerical model of tsunami propagation and coastal inundation. The model is based on a set of non-linear shallow water equations with bottom friction in the form of Manning's formula according to the land use condition. The equations are discretized by the Staggered Leap-frog finite difference scheme.

To create the computational grids for tsunami model, we use the GEBCO digital bathymetry / topography data³⁾, SRTM data⁴⁾, local bathymetric charts of northern Sumatra (1:500,000 and 1:125,000) and land elevation data obtained by digital photogrammetric mapping. The grid size varies from 1860 m to 23 m from the source region to the coast of Banda Aceh, constructing a nested grid system as shown in Figure 1. The Final grid size within the city of Banda Aceh to model

tsunami inundation on the land is 23 m, and the data is based on the land elevation data provided by JICA.

3. TSUNAMI SOURCE MODEL

Table 1 indicates the fault dimension for the present tsunami source model. The inferred fault structure is a thrust fault system that consists of 6 segments, dipping eastward with a total rupture area of 850 km by 150 km. The amount of fault slip was adjusted to provide surface displacements that are reasonably consistent with the reported subsidence along the coast of Sumatra Island. The resulting total seismic moment for the seismic source model is 4.70×10^{22} Nm, corresponding to an earthquake magnitude $M_w=9.05$. We assume that instantaneous displacement of the sea surface identical to the vertical sea floor displacement⁵⁾ shown in Figure 2. Also, the numerical model result with the present source model is validated with Jason-1 altimetry data⁶⁾ that captured the spatial extent of tsunami propagation across the Indian Ocean approximately 2 hours after the earthquake.

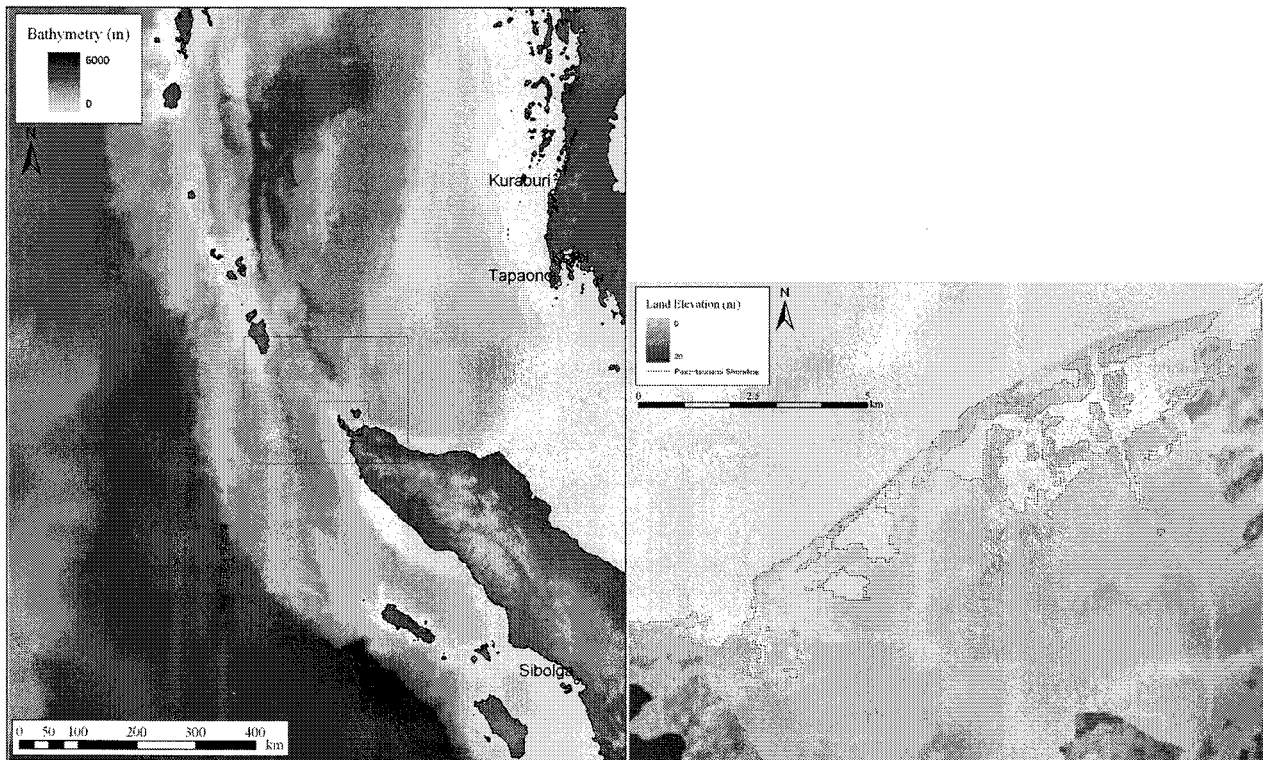


Figure 1 The computational domain for the model of tsunami propagation (left figure) and run-up to the city of Banda Aceh. The grid size varies from 1860 m to 23 m constructing nested grid system. Final grid size is 23 m within the city of Banda Aceh (right figure).

Table 1 Dimension of fault and source parameters for the present study.

Segment	Dislocation (m)	Length (km)	Width (km)	Depth (km)	Strike (deg.)	Dip (deg.)	Slip (deg.)
1	11	200	150	10	305	15	90
2	20	125	150	10	329	15	90
3	15	125	150	10	335	15	90
4	20	55	150	10	335	15	90
5	8	145	150	10	358	15	90
6	8	200	150	10	358	15	90

4. TSUNAMI INUNDATION AND VULNERABILITY WITHIN THE CITY OF BANDA ACEH

The city of Banda Aceh with an area of 61 km² is located at the coast of northern end of Sumatra Island. As shown in Figure 1, the topography of the center of the city is characterized with the low land with elevation of approximately lower than 3 m. Figure 3 shows the post-tsunami satellite imagery of Banda Aceh (IKONOS as of 29 December 2004 and 29 January 2005). Approximately 2 km inland from the coastline is wetland or swamp and was used for aquaculture. Densely populated region is 2 to 2.5 km inland from the coastline. The tsunami penetrated 3 to 4 km inland throughout the city.

Figure 4 indicates the computed inundation depth distribution within the city of Banda Aceh and the local inundation depth measured from the surface of the ground to the indicators such as debris, watermarks on buildings⁷⁾. The model results are consistent both with the measured inundation depth and extent of inundation zone. Note that the discontinuity of the inundation zone at south-western coast is because of the lack of high accuracy land elevation data. The tsunami wave height was estimated at 8-10m along the coastline.

Figure 5 shows the post-tsunami survey results in terms of damage on houses and structures within the inundation zone. By the interpretation of satellite imagery (IKONOS, acquired after 26 December, 2004), JICA study team counted the number of totally and partially destroyed houses and buildings (number of damaged structures within the inundation zone reached 12,972), and classified the damage every 100 m grid in the city with 4 damage classes, red (100-85% of houses were destroyed or washed away), orange (85-50% were destroyed or washed away), yellow (50-0%) and blue (only inundation) respectively¹⁾. Also, JICA study team estimated number of casualties by using population census data. Figure 6 shows the distribution of number of casualties estimated every Desa. According to the report of JICA¹⁾, number of casualties (dead or missing) in the city reached 71,435 as of 12 April 2005. We can see that almost all the residents within the inundation zone were significantly impacted.

In the situation we have no actual information in terms of distribution of inundation depth of tsunami, the numerical model result, if it is credible enough, enables us to relate the hazard information with the quantitative information in terms of the post-tsunami damage (vulnerability information). By using GIS analysis, Aceh's vulnerability against tsunami disaster is estimated as a form of inundation depth-damage diagram shown in Figure 7. The upper panel shows the relationship between estimated local inundation depth and damage on structures. And the lower is the relationship between local inundation depth and number of casualties or death rate of the residents. By using this diagram, we can explore the critical condition of tsunami inundation to cause the significant damage on structures and human beings. We can see that number of destroyed structures, i.e. number of cells interpreted as almost completely destroyed, and the percentage of casualties significantly increase for 2 or 3 m as local tsunami inundation depth. Throughout the analysis presented here, the future reconstruction planning for tsunami disaster mitigation should consider possible countermeasures such as sea walls or vegetations in order to reduce the local tsunami inundation depth to at least 2m.

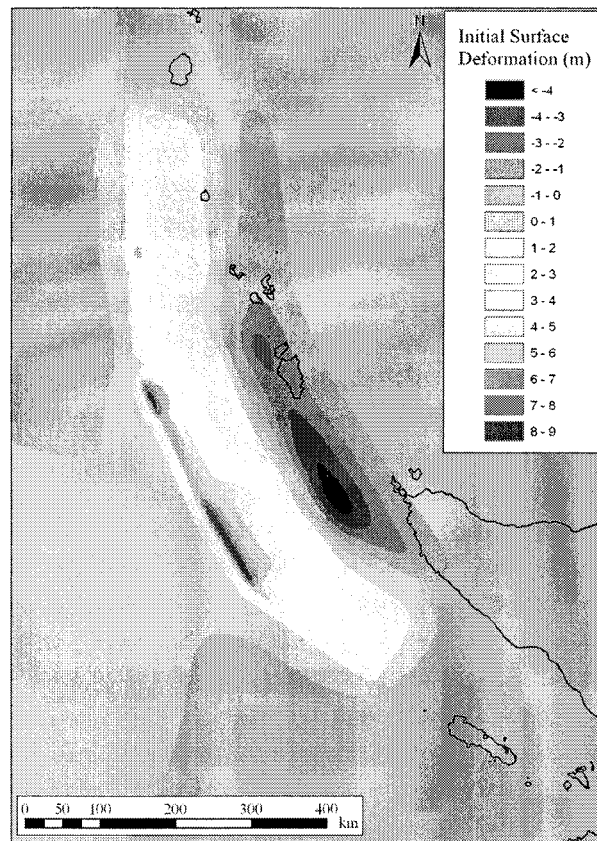


Figure 2 Computed sea floor displacement of the 2004 Sumatra earthquake. We assume that the instantaneous sea floor displacement pushes up/draws down overlying water to generate the initial sea surface profile of the tsunami.

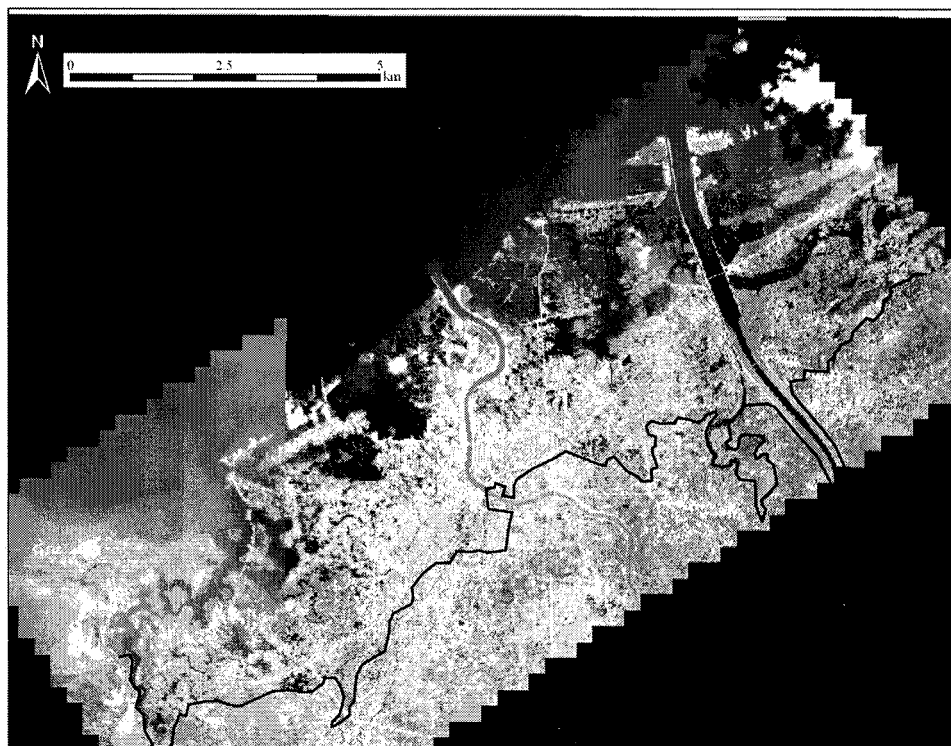


Figure 3 Post-tsunami satellite imagery of Banda Aceh (IKONOS as of 29 December 2004 and 29 January 2005). The solid line indicates the extent of tsunami inundation zone inferred from the satellite imagery.

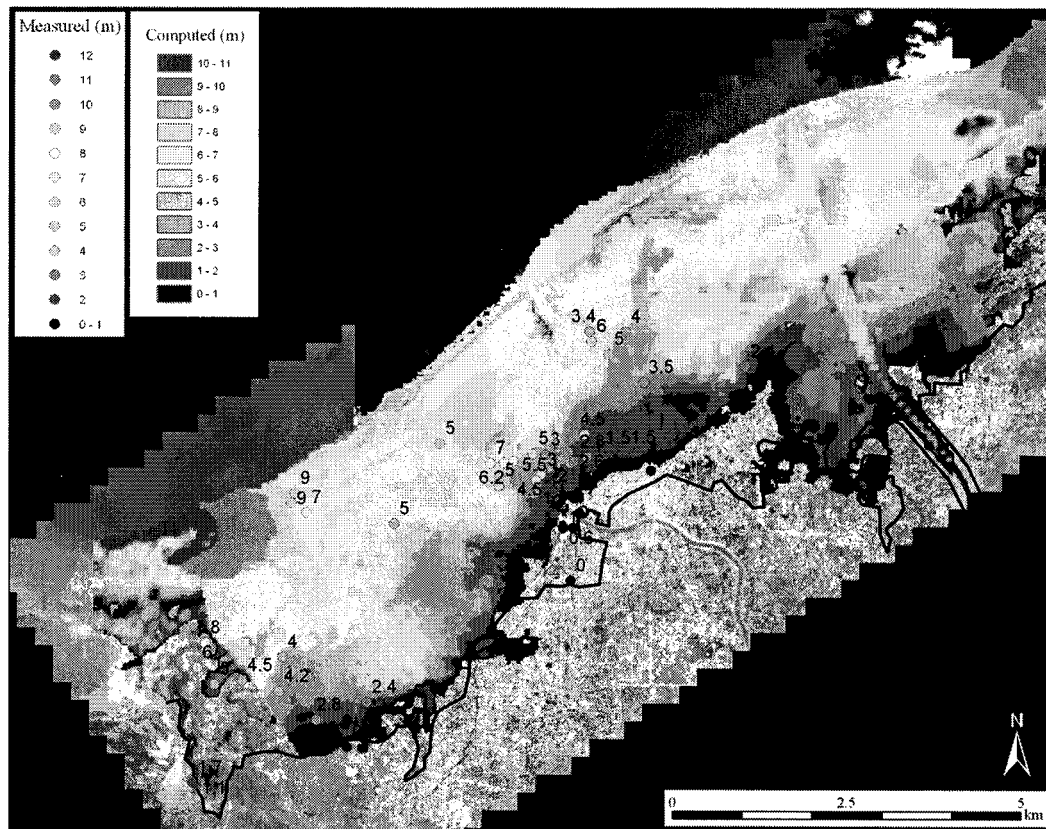


Figure 4 Comparison of computed and measured tsunami inundation depth within the city of Banda Aceh The number in the figure is the measured value of tsunami inundation depth from the ground to the indicators such as debris, watermarks on buildings (Borrero, 2005).

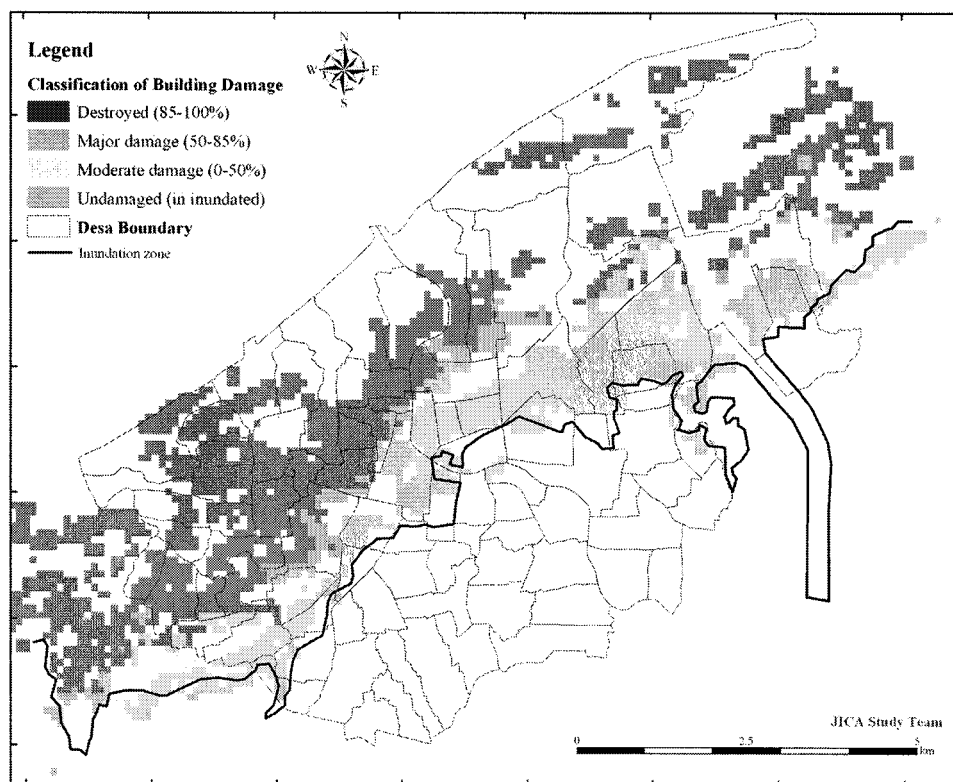


Figure 5 Tsunami damage classification for the city of Banda Aceh (JICA, 2005)

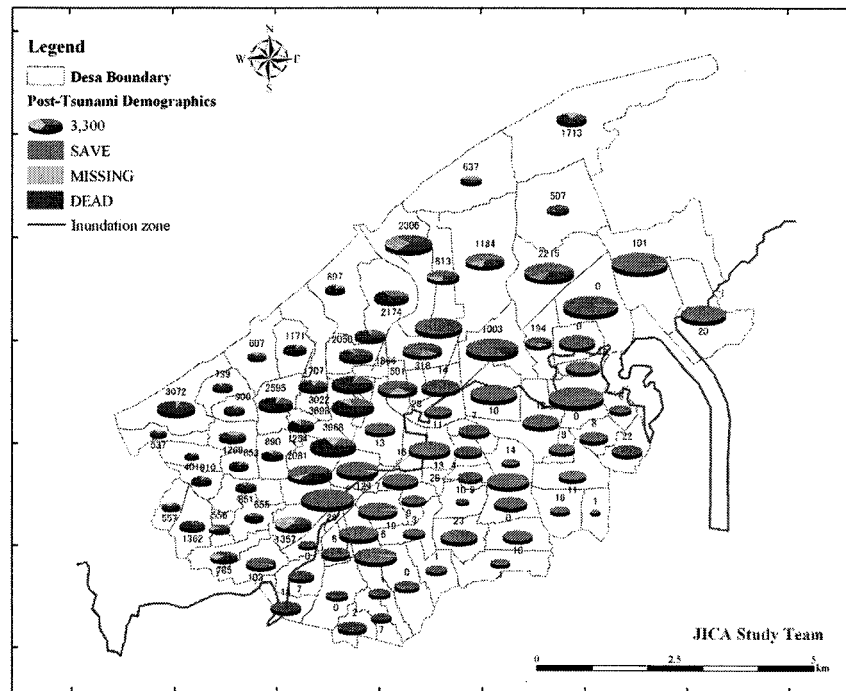


Figure 6 Distribution of tsunami casualties within the tsunami inundation zone (JICA, 2005). The number in the figure is the number of dead people.

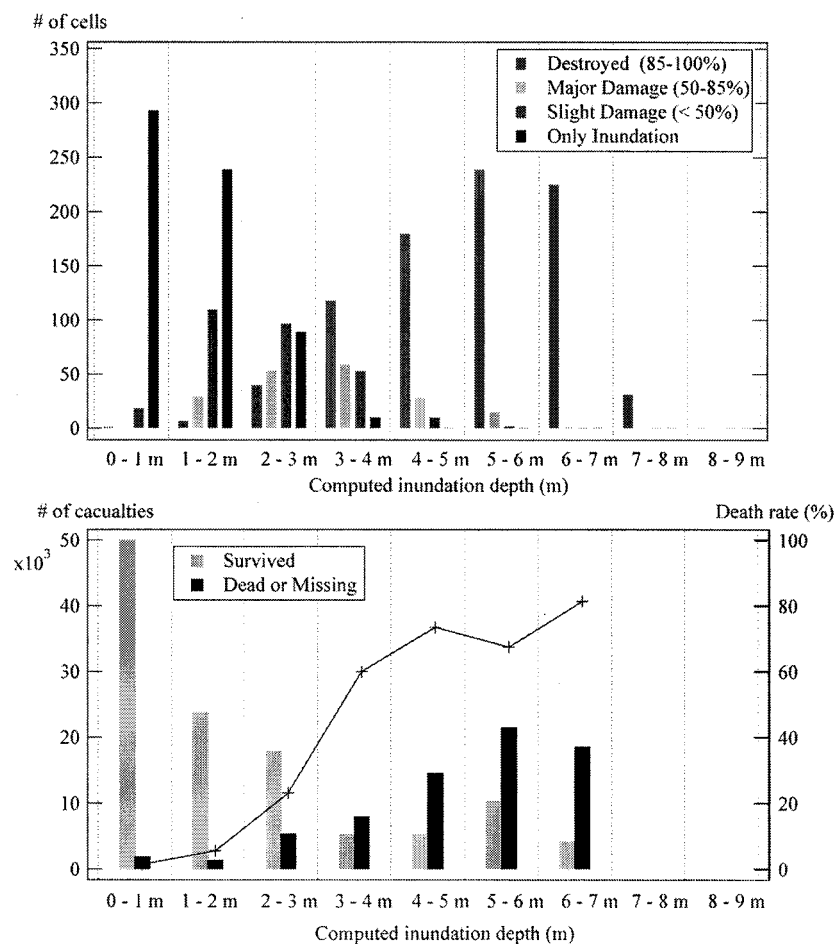


Figure 7 Tsunami inundation depth-damage diagram to understand Aceh's vulnerability against tsunami disaster (Upper : inundation depth vs. damage on structures, Lower : inundation depth vs. number of casualties).

5. SUMMARY

Using the high accuracy land elevation data, we performed a coastal inundation modeling for the 2004 Indian Ocean tsunami that attacked the city of Banda Aceh. The model results in terms of local inundation depth and the extent of inundation zone are consistent with the actually measured and interpreted data from satellite imagery. Also, using GIS analysis combined with the detailed survey data in terms of the damage on structures and casualties, we developed the tsunami inundation depth-damage diagram to understand Aceh's vulnerability against tsunami disaster. Throughout the present analysis, we found that number of destroyed structures and the percentage of casualties significantly increase for 2 or 3 m as local tsunami inundation depth. In order to reduce the tsunami hazard and mitigate the damage of possible tsunami disaster, Aceh's reconstruction planning should consider the possible countermeasures such as sea walls or vegetations in order to reduce the local tsunami inundation depth to at least 2m.

References

- 1) Japan International cooperation Agency, The study on the urgent rehabilitation and reconstruction support program for Aceh province and affected areas in north Sumatra, Final Report (1), 2005.
- 2) Geographical Survey Institute of Japan, Tsunami Damage estimation in Banda Aceh using high resolution satellite imagery (in Japanese), http://www1.gsi.go.jp/geowww/EODAS/banda_ache/banda_ache.html
- 3) The General Bathymetric Chart of the Oceans (GEBCO), <http://www.ngdc.noaa.gov/mgg/gebco/>
- 4) NASA , SRTM (Shuttle Radar Topography Mission) , <http://srtm.usgs.gov/>
- 5) Okada, Y. , Surface deformation due to shear and tensile faults in a half space, Bull. Seismol. Soc. Am., 75(4), 1135-1154, 1985.
- 6) Gower, J., Jason 1 detects the 26 December 2004 Tsunami, EOS, Transactions, American Geophysical Union, Vol. 86, No. 4, 37-38, 2005
- 7) Borrero, J., Field survey of northern Sumatra and Banda Aceh, Indonesia after the tsunami and earthquake of 26 December 2004, Seismological Research Letters, Vol. 76, No. 3, pp.309-317, 2005.

PRELIMINARY RESULTS OF THE OFFSHORE TSUNAMI OBSERVATION BY THE KURIL ISLANDS EARTHQUAKE OF 15 NOVEMBER 2006

H. Matsumoto¹⁾, K. Kawaguchi²⁾, and K. Asawaka³⁾

1) Research Scientist, Japan Agency for Marine-Earth Science and Technology, Japan

2) Research Scientist, Japan Agency for Marine-Earth Science and Technology, Japan

*3) Senior Scientist, Japan Agency for Marine-Earth Science and Technology, Japan
hmatsumoto@jamstec.go.jp, kawak@jamstec.go.jp, asakawa@jamstec.go.jp*

Abstract: Tsunami from the mega-thrust earthquake off the Kuril Islands on 15 November 2006 was observed by the offshore permanent observatory off Hokkaido, Japan. About one hour later, a series of the tsunami signal was observed by three bottom pressure sensors, two of them are permanent observatories and the other is temporarily deployed. Tsunami amplitudes observed offshore were approximately 5 cm, while those observed at the coast were a few tens of centimeters. An acoustic Doppler current profiler (ADCP) at the ocean-bottom, however, could not record any current anomaly by the tsunami propagation. This is because a particle velocity by the tsunami propagation is very slow (< 1 cm/s), whereas a phase velocity is more than 100 km/h. In the present study, the tsunami computation has been also done, and its results have been compared to the observations.

1. INTRODUCTION

On 15 November 2006 at 11:14:16 UTC, a mega-thrust earthquake (Mw8.3) took place off the central Kuril Islands. Because the Pacific plate is subducting beneath the Okhotsk plate with a velocity of about 90 mm/year at the epicentral area of the earthquake, a tsunamigenic earthquake possibly occurs once every century. According to the historical earthquake catalog, the recent largest earthquake had occurred in 1915 with its magnitude 7.9 in this central Kuril Islands' region. On the other hand, to the southwest and to the northeast of the earthquake, the largest earthquake occurred in 1963 and 1952, respectively. The detailed review of the earthquake is described in USGS (2006).

Focal mechanism by the USGS fast moment tensor solution shows a thrust faulting with shallow dipping, indicating a plate boundary earthquake. And the aftershock distribution for one day suggests that the fracture area extends to NE from the epicenter and its length is approximately 200 km along the trench (Fig. 1a).

In general, thrust faulting potentially produces larger tsunami. Following the earthquake, the first tsunami warning was issued by the Pacific Tsunami Warning Center (PTWC) at 11:30 UTC to the Pacific region, in particular Russia and Japan. The earthquake's magnitude was estimated to be 7.7 at that time, which was 0.6 lower than the revised magnitude using the further analysis. One hour after the earthquake, the second warning was issued, and the magnitude was modified to 8.1. In Japan, on the other hand, Japan Meteorological Agency (JMA) had issued tsunami warning as "tsunami" for Hokkaido and "tsunami attention" for the Pacific coast of NE Japan, that are the second and the third cautious categories in the Japanese tsunami warning. JMA withdrew all of tsunami warnings for Japan at 16:30 UTC on the same day. Three hours after the cancellation, the largest tsunami, however, was observed at Miyake Island, southern Japan. Tsunamis from the Kuril Islands

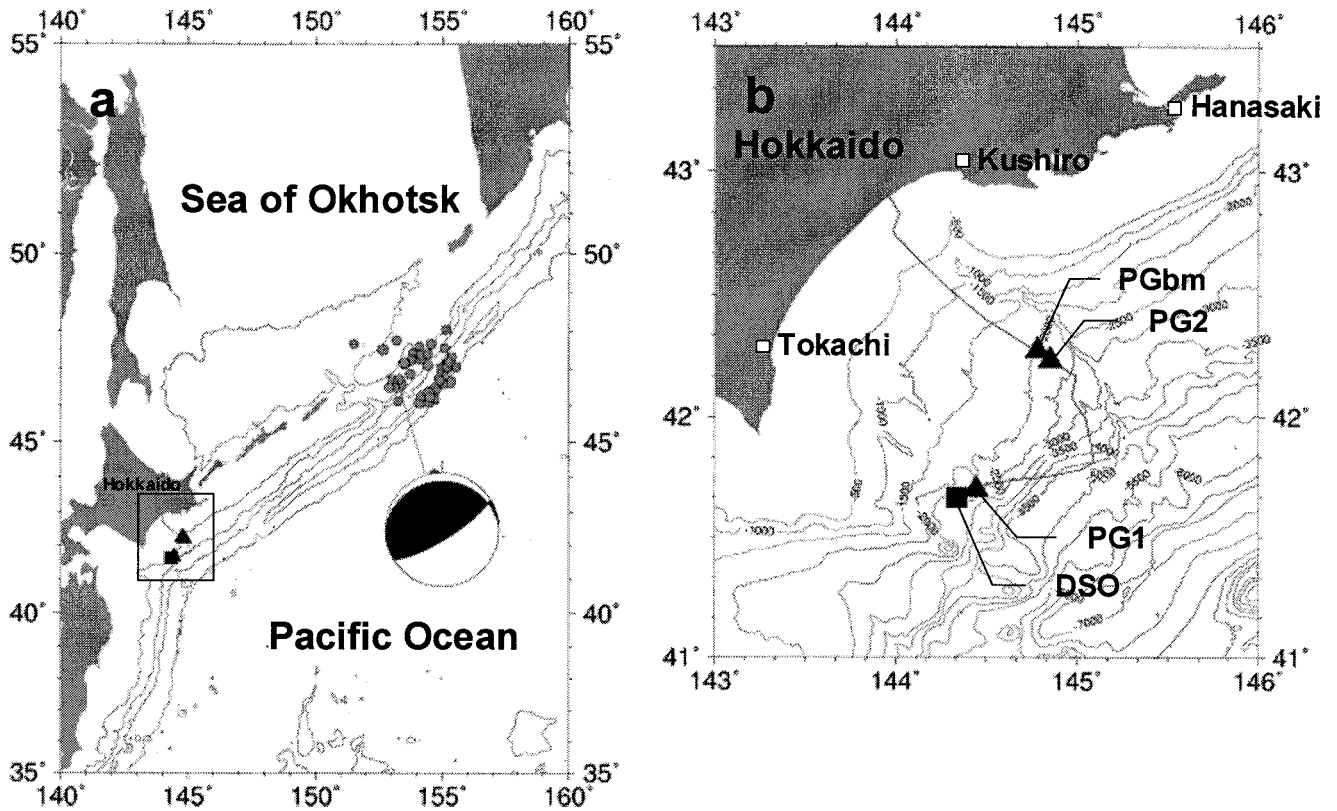


Figure 1 Map showing source area of the 2006 Kuril Islands earthquake and the offshore observatory. (a) Focal mechanism of the earthquake is based on the USGS fast moment tensor solution. Dots represent the aftershock distribution for one day after the earthquake by USGS. (b) Triangles and square show the pressure sensors and the cable end station of the off Kushiro real-time observatory.

Table 1 Position list of the pressure sensors and the cable end station of the off Kushiro real-time observatory.

	Latitude (deg. N)	Longitude (deg. E)	Water depth (m)
PG1	41.7040	144.4375	2218
PG2	42.2365	144.8454	2210
PGbm	42.2740	144.7811	2069
Cable end station (DSO)	41.6677	144.3409	2625

earthquake arrived at the eastern coast of Hokkaido about 1 hour later, at the northeast coast of Japan about 2 hours later. Tsunami toward the Pacific Ocean hit Hawaii, and then it arrived at the western coast of North America about 6 to 8 hours later, besides.

2. OFFSHORE TSUNAMI WAVEFORMS

Japan Agency for Marine-Earth Science and Technology (JAMSTEC) has deployed an offshore real-time observatory off Kushiro in 1999 (Hirata et al., 2002). Two permanent pressure sensors (PG1 and PG2) and one temporary pressure sensor (PGbm) were working during the earthquake (Fig.1b). PG1, PG2, and PGbm are deployed at the water depth of 2218 m, 2210m, and 2069m, respectively. Locations of PG2 and PGbm are close each other, while PG1 is located SW from other

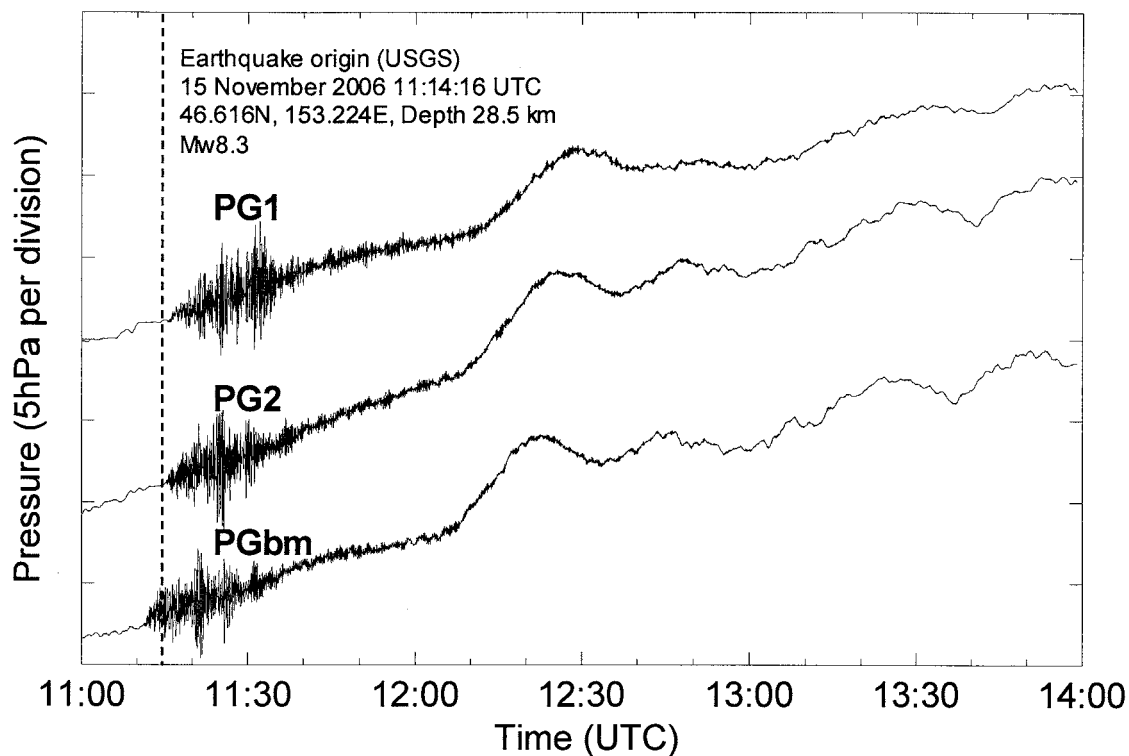


Figure 2 Pressure waveforms on 15 November 2006 after applying the moving average at 60 s. Vertical dashed line represents the origin time of the earthquake. The first tsunami arrived at the offshore pressure sensors at 12:09, 12:09, and 12:13 at PG2, PGbm, and PG1, respectively. The amplitude of the tsunami signal observed by the pressure sensors is about 5 hPa, i.e., ca. 5 cm in water level.

two sensors. The locations of the pressure sensors are listed in Table 1. PGbm has been temporarily deployed since 2004 by directly connecting to the branching mux unit of the off Kushiro system. PGbm needs an additional battery supplying electric power lasting approximately one year. Fortunately, we have replaced new battery last summer, so PGbm successfully recorded pressure waveforms during the earthquake. Three pressure sensors are located approximately 800 to 900 km from the epicenter of the Kuril Islands earthquake (Fig. 1a).

Figure 2 shows the observed pressure waveforms during the earthquake, to which a moving average at 60 s has been applied in order to remove seismic noise. This procedure makes possible to recognize tsunami signal from the bottom pressure sensors as done by similar studies before (e.g., Hino et al., 2001, Matsumoto and Mikada, 2005). It should be noted that astronomical tide still remains in the recorded dataset.

The first rises due to the tsunami signals can be seen at 12:09, 12:09 and 12:12, at PGbm, PG2, and PG1, respectively. Because two locations of PG2 and PGbm are close, the waveforms are similar each other. Amplitudes of the initial rise of PG2 and PGbm are 5 hPa, whereas that of PG1 somewhat seems smaller. Since 1 hPa in water pressure change corresponds to 1 cm in static water column, the initial tsunami height can be estimated to be ca. 5 cm at the location of the pressure sensors. On the other hand, according to the report of the tsunami observation released by Pacific Tsunami Warning Center, the initial tsunami arrivals were 12:29 to 12:46 by the tide gauge stations along the Hokkaido coast with their amplitude of 40 to 80 cm. Offshore pressure sensors could detect the initial tsunami arrival at least 20 min in advance, for example, compared to that at Hanasaki, the nearest tide gauge station to the epicenter. And the tsunami was amplified by ten times larger due to the shoaling effect.

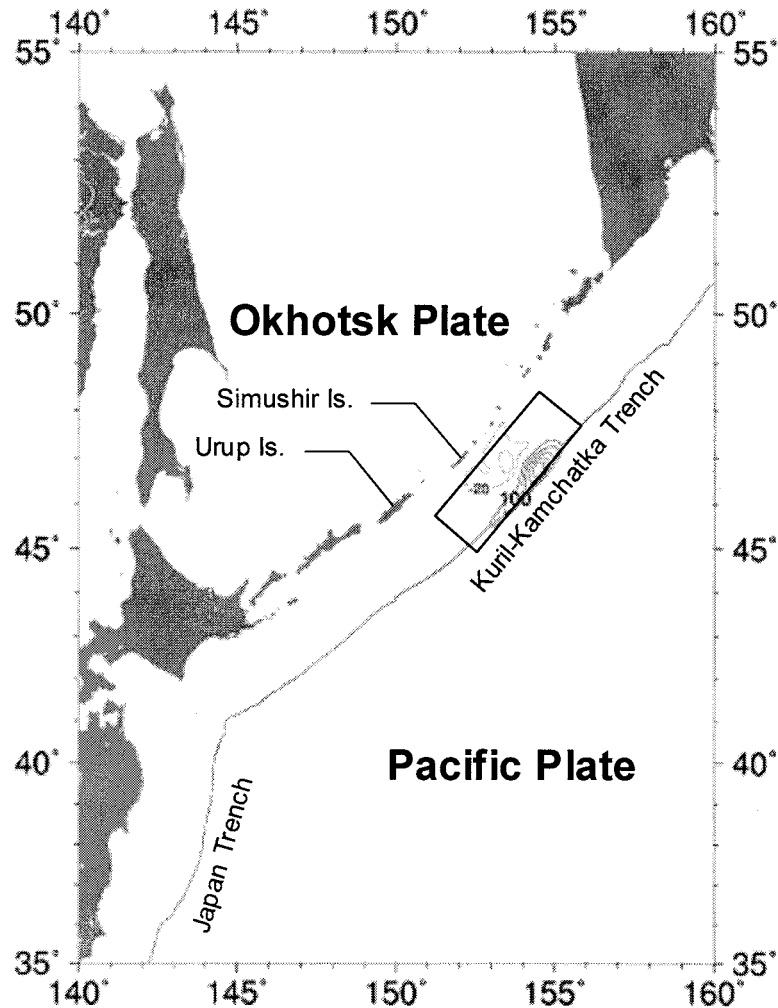


Figure 3 Coseismic deformation pattern from the fault model by USGS (2006). Rectangle denotes the surface projection of the seismic fault model, i.e., fracture area by the seismic faulting. Solid contours show uplift of every 50 cm, while dashed contours show subsidence of every 20 cm.

3. TSUNAMI SIMULATION FROM THE SEISMIC FAULTING

We would like to reproduce the offshore pressure waveforms associated with the tsunamis in order for better understanding how the tsunami propagate and how it affects to Japan from mega-thrust earthquake taking place along the Kuril-Kamchatka trench. In the present study, although we use simplified tsunami computation, three-dimensional fluid computation has been done.

Fault model causing water mass movement is from USGS (2006), which is based on the teleseismic body waves. The size of the fault plane is 400 km along the trench and 137.5 km normal to the trench, in which 220 sub-faults are consisted. We first calculate coseismic ocean-bottom deformation formulated by the dislocation theory (Okada, 1985), and then it is used for reproducing tsunami. Estimated coseismic deformation pattern from the fault model (USGS, 2006) is shown in Fig. 3. Uplift over 200 cm appears near the trench, while subsidence of 40 cm appears near Simushir Island. We expect that visible coseismic deformation at the Kuril Islands does not appear by the mainshock.

Our tsunami computation has some assumptions as follows. Although the fault fracturing must be running, we assume that the rupture velocity is infinite. To demonstrate this assumption, a tsunami rise time of 100 s is employed, which is equal to the duration of source time function, and we input coseismic deformation to the 3D fluid volume instantaneously as a linear ramp time function

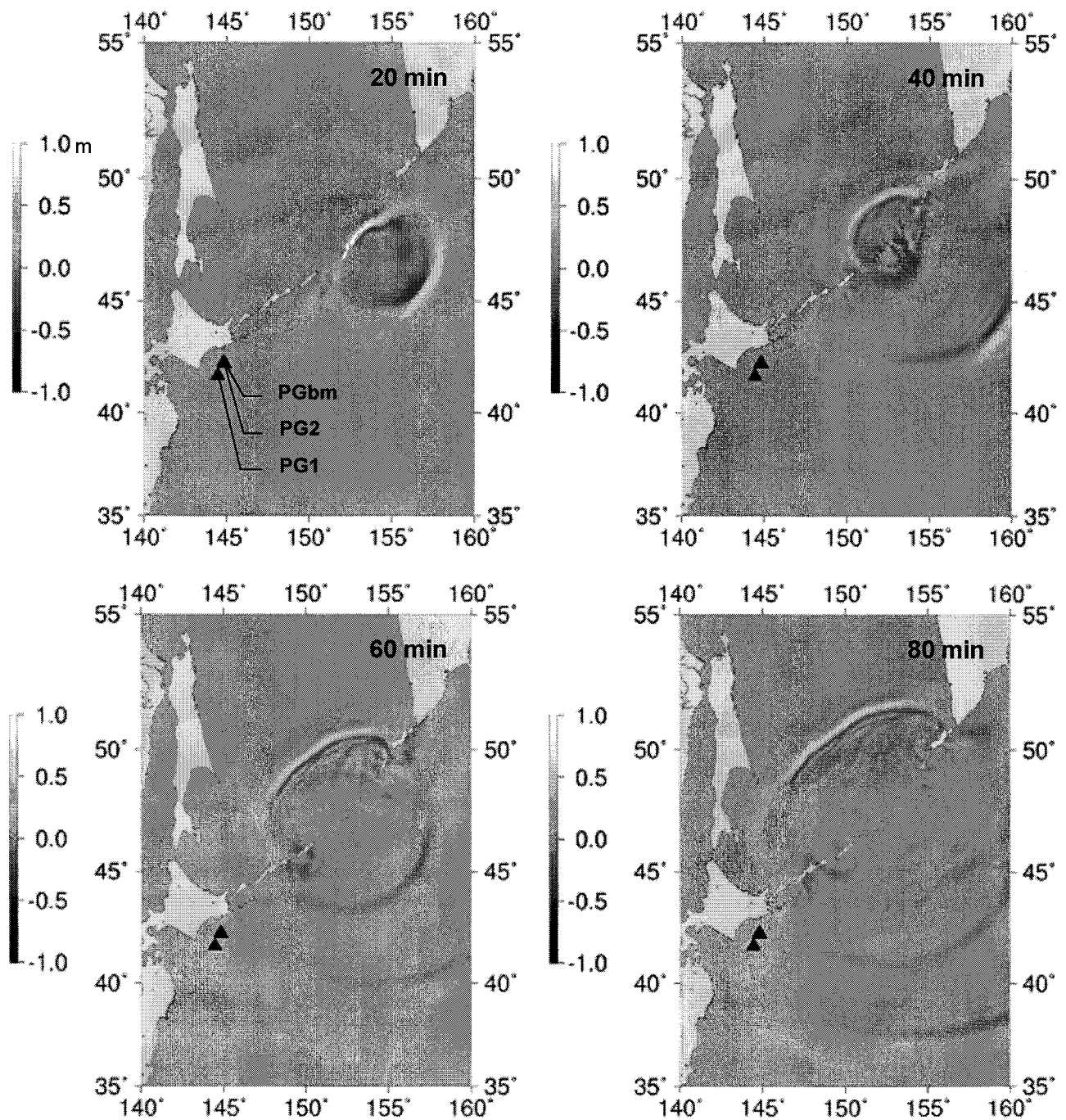


Figure 4 Snapshots of the tsunami propagation every 20 min. It can be seen that the initial phase of the tsunami arrived at the location of the pressure sensors 60 to 80 min later.

with a duration time of 100 s. In our tsunami computation, dynamic motion of the ocean-bottom is considered, but the rupture effect of seismic faulting is not taken into account. The computational domain is same as the area in Fig. 1, which extends from 35.0N to 55.0N in latitude and from 140.0E to 160E in longitude. 2 min in arc gridded bathymetric dataset made from GEBCO (British Oceanographic Data Centre, 1997) and 1000 m grid in depth direction, and time step of 0.5 s are used in our tsunami computation. This means the total grid points result in more than 3.2 millions. The basic equations and detailed techniques of our tsunami computation are described in Ohmachi et al. (2001).

Snapshots of the sea surface response at 20, 40, 60, and 80 min are shown in Fig. 4. At 20 min, the first tsunami arrived at the islands nearby to the tsunami source, and wave height became larger

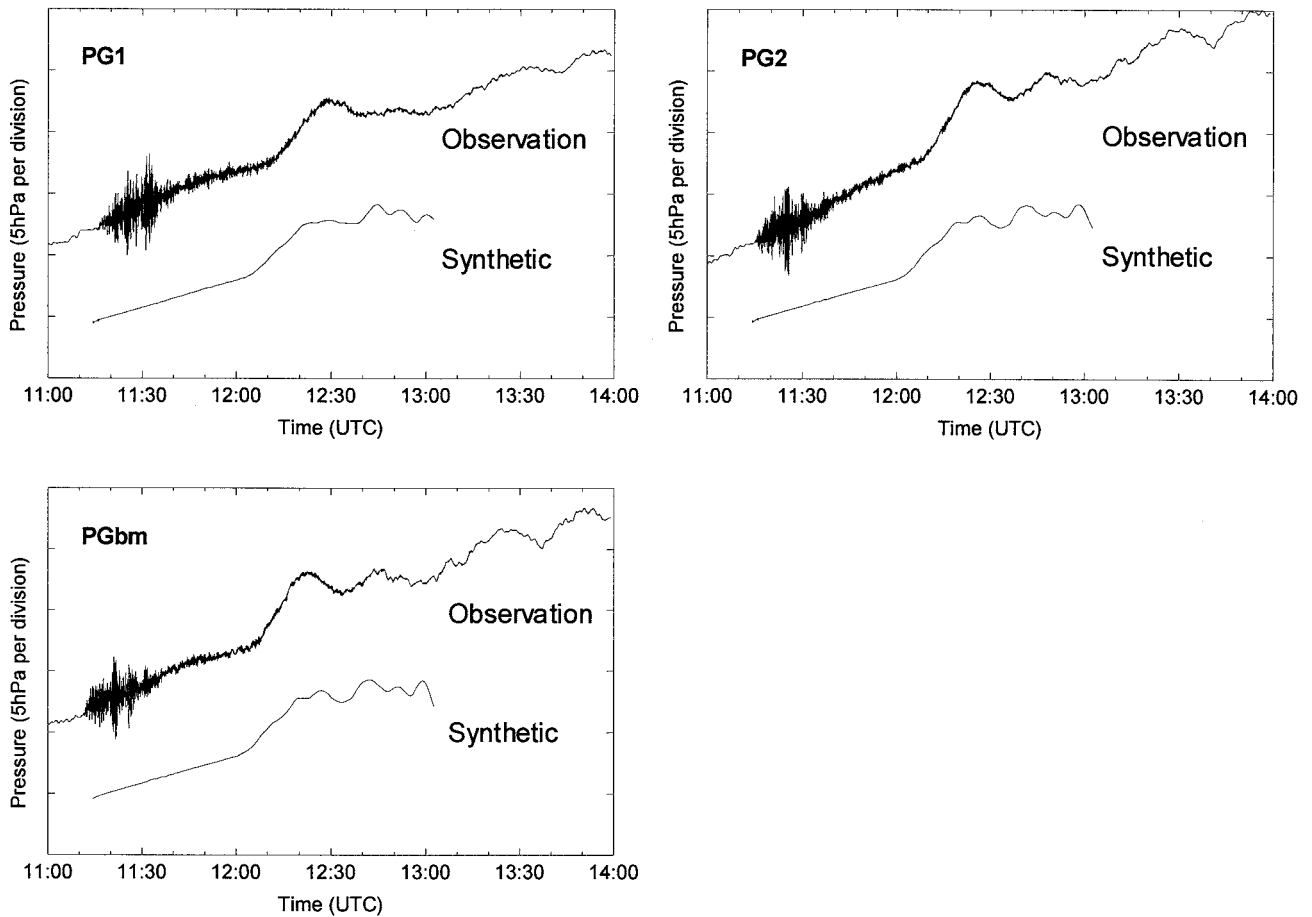


Figure 5 Comparison of the observed and the computed pressure waveforms at PG1, PG2, and PGbm during the earthquake. Black and red lines represent the observed and the computed waveforms, respectively.

than that toward the Pacific Ocean. From 40 to 60 min, the tsunami penetrated to the Sea of Okhotsk, while reflected waves by the Kuril Islands are excited, and it is propagated in the Pacific Ocean as the second wave. Because the Pacific Ocean is deeper than that of the Sea of Okhotsk, tsunami propagating toward the Pacific Ocean is faster than that in the Sea of Okhotsk. However, tsunami of the Sea of Okhotsk is higher than that of the Pacific Ocean, because of the shoaling effect. In general, tsunami energy is relatively large toward the normal of the fault strike direction (e.g., Satake et al., 2006). In the case of the Kuril Islands earthquake, the tsunami energy spreads toward the Pacific Ocean and the Sea of Okhotsk, since the fault strike is parallel to the Kuril-Kamchatka trench axis. Our tsunami computation qualitatively demonstrates this phenomenon. According to Fig. 4, the first tsunami from the earthquake reaches the offshore pressure sensors at 60 to 80 min.

The synthetic pressure waveforms are compared to the observations at PG1, PG2, and PGbm locations (Fig. 5). Because the actual pressure contains the astronomical tide in addition to the tsunami, we calculate the pressure caused by the astronomical tide given by Matsumoto et al. (2000), and its result is added to our tsunami computation. The arrivals of the first peak/trough of our computation are a few minutes earlier than that of the observations. The amplitudes of the first tsunami are fit to the observations. Although, two small peaks divided at the first tsunami crest computed at PG2 and PGbm are caused from the tsunami source, these small peaks could not be seen in the observations. The phases followed by first tsunami are not still fit to the observations. We realized that some discrepancies between the observations and our computations are still remaining, e.g., arrival time and later phase.

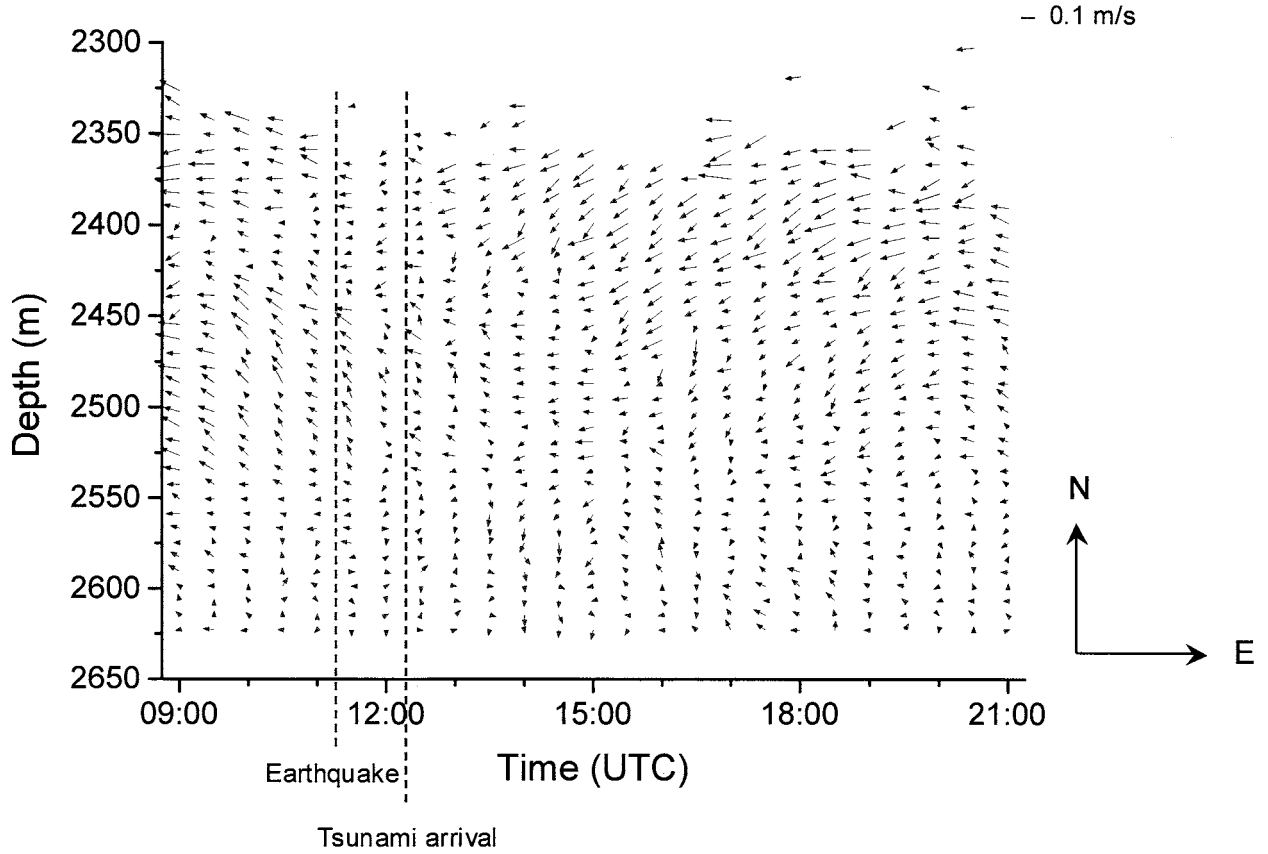


Figure 6 Time history of the current vector recorded by the acoustic Doppler current profiler (ADCP) at the cable end station during the earthquake. Left and right dashed lines show the clocks of the earthquake occurrence and the first tsunami arrival, respectively.

4. DEEP-SEA CURRENT BY THE TSUNAMI

The cable end station consists of an acoustic Doppler current profiler (ADCP) on the ocean-bottom at a depth of 2630 m (Fig. 1b). The benthic storm due to a debris flow or a turbidity current could be observed with a velocity of 1.4 m/s during the 2003 Tokachi-oki earthquake (Mikada et al., 2006). Fortunately, the vertical profile of the current speed was recorded by the ADCP during the earthquake as shown in Fig. 6. However, unfortunately, the ADCP does not always record continuous dataset, i.e., it works every 30 min. The maximum possible measured depth is 280 m above the ocean-bottom. We should note that the ADCP has relatively low resolution at far layer from the sensor. As shown in Fig. 6, no significant changing could be observed in the ADCP dataset both during the earthquake followed by the tsunami. As it is well known, a current velocity inside the shallow wave u is expressed as,

$$u = \sqrt{\frac{g}{h}}\eta = \frac{c}{h}\eta \quad (1)$$

in which g , h , η and c are gravity acceleration, water depth, wave height, and phase velocity, respectively. This equation means that a current velocity associated with tsunami is small compared to its phase velocity. In the case of the Kuril Islands earthquake, the current velocity at the cable end station due to the tsunami propagation is theoretically estimated to be 3 mm/s. In our tsunami computation, on the other hand, the current velocity during the tsunami propagation results in 1.2 mm/s. Since the threshold of the slowest current by the ADCP is 0.1 m/s, it was impossible to detect

the current caused by the tsunami. Thus, the tsunami is too small to be detected by the ADCP, suggesting that it seems difficult to detect tsunami itself by the present ADCP.

5. CONCLUSIONS

We have preliminarily reported the offshore tsunami waveforms observed by the bottom pressure sensors during the mega-thrust earthquake taken place off Kuril Islands on 15 November 2006. About 60 min after the earthquake, the initial rising motion of the tsunami could be observed with its height of ca. 5 cm. This is the earliest detection of the tsunami all over Japan, which is 20 min prior to its arrival at eastern tip of Hokkaido. We also carried out the tsunami computation from the latest seismic fault model, and we found that there are still discrepancies with respect to arrival time and the later phase of tsunamis between the observed and the computed waveforms.

The other instrument deployed at the deep ocean-bottom such as the ADCP could not detect the current anomaly associated with the tsunami propagation in the recorded dataset. The current excited by the tsunami propagation is much smaller than the phase velocity. The ADCP needs more sensitive resolution to detect tsunami signals.

In the end, we would like to note that three pressure sensors of the off Kushiro real-time observatory possibly become key instruments in the viewpoint of early warning for tsunamis coming from the Kuril-Kamchatka trench.

Acknowledgements:

The authors acknowledge all members of Submarine Cable Data Center, JAMSTEC, for their daily maintenances and data processing of the observatory. This research was partially supported by Ministry of Education, Culture, Sports, Science and Technology (MEXT), Grant-in-Aid for Young Scientists' Research (B), No.17710160. Some figures have been prepared using the GMT software made by Wessel and Smith (1995).

References:

- British Oceanographic Data Centre (1997), "The centenary edition of the GEBCO digital atlas (CD-ROM)".
- Hino, R., Y. Tanioka, T. Kanazawa, S. Sakai, M. Nishino, and K. Suyehiro (2001), "Micro-tsunami from a local interplate earthquake detected by cabled offshore tsunami observation in northeastern Japan", *Geophys. Res. Lett.*, **28**, 3533-3536.
- Hirata, K., M. Aoyagi, H. Mikada, K. Kawaguchi, Y. Kaiho, R. Iwase, S. Morita, I. Fujisawa, H. Sugioka, K. Mitsuzawa, K. Suyehiro, H. Kinoshita, and N. Fujiwara (2002), Real-time geophysical measurements on the deep seafloor using submarine cable in the southern Kurile subduction zone, *IEEE J. Ocean. Eng.*, **27**, 170-181.
- Matsumoto, H. and H. Mikada (2005), "Fault geometry of the 2004 off the Kii peninsula earthquake inferred from offshore pressure waveforms," *Earth Planets Space*, **57**, 161-166.
- Matsumoto, K., T. Takanezawa, and M. Ooe (2000), "Ocean tide models developed by assimilating TOPEX/POSEIDON altimeter data into hydrodynamical model: A global model and a regional model around Japan," *J. Oceanography*, **56**, 567-581.
- Mikada, H., K. Mitsuzawa, H. Matsumoto, T. Watanabe, S. Morita, R. Otsuka, H. Sugioka, T. Baba, E. Araki, and K. Suyehiro (2006), "New discoveries in dynamics of an M8 earthquake -Phenomena and their implications from the 2003 Tokachi-oki Earthquake using a long term monitoring cabled observatory-", *Tectonophysics*, **426**, 95-105.
- Ohmachi, T., H. Tsukiyama, and H. Matsumoto (2001), "Simulation of tsunami induced by dynamic displacement of seabed due to seismic faulting," *Bull. Seism. Soc. Am.*, **91**, 1898-1909.
- Okada Y. (1985), "Surface deformation due to shear and tensile faults in a half-space", *Bull. Seism. Soc. Am.*, **75**, 1135-1154.
- Satake, K., T. T. Aung, Y. Sawai, Y. Okamura, K. S. Win, W. Swe, C. Swe, T. L. Swe, S. T. Tun, M. M. Soe, T. Z. Oo, S. H. Zaw (2006), "Tsunami heights and damage along the Myanmar coast from the December 2004 Sumatr-Andaman earthquake" *Earth Planets Space*, **58**, 243-252.
- U.S. Geological Survey (2006), "Rupture process of the 2006 NOV 15 Magnitude 8.3 - KURIL Island Earthquake (Revised)", <http://earthquake.usgs.gov/eqcenter/eqinthenews/2006/usvcam/>.
- Wessel, P. and W. H. F. Smith (1995), "New version of the Generic Mapping Tools released", *EOS Trans. AGU*, **76**, 329.

EFFECT OF TSUNAMIS ON THE GULF OF THAILAND

A. Ruangrassamee¹⁾, and N. Saelem²⁾

1) Assistant Professor, Department of Civil Engineering, Chulalongkorn University, Thailand

2) Structural Engineer, Thai Nippon Steel Co.Ltd., Thailand

fcearr@eng.chula.ac.th, nopporn-s@tns.th.com

Abstract: The infrastructures in the Gulf of Thailand, for example, gas pipelines and platforms can be affected by tsunamis that are generated by earthquakes in the western part of the Philippines. In this study, the simulation of tsunamis in the Gulf of Thailand is conducted. Six cases of fault ruptures are considered for earthquakes with magnitudes of 8.0, 8.5, and 9.0 corresponding to earthquake return periods of 63, 205, and 667 years, respectively. The linear shallow water wave theory in spherical coordinate system is used for tsunami simulation in the large area covering Southeast Asia while the nonlinear shallow water wave theory in Cartesian coordinate system is used for tsunami simulation in the Gulf of Thailand. It is found that tsunamis arrives the southern part of Thailand in 11 hrs after an earthquake and arrives Bangkok in 20 hrs. The current velocity in the Gulf is about 0.1 m/s and the tsunami height is about 0.65 m near the shore of the southern peninsula for the Mw 9 earthquake.

1. INTRODUCTION

The 26 December 2004 Indian Ocean tsunami was generated by the Mw 9.0+ earthquake off the shore of northwestern Sumatra. The first wave of the tsunami struck the coast of Thailand, Malaysia, and other countries in the Andaman Sea about two hours after the earthquake. The tsunami caused human loss and devastating damage to civil engineering structures along the west coast of southern Thailand (TCLEE 2005). The event has drawn alerts in the engineering community in re-evaluate the tsunami hazard in Thailand. The infrastructures in the Gulf of Thailand, for example, gas pipelines and platforms can be affected by tsunamis generated by earthquakes in the seismically-active western part of the Philippines. In this study, the simulation of tsunamis in the Gulf of Thailand is conducted to investigate the arrival time, wave height, and current velocity.

2. EARTHQUAKES IN THE PHILIPPINES AND FAULT PARAMETERS

Bautista et. al. (2001) studied the geometry of subducting slabs in the Philippines. A new model of the subducting slab of the Eurasian plate beneath the Manila trench was proposed. Several earthquakes have occurred along the interface. The focal mechanism data of earthquakes in the subduction zone were analyzed and geometry of the subducting slabs was proposed.

In this study, the data of earthquakes generated around the Manila Trench and the Philippines are collected from Advanced National Seismic System (ANSS) from 1963 to 2006. The recurrence rate and magnitude relation based on the Gutenberg-Richter recurrence law is presented in Figure 1. The return period for each magnitude is summarized in Table 1.

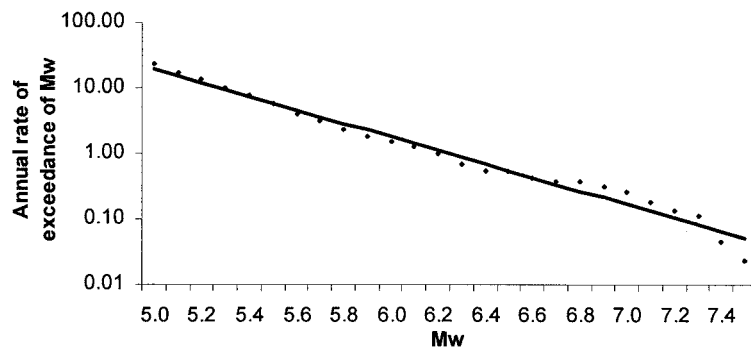


Figure 1 Relation between the annual rate of exceedance and the magnitude

Table 1 Return period for each magnitude

Magnitude Mw	Return Period (Years)
7.0	6
7.5	19
8.0	63
8.5	205
9.0	667

Papazachos et. al. (2004) proposed empirical equations for estimating fault parameters from earthquake magnitudes. The equations were developed from global earthquakes classified into strike-slip faults, dip-slip continental faults, and dip-slip faults in subduction regions. Based on the equations for dip-slip faults in subduction regions, the fault parameters which are the length, width, and displacement are predicted and summarized in Table 2.

Table 2 Predicted fault parameters

Magnitude Mw	Length (km)	Width (km)	Displacement (m)
8.0	162	71	2.2
8.5	305	102	4.5
9.0	575	145	9.5

The dip angle of a fault plane is assumed equal to that proposed by Bautista etl al. (2001). Then the vertical sea-bottom deformation is determined using the solution by Mansinha and Smylie (1971). Six cases of fault ruptures are considered for earthquakes with magnitudes of 8.0, 8.5, and 9.0 which correspond to return periods of 63, 205, and 667 years, respectively. The fault planes for all six cases

are located on the subducting slab in the Manila Trench as shown in Figure 2.

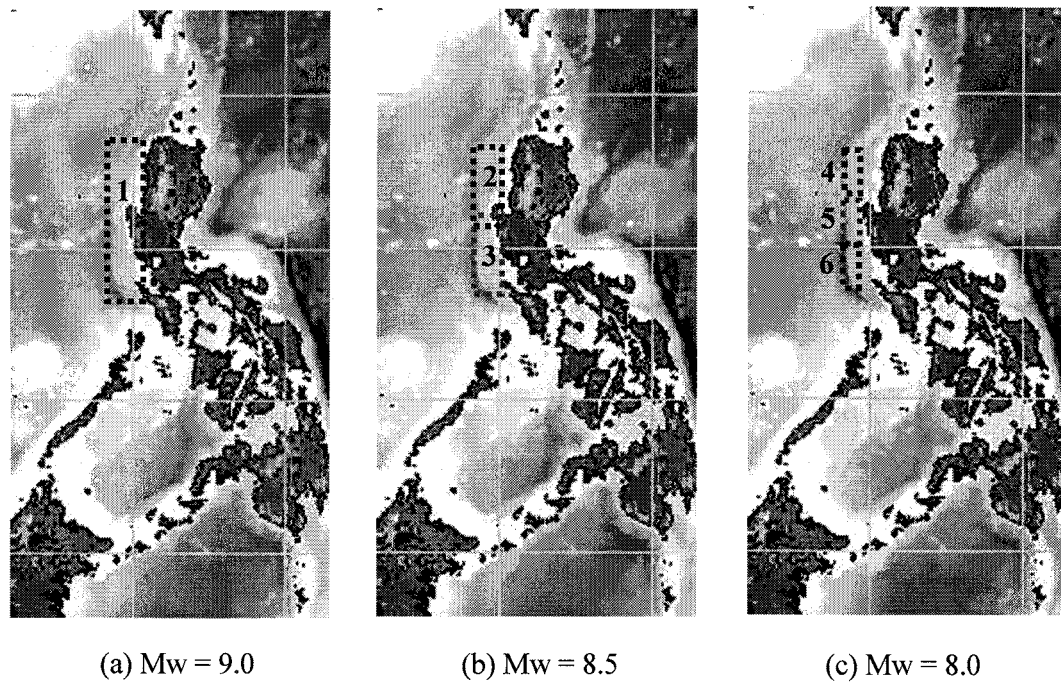


Figure 2 Location of faults for six cases in analysis

3. ANALYTICAL SCHEME AND CONDITIONS

Figure 3 shows the areas covered in the analysis. The sea depth off the shore of the Philippines is about 4,000 m, while the maximum sea depth in the Gulf of Thailand is about 60 m. The linear shallow water wave theory in spherical coordinate system is used for tsunami simulation in the large area covering Southeast Asia (Region 1) while the nonlinear shallow water wave theory in Cartesian coordinate system is used for tsunami simulation in the Gulf of Thailand (Region 2). The numerical simulation is conducted using TUNAMI codes with modifications to simultaneously solve tsunami propagation in the two regions. The grid size in Region 1 is 2 min, and that in Region 2 is 15 sec. ETOPO2 bathymetric data is used for Region 1. The bathymetry in Region 2 is digitized manually from the nautical chart by Hydrographic Department, Royal Thai Navy. The integration time step size is selected such that the stability condition is satisfied and response is close to the response obtained from smaller time step sizes. Hence, a time step of 5 sec is used in the analysis.

4. ANALYTICAL RESULTS

Analysis is conducted for all six cases to obtain the arrival time, tsunami height, and current velocity which are crucial for tsunami warning and evaluation of effects on off-shore structures. The tsunami arrives the southernmost province in 11 hrs and Bangkok in 20 hrs. It is found that the arrival time is slightly affected by the earthquake magnitude. Figure 4 show the contour map of tsunami arrival time. Since the Gulf of Thailand has a shallow depth of about 60 m, the propagation speed of the tsunami in the gulf is slow.

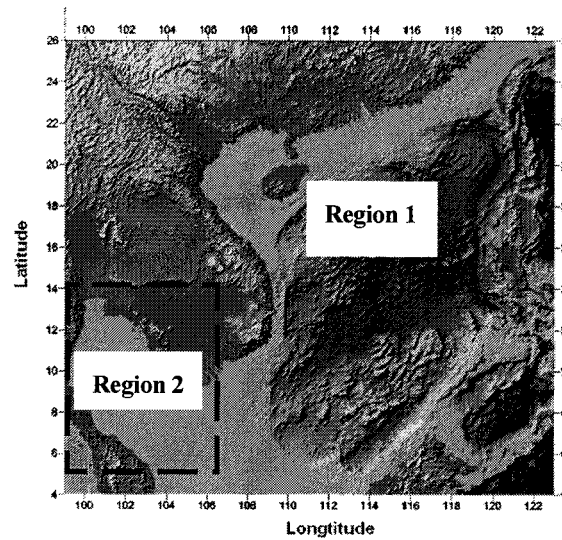


Figure 3 Regions for analysis

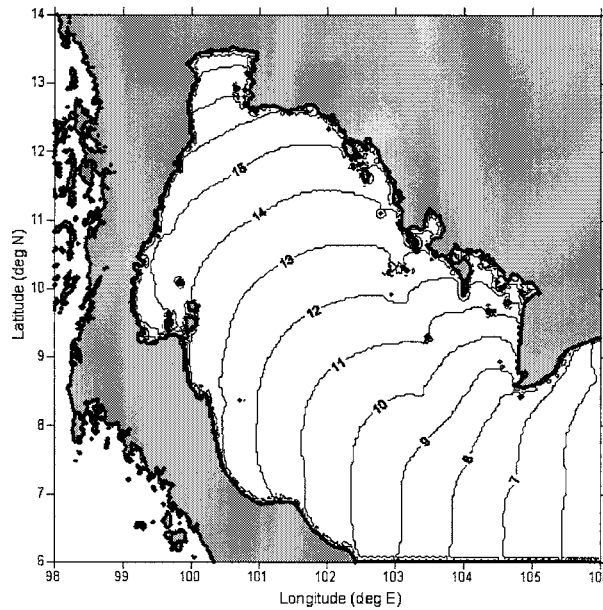


Figure 4 Tsunami arrival time for the Mw 9 earthquake

The tsunamis generated by fault ruptures in the Manila Trench mostly affects the Philippines and Vietnam. It is because of the directivity of tsunamis. At the central coast of Vietnam, the tsunami height is 3.8 m and the current velocity is 1.7 m/s at a sea depth of 20 m. The distribution of maximum tsunami height in the Gulf of Thailand for the Mw 9 earthquake is shown in Figure 5. The maximum tsunami height in the gulf is about 0.3 m. It is obvious that tsunamis diffracting around the southern part of Vietnam and entering the Gulf of Thailand have less effects to Thailand. The effect of magnitudes on the tsunami height at the coastline is presented in Table 3. As the earthquake magnitude increases from 8.0 to 8.5, the tsunami height increases by 3 times. And when the earthquake magnitude increases from 8.5 to 9.0, the tsunami height increases by 2 times.

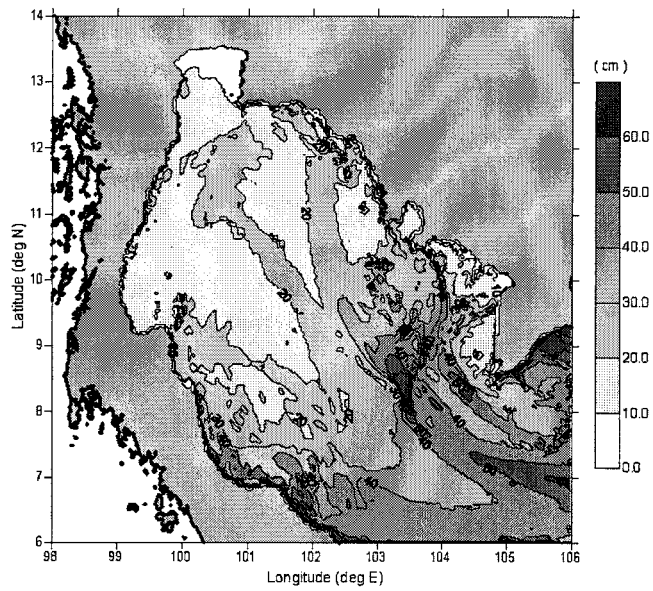


Figure 5 Tsunami height for the Mw 9 earthquake

Table 3 Maximum tsunami height at the coastline in Songkla

Magnitude Mw	Case	Maximum height (m)
9.0	1	0.65
8.5	2	0.20
	3	0.20
8.0	4	0.05
	5	0.05
	6	0.05

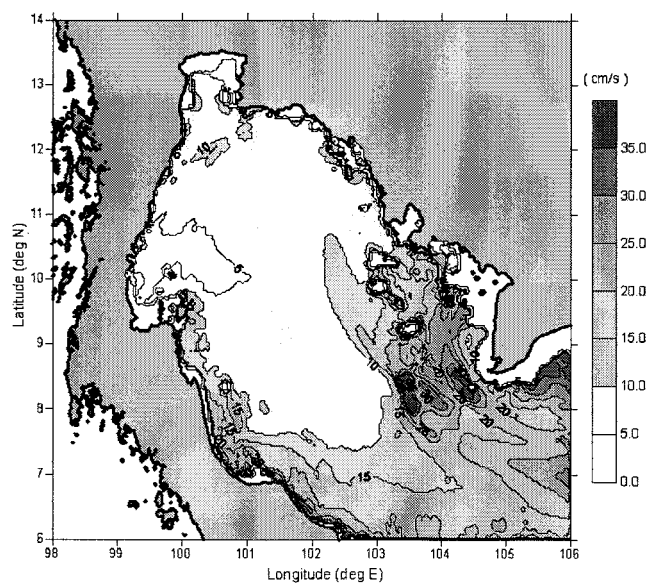


Figure 6 Current velocity for the Mw 9 earthquake

For an earthquake magnitude of 9.0, the maximum current velocity is 0.27 m/s at a sea depth of 15.6 m in the southernmost province. In the middle of the gulf where pipeline facilities are located, the velocity is about 0.1 m/s (Figure 6). The effect of earthquake magnitudes on current velocity is investigated. As the earthquake magnitude increases from 8.0 to 8.5, the current velocity increases by 2 times. And when the earthquake magnitude increases from 8.5 to 9.0, the current velocity increases by 2 times. It is obvious that the earthquake magnitude current velocity.

5. CONCLUSIONS

The tsunami arrival time, wave height, and current velocity are analyzed in this study. The Gulf of Thailand is less affected by the tsunamis generated by fault ruptures off the shore of the Philippines because of the diffraction of tsunamis at the southern part of Vietnam. Lifeline facilities in the Gulf of Thailand and coastal zones should be well prepared for the disaster.

Acknowledgements:

The research is financially supported by PTT PCL. The support is highly acknowledged.

References:

- Baulista, B. C., Baulista, M. L. P., Oike, K., Wu., F. T., Punongbayan, R. S. (2001), "A New Insight on the Geometry of Subducting Slabs in Northern Luzon, Philippines," *Tectonophysics*, 279-310.
- Mansinha, L., and Smylie, D. (1971), "The Displacement Fields of Inclined Faults," *Bulletin of the Seismological Society of America*, **61**(5), 1433-1440.
- Papazachos, B. C., Scordilis, E. M., Panagiotopoulos, D. G., Papazachos, C. B., and Karakaisis, G. F. (2004), "Global Relations between Seismic Fault Parameters and Moment Magnitude of Earthquakes," *Bulletin of the Geological Society of Greece*, 36, 1482-1489.
- Technical Council on Lifeline Earthquake Engineering (TCLEE) (2005), "Sumatra-Andaman Islands Earthquake and Tsunami of December 26, 2004- Lifeline Performance," *ASCE-TLCEE Monograph No. 29*, American Society of Civil Engineers.

DEVELOPMENT OF NUMERICAL TSUNAMI SIMULATION TECHNIQUE IN NEAR FAULT AREA

S. Inoue¹⁾, G. Kubo²⁾ and T. Ohmachi³⁾

1) Research Associate, Department of Built Environment, Tokyo Institute of Technology, Japan

2) Master course student, Department of Built Environment, Tokyo Institute of Technology, Japan

3) Professor, Department of Built Environment, Tokyo Institute of Technology, Japan

shusaku@enveng.titech.ac.jp, gotakubo@enveng.titech.ac.jp, ohmachi@enveng.titech.ac.jp

Abstract: In this paper, we built in the tsunami runup simulation technique to the existing dynamic tsunami simulation technique, and enabled it to simulate tsunami behavior including its generation, propagation, and runup by using SOLA and height function method. We confirmed our simulation results by comparing with runup height of solitary wave derived from theoretical and experimental equations. As much as we could prepare enough resolution mesh in coastal area, it could obtain accurate results. Finally we showed a preliminary 3-D tsunami simulation.

1. INTRODUCTION

People living in costal area of Japan are always exposed to tsunami risks because our country has a long costal line and active seismicity. Therefore, it is important to reveal tsunami behaviors and many researchers in practice investigate them by experiments and computer simulations. Especially lots of computer simulations are carried out and lots of simulation techniques are developed. In this paper, we reported a new tsunami simulation technique which is thought to be efficient in the near fault area.

In the conventional tsunami simulation technique, the simulation method which is based on the shallow water equation derived from long wave approximation is used in the world. Long wave approximation is theoretical equation which assumes that the horizontal current velocity is constant for the vertical direction and water pressure is described as hydrostatic pressure. These assumptions are applied because the wave length of the tsunami is much longer than the water depth and wave height. This simulation technique is practically used for research works, tsunami hazard maps and a tsunami warning system of the Japan Meteorological Agency.

However, it has been pointed out that the conventional tsunami simulation sometimes could not explain the field survey data when the tsunami occurred near the coastal line. For example, arrival times and wave heights observed by the field investigation does not correspond to the simulation results and it is often reported that the fault models estimated from the seismic waves tend to be smaller than that from the tsunami waves. Ohmachi et al. (2001) thought that these problems were caused by two factors which are the assumptions of the initial tsunami profile and long wave approximation. For this reason, they developed a new simulation technique which took into account the dynamic sea bed displacement to excite the initial tsunami profile and Navier-Stokes equation as the governing equation of the fluid domain. This simulation technique has been obtained useful results, but it has some problems remaining. One of them is that it can not calculate the tsunami runup which is most important for the tsunami disaster prevention.

As above, the purpose of this research is to develop the tsunami simulation technique which can calculate the combination of the tsunami generation, propagation and runup by improving the tsunami simulation technique developed by Ohmachi et al (2001). Our tsunami simulation technique in particular targets the tsunami in near fault area.

2. ANALYTICAL PROCEDURE

In the present tsunami simulation technique, weak coupling is assumed between the seabed and the seawater. Consequently, the motion of the seawater is influenced by that of the seabed, but the motion of the seabed is not influenced by that of the seawater. Based on this assumption, the present analysis consists of a two-step simulation. The first step is to simulate the dynamic seabed displacement resulting from a seismic faulting, and the second is to simulate the generation of the seawater disturbance followed by its propagation and runup. The seawater disturbance, including tsunamis, is simulated by imposing the velocity of the dynamic seabed displacement associated with seismic faulting as an input to fluid domain at the seabed (Ohmachi and Nakama, 1997). This type of analysis is hereafter called dynamic analysis, in contrast with the conventional one called the static analysis in which only the static seabed displacement is considered.

Among the numerical methods, the first step involves the simulation of the seabed displacement; the boundary element method (BEM) is employed here because it can give us time histories of dynamic displacement of irregular seabed resulting from a seismic faulting with a satisfactory level of accuracy (Kataoka and Ohmachi, 1997). As the second step, simulation of the seawater disturbance is conducted with the finite difference method (FDM). The analytical methods of fluid domain used for the present analysis are outlined in the following.

2.1 Fluid Domain Analysis

In the fluid domain analysis, the Navier-Stokes equation shown in equation (1) is used as a governing equation, and the eq. (1) and the mass conservation equation (2) are used to calculate the fluid domain by FDM.

$$\begin{aligned} \frac{\partial u}{\partial t} + u \frac{\partial u}{\partial x} + v \frac{\partial u}{\partial y} + w \frac{\partial u}{\partial z} &= -\frac{1}{\rho} \frac{\partial p}{\partial x} + \nu \left(\frac{\partial^2 u}{\partial x^2} + \frac{\partial^2 u}{\partial y^2} + \frac{\partial^2 u}{\partial z^2} \right) \\ \frac{\partial v}{\partial t} + u \frac{\partial v}{\partial x} + v \frac{\partial v}{\partial y} + w \frac{\partial v}{\partial z} &= -\frac{1}{\rho} \frac{\partial p}{\partial y} + \nu \left(\frac{\partial^2 v}{\partial x^2} + \frac{\partial^2 v}{\partial y^2} + \frac{\partial^2 v}{\partial z^2} \right) \\ \frac{\partial w}{\partial t} + u \frac{\partial w}{\partial x} + v \frac{\partial w}{\partial y} + w \frac{\partial w}{\partial z} &= g_z - \frac{1}{\rho} \frac{\partial p}{\partial z} + \nu \left(\frac{\partial^2 w}{\partial x^2} + \frac{\partial^2 w}{\partial y^2} + \frac{\partial^2 w}{\partial z^2} \right) \end{aligned} \quad (1)$$

$$\frac{1}{a^2} \frac{\partial p}{\partial t} + \rho \left(\frac{\partial u}{\partial x} + \frac{\partial v}{\partial y} + \frac{\partial w}{\partial z} \right) = 0 \quad (2)$$

where u , v and w are velocities of x , y and z direction, and p , ρ , a , ν and g are pressure, density, sound velocity of water, kinematic viscosity of the fluid and acceleration of gravity. As the simulation algorithm, we applied SOLA method (C. W. Hirt et al., 1975) with height function for the free surface. We generally have two choices to calculate free surface of the fluid in SOLA method, one is to use height function and another is to use volume of fluid (VOF) method. In this simulation, the reasons we adopted the height function are easiness to build in our program and to reduce the computation time.

2.2 Boundary Condition of Tsunami Runup

The main point of tsunami runup simulation is how to calculate the moving boundary. The height function method used in our simulation is suitable to simulate water in container boxed by vertical walls but is basically unsuitable for calculating water moving along the inclined walls. In this simulation, we set water, whose thickness is zero (Fig. 1), on the ground for convenience to calculate tsunami runup.

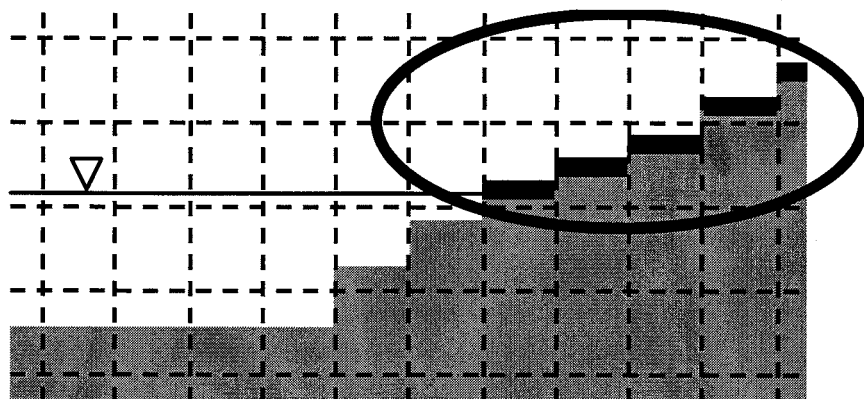


Figure 1 Tsunami runup analysis model

2.3 Nested mesh of Fluid Domain

When we calculate the tsunami from its generation to its runup, we should consider a very wide area including the seismic faults and the affected coastal area. Also, to simulate tsunami propagation, we should consider a long tsunami propagation time. Therefore, to conduct tsunami simulation with small meshes which have enough resolution for tsunami runup in coastal area is very hard for the computer, and almost impossible. For that reason, it is needed to change the mesh size gradually with large mesh in offshore and small mesh in coast area (Fig. 2).

In this simulation, we improved our program to be able to exchange the calculation data between large mesh and small mesh.

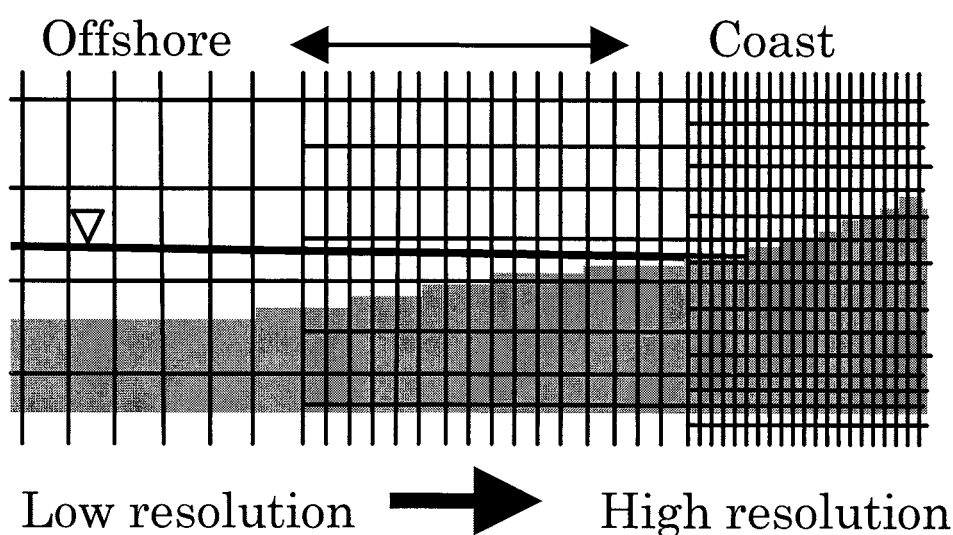


Figure 2 Image of the nested mesh

3. TEST SIMULATION OF A SOLITARY WAVE

To check our new developed simulation program, we conducted numerical experiments. In the numerical experiments, we inputted a solitary wave as an incident wave and compared the runup height derived from our simulation technique with that derived from theoretical and experimental equations (Synolakis, 1987). As shown in Fig. 3, we simulated that a solitary wave starts on the offshore, propagates to coast and runs up on the coast. Figure 4 showed the snapshots of the tsunami runup in case of $H/D = 0.15$.

First we conducted the simulation with constant $dz (=0.05)$. The results, which are shown as simulation 2 in Fig. 6, did not give good agreement with the experimental results when H/D is small, and we could not calculate the runup simulation in case of $H/D = 0.03$. Next we carried out the simulation with smaller constant $dz (=0.025)$ (simulation 2 in Fig. 6), these results gave good agreement with the theoretical and experimental results. From these results, we found out that our simulation program could obtain good results when the mesh size is enough small to calculate the tsunami runup. Finally we performed the simulation with nested mesh, and these results also showed good agreement.

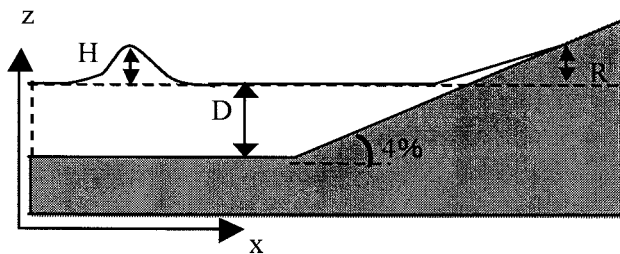


Figure 3 A simulation model for tsunami runup analysis.

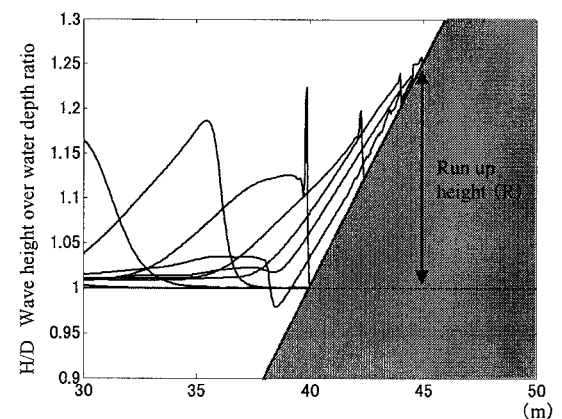


Figure 4 Edge of the tsunami runup in case of $H/D = 0.15$

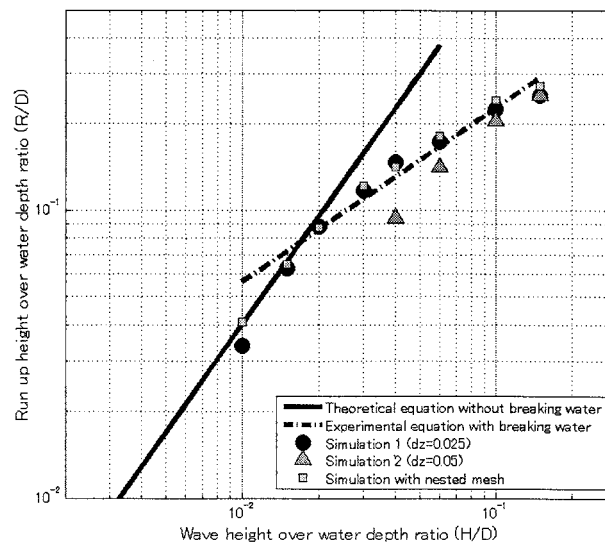


Figure 5 Comparison between our simulation results and theoretical and experimental results.

4. PRELIMINARY TSUNAMI SIMULATION IN NEAR FAULT AREA

In this section, we carried out the preliminary 3D tsunami simulation including its generation, propagation and runup. Figure 6 showed the simulation area and fault parameters. The area is divided into 5 regions and the largest region covers 100km square and the smallest region covers 700m by 400m. In this simulation, we calculate the 5 regions at the same time interval $dt = 0.1s$.

Figure 7 showed snapshots of tsunami generation in the largest region (region 1), and figure 8 showed tsunami runup in the smallest region (region 5). From these figures, our simulation results look working well, but it has some problems yet, for example, it sometime stops the calculation when the tsunami wave begin to retreat.

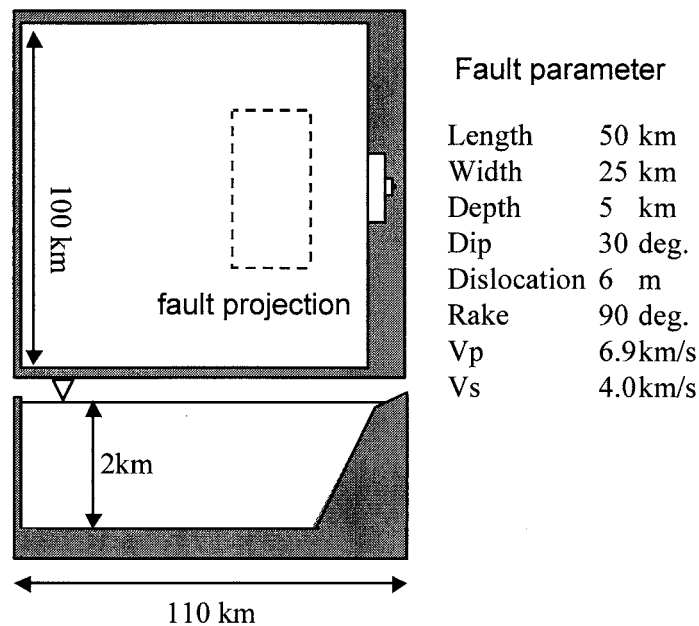


Figure 6 Analytical model and fault parameter employed.

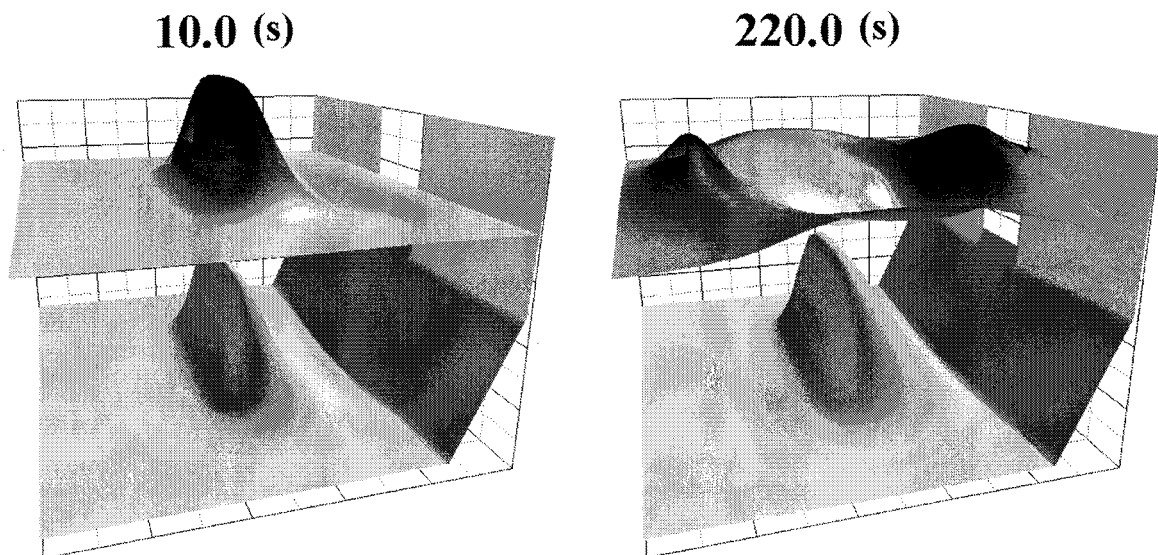


Figure 7 Tsunami generation and propagation in region 1.

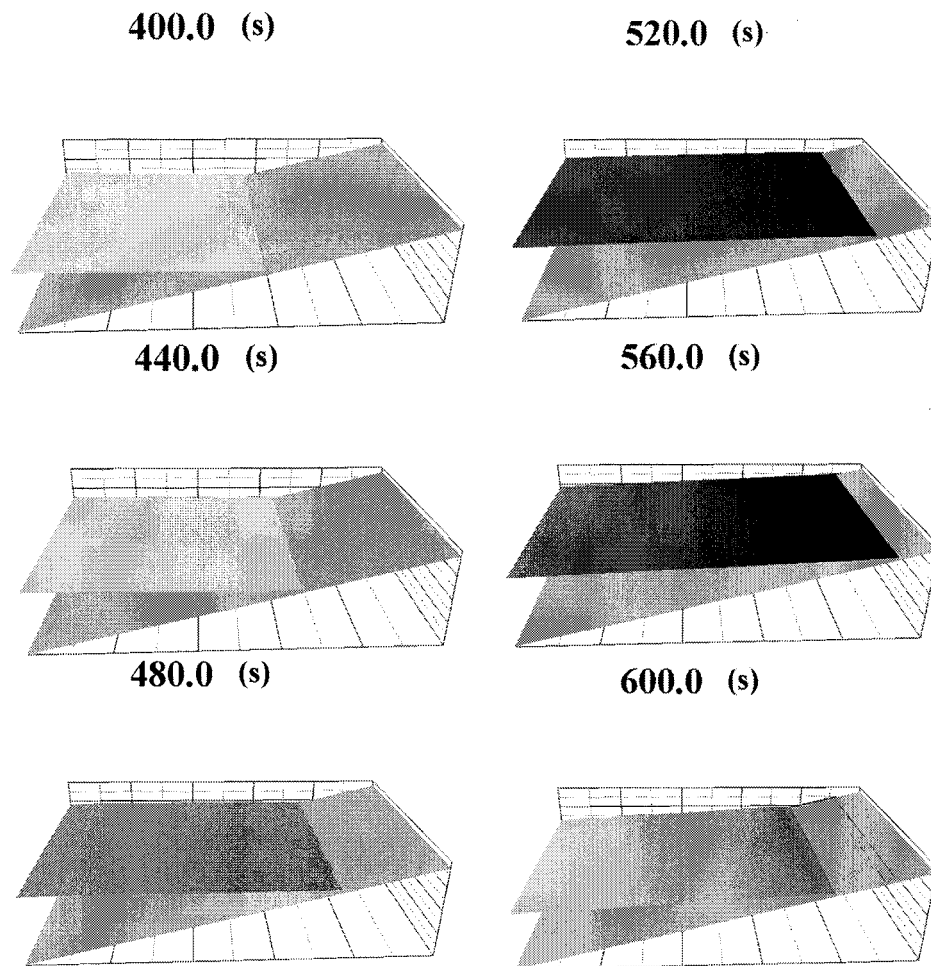


Figure 8 Tsunami runup in region 5

5. CONCLUSION

We built in the tsunami runup simulation technique to the existing dynamic tsunami simulation technique, and enable it to simulate tsunami behavior including its generation, propagation, and runup by using SOLA and height function method. In this paper, we confirmed our simulation results by comparing with runup height of solitary wave derived from theoretical and experimental equations. As much as we can prepare enough resolution mesh in coastal area, it could obtain accurate results. Finally we showed a preliminary 3-D tsunami simulation.

On the other hand, our simulation program has a few problems. For example, it sometimes does not work well when calculating the retreat waves. We will improve remaining problems as future works.

References:

- Ohmachi, T., Tsukiyama, H., and Matsumoto, H. (2001), "Simulation of Tsunami Induced by Dynamic Displacement of Seabed due to Seismic Faulting," *Bulletin of the Seismological Society of America*, Vol. 91, No. 6, pp. 1898-1909.
- Ohmachi, T., and Nakama, T. (1997), "Numerical analysis on tsunami propagation produced by dynamic seismic faulting," *Proc. Coastal Eng. Jpn., JSCE Vol. 45*, pp. 311-314 (in Japanese).
- Kataoka, S., and Ohmachi, T. (1997), "3-D simulation of near-field motion in irregular ground," *J. Struct. Mech. Earthquake Eng., JSCE*, 556, pp. 139-149.
- Hirt, C. W., Nichols, B. D., and Romero, N. C. (1975), "SOLA, A Numerical Solution Algorithm for Transient Fluid Flows," *Los Alamos Scientific Laboratory report*, LA-5852.
- Synolakis, C. E. (1987), "Runup of solitary wave," *J. Fluid Mech.*, Vol. 185, pp. 523-545.

DEVELOPMENT OF TSUNAMI SIMULATOR WITH CIP/MULTI-MOMENT FINITE VOLUME METHOD

R. Akoh¹⁾, S. Ii¹⁾ and F. Xiao²⁾

1) Graduate student, Dept. of Energy Sciences, Tokyo Institute of Technology, Japan

*2) Associate professor, Dept. of Energy Sciences, Tokyo Institute of Technology, Japan
d06akou@es.titech.ac.jp, d06ii@es.titech.ac.jp, xiao@es.titech.ac.jp*

Abstract: This paper presents a numerical model for shallow water equations, as an essential part of a multi-scale Tsunami simulation system. The underlying numerical framework is the CIP/Multi-Moment finite volume method. Accurate spatial discretization is constructed by making use of two kinds of so-called moments, namely volume integrated average (VIA) and point value (PV), of the physical fields. Particular efforts have been made to develop a model on a triangular unstructured grid with the source term of topography being well balanced to the flux terms. Thus, the resulting code is well suited for the simulation in presence of complex seabed topography and coastal line. Numerical validations for the model and a real-world case simulation of Tsunami will be given as well.

1. INTRODUCTION

After the huge tsunami triggered by the 2004 Indian Ocean Earthquake, people around the world have become increasingly aware of the importance of Tsunami disaster prevention. More accurate and reliable numerical models for Tsunami simulation and prediction are highly demanded. Efforts have been made in our group to establish a multi-scale Tsunami prediction and warning system. The system integrates two coupled models that respectively based on the 2D shallow water equations and the 3D Navier-Stokes equations with embedded free interface, and is able to simulate the motions ranging from large scale water waves to the local impact of water front. With the 3D model separately developed as a multi-fluid Navier-Stokes solver, we in this paper focus on the numerical model for the shallow water equations.

Although one can find some widely used Tsunami models that are based on the shallow water equations, as shown in the work by F.Imai et al. (1995) and C.Thaicharoen et al. (2005), and are able to provide the prediction of the arrival time and the height of Tsunami in the coastal region with reliability to some extent, the numerical models are far from being adequately accurate and still required further investigation. In this paper, we describe a newly developed shallow water equation model on an unstructured grid, aiming at the substantial improvement in representing the complex coastal line. Moreover, in the present model, the source term of the topographic effects is computed so as to well balance the numerical flux terms.

2. CIP/MULTI-MOMENT FINITE VOLUME METHOD

The basic concept of CIP/MM FVM is to make use of not only the volume integrated average

(VIA) but also other quantities, so-called moments, such as the point values (PV) or even the derivative values, as the model variables that are then updated temporally by different ways. CIP/MM FVM provides a flexible framework for building numerical models and has been so far applied to the simulations of various flows (F.Xiao 2005).

Considering the following two dimensional hyperbolic conservation law,

$$\frac{\partial \mathbf{U}}{\partial t} + \frac{\partial \mathbf{F}(\mathbf{U})}{\partial x} + \frac{\partial \mathbf{G}(\mathbf{U})}{\partial y} = 0. \quad (1)$$

where \mathbf{U} is the conservative variables and \mathbf{F} and \mathbf{G} are the flux functions in x and y directions respectively.

In the present CIP/multi-moment finite volume formulation, we use both the volume-integrated average (VIA) over a control volume and the point value (PV) at a specified point as the moments for the conservative variables, which are defined as

- VIA :

$$\overline{^V \mathbf{U}} \equiv \frac{1}{|V|} \int_V \mathbf{U}(\mathbf{x}, t) dV \quad \text{and} \quad (2)$$

- PV :

$$\overline{^P \mathbf{U}} \equiv \mathbf{U}(\mathbf{x}, t), \quad (3)$$

where V denotes the control volume. As shown later, the VIA is computed by a flux-based finite volume formulation and thus referred to VIA as the conservative moment. The PV, however, can be updated by a scheme that needs not to be numerically conservative, and can be referred to as non-conservative moment.

In the scheme based on multi-moment concept, different moments can be temporally updated by different approaches. The conservative moments have to be updated by flux-form to maintain the numerical conservation.

Integrating equation (1) over V and applying the theorem of Green-Gauss, we have the evolution equation for VIA as,

$$\frac{d \overline{^V \mathbf{U}}}{dt} = -\frac{1}{|V|} \oint_s (\mathbf{F}(\mathbf{U}) \cdot \mathbf{n}_x + \mathbf{G}(\mathbf{U}) \cdot \mathbf{n}_y) ds, \quad (4)$$

where s is the surface area of the control volume, $\mathbf{n} = (n_x, n_y)$ is the outward normal unit vector in x and y directions, and $\hat{\mathbf{F}}$ and $\hat{\mathbf{G}}$ are the flux functions. It is obvious that the equation (4) exactly guarantees the conservation of $\overline{^V \mathbf{U}}$. As discussed later, the numerical fluxes $\hat{\mathbf{F}}$ and $\hat{\mathbf{G}}$ are computed by using the PVs on the control volume surface.

The non-conservative moments, which need not to be rigorously conserved, are updated by solving the local Riemann problems in terms of the derivatives of flux functions at each discrete point.

The updating of the non-conservative moment PV is carried out with the governing equation (1) written at a point as follows,

$$\begin{aligned} \frac{d \overline{^P \mathbf{U}}}{dt} &= \frac{\partial \mathbf{F}(\mathbf{U})}{\partial x} - \frac{\partial \mathbf{G}(\mathbf{U})}{\partial y}, \\ &= -\left(\hat{\mathbf{F}}_x + \hat{\mathbf{G}}_y\right), \end{aligned} \quad (5)$$

where $\hat{\mathbf{F}}_x$ and $\hat{\mathbf{G}}_y$ denote the consistent numerical formulations for the derivative flux functions. $\hat{\mathbf{F}}_x$ and $\hat{\mathbf{G}}_y$ are eventually approximated through a derivative Riemann solver from the "left" and "right"

states that are piecewisely constructed based on both VIA and PV for a given physical field. As mentioned above, the PV is then used in the numerical fluxes needed in (4) for updating the VIA. The time integration of (4) and (5) is carried out by the third-order TVD Runge-Kutta method (C.W.Shu 1998).

With both VIA and PV treated simultaneously as the model variables and predicted in time, one can construct high order spatial interpolation function over just a single mesh cell. Thus, it is easy to implement the CIP/multi-moment finite volume method to unstructured grids.

3. NUMERICAL FORMULATION FOR SHALLOW WATER EQUATIONS

In this section, we first describe the formulation for shallow water equations without the source terms, then show how to compute the source term of topographic effects in a way that balances to the numerical flux of the hyperbolic part.

3.1 Shallow water equations without source term

Without source terms, the homogeneous shallow water equations read as

$$\frac{\partial \mathbf{U}}{\partial t} + \frac{\partial \mathbf{F}}{\partial x} + \frac{\partial \mathbf{G}}{\partial y} = 0, \quad \mathbf{U} = \begin{bmatrix} h \\ hu \\ hv \end{bmatrix}, \quad \mathbf{F}(\mathbf{U}) = \begin{bmatrix} hu \\ hu^2 + \frac{1}{2}gh^2 \\ huv \end{bmatrix}, \quad \mathbf{G}(\mathbf{U}) = \begin{bmatrix} hv \\ huv \\ hv^2 + \frac{1}{2}gh^2 \end{bmatrix}, \quad (6)$$

and the Jacobian matrix for the flux is defined as follows

$$\mathbf{A} = \frac{\partial \mathbf{F}}{\partial \mathbf{U}} = \begin{bmatrix} 0 & 1 & 0 \\ c^2 - u^2 & 2u & 0 \\ -uv & v & u \end{bmatrix}, \quad \mathbf{B} = \frac{\partial \mathbf{G}}{\partial \mathbf{U}} = \begin{bmatrix} 0 & 0 & 1 \\ -uv & v & u \\ a^2 - v^2 & 0 & 2v \end{bmatrix} \quad (7)$$

where h is the water depth, u, v are respectively the x, y components of velocity, and g is the gravitational acceleration. $c = \sqrt{gh}$ is the speed of the gravitational wave. We then have quantities, $\mathbf{U}_x, \mathbf{F}_x, \mathbf{U}_y$ and \mathbf{G}_y as follows,

$$\mathbf{U}_x = \begin{bmatrix} h_x \\ (hu)_x \\ (hv)_x \end{bmatrix}, \quad \mathbf{F}_x = \begin{bmatrix} (hu)_x \\ 2u \cdot (hu)_x + (c^2 - u^2) \cdot h_x \\ -uv \cdot h_x + v \cdot (hu)_x + u \cdot (hv)_x \end{bmatrix}, \quad (8)$$

$$\mathbf{U}_y = \begin{bmatrix} h_y \\ (hu)_y \\ (hv)_y \end{bmatrix}, \quad \mathbf{G}_y = \begin{bmatrix} (hu)_y \\ -uv \cdot h_y + u \cdot (hv)_y + v \cdot (hu)_y \\ 2v \cdot (hv)_y + (c^2 - v^2) \cdot h_y \end{bmatrix}. \quad (9)$$

Here, we solve the shallow water equation over unstructured triangular grid. The quadratic interpolation function is constructed over each cell element shown in Fig.1(a). We define the VIA over the control volume, and the PVs at the cell vertices and the middle points of each boundary edge for the conservative variables \mathbf{U} . Additionally, to remove numerical oscillations associating with the discontinuous solutions, like shock wave, we use the x, y gradients at the center of each cell as an extra constraint condition. One may refer to the references by S.Ii et al. (2005) for more details of the interpolation reconstructions.

Given a triangular mesh element i , we write eq.(1) as,

$$\frac{d^V \mathbf{U}_i}{dt} = -\frac{1}{\Delta S_i} \sum_{j=1}^3 \int_{l_{ij}} \left(\hat{\mathbf{F}} \cdot \mathbf{n}_x + \hat{\mathbf{G}} \cdot \mathbf{n}_y \right) dl, \quad (10)$$

where Δs is the area of cell i . Applying the Simpson's rule, the line integrals over the cell boundary are estimated by the PVs defined at the corresponding cell boundary. I.e., as mentioned previously, the numerical fluxes are computed directly from the PVs.

Concerning the updating of the PVs, the numerical fluxes of the equations (5) are computed by solving the derivative Riemann problems in respect to x and y directions with the values on both sides in each direction known (Fig. 1(b)). $U_x^{R,L}$ and $U_x^{T,B}$ are estimated by the gradients of the quadratic interpolation functions constructed over each cell in terms of both VIA and PVs.

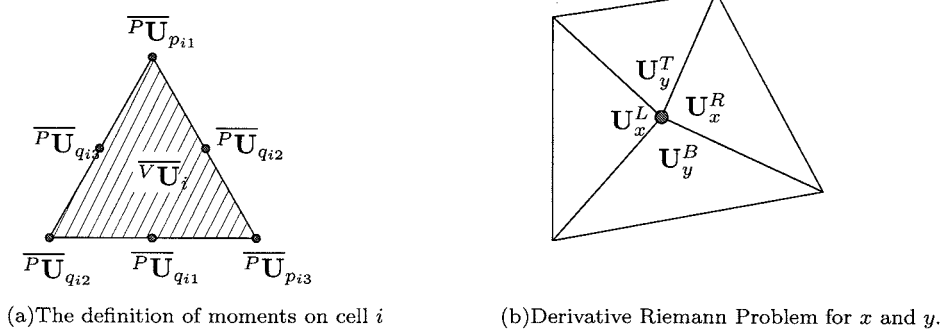


Figure 1: 2D model with the unstructured triangular grid

In this paper, we apply the approximate Riemann solver known as flux difference splitting (FDS) to estimate the numerical fluxes at each point as,

$$\hat{F}_x = -\frac{1}{2}F_x^R + F_x^L - \frac{1}{2}|A|(U_x^R - U_x^L), \quad (11)$$

$$\hat{G}_y = -\frac{1}{2}G_y^T + G_y^B - \frac{1}{2}|B|(U_y^T - U_y^B). \quad (12)$$

It should be noted that with PVs updated at every time step, different from the conventional FDS method, one can estimate the eigenvalues λ^p and the eigenvectors r^p directly from the corresponding PVs even without the Roe averages.

3.2 Treatment of a source term

The shallow water equations with a source term due to the bottom topography z read as

$$\frac{\partial U}{\partial t} + \frac{\partial F}{\partial x} + \frac{\partial G}{\partial y} = S, \quad S = \begin{bmatrix} 0 \\ -gh \frac{\partial z}{\partial x} \\ -gh \frac{\partial z}{\partial y} \end{bmatrix} \quad (13)$$

For the static condition ($h + z = H = \text{const}$, $hu = 0$, $hv = 0$), it is not trivial to get the balance between the numerical flux and the source term, known also as the "C-property". We need to consider the balance in the second and third equation of (13), i.e.

$$\frac{\partial}{\partial x} \left(\frac{1}{2}gh^2 \right) = -gh \frac{\partial z}{\partial x}, \quad \text{and} \quad \frac{\partial}{\partial x} \left(\frac{1}{2}gh^2 \right) = -gh \frac{\partial z}{\partial y}. \quad (14)$$

If a formulation does not preserve these balances between the source terms and the flux gradients at the discrete level, it may result in spurious oscillations. It is still an unsolved problem even in some operational Tsunami models. For simplicity, we only discuss the case in x direction. It is easy to show that we can obtain the exact C-property by combine the hyperbolic flux function and the source

term, i.e. $\mathbf{F}_x + \mathbf{S} \equiv \mathbf{F}'_x$, as follows,

$$\mathbf{F}'_x = \begin{bmatrix} (hu)_x \\ 2u \cdot (hu)_x + (c^2 - u^2) \cdot h_x + c^2 z_x \\ -uv \cdot h_x + v \cdot (hu)_x + u \cdot (hv)_x \end{bmatrix} = \begin{bmatrix} (hu)_x \\ 2u \cdot (hu)_x + c^2 \cdot H_x - u^2 \cdot h_x \\ -uv \cdot h_x + v \cdot (hu)_x + u \cdot (hv)_x \end{bmatrix}. \quad (15)$$

It is obvious that \mathbf{F}'_x exactly vanishes under the static condition ($(hu)_x = 0, H_x = 0, u = 0$). Thus, if we compute the H_x in the place of h_x and solve the Riemann problems in terms of H_x , the resulting $\hat{\mathbf{F}}'_x$ becomes zero under the static condition, and numerical formulation satisfies the C-property.

4. NUMERICAL RESULTS

In this section, we present numerical results of several test problems for the 1-dimensional and 2-dimensional shallow water equations.

4.1 1D dam-break flow

In the first numerical test, the one-dimensional dam-break is solved in a domain of $[0, 200]$. The mesh number is 201 and the time step is 0.1[s]. The initial conditions are

$$h_0(x) = \begin{cases} 1.0[\text{m}] & 0.0 \leq x \leq 100.0, \\ 0.1[\text{m}] & 100.0 \leq x \leq 200.0 \end{cases} \quad (16)$$

$$u_0(x) = 0.0[\text{m/s}] \quad (17)$$

After the instantaneous collapse of the dam, the numerical solution is computed until 20.0 [s].

The simulated water depth h and the velocity u are depicted against the exact solutions in Figure. 2. Both the shock wave and the rarefaction wave are accurately resolved. The conservativeness of the VIA quantities guarantees the correct location of the shock wave.

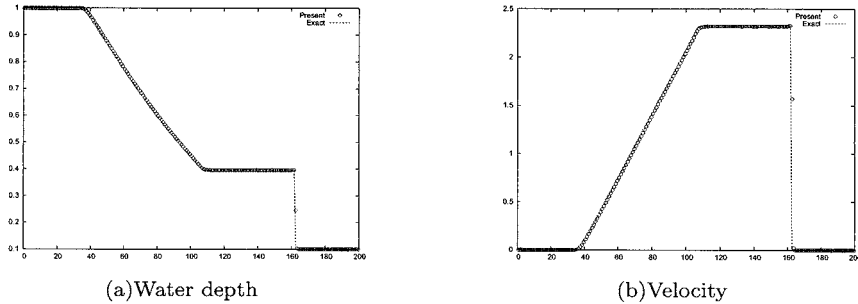


Figure 2: Numerical results of water depth (left) and velocity (right) at 20.0 [s].

4.2 1D Perturbation of a lake at rest

The purpose of the second problem is to test the present formulation for source term in the case of a small perturbation of a lake at rest with variable bottom topography. The bottom topography is given by

$$z(x) = \begin{cases} 0.25(1.0 + \cos(10.0\pi(x - 0.5))) & \text{if } 1.4 \leq x \leq 1.6, \\ 0.0 & \text{otherwise,} \end{cases} \quad (18)$$

where $[0, 2]$. The initial conditions are

$$H_0(x) = \begin{cases} 1.001[\text{m}] & \text{if } 1.1 \leq x \leq 1.2, \\ 1.0[\text{m}] & \text{otherwise} \end{cases} \quad (19)$$

$$u_0(x) = 0.0[\text{m/s}] \quad (20)$$

The results at 0.2[s] are shown in Fig.3. From these results that do not have spurious numerical oscillations, we know that the present formulation for source term preserves exactly the balance between the source term and flux gradient.

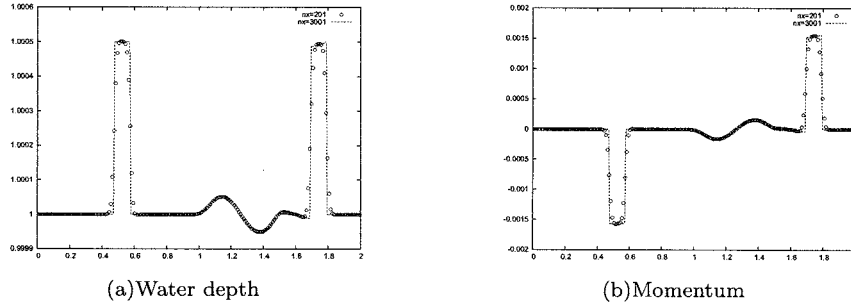


Figure 3: Numerical results of total height (left) and momentum (right) at 0.2[s].

4.3 A small perturbation of a steady-state lake in 2D

The third numerical test is widely used to evaluate numerical schemes for shallow water equations with source terms of bottom topography in 2D. The computational domain is $[0, 2] \times [0, 1]$, and the bottom topography is given by,

$$z(x, y) = 0.8 \exp(-5.0(x - 0.9)^2 - 50.0(y - 0.5)^2). \quad (21)$$

The initial condition is given as follows,

$$H_0(x, y) = \begin{cases} 1.01[\text{m}] & \text{if } 0.05 \leq x \leq 0.15, \\ 1.0[\text{m}] & \text{otherwise,} \end{cases} \quad (22)$$

$$u_0(x, y) = 0.0[\text{m/s}], \quad v_0(x, y) = 0.0[\text{m/s}].$$

Fig.4 show 30 uniformly spaced contour lines of the surface level H at 0.12, 0.36, 0.6[s]. The results obtained with the unstructured triangular grid appear on the left side, while on the right we find the numerical solution of the reference (Y.Xing et al 2006). The results indicate that numerical models can resolve the small-scale features of the flow very well.

4. EXPERIMENT WITH REAL GEOGRAPHICAL DATA

As the preliminary test for real case, we computed the simulations with complex coastal-line and bottom topography based on the real geographical-data in PhiPhi island region of Thailand (Fig.5). From these results, it is observed the overall behavior of the surface waves has been captured with reasonable accuracy. We will further validate and improve the present models and make them more reliable for real cases.

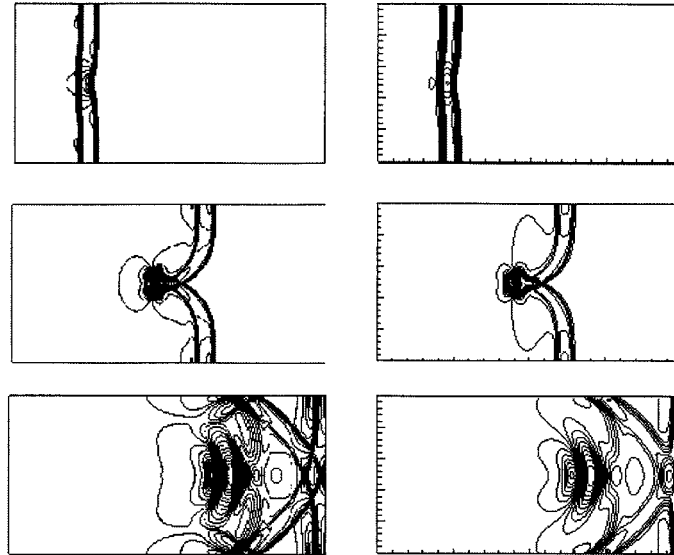


Figure 4: Numerical results of total height with present model (left) and references (right).

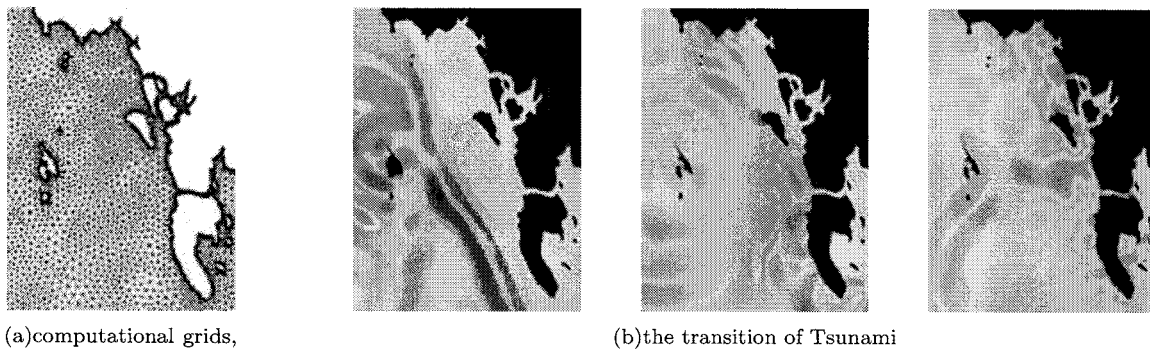


Figure 5: Simulation of Tsunami around PhiPhi island, Thailand.

5. CONCLUSIONS

We have constructed an accurate and robust numerical model for shallow water equations by applying some state-of-the-art numerical formulations. The numerical models have been validated by some idealized and "real-case" numerical experiments. The numerical results are quite promising. Further validations and applications of the present model are still needed. The coupling with the 3D Navier-Stokes model for free interface flows which have been separately developed in our group, will be carried out to build an integrated system for evaluating various waves of different scales.

References:

- F. Imamura. (1995), "Tsunami Numerical Simulation with the staggered Leap-frog scheme (Numerical code of TUNAMI-N1 and N2)," *School of Civil Engineering, Asian Inst. Tech. and Disaster Control Res. Cntr.*, Tohoku Univ.
- C. Thaicharoen, S. Weesakul, A. D. Gupta. (2005), "TSUNAMI PROPAGATION TO THAILAND A CASE STUDY: PHI PHI ISLAND," *MTERM International Conference*, 06.
- F. Xiao. (2005), "CIP/Multi-Moment Finite Volume Method", *J. Japan Soc. Comput. Engrg. Science*, Vol.10, 1243.(in Japanese)
- C. W. Shu. (1998), "Total variation diminishing time discretizations", *SIAM J. Sci. Statist. Comput.*, **9**, 1073.
- S. Ii, M. Shimuta, F. Xiao. (2005), "A 4th-order and single-cell-based advection scheme on unstructured grids using multi-moments", *Comput. Phys. Comm.* **173**, 17.
- Y. Xing, C. -W. Shu. (2006), "High order well-balanced finite volume WENO schemes and discontinuous Galerkin methods for a class of hyperbolic systems with source terms", *J. Comp. Phys.* **214**, 567.

LARGE MODEL TESTS OF SURGE FRONT TSUNAMI FORCE

T. Arikawa

*Project Researcher, Tsunami Research Center, Port and Airport Research Institute, Japan
arikawa@pari.go.jp*

Abstract: This report describes about the surge front tsunami force by using the physical model experiments. The characteristics of the tsunami force attacking on the structures on the land are investigated, and it is clarified that the maximum tsunami force is related with not only the inundation height but also the Froude number. The wooden wall of a wooden house is installed in the flume, and the mechanism of destruction of land structures due to the tsunami force is observed.

1. INTRODUCTION

The Indian Ocean Tsunami on 26th December affected the many countries around the Indian Ocean. A lot of people died and many buildings and houses were damaged by this tsunami. The terrific of power that huge tsunami brought was recognized again.

The tsunami force attacking on structures in the land is called the surge front tsunami force (Matsutomi, 1991). There are a few reports of the surge front tsunami force. Iizuka and Matsutomi (2000) proposed the empirical formula based on logic that the surge front tsunami force was proportional to the square of flow velocity. Asakura et al. (2000) suggested that the force has triangular distribution that height to act on supposed to be 3 times of inundation height.

Photo 1 shows the damage of a house at Galle city in Sri Lanka. Tsunami with average inundation height of about 2.5m attacked in the place. The Tsunami trace showed that the maximum inundation height was around 3.8m. The wall of this house was made of mortar and brick. It is necessary to investigate what kind of power acted and how it broke. However, since what kind of tsunami attacked had many unknown points, the fundamental experiments about Surge front tsunami force were conducted. Moreover, development of the numerical computation technique which can carry out the simulation of such power was tried.



Photo 1: Damage of houses at Galle City in Sri Lanka taken on 21st, Apr. 2005.

2. SURGE FRONT TSUNAMI FORCE

2.1 Type of Surge Front Tsunami Force

Surge front tsunami force may qualitatively divide into the following types (see Figure 1) from past researches and the experiments conducted so far. It seems to be classified according to the speed and wave profile of inundated tsunami. Type 1 shows the case where the overflow with slow speed acts on the structures. Suppose that such a situation is called overflow type in this paper. Type 2 shows the case where overflow with quick speed acts. When the inundated tsunami carries out soliton fission or becomes bore, it may be accompanied by the flow quick in this way. It is called bore type in this paper. Type 3 shows the case where tsunami breaks in front of structures. This type may cause when the structures are near the coast line and slope of seabed is steep, which is called breaking type. If the inundated height of tsunami is same, then it is thought that the maximum force becomes large as it becomes breaking type from overflow type. However, it is not clear how large the force is and where a boundary line of type is.

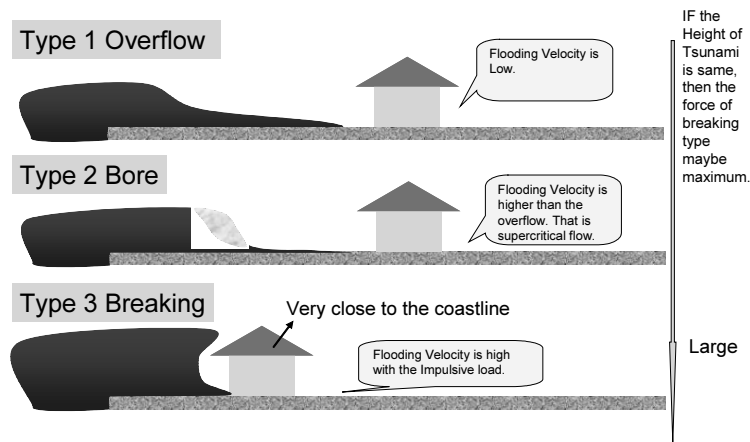


Figure 1: Type of surge front tsunami force

2.2 Definition of Surge Front Tsunami Force

Figure 2 shows the typical time history of surge front tsunami pressure. Since the period of Tsunami is longer than several minutes, the main part of tsunami attack is in the almost same state as a steady flow acts continuously. The pressure in such a state is called the sustainable pressure in this paper. On the other hand, the tsunami pressure of a front portion, that is called the bore pressure, is greatly dependent on a wave profile and may become larger than main portions depending on the case.

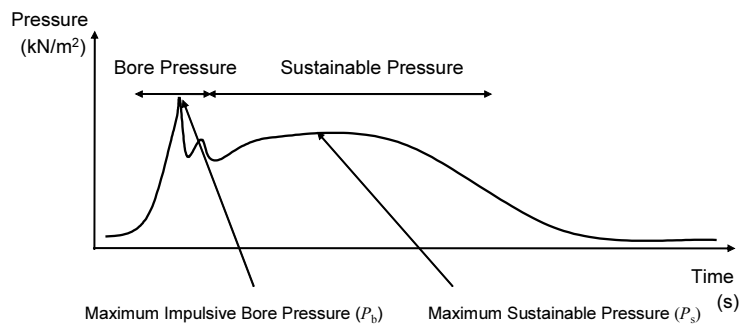


Figure 2: Typical time history of tsunami pressure

Asakura et al. (2000) mainly researched about the sustainable pressure and its vertical distribution. They proposed the following empirical formula (Eq. (1)).

$$p(z)/\rho g \eta_{\max} = 3(1 - z/3\eta_{\max}) \quad \text{for } 0 \leq z/\eta_{\max} \leq 3 \quad (1)$$

Where p is pressure, z is vertical axis, η_{\max} is the maximum height of the inundated tsunami, ρ is

the density of water, and g is the gravity acceleration. This formula indicates that the vertical distribution of maximum sustainable pressure is the same as the distribution of hydrostatic pressure. They also proposed the empirical formula (Eq. (2)) of the pressure when the inundated tsunami became soliton fission.

$$p(z)/\rho g \eta_{\max} = \max\{5.4(1 - z/1.35\eta_{\max}), 3(1 - z/3\eta_{\max})\} \quad \text{for } 0 \leq z/\eta_{\max} \leq 3 \quad (2)$$

It seems that they have proposed this formula as the maximum sustainable pressure. Since pressure is the force of acting on per unit area, the distribution of pressure is needed.

Iizuka and Matsutomi (2000) proposed that the empirical formula of the force in the state of steady flow (Eq. (3)).

$$F_H = 1/2 \rho C_D u^2 h_f B_h \quad (3)$$

Where F_H is the horizontal sustainable force of a structure, u is the velocity of inundated tsunami, C_D is the drag coefficient ($=1.1$ to 2.0), h_f is the inundated tsunami height in front of a structure, and B_h is the width of a structure. u is proportional to a square root of the height of inundated tsunami, so F_H is proportional to a square of the inundated height.

Although it seems that the part in the formula (Eq. 2) is a maximum impulsive pressure, there is no clear description. It is unknown what kind of vertical distribution the maximum impulsive pressure has and how large it is. Eq. 3 indicated that the force is proportional to the speed of velocity, but the effect of the velocity is not included in Eq. (1) and (2).

3. EXPERIMENTS OF SURGE FRONT TSUNAMI FORCE

3.1 Large Hydro Geo Flume

The size of the large hydro geo flume is 184m long, 3.5m wide and 12m deep at the maximum. This wave flume has the 14m stroke and can generate the 2.5m height tsunami. It can make the positive and negative tsunami. Figure 3 shows the relation between the stroke of wave paddle and tsunami height as positive tsunami, that is the height of crest above the still water level. In the figure, H_T is tsunami height, S is stroke, and T_D is the duration time while the wave paddle is moving. The motions of wave paddle use a sine function (see Figure 4).

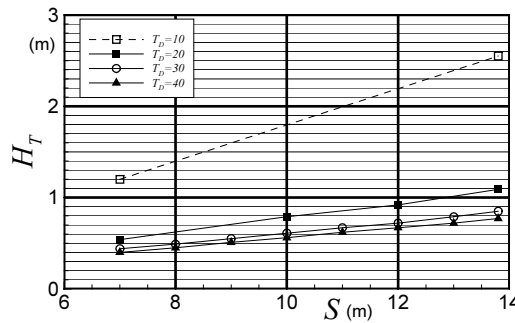


Figure 3: the relation between the stroke and tsunami height

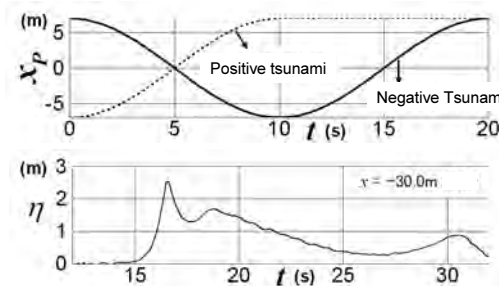


Figure4: example of motion of wave paddle (upper), tsunami profile (lower)

3.2 Dynamic Loading Tests

(1) Experimental set up

In order to see the difference in pressure by the difference in the type of inundated tsunami, the large-scale model experiments were conducted. Figure 5 shows the cross section of experiments about large model tests. The 1/10 slope was installed in the middle of the wave flume, and a flat part 20m in length was prepared from the termination part of the slope. The rigid boxes with 80cm high were put on the flat part with 6.0m from the end of the slope (see Figure 6.). The pressure gauges are attached in the central part of a box in the position of 10cm, 40cm, and 70cm from the bottom, respectively. The rated capacity of pressure gauges in a height of 10cm was 196kN/m^2 , and that of other pressure gauges was 19.6kN/m^2 . The sampling interval was set to 400Hz. The propeller type velocimeters with rated capacity 10.0m/s were installed 1.0m ahead and 0.8m behind the box.

Tsunami conditions were following: the periods 20s, 25s, 30s, 40s, and 60s, the tsunami height 40cm to 80cm, positive and negative initial movements.

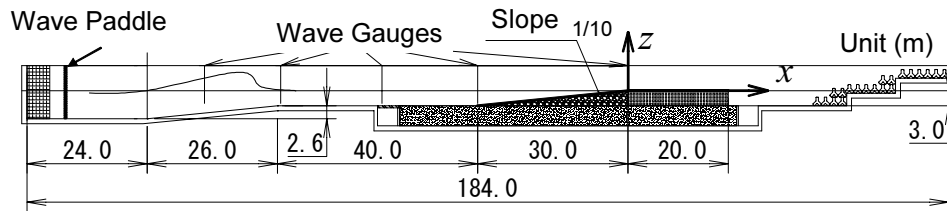


Figure 5: Cross section of experiments

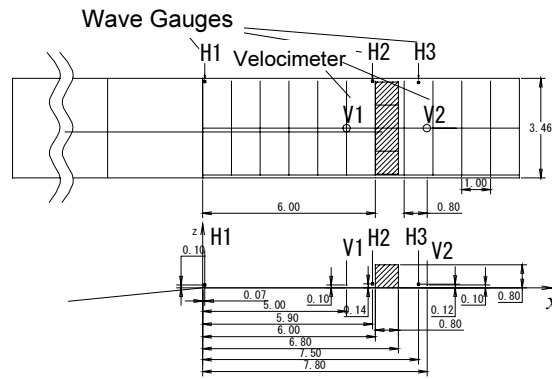


Figure 6: Boxes set up

(2) Inundated tsunami standardizing tests

The inundated height and velocity were measured in the state where there were no structures. Figure 7 shows the relation between the inundated tsunami height and velocity under this experiment series, where H_{sv} and v_{sv} are the maximum sustainable inundated tsunami height and velocity, respectively. It indicated that the Froude number is up to about 1.5 from these results.

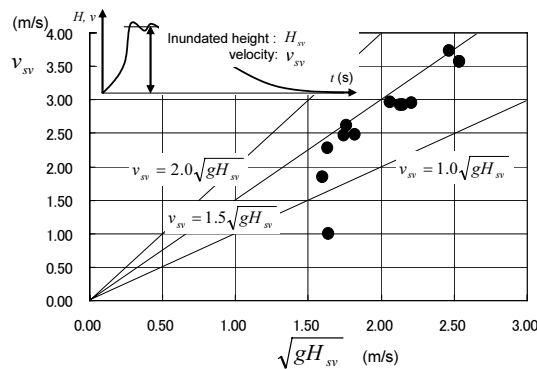


Figure 7: Relation between inundated height and velocity under this experiment series

(3) Results of the maximum sustainable pressure

The maximum sustainable pressure (P_s) is related with the maximum sustainable inundated tsunami height (H_{sv}). First, the vertical distribution of P_s is shown in Figure 8. $P_s(z)$ is less than $\rho g H_{sv} (3.0 - z/H_{sv})$ ($0 \leq z \leq 3.0 H_{sv}$). Figure 9 shows the relation between Froude number and the dimensionless P_s . Discrepancies exist in the results at the point where the Froude number is 1.5. One of the reasons is influence of the height of boxes. The height of boxes is smaller than $3.0 H_{sv}$ in some cases. Roughly speaking, the dimensionless P_s seems to be in proportional to the Froude number. From this result, the P_s can be expressed with the following formula;

$$P_s = \rho g H_{sv} (\alpha - z') \quad \text{for } (0 \leq z' \leq \alpha) \quad (4)$$

where α is in proportional to the Froude number. In this experiment series, on average $\alpha \cong 1.5 Fr$ and $\alpha \cong 2.0 Fr$ as the maximum.

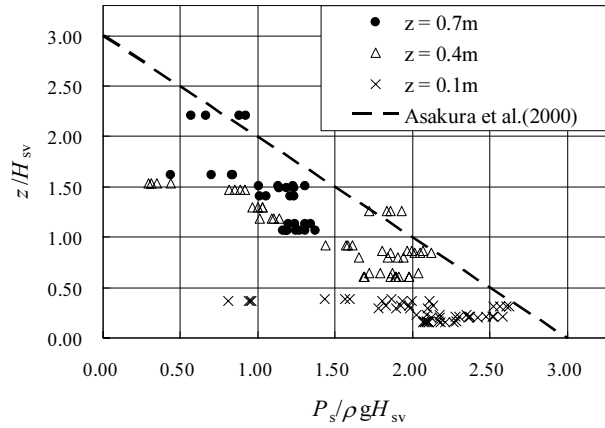


Figure 8: Results of vertical distribution of maximum sustainable pressures

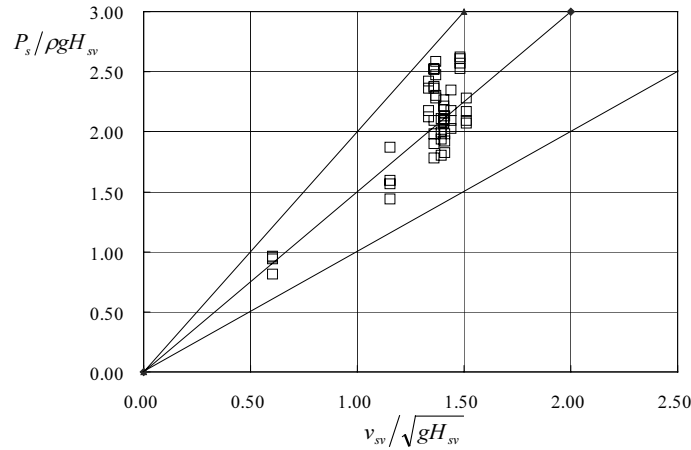


Figure 9: Relation between the Froude number and the dimensionless P_s

(4) Results of the maximum impulsive bore pressure

The inundated tsunami with ‘Breaking’ type attacked on boxes (see Photo 2). The inundated tsunami was breaking in front of boxes. Figure 10 shows the time history of the pressure, force, velocity and wave profile, where x starts the end of 1/10 slope and force is calculated by summarizing 3 pressure gauges. Large impulsive bore force acted on the boxes.

Figure 11 shows the vertical distribution of the maximum impulsive bore pressure (P_b) in this experiment series, where solid line means the Eq. (2) for soliton fission type. From this result, the maximum impulsive bore pressure is much larger than Eq. (2) according to circumstances. The relation between the Froude number and P_b is shown in Figure 12. It indicated that the P_b does not occur when the Froude number is less than at least 1.15 in this experiment series. The discrepancies of

data are according to the wave profile, such as breaking or after breaking profile. So, accurate prediction of wave profile is important to predict P_b , Matsutomi (1991) also pointed out.

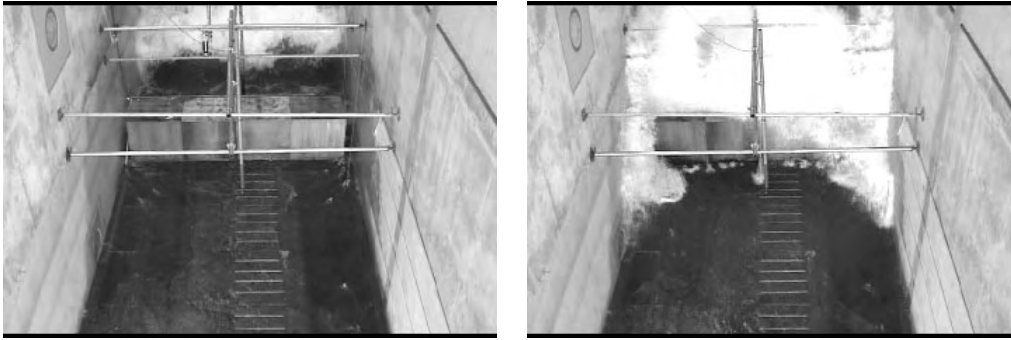


Photo 2 : Breaking type inundated tsunami attacked on boxes

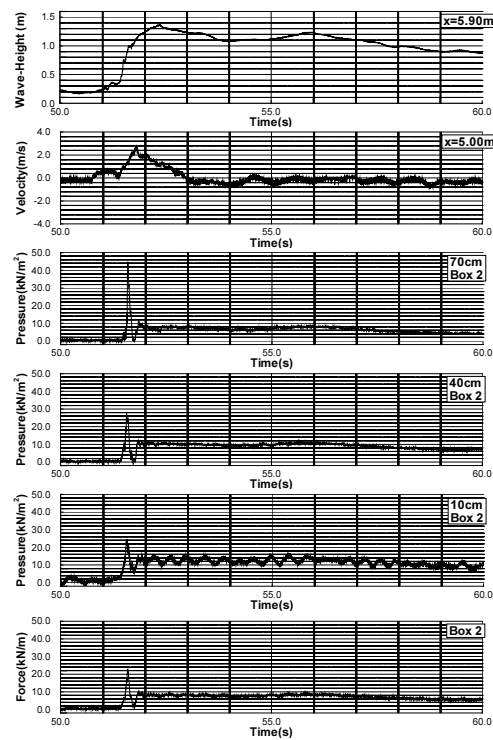


Figure 10: time history of wave profile, velocity, pressure, and force.

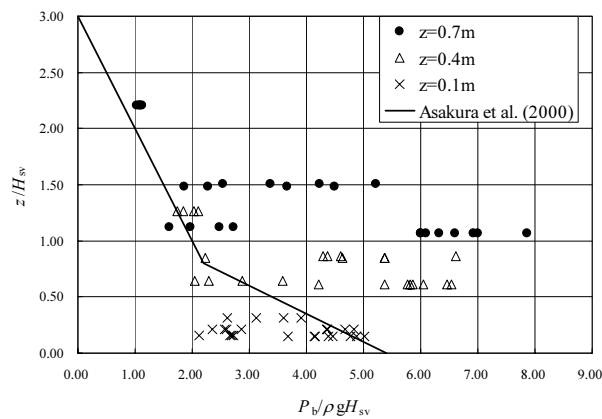


Figure 11: Vertical distribution of maximum impulsive bore pressure

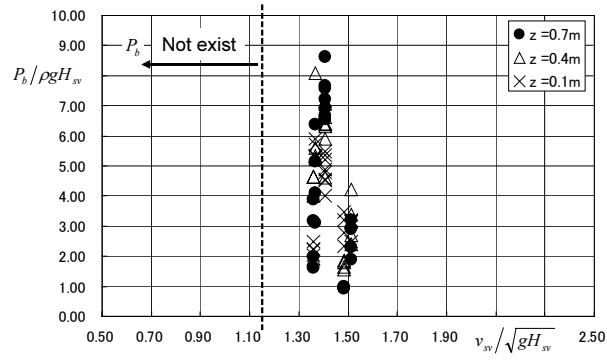


Figure 12: relation between the Froude number and P_b

3.3 Interaction between fluid and structures

(1) Experimental set up

The wooden wall of a wooden house is put in the flume in order to investigate the mechanism of destruction of land structures due to the tsunami force (see Figure 13). The 2.5m positive tsunami, which profile is shown in Figure 4, is generated.

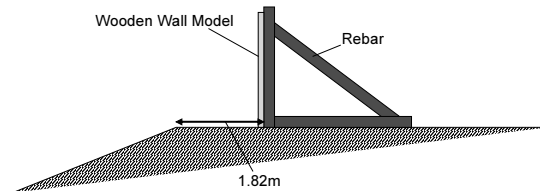


Figure 13: Cross section of the experimental setup

(2) Pressure distribution and the state of destruction

Photo 3 shows the state of destruction of a wooden wall. Photo 4 shows the plan view of the instance that the front part of tsunami attacks. Those photos indicate that the wall is broken in the moment water attacked on the wall.



Photo 3: The state of destruction of wooden wall



Photo 4: Plan view of the moment that tsunami attacks the wall

4. SUMMARY

The characteristics of surge front tsunami force are investigated. Some series of experiments are conducted, and it is clarified that the maximum sustainable pressure is proportional to the Froude number. It also makes clear that the impulsive bore pressure is not occurred if the Froude number is less than 1.15 under this experiment conditions and its maximum value is much larger than the maximum sustainable pressure.

The wooden wall of a wooden house is put in the flume in order to investigate the mechanism of destruction of land structures due to the tsunami force. The wall is broken in the moment 2.5m tsunami force attacked on the wall.

References:

- Matsutomi, H. (1991), "Distribution of impulsive pressure and impulsive force due to the collision of bore," *Proceedings of Coastal Engineering*, JSCE, **38**(1), 626-630. In Japanese.
- Iizuka, H. and Matsutomi, H. (2000), "Damage due to the Flooding Flow of Tsunami," *Proceedings of Coastal Engineering*, JSCE, **47**(1), 381-385. In Japanese.
- Asakura, R., Iwase, K., Ikeya, T., Kaneto, T., Fujii, N. and Omori, M. (2000), "An experiment study on wave force acting on on-shore structures due to overflowing tsunamis", *Proceedings of Coastal Engineering*, JSCE, **47**(1), 911-915. In Japanese.

A SCENARIO OF EARTHQUAKE-TSUNAMI DISASTER AND A POLICY OF MEASURES FOR ROAD NETWORKS

KATAOKA Shojiro¹⁾

*1) Senior Researcher, National Institute for Land and Infrastructure Management, Japan
kataoka-s92rc@nilim.go.jp*

Abstract: Disaster scenarios are now widely used for improving understanding and planning disaster mitigation measures. There is, however, no established method of evaluating tsunami damage to road bridges that can be used to develop a tsunami disaster scenario for road networks. In this paper, a simple procedure is proposed for evaluating of tsunami damage to road bridges, and its application to the development of a disaster scenario is presented. The scenario includes damage to road bridges and embankments, and inundated road sections caused by a hypothetical Nankai earthquake and its tsunami. The policy of measures for road networks is also discussed.

1. INTRODUCTION

Great earthquakes often have occurred at the boundaries of continental and oceanic plates around Japan. These earthquakes generate not only ground shaking but also tsunami and hence have caused major disasters especially along the Pacific coast. Scenarios of earthquake and tsunami disaster are useful to help decision-makers plan disaster mitigation measures and for people to understand disasters for which they must be prepared. Since there is only limited time between the occurrence of an earthquake and arrival of the tsunami, tsunami disaster scenarios are vital to consider in advance how to evacuate or respond properly after one feels the ground shaking.

Disaster scenarios have been developed and widely used in local governments in recent years but earthquake and tsunami damage to road networks are usually not taken into account. This is because there has been no established method of evaluating the degree of damage to road bridges caused by tsunami, whereas methods of evaluating seismic damage to road bridges and embankments, and tsunami damage to embankments are available (Kobayashi and Unjoh, 2005; Public Works Research Institute, 2003; Shuto, 1997).

In this paper, a simple procedure is proposed for evaluating tsunami damage to road bridges based on a series of wave channel experiments, and is applied to the development of an earthquake and tsunami disaster scenario. The scenario includes damage to road bridges and embankments, and inundated road sections caused by a hypothetical Nankai earthquake and its tsunami.

2. WAVE CHANNEL EXPERIMENTS

We conducted a series of experiments using a wave channel and bridge girder models to investigate wave force acting on a bridge girder struck by a tsunami. The experimental setup of one of the bridge girder models in the wave channel is shown in Figure 1. The wave channel is 140m

long, 2m wide, and 5m deep. A fixed bed slope had been constructed and the bridge girder model, which is made of metal, was installed on the slope. As shown in Table 1, 15 combinations of still water level, h , and initial wave height, H_0 , of solitary wave were set and the experiment with each combination was executed three times.

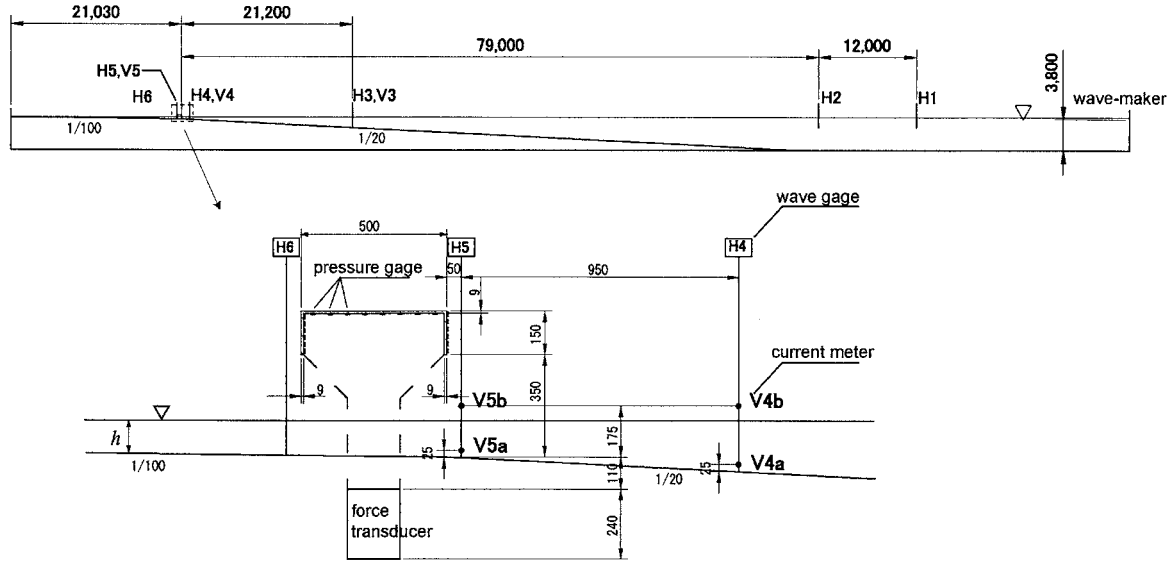


Figure 1: Experimental setup of a bridge girder model in the wave channel (unit: mm).

Table 1: Still water level, h , set for each initial wave height, H_0

H_0 [cm]	h [cm]
20	15, 30
30	7.5, 10, 12.5, 15, 30
40	7.5, 10, 12.5, 15, 17.5, 20, 22.5, 30

Photo 1 shows the moment when the horizontal force acting on the bridge girder reached the peak during the experiment with $H_0 = 40\text{cm}$ and $h = 17.5\text{cm}$. The solitary wave was breaking at this moment and hence the peak of both horizontal and vertical forces with this combination of H_0 and h were the largest among all combinations. The time histories of horizontal and vertical wave forces during the experiment with $H_0 = 40\text{cm}$ and $h = 17.5\text{cm}$ are shown in Figure 2. The time histories consist of impulsive force with short duration and drag that slowly decreases. Since the peak value of the impulsive force was found to highly depend on whether the wave is breaking, it cannot be represented in a simple manner.

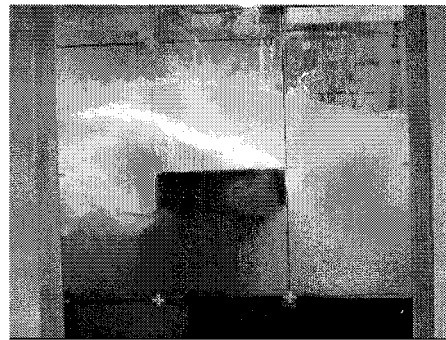


Photo 1: Solitary wave striking the bridge girder model ($H_0 = 40\text{cm}$, $h = 17.5\text{cm}$).

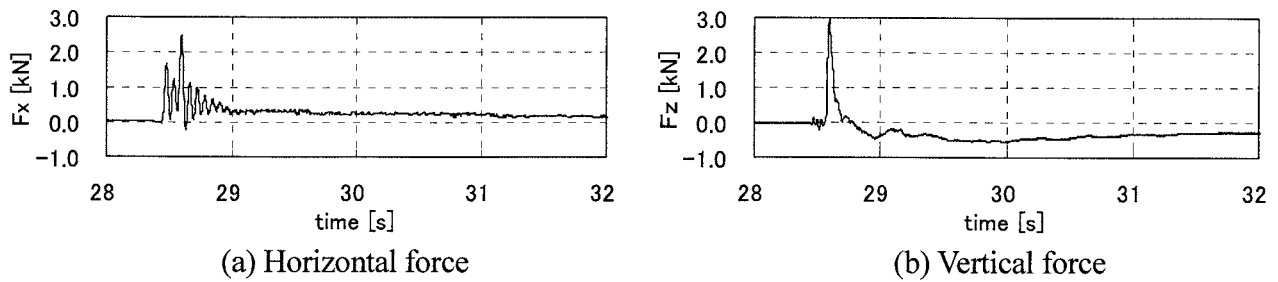


Figure 2: Time histories of wave force on the bridge girder model ($H_0 = 40\text{cm}$, $h = 17.5\text{cm}$).

Figure 3 compares the drag obtained from the experiments and wave force calculated by the formula, which is represented as shown in Figure 4, used in the standard for port facilities (Japan Port and Harbour Association, 1999; called “standard formula” from now on). The drag shown in Figure 3 is the average through 0.5s and is approximated well with some safety margin by the standard formula. Thus, we use the standard formula for evaluating the washout of a bridge girder.

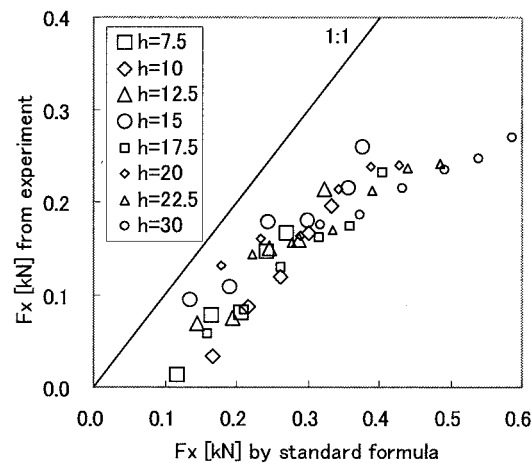


Figure 3: Comparison between the drag obtained from the experiments ($H_0 = 40[\text{cm}]$) and wave force calculated by the standard formula (Japan Port and Harbour Association, 1999).

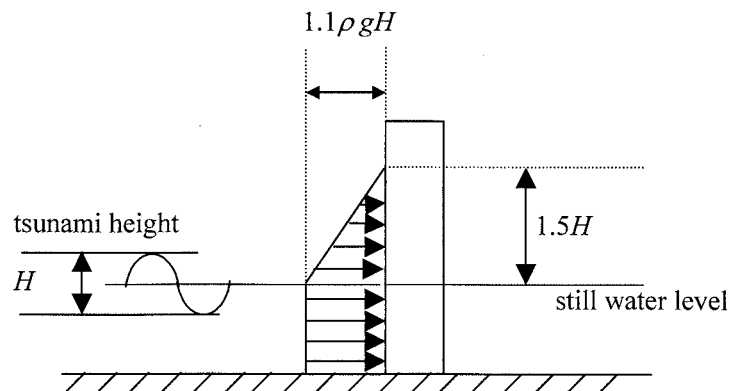


Figure 4: Representation of tsunami wave pressure used in the standard formula.

3. PROCEDURE FOR EVALUATION OF TSUNAMI DAMAGE TO ROAD FACILITIES

In this study, we propose the flowchart shown in Figure 5 for evaluating tsunami damage to road bridges. This flowchart is based on the following facts and concepts: (a) since the road bridges designed according to specifications after the 1995 Kobe earthquake have enough strength to withstand strong seismic force equivalent to that observed during the earthquake, we assumed those bridges are able to withstand tsunami striking; (b) the drag acting on a girder is evaluated by the standard formula as mentioned above; (c) the friction force is derived from the product of underwater weight of a girder by a friction coefficient that is assumed to be 0.6 (Rabbat and Russell, 1985); (d) displacement restriction devices and falling prevention devices can prevent the girder falling as was seen in Banda Aceh, Indonesia, after the 2004 Indian Ocean tsunami struck the city (Unjoh, 2005).

Since it is difficult to evaluate the impulsive force acting on a girder and strength of bearing against it, we assumed that the bearing is severely damaged if the tsunami flows over the bridge girder. Thus, the comparison between impulsive force and strength of bearings, which is shown in Figure 5, is not carried out in this study.

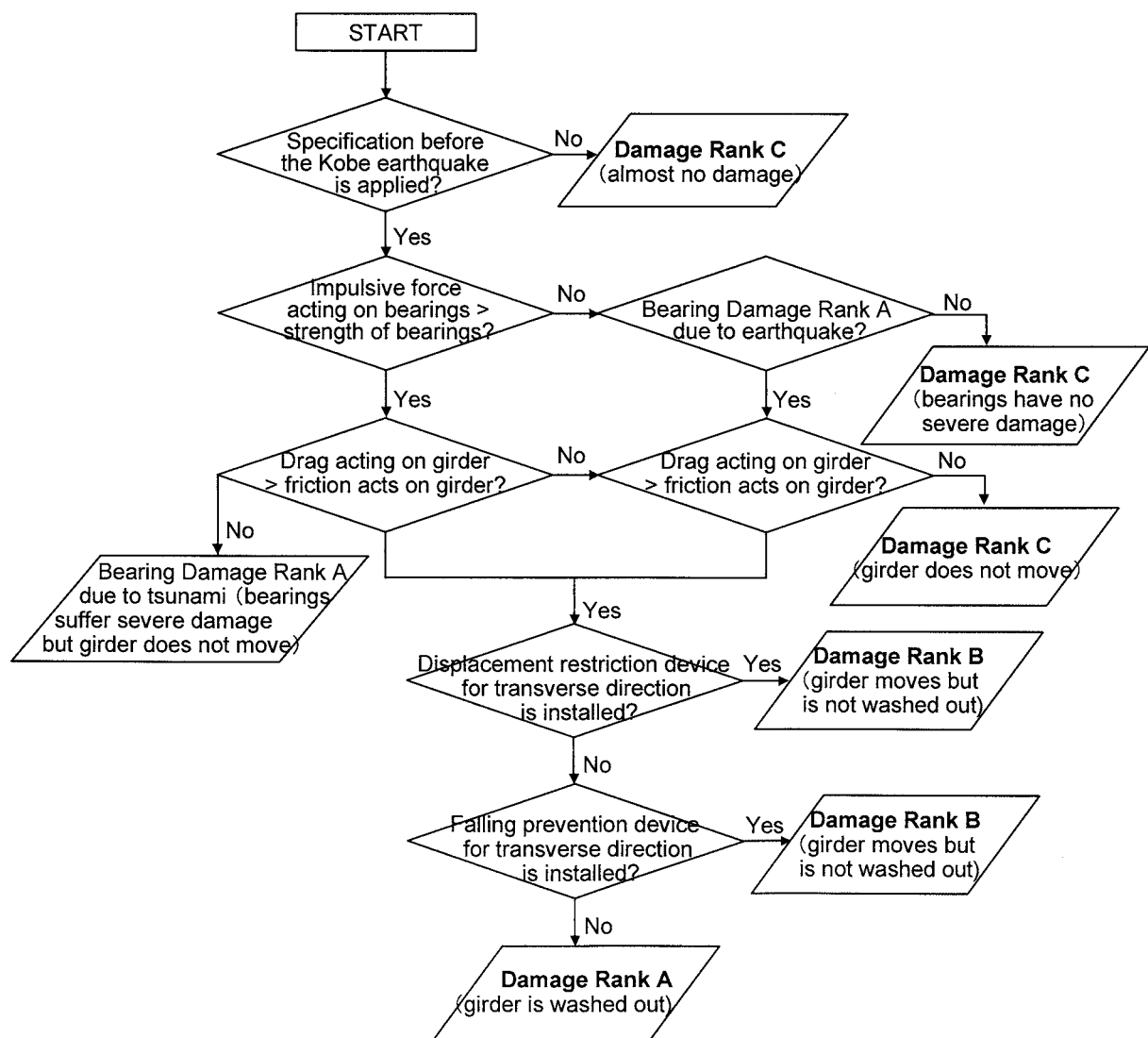


Figure 5: Flowchart for evaluation of tsunami damage to girder bridges. Damage rank A means severe damage including girder falling, B moderate damage, and C a little damage.

Figure 6 shows damage criteria for embankments due to tsunami overflow proposed by Shuto(1997) based on the data obtained from 17 road and railroad embankments damaged by tsunami in the past. We employ these criteria for evaluating tsunami damage to road embankments.

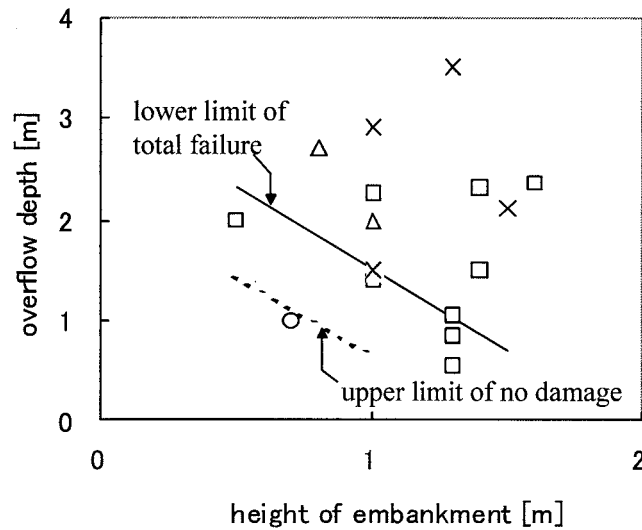


Figure 6: Damage criteria for embankment due to tsunami overflow (Shuto, 1997). The crosses, open triangles, open squares, and open circles denote total damage, major damage, partial damage, and no damage but inundation, respectively.

4. APPLICATION TO AN EARTHQUAKE-TSUNAMI DISASTER SCENARIO

We used the data of predicted ground motion and tsunami during a hypothetical Nankai earthquake ($M_w = 8.4$) provided by Kochi prefecture. Seismic damage to road bridges and road embankments were evaluated by the simple procedures proposed by Kobayashi and Unjoh (2005) and Public Works Research Institute (2003), respectively. Suzaki city, Kochi was chosen as the target area for developing an earthquake and tsunami disaster scenario because the city is predicted to have a large inundation area due to the tsunami of the Nankai earthquake. The locations of Suzaki city and source region of the Nankai earthquake are shown in Figure 7. The national highways in the area is administrated by Tosa National Highway Office, Shikoku Regional Development Bureau, Ministry of Land, Infrastructure and Transport.

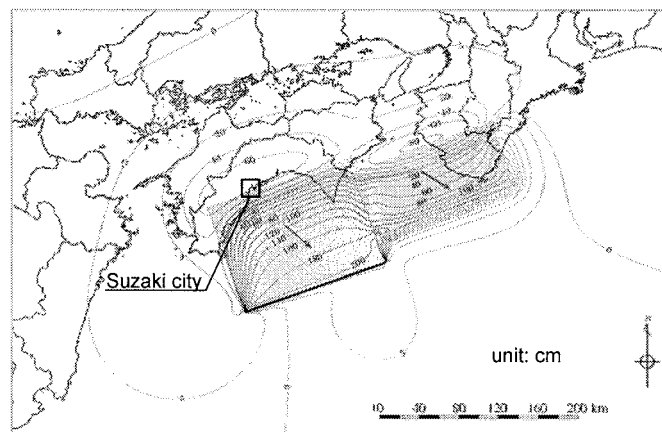


Figure 7: Locations of Suzaki city and the source region of the Nankai earthquake. Numbers in the figure denote vertical displacement due to fault slip.

Figure 8 shows the result of evaluating of earthquake and tsunami damage to road facilities and inundated road sections. There are three bridges evaluated to be Damage Rank A due to ground motion and two of them are located within the inundation area. These two bridges might hamper an urgent response and rehabilitation of the inundation area. Therefore, seismic retrofitting of the bridges in advance may be proposed to avoid such troubles.

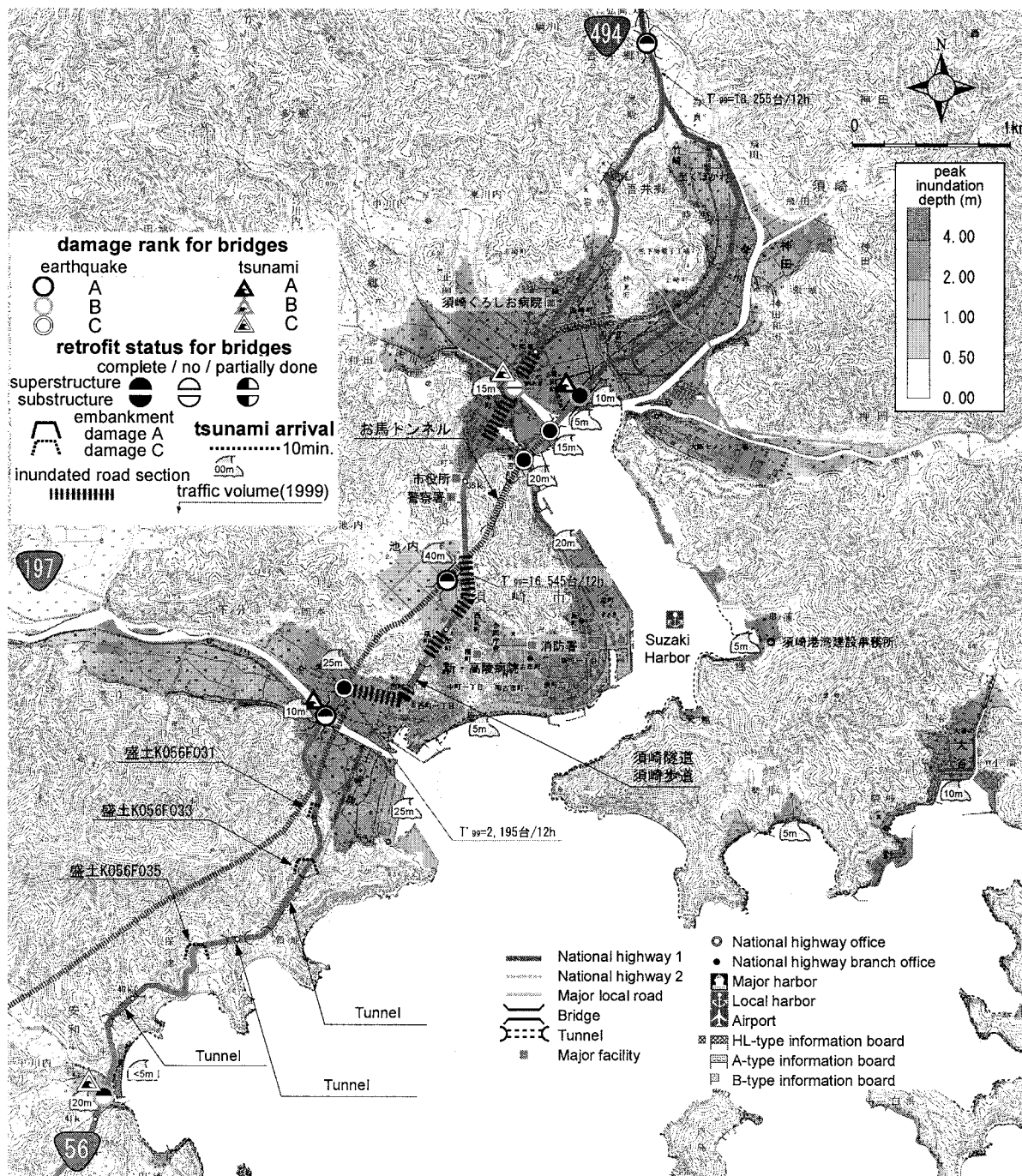


Figure 8: Disaster scenario map (draft) of Suzaki city, Kochi prefecture caused by the Nankai earthquake and its tsunami.

5. POLICY OF MEASURES FOR ROAD NETWORKS

Tosa National Highway Office and National Institute for Land and Infrastructure Management have been jointly investigating effective measures for road networks against earthquake-tsunami disasters. The measures include the tsunami information service, evacuation spaces and routes, emergency restoration plan, retrofitting plan for the bottleneck facilities that slow down the emergency restoration, and retrofitting and/or planning detours for improving the redundancy of the road networks. The outline of the policy of planning the above-mentioned measures is illustrated as Figure 9. The two organizations will discuss and conclude a practical plan of measures for the road network in the near future.

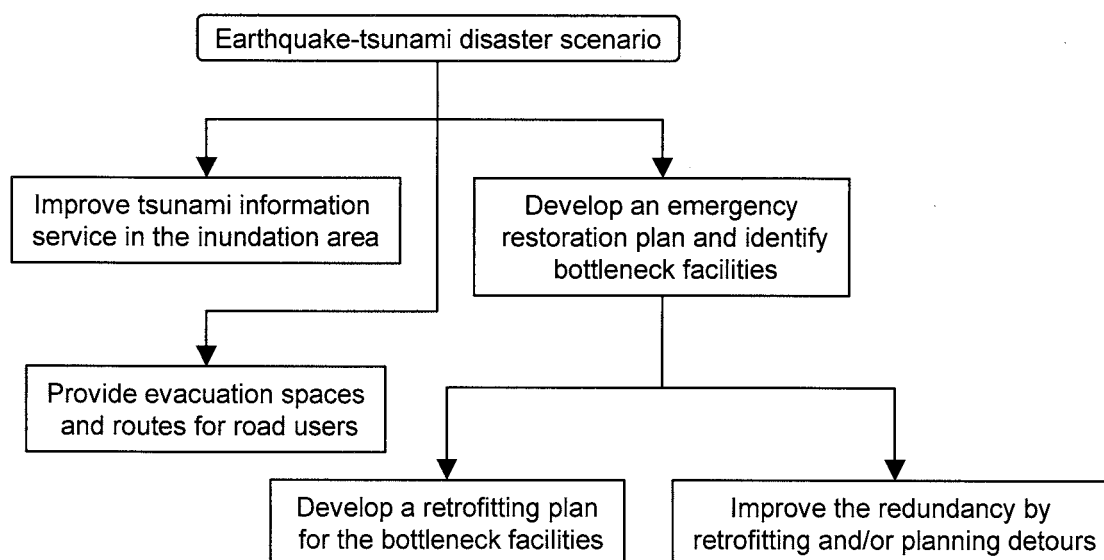


Figure 9: Outline of the policy of planning measures for road networks against earthquake-tsunami disaster based on a disaster scenario

6. CLOSING REMARKS

In this paper, an earthquake-tsunami disaster scenario that includes damage to a road network was presented. We have been studying the procedure for developing an integrated disaster scenario map that includes damage to coastal, port, and river facilities besides road facilities. The integrated map is expected to help us to develop a standard procedure for planning comprehensive earthquake-tsunami disaster measures, taking account of various possible problems.

Acknowledgements:

The author thank the Risk Management Division of Kochi Prefecture which provided the predicted ground motion and tsunami data, and the Shikoku Regional Development Bureau and Tosa National Highway Office which provided the data of the road facilities under their administration.

References:

- Japan Port and Harbour Association (1999): *Technical standards and commentaries of port and harbour facilities*.
Kobayashi, H. and Unjoh, S. (2005): Development of simplified seismic damage assessment method of road bridges based on past damage experiences, *Doboku Gijutsu Shiryou (Civil Engineering Journal)*, 47(12), 48–53.

- Public Works Research Institute (2003): A simple method for evaluation of seismic performance of road embankments (draft).
- Rabbat, B. G. and Russell, H. G. (1985): Friction coefficient of steel on concrete or grout, *J. Struct. Eng.*, ASCE, **111**(3), 505–515.
- Shuto, N. (1997): On traffic disorder after a tsunami attack, *Tsunami Engineering Technical Report*, **14**, 1–31.
- Unjoh, S. (2005): Damage to transportation facilities, *The damage induced by Sumatra earthquake and associated tsunami of December 26, 2004*, 66–76, <http://www.jsce.or.jp/committee/2004sumatra/report.htm>

DYNAMIC IMPACT OF TSUNAMI WATERBORNE MASSIVE OBJECTS ON STRUCTURES

M. A. K. M. Madurapperuma¹⁾, A. C. Wijeyewickrema²⁾ and K. Shakya³⁾

1) Graduate Student, Department of Civil Engineering, Tokyo Institute of Technology, Japan

2) Associate Professor, Department of Civil Engineering, Tokyo Institute of Technology, Japan

*3) Graduate Student, Department of Civil Engineering, Tokyo Institute of Technology, Japan
ma.k.aa@m.titech.ac.jp, wijeyewickrema.a.aa@m.titech.ac.jp, shakya.k.aa@m.titech.ac.jp*

Abstract: Tsunami field survey observations show that building destruction is often exacerbated by the impact of tsunami waterborne massive objects such as maritime cargo containers, small boats, automobiles, lumber and other debris. According to new tsunami resistant design concepts being proposed by different researchers, the lower level of the building should be elevated above the flood level by means of reinforced concrete piers or columns. It is of paramount importance to design these columns and piers to withstand dynamic impact loads of waterborne massive objects during a tsunami. In this paper dynamic impact on a reinforced concrete frame structure is considered by using an advanced fiber-based discretization model in OpenSees software. Parametric studies are conducted to investigate nonlinear structural response of the RC frame structure for impact due to shipping containers by changing the point of impact. In addition the dimensions of the impacted column are changed to study tsunami retrofitting. The retrofitted column shows that the structure will not collapse for the container masses considered. This will be useful for structural engineers to design tsunami resistant buildings in tsunami hazard zones particularly for buildings used for evacuation purposes.

1. INTRODUCTION

1.1 Background

The main issue associated with buildings within the tsunami hazard zones is to evaluate the design requirements for a structure to survive tsunami forces. Some of the main forces acting on structures due to tsunami are hydrostatic (vertical and lateral), hydrodynamic, impact, surge, wave and breaking wave loads (Yeh et al. 2005). Past tsunami field survey observations show that building destruction is often exacerbated by the impact of tsunami waterborne massive objects such as maritime cargo containers, small boats, automobiles, lumber and other debris. Many RC columns failed due to the impact of large and heavy objects in the tsunami debris as shown in Figure 1.

According to new tsunami resistant design concepts being proposed by different researchers, the lower level of the building should be elevated above the flood level by means of reinforced concrete piers or columns. An example of proposed multi-story building with concrete framework and open space at the first floor level is shown in Figure 2. Since there are no infill walls between the columns, the water pressure is equalized all around the column and therefore, the failure could occur entirely due to the impact of tsunami waterborne massive objects. It is of paramount importance to design these columns and piers to withstand impact loads of waterborne massive objects in the event of a tsunami.

Impact loading is a special case of impulsive loading, which in turn is a particular case of dynamic loading. In this type of loading, load reaches maximum value instantaneously and remains for a very

short time and structures will not behave elastically under such loadings. Structural design codes do not provide sophisticated provisions for dynamic impact loads due to tsunami waterborne massive objects when designing structures located in potential tsunami hazard zones. Therefore, a complete assessment of the tsunami resistant design of RC structures often requires a nonlinear dynamic analysis.

Numerical modeling of dynamic impact on structures due to waterborne massive objects is complex because of associated uncertainties in determination of the maximum impact force and the impact duration. Substantial amount of research is reported on the effect of impact loading on RC elements. For instance, Haehnel and Daly (2002) developed a one-degree of freedom model of a collision between woody debris and a rigid structure. The proposed model has been verified with series of laboratory tests and test results are discussed in detail. Haehnel and Daly (2004) used experimental procedures to estimate the maximum impact force of woody debris on floodplain structures. Series of laboratory tests were performed to investigate the effect of collision geometry and construction material of the structure face on the impact force. Consolazio and Cowan (2005) considered dynamic impact on bridge piers due to the collision from transport vessels such as barges. However, the authors have not come across any rigorous analysis or accurate quantitative prediction regarding the study of RC structures under impact loading due to tsunami waterborne massive objects. More advanced method should be used to model the dynamic impact on RC structure in order to design impact resistant buildings in tsunami inundation zones.



Figure1. Damage due to Impact of Waterborne Massive Objects of the Tsunami caused by the Sumatra-Andaman Earthquake of December 26, 2004 (Ghobarah et al. 2006).

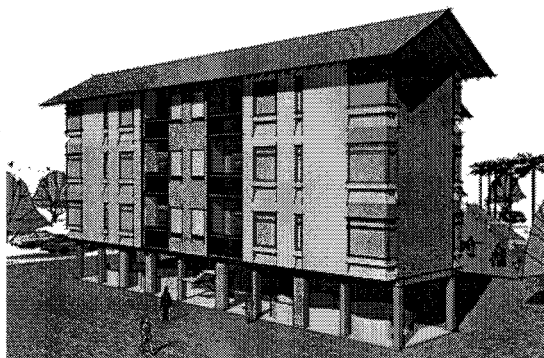


Figure 2. A Proposed Multi-Story Building with Concrete Framework and Open Space at the First Floor Level.

1.2 Scope and Objectives of Research

Dynamic impact on RC frame structure due to tsunami waterborne massive objects is considered in this paper by using an advanced fiber-based discretization model in OpenSees software. OpenSees (2006) is an advanced object-oriented framework for finite element analysis developed by the University of California, Berkeley. The force-based formulation implemented in OpenSees is an advance application of the fiber-section model in that a force-based formulation is used to facilitate the

modeling of the spread of plasticity along the member. Parametric studies are conducted to investigate nonlinear structural response of the RC frame structure for impact due to shipping containers, by changing the point of impact. In addition the dimensions of the impacted column are changed to study tsunami retrofitting. This will be useful for structural engineers to design tsunami resistant buildings in tsunami hazard zones particularly for buildings used for evacuation purposes.

2. STRUCTURAL MODELING

2.1 Building Design

The building considered is a three dimensional school building that can also be used for evacuation purposes in the event of a tsunami. The building is a RC frame structure with three stories and two bays. The first floor is open space with only columns allowing free flow of tsunami waves as shown in Figure 3(a). The live load of 4 kN/m^2 is considered on floor and roof slabs since the building is to be used for evacuation purposes. The frame structure is designed according to the RC design code, BS 8110-1:1997 using SAP2000. The required dimensions of columns and beams as well as quantity of reinforcements for the 2D frame structure are given in Figure 3(b).

2.2 Structural Model for Impact Simulation

Dynamic impact simulation is carried out using two-dimensional structural frame shown in Figure 3(b). The frame structure consists of beams and columns, and modeled as one-dimensional distributed plasticity type elements connected at nodes. These elements take into account spread of inelastic behaviour both over the cross-section and along the deformable region of the member length (Mazzoni et al. 2006). In order to accurately model the actual behaviour of the column in the area that impact takes place the deformable height of the column is divided into number of elements. The cross-section analysis that is performed at the control sections (integration points) is based on the fiber model. This will be described in detail in the next section. The gravity loads on 2D frame are calculated based on the geometry of the frame structure in the building model. The lumped mass approximation is considered and the mass of the structure is taken as $M = (G + 0.3Q)/g$ where G is the gravity load, Q is the live load and g is the gravitational constant (Karayannis and Favvata, 2005).

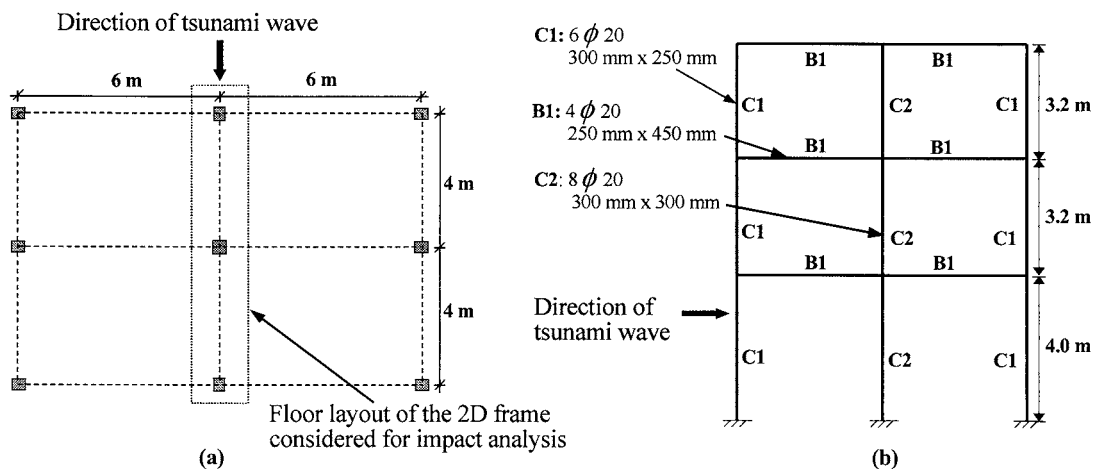


Figure 3. (a) Building First Floor Layout, and (b) Structural System and Column/Beam Reinforcement of 2D Frame.

2.3 Fiber-based Discretization

Recent advances in modeling the inelastic behaviour of RC structures subjected to dynamic loads involve the use of a fiber-based discretization of the member cross-section along the member length. Fiber models offer reliable nonlinear algorithms for their implementation in the nonlinear dynamic

impact analysis of RC structures that might experience considerable local damage and partial loss of load carrying capacity. In the fiber models the element is subdivided into longitudinal fibers, and the geometric characteristics of the fiber are its location in the local coordinate system and the fiber area. The nonlinear/inelastic behaviour of a fiber section is defined by the stress-strain response of the materials used to define it. The inelastic materials are assigned to each layer of fibers (steel) and patch of fibers (concrete) in the section. The material properties are defined independently for confined core concrete and unconfined cover concrete. Therefore, a fiber-section model relies entirely on the ability of material properties to represent the overall inelastic behaviour of the member. Material nonlinearity can take place at any element section and the flexural and axial behaviour of the element are derived by integration of the section response. Only the selected sections at the integration points are monitored during the numerical integration (Mazzoni et al. 2006).

3. ESTIMATING TIME HISTORY OF IMPACT FORCE

Estimating the maximum impact force on the structure is complex because the force is influenced by the properties of the waterborne object, particularly its mass, velocity and orientation on impact, and the properties of the structure itself, especially its stiffness and inertia. In the present study, the recommendations of FEMA (2000) are followed. The determination of maximum impact force is based on momentum approach that equates the momentum of the waterborne object and the impulse imparted on the structure. Hence, the maximum impact force F_I can be expressed as

$$F_I = m \frac{u}{\Delta t} \quad (1)$$

where m is the mass of the waterborne object, u is the velocity before impact and Δt is the duration of impact (pg 23, FEMA 2000).

The velocity of the waterborne object u is assumed to be the same as the tsunami velocity u_t . The estimation of tsunami velocity u_t in coastal tsunami hazard zones is subject to considerable uncertainty. Due to associated uncertainties about direction, topography, distance from the shoreline and proximity to other buildings or obstructions tsunami velocity u_t in a tsunami inundation zone is calculated from

$$u_t = 2\sqrt{gd} \quad (2)$$

where d is the inundation depth and g is the gravitational constant (pg 10, FEMA 2000).

Tsutsumi et al. (2000) reported that for a tsunami inundation depth of more than 4.5 m the maximum tsunami velocity was in the range of 10-18 m/s, which is in agreement with Eq. 2.

Uncertainty about the duration of impact, i.e. the time from initial impact, through the maximum deflection caused by the impact, to the time the object leaves, is influenced primarily by the natural frequency of the building, which is a function of the building's stiffness. For the present analysis impact duration is taken as 0.1 s (pg 24, FEMA 2000). Here the shape of the impact load time history is assumed to be triangular shape. Consolazio and Cowan (2005) who modeled barge collisions and Yukihiro et al. (2000) who considered aircraft impact on buildings also assumed a triangular shape.

4 NUMERICAL RESULTS

The frame structure is modeled in OpenSees using element "nonlinear beam column" which is a distributed plasticity type element, with fiber sections accounting for the spread of plasticity along the member length. The material type Concrete02 and the material type Steel02 are used to define material

properties for concrete and steel, respectively. The material parameters are defined independently for confined core concrete, unconfined cover concrete and steel (Tables 1-2). The material parameters for an elastic section are given in Table 3. The Rayleigh damping parameters are calculated with a 5% damping ratio. Dynamic analyses are performed using the Modified Newton solution algorithm and the Newmark method for time integration with $\beta = 0.25, \gamma = 0.5$. The time step is taken as $\Delta t = 0.0005$ s for all analyses.

Table 1. Material Properties for Concrete.

Concrete Material Properties	Unconfined Cover Concrete	Confined Core Concrete
Maximum compressive stress (N/mm ²)	25	32.5
Maximum compressive strain	0.003	0.00275
Ultimate stress (N/mm ²)	5.0	6.5
Ultimate strain	0.01	0.05497
Ratio between unloading slope and loading slope	0.1	0.1
Tensile strength (N/mm ²)	3.5	4.55
Tension softening stiffness (N/mm ²)	1750	1750

Table 2. Material Properties for Steel.

Yield stress (N/mm ²)	460
Modulus of elasticity (N/mm ²)	200,000
Strain hardening ratio	0.01

Table 3. Elastic Section Properties for Concrete.

Compressive stress (N/mm ²)	30
Elastic modulus (N/mm ²)	23,650

Numerical implementation of dynamic impact on 2D RC frame structure in OpenSees is compared with SAP2000 when homogeneous concrete sections with elastic parameters (Table 3) are considered. The results show a good agreement of displacement response (Figure 4). Since fiber-section model relies entirely on the ability of material properties used to define it to represent the overall inelastic behaviour of the member, the OpenSees fiber model results deviate from SAP2000 results as expected.

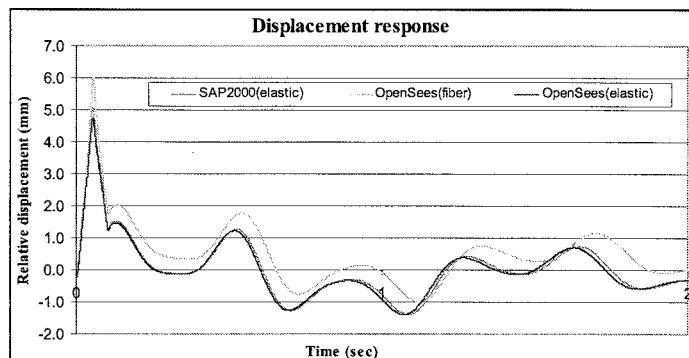


Figure. 4. Comparison of Displacement Time Histories for 2000 kg Mass Container Impacting at 2.0 m above Ground Level.

Displacement response and shear response at the impacted point of the column are investigated using different masses of watertight containers ranging from 2000-3500 kgs. This range of mass includes tare mass (i.e., mass of empty container) of 6.0 m × 2.4 m × 2.6 m box container (i.e., 20' box) plus its half loaded contents (Export 911, 2007). It is assumed that the container carried by tsunami impacts the column at the water level. The calculated maximum impact forces are given in Table 4.

Table 4. Maximum Impact Force (kN) for different Masses and Water Depths.

Water Depth from GL (m)	Container Velocity (m/s)	Mass of Container			
		2000 kg	2500 kg	3000 kg	3500 kg
2.0	8.86	177	221	266	310
3.0	10.85	217	271	325	380
3.5	11.72	234	293	352	410
4.0	12.53	251	313	376	438

All displacements are relative to the ground. The displacement response and shear response are presented in Figure 5.

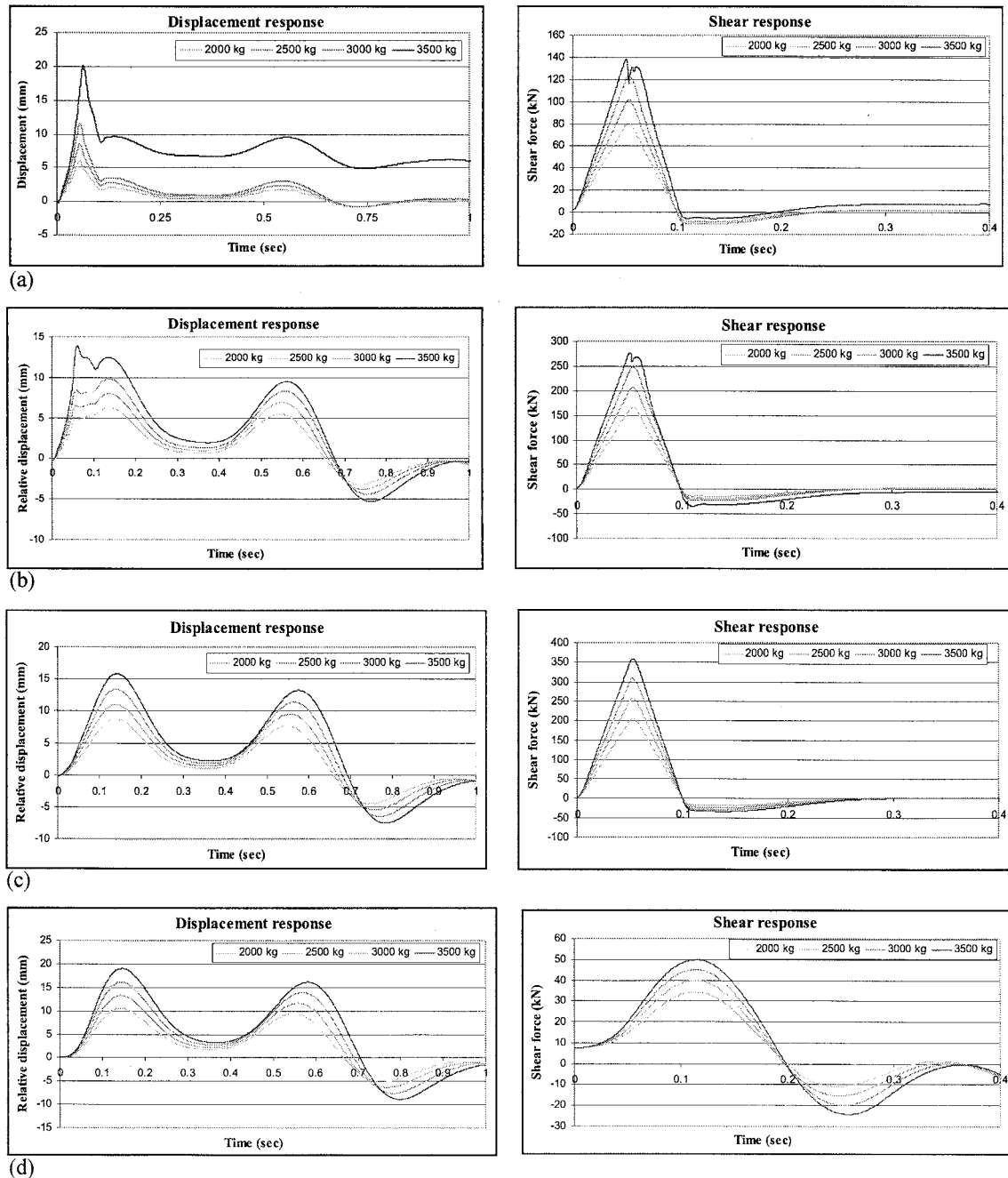


Figure 5. Displacement and Shear Response at different Heights above Ground Level (m): (a) 2.0 (b) 3.0 (c) 3.5, and (d) 4.0 (First Floor Level).

The shear response of the impacted cross-section follows a similar trend of the impact load time history for the impact duration in Figures 5(a), (b) and (c). The shear force in Figure 5(a) and (b) increases with increase in impact force up to certain magnitude and sudden drop of shear force can be observed. The section at the impacted point reaches to the nonlinear stage and local failure of the column by cracking of concrete can be expected. Figure 5(d) indicates that the shear force at the impacted cross-section is smaller when the container impacts the column at the floor level because the impact load directly transfers to other columns through beams of the frame structure.

Figure 6 show the response behaviour after the seaside corner column (C1) is replaced with mid column (C2) section properties. This can be considered as a tsunami retrofit of the building. The column displacement at the impacted point reduced by 32% after retrofitting (Figure 6(a)). The shear force and moment time histories of the impacted cross-section after retrofitting have a triangular shape similar to the impact load time history for the impact duration (Figures 6(b)-(c)).

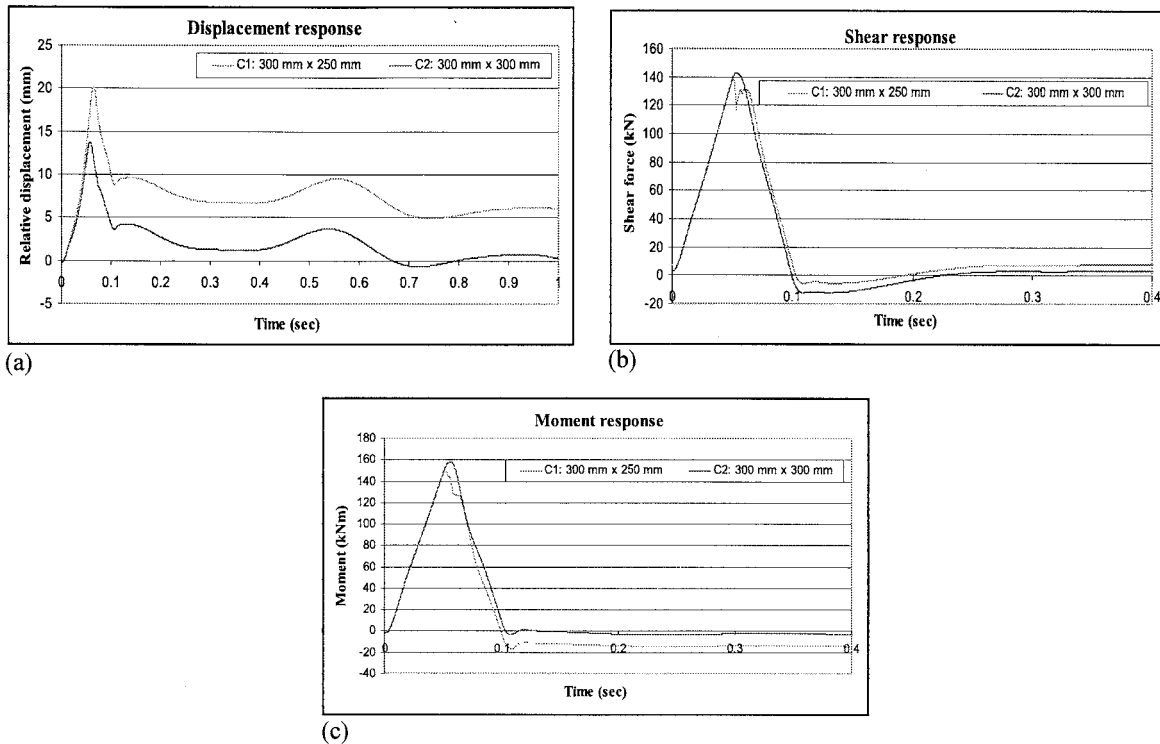


Figure 6. (a) Displacement Response, (b) Shear Response, and (c) Moment Response: at 2.0 m above Ground Level for 3500 kg Container after Retrofitting.

3. CONCLUSIONS

The dynamic impact of tsunami waterborne massive objects on a 2D RC frame structure is carried out using fiber-based discretization using OpenSees software. Displacement response and shear response of a ground floor seaside corner column is investigated using different watertight containers as the massive waterborne objects carried by tsunami. It is observed that impact at the mid section of the column is more critical than impact close to the floor level. The retrofitted column shows that the structure will not collapse for the container masses considered. More studies and research are needed to verify the validity of the assumptions made regarding impact load time history and the location and orientation of the impact. Furthermore, multiple impacts, 3D effects and distributed impact need to be consider in order to accurately simulate the dynamic impact on RC structures from tsunami waterborne massive objects.

Acknowledgements:

The first and the third authors gratefully acknowledge Monbukagakusho scholarships for master students from the Japanese government. The authors are very grateful to Prof. Tatsuo Ohmachi, COE Program Leader of Center for Urban Earthquake Engineering (CUEE), Tokyo Institute of Technology, and Prof. Kohji Tokimatsu, COE Program Sub-leader of CUEE, for their advice and support. Financial support from CUEE is gratefully acknowledged.

References:

- BS 8110 (1997), "Structural Use of Concrete," Part 1: Code of Practice for Design and Construction, British Standard Institution.
- Consolazio, G. R. and Cowan, D. R. (2005), "Numerical Efficient Dynamic Analysis of Barge Collisions with Bridge Piers," *Journal of Structural Engineering*, ASCE, **131**(8), 1256-1266.
- Export 911 (2007), "Container Dimensions and Capacity," Shipping department, <<http://www.export911.com/e911/ship/dimen.htm>> (Jan. 30, 2007).
- FEMA (2000), "Determining Site-Specific Loads," FEMA 55, Coastal Construction Manual, **2**, ch.11.
- Ghobarah, A., Saatcioglu, M. and Nistor, I. (2006), "The Impact of the 26 December 2004 Earthquake and Tsunami on Structures and Infrastructure," *Engineering Structures*, **28**, 312-326.
- Haehnel, R. B. and Daly, S. F. (2004), "Maximum Impact Force of Woody Debris on Floodplain Structures," *Journal of Hydraulic Engineering*, ASCE, **130**(2).
- Haehnel, R. B. and Daly, S. F. (2002), "Maximum Impact Force of Woody Debris on Floodplain Structures," Rep. No. ERDC/CRREL TR-02-2, USA Cold Regions Research and Engineering Laboratory, Engineering Research and Development Center, Hanover, N.H.
- Karayannis, C. G. and Favvata, M. J. (2004), "Earthquake-induced Interaction between adjacent Reinforced Concrete Structures with Non-equal Heights," *Journal of Earthquake Engineering and Structural Dynamics*, **34**, 1-20.
- Mazzoni, S., McKenna, F., Scott, M. H., Fenves, G. L. (2006), "OpenSees Command Language Manual", Pacific Earthquake Engineering Research Center, University of California at Berkeley, <<http://opensees.berkeley.edu/OpenSees/manuals/ExamplesManual/HTML/>>.
- OpenSees (2006), "Open System for Earthquake Engineering Simulation," Version 1.7.3, Pacific Earthquake Engineering Research Center, University of California at Berkeley, Open source software available at: <<http://opensees.berkeley.edu>, 2006>.
- Tsutsumi, A., Shimamoto, T., Kawamoto, E. and Logan, J. M. (2000), "Nearshore Flow Velocity of Southwest Hokkaido Earthquake Tsunami," *Journal of Waterway Port Coastal, and Ocean Engineering*, **126**(3).
- Yeh, H., Robertson, I. and Preuss, J. (2005), "Development of Design Guidelines for Structures that Serve as Tsunami Vertical Evacuation Sites," *Open File Report 2005-4*, Washington State Department of Natural Resources, 33 pp.
- Yukihiro, O., Eiji, F., Norihide, K., Hiroshi, M. and Ryusuke, F. (2000), "Structural Responses of World Trade Center under Aircraft Attacks," *Journal of Structural Engineering*, ASCE, **131**(1).

ADVANCED DAMAGE DETECTION FOR HURRICANE KATRINA INTEGRATING REMOTE SENSING AND VIEWSTTM FIELD RECONNAISSANCE

Beverley J. Adams¹⁾, J. Arn Womble²⁾, and Ronald T. Eguchi³⁾

1) Managing Director, ImageCat Ltd, London, UK

2) Consultant, LNSS, Lubbock, Texas, USA

3) CEO, ImageCat, Inc., Long Beach, California, USA

bja@imagecatinc.com, ArnWomble@aol.com, rte@imagecatinc.com

Abstract: This paper discusses the use and deployment of remote sensing technologies to quantify the extent of damage from storm surge and flooding after Hurricane Katrina. Damage results are presented at several different levels including regional and neighborhood levels. The work presented in this paper is significant in that it represents the first comprehensive assessment of impacts caused by multiple hazards in a catastrophic natural hazard event. This work was sponsored by the National Science Foundation through a grant made to the Multidisciplinary Center for Earthquake Engineering Research, now officially known as MCEER (EEC-9701471).

1. INTRODUCTION

In the aftermath of extreme events such as Hurricane Katrina, the rapid and accurate characterization of the extent and severity of urban damage is a high priority. Timely damage data generated through reconnaissance activities, provide critical decision support for numerous applications, ranging from emergency response to loss estimation. It is increasingly recognized that advanced technologies such as remote sensing and GIS have key roles to play in rapid damage assessment, providing a holistic perspective of damage sustained in locations that are often inaccessible for a number of days after the event.

Researchers working under MCEER's Thrust Area 3 Program (Response and Recovery) have made significant progress with the development of remote-sensing-based damage detection methodologies. The 1999 Marmara (Turkey) earthquake constituted the initial implementation of moderate-resolution imagery for detecting urban damage within the cities of Golcuk and Adapazari (Eguchi et al., 2000; Adams, 2004; and Huyck et al., 2004). The 2003 Boumerdes (Algeria) and Bam (Iran) earthquakes in turn marked the primary deployment of high-resolution imagery for building damage assessment (Adams, 2004; Adams et al., 2004a; Gusella et al., 2004; Yamazaki et al., 2005; Vu et al., 2006). From a multi-hazard standpoint, the 2004 U.S. hurricane season saw the first utilization of high-resolution QuickBird and IKONOS satellite imagery for assessment of windstorm damage (Adams et al., 2004b, 2004c; Womble et al., 2005a; Womble, 2005)

and for mapping effects of the Indian Ocean tsunami (Adams et al., 2005a, 2005b; Chang et al., 2006; Ghosh et al., 2005).

Hurricane Katrina in 2005 presented a unique opportunity to apply previous damage detection research findings in a multi-hazard context. The present paper describes the implementation of selected remote-sensing datasets for identifying urban damage caused by:

1. Storm surge, and
2. Flood inundation

This paper discusses the investigations that were conducted by MCEER researchers to quantify the damage caused by storm surge and flooding after Hurricane Katrina using a variety of remote sensing technologies. This paper extracts material from a more comprehensive report prepared by the first two authors of this paper (Womble et al., 2006)

2. DAMAGE ASSESSMENT

The implementation of moderate and very-high-resolution imagery for post-earthquake damage detection may be conceptualized within a three-stage Tiered Reconnaissance System, see Figure 1. Regional information garnered from Tier 1 guides the identification of severely impacted areas for the focus of Tier 2. Tier 2 (neighborhood) findings offer guidance for detailed study-site selections undertaken in Tier 3.

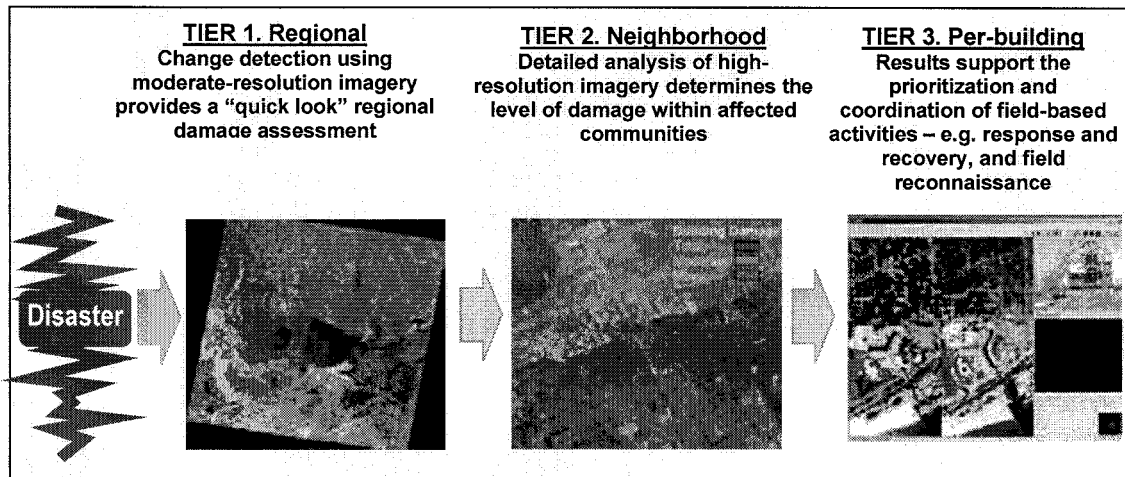


Figure 1. Schematic Representation of the Post-Disaster Tiered Reconnaissance System

In terms of advanced technology implementation, at Tier 1 moderate-resolution sensors such as Landsat-5 Thematic Mapper™ offer a “quick-look” region-wide perspective for establishing the broad scale extent of the event (Adams 2004; Adams et al., 2005a, b). At Tier 2, high-resolution imagery next distinguishes both the hardest-hit and lesser-affected neighborhoods (e.g., Adams et al., 2004a; Saito et al., 2004; Chiroiu et al., in press). At Tier 3, high-resolution imagery guides detailed site selection to the level of individual buildings. In the specific case of damage assessment, Tier 3 technology may further facilitate structural damage assessment through expert

interpretation (Womble 2005) and its integration into field-reconnaissance tools such as VIEWS™ (Adams et al., 2006).

The remaining discussions center on specific investigations that were carried out by the research team to quantify damage caused by storm surge and flooding after Hurricane Katrina.

2.1 Storm Surge (Mississippi Coast)

From the suite of remote sensing datasets, a combination of moderate and high-resolution imagery was used to provide first a *region-wide* and then a more detailed *neighborhood-scale* perspective on storm surge damage.

2.1.1 Region-wide Damage Detection Using Landsat-5 Imagery

Moderate spatial resolution and extensive geographic coverage afforded by Landsat-5 Thematic Mapper (TM) imagery provides a holistic perspective of post-disaster damage. Although Landsat-7 ETM imagery offers greater detail for the same extent, failure of the scan line corrector in 2003 limits the use of this data, due to the presence of ‘no-data’ gaps (appearing as black lines in the imagery).

Landsat-5 TM imagery was captured immediately after Hurricane Katrina on August 31, with the next overpass occurring on September 16, 2005. However, as shown by Figure 2, the coverage from August 31 was subject to considerable cloud cover, and as such proved to be of limited value for storm-surge damage detection. The analysis instead employed the next available dataset, together with pre-storm imagery dating from May 27, 2005.

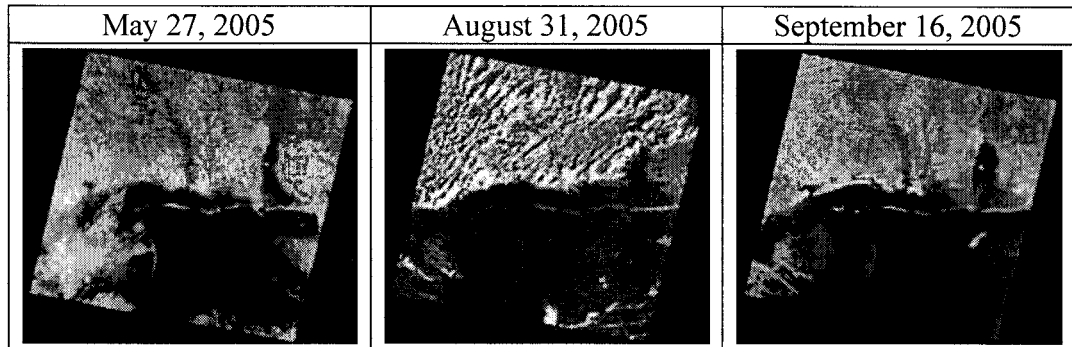


Figure 2. Pre- and post-Katrina Landsat-5 TM imagery (Path 21 Row 39) used to detect storm surge damage in Mississippi (Landsat imagery from USGS and NASA).

From a methodological standpoint, Figure 3 outlines the multi-temporal change detection algorithm used to locate the hardest hit areas. Originally developed to detect inundated coastal tracts in the aftermath of the December 2005 Indian Ocean tsunami (Adams et al., 2005b, Chang et al., 2006), the algorithm identifies urban damage as a function of changes in land surface cover between the pre- and post-disaster images.

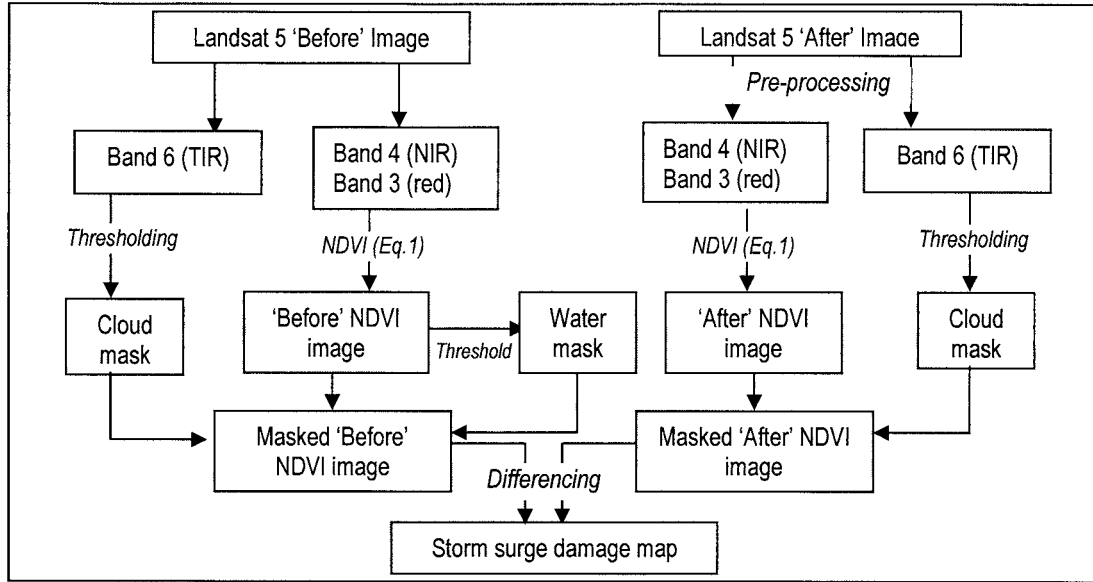


Figure 3. Methodology employed for region-wide storm surge damage detection.

Following an initial pre-processing registration step to ensure spatial alignment of the pre- and post-storm images, landcover is effectively quantified using the Normalized Difference Vegetation Index (NDVI). From Equation 1, the NDVI is defined as the ratio between spectral information contained in Landsat-5 TM near-infrared (NIR) and red bands.

$$NDVI = \frac{(Near-infrared) - (Red)}{(Near-infrared) + (Red)} \quad (1a)$$

$$NDVI = \frac{(Landsat-5 TM Band 4) - (Landsat-5 TM Band 3)}{(Landsat-5 TM Band 4) + (Landsat-5 TM Band 3)} \quad (1b)$$

To minimize the occurrence of false positives, potential non-damage-related sources of change were eliminated by masking. A cloud mask was obtained by thresholding Landsat-5 TM Band 6, which records thermal-infrared (TIR) emissions. Clouds have a distinctive signature within TIR imagery, recording a characteristically low value, as they are cold compared with the earth's surface. Water surfaces are another potential source of change, due to differences in tidal height, surface illumination and roughness. A water surface mask was obtained by thresholding the 'before' NDVI image. Since flooding can be a bonafide source of damage in hurricane affected areas, the water mask was not applied to the 'after' images. Adjusted 'before' and 'after' NDVI images were produced by applying the respective masks. The extent of damage created by the storm surge was finally determined as a function of the difference (computed as 'after' – 'before') between the adjusted NDVI scenes.

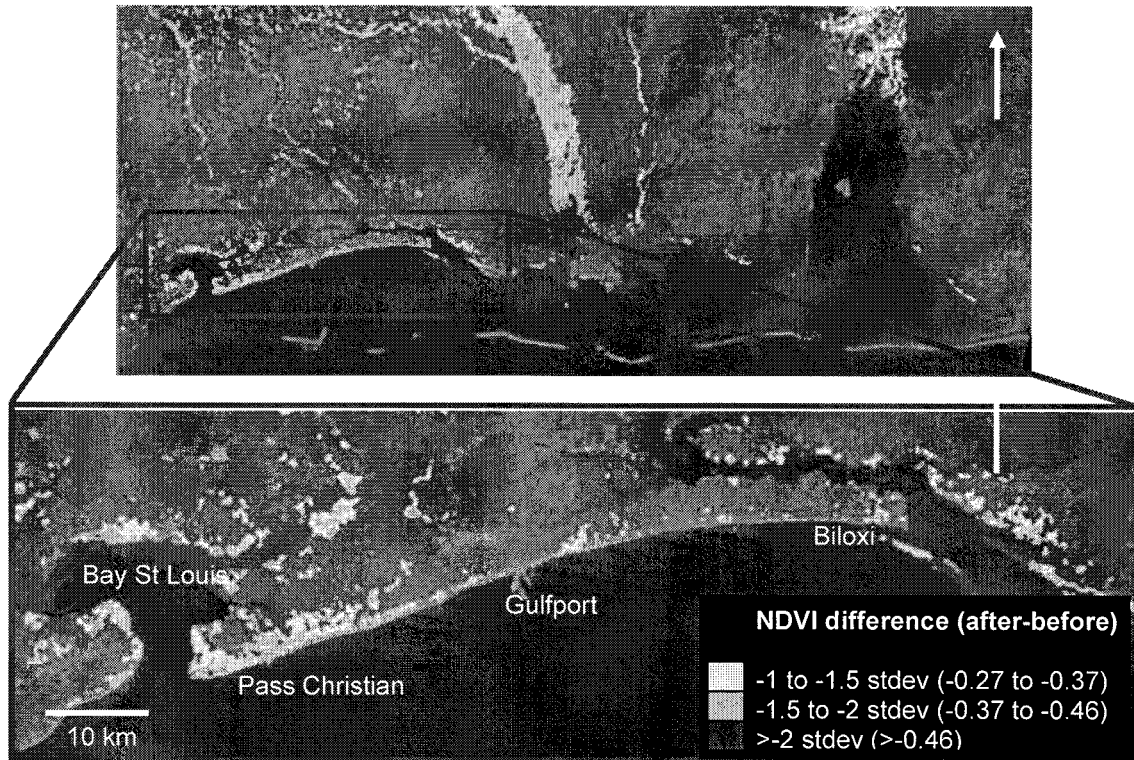


Figure 4. Region-wide storm surge damage map for the Mississippi coast. Damage is measured in terms of change in NDVI between pre- and post-hurricane Landsat-5 TM images. Extreme changes are evident within a narrow coastal strip between Biloxi and Bay St. Louis where coastal development has been replaced by bare soil and debris (Landsat imagery from USGS).

Figure 4 summarizes the results obtained. Measured in terms of standard deviation about the image-wide mean, extreme changes in NDVI are evident along the Mississippi coastline between Biloxi and Bay St. Louis. The negative difference indicates that NDVI readings are lower in the 'after' than in the 'before' image. This finding suggests that the surface has experienced extreme scouring, with the urbanized environment of buildings, roads, and vegetation replaced by bare soil and debris. A similar reduction in NDVI was observed along the tsunami-affected coast of Thailand where the land surface was scoured and buildings were destroyed by the high-velocity tidal wave (Adams et al., 2005a).

Despite the application of cloud and water masks to the NDVI scenes, other sources of significant change are also apparent. The waterways of the Pascagoula, Mobile, and Tensaw Rivers also exhibit a major reduction in NDVI between the pre- and post-hurricane images. From visual inspection, these areas comprise wetland vegetation rather than urban landuse. According to experts at the Mississippi Department of Marine Resources (G. Larsen, personal communication), this reduction in spectral response from the wetland vegetation may be attributable to a combination of browning and leaf loss induced by the windstorm and to blanketing debris. To minimize the effect of this ecologically-based source of change, MCEER researchers at ImageCat surmised that an additional non-urban mask should be applied to subsequent analyses.

2.1.2 Neighborhood Damage Detection Using NOAA Aerial Photography

High-resolution aerial photography captured by NOAA in the days following the hurricane provides a valuable neighborhood-scale perspective on damage within the storm-surge affected regions stretching from Bay St. Louis/Waveland to Biloxi. This imagery was rapidly posted on the NOAA website in non-georeferenced format. Figure 5 includes a sample of the NOAA coverage for Biloxi. From visual inspection, the surge-affected region is characterized by a significant increase in exposure of the underlying ground surface, where features of the urban landscape ranging from buildings to roads and vegetation have been removed. This serves to verify findings from the NDVI region-based analysis that scouring by the incoming wave replaced coastal developments with little more than bare soil and debris.



Figure 5. Sample of NOAA aerial imagery (ID 24330689) at Gulfport, Mississippi.

Figure 6 summarizes the methodology employed for damage assessment. To delineate the position of the surge line, and thereby identify neighborhoods experiencing a high proportion of collapsed structures, MCEER researchers at ImageCat began by downloading and archiving the online NOAA database, which initially comprised ~350 (and was subsequently expanded to several thousand) images, using a proprietary routine. The archived images were then georeferenced using an accompanying file comprising limited geospatial information for each scene. Since these data had insufficient “header” information to perform standard registration procedures, warping, and geo-referencing procedures, a custom “NOAA-Reg” algorithm was developed to generate new positional information.

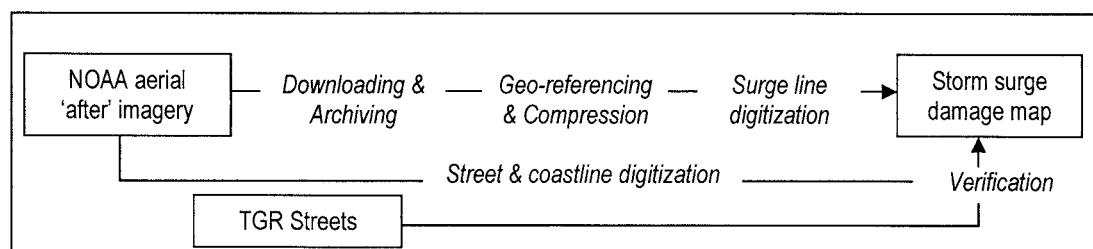


Figure 6. Methodology employed for neighborhood-scale storm-surge damage detection.

A “high confidence” surge line was delineated within coastal communities, based on expert interpretation of the georeferenced NOAA imagery on a frame-by-frame basis. Figure 7 shows that the Mississippi coast was divided into seven tracts comprising multiple frames of NOAA data, running from Biloxi in the east through to Pass Christian in the west. This division was necessary to maintain efficiency of the digitization process, given the large number of images involved. Finally, the surge lines for the respective frames within the seven tracts were fused together using GIS-based integration functions.

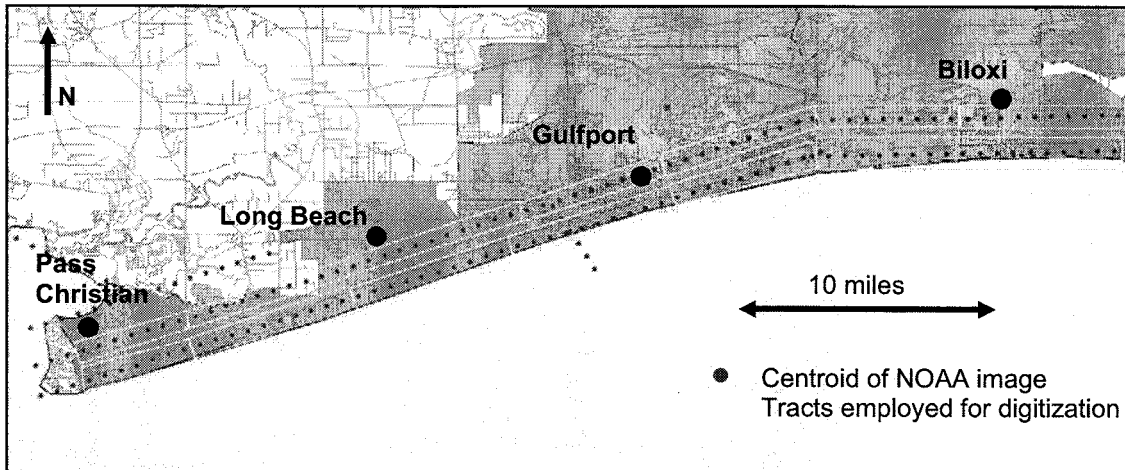


Figure 7. NOAA aerial coverage for the Mississippi Coast, divided into seven tracts for efficient digitization of the storm surge line.

During the surge-line delineation, a series of ‘quality control’ features were identified within each frame, including the coastline and street networks (as shown in Figure 8). To serve as independent verification that the NOAA coverage and surge line were correctly scaled and positioned, these control features were compared against the TIGER street network database (U.S. Census Bureau, 2002).

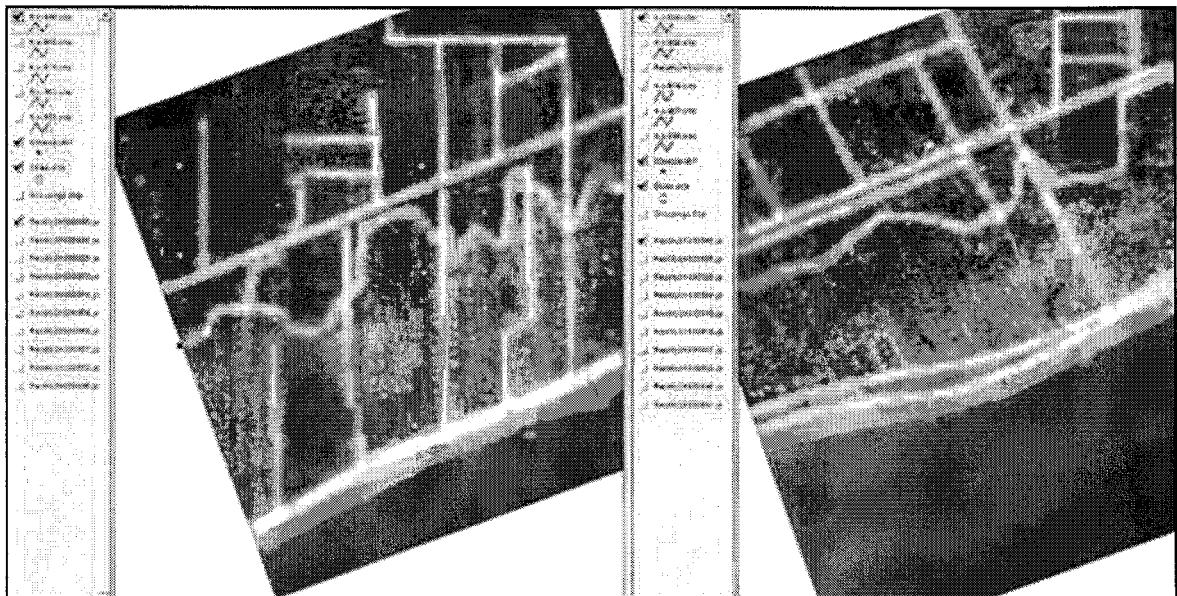


Figure 8. Extraction of “quality control” features within surge-affected regions to verify the geographic accuracy of the surge line (Base images from NOAA).

The damage assessment results shown in Figure 9 indicate that the entire coastal strip between Pass Christian and Biloxi was affected by the storm surge. On average, the most extreme damage where 90-100% of buildings were completely destroyed occurred within about 1 mile of the shore. In many locations, the landward limit of this devastation zone is demarcated by a wide debris line comprising housing materials and scoured vegetation. From visual inspection during the digitization process, particular land surface features served to mitigate the effect of the surge. For example, the debris line fell seaward of the average position where densely vegetated areas such as woodland were encountered. Also, large buildings such as factories and warehouses appeared to partially divert the incident surge, affording some protection to other building situated in their wake.

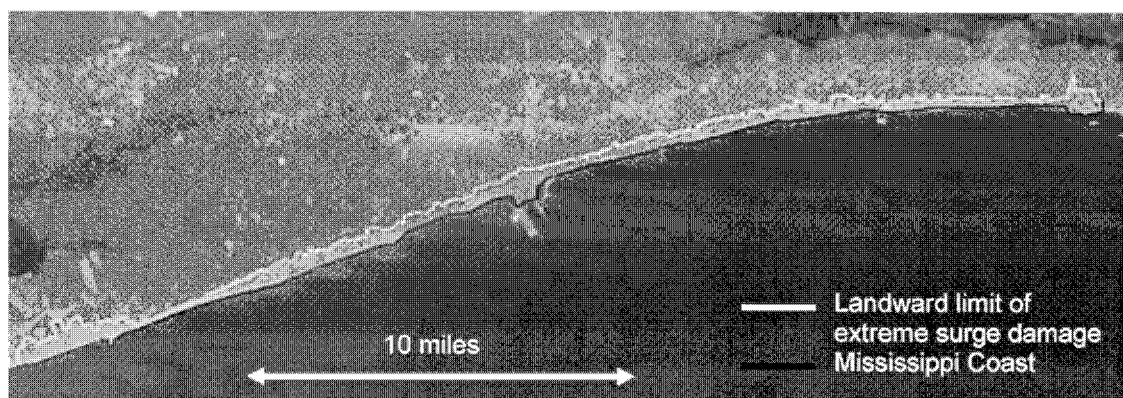


Figure 9. Mississippi coastal zone between Pass Christian and Biloxi experiencing extreme storm surge damage. The digitized surge line is overlaid with a false-color composite Landsat-5 TM image acquired on September 16, 2005 (Landsat imagery from USGS)

2.2 Flood Inundation (New Orleans)

In the days following Hurricane Katrina, it became apparent that rather than a single event, this was in fact a series of disasters. After the initial impact of wind pressure and storm surge, additional disasters unfolded as levees breached and floodwaters poured into New Orleans. With access to the city severely restricted as major highways were submerged, remote sensing played a central role in reconnaissance activities. MCEER researchers at ImageCat initially used imagery to *rapidly* assess the severity of flooding effects and subsequently to provide *region* and detailed *city-wide* perspectives on the damage extent.

2.2.1 Rapid Post-disaster Damage Verification (PDV)

In response to increasing demand for damage information in the hours following a disaster, ImageCat launched a rapid Post-disaster Damage Verification (PDV) initiative for the 2005 hurricane season. The aim of the PDV program is to acquire and distribute high-resolution aerial imagery *within 24-48 hours of the event*. The data-collection system comprises a high-definition video (HDV) camera, controlled through the

VIEWS™ reconnaissance system. Acquired along a linear flight path with a spatial resolution ranging from 5-15cm (depending on the altitude of the aircraft), the imagery provides extremely detailed coverage of damage conditions. Notably, the PDV program offers a transect-based perspective on damage, compared with the regional coverage offered by satellite platforms. However, the data can be acquired more quickly and are more resilient to limitations affecting optical satellite systems, such as cloud cover.

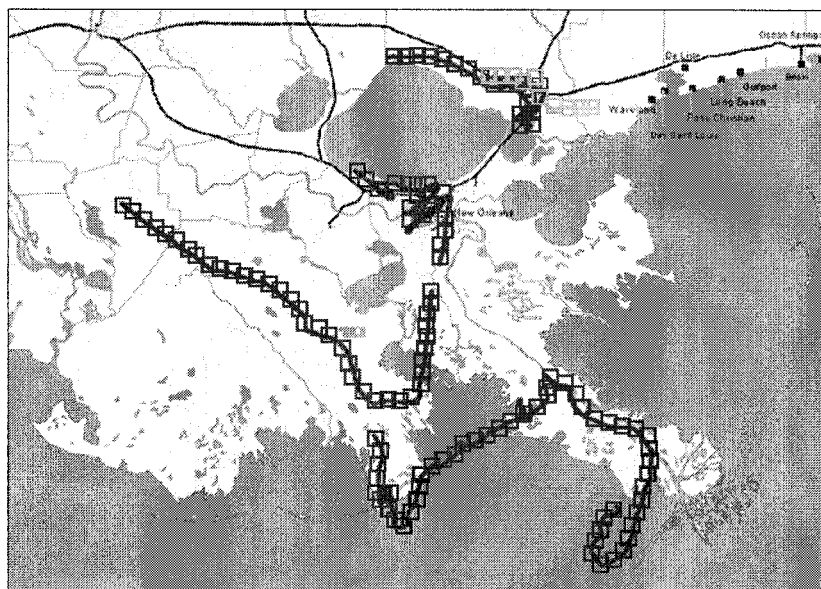


Figure 10. Locations of PDV aerial surveys of flood damage conducted within New Orleans and surrounding areas in the aftermath of Katrina. Damage information was distributed within 24-48 hours of the event.

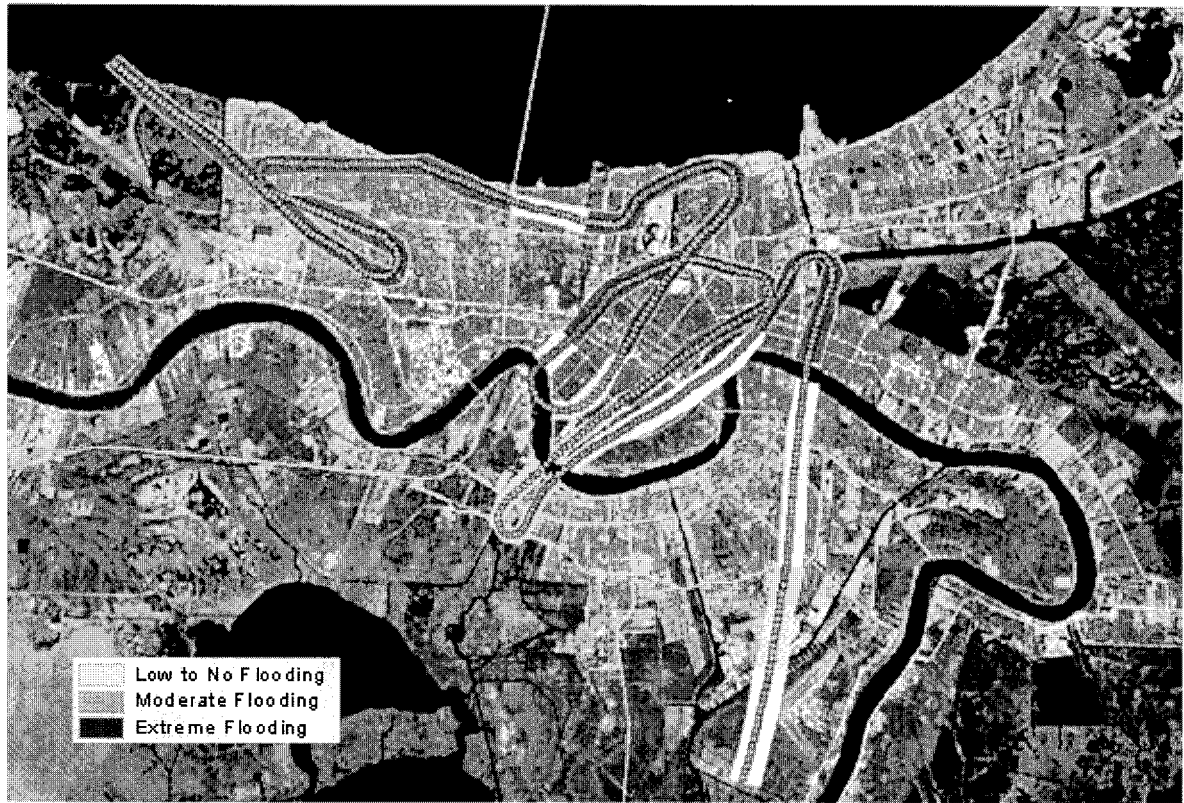


Figure 11. Damage assessment of flooding severity on August 30, based on expert interpretation of PDV VIEWSTM footage (Landsat base image from USGS).

2.2.2 Region-wide Damage Detection Using Landsat-5 Imagery

As previously observed in the case of storm-surge damage, the moderate spatial resolution and extensive geographic coverage afforded by Landsat imagery provide a region-wide perspective of post-disaster damage. In terms of flood damage detection, Landsat-7 ETM imagery was collected on August 30. Although this dataset provides reasonable coverage for downtown New Orleans, it is of limited value on a region-wide scale due to the no-data gaps (black lines) radiating outwards from the center of the scene (Figure 12), caused by failure of the scan line corrector in 2003. The present analysis instead employed the first set of Landsat-5 TM imagery captured after Hurricane Katrina on September 7, together with pre-storm imagery dating from June 19, 2005.

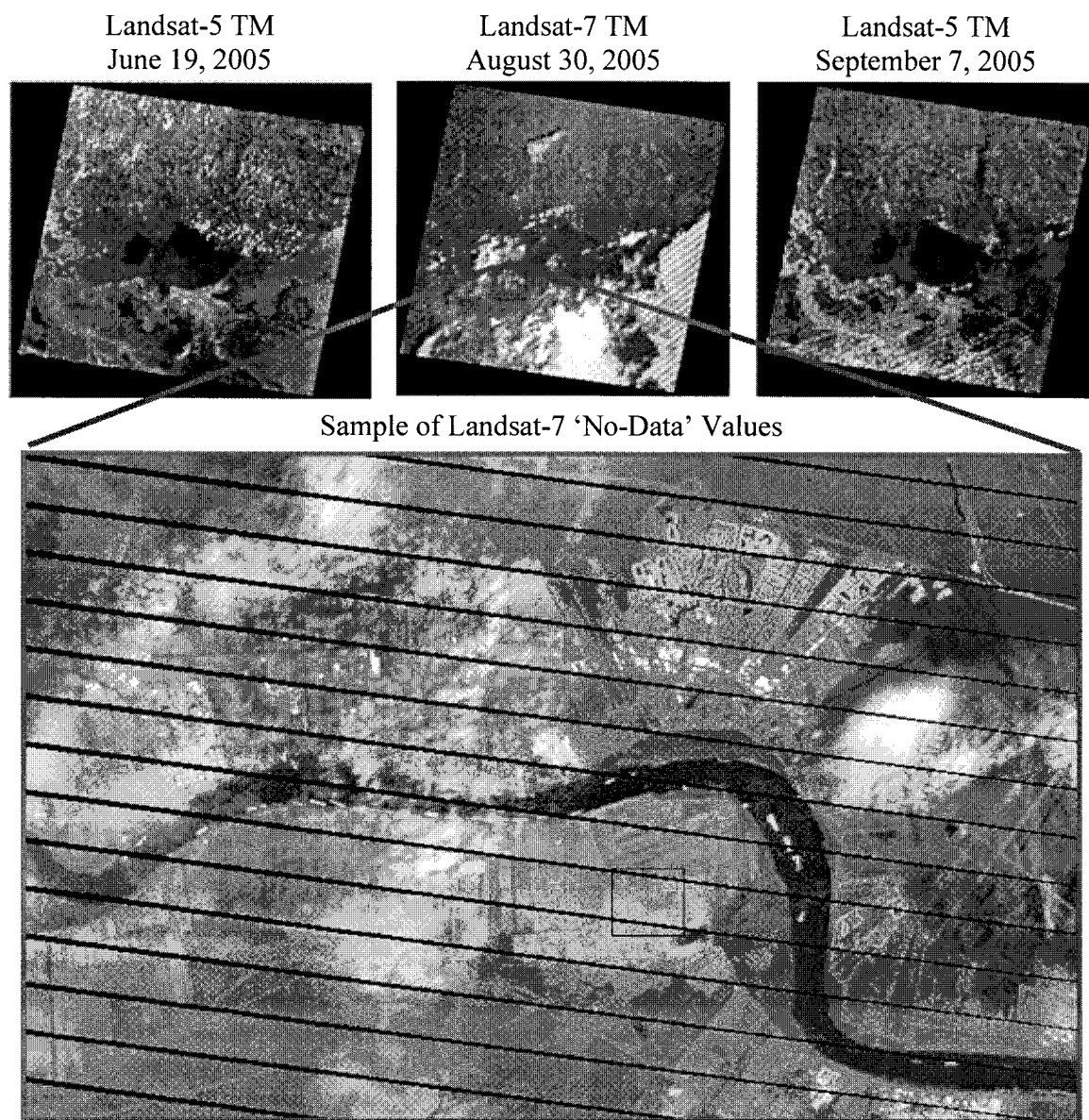


Figure 12. Pre- and post-Hurricane Katrina Landsat-7 imagery (Path 22 Row 39) used to detect flood damage in Louisiana. The Landsat-7 TM imagery captured on August 30 illustrates the 'no-data' values (black lines) that precluded use of this imagery for region-wide change detection (Landsat imagery from USGS and NASA).

Figure 13 summarizes the methodology used to assess urban damage on a region-wide basis. For the storm-surge analysis, an initial pre-processing step involved registering the pre-and post-storm imagery to ensure spatial alignment. Landcover within the co-registered pre-and post-disaster scenes was quantified using the NDVI defined in Equation 1. A set of masks was then applied to minimize the occurrence of false positives commensurate with non-damage-related sources of change. A cloud mask was obtained for each image by thresholding the Landsat-5 TM Band 6 coverage to identify their characteristically cold signature. The water surface mask was obtained by thresholding the pre-storm NDVI image.

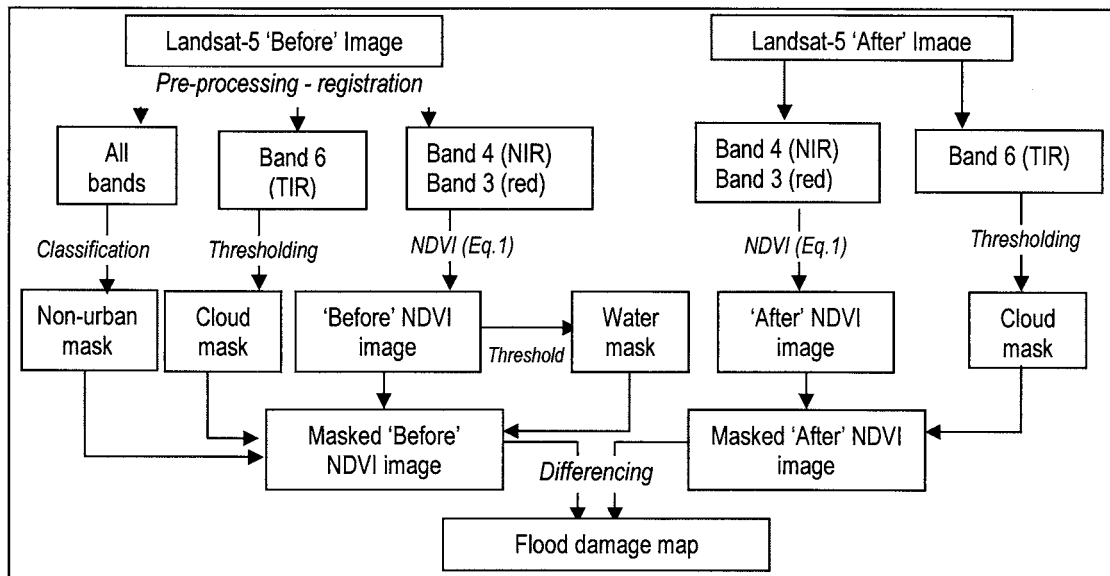


Figure 13. Methodology employed for region-wide flood damage detection.

Learning from the storm-surge analysis in the previous section, an additional non-urban mask was also applied to eliminate potential ecologically based changes where the hurricane caused browning or leaf loss. A supervised classification of the pre-storm image was used to create the mask. Training sites were selected for 8 dominant classes: (1) urban; (2) vegetated land; (3) wetland; (4) cleared agricultural land; (5) river/ocean; (6) cloud; (7) shadow; and (8) unclassified. For a sample of landcover classes, Figure 14 shows (a) the input image and (b) classified output image following application of a 9x9-pixel majority filter used to minimize isolated pixels within an otherwise homogenous class.

Adjusted 'before' and 'after' NDVI images were produced by applying the cloud, water, and urban masks to the 'before' image and the cloud mask to the 'after' image. The extent of flooding caused by the hurricane and levee breach was finally determined as a function of the difference (computed as 'after' – 'before') between the adjusted NDVI scenes, also expressed as a measure of standard deviation about the image-wide mean.

Figure 15 shows the flood inundation map for Louisiana, as of September 7, 2005. Areas within Jefferson and St. Bernard Parishes exhibit a significant change between the pre- and post-hurricane coverage, synonymous with inundation caused by flooding. The negative difference in NDVI indicates a reduction in spectral response in the red and near-infrared bands within the 'after' scene. Whereas a similar reduction along the Mississippi coast was attributed to surface scour by the storm-surge wave, in this instance the relatively bright reflection from buildings and vegetation comprising urbanized surfaces is replaced by the comparatively dark reflection from floodwaters.

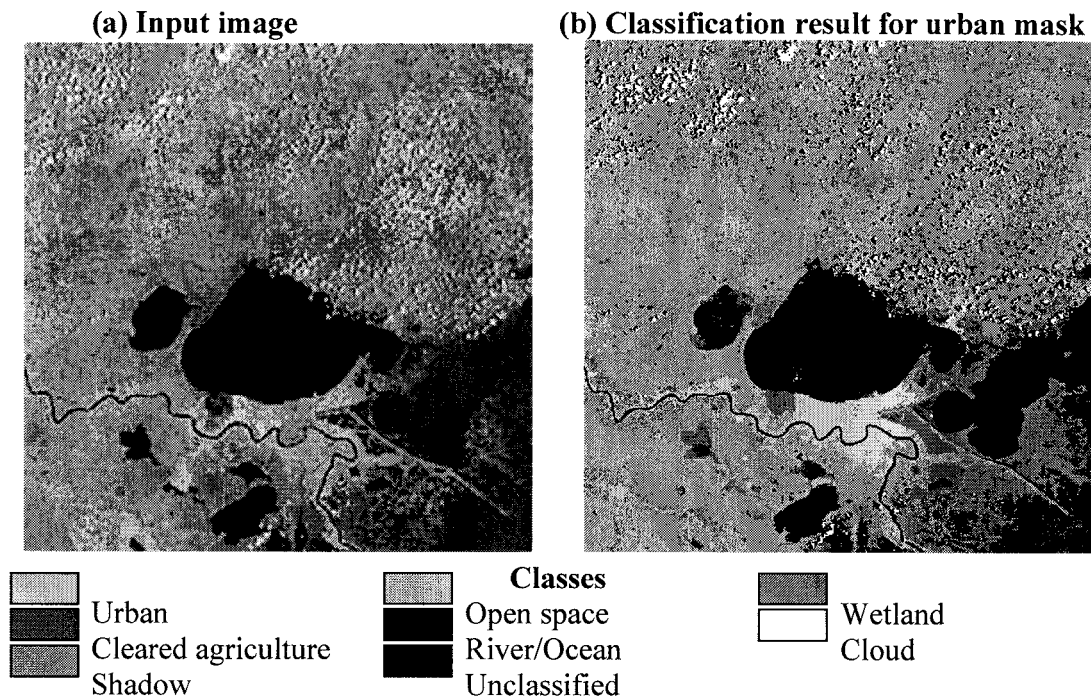


Figure 14. (a) Input Landsat-5 TM image (Bands 7,4,2) for New Orleans area, and (b) output classification result, subject to a 9x9 majority filter to mitigate the effect of isolated pixel classes. The 'urban' class was used to create a mask in order to eliminate ecologically-based changes (Landsat base images from USGS).

The study of Hurricane Katrina damage from a remote-sensing perspective reinforces the value of an integrated approach to damage assessment, which combines rapid survey with regular monitoring (i.e., situation assessment) during the following days and weeks. Figure 16 shows a temporal comparison of New Orleans images captured before and after the hurricane, from June to October 2005.

Comparison of the pre-storm Landsat imagery from June 2005 (Figure 16a) with post-event Landsat imagery from August 30, 2005 (Figure 16b) suggests that in the immediate aftermath of Hurricane Katrina, flooding occurred throughout western, eastern, and central districts of New Orleans. Multi-temporal analyses are also useful for monitoring the evolving disaster situation. For example, while flooding remains evident throughout central and eastern districts in the September 7 Landsat-5 imagery (Figure 16c), inundation that was observed during the PDV survey and Landsat coverage of August 30 (noted in yellow in Figure 16b) is no longer apparent. This finding suggests that flood waters retreated at different rates throughout the city, which may in turn be linked to the source of flood water (overtopping versus levee breach).

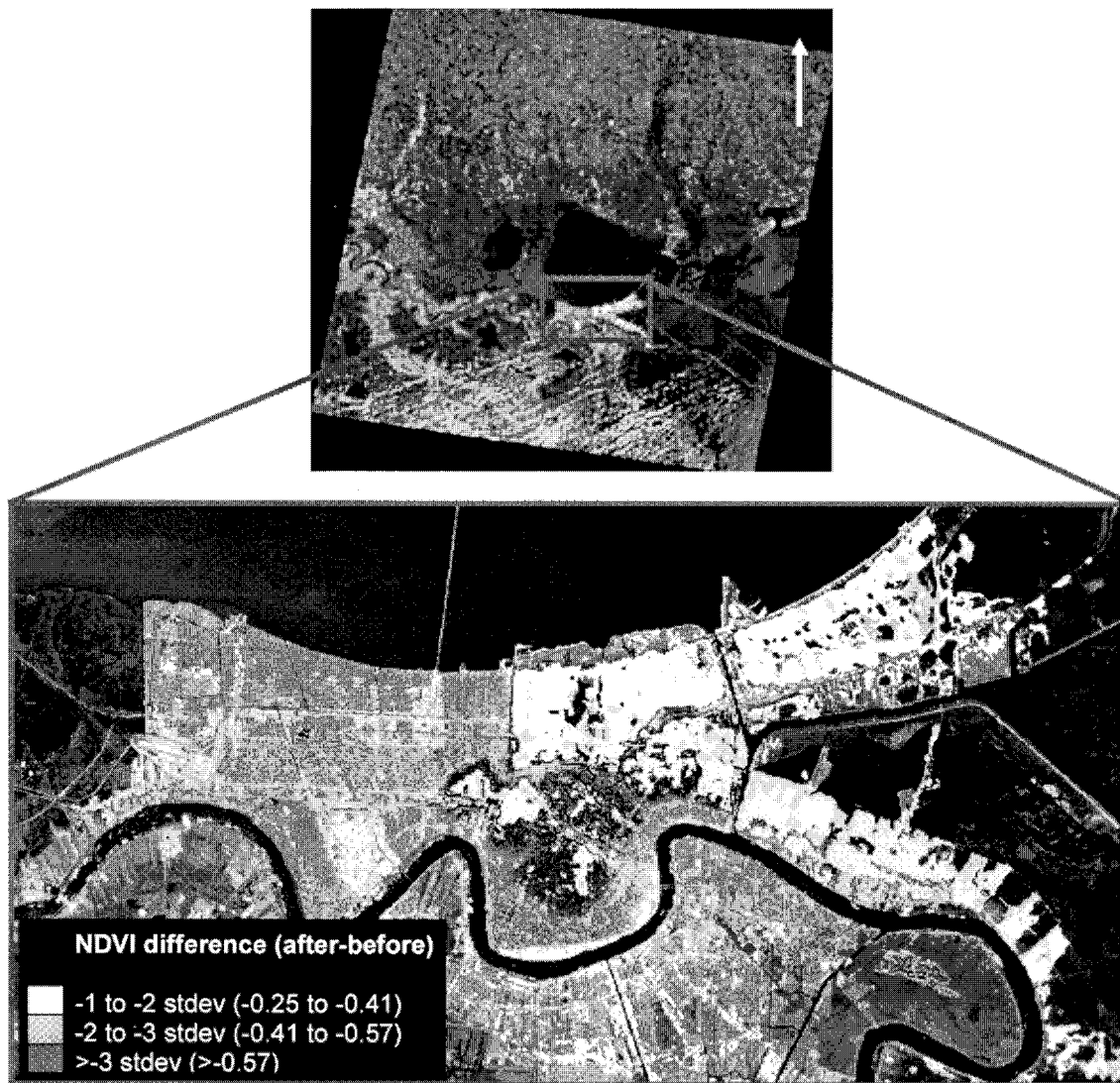


Figure 15. Region-wide flood damage map for the New Orleans area overlaid on the Landsat-5 TM image of September 7. Damage is measured in terms of change in NDVI between pre- and post-hurricane images. Extreme changes are evident within Jefferson and St. Bernard parishes (Landsat imagery from USGS).

The September 7 coverage in Figure 16c clearly depicts widespread inundation within central and eastern districts; due to dense cloud cover and no-data values, it is difficult to determine if these areas are also inundated in the August 30 Landsat-7 scene. Within the false-color composite comprising near-infrared, red, and green bands, flooding is characterized by a low spectral return (dark reflection). From detailed visual inspection, this low return can be traced to the location of levee breaches.

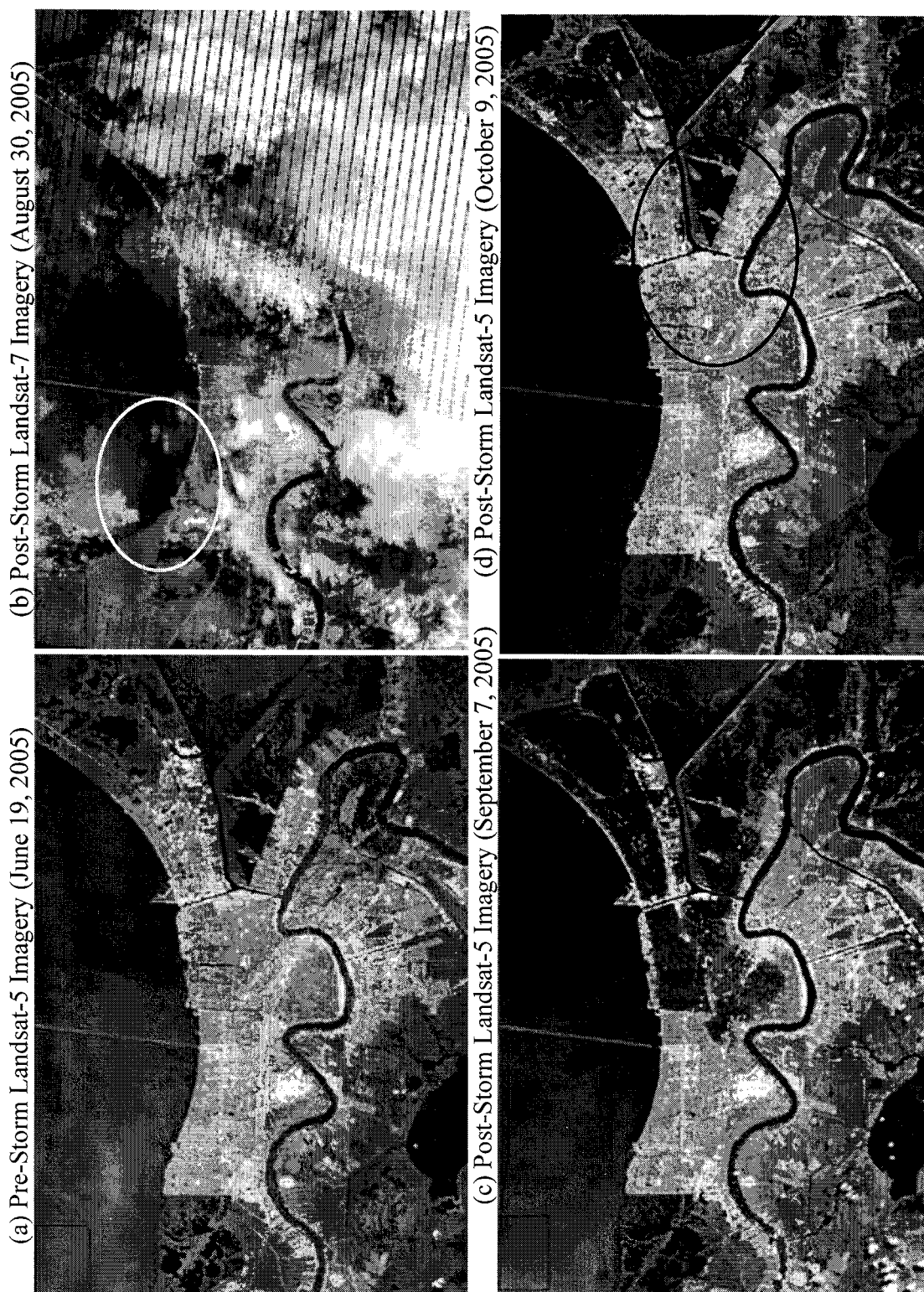


Figure 16. Temporal sequence of false-color composite images (Landsat-5 Bands 4,3,2) for New Orleans, acquired before and after Hurricane Katrina. Flooding that is evident in western districts on August 30 (see yellow annotation) is no longer apparent on September 7. Extensive flooding within central and eastern districts has subsided by October 9, leaving a distinctive spectral signature (see blue annotation). (Landsat base images from USGS.)

By October 9, when the fourth image in the sequence was acquired (Figure 16d), the floodwaters have subsided, and the inundated region exhibits a new signature. Compared with the pre-storm scene, spectral return is markedly lower at near infrared wavelengths, resulting in a blue/grey appearance. Judging from experience garnered following the Indian Ocean tsunami (Adams et al., 2004b) and through analysis of the Hurricane Katrina surge line in Mississippi, this effect is likely due to the die-back of surface vegetation, together with the in-situ deposition of waterborne sediments and debris.

In an applied context, this evaluation of temporal changes in flooding extent and severity has far-reaching implications for loss assessment within affected communities. During the days and weeks following the event, usual ground-based routes of access employed by insurance companies to assess the severity of damage were unavailable. The remote access offered by satellite and aerial imagery provides an accurate and holistic picture of the unfolding scene. Such data could serve as key benchmarks from which claims assessors could identify the probable degree of damage, and prioritize post-disaster business activities.

2.2.3 Neighborhood Damage Detection Using QuickBird Imagery

In addition to the swift identification of hurricane-affected areas through transect-based rapid PDV visualization and the broad scale extent of damage using moderate-resolution Landsat-5 coverage, high-resolution QuickBird satellite imagery offers a detailed neighborhood-based flood damage assessment for the entire city of New Orleans. This neighborhood evaluation serves as an exemplary case for the way in which the collection, ordering, delivery, and processing of satellite imagery can be streamlined to facilitate rapid response activities.

Figure 17 summarizes the methodology used to determine the status of communities in New Orleans as of Saturday September 3, 2005. High-resolution near-nadir QuickBird imagery was acquired by DigitalGlobe during the afternoon of September 3 and made available for ordering the same afternoon. An imagery order for a 618-km² area was placed on the night of Saturday September 3, as a “Rush-Archive” request, which promotes the order to the head of DigitalGlobe’s processing schedule. The processed imagery became available less than 24 hours later and was downloaded overnight via the Internet (ftp) to make the data available for analysis on Monday morning, September 5.

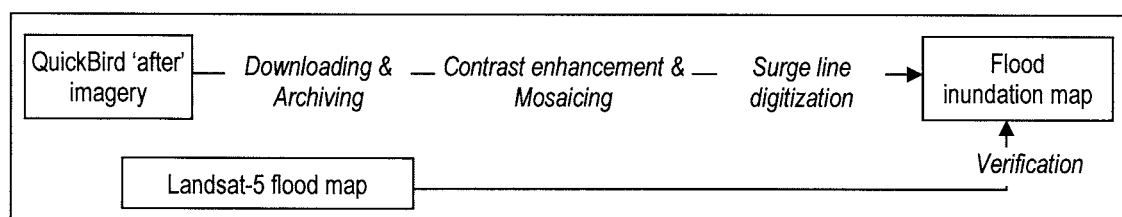


Figure 17. Methodology employed for neighborhood flood-damage detection.

The post-hurricane QuickBird imagery covering the New Orleans area was delivered as a series of 34 individual tiles in order to streamline the processing activities and to avoid large file size issues. To highlight the flood area in preparation for expert interpretation, a series of processing steps were performed. First, a contrast-enhanced false color-composite comprising near-infrared, red, and green bands was produced for each image tile in an attempt to capitalize on the distinctive signature (dark reflection) of the inundation zone and to minimize the effect of cloud and shadow. Next, the image tiles were converted to a GIS-compatible format in preparation for flood-line digitization. Finally, as shown in Figure 18, the tiles were mosaiced together within a GIS environment.

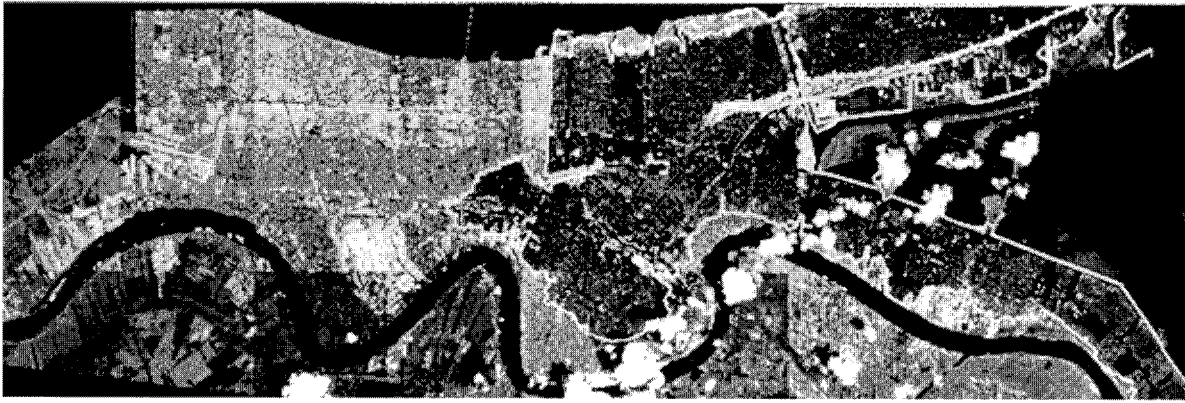


Figure 18. Expert-interpretation-based flood limit (delineated in yellow) overlaid with the QuickBird false-color composite image of New Orleans for September 3, 2005 (from which the flood zone was derived), comprising 34-contrast enhanced and mosaiced tiles (QuickBird Imagery from DigitalGlobe, Inc., www.digitalglobe.com).

The boundary of inundation was delineated for New Orleans as a series of polygons, based on expert interpretation of the spectrally-enhanced September 3 QuickBird coverage. For the Landsat-5 coverage (see Figure 16), the flooded area was identified based on the lower reflectance of water as compared with non-flooded ground-surface features. Given the high spatial resolution of the imagery, it was possible to distinguish inundated areas to within the nearest city block. There were several isolated areas surrounded by flooding, for which polygons appear as “non-flooded islands”.

The expert-defined flood boundary for September 3rd was visually compared with the NDVI-based flood map developed using Landsat-5 TM coverage for September 7 (see Figure 19). There is a close correspondence between the two extents, with flooding concentrated in the central and eastern districts of the city. An area of discrepancy is present within southern districts, where the NDVI analysis did not identify significant flooding. This discrepancy may be a function of the flooding severity.

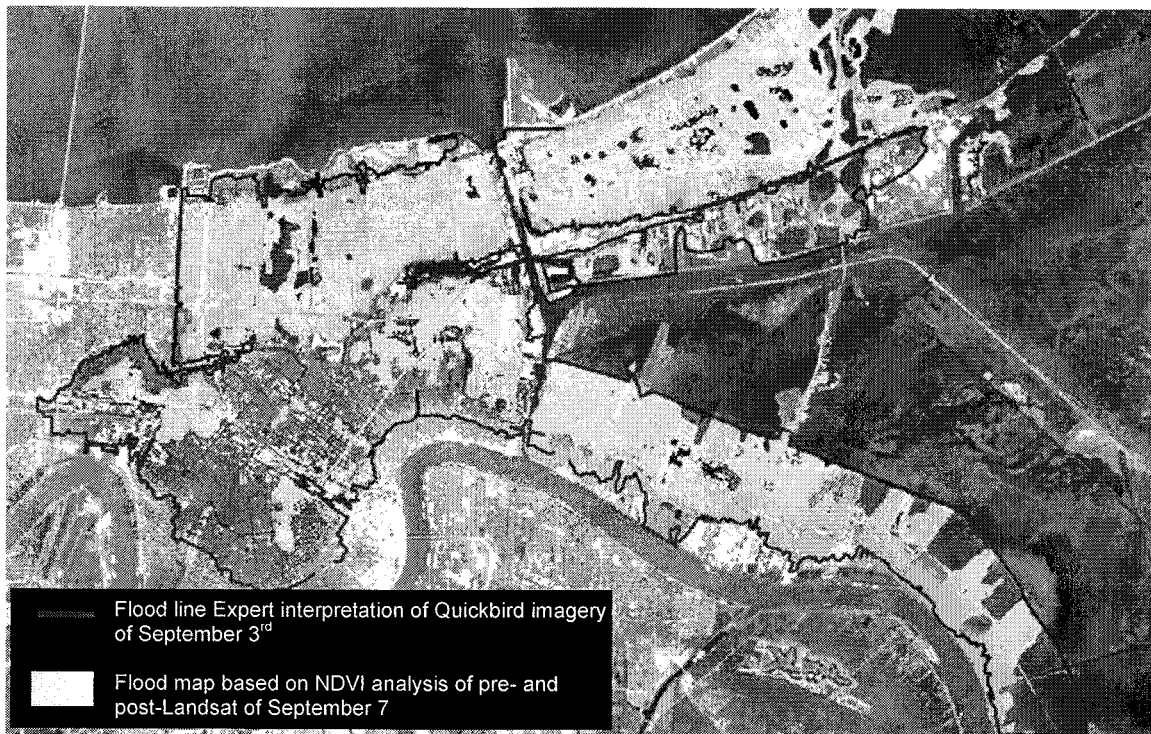


Figure 19. Independent verification of the QuickBird flood line, using the NDVI flood map developed with pre-hurricane Landsat-5 TM imagery and post-coverage for September 7 (QuickBird Imagery from DigitalGlobe, Inc., www.digitalglobe.com).

3. KEY FINDINGS

As a natural disaster, Katrina was record-breaking because of the unique convergence of multiple hazards within a single event (namely windstorm, storm surge, flooding, and levee breach), and also due to its status as the costliest U.S. hurricane on record. From a technology standpoint, hurricane Katrina is also important, as it marks the first event where the ‘eye in the sky’ was used operationally to assess the unfolding situation and record damage from multiple hazards.

- Within a Tiered Reconnaissance System (TRS) framework, remote sensing images acquired by satellites and aircraft can be used to guide and inform reconnaissance activities. Following Hurricane Katrina, activities conducted by MCEER researchers at ImageCat and MCEER advanced technology field teams spanned: (1) Tier 1 - the ‘regional’ evaluation of damage extent; (2) Tier 2 – recording the severity of damage at a ‘neighborhood’ scale; and (3) Tier 3 – detailed ‘per-building’ assessment damage . At Tier 3, detailed reconnaissance was completed using a combination of the VIEWSTM in-field system and remote sensing data from satellites, NOAA and the PDV program.
- Hurricane Katrina presented a unique opportunity to operationally deploy damage assessment research outputs from MCEER Thrust area 3 (Response and Recovery) for analyzing: (1) storm surge; and (2) flood inundation.
- Storm surge extent throughout Mississippi was evaluated using: (1) an analysis of ‘before’ and ‘after’ Landsat 5 satellite imagery from USGS/NASA, which suggested that the entire coast was affected; and (2) an evaluation of NOAA airborne imagery, which showed that 90-100% of buildings were completely destroyed within about ~1 mile of the shore. Remote sensing images quickly showed that in this area, storm surge proved far more damaging than wind pressure.

- The New Orleans flooding situation was assessed: (1) within 48-hours of the event using the ImageCat PDV program, capturing inundation within western districts that was absent from assessments conducted one week later; (2) for the entire city using a 'before' and 'after' sequence of Landsat-5 imagery; and (3) at a neighborhood-scale using multi-spectral QuickBird satellite imagery.

Acknowledgements:

The authors would like to acknowledge the support of MCEER through a grant from the Earthquake Engineering Research Centers Program of the National Science Foundation (supplement to award number EEC-9701471), funding from the New York State, and other sponsors.

The opinions, findings, conclusions or recommendations expressed in this paper do not necessarily reflect the views of these sponsors or the Research Foundation of the State of New York.

References:

- Adams, B.J. (2004), "Improved Disaster Management through Post-earthquake Building Damage Assessment Using Multitemporal Satellite Imagery," *Proceedings of the ISPRS XXth Congress*, Volume XXXV, Istanbul.
- Adams, B.J., Huyck, C.K., Mansouri, B., Eguchi, R.T., and Shinozuka, M. (2004a), Application of High Resolution Optical Satellite Imagery for Post-Earthquake Damage Assessment: The 2003 Boumerdes (Algeria) and Bam Earthquakes, *MCEER Research and Accomplishment 2003-2004*, MCEER, Buffalo, NY.
- Adams, B.J., Womble, J.A., Mio, M.A., Turner, J.B., Mehta, K.C., and Ghosh, S. (2004b), "Field Report: Collection of Satellite-Referenced Building Damage Information in the Aftermath of Hurricane Charley," *Response*, MCEER, <http://mceer.buffalo.edu/research/Reconnaissance/Charley8-13-04/04-SP04.pdf>.
- Adams, B.J., S. Ghosh, S., Wabnitz, C., and Alder, J. (2005a), "Post-tsunami Urban Damage Assessment in Thailand, Using Optical Satellite Imagery and the VIEWS™ Field Reconnaissance System, Proceedings of the Conference on the 250th Anniversary of the 1755 Lisbon Earthquake, Lisbon, Spain.
- Adams, B.J., Wabnitz, C., Ghosh, S., Alder, J., Chuenpagdee, R., Chang, S.E., Berke, P.R., and Rees, W.E. (2005b), "Application of Landsat 5 & High-resolution Optical Satellite Imagery to Investigate Urban Tsunami Damage in Thailand as a Function of Pre-tsunami Environmental Degradation," *Proceedings of the 3rd International Workshop on Remote Sensing for Disaster Response*, Chiba, Japan.
- Chang, S.E., Adams, B.J., Alder, J., Berke, P.R., Chuenpagdee, R., Ghosh, S., and Wabnitz, C., (2006), "The Great Sumatra Earthquakes and Indian Ocean Tsunamis of 26th December 2004 and 28th March 2005: A Reconnaissance Report," *Earthquake Spectra*, Special Issue III, Volume 22, June 2006.
- Eguchi, R.T., Huyck, C.K., Houshmand, B., Mansouri, B., Shinozuka, M., Yamazaki, F., Matsuoka, M., and Ulgen, S. (2000), "The Marmara, Turkey Earthquake: Using Advanced Technology to Conduct Earthquake Reconnaissance," *MCEER Research and Accomplishments 1999-2000*, MCEER, Buffalo, NY.
- Ghosh, S., Huyck, C.K., Adams, B.J., Eguchi, R.T., Yamazaki, F., and Matsuoka, M. (2005), *Preliminary Field Report: Post-Tsunami Urban Damage Survey in Thailand, Using the VIEWS Reconnaissance System*, MCEER, Buffalo.
- Gusella, L., Adams, B.J., Bitelli, G., Huyck, C.K., and Mognol, A. (2004), "Object-Oriented Approach to Post-Earthquake Damage Assessment for Bam, Iran, Using Very High-Resolution Satellite Imagery," *Proceedings of the Second International Workshop on the Use of Remote Sensing for Post-Disaster Response*, Newport Beach, CA.
- Huyck, C.K., Adams, B.J., Cho, S., Eguchi, R.T., Mansouri, B., and Houshmand, B. (2004), *Methodologies for Post-earthquake Building Damage Detection Using SAR and Optical Remote Sensing: Application to the August 17, 1999 Marmara, Turkey Earthquake*, MCEER-04-004 Technical Report, MCEER, Buffalo, NY.
- U.S. Bureau of Census (2002), *Tiger Street Network Database*.
- Vu, T.T., Matsuoka, M., and F. Yamazaki (2005), "Detection and Animation of Damage Using Very High-Resolution Satellite Data Following the 2003 Bam, Iran, Earthquake," *Earthquake Spectra*, Special Issue 1, Volume 21, Dec.
- Womble, J.A. (2005), *Remote-Sensing Applications to Windstorm Damage Assessment*. Doctoral Dissertation, Wind Science and Engineering Program, Texas Tech University.
- Womble, J.A., Adams, B.J., and Mehta, K.C. (2005), "Windstorm Damage Surveys Using High-Resolution Satellite Images," *Proceedings, 10th Americas Conference on Wind Engineering*, Baton Rouge, LA.
- Womble, J.A., Ghosh, S., Adams, B.J., and C. Friedland (2006), *Advanced Damage Detection for Hurricane Katrina: Integrating Remote Sensing and VIEWS™ Field Reconnaissance*, Volume 2 of MCEER Special Report Series, Engineering and Organizational Issues Before, During and After Hurricane Katrina, MCEER-06-SP02, March 2006.
- Yamazaki, F., Yano, Y., and M. Matsuoka (2005), Visual Damage Interpretation of Buildings in Bam City Using QuickBird Images Following the 2003 Bam, Iran, Earthquake," *Earthquake Spectra*, Special Issue 1, Volume 21, December.

BUILDING DAMAGE ASSESSMENT AFTER THE 2006 CENTRAL JAVA EARTHQUAKE USING HIGH-RESOLUTION SATELLITE IMAGES

H. Miura ¹⁾, M. Matsuoka ²⁾, and F. Yamazaki ³⁾

1) Post-Doctoral Research Fellow, Center for Urban Earthquake Engineering, Tokyo Institute of Technology, Japan

2) Team Leader, Earthquake Disaster Mitigation Research Center, NIED, Japan

3) Professor, Dept. of Urban Environment Systems, Chiba University, Japan

hmiura@enveng.titech.ac.jp, matsuoka@edm.bosai.go.jp, yamazaki@tu.chiba-u.ac.jp

Abstract: In order for efficient post disaster management, it is important to develop a methodology to capture affected areas from remote sensing data. In this paper, the areas damaged by the 2006 Central Java earthquake are identified from the high-resolution satellite images. Based on the field survey for the spectral reflectance of surface materials, the image classification technique is applied to post-earthquake QuickBird images to detect the areas covered with bricks (damaged buildings) and the areas covered with roof tiles (undamaged buildings). The distribution of the building damage is evaluated by computing Damage Index from the classified images. The severely damaged areas are distributed not only in Bantul and Imogiri, located near the epicenter, but also in Gantiwarno, the southern part of Klaten located 20-30km away from the epicenter. The distribution of the DI is compared with the damage statistics by the field survey. The result shows that the DI almost agrees with the severe damage ratio.

1. INTRODUCTION

The 2006 Central Java earthquake (Mw6.3) occurred in the state of Yogyakarta, Indonesia on May 27, 2006. More than 5,700 human lives were lost, 36,000 people were injured due to the earthquake. Approximately 140,000 houses were collapsed and 200,000 were damaged. After the earthquake, the field survey of the affected areas had been conducted by many researchers to investigate the distribution of the damage and their causes. However, the identification of the damaged area by the field survey is time-consuming in case of a large-scale disaster. For early rescue activities and efficient post disaster management, it is important to develop a methodology to quickly identify the distribution of the damaged areas.

Remote sensing data observed from satellites would be useful to detect the affected areas since the surface condition of vast area can be identified from the images. Recently, commercial high-resolution satellite images, such as QuickBird (QB) or IKONOS, are easily available. After the 2006 Central Java earthquake, the International charter of "Space and major disaster" (International Charter of Space and Major Disaster, 2006) had activated to obtain satellite remote sensing images of the severely damaged area. Especially, UNOSAT (UNOSAT, 2006) had published the damage distribution map estimated from the high-resolution satellite images on their web site. Figure 1 shows the damage distribution estimated by UNOSAT overlaid on the satellite ASTER image. The map is very useful to grasp the distribution of the building damage in the early-stage of the post disaster. The map shows the building damage is concentrated in the south of Yogyakarta, such as Bantul and Imogiri. However, according to the damage statistics (Murakami *et al.*, 2006), the building damage is distributed to the east of Yogyakarta, such as Gantiwarno in Klaten where the

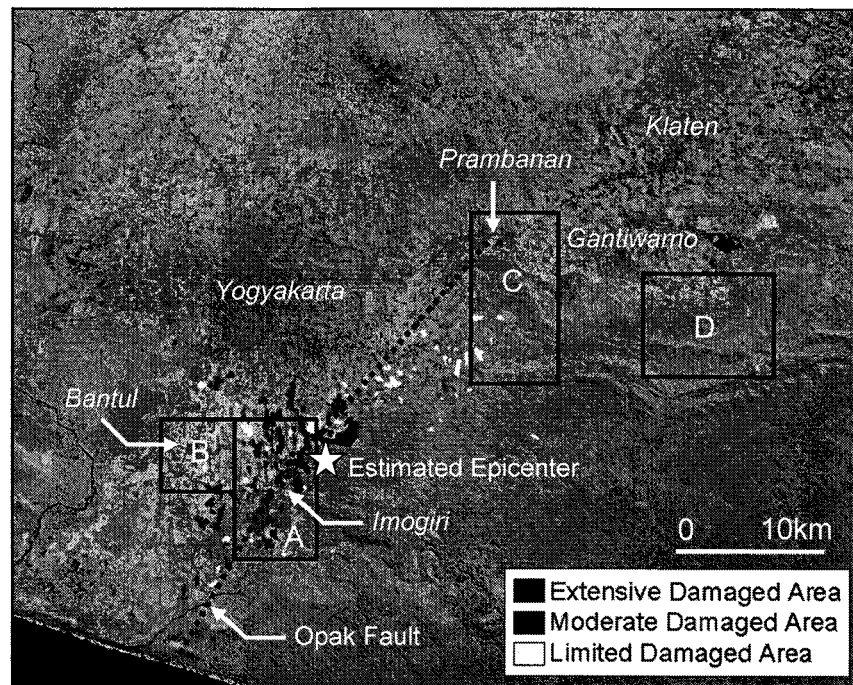


Fig. 1 Coverage of QuickBird images (A-D) and damage distribution estimated by UNOSAT(2006) overlaid on ASTER image.

damage is not described in the map. This is because the images in the southern part of Klaten are not used in the UNOSAT map.

The visual interpretation technique was applied to identify the damage are in the UNOSAT map. The technique requires great demand of time and labor, although it can provide the distribution of the reliable building damage. Therefore, more efficient technique is necessary for more quick identification of the building damage distribution. The image classification is one of the damage detection techniques and had been applied to the Landsat/TM images (spatial resolution=30m) in the 1995 Kobe earthquake (Matsuoka *et al.*, 2000). The applicability of the image classification technique for damage detection using high-resolution satellite image has never discussed in detail. In this paper, the image classification technique is applied to identify the building damage distribution using the post-earthquake QB images based on the observed spectral reflectance characteristics of the surface materials.

2. MEASUREMENT OF SPECTRAL REFLECTANCE

Since the radiation reflected from surface materials is observed in the optical images, such as Landsat/TM, QB, and IKONOS images, it is important to collect the spectral reflectance data by the in-situ observation for applying reliable image classification. We conducted the field survey and measured the spectral reflectance of the surface materials using the handy spectrometer (MS-720 of Eko Instruments Co., Ltd.). In order to grasp the reflectance of building materials, the reflectance of roof tile and brick are observed. We also measured the reflectance of asphalt, vegetation, soil and so on. Figure 2(a) shows the photograph during the observation of surface reflectance. The reflectance is computed from the irradiance of the target material divided by the irradiance of referenced white plate.

Figure 2(b)-(d) show the observed reflectance of the materials. Horizontal axis indicates the wavelength in nanometer and vertical axis indicates reflectance in percentage. Figure 2(b) represents that the reflectance of brick is high in red band range (600-700nm) while the reflectance of roof tile

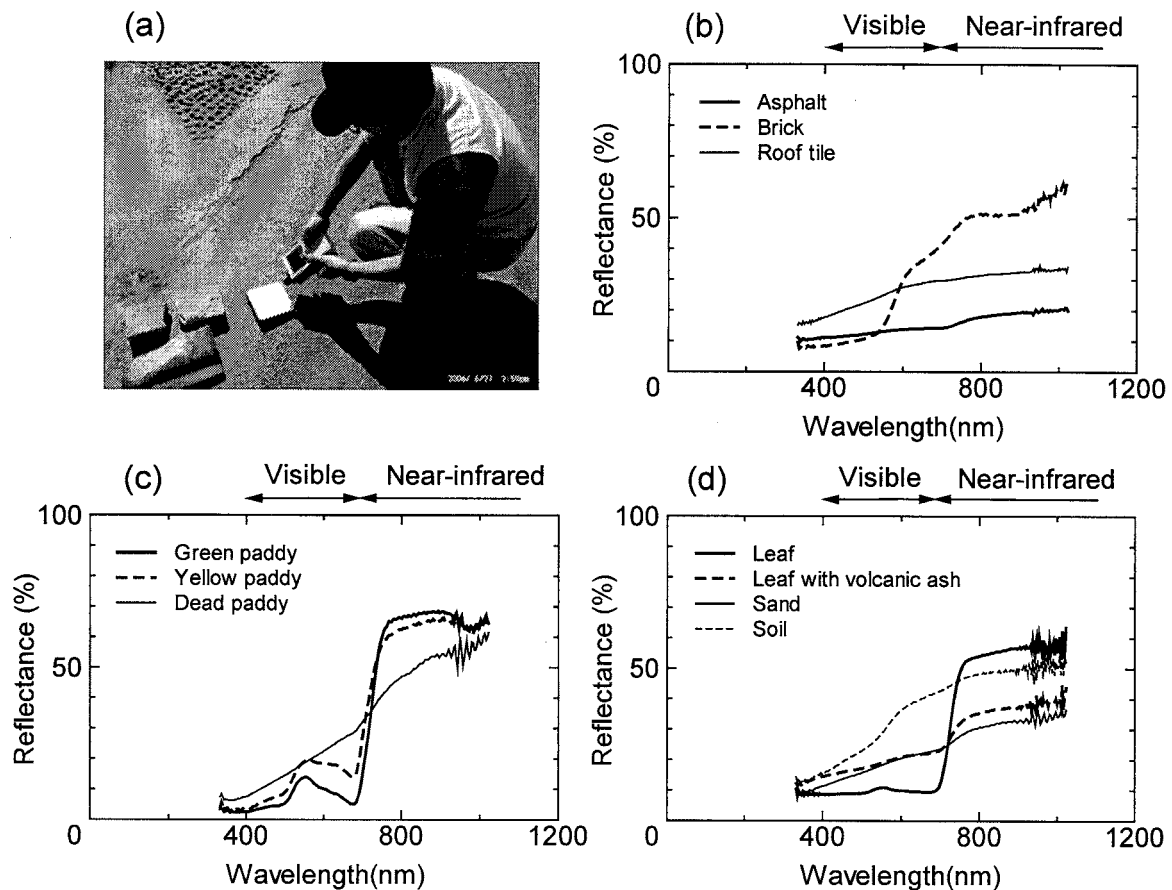


Fig. 2 (a) Observation of surface reflectance.
(b)-(d) Reflectance of surface materials.

and asphalt is low in the all ranges. Figure 2(c) shows the comparison of green healthy paddy, yellow unhealthy paddy and dead paddy. A rapid increase in reflectance between visible band and near infrared band is observed for the green paddy, while this characteristic is reduced for the yellow paddy, and it is lost for the dead paddy. These trends are also observed for between healthy leaf and volcanic ash-covered leaf as shown in Fig. 2(d). The characteristics of dead paddy and ash-covered leaf are similar with those of soil and sand, respectively.

3. DAMAGE ESTIMATION BY IMAGE CLASSIFICATION

In order to identify the distribution of the building damage, post-earthquake QB images are used in this study. The coverage of the QB images is shown by solid squared area (A-D) in Fig. 1. The pan-sharpened images whose spatial resolution is 0.6m are converted from the multi-spectral and panchromatic images using the Brovey transformation (Pohl and Van Genderen, 1998). The characteristics of the images are shown in Table 1. The images were observed from June to July 2006. The images of A and B cover the severely damaged areas such as Imogiri and Bantul, respectively. The images of C and D include the area around the Prambanan heritage and Gantiwarno in southern part of Klaten, that are also severely damaged area (Murakami *et al.*, 2006).

The close-ups of the images are shown in Fig. 3. Figure 3(a) represents the completely damaged buildings (top) and undamaged building (bottom) comparing with the pre-event images observed in 2003 and the ground photographs of the building. As shown in the figure, the color of the severely damaged building is turned to white because the bricks of the walls and the debris are exposed on the surface ground. On the other hand, the undamaged building is covered with roof

Table 1 Characteristics of QuickBird images

Image	Date	Time	Satellite		Sun		Spatial Resolution (m)
			Azimuth (deg.)	Elevation (deg.)	Azimuth (deg.)	Elevation (deg.)	
A	Jun. 8, 2006	AM 10:09	N134E	43	N35E	53	0.6
B	Jun. 13, 2006	AM 10:14	N118E	61	N33E	53	0.6
C	Jun. 13, 2006	AM 10:14	N118E	61	N33E	53	0.6
D	Jul. 7, 2006	AM 10:25	N247E	73	N32E	55	0.6

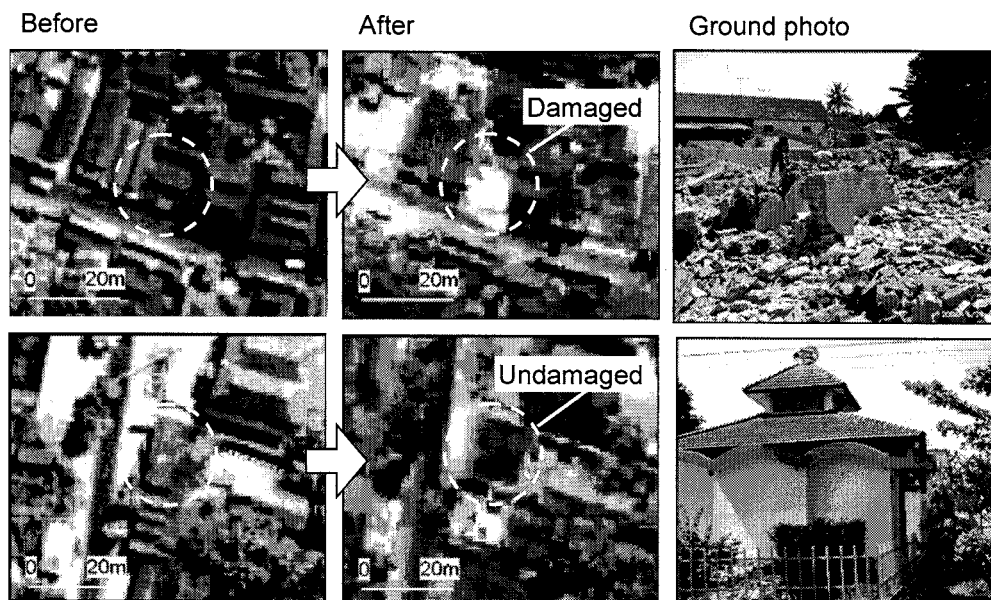


Fig. 3 Comparison of pre-, post-earthquake images and ground photos in severely damaged building and undamaged building

tiles in both of the pre- and post-event images. As shown in Fig. 2, the spectral characteristic of brick is different from that of roof tile. These suggest that it is possible to extract severely damaged area by discriminating the areas covered with bricks from the areas covered with roof tiles.

The supervised image classification technique is applied to the post-earthquake QB images to identify the damage distribution. The area of the collapsed buildings covered with bricks, undamaged buildings covered with roof tile, vegetation (tree and paddy), bare ground, water of river and so on are extracted for the supervised data of the image classification. About 5,000-10,000 pixels for each material are selected and the maximum likelihood image classification (Takagi and Shimoda, 2004) is applied to the images. The time required for the selection of the supervised data and applying the classification is much less than that for the visual interpretation. It means the identification of the damage by the image classification is faster than that by the visual interpretation.

The original QB image and the results of the classification are shown in Fig. 4(a) and (b), respectively. In Fig. 4(b), black pixels indicate bricks classified as collapsed buildings while gray pixels indicate roof tiles classified as undamaged buildings. The close-up of the central part of Imogiri is shown in Fig. 5 that covers the solid squared area in Fig. 4. The pre- and post-earthquake images are also shown in the figure. The comparison between pre- and post-earthquake images reveals that the completely collapsed buildings are covered with the white materials, such as bricks and debris. In the classified image, they are almost correctly classified as bricks.

In order to identify severely damaged areas, the images are segmented to 100m square meshes and the number of pixels classified as the damaged building in a mesh is computed. Here, ND and

A

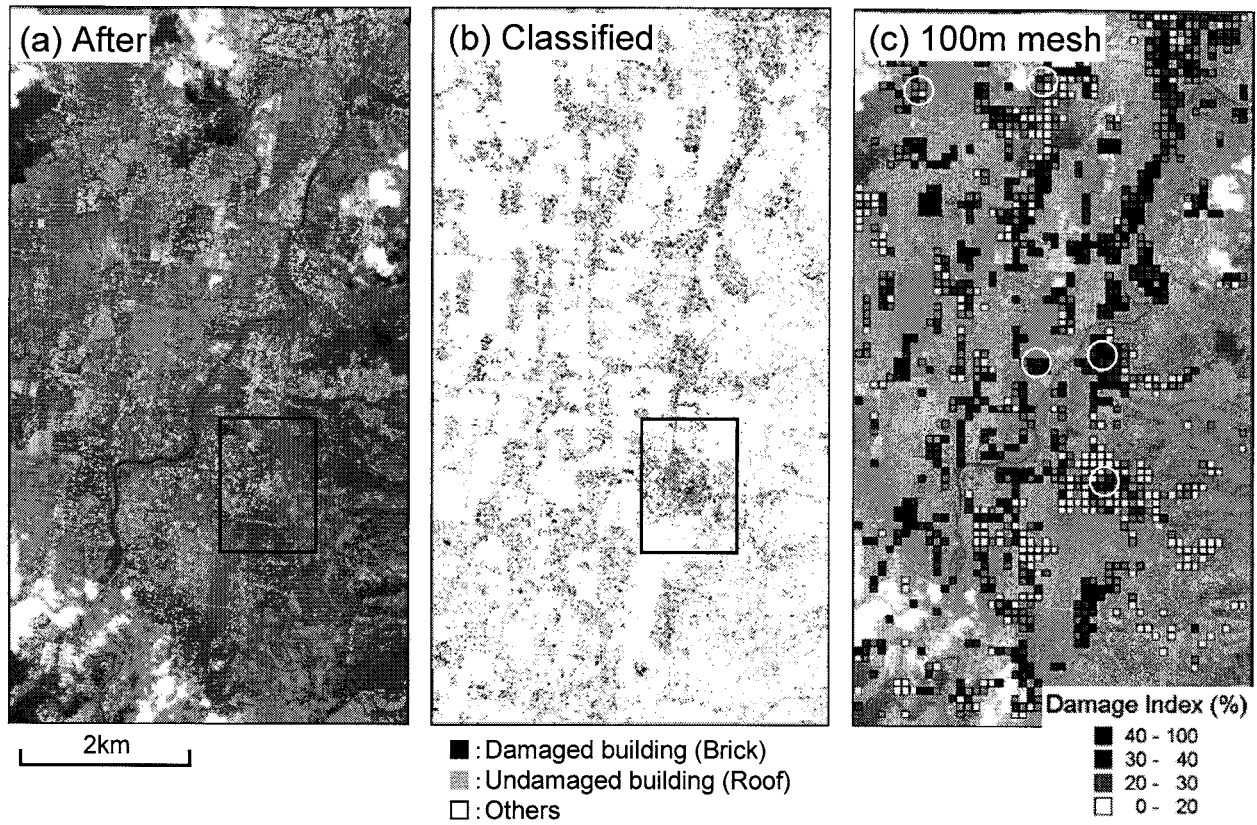


Fig. 4 (a) QuickBird image A, (b) Classified image, (c) Damage distribution estimated from classified image.

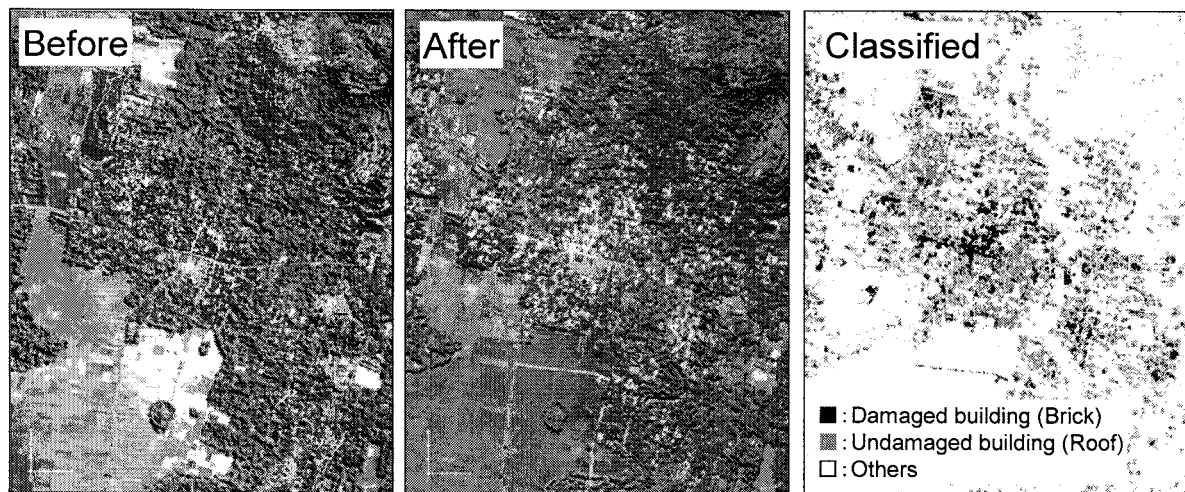


Fig. 5 Comparison between pre-, post-earthquake QB images and classified images.

NU is defined as the number of pixels classified as damaged building (brick) and undamaged building (roof tile), respectively. In order to avoid the meshes that do not contain settlement area, the meshes that the sum of ND and NU is less than 20% of total pixels in a mesh are eliminated in the analysis. DI (Damage Index) is computed in each mesh based on the following equation.

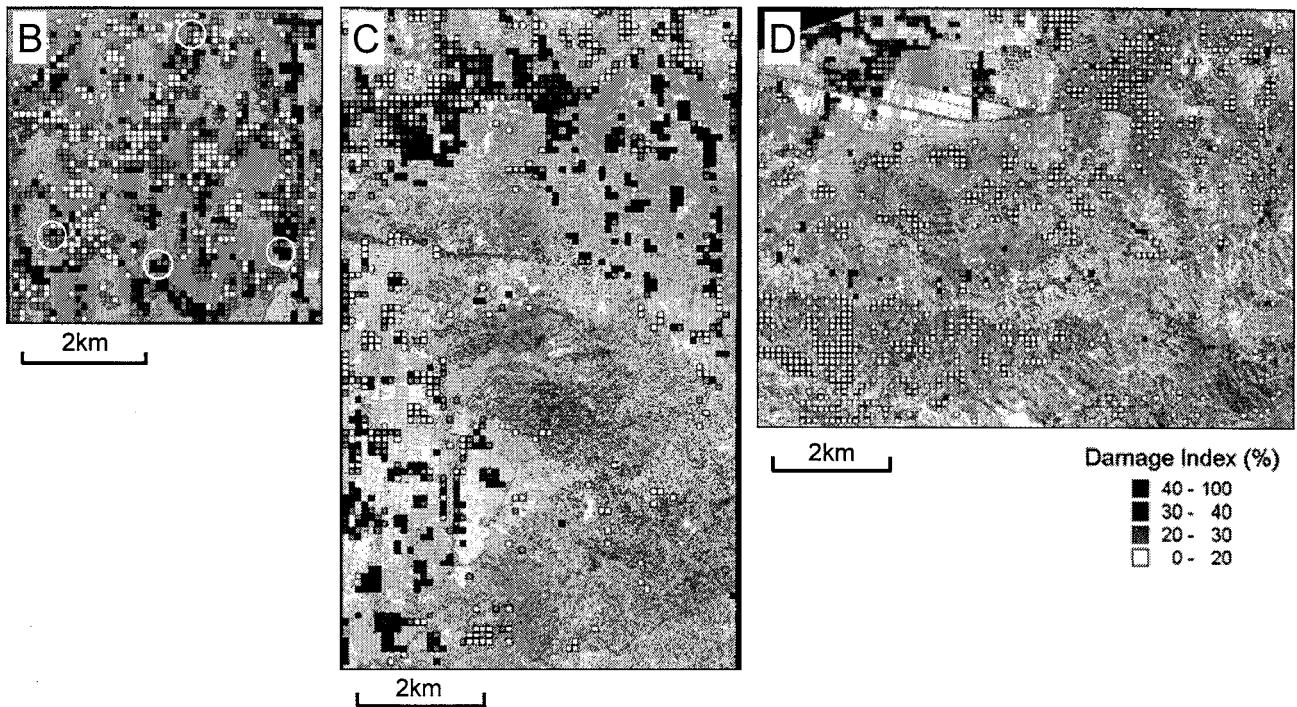


Fig. 6 Estimated damage estimation of image B, C, and D.

$$DI = ND / (ND + NU) \times 100 \quad (1)$$

Higher DI indicates larger area occupied by severely damaged buildings in the classification. The distribution of DI computed from the classified image (A) are illustrated in Fig. 4(c). The figure shows that high DI area that indicates severely damaged area is widely distributed. The distributions of DI in the images (B, C, and D) are shown in Fig. 6. As shown in the B image, the damage in the central part of Bantul is not so severe while extensive damage is observed in the southern and eastern area. The estimated damage distribution in Bantul and Imorigi almost agree with the UNOSAT map. The high DI areas are also observed in the northern and southern part of C image and the north-western part of D image. These results suggest the building damage is also severe in the southern part of Klaten located in relatively far from the epicenter.

4. COMPARISON WITH DAMAGE STATISTICS

In the epicentral region, such as Bantul and Imogiri, the field survey for building damage was conducted by the Japanese survey team of structural engineers (Maeda *et al.*, 2007). The open circles in the image A of Fig. 4 and the image B of Fig. 5 indicates the survey points. The centers of the points indicate the locations of the public buildings (schools and town offices) whose damage levels were minutely investigated by the survey team. The damage statistics for the residential houses were also collected in an about 250m radius of the public buildings. The damage level of each building was classified into three categories (Severe, Moderate, and Limited). Approximately from 15 to 60 buildings are investigated in each survey area.

Figure 7 shows the comparison between the damage ratio of severe damaged buildings in the damage statistics and the DI computed from the classified images. Since the survey area covers a dozen of meshes, the averages and their standard deviations of DI are indicated by circle and error bar, respectively. In this figure, as the damage ratio increases, DI also seems to increase, although the

standard deviations vary widely. The trend of the computed DI almost agrees with the severe damage ratio. The results show that the image classification technique and the computation of DI are valid for the identification of the building damage. In the future works, the result of the image classification of not only post-earthquake images but also pre-earthquake images would be included in the analysis for more reliable classification.

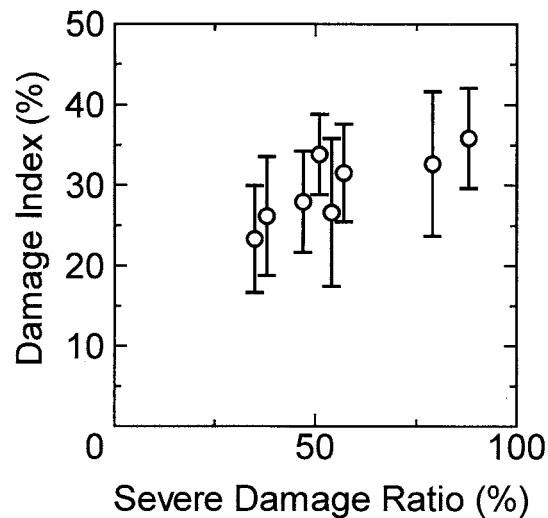


Fig. 7 Comparison between observed damage ratio (severe damage) and damage index computed from classified image

5. CONCLUSIONS

In this study, the areas damaged by the 2006 Central Java earthquake are identified from the high-resolution satellite images. Based on the field survey for the spectral reflectance of surface materials, the image classification technique is applied to post-earthquake QuickBird images to detect the areas covered with bricks (damaged buildings) and the areas covered with roof tiles (undamaged buildings). The distribution of the building damage is evaluated by computing Damage Index (DI) from the classified images. The severely damaged areas are distributed not only in Bantul and Imogiri, located near the epicenter, but also in Gantiwarno, the southern part of Klaten located 20-30km away from the epicenter. The distribution of the DI is compared with the damage statistics by the field survey. The result shows that the DI almost agrees with the severe damage ratio. The image classification allows us to analyze the wide-area image quickly compared with the visual interpretation. Although the coverage of the high-resolution satellite images is narrower than that of other optical images, such as Landsat/TM and ASTER images, the detailed damage distribution can be identified if the required images are available.

Acknowledgements:

This study was partially supported by the Ministry of Education, Science, Sports, and Culture, Grant-in Aid for Special Purpose No.1890001 (Representative: Prof. Hiroshi Kawase) and the Center for Urban Earthquake Engineering, Tokyo Institute of Technology. The authors gratefully acknowledge Prof. Yukio Kosugi, Tokyo Institute of Technology for providing one of the QuickBird images.

References:

- International Charter "Space and Major Disaster" (2006), <http://www.disasterscharter.org/>.
- Maeda, T., Kono, S., Sanada, Y. and Takahashi, N. (2007), 5.3.3 Damage of Residential Houses, *Reconnaissance Report of Building Damage due to the 27 May 2006 Central Java, Indonesia Earthquake*, Architectural Institute of Japan (in press).
- Matsuoka, M., Yamazaki, F. and Midorikawa, S. (2000), Characteristics of Satellite Optical Images in Areas Damaged by the 1995 Hyogo-Ken Nanbu Earthquake, *Journals of the Japan Society of Civil Engineers*, No.668/I-54, pp.177-185 (in Japanese with English abstract).
- Murakami, H., Pramitasari, D. and Kawase, H. (2006), Damage Distribution and Seismic Intensity Estimation in the 2006 Central Java Earthquake, *Proceedings of the Annual Conference of the Institute of Social Safety Science*, No.19, pp.43-46 (in Japanese with English abstract).
- Pohl, C. and Van Genderen, J. L., (1998), Multisensor Image Fusion in Remote Sensing: Concepts, Methods and Applications, *International Journal of Remote Sensing*, Vol.19, No.5, pp.823-854.
- Takagi, M. and Shimoda, H. (2004), *Handbook of Image Analysis (Revised Edition)*, University of Tokyo Press, 1991p.
- UNOSAT (2006), Indonesia Maps, <http://unosat.web.cern.ch/unosat/asp/>.

DAMAGE DETECTION TECHNIQUE USING SATELLITE SAR IMAGERY AND ITS APPLICATION TO RECENT EARTHQUAKES

M. Matsuoka ¹⁾, F. Yamazaki ²⁾, K. Horie ³⁾, and H. Ohkura ⁴⁾

1) Team Leader, Earthquake Disaster Mitigation Research Center (EDM), NIED, Japan

2) Professor, Dept. of Urban Environment Systems, Chiba University, Japan

3) Researcher, Disaster Reduction and Human Renovation Institute, Japan

*4) Senior Researcher, National Res. Inst. for Earth Sci. and Disaster Prevention (NIED), Japan
matsuoka@edm.bosai.go.jp, yamazaki@tu.chiba-u.ac.jp, horiek@dri.ne.jp, ohkura@bosai.go.jp*

Abstract: Synthetic aperture radar (SAR) has the remarkable ability to examine the Earth's surface, regardless of weather or sunlight conditions. A SAR-based remote sensing system can assess the damage to areas affected by large-scale disasters at an early stage. This can aid in recovery planning. An earthquake of magnitude (Mw) 6.5 occurred in the Chuetsu area, Niigata prefecture, Japan on October 23, 2004 and caused serious damage. Canadian satellite, Radarsat, captured the affected area using SAR sensor before and after the earthquake. On May 27, 2006 an earthquake struck Yogyakarta, Central Java, Indonesia, causing human suffering and severe building damage. PALSAR (Phased Array Type L-band Synthetic Aperture Radar) onboard the Japanese ALOS "Daichi" imaged the affected areas on the morning following the earthquake. This paper applies a damage detection technique based on the difference of pre-seismic and co-seismic correlation coefficients calculated from the three time-series images of the SAR dataset for both earthquakes. From a macroscopic point of view to the 2004 Niigata earthquake, the distributions of difference value of the correlation coefficients in built-up areas were in good agreement with damage reported in survey reports. In Yamakoshi village, located in the highlands, we could also identify large-scale landslides with accuracy as good as that of interpretation from aerial photos. From the Central Java earthquake, the estimated damage distribution closely matched damage assessment derived from high-resolution satellite images and field surveys. Then, we examine the relationship between the difference in correlation coefficients and severe building-damage ratio derived from the field survey data. Finally, the sub-district-based mapping of severe damage ratio using SAR imagery is performed and we demonstrate that the estimated result shows the good agreement to the damage statistics of the earthquake.

1. INTRODUCTION

Recently, international frameworks have been formed to exploit the observation data of satellites launched by various countries, and remote sensing technology has been increasingly used as a means of early detection of the extent of the disasters that are occurring frequently across the globe. One such framework is the International Charter "Space and Major Disaster" (International Charter 1999), which aims to promote the contribution of earth observation satellites to disaster management. Since 2003, the charter has been activated more than 20 times a year, which indicates that large-scale natural disasters are occurring at the frequency of about twice a month globally, and produced baseline and damage maps of the affected areas. However, since these visual interpretations are based on optical sensor images, damaged areas may not be visible due to clouds and cloud shadows, even if there is an early opportunity for observation. Satellites loaded with a synthetic aperture radar (SAR) are capable of observing the ground surface condition of a disaster-stricken area through clouds by day or night, but visual damage interpretation from SAR images is difficult, except in situations that have

significant influences on backscattering properties, such as inundation due to flood. The International Charter has published a few SAR-based thematic maps of damage to buildings, roads, and other social infrastructure. To use SAR images for damage detection, appropriate image processing is essential.

From the experiences of the 2004 Niigata-ken Chuetsu, Japan earthquake, we, the authors, have proposed a technique to automatically detect areas of large-scale damage, such as collapsed buildings (Matsuoka et al. 2006), based on the two pairs (pre-seismic and co-seismic) of SAR images to identify smaller building damage ratios in less densely built-up areas as compared to the previous technique (Matsuoka and Yamazaki 2004). In this paper, we show the result of damage estimation for the 2004 Niigata-ken Chuetsu earthquake and we also apply the technique to the 2006 Central Java, Indonesia earthquake. The two damage estimates are then compared with the damage assessment through field surveys and high-resolution satellite imagery.

2. DAMAGE DETECTION TECHNIQUE

Backscattering intensity is affected by the microwave wavelength and its incident angle, as well as the variability and dielectric characteristics of the ground. When only considering ground variability, microwaves aimed at urban areas backscatter more due to multiple reflections. The interaction between structures and the ground is called the “cardinal effect.” Due to multi-directional scattering, microwaves aimed at open spaces or areas with collapsed buildings experience less backscattering. Based on these properties of microwave scattering, we have developed an automated method for detecting areas with severe damaged buildings using pre- and post-event SAR images from the Kobe earthquake (Matsuoka and Yamazaki 2004).

A recent application of this method to the 2004 Niigata-ken Chuetsu earthquake in Japan revealed the limitations of this method for damage assessment in rural areas (Matsuoka et al. 2006). By using an additional pre-event SAR image, we proposed a new technique that uses two pairs of SAR images to identify the smaller building damage ratios than that was possible with the previous technique, even in less densely developed areas. The crux of this technique for estimating building damage involves calculating the difference between the correlation coefficients of pre-seismic and co-seismic pairs to minimize the effect of signal noise and surficial changes over time.

To identify damaged areas, the following steps are performed: First, three multi-looked intensity images are prepared: two taken before the earthquake and one taken after. The dates on which the images were acquired should be as close as possible to the day the earthquake occurred and the conditions under which the images were collected should be as similar as possible. After co-registering the SAR images, each image is filtered using a filter (Lee 1980) with a 21×21 pixel window. The correlation coefficient r within a local window (13×13 pixels) is calculated from the two filtered images. From the pair of pre-event images and the pair of images (one pre-event and one post-event) spanning the seismic event, the correlation coefficients, r_{bb} and r_{ab} , are derived. Finally, the difference in the correlation coefficients, $r_{dif} = r_{ab} - r_{bb}$, is calculated for areas where the correlation coefficient r_{bb} is larger than 0.8. The magnitude of the decrease in the r_{dif} value indicates increased surficial change (indicative of damage).

3. EARTHQUAKE AND SAR DATA

3.1 The 2004 Niigata-ken Chuetsu, Japan Earthquake

On October 23, 2004, an earthquake of magnitude (Mw) 6.5 occurred in the Chuetsu area, Niigata Prefecture, and caused serious damage: 40 people died, approx. 3, 000 people were injured, and more than 10,000 residential houses collapsed completely or partially. The earthquake also caused

significant damage to road facilities, agricultural facilities, and lifelines due to slope failures, liquefactions, etc. Particularly, in the former Yamakoshi village, located close to the epicenter, where the frequency of landslide occurrences is one of the highest in Japan, many slope failures and landslides occurred. Since the earthquake occurred in the evening, damage information collected immediately after the earthquake was limited. Two days after the earthquake, the Canadian Space Agency's SAR-loaded Radarsat satellite observed the disaster-stricken area in fine mode (C band, HH polarization, approx. 9m spatial resolution). For our study, we performed a geometric correction and conversion on backscattering intensity from SLC (Single Look Complex) data. Figure 1(a) shows the area of the image. There are also two pre-earthquake observational images of September 7 and October 1, 2004. Figure 2 shows the series of backscattering intensity images of the damaged areas. The incident angle is approx. 36 degrees for all images.

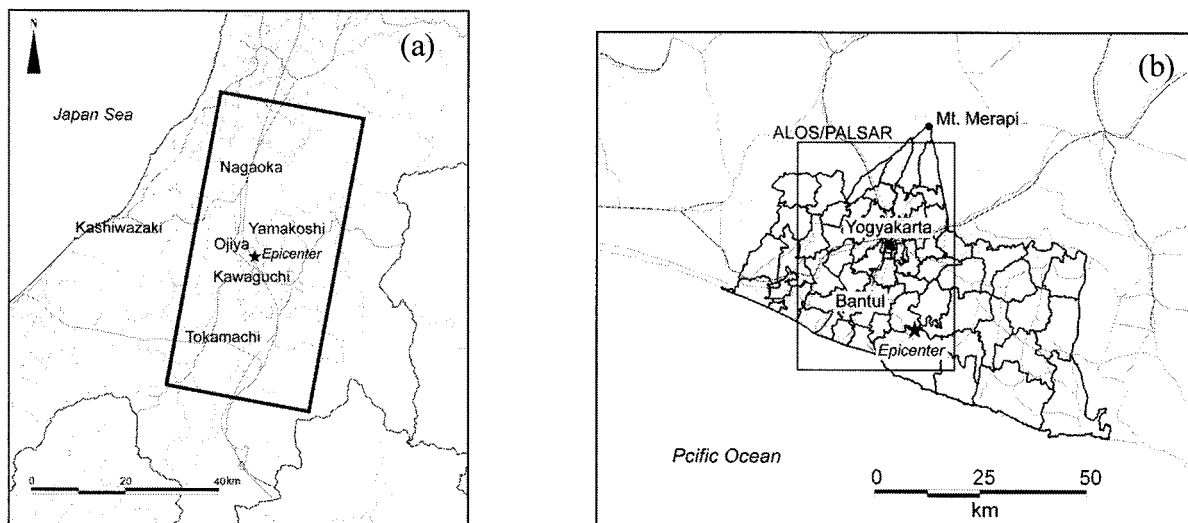


Figure 1 Scope of Analysis Area (a) the 2004 Niigata-ken Chuetsu Earthquake, (b) the 2006 Central Java Earthquake

3.2 The 2006 Central Java, Indonesia Earthquake

The Advanced Land Observing Satellite, ALOS (nicknamed “Daichi”), was launched on January 24, 2006, by the Japan Aerospace and Exploration Agency (JAXA). The onboard sensors [PRISM, AVNIR-2, and PALSAR (Phased Array Type L-band Synthetic Aperture Radar)] on ALOS have acquired images soon after natural disasters, including the Leyte Island mudslide that occurred in the Philippines on February 17; the volcanic eruptions of Mt. Merapi, Indonesia from April to May; and the flooding in the northern portion of the Kingdom of Thailand on May, 2006.

Then, a strong earthquake (Mw 6.3) occurred near Yogyakarta, Indonesia, in the early morning on May 27, 2006. The earthquake killed over 5,700 people, injured between 40,000 and 60,000 more, and left over 200,000 people homeless. Approximately 150,000 houses were destroyed and 200,000 were damaged (BAPPENAS 2006). Through the disaster charter, the abilities of the L-band SAR system, PALSAR (HH polarization, 9-meter resolution) onboard ALOS to detect damage were tested. The impact of the May 27 earthquake was observed in Yogyakarta and the Central Java provinces by using a microwave transmission angle of 36.9 degrees off-nadir angle on the day following the earthquake. The area imaged and analyzed is shown in Figure 1(b). Two PALSAR images taken prior to the event on April 29 and May 16, 2006 (with transmission angles of 34.3 and 30.8 degrees off-nadir, respectively) were used to evaluate the effect of signal noise and stationary temporal changes. Figure 3 shows the series of PALSAR backscattering intensity images of the damaged areas.

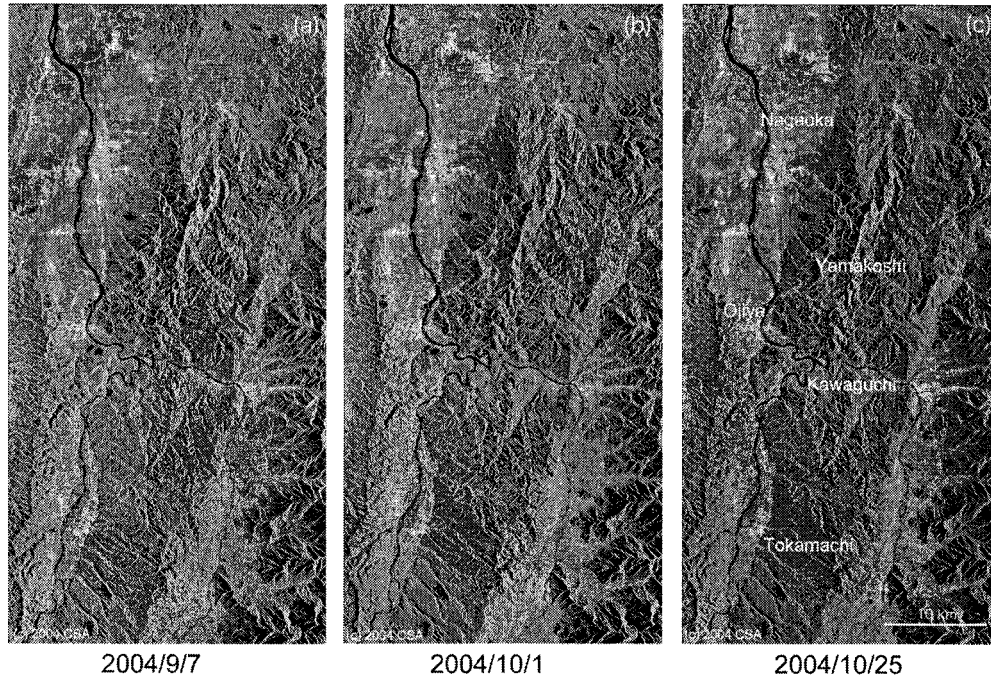


Figure 2 Backscattering Intensity Images of Niigata-ken Chuetsu Region Observed by Radarsat

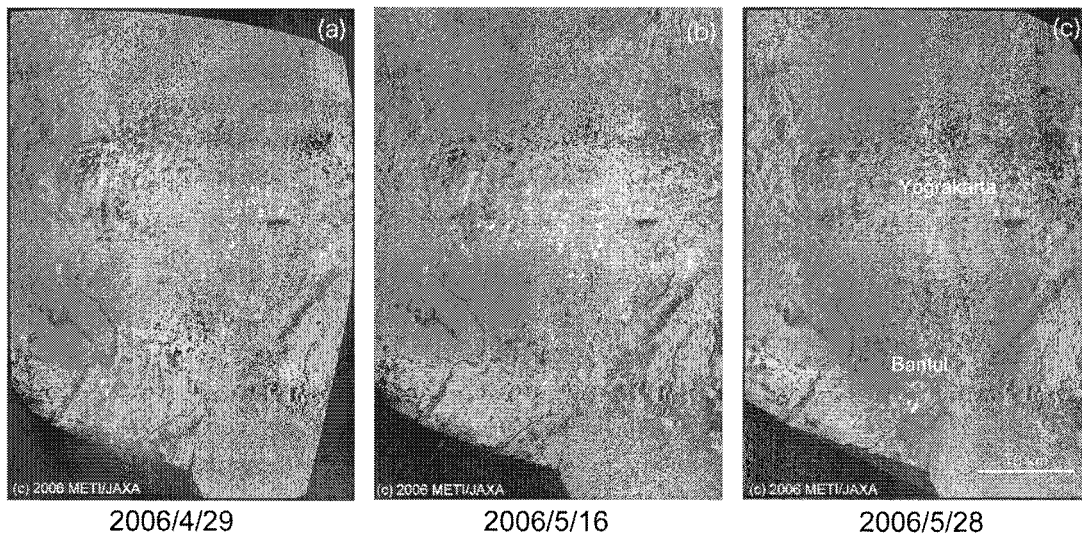


Figure 3 Backscattering Intensity Images of Central Java Observed by ALOS/PALSAR

4. DAMAGE ESTIMATION AND COMPARISON WITH ACTUAL DAMAGE

We applied the above described damage detection technique to the SAR dataset. For the Niigata-ken Chuetsu earthquake, Figure 4 shows the distribution of the difference of correlation coefficients r_{dif} overlaid on the intensity image. Areas that have a higher probability of damage are painted with darker colors. The areas with small r_{dif} value are distributed from Ojiya city to Kawaguchi-machi, the areas which suffered severe damage. On the other hand, in Nagaoka city and

Tokamachi city, the values are large. This is in good agreement with the report (Yoshimi et al. 2005) that investigated the building damage over a wide area. The areas where the severe-damaged building rate is 50% or above almost correspond to the area where the r_{dif} value is -0.15 or below. In the figure, areas with small r_{dif} values are present locally in the mountainous areas around former Yamakoshi village, and their distribution is in good agreement with the locations of slope failures (Geological Survey Institute 2004) interpreted from aerial photographs and with the damaged area estimated from the vegetation index of the IKONOS satellite (Miura and Midorikawa 2006). We consider the correlation coefficient to have been reduced as the irregularity of the ground surface changed due to landslides and slope failures. As to the mountainous areas, however, due to the influences of lay over, foreshortening, and shadow effects peculiar to SAR images, there are cases that are difficult to detect depending on their locations.

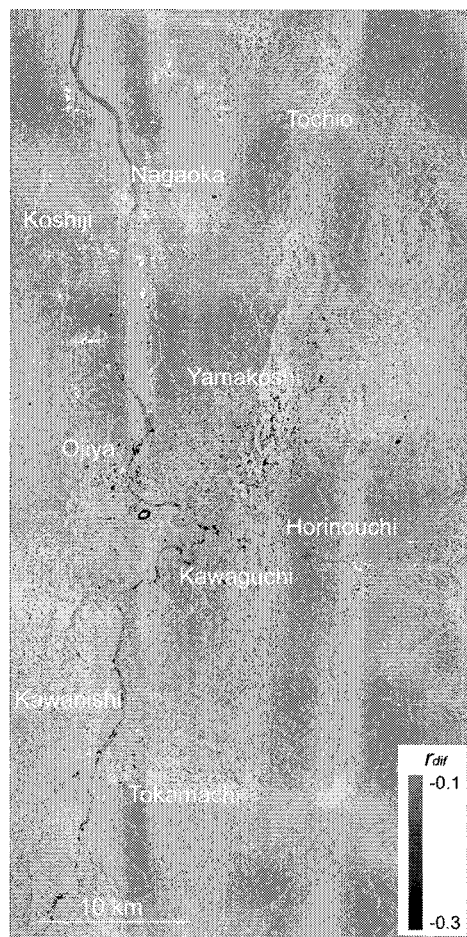


Figure 4 Distribution of the Difference, r_{dif} , between Correlation Coefficients Calculated from Radarsat/Fine Images of the 2004 Niigata-ken Chuetsu Earthquake (The background represents the pre-event intensity image taken on October 1, 2004.)

For the Central Java earthquake, the distribution of the difference, r_{dif} , between the r_{bb} value of the two pre-event images and the r_{ab} of the pre- and post-event images overlain on the PALSAR intensity image is shown in Fig. 5. In Yogyakarta province, the lower r_{dif} areas are distributed from southwest to northeast and correlate well with the damage estimates from visual surveys by high-resolution satellite images (UNOSAT 2006). A Japanese field team surveyed buildings and calculated the ratio of severely damaged buildings (Maeda et al. 2007). Figure 5 also shows twelve areas (white-hollow-circles) investigated according to the r_{dif} distribution.

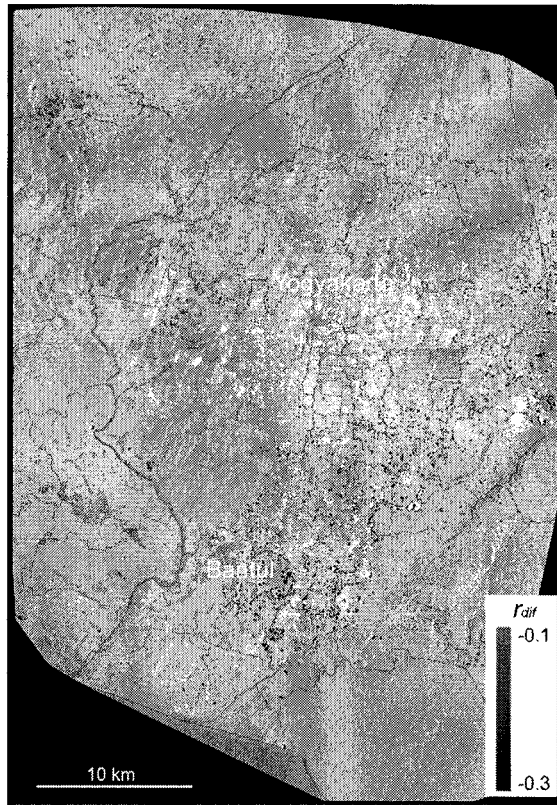


Figure 5 Distribution of the Difference, r_{dif} , between Correlation Coefficients Calculated from ALOS/PALSAR Images of the 2006 Central Java Earthquake (The background represents the pre-event intensity image taken on May 16, 2006. White circles indicate areas surveyed by ground teams (Maeda et al. 2007).)

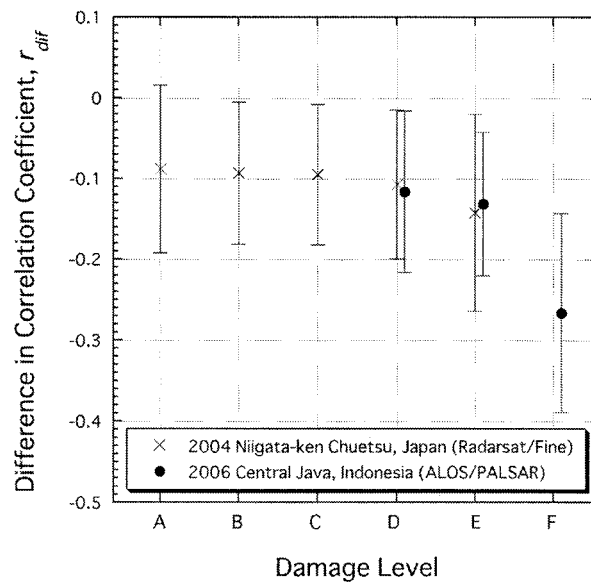


Figure 6 Relationship between Building Damage Levels and the r_{dif} (Damage levels is classified as A, B, C, D, E, and F corresponding to damage ratios of 0-6.25%, 6.25-12.5%, 12.5-25%, 25-50%, 50-75% and 75-100%, respectively.)

Table 1 Range of the r_{dif} for Corresponding to Building Damage Level

Damage Level	Severe Damage Ratio (%)	Difference in Correlation Coefficient, r_{dif}
A	0 — 6.25	— (-0.08)
B	6.25 — 12.5	(-0.08) — (-0.09)
C	12.5 — 25	(-0.09) — (-0.10)
D	25 — 50	(-0.10) — (-0.13)
E	50 — 75	(-0.13) — (-0.19)
F	75 — 100	(-0.19) —

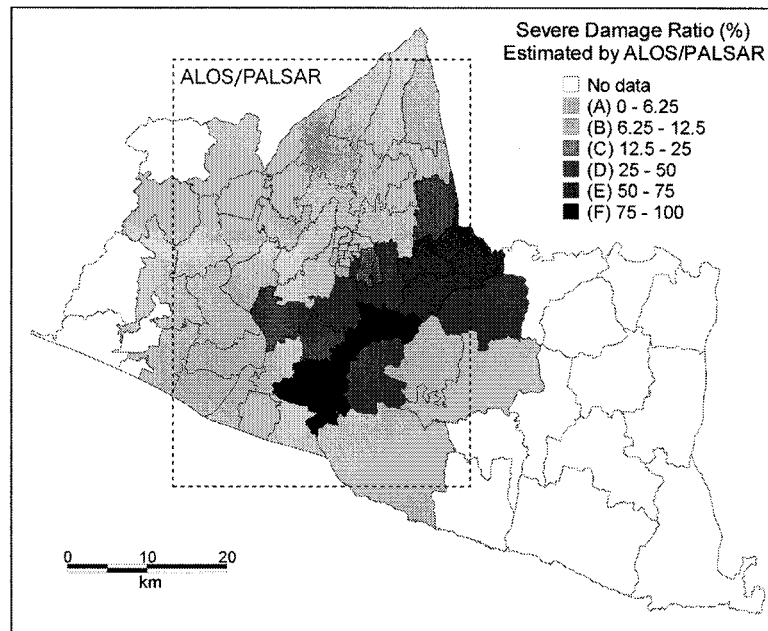


Figure 7 Sub-district-based Distribution of Building Damage Rates Estimated from the r_{dif} of ALOS/PALSAR Imagery

For our quantitative analysis, we chose pixels within the circles examined by field survey teams and calculated average values and standard deviations for the r_{dif} in each damage level. Considering precedent studies (Matsuoka et al. 2006), the severe damage rates 0 to 6.25%, 6.25 to 12.5%, 12.5 to 25%, 25 to 50%, 50 to 75%, and 75 to 100% are defined to be damage level A, B, C, D, E, and F respectively. Figure 6 shows the relationship between the damage level based on the data of the damage survey and the difference value, r_{dif} , adding the result of Ojiya city damaged by the Niigata-ken Chuetsu earthquake (Matsuoka et al. 2006). In Fig. 6, as the damage level increases, the difference between correlation coefficients decreases, although standard deviations vary widely. To evaluate simply, the thresholds and ranges of r_{dif} value are estimated for corresponding to the damage levels (Table 1). Overlaying the r_{dif} distribution on the GIS data of sub-district borderline, we extracted the image pixels and calculated the average value of the r_{dif} for each sub-district area. Using the relationship shown in Table 1, the sub-district-based damage mapping was estimated from the dataset of PALSAR imagery, as shown in Fig. 7. The result correlates well with the damage statistics report (Murakami et al. 2006).

5. CONCLUSIONS

We applied the building damage area detection technique, which is based on difference, r_{dif} value, of pre-seismic and co-seismic correlation coefficients calculated from the three time-series images of the SAR dataset for the 2004 Niigata-ken Chuetsu, Japan and the 2006 Central Java, Indonesia earthquakes and studied the r_{dif} value's relationship to the severe-damaged building rates. As a result, it was proved that the r_{dif} value and the damage levels closely correspond, and that damage can be detected even in less densely built-up areas. The technique also suggests the possibility of detecting areas of slope failures. In the case of damage detection, areas where water boundaries change significantly, such as river bars and regulating reservoirs, are also detected (see Fig. 4). To avoid these misinterpretations, it is essential to compare the detection result with the original image rather than reading the damaged area solely from the detection result based on image processing.

Acknowledgements:

A part of this research was made possible by the grant-in-aid for scientific research (Research No. 17510155 and 1890001). ALOS data was provided by the Japan Aerospace Exploration Agency (JAXA) under the collaborated research project. Radarsat is owned by the Canadian Space Agency. We would like to extend our thanks to these supports.

References:

- BAPPENAS, Provincial and Local Government of D.I.Yogyakarta and Central Java (2006), *Preliminary Damage and Loss Assessment, Yogyakarta and Central Java Natural Disaster*, 15th Meeting of the Consultative Group on Indonesia, Jakarta, Indonesia.
- Geological Survey Institute (2004), *Disaster Map: Distribution of Landslide due to the 2004 Niigata-ken Chuetsu Earthquake*, <http://zgate.gsi.go.jp/niigatajishin/> (in Japanese).
- International Charter "Space and Major Disaster," (1999), <http://www.disasterscharter.org/>.
- Lee, J.S. (1980), "Digital Image Enhancement and Noise Filtering by Use of Local Statistics," *Transactions on Pattern Analysis and Machine Intelligence*, **2**(2), 165–168.
- Maeda, T., Kono, S., Sanada, Y., and Takahashi, N. (2007), "5.3.3 Damage of Residential Houses," *Reconnaissance Report of Building Damage due to the 27 May 2006 Central Java, Indonesia Earthquake*, Architectural Institute of Japan (in press).
- Matsuoka, M. and Yamazaki, F. (2004), "Use of Satellite SAR Intensity Imagery for Detecting Building Areas Damaged due to Earthquakes," *Earthquake Spectra*, **20**(3), 975–994.
- Matsuoka, K., Horie, K., and Ohkura, H. (2006), "Damage Detection for the 2004 Niigata-ken Chuetsu Earthquake Using Satellite SAR," *Proc. of SPIE Asia-Pacific Remote Sensing Symposium*, Paper No.6412-24.
- Miura, H. and Midorikawa, S. (2006), "Slope Failure by the 2004 Niigata-ken Chuetsu, Japan Earthquake Observed in High-resolution Satellite Images," *Proc. of 4th International Workshop on Remote Sensing for Post-Disaster Response*, CD-ROM.
- Murakami, H., Pramitasari, D., and Kawase, H. (2006), "Damage Distribution and Seismic Intensity Estimation in the 2006 Central Java Earthquake," *Proc. of the Annual Conference of the Institute of Social Safety Science*, (19), 43–46 (in Japanese).
- UNOSAT (2006), *Indonesia Maps*, <http://unosat.web.cern.ch/unosat/asp/>.
- Yoshimi, M., Komatsubara, T., Miyachi, Y., Kimura, K., Yoshida, K., Sekiguchi, H., Saeki, M., Ozaki, M., Nakazawa, T., Nakashima, R., Kunimatsu, S., and Saomoto, H. (2005), "Preliminary Report on the 23 October 2004 Niigata-ken Chuetsu Earthquake: Landforms and Local Site Effects in Heavily Damaged Areas," *Chishitsu News*, (607), 18–28 (in Japanese).

STUDY ON DISASTER INFORMATION LINKAGE BETWEEN FIRE HEADQUARTERS AND LOCAL GOVERNMENT — A CASE STUDY FOR LANDSLIDE DISASTER —

T. Mizuta¹⁾ and K. Asano²⁾

1) Associate Professor, Dept. of Civil and Environmental Engineering, Akita National College of Technology, Japan

2) Associate Professor, Dept. of Architecture and Environment Systems, Akita Prefecture University, Japan

t-mizu@ipc.akita-nct.ac.jp, asano@akita-pu.ac.jp

Abstract: Objective in this study is implementation of two-way information support system between residents, Fire Headquarters and local government to prevent and reduce damage from landslide disaster. First, real-time slope failure potential prediction system is experimentally constructed by using rainfall observation information. Second, a system is developed for Fire Headquarters to be able to specify the disaster location by extracting area descriptions from reporter when precise location information cannot be given on emergency call. Third, support system is built to contribute to following situations: Residents, Fire Headquarters and local government share disaster information that has likely been a fragment; local government confirms and reconstructs the critical location; Fire Headquarters take quick action when disaster occurs.

1. INTRODUCTION

In recent years, online provision of real-time observation information for such rainfall and groundwater level is growing. Therefore utilization of Internet is expected for disaster prevention. Releasing such time series disaster information of slope failure from local government to Fire Headquarters is considered to reduce disaster damage.

Since the enactment of “promotion of security measure for disaster prevention in danger area” on April 2001, security plan has been promptly reviewed throughout the country. However, this is not helping its improvement (Ushiyama et al. 2003). One reason can be an undeveloped system structure to share necessary information between residents and Fire headquarters.

Therefore, this study reports the result by investigating experimental system that supports; residents, Fire Headquarters and local government to share disaster information that has been likely fragment between them; local government to confirm and reconstruct critical location in usual situation; and Fire Headquarters take quick action when disaster occurs.

2. OUTLINE OF SLOPE FAILURE INFORMATION SYSTEM

Fig.1 shows the outline of slope failure information system. This is the two-way information support system between Fire Headquarters, local government and residents, which contributes to prevent and reduce damage from landslide disaster. Public release system of landslide disaster, fast information-gathering system of disaster site and Municipal information system have been a joint

development of River management and Sabo Division of Akita Prefecture Department of Public works & Transportation, and Yurihonjo city government. Now the system is in process to be implemented. Black shaded part in the Fig.1 is the newly developed system.

“Real-time information processing system (Mizuta and Sugawara 2006)” and “Site determination system (Asano et al. 2005)” have been prepared by 2005, and basic system structure to realize two-way information support system between Fire headquarters, local government and residents was constructed. Connection of these systems can contribute to shorten rescue’s arrival time against the emergency call from mountain area where the site determination is difficult.

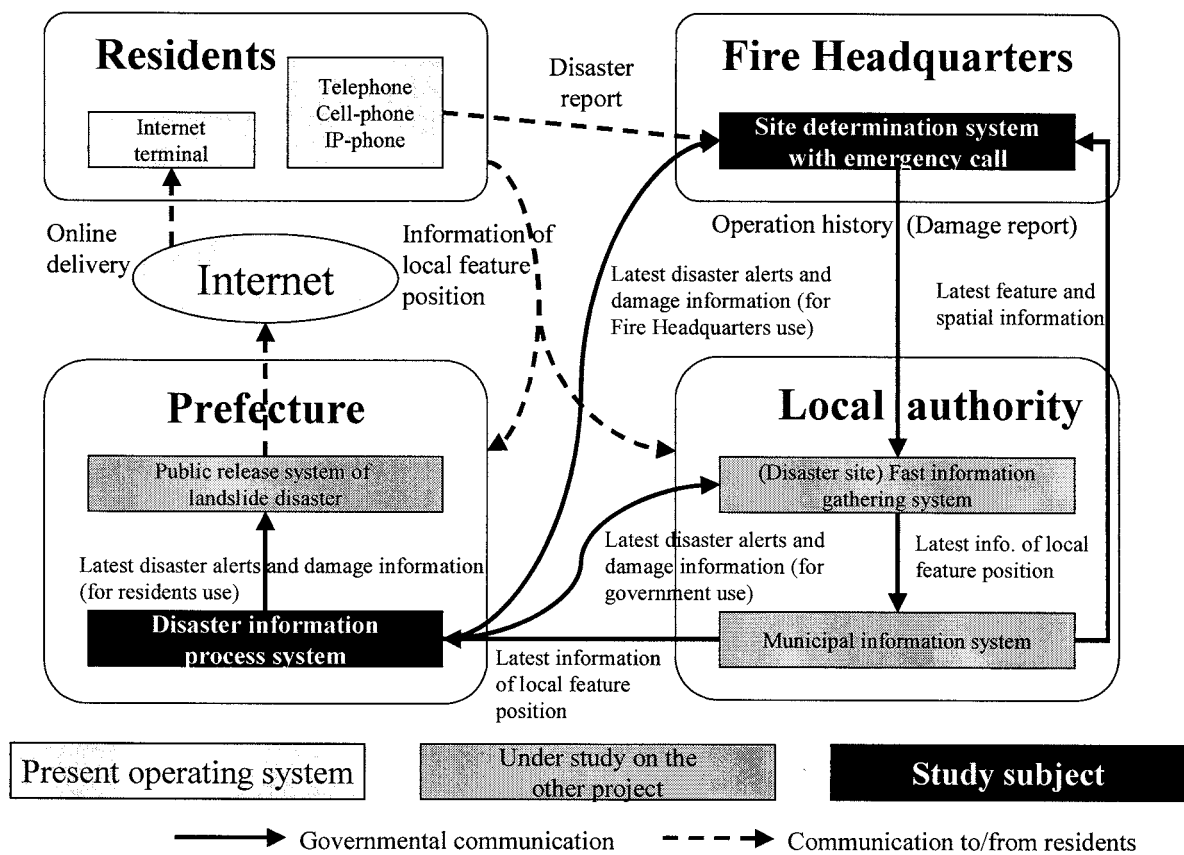


Figure 1 Slope Failure Information System

3. REAL-TIME CALCULATION SYSTEM OF SLOPE FAILURE INFORMATION

3.1 Use of Real-time Observation Data

Akita prefecture gathers rainfall information from over 40 observation stations. The rainfall information is instantly provided to related Sabo organs by using private line. With this circumstance, real-time Web delivery system for rainfall information of actually observed data is created by connecting to this rainfall observation system. Utilize this system, immediate action of import and application of the actually observed rainfall data is investigated. Fig.2 shows the example of the system.

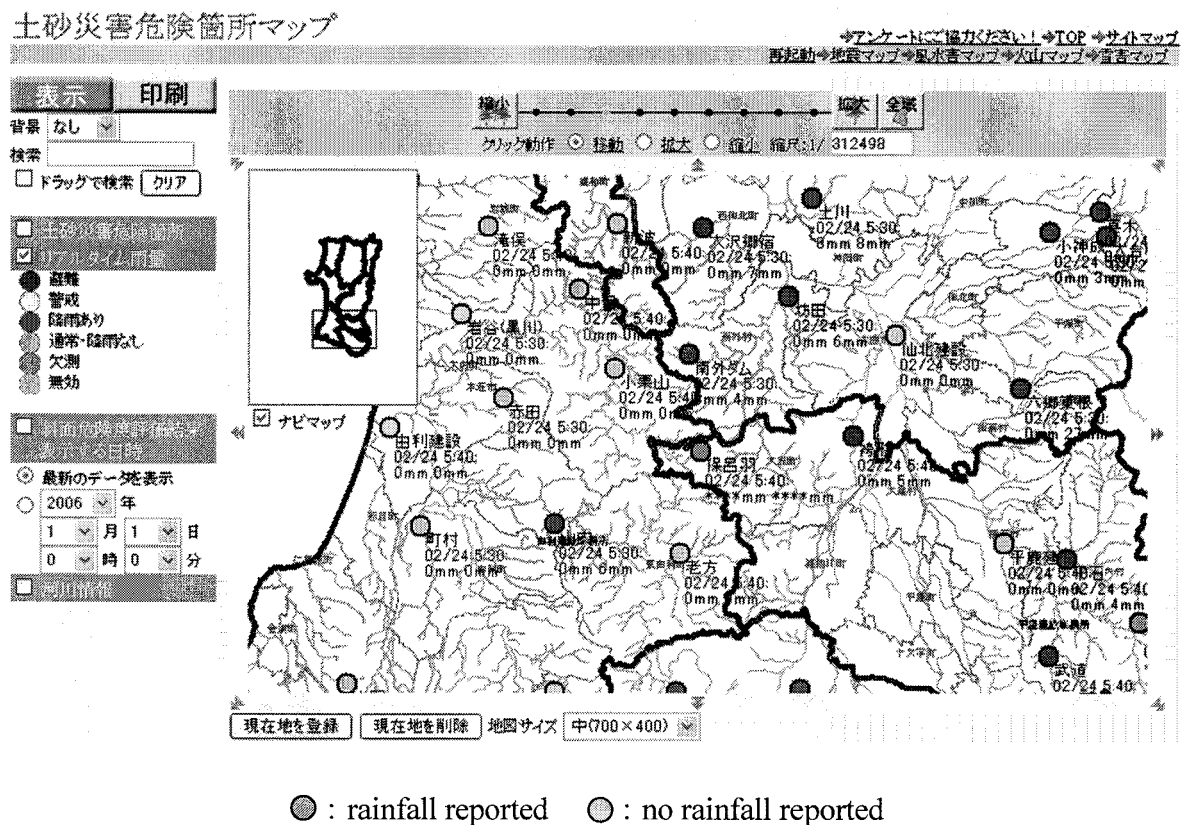


Figure 2 Web Delivery System for Rainfall Information

3.2 Experimental Model of Real-time Information Processing System

Real-time information processing system calculates slope failure potential in real time and provides Fire Headquarters a real-time slope failure risk information, which has been thought impractical. And thus, construction of real-time slope failure evaluation system, which is shown in Fig.3, is necessary for providing real-time information of slope failure risk information.

Experimental calculation system for slope failure potential was constructed by connecting the evaluation system to the rainfall observation system of Akita Sabo division (Fig. 4).

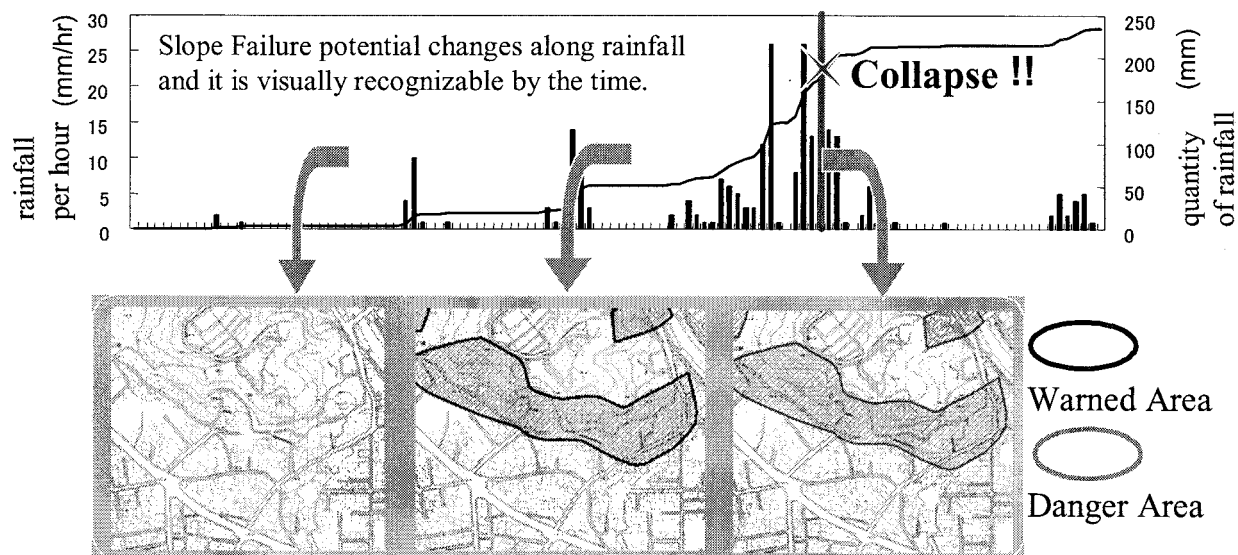


Figure 3. Outline of Real-time slope failure potential prediction system

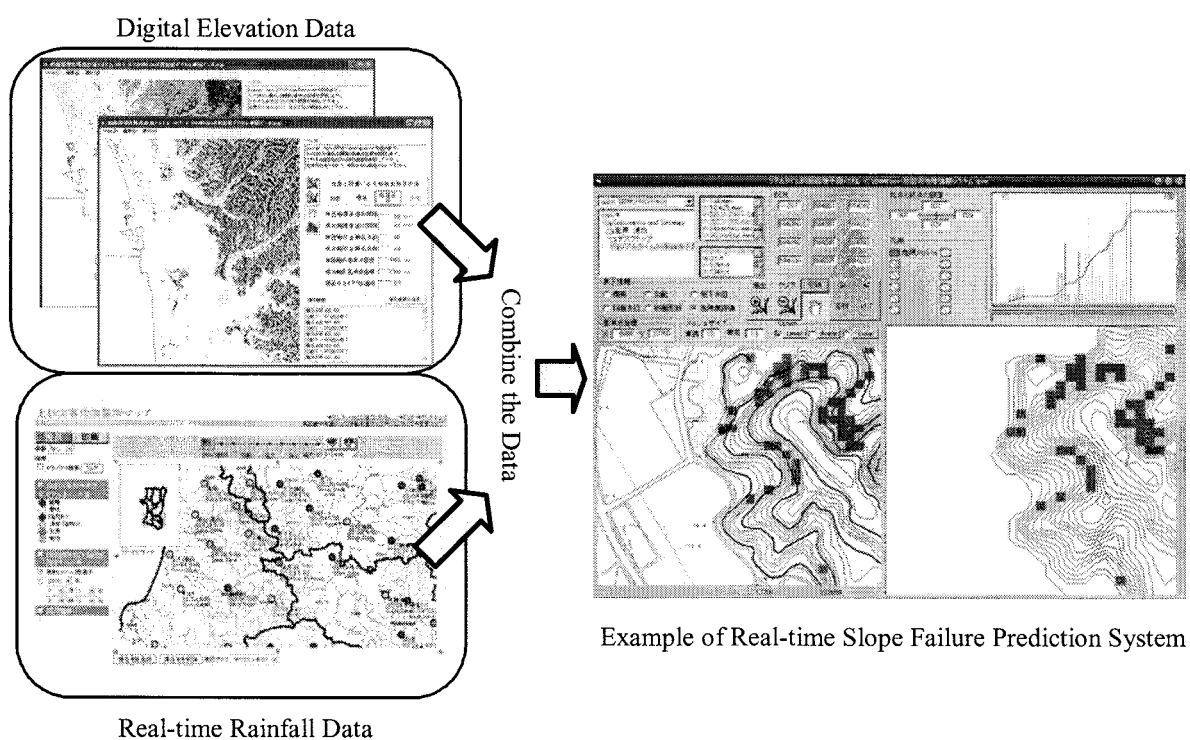


Figure 4 Real-time calculation system of slope failure information

4. SITE DETERMINATION SUPPORT SYSTEM

Based on the result of experiment of Real-time information processing system, Site determination support system is experimentally constructed to specify the accident/disaster site, including landslide disaster, against the emergency call.

4.1 Experimental Model of Fast Advanced Search System for Disaster Site

In the situation that cell phone and IP phone are difficult to be specified with their reporting points, there are growing cases that reporter can hardly describe their location in detail. Moreover, the emergency call from mountain area is also difficult for the location specification. Therefore, in case the reports made by cell phone and IP phone with no detailed description about local information, the experimental system has been constructed with a function that searches disaster site quickly by the information of neighbor features.

Flow chart of this experimental system is shown in the Fig.5. Firstly, reporter's present location with specific address or neighbor facility is asked. In case those are not effectively available, landmark of the site is then asked. If specific names or numbers (such as bus stop, power poll or taxi ID) are possibly reported, the location can be searched along given information. If no specific information is available, search will be made by combining informed features. In case the information is so few and imprecise, a rough determination will be made by asking reporter about the route to the present location.

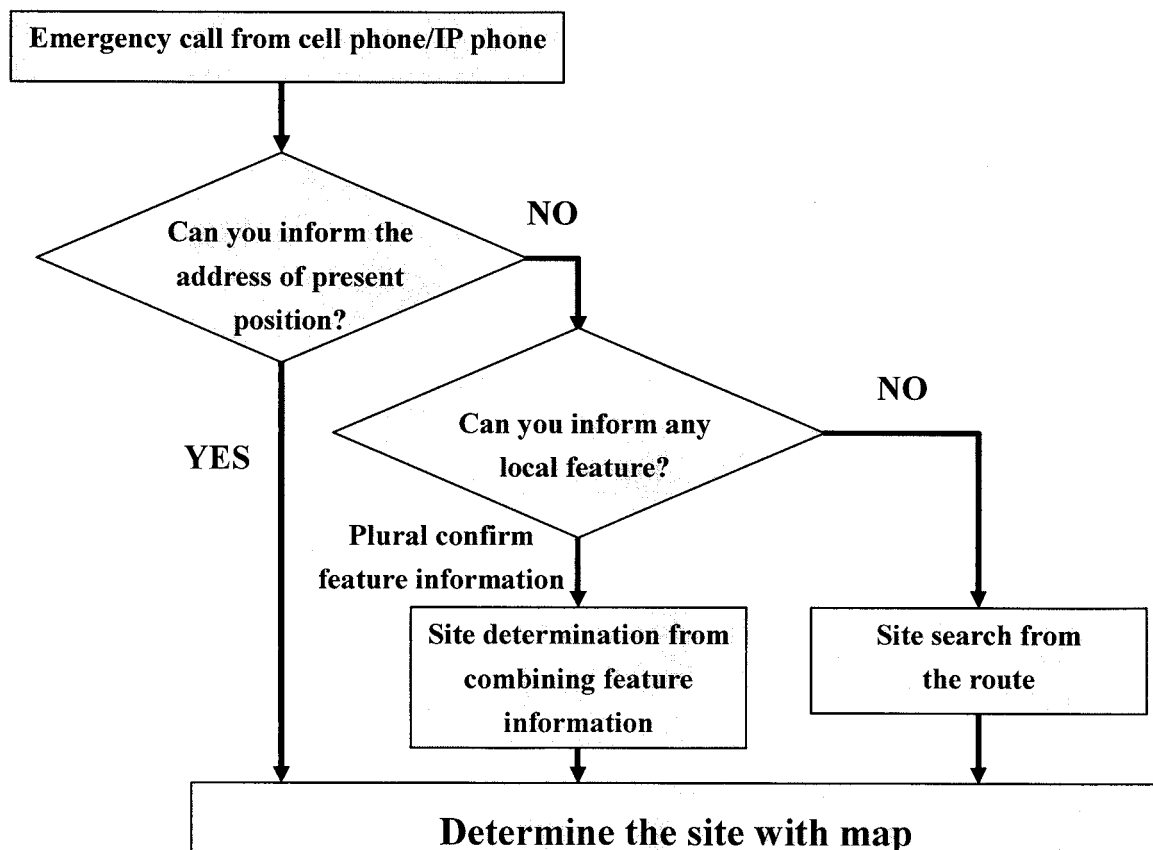


Figure 5 System flow chart

Fig.6 shows the example of fast advanced search system for disaster site that is consisted by 12 features, including post box, bus stop and vending machine. And, when alternate confirmation about location is needed, it can specify the site by checking visual data of QuickTimeVR movie, which liaises with GIS, with reporter. Fig.7 shows the example of image display to confirm report site.

Firefighter said that pan control of QuickTimeVR wouldn't be easy at the emergency situation. However, after consideration of changing operation to touch panel and adding diagram of viewing angle, they said that it would be effective in the case they station staff. Moreover, considering the viewpoint of Yurihonjo Fire station, we made site search and estimation available by using road network information that is used for giving route information when reporter reached the site by vehicle.

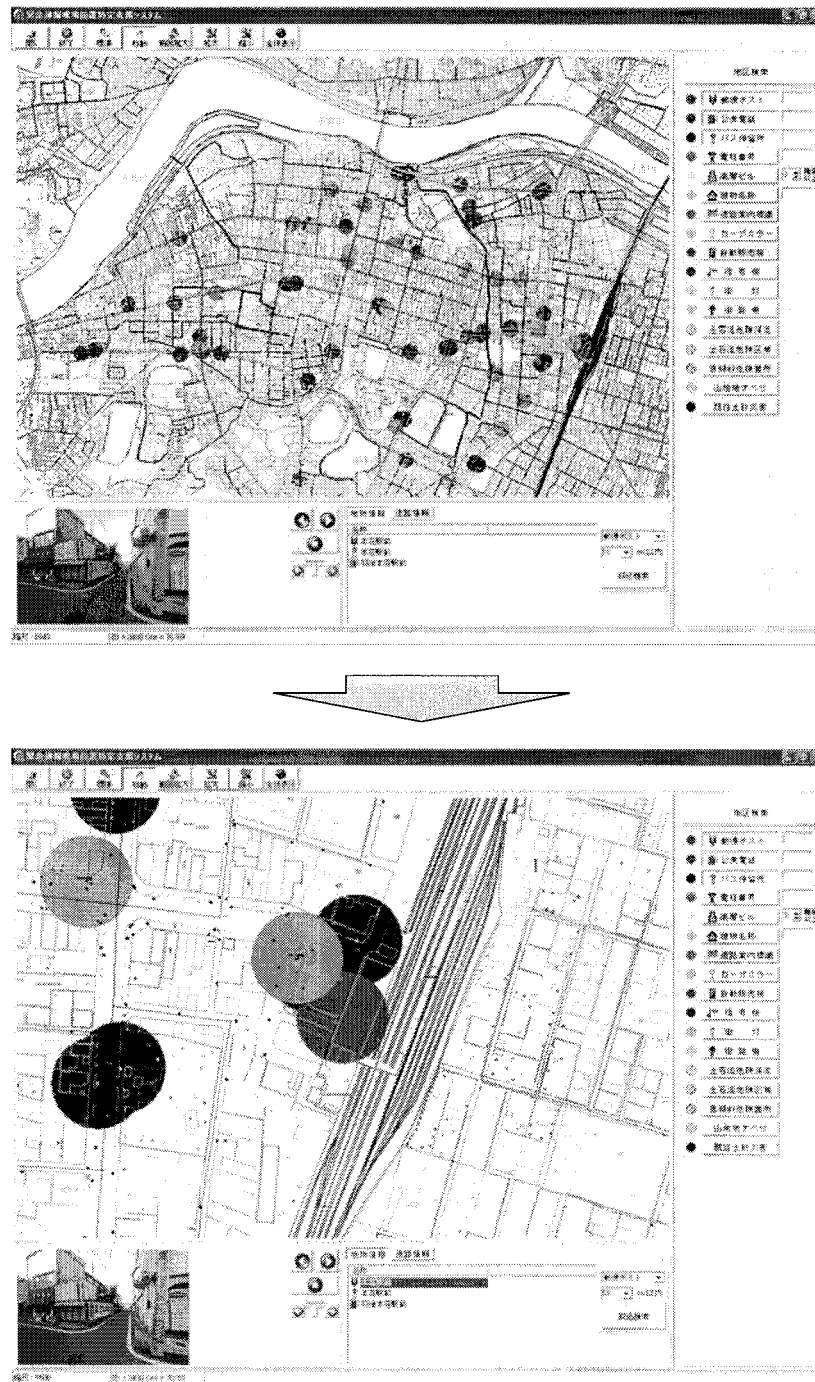


Figure 6 Fast advanced search system for disaster site
(Upper: search result from feature information Lower: example of report source determination)

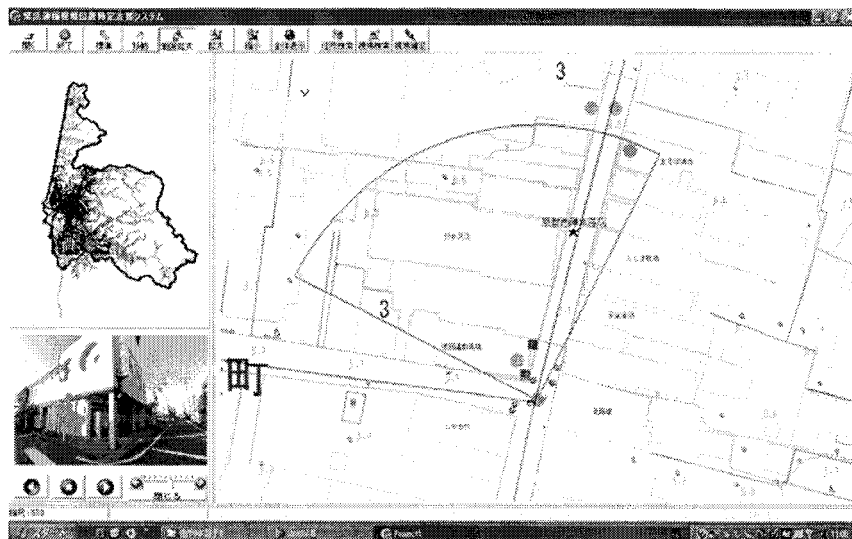


Figure 7 Image display to confirm report site (QuickTimeVR)
(Viewing indicator on the map rotate as tool button operated in lower left)

4.2 Share of Slope Failure Warning Function

Usually, danger area is prescribed on the system. However in alert condition, it's more effective if notification is made for imminent slope failure hazard by indicating selected location with real-time calculation system. Unlikely to traffic accident, site of slope failure can be estimated preliminarily.

Adding to the search object such as address, name of facility, feature information and the route on this system, this experimental system shares the information of various danger/warned area indicated by the law of disaster prevention and slope failure area information given by real-time calculation system as the effective search object for the emergency call.

According to this system, firefighter can shorten reach time and contribute to quick rescue when emergency call is made from mountain site that has been difficult to be specified. Actual hazard information is delivered to municipal Fast information gathering system by tracking operation record of Site determination support system (Fig.8).

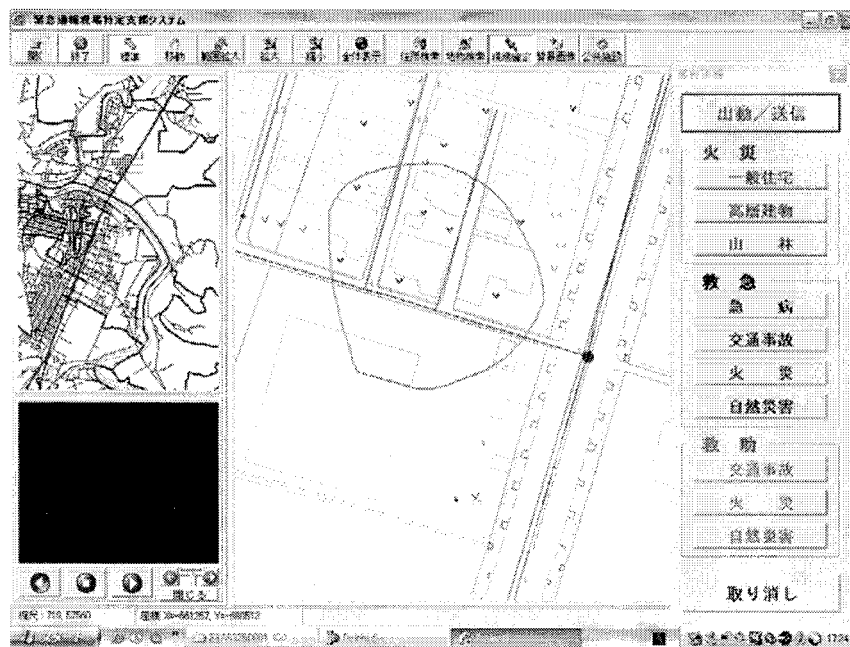


Figure 8 Example of supervise the operation after site determination

5. CONCLUSIONS

In this study, support system was experimentally developed for Fire Headquarters to take quick action when slope failure occurs. Hereafter, adequacy for result of real-time slope failure potential calculation will be examined. Slope failure is considered to be variable. For now the time of small data of rainfall and soil information at the slopes, further examination is necessary on the use of data and its adequacy.

Also an evaluation of effectiveness of the support system will be made by having disaster drill on the map with some citizen volunteers.

Acknowledgements:

The writer is grateful to Mr. Tsuneo Miura, Fire fighter of Yurihonjo, for his support on this study.

References:

- Asano, K., Mizuta, T., Kitano, K. and Miura, T. (2005), "study on Emergency report System Improvement to Specify Accident/Disaster Location Effectively Using Spatial-Temporal GIS — Landslide Disaster Information System for Fire Prevention Activity (2) —" *Papers and Proceedings of the Geographic Information Systems Association*, Vol.14, 493-496 (in Japanese).
- Mizuta, T. and Sugawara, T. (2006), "Construction of Real-Time Landslide Risk Estimation System Based on Digital Elevation Model in Case of Heavy Rain — A Case Study for Akita Prefecture —," *Journal of Social Safety Science*, No.8, 7-14 (in Japanese).
- Ushiyama, M., Imamura, F., Katada, T. and Koshimura, S. (2003), "A research of How to Use Disaster Information by Local Governments for Heavy Rainfall," *Annual Journal of Hydraulic Engineering*, Vol. 47, 349-354 (in Japanese).

WHAT WE LEARN FROM DAMAGES AND HUMAN BEHAVIOR IN CONDOMINIUM BUILDINGS IN THE 2005 WEST OFF FUKUOKA PREFECTURE EARTHQUAKE

H. Murakami¹⁾, A. Kawano²⁾, and K. Sakino³⁾

*1) Associate Professor, Division of Environmental Science and Engr.,
Graduate School of Science and Engr., Yamaguchi University, Ube, Japan*

*2), 3) Professor, Dept. of Architecture and Urban Design
Faculty of Human Environmental Studies, Kyushu University, Fukuoka, Japan
hitomim@yamaguchi-u.ac.jp, kawano@arch.kyushu-u.ac.jp, sakino@arch.kyushu-u.ac.jp*

Abstract: This paper examines causes and distribution of human casualty in the 2005 West off Fukuoka Prefecture earthquake. Questionnaire survey was conducted for condominium residents, of which some buildings sustained extensive non-structural damages. The results indicated that damaged non-structural walls and distorted doors disrupted evacuation route for many occupants, and furniture and content damage on upper floors become severer resulting in high rate of human casualty. Earthquake preparedness for indoor safety was raised to 50% after the earthquake, though further safety measures can be advised. In the phase of post-earthquake emergency and restoration period, residents' organizations and play important roles, so that neighborhood activities to promote communication networks are important in urban environment of aging population.

1. INTRODUCTION

The 2005 west off Fukuoka prefecture earthquake occurred on March 20, Sunday at 10h53m in the morning. The JMA magnitude (Richter Scale) is 7.0 and the epicenter was located at 33 deg. 44.35 min N in Longitude and 130 deg. 10.58 min. E in Latitude, which is near Genkai Island in Fukuoka city. Maximum JMA seismic intensity of 6- was reported for Central ward and East ward of Fukuoka city, Maebaru city and Miyaki town in Saga Prefecture. The maximum PGV observed in the K-net strong motion observation network by NIED was 64.4 cm/s at FKOS01 station in the Central Ward of Fukuoka city, and the maximum PGA observed in the same network was 361.8 Gal in Jonan Ward of Fukuoka city.

Human casualty in this earthquake is 1 human loss by collapse of concrete block wall, 75 serious injury, and 994 light injuries as reported by Fukuoka prefectural government on March 13, 2005. In Fukuoka city with 1.4 million populations, damages in Genkai Island were severest with most dwellings in steep slope damage, and damages in Central ward were serious for mid-rise condominium buildings. Many condominiums suffered non-structural damage with infill walls cracked, however they often disabled opening of the door and evacuation route, and forced the residents to stay at earthquake shelters. The authors made questionnaire survey to the residents of several condominium buildings to elucidate relations of indoor architectural damage, occupants' behavior, evacuation, and risk of casualty. This paper summarizes the results of the survey and discusses what we should learn from the experiences of this earthquake. Detailed survey result is reported in Murakami, et al. (2005).

2. HUMAN CASUALTY

In Fukuoka city, 873 human casualties were reported by Fukuoka municipal government as of April 17, 2005. In Fukuoka prefecture, 87% of human loss and 95% of heavily damaged or partially damaged dwellings occurred in Fukuoka city. Figure 1 shows relation of JMA seismic intensity scale and casualty rate in log scale. There were no strong motion records in Genkai Island, so that intensity of 6+ (6.3) is assumed here. Normal correlation can be observed. Comparing this relation with other earthquakes in Japan, there is a tendency that casualty rate is smaller in Fukuoka earthquake, possibly because of earthquake occurrence in day time when few kitchen fires could be used.

According to the Fukuoka Municipal Fire Department, 109 cases of emergency medical transfer (ambulance transfer) were provided as earthquake related causes. Figure 2 shows causes of casualty in the ambulance transfer cases by Fukuoka City Fire Department. Injury due to one's falling is 29% and highest, while falling objects or furniture and burn due to hot water or cooking pan follow with 17% each. Collapsed structure is 11% and could result in serious injury or fatality. As for the sex distribution, 36 (33%) are male and 73 (67%) are female. Elderly people over 60 share 60% of the ambulance cases, which is 3 times higher than population in Fukuoka city (Figure 2). Compared with the 2004 Niigata Chuetsu earthquake, urgent illnesses such as heart disorder or a cerebral hemorrhage seem to be lower in Fukuoka earthquake. In case of Chuetsu earthquake, very severe and frequent aftershock sequence followed the main shock and increased illnesses causing 32% out of 46 human losses (Murakami, 2006). In case of Fukuoka earthquake, day time Sunday occurrence when many family were together, and less elderly population in urban area could have been rather fortunate conditions.

3. DAMAGE TO CONDOMINIUMS AND OCCUPANT BEHAVIOR

3.1 Survey Method

In Central ward of Fukuoka city, where active Kego fault runs underground, serious damages to mid-rise condominium and apartment buildings were observed. According to the damage report by Fukuoka city (as of May 6, 2005), heavily damaged 3 buildings, partially damaged 19 buildings were counted for RC or steel condominium or apartment buildings. We made questionnaire survey for the 8 condominium buildings with 364 households to ask architectural and indoor damage and human behavior of the occupants. Figure 3 shows location of Kego active fault in Fukuoka city and Figure 4 shows locations of the survey buildings. Table 1 indicates outline of the buildings for the survey. The questionnaire asks indoor architectural damage conditions, human response during and after the earthquake, location of family members and casualty, evacuation behavior, preparedness before and after the earthquake.

The questionnaires were distributed in late May, 2005 and were collected up to August, 2005 via each condominium management organization. We collected 198 cases (53.8%) out of 364 households. Total number of family members listed in the questionnaire is 219 persons.

3.2 Architectural and Indoor Damage

Floor of residence varies from ground level to 14th floor, while most data are from 2nd thru 8th floors. As for architectural damage, disabled opening of the entrance door is 7%, difficulty in opening the entrance door is 16%. As for the wall damage, two thirds answer cracks, and 20% answer fracture, displacement or falling of the walls. Some occupants had to evacuate thru balcony partition to their neighbouring dwelling units. Figure 5 shows changing architectural damage rate along floor levels.

As for the interior contents damage, Figure 6 indicates rate of falling furniture along floor levels. Rates of falling in 10-14th floors are 2 to 4 times higher than those in 1-3rd floors as reasonably explained by higher floor response in upper floors. Falling rate is highest for bookshelf and TV, and is medium for wardrobe and cupboard. Extents of interior scattering damage level are compared among types of rooms in Figure 7. Damages are severest for living rooms and kitchens followed by bedrooms.

3.3 Characteristics of Human Casualty

Effective responses for family member of 339 cases are examined here regarding casualty risk. They consist of 14% of elderly, 13% of children, and 73% adults. Males are 39% and females are 61%. Sixty two % of people were at home, 20% were indoors except for one's home, 10% were outdoors at the time of the earthquake occurrence.

Injury rate of those 339 people reach as high as 13.1%. Causes of injury are falling furniture (31%), broken glass (29%), one's falling (19%) and falling objects (14%). Out of the injury cases, 26.8% were treated as out-patient or were hospitalized. Rate of injury cases who were treated by medical facilities can be estimated as $0.131 \times 0.268 = 0.035$, that is, 3.5%. This rate is much higher than 0.2% in Chuo Ward in Figure 1. Casualty rate along floor levels (Figure 8) indicates steep rise of the rate to 30% especially in the floors of 10th thru 14th. Many responses of the highest floors come from one condominium building, in which architectural and contents damage were severest in Imaizumi area, and that may have affected very high rate of casualty.

Fire usage rate is 2% and is small, though, half cases turned off the devise, in the left cases, automatic shut off device were activated. The rate of responses who think there was a risk of fire occurring from their own home reaches 13%, warning danger of human loss by combination of fire occurrence and disabled evacuation route with entrance door destroyed.

3.4 Earthquake Preparedness

As for the earthquake preparedness at home, 2% answered that they had taken measures to prevent falling furniture before the earthquake, which seem to be much lower than other survey results in Tokyo metropolitan area and other regions, reflecting Fukuoka citizens' belief that Fukuoka was free from attack of any damaging earthquakes. After the earthquake, 52% answered that they took measures to prevent falling furniture, still it is significant the left of the respondents are not prepared for earthquake safety at home.

Figure 9 shows respondents' attitude to ask earthquake safety and structural conditions of the condominium building when they made decisions to purchase or to lend the dwelling unit. Majority of 73% say they didn't make any inquiry, and 21% say they asked few questions. It is important for lay people to ask for due explanation of earthquake safety, ground conditions, structural safety levels and expected level of damage in case of major earthquakes, because seismic code allows non-structural damage affecting architectural elements, utilities, etc. in case of rare but possible maximum input seismic motions. After the Anaha cases of farcified seismic design data exposed, public enormously raised concern and disbelief in the seismic safety of condominium buildings. It is crucial to improve the mechanism and the system to provide incentives to make safer buildings.

The partially damaged condominium had great difficulty in making decisions how to repair or to retrofit the building collectively owned by around 40 households. Owners and residents management organizations play crucial role in case of emergency and post-earthquake recovery phase. With aging occupants of urban condominiums, daily communication and kind and familiar relationship is important, even if many residents seek privacy and are mukanshin to their neighbors.

4. CONCLUDING REMARKS

Fukuoka city with 1.4 million populations was hit by strong earthquake occurrence in March 2005. The authors collected human casualty information from the municipal government and fire departments to find out causes and distribution of human casualty. Rate of casualty increase as seismic intensity rises. Causes of casualty in EMT cases showed higher risk of casualty in elderly population.

Questionnaire survey was conducted for condominium residents in Chuo ward, Fukuoka city to elucidate architectural damage and human behavior and risk of injury. In a third# of cases, severe damage to non-structural walls and distorted entrance door disrupted the occupants' evacuation routes. Architectural and contents damages become worse at higher floors resulting in higher casualty rates. Earthquake preparedness measures prior to the earthquake to prevent furniture falling were only 2% and much lower than that in other regions with more frequent earthquake occurrence. Rate of respondents to take measures to prevent furniture falling or indoor safety after the earthquake is improved to 51%, though, suggesting needs to improve further seismic safety awareness and actions. Active Kego fault of 25 long located in the middle of Fukuoka city towards Dazaihu city in the south are major concern of future earthquake disaster, though the probability of earthquake occurrence in this fault is rather low. Kawase et al. (2003) estimated ground motion and building damage distribution in Fukuoka city area assuming different rupture scenario in Kego fault earthquake. In the worst scenario, wooden dwelling, RC buildings, and steel buildings with major damage may reach 32,000, 440, and 5,773 respectively. Promoting earthquake safety is important and assisting seismic retrofit of condominium buildings is crucial issue. Measures to improve indoor safety and daily communication would help reducing people injured and increasing people to assist neighbors in the emergency of earthquake disaster.

Acknowledgements:

The authors acknowledge the condominium residents in Fukuoka city for their kind cooperation to answer the questionnaire as well as the owners' management organization to distribute and collect the questionnaires. Former student of Yamaguchi University, Ms. Saori Yanagi contributed significantly for data collection and analysis. The research was funded as No. 17800001, in which chief investigator is Prof. H. Kawase of Kyushu University, by Japan Ministry of Education, Culture, Sport, Science, and Technology (MEXT).

References:

- Kawase, H., Nagato, K., and Nakamichi, S. (2003), "Damage Prediction of Fukuoka City for a Scenario Earthquake Based on Strong Ground Motions Evaluated by a Hybrid Technique," *Proc. Structural Engineering*, **49B**, pp.1-10, AIJ.
- Murakami, H. (2006), "Factor Analysis of Human Casualty and Indoor Contents Damage of Condominium Buildings due to the West off Fukuoka Prefecture Earthquake," *Investigation Research Report of the Strong Ground Motion and Structural Damage in the West off Fukuoka Prefecture Earthquake*, pp. 218-229, Kyoshu University.
- Murakami, H. (2006), "Human Casualty and SAR Emergency Medical Activity in the 2004 Niigata Chuetsu Earthquake -Role of Communication and Transportation Network-," *Report of Studies in Life Saving Life-line Functions in Earthquakes and Human Casualty Mitigation*, pp.15-30, Kobe University.

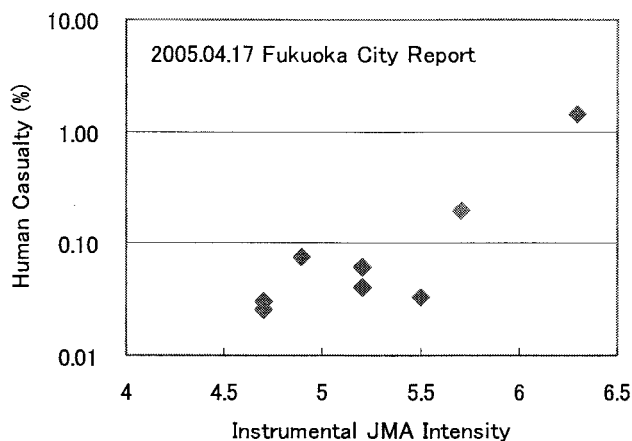


Figure 1 Relation of Casualty Rate (%) in Log Scale vs. JMA Seismic Intensity for Fukuoka city. Highest casualty of 1.4% is for Genkai Island, where seismic intensity of 6.3 is temporally assigned.

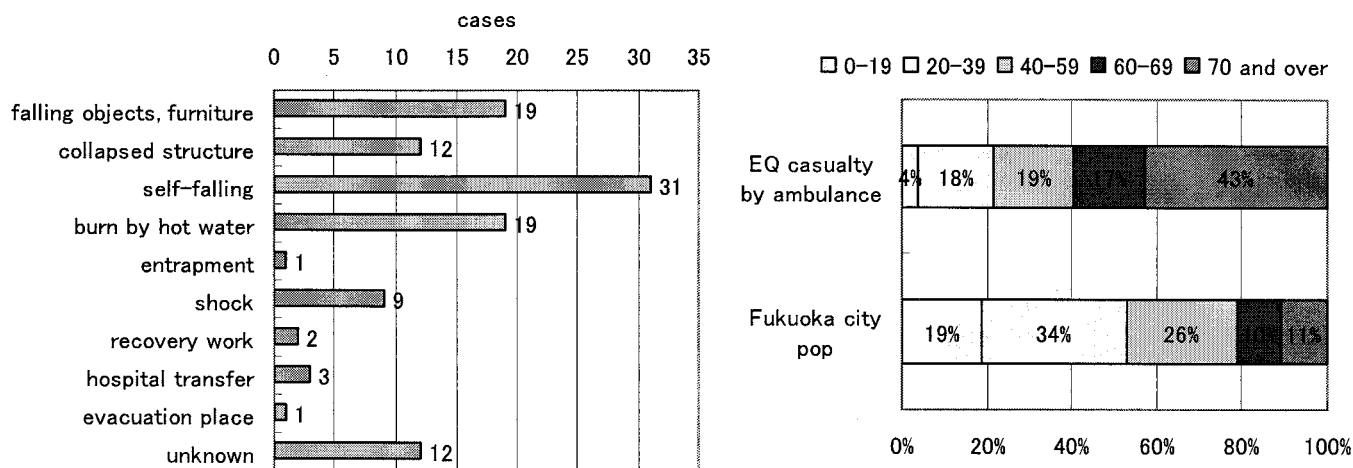


Figure 2 Causes of Casualty (left) and Age Distribution (right) in Ambulance Transfer Cases by Fukuoka Municipal Fire Department (N=109 cases).

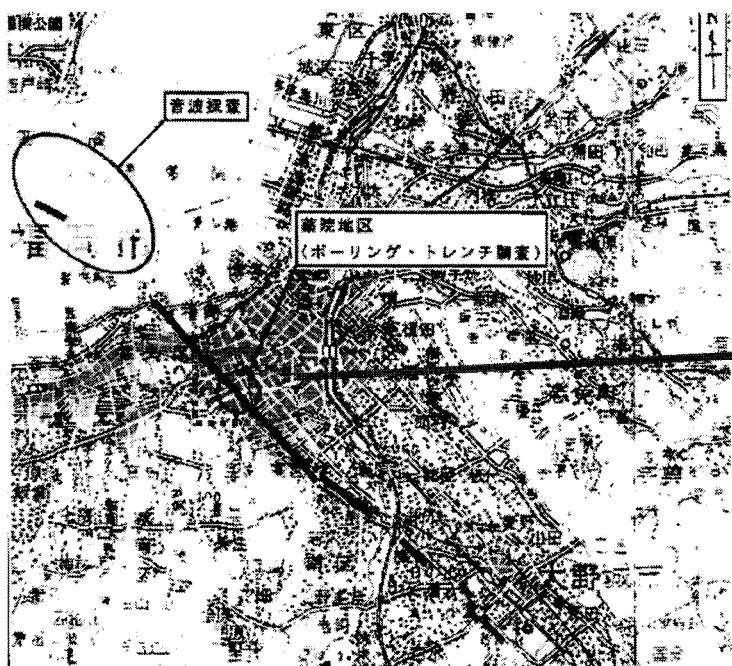


Figure 3 Map of Fukuoka city with Kego Fault (L=22km) in black line
<http://bousai.city.fukuoka.jp/kegodansou.htm>

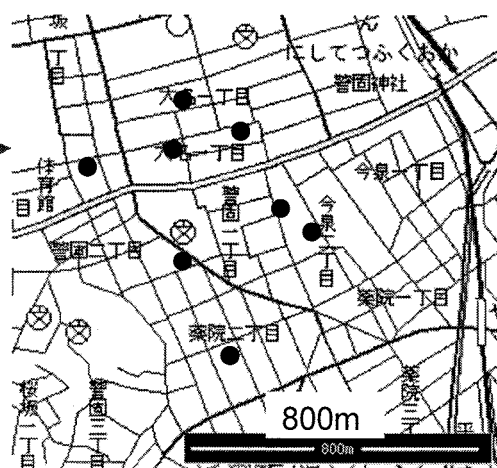


Figure 4 Location of the Condominium Buildings for the Questionnaire Survey in Fukuoka Map. (base map: denshi kokudo by GSI of Japan)

Table 1 List of the 8 Condominium Buildings for Questionnaire Survey in Fukuoka City

id	address	Intensity *	year built	year of age	no of floors	structur e	damage	no of units	no collecte
7	Imaizumi 2	5.8	1981	23	11	SRC	D2	66	19
9	Yakuin 2	4.9	1979	25	11	SRC	D0	51	30
8	Kego 2	4.9	1963	42	8	RC	D2	45	24
3	Daimyo 1	5.7	1975	30	6	S	D1	26	20
2	Daimyo 1	5.7	1987	17	10	SRC	D0	44	18
4	Daimyo 1	5.7	1998	6	15	SRC	D2	38	26
1	Akasaka 1	5.1	1985	19	10	SRC	D0	46	29
5	Imaizumi 2	5.8	1999	5	14	SRC	D3	48	30
* estimated by intensity questionnaire survey (Narahashi, 2005)								sum	196

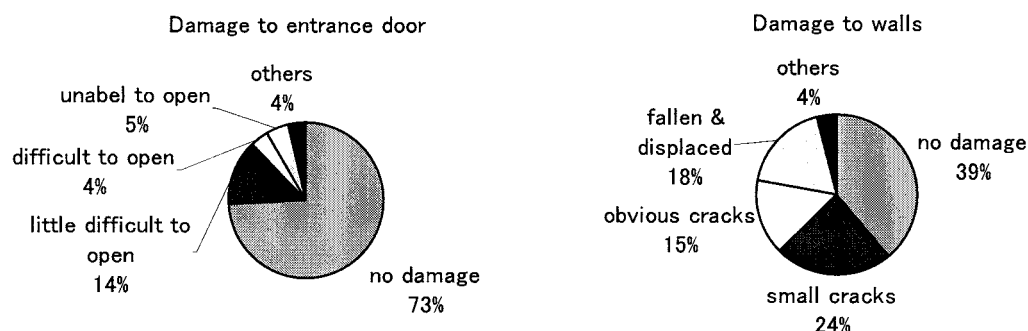


Figure 5 Damages of Entrance Doors (N=189 cases) and Non-Structural Walls (N=190 cases).

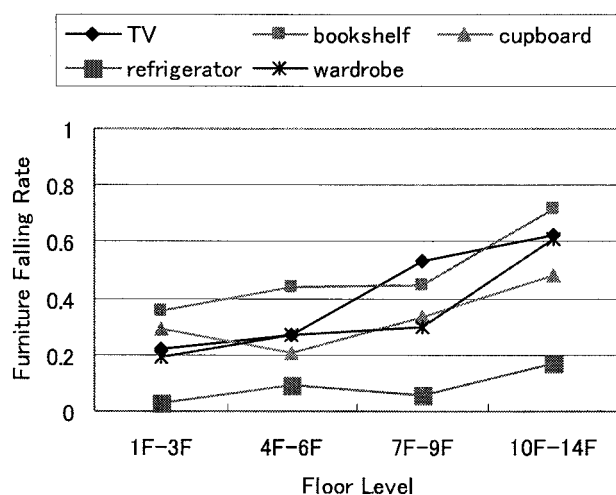


Figure 6 Rate of Furniture Falling along Floor Levels.

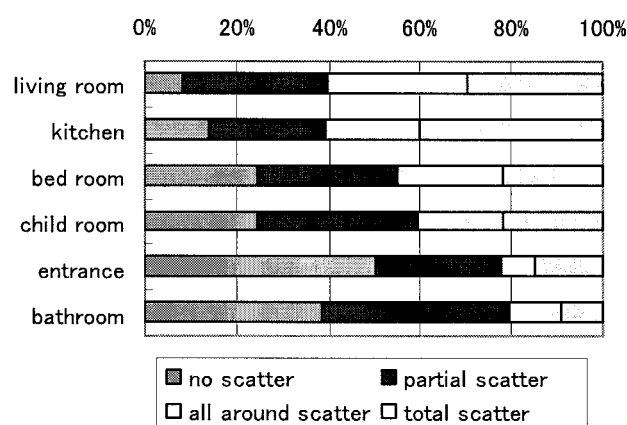


Figure 7 Comparison of Scattering Damages of Use of Rooms.

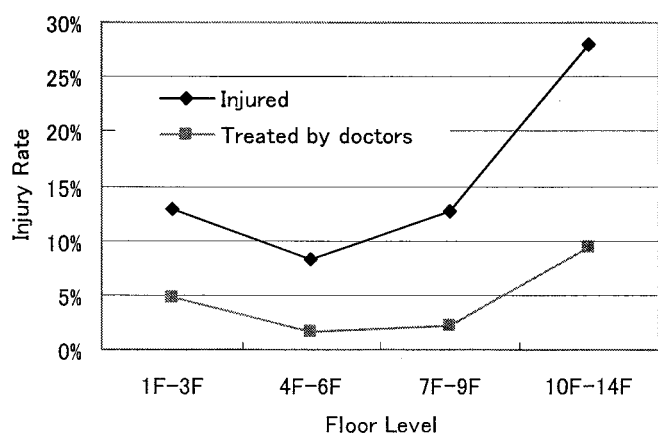


Figure 8 Injury Rate along Floor Levels.

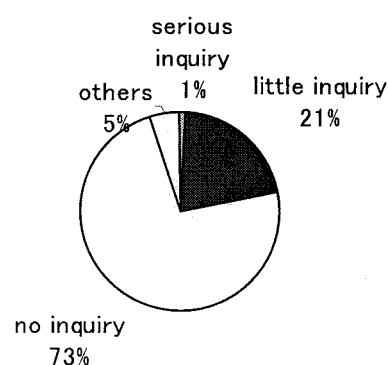


Figure 9 Inquiry for Structural and Earthquake Safety at the Time of Purchasing Condominiums or Renting Apartments (N=185 cases).

SEISMIC RISK PERCEPTION AND COMMUNICATION

S. Fujii¹⁾

*1) Professor, Tokyo Institute of Technology
fujii@plan.cv.titech.ac.jp*

Abstract: Seismic risk perception and communication is very important for seismic risk management. Where, risk perception denotes how people perceive seismic risk, and risk communication denotes how people and seismic experts communicate each other. These two components, i.e. risk perception and communication, are expected to directly determine how people and society respond to seismic risk before and after the hit by earthquake. In this paper, I will explain fundamental psychological and cognitive model about risk perception and communication. That is Contingent Focus Model.

1. INTRODUCTION

Seismic risk perception and communication is very important for seismic risk management. Where, risk perception denotes how people perceive seismic risk, and risk communication denotes how people and seismic experts communicate each other. These two components, i.e. risk perception and communication, are expected to directly determine how people and society respond to seismic risk before and after the hit by earthquake. In this paper, I will explain fundamental psychological and cognitive model about risk perception and communication. That is Contingent Focus Model.

Identical decision problems under risk may lead to different decisions because of subjective decision framing, in which the decision-making process depends on how the situation is described. This is called the framing effect (Tversky & Kahneman, 1981). For instance, when a decision needs to be made concerning whether or not one agrees to undergo a surgical operation, the decision may be different when a doctor tells one that there is a 95% probability of living following the surgery, as compared to when one is told that there is a 5% probability of dying. This effect violates the principle of description invariance, which states that different representations of the same choice problem should yield the same preference (Tversky & Kahneman, 1986).

Tversky and Kahneman (1981) posed a question under the following two framing conditions; this typical and well-known example, known as the Asian disease problem, allows subjects to make a choice under each condition and results in the framing effect.

[Problem 1]

Positive frame condition:

“Imagine that the U.S. is preparing for the outbreak of an unusual Asian disease, which is expected to kill 600 people. Two alternative programs to combat the disease have been proposed. Assume that the exact scientific estimates of the consequences of programs are as follows. Which of the two programs would you favor?”

If program A is adopted, 200 people will be saved.

If program B is adopted, there is 1/3 probability that 600 people will be saved, and 2/3 probability that no people will be saved. (p.193.)”

Negative frame condition:

The question is the same except for the description of programs, which were changed as follows:

“If program C is adopted, 400 people will die.

If program D is adopted, there is 1/3 probability that nobody will die, and 2/3 probability that 600 people will die. (p.193)”

Here, although the program descriptions are different, it is clear that programs A and C, and programs B and D, respectively, have equivalent meanings. “Be saved” equals “not die,” and “not be saved” equals “die.” Tversky and Kahneman (1981) reported that when a profitable position was emphasized in the description of a positive frame condition, most subjects chose risk averse programs, i.e., program A. But, if a losing position was emphasized in the description of a negative frame condition, most subjects chose the risk taking program, i.e., program D.

Tversky and Kahneman (1981, 1986) reported that the framing effect is a robust phenomenon and suggested that, similar to visual illusion, the framing effect leads to a paradoxical result, even though the paradox may only be recognized afterwards. Framing effects have been reported to occur in relation to medical judgments made by doctors (McNeil, Pauker, Sox, & Tversky, 1982), in managerial decision making (Qualls & Puto, 1989), and in many other decision making situations (Wang, 1996; Kühberger, 1998; Shafir & LeBoeuf, 2002; LeBoeuf & Shafir, 2003).

1.1 Prospect theory and Reference Point

Tversky and Kahneman (1979) proposed prospect theory as a way of explaining framing effects. They highlighted a difference in subjective values between gains and losses associated with choice behavior. The value function in prospect theory is concave in the gain area and convex in the loss area, which implies that a decision maker is risk averse in the gain area but chooses to take risks in the loss area. prospect theory also assumes that original points of the value functions, i.e., reference points, shift depending on the description of a decision problem. Prospect theory explains framing effects by a shift of the reference point. When a reference point is greater than an outcome, the outcome is interpreted as a gain. However, if the reference point shifts to be less than the outcome, it then comes to be regarded as a loss. Since prospect theory assumes that subjects avoid risks when outcomes are framed as gains (i.e., positive frame), and that subjects take risks when outcomes are framed as losses (i.e., negative frame), the theory predicts that attitudes toward risk change, depending on the frame condition.

A reference point is necessary for prospect theory to explain decision making under risk because attitude toward risk, which determines a decision, depends on the relation between a reference point and an outcome. This implies that one must be able to predict the position of a reference point and its shift due to contextual factors, including positive/negative frame conditions, in order to predict decision making under risk in an actual environment, in which numerous contextual factors are embedded.

Does prospect theory, then, provide a theoretical and quantitative explanation as to the shift of a reference point per se? With respect to this question, Tversky and Kahneman (1981) stated briefly the following:

“The frame that a decision maker adopts is controlled partly by the formulation of the problem and partly by the norms, habits, and personal characteristics of the decision maker” (p. 453)

In line with this conjecture, Fischhoff (1983) reported the experiment that investigated reference point positions while postulating the validity of prospect theory. However, he found that it was difficult, or even impossible, to identify a reference point position from external observations, i.e.

actual choices. In addition, he found an inconsistency between a reference point that is derived from actual choice based on prospect theory, and a self-reported reference point. To the present time, a methodology to identify reference point position does not seem to have been proposed.

While prospect theory postulates one reference point, a decision maker may actually use multiple reference points. For instance, Takemura (2001) proposed the mental ruler theory that postulates two reference points to explain numerical judgments. He confirmed that the theory provides a better fit to judgmental data than other theories. In addition, Maule (1989) collected verbal protocol data in decisions involving the Asian disease problem and found that 5 subjects out of 12 made their decisions while adopting two different reference points.

1.2 Contingent Focus Model

The reference point concept is useful with respect to explaining the framing effect. However, it is difficult to define a reference point and to predict its position and shift; furthermore, prospect theory cannot explain decision making when a decision maker has multiple reference points. For these reasons, one of the authors of the present study proposed the contingent focus model, which does not employ the concept of reference point to explain the framing effect (Takemura, 1994a; Fujii & Takemura, 2000, 2001, 2003).

The basic assumption of the contingent focus model is that framing effects emerge, not when a reference point shifts, but when a decision maker changes focus on possible outcomes and probabilities, depending on the frame conditions of decision problems. As shown in Figure 1, under positive frame conditions, a decision maker is assumed to pay more attention to probabilities than to possible outcomes, which results in the decision maker being risk averse. On the other hand, under negative frame conditions, a decision maker is assumed to pay more attention to possible outcomes than to probabilities, which results in the decision maker being risk inclined. In other words, a decision maker is assumed to attend to negative outcomes (i.e., loss) more intensely than to positive outcomes (i.e., gain).

This hypothesis is in line with the loss sensitivity principle (Gärling, et al., 1997; Romanus & Gärling, 1999), which presumes that a decision maker is more sensitive to a negatively framed outcome (i.e., loss) than to a positively framed outcome (i.e., gain). Prospect theory hypothesizes that the value function of outcomes is steeper for losses than for gains, which is also congruent with the hypothesis, since the curvature of the value function implies the decision maker's sensitivity to outcome.

Furthermore, Kahneman & Tversky (1984) have argued that "losses loom larger than gains (p. 348)." We can then infer that a decision maker pays more attention to outcomes under negative frame conditions than under positive frame conditions, as is assumed in the contingent focus model.

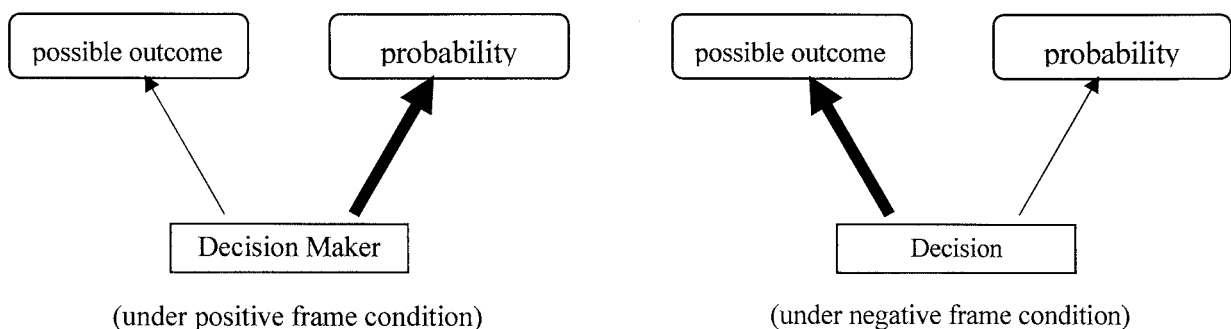


Figure 1. Contingent focus model (Takemura, 1994a)

As in prospect theory (Kahneman & Tversky, 1979) and subjective expected utility theory (Von Neumann and Morgenstern, 1944; Savage, 1954), the contingent focus model also describes

decision making under risk. Within the contingent focus model, it is hypothesized that a decision maker chooses an alternative whose subjective decisional value is maximum from among possible alternatives. The value is formulated as follows.

$$U(X, P) = F(X)aG(P) (1-a) \quad (1)$$

where X denotes possible outcome, P denotes the probability that a decision maker gets X , $U(X, P)$ denotes a subjective decisional value of an alternative of X and P , $F(X)$ denotes the subjective value of a possible outcome X ($F(X) \geq 0$), $G(P)$ denotes the subjective value of P ($G(P) > 0$), and a denotes a parameter ($0 \leq a \leq 1$) indicating the degree of focus on outcome X . We label this parameter the focal parameter. As the focal parameter a approaches 1 from 0, a decision maker makes riskier decisions. When a equals 1, only outcomes influence the decision making, and a decision maker is making extremely risky choices. On the other hand, as a approaches 0 from 1, a decision maker becomes risk averse. When a equals 0, only probabilities influence the decision making, and a decision maker is extremely risk averse. This hypothesis, which explains how focusing on possible outcomes and probabilities determines risk attitudes, is called the focusing hypothesis.

The hypothesis that focal parameter a changes depending on contextual factors, including frame condition, is the contingent focus hypothesis. Thus, in the contingent focus model, framing effects are ascribed to changes of the focal parameter a and not to reference point shifts. This contingency of the focal parameter is formulated as follows:

$$a = \Psi(\theta) \quad (2)$$

where θ denotes a vector of contextual factors and Ψ denotes a function indicating the contingency of the focal parameter a on θ . Contextual factors (θ) include positive/negative frame conditions. The basic contention within the contingent focus model, that a decision maker attends to negative outcomes more intensely than to positive outcomes, indicates that the focal parameter a will be larger under negative frame conditions than under positive frame conditions.

Figure 2 summarizes the contingent focus model hypothesis that contextual factors, including frame conditions, affect attention on possible outcomes and probabilities, and that attention, in turn, determines risk attitudes.

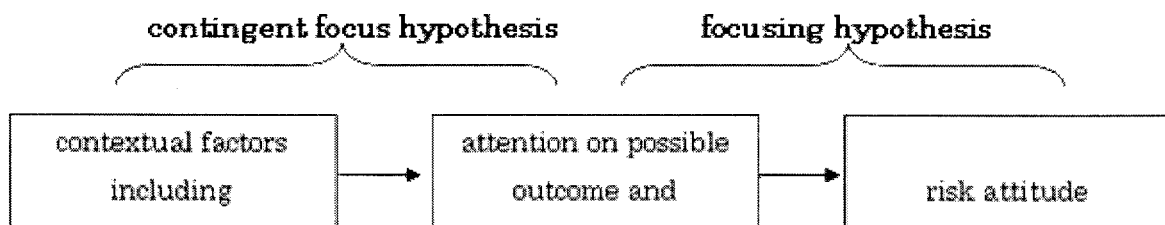


Figure 2. Two hypotheses within the contingent focus model: the contingent focus hypothesis and the focusing hypothesis.

1.3 Empirical Hypotheses

The hypotheses of the contingent focus model, i.e., the focusing hypothesis and the contingent focus hypothesis, are supported by data from previous studies. Two experiments manipulated the size of letters describing outcomes and probabilities in decision problems under risk (Fujii & Takemura,

2000). Results were compatible with predictions; that is, the subjects more frequently selected risky options when outcomes were emphasized. The data from an experiment using an information board technique, which manipulated time to display possible outcomes and probabilities, also supported the hypothesis. Results indicated that participants accepted more risk as possible outcomes were displayed longer (Takemura, H u & Fujii, 2001). We also applied the model to a psychometric meta-analysis of subjects' responses in 4 experiments of the Asian disease problem reported in Tversky & Kahneman (1981), Takemura (1994b) and Fujii & Takemura (2000). The results reported in Fujii & Takemura (2001) were also compatible with predictions derived from the hypotheses; a ratio developed by calculating the weighting parameter of possible outcomes to probabilities under negative frame conditions was significantly greater than that under positive frame conditions.

While the two hypotheses of the contingent focus model are supported by experimental data, attention to possible outcomes and probabilities was not explicitly observed in previous studies.

In the present study, we used an eye gaze recorder to record the time that the participants gazed at words representing possible outcomes and probabilities in a decision problem involving risk. Based on the contingent focus hypothesis, it was predicted that the ratio of time to gaze at words representing possible outcomes to time to gaze at words representing probabilities would be greater under negative frame conditions than under positive frame conditions (Hypothesis 1). Based on the focusing hypothesis, we predicted that the ratio of time to gaze at possible outcome words to the time to gaze at probability words would be greater for risk-taking participants than for risk-averse participants (Hypothesis 2).

2. METHOD

2.1 Participants

Thirty-three undergraduate university students (25 men and 8 women) at the Tokyo Institute of Technology participated in the experiment in return for the equivalent of \$xx. The mean age of the participants was 22.18 years ($Sd = 1.97$), within a range of 19 to 24 years. Subjects were randomly assigned to two conditions: the negative frame condition ($n = 18$) and the positive frame condition ($n = 15$).

2.2 Materials

We adopted the Asian disease problem and reflection-effect problem used in Tversky and Kahneman's (1981) original framing study. Eye gaze recorder equipment (NAC EMR-8) was used to test the present hypotheses. This equipment used the pupil-center/corneal reflection method, which has the same function as the eye-tracking equipment used in previous decision research (Lohse & Johnson, 1996; Boe, Selart, & Takemura, 2000; Selart, Boe, & Takemura, 2000).

2.3 Procedure

Each participant was individually invited to an experimental room and sat in a chair placed 2 meters in front of a screen on the wall. The screen was approximately 1.5 meters high and approximately 2 meters wide. After s/he sat in a chair, s/he put on a cap equipped with a small camera to detect movement of the right eye. An experimenter then calibrated the eye gaze recorder to detect the participant's eye movement, a process that averaged two minutes. The eye movement was recorded in the video picture of the angular range of view that was simultaneously captured by another camera. After the calibration, the participant was instructed to say "yes" immediately after s/he understood the instructions displayed on the screen, and was also instructed to verbally answer the questions displayed on the screen immediately after making a decision.

"Which do you choose if you have to choose from 2 alternatives?" was then displayed on the screen. If s/he said "yes," the experimenter changed the display.

The following two options were displayed for the participants assigned to the positive frame condition:

[A]

certainly gain 20,000 yen

[B]

a lottery with a 50 % chance to gain 40,000 yen and
a 50 % chance for no gain.

For the participants assigned to the negative frame condition, the following two options were displayed:

[A]

certainly lose 20,000 yen

[B]

a lottery with a 50 % chance to lose 40,000 yen and
a 50 % chance for no loss.

We labeled this the “reflection-effect problem”, as it is a version of a decision problem that exhibits the reflection effect (Kahneman & Tversky, 1979).

After s/he reported hers/his choice, the experimenter again changed the display so that instructions for the Asian disease problem (Tversky and Kahneman, 1981) were displayed. After the participant finished reading, s/he said “yes,” and the experimenter changed the display to the following for the participants assigned to the positive frame condition:

[program A]

200 people will be saved.

[program B]

there is 1/3 probability that 600 people will be saved,
and 2/3 probability that no people will be saved.

For the participants assigned to the negative frame condition, the following was displayed:

[program A]

400 people will die.

[program B]

there is 1/3 probability that nobody will die,
and 2/3 probability that 600 people will die.

After s/he said “A” or “B,” the experiment was concluded.

3. RESULT

2.1 Choice Data

As can be seen in Table 1, participants preferred a risk-taking option to a risk-averse option in the negative frame condition and preferred a risk-averse option to a risk-taking option in the positive frame condition for both the reflection-effect problem and the Asian disease problem. The results from the reflection-effect problem supported the reflection effect, and the results from the Asian disease problem supported the framing effect. A χ^2 test was significant for the reflection effect data (χ^2 [df = 1] = 3.91, $p < .05$), but did not reach significance for the framing effect data (χ^2 [df = 1] = 13, $p = .25$).

Table 1. Distributions of participants' choices between the risk-taking and risk-averse options under negative and positive frame conditions.

	reflection-effect problem		Asian disease problem	
	negative frame condition (n = 18)	positive frame condition (n = 15)	negative frame condition (n = 18)	positive frame condition (n = 15)
risk-taking	11 (61.1%)	4 (26.7%)	12 (66.7%)	7 (46.7%)
risk-averse	7 (38.9%)	11 (73.3%)	6 (33.3%)	8 (53.3%)

2.2 Recoding of the eye fixation data

We created the ROF variable, Rate of Outcome Focusing, for each choice problem using data from the eye gaze recorder.

$$\text{ROF} = T(\text{outcome}) / [T(\text{outcome}) + T(\text{probability})]$$

where $T(\text{outcome})$ is the total time to gaze at possible outcome words after the participant read sentences on the screen and $T(\text{probability})$ is the total time to gaze at probability words after the participant read sentences on the screen. The possible outcome words in the reflection-effect problem for both frame conditions were "20,000 yen," "40,000 yen," and "no." The probability words in the problem for both frame conditions were "certainly" and "50%." The possible outcome words in the Asian disease problem for the positive frame condition were "200 people," "600 people," and "no people;" those for the negative frame condition were "400 people," "600 people," and "nobody." The probability words in the Asian disease problem for both frame conditions were "1/3" and "2/3." Since the time required to acquire information using eye fixations varies between 200 ms to 400 ms (Russo, 1978; Card, Moran, &, Newell, 1983), we defined "gazing at a word" as gazing at the word for more than 200 ms. We defined the total time to gaze at a word as the sum of time to gaze at the word longer than 200 ms.

Table 2. ROF (rate of outcome focusing) under negative and positive frame conditions.

	reflection-effect problem		Asian disease problem	
	negative frame condition (n = 15)	positive frame condition (n = 13)	negative frame condition (n = 12)	positive frame condition (n = 12)
$M^{\dagger 1}$	65.0%	47.2%	59.0%	44.6%
$SEM^{\dagger 2}$	(5.1%)	(6.5%)	(5.6%)	(7.4%)

$^{\dagger 1}$ mean

$^{\dagger 2}$ standard error of the mean

2.3 Hypothesis 1

Table 2 presents ROFs for each condition and each decision problem. Data from instances where eye movement data indicated that participants did not read sentences of each option to the end were eliminated from the following analyses. The ROF was larger under the negative frame condition than under the positive frame condition for both the reflection-effect problem and the Asian disease problem. The difference in ROF for the reflection-effect problem was significant ($t [26] = 2.19$, $p < .019$), and the difference for the Asian disease problem was marginally significant ($t [22] = 1.56$, $p = .067$). These results support Hypothesis 1 that predicted, based on the contingent focus hypothesis, that decision makers attend more to possible outcomes under negative frame conditions than under positive frame conditions.

2.4 Hypothesis 2

In order to test Hypothesis 2, which was derived from the focusing hypothesis, we compared ROF means from those who chose a risk-taking option with those who chose a risk-averse option. According to Hypothesis 2, the ROF for those who chose the risk-taking option would be greater than the ROF for those who chose the risk-averse option. Table 3 presents data that support this prediction. The mean ROF for risk-taking participants was greater than 50 % for both decision problems, but the mean ROF for risk-averse participants was less than 50 %. The difference in ROF between risk-taking participants and risk-averse participants was significant for the reflection-effect problem ($t [26] = 3.02$, $p < .005$), and was marginally significant for the Asian disease problem ($t [22] = 1.57$, $p = .065$).

Table 3. ROF (rate of outcome focusing) of risk-taking participants and risk-averse participants.

	reflection-effect problem		Asian disease problem	
	risk-taking (n = 13)	risk-averse (n = 15)	risk-taking (n = 14)	risk-averse (n = 10)
M ^{†1}	69.1%	46.0%	58.0%	43.2%
SEM ^{†2}	(5.3%)	(5.4%)	(6.5%)	(6.5%)

†¹mean

†²standard error of the mean

2.5 Mediation Analysis

We performed a set of binary logit analyses of the choice data. The results of the logit analyses for the reflection-effect problem are presented in Table 4, and those for the Asian disease problem are presented in Table 5. Frame condition had a significant effect on choice for the reflection-effect problem, if ROF was not included in the model (Table 4). The effect of a negative-frame dummy was significantly positive for the case without ROF, which implies that the probability that participants will select the risk-taking option is larger under negative frame conditions than under positive frame conditions, supporting the reflection effect. However, Table 4 also shows that the effect of frame condition disappeared if ROF was included as an explanatory variable, while the effect of ROF was significantly positive, which indicates that the probability of choosing the risk-taking option increases as ROF increases. Since we found that frame condition was related to ROF in the reflection-effect problem (Table 2), the logit analyses tell us that the effect of frame

condition on choice in the reflection-effect problem (the reflection effect) was indirectly mediated by ROF.

Table 4. Estimation of logit regression analysis of choice^{†1} of the reflection-effect problem with and without ROF as an explanatory variable.

	without ROF			with ROF		
	$\beta^{\dagger2}$	t	p	$\beta^{\dagger\dagger}$	t	p
constant	-0.45	-0.93	.175	3.47	1.90	.028
negative-frame dummy ^{†3}	1.46	1.93	.027	-0.64	-0.71	.240
ROF				6.22	2.15	.016
sample size	33			28		
L (C) ^{†4}	-18.64			-5.15		
L (B) ^{†5}	-14.09			-3.14		

^{†1} The dependent variable of the logit regression analysis = 1 if the risk-taking option was chosen, = 0 if the risk-averse option was chosen. Therefore, if an explanatory variable whose coefficient is positive increases, the probability of choosing the risk-taking option increases.

^{†2} standardized coefficient.

^{†3} = 1 if negative-frame condition, = 0 otherwise.

^{†4} log-likelihood for the model only with constant.

^{†5} log-likelihood for the model with constant and the other variables.

Table 5. Estimation of logit regression analysis of choice^{†1} of the Asian disease problem with and without ROF as an explanatory variable.

	without ROF			with ROF		
	$\beta^{\dagger2}$	t	p	β	t	p
constant	-0.69	-1.39	.083	1.70	1.17	.120
negative-frame dummy ^{†3}	0.83	1.15	.125	0.51	0.54	.794
ROF				3.50	1.53	.063
sample size	33			24		
L (C) ^{†4}	-15.61			-3.90		
L (B) ^{†5}	-14.19			-3.22		

^{†1} The dependent variable of the logit regression analysis = 1 if the risk-taking option was chosen, = 0 if the risk-averse option was chosen. Therefore, if an explanatory variable whose coefficient is positive increases, the probability of choosing the risk-taking option increases.

^{†2} standardized coefficient.

^{†3} = 1 if negative-frame condition, = 0 otherwise.

^{†4} log-likelihood for the model with constant only.

^{†5} log-likelihood for the model with constant and the other variables.

Similar results were obtained for the Asian disease problem. Table 5 shows that the negative-frame dummy had a negative effect on the responses, suggesting that participants are more

likely to select a risk-taking option under negative frame conditions than under positive frame conditions. Although this framing effect did not reach significance, the standardized coefficient for the framing effect and its t-statistics decrease when ROF was included as an explanatory variable. ROF had a marginally significant positive effect, compatible with our Hypothesis 2 derived from the focusing hypothesis. Since frame condition was related to ROF in the Asian disease problem (Table 3), the logit analyses imply that the effect of frame condition on choices in the Asian disease problem (the framing effect) was indirectly mediated by ROF.

4. DISCUSSION

The contingent focus model incorporates two basic hypotheses: the focusing hypothesis and the contingent focus hypothesis. The focusing hypothesis states that risk attitudes depend on the extent to which a subject focuses on possible outcomes and probabilities. The contingent focus hypothesis states that focusing on possible outcomes and probabilities, or attending to possible outcomes and probabilities, is contingent on decisional contexts. These hypotheses have been supported by experimental data and psychometric tests (Fujii & Takemura, 2000, 2001, 2003; Takemura, Hu, & Fujii, 2001). In the past, however, attention to possible outcomes and probabilities was not explicitly observed, so in the current study we used an eye gaze recorder to observe eye movement during decision making, which may be related to attention to possible outcomes and probabilities.

The choice data from the reflection-effect problem supported the reflection effect; that is, participants preferred a risk-taking option more strongly under negative frame conditions than under positive frame conditions. The choice data from the Asian disease problem indicated that more participants preferred a risk-taking option under negative frame conditions than under positive frame conditions, although the difference between frame conditions was not significant. The effect of frame condition on choice in the reflection-effect problem disappeared, and the effect of frame condition on choice in the Asian disease problem decreased when eye movement data were included as a covariate. These results imply that the effects of frame condition on choice, i.e., the framing effect and the reflection effect, may be mediated by attention.

In the current study, ROF (the ratio of total time to gaze at possible outcome words compared to the total time to gaze at possible outcome words and probability words) was used to analyze the eye movement data. For both the reflection-effect problem and the Asian disease problem, ROFs were larger under negative frame conditions than under positive frame conditions, and participants with higher ROFs were more likely to choose a risk-taking option than those with lower ROFs. The former result supports the contingent focus hypothesis and the latter supports the focusing hypothesis.

Results overall support the contingent focus model's explanation of the reflection and framing effects; the decision maker attends to possible outcomes more strongly under negative frame conditions than under positive frame conditions, and those who attend strongly to possible outcomes are likely to prefer a risk-taking option. Decision makers thus prefer risk-taking options more strongly under negative frame conditions than under positive frame conditions.

It should be noted that although predicted effects for the reflection-effect problem achieved significance, predicted effects for the Asian disease problem did not. Lack of significance for the framing effect in the Asian disease problem is inconsistent with the original experiment by Tversky and Kahneman (1981); in this respect, the "elaboration effect" (Fujii & Takemura, 2003; Takemura, 1992, 1993, 1994b) may provide an explanation. The elaboration effect refers to the inhibition of the framing effect when decision makers are asked to elaborate their decision making process. Participants in the current experiment might have elaborated their decision making process in the Asian disease problem more than did participants in the original experiment by Tversky and Kahneman (1981) because those in the current study were requested to respond while alone in an experimental room. Although the framing effect was not significant for the Asian disease problem, both the effect of frame

condition on eye movement and the effect of eye movement on decisions were marginally significant in the direction compatible with the predictions of the contingent focus model.

In anyway, this model is expected to be used for analysis of people's decision making under seismic risk and psychological effects of risk communication.

References:

- Boe, O., Selart, M., Takemura, K. (2000) Perspectives on information acquisition: Rethinking its role in the construction of reason-based preferences. *Goteborg Psychological Reports*, 30, No.2, Goteborg University, Sweden.
- Card, S.K., Moran, T.P. & Newell, A. (1983) *The psychology of human-computer interaction*. Hillsdale, NJ; Erlbaum.
- Fischhoff, B. (1983) Predicting frames. *Journal of Experimental Psychology: Learning, Memory, & Cognition*, 9, 103-116.
- Fujii, S. and Takemura, K. (2000) Attention and risk attitude: Contingent focus model of decision framing, *International Journal of Psychology*, 35 (3/4), p. 269.
- Fujii, S. and Takemura, K. (2001) A psychometric meta-analysis of framing effect by Contingent Focus Model, Paper presented at International Meeting of the Psychometric Society 2001, Osaka, Japan.
- Fujii, S. and Takemura, K. (2003) Contingent focus model of decision framing under risk, Technical Report 67, Department of Civil Engineering, Tokyo Institute of Technology, 51-67.
- Gärling, T & Romanus, J. (1997) Integration and segregation of prior outcomes in risky decisions. *Scandinavian Journal of Psychology*, 38, 289-296.
- Kahneman, D. & Tversky, A. (1979) Prospect theory: An analysis of decision under risk. *Econometrica*, 47, 263-291.
- Kahneman, D. & Tversky, A. (1984) Choices, values, and frames. *American Psychologist*, 39, 341-350.
- Kühberger, A. (1998) The influence of framing on risky decisions: a meta-analysis. *Organizational Behavior and Human Decision Processes* 75(1), 23-55.
- LeBoeuf, R.A. & Shafir, E. (2003) Deep thoughts and shallow frames: on the susceptibility to framing effects, *Journal of Behavioral Decision Making*, 77-92.
- Lohse, G.L., and Johnson, E.J. (1996) A comparison of two process tracing methods for choice tasks. *Organizational Behavior and Human Decision Processes*, 68, 28-43.
- Maule, A. J. (1989) Positive and negative decision frames: A verbal protocol analysis of the Asian disease problem of Tversky and Kahneman, in H. Montgomery and O. Svenson, *Process and structure in human decision making*, John Wiley & Sons Ltd, New York.
- Romanus, J., & Gärling, T. (1999) Do changes in decision weights account for effects of prior outcomes on risky decisions? *Acta Psychologica*, 101, 69-78.
- Russo, J.E. (1978) Adaptation of cognitive processes to eye movement systems. In Seders, J.E., Fisher, D.F., & Monty, R.A.(Eds.), *Eye movements and higher psychological functions*, Hillsdale, NJ; Erlbaum, pp. 89-109.
- Savage, I.R. (1954) *The foundations of statistics*. New York: Wiley.
- Shafir, E. and LeBoeuf, R.A. (2003) Rationality, *Annual Review of Psychology*, 53, 491-517.
- Selart, M., Boe, O., and Takemura, K. (2000) How do decision heuristics and social value orientation influence the building of preferences? *Göteborg Psychological Reports*, 30 (6), Göteborg University, Sweden.
- Takemura, K., Hu, K. & Fujii, S. (2001) Examination of contingent focus model using a method of monitoring information acquisition, Paper Presented at the Japan Society for Kansei Engineering, Tokyo, Japan.
- Takemura, K. (2001) Contingent decision making in the social world: Mental ruler theory. In C. M. Allwood, & M. Selart (Eds.), *Decision making: Its creative and group dimensions*. Dordrecht, Netherlands: Kluwer Academic, pp.153-173.
- Takemura, K. (1992) Effect of decision time on framing of decision: A case of risky choice behavior. *Psychologia*, 35, 180-185.
- Takemura, K. (1993) The effect of decision frame and decision justification on risky choice. *Japanese Psychological Research*, 35, 36-40.
- Takemura, K. (1994a) Framing kouka no rironteki setumei: risk ka ni okeru ishikettei no jyokyoku-izonteki-syouten-model, *Shinrigaku Hyoron*, 37(3), 270-291. (Theoretical explanation of framing effect: Contingent focus model of decision framing, *Japanese Psychological Review*, 37 (3), 270-291.)
- Takemura, K. (1994b) The influence of elaboration on the framing of decision. *The Journal of Psychology*, 128, 33-39.
- Tversky, A., & Kahneman, D. (1981) The framing of decisions and the psychology of choice. *Science*, 211, 453-458.
- Tversky, A., & Kahneman, D. (1986). Rational choice and the framing of decisions. *Journal of Business*, 59, 251-278.
- Von Neumann, J., & Morgenstern, O. (1944). *Theory of games and economic behavior*. Princeton, NJ: Princeton University Press (see also 2nd ed., 1947; 3rd ed., 1953).
- Qualls, W.J., & Rodin, P.A. (1989) Organizational climate and decision framing: An integrated approach to analyzing industrial buying decisions. *Journal of Marketing Research*, 26, 179-192.
- Wang, X.T. (1996). Framing effects: Dynamics and task domains. *Organizational Behavior and Human Decision Processes*, 68, 145-157.

EFFECTIVENESS OF FLOOR AREA RATIO SYSTEM BY STRUCTURES FOR THE REDUCTION OF FIRE-SPREADING RISK

Y. Meshitsuka¹⁾

*1) Assistant Professor, Department of Architecture and Building Engineering, Tokyo Institute of Technology, Japan
meshi@mail.arch.titech.ac.jp*

Abstract: The aim of this study is to propose floor area ratio system by structures and to show how it works on future fire-spreading risk. To this end, a behavior model of building-clients was constructed. In this model, a utility of each building was represented by two indexes, namely benefit index and cost index. The former was represented by the total amount of floor area. The latter was represented by the annual cost of building and its lot. The parameters of the model were coordinated by building database at two different observation times. Based on the simulation by the above model, changes of an index of fire-spreading risk were estimated. As a result, when the ratio of fireproof building was enlarged 3 times as much as a wooden building, future index of fire-spreading risk was reduce more than 4 times of the case without the system. These results show the good effectiveness of this system.

1. INTRODUCTION

1.1 Background and Objectives

In urban district where many old wooden buildings are included, it is a serious concern that their damage can be increased because of fire-spreading after a big earthquake. In order to reduce this damage, it is required not only to enrich infrastructures such as road base and fire fighting system but also to improve fire-prevention performance of each building. However a lot of buildings having minimum fire-prevention performance have been built, because the higher fire-prevention performance is, the more building construction cost is, and a big earthquake extremely rarely occurs. In order to improve fire-prevention performance, clear incentives are required. In this study, we propose floor area ratio system by structures and try to verify the effect of this system.

1.2 Floor Area Ratio System by Structures

In the volume restriction system of Japan, there is a fixed upper limit volume that has no connection with its structure and use. In floor Area Ratio System by Structures, an extra volume is added to fire-prevented buildings (such as RC building) and some volume is subtracted from combustible buildings (such as wooden building). It is expected that fire-prevented buildings come to be built more by this system (Figure 1).

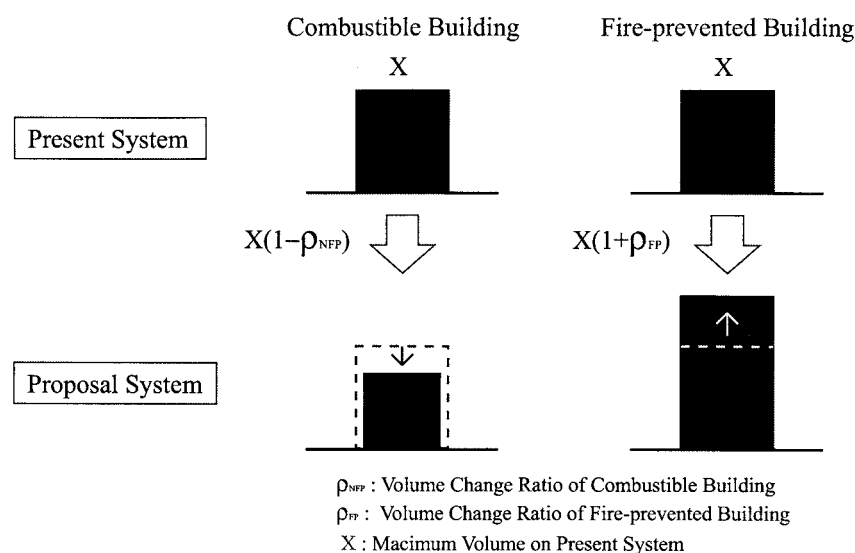


Figure 1 : Floor Area Ratio System by Structure

1.3 Method and Using Data

To verify an effect of the proposal system, a behavior model of building-clients was constructed. With above model, we tried to estimate how the ratio of newly built fire-prevented buildings to the total new buildings changes by our proposed system.

Data used in this study is Tokyo City Planning Geographical Information System at 1991 and 1996. This is a vector type data, and the two dimensional shape of buildings are related to various information such as structure, use, area, number of floors and total floor area conversion code. Structure of buildings is classified into 4 categories of Fireproof (Taika), Semi-fireproof (Jyuntaika), Slow-burning (Bouka), and Wooden (Mokuzo) buildings in the original data. Fireproof and Semi-fireproof building were treated as one category "Fireproof". Slow-burning and Wooden building were sometimes treated as one category "Non-fireproof" (Table 1). Use of buildings is classified into 38 categories in the original data, but those were re-classified into the following 4 categories, Business, Housing, Industry, and Others in this study (Table 2).

2. BEHAVIOR MODEL OF BUILDING-CLIENTS AND ITS CALIBRATION

2.1 BEHAVIOR MODEL OF BUILDING-CLIENTS

Behavior model of building-clients is modelled based on a general utility model. In this model, a utility of some building (u_i) is expressed with a sum of "Charm" and "Cost".

$$u_i = a \cdot \text{Charm} + b \cdot \text{Cost} + \varepsilon$$

When the probable error ε distributes Gumbel-distribution, choice probability p_i is represented as follow. Where m is a number of charm type and n is a number of cost type.

Table 1 : Classification of building structure in Urban Planning GIS of Tokyo

Code	Class in Urban Planning GIS of Tokyo	Our class
22	Wooden building (Mokuzo-tatemono)	Non-fireproof
21	Slow-burning building (Bouka-tatemono)	
12	Semi-fireproof building (Jyuntaika-tatemono)	Fireproof
11	Fireproof building (Taika-tatemono)	

Table 2 : Classification of building use in Urban Planning GIS of Tokyo

Code	Class in Urban Planning GIS of Tokyo	Our class
121	Office	Business (U2)
122,123	Commerce	
124	Lodging, amusements	
125	Sports, show business	
131	Detached house	Housing (U3)
132	Collective housing	
141,142	Factory	Industry (U4) Agriculture (U5)
143	Warehouse, transport	
150, etc.	Agriculture, etc.	
111	Government and municipal	Other (U1)
112	Education and culture	
113	Medical and welfare	
114	Supply and disposal	

Table 3 : Floor Area Conversion Codes and Coefficients in Urban Planning GIS of Tokyo

Code	Coefficient				
	1 st floor	2 nd floor	3 rd floor	4 th floor -11 th floor	12th floor -
1	1.0				
2	1.0	0.9	0.9	0.8	
3	1.0	0.7	0.6	0.5	0.4

$$p_i = \exp(u_i) / \sum_{i=1}^{mn} \exp(u_i)$$

2.1.1 Attraction Model

Charm-model is estimating from total floor area of each building. The total floor area is estimated from building area, a number of floors and a floor area conversion coefficient. Floor area conversion coefficient is a coefficient to calculate a floor area considering three-dimensional shape of buildings. Building area multiplied by floor area conversion coefficients for each floor is its floor area, and their total sum gives total floor area (Table 3).

2.1.2 Cost Model

Cost-model is estimated from an annual cost of construction and cost for its site. The detail will be described as below.

1) Annual construction cost

A construction cost is the product of the construction unit price according to structure and the floor area. A construction cost is divided by building life span to obtain an annual construction cost. The construction unit price of fireproof building is 207 thousand yen per meter square, and non-fireproof building is 153 thousand yen per meter square. These prices were calculated from "Research of Building Construction Started (1996)" by Ministry of Land, Infrastructure and Transport (MLIT).

2) Building life span

Building life span is considered to be a period from the construction to the elimination. In this study, we use following settings (Table 4).

Table 4 : Building Life Span

	Business	Housing	Industry
Fireproof	35 years	41 years	35 years
Non-Fireproof	29 years	39 years	29 years

3) Annual site cost

Annual site cost is very different depending whether building client is an owner of its site or a leaseholder. In this study, all building client is considered to be a leaseholder, and annual lease cost is estimated to be 5% of the land price. A land price of each site is a price of the nearest evaluation point from the price of official announcement of land price of "Numerical Land Information" by MLIT.

2.2 Calibration of Parameters

2.2.1 Extraction of replaced building

Parameters of behavior model are estimated from sample data (Figure 2). In this study, we tried to distinguish the rebuilt in the meantime based on a difference of data at two points of time, because there are few data which recorded the rebuilt of buildings.

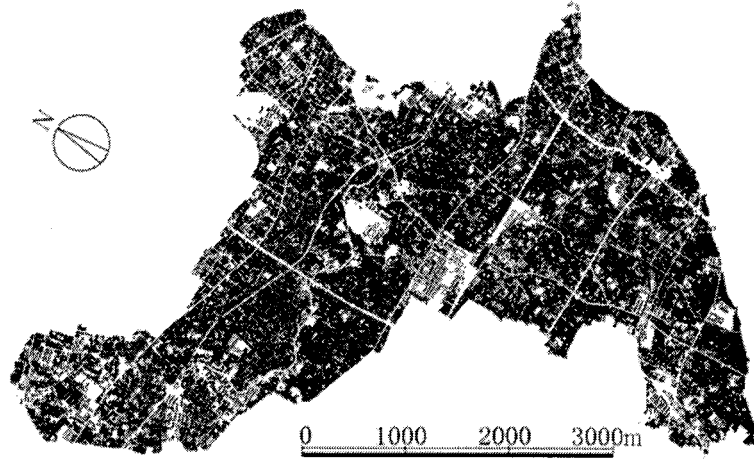


Figure 2: Sample Data

It was considered that the building which satisfied either one of the following conditions was rebuilt during the period of time. (1) The structures of buildings are different. (2) The number of floor is different. (3) Building shapes are clearly different.

2.2.2 Calibration Parameters

When N is the number of building that built in a period of time, and N_i is the number of building of plan i ,

$$p_i^* = N_i / N, \quad N = \sum_{i=1}^{mn} N_i.$$

When $p_i^* \neq 0$ and $p_j^* \neq 0$,

$$\frac{P_i^*}{P_j^*} = \frac{N_i / N}{N_j / N} = \frac{N_i}{N_j}.$$

On the other hand,

$$\frac{p_i}{p_j} = \frac{\exp(u_i) / \sum_{i=1}^{mn} \exp(u_i)}{\exp(u_j) / \sum_{j=1}^{mn} \exp(u_j)} = \frac{\exp(u_i)}{\exp(u_j)}.$$

When a client of building follows above behavior model, a following equation is established because p_i and p_i^* become equal.

$$\frac{p_i}{p_j} = \frac{p_i^*}{p_j^*}.$$

Hence,

$$\frac{N_i}{N_j} = \frac{\exp(u_i)}{\exp(u_j)}.$$

A logarithm of above equation is,

$$\log \frac{N_i}{N_j} = \log \left(\frac{\exp(u_i)}{\exp(u_j)} \right) = \log(\exp(u_i)) - \log(\exp(u_j)) = u_i - u_j.$$

Therefore, parameter a, b minimizes following L.

$$L = \sum_{i,j}^{mn} \left(u_i - u_j - \log \frac{N_i}{N_j} \right)^2 = \sum_{i,j}^{mn} \left(ax_i + by_i - ax_j - by_j - \log \frac{N_i}{N_j} \right)^2$$

Parameter a is 6.14×10^{-2} and parameter b is -1.95×10^{-8} in sample area, when we specified these parameters by the quasi-Newton method.

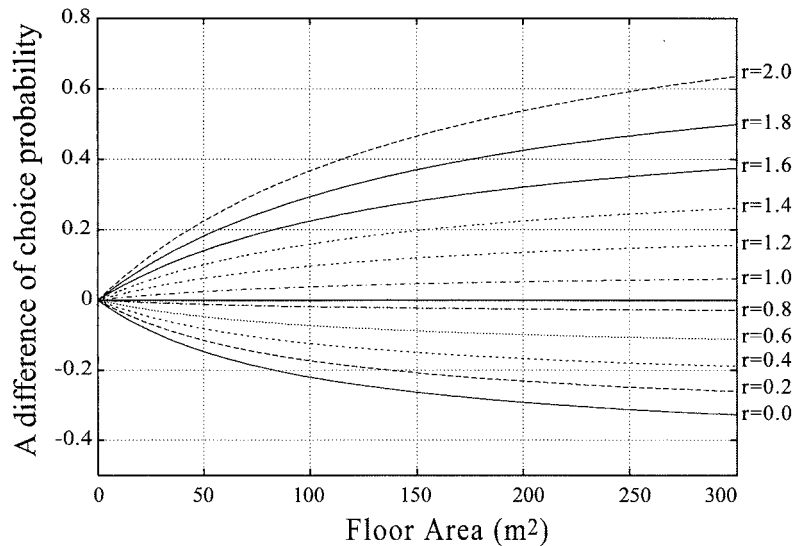


Figure 2: A Difference of Choice-probability

With these parameters, choice-probability of fireproof building grew big as a rate of extra volume became big (figure 2).

3. VALIDITY OF PROPOSED SYSTEM

3.1 Simulations Setting

To verify a validity of proposed system, we estimate how a ratio of fireproof buildings to occupy to buildings built newly by our proposal system changes. The detail of simulation will be described as below.

- 1) Targeted area of this simulation is a part of sample area.
- 2) Building change happen at random.
- 3) The upper limit of the cost that the client of building can pay is not set.
- 4) The bottom of a floor space is not set.
- 5) A use of a building is not changed at rebuilding.
- 6) A use in case of new construction is decided at random.
- 7) Structure of a building is fireproof or slow-burning or wooden.
- 8) A floor space of a building and building area are the greatest areas forgiven by a law.
- 9) Floor area ratio sets it according to the existing law.
- 10) When width of front road is narrower than 12m, according to the existing law, floor area ratio of house assumes 0.4 times of road width and floor area ratio of business assumes 0.6 times of road width.
- 11) Site distributed land polygon proportionally in building area of a building polygon in a polygon.
- 12) The following fire-spreading velocity ratio α is used to catch a tendency of fire-prevention of sample area. Where s is wooden building ratio and t is slow-burning building ratio.

$$\alpha = (s + t)^2 / (s + \frac{t}{0.6})$$

3.2 Result of simulation

As a result of simulation, the fire-spreading velocity ratio had great decrease as a rate p was big. For example, when the ratio of fireproof building was enlarged 3 times as much as a wooden building, future index of fire-spreading risk was reduce more than 4 times of the case without the system. This shows that disaster prevention characteristics of a town area may improve by a proposed system more quickly.

4. CONCLUSIONS

In this study, floor area ratio system by structure was proposed, and a behavior model of building-clients was constructed in order to verify an effect of the proposed system. As a result of simulations, fire prevention performance of a town area might improve by proposed system

immediately.

It is necessary to consider regionalities in future study. In addition, it is also necessary to examine a method to increase the number of rebuilding because there are enormous numbers of old wooden combustible buildings in the suburbs of downtown area.

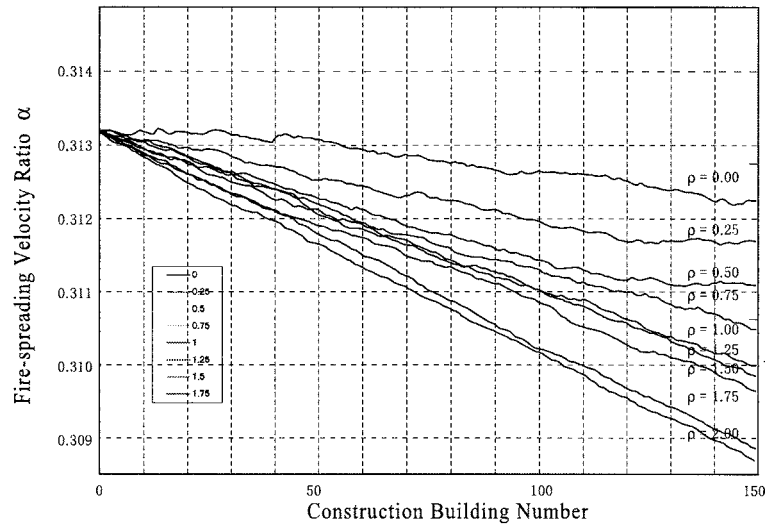


Figure 3: Fire-spreading Velocity Ratio α and Extra Volume Rate ρ

References:

- Yasuhisa KATO, Yukio KOMATSU : “A Statistical Study on Life Time of Japanese Wooden Houses”, Journal of Architecture, Planning and Environmental Engineering (Transaction of AIJ), No.363, 20-26,1986 (in Japanese)
- Minoru HAMADA : “Fire-spreading velocity”, Research of fire, vol.1, Sagami publishing, 1951(in Japanese)
- Tokyo Metropolitan Government: Definition Note of Urban Planning GIS, 1998
- Economic Research Association: “Quarterly Unit Price Data of Building Construction 2006 Spring”, 2006 (in Japanese)

DISCRETE CHOICE ANALYSIS OF TEMPORARY HOUSING CHOICE AFTER URBAN EARTHQUAKE DISASTER

K. Sato¹⁾, I. Nakabayashi²⁾ and S. Midorikawa³⁾

1) Post-doctoral Research Fellow, Center for Urban Earthquake Engineering, Tokyo Institute of Technology, Japan

2) Professor, Graduate School of Urban Science, Tokyo Metropolitan University, Japan

3) Professor, Center for Urban Earthquake Engineering, Tokyo Institute of Technology, Japan
ksato@enveng.titech.ac.jp, nakabasi@comp.metro-u.ac.jp, smidorik@enveng.titech.ac.jp

Abstract: This paper aims to develop a temporary housing choice model of households who lose their houses after urban earthquake disaster for integration into a micro simulation of a temporary housing situation. Disaggregate behavioral analysis is used for the choice model. As a result of parameter estimation, many statistically significant parameters were obtained. Also, Positive and negative relations between attributes variables and estimated parameters for calculating choice probabilities were examined, and reliability of the response data was confirmed. However, hitting ratio of the model was not high enough. The value of estimated parameter showed the importance of location at temporary housing choice. Therefore we considered that parameter estimation using questionnaire data separated by each residential area is required.

1. INTRODUCTION

In the 1995 Kobe earthquake disaster, approximately 48,000 units of prefabricated temporary houses (hereinafter called prefabs) were supplied. The prefabs had many problems such as poor quality of residential environment and local community disruption (Maki 1997). After the earthquake, the Natural Land Agency reported the importance of utilizing vacancies in rental housing as temporary housing countermeasures after urban disaster (Natural Land Agency 2000). The use of the prefabs is not a universal countermeasure as exemplified by events after the Taiwan Earthquake in 1999, wherein approximately 800 thousands victims chose rent subsidies (Shao 2001). In 2004, the Japanese Natural Disaster Victims Relief Law was reformed, and a system of rent subsidies for temporary housing countermeasures after disaster was established. In Japan, occurrences of large earthquakes such as the Tokai Earthquake and the Tokyo metropolitan earthquake are the concern of researchers in seismology (Headquarters for Earthquake Research Promotion 2007). In the event of a large urban earthquake, it is not clear whether the new system of rent subsidies will perform effectively. In order to design institutional arrangements as well as to make preliminary considerations, a micro simulation of temporary housing that can treat policy variables is necessary. In this study, we tried to develop a model that looked at the temporary housing choice of households who lose their homes after an urban earthquake disaster in order to construct the micro simulation.

2. DESIGN OF QUESTIONNAIRE SURVEY

2.1 Target Area of Questionnaire Survey

First, we set a target area for data collection in the form of questionnaire survey. The Tokyo

metropolitan area has 5 prefectural governments with about 300 city governments. Because size of administrative segmentation is not appropriate for questionnaire survey, we divided the area into original 24 sections. Then, based on damage assessment by the Cabinet Office (2004), if a M7.3 earthquake occurs at the northern part of Tokyo Bay, housing damage will cover wide areas within the circumference of the bay. From a damage map of the Cabinet Office's assessment, we extracted 15 areas for questionnaire distribution.

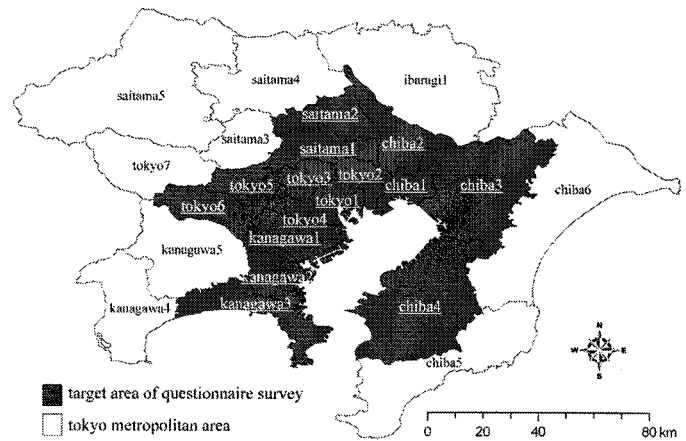


Figure 1 Target Area of the Survey

2.2 Survey Method

The survey that we wanted to pursue has several unique characteristics. First, it has a huge total target area. Second, it needs at least 300 to 500 samples from each selected area as a requirement of disaggregate behavior analysis (JSCE 1995). And last, it can make use of the rental housing database on Tokyo metropolis. With these characteristics, traditional paper-based questionnaire survey becomes unsuitable mainly due to the enormous cost it would incur. For the cost and effort of the survey, we conducted an internet-based questionnaire survey.

For the main purpose of this study, it is preferable that the temporary housing choice model treat conditions of housing and households. From this viewpoint, there are several methods of analysis such as conjoint analysis, analytic hierarchy process (AHP), and disaggregate behavioral analysis. Conjoint analysis and AHP can treat conditions of housing and households but results of these methods are not suitable to use for prediction or simulation. In contrast, disaggregate behavioral analysis creates choice probabilities and its results are suitable for prediction and simulation. Thus, we used discrete choice analysis in this survey.

2.3 Constructing of Choice Set

In accord with the housing shift after the Great Hanshin-Awaji Earthquake (Kimura et al., 2001), we made a fundamental model of temporary housing choices as shown in Figure 2. Choices were divided into three categories: prefabricated temporary house, rental housing, and others such as leads on a temporary residence.

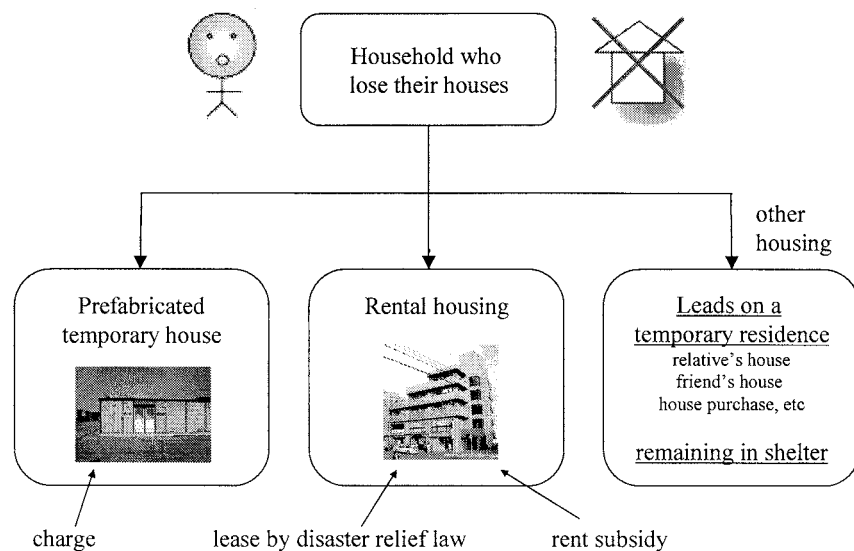


Figure 2 Fundamental model of temporary housing choice

Based on the fundamental model, internet-based questionnaire system showing in the Figure 3 was constructed. In the system, common gateway interface (CGI) program which make conditions of temporary housing (such as location and rent) by a respondent's conditions and data base of rental housing was developed. In more detail, following three CGI program was developed in the system.

The 1st program selects one rental housing at random using data base and respondent's conscious of rental housing. The database was constructed from the internet site of CHINTAI (<http://www.chintai.net/>) with the following details;

- Target area : Tokyo metropolitan area (Tokyo metropolis, Kanagawa Pref., Saitama Pref. Chiba Pref., and a part of Ibaragi Pref.)
- Period of gathering : October 2006
- Amount of data : 144,902 rental housing (after erasing double count data and illogical data)

The second program fixes conditions of prefabs using respondent's attributes. A rule of fixing follows the actual countermeasures at Kobe earthquake and Mid-niigata earthquake. Room layout of the prefabs is fixed from number of people in a household. Location of the prefabs is fixed from present address; one location is in the same city, the two locations are in the other city of the same prefecture, and the one location is out of the present prefecture.

The third program fixes four administrative subsidy pattern; no administrative support, rent subsidy by the Natural Disaster Victims Relief Law, lease of rental housing by the Disaster Relief Law, and virtual rent subsidy (random value from 10 to 80 thousand JPY which is provided every month).

The choice experiments were created in an HTML form. At first, a respondent who accesses a questionnaire web site answer their household's attribute. After that, the HTML form as showing in the Figure 3 comes to respondent's computer, and they select one choice.

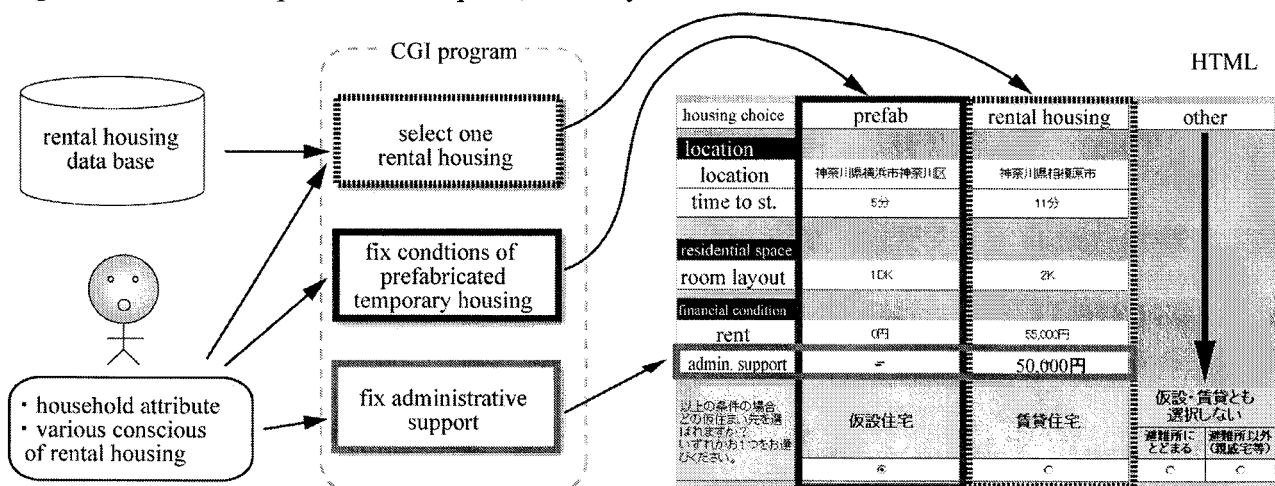


Figure 3 outline of Internet-based questionnaire survey

3. RESULT OF QUESTIONNAIRE SURVEY

3.1 Attributes of Respondents

The internet-based questionnaire was conducted from January 9th on 12th, 2007 and responses 2869 households were collected. Attributes of the respondents are summarized in Table 1. In residential areas, over 200 respondents were retrieved in each location except for Tokyo 6 and Chiba 4. In householder's age, respondents of over 70's couldn't retrieve but other ages could retrieve relatively uniform. With respect to the number of persons per household, respondents ranged from a single head household to more than five heads. With respect to a house's form of ownership, households who own their houses were about 67%, and households who rent their houses were about 34%. Lastly, a wide range of information with respect to annual household income was collected.

Table 1 attributes of the respondents

household's attribute	category1		category2		category3		category4		category5	
	number	percentage	number	percentage	number	percentage	number	percentage	number	percentage
residence area	tokyo1		tokyo2		tokyo3		tokyo4		tokyo5	
	200	7.0%	200	7.0%	200	7.0%	200	7.0%	268	9.3%
	tokyo6		kanagawa1		kanagawa2		kanagawa3		saitama1	
	130	4.5%	204	7.1%	200	7.0%	200	7.0%	200	7.0%
	saitama2		chiba1		chiba2		chiba3		chiba4	
householder's age	20's		30's		40's		50's		60's	
	250	8.7%	759	26.5%	694	24.2%	577	20.1%	589	20.5%
numbers of persons	single		two persons		three persons		four persons		over five persons	
	363	12.7%	714	24.9%	766	26.7%	732	25.5%	294	10.2%
ownership form of a house	own		rental							
	1905	66.4%	964	33.6%						
annual income	under 3millionJPY		3's million JPY		4's million JPY		5's million JPY		6's million JPY	
	307	10.7%	263	9.2%	354	12.3%	343	12.0%	323	11.3%
	7's million JPY		8's million JPY		9's million JPY		10-14's million JPY		over 15 million JPY	
	305	10.6%	215	7.5%	234	8.2%	409	14.3%	115	4.0%

3.2 Existence of Leads on Temporary Residence

Existence of leads on a temporary residence is summarized in Table 2. The highest rate of the existence is about 65% in relative's home. The second is about 38% in self-build prefabs on their home garden. Added to this, about 20% of respondents have friend's home or employee's house. It can say that the rates of existence of leads on a temporary residence are not low and the leads such as relative's home have important role after Earthquake occurring near Tokyo metropolis.

Table 2 existence of leads on temporary residence

	self-build prefabs on home garden		relative's home		friend's home		employee's house	
	impossible	possible	no exist	exist	no exist	exist	no exist	exist
number	1792	1077	1013	1856	2257	612	2164	705
percentage	62.5%	37.5%	35.3%	64.7%	78.7%	21.3%	75.4%	24.6%

3.3 Results of Discrete Choice

Results of the discrete choices using the internet-based questionnaire system are summarized in Figure 4. The choice problem has four variations of administrative supports as described in the figure. If there is no administrative support, about 54% of the respondents would choose the prefabs. The rent subsidy offered by the Natural Disaster Victims Relief Law did not make much impact to choice results. However, if a rent subsidy with random value from one to eight provided every month exists, the rate of rental housing increased to about 14% given this fictitious option. Lastly, if there are leases of rental housing by the Disaster Relief Law, the rental housing was chosen by 3% more of the respondents

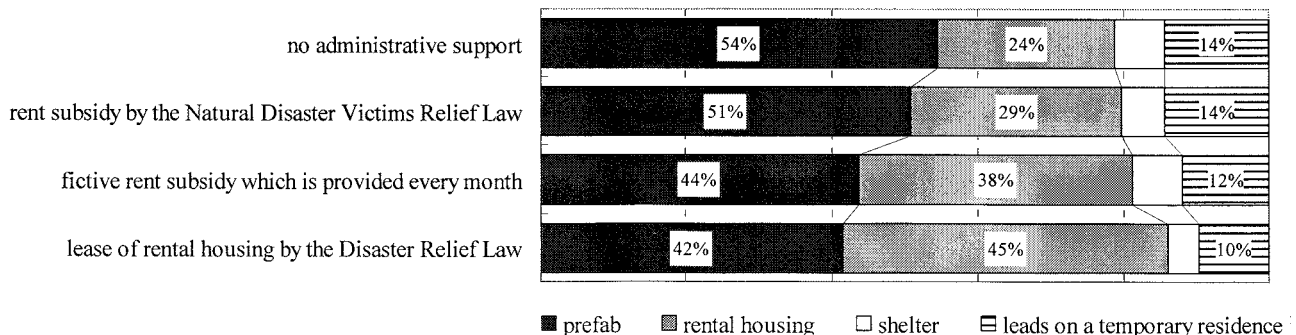


Figure 4 Results of the Choice problem

as compared to the prefabs. These results are based on a virtual setting of discrete choices such that the value of the rate has minimum importance but rate changes indicate the importance and impact of administrative supports.

4. PARAMETER ESTIMATION

4.1 Outline of Multinomial Logit Model

According to transportation research (i.e., Ben-Akiva et al. 1985), multinomial logit model is based on random utility theory. Let U_{ij} be the utility of the j th alternative for the i th individual. Further assume each utility value can be partitioned into two components: a systematic component, V_{ij} , and a random component, where e_{ij} , reflects unobserved individual idiosyncrasies of tastes. Then,

$$U_{ij} = V_{ij} + e_{ij} \quad (1)$$

V_{ij} is assumed to be linear, additive functions in the attributes x_{mij} which determine the utility of the j th alternative. That is, let V_{ij} be written as:

$$V_{ij} = \sum_m \beta_m x_{mij} \quad (2)$$

The probability that an individual drawn randomly from the population and given the alternatives $1, \dots, J$ will choose i equals

$$P_{ij} = P(U_{ij} > U_{ik}; \text{ for all } k \neq j) = P(V_{ij} - V_{ik} > e_{ik} - e_{ij}; \text{ for all } k \neq j) \quad (3)$$

By assuming that e_{ij} are independently and identically distributed with the double exponential distribution, the choice probability for alternative i can be written as:

$$P_{ij} = \exp(V_{ij}) / \sum_k \exp(V_{ik}) \quad (4)$$

The likelihood function L can be simplified somewhat by defining a dummy variable d_{ij} , such that $d_{ij}=1$ if alternative j is chosen and $d_{ij}=0$ otherwise.

$$L = \prod_i \prod_j P_{ij}^{d_{ij}} \quad (5)$$

Given L in the above equation, the log likelihood function LL can be written as in equation 6 and the parameter β_m can be calculated by maximum likelihood method.

$$LL = \ln(L) = \sum_i \sum_j d_{ij} \ln(P_{ij}) \quad (6)$$

4.2 Formulation of Temporary Housing Choice

A systematic component of utility of prefabricated temporary housing

$$\begin{aligned} V_{i \text{ temp}} = & \beta_1 time_{i \text{ temp}} + \beta_2 floor_{i \text{ temp}} + \beta_3 rent_{i \text{ temp}} + \beta_4 tokyo1_{i \text{ temp}} + \dots + \beta_{27} ibaragi1_{i \text{ temp}} \\ & + \gamma_{1_temp} age + \gamma_{2_temp} number + \gamma_{3_temp} own + \gamma_{4_temp} income + \gamma_{5_temp} month + \gamma_{6_temp} ate \\ & + \gamma_{7_temp} support1 + \gamma_{8_temp} support2 + \gamma_{9_temp} support3 \end{aligned} \quad (7)$$

A systematic component of utility of rental housing

$$\begin{aligned} V_{i \text{ rental}} = & \beta_1 time_{i \text{ rental}} + \beta_2 floor_{i \text{ rental}} + \beta_3 rent_{i \text{ rental}} + \beta_4 tokyo1_{i \text{ rental}} + \dots + \beta_{27} ibaragi1_{i \text{ rental}} \\ & + \gamma_{1_rental} age + \gamma_{2_rental} number + \gamma_{3_rental} own + \gamma_{4_rental} income + \gamma_{5_rental} month + \gamma_{6_rental} ate \\ & + \gamma_{7_rental} support1 + \gamma_{8_rental} support2 + \gamma_{9_rental} support3 + d02 \end{aligned} \quad (8)$$

A systematic component of utility of other housing

$$V_{i \text{ other}} = d03 \quad (9)$$

Definitions of each variable in formulations are summarized in Table 3. If formula 7 to 9 are applied to a formula 5, probability of temporary housing choice can be calculated by attributes of household and housing.

Table 3 Definition of variables in formulation

①housing attributes	
time	The time required form a nearby station(minutes)
floor	room layout (1:1R・1K, 2:1DK・2R・2K, 3:1LDK・2DK, 4:2LDK・3DK, 5:3LDK or more)
rent	rent(10 thousand JPY)
tokyo1	location(1:tokyo1, 0:other 23areas) other 23 areas are same format
d02	dummy variables (rental housing)
d03	dummy variables (other housing)
②household's attributes	
age	householder's age (1:20's 2:30's, ...5:over 60's)
number	number of household (person)
own	housing ownership (0:rental dwelling, 1:house ownership)
income	annual income (1:under3millionJPY, 2:3million's, ...9:10~14millionJPY, 10:over15millionJPY)
month	month which has passed sinse a earthquake disaster(0:1month, 1:6months)
ate	existence of the leads on temporary residence(0:nonexistent , 1:exist)
③policy variables	
support1	lease of a rental housing by the Disaster Relief Law
support2	rent Subsidy furnished by Natural Disaster Victims Relief Law(10 thousand JPY)
support3	fictive rent subsidy which is provided every month(10 thousand JPY per month)

4.3 Result of Parameter Estimation

Parameters were estimated by Broyden-Fletcher-Goldfarb-Shanno (BFGS) method (i.e., Broyden 1970) of “optim” function of R language using all questionnaire reply. The results are summarized in Table 5 and the features are listed below.

- The time required from a nearby station and systematic component of utility have a negative relation.
- If room layout becomes large, systematic component of utility increases.
- The rent of temporary housing and systematic component of utility have a negative relation.
- If the location of temporary housing is suburb such as tokyo6, tokyo7, kanagawa4, kanagawa5, saimata4, saitama5, chiba5, chiba6 and ibaragi1, systematic component of utility decreases.
- If the household have leads on temporary residence, the both systematic components (prefabs and rental housing) decrease.

As previously mentioned, we can be fairly certain that positive and negative relations between estimated parameter and variables are logically correct. Thus, we can say that the reliability of the response data was confirmed. And the value of estimated parameter shows the importance of location at temporary housing choice because estimated parameters of location are larger than other parameters.

Moreover, we can get some features between household attributes and temporary housing choice described below.

- When the choice is rental housing or other housing, systematic component of utility decreases. It shows that the prefabs are preferred by residents of Tokyo metropolitan area.
- The householder's age and the systematic component of prefabs have a positive relation.
- If the household own their houses, the systematic component of rental housing decreases.
- The annual income and the systematic component of rental housing have a positive relation.
- From value of each parameter, we can say that householder's age and month which has passed since earthquake disaster doesn't have strongly effect to temporary housing choice.

Added to this, relations between policy variables and temporary housing choice were observed. Lease of rental housing by the Disaster Relief Law have strong positive influence to utility of rental housing. We also observed that fictive rent subsidy which provided every month have positive influence to utility of rental housing.

Although the adjusted likelihood ratio of the model used for prediction was about 0.2 to 0.3, the

ratio from actual results was 1.3. In order to construct a micro simulation using disaggregate behavior model, it is necessary to adjust the model and to raise the adjusted likelihood ratio.

Table 5 Result of parameter estimation

	attributes		parameter estimated	standard error	t-value	p-value
	names of attributes	details				
choice attributes	time	-	-0.021	0.002	-13.347	0.000 ***
	floor	-	0.155	0.026	6.057	0.000 ***
	rent	-	-0.100	0.006	-16.557	0.000 ***
	location	tokyo1	0.127	0.114	1.108	0.268
		tokyo2	-0.064	0.117	-0.550	0.582
		tokyo3	-0.061	0.116	-0.530	0.596
		tokyo4	0.166	0.121	1.364	0.173
		tokyo5	-0.394	0.110	-3.584	0.000 ***
		tokyo6	-0.377	0.125	-3.005	0.003 ***
		tokyo7	-1.019	0.141	-7.199	0.000 ***
		kanagawa1	-0.083	0.113	-0.728	0.466
		kanagawa2	-0.115	0.116	-0.992	0.321
		kanagawa3	-0.263	0.120	-2.190	0.029 **
		kanagawa4	-1.111	0.138	-8.066	0.000 ***
		kanagawa5	-0.804	0.142	-5.680	0.000 ***
		saitama1	-0.221	0.116	-1.898	0.058 *
		saitama2	-0.030	0.124	-0.243	0.808
		saitama3	-0.935	0.161	-5.818	0.000 ***
		saitama4	-1.230	0.131	-9.371	0.000 ***
		saitama5	-1.493	0.181	-8.245	0.000 ***
		chiba1	0.083	0.121	0.687	0.492
		chiba2	-0.198	0.118	-1.676	0.094 *
		chiba3	-0.528	0.113	-4.663	0.000 ***
		chiba4	-0.593	0.141	-4.212	0.000 ***
		chiba5	-1.194	0.317	-3.770	0.000 ***
		chiba6	-1.631	0.159	-10.273	0.000 ***
		ibaragi1	-1.716	0.213	-8.070	0.000 ***
	d02	rental	-0.389	0.115	-3.372	0.001 ***
	d03	other	-1.518	0.168	-9.018	0.000 ***
household attributes	age	prefab	0.039	0.022	1.722	0.085 *
		rental	-0.010	0.024	-0.400	0.689
	number	prefab	-0.002	0.025	-0.087	0.931
		rental	-0.118	0.028	-4.262	0.000 ***
	own	prefab	-0.012	0.065	-0.179	0.858
		rental	-0.422	0.069	-6.136	0.000 ***
	income	prefab	0.004	0.011	0.380	0.704
		rental	0.143	0.012	11.862	0.000 ***
	month	prefab	-0.055	0.052	-1.051	0.293
		rental	0.044	0.056	0.797	0.426
	ate	prefab	-0.299	0.067	-4.469	0.000 ***
		rental	-0.384	0.071	-5.436	0.000 ***
variable	support1	prefab	0.160	0.069	2.309	0.021 **
		rental	1.020	0.076	13.381	0.000 ***
	support2	prefab	0.000	0.002	-0.138	0.890
		rental	0.013	0.002	5.402	0.000 ***
	support3	prefab	0.003	0.013	0.252	0.801
		rental	0.087	0.020	4.358	0.000 ***

L(0)=-12607.67 , Lmax=-10950.24 ,adjusted likelihood ratio=0.130 ,AIC=21994.49, hitting ratio=0.550

Signif. codes: 0 '***' 0.01 '**' 0.05 '*' 0.1

4.4 Hitting Ratio

Finally, hitting ratio of the estimated model was calculated. In the calculation, choice probability of each answer was calculated using questionnaire data (such as estimated parameter, housing attributes, household attributes) based on equation 5. The cross table of the anticipated result at assuming that the choice which has biggest estimated probability is chosen and the result of questionnaire is Table 4. According to Table 4, existence of multiple hits can be checked. However the hitting ratio is not so

high at 55%. In addition to this, the rate of choosing other housing is only 1.7% even though the questionnaire result is 18.7%. The low level of prediction for the other housing option is considered one of the possible causes of mismatch. In this case, the formulation of a systematic component of utility of other housing (equation9) should be adjusted by inserting household attributes.

Table 4 cross table of the prediction and the questionnaire

		result of questionnaire				
		prefabs	rental housing	other housing	total(frequency)	total(%)
prediction result	prefabs	4360	1957	1365	7682	66.9%
	rental housing	1055	1875	670	3600	31.4%
	other housing	54	53	87	194	1.7%
	total(frequency)	5469	3885	2122	11476	100%
	total(%)	47.7%	33.9%	18.5%	100%	hitting ratio = 55%

5. CONCLUSIONS AND FUTURE REMARKS

In this paper, the temporary housing choice model based on multinomial logit model was developed. Many statistically significant parameters were obtained. Positive and negative relations between attributes variables and estimated parameters were examined, and reliability of the response data was confirmed. The estimated parameter showed the importance of location at temporary housing choice. After parameter estimation, choice probability of each answer was calculated using questionnaire data, and the hitting rate was calculated. As the result, the hitting rate was not high enough. In order to construct a more reliable model, parameter estimation using questionnaire data separated by each residential area is required. Also the formulation of each systematic component of utility should be rearranged. In addition, it should be noted that applying the other models of disaggregate behavior analysis (such as Nested logit, Mixed-logit) should be also considered. After enhancing the choice model, we want to develop a micro simulation of temporary housing after Tokyo Metropolitan earthquake.

Acknowledgements:

This research was supported in part by grants from the Center for Urban Earthquake Engineering (Tokyo Institute of Technology) and the Nakayama Foundation for Human Science. Thanks are due to Associate Professor Y. Muromachi (Tokyo Institute of Technology) for advice of questionnaire design and Mrs. Janila R. Baul-Deocampo (Tokyo Institute of Technology) for helpful suggestions of English expression.

References:

- N.Maki(1997), "History and Planning Method of Emergency Housing after Natural Disaster," Doctoral thesis, Kyoto University. (in Japanese)
- Natural Land Agency (2000), http://www.bousai.go.jp/oshirase/h13/130126chubo/shiryo5_mokuji.html, 2007/01/31. (in Japanese)
- P.Shao and Y.Murosaki(2001), "Emergency Housing Policies for Taiwan Earthquake – Actual Condition and Evaluation of Rent Subsidies Policy –," "Journal of Social Safety Science, No.3, 157-162. (in Japanese)
- Headquarters for Earthquake Research Promotion (2007) "List of Long-term evaluation," http://www.jishin.go.jp/main/p_hyoka02_chouki.htm, 2007/01/31.(in Japanese)
- Cabinet Office(2004), "Reference Data of Damage Assessment of Tokyo Metropolitan Earthquake," <http://www.bousai.go.jp/jishin/chubou/shutochokka/13/shiryo2-2.pdf>, 2007/01/31.(in Japanese)
- Japan Society of Civil Engineers (1995), "Disaggregate Behavior Analysis : Theory and Application," JSCE, 113-114.(in Japanese)
- Reo KIMURA, et al. (2001), "Determinants and Timing of Housing Reconstruction Decisions by the Victims of the 1995 Hanshin-Awaji Earthquake Disaster," Journal of Social Safety Science No.3, 23-32.(in Japanese)
- Ben-Akiba, M. and S.R.Lerman (1985), "Discrete Choice Analysis : Theory and Application to Travel Demand," MIT Press.
- Broyden C. G. (1970), "The Convergence of a Class of Double-rank Minimization Algorithms," Journal of the Institute of Mathematics and Its Applications, 6, 76-90.

SPACE-TIME DISTRIBUTION OF RAILROAD PASSENGERS FOR DISASTER PREVENTION PLANNING

T. Osaragi¹⁾, and I. Otani²⁾

*1) Associate Professor, Dept. of Mechanical and Environmental Informatics,
Graduate School of Information Science and Engineering, Tokyo Institute of Technology, Japan*

*2) Graduate Student, Dept. of Mechanical and Environmental Informatics,
Graduate School of Information Science and Engineering, Tokyo Institute of Technology, Japan
osaragi@mei.titech.ac.jp*

Abstract: In the field of urban disaster prevention planning, it is important to understand the characteristics of the space-time distribution of the population when considering provisions for human damage due to a large earthquake. In this paper, we construct a model which simulates, on geographic information systems, the route choice behavior and transfer behavior of railroad users. The space-time distribution of users is estimated by applying the model to the Tokyo metropolitan area, using data taken from a person-trip survey. Some numerical examples using the proposed model are shown for more detailed disaster prevention planning.

1. INTRODUCTION

In recent years, there has been growing concern about disaster prevention planning for an earthquake directly below Tokyo, and numerous investigations and studies have been done regarding estimation of damage. Most previous estimates of human damage have been based on static population distributions, such as the daytime population distribution or nighttime population distribution obtained from the national census or other sources. However, the actual population distribution varies from hour to hour, and the degree of human damage and the spatial distribution of that damage are thought to be intimately related to the time when the disaster occurs. In particular, the time variations of railroad users are extremely large, and cannot be ignored.

Thus the purpose of this research is to build a model for estimating the space-time distribution of railroad users, using the data from the Tokyo metropolitan area person-trip survey of 1998 (hereafter referred to as “PT data”), and thereby develop a detailed understanding of the time variation and space variation of railroad users. The constructed model was also used to study the space-time distribution of persons with difficulty returning home.

2. METHOD OF ESTIMATING THE SPACE-TIME DISTRIBUTION OF RAILROAD USERS

2.1 Construction of a model for estimating the space-time distribution of railroad users

By using PT data, a model was constructed to estimate the dynamically varying space-time distribution of railroad users—i.e. to answer the question “what kind of people (attributes such as age, sex, etc.) use the railroad, and when (time), where (position coordinates), and for what reason

(purpose) do they use it?” More specifically, position information and time information for the departing/arriving stations of railroad trips were extracted from PT data, and based on that information, time specific position information was found for railroad users by recreating spatial movements on railroad lines using the network analysis in geographical information systems (GIS). Figure 1 shows details of the model for estimating the space-time distribution of railroad users.

Using PT data, it is possible to determine position information and time information for the departing/arriving stations of railroad users. However, it is not possible to directly determine data such as the movement route or transfer stations between the departing and arriving stations. Thus the spatial movement of railroad users was modeled by regarding them as “moving by selecting the route which minimizes the cost needed to move (time cost).” However, it is likely that the route selection of railroad users is also affected by factors such as the train waiting time, physical fatigue, and psychological load involved in changing trains, and the base fares which arise when switching between lines under different management (operators). Also, changing trains is generally done within the same station or between stations with the same name, but there are cases where users change trains by walking between stations located in close proximity (walking transfer). Thus, the various resistances which arise when changing trains were all converted to time cost and incorporated into the model. The following discusses the specific method of setting time cost.

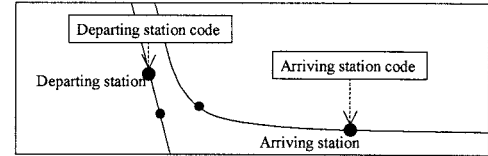
For movement on a line, the movement time was found from the distance between stations and the railroad velocity, and taken to be the “railroad movement cost.” However, the railroad velocity is likely to vary depending on the lines. Thus a model describing the railroad velocity was developed by using the average distance between stations for each line. On the other hand, for changing trains between lines, the movement time on the station premises, the waiting time for the train, and resistance to changing trains (i.e. the psychological load which arises due to changing trains) were converted to time cost, and the total of those values was taken to be the “in-station transfer cost.” However, movement time on the station premises is thought to depend on the size of the station. Thus, it was decided to indicate the size of the station by the number of connected lines. The in-station transfer cost is set for links connecting a group of boarding/disembarking points of lines of the same operator with the same station name (corresponding to platforms) and their representative point (center of gravity of the group of boarding/disembarking points: corresponding to the station representative point for each operator). Furthermore, the movement time between stations of lines of different operators with same name, and resistance to changing trains between lines of different operators (base fare resistance) were converted to time cost, and the total value was taken to be “inter-station transfer cost.” Inter-station transfer cost is set for links which connect between the station representative points of lines of different operators with the same station name. Also, the walking time between stations with different names and the resistance to walking transfer (resistance due to the necessity of moving a long distance by walking) were converted to time costs, and the total of those values was taken to be the “walking transfer cost.” Walking transfer cost is set for links connecting between station representative points where the distance between stations with different names is 500 meters or less.

2.2 Estimation of time cost parameters

Estimation of the time cost parameters for the line network was performed in a trial and error fashion while confirming coordination with statistical values relating to the total number of users per day at major stations (number of persons boarding/disembarking, number of persons changing trains) prepared by the Institution for Transport Policy Studies (2003). More specifically, parameters were estimated, using approx. 1% of the railroad trips of railroad users, so as to minimize the absolute error between the estimated values for the number of users of stations with multiple connected lines and stations with a single connected line, and the statistical values in the Urban Transport Yearbook.

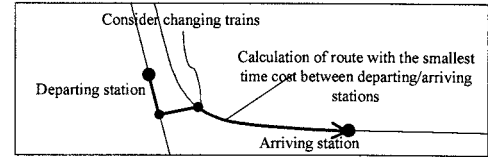
(1) Extraction of departing/arriving station

Using GIS, station points are extracted corresponding to the position information (departing/arriving station code) for the departing/arriving station of a railroad user obtained from person-trip survey data. Also, time information (departing/arriving time) obtained at the same time is added to the station point.

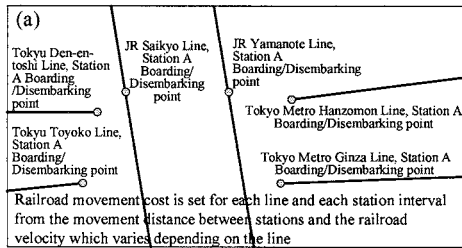


(2) Modeling of spatial movement between departing/arriving stations

In order to understand the movement route and stations for changing trains between the departing/arriving stations, the route which minimizes the time required for movement (time cost)—i.e. the route with the shortest time cost—is calculated using GIS network analysis. However, considering that route selection is affected by factors such as the train waiting time, physical fatigue and psychological load involved in changing trains, and the base fares which arise between lines under different management (operators), the various resistances which arise when changing trains are all converted to time cost, and the following sort of time costs are set in the line network.



Time cost setting in line network



(a) Railroad movement cost C_1

Movement time found from movement distance between stations (L_i) and railroad velocity (V_i) which varies depending on the line.

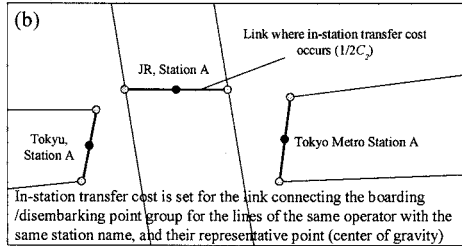
$$C_1 = \frac{\text{Movement distance } L_i}{\text{Railroad velocity } V_i}$$

(b) In-station transfer cost C_2

Total of the movement time on station premises between lines of the same operator with the same station name (T_a), the train waiting time (W_a), and the value (C_a) obtained by converting resistance to changing trains (psychological load of changing trains rather than traveling to the arriving station on one line) to time cost.

$$C_2 = \frac{\text{Movement time } T_a}{\alpha R_{ki}} + \frac{\beta}{\text{Train waiting time } W_a + \text{Resistance to changing trains } C_a}$$

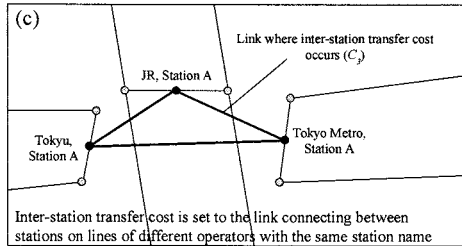
where, the movement time (T_a) shall be the value proportional to the number of connecting lines R_{ki} of the same operator i for each station k .



(c) Inter-station transfer cost C_3

Total of the movement time between stations on lines of different operators with the same station name (T_b), and the value (C_b) obtained by converting resistance to changing trains (resistance to the base fares which are incurred) to time cost.

$$C_3 = \frac{\gamma}{\text{Inter-station movement time } T_b} + \text{Resistance to changing trains between stations } C_b$$

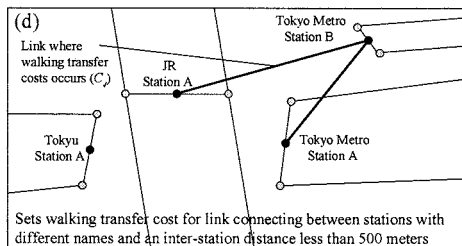


(d) Walking transfer cost C_4

Total of the movement time due to walking between stations with different station names and a distance between stations of less than 500 m (T_c), and the value (C_c) obtained by converting the resistance to walking transfer (resistance to the effort of walking) to time cost.

$$C_4 = \frac{\text{Movement distance}}{\text{Walking velocity}} + \frac{\delta}{\text{Resistance to walking transfer } C_c}$$

where, the walking velocity V_w is assumed to be a uniform value.



[Transfer costs $C(k, l)$ which arise due to time cost setting]

Transfer cost $C(ki, ki)$ between lines of the same operator (i to i) at station k	
$C(ki, ki) = 1/2 (\alpha R_{ki} + \beta) + 1/2 (\alpha R_{ki} + \beta) = \alpha R_{ki} + \beta$	
Transfer cost $C(ki, kj)$ between lines of different operators (i to j) at station k	
$C(ki, kj) = 1/2 (\alpha R_{ki} + \beta) + \gamma + 1/2 (\alpha R_{kj} + \beta) = 1/2 (\alpha (R_{ki} + R_{kj}) + \beta) + \gamma$	
Transfer cost $C(ki, lj)$ between station k (operator i) and station l (operator j)	
$C(ki, lj) = 1/2 (\alpha R_{ki} + \beta) + (T_c + \delta) + 1/2 (\alpha R_{lj} + \beta) = 1/2 \alpha (R_{ki} + R_{lj}) + \beta + \delta + T_c$	

(3) Extraction of positions by time between departing/arriving stations

Position for each unit time is calculated from the movement route based on departing/arriving station time information (departing/arriving time) for railroad users, obtained from person-trip survey data.

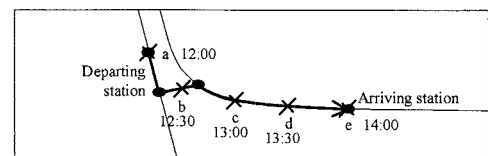


Figure 1 Model for Estimating Space-time Distribution of Railroad Users

3. ESTIMATION OF THE SPACE-TIME DISTRIBUTION OF RAILROAD USERS

3.1 Space-time distribution of railroad users

When figures are compared by time (Figure 2), the number of persons moving at 8:00 is 10 times the number at 12:00 and 2 times the number at 18:00. There is a possibility that people moving on lines will be later in starting evacuation than persons present on the station premises, and the danger will increase when moving at high-density and high-speed. Disaster countermeasures must be taken while taking into consideration the amount of concentration and the concentration points on lines around 8:00 and after 18:00.

Looking at the spatial distribution (Figure 3), it is evident that the distribution moves from the suburbs to the city center from 7:00 to 9:00, and then moves in reverse from 18:00 to 20:00. Also, if an earthquake occurs in these time periods, there is a risk that the damage will extend over a larger scope. Hence, measures for reducing the peak in railroad usage (recommendation of time staggered commuting, etc.) can not only improve comfort, but are also an important issue for disaster prevention.

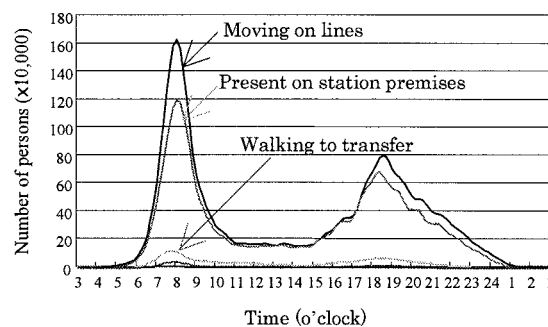


Figure 2 Time Variations of Railroad Users

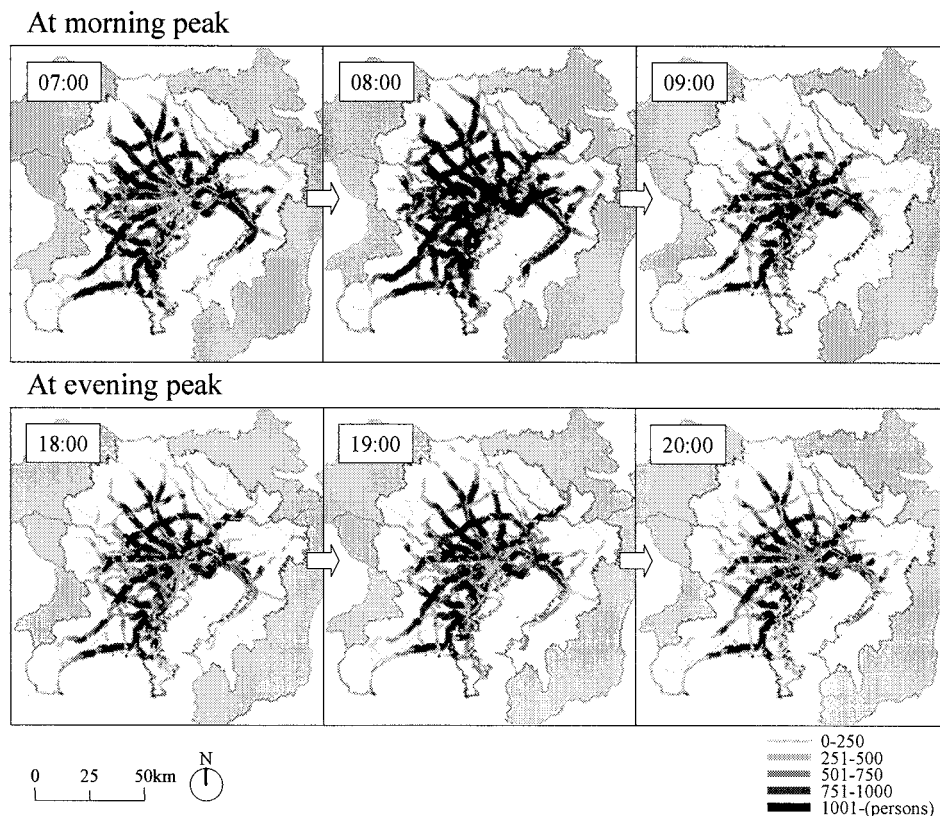


Figure 3 Number of Persons Moving on Railroad Lines

3.2 Space-time distribution by movement purpose of railroad users

The space-time distribution of railroad users, estimated in the previous section, was broken down by movement purpose. In the morning and evening, the percentage of persons with the purpose of commuting to work is high, but in the daytime, the percentage of persons with purposes such as shopping is high, and, in particular, accounts for half of the total at around 15:00. Unlike persons with the purpose of commuting to work or school, there is a high probability that persons with purposes such as shopping are not following a determined route, and if an earthquake happens in the daytime, there is likely to be a large percentage of people affected by the earthquake in areas they are unfamiliar with. Looking at the spatial distribution (Figure 4), there is a close resemblance between the morning and evening in terms of the spatial distribution of persons with the purpose of commuting to work or school, but the distribution is different in the morning and evening for persons with purposes such as shopping. Also, persons with the purpose of commuting to school are distributed over a wide range in both the morning and evening, and this indicates that high schools, universities, and other schools are distributed widely over the Tokyo Metropolitan area, and that persons commuting to work move over a wide range using railroads.

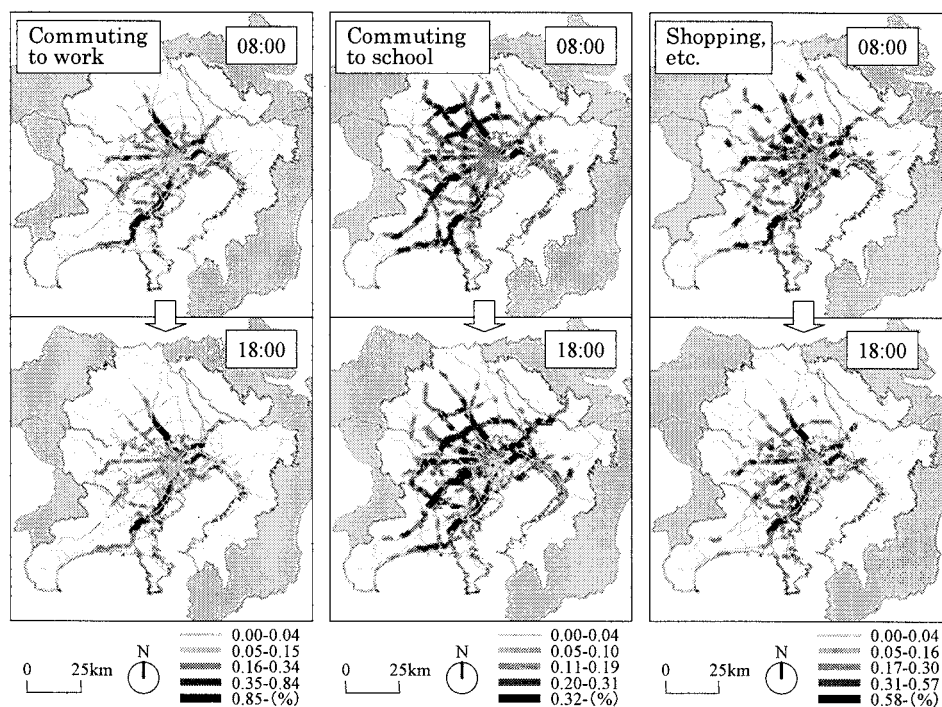


Figure 4 Percentage of Persons with Each Type of Purpose on Railroad Lines

4. ESTIMATING THE SPACE-TIME DISTRIBUTION OF PERSONS WITH DIFFICULTY RETURNING HOME

4.1 Method of estimating the space-time distribution of persons with difficulty returning home

Estimation of the space-time distribution of persons with difficulty returning home was done using the method of anticipating difficulty returning home in Tokyo Metropolitan Government (1997). More specifically, the ability/difficulty of returning home was determined in accordance with the distance to return home by letting the distance to return home be the distance from the time-specific position coordinates of the railroad user calculated in the previous chapter, to the center coordinates of the residential sub-zone (a statistical unit of PT data). (However, the time-specific position coordinates in the case when railroads are not being used are represented with the center coordinates of the

sub-zone.) Actually, it is likely that the distance over which a person can return home by walking differs depending on the time when the earthquake occurs and the degree of damage. However, at present it is not clear how the decision of whether it is possible to return home or difficult to return home will be made. Therefore, we decided to use a simple past history method (Tokyo Metropolitan Government, 1997). Also, in the following we focused only on railroad users. Therefore, caution must be given to the point that the figures are underestimates compared to studies focusing on all persons who are outside their homes. However, if we consider the fact that many of the persons who move over long distances and can easily become persons with difficulty returning home are railroad users, then this is one important estimate.

4.2 Space-time distribution of persons with difficulty returning home

The number of persons with difficulty returning home abruptly increases from 7:00 to 9:00, and gradually decreases from 18:00 to 24:00 (Figure 5). The number of persons with difficulty returning home reaches a maximum at around 14:00, and the number is approx. 4.2 million persons. In terms of a percentage, this is extremely high—about 45% of all railroad users—and if an earthquake occurs in this time period and transportation facilities stop, it is anticipated that there will be large numbers of persons with difficulty returning home. Also, Figure 5 shows that many people are moving to destinations in the morning and evening, and if an earthquake occurs in the evening in particular, it will be necessary to urgently provide facilities which can accept persons with difficulty returning home. Looking at the spatial distribution, it is evident that persons with difficulty returning home are distributed in the morning along railroad lines, and spread out during the day from the city center to the west side, and at night many are distributed in the center of the city core (Figure 6).

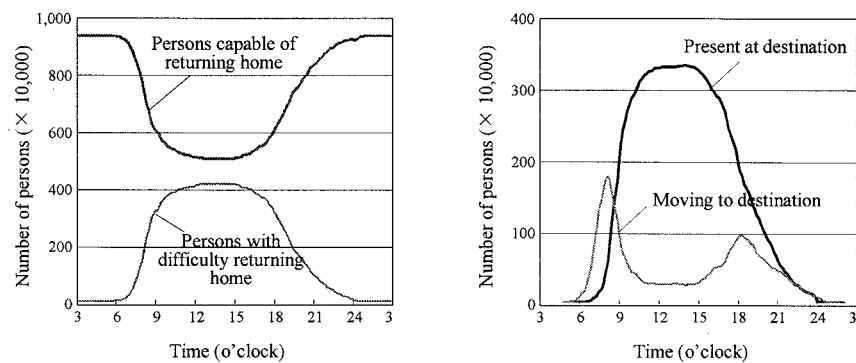


Figure 5 Number of Persons with Difficulty Returning Home

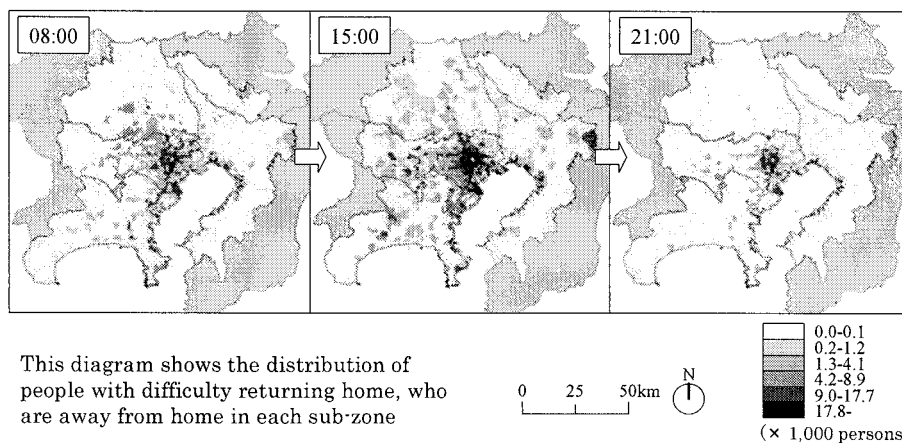


Figure 6 Number of Persons with Difficulty Returning Home in Each Sub-zone

4.3 Space-time distribution of persons with difficulty returning home by personal attributes

The percentage of the total accounted for by persons with difficulty returning home in the age group 5–18 who are pupils, children, and kindergartners temporarily becomes high at around 8:00, and during the day, the percentage of persons over 70, housewives and househusbands, and the unemployed increases (Figure 7). It will be crucial to respond to students, children, kindergartners, and other underage persons in the age group 5–18 if an earthquake occurs during the time period of commuting to school in the morning.

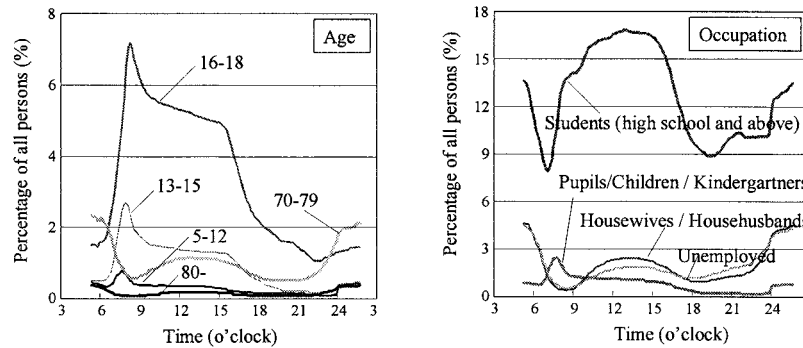


Figure 7 Percentage of Persons with Difficulty Returning Home (1)

4.4 Space-time distribution of stranded persons by movement purpose

During the day, there is a high percentage of persons with difficulty returning home who are moving for purposes such as shopping (Figure 8). Also, in the day, there is a high percentage of persons with difficulty returning home who are at their place of work or school, but at night there is a high percentage at locations outside the home for purposes such as shopping. Looking at the space distribution (Figure 9), while there is a tendency for persons with difficulty returning home and the purpose of commuting to work to concentrate in the city core, persons with the purpose of commuting to school are distributed over a wide range throughout the day. Persons with purposes such as shopping tend to be distributed over a wide range in the morning, and concentrated in the city center in the evening. There is concentration in the city center when viewed in terms of persons with difficulty returning home as a whole. When viewed by purpose, distinguishing characteristics are evident, such as the distribution over a wide area, depending on the time period, of persons with the purpose of commuting to kindergarten or school, including young children who must be met by their parents or guardians, and persons with purposes such as shopping who do not belong to any organization. That is, the need for measures to handle persons with difficulty returning home is not limited to the city core.

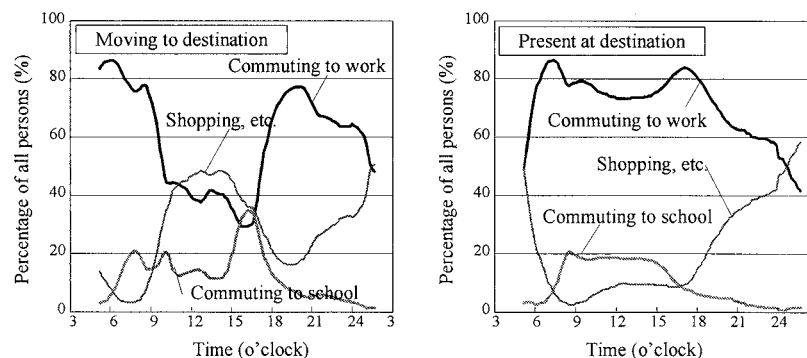


Figure 8 Percentage of Persons with Difficulty Returning Home (2)

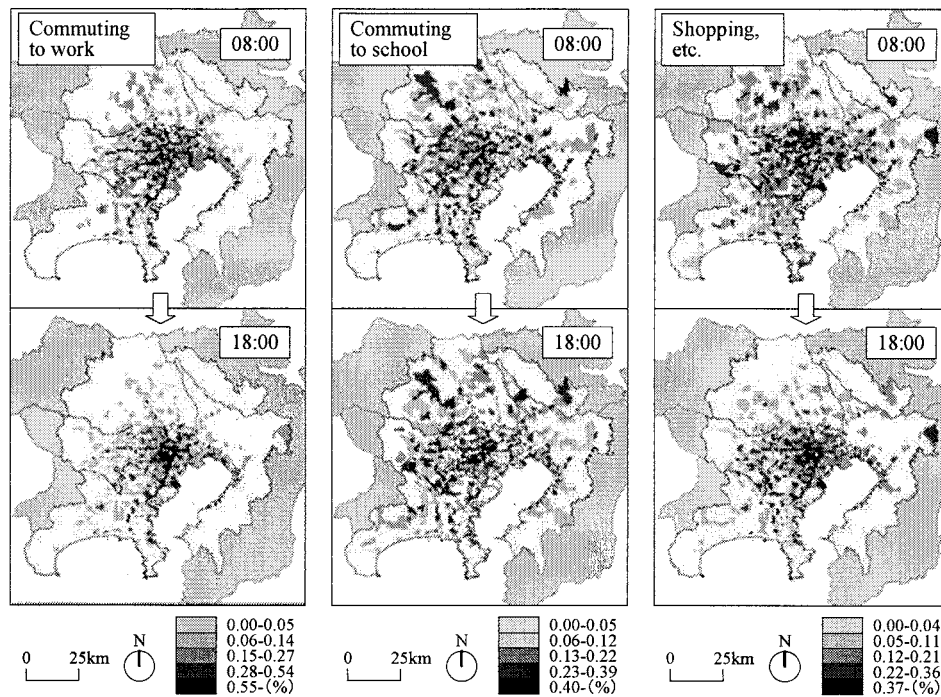


Figure 9 Space-time Distribution of Persons with Difficulty Returning Home

3. CONCLUSIONS

We constructed a model for estimating the space-time distribution of railroad users based on PT data, and developed an understanding of the time variation and space variation of railroad users by personal attributes and movement purpose. Using this model, it became possible to understand factors which previously could not be understood—i.e. the degree of human damage, and the specific profile of persons affected by the earthquake, which vary greatly depending on the time and location. By combining the profile of affected persons and their space-time distribution, it should be possible to provide assistance for more detailed disaster prevention planning suited to the time and location.

References:

Tokyo Metropolitan Government (1997), 東京における直下地震の被害想定に関する調査報告書.
Institution for Transport Policy Studies (2003), The Urban Transport Yearbook (2002).

**EXAMINATION ABOUT RELATIONS BETWEEN STIFFNESS OF FLOOR
AND INITIAL INCLINATION OF FURNITURE AT EARTHQUAKE
FUNDAMENTAL STUDY ON ESTABLISHMENT OF EVALUATION METHOD
FOR SEISMIC RESISTANCE OF FLOOR FINISHING SYSTEM Part 3**

Y. Yokoyama¹⁾, T. Yokoi²⁾, and Y. Yoshida³⁾

1) Assoc. Prof., Dep. of Architecture and Building Eng., Tokyo Institute of Technology, Japan

2) 21st Century COE Postdoctoral Fellowship, Tokyo Institute of Technology, Dr. Eng.

3) Tokyo Institute of Technology

tyokoi@mail.arch.titech.ac.jp

Abstract: A behavior of furniture is influenced by characteristics of floor greatly. This research tries to clear a relation between floor characteristics and tumble of furniture. As a fundamental stage, a relation between characteristics and initial inclination of furniture is investigated by experimental study.

When acceleration of earthquake is comparatively large, furniture begins to incline. It was found that boundary acceleration was in proportion to a static pulling load that furniture begin to rock. And it was also found that response sensibility of furniture to earthquake wave could be explained by an energy used until one side of mock furniture base floated. From these knowledge, the method to presume initial inclination of furniture was set.

1. INTRODUCTION

Tumble and movement of furniture are one of the causes of human suffering under seismic disaster. Stiffness, flatness, slipperiness, etc. of a floor are considered as characteristics that greatly influence a behavior of furniture. However, except for coefficient of floor friction, these factors are not considered in previous research using analysis method. This research aims to present evaluation methods of stiffness, flatness, slipperiness, etc. according to a behavior of furniture during earthquake. As a fundamental stage, this report describes a result of investigation of a relation between stiffness of floor and initial inclination of furniture.

2. OUTLINE OF EVALUATION METHOD AND DIVISION OF THIS REPORT

Under a large earthquake, if furniture dose not slide, one side of a furniture base floats and the furniture inclines. At this time, the furniture falls if an inclination is large. Or, if an inclination is small and a center of gravity remains inward of fulcrum, the furniture's weight act to restore the inclination and the furniture begins to rock. Moreover, when rocking cycle synchronizes with phase of the earthquake, the inclination increases and the furniture tumble at the worst. Therefore the evaluation of floors should be done under following 3 sections.

1: Distinction of movement and inclination

2: Presumption of initial inclination

3: Presumption of furniture behavior considering with influence of synchronization with phase of earthquake

This report describes about the 2nd section in this flow.

3. MEASUREMENT OF FLOOR CHARACTERISTIC

Table 1 shows an outline of 4 kinds of specimen floors used in experiment. At a selection of these specimen floors, it was noticed that stiffness of sample floors were vary in each floors.

Then a characteristic of these specimen floors were measured. The initial inclination under an earthquake depends on easiness to be inclined, so a load and a inclination during pulling the gravitational center of the mock furniture is measured as shown in **Figure 1**. The gravitational center is pulled horizontally at constant speed (1 cm/sec). **Figure 2** shows an outline of the mock furniture. This is imitating of a bookshelf and this was set in previous report¹⁾. The ratio of thickness and height was 0.2 that is considered to be in dangerous side within actual range. A position of gravitational center is set on a center of the mock furniture. And weights of the mock furniture are 236.5 kgf as bookshelf is full of books. The mock furniture touches a floor by four points (30×30 mm).

Figure 3 shows relations between the pulling load and the inclination as results of measurement. The mock furniture began to incline at L point. Until M point, specimen floor transformed and the base of mock furniture does not float yet. After M point, one side of mock furniture base floats and load begins to decrease, and finally, at N point, the gravitational center goes outward of fulcrum and the mock furniture tumbles. Generally, in soft floor, the load at L point (P_L) is small and the angle at M point (θ_M) is large.

Table 1 Outline of Specimen Floors

No.	Outline
1	Resin Seat (2 mm thick)
2	Rubber Seat (7 mm thick)
3	No. 1 + Foam Polyurethane Seat (5 mm thick)
4	No. 1 + Foam Polyurethane Seat (30 mm thick)

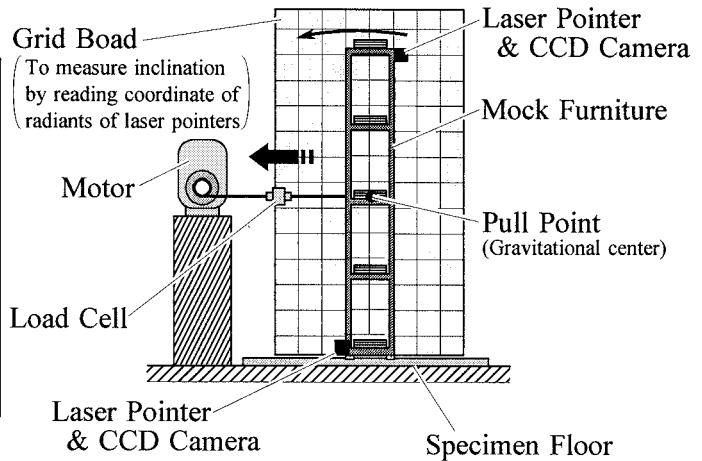


Figure 1 Measurement Method of Easiness to be Inclined

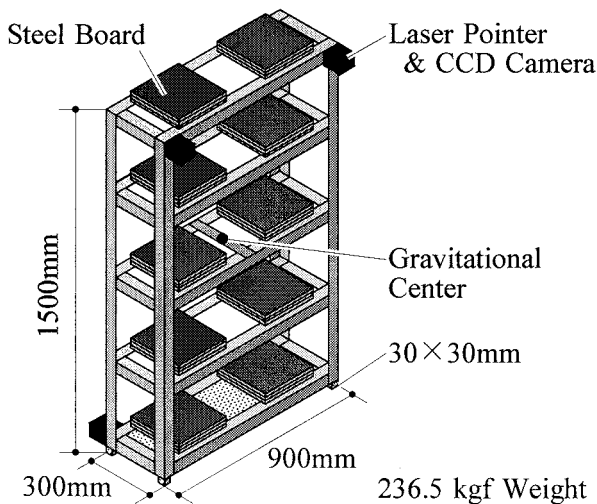


Figure 2 Outline of Mock Furniture

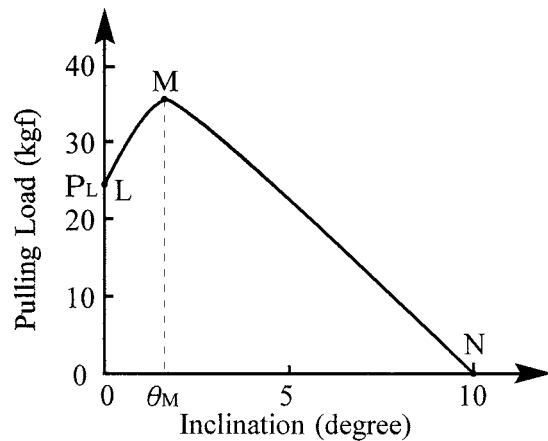


Figure 3 Relations between Pulling Load and Inclination

4. MEASUREMENT OF INITIAL INCLINATION

Shaking test was done by using the simple vibration table, and initial inclinations of furniture on the specimen floors were measured. **Figure 4** shows an outline of the simple vibration table developed at previous research²⁾. This vibration table can generate an input wave shown in **Figure 5**. The main part of this input wave is sign wave. And there are pre-position part and post-position part those accelerations change linearly. An acceleration amplitude (" a_{MAX} "), number of waves (" n "), frequency (" f ") of sign part and time (" t ") of pre-position and post-position part can be controlled. In this research, 3 kinds of input waves of $f=1, 2, 3$ Hz, $n=3$ and $t=1.5$ s were used. It depends on the following reasons those were found by the research¹⁾ targeted on random-access floor.

- A main range of frequency in real earthquake waves is 1-3 Hz.
- Few waves before and behind the largest part in real earthquake waves influence a furniture behavior mostly.

At the shaking test, the a_{MAX} was increased step by step till the mock furniture tumbled. And time-change of the inclination and the acceleration were measured. **Figure 6** shows an example of the result. At this time, following codes are defined.

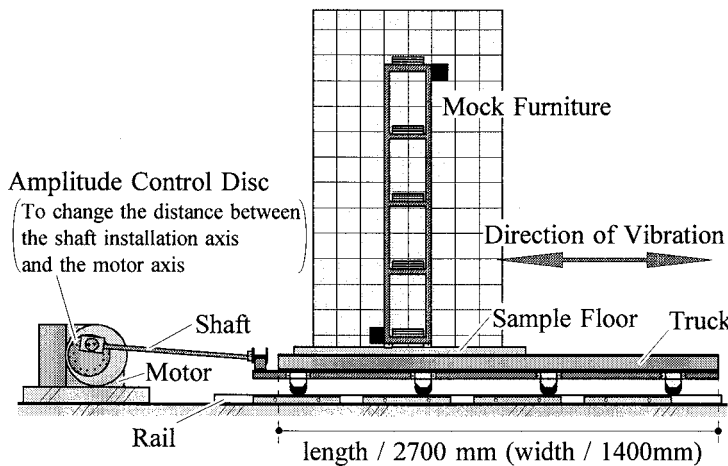


Figure 4 Outline of Simple Vibration Table

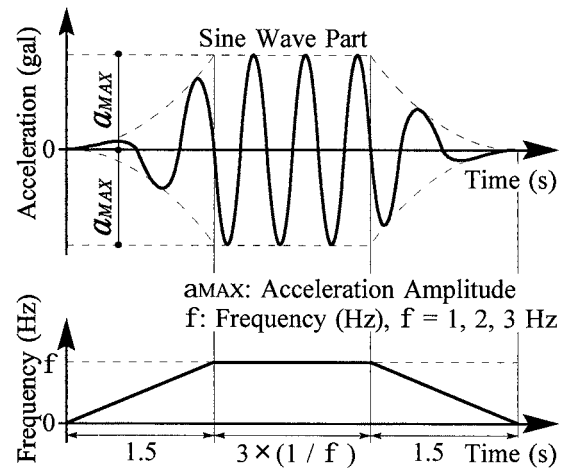


Figure 5 Outline of Input Wave

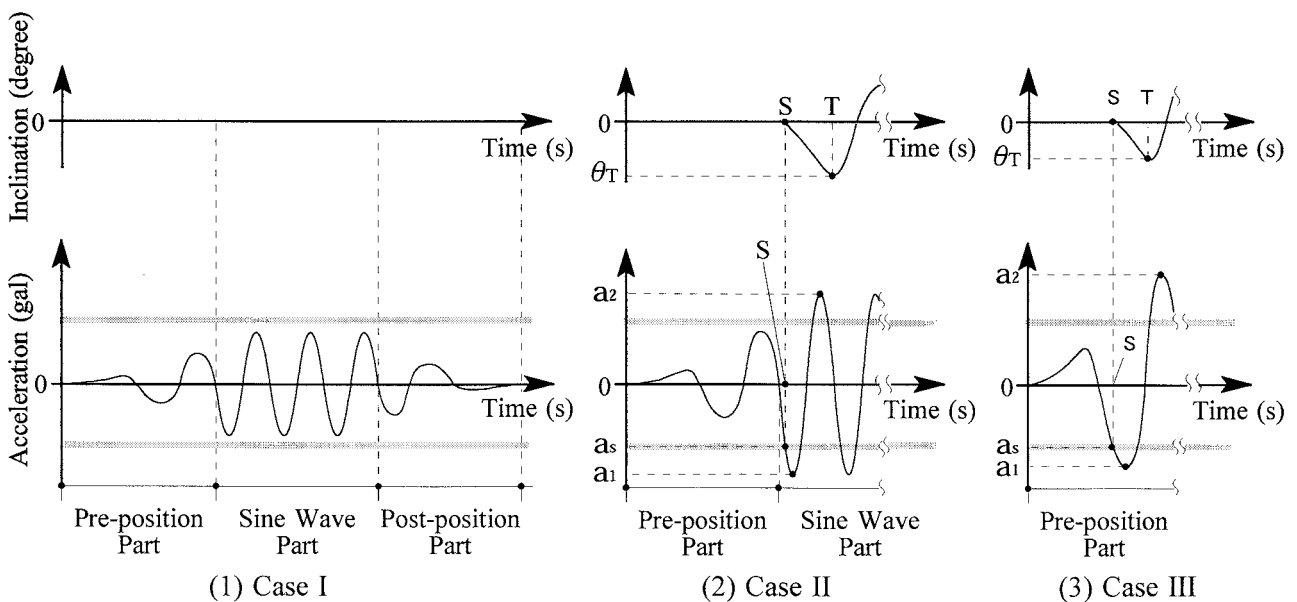


Figure 6 Time-Change of Inclination and Acceleration

S: The point that one side of mock furniture base floats

T: The point that the inclination of mock furniture become a peak at first time after S point

a_s : The absolute value of acceleration at S point

a_n : The absolute value of acceleration amplitude at the point that acceleration become a peak.

n is a number of times from S point

θ_T : The absolute value of inclination of mock furniture at T point

From **Figure 6** (2) and (3), it can be shown that the mock furniture's base floated at S point. At this time, it was found that a_s is peculiar to each specimen floor independent on f . And as shown in the following description, a behavior of the mock furniture is vary between the case that a_1 and a_2 are nearly same (shown in (2)) and the case that a_2 is larger than a_1 (shown in (3)). In this report, the former case is defined as "Case II", and the latter case is defined as "Case III". On the other hand, as shown in (3), when a_{MAX} is smaller than a_s , the base of mock furniture did not floated. This case is defined as "Case I".

Figure 7 shows relations between θ_T and a_1 . As shown in this figure, every specimen floor have a boundary acceleration value to divide Case I and others. And when a_1 is larger than the boundary value, θ_T is related to a_1 independent on f , however a tendency of the correspondence is different between Case II and Case III.

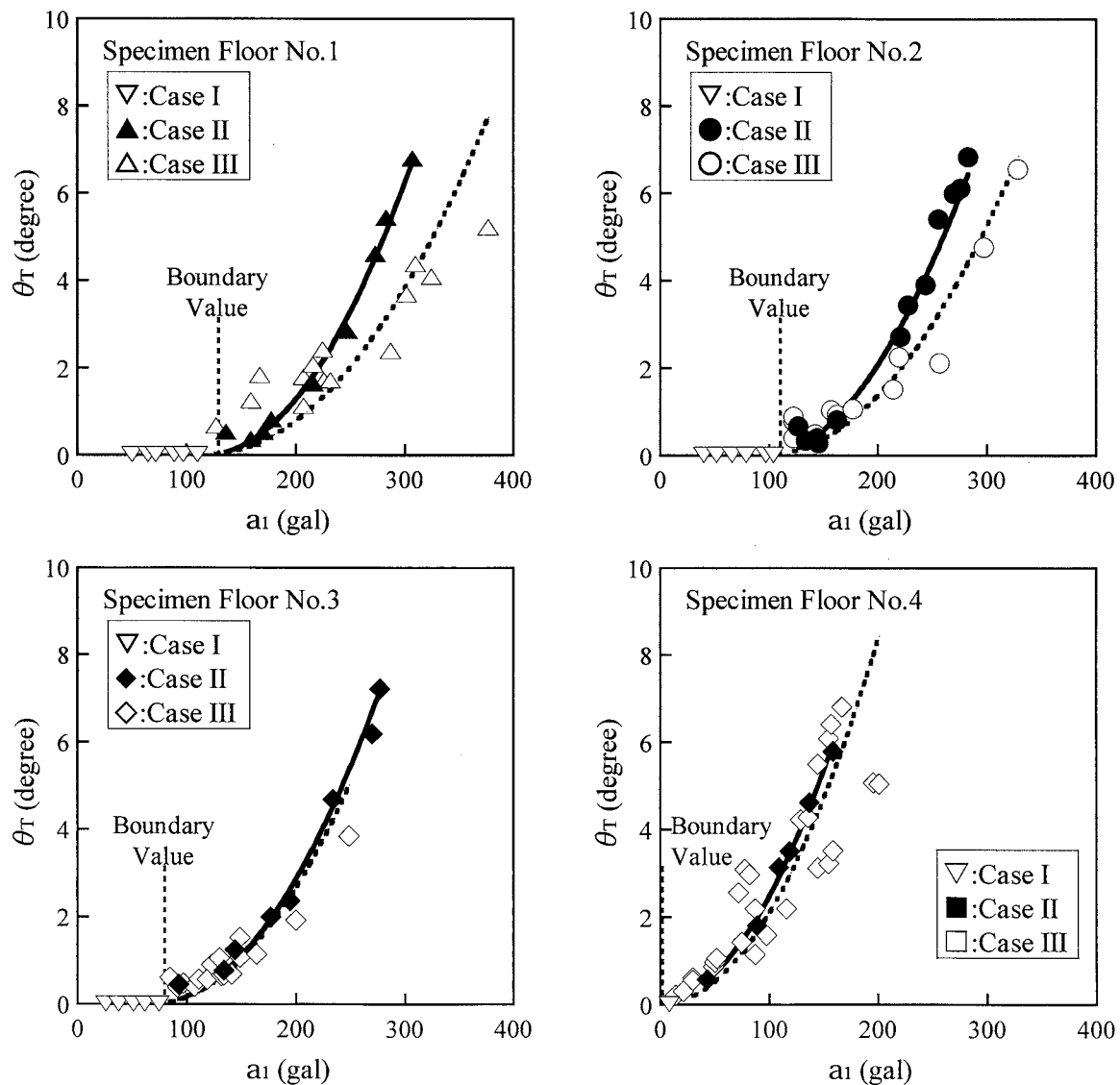


Figure 7 Relation between θ_T and a_1

Table 2 Regression Equation and Correlation Coefficients

No.	Case II	Case III
1	$\theta_T = 0.000186 \times (a_1 - 117.238)^2$ $r = 0.996$	$\theta_T = 0.000114 \times (a_1 - 117.238)^2$ $r = 0.963$
2	$\theta_T = 0.000191 \times (a_1 - 96.438)^2$ $r = 0.997$	$\theta_T = 0.000127 \times (a_1 - 96.438)^2$ $r = 0.974$
3	$\theta_T = 0.000164 \times (a_1 - 67.872)^2$ $r = 0.996$	$\theta_T = 0.000152 \times (a_1 - 67.872)^2$ $r = 0.970$
4	$\theta_T = 0.000242 \times (a_1 - 0)^2$ $r = 0.999$	$\theta_T = 0.000209 \times (a_1 - 0)^2$ $r = 0.982$

From the tendency of the correspondence, the relation between a_1 and θ_T is thought to be regulated by parabola curve those peak is on the horizontal axis, when a_1 is larger than the boundary value. Therefore, a following equation is supposed and regression analysis was done.

$$\theta_T = A \times (a_1 - B)^2 \text{ ----- (1)}$$

A: Constant that shows a response sensibility of furniture to input wave

B: Constant that shows a boundary value of beginning to rock

Regression lines are shown in **Figure 7** together, and values of A, B and correlation coefficients are shown in **Table 2**. In this figure, regression lines are suited enough to the correspondence of a_1 and θ_T .

5. INVESTIGATION ABOUT RELATION BETWEEN INITIAL INCLINATION AND FLOOR CHARACTERISTIC

Relation between initial inclination and floor characteristic were investigated. From the Lord-Inclination curve shown in **Figure 2**, quantitative values those correspond to A and B were found.

At first, because A could be considered to be a response sensibility of furniture to input wave, it was thought that A was closely related to energy used until one side of mock furniture base floated. Therefore, the energy until M point (U_M) was calculated. **Figure 8** shows a relation between A and U_M . From the figure, it can be known that both correspond comparatively well.

On the other hand, because B could be considered to be a boundary value of beginning to rock, it was thought that B was closely related to the load when the mock furniture began to incline (P_L). **Figure 9** shows a relation between B and P_L . From the figure, it also can be known that both correspond comparatively well.

Conclusively, initial inclination of furniture during earthquake can be presumed from input wave by following process.

1: Measuring U_M and P_L of the objective floor

2: Referring A and B of **Equation 1** to **Figure 8** and **9**.

3: Substituting a_1 (the first peak acceleration beyond the boundary acceleration B) for **Equation 1** and calculate θ_T .

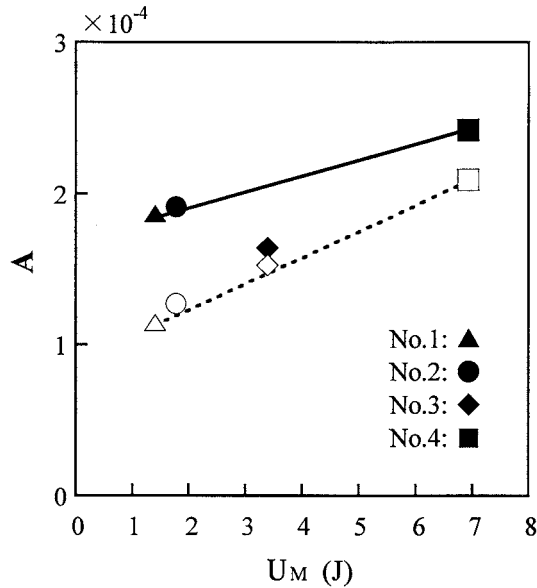


Figure 8 Relation between A and U_M

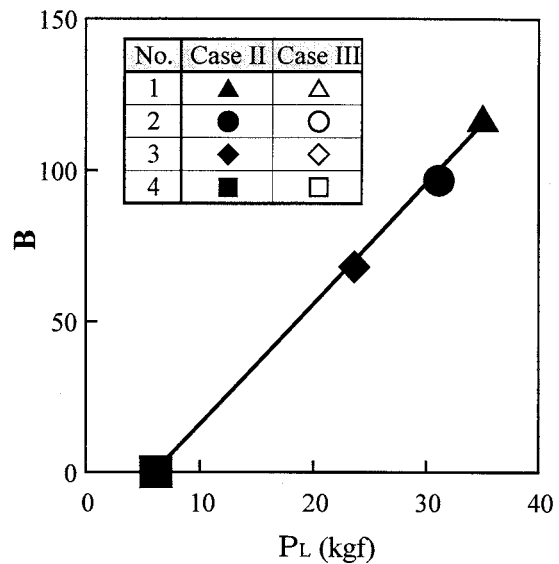


Figure 9 Relation between B and P_L

6. CONCLUSION

Through the investigation about the relation between behavior of furniture during earthquake and floor characteristic, the method to presume initial inclination of furniture according to input wave by using floor characteristic as parameter was set. However, this result is only one example by the experiment that limited conditions such as furniture's shape, weight and the input waves. Therefore, examinations under various conditions should be done in the future.

References;

- 1) Yokoyama, Y., Katagi, U., Yokoi, T. and Ono, H. (2005.9), "Configuration of Input Wave for Evaluating Seismic Resistance on Free access Floor", *Journal of Structural and Construction Engineering*, A.I.J., No. 586, 37-44
- 2) Yokoyama, Y., Yokoi, T., Iida, R., (2006.3), "Influence of Floor Characteristics on Furniture Behavior during Earthquake, Fundamental Study on Establishment of Evaluation Method for Seismic Resistance of Floor Finishing System Part 2", *3rd International Conference on Urban Earthquake Engineering*, CUEE, 689-696

AN ATTEMPT TO IMPROVE THE EVACUATION DRILL WITH THE MULTI-AGENT SIMULATION

K. Hashimoto¹⁾, T. Ohmachi²⁾, and S. Inoue³⁾

1) Doctoral Student, Department of Built Environment, Tokyo Institute of Technology, Japan

2) Professor, Department of Built Environment, Tokyo Institute of Technology, Japan

3) Assistant, Department of Built Environment, Tokyo Institute of Technology, Japan

khashimo@enveng.titech.ac.jp, ohmachi@enveng.titech.ac.jp, shusaku@enveng.titech.ac.jp

Abstract: It is urgently needed to establish a school-wide consensus on post-earthquake evacuation procedures. As a first step to do this, an evacuation drill actually conducted in a high school in Tokyo, was simulated by using a multi-agent technique. Through comparison with the actual drill and the simulation, some characteristics of the mass evacuation were pointed out. They are, for example, average walking velocity was about 70m/min on a wide corridor which is almost the same as on a wide stair, but the velocity remarkably decreases at narrow entrances. A kind of mass concentration is likely to take place even when one or two students walk slowly. The multi-agent simulation taking into account these characteristics seems promising to suggest a procedure to maximize post-earthquake students safety.

1. INTRODUCTION

Although most Japanese schools hold an evacuation drill regularly, it is often pointed out that the substance of the drill is lost and many teachers as well as students could not feel the actual effect. For the schools, a crowd evacuation is an invaluable characteristic because it may cause the route congestion and delay in evacuation when everyone focuses on the same route. However, to grasp the crowd evacuation at school and find the effective evacuation method, trying many patterns of evacuation behavior with a bunch of people is not realistic, but forecasting the crowd evacuation with the simulation in place of actual movement has no other choice. Based on this standpoint, many researchers have previously studied about the evacuation simulation and recently the objected-oriented simulation, especially the multi-agent simulation, has a focus on attention as shown in the work by Ebihara et al. (1995) and Fujioka et al. (2002). These works tried to make the complex modeling to achieve the real human behavior, however, often fail to examine the correctness of the assumed human behavior. On other front, work is proceeding with the characteristic of human behavior from many view points such as the walking trajectory and the distance of human to human, for example, as shown in the work by Watanabe (1982). However, the characteristic of human behavior varies according to the target and situation, so that the characteristic of crowd evacuation at school should be examined independently in the same or close situation such as the evacuation drill hold regularly by most schools.

The purpose of this research is to grasp the characteristic of a crowd evacuation at schools in comparison with the real evacuation drill to the multi-agent simulation that every human move independently on the three-dimensional model of the accurate school buildings and ground.

2. THE EVACUATION DRILL

This study turn the evacuation drill hold at the Tokyo Tech High School of Science and Technology in 2005 into the contract of the real drill to the simulation. Fig.1 indicates the positional relation of buildings and Fig.2 shows one scene of this drill.

The drill started from 15:10 in the integrated study periods on November 25 in 2005 and was jointed by about 600 students, homeroom teachers and the other faculty. In this drill, the start location was changed from the past. In the past the start locations for all class were specified the homerooms and focused on the fourth building in Fig.1. Meanwhile, this drill specified the separate start locations were specified for each class such as usually used practical rooms and lecture rooms that are dotted all over the school. The meeting place was the ground because of the sunny day.

Additionally, this drill instigated some attempts at achieving the ability of students to evacuate independently. Students had preliminarily prepared two evacuation routes such as the evacuation routes if and not if the fire breaks in their located building, and chose between them when listening the announcement on the day of drill. Homeroom teachers accompanied the evacuation of students without any assignment. As the announcement was “the fire breaks in the fourth building”, the classes in the fourth building expected to choose the route if the fire breaks and the other classes expected the route not if. Practically most classes chose the expected the route and a few classes chose the opposite route.

In this drill, all classes finished to call over the names in about seven and half minutes after the announcement. In this regard, however, all students arrived at the ground in four minutes and just formed up in line and call over on the rest of the time.

We participated in the drill from the beginning and made films of the drill about five locations considered proper to observe a characteristic of crowd evacuation as forecasting with the simulation.

This paper will discuss about the characteristic of crowd evacuation at the three locations as shown in Fig.3 and Table1. Observation point [1] shows the characteristic of walking around the door and corridor for class A. As counting the transit time on both ends of the five meters corridor (as shown in Fig.3 as [1]-1 and [1]-2), the different leads to the walking speed on the corridor. Observation point [2] shows the characteristic of walking on the stairway for class B. In a similar way, as counting the transit time on both ends of the stairway (as shown in Fig.3 as [2]-1 and [2]-2), the different leads to the walking speed on the stairway. Observation point [3] shows the characteristic of walking around the gate to the ground, in the open air and through the crowd for about 400 students including class A and B. As counting the transit time on both ends of the eight meters outside road (as shown in Fig.3 as [3]-1 and [3]-2), the different leads to the walking speed on the outside road. In the forth chapter, the characteristic of the crowd evacuation will be discussed to use these actual measurement.

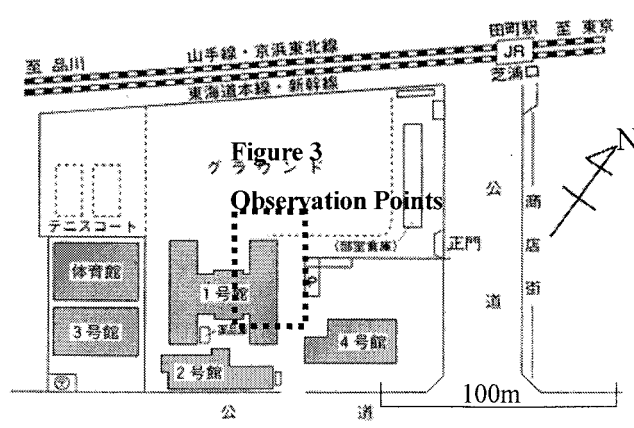


Figure 1 School Layout



Figure 2 Snapshot of Evacuation Drill

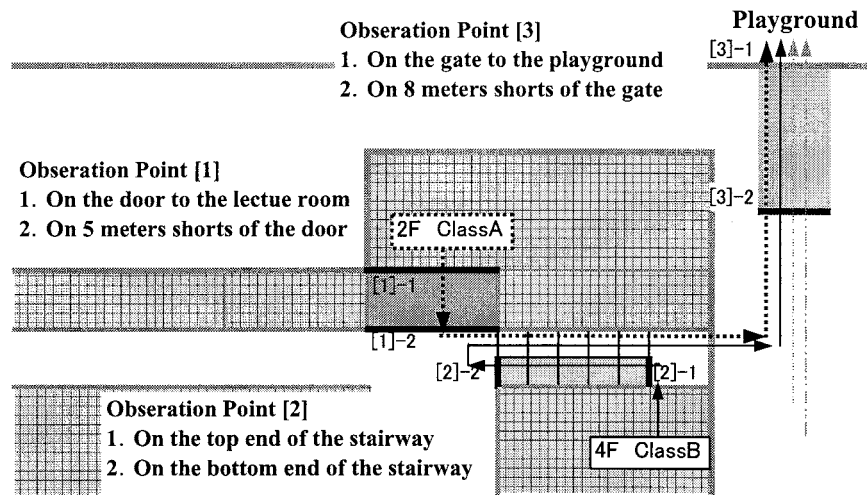


Figure 3 Observation Points [1]~[3] (see Figure 1)

Table 1 Details of Observation Points

Observation points	Characteristics	Transit people	Evacuation routes
[1] In front of the lecture room on the 2 nd floor in the 1 st building	Around the door and the corridor	Class A 37 students	Lecture room (2F, 1 st building) →the corridor→the stairway→outside road→the gate to the ground
[2] The stairway on the 2 nd floor in the 1 st building	The stairway	Class B 43 students	Lecture room (4F, 1 st building) →the corridor→the stairway→outside road→the gate to the ground
[3] The outside roads in front of the gate to the ground	Outside road, the crowd and the gate to the ground	About 400 students	

3. EVACUATION SIMULATION

3.1 Systems of the Simulation

Our evacuation simulation is the three-dimensional multi-agent system that consists of four independent components such as “the agent component”, “the scenario component”, “the infrastructure component” and “the disaster component” as be outlined in the homepage of CAS research. Fig.4 indicates the relationship between four components. “The agent component” means the individual human that move independently on “the infrastructure component”. “The infrastructure component” consists of the mesh elements that section the human passing area such as rooms, corridors, staircases and outside road, and that have the information of “possession” if something such as the agent and the disaster is on the element or “vacancy” not if. All “the agent components” and “the disaster components” are connected with “this infrastructure component”, and can get the information of the other through it. “The scenario component” independence grants to the information of each agent behavior such as the evacuation route as shown in the most right column in Table 1.

Each agent move based on the flowchart in Fig.5. The agent confirms the information of the next behavior from “the scenario

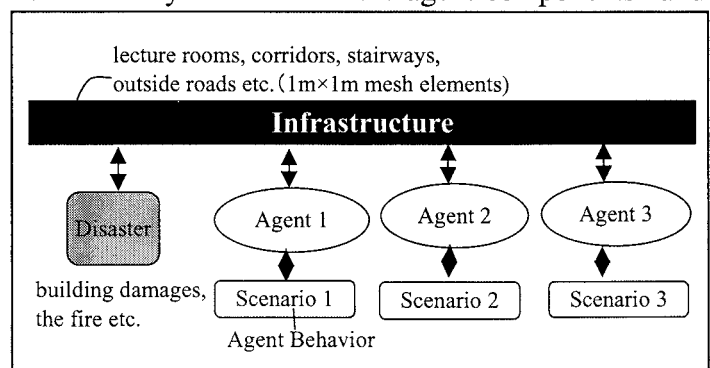


Fig.4 Objects relationship diagram

component”, obtains the information of the mesh elements around him from “the infrastructure component” and then determines the mesh element to move next in accordance with the decision priority as shown in the figure on the bottom-right corner in Fig.5. First priority is the neighbor mesh element in the same direction of the scenario information (①), next priority is the mesh elements on both sides of first priority (②), third priority is the mesh element on both sides of his present position (③). If all these mesh elements are “possession”, the agent rests for a definite period (0.1 seconds in this time), then repeat from obtaining the information of “the infrastructure component”, and after all the agent has no choice to back away. When determining the mesh element, the information of “the infrastructure component” is changed as that the present mesh element becomes “vacancy” and the determined mesh element becomes “possession” and then starts to move to the determined mesh element.

“The disaster component” such as the fire and the building damage can affect the agent behavior with leaving the information of “possession” in “the infrastructure component” as in the case of the agent.

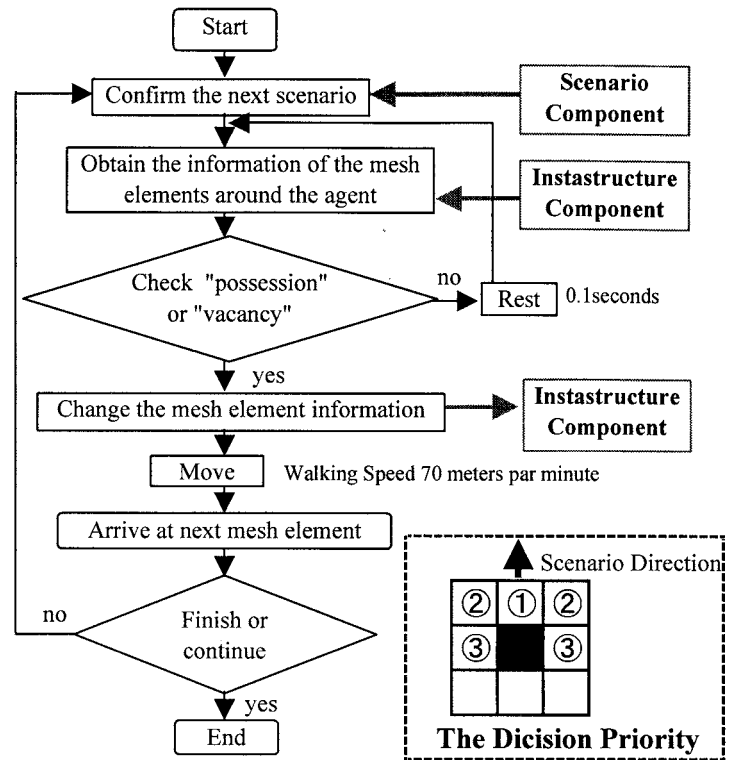


Fig.5 Movement of an agent

3.2 Customization for the Evacuation Drill

In this study, based on the actual measurement obtained from the evacuation drill, the parameters of the simulation model were finally customized as below.

1. The agent component:

In the actual measurement, an average of the walking speed was about 65 meters par minute in the situation of no congestion and it takes about 4 minutes that all students arrived at the ground.

The simulation is approximately consistent with the actual measurement of the end time to evacuate, when the walking speed of each agent is distributed evenly in the range of plus and minus 10 percents of the 70 meters par minute that was obtained from some trials with taking into consideration the delay of evacuation by a crowd.

2. The scenario component:

“The scenario component” follows the evidence by some students and homeroom teachers to be customized, because actually some classes did not choose the expected scenario out of two prepared scenarios. And although each class actually started to evacuate in the different time, the simulation specified the same starting time of all classes because no further information is available.

3. The infrastructure component:

“The infrastructure component” was constructed with the floor plan and the building arrangement.

All mesh elements measure one meter square, because human is usually considered to walk with a distance of one meter around between the other. In this regard, however, the door of room consists of one mesh element and the gate to the ground is modeled as three mesh elements.

4. The disaster component:

The fire on the fourth floor in the fourth building was assumed in the actual drill so that the simulation built it into “the disaster component”. The fire in the simulation causes the smoke spreading after students evacuate and do not affect the student evacuation.

3.3 Accuracy of the Simulation

Fig.6 shows one scene of the simulation on the evacuation drill. Fig.7 indicates the comparison between the actual measurement and the computational result of accumulated head-count at the gate the playground, as shown the observation point [3] in Fig.3, that about two-thirds of the whole students passed through.

This result can be said to emulate the accumulated community as the characteristic of the crowd evacuation that is caused by the difference between the inflow (on the point [3]-2 as 8 meters shorts of the gate) and the outflow (on the point [3]-1 as the gate) because of the narrow gate.

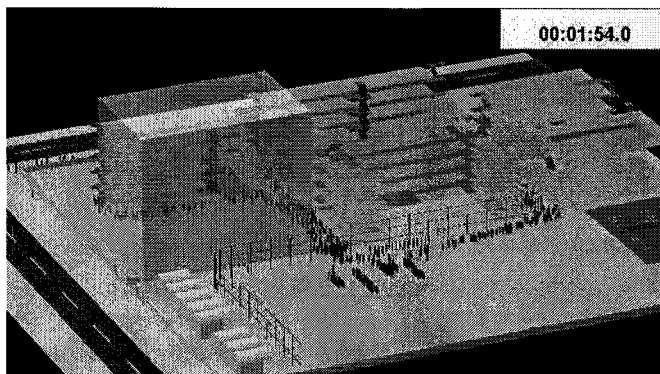


Fig.6 Snapshot of evacuation simulation

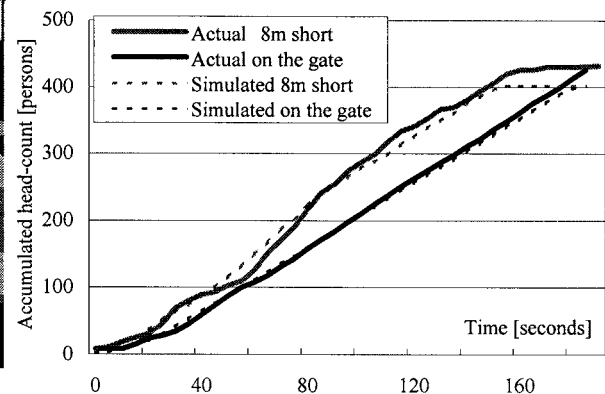


Fig.7 Accumulated head-count at the gate to the playground

4. CHACACTARISTICS OF THE CROWD EVACUATION AT SCHOOL

This chapter shows the comparison between the actual measurement and the computational result according to location and discusses about the characteristic of the crowd evacuation behavior at school.

4.1 Observation Point[1] : Around the door

Fig.8 indicates the comparison of the accumulated head-count at the room exit, as shown at the observation point [1]-1 in Fig.3, and the slope in this figure means head-count par second. The average of the actual measurement is 0.97 persons par second, meanwhile the average of the simulated result is 0.72 persons par second. This difference is considered to cause by three factors such as the walking speed, the number of persons arranged in rows and the distance with the front person. The quick walking causes the many passing heads, and both marching the double persons abreast and walking at the half distance with the front person cause the double passing heads. The averages of the walking speed are 55 meters par minute by actual measurement and 68 meters par minute by simulation. The numbers of persons arranged in rows are one person by both. And the distances with the front person are 50 centimeters around by actual measurement and 1 meter across the board by simulation. Consequently, the difference at the observation point [1] can be considered to cause by the difference of the distances with the front person around the door.

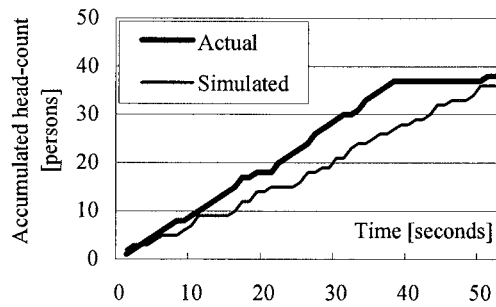


Figure 8 Accumulated head-count at the room exit

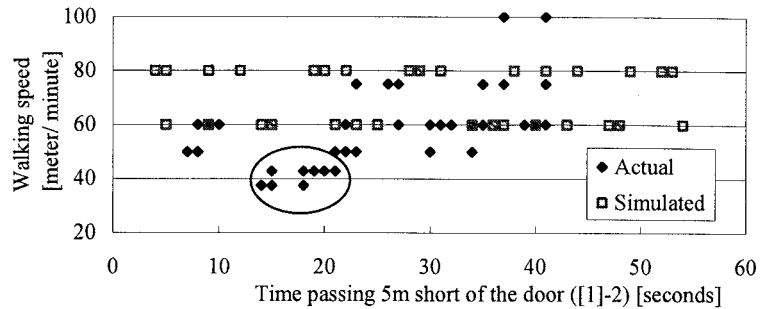


Figure 9 Walking speed on the corridor

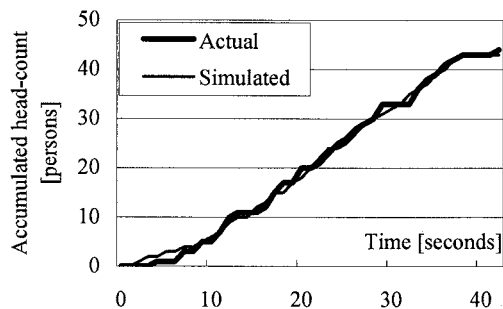


Figure 11 Accumulated head-count passing through the stairways

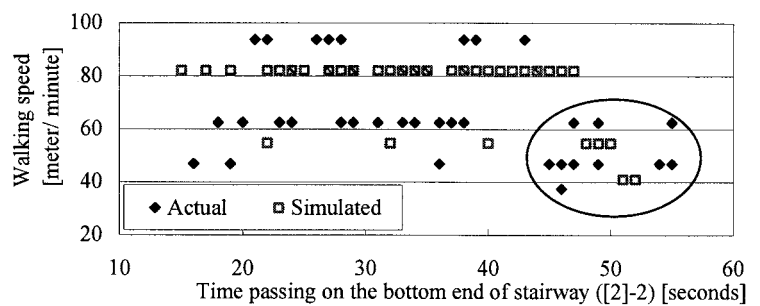


Fig.10 Walking speed on the stairways

4.2 Observation Point[1] :On the Corridor

On the corridor the following characteristic was observed. One or two persons walked abreast, and in case of a three-member group one person tended to follow after the other two persons. The distance with the front person was usually one meter around, and in case of a three-member group the distance between the two persons and the following person was often 50 centimeter around.

And there was the situation bunching up together behind the slow persons because of the narrow corridor that is named “collectivization” tentatively afterward. Figure 9 shows the walking speed obtained from the measurement of the transit times on both ends of the five meters corridor. Horizontal axis indicates the transit time at the five meters mark from the door of the lecture room and the finishing time to pass through the corridor. As seen in Figure 9, the range of the walking speed in simulation is less because the person in this simulation gets ahead of the slow person, meanwhile in the actual drill the class split up into the quick and slow groups. As a specific case of the collectivization, there was a slow group in the actual drill from 12 seconds to 25 seconds, as seen in the figure as a circle, because two students at the head of this group walked very slowly and the following students could not get ahead of them in the narrow corridor. Additionally, this slow group has the characteristic to increase the distance with the previous group and actually to go this group was 1 second at the door and then 4 seconds after walking on the 5 meters corridors from the previous group.

4.3 Observation Point[2] : On the Stairway

On the stairway the two types of students who went down rhythmically at a dogtrot and slowly were observed Figure 10 indicates the walking speed to go down the 8 steps and the students waking faster than 60 meters par minute seemed to go down at a dogtrot in the actual drill. As seen in this figure, the average of the actual waking speed was 62 meters par minute that means many students went down at a dogtrot and walking on the stairway is slightly faster than on the corridor. And this figure also shows that there was the collectivization according to a slow group passing on the 45 second around.

In the actual drill, three persons can walk abreast on the stairway and the distance with the front

person was from 2 steps to 4 steps that is around 1 meter. Because the distance with the other in the simulation is 1 meter across the board, persons in the simulation walk slightly faster and fewer persons as only two can walk abreast, and the distance with the front person is almost same with the actual.

Figure 11 shows the accumulated head-count passing through on the top end of the stairways. The slopes in this figure of both the actual and the simulation indicate that 1.1 persons pass through for a second.

4.4 Observation Point[3] : Outside road

On the outside road in front of the gate to the playground more than 10 persons can walk abreast. In case of no congestion, three or four persons usually have walked abreast with a 1 meters distance from the front person and the average of their walking speed was 64 meters par minute by the observation. The congestion decreased the distance with the front and increased the number of rows, in this regard, however more than nine persons did not walk abreast.

Around the gate to the playground the characteristic is similar with the one around the door of room. The distance with the front person around the gate, that is closer than the distance on the usual outside road, was usually 50 centimeters around and became from 20 to 30 centimeters due to the congestion. And the gate to the playground was usually passed through in two rows, but sometimes during rush hours became in three rows with rotating the body.

The thick line of the dark color in Figure 12 indicates the 15 minutes mean head-count passing through the gate to the playground in the actual drill. The head-count increased gradually due to the congestion and converged on the 2.5 persons around. It is considered to cause by the increasing rows and the decreasing distance with the front person, and the maximum 2.5 persons can pass through this gate for a second so that the gate in the simulation was established as three mesh elements in rows. The dark thin line in the figure is the simulated result, and the thick and thin lines of the light color are the head-count passing through the point 8 meters short of the gate. To focus attention on the difference between the simulated results and the actual measurement, for example, there are some movements in the actual measurement that the simulated result does not have from 50 seconds to 80 second at the point 8 meters short of the gate. During this period, a big group came at about 50 seconds in the actual drill and then few students came, that is considered to caused by the time differences starting to evacuate for each class and the phenomenon to increase the distance with the previous group as shown at the other observation points.

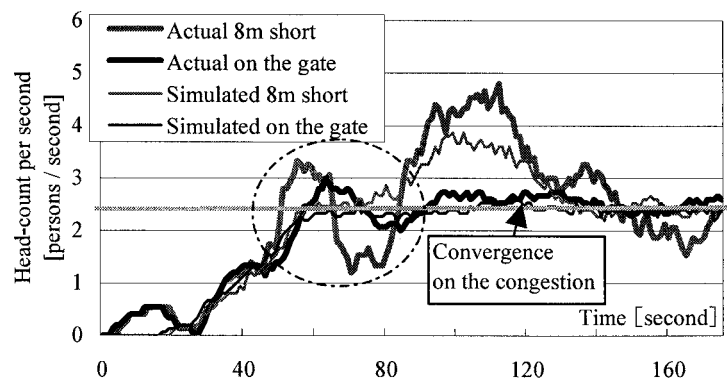


Figure 12 Head-count passing the gate to the playground

5. CONCLUSIONS

This study discussed about the characteristic of the crowd evacuation at school by comparison between the simulated result and the actual measurement. The crowd evacuation were found to have some characteristics that the distance with the neighbor persons is decreased around the gate compared with on the corridor and the outside road, and the students split up into the quick and slow groups and evacuate together. And the congestion is remind quantitatively to cause to decrease the distance with the neighbor persons anyplace. These characteristics are considered not to fall into the school observed in this study, but into the crowd evacuation in general.

The simulation system will be developed with these characteristics, the differences between the

disaster and the drill, and “the disaster component” to find the effective evacuation method in our future work

Acknowledgements:

The authors acknowledge support from Tokyo Tech High School of Science and Technology for observing the actual evacuation drill at school.

References:

- Ebihara, M. and Kakegawa, S. (1995), “Simulation Model of Evacuation and Rescuing Behavior Using an Object-Oriented Modeling Technique”, *Journal of architecture, planning and environmental engineering*, Architectural Institute of Japan, **467**, 1-12
- Fujioka, M., Ishibashi, K., Kaji, H. and Tsukagoshi, I. (2002), “Assessment for Estimated Evacuees Behavior Using Multi Agent Based Simulation Model”, *Journal of social safety science*, Institute of Social Safety Science, **4**, 57-63
- Watanabe, H. (1982), “Shin-Kenchiku-gaku Taikei”, Shokokusha Publishing Co.,Ltd , **11**, 153-234
- Homepage of CAS research, <http://www.cas.fussa.tokyo.jp/>

DEVELOPING OF NOVEL ROOM RELAYOUT TOOL USING REAL-TIME PHYSICS SIMULATION AND PORTABLE VR SYSTEM FOR PREPAREDNESS OF EARTHQUAKE DISASTER

J. Ryu¹⁾ and R. Ohno²⁾

1) *Postdoctoral Research Fellow, Department of Built Environment, Tokyo Institute of Technology, Japan*

2) *Professor, Department of Built Environment, Tokyo Institute of Technology, Japan*

jahoryu@enveng.titech.ac.jp, rohno@enveng.titech.ac.jp

Abstract: Based on the results of survey about disaster education facilities of major cities in Japan, we have developed an educational VR system, which is design to help people reconsider safer layout of furniture in their own room. In this earthquake disaster education program we apply the virtual reality technology to this system that is used in many industrial field. Not only showing the visual effects but also representing the real-time physics simulation of virtual objects has become possible that could make high presence sense during the disaster education process, which is expected to enhance the effectiveness of education. Portable VR system, consisting of three screens (2M X 1.8M size), was invented to give the disaster education without visiting disaster education facilities, which is easily assembled and disassembled for transportation. This system can display both the real-timely generated computer graphics and moving picture on the screen.

1. INTRODUCTION

In Japan, the probability of occurrence of earthquake is relatively quite high compared with other countries because the location of country is near to the seismogenetic area. Therefore the major cities in Japan like Tokyo makes great efforts to inform the citizen about the earthquake disaster through several disaster education facilities. These facilities play a central role in disaster education system that executes various kinds of training. We have surveyed these facilities to find some guidelines for development of earthquake disaster education tool in the previous research (Ryu et al., 2006). The target of analysis includes the several representative facilities in Tokyo and Kobe. Especially, the disaster preparedness education on earthquake is very important because its damage can be reduced quite a lot, if the daily preparedness is properly conducted. Since earthquake usually come to occur suddenly with no coping time to react, the daily preparedness is more important than other types of disaster. For example, the statistic analysis about the causes of injured people in Kobe earthquake in 1995 shows the tumbling of furniture in house is the biggest one among the several reasons, which could be prevented by the daily carefulness or disaster awareness education program (AIJ, 1996).

As an effective disaster education tool we have developed a program for testing safety of furniture layout using virtual reality technology. There are several expected merits of using virtual reality technology. For example, the disaster education program using the effective virtual reality tool will help to enable the educatee to understand the education program easily and intuitively, which will result in a mitigation of damages by earthquake disaster.

As a room layout design tool for preparedness of earthquake disaster using real-time physics simulation, we are developing a prototype of VR tool using physics simulation engine, PhysX (formerly called NovodeX), that is partly open library for non-commercial use. We could substitute this system using the real-time physics simulation for the real object simulation tool such as shaking room model box tool in the earthquake disaster education facilities in Kobe (Fig. 1). There are several expected advantages of using virtual reality in the earthquake disaster education program such as the easy comprehensive process, cost-economic for making various models, and high effectiveness of education through the attraction of the educatee interests.

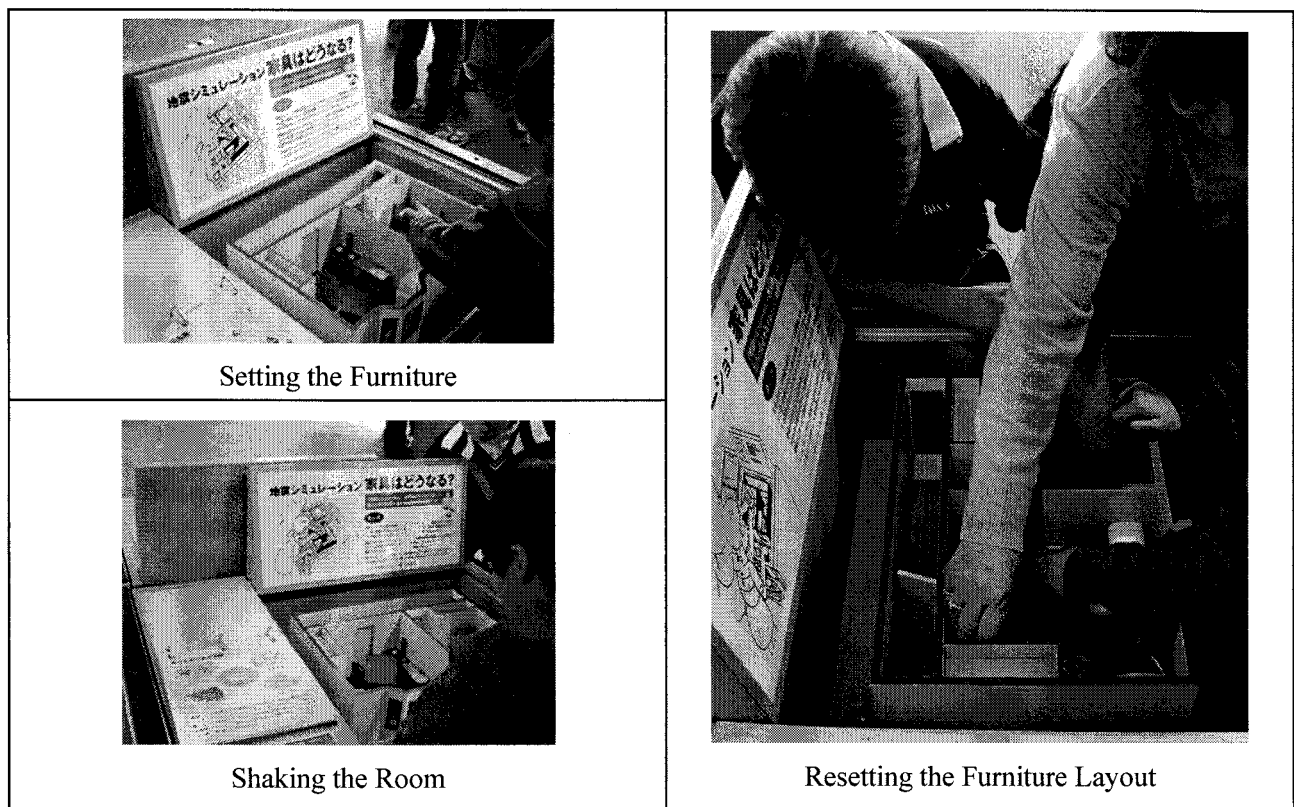


Figure 1 Earthquake education tool for verifying the collapse of furniture during the earthquake disaster using real objects in DRI(Disaster Reduction and Human Renovation Institution) in Kobe

2. REAL-TIME PHYSICS SIMULATION IN VR

2.1 Real-time Physics Simulation

In virtual world, the realistic movement of objects has been requested for a longtime in order to give viewer with high presence sense. Before achieving the real-time physics simulation, the pre-calculated animated sequence was used to show the realistic behavior of objects in virtual world. One of the obstacles to use the real-time physics simulation in VR was the calculation time to get the results, which took long time to show the continual movie sequence for viewer.

At the real-time physics simulation the physics engine simplifies its calculation and lower the accuracy so that they can render the scene at an appropriate rate for continual move image. Recently, the real-time physics simulation begin to be adapted to the VR world and game application from the rapid developing of the physics simulation algorithm and hardware. Realization of the proper object movement in VR space makes improve the presence sense of viewer.

There are open source physics engine such as ODE (Open Dynamic Engine), Bullet, OPAL and commercial one such as Havok, PhysX (formerly called NovodeX) and so on. At the sametime there is

a proposal for using Physics Processing Unit (PPU) from AEGIA PhysX, such as CPU (Central Processing Unit) and GPU (Graphics Processing Unit) to accelerate the calculation for the physics process. In this research, we have chosen the PhysX engine because of the stability of simulation and many developing support documents which help making new code for our system. Through using the computer simulated physics process, we can have the physics-based environments that could give us higher presence sense.

2.2 Force-feedback Interface for Interaction

Also, we are planning to use the SPIDAR, wire based force-feedback interface, to realize the user's direct manipulation of furniture in VR room (Buoguila et al., 1997). One of the characteristics of our VR system is that user can experience the interaction with the virtual space through the SPIDAR-G, string based force-feedback human scale interface. The user can touch and manipulate the object in the virtual space with force-feedback interaction. This is the on the way of developing that will be installed to system in the near future. This device will reinforce the immersion of user through sense of touch and force-feedback in the virtual space.

3. ROOM RELATOUT TOOL FOR EARTHQUAKE DISASTER PREPAREDNESS

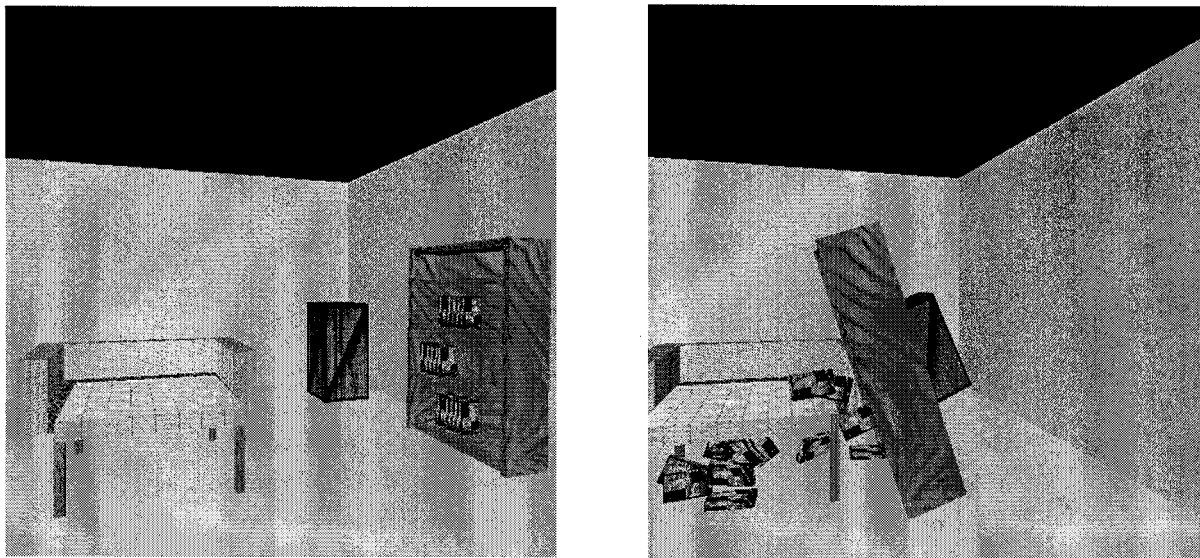


Figure 2 Real-time Earthquake Simulator Before and After

The purpose of this system is the reconsideration of the status of room through the simulation of earthquake occurrence situation. After setting the furniture, educatee will verify the extents of the damage caused by inappropriate layout of furniture in their room such as shown in Figure 2. For example the high stand furniture would tumble into the wide range of area that needs to be avoided through not to install it near to the bed. Furthermore, the heavy furniture must not be installed in the high places or near to sitting and sleeping area. In our prototype of the room relayout tool, users can control the furniture in virtual room and change the layout of it using the popup menu or force-feedback interface. After setting the furniture they can verify the degree of danger of their room from the earthquake disaster in the virtual room, which will probably lead to an appropriate new layout of furniture.

The user set the furniture similar his room layout. The methods of the setting the furniture are possible in the several ways with keyboard or exclusive haptic interface. The using keyboard and mouse input is illustrated in the Figure 3. The user can move the position of furniture through popup

menu on screen. This is very familiar way of setting the furniture for regular user of computer because they are doing similar task like this everyday. Another possible option could be the using of the haptic interface for manipulating the virtual furniture. The prototype of wire based haptic interface for manipulating objects have been proposed in the previous study (Ryu et al., 2004).

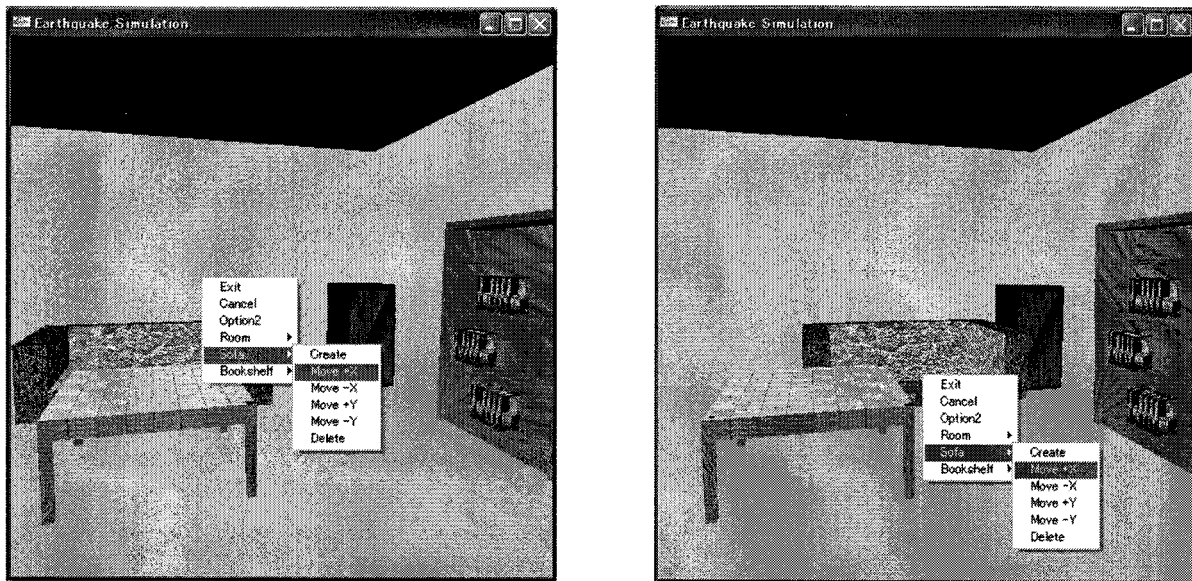


Figure 3 Using Keyboard and Mouse input for setting the furniture layout

Now, we are in the stage of preparing the sole use for this system from the former study. The system can represent the situation of occurrence of earthquake with visual display and sound effects. This software can be carried out in stand-alone computer or immersive three-side screen system that will be completed in the late of January 2007. The impact of verifying the results of earthquake disaster is supposed to influence the educatee to change the environments of their room, which will mitigate the actual damage from the real earthquake. As the future works, we are planning to carry out the education program for children with the Portable VR system. Also we have plan to investigate the effectiveness of education itself and the influence of the using VR tool compared with the other education media such as text or picture based education.

4. DEVELOPING OF PORTABLE VR SYSTEM

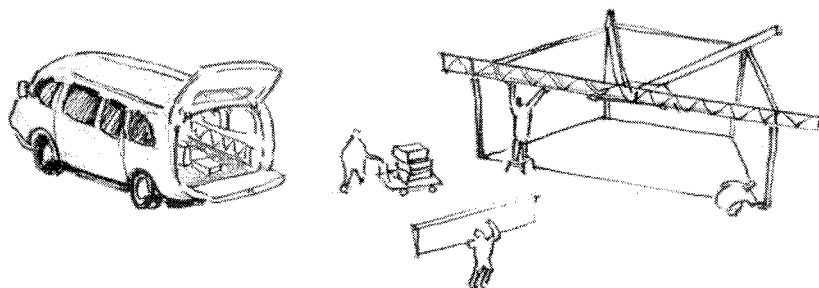


Figure 4 Concept of Portable VR System (Assembling and Disassembling)

To achieve the effective results of earthquake disaster preparedness education through the high presence sense, we have designed a portable human-scale immersive VR system composed of three screens with 2.0M (width) x 1.8M (height) in size for safer room relayout as a design tool. There are

two main focuses of developing of new Portable VR system that are portability and compact size because we are assuming that we need to convey the system even to the small space room. This system was the embodiment of the interviews that showed the need of the transition of VR system in order to enhance the effectiveness of the education for children through providing the virtual experience of disaster situation. One of the great characteristics of this system is the portability. We have hardly tried to achieve the portability of system by simplifying the structure, electrical connection, and the reduction of the frame size from assembling of the small parts.

4.1 Configuration of Portable VR

Portable VR system has two main functions to making virtual experience for earthquake disaster preparedness. First function is presenting the real-time CG image that is generated by render computer, synchronizing the three computers to make whole one image for 120 degrees jointed three screens. The other function is presenting the high quality movie image on the wide screen that is composed by three projectors. The total resolution of three screens reaches about 3000 pixels X 1000 pixels because the screen consists of three projectors that have the resolution of SXGA (1280 X 1024). The total resolution is almost similar with or higher than the high-definition (HD) video image that is 1920 X 1080. The three rendering computers, which are charge of each projector, are connected through the Gigabit Ethernet. The broad band of network helps the fast traffic of data to synchronize the images.

4.2 Structural Frame for Portable VR

The hexagonal plan of frame was invented to support the three projectors and three screens for easy assembling process. The hexagonal shape has merits of structural stability and economic space occupancy. The adoption of the front projection method within the hexagonal frame saves the installation room space a lot. To avoid the making the shadow area of viewers inside of system, the mirror system was adapted to heighten the starting point of projection. Even the system can be installed in the 4M X 4M room space including the computer related hardware. Not only the small room space of assembled frame of system but also the occupied space of disassembled parts is quite small in order to be loaded to mini van that has the 3.0M X 1.3M X 1.5M size cargo volume.

The assembling and disassembling process requires just a couple of hours that is not the obstacle of moving the system to other place. The Figure 5 and Figure 6 shows the hexagonal plan of the system frame and the projection methods of system by using mirror. The total number of people who can watch the screen all together at same time is 15 persons.

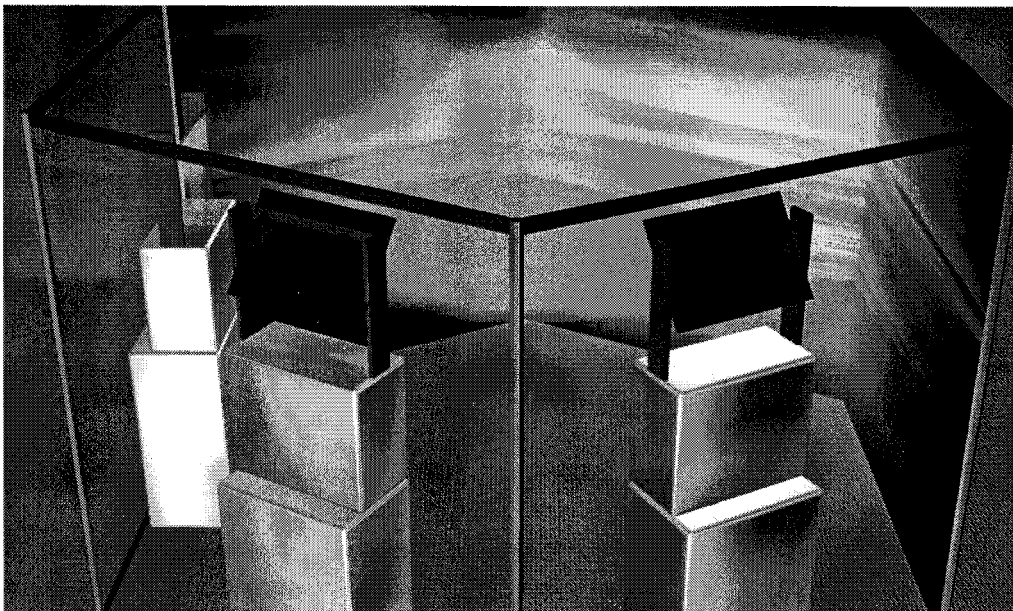


Figure 5 Image of Portable VR System

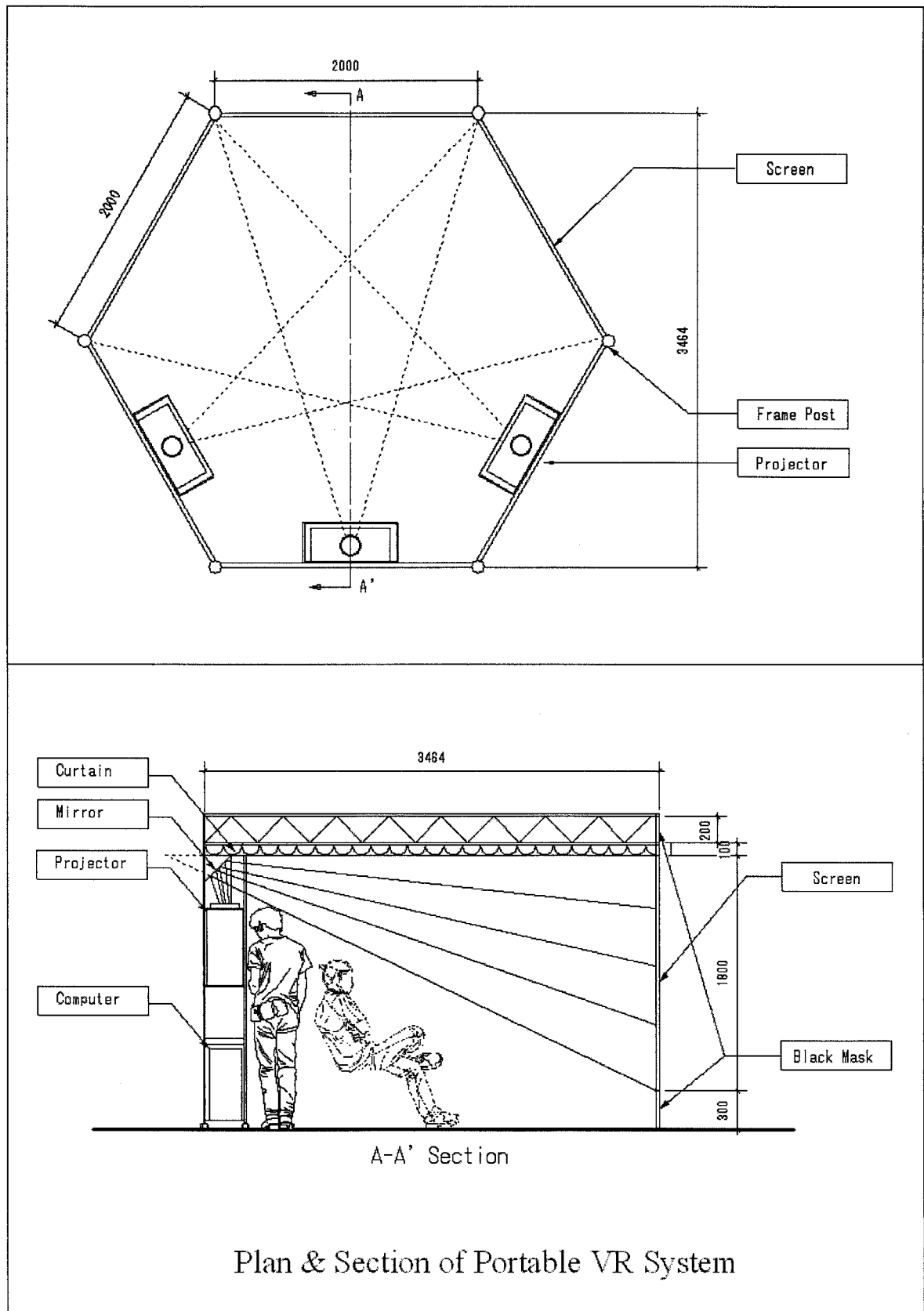


Figure 6 Plan of Portable VR System

6. CONCLUSION

We have developed a novel room layout design tool for preparedness of earthquake disaster using real-time physics simulation and force-feedback interface through the survey of several disaster education facilities in Kobe and Tokyo. Also, we have invented a portable VR system that is very compact and portable system for high presence sense of visual presentation. The visual presentation and high presence sense of system have some merits of easy understanding and continued interests than literature presentation. As the future works, we have a plan to upgrade the education contents for the disaster preparedness and the technical aspects such as physical simulation and furniture manipulation interfaces. Also a post education survey needs to be carried out for evaluation of effectiveness of the system.

References

- Architectural Institute of Japan (1996), "Report of Damage Occurred Inside of Houses at Hanshin-Awaji Great Earthquake," AIJ (Japanese)
- Ryu, J., Soeda, M., and Ohno, R., (2006), "Development of an effective tool for virtual experience of environmental hazard –A survey of disaster education facilities in Japan," Third International Conference on Urban Earthquake Engineering March 6-7, Tokyo, Japan, 197-203.
- Cruz-Neira, C., Sandin D., and DeFanti, T., (1993), "Surround-Screen Projection-Based Virtual Reality: The Design and Implementation of the CAVE," Proceedings of ACM SIGGRAPH'93, 135–142.
- Hill II, L.C., Chan, C-S., and Cruz-Neira, C., (1999), "Virtual Architecture Design Tool (VADeT)," Third International Immersive Projection Technology Workshop (IPT 1999)
- Leigh, J., Johnson, A., Vasilakis, C., and DeFanti, T., (1996), "Multi-perspective collaborative design in persistent networked virtual environment," Proceedings of IEEE Virtual Reality Annual International Symposium'96, Mar. 20 –Apr. 2, 1996, 253-260.
- Ryu, J., Hasegawa, S., Hashimoto, N., and Sato, M., (2004), "Multi-Projection Display System for Architectural Design Evaluation," The 9th Conference on Computer-Aided Architectural Design Research in Asia (CAADIRA), Paper Number 81, 901-910.
- Buoguila, L., Cai, Y., and Sato, M., (1997), "New Haptic Device For Human Scale Virtual Environment: Scaleable-SPIDAR," ICAT'97, Tokyo, 93-98.
- http://en.wikipedia.org/wiki/Physics_engine
- <http://www.tfd.metro.tokyo.jp/ts/museum.htm>: Fire Museum of Japan & Disaster preparedness Center
- <http://www.dri.ne.jp/index.html>: Disaster Reduction and Human Renovation Institution of Kobe City
- <http://www.disastereducation.org>: The National Disaster Education Coalition (NDEC) of USA

RECOVERY CONDITION AND BEHAVIOR OF THE AFFECTED PEOPLE -a Case of May 27th, 2006 Central Java Earthquake-

Syam, Rachma Marcillia¹⁾ and Ohno, Ryuzo²⁾

*Research Student, Department of Build Environment, Tokyo Institute of Technology, Japan
Professor, Department of Build Environment, Tokyo Institute of Technology, Japan
rachma3382@yahoo.com, rohno@n.cc.titech.ac.jp*

Abstract: The aim of this survey is to assess and evaluate current survivors' recovery condition and behavior after May 27th Central Java earthquake. The survey consists of photos documentation, questionnaires and one on one interview with the residents. There are three main aspects being surveyed: individual aspect, community aspect and information aspect. Concerning individual aspect, we observed and interviewed individual post-disaster physical and mental conditions. Concerning community aspect, we observed and analyze role of the social networks, traditional lifestyle, tradition and custom and community facilities for recovery. As for information aspect, we observed what kind of information need, when and how the survivors get it, and their risk perception for future disaster. It is expected that this report will be useful as an overview to take measures for disaster relief programs and precautions for future disaster.

1. INTRODUCTION

Earthquake measuring M6.3 (USGS and ERI) struck the Indonesian island of Java with the epicenter of about 20km south of Yogyakarta city at 5.53 AM local time on Saturday, 27th May 2006. Even though the earthquake lasted for only 57 seconds with an aftershock occurring at 10.15 AM, it killed over 5,000 people, injured thousands and displaced up to 200,000 people from their homes.

The earthquake had left tremendous damage in the lives of the residents both physically and psychologically. The physical damage causes and effects of the earthquake had been investigated in various researches but the social behavioral condition of the residents has not been clearly observed and proved by data. Since both physical damage and social behavioral effects are inseparable post disaster condition of the residents, we conducted a survey in October and November 2006 as an integral and continuous survey with the previous survey conducted in June 2006. The necessities of gathering information on what are the effects of the earthquake on their lives, what is their current condition and necessities and how the survivors' coping behavior to manage and continue their lives is very important to take measures for disaster relief programs and rehabilitation.

2. SURVEY METHOD

In order to compare the influence of residential houses damage and community type on the condition of the residents, a survey was conducted in 12 sub-villages in October and November 2006. The respondents were selected considering their previous house damage and current conditions.

The survey was divided into two periods. In the first period, six sub-villages were chosen from high damage areas, where majority of the house structures were brick masonry with/without reinforcement. Most respondents are people whose houses were collapsed right after the earthquake.

In the second period, other six sub-villages were chosen based on their community unique characters that divided into three categories; suburban, rural village and Old Town (full description in Table 1). Most of the respondents are those who live in houses that are still standing and reused (in most cases those houses are traditional wood structure with brick wall or wood wall).

Table 1: Three Categories of House Settlement and Community

Community Type	Description of Characteristics
Suburban	Outlying areas of the city, most of the house are brick masonry with/without RFC, but there are some wood structure house still standing and reuse. People who with collapsed house still in temporary shelter/tent while other live in their reused house. People previous occupations are traders, employee and construction labor.
Rural village	Remote village area, mostly with less/little damage wooden house, majority people occupation are farmers, mostly now live in previous house being reuse/rehabilitate
Old Town	Old Town in Yogya City, one of cultural and heritage area. Majority are wood house structure with brick infill with less damage and age more than 50 years. People occupations are government employee and traders. Have very strong community relation that has been going on in centuries.

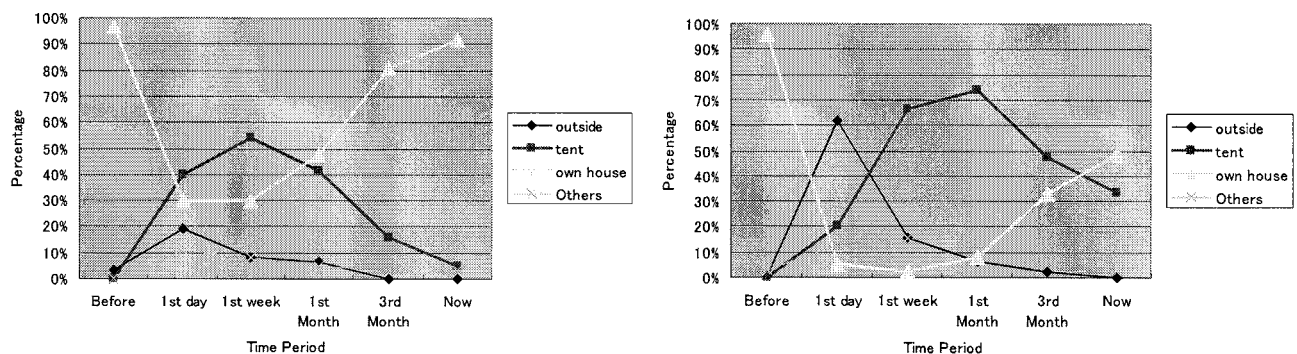
Both two periods of survey were conducted through visual observation, documentation and information collection from local residents with the same questionnaires and interviews with the help of 6 volunteers from Gadjah Mada University

3. INDIVIDUAL ASPECTS

3.1 Post Disaster Recovery Residents' Conditions

3.1.1 Shelter Recovery

Shelter recovery within 6 months after the earthquake was investigated. Fig. 1 shows that since the first day, when earthquake occurred, there are less people who lived outside and in temporary tent for residents who previously live in little/no damage houses and in 6 months 90% of them have lived back in their own house. Contrastively, there are only 50% of high damage residents have returned to their own house and 40% still have to live in temporary tents.



(a) Shelter recovery for little/no damage residents

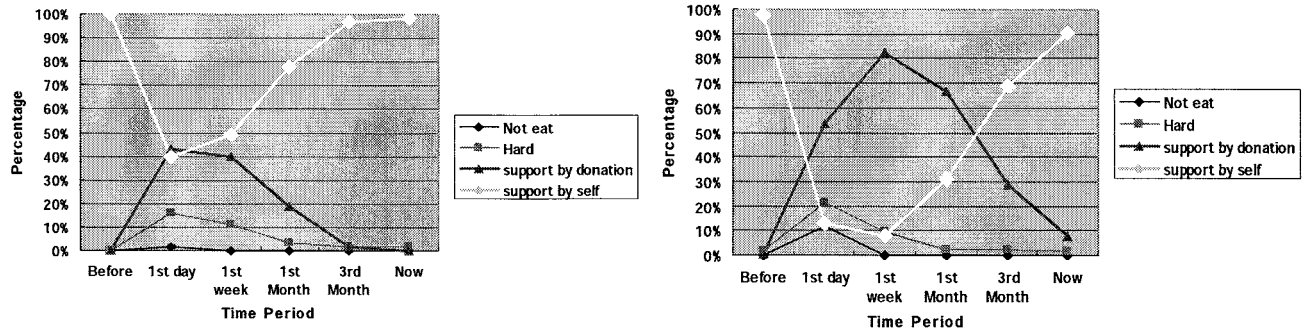
(b) Shelter recovery for high damage residents

Fig. 1 Changes in Shelter Recovery Condition

From previous research (Ohno and Syam, 2006 in press), most of little/no damage residents are those who previously lived in wood house structures that survived and being re-used or rehabilitated. Unlike majority of the high damage residents, who previously lived in brick masonry that collapsed, recovery process takes longer period from being living outside, in temporary tent, temporary shelter and finally permanent house. It then conceded that some of the little/no damage residents have been using the reused/rehabilitated houses again even right after the earthquake. This resulted in a faster shelter recovery process.

3.1.2 Food and Health Recovery

In both high and little/no damage residents, more than 90% food consumption is already self-supported, even though the quantity and quality of the food had decreases compared to before the earthquake. But it was revealed that there are differences in the recovery process period. For high damage residents, even until the 3rd month, 30% of their food consumption still depends on donation. Contrastively, for little/no damage residents this situation happened only until the 2nd week.



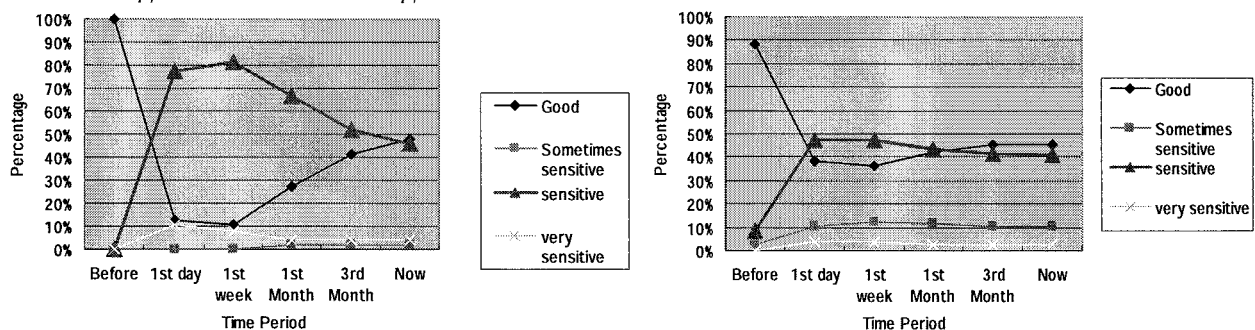
(b) Food condition for little/no damage residents

(b) Food condition for high damage residents

Fig.2 Changes in Food Condition

Moreover, there are still concerns for health and psychological aspects, because until now 40-50% in both high and little/no damage residents still suffered from trauma and health problem such as insomnia. Even though there are no more frequent after-shocks that is happening after the second month, but small shaking or rumbling sound and sudden movement will evoke their trauma.

Interestingly this situation is actually worse in rural village area with little/no damage residents instead of sub-urban area with high damage residents, especially during the first 3 months. One of the reasons might be caused by lack of information received in rural area about earthquake and disaster prevention and mitigation, because of lesser information distribution and disaster education program in rural village with less/no damage.



(c) Health condition for little/No damage residents

(b) Health condition for High damage residents

Fig.3 Changes in Health Condition

3.1.3 Occupation changes and Kinship

Residents' daily activities also had been resumed even though there had been some temporary occupation changes occurred especially for men. Before the earthquake, generally residents were villagers who work as farmers, construction labors, government employees or traders. Now, majority of men work for the reconstruction program, even government employees during morning-afternoon they work as usual but in the evening-night they will continue to work on their own house reconstruction. The reason for the phenomenon is because the need of construction labors had increases drastically, especially since all reconstruction programs for temporary shelters and permanent houses are undergoing as a mass construction and at the same time.

After the disaster, there is a 30-40% inclination of closeness in kinship. It happened not only within nuclear family members but also relationship between each person in the community, which had more sympathy and tolerance with each other.

4. COMMUNITY ASPECTS

4.1 Influence of Cultural Aspects and Place Attachment on the Recovery Process.

4.1.1 Role of Traditional Lifestyle

More than 90% of high and little/no damage residents still cherish traditional Javanese society lifestyle and spirit such as '*Gotong Royong*' (state of action and spirit from Javanese people to help each other in good and bad time) and '*Kekeluargaan*' (an extended kinship feeling of being one big family in Javanese communities) and after the earthquake more than 60% said that these values are even more significance. Many recovery programs undergoing in Bantul and Klaten by NGOs and Government were community-based works that consider taking benefit of the traditional lifestyle to advance the recovery process.



(a) A temporary tent shared by five different families, bound together because of sharing the same experience and feeling



(b) *Kekeluargaan* between Housewives gather to share and make public use of a well that is still usable



(c) *Gotong royong* spirit of youths and elders to help each other cleaning vicinities area and making reconstruction of temporary shelter.

Photo 1 Traditional Lifestyle and Spirit in Javanese Community Lifestyle

The previous social networks in the communities itself plays vital role in rehabilitation process. '*Rukun Tetangga*' (RT) as the lowest sociopolitical hierarchy is not only works as a sociopolitical territorial unit but moreover as a community unit where they work and help each other. Other prior community organizations such as '*Karang Taruna*' (the youth organization), '*PKK*' (the woman organization), etc give a lot of contribution in the recovery programs (see Table 2 for community activities). This traditional lifestyle, spirit and social networks had been going on for centuries in Javanese communities.

Table 2: Community Activities

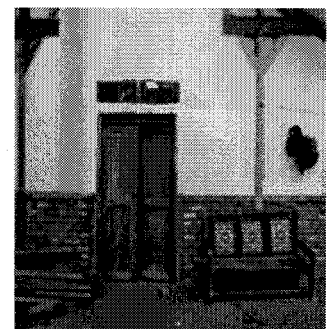
Community Organization	Activities before Earthquake	Frequency	Activities after Earthquake	Starts from
RT/RW	beurocracy, sharing information, organized plan for community, etc	1-2x a month/in event	beurocracy, distribute donation, information post, education lecture and training, arrange recovery program	earliest 1st week
Karang Taruna	community event organizer such as wedding, independence, funeral, etc.	1-4x a month/in event	Cleaning up the debris, distribute donation, reconstruction public facilities.	earliest 1st week
PKK	sharing information for housewives, arrange health programs for mom and kids, lottery, preach, etc.	1-2x a month	public kitchen works, arrange public toilet use and wheel, psychological recovery program, etc.	earliest 1st week
Pos Kamling	Community security night watch guarding	every night	Community security night watch guarding	earliest 1st week
Takmir Masjid	arrange preaching, Friday pray, Islam religious occasion	1x a week	preaching, Friday pray, psychological recovery program	earliest 1st week

4.1.2 Role of Tradition and Custom

Considering tradition and custom practices in individual and community are also essential to progress the recovery. In one of a community base reconstruction project lead by Mr. Eko Prawoto at Ngibikan, Canden, Jetis Bantul, rituals were carried out after completing the highest part of the new rebuild house. Personalization of individual house from the same structure module was also undertaken by each family; see Photos 2 (a), (b)&(c). The reason for all of these actions is to give self-assurance for the residents that each house is not only as a 'shelter' but moreover as a sense of being 'themselves' and 'home'. It is because reconstruction is not only about making sure that no one is homeless anymore, but furthermore it is about rebuilding residents' self confidence in life, which will progress the recovery process.



(a) & (b) Different house façade of the same house structure module



(c) Previous house parts being reused to make personalization.

Photo 2 Personalization of Same Module House Structure in Canden

4.1.3 Role of Community Public Facilities

Cultural influence is not only reflected on community lifestyle and tradition but also on the usage of their public facilities. The so-called '*Alun-alun*' (open area/field owned and used by the community as sport field, night market, and other events), '*Gardu ronda*' (public security guard post) and '*Balai Desa*' (public hall owned by the community used for public discussion, meeting, etc) are some of the public facilities that traditionally had been used as community gathering places. In the case of May 27th earthquake, '*Alun-alun*' was used as temporary emergency areas such as shelter and evacuation areas, *Gardu ronda* used as emergency information post meanwhile the '*Balai Desa*' was used as donation and gathering posts. Now, after 6 months, '*Alun-alun*' is used as temporary school area, *Gardu ronda* back to original use, while '*Balai Desa*' is used as information and training center.

Table 3 Community Facilities Usage

Community Facilities	Activities before earthquake	Frequency	Activities after earthquake	Time period after earthquake
Balai Desa	RT/RW meeting, share information, event organizing	1-2x a month	Food Donation	1st week-2 months
			Health Donation	1st week-1st month
			Psychological program	2nd-3rd month
			Lectures	depend schedule
			Information post	1st week
Mosque	Preaching, Friday Pray, information distribution	1x a week	Preaching, Friday Pray, information distribution	1st week-now
			Health Donation	1st week-1st month
			Psychological program	
Alun-Alun	Specific event such as independence, sports, night market.	Event only, sports every afternoon.	temporary shelter	2 week-now
			Food Donation	1st week-2 months
			Psychological program	2nd-3rd month
			Health Donation	1st week-1st month
			Cleaning up debris	1st week-1st month
Gardu Ronda	pos kamling/night watch community security	every night	pos kamling	every night
			information post	1st week



(a)&(b) Two weeks after the earthquake, alun-alun used as temporary tent areas and evacuation sites in Wonokromo. (c) The same alun-alun now used as temporary school areas.

Photo 3 Usage of public facilities

4.2 Influence of Place Attachment on the Recovery Process.

Another factor that is also important to advances the recovery process is the residents' place attachment to their neighborhoods. It was revealed that more than 90% of the residents still live in their own property and almost 80% of them are not willing to be relocated to a new resettlement area.

The reason for this preference might be caused by their familiarity to the surroundings and better access to the physical source, family supports and social networks. In most recovery cases, residents made their own motivation and efforts to progress their own recovery in fulfilling their needs and rebuilding their own house.

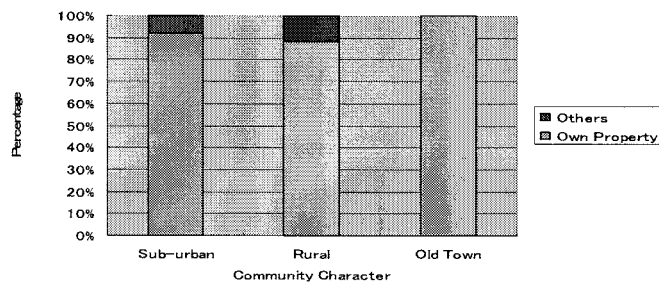


Fig.4 Residential properties based on community character

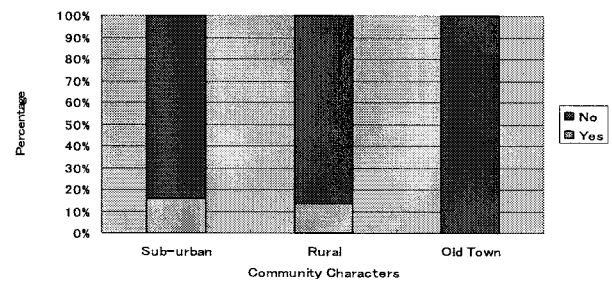


Fig.5 Willingness to move to new resettlements

5. INFORMATION ISSUES and RISK PERCEPTION

5.1 Information Necessities.

From researches conducted in the damage areas, general reason for the high damage of residential houses is failure of structural design for safety, poor quality and insufficient material used for reinforcement. This tendency was not only influenced by economic reason but also low educational background that affect how they build their house (Most people build their own house, but less than 50 % of the residents have chance to go to high school).

Concerning information importance, how to build a safe house is the highest information needed by the residents now (more than 60%) and sequentially after that are 'what to do if there is earthquake', 'whether the previous house is safe enough to be live in again', and 'knowledge on what is earthquake'. Other information that they want to know is 'how to get donation'.

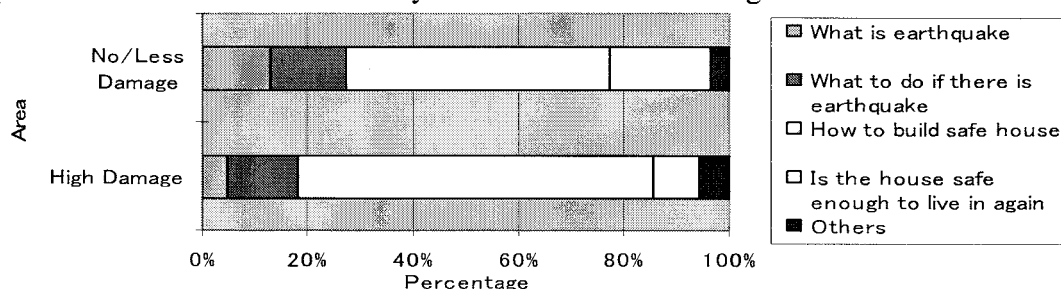
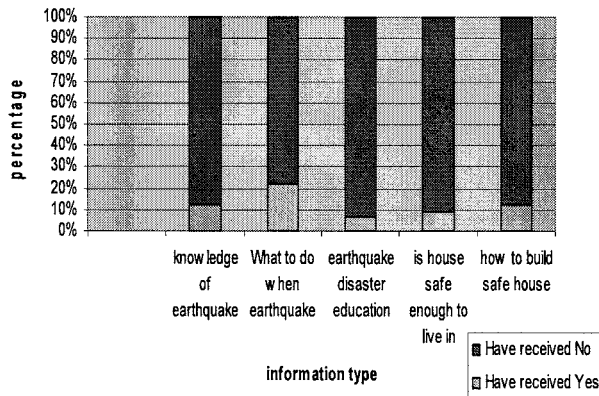


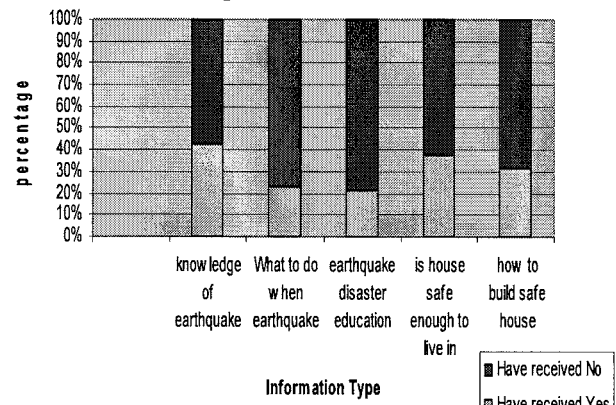
Fig.6 Information needed by the residents

5.2 Information Distribution (Disaster Education)

In Figure 7 shows that less than 50% information about earthquake and disaster prevention and mitigation is received by suburban residents and less than 20% received by rural residents. This difference is corroborating by the facts that information distribution is not equal throughout all areas yet. More than 20% suburban residents received information through other source such as training and lectures by experts and volunteers and also other technical information distribution by poster and construction manual on site. Contrastively, the rural area only received information through mass media such as TV and radio. Nevertheless, it seems that inadequate information distribution in both residents had been one of the reasons of why the trauma level is still high now.

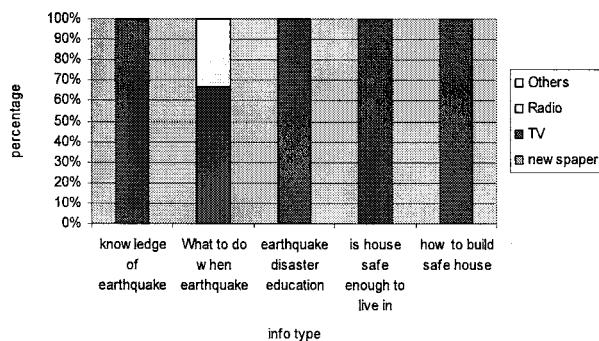


(a) Information received by rural residents

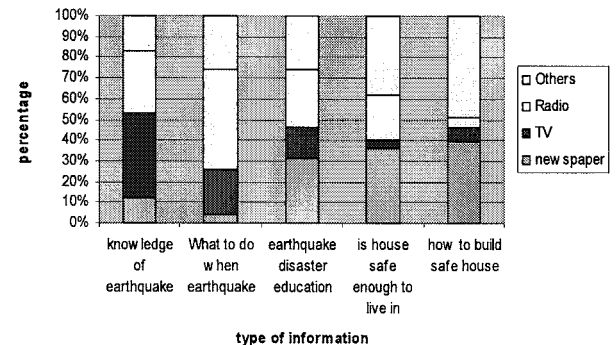


(b) Information received by suburban residents

Fig. 7 The content of information received by the residents



(a) Rural residents



(b) Suburban residents

Fig. 8 The media of information used by the residents

5.3 Risk Perception for Future Disaster

Concerning the prediction of reoccurrence, 30% of suburban and Old Town residents anticipate the possibilities of future earthquakes higher than those in rural area, see Fig.9. Respectively, when they were asked their attitude for future disaster, 30% of suburban and Old Town residents believed that if they were given knowledge on disaster education, they can prevent or at least minimize the impact of the disaster higher than the rural residents. It seems that the higher the earthquake damage experience and the more the information received have raised the concern of its risk, contrastively those who lived in rural area with less damage and information received had pay less attention .

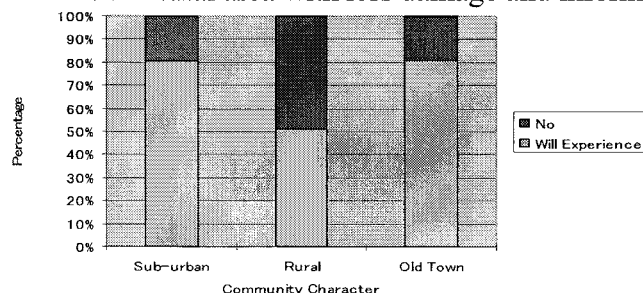


Fig. 9 Possibility of future earthquake

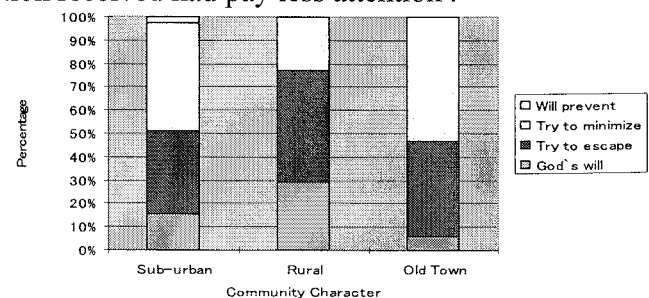


Fig.10 Attitude toward future disaster

6. CONCLUSIONS

Overall, residents have resumed their daily activities even though recovery process periods are different between those with high and no/less damage. Nevertheless, there are still concerns of shelter recovery for high damage residents and trauma/health condition for both high and less/no damage residents.

Cultural aspects had a great influence in the post disaster recovery process. The traditional life-style and spirit, custom, community facilities and place attachment play quite an important role, therefore it should be taken into consideration to assist rehabilitation of the disaster area. Reconstruction of a house is not merely making a “shelter” but creating “home” for the residents as a firm basis to rebuild their self-confidence in life.

Lack of information and ignorance about the disaster education has caused insistent trauma and distress from the earthquake. The necessity for information distribution is urgent to give both high damage and no/less damage residents a faster physical and psychological recovery. These will include information on reconstruction, disaster education and mitigation, etc. Information system not only through formal education programs in schools and mass media, but also include traditional information system through local gathering communities and public facilities such as billboard, ‘Balai desa’, etc. Information distribution through lectures and socialization also need to be followed with on site training so that the community can get better understanding by experience it themselves.

Risk perception of those who received higher the earthquake damage experience and more information are higher than those received less damage and information.

Acknowledgements:

Financial support from Center for Urban Earthquake Engineering (CUEE), Tokyo Institute of Technology, to undertake this survey to Yogyakarta, is gratefully acknowledged.

This field visit was successfully completed with the help of Ms.Puput Puji P., Mr. Arief Budiman, Mr. Nanang Nurseta, Mr. Ardiyan, Mr. Nurcholis, Mr. Hikmat Rizki and Ms. Puji from Gadjah Mada University, who help in obtaining the data. The field survey and discussion with Mr. Eko Prawoto is also gratefully acknowledged.

Last but not least, we would like to thank to the residents for the sincerity in the interviews and extent our deepest condolences for the loss of family members and properties in this earthquake.

Note: A part of this paper has been published in the previous paper (Ohno and Syam, 2006 in press).

References:

- R.Ismunandar K. (2001).” Joglo; Arsitektur Rumah Tradisional Jawa”. Semarang: Effhar Press. P. 48, 89, 91,106,118,144
- Arya Ronald (2005). “Nilai-nilai Arsitektur Rumah Tradisional Jawa”,. Yogyakarta: Gadjah Mada University Press. P-130-151
- Ohno, R, Syam, R.M. : Field Survey of the damage caused by Central Java Earthquake of May 27, 2006 in Research Report on Earthquake Engineering no.99, supported by Center for Urban Earthquake Engineering, Tokyo Institute of Technology. (Pp.65-76, 2006)
- Ohno,R, Syam, R.M : Earthquake Damage in Yogyakarta due to The Central Java Earthquake of May 27, 2006 Preliminary Survey in CUEE newsletter no.5, 2006
- Ohno,R, Syam, R.M. An analyses of the residents' condition and behavior based on interview, in (H. Kawase ed.) Report on the Damage Investigation of the 2006 Central Java Earthquake, Architectural Institute of Japan (in press)

SEISMIC ANALYSIS OF UNDERGROUND REINFORCED CONCRETE STRUCTURES AND A NEW CHALLENGE FOR NUMERICAL SOLUTION

Ha-Won Song¹⁾, Sang-Hyeok Nam²⁾, and Sung-Hwan Jang³⁾

1) Professor, School of Civil and Environmental Engineering, Yonsei University, Korea

2) Research Professor, School of Civil and Environmental Eng., Yonsei University, Korea

3) Graduate Student, School of Civil and Environmental Eng., Yonsei University, Korea
song@yonsei.ac.kr, salute@cmme.yonsei.ac.kr, jsh1981@cmme.yonsei.ac.kr

Abstract: In this paper, an elasto-plastic interface model which considers the thickness of interface between underground reinforced concrete (RC) structure and surrounding soil media is proposed for seismic analysis of underground RC structures and a new solution technique which controls the volume change of RC structures is also proposed for nonlinear analysis of RC structures subjected to cyclic loading. In the seismic analysis of underground RC structures surrounded by soil media, the effects of the interface between the structure and soil media and the effect of stiffness in the RC structure due to reinforcement to seismic behavior of underground RC box structures are analyzed. Nonlinear constitutive models for reinforced concrete, soil and interface are presented and failure mechanisms of underground RC structure under seismic action are discussed through seismic analysis of underground RC subway station structure. As an attempt for performance based seismic design, the failure mode of subway station structures and the damage level of the structures due to different design options are also discussed. As another attempt for performance based evaluation of RC shell structures under static and dynamic loading, the so-called volume control technique is also presented. The volume control technique is a nonlinear solution technique which overcomes the instability problem of the conventional force-control method and improves the displacement-control method. For the post-peak softening behavior of RC shell structures, the volume control method can analyze post-peak behavior of RC shell structures by adding a pressure node on the shell elements. The distinctive characteristic of this shell element equipped with a pressure node is its capability to simulate the behavior of RC shell structures under cyclic loads even for post-peak softening range. In this paper, a path-dependent volume control method using the pressure node is presented and finite element failure analysis of RC shell structures discretized with multi-layered shell elements and implemented with in-plane two dimensional constitutive equations are carried out. The results of the analysis for RC box culvert, RC tank, and RC hollow columns subjected to cyclic load are compared with experimental results.

1. INTRODUCTION

Although design, construction and performance evaluation techniques of reinforced concrete structures have been improved considerably, there are still many problems to be solved, for example, the problem in seismic analysis of underground structures due to interaction of structures with surrounding media and instability problem during numerical solution stages due to geometrical and material nonlinearity and cracks of reinforced concrete. The importance and cost of underground concrete structures make it necessary to analyze the behavior of underground structural system including surrounding soil media accurately because underground structures are mostly infrastructures and large-scale structures (An, 1996). Nonlinear finite element analysis is an effective tool for performance based design and evaluation to design RC structures subjected to both static and dynamic loading. For nonlinear finite element analysis of the structures, an accurate constitutive equation which

can predict post-peak behavior after cracking is necessary. Most of the research has been focused on finding an efficient element development and crack models for the implementation of realistic constitutive models to accurately analyze RC shell structures. However, effective algorithms to overcome instability in the post-peak failure behavior of the shell structures are limited. Furthermore, conventional analysis technique is not sufficient to predict non-linear behaviors satisfactorily due to the complexity of the structural geometry, boundary conditions and highly non-linear behavior (Song et al., 2002a). Since seismic behavior of large underground RC structure with surrounding soil medium is difficult to be simulated through experiment, an analytical method can be used for the analysis very effectively and a solution technique which analyzes an entire structural system including structural members like beam, slab, and column as well as surrounding soil media up to failure is very much necessary for the performance based design of RC structures. For the analysis, a path-dependent constitutive model for soil is necessary for dealing with kinematic interaction of RC-soil entire system under static and dynamic loads. Interfacial behavior should also be considered in the analysis because the interaction between the concrete structure and soil media most likely occurs along the interfacial zone (Yin et al., 1995). As the first part of this paper, an elasto-plastic interface model with thickness is presented for simulating the interfacial behavior more accurately, and the effect of interfacial behavior is studied through analysis of underground RC box structure. A finite element analysis technique is also developed for seismic analysis of underground RC subway station. Failure mechanisms including failure modes and damage levels of the RC subway station structure under seismic action are also analytically evaluated for the cases of several design attempts for the underground RC station structure.

For the post-peak softening behavior of reinforced concrete shell structures, the so-called volume control method, which can analyze post-peak behavior including ultimate failure of RC shell structures, was developed by adding a pressure node on the shell elements. The pressure node has a single degree of freedom, namely, the uniform change of pressure on finite element. The distinctive characteristic of volume control technique is its capability to simulate the behavior of reinforced concrete shell structures under cyclic loads even for post-peak softening range. With the pressure node formulation, the change in volume enclosed by the shell structures and the required change in load can be determined. Thus, the pseudo-volume control method with a pressure node can overcome the instability problem of the conventional force-control method. This method also overcomes the difficulty of selecting a local characteristic point to control the local displacement which governs the global behavior of shell structures in the conventional displacement-control method (Song et al., 1999, 2002b).

As the second part of this paper, the so-called path dependent volume technique is presented as a new challenge for solution technique in the nonlinear analysis of RC shell structures. The path-dependent volume control technique is an extension of the volume control technique for the path-dependent analysis of RC shell structures under cyclic loading. The technique can obtain increase or decrease of applied force effectively by controlling volume change of the structure subjected to reverse cyclic loading include loading, unloading, and reloading paths. In order to develop a generic, path-dependent, three-dimensional RC shell element, an in-plane two-dimensional constitutive equations and a layered formulation are utilized. For modeling of a shell structure, a multi-layered shell element is adopted. Then, a set of constitutive models based on the averaged stress-strain fields of cracked concrete and reinforcement is applied to each layer of the shell element. For the nonlinear analysis of cracked RC shell element, orthogonal two-way fixed crack model is applied. The validity of the proposed analytical technique is verified by comparing the results for RC culvert, tank and hollow columns with the experimental data. Results show that the path-dependent volume control technique in this paper can be used effectively for performance based design and evaluation of RC structures if the structures can be modeled with finite shell elements.

2. NONLINEAR CONSTITUTIVE MODELS

2.1 Constitutive model for reinforced concrete

Reinforced concrete material model has been constructed by combining constitutive laws for cracked concrete and for reinforcing bars. The constitutive equations are given as the relationships between the average stress and average strain. Crack spacing or density and diameter of reinforcing bars have negligible effect on spatially averaged stress-strain relation defined on RC in-plane control volume. So, the constitutive equations satisfy the uniqueness for compression, tension and shear of cracked concrete and tension of reinforcing bar inside concrete. The constitutive model for the reinforcing bar inside concrete is modeled by bilinear average stress-strain formulation considering strain hardening. Kato's model for bare bar under reversed cyclic loading and the assumption of stress distribution denoted by cosine curve are used for calculating the mechanical behaviors of reinforcing bars in concrete under reversed cyclic loadings (Okamura and Maekawa, 1995; Maekawa et al. 2003).

2.2 Constitutive model for soil

A path-dependent constitutive model for soil is indispensable to simulate behavior of RC-soil entire system accurately. Furthermore, nonlinear characteristic in shear governs the magnitude of ground acceleration which in turn generates induced forces of underground RC. Therefore, it is important for use a constitutive model for soil which can simulate nonlinear characteristics of soil. In this paper, the so-called Ohsaki's soil model which can predicts nonlinear response of layered soil is applied to finite element analysis. The Ohsaki's model defines a nonlinear relation between the shear stress and strain for soil as equation (1) (Ohsaki, 1982).

$$\frac{J_2'}{M} = \frac{J_2}{2G_0M} \left(1 + A \left| \frac{J_2}{S_u M} \right|^B \right) \quad (1)$$

where, J_2 , J_2' : second invariants of deviatoric stress and strain

$$J_2 = \frac{1}{2} S_{ij} S_{ij}, \quad J_2' = \frac{1}{2} e_{ij} e_{ij}, \quad S_{ij} = \sigma_{ij} - I_1 \delta_{ij}, \quad e_{ij} = \varepsilon_{ij} - I_1' \delta_{ij}$$

$$A = \frac{G_0}{100S_u} - 1, \quad S_u: \text{maximum shear strength}$$

B; soil type factor (1.4 for clay, 1.6 for sand)

M; hysteric coefficient (1.0 for loading, 2.0 for unloading and reloading)

2.3 Constitutive model for interface between RC and soil

The interaction between soil and structure is affected by the simultaneous dynamic responses of both soil and structure and must be solved by coupled equation of motions for the integrated soil-structure system as a single unit. From a different viewpoint, the soil-structure interaction may be regarded as the energy transfer between soil and structure through the interface. It is obvious that, besides nonlinear behaviors of soil and structure, the interface property also has an influence on the soil-structure interaction. Since soil and structure have different nonlinear behaviors and stiffness characteristics, complete contact at the interface is not always assured. In fact, under reversed cyclic shear, soil and structure do not displace equally, but relative displacements, e.g. sliding and separation, tend to occur along the interfacial zone. These have to be considered as a source of energy dissipation between soil and structure. In order to account for this interfacial kinematics, a model for RC-soil interface is required (Samtani et al., 1996).

Initial interface of soil and structure is naturally in complete contact under static loading conditions

(self-weight, moving load and service load) because of the horizontal earth pressure that soil exerts on the structure. This pressure results from the self-weight of surrounding soil. Although the assumption of perfect bonding between soil and structure surface is acceptable under static conditions, rocking of a structure can cause high tensile and shear stress at soil-structure contact under reversed cyclic loads or strong seismic excitations, which brings about the interface separation and sliding.

2.3.1 Interface model with thickness

The macroscopic interface between structure and soil has no thickness. The interface element without thickness can be suitable for its numerical simulation. However, the sliding of RC-soil interface may occur in soil close to the interface, not exactly along it, so that the interface element without thickness can not simulate deformational behavior near the interface. Therefore, it is necessary to use an interface element with thickness. The slide deformation on the interface may have three forms as below as shown in Fig. 1;

- 1) Slide take place just along the concrete surface if interface is ideally smooth (Fig. 1(a)).
- 2) The slide surface is located in the soil adjacent to the concrete if the concrete surface is rough (Fig. 1(b)).
- 3) There exists a failure area, which consists of a lot of slide surface (Fig. 1(c)).

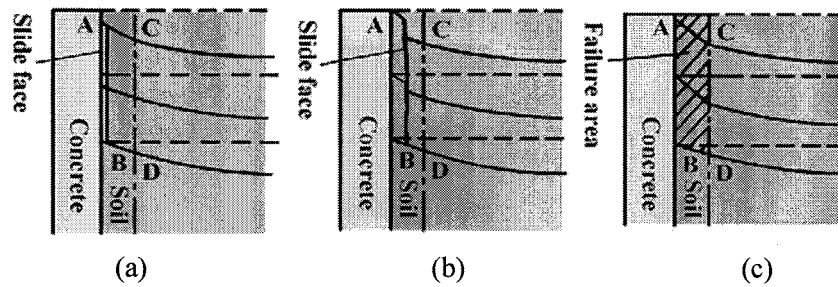


Fig. 1 Three forms of the slide deformation on RC-soil interface

In the Fig. 1, the dotted lines represent the soil surface before deformation, and the solid lines represent it that after deformation. In all these forms, there exists a large relative slide displacement in a narrow area adjacent to the surface, as shown by ABCD in the figure. Thus, interface elements with thickness can simulate the deformation behavior more realistically on the interface together with the narrow adjacent soil area (Yin et al., 1995).

2.3.2 Elastoplastic interface model

The interface behavior involves primarily shear deformation under normal stress (σ_n), and shear stress (τ) as shown in Fig. 2(a). The dominant deformation pattern observed in many interfaces involves a simple shear strain condition as shown in Fig. 2(b), where u and v are deformations in the local x and y coordinate directions, while u_r and v_r are relative shear and normal displacements, respectively. In this paper, the interface is represented by an 8-node rectangular element with a width B , and thickness t as shown in Fig. 2(c). An elastoplastic constitutive equation is applied to the interface element for simulating RC-soil interface behavior (Nam et al., 2006).

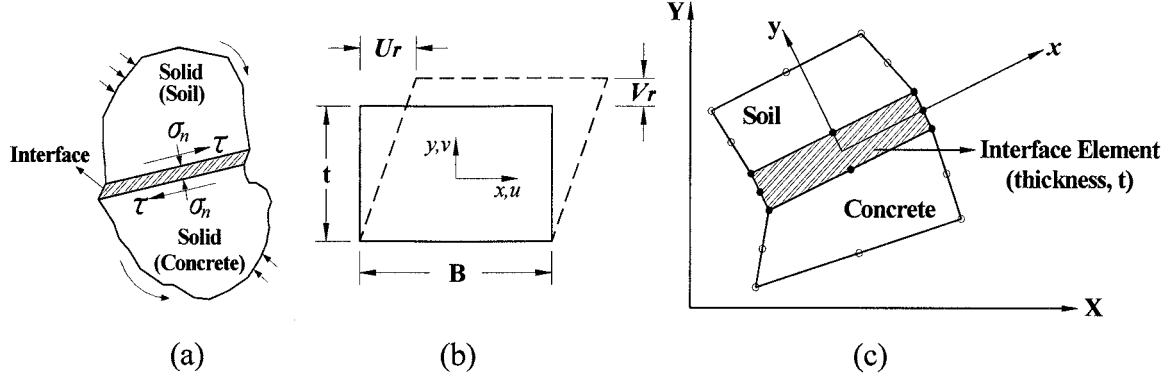


Fig. 2 Formulation of elastoplastic interface model with thickness

After initial yielding, the behavior of interfacial area will be partly elastic and partly plastic. During any increment of stress, the changes of strain are assumed to be divisible into elastic and plastic components as equation (2).

$$d\epsilon_{ij} = (d\epsilon_{ij})_e + (d\epsilon_{ij})_p \quad (2)$$

In equation (2), elastic strain component can be decomposed into their deviatoric and hydrostatic components, and plastic strain component is proportional to the stress gradient of a quantity f called plastic potential. Thus, the complete incremental relationship between stress and strain for elasto-plastic deformation can be written as equation (3).

$$d\epsilon_{ij} = \frac{dS_{ij}}{2\mu} + \frac{(1-2\nu)}{E} \delta_{ij} d\sigma_{kk} + d\lambda \frac{\partial f}{\partial \sigma_{ij}} \quad (3)$$

Equation (3) can be immediately rewritten as equation (4).

$$d\epsilon = [D]^{-1} d\sigma + d\lambda \frac{\partial F}{\partial \sigma} \quad (4)$$

Therefore, we obtain the stress-strain relation as equation (5). So, the complete elasto-plastic incremental stress-strain relation of interface element can be represented as equation (6).

$$d\sigma = D(d\epsilon - d\epsilon^p) = D(d\epsilon - a \, d\lambda) \quad (5)$$

$$d\sigma = D_{ep} \, d\epsilon \quad (6)$$

$$\text{where, } D_{ep} = D - \frac{d_D \, d_D^T}{H + d_D^T a}, \quad d_D = D \, a$$

3. PATH-DEPENDENT VOLUME CONTROL METHOD

3.1 Volume change of shell element

The Volume V of a shell element surrounded by boundary b can be defined as equation (6) using divergence theorem.

$$V = \int_b \mathbf{n}^T \cdot \mathbf{x} \, db \quad (6)$$

Where, $\mathbf{x} = \{x^I, y^I, z^I\}^T$ and \mathbf{n} is a unit vector normal to the element boundary.

The coordinate of shell element subject to external load can be updated as

$$\mathbf{x}'_k = \mathbf{x}_k + \mathbf{u}_k \quad (7)$$

where \mathbf{u}_k is a displacement vector by associated load.

A change in volume by loading history can be obtained from equation (6) using the updated co-ordinate as equation (8).

$$V' = \int_b \mathbf{n}^T \cdot \mathbf{x}'_k db \quad (8)$$

Finally, the pseudo-volume of the shell element can be formulated as equation (9), and presented as equation (10) using shape function N.

$$\Delta V = V' - V \quad (9)$$

$$\begin{aligned} \Delta V &= \int_b \mathbf{n}^T \cdot \mathbf{u}_k db \\ &= \left(\int_{b^e} \mathbf{n}^T \cdot N db^e \right) \mathbf{U}_k \end{aligned} \quad (10)$$

Where, $\mathbf{u}_k = N \mathbf{U}_k$.

3.2 Pressure node formulation

The basic idea of pressure node formulation for the so-called volume control method is as follows. The pressure node has a single degree of freedom, namely, the uniform change of pressure on finite shell element, denoted by Δp (Song and Tassoulas, 1994). Thus, a multi-layered shell element in this study has 49-degree-of-freedom by adding a pressure node to 8-noded multi-layered shell element that has 6-degree-of-freedom per node. Since the traction increment $\Delta \mathbf{t}$ on element boundaries due to Δp is approximated by $-\Delta p \mathbf{n}$ as equation (11), the traction term in the element load vector is given by equation (12).

$$\Delta \mathbf{t} \cong -\Delta p \mathbf{n} \quad (11)$$

$$\int_{b^e} N^T (\mathbf{t} + \Delta \mathbf{t}) db^e = -(p + \Delta p) \int_{b^e} N^T \mathbf{n} db^e \quad (12)$$

Multi-layered shell element with a pressure node can be formulated as equation (13) satisfying equilibrium condition in pressure-volume relation with traction term in the load vector of finite element method.

$$\mathbf{K}_e \mathbf{U}_k = -(p + \Delta p) \int_b N^T \mathbf{n} db^e + \mathbf{F}_e \quad (13)$$

Absorbing the term involving Δp into the stiffness matrix in equation (13) and inserting an additional equation (10) for the change in volume, the element equilibrium equation with matrix form is now given by equation (9).

$$\begin{bmatrix} \mathbf{K}_e & \int_{b^e} N^T \mathbf{n} db^e \\ \int_{b^e} \mathbf{n}^T N db^e & 0 \end{bmatrix} \begin{bmatrix} \mathbf{U}_k \\ \Delta p \end{bmatrix} = \begin{bmatrix} -\mathbf{p} \int_{b^e} N^T \mathbf{n} db^e + \mathbf{F}_e \\ \Delta V \end{bmatrix} \quad (14)$$

The last row and column in modified stiffness matrix correspond to the additional degree of freedom, while the load vector now contains an additional component ΔV . The presence of ΔV in the load vector indicates the change in volume enclosed by structures and determines the required change in pressure. Thus, by controlling the volume in non-linear iterative analysis, the required increase or decrease in pressure along equilibrium paths around the ultimate point of pressure can be calculated.

The technique can overcome the instability problem of the conventional force-control method as well as the difficulty of selecting a local characteristic point to control the local displacement which governs the global behavior of shell structures in the conventional displacement-control method (Song and Tassoulas, 1994). An iterative procedure based on Newton-Raphson method is applied to the volume control technique. The iterations are repeated until external volume increment by means of load equilibrated with internal volume change due to associated deformation within a prescribed tolerance for every step during non-linear analysis. Therefore, the displacement increment \mathbf{U}_k and pressure increment Δp by external volume increment ΔV^{ext} can be decided from equation (15).

$$\begin{bmatrix} \mathbf{U}_k \\ \Delta p \end{bmatrix} = \begin{bmatrix} \mathbf{K}_e & \int_{b^e} \mathbf{N}^T \mathbf{n} db^e \\ \int_{b^e} \mathbf{n}^T \mathbf{N} db^e & 0 \end{bmatrix}^{-1} \begin{bmatrix} -p \int_{b^e} \mathbf{N}^T \mathbf{n} db^e + \mathbf{F}_e \\ \Delta V_m^{ext} \end{bmatrix} \quad (15)$$

Internal volume increment ΔV_i^{int} can be obtained from displacement increment \mathbf{U}_k . Internal volume increment ΔV_i^{int} and external volume increment ΔV^{ext} should satisfy with volume equilibrium equation (16) in the step $t + \Delta t$. If not, divergence volume increment ΔV_i^R is calculated, and iterations are repeated after ΔV_i^R turns into external volume increment.

$${}^{t+\Delta t}V^R - {}^{t+\Delta t}V^{int} = 0 \quad (16)$$

$$\Delta V_i^R = \Delta V_m^{ext} - \Delta V_i^{int} \quad (17)$$

Namely, divergence volume increment ΔV_i^R is included in load vector in next iteration step, and displacement increment $\delta \mathbf{U}^{i+1}$ and pressure increment δp^{i+1} are decided by equation (15). Total displacement increment and total pressure increment in one step is given by equation (18). Fig. 3 presents the iterative flow for path-dependent volume control method.

$$\begin{aligned} \mathbf{U}^{i+1} &= \mathbf{U}^i + \delta \mathbf{U}^{i+1} \\ \Delta p^{i+1} &= \Delta p^i + \delta p^{i+1} \end{aligned} \quad (18)$$

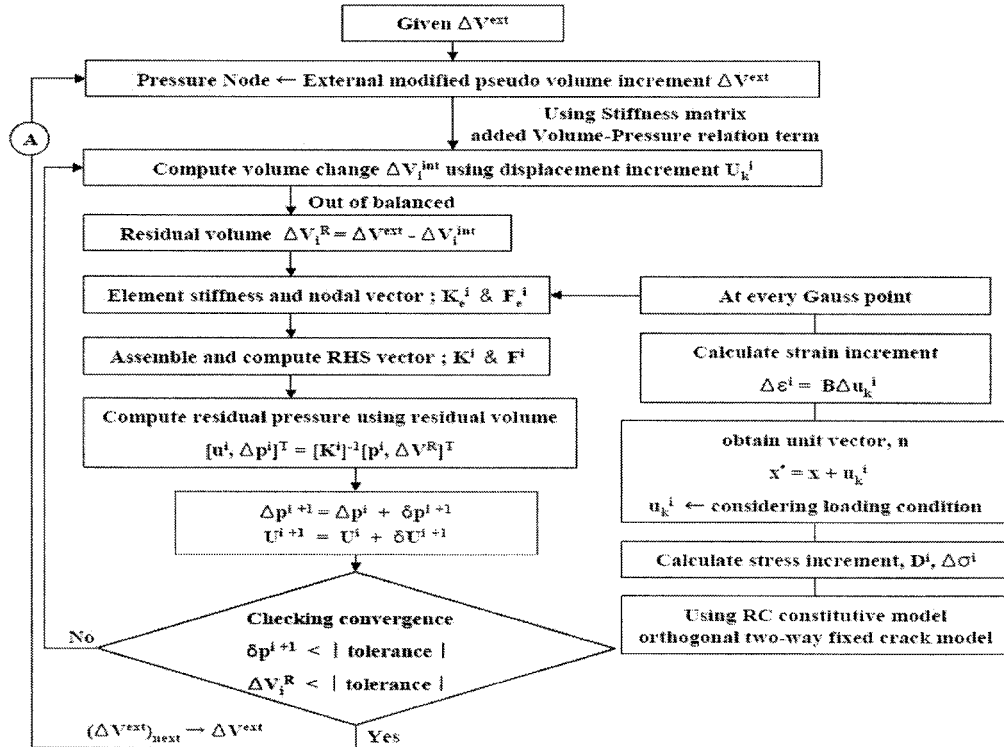


Fig. 3 Flow chart for path-dependent volume control iterative method

3.3 Path-dependent volume control method

In path-dependent volume control method, volume change is modified according to loading history (loading, unloading, reloading) until it satisfies convergence condition. Tangent stiffness matrix is calculated step by step in iteration procedure, and volume changes under loading, unloading and reloading conditions are modified automatically by the gradient of tangent stiffness matrix.

As shown in Fig. 2, applied pressure (or load) on V_{next} normalized by initial volume depends on deformation history of structure. So volume change is given by equation (19)

$$V_{next} = f(P_{1next}, P_{2next}, P_{3next}) \quad (19)$$

Therefore, in path-dependent volume control method, it can have three different pressure values in same volume according to deformation history of the structure. It can also be known that control volume for next step depends on the deformation history of the structure. Fig. 4 presents the analysis flow of overall path-dependent volume control method.

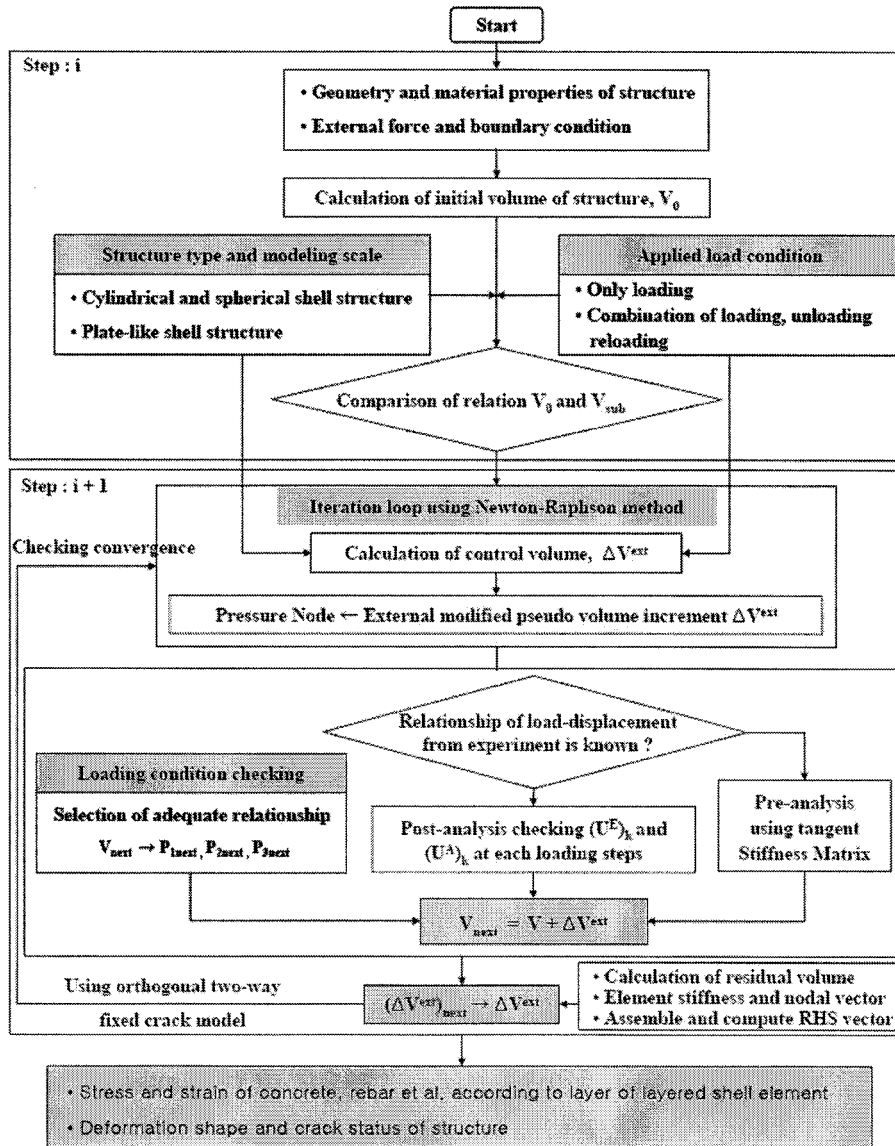


Fig. 4 Flow chart for overall path-dependent volume control method

4. SEISMIC ANALYSIS OF RC SUBWAY STATION STRUCTURE

4.1 Target RC structure for analysis

Fig. 5 shows the shape and dimension of the two-story box culvert section consisting of sidewalls, top and bottom slabs and intermediate columns. The intermediate column has a rectangular cross-section of $0.7 \times 1.4\text{m}$ for the upper level and $0.6 \times 1.5\text{m}$ for the lower level, with the average reinforcement ratio of 6.0%. The columns are idealized as completely fixed to the slabs. The whole structure is located inside the soil with 5.0m soil surcharge.

The finite element discretization is also shown in Fig. 5. Both soil and RC underground structures are represented by 8-node isoparametric two-dimensional elements. And the earthquake wave used as the input for seismic analysis was recorded at the Kobe meteorological observatory. The Kobe wave has maximum horizontal wave of 818gal and maximum vertical wave of 332gal with a very short period.

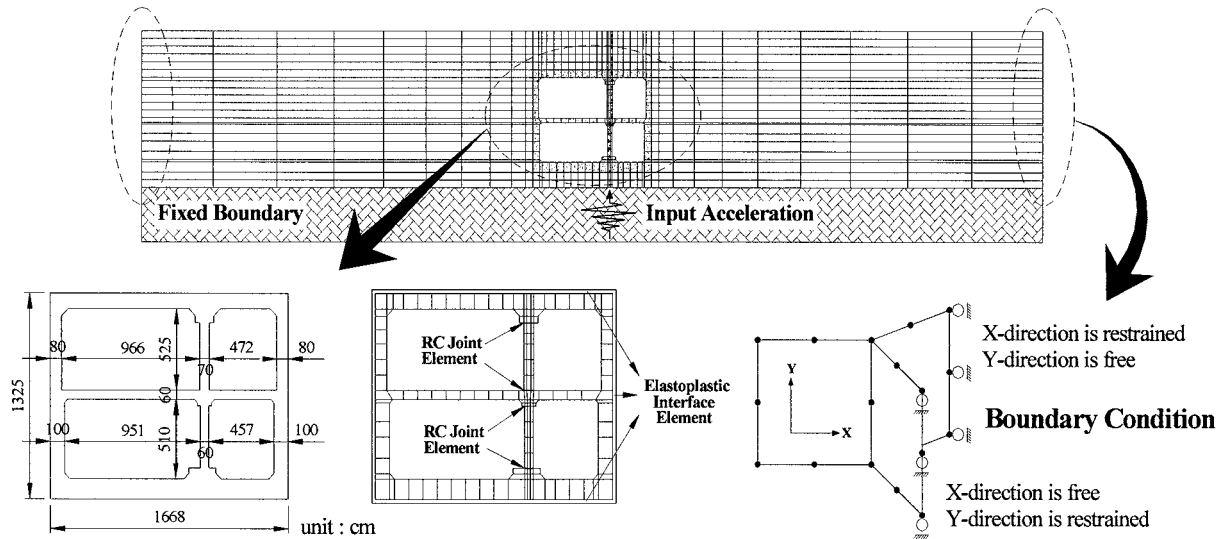


Fig. 5 Finite element mesh of RC-soil system and boundary condition

4.2 Collapse simulation

4.2.1 Damage level

The analysis was performed with different reinforcement ratios of intermediate column as shown in Table 1 to investigate the behavior of structure including the change of shear capacity and ductility. Fig. 6 shows the average induced shear force to RC and Fig. 7 shows the inelastic strain of the RC frames in time domain. These indexes are used to qualitatively present how much damage to the RC structure and how much deformation resided after the dynamic action, respectively. The figures show the difference of failure time in each case, i.e., RC structure with low shear strength due to less web reinforcement was failed, but the RC structure with higher shear strength and ductility survived during the earthquake.

Table 1 Variation of reinforcement ratio in intermediate column for each case

Reinforcement Ratio	Case A	Case B	Case C
Longitudinal Reinforcement	5.1%	5.1%	3.67%
Web Reinforcement	0.15%	0.76%	0.76%

4.2.2 Crack pattern and failure mode

To clearly identify the failure mode and the location of failure, the crack pattern of the structure and the deformation profile were investigated. As shown in Fig. 8 and Fig. 9, it can be seen that large cracks are concentrated in the upper column in case A. On the contrary, the lower column and other parts of the structures have just a few cracks. All cracks shown in this figure were computationally predicted at the failure step. It can clearly be seen that very large shear cracks appear at this step in the upper column only, which finally brings to failure. In case B, the deformation is concentrated at the corner of the RC outer frame and the failure took place at the upper slab accompanying diagonal cracking. Unlike the case A, no localization of deformation occurred in the column since it was more strongly reinforced in shear. In case C, the induced shear stress to slab is decreased by reducing the flexural capacity of the column and increased ductility by use of less longitudinal reinforcement. This is simply because the moments at the column end become lower, thus inducing lower moments and shear forces on the connecting slabs. It can be concluded that both the shear capacity and the ductility are important factors in seismic resistant performance.

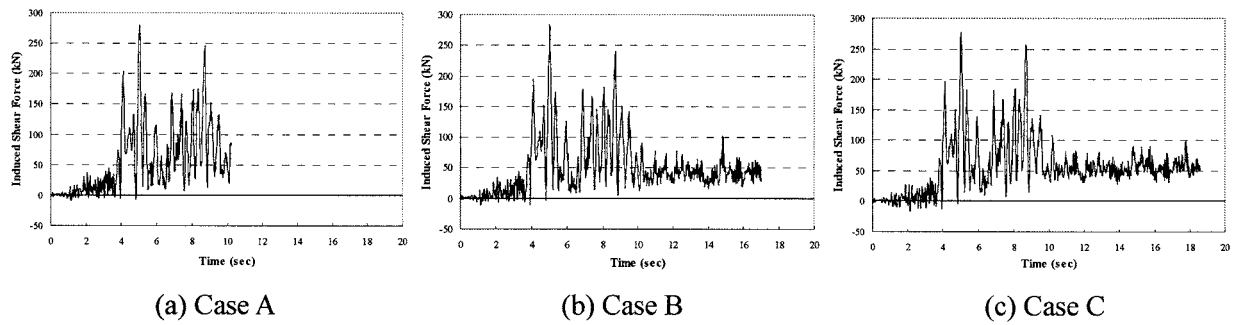


Fig. 6 Average induced shear force to RC

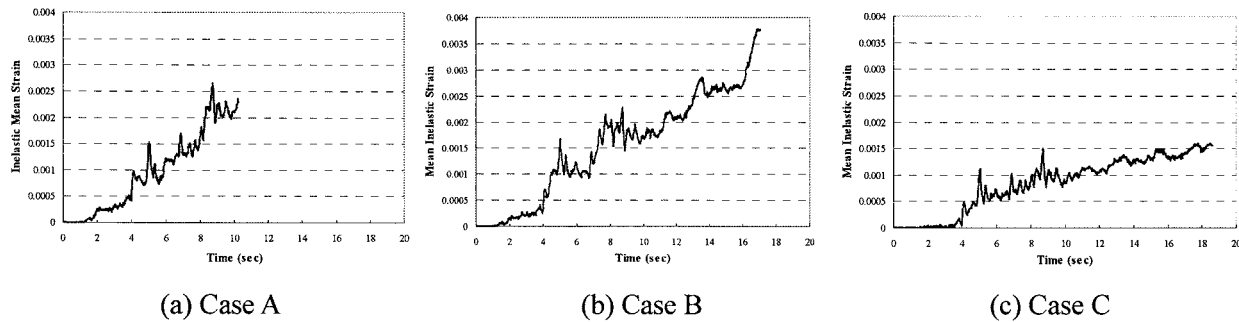


Fig. 7 Inelastic strain representing damage in time domain

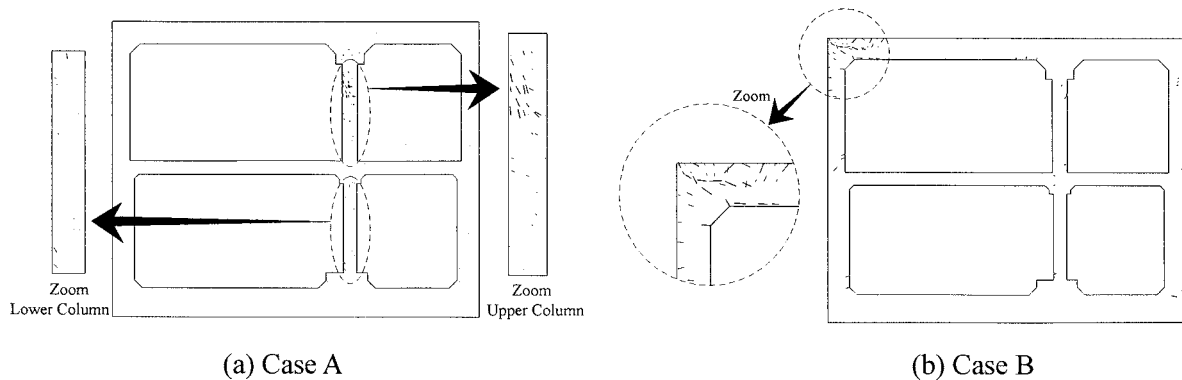


Fig. 8 Crack pattern of RC structure at the failure

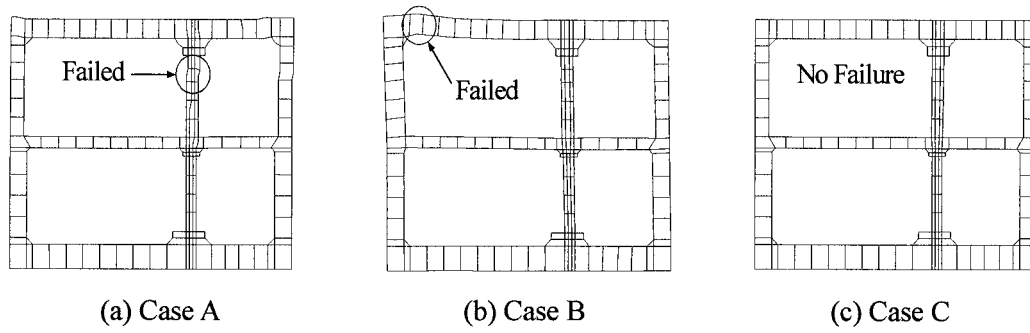


Fig. 9 Deformation profile of RC structure

5. NONLINEAR ANALYSIS OF RC STRUCTURES USING PATH-DEPENDENT VOLUME CONTROL METHOD

5.1 RC box culvert subjected to cyclic loading

A test conducted on RC box culvert subjected to reversed cyclic load at the University of Tokyo (Irawan, 1995) is selected to verify the applicability of path-dependent volume control method. Fig. 10 shows the details of RC box culvert and finite element discretization.

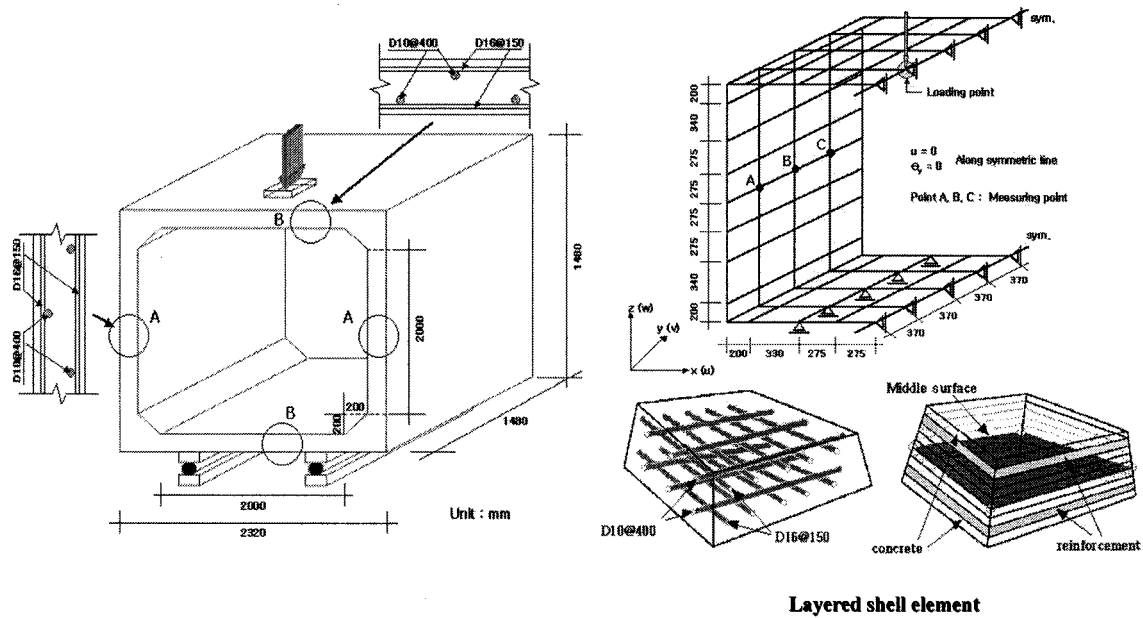


Fig. 10 Details of RC box culvert specimen and finite element discretization

The bar spacing is 150mm each side in the height direction (main reinforcement volumetric ratio of 1.87%, D16), and 400mm each side in the depth direction (side reinforcement volumetric ratio of 0.27%, D10). For the top and bottom slab, the main reinforcement volumetric ratio in the width direction is 1.66% and the side reinforcement volumetric ratio in the depth direction is 0.24%. Material properties of concrete and steel bars are given in Table 2. Tensile strength of concrete is assumed as 1/12 of compressive strength.

Table 2 Material properties of RC box culvert

Concrete		Reinforcement	
f'_c (MPa)	50	f_y (MPa)	400
f_t (MPa)	4.12	Yield strain (μ)	1,900
E_c (MPa)	32,438	E_s (MPa)	205,800

Comparison of experimental and analytical (path-dependent volume control method) results are shown in Fig. 11 for the load-displacement relations at the loading point. Generally, the analysis could predict all experimental results well in both load-displacement envelopes and cyclic loops.

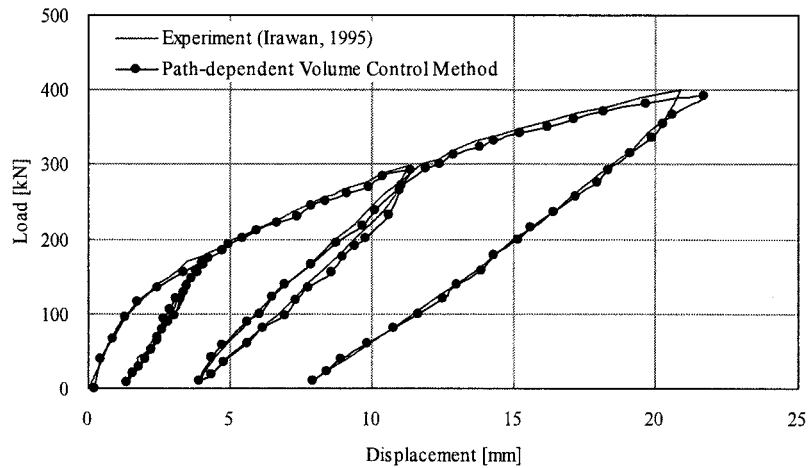


Fig. 11 Load-displacement relation at loading point of box culvert

5.2 Reinforced concrete cylindrical tank subjected to reversed cyclic loading

Harada et al.(2001) tested a reduced-scale lightly reinforced RC tank subjected to reversed cyclic loading to investigate its deformation capacity and failure characteristics. The specimen is a cylindrical RC tank, as shown in Fig. 12. The reinforcement ratios in circumferential and vertical directions are 0.8%, equal in both directions. Properties of concrete and steel bars are given in Table 3.

The load is applied to the specimen by a ventral hydraulic jack and two actuators at the loading plate attached to the top of specimen. The applied loading is reversed cyclic, applied at 0° and 180° to the faces as shown in Fig. 12. Taking advantage of symmetry, only half of the tank needs to be discretized for the finite element analysis. For each element, 7 concrete layers and 2 reinforcing bar layers were used for the integration along the depth of three-dimensional multi-layered shell element.

The comparison of experimental and analytical results is presented in Fig. 13. The analysis result is in a fair agreement with experimental facts. Under horizontal reversed cyclic loading, in-plane diagonal cracks are formed and the stiffness gets reduced.

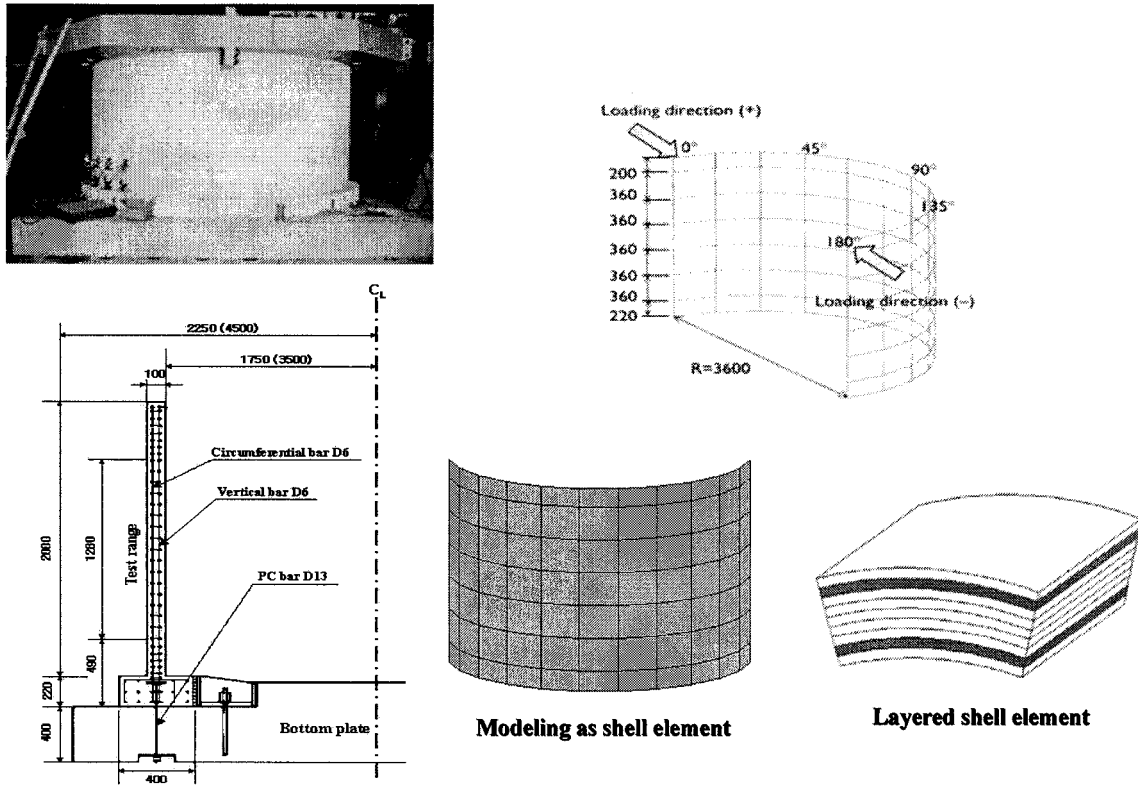


Fig. 12 Shape of RC tank and finite element discretization

Table 3 Material properties of RC tank

Concrete		Reinforcement	
f'_c (MPa)	28	f_y (MPa)	386
f_t (MPa)	2.2	Yield strain (μ)	1,900
E_c (MPa)	22,600	E_s (MPa)	200,000

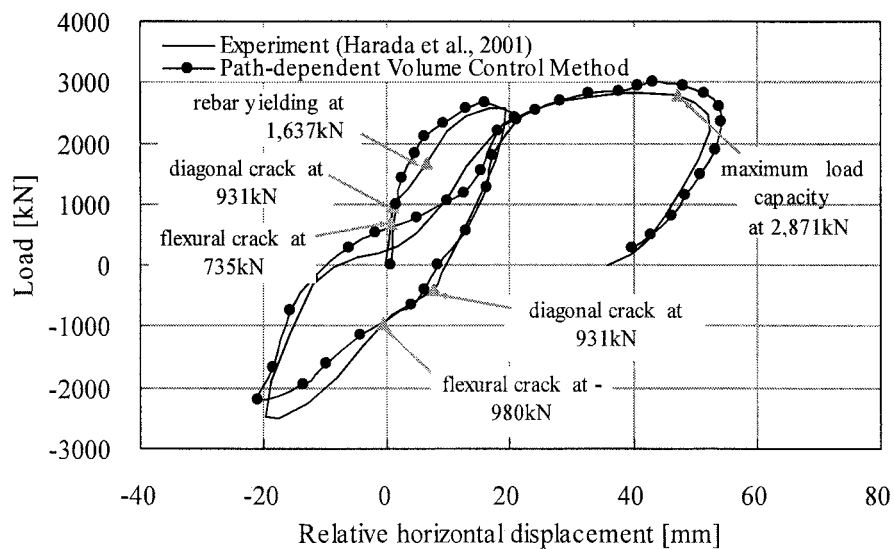


Fig. 13 Load-displacement relationship of RC tank

5.3 Reinforced concrete hollow column subjected to reversed cyclic loading

An experiment on the RC square and circular full-size hollow columns subjected to reversed cyclic loading were performed by Cheng et al (2003). The square column has a 150 x 150cm cross-section with 90 x 90cm hole in the center. The circular column has a 150cm outer diameter and 90cm inner diameter. The column heights are 4m for square one, and 6m for circular one. Columns are longitudinally reinforced with 64D22 bars. The specimens were tested under constant axial load 3,600kN, representing $0.08 f'_c A_g$ for rectangular section and $0.1 f'_c A_g$ for circular section. And then reversed cyclic loading is applied to 50cm away from top of the column with sequential displacement increments. Fig. 14 shows specimen layouts and reinforcement arrangements of square and circular hollow columns.

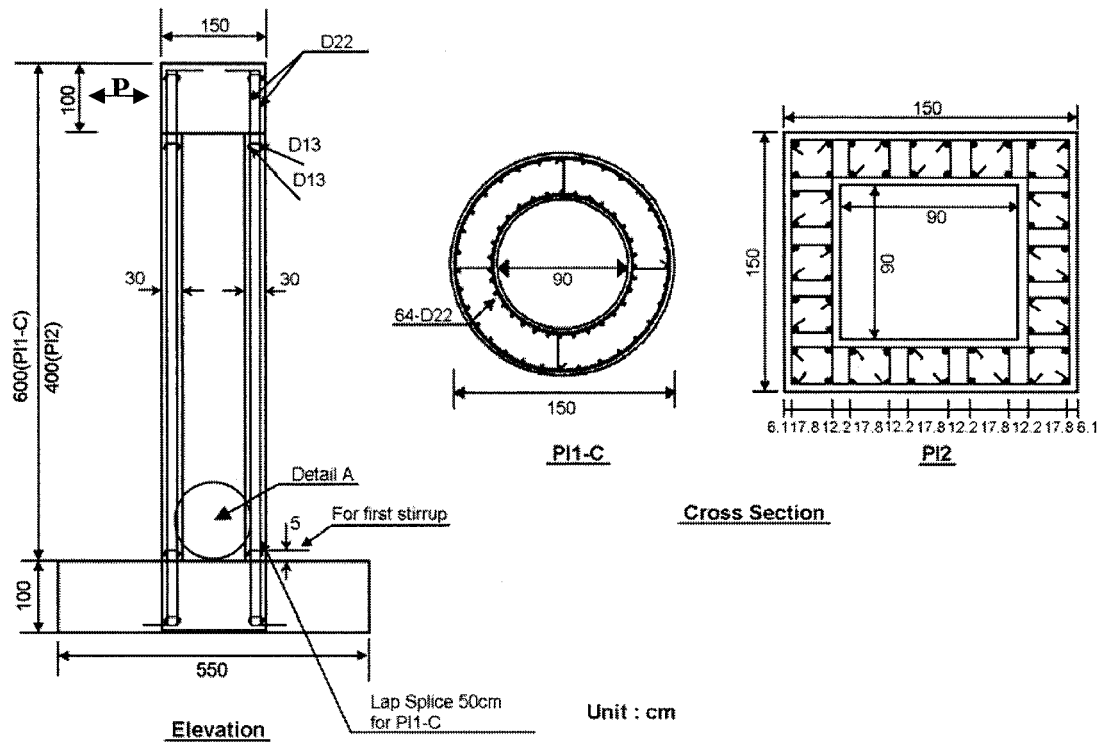


Fig. 14 Details of RC square and circular hollow columns

The hollow parts of columns are modeled by 40 shell elements (square one) and 120 shell elements (circular one). And then upper solid parts are modeled by solid elements. Reinforcement layer is composed of two-way orthogonal reinforcement with an equal amount of top and bottom reinforcement to make a same condition with experiment. Material properties and reinforcement ratios are given in Table 4 and Table 5 for square and circular hollow columns each.

Comparisons of analytical and experimental results conducted on RC square and circular hollow columns under reversed cyclic loading are given in Fig. 15 and Fig. 16, respectively. As shown in the figures, analysis results by path-dependent volume control method predict the experimental results with good agreement.

Table 4 Material properties of square column

Concrete		Reinforcement		
			Longitudinal bar	Stirrup bar
f'_c (MPa)	32.6	f_y (MPa)	423.3	392
f_t (MPa)	3.21	f_u (MPa)	531	483
E_c (GPa)	21.7	E_s (GPa)	200	200
ν	0.18	ρ (%)	1.01	0.26

Table 5 Material properties of circular column

Concrete		Reinforcement		
			Longitudinal bar	Stirrup bar
f'_c (MPa)	33.8	f_y (MPa)	418.2	410
f_t (MPa)	3.35	f_u (MPa)	514.3	507
E_c (GPa)	21.7	E_s (GPa)	200	200
ν	0.18	ρ (%)	1.72	0.29

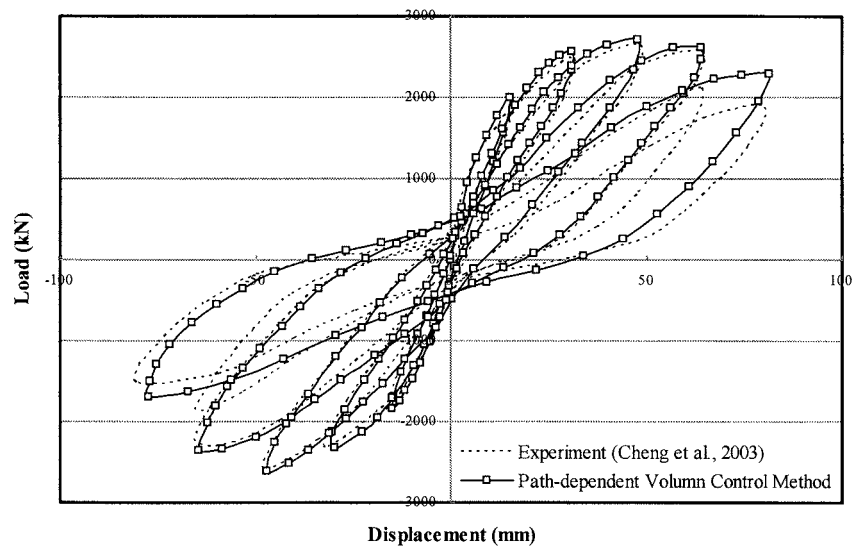


Fig. 15 Comparison of analytical and experimental result (square column)

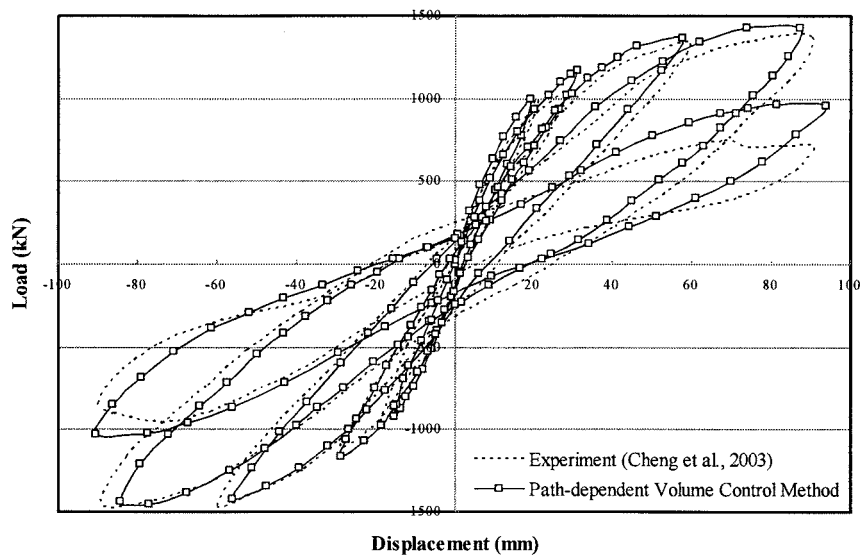


Fig. 16 Comparison of analytical and experimental result (circular column)

6. CONCLUSIONS

For the performance based design and evaluation of RC structures subjected to both static and dynamic loading including seismic loading, the analysis should be carried out for an entire structural system rather than for individual members by considering interface between structure and surrounding soil media if an RC structure is underground RC subway station structure. The nonlinear finite element analysis can be an effective tool for the performance based design and evaluation. For the nonlinear finite element analysis of RC structures, an effective solution technique which can predict post-peak behavior of RC structures after peak strength due to geometrical and material nonlinearity including cracking is also necessary. In this paper, an elasto-plastic interface element with thickness is developed, and failure mechanisms and crack patterns of underground RC station structure subjected to seismic load are numerically derived through seismic analysis of underground RC station structure considering elasto-plastic interface model with thickness. It is shown that the shear capacity and the ductility of underground RC structures which were obtained quantitatively from the analysis are important factors for the design of underground RC structure to have higher seismic resistant performance. The path-dependent volume control technique has been also presented for the failure analysis of reinforced concrete structures. Through layered formulation for a layered shell element equipped with a pressure node, path-dependent constitutive models of cracked concrete were successfully utilized. The path-dependent volume control technique implemented in nonlinear finite element method can be used to analyze the nonlinear behavior of RC structures according to the loading path and loading history effectively. The validity of proposed analysis technique is verified by comparing analytical results with experimental data on RC box culvert, RC tank, and RC hollow columns subjected to cyclic load or reversed cyclic load.

Acknowledgements:

The authors gratefully acknowledge support from a Infra-Structure Assessment Research Center (ISARC) and a research group for improving the performance of bridge (IPET Bridge), Korea.

References:

- Aghayere, A. O. and MacGregor, J. G. (1990), "Tests of Reinforced Concrete Plates under Combined In-Plane and Transverse Loads", *ACI Structural Journal*, **87**(6), 615-622.
- An X. (1996), "Failure Analysis and Evaluation of Seismic Performance for Reinforced Concrete in Shear", Ph.D. Dissertation, University of Tokyo, Tokyo, Japan.
- Cheng, C. T., Yang, J. C., Yeh, Y. K. And Chen, S. E. (2003), "Seismic Performance of Repaired Hollow-Bridge Piers", *Construction and Building Materials*, **17**, 339-351.
- Hara, T., Shigematsu, T., Kusunoki, M. and Kuboyama, H. (2000), "Numerical Analysis of Cylindrical Shell under Cyclic Loading", *6th Asian Pacific Conference on Shell and Spatial Structures*, 557-564.
- Hara, T., Shigematsu T., and Tamura T. (2003), "Behavior of R/C cylindrical shell under lateral load", *Structural Engineering and Mechanics*, **16**(3), 361-369.
- Harada, M., Onituka, S., Adachi, M., and Matsuo, T. (2001), "Experimental Study on Deformation Performance of Cylindrical Reinforced Concrete Structure", *Proceedings of Japan Concrete Institute*, **23**(3), 1129-1134.
- Irawan, P. (1995), "Three Dimensional Analysis of Reinforced Concrete Structures", PhD Thesis, University of Tokyo, Tokyo, Japan.
- Irawan, P. and Maekawa, K. (1997), "Path-Dependent Nonlinear Analysis of Reinforced Concrete Shells", *Proceedings of JSCE*, **34**(557), 121-134.
- Maekawa K., Pimanmas P., and Okamura H. (2003), "Nonlinear Mechanics of Reinforced Concrete", Spon Press.
- Nam S. H., Song H.-W., Byun, K. J., and Maekawa K. (2006), "Seismic analysis of underground reinforced concrete structures considering elasto-plastic interface element with thickness", *Engineering structures*, **28**, 1122-1131.
- Ohsaki, Y. (1982), "Dynamic Nonlinear Model and One-Dimensional Nonlinear Response of Soil Deposits", *Research Report 82-02*, Dept. of Architecture, University of Tokyo.
- Okamura H. and Maekawa K. (1995), "Nonlinear Analysis and Constitutive Models of Reinforced Concrete", Gihodo-Shuppan, Tokyo, Japan.
- Owen D. R. J. and Hinton E. (1980), "Finite Elements in Plasticity : Theory and Practice", Pineridge Press Limited, U.K.
- Samtani N. C., Desai C. S., and Vulliet L. (1996), "An Interface Model to Describe Viscoplastic Behavior," *International Journal for Numerical and Analytical Methods in Geomechanics*, **20**, 231-252.
- Shawky A. A. (1994), "Nonlinear Static and Dynamic Analysis for Underground Reinforced Concrete", Ph.D. Dissertation, University of Tokyo, Tokyo, Japan.
- Song, H.-W., Bang, J. Y., Byun, K. J., and Choi, K. R. (1999), "Finite Element Analysis of Reinforced Concrete Reactor Containment Vessels subjected to Internal Pressure", *Transactions of the 15th International Conference on Structural Mechanics in Reactor Technology (SMiRT-15)*, Seoul, Korea, Aug. 15-20, VI341-348.
- Song, H.-W., Shim, S. H., Byun, K. J., and Maekawa, K. (2002a), "Failure Analysis of RC Shell Structures using Layered Shell Element with Pressure Node", *Journal of the Structural Engineering*, **128**(5), 655-664.
- Song, H.-W., Shim, S. H., Byun, K. J. (2002b), "Finite Element Analysis of Prestressed Concrete Containment Vessel subjected to Internal Pressure", *Proceeding of the Third DIANA World Conference*, Tokyo, Japan.
- Song, H.-W. and Tassoulas, J. L. (1994), "Large Deformation Buckle Analysis of an Inelastic Ring under External Pressure", *Computers and Structures*, **51**(2), 225-233.
- Yin Z. Z., Zhu H., and Xu G. H. (1995), "A Study of Deformation in the Interface between Soil and Concrete", *Computers and Geomechanics*, **17**, 75-92.

RC PILE FOUNDATION-SOIL INTERACTION ANALYSIS USING 3-D FINITE ELEMENT METHOD

T. Maki¹⁾, R. Tuladhar²⁾ and H. Mutsuyoshi³⁾

1) Associate Professor, Department of Civil and Environmental Engineering, Saitama University, Japan

2) JSPS Post Doctoral Fellow, Department of Civil and Environmental Engineering, Saitama University, Japan

3) Professor, Department of Civil and Environmental Engineering, Saitama University, Japan

maki@post.saitama-u.ac.jp, rabin@mtr.civil.saitama-u.ac.jp, mutuyosi@mtr.civil.saitama-u.ac.jp

Abstract: Seismic behavior of a structure is highly influenced by the response of the foundation and the ground. Hence, the modern seismic design codes stipulate the analysis of an overall structural system considering soil-structure interaction. In this paper, 3D FEM analysis was carried out to study the behavior of the pile and soil during earthquakes. Numerical simulations were carried out based on the two different experimental studies: a) Cyclic loading test of RC model piles embedded into sandy soil and b) lateral loading test on real-scale piles embedded into cohesive soil. The 3D FEM analysis used in the study could adequately simulate the behavior of the experimental specimens.

1. INTRODUCTION

For the development of comprehensive analytical tools for structures considering soil-structure interaction, it is first important to clarify the pile-soil interaction during earthquakes. Presently available analytical tools mostly simplify the soil media as discrete spring models. The discrete spring models, however, ignores the soil continua, and hence, can not take the damping and inertial effect of soil into account. On the other hand, 3-D finite element analysis (FEM) inherently takes soil continua into consideration. Moreover, the nonlinearities of soil and pile can be modeled more rigorously in 3-D FEM analysis (Wakai et al. 1999). There are still various issues which have to be addressed for the successful implementation of 3-D FEM analysis for pile-soil interaction problems. With this in view, comprehensive 3-D FEM analysis has been carried out to study the seismic behavior of reinforced concrete pile and soil.

In this study, numerical simulations were conducted using 3-D FEM analysis for the two different experiments: a) Cyclic loading test of RC model piles embedded into sandy soil, and b) Lateral loading test of real-scale PC piles embedded into cohesive soil. In all of the analyses cases, both pile and soil were modeled by 20-node solid element. The paper addresses various issues that have to be taken into consideration for sandy soil and cohesive soil for the accurate simulation of seismic behavior of pile and soil during earthquakes.

2. NUMERICAL SIMULATION OF LATERALLY LOADED RC PILES EMBEDDED INTO SANDY SOIL

2.1 Lateral Cyclic Loading Test of Single RC Piles

Figure 1(a) shows the experimental setup (Maki and Mutsuyoshi 2004). A single RC pile specimen with square cross section was fastened to a rigid steel box, and the box was filled with dry sand having

a uniform grain diameter. The properties of the sand are listed in Figure 1(c). Lateral reversed cyclic displacements were applied at the pile head through a loading actuator. A constant axial load was applied at the pile head by a vertical loading jack during lateral loading. The pile specimen was securely fastened to the bottom of the steel box to prevent rotation, whereas the pile head was allowed to rotate freely. Overall soil deformation was confined by the rigid steel box during loading. Although this soil condition differs from the real condition, it was chosen to provide clear boundary conditions so that the results could be used in subsequent analyses.

The experimental parameters consisted of the longitudinal reinforcement ratio, the axial stress level and the relative density of soil. All the six experimental cases are summarized in Table 1. Figure 1(b) shows the cross section of the specimen. All of the specimens had an equal width of 100 mm in the loading direction. Deformed bars having a diameter of 6 or 10 mm were used as longitudinal reinforcements and deformed bars having a diameter of 3.2 mm were arranged with 100 mm spacing as lateral reinforcements. The relative density of the soil was controlled in the experiment, and the resulting values of density are listed in Table 1.

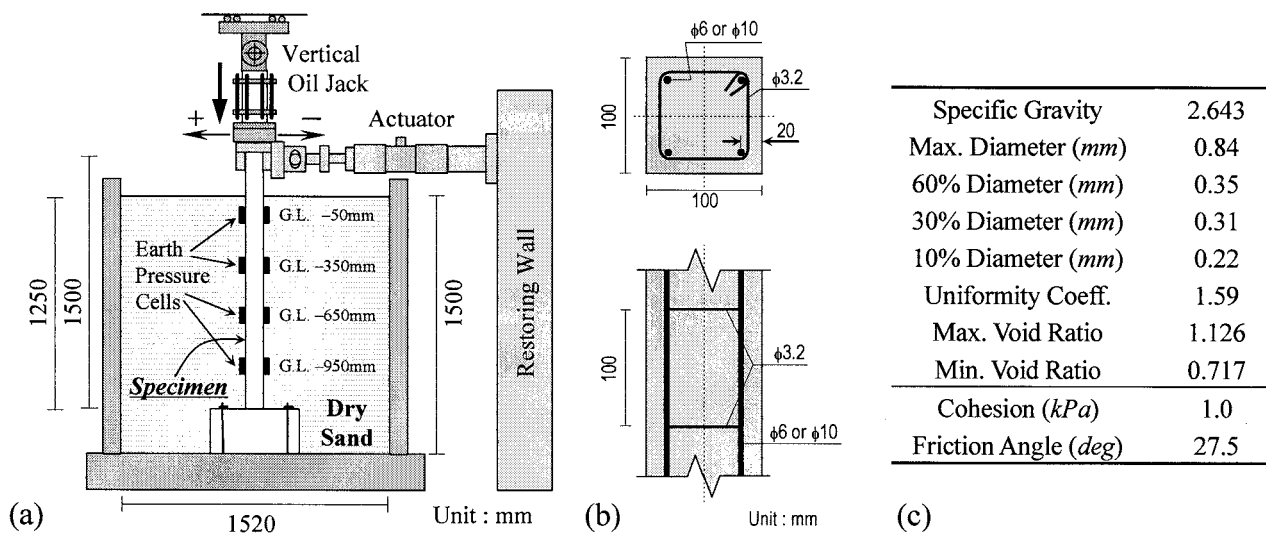


Figure 1 (a) Loading Setup, (b) Cross Sectional Detail of Specimen, and (c) Properties of Sand

Table 1 Experimental Variables

Case	Pile Specimen			Soil		Note
	ρ_s (%)	f'_c (MPa)	σ'_n (MPa)	D_r (%)		
RX-0-L	2.85 ^{*1}	43.0	0	55.5	Loose	ρ_s : Longitudinal Reinforcement Ratio ^{*1} : 4- ϕ 10 ($f_y = 345$ MPa) ^{*2} : 4- ϕ 6 ($f_y = 345$ MPa) ^{*3} : 4- ϕ 6 ($f_y = 295$ MPa)
RR-0-L	1.27 ^{*2}	45.3	0			
RR-2-L	1.27 ^{*3}	46.6	2			
RR-0-D	1.27 ^{*2}	42.3	0	70.3	Dense	f'_c : Compressive Strength of Concrete σ'_n : Axial Stress applied at Pile Head D_r : Relative Density of Sand
RR-2-D	1.27 ^{*3}	45.5	2	83.2		
RR-4-D		52.6	4	86.4		

2.2 Numerical Models

Figure 2(a) shows the FE mesh used in the numerical simulations of the laterally loaded RC piles. Based on the assumption of symmetry, 1/2-model was applied in the simulation here. The pile specimen and the soil were modeled using 20-node isoparametric solid elements. For the pile specimen, RC solid element was applied, which was formulated by the three-dimensional nonlinear

path-dependent constitutive laws for reinforced concrete proposed by Okamura and Maekawa (1991, 2003).

The Osaki's model (Osaki 1980) was used as a nonlinear constitutive model for soil, which defines the relationship between the second deviatoric stress invariant J_2 and strain invariant J_2' as shown in

$$\frac{J_2'}{M} = \frac{J_2}{2G_0M} \left\{ 1 + \left(\frac{G_0}{100S_u} - 1 \right) \left| \frac{J_2}{S_uM} \right|^B \right\} \quad (1)$$

where G_0 is the initial shear modulus, S_u is the shear strength at 1% shear strain, B is the material parameter (1.6 for sand and 1.4 for clay), and M is the loading parameter (1.0 when loading, and 2.0 when unloading and reloading). The initial shear modulus (G_0) and the shear strength (S_u) were determined from the experimental conditions by using the following equation (2):

$$G_0 = 630 \frac{(2.17 - e)^2}{1 + e} \sigma_c^{0.321} \quad (2)$$

where G_0 is in kgf/cm^2 , σ_c is the initial confining pressure in kgf/cm^2 , and e is the void ratio. The average (volumetric) component in the formulation of soil element was assumed to be linear elastic, in which the volumetric elasticity was calculated from the initial shear modulus and Poisson's ratio (a constant value of 0.3 is assumed). In this soil material model, the effect of confinement (average stress state) on the shear behavior was ignored.

16-node joint interface element, as shown in Figure 2(b), was placed between RC element and soil element in order to consider contact, separation and shear slip at the surface of the pile. This interface element had high rigidity in compression (close) to avoid excess overlapping of the elements, while small values were given for the tensile (open) and two directional in-plane shear rigidities.

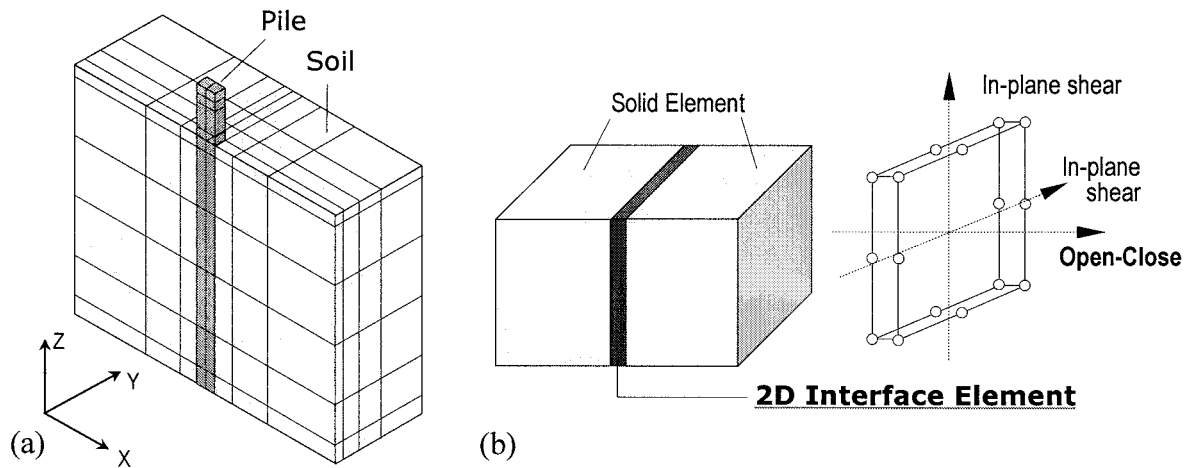


Figure 2 (a) Finite Element Mesh, and (b) Configuration of Interface Element

2.3 Analytical Results and Discussions

The hysteresis and skeleton curves of the lateral load and displacement relationships are shown in Figure 3 and Figure 4, respectively. The calculated skeleton curves had a reasonably good agreement with the experimental ones. However, thinner shapes of the inner hysteresis loops could be observed in the analytical results. Figure 5 shows the variations of the equivalent damping factors calculated from the hysteresis curves. The factors in the analyses for the cases without axial load were underestimated by about 10% compared with those in the experiments, whereas 15% or more underestimation could be observed in the cases with axial load. In the experiment, dry sand was used as soil media; however,

the Ohsaki's model cannot properly simulate the effects of hysteretic behavior of dry sand soil. Therefore, more reasonable result will be obtained if the soil model is modified. From the macroscopic point of view, it can be concluded that the applied analytical method is verified for the nonlinear behavior of laterally loaded small-scale piles under ground.

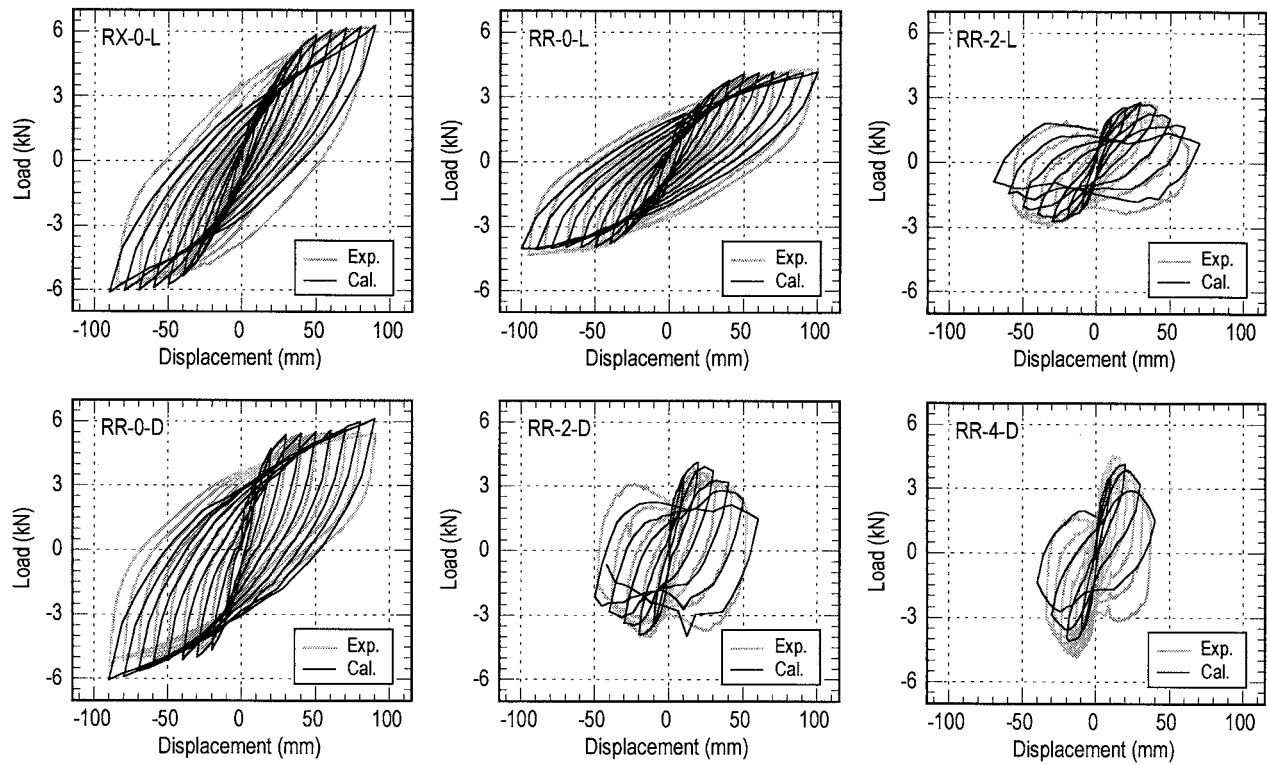


Figure 3 Load and Displacement Relationships of RC Pile Specimens

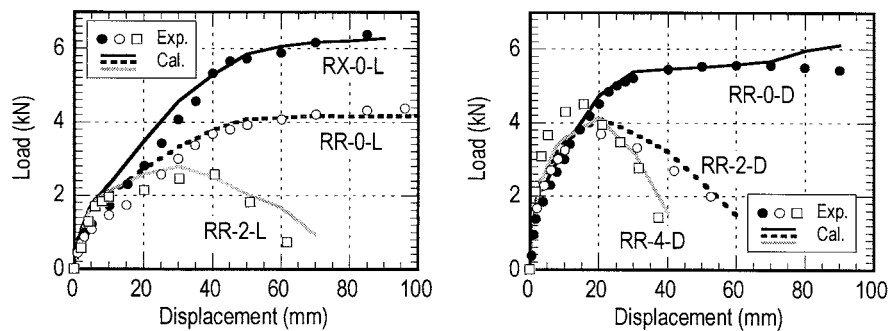


Figure 4 Skeleton Curves of Load and Displacement Relationships

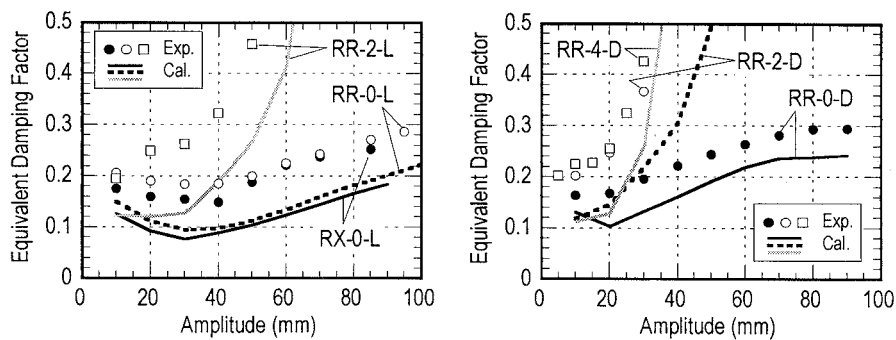


Figure 5 Variations of Equivalent Damping Factors

3. NUMERICAL SIMULATION OF Laterally LOADED REAL-SCALE CONCRETE PILES EMBEDDED INTO COHESIVE SOIL

3.1 Lateral Loading Test of Real-Scale PC Piles

Lateral loading test was carried out on two real-scaled concrete piles embedded into the ground. One of the test piles was subjected to monotonic loading (A-1), whereas, another test pile was subjected to reversed cyclic loading (A-2). Both of the test piles were hollow precast prestressed concrete piles with a diameter of 450mm and a thickness of 70mm, as shown in Figure 6(a). Twelve prestressing deformed tendons of 7mm diameter were used as longitudinal reinforcement, and spiral hoops with 3mm diameter were placed with 100mm pitch as confining reinforcement. Compressive strength of concrete was 79MPa and yielding stress of longitudinal prestressing steel was 1325MPa. The effective prestress on the piles was 5MPa. The bending test of the pile was carried out by using a 8m-long pile with the same cross-sectional properties as the test piles. The moment-curvature curve from the bending test is shown in Figure 6(b).

Piling was carried out by inside drilling method. Auger with 270mm diameter was inserted into the hollow pile and drilling was carried out inside the pile while the pile was installed into the ground. The test pile were embedded up to 12.8m from the ground level (GL), and the height of the pile head was 1.2m from GL. Lateral monotonic or cyclic displacements were applied at the height of 0.6m from GL. Figure 7 shows the experimental setup in the loading tests. Reaction frames were setup on six reaction piles. The reaction piles were driven up to the depth of 10m from GL.

The standard penetration test (SPT) was carried out at the experimental site to investigate the relevant soil parameters. The N-SPT values obtained from the test are shown in Figure 8 along with the soil type. The depth of water-table was 1.3m from GL.

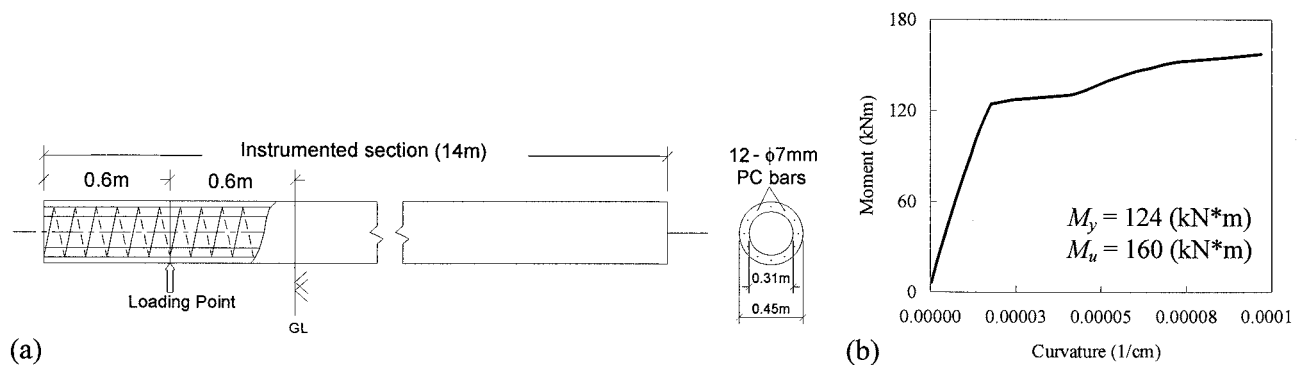


Figure 6 (a) Detail of Pile Specimen, and (b) Test Result of Bending Test

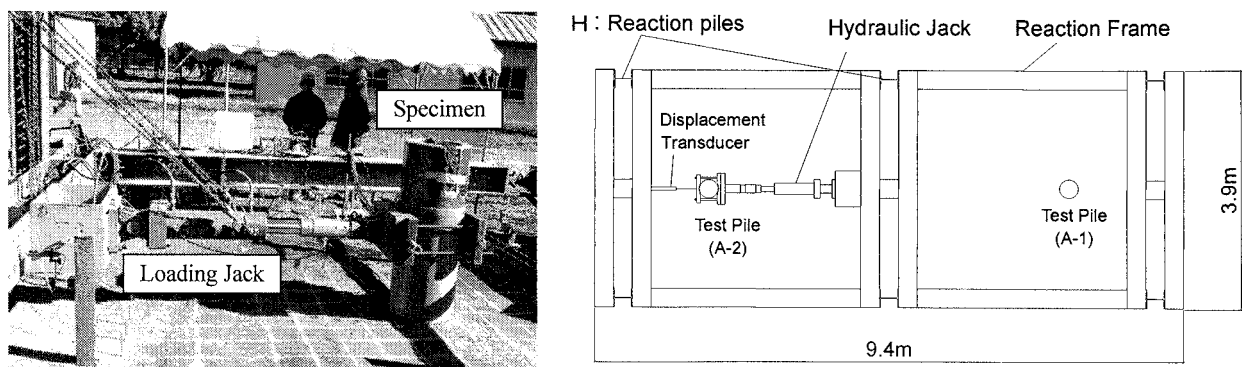


Figure 7 Loading Test Setup

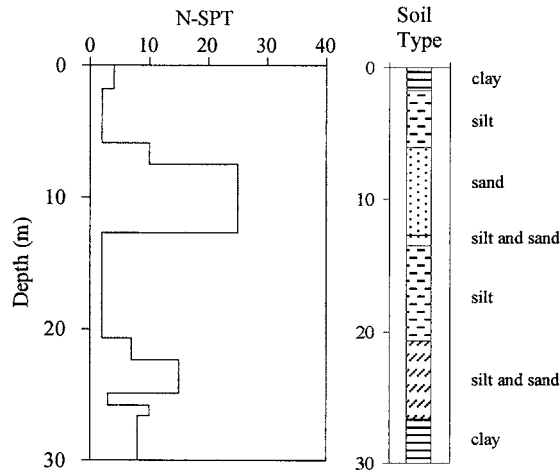


Figure 8 Soil Profile at Test Site

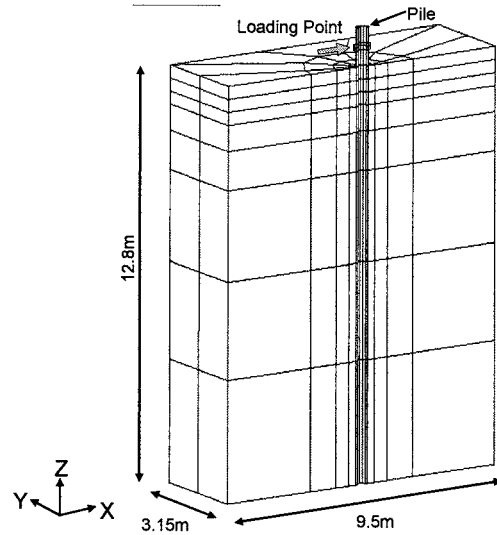


Figure 9 Finite Element Mesh

3.2 Numerical Models

Figure 9 shows the FE mesh used in the numerical simulations of the laterally loaded RC piles. Based on the assumption of symmetry, 1/2-model was applied in the simulation here. The pile specimen and the soil were modeled using 20-node isoparametric solid elements, similarly as the modeling in the previous section. The pile specimen was modeled with RC solid element, whereas the soil was modeled by the soil solid element with the Osaki's model (Osaki 1980). The depth of the model was 12.8m, equal to the embedded length of the pile. The widths of the model in x- and y-direction were 9.5m and 3.15m, respectively, which were 20D and 7D, respectively, where D is a diameter of the pile. The initial shear modulus (G_0) and the shear strength (S_u) were calculated by the following equations (3) and (4):

$$G_0 = 11.76 N^{0.8} \quad (3)$$

$$\begin{aligned} S_u &= G_0 / 1100 \text{ (for Sand)} \\ &= G_0 / 600 \text{ (for Clay)} \end{aligned} \quad (4)$$

where G_0 and S_u are in MPa, and N is the N-SPT value. 16-node joint interface element was placed between RC element and soil element, similar to the previous numerical model.

3.3 Analytical Results and Discussions

Figure 10(a) and 10(b) show the analytical results of load-displacement relationships. For the monotonic loading test, the analytical result had a good agreement with the experimental one. On the contrary, the analysis overestimated the lateral load in the reversed cyclic loading case, although the same finite element mesh was used.

The reduction in shear modulus and undrained shear strength in soft clay due to cyclic loading has been studied by means of undrained cyclic triaxial and simple shear tests on clay by several researchers (Thiers and Seed 1968, etc.). Thiers and Seed (1968) observed from cyclic shear testing on clay specimen that for constant peak shear strain, shear modulus decreases with number of cycles. Shear modulus was found to decrease approximately 20% for peak strain of 1% while reduction was about 50-80% for peak strain of 3%. It was also observed that undisturbed shear strength of clay was reduced by 10% at peak strain level of 2% to 3%. Theirs concluded that cyclic straining has little effect on soil shear strength; however, it has considerable effect on shear modulus of clay.

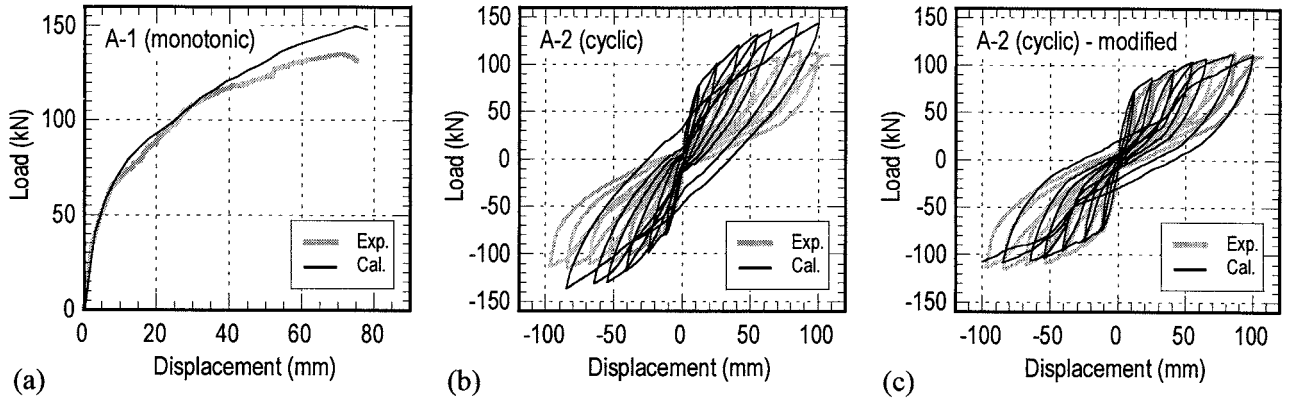


Figure 10 Load-Displacement Relationships for (a) A-1, (b) A-2, and (c) A-2 with Modified Model

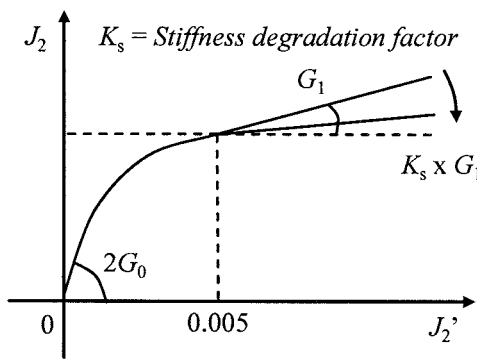


Figure 11 Concept of Stiffness Degradation Factor

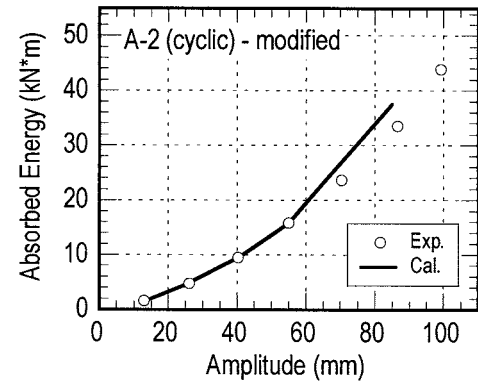


Figure 12 Variation of Absorbed Energy

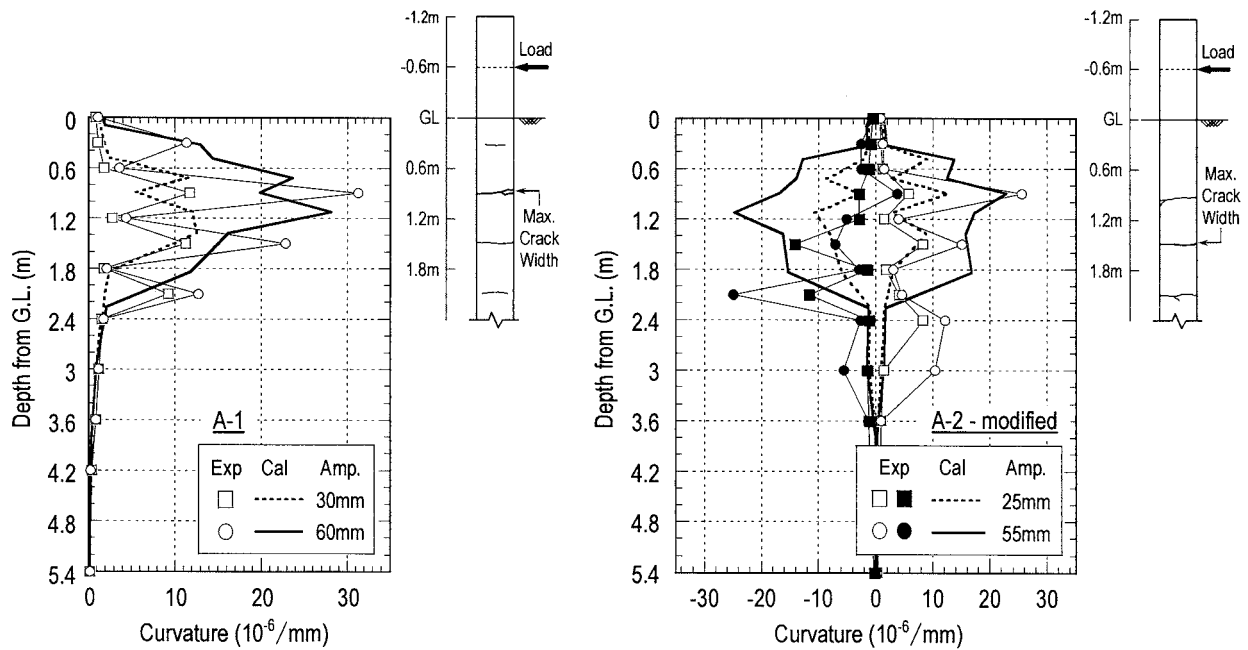


Figure 13 Curvature Distributions along the Depth and Crack Patterns of the Piles

In the Ohsaki's soil model applied in the current analysis, the shear stress-strain relationship was formulated only up to 1% engineering shear strain level. Therefore, constant shear modulus G_1 , which

is equal to the tangential stiffness at 1% shear strain, was assumed even after 1% strain in the analysis, as shown in Figure 11. In order to incorporate the above-mentioned stiffness degradation due to cyclic loading, the shear modulus after 1% shear strain was reduced parametrically using stiffness degradation factor (K_s) considering the experimental result.

Figure 10(c) shows the modified analytical result of the load-displacement relationship with the stiffness degradation factor K_s equal to 0.2. This result tends to agree with the experimental result, as well as the result of the absorbed energy does, as shown in Figure 12. Hence, the stiffness degradation of clay due to cyclic loading should be considered to accurately calculate the cyclic behavior of piles.

Figure 13 shows the curvature distributions and the crack patterns of the piles along the depth. The experimental results of curvature values were calculated from the strains of the prestressing bars inside the piles. In the curvature diagrams, the experimentally-obtained distributions exhibited zigzag shape due to strain localization of the prestressing bars at the cracks. In both cases A-1 and A-2, maximum curvature occurs at around 1.2m from the GL which agrees well with the experimental observations.

4. CONCLUSIONS

In this study, numerical simulations using 3-D finite element analysis were conducted for the two different experiments. One was the cyclic loading test of RC model piles embedded into sandy soil, and the other was the loading test of real-scale PC piles embedded into cohesive soil. In the analysis, both pile and soil were modeled by 20-node solid element. The analysis verified that 3D FEM analysis can accurately simulate the behavior of pile-soil interaction.

For the case of lateral loading test on RC model piles embedded into sandy soil, the 3D FEM analysis could adequately simulate the skeleton of load displacement hysteresis curves. The equivalent damping factors for the hysteresis curves were, however, underestimated from the analysis compared to the experimental results. More reasonable results can be expected by improving the Ohsaki's model to incorporate the affects of dry sand soil. On the other hand, for the case of lateral loading test on real-scale RC piles embedded into cohesive soil, the analytical results could accurately simulate the monotonic behavior of pile. However, for the reversed cyclic loading, the analysis could accurately simulate the load displacement curve only after considering the degradation of stiffness of soil due to cyclic loading. The next stage of this research is to investigate its applicability of 3D FEM to simulate the behavior of group pile foundations and the dynamic analysis for overall response of structure-foundation-soil system.

Acknowledgements:

The authors acknowledge support provided by Prof. Koichi Maekawa of The University of Tokyo for using 3-D nonlinear FE program COM3 in this study, as well as cooperation in the experimental works made by the members in the Structural Material Laboratory in Saitama University.

References:

- Wakai, A., Gose, S., and Ugai, K. (1999), "3-D Elasto-plastic Finite Element Analysis of Pile Foundations Subjected to Lateral Loading", *Soils and Foundations*, Japanese Geotechnical Society, **39**(1), 97-111.
- Maki, T. and Mutsuyoshi, H. (2004), "Seismic Behavior of Reinforced Concrete Piles under Ground," *Advanced Concrete Technology*, **2**(1), 37-47.
- Maekawa, K., Pimanmas, A., and Okamura H. (2003), "Nonlinear Mechanics of Reinforced Concrete," Spon Press, London.
- Ohsaki, Y. (1980), "Some notes on Masing's Law and Non-linear Response of Soil Deposits," *Journal of the Faculty of Engineering*, The University of Tokyo, **35**(4), 513-536.
- Thiers, GR. and Seed, HB. (1968), "Cyclic stress-strain characteristics of clay, Journal of the Soil Mechanics and Foundation Division," *Proceedings of the American Society of Civil Engineers*, **94**(SM2), 555-569.

MULTI-LEVEL SEISMIC PERFORMANCE ASSESSMENT OF A DAMAGE-PROTECTED BEAM-COLUMN JOINT WITH INTERNAL LEAD DAMPERS

K. M. Solberg ¹⁾, B.A. Bradley ²⁾, J.B. Mander ³⁾, R. P. Dhakal ⁴⁾, G.W. Rodgers ⁵⁾, J.G. Chase ⁶⁾.

1) M. E. Candidate, Department of Civil Engineering, University of Canterbury, NZ

2) Ph.D. Candidate, Department of Civil Engineering, University of Canterbury, NZ

3) Professor, Department of Civil Engineering, University of Canterbury, NZ

4) Senior Lecturer, Department of Civil Engineering, University of Canterbury, NZ

5) Ph.D. Candidate, Department of Mechanical Engineering, University of Canterbury, NZ

6) Professor, Department of Mechanical Engineering, University of Canterbury, NZ

kms@mka.com, bab54@student.canterbury.ac.nz, rajesh.dhakal@canterbury.ac.nz, john.mander@canterbury.ac.nz,
gwr37@student.canterbury.ac.nz, geoff.chase@canterbury.ac.nz.

Abstract: A multi-level seismic performance assessment is performed on a near full scale beam-column subassembly. The physical model is taken from a 3D exterior connection of a jointed precast concrete frame structure that is designed for damage avoidance. Unbonded post-tensioned prestress is provided by high-alloy high-strength thread-bars. Draped and straight tendon profiles are used in the transverse and orthogonal directions, respectively. The joint region is armoured to avoid damage by providing steel plates at the beam-column contact points. Supplemental energy dissipation is provided by high-performance lead-damping devices cast internally in each beam. Bi-directional quasi-earthquake displacement profiles are applied meaning the input displacement profiles are taken directly from the results of inelastic dynamic analysis. Three input earthquakes are selected probabilistically to represent multiple levels of seismic demand. Results from physical testing are critically discussed.

1. INTRODUCTION

Research and development of jointed precast concrete structures has gained considerable momentum over the past two decades, with significant research on so-called PRESSS systems being conducted in the United States for buildings (Priestley et al., 1999) and Damage Avoidance Design (DAD) bridges (Mander and Cheng, 1997). These systems, which exhibit non-linear response by connection opening rather than by the formation of a ductile plastic hinge, have markedly less inherent energy dissipation than ductile monolithic systems. Therefore, supplemental energy dissipation devices are often provided to help reduce displacement response from earthquakes. Various dissipation devices have been investigated (Stanton et al., 1997; Amaris et al., 2006), and are limited by the fact that, for various reasons, they must be replaced following a seismic event. It then becomes apparent that a more robust form of energy dissipation is needed which satisfies several objectives: (i) the damper should not be at risk of low-cycle fatigue fracture; (ii) the damper should, ideally, be located internally within the beam-end region; (iii) residual compression forces in the damper device should creep back towards zero over time; and (iv) the damper device should be economically feasible.

In response to these objectives, the application of *lead-extrusion* (LE) dampers was developed as part of this study. To provide a reliable form of energy dissipation and an architecturally pleasing finish, LE dampers (Cousins and Porritt, 1993) are buried within the beam-end regions. Attention is given to the detailing of the joint region to reduce materials and improve constructability while still

adhering to the overall objective of ensuring that elements remain damage-free.

This paper presents results of an experimental study using a *Multi-Level Seismic Performance Assessment* (MSPA) of a 3D subassembly, where earthquakes representing multiple levels of seismic demand are selected probabilistically from a comprehensive computational incremental dynamic analysis (IDA).

2. EXPERIMENTAL INVESTIGATION

2.1 Subassembly Development

An 80 percent scale 3D subassembly representing an interior joint on a lower floor of a 3x3-bay 10-storey building was developed. The subassembly consisted of two beams cut at their midpoints and an orthogonal beam cut at its midpoint (the approximate location of the point of contraflexure). All beams were 560mm deep and 400mm wide and all framing into a central 700mm square column. The orthogonal beam, referred to herein as the gravity beam, was designed for one-way precast flooring panels, while the other two beams, referred to herein as the seismic beams, were designed for predominantly seismic forces.

Prestress was provided by two 26.5mm MacAlloyTM thread-bars ($f_y = 1100\text{MPa}$). The prestress system in the seismic direction utilized a straight profile, along the longitudinal axis of the beams. The thread-bars in the gravity beam were draped to provide load balancing with the gravity loading from the one-way floor panels. Shear from gravity and seismic loads were carried by four 30mm shear keys located at each corner of the connecting beam. Details of the longitudinal and transverse reinforcement are given in Figure 1.

A 300mm cast insitu 'wet' joint was provided at the end of each beam. The detailing strategy of the cast insitu joint in the seismic direction is illustrated in Figure 2a. This joint was designed to accommodate the LE damper with maximum dimensions of 150mm by 150mm. This space was provided in the centre of the joint in the seismic beams, and at a 50mm offset from centreline in the gravity beam. A 180PFC channel was used top and bottom to provide the armouring contact surface. The channel also served as a means of mechanically anchoring the longitudinal reinforcing. This was accomplished by providing cuts on the interior flange of the channel whereby the longitudinal thread-bar reinforcing steel could be locked into it using nuts. Furthermore, these nuts provided a means of adjusting the channel flush with the column face during final on-site fabrication. Four 25x10x500mm rods were welded in the corners of each flange. These were provided to help stiffen the joint region to ensure rocking behaviour occurred in a rigid manner. Finally, four 1m threaded rods were spaced at 100mm centres to provide an attachment and anchoring point for the LE damper device.

One of the primary objectives of this study was to improve beam-column joint detailing by improving constructability. In the column, end-plates were sized to provide a full contact surface for the beam's armouring (180 PFC channel, see Figure 2a), and to provide a 10mm extension on all sides. In keeping with *Damage Avoidance Design* (DAD) principles, the column end-plate design was checked to ensure concrete crushing in the column did not occur at the design strength of the connection.

2.2 The lead-extrusion dampers

Supplemental damping was provided by LE dampers, as shown in Figure 3. A single LE damper was designed to fit within in the ends of each beam (Figure 2a). A 30mm rod with one threaded end was used as the damper shaft (Figure 3a). This rod was designed to be coupled to a threaded rod in the column of the same size. Four 18mm threaded rods at 100mm centres were cast into the beam-end and used to anchor the device during the closure pour. The holes on the devices were oversized to allow the device to be adjusted when coupled to the threaded rod in the column.

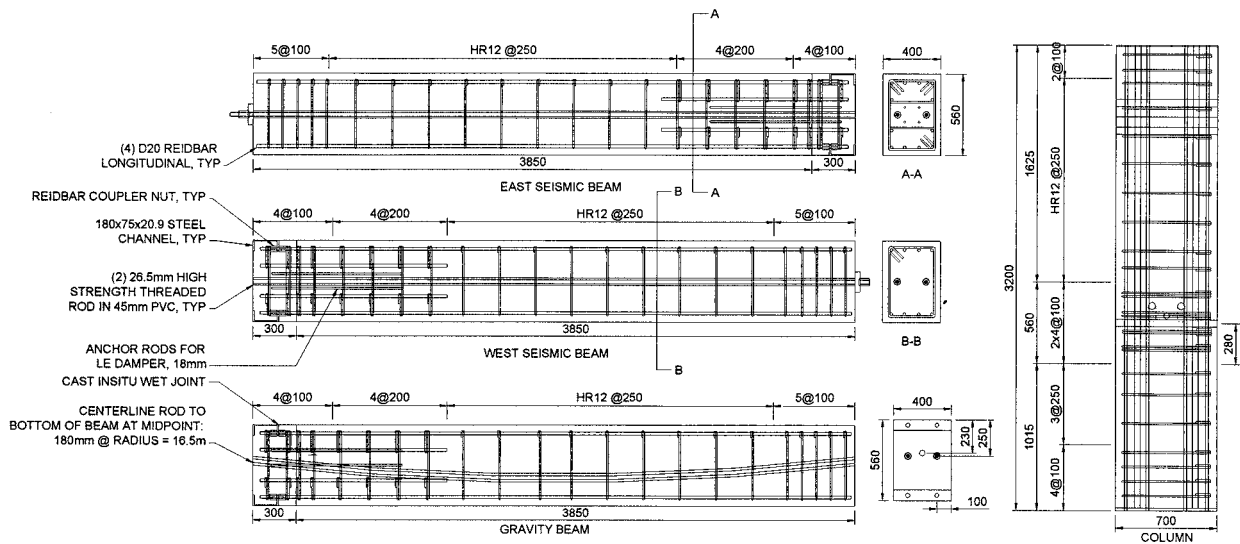
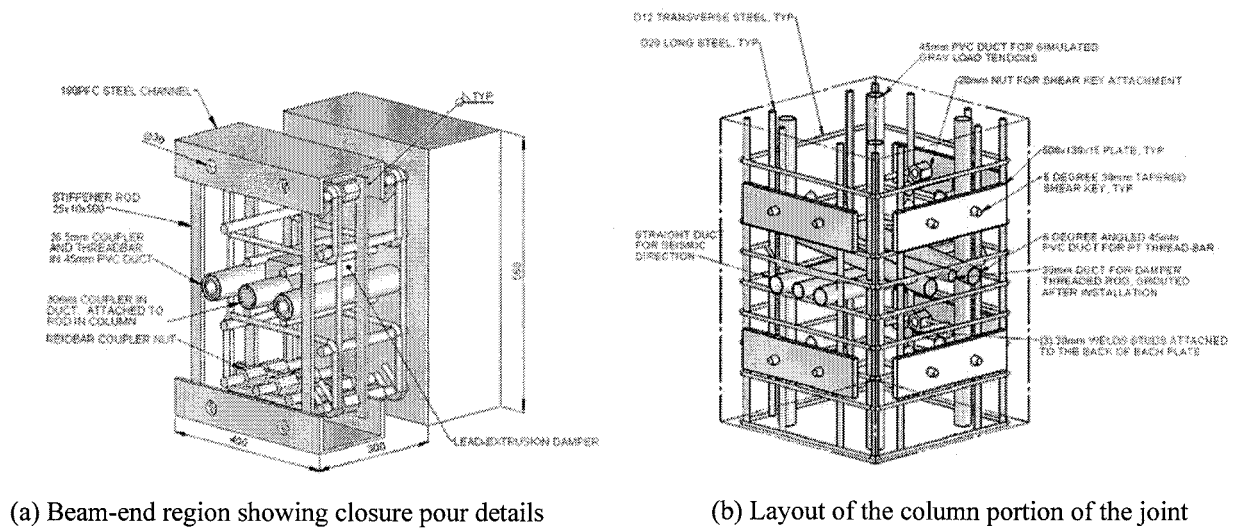


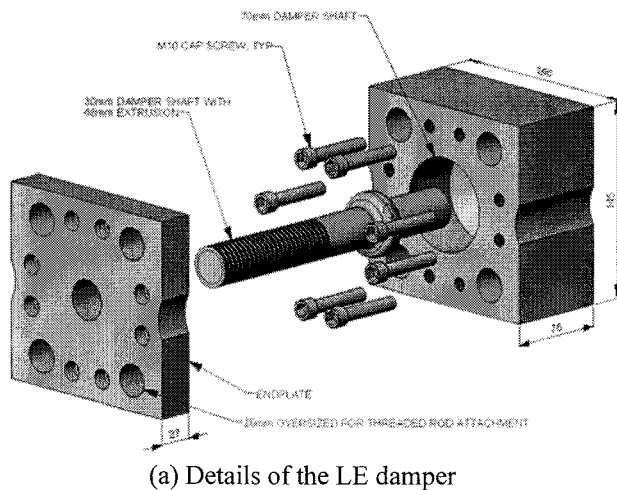
Figure 1: Reinforcement details of the beam-column subassembly elements



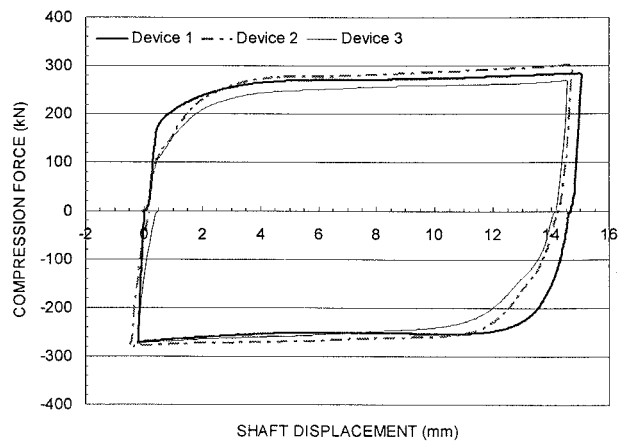
(a) Beam-end region showing closure pour details

(b) Layout of the column portion of the joint

Figure 2: Components of the precast beam-column joint region



(a) Details of the LE damper



(b) Force-displacement response of the damper

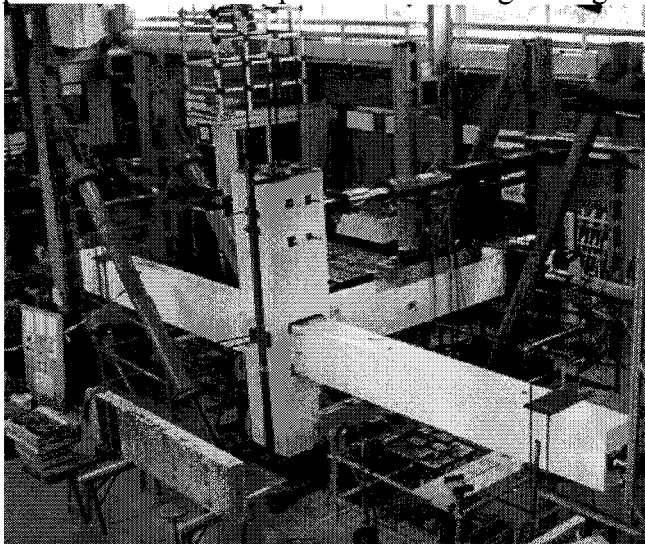
Figure 3: Details and results of the LE damper

Given the initial prestress force of 250kN per thread-bar, the dampers were designed for a 250kN yield force. This corresponds to a re-centering moment ratio of 1.23 and 1.06 in the NS direction for positive and negative moment, (considering over-strength in the dissipator and reduced prestress force) and 1.13 in the EW direction.

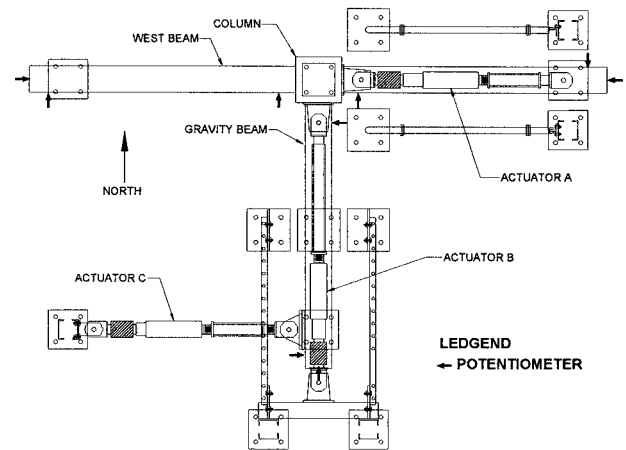
3. EXPERIMENTAL SETUP

A photograph of the specimen and the test setup is given in Figure 4a, and a plan view is given in Figure 4b. Displacement of the column was provided by two orthogonal actuators attached at the top of the column, while a third actuator was located at the end of the gravity beam to stabilise the specimen. The column was pinned to the floor using a universal joint, additional pins were provided on the struts of each beam. Rotary potentiometers were installed against the opposite face of each actuator. A vertically oriented hydraulic jack was installed at mid-height of the gravity beam to simulate the presence of precast one-way floor panels. This load was spread over a 1.5m timber block. The load was applied at a constant force of 120kN. The base of the column was pinned with a universal joint, allowing free rotation in both the EW and NS direction.

At one end of each prestress thread-bar anchor, load cells were installed to measure the magnitude of the unbonded prestress throughout testing. Four 32mm high strength thread-bars located along the longitudinal axis of the column were each stressed to 500kN to simulate a total axial load of 2000kN ($0.1f_c A_g$). Potentiometers were located at various locations around the specimen to record displacements during testing.



(a) View of specimen in laboratory



(b) Plan view of the specimen test setup

Figure 4: Isometric view of the specimen test setup

4. EXPERIMENTAL METHODS

Experiments were conducted on the specimen using the *quasi-earthquake displacement* (QED) test method. Details of the QED test method may be found in Dutta et al., (1999). The QED testing method is intended to serve as a more realistic testing protocol, capturing the behaviour of the specimen under ‘real’ earthquake ground motion. This has three advantages: (i) unlike QS testing which uses controlled cyclic displacements in ascending order, QED testing realistically captures small loading cycles following severe displacement demand from initial pulses; (ii) P-Δ effects can be considered in the analytical model, thus capturing any non-uniform displacement due to

excessive yielding in a single direction; (iii) the behaviour of the specimen subject to QED displacement profiles can be extrapolated to infer likely damage at multiple levels of excitation.

The data generated from preliminary quasi-static tests was used to create an equivalent analytical model of the specimen. This is illustrated in Figure 5a, showing the modelling strategy adopted. A thorough discussion of the development of the 3D analytical model is given elsewhere (Bradley et al., 2006). The natural period of the prototype structure was found to be 1.5s. With the development of a reliable analytical model of the structure, it was then possible to generate a displacement profile at the node of interest which could be used for physical testing. This required the identification of earthquakes likely to represent various levels of demand, considering both rare and relatively frequent earthquakes. A procedure described by Dhakal et al. (2006) was adopted to define three key earthquake records representing multiple levels of seismic demand. This procedure consists of performing an *Incremental Dynamic Analysis* (IDA) (Vamvatsikos and Cornell, 2002) to identify the response of the structure from various earthquakes. Using this data, earthquakes representing non-exceedance probability (percentile) levels at various earthquake intensities can be identified and used for subsequent analysis.

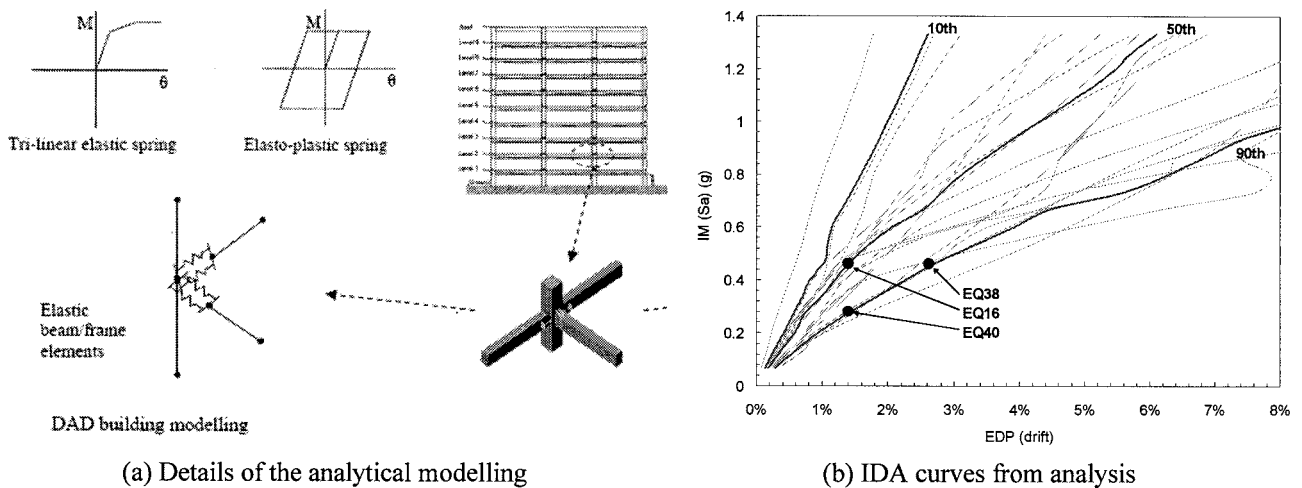


Figure 5: QED methodology

Assuming a firm soil site in Wellington, New Zealand (a high seismic zone) three levels of seismic demand were identified. These demand levels were: (i) a 90th percentile *design basis earthquake* (DBE); (ii) a 50th percentile *maximum considered earthquake* (MCE); and (iii) a 90th percentile MCE. The DBE and MCE were defined as an earthquake with a return period of 475 years (10% in 50 years) and 2475 years (2% in 50 years), respectively. For the site of interest, this corresponds to a *peak ground acceleration* (PGA) of approximately 0.4g and 0.8g for the DBE and MCE, respectively, based on the seismic hazard model presented in Stirling et al. (2002). Given these levels of demand, several performance objectives can be defined. Following current trends, each level was related to serviceability and life-safety. For the 90th percentile DBE, this corresponded to a high probability that the structure would remain operational following an earthquake of that intensity. After the MCE it would be expected the structure is repairable with a moderate probability (50th percentile MCE) and a high probability that the structure would not collapse (90th percentile MCE).

Due to the lack of large earthquakes in the Wellington region over the past 100 years, despite its known large seismicity, there are insufficient regional ground motion records to carry out a performance-based assessment. Therefore ground motion records were selected from a suite of 20 bi-direction ground motion records used in the SAC steel project (SAC, 1995), representing both near-source and medium-source distance accelerograms. Following current practice, the spectral acceleration (S_a) at the fundamental period of the structure was selected as the *intensity measure*

(IM). Thus, from the Stirling et al (2002) hazard model the S_a at the DBE and MCE intensity levels were 0.27g and 0.48g, respectively. The resulting IDA data is plotted in Figure 5a, showing the 10th, 50th, and 90th percentile fractal curves. The three selected records are noted in the figure. These records corresponded to peak (radial) interstorey drifts of 1.6, 1.6 and 2.8 percent for the 90% DBE, 50% MCE, and the 90% MCE, respectively.

5. EXPERIMENTAL RESULTS

Although the experiments were conducted using concurrent bi-directional earthquake motions, for the sake of brevity, this section will focus on the results of the QED tests in the EW direction—this is where the major drift levels were observed. Results from QED testing for the EW direction are presented in Figure 6. These plots show the force-displacement response, the bi-directional orbit of the column, and the displacement profile versus time. In all cases, the specimen exhibited good hysteretic response, showing a flag-shaped hysteresis loop with good energy dissipation. The response in the NS direction was not as stable as in the EW direction. This was especially the case for the 50 percent MCE. In this case, the specimen exhibited some stiffness degradation, possibly as a result of bi-directional rocking coupled with non-uniform displacement cycles. Damage to the specimen was minimal. Throughout all tests, only a few slight cracks near the joint region were observed. These cracks generally tended to close entirely when the applied drift was passing through zero and also at the end of testing.

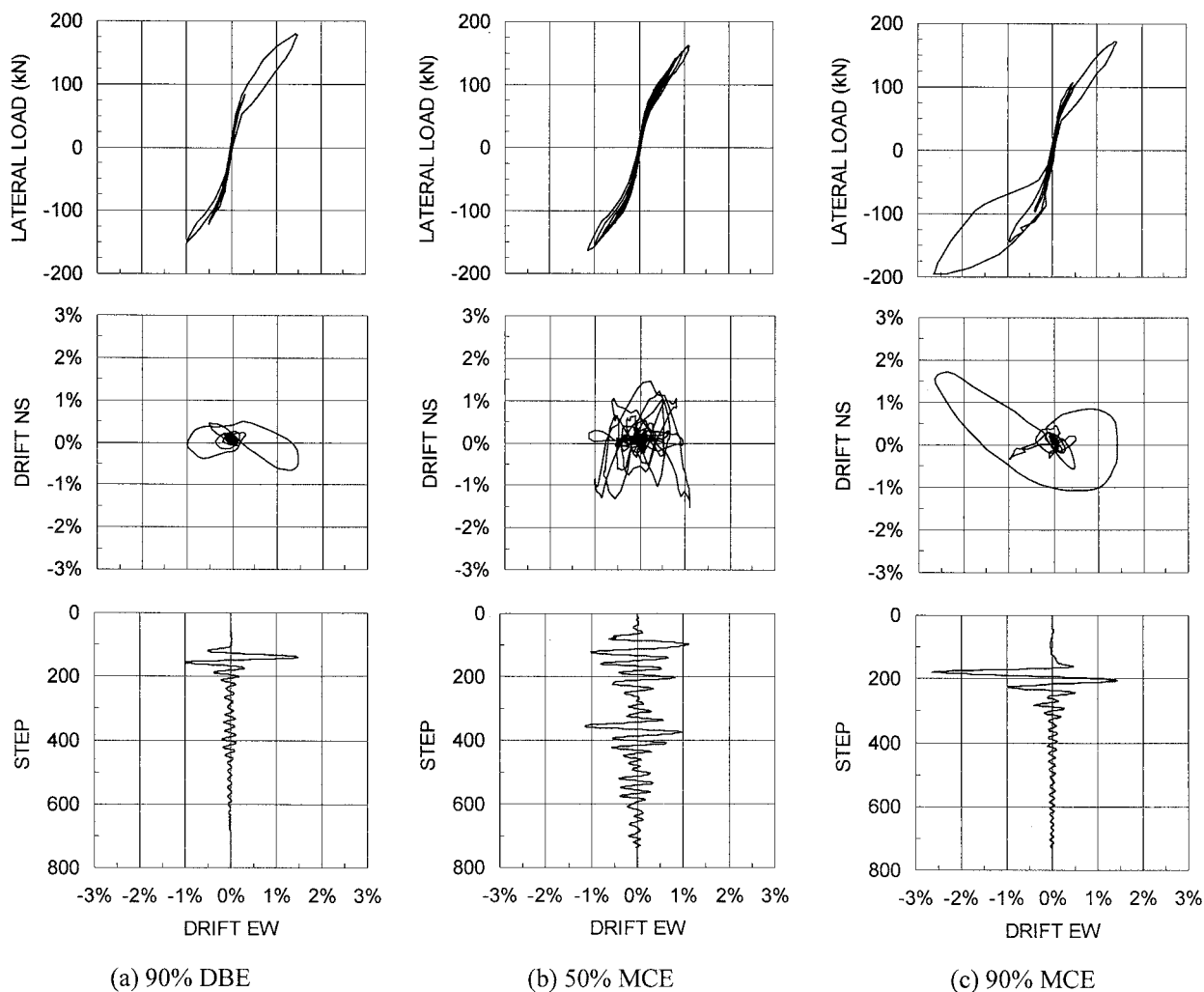


Figure 6: Results from QED testing in the EW direction

Some prestress loss was detected. This was generally in the order of 0-15kN, and may be ascribed to the “bedding-in” of the thread-bar anchorages.

The LE dampers performed very well, especially at higher drift levels. As apparent from Figure 6b, at low drift levels the dampers did not engage and the response was elastic. This can be attributed to some elasticity and minor thread-slop in the connecting elements, delaying full engagement of the devices. Clearly, most hysteretic energy dissipation was observed in the final test (Figure 6c). Upon unloading after this test the compression force in the LE dampers remained at about 200kN. Over several hours, this force reduced by about 50 percent with further reduction over time following logarithmic decay, thus validating the ‘resetable’ nature of the device.

The first performance objective dealt with serviceability. Given a design level earthquake, there must be a high confidence that the structure will not sustain damage which causes a disruption to its normal function. The displacement profile (Figure 6a) consisted mainly of a single large displacement cycle to an interstory drift of 1.6 percent, followed by a slow reduction in displacement. Residual drift was negligible. Observed damage from this level of shaking was minimal. Flexural cracks were observed in the beams and small (50mm) cracks were observed in the beam’s joint region. These cracks closed after testing. The LE dampers performed well, with some hysteretic energy dissipation on the first pulse, followed by near-elastic behaviour. The specimen did not suffer any stiffness or strength degradation. Given these results, the specimen satisfied the first requirement of the MSPA.

The second performance objective relates to repairability. In this case, one must be moderately confident the structure is repairable following a very rare earthquake. The displacement demand (Figure 6b) was most severe in the NS (gravity) direction, corresponding to a maximum interstory drift of 1.6 percent. Again, the specimen performed very well. Only a few additional cracks near the armoured beam-ends armouring were observed. In the EW direction, the specimen behaved elastically, with no stiffness or strength degradation. In the NS direction, some minimal stiffness degradation was observed. This was attributed to the draped thread-bar profile which would bind within the duct. Nevertheless, this effect was minimal and did not affect subsequent performance. Therefore the specimen met the second requirement of the MSPA.

The third and final performance objective related to life-safety and collapse prevention. In a maximum considered event there must be a high level of confidence the structure must not collapse following a very rare earthquake. The displacement of the structure (Figure 6c) consisted of one primary pulse to a 2.8 percent interstorey drift, followed by several small displacement cycles. As with the previous two earthquakes, damage to the specimen was minimal. Some of the previously developed cracks propagated away from the joint approximately another 100mm. A few additional cracks formed behind the armoured beam-end region. Most of these cracks closed following testing. During the first pulse, a considerable amount of hysteretic energy dissipation was observed. It should be emphasised that this was not from the structural elements, but primarily from the LE dampers. Subsequent displacement cycles were elastic, with the full stiffness and strength of the specimen preserved. Some prestress losses were recorded, in the order of 0 to 5 percent, likely caused by “bedding-in” at in the anchorage regions. These losses were deemed too small to necessitate re-stressing the thread-bars. Given the damage outcome from this level of demand, the structure easily satisfied the final objective of life-safety and collapse prevention.

6. DISCUSSION

The experimental-based MSPA investigation has verified that the specimen performance, and indirectly the frame of a DAD structural system, is capable of remaining essentially damage-free given severe ground shaking. All performance objectives related to serviceability and life-safety were achieved. This structure, designed to resist damage by rocking at specially detailed joints,

offers an attractive alternative to conventional monolithic design and construction. An equivalent monolithic structure would have likely undergone cyclic rotations at its plastic hinges, resulting in damage locally and residual displacement of the global system. The MSPA method relies heavily on the analytical model developed in conjunction with the experimental specimen. In order for realistic displacement profiles to be extracted from the model, the response of the two must be reasonably identical. Furthermore, non-structural damage, which constitutes a large portion of overall damage, should be considered for a more complete conclusion to be drawn. Nevertheless, the MSPA method has demonstrated a sound means of experimentally verifying the performance of structures at various levels of seismic demand.

7. CONCLUSIONS

Based on the findings of this research the following conclusions are drawn:

1. The specimen satisfied all performance objectives related to serviceability, life-safety and collapse-prevention. After being subject to displacement paths representing a design level earthquake and more severe rare earthquakes, the specimen remained essentially damage-free, thus validating the DAD philosophy.
2. The lead-extrusion damper was able to provide a reliable form of energy dissipation to the specimen. Residual compression forces in the devices at the end of testing were shown to creep back towards zero, with half the force being lost over the first few hours. Therefore, the devices would not have to be replaced following an earthquake.
3. Precast concrete framed structures constructed in accordance with the principles of Damage Avoidance Design (DAD) now appears to be a viable alternative to the conventional monolithic construction of concrete structures that possess ductile details. The next step is to investigate detailing methods of mitigating damage to the floor system within such DAD frames.

References:

- Amaris A, Pampanin S, Palermo A. 2006. Uni and bi-directional quasi-static tests on alternative hybrid precast beam column joint subassemblies. *Proceedings of the 2006 New Zealand Society for Earthquake Engineering (NZSEE) Conference*. Napier, New Zealand, Paper #24.
- Bradley, B.A. Dhakal, R.P. Mander, J.B. 2006 Dependency of current Incremental Dynamic Analysis to source mechanisms of selected records. *19th Biennial Conference on the Mechanics of Structures and Materials*; Christchurch, NZ.
- Cousins WJ and Porritt T E. 1993, Improvements to lead-extrusion damper technology. *Bulletin of the New Zealand National Society for Earthquake Engineering*; **26**:342-348.
- Dhakal, R.P. Mander, J.B. Mashiko, N. 2006. Identification of Critical Earthquakes for Seismic Performance Assessment of Structures, *Earthquake Engineering and Structural Dynamics*; **35**(8):989-1008.
- Dutta, A, Mander JB, Kokorina. T. 1999. Retrofit for Control and Repairability of Damage. *Earthquake Spectra* **15**(4), pp. 657-679.
- Mander, J.B. and Cheng, C.-T. 1997 Seismic resistance of bridges based on Damage Avoidance Design", NCEER, Technical Report NCEER-97-0014, Buffalo USA.
- Priestley MJN, Sritharan S, Conley JR, Pampanin S. 1999. Preliminary Results and Conclusions from the PRESSS Five-Storey Precast Concrete Test Building. *PCI Journal*, **44**(6):43-67.
- Stanton JF, Stone WC, and Cheok GS. 1997. A Hybrid Reinforced Precast Frame for Seismic Regions. *PCI Journal*, **42**:20-32.
- Stirling M.W., McVerry G.H., Berryman K.R., 2002, A New Seismic Hazard Model for New Zealand, *Bulletin of the Seismological Society of America*. **92**(5) pp 1878-1903.
- Vamvatsikos, D. and Cornell, C.A. 2002. Incremental Dynamic Analysis. *Earthquake Engineering and Structural Dynamics*; **31**:491-514.

HYSTERETIC BEHAVIOR OF R/C CORNER JOINT WITH HEADED REINFORCEMENTS

Soo-Yeon Seo¹⁾, Seung-Joe Yoon²⁾, and Gi-Bong Choi³⁾

1) Assistant Professor, Department of Architectural Engineering, Chungju National University, Chungju, Korea

2) Professor, Department of Architectural Engineering, Chungju National University, Chungju, Korea

3) Professor, Department of Architectural Engineering, Kyungwon University, Seongnam, Korea

syseo@cjnu.ac.kr, sjyoon@cjnu.ac.kr, kbchoi@mail.kyungwon.ac.kr

Abstract: This study offers a various details for corner joint anchored with *headed reinforcement*, examines their structural properties, and endeavors to provide a database to develop efficient details for fabrication and construction of RC frame structure. To evaluate the performance of the corner joint details that are subjected to repetitive stress, five specimens with different anchorage details in joint were designed and tested.

Test results shows that if the head is anchored to avoid complicated steel reinforcing at the joint, the risk of brittle failure is heightened. Therefore, more development for applicable specification to effectively restrain concrete is requested. Especially when the reinforcements of beam and column are anchored in the corner joint only with head anchorage, the joint is to show low strength and rapid brittle failure under opening moment. To prevent this, additional transverse reinforcement is needed within the joint to restrain concrete adequately.

1. INTRODUCTION

When a building structure is put under repetitive stress (e.g. seismic loads), a stress is converged into the joint where vertical and horizontal members cross, and causes inelastic deformation. In constructing a building against lateral loads, the joint parts are especially important because the non-linear behavior affects the entire structure. Generally the first inelastic deformation takes place in the bottom joint, which is why the research has been concentrated on the subject so far; however, further research on the top corner joint is needed because issues frequently arise such as reinforcement congestion or lack of concrete filling in the area. The demand for research is increasing as the diminishing section area and the use of high-strength materials makes it hard to secure sufficient length for placing reinforcements.

Recently researches have been presented on *headed reinforcement*, a combination of anchoring hardware over the reinforcing steel bars, as an alternative to the standard hooks that are used for the joint area. The experiments show that the head improves anchorage capacity of the reinforcing bars, thus requiring shorter length for embedment.

In case of corner joints, as they connect columns and beams together, reinforcement congestion is likely to occur; thus a detailing can be very useful by using mechanical anchoring. *Headed reinforcement* is expected to improve the performance in corner joints, but if the concrete is not adequately restrained, it could easily lead to brittle failure.

This study offers a various details for corner joint anchored with *headed reinforcement*, examines their structural properties, and endeavors to provide a database to develop efficient details for the fabrication and construction.

2. BEHAVIOR OF CORNER JOINT

The behavior of a corner joint in steel-concrete structure is largely divided into two kinds. One is a joint under positive moment to be opened; the other is that under negative moment to be closed. The moment is influenced by the tensile failure for opening, and by compressive strength for closing.

When the positive moment acts, the principle tensile stress occurs at the center of joint and inner corner. And the compressive stress at the outside of diagonal crack pushes triangle as shown in Figure 1(c) so that only internal tensile force resists the diagonal force. On the contrary, when the negative moment acts, the tensile stress in the joint governs as shown in Figure 2(b). In Figure 2(a), the force causing the diagonal cracks in joint is assumed to be induced as a type of equal shear stress by bond force. The summed equal shear stress makes the splitting cracks as shown in Figure 2(d). These diagonal cracks appear when concrete reaches the tensile strength.

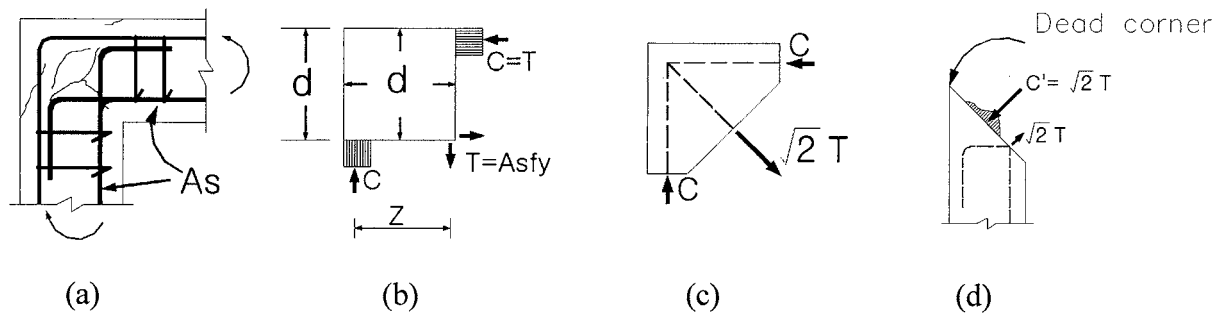


Figure 1 Stress of corner joint at positive moment (Opening moment)

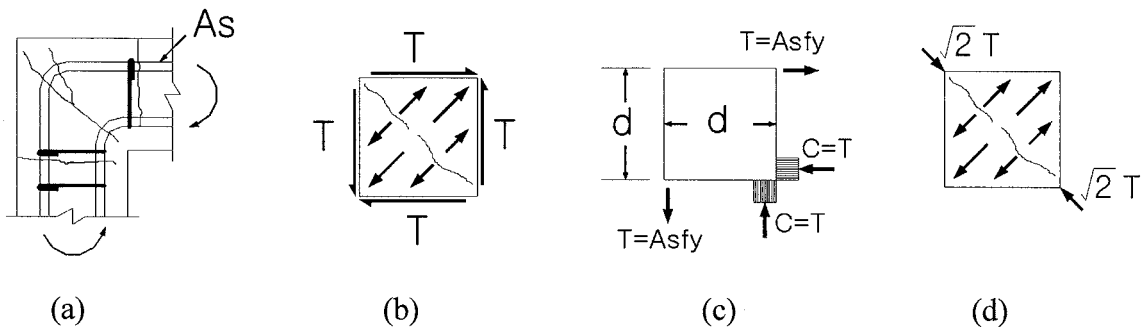


Figure 2 Stress of corner joint at negative moment (Closing moment)

Generally, the opening moment is relatively subject to the reinforcing of the steel bar (Mayfield *et al*, 1971; Nilsson and Losberg, 1976). Accordingly, most experiments have focused on the opening moment (Mayfield, 1971; Mayfield and Bennison, 1972; Nilsson, 1973) and details that influence the opening moment (Morgan Johansson, 2001).

However, as was explained earlier, the joint can be easily burdened with reinforcement congestion, which complicates the construction and also discourages effective resistance against lateral force. Moreover, the corner joint has low restraint strength due to the absence of an upper column, which further deteriorates shearing strength.

To improve the property of the corner joint, a construction method that uses mechanical anchoring of the steel bars was suggested and the evaluation of its performance under various details was conducted by John Wallace *et al* (1998). *Headed reinforcement* was reported to enforce the internal force of the joint, but under closing moment, the strength plummeted. As a result, the additional transverse reinforcement was recommended within the joint.

Based on these premises, this study evaluates the performance of various details using *headed reinforcement* through experiments.

3. EXPERIMENTS

3.1 Planning of specimens

To evaluate the performance of the corner joint details that are subject to cyclic load, five specimens were designed (KJ-1 ~ KJ-4, KJ-7). In KJ-1, *head* was used to anchor beam top bar after 90-deg-hooked; the reinforcement in beam bottom and column were also anchored with *headed reinforcement*. In KJ-2, only *headed reinforcement* was used without a hook. In KJ-3, to oppress push-out around beam in KJ-2, a stirrup was added. In KJ-4, to distribute the destructive force on the exterior corner of the joint, exterior beam-column joint was anchored with *headed reinforcement* in 90 deg hook. In KJ-7, the amount of reinforcing within the joint was diminished compared to KJ-4, and the head was removed from the lower beam reinforcements. This is to observe the minimum reinforcement requirement and the effect of the head in the lower beam.

Table 1 Detail of test specimen

Specimen Name	Anchorage detail of outer reinforcement in column	Anchorage detail of upper reinforcement in beam	Shear reinforcement in joint
KJ1	Head anchor	90°Hook+Head	3-HD10
KJ2		Head	3-HD10
KJ3*		Head	3-HD10
KJ4	90°Hook+Head	90°Hook+Head	3-HD10
KJ7	90°Hook+Head	90°Hook+Head	1-HD10

* Additional stirrup is added in joint.

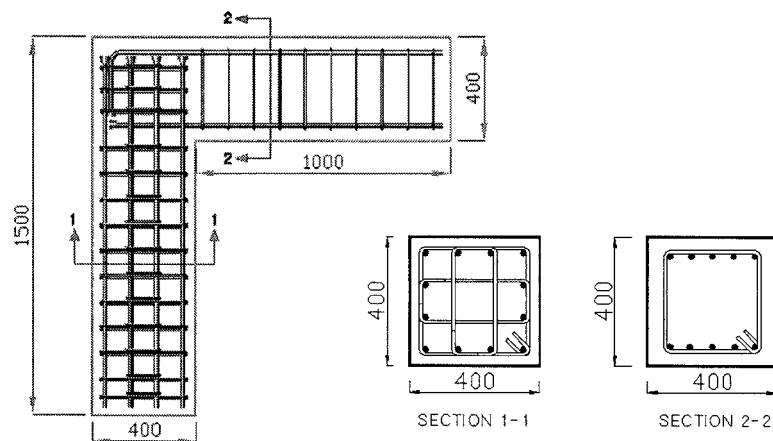


Figure 3 Dimension of test specimen (Unit: mm)

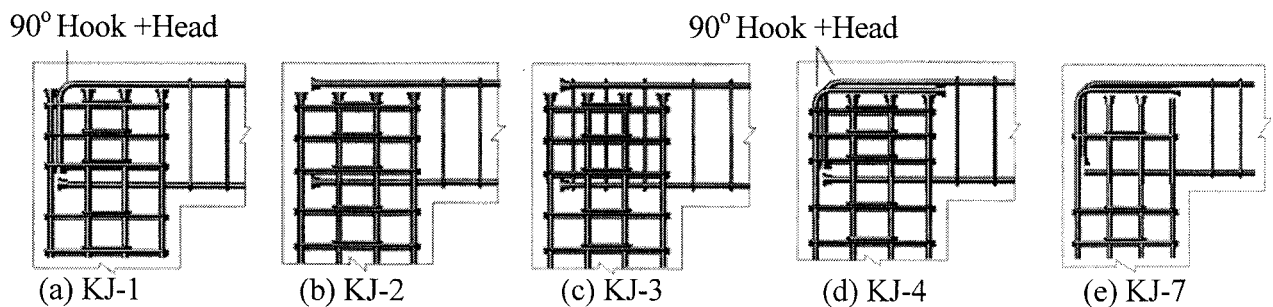


Figure 4 Joint details of specimens

The detailed specimen outline is shown in Table.1; the dimension and reinforcement details are illustrated in Figure 3 and Figure 4.

3.2 Characteristics of the materials

The head used in the experiment is composed of connecting part and anchoring board as illustrated in Photo 1. The head and reinforcements are connected by upset-end-type method. As for the connecting part, the diameter is 28mm, thickness 23mm; for anchoring board, diameter 38mm, and thickness 10mm.

Ready-mixed concrete was used (strength 24MPa, slump 15cm); concrete cylinders for the evaluation of compressive strength were made by using 100 x 200mm mould, which were cured in the same condition with the test specimens. The reinforcement is SD400 (D19 for main bars; D10 for stirrup and hoop). The result of tensile strength test for the material is shown in Table.2.

Figure 5 shows the pull-out test of *headed reinforcement* by Sung-Chul Chun (2001), its internal strength by different embedment depth. It compares the hypothetical outcome of formula ACI 349 (1997) and CCD (Concrete Capacity Design; Werner *et al*, 1995) and the actual result from the experiment. When the anchoring depth was 9, 12, 15cm, “cone” failure occurred. When the depth exceeded 18cm, the steel bar yielded first then the “cone” failure followed. And in case of 21, 24cm, the steel bars were deteriorated. In the figure, F_t indicates maximum tensile strength; F_y for yield stress.

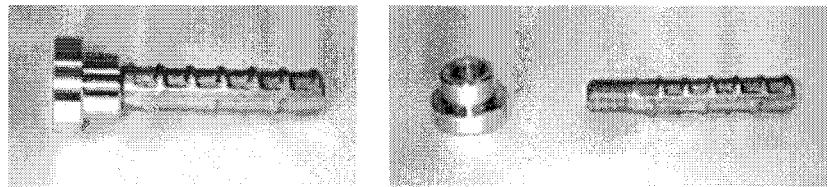


Photo 1 Headed reinforcement detail

Table 2 Mechanical properties of reinforcements

Type	f_y (MPa)	ε_y ($\times 10^{-6}$)	f_u (MPa)	E_s ($\times 10^5$, MPa)	Elongation ratio (%)
D10	408	2,090	549	1.95	16.3
D19	511	4,310	897	1.94	11.6

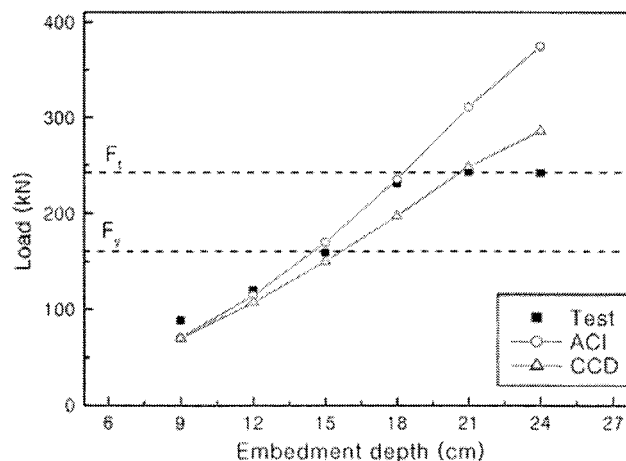


Figure 5 Tensile strength of embedded headed reinforcement (S. Chun, 2001)

3.3 Loading and measuring of instruments

In order to simulate the hysteretic behavior of the corner joint under earthquake loads, an actuator is installed on the end of beam. Also, the end of column is supported with pin like the contra-flexure point in real building. The opening or closing moment can be applied to the joint by changing the actuator stroke. Figure 6 shows the test layout.

The displacement is controlled by the prepared story drift following the procedure proposed by ACI (1999) that is codified for the test to simulate the hysteretic behavior of structure in high seismic region. Three cycle loadings are applied at every story drifts such as 1/1000, 1/700, 1/350, 1/250, 1/180, and 1/130.

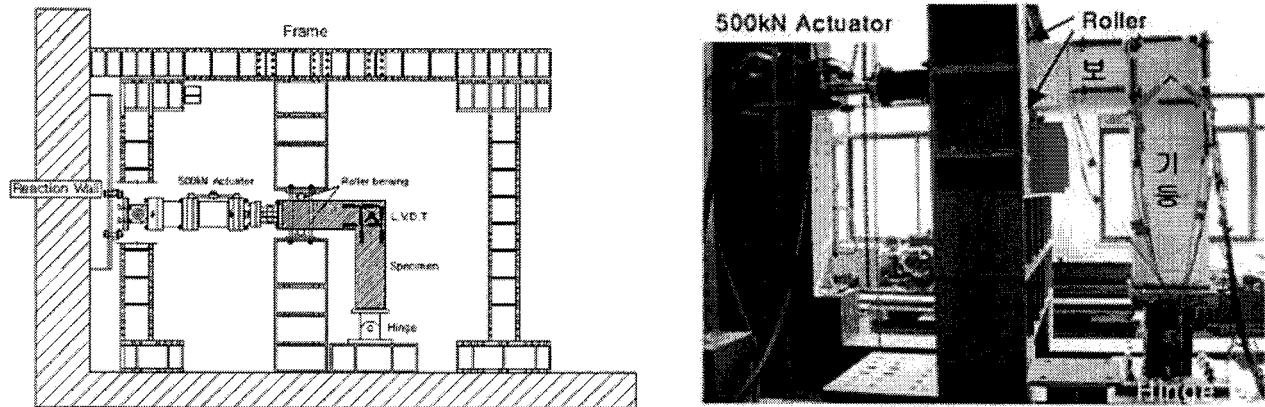


Figure 6 Test set up

4. TEST RESULTS

4.1 Crack pattern

Both in KJ-1 that used *headed reinforcement* in beam top with 90 deg standard hook, and in KJ-4 that used *headed reinforcement* in beam top as well as column exterior with 90 deg standard hook, shearing failure occurred, and the initial crack took place at inner joint in vertical and horizontal pattern. Then, as the diagonal crack appeared due to opening and closing moment, the cracks became prominent in the center part of the joint. Finally the crushing of concrete followed, and the concrete split.

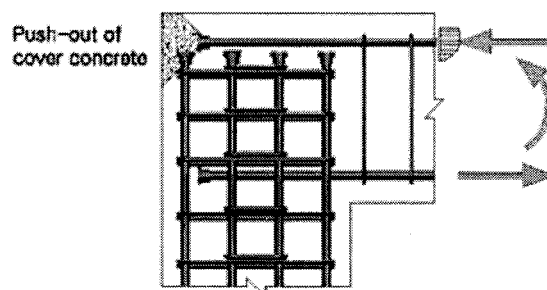


Figure 7 Push-out of headed reinforcement in compression

In KJ-2 and KJ-3, the head was used instead of ACI standard hook; the initial crack pattern was same as above, and deterioration occurred by the failure of anchorage and bonding, and “push-out” occurred as the cover was stripped by the head (Fig.7). In the final stage, the failure of anchorage and bonding was observed as the beam top and the joint area fell apart. In KJ-3 where a stirrup was added, “push-out” as well as the failure of anchorage and bonding were observed. In KJ-7 where the amount

of reinforcing within the joint was diminished and the beam top and outer column bars were anchored with 90 deg hook, a diagonal crack started from the inner part of the joint and progressed to the outer side as the stress increases; finally, X-shaped crack occurred at the inner joint leading to splitting. Failure pattern of all specimens is shown in Photo 3.

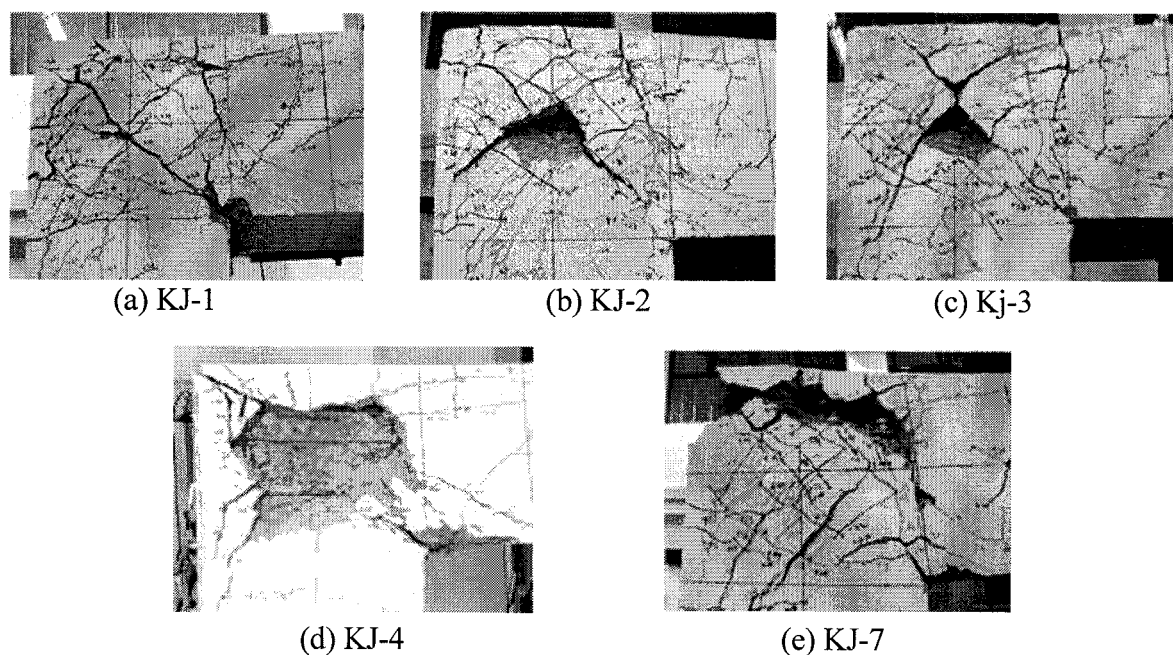
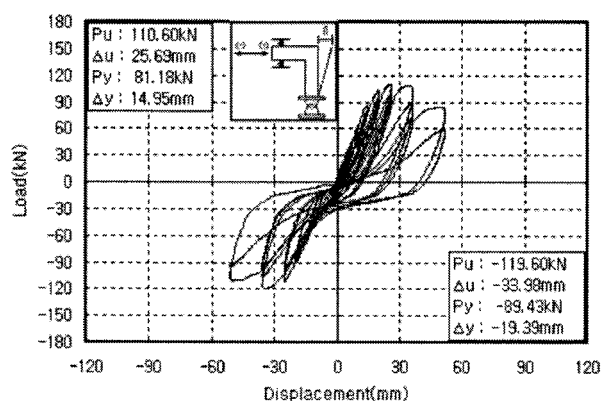


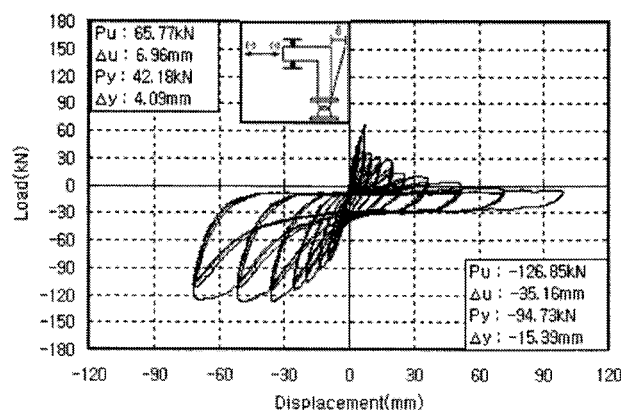
Photo 3 Failure pattern

4.2 Load-displacement curve

Figure 8 plots curves that show the correlation between the applied load and the displacement. In KJ-1, the maximum strength showed 110.6kN for positive stress and 119.6kN for negative stress: a *hysteresis loop* that shows symmetrical result for two loads. In KJ-2, in applying positive loading (negative moment), the strength decreased after the diagonal crack took place, then further declined by the “push-out”. In KJ-3, the maximum strength increased 80% compared to KJ-2; yet the “push-out” still kept the strength low. In all cases except KJ-7, the *hysteresis loop* showed similar patterns, indicating that when the head is anchored in beam bottom for reinforcing, sufficient strength and ductility capacity can be acquired.



(a) KJ-1



(b) KJ-2

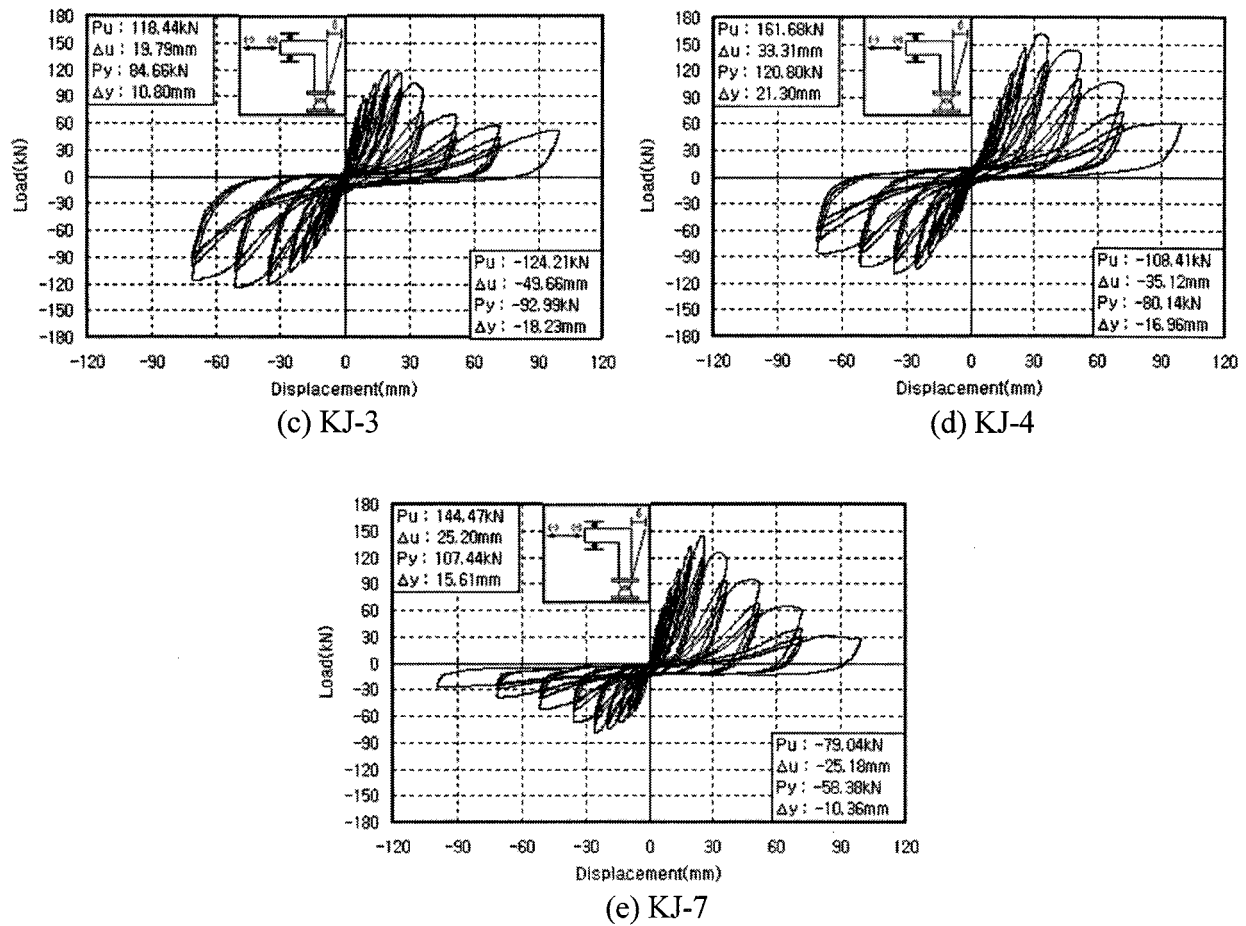


Figure 8 Load-displacement curves

KJ-4 showed the highest maximum strength, 37% more than KJ-3 under positive stress. However, the degree of declining was still unavoidable as the stress increases. KJ-7 showed performance that reached 89% and 73% of KJ-4's maximum strength under positive and negative stress, respectively. Its weak performance resulted from the lack of transverse reinforcement within the joint under positive stress, and missing head in the beam bottom under negative stress.

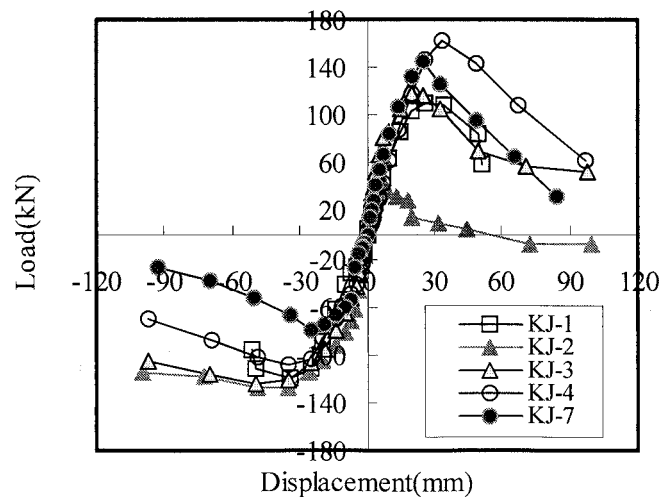


Figure 9 Envelop of all specimens

4.3 Comparing maximum strength

In the load-displacement curve, it was noted that the ultimate strength in each cycle declined due to the crack and the yield of steel bars. Figure 9 shows that KJ-4 bore the maximum strength under the positive stress; KJ-2, reinforced with only the head, showed lowest resistance. In contrast, KJ-3 reinforced with a stirrup in joint showed relatively satisfactory performance. KJ-7, with less reinforcement compared to other specimens, showed relatively higher strength under negative moment as the hook held the column and the beam; yet under positive moment, the lack of the head in beam bottom critically eroded the strength. It can be induced that the reinforcement inside the joint is critical in preparation for the repetitive stress.

Table 3 Test result

Specimen Name		$P_y(\text{kN})^{1)}$	$\Delta_y(\text{mm})^{2)}$	$P_u(\text{kN})^{3)}$	$\Delta_u(\text{mm})^{4)}$	Ductility(μ)	Dissipated energy ($\text{kN}\cdot\text{mm})^{6)}$
						$\mu_u^{5)}$	
Knee joint-1	(+)	81.18	14.95	110.60	25.69	1.72	18710
	(-)	89.43	19.39	119.60	33.98	1.75	
Knee joint-2	(+)	42.18	4.09	65.77	6.96	1.70	826
	(-)	94.73	15.39	126.85	35.16	2.28	
Knee joint-3	(+)	84.66	10.80	118.44	19.79	1.83	12385
	(-)	92.99	18.23	124.21	49.66	2.72	
Knee joint-4	(+)	120.80	21.30	161.68	33.31	1.56	19383
	(-)	80.14	16.96	108.41	35.12	2.07	
Knee joint-7	(+)	107.44	15.61	144.47	25.20	1.61	11643
	(-)	58.38	10.36	79.04	25.18	2.43	

1) P_y : Yield load, 2) Δ_y : Yield displacement, 3) P_u : Ultimate load, 4) Δ_u : Displacement at P_u , 5) μ_u : Δ_u/Δ_y , 6) Accumulated dissipated energy ($\text{kN}\cdot\text{mm}$) at failure point (at 75% load beyond the peak load)

4.4 Capacity for energy dissipation

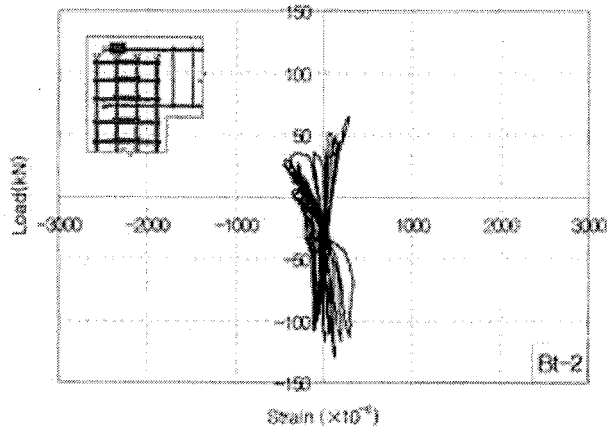
Table 3 shows the accumulative energy from the maximum strength to the point where the maximum strength dropped by 75% (starting point of deterioration). KJ-1 and KJ-4 with hook-shaped head showed better ductility capacity and dissipation of energy compared to KJ-2 and KJ-3 with only a head after the maximum strength was reached.

KJ-2 that simply anchored the head for beam and column exterior bars showed lowest dissipation of energy; this indicates that to apply this detail to the corner joint to resist a seismic force, a proper reinforcement is required to prevent brittle failure.

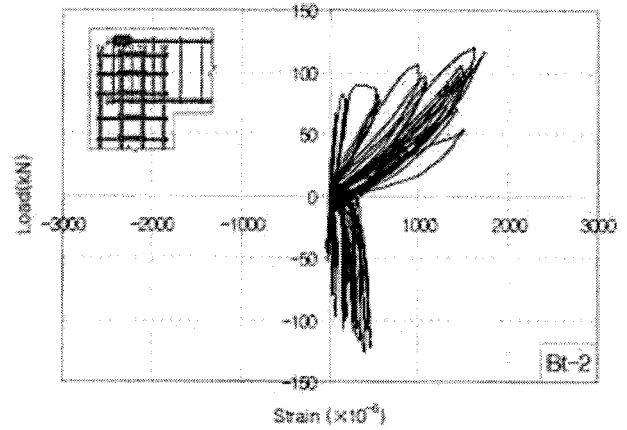
4.5 Strain variation of beam reinforcements in joint

Figure 10 shows the strain variation of beam top bars that are anchored in the inner joint of KJ-2 and KJ-3. Generally the strain should be substantial due to the tensile force applied under negative stress. Yet the KJ-2 that is anchored with the head did not show significant variation in case of positive stress.

Figure 11 shows the strain variation of beam bottom bars in conditions where the head was anchored (KJ-3) or not (KJ-7). If the head was used, the strain occurred extensively under negative stress (opening moment); meanwhile if the head was not used, the degree of strain was negligible. It can be drawn that steel bars are not effectively restrained if both 90 deg hook and the head are missing.

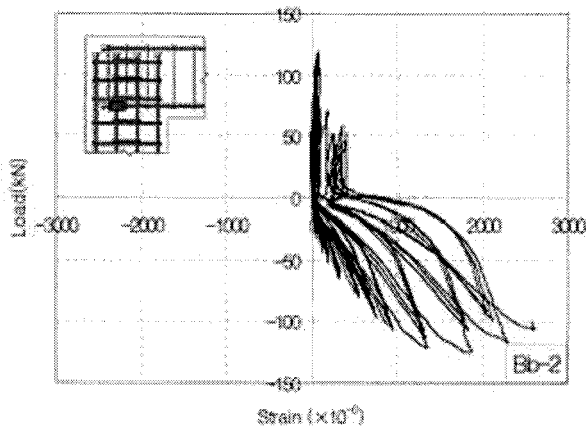


(a) KJ-2 (with only head)

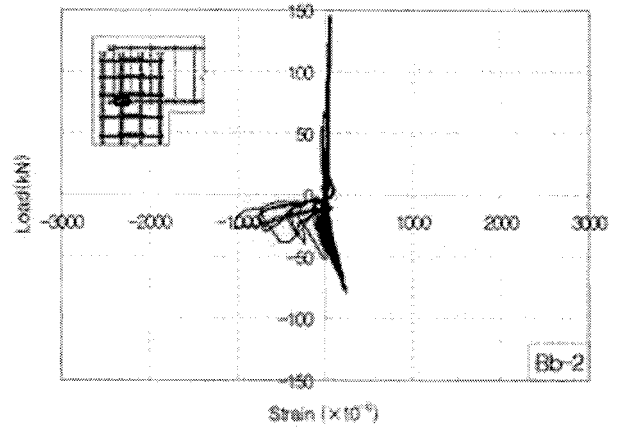


(b) KJ-3 (with head + 90° hook)

Figure 10 Load-strain curve of beam top bar in joint



(a) KJ-3 (with head)



(b) KJ-3 (without head)

Figure 11 Load-strain curve of beam bottom bar in joint

5. CONCLUSIONS

- 1) When repetitive stress is applied in the beam-column corner joint where *head reinforcement* was anchored, the exterior joint was exposed to the risk of brittle failure.
- 2) Especially when the exterior column and the beam were placed with only the head, the structure was subject to low inner strength and rapid brittle failure under opening moment. To prevent this, additional transverse reinforcement is needed within the joint to restrain concrete adequately.
- 3) If the exterior column bars and beam bars were 90 deg hooked then anchored with the head, the placement was most effective; even better than using additional reinforcement without 90 deg hooks. However, it is hard to prevent weakening under closing moment, which calls for a further study of details.
- 4) If the bottom reinforcement of beam was not anchored with 90 deg hook or the head, the compressive force under the opening moment could not be transmitted sufficiently to the anchoring parts, and the strength declined substantially.
- 5) If the head is anchored to avoid complicated steel reinforcing at the joint, the risk of brittle failure is heightened. Therefore, more development for applicable specification to effectively restrain concrete is requested.

Acknowledgements:

This research was supported by a grant (06ConstructionCoreB04) from Construction Core Technology Program funded by Ministry of Construction & Transportation of Korean government.

References:

- ACI Innovation Task Group and Collaborators (1999), "Acceptance Criteria for Moment Frames Based on Structural Testing," American Concrete Institute. Farmington Hills. MI.
- ACI 349-97 (1997), "Code Requirements for Nuclear Safety Related Concrete Structures," Appendix B- Steel Embedment.
- B. Mayfield, F. K. Kong, A. Bennison, and J.C.D Davis (1971), "Corner Joint Detail in Structural Lightweight Concrete," *ACI Structural Journal*, American Concrete Institute, Proceedings .68(5), May, 366-372
- B. Mayfield, F. K. Kong, A. Bennison (1972), "Strength and Stiffness of Lightweight Concrete Corners," *ACI Structural Journal*, American Concrete Institute, Proceedings 69(7), July, 420-427
- Hashim M. S. Abdul-Wahab and Waleed M. Ali (1989), "Strength and Behavior of Reinforced Concrete Obtuse Corners under Opening Bending Moments," *ACI Structural Journal*, American Concrete Institute, November-December
- Hashim M. S. Abdul-Wahab and Shamil A. R. Salman (1999), "Effect of Corner Angle on Efficiency of Reinforced Concrete Joints under Opening Bending Moment," *ACI Structural Journal*, American Concrete Institute, 96(1), January-February
- I. H. E. Nilson, and A. Losberg (1976), "Reinforced Concrete Corners and Joints Subjected to Bending Moment," Proceedings ASCE, American Society of Civil Engineers, 102(6), June, 1229-1253
- John W. Wallace, Scott W. McConnell, Piush Gupta, and Paul A. Cote (1988), "Use of Headed Reinforcement in Beam-Column Joints Subjected to Earthquake Loads," *ACI Structural Journal*, American Concrete Institute, September-October
- M. J. N. Priestley, F. Seible, and G. M. Calvi (1996), "Seismic Design and Retrofit of Bridges," John Wiley & Sons, Inc.
- Morgan Johansson (2001), "Reinforcement Detailing in Concrete Frame Corners," *ACI Structural Journal*, American Concrete Institute, January-February
- Morgan Johansson (2002), "Nonlinear Finite-Element Analysis of Concrete Frame Corners," *ASCE Journal of Structural Engineering*, American Society of Civil Engineers, February, 190-199.
- Nuttawat Chutarat and Riyad S. Aboutaha (2003), "Cyclic Response of Exterior Reinforced Concrete Beam-Column Joints with Haded Bars Experimental Investigation," *ACI Structural Journal*, American Concrete Institute, March-April, 259-264
- R. Park, and T. Paulay (1971), "Reinforced Concrete Structures," John Wiley & Sons, Inc.
- Sung-Chul Chun, Dae-Young Kim (2001), "Design Consideration and Pull-Out Behavior of Mechanical Anchor of Reinforcement," *Journal of the Korea Concrete Institute*, Korea Concrete Institute, 13(6), 593-601
- Werner, F., Rolf, E., and John E. B. (1995), "Concrete Capacity Design (CCD) Approach for Fastening to Concrete," *ACI Structural Journal*, American Concrete Institute, 92(1), Jan.-Feb., 73-94
- Y.H.Luo, A.J. Durrani, Shaoliang Bai, and Jixing Yuan(1994), "Study of Reinforcing Detail of Tension Bars in Frame Corner Connections," *ACI Structural Journal*, American Concrete Institute, July-August

LATERAL FORCE-RESISTING MECHANISM OF SHEAR-CRITICAL REINFORCED CONCRETE SHEAR WALL ESTIMATED FROM ITS LOCAL SHEAR FORCES

Y. Sanada¹⁾ and T. Kabeyasawa²⁾

1) Associate Professor, Department of Architecture and Civil Engineering, Toyohashi University of Technology, Japan

2) Professor, Earthquake Research Institute, University of Tokyo, Japan

sanada@tutrp.tut.ac.jp, kabe@eri.u-tokyo.ac.jp

Abstract: Static loading tests of two reinforced concrete shear walls were carried out to investigate their lateral force-resisting mechanism. The test program and results are summarized herein. Although one of the specimens was a conventional type, the other was specially designed to measure its local forces on the critical section. As a result, the shear force on the critical section was shifted toward the compression zone according to the damage, which might be related to the flexural behaviors of the wall. Therefore, in this paper, a new concept to evaluate ultimate seismic performances for shear walls was presented and verified based on the test results.

1. INTRODUCTION

Accurate numerical modeling of structures or structural elements plays an important role in the performance based design. Sophisticated models based on material properties can be used resulting from recent innovative developments of computers. Although such models are usually verified through comparing to data from tests or observations, experimental data on stress or local forces in cross-sections of structural elements is extremely limited because of technical difficulties in measuring them. Therefore, in this study, static loading tests of reinforced concrete shear walls were carried out to obtain experimental data on local forces, which are summarized herein. This paper discusses a new concept to evaluate ultimate seismic performances for shear walls based on the test results.

2. OUTLINE OF THE SHEAR WALL TEST TO MEASURE LOCAL FORCES

Since the test program and results have been reported in detail by the authors (Sanada and Kabeyasawa 2006), they are briefly summarized in this paper.

2.1 Specimens

Two 1/3 scale reinforced concrete shear-critical wall specimens, representing the lower part of a multi-story shear wall, were designed. One is a normal type specimen (Type-N) which has a massive base as conventional wall specimens, the other is a specially designed one (Type-S) which has split bases along the wall length to measure its local forces on the critical section. Details of the specimens are shown in Figure 1. The local shear and axial forces of Type-S were measured using the biaxial load cells fixed under the split bases as shown in the figure. The material properties of the specimens are shown in Table 1.

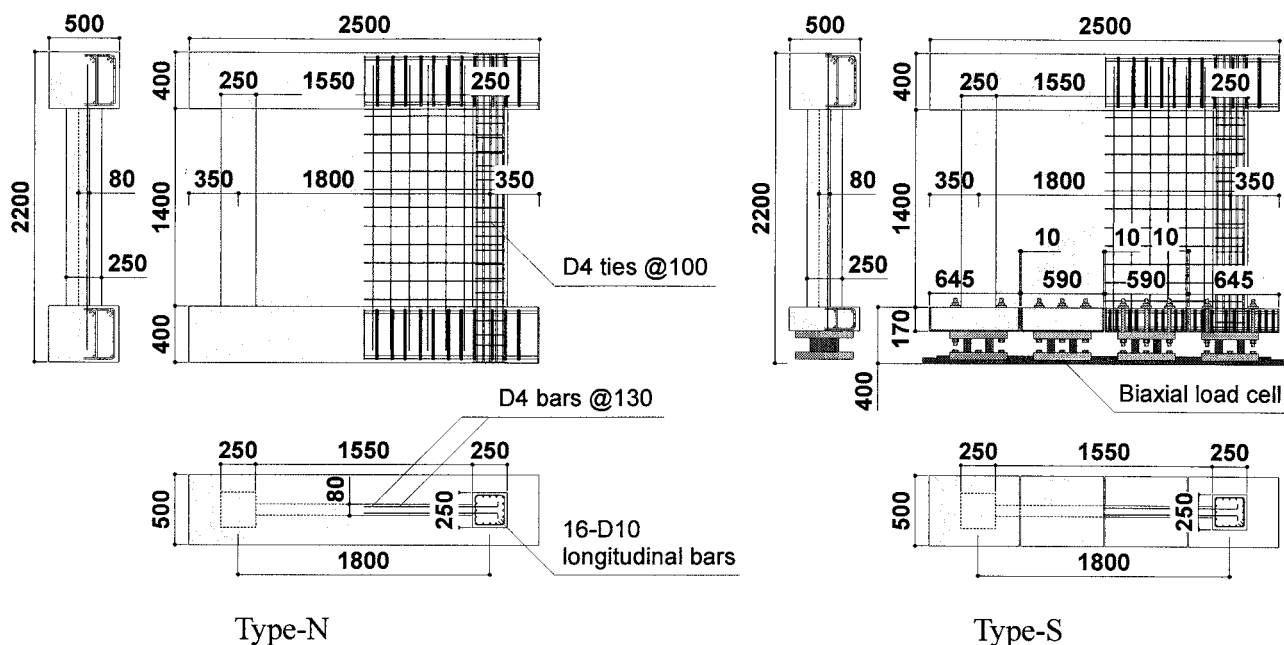


Figure 1 Details of the Specimens

Table 1 Material Properties
Concrete

Specimen	Age, day	E_c , GPa	f_c , MPa	ϵ_c , μ	f_{cr} , MPa
Type-N	41	24.7	22.4	1590	1.7
Type-S	52	25.6	24.5	1765	2.1

where, E_c : initial modulus of concrete, f_c : peak compressive strength of concrete cylinder, ϵ_c : strain at peak compressive stress in concrete cylinder, f_{cr} : cracking stress of concrete in tension.

Steel

Bar no.	Type	d , mm	E_s , GPa	f_y , MPa	ϵ_y , μ	f_t , MPa
D10	Deformed	9.5	172	398	2440	557
D4	Deformed	4.1	159	340	4140	560

where, d : nominal diameter of reinforcement, E_s : initial modulus of reinforcement, f_y : yield stress of reinforcement, ϵ_y : yield strain of reinforcement, f_t : peak strength of reinforcement.

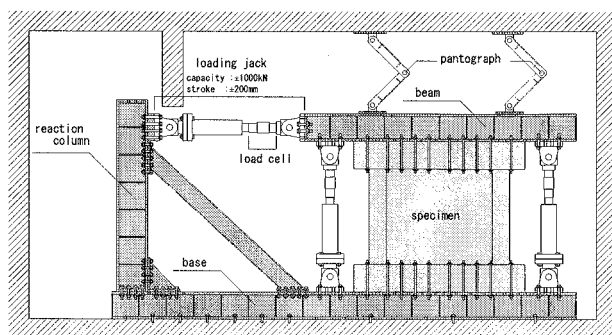
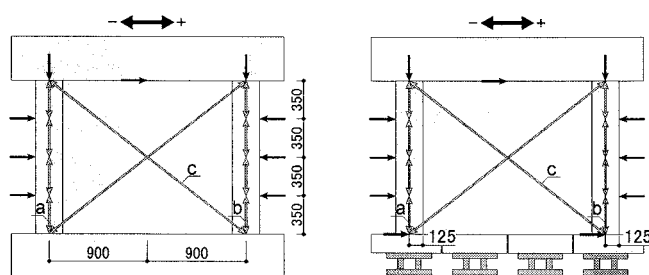


Figure 2 Loading System



Type-N

Type-S

Figure 3 Transducers Set-up

2.2 Test System and Loading Program

The tests were carried out at a testing facility in Earthquake Research Institute, University of Tokyo, shown in Figure 2. The specimens were subjected to cyclic lateral loading under constant axial loading of 600kN ($\approx 0.1A_w f_c$, where, A_w : cross sectional area of the specimen), whereas the shear span to depth ratio of 1.0 was maintained by controlling both vertical jacks shown in Figure 2. Figure 3 shows the set-up of the displacement transducers. Crack widths were also observed at the peak and residual drifts during the tests.

2.3 Test Results

Figure 4 compares envelope curves of the lateral force-drift ratio relationships of Type-N and -S, obtained during the negative loading when both specimens finally failed. This figure also shows the observed yielding and ultimate points, and the calculated flexural and shear strength of Type-N according to the AIJ guidelines (AIJ 1990). These specimens behaved similarly during the tests and failed in shear soon after flexural yielding. Although the initial stiffness of Type-S was a little lower than that of Type-N owing to horizontal cracking on a split base of Type-S caused before the test, the performances at relatively large deformations, such as the maximum strength, the secant stiffness at yielding, and so on, were consistent between both specimens. Figures 5 and 6 compare the final crack patterns and the maximum crack widths at the peak and residual drifts, which were measured using crack gages, respectively. Typical crack patterns after shear failure were obtained from both specimens, which were very similar to each other. The observed maximum crack widths of Type-S were as large as those of Type-N not only at the peaks but also at the residual drifts. These results mean that Type-S could substantially reproduce the behaviours of Type-N in spite of different details around the bases.

The distributions of local shear forces obtained through the test of Type-S are shown in Figure 7. The shear force on the critical section of Type-S shifted toward the compressive side according to its damages. Almost no shear transfer was observed around the tensile column bottom from the relatively small drift level. On the contrary, about 70% of the total shear force was carried around the compressive column bottom at the shear failure.

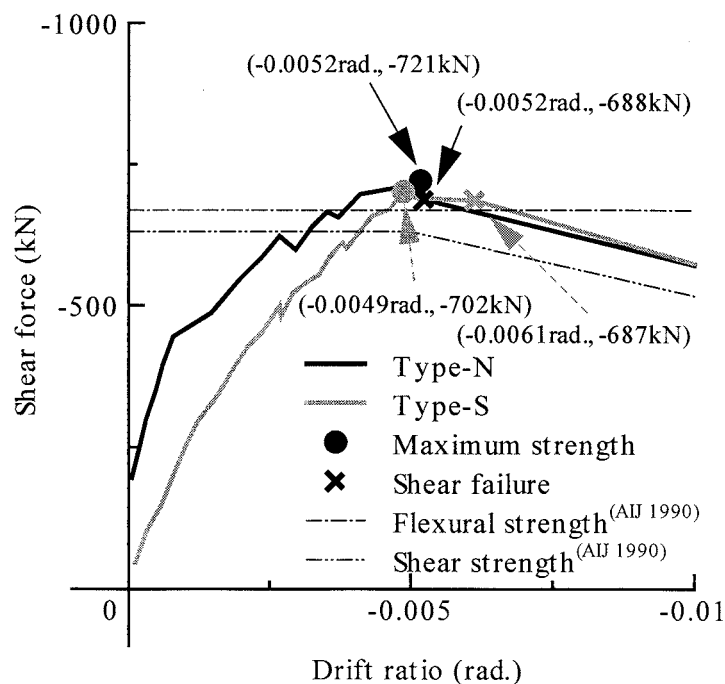


Figure 4 Comparison of the Envelope Curves of the Lateral Force-Drift Ratio Relationships

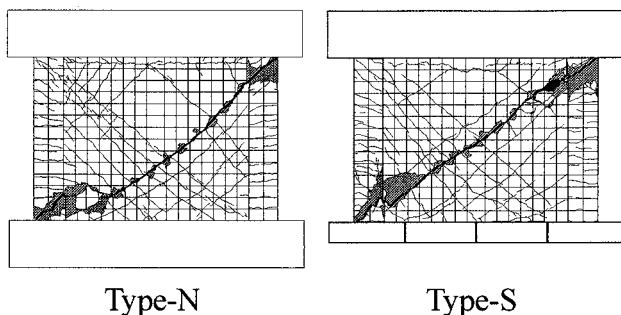


Figure 5 Comparison of the Final Crack Patterns

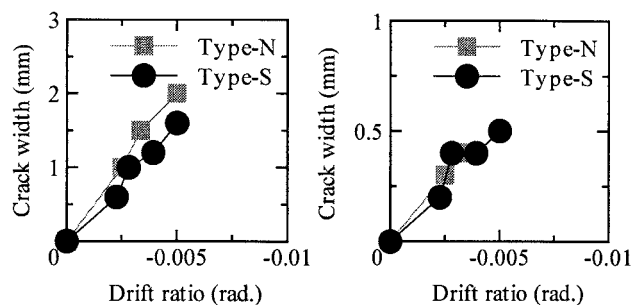


Figure 6 Comparisons of the Maximum Crack Widths at the Peak and Residual Drifts

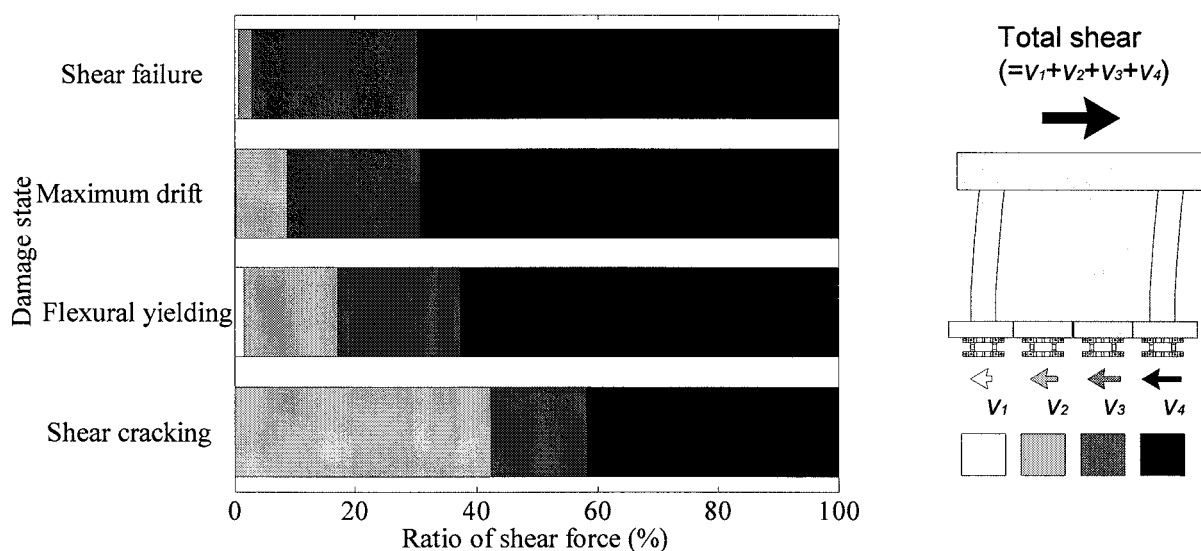


Figure 7 Distributions of the Local Shear Forces

3. LATERAL FORCE-RESISTING MECHANISM ESTIMATED FROM THE TEST RESULTS

3.1 Correlation between the Shear and Flexural Behaviors

The location of centroid of the observed local shear forces was calculated according to Eq. (1) (see Figure 8) and the location of zero normal strain on the critical section was also calculated by Eq. (2) using the data from the transducers a and b in Figure 3. In these equations, however, each location was represented as a distance from the wall edge on the compressive side.

$$L_c = \frac{\sum_{i=1}^4 v_i l_i}{\sum_{i=1}^4 v_i} \quad (1)$$

$$L_n = \frac{-\delta_c}{\delta_t - \delta_c} l_w + \frac{d_c}{2} \quad (2)$$

where, L_c : distance to the centroid of local shear forces, v_i : local shear force measured by the i -th load cell in Figure 8, l_i : distance to the center of i -th load cell in Figure 8, L_n : distance to the location of zero normal strain on the critical section, δ_c : axial deformation at the compressive column bottom measured by the transducers a or b in Figure 3, δ_t : axial deformation at the tensile column bottom measured by the transducers a or b in Figure 3, l_w : span length between the center of boundary columns, d_c : depth of boundary column.

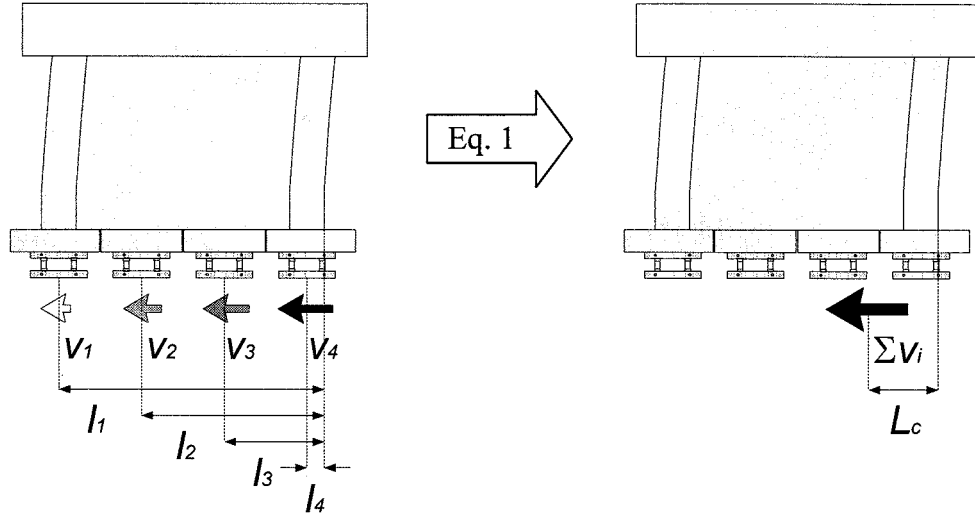


Figure 8 Evaluation of the Location of Centroid of the Local Shear Forces

L_c and L_n at each damage state shown in Figure 7 are compared in Figure 9. They decreased according to the damages of the shear wall. Then, the centroid of the compression zone on the critical section, which was assumed to be from the wall edge to L_n , was also evaluated using L_n and plotted as L_n' in the figure. The centroid of compression zone was also located around that of the local shear forces at the large drift levels, which indicates that the distributions of shear stress on the critical section may be related to the flexural behaviors.

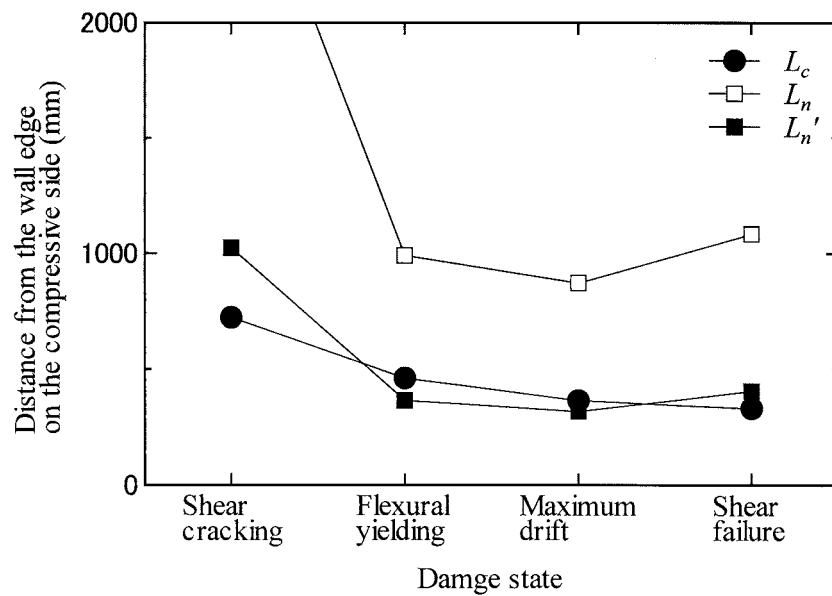


Figure 9 Shifts of L_c , L_n , and L_n'

3.2 Evaluation of Shear Strength Considering Flexural Behaviors

The shear stress seems to be almost carried on the compression zone of the critical section, based on Figure 9 where L_n is located around the midspan of the wall, and Figure 7 where 97 % of the total shear force is carried on two split bases on the compressive side. In the following, then, the lateral force-resisting mechanism of shear walls is discussed based on these test results.

Assuming that lateral forces are resisted by an inclined compression strut, which is formed approximately along the shear cracks illustrated in Figure 5, as shown in Figure 10(a), the compression zone on the critical section can be regarded as the horizontal projection of the strut. Eq. (3) represents the equilibrium among three forces shown in Figure 10(a).

$$V = C \sin \theta \approx \bar{\tau} A_c \quad (3)$$

where, V : lateral force acting on the wall, C : compression force transferred in the strut, $\bar{\tau}$: shear stress carried on the compression zone of the critical section, A_c : cross sectional area of the compression zone on the critical section.

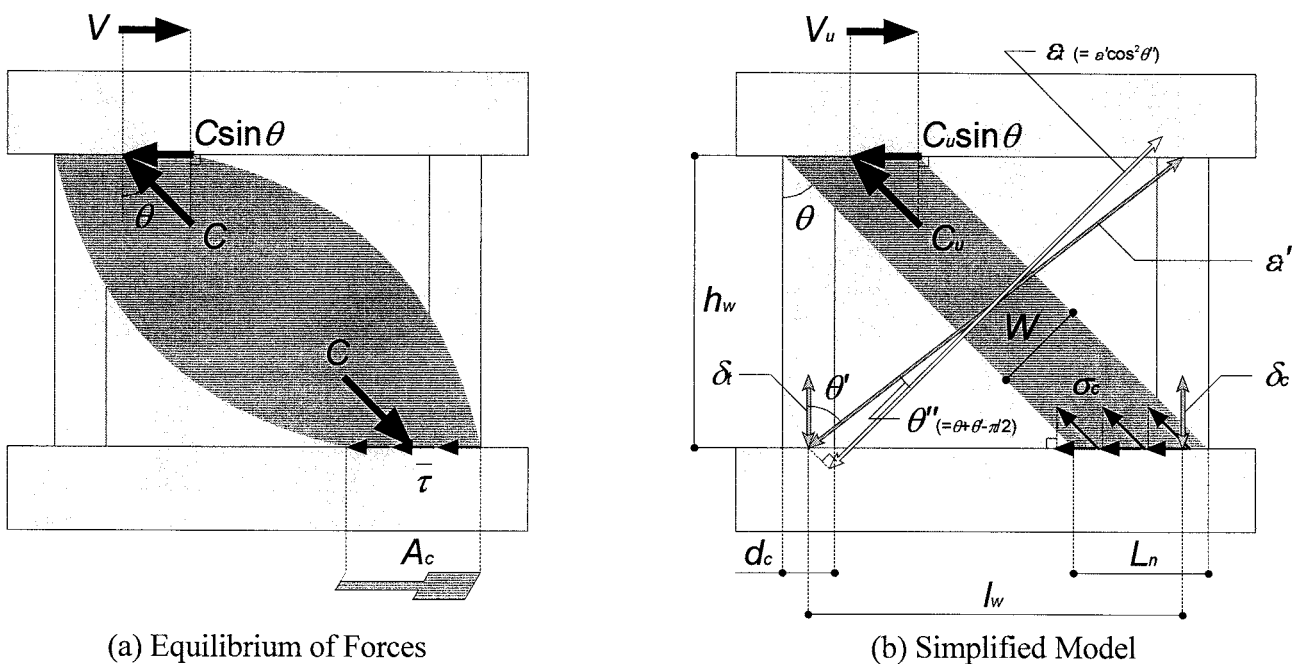


Figure 10 Assumed Lateral Force-Resisting Mechanism

Moreover, assuming that both the strut width and the stress distribution along the width are uniform as shown in Figure 10(b), the width and the compressive strength of the strut are calculated by Eqs. (4) and (5). If the tensile strain orthogonal to the strut can be evaluated, the two-dimensional constitutive law of concrete by Vecchio (1989), shown in Eq. (6), can be considered in Eq. (5).

$$W = L_n \cos \theta \quad (4)$$

$$C_u = t_w W \sigma_c \quad (5)$$

$$\sigma_c = \frac{1}{0.8 - 0.34 \varepsilon_t / \varepsilon_{c0}} \sigma_{c0} = \beta \sigma_{c0} \quad (6)$$

where, W : strut width, t_w : wall thickness, σ_c : biaxial compressive strength of concrete, ε_c : strain at compressive strength of concrete, ε_t : tensile strain orthogonal to the strut, β : reduction factor of compressive strength of concrete.

Then, substituting Eqs. (4) and (5) for Eq. (3), and eliminating θ by Eqs. (7a) and (7b) based on Figure 10(b), the ultimate lateral strength of shear walls can be evaluated as a function of L_n by Eq. (8). This equation indicates that effects of flexural behaviors of shear walls on their ultimate shear strength can be considered rationally.

$$\sin \theta = \frac{l_w + d_c - L_n}{\sqrt{(l_w + d_c - L_n)^2 + h_w^2}} \quad (7a)$$

$$\cos \theta = \frac{h_w}{\sqrt{(l_w + d_c - L_n)^2 + h_w^2}} \quad (7b)$$

$$\begin{aligned} V_u &= C_u \sin \theta = t_w L_n \sigma_c \sin \theta \cos \theta \\ &= t_w \frac{(l_w + d_c - L_n) h_w L_n}{(l_w + d_c - L_n)^2 + h_w^2} \sigma_c \end{aligned} \quad (8)$$

To verify Eq. (8), the observed shear strengths of both specimens were compared to the estimations by this equation, which were calculated using the data from the transducers a, b, and c in Figure 3 for δ_c and δ_t in Eq. (2) and ε_t in Eq. (6), respectively. At the shear failure of both specimens, the measured value of each transducer a, b, and c was -0.49 , 0.62 , and 4.67 mm for Type-N and -0.53 , 0.46 , and 6.00 mm for Type-S. However, the data from transducer c for ε_t was converted to the averaged tensile strain orthogonal to the compression strut. As a result, the evaluated strength of Type-N was 662.7 kN and that of Type-S was 762.9 kN. Although the former gives good agreement with the test result, the latter was a little higher than the observed. This might be caused by several assumptions that were applied to simplify the lateral force-resisting mechanism of shear walls. Therefore, detailing analytical data is needed to verify these assumptions. In this paper, however, a new concept could be derived to evaluate ultimate strength of shear walls considering effects of flexural behaviors.

4. CONCLUSIONS

Static loading tests of reinforced concrete shear walls were carried out to obtain experimental data on local forces. In this paper, the test results were discussed for evaluating ultimate seismic performances of shear walls. Major findings are summarized below.

1. According to the test results, the shear stress on the critical section was almost carried on the compression zone at the large deformation.
2. Based on this test result and several assumptions, ultimate lateral strength of shear-critical walls can be evaluated considering effects of flexural behaviors.
3. The ultimate strengths of the test specimens were compared to the estimations by the derived equation. Although the strength of Type-N can be evaluated very well, that of Type-S was evaluated a little higher.

Detailing analytical data is needed to verify several assumptions applied to simplify the lateral

force-resisting mechanism of shear walls. In this paper, however, a new concept for evaluating ultimate seismic performances of shear walls could be presented based on the test results.

Acknowledgements:

The authors acknowledge support by Grant-in-Aid for Young Scientist (A) (No. 16686033), Japan Ministry of Education, Culture, Sport, Science, and Technology (MEXT).

References:

- AIJ (Architectural Institute of Japan) (1990), "Design Guidelines for Earthquake Resistant Reinforced Concrete Buildings Based on Ultimate Strength Concept." (in Japanese)
- Sanada, Y. and Kabeyasawa, T. (2006), "Local Force Characteristics of Reinforced Concrete Shear Wall," *Proceedings of the 8th U.S. National Conference on Earthquake Engineering*, Paper No. 324.
- Vecchio, F.J. (1989), "Nonlinear Finite Element Analysis of Reinforced Concrete Membranes," *ACI Structural Journal*, American Concrete Institute, **86**(1), 26-35.

ULTIMATE STRENGTH EQUATIONS FOR R/C MEMBERS RETROFITTED BY CIRCULAR STEEL TUBE

Y. Sun¹⁾ and T. Fujinaga²⁾

1) Professor, Department of Architecture, Kobe University, Japan

*2) Research Associate, Department of Architecture, Kobe University, Japan
sunlili@people.kobe-u.ac.jp, fatake@kobe-u.ac.jp*

Abstract: This paper is to propose simple design equations for computing the ultimate flexural and shears strengths of reinforced concrete columns retrofitted by circular steel tubes. The proposed design equation for ultimate flexural strength has a very simple mathematical expression so that structural engineer can calculate ultimate moment capacity of the circularly retrofitted columns by hand. Another significant feature of the proposed flexural strength equation is that it can take account of confinement effect by the circular steel tubes on the ultimate moment capacity. The shear strength equation is derived by considering equilibrium of forces acting along shear-cracked surface and Mohr-Coulomb failure criteria. Previous tests are compared with the theoretical predictions by the proposed equations. Good agreements between the experimental results and the predicted indicate validity of the proposed equations.

1. INTRODUCTION

Several recent earthquakes (e.g., Northridge, 1994; Hyogoken-Nanbu, 1995; Taiwan, 1999; India Gujarat, 2001) have caused substantial damages to a great number of reinforced concrete bridge piers and building columns. Severe damages observed in many concrete frame buildings during these earthquakes demonstrated inadequacy of the previous design and emphasized again the urgent need to enhance the earthquake-resisting capacity of older concrete structures and/or their members.

Jacketing a reinforced concrete column with steel tube or plate is one of the effective measures to upgrade earthquake-resistant capacities of the existing columns. While several researches (Tomii et al (1987), Sakino et al (1989), and Priestley et al (1991, 1994)) have experimentally verified effectiveness of the lateral confining steel tube in enhancing flexural and shear strengths of concrete columns, there has not yet been a rational design equation available to compute the ultimate strength of retrofitted concrete columns. This is particularly true for the columns retrofitted by circular steel tubes.

To authors' knowledge, no design equation, which is directly applied to compute the ultimate capacities of circular concrete members, are shown or recommended currently even in the major concrete design codes or standards such as ACI code (ACI 1999) and AIJ standards (AIJ, 1999). Due to lack of information on the ultimate properties of circular concrete members, in lieu of giving a direct design equation, some of design standards recommend or mention substitute method to evaluate the ultimate flexural and shear strengths for circular members. In Japan, for example, the so-called equivalent section method has been conventionally recommended for this computation.

Figure 1 shows concepts of the equivalent section method recommended in Japan (AIJ, 1999). According to the equivalent section method, ultimate capacities of a circular column will be calculated by the following procedures: 1) replacing the circular section with a square or rectangular section that has the same area as the circular section, 2) distributing the longitudinal steels uniformly along the

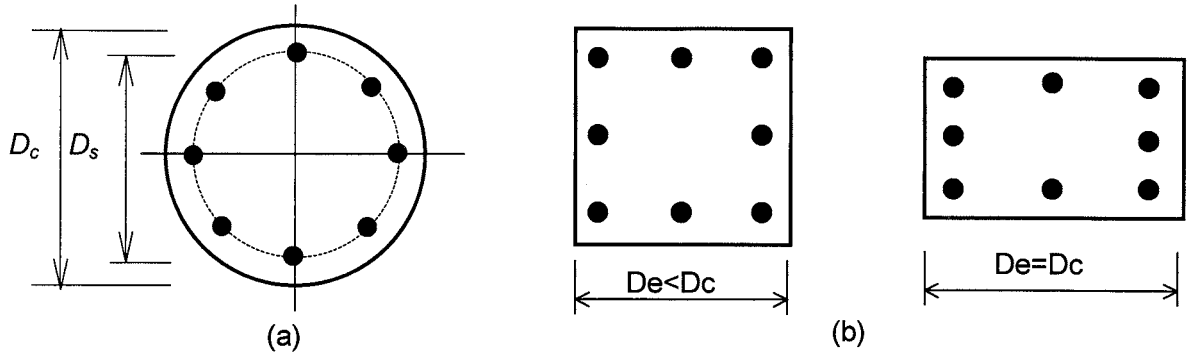


Figure 1 Concept of the Equivalent Section Method: (a) circular section, (b) equivalent section

perimeter of the equivalent section, and 3) calculating the ultimate capacities by utilizing the design equations available for the rectangular section.

The equivalent method is only a convenient substitute for circular members. There are apparently several problems concerning with accuracy of the calculated ultimate capacities inherent in the equivalent method as listed below:

1. Since the compressed portion in the equivalent square or rectangular section differs from that in the circular section, contribution of the compressed concrete to the moment capacity cannot be accurately evaluated.
2. Locations of the longitudinal steels in the equivalent sections are obviously changed, and then the moment carried by the steels cannot be correctly computed.
3. The equivalent square section has smaller section depth than the circular section. The reduced section depth results in larger shear span ratio, which may underestimate the shear strength of the original circular members.

In order to overcome above-mentioned problems, this paper introduces two design equations, one of which is used to evaluate the ultimate flexural strength for circular concrete members, and the other for the computation of the shear strength. The design equations proposed here involve no changes in the section shape and the location of longitudinal steels. Meanwhile, the proposed equations can take confinement effect on flexural strength and shear effect by the circular steel tube into consideration.

2. EQUATION FOR ULTIMATE FLEXURAL STRENGTH

2.1 Confinement Effect by Circular Steel Tubes

In the concrete members retrofitted by circular steel tubes, the steel tubes are generally used to provide lateral confining pressure to the concrete rather than the direct resistance to the axial stresses induced by the axial load and bending moment. Therefore, the steel tubes are under uniaxial stress, which acts in transverse hoop direction. If we measure the confinement degree by the steel tubes in terms of strength enhancement ratio of the confined concrete as conventionally, applying famous Richart formula can derive the following equation to calculate the strength enhancement ratio for the concrete confined by circular steel tube.

$$K = \frac{f_{cc}}{f_p} = 1 + 4.1 \frac{2}{D/t - 2} \frac{f_{yt}}{f_p} \quad (1)$$

where K is the strength enhancement ratio, f_{cc} is the confined concrete strength, f_p is the unconfined concrete strength, f_{yt} , t , and D are the yield strength, thickness, and outside diameter of the steel tube, respectively.

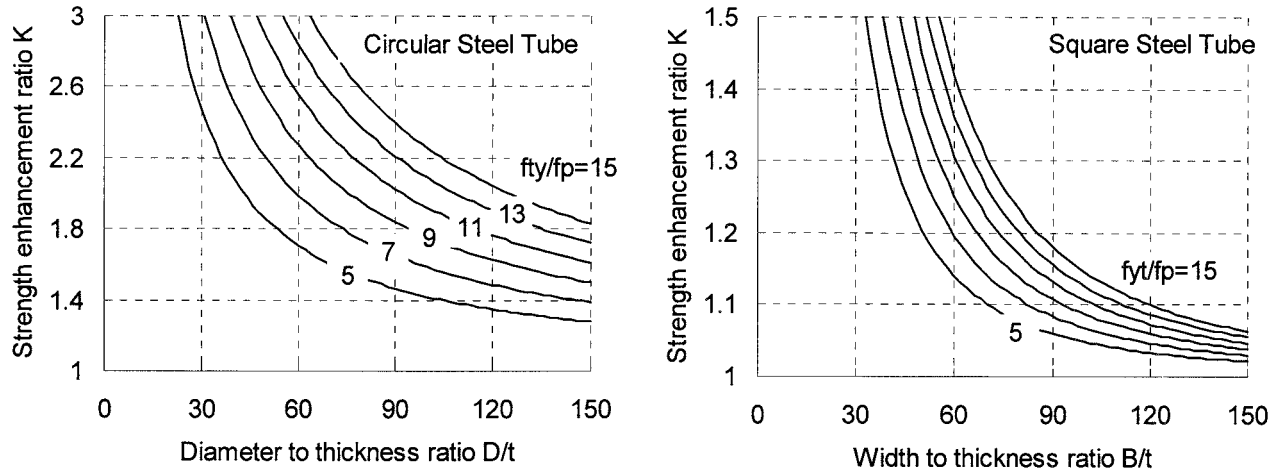


Figure 2 Examples of Strength Enhancement Ratios of Confined Concrete

Figure 2 shows relationships between the strength enhancement ratio and the wall thickness of circular steel tube. For comparison, the same relationships for the concrete confined by square steel tubes (Sakino and Sun, 1994) are also plotted in Figure 2. One can see from Figure 2 that confinement effectiveness of circular steel tube is much higher than that of square steel tube. For a column of 1000 mm in diameter, retrofitting the column with 6mm thick circular steel tube having $f_{yt} = 300$ MPa could bring 53% strength gain to the concrete with $f_p = 30$ MPa as compared with the only 2% strength gain provided by the confinement of square steel tube having same thickness.

2.2 Equation for Ultimate Flexural Strength

Interaction diagram between the axial load N and the ultimate moment M (referred to as N - M interaction diagram hereafter) is usually adopted to compute the flexural strength of concrete columns. Generally, for a given column, the N - M interaction diagram can be obtained by conducting flexural analysis, i.e., by computing the moment-curvature response of the column section under various levels of axial load. If a sound stress-strain model for the confined concrete is assumed, the flexural analysis can give fairly accurate prediction of the flexural strength, in which confinement effect of transverse steels can be taken into account. This general approach, however, is very tedious and needs help of a computer program, since it involves an iterative procedure to find the depth of the neutral axis for the internal forces to balance the external applied load. Due to its complexity, this approach isn't a favorite method for structural engineers. Therefore, a simple and reasonable calculation method for the ultimate flexural strength is desirable.

To develop a simple method to compute the ultimate capacities for circularly confined concrete members, Sun et al (2001) have proposed an equivalent rectangular stress block to replace the actual stress state for the compressed concrete in circular section by conducting parametric study of flexural response of circularly confined concrete columns, and verified validity of the proposed stress block. To further simplify the calculation of the flexural strength for circularly confined concrete members, after intensive analysis of the properties of the N - M interaction diagrams, Sun et al (2001) developed a simple equation to define the N - M interaction diagrams in form of:

$$m = \begin{cases} m_0 \left[1 - \left(\frac{n - n_0}{n_0 + r} \right)^2 \right], & n \leq n_0 \\ m_0 \left[1 - \left(\frac{n - n_0}{n_0 - K - r} \right)^2 \right], & n > n_0 \end{cases} \quad (2)$$

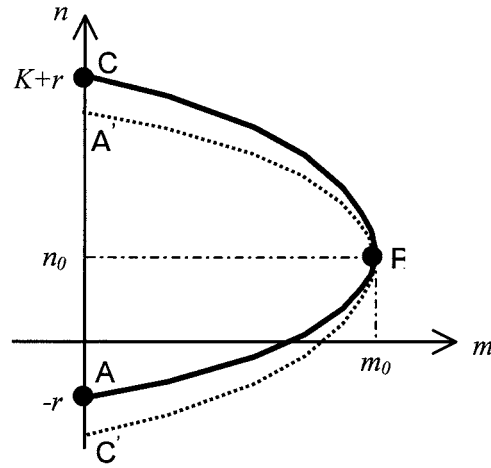


Figure 3 Idealization of the Ultimate n - m Interactive Diagram

In Equation (2), n and m are the normalized axial force the normalized moment, respectively, K is the strength enhancement ratio defined by Equation (1), n_0 and m_0 are the normalized axial force and moment at the peak of the design curve (See Figure 3), and r is the normalized steel ratio of the longitudinal bars. Definitions and expressions for these parameters are given as follows:

$$n = \frac{N}{A_g f_p}, \quad m = \frac{M}{A_g D_c f_p}, \quad r = \frac{p_g f_{ys}}{f_p} \quad (3)$$

$$n_0 = \frac{1}{\pi} (0.1K^2 + 1.3K - 2.2K^{-1} f_p \times 10^{-3}) \quad (4)$$

$$m_0 = \frac{1}{\pi} \left[0.31K + (0.61K - 0.85) f_p \times 10^{-3} + r \frac{D_s}{D_c} \right]$$

where N is the applied axial load, M is the ultimate moment capacity corresponding to the N , A_g is the gross sectional area of the column, D_c is the diameter of the column section, and D_s is the distance between the centroids of longitudinal steels located at the extreme compressive and tensile side.

As obvious from Equation (2) through Equation (4), besides its simplicity, the design equation by Sun et al (2002) can take account of confinement effect by the transverse steels on the flexural strength. Therefore, just substituting the strength enhancement ratio K defined by Equation (1) for the confinement by circular steel tubes, Equation (2) can be simply applied to evaluate ultimate flexural strength of concrete columns retrofitted by circular steel tubes.

It should be noted that as applying Equation (2) to calculate ultimate flexural strength of circularly retrofitted concrete column, considering that concrete strength in actual members may be less than material strength, the f_p will be taken as $0.85f'_c$, the compressive strength of standard concrete cylinder.

3. EQUATION FOR ULTIMATE SHEAR STRENGTH

By assuming that the shear-cracked surface is at an angle of 45° to the longitudinal axis of the concrete member, and that the concrete along the shear-cracked surface follows Mohr-Coulomb failure criteria, Sun and Miyake (2005) have recently developed a design equation to directly calculate the ultimate shear strength of circular reinforced concrete members transversely confined by circular spirals or hoops. Figure 4 shows outlines of the shear-cracked surface in a circular concrete member failing in shear.

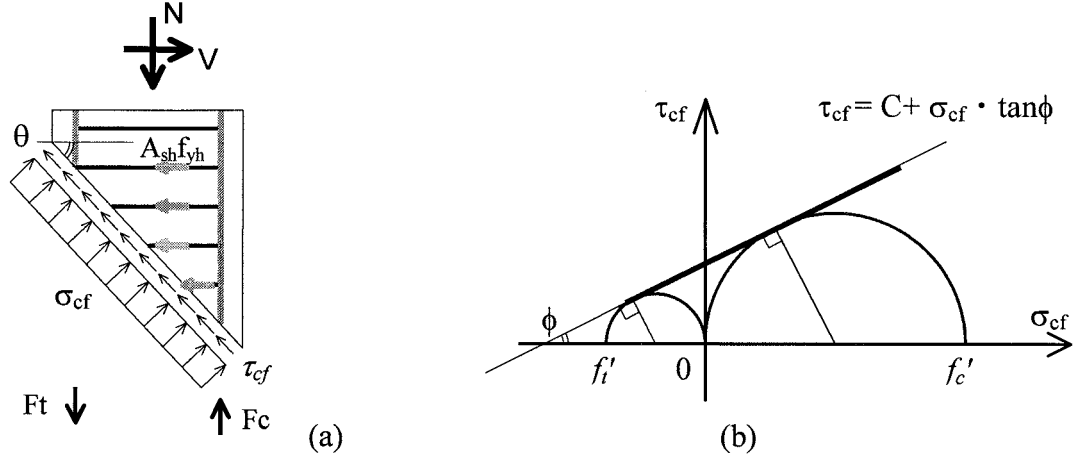


Figure 4 Outlines of the Shear-Cracked Surface: (a) equilibrium of force, (b) Mohr-Coulomb criteria

Applying the above-mentioned assumptions and considering the equilibrium of forces acting at the shear-cracked surfaces (see Figure 4), Sun and Miyake has derived the following equation to directly compute the ultimate shear strength V_u for circular concrete members:

$$V_u = (0.175 \cdot n + 0.13) \cdot \nu_c \cdot f'_c \cdot A_g + \frac{\pi}{4} \cdot A_{sh} \cdot f_{yh} \cdot \frac{D}{s} \quad (5)$$

where n is the axial load ratio defined by Equation (3), f'_c is the concrete cylinder strength, A_g is the gross sectional area of the concrete, A_{sh} is the area of circular spiral or hoop within a distance s , f_{yh} is the yield strength of circular hoop or spiral, D is the depth of column section, s is the spacing of shear reinforcement in the direction perpendicular to longitudinal reinforcement (rebar), and ν_c is the reduction factor for concrete strength, which is obtained by

$$\nu_c = \left(1.4 - \frac{D}{740}\right) \cdot \exp\left(-\frac{f'_c}{41}\right) \geq 0.5 \exp\left(-\frac{f'_c}{41}\right) \quad (6)$$

Since the circular steel tube can be considered approximately as circular hoop having spacing of zero, by conducting a simple permutation in Equation (5), the following equation can be obtained to directly evaluate ultimate shear strength of concrete columns retrofitted by circular steel tubes.

$$V_u = \left[(0.175 \cdot n + 0.13) \cdot \nu_c \cdot f'_c + \frac{2t}{D} \cdot f_{yt} \right] \frac{\pi D_c^2}{4} \quad (7)$$

where t and D are the thickness and diameter of circular steel tube used for retrofit, respectively, f_{yt} is the yield strength of circular steel tube, and D_c is the diameter of the concrete section contained in circular steel tube.

4. VERIFICATION OF THE DESIGN EQUATIONS

The experimental results by Tomii et al (1987), Sakino et al (1989), and Priestley et al (1991, 1994) are used to validate the proposed design equations. These previous tests comprise of twenty-one reinforced concrete columns retrofitted by circular steel tubes and cover wide ranges of structural factors such as the concrete strength (from 25.3 MPa to 58.8 MPa), the size of column section (from 166mm to 620mm), the amount of longitudinal reinforcement (from 2.45% to 5.87%), the wall thickness of steel tubes, and the shear span ratio of column. The wall thickness, expressed in terms of diameter-to-thickness ratio (D/t ratio) varied from 30 to 199, while the shear span ratio were between 1.0 to 6.0, covering every short columns as well as slender columns.

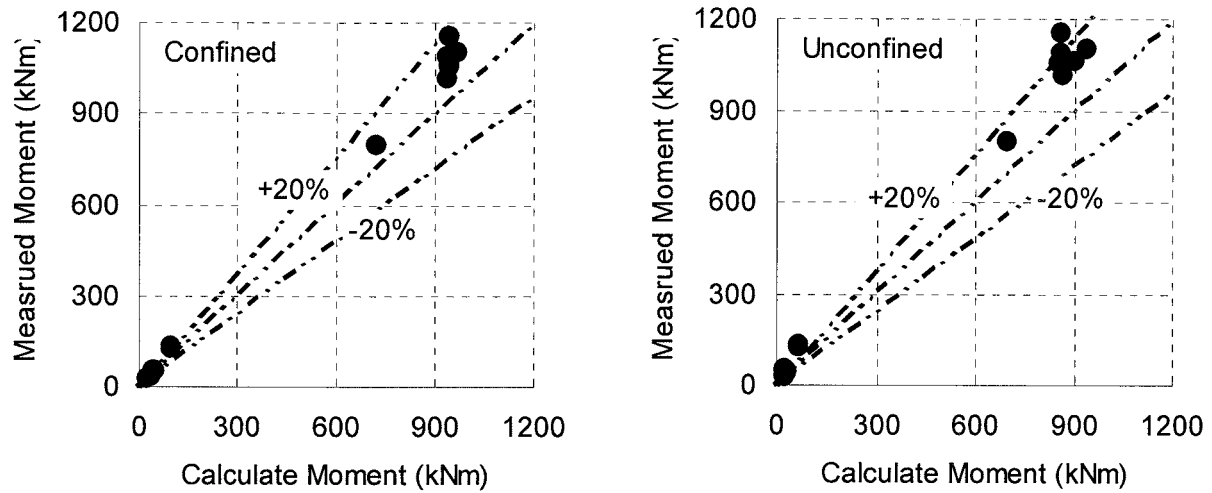


Figure 5 Comparison Between the Measured and Predicted Flexural Strength

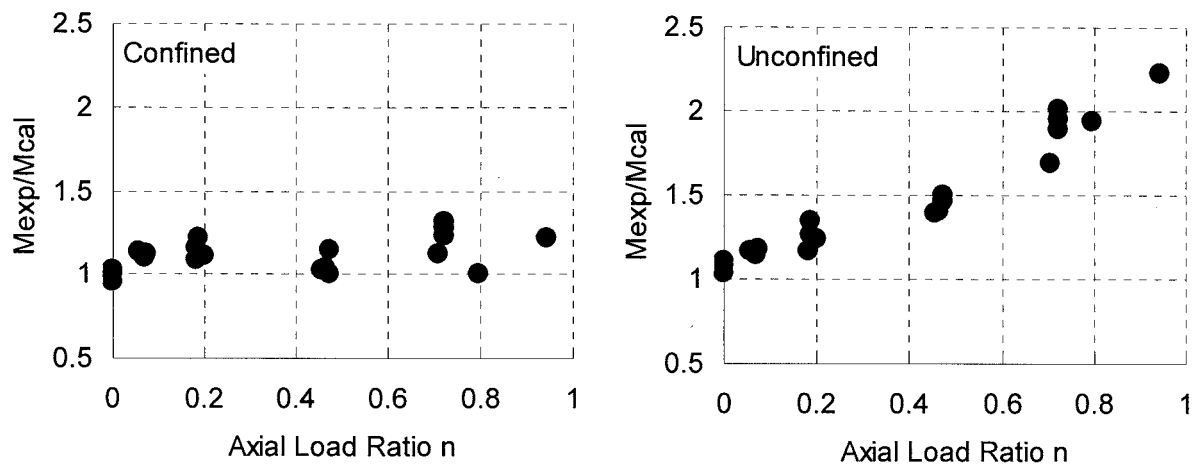


Figure 6 Influence of Axial Load Level on The Calculated Flexural Strength

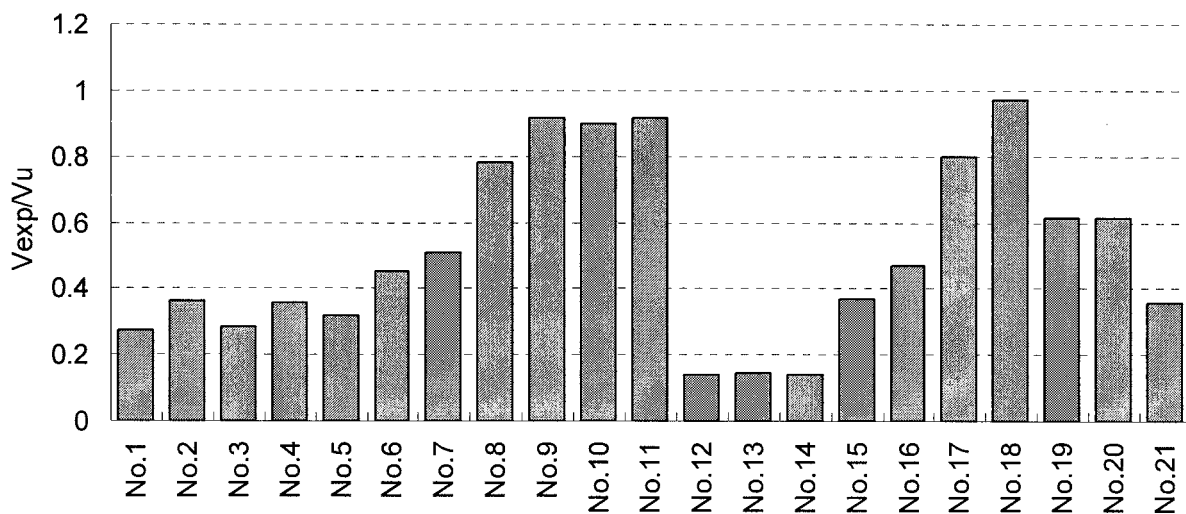


Figure 7 Distribution of the Calculated Shear Strength

Figure 5 shows comparisons between the experimental moment capacities and the theoretical results calculated by the proposed design Equation (2). For comparison, the calculated moments where

confinement effect by steel tubes is ignored are also compared with the measured results in Figure 5 with the label Unconfined. Since all the test columns failed in flexure and experienced large lateral deformation till the end of experiments, in the experimental flexural strengths, the secondary moment due to the axial load and the large lateral deformation are also included.

It can be seen from Figures 5 that the theoretical flexural strengths by Equation (2) agree very well with the measured results. The ratio of measure strength to predicted one has an average of 1.10 and a standard deviation of 0.103. On the other hand, if ignoring confinement effect by circular steel tubes, the calculated flexural strengths underestimate the experimental results by 44% on average, and the discrepancy becomes larger as the applied axial load level is higher (see Figure 6). These observation indicates that the proposed design equation does provide engineers a useful and simple tool to predict ultimate flexural strength of circularly retrofitted concrete columns.

Since all the previous test columns were reported failing in flexure, these tests cannot be used to directly verify validity of the proposed shear strength equation, i.e. Equation (7). By comparing the ratios of the calculated shear strengths V_u to the measured maximum lateral load capacities V_{exp} with the observed failure pattern, however, validity of the proposed equation can be indirectly verified. Figure 7 shows distribution of the V_{exp} to V_u ratios of the tests columns. As obvious from Figure 7, for all the columns, their V_{exp} to V_u ratios are less than 1.0, which means that these columns are theoretically predicted failing in flexure, and which coincides with the observed failure pattern. This observation implies that the proposed shear strength equation may give a reasonable prediction to the ultimate shear strength for concrete members retrofitted by circular steel tubes.

5. CONCLUSIONS

Simple design equations have been proposed in this paper to calculate the flexural and shear strengths of reinforced concrete columns retrofitted by circular steel tubes. The Proposed design equations have concise expressions and can take account of confinement effect of steel tubes on the flexural and shear strengths. Comparing the measured moments and the lateral load-carrying capacities with the predicted results by the proposed equations has verified validity and accuracy of these equations. Because of their simplicity and comprehensiveness, the proposed design equations can provide a powerful tool enabling structural engineers to conduct rational retrofitting design for the existing concrete columns.

References:

- ACI Committee (1999), "Building Code Requirements for Structural Concrete," American Concrete Institute
- AII (1999), "Standards for Structural Calculation of Reinforced Concrete Structures," Japan Architectural Institute
- Tomii, M., et al. (1987), "Ultimate Moment of Reinforced Concrete Short Columns Confined in Steel Tube," Proceedings of Pacific Conference on Earthquake Eng., 11-22.
- Sakino, K. et al. (1989), "Seismic behavior of Reinforced Concrete Short Columns Confined by Thin Steel Tubes," Proceedings of the Japan Concrete Institute, Vol. 11, No. 2, 513-518. (in Japanese)
- Priestley, M.N.J., et al. (1991), "Seismic Retrofit of Circular Bridge Columns for Enhanced Flexural Performance," *ACI Structural Journal*, **88**(5), pp.572-584
- Priestley, M.N.J., et al. (1994), "Steel Jacketing Retrofitting of Reinforced Concrete Bridge Columns for Enhanced Shear Strength," *ACI Structural Journal*, **91**(5), pp.537-551
- Sakino, K. and Sun, Y. (1994), "Stress-Strain Curve of Concrete Confined by Rectilinear Reinforcement," *J. of Struct. Constr. Eng.*, AII, No. 468, pp. 94-103 (in Japanese)
- Sun Y. and Sakino K. (2001), "Simplified Design Method for Ultimate Capacities of Circularly Confined High-Strength Concrete Columns," The ACI special Publication SP193, pp.571-585.
- Sun, Y. et al. (2001), "Equation for Computing Ultimate Flexural Strength of Circularly Retrofitted Concrete Columns," *J. of Architecture and Urban Design of Kyushu University*, Vol. 1, No.1
- Sun, Y. and Miyake, Y. (2005), "A Proposal of Shear Strength Equation for Circular Concrete Columns," Proceedings of the Japan Concrete Institute, Vol. 27, No. 2, 229-234. (in Japanese)

BEHAVIOR OF REINFORCED CONCRETE BEAMS STRENGTHENED WITH COMPOSITE PLATES

Y. C. Wang¹⁾ and K. Hsu²⁾

1) Associate Professor, Department of Civil Engineering, National Central University, Taiwan

2) ME Students, Department of Civil Engineering, National Central University, Taiwan

wangyc@cc.ncu.edu.tw

Abstract: The results of an analytical study on the behavior of reinforced concrete T-beams retrofitted with carbon fiber reinforced polymer (CFRP) plates for flexure and glass fiber reinforced polymer (GFRP) plates for shear are discussed in this paper. A test series comprising four five meters long simply supported beams were tested under monotonic load to verify the analytical model. Particular emphasis was given to the performance of predicted model building upon discrete element analytical methodology incorporating the dual effects of flexure and shear in beams. The effects of curtailed longitudinal CFRP plates bonded to the soffit of test beams were also analyzed to examine the prediction accuracy of the model. An important conclusion in this paper is that the predicted model can be used to accurately predict the behavior of load versus displacement and FRP plate bond stresses

1. INTRODUCTION

Analytical prediction of the behavior of beams with bonded FRP plates has been mainly based on two approaches. The first approach used non-linear finite element analysis (Malek et al. 1998 and Nitereka et al. 1999). Such approach is complex, time consuming, sensitive to element modeling and, at present, does not always lead to reliable predictions. Arduini and Nanni (1997) developed a second approach, termed the discrete element analysis. This is a rather simple model that accounts for the mechanical properties of the constituent materials and the characteristics of the concrete-to-FRP interface. The resultant tensile forces are found from a sectional moment-curvature analysis at the ends of each discrete element. This approach can be used to find the maximum bond stresses at the FRP plate and concrete interface as well as the bond stress distribution at the interface throughout the beam length. The approach proposed by Arduini and Nanni is computationally attractive but it has the disadvantage that it does not consider the effects of diagonal tension cracking in the shear span of a beam. As a result, the model can not fully represent the FRP plate-concrete interface bond stress distribution. Meier and Kaiser (1991) had pointed out earlier that plate separation in beams could be largely influenced by shear. This paper builds on the work developed by Arduini and Nanni and incorporates the effects of diagonal tension cracking resulting from the presence of shear forces in a beam.

A series of tested reinforced concrete beams with carbon fiber reinforced polymer (CFRP) plates bonded to their soffit and glass fiber reinforced polymer (GFRP) plates bonded to their sides was used to verify the proposed analytical model.

2. ANALYTICAL MODEL

The main assumptions considered in the analytical model using the technique of discrete element analysis are:

- (a) Plane sections remain plane under bending;
- (b) The behavior of concrete in tension is ignored in the flexural calculations but accounted for in the shear calculations;
- (c) Perfect bond exists between composite plate and concrete beam; and
- (d) The presence of the adhesive layer between the composite plate and the reinforced concrete beam is ignored.

The model improved from the discrete element analysis (Arduini and Nanni 1997) considers the effects caused by diagonal tension cracking and incorporates a refinement in the numerical evaluation of the bond stress at the FRP plate-to-concrete interface.

2.1 Material Properties

The constitutive law of the three materials, namely steel, concrete and FRP, are considered in the analytical model. The stress-strain relationship of reinforcing steel is assumed to be tri-linear. Hongnestad's parabola to idealize the stress-strain relationship for concrete is used. Normally the strain ϵ'_c at maximum concrete compressive strength is assumed equal to 0.2% and the maximum strain ϵ_{cu} is 0.3%. Note that the presence of confining reinforcement in beams is unlikely to significantly affect the load-deflection response. For this reason the simple parabolic representation of the stress-strain behavior has been adopted in the study. In general the FRP laminates behave in a linear elastic manner up to failure. A wide range of composites with different mechanical properties is available.

2.2 Flexural Analysis

The analytical model incorporates a conventional moment-curvature analysis for a beam subjected to flexure (Park and Paulay 1975). The strains and stresses in the FRP plate, steel longitudinal reinforcement, and concrete, as well as curvature, are calculated using an incremental deformation technique. For convenience of calculations, the strain in the extreme concrete compressive fiber is increased in small steps to generate a moment-curvature relationship.

The strain in the extreme fiber of the beam, ϵ_{ct} , is increased until failure is reached. It is assumed that failure is reached when either the concrete strain reaches $\epsilon_{cu}=0.003$ or the composite plate reaches its ultimate tensile strain. The strains in the reinforcing bars in the composite plate are calculated in terms of ϵ_{ct} using strain compatibility.

The distribution of concrete stresses in the compression zone is found from the stress-strain curve of concrete. The reinforcing steel stresses f_{si} and the FRP plate stress f_p corresponding to strains ϵ_{si} and ϵ_p are also found by the stress-strain relationship. Then the magnitude of the concrete compressive force C_c , the steel force T_s , and the FRP plate force T_p are found by multiplying the stresses by their corresponding areas.

The location of the neutral axis c obtained from the equilibrium of internal forces is solved iteratively until equilibrium of forces across the depth of the cross section is satisfied. The internal moment of resistance is then obtained by taking the moments of internal forces about neutral axis. The curvature is then obtained by the ratio of ϵ_{ct} to neutral axis c .

2.3 Shear Analysis

Modified Compression Field Theory (MCFT) developed by Collins and Mitchell (1991) is adopted into the shear analysis. In the MCFT, reinforced concrete is treated as a composite material with its own stress-strain characteristics. Equilibrium, compatibility, and constitutive relationships

are formulated in terms of average stress and average strain. Variability in the angle of inclination of the diagonal compression stress field and strain softening in the response are considered. The MCFT can be applied to the analysis of reinforced concrete beams subjected to shear, moment, and axial load at any loading level, including beams which are reinforced in flexure and shear with elastic materials as FRP plates. Hence, the MCFT is implemented in this study as part of the refined analytical model for the prediction of the behavior of FRP composite beam at any load level.

The detail procedure for predicting the response using the MCFT of a beam with a FRP plate applied to its soffit and loaded in shear and bending moment is described in reference (Wang and Chen 2003). Fig. 1 shows many variables will be mainly explained in the segmental model with FRP plates. The MCFT calculate the strength of the diagonal compression stress field by equation 1a and 1b.

$$f_2 = f_{2\max} \left[2 \left(\frac{\varepsilon_2}{\varepsilon'_c} \right) - \left(\frac{\varepsilon_2}{\varepsilon'_c} \right)^2 \right] \quad (1a)$$

$$\frac{f_{2\max}}{f'_c} = \frac{1}{0.8 + 170\varepsilon_1} \leq 1.0 \quad (1b)$$

where ε_1 and ε_2 are the principal concrete tensile and compressive strain. After that, we determine an equivalent axial force caused by an equivalent axial strain ε_x , found by setting at the level of $jd/2$ in the sectional strain distribution that corresponds to a given moment. Considering the equilibrium of the internal axial force, the relationship of shear and principal concrete tensile stress field will be obtained.

2.4 Summation of Section Force

With reference to Fig. 2, the resulting sectional forces of an analytical segment can be estimated. The T_k and C_k are the sectional forces, resulting from bending, in tensile and compressive chord respectively. f_1 is the tensile stress resulting from the diagonal tension field and f_2 is the compression stress resulting from the diagonal compression stress field. $N_{v,k}$ is the equivalent axial force due to shear.

The total resultant forces in tensile chord, T'_k , can further be divided into two component forces, $T'_{s,k}$ and $T'_{p,k}$. $T'_{s,k}$ is the steel component forces and $T'_{p,k}$ is the FRP component forces of the reinforcement in the tensile chord. In Fig. 2(e), it can evaluate the concrete-to-FRP plate interface bond stresses.

2.5 FRP Bond Stresses

The actual distribution of the concrete-to-FRP plate interface bond stress generally follows a nonlinear behavior. However, the appropriate explanation in deriving the concrete-to-FRP interface bond stresses may be determined in relation to Fig. 2(f). In each segment, the FRP plate forces at both ends are obtained previously and then a mean bond stress in the segment can be evaluated.

Although the actual bond stresses, $\tau_{p,k-1}$ and $\tau_{p,k}$, at the ends of each segment cannot be achieved in the analytical method, a mean value of bond stress in each segment can be determined as

$$\bar{\tau}_{p,k} = \frac{T'_{p,k} - T'_{p,k-1}}{b_p \Delta x} \quad (2)$$

3. MODEL VERIFICATION BY EXPERIMENTAL RESULTS

In order to verify the model of discrete element analysis proposed by the study, four 5m long simply supported T-beams were tested under monotonic loading. Fig. 3 shows the details of steel and FRP reinforcement layout. Two beams (Units F1 and F2) were strengthened with CFRP plates for flexure only and two beams (Units S1 and S2) were strengthened with CFRP plates for flexure and GFRP plates for shear. Among these beams, Units F1 and S1 had full-length CFRP plates whereas Units F2 and S2 had staggered CFRP plates. Table 1 represents the mechanical properties of the materials used in the test. All units were subjected to six-point loading to closely simulate uniform loading, as depicted in Fig. 4.

The strain on the extreme bottom fiber of concrete surface and CFRP plate was measured by hand-held mechanical gauges to endorse the assumption of strain compatibility made when analyzing beams incorporating CFRP plates. Fig. 5 shows the longitudinal strains measured in CFRP plates and in the concrete surface next to the plates in Units F1 and F2 when approaching ultimate load. It is clear that the strains measured on the concrete surface and on the plates are very similar. In conclusion, the observed behavior confirms that the assumption of no bond slip between the concrete and a bonded plate is adequate for analysis and design.

Fig. 6 compares the measured and predicted load-deflection response of all units. For Units F1 and F2, the predicted and measured response shows good agreement overall. The difference in the elastic response is due to the fact that the behavior of concrete in tension was not considered in the moment-curvature calculations. However, the predicted initial stiffness coincides very well with the secant stiffness of the member at a load level approaching the elastic limit. The ultimate load in Units F1 and F2 was underpredicted as the ultimate tensile strain of the CFRP plate obtained from a coupon was smaller than that recorded in the bonded plate at failure. In contrast, the model overpredicted the ultimate load for Units F1 and F2 because the prediction was carried out before the tests using limited information available for predicting the location and capacity of the observed localized shear failures in these units. For Units S1 and S2, there is excellent agreement between the theoretical and observed response.

4. EFFECT OF THE SEGMENT LENGTH

In general, the test beams were modeled with segment lengths varying between $0.1h$ and $0.6h$. The appropriate segment length for the analytical model was discussed by means of sensitive analysis. Hence, a tee-section simple supported beam with 5m long, identical to prototype Unit P1 as depicted in Fig. 3, was chosen for conducting the case study. Fig. 7 shows several analytical beams with different modeled length and CFRP layout subjected to a uniform load. The materials given in Table 1 were adopted in the analysis.

To observe the effect caused by the length of a discrete segment, a beam was partitioned with segments varying from $0.05h$ to $0.6h$ in length as shown in cases 1 to 5 of Fig. 7. Fig. 8 shows the results of stress distribution in the CFRP laminates and the interface bond stresses. The stress distribution in the CFRP laminate is not sensitive to the length of the segment. However, the interface stress varies depending on the length of the segment. This is because the bond stress between the concrete and the CFRP laminate were calculated assuming a linear variation of the longitudinal tensile stress in the segment. This situation can be explained by a concept of average stress calculated in a given segment length. If a smaller segment length is considered, a more pronounced local peak stress is obtained. On the other hand, the longer the segment length chosen, the average stress in the segment is obtained.

Since the segment length affects the analytical result of the laminate bond stress, special

attention must be given to the choice of appropriate segment widths for a reasonable analysis. The sensitivity analysis carried out suggests that a beam can be separated in segments with lengths varying between 0.1h and 0.6h. Smaller length segments are required for at least a distance 0.2h from the CFRP cut-off points and for a zone of higher shear if the bond stress concentration is to be observed. An example was selected by a more complicated condition of the beam with curtailed CFRP laminates as presented in Cases 6 and 7 of Fig. 7. The beam in case 6 was analyzed with equal segment lengths of 0.1h over the span while the beam in case 7 was represented by 0.1h short segments ranging from the beam end to the CFRP laminate cut-off point and by 0.6h long segments elsewhere. Fig. 9 shows the results of Cases 6 and 7 are nearly identical. The modeling of beams with the arrangement used for Case 7 was adopted previously for the analysis of the beams tested in the experimental program.

5. CONCLUSION

1. The proposed model, using discrete segment analysis and considering the effect of bending moment and shear with diagonal tension cracking in each segment, is used to analyze the beams externally bonded with FRP laminates to their soffit and sides. This allows simulation of the failure of the strengthened beams in a more practical manner than other analytical models.
2. Experimental work consisting of two beams which had CFRP plates bonded to their underside and two beams which had CFRP plates bonded to their underside and GFRP U-shaped plates bonded to their sides was carried out to verify the proposed model. These tested beams were subjected to monotonic loading up to failure.
3. Test results confirmed the model assumption of strain compatibility and no bond slip between concrete surface and FRP plate is satisfactory.
4. The sensitivity analysis carried out suggests that the beam can be discretized in segments with lengths varying between 0.1h and 0.6h. Smaller length segments are required for at least a distance 0.2h from the FRP cut-off points and for a zone of higher shear if the bond stress concentration is to be observed.
5. The model described in this study was used to accurately predict the load-displacement behavior of the units tested. Excellent agreement was also found between the measured plate strains and the strains predicted by the model.

References:

- Malek A. M., Saadatmanesh H., Ehasani, M. R. (1998), "Prediction of failure load of R/C beams strengthened with FRP plate due to stress concentration at the plate end." *ACI Struct J* **95**(1), 142-52.
- Nitereka C., Neale K. W. (1999), "Analysis of reinforced concrete beams strengthened in flexure with composite laminates." *Canadian J Civil Eng* **26**, 646-54.
- Arduini M., Nanni A. (1997), "Parametric study of beams with externally bonded FRP reinforcement." *ACI Struct J* **94**(5), 493-501.
- Meier U., Kaiser H. (1991), "Strengthening of structures with CFRP laminates." In: *Proceedings of the Conference on Advanced Composite Materials in Civil Engineering Structures*. ASCE, 224-32.
- Collins M.P., Mitchell D. (1991), "Prestressed concrete structures." *Prentice Hall Inc.*
- Park R., Paulay T. (1975), "Reinforced Concrete Structures." *John Wiley & Sons Inc.*
- Fyfe Co. LLC. Design manual for Tyfo Fibrwrap System – Rev.1. San Diego, CA, USA 1988.
- Wang Y. C. and Chen C. H. (2003) "Analytical study on reinforced concrete beams strengthened for flexure and shear with composite plates." *Composite Structures* **59**, 137-148

Table 1. Mechanical properties

Materials	A_s (mm ²)	f_y (MPa)	f_u (MPa)	E (GPa)	ϵ_{sh} (%)	ϵ_u (%)
Concrete $f_c' = 19\text{MPa}$	-	-	-	21	-	0.3
Rebar R6	28.3	365	504	203	1.2	13
Rebar D6	78.5	325	458	192	3.2	28
Rebar D12	113.1	316	470	197	3.2	27
CFRP Plate	-	-	658	65	-	1.0
GFRP Plate	-	-	374	20	-	1.9

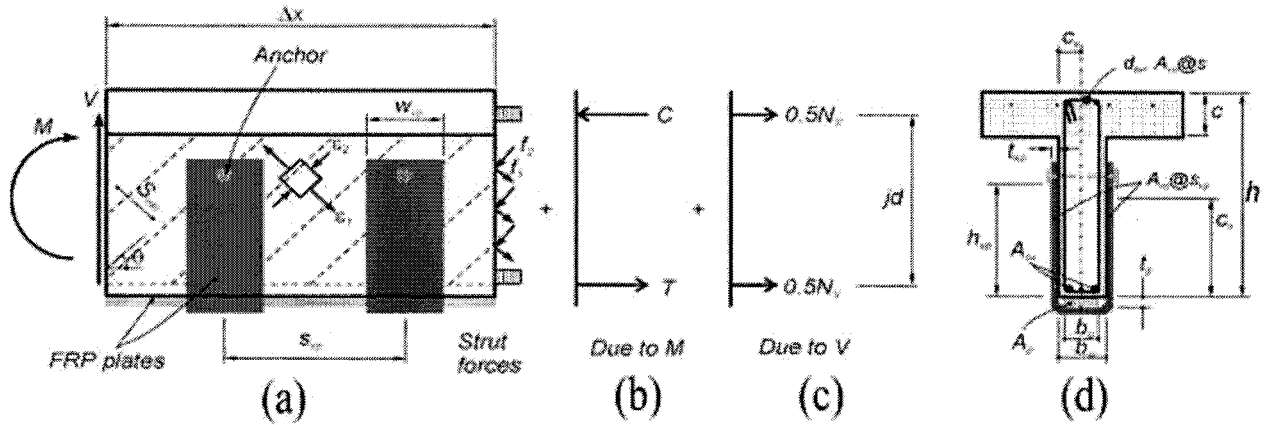


Fig. 1. MCFT model for beams with FRP laminates: (a) segment; (b) sectional forces due to flexure at end; (c) forces due to shear; (d) cross section.

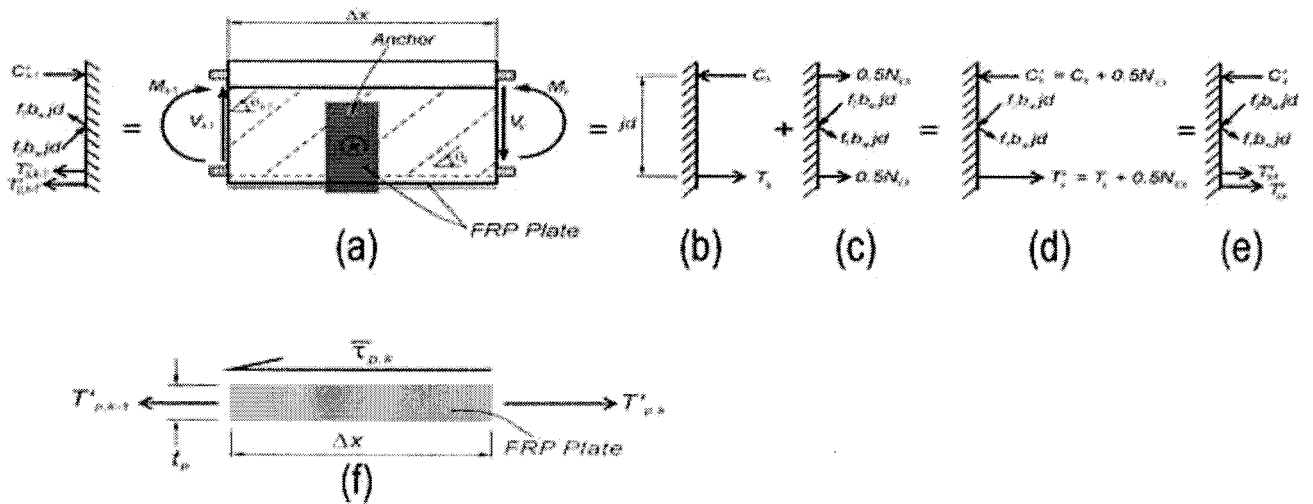


Fig. 2. Diagrams for segmental components: (a) segment k ; (b) sectional forces due to flexure; (c) forces due to shear; (d) resultant forces; (e) detailed component forces acting at tension chord; (f) FRP laminate bond stress.

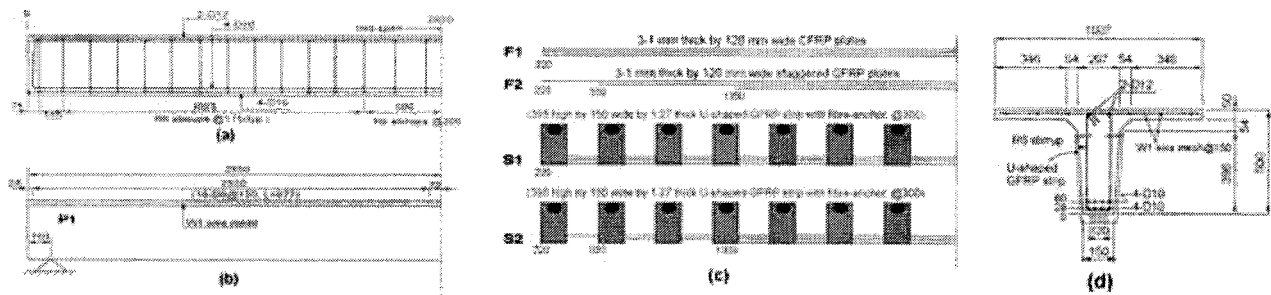


Fig. 3. Steel reinforcement and FRP layout for test units: (a) rebar arrangement of prototype unit; (b) geometry and steel reinforcement of slab; (c) FRP layout for retrofitted units; (d) cross section.

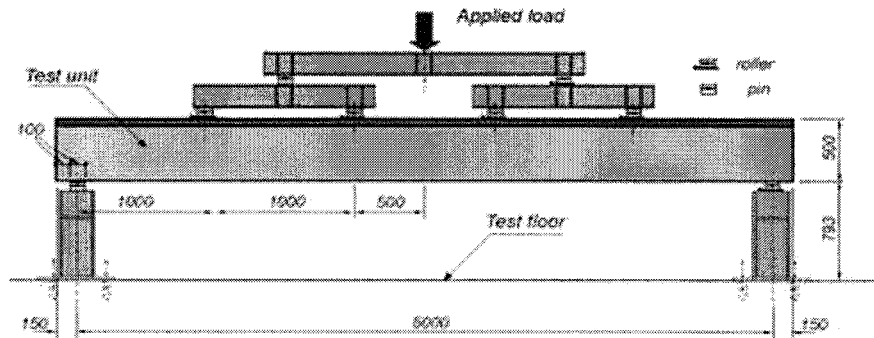


Fig. 4 Test setup

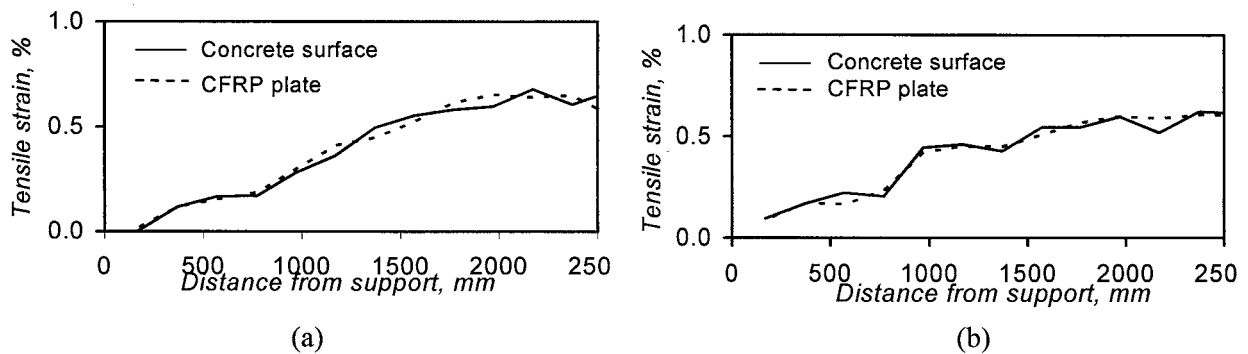


Fig. 5. Measured concrete surface and CFRP plate longitudinal strains: (a) Unit F1 at the load of 218 kN; (b) Unit F2 at the load of 211 kN.

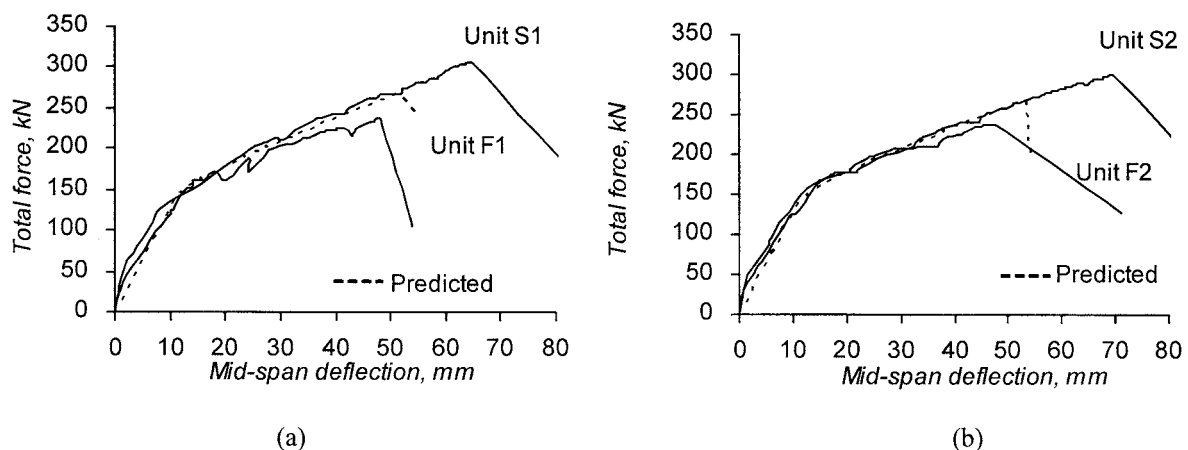


Fig. 6. Comparison of load versus deflection between measured and predicted values: (a) Units F1 and S1; (b) Units F2 and S2.

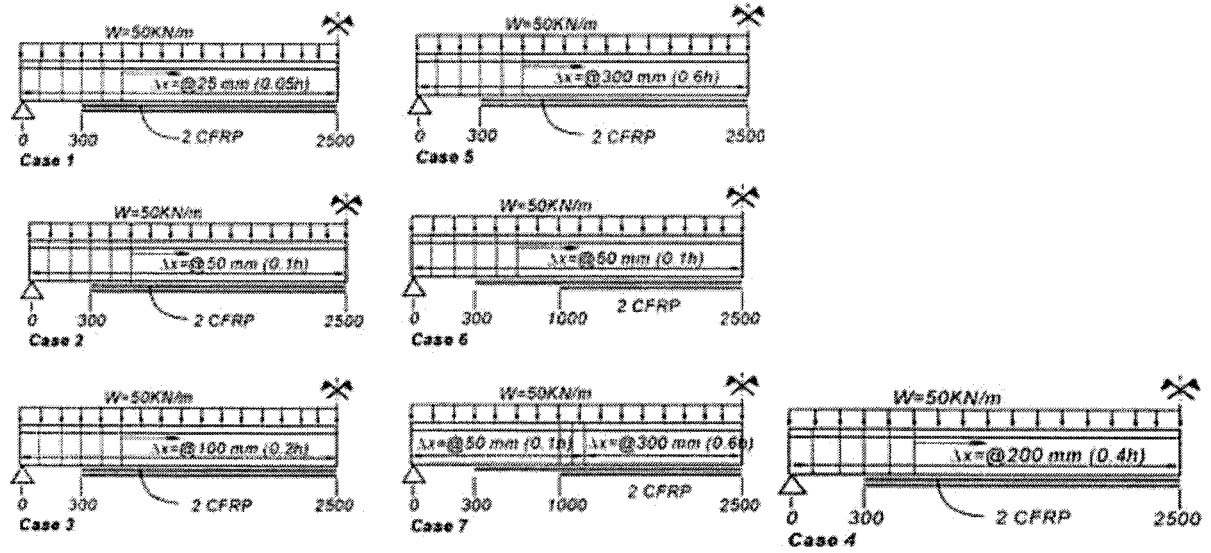


Fig. 7 Case studies in analysis on the effect of segmental length.

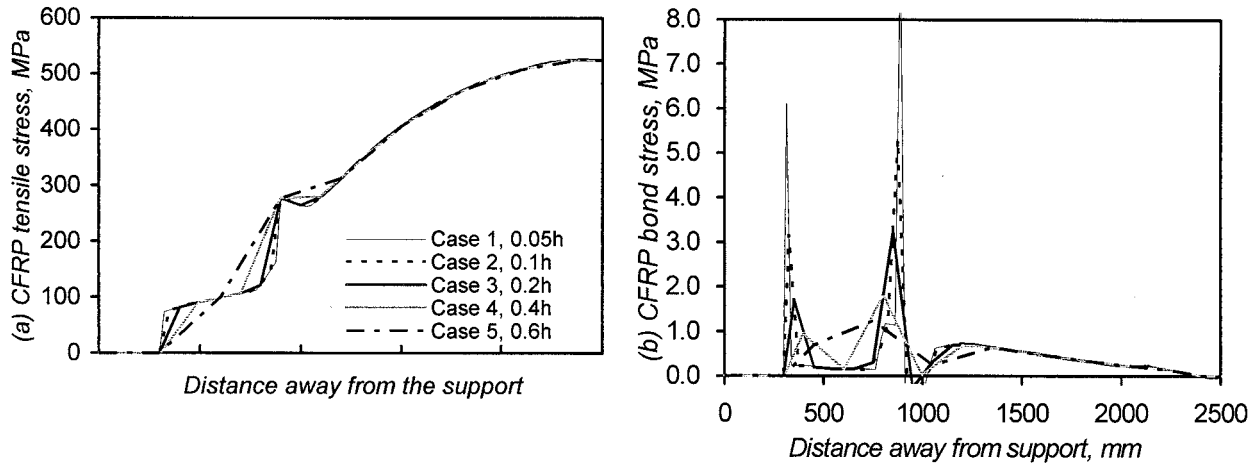


Fig. 8 Analytical results of different modeled lengths for cases 1 to 5: (a) CFRP plate longitudinal stress; (b) interfacial CFRP bond stress.

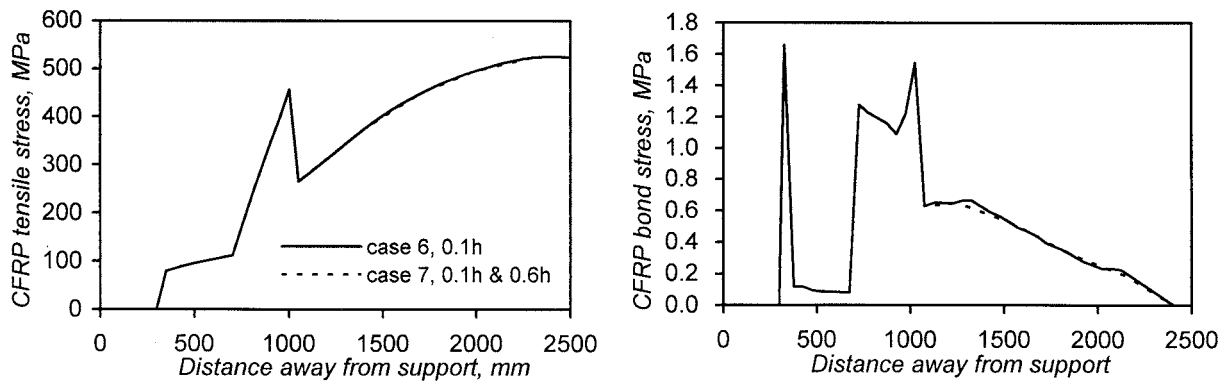


Fig. 9 Analytical results of different modeled lengths for cases 6 and 7: (a) CFRP plate longitudinal stress; (b) interfacial CFRP bond stress.

STRUCTURAL PERFORMANCE OF RC COLUMNS SUBJECTED TO REBAR CORROSION

M. Iwanami¹⁾, E. Kato²⁾, and H. Yokota³⁾

1) Senior Researcher, Structural Mechanics Division, Port and Airport Research Institute, Japan

2) Project Researcher, LCM Research Center for Coastal Infrastructures, Port and Airport Research Institute, Japan

3) Executive Researcher, Port and Airport Research Institute, Japan

iwanami@pari.go.jp, kato-h-e@pari.go.jp, hiroy@pari.go.jp

Abstract: Some infrastructures in urban districts, particularly, RC structures in marine environments, suffer from material deterioration, such as rebar corrosion. To ensure structural safety of the infrastructures against great earthquakes, it is necessary to evaluate influence of material deterioration on structural performance of the infrastructures. In this study, focusing on RC bridge piers subjected to rebar corrosion, influence of rebar corrosion on structural performance of RC column members was experimentally investigated by performing reversed cyclic loading tests. Corrosion of rebars in concrete was artificially generated by an electrolytic test before load application. The experimental results were analyzed in terms of load carrying capacity, ductility, and failure process of RC columns. From the results, load carrying capacity and ductility decreased due to corrosion of main bars and stirrups. Load carrying capacity of RC columns was influenced by localized corrosion of main bars, and the ductility was especially influenced by localized corrosion of stirrups. It was found to be very important to consider localized corrosion of rebars in concrete and the consequent localized deformation when evaluating structural performance of RC column members damaged by rebar corrosion.

1. INTRODUCTION

Some infrastructures in urban districts, particularly, reinforced concrete (RC) structures in marine environments, suffer from material deterioration. When RC structures are built in marine areas, a typical and important deterioration phenomenon is corrosion of rebars embedded in concrete. Once the corrosion starts, concrete cracks along the rebar are initiated due to volume expansion of corrosion products. Such cracks may accelerate further corrosion, and subsequently structural performance such as load carrying capacity and ductility will be degraded when rebar corrosion progresses to a certain limit degree. To ensure structural safety of urban infrastructures against great earthquakes, it is necessary to evaluate influence of material deterioration on seismic behaviour and structural performance of the infrastructures. However, the relationship between the degree and state of material deterioration and the structural performance is not made clear to date.

In this study, focusing on RC bridge piers subjected to rebar corrosion, influence of rebar corrosion on structural performance of RC column members was experimentally investigated by performing reversed cyclic loading tests on models of RC piers. Rebar corrosion was artificially generated by an electrolytic test before load application, at which the electric current was controlled by its period to obtain the target degree of rebar corrosion. The experimental results were analyzed focusing on load carrying capacity, ductility, and failure process of RC columns.

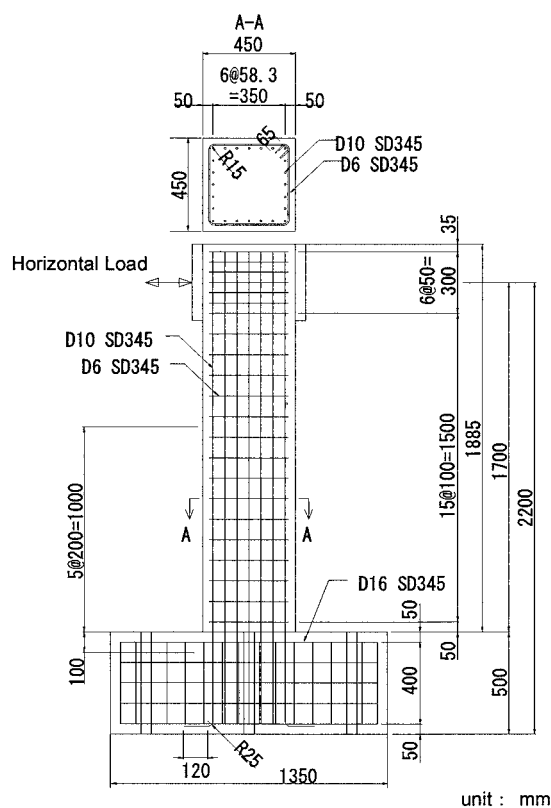


Figure 1 Test Model

Table 1 Properties of Concrete and Rebars

Type	Concrete		Reinforcement			
	Compressive strength	Young's modulus		Yield strength	Tensile strength	Young's modulus
N	42.0	3.2×10^4	Main	388	587	2.0×10^5
			Stirrup	319	507	2.0×10^5
A, B	36.0	3.3×10^4	Main	377	607	1.9×10^5
			Stirrup	324	544	1.9×10^5

Unit: N/mm^2

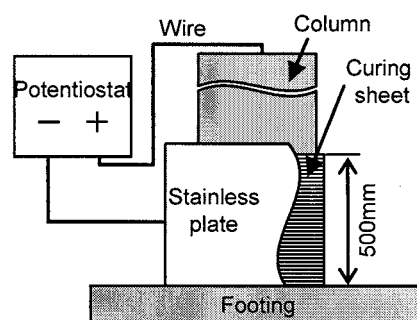


Figure 2 Setup of Electrolytic Test

2. EXPERIMENTAL PROCEDURES

2.1 Test Model of RC Column

The geometrical shape, dimensions, and rebar arrangement of test models used in this study are shown in Figure 1. The column part of the model had a square cross section of 450 mm by 450 mm, and its height of the column was 1885 mm. The total height of the test model was 2385 mm, including the footing part that was 1350 mm wide and 500 mm high. Three test models were prepared for the experiment; one was sound, that is, without rebar corrosion (Model N) and the other two were deteriorated, that is, with rebar corrosion (Models A and B). The test models were designed to fail in bending at the joint of column and footing, according to the Specifications for Highway Bridges (Japan Road Association 2002).

Compressive strengths and Young's moduli of concrete used are also shown in Table 1, obtained from compressive tests on 100 mm diameter by 200 mm high concrete cylinders at the time of reversed cyclic loading test. Also, mechanical properties of rebars used in test models are presented in the same table.

2.2 Electrolytic Corrosion Test

Models A and B had 24 wires connecting to the top of main bars in order to apply electric direct current by a potentiostat, as shown in Figure 2. The direct current was applied to the area of 500 mm in height from the joint of column and footing. To keep the concrete of this area in fully wet condition, the concrete surface was covered with a curing sheet which contained seawater. To control the degree of rebar corrosion in Models A and B, duration of application of direct current was changed. In case of Model A, application of direct current was ceased before cracks due to rebar corrosion appeared on the concrete surface. On the other hand, in case of Model B, direct current was continued to apply even

after the cracks occurred in order to make the model heavily deteriorated.

2.3 Reversed Cyclic Loading Test

With the footing fixed on a load bearing floor by PC bars, reversed cyclic loads were applied to the column by an actuator fixed to a load bearing wall. The capacity of the actuator was 1000 kN and its maximum stroke was 400 mm. The horizontal loads were applied at the position 1700 mm high from the joint. Therefore, ratio of shear span to effective height was 4.25. The vertical load was constantly applied onto the top of the column by a hydraulic jack. The resultant compressive stress acting in the column section was 1.0 N/mm^2 . The set-up of reversed cyclic loading test is shown in Figure 3.

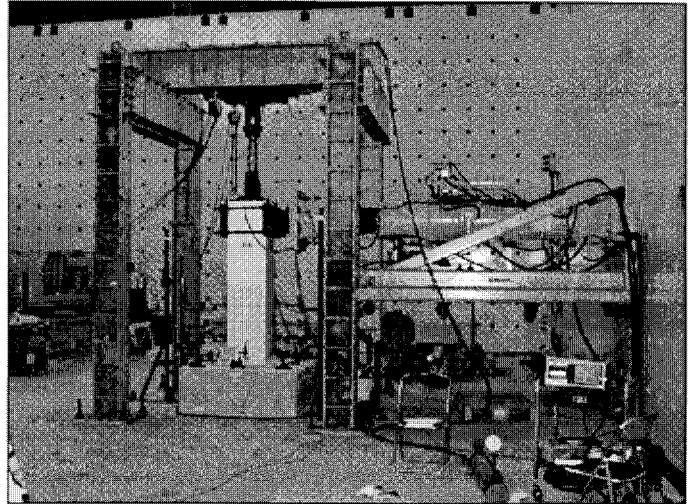


Figure 3 Reversed Cyclic Loading Test

The first loading cycle was performed by gradually applying horizontal loads in a direction (pushing-side direction) until the main bars probably reached the yield state. The corresponding horizontal displacement at the horizontal loading position, $\delta_{y,exp}$, was recorded and the loads were completely released. The same procedure was repeated in the opposite direction (pulling-side direction). This cycle of loading-releasing was performed three times for each displacement of $\pm\delta_{y,exp}$, $\pm 2\delta_{y,exp}$, $\pm 3\delta_{y,exp}$, and so on, until the ultimate failure was observed. Since the models were subjected to electrolytic corrosion, no strain gauge was attached on the main bars before casting concrete. Therefore, the first yield of main bars was determined by the load-horizontal displacement curve recorded during loading. The first $\delta_{y,exp}$ of each model was presented in Table 2. In this study, the ultimate load was defined as the maximum load recorded during loading, and the ultimate displacement was defined as the horizontal displacement at which the applied horizontal load decreased below the first yield load after the maximum load.

During the loading test, horizontal load, vertical load, horizontal displacement at the loading position and slip-out of column from footing were measured. Slip-out of Model N and Models A and B were measured 50 mm and 30 mm high from the joint, respectively. Because the measurement point of slip-out in each model was different, the measured slip-out had a possibility to be influenced by flexural deformation of the column. Regardless of the measurement conditions, horizontal displacement and slip-out were almost proportional and were unrelated to the degree of corrosion.

Table 2 First $\delta_{y,exp}$

Model	N	A	B
+ (pushing-side)	4.9 mm	4.5 mm	4.0 mm
- (pulling-side)	4.9 mm	5.5 mm	4.0 mm

2.4 Measurement of Amount of Rebar Corrosion

After the loading test, all the main bars and stirrups were taken out from the electrolytic area of Models A and B. Two pieces of rebar, 0 to 150 mm and 150 to 400 mm distance from the joint were collected from the main bars. Four pieces of each stirrup were cut from the straight part of about 200 mm long. The length of each piece cut from the main bar was measured according to the originally

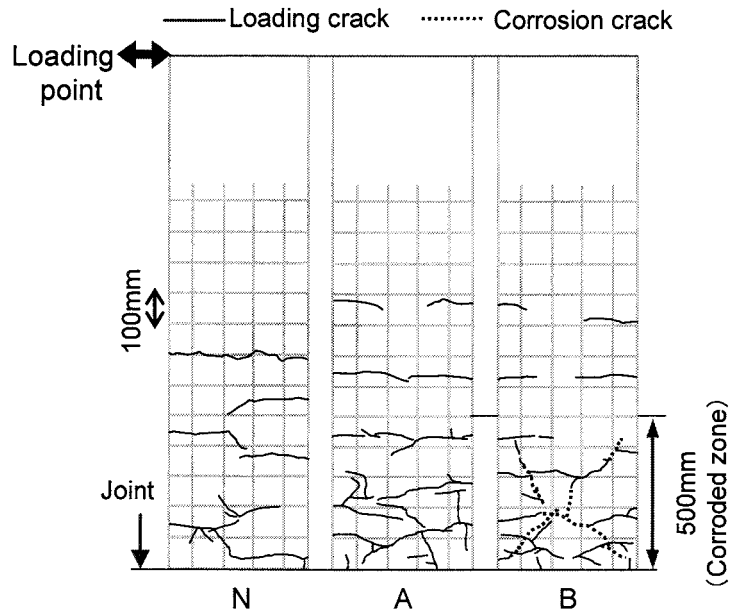


Figure 4 Crack Pattern

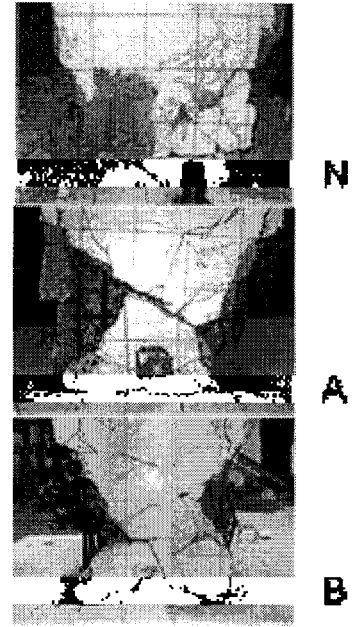


Figure 5 Ultimate Failure State

designed length, although that of stirrup was measured directly. The weight loss of rebar was measured by the following procedures: at first, sampled rebars were sand-blasted to remove corrosion products and concrete sticking to the rebar surface. Then, the rebars were immersed in 10% diammonium hydrogen citrate solution to completely remove corrosion products. The average, maximum and minimum weight loss of rebar taken from Models A and B are listed in Table 3, respectively. In the same table, 'Average' shows the averaged weight loss of all the measured values of main bars. '+' and '-' show those of 7 main bars at the edge of each tension side.

Table 3 Weight Loss of Rebar

Model Rebar Type		A			B		
		Average	+	-	Average	+	-
Main Reinforcement	Average	2.9	3.6	2.2	6.2	9.4	4.6
	Maximum	6.2	6.2	4.7	13.2	13.2	12.0
	Minimum	0.5	1.7	0.5	0.7	5.2	1.5
Stirrup	Average	5.6			20.0		
	Maximum	9.5			37.3		
	Minimum	1.3			12.0		

[Unit : %]

3. RESULTS AND DISCUSSION

3.1 Failure Process of Test Model

The crack pattern of each model observed at the horizontal displacement of $\pm 5\delta_{y,exp}$ is shown in Figure 4. After the electrolytic corrosion test, cracks were formed on the surface of Model B as shown

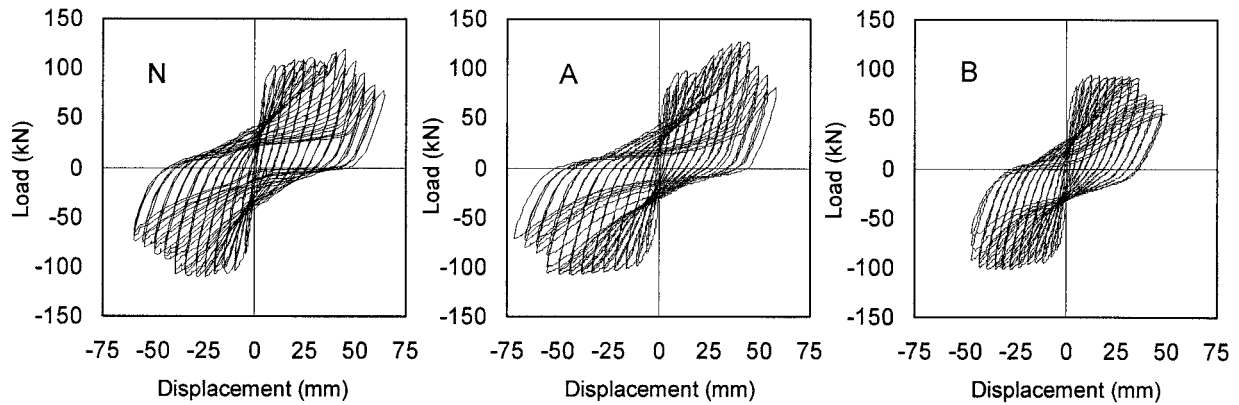


Figure 6 Load-Displacement Relationship

in the dotted lines in the same figure. Cracks, which were considered to be due to corrosion but not observed before the loading test, were formed on the surfaces of Models A and B during loading. According to the previous research on deteriorated RC beams, rebar corrosion decreases crack distribution performance because of bond deterioration between corroded rebar and concrete (Kato et al. 2006). In this study, however, decrease in crack distribution performance was not remarkably observed in column members. It was considered to be caused by localized deformation of column near the joint. Spalling of cover concrete near the joint was observed at $9\delta_{y,exp}$ in Model N, where it was observed at $13\delta_{y,exp}$ in Models A and B. One main bar was first broken at $10\delta_{y,exp}$ and $12\delta_{y,exp}$ in Model N and Models A and B, respectively, while breakage of stirrups was not observed in all the models. Figure 5 shows failure state of column near the joint after the reversed cyclic loading test. Regardless of the corrosion degree of each model, plastic hinge was observed in all the models.

3.2 Load-Displacement Relationship

Figure 6 shows the relationships between applied horizontal loads and horizontal displacements at the loading point obtained from the reversed cyclic loading test. The ultimate load and the ultimate displacement of Model B were smaller than those of Model A, which had the smaller corrosion degree than Model B. In Model A, the applied horizontal loads remarkably increased during $+6\delta_{y,exp}$ from $+10\delta_{y,exp}$. Because this increase in load was considered to be caused by unexpectable friction between the loading device and the test model, the ultimate load and displacement of Model A in the pushing-side direction were excluded in the following discussion.

Table 4 Structural Performance of Test Models

Index \ Model	N		A		B	
	+	-	+	-	+	-
First Yield Load (kN)	83.9	87.8	80.4	85.1	79.3	81.1
First Yield Displacement, δ_y (mm)	5.3	4.4	4.1	5.4	4.3	4.4
Ultimate Load (kN)	119.4	111.1	—	107.5	94.0	102.0
Ultimate Displacement, δ_u (mm)	59.9	48.2	—	61.3	39.5	46.1

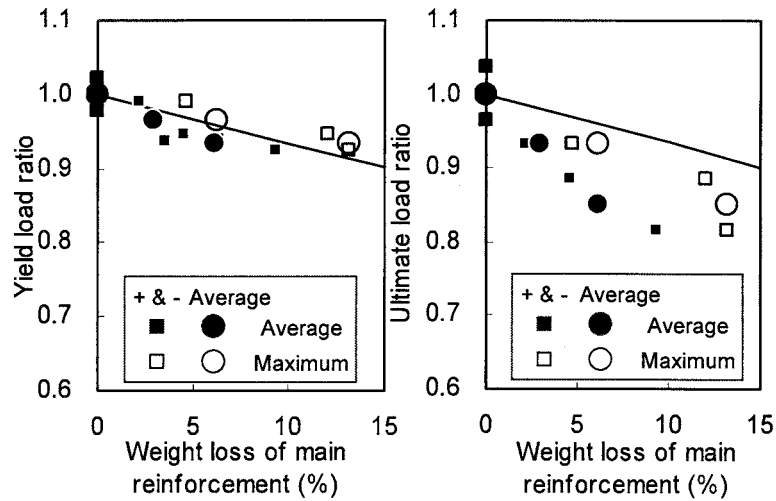


Figure 7 Load Carrying Capacity vs. Weight Loss of Rebar

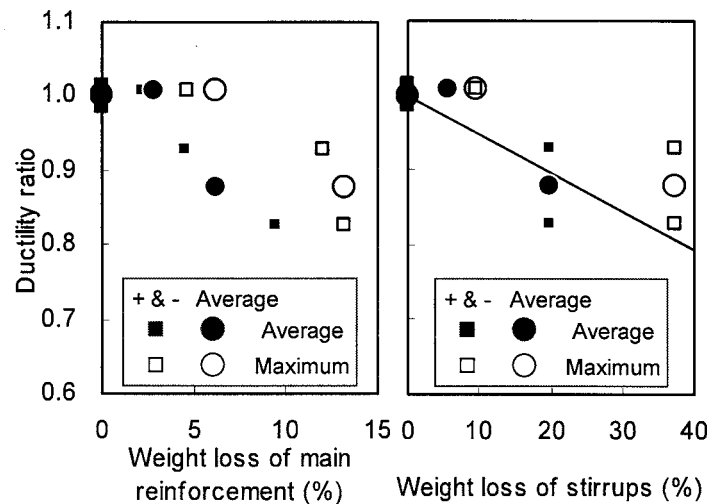


Figure 8 Ductility vs. Weight Loss of Rebar

Table 4 summarizes experimental structural performance of each model. The first yield and ultimate displacements, δ_y and δ_u , in this table were calculate from measured horizontal displacements with consideration of rotation of column due to loading. Therefore, the first yield displacement, δ_y , was different from the corresponding horizontal displacement measured at the first yield state, $\delta_{y,exp}$, described before. The load carrying capacity was degraded with increase in corrosion degree. The ultimate displacement in Model B in the pushing side, in which main bars in the tensile edge and stirrups were heavily corroded, remarkably decreased compared with that in Model N, although their first yield displacements were almost the same.

3.3 Influence of Corrosion on Structural Performance of RC Column

To understand influence of corrosion on structural performance of column members, the relationships between the average and the maximum weight losses of main bars and the first yield and ultimate load ratios are shown in Figure 7. Because compressive strength of concrete and yield strength of reinforcement of each column were slightly different, the load ratios in Figure 7 were corrected according to their specifications. The first yield and ultimate load ratios were normalized by

corresponding loads of Model N. In the same figure, the calculated first yield and ultimate load ratios according to the Specifications for Highway Bridges (Japan Road Association 2002) taking into account cross-sectional loss of main bars are also plotted as straight lines in Figure 7. Here, it was assumed that cross-sectional loss of rebars was equivalent to weight loss of rebars.

Although the experimental first yield load can be evaluated by the calculation considering the maximum weight loss of main bars, the experimental ultimate load ratio was smaller than the calculated result. According to the JCI Committee Report on Rehabilitation of Concrete Structures (Japan Concrete Institute 1998), rebar corrosion brings about decrease in mechanical properties of rebar itself, such as yield stress, elongation etc., in addition to decrease in cross-section. Moreover, decrease in bond between corroded rebar and concrete was considered to have influence on the structural performance. The bond deterioration was considered to prevent stresses from smoothly transmitting between corroded main bars and concrete (Yokota et al. 2003). Therefore, it can be concluded that influence of corrosion of main bars on the ultimate load was larger than that on the first yield load. According to our previous research work on the structural performance of corroded RC beams, the first yield and ultimate loads can be approximately evaluated by considering averaged weight loss of main bars. However, in this paper, load carrying capacity of RC columns under axial loading condition was greatly influenced by localized corrosion of main bars compared with that without axial loads. In addition to this, localized deformation of column might result in decrease in load carrying capacity of corroded RC column.

The relationships between weight losses of main bars or stirrups and ductility ratios are shown in Figure 8. A ductility ratio is defined as ratio of the ultimate displacement to the first yield one, δ_y/δ_u . The ductility ratio is normalized by the averaged ductility of Model N. The calculated ductility ratio according to the Specifications for Highway Bridges (Japan Road Association 2002) taking into account cross-sectional loss of stirrups is also shown in the same figure. Similar to calculation of load carrying capacity, it was assumed that cross-sectional loss of rebars was equivalent to weight loss of rebars. The calculated ductility ratios taking into account cross-sectional loss of main bars are not plotted because the ratios do not decrease with decrease in cross section of main bars in theory. The experimental ductility ratios became small as the weight losses increased. Focusing on main bars with about 3% weight loss, influence of corrosion on ductility was smaller than that on load carrying capacity. On the other hand, the experimental ductility ratio can be evaluated by calculated ductility ratio considering the weight loss of stirrups. Moreover, the experimental ductility ratios were evaluated in the safe side by the calculation considering the maximum weight loss of stirrups. Ductility of RC columns under axial loading condition was considered to be influenced by localized corrosion of stirrups. In Model B, heavy corrosion of stirrups was observed at the region 50 mm high from the joint, in which localized deformation was observed. Therefore, in evaluating ductility of corroded RC column, it can be concluded that it becomes important to take into account localization of deformation as well as localized corrosion.

4. CONCLUSIONS

In this study, structural performance of corroded RC columns was experimentally investigated through the reversed cyclic loading test. From the result, it was concluded that load carrying capacity and ductility were degraded due to corrosion of main bars and stirrups. Load carrying capacity of RC columns was greatly influenced by localized corrosion of main bars, where ductility was especially influenced by localized corrosion of stirrups. It was found to be very important to take into account localized corrosion and the consequent localized deformation when evaluating structural performance of RC column members damaged by rebar corrosion.

References:

- Japan Road Association (2002), "Specifications for Highway Bridges," Part V. (in Japanese)
- Kato, E., Iwanami, M., and Yokota, H. (2006), "Deterioration in Ductility of RC Beams with Corroded Reinforcement," *Proceedings of 2nd International fib Congress*, Naples, Italy, ID15-14.
- Japan Concrete Institute (1998), "Committee Report on Rehabilitation of Concrete Structures." (in Japanese)
- Yokota, H., Iwanami, M., and Sato, F. (2003), "Quantitative Evaluation of Structural Performance of Reinforced Concrete Beams Damaged by Corrosion of Reinforcement," *Proceedings of the 6th CANMET/ACI International Conference on Durability of Concrete*, Thessaloniki, Greece, 555-570.

DEVELOPMENT OF HIGH STRENGTH RC FLAT BEAM SYSTEM AND SRC FLAT BEAM SYSTEM

K. Nishimura¹⁾, K. Takiguchi²⁾, H. Hotta³⁾,
Y. Masui⁴⁾, Y. Tsuneki⁵⁾, Y. Koitabashi⁵⁾, and N. Nakanishi⁵⁾

1) Assistant Professor, Dept. of Architecture and Building Engineering, Tokyo Institute of Technology, Japan

2) Professor, Dept. of Mechanical and Environmental Informatics, Tokyo Institute of Technology, Japan

3) Associate Professor, Dept. of Architecture and Building Engineering, Tokyo Institute of Technology, Japan

4) Sumitomo Realty & Development Co., Ltd.

5) NIKKEN SEIKKEI, Japan

knishimu@tm.mei.titech.ac.jp, ktakiguc@tm.mei.titech.ac.jp, hotta@arch.titech.ac.jp,

masui.yasushi@sumitomo-rd.co.jp, tsuneki@nikken.co.jp, koitabashi@nikken.co.jp, nakanishin@nikken.co.jp

Abstract: A RC flat beam system, which was rigid frame construction that consisted with RC flat beams and normal RC columns, were researched and developed by the authors (Nishimura et al. 2006). In this project, the flat beam system was supposed to be used at exterior frame of residential buildings, and SRC or high strength RC was used for the flat beam system. In order to investigate possibility of these systems, cyclic loading tests of three beam-column joint specimens were carried out. One is high strength RC cross-shape joint specimen, another is high strength RC corner joint specimen, and the other is SRC cross-shape joint specimen. As results, it can be said that there were no serious problem. All the specimens showed restoring force characteristics of flexural type. Strength of two high strength RC specimens could be estimated by traditional ways, and estimating methods of flexural strength of SRC flat beam were proposed.

1. INTRODUCTION

A RC flat beam system, which was rigid frame construction that consisted with RC flat beams and normal RC columns, were researched and developed by the authors (Nishimura et al. 2006). In the previous study, seven cross-shape RC beam-column joint specimens, which concrete strengths were about 30N/mm^2 , were subjected to cyclic load. In this project, the flat beam system was supposed to be used at exterior frame of residential building, and SRC or high strength RC was used for the flat beam system. High strength concrete and reinforcements must be used in case of high-rise buildings. Characteristics of flat beam and corner column joint, what is called corner joint in this paper, aren't clear. In case of SRC structures, section steel in the flat beam might be eccentric. Some fears can be indicated as follows;

- 1) Whether beam-column joints suffer undesirable damage due to using high strength materials.
- 2) Whether stress can be transmitted well between corner column and flat beam.
- 3) Whether SRC flat beam and column joint can perform expectative strength.

In order to investigate these, cyclic loading tests of three beam-column joint specimens were carried out. One was high strength RC cross-shape joint specimen, another was high strength RC corner joint specimen, and the other was SRC cross-shape joint specimen.

2. EXPERIMENTAL PROGRAM

2.1 Specimens

Three specimens were prepared for the tests. High strength RC cross-shape joint specimen, High strength RC corner joint specimen, and SRC cross-shape joint specimen were numbered No.1, No.2, and No.3, respectively. Dimension of specimens and mechanical properties of reinforcements, H-shape steel used for SRC specimen, and concrete are shown in Table 1, 2, 3, and 4, respectively. Figure 1 and 2 show details of specimens. Concrete strength and yield strength of longitudinal bars of No.1 and No.2 were about 60 N/mm² and 470N/mm². Concrete strength of No.3 was about 30N/mm², and yield strength of longitudinal bars in beam and column were about 390N/mm² and 370N/mm², respectively.

All the specimens had additional reinforcements at beam end and dense stirrup around assumed plastic hinges. The assumed plastic hinge sections are shown in Figure 3. No.2 had anchor heads of longitudinal bar and additional reinforcement at beam end. Another additional reinforcement at protrusion part of joint was placed in No.2 at the center of beam depth. No.3 had H-shape steel in column and beam. Flange of beam had 90mm width at beam end and 60mm width at middle part of span, and had haunch between different widths. The end of haunch was agreed with the center of hook of additional reinforcement at beam end, which was assumed as plastic hinge section as shown in Figure 3. No.2 had a part of normal SRC beam in orthogonal direction. All the specimens had 30φ or 35φ of holes for plumbing on the flat beam near the beam-column connection.

Strain gages were pasted on four corner longitudinal bars in the beams of No.2 and No.3 at distances of 20mm and 37mm from the assumed plastic hinge section of No.2 and No.3, respectively, and pasted on flanges of H-shape steel in the beams of No.3 at a distance of 20mm from the assumed plastic hinge section.

Table 1 Dimension of Specimens

Name of specimens	Dimension b x D[mm]		Main reinforcements		Steel frame Web x Flange [mm]	
	Column	Beam	Column	Beam	Column	Beam
No.1 [HRC Cross-Shape Joint]	200 x 200	360 x 120	16-D10	16-D10		
No.2 [HRC Corner Joint]						
No.3 [SRC Cross-Shape Joint]	240 x 240	500 x 160	8-D13	8-D10	130 x 130 x 9 x 16	80 x 90 x 4.5 x 12 ^{*1} 80 x 60 x 4.5 x 12 ^{*2}

*1: beam end; *2: middle part of span; *3: compressive strength of concrete cylinder

Table 2 Mechanical Properties of Reinforcements

Name of deformed bar	D6	D10		D13	
Specimen	No.1, No.2, No.3	No.1, No.2	No.3	No.2	No.3
Nominal section area [mm ²]	31.67	71.33		126.7	
Yield strength [N/mm ²]	419 *	466	394	366	370
Tensile strength [N/mm ²]	600	656	539	515	522
Young's modulus [kN/mm ²]	201	202	196	196	197

*: 0.2% offset method

Table 3 Mechanical Properties of H-Shape Steel in Specimen No.3

	Beam		Column	
	Web	Flange	Web	Flange
Yield strength [N/mm ²]	376	296	323	279
Tensile strength [N/mm ²]	473	435	455	451

Table 4 Mechanical Properties of Concrete

Specimen	No.1	No.2	No.3
Age of concrete [days]	34	37	32
Compressive strength [N/mm^2]	60.6	61.8	30.1
Splitting tensile strength [N/mm^2]	4.2	4.0	3.0

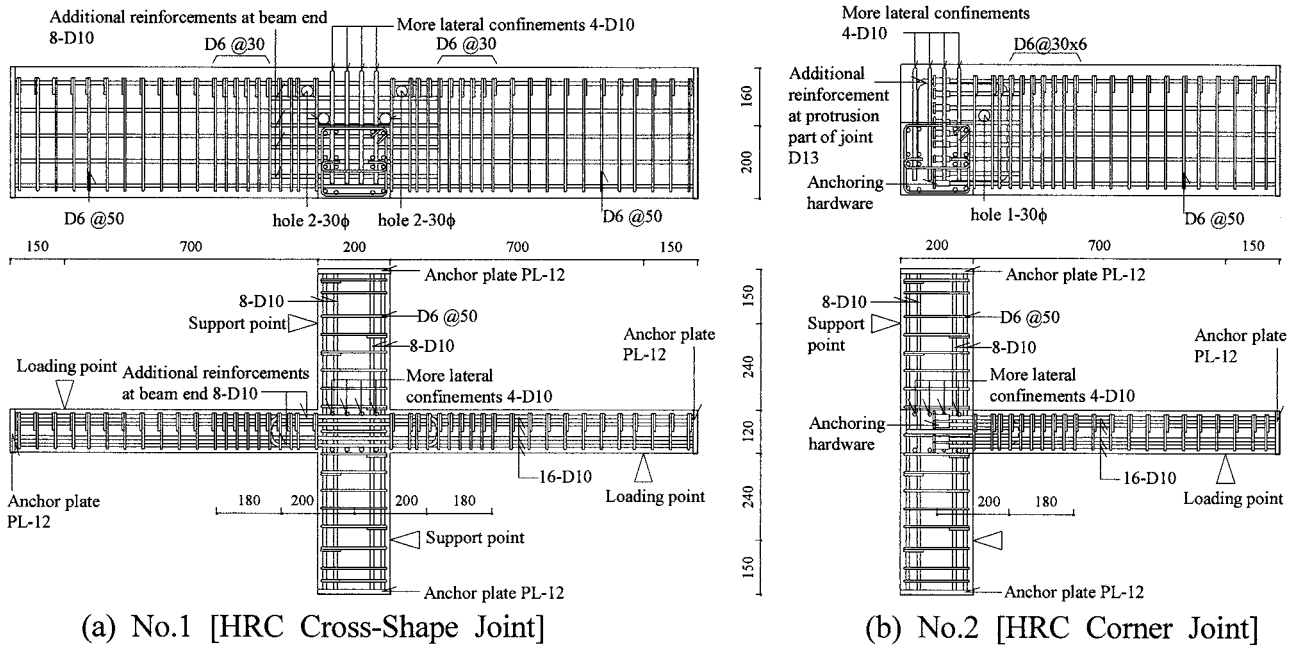


Figure 1 Details of No.1 and No.2

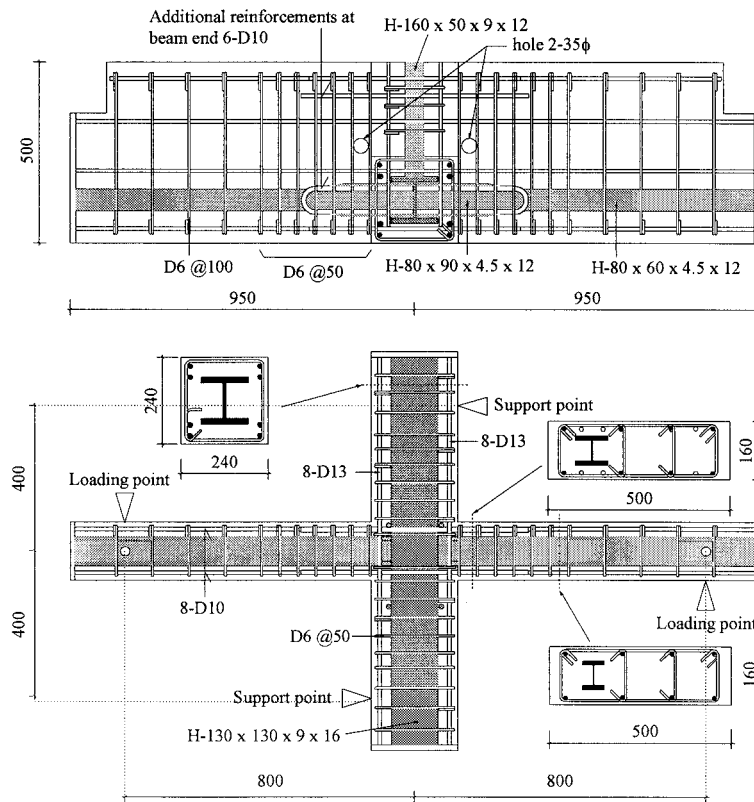


Figure 2 Detail of No.3 [SRC Cross-Shape Joint]

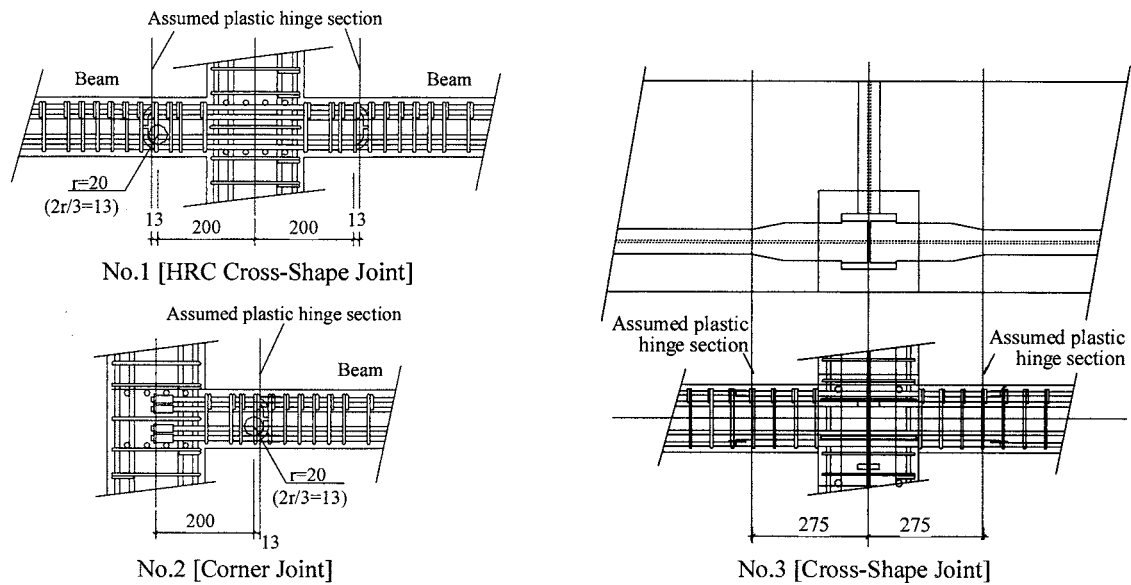


Figure 3 Assumed Plastic Hinge Sections

2.2 Loading Setup and Loading Plan

As shown in Figure 4 and 5, the column was laid and supported. Cyclic loads were applied to No.1, No.2, and No.3 by four, three, and two hydraulic jacks, respectively. Axial load was applied on No.2 by hydraulic jack as reaction of cyclic load on beam. The beams and the columns were fastened by two steel plates, which had 20mm thickness, at loading points and supporting points. Displacements in orthogonal direction of loading direction were restricted at side of beam near the loading points. Tensile reactions against torsion were taken at column sides of No.1 and No.2 by PC bars of 15 ϕ . Displacement transducers measured displacements of loading points. The cyclic loads were applied as shown in Figure 6.

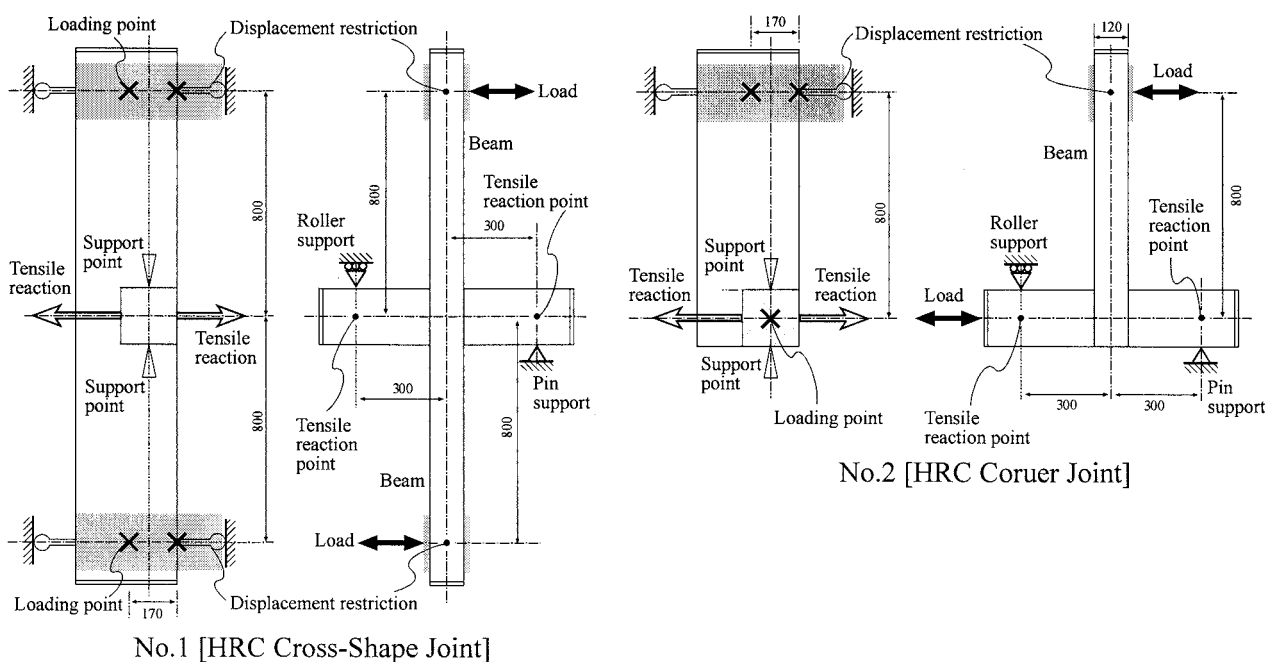


Figure 4 Loading Setups of No.1 and No.2

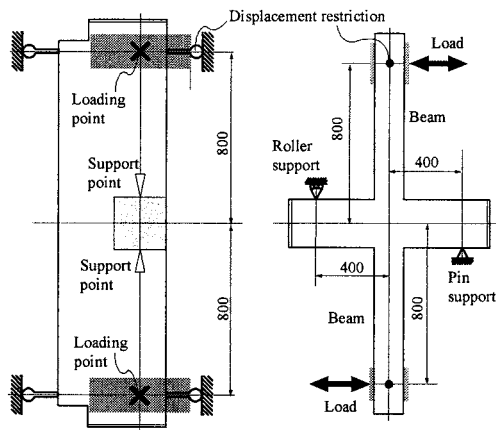


Figure 5 Loading Setup of No.3

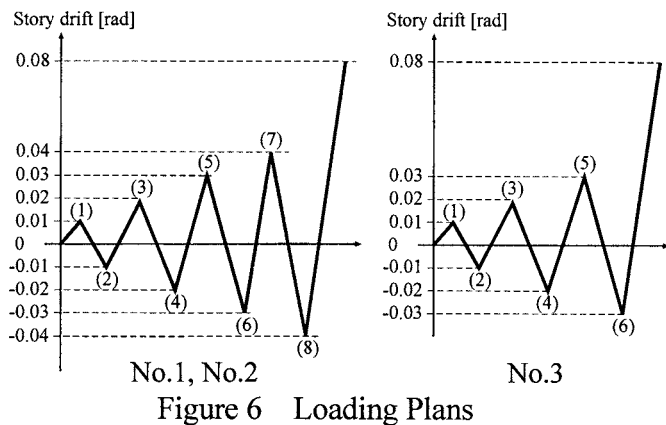


Figure 6 Loading Plans

3. TEST RESULTS AND CONSIDERATION

3.1 Restoring Force Characteristics

Figure 7 and 8 show test results and pictures of three specimens, respectively. Horizontal and vertical axis in Figure 7 is story drift and shear force of beam, respectively. Broken lines are calculated bending strengths, which were computed on condition that bending moment was equal to yield moment or ultimate moment at assumed plastic hinge section.

The calculated bending strengths of No.1 and No.2 were computed by two methods, which one method was based on AIJ standard (AIJ, 1999) and another was based on the additional theorem. The strengths based on the additional theorem were calculated with assumption that concrete and longitudinal bars had rigid-perfectly plastic body, which strength were 0.85 times of concrete compressive strength shown in Table 4 and yield strength of reinforcements shown in Table 2. Bending moment of concrete section and reinforcement section were added as the additional strength became the maximum.

On the other hand, the calculated bending strengths of No.3 were also computed by two methods, as shown in Figure 9, which were both based on the additional theorem, and strengths used on computing were 0.85 times of concrete compressive strength shown in Table 4 and yield strength of reinforcements shown in Table 2. One method was that beam section was divided into two sections, which were SRC section and RC section, and strengths of two sections were added. Another was that strengths related to rotation around the X and Y axes were calculated and calculated strength points on X-Y plane were interpolated by two ellipses, which was assumed as strength curve. The strength shown in Figure 7 was calculated on the condition that bending moment around Y axis is equal to zero.

As shown in Figure 7, it can be said that yield strength and maximum strength of No.1 and No.2 could be estimated to be the calculated bending strengths based on AIJ standard and the additional theorem could, respectively. In case of No.3, maximum strength could be expected to be the calculated strengths of Method 1 and Method 2 those results were almost same as shown in Figure 7. All the specimens didn't degrade its strength under large deformation. No.1 and No.2 showed good loops of flexural type, and No.3 showed better loop than No.1 and No.2 because of its steels. Stiffness of No.2 was a little higher than that of No.1. Stress of column and joint were smaller than that of No.1 because No.2 had one beam, therefore deformation of column and joint were smaller.

All the specimens had wide bending crack near the assumed plastic hinge section, and deformation was concentrated on the assumed plastic hinge. No.2 had some cracks on protrusion part of joint, which weren't seen on the same part of No.1. However there are no remarkable effects of these cracks on restoring force characteristics.

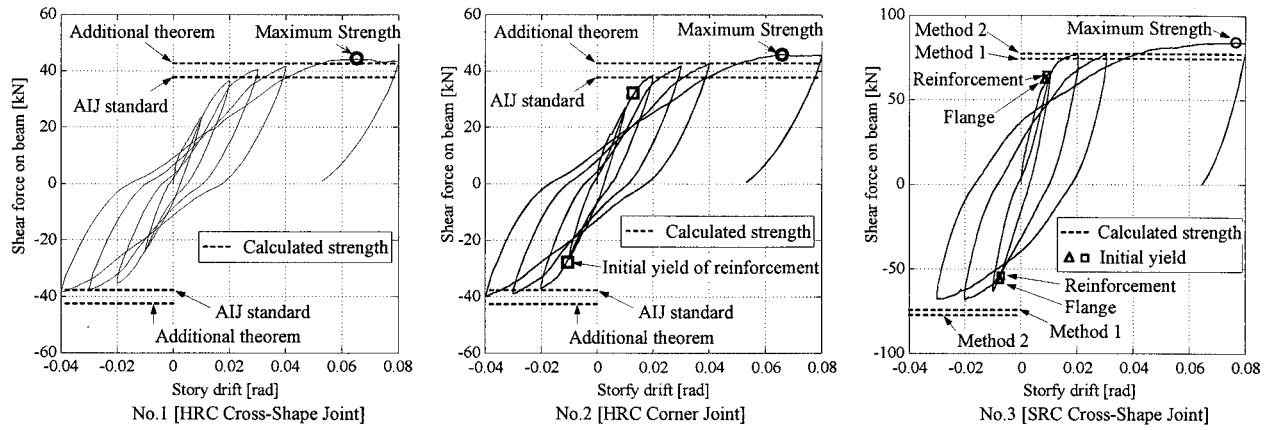
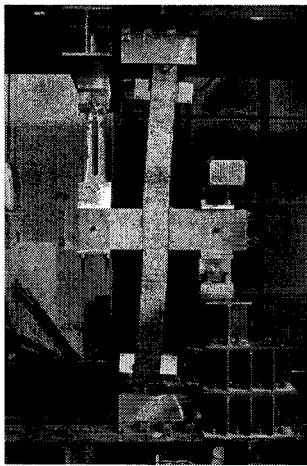
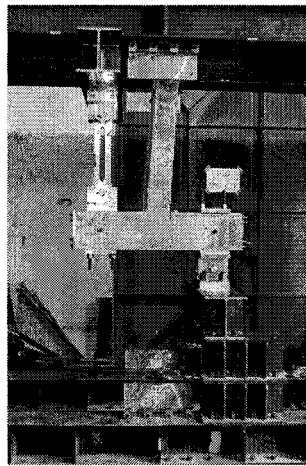


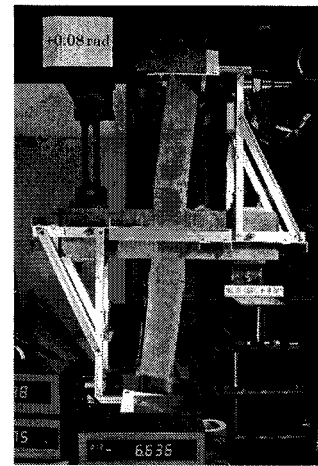
Figure 7 Story Drift and Shear Load Relationships



No.1 after the test



No.2 after the test



No.3 at maximum deformation

Figure 8 Pictures of Specimens

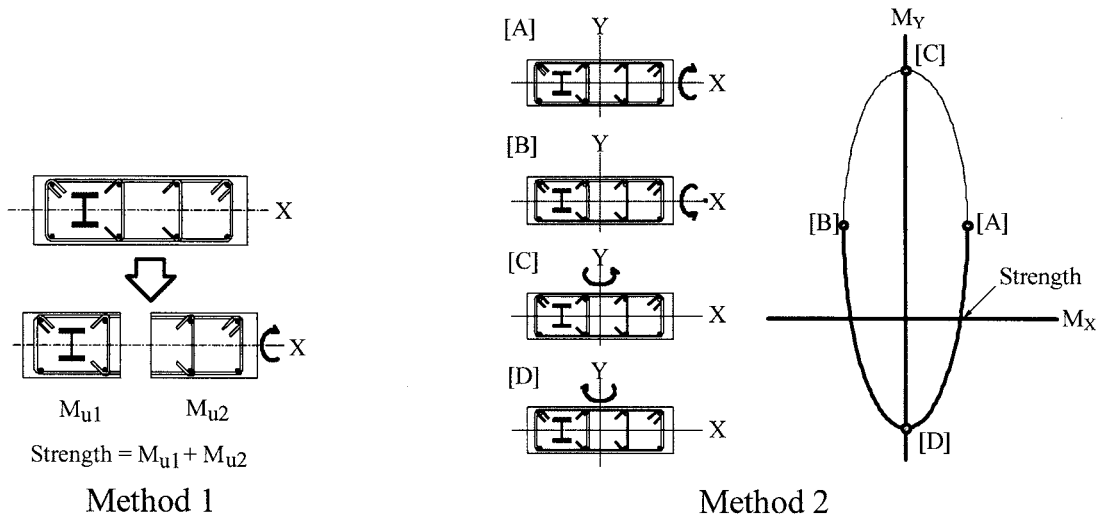


Figure 9 Calculation Methods of Bending Strength of SRC Flat Beam Section

3.2 Strain of Reinforcement and Flange

Figure 10 shows strains of reinforcements and flanges of No.2 and No.3. Numbers of horizontal axis were corresponded to numbers shown in Figure 6. As shown in the results of No.2, tensile strain of tensile reinforcement of column side was a little larger than that of protrusion side, which wasn't

observed in the results of cross-shape joint specimens. A reason could be considered that torsional rigidity of protrusion part of corner joint was softer than that of cross shape joint. However, difference between cross-shape joint and corner joint didn't effect on restoring force characteristics, as shown in Figure 7. One of the features in the result of No.3 was compressive strain of compressive reinforcement was large. This fact is one of the evidences for appropriateness of calculating method of bending strength shown in Figure 9.

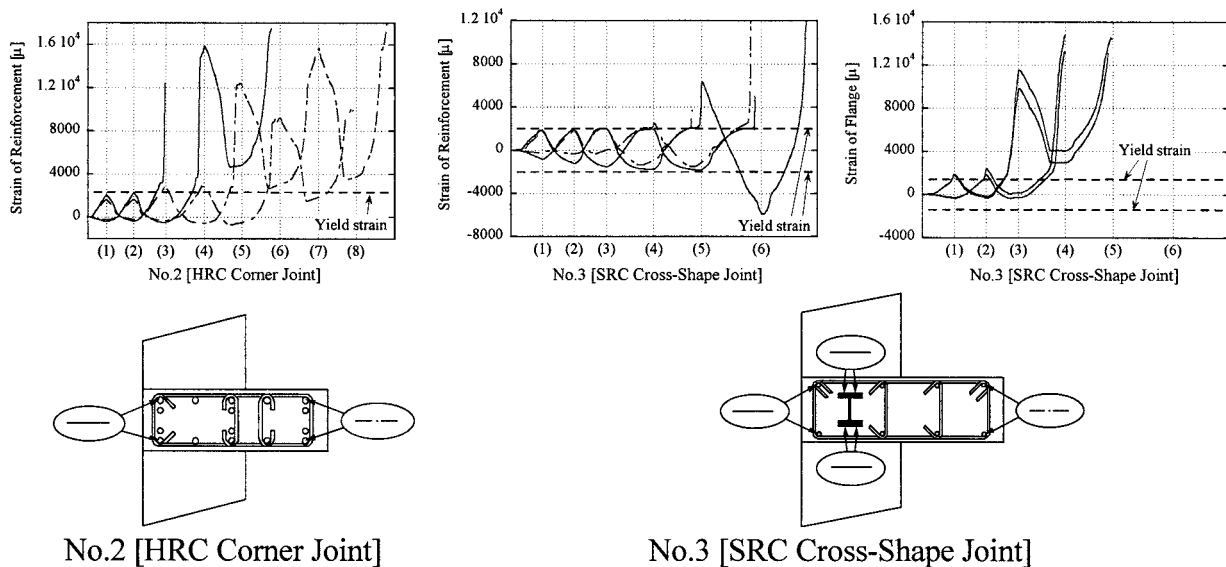


Figure 10 Strains of Reinforcements and Flanges

4. CONCLUSIONS

Three flat beam and column joint specimens were subjected to cyclic loading tests, which one was high strength RC cross-shape joint specimen, another was high strength RC corner joint specimen, and the other was SRC cross-shape joint specimen. As results, the following conclusion could be found.

1. Maximum strength can be expected to be calculated bending strength.
2. Eccentricity of steel section in SRC beam must be considered when bending strength of SRC flat beam was calculated.
3. High strength RC flat beam and column joint performed flexural type of restoring force characteristics, and SRC joint showed better loops of force-deformation relationship than RC joint.
4. Restoring force characteristics of corner joint were equivalent to that of cross-shape joint.

References:

- Architectural Institute of Japan (1999), "Standard for Structural Calculation of Reinforced Concrete Structures –Based on Allowable Stress Concept," Architectural Institute of Japan.
- Nishimura, K., Takiguchi, K., Hotta, H., Tsuneki, Y., Koitabashi, Y., Nakanishi, N., and Masui, Y. (2006), "Research and Development of RC Flat Beam and Column Joint System", *Proceedings of the Tenth East Asia-Pacific Conference on Structural Engineering and Construction (EASEC-10)*, Real Structures, 401-406

MECHANICAL PROPERTIES OF COMPOSITE PC BRIDGES USING UFC TRUSS

H. Murata¹⁾, T. Miki²⁾ and J. Niwa³⁾

1) Ph.D. Candidate, Department of Civil Engineering, Tokyo Institute of Technology, Japan

2) Assistant Professor, Department of Civil Engineering, Tokyo Institute of Technology, Japan

3) Professor, Department of Civil Engineering, Tokyo Institute of Technology, Japan

hmurata@cv.titech.ac.jp, mikitomo@cv.titech.ac.jp, jniwa@cv.titech.ac.jp

Abstract: In the improvement of the seismic performance of a bridge structure, the weight reduction of the girder is one of the significant factors. To reduce the self-weight of the girder, composite prestressed concrete (PC) girders, with webs made of steel truss, have been recently developed. However, due to the problem of durability in steel truss, composite PC girders using Ultra High Strength Fiber Reinforced Concrete (UFC) truss as web have been introduced in this study. UFC provides highly advanced mechanical properties, such as high compressive strength, 200N/mm^2 , high durability and high ductility. Therefore, UFC can be applied, instead of using steel, for solving the problem of durability. Due to its high compressive strength, high prestress can be applied to UFC members. The self-weight of composite PC girders using prestressed UFC truss can be reduced as well similar to the steel truss web composite PC girder. The aim of this research is to investigate the mechanical properties of composite PC girders using prestressed UFC truss. Then, mechanical properties of composite PC girders using prestressed UFC truss are compared with that of the actual steel truss web composite PC girders with the same self-weight.

1. INTRODUCTION

In order to improve the seismic performance of a bridge, the weight reduction of the superstructure is important. A composite prestressed concrete (PC) girder, of which the web member is made out of a different material from the flange member, has been developed in the world. Because of the high strength of the web member, its cross sectional area can be reduced. As a result of volume reduction, the total weight of the bridge girder is also reduced. Moreover, the construction on the site can be simplified because the web member is manufactured beforehand at a factory and only the flange part is cast at the site.

Recently, steel truss web composite bridges have been given special considerations (JPCEA, 2005). However, the steel truss has a problem of durability. The corrosion occurs at the joint part between the flange and the steel web. Therefore, it is suggested to use Ultra High Strength Fiber Reinforced Concrete (UFC) (JSCE, 2004) instead of steel for the web in this study.

UFC has been developed since 1994 (Rechard et al., 1994). This material provides high compressive strength around 200 N/mm^2 , and high ductility because of the existence of steel fiber. Moreover, UFC has excellent resistance to carbonation, chloride attack, freeze-thaw action and alkali silica reaction. In addition, due to high workability, members with various shapes can be made.

The author has studied about mechanical properties of composite PC structures using UFC for the web (Murata et al., 2005) and proposed a new joint system between UFC truss and flange concrete (Murata et al., 2006). In this study, composite PC girders utilizing prestressed UFC truss as web members (prestressed UFC truss web composite PC girders) are focused upon the prestressed UFC truss web composite PC girder is compared with that of Kinokawa viaduct, which is the first steel truss

web composite viaduct in Japan. By using the two-dimensional nonlinear finite element analysis, the mechanical behavior of Kinokawa viaduct girder and the prestressed UFC truss web composite PC girder, that would replace the web of the Kinokawa viaduct by the UFC truss member, was simulated and compared.

2. ANALYTICAL PROCEDURE

2.1 Target of Analysis

The target of analysis is the span from P1 to P2 of Kinokawa viaduct as shown in Figure 1. The length of this span is 85 m and the height of the girder is 6 m. In Kinokawa viaduct, diagonal members are round shape steel pipes with 406 mm diameter. In the analysis, the total weight of the UFC diagonal members of the composite PC girder was chosen to be the same with the total weight of the steel diagonal members of Kinokawa viaduct. The shape of the UFC diagonal members is a hollow box which has the cross section of 500 × 300 mm.

Table 1 tabulates the thickness of a UFC hollow box that replaces each steel pipe. In the span of Kinokawa viaduct to be analyzed, four types of steel pipe were used. For each of the four types, the

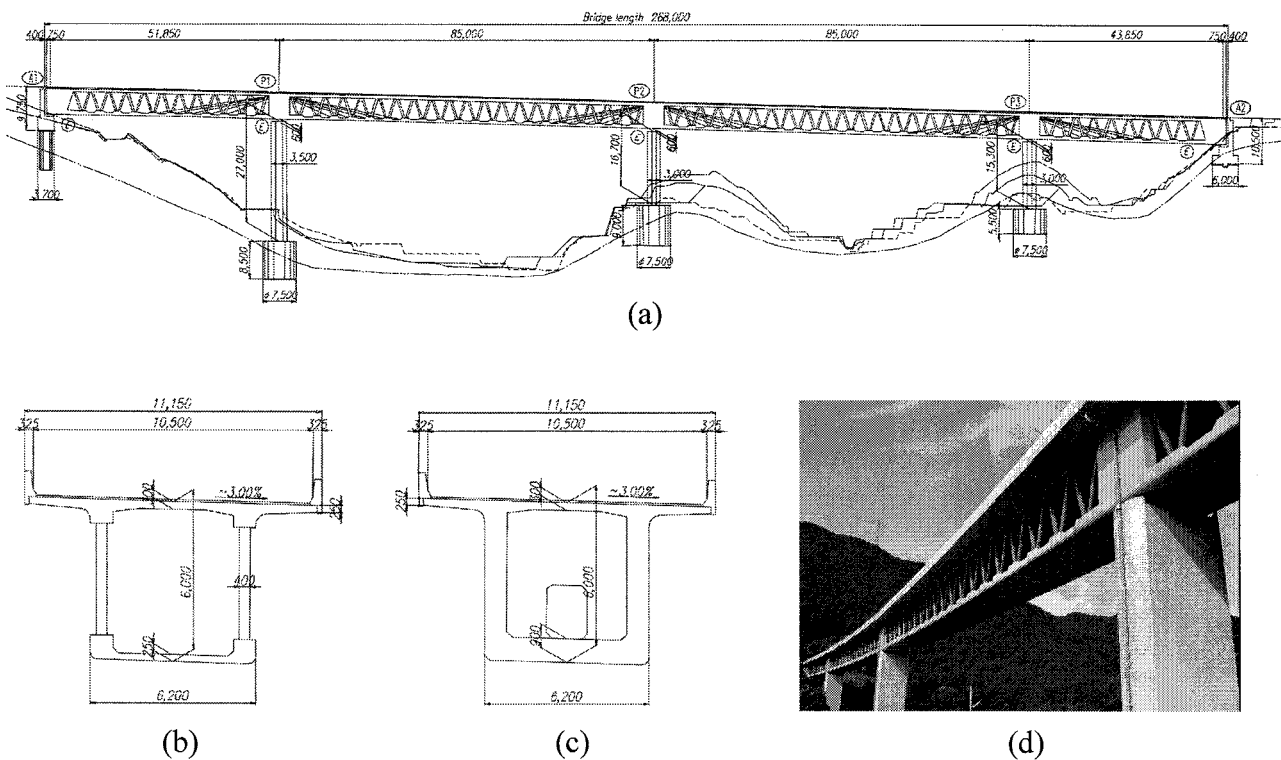


Figure 1 Outlines of Kinokawa viaduct: (a) Side view, (b) Cross section (center of the span (P1 - P2)), (c) Cross section (over the pier (P1 or P2)), and (d) Picture

Table 1 Thickness of UFC hollow box corresponding to each steel pipe

Steel pipe ($\phi = 406$ mm)	9.5	12	16	19
UFC hollow box (500 × 300 mm)	69	77	84	94

Note: unit is mm

thickness of the steel pipe is 9.5, 12, 16 and 19 mm, respectively. In addition, in order to prevent buckling, the compressive diagonal members of the Kinokawa viaduct were filled with concrete. In this consideration, the thickness of the UFC hollow box was determined by making the total weight of the tensile diagonal member and the compressive diagonal member including the filling concrete in Kinokawa viaduct equal to the weight of two UFC hollow boxes. For example, the total weight of two steel pipes with 9.5 mm thickness and concrete filled into the steel pipe was the same with the weight of two UFC hollow boxes with 69 mm thickness.

2.2 Details of Analysis

To calculate the thickness of a UFC hollow box, the densities of steel pipe, concrete and UFC were assumed to be 7.85, 2.3, 2.5 t/m³, respectively. These densities were also used in the analysis. The cross-section of the prestressed UFC truss web composite PC girder was considered to be the same with the real girder of the Kinokawa viaduct, except for the truss part which replaced the steel pipe by the UFC hollow box. The parameter in the analysis is the prestress level in UFC truss web. A prestress of 20, 30 or 40 N/mm² was introduced to both compressive and tensile diagonal members of the UFC truss.

Two dimensional nonlinear finite element analysis was performed by DIANA 8.1. Figure 2 shows the mesh discretization. Four nodes and three nodes isoparametric plane stress elements were applied for concrete. Beam elements in which bending can be considered were adopted for the diagonal members. Truss element without the consideration of bending was used for the external cables. Embedded reinforcement elements were applied for the steel bars and the internal cables. In both of the prestressed UFC truss web composite PC girder and Kinokawa viaduct girder, it was assumed that the joint between the truss and the flange was completely bonded. Figure 3 shows the joint systems in the Kinokawa viaduct girder and the prestressed UFC truss web composite PC girder. Figure 3(a) shows the joint system of Kinokawa viaduct girder in the practical construction and Figure 3(b) shows the image of the joint system of prestressed UFC truss web composite PC girder.

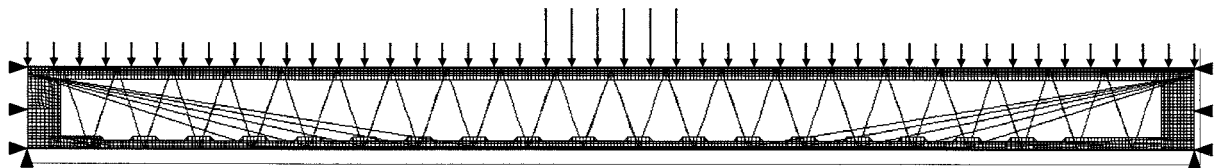


Figure 2 Mesh discretization

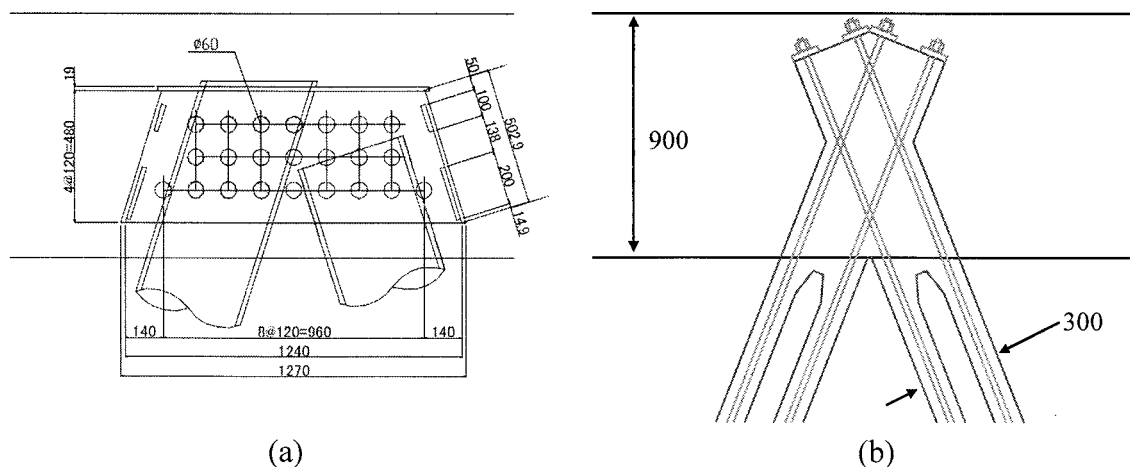


Figure 3 Joint systems: (a) Steel truss, and (b) UFC truss

In the analysis, the loading order is the prestress, dead-weight and live load. At the time of loading of the dead-weight, densities of reinforced concrete and external cable were determined as 2.5 t/m^3 and 7.85 t/m^3 , respectively. As for the live load, the primary load was provided at the center of the span, and then the load was increased by 0.2 times each of live load of type B (Japan Road Association, 2002). Analyses were performed by the load control, and Quasi-Newton method (secant method) was used for the iteration. In the calculation for the convergence, the tolerance for convergence was 0.01%. When the variation of internal energy has become less than 0.01% of the internal energy of the first iteration, it is assumed that the convergence has been obtained and the iteration is stopped. After that, the calculation continues with the next step.

2.3 Analytical Model

For the crack model of concrete and UFC, the rotating crack model was used. It was assumed that only one crack occurs in an element and the average strain in the element was determined by dividing the crack width by the equivalent length, L_{eq} . L_{eq} was set to be the average of square root of the element area for quadrangular elements and the average of square root of twice the element area for triangular elements. L_{eq} was 250 mm in either shape of elements. In beam elements for UFC diagonal members, L_{eq} was 770 mm (the length of the beam element).

For UFC, from experimental results in the previous work (Kakei et al., 2003), constitutive models as shown in Figure 4(a) for compression and Figure 4(b) for tension were applied. For concrete, Thorenfeldt's model (Thorenfeldt et al., 1987) with compressive fracture energy, G_{FC} , was applied for compression (Figure 5(a)). As the area of the gray zone in Figure 5(a) became equal to the value that divided G_{FC} by equivalent length, L_{eq} , the curve in the post peak of Thorenfeldt's model was extended

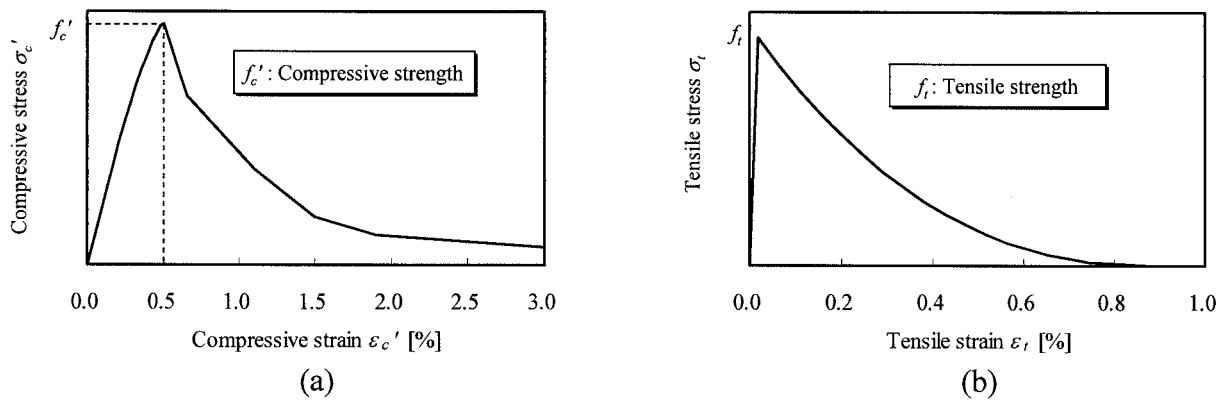


Figure 4 Stress-strain relationships of UFC: (a) Compression, and (b) Tension

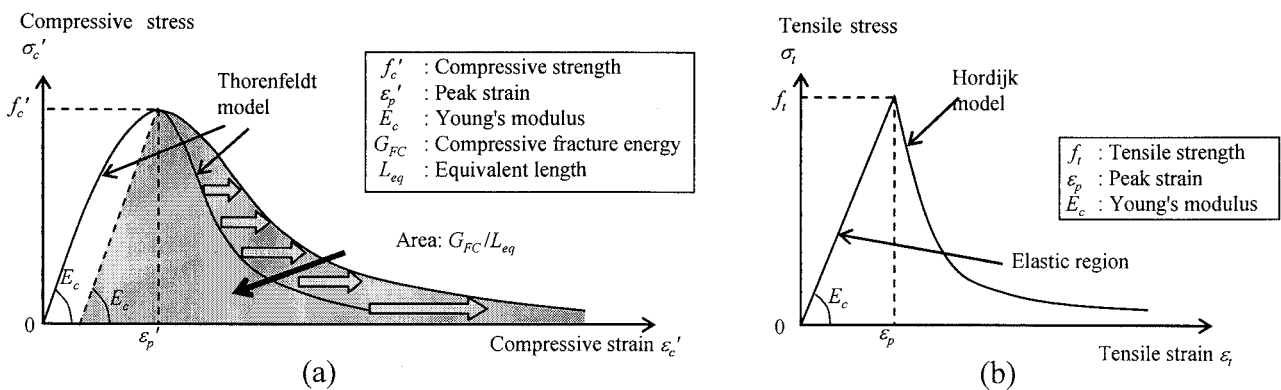


Figure 5 Stress-strain relationships of concrete: (a) Compression, and (b) Tension

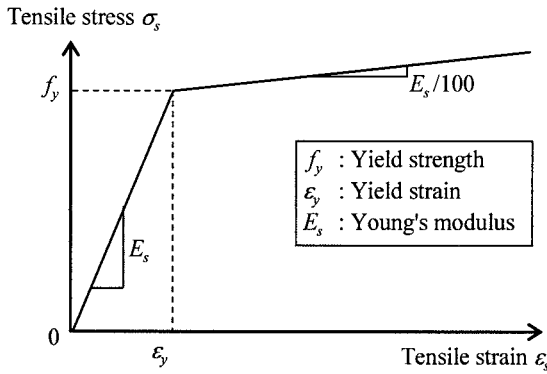


Figure 6 Stress-strain relationship of reinforcements and PC cables

Table 2 Material properties

Materials	Strength [N/mm ²]	<i>E</i> [kN/mm ²]
Concrete	f'_c : 40 f_t : 3.0	31
UFC	f'_c : 180 f_t : 8.8	50
Steel pipe	f_y : 325	200
Reinforcement	f_y : 345	200
Internal cable	f_y : 1600	200
External cable	f_y : 1600	200

Note: f'_c is compressive strength,
 f_t is tensile strength
 f_y is yield strength
 E is Young's modulus.

in the direction of strain axis. G_{FC} [N/mm] was set as Eq. (1) (Nakamura et al., 2001) (f'_c is compressive strength [N/mm²]).

$$G_{FC} = 8.77 \times \sqrt{f'_c} \quad (1)$$

For tension, concrete was assumed to be elastic with the elastic modulus, E_c , until it reaches the tensile strength, f_t . In the post peak region, Hordijk's model (Hordijk, 1991) was applied (Figure 5(b)). Reinforcements and PC bars were assumed to be elastic with the elastic modulus, E_s , until it reaches the yield strength, f_y , and the stress increases gradually with $0.01E_s$ after it reaches f_y as shown in Figure 6.

The material characteristics of concrete, UFC, internal cable, external cable, and steel bar were determined as shown in Table 2. As for the concrete strength, the specified concrete strength of Kinokawa viaduct was used. The specified value by each design code was adopted to another strength.

3. RESULTS AND DISCUSSIONS

Figure 7 shows the load-deflection curves. The load was calculated from the sum of left and right support reactions. Before introducing the prestress, the load and deflection showed zero values. Because the load control method was used in all cases, the post peak behavior cannot be predicted. In the graph, the response is valid until the convergence. Figure 8 shows the relationship of multiple of live load and deflection. The multiple of live load in the vertical axis was designated as 1 corresponding to B live load. The origin of the graph illustrated in Figure 8 is considered to be the condition after the prestress was introduced and the effect of self-weight was included. Figure 9 shows the minimum principal stress of concrete with its deformation at the peak load in each case.

From Figure 7, the prestressed UFC truss web composite PC girders which were designed as having the same web weight as the steel truss web composite PC girder, have the same initial stiffness with the steel truss web composite PC girder. The stiffness of steel truss web composite PC Bridge did not change until the load of 45000 kN, and finally the girder failed in compression mode at the lower flange near by the left support point (the part surrounded with circle in Figure 9).

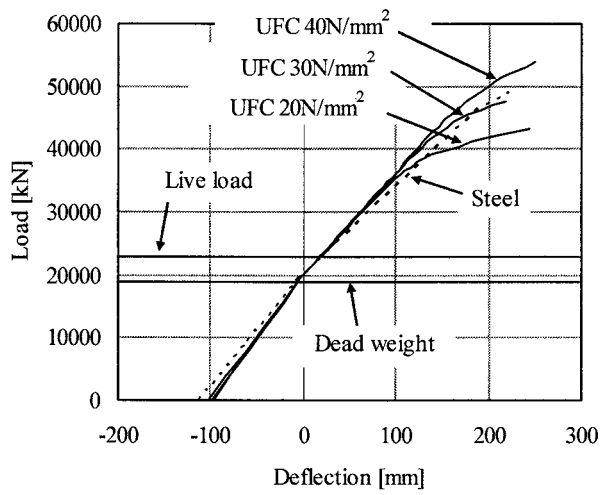


Figure 7 Load-deflection curves

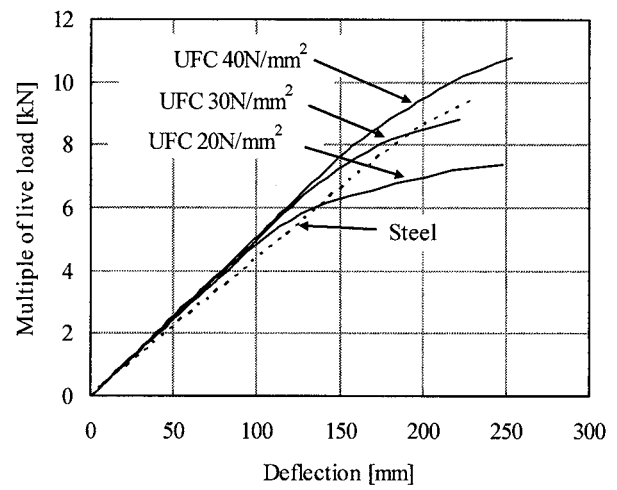


Figure 8 Live load-deflection curves

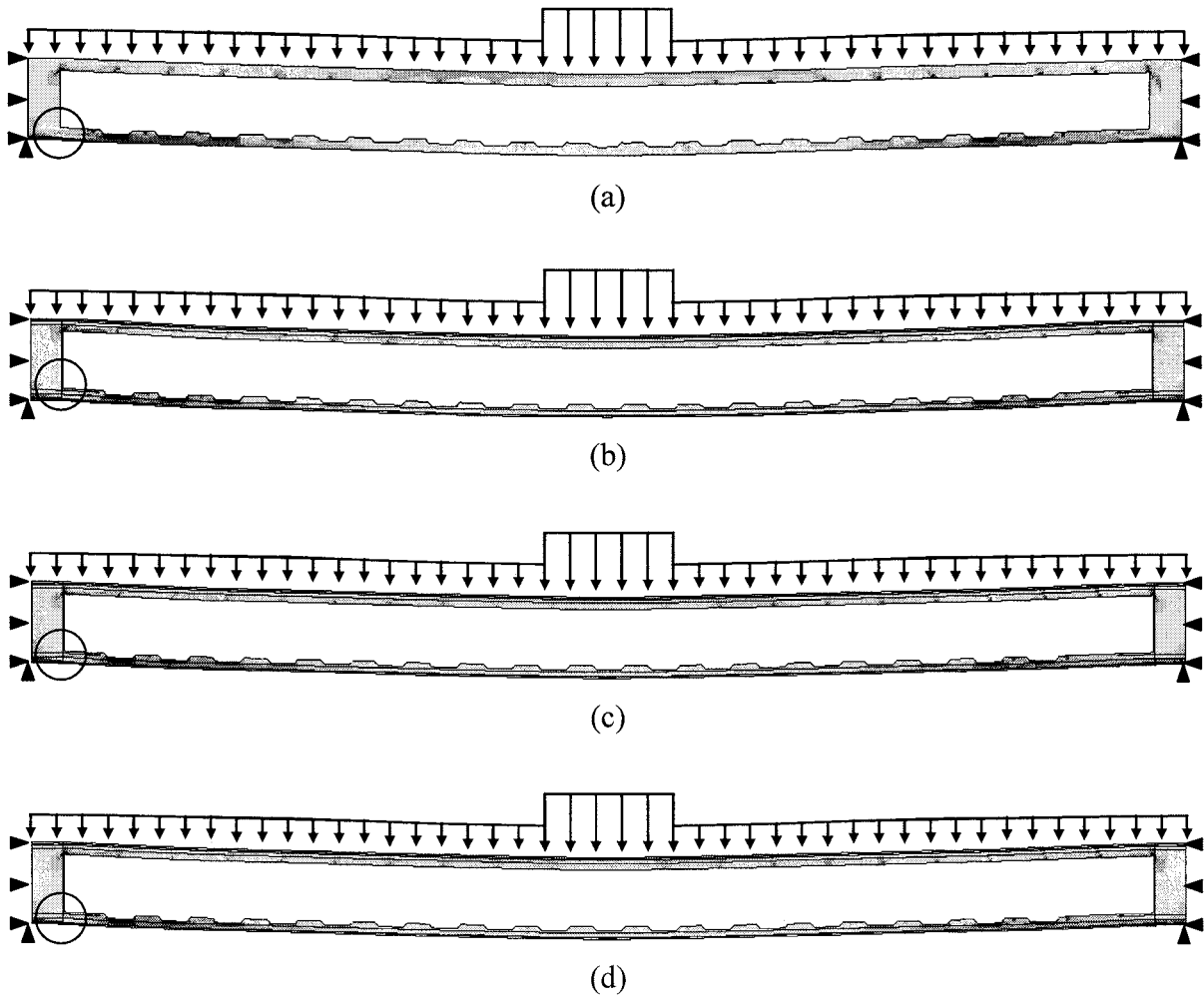


Figure 9 Minimum principal stress and its deformation: (a) Steel truss, (b) UFC truss (20 N/mm²), (c) UFC truss (30 N/mm²), and (d) UFC truss (40 N/mm²)

As for the prestressed UFC truss web composite PC Bridge, the crack for UFC tensile diagonal member occurred at load 35000, 40000 and 45000 kN for the level of prestress of 20, 30 and 40 N/mm² applied to UFC cases, respectively. In 20 N/mm² type, the maximum load could not reach the maximum load of the steel truss web composite PC girder. However, the 30 N/mm² type had almost the same load carrying capacity as the steel truss web composite PC girder. Moreover, 40 N/mm² type showed much larger load carrying capacity than the steel truss web composite PC girder.

In all cases of prestressed UFC truss web composite PC girders, the girders failed at the lower flange nearby the left support point (Figure 9). The boundary condition due to the continuous girder caused this failure mode.

From Figure 8, for the steel truss web composite PC girder, the peak load was 9.4 times the B live load. In the prestressed UFC truss web composite PC girder with 20 N/mm² prestress, the crack of tensile diagonal members nearby the support point occurred at about 5 times the B live load and then the stiffness decreased. Finally, cracks in most of the tension diagonal members occurred as shown in Figure 10 and the girder failed at 7.4 times the B live load. In 30 N/mm² type, the stiffness decreased at about 7 times the B live load and the peak load was 8.8 times the B live load. In 40 N/mm² type, the stiffness decreased at about 9 times the B live load and the ultimate load was 10.8 times the B live load. In 30 N/mm² and 40 N/mm² types, the crack occurred only in 7 tension diagonal members (Figure 10). From these results, even though the stiffness of the prestressed UFC truss web composite PC girder with 30 N/mm² prestress slightly decreased, it is confirmed that it provides almost the same capability of the steel truss web composite PC girder. In addition, when a prestress of 40 N/mm² is applied to the UFC truss, the load carrying capacity exceeds that of the steel truss web composite PC girder.

Thus, the composite PC girder using prestressed UFC truss web that has the same self-weight as the steel truss web composite PC girder has slightly higher stiffness and approximately the same load carrying capacity relative to the steel truss web composite PC girder. Especially, introducing a prestress of 40 N/mm² to the UFC truss provides higher load carrying capacity than the steel truss web composite PC girder. From these results, the prestressed UFC truss web composite PC girder can

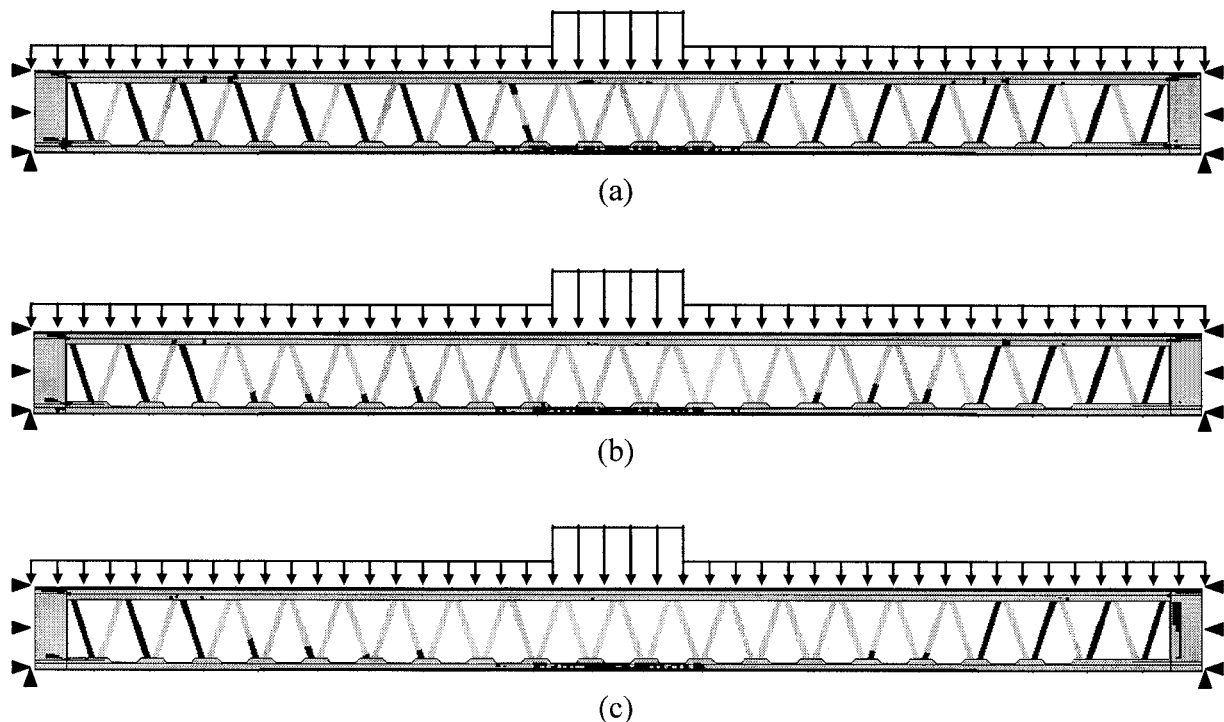


Figure 10 Cracked part (The black part is cracked): (a) Steel truss, (b) UFC truss (20 N/mm²), (c) UFC truss (30 N/mm²), and (d) UFC truss (40 N/mm²)

reduce the self-weight of the superstructure as much as steel truss web composite PC girder can and contributes to the improvement of seismic performance of the bridge compared with the conventional normal PC girder bridges.

4. CONCLUSIONS

In this study, the comparison of mechanical properties between the steel truss web composite PC girder (Kinokawa viaduct) and prestressed UFC truss web composite PC girders having the same web weight was carried out. The summary of this paper is as follows:

- 1) The initial stiffness of the prestressed UFC truss web composite PC girders that replaced the steel truss of Kinokawa viaduct by the UFC truss is slightly higher than the steel truss web composite PC girder.
- 2) When a prestress of 30 N/mm^2 is introduced to the UFC truss, the stiffness of the prestressed UFC truss web composite PC girder near the ultimate state decreases because of the cracks in the tension diagonal members but the load carrying capacity is almost the same with the steel truss web composite PC girder.
- 3) When a prestress of 40 N/mm^2 is introduced to the UFC truss, the stiffness of the prestressed UFC truss web composite PC girder does not decrease near the ultimate state and the load carrying capacity exceeds that of the steel truss web composite PC girder.
- 4) The prestressed UFC truss web composite PC girder can reduce the self-weight of the superstructure as much as the steel truss web composite PC girder can and contributes to the improvement of the seismic performance of the bridge.

Acknowledgements:

Sincere gratitude is expressed to Taiheiyo Cement Corporation, Taisei Corporation and Kajima Corporation for their cooperation. The authors also would like to express their gratitude to the COE program for providing financial support to accomplish this research.

References:

- Hordijk, D. A. (1991), "Local Approach to Fatigue of Concrete," *PhD thesis, Delft University of Technology*.
- Japan Road Association (2002), "Specification for Highway Bridges [Concrete Bridges]," Maruzen Co., Ltd.
- Japan Prestressed Concrete Engineering Association (JPCEA) (2005), "Standards for Design and Construction of Composite bridges," Gihodo Shuppan Co., Ltd.
- Japan Society of Civil Engineers (JSCE) (2004), "Recommendations for Design and Construction of Ultra High Strength Fiber Reinforced Concrete Structures - Draft," *Concrete Library of JSCE*, No.113.
- Takei, T., Kawaguchi, T., Niwa, J. and Hyodo, H. (2003), "Fracture Properties of Ultra High Strength Steel Fiber Reinforced Cementitious Composites," *Proceedings of Cement and Concrete*, **57**, 230-231.
- Minami, H., Yamamura, M., Taira, Y. and Fruichi, Y. (2002), "Design of the Kinokawa Viaduct Composite Truss Bridge," *Proceedings of the first fib Congress*, Session 5, 371-380.
- Murata, H., Niwa, J., Sivaleepunth, C., Kawaguchi, T. and Hyodo, H. (2005), "Proposal of New Type Composite PC Structures Using UFC Truss as the Web Member," *Journal of Materials, Concrete Structures and Pavements, JSCE*, No.795/V-68, 145-155.
- Murata, H., Niwa, J., Tanaka, Y. and Katagiri, M. (2006), "Mechanical Properties of Composite PC Girders Using Prestressed UFC Truss," *Proceedings of the EASEC-10 (10th East Asia-Pacific Conference on Structural Engineering and Construction)*, Materials, Experimentation, Maintenance and Rehabilitation, 437-442, Bangkok
- Nakamura, H. and Higai, T. (2001), "Compressive Fracture Energy and Fracture Zone Length of Concrete," *Modeling of RC Structures under Seismic Loads, ASCE*, 471-487.
- Richard, P. and Cheyrezy, M. H. (1994), "Reactive Powder Concretes with High Ductility and 200-800 MPa Compressive Strength," *ACI Spring Convention*, SP144-24, 507-517.
- Thorenfeldt, E., Tomaszewicz, A. and Jensen, J. J. (1987), "Mechanical Properties of High-strength Concrete and Applications in Design," *Symposium Proceedings of Utilization of High-Strength Concrete*, Norway.

SHEAR STRENGTH OF R/C MEMBERS BASED ON PLASTIC THEORY TAKING ACCOUNT OF INFLUENCE OF AXIAL FORCE AND AMOUNT OF LONGITUDINAL REINFORCEMENT

H. Hotta¹⁾ and T. Harada²⁾

1) Assoc. Prof., Graduate School of Science and Engineering, Tokyo Institute of Technology, Dr. Eng.

2) Graduate Student, Graduate School of Science and Engineering, Tokyo Institute of Technology

Abstract: In this paper, considering the fracture mechanism putting yield limit of longitudinal reinforcement, we propose theoretical formula based on upper bound theorem. The formula can prove qualitatively the rise of shear strength by rise of shear reinforcement, longitudinal reinforcement, or axial force. By introducing the effective coefficient to the formula, we got the semi-theoretical formula that reflects experimental results.

1. INTRODUCTION

In AIJ's "Design Guidelines for Earthquake Resistant Reinforced Concrete Buildings Based on Inelastic Displacement Concept" [1999], an evaluation method of shear strength of R/C members based on plastic theory is recommended. According to this method, shear strength can be calculated as sum of the one due to arch action and truss action. Shear resisted by truss action originated from Nielsen's work [1984] and is that modified by Ichinose [1992] so as to be able to consider the influence of interval and diameter of shear reinforcement, however, influence of axial load and longitudinal reinforcement that is recognized in numbers of empirical examinations can not be considered in the method because it is assumed longitudinal bars do not yield. In this paper, theoretical shear strength due to truss action is reconsidered by allowing the yielding of longitudinal reinforcement.

2. THEORETICAL SHEAR STRENGTH OF R/C MEMBERS DUE TO TRUSS ACTION IN THE CASE OF ASSUMING LONGITUDINAL BARS HAVE A CERTAIN YIELD LIMIT

In line with Nielsen and Ichinose's method, a theoretical shear strength resisted by truss action is induced minimizing an upper bound solution through the following assumptions and procedures.

A concrete strip with thickness δ and at angle β with the longitudinal direction is assumed to fail due to shear force V as shown in Fig.1. The upper part of the concrete strip is detailed in Fig.2. The virtual displacement along the direction of the shear force V is assumed u and axial displacement $u \tan \alpha$ is accompanied. That is different from Nielsen and Ichinose's assumption. They assumed that the longitudinal bars never yield. By contrast, in this paper it is assumed that the longitudinal bars also yield.

In the assumed failure mechanism, virtual external work is given as $W_e = Vu$ and virtual internal work is given as $W_i = W_{i\text{hoop}} + W_{i\text{long}} + W_{i\text{conc}}$, where $W_{i\text{conc}}$ = virtual work done by concrete, $W_{i\text{hoop}}$ = virtual work done by stirrup, and $W_{i\text{long}}$ = virtual work done by longitudinal reinforcement.

The virtual internal work done by stirrup and longitudinal reinforcement is expressed as

$$W_{i\text{hoop}} = bjp_w \sigma_y u \cot \beta \quad (1)$$

$$W_{i\text{long}} = bjp_g \sigma_y u \tan \alpha \quad (2)$$

respectively, where b =breadth of the member, j =effective depth for truss action, p_w =hoop ratio, σ_y =yield strength of stirrup, p_g =ratio of longitudinal reinforcement and σ_y = its yield strength.

The strain of the concrete strip is uniform and it can be expressed as the following equations under x-y coordinate determined as shown Fig.2.

$$\epsilon_{xx} = 0 \quad (3)$$

$$\epsilon_{yy} = \frac{\Delta_y}{\delta} = \frac{1}{\delta} \frac{u}{\cos \alpha} \sin \left(\frac{\pi}{2} - \beta + \alpha \right) \quad (4)$$

$$\gamma_{xy} = \frac{\Delta_x}{\delta} = \frac{1}{\delta} \frac{u}{\cos \alpha} \cos \left(\frac{\pi}{2} - \beta + \alpha \right) \quad (5)$$

The compressive principal strain is given as

$$\epsilon_2 = -\frac{1}{2\delta} \frac{u}{\cos \alpha} \{1 - \cos(\beta - \alpha)\} \quad (6)$$

Assuming the yield criterion of concrete as shown in Fig.3, virtual internal work done by concrete is given by integrating $-\epsilon_2 \sigma_B$ in the region of the concrete strip as

$$W_{i\text{conc}} = bj\sigma_B \frac{u}{2 \sin \beta \cos \alpha} \{1 - \cos(\beta - \alpha)\} \quad (7)$$

As the external work should be equal to the internal work, the following upper bound solution is obtained as a result.

$$V = bjp_w \sigma_y \cot \beta + bjp_g \sigma_y \tan \alpha + \frac{bj\sigma_B}{2 \sin \beta \cos \alpha} \{1 - \cos(\beta - \alpha)\} \quad (8)$$

Using non-dimensional parameters $\tau = V/bj$, $\lambda = p_w \sigma_y / \sigma_B$ and $\phi = p_g \sigma_y / \sigma_B$, eq.(8) can be rewritten as

$$\frac{\tau}{\sigma_B} = \frac{1 - (1 - 2\lambda) \cos \beta \cos \alpha - (1 - 2\phi) \sin \beta \sin \alpha}{2 \sin \beta \cos \alpha} \quad (9)$$

Shear strength given by eq.(9) is one of the upper bound solution, therefore the minimum strength is true theoretical shear strength. As for angle β , $\beta = \pi/2$ gives the minimum τ in the case $\lambda \geq 0.5$, and in the case $\lambda \geq 0.5$ the minimum τ is given when

$$\cos \beta = (1 - 2\lambda) \cos \alpha \quad (10)$$

As for angle α , $\alpha = 0$ minimizes τ in the case $\phi \geq 0.5$, and in the case $\phi \leq 0.5$, τ is minimized when

$$\sin \alpha = (1 - 2\phi) \sin \beta \quad (11)$$

Eventually we get the following theoretical equations.

$$\tau / \sigma_B = 2\sqrt{\lambda(1-\lambda)\phi(1-\phi)} \quad \lambda \leq 0.5, \phi \leq 0.5 \quad (12)$$

$$= \sqrt{\phi(1-\phi)} \quad \lambda \geq 0.5, \phi \leq 0.5 \quad (13)$$

$$= \sqrt{\lambda(1-\lambda)} \quad \lambda \leq 0.5, \phi \geq 0.5 \quad (14)$$

$$= 0.5 \quad \lambda \geq 0.5, \phi \geq 0.5 \quad (15)$$

The relationship between τ given by eqs.(12)-(15) and λ is drawn in Fig.4. In the case $\phi \geq 0.5$, proposed formula is coincident with Nielsen's one, however, in the case $\phi \leq 0.5$, the maximum shear strength is dependent on the amount of longitudinal reinforcement and less than the one given by Nielsen and Ichinose.

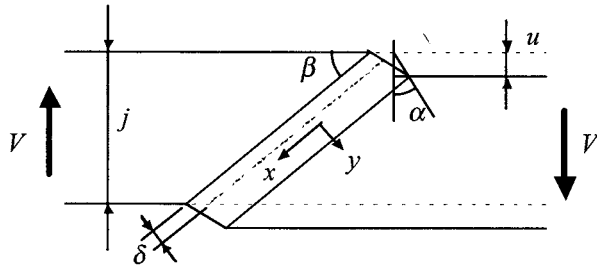


Figure 1 Failure mechanism

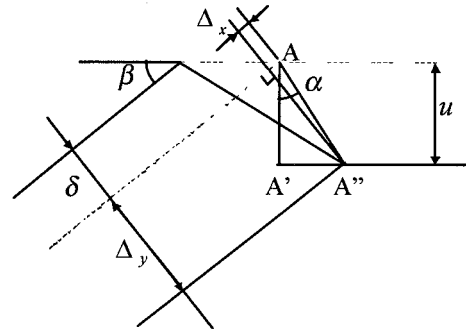


Figure 2 Strain of concrete strip

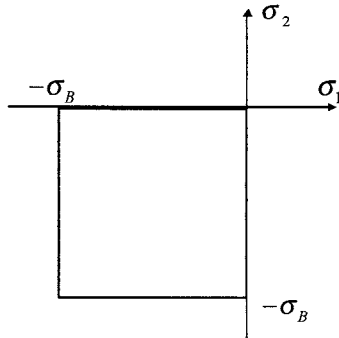


Figure 3 Yield criterion of concrete

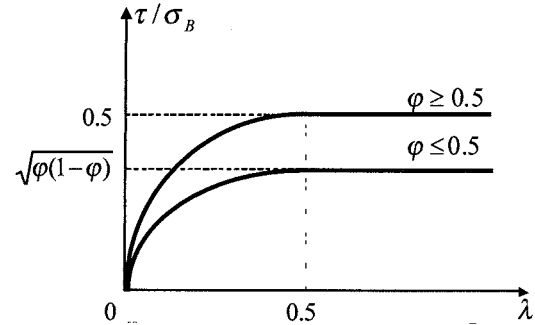


Figure 4 Relationship between shear strength and amount of stirrup

3. THEORETICAL TENSILE FORCE RESISTED BY LONGITUDINAL BARS AT SHEAR SLOPING SURFACE

Tensile force resisted by longitudinal reinforcement is discussed in this section. The stress of concrete at the failure surface is shown in Fig.5. The direction of the compressive principal stress is coincident with the direction of the principal strain given by eq.(6) and it crosses at angle $(\beta - \alpha)/2$ with the shear slipping surface. Each components of the stress vector in x-y coordinate can be written as

$$\sigma_{yy} = -\frac{1}{2}\sigma_B \{1 - \cos(\beta - \alpha)\} \quad (16)$$

$$\tau_{yx} = \frac{1}{2}\sigma_B \sin(\beta - \alpha) \quad (17)$$

The following equation is given due to the balance of force in the axial direction.

$$N_g + \frac{bj}{\sin \beta} \sigma_{yy} \sin \beta - \frac{bj}{\sin \beta} \tau_{yx} \cos \beta = 0 \quad (18)$$

where N_g =tensile force resisted by longitudinal reinforcing bars. Substituting eqs.(16)and (17) into eq.(18), we get

$$N_g = \frac{1}{2}bj\sigma_B \left(1 - \frac{\sin \alpha}{\sin \beta}\right) \quad (19)$$

Moreover, eq.(19) can be rewritten as follows from the relationship between $\sin \alpha$ and $\sin \beta$ given by eq.(11),

$$N_g = bj\phi\sigma_B \quad (20)$$

The above equation shows that tensile force of the longitudinal bars is equal to the yield force. That accords with the initial assumption. On the other hand, as $\alpha = 0$ according to Nielsen's assumption, tensile force of the longitudinal bars is given by

$$N_g = \frac{1}{2}bj\sigma_B \quad (21)$$

Hence in Nielsen's assumption, tensile force equivalent to $\phi = 0.5$ is always expected to the longitudinal reinforcement regardless of its amount.

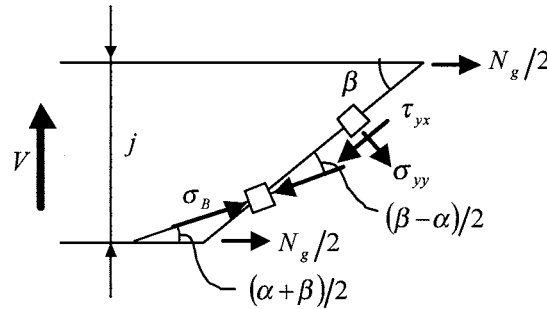


Figure 5 Stress of concrete at the failure surface

4. BASIC CHARACTERISTICS OF PROPOSED SHEAR RESISTANCE

In Fig.6, proposed shear strength considering the yield strength in the case $\phi = 0.2$ and other several significant characters are compared with those of Nielsen. The characters are ratio of axial elongation to lateral displacement $\tan \alpha$, angle between slipping surface and longitudinal axis of members β , and angle between direction of concrete strut and longitudinal axis of members $(\alpha + \beta)/2$. In the figure, solid and broken lines stand for Nielsen's and proposed ones respectively.

The maximum shear strength is expected $\tau/\sigma_B = 0.4$ when $\phi = 0.2$. Axial elongation is always equal to zero in Nielsen's theory, however, in the proposed formula, the axial elongation amounts to almost 80% of lateral displacement in the case $\phi \geq 0.5$. The angle of slipping surface β is not significantly affected by the amount of the longitudinal reinforcement, however, the angle of concrete strut is much influenced. In the case $\phi = 0.2$ and $\lambda \geq 0.5$, the angle between concrete strut and member axis becomes more than $\pi/4$.

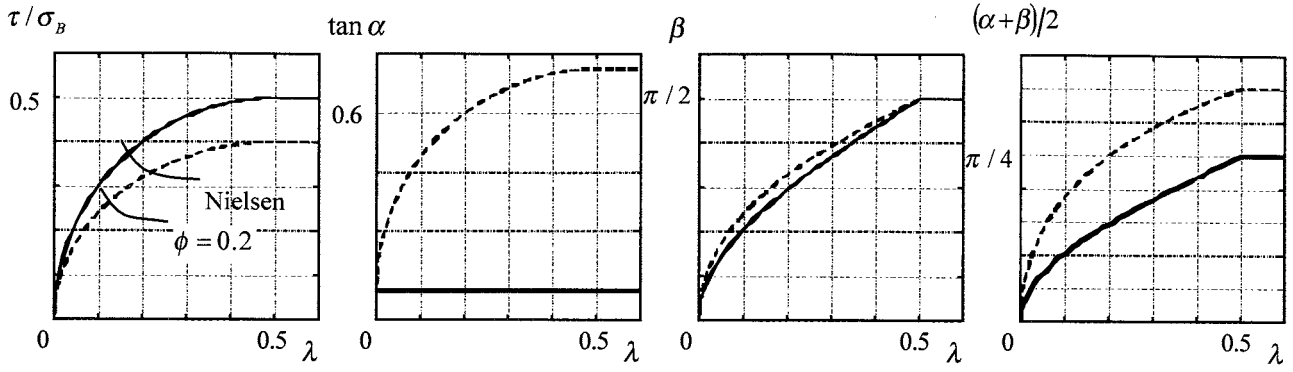


Figure 6 Comparison between proposed shear strength and Nielsen

5. THEORETICAL SHEAR STRENGTH OF R/C MEMBERS SUBJECT TO AXIAL COMPRESSION

Theoretical shear strength of R/C members subject to axial compression is proposed in this section by means of the similar method described in section 2.

External virtual work can be written as follows using axial force N , in which compression is positive,

$$W_e = Vu - Nu \tan \alpha \quad (22)$$

Determining axial compression ratio as $\eta = N / bj\sigma_B$, the second term of eq.(22) can be rewritten as

$$Nu \tan \alpha = \eta bj\sigma_B u \tan \alpha \quad (23)$$

that is the same form as eq.(2), therefore the following upper bound solution can be obtained replacing ϕ to $\eta + \phi$ in eq.(9) in the case $\alpha \geq 0$.

$$\frac{\tau}{\sigma_B} = \frac{1 - (1 - 2\lambda)\cos\beta\cos\alpha - (1 - 2\eta - 2\phi)\sin\beta\sin\alpha}{2\sin\beta\cos\alpha} \quad (24)$$

In the case $\alpha \leq 0$, the following equation gives an upper bound solution.

$$\frac{\tau}{\sigma_B} = \frac{1 - (1 - 2\lambda)\cos\beta\cos\alpha - (1 - 2\eta + 2\phi)\sin\beta\sin\alpha}{2\sin\beta\cos\alpha} \quad (25)$$

Minimizing those upper bound solutions, we can obtain the following theoretical shear strength.

$$\tau / \sigma_B = 2\sqrt{\lambda(1-\lambda)(\eta+\phi)(1-\eta-\phi)} \quad 0 \leq \eta \leq 0.5 - \phi \quad (26)$$

$$= \sqrt{\lambda(1-\lambda)} \quad 0.5 - \phi \leq \eta \leq 0.5 + \phi \quad (27)$$

$$= 2\sqrt{\lambda(1-\lambda)(\eta-\phi)(1-\eta+\phi)} \quad 0.5 + \phi \leq \eta \quad (28)$$

How the shear strength given by eqs.(26)-(28) changes according to axial force ratio is drawn in Fig.7. According to the proposed formula, shear strength increases according as the axial force increases until $\eta = 0.5 - \phi$ and it keeps the maximum value until $\eta = 0.5 + \phi$. Under more axial compression, the strength gradually decreases according to the magnitude of axial compression. Another important property induced by the proposed theory is that the influence of axial force changes according to the amount of longitudinal reinforcement.

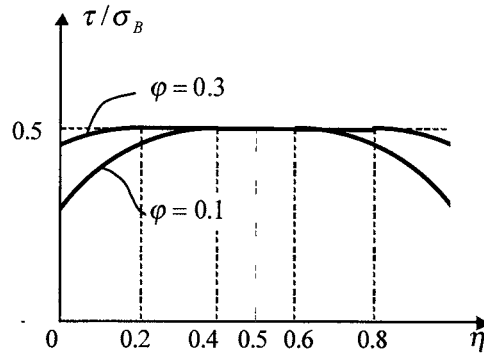


Figure 7 Relationship between shear strength and axial force ratio

6. MODIFICATION OF THEORETICAL EQUATION SO AS TO BE ADAPTED TO THE PAST EMPIRICAL DATA BY MEANS OF SEVERAL EFFECTIVE COEFFICIENTS

By mean of the past empirical data, we made a database concerned with shear strength of R/C members subject to a certain axial load. The source is recent papers published in AIJ transactions during 1984-2006 and reports at AIJ annual meeting(1985-2005.) 124 data that came under the following classifications were chosen as a result.

Dimension of the cross section is more than $250\text{mm} \times 250\text{mm}$.

Compressive strength of the concrete is less than 60Mpa.

Situ-in-place concrete is used.

The amount of shear reinforcement is more than $0.1v_0$, where v_0 is effective coefficient of concrete strength presented in AIJ guideline previously mentioned.

The reason the data of the specimens having less than $0.1v_0$ shear reinforcement were abandoned is that the arch mechanism would be distinguished in those specimens. How the parameters are distributed is indicated in Table 1.

Table 1 Distribution of parameters of specimens

	$0.04 \leq \lambda < 0.08$			$0.08 \leq \lambda < 0.12$			$0.12 \leq \lambda < 0.39$			Total		
$0.0 \leq \phi < 0.4$		5	5		2	3		1		0	8	8
	3	3	16	5	1	11	2	1	4	10	5	31
$0.4 \leq \phi < 0.7$		11	3	3		5		2	9	3	13	17
	1	1	16	7	4	19	2	1	14	10	6	49
$0.7 \leq \phi < 2.0$	2	1	5			11	6		9	8	1	25
	3	4	15	1		12	2		17	6	4	44
Total	2	17	13	3	2	19	6	3	18	11	22	50
	7	8	47	13	5	42	6	2	35	26	15	124

Range of η			$\eta = 0.0$	$0.0 < \eta < 0.2$	$0.2 \leq \eta < 0.4$
			$0.4 \leq \eta < 0.6$	$0.6 \leq \eta$	Total

Relationship between empirically obtained shear strength and amount of shear and longitudinal reinforcement is shown in Figs.8 and 9 respectively. Though the plots are considerably scattered, the shear strength has a tendency to increases depending on the amount of reinforcement and to become constant when the amount of the reinforcement goes over a certain border. That tendency is similar to the one recognized in the proposed theory, however, the maximum shear strength is much smaller than the theoretical one proposed in the previous sections and the borders are different from the ones given by the theory.

How the strength changes according to axial compression is indicated in Fig.10. In the figure, the data divide into 3 ranges according to the degree of axial compression. Three lines shown in Fig.10 are the approximate ones of the data which belong to each range and their slope is dependent on the degree of axial compression. High compression decreases the slope, however, low increases the one. This tendency of the influence of the axial load is also similar to the theory, however, negative influence of the axial load recognized in the theory cannot be observed in Fig.10.

It is considered that those differences between practice and theory are caused by the difference of the quantitative effect of materials. Therefore theoretical equations given by eqs.(26)-(28) is modified so as to fit to the practical data by giving effective coefficient to every parameter in the equations. Equations (26)-(28) are modified by replacing σ_B , σ_y , σ_y , and N to $v\sigma_B$, $v_\lambda\sigma_y$, $v_\phi\sigma_y$, and $v_\eta N$ respectively, and it is assumed that the effective coefficient for concrete strength can be given as linear function of concrete strength in line with Nielsen as $v = v_a\sigma_B + v_b$. As for five effective coefficients, the optimum values are obtained by means of the method of least squares as

$$\{v_a, v_b, v_\lambda, v_\phi, v_\eta\} = \{-0.0032, 0.52, 1.4, 0.15, 0.23\} \quad (29)$$

Theoretical curves given by the modified equations using the above coefficients are compared with the empirical data in Figs.11-13. It can be recognized from the figures and the values of the effective coefficients that the influence of longitudinal reinforcement and axial load on shear strength is much lower than that of shear reinforcement. The accuracy of the estimate obtained by the proposed formula and other typical ones are compared with each other in Table 2, where V_{exp}/V_{cal} is ratio of empirical shear strength to calculated one. The proposed formula gives the best estimate in the table.

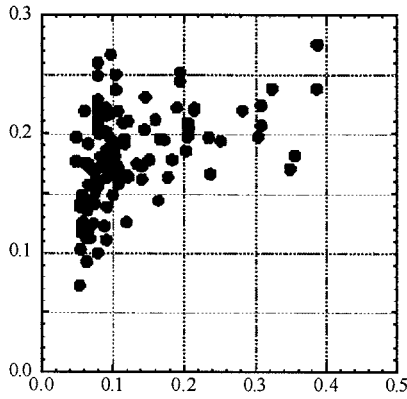


Figure 8 Relationship between shear strength and amount of stirrup

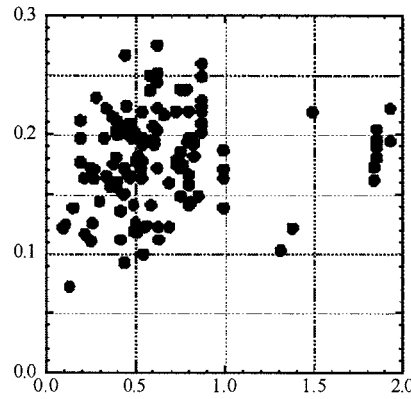


Figure 9 Relationship between shear strength and amount of longitudinal reinforcement

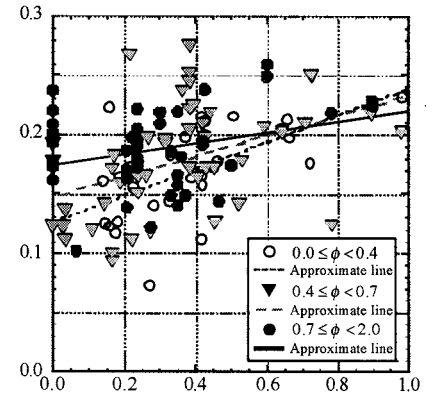


Figure 10 Relationship between shear strength and axial force ratio

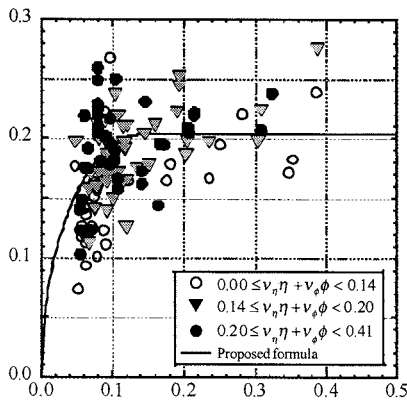


Figure 11 Relationship between shear strength and amount of stirrup

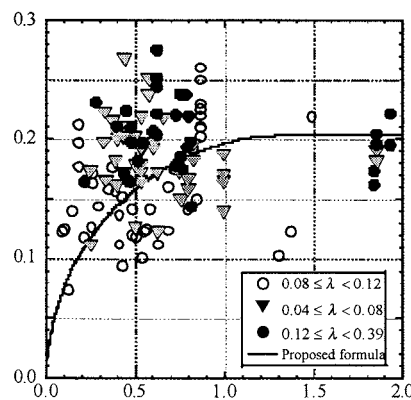


Figure 12 Relationship between shear strength and amount of longitudinal reinforcement

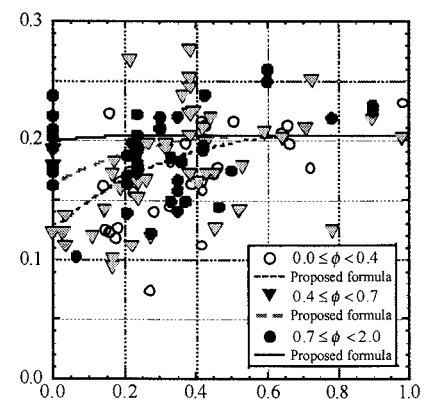


Figure 13 Relationship between shear strength and axial force ratio

Table 2 Statistics of V_{exp}/V_{cal} of proposed formula and other typical ones

	Proposed formula	AIJ recommendation	Empirical formula proposed by Hisosawa[1972]
Mean	1.00	1.18	2.09
Standard deviation	0.18	0.24	0.41
Coefficient of variation	0.18	0.21	0.20

7. CONCLUSIONS

- (1) Theoretical formula on shear strength of R/C members anew proposed based on plastic theory considering the yield strength of longitudinal reinforcement can qualitatively explain the influence of longitudinal reinforcement and axial load on the shear strength of members.
- (2) Shear strength formula modified to fit the empirical data by means of effective coefficients gives more accurate estimate than the ordinary ones such as AIJ recommendation's and an empirical ones proposed by Hirosawa give.

References:

- AIJ Guidelines for Earthquake Resistant Reinforced Concrete Buildings Based on Inelastic Displacement Concept, rev.1999 (in Japanese)
- Nielsen M.P. (1984), "Limit Analysis and Concrete Plasticity," Prentice Hall Inc.
- Ichinose, T. and Yokoo, S. (1992), "Effects of Sparseness of Shear Reinforcement on Shear Strength of R/C Beam," *Journal of Structural and Construction Engineering (Transaction of Architectural Institute of Japan)*, 437, 97-103.(in Japanese)
- Hirosawa, M. and Goto, T. (1972), *Summaries of Technical Papers of Annual Meeting Architectural Institute of Japan*, 819-820.(in Japanese)

BI-AXIAL NON-LINEAR MACROSCOPIC RESPONSE ANALYSIS OF SLIPPING TYPE R/C STRUCTURE TO STRONG EARTHQUAKE MOTION

H.H. Nguyen¹⁾, K. Nishimura²⁾, and K. Takiguchi³⁾

1) Doctor Candidate, Dept. of Mechanical and Environmental Informatics, Tokyo Institute of Technology, Japan

2) Assistant Professor, Dept. of Architecture and Building Engineering, Tokyo Institute of Technology, Japan

3) Professor, Dept. of Mechanical and Environmental Informatics, Tokyo Institute of Technology, Japan
huyhoang76@tm.mei.titech.ac.jp, knishimu@tm.mei.titech.ac.jp, ktakiguc@tm.mei.titech.ac.jp

Abstract: Based on the test result of pre-research on behavior of slipping type R/C member subjected to multi-axial force, this paper firstly present a multi-axial restoring force model proposed for slipping type R/C structure. The restoring force model was formulated and based on an analogy to the theory of plasticity. Using proposed bi-axial model, bi-axial non-linear response analysis of R/C structure to strong earthquake motion was carried out by using one mass system with input data were North-South and East-West axis ground motion, which recorded in El Centro 1940 earthquake. Natural period of the model was in a range of 0.1 sec to 0.9 sec. As a result, comparison between numerical results of earthquake response analysis using proposed model with three types of slip coefficient is concerned.

1. INTRODUCTION

Earthquake is a terrible threatening to the human life because of its severe damages to human-used facilities such as building, bridges or transportation system. In order to reduce losses which caused by earthquake, response analyses of structures subjected to strong motions is highly essential. Modeling restoring force characteristic of structure plays an important role in such kind of the analyses.

Considering restoring force characteristic of RC members subjected to one-directional lateral force, there appeared slipping behavior, in which variation of lateral deformation caused non-remarkable variation of lateral force at low load condition. Slipping behavior takes characteristics of slipping type, which was well considered and modeled in one-axial behavior (for example Akiyama, H.1985). However, study on multi-axial restoring force model of slipping type is still limited.

Based on the test result of pre-research on behavior of slipping type R/C member subjected to multi-axial force, this paper firstly present a multi-axial restoring force model proposed for slipping type R/C structure (Nishimura, K. Nguyen, H.H. Takiguchi, K. 2006). The restoring force model was formulated and based on an analogy to the theory of plasticity. Using proposed bi-axial model, bi-axial non-linear response analysis of R/C structure to strong earthquake motion was carried out by using one mass system with input data is ground motion, which recorded in El Centro 1940 earthquake. Natural period of the model in the analysis ranged from 0.1 sec to 0.9 sec. By keeping the value of lateral strength fixed in the same natural period, the earthquake analysis was carried out with three types of slip coefficient. One of them is elastic-perfectly plastic model, which is very common in earthquake response analysis of building structure. As a result, comparison between numerical results of earthquake response analyses using proposed model with three types of slip coefficient is concerned.

2. BI-AXIAL SLPPING TYPE RESTORING FORCE MODEL

2.1 Concept and Proposed model

Figure 1 show the restoring force model concept by imaging on mechanical vibration system. The model contains a roller connected to mass point P by elastic mass-less spring stiffness K^e ; the system then was imaged to move smoothly inside a surrounding wall. The inside area of surrounding wall is slipping area. Total displacement vector $\{\delta\}$ was assumed to consist of three components: elastic displacement vector $\{\delta^e\}$, slip displacement vector $\{\delta^s\}$ and center vector of slip area $\{\delta^c\}$:

$$\{\delta\} = \{\delta^e\} + \{\delta^s\} + \{\delta^c\} \quad (2.1.1)$$

in the expression (1) $\{\delta\} = (\delta_x, \delta_y)^T$; $\{\delta^e\}$, $\{\delta^s\}$ and $\{\delta^c\}$ were expressed similarly.

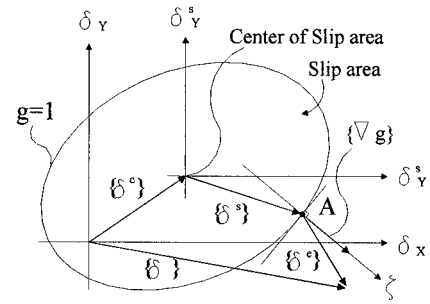
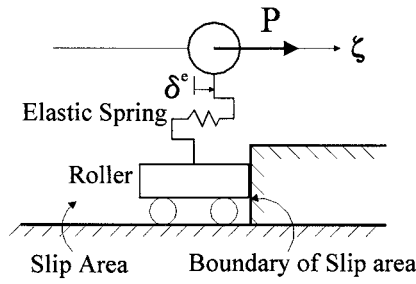


Figure 1. Concept of the Model Figure 2. Loading direction in displacement space

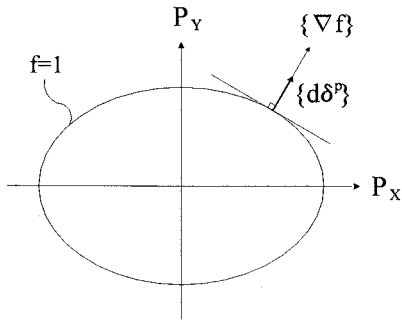


Figure 3. Yielding surface

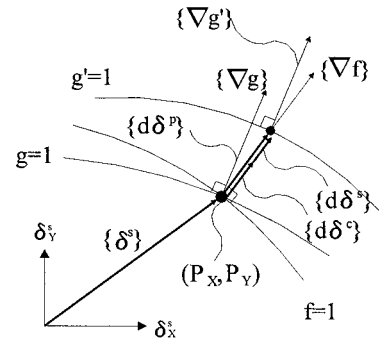


Figure 4. Yielding surface

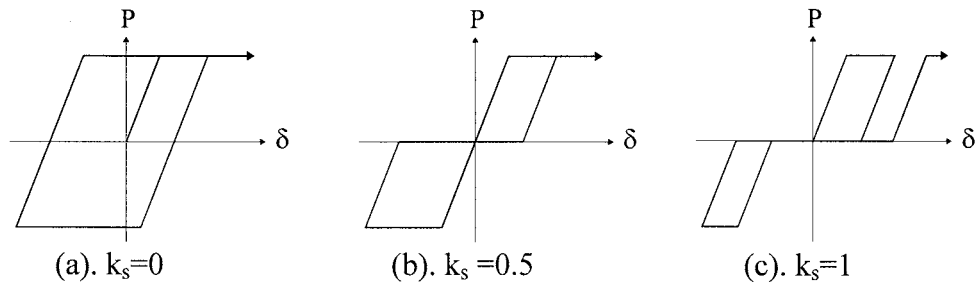


Figure 5. Three cases of Slip coefficient

The limitation of slip area was expressed by a function g of $\{\delta^s\}$ and $g=1$. As shown in figure 1, when the roller comes to standstill at certain position A, direction of force P is the same with that of

normal vector at the point A. From this significant suggestion, the following expression was established:

$$\{P\} = \kappa \cdot \{\nabla g\}, (\kappa \geq 0) \quad (2.1.2)$$

where $\{\nabla g\} = (\nabla g_x, \nabla g_y)^T = (\partial g / \partial \delta^s_x, \partial g / \partial \delta^s_y)^T$
 $\{P\} = (P_x, P_y)^T$ was expressed by elastic stiffness matrix $[K^e]$ as follows:

$$\{P\} = [K^e] \{\delta^e\} \quad (2.1.3)$$

In this paper, yielding surface was assumed as a circle and the loading state after yielding was perfectly plastic. The yielding surface was expressed by function $f=1$ as shown in the Fig.2

$$f = \{P\}^T [U] \{P\} \quad (2.1.4)$$

Ex (2.1.2),(2.1.4) resulted in an expression of κ follows:

$$\kappa = \sqrt{\frac{\{P\}^T [U] \{P\}}{\{\nabla g\}^T [U] \{\nabla g\}}} \quad (2.1.5)$$

Plastic displacement increment $\{d\delta^p\}$ was calculated by the flow rule of the theory of plasticity:

$$\{d\delta^p\} = d\lambda \cdot \{\nabla f\} \quad (2.1.6)$$

where $\{\nabla f\} = (\nabla f_x, \nabla f_y)^T = (\partial f / \partial P_x, \partial g / \partial P_y)^T$ is normal vector of yielding surface.
In order to investigate slip behavior, the following expressions were proposed:

$$\{\delta^s\} = [D] \{n\} \quad (2.1.7)$$

$$[dD] = \frac{k_s}{\{d\delta^p\}} \cdot \begin{bmatrix} d\delta_x^{p^2} + k_o \cdot d\delta_y^{p^2} & (1-k_o) \cdot d\delta_x^p \cdot d\delta_y^p \\ (1-k_o) \cdot d\delta_x^p \cdot d\delta_y^p & d\delta_x^{p^2} + k_o \cdot d\delta_y^{p^2} \end{bmatrix} \quad (2.1.8)$$

$$\{d\delta_c\} = (1-k_s) \cdot \{d\delta^p\} \quad (2.1.9)$$

$[D]$ is a matrix express slip area. $\{n\}$ is used as a unit vector of slip displacement vector $\{\delta^s\}$, $|\{n\}| < 1$. Figure 3 describes transformation and expansion of slip area in the lateral force and displacement vector space. In figure 3, the force point does not move, therefore $\{\nabla g\}$ and $\{\nabla g'\}$ have the same direction. Slip area moves $(1-k_s) \cdot \{d\delta^p\}$ and expand $k_s \cdot \{d\delta^p\}$, slip displacement vector increases $\{d\delta^s\} = k_s \cdot \{d\delta^p\}$. Coefficient k_s expressed slip level, and k_o is expansion coefficient to orthogonal direction of slip vector. When $k_s = 0$ proposed model becomes elastic perfectly plastic model. Figure 4 shows one- axial restoring force characteristic of proposed model in three cases of $k_s = 0$, $k_s = 0.5$ and $k_s = 1$.

Because slip area boundary $g=1$ and $[D]$ is a symmetric matrix, therefore from (2.1.7):

$$g = \{\delta^s\}^T \cdot [D]^{-1} \cdot [D]^{-1} \cdot \{\delta^s\} \quad (2.1.10)$$

Normal vector of slipping area limitation was calculated from (2.1.10) as follows:

$$\nabla g = 2 \cdot [D]^{-1} \cdot [D]^{-1} \cdot \{\delta^s\} \quad (2.1.11)$$

From (2.1.2), (2.1.11), following expression is established:

$$\{P\} = \kappa.[T]\{\delta^s\} \quad \text{where} \quad \{T\} = 2.[D]^{-1}.[D]^{-1} \quad (2.1.12)$$

2.2 Force- Displacement Increment Relationship

From expression (2.1.1), total displacement increment

$$\{d\delta\} = \{d\delta^e\} + \{d\delta^s\} + \{d\delta^c\} \quad (2.2.1)$$

Force increment was expressed by stiffness matrix $[K^e]$ as follows:

$$\{dP\} = [K^e] \cdot \{d\delta^e\} \quad (2.2.2)$$

Force- displacement relationship was divided into 4 separate states: displacement point is still in elastic range was named as E- state; displacement point is inside of slip area was named as S-state; In case of displacement point is outside of slip area but still elastic range named as ES-state; displacement point is outside of slip area and plastic state appears named as ESP-state.

*E-state

In the E-state, $\{d\delta^s\}=0$, $\{d\delta^c\}=0$, therefore $\{d\delta\}=\{d\delta^e\}$; (2.2.3)

Force- displacement increment relationship was expressed by following:

$$\{dP\} = [K^e] \cdot \{d\delta\} \quad \text{where} \quad [K^e] = \begin{bmatrix} k^e & 0 \\ 0 & k^e \end{bmatrix} \quad (2.2.4)$$

*S-state

In the S-state, because force point does not move, while the roller moves inside of slip area, therefore $\{d\delta^e\}=0$, $\{d\delta^c\}=0$.

$$\{d\delta\} = \{d\delta^s\} \quad (2.2.5)$$

Force- displacement increment relationship was expressed as follows:

$$\{dP\} = [K^s] \cdot \{d\delta\} \quad \text{where} \quad [K^s] = \begin{bmatrix} 0 & 0 \\ 0 & 0 \end{bmatrix} \quad (2.2.6)$$

*ES-state

In the ES-state, from ex. (2.1.9) $\Rightarrow \{d\delta^c\}=0$ replace into (2.2.1)

$$\{d\delta\} = \{d\delta^e\} + \{d\delta^s\} \quad (2.2.7)$$

Force-displacement increment relationship in ES-state:

$$\{dP\} = [K^{es}] \{d\delta\} \quad (2.2.8)$$

where

$$[K^{es}] = [K^e].[A]^{-1} \frac{\{\nabla g\} \cdot \{\nabla g\}^T}{\{\nabla g\}^T \cdot [A]^{-1} \cdot \{\nabla g\}} \cdot [A]^{-1} \cdot [K^e] + \kappa.[T].[A]^{-1} \cdot [K^e]$$

Slipping increment vector was re-write as follows:

$$\{d\delta^s\} = ([I] - [K^e]^{-1} \cdot [K^{es}]) \cdot \{d\delta\} \quad [I] \text{ is unit matrix.}$$

* ESP-state

Total displacement increment was evaluated as expression. (2.2.1). Force-displacement increment

relationship in ES-state:

$$\{dP\} = [K^{esp}] \{d\delta\} \quad (2.2.9)$$

$$\text{where } [K^{esp}] = [K^{es}] - \frac{[K^{es}] \{\nabla f\} \{\nabla f\}^T [K^{es}]}{\{\nabla f\}^T [K^{es}] \{\nabla f\}}$$

Slip center increment vector $\{d\delta^c\}$, slip increment vector $\{d\delta^s\}$ and slip area increment matrix were calculated as follows:

$$\{d\delta_c\} = (1 - k_s) \{d\delta^p\} = (1 - k_s) d\lambda \{\nabla f\}$$

$$\{d\delta^s\} = ([I] - [K^e]^{-1} [K^{esp}]) \{d\delta\} - (1 - k_s) d\lambda \{\nabla f\}$$

$$[dD] = \frac{k_s}{d\lambda \|\{\nabla f\}\|} \begin{bmatrix} d\lambda^2 \nabla f_x^2 + k_o \nabla f_y^2 d\lambda^2 & (1 - k_o) d\lambda^2 \nabla f_x \nabla f_y \\ (1 - k_o) d\lambda^2 \nabla f_x \nabla f_y & d\lambda^2 \nabla f_y^2 + k_o \nabla f_x^2 d\lambda^2 \end{bmatrix}$$

$$\text{where } d\lambda = \frac{\{\nabla f\}^T [K^{es}] \{d\delta\}}{\{\nabla f\}^T [K^{es}] \{\nabla f\}}$$

3. EARTHQUAKE RESPONSE ANALYSIS

3.1 Numerical program

The equation of motion for one- mass system subjected to earthquake ground motion is expressed as follows:

$$M\ddot{x} + C\dot{x} + F(x) = -M\ddot{z} \quad (3.1.1)$$

M: mass, Cx': damping force; F(x) restoring force; x: displacement; z: ground motion.

Earthquake response analysis was carried out with one-mass system using proposed restoring force model with three types of slip coefficient, $k_s=0, 0.5$ and 1 . Expansion coefficient to the orthogonal direction of slip vector was 0.2 . Newmark method $\beta=1/4$ was used in the numerical program with input data is the ground motion in North-South (NS) and East-West (EW) axis of El-Centro 1940 earthquake, time interval $dt=0.002$ sec. The model was assumed to be isotropic in X and Y axis and the yielding surface was a circle. Damping ratio gets the value of 0.03 .

Parameter of the earthquake response analysis consists of natural period ranged from 0.1 to 0.9 sec. Lateral strength was decided by total energy input attributable to damage (Akiyama, H. 1985) of one-axial earthquake response as follows: For each natural period, the one-directional numerical program was ran with proposed restoring force model with slip coefficient $k_s=0$ to get maximum energy input, then the lateral strength was calculated as the maximum energy input value reach to the value of η as shown in figure 5. In this paper, the value of $\eta=5$ and 10 . This lateral strength was common used for numerical program with proposed restoring force model with $k_s=0.5$ and 1 which has the same natural period.

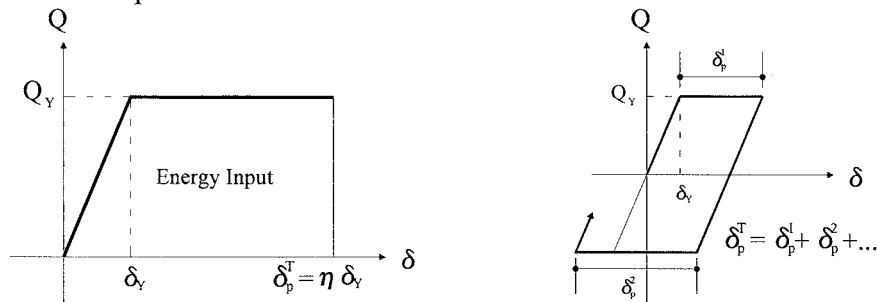


Figure 5. Energy Input and Total plastic displacement

3.2 Numerical Result and Consideration

Figure 6 to 9 show numerical results with input data is El Centro earthquake 1940 ground motion. Lateral strength of the model was decided according to the energy input of one-axial earthquake response using proposed model with $k_s=0$. D, A, V, V_E , T expressed maximum lateral displacement, maximum lateral acceleration, maximum lateral velocity, equivalent velocity of total energy input, and natural period of the system, respectively.

The value of maximum lateral displacement D is calculated as follows:

$$D = \sqrt{\delta_{NS}^2 + \delta_{EW}^2} \quad (3.2.1)$$

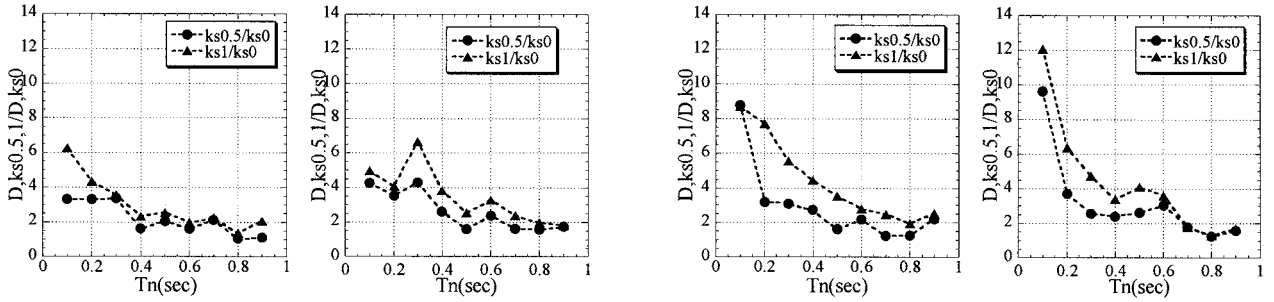
The value of maximum lateral acceleration A and maximum lateral velocity V is calculated in the same method as D.

V_E can be given as follows, where E and M are energy input and mass of system, respectively.

$$V_E = \sqrt{\frac{2E}{M}} \quad (3.2.2)$$

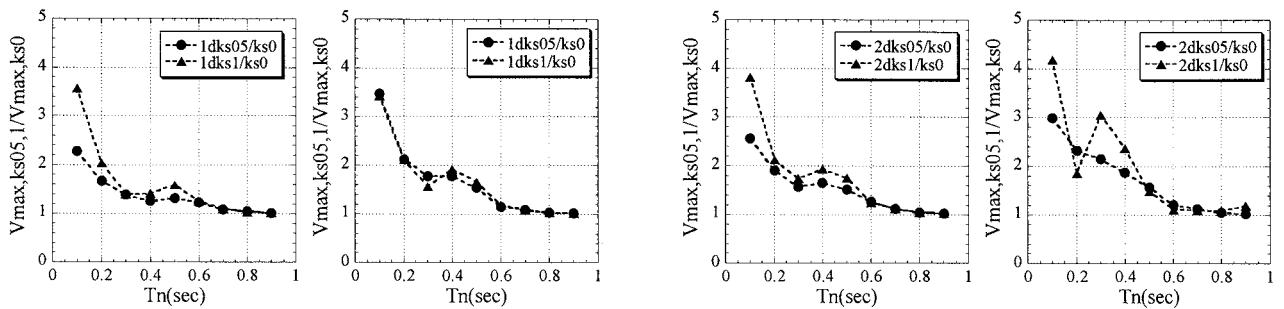
Circle and triangle mark in figure 6, 7, 9 are represented the ratio between maximum lateral displacement, lateral velocity and equivalent velocity of the earthquake response analysis with $k_s=0.5$, 1 and $k_s=0$. Circle, square and diamond marks in figure 8 show the numerical result of maximum lateral acceleration in case k_s is 0, 0.5 and 1, respectively.

As can be seen in figure 8 to figure 10, A, V and V_E of one-axial and bi-axial earthquake response with $k_s=0.5$ and $k_s=1$ are almost equal. As can be seen in figure 7 and figure 9, comparing with numerical result of the earthquake response with $k_s=0$, the value of maximum lateral velocity V and equivalent velocity V_e of response with $k_s=0.5$ and 1 is large as the natural period is short; as the natural period is long ($T_n=0.4\sim0.9$ sec), numerical result of V and V_e with three types of k_s tend to be equal. Moreover, equivalent velocity of bi-axial earthquake response is much bigger than that of one-axial response analysis in short natural period.



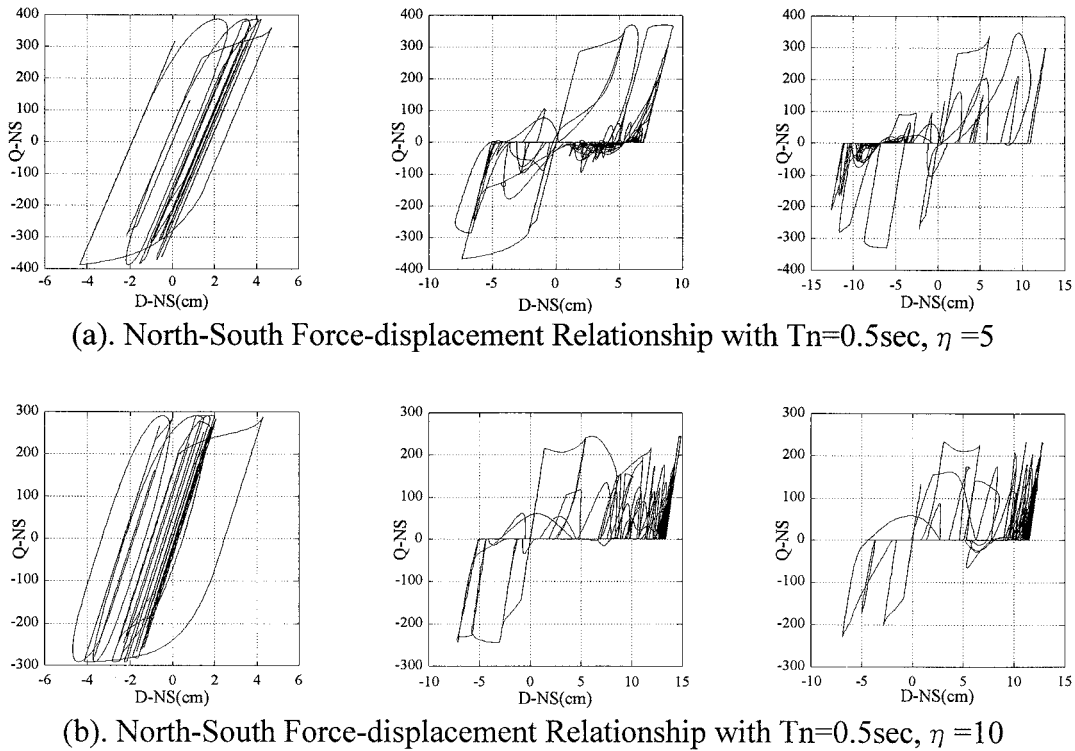
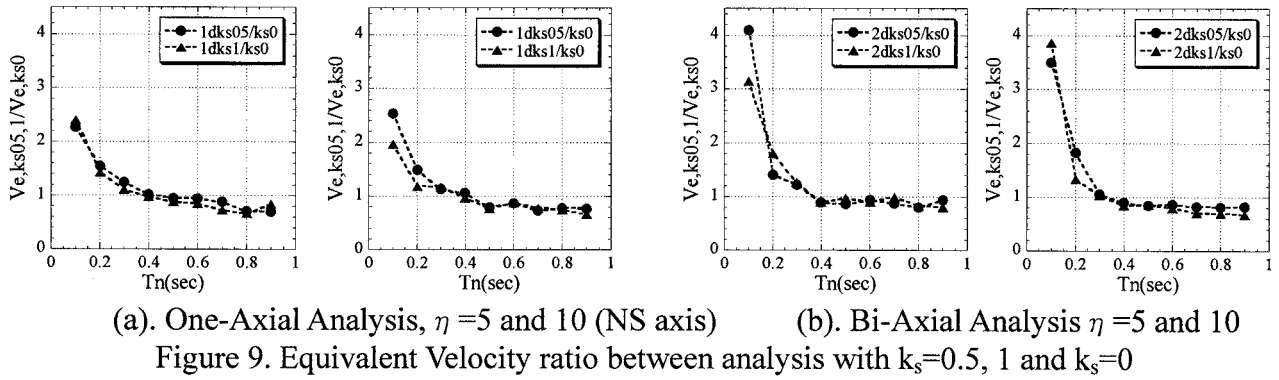
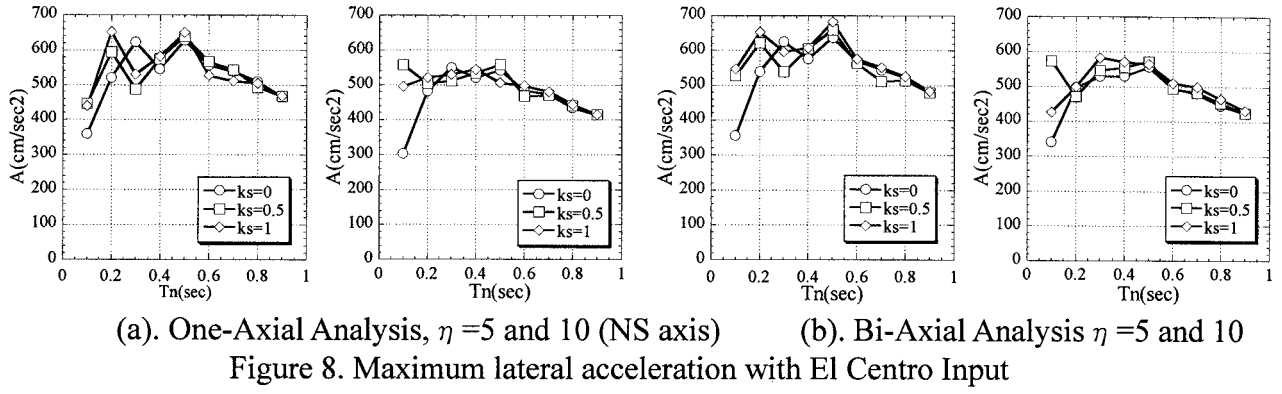
(a). One-Axial Analysis, $\eta = 5$ and 10 (NS axis) (b). Bi-Axial Analysis, $\eta = 5$ and 10

Figure 6. Lateral displacement ratio between analysis with $k_s=0.5$, 1 and $k_s=0$



(a). One-Axial Analysis, $\eta = 5$ and 10 (NS axis) (b). Bi-Axial Analysis $\eta = 5$ and 10

Figure 7. Maximum lateral velocity ratio between analysis with $k_s=0.5$, 1 and $k_s=0$



Considering maximum lateral acceleration in figure 8, A of both one-axial and bi-axial earthquake response with $k_s=0$ is almost agree with that of analysis with $k_s=0.5$ and 1 when natural period ranged from 0.2 to 0.9 sec. The value of maximum acceleration is in a range of 400~700 cm/s^2 . However, the differences can be seen clearly in the numerical result of maximum lateral displacement. As shown in figure 7, the lateral displacement of the bi-axial earthquake response

with $k_s=0.5$ and 1 were much bigger than that of the one-axial analysis in short natural period. Moreover, maximum lateral displacement of both one-axial and bi-axial response analysis with $k_s=1$ is generally bigger than that of response with $k_s=0.5$.

The earthquake response analysis is now continuing to estimate numerical result using proposed restoring force model and the value of η was decided 5 or 10 for each type of slip coefficient. Figure 10 show the earthquake response in terms of lateral force –displacement with input data is El Centro 1940 earthquake ground motion. The natural period of the analysis is 0.5 sec, and the value of η is 5 and 10 for each slip coefficient is 0, 0.5, and 1. As can be seen in figure 10, the responses somewhat show agreement with characteristic of the proposed restoring force model.

4. CONCLUSIONS

Based on the test result of pre-research on behavior of slipping type R/C structure subjected to multi- axial force, this paper firstly present a multi-axial restoring force model proposed for slipping type R/C structure. The restoring force model was formulated and based on an analogy to the theory of plasticity. Using proposed multi-axial restoring force model, bi-axial non-linear response analysis of R/C structure to strong earthquake motion was carried out by using one mass system with three types of slip coefficient $k_s=0, 0.5$ and 1. With $k_s=0$, the proposed model becomes elastic-perfect plastic model. In case of $k_s=0.5$ and 1, slipping behavior was appeared in the proposed restoring force model with varying slip level. Input data for the analysis were North-South and East-West axis ground motion, which recorded in El Centro 1940 earthquake. Natural period of the model was in a range of 0.1 sec to 0.9 sec. The main findings were obtained as follows:

1. The lateral displacement and total energy input of the bi-axial earthquake response with $k_s=0.5$ and 1 were much bigger than that of the one-axial response in short natural period.
2. Maximum lateral acceleration of numerical result of both one- axial and bi-axial earthquake response with three types of slip coefficient were almost equal when natural period was ranged from 0.2 to 0.9 sec. The value of maximum acceleration is in a range of 400~700 cm/s^2 .
3. Comparing with numerical result of the earthquake response with $k_s=0$, the value of maximum lateral velocity and total energy input of both one-axial and bi-axial response with $k_s=0.5$ and 1 were large as the natural period is short; as the natural period is long, numerical result of maximum lateral velocity and total energy input with three types of k_s tend to be equal.

References:

- Akiyama, H. (1985). *Earthquake-Resistant Limit-State Design for Buildings*. University of Tokyo Press, Tokyo, Japan.
- Nishimura, K. Nguyen, H.H. and Takiguchi, K. (2006), "Study on formulation of Slipping Type Multi-Axial Restoring Force Characteristic of R/C member" *Transaction of the Architectural Institute of Japan*, Architectural Institute of Japan, 609,147-154(in Japanese).
- Takiguchi, K., Kokusho, S., K., Ishida, A., and Kimura, M. (1979), "Study on the Restoring Force Characteristics of Reinforced Concrete Columns to Bi- Directional Displacements, Part 1 Development and Examination of Loading Apparatus for Testing Reinforced Concrete Columns Subjected to Bi- Directional Horizontal Force and Axial Force," *Journal Structural and Construction Engineering*, Architectural Institute of Japan, 286,29-35,(in Japanese).
- Takiguchi, K., (1977), "Deforming Characteristics of RC Members with and Without Bond. II," *Transaction of the Architectural Institute of Japan*, Architectural Institute of Japan, 262,53-59(in Japanese).
- Takiguchi, K., Okada, K., Sakai, M. (1976), "Deforming Characteristics of RC Members with and without Bond," *Transaction of the Architectural Institute of Japan*, Architectural Institute of Japan, 249,1-10(in Japanese).
- Takizawa, H., and Aoyama, H. (1976). Biaxial effects in modeling earthquake response of R/C structures. *Earthquake Engineering and Structural Dynamics*, Vol.4, 523-552.

EVALUATION ON SHEAR MECHANISM OF CORRODED RC BEAMS BY LATTICE MODEL ANALYSIS CONSIDERING BOND DETERIORATION

T. Miki¹⁾ and J. Niwa²⁾

1) Assistant Professor, Department of Civil Engineering, Tokyo Institute of Technology, Japan

2) Professor, Department of Civil Engineering, Tokyo Institute of Technology, Japan

mikitomo@cv.titech.ac.jp jniwa@cv.titech.ac.jp

Abstract: This paper presents an analytical study to evaluate the residual structural performance of RC members damaged due to steel corrosion. A lattice model is focused on and developed to evaluate the shear resisting mechanism of corroded RC beams. An interface element is modeled the bond behavior between corroded steel reinforcement and concrete and is incorporated into the lattice model. Using this element, the lattice model analysis is conducted on RC beams corroded by the electrolytic method. The analysis shows that the shear carrying capacity of the RC beams increases when the bond between the longitudinal reinforcement and concrete degrades as the corrosion proceeds.

1. INTRODUCTION

Analytical technique to predict the mechanical response of RC structures has significantly improved. The technique benefits from the rapid development of computer technology that made possible the reduction of processing time required for the analysis and yielded higher accuracy by means of realistic material constitutive models. The analytical prediction method can be extended to solve a keen issue for durability problems on RC structures in terms of structural performance evaluation. The actual RC structures are going to be more or less subjected to environmental menaces. The environmental actions cause the structures many possible conditions of deterioration. The deterioration due to chloride ions is one of the most serious problems of durability of the reinforced concrete found in many existing RC structures. When the corrosion of steel reinforcement occurs in the RC structures, the cross-section of the reinforcement decreases and the corroded products result in the bond degradation between the reinforcement and concrete. Therefore, it is necessary to consider actual damages of the structure caused by steel corrosion when a nonlinear analysis is conducted for the performance assessment of structures in their service life.

In the practice, an objective, simple, accurate nonlinear analytical model is strongly required to simulate the structural performance of RC structures. The purpose of this study is to apply the easy-to-use method of lattice model analysis (Niwa et al. 1995) in order to analytically explain the shear resisting mechanism and the mechanical behavior of damaged RC members (ex. steel corrosion). In the conventional lattice model, nodes of longitudinal reinforcement members correspond to those of flexural tension members of concrete, because these elements are assumed to perfectly bond to one another. The modeling to separate these nodes is required to describe the bond deterioration between concrete and longitudinal reinforcement. The study also aims to propose the interface model of bond behavior and incorporate into the lattice model analysis being able to consider the actual conditions of steel corrosion.

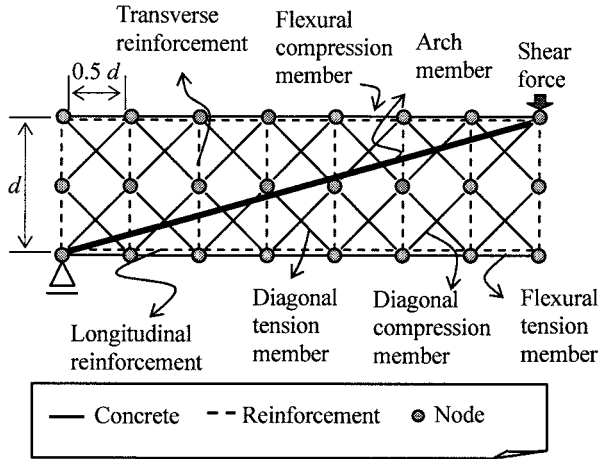


Figure 1 Outlines of 2D Lattice Model

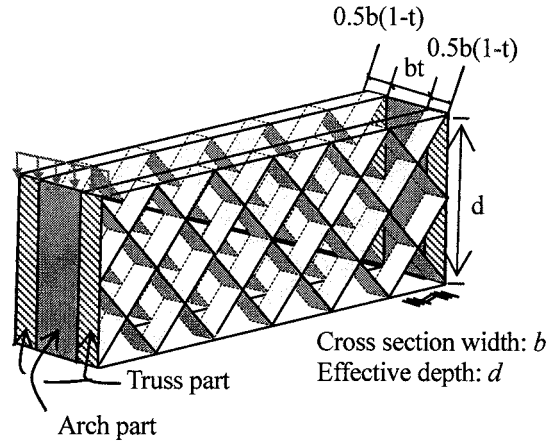


Figure 2 Cross Section of a RC Beam Modeled by 2D Lattice Model

2. ANALYTICAL MODEL

2.1 Outlines of 2D Lattice Model

The 2D lattice model consists of members of concrete and reinforcement, as shown in Figure 1. In a RC beam, the concrete is modeled into flexural compression members, flexural tension members, diagonal compression members, diagonal tension members and an arch member. The longitudinal and transverse reinforcements are modeled into horizontal and vertical members, respectively. The diagonal members are arranged at regular intervals with inclined angles of 45 and 135 degrees with respect to the longitudinal axis of the beam. The arch member connecting the nodes at the opposite diagonal corners between the loading point and the bottom of the beam is arranged according to the direction of the internal flow of compressive stresses. Figure 2 illustrates a schematic diagram of cross section of the RC beam. The concrete is divided into the truss and arch parts. When the value of t is defined as a ratio of the width of arch part to the width of cross section, the widths of the arch part and the truss part are given as bt and $b(1-t)$, respectively, where t ranges from 0 to 1. The value of t is determined based on the theorem of the minimization of the total potential energy for the lattice model with the initial elastic stiffness. The total potential energy is obtained from the difference between the summations of the strain energy in each element and the external work. The pre-analysis using the lattice model is carried out to determine the value of t .

2.2 Material constitutive model

(a) Concrete Model

To consider the effect of lateral confinement of concrete due to suitable arrangement of transverse reinforcement, the stress-strain relationship of confined concrete proposed by Mander et al. (1998) is applied to the diagonal compression members and to the arch member. For cracked concrete, the compressive softening behavior of concrete proposed by Vecchio and Collins (1986) is considered. Using the model, we can consider the fact that the ability of cracked concrete to resist the compressive stress decreases as the transverse tensile strain increases. For the flexural compression

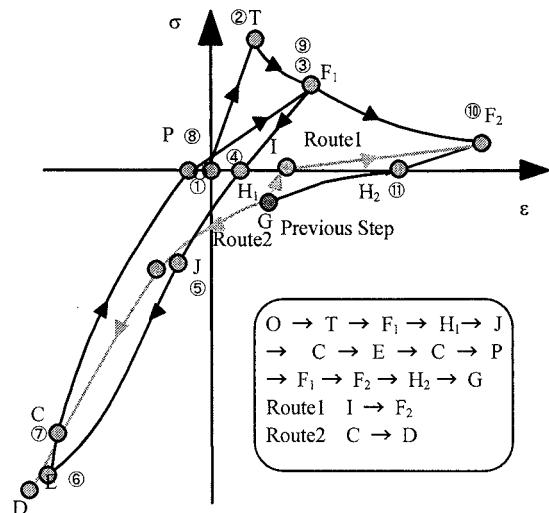


Figure 3 Concrete Model under Cyclic

members, the stress-strain relationship proposed by Okamura and Maekawa (1991) is used. For the flexural tension members of concrete, which are provided near the reinforcing bars, the tension-stiffening model (Okamura and Maekawa 1991) is applied in order to consider the bond effect between the concrete and the reinforcing bars. On the other hand, for the diagonal tension members, the 1/4 tension-softening model (Rokugo et al. 1989) is applied.

For the cyclic behavior of concrete under both compression and tension, the cyclic stress-strain relationships proposed by Naganuma et al. (2000) are used. Figure 3 indicates the concrete model under cyclic loading. The compressive model can evaluate the decrease in the stiffness of concrete during unloading and reloading paths as the maximum compressive strain increases. In the loading process from tension to compression, the compressive stress is transmitted to the concrete across the crack surface, even though the strain of the concrete becomes zero. The stress-strain model can evaluate the contact stress at crack surfaces during the cyclic behavior.

(b) Reinforcement Model

The envelope curve for the stress-strain relationship of reinforcement in tension is modeled as the average behavior in concrete by Okamura and Maekawa (1991). The envelope curve for the stress-strain relationship in compression of reinforcing bars is modeled as bi-linear in which the tangential stiffness after yielding is 0.01 E_s , where E_s denotes the Young's modulus of steel.

2.3 Interface Element between Longitudinal Reinforcement and Concrete

In this study, the nodes of longitudinal reinforcement members and flexural tension members of concrete are considered to be independent. Figure 4 shows the outline of the interface element. The nodes are arranged such that the nodes of steel are located between the neighboring nodes of concrete.

The thickness of the joint element is assumed to be the diameter of longitudinal reinforcement, D . These nodes are connected with vertical springs transmitting the vertical stress and lateral springs transmitting the shear stress. Constitutive models are provided for each spring. The vertical spring is modeled as linear elastic spring in which the tangential stiffness is E_c , where E_c denotes the Young's modulus of concrete. In the lateral spring, it is assumed that the bond stress is uniformly distributed on the surface area of the longitudinal reinforcement and the bond force is calculated by the bond stress being multiplied by the steel surface. In this study, the relationship between the bond stress, τ and the slip between steel and concrete, s , as shown in Figure 5, is applied to the lateral spring. The parameters in this model are maximum bond stress, τ_{\max} , the slip displacement at τ_{\max} , s_1 , the slip displacement at $\tau = 0$, s_2 and exponential coefficients, a and b . Herein, the exponents a and b are assumed to be constant; $a = 1$ and $b = 4$. Then, the bond stiffness k_1 can be determined by τ_{\max} and s_1 . In the next section, parameters of τ_{\max} , s_1 and s_2 will be determined.

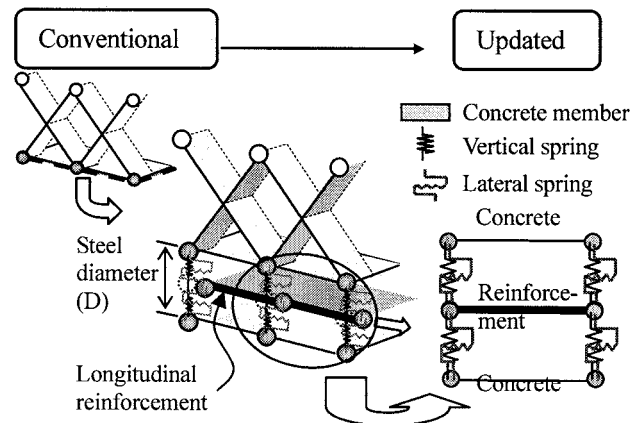


Figure 4 Interface Elements

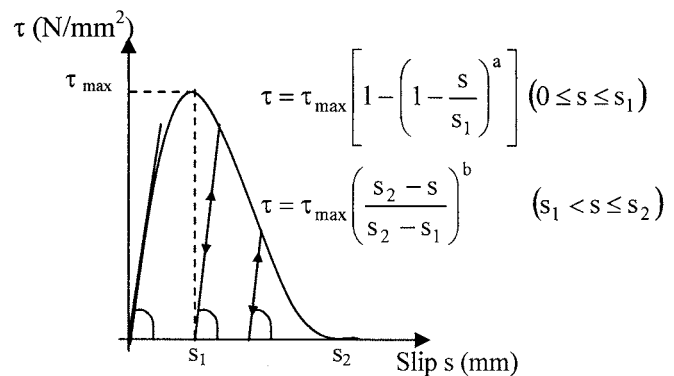


Figure 5 Bond Property of the Lateral Spring

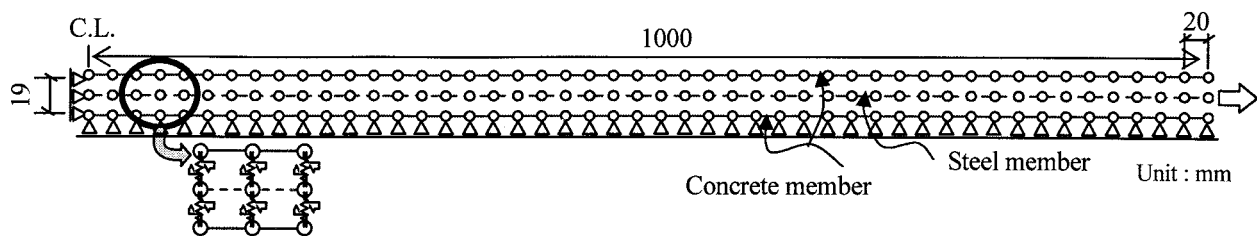


Figure 6 Analytical Model for the Experiment (Kato et al. 2003)

2.4 Constitutive Model of Lateral Springs in the Interface Element

The 2D lattice model analysis is conducted to obtain the optimal solution for each parameter of the constitutive model in the lateral spring by comparing experimental results with analysis. In this study, the experimental test conducted by Kato et al. (2003) is adopted. This experiment consists of uniaxial loading tests in tension to confirm the effects of the bond deterioration induced due to steel corrosion on the tension stiffening of RC members. The specimens were RC members with reinforcement of D19 embedded in the center of the concrete. The specimen was 2000 mm in length having the cross section of 200 mm in width and 150 mm in depth. The embedded reinforcement had the yield strength of 362 N/mm². The compressive strength of concrete was 39.3 N/mm². The specimen was subjected to tensile loading directly at the each end of reinforcement. The 2D lattice model and boundary conditions used in the analysis are illustrated in Figure 6. The specimen is discretized with a symmetric model. An element is 20 mm in length. The concrete elements and steel elements are connected by the interface elements as also shown in Figure 6. Figure 7 shows the experimental results on the load-steel strain relationship. To obtain the optimal solutions of τ_{\max} , s_1 and s_2 , extensive parametric analyses are conducted to fit experimental results well. Figure 7 shows results using appropriate parameters for the bond behavior of the lateral spring. The results of the optimal values of τ_{\max} , s_1 and s_2 are listed in Table 1. In the specimens, it is clarified that the values of s_1 and s_2 can be fixed, 0.1mm and 0.8mm. Here, τ_{\max} (N/mm²) is expressed in Eq. (1).

$$\tau_{\max} = -0.16x + 4 \quad (1)$$

where, x (%) is the cross-sectional loss of steel.

Figure 8 shows the relationship of τ_{\max} and x obtained from the analysis and Eq. (1). In the later section, τ_{\max} is correlated with the cross-sectional loss of steel according to Figure 8, only in the case of a damaged specimen due to steel corrosion.

Table 1 Parameters in Lateral Spring

type	Cross-sectional loss (%)	τ_{\max} (N/mm ²)	s_1 (mm)	s_2 (mm)
No corroded	0	6.0	0.1	0.6
Corroded	0.8	4.0	0.1	0.8
	5.3	3.0	0.1	0.8
	10.2	2.5	0.1	0.8

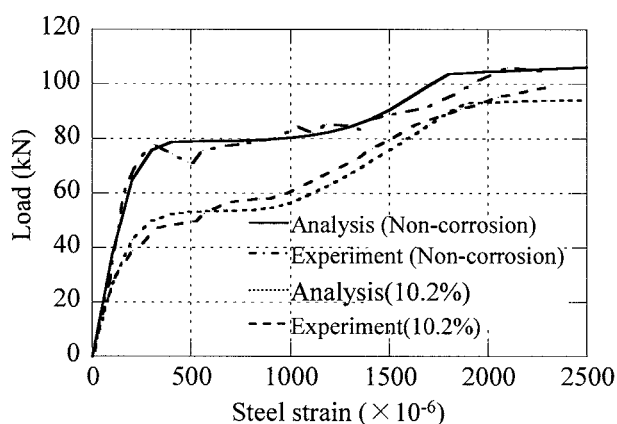


Figure 7 Load-steel Strain Relationships

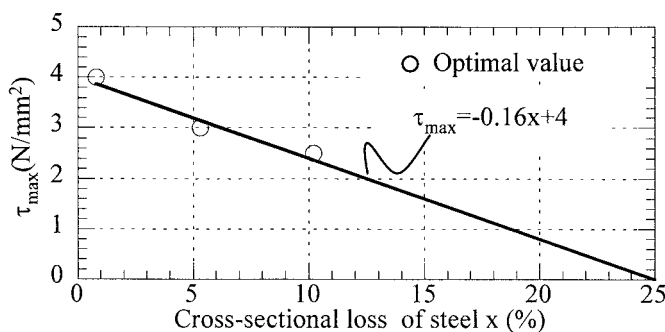


Figure 8 Prediction for τ_{\max}

3. SHEAR RESISTING MECHANISM OF DAMAGED RC BEAMS

3.1 Experimental Setups

The target is the shear loading tests conducted by Matsuo et al. (2004) on RC beams with the reinforcement artificially corroded by the electrolytic method. Since ion migration accelerated in a sodium chloride solution as shown in Figure 9, the corrosion of reinforcement occurred in this region. The specimens were RC beams with or without transverse reinforcement. The rectangular cross section had the width of 200 mm, the depth of 400 mm and the effective depth of 350 mm as shown in Figure 9. The corrosion target region which is soaked in the sodium chloride solution corresponds to the span between the supports (2400 mm).

The arrangement of reinforcement and loading condition are also illustrated in Figure 9. The longitudinal reinforcement ratio was 1.11%. In the specimen with transverse reinforcement, the transverse reinforcement ratio was 0.11%. The material properties of concrete and reinforcement are listed in Table 2. The experimental cases are listed in Table 3. The parameters of this experiment are the existence transverse reinforcement and the electrolytic corrosion time. The specimens with transverse reinforcement are called “A series” and the specimens without transverse reinforcement are called “N series”. Corrosion times that relate well to the degree of corrosion are clearly indicated in the name of specimens. Calculated τ_{\max} according to Eq. (1) is also shown in Table 3.

3.2 Analytical Model

The 2D lattice model is shown in Figure 10. The value of t , the number of nodes and elements are also shown in this figure. Cross-sectional loss of longitudinal and transverse reinforcements and the bond deterioration between longitudinal bar and concrete are considered in the lattice model in order to represent damaged RC beams as shown in Figure 11. In addition, the ruptured transverse reinforcement due to corrosion at lower corners was predicted not to be able to work at the anchorage in the concrete web. For taking into account the insufficient anchorage of transverse reinforcement, no transverse element is provided in the area near the longitudinal reinforcement as shown in Figure 11. In contrast, the anchorage of longitudinal reinforcement is strong enough in the shear loading test, since the anchorage zone at both ends of the beam is set to be outside of the corrosion area.

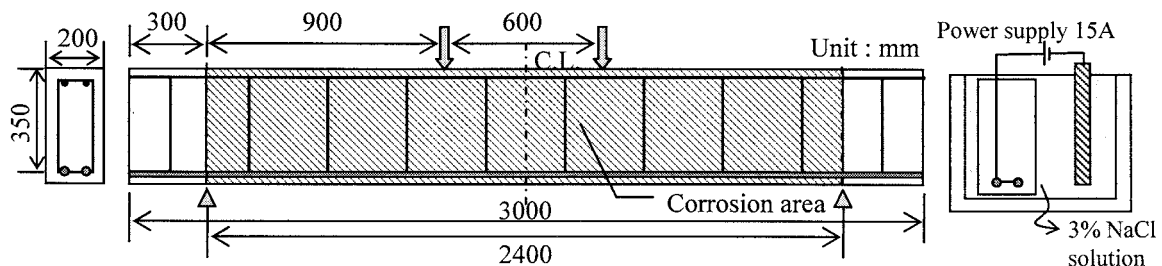


Figure 9 Specimen Details and Test Setup

Table 2 Material Properties

Concrete	
Compressive strength (N/mm ²)	47.8
Young's modulus (kN/mm ²)	36.4
Longitudinal reinforcements (D19)	
Yielding strength (N/mm ²)	429
Young's modulus (kN/mm ²)	191
Transverse reinforcements (D6)	
Yielding strength (N/mm ²)	279
Young's modulus (kN/mm ²)	191

Table 3 Experimental and Analytical Parameters

ID	Cross-sectional loss of steel (%)		τ_{\max} (N/mm ²)
	Longitudinal	Transverse	
A-0h	0	0	Perfect-bonded
A-36h	1.3	21.3	3.8
A-72h	2.8	38.0	3.55
A-144h	10.6	52.9	2.3
N-0h	0	/	6.0
N-36h	3.5		3.4
N-72h	7.3		2.83
N-144h	24.4		0.16

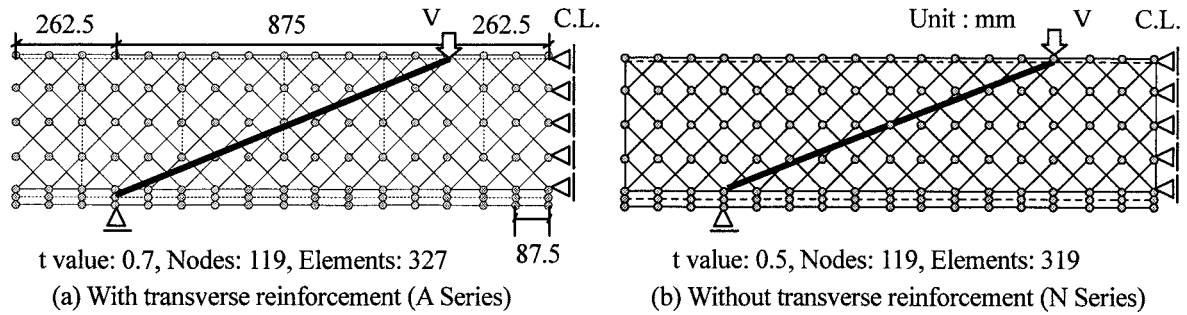


Figure 10 Analytical Models

3.3 Load-Displacement Relationships

Figure 12 shows the load-displacement relationships obtained from the experiment and lattice model analysis. In the analysis, it is assumed that the rapid compression softening behavior of the arch member leads to the brittle shear failure of RC beams. Therefore, if the compression softening of the arch member occurs before the yield of the longitudinal reinforcement, the diagonal tension failure will be predicted. The point of arch softening (C) and yielding of longitudinal bar (Y) obtained from the analysis are indicated in this figure. In addition, the failure modes of experiment and analysis are shown in this figure. The analysis shows a good agreement with the experiments. The beams N-0h, N-36h, A-0h and A-36h show brittle shear failures both in the experiment and analysis. In the experiment, the beam A-72h shows shear-compression failure while in the analysis shear failure was predicted. In the experimental and analytical results, the beams N-72h, N-144h and A-144h show flexural failure followed by the yielding of the longitudinal reinforcement. The loading capacity of the beam N-144h is lower than that of the beam N-72h. The flexural capacity decreased due to cross-sectional loss of the longitudinal reinforcement. Interestingly the analysis shows that the shear carrying capacity of the beams is improved with the increase in cross-sectional loss of the reinforcement.

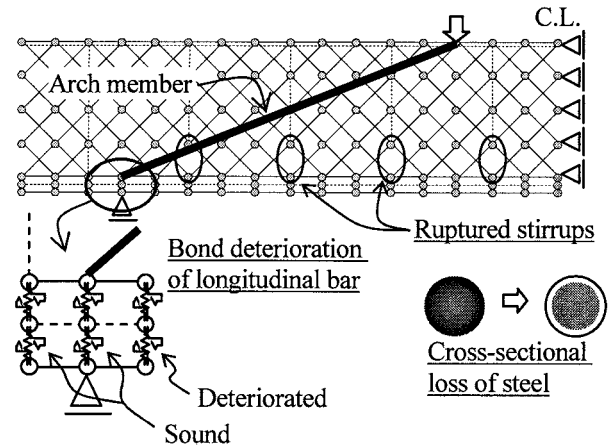


Figure 11 Modeling of Damaged RC Beams

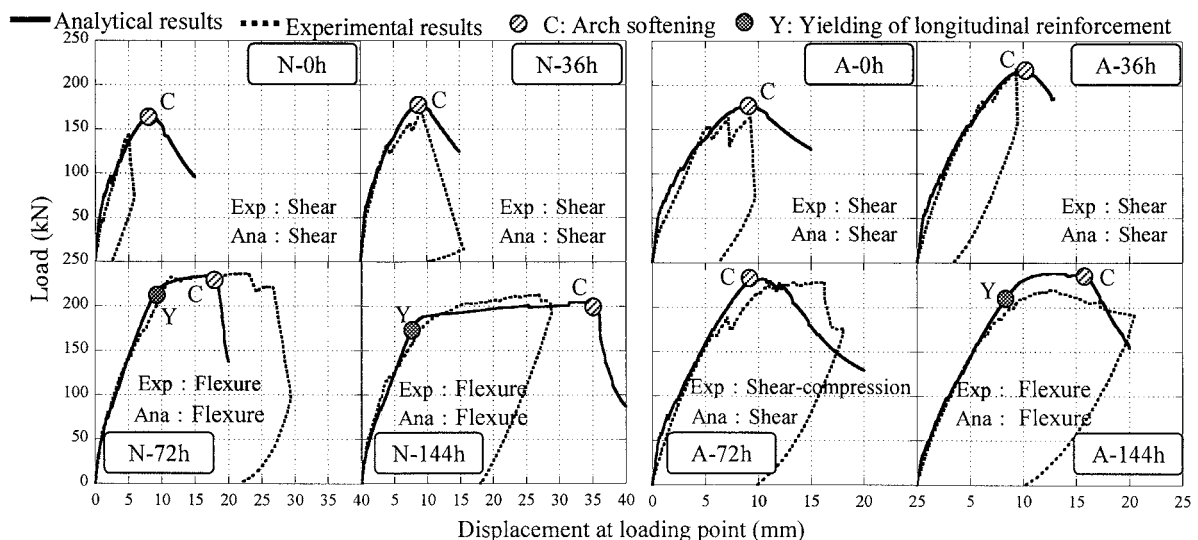


Figure 12 Load-Displacement Relationships

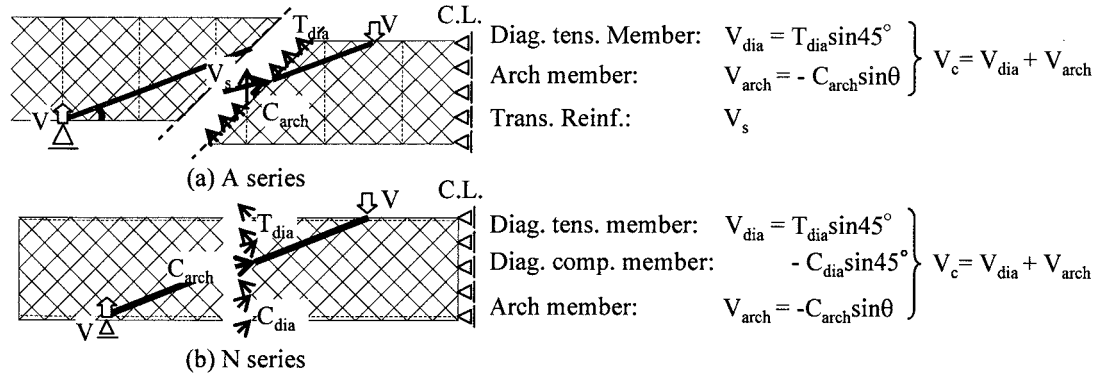


Figure 13 Free Body Diagrams of the Beams

3.4 Shear Resisting Mechanism of Damaged RC Beams

To understand why the shear carrying capacity of damaged RC beams is improved as corrosion of the reinforcement proceeds further, we evaluate the resisting mechanism of the beams in terms of the behavior of each member of the lattice model. Free body diagrams with specific cross section considered here are shown in Figure 13. For the beams with transverse reinforcement, the free body parallel with the diagonal compression member at the middle of shear span is focused on. Shear forces which are the resultant forces of internal force of each member are computed as shown in Figure 13(a). As for the beams without transverse reinforcement, the free body crossing transversely at the middle of the shear span shown in Figure 13(b) is considered. The contribution of the diagonal tension and compression members and the arch member to the shear force can be computed.

The analytical results of each member in the lattice model are illustrated in Figure 14. The analysis shows that the contribution of concrete (V_c) in the beam A-0h decreases just after the transverse reinforcement yields. On the other hand, for the beam A-144h, the shear force due to concrete V_c increases even though the transverse reinforcement yields. The beam A-144h is predicted to finally fail in flexure. As for the beams N-0h and N-144h, the behavior of the arch member is predicted to be dominant after the diagonal crack occurs. It is clearly found that the beginning of softening of the arch member corresponds to the shear carrying capacity of the RC beam.

Figure 15 shows the contribution of arch member to the shear force, V_{arch} in the beams of A series. The comparison with the results indicates that the analysis predicts the increase in the V_{arch} as the steel

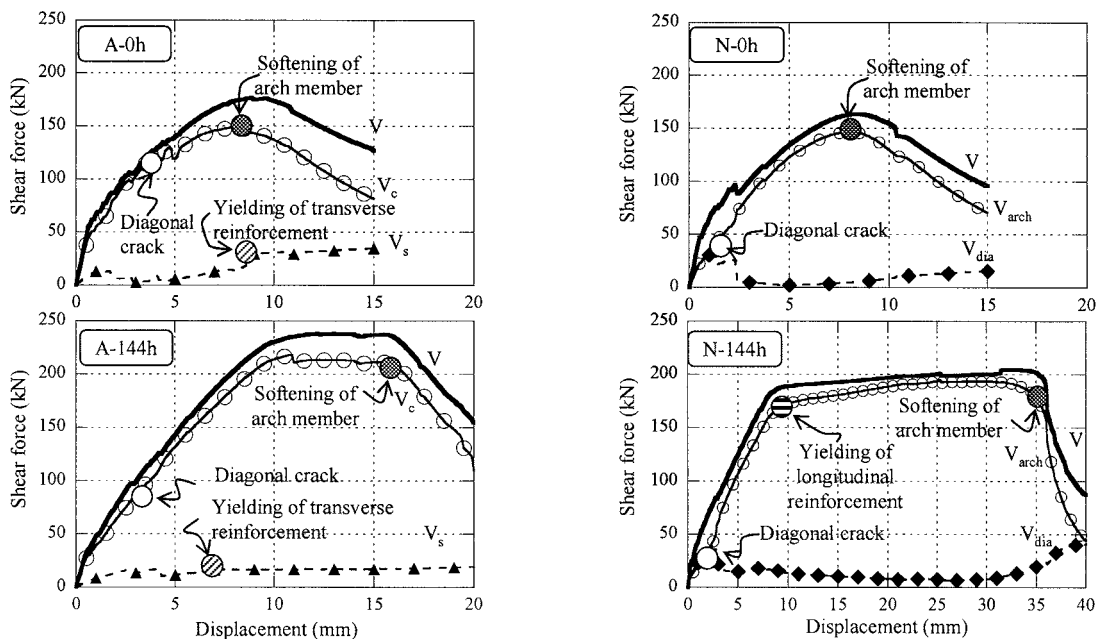


Figure 14 Contribution in the Shear Carrying Capacity of RC Beams

corrosion proceeds. In the analysis, especially in the beam A-144h, the bond between concrete and longitudinal reinforcement significantly degraded within the shear span of the beam. The arch member of concrete in the lattice model represents tied arch action in the shear carrying mechanism of the RC beam. Consequently, the increase in the shear carrying capacity can be explained by the premature formation of the tied arch mechanism in the RC beam. Previous research (Ikeda and Uji 1980) has indicated that RC beams without bond between the longitudinal reinforcement and concrete showed higher shear carrying capacity compared with the beams with sufficient bond. This behavior is similar to the predicted behavior of the beams. It should be noted that for all specimens in this study, the longitudinal reinforcement has been anchored properly. In addition, it was observed in the experiment that the crack along the longitudinal reinforcement resulted in the bond deterioration by the expansion pressure due to the steel corrosion.

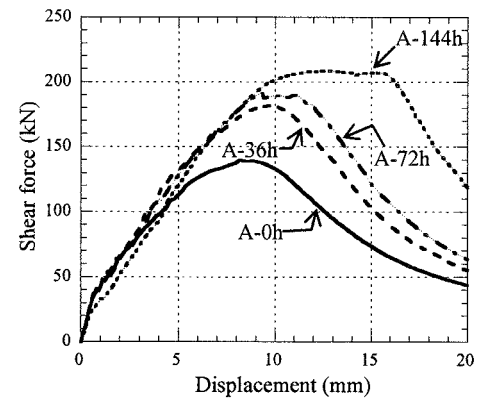


Figure 15 Contribution of Arch Member to the Shear Force (A series)

4. CONCLUSIONS

The conclusions of this study are drawn as follows:

1. The bond deterioration due to the corrosion of reinforcement is modeled using the relationship between the cross-sectional loss of reinforcement and maximum bond stress, τ_{\max} .
2. The lattice model analysis considering the cross-sectional loss of longitudinal and transverse reinforcements and the bond deterioration between concrete and reinforcement can appropriately predict the experimental load-displacement relationships of the RC beams.
3. The analysis shows that as corrosion proceeds, the shear carrying capacity of damaged RC beams increases when the bond between the longitudinal reinforcement and concrete degrades. This behavior can be explained by the premature formation of the tied arch mechanism in the beam.

References:

- Ikeda, S. and Uji, K. (1980), "Studies on The Effect of Bond on The Shear Behavior of Reinforced Concrete Beams," *Journal of Materials, Concrete Structures and Pavement*, JSCE, 293(5), 101-109.
- Kato, E., Iwanami, M., Yokota, H., Ito, H and Sato, F. (2003), "Bond Behavior between Corroded Rebar and Concrete," *Technical Note of the Port and Airport Research Institute*, 1044.
- Mander, J.B., Priestly, K.J.N. and Park, R. (1988), "Theoretical Stress-strain Model for Confined Concrete," *Journal of Structural Engineering*, ASCE, 114(8), 1804-1826.
- Matsuo, T., Sakai, M., Matsumura, T. and Kanazu, T. (2004), "An Experimental Study on Shear Resisting Mechanism of RC Beams with Corroded Reinforcement," *Concrete Research and Technology*, JCI, 15(2), 69-77.
- Naganuma, K. and Ohkubo, M. (2000), "An Analytical Model for Reinforced Concrete Panels under Cyclic Stresses," *Journal of Structural and Construction Engineering*, AIJ, 536, 135-142.
- Miki, T. and Niwa, J. (2004), "Nonlinear Analysis of RC Structural Members Using 3D Lattice Model," *Journal of Advanced Concrete Technology*, JCI, Vol.2, No.3, pp.343-358, 2004.
- Okamura, H. and Maekawa, K. (1991), "Nonlinear Analysis and Constitutive Models of Reinforced Concrete," Gihodo-Shuppan.
- Rokugo, K., Iwasa, M., Suzuki, T. and Koyanagi, W. (1989), "Testing Method to Determine Tensile Strain Softening Curve and Fracture Energy of Concrete," *Fracture Toughness and Fracture Energy*, Balkema, 153-163.
- Vecchio, F.J. and Collins, M.P. (1986), "The Modified Compression Field Theory for Reinforced Concrete Elements Subjected to Shear," *ACI Journal*, 83(2), 219-231.

SEISMIC POUNDING OF REINFORCED CONCRETE BUILDINGS WITH NON-EQUAL STORY HEIGHTS CONSIDERING EFFECTS OF UNDERLYING SOIL

K. Shakya¹⁾, A. C. Wijeyewickrema²⁾, and M. Madurapperuma³⁾

1) Graduate Student, Department of Civil Engineering, Tokyo Institute of Technology, Japan

2) Associate Professor, Department of Civil Engineering, Tokyo Institute of Technology, Japan

*3) Graduate Student, Department of Civil Engineering, Tokyo Institute of Technology, Japan
shakya.k.aa@m.titech.ac.jp, wijeyewickrema.a.aa@m.titech.ac.jp, ma.k.aa@m.titech.ac.jp*

Abstract: An analysis of seismic pounding of two typical reinforced concrete moment resisting frame buildings, 5-story and 4-story, with non-equal story heights including soil-structure interaction, is presented by using structural analysis software SAP2000. The response time history of the buildings and shear amplification factors are investigated. The underlying soil is modeled through a combination of mass-spring-damper and contact between the adjacent buildings is modeled through link elements composed of spring, gap element and damper. Fundamental time periods of buildings increase and shear amplification factors are reduced when the soil-structure-interaction is considered.

1. INTRODUCTION

Collision between two adjacent buildings may occur under seismic excitation if the separation between them is insufficient and when the buildings vibrate out of phase. This could lead to significant damage of the structures and even to total collapse. The characteristics of input ground motion, dynamic characteristics of structures and the gap between adjacent structures govern the magnitudes and the locations of impact. Though the provision of sufficient gap between the adjacent structures eliminates the pounding phenomena, due to increase in urban development and the associated increase in real-estate values, buildings are constructed even up to their property lines. Moreover, in order to fulfill functional requirements, adjacent buildings are constructed with non-equal heights resulting in mid column pounding during earthquakes. Very few studies have been conducted to investigate the response of the buildings considering the effects of underlying soil. The foundation soil highly influences the structural response not only in terms of seismic wave propagation but also affecting the fixity of the foundations of buildings. Hence, the underlying soil properties must be taken into consideration for the pounding analysis of buildings.

Many instances of damage and collapse of different structures have been reported due to pounding during past large earthquakes. Anagnostopoulos (2004) proposed an equivalent viscous damper for modeling inelastic impacts in earthquake pounding problems. Jankowski (2005) introduced non-linear viscoelastic modeling of earthquake-induced structural pounding and also provided the characteristics of steel to steel impact and concrete to concrete impact. Karayannis et al. (2005)

investigated the influence of the structural pounding on the ductility requirements and the seismic behavior of reinforced concrete structures with non-equal heights, designed according to Eurocode 2 and Eurocode 8. These studies do not include the effect of underlying soil. Rahman et al. (2001) highlighted the influence of soil flexibility effects on seismic pounding of a case of adjacent multiple-story buildings of different total heights using coefficients proposed by Mullikan and Karabalis (1998) by means of 2-D structural analysis software, RUAUMOKO.

The present paper is a study of pounding of two typical reinforced concrete moment resisting frame buildings, 5-story and 4-story, with non-equal story heights considering underlying soil. The main objective of this paper is to investigate the influence of underlying soil on the structural pounding between non-equal story height buildings under seismic excitation.

2 SOIL-STRUCTURE INTERACTION

Typically, buildings are analyzed and designed considering fixed foundation assuming underlying soil is very stiff. But the consideration of the soil-structure interaction effects may alter the effect of input seismic excitation on the structures and accordingly the seismic performance of buildings. The study of earthquake motions showed that the rock motions could be amplified at the base of a structure by over a factor of five (Wilson, 2002). The ground motion at the free-field will either be amplified or attenuated depending on characteristic of the bed rock, soil profile, topography of site and soil characteristics. The adaptation of soil supports increases the degree of freedom at the foundations and accordingly the vibration modes of the structure are increased. Furthermore, base shear and moments are modified; consequently the distribution of lateral forces as well as inertial forces vary along the height of the structure. The natural time period of the structure gets lengthened and more energy dissipation takes place at the foundation-soil interface causing increase in damping of the system.

3 MODELING OF SOIL-STRUCTURE INTERACTION

For 3-D soil-structure systems, the most common soil-structure interaction model is based on the “added motion” formulation, which is simple, easy to automate and use within a general linear structural analysis program (Wilson, 2002). Another way of modeling soil structure interaction is by using springs and dampers at the base of a structure. In this paper, combinations of frequency independent mass-spring-damper systems have been used. The schematic diagram of the mass-spring-damper is shown in Figure 1. The mass-spring-damper properties can be obtained from Table 1.

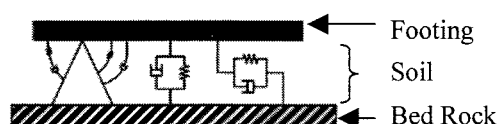


Figure 1. Discrete-Element Model to Represent Degree of Freedom of Soil Mass Beneath Footing

Table 1. Coefficients for 1-D Discrete Element Model for Square Footing (Rahman et al. 2001)

MOTION	HORIZONTAL	VERTICAL	ROCKING
Mass (inertia) ratio, β	$\frac{m(7-8\nu)}{32\rho r_0^3(1-\nu)}$	$\frac{m(1-\nu)}{4\rho r_0^3}$	$\frac{3(1-\nu)}{8\rho r_0^5}$
Equivalent radius, r_0	$2a/\sqrt{\pi}$	$2a/\sqrt{\pi}$	$2a/\sqrt[4]{3\pi}$
Virtual soil mass (inertia), m_v	$0.095m/\beta$	$0.27m/\beta$	$0.24m/\beta$
Discrete element model, K (static stiffness) and C (damping)	$K = 9.2Ga/(2-\nu)$ $C = 0.163Ka/V_s$	$K = 4.7Ga/(1-\nu)$ $C = 0.8Ka/V_s$	$K = 4.0Ga^3/(1-\nu)$ $C = 0.6Ka/V_s$

The coefficients for rectangular footings can be calculated by using equations (1)~(9) and Table 2 (Wolf, 1988).

$$K_{hx} = Gb/(2-\nu) * [6.8(l/b)^{0.65} + 2.4][1 + \{0.33 + 1.34/(1+l/b)\}(e/b)^{0.8}], \quad (1)$$

$$K_{hy} = Gb/(2-\nu) * [6.8(l/b)^{0.65} + 6.8l/b + 1.6][1 + \{0.33 + 1.34/(1+l/b)\}(e/b)^{0.8}], \quad (2)$$

$$K_v = Gb/(1-\nu) * [3.1(l/b)^{0.75} + 1.6][1 + (0.25 + 0.25b/l)\{e/b\}^{0.8}], \quad (3)$$

$$K_{rx} = Gb^3/(1-\nu) * [3.2l/b + 0.8][1 + e/b + \{1.6/(0.35 + l/b)\}(e/b)^2], \quad (4)$$

$$K_{ry} = Gb^3/(1-\nu) * [3.73(l/b)^{2.4} + 0.27][1 + e/b + \{1.6/(0.35 + (l/b)^4)\}(e/b)^2], \quad (5)$$

$$K_t = Gb^3 * [4.25(l/b)^{2.45} + 4.06][1 + \{1 + (1.3 + 1.32b/l)\}(e/b)^{0.9}], \quad (6)$$

$$K_{hxy} = e/3 * K_{hx}, \quad K_{hyx} = e/3 * K_{hy}, \quad (7)$$

$$C_0 = b/V_s * K\gamma_0, \quad C_1 = b/V_s * K\gamma_1, \quad (8)$$

$$M_0 = b^2/V_s^2 * K\mu_0, \quad M_1 = b^2/V_s^2 * K\mu_1, \quad (9)$$

where, G is shear modulus, ν is Poisson's ratio, a side of square footing, l and b are length and breadth of rectangular footing, e is embedment and V_s is shear wave velocity.

Table 2. Dimensionless Coefficients of Discrete Model for Rectangular Foundation (Wolf, 1988)

	Dampers		Masses	
	γ_0	γ_1	μ_0	μ_1
Horizontal h_x h_y	$0.75 + 0.2(l/b - 1)$	-	-	-
Vertical	$0.9 + 0.4(l/b - 1)^{2/3}$	0.3	-	0.14
Rocking r_x	-	0.45	-	0.34
r_y	-	$0.45 + 0.23(l/b - 1)$	-	$0.34 + 0.55(l/b - 1)$
Torsional	-	$0.35 + 0.12(l/b - 1)$	-	$0.28 + 0.63(l/b - 1)$

4 POUNDING FORCE AND ELEMENTS

In order to model pounding between two colliding objects, linear spring-damper (Kelvin-Voigt model) can be used. The viscous component of the linear spring-damper element is activated with the same damping coefficient during the whole time of contact. But in reality, most of energy is dissipated during the approach period and minor energy dissipation is observed during restitution period. However, for simplicity, to simulate the structural pounding the linear viscoelastic model has been widely used. The force, $F(t)$ in the linear viscoelastic model during impact is expressed as

$$F(t) = k\delta(t) + c\dot{\delta}(t), \quad (10)$$

where, $\delta(t)$ is the deformation of colliding structural elements, $\dot{\delta}(t)$ is the relative velocity between colliding elements, k is the stiffness of contact element and c is the damping of contact elements and is given by

$$c = -2 \ln e \sqrt{k \frac{m_1 m_2}{(m_1 + m_2) \sqrt{\pi^2 + (\ln e)^2}}}, \quad (11)$$

where, e is a coefficient of restitution, m_1 and m_2 are masses of structural members. Jankowski (2005) proposed that for concrete-to-concrete impact, $k = 93,5000$ kN/m and $e = 0.65$ provides good correlation between experimental and theoretical results.

Contact of buildings and pounding force are simulated by link elements, which are inserted between buildings (Figure 2(a)). A link element having gap property (Figure 2(b)) and one with linear property are used. The purpose of gap property is to transmit the force through link element only when contact occurs and the gap is closed. The force-deformation relationship of gap element is given by

$$f_G = \begin{cases} -k_G[(u_i - u_j) - open] & \text{if } u_i - u_j > open, \\ 0 & \text{if } u_i - u_j < open, \end{cases} \quad (12)$$

where, k_G is the spring constant, u_i and u_j are the displacements of the element's end nodes and $open$ is the initial gap opening.

The stiffness of gap element is considered as 100 times that of linear element to avoid error in convergence and to ensure that it works nearly rigidly when the gap is closed.

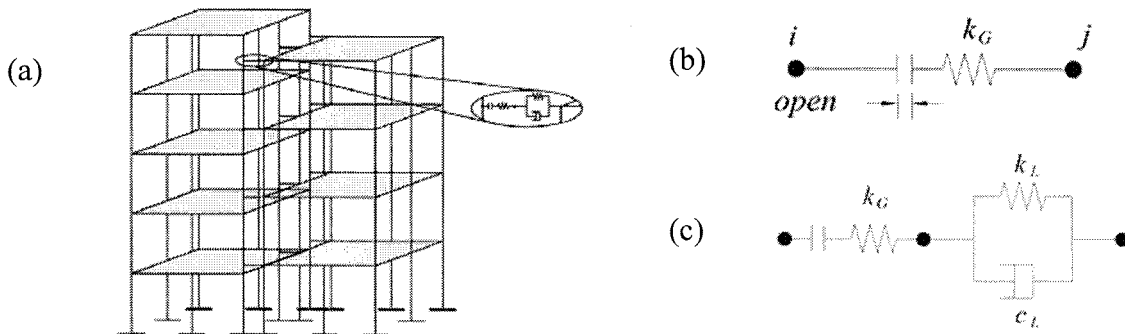


Figure 2. (a) Buildings Connected with Link Elements, (b) Link Element with Gap Property, and (c) Link Element with Gap Property Combined with Kelvin-Voigt Element

5 PROBLEM STATEMENT

A 4-story and a 5-story moment resisting reinforced concrete buildings as shown in Figure 3 are considered for the analysis. Both of these buildings are constructed up to their property lines, so the gap between them is considered to be 2 mm. In order to avoid eccentric footings in 5-story building, 1.2 m offset is provided for the location of columns nearby adjacent building and beams are projected up to the property line. The buildings are analyzed and designed separately without considering pounding according to Indian Standard 456:2000 and considering earthquake loads as per Indian Standard 1893:(part1) 2002. For the analysis and design M20 grade concrete and Fe415 grade steel is used. The unit weight of concrete is considered as 25 kN/m^3 , modulus of elasticity 22360 N/mm^2 and Poisson's ratio 0.2. Analyses of the structures are performed using SAP2000 and the structural members including foundations are designed according to the acquired output results. The slab thickness of 120 mm, 300 mm x 300 mm columns and 230 mm x 356 mm beams are found to be sufficient. The designed sizes of the footings and steel reinforcements in columns are shown in Appendix A. In order to investigate structural pounding, the N-S component of acceleration record of the 1989 Loma Prieta earthquake recorded at station 47379 Gilroy Array #1 is used as input earthquake motion along x-axis (<http://peer.berkeley.edu.smcat/search.html>). Newmark method with $\beta = 0.25$, $\gamma = 0.5$ and time step, $\Delta t = 0.005 \text{ sec}$ is adopted for time history analysis of buildings. To find out the mass-spring-damper properties soil density, Poisson's ratio of soil and shear modulus of soil are taken as 16.5 kN/m^3 , $1/3$ and 18.75 kN/m^3 respectively. Due to the presence of very small gap between the buildings and also non-equal heights of buildings, mid column pounding is inevitable. To find the structural response of models with two different foundation types are prepared and analyses are performed using SAP2000.

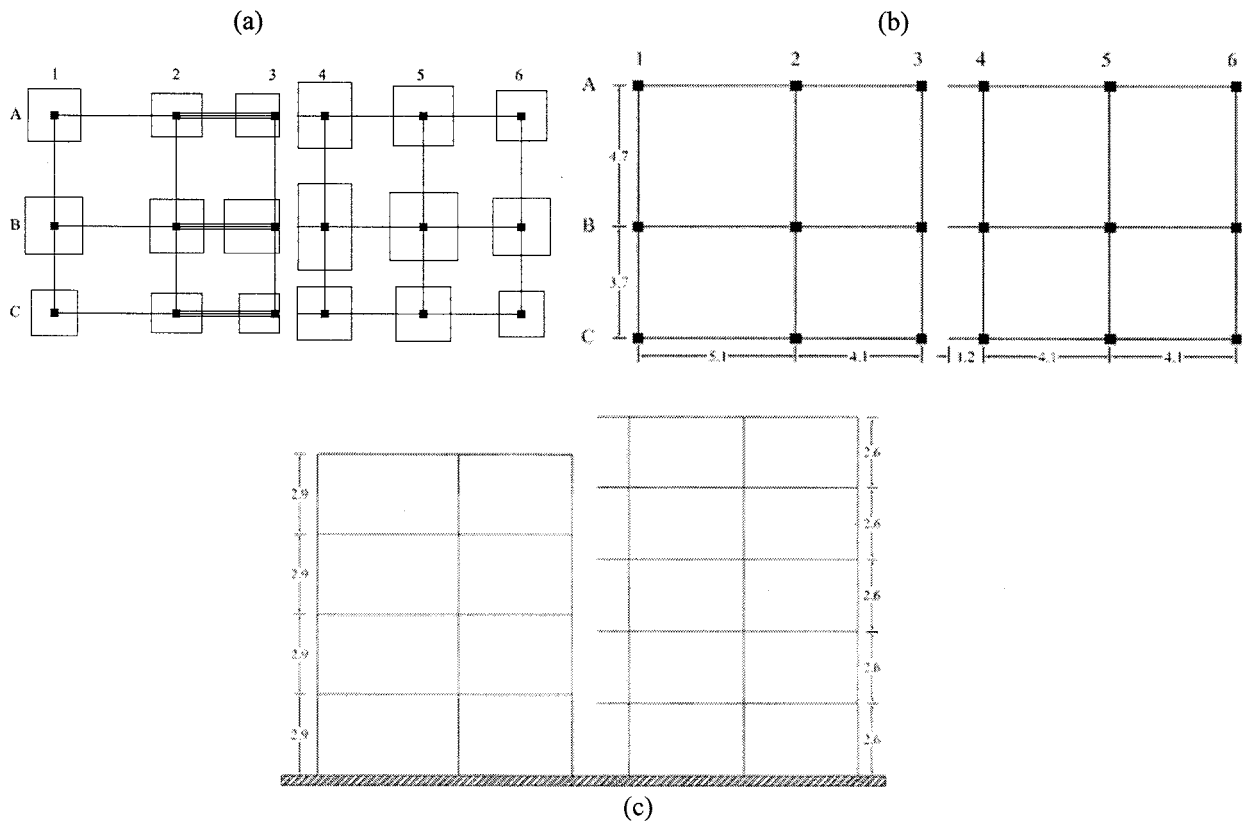


Figure 3. (a) Foundation of Buildings, (b) Plan and (c) Elevation

6 NUMERICAL RESULTS

In this section, the effect of soil on the dynamic response of the structure and structural pounding are presented. The fundamental time periods of the buildings are given in Table 3, where it can be seen that when the underlying soil is considered, the fundamental time periods increased.

Table 3. Fundamental Time Period of Buildings

Foundation Type	Time Period (sec)	
	5-Story	4-Story
Fixed	0.66215	0.61975
Flexible (Soil)	0.68888	0.64706

Figure 4 shows the displacement time history of grid-C3 and grid C4 for fixed foundation and it can be seen that the buildings are vibrating out of phase. The response of buildings upon considering soil-structure-interaction and during pounding is represented in terms of shear amplification factor, which is defined as the ratio of maximum shear resulting from pounding to that of no pounding case. The shear amplification factors are shown in Figure 5. The results illustrate that the shear force in the 4-story building is highly amplified and is prone to more damage compared to 5-story building. In both 4-story and 5-story buildings, the shear amplification factors in the buildings with fixed foundation are higher than those of buildings with flexible foundation except at the top floor of the 4-story building (Figure 5(a)). Due to mid column pounding in 4-story building, shear at the section of impact is relatively high and accordingly the story shear increased causing significant increment in the shear amplification factors, whereas for the 5-story building, pounding takes place at the floor level due to which the shear amplification factors are comparatively low. These increments in shear amplification factors indicate the vulnerability of mid column pounding. The shear is amplified more than 1.7 times in 4-story building.

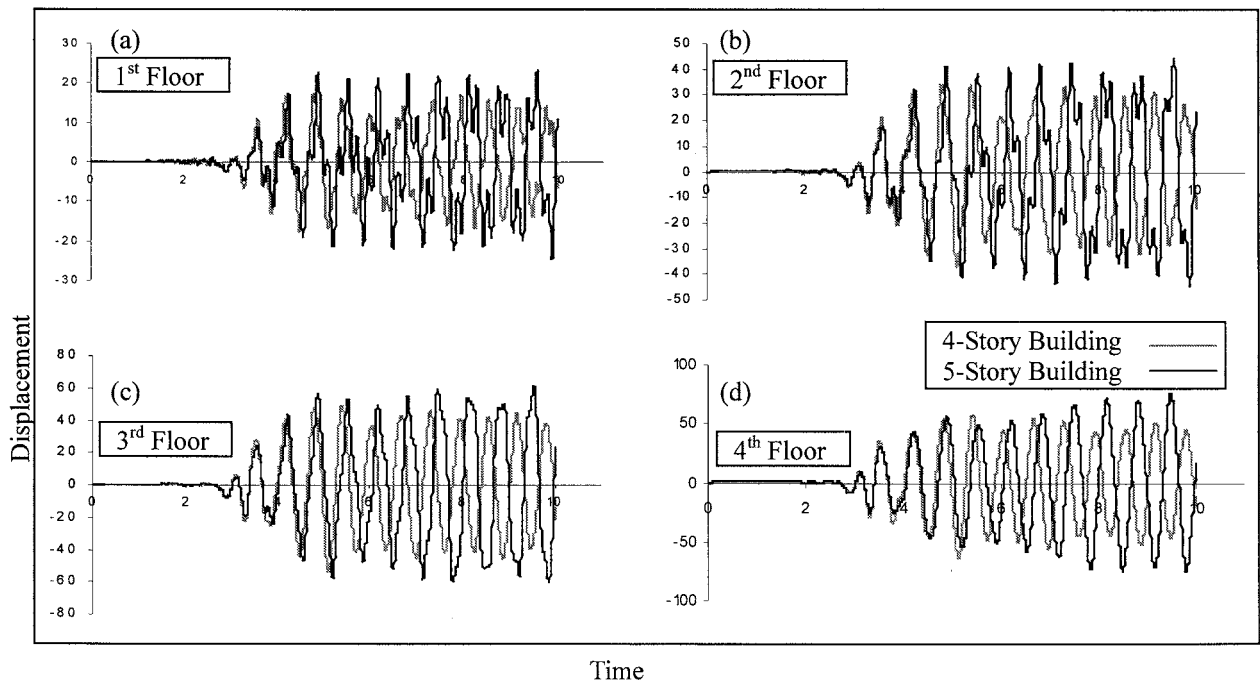


Figure 4. Displacement of Buildings for Fixed Foundation: (a) 1st Floor, (b) 2nd Floor, (c) 3rd Floor, and (d) 4th Floor

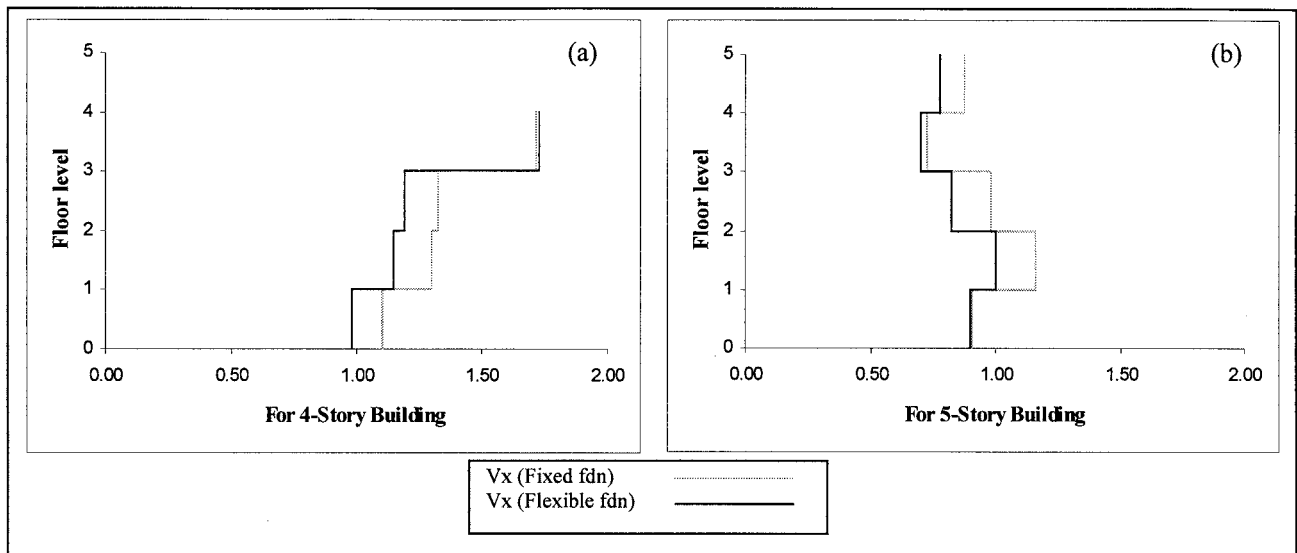


Figure 5. Shear Amplification Factor at Different Floor Level

7 CONCLUSIONS

To find the structural responses under seismic excitation, 4-story and 5-story reinforced concrete moment resisting frame buildings with non-equal heights are modeled and analyzed with different foundation types using SAP2000. The fundamental time period of buildings are increased when the effect of underlying soil is considered in the analysis. As the fundamental time periods of the buildings are different, out of phase vibration is observed. Furthermore, the 4-story building is more affected when soil-structure-interaction is considered. The shear amplification factors are always higher for 5-story building when the effect of underlying soil is not taken in account but only at the top floor of the 4-story building the shear amplification factor is marginally large when underlying soil is considered. The effect of soil-structure-interaction considerably increases with increase in the height of buildings.

Acknowledgements:

The first and the third authors gratefully acknowledge Monbukagakusho scholarships for master students from the Japanese government. The authors are very grateful to Prof. Tatsuo Ohmachi, COE Program Leader of Center for Urban Earthquake Engineering (CUEE), Tokyo Institute of Technology, and Prof. Kohji Tokimatsu, COE Program Sub-leader of CUEE, for their advice and support. Financial support from CUEE is gratefully acknowledged.

References:

- Anagnostopoulos, S.A. (2004), "Equivalent Viscous Damping for Modeling Inelastic Impacts in Earthquake Pounding Problems", *Earthquake Engineering and Structural Dynamics*, **33**, 897-902.
- IS 456:2000, "Indian Standard Code of Practice for Plain and Reinforced Concrete", (Fourth Revision), *Bureau of Indian Standards*.
- IS 1893:(Part1) 2002, "Indian Standard Criteria for Earthquake Resistant Design of Structures, Part 1 General Provisions and Buildings" (Fifth Revision), *Bureau of Indian Standards*.
- Jankowski, R. (2005), "Non-Linear Viscoelastic Modelling of Earthquake-Induced Structural Pounding", *Earthquake*

- Engineering and Structural Dynamics*, **34**, 595-611.
- Karayannis, C.G., Favvata, M.J. (2005), "Earthquake-Induced Interaction Between Adjacent Reinforced Concrete Structures with Non-Equal Heights", *Earthquake Engineering and Structural Dynamics*, **34**, 1-20.
- Mullikan, J.S., Karabalis, D.L. (1998), "Discrete Model for Dynamic Through-The-Soil Coupling of 3-D Foundations and Structures", *Earthquake Engineering and Structural Dynamics*, **27**, 687-710.
- Ohta, R., Wijeyewickrema, A.C., Farahani, A. (2006), "Structural Pounding between Adjacent Buildings in a Row", *Taiwan-Japan Symposium on the Advancement of Urban Earthquake Hazard Mitigation Technology*, A12(1-8).
- Rahman, A.M., Carr A.J., Moss P.J. (2001), "Seismic Pounding of a Case of Adjacent Multiple-Storey Building of Differing Total Heights Considering Soil Flexibility Effects", *Bulletin of The New Zealand Society for Earthquake Engineering*, **34**(1), 40-59.
- Wilson, Edward L. (2002), "Three-Dimensional Static and Dynamic Analysis of Structures", Computers and Structures Inc.
- Wolf, J.P. (1988), "Soil-Structure-Interaction Analysis in Time Domain", Prentice Hall Inc.

Appendix A:

Table A1. Footing Description

Grid	1	2	3	4	5	6
A	2.2x2.2x0.42	2.1x1.8x0.46	1.8x1.8x0.39	2.2x2.8x0.42	2.5x2.5x0.43	2.1x2.1x0.37
B	2.4x2.4x0.39	2.25x2.25x0.47	2.25x2.25x0.47	2.2x3.6x0.38	2.85x2.85x0.48	2.4x2.4x0.41
C	1.9x1.9x0.33	2.1x1.65x0.45	1.65x1.65x0.38	2.25x2.25x0.38	2.3x2.3x0.40	1.9x1.9x0.33

All dimensions are in m

Table A2. Column Main Steel Reinforcement

Floor	Grid	1	2	3	4	5	6
1	A	4-20Ø+4-16Ø	8-20Ø	8-16Ø	4-20Ø+4-16Ø	8-20Ø	8-16Ø
2		4-20Ø+4-16Ø	8-20Ø	8-16Ø	4-20Ø+4-16Ø	8-20Ø	8-16Ø
3		8-16Ø	4-20Ø+4-12Ø	4-16Ø+4-12Ø	8-16Ø	4-20Ø+4-12Ø	4-16Ø+4-12Ø
4		8-16Ø	4-20Ø+4-12Ø	4-16Ø+4-12Ø	8-16Ø	4-16Ø+4-12Ø	4-16Ø+4-12Ø
5					8-16Ø	4-16Ø+4-12Ø	4-16Ø+4-12Ø
1	B	8-20Ø	4-25Ø+4-16Ø	8-16Ø	4-25Ø+4-16Ø	4-25Ø+4-20Ø	4-20Ø+4-16Ø
2		8-20Ø	4-25Ø+4-16Ø	8-16Ø	4-20Ø+4-16Ø	8-20Ø	4-20Ø+4-12Ø
3		8-16Ø	8-16Ø	8-12Ø	8-16Ø	4-20Ø+4-12Ø	4-16Ø+4-12Ø
4		8-16Ø	8-16Ø	8-12Ø	4-16Ø+4-12Ø	8-12Ø	8-12Ø
5					8-12Ø	8-12Ø	8-12Ø
1	C	8-16Ø	8-16Ø	8-12Ø	8-16Ø	8-16Ø	8-12Ø
2		8-16Ø	8-16Ø	8-12Ø	8-16Ø	8-16Ø	8-12Ø
3		8-16Ø	8-12Ø	8-12Ø	8-12Ø	8-12Ø	8-12Ø
4		8-16Ø	8-12Ø	8-12Ø	8-12Ø	8-12Ø	8-12Ø
5					8-12Ø	8-12Ø	8-12Ø

SIMULATION OF CUTTING AND FILLING GROUND IN NIIGATA-KEN CHUETSU EARTHQUAKE 2004

K. Fukutake¹⁾, and A. Onoue²⁾

1) Senior Researcher Institute of Technology, Shimizu Corporation, Tokyo, Japan

*2) Professor, Department of Civil Engineering, Nagaoka National College of Technology, Niigata, Japan
kiyoshi.fukutake@shimz.co.jp, onoue@nagaoka-ct.ac.jp*

Abstract: Numerous artificially embanked slope failures were caused by the 2004 Niigata-ken Chuetsu Earthquake. The cause of destructive damage of a school building at Nagaoka National College of Technology was examined by three-dimensional dynamic FEM based on effective stress analysis. From the analysis results, it was confirmed that the building was pulled and twisted by the landslide of the bank shotcrete accompanied with pile fracture.

1. INTRODUCTION

Nagaoka National College of Technology (NNCT) has suffered from serious damage by the 2004 Niigata-ken Chuetsu Earthquake. Many damaged buildings and facilities locate at the peripheral zone of the campus, which was constructed by filling of soil. Since the school building No.3 has been built on the site that consists of cutting and filling ground at the exit of old valley topography, the vibration of the ground was very complicated.

In order to examine such complicated vibration of the ground, a dynamic simulation model of an equivalent linear analysis and a nonlinear effective stress analysis based on finite element method were used. The present study aims to clarify the main cause of the split destruction of Building No.3 through comparing the observation results and analyzed ones.

2. SEISMIC DISASTER IN NNCT BY EARTHQUAKE

2.1 Outline of the site

The campus of NNCT was originally a small hill with the summit; 75 m in elevation. The axis of the ridge locates almost Northwest-Southeast in compass as shown in Fig. 1. Several buildings, located along the southeast edge of the campus, are superimposed on the contour lines of original geography in this figure. The original stratigraphy was as follows; the volcanic ash cover, Oyama layer of Pleistocene deposit and Uonuma layer sedimented by early Diluvium, from the top to downward.

In 1960, the northwestern area of the hill was improved and terraced: At the elevation (hereafter: EL) of 62.8 m for the athletic field, at EL=65 m for the main campus, and at EL=68.2 m for the level ground in the southeastern area. In Fig. 1, the gray and white color areas show the cutting ground and the filling ground respectively. In the first cutting and filling ground construction, the west slopes and valleys were filled with cut soil for the enlargement of each terrace in both directions; west and southwest.

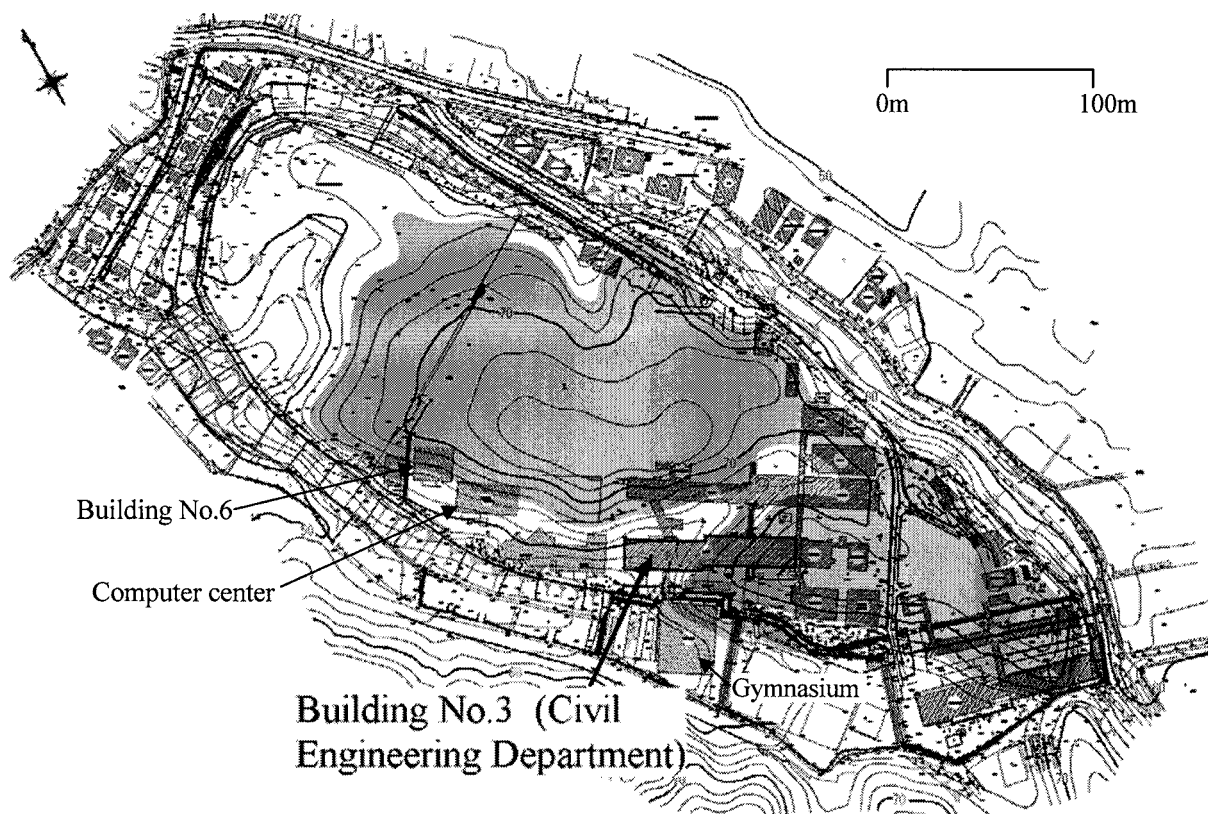


Figure 1 Super imposed buildings and contour map before construction of the site by cutting and filling

The construction of the present campus has been completed in 1968 after the second filling construction for further enlargement of the site at each elevation. The slopes of northeast and northwest have partially natural shapes of the original hill.

From the comparison between Fig. 1 and present campus condition, we can see two deep and long hidden valleys, which must have been already filled many years ago. One is buried under the athletic field and the other is under the middle of the campus. Both of the old valleys open into the southwest edge of the present campus.

The filling ground spreads to the area where the original elevation is lower than 65 m. The connecting passage and the southwest half of Building No.3 locate at the exit of the old valley which sweeps deeply off to the east direction. All buildings that locate on the filling ground are supported by bearing piles except for connecting passage and machinery factory. All buildings and facilities locating on the filling ground except Building No.6 and Computer center displaced and/or inclined due to the earthquake, and were demolished afterward.



(a) View from southwest direction



(b) View from south direction

Figure 2 Building No.3

2.2 Feature of Building No.3 and the ground

Figure 2(a) shows the picture, taken from southwest direction, of Building No.3 behind the parking lot for bicycles. Gymnasium No.2 is seen on the right. It should be noted that there is a difference of 5.2 m in ground elevation between the front and the back, both of which are filling ground. Figure 2(b) is a view from south direction, where the left hand side of Building No.3 is of three- stories and the right hand side is two-stories. The two-story portion of Building No.3 and athletic clubhouse, shown at the front, locate at the cutting ground, although the three-story portion of Building No.3 is on the filling one.

2.3 Damage of Building No.3 due to the earthquake

Figure 3 is the plan of damaged Building No.3 and the displacement due to the earthquake. The three-story portion; 40m long at northwest side and the two-story portion; 24m long at the middle portion of the building locate on the ground of EL=65m. The single story portion; 16m long at southeast side locates on EL=68.2 m for the convenience to connect to the second floor of the middle portion. During the earthquake, the three-story portion turned anti clockwise, and the displacement of the northwest end of the building reached 77cm to southwest direction. The displacement of the ground reached 95cm to southwest direction because of the crack, 18 cm in width, beside the great beam. At the same time, the subsidence of the ground reached 47cm and 59cm at the points b and c, respectively.

Figure 4 shows the footing, and two of the three-combined piles at the corner. They are reinforced concrete piles with a diameter of 30 cm. As shown clearly in the pictures, the movement of the piles is larger than that of the footing. The displacement of the piles toward southeast is under 20cm, and that

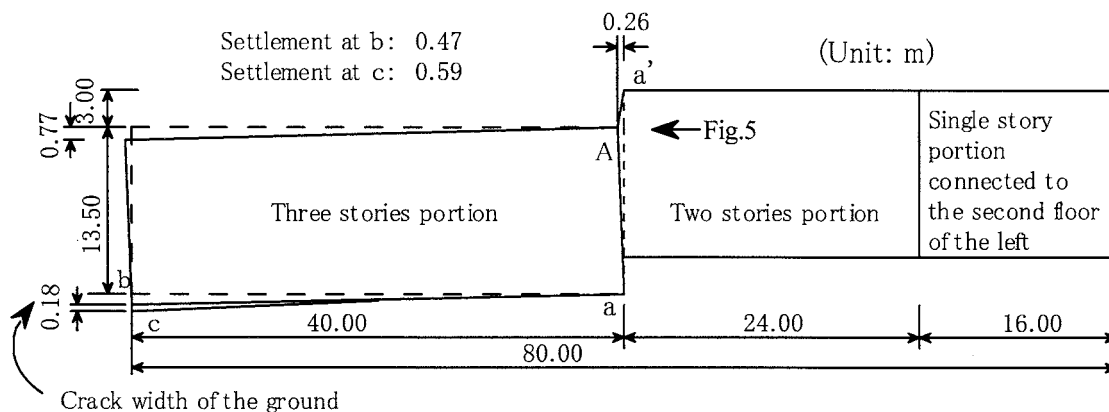


Figure 3 Disconnection of Building No.3 and displacements

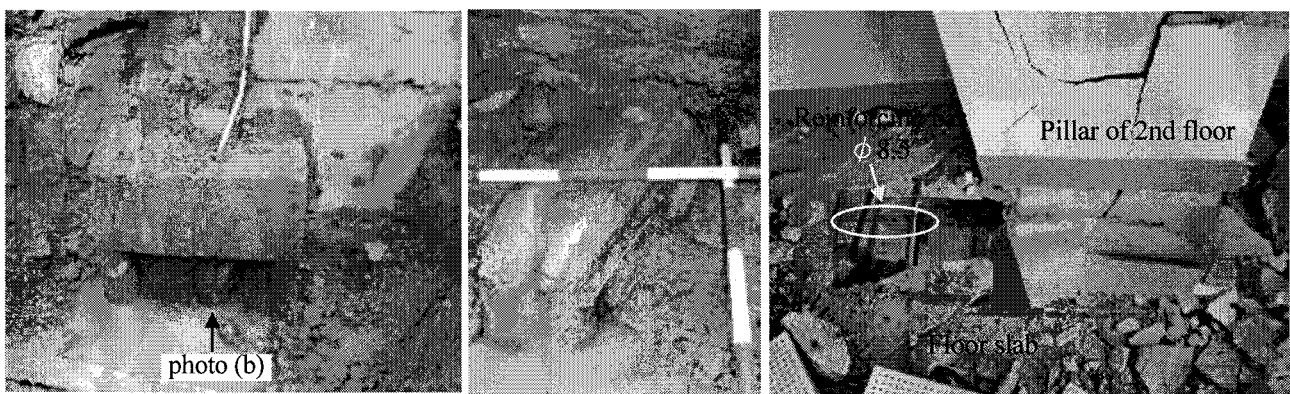


Figure 4 Footing and RC-piles($\phi 300 \times 3$) at Southeast corner

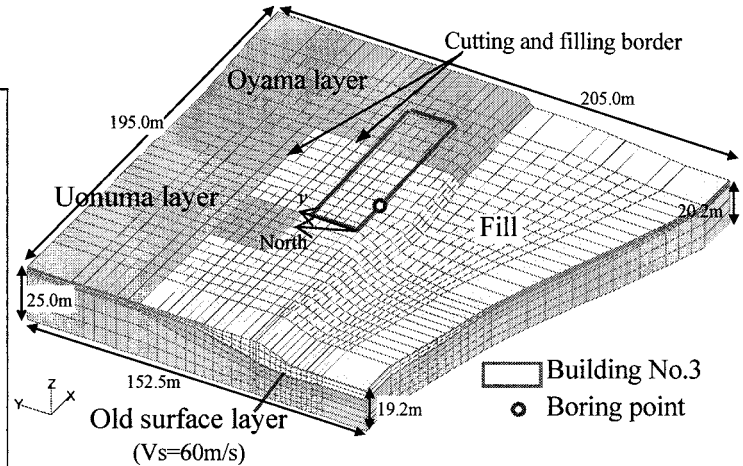
Figure 5 Disconnected second floor at point A in Fig.18

toward northwest is over 35cm, which is larger than those of the footing. The pile heads were destroyed as long as 60 cm. From the result shown in Fig.4, we can see that the ground has moved together with the piles.

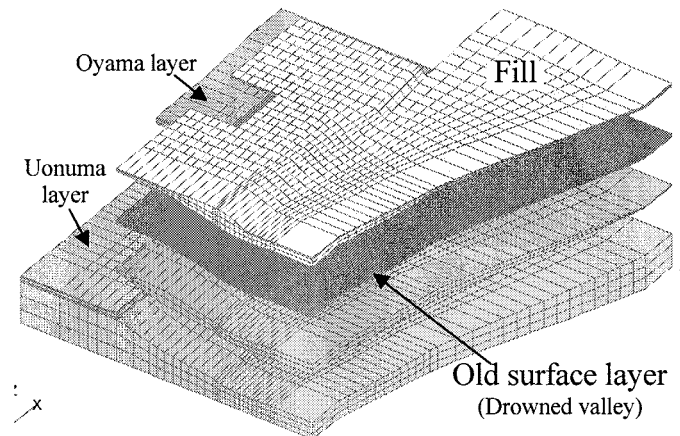
Figure 5 is the picture of the column and the second floor at Point A, taken from the direction of the arrow shown in Fig.3. The column was displaced 26cm, resulting in an opening in the floor. Through the opening of the second floor, we can see a part of the column of the first floor. The floor is made up of double reinforced concrete with the thickness of 13cm, and the rebar, 9mm in diameter, with 17 cm in spacing.

Table 1 Boring log and soil properties

m	Layer	Soil type	V_s (m/s)	γ_t (kN/m ³)	$\gamma_{0.5}$ ($\times 10^{-4}$)	h_{max}
0		Fill				
1						
2			100	16.2	8.7	0.20
3						
4	Fill					
5						
6		Filling loam	130	16.2	14.3	0.20
7						
8	Old surface soil	Organic soil	60	13.7	16.2	0.20
9						
10		Volcanic clay			Above water table:	
11	Oyama layer		150	16.7	17.7	0.20
12		Medium sand			Below w.t.: 8.8	
13						
14	Uonuma layer	Clayey sand and gravel	300	17.6	Above: 4.3 Below: 1.8	0.22
15						



(a) Analysis area, building No.3, boring point



(b) Mesh configuration

3. SEISMIC RESPONSE ANALYSIS OF THE GROUND

3.1 Analysis model

The analysis model shown in Fig. 6(a) was applied to the ground in the vicinity of Building No.3. Figure 6(b) shows the FEM mesh configuration, where the viewing directions are different between (a) and (b). The gradient of the slope in the third quadrant is in the range from 25° to 28° , and the high step (between Building No.3 and the bicycle parking lot) is retained by the stone block retaining wall.

The boring log at the point indicated in Fig. 6(a) is shown in Table 1, together with the input soil properties for FE analysis. There is the extremely weak organic soil layer whose N value is 0 just under the filling loam layer of about 8m thick, having a N value of less than 6. This organic soil had covered the original hill of Oyama layer before the filling construction for campus extension, and it spreads to the border between the cutting and filling ground. The depth of water table is 3.5 m.

The analysis model shown in Fig. 6(a) is assumed to be a part of the infinite model, and the all

boundaries are surrounded by the special elements deformable only for shear. In other words, the displacements in three directions of the all peripheral nodes were assumed to be equal to those of the corresponding nodes at one line inside by applying the Multi-Point Constraint function.

3.2 Method of analysis

The configuration of soil and the shape of ground is three dimensional, and the behavior of the saturated organic soil play a key role. It is, therefore, reasonable for this particular case to apply a 3-D effective stress analysis. The dynamic analysis conducted here is the one that satisfies this condition, “HiPER” (Fukutake, 1997). The modified Ramberg-Osgood model extended to three dimensions was used for the stress-strain relationship, and the bowl model was used for the strain-dilatancy relationship (Fukutake and Matsuoka, 1993). The values of R-O model’s parameters in Table 1 were assumed based on the existing $G_0-\gamma$ and $h-\gamma$ relationships (Imazu and Fukutake, 1986). In the bowl model, the monotonously compressive component of dilatancy was expressed by the following cumulative shear strain, G^* , and the reversibly dilative component, namely the vibration component, was expressed by the following resultant shear strain, Γ .

$$\Gamma = \sqrt{\gamma_{zx}^2 + \gamma_{zy}^2 + \gamma_{xy}^2 + (\varepsilon_x - \varepsilon_y)^2 + (\varepsilon_y - \varepsilon_z)^2 + (\varepsilon_z - \varepsilon_x)^2} \quad (1)$$

$$G^* = \sum \Delta G^* = \sum \sqrt{\Delta \gamma_{zx}^2 + \Delta \gamma_{zy}^2 + \Delta \gamma_{xy}^2 + \Delta (\varepsilon_x - \varepsilon_y)^2 + \Delta (\varepsilon_y - \varepsilon_z)^2 + \Delta (\varepsilon_z - \varepsilon_x)^2} \quad (2)$$

The dilatancy, ε_v^s , is accordingly expressed as Eq. (3).

$$\varepsilon_v^s = A \bullet \Gamma^B + \frac{G^*}{C + D \bullet G^*} \quad (3)$$

Applicability of this constitutive model for clay material has been already confirmed by Tamura et al (2006). The values of A , B , C and D used in the present analysis are -0.2, 1.4, 2.5 and 40.0, respectively, and the value of $C_s/(1+e_0)$ is assumed to be 0.05 for all layers, where C_s is the swelling index. These values were determined based on the study done by Fukutake (1997) and Tamura et al (2006). The minimum value of the liquefaction resistance, R , namely X_i , is 0.05 for the organic soil and 0.1 for all other layers. The shear modulus for each layer is calculated from the V_s value.

The seismic waves observed at the base rock of 100 m deep in the ground at Nagaoka KiK-net station (2004) in Nagaoka Institute of Snow and Ice Studies, which is just about 700m far from NNCT, were used with the slight correction of the coordinate direction from compass, shown in Fig. 6(a).

Figure 7 shows the horizontal accelerations being input as $E+F$ waves at the base of the analysis model. We can see the long period components due to surface waves at the latter half in this figure. The vertical acceleration was disregarded because of its negligible influence on the calculation results shown in the previous study (Fukutake et al., 2005). The major axis of the input acceleration almost coincides with y-direction, and the maximum acceleration values in x- and y-components are 313 Gal and 477 Gal, respectively. The predominant frequencies of x-direction are 0.5 Hz and 2.0 Hz, and those of y-direction are 0.6 Hz and 2.0 Hz.

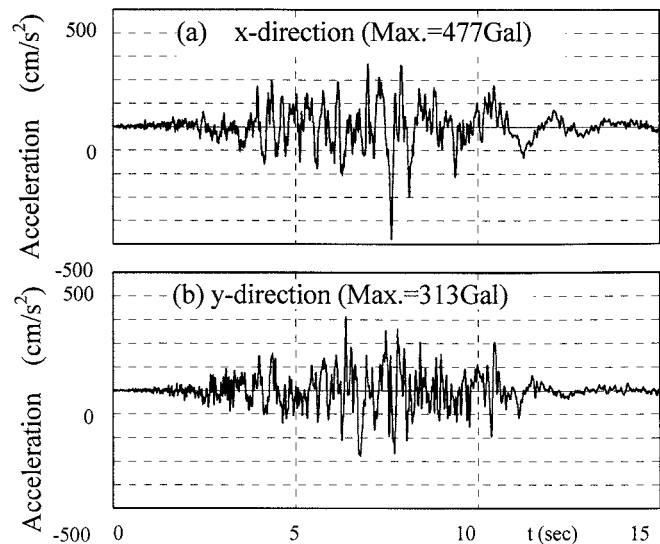


Figure 7 Input seismic wave ($E+F$ wave)

3.3 Analysis results and discussions

Figure 8(b) shows the distribution of the maximum accelerations in the whole duration. The y -components almost coincide the major axis, and they are larger than the x -components. The largest acceleration by effective stress analysis was 720 Gal, which is observed along the top of the high step of Oyama layer between Building No.3 and the tennis court in the fourth quadrant. We can see that the maximum accelerations of the filling ground (on the old surface layer of weak organic soil) are relatively small in comparison with those of the cutting ground. This means that the old surface layer played the role of an isolation layer due to high nonlinearity. On the other hand, the largest acceleration by equivalent linear analysis was 1000Gal, which is observed along the top of the high step of Oyama layer in the third quadrant shown in Fig.8(a) in the red zone.

Figure 9 is the panel diagram, which shows the distribution of the maximum pore water pressure ratio, r_u . The largest r_u value exceeds 70 % in the old surface layer. The r_u is larger than 50 % at the bottom of the filling loam and at the top of Oyama layer between which the old surface layer is sandwiched.

Figure 10 shows the time history of the excess pore water pressure ratio in the old surface layer just below the origin of the coordinates. It rapidly reached 60 % by 4.5 sec, namely soon after the beginning of the seismic motion and prior to the following several large shocks.

Figure 11 shows the distribution of the maximum resultant shear strain, Γ . The largest value of Γ reached as large as 15% in the old surface layer, which indicates that the landslide of this layer has occurred.

Figure 12 shows the birds-eye view of deformation and r_u at the end of vibration, $t=15$ sec. The ground moved toward down stream of the buried valley, with subsidence. The large deformation mainly occurred in thin old surface layer, thus it seemed that the ground caused slip failure.

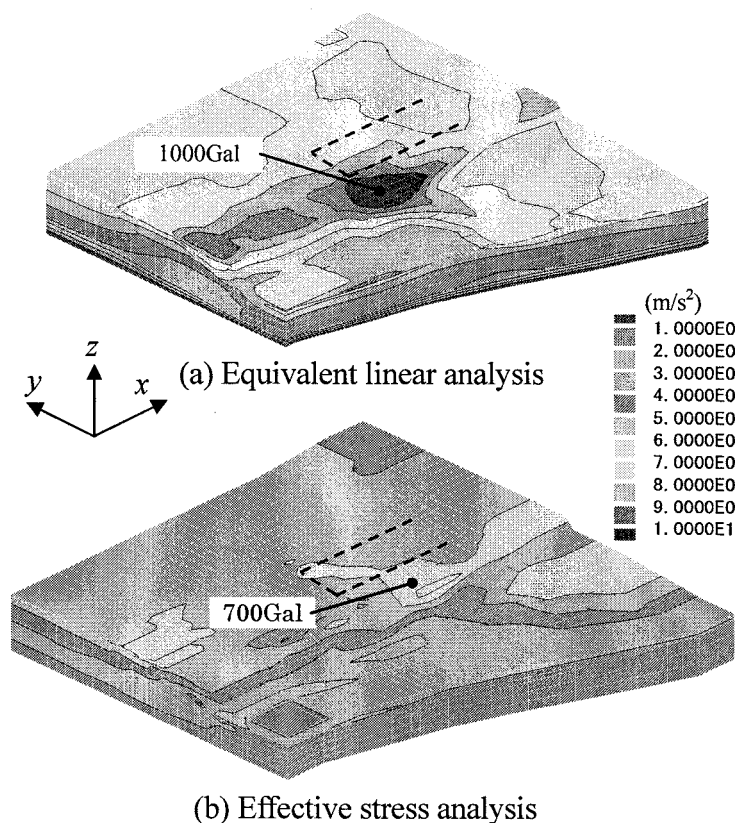


Figure 8 Distribution of maximum acceleration (y -direction)

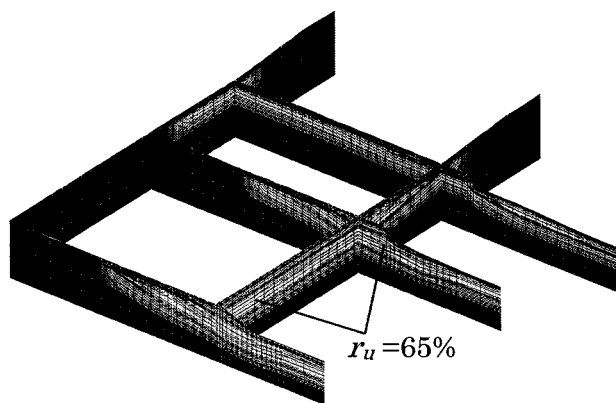


Figure 9 Distribution of maximum pore pressure ratio, r_u

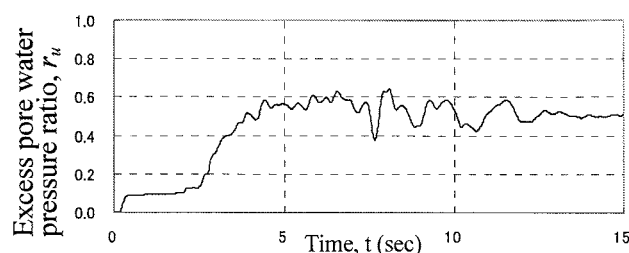


Figure 10 Time history of excess pore water pressure ratio, r_u , of Old surface layer at the southwest corner of Building No.3

Figure 13 shows the deformation of the ground surface at the end of vibration, $t = 15$ sec. The rectangular in this figure shows the three- and two-story portions of Building No.3. The left two third of it locates on the filling ground, whereas the right one third stands on the cutting one. As shown in this figure, although the deformation of the cutting ground is small, the filling ground moved remarkably to both left and lower directions. This indicates that the filling ground slid together with the piles, and twisted the three-story portion of the building anti-clockwise. During this movement, the pile heads were broken as shown in Fig. 4. The maximum analyzed displacement of the ground at the origin of the coordinates is 11 cm, whereas the actual movement was more than 95 cm. This discrepancy will be attributed to the following imperfection in the analysis;

1) The present analysis can not evaluate the magnitude of the cracks in the ground.

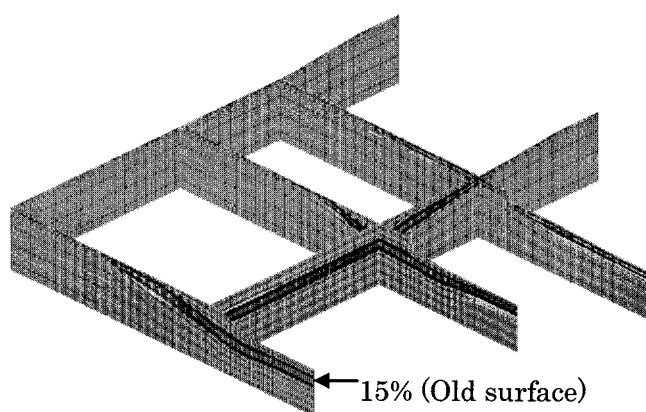
2) All the layers on the water table are united as a continuum.

3) In the FEM analysis, discontinuous displacement like a sliding failure is difficult to treat.

4. CONCLUSIONS

Destructive damage of Building No.3 at Nagaoka National College of Technology (NNCT) was investigated by a 3-D effective stress dynamic FEM. The following conclusions were obtained from the present work;

1) A landslide occurred at the filling ground where the half building located. There is no sliding on the other half stand of the neighboring cutting ground. The sliding occurred in the old surface layer of weak organic soil, which had covered the original



$$\Gamma = \sqrt{\gamma_{zx}^2 + \gamma_{zy}^2 + \gamma_{xy}^2 + (\epsilon_x - \epsilon_y)^2 + (\epsilon_y - \epsilon_z)^2 + (\epsilon_z - \epsilon_x)^2}$$

Figure 11 Distribution of resultant shear strain, Γ

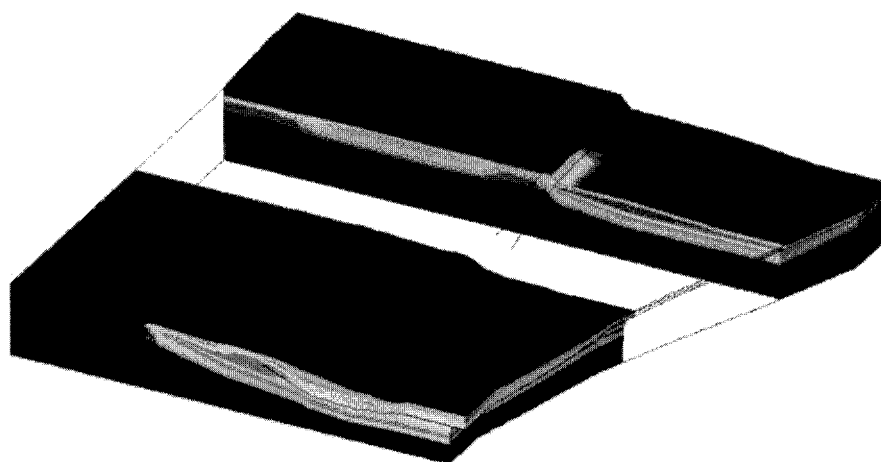


Figure 12 Birds-eye view of deformation and r_u at 15 sec after the beginning of earthquake

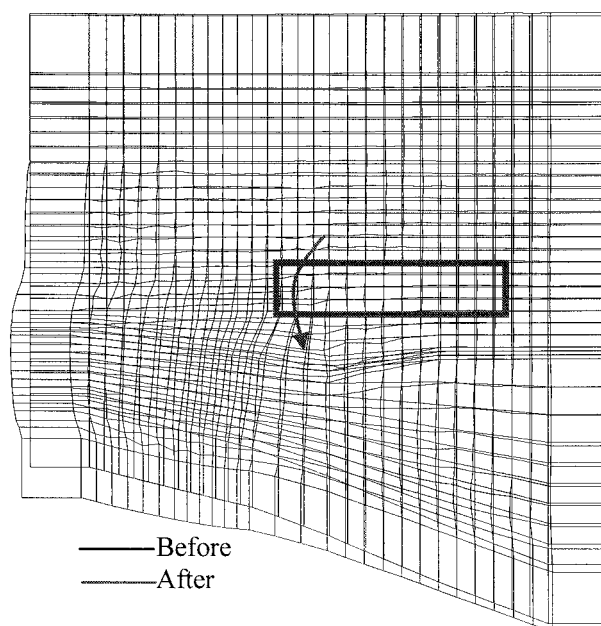


Figure 13 Plan of deformation at 15 sec after the beginning of earthquake

hill before filling construction on it. The filling soil slid with piles, and the piles pulled and rotated the building. As the result, the disconnection of the building occurred at the border between the cutting and filling ground.

2) According to the effective stress analysis, the sliding occurred approximately 4 sec after the beginning of the seismic wave recording.

3) In the organic soil, the excess pore water pressure ratio reached 65%, and shear strain occurred more than 15%. These results support that the ground moved toward down stream of the buried valley, and large deformation mainly occurred in thin old surface layer.

4) The horizontal accelerations on the ground surface especially along the top of the high step are the double of those at the base rock. The maximum acceleration by effective stress analysis is smaller than that by equivalent linear analysis due to the high nonlinearity of the organic soil.

Acknowledgements:

This study was conducted in “Emergency Research on the 2004 Niigata-ken Chuetsu Earthquake” supported by the Special Coordination Funds for Promoting Science and Technology (MEXT).

References:

- Fukutake, K. (1997), “Studies on three-dimensional liquefaction analyses of soil-structure system considering multi-directional shearing of soil” (in Japanese), doctoral thesis of Nagoya Institute of Technology.
- Fukutake, K. and Matsuoka, H. (1993), “Stress-strain relationship under multi-directional cyclic simple shearing” (in Japanese), *Proc. Annual congress of Japan Society of Civil Engineers*, **463/III-22**, 75-84.
- Fukutake K., Hotta H. and Onoue A. (2005), “Stability of cutting and filling ground using 3-dimensional equivalent linear analyses during Chuetsu Earthquake” (in Japanese), *Proc. Proc. Symposium on safety and performance evaluation of ground for housing*, JGS, 39-46.
- <http://www.kik.bosai.go.jp/kik/>, (2004).
- Imazu, M. and Fukutake, K. (1986), “Dynamic shear modulus and Damping of Gravel materials” (in Japanese), *Proc. of the 21st Japan national conference on geotechnical engineering*, 509-512.
- Tamura, T., Shamoto, Y. and Hotta, H. (2006), “Estimation of earthquake-induced residual deformation of foundation structure on cohesive ground” (in Japanese), *Journal of structural and construction engineering* (Transactions of AIJ), **602**, 179-185.

SAFETY – AN EARTHQUAKE DISASTER MITIGATION MEASURE CONSIDERING COST -PERFORMANCE AND ENVIRONMENTAL IMPACT

H. Hazarika

*Senior Research Engineer, Geotechnical and Structural Engineering Department, Port and Airport Research Institute,
Japan
hazarika@pari.go.jp*

Abstract: Cost, environment and structural performance are three key factors that dictate the final design of today's infrastructures. SAFETY (Stability And Flexibility of structures during Earthquake using Tyres) is one such earthquake disaster mitigation technique in which scrap tire derived recycled materials are used to reduce the earthquake induced lateral deformation of geotechnical structures. In this research, a model 1G shaking table experiment was conducted to validate the performance of SAFETY technique. The test results have demonstrated that such technique not only reduces the seismic load but also the earthquake induced permanent displacement of structures. Such mitigation measures could also contribute towards the cost-effective design and retrofitting of geotechnical structures by reducing the materials and structural cost.

1. INTRODUCTION

Fears loom large over three large-scale devastating earthquakes (Tokai Earthquake, Tonankai-Nankai Earthquake, Strong metropolitan Earthquake) that are predicted to strike the Tokai area, the Nankai area and the Kanto area of Japan any time in the near future. The central disaster management council, government of Japan (<http://www.bousai.go.jp>, 2006), have been making concerted efforts designed to mitigate the disasters and minimize the economic implications from these earthquakes. With tough government policy of cutting expenditure on infrastructural projects, demands on engineers are mounting for developing novel and cost-effective disaster mitigation technique that can protect and reduce the damages of geotechnical structures during devastating earthquakes. Emerging design methodology called the performance based design, thus, is becoming the norm of the present design codes to meet some of these demands.

On the other hand, used tires have become an increasingly problematic global problem whose disposal is posing dangers to our environment. Statistics reveal that in most of the countries they are mostly used for thermal recycling, which produces greenhouse gases such as CO₂ jeopardizing the effective implementation of the Kyoto Protocol (<http://unfccc.int>, 2005). Thus, efforts are increasing to reduce the thermal recycle of scrap tires and instead use them as materials. Use of scrap tires as materials reduces the environmental impact (CO₂ emission in material recycling is 1/4th that of the thermal recycling) from scrap tires, and thus contributes towards a sustainable environment.

In the 21st century, cost, environment and structural performance are going to be three decisive factors in the design and retrofitting of urban infrastructures against earthquake loading. Concerns have been growing on the seismic stability of the existing and newly built port and harbor facilities in Japan after her bitter experiences of the 1995 Hyogoken-Nanbu earthquake, Kobe. The earthquake caused severe damage to more than 90% of the waterfront structures (Inagaki et al., 1996; Ishihara, 1997; JGS/JSCE, 1996; Kamon et al, 1996; Towhata et al., 1996).

Typical waterfront structure such as gravity type quay wall has rubble backfill immediately behind the wall. One of the reasons for using rubble backfill is to reduce the earth pressure due to friction. However, such granular material is vulnerable to deformation under seismic load, and hence can cause large permanent deformations to the structures. If we can substitute this material with some other lightweight granular materials with other beneficial characteristics, then the earth pressure during earthquake can be reduced to a greater extent along with the curtailment of earthquake induced permanent deformation of the structures. One material of choice, is an emerging geomaterial material known as tire chips, derived from used tires (Humphrey, 1998). Tire chips is a recycled material that is lightweight, elastic, compressible, highly permeable, earthquake resistant, thermally insulating and durable. Such material has been coined a *smart geomaterial* by Hazarika et al (2006a).

In this research, an innovative cost-effective disaster mitigation technique is developed using tire chips, a newly emerging geomaterial, which can be utilized as a seismic performance enhancer of geotechnical structures. The technique is called SAFETY (Stability And Flexibility of structures during Earthquake using TYres). The objective of this research is to examine whether SAFETY technique can reduce the earthquake related damages to structures. To that end, an underwater shaking table test (1G condition) was performed using the actual earthquake loading of the 1995 Hyogoken-Nanbu earthquake, Kobe and the structural performances under such level 2 earthquake motion (PIANC, 2001) were investigated.

2. DESCRIPTION OF SAFETY TECHNIQUE

SAFETY is a novel technique that involves placing cushion layer made out of tire chips as a vibration absorber immediately behind the structures. In addition, vertical drains made out of tire chips are installed in the backfill as a preventive measure against soil liquefaction. Yasuhara et al. (2004) used such tire chips as vertical drains for reducing liquefaction induced deformation. Figure 1 shows typical cross section of the earthquake resistant SAFETY technique. One function of the cushion is to reduce the load against the structure, due to energy absorption capacity of the cushion material. Another function is to curtail permanent displacement of the structure due to inherited flexibilities derived from using such elastic and compressible material.

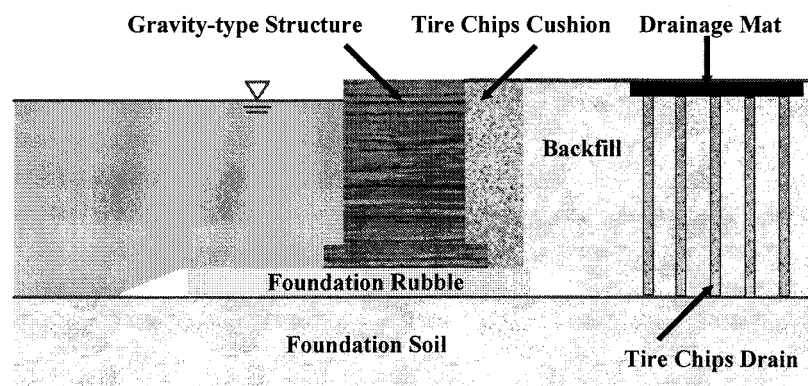


Figure 1 SAFETY Technique

3. MODEL SHAKING TABLE TEST

3.1 Experimental Setup

The large three dimensional underwater shaking table assemblies of Port and Airport Research

Institute (PARI) was used in the testing program. The shaking table is mounted on a 15 m long by 15 m wide and 2.0 m deep water pool, and thus can simulate the actual state of waterfront structure.

A caisson type quay wall (model to prototype ratio of 1/10) was used in the testing. Figure 2 shows the cross section of the soil box, the model caisson and the locations of the various measuring devices (load cells, earth pressure cells, pore water pressure cells, accelerometers and displacement gauges). The model caisson (425 mm in breadth) was made of steel plates filled with dry sand and sinker to bring its center of gravity to a stable position. The caisson consists of three parts; the central part (width 500 mm) and two dummy parts (width 350 mm each). All the monitoring devices were installed at the central caisson to eliminate the effect of sidewall friction on the measurements.

The soil box was made of a steel container 4.0 m long, 1.25 m wide and 1.5 m deep. The foundation rubble beneath the caisson was prepared using Grade 4 crushed stone with particle size of 13 mm ~ 20 mm. The backfill and the seabed layer were prepared using Sohma sand (No. 5). Backfill was prepared in stages using free falling technique, and then compacting using a manually operated vibrator to achieve the target relative density of 50%. After constructing the foundation and the backfill, and setting up of the devices, the pool was filled with water gradually elevating the water depth to 1.3 m to saturate the backfill. This submerged condition was maintained for two days so that the backfill attains a complete saturation stage.

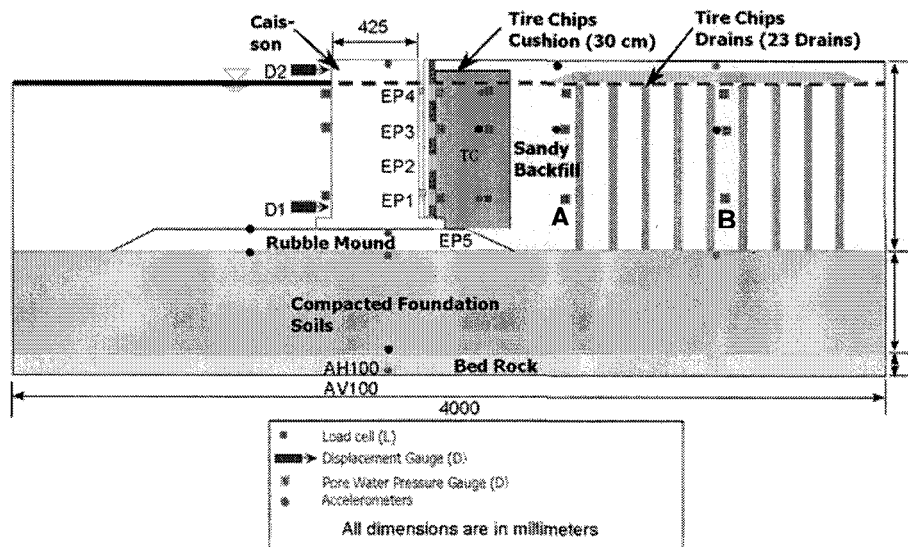


Figure 2 Cross Section of the Test Model

3.2 Test Procedures

Two test cases were examined using the same soil box by mounting two gravity type model quay walls with different backfill conditions. In one case, a caisson with a rubble backfill with conventional sandy backfill behind it was used. In another case, behind the caisson, a cushion layer of tire chips (average grain size 20 mm) was placed vertically down. Also, vertical drains made out of tire chip (average grain size 7.0 mm), were installed in the backfill as shown in Figure 2. The cushion thickness was adopted to be 0.4 times of the wall height. In actual practice, the design cushion thickness will depend upon a lot of other factors such as height and rigidity of the structure, compressibility and stiffness of the cushion material. The effect of cushion thickness using a small-scale model shaking table test has been described in Hazarika et al (2006b). The average dry density of the tire chips cushion achieved after filling and tamping was 0.675 t/m³.

The relative densities that was achieved after the preparation of the backfill were between 50% to 60%. This implies that the backfill soil is partly liquefiable. Since liquefaction tends to increase the earth pressure, the presence of tire chips cushion is expected to protect the structure from the adverse effect of liquefaction within a limited region surrounding the structures during earthquake. Liquefiable

backfill was thus selected on purpose. On the other hand, the foundation soils were compacted with mechanical vibrator to achieve a relative density of about 80%, implying a non-liquefiable foundation deposit.

Vertical drains made out of tire chip (average grain size 7.0 mm), were installed in the backfill. Geotextile bags with the specific drain size were first prepared, which then were filled with the tire chips with a pre-determined density. They were then installed with a spacing of 150 mm in triangular pattern. The drain diameter was chosen to be 50 mm. The top of the entire drains were covered with a 50 mm thick gravel layer underlying a 50 mm thick soil cover. The purpose of such cover layer is twofold: one is to allow the free drainage of the water and other is to prevent the likely uplifting of the tire chips during shaking due to its lightweight nature.

The input motion used was the N-S component of the strong motion acceleration recorded at the Port Island, Kobe, Japan during the 1995 Hyogo-ken Nanbu earthquake (M 7.2). The wave record of the motion is shown in Figure 3. The similitude of various parameters in 1g gravitational field for the soil-structure-fluid system were calculated using the relationship given in Iai (1989) for a model to prototype ratio of 1/10. Durations of the shaking in the model testing were based on the time axes of these accelerograms, which were reduced by a factor of 5.62 according to the similitude relationship.

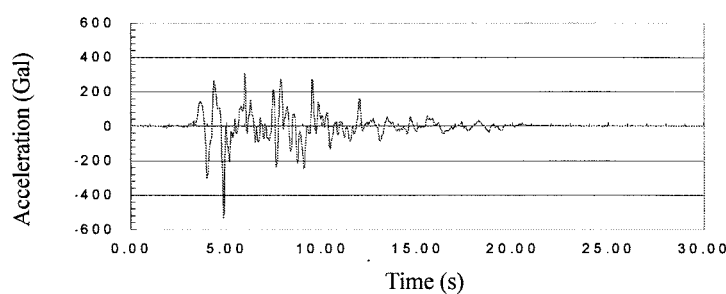


Figure 3 Input Earthquake Motion (PI Wave of the 1995 Hyogoken Nanbu Earthquake)

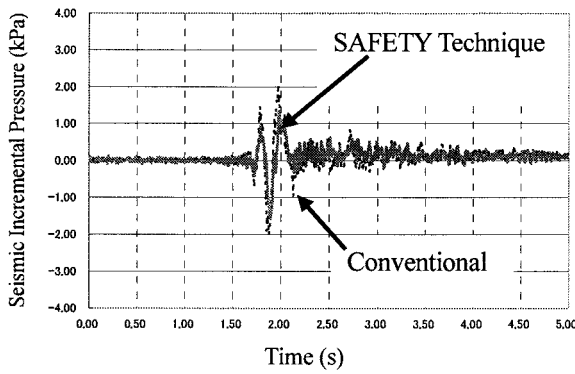
4. TEST RESULTS

4.1 Seismically Induced Lateral Thrust

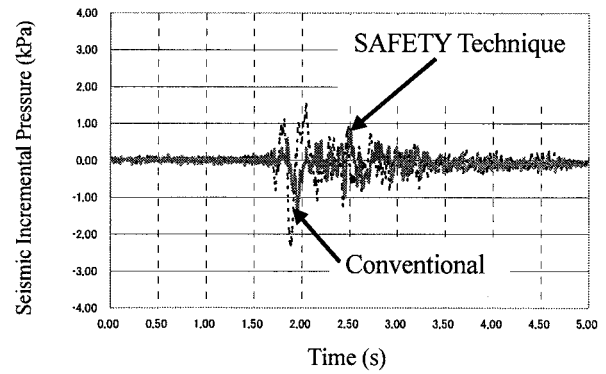
Figures 4(a) and 4(b) show the time history of the increment of the seismic earth pressure acting on the quay wall at the lower middle and the upper middle part of the caisson. It can be observed that as compared to conventional backfill condition, the seismic increment is decreased to a considerable extent in tire chips reinforced backfill using SAFETY technique. Considering the fact that the static earth pressure itself will also be reduced (Hazarika et al., 2006a) due to low weight and compressible characteristics of the cushion materials, the total seismic thrust acting on the structure can, thus, be reduced to a greater extent. The end result, thus, is the reduction of the total earth pressure, which will contribute towards the stability of the structure during earthquakes.

4.2 Liquefaction Potential of the Backfill

In order to evaluate, whether the SAFETY technique can minimize the liquefaction related damages, the time histories of the excess pore water pressure during the loading at a particular locations (B in Figure 2) for the two test cases are compared in Figures 5(a) and 5(b). Comparisons reveal that the pore water pressure build up is restricted due to dissipation by the permeable backfill condition. In the case of conventional backfill, the pore water pressure builds up and it takes considerable time (about 25 second) to dissipate. However, in the case of backfill with SAFETY technique, the built up pore water pressure dissipates within a very short interval (2.5 second), preventing any chance for the backfill to liquefy.

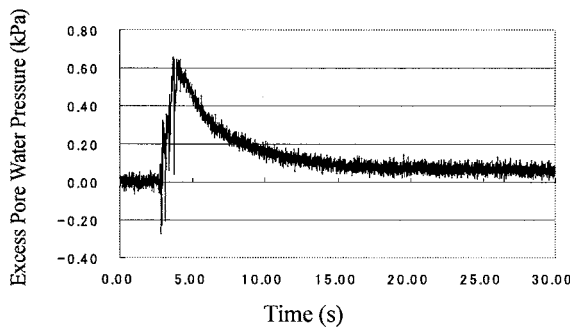


(a) At lower middle (EP2 of Fig. 2)

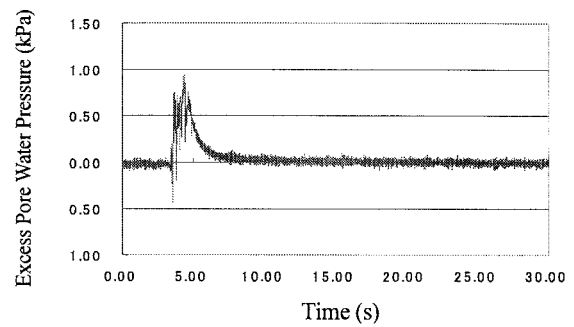


(a) At upper middle (EP3 of Fig. 2)

Figure 4 Lateral Seismic Pressure on the Quay Wall



(a) Conventional backfill

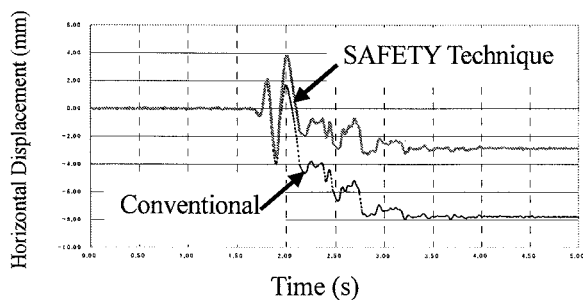


(b) SAFETY Technique

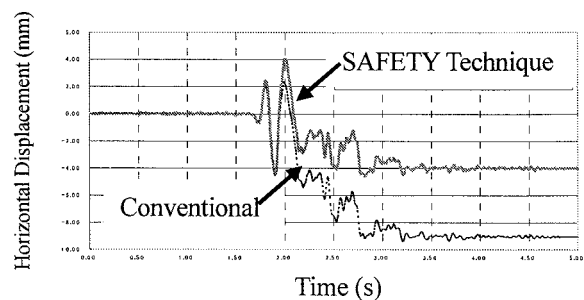
Figure 5 Prevention of Liquefaction

4.3 Seismically Induced Horizontal Displacement

The time histories of the horizontal displacements (D1 and D2 in Figure 2) during the earthquake loading for the two test cases are compared in Figures 6. Comparisons reveal that the maximum displacement experienced by the quay wall with SAFETY technique (thick continuous line) is toward the backfill in contrast to the quay wall without any earthquake resistant reinforcement (shown in dotted line), in which case it is seaward. The compressibility of the tire chips renders flexibility to the soil-structure system, which allows the quay wall to bounce back under its inertia force, and this tendency ultimately (at the end of the loading cycles) aids in preventing the excessive seaward deformation of the wall. However, the wall with conventional backfill experiences very high seaward displacements right from the beginning due to its inertia. As a consequence, the structure can not move back to the opposite side and ultimately suffers from a huge permanent seaward displacement.



(a) Bottom of the quay wall (D1)



(b) Top of the quay wall (D2)

Figure 6 Measured Structural Performance

5. CONCLUSIONS

SAFETY technique described and evaluated here, involves three most important and beneficial elements: low cost, high performance and sustainable environment. 1G shaking table tests on model quay walls have indicated that the SAFETY technique contributes not only to reduction of the seismic load, but also the seismically induced permanent displacement of the structure. Reduction of the load against structure implies lowering of the design seismic load, which in turn yields a slim structure with reduced material cost. Such applications of scrap tire derived material, thus, not only reduce considerably the execution and construction cost of a project, but also contributes towards a sustainable environment by recycling of the scrap tires as materials. If adequate design method is established, the SAFETY technique described here, could also be applied for upgrading (retrofitting) of the existing structures that run the risk of damages during devastating future earthquakes (such as strong metropolitan earthquake, Tokai earthquake, Tonankai-Nankai earthquake).

Acknowledgements:

The author acknowledges the support from Prof. Kazuya Yasuhara, Ibaraki University, Japan, Dr. Takao Kishida, Toa Corporation, Japan and Mr. Hideo Takeichi, Bridgestone Corporation, Japan in the course of this research. The author also gratefully acknowledges the financial support from Japan Ministry of Education, Culture, Sport, Science, and Technology (MEXT), Japan under the Grant-in-Aid for scientific research (Grant No. 18206052).

References:

- Hazarika, H., Kohama, E., Suzuki, H., and Sugano, T.: "Enhancement of Earthquake Resistance of Structures using Tire chips as Compressible Inclusion", *Report of the Port and Airport Research Institute*, Vol. 45, No. 1, pp. 1-28, 2006a.
- Hazarika, H., Sugano, T., Kikuchi, Y., Yasuhara, K., Murakami, S., Takeichi, H., Karmokar, A.K., Kishida, T., and Mitarai, Y.: "Model Shaking Table Test on Seismic Performance of Caisson Quay Wall Reinforced with Protective Cushion", *International Society of Offshore and Polar Engineers (ISOPE) Transaction*, Vol. 2, San Francisco, USA, pp. 309-315, 2006b.
- <http://www.bousai.go.jp>: "Cabinet Office, Government of Japan: Central Disaster Management Council", Available: <http://www.bousai.go.jp/jishin/chubou>, 2006 (in Japanese).
- <http://unfccc.int> (2005): "Kyoto Protocol to the United Nations Framework Convention on Climate Change", <http://unfccc.int/resource/docs/convkp/kpeng.html>.
- Humphrey D.N.: Civil Engineering Applications of Tire Shreds, *Manuscript Prepared for Asphalt Rubber Technology Service*, SC, USA, 1998.
- Iai, S.: Similitude for Shaking Table Tests on Soil-structure-fluid Model in 1g Gravitational Field, *Soils and Foundations*, Japanese Geotechnical Society, Vol. 29, No. 1, pp. 105-118, 1989.
- Inagaki, H., Iai, S., Sugano, T., Yamazaki, H., and Inatomi, T.: "Performance of Caisson Type Quay Walls at Kobe Port", *Special Issue, Soils and Foundations*, Vol. 1, pp. 119-136, 1996.
- Ishihara, K.: "Geotechnical Aspects of the 1995 Kobe Earthquake", *Terzaghi Orientation, 14th Intl. Conf. of International Society of Soil Mechanics and Geotechnical Engineering*, Hamburg, Germany, Vol. 4, pp. 2047-2073, 1997.
- Japanese Geotechnical Society (JGS) and Japan Society for Civil Engineers (JSCE): Joint Report on the Hanshin-Awaji Earthquake Disaster, 1996 (In Japanese).
- Kamon, M., Wako, T., Isemura, K., Sawa, K., Mimura, M., Tateyama, K., and Kobayashi, S.: "Geotechnical Disasters on the Waterfront", *Special Issue of Soils and Foundations*, Vol. 1, pp. 137-147, 1996.
- PIANC: *Seismic Design Guidelines for Port Structures*, Balkema Publishers, Rotterdam, 2001.
- Towhata, I., Ghalandarzadeh, A., Sundarraj, K.P., and Vargas-Monge, W.: "Dynamic Failures of Subsoils Observed in Waterfront Area", *Special Issue of Soils and Foundations*, pp. 149-160, 1996.
- Yasuhara, K., Unno, T., Komine, H., and Murakami, S.: Gravel Drain Mitigation of Earthquake-induced Lateral Flow of Sand, *13th WCEE*, No. 146(CD-ROM), 2004.

EVALUATION OF SEISMIC STABILITY OF FOUNDATIONS ON SLOPE

M. Okamura¹⁾, and Y. Sugano²⁾

1) Associate Professor, Graduate School of Science and Engineering, Ehime University, Japan

*2) Graduate student, Graduate School of Science and Engineering, Ehime University, Japan
okamura@dpc.ehime-u.ac.jp*

Abstract: In this study, a series of bearing capacity tests on a strip footing at the shoulder of 30 degree slope is conducted and footing responses under combined vertical, horizontal and moment loadings are observed. The failure envelope and the displacement potential in the general load space were prescribed. The derived failure envelope and displacement potential are incorporated to the displacement prediction method which is capable of calculating fully coupled displacement under earthquake loadings. Shaking table tests of strip footings resting on the shoulder of the sand slope were carried out. The method is validated through comparison between calculated results and test observations.

1. INTRODUCTION

Shallow foundations near slopes have often been damaged during past large earthquakes. Such foundations failed in the mechanism of bearing capacity failure under the action of combined effects of vertical, horizontal and moment loads arisen from earthquake inertia forces. Figure 1 shows a house rested on the shoulder of a slope and was damaged by the Niigataken-Chuetsu earthquake of 2004.



Figure 1 A house near slope damaged by Niigataken-Chuetsu Earthquake

For footings on a level ground surface subjecting eccentric and inclined loadings, Meyerhof (1953, 1963) introduced the inclination factors in the bearing capacity formula and the concept of 'effective foundation width' to account for the load inclination and eccentricity, respectively. More recently, an alternative approach for estimating bearing capacities of footings under combined vertical (V), horizontal (H) and moment (M) loads has been developed (Butterfield and Ticof, 1979; Georgiadis and Butterfield, 1988; Butterfield and Gottardi, 1994; Okamura et al., 2002) in which a macroscopic

failure envelope of an entire soil-footing system was considered in the V - H - M/B general load space. Note that M is divided by footing width, B , to preserve dimensional homogeneity. The displacement potential of such a soil-footing system, which prescribes incremental footing displacement components, has also been investigated. The macroscopic failure envelope prescribed in the V - H - M/B load space in conjunction with the displacement potential has an apparent advantage. Assuming the soil as a rigid-perfectly plastic media, the failure envelope with the displacement potential is capable of directly describing footing response under general combined loads. The idea has been successfully applied to predict seismic displacement of footings and retaining walls (Okamura and Matsuo, 2002). Since there is an apparent trend to switch over to design based on a specified limit displacement in recent years, such a method to estimate the displacement under earthquake loading have increased in importance.

While for footing near slopes, effects of slopes on the bearing capacity of vertically loaded footings have been investigated (Shields et al., 1977; Kusakabe et al., 1981). The results were summarized in the form of the degradation factor of bearing capacity. However, effects of load inclination and eccentricity on the bearing capacity of footings near slopes have not been well understood yet. Information about the shape of the failure locus and the displacement potential is very limited. Accumulation of test data for footings on a slope is desired.

In this study, a series of bearing capacity tests on a footing near slope is conducted, aiming at prescribing the failure envelope and the displacement potential of strip footings near the slope. Two types of loading tests were conducted to this aim; (1) constant rate loading tests in which the ratio $V : H : M$ is kept constant throughout the loading sequence, and (2) moment swipe and horizontal swipe tests in which rotation or horizontal displacement is applied after the footing penetrated vertically to the predetermined vertical load while the footing is exhibited to displace vertically. The load path during the swipe test is expected to follow the yield locus.

The derived failure locus and displacement potential are incorporated to the displacement prediction method which is capable of calculating fully coupled displacement, that is vertical, horizontal and rotational displacement, of foundation on slope under earthquake loading. Shaking table tests of footing resting on the shoulder of the sand slope were carried out. The method is validated through comparison between calculated results and test observations.

2. FAILURE LOCUS AND DISPLACEMENT POTENTIAL

2.1 Footing on level ground surface

It has been reported that the combination of vertical and horizontal loads, as well as vertical and moment loads can be well approximated by simple parabolas on the H - V plane and M/B - V plane, respectively (Georgiadis and Butterfield 1988). Small scale 1g footing tests on the Toyoura sand bed prepared at relative densities between 85 % and 90 % revealed that the failure locus on the planes are well approximated by equations (1) and (2) with constants ϕ and μ for the best-fitted parabolas of 0.37 and 0.54, respectively (Hori et al. 2005). Note that the center of the footing base was taken as the reference point of the moment load and the loads are normalized with respect to the maximum vertical load V_{\max} where V_{\max} is the peak load intensity for the purely vertical loading.

$$\frac{M}{BV_{\max}} = \frac{V}{\phi V_{\max}} \left(1 - \frac{V}{V_{\max}} \right) \quad (1)$$

$$\frac{H}{V_{\max}} = \frac{V}{\mu V_{\max}} \left(1 - \frac{V}{V_{\max}} \right) \quad (2)$$

On the normalized H - M/B plane the ellipse with the axis rotated at 17 degree approximated the test results fairly well. The failure envelope in the V - H - M/B load space for the strip footing with 40 mm breadth on dense Toyoura sand was, following the formula proposed by Butterfield and Gottardi (1994), expressed as

$$F = \left(\frac{H}{0.54V_{\max}} \right)^2 + \left(\frac{M}{0.37BV_{\max}} \right)^2 - \frac{2.44HM}{BV_{\max}^2} - \left[\frac{V}{V_{\max}} \left(1 - \frac{V}{V_{\max}} \right) \right]^2 = 0 \quad (3)$$

The perspective illustration of the failure envelope is given in Fig. 2 (Hori et al., 2005). The apparent advantage of the failure envelope in this form is that equation (3) is valid irrespective of the footing geometry and the relative density of foundation beds with minor variations of the three constants in the equation.

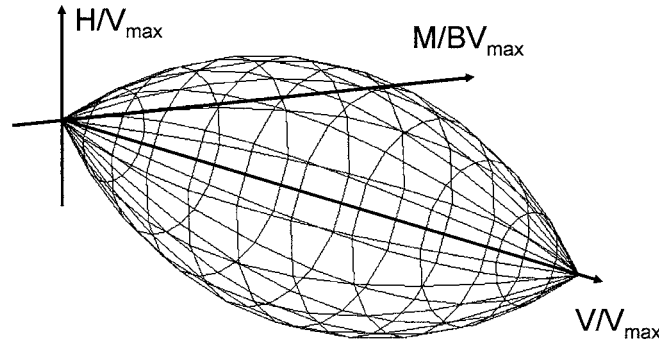


Figure 2 Perspective view of failure envelope in normalized general load space

In order to prescribe the displacement characteristics the flow rule has been examined, in which a macroscopic constitutive law for the entire soil-footing system was considered. Applicability of the associated flow rule has been investigated by several researchers (Nova and Montransio, 1991; Gottardi and Butterfield, 1995; Martin and Houlsby, 2000), where the failure envelope also describes the plastic potential defining the relative magnitudes of the incremental displacement during failure. It was reported, however, that the incremental displacement vectors are generally not normal to the failure locus and this is more apparent as V/V_{\max} decreases. Since the safety factor for the bearing capacity of most shallow foundations is more than two or three, the associated flow rule may not be applicable for practical purposes (Gottardi and Butterfield, 1995; Okamura et al., 2002). This fact suggests the clear need of separate displacement potential to describe foundation behavior. Recent experiments (Hori et al., 2005) established the displacement potential in the general load space for Toyoura sand at the particular relative density.

2.2 Bearing capacity tests of footing near slope

Toyourea sand ($D_{50} = 0.19$ mm, $G_s = 2.64$, $e_{\max} = 0.973$ and $e_{\min} = 0.609$) with a relative density Dr ranging between 85 and 90% was used in all tests reported in this paper. Dry Toyoura sand was

rained from a hopper to a depth of about 200 mm into the rigid model container with internal dimensions of 900 mm long, 200 mm wide and 300 mm deep. The hopper was manually moved back and forth and free falling height was kept constant to provide uniform sand deposits with the desired relative density. The 30 degree slope was made by sucking in sand with a vacuum pump. A 40 mm wide steel footing with the rough base was placed at the shoulder of the slope as shown in Fig. 3. The footing was equipped with a pair of two-component load cells which are capable of measuring vertical and horizontal load independently. The load cells were hinged to loading rams so that any moment load is transmitted to the load cells. The loading system used in this study consists of two vertical loading jacks with electric motors fixed on a table. The table can be move horizontally on a pair of linear way guides by the another motor. The computer, which controls the three motors, enable to conduct load control or displacement control tests referring to the load cells or displacement transducers readings.

In the testing program, constant rate loading tests and swipe tests were carried out. The constant rate tests, in which ratios of vertical, horizontal and moment loads were kept constant throughout the loading sequence, included the purely vertical loading ($H=M=0$), inclined loading ($M=0$), eccentric loading ($H=0$) and combined loading of V , H and M . For the swipe tests, the footing was vertically loaded with horizontal displacement and rotation being zero until predetermined load (V_i) was attained, following the horizontal displacement or the rotation increased while the other two displacement component being kept constant. The sign conventions employed in this study is depicted in Fig. 4.

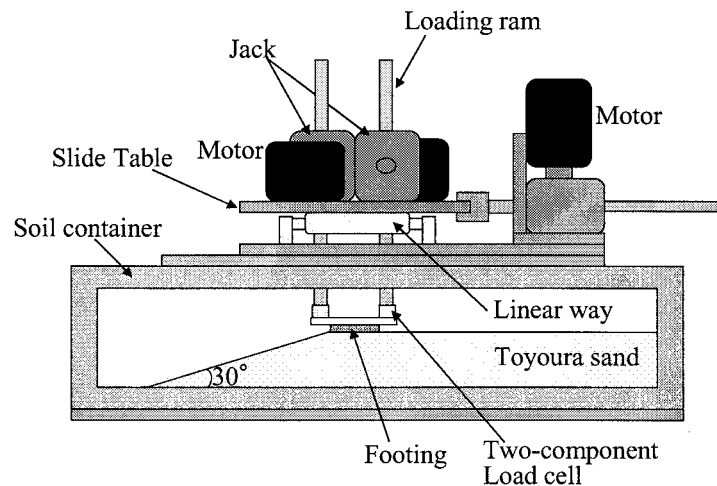


Figure 3 Setup for bearing capacity test on footing at shoulder of slope

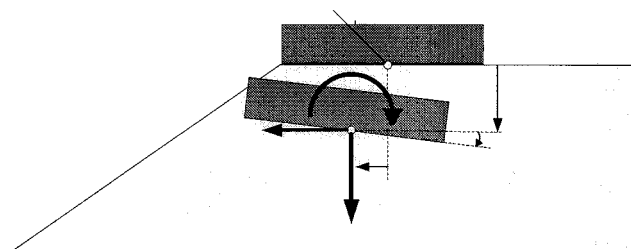


Figure 4 Definition of sign conventions

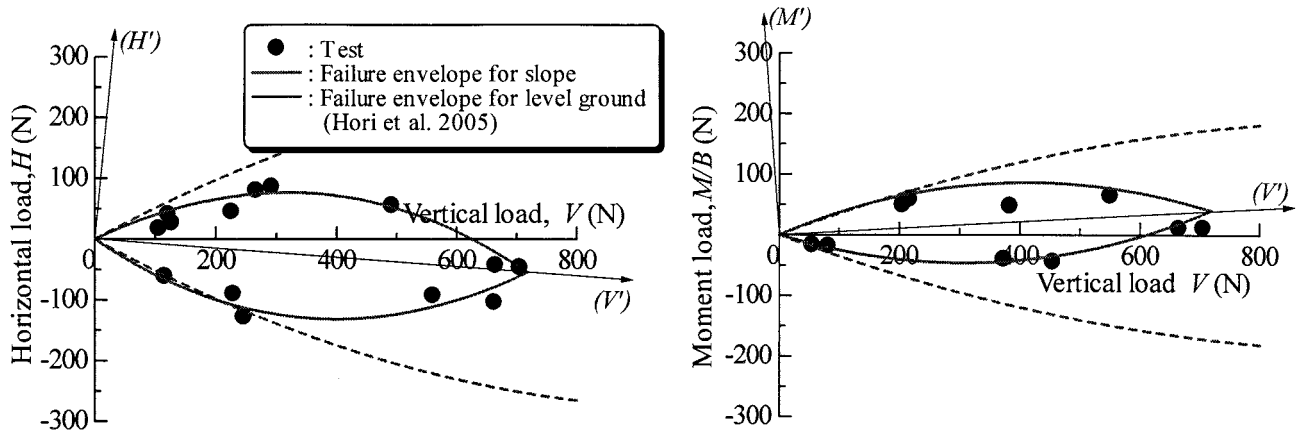


Figure 5 Failure envelope for 40mm breadth strip footing on 30 degree sand slope

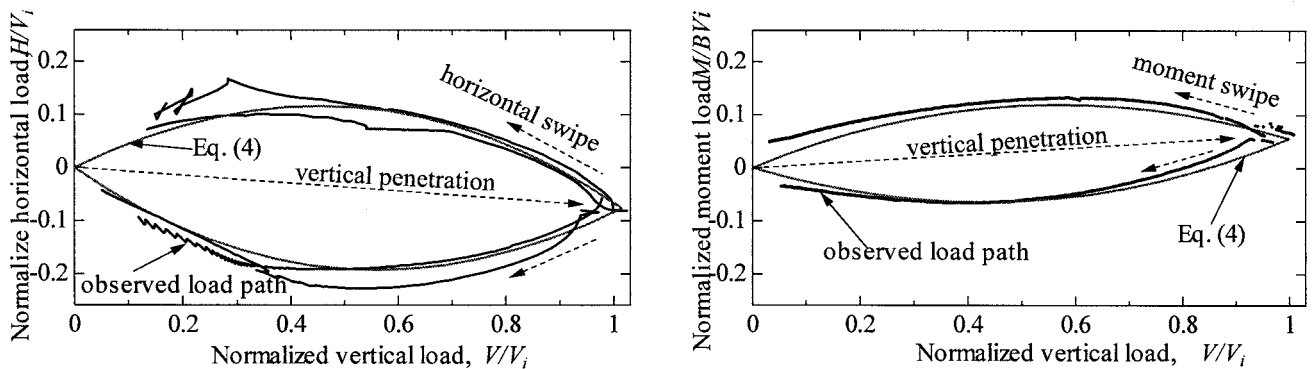


Figure 6 Yield locus and load paths observed in (a) horizontal swipe and (b) moment swipe tests

The loads at failure observed in the tests are plotted on H - V and M/B - V planes in Fig. 5, together with the best fit parabolas. A part of failure envelopes for level ground are also provided in the figure.

Figure 6 shows load paths for the swipe tests and failure loads for the constant rate tests plotted on the normalized load plane. The vertical loads V_i at the beginning of the swipe were used to normalize the loads. It can be seen that the load paths on the normalized load plane agree well with the failure envelope obtained from the constant rate tests.

For cases of inclined loading, horizontal loads at failure are essentially the same as those for level ground if the load inclined the direction opposite from the slope, although the failure envelope for the slope is much smaller than that for level ground (Fig. 5 (a)). This is consistent with deformation mechanism that the slip line appeared in the sand was extended from footing edge on the slope shoulder toward level ground surface when the load inclination ratio H/V lower than -0.4 . On the other hand, for cases of $H/V > -0.2$, the slip surface was observed to extend from the opposite footing edge to the slope and horizontal loads at failure were much lower than those for level ground.

For cases of eccentric loading (Fig. 5(b)), failure loads for the eccentricity, M/BV , higher than 0.3 fell on the failure envelope of the level ground. This is because that the effective footing width where the footing base contacted effectively with ground surface is away from the slope shoulder. As the load eccentricity decreases, the influence of slope on the failure mechanism is more apparent and moment loads at failure for a certain vertical load decrease significantly.

The failure envelope is best approximated by the parabolas with $\phi = 0.37$ and $\mu = 0.57$, and with their axis inclined 4 degree and 3 degree on the H - V plane and M/B - V plane, respectively. The

failure envelope in the general load space is expressed as,

$$F = \left(\frac{H'}{0.57V_{\max}} \right)^2 + \left(\frac{M'}{0.36BV_{\max}} \right)^2 - \frac{4.2H'M'}{BV_{\max}^2} - \left[\frac{V'}{V'_{\max}} \left(1 - \frac{V'}{V'_{\max}} \right) \right]^2 = 0 \quad (4)$$

Where V' , H' and M' are loads on the coordinates which is rotated around the origin 4 degree and 3 degree on the H - V plane and M / B - V plane, respectively.

The section of the locus on H - M/B plane is the ellipse with the axis rotated at 21 degree.

Figure 7 depicts residual loads of the constant rate tests plotted on load planes. It appears that the residual loads can be well approximated by the same equation as failure envelope with V_{\max} replaced by $V_{\max r}$. For the 30 degree slope, $V_{\max r}$ was 160 N, about 22 % of V_{\max} .

$$Q = \left(\frac{H'}{0.85V_{\max}} \right)^2 + \left(\frac{M'}{0.50BV_{\max}} \right)^2 - \left[\frac{V'}{V'_{\max}} \left(1 - \left(\frac{V'}{V'_{\max}} \right)^2 \right) \right]^2 = 0 \quad (5)$$

Figure 8 illustrates the proposed displacement potential in load planes superimposed with observed incremental displacement vectors at peak loads.

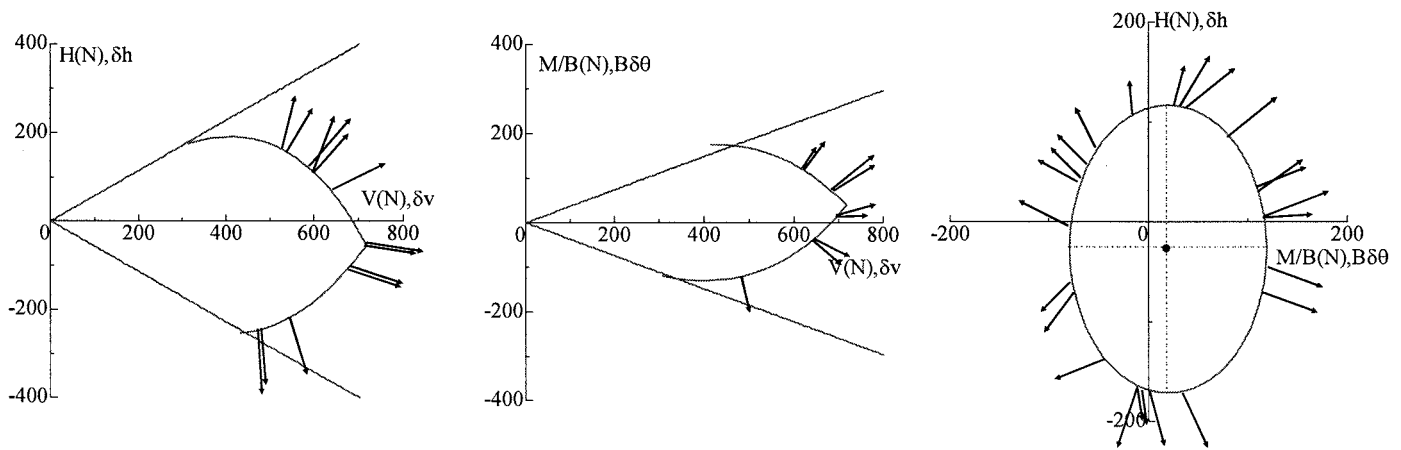


Figure 8 Displacement potential superimposed with observed incremental displacement vectors at peak load intensity

3. APPLICATION OF MACROSCOPIC ELEMENT MODEL FOR SEISMIC DISPLACEMENT PREDICTION

3.1 Shaking table test

Shaking table tests on the seismic behavior of a strip footing near a sand slope were conducted. Figure 9 sketches a side view of the plane strain models prepared in a rigid model container. The foundation bed were prepared in much the same way as the bearing capacity tests described above. The angle of shear resistance of the sand, ϕ' , obtained from triaxial tests under a confining pressure of 49 kPa was 42 degrees. The footing had comprised of 40 mm wide acrylic plates and brass plates. The height the center of gravity from the base was varied from 29 mm to 38 mm by changing the

order of stacking the plates. The total mass of the footing was either 2.7 kg or 4.9 kg, giving rise to a safety factor against static purely vertical bearing capacity failure of 27 or 15, respectively. The locations of instrumentation including five accelerometers and three laser displacement transducers are shown in the figure.

The models were excited by a sinusoidal input for 2 seconds parallel to the base of the container with nearly uniform acceleration amplitude. Several excitation events were imparted to each model intermittently with the acceleration amplitude and the frequency of the input motions varied between the events. Test conditions are summarized in Table 1.

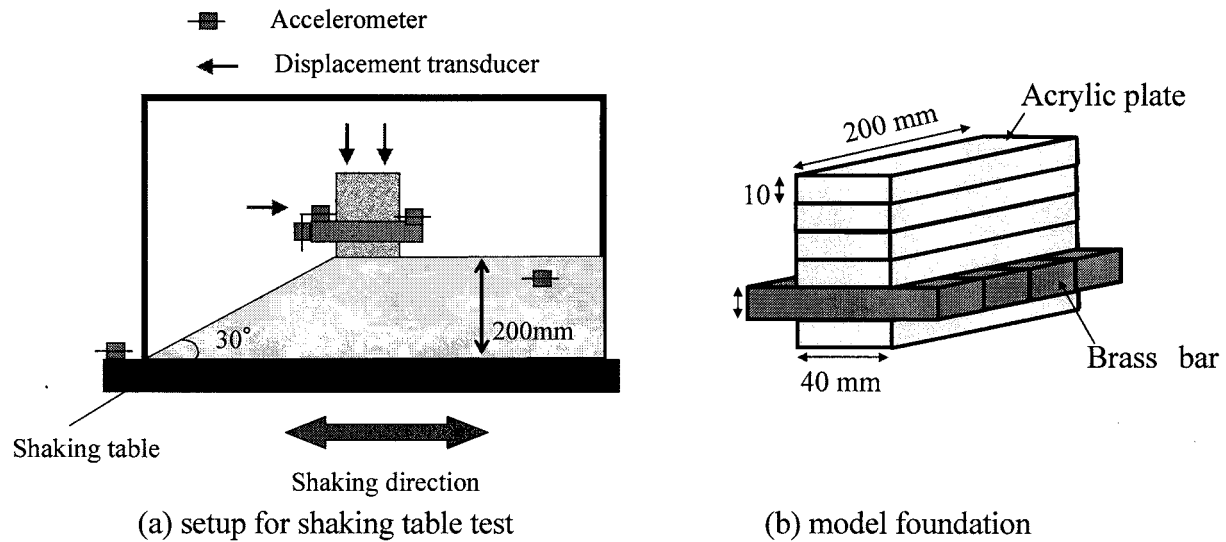


Figure 9 Test setup for shaking table test

Table 1 Summary of test conditions

Test code	Model foundation				Input acceleration amplitude (gal)
	Width (mm)	Weight (kg)	Height of center of gravity (mm)	Pola moment of inertia (g m^2)	
H1	40	4.9	29	59	100, 200
H2		4.9	38	85	100, 200
L1		2.7	32	38	100, 200, 300
L2		2.7	39	50	100, 200, 300

3.2 Displacement prediction

In this section, the computational procedure for footing displacement during an earthquake is briefly described. The important aspect of the bearing capacity characteristics under combined loading discussed in the preceding section is that the subgrade reaction force during failure is located on the failure envelope and its location on the envelope is determined by the flow rule with the incremental displacement vector of the foundation.

Assumptions made in the procedures are as follows.

(a) The failure envelope of the ground in the load space can be defined as

$$F = F(V, H, M/B) = 0 \quad (6)$$

- (b) In a manner typical of sliding block analysis (Newmark 1965), the foundation soil is assumed to be a rigid-perfectly plastic media. The subgrade reaction forces (V , H , M/B) have to be within the failure envelope ($F < 0$) or on the failure envelope ($F = 0$).
- (c) In a manner consistent with the theory of plasticity, in which the ratio of incremental plastic strain is related to the state of stress, “displacement potential”, Q , is defined. The incremental displacement vector in the work-conjugate displacement space, δ , is assumed to be orthogonal to the plastic displacement potential. Thus we have,

$$\delta = \{\delta v, \delta h, B\delta\theta\} = \lambda \frac{\partial Q}{\partial R} \quad (7)$$

in which v and h are vertical and horizontal displacement at the center of the footing base relative to the foundation soil, θ is rotation, R is the subgrade reaction force vector and λ is a constant.

Note that the rotation θ is multiplied by B to preserve dimensional homogeneity. These assumptions indicate that when the footing is moving at velocity δ , the ground is in the failure condition and the vector R is determined by the following two conditions:

- (i) R is on the failure envelope ($F = 0$), and
- (ii) the vector δ is normal to the displacement potential.

The difference between the external load and the subgrade reaction accelerate or decelerate the footing and the movement of the footing is described by the equation of motion. More information regarding computational procedure can be found elsewhere (Okamura and Matuo 2002).

Foundation displacements were predicted using two type of load-displacement relationship; one is the rigid-perfectly plastic response with the peak load intensity (equation.(4)) always mobilized. The other is that the peak load intensity is invoked but the bearing capacity drops to the residual load intensity (22% of peak load intensity) as soon as the foundation started moving.

3.3 Discussions

The input base acceleration and typical displacement time histories observed in the test H1 are depicted in Fig. 10. The calculated displacements using the proposed method are also shown in the figure. It should be noted that the observed horizontal displacement increased slowly until the displacement reached about ten millimeters, and after that the displacement accumulated at a higher rate. In the calculated result, however, the displacements accumulated more or less at the constant rate through the course of the shaking event. This difference may have arisen from the change in geometry which is not taken into consideration in the calculation. This is more significant for footing on a slope than on a level ground because a horizontal displacement of a footing toward slope results in complete loss of the contact pressure of footing base near the edge.

The predicted displacements in which the peak load intensity was invoked in the calculation underestimated the observed displacements. This is probably due to the sharp decrease in the bearing capacity after the peak load, which is typical for the footing near the slope. The utilize of the residual load capacity provides a much improved prediction.

Figure 11 indicate relationships between displacement and weight of foundation. It was observed that the displacement increased with weight of foundation. The displacement slightly increased with the height of the center of gravity of the foundation getting higher. Predicted displacement also increased with the foundation weight and the height of the center of gravity. It can be seen that the two predictions provide the upper and lower limit of displacement.

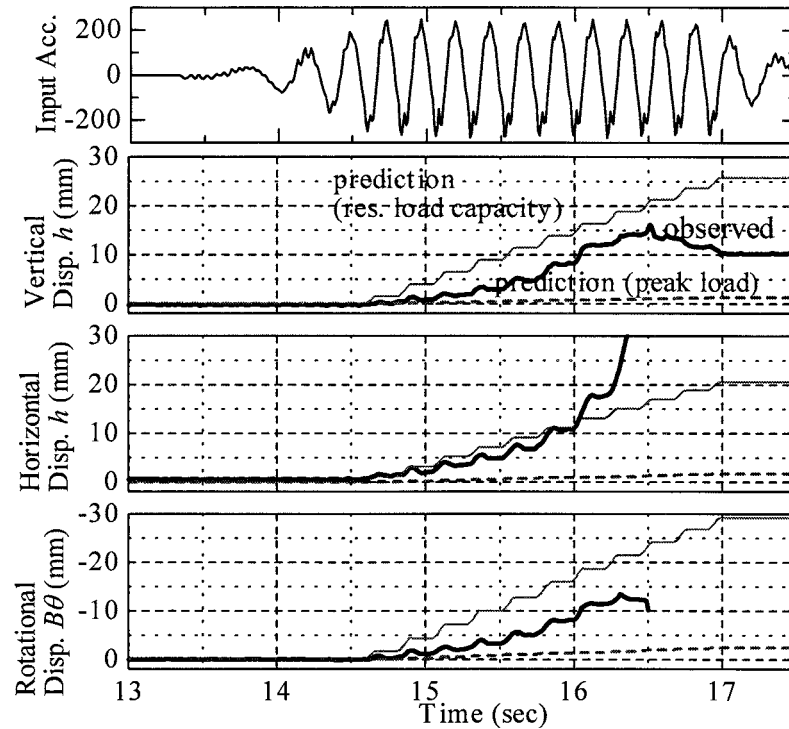


Figure 10 Time histories of observed and calculated footing responses (test H1)

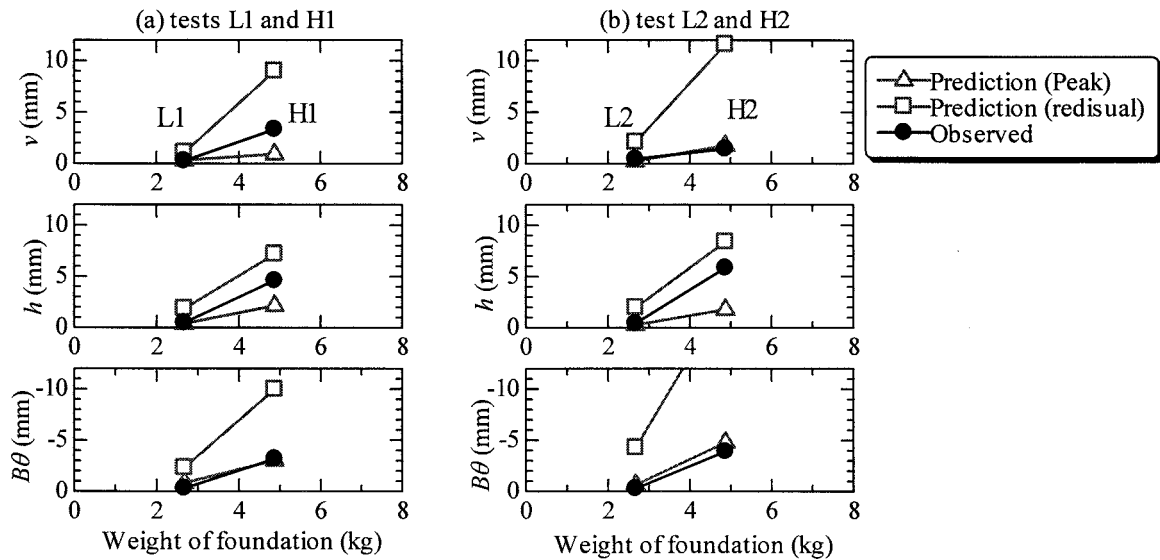


Figure 11 Comparison of predicted displacements with observations

4. CONCLUSIONS

In this study, a series of bearing capacity tests on a strip footing at the shoulder of 30 degree slope is conducted and footing responses under combined vertical, horizontal and moment loadings are observed. The failure envelope and the displacement potential in the general load space were prescribed. It was found that failure envelope for footing near slope is more or less similar in shape to the that for level ground. Axis of the failure envelope inclined 4 degree and 3 degree in H - V plane and M/B - V plane, respectively. The envelope for the residual state was appeared to be the same in

shape but about 5 times smaller as compared with the peak load condition.

The derived failure envelope and displacement potential are incorporated to the displacement prediction method which is capable of calculating fully coupled displacement under earthquake loadings. Shaking table tests of strip footings resting on the shoulder of the sand slope were carried out. The method is validated through comparison between calculated results and test observations. It was found that the prediction using the failure envelope corresponding to the peak load underestimated the observations. While the prediction with the load degradation after the peak load being taken into account provides upper bound of the observed displacements, in which the failure envelope for peak load was used until the footing firstly started to move and the subgrade reaction was estimated using the envelope for residual condition throughout the calculation after the footing once started to move. This holds true irrespective of the weight and the height of the center of gravity of foundations

References:

- Butterfield, R. and Gottardi, G. (1994), "A complete three-dimensional failure envelope for shallow footings on sand," *Geotechnique*, 44(1), 181-184.
- Georgiadis, M. and Butterfield, R. (1988), "Displacements of footings on sand under eccentric and inclined loads," *Can. Geotech. J.*, 25, 199-212.
- Gottardi, G. and Butterfield, R. (1995), "The displacement of a model rigid surface footing on dense sand under general planar loading," *Soils and Foundations*, 35(3), 71-82.
- Hori, M., Okamura, M. and Sugano, Y. (2005), "Bearing capacity and deformation characteristics of sand under combined loading," *Proc. 40th Japan National Conference on Geotechnical Engineering*, CD-ROM
- Kusakabe, O., Kimura, T. and Yamaguchi, H. (1981), "Bearing capacity of slopes under strip loads on the top surfaces," *Soils and Foundations*, 21(4), 29-40.
- Meyerhof, G. G. (1953), "The bearing capacity of foundations under eccentric and inclined loads," *Proc. 3rd ICSMFE*, 1, 440-445
- Meyerhof, G. G. (1963), "Some recent research on the bearing capacity of foundations," *Can. Geotech. J.*, 1(1), 16-26
- Okamura, M. and Matsuo, O. (2002), "A displacement prediction method for retaining wall," *Soils and Foundations*, 42(1), 131-138.
- Okamura, M., Mihara, A., Takemura, J. and Kuwano, J. (2002), "Effects of footing size and aspect ratio on the bearing capacity of sand subjected to eccentric loading," *Soils and Foundations*, 42(4), 43-56.
- Shields, D. H., Scott, J. D., Baner, G. E., Deshenes, J. H. and Barsvary, A. K. (1977) "Bearing capacity of foundations near slopes," *Proc. 9th Int. Conf. SMFE*, 1, 715-720.

EFFECTS OF NEAR FAULT STRONG GROUND MOTION ON A CIRCULAR TUNNEL

A. Farahani¹⁾, A. C. Wijeyewickrema²⁾, and T. Ohmachi³⁾

1) Post Doctoral Researcher, Center for Urban Earthquake Engineering, Tokyo Institute of Technology, Japan

2) Associate Professor, Department of Civil Engineering, Tokyo Institute of Technology, Japan

3) Professor, Department of Built Environment, Tokyo Institute of Technology, Japan

farahani.a.aa@m.titech.ac.jp, wijeyewickrema.a.aa@m.titech.ac.jp, ohmachi@enveng.titech.ac.jp

Abstract: In this paper fault rupturing during strong ground motion is simulated and the effects of faulting on a nearby circular tunnel surrounded by a soft soil are studied using the finite element technique. In the near fault region, depending on the distance from the source, very complex wave patterns are produced, where the body and Rayleigh waves on the ground surface are neither well separated nor plane. In order to apply dynamic rupturing forces to the system, the *split-node technique* is used to introduce relative slip in the adjacent elements on the opposite sides of the fault. The fault source parameters which are considered during this study are dip-slip angle, rupture velocity, rise-time of the fault slip, final depth of fault tip and the permanent slip. The effects of these parameters on displacement field in the near fault region and ovality factor of the tunnel which represents the deformation of the tunnel relative to its original shape are investigated. Finally the maximum hoop stress inside the concrete lining is plotted. The ovality factor together with internal forces of the tunnel can be used to predict or quantify damage to tunnels due to deformation.

1. INTRODUCTION

In principle, the transient response of an elastic medium containing a cavity or inclusion can be obtained by first decomposing the input motion into its simple harmonic components by means of the Fourier integral, calculating the response of the medium to each harmonic component and finally by superposing the inverse Fourier transform of all the harmonic responses. Baron and Matthews (1961) investigated the diffraction of pressure waves by a cylindrical cavity in an elastic medium using the integral transform technique. Eringen and Suhubi (1975) solved the scattering of plane P-wave and S-wave pulses by a cylindrical cavity. In particular, the key monograph by Pao and Mow (1973) contains a comprehensive account of diffraction of plane waves by cylindrical and spherical inclusions. Using Laplace transform and Fourier synthesis technique combined with mode superposition they transferred the stresses around the cavity from frequency domain into time domain to study the transient effects of the scattered waves. Tadeu *et al.* (2002) used BEM to simulate 3D scattering of waves around a cylindrical irregular cavity of infinite length and arbitrary cross section due to spatially harmonic line loads. He chose a source whose temporal variation is given by Ricker wavelet and its Fourier transformation is defined as well. By superposition of the responses of mother wavelets, the total response of the cavity in time domain can be obtained.

In the previous studies either the problems are limited to incident plane waves or solved for simple cases of line loads as sources. In reality the near fault region wave field is much more complicated. In the strong ground motion region, the Rayleigh wave may not be formed clearly and the propagated energy from the rupture is carried by non-planar P-waves and S-waves. It is also possible that the tunnel is located in the region that is permanently deformed by the fault rupture.

In order to estimate the possible damage to structures near the faulting zone, the fault rupture phenomenon should be simulated. Analytical solutions for internal and surface soil deformations due to a buried finite fault in a homogeneous half-space were obtained by Okada (1985, 1992). Sato and Matsu'ura (1973) and Ma and Kuszniir (1992) investigated the static deformations of a layered elastic medium. Static as well as dynamic deformation of a soft surface layer above a fault were studied by Honda and Yomogida (2003) and compared with the solutions for a half-space.

In this paper the elastic medium and circular tunnel is discretized using finite elements and the fault rupture is modeled using the *split-node technique* introduced by Melosh and Raefsky (1981). The effects of dip-slip angle, final depth of fault tip, rupture velocity, rise-time of the fault slip and the permanent slip on soil deformation (Aki and Richards 1980) and response of a circular tunnel are investigated.

2. APPLYING FAULT SLIP USING SPLIT-NODE TECHNIQUE

In the *split-node technique* the fault slip is simulated by forces which are applied on fault elements and produce the same amount of displacements in the medium as the actual rupture. Fault elements are the elements which have at least one shared node on the fault line (shaded elements in Fig. 1(a)). For simplicity only one element on each side of the fault line is depicted in Fig. 1(b). The geometry of the two elements at time t has been shown by $IMNJ$ and $MKLN$. From time t to $t + \Delta t$, the left and right elements move to the new locations $I'M'N'J'$ and $M'K'L'N'$, and nodes M' and N' split virtually. The displacement of node M in the left and right elements at $t + \Delta t$ are calculated by $U_M^L = \langle U_M \rangle + \Delta U_M$ and $U_M^R = \langle U_M \rangle - \Delta U_M$, where $\langle U_M \rangle$ is the displacement mean value of the node M' relative to M , which is calculated from solving the complete system of the equations of motion together with relevant boundary conditions, and ΔU_M is the input relative slip of the elements at node M' . Using the same definition, the displacement of node N in the left and right elements at $t + \Delta t$ are calculated as $U_N^L = \langle U_N \rangle + \Delta U_N$ and $U_N^R = \langle U_N \rangle - \Delta U_N$, respectively. By calculating the new locations of the nodes and the stiffnesses of fault elements, the induced forces at the nodes of the fault elements due to the slip can be calculated (Melosh and Raefsky 1981). These induced forces are applied to the original model with the opposite sign.

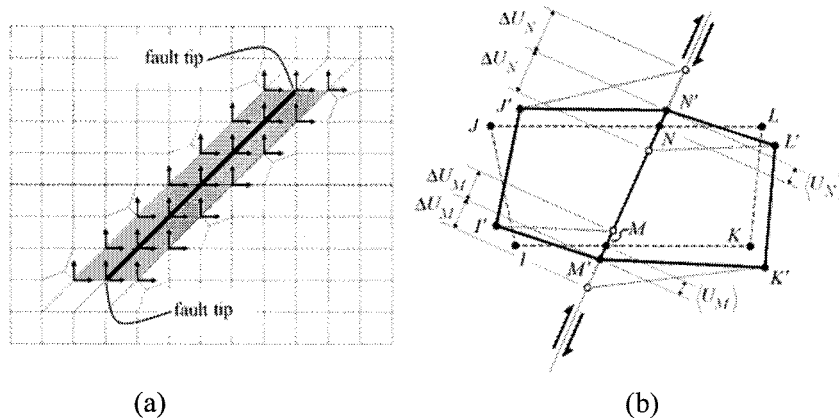


Figure 1. Split-node technique fault elements: (a) Nodal forces applied on fault elements; (b) Deformations of fault elements on both sides of fault line.

To simulate the propagation of the rupture, the split-node forces can be applied with time delay along the fault line. The relative slips and hence equivalent split-node forces reach the final values according to the prescribed slip function (Haskell 1969).

3. THE PARAMETRIC STUDY

To study the effects of near fault motions on underground structures, the following model has been considered. An isotropic elastic half plane with a circular cylindrical tunnel has been discretized with plane strain 4-node elements. The sizes of the elements decrease near the tunnel to reduce spurious reflections. The outside diameter of the tunnel is 15 m with 0.8 m thickness, and 47,500 nodes and 46,900 elements are used in this model (Fig. 2). Material properties of the isotropic elastic soil medium are: Young's modulus $E_s = 8.512\text{E}8 \text{ N/m}^2$, Poisson's ratio $\nu_s = 0.4$, and mass density $\rho_s = 1900.0 \text{ kg/m}^3$, which yield P-wave and S-wave velocities of $V_p = 979.8 \text{ m/s}$ and $V_s = 400.0 \text{ m/s}$, respectively. Material properties of the concrete are: Young's modulus $E_c = 2.4\text{E}10 \text{ N/m}^2$, Poisson's ratio $\nu_c = 0.15$, and mass density $\rho_c = 2500.0 \text{ kg/m}^3$. The variables in this parametric study are dip-slip angle θ , final depth of fault tip H (Fig. 3(a)), rupture velocity V_{rup} , rise-time of the fault slip T_0 , and the permanent slip D (Fig 3(b)). For all cases, the fault slip originates from a depth of 3600 m. In the following numerical examples the prescribed permanent slip $D = 1.0 \text{ m}$. As the circular cylindrical tunnel deforms due to the fault motion, an important response parameter is the ovality factor $\beta = a/b$, where a and b are the maximum and minimum deformed diameters of the tunnel. The ovality factor together with internal forces of the lining can be used to predict or quantify damage to tunnels due to deformation.

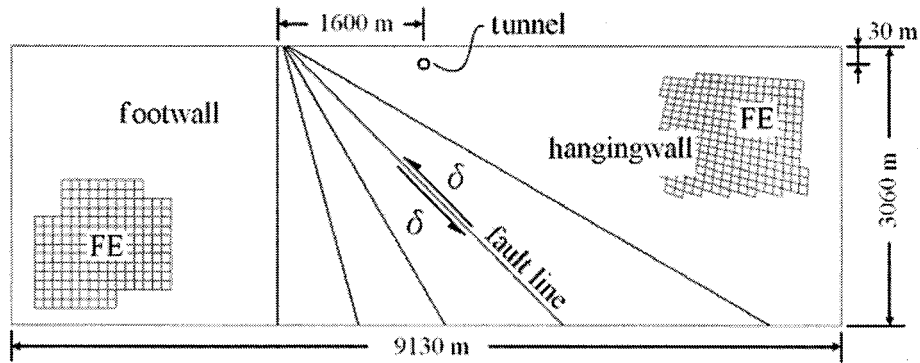


Figure 2. Dimensions of the medium for simulation of thrust fault.

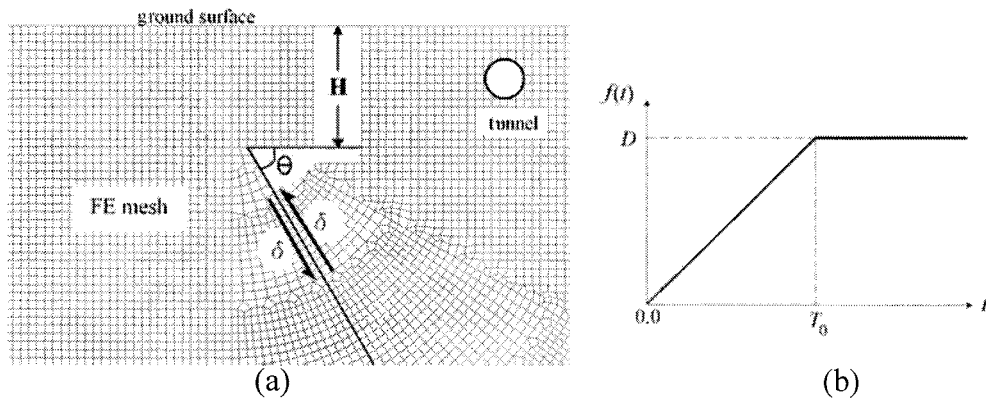


Figure 3. (a) Definition of dip-slip angle and final depth of fault tip; (b) Ramp slip function

At the boundaries of the truncated model, simple dashpots have been used to reduce reflection of the outgoing waves back into the system (Lysmer and Kuhlmeyer 1969).

3.1 Effects of Dip-Slip Angle

For a surface breaking fault ($H = 0.0$ m), the effect of dip-slip angle is studied for the prescribed parameters $V_{rup}/V_s = 0.75$ and $T_0 = 1$ sec. In Fig. 4 the ovality factor β is plotted for the dip-slip angles $\theta = 30^\circ, 45^\circ, 60^\circ, 75^\circ$, and 90° . For each dip-slip angle there is at least one major peak which occur at different times since the initiation of rupture takes place at different locations. It is seen that the maximum ovality factor occurs when $\theta = 30^\circ$ and 45° .

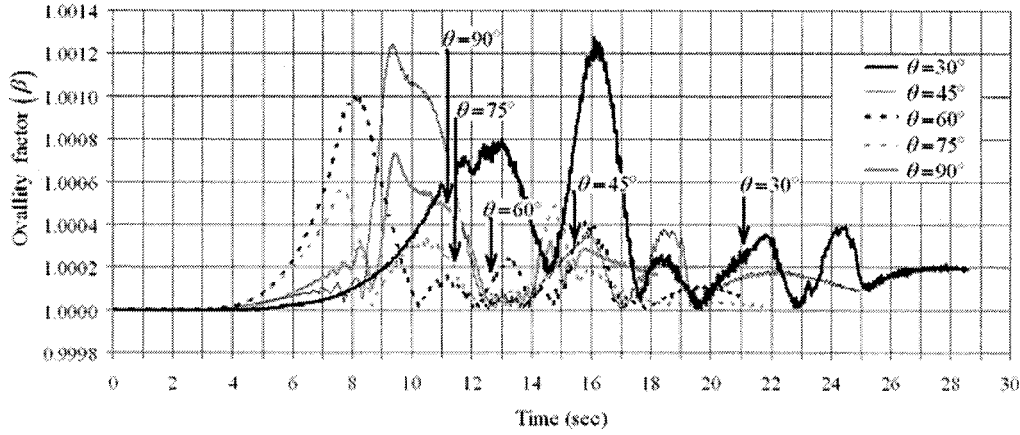


Figure 4. Ovality factors for different dip-slip angles of fault rupturing, where $H = 0.0$ m, $V_{rup}/V_s = 0.75$ and $T_0 = 1$ sec. Arrows indicate the time rupture ends.

For $\theta = 45^\circ$, the displacement amplitude increment at $t = 9.34$ sec which corresponds to the maximum ovality factor β , is plotted in Fig. 5. It can be seen that the maximum displacement amplitude increment is at the fault tip and is directed towards the tunnel. The response of the tunnel is due to the superposition of direct incident waves from the rupture and reflected waves from the ground surface.

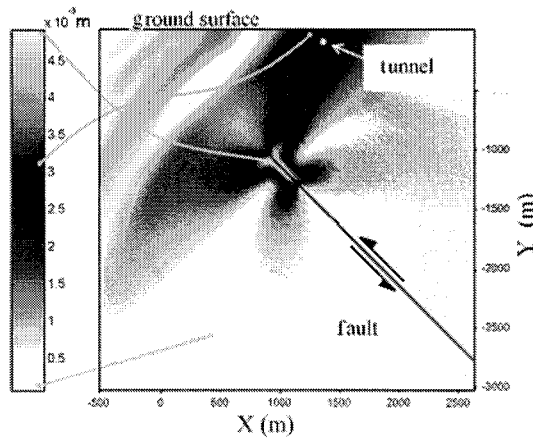


Figure 5. Incremental displacement amplitude for $\theta = 45^\circ$, $V_{rup}/V_s = 0.75$ and $T_0 = 1$ sec at $t = 9.34$ sec.

3.2 Effects of rupture velocity

In this section, the effect of rupture velocity is investigated where the prescribed parameters are $\theta = 45^\circ$, $H = 0.0$ m and $T_0 = 1$ sec. The ovality factor is shown in Fig. 6 for $V_{rup}/V_s = 0.65, 0.75$ and 0.85 . It is seen that the ovality factor for fast rupturing ($V_{rup}/V_s = 0.85$)

produces a higher peak of shorter duration when compared to slow rupturing. Hence, it shows that fast rupturing can cause more damage to tunnels.

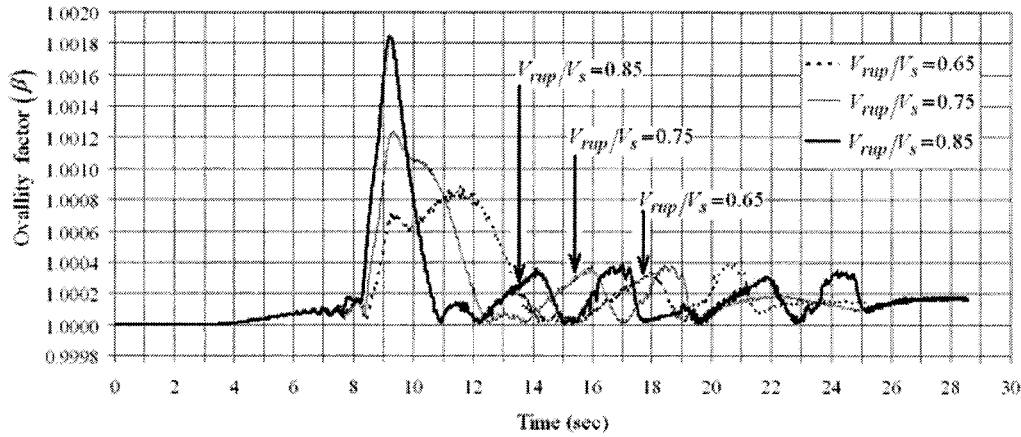


Figure 6. Ovallity factors for different rupture velocities, where $\theta = 45^\circ$, $H = 0.0$ m and $T_0 = 1$ sec. Arrows indicate the time rupture ends.

3.3 Effects of rise-time

Here the prescribed parameters are $\theta = 45^\circ$, $H = 0.0$ m and $V_{rup}/V_s = 0.75$. Figure 7 shows that for $T_0 = 1, 2$ and 3 sec, the rise-time has little effect on ovallity factor. By increasing the rise-time, the ovallity factor becomes smaller with longer duration.

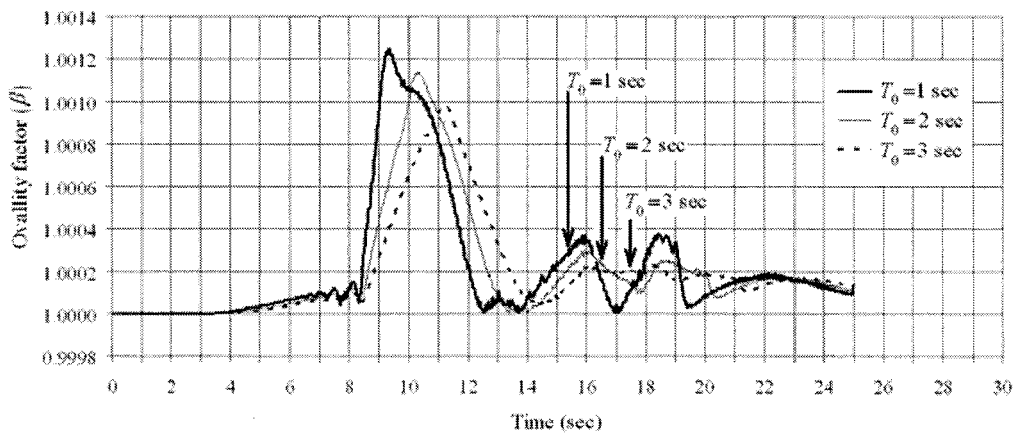


Figure 7. Ovallity factors for different rise-time, where $\theta = 45^\circ$, $H = 0.0$ m and $V_{rup}/V_s = 0.75$. Arrows indicate the time rupture ends.

3.4 Effects of the depth of the fault tip

In this section the prescribed parameters are $\theta = 45^\circ$, $V_{rup}/V_s = 0.75$ and $T_0 = 1$ sec. The ovallity factor for $H = 0.0, 500$ and 1000 m is plotted in Fig. 8. As expected, the maximum ovallity factor is the same because the rupture path, rupture velocity and rise-time are the same. The permanent ovallity factor from a surface breaking rupture is less than a buried rupture.

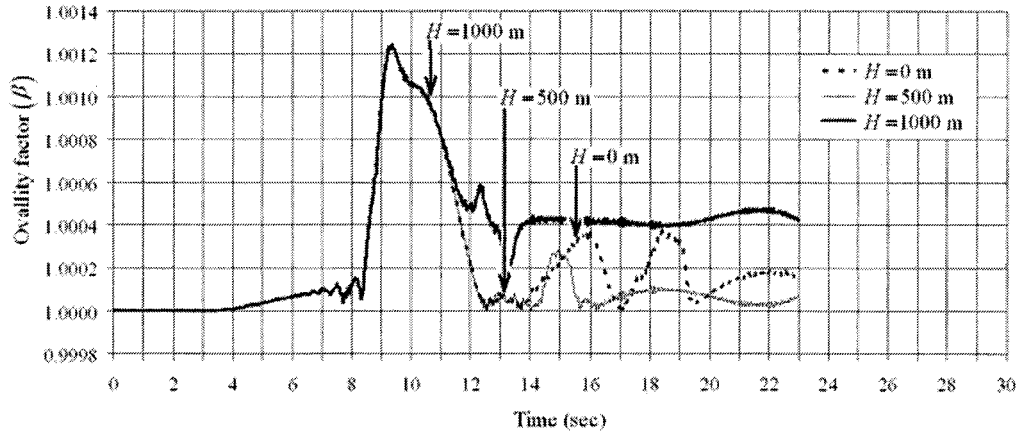


Figure 8. Owallity factors for different depth of the fault tip, where $\theta = 45^\circ$, $V_{rup}/V_s = 0.75$ and $T_0 = 1$ sec. Arrows indicate the time rupture ends.

In order to interpret this behaviour, the displacement field around the rupture tip is investigated. For instance at $t = 16$ sec around the rupture tip, the displacement field is non-uniform, but on either side of the rupture line the displacement field becomes uniform away from the rupture tip (Fig. 9). If the rupture stops near the tunnel, this non-uniform displacement field applies permanent non-uniform deformation to the lining.

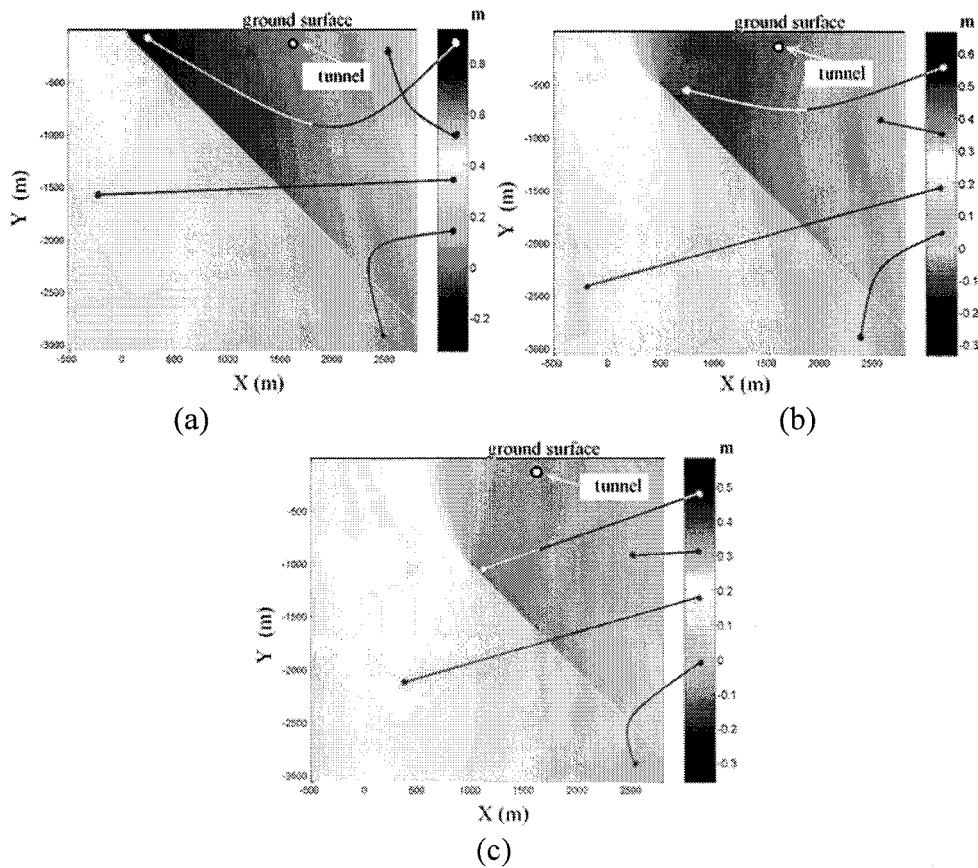


Figure 9. Vertical displacement component u_y near the fault tip at $t = 16$ sec, for (a) $H = 0$ m; (b) $H = 500$ m; (c) $H = 1000$ m.

4. EFFECT OF THE RUPTURE VELOCITY ON THE HOOP STRESS OF THE LINING

In this section, the effect of rupture velocity on hoop stress is investigated, where the prescribed parameters are $\theta = 45^\circ$, $H = 0.0$ m and $T_0 = 1$ sec. The maximum hoop stress is shown in Fig. 10 for $V_{rup}/V_s = 0.65, 0.75$ and 0.85 . It shows that fast rupturing can cause higher hoop stress in tunnels.

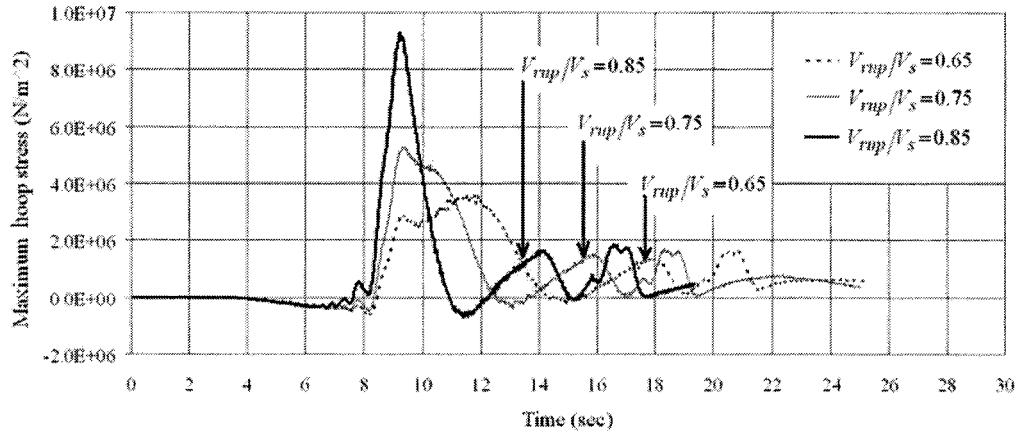


Figure 10. Maximum hoop stress for different rupture velocities, where $\theta = 45^\circ$, $H = 0.0$ m and $T_0 = 1$ sec. Arrows indicate the time rupture ends.

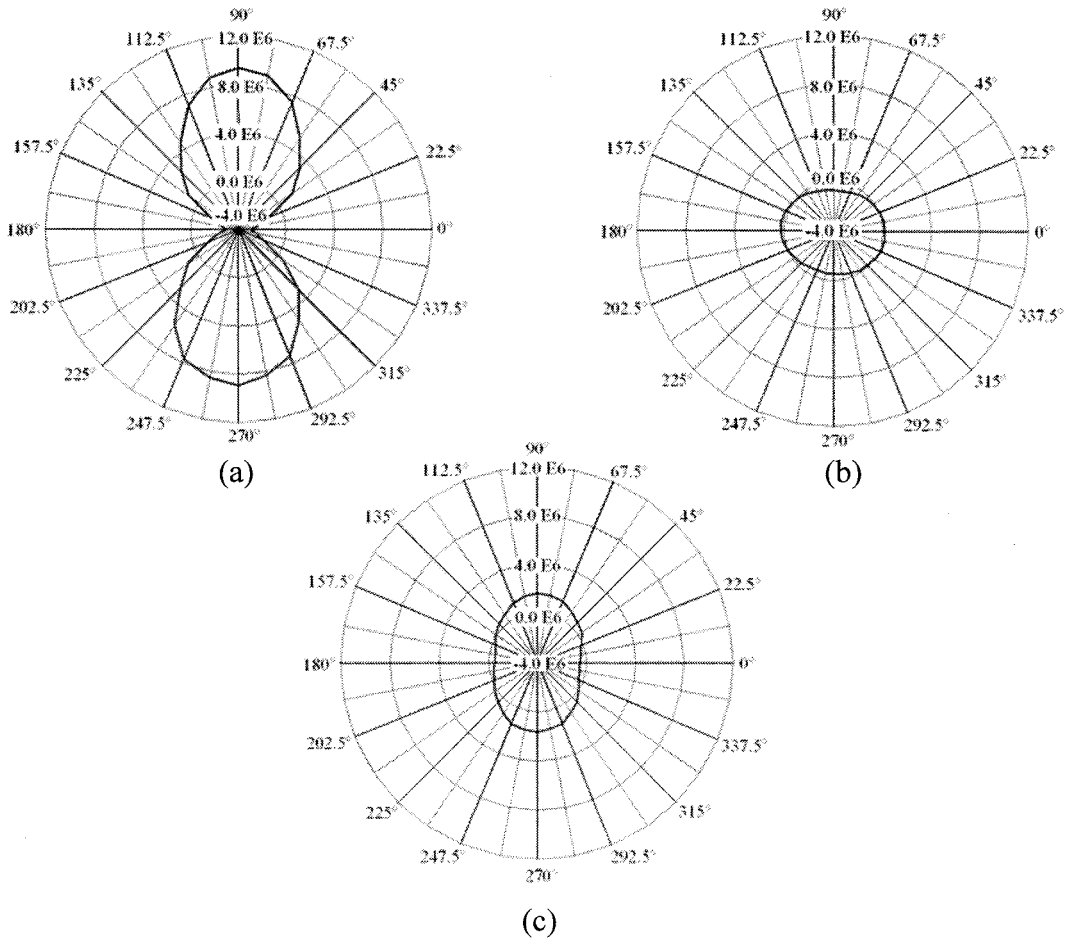


Figure 11. Angular distribution of maximum hoop stress (N/m^2), where $\theta = 45^\circ$, $H = 0.0$ m, $V_{rup}/V_s = 0.75$ and $T_0 = 1$ sec for: (a) $t = 9.24$ sec; (b) $t = 11.39$ sec; (c) $t = 14.19$ sec.

Figure 11 shows the hoop stresses inside the lining at $t = 9.24, 11.39, \text{ and } 14.19 \text{ sec}$, which correspond to the first three maximum and minimum values of the hoop stress.

5. CONCLUSIONS

Among the fault source parameters, dip-slip angle and rupture velocity have more effect on ovality factor of a circular tunnel than rise-time and final depth of fault tip. Shorter rise-time produces high frequency waves which increase the ovality factors of tunnels. If the fault stops near a tunnel, the non-uniform displacement field around the fault tip applies permanent non-uniform deformation to the tunnel. Fast rupturing applies more deformation and internal forces to tunnels than slow rupturing.

Acknowledgment:

The first author gratefully acknowledges a post doctoral fellowship from the Center for Urban Earthquake Engineering (CUEE), Tokyo Institute of Technology. Financial support of CUEE for strong ground motion studies are very much appreciated and kindly acknowledged.

References:

- Aki, K. and Richards, P.G. (1980), "Quantitative seismology, Theory and methods." Freeman and Co., New York.
- Baron, M.L. and Matthews, A.T. (1961), "Diffraction of a pressure wave by a cylindrical cavity in an elastic medium," *Journal of Applied Mechanics (ASME)*, **28**, 347-354.
- Eringen, A.C. and Suhubi, E.S. (1975), "Elastodynamics, Volume II: Linear Theory." Academic Press, New York.
- Haskell, N.A. (1969), "Elastic displacements in the near-field of a propagating fault," *Bulletin of the Seismological Society of America*, **59**(2), 865-908.
- Honda, R. and Yomogida, K. (2003), "Effects of a soft surface layer on near-fault static and dynamic displacements," *Geophysical Journal International*, **154**, 441-462.
- Lysmer, J. and Kuhlmeyer, R.L. (1969), "Finite dynamic model for infinite media," *Journal of Engineering Mechanics Division (ASCE)*, **95**, 859-877.
- Ma, X. and Kuszniir, N. (1992), "3-D subsurface displacement and strain fields for faults and fault arrays in a layered elastic half-space," *Geophysical Journal International*, **111**, 542-558.
- Melosh, H.J. and Raefsky, A. (1981), "A simple and efficient method for introducing faults into finite element computations," *Bulletin of the Seismological Society of America*, **71**(5), 1391-1400.
- Okada, Y. (1985), "Surface deformation due to shear and tensile faults in a half-space," *Bulletin of the Seismological Society of America*, **75**, 1135-1154.
- Okada, Y. (1992), "Internal deformation due to shear and tensile faults in a half-space," *Bulletin of the Seismological Society of America*, **82**, 1018-1040.
- Pao, Y.H. and Mow, C.C. (1973), "Diffraction of Elastic Waves and Dynamic Stress Concentrations." Crane and Russak, New York.
- Sato, R. and Matsu'ura, M. (1973), "Static deformation due to the fault spreading over several layers in a multi-layered medium," *Journal of Physics of the Earth*, **21**, 227-249.
- Tadeu, A.J.B., Anotnio, J.M.P. and Kausel, E. (2002), "3D scattering of waves by a cylindrical irregular cavity of infinite length in a homogeneous elastic medium," *Computer Methods in Applied Mechanics and Engineering*, **191**, 3015-3033.

VERIFICATION OF GENERALIZED SCALING RELATIONS FOR DYNAMIC CENTRIFUGE EXPERIMENTS

T. Tobita¹⁾ and S. Iai²⁾

1) Assistant Professor, Disaster Prevention Research Institute, Kyoto University, Japan

2) Professor, Disaster Prevention Research Institute, Kyoto University, Japan

tobita@geotech.dpri.kyoto-u.ac.jp, iai@geotech.dpri.kyoto-u.ac.jp

Abstract: Dynamic centrifuge tests for pile foundations are conducted to investigate the applicability of the generalized scaling relation proposed by Iai et al. (2005). In the centrifuge tests, geometrical scale of a model pile foundation (prototype/centrifuge model) is set as 100 ($= \mu \eta$). Five combinations of scaling factors of virtual 1 g model (μ) and centrifuge model (η) are tested. According to the combination of the scaling factors, values of flexural rigidity of a pile are determined in centrifuge model. Responses in prototype scale are compared each other for five pile foundation models tested under various centrifugal accelerations. Fairly good agreements are obtained for the amplitude of input displacement and input acceleration for all the cases, except the case of large input motion. Also for the case of lower centrifugal accelerations, the agreements are significant for the average amplitude of acceleration in soil. Not only the average amplitude of responses, but also bending moment profile of lower centrifugal accelerations shows fair agreements to justify the applicability of the generalized scaling relation. When centrifugal acceleration is larger, some responses become small and the exact cause of this is unknown yet.

1. INTRODUCTION

With recent demand from earthquake engineering community to carry out physical model testing of larger prototypes, a size of experimental facility is becoming larger and larger. For example, the world largest shaking table of 20 × 15 m has been built in the E-defense, Japan. It can shake a real scale 6-story reinforced concrete building (1,000 t) (Chen et al. 2006), or 2 wooden Japanese houses simultaneously (Suzuki et al. 2006). However, even with such a large shaking table, when dynamic behavior of a whole structure including its foundation buried into the ground is examined, a prototype has to be scaled down due to the limitation of the shaking table's capacity (Suzuki and Tokimatsu 2007).

In centrifuge modeling, geometrical scale of a model can be theoretically decreased by increasing the centrifugal acceleration. However, with decreasing model scale, the problem of scaling effects, i.e., dependence of model behavior on a relative size of structure and granular material (e.g., Honda and Towhata 2006), becomes more and more apparent. Other problem for dynamic testing under larger centrifugal acceleration is the requirement of more powerful actuator and its precise control (Chazelas et al. 2006).

To overcome these deficiency in centrifuge tests and increase the efficiency of small to medium size centrifuges, two stage scaling relationship called generalized scaling relationship for centrifuge tests was proposed by Iai et al. (2005) (Figure 1). In this scaling relation, a prototype is scaled down to a 1 g model with scaling factor for 1 g model tests (Iai 1989), and the 1 g model is further scaled down

to a centrifuge model with scaling factor for centrifuge model tests. By using this scaling relationship, model tests with scaling factor (prototype/physical model) of 100 or much higher may be possible.

In the present study, using a prototype and five centrifuge models scaled down to 1/100 with various scaling factors for 1 g and centrifuge model tests, the generalized scaling relation is investigated by comparing the responses of the five models in prototype scale.

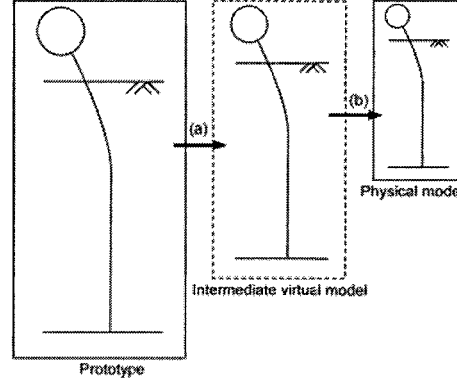


Figure 1. Concept of two stage scaling: (a) scaling relations for 1g field; (b) scaling relations for centrifugal field (modified after Iai et al., 2005).

2. GENERALIZED SCALING RELATIONSHIP

This section briefly reviews the derivation of generalized scaling relationship (Iai et al. 2005) of physical model tests based on the fundamental physical laws, for example, stress equilibrium, definition of strains, and a constitutive relation.

Stress equilibrium:

$$\frac{\partial \sigma_{ij}}{\partial x_j} + X_i = \rho \ddot{u}_i \quad (1)$$

Definition of strain:

$$\varepsilon_{ij} = \frac{1}{2} \left(\frac{\partial u_i}{\partial x_j} + \frac{\partial u_j}{\partial x_i} \right) \quad (2)$$

Constitutive relation:

$$\sigma_{ij} = C_{ijkl} \varepsilon_{kl} \quad (3)$$

where σ_{ij} is stress tensor, x_i is coordinate system, ρ is density, \ddot{u}_i is acceleration and dots mean temporal differentiation and $X_i = (0, -\rho g, 0)$, g is acceleration due to gravity, ε_{ij} is strain tensor and C_{ijkl} is tangential stiffness tensor. Here, the summation rule is supposed.

The scaling relations for centrifuge model tests are derived by introducing scaling factors for variables appearing in equations (1) - (3) as follows and by demanding that these variables must satisfy both the equations for prototype and the model.

$$(x_i)_p = \lambda(x_i)_m, \quad (\sigma_{ij})_p = \lambda_\sigma(\sigma_{ij})_m, \quad (u_i)_p = \lambda_u(u_i)_m, \quad (\rho)_p = \lambda_\rho(\rho)_m, \quad (g)_p = \lambda_g(g)_m, \quad (\varepsilon_{ij})_p = \lambda_\varepsilon(\varepsilon_{ij})_m,$$

$$(t)_p = \lambda_t(t)_m, \quad (C_{ijkl})_p = \lambda_C(C_{ijkl})_m$$

where subscripts “p” and “m” mean, respectively, “prototype” and “model.” By substituting variables for prototype into Eq. (1),

$$\frac{\partial(\sigma_{ij})_p}{\partial(x_j)_p} + (X_i)_p = (\rho)_p \frac{\partial^2(u_{ij})_p}{\partial(t)_p^2} \quad (4)$$

Then introducing scaling relations into Eq. (4),

$$\frac{\lambda_\sigma}{\lambda} \frac{\partial(\sigma_{ij})_m}{\partial(x_j)_m} + \lambda_\rho \lambda_g (X_i)_m = \lambda_\rho \frac{\lambda_u}{\lambda_t^2} (\rho)_m \frac{\partial^2(u_{ij})_m}{\partial(t)_m^2} \quad (5)$$

Since variables for model also satisfy Eq. (1), then all the coefficients of Eq. (5) must be equal as follows,

$$\lambda_\sigma / \lambda = \lambda_\rho \lambda_g = \lambda_\rho \lambda_u / \lambda_t^2 \quad (6)$$

Now, from the left hand side of Eq. (6), the scaling relation of stress is written as,

$$\lambda_\sigma = \lambda \lambda_\rho \lambda_g \quad (7)$$

From Eq. (2), (3) and (6) in the same way, the scaling relation of time, displacement and stiffness are given as,

$$\lambda_t = (\lambda \lambda_\epsilon / \lambda_g)^{0.5}, \quad \lambda_u = \lambda \lambda_\epsilon, \quad \lambda_c = \lambda \lambda_\rho \lambda_g / \lambda_\epsilon.$$

Now let us partition the scaling factors for length, density, acceleration, and strain as follows,

$$\lambda = \mu \eta, \quad \lambda_\rho = \mu_\rho \eta_\rho, \quad \lambda_g = \mu_g \eta_g, \quad \lambda_\epsilon = \mu_\epsilon \eta_\epsilon$$

where η and μ denote respectively the scaling factor of length for 1 g and centrifuge model tests. The value of the scaling factor for acceleration due to gravity in 1 g field is unity ($\mu_g = 1$) and that for centrifugal field is $\eta_g = 1/\eta$. The scaling factor for density and strain in centrifugal field are $\eta_\rho = \eta_\epsilon = 1$. Substituting these into the above relations yields the generalized scaling relationship,

$$\lambda = \mu \eta, \quad \lambda_\rho = \mu_\rho, \quad \lambda_g = 1/\eta, \quad \lambda_\epsilon = \mu_\epsilon$$

The generalized scaling relationships used in the present study are summarized in Table 1 with the scaling factor of density and strain $\mu_\rho = 1$ and $\mu_\epsilon = \mu^{0.5}$ in 1 g field (Iai 1989).

Table 1 Generalized scaling factors for centrifuge model tests (Iai et al. 2005)

	Partitioned		Generalised
	Virtual 1G field μ =Prototype /virtual model	Centrifugal field η =Prototype /physical model	Prototype /physical model
Length	μ	η	$\mu \eta$
Density	1	1	1
Time	$\mu^{0.75}$	η	$\mu^{0.75} \eta$
Stress	μ	1	μ
Pore water pressure	μ	1	μ
Displacement	$\mu^{1.5}$	η	$\mu^{1.5} \eta$
Velocity	$\mu^{0.75}$	1	$\mu^{0.75}$
Acceleration	1	$1/\eta$	$1/\eta$
Strain	$\mu^{0.5}$	1	$\mu^{0.5}$
Bending moment	$\mu^{4.0}$	$\eta^{3.0}$	$\mu^{4.0} \eta^{3.0}$
Flexial rigidity	$\mu^{4.5}$	$\eta^{4.0}$	$\mu^{4.5} \eta^{4.0}$

3. CONFIGURATION OF CENTRIFUGE TESTS

Experiments were conducted in a rigid wall container mounted on 2.5 m radius geotechnical centrifuge at the Disaster Prevention Research Institute, Kyoto University (DPRI-KU). Overall dimensions of the rigid container are 450 × 150 × 300 mm in length, width, and height, respectively. Dynamic excitation was given in the direction parallel to the cross-section shown in Figure 2. A shake table mounted on a platform was unidirectionally driven by a servo hydraulic actuator.

A vertical cross-section of the pile foundation model in a deposit of dry sand is depicted in Figure 2. Sand deposit (silica sand: $e_{\max} = 1.01$, $e_{\min} = 0.76$, and $D_{50} = 0.5$ mm) was prepared by air pluviation to the target relative density of 70 % in 250 mm lifts (model scale). The length of a pile was 300 mm (model scale) and a mass of 0.5 kg (model scale) was put on top of the foundation. Rotation was fixed on both top and bottom of piles. Ten pairs of strain gauges were attached at the specified height of the pile (Figure 2). As shown in Figure 2, the model was instrumented with four accelerometers, one laser displacement transducers. Sampling frequency was 5 kHz.

To investigate the generalized scaling relations, five individual pile foundation models were used. Models were designed so that the flexural rigidities, EI , were identical each other in prototype scale. The horizontal cross section of a model pile is rectangular and their thickness in the shaking direction is varied with the scaling factors.

Scaling factor of prototype/centrifuge model was set as 100 ($= \mu\eta$), and the scaling factors of 1 g (μ) and centrifugal (η) fields were varied with 5 patterns as shown in Table 2. Input frequency of prototype was set as 1.0 Hz, and by applying the generalized scaling factors, frequencies of input displacement in centrifugal fields were determined as shown in Table 3. In each case, three consecutive input displacements (amplitudes of 51, 72 and 97mm in prototype scale) were applied at the base of models. Converted input displacement amplitudes to the centrifugal fields are shown in Table 4. The input displacement (Figure 3) is tapered off in the beginning and at the end and has 20 s (prototype) of flat amplitude in between.

Table 2. Scaling factors of virtual 1 g field and centrifugal field used in the experiments.

Case	Virtual 1G field	Centrifugal field
	μ	η
1	2.1	48.1
2	2.6	38.5
3	5.2	19.2
4	10.4	9.6
5	20.8	4.8

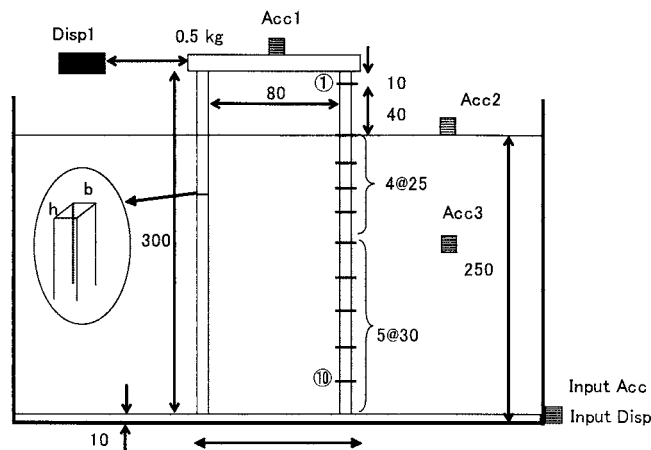


Figure 2. Cross section of centrifuge model (Units are in mm: model scale)

Table 3. Input frequency of prototype, virtual 1 g field and centrifugal field.

Case	Input frequency (Hz)		
	Prototype	Virtual 1G field	Centrifugal field
1	1.0	1.7	83.3
2		2.0	78.8
3		3.4	66.2
4		5.8	55.7
5		9.8	46.8

Table 4. Average input displacement of prototype, virtual 1 g field and centrifuge field.

Case	Amplitude of input displacement (mm)		
	Prototype	Virtual 1G field	Centrifugal field
1	51.0	16.8	0.4
2		12.0	0.3
3		4.2	0.2
4		1.5	0.2
5		0.5	0.1
1	72.0	24.1	0.5
2		17.2	0.4
3		6.1	0.3
4		2.1	0.2
5		0.8	0.2
1	91.0	32.2	0.7
2		23.1	0.6
3		8.1	0.4
4		2.9	0.3
5		1.0	0.2

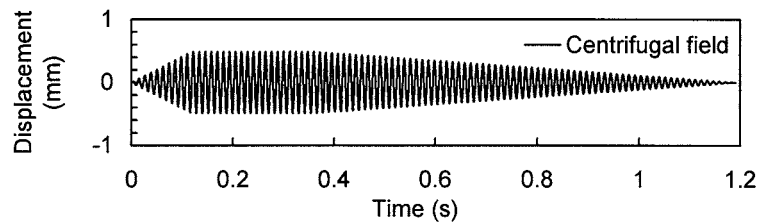


Figure 3. Example of input displacement in centrifugal field.

3. VERIFICATION OF GENERALIZED SCALING RELATION

Data obtained by the centrifuge tests are converted into the ones in prototype scale by applying the generalized scaling relation. For all the test cases, corresponding responses are supposed to be identical as long as the input motions are the same. To confirm this, Figure 4 compares average amplitudes of input displacements between specified and measured. “Specified” amplitudes are the target amplitude of each test. As shown in Table 4, these values are given as 51, 72, and 97 mm in prototype scale. “Measured” amplitudes are obtained by the gap sensor attached to the shaking table. In all cases in Figure 4, measured amplitudes are more or less off from the specified amplitude. This is due to the lack of precise control of shaking table. However, fairly good agreements are obtained for all the cases except 97 mm input of Case 2 that is 1.5 times larger than the specified amplitude.

The generalized scaling relations can be evaluated by comparing the average amplitude of measured responses. Prototype responses are compared in Figure 5(a-d) whose horizontal axis is the case number and vertical axis is the average value of measured response. If the scaling is correct, measured responses of each specified input displacement in all the cases coincide. In Figure 5(a), for the input displacement of 51 and 72 mm, almost identical amplitude is obtained for the measured input

displacement. For the input acceleration shown in Figure 5(b), average value is nearly the same except Case 2 that is slightly higher than the others. Average acceleration of Acc3 [Figure 5(c)] shows fairly good agreements for the input displacements of 51 and 72 mm of Case 3 to 5. However, for Case 1 and 2, the response is significantly lower than the others. One possible cause of this degradation is that the ground is vibrating with higher mode because input frequency in centrifugal field is 83.3 and 78.8 Hz for Case 1 and 2, respectively (Table 3). However, its effect was not clearly seen in time and frequency domain, and, therefore, thorough investigation is required. Average pile head displacements are more scattered than the other responses shown in Figure 5(a)-(c) except Case 3 to 5 of 72 mm of input displacement [Figure 5(d): (triangle makers)] which show almost the same level of response.

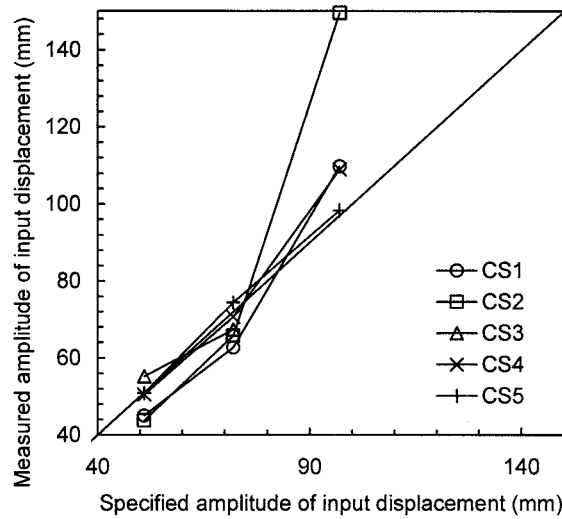


Figure 4. Specified versus measured amplitude of input displacement. Amplitude is an average.

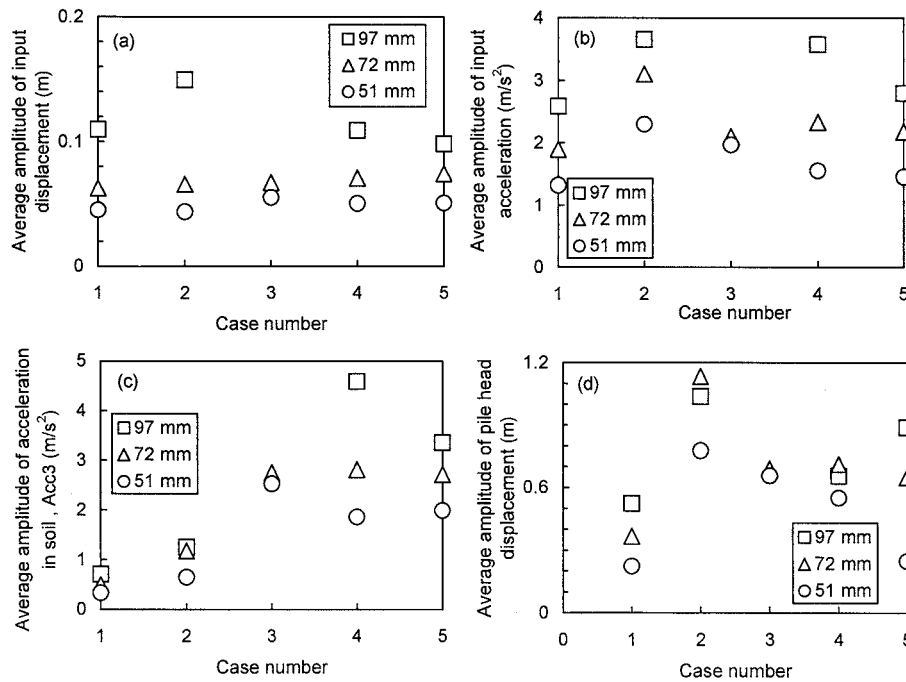


Figure 5. Average amplitude of input displacement (a), input acceleration (b), acceleration in soil, Acc3 (c), and pile head displacement (d).

Figure 6 shows vertical profiles of bending moment when the pile head displacement is absolute maximum. Profiles of Case 3 to 5 are similar in that the absolute maximum of bending moment is obtained at the depth of 13 m, while the profile of Case 1 is almost flat and of Case 2 shows reverse trend. When the input displacement becomes larger as shown in Figure 6(b) and (c), the profile of Case 4 and 5 approaches each other verifying the correctness of the generalized scaling relations.

To investigate the low amplitude of bending moment of Case 1, the horizontal scale of the profile of 72 mm of input displacement is enlarged [Figure 7(a)]. Also in Figure 7, plotted are the time histories of pile head displacement [Figure 7(b)] and bending moment at the depth of 10 m (Moment 4) [Figure 7(c)]. In these time histories, square markers indicate the time when the bending moment profile is plotted. In Figure 7, the profile with solid-square corresponds to the one at 20 s, while the one with solid-triangle is obtained by averaging over the period of 20 to 30 s. This profile shows slightly different shape of moment distribution in depth compared with Case 4 or 5 shown in Figure 6. The shape of moment distribution of Case 1 [Figure 7(a)] implies the incidence of higher mode of vibration in the model pile foundation. However, there was no evidence of the higher mode on records in both time and frequency domain.

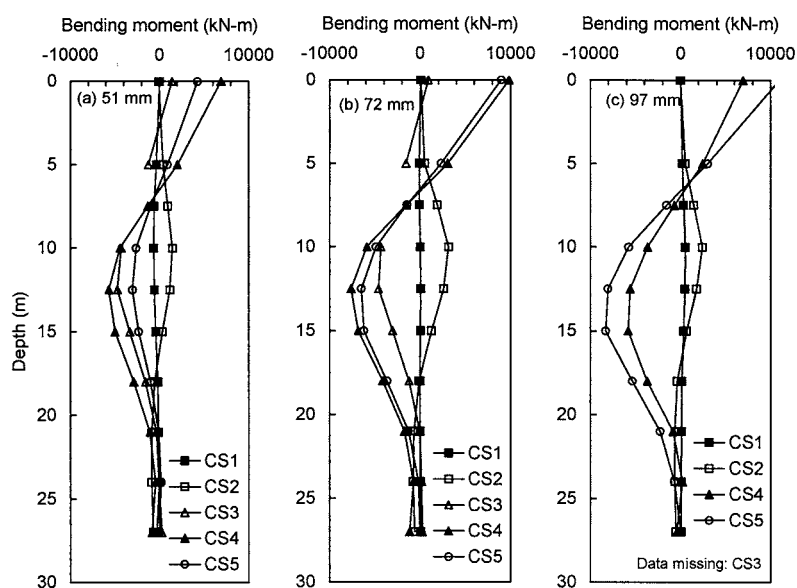


Figure 6. Vertical profile of bending moment when the pile head displacement is absolute maximum.

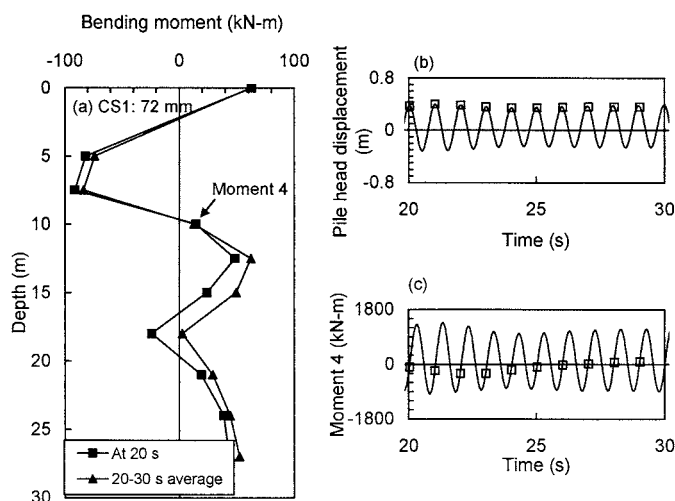


Figure 7. Vertical profile of bending moment of CS1 (specified input displacement amplitude of 72 mm) (a), time histories of pile head displacement (b) and bending moment of Moment 4 (c).

4. CONCLUSIONS

Comparing the results obtained through centrifuge tests with various combination of scaling factors, the generalized scaling relation for dynamic centrifuge tests proposed by (Iai et al. 2005) were verified conditionally. In the centrifuge tests, geometrical scale of a model pile foundation (prototype/centrifuge model) was 100 ($= \mu \eta$). Five combination of scaling factors of virtual 1 g model (μ) and centrifuge model (η) were tested. With the combination of the scaling factors, values of flexural rigidity of a pile were varied in centrifuge model. Responses in prototype scale were compared each other for five pile foundation models tested under various centrifugal accelerations.

Fairly good agreements are obtained for the amplitude of input displacement and input acceleration for all the cases, except the case of large input displacement (97 mm). Also for the case of lower centrifugal accelerations, agreements were significant for the average amplitude of acceleration in soil. Not only the average amplitude of response, but also bending moment profile of lower centrifugal accelerations shows fair agreements to justify the generalized scaling relation.

However, when the centrifugal acceleration is larger, the model ground as well as model piles might vibrate with higher mode. However, its effect was not clearly seen in time and frequency domain, and, therefore, thorough investigations on both modeling and centrifuge facility are required.

Acknowledgements:

The authors thank Mr. Kazuma Nishida for his assistance for conducting a series of centrifuge experiments as part of his graduation requirements.

References:

- Chazelas, J. L., Derkx, F., Thorel, L., Escoffier, S., Rault, G., Buttigieg, S., Cottineau, L. M., and Garnier, J. (2006), "Physical modelling of earthquakes in the LCPC centrifuge," *1st European Conference on Earthquake Engineering and Seismology*, 3-8 September, Geneva, Switzerland, ID 1064.
- Chen, S., Kabeyasawa, T., and Kabeyasawa, T. (2006), "Analytical research of full-scale reinforced concrete structure test on E-Defense," *Proceedings of the 100th Anniversary Earthquake Conference, San Francisco, California, USA, April 18-22*, 8NCEE-000666.
- Honda, T., and Towhata, I. (2006), "Study of similarity rules in centrifuge model tests on embankment during liquefaction," *The 41st Japan National Conference on Geotechnical Engineering, Kagoshima, Japan*, No. 928.
- Iai, S. (1989). "Similitude for shaking table tests on soil-structure-fluid model in 1g gravitational field," *Soils and Foundations*, **29**(1), 105-118.
- Iai, S., Tobita, T., and Nakahara, T. (2005), "Generalised scaling relations for dynamic centrifuge tests," *Géotechnique*, **55**(5), 355-362.
- Suzuki, H., and Tokimatsu, K. (2007), "Soil-pile-structure interaction during multi-dimensional shaking through physical model tests using E-Defense facility," *The Fourth International Conference on Urban Earthquake Engineering*.
- Suzuki, Y., Saito, Y., Okuda, T., Ogasawara, M., and Suda, T. (2006), "Large-scale shaking table tests of Kyoto's traditional wood houses," *The Annual Conference of Disaster Prevention Research Institute, Kyoto University*, E-07.

STRESS REDUCTION FACTORS IN SIMPLIFIED LIQUEFACTION SUSCEPTIBILITY ANALYSIS

A. Ansal¹⁾ and G.Tönük²⁾

1) Professor, Kandilli Observatory and Earthquake Research Institute, Boğaziçi University, Istanbul, Turkey

2) Ph.D. Student, Kandilli Observatory and Earthquake Research Institute, Boğaziçi University, Istanbul, Turkey
ansal@boun.edu.tr, gokce.tonuk@boun.edu.tr

Abstract: Two variables are required for the assessment of liquefaction susceptibility of sandy soil layers; the seismic demand expressed in terms of cyclic stress ratio, CSR; and the capacity of the soil layers to resist liquefaction, expressed in terms of cyclic resistance ratio, CRR. The variation of the safety factors with depth were determined for set of soil profiles where CSRs were calculated using stress reduction factors proposed in the literature and CRRs based on SPT blow counts. In addition, CSRs were also determined based on site response analyses. The results are compared and the differences are discussed in terms of the final evaluation of the liquefaction susceptibility.

1. INTRODUCTION

Liquefaction of soil layers has been a major cause of damage to soil structures, lifeline facilities and building foundations during the past earthquakes. The approach that has gained wide acceptance within the framework of urban planning is to establish liquefaction susceptibility microzonation maps to mitigate possible earthquake damage related to liquefaction (Ansal and Tönük, 2006, 2005; Ansal et al., 2004; Todorovska, 1998, Yasuda et al., 1995; Kavazanjian et al., 1985).

Two variables are required for the assessment of liquefaction susceptibility: (1) seismic demand on the soil layers, expressed in terms of cyclic stress ratio, CSR; and (2) capacity of the soil layers to resist liquefaction, expressed in terms of cyclic resistance ratio, CRR. Cyclic stress ratio is defined as the ratio of the average cyclic shear stress induced by earthquake excitations to the effective normal stress acting at the beginning of shaking on the plane where shear stress is applied.

The site response analysis code (Shake91), originally developed by Schnabel et al. (1972) later updated by Idriss and Sun (1992) was used to evaluate the effects of local soil stratification and to calculate the peak horizontal accelerations on the ground surface as well as the variation of maximum shear stress with depth. Previously recorded hazard compatible (in terms of estimated magnitude, rupture distance and fault mechanism) acceleration records were used as outcrop motion for site response analyses. These input acceleration time histories were scaled with respect to the peak acceleration obtained from earthquake hazard study (Ansal et al., 2006; Durukal et al., 2006).

2. EVALUATION OF LIQUEFACTION SUSCEPTIBILITY

The oldest and still the most widely used approach is the simplified procedure for assessing

liquefaction susceptibility originally proposed by Seed and Idriss (1971) based on SPT N-values and cyclic stress ratio calculated using stress reduction factor. The cyclic stress ratio, CSR, is expressed as;

$$CSR = \frac{\tau_{av}}{\sigma'_v} = 0.65 \frac{a_{max}}{g} \frac{\sigma_v}{\sigma'_v} r_d \quad (1)$$

where a_{max} = peak horizontal acceleration on the ground surface; g = acceleration of gravity; σ_v = total vertical overburden stress; σ'_v = effective vertical overburden stress; r_d = stress reduction factor.

There have been various studies concerning the definition of stress reduction factor in the literature (Cetin, et al., 2004; Idriss and Boulanger, 2003; Youd et al., 2001; Liao and Whitman, 1986). In most of these studies, different formulations were proposed to calculate the variation of cyclic stress ratio that would be induced by the design earthquake and almost all of them are only dependent on the depth in the soil profile. In the recent formulation proposed by Cetin et al. (2004), the effect of other factors such as peak acceleration on the ground surface, magnitude of the design earthquake, and soil stiffness at the top 12m in addition to the depth from the ground surface were considered as factors controlling the variation of stress reduction factor or in more general terms variation of maximum shear stresses with depth. Some of these different definitions for r_d may be given as;

a. by Liao and Whitman (1986)

$$\begin{aligned} r_d &= (1.00 - 0.00765z) & \text{for } z \leq 9.15\text{m} \\ r_d &= (1.174 - 0.00267z) & \text{for } 9.15\text{m} < z < 23\text{m} \end{aligned} \quad (2)$$

b. by Idriss (1999)

$$\begin{aligned} \ln(r_d) &= \alpha(z) + \beta(z)M & \text{for } z \leq 34\text{m} \\ \alpha(z) &= -1.012 - 1.126 \sin\left(\frac{z}{11.73} + 5.133\right) \\ \beta(z) &= 0.106 - 0.118 \sin\left(\frac{z}{11.28} + 5.142\right) \\ r_d &= 0.12 \exp(0.22M) & \text{for } z > 34\text{m} \end{aligned} \quad (3)$$

c. by Youd et al. (2001)

$$r_d = \frac{(1.00 - 0.4113z^{0.5} + 0.04052z + 0.001753z^{1.5})}{(1.00 - 0.4177z^{0.5} + 0.05729z - 0.006205z^{1.5} + 0.00121z^2)} \quad (4)$$

d. by Cetin et al. (2004)

$$r_d = \frac{\left\{ 1.00 + \frac{-23.013 - 2.949PGA/g + 0.999M + 0.0525V_{s12}}{16.258 + 0.201e^{0.341(-z + 0.0785V_{s12} + 7.586)}} \right\}}{\left\{ 1.00 + \frac{-23.013 - 2.949PGA/g + 0.999M + 0.0525V_{s12}}{16.258 + 0.201e^{0.341(0.0785V_{s12} + 7.586)}} \right\}} \quad (5)$$

where, z is the depth below ground surface in meters, velocity (V_{s12}) is the average shear wave velocity at top 12m in m/s, PGA is peak horizontal acceleration, M is the magnitude.

In the first stage of the study a set of borings were analysed to observe the variation of cyclic stress ratio CSR with depth based on site response analyses (Ansal et al., 2005). As input motion for the

site response analyses earthquake hazard compatible previously recorded three real acceleration time histories were used. These records were scaled with respect to peak ground acceleration determined by the earthquake hazard study conducted for the region. The CSR variations were calculated as the average of the CSRs from three site response analyses. The comparison of the variation of CSR calculated using the formulation proposed by Youd et al., 2001, Cetin et al. (2004) and site response analyses given in Figure 1 indicates significant differences among the three approaches. The differences are not consistent and it depends very much on the properties of the soil stratification, shear wave velocity profiles and peak ground accelerations. In general, CSRs calculated by site response analyses were higher while the formulation suggested by Cetin et al. (2004) gave lower values.

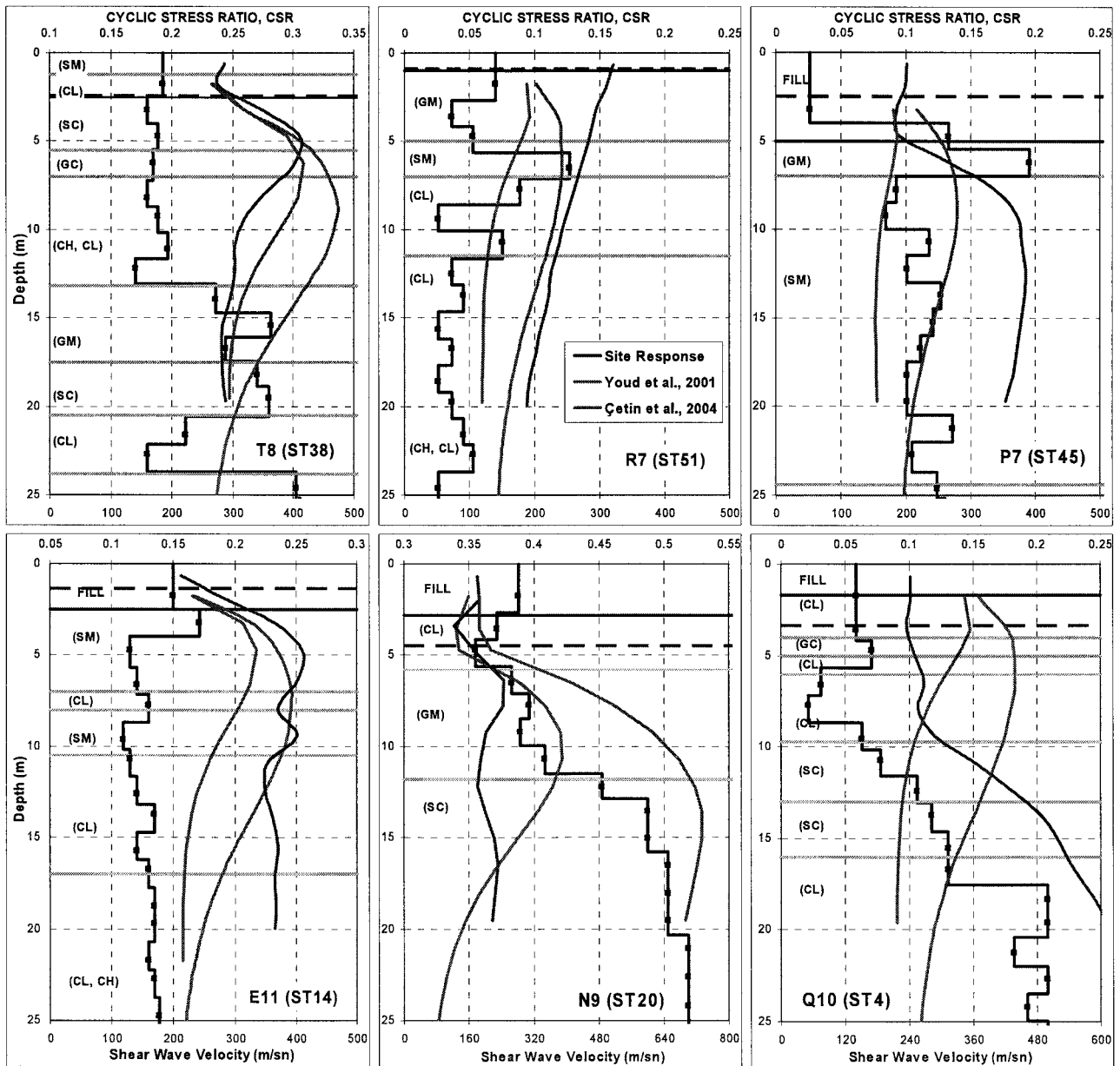


Figure 1. CSR by site response analyses and by the simplified procedures according to Youd et al., 2001 and Cetin et al., 2004

The CSRs calculated by the procedure suggested by Youd et al., 2001 depends only on depth of the element and ground water level and incapable to account for the changes in the soil profile. Depending on the soil stratification and stiffness of the soil layers the variation of CSRs obtained by

site response analysis could be considered more reliable.

It was also interesting to observe the variation of safety factors with respect to liquefaction susceptibility calculated using the r_d formulation proposed by Youd et al. (2001) and Cetin et al. (2004) in comparison to site response analyses as shown in Figure 2 for the same soil profiles. Even though the differences in the CSR variations appear significant (Figure 1), these differences are not reflected in the safety factor variations (Figure 2) except in one case (Boring P7) where the safety factors calculated by site response analysis and using stress reduction factors are radically different.

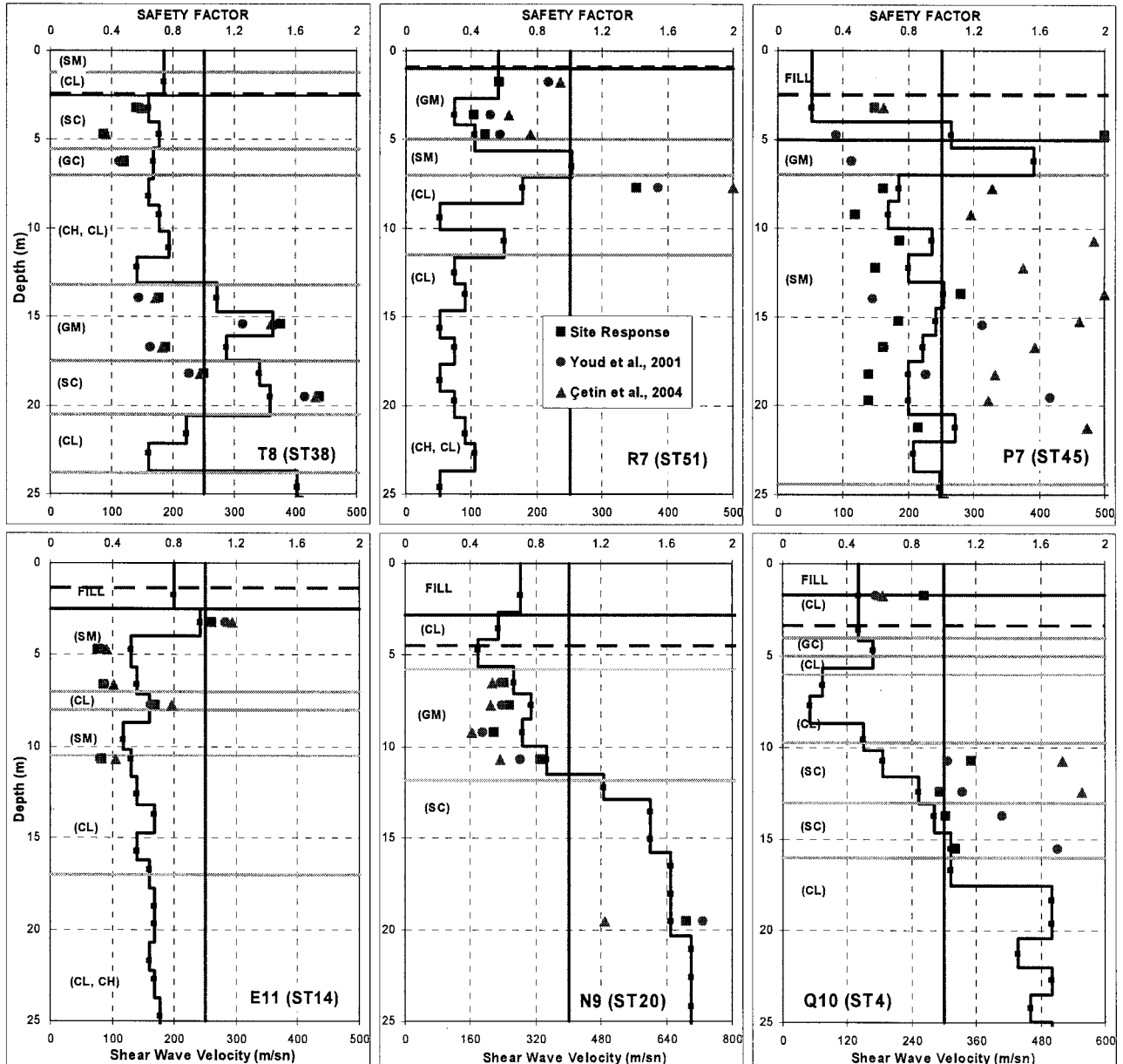


Figure 2. Safety factors with respect to liquefaction susceptibility by site response analyses and by the simplified procedures according to Youd et al. (2001) and Cetin et al. (2004)

In the second stage of the study, the effect of input motion on liquefaction susceptibility was evaluated for set of borings. In this case as shown in Figure 3, the variation of SPT blow counts as well as shear wave velocity profile determined by PS Logging in-hole seismic survey was utilised. Site response analyses were conducted using 21 previously recorded acceleration time histories that are compatible with the earthquake hazard for the investigated site. All of these acceleration records

were scaled to the same rock outcrop peak ground acceleration estimated by the earthquake hazard study for the region. The variations of stress reduction factor with depth back calculated from the site response analyses are shown in Figure 3. It is interesting to observe that even though all the real records selected are compatible with the earthquake hazard for the investigated site and even though they were all scaled to the same peak ground acceleration, the variations of back calculated stress reduction factors and thus cyclic stress ratio CSR are significantly different.

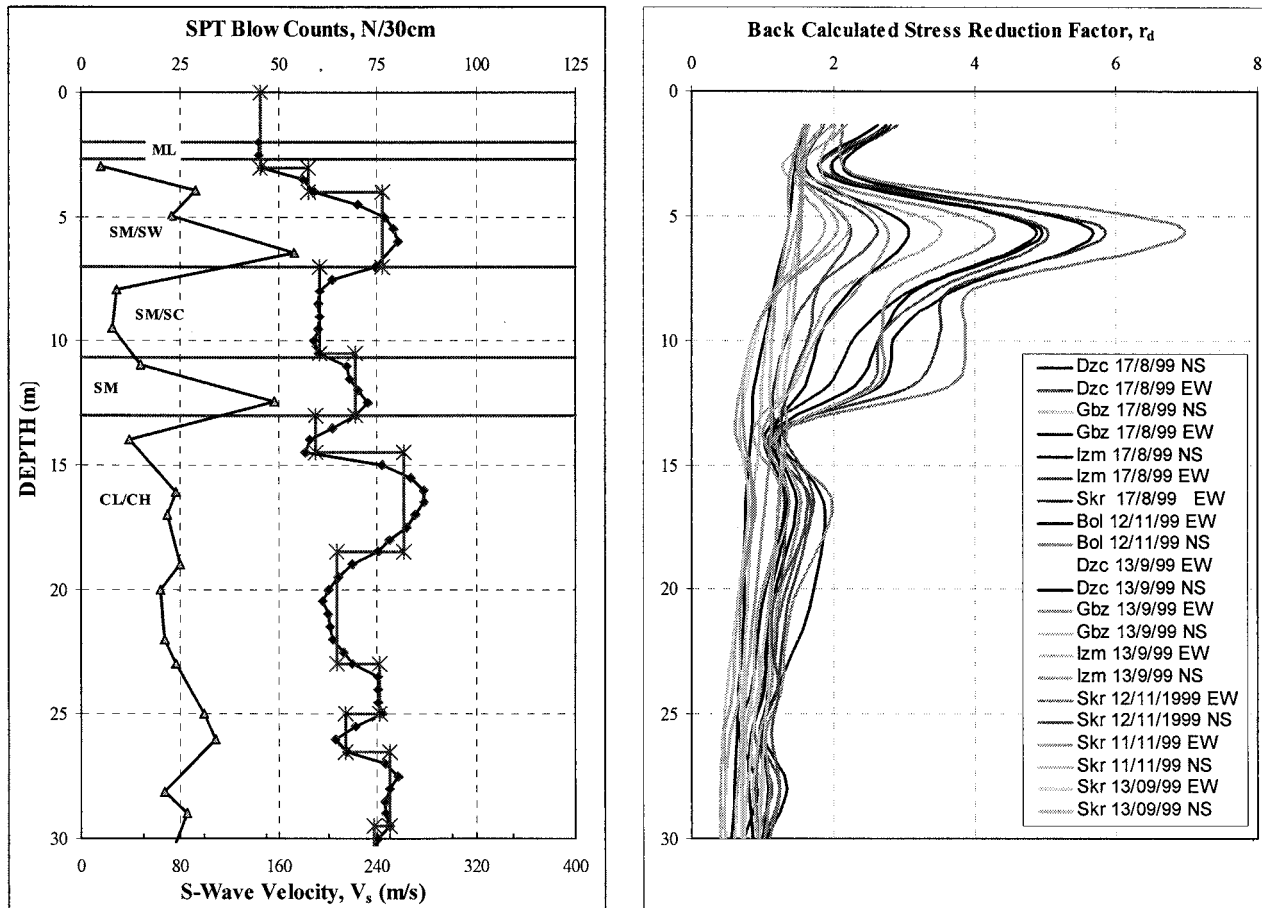


Figure 3. (a) A soil profile and (b) the results of site response analyses to evaluate liquefaction susceptibility

The variation of cyclic stress ratios calculated by Youd et al. (2001), Liao and Whitman (1986), Idriss (1999) and by site response analysis using Skr 12/11/1999 acceleration time history that yielded the highest CSRs (Figure 3) are given in Figure 4(a) along with the respective safety factors calculated. The variation of safety factors calculated based on site response analyses for sandy soil layers given in Figure 3(a) for 21 different input motions are shown in Figure 4(b) with respect to the variation of SPT blow counts.

It is interesting to observe that in terms of safety factors, the end results do not reflect the effects as much as the variability observed in CSRs as shown in Figure 4(a) or the stress reduction factor as shown in Figure 3(b) on the safety factors calculated shown in Figure 4(b).

There is a variability concerning the peak ground accelerations calculated by site response analyses. And if these PGAs are used along with the simplified liquefaction susceptibility analyses the variation of safety factors can have much larger range. For example in the case of 21 site response analyses conducted for the soil profile given in Figure 3(a), the calculated PGAs on the ground surface varied between the maximum of 0.88g and minimum of 0.44g, with the average of 0.63g and standard deviation of 0.12g.

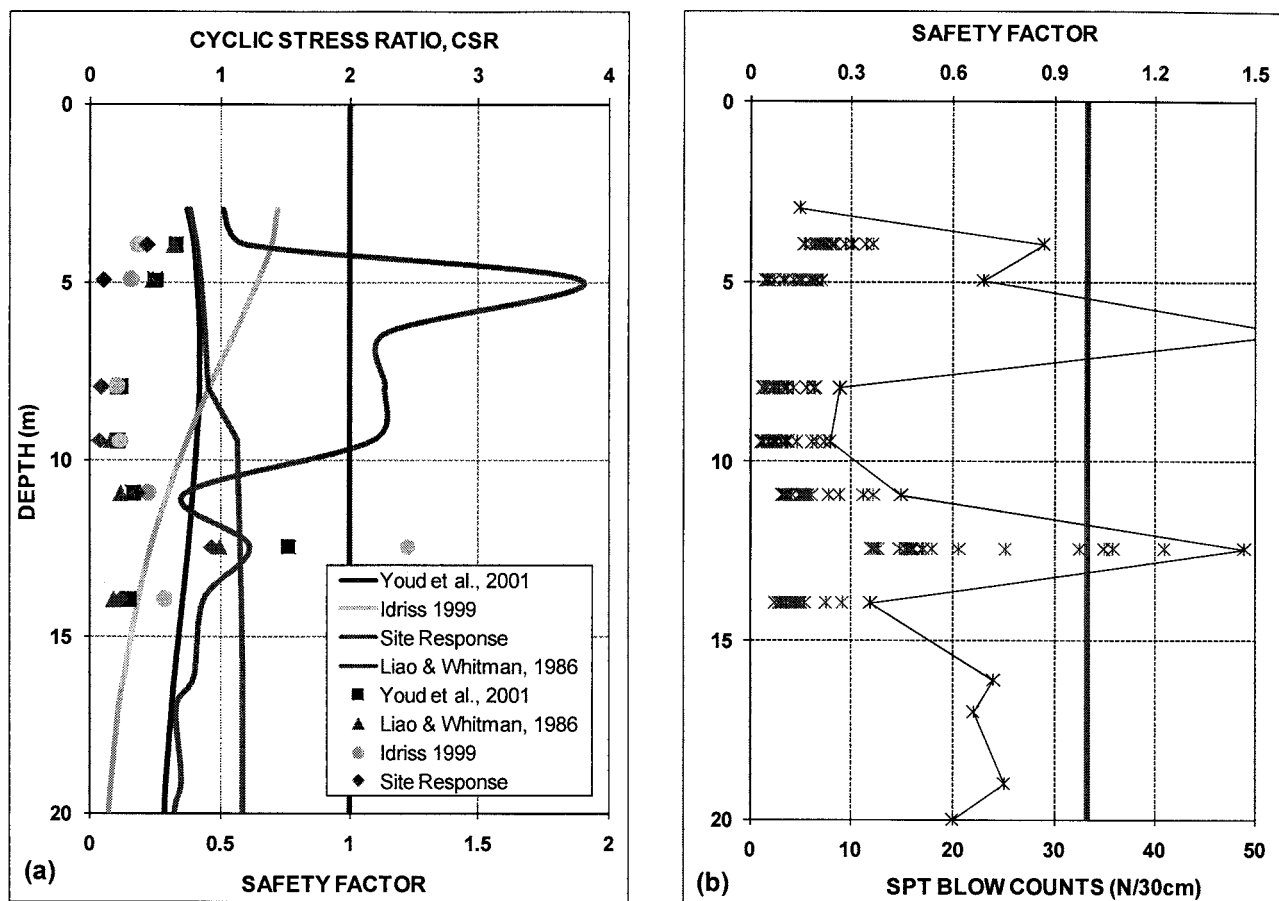


Figure 4. (a) Variation of CSRs and Safety Factors for liquefaction susceptibility with respect to different formulation
(b) Variation of Safety Factors for liquefaction susceptibility based on 21 site response analyses

3. CONCLUSIONS

The evaluation of liquefaction susceptibility of soil layers in nature for engineering purposes is performed based on empirical procedures developed using Standard Penetration Test results obtained by in-situ testing. One of the most popular procedures was originally developed by Seed and Idriss (1971) and later summarised by Youd et al., 2001. Two variables are required for the assessment of liquefaction resistance of sandy soil layers; the seismic demand expressed in terms of cyclic stress ratio, CSR; and the capacity of the soil layers to resist liquefaction, expressed in terms of cyclic resistance ratio, CRR. The variation of the safety factors with depth were determined for set of boreholes where CSR is calculated using stress reduction factors and CRR based on SPT blow counts. In addition CSRs were calculated based on site response analyses and using the stress reduction formulation suggested by Cetin et al., (2004). As expected all three procedures gave different results. Assuming that site response analyses would yield more reliable results, the two procedures suggested by Youd et al. (2001) and Cetin et al. (2004) yielded results on the unsafe side. Thus even though r_d procedures to estimate the variation of CSR with depth are simpler and could be applied much faster, the calculated safety factors may not always be on the safe side.

References:

- Ansal, A. and Tönük, G. (2006), "Evaluation of Liquefaction Susceptibility for Microzonation and Urban Planning," *Proceedings of Int. Conf. on Geohazards - Technical, Economical and Social Risks*, Lillhammer, Norway.
- Ansal, A., Durukal E., Tönük G. (2006), "Selection and Scaling of Real Acceleration Time Histories for Site Response Analyses," *Proceedings of ETC12 Workshop*, Athens, Greece.
- Ansal, A. and Tönük, G. (2005), "Liquefaction Susceptibility and Microzonation," *Proceedings of Int. Con. on Problematic Soils, Eastern Mediterranean University*, Famagusta, N. Cyprus.
- Ansal, A., Tönük, G., and Bayrakli, Y. (2005), "Microzonation for Site Conditions for Bakirköy, Gemlik, Bandırma, Tekirdağ, Eskisehir and Körfez, Microzonation and Hazard Vulnerability Studies For Disaster Mitigation in Pilot Municipalities," Bogazici University, Kandilli Observatory and Earthquake Engineering Research Institute, Turkey.
- Ansal, A., Erdik, M., Studer, J., Springman, S., Laue, J., Buchheister, J., Giardini, D., Faeh, D., Koksall, D. (2004), "Seismic Microzonation for Earthquake Risk Mitigation in Turkey," *Proceedings of 13th World Conference of Earthquake Engineering*, Paper.1428. Canada.
- Cetin, K.O., Seed, R.B., and Der Kiureghian, A., Tokimatsu, K., Harder, L.F., Kayen, R.E. Moss, R.E.S. (2004), "Standard penetration Test-Based Probabilistic and Deterministic Assessment of Seismic Soil Liquefaction Potential," *ASCE, JGGE*, 130(12), pp1314-1340.
- Durukal, E., Ansal, A., and Tönük, G. (2006), "Effect of Ground Motion Scaling and Uncertainties in Site Characterisation on Site Response Analyses," *Proceedings of the 100th Anniversary Earthquake Con. Commemorating the 1906 San Francisco Earthquake*, USA.
- Idriss, I. M. and Boulanger, R. W. (2003) "Semi-Empirical Procedures For Evaluating Liquefaction Potential During Earthquakes," *Proceedings of the 11th ICSDEE*, pp 32 – 56.
- Idriss, I.M. (1999) "TRB Workshop on New Approaches to Liquefaction Analysis", *Publ. No. FHWA-RD-99-165*, Transportation Research Board (TRB), Federal Highway Administration, Washington, D. C. (on CD-ROM),
- Idriss, I. M. and Sun J. I. (1992) "Shake91, A Computer Program for Conducting Equivalent Linear Seismic Response Analysis of Horizontally Layered Soil Deposits," Modified based on the original SHAKE program by Schnabel, Lysmer and Seed, 1972.
- Kavazanjian, E. Jr., Roth, R.A., and Echezuria, H. (1985), "Liquefaction potential mapping for San Francisco," *J. Geotech. Eng. ASCE*, 111(1), pp. 54-76.
- Liao, S.S.C. and Whitman, R.V. (1986) "Overburden correction factor OS for SPT in sand," *ASCE, Journal of Geotechnical Engineering*, 112(3), pp. 373-377.
- Schnabel, P.B., Lysmer, J. and Seed, H.B. (1972) "Shake-A Computer Program for Earthquake Analysis of Horizontally Layered Sites," *EERC Report No. 72-12*, Uni. of Cal., Berkeley.
- Seed, H.B., Idriss, I.M. (1971), "Simplified Procedure for Evaluating Soil Liquefaction Potential," *Journal of the Soil Mechanics and Foundations Div. ASCE*, 97, 1249-1273.
- Todorovska, M.I. (1998), "Quick reference liquefaction opportunity map for a metropolitan area," *Proceedings of 3rd ASCE Speciality Conf. on Geotech. Earthquake Eng. Soil Dynamics*, ASCE Spl. Pub. No., 75(1), pp. 116-127.
- Yasuda, S., Negishi, S., Yoshikawa, Y., and Morimoto, I. (1995) "Microzonation for liquefaction to detect liquefaction sites immediately after an earthquake," *Proc. of the 5th Int. Conference on Seismic Zonation*, Nice, FRANCE, pp. 657-664.
- Youd, T.L., Idriss, I.M., Andrus, R.D., Arango, I., Castro, G., Christian, J.T., Dobry, R., Finn, L.W.D., Harder Jr., L.F., Hynes, M.E., Ishihara, K., Koester, J.P., Liao, S.S.C., Marcuson III, W.F., Martin, G.R., Mitchell, J.K., Moriwaki, Y., Power, M.S., Robertson, P.K., Seed, R.B., Stokoe II., K.H. (2001), "Liquefaction Resistance of Soils: Summary Report from the 1996 NCEER and 1998 NCEER/NSF Workshops on Evaluation of Liquefaction Resistance of Soils," *JGGE*, 127(10).

A TWO MOBILIZED-PLANE MODEL FOR SOIL LIQUEFACTION ANALYSIS¹

S.-S. Park¹⁾, P. M. Byrne²⁾, and D. Wijewickreme³⁾

1) Post-Doctoral Researcher, Dept. of Civil Engineering, Kyungpook National University, Korea

2) Emeritus Professor, Dept. of Civil Engineering, University of British Columbia, Vancouver, Canada

3) Associate Professor, Dept. of Civil Engineering, University of British Columbia, Vancouver, Canada
sungpark@knu.ac.kr, pmb@civil.ubc.ca, dwije@civil.ubc.ca

Abstract: A Two Mobilized-plane Model is presented for monotonic and cyclic soil response including liquefaction. This model is based on two mobilized planes: a plane of maximum shear stress, which rotates, and a horizontal plane which is spatially fixed. By controlling two mobilized planes, the model can simulate the principal stress rotation effect associated with simple shear loading from different K_0 states, which can significantly influence soil behavior. The proposed model gives a similar skeleton behavior for soils having the same mean stress, regardless of K_0 conditions as observed in laboratory tests. The soil skeleton behavior observed in cyclic drained simple shear tests, including compaction during unloading and dilation at large strain is captured in the model. Undrained monotonic and cyclic response is predicted by imposing the volumetric constraint of the water on the drained or skeleton behavior. This constitutive model is incorporated into the dynamic coupled stress-flow finite difference program FLAC (Fast Lagrangian Analysis of Continua). The model was first calibrated with drained monotonic and cyclic simple shear tests on Fraser River sand, and verified by comparing predicted and measured undrained monotonic and cyclic behavior of Fraser River sand.

1. INTRODUCTION

The effect of principal stress rotation significantly influences soil behavior and has received substantial attention since Arthur et al. (1980). A few different types of numerical models considering principal stress rotation effects have been proposed. These are mainly based on plasticity. One of them is a multi-laminate model proposed by Pande and Sharma (1983). Recently, Lee and Pande (2004) presented its extension to soil liquefaction analysis. This model was originally proposed to study rock joint behavior by considering many slip planes. Alternatively, Matsuoka (1974) proposed a similar idea but a different concept called multimechanism that used only a maximum obliquity plane, $45 + \phi / 2$ for three different shearing mechanisms. Each shearing mechanism is based on two of three principal stresses (i.e. σ'_1 and σ'_2 , σ'_2 and σ'_3 , σ'_3 and σ'_1). Kabilamany and Ishihara (1991) also proposed a similar concept in three dimensional stress space. In their models, plastic strains from three mechanisms are independently produced and superimposed. The practicality of utilizing such numerical models depends on their simplicity and robustness (Kolymbas 2000). This is particularly so for dynamic analyses. Consequently, the practical application of models for dynamic analyses has been limited to few cases.

A plasticity based constitutive model has been developed at the University of British Columbia (UBC) to handle plastic unloading and principal stress rotation associated with anisotropic

¹ A similar version of this paper has been presented at the 16th ICSMFE in Osaka.

consolidation, or K_0 state and is presented here. The proposed model uses two mobilized planes, a maximum shear stress plane which rotates with as the direction of the principal stress rotates, and a horizontal plane which is spatially fixed. Under simple shear conditions the plane of maximum shear is initially at 45 degrees to the horizontal and as the shear stress is applied the plane rotates and becomes nearly horizontal at failure. This concept is referred to as a Two Mobilized-plane Model. The characteristics of this model and its formulation are introduced, and a comparison with laboratory data is presented.

2. SIMPLE SHEAR BEHAVIOR UNDER ISOTROPIC AND K_0 CONDITIONS AND ITS MODELLING

Rotation of principal stresses occurs in simple shear loading and its effect depends very much on the initial K_0 consolidation state. If $K_0 = 1.0$, then as soon as any horizontal shear stress is applied, the horizontal plane become the plane of maximum shear and essentially remains so for the rest of the loading. For this case the plane of maximum shear is horizontal for the duration of loading, and there is no rotation effect. Classical plasticity with a single rotating plane of maximum shear simulates this condition very well. If $K_0 = 0.5$, then a large shear stress acts on the 45 degree plane. As the horizontal shear stress is applied, the plane of maximum shear gradually rotates and becomes approximately horizontal at failure (Roscoe 1970). Thus, there is a gradual rotation of principal stress during the loading process. A classical plasticity approach with a single plane cannot capture the observed response in this case. We have found that the observed response can be captured by adding a plastic contribution from the horizontal plane.

From drained monotonic torsional tests using hollow cylindrical samples, Wijewickreme and Vaid (2004) found that the shear stress-shear strain behavior on a horizontal plane under the same mean stress is independent of stress path at small strain ranges (shear strain $\gamma < 0.5\%$) for loose sand. In simple shear, this finding can infer that shear stress-strain behavior of loose sands is the same at small strain level regardless of K_0 state as long as initial mean stresses are the same.

Ishihara (1996) showed that K_0 has a significant effect on liquefaction resistance of sands based on a series of torsional tests with lateral confinement. He found that the cyclic resistance ratio, τ/σ_{v0}' where σ_{v0}' is the initial vertical effective stress, under $K_0 = 1.0$ condition is stiffer and stronger than that observed under $K_0 = 0.5$ condition. On the other hand, there was no significant difference between the $K_0 = 1.0$ and 0.5 conditions when the cyclic resistance was examined in terms of τ/σ_{m0}' where σ_{m0}' is the initial mean effective stress. Iai et al. (1992) considered K_0 consolidated elements using a generalized plasticity approach. They mentioned that conventional plasticity models cannot simulate $K_0 = 0.5$ simple shear tests because they involve effects of rotation of principal stress. The proposed plasticity model can simulate rotation effects associated with K_0 simple shear loading by incorporating two mobilized planes rather than one. Numerical simulations under two K_0 conditions, 0.5 and 1.0, are compared with measured liquefaction behavior.

The proposed model referred to as a Two Mobilized-plane Model is an extension of a simpler model called UBCSAND to include plastic unloading and rotation of principal planes associated with simple shear loading. UBCSAND originally considered unloading as elastic. From a practical point of view, elastic unloading may be adequate for preliminary analysis. However, laboratory data indicate that significant plastic deformation always occurs during the unloading phase. Plastic unloading is particularly important following a large stress cycle that has induced dilation. In the proposed constitutive model, plastic unloading is incorporated by mobilizing plastic deformation on a horizontal plane.

3. A TWO MOBILIZED-PLANE MODEL

The UBCSAND modifies the Mohr-Coulomb model incorporated in FLAC (Fast Lagrangian Analysis of Continua) Version 4.0 (Itasca 2000) to incorporate the plastic strains that occur at all stages of loading. This model has been substantially improved to better model observed sand behavior and include the effects of rotation of principal planes or K_0 effect, and plastic unloading as mentioned earlier. These two factors incorporated into the Two Mobilized-plane Model are presented in this paper. It is also referred to as UBCSAND2 from its extension of UBCSAND. The concept and formulations of this model are described in this section including plastic deformations mobilized on two planes.

3.1 Concept of Two Mobilized-plane Model

The concept of Two Mobilized-plane Model is described here. Shear stress increments on two planes causing plastic strains are illustrated in Figure 1 for simple shear conditions with $K_0 = 0.5$. Figure 1(a) represents conditions at the start of shearing when $\tau_{xy} = 0$ and a small increment $\Delta\tau_{xy}$ is applied. In this case the plane of maximum shear is at 45 degrees ($\beta = 45^\circ$) as illustrated in Figures 1(a) and 2(a), and while there is a large shear stress from the K_0 condition, the increments of shear and normal stresses $\Delta\tau$ and $\Delta\sigma$ on this plane are both zero, and hence no plastic strains are predicted. This results in an initial very stiff elastic response from classical plasticity based on a single plane. However, the stress increment on the horizontal plane, $\Delta\tau_{xy}$ will cause plastic strains on the horizontal plane and all other planes except for the 45 plane. When this second plane is considered, a much softer response is predicted as shown in Figure 3, condition A.

A later stage of loading is depicted in Figure 1(b). Here τ_{xy} is approaching its failure value and the plane of maximum shear has swung around to become nearly horizontal as illustrated in Figures 1(b) and 2(b). Now the $\Delta\tau \approx \Delta\tau_{xy}$ and both planes essentially coincide. Consideration of both planes would essentially predict double the plastic strain. This is accounted for by gradually phasing out the plastic strain increment from the horizontal plane as the plane of maximum shear becomes horizontal. This stress strain condition is depicted as condition B on Figure 3. Note that if $K_0 = 1$ then the plane of maximum shear becomes horizontal as soon as the first increment of $\Delta\tau_{xy}$ is applied and the horizontal plane contribution is not needed. It is depicted in Figure 2(b).

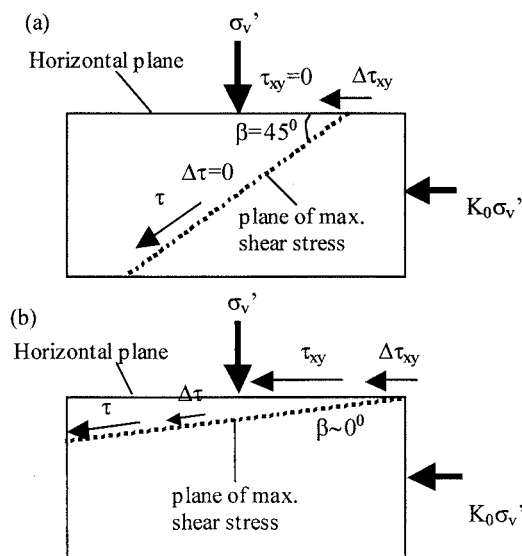


Figure 1 Stress conditions on two mobilized planes: (a) at small strain level and (b) at large strain level

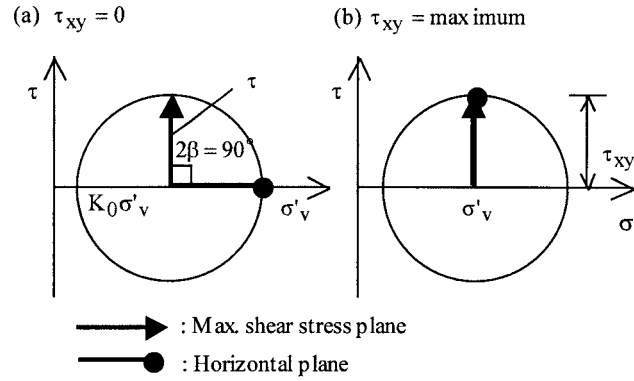


Figure 2 Rotation of the plane of maximum shear stress under K_0 condition

In summary, for simple shear conditions, the predicted response from classical plasticity will be too stiff if only the plane of maximum shear is considered as depicted in Figure 3. By including the plastic strain increments from the horizontal plane a softer response in keeping with observed response is predicted. For the special case of $K_0 = 1$, the plane of maximum shear is approximately horizontal throughout simple shear loading, and there is no need to consider a second plane. For cyclic triaxial tests the direction of principle stress remains vertical and there is no rotation of principle stress and no need to consider a second plane. However, earthquakes induced loading conditions are much closer to simple shear than conventional triaxial loading, and it is important therefore to consider a second plane for seismic loading.

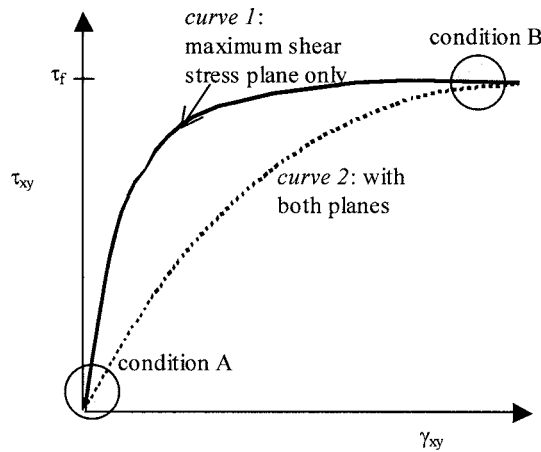


Figure 3 Shear stress-strain curves using two mobilized planes under K_0 condition

3.2 Elastic Behavior

Elastic behavior is assumed isotropic and expressed in terms of bulk and shear moduli. The elastic bulk modulus, B , and shear modulus, G , are stress level dependent and described by the following relations, where κ_B^e and κ_G^e are modulus numbers, P_A is atmospheric pressure, and σ'_m is the mean effective stress:

$$B = K_B^e \cdot P_A \cdot \left(\frac{\sigma'_m}{P_A} \right)^{0.5} \quad (1)$$

$$G = K_G^e \cdot P_A \cdot \left(\frac{\sigma'_m}{P_A} \right)^{0.5} \quad (2)$$

3.3 Plastic Behavior on Maximum Shear Stress Plane

The formulation is based on classical plasticity. Yield loci are radial lines from the origin of stress space corresponding to the mobilized friction angle. The proposed model is a Mohr-Coulomb type of model (Vermeer 1980). Since the sine of a mobilized friction angle corresponds to the ratio of shear stress to mean stress, τ/σ'_m , yield loci f_1 are assumed to be radial lines of constant stress ratio as shown in Figure 4 and expressed by

$$f_1 = \tau_1 - \sigma'_m \cdot \sin(\phi_{mob})_1 \quad (3)$$

where τ_1 = the maximum shear stress, and $(\phi_{mob})_1$ = the friction angle mobilized on the maximum shear stress plane. Reloading induces plastic response but with a stiffened plastic shear modulus. The plastic shear modulus relates the shear stress and the plastic shear strain and is assumed to be hyperbolic with stress ratio as shown in Figure 5. Moving the yield locus from A to B in Figure 4 induces a plastic shear strain increment, $d\gamma^P$, as shown in Figure 5, and is controlled by the plastic shear modulus, G^P . The flow rule defines the direction of the plastic strain increments and is non-associated here. The plastic potential g_1 used in the flow rule is a function of dilation angle as follows:

$$g_1 = \tau_1 - \sigma'_m \cdot \sin(\psi)_1 \quad (4)$$

where $(\psi)_1$ is the dilation angle based on laboratory data and energy considerations and is approximated by

$$\sin(\psi)_1 = \sin \phi_{cv} - \sin(\phi_{mob})_1 \quad (5)$$

where ϕ_{cv} is the phase transformation or constant volume friction angle and $(\phi_{mob})_1$ describes the current yield locus. A positive value of $\sin(\psi)_1$ corresponds to contraction. Contraction occurs for stress states below ϕ_{cv} and dilation above. The associated plastic volumetric strain increment, $d\varepsilon_v^P$, is obtained from $d\gamma^P$ and the dilation angle $(\psi)_1$:

$$d\varepsilon_v^P = d\gamma^P \cdot \sin(\psi)_1 \quad (6)$$

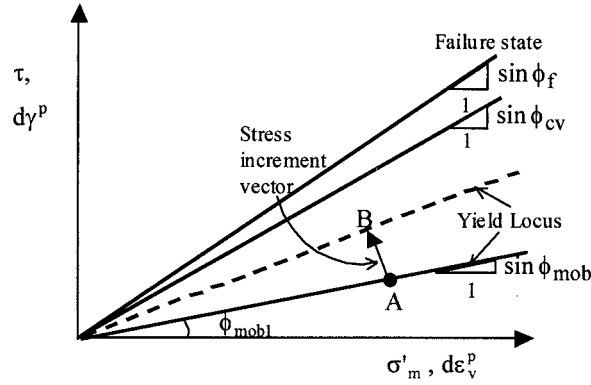


Figure 4 Failure and yield conditions

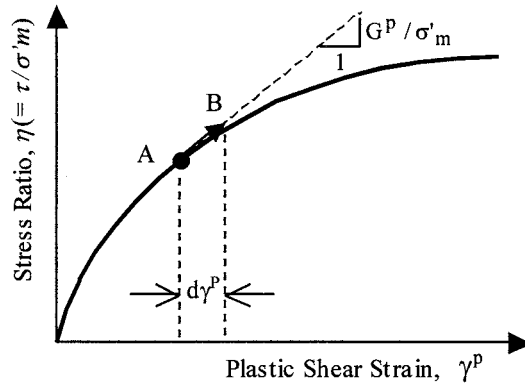


Figure 5 Hardening rule

3.4 Plastic Behavior on Horizontal Plane

Yield loci associated with the horizontal plane, f_2 , have the same shape as those for the maximum shear stress plane and are expressed by

$$f_2 = \tau_2 - \sigma'_m \cdot \sin(\phi_{mob})_2 \quad (7)$$

where $\tau_2 = \tau_{xy}$, the shear stress acting on a horizontal plane, and $(\phi_{mob})_2$ = the friction angle mobilized on a horizontal plane. The horizontal plane will contribute to both loading and unloading component. In terms of the amount of plastic strains, this contribution will be maximum when shearing starts under a K_0 state. It will gradually decrease as the plane of maximum shear stress rotates. After the maximum shear stress plane becomes horizontal, the contribution from this horizontal plane becomes zero. The plastic volumetric strain increment and dilation angle are similar to those in Eq. 5 and Eq. 6. However, the dilation angle, $\sin(\psi)_2$, is based on a mobilized angle on a horizontal plane, $\sin(\phi_{mob})_2$ and expressed by

$$\sin(\psi)_2 = \sin \phi_{cv} - \sin(\phi_{mob})_2 \quad (8)$$

3.5 Hardening Rule and Elasto-plastic Behavior

The hardening rules are similar for both maximum shear stress and horizontal planes. The only difference is the stress ratio, η . The plastic properties used by the model are the peak friction angle ϕ_P , the constant volume friction angle ϕ_{cv} , and plastic shear modulus G^P , where

$$G^P = G_i^P \cdot \left(1 - \frac{\eta}{\eta_f} R_f\right)^2 \quad (9)$$

$G_i^P = \alpha G$ and α depends on relative density, η ($= \tau_1/\sigma'_m$ or τ_2/σ'_m) is the stress ratio, η_f is the stress ratio at failure, and R_f is the failure ratio used to truncate the hyperbolic relationship.

For loading on the plane of maximum shear, the position of the yield locus $(\phi_{mob})_1$ is initially specified for each element. As the stress ratio increases and plastic strain is predicted, the yield locus for that element is pushed up by an amount $d(\phi_{mob})_1$ as given by Eq. 10.

$$d(\phi_{mob})_1 = \left(\frac{G^P}{\sigma'_m}\right) \cdot d\gamma^P \quad (10)$$

Upon unloading, plastic deformation is controlled by conditions on the horizontal plane using an incremental formulation of Eq. 7 and expressed in Eq. 11. The initial yield locus is set at the stress reversal point C in Figure 6 and plastic shear strain, $d\gamma^P$, upon unloading is predicted based on Eq. 11 until the shear stress changes sign, or reversal occurs.

$$df_2 = d\tau_2 - d\sigma'_m \cdot \sin(\phi_{mob})_2 - G^P \cdot d\gamma^P = 0 \quad (11)$$

During unloading and reloading, plastic shear moduli are based on modified shear stresses as given by Eq. 12 and illustrated in Figure 6, where $\eta^* = \tau^*/\sigma'_m$ and $\eta_f^* = \tau_f^*/\sigma'_m = (\tau_r + \tau_f)/\sigma'_m$. Reloading then occurs with a stiffened modulus:

$$G^P = G_i^P \cdot \left(1 - \frac{\eta^*}{\eta_f^*} R_f\right)^2 \quad (12)$$

The plastic volumetric strain increment is obtained from Eqs. 13 and 14 through dilation angle, $\sin(\psi)_2$. Eq. 13 is for loading and Eq. 14 is for unloading as illustrated in Figure 7. These equations are based on stress-dilatancy theory as well as the results of drained cyclic simple shear tests, Lee (1991). His results showed that dilation angle depended on stress ratio, η , and whether loading or unloading is occurring, but was not influenced by the initial density, normal stress, or number of cycles.

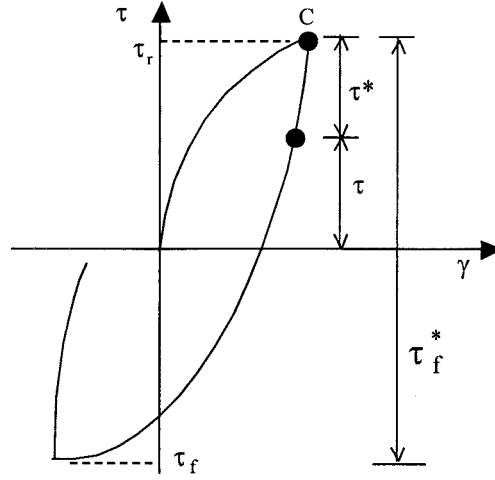


Figure 6 Stress ratio during unloading and reloading

$$\frac{d\varepsilon_v^p}{|d\gamma^p|} = (\sin \phi_{cv} - \eta) = \sin(\psi)_2 \quad (13)$$

$$\frac{d\varepsilon_v^p}{|d\gamma^p|} = (\sin \phi_{cv} + \eta) = \sin(\psi)_2 \quad (14)$$

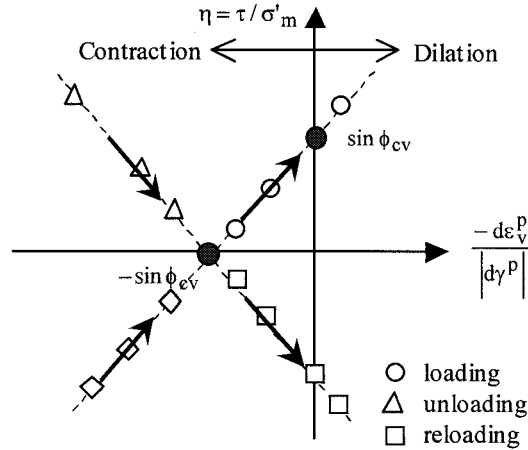


Figure 7 Shear volume coupling

Plastic shear and volumetric strain increments from both the plane of maximum shear and the horizontal plane are simply added as shown in Eq. 15.

$$(d\varepsilon^p)_k = \lambda_k \cdot \frac{\partial g_k}{\partial \sigma} \quad (15)$$

where k indicates each mobilized plane causing plastic deformation (i.e. $k = 1, 2$), λ is a scalar number, and determined by a consistency condition (i.e. $df = 0$). Plastic strain increments resulting from principal stress rotation during both loading and reloading are considered on the horizontal plane.

Their contribution gradually decreases as principal stresses rotate and becomes zero when both planes are coincident. A scalar number λ_2 on a horizontal plane is adjusted to λ_2^* as follows

$$\lambda_2^* = \lambda_2 \cdot (\cos 2\alpha_\sigma)^\chi, \text{ where } 0 \leq (\cos 2\alpha_\sigma)^\chi \leq 1.0 \quad (16)$$

where α_σ is a principal stress rotation angle from the vertical, and χ is an adjusting parameter to give a best fit. When both planes are coincident, $\lambda_2^* = 0$.

The response of sand is controlled by the skeleton behavior. A fluid (air water mix) in the pores of the sand acts as a volumetric constraint on the skeleton if drainage is curtailed. It is this constraint that causes the pore pressure rise that can lead to liquefaction. Provided the skeleton or drained behavior is appropriately modeled under monotonic and cyclic loading conditions, and the stiffness of the pore fluid (B_f) and drainage are accounted for, the liquefaction response can be predicted. This concept is incorporated in the Two Mobilized-plane Model.

4. CALIBRATION

A series of simple shear tests were performed on Fraser River sand at UBC and used as a database to calibrate the numerical model element response. Test data are available on web site (<http://www.civil.ubc.ca/liquefaction/>). The samples were prepared by air pluviation method, which is normally adopted in centrifuge tests. The details including test results can be found in Wijewickreme et al. (2005) and Sriskandakumar (2004). Drained behavior of the sand was first captured by the model as shown in Figure 8.

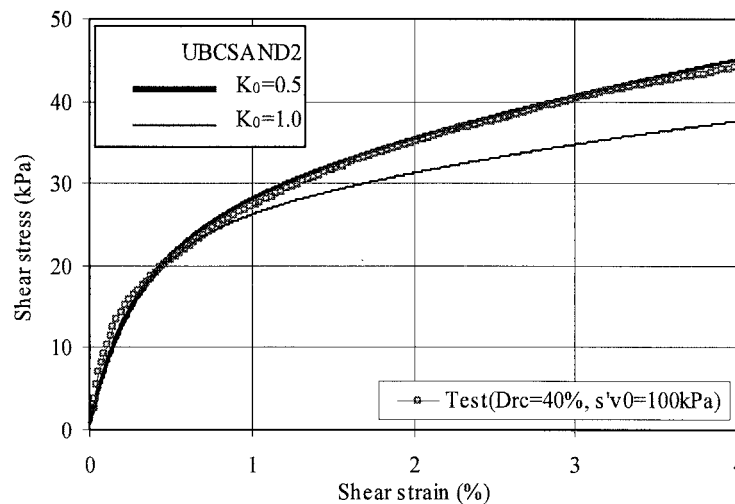


Figure 8 Numerical simulations of $K_0 = 0.5$ and 1.0 with the same initial mean stress

Two numerical predictions with the same initial mean stress for the test ($D_{rc} = 40\%$ and $\sigma'_{v0} = 100$ kPa) give similar response at small shear strain ($\gamma < 1\%$), regardless of K_0 conditions. Upon further shearing, the $K_0 = 0.5$ case (thick line) gives a stiffer response because the horizontal stress rises and increases σ'_m .

Samples were also subjected to cyclic shear for a range of cyclic stress ratios under constant volume conditions that simulate undrained response. Tests were carried out for four different CSRs (Cyclic Stress Ratio), 0.08, 0.1, 0.12 and 0.15. Typical results of measured response of $D_{rc} = 40\%$ for

CSR = 0.1 are shown in Figures 9a and 9b. Test data are shown as the heavy lines. The thin lines are the numerical predictions for $K_0 = 0.5$. When CSR = 0.1, liquefaction occurred in 6 cycles. It is observed that the first and last cycles generated large excess pore pressures. Once the pore pressure ratio reached unity, large cyclic strains developed referred to as cyclic mobility.

The CSR versus number of cycles to liquefaction is shown in Figure 10. Liquefaction triggering was defined as $\gamma > 3.75\%$, and at this point R_u (pore pressure ratio) is 90 - 95 %. This strain level is equivalent to reaching a 2.5% single-amplitude axial strain in a triaxial sample, which also is a definition for liquefaction previously suggested by the National Research Council of United States (NRC 1985).

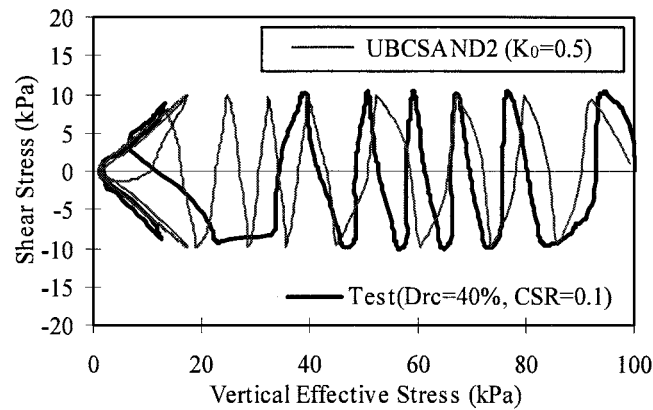


Figure 9a Predicted stress path under $K_0 = 0.5$ and test result

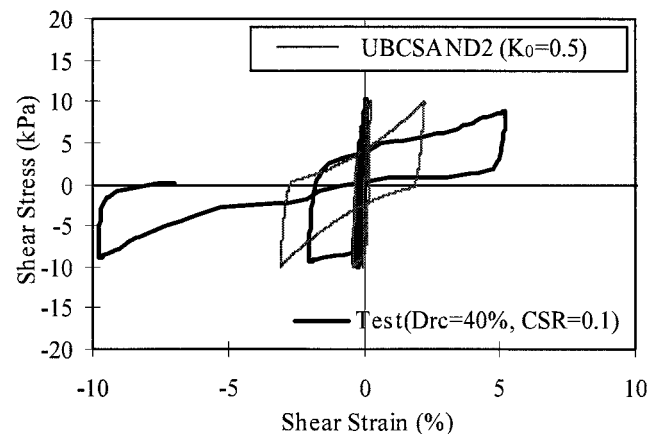


Figure 9b Predicted stress-strain curve under $K_0 = 0.5$ and test result

The calibration was carried out in the same way as the tests, i.e. under constant volume. The test sample was subjected to an initial vertical stress of 100 kPa under K_0 conditions. It was assumed that the initial horizontal stress in the test was 50 kPa, i.e., $K_0 = 0.5$. The same initial stresses were assumed in the numerical simulation. A single element was used. The elastic and plastic parameters selected for calibration were the same for all cases having the same D_r and tabulated in Table 1. The predicted stress-strain and stress paths for $K_0 = 0.5$ and CSR = 0.1 are shown in Figures 9a and 9b as “thin” lines. The predictions generally give a reasonable representation of the observed response including plastic unloading, sudden drop of effective stress during stress reversal after dilation, and cyclic mobility.

Table 1 Input parameters for $D_{rc} = 40\%$ Fraser River sand

Parameters	K_G^e	K_B^e	α	ϕ_{cv}	η_f	R_f
Values	622	249	0.4	33	0.58	0.99

If test condition were $K_0 = 0.5$, the predicted triggering of liquefaction shows a good agreement with measurements as shown in Figure 10.

An examination of the effect of K_0 on prediction of liquefaction resistance is shown in Figure 11. The $K_0 = 0.5$ case had initial stresses of 100 kPa and 50 kPa, and thus a mean stress of 75 kPa. The $K_0 = 1.0$ case had stresses of 75 kPa, and thus a mean stress of 75 kPa also. The predicted results show that both $K_0 = 0.5$ and $K_0 = 1.0$ states liquefaction in about the same number of cycles. This is in agreement with the test results of Ishihara (1996) who found that samples at the same density and mean stress had similar liquefaction response.

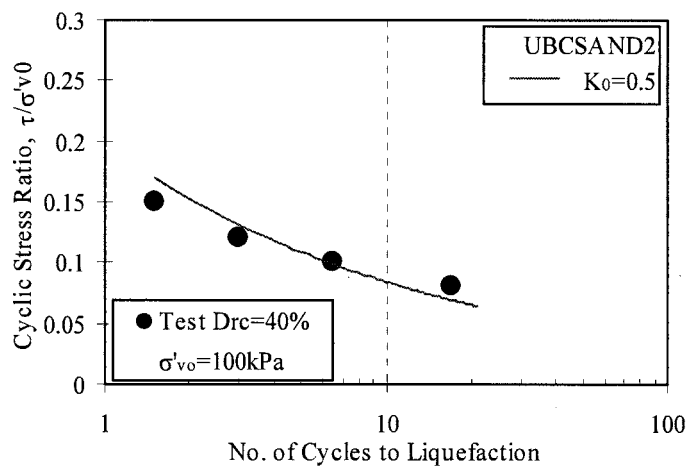


Figure 10 Predicted liquefaction resistance under $K_0 = 0.5$ and test result in terms of τ/σ'_{v0}

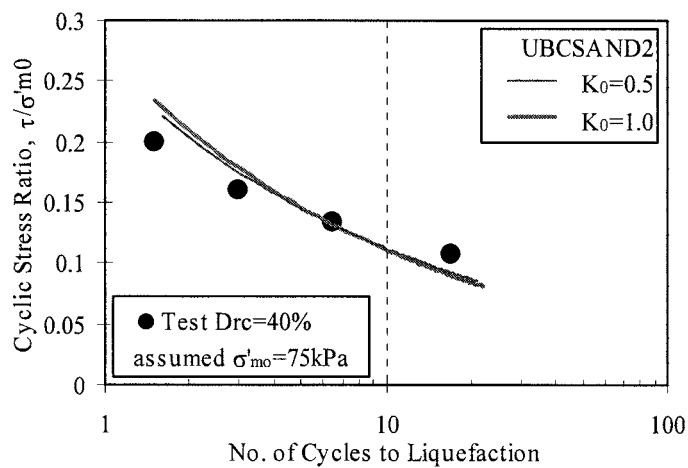


Figure 11 Predicted liquefaction resistance in terms of τ/σ'_{m0} under $K_0 = 0.5$ and 1.0 and test result

5. CONCLUSIONS

A Two Mobilized-plane Model for predicting the stress-strain response of sand under monotonic as well as cyclic loading conditions is presented. The model is focused on simple shear loading conditions, as this is most representative of seismic loading conditions in the field. The proposed model addressed two key features; rotation of principal planes and plastic unloading. It uses two mobilized planes; a maximum shear stress plane, and a horizontal plane. The model was calibrated based on drained and constant volume simple shear tests and showed the same characteristic response as observed in the laboratory tests. The model captured the large soil compaction effect during stress reversal after dilation and general cyclic soil behavior including cyclic mobility after triggering of liquefaction. The model also predicts that elements having the same initial density and mean stress will have similar liquefaction response, in agreement with laboratory element tests.

Acknowledgements:

Authors acknowledge that a series of simple shear tests for numerical model validation presented herein were carried out by Mr. Sriskandakumar during his MASc studies at the University of British Columbia under the supervision of Dr. Wijewickreme at UBC. The authors also acknowledge NSERC support through grant No. 246394, without which this work would not have been possible. The first author acknowledges support from the Center for Urban Earthquake Engineering (CUEE) in Tokyo Institute of Technology.

References:

- Arthur, J. R. F., Chua, K. S., Dunstan, T. and Rodriguez del C. J. I. (1980), "Principal stress rotation: a missing parameter," *Journal of the Geotechnical Engineering Division*, 106(GT4), 419-433
- Iai, S., Matsunaga, Y., and Kameoka, T. (1992), "Analysis of undrained cyclic behavior of sand under anisotropic consolidation," *Soils and Foundations*, 32(2), 16-20.
- Ishihara, K. 1996. *Soil behaviour in earthquake Geotechnics*. Clarendon Press, Oxford.
- Itasca. 2000. FLAC, version 4.0. Itasca Consulting Group Inc., Minneapolis.
- Kabilamany, K., and Ishihara, K. (1991), "Cyclic behaviour of sand by the multiple shear mechanism model," *Soil Dynamics and Earthquake Engineering*, 10(2), 74-83.
- Kolymbas, D. (2000), "The misery of constitutive modeling," *Constitutive modelling of granular materials*. Edited by Dimitrios Kolymbas: 11-24.
- Lee, C.- J. (1991), "Deformation of sand under cyclic simple shear loading," Proceedings of the Second International Conference on Recent Advances in Geotechnical Earthquake Engineering and Soil Dynamics, March 11-15, St. Louis, Missouri, 1, 33-36.
- Lee, K.-H. and Pande, G. N. (2004), "Development of a two-surface model in the Multilaminate framework," Proceedings of the 11th Conference on Numerical Models in Geomechanics, Ottawa, pp. 139-144.
- Matsuoka, H. (1974), "Stress-strain relationships of sands based on the mobilized plane," *Soils and Foundations*, 14(2), 47-61.
- NRC. (1985), Liquefaction of soils during earthquakes. National Research Council Report CETS-EE-001, National Academic Press, Washington, D.C.
- Pande, G. N., and Sharma, K. G. (1983), "Multi-laminate model of clays-a numerical evaluation of the influence of rotation of the principal stress axes," *Int. Journal for Numerical and Analytical Methods in Geomechanics*, 7, 397-418.
- Roscoe, K.H. (1970), "The influence of strains in soil mechanics," *Geotechnique*, 20, 129-170.
- Sriskandakumar, S. (2004), "Cyclic loading response of Fraser River sand for validation of numerical models simulating centrifuge tests," MASc Thesis, Department of Civil Engineering, UBC.
- Vermeer, P. A. (1980), "Formulation and analysis of sand deformation problems," Report 195 of the Geotechnical Laboratory, 142p. Delft University of Technology.
- Wijewickreme, D. and Vaid, Y. P. (2004), "A descriptive framework for the drained response of sands under simultaneous increase in stress ratio and rotation of principal stresses," Submitted to *Soils and Foundations*.
- Wijewickreme, D., Sriskandakumar, S., and Byrne, P.M. (2005), "Cyclic Loading Response of Loose Air-pluviated Fraser River Sand for Validation of Numerical Models Simulating Centrifuge Tests," *Canadian Geotechnical Journal*, 42(2), 550-561.

A UNIFIED PREDICTION FOR LIQUEFACTION AND SETTLEMENT OF SATURATED SANDY GROUND

R. Uzuoka¹⁾, Y. Shimizu²⁾, A. Kamura²⁾, N. Sento³⁾ and M. Kazama⁴⁾

1) Associate Professor, Dept. of Civil Engineering, Tohoku University, Japan

2) Graduate student, Dept. of Civil Engineering, Tohoku University, Japan

3) Research Associate, Dept. of Civil Engineering, Tohoku University, Japan

4) Professor, Dept. of Civil Engineering, Tohoku University, Japan

uzuoka@civil.tohoku.ac.jp

Abstract: A unified prediction model for liquefaction and settlement of saturated sandy ground based on the minimum effective stress concept is proposed. Minimum effective stress can be easily applied to existing constitutive models proposed for liquefaction analyses. Performance of the new prediction method was verified through numerical simulations, based on the dynamic soil-water coupled theory, on laboratory tests as well as the dynamic centrifuge tests. Both liquefaction process during the excitation and consequent ground settlement during the excess pore water pressure dissipation process were well reproduced with the simulations.

1. INTRODUCTION

Although the settlement of liquefied ground has caused serious damages of structures (e.g. Ishihara 1993), a unified prediction for the occurrence of liquefaction and accompanying settlement of saturated sandy ground has not been achieved. Liquefaction analysis has been developed since 1980's by many researchers. The field equations of these liquefaction analyses are mainly based on Biot's porous media theory (1962). Although several formulations, which use different unknown variables, for example, $u-U$, $u-w$ and $u-p$ formulations, have been used, their differences are not significant in the earthquake applications (Zienkiewicz and Shiomi, 1984). The performance of constitutive models, on the other hand, affects analytical results considerably, because the applicability of current constitutive models has not yet been sufficiently confirmed (Arulanandan and Scott, 1994). Further validation and modification of constitutive models in liquefaction analyses are necessary through simulations of laboratory tests, model experiments and case histories.

The volumetric compression of sand after liquefaction has been investigated with laboratory tests including undrained shear process and consequent drained compression process with dissipation of excess pore water pressure after liquefaction. It is reported that volumetric strain characteristics after liquefaction depends on the experienced strain histories (e.g. Lee and Albaisa 1974, Nagase and Ishihara 1988, Sento et al. 2004). Recent research (Sento et al. 2004) pointed out that liquefied sand experienced large strain histories yields large volumetric strain change during the dissipation of excess pore water pressure. Although some simplified evaluation methods of settlement of liquefied ground have been proposed (e.g. Tokimatsu and Seed 1987, Ishihara and Yoshimine 1992), most liquefaction analyses mainly focused on the liquefaction process and the shear deformation of the ground. Few analyses qualitatively discussed the settlement of liquefied ground after the dissipation of excess pore water pressure (Yoshida and Finn 2000). This study proposes a unified prediction model for

liquefaction and settlement of saturated sandy ground based on the concept of minimum effective stress. Utilizing the dynamic soil-water coupled analysis with the proposed model numerical simulations are performed on dynamic centrifugal model tests, and find the proposed method can reproduce a unified behavior of saturated sandy ground during and after liquefaction.

2. CONCEPT OF MINIMUM EFFECTIVE STRESS

A concept of minimum effective stress is introduced in order that the constitutive model can quantitatively reproduce the amount of volumetric strain with the dissipation of excess pore water pressure after liquefaction. Here we assume a simplified condition as shown in Figure 1 in which isotropically consolidated sand is subjected to undrained cyclic shear and the excess pore water pressure dissipates after liquefaction as shown in Figure 1. From the view point of the elasto-plastic theory, the increment of volumetric strain can be expressed as follows:

$$dv = dv^E + dv^P = \frac{\kappa}{(1+e)\sigma'_m} d\sigma'_m + Dd\gamma^P \quad (1)$$

where dv is the volumetric strain increment, dv^E is the elastic volumetric strain increment, dv^P is the plastic volumetric strain increment, κ is the swelling index, e is the initial void ratio, $d\sigma'_m$ is the mean effective stress increment, D is the dilatancy coefficient and $d\gamma^P$ is the second invariant of incremental deviatoric strain tensor. The dissipation process of the excess pore water pressure after liquefaction can be assumed as an elastic process because no plastic volumetric strain changes in the overconsolidation region without shear deformation. By neglecting plastic volumetric components, we can use the elastic linear relationship between the logarithms of mean effective stress and void ratio as shown by the broken line shown in Figure 1. In addition, the minimum effective stress σ'_{ml} as follows is defined as the intersection between the undrained path and dissipation path shown in Figure 1:

$$\sigma'_m \geq \sigma'_{ml} = R_{lim} \sigma'_{m0} \quad (2)$$

where R_{lim} is the ratio of σ'_{ml} for the initial mean effective stress σ'_{m0} (parameter of liquefaction intensity). The typical measured path during the dissipation process is also shown in Figure 1. The measured minimum effective stress does not always coincide with the theoretical minimum effective stress σ'_{ml} due to the limit of measurement.

Sento et al. (2004) measured the volumetric strain of liquefied sand after dissipation of excess pore water pressure with torsional shear tests under various shear strain histories, and reported the limit of

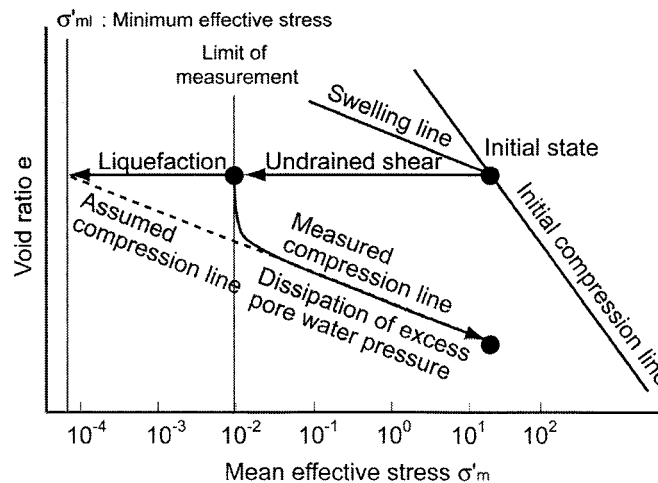


Figure 1 Concept of minimum effective stress

measurement for small mean effective stress at a liquefied state as shown in Figure 1. Thereby, they changed σ'_{ml} with the density of sand and strain history as follows:

$$R_{lim} = 10^{-x} \quad x = \frac{a\gamma^p}{1 + \gamma^p / b} \quad (3)$$

where a and b are the material parameters. γ^p is the accumulated shear strain which is the summation of the second invariant of incremental deviatoric strain from the initial state. The small R_{lim} implies a high intensity of liquefaction caused by large accumulated shear strain.

Utilizing the equations (1) - (3), we can calculate the elastic volumetric strain in the framework of the elasto-plastic model. Although the minimum effective stress can be related to the plastic volumetric strain during shear deformation, this simplified method is easy to be applied to practical problems. The minimum effective stress σ'_{ml} is also the lower bounds of the mean effective stress to keep numerical stability. It is noted that the σ'_{ml} has physical meaning previously discussed as equation (2) in this study, although it has been treated as a numerical parameter in past liquefaction analyses.

3. VALIDATION OF THE PROPOSED CONSTITUTIVE MODEL

3.1 Modification of existing constitutive model

By adopting the minimum effective stress concept, an existing elasto-plastic constituting model (Oka et al. 1999) is modified. The existing constitutive equation is formulated based on the following concepts; 1) the elasto-plastic theory, 2) the non-associated flow rule, 3) the concept of the overconsolidated boundary surface, 4) the non-linear kinematic hardening rule and 5) the plastic strain-dependent plastic and elastic modulus. Oka et al. (1999) applied the constitutive model to the cyclic undrained behavior of sand through the numerical simulation of hollow cylindrical shear tests, and showed that the simulation reproduced experimental results well under various stress conditions, such as isotropic and anisotropic consolidated conditions, with and without the initial shear stress conditions, principal stress axis rotation, etc.

The modification of the existing constitutive model is easy if the constitutive model is based on the same assumption as equation (1). Although Oka's constitutive model assumes the equation (1), the swelling index (or elastic bulk modulus) is dependent on plastic strain history. Hence the swelling index is modified to be constant in this study.

3.2 Laboratory Tests

Undrained and drained torsional shear tests were performed with careful evaluation of mean effective stress of the specimen. The specimen of the hollow cylindrical torsional shear test was 100 mm in outer diameter, 60 mm in inner diameter, and 100 mm in height. We used Toyoura sand as a testing material, which is the same material as that used in the dynamic centrifugal tests as mentioned later. Specimens were prepared by the air pluviated procedure and the relative density of about 40%, 65% and 80% at the end of the consolidation. The test samples were isotropically consolidated, the initial effective stress was 100 kPa with a backpressure of 200 kPa, and the B value was maintained at more than 0.95. The cyclic shear strain was applied under undrained condition in uniform triangular cycles with a constant strain rate. The shear strain amplitude increased from 0.1% (5 cycles), 0.2% (5 cycles), 0.5% (3 cycles), 1.0% (3 cycles), 2.0% (3 cycles) to 5.0% (1 cycle) in 6 stages. After undrained shear process, the liquefied specimen was isotropically reconsolidated with the drainage rate of 0.04%/min until the mean effective stress recovered the initial value. The responses of shear stress and pore water pressure were recorded. The recorded shear stress was corrected with a membrane tensile stress. The volumetric strain was also corrected with a membrane penetration effect (Vaid and Negussey 1984, Tokimatsu and Nakamura 1986, Goto 1986). The mean effective stress was

calculated from vertical and lateral effective stress. The lateral effective stress was the measured differential pressure between inside the specimen and the outer cell pressure. The vertical effective stress was the sum of axial effective pressure and the self-weight of the specimen at the middle in height.

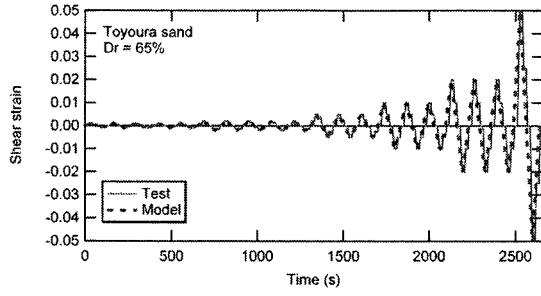
3.3 Simulation of Laboratory Tests

Model parameters of Toyoura sand with various relative densities are summarized in Table 1. Detailed description about the parameters can be referred to corresponding references (Oka et al., 1999). The following parameters, e_0 , λ , κ , OCR^* , M_m^* , M_f^* and G_0/σ'_m were directly determined by physical property tests, isotropic consolidation process and undrained shear process. The parameters of R_{lim} were determined based on the results of volume compression tests (Sento et al. 2004). Although, in principle, remaining parameters could be determined by physical property tests and undrained monotonic and cyclic shear tests, the data adjusting method is more practical to determine the soil parameters. The values of material parameters were calibrated in order to provide a good description of the stress-strain relations and effective stress paths during undrained shear process.

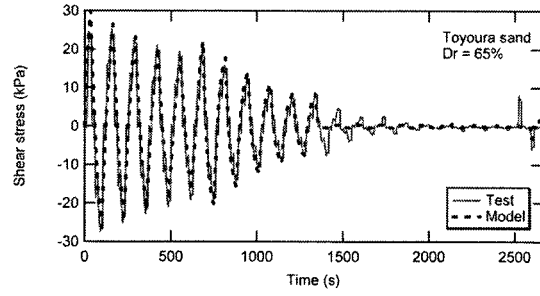
The undrained shear and reconsolidation processes were simulated with the proposed constitutive model. The simulations of undrained shear and reconsolidation processes were performed with controlling the shear strain and the volumetric strain respectively. The increment of the strain was determined sufficiently small to keep the numerical accuracy. Figure 2 shows the measured and computed results of undrained shear process for the relative density of about 65%. The shear strain histories (a) were imposed to the specimen, and the shear stress and effective mean stress were computed. The constitutive model with calibrated material parameters can reproduce the test results very well. Figure 3 shows the measured and computed results of drained reconsolidation processes for the relative density of about 40% and 65%. The constitutive model with calibrated material parameters can reproduce the final volumetric strain qualitatively and quantitatively. The measured mean effective stress less than about 0.5 kPa contains some measurement errors due to the electrical noise during the measurement. Although the compression curve is assumed to be linear in the constitutive model, the measured compression curves show some negative curvatures. This results show that the volumetric

Table 1 Material parameters

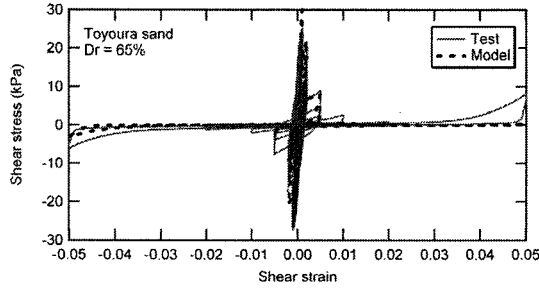
Name of soil profile		Toyoura sand Dr=40%	Toyoura sand Dr=65%	Toyoura sand Dr=80%
Density	ρ (t/m ³)	1.91	-	-
Coefficient of permeability	k (cm/s)	0.0065	-	-
Initial void ratio	e_0	0.829	0.726	0.656
Compression index	λ	0.0045	0.0036	0.0031
Swelling index	κ	0.0032	0.0030	0.0026
Quasi-overconsolidation ratio	OCR^*	1.0	1.0	1.0
Failure stress ratio	M_f^*	1.097	1.170	1.290
Phase transformation stress ratio	M_m^*	0.714	0.714	0.714
Initial shear modulus ratio	G_0/σ'_m	354	436	555
Dilatancy parameter	D_0^*	1.5	1.0	1.0
	n	0.0	0.0	0.0
Hardening parameter	B_0^*	1100	1500	1800
	B_1^*	30	100	94
	C_f	500	1100	2000
Reference strain parameter	γ_r^{p*}	0.01	0.001	0.001
	γ_r^{E*}	0.01	0.05	0.1
R_{lim} parameter	a	24.0	15.0	8.6
	b	0.5	0.5	0.5



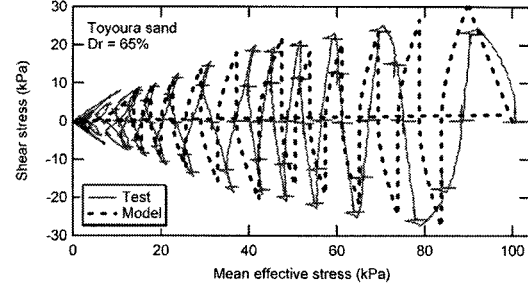
(a) shear strain histories



(b) shear stress histories

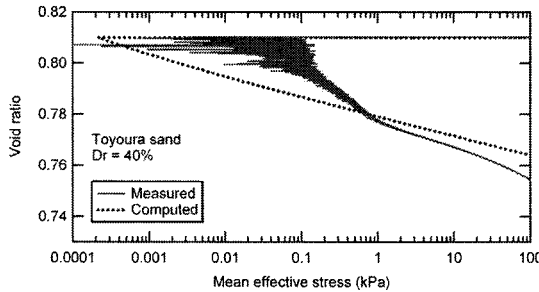


(c) stress – strain relations

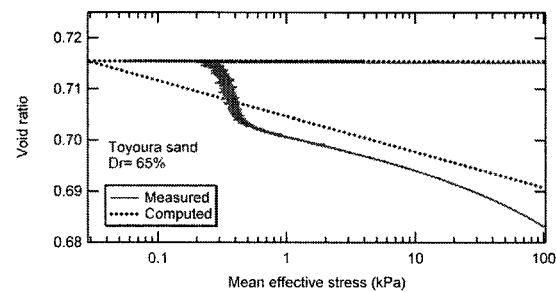


(d) effective stress paths

Figure 2 Measured and computed results of undrained shear process ($D_r = 65\%$)



(a) $D_r = 40\%$



(b) $D_r = 65\%$

Figure 3 Measured and computed results of drained reconsolidation process ($D_r = 40$ and 65%)

compression behavior of sand is not elastic even in overconsolidation region; therefore further investigation on modeling of volumetric compression behavior is necessary.

4. SIMULATION OF LIQUEFACTION-INDUCED SETTLEMENT

4.1 Dynamic Centrifugal Tests

The dynamic centrifugal tests were carried out with a circular laminar box under the 50 times gravity acceleration (Kawasaki et al. 1998). The horizontal model ground was made of homogeneous saturated Toyoura sand with the relative density of about 40%. The thickness of the model ground was 17.5m in prototype scale. The ground water level was set at the ground surface. The pore fluid was silicon oil with 50 times viscosity of water. The input acceleration at the table was a sinusoidal wave with the frequency of 1 Hz and the number of cycles of 20 in prototype scale. The amplitudes of acceleration were about 60 Gal in Case 1 and 90 Gal in Case 2 respectively. The measurements of pore water pressure, ground acceleration and settlement at the ground surface were made during and after the shaking.

4.2 Numerical Method

The numerical method is briefly described in this section. A dynamic soil-water coupled problem is formulated based on a u-p formulation (Oka et al., 1994). The finite element method (FEM) is used for the spatial discretization of the equilibrium equation, while the finite difference method (FDM) is used for the spatial discretization of the pore water pressure in the continuity equation. Oka et al. (1994) verified the accuracy of the proposed numerical method through a comparison of numerical results and analytical solutions for transient response of saturated porous solids. The governing equations are formulated basing on the following assumptions; 1) the infinitesimal strain, 2) the smooth distribution of porosity in the soil, 3) the small relative acceleration of the fluid phase to that of the solid phase compared with the acceleration of the solid phase, 4) incompressible grain particles in the soil. The equilibrium equation for the mixture is derived as follows:

$$\rho \ddot{\mathbf{u}}^S - \text{div} \boldsymbol{\sigma} - \rho \mathbf{b} = \mathbf{0} \quad (4)$$

where ρ is the overall density, $\ddot{\mathbf{u}}^S$ is the acceleration vector of the solid, $\boldsymbol{\sigma}$ is the total stress tensor and \mathbf{b} is the body force vector. The continuity equation is derived as follows:

$$\frac{n}{K^F} \dot{p} + \dot{\varepsilon}_v^S + \text{div} \left\{ \frac{k}{\gamma_w} (-\text{grad } p + \rho^F \mathbf{b} - \rho^F \ddot{\mathbf{u}}^S) \right\} = 0 \quad (5)$$

where n is porosity, K^F is the bulk modulus of the fluid, p is the pore water pressure, $\dot{\varepsilon}_v^S$ is the volumetric strain rate of the solid, k is the coefficient of permeability, γ_w is the unit weight of the fluid, and ρ^F is the real density of the fluid. Newmark implicit method was used for time integration.

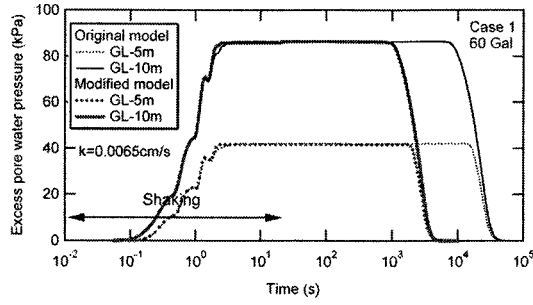
4.3 Numerical Data

A one-dimensional soil column model for the model ground was used for the simulation. The soil column comprised 35 isoparametric 4-noded solid elements. Only the ground water table at the surface was set to be permeable and the other boundaries were impermeable. The horizontal and vertical displacements at two nodes with the same depth were tied to reproduce free-field motion. The bottom of the soil column where the shaking motions were input is set to be rigid. The initial stress components for all elements were calculated by assuming the lateral earth pressure coefficient of 0.5. The proposed constitutive model was applied to all elements. The material parameters of Toyoura sand with the relative density of 40% were used in the simulation because the same material was used in the centrifugal tests.

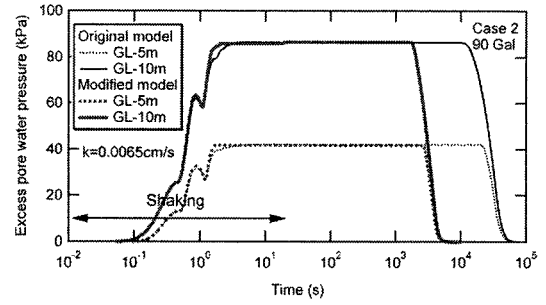
A time integration step of 0.001 second was adopted to ensure the numerical stability. The hysteresis damping by the constitutive model was basically used, and Rayleigh damping proportional to initial stiffness was used in order to describe the damping especially in the high frequency domain. The factor of Rayleigh damping which was proportional to the initial ground stiffness was set to be 0.0025. The parameters in Newmark method were set to be 0.3025 and 0.6 to ensure the numerical stability.

4.4 Numerical Results

Figure 4 and Figure 5 show the time histories of computed pore water pressures and ground accelerations respectively in both cases. The excess pore water pressures are picked up at the depth of 5 m and 10 m. The computed results with the original constitutive model also are shown in both figures. The complete liquefaction can be confirmed at about 3 seconds when the excess pore water pressure attains the initial effective overburden pressure and the ground acceleration becomes small. It is noted that both original and modified model show similar results before complete liquefaction; therefore it is easy to apply the proposed method to existing constitutive model. The discrepancy between the original and modified model is shown during the dissipation of excess pore water pressure. The dissipation with original model is much slower than that with modified model. This discrepancy will be discussed later.

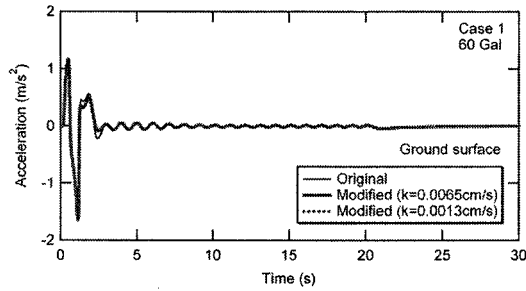


(a) Case 1 (60 Gal)

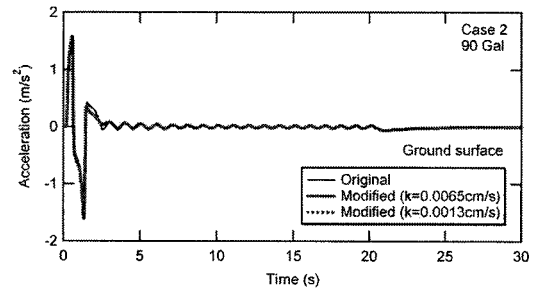


(b) Case 2 (90 Gal)

Figure 4 Computed time histories of excess pore water pressures

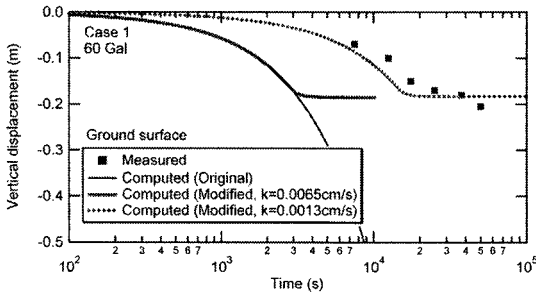


(a) Case 1 (60 Gal)

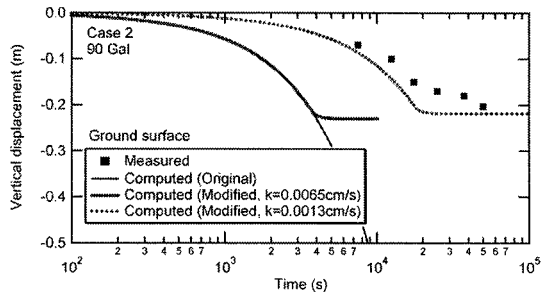


(b) Case 2 (90 Gal)

Figure 5 Computed time histories of ground accelerations



(a) Case 1 (60 Gal)



(b) Case 2 (90 Gal)

Figure 6 Computed and measured time histories of ground settlements

Figure 6 shows the time histories of computed and measured ground settlements in both cases. The settlements with original model largely overestimate the measured ones because the material parameters of original model were calibrated only for the undrained shear process without the minimum effective stress concept. This overestimation of volumetric compression causes the delay in the dissipation of excess pore water pressure. The final settlements with modified model agree with the measured ones; however the convergence of settlement is earlier than the measurement in the case with the initial permeability of 0.0065 cm/s. The parametric cases with the permeability of 0.0013 cm/s are also shown in Figure 5 and 6. The results with the permeability of 0.0013 cm/s agree with the measurements. Although the decrease in permeability of liquefied ground is reasonable due to decrease in the void ratio, we need further investigation on the permeability of liquefied sand.

5. CONCLUSIONS

A unified prediction model for liquefaction and settlement of saturated sandy ground based on

minimum effective stress concept is proposed. Minimum effective stress concept can be easily applied to existing constitutive models proposed for liquefaction analyses. The modified constitutive model was validated based on the results of undrained shear and consequent drained compression tests. The constitutive model with calibrated material parameters can quantitatively reproduce the final volumetric strain after liquefaction. Dynamic centrifugal model tests with saturated sandy ground were simulated with the dynamic soil-water coupled analysis incorporating the proposed model. The simulations reproduced the occurrence of liquefaction during the shaking process and consequent ground settlement during the dissipation process of excess pore water pressure. The computed ground settlements with the modified permeability quantitatively agree with the measured ground settlements.

Acknowledgements:

The support of Special Project for Earthquake Disaster Mitigation in Urban Areas by Ministry of Education, Culture, Sports, Science and Technology is gratefully acknowledged. The authors wish to thank the research group chaired by Professor Tadanobu Sato, Waseda University and Professor Susumu Iai, Kyoto University. The authors thank Dr. Kenichi Horikoshi and Dr. Tadafumi Fujiwara, Taisei Corporation for their providing information about the centrifuge tests.

References:

- Arulanandan, K. and Scott, R.F. (ed.). (1994). "Verification of Numerical Procedures for the Analysis of Soil Liquefaction Problems," Vol. 2, Balkema, Rotterdam.
- Biot, M.A. (1962). "Mechanics of deformation and acoustic propagation in porous media," *J. Applied Physics*, 33, 1482-1492.
- Goto, S. (1986). "Strength and characteristics of granular materials in triaxial tests," Doctoral Thesis, University of Tokyo, (in Japanese).
- Ishihara, K. and Yoshimine, M. (1992). "Evaluation of settlements in sand deposits following earthquakes," *Soils and Foundations*, 32(1), 173-188.
- Ishihara, K. (1993). "Liquefaction and flow failure during earthquakes," *Geotechnique*, 43(3), 351-415.
- Kawasaki, K., Sakai, T., Yasuda, S. and Satoh, M. (1998). "Earthquake-induced settlement of an isolated footing for power transmission tower," *Proc. Centrifuge 98*, Tokyo, 271-276.
- Lee, K.L. and Albaisa, A. (1974). "Earthquake induced settlements in saturated sands," *Journal of the Geotechnical Engineering Division, ASCE*, 100, GT4, 387-406.
- Nagase, H. and Ishihara, K. (1988). "Liquefaction-induced compaction and settlement of sand during earthquakes," *Soils and Foundations*, 28(1), 65-76.
- Oka, F., Yashima, A., Shibata, T., Kato, M. and Uzuoka, R. (1994). "FEM-FDM coupled liquefaction analysis of a porous soil using an elasto-plastic model," *Applied Scientific Research*, 52, 209-245.
- Oka, F., Yashima, A., Tateishi, A., Taguchi, Y. and Yamashita, S. (1999). "A cyclic elasto-plastic constitutive model for sand considering a plastic-strain dependence of the shear modulus," *Geotechnique*, 49, 661-680.
- Sento, N., Kazama, M. and Uzuoka, R. (2004). "Experiment and idealization of the volumetric compression characteristics of clean sand after undrained cyclic shear," *J. Geotechnical Engineering, JSCE*, 764/III-67, 307-317 (in Japanese).
- Tokimatsu, K. and Nakamura, K. (1986). "A liquefaction test without membrane penetration effects," *Soils and Foundations*, 26(4), 127-138.
- Tokimatsu, K. and Seed, H.B. (1987). "Evaluation of settlements in sands due to earthquake shaking," *Journal of Geotechnical Engineering, ASCE*, 113(8), 861-878.
- Vaid, Y.P. and Negussey, D. (1984). "A critical assessment of membrane penetration in the triaxial test," *Geotechnical Testing Journal*, 7(2), 70-76.
- Yoshida, N. and Finn, W.D.L. (2000). "Simulation of liquefaction beneath an impermeable surface layer," *Soil Dynamics and Earthquake Engineering*, 19, 333-338.
- Zienkiewicz, O.C. and Shiomi, T. (1984). "Dynamic behavior of saturated porous media: The generalized Biot formulation and its numerical solution," *International Journal for Numerical and Analytical Method in Geomechanics*, 8, 71-96.

PUSH-OVER ANALYSES OF PILES IN LATERALLY SPREADING SOIL

Scott A. ASHFORD¹ and Teerawut JUIRNARONGRIT²

ABSTRACT: This paper presents the assessment of push-over analyses of single pile and pile groups in laterally spreading ground using p-y approach. The results from full-scale blast induced lateral spreading experiments in Japan were used to evaluate the numerical model. For the single pile, the pile responses were determined by imposing the measured free field displacements to the Winkler spring model. For pile groups, the piles in the group were modeled as an equivalent single pile, together with reduced stiffness p-y springs to account for the effect of pile group. A rotational spring was also introduced into the model to represent the rotational pile group stiffness. The results from the analyses for both single pile and pile groups were in good agreement with the measured responses from the experiments, thus suggesting that this method may be used in common design practice for piles in laterally spreading ground problems.

KEYWORDS: piles, pile group, pile tests, lateral spreading, liquefaction, soil-pile interaction.

1. INTRODUCTION

A pseudo-static push-over analysis using the p-y analysis method is widely used in current design practice to analyze the response of laterally loaded piles due to its simplicity in modeling compared to the 2D or 3D finite element method (FEM). Despite its simplicity, the p-y approach has the capability to provide key design parameters (i.e., pile maximum moment and pile head displacement). Application of this method in current design practice is mainly focused on the analysis of piles under inertial loading, with movement relative to a stationary soil mass [1-2]. For the case of moving soil mass such as piles in lateral spreading soil, the moving soil mass will exert the load on the pile and displace the pile a certain amount depending on the relative stiffnesses between the pile and the soil. For this kind of application, it requires the free-field soil movement (see Figure 1) as an input to the boundary ends of the Winkler springs [3-5]. When the expected free-field displacement is large enough to cause the ultimate pressure of laterally spreading soils to be fully mobilized, the ultimate pressure, instead of free-field soil displacement, may be used. Estimates of the ultimate pressure of liquefied soils have been developed based on calibration with piles damaged in the 1995 Kobe earthquake [6], and centrifuge test data [7].

¹ Professor, University of California, San Diego, USA

² Post Doctoral Researcher, University of California, San Diego, USA

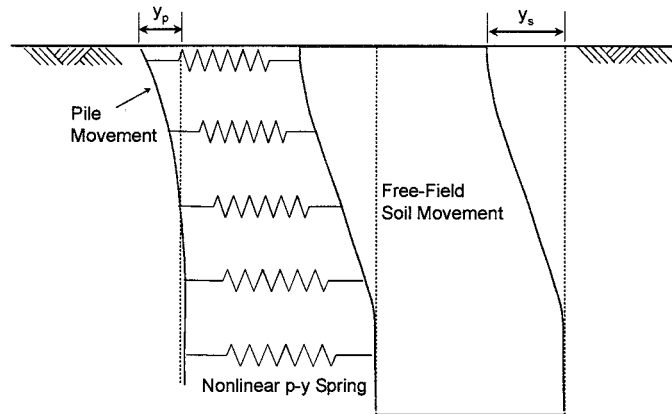


Figure 1. The p-y analysis model for pile subjected to lateral spreading

2. SITE DESCRIPTIONS

Two full-scale lateral spreading experiments were conducted at the Port of Tokachi, Hokkaido Island, Japan to study the behavior of single piles and pile groups subjected to lateral spreading. A layout of the test site for the first test is shown in Figure 2. The test site was approximately 25 m wide by 100 m long with 4% surface slope test bed. The site was bordered by a traditional design of quay walls (e.g., no consideration of seismic force in the design) on one end. The quay wall was fixed to H-piles using a series of tie-rods to reduce the movement of quay wall. The test piles were located 19.0 m away from the quay wall, which consisted of a UCSD single pile, a group of Waseda University (WU) single piles, a 4-pile group, and a 9-pile group. The piles were instrumented with strain gauges to measure moments during lateral spreading. All the single piles had the free-head condition, while the pile groups were fixed to a rigid pile cap. Controlled blasting was used to liquefy the soil at the test site, and thus induce lateral spreading. The blast holes were spaced at 6.0 m on center in the regular grid pattern with the blasting starting from the southwest corner of the embankment and continuing toward the quay wall as shown in Figure 2. More details on the site information and detail for the second lateral spreading test can be obtained elsewhere [8].

The soil at the test site consisted of 7.5 m of hydraulic fill, underlain by 1 m of medium dense sand overlying a very dense gravel layer (see Figure 3). The ground water table was approximately 1 m below the ground surface. The hydraulic fill consisted of a 4-m layer of very loose to loose silty sand (SM), underlain by a 3.5-m layer of very soft lean to fat clay with sand (CL to CH). Using the US criterion for liquefaction susceptibility evaluation [9], the first and second sand layers below the ground water table are susceptible to liquefaction. A summary of soil properties used in the push-over analyses is also given in Figure 3.

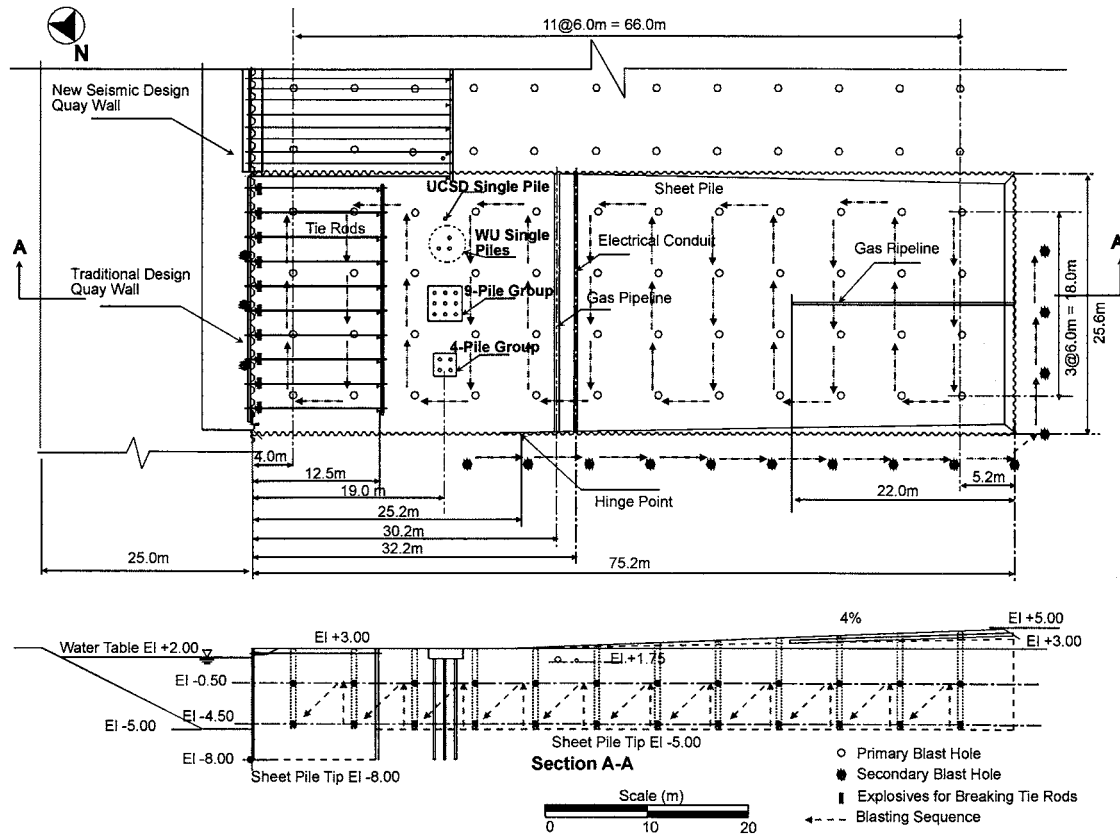


Figure 2. Site layout for 1st lateral spreading test

3. PUSH-OVER ANALYSES

3.1 SINGLE PILE

To predict the behavior of piles subjected to lateral spreading, the free-field soil displacement, y_s , needs to be known first, then imposed to the boundary ends of the Winkler soil springs along depths as shown in Figure. 3. The free-field soil movement profiles (i.e., no influence from pile foundations) at the end of both the first and second experiments were obtained from the measured soil displacement profiles of a slope inclinometer between the pile groups. Based on these data, simplified linear displacement profiles of the free-field soil movements were used for the boundary condition at the end of soil springs with the largest displacements at the ground surface of 0.43 m for the first test and additional 0.46 m from the second test for a total of 0.89 m. Soil springs at different depths were calculated based on standard p-y springs available in the literature. The p-y curves for non-liquefied cohesionless soil were developed based on Reese et al.'s (1974) recommendations [1], while the p-y curves for soft clay were obtained based on Matlock's (1970) recommendations [2]. Since the maximum response of the piles due to lateral spreading occurred at the end of the test, where the soil had already been liquefied, the p-y curves for liquefied soil were used for the saturated sand layers. Details of p-y curves for liquefied sand used in this study are described below.

Review of current research based on results from various physical modeling techniques suggests that the characteristics of p-y curves of liquefied soil may depend on the initial relative density of the soil. For loose sand with relative density, D_r , of less than 40% [10-11], the p-y curves are flat, inferring that the soil pressure from liquefied soil is negligible, while for medium dense and dense sand with relative density of greater than 55% [10-12], the p-y curves are concave up due to soil dilation. The relative densities at the Tokachi test site was slightly over 30% for the first 4-m of the sand layer and about 45% for the second sand layer at depths between 7.5 m and 8.5 m (see Figure 3). Based on the low

initial relative density, the liquefied soil layer at the Tokachi site should not provide any resistance to pile movement. Therefore, zero soil spring stiffness was used for the liquefied soil layers (i.e., from depths of 1 m to 4 m and from depths of 7.5 m to 8.5 m). In addition, recommendations for passive pressure of liquefied sand using a p-multiplier of 0.1 to reduce ultimate pressure obtained from Reese et al.'s sand p-y curves [13-14] were also used in this study for comparison. All the analyses in this paper were conducted using the LPILE Plus 4.0m computer code [15].

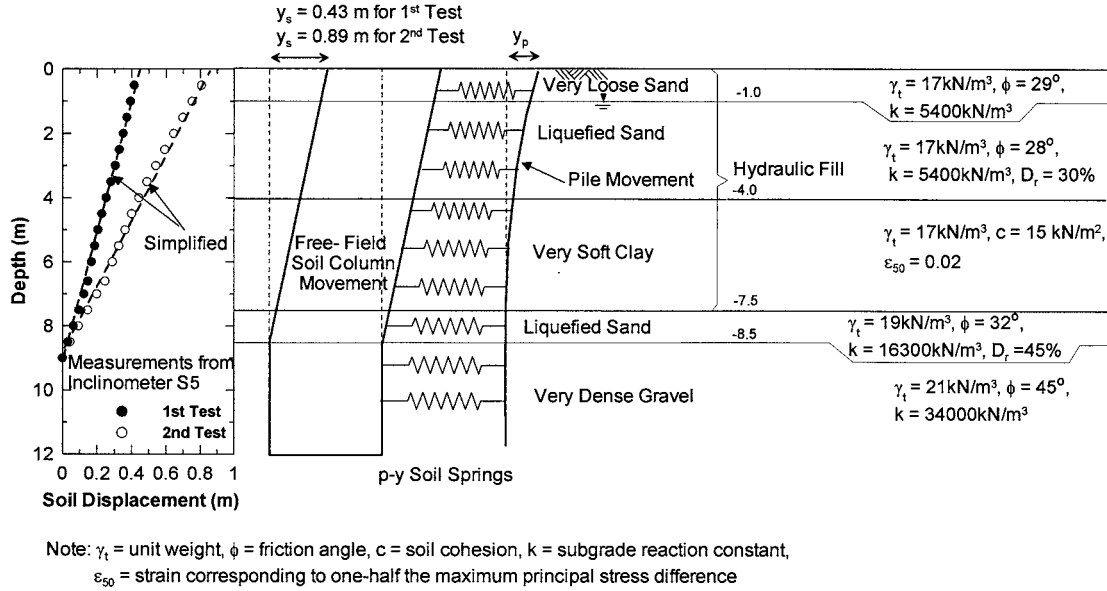


Figure 3. Soil displacement profiles from 1st and 2nd tests at Tokachi, and p-y analysis model for single pile

3.2 PILE GROUPS

Two special considerations incorporated into the analysis of the pile groups were the effect of pile head restraint at the pile cap and the effect of pile groups. The approach used to analyze pile group behavior in this study was adopted from the method proposed by Mokwa [16-17]. In this method, it is recommended that the piles in a group can be modeled as an equivalent single pile with a flexural stiffness equal to the number of piles in the group multiplied by the flexural stiffness of a single pile within the group. Figure 4 shows a schematic of the numerical model used for the analysis of 4-pile group subjected lateral spreading. The p-multiplier approach was used to reduce the soil stiffnesses for each pile in the group to account for group effects. The reduced soil spring stiffnesses were then summed to develop the combined soil springs for the pile group. For the soil passive pressure acting on the pile cap, it was modeled using the sand p-y curves [1], considering the width of pile cap as a pile diameter. In addition, the pile head boundary condition of the group-equivalent pile was determined by estimating the rotational restraint provided by the piles and pile cap and was represented by a rotational spring as suggested by Mokwa [16]. Finally, the group-equivalent pile, incorporating both the effect of pile head restraint and the effect of pile group behavior was analyzed by imposing the free-field soil movement profile at the boundary end of each soil spring. The input free-field soil movement profiles were the same as that used in the single pile.

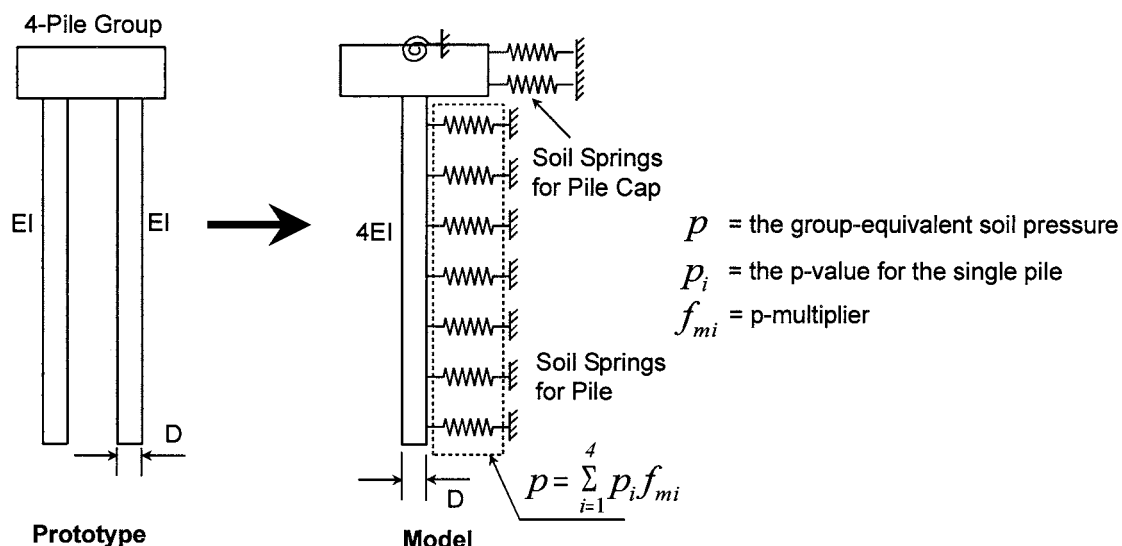


Figure 4. p-y analysis model for pile group

4. ANALYSIS RESULTS

4.1 SINGLE PILE

Figure 5 presents a comparison between computed and measured pile responses of the single pile for the first and second experiments. When using zero spring stiffness for liquefied soil, the predicted pile head displacements (Figure 5a), pile head rotations (Figure 5b) and moment profiles (Figure 5c) were in very good agreement with the pile responses measured from both tests. Figure 5 also shows that using the p-multiplier approach for the liquefied soil layers overestimated the pile displacement, rotation, and moment. Because the behavior of liquefied soil at the test site could be well represented by using zero spring stiffness, only this method was used to analyze the behavior of pile groups in the subsequent sections of this paper.

Figure 5a shows that for the first 8 m, the movement of the free-field soil mass was greater than the movement of the pile, which implies that the soil provided the driving force to the pile, as is also shown by the positive soil reaction in Figure 5d, except for the liquefied layer where zero reaction was assumed. Negative soil resistance indicates that the soil mass moved less than the pile, and therefore the soil provided the resistance force to the pile, as mostly occurred in very dense gravel layer (Figure 5d).

The lateral responses of the pile are dependent on the magnitude of free-field soil displacement; increasing the free-field soil displacement results in higher maximum moment and pile head displacement. However, if the free-field soil movement is large enough to cause the lateral soil pressure to be fully mobilized, the response of the pile will be independent of the free-field soil movement. Analyses were conducted to determine the magnitude of surface displacement required to cause the soil to reach its ultimate, or limiting, pressure. The pile stiffness was assumed to remain linear-elastic throughout the analyses. The analyses were carried out by gradually increasing the ground surface displacement while the soil displacement profile was assumed to be linear as shown in Figure 3. Figure 6a shows that once the ground surface displacement is larger than 1.4 m, the laterally spreading soil reaches its ultimate pressure, resulting in no change in the pile head displacement and pile moment. The analysis results indicate that the maximum moment (537 kN-m) in the pile, assuming linear pile behavior, is greater than the yield moment (460 kN-m); therefore, the pile will yield before the soils reach the ultimate pressure, which was indeed observed from pile data in the second test. Additional analyses were then conducted using actual nonlinear pile properties. Figure

6b shows the analysis results of a nonlinear pile which indicates that the pile yields when the soil surface displacement reaches 0.65 m. Because of the pile yielding, increasing the ground displacement increases the pile head displacement. The measured pile displacements and maximum moments from both tests are also plotted in Figure 6b, indicating good agreement between the p-y analysis method and the test results for the single pile.

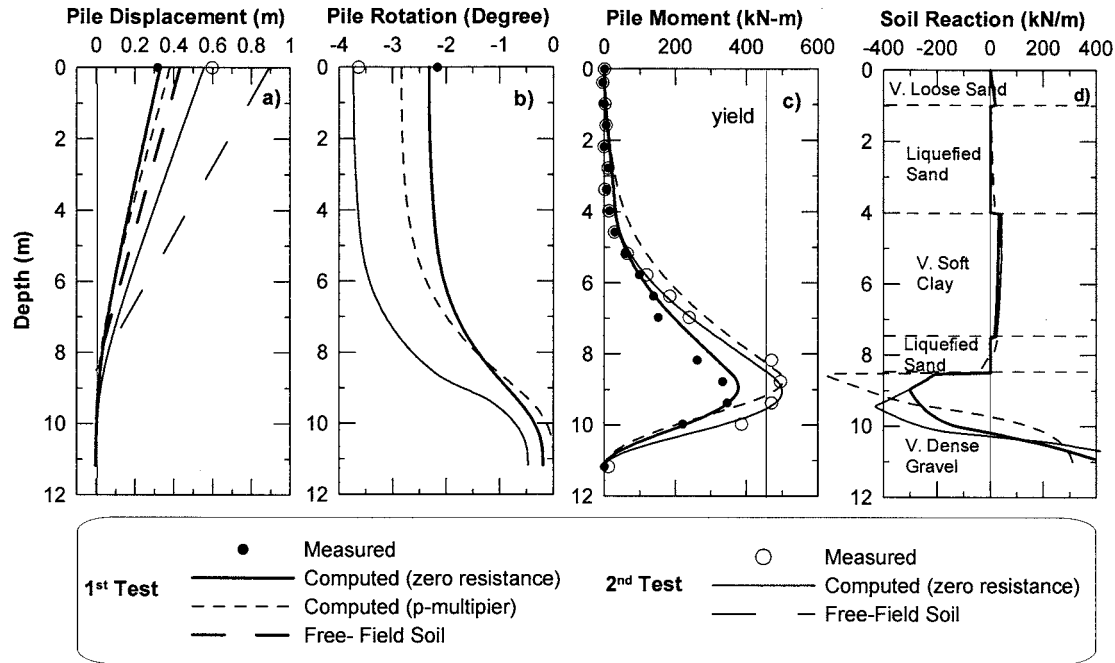


Figure 5. Comparison between measured and computed pile responses for the single pile

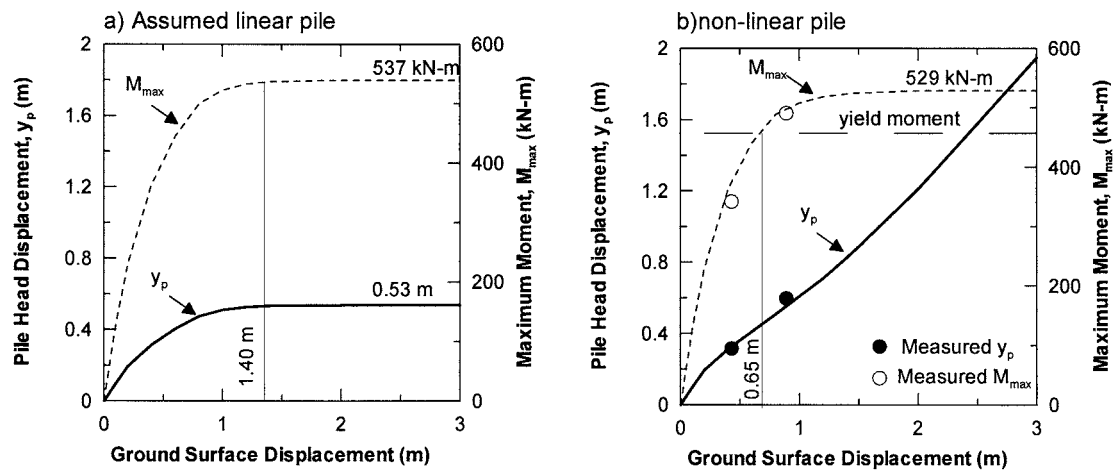


Figure 6. Pile head displacement and maximum moment vs. ground surface displacement for UCSD single pile; a) assumed linear pile behavior; b) non-linear pile behavior

4.2 PILE GROUPS

Although observations from the Tokachi experiments [8] indicated that small rotations might have occurred at the connection between the pile heads and the pile cap due to the cracking of the concrete

around the embedded piles and the elongation of the anchor bars, this effect was assumed to be small, especially for the first test (i.e., the maximum negative moment at the pile head was significantly lower than the ultimate moment capacity at the connection). As a result, the rotations of the cap and the pile heads were assumed to be identical. However, for the second test, this assumption might not be valid and the effect of the difference in the rotations between the cap and the pile heads has to be taken into consideration. Due to the limitation of incorporating this effect into the numerical model used in this study, the analyses were only conducted to predict the results from the first experiment and are presented below.

Figure 7 and Figure 8 present the results of calculated and measured pile responses of the 4-pile group and the 9-pile group, respectively. The same soil properties and free-field soil displacement profile used in the case of single pile were also used for analyzing the behavior of pile groups. Three types of boundary conditions at the pile head were considered for the purpose of comparison; these include the free head condition, fixed head condition, and rotationally restrained pile head boundary condition. Neither the free head nor fixed head conditions provided a reasonable estimate of the measured pile behavior. The free-head case overestimated the maximum positive moment at depth, and gave zero moment at the pile head, while the fixed-head case under-predicted the maximum positive moment but overestimated the maximum negative moment. The deflections at the pile head obtained from the fixed-head case were smaller than that measured by approximately 50% for both the 4- and 9-pile groups. The free-head case over-predicted the pile head deflection by 53% and 60% for the 4-pile group and the 9-pile group, respectively.

The analysis results obtained using the rotationally restrained pile head boundary condition considerably improved the agreement between measured and computed responses for both 4-pile group and 9-pile group, as shown in Figure 7 and Figure 8, respectively. The computed pile moments were within a reasonable range of the measured moment from the test. The errors between computed and measured pile group displacements were 3% for the 4-pile group and 13% for the 9-pile group. Pile head rotation was somewhat overestimated on the 9-pile group as shown in Figure 7b, likely due to the difference in the amount of rotation between the pile heads and the pile cap.

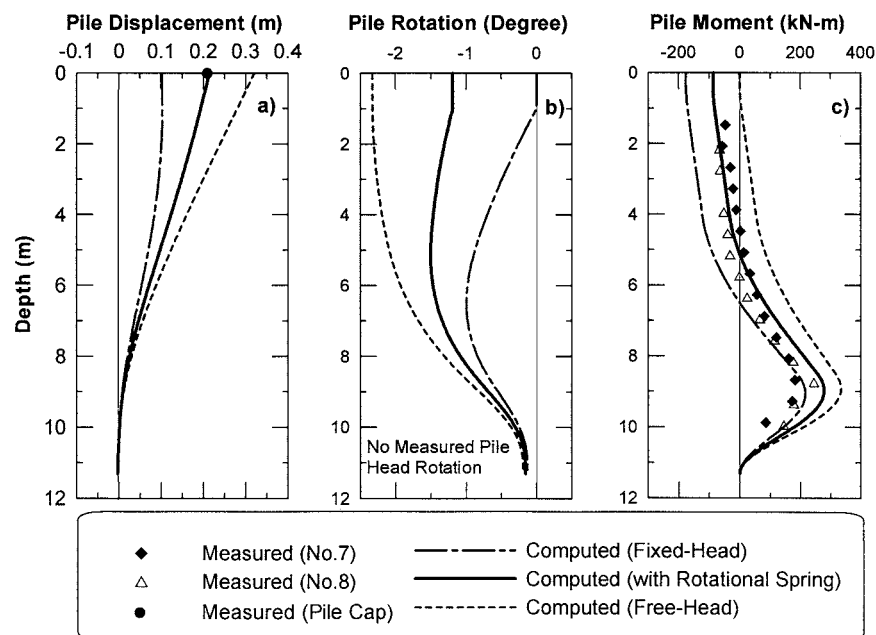


Figure 7. Comparison between measured and computed pile responses for 4-pile group for 1st test

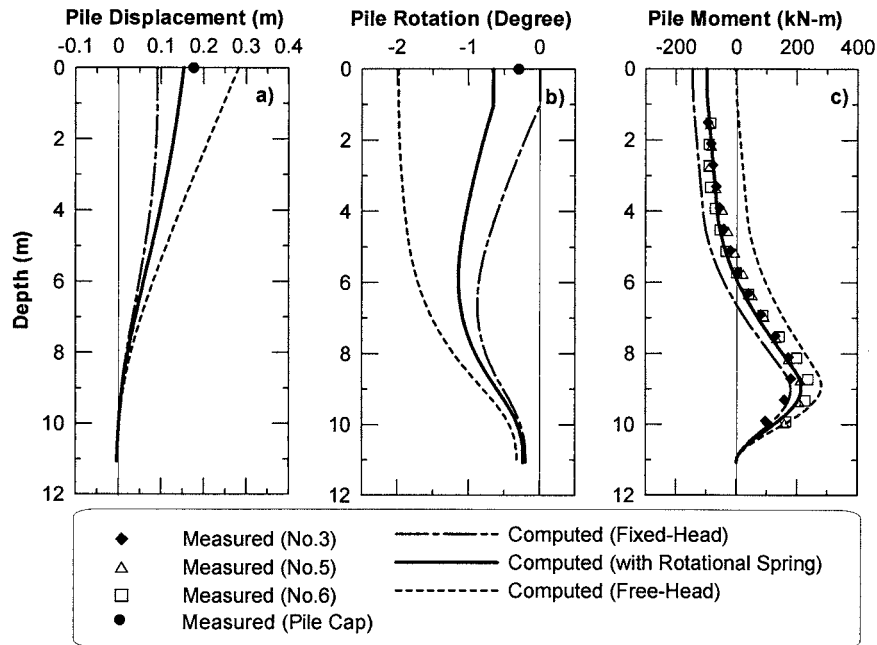


Figure 8. Comparison between measured and computed pile responses for 9-pile group for 1st test

5. CONCLUSIONS

In this study, the push-over analysis using p-y approach was used to predict the behavior of single pile and pile groups subjected to lateral spreading using a single set of baseline soil properties. The analysis results were compared to the results from the full-scale lateral spreading tests in the Port of Tokachi, Japan. Responses of the single piles subjected to lateral spreading were determined by imposing the known free-field soil movement profile measured during the tests to the boundary condition of Winkler springs. Standard p-y springs available in the literature were used to model the stiffnesses of non-liquefied soil layers, while no soil resistance was used for the liquefied soil layer. For the case of pile groups, the piles in the groups were modeled as an equivalent single pile with a flexural stiffness equal to the number of piles in the group multiplied by the flexural stiffness of a single pile within the group. The rotational spring and a decrease of soil spring stiffnesses using p-multiplier approach were incorporated into the pile group model to account for the rotational pile group stiffness and the pile group effect, respectively. Then, the analyses for the case of pile group can be conducted in similar way as the single pile case. Computed pile responses for each pile foundation were compared to the measured responses obtained from the tests. Reasonably good agreement for all types of pile foundations considered in this study was obtained between the computed and measured responses. The results provide justification for the use of push-over analysis using p-y approach in piles subjected to lateral spreading problems.

6. ACKNOWLEDGMENTS

This research was sponsored by the PEER Lifelines Program with support from Caltrans, Pacific Gas & Electric and the California Energy Commission under Contract No. 65A0058, as well as by the Pacific Earthquake Engineering Research Center under NSF Contract No. EEC-9701568.

7. REFERENCES

1. Reese, L. C., Cox, W. R., and Koop, F. D. (1974). "Analysis of laterally loaded piles in sand." *Proc. 6th Offshore Technology Conference*, Paper 2080, Houston, Texas, 473-483.
2. Matlock, H. (1970). "Correlations for design of laterally loaded piles in soft clay." *Proc., 2nd Annual Offshore Technology Conf.*, Paper No. OTC 1204, Houston, Texas, 577-594.

3. Boulanger, R. W., Kutter, B. L., Brandenberg, S. J., Singh, P., and Chang, P. (2003). *Pile Foundations in Liquefied and Laterally Spreading Ground during Earthquakes: Centrifuge Experiments and Analyses*, Report No. UCD/CGM-03/01, Department of Civil and Environmental Engineering, University of California at Davis.
4. Meyersohn, W. D. (1994). "Pile response to liquefaction induced lateral spread." Ph.D. thesis, Dept. of Civil and Environmental Engineering, Cornell University, Ithaca, N.Y.
5. Tokimatsu, K., and Asaka, Y. (1998). "Effects of liquefaction-induced ground displacements on pile performance in the 1995 Hyogoken-Nambu earthquake." *Soils and Foundations*, Special Issue on Geotechnical Aspects of the January 17, 1995 Hyogoken-Nambu Earthquake, 163-177.
6. Japanese Road Association (JRA). (2002). *Specifications for Highway Bridges*, Japan Road Association, Preliminary English Version, prepared by Public Works Research Institute (PWRI) and Civil Engineering Research Laboratory (CRL), Japan, November.
7. Dobry R., Abdoun, T., O'Rourke, T., and Goh, S. H. (2003). "Single piles in lateral spreads: Field bending moment evaluation." *Journal of Geotechnical and Geoenvironmental Engineering*, ASCE, 129 (10), 879-889.
8. Ashford, S. A., and Juirnarongrit, T. (2004). "Performance of lifelines subjected to lateral spreading." *Report No. SSRP-04/18*, Department of Structural Engineering, University of California, San Diego.
9. Seed, H. B., and Idriss, I. M. (1971). "A simplified procedure for evaluating soil liquefaction potential." *JSMFD*, ASCE, 97(9), 1249-1274.
10. Wilson, D. W., Boulanger, R. W., and Kutter, M. L. (2000). "Observed seismic lateral resistance of liquefying sand." *Journal of Geotechnical and Geoenvironmental Engineering*, ASCE, 126(10), 898-906.
11. Tokimatsu, K., Suzuki, H., and Suzuki, Y. (2001). "Back-calculated p-y relation of liquefied soils from large shaking table tests." *Fourth International Conference on Recent Advances in Geotechnical Earthquake Engineering and Soil Dynamics*, S. Prakash, ed., University of Missouri-Rolla, paper 6.24.
12. Ashford, S. A., and Rollins, K. M. (2002). *TILT: Treasure Island Liquefaction Test Final Report*, Report No. SSRP-2001/17, Department of Structural Engineering, University of California, San Diego.
13. Liu, L. and Dobry, R. (1995). "Effect of liquefaction on lateral response of piles by centrifuge model tests." *NCEER Bulletin*, Vol. 9, No. 1, 7-11.
14. Wilson, D. W., Boulanger, R. W., and Kutter, B. L. (1999). "Lateral resistance of piles in liquefying soil." *OTRC'99 Conf. On Analysis, Design, Construction & Testing of Deep Foundations*, J. M. Rosset, ed., Geotechnical Special Publication No. 88, ASCE, 165-179.
15. Reese, L. C., Wang, S. T., Isenhower, W. M., and Arrellaga, J. A. (2000). *Computer Program LPILE Plus Version 4.0 Technical Manual*, Ensoft, Inc., Austin, Texas.
16. Mokwa, R. L. (1999). "Investigation of the resistance of pile caps to lateral spreading." Ph.D. thesis, Dept. of Civil Engineering, Virginia Polytechnic Institute and State University, Blacksburg, Virginia.
17. Mokwa, R. L., and Duncan, J. M. (2003). "Rotational restraint of pile caps during lateral loading." *Journal of Geotechnical and Geoenvironmental Engineering*, ASCE, 129(9), 829-837.

ANALYSIS OF PILES IN LIQUEFYING SOILS

M. Cubrinovski¹⁾

*1) Senior Lecturer, Department of Civil Engineering, University of Canterbury, Christchurch, New Zealand
misko.cubrinovski@canterbury.ac.nz*

Abstract: Two methods for analysis of piles in liquefying soils are discussed and comparatively examined in this paper: an advanced method for dynamic analysis based on the effective stress principle and a simplified analysis based on the pseudo-static approach. The former method aims at an accurate simulation of the complex liquefaction process and soil-pile interaction while the latter is a design-oriented approach aiming at an optimum trade-off between the accuracy and simplicity required in the preliminary assessment and design of piles. Typical models, analysis procedures and characteristic features of both methods are discussed in order to illustrate their advantages and shortcomings and hence provide guidance for their application to the evaluation of seismic performance and design of piles.

1. INTRODUCTION

Soil liquefaction during strong earthquakes significantly affects the performance of pile foundations leading to damage and even collapse of piles. In the 1995 Kobe earthquake, for example, massive liquefaction of reclaimed fills caused damage to numerous pile foundations of buildings, storage tanks and bridge piers. The unprecedented level of damage to foundations of modern structures instigated a great number of research studies in an effort to better understand soil-pile interaction in liquefied soils and to improve the seismic performance of pile foundations. In the initial stage of these studies, detailed field investigations on the damage to piles, in-situ soil conditions and features of permanent ground displacements were conducted. The field investigations were then followed by experimental studies aiming to clarify the mechanism of the damage by means of seismic centrifuge tests, 1-g shake table tests and benchmark experiments on full-size piles. Based on these studies, analysis concepts and procedures have been proposed and examined in an effort to explore design methodologies for piles in liquefied soils. This paper discusses two analysis methods that received particular attention either because of their high potential in modelling the complex soil-pile interaction in liquefying soils or due to the capacity to model the salient features of pile behaviour by a simple approach that is practical for engineering applications.

2. SOIL-PILE INTERACTION IN LIQUEFYING SOILS

Soil-pile interaction in liquefying soils is a very intense dynamic process that involves significant changes in the soil characteristics and interaction loads over a relatively short period of time during and immediately after the ground shaking. In what follows, we will illustrate some typical features of the ground response and loads on piles in liquefying soils through the use of Figure 1.

During the intense ground shaking in loose saturated sandy deposits, the excess pore water pressure rapidly builds up until it eventually reaches the effective overburden stress σ_v , as shown in

Figure 1a. At this stage, the effective stress practically drops to zero and the soil liquefies. In the example shown in Figure 1a from the 1995 Kobe earthquake, the excess pore pressure reached its maximum in just 6-7 seconds, and this was practically the time over which the soil stiffness reduced from its initial value to nearly zero. This intense reduction in stiffness and strength of the soil was accompanied with equally rapid increase in the ground deformation as illustrated with the solid line in Figure 1b where horizontal ground displacements within the liquefied layer are shown. Note that these displacements are cyclic in nature and representative for a free field level ground response. The peak displacements of about 40 cm occurred just before or at the time of development of complete liquefaction and were accompanied with relatively high ground accelerations of about 0.4g. During this phase of intense ground shaking and development of liquefaction, the piles are subjected to both kinematic loads due to ground movement and inertial loads from the vibrations of the superstructure. Both these loads are oscillatory in nature with magnitudes and spatial distributions dependent on a number of factors including ground motion characteristics, soil density, presence of non-liquefied crust layer, and predominant periods of the ground and superstructure, among others.

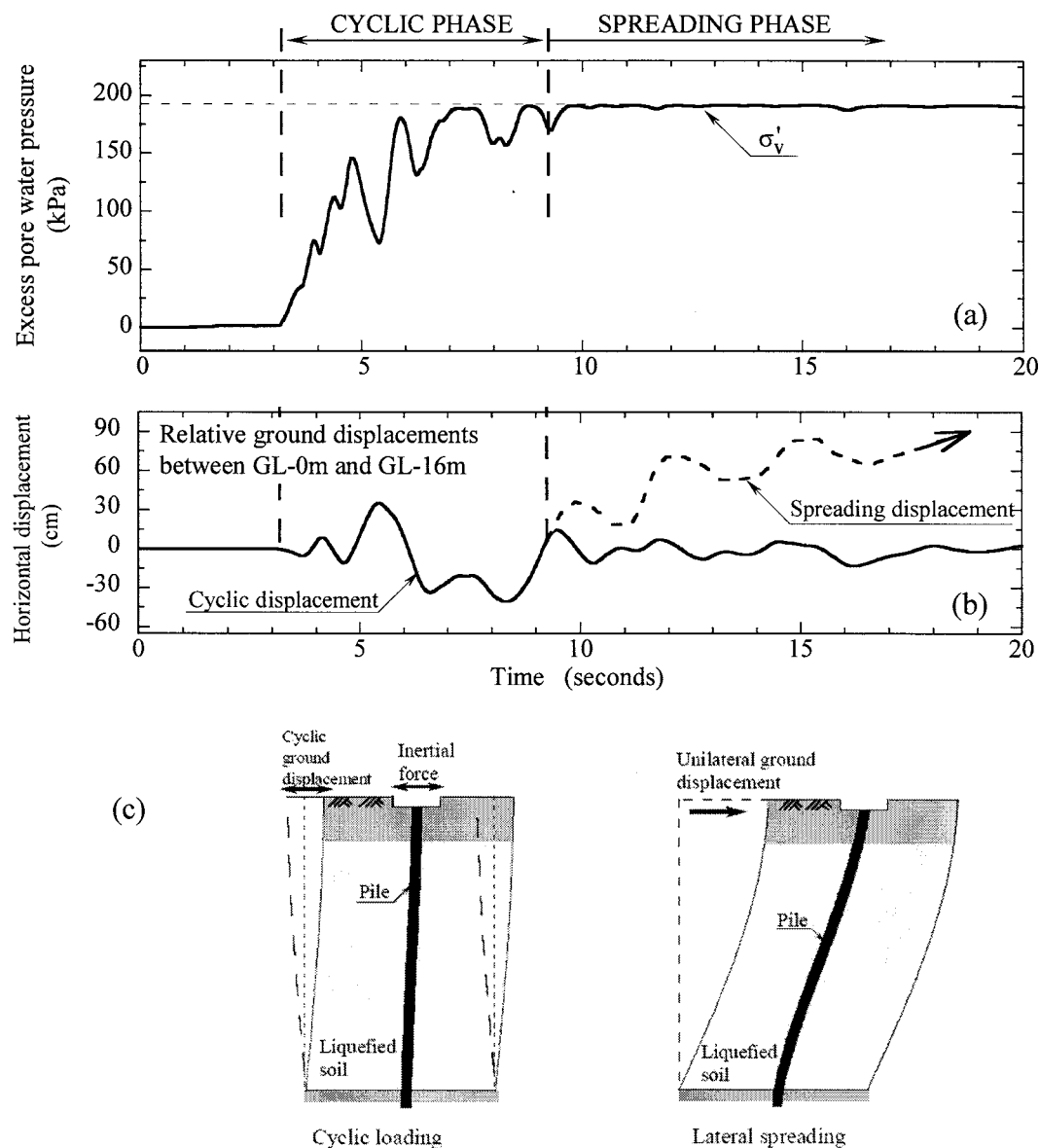


Figure 1. Illustration of ground response in liquefied soils and effects on piles: (a) excess pore water pressure; (b) lateral ground displacements; (c) loads on piles during cyclic loading and lateral spreading

In the subsequent phase of the response following the liquefaction, the stiffness and strength of the liquefied soil remain very low, and hence large unilateral ground displacements may develop due to lateral spreading, as indicated with the dashed line in Figure 1b. Lateral spreads typically develop in sloping ground or in loose backfills behind waterfront structures and often result in excessive permanent displacements of up to several meters in the down-slope or seaward direction. The spreading may be initiated either during the intense pore pressure build up, at the initiation or well after the development of complete liquefaction and hence there are no general rules for combining the kinematic and inertial loads on piles during the spreading phase. In general, however, the ground displacements are approximately one order bigger and the inertial loads are relatively small as compared to those in the cyclic phase of the response, as illustrated schematically in Figure 1c. Thus, when analyzing the behaviour of piles in liquefying soils, it is often useful to distinguish between the cyclic phase and lateral spreading phase of the pile response because the soil characteristics and loads on the pile are quite different between these two phases.

3. METHODS OF ANALYSIS

There are several methods available for analysis of piles in liquefying soils including sophisticated finite element analysis based on the effective stress principle and simplified design-oriented methods based on the pseudo-static approach. The effective stress analysis permits evaluation of seismic soil-pile interaction while considering the complex effects of excess pore water pressure and highly nonlinear stress-strain behaviour of soils in a rigorous dynamic analysis. This method basically aims at very detailed modelling of the complex liquefaction process through the use of advanced numerical procedures. The pseudo-static analysis of piles, on the other hand, is a practical engineering approach for assessment of piles based on routine computations and use of relatively simple models.

3.1 Dynamic Effective Stress Analysis

The dynamic analysis based on the effective stress principle has been established as one of the principal tools for analysis of liquefaction problems. Over the past two decades, the application of the effective stress analysis gradually has expanded from the 1-D analysis of a free-field ground to more complex 2-D analyses involving earth structures and soil-structure interaction systems. Recently, attempts have been made to apply this method to a three-dimensional analysis of large-deformation problems. In what follows, the requirements and advantages of such analysis are illustrated on the example of a 2-D SSI analysis for the analytical model shown in Figure 2.

3.1.1 SSI Model

Figure 2 shows an FEM model of a storage tank on pile foundation embedded in liquefiable soils. Solid elements are used for modelling the soil while beam elements are used for modelling the piles, foundation mat and the tank. Note that the finite element mesh extends throughout the whole model, but was removed from the central part in the figure in order to clarify the foundation soils and geometry. Several important features are apparent in this model. Clearly, the discretization of the soil into finite elements allows a complex geometry and variable soil properties to be modelled. Hence, multiple liquefiable layers with different liquefaction resistance including ground improvement by sand-compaction piles along the perimeter of the pile foundation are incorporated in the model. The model is subjected to an earthquake excitation specified by an acceleration time history at the base of the model.

An elastic-plastic constitutive law is used for modelling the highly nonlinear stress-strain behaviour of the soil including practically all aspects of cyclic undrained behaviour of liquefiable soils. It allows for dilatancy effects, stiffness degradation including the extreme strain-softening and precise simulation of the cyclic strength or liquefaction resistance observed in laboratory tests. Hence the

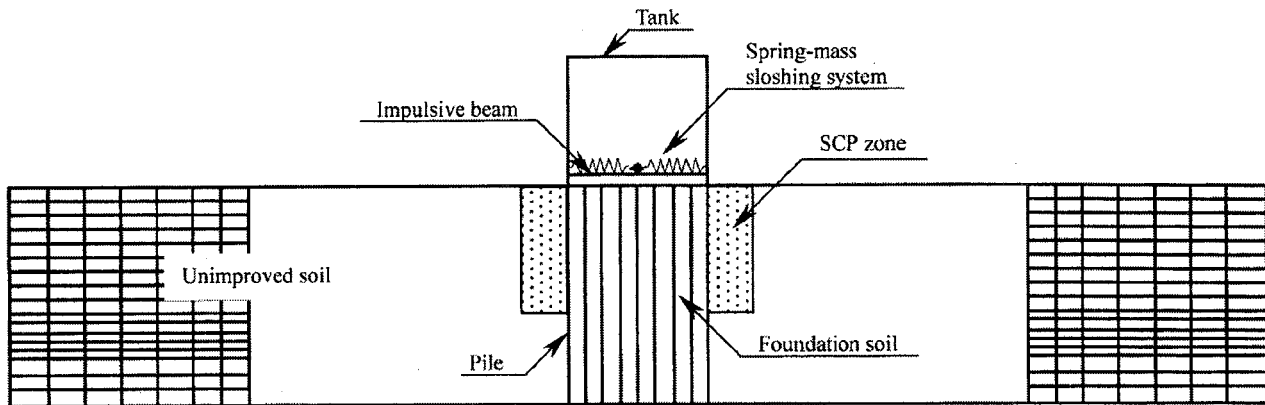


Figure 2. Finite element model for seismic effective stress analysis of a soil-pile-tank system

model shown in Figure 2 permits to analyze the soil-pile-structure-fluid system under dynamic excitation in a step-by-step procedure by considering the key features of liquefaction including development of excess pore pressure and its effects on the variation of stiffness and strength of soils.

3.1.2 Implementation

Whereas the predictive capacity of the effective stress analysis has been verified in many studies (e.g. Ishihara and Cubrinovski, 2005; Cubrinovski et al., 2005), its application in engineering practice is constrained by two key requirements of this analysis, namely, the required high-quality data on in-situ conditions, physical properties and deformational behaviour of soils, and quite high demands on the user regarding the knowledge and understanding of the phenomena considered and the particular features of the adopted numerical procedure.

By and large, an effective stress analysis involves the following steps:

1. *Determination of parameters of the constitutive model*
2. *Definition of the numerical model*
3. *Dynamic analysis and interpretation of results*

Figure 3 summarizes these steps including the details described below.

In the first step, parameters of the constitutive model are determined using results from laboratory tests on soil samples and data from in-situ investigations. The types of laboratory tests are usually model-specific and usually include tests for determination of stress-strain relationships of soils and liquefaction tests. Whereas most of the constitutive model parameters can be directly evaluated from the laboratory tests and in-situ data, some parameters are determined through a calibration process in which best-fit values for the parameters are identified in simulations of laboratory tests (element test simulations).

Following the selection of appropriate element types, mesh size and geometry, key issues in the definition of the numerical model are the determination of the initial stress state and selection of appropriate boundary conditions for the dynamic analysis including treatment of discontinuities. Stress-strain behaviour and liquefaction resistance of soils are strongly affected by the initial stress state, and therefore, an initial stress analysis is required to determine the static normal and shear stresses in all elements of the model. Selection of appropriate boundary conditions along end-boundaries and soil-pile-footing interfaces are equally important for an unconstrained response and development of relevant deformation modes.

Considering the geometry of the problem and anticipated behaviour, numerical parameters such as computational time increment and numerical damping are eventually adopted, and the dynamic effective stress analysis is then executed. The analysis is quite demanding on the user in all these steps including the final stages of post-processing and interpretation of results since it requires a good

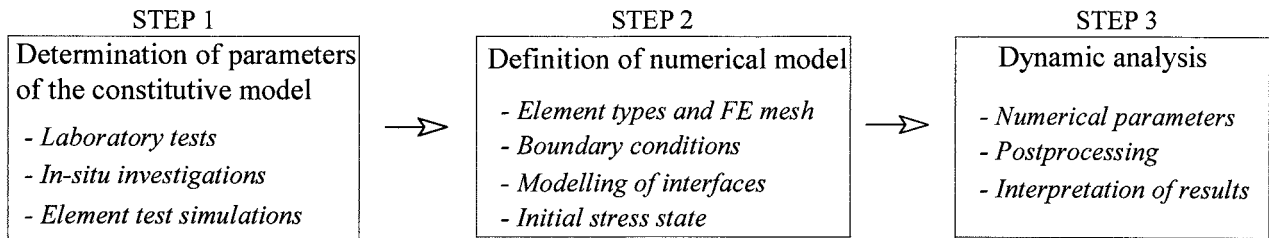


Figure 3. Principal steps in the implementation of effective stress analysis

command of the numerical tools and understanding of the problem and stress-strain behaviour of soils and piles.

3.2 Pseudo-Static Analysis

For preliminary assessment and design of piles, a simplified analysis may be more appropriate provided that such analysis: (i) captures the mechanism associated with liquefaction and lateral spreading; (ii) permits estimation of the inelastic response and damage to piles, and (iii) addresses the uncertainties associated with liquefaction and lateral spreading. The pseudo-static analysis of piles in liquefying soils introduced below was developed based on these premises.

Unlike the effective stress analysis which aims at simulating the very complex process in detail as it develops through time, the pseudo-static analysis aims at estimating the maximum pile response by using the salient mechanism of deformation and a relatively simple model. The key issue in such analysis is thus the selection of appropriate values for the deformational properties and loads on the pile that represent the soil and loading conditions at the time when the maximum response of the pile develops. As discussed in Section 2, the liquefaction characteristics and lateral loads on piles vary significantly in the course of ground shaking and are therefore quite different between the cyclic phase and subsequent lateral spreading phase of the pile response. For this reason, the cyclic phase and lateral spreading phase are treated separately in the pseudo-static analysis.

3.2.1 Soil-pile model

The most frequently encountered soil profile for piles in liquefied deposits consists of three distinct layers, as shown in Figure 4 where the liquefied layer is sandwiched between a non-liquefied crust layer at the ground surface and non-liquefied base layer. It is commonly assumed that during the

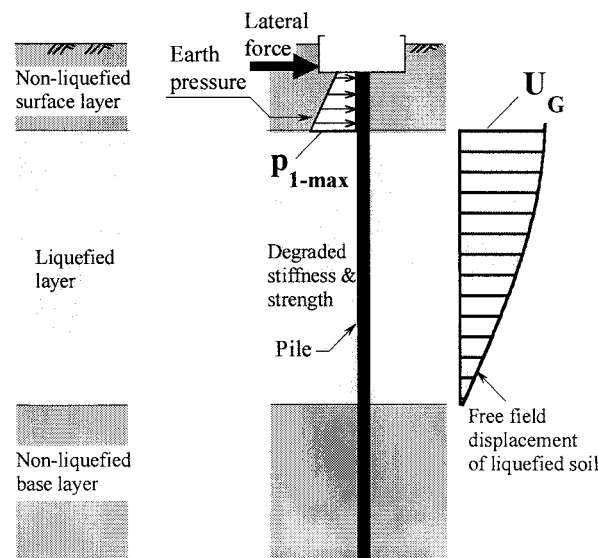


Figure 4. Simplified kinematic mechanism for piles in liquefiable soils

lateral ground movement in the course of shaking and spreading, the non-liquefied layer at the ground surface is carried along with the underlying spreading soil, and when driven against embedded piles, the crust layer is envisioned to exert large lateral loads on the piles, as indicated with the earth pressure in Figure 4. Thus, key features that need to be considered in the simplified pseudo-static analysis are the significant stiffness and strength reduction in the liquefied layer, excessive lateral movement of the liquefied soil, large lateral loads from the crust layer, and lateral load at the pile head due to inertial effects.

Based on these assumptions, both conventional discrete beam-spring models (Figure 5) and closed-form solutions based on simplified three-layer models (Cubrinovski and Ishihara, 2004) have been developed for the pseudo-static analysis of piles. The former approach permits more rigorous analysis because it allows variation of soil (spring) properties and irregular distribution of ground displacement throughout the depth; the latter approach, on the other hand, is appealing to the engineering practice because of its simplicity both in the preparation of input data and interpretation of results.

3.2.2 Key parameters and uncertainties

Input parameters for the three-layer model and adopted simple characterization of nonlinear behaviour of the soil and pile are shown in Figure 6. As indicated in Figures 5 and 6, the lateral ground displacement (kinematic load) and force at the pile head (load transferred through the upper foundation including inertial effects) are the only external loads applied to the soil-pile model. It is very difficult to reliably predict this loads, however, in particular the magnitude and spatial distribution of spreading displacements, and the combination of lateral ground displacement and inertial load relevant for the cyclic phase of the response.

The bilinear p - δ relationships for the soil shown in Figure 6 are defined by the initial stiffness through the conventional subgrade reaction approach and by the ultimate lateral soil pressure, p_{max} . The subgrade reaction coefficients k can be evaluated using empirical correlations based on the elastic property of the soil or SPT blow count while the ultimate lateral pressure for the non-liquefied layers can be estimated based on the Rankine passive pressure, as described in Cubrinovski and Ishihara (2004).

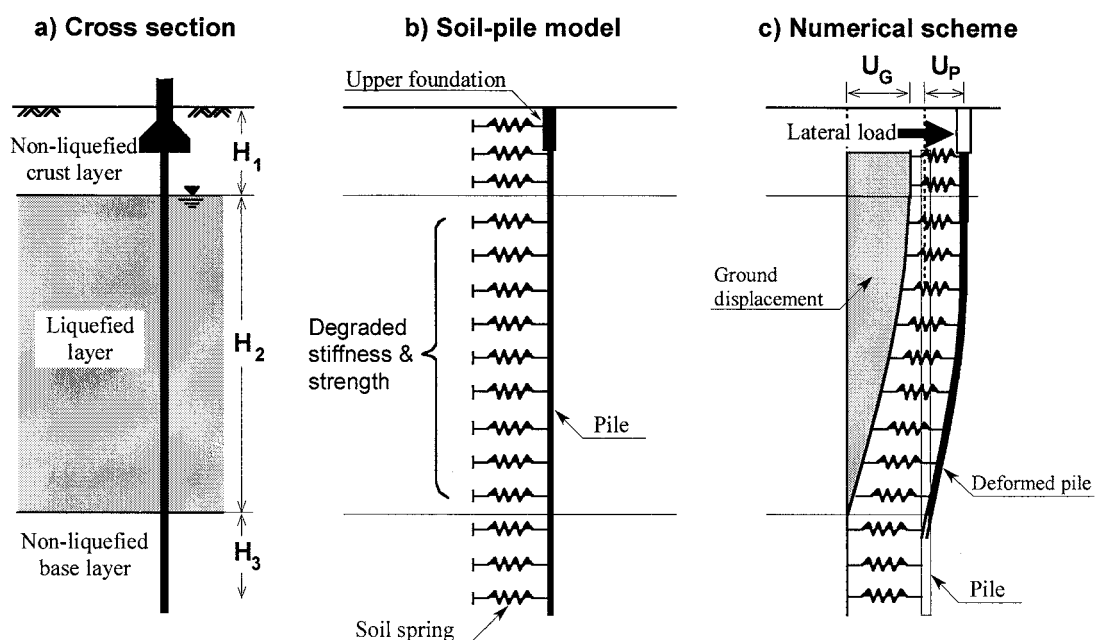


Figure 5. Typical FEM beam-spring model for pseudo-static analysis of piles

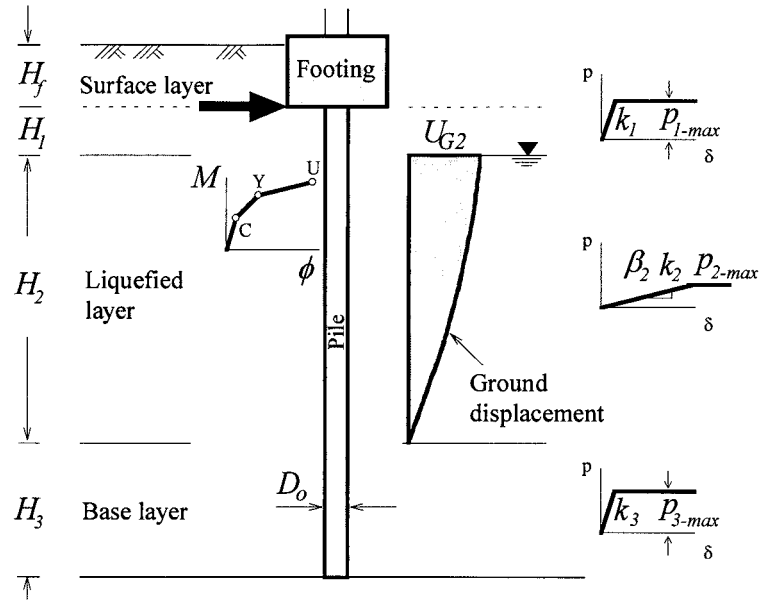


Figure 6. Characterization of nonlinear behaviour and input parameters for pseudo-static analysis

Here, particularly influencing for the pile response is the ultimate pressure from the crust layer, p_{1-max} because of the unfavourable point of application of this load and its large magnitude; for single piles under passive loading, this pressure was found to be 4.5 times the Rankine passive pressure (Cubrinovski et al., 2006).

The largest uncertainty is associated with the level of degradation in stiffness and strength of the liquefied soils. In the model, this degradation is accounted through the stiffness degradation factor β_2 and use of the residual strength of liquefiable soils for determining the ultimate pressure p_{2-max} . Experiments on piles and back-calculations from case histories indicate a large variation in these parameters. Typically, β_2 takes values in the range between 1/50 and 1/10 for cyclic liquefaction and between 1/1000 and 1/50 for lateral spreading (Tokimatsu and Asaka, 1998; Cubrinovski et al., 2006). The residual strength can be evaluated using the empirical correlation between the undrained strength and SPT blow count proposed by Seed and Harder (1991), but the scatter of the data is quite large and hence the value of the residual strength may vary significantly for a given SPT blow count, e.g. $S_u = 5$ to 27 for $(N_I)_{60} = 10$.

Because of the uncertainties in the values of key parameters of the model, it is critically important to conduct parametric studies and evaluate the pile response by considering a relatively wide range of relevant values for U_{G2} , β_2 and p_{2-max} in particular. In addition, pile group effects have to be considered since the pseudo-static analysis is commonly conducted by using a single pile model. Provided that variations in the applied loads and key parameters as above are properly considered, the pseudo-static analysis permits to estimate the range of pile response and expected level of damage to pile for the adopted ground and loading conditions. More details on the pseudo-static analysis of piles in liquefying soils can be found in Cubrinovski et al., 2007.

4. CONCLUDING REMARKS

The key characteristics of the dynamic effective stress analysis and pseudo-static analysis of piles in liquefying soils are summarized in Figure 7.

The effective stress analysis aims at detailed modelling of the complex soil-pile interaction in liquefied soils, and hence, this analysis procedure is quite complex and burdened by the large number

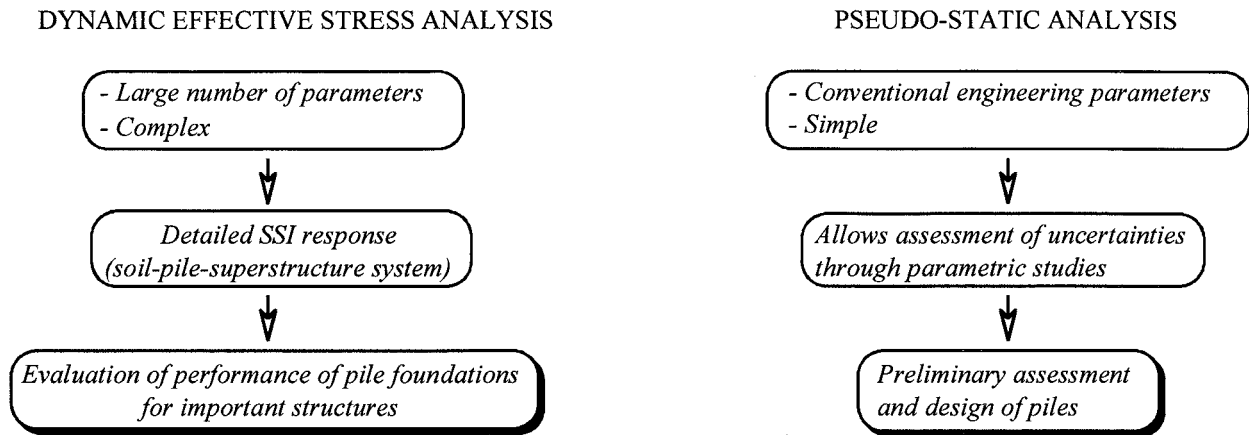


Figure 7. Features of effective stress analysis and pseudo-static analysis of piles in liquefying soils

of parameters and expertise needed for its execution. This analysis, however, permits detailed modelling of the stress-strain behaviour of soils and effects of excess pore pressures throughout the intense ground shaking and subsequent lateral spreading, and hence, allows accurate simulation of the soil-pile interaction including effects from the superstructure. For these reasons, the effective stress analysis is very suitable for a rigorous evaluation of the seismic performance of pile foundations of important structures.

The pseudo-static analysis is a simple design-oriented approach that uses conventional engineering parameters and modelling. For these reasons, it is suitable for preliminary assessment and design of piles. Because of the gross simplification of the problem and significant uncertainties associated with liquefaction and lateral spreading, however, the key parameters in the analysis are not uniquely defined, but rather they may vary over a wide range of values. Thus, when analysing piles with the simplified pseudo-static approach, parametric studies need to be conducted and in order to evaluate the possible range of responses and damage level to the pile. The cyclic phase and lateral spreading phase of the pile response should be treated separately in the pseudo static analysis.

References:

- Cubrinovski, M. and Ishihara, K. (2004), "Simplified method for analysis of piles undergoing lateral spreading in liquefied soils," *Soils and Foundations*, 44(25), 119-133.
- Cubrinovski, M., Sugita, H., Tokimatsu, K., Sato, M., Ishihara, K., Tsukamoto, Y., and Kamata, T. (2005). "3-D numerical simulation of shake-table tests on piles subjected to lateral spreading," *Proc. Geotechnical Earthquake Engineering Satellite Conf.*, Osaka, September 2005, 199-206.
- Cubrinovski, M., Kokusho, T. and Ishihara, K. (2006), "Interpretation from large-scale shake table tests on piles undergoing lateral spreading in liquefied soils," *Soil Dynamics and Earthquake Engineering*, 26, 275-286.
- Cubrinovski, M., Ishihara, K. and Poulos, H. (2007), "Pseudostatic analysis of piles subjected to lateral spreading," *Special Issue Bulletin of NZ Society for Earthquake Engineering* (to be published).
- Ishihara and Cubrinovski (2005), "Characteristics of ground motion in liquefied deposits during earthquakes," *Journal of Earthquake Engineering*, Vol. 9, Special Issue 1, 1-15.
- Seed, R.B. and Harder, L.F. (1991), "SPT-based analysis of cyclic pore pressure generation and undrained residual strength," *H. Bolton Seed Memorial Symposium Proc.*, Vol. 2, 351-376.
- Tokimatsu, K. and Asaka, Y. (1998), "Effects of liquefaction-induced ground displacements on pile performance in the 1995 Hyogoken-Nambu earthquake," *Special Issue of Soils and Foundations*, September 1998: 163-177.

EFFECTS OF CYCLIC LOADING ON MOBILISATION OF EARTH PRESSURE ACTING ON PILE CAPS

A. Takahashi¹⁾, H. Sugita²⁾, and S. Tanimoto³⁾

1) Senior Researcher, Earthquake Disaster Prevention Research Group, Public Works Research Institute, Japan

2) Team Leader, Earthquake Disaster Prevention Research Group, Public Works Research Institute, Japan

3) Researcher, Earthquake Disaster Prevention Research Group, Public Works Research Institute, Japan
aki-taka@pwri.go.jp, sugita@pwri.go.jp, s-tanimo@pwri.go.jp

Abstract: A series of centrifuge model tests were conducted to examine the effect of strain history on the mobilization of lateral earth pressure acting on pile caps. The test results demonstrate the importance of considering strain history when modelling the interaction between a surface soil layer and a pile cap.

1. INTRODUCTION

In lateral resistance of piles with a pile cap, marked contribution of the pile cap resistance can be expected. Recent lateral loading tests on full scale piles with a pile cap (Mokwa & Duncan 2001, Rollins & Sparks 2002, Rollins & Cole 2006, among others) reveal that the pile cap provides large portion (40-50% in the cited papers) of the overall lateral resistance of the pile groups to lateral loads.

Apart from the positive side mentioned above, a pile foundation is vulnerable from the lateral force acting on the pile cap when the foundation soils are susceptible to laterally spread due to liquefaction. Piles have been severely damaged in past earthquakes by a non-liquefied surface layer spreading laterally over an underlying liquefied soil layer and the load induced by the interaction of this surface “crust” with the structure is believed to dominate the response of pile foundations subjected to these conditions (e.g., Berrill & Yasuda 2002, Finn & Fujita 2005).

In any case, mobilisation of the earth pressure acting on pile caps, induced by interactions between the pile cap and surrounding soils, has to be properly considered in pile foundation performance assessments. In this study, a series of centrifuge model tests were conducted to examine the effect of strain history on the mobilization of lateral earth pressure acting on pile caps. This paper shows the importance of considering strain history when modelling the interaction between a surface soil layer and a pile cap.

2. OUTLINE OF PHYSICAL MODEL TESTS

2.1 Model setup

Because the focus of this study was the examination of lateral earth pressure acting on pile caps (and not the pressure acting the piles themselves), a pile cap only —without piles— was modelled. Figure 1 shows a diagram of the centrifuge model package. In a real foundation, the earth pressure acting on a pile cap is the result of the interaction between the moving surface soil layer and foundation. However, because this is difficult to simulate in a centrifuge while controlling the relative displacement between the pile cap and the surrounding soil, the relative displacement was created by horizontally displacing a model pile cap in motionless model ground, using an electric

actuator. In the tests, the model surface layer was relatively thick as shown in Fig. 1. However, as (1) Rollins & Sparks (2002) pointed out that a weak soil layer under the surface layer could make the required displacement to mobilise the full passive pressure larger and (2) Brandenberg et al. (2007) demonstrated such effects using simple load transfer models, the obtained displacement to mobilise the passive earth pressure in this study could be smaller than the cases with a weak soil layer just below pile caps.

A front view of the model pile cap is illustrated in the lower left of Fig. 1. Two 2-directional load cells were placed on the front face of the pile cap to measure the normal and shear stresses acting on the centre and edge of the cap. In order to minimize friction between the pile cap and the surrounding ground at the top, bottom and sides, 0.3mm-thick latex membranes were attached to those faces with grease. Particles of Toyoura sand were glued to the front face, to roughen that surface.

Load tests were performed at 50g by changing the geomaterial, the depth of the pile cap, and the loading pattern, as shown in Table 1. A typical road bridge foundation in Japan has pile caps about 8m wide and 2m thick when it has three cast-in-place concrete piles in a row. According to scaling laws for the geotechnical centrifuge modelling, the model pile cap should be 1/50 of that size when the tests are conducted at 50g. However, due to the limited capacity of the electric actuator used, the tests were performed on a 1/100 model at 50g.

2.2 Materials used

For the tests using Toyoura sand, specimens were prepared by the air-pluviation method, using air-dried sand. For the tests using Edosaki sand, specimens with a near-optimum water content of 15% were compacted in layers to a dry density of 1.49Mg/m^3 (bulk density $\rho_t = 1.72\text{Mg/m}^3$) on the laboratory floor, corresponding to a relative compaction of 90%. However, drainage induced during centrifugal acceleration of the model ground to 50g resulted in a final estimated average water content of about 10%, $\rho_t \approx 1.65\text{Mg/m}^3$. The strength parameters for the material used are summarised in Table 2.

2.3 Test conditions

Two cyclic loading conditions were adopted in this study: (1) One is to gradually increase horizontal relative displacement between the surface layer and pile cap during cyclic loading, and (2) “two-way” cyclic loading followed by the monotonic loading. The former may correspond to a soil-abutment interaction (as seen in Takahashi et al., 2007) or soil-pile foundation interaction in the laterally spreading soil during earthquake. These impose different strain histories on the surface soils, along with a potential for differences in the mobilization of lateral earth pressure acting against a pile cap. To investigate these types of strain history effects on lateral earth pressure mobilization, three loading patterns were employed, as shown in Table 1. “Cyclic1” corresponds to the first loading pattern described above, while “Cyclic2” is the second. In addition to these two patterns, monotonic loading was also conducted. Typical loading patterns are illustrated in Fig. 2. The tests were performed “statically” in order to remove potential inertia forces; a very slow loading rate (3mm/min) was used in all the loading cases.

3. TEST RESULTS AND DISCUSSION

3.1 Overall soil responses during cyclic loading

Figure 3 shows how the mobilized earth pressure coefficient, $K = \sigma_h / \sigma_v$, varies with the normalized horizontal displacement of the pile cap, u/H , for the air-dried Toyoura sand cases. The mobilized earth pressure coefficient was calculated from the average horizontal stress acting on the pile cap, which was measured at L1 and L2. The displacement required to reach the first peak is smallest for the Cyclic2 loading pattern, largest for the Monotonic loading, and intermediate for Cyclic1. Even though the graph in Fig. 3 is crowded with data points in the small displacement

region, this behaviour can be seen for both of the pile cap embedment depths that were tested. This indicates that sand which has undergone many strain cycles (amplitudes of the imposed strain may also affect the result though) before reaching a first peak in mobilized earth pressure will reach that first peak after a smaller displacement than a sand that has been subject to a small number of strain cycles (cf. Fig. 4 in the following subsection). The results also show, as expected, that increasing the pile cap embedment depth will increase the amount of horizontal displacement necessary to reach the first earth pressure peak.

These results may be related to the relocation of soil adjacent to the pile cap that occurs when the cap moves away from the soil during the unload phase of an unload-reload cycle. Leftward movement ($\Delta u < 0$) of the cap creates an active state in the soil adjacent to the cap, as shown by a rapid drop in the earth pressure (cf. Fig. 4 in the following subsection). This allows the soil adjacent to the cap to move downward, filling a gap that has formed between the cap and the surrounding soil, i.e., the local failure of the ground occurs during this process. Successive reloading cycles ($\Delta u > 0$) act to compact the in-filled sand. Particularly near the bottom of the pile cap, as the gap is fully filled with sand as long as the enough sand supply from the top exists, this compaction hardens the adjacent soil and causes higher strains in the soil distant from the cap than would be likely to occur without such cycles. Therefore, a pile cap that has experienced cyclic displacement relative to the surrounding soil requires a smaller displacement to cause general shear failure of the soil in front of the cap. (However, the Edosaki sand cases showed different soil responses, as discussed in the following subsection.)

Displacement beyond the first peak in earth pressure resulted in large geometrical changes to the ground surface, and the earth pressure vs. displacement curves become more complicated. In every case except for monotonic loading with $D/H = 2$ [†], the first peak is followed by several more peaks (e.g., local maximal points can be seen at $u/H = 6, 36, 75\%$ for Cycle1 with $D/H = 1$). The interval between peaks depends upon the loading history and the embedment depth of the pile cap, as follows: (1) the larger the number of loading cycles (Cycle2, Cycle1 and Monotonic, in descending order), the shorter the interval between peaks, and (2) the larger the pile cap embedment depth, the longer the interval between peaks. Visual observation of the ground surface during the tests revealed that the drop in the earth pressure coincided with the appearance of the edge of a slip plane on the ground surface (a shear zone); outer slip surfaces, further from the pile cap, were observed during subsequent drops in the earth pressure.

In brief, the large displacement of the pile cap greatly changes the geometry of the ground surface and hence causes many local maximal points in the earth pressure vs. displacement curves depending on the strain history. In many cases implementation of this feature may not be relevant in design practice. However, in the case that the lateral spreading of liquefiable soils dominates the pile foundation responses, consideration of fluctuation of the passive earth pressure or determination of representative value for the upper limit of the earth pressure can be a crucial factor.

Apart from the geometrical change of the ground surface, the process of the local failure and compaction of the soil adjacent to the pile cap in the cyclic loading can make larger the strain imposed to the soil distant from the cap, resulting in a smaller displacement to cause general shear failure of the soil in front of the cap. Not only the timing of the passive earth pressure mobilisation, but also the relationship between the earth pressure and displacement during cyclic loading before reaching the passive state are affected by the response of the soil adjacent to the pile cap. Detailed observation of the adjacent soil behaviour during the cyclic loading is described and discussed in the following sections.

3.2 Responses of dry clean sand

Relationships between the earth pressure and displacement for the Toyoura sand (air-dried sand)

[†] If the larger displacement is imposed, several peaks could be observed for this case as well.

are shown in Fig. 4, together with the evolutions of the heave of the ground surface in the proximity of the cap at DV3 (see Fig. 1). In all the cases, the mobilised earth pressure rapidly drops down to the active state when unloaded. After that, as soon as the re-loading starts, the earth pressure starts increasing to reach the passive state and the state points in the earth pressure vs. displacement plane seems to move toward the unloading point whose displacement is the largest in a loading history, once the earth pressure reaches the passive state.

Addition to these, detailed observation reveals the followings: (1) In Cyclic2, the mobilised earth pressure increases with each successive loading cycle in a loading phase when the earth pressure is well below the passive earth pressure, while it shows degradation in the earth pressure vs. displacement curve when the earth pressure is proximity to or reaches the passive state*. (2) In Cyclic1, the state point in the earth pressure vs. displacement plane moves toward the unloading point whose displacement is the largest in a loading history in Phases 1 and 2 ($u/H < 50\%$) even after reaching the first peak in the earth pressure vs. displacement curve, while it shows similar trend observed in Cyclic2 and the degradation occurs when the imposed displacement becomes large ($u/H > 50\%$) as seen in Fig. 3. Although the degradation due to the cyclic loading is reported in the published papers for piles and pile caps (Shirato et al. 2006, Rollins & Cole 2006, among others) the increase of the mobilised earth pressure with each successive loading cycle does not seem to emphasis in the previous works.

3.3 Differences between dry clean sand and partially saturated compacted sand with fines

The earth pressure vs. displacement curves for the Edosaki sand are shown in Fig. 5, together with the evolutions of the heave of the ground surface in the proximity of the cap at DV3. The Edosaki sand tests were designed to model more realistic conditions, in which the surface soil may be partially saturated, and is likely to contain fines. When $D/H = 1$, pre-peak strains in the Edosaki sand have an effect similar to the effect seen in the Toyoura sand: a certain number of strain cycles before the first peak in mobilized earth pressure results in a smaller required displacement to reach that peak, although no large difference was observed in the earth pressure vs. displacement curves between Cyclic1 and Cyclic2. On the other hand, when $D/H = 2$, this effect was not seen, at least not in the small displacement region where $u/H < 20\%$ and the envelopes of the curve are approximately identical, irrespective of the loading pattern (although some effect can be seen in the larger displacement region).

Before describing observations for the Edosaki sand cases in detail, the following fact should be noted: In the cases where $D/H = 1$, i.e., the no covering soil existed above the top surface of the pile cap, excessive evaporation occurred and it may have led to drying and desiccation of the soil surface exposed to the air at the gap between the pile cap and adjacent soil as well as the ground surface in Cyclic1 and Cyclic2, due to the spinning of the centrifuge. This desiccation reduced the water content of the soil adjacent to the pile cap and probably made the adjacent soil stiffer and stronger during the course of the cyclic loading, resulting in the large passive earth pressure in Cyclic1 and Cyclic2, while such large difference was not observed in the cases where $D/H = 2$ since the gap between the pile cap and adjacent soil was not exposed and the drying and desiccation of the soil surface little affected on the passive resistance. Due to this fact, hereafter detailed comparisons of the soil responses between monotonically and cyclically loaded soils for the Edosaki sand cases where $D/H = 1$ will not be made.

In the Edosaki sand cases, irrespective to the embedment depth of the pile cap, the reload curve retraces the unload curve, suggesting that ‘refilling’ of the soil did not occur during unload—reload cycles due to the apparent cohesion, at least, before reaching the passive earth pressure. Once the mobilised earth pressure reaches the passive state, the gap seems to be partially filled by the soil during the unloading stage in the larger displacement region ($u/H > 10\%$) for the cases where

* Due to the limited number of pages, the figures that explain these features could not be included in the paper.

$D/H = 2$. Tokimatsu (2003) performed a series of large scale shake table tests on a pile foundation in horizontally layered sand with fines ($F_c = 5.4\%$) and observed a similar trend in the mobilization of the lateral earth pressure acting on pile caps. Rollins and Cole (2006) conducted a series of the cyclic loading tests on piles with a pile cap and used four different materials (from the fine sand to coarse gravel) for the backfill. They also reported that the gap appeared during the one-way cyclic loadings and got larger with increase of the input displacement magnitude. What these, including the Edosaki sand cases in this study, have in common is the fact that the soils surrounding the pile caps are partially saturated, which is contrast to the condition for the dry Toyoura sand cases described in the previous subsections. These results suggest that the mechanism causing changes in the earth pressure mobilization in Edosaki sand with apparent cohesion is different from the mechanism at work in the dry Toyoura sand tests.

For $D/H = 2$, the heaving near the cap as well as the envelopes of the earth pressure vs. displacement curve are approximately identical, irrespective of the loading pattern in the small displacement region. The small and similar heave of the ground surface in the proximity of the cap during that stage suggests that pile cap displacement contributes to localised deformation of the soil adjacent to the cap, but does not have a large effect on strains in the soil distant from the cap. As a result, no marked difference could be seen in the envelopes of the curve.

3.4 Soil stiffness in unloading stages

The process of the local failure and compaction of the soil adjacent to the pile cap in the cyclic loading did have effects on the earth pressure mobilisation in the dry sand while it had little effects for the compacted pit run (Edosaki) sand. For the latter, the earth pressure vs. displacement curve can be modelled, provided (1) the backbone curve for the earth pressure and displacement relation and (2) the slope of the curve when unloaded, as the backbone curve is almost identical irrespective to the loading patterns and the reload curve retraces the unload curve.

Figure 6 plots relationships between the soil stiffness in unloading and the earth pressure just before unloading. The soil stiffness is taken as the slope of a linear portion of the unloading curve. Even though the plots are scattered, the soil stiffness in unloading stages increases with the earth pressure just before unloading. This suggests that the soil stiffness in unloading stages can be modelled as a function of the earth pressure just before unloading, especially for the Edosaki sand. However, Cole and Rollins (2006) reported different tendency in the soil stiffness change: They performed a series of the cyclic loading tests on full-scale piles with a pile cap and plotted the soil stiffness for reloading, which is equivalent to that for unloading in a previous loading stage, against the displacement and concluded that the soil stiffness “reduction” relationship with displacement can be modelled by nonlinear hyperbolic relationship, i.e., the soil stiffness in the very first loading is the maximum and degrades with displacement. (The larger the displacement, the larger the mobilised earth pressure in their tests.) Since they extracted the relationship between the earth pressure acting on a pile cap and displacement from the pile loading tests with some assumptions for the piles’ contributions, perhaps their results are affected by the existence of piles.

4. SUMMARY

Centrifuge model tests were conducted to demonstrate the importance of considering the effect of strain history on the load-displacement characteristics of a surface soil layer in the soil-pile cap interaction.

The tests on dry sand show that pre-peak cyclic strains in the surface soil markedly reduce the relative displacement between the soil and pile cap that is required to reach the maximum lateral earth pressure. The process of the local failure and compaction of the soil adjacent to the pile cap in the cyclic loading can make larger the strain imposed to the soil distant from the cap, resulting in a smaller displacement to cause general shear failure of the soil in front of the cap. Not only the timing of the

passive earth pressure mobilisation, but also the relationship between the earth pressure and displacement during cyclic loading before reaching the passive state are affected by the response of the soil adjacent to the pile cap. This tendency is more prominent when the covering soil thickness is small.

When the surface layer is partially saturated and compacted sand with fines (like a real pit-run sand), these features were less pronounced. For such soils, the earth pressure vs. displacement curve can be modelled, provided (1) the backbone curve for the earth pressure and displacement relation and (2) the slope of the curve when unloaded, as the backbone curve is almost identical irrespective to the loading patterns and the reload curve retraces the unload curve. The test results suggest that the soil stiffness in unloading stages can be modelled as a function of the earth pressure just before unloading.

References:

- Berrill, J. & Yasuda, S. (2002), "Liquefaction and piled foundations: some issues," J. Earthquake Eng., Vol.6, Special Issue 1, 1-41.
- Brandenberg, S.J., Boulanger, R.W., Kutter, B.L. & Chang, D. (2007), "Liquefaction-induced softening of load transfer between pile groups and laterally spreading crusts," J. Geotechnical and Geoenvironmental Engineering, ASCE, Vol.133, No.1, 91-103.
- Cole, R.T. & Rollins, K.M. (2006), "Passive earth pressure mobilisation during cyclic loading," J. Geotechnical and Geoenvironmental Engineering, ASCE, Vol.132, No.9, 1154-1164.
- Finn, W.D.L. & Fujita, N. (2005), "Piles under seismic excitation and lateral spreading in liquefiable soils," Proc. Geotech. Earthquake Eng. Satellite Conf. -Performance based design in earthquake geotechnical engineering: concepts and research-, Osaka, Japan, 207-214.
- Mokwa, R.L. & Duncan J.M. (2001), "Experimental evaluation of lateral-load resistance of pile caps," J. Geotechnical and Geoenvironmental Engineering, ASCE, Vol.127, No.2, 185-192.
- Rollins, K.M. & Cole, R.T. (2006), "Cyclic lateral load behavior of a pile cap and backfill," J. Geotechnical and Geoenvironmental Engineering, ASCE, Vol.132, No.9, 1143-1153.
- Rollins, K.M. & Sparks, A. (2002), "Lateral resistance of full scale pile cap with gravel backfill," J. Geotechnical and Geoenvironmental Engineering, ASCE, Vol.128, No.9, 711-723.
- Shirato, M., Koseki, J. & Fukui, J. (2006), "A new nonlinear hysteretic rule for Winkler type soil-pile interaction springs that considers loading pattern dependency," Soils and Foundations, Vol.46, No.2, 173-188.
- Takahashi, A., Sugita, H. & Tanimoto, S. (2007), "Forces acting on bridge abutments over liquefied ground," Accepted for publication in Soil Dynamics and Earthquake Engineering as of 22 December 2006.
- Tokimatsu, K. (2003), "Behavior and design of pile foundations subjected to earthquakes," Proc., 12th Asian regional conference on soil mechanics and geotechnical engineering, Vol.2, 1065-1096.

Table 1: Centrifuge model tests conditions

Materials:	Dry Toyoura sand ($\rho_s = 2.66 \text{ Mg/m}^3$, $D_{50} = 0.18 \text{ mm}$, $D_r = 70\%$) or Partially saturated Edosaki sand ($\rho_s = 2.68 \text{ Mg/m}^3$, $D_{50} = 0.25 \text{ mm}$, $F_C = 8.2\%$, $w_{opt} = 15\%$, $w \approx 10\%$, $\rho_t \approx 1.65 \text{ Mg/m}^3$, Relative compaction = 90%)
Depth of pile cap, D :	$D/H = 1$ or 2 (H = Pile cap height)
Loading patterns:	<ul style="list-style-type: none"> Monotonic Cyclic1 (Horizontal relative displacement between soil and pile cap gradually increases during cyclic loading.) Cyclic2 ("Two-way" cyclic loading followed by monotonic loading)

Table 2: Peak strength parameters from direct shear tests

Material	ϕ	c	Range of σ_v (kPa)
Toyoura sand	40.8	7.5	9.8 – 98
Toyoura sand and pile cap	33.2	11.9	49 – 196
Edosaki sand	37.1	9.7	9.8 – 98
Edosaki sand and pile cap	33.7	17.2	49 – 196

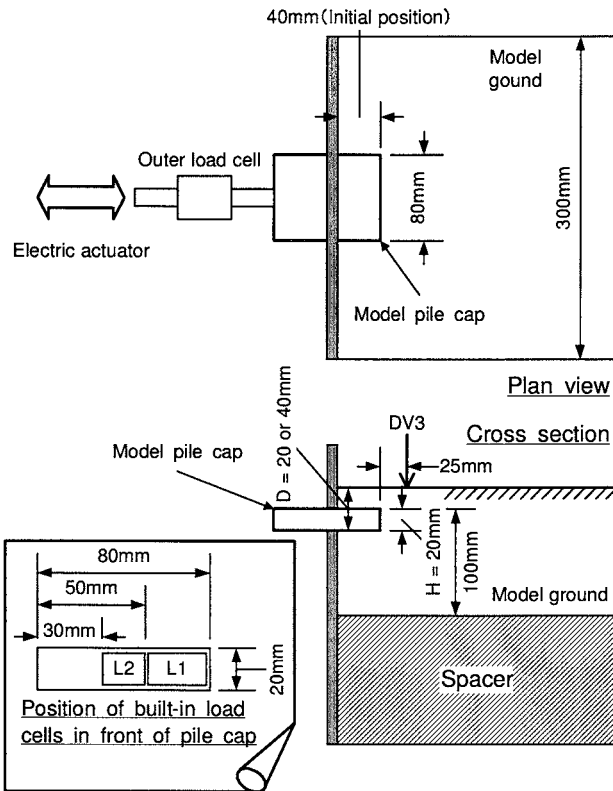


Figure 1: Centrifuge model package

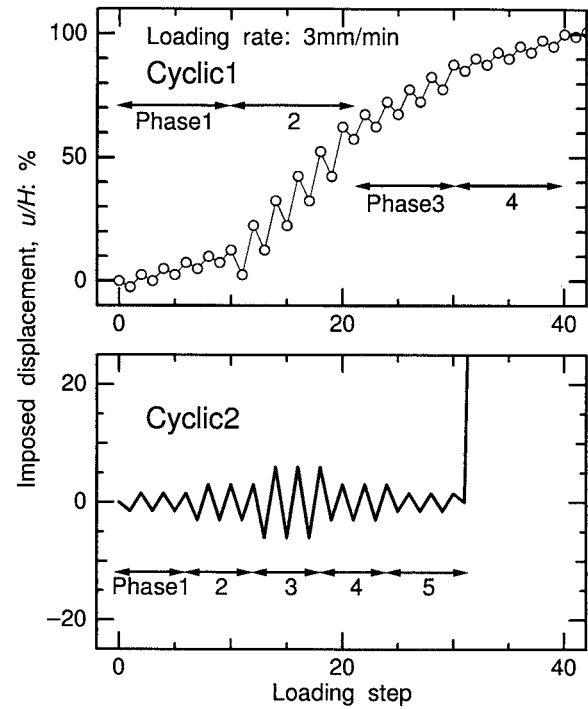


Figure 2: Typical loading patterns

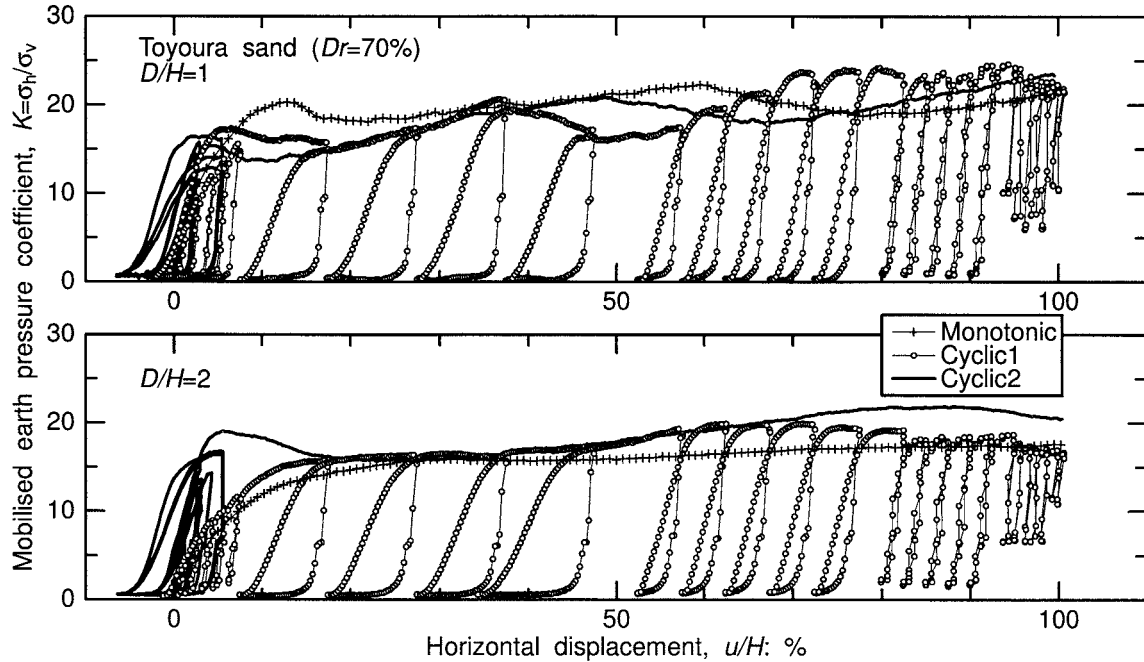


Figure 3: Mobilised earth pressure coefficient, $K = \sigma_h / \sigma_v$, against normalised horizontal displacement of the pile cap, u/H , for Toyoura sand cases

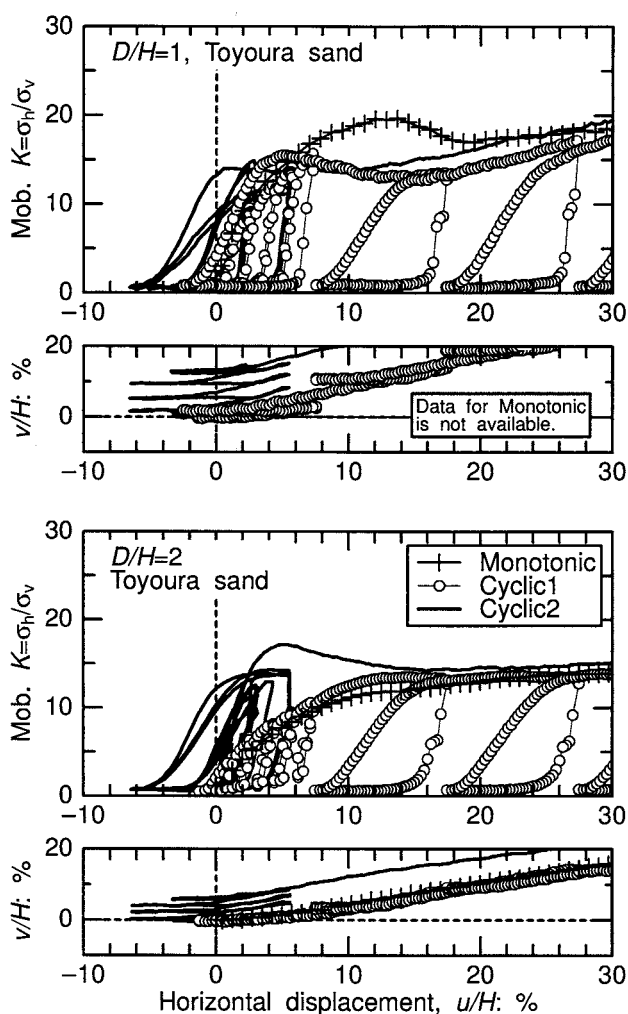


Figure 4: Mobilised earth pressure coefficient, $K = \sigma_h / \sigma_v$, normalised vertical heaving at DV3, v/H , against normalised horizontal displacement of the pile cap, u/H , measured at centre of pile cap (L2) for Toyoura sand cases

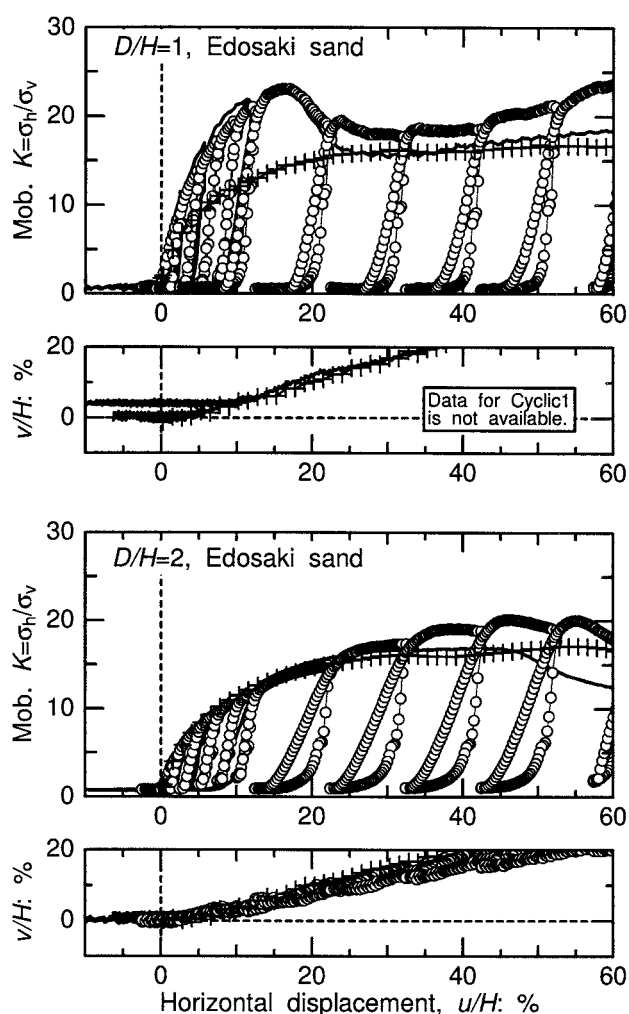


Figure 5: Mobilised earth pressure coefficient, $K = \sigma_h / \sigma_v$, normalised vertical heaving at DV3, v/H , against normalised horizontal displacement of the pile cap, u/H , measured at centre of pile cap (L2) for Edosaki sand cases

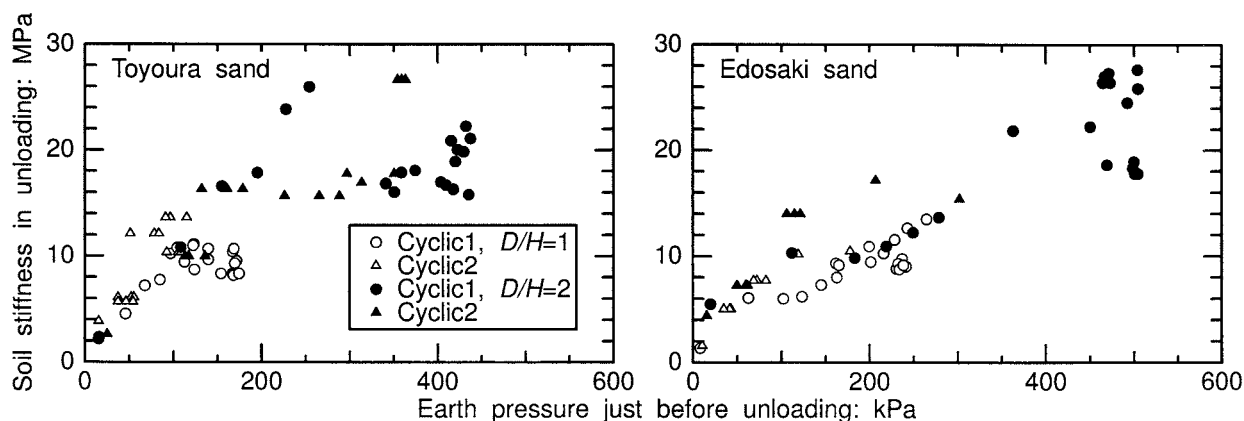


Figure 6: Relationships between soil stiffness in unloading and earth pressure just before unloading

FRAGILITY CURVES FOR LATERAL-SPREADING INDUCED DAMAGE TO THE LANDING ROAD BRIDGE

P. Kashighandi¹⁾, and S.J. Brandenburg²⁾

1) Graduate Student, Dept. of Civil and Env. Engineering, University of California, Los Angeles, United States

2) Assistant Professor, Dept. of Civil and Env. Engineering, University of California, Los Angeles, United States
pirooz@ucla.edu, sjbrandenberg@ucla.edu

Abstract: Fragility curves are developed for damage caused to the Landing Road Bridge by liquefaction and lateral spreading of the surrounding soils. The bridge suffered moderate damage due to lateral spreading of up to 2 m of the surrounding soils due to the 1987 Edgemoor earthquake. Suites of beam on nonlinear Winkler foundation analyses are performed using the software package OpenSees to characterize the influence of uncertainty in the input parameters and loading conditions on the predicted damage. The fragility curves predict an 82% probability of the bridge being in at least damage state 3 (moderate damage), a 42% probability of being in at least damage state 4 (extensive damage) and a 5% probability of collapse for 2 m of lateral spreading displacement. These results are consistent with the moderate damage observed to the Landing Road Bridge. Crust load and soil displacement profile were the input parameters whose uncertainty most affected the analysis results. Increasing the crust thickness from 1.2 m to 1.7 m causes the predicted probability of collapse to increase from 5% to 60%.

1. INTRODUCTION

Bridges are susceptible to damage in areas of liquefaction, particularly when a nonliquefied crust spreads laterally on top of underlying liquefiable layers. Recent research has clarified many aspects such as load transfer behavior between piles and liquefied sand, load transfer between pile caps and laterally spreading crusts, and effects of pinning forces exerted by bridge components on spreading finite-width approach embankments (e.g., Boulanger and Tokimatsu 2005). These fundamental findings provide important guidance for improving our analytical predictions of bridge response, but evaluation with case history data is required to assess the reliability of the design methods.

A range of bridge damage has been observed in areas of liquefaction and lateral spreading in past earthquakes. Analytical methods are often calibrated based on their ability to predict collapse (e.g., Dobry et al. 2003), while the ability to predict intermediate structural damage is often left unexplored. However, there is a need for analyses to be able to predict the gamut of potential damage states, and to account for the various sources of uncertainty in the input parameters and loading conditions. Kiremidjian et al. (2006) performed transportation network analyses that used the fragility curves for liquefaction-induced damage to bridges inherent to the program HAZUS (1999), and predicted unrealistically widespread bridge collapse caused by liquefaction. These analyses identified a need for improved, more realistic fragility curves for probabilistically predicting damage to bridges caused by liquefaction and lateral spreading. Furthermore, the California Department of Transportation (Caltrans) has screened its approximately 13,000 bridges for damage potential due to ground shaking, while damage caused by liquefaction and lateral

spreading has not been systematically evaluated for every bridge. Improved fragility functions are needed to screen these bridges for liquefaction-induced damage because the large number of bridges prohibits individual analysis.

This paper uses static pushover methods recommended by Brandenberg (2005) to derive fragility curves that relate damage state to free-field ground displacement for the Landing Road Bridge, which experienced moderate damage as a consequence of lateral spreading during the 1987 Edgecumbe earthquake in New Zealand (Berrill et al. 2001). The fragility curves inherent to HAZUS unrealistically predict the bridge would collapse. Hence this case history provides an opportunity to (1) use recent design guidelines to analyze a bridge that experienced some damage, but did not collapse, and (2) evaluate the ability of static pushover methods to generate improved fragility curves for bridges in lateral spreads.

2. LANDING ROAD BRIDGE CASE HISTORY

Lateral spreading affected the Landing Road Bridge as a result of the M_L 6.3 1987 Edgecumbe Earthquake. The case history was thoroughly documented by Berrill et al. (2001), Berrill et al. (1997) and Keenan (1996). The bridge was constructed in 1962 and comprises 13 spans, each 18.3 m long, constructed of five precast post-tensioned concrete I-beams bearing on 16 mm rubber pads. The spans are bolted together and to the abutments, and the beams are bolted to the piers, forming stiff, moment-resisting connections. The substructure comprises concrete pier walls running the full width of the superstructure, each supported by eight 0.41 m square prestressed concrete piles at a 6:1 batter. The piles were fixed into pile caps embedded about 0.5 m below the ground surface, and pile cap dimensions were approximately 10 m long (in the transverse bridge direction) 2 m wide and 0.76 m thick.

The liquefiable geologic feature was the flood plain on the left bank of the Whakatane River in which five of the bridge piers and the left abutment were founded. The deposit consisted of a nonliquefiable silty crust over loose liquefiable clean sand, over dense nonliquefiable material. Lateral spreading of the crust layer extended 300 meters back from the river bank, and spread by as much as 2 m at the river bank. Spreading is believed to have occurred in a static mode after strong shaking based on eye witness accounts that the road was passable immediately after the earthquake, but not an hour later. Such delayed failures can be caused by void redistribution (e.g., Kulasingam et al. 2004). The 1.2-m thick nonliquefiable crust was composed of silty materials with mixed in wood chips that had been deposited on the banks of the river by a nearby cardboard mill. The unit weight of the crust material was about 12.5 kN/m^3 , which is lower than for typical soils due to the presence of the wood chips. Sampling and soil strength testing was complicated by the wood chips, and their tensile reinforcing behavior resulted in a high friction angle over 40° based on large-scale in situ direct shear tests near one of the piers. The cohesion intercept was about 10 kPa.

The bridge superstructure did not sustain any significant damage as a result of the lateral spreading, though buckled footpaths indicated compressive forces were mobilized in the superstructure. Cracks observed in some of the piers were repaired with epoxy resin. Small cracks were also observed near the heads of some of the piles. Rotations of about 1° were measured at some of the piers. Ground settlements of 0.3 to 0.5 m were observed at the northern abutment. Structural analyses by Berrill et al. (2001) predicted that collapse loads were nearly mobilized against the bridge, and they acknowledged significant sources of uncertainty in estimating the loads and resistances for the bridge. The Landing Road Bridge is a particularly interesting case history to evaluate because it performed reasonably well despite widespread liquefaction and lateral spreading.

3. ANALYTICAL METHOD

Beam on nonlinear Winkler foundation analyses were performed using the finite element modeling platform OpenSees. The piles and pier wall were modeled using nonlinear beam column elements, while the pile cap was modeled using stiff (essentially rigid) elastic beam column elements (Fig. 1). The nonlinear beam column elements were bilinear, with the elastic stiffness based on the cracked section modulus. Plastic moments for the piers and piles were computed by Berrill et al. (2001) based on section analyses that utilized nominal material strengths, and these values were adjusted up by 13% for this study to account for the average discrepancy between actual and nominal steel strengths (Table 1). Post-yield stiffness was set to 5% of the elastic stiffness. The moment resisting connection at the top of the pier was represented by fixing the translational and rotational degrees of freedom of the pier wall beam column element. The actual restraint at the top of the pier is likely flexible due to deformations of the bridge superstructure, but was modeled as a fixed connection for simplicity.

Soil-structure interaction was modeled using p-y springs distributed along the embedded portion of the pier wall, on the pile cap, and along each pile. The p-y springs on the piles were oriented perpendicular to the pile axis. Soil-structure interaction along the axis of the piles was modeled using t-z springs along the pile shaft, and q-z springs at the pile tips. The t-z and q-z springs were oriented parallel to the pile axis. Each of the two rows of four piles was modeled as a single pile with the structural properties and p-y and t-z material properties multiplied by four. Lateral spreading demands were modeled by imposing displacements on the free ends of the p-y springs, with a maximum crust displacement of 2 meters (sufficient to mobilize passive pressures). Passive pressure was estimated using Rankine theory based on the soil properties in Table 2. A correction for three-dimensional loading conditions was applied (Ovesen 1964). Friction forces between the pile cap and the crust were found to be important for the pile groups tested by Brandenburg et al. (2005), but were relatively insignificant contributors (i.e. only about 1% of the passive pressure) for the pile caps in Landing Road Bridge because (1) the area on the sides of pile cap in contact with the crust was small, (2) the shear strength of the soil was relatively small, and (3) the base of the pile cap was not in contact with the crust. Nevertheless, the friction forces were included in the estimate of crust load. Load transfer between pile groups and spreading crusts was observed by Brandenburg et al. (2007) to be much softer when underlying layers are liquefied, hence the springs in the crust layer were softened to account for this effect. Inertia forces can occur

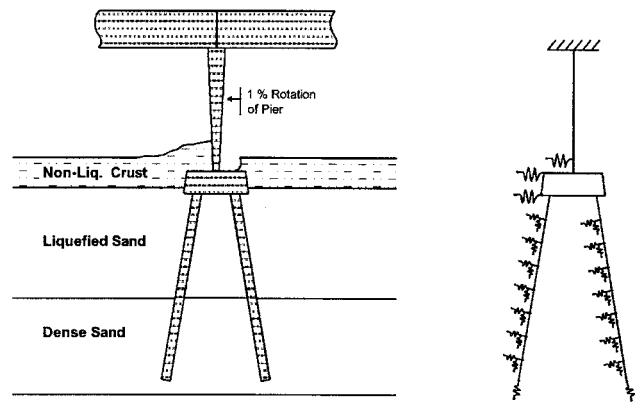


Figure 1: Schematic of Landing Road Bridge and beam on nonlinear Winkler foundation analyses.

Table 1: Structural Properties.

	El (kN·m ²)	My (kN·m)	Length (m)
Pier	119000	690	4.2
Piles	1900	230	9

Table 2: Soil Properties.

Soil Layer	Depth to Top of Layer (m)	Unit Weight, γ (kN/m ³)	Friction Angle, ϕ (deg)	Cohesion, c (kPa)
Crust	0	12.5	42	8
Loose Sand	1.2	17	35	0
Dense Sand	6.2	18	38	0

simultaneously with lateral spreading loads (Brandenberg et al. 2005), but were not imposed simultaneously with ground displacements based on eye witness accounts of the bridge damage occurring after shaking.

Results for the baseline analysis utilizing the mean values from Tables 1 and 2 are presented in Fig. 2. The lateral spreading demands yielded the pier wall beam columns, mobilizing a pier drift of about 1%, which matches post-earthquake measurements of pier rotations, and is consistent with the damage experienced by the bridge. The reasonable agreement between predicted and observed bridge damage suggests that the mean values of the parameters are reasonable, and that static pushover methods have the ability to accurately predict performance levels.

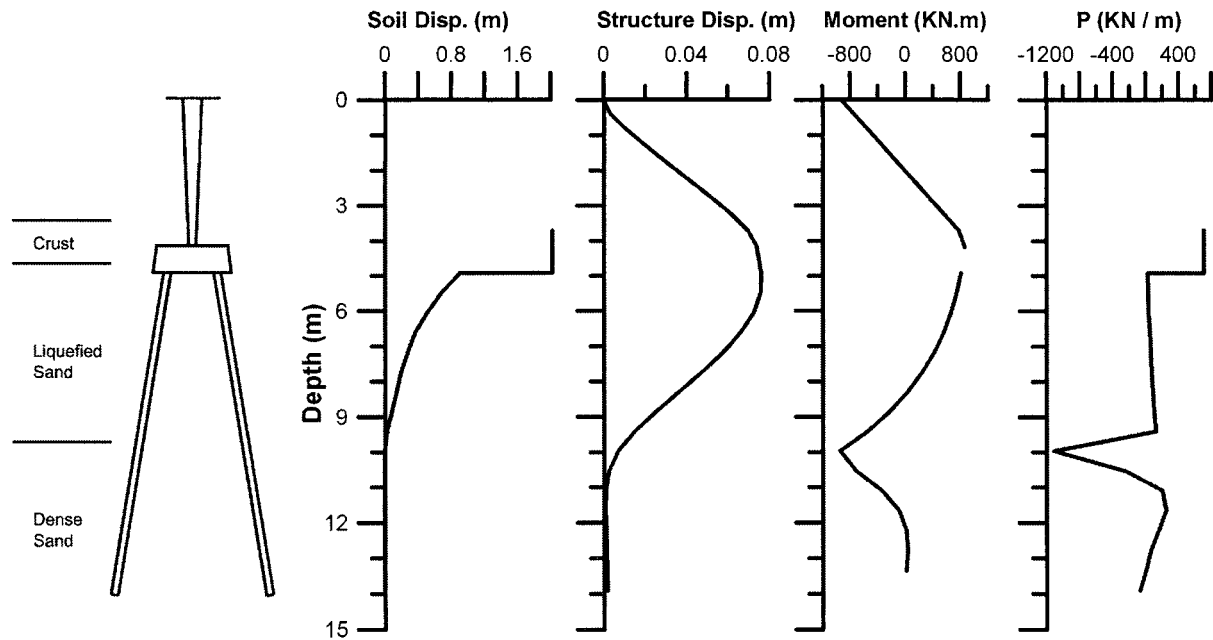


Figure 2: Analysis utilizing baseline input parameters.

4. FRAGILITY CURVES

Fragility curves that relate bridge damage state to free field ground displacement were derived by treating the following variables probabilistically: maximum crust load, maximum subgrade reaction load from the liquefiable layer, structural strength of the piles and pier, ground displacement profile, stiffness of the p-y springs in the crust layer, and the capacity of the t-z and q-z springs. Mean values and standard deviations are presented in Table 3. Measurements were used when available to estimate the standard deviations or ranges in the variables, but the data, if available, are insufficient to

Table 3: Probabilistic variables.

Parameter	Mean	Distribution	Standard Deviation or Range ¹
Crust Load	850 kN	Normal	250 kN
$\Delta_{\text{sand}} / \Delta_{\text{crust}}^2$	0.5	Uniform	0 - 1
Yield Moment, Piles	230 kN·m	Normal	23 kN·m
Yield Moment, Pier	690 kN·m	Normal	69 kN·m
P-multiplier	0.05	Normal	0.02
y_{50} for p-y springs in crust ³	0.1 m	Normal	0.05 m
Axial Capacity	500 kN	Normal	250 kN

¹ Standard deviations are assigned to normally distributed parameters, and ranges to uniformly distributed parameters.

² $\Delta_{\text{sand}} / \Delta_{\text{crust}}$ is the ratio between the displacement at the top of the loose sand to the displacement of the crust.

³ y_{50} = displacement in p-y spring at 1/2 of ultimate capacity.

accurately characterize the uncertainty in these input parameters. Hence, the values selected for the standard deviations are admittedly subjective. Standard deviation for the maximum crust load was estimated based on scatter in direct shear measurements (Berrill et al. 1997). Standard deviations for yield moment were based on the observation that the strength of steel has a coefficient of variation of approximately 10%.

Table 4: Damage states.

Damage State	Description	Drift (%)
1	No Damage	< 0.5
2	Slight / Minor	0.5 - 1.0
3	Moderate	1.0 - 2.0
4	Extensive	2.0 - 5.0
5	Collapse	> 5.0

The probability density functions for each parameter were discretized into three bins with equal areas of 1/3, and representative values were selected at the centroid of each bin. A total of $3^6 = 729$ analyses were performed using the automation capabilities of the Tcl scripting language that controls OpenSees. Basoz and Mander (1999) related bridge damage states to pier drift ratios for bridges with weak piers and strong bearings (Table 4), and these relations were adopted in this study. Ground displacements were imposed incrementally and the drift ratio was monitored at each increment. Ground displacement was recorded at transition points from one damage state to the next. After all analyses had finished, ground displacements associated with each damage state were sorted and represented as a cumulative distribution of probability of exceeding the damage state at each ground displacement. These fragility curves are plotted in Fig. 3. Some fragility curves do not reach a cumulative probability of 1 because the ground breaks up and flows around the bridge foundation without causing collapse. The free-field ground displacements measured at Landing Road Bridge were about 1 to 2 m, which corresponds to about a 40% probability of being in damage state 4 or worse, and a 80% probability of being in DS3 or worse. DS5 had 5% probability of being exceeded, while DS2 had 100% probability of being exceeded. These results are consistent with the moderate repairable damage observed following the Edgecumbe earthquake. The fragility curves inherent to HAZUS would predict collapse of the bridge since the ground displacement exceeded 0.35 meters. Hence, the fragility curves generated by the static pushover analyses provide a marked improvement over the existing fragility functions.

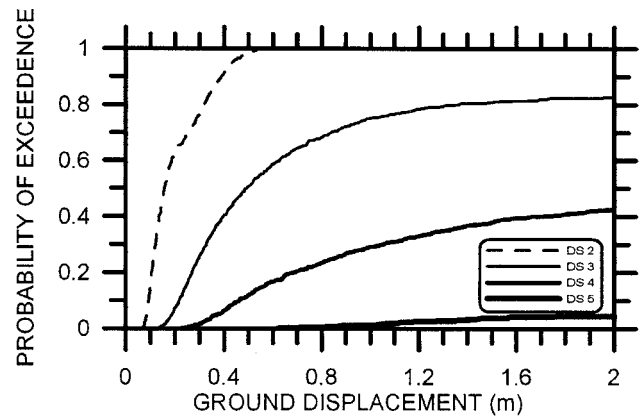


Figure 3: Fragility curves for Landing Road Bridge.

5. DISCUSSION

Disaggregation of probabilistic analyses can identify the variables whose uncertainty has the largest impact on the predictions. Disaggregation was performed by independently varying each parameter by a constant number of standard deviations with all other parameters set to their mean values, and observing the ground displacement required to reach a given damage state. In this case the variables the points were selected at the centroids of the equal-probability bins for the analyses performed in the Monte-Carlo simulations. The range in ground displacement associated with the variation in each parameter was computed, results were sorted and presented as floating bar charts (sometimes called tornado diagrams due to their characteristic shape) in Fig. 4 for damage states 2 and 3. Displacement of the sand layer had the most influence on crust displacements that mobilized DS2, while crust load had the most influence on crust displacements that mobilized DS3. The range in the tornado diagrams for each parameter reflects a combination

o f

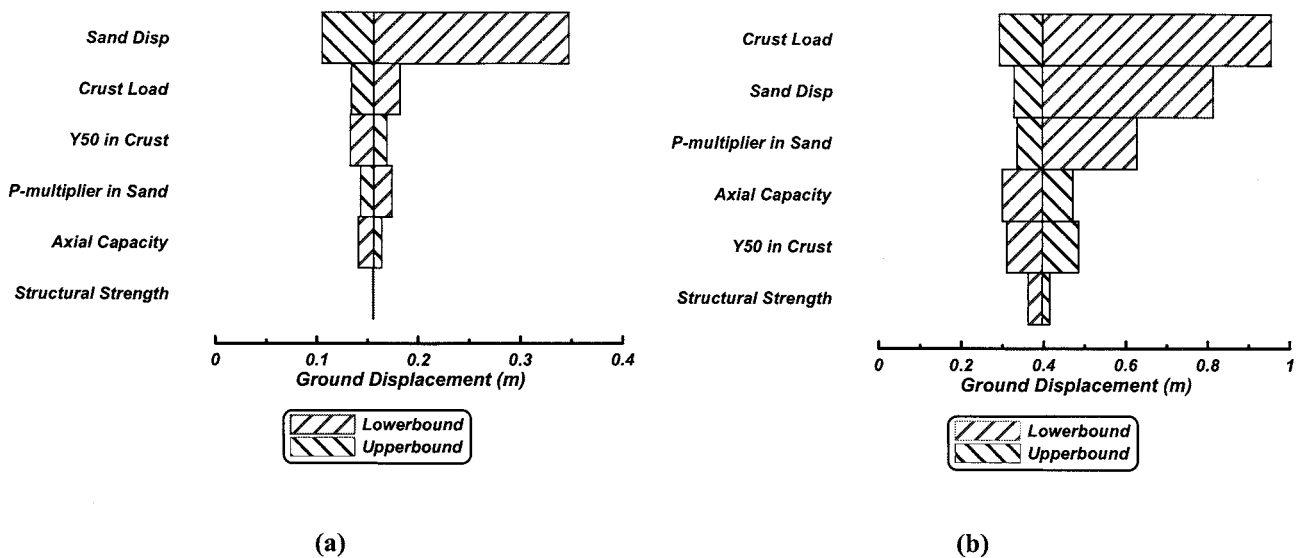


Figure 4: Tornado diagrams for (a) damage state 2 and (b) damage state 3.

the importance of the parameter on the analysis results and the parameter's uncertainty. Displacement profile is highly uncertain, and hence has a high influence. Structural strength may be very important, but is not highly uncertain compared with the other inputs and appears at the bottom of the tornado diagrams. The relative influence of probabilistic variables can depend on the target performance level. Tornado diagrams are analysis-specific and should not be generalized to other cases (e.g., see Brandenburg 2005).

Crust load was identified to be an important parameter in the analyses in this paper, and Berrill et al. (2001) concluded that the bridge could not structurally tolerate any additional crust loads. The impact of increasing the crust thickness by 0.5 meters (approx. 80 % increase in crust load) is shown in the fragility curves in Fig. 5. There is now a 60% probability of collapse (DS5) and a 96% probability of at least extensive damage (DS4) for a free-field ground displacement of 2 m. This significant change in the fragility curves verifies the observation that the bridge could not tolerate a modest increase in crust load, and illustrates that the thickness and strength of any nonliquefiable crust layer is likely an important design consideration.

Estimation of bridge damage in a transportation network due to liquefaction and lateral spreading involves (1) prediction of liquefaction triggering, (2) prediction of ground displacement, and (3) prediction of bridge damage associated with estimated ground displacement. Predictions of liquefaction triggering and lateral spreading displacements carry their own uncertainties that must be considered in probabilistic analyses of bridge damage.

Free-field ground displacements may not be an appropriate representation of lateral spreading demands for cases where a finite-width approach embankment spreads against a bridge (TRB 2002, Boulanger et al. 2005). Forces mobilized by the foundation and bridge superstructure can pin the spreading embankment, thereby reducing the lateral spreading demands. Pinning effects were not included in the analyses in this paper because the analyses were restricted to a single

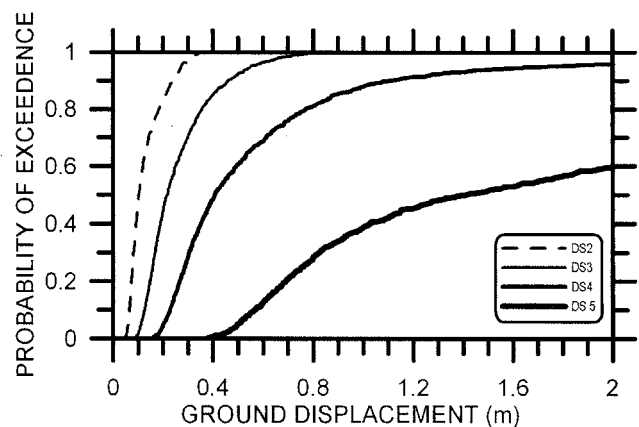


Figure 5: Fragility curve for Landing Road Bridge, but with crust thickness increased from 1.2 m to 1.7

bridge bent embedded in a large mass of spreading soils, and spreading of the approach embankment at the left abutment was left unexplored. Future analyses are required to assess the influence of pinning at the left abutment.

Inertia forces can occur simultaneously with lateral spreading forces (Tokimatsu 2003, Brandenberg et al. 2005), and constitute an extra demand that was not considered in this paper. Inertia forces were disregarded based on eye-witness accounts that the ground failure occurred after strong shaking, and that the road was passable shortly after the earthquake. It is conceivable that some of the damage to the bridge was caused during shaking by a combination of inertia forces and transient ground lurching, with the remaining damage occurring after shaking. Inertia forces should be included simultaneously with lateral spreading displacements for design calculations where the phasing of load components is not known apriori.

The integration scheme applied to the probability density functions (pdf's) in this study, which discretized the pdf's into equal-sized bins with values sampled at the means of the bins, is known result in errors sampling the moments of the pdf's. The error in sampling the standard deviation of normally distributed variables in this study would be anticipated to be approximately 20% (e.g., Miller and Rice 1983). Such errors can be avoided using a Gaussian quadrature approach to numerical integration, which is currently being considered, but was not completed at the time of publication of this paper.

6. CONCLUSIONS

Fragility curves were derived for liquefaction and lateral spreading against the Landing Road Bridge, which suffered moderate damage as a result of the 1987 Edgecumbe earthquake in New Zealand. The level of damage predicted by the fragility curves is consistent with the observations of moderate damage (reparable cracks, limited settlement, etc.), and is a significant improvement over the fragility curves inherent to HAZUS (1999) that predict collapse of the bridge. Crust load and the displacement profile were the input parameters whose uncertainty most influenced the probabilistic analysis. A modest increase in crust thickness from 1.2 m to 1.7 m increases the probability of collapse from 5% to 60% for 2 m of free-field ground displacement.

Ongoing studies similar to those in this paper are being conducted to develop fragility curves for various classes of the more than 13,000 bridges owned by the California Department of Transportation. The purpose of these fragility curves is to (1) improve predictions of liquefaction-induced bridge damage for transportation network analyses and (2) provide a screening tool for prioritizing retrofit efforts to improve performance of bridges exposed to seismic hazard.

7. ACKNOWLEDGEMENTS

Funding for this work is provided by the Pacific Earthquake Engineering Research Center under project no. 2572005, and by the Pacific Earthquake Engineering Research Center Lifelines program under project task no. 9C. The contents of this paper do not necessarily represent a policy of either agency or endorsement by the state or federal government.

8. REFERENCES

- Basoz, N., and J. Mander (1999), *Enhancement of the Highway Transportation Module in HAZUS*, in *Report to National Institute of Building Sciences*. Washington, D.C.
- Berrill, J.B., Christensen, S.A., Keenan, R.P., Okada, W., and Pettinga, J.R. (2001). "Case study of

- lateral spreading forces on a piled foundation." *Geotechnique*, 51(6). 501-517.
- Berrill, J.B., Christensen, S.A., Keenan, R.J., Okada, W., and Pettinga, J.R. (1997). "Lateral-spreading loads on a piled bridge foundation." *Seismic Behavior of Ground and Geotechnical Structures*, Seco e Pinto ed., Balkema, Rotterdam.
- Boulanger, R.W., Chang, D., Gulerce, U., Brandenburg, S.J., and Kutter, B.L. (2005). "Evaluating pile pinning effects on abutments over liquefied ground." *Simulation and Performance of Pile Foundations in Liquefied and Laterally Spreading Ground*, Geotechnical Special Publication, ASCE, 306-318.
- Boulanger RW, and Tokimatsu K (2006) Geotechnical Special Publication No 145: Seismic performance and simulation of pile foundations in liquefied and laterally spreading ground. ASCE Press, Reston, VA, 321 p
- Brandenberg, S.J., Boulanger, R.W., Kutter, B.L., and Chang, D. (2007). "Liquefaction-induced softening of load transfer between pile groups and laterally spreading crusts." *J. of Geotech. Geoenviron. Eng.* 133(1). 91-103.
- Brandenberg, S.J. (2005). "Behavior of pile foundations in liquefied and laterally spreading ground." Ph.D. Dissertation. University of California, Davis.
- Brandenberg, S. J., Boulanger, R. W., Kutter, B. L., and Chang, D. (2005). "Behavior of pile foundations in laterally spreading ground during centrifuge tests." *J. Geotech. Geoenviron. Eng.*, 131(11), 1378-1391.
- Dobry, R., Abdoun, T., O'Rourke, T.D., and Goh, S.H. (2003). "Single piles in lateral spreads: Field bending moment evaluation." *J. Geotech. Geoenviron. Eng.*, 129(10), 879-889.
- HAZUS (1999), Earthquake Loss Estimation, Technical Manual, National Institute of Building Sciences, Washington D.C.
- Keenan, R.P. (1996). "Foundation loads due to lateral spreading at the Landing Road Bridge, Whakatane", MEng Report, University of Canterbury, Christchurch, New Zealand.
- Kiremidjian, A., Moore, J., Fan, Y.Y., Basoz, N., Yazali, O., and Williams, M. (2006) "Pacific Earthquake Engineering Research Center highway demonstration project." *Pacific Earthquake Engineering Research Center*, Report No. PEER 2006/02.
- Kulasingam, R., Malvick, E. J., Boulanger, R. W., and Kutter, B. L. (2004). "Strength loss and localization at silt interlayers in slopes of liquefied sand." *J. Geotech. Geoenviron. Eng.*, 130 (11), 1192-1202.
- Miller, A.C. III, and Rice, T.R., (1983). "Discrete approximations of probability distributions." *Management Science*. 29(3). 352-362.
- Ovesen, N. K. (1964). *Anchor slabs, calculation methods and model tests*. Bulletin No. 16, The Danish Geotechnical Institute, Copenhagen.
- Tokimatsu, K. (2003). "Behavior and design of pile foundations subjected to earthquakes." *Proc. 12th Asian Regional Conference on Soil Mechanics and Geotechnical Engineering*, Singapore, August 4th – 8th.
- Transportation Research Board (TRB). (2002). *Comprehensive specification for the seismic design of bridges*. National Cooperative Highway Research Program (NCHRP) Report 472, National Research Council, 47 pp.

E-DEFENSE SHAKING TABLE TEST OF MODEL GROUND WITH A QUAY WALL ON LIQUEFACTION-INDUCED LATERAL SPREADING

K. Tabata¹⁾, M. Sato²⁾, K. Tokimatsu³⁾, H. Suzuki⁴⁾ and H. Tokuyama⁵⁾

1) Researcher, National Research Institute for Earth Science and Disaster Prevention (NIED), Japan

2) Principal Senior Researcher, NIED

3) Professor, Tokyo Institute of Technology, Japan, and Visiting Researcher, NIED

4) Research Associate, Tokyo Institute of Technology, Japan

5) Visiting Scholar, NIED

tabata@bosai.go.jp, m.sato@bosai.go.jp, kohji@o.cc.titech.ac.jp, hsuzuki@arch.titech.ac.jp, tokuyama@bosai.go.jp

Abstract: To investigate the behavior of liquefaction-induced lateral spreading and the mechanism of its influencing failure of structures, a shaking test of large-scale model ground was conducted at E-Defense shaking table facility. The model ground in a container of 16 m long, 4 m wide and 5 m high included quay wall and group-pile-supported structure. 883 sensors were distributed to the model, acquiring precise displacements, water pressures, strains, and so on. Two-dimensional, horizontal and vertical strong motions from 80-percent-adjusted JR Takatori station record generated extensive liquefaction and horizontal displacements of the quay wall and ground of more than 1 m to waterside. This lateral spreading and structure's inertia, in turn, caused deformation of the structure to waterside, elephant-foot buckling at each pile head and following inclination of the structure. During the shaking, excess pore water pressure build-up began from the ground surface to the bottom, while the pressure dissipated inversely from the bottom to the surface. Moreover, at the same level of the ground layer, pore water pressure started decreasing earlier in the soil closer to the deformed quay wall.

1. INTRODUCTION

Many earthquakes caused severe damages to various structures. In 1995 Kobe earthquake, especially a lot of pile-supported structures behind quay walls in harbor areas were collapsed due to liquefaction and its resulting lateral spreading of ground. Such harbor structures are very essential as facilities for rescue supplies to disaster areas as well as economical distribution systems in rehabilitation process. Therefore, the resolution of the lateral spreading behavior of liquefied ground and the failure mechanism of pile structures are important problem in geotechnical earthquake engineering discipline in order to mitigate the earthquake disaster. However, the lateral spreading can be hardly reproduced not only during shaking but also after shaking in model ground on centrifuge apparatus or conventional shaking table because mainly of insufficient size of the small model, so that the influences of the lateral spreading on structures still have not been revealed completely. This implies that progress of the study on the behavior and its influences needs to execute shaking tests of "large-scale" model ground with a structure subjected to earthquake motions with actual magnitude.

From this point of view, the authors conducted the test of a large-scale model with quay wall and group-pile-supported structure in saturated sandy ground on lateral spreading behavior due to liquefaction using the "E-Defense" jumbo shaking table (MEXT and NIED, 2006). E-Defense is the nickname of a full-scale three-dimensional earthquake testing facility in Miki city adjacent to Kobe and operated by National Research Institute for Earth Science and Disaster Prevention (Ohtani et al., 2003). The objective of this shaking test is reproduction of the liquefaction-induced lateral spreading

in order to observe phenomena of the model ground and structures in detail during and after excitation. Such experimental study encompasses to reveal the failure mechanism of the pile-supported structure behind the quay wall. This paper presents the program, the sketches after shaking and results of the shaking test.

2. OUTLINE OF THE TESTING

2.1 Model specification

Figure 1 and Photo 1 show the specimen modeled on liquefiable ground in waterfront with quay wall and structure supported by a 3-by-2 pile group. The model ground was employed in a rectangular container of 16 m long, 4 m wide and 5 m high.

The liquefiable deposit was made of silica sand compacted to 60-percent relative density and saturated by de-aired water before testing. The properties, indices and deformation characteristics of the sand are presented by Yasuda et al. (2006). The deposit was divided by a sheet-pile quay wall into 3.2-meter-thick “waterside” and 4.5-meter-thick “landside” deposits. The water table was 0.5 m below the landside ground surface, i.e., 0.8 m above the waterside ground surface.

In the landside deposit, the pile structure was installed behind the quay wall, consisting of six hollow steel piles, footing and weight. The six steel piles were aligned with three paralleled to the quay wall in two rows and fixed rigidly to the footing and pinned at the bottom. The footing was penetrated into the landside deposit with a depth of 0.5 m. The weight was placed on the footing, generating inertia by a 12-ton superstructure.

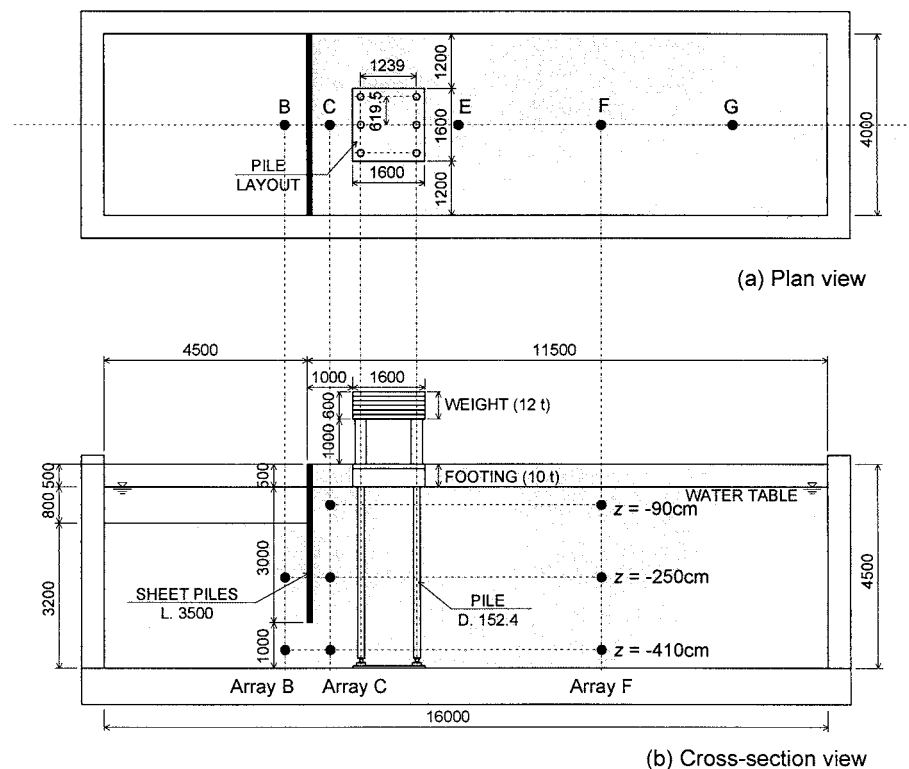


Figure 1 Illustration of the specimen and the locations of measurement points represented by dots: (a) plan view and (b) cross-section view.

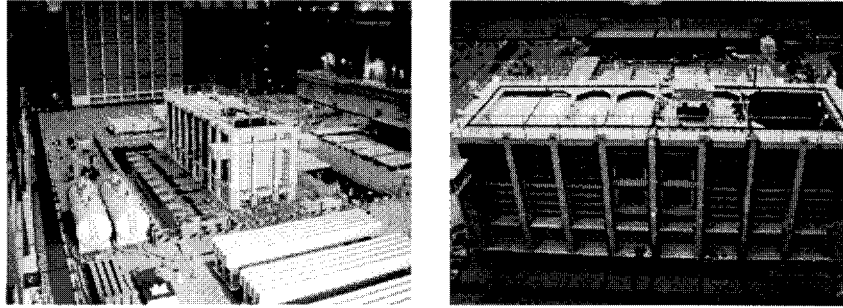


Photo 1 Bird's-eye views of the specimen

2.2 Measurement installations

For achievement of the objective explained in the introduction section, measurement devices listed below were installed to the specimen:

- Strain gauges, accelerometers and laser- and wire-type displacement transducers to observe the behaviors of the pile structure and quay wall.
- Earth pressure transducers on the piles, and pore water pressure transducers in the ground and on the piles to evaluate the effect of earth pressure on the piles.
- Accelerometers and displacement transducers set on footing and weight to observe structure's inertia.
- Accelerometers and pore water pressure transducers in the ground, and displacement transducers on the ground surface to observe the behavior of the ground.

Table 1 describes the numbers of sensors installed. The table presents a total of 883 sensors were mounted to observe the behaviors in detail, which were almost close to the maximum 896 sensors connecting to the E-Defense data acquisition system.

Additionally, a unique three-dimensional displacement measuring system was introduced to investigate the motions of ground surface and structures. In this system, displacement is measured by digital video cameras capturing fluorescent spherical markers attached on an object. The results are shown later in Figures 5 and 7.

Table 1 Numbers of sensors installed to the specimen.

Type of sensor	Ground	Quay wall	Piles (3 x 2)	Weight	Columns between weight and footing	Footing	Container	Total
Strain gauge		34	216		48			298
Accelerometer	122	12	22	12		12	24	204
Displacement transducer	11	6		7		4		28
Earth pressure transducer		13	104			16		133
Water pressure transducer	117	13	72					202
Load cell			18					18

2.3 Testing program

The model ground on the table was shaken under two-dimensional, horizontal and vertical motions

with 80-percent-adjusted north-south and up-down motions recorded at JR Takatori station in 1995 Kobe earthquake. In the test, north-south component applied to the specimen's long direction, while up-down component to the vertical direction. The peak table accelerations were approximately 6 and 2 m/s^2 in horizontal and vertical directions, respectively, and the shaking duration was about 42 seconds. Figure 2 shows the acceleration time histories of the target input motion and actual table motion from zero (data acquiring start time) to 20 second. Because the nature of the specimen was extremely changed due to liquefaction by strong motions, the table's control system could hardly follow such specimen's change and reproduce the table motions identical to the target. However, as shown in Figure 3, the both shapes of Fourier spectrum are very similar, especially in the domain of lower frequencies.

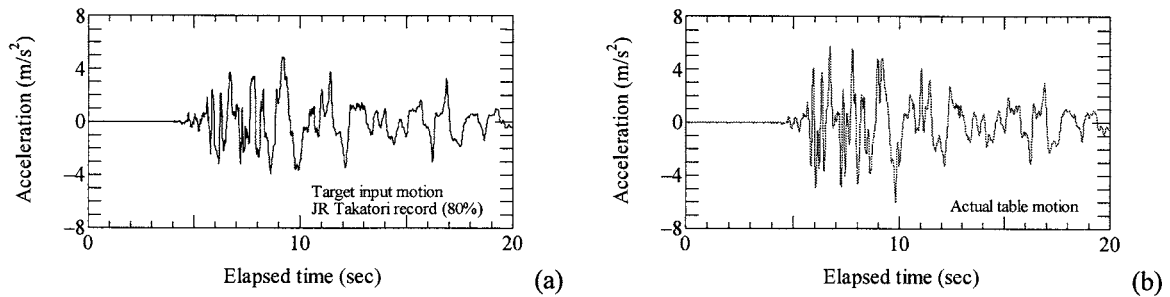


Figure 2 Acceleration time histories of (a) target input motion signaled to the table and (b) actual table motions.

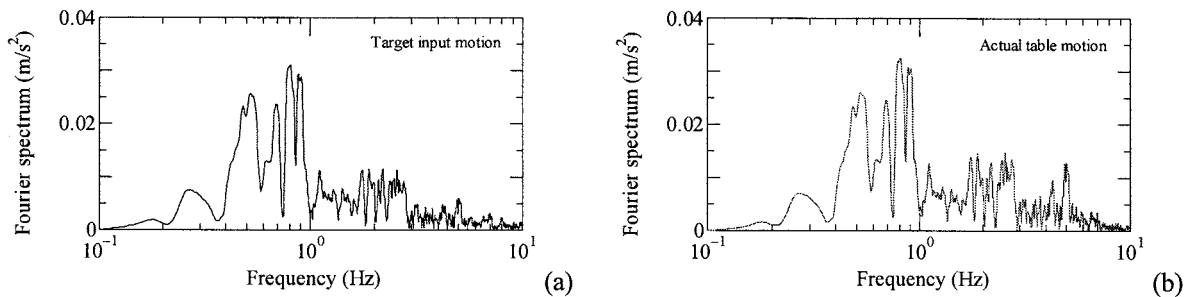


Figure 3 Fourier spectra of acceleration of (a) target input motion and (b) actual table motion.

3. TESTING RESULTS

3.1 Observation of the specimen after test completion

Figure 4 illustrates the specimen after shaking and following dissipation process of excess pore water pressure. The figure also includes horizontal and vertical displacements of the measurement points on ground surface, quay wall and pile heads. Liquefaction triggered by intensive strong motions in a few seconds after shaking start induced the large displacement of the quay wall in horizontal direction ranging from 1.1 to 1.2 m toward waterside but a little in vertical (Photo 2). This, in turn, caused horizontal deformation of the pile structure with the displacement toward waterside ranging between 1.1 and 1.4 m at a pile head and 20-degree decline of the weight and footing in landside. Such extensive movement also formed elephant-foot buckling at all six pile heads just below the footing (Photo 3). Additionally, in three landside piles, breakage of the connections at the bottom was found and may be considered as the reason of structure's decline in landside.

As shown in the figure, the horizontal displacement of landside ground surface ranged up to 1 m and decreased with the distance from the quay wall. The liquefaction and resulting lateral spreading also caused swell of waterside ground surface with about 35 cm and settlement in landside of more

than 20 cm.

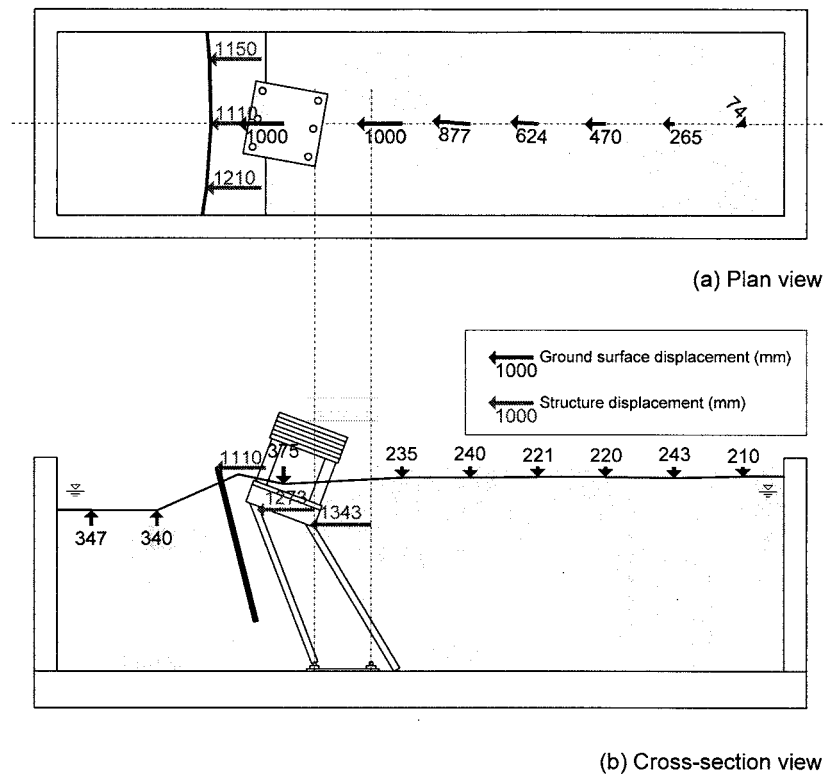


Figure 4 Illustration of the specimen after test completion

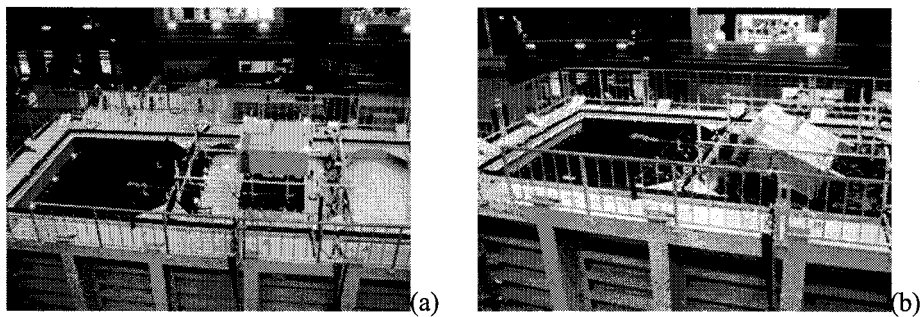


Photo 2 Quay wall and pile structure (a) before shaking and (b) after test completion.

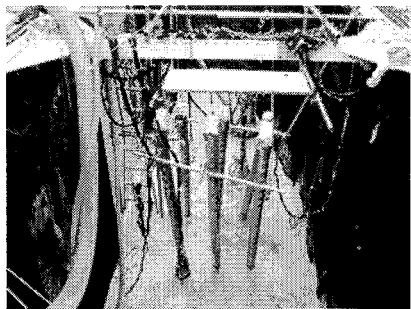


Photo 3 Piles after excavation.

3.2 Observation of the structure and ground surface during and after shaking

Figure 5 presents the displacements of ground surface and structures during shaking. The displacement of the quay wall could not be captured after $t = 8$ second because of the fluorescent

marker lost. The figure shows the displacement of the weight was larger than of the ground before $t = 9$, equaled around $t = 10$ and then became smaller after $t = 11$. To understand the behavior and interaction between ground and structure, Figure 6 demonstrates the change of bending strain distribution in depth of corner and center landside piles. In Figure 6(a) for the corner pile, it is found that large bending strain was occurred at $t = 9$ and its pile head possibly buckled. This observation is almost same in the other corner. Similarly, the pile head of the center pile buckled around $t = 14$, as shown in Figure 6(b). These facts indicate that the structure's deformation was caused mainly by its inertia before $t = 9$ or 10 at which the corner piles buckled. After this moment, following center pile's buckling, the structure reached to failure, so that the ground displacement exceeded.

Figure 7 shows the displacements of landside ground surface at Points E, F and G during and after shaking (Figure 1). The displacement of Point E could not be measured after $t = 20$ because severely liquefied ground flowed the fluorescent marker toward waterside. The figure presents the displacements at Points E, F and G accumulated during shaking. Following the accumulation, no or little displacement change was observed under no shaking motions, i.e., lateral spreading behavior could not be reproduced in the model ground after shaking.

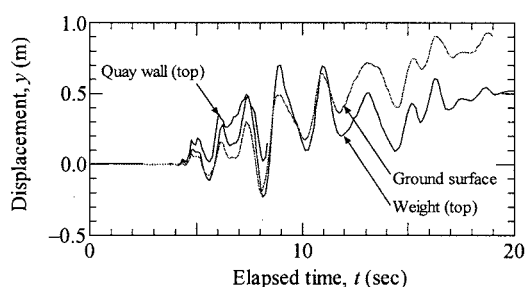


Figure 5 Displacement time histories of ground surface and structures measured by the three-dimensional displacement measuring system.

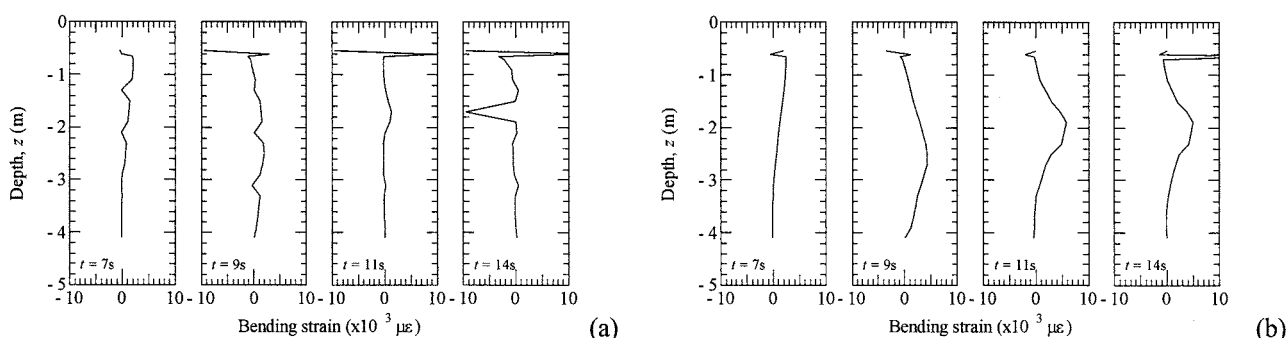


Figure 6 Bending strain distribution change of landside piles: (a) corner pile and (b) center pile.

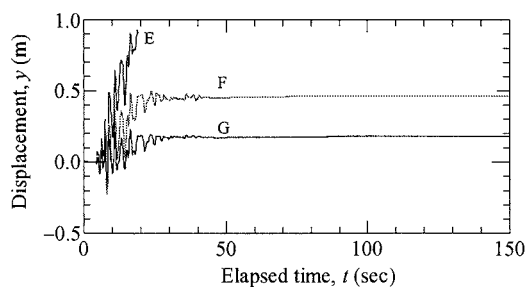


Figure 7 Displacement time histories of the points on landside ground surface.

3.3 Excess pore water pressure change during and after shaking

Figure 8 shows the changes of excess pore water pressure, Δu , at three different levels (90, 250

and 410 cm from the landside surface) in sensor arrays B, C and F during and after shaking. Arrays B and C were located just next to the quay wall and Array F was in the middle of the landside ground far from the structures (Figure 1). As shown in Figures 8(a) to (c), Δu build-up and its resulting liquefaction occurred from the surface to the bottom, while the Δu dissipation started inversely, i.e., from the bottom to the surface layer. This means liquefied ground became dense from the bottom to the surface in dissipation process of Δu . In addition, the dissipation took place earlier in deeper layer while later in shallower. Especially in Array F shown in Figure 8(c), Δu began to dissipate when its pressure level reached to the level of lower layer.

Figures 8(d) to (f) show the Δu change at the levels of 90, 250 and 410 cm from the landside surface in different locations. The levels of 90 and 250 cm were above the bottom of the quay wall, while the level of 410 cm was below. In Figures 8(d) and (e), Δu started decreasing earlier in closer to the quay wall while slower in farther. This implies that the deposit close to the quay wall can be denser than that far from the wall during dissipation process. In Figure 8(f), there is no or little difference among the trends. In terms of Δu change in this model ground, the layer deeper than that with horizontal deformation may not take an active role in the lateral spreading behavior.

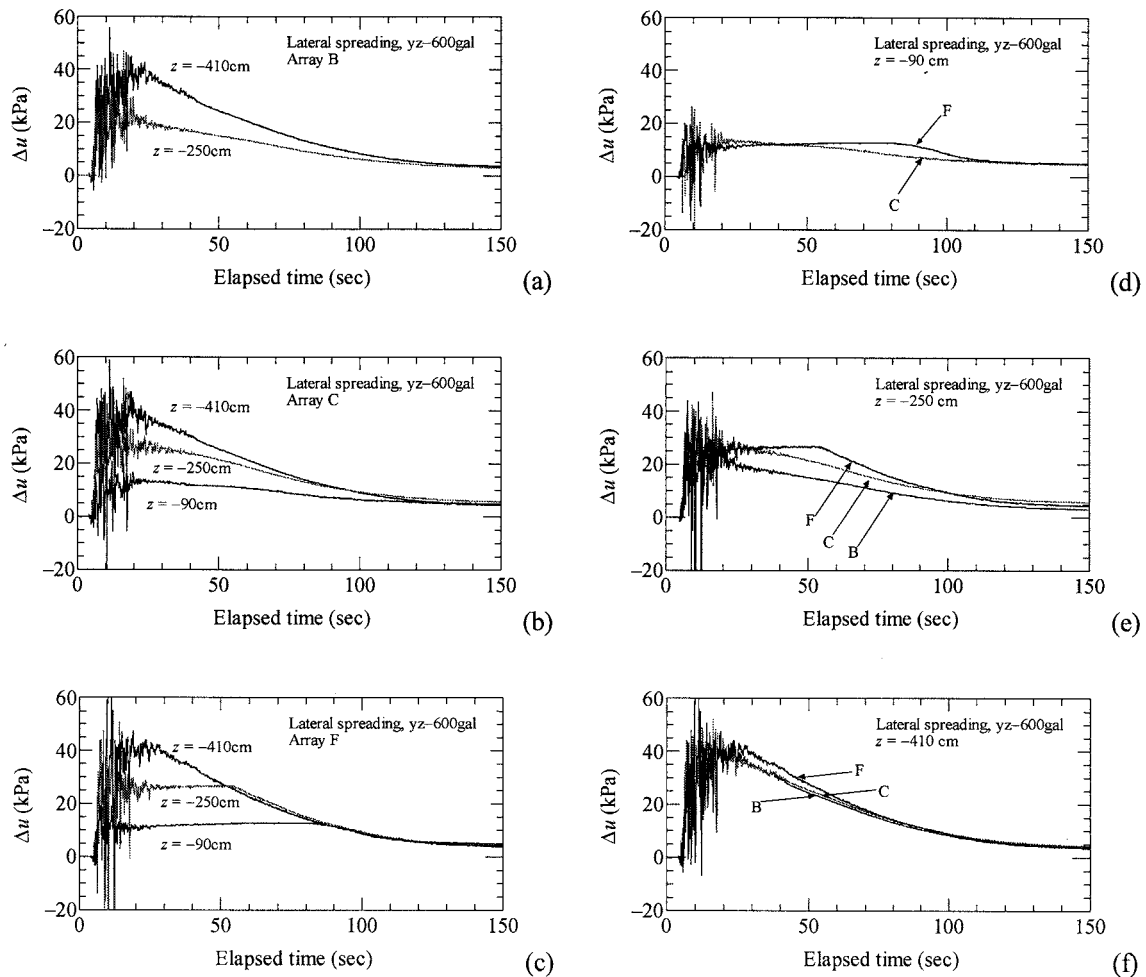


Figure 8 Time histories of excess pore water pressure, Δu , in deposit:
(a) to (c) Δu changes at different levels in Arrays B, C, and F, and
(e) to (f) Δu changes at the level of 90, 250 and 410 cm from the landside surface in different arrays.

4. SUMMARY AND CONCLUSIONS

In order to investigate the behavior of lateral spreading due to liquefaction and the mechanism of

its influencing failure of structures, a shaking test of large-scale model ground with sheet-pile quay wall and group-pile-supported structure assumed as harbor areas was conducted by the E-Defense jumbo shaking table. 883 sensors including accelerometers, strain gauges, displacement and pore water pressure transducers were installed to the ground and structures, and, in addition, the three-dimensional displacement measuring system was employed to observe large deformations. The model ground was shaken under two-dimensional motions with 80-percent-adjusted north-south and up-down motions recorded at JR Takatori station in 1995 Kobe earthquake.

Extensive liquefaction induced by strong motions caused large horizontal displacements of the quay wall and pile structure of approximately 1.2 m toward waterside. The horizontal displacement of ground surface was about 1 m at the measurement point close to the quay wall and decreased with the distance from the wall.

In a few seconds after shaking start, the horizontal displacement of the structure was larger than of the ground surface, and then elephant-foot buckling at each pile head was generated mainly by inertial force of the structure. Following that, the structure's displacement became smaller because of structure's failure. After the shaking, no or little horizontal displacement of the ground surface was observed.

Excess pore water pressure build-up started from the surface layer to the bottom. In contrast, its dissipation occurred from the bottom to the surface, i.e., the densification of liquefied ground took place from the bottom to the surface. At each layer of same depth in the ground, pore water pressure decreased earlier in soil deposit closer to the quay wall, meaning the deposit close to the wall deformed largely could be denser than that far from the wall during dissipating.

Note that these conclusions and considerations are based on the model testing results, meaning the observing area is still limited comparing to actual fields. Hence, to apply the knowledge from this study to the field and understand the behaviors in detail, other research procedures, such as parametric testing of small models, field observation and computational analyses, as well as more full-scale model testing are needed.

Acknowledgements:

The testing program described is a part of "Special project for mitigation of earthquake disaster in urban areas" supported by Japan Ministry of Education, Culture, Sports, Science and Technology, which was launched in 2001. In addition, the participation of the fifth author was financially supported by Tokyo Soil Research Co., Ltd. These financial supports are gratefully acknowledged.

References:

- Ministry of Education, Culture, Sports, Science and Technology (MEXT) and National Research Institute for Earth Science and Disaster Prevention (NIED) (2006), Research Theme No.2 Annual Report of the fiscal year 2005, Special project for earthquake disaster mitigation in urban areas, 831p. (in Japanese).
- Ohtani, K., Ogawa, N., Katayama, T. and Shibata, H. (2003), "Construction of E-Defense (3-D full-scale earthquake testing facility)," Proc., 2nd International Symposium on New Technologies for Urban Safety of Mega Cities in Asia, pp.69-76.
- Yasuda, S., Saito, S. and Suzuki, S. (2006), "Effect of confining pressure on liquefaction behavior of sand," Proc., 61st Annual Symposium, Japan Society of Civil Engineers, 3-276 (CD-ROM; in Japanese).

SEISMIC STABILITY OF RECTANGULAR TUNNELS WITH COUNTERMEASURES

J. Izawa¹⁾, O. Kusakabe²⁾, H. Nagatani³⁾, T. Yamada³⁾ and N. Ohbo³⁾

1) Research Associate, Dept. of Civil Engineering, Tokyo Institute of Technology, Japan

2) Professor, Dept. of Civil Engineering, Tokyo Institute of Technology, Japan

*3) Kajima Technical Research Institute, Japan
jizawa@cv.titech.ac.jp, kusakabe@cv.titech.ac.jp*

Abstract: Centrifuge shaking table tests were conducted in order to investigate the behavior of a rectangular tunnel in this study. Furthermore, three countermeasures, such as improvement of the ground surrounding the tunnel by cement, installation of a thin flexible layer surrounding the tunnel as isolation layer and combination of soil improvement and isolation layer, were picked up and their effectiveness was compared. Beside the centrifuge shaking table test, the static shear tests were conducted in order to confirm the applicability of the seismic displacement method to the rectangular tunnel by using an active type shear box in the centrifuge. Results of the centrifuge tests indicated effectiveness of countermeasures and the applicability of the seismic displacement method for a rectangular tunnel.

1. INTRODUCTION

Recent development of driving machine for shield tunnel has made it possible to construct some kinds of tunnel with complex and large cross-section. Here, some construction projects of circular routed highways under urban area are planned in Japan. Figure 1 shows the overview of the example of underground highway. As Figure 1 shows, underground highway has some complex cross-sections, such as ramp area and rectangular cross-section area. It is likely that the seismic stability of the rectangular tunnel is lower than that of a usual circular tunnel. For example, Daikai station, which is a subway station, collapsed due to 1995 Hyogoken-Nambu Earthquake (Iida, et al. 1996), although it was constructed by cut and cover method. Seismic stability of a circular tunnel has been reported, but little is known about a rectangular tunnels. The purpose of this study is to examine the seismic stability of the rectangular tunnel through the centrifuge shaking table test. In addition to the examination of the seismic stability, some kinds of countermeasures for the rectangular tunnel are referred to in this paper.

Seismic stability of an underground structure is usually evaluated by means of the seismic displacement method. The method evaluates stress resultants of tunnel by applying the lateral movement of ground to the tunnel statically because effects of inertia force acting to the underground structure can be negligible as compared with super structures. Therefore, beside the shaking table test (the dynamic loading test) series, the static loading tests, which can simulate the seismic displacement method, were conducted in this study. Concepts of the dynamic and static loading test are indicated in Figure. 2. Finally, the applicability of seismic displacement method to a rectangular tunnel was examined by comparing the results of shaking and shear tests.

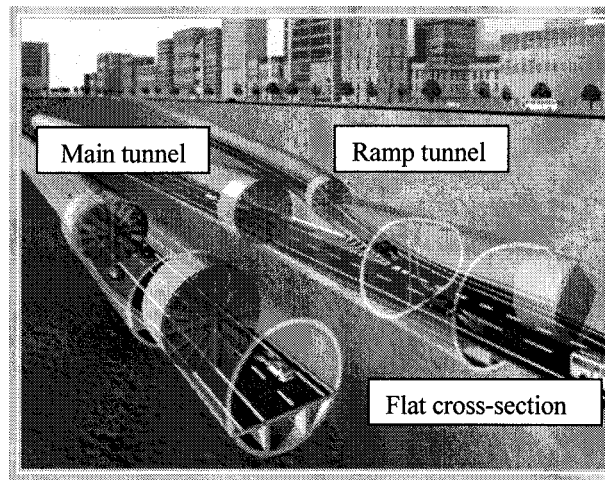


Figure 1. Overview of an example of ramp structure in tunnel

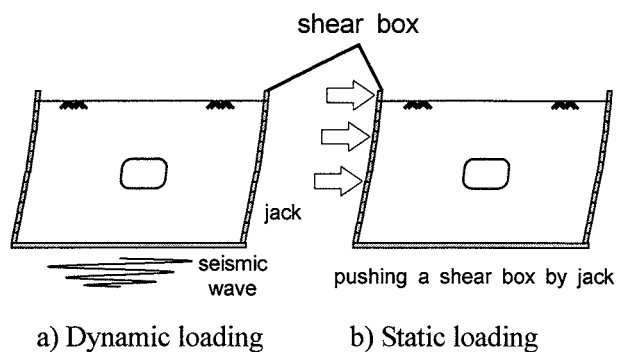


Figure 2. Concept of the dynamic and static loading test

2. OUTLINE OF THE TEST

2.1 Test Procedure

As mentioned above, two types of the centrifuge test were conducted. The centrifuge shaking table tests were conducted in a centrifugal acceleration of 50G in Kajima Research Institute. Four sinusoidal waves with the frequency of 100Hz and 20 waves were applied to the model and the typical acceleration time histories are shown in Figure 3. Model ground was set up in a laminar shear box with 500mm in height, 450mm in width and 200mm in breadth.

The Tokyo Tech. Mark3 Centrifuge was used in the static loading test. Shear displacement was applied to the model by using the active type shear box apparatus in 50G (Takahashi, et al. 2001). The shear box consists of thirteen-stacked 24 mm-thick duralumin rings. The size of the shear box is 452mm in width, 202mm in breadth and 312mm in height. Three actuators are connected with three rings and lateral forces are transmitted to the other rings through thin plate springs. A sinusoidal wave with a frequency of 0.01Hz and a period of 0.5 was applied to the shear box. Attempted distribution of the lateral displacement was linear in vertical direction and a value of lateral displacement at the 13th ring was about 6mm. Figure 4 shows a distribution of shear displacement obtained from displacement transducer attached to each shear ring.

2.2 Tunnel model & its Countermeasures

A tunnel model was made of aluminum of 2mm thickness. Aluminum was selected in order to measure the stress resultant clearly although its shear modulus was much higher than that of a prototype tunnel. Figure 5 a) and b) show the schematic views of the model tunnels and locations of strain gage in the dynamic and static loading test respectively. Previously, lower seismic stability of

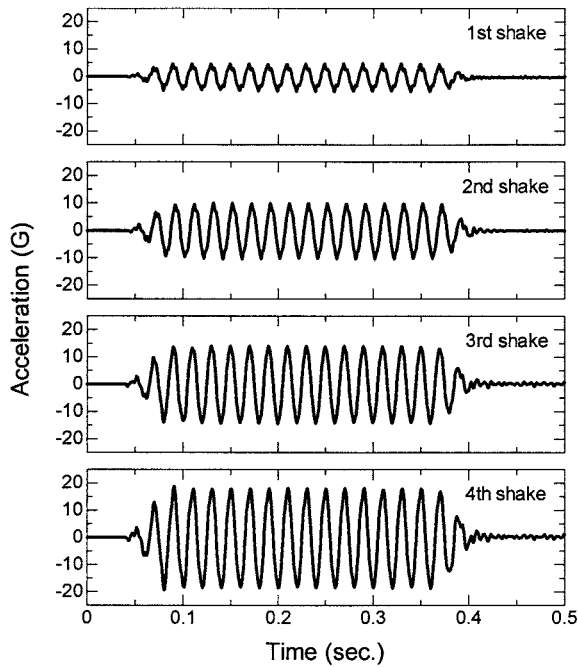


Figure 3. Examples of input waves

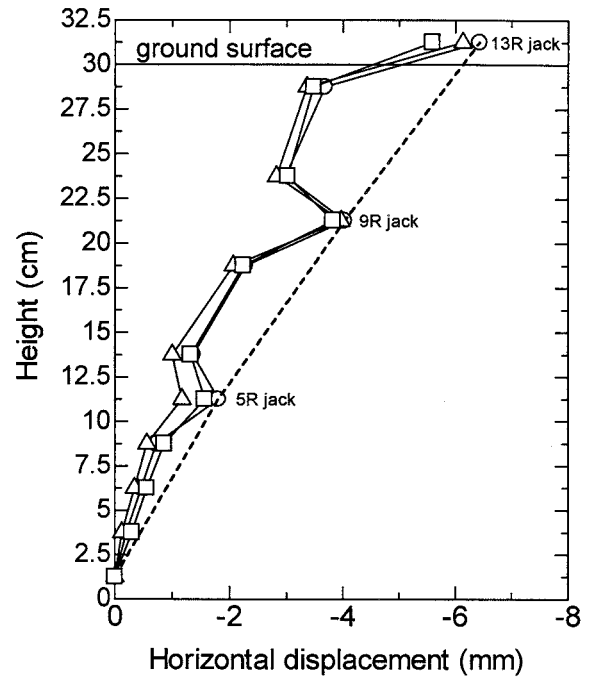
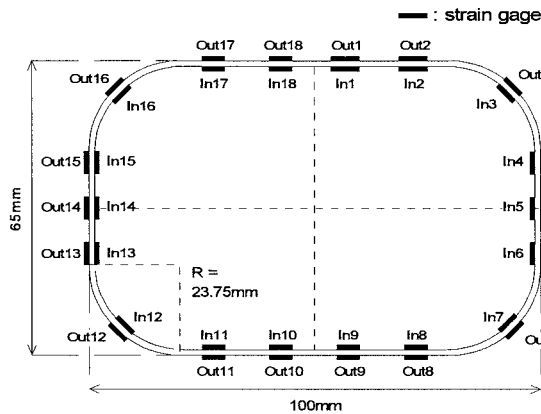
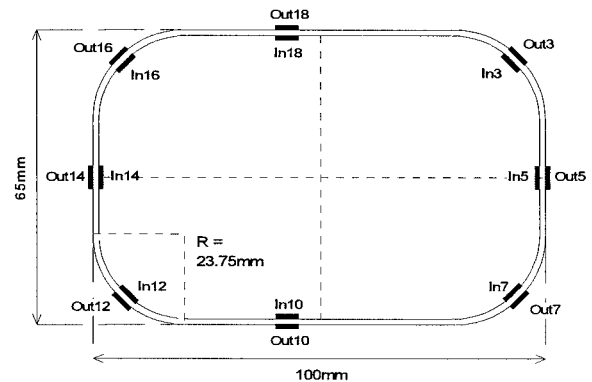


Figure 4. Distributions of lateral movement in the static loading tests



a) for the dynamic loading test



b) for the static loading test

Figure 5. Tunnel model

rectangular tunnels to a circular one and effectiveness of some kinds of countermeasure were demonstrated by the centrifuge tests with mortal tunnel model (Yamada, et al. 2004).

On the basis of the result, three kinds of countermeasures, a thin flexible layer surrounding the tunnel in order to avoid the shear force from ground, improvement of the ground surrounding the tunnel by cement and combination of soil improvement method and flexible membrane, were picked up. A rubber membrane of 1.0mm thickness and elastic modulus of 1.5MPa was glued around the outer surface of the tunnel as an isolation layer. This case is called "RM" case. Round shaped soil cement ground, of which diameter was 135mm and unconfined compression strength was 1.0MPa, was arranged surrounding tunnel as ground improvement. Hereafter this case is called "SC" case. Rubber membrane and soil cement were applied to the combination case, which is called as "RM+SC" case. In addition, a non-reinforced case, "NC" case, was conducted for reference.

Model setups were shown in Figure 6 a) and b). Toyoura sand ($D_r=80\%$, $D_{50}=0.19\text{mm}$, $U_c=1.56$, $\phi'=42\text{deg.}$) was used as ground material. Accelerometers were laid in the ground only in the dynamic

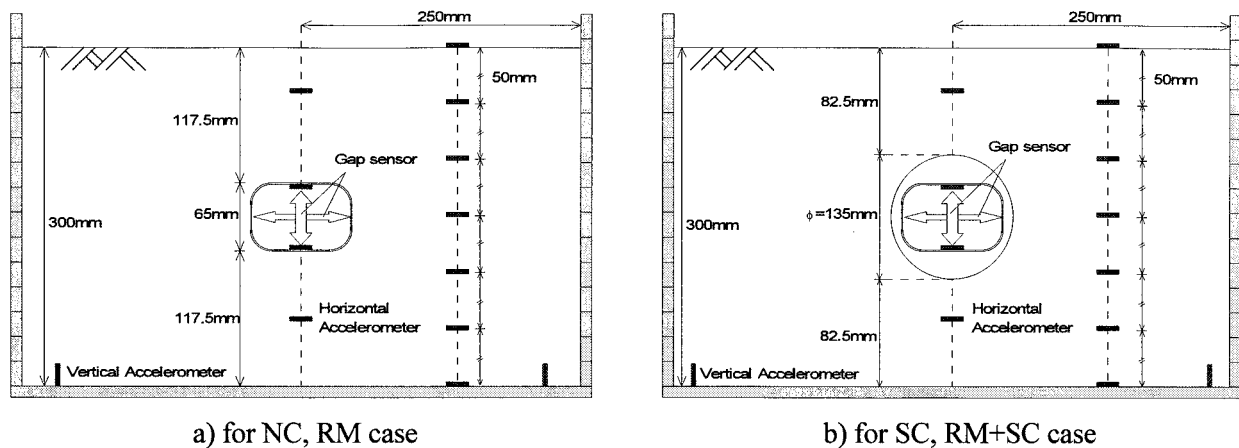


Figure 6. Model setup

loading test. Some displacement transducers were attached to each ring to measure the lateral ground displacement. Lateral and vertical convergences were measured by gap sensors.

3. RESULT AND DISCUSSION

3.1 Stability at 50G

Figure 7 shows the relationships between vertical convergence obtained by gap sensor and centrifugal acceleration in the dynamic loading table tests. Large convergences were observed in NC case, which was the non-reinforced rectangular tunnel case. That of RM case was almost the same with NC case at 50G, although it was slightly smaller up to about 15G. The result indicated that rubber membrane could avoid the transfer of the shear stresses due to weight of surrounding ground to some degrees. Deformation could be reduced in SC and RM+SC case. Reduction ratio of vertical convergence due to the soil improvement and the combination method was about 66% and 23% respectively. That is to say, it was more effective to improve the surrounded ground only by soil cement as compared with the combined method.

Figure 8 show the distributions of the bending moment and axial force at 50G respectively. Large bending moment was observed at the center of upper and lower slab and side wall in all cases. The axial force also shows the peak value at the same are, but it was not so remarkable compared with bending moment. There were little differences in both bending moments and axial forces between NC and RM. Those in RM+SC case were slightly smaller than NC and RM. The smallest bending moments were observed in SC. Although the same trend applied to axial forces with respect to NC, RM and RM+SC case, the largest values were observed in SC case. That is, it is effective to improve the surrounding ground around the rectangular tunnel against deformation or bending moment due to loading from weight of surrounded ground. However, large axial forces were generated in SC case. It could be reduced by gluing the rubber membrane around outer surface of a tunnel.

3.1 Results of shaking table test

The vertical and horizontal residual convergences at each step were plotted against the maximum acceleration in Figure 9 a) and b) respectively. Here, the data shown are the increments from 50G. Both vertical and horizontal convergences showed almost linear relations with maximum accelerations. Large vertical convergences were observed in the case of SC and RM+SC as compared with NC and RM case. But values of them seem to be much smaller than horizontal ones as it is possible to be negligible in all cases. With respect to the horizontal convergence, almost the same values were shown in the case of NC, RM and RM+SC and only those in SC case were slightly smaller.

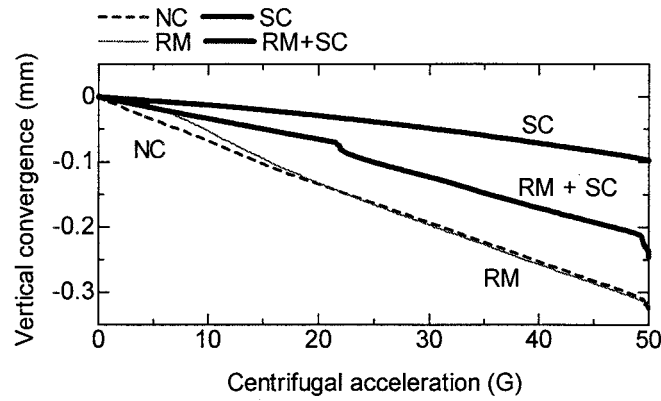


Figure 7. Vertical convergence vs centrifugal acceleration in the dynamic loading test

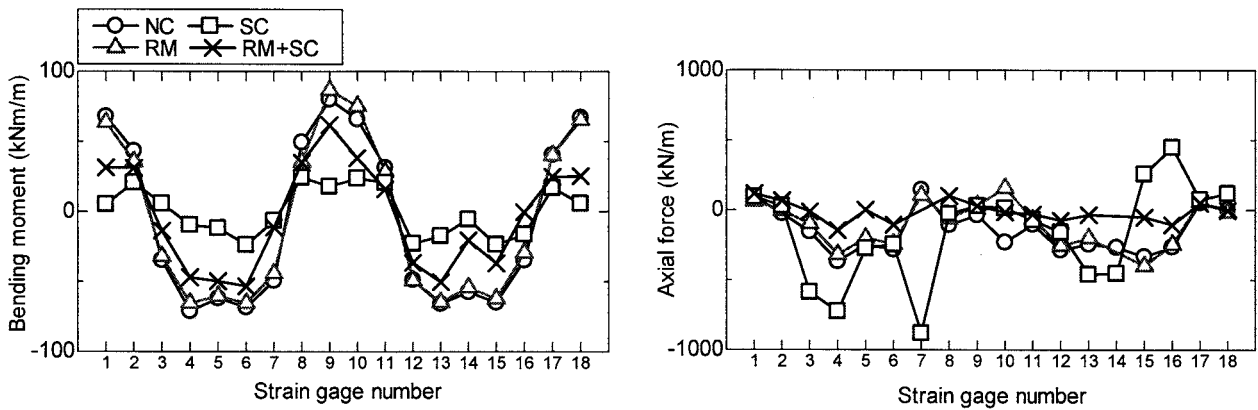


Figure 8. Distributions of stress resultants under 50G

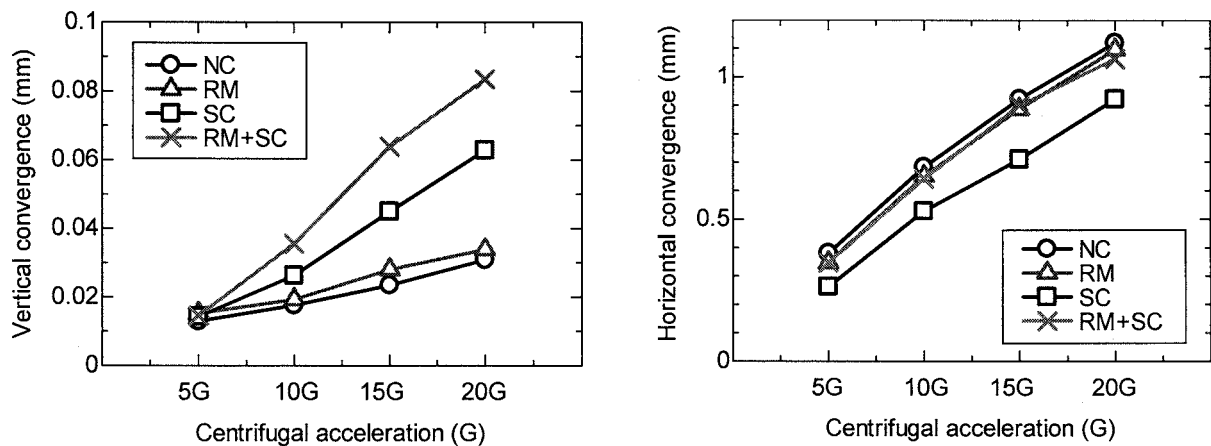


Figure 9. Residual convergence at each shaking step

Figure10 show the distributions of stress resultant in all cases. In a similar fashion with the convergences, the stress resultants were increments from 50G. The bending moment and the axial force showed the peak values at each corner in the case of NC, RM and RM+SC. On the contrary, in SC case, remarkable large axial forces were observed at the side walls although the distribution of the bending moment was almost the same trend with the other cases. The same trend of axial forces in SC cases can be shown in the former studies of a circular tunnel (Yamada, et al. 2002). Such concentration of axial force could be reduced by applying the isolation layer surrounding the tunnel surface.

There were little differences between NC and RM case. Rubber membrane method was not effective. It has been recognized that the seismic isolation layer is effective in reduction of the dynamic sectional forces due to isolating the transmission of seismic ground strain to a tunnel body

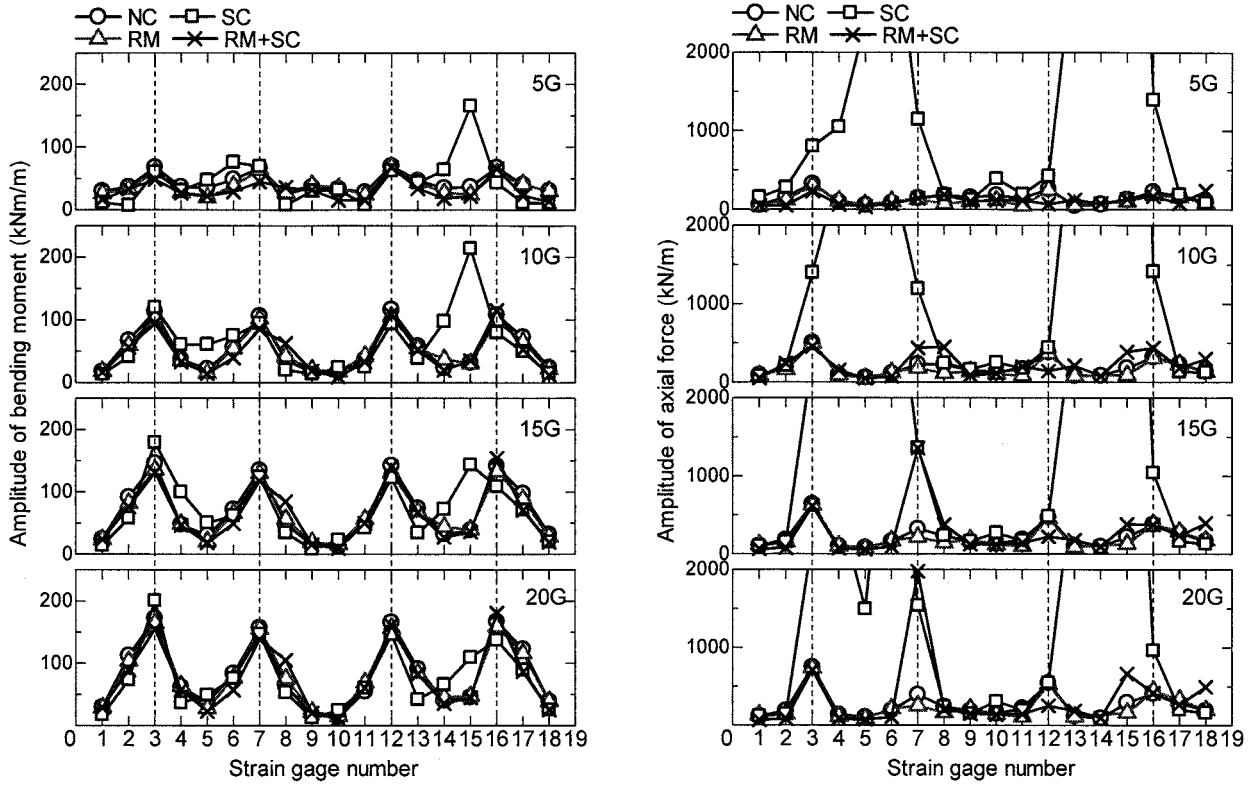


Figure 10. Distribution of stress resultant at each shaking step

(Suzuki, et al. 2000). The effectiveness of it depends on the ratio of shear modules between isolation layer and ground. Furthermore, it was reported that the ratio should be smaller than 0.01(Zhi, et al. 1993). The ratio in this study varied from 0.05 to 0.10 in consideration of strain dependency of shear modules of ground and it was larger. It seems to be a reason why the effectiveness of RM was not clear in this study.

3.2 Comparison with each test series

Static loading test was conducted in order to compare the results of shaking table test and verify the applicability of seismic deformation method to the non-reinforced and some reinforced rectangular tunnels. In this chapter, distribution of stress resultant and deformation behavior between dynamic and static loading test was compared.

Figure11 shows the distributions of bending moment and axial force in the dynamic and static loading test. The values at the same horizontal convergence between dynamic and static loading test were picked up. As a whole, almost the same tendency and values with dynamic loading test about the distributions and the values of bending moments and axial forces can be shown in static loading test. Distribution and value of stress resultant were almost the same between dynamic and static loading test when the same convergence occurred.

Figure12 shows the relationships between horizontal convergence. δ_R and δ_{TH} are relative displacement of tunnel and ground respectively. δ_R was determined from the relative displacement between two shear rings, which was located near upper and lower slabs of tunnel. The dotted lines in Figure12 were Skelton curves of TH-R relations in dynamic loading tests. They corresponded to the TH-R curves obtained in the static loading tests. The relationships between deformation of ground and convergence were almost the same in the dynamic and static loading tests.

Thus, if the same convergence was applied to the tunnel, the same stress resultants occurred in the tunnel regardless of the dynamic or static loading. Furthermore, if the same lateral movement was applied to the ground, the same deformation was occurred in the tunnel. In conclusion, if the same

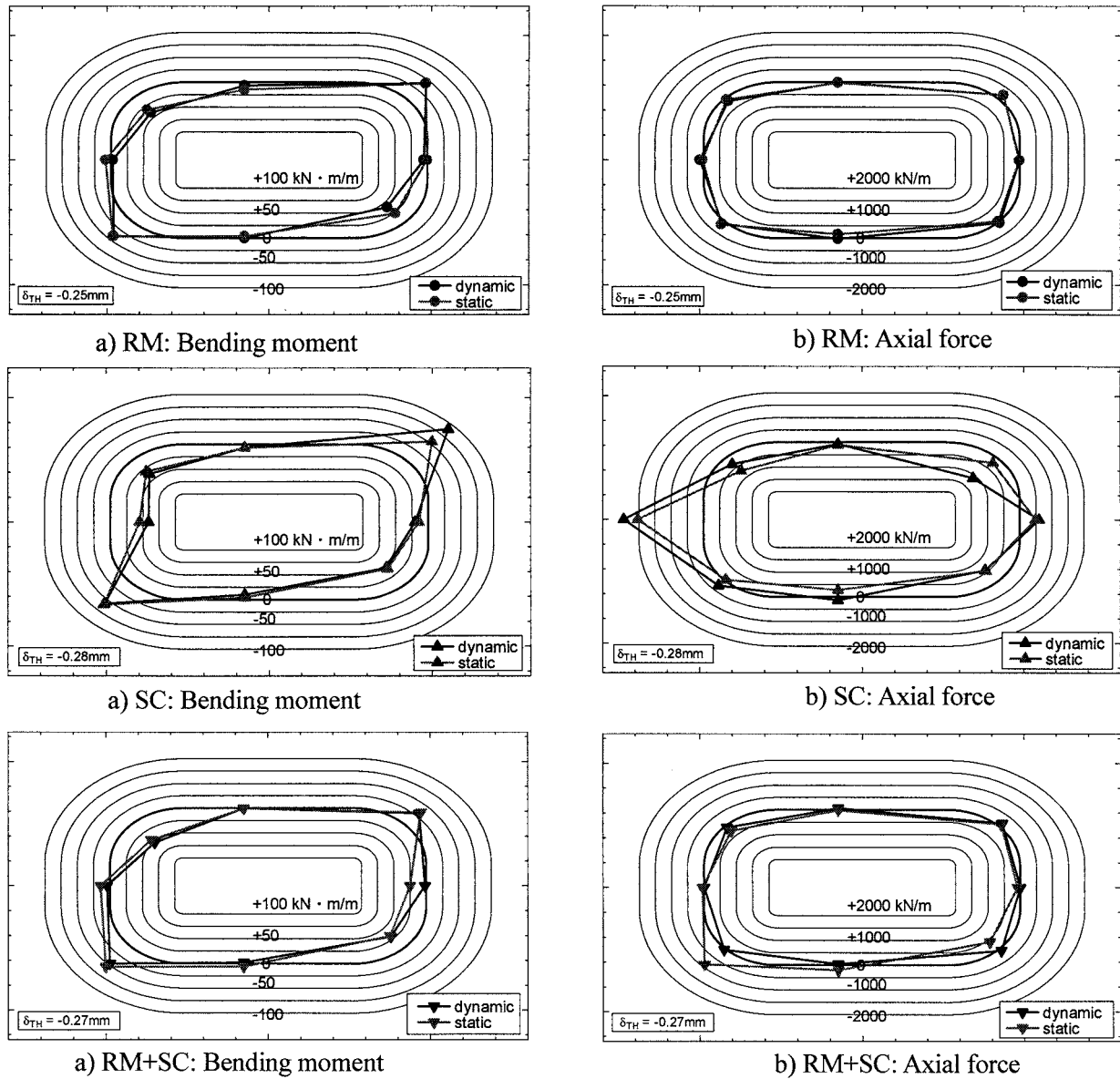


Figure 11. Comparison of stress distribution between dynamic and static loading test

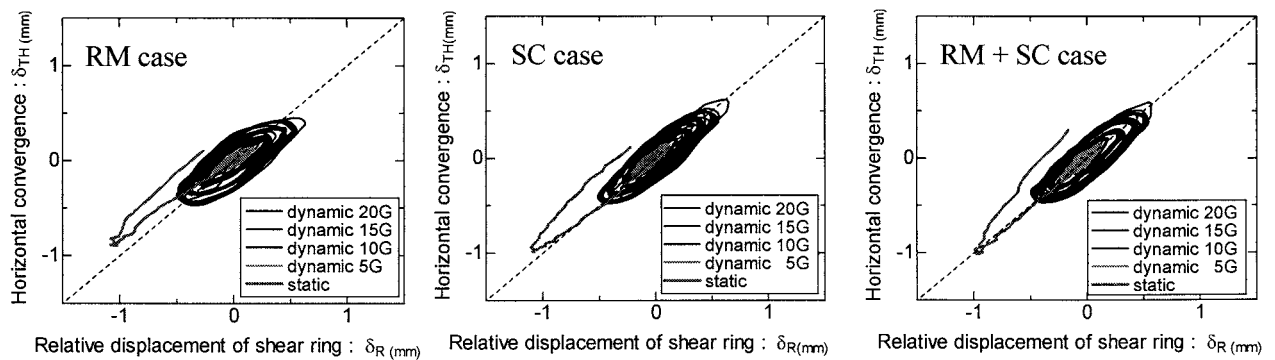


Figure 12. Relationships between horizontal convergence and relative displacement of shear rings

lateral movement was applied to the ground, the same stress resultants occurred in the tunnel regardless of the dynamic or static loading. It follows that the seismic deformation method can be applied to the non-reinforced and reinforced rectangular tunnels.

4. CONCLUSIONS

In conclusion, the following results were obtained.

1. Large bending moment was observed at the center of upper and lower slab and side wall in the rectangular tunnels in 50G. On the other hand, the bending moment and the axial force showed the peak values at each corner in the dynamic and static shear loading test.
2. It was not so effective to install the isolated layer surrounding the tunnel for reducing the deformation and the stress resultant in tunnel in this study. One of the possible reason is that the ratio of shear modules between isolation layer and ground was much larger.
3. If the surrounding ground was improved by soil cement, deformation of the tunnel could be reduced. On the contrary, large axial forces occurred at the side wall. Such concentration of axial force could be reduced by applying the isolation layer surrounding the tunnel surface.
4. If the same lateral movement was applied to the ground, the same stress resultants occurred in the tunnel regardless of the dynamic or static loading. It follows that inertia force can be negligible and the seismic deformation method can be applied to the non-reinforced and reinforced rectangular tunnels.

References:

- Iida, H., Hiroto, T., Yoshida, N., & Iwafuji, M. (1996) SPECIAL ISSUE on Geotechnical Aspects of the January 17 1995 Hyogoken-Nambu Earthquake, *Soils and Foundations*, No. 1, pp. 283- 300
- Suzuki, T. (2000) The Axisymmetric Finite Element Method Developed as a Measure to Evaluate Earthquake Responses of Seismically Isolated Tunnels, *Proc. of 12th World Conference on Earthquake Engineering*
- Takahashi, A., Takemura, J., Suzuki, A. & Kusakabe, O. (2001) Development and performance of an active type shear box in a centrifuge, *International Journal of Physical modelling in Geotechnics*, Vol. 1, No.2, pp. 1-18
- Yamada, T., Nagatani, H., Kobayashi, I., Kusakabe, O. & Izawa, J. (2004) Seismic resistant performance of large cross-section flat tunnel and its countermeasure, *CD-ROM of 13th World Conference of Earthquake Engineering*
- Yamada, T., Nagatani, H., Igarashi, H. & Takahashi, A. (2002) Centrifuge model tests on circular and rectangular tunnels subjected to large earthquake-induced deformation, *Geotechnical Aspects of Underground Construction in Soft Ground*, pp. 673-678
- Zhi, H., Otsuka, H. & Toyonaga, S. (1993) Isolation Analysis of Underground Structure, *Memories of the Faculty of Engineering, Kyushu Univ.*, Vol. 59, No. 1, pp. 21-29

SOIL-PILE-STRUCTURE INTERACTION DURING MULTI-DIMENSIONAL SHAKING THROUGH PHYSICAL MODEL TESTS USING E-DEFENSE FACILITY

K. Tokimatsu¹⁾, H. Suzuki²⁾, M. Sato³⁾ and K. Tabata⁴⁾

1) Professor, Dept. Architecture and Building Engineering, Tokyo Institute of Technology, Visiting Researcher, NIED, Japan

2) Research Associate, Dept. Architecture and Building Engineering, Tokyo Institute of Technology, Japan

3) Principal Senior Researcher, Disaster Prevention System Research Center, NIED, Japan

4) Researcher, Hyogo Earthquake Engineering Research Center, NIED, Japan

kohji@o.cc.titech.ac.jp, hsuzuki@arch.titech.ac.jp, m.sato@bosai.go.jp and tabata@bosai.co.jp

Abstract: To investigate inertial and kinematic effects on failure and deformation mode of piles during three-dimensional shaking, physical model tests were conducted at E-Defense, one of the largest shaking table facilities in the world. A 3x3 steel pile group supporting a foundation with or without a superstructure was set in a dry sand deposit prepared in a cylindrical laminar box with a height of 6.5 m and a radius of 8.0 m. The tests were conducted under one-, two- or three-dimensional shaking with three types of ground motion having a peak acceleration of 0.3 m/s² to 8.0 m/s². Bending strains become larger in the leading piles than in the trailing piles due to group pile effects. The piles yielded and buckled not only at their heads but also at depths from 0.7 m to 1.2 m during the shaking with peak input accelerations of 6.0 m/s² and 8.0 m/s², resulting in permanent deformation of piles as well as the inclination of the superstructure. The direction of pile deformation corresponds to those of the strong axis of ground displacement and inertial force.

1. INTRODUCTION

To establish reliable seismic design of pile foundations, it is important to clarify soil-pile-structure interaction under actual earthquake loading conditions; i.e. multi-dimensional shaking. Most of previous studies, however, concentrated on the effects of one-dimensional loading (e.g. Mizuno et al., 1997, Tamura et al., 1998 and Boulanger et al., 1999) and rarely looked upon the effects of multi-dimensional shaking. Saito et al. (2002) conducted a soil-pile-structure interaction study using three-dimensional ground motions caused by mine blasting. The test using mine blasting was, however, insufficient to estimate inertial and kinematic effects on deformation and failure modes of pile group in detail due to reproduction of ground motions and limited number of sensors used.

To investigate inertial and kinematic effects on failure and deformation modes of pile group during three-dimensional shaking, physical tests on soil-pile-structure models were conducted (Tabata and Sato, 2006, and Tokimatsu et al., 2006) using the E-Defense at the Hyogo Earthquake Engineering Research Center of the National Research Institute for Earth Science and Disaster Prevention (NIED). The E-Defense was one of the largest shaking table facilities in the world, opened in 2005, commemorating the tenth anniversary of the 1995 Kobe earthquake. The objective of this study is to investigate dynamic soil-pile-structure interaction involving failure mechanism of pile foundation, based on shaking table tests conducted at the E-Defense.

2. SHAKING TABLE TESTS WITH SOIL-PILE-STRUCTURE MODELS AT E-DEFENSE

The E-Defense shaking table platform has a dimension of 15 m long and 20 m wide. It is supported on fourteen vertical hydraulic jacks and connected to five hydraulic jacks each in the two orthogonal horizontal directions. Fig. 1 and Photo 1 show a test model constructed in a cylindrical laminar box, with a height of 6.5 m and a radius of 8.0 m, placed on the large shaking table. The cylindrical laminar box consists of forty-one stacked ring flames, enabling shear deformation of the inside soil during two-dimensional horizontal shaking.

Albany sand, imported from Australia, was used for preparing the sand deposit. Fig. 2 shows the grain size distribution of the sand. The sand had a mean grain size D_{50} of 0.31 mm and a coefficient of uniformity U_c of 2.0. After setting the pile group in the laminar box, the sand was air-pluviated and compacted to a relative density of about 70 % to form a uniform sand deposit with a thickness of 6.3 m. The natural period of the ground is about 0.2s.

A 3x3 steel pile group was used for the test. The piles are labeled A1 to C3 according to their locations within the pile group, as shown in Fig. 1. Each pile had a diameter of 152.4 mm and a wall thickness of 2.0 mm. The piles were set up with a horizontal space of four-pile diameters center to center. Their tips were jointed to the laminar box base with pins and their heads were fixed to the foundation of a weight of 10 tons.

A total of five test series named A to E was conducted, in which the presence of foundation embedment and superstructure, and the natural period of the superstructure, as well as the type of input motions including predominant period and maximum acceleration were varied. Table 1 shows the list of the test series. The foundation carried the superstructure of a weight of 28 tons in all series except for series C and had embedment except for series E. The superstructure had a natural period of 0.1, 0.2 or 0.6 s. This was achieved by changing the height and/or the rigidity of the four columns supporting the superstructure. The superstructure in series A was carried on four steel columns 0.3 m high, that in series B on four rubber columns 0.3 m high, and those in series D and E on four steel

Table 1 Test series

	Embedment	Superstructure	Natural period (s)	Maximum input acceleration (m/s ²)									
				JR Takatori				Taft and Tottori					
				X	Y	XY	XYZ		X	Y	XY	XYZ	
A	Yes	Yes	0.1	0.3, 0.8				-		0.3, 0.8			
B	Yes	Yes	0.6										
C	Yes	No	-					0.3, 0.8					
D	Yes	Yes	0.2	0.3, 0.8				0.3, 0.8					
E	No	Yes						0.3, 0.8				0.3, 0.8, 6.0, 8.0	

Table 2 Number of sensor channels

	Strain gauge	Accelerometer	Velocity meter	Earth pressure transducer	Displacement meter	Settlement meter	Load cell
Super-structure	0	12	4	0	7	0	0
Column	48	0	0	0	0	0	0
Foundation	0	12	0	16	4	0	0
Pile	476	28	0	52	0	0	27
Ground	0	63	0	0	2	5	0
Laminar box	0	82	0	0	24	0	0
Total	524	197	4	68	37	5	27

columns 1.0 m high. The natural period of the superstructure is smaller than that of the ground in series A, but closed to that of the ground in series D and E and larger than that of the ground in series B.

Table 2 shows the number of sensors used in the tests. Many strain gauges, accelerometers, velocity meters, earth pressure transducers, displacement transducers, settlement meters and load cells, about 900 sensors in total, were placed in the deposit as well as on the pile-structure model.

The tests were conducted under one-, two- or three-dimensional shaking with three different ground motions recorded at Takatori in the 1995 Kobe earthquake, at Lincoln School in the 1952 Taft earthquake and at Akasaki in the 2000 Tottori earthquake (hereby named Takatori, Taft, and Tottori). Fig. 3 shows the acceleration response spectra of those motions, which were computed from acceleration records, on the assumption that a damping was 5 %. The acceleration response spectra of the horizontal motions at Tottori dominate only in a short period range with a sharp spectral peak at about 0.1 s (Fig. 3(c)), whereas those at Takatori and Taft dominate over a wide period range covering from 0.1 s to 1.0 s (Fig. 3(a)(b)). In each test series, either or both of the two horizontal or three-component motions were used as input to the shaking table with the largest horizontal acceleration being scaled to a value listed in Table 1. The NS and EW components of the ground motion were

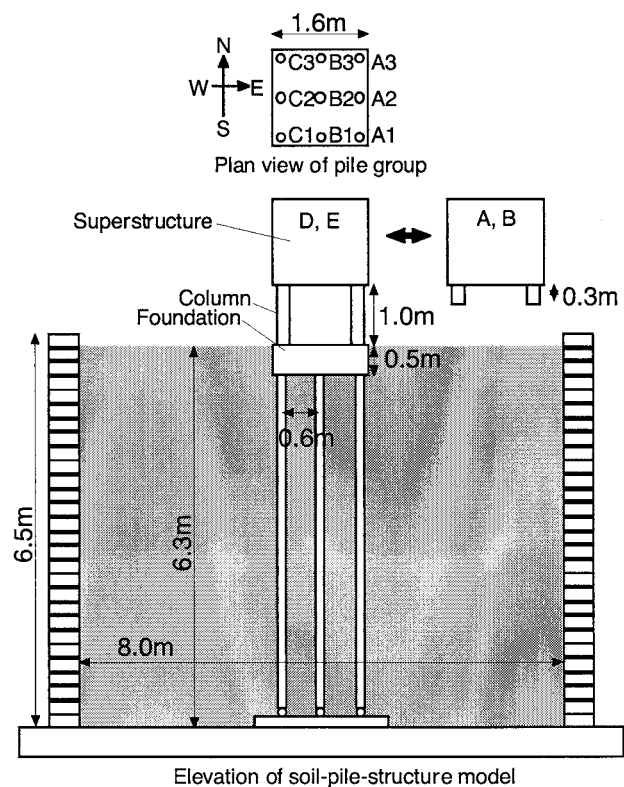


Fig. 1 Soil-pile-structure model

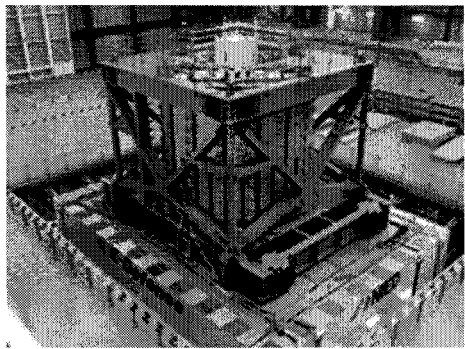


Photo 1 Test model on shaking table

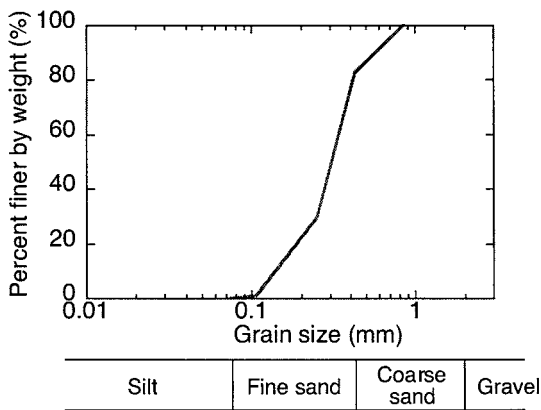


Fig. 2 Grain size of Albany sand

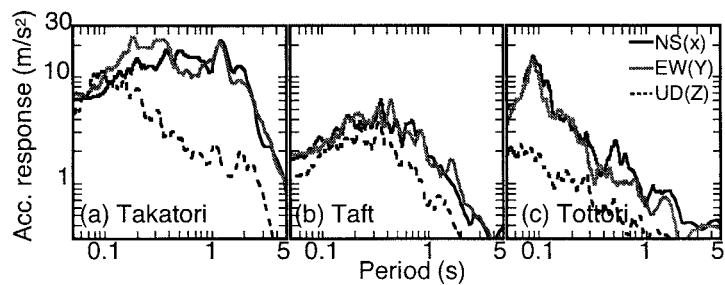


Fig. 3 Acceleration response spectrum

applied to the NS (X) and EW (Y) directions as shown in Fig. 1, with the UD (Z) component to the vertical direction. This paper describes inertial and kinematic effects on deformation and failure mode of piles based on test series E with Takatori motion having maximum input accelerations of 0.8 m/s^2 and 6.0 m/s^2 . The strains induced in the piles were within the elastic range with a maximum input acceleration of 0.8 m/s^2 . The piles, however, yielded at the pile heads as well as at 0.7 to 1.2 m below their heads with a maximum input acceleration of 6.0 m/s^2 .

3. INERTIAL AND KINEMATIC EFFECTS ON BENDING STRESSES WITHIN PILE GROUP

Figs. 4 and 5 show the time histories of accelerations of superstructure, ground surface and shaking table in the NS, EW and UD directions and of bending strains of the NS and EW directions and axial strains at the heads of Piles A1, B2 and C3. The maximum acceleration of shaking table is 0.8 m/s^2 in the horizontal directions and 0.4 m/s^2 in the vertical directions (Fig. 4(c)(f)(i)). The horizontal ground surface accelerations are more than twice as large as those of the shaking table (Fig. 4(b)(c)(e)(f)), and those of the superstructure are significantly larger than those of the ground surface (Fig. 4(a)(b)(d)(e)). The bending and axial strains tend to increase with increasing superstructure acceleration. The absolute axial strains in Piles A1 and C3 are almost the same with each other, but

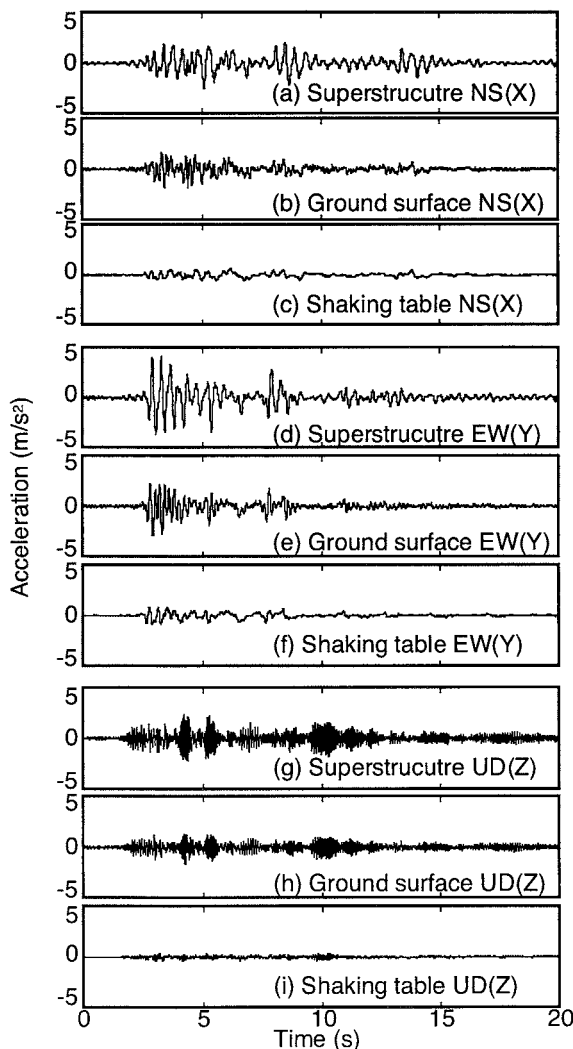


Fig. 4 Time histories of accelerations

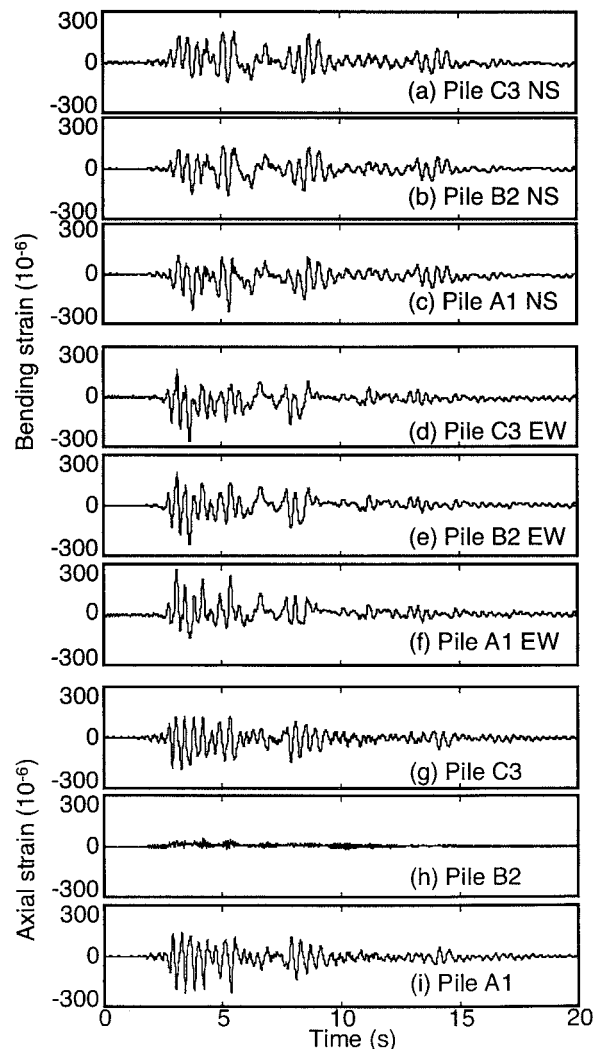


Fig. 5 Time histories of bending and axial strains

have opposite signals (Fig. 5(g)(i)). This is because Piles A1 and C3 are located on the opposite sides within a pile group and their axial forces due to overturning moment of the superstructure are reversed. The axial strain in Pile B2 is significantly smaller than those in Piles A1 and C3 (Fig. 5(g)(h)(i)), probably because Pile B2 is located in the center within the pile group. The bending strain in the EW direction is smaller on the negative side than on the positive side in Pile A1 but is smaller on the positive side than on the negative side in Pile C3 (Fig. 5(d)(f)). The bending strain in the NS direction, in contrast, is smaller on the positive side than on the negative side in Pile A1 but is smaller on the negative side than on the positive side in Pile C3 (Fig. 5(a)(c)). This suggests that the bending strain varies depending on the location within the pile group, as is the case in axial strain.

To investigate the variation of bending strain within the pile group, Fig. 6 shows loci of the inertial force of structure, ground surface displacement and bending strain of nine piles on the horizontal plane. The inertial force was computed from the observed accelerations of superstructure and foundation. In Fig. 6, the horizontal axis indicates a component in the EW direction and the vertical one indicates a component in the NS direction. The inertial force is larger in the EW direction than in the NS direction and its two-dimensional locus shows a spindle shape with its longer axis in the EW direction (Fig. 6(a)). The loci of bending strain show the same trends as those of the inertial force. In addition, whenever the inertial force acts southeastward, the bending strain becomes the largest in Pile A1 located at the southeast side of the pile group (Fig. 6(k)). In contrast, whenever the inertial force acts northwestward, the bending strain becomes the largest in Pile C3 located at the northwest side (Fig. 6(c)). This indicates that the bending strain is the largest at the leading pile within the pile group. The ground displacement is significantly small and its locus shows a different shape from those of inertial force and bending strains (Fig. 6(b)). This suggests the ground displacement plays an insignificant role in an increase in pile stresses in the test with small shaking.

To estimate difference in bending strain within the pile group, Fig. 7 shows the distributions with depth of bending strains computed by a sum of NS and EW components for the nine piles when the inertial force takes the largest peak on the southeast, as shown by a circle in Fig. 6(a)(b). At this moment, Pile A1 is the leading corner pile and Pile C3 is the trailing corner pile. The bending strains at the pile head as well as at a depth of about 1.0 m become the largest at the leading corner pile, i.e., Pile A1 (Fig. 7(i)), and become the smallest at the trailing corner pile, i.e., Pile C3 (Fig. 7(a)). In addition, the depth at which the bending strain takes the inflection tends to be smaller in the leading pile, i.e., Pile A1 (Fig. 7(i)) than in any other trailing pile. These trends confirm that the pile stresses vary within the pile group and that bearing load is the largest in the leading corner pile.

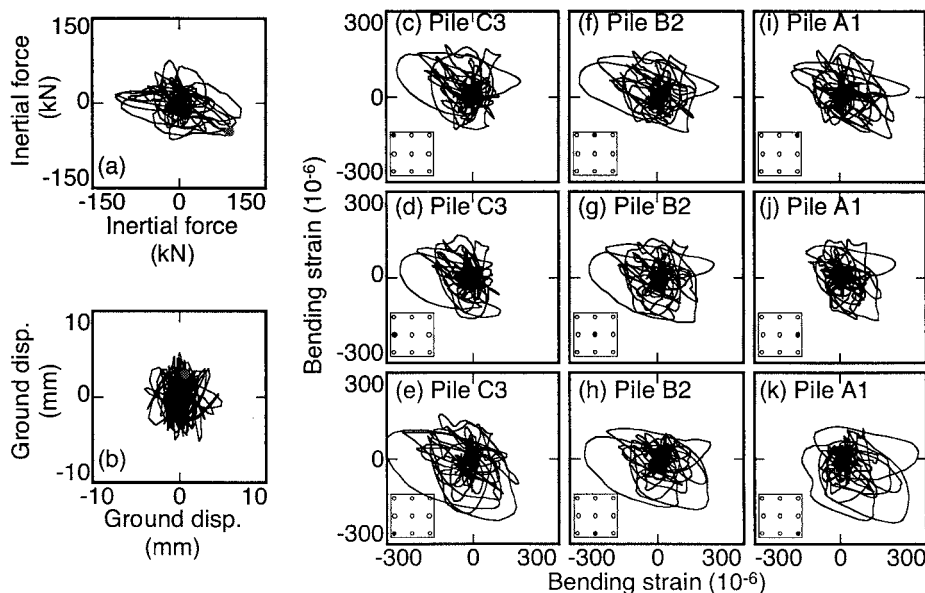


Fig. 6 Loci of inertial force, ground surface displacement and bending strains

4. INERTIAL AND KINEMATIC EFFECTS ON PILE DEFORMATION AND FAILURE MODE

To estimate inertial and kinematic effects on pile deformation and failure mode, Fig. 8 shows the time histories of inertial force of structure, ground surface displacement and bending strains of the corner piles (Piles A1, A3, C1 and C3) in the test with a maximum acceleration of 6.0 m/s^2 . Despite large difference in maximum input acceleration, the maximum inertial force of the structure of this test is almost the same as that in the test with a maximum acceleration of 0.8 m/s^2 (Figs. 6(a) and 8(a)(b)). In contrast, the maximum ground surface displacement of is significantly larger than that in the test with a maximum acceleration of 0.8 m/s^2 (Figs. 6(b) and 8(c)(d)). In spite of almost the inertial force between the two tests, the bending strains are significantly larger in the test with a greater input acceleration, showing residual values in some of the piles after about 6 s (Fig. 8(e)-(l)), particularly in Pile A3 (Fig. 8(i)(j)). At the instant shown by lines in the figures, when the bending strain in Pile A3 increases significantly, both the ground surface displacement and the inertial force increase northeastward (Fig. 8(a)-(d)). This indicates that both inertial and kinematic effects might have played important roles in increasing bending strain.

To investigate inertial and kinematic effects on deformation and failure mode of piles, Fig. 9 shows the distributions with depth of bending strains of the nine piles at about 6 s after the start of shaking at which the piles start yielding. The inertial force and ground surface displacement increase northeastward, making Pile A3 the leading corner pile. The figure shows that the bending strains at about 1 m depth in Piles A1, A2, and A3 exceed the elastic limit because of the combined effects of inertial and kinematic forces acting on the same directions at this moment (Fig. 9(g)-(i)). This indicates that the leading piles including Pile A3 bear larger forces than others and might have failed first.

After the test with a maximum acceleration of 6.0 m/s^2 , a high input motion with a maximum acceleration of 8.0 was applied to the test model. The ground deformed significantly with the strong axis of the northeast-southwest direction. The superstructure began to incline toward northeast during the test. Fig. 10 shows the residual deformation of the foundation, indicating that it not only

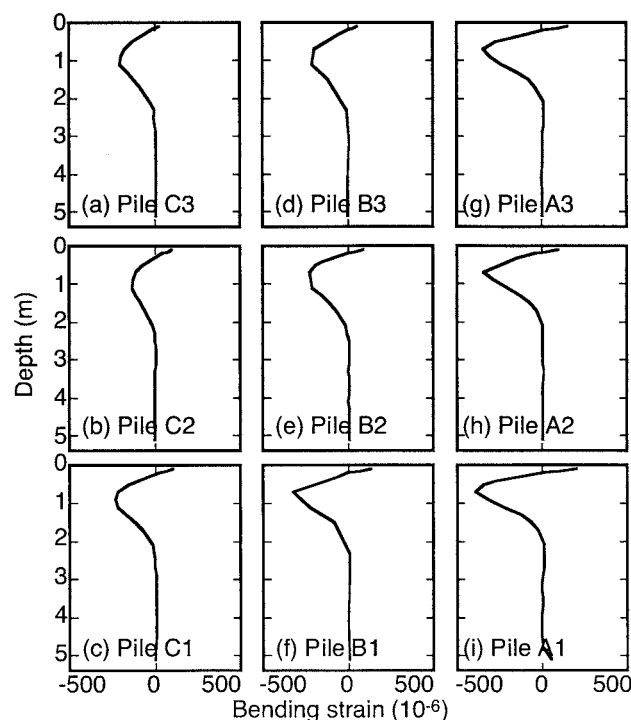


Fig. 7 Distributions of bending strain in test with maximum acceleration of 0.8 m/s^2

moved northeastward but also rotated clockwise. Photo 2 shows the damage to pile foundations after excavation. Piles A1-A3 buckled at 1.2 m below their pile heads, the depth of which corresponds to the depth at which the measured bending strains take a peak (Fig. 9(g)-(i)). In contrast, Piles C1-C3 deform at 0.7 m below their pile heads, the depths of which do not correspond to the depths at which the measured bending strains take a peak, i.e., a depth of 1.0 m (Fig. 9(a)-(c)). This is probably because the damage firstly occurring in Piles A1-A3 led to redistribution of bearing load within the pile group, causing subsequent pile buckling at a smaller depth for the other piles.

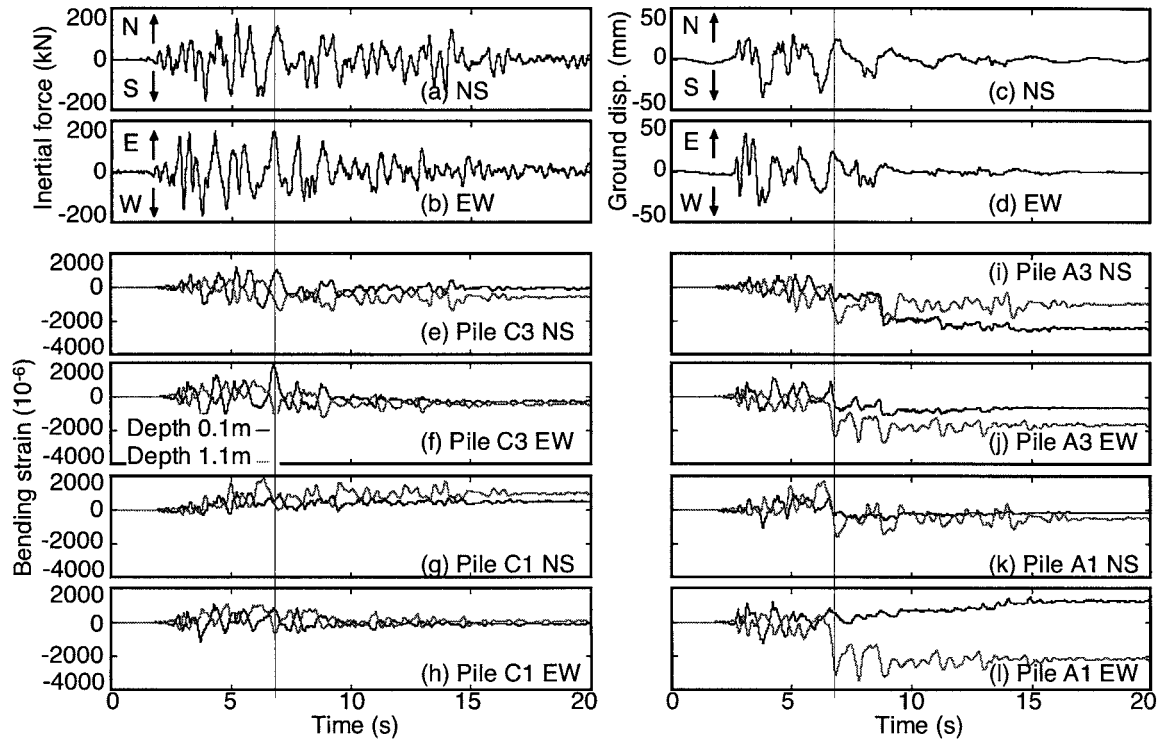


Fig. 8 Time histories of inertial force, ground surface displacement and bending strains

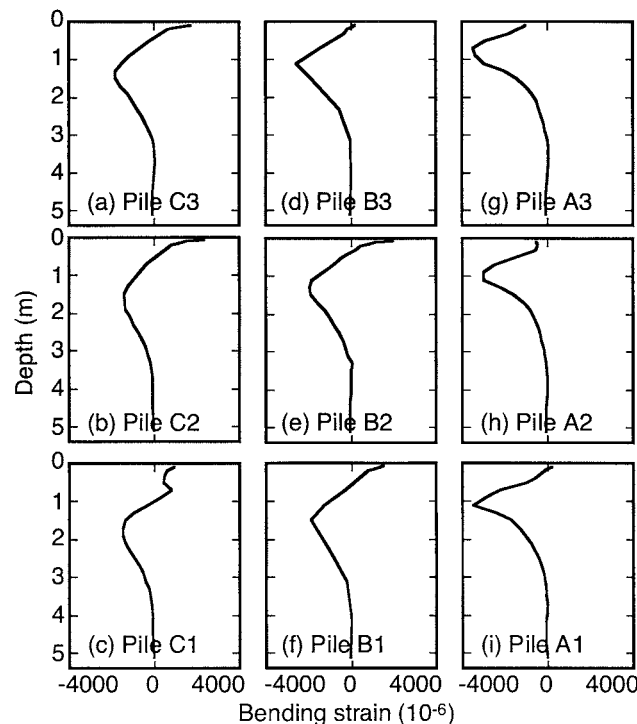


Fig. 9 Distributions of bending strain in test with maximum acceleration of 6.0 m/s²

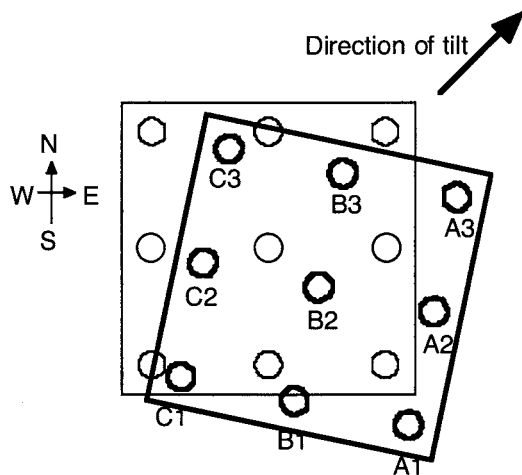


Fig. 10 Residual deformation of foundation

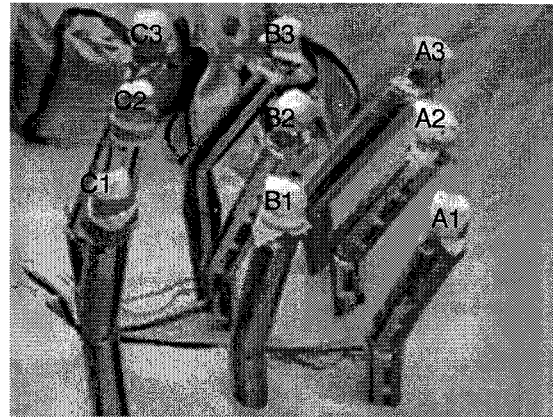


Photo 2 Damage to piles after shaking

5. CONCLUSIONS

To investigate inertial and kinematic effects on failure and deformation mode of piles, physical model tests on soil-pile-structure systems were conducted using the large shaking table at E-Defense, NIED. The test results and discussions have led the following:

- 1) The bending strain is larger in the leading piles than in the trailing piles probably due to group pile effects and the depth at which the inflection of bending strains occurs is shallower in the leading piles than in the trailing piles.
- 2) The piles yielded and the superstructure inclined under the high input motion. The piles not only suffered local buckling at their heads but also deformed significantly at 0.7 m to 1.0 m below their heads. The direction of permanent pile deformation corresponds to those of the strong axis of inertial force and ground displacement.

Acknowledgements:

The study described herein was made possible through Special Project for Earthquake Disaster Mitigation in Urban Areas, supported by the Ministry of Education, Culture, Sports, Science and Technology (MEXT). The authors express their sincere thanks to the above organization.

References:

- Saito, H., Tanaka, H., Ishida, T., Koyamada, K., Kontani, O. and Miyamoto, Y. (2002), "Vibration tests of pile-supported superstructure in liquefiable sand using large-scale blast (Outline of vibration tests and responses of soil-pile-structure)", *Journal of Structural and Construction Engineering*, **553**, 41-48 (in Japanese).
- Mizuno, H., Sugimoto, M., Iiba, M., Hirade, T. and Mori, T. (1997), "Evaluation of seismic behavior of pile foundations and seismic action on piles by shaking table tests of large-scale shear box (Part 5 Plan and intention of shear box shaking table tests (liquefaction) and soil characteristics)", *Proc. of Japan National Conference on Architecture and Building Engineering*, **B-2**, 377-378 (in Japanese).
- Tamura, S., Minowa, C., Fujii, S., Yahata, K., Tsuchiya, T., Kagawa, T. and Abe, A. (1998), "Shaking table test of reinforced concrete pile foundation on liquefied soil using large scale laminar box (Part 1 Outline of test)", *Proc. of Thirty-third Japan National Conference on Geotechnical Engineering*, **1**, 819-820 (in Japanese).
- Boulanger, R. W., Curras, J. C., Kuter, B. L., Wilson, D. W. and Abghari, A. (1999), "Seismic soil-pile-structure interaction experiments and analyses", *Journal of Geotechnical and Geoenvironmental Engineering*, ASCE, **125** (9), 750-759.
- Tabata, K. and Sato, M. (2006), Report of special project for earthquake disaster mitigation in urban areas, Ministry of Education, Culture, Sports Science and Technology, 489-554, (in Japanese).
- Tokimatsu, K., Sato, M., Tabata, K. and Suzuki, H. (2006), "Shaking table tests conducted on soil-pile-structure model in laminar box by using E-Defense", *Proc. of 12th Japan Earthquake Engineering Symposium*, 682-685 (in Japanese).

EFFECTS OF NONLINEAR DYNAMIC PROPERTIES OF SURFACE SOILS ON SEISMIC GROUND MOTION AND BUILDING DAMAGE IN OJIYA DURING 2004 MID NIIGATA PREFECTURE EARTHQUAKE

K. Tokimatsu ¹⁾, T. Sekiguchi ²⁾ and H. Arai ³⁾

1) Professor, Structural Engineering Research Center, Tokyo Institute of Technology, Japan

2) Graduate Student, Dept. of Architecture and Building Engineering, Tokyo Institute of Technology, Japan

3) Research Engineer, National Research Institute for Earth Science and Disaster Prevention, Japan.

Kohji@o.cc.titech.ac.jp, tsekiguc@mail.arch.titech.ac.jp, arai.h@bosai.go.jp

Abstract: In order to examine the effects of nonlinear site amplification characteristics on strong ground motions and damage to wooden houses in Ojiya during the Mid Niigata Prefecture earthquake, strong ground motions are simulated for several damaged sites in the city with the investigated soil profiles. Using the simulated ground motions and simplified wooden structural models, maximum responses of wooden houses are also estimated at the sites. The house responses evaluated are consistent with the damage statistics available at the sites. It is shown that the surface soils including their nonlinear soil properties might have had a significant effect on the damage distribution of house buildings in Ojiya city during the earthquake.

1. INTRODUCTION

The Mid Niigata Prefecture earthquake in 2004 caused severe damage to many wooden houses in Ojiya city located immediately west of the epicenter, inducing quite different ground motions at two stations (K-NET and JMA) in the city. Tokimatsu et al. (2006) showed that near surface soil conditions including nonlinear soil properties might have played an important role on the difference in ground motions at K-NET and JMA during the earthquake. With the advance of high-density strong motion observation network, it has been revealed that seismic ground motions and resulting building damage can vary significantly even between neighboring areas, depending on the difference in local geological and geophysical conditions.

Horie et al (2005) analyzed the building damage in Ojiya city caused by the earthquake and showed that the building damage ratio in the western area of the city is higher than that in the central area. It seems that seismic ground motions in the western area of the city during the earthquake might have been amplified by the surface soils more than those in the central area. There exist, however, few geological and geophysical data available for examining such local site effects.

The objective of this study is to evaluate the site effects on the building damage in the city during the Mid Niigata Prefecture earthquake (hereafter called "main shock"). Microtremor and seismic ground motion observation are conducted along a line across the central and western areas of the city. Field investigations including boring and spectral analysis of surface wave methods are conducted to evaluate surface soil profiles at several damaged sites. Dynamic analysis is then conducted using the soil profiles to simulate strong ground motions during the earthquake for the sites. Using the simulated ground motions and simplified wooden structural models, maximum responses of wooden houses are also estimated at the sites.

2. BUILDING DAMAGE DISTRIBUTION IN OJIYA CITY

Figure 1 shows the distribution of total collapse ratio of house buildings in Ojiya city analyzed by Horie et al. (2006) after the earthquake, using about 250 m square meshes. The total collapse ratio is defined as the ratio of total collapsed buildings to all buildings in the area. In the area where mesh is not shown, the total collapse ratio is not calculated because of a scarcity of house buildings. Widespread damage to house buildings occurred in the city, with higher damage ratios in Tokimizu and Yoshitani located in the west and southwest of the city (hereafter called “western area”) than in the central area. Since large ground deformation in the western area is not reported, it seems that the building damage in this area is due to ground shaking during the earthquake.

3. MICROTREMOR AND WEAK SEISMIC GROUND MOTION CHARACTERISTICS IN OJIYA CITY

Microtremor measurements with a three-component sensor were conducted at 24 sites along line A-A' across the central area and the western area as well as other two sites in the western area, as shown with open circles in Fig. 1. Figure 2 (a) shows spatial variations of H/V spectra calculated from the three component motions of microtremors observed along the line A-A' using the gradations shown in the legend. The H/V spectra have a prominent peak at about 0.4-0.5 s, at such sites as No. 5 station in the western area where the damage ratios are high, at No. 4 station near Kanetsu expressway and No. 2 station in the central area. The H/V spectra at other sites, in contrast, have a prominent peak at less than 0.4 s (K-NET, No. 1 station, JMA), or do not have any prominent peak (No. 3 station).

Figure 2 (b) shows damage ratios of house building (Horie et al. 2006) around the microtremor observation sites along line A-A'. The total collapse ratio near No. 5 station in the western area is relatively high, i.e., more than 40%, whereas it is almost zero in the central area, with a partial damage ratio of about 20-30 %.

Seismic array observation was initiated at Nos. 1-6 stations on November 3rd, 2005 to examine seismic ground motion characteristics of each site. Seismic ground motions of 10 earthquakes ($M_J = 2.7-4.8$) at those stations have been simultaneously recorded as of February 10, 2007. Figure 3 shows the velocity response spectra with a damping ratio of 5% for the EW component recorded at

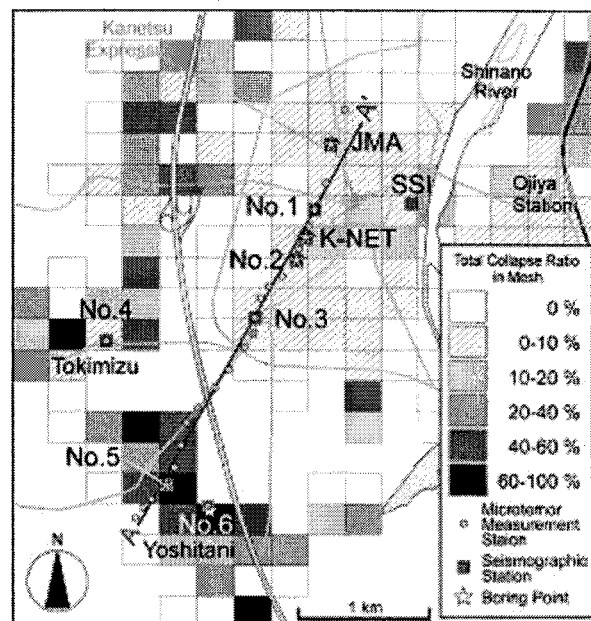


Figure 1 Map showing distribution of total collapse ratio of house buildings [Horie et al., 2006], microtremor and ground motion observation stations, and boring investigation sites in Ojiya city

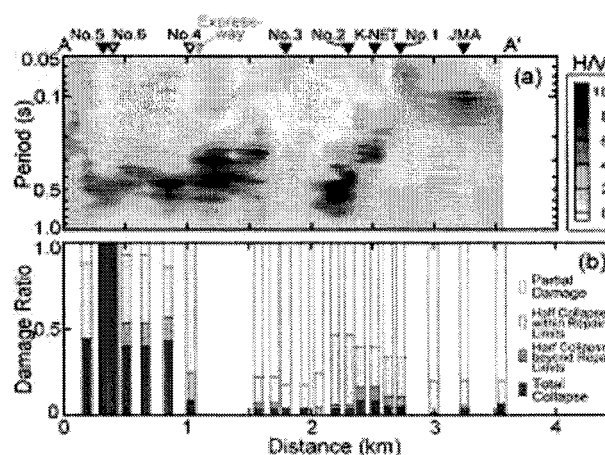


Figure 2 Spatial variations of (a) microtremor H/V spectra and (b) building damage ratios along line A-A' shown in Figure 1

Nos. 1-6, K-NET and JMA stations during the earthquake of November 4, 2005. The spectral amplitudes at Nos. 4-6 stations in the western area and No. 2 station in the central area are larger than those at the other stations, with a longer spectral peak period and/or more prominent peak than those of the other sites including K-NET and JMA, and Nos.1, 3 stations.

The above findings indicate that microtremor and weak seismic ground motions at Nos. 4-6 stations in the western area and No. 2 station show similar spectral characteristics, but the damage ratio of house building in the western area is significantly higher than that around No. 2 station.

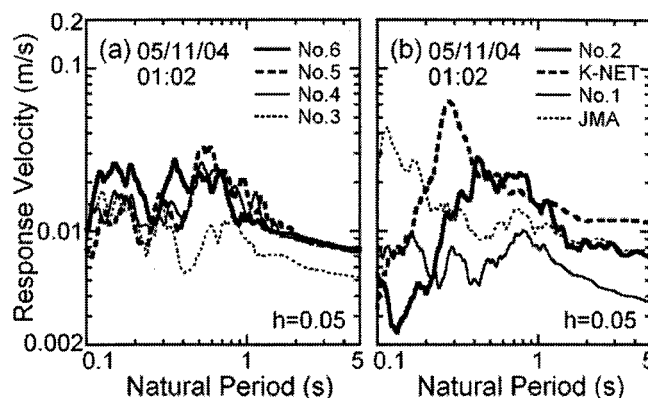


Figure 3 Comparison of velocity response spectra observed at several stations in Ojiya during an earthquake of Nov. 4, 2005

4. FIELD INVESTIGATION

Field investigations including boring and spectral analysis of surface wave methods were conducted at selected stations to evaluate surface soil profiles at the stations and then to examine the cause of the difference in building damage ratio with in the city identified in the previous chapter.

4.1 Geological Logs from Current and Previous Studies

Boring survey was conducted at Nos. 2 and 5 to determine their surface soil properties down to a depth at which stiff/dense soil occurs. Figure 4 shows the boring logs at No. 2 and No. 5 stations together with those at No. 6 and K-NET stations from the previous investigations (Tokimatsu et al. 2006). The surface soil at No. 2 station, which is very similar to that of K-NET station, is extremely soft, mainly consisting of peat, and is underlain by gravel occurring at a depth of 5 m. The surface soil at Nos. 5 and 6 stations in the western area, in contrast, consists of thicker soft soils such as silty clay, silt, and sand, which is underlain by gravel occurring at a depth of about 15-20 m.

4.2 Shear Wave Velocity Profiles from Spectral Analysis of Surface Wave Methods

Active and passive techniques of spectral analysis of surface wave methods were also performed at Nos. 1-6 stations to estimate the shear wave velocity profiles to a depth of about 25 m. In the active method of exploring shallow soil profiles, an artificially generated point source was observed with different linear arrays of several vertical sensors distributed at an equal spacing of 0.5 to 2 m on a line with the source. In the passive method of exploring deep soil profile, microtremors were measured with different circular arrays of different radius of 5 to 40 m. Based on the F-k spectral analysis of the observed vertical motions, dispersion characteristics at the six stations were computed. Figures 5 shows the computed phase velocities at Nos. 2, 5 stations plotted against periods with symbols

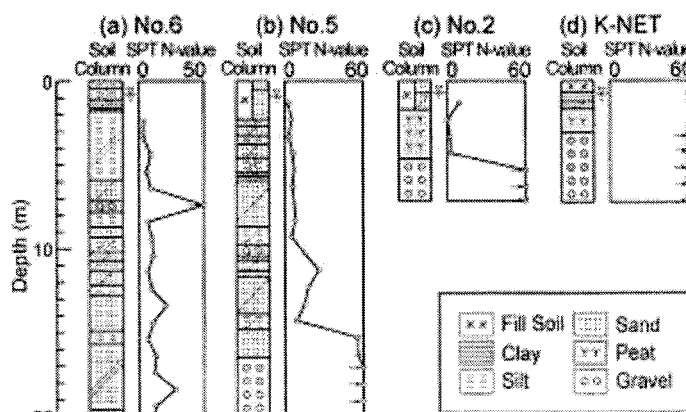


Figure 4 Boring logs at several sites in Ojiya

corresponding to the sensor distances used.

The H/V spectra were calculated from the three component motions of microtremors at the six stations. Figure 6 shows the H/V spectra at Nos. 2 and 5 stations with open circles.

Shear wave velocity profiles down to a depth of 25 m for the six stations were back-calculated based on an inverse analysis using both dispersion curves and H/V spectra (Arai and Tokimatsu, 2005). The solid lines in Figs. 5 and 6 show the theoretical dispersion curves and H/V spectra for the inverted shear wave velocity profiles. The computed values are in fairly good agreement with the observed ones, suggesting that the inverted V_s profiles are reasonably reliable.

Figure 7 shows the estimated shear wave velocity profiles to a depth of 25 m. The impedance contrasts between the bottom layer with V_s of about 400 m/s (engineering base layer) and the surface soil layers at the stations other than Nos. 1 and 3 are significantly high, which might have induced the large amplification near the spectral peak period at these stations, as observed in Fig. 3. A comparison between Figs. 4 and Fig. 7 suggests that the estimated bottom layer with V_s of about 400 m/s at each station corresponds to the gravel layer shown in Fig. 4 and the depth at which such gravel layer occurs at any station in the western area (Nos. 4-6) is much deeper than that in the central area (No. 2 and K-NET stations).

5. DYNAMIC RESPONSE ANALYSIS

To estimate the strong motions at Nos. 1-6 stations during the main shock, one-dimensional nonlinear dynamic response analysis was conducted. Modified Ramberg-Osgood model was used to represent the stress strain relation. Figure 8 shows the nonlinear dynamic soil properties used for the analysis, most of which are based on the study by Imazu and Fukutake (1986). Only exceptions are those of peat that is based on the laboratory test results by Tokimatsu and Sekiguchi (2006) shown with symbols in Fig. 8. The soil types of the surface layers at the stations were assumed to be those shown in Fig. 7, based on the boring logs shown in Fig. 4. The EW component

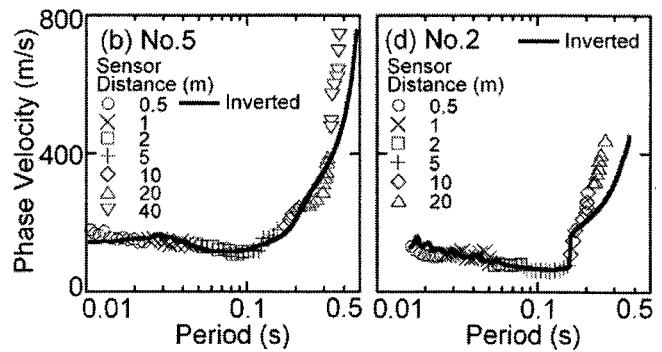


Figure 5 Surface wave dispersion curves

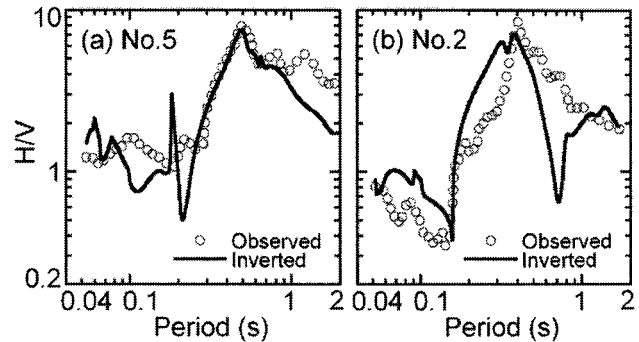


Figure 6 Microtremor H/V spectra

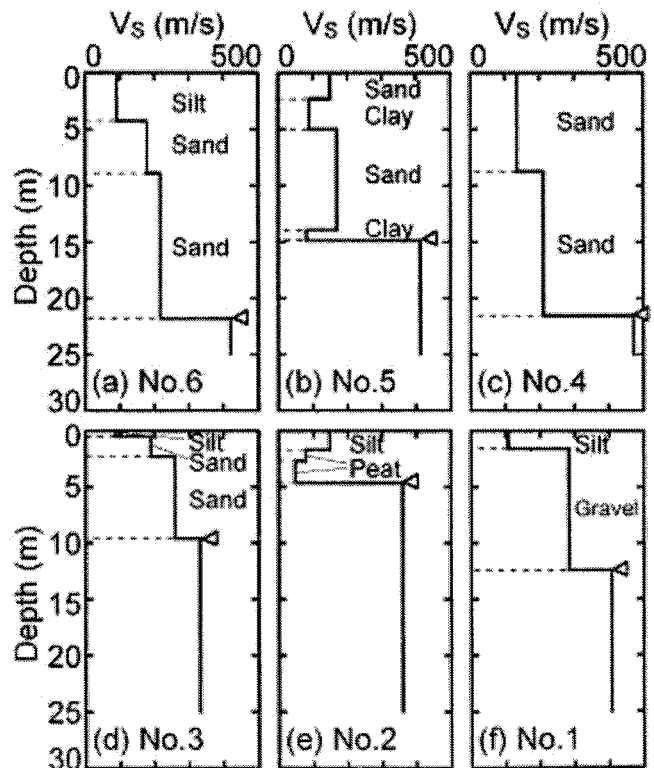


Figure 7 Shear wave velocity profiles estimated from surface wave methods and soil types used for dynamic analysis

of the engineering base outcrop motions recorded at SSI shown in Fig. 1 (Tamari and Tokida, 2004) was used as input motion to the assumed base outcrop layer at each station shown with a triangular symbol in Fig. 7. The shear wave velocities of the base layers are almost the same as that of the outcrop rock at SSI.

Figure 9 shows the acceleration response spectra with a damping ratio of 5% for the computed motions at Nos. 1-6 stations and the observed motions at K-NET and JMA during the main shock, with the natural site periods of all the stations. The peak period at No. 2 station during the main shock is about 0.6 s, which is about 1.5 times the natural site period during small earthquakes. The peak periods at Nos. 4-6 stations in the western area are elongated to as much as about 1 s from the natural site period of 0.4-0.5 s during small earthquakes. The difference in elongation of the spectral peak period between No. 2 and Nos. 4-6 stations is due to the difference in nonlinear dynamic soil properties of the surface soils and, in particular, the weaker nonlinearity of peat at No. 2 station shown in Fig. 8.

Superimposed in Fig. 9 are the equivalent-performance response spectra (EPRS) presented by Hayashi (2002) for two-storied wooden houses with base shear coefficients, C_y , of 0.2, 0.4 and 0.6 (Morii et al., 2005). The intersection between the response spectra of the ground motion and EPRS yields the maximum response drift angle R_{\max} of a building for the given base shear coefficient and for the given ground motion.

Figure 10 shows the distribution of the estimated R_{\max} within the city. R_{\max} at Nos. 4-6 stations in the western area are about 0.07 for buildings with any C_y , which are larger than any other station in the central area including No. 2 station. This tendency agrees reasonably well with the damage distribution of wooden houses shown in Figs. 1 and 2 (b), indicating that the surface soils including their nonlinear soil properties might have had a significant effect on the damage distribution of house buildings in Ojiya city during the Mid Niigata Prefecture earthquake.

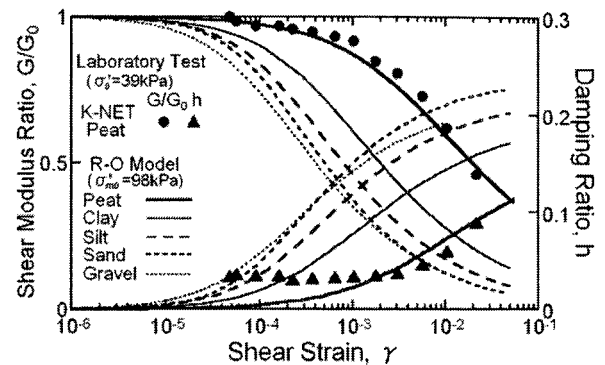


Figure 8 Relations of shear modulus ratio and damping ratio with shear strain used for dynamic analysis and for sample obtained at K-NET in Ojiya.

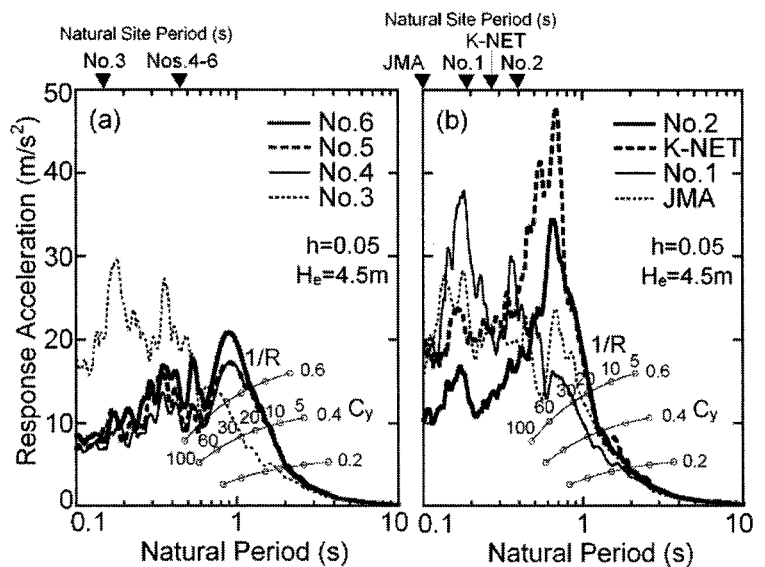


Figure 9 Comparison of acceleration response spectra estimated at Nos. 1-6 stations and observed at K-NET and JMA during main shock with equivalent-performance response spectra for two-storied wooden houses [Hayashi, 2002]

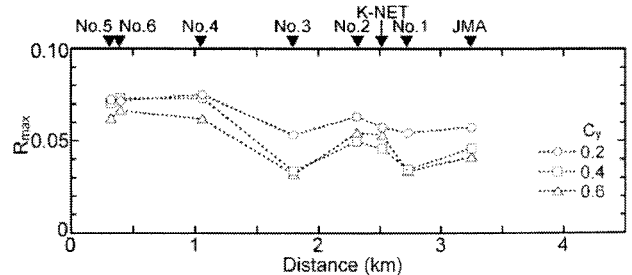


Figure 10 Distribution of estimated maximum response drift angles of wooden houses during main shock at Nos. 1-6, K-NET and JMA stations

6. CONCLUSIONS

The effects of local site conditions on the strong ground motion and building damage in Ojiya during the Mid Niigata Prefecture earthquake were examined based on the field investigations and subsequent analyses. Based on the results and discussions, the following conclusions may be made:

- (1) The surface soil properties and depths of engineering base layers as well as the shear wave velocity profiles at Nos. 4-6 stations in the western area are quite different from those around No. 2 station in the central area, although microtremors and ground motions during small earthquakes at these stations show similar spectral characteristics.
- (2) The strong input motions during the main shock elongated the natural site period of the western area by a factor of more than 2 from 0.4-0.5 s to 1 s, amplifying ground motions in a period range of 1-3 s more than those in the central area where less elongation of natural site period (0.4 s to 0.6 s) occurred. The difference in elongation of natural site period between the two areas is probably due to the difference in nonlinear dynamic properties of surface soils between the two areas.
- (3) The difference in the surface soils including nonlinear dynamic properties might have caused significant difference in collapse ratio of house buildings between the western area and the central area of the city during the Mid Niigata Prefecture earthquake.

Acknowledgements:

The strong motion records at K-NET and JMA used in this study were provided by K-NET (NIED) and Japan Meteorological Agency. The strong motion records at SSI were provided by Ojiya Polyclinic, Mitsubishi Jisho Sekkei and Taisei Corporation. The geological log at No. 6 station was provided by Ojiya City Office.

References:

- Arai, H. and Tokimatsu, K. (2005), "S-Wave Velocity Profiling by Joint Inversion of Microtremor Dispersion Curve and Horizontal-to-Vertical (H/V) Spectrum," *Bulletin of the Seismological Society of America*, **95**(5), 1766-1778.
- Hayashi, Y. (2002), "Evaluation of Seismic Design Load based on Equivalent-Performance Response Spectra," *Proceeding of the 11th Japan Earthquake Engineering Symposium*, 651-656 (in Japanese with English abstract).
- Horie, K., Hayashi, H., Maki, N., Yoshitomi, N., Shigekawa, K., Tanaka, S., Okimura, T., and Torii, N. (2005), "A Study on Spatial Distribution of Building Damage in Ojiya City During the 2004 Niigata-ken Chuetsu Earthquake," *Proceedings of the 24th Annual Meeting, Japan Society for Natural Disaster Science*, 7-8 (in Japanese).
- Horie, K., Hayashi, H., Maki, N., Yoshitomi, N., and K., Tanaka, S. (2006), "A Study on Process of Housing Damage Certification During the 2004 Niigata-ken Chuetsu Earthquake Based on Damage Survey Data of Local Governments," *Proceedings of the 25th Annual Meeting, Japan Society for Natural Disaster Science*, 39-40 (in Japanese).
- Imazu, M. and Fukutake, K. (1986), "Dynamic Shear Modulus and Damping of Gravel Materials," *Proceeding of the 21st Japan National Conference on SMFE*, 509-512 (in Japanese).
- Japan Meteorological Agency, available from: http://www.jma.go.jp/JMA_HP/jma/index.html
- Kyoshin Network K-NET, National Research Institute for Earth Science and Disaster Prevention, available from : <http://www.kyoshin.bosai.go.jp/k-net/>
- Morii, T., Hayashi, Y. and Saratani, A. (2005), "Semiempirical Method for Predicting Seismic Damage of Wood Houses Based on Seismic Performance," *Journal of Social Safety Science*, **7**, 281-289 (in Japanese with English abstract).
- Tamari, T. and Tokida, T. (2004), "Earthquake Motion records and Vibration Analysis Results of a Base Isolated Building," *Report on Damage Caused by the Mid Niigata Prefecture earthquake in 2004*, Japan Association of Earthquake Engineering (in Japanese).
- Tokimatsu, K., Sekiguchi, T., Miura, H. and Midorikawa, S. (2006), "Nonlinear Dynamic Properties of Surface Soils Estimated from Strong Motion Accelerograms at K-NET and JMA Stations in Ojiya," *Journal of Struct. Constr. Eng.*, **600**, 43-49 (in Japanese with English abstract).
- Tokimatsu, K. and Sekiguchi, T. (2006), "Relation of Nonlinear Dynamic Soil Properties Observed in Strong Motion Records at K-NET and JMA Stations in Ojiya with those Obtained from Laboratory Test," *Journal of Struct. Constr. Eng.*, **603**, 63-68 (in Japanese with English abstract).

PULLOUT RESISTANCE OF ANCHOR BOLTS IN CEMENTED SAND SUBJECTED TO SHEAR STRAIN

J. Takemura¹⁾, Y. Miyamoto²⁾, and J. Izawa³⁾

1) Associate Professor, Department of Civil Engineering, Tokyo Institute of Technology, Japan

2) Engineer, Kajima Corporation, Japan

3) Research Associate, Department of Civil Engineering, Tokyo Institute of Technology, Japan

jtakemur@cv.titech.ac.jp, jizawa@cv.titech.ac.jp

Abstract: In order to investigate the pullout behavior of anchor bolt in cemented sand subjected to shear deformation, centrifuge model tests have been conducted using an active type shear box. The artificial cemented sand used in the study was made by mixing silica sand, cement, admixture and water. The solidified model ground with model anchor bolts was placed in the active type shear box and sheared under 50g centrifugal acceleration. Pullout tests were conducted after applying various shear deformation to the ground. From the test results, the effects of shear deformation on the maximum pullout resistance and the coefficient of pullout resistance of the anchor bolts in cemented sand were discussed.

1. INTRODUCTION

NATM tunnels are commonly used in rock with rock bolts and shotcrete as a part of tunnel lining. Recently the NATM tunnels have been applied in a sand/gravel deposit if it has a certain cementation. The cemented sandy soil can also be a bearing layer of anchor bolts for supporting geotechnical structures and slopes. However, the cementation of the sand is expected to deteriorate by some disturbances, such as shear deformation due to seismic motion, which may lower the strength mobilized on the bonding area between the bolts and soils and decrease the pullout resistance of the bolts. As a result, stability of the structures supported by the bolts may decrease. The mechanical properties of cemented sand are very complicated, because the mobilizations of cohesion and friction when sheared depend on many factors, e.g., pre shear, stress level, etc.. The objective of this study is to investigate the pullout behavior of anchor bolt in cemented sand subjected to shear deformation by using centrifuge model tests.

Ground aimed in this study is unconsolidated sand but with cementation, which is common in Pleistocene deposits where urban NATM tunnel can be applied. The artificial cemented sand used in the study was made by mixing silica sand, cement, admixture and water. The solidified model ground with model anchor bolts was placed in the active type shear box and sheared under 50g centrifugal acceleration. Pullout tests were conducted after applying various shear deformation to the ground. From the test results, the effects of shear deformation on the pullout resistance of anchor bolts in cemented sand were discussed.

2 ARTIFICIAL CEMENTED SAND

2.1 Preparation of artificial sand

In this study, mixture of sand, cement, admixtures and water are used to replicate the cemented sand refereeing a previous study (Kojima et al., 2003). Silica sand 6 with the physical properties given in Table 1 and high early strengthening portland cement are used. As the admixtures, high-range water reducing agent (Rheobuild 4000, NMB Co. Ltd) and Methylcellulose (Metolose SC2300, Sinetsukagaku) are used to secure flowability with relatively low water content and high viscosity for preventing material segregation in placing the slurry form mixture in the model container.

To make test specimens used for mechanical property tests, these materials are mixed by a mortar mixer for 1 hour under vacuum. The slurry type mixture is then poured into a mold by three layers. Vibration is applied to the mold to get rid of air bubbles from the specimen. The mold is covered by a plastic sheet and stored in a container under wet condition with curing temperature about 20°C.

Table 1 Physical properties of Silica sand 6

Specific gravity G_s	Mean particle dia. D_{50} (mm)	D_{30} (mm)	D_{10} (mm)	Uniformity coef. U_s	Max. void ratio e_{max}	Min. void ratio e_{min}
2.65	0.5	0.25	0.18	2.22	1.132	0.711

2.2 Mechanical properties

To determine the mixing proportion of the materials of the artificial cemented sand used for the model tests, various test specimens with different mixing ratio were prepared as shown in Table 2 and unconfined compression tests and consolidated constant pressure direct shear tests were performed for them. Void ratio e , unit weight, and water content in the table are values under assumption that the soil is totally saturated.

Table 2 Mixing condition of artificial cemented sand

sample No.	cement C (g)	water W (g)	sand S (g)	W/C	HRWR A (g)	Metolos e (g)	water content w (%)	unit weight γ_{sat} (g/cm ³)	cement content (kg/m ³)	ave G_s
F	50	150	500	3.0	1.13	1.5	27.3	1.96	140	2.69
G	40	150	500	3.8	0.904	1.5	27.8	1.95	113	2.69
H	30	150	500	5.0	0.678	1.5	28.3	1.94	85	2.68
I	20	150	500	7.5	0.452	1.5	28.8	1.93	58	2.67

(1) Unconfined compression tests

After curing the specimens, unconfined compression tests were conducted at the axial strain rate of 1% per minute. Figure 1 shows the evolutions of unconfined compressive strength q_u , and secant modulus of deformation E_{50} with curing period for Sample I. Although there is scattering in the unconfined compressive strength and the modulus of deformation, they increase with curing period in early stage. However after 1 week, no significant increase was observed both in strength and stiffness. In Figure 2, the unconfined compression strengths at curing time of one week were plotted against the water-cement ratio (W/C) and the cement content in double logarithmic scale. The q_{us} increase with decreasing W/C and increasing cement content. With the mixing conditions adopted in this study, there are linear relations between the unconfined strength and both the W/C and the cement content in log-log scale.

(2) Consolidated constant pressure direct box shear test

Consolidated constant pressure direct box shear test was conducted to the samples with curing

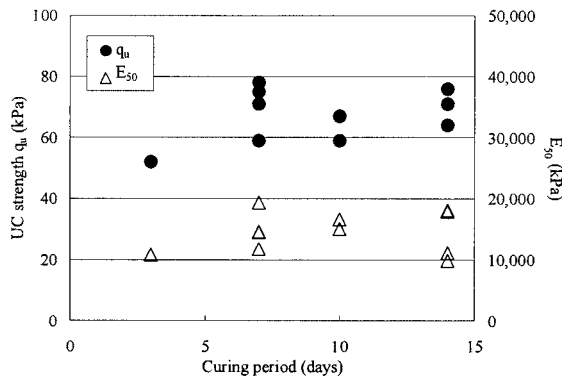


Figure 1 Evolution of q_u and E_{50} with curing time

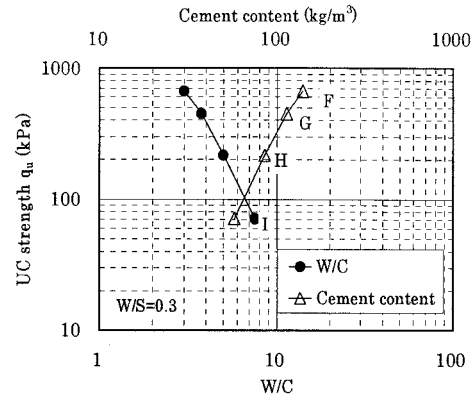


Figure 2 Relationships between q_u and W/C and cement content

period of 7 days. The specimen with the size of $\phi 60 \times 20 \text{ mm}$ was sheared by the rate of 0.12 mm/min under constant vertical stress σ'_v of , 49, 98, and 196 kPa.

In all cases, the compression was first observed, followed by expansion (dilation) after certain horizontal displacement. Figure 3 shows relationships between vertical stress σ'_v and maximum shear stress τ_{\max} for Samples I and H together with that of the silica sand. In the figure the strength

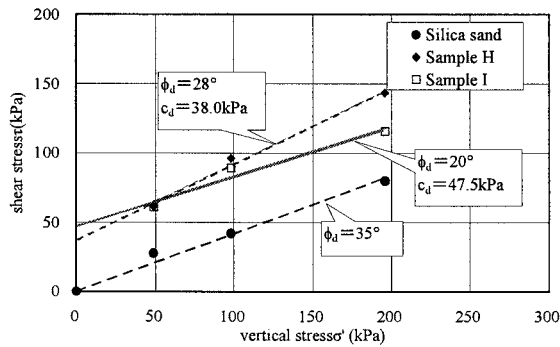


Figure 3 Results of constant pressure direct shear test

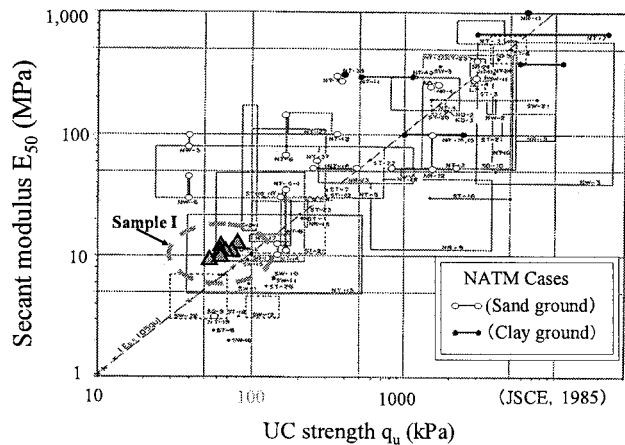


Figure 4 Relationship between q_u and E_{50} of unconsolidated soils at NATM tunnel sites

parameters c' and ϕ' obtained from the linear regression are shown. But it should be noted that actual failure envelopes are more like convex shape rather than straight.

2.3 Determination of mixing proportion for the centrifuge tests

From the experiences in the element tests, the mixing proportion condition of Sample I was selected as that of the sand used in the centrifuge tests. The main reason for this selection was high flowability maintained when casting, therefore uniform samples can be prepared.

Figure 4 shows relationship between the unconfined compression strength and the secant modulus of the soils collected at earth/ground tunnel sites (JSCE,1985). There is nearly a linear relationship between q_u and E_{50} ranging from 50kPa and 2000kPa of q_u . The data on Sample I are also plotted in the figure. The strength and stiffness of Sample I satisfy the overall relationship for sandy ground at the lower bound in the range.

3 Model tests

3.1 Active type shear box

Active type shear box shown in Figure 5 was used for the centrifuge tests. The height of the shear box, length and width are 500mm, 450mm and 200mm respectively. Horizontal displacement of laminae were controlled by four pairs of actuators fixed the side the box through plate springs. The maximum horizontal displacement at the height 500mm is 20mm in maximum, which is equivalent to 4% shear strain. The shear box was designed and built for Mark III Tokyo Tech Centrifuge (Takahashi et al., 2001) and renovated from the original one to increase the height of box (Takemura et al., 2006).

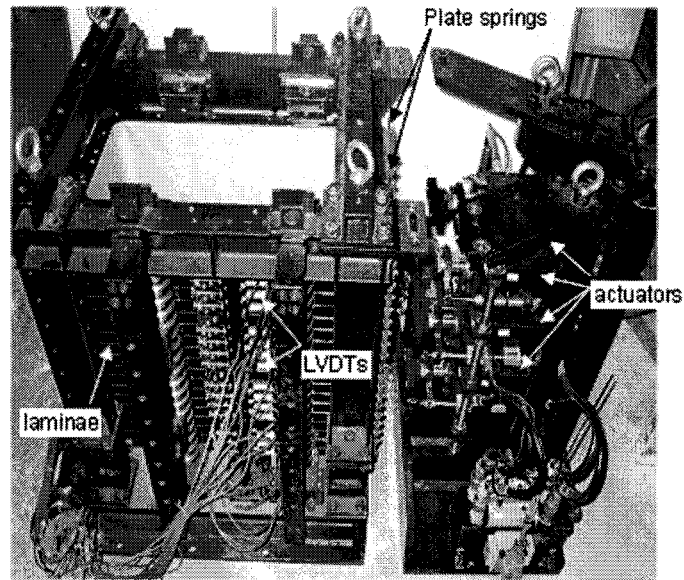


Figure 5 active type shear box

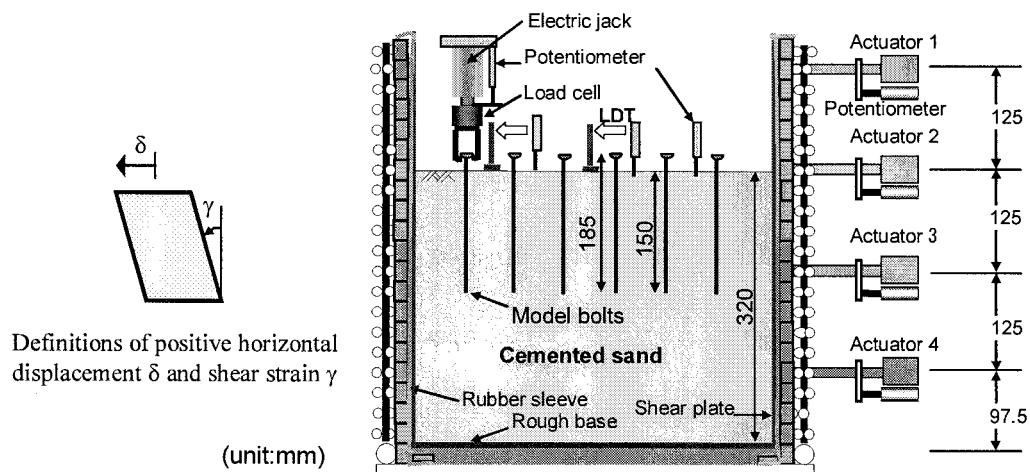


Figure 6 Setup of pullout test in Active Type Shear Box and definitions of displacement and shear strain

3.2 Model preparation and test procedures

After casting the cement mixed sand with the same mixing condition of Sample I and the procedure explained in 2.1, the sand was placed in a container with the same inner dimension of the

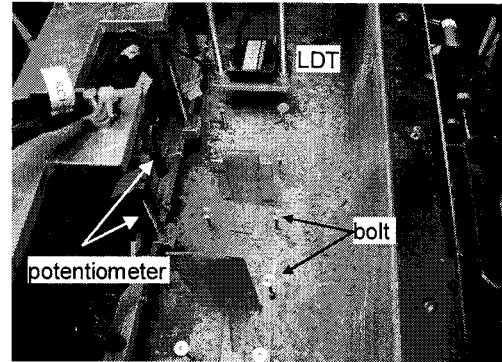
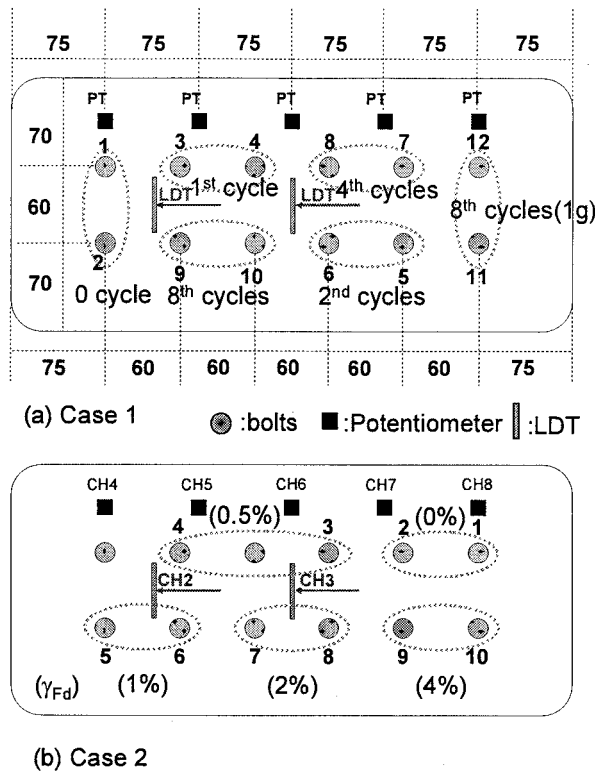


Figure 8 Top view of the model in shear box

Figure 7 Location of sensors and bolts, and conditions of shear strain of the bolts

shear box. 20mm thick bottom plate with 1mm thin plates were placed in the container, the surface of the plates were made rough to generate shear stresses on the surface. Having cast, stainless steel made bolts with 185mm length, 3mm diameter, 0.2mm screw pitch and 10g weight were inserted into the sand vertically before the solidification of the sand.

After curing period of 8days in the casting container, solidified sand was removed from the container with the bottom and side plates and placed into the active type shear box as shown in Figure 6. Potentiometers and Laser displacement transducers (LDTs) were mounted to measure the vertical and horizontal displacement of the sand surface.

Locating the pullout hook at the curved nut fixed at the top of bolt as shown in Figure 6, the centrifuge was spun up 50G and pullout test was then conducted after giving the shear strain to the sand. The centrifuge was once stopped to relocate the jack for the pullout test of the other bolt.

Two centrifuge tests were conducted with different imposed shear strain conditions. In Case 1, the shearing of box strain amplitude $\gamma_{Fd} = 4\%$ with 0.01 Hz sinusoidal form was imposed 8 cycles. Pullout tests were conducted before shearing and after imposing one, two, four and eight cycles. The tests were also done in 1g conditions after stopping the centrifuge. In Case 2, the shear strain amplitude was increased from 0 to 4 % and the pullout tests were conducted after imposing two cycles of shearing of each amplitude. The location of the bolts and their shearing condition when pulled are shown in Figures 7 and 8.

The pullout tests were also conducted for non-sheared cemented sand and the silica sand with void ratio $e=0.90$, using the strong box at different centrifuge acceleration, 1G, 10G, 30G and 50G.

4 Results and discussion

4.1 Deformation of model ground by the active shear box

Figures 9 and 10 show shear strain of the model ground imposed by the active type shear box in

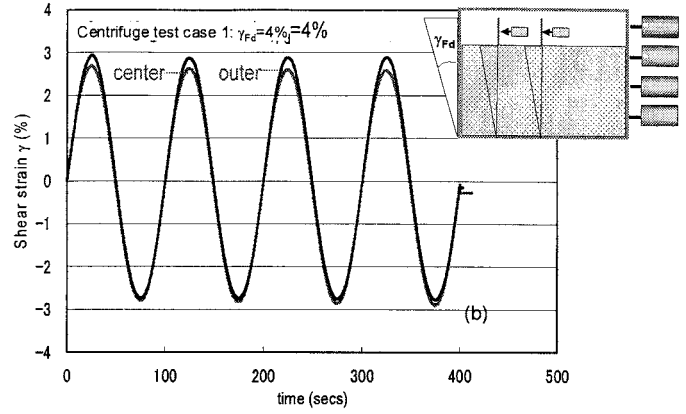
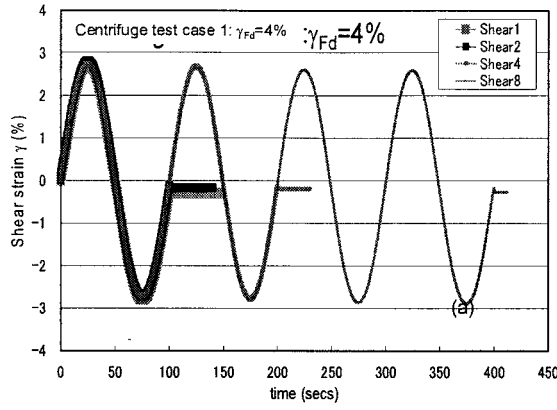


Figure 9 Shear deformation of the model ground in centrifuge: Case 1

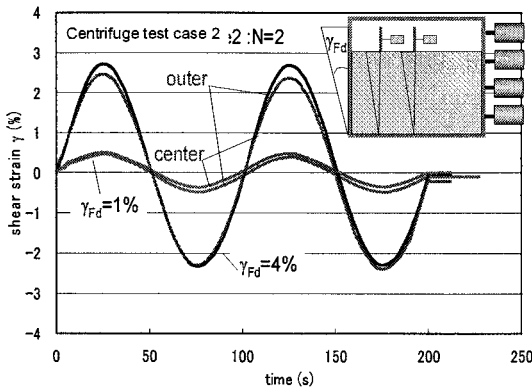


Figure 10 Shear deformation of the model ground in centrifuge: Case 2

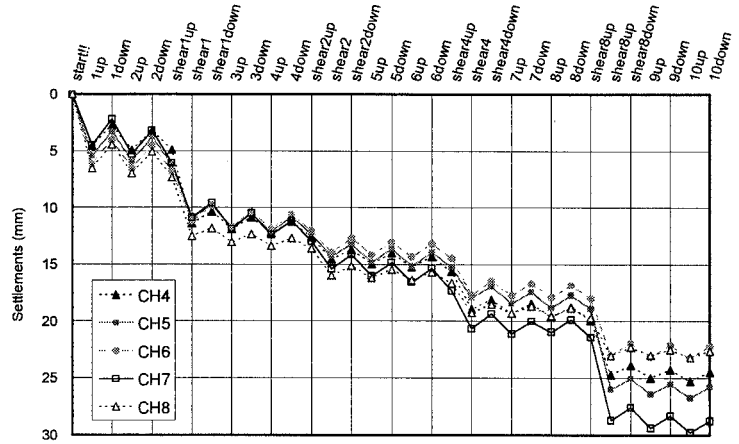


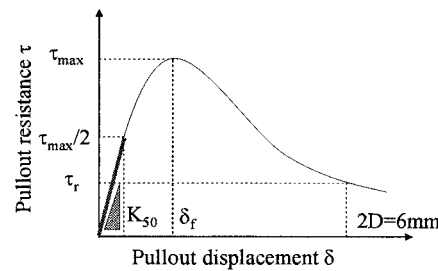
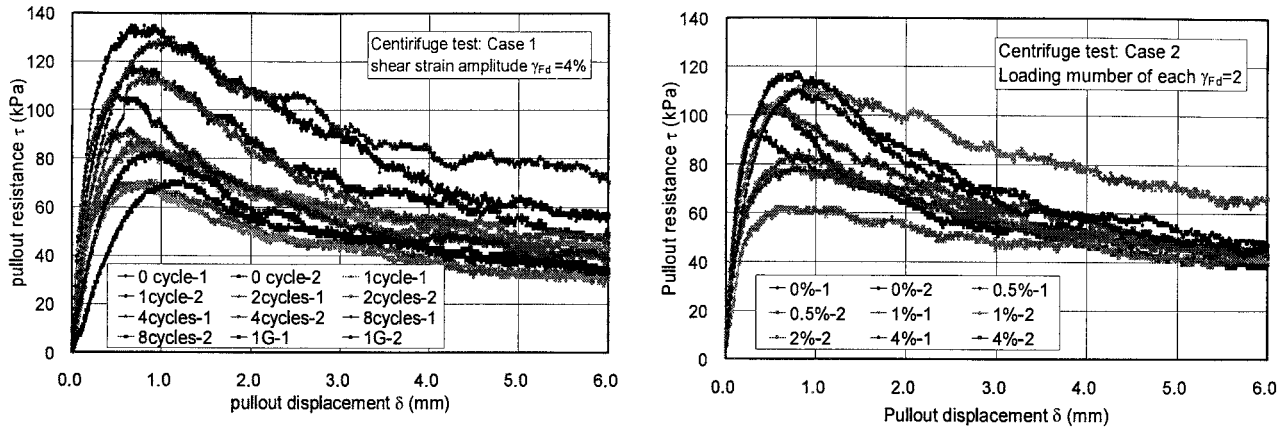
Figure 11 Settlements of the model ground during centrifuge test: Case 1

centrifuge, which were evaluated by the horizontal displacements at the ground surface. As shown Figure 9(a) for Case 1, imposed shear deformation in all cycles e.g., are almost the same at the center of the ground and the amplitude of shear strain γ are about 70% of that of the box ($\gamma_{Fdmax}=4\%$). Comparing the center and outer positions of the ground, γ of the center position is slightly lower than that of the outer one for the cases with $\gamma_{Fd}=4\%$. The amplitude of γ imposed by $\gamma_{Fdmax}=4\%$ in Case 1 are little larger than that in Case 2. This can be attributed to the difference of ground conditions between the two cases, the measured densities of the former slightly larger than the latter.

Figure 11 shows the settlements of the ground surface observed in the centrifuge test Case1. The settlement due to acceleration change was quite elastic, but the positive plastic compression took place by shearing. In both Cases 1 and 2, the total settlement was about 25mm, which equivalent to the change of average density of the sand from $\rho_t=1.97\text{g/cm}^3$ to 2.13g/cm^3 .

4.2 Pullout tests in centrifuge

Figure 12 shows the relationship between the pullout resistance (τ) and displacement (δ) in the centrifuge tests. This pullout resistance τ is defined by the pullout force divided by the surface of perimeter of embedded portion of the bolt, meaning the averaged mobilized frictional stress on the bolt surface. From the τ - δ curves, maximum resistance (τ_{max}), residual resistance (τ_r), coefficient of pullout resistance (K_{50}), and pullout displacement at τ_{max} were obtained as shown in Figure 13. (τ_r) is defined by τ at $\delta=6\text{mm}$ ($=2D$:diameter of the bolt). K_{50} is secant coefficient defined by the following equation.



$$K_{50} = \frac{\tau_{\max}/2}{\delta_{\tau=\tau_{\max}/2}} \quad (1)$$

The variations of these values with the number of shearing cycle (N) for Case 1 are shown in Figures 14 and 15. The all values decreased by shearing with large strain of about $\gamma=3\%$ especially for τ_{\max} and K_{50} . After a certain number of shear strain cycles, they turned to increase, which can be attributed to the densification of the sand due to shearing as shown in Figure 11. As there was no clear difference in the values at different location from the side wall, it can be said that the difference of shear deformation between center and outer side (Figure 9) were not so significant that affected the results.

Figure 16 shows the relationship between loading cycles and these values normalized by the values before shearing. From the figure, it can be said that the stiffness of the cemented sand is more severely affected by shearing than the strength. The effect of the shearing cycles can be seen for the larger number in the coefficient but not in the resistances and δ_f .

The same trend can be confirmed in Case 2 as shown in Figure 17 on the variation of the normalized values with the shear strain amplitude. But in Case 2 where the applied shear strain was increased gradually, τ_{\max} decreased to $\tau_d=2\%$. It is interesting to note that failure displacement δ_f increased without showing the decrease in the first shearing. This may be because the density of the ground in Case 2 is smaller than that in Case 1.

4.3 Mobilizations of cohesion and friction

Beside centrifuge tests on the sheared cemented soil, pullout tests were conducted in dry uncemented silica sand under various centrifugal acceleration and in the cemented sand under 1g without shearing. From the pullout resistance and displacement curves shown in Figure 18, clear effects of g-level, that is, confining stress in the pullout behavior can be seen. The higher the

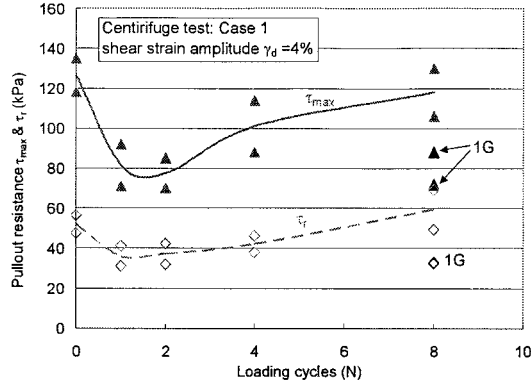


Figure 14 Relationships between τ_{max} & τ_r , and shearing cycle (N) : Case 1

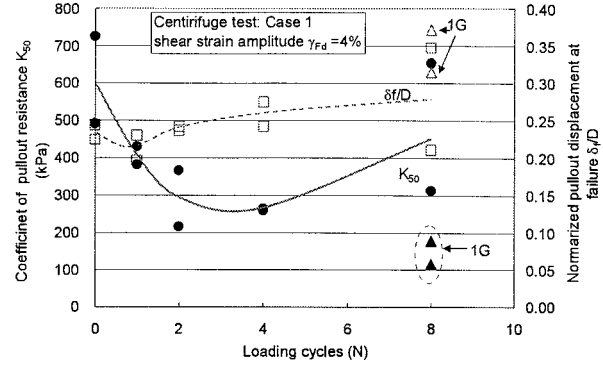


Figure 15 Relationships between K_{50} and δ_f/D , and shearing cycle (N): Case 1

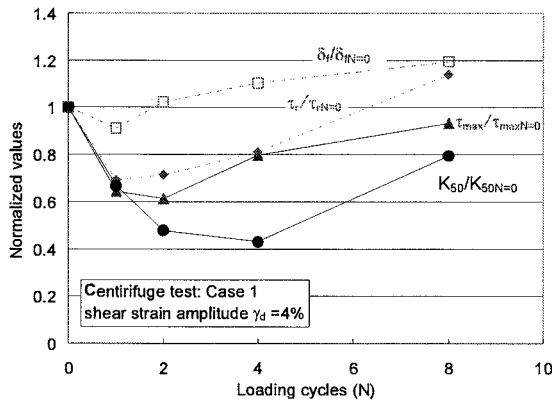


Figure 16 Effect of shearing cycle on the pullout behavior: Case 1

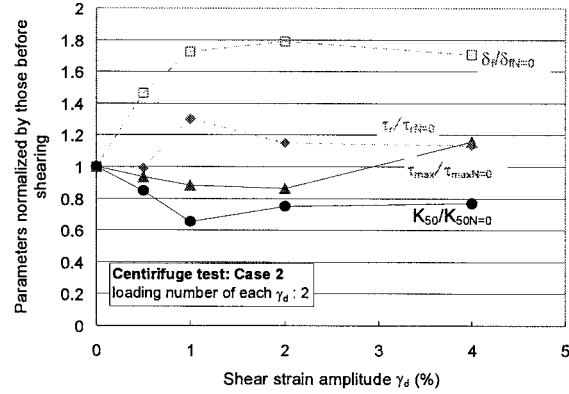


Figure 17 Effect of shear strain amplitude on the pullout behavior: Case 1

pullout resistance of the cohesionless sand is the function of friction angle ϕ' and horizontal pressure coefficient K . If the frictional angle of 40° is assumed as the common value of the loose silica sand under ax-symmetrical condition, the K value of about 2 can explain the maximum resistance of the sand. It is also interesting to note that decrease of the resistance after the peak is more significant in the dry sand than the cemented sand.

Figure 19 shows the relationship between maximum pullout resistance τ_{max} and centrifugal acceleration obtained from the dry silica sand and cemented sand without shearing. The pullout resistances observed in Case 1 are also compared in 50g and 1g in the figure. Although there are some scatters in the model, the pullout resistances of the cemented sand in 1g are much bigger than that of 1g dry sand, which clearly showing the effect of cementation. For the dry sand τ_{max} is nearly increases in proportion to g-level showing the mobilizations of frictional angle at the peak are almost the same in different g-level, although some effect of confining stress on ϕ' value can be seen.

On the other hand, the difference of maximum resistance between 1g model and 50g model is very small for the cemented sand. τ_{max} are the almost same between 1g and 50g models for the case without shearing. While for the case with preshearing, τ_{max} of the 1g model is about 30% smaller than that of 50g model, which is much smaller than the difference of dry sand.

As the contribution of confining stress or frictional stress in 1g model is minimal as shown in the result of dry sand, it can be said that the resistance in 1g cemented sand comes from the cohesion. But this cohesion cannot last during pullout process and decrease with pullout displacement to the residual value. Mobilization of cohesion with the displacement is different from that of frictional angle. This

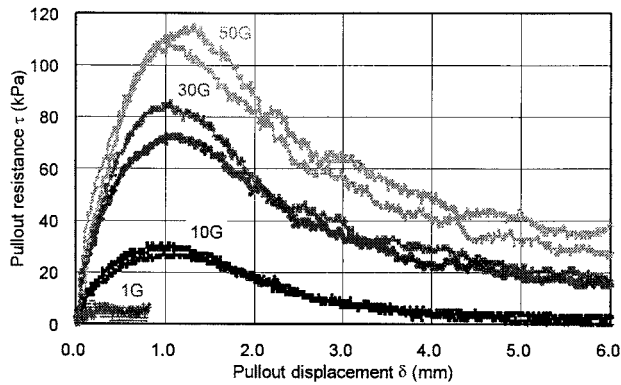


Figure 18 Variation of average pullout resistance with displacement observed in silica sand

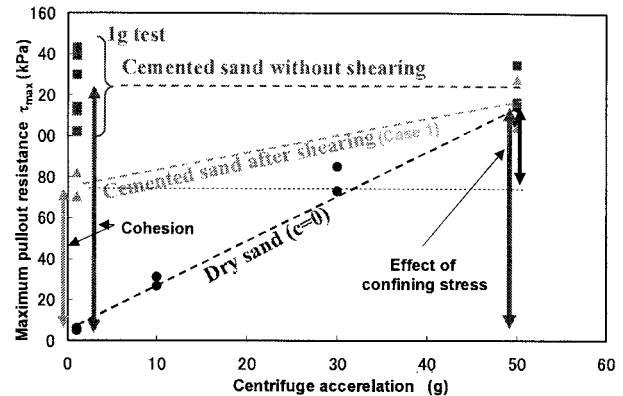


Figure 19 Relationships between τ_{\max} and centrifugal acceleration

might be the reason why the effect of confining stress cannot be clearly seen in for the cemented sand cases.

5 Conclusions

In this study, model cemented sand was made and the pullout tests of anchor bolts in the cemented sand were conducted after being sheared by active type shear box in 50g. The following conclusions are derived.

1. Model cemented sand can be prepared by mixing silica sand, strengthening Portland cement, super plasticizer, Metolose and water.
2. Effect of shear strain on pullout out behavior can be clearly seen in the maximum resistance and coefficient of pullout resistance, especially for the latter.
3. The densification of sand by the shear causes the recover of the pullout resistance.
4. In cemented sand, the confining stress does not contribute the increase of resistance compared to the dry sand, which can be explained by the difference of the mobilization of cohesion and friction with displacement in different confining stress level.

Acknowledgement

The authors gratefully acknowledge the funding for this research from Ground Anchor Association.

References:

- Kojima, H., Yoshikawa, K., Yashiro, K., Noma, T., Asakura, T. and Tsuchiya, T.(2003), "Ground surface loading model test on deformation behavior of tunnel lining", Journal of Geotechnical Eng., JSCE, No. 729/III-62, 73-86(in Japanese).
- JSCE (1985) Technical Report by the JSCE committee on mountain tunneling:
- Takahashi, A. Takemura, J. Suzuki, A. and Kusakabe, O. (2001), "Development and Performance of an Active Type Shear Box in a Centrifuge", International Journal of Physical Modelling in Geotechnics, Vol.1, No.2, pp. 1-17.
- Takemura, J., Izawa, J., Shibayama, S. and Kusakabe, O. (2006)" Active type shear box and its application on a stability of shallow tunnel in a centrifuge", Proc. 3rd Intn Conf. on Urban Earthquake Engineering, 639-646.
- Tsuchiya, T. (1987) "The Experimental Study on the Reinforcing Effect of Rock-Bolt and its Optimum Design as Tunnel Support", Railway Technical Research Report, No.1342.(in Japanese)

A SERIES OF MICRO-TREMOR MEASUREMENTS AT A FILL DAM DAMAGED BY THE 2004 NIIGATA-CHUETSU EARTHQUAKE

T. Ohmachi¹⁾, S. Inoue²⁾ and S. Tomita³⁾

1) Professor, Center for Urban Earthquake Engineering, Tokyo Institute of Technology, Japan

2) Research Associate, ditto

3) Civil Engineer, JR East Consultant Company Ltd., Japan

ohmachi@envng.titech.ac.jp, shusaku@envng.titech.ac.jp, tomita@jrc.jregroup.ne.jp

Abstract: The Niigata-ken Chuetsu earthquake ($M_j6.8$), Japan, occurred on October 23, 2004. It caused more or less damage to several fill dams located in and around the near field. Among them is 42.4m-high Shin-yamamoto dam, completed in 1990. The dam suffered settlement of the crest exceeding 80cm and sand liquefaction. Thick deposit in front of the drain layer was presumably responsible for the liquefaction. After close investigation of the damage, restoration work was conducted from April through November 2005, removing the damaged portions of surface layers followed by re-banking. Before and after the repair work, and also after impoundment of reservoir water, micro-tremor measurements were conducted along the crest of the dam. The measurements showed a little change in the vibration period of the dam, especially around the seriously damaged portion, implying effects of the restoration and impounded water.

1. INTRODUCTION

The Niigata-ken Chuetsu earthquake ($M_j6.8$), Japan, occurred at 17:56 (local time) on October 23, 2004 (Fig. 1). Forty people were killed, and numerous landslides of various types took place on natural slopes and man-made banks. The highest seismic intensity of 7 on the JMA scale was registered at Kawaguchi town. Strong motion accelerometers of the K-net registered peak acceleration of 1501gal at Ojiya, and 1750gal at Tokamachi during the main shock. The main shock was followed by many strong aftershocks for weeks (Midorikawa et al 2005).

Several fill dams built for hydroelectric power generation or agricultural irrigation were damaged by the earthquake (Ohmachi, 2005). Due to the end of a harvest season, those dams for irrigation were empty of reservoir water at the time of the main shock, which served to avoid secondary damage to the downstream. While three dams for power generation were impounded with water from the Shinano river, the longest river in Japan. The three dams were Yamamoto Dam and Shin-yamamoto Dam located in Ojiya, 6 and 5km from the epicenter respectively, and Asagawara Dam in Tokamachi, 22km from the epicenter (see Figure 1). The electric power generated with the water from these dam is used to drive JR trains in the Tokyo metropolitan area. Since much of the electric power is used during morning and evening rush hours, these dams are always subjected to rapid draw down of the water level twice a day. Although these three dams suffered earthquake damage, there was no secondary damage to the downstream because the storage water was safely released from each reservoir after the damage to the dams was discovered. Although the first author has been one of the members of a committee established by the owner of the dam (JR East) and given much information to be described in this paper, he is solely responsible for any errors and misunderstanding.

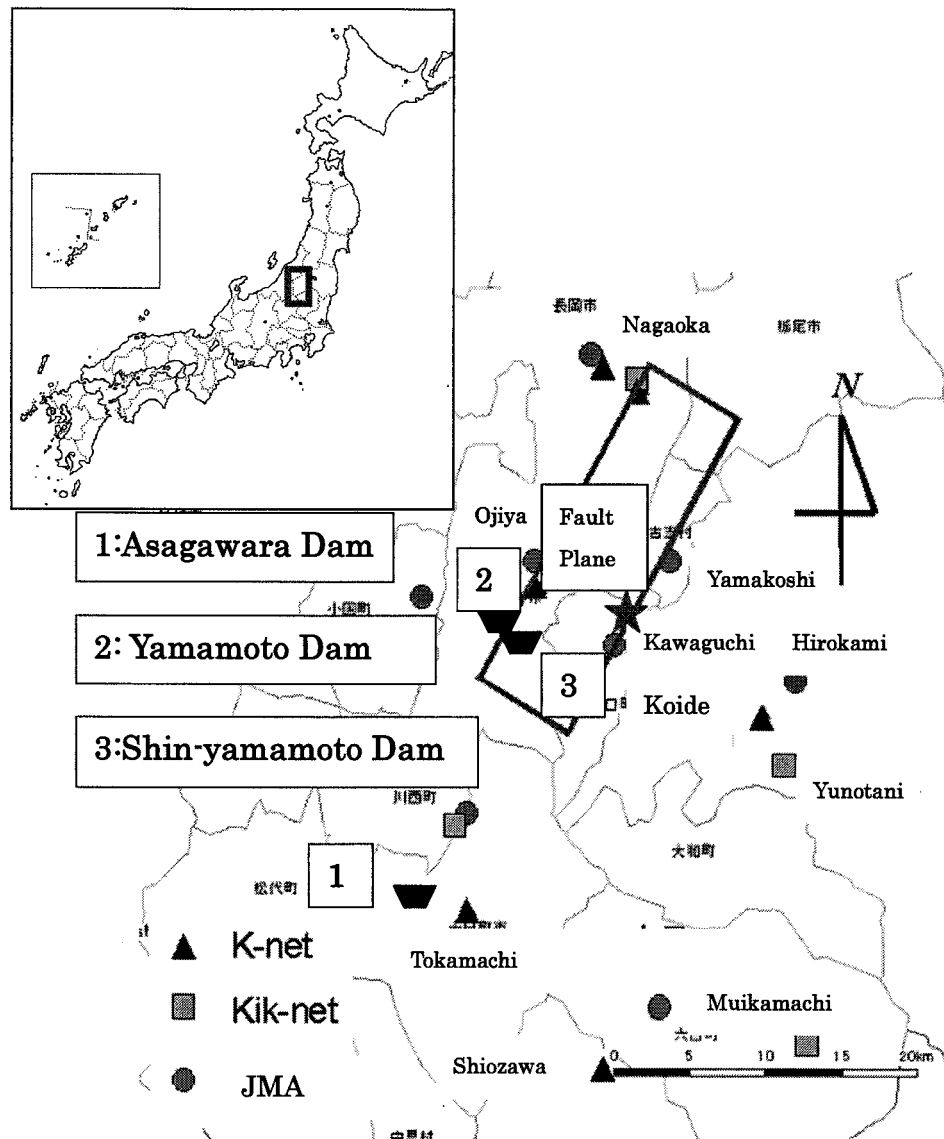


Figure 1 Location Map

2. DAMAGE TO SHIN-YAMAMOTO DAM AND RESTORATION

Shin-yamamoto dam was built in 1990. The dam is 42.4m high, and has a crest length of 1,392m with a standard cross section shown in Figure 2. This is a zoned fill dam with a dam axis of a semi-circular shape as shown in Figure 3, where numbered circles indicate micro-tremor observation points described later. Both right and left ends of the dam are plunged into natural slopes. To facilitate the rapid draw down of the water level, there is a horizontal drain layer on the upstream side at the elevation of EL.143.8m~147.3m, which is just above the low water level of EL. 143.8m.

The strong shaking of the main shock and aftershocks caused considerable damage to the dam (Ohmachi and Inoue, 2006). Settlement of the crest was about 10~40cm on the right half side of the dam, while it was about 50~90cm on the left half side. The crest was also displaced upstream about 20~40cm on the left half side, while downstream about 3~10cm on the right half side. Due to the large settlement, a top of an H-shaped steel beam which was embedded to protect monitoring cables from bottom to crest in the filter zone was observed protruding about 30cm from the asphalt pavement, and several water pools were observed on the dam crest after rainfall, as shown in Figure 4(b).

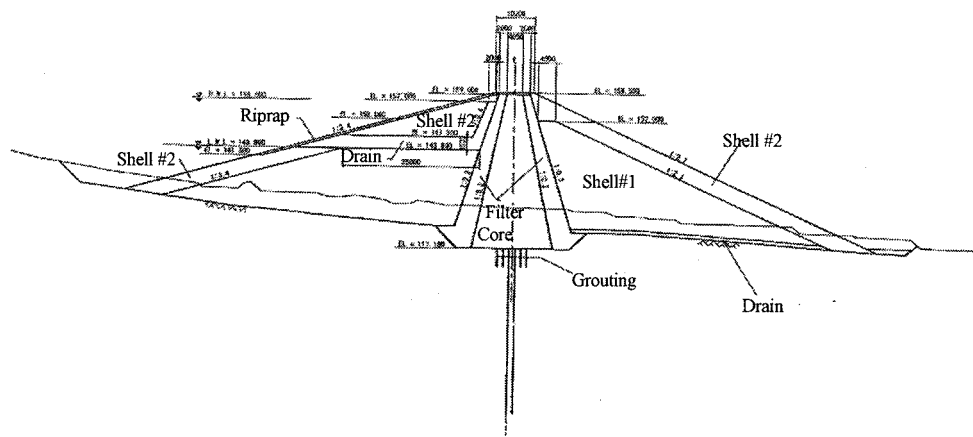


Figure 2 Standard Cross Section of Shin-yamamoto Dam

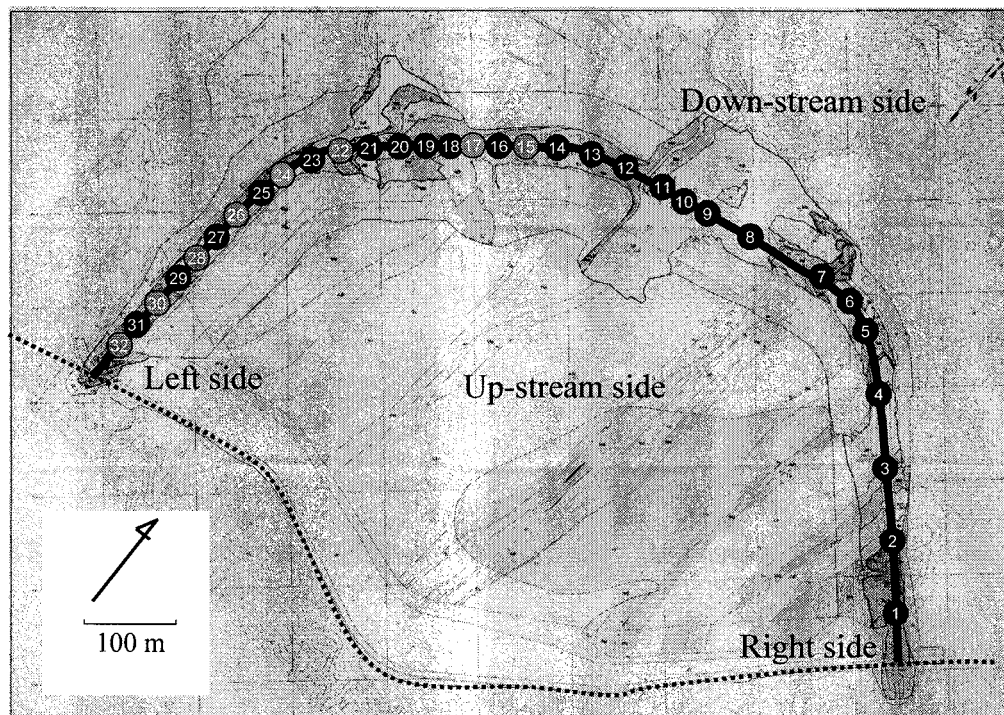


Figure 3 Plan of Shin-yamamoto Dam and Location of Measurement Points

On the upstream side near the left end, boiled sand was found at several places on the riprap surface at EL. 145~150m and nearby deposit as shown in Figure 4 (a). Trenches were excavated to investigate origin of the boiled sand and soil properties such as permeability and grain size distribution in and around the liquefied areas. The origin of the boiled sand was mostly concentrated in and around the drain layer whose sand content was higher than that at the construction stage. In addition, near the left end of the dam, it was noted that deposit of fine particles was thick enough to cover the mouth of the drain layer. Hence, it seemed reasonable to think that the thick sedimentation in front of the drain layer caused pore water pressure buildup under the strong shaking followed by the liquefaction.



(a) Boiled Sand indicating Liquefaction on the Left Upstream-side.



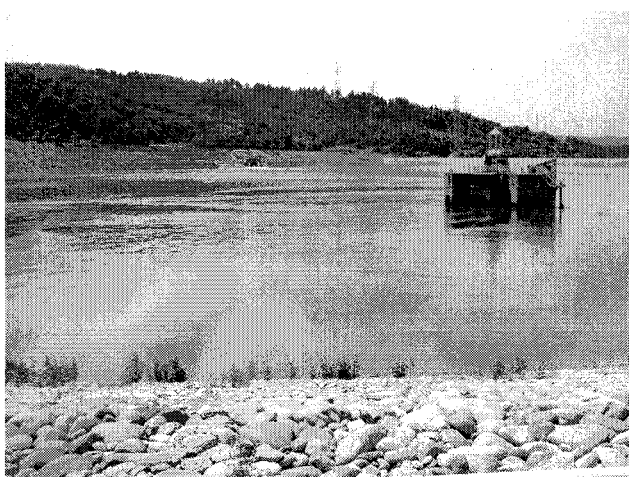
(b) 1st Measurement along the Dam Crest with Pools due to Large Settlement.



(c) Left Ban-side after Restoration for which Fine Deposits were Removed.



(d) 2nd Measurement along the Dam Crest at the final stage of the Repair Work.



(e) Reservoir Impounded with Water whose Inflow is seen at the Far End



(f) 3rd Measurement along the Dam Crest with the Reservoir almost Full of Water.

Figure 4 Pictures Related to the Micro-tremor Measurements at Shin-yamamoto Dam

Various kinds of investigation were conducted such as excavation of trenches and borings in and around the liquefied and/or settled areas, and removal of asphalt concrete and base course material of the crest for visual inspection of the clay-core. As a result, the clay-core was found to be free from the damage. For restoration of the dam, in principle, damaged portions of the dam body such as upper ripraps and outer drain-layer were removed and banked again to the original design. Special care was paid to compaction during the re-banking to attain higher density of the dam material. The restoration work took more than seven months, from April through November, 2005.

The first filling of water after the restoration began in December, 2005, and successfully finished in the middle of March, 2006. Following the success, the power generation was put into full operation on March 14, 2006.

3. VIBRATION CHARACTERISTICS DETECTED BY MICROTREMOR MEASUREMENTS

3.1 Micro-tremor Measurements and Data Processing

Micro-tremor measurements at the dam were conducted three times as shown in Figure 4(b), (d) and (f); on November 22, 2004, immediately after the earthquake damage, on November 28, 2005, at the final stage of the restoration work, and August 28, 2006, after filling the reservoir with water. In all of the three cases, the measurements were done at the same 32 points along the crest shown with numbered circles in Figure 3.

At each measurement point on the dam crest, three-component micro-tremor in terms of velocity was observed simultaneously with a sampling rate of 1/100 s. The three components were two horizontal ones in the normal and parallel to the dam axis directions, and vertical one. Using the Fourier spectra of the observed time histories, the H/V spectral ratios which are often used to estimate ground motion characteristics from micro-tremor data were calculated to find vibration characteristics of the dam. As shown in Figure 5, the H/V spectral ratios indicate some peaks and troughs, and it is difficult to find vibration periods of the dam from the peaks in the H/V spectral ratios at one observation point only. To cope with the difficulty, the H/V spectral ratios at all the observation points are arranged in numeric order from No.1 through No.32, which is tentatively called an H/V spectral ratio map. In the maps shown in Figure 8, several dotted lines are drawn by connecting peaks observable in adjacent H/V spectral ratios to find the periods associated with the dam vibration, the ground and others. The detailed data processing is omitted here, because it has been described elsewhere (ohmachi and Inoue, 2006).

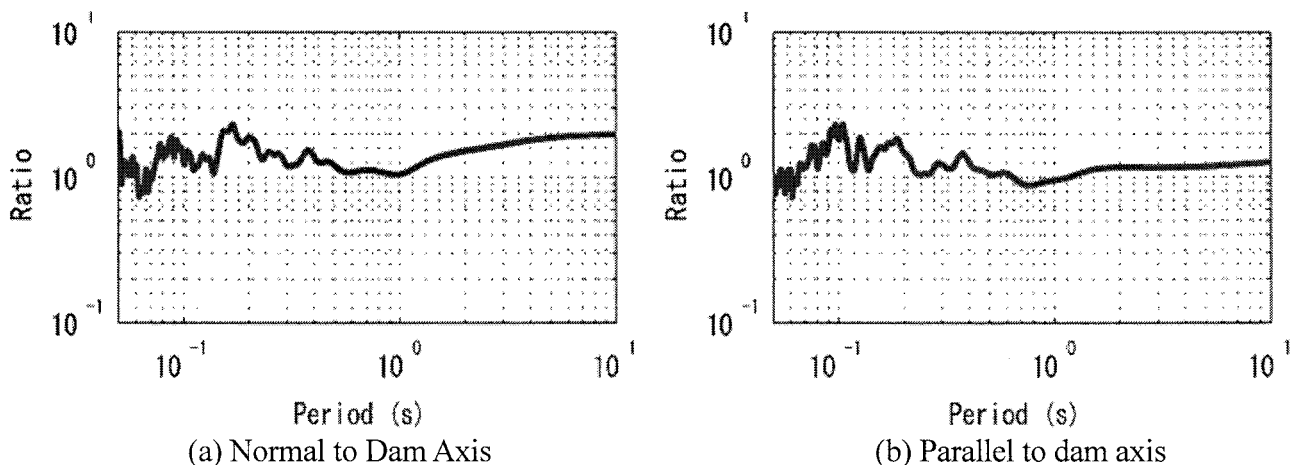
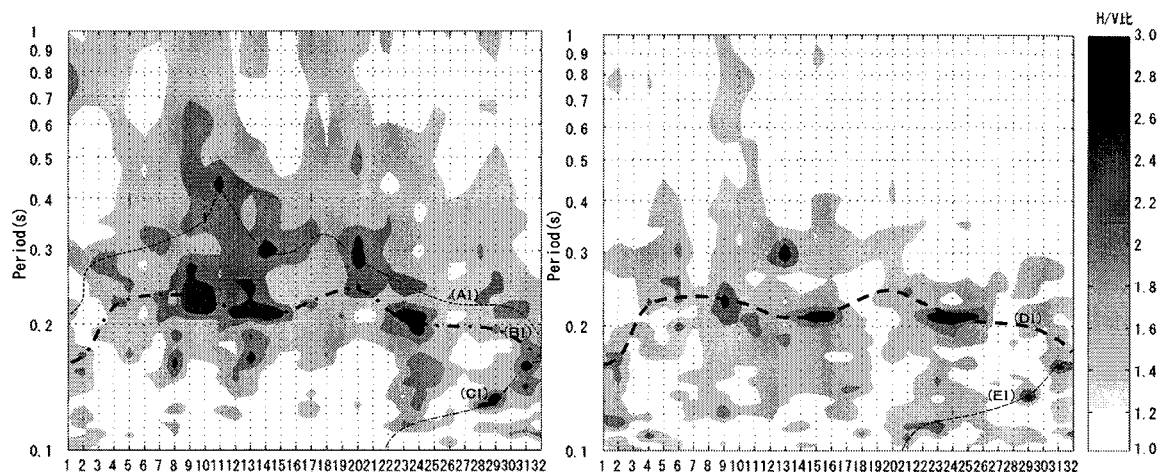


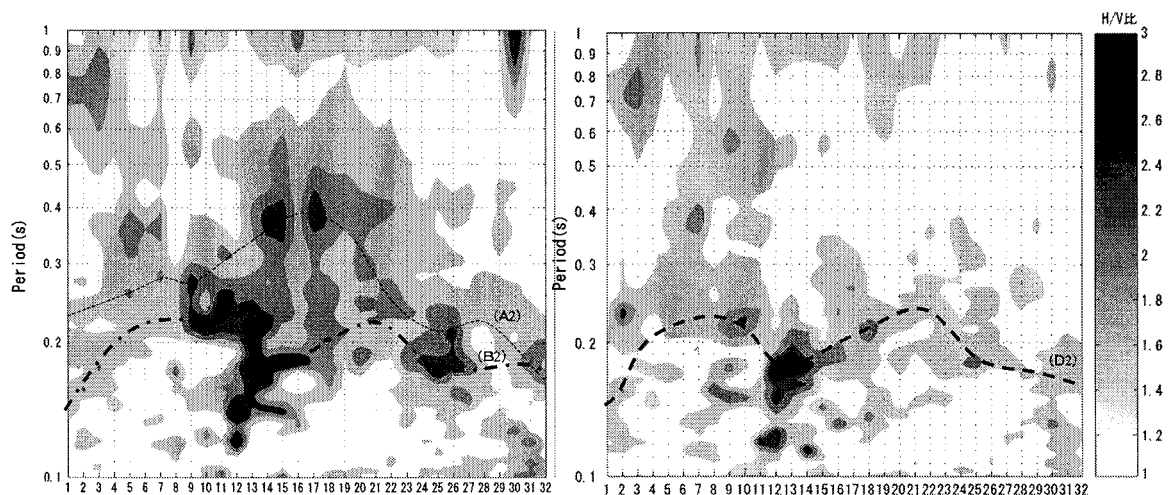
Figure 5 Examples of H/V Spectral Ratios from Fourier Spectra

Normal to Dam Axis

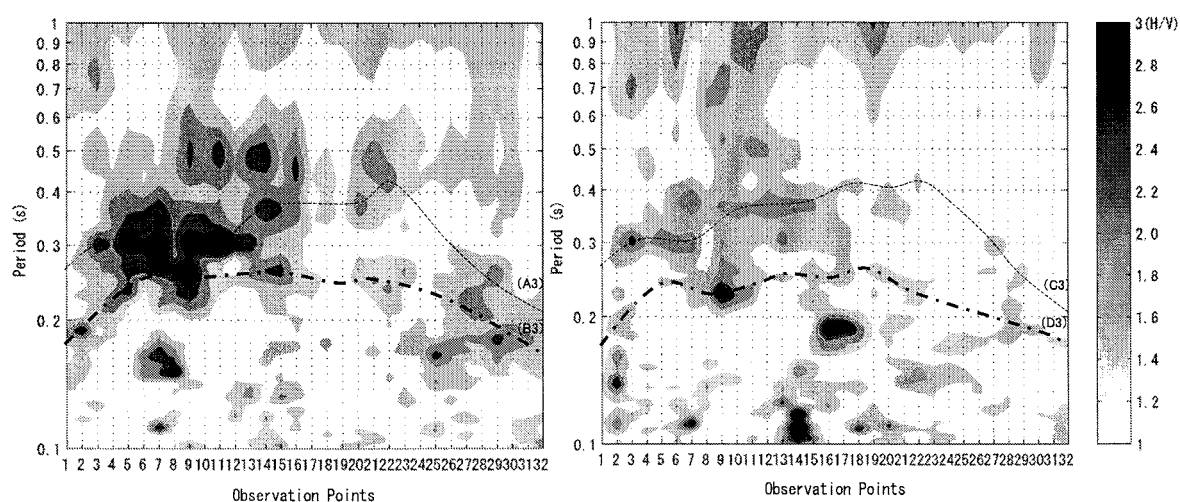
Parallel to Dam Axis



(a) H/V Spectral Ratios from the 1st Measurement



(b) H/V Spectral Ratios from the 2nd Measurement



(c) H/V Spectral Ratios from the 3rd Measurement

Figure 6 H/V Spectral Ratio Maps from a Series of Micro-tremor Measurements

3.2 Vibration Characteristics of the Dam

As a rule of thumb, the fundamental period of rockfill dams is empirically given by $T=H/200$, where T and H are the period in second and the dam height in m, respectively. When $H=42.4\text{m}$ for Shin-yamamoto dam is substituted in this equation, an estimate of the period of the dam is $T=0.21\text{s}$. Considering that the vibration period of the dam is proportional to the dam height, it is possible to draw a continuous line connecting peaks in each H/V ratio map in Figure 6, such as the dashed lines B1 to B3 in the normal to dam axis direction, and D1 to D3 in the parallel to the dam axis directions, as shown in Figure 6.

Besides the lines B1- B3 and D1 – D3, it seems possible to draw the lines C1 and E1 which are supposedly related to the fine deposits at the left end side of the dam, and A1 to A3 which seems to be related to some other factors like the dam-foundation interaction.

When it comes to the vibration period of the dam estimated from the three measurements, as a whole, it shows a little decrease after the restoration, and then a little increase after the impoundment of reservoir water. Probably, the first decrease is attributed to the compaction during the re-banking process, and the next increase is attributed to the increase in the mass and the decrease in the rigidity of the dam material mainly due to saturation with water. The period change on the left side of the dam looks slightly different from that on the right side. For example, the periods at the point 10 are 0.22s, 0.22s and 0.23s from the 1st, 2nd and 3rd measurements respectively, while they are 0.23s, 0.22s and 0.25s at the point 19. This difference in the period change may be attributable to the difference in the restoration work, because the work was rather concentrated on the left side of the dam. Further study is needed to find causes and effects of the period change of the dam.

4. CONCLUSIONS

The strong shaking in the near field of the 2004 Niigata-ken Chuetsu earthquake caused considerable damage to Shin-yamamoto dam. With a special attention focused on the large settlement and boiled sand observed on left half side of the dam, restoration of the dam was conducted followed by the first filling of the reservoir with success.

A series of micro-tremor measurements along the dam crest showed a perceptible change in the vibration period of the dam, when they are compared between before and after the restoration work, and before and after the impoundment of the reservoir water. The period change implies that rigidity of the dam was increased by the adequate compaction during the re-banking process, and that it was decreased by the water impoundment.

As shown here, the micro-tremor measurement has demonstrated to be useful as a handy tool to diagnose the state of dams, when it is properly applied.

References:

- Midorikawa, S. and Miura, H. (2005), "Strong Motion Records Observed in the 2004 Niigata-ken-chuetsu Earthquake," pp. 21-35, Proceedings of the 2nd International Conference on Urban Earthquake Engineering.
- Ohmachi T. (2005), "Safety of Fill Dams under Level 2 Earthquake Motions: Lessons from the 2004 Nigata-chuetsu Earthquake", pp.45-52, Proceedings of the 2nd International Conference on Urban Earthquake Engineering.
- Ohmachi T. and Inoue, S. (2006), "Micro-tremor Measurements at a Fill Dams damaged by the 2004 Nigata-chuetsu Earthquake", pp.681-688, Proceedings of the 3rd International Conference on Urban Earthquake Engineering.

SIMULATING EARTHQUAKE-INDUCED FRACTURES IN STEEL STRUCTURES: MODELS AND METHODS

A.M. Kanvinde¹⁾ and G.G. Deierlein²⁾

1)Assistant Professor, Dept. of Civil and Environmental Engineering, University of California, Davis, CA 95616

*2)Professor, Dept. of Civil and Environmental Engineering, Stanford University, Stanford, CA 94305
kanvinde@ucdavis.edu, ggd@stanford.edu*

Abstract: Recent advances in modeling fatigue and fracture in steel structures are outlined. Current approaches to simulate earthquake induced fracture and fatigue in steel structures rely on experimental and semi-empirical methods, or conventional fracture mechanics. While the semi-empirical methods cannot be generalized to a wide range of structural details, conventional fracture mechanics can be reliably used only to simulate brittle fractures similar to those observed during the Northridge earthquake, where large scale yielding is absent. The physics-based micro-models similar to the one described in this paper seek to simulate the fundamental processes of void growth and coalescence and granular cleavage responsible for fracture and ultra low cycle fatigue in structures. These models are relatively free from assumptions regarding behavior and can be used with accuracy to simulate fracture and fatigue in a general sense under a variety of conditions. Thus, these micro-models, relying on fundamental physics are equally applicable to situations that are regarded as “brittle” or “ductile” at the structural or component level. Examples to illustrate the use of one such model – the Cyclic Void Growth Model (CVGM) to simulate fracture through continuum finite element analyses are presented. Areas for refinement of the models and future work are outlined.

1. INTRODUCTION

Accurate assessment of earthquake-induced fracture is critical to developing fracture-resistant design provisions and for evaluating structural performance. Widespread damage to steel-framed buildings during the 1994 Northridge earthquake highlighted the importance of fracture limit states in structural engineering. The ensuing SAC Joint Venture investigation in the US (FEMA, 2000) confirmed the significant likelihood of fracture in steel moment frame connections and the sensitivity of response to local effects that are difficult to quantify with conventional structural engineering and fracture mechanics models. The SAC investigation and related studies have mitigated the immediate problem of premature brittle fractures through the development of improved connection details that employ tougher materials and reduced fracture toughness demands (through smaller flaw sizes and reduced stresses). However, even these post-Northridge connections can potentially fracture, although in a ductile manner (Stojadinovic et al, 2000). Moreover, there are many situations outside the scope of the SAC investigation where fracture is likely to compromise the seismic safety of the system, such as brace and connection fracture in concentrically braced frames (Tremblay et al, 2003, Uriz and Mahin, 2004), or link-column connection fractures in eccentrically braced frames (Okazaki et al, 2006). Finally, as we move further into the realm of performance based design, methods and tools are needed to quantify fracture behavior over a range

of seismic demands (hazards), as opposed to simply “qualifying” the structure to perform “adequately” for a single limit state.

Given the importance of fracture, this paper addresses the issue in a wider scientific context by examining the accuracy, feasibility and validity of traditional and evolving approaches to characterize earthquake-induced fracture in steel structures. The approaches discussed in this paper encompass various scales of simulation (micro to structure scale), levels of sophistication, and computational resources required to predict fracture. Some key questions to consider are (1) Are traditional fracture and fatigue prediction techniques accurate and general enough to be applied to a wide range of structural configurations under various loading conditions? (2) If not, are more fundamental models available to improve the assessment of fracture? (3) Is the application of these advanced models computationally feasible? (4) If so, what are the major challenges (conceptual or practical) to the implementation of these models?

The paper addresses these questions in the light of recent development and validation of micromechanics-based models for simulating ductile fracture and Ultra-Low Cycle Fatigue (ULCF) in steel structures. The paper begins by briefly and qualitatively describing processes responsible for earthquake-induced fracture, and then reviewing the state of the art of earthquake-induced fracture and fatigue prediction in steel structures. Important limitations of the existing approaches are described and newer physics-based approaches, including the recent development of models for ULCF are introduced. Issues regarding the implementation of these approaches are discussed. The paper concludes by outlining a framework for model-based simulation of earthquake-induced fracture, and identifying knowledge gaps that need to be filled to realize this framework.

2. EARTHQUAKE-INDUCED FRACTURE DUE TO ULTRA LOW CYCLE FATIGUE AND REVIEW OF CONVENTIONAL APPROACHES TO SIMULATE ULCF

This section introduces the phenomenon of earthquake-induced ULCF from a physical standpoint, and reviews various techniques that are commonly used to characterize ULCF in steel structures, before describing the micromechanics-based approach to ULCF.

Earthquake-induced fracture in structures maybe classified as a fatigue problem, because it is typically preceded by a small number of high-amplitude cyclic strain or load reversals. The traditional view of fatigue encompasses crack initiation and propagation under a large number of load reversals, ranging from several hundred to a few million cycles. For example, fatigue typically occurs in bridges or mechanical and aerospace components, where the amplitude of the cyclic demands is small relative to the yield stress of the material and the number of cycles to failure is large (on the order of 10^2 to 10^6 cycles). Within this range, fatigue is commonly distinguished between low-cycle or high-cycle fatigue. In contrast to classical high or low cycle fatigue encountered in bridges or mechanical components, earthquake-induced fatigue involves fewer than ten cycles with large strain amplitudes, on the order of ten or more times the yield strain. Termed Ultra Low Cycle Fatigue (ULCF), this type of fatigue/fracture occurs in modern steel structures that are designed to absorb seismic energy by sustaining large inelastic deformations under cyclic loads. Plastic hinging of beam-column connections and inelastic cyclic buckling of steel braces are two primary examples where ULCF fracture is the ultimate limit state. An example of ULCF fracture for a steel brace is shown in Fig. 1.

While ULCF type behavior has long been recognized in seismic design, the fundamental physical processes responsible for this type of fatigue are not well understood. As a result, earthquake engineering and other situations involving ULCF have relied on various empirical or semi-empirical approaches which are difficult to generalize because (1) They often rely on costly testing for their implementation and (2) They fail to directly simulate the physical processes of ULCF relevant to earthquake engineering. Some of these approaches are now reviewed.

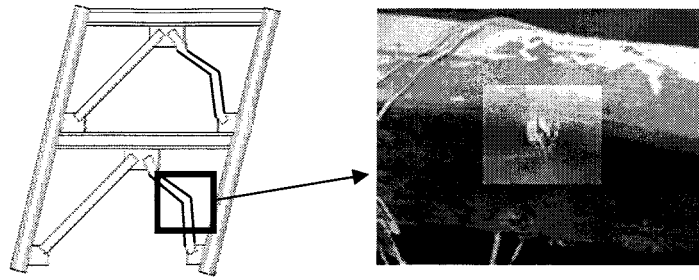


Figure 1 Ultra Low Cycle Fatigue in Concentric Steel Braces (Fell et al, 2006)

2.1 Experimental Modeling

Experiment-based empirical methods remain the most popular approaches to assess the fracture susceptibility of steel structures and components. These approaches involve testing structural subassemblies under pre-defined monotonic or cyclic loading protocols and then using gross measures of deformations (interstory drift, joint rotation) to establish performance limits, and to infer fracture or fatigue capacity. Past research e.g. Uang et al, (2001), including several studies within the SAC project have employed these types of approaches.

Experiment-based modeling is attractive mainly because, for a given component, it is relatively free from assumptions (except an accurate representation of boundary conditions), and incorporates most aspects of behavior and various physical phenomena (e.g. local buckling, material variability, contact, gapping etc). Despite its advantages, experiment based modeling cannot be conveniently generalized to structural details that are significantly different from the tested components in terms of geometry or material types. Due of the high cost of experiments, sensitivity and parametric studies and the use of alternate loading histories is often not possible. In fact, a fair bit of judgment is needed to generalize the experimental results, which may result in conservative characterizations of the adequacy of a given component, rather than a performance assessment over the full range of behavior. Finally, modeling at the component or structural scale does not provide insights into localized effects that may be responsible for fracture.

2.2 Conventional Fracture and Fatigue Mechanics

Conventional fracture mechanics (CFM) typically involves the determination of a single parameter at a crack tip that is assumed to quantify the fracture toughness demand. Consequently, the fracture toughness capacity, too, is expressed in terms of a similar parameter. The toughness demand parameter (such as the stress intensity factor K_I , or the J-integral, or the Crack Tip Opening Displacement – CTOD), is typically determined either through analytical formulae or finite element simulations. The corresponding material toughness capacity K_{IC} or J_{IC} (critical stress intensity factor or J-integral), is typically determined from standard tests. The fracture toughness corresponds to the energy release rate (per unit advance of the crack front). Conventional fracture mechanics is further classified as Linear Elastic Fracture Mechanics (featuring K_I) and Elastic Plastic Fracture Mechanics (featuring J and CTOD), suitable for different levels of crack-tip plasticity.

While CFM has been used extensively by the mechanical and aerospace research and practice, efforts to apply these approaches to civil structures have been fairly recent (Chi, 2000), where CFM type approaches were used to characterize the fracture susceptibility of pre- and post-Northridge beam column connection details. The Chi study demonstrated that CFM-type approaches could be used to characterize the ductility of pre-Northridge type details. However, CFM-based methods can reliably describe the fracture process only in situations where the yielding is limited in extent, and when a sharp crack is present. They are less suited to conditions of large-scale yielding or details without sharp cracks, such as commonly encountered in post-Northridge connection details. Moreover, as discussed earlier, earthquake-induced fracture is a fracture-fatigue interaction problem, and thus CFM type approaches that do not explicitly include effects of reversed cyclic loading cannot be conveniently applied to situations of earthquake-induced fatigue.

In addition to the CFM approaches, traditional fatigue mechanics approaches are often adapted and used in conjunction with experimental analysis or finite element methods. One such common method involves dividing the loading history at the component or strain level into equivalent cycles of fixed amplitude and then comparing the accumulated cycles to the “strain-life” determined from other experiments on similar details (Coffin, 1954). These conventional fatigue mechanics methods, too are limited in scope mainly because they are difficult to generalize to various arbitrary structural details, since ULCF is caused by interactions of local stress and strain histories and because earthquake loading histories are extremely random, with very few cycles, making them difficult to adapt to conventional cycle counting techniques such as Rainflow analysis (Tatsuo et al, 1974).

These limitations create the need for improved understanding of the ULCF process and the development of methods to predict it. Micromechanics-based models (discussed in the next section) that simulate the fundamental physical processes (void growth, coalescence) underlying ULCF are relatively free from assumptions regarding component level response – i.e. strain distributions, large versus small scale yielding etc, and may offer accurate predictions of response that can be conveniently generalized across different component configurations. These models (also referred to as “local fracture mechanics”) are applied at the continuum level (in contrast to the component or structure level) through interpretations of stress and strain histories that may be computed through detailed finite element (FE) analysis. The subsequent sections describe the application of one such model (the Cyclic Void Growth Model – CVGM) to structural details.

3. THE CYCLIC VOID GROWTH MODEL TO PREDICT EARTHQUAKE-INDUCED ULCF IN STEEL STRUCTURES

Referring to the preceding discussion, earthquake-induced fracture in structures presents a complex problem involving the complex interactions of material microstructure, irregular loading histories, and uncertainties in crack initiation and subsequent propagation processes. Fundamental micromechanics-based models show promise in predicting fracture and fatigue under such situations, because they are based on the physical processes of void growth and coalescence responsible for ULCF, and are relatively free from many assumptions that limit the applicability of other common approaches. Several such models have been used for ductile fracture conditions under monotonic loading for pressure vessel type steels (e.g. Hancock and Mackenzie, 1976). The use of such models in structural engineering has been fairly recent – e.g. El-Tawil et al, (1999) and Chi et al, (2006) have applied micromechanics-based models in a qualitative sense to assess the fracture-susceptibility of moment connections and shear panel zones. This section discusses the recently introduced Cyclic Void Growth Model (CVGM), and then describes a procedure to apply it along with validation data obtained from a recent NEESR project. For monotonic loading, ductile fracture in steel is caused by the processes of void nucleation, growth, and coalescence (Anderson, 1995). On the application of a triaxial stress field in steel, voids nucleate and grow around inclusions (mostly carbides in the steel material matrix) to coalesce until a macroscopic crack is formed (see Fig. 3). Previous research, Rice and Tracey (1969) has shown that under monotonic loading, void growth is controlled by the equivalent plastic strain, ε_p , and stress triaxiality $T = \sigma_m/\sigma_e$, where σ_m is the mean or hydrostatic stress and σ_e is the von Mises stress. For ULCF, both void growth and void collapse need to be explicitly considered, due to the reversed cyclic nature of the load. Recent research (refer Kanvinde and Deierlein, 2004 for more details) led to the development of a model that simulates the micromechanisms of void growth, collapse and cyclic degradation that are responsible for ULCF.

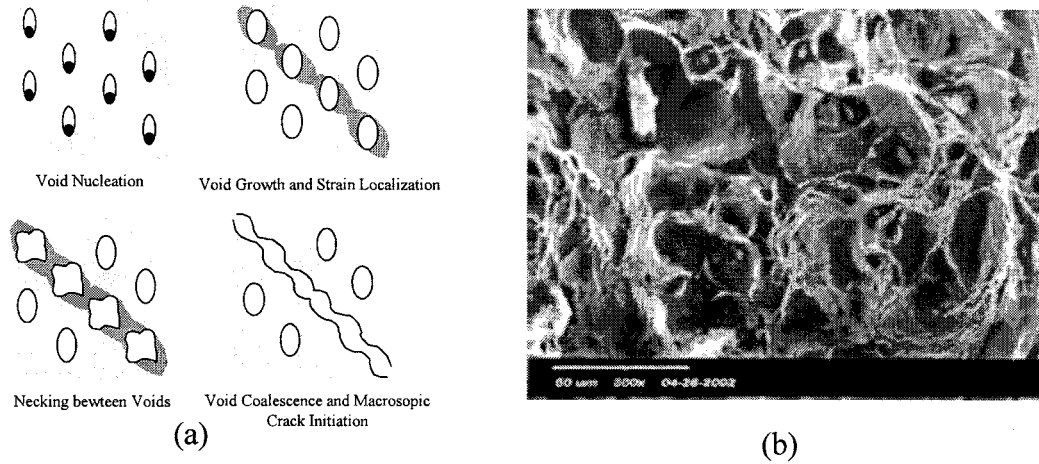


Figure 2 (a) Void growth and coalescence leading to ductile fracture in steel and (b) The corresponding dimpled fracture surface

Equation (1) describes the critical condition of the CVGM that must be attained to trigger ULCF initiation. The numerator of the equation reflects the cyclic micromechanical void growth demand and is based on strains and stresses inferred through finite element analysis, and the denominator reflects material capacity, calibrated through convenient small scale tests, such that ULCF is assumed to initiate when the Fracture Index (FI) exceeds 1. The model contains one additional parameter (quantifying the rate of capacity degradation) that is calibrated through multiple cyclic tests of notched bar specimens.

$$Fracture\ Index = \frac{\sum_{tensile-cycles} \int_{\epsilon_1}^{\epsilon_2} \exp(|1.5T|) d\epsilon_p - \sum_{compressive-cycles} \int_{\epsilon_1}^{\epsilon_2} \exp(|1.5T|) d\epsilon_p}{VGI_{monotonic}^{critical} \exp(-\lambda \epsilon_p^{accumulated})} > 1 \quad (1)$$

The CVGM model has been validated using fractographic studies (that suggest the likely micromechanism – void growth and collapse) as well as small, medium and large scale tests, most recently as part of a NEESR project. The next section discusses the calibration and application of the CVGM model in more detail.

4.1 Procedure for predicting Ultra Low Cycle Fatigue in structural components using the Cyclic Void Growth Model

Figure 3 schematically illustrates the various steps of predicting ULCF based on CVGM, and their inter-relationships. As discussed earlier, the Cyclic Void Growth Model has two material parameters ($VGI_{critical}$ and λ) that can be calibrated from small scale tests and complementary FE analysis of notched bar specimens such as the one shown in Fig. 3a. A detailed calibration procedure is discussed in detail in Kanvinde and Deierlein (2004). Once the parameters have been calibrated, detailed FE analysis of large scale components can be conducted to determine the stress and strain histories at each continuum point. Recently, the authors tested 19 large scale concentric brace elements cyclically to validate the CVGM model for full scale specimens. Figure 3b shows a photograph of a representative brace specimen as it buckles, while Fig. 3c includes the axial load deformation plot for the specimen, as well as the instant during the loading history when fracture initiation was first observed. A detailed description of the testing program can be found in Fell et al, 2006. Figure 3d shows a FEM simulation (performed on ABAQUS, 1998) of this specimen. The simulation considers all the relevant aspects of behavior, including multiaxial plasticity. To simulate the local buckling accurately, initial imperfections must be prescribed to perturb the analysis. A simulation-based load deformation plot is overlaid on the experimental plot in Fig. 3c, and the agreement between the two is encouraging.

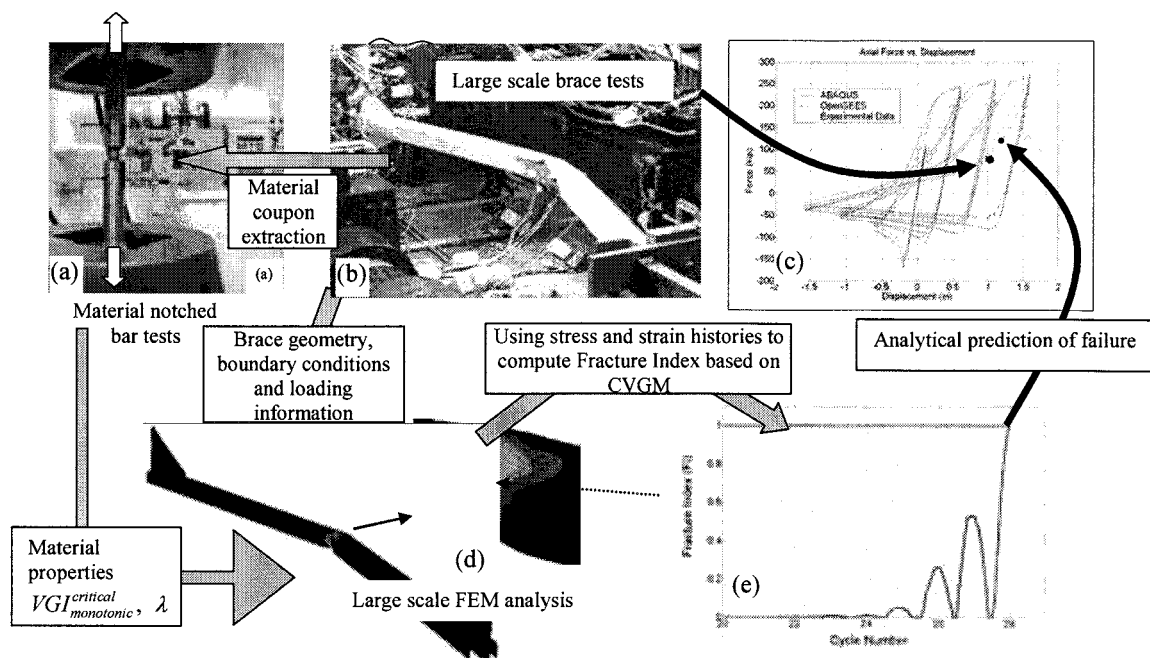


Figure 3 Prediction of ULCF in a concentric brace using the Cyclic Void Growth Model

To predict the location and instant of ULCF initiation, the stress and strain histories are determined from the FEM simulation over the entire plastic hinge region as the loading progresses, and the Fracture Index (FI) is determined as per Equation (1) at each loading step. It is important to note that FI is determined at each continuum location in the FEM model, and is dependent on material parameters $VGI_{critical}$ and λ . Thus, the FI can be determined in a general sense for any component once the material properties have been calibrated using the small scale tests. ULCF is assumed to initiate at a given continuum location when the micromechanical cyclic void growth demand exceeds degraded void size capacity, or mathematically, FI at that location exceeds 1. Fig. 3e plots the FI at the critical location in the locally buckled cross-section profile (indicated by the arrow in Fig. 3d), versus the loading time step. This point is shown as circle on Fig. 3c. Comparing this point to the experimental fracture instant (shown as a circle in the figure) demonstrates the accuracy of the ULCF models. Furthermore, as is evident from Fig. 3c, the instant of ductile crack initiation predicted from the analysis is very close to that observed during the experiment. Moreover, the physical location of ULCF is predicted with exact precision by the CVGM model.

Similar agreement between experimental and analytical fracture is observed for all 19 specimens. Given that the test matrix included specimens with different cross section geometries, different steel materials and loading histories, the agreement between experimental and CVGM predictions of fracture indicates that the CVGM simulates fundamental physical processes and material properties that control fracture.

4. AREAS FOR REFINEMENT OF THE MICROMECHANICS-BASED MODELING APPROACH

While the CVGM and similar micromechanical models provide a fairly general and accurate framework for predicting earthquake induced fracture in steel structures, several issues need to be addressed to successfully and routinely apply these models in structural simulations. Some of these issues are now summarized.

1. Because the micromechanics-based models are applied at the continuum level, their success is contingent on an accurate characterization of the local stress and strain histories at critical locations. Thus, sophisticated modeling of various physical phenomena that affect these stresses and

strains is required. For example, the brace specimens described in this paper required simulation of global and local buckling, which in turn required a detailed definition of initial member imperfections. One can envision that in other situations, various mechanisms may become critical, e.g. gapping and contact in connections including fillet welds, or the loosening of bolts in bolted connections.

2. In many situations such as welded connections (that include base and weld metal and heat affected zones) it is necessary to consider the spatial gradients and statistical variability in material properties and capacities that may affect the instant and location of ULCF initiation.

3. While the model discussed in this paper addresses mainly ULCF initiation, often the fracture propagates in a ductile manner for a considerable duration of time before the component fractures completely, and these need to be addressed separately through propagation models.

4. Another important issue to consider with regard to the micromechanics-based models is that they typically focus on a single mechanism for failure (e.g. microvoid growth and coalescence). However, depending on stress conditions and material properties, various other mechanisms may be possible, such as intragranular cleavage or intergranular fracture. Thus, appropriate models need to be chosen for a given situation. CVGM may be appropriate for many structural engineering situations where fracture initiates in a ductile manner.

Thus, while the micromechanics-based models offer an attractive and physics-based approach to predicting ULCF, they also require more sophisticated modeling of many physical phenomena and knowledge of potential micromechanisms of failure.

5. SUMMARY

This paper reviews various methods to predict earthquake-induced fracture in steel structures, and presents the physics-based micromechanical approach as a general, accurate and viable approach. Unlike high-cycle fatigue or low-cycle fatigue observed in bridges or mechanical components that are subjected to thousands or millions of cycles, earthquake-induced Ultra-Low Cycle Fatigue (ULCF) is characterized by a very small number (<10) of random, high amplitude cycles. However, fundamental approaches to predict ULCF in steel structures are not well developed. Traditional models to characterize earthquake-induced fracture have relied on experimental or empirical approaches, or on adaptation of techniques originally developed for other problems (such as high-cycle fatigue). Consequently, predictions from these models cannot be generalized to components and situations beyond those that are experimentally tested. Moreover, these costly approaches do not provide insights into local effects that are responsible for fracture. More recently, Conventional Fracture Mechanics (CFM) methods have been used to assess the fracture susceptibility of structural components. While an improvement over experiment-based methods, the CFM methods are limited by assumptions of small-scale yielding and monotonic loading that are not typical to ductile details subjected to earthquake-type ULCF.

Physics-based models that simulate the fundamental micromechanics of the fracture-ULCF process are presented as an attractive alternative to traditional methods. These are fracture criteria based on continuum stress and strain quantities, and thus can be applied to a variety of structural details once the material properties are calibrated. The Cyclic Void Growth Model (CVGM), presented in this paper is one such model that simulates the micromechanical processes of cyclic void growth, collapse and damage to predict ULCF initiation. The application of the CVGM model requires the calibration of two material parameters. This is done through fairly economical small scale notched bar cyclic tests. A procedure for predicting ULCF initiation based on CVGM is outlined, and validation experiment results are presented which suggest that the CVGM simulates fundamental material behavior and can be applied in a general sense to a wide variety of structural components and configurations. However, being highly dependent on the accurate characterization

of local stress and strain histories, these micromechanical models require the simulation of other physical processes such as global and local buckling, contact, gapping etc. Also important are aspects such as the spatial gradients and statistical variability in material properties. Moreover, these models are typically focused on a single micromechanism, so multiple models (e.g. addressing void growth, cleavage) may need to operate simultaneously for an accurate simulation.

It is important to note that micromechanics-based earthquake-induced fracture prediction approaches are relatively recent, and need refinement to be widely accepted. However, given their fundamental appeal, flexibility and generality, coupled with the research community's shift towards model-based simulation, they may be a viable alternative to experimental approaches in the future.

Acknowledgements:

This research was supported by the National Science Foundation (NSF Grant CMS 0421492), the George E. Brown Jr. Network for Earthquake Engineering Simulation (NEES), and the Structural Steel Educational Council (SSEC). The advice and guidance of Helmut Krawinkler (Stanford University), Stephen Mahin (University of California at Berkeley), Charles Roeder (University of Washington) is greatly appreciated. In addition, the knowledgeable support of the UC Berkeley NEES lab personnel was extremely important in the experimental aspect of this study. The authors also acknowledge support from the John A. Blume Earthquake Engineering Center at Stanford University and the University of California at Davis.

References:

- ABAQUS (1998), Abaqus User Manual.
- Anderson, T.L (1995), *Fracture Mechanics*, 2nd Ed., CRC Press, Boca Raton, FL.
- Chi, W-M (2000), "Prediction of steel connection failure using computational fracture mechanics," Ph.D. Thesis, Stanford University, Stanford, CA.
- Chi, W-M, Kanvinde, A.M., and Deierlein, G.G. "Prediction of Ductile Fracture In Welded Connections Using the SMCS Criterion," *Journal of Structural Engineering, ASCE*, **132**(2), 171-181.
- Coffin, L. F., Jr (1954), "A Study of the Effects of Cyclic Thermal Stresses on a Ductile Metal," *Trans. ASME*, **76**, 931-950.
- El-Tawil, S., Vidarsson, E., Mikesell, T., and Kunnath, K (1999), "Inelastic behavior and design of steel panel zones," *Journal of Structural Engineering, ASCE*, **125**(2), 183-193.
- Fell, B.V., Kanvinde, A.M., Deierlein, G.G., Myers, A.T., and Fu, X (2006), "Buckling and fracture of concentric braces under inelastic cyclic loading," *SteelTIPS, Technical Information and Product Service*, Structural Steel Educational Council.
- FEMA (2000), "Recommended Design Criteria for New Steel Moment-Frame Buildings FEMA-350," Federal Emergency Management Agency.
- Hancock, J. W. and Mackenzie, A. C (1976). "On the mechanics of ductile failure in high-strength steel subjected to multi-axial stress-states," *Journal of Mechanics and Physics of Solids*, **24**(3), 147-169
- Kanvinde, A. M. and Deierlein, G.G. (2004), "Micromechanical Simulation of Earthquake Induced Fracture in Steel Structures," Technical Report 145, John A. Blume Earthquake Engineering Center, Stanford University, CA.
- Okazaki, T., Engelhardt, M., Nakashima, M., and Suita, K (2006), "Experimental Performance of Link to Column Connections in Eccentrically Braced Frames," *Journal of Structural Engineering, ASCE*, **132**(8), 1201-1211.
- Panontin, T. L. and Sheppard, S. D. "The relationship between constraint and ductile fracture initiation as defined by micromechanical analyses," *Fracture Mechanics: 26th Volume*. ASTM STP 1256. 1995. 54-85.
- Rice, J. R. and Tracey, D. M. (1969), "On the ductile enlargement of voids in triaxial stress fields," *Journal of the Mechanics and Physics of Solids*, **35**, 201-217
- Stojadinovic, B., Goel, S., and Lee, K.H. (2000), "Development of post-Northridge steel moment connections," *Proceedings of the 12th World Conference on Earthquake Engineering*, New Zealand, paper 1269.
- Tatsuo, E., Koichi, M., Kiyohumi, T., Kakuichi, K., Masanori, M. (1974), "Damage evaluation of metals for random of varying loading – three aspects of rain flow method," *Journal of the Institution of Water Engineers and Scientists*, 371-380
- Tremblay, R., Archambault, M-H, Filiatrault, A. "Seismic performance of concentrically braced steel frames made with rectangular hollow bracing members," *Journal of Structural Engineering, ASCE*, Vol. 129(120). 2003. 1626-1636.
- Uang, C.M and Fan, C.C. (2001), "Cyclic Stability Criteria for Steel Moment Connections with Reduced Beam Section," *Journal of Structural Engineering, ASCE*, **127**(9) 1021-1027.
- Uriz, P., and Mahin, S., (2004). "Seismic Performance Assessment of Concentrically Braced Steel Frames," *Proceedings of the 13th World Conference on Earthquake Engineering*, Vancouver, Canada,

PERFORMANCE OF PREFABRICATED STEEL STAIR ASSEMBLIES UNDER SEISMIC AND GRAVITY LOADS

Christopher Higgins

*Associate Professor, Department of Civil and Construction Engineering, Oregon State University, USA
chris.higgins@oregonstate.edu*

Abstract: Tests were performed on full-size prefabricated steel stair assemblies to assess seismic interstory drift response combined with factored gravity loads. The stair assemblies were production-run units of a standard system and were designed for a typical steel frame building. Two different stair assembly units were tested: one with checker plate and one with concrete filled pans. A testing protocol was developed to evaluate the seismic performance using seismic and gravity load combinations. Lateral drifts were imposed in both orthogonal stair directions followed by factored live and dead loads. Imposed lateral drift placed high deformation demands on the stair-to-landing connections and overall performance is dependent on these connections. Careful detailing, fabrication, and inspection of welds joining the landing connection plates are required to ensure desired performance.

1. INTRODUCTION

Stairs serve as a primary means of egress from a structure after an earthquake or other disaster and thus their role in achieving life-safety performance for a building is critical. As a result of newly adopted performance-based design provisions for buildings in the US, the lateral drift performance of prefabricated stair assemblies during seismic events has become of interest to some designers. No standardized testing methods or loading protocols are currently available for evaluating the seismic performance of prefabricated stair assemblies. Further, data on the structural performance of stair assemblies under lateral and combined lateral and gravity loading are lacking. Research was undertaken to develop a testing protocol to evaluate the anticipated seismic performance of production-run prefabricated steel stair assemblies. Laboratory tests of two full-size stair assemblies were conducted in the Structural Engineering Research Laboratory at Oregon State University to assess seismic performance and the results of this study are reported here.

2. SPECIMEN DESCRIPTION

Two full-size stair assemblies were fabricated. The stairs were production-run units designed for a typical steel frame building with 3.6 m story heights, a common design used in the United States. Each stair set consisted of two flights, a single intermediate landing, and 4 support columns as illustrated in Fig. 1. The two stair assemblies were similar except for the stair tread and landing surface. One set was fabricated with 14 gauge diamond or checker plate (Checker), the other was fabricated with 14 gauge steel pans to permit concrete in-fill (Infill). Each of the two flights of stairs consisted of 10 treads with each tread having a 166 mm rise and 279 mm run. Stringers consisted of ASTM-A36 6x 254 mm plate. Stair tread plates were fillet welded to the stringers. The landing area was 1.2 x 2.39 m

and supported by ASTM-A36 channel framing. Vertical support to the landing was provided by four ASTM-A36 63x63x6 angle columns bolted to each corner of the landing. Connections at the base of each flight of stairs consisted of ASTM-A36 127x76x6 angle fillet welded to the stringers. Connections at the top of each flight of stairs consisted of ASTM-A36 6x101 mm plate fillet welded to the stringers. The top and bottom connections to the flight were made with two 16 mm diameter A325 tension-controlled (TC) bolts. The Infill test specimen required placement of concrete in the tread form pans and landing. The landing consisted of 20 gauge 'BR' decking with the ribs oriented in the short landing dimension. Minimum height of the concrete overfill in the decking and treads was 16mm. Concrete consisted of 9.5 mm maximum size aggregate with an average compressive strength on the first day of testing (7 day strength) of 13.8 MPa.

After assembly of the components in the laboratory, instruments were applied to stair specimens to measure specimen deformations and internal stresses as well as applied lateral force as illustrated schematically in Fig. 1. Sensor data were acquired using 16-bit PC-based data acquisition system with commercially available software used to control acquisition and data storage.

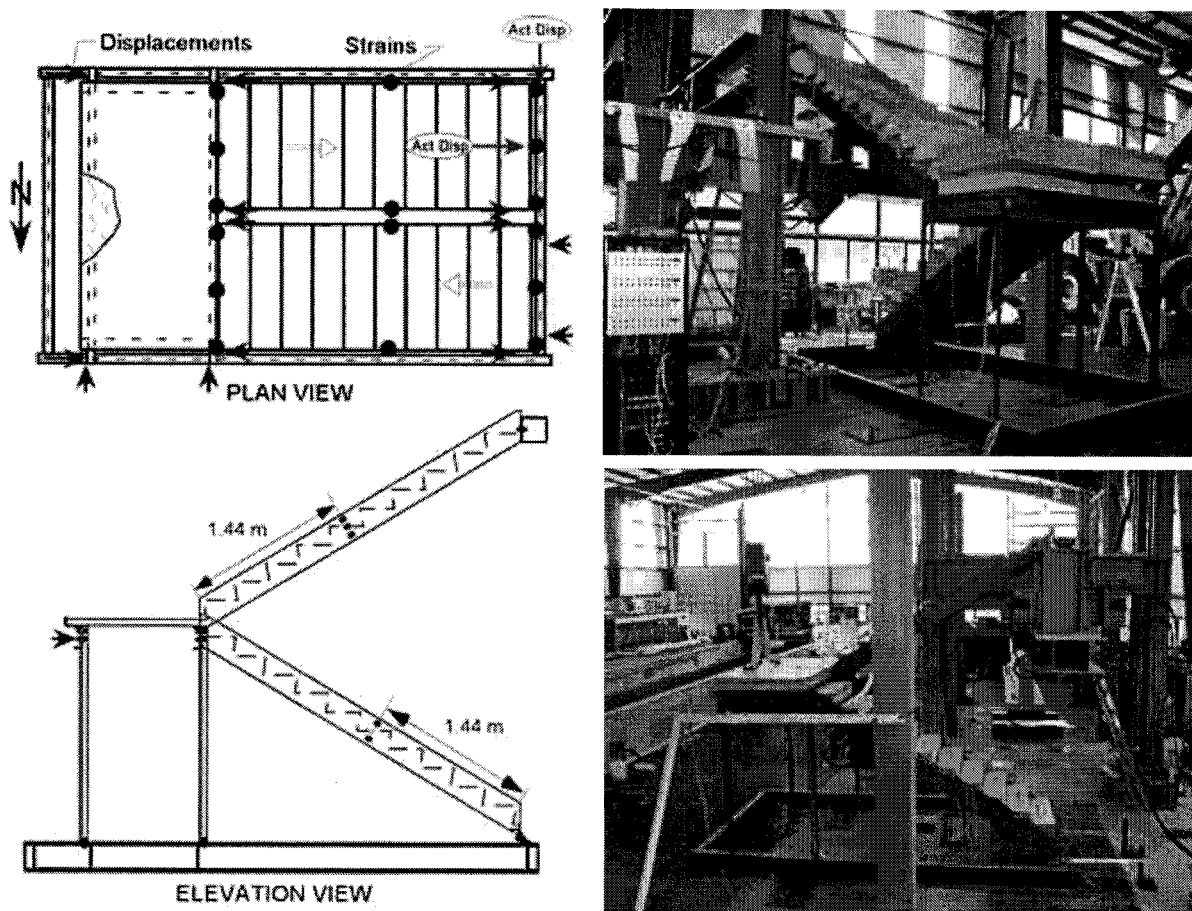


Figure 1 Prefabricated stair assembly and overall test setup

3. TEST SETUP AND METHODOLOGY

The stair assemblies were placed in a loading frame as shown in Fig. 1. A base frame consisting of beam sections was welded to 19 mm thick steel plates that were bolted to the structural laboratory strong-floor. An ASTM-A36 76x76x6 angle was fillet welded to the flange of the beams to permit

connection of the first stair flight to the base frame. Stiffeners were added to the angle to minimize distortion during tests. The landing posts were bolted through the top flange of the base frame with a single A325 TC bolt. Single-sided 6 mm web stiffeners were located near each of the column post connections.

The top landing was attached to an ASTM A600 152x152x6 mm tube. The tube dimensions were selected to approximate the concrete landing slab dimensions and force transfer mechanism for an actual stair assembly in a building. A unique guiding system was developed to permit only in-plane deformations at the top landing attachment location as shown in Fig. 2. This was necessary to prevent uplift and out-of-plane deformations during lateral tests that are not possible when the stairs are located in an actual building subjected to lateral drift. Special radial and axial bearings were mounted to the steel tube and guided by special profile rails to restrict deformations to the in-plane directions. Stair tests were performed in each direction separately and the guide assembly had to be reconfigured for each of the test directions. The steel tube landing was displaced during testing using a hydraulic actuator that was operated under displacement control using a closed-loop servo-hydraulic system.

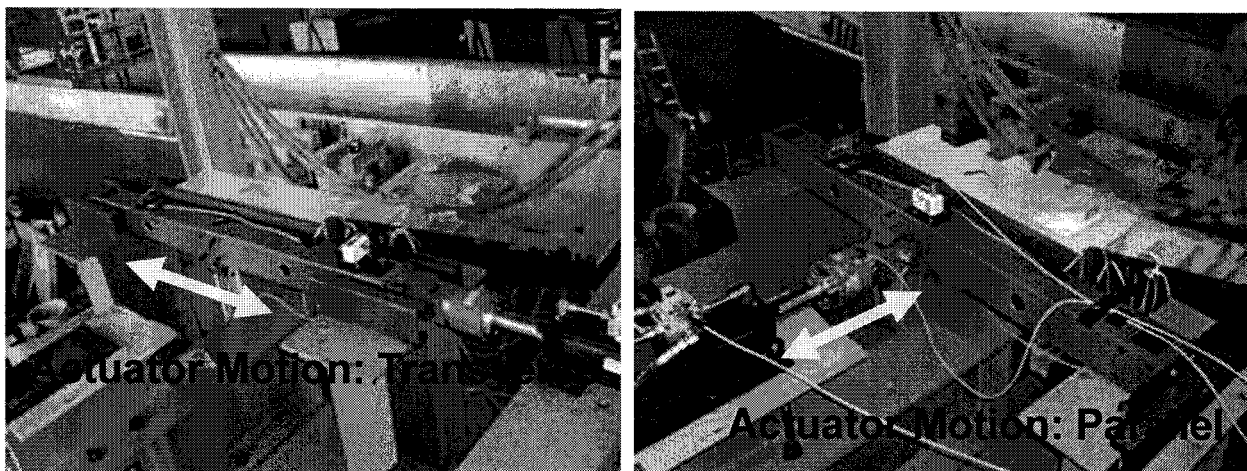


Figure 2 Top landing loading and guide assembly for two orthogonal directions

Currently, no standardized seismic testing protocols for prefabricated stair assemblies exist. However, ATC-24 (1992) provides guidelines for cyclic seismic testing of components of steel structures. In general, these procedures are based on the yield level of the component, which may not be appropriate for a stair assembly. The stair assembly within a building, does not provide significant lateral stiffness or force resistance, but is instead compliant with the building deformations. The production-run stair assemblies were considered for a typical application in a steel moment resisting frame (MRF). For a typical steel MRF, the interstory drift angle considered for the 2/3 MCE event was 2.5%, which corresponds to a peak lateral displacement (Δ_{bm}) of ± 91 mm. Using Δ_{bm} as the maximum cyclic displacement to be imposed on the stair specimen, the cycle amplitudes for three previous sequences of displacement cycles were scaled in proportion as $\frac{3}{4}$, $\frac{1}{2}$, and $\frac{1}{4}$ of Δ_{bm} . Four cycles were imposed at these amplitudes as compared to the two or three cycles used in the ATC24 protocol for cycles imposed after yielding. At the start of testing, two sets of small amplitude cyclic displacements (2 cycles at 3 mm and 2 cycles at 6 mm) were applied to ensure data sensors were seated and data acquisition was properly functioning. Following these small amplitude initial cycles, six cycles were imposed at ± 13 mm. The complete lateral loading history is shown in Fig. 3. Because the stairs are compliant with the building deformations, and steel MRFs tend to be more flexible than many other types of lateral force resisting structural systems, the test displacement history would likely impose higher demands on the stair assembly than those required for many other building types.

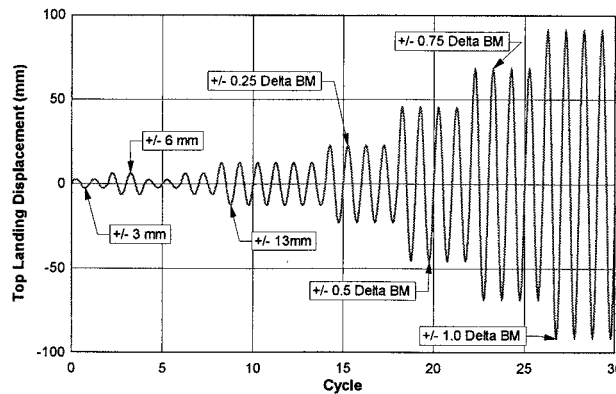


Figure 3 Imposed lateral displacement history

Current AISC LRFD (2003) specification load combinations require consideration of live and dead loads with earthquake loading. The specified load combination is:

$$U = 1.2D + 0.5L + 1.0E \quad (1)$$

where U is the factored load combination, D is the dead load, L is the service live load, and E is the earthquake load. The applied lateral load was considered to be at the load factor of 1.0 and the in-place stair assembly represented $1.0D$, however additional gravity load was required to account for the additional 20% dead load and 50% service live load. For stairs, the specified service live load is 4.8 kPa. The dead load of the stairs was provided by the manufacturer as 6.5 kN and 5.6 kN for the checker plate and infill concrete treads (without concrete), respectively. The total dead load of the concrete in-fill stair including the weight of concrete was approximately 14.7 kN assuming normal weight concrete. Individual concrete blocks weighing approximately 0.9 kN were cast for each step and two large blocks weighing 7.4 kN total were cast for the landing. The total weight of the blocks applied to the stair specimen was 25.4 kN and exceeded the load factor combination in Eq. 1 for both specimens. The blocks were placed on the specimen prior application of the lateral load and remained in place during lateral displacement testing (as seen in Fig. 1).

After completion of lateral displacement testing protocol, the top landing displacement was returned to the original neutral position. The AISC LRFD (2003) specification full design live load combination was applied to the specimen as:

$$U = 1.2D + 1.6L \quad (2)$$

Additional concrete blocks were placed on the specimen to represent the additional factored live load (5.3 kPa above the previous level in Eqn. 1). Individual concrete blocks weighing approximately 1.8 kN were placed on each step and two large blocks weighing 15.5 kN total were placed on the landing. These new blocks were placed on top of the previous sets of blocks. The total weight of the blocks applied to the stair specimens was 75.8 kN (two sets of blocks stacked on top of each other) and exceeded the load factor combination in Eqn. 2 for both specimens.

To account for a possible aftershock event that may occur as the stairs are subjected to the full design live load, the following load combination was also considered:

$$U = 1.2D + 1.6L + 0.5E \quad (3)$$

For this test, four (4) cycles of lateral displacement of $\pm 0.5 \Delta_{bm}$ ($= \pm 45$ mm) were applied when the specimen was loaded with the concrete blocks representing the full design live load.

Each stair specimen was subjected to lateral displacements imposed in the two orthogonal directions separately. To achieve the performance requirements, the specimen was expected to sustain

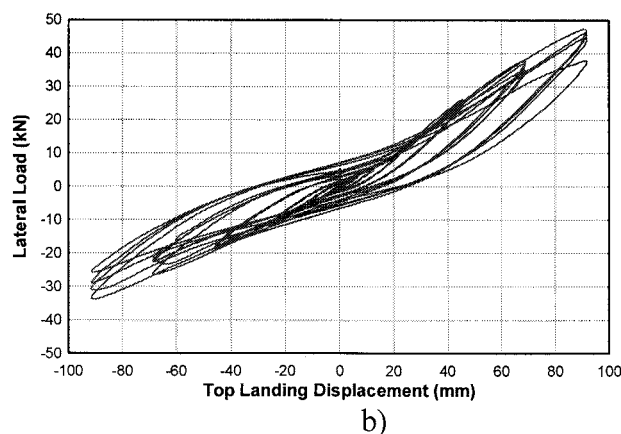
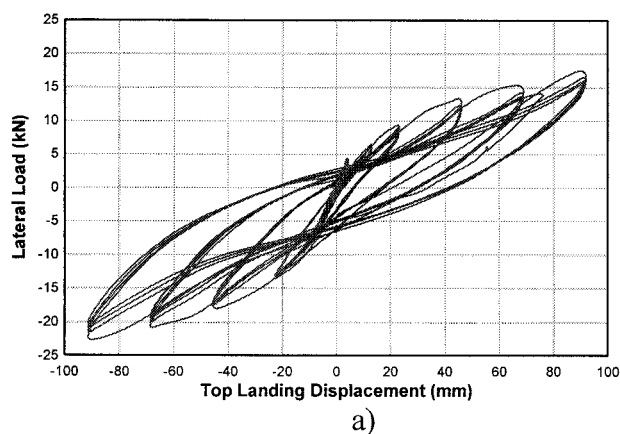
both events without loss of gravity load carrying capacity. The combined testing history for each specimen consisted of the following:

- Application of 0.2D+0.5L gravity load blocks
- Application of complete lateral displacement history in Fig. 3 (transverse for checker plate specimen; parallel for infill specimen) [Meets Eqn. 1]
- Application of additional 1.1L gravity load blocks [Meets Eqn. 2]
- Application of four cycles $\pm 0.5 \Delta_{bm}$ [Meets Eqn. 3]
- Removal of additional 1.1L gravity load blocks
- Switch actuator direction
- Application of complete lateral displacement history in Fig. 3 (parallel for checker plate specimen; transverse for infill specimen) [Meets Eqn. 1]
- Application of additional 1.1L gravity load blocks [Meets Eqn. 2]
- Application of four cycles $\pm 0.5 \Delta_{bm}$ [Meets Eqn. 3]
- Test complete for one specimen

4. TEST RESULTS

Test specimens were initially loaded with concrete blocks simulating gravity load. Strains gages on the stringers indicated bending along the weak-axis of the stair run under the gravity load. The internal moment determined from measured strains indicated some degree of moment restraint was provided by the landing connections (the runs are not simply supported at ends). Strains on the connection plates and angles were negligible and relative displacement between connected parts were also negligible.

The checker plate specimen was first subjected to lateral displacements in the transverse to stair run (north-south direction in Fig. 1), while the in-fill specimen was initially loaded in the parallel to stair run direction (east-west direction in Fig. 1). Overall force-deformation response for the lateral loading cases are shown in Fig. 4a and 4b and Fig. 4c and 4d for the checker and infill specimens, respectively. As seen in these figures, the specimens provided relatively little lateral stiffness and energy dissipation. The stair assemblies had higher strength and stiffness in the parallel to stair loading direction as compared to the transverse loading case.



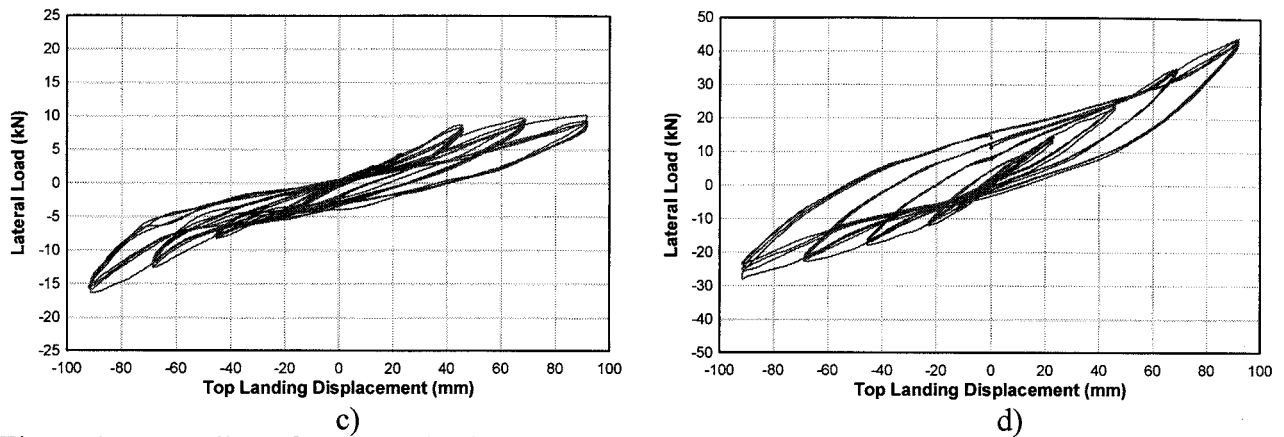


Figure 4 Overall top force- top displacement response for the checker plate specimen (a) Transverse (b) Parallel loading and Infill concrete specimen (c) Transverse (d) Parallel loading

The larger stiffness and energy dissipation seen for both stair specimens during the initial loading direction (transverse for the checker plate and parallel for the infill concrete) was due to the initial undamaged installation conditions that provided original contact between connecting stair components. After the actuator was moved to the orthogonal direction for the second sequence, specimens exhibited softer response with some stiffening and very little energy dissipation. This is because the connection parts were already yielded and residual connection gaps were produced during the previous loading history and thus the observed response for this second loading case does not correspond to that of a new undamaged specimen. Connection strains indicated initial yielding at low lateral displacements (approximately ± 10 mm). Stringer strains indicated a relatively small amount of bending in the strong-axis of the stair run at the instrumented locations. Parallel loading produced single curvature in the stair runs, while transverse loading produced double curvature in the stair runs. Transverse loading produced higher demand at the upper landing connections. Parallel loading produced higher demands at the lower landing connection. Displaced shapes for the stair assemblies are shown in Fig. 5 in the two loading directions. The intermediate landing moved primarily in the north-south direction with relatively small displacements in the east-west direction for the transverse loading case. Indeed almost no motion of the intermediate landing was observed in the west direction for this case. For the parallel loading case, the intermediate landing exhibited relatively large motions and rotated about the bottom landing connection.

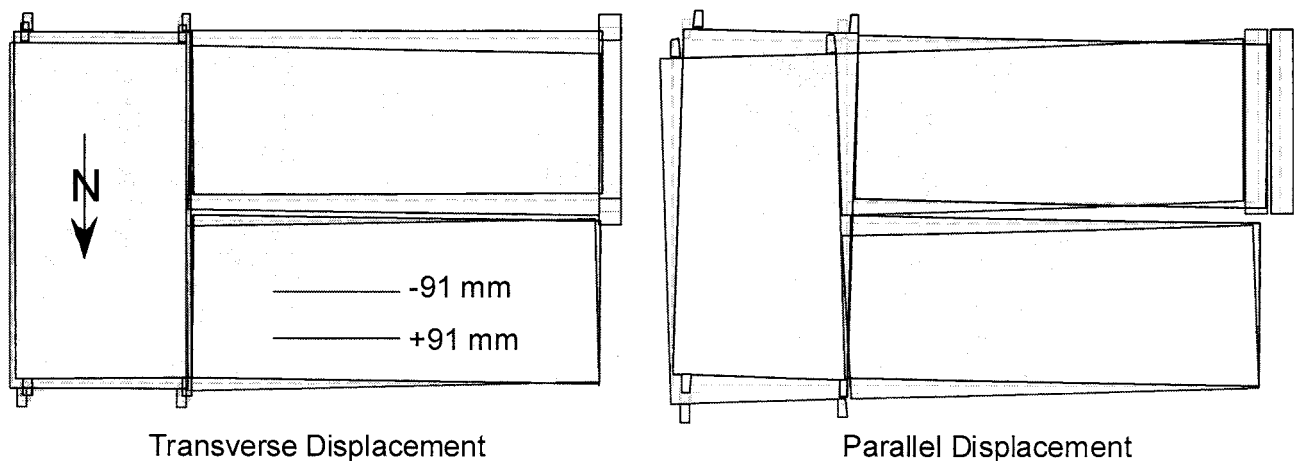


Figure 5 Displaced shape for stair assembly loaded in the transverse and parallel directions

Relative displacements between the stringer ends and the landing connections were observed during loading. Under the imposed transverse displacements, the stringers are alternatively pulled away from and compressed against the landing connections as seen in Fig. 6. Under the imposed parallel displacements, the stringers are alternatively pulled away from and pushed against the landing connections. The deformed shape of the connection plate appeared to be fixed at the vertical weld line and primarily fixed at the bolt location as seen in Fig. 6. Due to connection yielding, there were residual displacements in the form of gaps that remained when the stairs were returned to the original neutral position. Displacement measurements of the base connection and laboratory floor were small and the base connection appeared to reasonably approximate that of a stiff slab connection typical of in-situ building conditions.

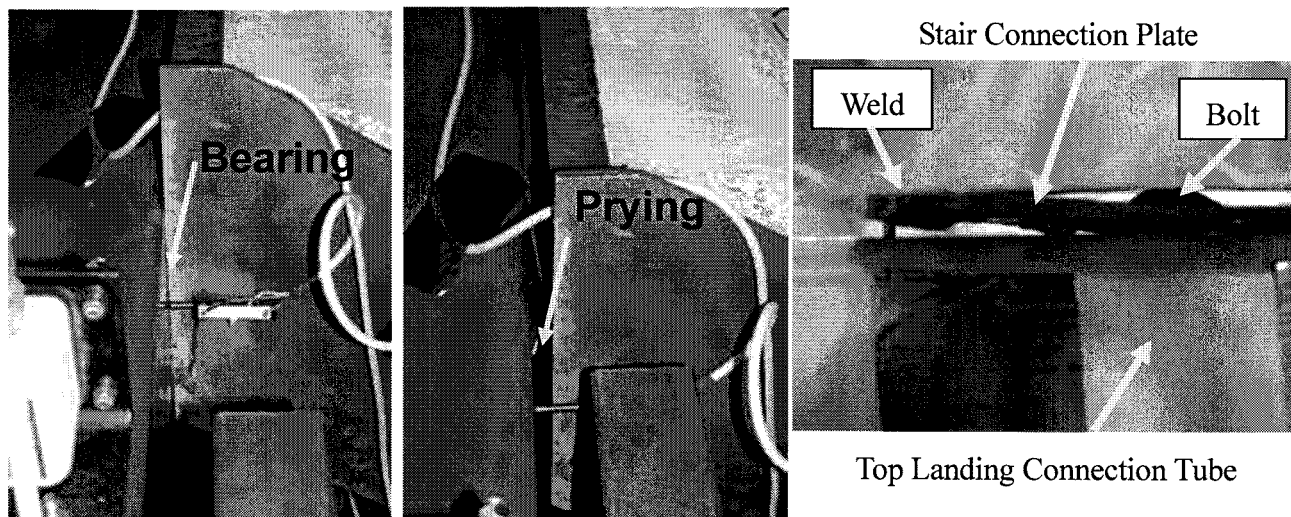


Figure 6 Alternating top landing connection bearing and prying during transverse loading

After applying the lateral displacements of Fig. 3, the specimens were returned to the original neutral position and loaded with additional concrete blocks simulating Eqn. 2 level gravity loads. The specimens sustained the applied load. Strains gages on the stringers indicated additional in-plane bending of the stairs under the gravity load and again showed some moment restraint was provided by the landing connections. The specimens were then subjected to 4 cycles of lateral loading with maximum displacement amplitude of $\pm 0.5\Delta_{bm}$ while under the full factored design gravity load. The specimens exhibited stable and repeatable cyclic performance during the four cycles. After the first lateral loading position was completed, the top layer of concrete blocks was removed and the lateral loading actuator orientation was changed to permit testing of the specimen in the orthogonal direction. The resulting overall force-deformation responses for the second sequence are shown in Fig. 4b and 4c for the two specimens (the diminished performance was again due to the residual damage from the first loading orientation). After lateral displacements of Fig. 3 were imposed for the orthogonal direction, the specimens were returned to the original neutral position and loaded with additional concrete blocks simulating Eqn. 2 level gravity loads. The specimens again sustained the applied gravity load. The specimens were subjected to 4 cycles of lateral loading with maximum displacement amplitude of $\pm 0.5\Delta_{bm}$ while under the full factored design gravity load (Eqn. 3) and exhibited stable cyclic performance during the four cycles. Both the checker plate and infill concrete stair specimens satisfied the loading protocol by sustaining the factored gravity loads under the design lateral motions in the two orthogonal directions and demonstrating full design gravity load carrying capacity combined with the aftershock lateral displacements.

A final visual inspection of the specimen was performed after all the concrete blocks were

removed. Cracks were observed in the wrap-around welds along the bottom of the connection plate resulted in tearing of the checker plate material. Based on dye-penetrant inspection, cracks in the wrap-around weld did not propagate into the vertical weld joining the connection plate to the stringer. To investigate the condition of the vertical weld along the stringer to landing connection plate, connections were removed from the specimen after disassembly of the stair specimen from the loading system. Cracks were visible along the weld toe at the stringer-plate boundary. Three slices of the weld were machined from the section and inspected. There was evidence of crack propagation initiating at the lack of fusion zone. One section indicated almost no weld penetration although it appeared from the surface to be similar to the adjacent areas. While the weld conditions were not sufficient to hinder the overall stair performance, welding procedures and inspection protocols for stringer to landing connections should be further emphasized to ensure desired connection strength and performance.

5. CONCLUSIONS

Laboratory tests were performed to assess the anticipated seismic performance of prefabricated steel stair assemblies. Two different production-run stair assembly units were tested: checker plate and concrete filled pans. The stair assemblies were subjected to combined AISC factored gravity loads with lateral displacements simulating seismic interstory drift demands. Peak lateral displacements on the stair assemblies were based on an interstory drift angle of $\pm 2.5\%$ for a steel frame building having 3.6 m story heights and displacements were imposed to the stair assemblies at the top landing location in each direction (parallel to stair run and transverse to stair run) separately. The testing apparatus constrained the top landing displacements to the plane of loading considered, thereby imposing deformations and stresses consistent with in-situ building conditions. Both stair assemblies successfully completed the testing protocol by demonstrating full design gravity load capability after undergoing lateral displacements in both orthogonal directions and there were no appreciable differences between the performance of the two different stair assemblies. Parallel loading produced single curvature in the stair runs and produced the highest deformation demand in the bottom landing angle connection. Transverse loading produced double curvature in the stair runs and produced the highest deformation demands in the top stair to landing connection plate and weld. Strain measurements in stringers indicated the stairs carry gravity loads as semi-rigid beams along the horizontal projected length. The stair-landing connections appeared to provide some moment restraint that was reduced after lateral loading produced separation at the landing connections. Stringers are subject to combined stringer bending (both strong-axis from seismic and weak-axis from gravity load) and axial force from seismic loading. Stair performance was dependent on the landing connections and the vertical weld joining the connection plate to the stringer. Inspection of the weld after testing indicated lack of penetration of the weld along the stringer edge. Fabrication procedures and inspection of the welds joining the connection plate to the stringer should be further emphasized to ensure best practices and desired performance.

Acknowledgements:

The author would like to acknowledge the financial support for this research by Pacific Stair Co. of Salem, Oregon, USA. The findings and conclusions are those of the author and do not necessarily reflect those of the project sponsor.

References:

- American Institute of Steel Construction (AISC). (2003). 3rd Edition, "Load and Resistance Factor Design Specification for Structural Steel Buildings." Chicago, Illinois.
- Applied Technology Council. (1992). ATC-24. "Guidelines for Cyclic Seismic Testing of Components of Steel Structures." Redwood City, California.

EARTHQUAKE RESISTANCE PERFORMANCE OF FLEXIBLE-STIFF MIXED STRUCTURE FOR EFFECTIVE USE OF HIGH-STRENGTH STEEL

Sang-Hoon Oh ¹⁾

*1) Steel Structure Research Laboratory, Research Institute of Science & Technology,
Dongtan, Hwasung, Kyungk-Do 445-810, Korea*

Abstract: Nowadays, various grades of high-strength steels are available. The application of ultra-high grades of steels for building structures, however, is limited only to the elements stressed under tension. The highest grade of steels generally used has a tensile strength of around 600N/mm². Most research is focused on lower yield ratios of high strength steel in the inelastic range to ensure the stability of structures. In this paper, however, the possibility of an effective application of high strength steel with high yield ratio to building structures is discussed. An efficient structural system and a design method based on earthquake response analysis and experimental results are proposed.

1. INSTRUCTIONS

Recently high strength steels have been developed and applied to machines, pressure vessels, ships, etc., and the need for high strength steels in building structures is increasing. In contrast to the design method for pressure vessels and machines, buildings are designed to expect the plastic deformation capacity under earthquake. The stress-strain relationship of steels has a basic trend in accordance with their grades as follows.

- 1) Young's modulus takes almost a constant value.
- 2) To increase the yield point stress, σ_y is easier than to increase the tensile strength, σ_u . Therefore, the yield ratio $Y(= \sigma_y / \sigma_u)$ becomes higher as the tensile strength increases.
- 3) The elongation capacity decreases as the tensile strength increases.
- 4) Welding becomes difficult to apply as the tensile strength increases.

Under tensile stresses, high strength steels develop their intrinsic advantageous nature as is demonstrated in the isolated use of struts and cables. Under compressive stresses, the buckling strength cannot be drastically improved due to the constancy of Young's modulus. Therefore, the high-strength does not result in the reduction of material used, since building structures are governed by not only tensile stresses but also compressive stresses. Also, the constancy of Young's modulus produces larger deformations at the elastic limit as the tensile strength increases. Thus, the structures are softened by the application of high-strength steels. The inelastic deformation capacity (energy absorption capacity) of members and frames decreases as the tensile strength increases, since the inelastic deformation capacity is primarily influenced by the yield ratio and elongation capacity of materials. Therefore, development of new structural systems is required to improve the defects of high strength steel, mainly the high yielding ratio, and to develop an optimal and economical design.

In this paper, therefore possibilities of an effective application of high yielding ratio-high strength steel to building structures, the flexible-stiff mixed structural system is suggested. The efficiency of this structural system is investigated by earthquake response analysis and experimental tests.

2. FLEXIBLE-STIFF MIXED STRUCTURE FOR APPLICATION OF HIGH STRENGTH STEEL

Members should behave in the elastic range because of the low plastic deformation capacity of high strength steel. However flexible-stiff mixed structures proposed by AKIYAMA1) increase the possibility of usage of high strength steel. Flexible-stiff mixed structures consist of flexible elements (very small bending stiffness) and stiff elements (very large bending stiffness) all put into one story. This mixture of structural elements, which have different stiffness, enables an increase in the capacity of structures to resist earthquake load. The restoring force characteristics of flexible-stiff mixed structure are the summation of those of stiff elements and flexible elements as represented in Figure 1.

Therefore, flexible members would stay in the elastic range when stiff members absorb energy produced by plastic deformation at the ultimate state. To improve the efficiency of a flexible-stiff mixed structure, the development of energy absorption devices using stiff elements is required and appropriate installation of flexible elements, having large elastic deformation to stay in the elastic range at the limit of energy absorption of stiff elements is recommended.

The application of high yielding ratio-high strength steel makes it profitable to design a flexible element which resists vertical load, such as live load and dead load, and have small bending stiffness.

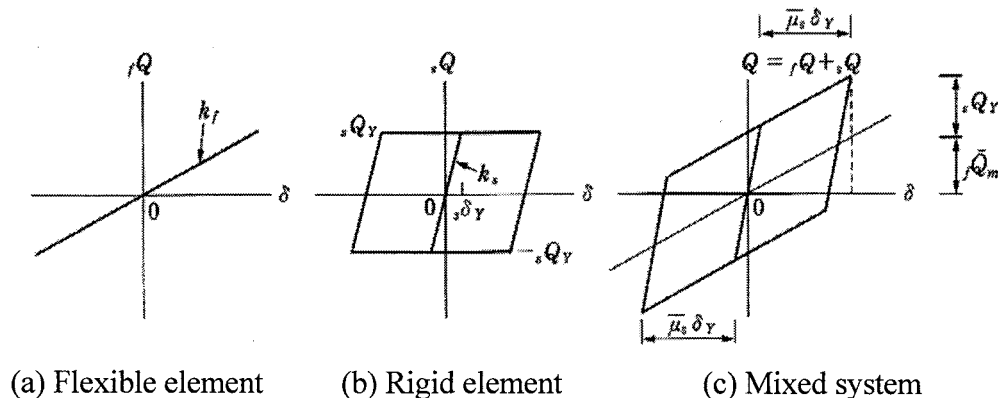


Figure 1. Flexible-stiff mixed structure.

3. RESPONSE ANALYSIS RESULTS OF FLEXIBLE-STIFF MIXED STRUCTURE

3.1 Analysis results for single story

To investigate the application method of high strength steel on the flexible-stiff mixed structure, earthquake response analysis was carried out. The analysis model established for response analysis is shown in Figure 2. This model consists of two stiff columns (ordinary mild steel) and a flexible column (high strength steel). The beam member was assumed as rigid element. The following parameters are taken as variables on the design of analysis model.

- 1) Stiffness ratio (K_s/K_f) between stiffness of stiff column (K_s) and flexible column (K_f).

This range is from 1.0 to 10.0

- 2) Strength ratio (M_f/M_s) between yielding strength of flexible column (M_f) and stiff column (M_s).

The range is from 0.7 to 1.4

The restoring force characteristics adopted for the stiff and flexible columns are shown in Figure 3. The seismic input consists of four recorded earthquakes: the El-Centro earthquake (NS component), the Hachinohe earthquake (EW component), the Kobe earthquake (NS component) and artificial earthquakes. The acceleration records are scaled so that the total energy input is expressed in terms of a pseudo velocity of $V_E=120\text{cm/sec}$.

V_E is defined as shown below:

$$V_E = \sqrt{\frac{2E}{M}} \quad (1)$$

where, E = the total energy input on the building by earthquake, M = the total mass of the system.

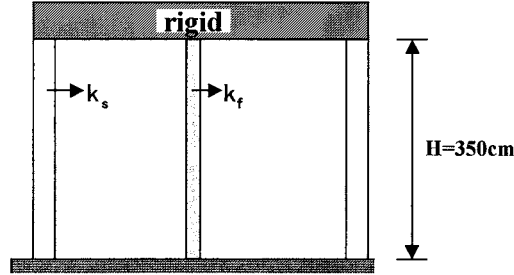


Figure 2. Analysis model.

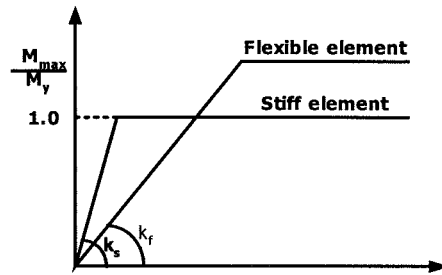


Figure 3. Restoring force characteristics of columns.

The results of earthquake response analysis are shown in Figure 4. This figure shows the relation between yield deformation ratio ($\delta_y/s\delta_y$) of stiff column ($s\delta_y$) and flexible column (δ_y) and the damage when the energy input was reached at the ultimate state of the structure.

The damage ratio of the flexible column will be approximated by the following equation

$$\frac{W_f}{W_f + W_s} = \frac{1}{\left(\frac{\delta_y}{s\delta_y}\right)^2} \times \frac{n_f}{n_f + n_s} \quad (2)$$

where, W_f = Inelastic strain energy of flexible element, W_s = Inelastic strain energy of stiff element, δ_y = yielding deformation of flexible element, $s\delta_y$ = yielding deformation of stiff element, n_f = number of flexible elements, n_s = number of stiff elements

The approximate curve of eq. (2) is represented by the solid line in Figure 4.

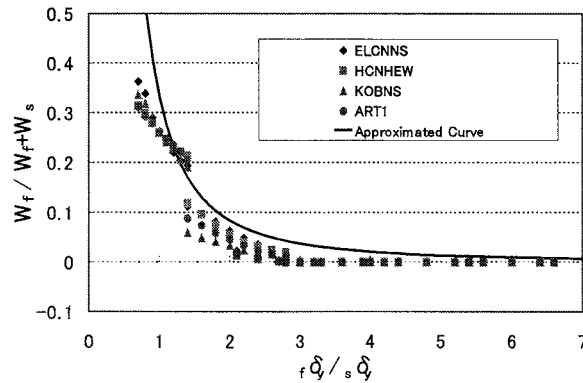


Figure 4. Damage ratio of flexible and stiff columns.

3.2 Analysis results for multi story model

The earthquake response analyses were performed using a multi story model to expand the application of the flexible-stiff mixed structure. Figure 5 shows the analysis model. The analyses were carried out for 6 stories, 9 stories and 20 stories moment-framed buildings. The design method of model and analysis method are same as those of one story structure.

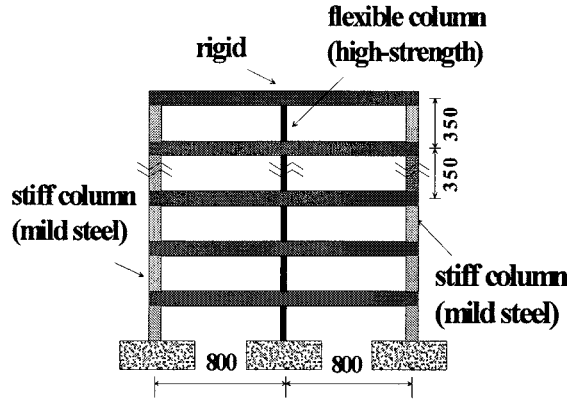


Figure 5. Multi story analysis model.

One example of earthquake response analysis result for 6-story frame is shown in Figure 6. The strength of flexible and stiff elements is same but the stiffness ratio (K_s/K_f) is changed. So, this figure shows the trend of damage distribution by difference of stiffness between flexible and stiff elements. Generally, the damage is concentrated to first story. If the strength and stiffness of flexible and stiff element are same (Figure 6(a)), inelastic strain energy occurred in flexible element is almost same as that of stiff element. But if stiffness ratio (K_s/K_f) is greater than 4.0, flexible element remains elastic. As the stiffness ratio becomes larger, the damage concentration to 1st story becomes smaller.

Figure 7 shows the relationship between yielding deformation ratio ($\delta_y/s\delta_y$) and inelastic strain energy ratio of 1st story. Regardless of number of story, as the yielding deformation ratio becomes larger, the inelastic strain energy becomes smaller, and the flexible element remains in the elastic region for the $\delta_y/s\delta_y$ is greater than 3.0~4.0.

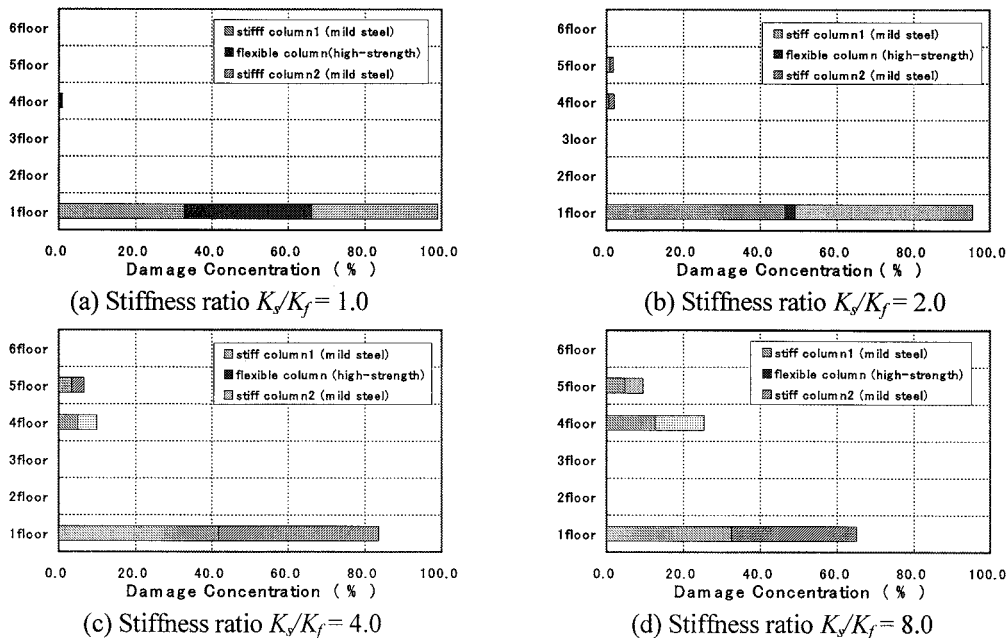


Figure 6. Damage distribution of 6-story building (strength ratio $M_f/M_s=1.0$).

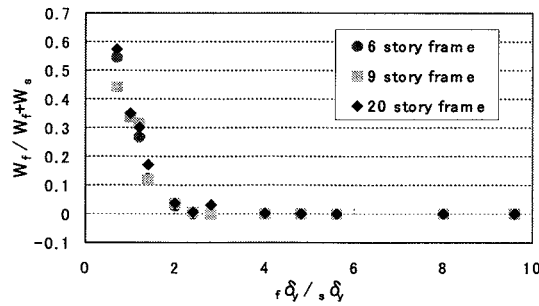


Figure 7. Damage ratio of flexible member in 1st story.

4. EXPERIMENTAL INVESTIGATION ON THE FLEXIBLE-STIFF MIXED STRUCTURE

4.1 Description of Experiments

The test set-up was designed for the application of lateral load and lateral displacement as shown in Figure 8. The specimens, which are showed by thick line in this figure, consist of two exterior columns (used as stiff element) and an interior column (used as flexible element). The features of the specimens and test parameters are described in Table 1. In the tests, exterior columns are the stiff parts (ordinary mild steel) of the system, and interior column are the flexible part (high yielding ratio-high strength steel) of the system. The ratio of yielding deformation between the interior column and the exterior columns is a variable to give different hysteretic characteristics in the tests. For a unit ratio the specimens have same exterior columns; otherwise the section of the interior column of high strength steel with high yield ratio is changed.

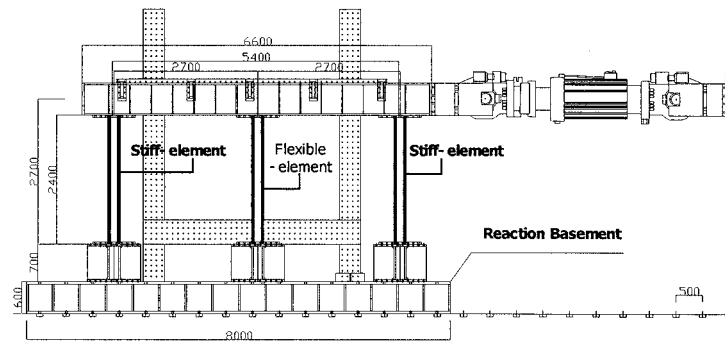


Figure 8. Drawing of Set-up.

Table 1. Test parameters of specimen.

Specimen	Exterior Column	Interior Column	Ratio of Stiffness	Ratio of Yield disp.
SS100	SS400	SS400	1.00	1.00
SM100	SM570	SM570	1.00	1.00
SA100	SSA440	SSA440	1.00	1.00
FSM282	SS400	SM570	1.72	2.82
FSM327	SS400	SM570	2.72	3.27
FSM417	SS400	SM570	5.71	4.17
FSM225	SS400	SM570	1.56	2.25
FSM290	SS400	SM570	3.39	2.90
FSA273	SS400	SSA440	2.07	2.73
FSA321	SS400	SSA440	2.76	3.21
FSA334	SS400	SSA440	3.80	3.34
FSA430	SS400	SSA440	6.60	4.30
FSA494	SS400	SSA440	10.17	4.94

The mechanical properties of the materials used for the specimens are shown in Table 2. The yield ratio for the SS400 steel that is used as the exterior columns was 0.69, and those of the SSA440 and SM570 material used as the interior column were from 0.81 to 0.92.

Table 2. Material tensile test result

	σ_y	σ_u	E	E_y	ϵ_{st}	σ_y/σ_u	Elongation
	N/mm ²	N/mm ²	N/mm ²	10 ⁻⁶	10 ⁻⁶		%
SS400	316	461	2125	1518	1518	0.69	22.79
SM570(9t)	572	620	2142	2728	2612	0.92	16.78
SM570(19t)	572	640	2238	2622	2974	0.89	18.38
SSA440	514	637	2135	2457	3236	0.81	17.27

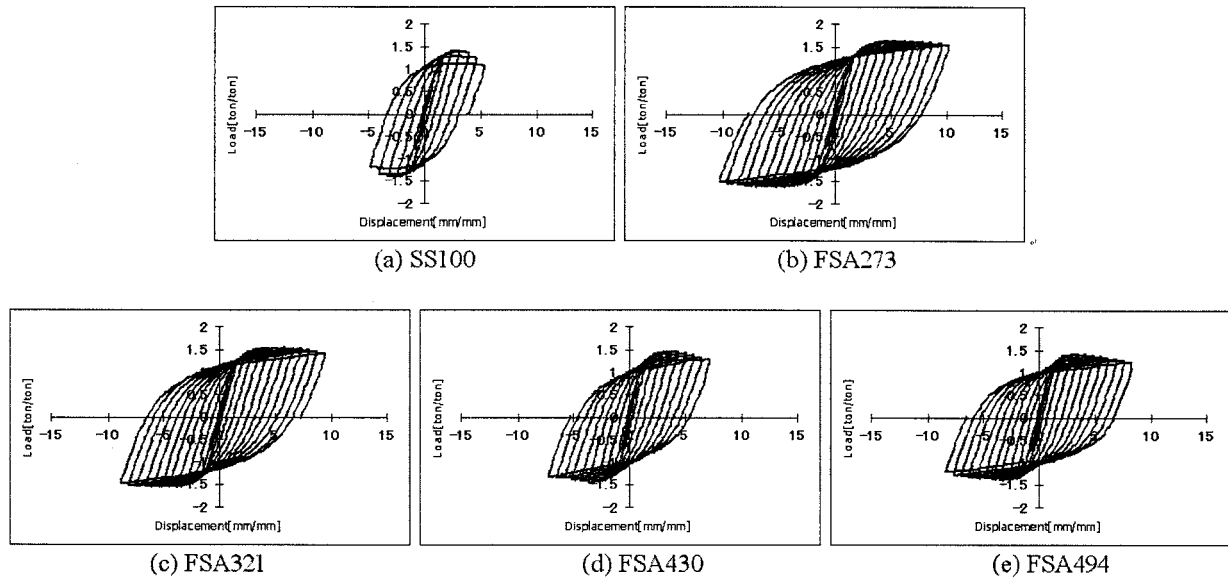


Figure 9. Load-displacement relationship (divided by yielding load and displacement).

4.2 The Lateral Load-Displacement Relation

The envelope curves of the lateral load-displacement relationship of specimens SS100 and FSA series are shown in Figure 9. Dividing the abscissa and ordinate by the yield deformation and strength has normalized these curves. In a comparison between load-displacement relationships, there is a specific difference that shows the range of plastic deformation. The increase in strength after the yield strength and deformation capacity of the FSA series specimen, disregarding high yielding-high strength steel (SSA440) used for the interior column, were greater than SS100 specimen which consisted solely of low yielding ratio-mild steel (SS400) columns. And as the yield displacement ratio between the interior column (flexible element) and exterior column (stiff element) becomes larger, the plastic deformation capacity of frames becomes larger.

4.3 The Strain-Rotation Angle Relation

The relations of the strain-accumulative rotation angle are shown in Figure 10 and Figure 11. Figure 10 represents the test result of an SS100 specimen where the whole column section and material (SS400) are the same. On the other hand, Figure 11 shows the results of the FSM series, which are mixed SS400 and SM570. The abscissa axis represents accumulative rotation angle under the cyclic load, and the ordinate axis represents the strain of each specimen. In Figure 11, the horizontal thick line represents the yield strain of the SM570 material.

In the case of the specimen composed of the same steel, the strain of the exterior and interior

column increases because of local buckling. Hence, in case of a flexible-stiff mixed system, the strain of exterior columns increases as much as that of the exterior columns of the SS100 specimen, however, the strain of the interior column in a flexible-stiff mixed system is not affected less than exterior columns. And, if the yielding deformation ratio between interior column and exterior column is greater than 3.0, the strain of interior column remains in elastic range although exterior columns reach at ultimate condition. Therefore, in case of flexible-stiff mixed column, stiff element which it has so much elastic stiffness and plastic deformation ability absorbs energy much enough.

Thus, it is obvious that the most of energy by external forces (horizontal forces) were absorbed by the columns that have a larger stiffness.

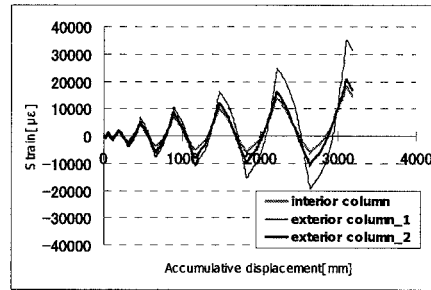
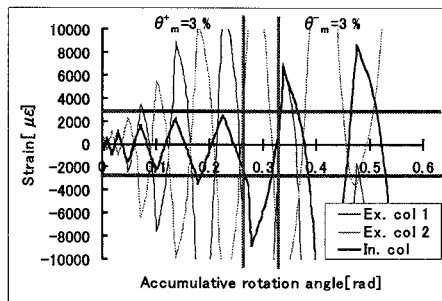
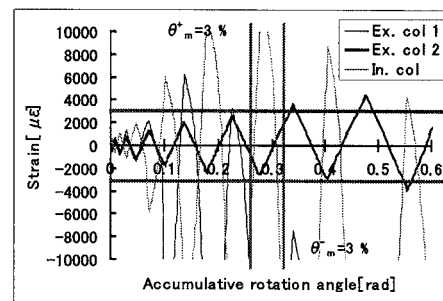


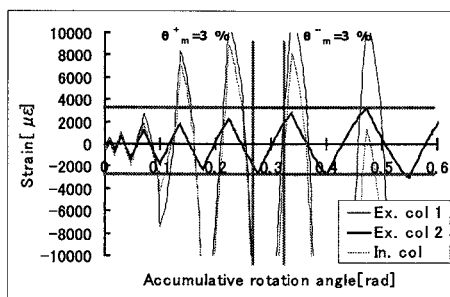
Figure10. Strain-cumulative rotation angle relationship of SS100



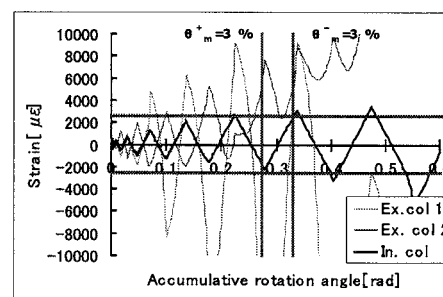
(a) FSM225



(b) FSM290



(c) FSM327



(d) FSM417

Figure 11. The comparison of strain distribution between interior column and exterior columns.

4.4 Energy Absorption Capacity

As shown in Figure 12, the load-deformation relation of the steel member subjected to cyclic load was decomposed into three parts: the skeleton part, the elastically unloaded part and the softened part due to Baushinger effect.

The comparison of capacity of energy absorption of each specimen is shown in Figure 13. The total absorbed energy of each specimen represents the sum of the three parts indicated in Figure 12. In the case of specimen composed of the same steel, the energy absorption capacity of SS100, which has

low yield ratio, is 5.54 times as much as that of SM100 used as the high yielding ratio steel in Baushinger part. In case of SA100, it absorbed more energy in the skeleton part because the load increased steadily. In case of the flexible-stiff mixed column, the energy absorption capacity is almost same as the SS100 in the skeleton part, but it represents more than that of SS100 in the Baushinger part. Finally, the energy absorption capacity of the FSM290 specimen was 4 times as much as the SS100 specimen, and that of the FSA273 specimen showed 4.57 times as much as the SS100 specimen.

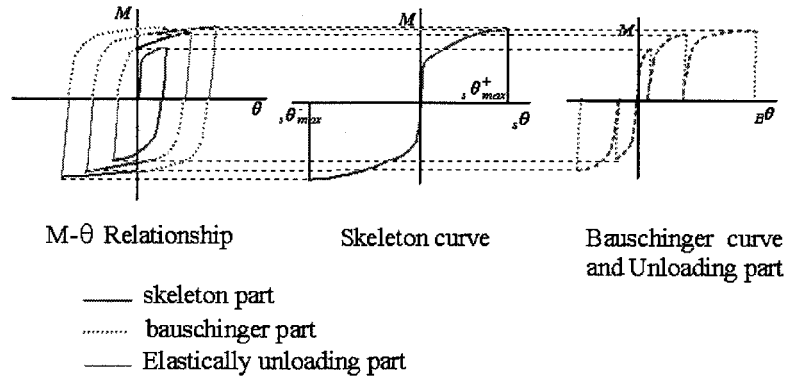


Figure 12. Example of decomposition of a cyclic curve.

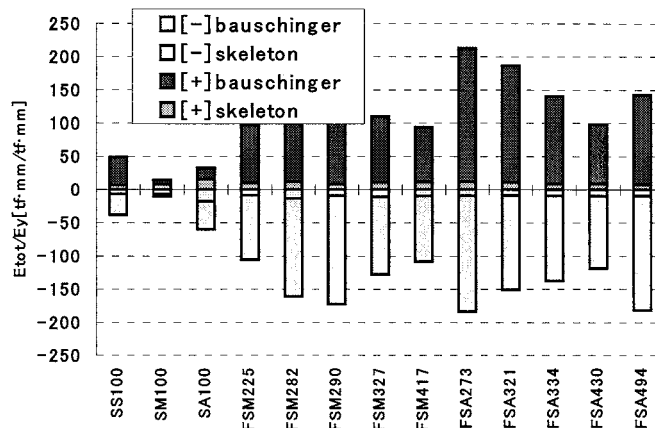


Figure 13. The ultimate energy absorption capacity of each specimen.

5. CONCLUSION

In this study, to clarify whether high strength steel with high yield ratio can be used as structural members, the earthquake response analysis and experimental tests of a flexible-stiff mixed structure consisting of flexible and stiff members were carried out. As a result, the following conclusions can be made:

- 1 When the yield deformation ratio between flexible element and stiff element is greater than 3.0, the flexible element using high strength steel with high yield ratio can be remain in the elastic region although the stiff elements reach the ultimate condition.
- 2 The ultimate energy absorption of a flexible-stiff mixed structure, where the high yield ratio-high strength steel is used as flexible element, is greater than that of structure consisting of mild steel only. It is greatest at the 3.0~4.0 of yield deformation ratio of flexible to stiff element.
- 3 Design with high yielding ratio-high strength steel is possible by application of a reasonable arrangement of columns with high strength and ordinary mild steel. This enables the high yielding

ratio-high strength columns to remain in elastic region. This design method is applicable to various buildings according to their characteristics.

REFERENCES

- Akiyama, H. 1985. *Earthquake-Resistant Limit-State Design for Buildings*. University of Tokyo Press.
- Akiyama, H. & Takahashi, M. 1990. *Influence of Baushinger Effect on Seismic Resistance of Steel Structures*. Trans. of A.I.J., No.418.
- Harada, Y. & Akiyama, H. 1995. *Seismic design of Flexible-stiff Mixed Frame with Energy Concentration*. J. Struct. Const. Eng., A.I.J. No.472.
- Kato, B. & Akiyama, H. 1973. *Theoretical Prediction of the Load-Deflection Relationship of Steel Members and Frames*. IABSE Symposium, Preliminary Publication, Lisbon.

MULTIOBJECTIVE HEURISTIC APPROACHES TO PERFORMANCE-BASED SEISMIC DESIGN

M. Ohsaki¹⁾, T. Kinoshita²⁾, and P. Pan³⁾

1) Associate Professor, Dept. of Architecture and Architectural Eng., Kyoto University, Japan

2) Graduate Student, Dept. of Architecture and Architectural Eng., Kyoto University, Japan

3) Lecturer, Dept. of Civil Engineering, Tsinghua University, P. R. China

ohsaki@archi.kyoto-u.ac.jp, is.kinoshita@archi.kyoto-u.ac.jp, panpeng@tsinghua.edu.cn

Abstract: Seismic design problem of a steel moment-resisting frame is formulated as a multiobjective programming problem. The total structural (material) volume and the plastic dissipated energy at the collapse state against severe seismic motions are considered as performance measures. Simulated Annealing (SA) and Tabu Search (TS), which are categorized as single-point-search heuristics, are applied to the multiobjective optimization problem. It is shown in the numerical examples that the frames that collapse with uniform interstory drift ratios against various levels of ground motions can be obtained as a set of Pareto optimal solutions.

1. INTRODUCTION

In the framework of performance-based design of steel moment-resisting frames, several performance states such as immediate occupancy and collapse prevention should be investigated against seismic motions with specified levels. In this paper, we consider the collapse state defined so that the roof displacement reaches the specified value (Whittaker et al. 1998; Hasan et al. 2002).

One of the most important seismic design criteria is that the load level should be large enough at the predefined collapse state, and the collapse mechanism should not consist of unfavorable local deformation. In the inelastic design of frames, the collapse mechanism with widely distributed plastic hinges at beam ends are preferred. Such a design can be obtained by maximizing the dissipated energy for specified displacement at collapse state. On the other hand, the amount of the energy to be dissipated under specified deformation is strongly related to the total structural (material) volume. Hence, the structural volume controls the level of seismic motion that leads to the collapse state. Therefore, a design with favorable collapse mechanism with uniform interstory drift ratios can be obtained by simultaneously minimizing the total volume and maximizing the dissipated energy, which is formulated as a MultiObjective Programming (MOP) problem (Marler and Arora 2004).

If the cross-sections of the beams and columns of the steel frames are to be chosen from a list or a catalog of the available standard sections (Huang and Arora 1997), the design problem turns out to be a combinatorial optimization problem for which the global optimal solution is very difficult to obtain. Heuristic approaches (or heuristics for simplicity) have been developed to obtain approximate optimal solutions within reasonable computational cost, although there is no theoretical proof of convergence (Reeves 1995).

In this paper, Pareto optimal solutions are generated for a plane frame by improved multiobjective SA (Aarts and Korst 1989) and TS (Glover 1989). The responses at the collapse state under seismic

motions are computed by time-history analysis considering geometrical nonlinearity, where the peak ground velocities of the recorded motions are incrementally scaled to the level leading to the collapse state. The computational performances of the methods and the characteristics of the solutions are discussed by using a 5-story 4-span plane frame.

2. EVALUATION OF SEISMIC PERFORMANCE

It is important in the seismic design of moment-resisting frames that the local story mechanism should be avoided to ensure the required energy dissipation capacity before reaching the collapse state. Therefore, if the collapse state is defined by deformation level such as the roof displacement, the plastic dissipated energy E_p is to be maximized.

The typical three recorded motions; (i) El Centro NS (1940), (ii) Hachinohe NS (1968), and (iii) Taft EW (1952) are used after scaling by the Peak Ground Velocity (PGV). Let z denote a representative response quantity such as a story displacement, the plastic dissipated energy, and so on. The maximum response z^{\max} is defined as the maximum absolute value among the responses z^i , z^{ii} and z^{iii} for the three motions (i), (ii) and (iii).

The maximum responses are computed by time-history analysis considering both geometrical and material nonlinearities modeled by a generalized plastic hinge considering the interaction between the bending moment and axial force in yield condition. Since the geometrically nonlinear inelastic responses are not proportional to the magnitude of the input seismic motion, z^{\max} is evaluated by an incremental dynamic analysis (Hamburger et al. 2000).

Denote by H and d^{\max} the total height of the frame and the maximum response displacement at the roof level, respectively. The collapse state is defined by

$$d^{\max} = \beta H \quad (1)$$

where β is the specified average interstory drift ratio. The PGV of the ground motion is increased until the collapse condition (1) is satisfied.

The PGV v_k^{\max} of the k th-level ground motion is defined by

$$v_k^{\max} = v_1^{\max} + \Delta v^{\max}(k - 1) \quad (2)$$

where v_1^{\max} is the specified PGV for the smallest motion, and Δv^{\max} is the increment of the PGV. A value corresponding to the k th-level motion is indicated by subscript $()_k$. The responses at collapse state are evaluated by the following incremental dynamic analysis with interpolation:

Step 1: Set v_1^{\max} and Δv^{\max} , and initialize the ground motion level as $k = 1$.

Step 2: Calculate PGV by (2), and carry out time-history analysis to compute the maximum roof displacement d_k^{\max} and the maximum values $z_k^{(i)\max}$ of the preselected responses $z_k^{(i)}$ ($i = 1, \dots, q$), where q is the number of response quantities.

Step 3: If $d_k^{\max} < \beta H$, let $k \leftarrow k + 1$ and go to Step 2. Otherwise, let $s = k$, and linearly interpolated z^{\max} at collapse between the values for $s - 1$ and s as

$$\alpha = \frac{\beta H - d_{s-1}^{\max}}{d_s^{\max} - d_{s-1}^{\max}} \quad (3)$$

$$z^{(i)\max} = (1 - \alpha)z_{s-1}^{(i)\max} + \alpha z_s^{(i)\max}, (i = 1, \dots, q) \quad (4)$$

3. SEISMIC DESIGN PROBLEM

Suppose a list of the available standard sections is given for each member of a moment-resisting steel frame. The cross-sectional property of the member i is defined by the cross-sectional area A^i , the second moment of inertia I^i and the plastic section modulus Z_p^i , which are to be selected from the list M^i as $M^i = \{(A_1^i, I_1^i, Z_{p1}^i), \dots, (A_{r_i}^i, I_{r_i}^i, Z_{pr_i}^i)\}$, where r_i is the number of elements in the list.

The integer variable J_i defines the cross-section of the i th member. Let m denote the number of members. If $J_i = j$ ($i = 1, \dots, m$), the j th section (A_j^i, I_j^i, Z_{pj}^i) in M^i is assigned to the i th member. Hence, the mechanical property of the frame is defined by the vector $\mathbf{J} = \{J_i\}$, which is taken as the integer design variable vector.

The total structural volume to be minimized is denoted by $V(\mathbf{J})$. E_p^{\max} is also chosen as the objective function to be maximized. Hence, the multiobjective structural optimization problem is formulated as (Marler and Arora 2004)

$$\text{MOP : minimize } V(\mathbf{J}) \text{ and } -E_p^{\max}(\mathbf{J}) \quad (5)$$

$$\text{subject to } R^{\max}(\mathbf{J}) \leq \bar{R}^{\max}, \quad (6)$$

$$J_i \in \{1, \dots, r_i\}, \quad (i = 1, 2, \dots, m) \quad (7)$$

where R^{\max} denotes the maximum interstory drift ratio among all stories corresponding to all the seismic motions for the initial PGV level v_1^{\max} . If R^{\max} exceeds the moderately large upper bound \bar{R}^{\max} , then the solution is simply rejected and the incremental process is not carried out, because the frame will collapse prematurely exhibiting unfavorable story mechanism. This way, the computational cost for performance evaluation at each step of optimization is reduced.

Let $F_1(\mathbf{J}) = V(\mathbf{J})$ and $F_2(\mathbf{J}) = -E_p^{\max}(\mathbf{J})$. For two feasible solutions \mathbf{J}^1 and \mathbf{J}^2 satisfying the constraints, if $F_i(\mathbf{J}^1) \leq F_i(\mathbf{J}^2)$ for $i = 1, 2$ and $F_j(\mathbf{J}^1) < F_j(\mathbf{J}^2)$ for $j = 1$ or 2 , then \mathbf{J}^2 is said to be dominated by \mathbf{J}^1 . If there is no solution that dominates \mathbf{J}^* , then \mathbf{J}^* is called *nondominated solution*, *noninferior solution*, *compromise solution* or *Pareto optimal solution*, which is called Pareto solutions, for simplicity, in the remainder of this paper.

4. HEURISTIC APPROACHES

Several heuristics have been developed for simultaneously generating a diverse set of Pareto solutions. Among them, we use SA and TS, which are categorized as single-point-search heuristics. SA has been shown to be very effective to the problems with many local optimal solutions, because it allows a move to a non-improving solution. Recently, SA has been extended to MOP (Whidborne et al. 1997), and we follow the basic framework in (Jilla and Miller 2001). The following options are introduced to improve the convergence property to the Pareto solutions with enough diversity:

- In the process of generating neighborhood solutions, all the variables are modified, and the magnitude of modification is governed by the normal distribution of probability.
- The neighborhood solution in the direction that has been rejected at the previous step is automatically rejected to reduce the computational cost for function evaluation.
- Local search is conducted several times at the same temperature level.
- A sharing function approach developed for genetic algorithms (Goldberg and Richardson 1987) is used to maintain diversity of the Pareto solutions.

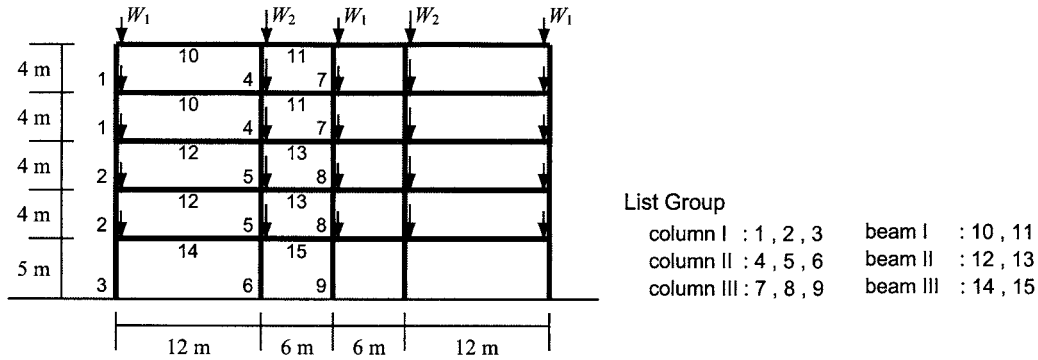


Figure 1 A 5 story 4 span planar frame model.

TS, which is originally developed for single objective problem (Glover 1989), has also been proven to be effective to MOP (Hansen 1997). In TS, the best solution in the neighborhood is selected as the next candidate, and a tabu list is used to prevent a local cyclic search among small number of solutions. We modify the approach in (Baykasoglu et al. 1999) as

- The best solution in the candidate list is selected as the seed solution for the next step; whereas it was randomly selected in the original algorithm.
- A sharing function and niche count are used for modification of the performance function of a solution.

5. NUMERICAL RESULTS

5.1 Analysis Model

Pareto solutions are found for a 5-story 4-span plane frame as shown in Fig. 1. Only the mass of the slab is included in the story mass that does not depend on the sizes of the columns and beams. The vertical load due to the story mass is applied at each beam-to-column connection before conducting time-history analysis, where $W_1 = 245$ kN and $W_2 = 343$ kN. The following two kinds of groups are utilized for definition of the design variables:

Member Group: Symmetrically located members have the same section.

List Group: The sections of the vertically aligned columns and the beams in the same floor, respectively, are selected from the same lists.

The numbers 1, 2, 3, ... in Fig. 1 denote the Member Groups. The List Groups are shown below the frame in Fig. 1; e.g., the members in Member Groups 1, 2 and 3 are selected from the same list. See Ohsaki et al. (2006) for details.

The average drift ratio β for the definition (1) of the collapse state is 0.02. Note that any larger value can be used for β , if necessary. The initial value of PGV in (2) is $v_1^{\max} = 0.5$ m/s, which is equal to the level of the severe earthquake motion for inelastic design that is traditionally used in Japan. The increment is given as $\Delta v^{\max} = 0.05$ m/s. The upper bound \bar{R}^{\max} for the interstory drift ratio for $v_1^{\max} = 0.5$ m/s is 1/75, which is slightly larger than the upper bound 1/100 adopted in Japan to allow more variety of designs in the framework of performance-based design. Time-history analysis is carried out by CLAP (Ogawa and Tada 1994), where the P - Δ effect is considered, and the material nonlinearity is modeled by the generalized plastic hinge. Young's modulus is $E = 205.8$ kN/mm²,

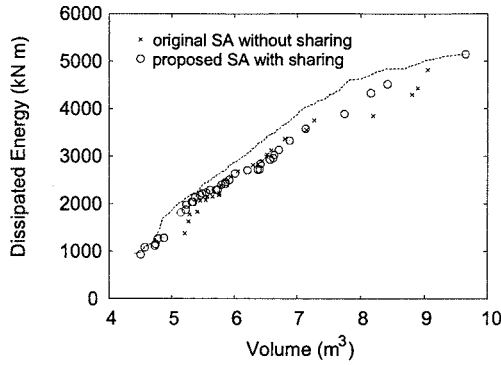


Figure 2 Comparison of solutions obtained by original and proposed SAs with 3000 analyses. Dotted line: Pareto front by 30000 analyses.

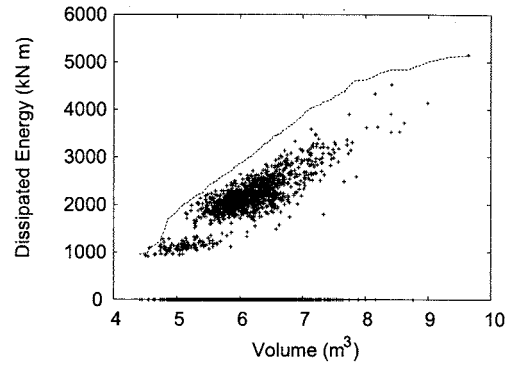


Figure 3 All solutions generated by proposed SA with 3000 analysis. Dotted line: Pareto front by 30000 analyses.

Table 1 Comparison of the results by the proposed SA and TS to the original methods without sharing functions.

	Volume [m ³]		Dissipated Energy [kJ]		No. of solutions	No. of superior solutions
	Min.	Max.	Min.	Max.		
SA (original)	5.21	9.05	1382.07	4819.92	26	12
SA (proposed)	4.50	9.65	937.45	5153.14	37	31
TS (original)	7.37	9.36	3710.52	5153.14	101	21
TS (proposed)	6.94	9.27	3484.76	5103.31	103	74
Pareto Front	4.40	9.65	961.75	5153.14	-	-

Poisson's ratio is 0.3, and the yield stress is 265 kN/mm². The bilinear stress-strain relation with kinematic hardening is used, where the stiffness after yielding is 0.01 E . The stiffness-proportional damping is used, where the damping ratio for the fundamental mode is 0.02.

5.2 Pareto Optimal Solutions in the Objective Space.

The Pareto solutions found by the proposed SA with sharing function is shown by \circ in Fig. 2 in the space of the objective functions. Three sets of optimization process with 1000 analyses from different initial solutions are combined to find Pareto solution with 3000 analyses, because no significant improvement of solutions has been observed after 1000 analyses for each set. The Pareto front obtained by 30000 preliminary analyses, which is regarded as an accurate set of the Pareto solutions, is plotted by the dotted line. The \times marks in Fig. 2 are the Pareto solutions found by three sets of 1000 analyses by the original SA without sharing function. Note that only the effect of the use of sharing function is investigated, because it is the most effective option for both of SA and TS. The range of the solutions and the number of Pareto solutions obtained by the original and proposed SAs are shown in Table 1. The number of Pareto solutions obtained by proposed SA that dominate those by the original SA, or vice versa, which are called superior solutions for simplicity, are also listed in Table 1. The range of the Pareto front is also shown in the last row of Table 1. It is seen from these results that more solutions distributed in wider range can be found by incorporating sharing function. The increase of the number of superior solutions also indicates improvement of accuracy of the solutions.

Fig. 3 shows all the solutions generated in the process of SA with 3000 analyses. Note that the solutions with $E_p^{\max} = 0$ located along the abscissa do not satisfy the constraint (6) on the maximum interstory drift ratio at the first analysis with $k = 1$, where the PGV is equal to 0.5 m/s. These solutions are unconditionally rejected without further carrying out incremental dynamic analysis. Thus the total computational cost can be reduced by utilizing the constraint (6) on the interstory drift ratio. The ratio of the number of these rejected solutions to the number of total solutions is 44.2%; i.e., almost half

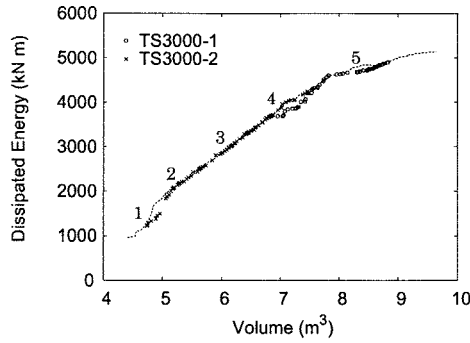


Figure 4 Two sets of Pareto solutions obtained by proposed TS with 3000 analyses. Dotted line: Pareto front by 30000 analyses.

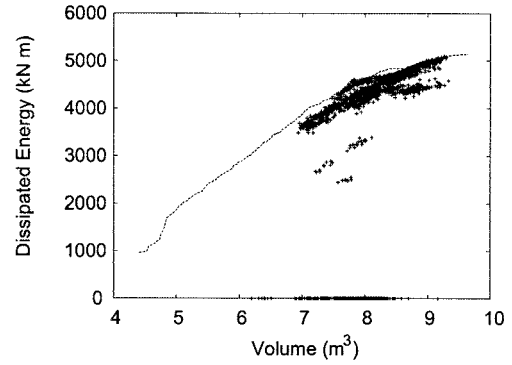


Figure 5 All solutions generated by TS3000-1. Dotted line: Pareto front by 30000 analyses.

of the solutions are infeasible. As can be seen from Fig. 3, SA searches a wide range in the objective space, but cannot reach the Pareto front. This is a general property of SA that has been observed in the results with different initial solutions.

The two sets of Pareto solutions found by the proposed TS with 3000 analyses are shown in Fig. 4, where the Pareto front obtained by 30000 preliminary analyses is also plotted. TS3000-1 and TS3000-2 are the results from different initial solutions. Fig. 5 shows all the solutions generated by TS3000-1. As can be seen, TS searches the solutions near the Pareto front.

It is seen from Figs. 2 and 4 that the TS has more accuracy than SA, and has good diversity if the results of the two sets of 3000 analyses are combined. However, the search space of TS depends on the initial solution as observed in Fig. 4, where the region with larger V and E_p^{\max} are searched by TS3000-1 and the remaining region is searched by TS3000-2. The ratios of the numbers of the rejected solutions along the abscissa of Fig. 5 to the number of total solutions is 16.7% which is much smaller than that of SA. Therefore, TS has the advantage in searching the space of the feasible solutions.

The results by the proposed TS is compared in Fig. 6 with those of the original TS without sharing function. Although no drastic increase is observed in the range and number of solutions, the number of the superior solutions by the proposed TS is more than three times of that by the original TS. Therefore, the accuracy of the Pareto solutions is improved by incorporating the sharing function.

5.3 Properties of the Pareto Optimal Solutions.

The properties of the Pareto solutions are discussed based on the results of TS3000-2. Fig. 7 shows the relation between the objective functions V and E_p^{\max} of the Pareto solutions. Each mark distinguishes the PGV at the collapse state, which increases as V is increased. Even for the frames that collapse under the seismic motions of the same PGV, E_p^{\max} is an increasing function of V so as to form the smooth Pareto front. A design with widely distributed plastic hinges can be obtained by selecting a solution from the set of Pareto solutions. Thus, the most preferred solutions for various levels of PGV at collapse can be obtained.

The characteristics of the Pareto solutions are investigated for the solutions that collapse under seismic motions with $v_k^{\max} = 1.2$ m/s. The typical designs named Solutions 1–5 are selected as indicated in Fig. 4. The cross-sectional areas of Solution 3 are as shown in Fig. 8, where the width of each member is proportional to its cross-sectional area. It can be observed from Fig. 8 that Solution 3 has large sections for internal beams and columns. The total volume, dissipated energy and the story drift ratios of Solutions 1–5 are listed in Table 2. It is seen that the The members in the lower 3 stories have

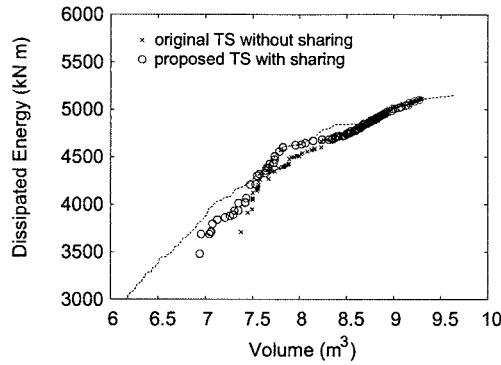


Figure 6 Two sets of Pareto solutions obtained by proposed TS with 3000 analyses. Dotted line: Pareto front by 30000 analyses.

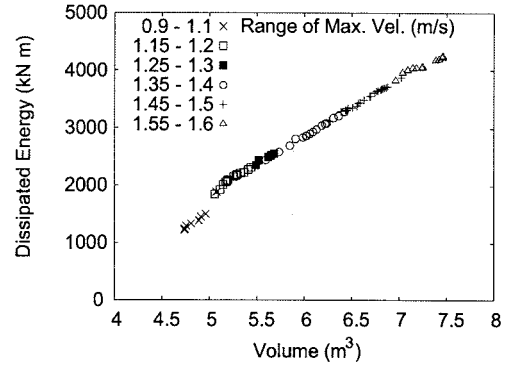


Figure 7 Comparison of the solutions by original and proposed TSs with 3000 analyses; close view in the larger region of the objective functions of TS3000-1.

Table 2 Total volume, dissipated energy and interstory drifts of Solutions 1–5.

Solution	Volume (m³)	Dissipated Energy (kN · m)	Story Drift Ratio ($\times 10^{-2}$)				
			1	2	3	4	5
1	4.715	1269.9	3.6160	2.8926	2.7763	2.4588	1.2720
2	5.328	2212.7	3.2760	2.6208	2.6657	2.0847	1.5753
3	6.127	2993.1	3.4085	2.7268	2.8153	2.4748	1.8625
4	7.013	3889.6	3.6018	2.8814	2.4655	2.4818	1.8150
5	8.330	4770.3	3.9145	3.1316	2.5125	2.0860	1.3488

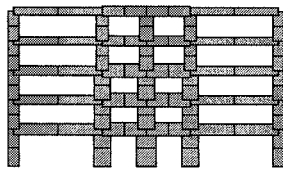


Figure 8 Cross-sectional areas of Solution 3.

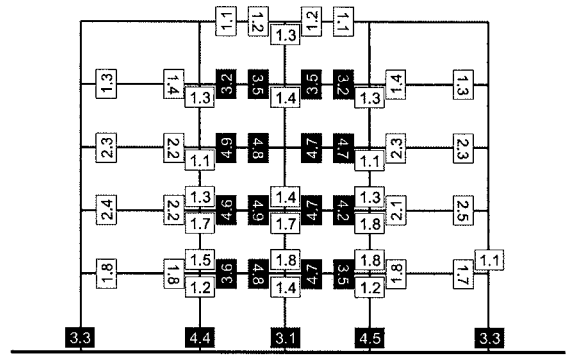


Figure 9 Ductility ratios of Solution 3.

almost the same maximum drift ratios; i.e. the frames collapse uniformly. Fig. 9 shows the maximum ductility ratios of the plastic hinges at the ends of each member of Solution 3. The member ends without the values in Fig. 9 remain elastic at the collapse state. The ductility ratios greater than 3.0 are written in a white number in a black box. Note that large plastic deformation exists in the column base and the internal beams, and no large deformation can be found in the columns except at the base. This way, the Pareto solutions with favorable uniform story collapse can be generated by solving the multiobjective optimization problem, and many alternative designs can be simultaneously obtained.

6. CONCLUSIONS

An MOP problem has been formulated to simultaneously minimize the total structural volume and maximize the plastic dissipated energy at the collapse state. Incremental dynamic analysis is carried out to determine the PGV of the seismic motion that leads to the collapse state. The design variables are cross-sectional properties that are selected from the list of the standard sections. SA and TS have been used to obtain the set of Pareto solutions. The conclusions obtained from this study are

summarized as follows:

- A frame that collapses with a uniform interstory drift ratio can be obtained as a Pareto solution that simultaneously minimize the structural volume and maximize the dissipated energy at collapse state. Many alternative designs or compromise solutions can be obtained as a set of Pareto solutions.
- The optimal cross-sections, which are to be selected from the list of available standard sections, can be found by solving a combinatorial optimization problem.
- SA and TS can be successfully used for a multiobjective structural optimization problem that demands large computational cost for the function evaluation. However, TS is an advantage over SA in view of the diversity of the Pareto solutions and the ability of searching the solutions near the Pareto front.

Acknowledgement:

The authors are grateful to Prof. M. Tada of Osaka University of Japan for kindly offering "CLAP" source code.

References:

- Aarts, E. and J. Korst (1989). *Simulated Annealing and Boltzmann Machines: A Stochastic Approach to Combinatorial Optimization and Neural Computing*. Chichester, England: Wiley.
- Baykasoglu, A., S. Owen, and N. Gindy (1999). A taboo search based approach to find the pareto optimal set in multiple objective optimization. *Eng. Opt.* 31, 731–748.
- Glover, F. (1989). Tabu search – part I. *ORSA J. on Computing* 1, 190–206.
- Goldberg, D. E. and J. Richardson (1987). Genetic algorithms with sharing for multimodal function optimization. In *Proc. 2nd Int. Conf. Genetic Algorithms*.
- Hamburger, R. O., D. A. Foutch, and C. A. Cornell (2000). Performance basis of guidelines for evaluation, upgrade and design of moment-resisting steel frames. In *Proc. 12th World Congress of Earthquake Eng.*, pp. Paper No. 2543.
- Hansen, M. P. (1997). Tabu search for multiobjective optimization: Mots. In *Proc. 13th Int. Conf. on MCDM*, Cape Town, pp. 6–10.
- Hasan, R., L. Xu, and D. Grierson (2002). Push-over analysis for performance-based seismic design. *Comp. & Struct.* 80, 2483–2493.
- Huang, M.-W. and J. S. Arora (1997). Optimal design of steel structures using standard sections. *Struct. Multidisc. Optim.* 14, 24–35.
- Jilla, C. D. and D. W. Miller (2001). Assessing the performance of a heuristic simulated annealing algorithm for the design of distributed satellite systems. *Acta Astronautica* 48(5), 529–543.
- Marler, T. and J. S. Arora (2004). Survey of multi-objective optimization methods for engineering. *Struct. Multidisc. Optim.* 26(6), 369–395.
- Ogawa, K. and M. Tada (1994). Computer program for static and dynamic analysis of steel frames considering the deformation of joint panel. In *Proc. 17th Symp. on Comp. Tech. of Information, Sys. and Appl.*, pp. 79–84. (in Japanese).
- Ohsaki, M., T. Kinoshita, and P. Pan (2006). Heuristic approaches to performance-based design of steel frames with standard sections. In *Proc. Behavior of Steel Structures in Seismic Areas, STESSA 2006*, Yokohama, pp. 67–72. Taylor & Francis.
- Reeves, C. (1995). *Modern Heuristic Techniques for Combinatorial Problems*. New York: McGraw-Hill.
- Whidborne, J. F., D. W. Gu, and I. Postlethwaite (1997). Simulated annealing for multiobjective control system design. *IEE Proc. Control Theory Appl.* 144(6), 582–588.
- Whittaker, A., M. Constantinou, and P. Tsopelas (1998). Displacement estimates for performance-based seismic design. *J. Struct. Eng., ASCE* 124(8), 905–912.

Collapse Test of Steel Structural Model under High Gravity Force Field

A. Wada¹⁾, S. Yamada²⁾, M. Takazawa³⁾, M. Seki⁴⁾,
H. Katsumata⁴⁾, S. Higuchi⁴⁾, H. Okuda⁴⁾, and R. Okada⁵⁾

1) Professor, Structural Engineering Research Center, Tokyo Institute of Technology, Japan

2) Associate Professor, Structural Engineering Research Center, Tokyo Institute of Technology, Japan

3) Engineer, Taisei Corporation, Japan

4) Research Engineer, Technical Research Institute, Obayashi Corporation, Japan

5) COE researcher, CUEE, Tokyo Institute of Technology, Japan

wada@serc.titech.ac.jp, naniwa@serc.titech.ac.jp, tkzmsy00@pub.taisei.co.jp,

seki.matsutaro@jica.ro, katsumata.hideo@obayashi.co.jp, higuchi.shunichi@obayashi.co.jp,

okuda.hirofumi@obayashi.co.jp, rokada@serc.titech.ac.jp

Abstract: In this paper, the results of vibration tests concerning the scale model of steel structure under high gravity force field are shown. Due to many difficulties of shaking tests for full scale structure, there have been few experiments about the collapse behavior of structure subject to earthquake excitation. On the other hand, in the scale model test, it is difficult to reproduce the stress field on the scale model. In our tests, the appropriate stress field on the scale model is generated by the high gravity field using the centrifugal force. This experimental system is used, for the first time, to analyze the seismic behaviors of superstructures, although it has been used to verify the phenomena about soils and underground structures. The structural model is set on the shaking table located in the large centrifuge. The behaviors of three-story structural model are simulated successfully in the experiment. The outlines of the large centrifuge and the specimen are presented. And the experimental results are shown.

1. INTRODUCTION

It is important to clarify the collapse mechanism of structures in safety under the strong seismic motion. The most accurate experimental method to verify the collapse of structure would be the shaking table tests using full-scale structural models. However, due to several problems (i.e. performance limitation of shaking table, costs and safety of experiments), it is not easy to shake the structure to the level of complete collapse.

Meanwhile, there are many shaking table tests using the scale model. In these cases, the stress field on the model is underestimated by scale effects. In fact, in case of $1/N$ scale model (N : scale ratio), scale of area and weight become $1/N^2$ and $1/N^3$, respectively. So the scale of stress becomes $1/N$. The masses add to the test specimen in many dynamic tests for the structure, to adjust the stress distribution such as the compressive stress of the column.

In this study, as another approach for verifying the collapse mechanism, the shaking table tests in the high gravity force field are carried out. The gravity force field is actualized by the large centrifuge. In the civil engineering field, although this experimental system has been used for verifying the phenomena about ground (i.e. the liquefaction of ground and the lateral flow of ground) and underground structures (i.e. the pile group), it has not been used for verifying the seismic behaviors of superstructures. The aim of this study is to establish the experimental method for miniature size structural models using the large centrifuge. This paper describes the

specifications of the large centrifuge and the results of the pilot experiment of three-story steel structural model. The assumed collapse mode of this model is the story collapse at the 1st floor column. The influences of the P- Δ effects are confirmed quantitatively.

2. SPECIFICATIONS OF CENTRIFUGE

The centrifuge with shaking table owned by Technical Research Institute of Obayashi Corporation is used in this experiment. The picture of the centrifuge is shown in Figure 1. The specifications of the centrifuge and the shaking table on the centrifuge are shown in Tables 1 and 2, respectively.

Up to now, many experiments using this system have been performed only for soils and underground structures. So this study is the first experiment to use the shaking table for the superstructures.

Since the similarity law for the 1/N scale model (Table 3) holds true in a centrifuge, it can be said that experiments using a centrifuge are one of the most accurate methods to simulate the realistic behavior of actual structures under 1G ($=9.8 \text{ m/s}^2$) gravitational field. Particularly, the most valuable advantage of the centrifuge is that the same stress and strain field in actual structure under 1G field can be reproduced using 1/N scale miniature model subject to NG gravitational field.

Table 1 Specifications of centrifuge

Outer diameter of arm	16.67m
Height of arm	3.00m
Driving system	Direct current motor with Reduction gear
Radius to the platform	7.01m
Maximum payload	700g·t
Payload weight	7t
Platform space	2.2m × 2.2m
Test model height	2.5m
Number of platforms	2

Table 2 Specifications of shaking table

Payload mass	3t
Table area	2.2m(Length) × 1.07m(Wide)
Max. acceleration	500m/s ²
Max. velocity	90cm/s
Max. displacement	5mm
Max. drive force	1.176MN

Table 3 Similarity law for scale model

Quantity	Theoretical ratio (Model/Prototype)
Length	1/N
Density	1
Mass	1/N ³
Strain	1
Acceleration	N
Velocity	1
Displacement	1/N
Stress	1
Pressure	1
Young's modulus	1
Time	1/N
Frequency	N
Axial stiffness	1/N ³
Flexural rigidity	1/N ⁴

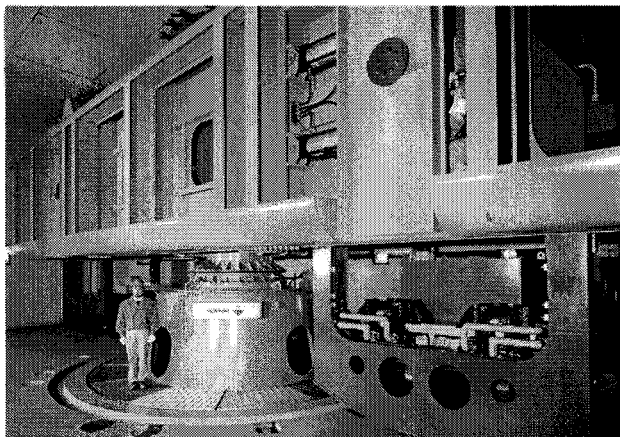


Figure 1 View of centrifuge

3. SUMMARY OF TEST SPECIMEN

3.1 Configurations of Moment-Resisting Frame model

Figure 2 shows the elevations and the plan of the test specimen and Figure 3 shows its picture. The specimen is 1/20-scale model. It is the steel moment resistant frame (three-story, one-span, weak-column, and strong-beam). The model is designed so that yielding would occur at the top and the bottom of the 1st story column. The plane frame of the specimen is 400mm (shaking

direction) x 225mm and floor height is 208mm. The cross section of all columns is 15.9(diameter) x 1.0(thickness) mm and the cross section of all beams is 16 x 16 mm. The base shear force ratio is 0.49 under a centrifugal acceleration of 20G and the axial force ratio is 0.12. Based on the free vibration test, it is found that the 1st natural period of the specimen is 0.041sec.

3.2 Measurement Plan

The absolute accelerations in horizontal and vertical directions are measured by acceleration meters installed on the beams in each floor. The floor displacements relative to the shaking table are measured by laser displacement meters. The axial force and shear forces at each story are measured by strain gauges. The sampling frequency of all measurements is equal to 1 kHz. The locations of the sensors for the accelerations, displacements, and forces are shown in Figure 2.

Moreover, the high-speed camera and the CCD camera are used to capture the collapse behavior of the structural model graphically.

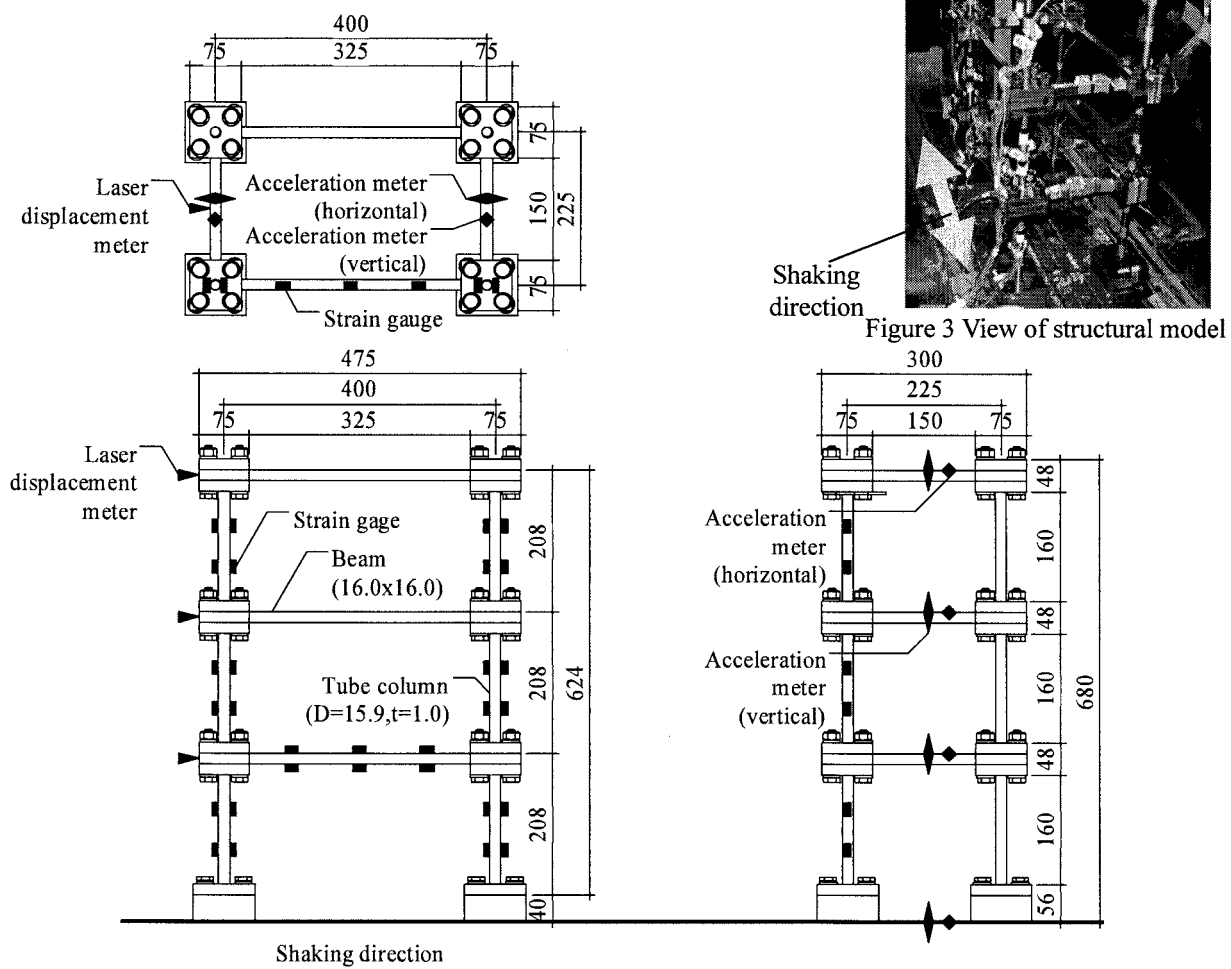


Figure 2 Elevations and plan of structural model [Dimensions in mm]

3.3 Input Wave Patterns and Process of Experiments

The wave patterns of the dynamic loadings are shown in Table 4. Kobe-NS wave is chosen as the input wave. The vertical acceleration by centrifugal acceleration is 20G.

While, the specimen behaved elastically, the input level is increased at approximately 0.5G (maximum acceleration) intervals. After that, the input acceleration level is increased at each step by 1G. Since the complete collapse did not occur by Kobe-NS wave, the centrifugal acceleration is increased to 30G. Then the input pattern of acceleration changes to sinusoidal wave. Its frequency is 20Hz (close to the 1st natural frequency of the structural model). Finally, when the sinusoidal wave (maximum input acceleration = 9.8G) is input, the structure collapsed.

Table 4 Input wave patterns

Run	1	2	3	4	5	6	7	8	9	10	11	12	13	14	15	
Input wave	Kobe NS															
Max. acc.[G]	0.5	0.7	1.0	1.4	1.9	1.7	2.4	3.1	3.2	3.7	3.4	4.1	4.6	4.5	5.9	
Run	16	17	18	19	20	21	22		23		24		25			
Input wave	Kobe NS						Sin wave(20Hz,50waves)									
Max. acc.[G]	6.6	7.8	8.6	9.4	10.4	11.5	1.8		3.6		6.9		9.8			

4. EXPERIMENTAL RESULTS

4.1 Elasto-plastic behaviors of the Structural model

The elasto-plastic motions in the case that Kobe-NS waves are acting on the structural model are shown. The maximum values of the ground motion acceleration are presented in Table 4.

Figure 4 shows the relations between the maximum relative story displacement and the ground motion acceleration ($a_{g,max}$). The maximum relative story displacements of the 2nd story and the 3rd story increase almost proportional to $a_{g,max}$, and the gradient of the maximum relative story displacement decreases when $a_{g,max}$ exceeds 20 m/s², and after 60 m/s², the maximum relative story displacement becomes almost constant. On the other hand, the gradient of the maximum relative story displacement of the 1st story continues to increase. Figure 5 shows the relations between the maximum acceleration response of each story and $a_{g,max}$. The gradient of the accelerations at all stories start to decrease as $a_{g,max}$ exceeds 20 m/s². When $a_{g,max}$ exceeds 40 m/s², the acceleration response remains almost constant. Figure 6 shows the relations between the maximum story shear force in each story and the $a_{g,max}$. The gradient of the maximum story shear force starts to decrease when $a_{g,max}$ exceeds 20 m/s². After that, the story shear force in the 3rd story increases gradually. However the story shear forces in the 1st story and the 2nd story do not increase significantly when $a_{g,max}$ is around 40 m/s². Figure 7 shows the relations between the maximum story force and the maximum relative story displacement. When the maximum relative story displacement of the 1st story exceeds 2.6mm, the values of displacement reach the top. On the other hand, the maximum relative story displacement and the story shear force at the 2nd story and the 3rd story are proportional. These results in this section say that the structural model yields at the column of the 1st story.

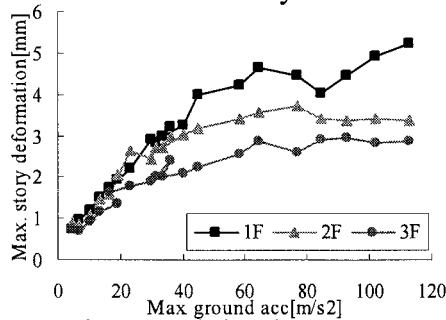


Figure 4 Relations between response deformation of story and max. ground acc.

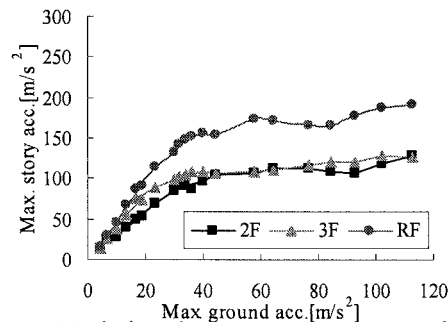


Figure 5 Relations between response acc. of story and max. ground acc.

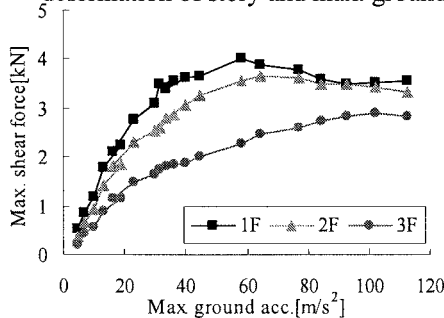


Figure 6 Relations between response shear force and max. ground acc.

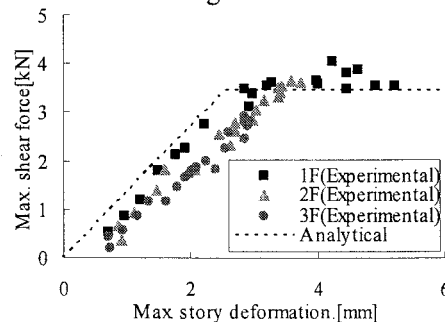


Figure 7 Relations between responses shear force and story deformation

4.2 Collapse Test

4.2.1 Transition of the axial force at the column

The transitions of the axial force are examined. The time-histories of the axial force in each member of the structural model are shown in Figure 8. At each figure, the locations to measure the axial force are also attached.

At approximately 1.5 sec., when the drift of the structural model occurs, the average of the axial force in all the right side columns decreases. The state of the axial forces changes rapidly from compression to tension around the final state.

Meanwhile, the axial forces of the left columns in the 2nd story and the 3rd story increase, and converge at the value greater than the initial axial force. However, the axial force of the 1st story at the right column converges at the initial axial force.

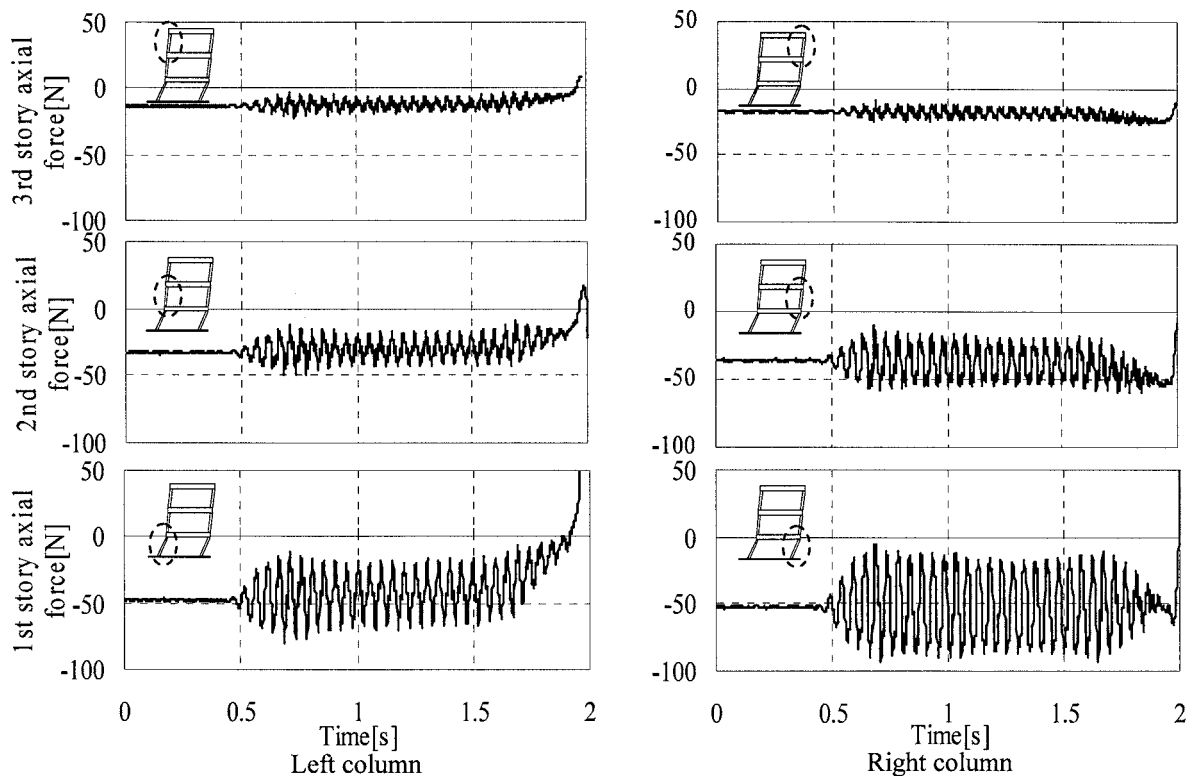


Figure 8 Time history of axial forces in each column of the structural model

4.2.2 Transition of the story shear force

To simulate the collapse phenomena of the structure, sinusoidal wave is used for the input wave. The centrifugal acceleration is 30G. In consideration of natural frequency of the structural model (24.4 Hz), the input frequency is 20.0Hz. In this case, 'the base shear coefficient' and 'the ratio of axial force to yield axial force' become 0.33 and 0.18, respectively. As a result, under the sinusoidal wave ($a_{g,max} = 9.8G$), the plastic hinges form at the top and the bottom of the 1st story, and the story-mechanism failure occurs.

Figure 9 shows the time-history of ground motion acceleration. Figure 10 shows the time history of the absolute displacement in each story. In these figures, black dots describe the peaks of each cycle at 2nd floor. So the absolute displacements in all stories are in the same phase. Moreover, the absolute displacements in all stories drift after 1.5 sec.. The displacement distributions of the structural model at the time indicated by the black dots in Figure 10 are shown in Figure 11. After 1.5 sec., the absolute displacement of the 2nd story increases significantly. It means the story collapse at 1st story is occurred. After that, the structure collapses at 1.9 sec..

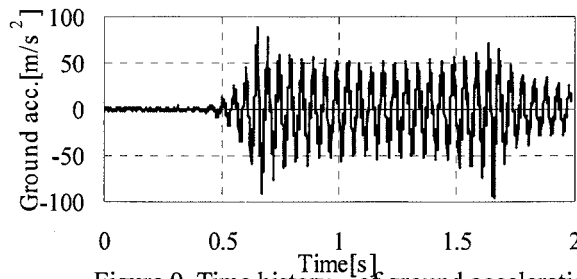


Figure 9. Time history of ground accelerations (sinusoidal wave input: Max.=9.8G)

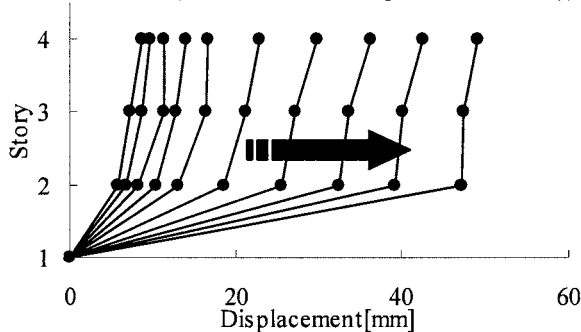


Figure 11 Displacement distributions along the height

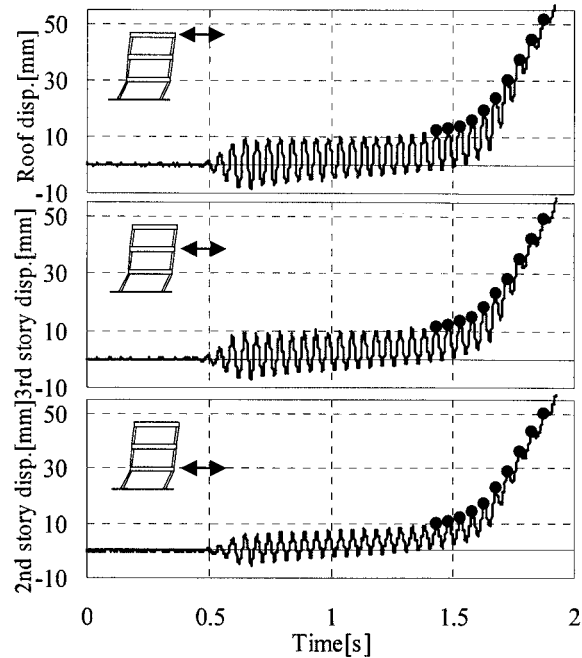


Figure 10 Time history of displacement in each story

Figure 12 shows the time-history of response acceleration at each story after the story failure occurs at 1.5 sec.. Figure 13 shows the time-history of story shear force at each story. The ground motion acceleration has almost constant amplitude after 1.7 sec.. However, the acceleration amplitude of each story begins to decrease significantly, and this value becomes 0 at 1.9 sec..

As a result, the story shear force begins to decrease significantly after 1.7 sec. and reaches to origin at 1.9 sec..

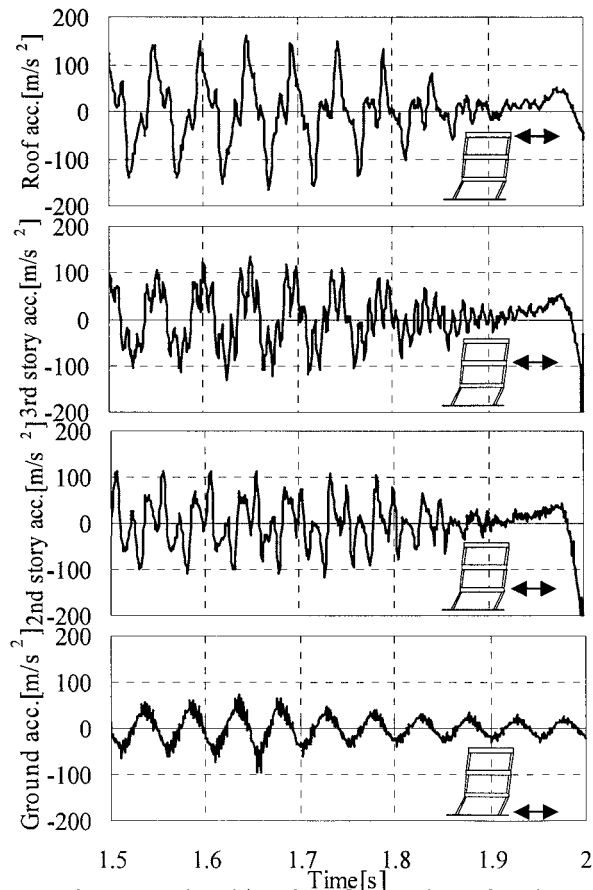


Figure 12 Time histories of ground acceleration and response acceleration in each story

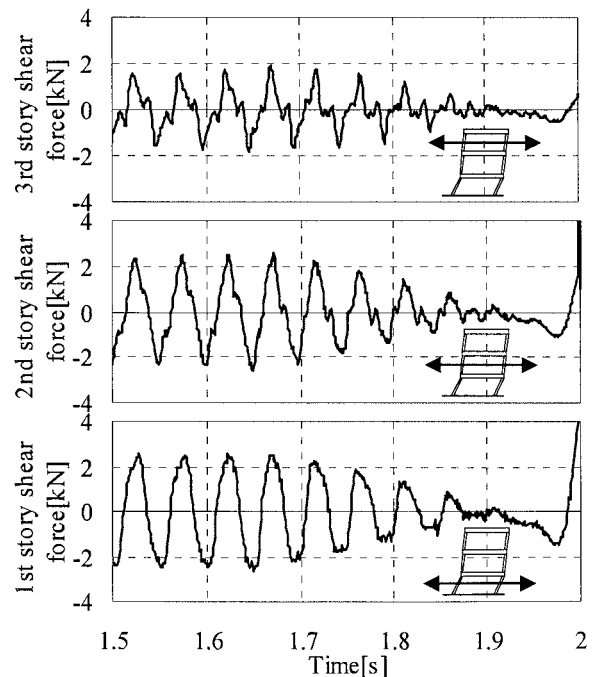


Figure 13 Time histories of shear force in each story

4.2.3 Relationships between shear force and shear deformation

In Figure 14, the relationship between the shear force and the shear deformation of the 1st story between 0.3 sec. and 1.5 sec. (before the story collapse occurs). The restoring force characteristics draw the hysteric loop around the origin point between 0.3 sec. and 0.7 sec.. However, the restoring characteristics after 0.7 sec. (when the deformation starts) have the center of the hysteric loop swaying in the direction of deformation.

Figure 15 shows the relationship between story shear force and the shear deformation in each story from 1.5 sec. (the story failure occurs) until 1.9 sec. (the complete failure occurs). The hysteric loop in the 2nd story has clearly elastic response. In the 2nd and the 3rd story, when the deformation increases, the hysteric loop is disturbed. On the other hand, the story shear force obtained from the envelope curve of the 1st story acceleration has a negative gradient in the horizontal restoring force and decreases as the deformation increases. It means that the 1st story collapses are influenced by the P- Δ effect from specimen weight. The envelope curves of the experimental results have a good agreement with the calculation results considering the P- Δ effect.

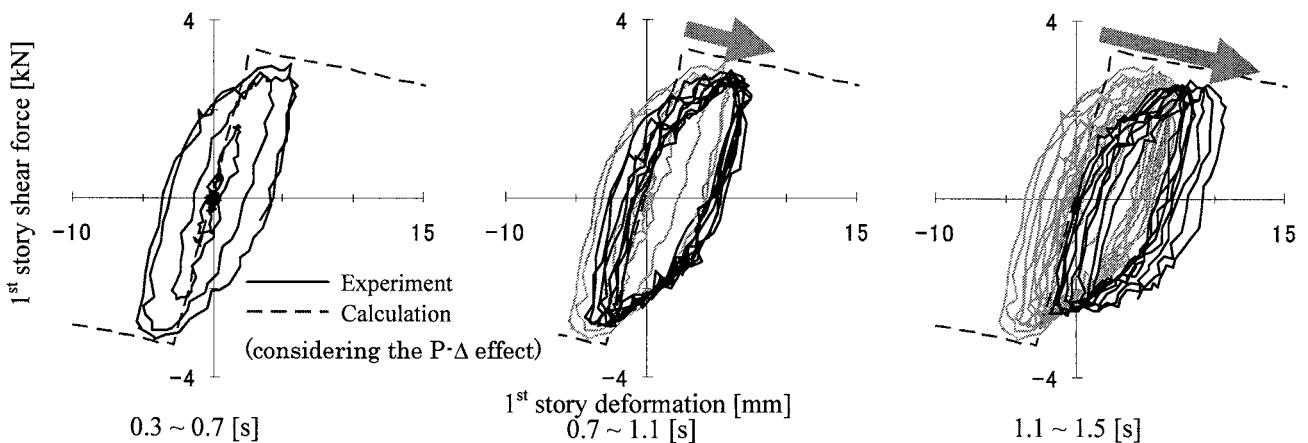


Fig. 14 Relationship between the shear force and the shear deformation at the 1st story

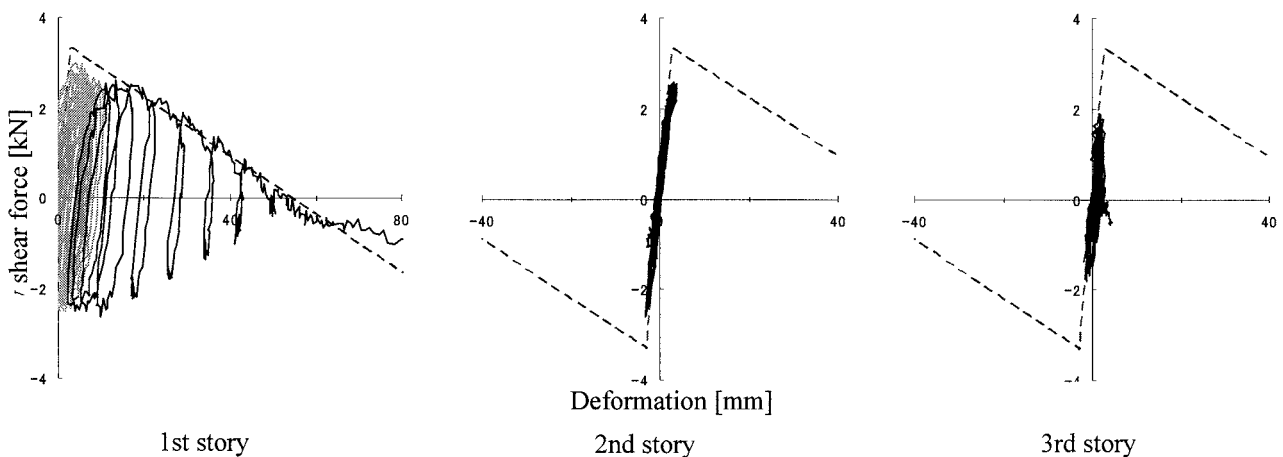


Fig. 15 Relationship between the shear force and the shear deformation at each story (15.0~19.0[s])

4.2.4 Observation of experimental model

Figure 16 shows the pictures obtained from the CCD camera. It is observed visually that the 1st story columns incline, and then story failure occurs. Figure 17 shows the pictures obtained from the high-speed camera installed at the top of the specimen. It is observed that after the story failure, the 2nd story and the 3rd story collapse.

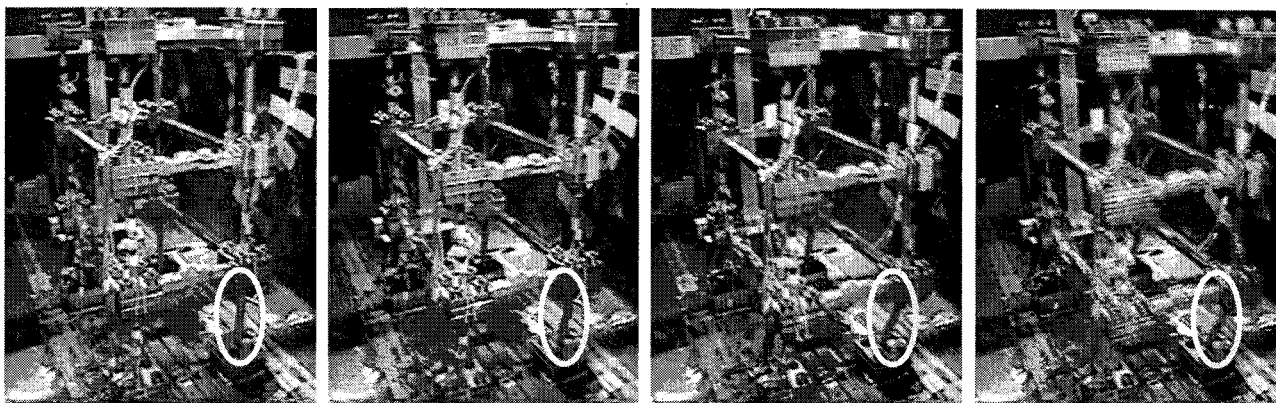


Figure 16 Pictures obtained from the CCD camera

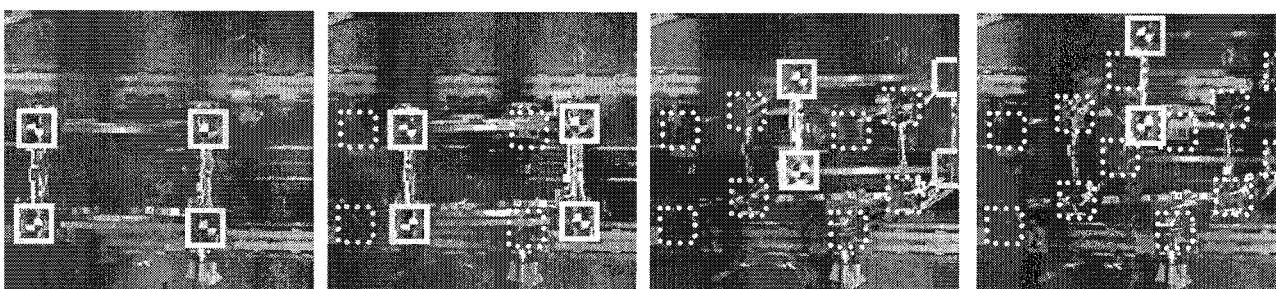


Figure 17 Pictures obtained from the high-speed camera

5. CONCLUDING REMARKS

- The collapse tests using the shaking table in the large centrifuge are carried out for the pilot model of superstructure. The results of this experiment are shown as follows.

- 1). The whole behavior (from elastic state to collapse) of three-story model which has weak-column and strong-beam is presented (i.e. displacement, acceleration, axial force of column, and shear force at the story failure)
- 2). The specimen collapsed completely due to P- Δ effects. It is confirmed that this effects are reproduced appropriately in this experiment.
- 3). Story mechanism due to column yielding is captured visually by the CCD and the high-speed camera.
- 4). The complete failure of the miniature model of superstructure can be realized using the centrifuge machine.

- Based on these experimental results, It can be expected to verify the collapse mechanism of various types of superstructures such as steel high-rise buildings and reinforced concrete buildings.

Acknowledgement

This project is supported by the Japan Society for the Promotion of Science (No. 17206057). We would like to express appreciation to the technical staffs of Obayashi Corporation, for helping us concerning whole procedure of these experiments.

References

- T. Matsuda and S. Higuchi, (2002), "Development of the Large Geotechnical Centrifuge and Shaking Table of Obayashi", Proceedings of ICPMG'02, Phillips, R., Guo, P. & Popescu, R. (eds): 63-68
- Takada N. and Kusakabe O. (1987), "Centrifuge model tests, 3. Principle", Tsuchi-to-kiso, Vol. 35, No. 12, pp. 89-94 (in Japanese).

CYCLIC MODELING OF BOLTED CONNECTIONS FOR A TYPE OF PRE-FABRICATED MEZZANINE FRAMES

A. Sato¹⁾ and C. M. Uang²⁾

1) *Visiting Scholar, Dept. of Structural Engineering, University of California San Diego, La Jolla, CA, USA
(Research Associate; Dept. of Architecture and Design, Nagoya Institute of Technology, Japan)*

2) *Professor, Dept. of Structural Engineering, University of California San Diego, La Jolla, CA, USA
atsato@ucsd.edu (asato@nitech.ac.jp), cmu@ucsd.edu*

Abstract: In order to evaluate the seismic performance of a type of pre-fabricated mezzanines with cold-formed HSS columns and double-channel beams full-scale cyclic testing was conducted at the University of California, San Diego in 2004. The study suggested that yielding should be confined in the bolted connections; columns and especially beams should be designed to remain elastic during a major seismic event. Accordingly, energy dissipation is expected to occur in the bolted connections. In an effort to develop a seismic design procedure for this type of frames, accurate modeling of the bolted connection under cyclic loading is needed for nonlinear time-history analysis. Extending the concept of instantaneous center of rotation for cyclic loading and combining it with a friction theory, this paper presents a mathematical model which provides a very good correlation with the test results.

1. INTRODUCTION

Full-scale cyclic testing of beam-column subassemblages was conducted at the University of California, San Diego (UCSD) to evaluate the cyclic performance of the bolted connections for a type of pre-fabricated mezzanines (Hong and Uang 2004); the system is composed of cold-formed Hollow Structural Section (HSS) columns and double-channel beams. A typical construction of mezzanines is shown in Figure 1. It is common that HSS columns and double-channel beams be connected by snug-tight high strength bolts. Contrary to the general belief that frames with cold-formed members could not deliver ductility, test results showed that all specimens exhibited a deformation capacity significantly larger than 4% story drift ratio, as shown in Figure 2 (Hong and Uang 2004). The study showed that the strong column-weak beam seismic design philosophy, as stipulated in the AISC Seismic Provision (AISC 2005) for typical moment-framed steel buildings, is not applicable for the type of system investigated. Instead, it was suggested that yielding should be confined in the bolted connection; columns and especially beams should be designed to remain elastic during a major seismic event. Therefore, energy dissipation is expected to occur in the bolted connections. Since building codes in US (e.g., AISI 1996; and AISC 2005) do not specifically address the seismic design of this type of system, understanding the bolted connection behavior is an important step toward developing a seismic design procedure for the system.

The purpose of this paper is to propose an accurate mathematical modeling of bolted connections under cyclic loading that can be used for nonlinear time-history analysis. In this study, test results reported by Hong and Uang (2004) are used for correlation purposes.

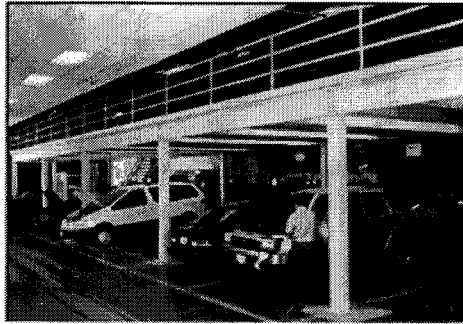


Figure 1. A Type of Mezzanines

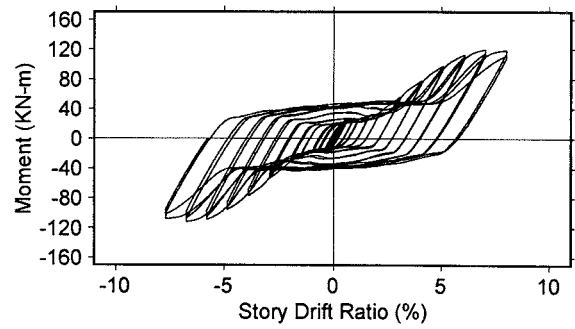


Figure 2. Typical Hysteresis Behavior of Cold-Formed Beam-Column Subassembly with Bolted Connection

2. EXPERIMENTAL TEST RESULTS

Test setup is shown in Figure 3, and the member sizes and bolt locations are summarized in Table 1. Material properties of beam and column are summarized in Table 2. Typical behavior of bolted connection is shown in Figure 5. As shown in Figure 5, it is clear that the bolted connection behavior is characterized by three ranges; slip range, hardening range, and unloading range.

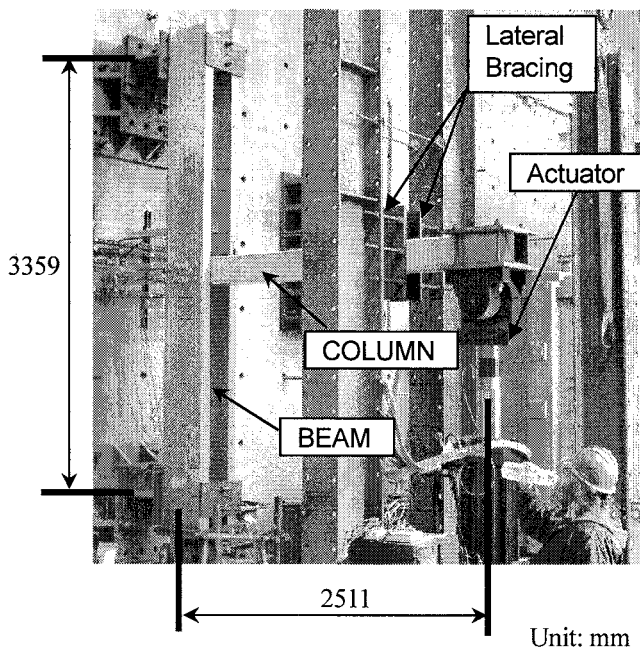


Figure 3. Test Setup (Hong and Uang 2004).

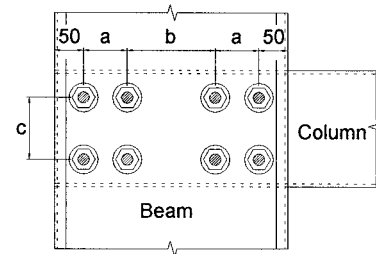


Figure 4. Connection Configuration.

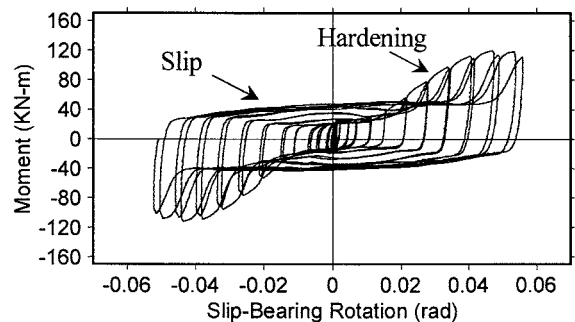


Figure 5. Bolted Connection Behavior (Specimen 3).

Table 1. Member Sizes

Specimen No.	Beam	Column	Connection*			Doubler Plates
			a	b	c	
1, 2	2C 305x89x2.66	HSS 203x203x6.35	63.5	76.2	108	3.42 (10 Ga)
3	2C 406x89x2.66	HSS 203x203x6.35	76.2	152.4	108	N/A
4	2C 406x89x2.66	HSS 203x203x6.35	76.2	152.4	108	3.42 (10 Ga)
5, 6, 7	2C 406x89x3.42	HSS 203x203x6.35	76.2	152.4	108	N/A
8, 9	2C 508x89x3.42	HSS 254x254x6.35	76.2	254	158.8	N/A

* See Figure 4, Bolt: 25.4-mm (1-in.) dia. A325 Bearing Type.

Table 2. Material Properties

Member	Component	F_y (N/mm ²)	F_u (N/mm ²)	Elong. ^a (%)
Beam	2C 305x89x2.66	350	519	21.0
	2C 406x89x2.66	316	444	22.8
	2C 406x89x3.42	372	509	21.4
	2C 508x89x3.42	400	512	23.6
Column	HSS 203x203x6.35	405	496	23.4
	HSS 254x254x6.35	336	441	27.5

^a Based on 51-mm gage length.

3. EVALUATION OF RESISTING MECHANISM

To model the bolted connection behavior, it is important to understand the resisting mechanism of the bolted connection under investigation. The resisting mechanism is composed of both friction and bearing.

The friction resistance of a single fastener, R_s , can be expressed by the following formula (AISC 2005):

$$R_s = k \cdot T \quad (1)$$

where k = coefficient of friction, T = snug-tight bolt tension.

The bearing resistance of a single fastener, R_b , can be expressed by the following formula (AISC 2005):

$$R_b = R_{ult} \cdot (1 - e^{-\mu\Delta})^\lambda \quad (2)$$

where R_{ult} = ultimate shear strength of the fastener ($= 3.0t d F_u$), Δ = local bearing deformation,

μ , λ = regression coefficients, e = base of natural logarithms,

t = thickness of member, d = bolt diameter, F_u = ultimate strength of member.

As can be seen from Figure 5, slip range shows a plateau strength; therefore, it is assumed that friction is the resisting mechanism (i.e., $R = R_s$). In the hardening range, the resisting mechanism includes both friction and bearing (i.e., $R = R_s + R_b$). Unloading range is approximately as a rigid unloading.

The coefficients and the snug-tight bolt tension used in this study are summarized in Table 3. Lacking data to derive coefficients, the tabulated values were shown to provide a good correlation in this study (AISC 2001; Crawford and Kaluk 1968; Fisher et al. 1963).

Table 3. Assumed Values

Specimen No.	k	T (KN)	μ	λ
1 to 7	0.33	44.5	5	0.55
8, 9	0.45	66.7		

4. EVALUATION OF ECCENTRICALLY LOADED FASTENER GROUP

4.1 Definition of Instantaneous Center of Rotation

The concept of instantaneous center (IC) of rotation is to reduce the translation and rotation of a bolted group to pure rotation. IC can be obtained when the distance r_0 (see Figure 6) satisfies the static equilibrium Eqs. (3-a), (3-b), and (3-c) simultaneously (Salomon and Johnson 1996).

$$\sum_{i=1}^n \frac{R_i y_i}{d_i} = 0, \quad \sum_{i=1}^n \frac{R_i x_i}{d_i} - P = 0, \quad P(e - r_0) - \sum_{i=1}^n R_i d_i = 0 \quad (3-a, b, c)$$

where R_i = bearing resistance, P = applied load, e = eccentricity,

r_0 = distance from center of bolt group, d_i = arm length = $\sqrt{x_i^2 + y_i^2}$

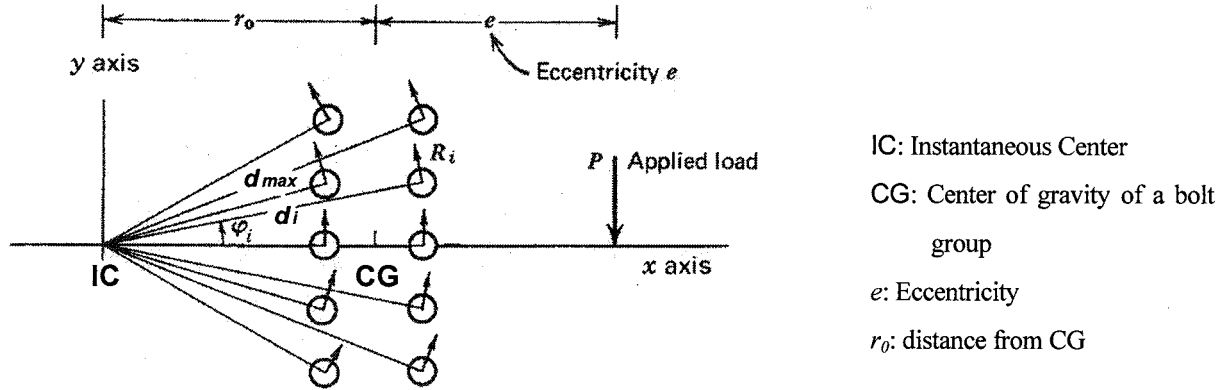


Figure 6. Eccentrically Loaded Fastener Group (Crawford and Kulak 1971).

4.2 Assumption in Calculation

In the slip range, the following assumptions are made (Kulak, G.L. et al. 2001; Nagae, T. et al. 2006):

- At a given load level, the connection rotates about the instantaneous center (IC) of rotation.
- At the slip load of the connection, slip strength of individual fastener is reached simultaneously.
- The slip resistance of each fastener can be represented by a force at the center of the bolt acting perpendicularly to the radius of rotation.
- Coefficient of friction (k) is similar in static and kinetic, i.e., $k_s = k_k$.

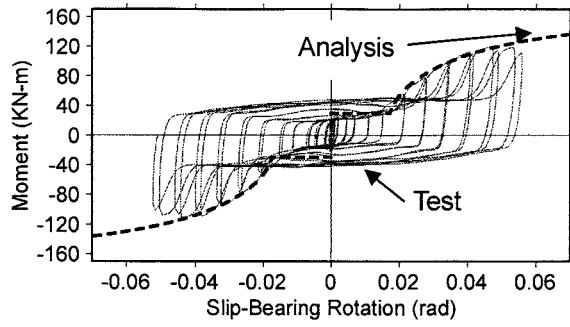
In the hardening range, the following assumptions are made (Kulak, G.L. et al. 2001; Nagae, T. et al. 2006):

- The connection rotates about the instantaneous center (IC).
- The deformation occurring at each fastener varies linearly with its distance from the instantaneous center.
- The fastener deformation and the resulting bearing resistance on the fastener act perpendicularly to the radius of rotation.
- Coefficient of friction (k) is similar in static and kinetic, i.e., $k_s = k_k$.

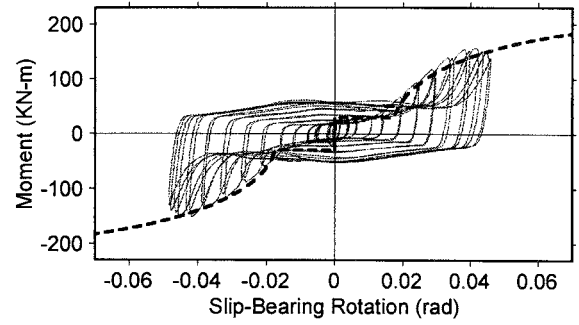
5. MONOTONIC LOADING ANALYSIS

Based on the assumptions made above, it is possible to obtain the relationship between moment and slip-bearing rotation of a bolted connection by iteration.

Sample correlations are shown in Figure 7. As shown in the figure, the predicted connection response shows a high agreement with the response envelope of the experimental results.



(a) Specimen 3



(b) Specimen 7

Figure 7. Moment versus Connection Rotation Relationship (Monotonic Loading Analysis).

6. CYCLIC LOADING ANALYSIS

A hysteresis rule can be proposed based on the monotonic loading analysis. However, as can be seen in Figures 5 and 7, the slip range grows due to hole ovalation from prior bolt bearing at lower drift cycles. To model accurately the cyclic behavior of the bolted connection, it is important to model the effect of hole ovalation.

6.1 Evaluation of Delayed Hardening

The proposed model to reflect such “delayed” hardening is shown in Figure 8. To explain that the starting point of hardening will start earlier than the previous maximum rotation (see Figure 8, where hardening will start at point 3 instead of point 3'), the variation of IC location and modeling of movement of IC are shown in Figures 9 and 10, respectively.

As shown in Figure 9, in the slip range, friction is the resisting mechanism and IC is stationary, i.e., $r_o = \text{constant}$. In the hardening range, IC moves and r_o is smaller than that in friction. Hence, as shown in Figure 10, the arm length (d_{max}) to calculate the slip rotation will be longer. Accordingly, as the deformation [$\Delta + (\text{IHO})$] in Figure 10] at the bolt is the same, the starting point of hardening will occur earlier than the previous maximum rotation.

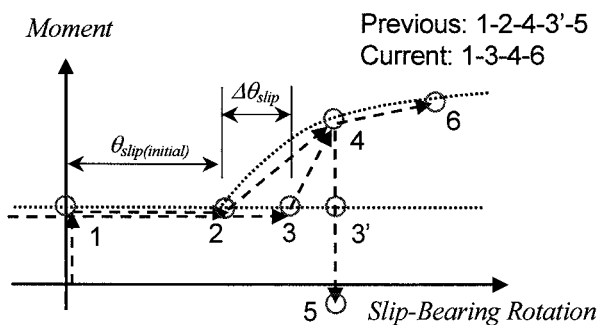


Figure 8. Model of Delayed Hardening.

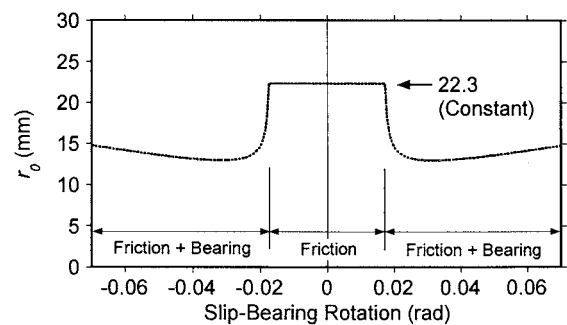


Figure 9. Predicted IC Location (Specimen 3).

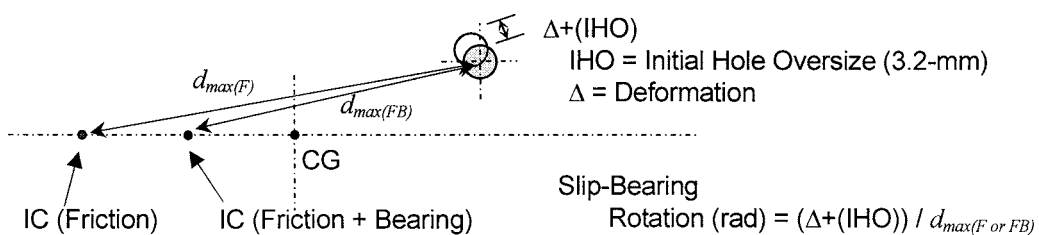


Figure 10. Movement of Instantaneous Center.

6.2 Analytical Result of Cyclic Loading

Sample correlations are shown in Figure 11. Note that the “delayed” hardening is well predicted, and the predicted cyclic response of the bolted connections correlates very well with the experimental results.

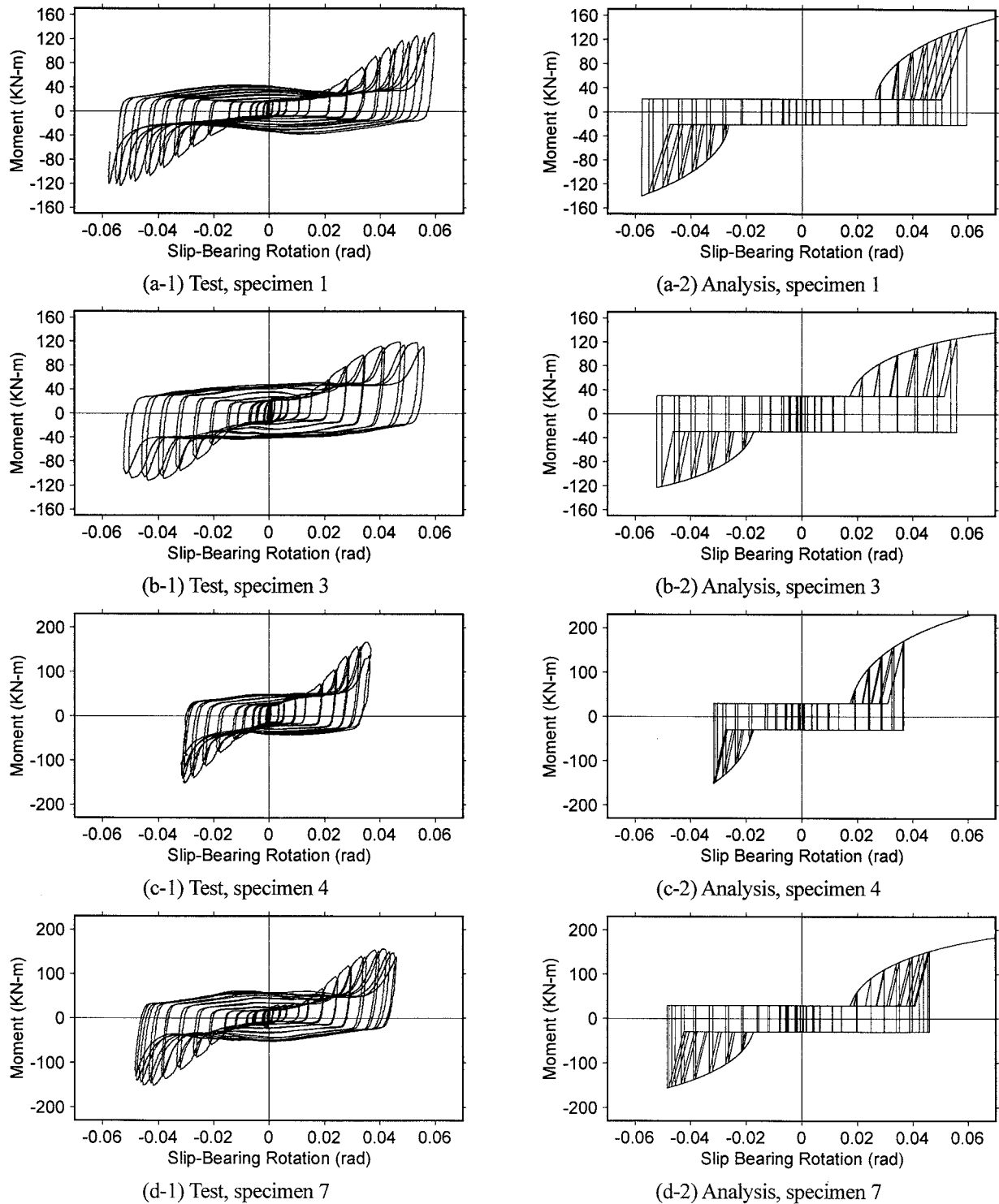
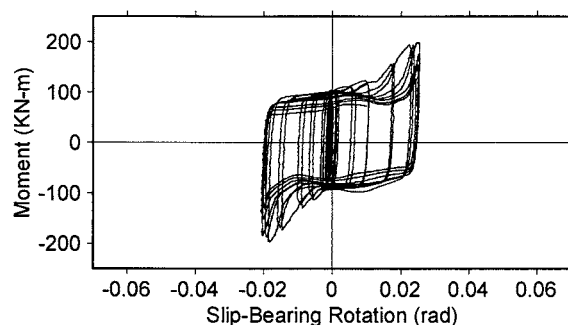
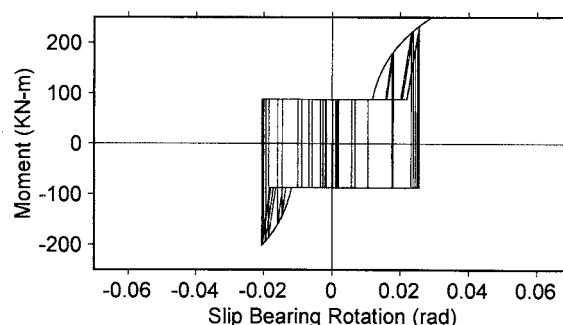


Figure 11. Moment versus Slip-Bearing Rotation Relationship (Cyclic Loading Analysis).



(e-1) Test, specimen 9



(e-2) Analysis, specimen 9

Figure 11. Moment versus Slip-Bearing Rotation Relationship (Cyclic Loading Analysis) (cont.).

7. CONCLUSIONS

A model to simulate the cyclic behavior of the bolted connections in a type of mezzanine structures is proposed; cyclic testing showed that the hysteresis behavior of the eccentrically loaded bolt group is characterized by 3 regions involving both friction and bearing mechanisms. The main conclusions are summarized as follows:

1. A mathematical model using the Instantaneous Center (IC) of rotation concept was proposed to simulate the bolted connection behavior.
2. Only the following information is needed to model the bolted connection behavior: (1) Fastener configuration, (2) Eccentricity of the load, and (3) Material property (ultimate strength).
3. Predicted connection monotonic response showed a high agreement with the response envelope of the experimental results.
4. A procedure was developed to account for the growth of slip range in cyclic response due to hole ovalation.
5. Predicted cyclic response of bolted connection correlated very well with the experimental results.

Acknowledgements:

This research is sponsored by American Iron and Steel Institute.

References:

- American Iron and Steel Institute. (AISI). (1996). *Cold-Formed Steel Design Manual*, 1996 Edition, Milwaukee, Wisconsin, USA.
- American Institute of Steel Construction (AISC). (2005). *Seismic Provision for Structural Steel Buildings*, Chicago, Illinois, USA.
- American Institute of Steel Construction (AISC). (2005). *Steel Construction Manual*, Thirteenth Edition, Chicago, Illinois, USA.
- Crawford, S.F. and Kulak, G.L. (1968). "Behavior of Eccentrically Loaded Bolted Connections," *Studies in Structural Engineering*, No.4, Department of Civil Engineering, Nova Scotia Technical College, Halifax, Nova Scotia.
- Fisher, J.W., Ramseier, P.O. and Beedle, L.S. (1963). "Strength of A440 Steel Joints Fastener with A325 Bolts," *Publication*, IABSE, 23.
- Hong, J.K. and Uang, C.M. (2004). "Cyclic Testing of Cold-Formed Steel Moment Connection for Pre-Fabricated Mezzanines" *Report No. TR-04/03*, University of California, San Diego, La Jolla, CA, USA.
- Kulak, G.L., Fisher, J.W. and Struik, J.H.A. (2001). *Guide to Design Criteria for Bolted and Riveted Joints*, Second Edition, American Institute of Steel Construction, Chicago, Illinois, USA.
- Nagae, T., Ikenaga, M., Nakashima, M. and Suita, K. (2006). "Shear Friction Between Base Plate and Base Mortar in Exposed Steel Base," *Journal of Structural and Construction Engineering*, Architectural Institute of Japan, No.606, 217-223.
- Salmon, C.G. and Johnson, J.E. (1996). *Steel Structure Design and Behavior*, 4th Edition, HarperCollin Publishers, New York, NY, USA.

EVALUATING SEISMIC PERFORMANCE OF STEEL REINFORCED CONCRETE MEMBERS

H.-L. Hsu ¹⁾, and J.-L. Juang ²⁾

1) Professor, Dept. of Civil Engineering, National Central University, Taiwan

*2) Post-doctoral research fellow, Research Center for Hazard Mitigation and Prevention,
formerly, graduate student, Dept. of Civil Engineering, National Central University, Taiwan
t3200178@ncu.edu.tw, jjl1@ncu.edu.tw*

Abstract: This paper presents an effective hysteretic model for the prediction and evaluation of the cyclic performance of steel reinforced concrete members. This model adopts the load-deformation relationship acquired from the monotonic loading tests and incorporates the modified pivot behavior to reflect the characteristics on the deteriorations of stiffness and strength when members are subjected to cyclic loading. Influence of Bauschinger effects is included in the hysteretic model to establish the cyclic load-deformation relationship. Comparisons between the results from cyclic loading tests and the analytical model validated the effectiveness of the proposed method.

1. INTRODUCTION

Steel reinforced concrete members possess sufficient stiffness and adequate ductility, thus are effective structural designs for earthquake-resistant purposes. Seismic behavior of steel reinforced concrete members involves complicated steel-concrete interaction as well as hysteretic characteristics. In order to effectively evaluate the seismic performance of such members, adequate analytical models to calculate the member strength as well as the deterioration in member strength and member stiffness during the inelastic stages must be established.

In general, hysteretic behavior of structural members can be evaluated by the finite element methods. However, such approaches require large amount of computations and iterations. This phenomenon applies to the prediction of steel reinforced concrete members as well, because performance evaluation of such designs raises further difficulty due to highly non-linear composite member behavior that makes the practical performance evaluation infeasible. Alternatively, a simplified polygonal hysteretic model (Sivaselvan and Reinhorn 1999), denoted PHM hereafter, which simulates the member behavior by composing the member behavior of piece-wise linear segments is more practical. This model adopts the backbone curve information obtained from the monotonic loading tests with adequate strength and stiffness deterioration rules to describe the member behavior in the elastic and inelastic stages. This model has been demonstrated to be effective analytical tool in the structural analysis of steel structures and concrete-related designs. However, information on the composite member performance evaluation, particularly the load-deformation relationship, is still limited. This paper is focused on the establishment of control parameters for the PHM model to evaluate the seismic performance of steel reinforced concrete members. A series of monotonic and cyclic loading tests were conducted to validate the effectiveness of the proposed method.

2. TEST PROGRAM

Six steel reinforced concrete members with various encased structural steel were fabricated for testing. Three types of structural steel were used. They were ASTM A36 H200x100x5.5x8, H194x150x6x9, and H200x200x8x12. The dimensions for the composite sections are listed in Table 1. Three of the specimens were used for monotonic loading tests, and the others were used for cyclic loading tests. A set of servo-hydraulic actuator was used to generate the required loading. Cyclic loading was generated by a series of prescribed increasing displacement commands. The load-deformation relationships for the tested members are shown in Figure 1.

Table 1 Test group and specimen

Test group	Specimen	Dimension Width x Depth (mm)	Steel section $d_s \times b_f \times t_w \times t_f$ (mm)	Longitudinal bar	$\frac{(EI)_s}{(EI)_{SRC}}$
Monotonic loading test	SRC100m	370x370	H200x100x5.5x8	4-#6	0.225
	SRC150m	370x370	H194x150x6x9	4-#6	0.299
	SRC200m	370x370	H200x200x8x12	4-#6	0.437
Cyclic loading test	SRC100c	370x370	H200x100x5.5x8	4-#6	0.225
	SRC150c	370x370	H194x150x6x9	4-#6	0.299
	SRC200c	370x370	H200x200x8x12	4-#6	0.437

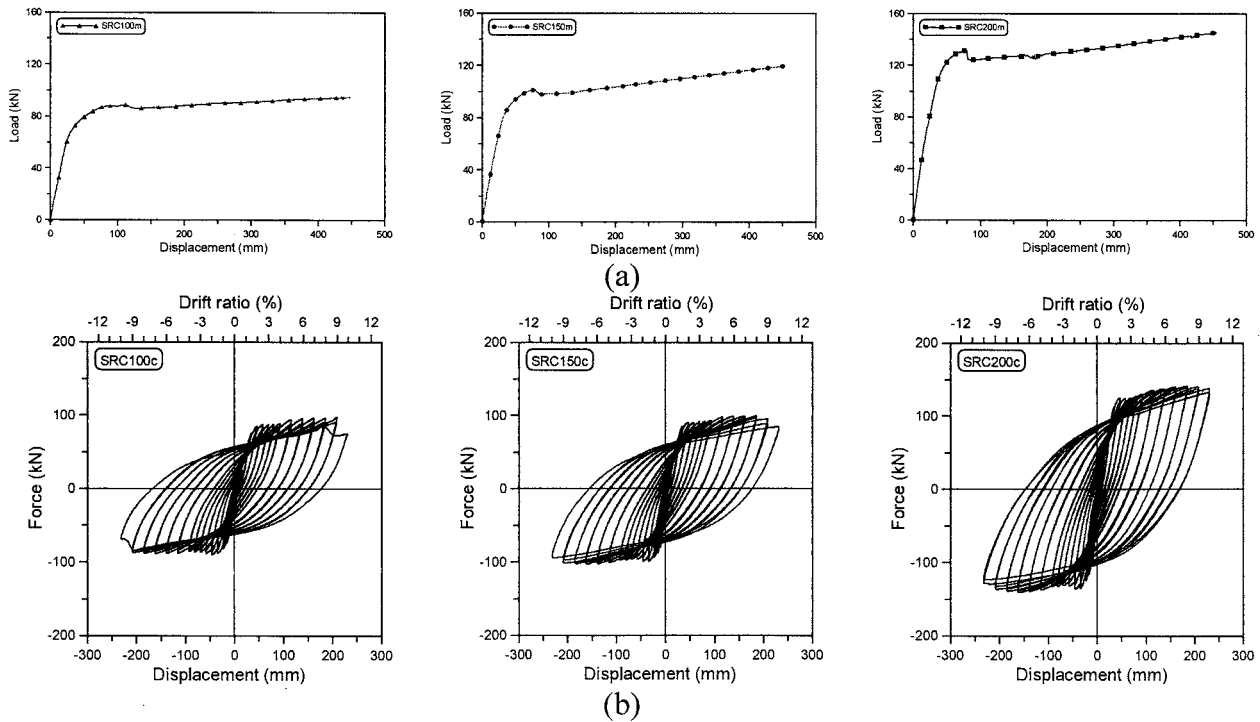


Figure 1 Load-deformation relationships for the specimens: (a)monotonic loading tests; (b)cyclic loading tests

3. STIFFNESS DETERIORATION

Deterioration in stiffness affects the achievable strength and the corresponding deformation. It has been indicated in many research studies that the stiffness deterioration of concrete-related members is greatly influenced by the loading histories. From several test results of reinforced concrete members subjected to cyclic loading (Takeda et al. 1970, Park et al. 1987, Kunnath et al. 1990, Valles 1996), the unloading stiffness of the members at various deformation stages coincided at a pivot point, as shown in Figure 2. Analytical methods involving this phenomenon were noted pivot model, and could be used to describe the softening characteristics of reinforced concrete at large deformation. According to the pivot model, the deteriorated member stiffness K_r under cyclic loading is determined by multiplying the original stiffness K_0 with a reduction factor as follows:

$$K_r = \frac{M_m + \alpha M_y}{K_0 \phi_m + \alpha M_y} K_0 \quad (1)$$

in which ϕ_y is the yielding curvature, ϕ_m is the largest curvature under the cyclic loading, α is a positive number that determines the location of pivot point, M_y is the yielding moment, M_m is the moment with respect to ϕ_m , and K_0 is the original stiffness.

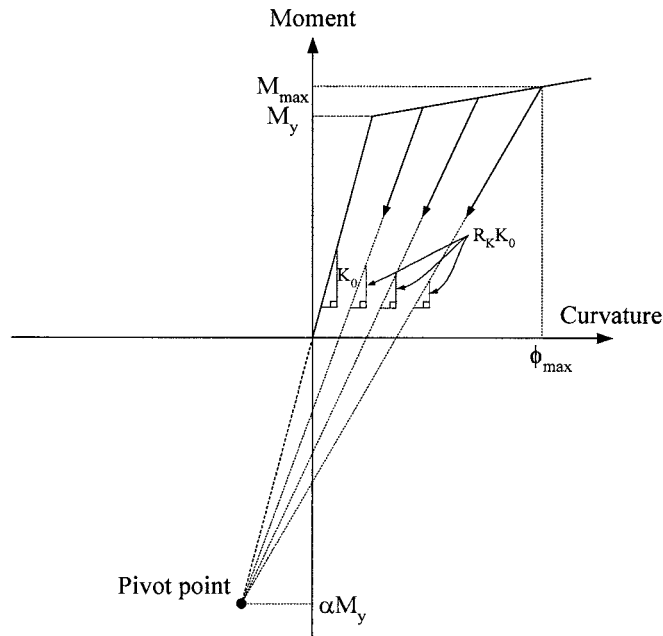


Figure 2 Modeling of stiffness deterioration by pivot model

This reduction factor accounts for the influence of member strength and the corresponding deformation at various loading stages. The pivot model usually provides sufficient accuracy when used to describe the behavior of reinforced concrete members. However, significant discrepancy raised when this model was used to predict the hysteretic behavior of steel reinforced concrete members, as shown in Figure 3. It can be observed in this figure that double pivot points, instead of single point, were exhibited when the members were subjected to cyclic loading. These two points, as shown in Figure 4, connected the unloading curves when members were subjected to smaller and

larger deformations, respectively.

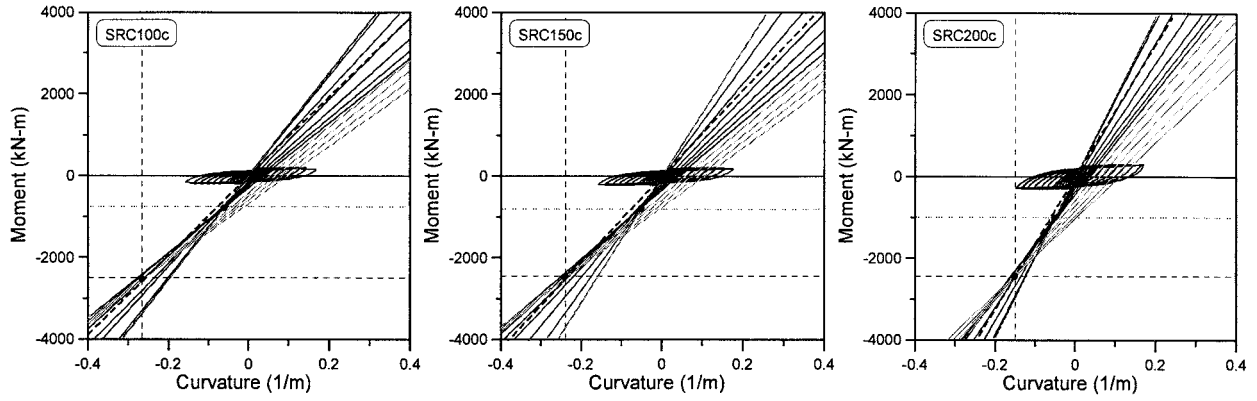


Figure 3 Stiffness deterioration of specimens

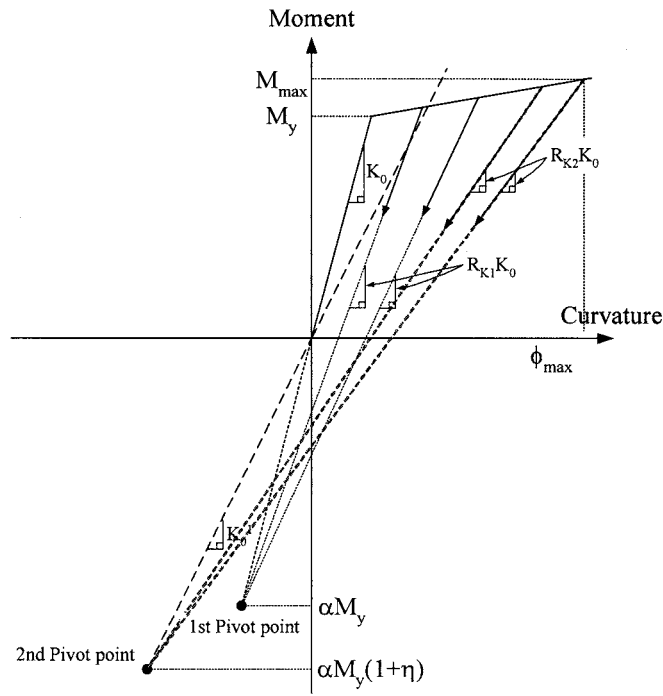


Figure 4 Modified pivot model with two pivot points

The location of the first pivot point, defined by the intersecting position of the unloading curves when member was subjected to smaller drifts, can be determined by the following values:

$$\phi_{pv1} = -\frac{\alpha M_y}{K_0} \quad (2)$$

$$M_{pv1} = -\alpha M_y \quad (3)$$

Therefore, the stiffness reduction factor at this stage, R_{K1} , can be expressed as:

$$R_{K1} = \frac{M_{\max} + \alpha M_y}{K_0 \phi_{\max} + \alpha M_y} \quad (4)$$

Shifting of the first pivot point to a lower position, defined as the second pivot point, was observed when the member deformation was increased. This point can be determined by the following values:

$$\phi_{pv2} = -\frac{\alpha M_y (1 + \eta)}{K_0^1} \quad (5)$$

$$M_{pv2} = -\alpha M_y (1 + \eta) \quad (6)$$

in which K_0^1 is the stiffness when member first reached the softening stage.

In order to account for the softening characteristics of the member at large deformation, a further reduction factor η_K was defined:

$$\eta_K = \frac{K_0^1}{K_0} \quad (7)$$

Therefore, the stiffness reduction factor at second pivoting stage, denoted R_{K2} , can be evaluated by the following expression:

$$R_{K2} = \frac{M_{\max} + \alpha M_y (1 + \eta)}{\eta_K K_0 \phi_{\max} + \alpha M_y (1 + \eta)} \quad (8)$$

Relationships between the stiffness reduction factors and the compositions of the sections are shown in Figure 5. It is observed from this figure that these parameters can be approximated by linear relationships, and can be expressed as follows:

$$\alpha = -5.144 \frac{(EI)_s}{(EI)_{SRC}} + 5.774 \quad \text{for} \quad 0.2 \leq \frac{(EI)_s}{(EI)_{SRC}} \leq 0.45 \quad (9)$$

$$\eta_K = 0.821 \frac{(EI)_s}{(EI)_{SRC}} + 0.368 \quad \text{for} \quad 0.2 \leq \frac{(EI)_s}{(EI)_{SRC}} \leq 0.45 \quad (10)$$

$$\eta = -4.108 \frac{(EI)_s}{(EI)_{SRC}} + 3.243 \quad \text{for} \quad 0.2 \leq \frac{(EI)_s}{(EI)_{SRC}} \leq 0.45 \quad (11)$$

in which $(EI)_s$ and $(EI)_{SRC}$ are the equivalent flexural rigidities of the structural steel and the composite section, respectively.

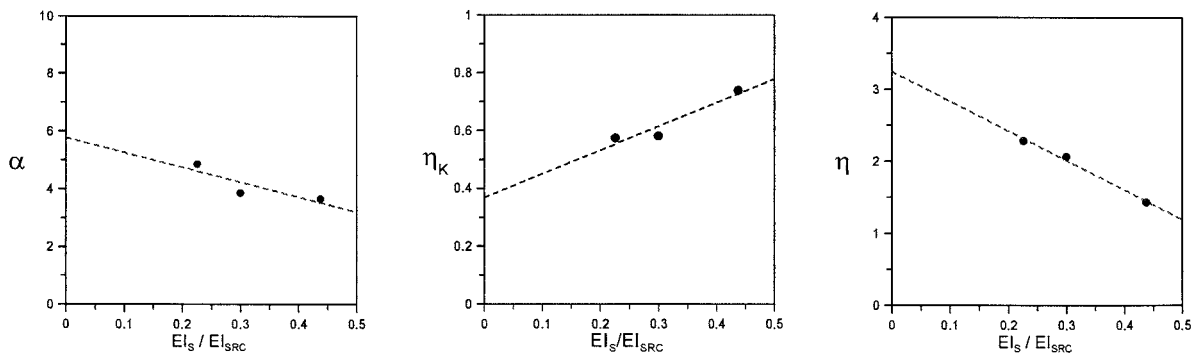


Figure 5 Relationships between stiffness deterioration parameters and the flexural rigidity ratios $((EI)_s/(EI)_{SRC})$: (a) α ; (b) η_K ; (c) η

4 STRENGTH DETERIORATION

Major parameters that affect the strength deterioration for members subjected to repeated loading include the magnitude of the deformation and the cumulative energy at various loading stages. It has been indicated in several behavior studies of reinforced concrete members (Powell 1975, Park et al. 1987, Valles 1996) that the relationship between strength reduction and the magnitude of deformation was nonlinear when the member was subjected to cyclic loading. These approaches are adopted in the performance evaluation of the steel reinforced concrete members, because the major strength of the composite is also contributed by the reinforced concrete. Therefore, the above-mentioned approaches should be applicable to the evaluation of the composite members, as long as the structural parameters were adequately defined.

In this regard, the reduction in strength in each loading cycle, denoted ΔM , could be evaluated from the yield strength at that loading stage, as expressed below:

$$\Delta M \approx M_{y0} \left[\left(\frac{\phi_m}{\phi_{mu}} \right)^{\frac{1}{\beta_1}} + \frac{\beta_2}{1 - \beta_2} \frac{\int dE}{E_{ult}} \right] \quad (12)$$

In this equation, M_{y0} is the member's yield strength, E_{ult} is the energy dissipation when member was subjected to monotonic loading, ϕ_m and ϕ_{mu} are the maximum curvatures when members are subjected to monotonic loading and cyclic loading, respectively; and β_1 and β_2 are the influence parameters accounting for the member ductility and energy dissipation, respectively. According to the test results as shown in Figure 1, the reduction in strength was not significant. Therefore, β_2 could be set to zero as suggested in relevant studies (Chai 2005), and the value of β_1 could be determined as 0.11 from test results calibrations.

5 VALIDATION OF PROPOSED METHOD

In order to validate the adequateness of the proposed parameters for the PHM model to predict the behavior of the composite members, the experimental and analytical load-deformation relationships for the test specimens were compared in Figure 6. It can be found from the comparisons that good relevance was achieved. Cumulative energy dissipation for the test specimens, as shown in Figure 7, further justified the applicability of the proposed information.

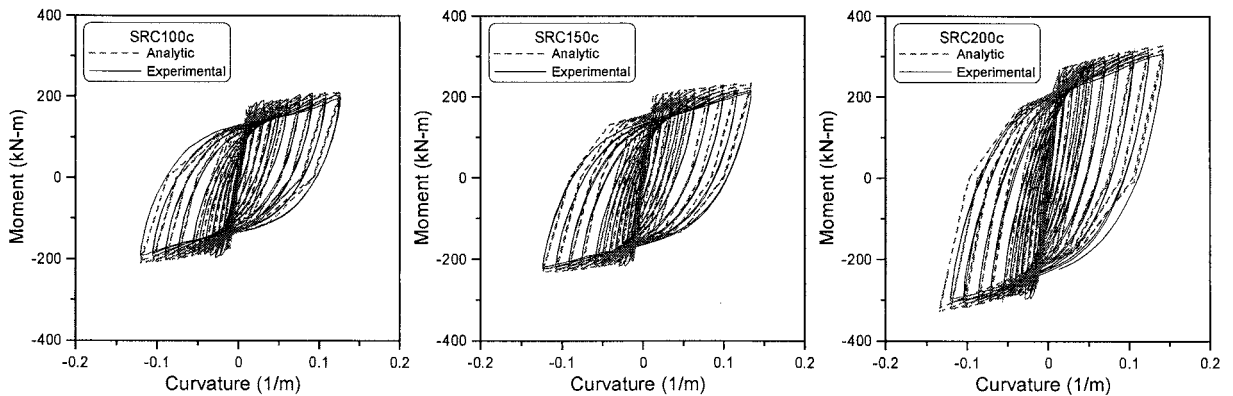


Figure 6 Comparisons of load-deformation relationships for the test specimens

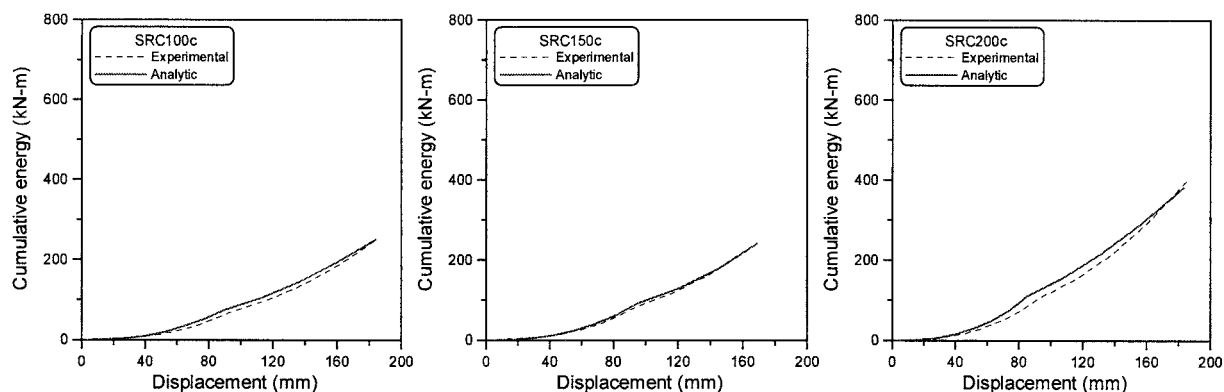


Figure 7 Comparisons of cumulative energy for the test specimens

6 CONCLUSIONS

This paper presents an effective hysteretic model for the prediction and evaluation of the cyclic performance of steel reinforced concrete members. Both stiffness and strength deteriorations were considered in the proposed model. Adequate structural parameters from test results were calibrated to evaluate the member performance. Comparisons between the results from cyclic loading tests and the analytical model validated the effectiveness of the proposed method.

Acknowledgements:

This study was partially supported by the National Science Council of the Republic of China under Grant No. NSC 95-2221-E-008-099, which is gratefully acknowledged.

References:

- Chai, Y. H. (2005). "Incorporating low-cycle fatigue model into duration-dependent inelastic design spectra," *Earthquake Engineering & Structural Dynamics*, **34**(1), 83-96.
- Kunnath, S. K., Reinhorn, A. M., and Park, Y. J. (1990), "Analytical Modeling of Inelastic Seismic Response of R/C Structures," *Journal of Structural Engineering, American Society of Civil Engineers*, **116**(4), 996-1017.
- Park, Y. J., Reinhorn, A. M., and Kunnath, S. K. (1987), "IDARC: Inelastic Damage Analysis of Reinforced Concrete Frame - Shear-Wall Structures," NCEER-87-0008, State University of New York at Buffalo.
- Powell, G. H. (1975), "Supplement to Computer Program DRAIN-2D," Supplement to Report, DRAIN-2D User's Guide, University of California, Berkeley.
- Sivaselvan, M. V., and Reinhorn, A. M. (1999), "Hysteretic Models for Cyclic Behavior of Deteriorating Inelastic Structures," MCEER-99-0018, State University of New York at Buffalo.
- Takeda, T., A., Sozen, M. A., and Nielsen, N. N. (1970), "Reinforced Concrete Response to Simulated Earthquake," *Journal of Structural Division, American Society of Civil Engineers*, **96**(ST-12), 2557-2573.
- Valles, R. E., Reinhorn, A. M., Kunnath, S. K., and Madan, A. (1996), "IDARC2D Version 4.0: A Computer Program for the Inelastic Damage Analysis of Buildings," NCEER-96-0010, State University of New York at Buffalo.

EXPERIMENTAL SIMULATION OF PROGRESSIVE FAILURE OF PERIMETER FRAMES IN FRAMED-TUBE STRUCTURES

H. Tagawa¹⁾, S. Sumitani²⁾, S. Yamada³⁾, and A. Wada⁴⁾

1) 21st Century COE Researcher, Tokyo Institute of Technology, Japan

2) Ove Arup & Partners Japan Ltd, Japan

3) Associate Professor, Tokyo Institute of Technology, Japan

4) Professor, Tokyo Institute of Technology, Japan

htagawa@serc.titech.ac.jp, Shinya.Sumitani@arup.com, naniwa@serc.titech.ac.jp, wada@serc.titech.ac.jp

Abstract: The framed-tube structures consist of rigid moment-resisting frames in the perimeters and floors which provide lateral supports to prevent buckling of the perimeter columns. However, when the perimeter columns deform toward the outside of the structure, simple connections between floors and the perimeter columns may rupture in tension. In this study, progressive failure of the perimeter columns in the framed-tube structures is simulated by the experiments using the simplified model. A number of the monotonic pseudo-static compressive tests are carried out for a steel column laterally supported by the aluminum boards with a notch in tension direction. Major findings include: (1) even 1% lateral support strength provide satisfactory behavior of the column before reaching the yield strength, (2) as the number of the lateral supports increases, the axial deformation of the column at the rupture of the lateral supports increases, (3) as the lateral support strength increases, the degradation of the column after the peak strength becomes smaller. These results indicate that the post-yield progressive failure of the perimeter columns in the framed-tube structures is mitigated by the increase of the strength and the number of lateral supports.

1. INTRODUCTION

Super high-rise framed-tube structures (Figure 1) often consist of rigid moment-resisting or truss frames in the perimeters and floors and gravity beams inside the building. Typical example of the framed-tube structure is the World Trade Center (FEMA403, 2002). These floors and gravity beams serve to limit the out-of-plane deformation of the perimeter frames and prevent perimeter column buckling by providing lateral supports. When the perimeter frames move toward the inside of the building during an earthquake, the floors and beams prevent this movement providing large compression force. However, when the perimeter frame moves toward the outside of the building, the simple connections (referred to as “link-elements” in this study) between the floors and the perimeter frames may fail in tension, and the perimeter frame may become unstable due to the lost of lateral supports from the link-elements. This small tension strength of connections between the perimeter frame and the floor is one of the reasons for progressive failure of the World Trade Center (FEMA403, 2002). The detail of such connection is shown in Figure 1(c).

To ensure the perimeter columns in the framed-tube structures subject to large compressive forces from earthquake loading, column buckling phenomena including lateral support failure in tension should be fully understood. In the past, many experiments have been carried out on the column

buckling with lateral supports modeled by elastic springs. However, none of experiments has been carried out to investigate the column buckling with lateral supports which (1) has asymmetric hysteretic forces in tension and compression and (2) is fragile in tension. In this study, to obtain the data on the necessary strength and stiffness of the link-elements to prevent the perimeter column buckling during an earthquake, the progressive failure of the perimeter column in the framed-tube structures is simulated by pseudo-static loading experiments using the simplified structural system.

2. EXPERIMENTAL SETUP

The simplified model to represent the major structural parameters of the framed-tube structures is illustrated in Figure 2. Here, one column of the perimeter frames is extracted and connected to in-plane moment frame through the link-element at each floor level without transferring moments. The in-plane moment frame is assumed to be rigid in this study. When the column moves toward the inside of the structure, the link-element and floors provide very large rigidity as shown in Figure 2. However, when the column moves toward the outside of the structure, the link-element may rupture in tension. In this study, to simulate the behavior of the perimeter columns subjected to increased axial force under an earthquake, the pseudo-static compressive loading tests are carried out for this structural system.

2.1 SPECIMEN AND EXPERIMENTAL APPARATUS

Figure 3 shows the specimen and experimental apparatus. The column specimen has 50(mm)×32(mm) rectangular section. Each story height is 185mm providing the slenderness ratio of 20 for each story. In this study, 6-story sub-frame is extracted, which is 1110mm in total height and the slenderness ratio of 120. The link-element (lateral support) is modeled by aluminum board with 3mm thickness (A1050) and the lateral support force is adjusted by inserting a notch. As shown in Figure 5, when the column specimen moves toward the inside of the structure, the floors attached to the stiffeners in the H-section steel column (H488x300x11x18), which simulate the in-plane moment frame in the framed-tube structures, prevent the movement. However, when the column specimen moves toward the outside of the structure, the outward forces are transmitted to the aluminum boards with a notch through the levers. When the aluminum board is subjected to the outward force equal to the tension strength of it, it ruptures. According to the monotonic tension tests for aluminum boards, the tension strengths are 3.69, 11.1, and 18.5kN for 10, 30, and 50mm widths of the aluminum board with a notch, respectively.

2.2 EXPERIMENTAL PARAMETERS

The experimental parameters are (1) the lateral support strengths, 1%, 3% and 5%, and (2) the number of the lateral supports, 1, 2, and 5. Also, assuming that the framed-tube structure has an atrium, the column is laterally supported at the mid-height and other floors are not constrained in both inward and outward directions. As a result, the total number of specimens is 10 as given in Table 1. The lateral support strength is represented by the ratio of the tension strength of the aluminum board with a notch at the rupture point to the yield strength of the column specimen. The representation using the ratio follows the design recommendation (AIJ, 1998), which requires that the lateral support force should be 3% or more of the column yield strength to prevent premature buckling. The lateral support force given in Table 1 is the nominal value. Based on the results of the monotonic tension tests for the aluminum boards, actual lateral support forces of the aluminum boards with a notch are 1.15%, 3.45%, and 5.74%, instead of 1%, 3%, and 5% of the nominal values, respectively.

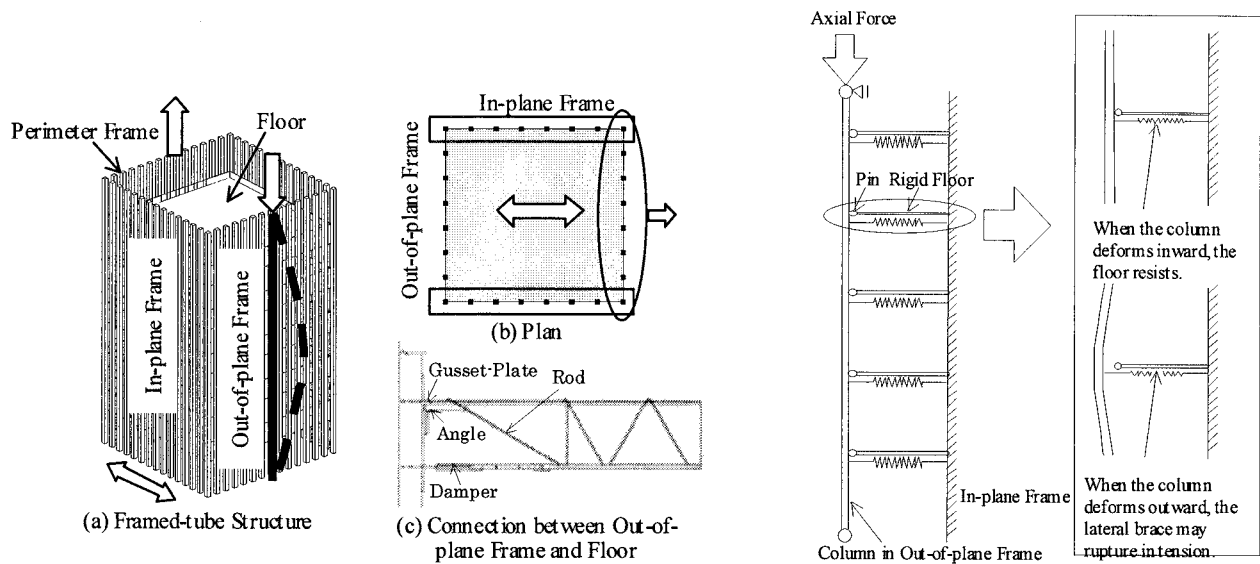


Figure 1: Overview of framed-tube structure Figure 2: Simplified model of framed-tube structure

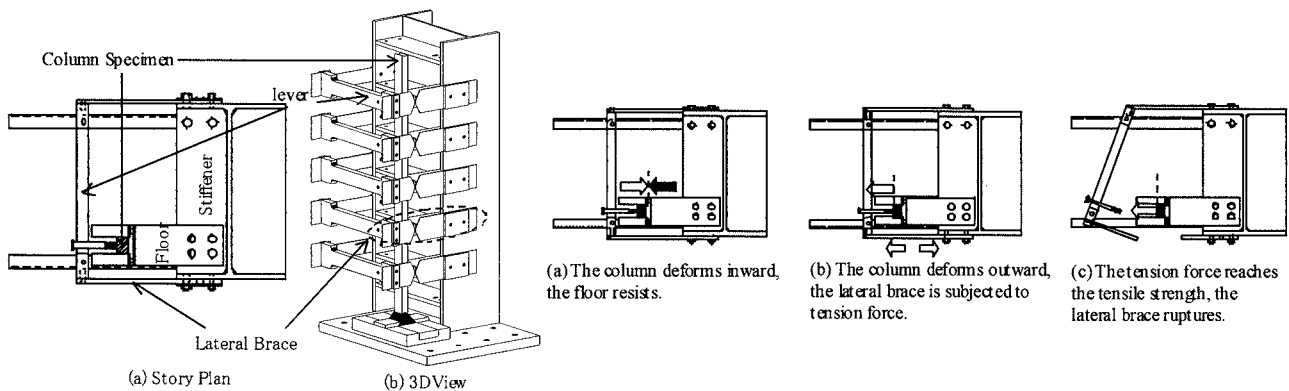


Figure 3: Experimental device

Figure 4: Mechanism of each floor

3. EXPERIMENTAL RESULTS

The pseudo-static compression tests are carried out for a column laterally supported by the aluminum boards with a notch. The total number of the specimens is 10. In this chapter, (1) the case of 5%_5 (5% lateral supports at all stories), (2) the comparisons of the three cases of the different number of lateral supports (5%_1, 5%_3, 5%_5), (3) the comparisons of the three cases of the different lateral support strengths (1%_5, 3%_5, 5%_5), and (4) the comparison of the cases with and without the atrium (1%_1(60), 1%_1, 3%_1) are discussed.

3.1 COLUMN BUCKLING WITH LATERAL SUPPORTS AT ALL FLOOR LEVELS

Figure 5 shows the vertical load (P) - vertical displacement (v) relationship for the column with 5% lateral supports at all floor levels (3%_5). Figure 6 shows the horizontal deformation of the column along the height at the stages of (1) $v/v_y = 0.5$, (2) peak strength, (3) right before the rupture of the lateral support at the 6th floor, (4) right after the rupture of the lateral support at the 6th floor, (5) right after the rupture of the lateral support at the 5th floor, (6) right before the rupture of the lateral supports

at the 4th, (7) right after the rupture of the lateral supports at the 4th, (8) right before the rupture of the lateral supports at the 2nd and 3rd floors, (9) right after the rupture of the lateral supports at the 2nd and 3rd floors, and (10) unloading. It is observed that the deflection increases significantly and its mode shape changes with the sudden decrease of the load after the progressive notch failure in tension. This is progressive failure.

3.2 COMPARISONS FOR NUMBER OF LATERAL SUPPORTS (5%_1, 5%_3, 5%_5)

Figure 7 compares the relationships of the axial force and axial displacement for the different number of lateral supports with 5% strength. All columns (5%_1, 5%_3, and 5%_5) reach the peak strengths greater than the short-term allowable strength for $\lambda = 60, 40$, and 20 specified by the design recommendation (AIJ, 1998). After the peak strength, the negative slope from the peak strength to the point where the aluminum board with a notch starts to rupture for the case of 5%_1 is -0.086, which is much larger than that of -0.043 for the case of 5%_5. This indicates that, as the number of the lateral supports increases, the degradation after the peak strength of the column becomes smaller. Therefore, the larger number of the lateral supports can delay and limit the progressive failure.

3.3 COMPARISONS FOR STRENGTH OF LATERAL SUPPORTS (1%_5, 3%_5, 5%_5)

Figure 8 shows the relationships of the axial force and axial displacement for the 1%, 3%, and 5% strengths of the lateral supports installed at all floor levels (i.e. 1%_5, 3%_5, 5%_5). When the strength is 1%, the tension forces transmitted to the lateral supports at the 5th and 6th floor levels increase dominantly compared with the other stories. When the tension forces in the lateral supports at the 5th and 6th floors reach the lateral support strength, the lateral supports in those stories rupture. Immediately after those ruptures, the lateral supports at the other stories are also subjected to the significant increase of the tension forces and finally rupture. After all lateral supports rupture, the displacement profile over the height becomes similar to the 1st mode shape. When the lateral support strengths are 3% or 5%, horizontal displacements increase in the upper stories and then the lateral supports rupture from the upper to the lower stories. As the lateral support force increases from 1%, to 3% and 5%, the axial displacement at the ruptures of the lateral supports increases, from $1.95\delta_y$ to $2.48\delta_y$ and $8.06\delta_y$. These indicate that larger lateral support strength can delay and limit the progressive failure of the column. However, in the perspective of the column design, the peak strength of the column reaches the yield strength of it in all cases. Therefore, if the perimeter column is designed so that it is subjected to the axial force smaller than the yield strength, the perimeter column in the framed-tube structures would perform well due to the lateral supports even with 1% strength, which is smaller than 3% strength specified in the design recommendation (AIJ, 1998).

3.4 COMPARISONS FOR CASES WITH AND WITHOUT ATRIUM (1%_1(60), 1%_1, 3%_1)

The column buckling tests are carried out for a column with one lateral support at the mid-height story with and without the atrium (1%_1(60) and 1%_1). First, the column is not attached to the floors assuming the original framed-tube structure has the atrium except at the 3rd floor level (1%_1(60)). The column reaches the short-term allowable design strength for a column with $\lambda = 60$ (AIJ, 1998). Also, the lateral support does not rupture and the displacement profile over the height is similar to the 2nd mode shape as shown in Figure 10. Next, when the lateral support at the mid-height is 1% and other stories are constrained (1%_1), right after the column reaches the peak strength, the lateral support ruptures and the significant degradation of the strength and stiffness occurs. Also, the specimen 3%_1 has the significant decrease of the strength right after the rupture of the lateral support. The results suggest that the constraints by the floors in the compression direction accelerate the rupture of the lateral support and then the failure of the perimeter column.

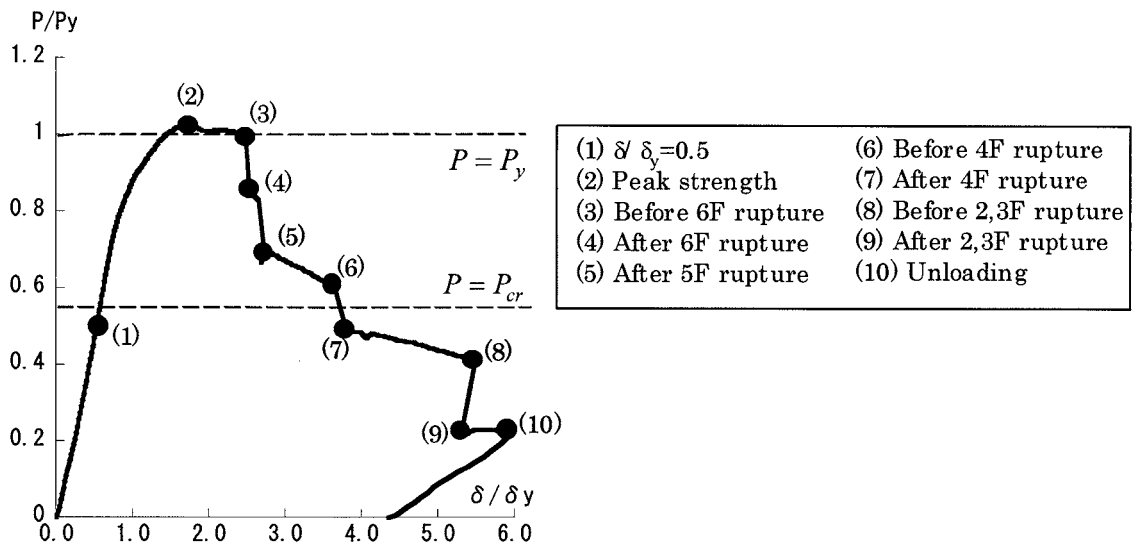


Figure 5: Load-axial deformation relationship for the specimen with 3% lateral strength at every floor.

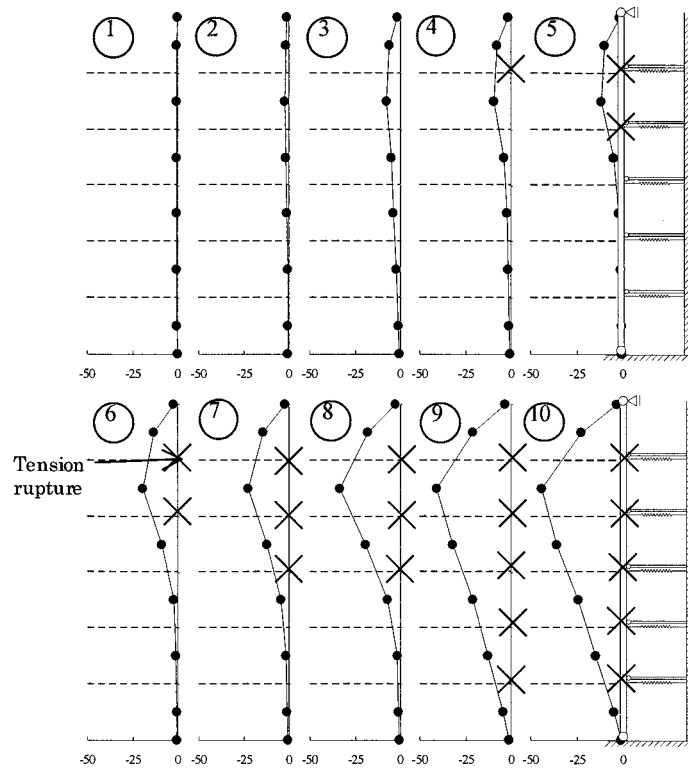


Figure 6: Deformation mode for the specimen with 3% lateral strength at every floor.

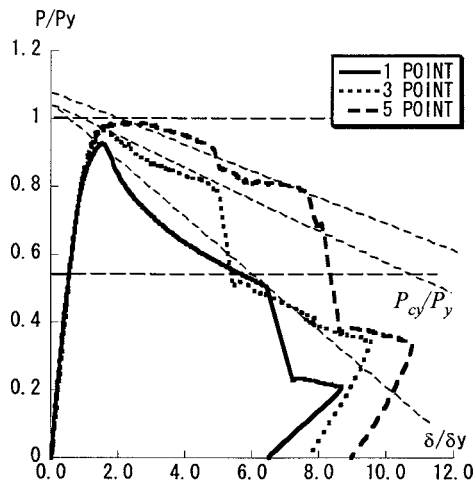


Figure 7: Difference in lateral support strength

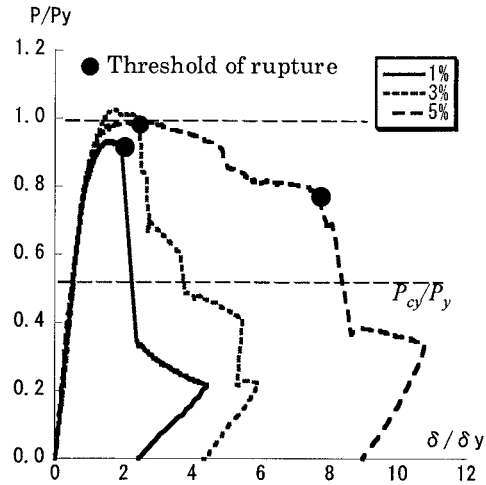


Figure 8: Difference in lateral support number

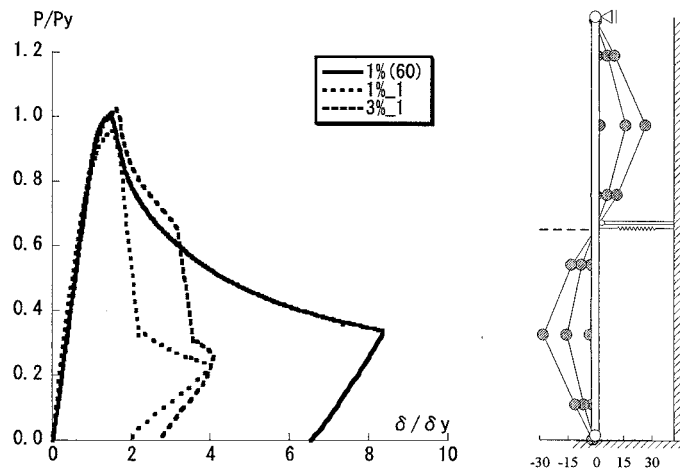


Figure 9: Response for the specimen with atrium

4. CONCLUSIONS

A number of pseudo-static compressive loading tests are performed for steel columns laterally supported by aluminum boards with a notch to simulate the perimeter columns in the framed-tube structures during earthquake loading. Major findings include:

1. The progressive failure of the perimeter columns in the framed-tube structures is simulated through pseudo-static experiments using simple structural models.
2. If the floor and gravity beams have stiffness and strength specified by the design recommendation (AIJ, 1998), the perimeter columns can be designed according to the short-term allowable design strength specified by the recommendation.
3. The progressive failure of the perimeter columns in the framed-tube structures can be delayed and limited by installing the lateral supports with larger strength and smaller spacing.

Acknowledgements:

This research work was sponsored by the Japan Society for the Promotion of Science (grant-in-aid for scientific research: 16206057, the leader of the project: Prof. Nonaka Taijiro, Chu-bu University).

References:

- Architectural Institute of Japan (1998), "Recommendation for Limit State Design of Steel Structures".
 FEMA403 (2002), "World Trade Center Building Performance Study: Data Collection, Preliminary Observations, and Recommendations", FEMA, Washington, DC.

EXPERIMENTAL VERIFICATION ON BUCKLING-RESTRAINT DESIGN OF KNEE BRACE DAMPER

Yuji Koetaka¹⁾, Yasuki Byakuno²⁾, and Kazuo Inoue³⁾

1) Research Associate, Dept. Architecture and Architectural Engineering, Kyoto Univ., Japan

2) Structural Designer, Tokyo Head Office, Obayashi Corporation, Japan

3) Professor, Dept. Architecture and Architectural Engineering, Kyoto Univ., Japan

koetaka@archi.kyoto-u.ac.jp, biyakuno.yasuki@obayashi.co.jp, inoue@archi.kyoto-u.ac.jp

Abstract An innovative structural system, named weld-free system, has been developed to overcome the difficulty in quality assurance encountered in construction of steel moment resisting frames with conventional welded connections. Wide flange columns and beams are connected by means of double angles and high strength bolts. And buckling-restrained braces, referred to as knee brace dampers, are implemented to improve lateral stiffness of the frame as well as to dissipate seismic input energy. In this paper, buckling-restraint design of the knee brace damper is presented, and an experimental verification that was conducted on sub-assembled test specimens is described. The test results clearly reveal that knee brace dampers can have large and stable hysteresis loop if they satisfy the proposed design criteria.

1. INTRODUCTION

In order to assure sufficient plastic deformation capacity of welded beam-to-column connections for steel structures, various suggestions have been made in the United States and Japan after the 1994 Northridge earthquake and the 1995 Hyogoken-Nanbu earthquake. For example, the reduced beam section design (FEMA, 2000) has been widely accepted in the United States as an effective and economic solution. On the contrary, based on the observation that cracks often initiated at the toe of the weld access hole, Japanese researchers placed more emphasis on connection details to mitigate stress concentrations at welds. Although modified connections have shown satisfactory performance in the laboratories, it is realized that the quality of welds is difficult to control in practice so long as the structural fabrication relies on workmanship. The defects as well as insufficient deposition are often of concern regardless of the connection details adopted. As compared with welded connections in the United States, the Japanese practice generally requires larger volume of weld, implying that the Japanese connections are more relevant to the quality assurance problems (Nakashima, 2000).

To overcome the difficulty in the weld quality assurance as well as stringent post-Kobe requirements for welding practice, an idea to mainly utilize high strength bolts in beam-to-column connections with the number of welds minimized is appealing. In this regard, an innovative structural system, the "weld-free" system has been proposed (Inoue et al., 2006). The distinctive feature of the proposed system is that, with wide flange steel adopted for beams and columns, the conventional welded beam-to-column connection is replaced by a mechanical joint equipped with buckling-restrained braces. The brace, named "knee brace damper," is implemented to improve lateral stiffness of the frame as well as to dissipate seismic input energy. In order to ensure that knee brace dampers have large and stable hysteresis loop as well as sufficient plastic deformation

capacity, it is important to design restraining members, bolted connections, and other details. This paper addresses not only buckling-restraint design of knee brace dampers but also experimental verification which was conducted on full-scale subassemblies.

2. STRUCTURAL SYSTEM

Fig. 1 shows beam-to-column connection of weld-free structural system. Wide-flange beams are connected to the wide-flange column only at the top flanges by means of double angles and high strength bolts. At the top and bottom of the beams, knee brace dampers are installed primarily to provide the structural system with sufficient lateral resistance against design seismic force and, at the same time, dissipate seismic input energy during a strong earthquake [see left side in Fig. 1]. In interior frames, to preserve the large opening, knee brace damper may be implemented only at the bottom of the beam [see right side in Fig. 1]. This connection arrangement would place the center of the beam rotation at the end of the beam top flange. As a result, knee brace dampers can freely deform without causing a significant damage to the concrete floor slab under large story drifts.

The buckling-restrained knee brace damper developed in this research is more compact than those devised previously (e.g., Iwata et al., 2000; Uang and Nakashima, 2004). As shown in Fig. 2, the core plate is made of a steel rectangular bar coated with a friction-reduced material, and is encased in a sheath called restraining member. The restraining member is made of two kinds of steel plates, which are named face plate and side plate, and these steel plates whose friction surfaces are treated by shot blasting are connected by high strength bolts. The side plates should be slightly thicker than the core plate to secure the clearance between the core plate and the face plate. The width at the end of the core plate is expanded to avoid yielding, and at the same time, the core plate is welded with full penetration to the end plates, which are connected to the beam flange or the column flange by high strength bolts. The only part in this system that requires highly skilled workmanship is welding at the end plates. To confine axial deformation of the knee brace damper to the core plate, a small gap is provided between the restraining member and the end plate so that they do not touch each other when the knee brace damper sustains contractions. And the face plate is held at the center of the core plate by welding, in order to keep the both gaps even.

The weld-free structural system employs the connection between the beam top flange and the column flange as a means for transferring gravity loads from the beams to the columns. Under a strong earthquake, significant yielding excursion is expected only at the knee brace dampers. Beams and columns are designed to respond in the elastic range, except at the base of the structure where some plastic deformations may be allowed in the columns. Accordingly, the behavior of the weld-free system can be regarded as "strong column-strong beam-weak brace."

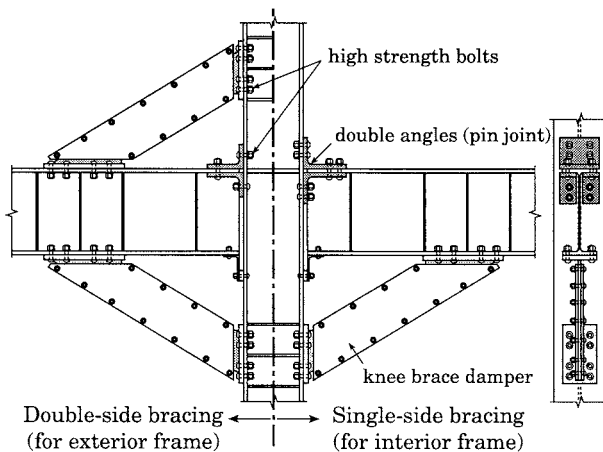


Figure 1. Details of beam-to-column connection of weld-free structural system

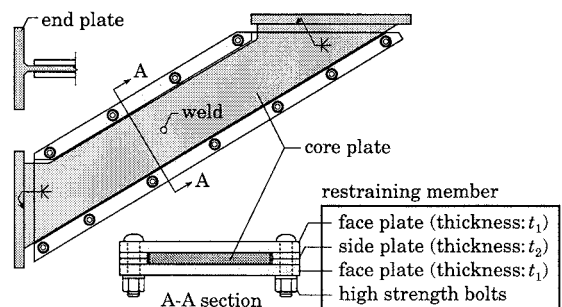


Figure 2. Details of buckling-restrained knee brace damper

3. BUCKLING-RESTRAINT DESIGN

The restraining member is designed to prevent both overall buckling and local failure. In order to prevent overall buckling, it is necessary that the restraining member must remain elastic (Inoue et al., 1993; Inoue et al., 2001), and at the same time, the slip between the face plate and the side plate must not occur. These requirements are called the condition of preventing flexural failure and the condition of preventing slip. As shown in Fig. 7 in the latter part of this section, the face plate can yield between the bolts in case the restraining member satisfies these conditions. Consequently, it needs to prevent the face plate from yielding, and this requirement is called the condition of preventing local failure.

3.1 The condition of preventing flexural failure : Design criteria (i)

Fig. 3 shows a mechanical model for buckling-restraint of knee brace damper. In Fig. 3, ${}_dN_{\max}$ means the maximum axial load for design of restraining member, and is defined by multiplying yield axial force ${}_dN_y$ by ${}_d\alpha$. The value of ${}_d\alpha$ is chosen from 1.4 to 1.5 by depending on steel grade of core plate. e means unavoidable fabrication error of welding between the core plate and the end plates. And s , which is calculated by subtracting thickness of the core plate from thickness of the side plate, means the clearance between the core plate and the face plate. If initial deflection of the restraining member is half-sine curve and initial deflection of the center of the restraining member is a , curvature of the restraining member is $d^2(u - u_0)/dx^2$. Consequently, equilibrium of bending moment of the restraining member in Fig. 3 is shown as Eq. (1).

$$E_B I_B \frac{d^2(u - u_0)}{dx^2} + {}_dN_{\max}(u + S + e) = 0 \quad (1)$$

$$u_0 = a \sin \frac{\pi x}{l}, \quad S = s \sin \frac{\pi x}{l} \quad (2a), (2b)$$

And length of the core plate l is defined by Fig. 4. The maximum bending moment of the restraining member is approximated by adopting up to the second order of formula by summation of series and assuming $\pi^2/8$ as 1, as shown Eq. (3).

$$M_C^B = \frac{a + s + e}{1 - {}_dN_{\max} / N_E^B} {}_dN_{\max} \quad (3)$$

In order to prevent the knee brace damper from overall buckling, it needs that the yield bending moment of the restraining member is larger than the maximum bending moment. Consequently, Eq. (4) is obtained from Eq. (3).

$$\left(1 - \frac{1}{n_E^B}\right) m_y^B > \frac{a + s + e}{l} \quad (4)$$

$$n_E^B = \frac{N_E^B}{{}_dN_{\max}} = \frac{\pi^2 E_B I_B}{{}_dN_{\max} l^2}, \quad m_y^B = \frac{M_y^B}{{}_dN_{\max} l} \quad (5a), (5b)$$

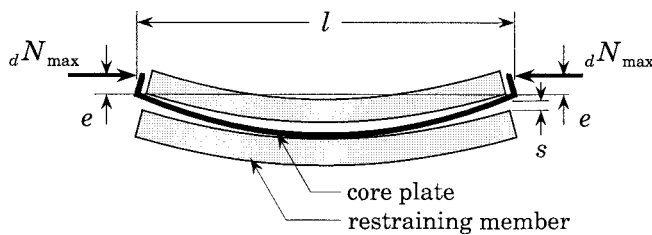


Figure 3. Mechanical model of the knee brace damper

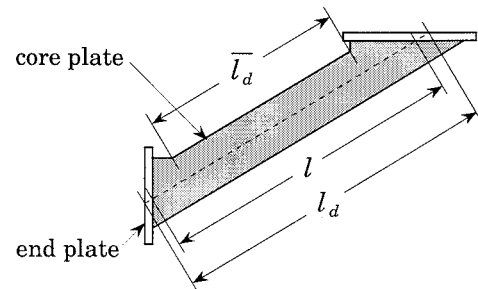


Figure 4. Definition of length of the core plate

3.2 The condition of preventing slip between face plate and side plate : Design criteria (ii)

If the slip between the face plate and the side plate occurs, geometrical moment of inertia of the restraining member decreases rapidly. Calculating the required bolts in number to prevent the slip is represented as follows.

Distribution of the bending moment of the restraining member is shown in Fig. 5 when knee brace damper sustains the maximum axial load for design ${}_dN_{\max}$. The maximum bending moment of the restraining member is shown in Eq. (3) and the minimum bending moment at the end of the restraining member is obtained by Eq. (6).

$$M_0^B = e {}_dN_{\max} \quad (6)$$

Set of forces at the center of face plates, as shown in Fig. 5, is obtained from the bending moment. Shear force Q_s , which is distributed on a half side of the restraining member, can be calculated by using the set of forces.

$$Q_s = \frac{M_C^B - M_0^B}{t_1 + t_2} \quad (7)$$

When Q_s acts between the face plate and the side plate in a half side of the restraining member, the required bolts in number of the restraining member is obtained by Eq. (8).

$$n_b \geq \frac{2Q_s}{\mu_f N_0} \quad (8)$$

Where, μ_f is a coefficient of friction and N_0 is initial tensile force of a bolt.

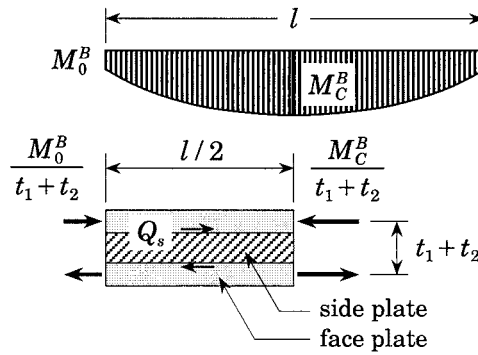


Figure 5. Bending moment and shear force acted on the restraining member

3.3 The condition of preventing local failure : Design criteria (iii)

The core plate pushes out the face plate after the core plate becomes a deformed high degree buckling mode under the compressive axial force, as shown in Fig. 6. Local failure occurs between bolts of the restraining member as shown in Fig. 7 if the face plate yields against the force B . Here, it is assumed that the flexural rigidity of the core plate which yields under the compressive axial force is negligible and the core plate sustains only axial force, and then the force B is obtained from Eq. (9).

$$B = \frac{4 {}_dN_{\max} s}{l_n} \quad (9)$$

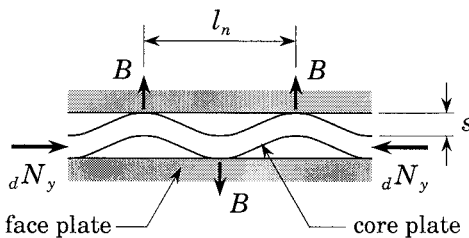


Figure 6. Force B acting on the face plate

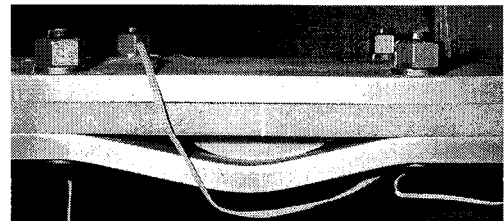


Figure 7. Local failure of the restraining member

In Eq. (9), l_n is the wavelength of buckling mode. If the wavelength does not vary after yielding, l_n is calculated by substituting ${}_dN_y$ for tangent modulus load of the core plate, as shown in Eq. (10).

$$l_n^2 = \frac{4\pi^2 E_t I_s}{{}_dN_y} \quad (10)$$

Where, E_t is tangent modulus of the core plate and I_s is geometrical moment of inertia around weak-axis of the core plate. E_t can not be decided in a theoretical sense, so that $0.05 E$ which is based on the experimental results (Shimokawa et al., 1998) is adopted in this paper, and E is Young's modulus. In order to prevent the face plate from yielding, the yield moment of the face plate M_y^f must be larger than the moment acted by the force B . The moment acted by the force B should be decided in consideration of the most disadvantageous situation, that is to say, the force B acts on the middle of bolt pitch l_p of the restraining member and the face plate is supported on the points of the bolts as pins. Consequently, the condition of preventing local failure is defined in Eq. (11).

$$M_y^f > \frac{B l_p}{4} \quad (11)$$

4. LOADING TESTS

4.1 Test Specimens

In order to verify buckling-restraint design, loading test was conducted. There are five specimens as shown in Table 2. The cross section of 175×16 mm is chosen for the core plate of all specimens. At the same time, elements such as thickness of the face plate, thickness of the side plate, friction surface, and number of bolts, that compose the restraining members, are different from each other. Here, 9+9, which is denoted in the column of thickness of the side plate t_2 , means that two pieces of plates with 9 mm thickness are applied, and the clearance between the core plate and the face plate is ensured to be 2 mm. And either shot blasted or "as it is" is selected as friction

Table 2. Test specimens

Specimen No.	t_1 (mm)	t_2 (mm)	s (mm)	friction surface	n_b (F10T M16)	Design criteria of the restraining member		
						(i)	(ii)	(iii)
No. 1	16	9+9	2	shot blasted	11	OK	OK	OK
No. 2	9	9+9	2	shot blasted	11	NG	NG	NG
No. 3	9	9+9	2	shot blasted	22	NG	NG	NG
No. 4	16	9+9	2	as it is	11	OK	NG	OK
No. 5	16	19	3	shot blasted	11	OK	OK	NG

signs

t_1 : thickness of the face plate,

t_2 : thickness of the side plate,

s : clearance between the core plate and the face plate, which equals to difference of t_1 and t_2 ,

n_b : number of high strength bolts of the restraining member.

Table 3. Mechanical properties of steel materials used for specimens

Sampled part (Specimen No.)	Steel grade	thickness (mm)	Yield stress (N/mm ²)	Tensile stress (N/mm ²)	Elongation (%)
The core plate (all specimen)	SN400B	16	289	428	33
The face plate (No. 1, 4, and 5)	SS400	16	262	428	32
The face plate (No. 2 and 3)	SS400	9	298	451	30

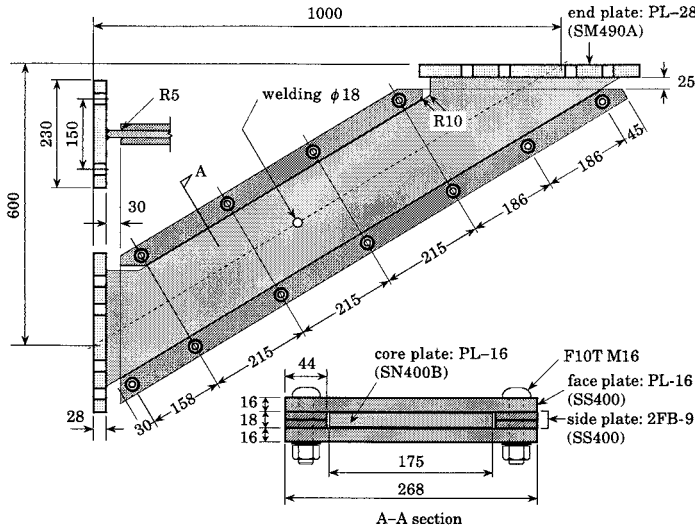


Figure 8. Details of knee brace damper (No. 1)

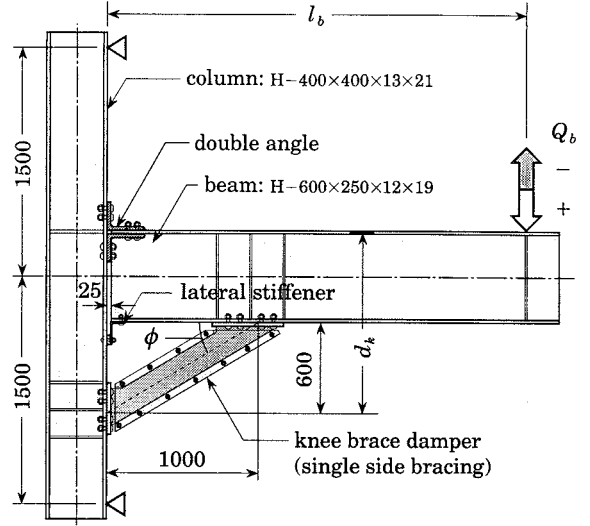


Figure 9. Test setup

surfaces of the face plates and the side plates, as it is, i.e., meaning the mill-scale is left on the surface of the plate. Experimental verification of coefficient of friction was conducted in addition to the test. As a result, the coefficient of friction by shot blasted is 0.42 and the coefficient of friction by "as it is" is 0.30. Mechanical properties of steel materials used for specimens are shown in Table 3.

Based on nominal strength and assumed $\alpha = l/1000$ and $e = 1$ mm as initial deflection, only No. 1 (to refer Fig 8) satisfies all design criteria, while other specimens don't satisfy either (i), (ii), or (iii) of criteria as shown in Table 2.

4.2 Test Setup and Loading Program

Fig. 9 shows test setup. Lateral length of knee brace damper is 1000 mm, vertical length of knee brace damper is 600 mm, and half span l_b is 2775 mm. And d_k , which is calculated by adding vertical length knee brace damper and beam depth and by subtracting half of thickness of beam flange besides, is 1190.5 mm. Lateral stiffener is attached at the end of the beam bottom flange in order to restrain lateral displacement of the beam.

Beam tip was loaded alternately with two cycles of $\varepsilon = \pm 2\%$, and subsequent cycles of $\varepsilon = \pm 4\%$ applied up to the ultimate state. Here, ε means average strain of the core plate and is obtained longitudinal deformation between end plates divided by the length of parallel part \bar{l}_d , which is shown in Fig. 4. As a result, story drift angle is almost equal to the average strain ε . It was expected that testing at the level of $\varepsilon = \pm 2\%$ would reveal the performance of the structures under a large earthquake. Loading was, however, applied up to $\varepsilon = \pm 4\%$ to explore the structural behavior under deformation significantly larger than that considered in seismic design codes. Axial force of knee brace damper is calculated by Eq. (12), assuming that the beam is connected to the column at the end of the beam top flange as pin joint.

$${}_dN = \frac{Q_b l_b}{d_k \cos \phi} \quad (12)$$

4.3 Test Results

Fig. 10 presents the axial force of knee brace dampers ${}_dN$, which is normalized by the yield axial force ${}_dN_y$ based on yield stress in Table 2, versus the average strain ε . The triangle marks in Fig. 10 mean the points that specimens form failure modes (to refer Fig. 11). Additionally, prediction of failure mode and test results of each specimen are shown in Table 4. The critical strengths ${}_1N_{cr}$, ${}_2N_{cr}$, and ${}_3N_{cr}$ correspond to limit of preventing overall buckling, slip between the face plate and the side plate, and local failure of the face plate, respectively. Firstly, ${}_1N_{cr}$ is obtained from Eq. (13) by substituting ${}_1N_{cr}$ to ${}_dN_{\max}$ and M_y^B to M_C^B in Eq. (3).

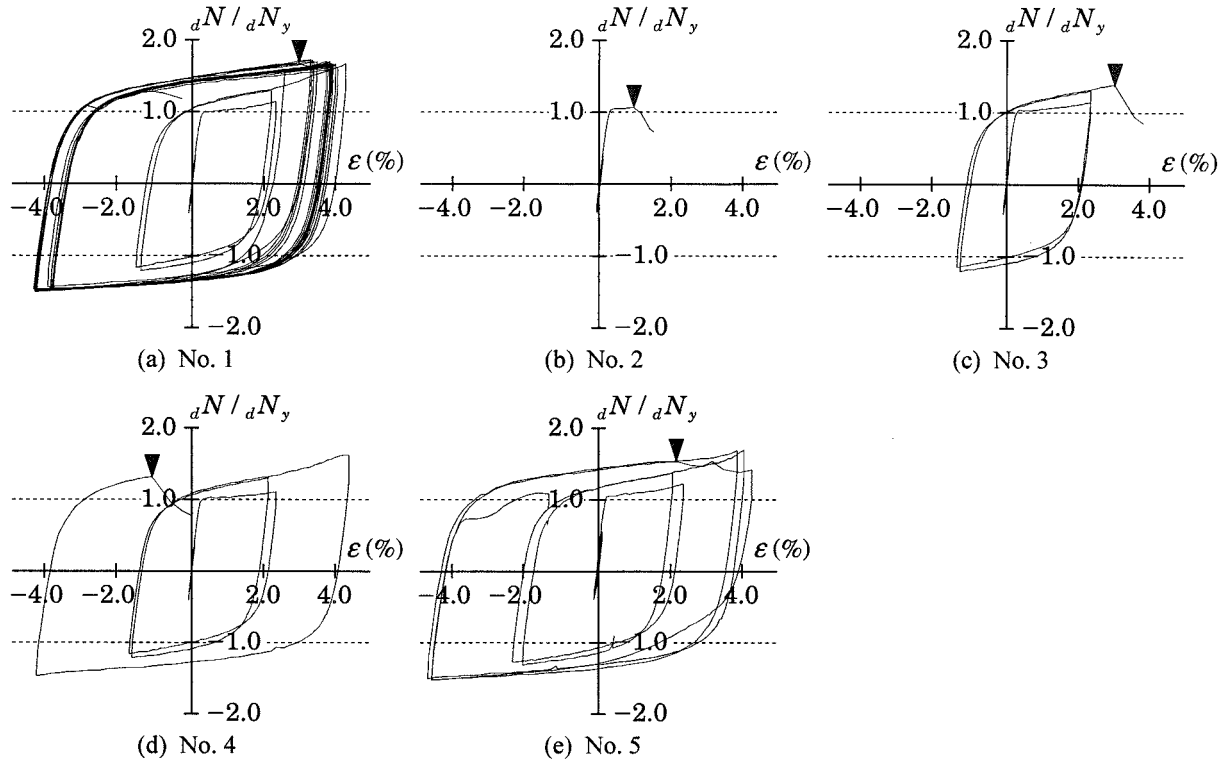


Figure 10. Axial force dN versus the average strain ε of knee brace dampers

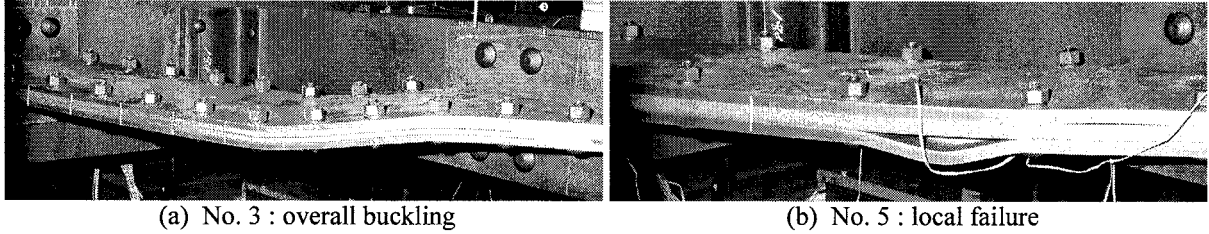


Figure 11. Examples of failure mode

$${}_1N_{cr} = \frac{M_y^B}{a + s + e + M_y^B / N_E^B} \quad (13)$$

Next, maximum moment at the center of the restraining member is presented in Eq. (14) in order to obtain ${}_2N_{cr}$.

$$M_C^B = \frac{a + s + e}{1 - {}_2N_{cr} / N_E^B} {}_2N_{cr} \quad (14)$$

Substituting Eq. (14) to Eq. (7), ${}_2N_{cr}$ can be calculated. And finally, ${}_3N_{cr}$ is obtained by Eq. (15).

$${}_3N_{cr} = \frac{M_y^f l_n}{s l_p} \quad (15)$$

In Table 4, bold text in the column of either ${}_1N_{cr}$, ${}_2N_{cr}$ or ${}_3N_{cr}$ means the minimum value among ${}_1N_{cr}$, ${}_2N_{cr}$ and ${}_3N_{cr}$. Failure mode is predicted to overall buckling if the minimum value is ${}_1N_{cr}$ or ${}_2N_{cr}$. On the contrary, failure mode is predicted to local failure if the minimum value is ${}_3N_{cr}$. As shown in Table 6, the prediction of failure mode agrees with the test results absolutely. And it is verified that the buckling-restraint design of knee brace damper is valid for practical design.

The details of test results are as follows. In No. 1 specimen, large and stable hysteresis loop was shown, and finally local failure occurred in the 17th cycle of $\varepsilon = \pm 4\%$. And it is verified that plastic

Table 4. Prediction of failure mode and test results

Specimen No.	Prediction					Test results		
	Failure mode	${}_1N_{cr}$ (kN)	${}_2N_{cr}$ (kN)	${}_3N_{cr}$ (kN)	$N_{cr} / {}_dN_y$	Failure mode	ϵ_{max} (%)	η
No. 1	local failure	2388	1219	1203	1.49	local failure	4.37	1744
No. 2	overall buckling	960	668	809	0.83	overall buckling	0.97	–
No. 3	overall buckling	960	971	1013	1.19	overall buckling	3.03	82
No. 4	overall buckling	2388	969	1203	1.20	overall buckling	4.40	182
No. 5	local failure	2273	1062	809	1.00	local failure	4.78	423

Here, $N_{cr} = \min \{ {}_1N_{cr}, {}_2N_{cr}, {}_3N_{cr} \}$,

ϵ_{max} : maximum strain of the core plate,

η : ratio of the cumulative plastic deformation of the core plate

($= \sum \epsilon_p / \epsilon_y$; $\sum \epsilon_p$ is the cumulative plastic strain and ϵ_y is the yield strain).

deformation capacity is as much as about 10 times against a strong earthquake if the knee brace damper satisfies with all design criteria. All of No. 2, No. 3, and No. 4 specimens, which didn't satisfy the condition of preventing either overall buckling or slip, formed overall buckling as shown in Fig. 11 (a). In No. 5 specimen, local failure occurred as predicted.

5. CONCLUSIONS

This paper has presented the experimental verification of the buckling restrained knee brace dampers which were equipped with beam-to-column connections in the proposed weld-free system. The test results clearly reveal that knee brace dampers can have large and stable hysteresis loop if they satisfy the proposed design criteria: the conditions of preventing flexural failure of the restraining member (Eq. (4)), the condition of preventing slip between the face plate and the side plate (Eq. (8)), and the condition of preventing local failure of the face plate (Eq. (11)).

Acknowledgments:

The loading test was supported by the Ministry of Education, Culture, Sports, Science, and Technology of Japan (No. 13305307). And the third author was the principal investigator of this project. The authors express to thank M. Nakashima and K. Suita of Kyoto University, and wish to thank the graduate students of Kyoto University.

References:

- Federal Emergency Management Agency (FEMA). (2000). "Recommended seismic design criteria for new steel moment-frame buildings," *FEMA350*, Washington, D.C.
- Inoue, K., Chang, P. Y., Mine, T., Hukuyama, K., and Inoue, K. (1993). "Stiffening design of the precast concrete panels to prevent the steel flat braces from buckling," *J. Constr. Steel*, (1), pp. 195-202, (in Japanese).
- Inoue, K., Sawaizumi, S., and Higashibata, Y. (2001). "Stiffening requirements for unbonded braces encased in concrete panels." *J. Struct. Eng.*, 127 (6), pp. 712-719.
- Inoue, K., Suita, K., Takeuchi, I., Chusilp, P., Nakashima, M., and Zhou, F. (2006) "Seismic-resistant weld-free steel frame buildings with mechanical joints and hysteretic dampers," *J. Struct. Eng.*, 132 (6), pp. 864-872.
- Iwata, M., Kato, T., and Wada, A. (2000). "Buckling-restrained braces as hysteretic dampers," *Proc., 3rd Int. Conf. on Behavior of Steel Structure in Seismic Areas (STESSA 2000)*, Montreal, pp. 33–38.
- Nakashima, M. (2000). "Quality assurance for welding of Japanese welded beam-to-column connections," *Proc., 3rd Int. Conf. on Behavior of Steel Struct. in Seismic Areas (STESSA 2000)*, Montreal, pp. 223-230.
- Shimokawa, H., Morino, S., Kamiya, M., Ito, S., Kawaguchi, J., Kamura, H., and Hirota, M. (1998). "Elasto-plastic behavior of flat-bar brace stiffened by square steel tube (Part 7)," *Summaries of Technical Papers of Annual Meeting Architectural Institute of Japan*, Structures III, pp. 843-844, (in Japanese).
- Uang, C. M., and Nakashima, M. (2004). "Steel buckling-restrained braced frames," *Earthquake engineering from engineering seismology to performance-based engineering*, Chap. 16, CRC, Boca Raton, Fla., pp. 1-37.

A Beam Element for Approximate Analysis of Truss Beam lateral Postbuckling behavior

S. Motoyui¹⁾, and S. Ogata²⁾

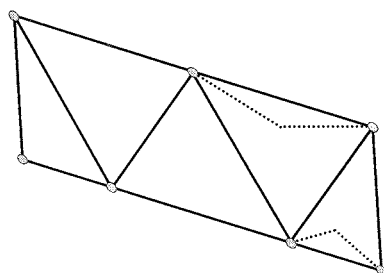
1) Associate Professor, Department of Built Environment, Tokyo Institute of Technology, Japan

2) Graduate Student, Department of Built Environment, Tokyo Institute of Technology, Japan
motoyui.s.aa@m.titech.ac.jp, ogata.s.ab@m.titech.ac.jp

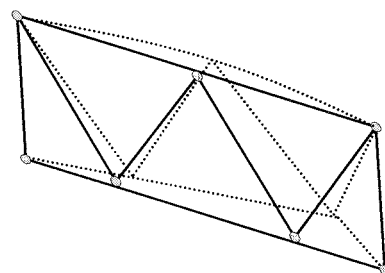
Abstract: The space frame structure has special characteristics that it is used as the temporary shelters while the catastrophe. Therefore it is generally designed as the member does not buckle and yield against the very rare large earthquake. It is because the space frame structure occurs quickly strength degradation after member's buckling and yielding and can not be expected the plastic deformation capacity like the layered structure. Therefore it is significant to grasp the collapse behavior of the space frame structure which is designed by elastic limit to account for the true safeness of it. One of the space frame structure's types is a pattern which consists of 2-D or 3-D continuously arranged truss beams. Its typical collapse phenomena are in-plane buckling and out-of-plane buckling of the chord member. This study focuses the out-of-plane postbuckling behavior of the chord member and proposes a simple numerical method for approximating the strength degradation caused by elastoplastic buckling with a small chord member's slenderness ratio. The validity of this method then is examined through some numerical examples.

1. INTRODUCTION

The collapse behavior of the truss beam is classified mainly into two patterns: in-plane buckling (Figure 1.a) and out-of-plane buckling (Figure 1.b). The in-plane buckling model is a very simple, that is, the axial force of this model is uniform to assume that each section separated by diagonal bracing is one model. In contrast, out-of-plane buckling model is complicated, that is, the axial force of this model is non-uniform to assume that both upper and lower chord members are single elements. One of authors has already researched on the elastoplastic postbuckling behavior of chord members in in-plane buckling and has suggested an effective continuous model for truss beams with chord member's elastoplastic buckling behavior [1]. However, to grasp the collapse behavior for all cases, the out-of-plane buckling of the truss beam has to be considered.



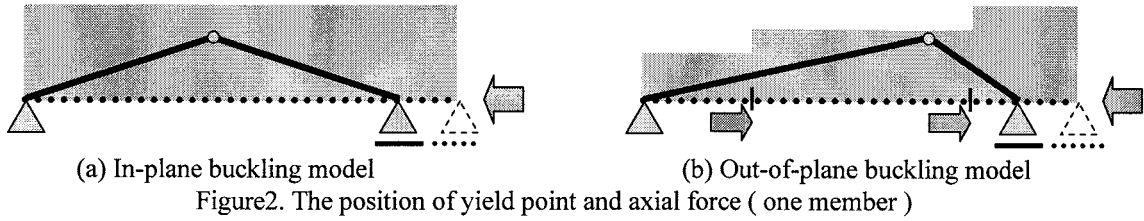
(a) In-plane buckling



(b) Out-of-plane buckling (Lateral buckling)

Figure1. Buckling mode

The axial force working on upper and lower chord members is non-uniform because there is axial external force working on the chord members, which comes from the axial force that works on the braces bearing the shear force of the truss beam. Therefore, when the upper and lower chord members yield to the elastoplastic buckling from the lateral buckling of the truss beam, the buckling point (the yield point) shifts a larger portion of axial force from the center of the members (Figure 2.). When dealing with lateral buckling of the truss beams, to take the constraint on out-of-plane with brace as well as warping torsion into consideration may be needed. However in this paper, a simplified model capable of pursuing the strength degradation for the elastoplastic buckling of upper and lower chord members under non-uniform axial force is proposed. This simplified model can be achieved by using the simplest plastic hinge model. The validity of our model then is examined through some numerical examples. The range of application for this model is when the chord member's slenderness ratio is much less. Using this restraint, a simple evaluation method can be proposed, which approximates total rotation θ by replacing θ for plastic components of rotation θ_p to handle the elastoplastic buckling problem in the same manner as the elastoplastic problem.



2. BASIC EQUATIONS OF CHORD MEMBER

First, the basic equations using the plastic hinge model are derived. Figure3 shows the chord member model which has n intermediate external forces of axial direction. To facilitate understanding of this formulation, the member is divided into two parts at the plastic hinge as shown in Figure3 (b,c). In addition, the shear force Q gives

$$Q = \frac{n}{2} \beta N \theta_L \quad (1)$$

Where β is an axial force ratio, N is external force, and θ_L is total left rotation. It is assumed that the Helmholtz free energy Ψ_R for the right-hand-side part in Figure3(c) can be written as

$$\Psi_R = \frac{1}{2} \frac{EA}{\alpha L} \left(u_C - u_B - u_{pR} + \frac{\alpha L}{2} \theta_R^2 \right)^2 + \frac{1}{2} \frac{3EI}{\alpha L} \left(\theta_R - \phi - \theta_{pR} \right)^2 \quad (2)$$

Where α is the coefficient which shows the position of plastic hinge, ϕ is the rotation of plastic hinge, and u_{pR} and θ_{pR} are plastic components of a stretch and a rotation. In this paper, it is assumed that θ is always positive and chord members do not buckle until these members yield. The right-hand-side of the Clausius-Duhem inequality, which holds under the second law of thermodynamics, can be expressed by

$$-\dot{\Psi}_R + N(\dot{u}_C + \dot{u}_B) + M(-\dot{\phi}) - Q(\alpha L \dot{\theta}_R) \geq 0 \quad (3)$$

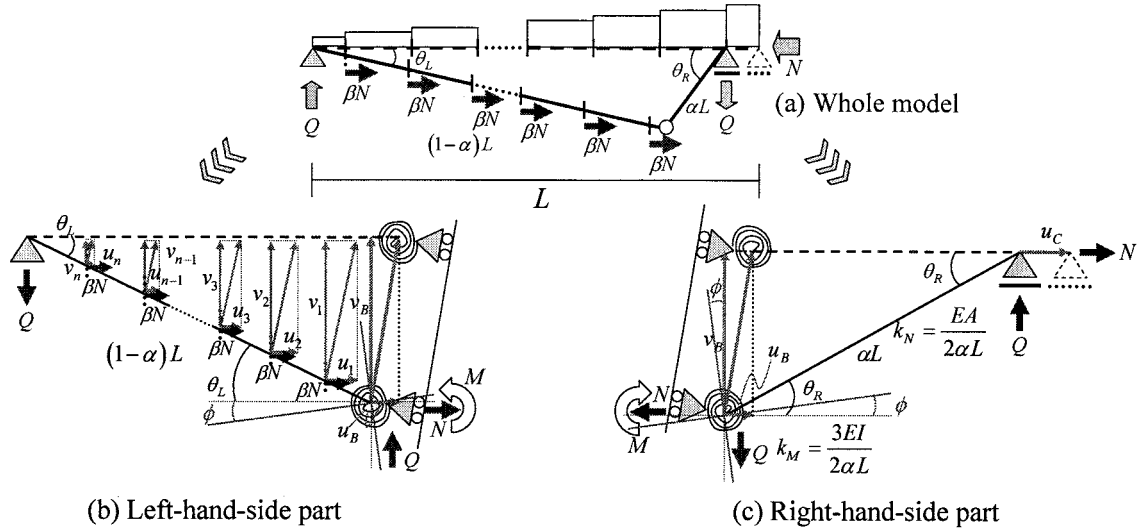


Figure3. Mechanical model

By substituting Eq.(2) into the Clausius-Duhem inequality, basic equations with right-hand-side part give:

$$N = \frac{EA}{\alpha L} \left(u_C - u_B - u_{pR} + \frac{\alpha L}{2} \theta_R^2 \right), \quad M = \frac{3EI}{\alpha L} (\theta_R - \phi - \theta_{pR}) \quad (4-a,b)$$

$$\Xi = -Q\alpha L - N\alpha L\theta_R - M = 0, \quad \Gamma = N\dot{u}_{pR} + M\dot{\theta}_{pR} \geq 0 \quad (4-c,d)$$

As with right-hand-side part, basic equations with left-hand-side part are obtained. Moreover, basic equations with whole model are obtained by considering the equilibrium of force about plastic hinge.

$$N = \frac{2}{2+n\beta} \frac{EA}{L} \left(u_C - u_p + \frac{\alpha(1-\alpha)L}{2} \theta^2 \right), \quad M = \frac{3EI}{L} (\theta - \theta_p) \quad (5-a,b)$$

$$\Xi = -\frac{(2-2\alpha+n\alpha\beta)\alpha}{2} NL\theta - M = 0, \quad \Gamma = N\dot{u}_p + M\dot{\theta}_p \geq 0 \quad (5-c,d)$$

where

$$\theta_R + \theta_L = \theta, \quad u_{pR} = u_{pL} = \frac{1}{2}u_p, \quad \theta_{pR} = \theta_{pL} = \frac{1}{2}\theta_p$$

Eq.(5-a) and Eq.(5-b) represent the elastic constitutive equations. Eq.(5-c) and Eq.(5-d) represent the equilibrium of the moment in plastic hinge and the plastic dissipation term. Here, the yield function for the chord members is defined as described below

$$\Phi(N, M) = \left(\frac{N}{N_y} \right)^2 - \left| \frac{M}{M_p} \right| - 1 \leq 0 \quad (6)$$

where N_y and M_p are yield axial force and full-plastic moment. Then, Eq.(6) can be rewritten by Eq.(5-c) as follows

$$\Phi(N, \theta) = \frac{|N|}{N_y} - \bar{\tau}(\theta) \leq 0 \quad (7-a)$$

$$\bar{\tau}(\theta) = \bar{\sigma}(\theta) - \frac{(2-2\alpha+n\alpha\beta)\alpha N_y L \theta}{4M_p}, \quad \bar{\sigma}(\theta) = \sqrt{1 + \left(\frac{(2-2\alpha+n\alpha\beta)\alpha N_y L \theta}{4M_p} \right)^2} \quad (7-b)$$

Here, the principle of maximum plastic dissipation is introduced to specify the post-buckling behavior. Therefore consider the Lagrangian, $L = -\Gamma + \dot{\lambda}_p \Phi$, where $\dot{\lambda}_p$ is a plastic consistent parameter. Differentiation of the Lagrangian with respect to N or θ gives

$$\dot{u}_p = \frac{N}{N_y^2} \frac{1}{\bar{\sigma}(\theta)} \dot{\lambda}_p, \quad \dot{\theta}_p = -\frac{\text{sgn}(N)}{2M_p} \frac{1}{\bar{\sigma}(\theta)} \dot{\lambda}_p \quad (8-a,b)$$

Eq.(8-a,b) are the plastic flow rule. Here, next approximation is introduced

$$\theta \cong \theta_p \quad (9)$$

Eq.(9) means that total rotation is plastic rotation, that is, elastic rotation does not exist. Therefore the range of application for this model is when the chord member's slenderness ratio is much less. Eq.(5-d), Eq.(7) and Eq.(8) can be rewritten by Eq.(9) as follows

$$\Gamma \cong N \dot{u}_p - \frac{(2-2\alpha+n\alpha\beta)\alpha}{2} NL \theta_p \dot{\theta}_p \geq 0, \quad \Phi(N, \theta_p) \cong \frac{|N|}{N_y} - \bar{\tau}(\theta_p) \leq 0 \quad (10-a,b)$$

$$\bar{\tau}(\theta_p) \cong \bar{\sigma}(\theta_p) - \frac{(2-2\alpha+n\alpha\beta)\alpha N_y L \theta_p}{4M_p}, \quad \bar{\sigma}(\theta_p) \cong \sqrt{1 + \left(\frac{(2-2\alpha+n\alpha\beta)\alpha N_y L \theta_p}{4M_p} \right)^2} \quad (10-c)$$

$$\dot{u}_p \cong \frac{N}{N_y^2} \frac{1}{\bar{\sigma}(\theta_p)} \dot{\lambda}_p, \quad \dot{\theta}_p \cong -\frac{\text{sgn}(N)}{2M_p} \frac{1}{\bar{\sigma}(\theta_p)} \dot{\lambda}_p \quad (10-d,e)$$

These equations are basic approximate equations. However, inequality (10-a) is not still proved. To prove this inequality, substituting in Eq.(10-a) from Eq.(10-d,e) gives

$$\Gamma \cong N \left(1 + \frac{(2-2\alpha+n\alpha\beta)\alpha N_y^2 L \theta_p}{4|N|M_p} \right) \dot{u}_p = N \dot{u}_{pb} = N \frac{\text{sgn}(N)}{N_y} \dot{\lambda}_p = \frac{|N|}{N_y} \dot{\lambda}_p \geq 0 \quad (11)$$

If the yield condition of Eq.(10-b) is active then the following Kuhn-Tucker complementary conditions must be satisfied $\Phi = 0$, $\dot{\Phi} = 0$ and $\dot{\lambda}_p \geq 0$. Therefore Eq.(11) is satisfied.

In next section, sectional forces of the chord member are represented as $N \Rightarrow N^c$, $N_y \Rightarrow N_y^c$, $M_p \Rightarrow M_p^c$.

3. EXTEND TO TRUSS BEAM

In this section, a whole model of the truss beam as shown in Figure4 (a) is extended to a beam element model as shown in Figure4 (b). This formulation is assumed that the chord member's

slenderness ratio is much less. In this case next assumption is satisfied.

$$\theta_k \cong \theta_k^p \quad k \in \langle \underline{upper}, \underline{lower} \rangle \quad (12)$$

The Helmholtz free energy Ψ for the whole of a truss beam can be given by the sum of upper chord member and lower chord member's Helmholtz free energy

$$\Psi = \Psi_u(u_u, u_u^p, \theta_u^p) + \Psi_l(u_l, u_l^p, \theta_l^p) \Leftrightarrow \Psi = \frac{1}{2} \tilde{\mathbf{u}}^e T \mathbf{k}^e \tilde{\mathbf{u}}^e \quad (13)$$

where $()^T$ signifies transpose, \mathbf{k}^e is an elastic stiffness matrix for an effective continuous model and $\tilde{\mathbf{u}}^e$ is the elastic component of the nodal relative displacement $\tilde{\mathbf{u}}$. And it is assumed that total component $\tilde{\mathbf{u}}$ can be rewritten by the form of additive decomposition.

$$\tilde{\mathbf{u}} = \tilde{\mathbf{u}}^e + \tilde{\mathbf{u}}^p + \tilde{\mathbf{u}}^b, \quad \tilde{\mathbf{u}} = \langle \tilde{\delta} \quad \tilde{\theta}_i \quad \tilde{\theta}_j \rangle^T \quad (14)$$

where $\tilde{\mathbf{u}}^p$ and $\tilde{\mathbf{u}}^b$ are the plastic and buckling components of the nodal relative displacement. Furthermore, the assumption of $\tilde{\mathbf{u}}^p \equiv \tilde{\mathbf{u}}^p(u_k^p)$ and $\tilde{\mathbf{u}}^b \equiv \tilde{\mathbf{u}}^b(\theta_k^p)$ is introduced.

$$\dot{\tilde{\mathbf{u}}}^p(u_k^p) = \sum_{k=u,l} \frac{\partial \tilde{\mathbf{u}}^p}{\partial u_k^p} \dot{u}_k^p \equiv \sum_{k=u,l} \mathbf{h}_k^p \dot{u}_k^p, \quad \dot{\tilde{\mathbf{u}}}^b(\theta_k^p) = \sum_{k=u,l} \frac{\partial \tilde{\mathbf{u}}^b}{\partial \theta_k^p} \dot{\theta}_k^p \equiv \sum_{k=u,l} \mathbf{h}_k^b \dot{\theta}_k^p \quad (15)$$

In this case, the Clausius-Duhem inequality can be rewritten as $-\dot{\Psi} + \mathbf{f}^T \dot{\tilde{\mathbf{u}}} \geq 0$. \mathbf{f} is the nodal forces; $\mathbf{f} = \langle N \quad M_i \quad M_j \rangle^T$. Then substituting in this inequality from Eq.(13) gives

$$-\dot{\Psi} + \mathbf{f}^T \dot{\tilde{\mathbf{u}}} = [\mathbf{f} - \mathbf{k}^e \tilde{\mathbf{u}}^e]^T \dot{\tilde{\mathbf{u}}} + \sum_{k=u,l} [\mathbf{f}^T \mathbf{h}_k^p \dot{u}_k^p + \mathbf{f}^T \mathbf{h}_k^b \dot{\theta}_k^p] \geq 0 \quad (16)$$

For this inequality equation to be true for all values of $\tilde{\mathbf{u}}$, their coefficients must be zero, giving

$$\mathbf{f} = \mathbf{k}^e \tilde{\mathbf{u}}^e, \quad \Gamma = \sum_{k=u,l} [\mathbf{f}^T \mathbf{h}_k^p \dot{u}_k^p + \mathbf{f}^T \mathbf{h}_k^b \dot{\theta}_k^p] \geq 0 \quad (17)$$

The second equation represents the dissipation term. By comparison with Eq.(10-a), it is understood that both \mathbf{h}_k^p and \mathbf{h}_k^b can be represented by \mathbf{h}_k which is defined by $N_k^c = \mathbf{f}^T \mathbf{h}_k$ (as shown in Figure5.).

$$\mathbf{h}_k^p = \mathbf{h}_k, \quad \mathbf{h}_k^b = -\frac{(2 - 2\alpha_k + n_k \alpha_k \beta_k) \alpha_k}{2} L \theta_k^p \mathbf{h}_k \quad (18-a,b)$$

And from Eq.(10-b), the yield function for a truss beam model can be expressed in the form

$$\Phi_k(\mathbf{f}, \theta_k^p) = \left| \frac{\mathbf{f}^T \mathbf{h}_k}{N_y^c} \right| - \tau_k(\theta_k^p) \leq 0 \quad (19)$$

The expression of Eq.(18) and Eq.(19) means that both plastic and buckling component rate are proportional to the gradient of the yield surface. Namely the associate flow rule is satisfied in this model. It is noted that Eq.(15) is similar to the extended Koiter's form. And the yield surface becomes to be so-called multi-surface in $(\mu_i, \mu_j, \nu) = (M_i / M_p, M_j / M_p, N / N_y)$ space as Eq.(19). Here an effective plastic-buckling component $\dot{\mathbf{u}}^{pb}$ is introduced, which is defined by $\dot{\mathbf{u}}^{pb} = \dot{\mathbf{u}}^p + \dot{\mathbf{u}}^b$ and $\dot{\mathbf{u}}^{pb} = \dot{\mathbf{u}}^p + \dot{\mathbf{u}}^b$. Substituting in the latter equation from Eq.(15) and comparing with Eq.(11) gives

$$\dot{\mathbf{u}}^{pb} = \sum_{k=u,l} \frac{1}{N_y^c} \frac{\mathbf{f}^T \mathbf{h}_k}{|\mathbf{f}^T \mathbf{h}_k|} \mathbf{h}_k \dot{\lambda}_k^p \Leftrightarrow \sum_{k \in \text{active}} \frac{1}{N_y^c} \frac{\mathbf{f}^T \mathbf{h}_k}{|\mathbf{f}^T \mathbf{h}_k|} \mathbf{h}_k \dot{\lambda}_k^p \quad (20)$$

This equation is the plastic flow rule for the present method. Furthermore, the hardening (softening) coefficient can be calculated by

$$\dot{\tau}_k(\theta_k^p) = \frac{\partial \tau_k}{\partial \theta_k^p} \dot{\theta}_k^p = \frac{(2 - 2\alpha_k + n_k \alpha_k \beta_k) \alpha_k N_k^c L}{4 M_p^c \bar{\sigma}_k(\theta_k^p)^2} \dot{\lambda}_k^p \quad (21)$$

The yield function, the plastic flow rule and the hardening (softening) property are clarified.

The present calculation method of a nodal force vector belongs to the Return Mapping Algorithm for the Multi-surface yield function (Simo et al. 1998). In this paper, the detail of the calculation method is skipped because this method is mostly the same as [1].

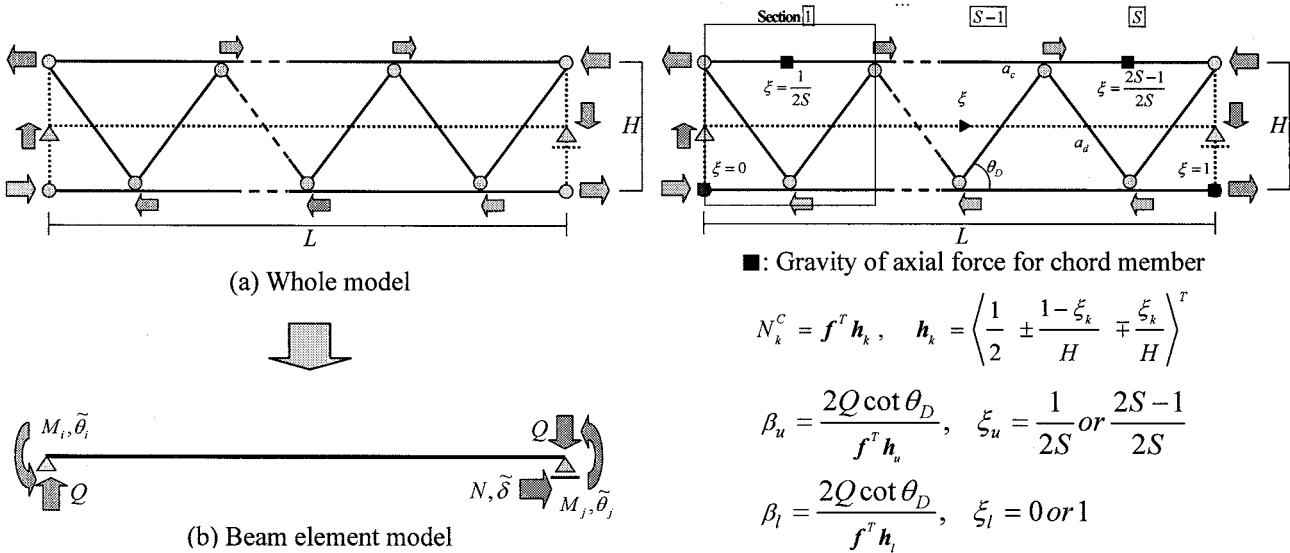
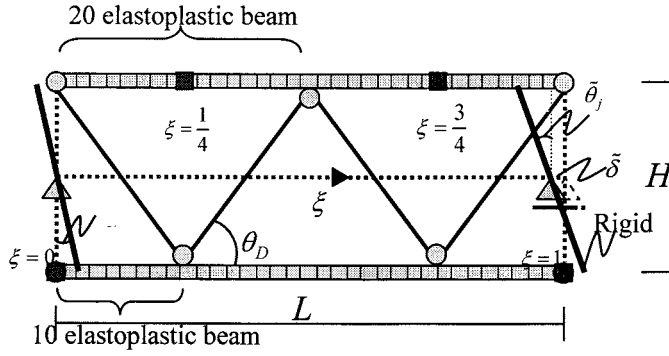


Figure4. Truss beam model

Figure5. Local coordinate system

4. NUMERICAL EXAMPLES

Figure7 shows analytical results to test the effectiveness of the present method. An example is subjected to monotonic loading: $\langle M_i = 0, \tilde{\delta} = -20\tilde{\theta}_j \rangle$. The present results are calculated with only one element, and another is done with the model as shown in Figure6. The mechanical properties are as shown in Figure6. Two equilibrium paths are close, that is, the present method is valid.



$$L = 115.47 \text{ (mm)}, \quad H = 50 \text{ (mm)}, \quad \theta_D = 60^\circ$$

$$S = 2, \quad a_c = a_d = 8 \text{ (mm)}$$

Figure6. Analytical model

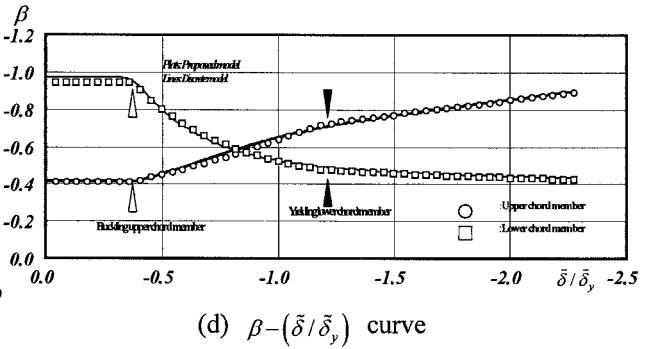
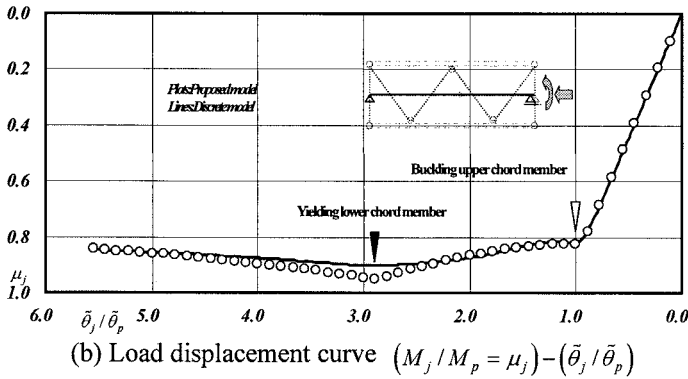
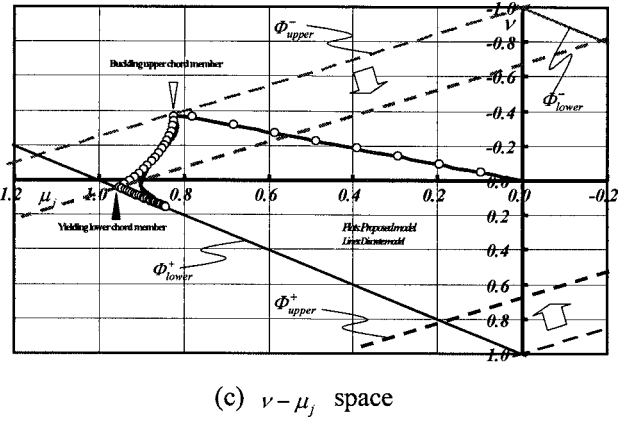
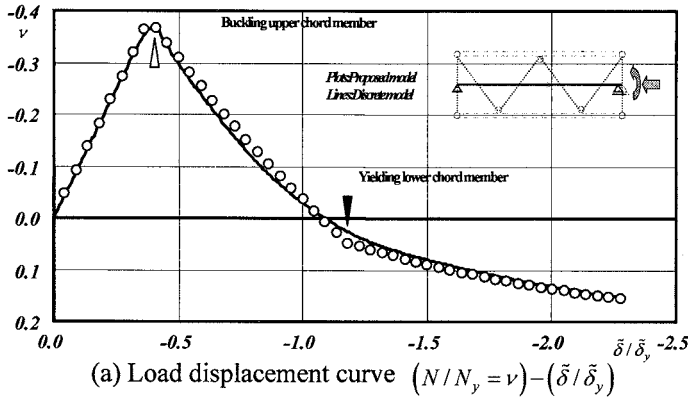


Figure7. Numerical results (monotonic loading)

5. CONCLUSIONS

In this paper, the consistent and convenient analytical method to simulate truss beam problems including the elastoplastic out-of-plane postbuckling behavior of chord members under the condition that a chord member's slenderness ratio is much less is proposed. Moreover, such problems reduce to the pure elastoplastic problems under this condition is clarified. Finally the validity of the present method was examined through the numerical examples.

References:

- [1]:Motoyui, S "Beam Element For Truss Beam With Elastoplastic-Buckling Behavior", First International Conference on Urban Earthquake Engineering, 2004, pp.71-76
- [2]:Simo, J, C., Kennedy, J. G., Govindjee, S., "Non-smooth Multisurface Plasticity and Viscoplasticity. Loading/Unloading Conditions and Numerical Algorithms", International Journal of Numerical Methods in Engineering, 1998, Vol.26,pp.2161-2185

A METHOD FOR EVALUATION OF ELASTIC BUCKLING STRENGTH OF H SHAPED STEEL MEMBER UNDER SHEAR BENDING

T.Wang¹, K.Ikarashi²

1)Graduate Student, Department of Architecture and Building Engineering, Tokyo Institute of Technology, Japan

2)Associate Professor, Department of Architecture and Building Engineering, Tokyo Institute of Technology, Japan

twan@o.cc.titech.ac.jp, ikarashi@arch.titech.ac.jp

Abstract: Local buckling behavior of web and flange are thought as a single plate under the assumption of boundary condition. But few researches about coupled instability of web and flange have been performed so far. As elements of H shaped steel members, the behavior of web and flange is affected by each other. Therefore, the purpose of this study is to understand the interaction between the plate elements of web and flange when coupled buckling happens. In this paper, the analysis is done by energy method. Buckling interrelation between web and flange is clarified. And a new method of evaluation about coupled buckling strength under shear bending is proposed by using parameter of geometrical shape about web and flange of H Shaped members.

1. INTRODUCTION

It is clarified in Ref.1 and 2 about local buckling behavior of H shaped steel members when they are acted under compression and bending or pure shear. However, H shaped beam will bend like Figure 1 generally because steel structures occur horizontal displacement while earthquake happens. Therefore, it is important to examine the elastic buckling behavior of H shaped beam under shear bending stress situation. In recent studies (Ref.3 and 4), a theoretical analysis has been done to derive elastic buckling strength of web under such a situation. On the other hand, since enormous local compression caused by shear bending may occur on flanges especially for long beams or columns in steel frame structures, the influence from flanges about the buckling behavior can not be ignored in such cases. As a result, buckling strength of H shaped steel can not be described by web or flange only. In general, coupled buckling happens on both web and flange at the same time. Therefore, it is necessary to consider the coupled buckling interrelation between web and flange. A lot of numerical analyses by finite element method, and experiments such as Ref.5 and 6 have been done. But it is difficult to find the important factors which can adequately express the

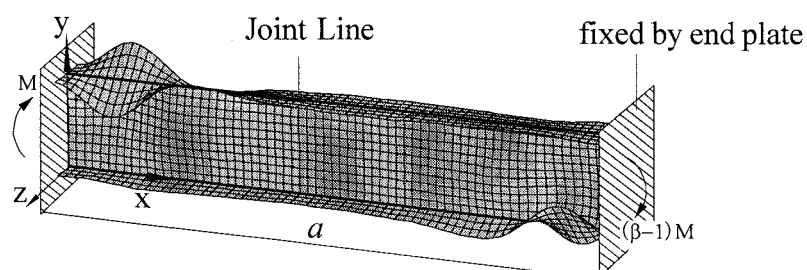


Figure 1 Analytical model

coupled buckling behavior.

In this study, as the analysis model shown in Figure1, both ends of beam are fixed by strong end plates, and the end of plates are only permitted to rotate around axis z. At the same time, the beam is forced to rotate under shear bending. At first, assume the boundary condition of Joint Line, and derive the bulking strength of web and flange separately. Then, derive the coupled buckling strength by considering the interaction between them. The geometrical parameter referring to Figure 2 shown below is used to do these analyses.

Table 1 Geometrical parameter used to evaluate the buckling strength

$\lambda_w = a/b_w$: aspect ratio of web
$\lambda_f = a/b_f$: aspect ratio of flange
A_f : section area of flange
A_w : section area of flange
b_w/t_w : width-thickness ratio of web
b_f/t_f : width-thickness ratio of flange
where, $\lambda_f / \lambda_w = \sqrt{2(b_w/t_w)/(b_f/t_f) \cdot A_w / A_f}$

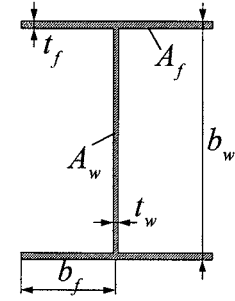


Figure 2 Dimension of H shaped section

In order to distinguish the difference among them, buckling strength of web and flange and coupled buckling strength are defined as the following formulas by appropriate marks and coefficients.

$${}_w\sigma_{cr} = K_{\sigma w} \cdot \frac{\pi^2 E}{12(1-\nu^2)} \cdot \frac{1}{b_w^2/t_w^2} \quad {}_w\tau_{cr} = K_{\tau w} \cdot \frac{\pi^2 E}{12(1-\nu^2)} \cdot \frac{1}{b_w^2/t_w^2} \quad (1.1)$$

$${}_f\sigma_{cr} = K_f \cdot \frac{\pi^2 E}{12(1-\nu^2)} \cdot \frac{1}{b_f^2/t_f^2} \quad {}_f\tau_{cr} = K_{\tau f} \cdot \frac{\pi^2 E}{12(1-\nu^2)} \cdot \frac{1}{b_w^2/t_w^2} \quad (1.2)$$

$$\sigma_{cr} = K_{\sigma} \cdot \frac{\pi^2 E}{12(1-\nu^2)} \cdot \frac{1}{b_w^2/t_w^2} \quad \tau_{cr} = K_{\tau} \cdot \frac{\pi^2 E}{12(1-\nu^2)} \cdot \frac{1}{b_w^2/t_w^2} \quad (1.3)$$

Where,

E: Young's modulus; ν : Poisson's ratio($\nu=0.3$ in this study).

${}_w\sigma_{cr}, {}_f\sigma_{cr}, \sigma_{cr}$: Critical value of $\sigma_w, \sigma_f, \sigma_w(=\sigma_f)$ shown in Figure 3 and 4 at each state of web, flange, coupled buckling.

$K_{\sigma w}, K_f, K_{\sigma}$: Coefficients used to calculate ${}_w\sigma_{cr}, {}_f\sigma_{cr}, \sigma_{cr}$

${}_w\tau_{cr}, {}_f\tau_{cr}, \tau_{cr}$: Critical value of average shear stress $\bar{\tau}$ shown in Figure 4 at each state of web, flange, coupled buckling.

$K_{\tau w}, K_{\tau f}, K_{\tau}$: Coefficients used to calculate ${}_w\tau_{cr}, {}_f\tau_{cr}, \tau_{cr}$ which are described as below.

$$K_{\tau w} = \frac{(1/6 + A_f/A_w)\beta}{\lambda_w} \cdot K_{\sigma w} \quad (1.4)$$

$$K_{\tau f} = \frac{(1/6 + A_f/A_w)\beta}{\lambda_w} \cdot \frac{b_w^2/t_w^2}{b_f^2/t_f^2} \cdot K_f \quad (1.5)$$

$$K_{\tau} = \frac{(1/6 + A_f/A_w)\beta}{\lambda_w} \cdot K_{\sigma} \quad (1.6)$$

β : bending incline

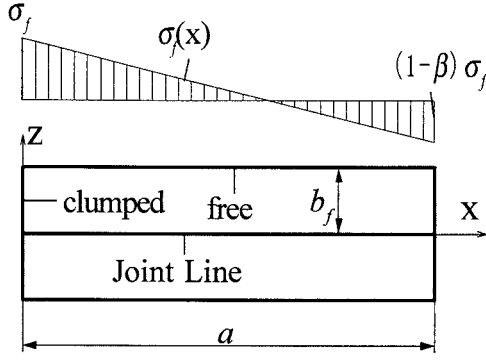


Figure 3 Distribution of compressive stress and boundary condition of flange

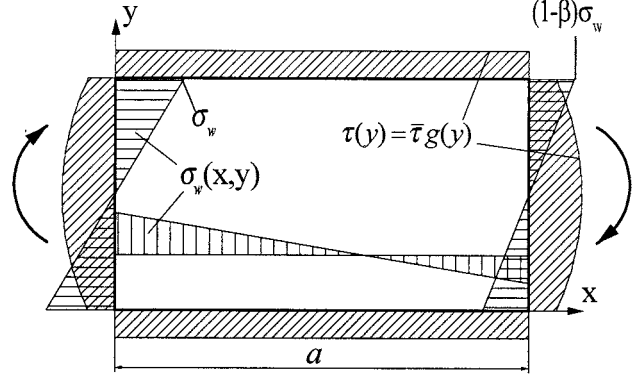


Figure 4 Distribution of in-plane stress of web

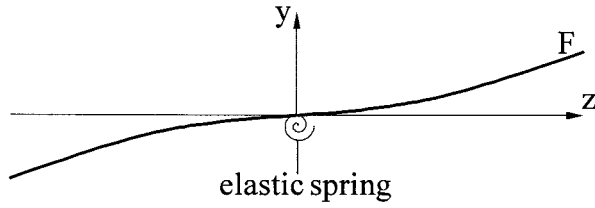


Figure 5 Out-of-plane deformed flange on elastic support condition of Joint Line

$$F = \sum_{m=1} \sum_{n=1} a_{mn} \cdot u_m \cdot v_n \quad (2.1)$$

$$u_m = \sin \frac{m\pi x}{a} \sin \frac{\pi z}{a} \quad v_n = (z/b_f)^n$$

2. ELASTIC BUCKLING STRENGTH OF FLANGE UNDER UNEQUAL COMPRESSION

According to the assumption of boundary condition given in Figure 2, Flange is thought as a single plate under the assumption of boundary condition in this chapter. The Joint Line keeps straight, and web acts as an elastic spring shown in Figure 5. The function F used to express out-of-plane deformation which is suitable to this boundary condition is shown by series of Eq.(2.1)

The twist rigidity C_{1w} and rotation rigidity C_{2w} of the spring are shown as follows.

$$C_{1w} = \frac{E}{6(1+\nu)} b_w t_w^3 \quad (2.2)$$

$$C_{2w} = \frac{4Et_w^3}{12b_w(1-\nu^2)} \quad (2.3)$$

In Figure 2, the distribution of compressive stress on upper flange($y=b_w$) is described as

$$\sigma_f(x) = \sigma_f \cdot \left(1 - \frac{\beta}{a} x\right) \quad (2.4)$$

The strain energy of flange and spring and the external work ΔU and ΔT are shown by the following two expressions.

$$\Delta U = \frac{1}{2} D_f \int_0^a \int_0^{b_f} \left\{ \left(\frac{\partial^2 F}{\partial x^2} + \frac{\partial^2 F}{\partial z^2} \right)^2 - 2(1-\nu) \left[\frac{\partial^2 F}{\partial x^2} \frac{\partial^2 F}{\partial z^2} - \left(\frac{\partial^2 F}{\partial x \partial z} \right)^2 \right] \right\} dx dz + \frac{1}{4} C_{1w} \int_0^a \left(\frac{\partial^2 F}{\partial x \partial z} \right)^2 \Big|_{z=0} dx + \frac{1}{4} C_{2w} \int_0^a \left(\frac{\partial F}{\partial z} \right)^2 \Big|_{z=0} dx \quad (2.5)$$

$$\Delta T = \frac{1}{2} K_f \frac{\pi^2 D_f}{b_f^2} \int_0^a \int_0^{b_f} \left(1 - \frac{\beta}{b_f \lambda_f} x \right) \left(\frac{\partial F}{\partial x} \right)^2 dx dz \quad (2.6)$$

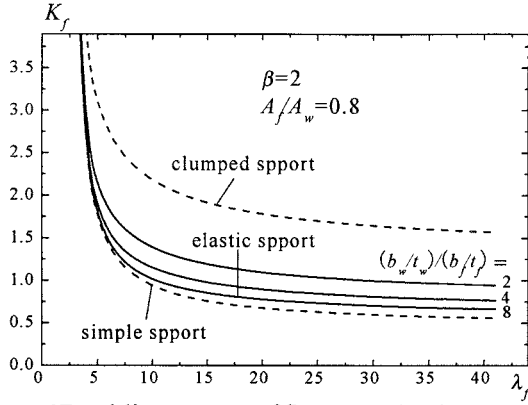


Figure 6 Buckling curves of flange under the assumption of boundary condition

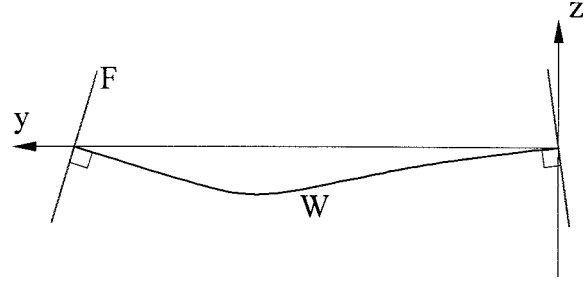


Figure 7 Out-of-plane deformation of H shaped members

Where, $D_f = \frac{Et_f^3}{12(1-\nu^2)}$: bending rigidity of flange

C_{1w} and C_{2w} are assumed to be 0 in Eq.(2.2) and (2.3) when the support condition in Joint Line is considered to be a simple support; and ν_n expressed in Eq.(2.1) is assumed to be $(z/b_f)^{n+1}$ when it is a clumped support. Moreover, buckling happens earlier in upper flange than in lower in range of bending incline $\beta < 2$. Here, the upper flange is considered only in such range because the upper and lower flange are symmetry. According to the mentioned above, a theoretical analysis is applied by using energy method. K_f in this analytical result is used to calculate buckling strength $f_{\sigma_{cr}}$ and $f_{\tau_{cr}}$ by Eq.(1.2) and (1.5).

For example, in Figure 6 which shows the correlation between the buckling curve of each boundary condition, It can be understood that the buckling value with clumped support in Joint Line is about three times of the value with simple support. Moreover, it can be forecasted that the support condition in Joint Line is much similar to simple support in many cases at present.

3. COUPLED BUCKLING STRENGTH OF H SHAPED MEMBERS UNDER SHEAR BENDING

In Chapter 2 of this paper and the past studies(Ref.4), it is understood that buckling strength of web and flange can be singly evaluated. Therefore, it is possible to evaluate the buckling strength of H Shaped steel members by using the smaller buckling strength value between web and flange. However, when the web or flange buckling occurs at first, there is also somewhat influence from the other one. Therefore, coupled buckling generally occurs on plates as shown in Figure 1 which can be thought that web and flange buckle at the same time.

3.1 Outline of Coupled Buckling Analysis

It is assumed that the Joint Line shown in Figure 1 keeps straight, so the overall buckling doesn't occur. As shown in Figure 7, fiber of web and flange still keeps vertical when Joint Line rotates, and the out-of-plane deformation function W and F of web and flange can be expressed by the following two expressions based on this assumption.

$$W = \sum_{m=1} \sum_{n=1} a_{mn} \left(\sin \frac{m\pi x}{a} \sin \frac{\pi x}{a} \right) \sin \frac{n\pi y}{b_w} \quad (3.1)$$

$$F = \sum_{m=1} \sum_{n=1} a_{mn} \frac{zn\pi}{b_w} \left(\sin \frac{m\pi x}{a} \sin \frac{\pi x}{a} \right) \cos \frac{n\pi y}{b_w} \Big|_{y=0, b_w} \quad (3.2)$$

When coupled buckling of web and flange occurs, the strain energy ΔU_1 and ΔU_2 accompanied

by out-of-plane deformation of web and flange are shown in Eq(3.3) and (3.4).

$$\Delta U_1 = \frac{1}{2} D_w \int_0^a \int_0^{b_w} \left\{ \left(\frac{\partial^2 W}{\partial x^2} + \frac{\partial^2 W}{\partial y^2} \right)^2 - 2(1-\nu) \left[\frac{\partial^2 W}{\partial x^2} \frac{\partial^2 W}{\partial y^2} - \left(\frac{\partial^2 W}{\partial x \partial y} \right)^2 \right] \right\} dx dy \quad (3.3)$$

$$\Delta U_2 = \frac{1}{2} D_w \left(\frac{A_f}{2A_w} \cdot \frac{b_w/t_w}{b_f/t_f} \right)^{\frac{3}{2}} \int_0^a \int_{-b_f}^{b_f} \left\{ \left(\frac{\partial^2 F}{\partial x^2} \right)^2 + \left(\frac{\partial^2 F}{\partial x^2} \right)^2 + 2(1-\nu) \left[\left(\frac{\partial^2 F}{\partial x \partial z} \right)^2 + \left(\frac{\partial^2 F}{\partial x \partial z} \right)^2 \right] \right\} dx dz \quad (3.4)$$

The distribution of compressive stress is also described as Eq.(2.4) on upper flange and the following Eq.(3.5) on lower flange(y=0).

$$\sigma_f(x) = \sigma_f \cdot \left(\frac{\beta}{a} x - 1 \right) \quad (3.5)$$

The in-plane stress of web shown in Figure 4 can be expressed as

$$\text{bending stress: } \sigma_w(x, y) = - \left(1 - \frac{\beta}{a} x \right) \left(1 - \frac{2}{b_w} y \right) \cdot \sigma_w = w(x, y) \cdot \sigma_w \quad (3.6)$$

$$\text{shear stress: } \tau(y) = \left[\frac{6A_f}{A_w + 6A_f} + \frac{6A_w}{A_w + 6A_f} \cdot \frac{y(b_w - y)}{b_w^2} \right] \cdot \bar{\tau} = g(y) \cdot \bar{\tau} \quad (3.7)$$

Where, $\bar{\tau} = \frac{(1/6 + A_f/A_w)\beta}{\lambda_w} \cdot \sigma_w$: average of shear stress

Since the direct stress of web and flange are the same value at the upper and lower Joint Line, σ_f is equal to σ_w in Figure 3 and 4. According to the expressions above, the external work are shown by Eq.(3.8) and (3.9).

$$\Delta T_1 = \frac{1}{2} K_\sigma \frac{\pi^2 D_w}{b_w^2} \int_0^a \int_0^{b_w} \left[w(x, y) \cdot \left(\frac{\partial W}{\partial x} \right)^2 - 2\alpha g(y) \frac{\partial W \partial W}{\partial x \partial y} \right] dx dy \quad (3.8)$$

$$\Delta T_2 = \frac{1}{2} K_\sigma \frac{\pi^2 D_w}{b_w^2} \sqrt{\frac{A_f}{2A_w} \cdot \frac{b_w/t_w}{b_f/t_f}} \int_0^a \int_{-b_f}^{b_f} \left(1 - \frac{\beta}{a} x \right) \left[- \left(\frac{\partial F}{\partial x} \right)^2 + \left(\frac{\partial F}{\partial x} \right)^2 \right] dx dz \quad (3.9)$$

Where, $D_w = \frac{E t_w^3}{12(1-\nu^2)}$: bending rigidity of flange

It is obvious that buckling strength is influenced by $(b_w/t_w)/(b_f/t_f)$ and A_f/A_w which show the section shape of H shaped members in these expressions. In this analysis, the strain energy and the external work are calculated as the whole plate members.

3.2 Interaction Between Buckling Strength of H Shaped Steel Member

As a sample of analysis results shown in Figure 8, the buckling curves of single plate and coupled curve are shown in the same graph. Boundary condition is assumed as clumped support on web and elastic support on flange in Joint Line when they are regarded as a single plate here. The horizontal axis shows aspect ratio of web λ_w . The correlation of buckling coefficient shown in vertical axis and buckling strength are expressed as follows.

$${}_w \tau_{cr} : {}_f \tau_{cr} : \tau_{cr} = K_{\tau w} : K_{\tau f} : K_\tau \quad (3.10)$$

From the Figure 8, it is obvious that τ_{cr} is smaller than ${}_w \tau_{cr}$ and ${}_f \tau_{cr}$, especially at the cycle where buckling strength of web and flange are same. Take the black cycle as a separation. It is clear that the coupled buckling curve 3 is much closer to the flange curve 2 when λ_w is larger than it at the cycle. On the contrary, the curve 3 becomes much closer to the web curve 1 when λ_w is

smaller than it at the cycle. Especially, in range far away from the cycle, coupled buckling strength is controlled by web or flange because the buckling strength of web and flange is extremely different from each other. That is to say, web or flange buckles without the influence from the other, and coupled buckling strength of H Shaped members can be evaluated by the smaller one of web and flange at such situation. But in the range of closing to the cycle where the buckling strength of web and flange is a little different from each other, web and flange buckle at the same time and affect each other which leads to reduce

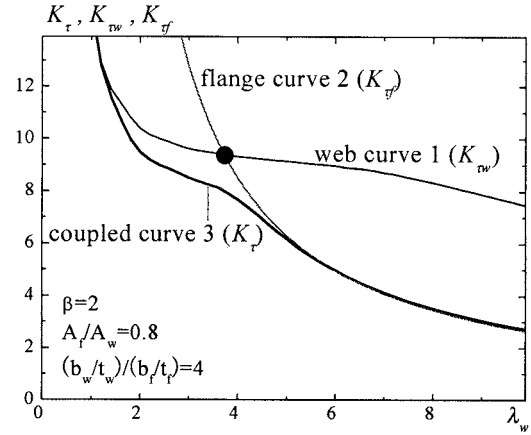


Figure 8 Interaction between buckling strength of H shaped member

4. PROPOSAL FOR EVALUATING BUCKLING STRENGTH OF H SHAPED MEMBERS UNDER SHEAR BENDING

In this chapter, based on the analyzing results, an evaluation method about coupled buckling is proposed by using the geometry parameter of H Shaped steel shown in Table 1. At first, evaluate the buckling strength of plate members separately since it is difficult to evaluate the coupled buckling strength directly. In the following statement, an approximate evaluation is done by using the least square method, and the concrete calculation procedure will not be shown here.

4.1 Approximate Evaluation About Buckling Strength Of Flange

In order to distinguish the coefficients in different support conditions, such as simple support, clumped support, and elastic support, ${}_pK_f$, ${}_cK_f$, ${}_eK_f$ are used here. Firstly, approximate evaluations are easily obtained in Eq.(4.1) and (4.2) when the support conditions in Joint Line are simple support and clumped support.

$${}_pK_f = 0.425 + 4/\lambda_f^2 + 2.4\beta/\lambda_f \quad (4.1)$$

$${}_cK_f = 1.28 + 3.5/\lambda_f^2 + 4.5\beta/\lambda_f \quad (4.2)$$

From Figure 9(a), it is clear that the calculable results by using Eq.(4.1) and (4.2) are accordant with analytical results. Since it is always ${}_cK_f < {}_pK_f$ and ${}_eK_f > {}_pK_f$ at any situation, C_f is defined as the

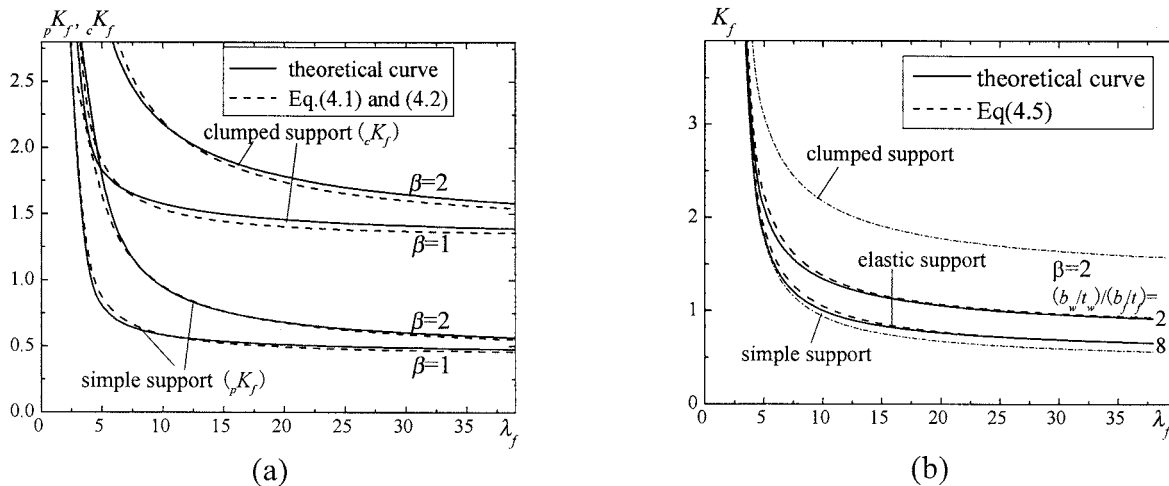


Figure 9 Evaluation of buckling strength of flange

increasing rate from the relation among ${}_pK_f$ and ${}_cK_f$ as follows.

$$C_f = (K_f - {}_pK_f) / ({}_cK_f - {}_pK_f) \quad (4.3)$$

Consider the effect of $(b_w/t_w) / (b_f/t_f)$ and A_f/A_w which control the support condition in Joint Line, The C_f is obtained approximately as Eq.(4.4) in the range of $0.4 < A_f/A_w < 2.5$.

$$C_f = \frac{7}{5A_f/A_w + 4} \cdot \frac{(b_f/t_f)}{(b_w/t_w)} \quad (4.4)$$

Since ${}_pK_f$ and ${}_cK_f$ are able to be calculated by Eq.(4.1) and (4.2), Eq(4.5) is easily obtained to evaluate the buckling strength of flange under elastic support condition in Joint Line.

$$K_f = {}_pK_f + ({}_cK_f - {}_pK_f) \cdot \frac{7}{5A_f/A_w + 4} \cdot \frac{(b_f/t_f)}{(b_w/t_w)} \quad (4.5)$$

Figure 9(b) shows that the approximate curve expressed by expression (4.5) is almost corresponding to the analytical curve. By such way, approximate evaluation about buckling strength of flange is proposed according to lots of analytical data. The approximate evaluation about buckling strength of web has also been obtained by the similar method in Ref.4.

4.2 Approximate Evaluation About Coupled Buckling Strength Of H Shaped Members

According to Chapter 3, coupled buckling strength sufficiently converges to the lower strength of web and flange when buckling strength of them is far different from each other. As approximate evaluation, coupled buckling strength is equal to the lower one of web and flange which buckling strength are evaluated as single plates under the assumption of boundary condition in such range. But in range which buckling strength of web closes to flange, decrease will occur somewhat. In order to derive coupled buckling strength more accurately, decreasing rate C_{wf} is defined in the following expression.

$$C_{wf} = \begin{cases} 1 - \tau_{cr}/{}_w\tau_{cr} & ({}_w\tau_{cr} < {}_f\tau_{cr}) \\ 1 - \tau_{cr}/{}_f\tau_{cr} & ({}_w\tau_{cr} \geq {}_f\tau_{cr}) \end{cases} \quad (4.6)$$

Then, coupled buckling strength is evaluated by expectation of decreasing rate C_{wf} by the following process.

According to the analysis data like Figure 8, C_{wf} become the largest which is defined as C_{wfo} when ${}_w\tau_{cr}$ is equal to ${}_f\tau_{cr}$. and C_{wfo} is only related to A_f/A_w which is approximately expressed as

$$C_{wfo} = 0.16(A_w/A_f) - 0.05 \quad (4.7)$$

In order to make τ_{cr} coverage to the lower value of ${}_w\tau_{cr}$ and ${}_f\tau_{cr}$ when the difference between ${}_w\tau_{cr}$ and ${}_f\tau_{cr}$ is perceptible extremely, the decreasing rate C_{wf} is expressed in the following expression.

$$C_{wf} = \begin{cases} C_{wfo} \cdot {}_w\tau_{cr} / {}_f\tau_{cr} & ({}_w\tau_{cr} < {}_f\tau_{cr}) \\ C_{wfo} \cdot {}_f\tau_{cr}^2 / {}_w\tau_{cr}^2 & ({}_w\tau_{cr} \geq {}_f\tau_{cr}) \end{cases} \quad (4.8)$$

According to the expectation of decreasing rate C_{wf} and correlation shown as Eq.(3.10). A approximate evaluation about coupled buckling strength of H Shaped members under shear bending is obtained as follows.

$$K_\tau = \begin{cases} K_{\tau w} - K_{\tau w}^2 / K_{\tau f} (0.16A_w/A_f - 0.05) & (K_{\tau w} < K_{\tau f}) \\ K_{\tau f} - K_{\tau f}^2 / K_{\tau w} (0.16A_w/A_f - 0.05) & (K_{\tau w} \geq K_{\tau f}) \end{cases} \quad (4.9)$$

As a sample, Figure 10 shows the coupled buckling strength curves of H Shaped members under shear bending. The approximate curves proposed by Eq.(4.9) are almost corresponding to

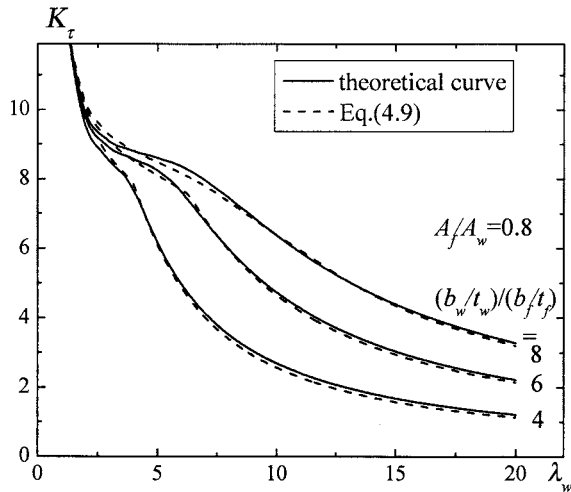


Figure 10 Evaluation of coupled buckling strength

the analytical curves.

According to all mentioned above, the process how to conduct the approximate evaluation about coupled buckling strength of H Shaped members under shear bending is shown by a flowchart in Figure 11.

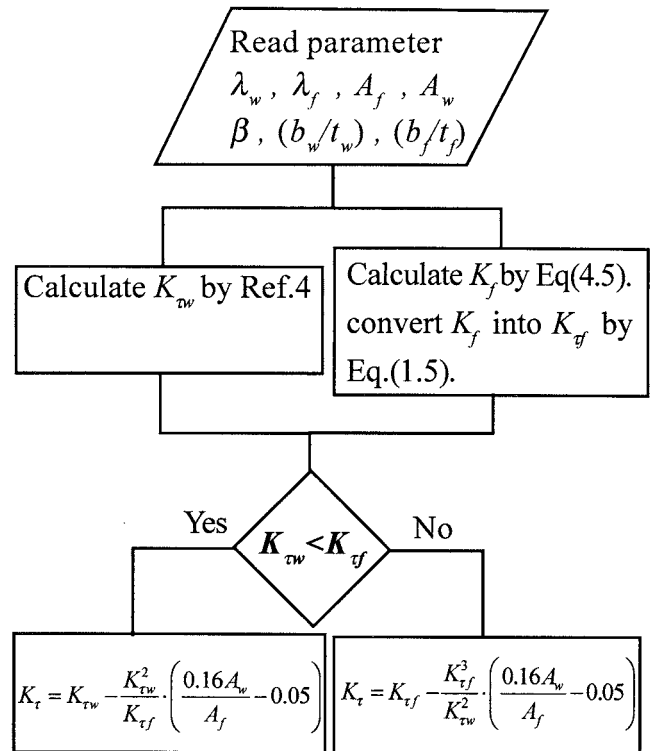


Figure 11 Flowchart for evaluating the coupled buckling strength

5. CONCLUSIONS

In this paper, coupled buckling strength of H Shaped members under complex stress situation is resolved by using energy method. It is understood that coupled buckling strength closes to the smaller strength of web or flange which buckles as a single plate under assumption of boundary condition. According to such property, the coupled buckling strength can be evaluated in expectation of the decreasing rate defined in this study. Moreover, based on the theoretical analysis results, a new approximate evaluation is proposed by using parameter regarding geometrical shape, such as aspect ratio, width-thickness ratio of plates, section area and bending incline etc.

Acknowledgements:

Financial support by CUEE (Center for Urban Earthquake Engineering, Tokyo Institute of Technology) are gratefully acknowledged.

References:

- [1] Timoshenko, Gere(1963), "Theory of Elastic Stability,"
- [2] Arch. Inst. of Japan(1996), "Recommendations for Stability Design of Steel Structures,"
- [3] Ikarashi,K.(2003), "Buckling Strength of simply Supported Web Plate under the action of Bending Shear Stress," *Journal of Structural and Construction Engineering, Arch, Inst. of Japan*, No.571,145-152.
- [4] Ikarashi,K. and Suzuki,T.(2004), "a Methode for Evaluating Buckling Strength of Plate under Bending-Shear and Axial Force," *Fourth International Conference on Coupled Instabilities in Metal Structures*.
- [5] Hasham,A.S., Rasmussen,K.J.R.(2002), "Interaction curves for locally buckled I-section beam-columns," *Journal of Constructional Steel Research* 58, 213-241
- [6] Salem,A.H., Aghoury,M.El., Dib,F.F.El. and Hanna,M.T.(2005), "Post local buckling strength of bi-axially loaded slender I-section columns," *Thin-Walled Structures*,No.43,1003-1019.

SHAKE TABLE COMPETITION TO STIMULATE UNDERGRADUATE INTEREST IN EARTHQUAKE ENGINEERING AND SEISMIC DESIGN

Scott A. ASHFORD¹, Michael J. GEBMAN², Scott J. BRANDENBERG³ and Lijuan CHENG⁴

ABSTRACT: An undergraduate seismic design competition was developed by graduate student members of the Pacific Earthquake Engineering Research (PEER) Center Student Leadership Council (SLC). This competition was designed to physically demonstrate aspects of PEER's performance-based earthquake engineering methodology, and to educate and stimulate engineering undergraduate students via a hands-on project in a team environment. Teams design a balsa wood model of a multi-level commercial office structure that is subjected to a sequence of scaled ground motions from El Centro, Northridge and Kobe earthquakes, and a sinusoidal sweep. Models are tested on a University Consortium on Instructional Shake Tables (UCIST) shaking table with simulated weights attached to each level. Accelerations are measured at the roof and base of the structure, and are subsequently processed to obtain measurements of engineering demand parameters (EDP's) that are correlated deterministically with dollar loss. EDP's are based on the drift ratio and on the roof acceleration, both of which teams must strive to minimize in their designs. The seismic performance is ultimately scored based on annual building revenue, which accounts for rent income, construction cost, and annual seismic cost. Three annual competitions have been held to date, sponsored by PEER. Two annual competitions have been held sponsored by the Multi-Disciplinary Center for Earthquake Engineering Research (MCEER).

KEYWORDS: Shake Table, Undergraduate Engineering Education, Seismic Design, Earthquake Engineering, Performance Based Design, Competition.

1. INTRODUCTION

Graduate student members of the Student Leadership Council (SLC) for the Pacific Earthquake Engineering Research (PEER) Center developed an undergraduate seismic design competition in 2004, with three annual competitions held to date. The competition, though still in its infancy, has already expanded nationally by involving teams from all three national earthquake research centers across the United States. The competition provides students with the opportunity to apply classroom knowledge in a team environment, similar to other well known competitions such as the American Society of Civil Engineers National Concrete Canoe Competition [1], and the American Institute of Steel Construction National Steel Bridge Competition [2]. This competition has three primary objectives. The first is to physically demonstrate aspects of performance-based earthquake engineering in the context of the PEER methodology. The second is to educate undergraduate students about earthquake engineering and stimulate them to contribute to the profession. The third is to demonstrate the value of PEER's Student Leadership Council (SLC) representatives and officers.

¹ Professor of Geotechnical Engineering, Department of Structural Engineering, University of California, San Diego, U.S.A.

² Ph.D. Candidate, Department of Structural Engineering, University of California, San Diego, U.S.A.

³ Assistant Professor, Department of Civil Engineering, University of California, Los Angeles, U.S.A.

⁴ Assistant Professor, Department of Civil Engineering, University of California, Davis, U.S.A.

This paper presents a brief overview of the technical and educational components of the seismic design competition. Detailed rules for the competition and results can be found on the PEER SLC website (<http://peer.berkeley.edu/students>) [3], and only an abbreviated summary is presented herein. The performance-based earthquake engineering scoring system is presented, with focus on the implementation of aspects of the PEER methodology. The experimental setup, data acquisition features, and data processing methods are presented second. Finally, the educational value of the seismic competition is discussed, including results from past competitions and goals for future competitions.

2. STRUCTURAL DESIGN TASK

Teams must design a multi-level commercial office building to resist severe earthquake loading, from scaled versions of ground motions recorded during the 1940 El Centro, 1994 Northridge and 1995 Kobe earthquakes. Teams need to also account for architectural and economic concerns (such as the maximization of premium office space) in their design. Teams are allowed to use lateral force resisting systems, which include: shear walls, moment connections, x-bracing, eccentric bracing, and dampers. To verify the seismic load resistance system teams must construct a scaled model from balsa wood, at a scale of 72:1, for testing on the UCIST shake table. Figure 1 shows two of the models from the third annual competition.

3. PERFORMANCE-BASED EARTHQUAKE ENGINEERING SCORING SYSTEM

The seismic competition physically demonstrates aspects of the performance-based earthquake engineering (PBEE) methodology as developed by the Pacific Earthquake Engineering Research (PEER) Center [4]. The PEER methodology involves four steps: 1. hazard analysis, 2. structural analysis, 3. damage analysis, and 4. loss analysis. Uncertainty in each step is integrated in the methodology, producing in the end estimates of the rate at which certain decision variables (e.g., dollar cost, loss of life) are exceeded. The seismic competition treats each of the components deterministically, and focuses primarily on the structural analysis component of the methodology. Treatment of each component is discussed in the sections that follow.

3.1 HAZARD ANALYSIS

The seismic hazard for the site is represented by a set of three ground motions (Figure 2). Scaled versions of motions recorded during the 1940 El Centro, 1994 Northridge, and 1995 Kobe earthquakes are applied in that sequence to the base of each of the model structures. The motion sequence corresponds to increasing spectral accelerations in the anticipated structural natural period range of 0.2 s to 1.0 s. Return periods assigned to the motions are 50, 150 and 200 years for the El Centro, Northridge and Kobe motions, respectively. Calculation of annual seismic cost depends on motion return period, as explained later.

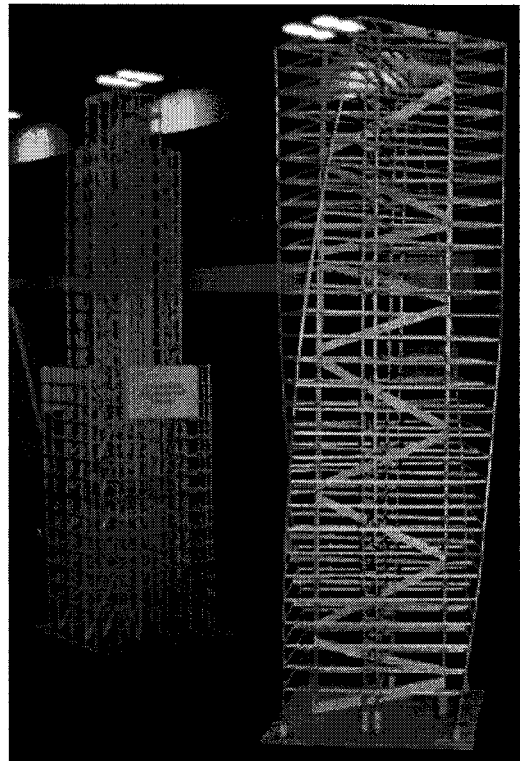


Figure 1. Typical models with a height of 1.5 m

3.2 STRUCTURAL ANALYSIS

During application of the base motions, accelerations are recorded at the base and roof of the structures and those measurements are processed to obtain two engineering demand parameters (EDP's). The first is the peak of the absolute value of drift between the roof and the base (EDP1), and the second is the peak of the absolute value of roof acceleration (EDP2). These two EDP's, stated in equations 1 and 2, were selected because they are easy to measure using the available data acquisition system and instrumentation, and to demonstrate that building fragility can depend on multiple engineering demand parameters. Displacements are computed from the measured accelerations by digitally filtering the records and subsequently double-integrating them in time.

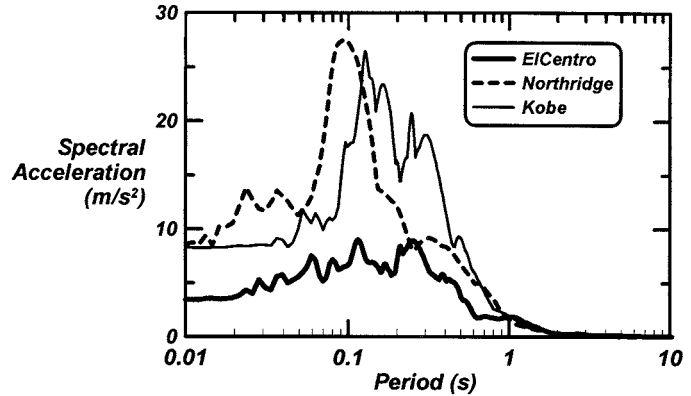


Figure 2. Acceleration response spectra for competition ground motions

$$EDP1 = \max \left(\left| \frac{\Delta_{Roof} - \Delta_{Base}}{H} \right| \right) \quad (1)$$

$$EDP2 = \max |Roof Acceleration| \quad (2)$$

3.3 DAMAGE ANALYSIS AND LOSS ANALYSIS

Damage and loss constitute separate analyses in the PEER methodology, each carrying its own uncertainty, but the two analyses were combined in this competition and loss was represented as deterministic functions of the EDP's. Structural damage was correlated with building drift (EDP1) and damage to non-structural equipment housed inside the building was correlated with peak roof acceleration (EDP2). Cost functions relating dollar loss to the EDP's are presented in Figure 3. Similar cost functions could be developed for any number of EDP's as the competition continues to evolve.

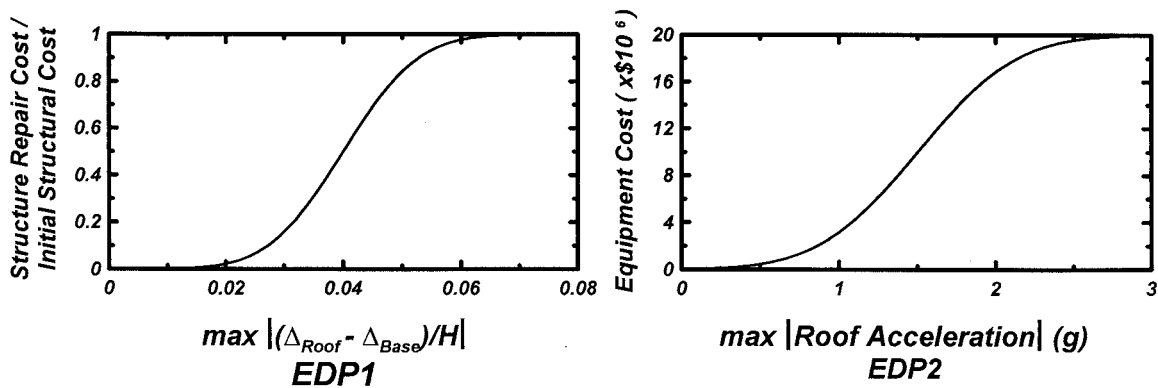


Figure 3. Cost functions relating dollar loss to engineering design parameters (EDP's)

3.4 COMPETITION SCORING

The competition is scored based on building annual revenue, which is analogous to the decision variable (DV) in the PEER methodology. Buildings receive annual rent income based on available floor space, and additional annual income can be earned in the presentation and poster components of the competition. The initial cost of the building is the sum of the cost of land (based on building footprint area) and the initial structural cost (based on the mass of the structural components). The initial building cost is represented annually by dividing by the 100-year design life of the building. Seismic cost for each motion is computed by measuring EDP1 and EDP2 for all three earthquake motions, and computing the associated cost for each EDP for each motion using the cost functions in Figure 3. Seismic cost for each motion is represented annually by dividing by the return period of that motion, and total annual seismic cost is computed as the sum of the annual costs for each motion. Finally, annual building revenue is computed as annual rent income minus annual initial building cost minus annual seismic cost plus any additional annual revenue for high placement in the presentation and poster components of the competition and a decrease in revenue for not complying with dimensional requirements. The team with the highest annual building revenue wins the competition.

4. EXPERIMENTAL SETUP AND TESTING

The ground motions are applied to the structures using an educational UCIST Shake Table II manufactured by Quanser. The table has plan-view dimensions of 457 x 457 mm (18 inch x 18 inch), a mass of 27.2 kg (60 lbf.), and can easily be transported in the trunk of a small car. The shake table operates using an electric motor, power amplifier, and WinCon control software, which interfaces with Matlab. A personal computer is required to operate the shaker. Four accelerometers can be attached to a test specimen and recorded using through the power amplifier. Models were fabricated with a base plate which a hole pattern corresponding to the shake table to allow for bolt attachment to the shake table. The shake table was bolted to a steel fabricated frame and a reaction mass of 204 kg (450 lb) to provide a fixed base reaction for the shake table, as shown in the test setup photograph of Figure 4. The operation PC, amplifier and other equipment were placed away from the direction of shaking, to prevent any damage to these items, or injury to personnel, in the event of a structural collapse. A model ready for testing is shown in Figure 4. Model testing is shown in Figure 5 with excitation of the second mode and in Figure 6 with the structural collapse of a model.

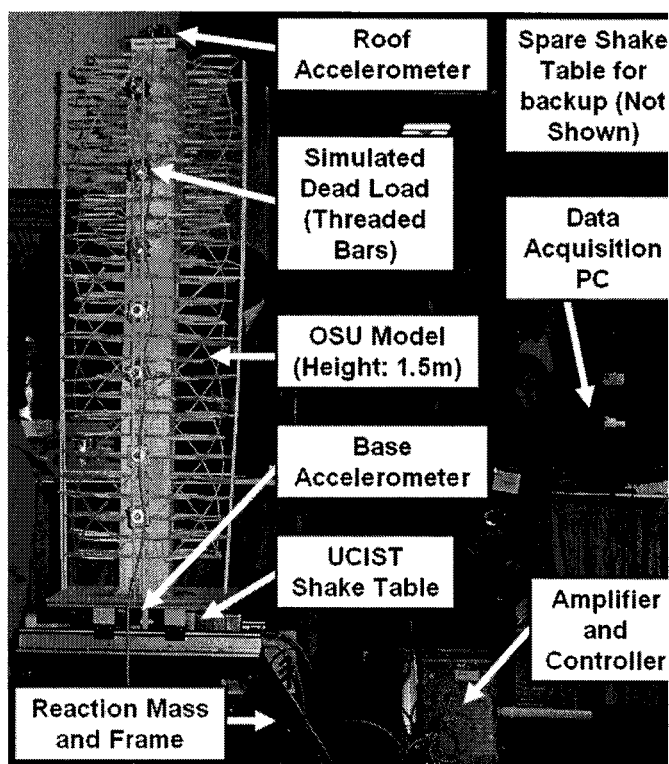


Figure 4. Competition test setup



Figure 5. Model testing underway



Figure 6. Model collapse due to shear failure in the base of the central core strong wall system (OSU model)

Accelerations during shaking are measured at the shake table base and at the roof of the structure. The measured acceleration records are transferred into the frequency domain using a Fourier transform. A third order Butterworth filter with a corner frequency of 0.8 Hz is used to filter the acceleration recordings in the frequency domain. Filtered acceleration records are then double integrated over time to obtain displacements. Data processing is performed using Matlab, and outputs (time series of accelerations and displacements, and computation of structure's score) are organized into html files that are subsequently posted on the SLC website.

A portion of the low frequency range of the raw acceleration signals must be removed using a digital filter prior to double integration because the low frequency content of the signals is small compared with the noise in the signals. Highly unrealistic displacements would be obtained if the raw data were integrated in time without first filtering off some of the low frequency content. An undesired but unavoidable consequence of the filtering is that the low frequency portion of the acceleration signals, which contains permanent displacements, must be removed. As a result, the displacements computed by double-integrating the acceleration records are transient displacements; the low-frequency permanent component is not contained in the computed displacement time series.

5. EDUCATIONAL VALUE AND OUTCOME

The three seismic design competitions held so far have provided a unique learning opportunity for undergraduates throughout the United States. The first PEER competition was held in conjunction with the annual National Science Foundation (NSF) review of the PEER Center. This provided undergraduates the opportunity to interact with PEER graduate students and faculty. The second PEER competition was held in conjunction with the PEER annual research meeting. This provided undergraduates, most of which have been juniors or seniors, the opportunity to attend a portion of the PEER annual research meeting, and to interact with the entire PEER research community. Some of these competing undergraduates have now continued to graduate programs in structural engineering and PEER funded research projects at the graduate level. The third competition, in April of 2006, was held at the Eighth U.S. National Conference on Earthquake Engineering, sponsored by the Earthquake

Engineering Research Institute (EERI). This conference commemorated the 1906 San Francisco Earthquake, and provided undergraduates the opportunity to attend sessions and to interact with industry and academia.

The 2006 competition had teams from: University of Washington (first place); University of California, Berkeley; University of California, Davis; University of California, San Diego; University of Buffalo/State University of New York; University of Hawaii; Georgia Institute of Technology and Oregon State University.

6. CONCLUSION

The undergraduate seismic design competition (1) demonstrated physical aspects of the PEER performance-based earthquake engineering methodology, (2) educated undergraduate students about earthquake engineering and stimulated them to contribute to the profession, and (3) demonstrated the value of PEER's Student Leadership Council representatives and officers. The competition demonstrated the emerging concept of performance based design, which is not yet in the academic curriculum, but making inroads in design practice. The competition provided undergraduates the opportunity to not only enhance their knowledge and interest in seismic design and earthquake engineering, but to also emphasize other skills that are not commonly used in the classroom environment. Those skills include project management, team work, and communication. This competition has provided a unique learning experience for hundreds of competing undergraduates, throughout the U.S., and will continue to do so into the future. The first phase of the competition was developing the rules and requisite software tools. The second phase was to encourage nationwide participation through the three NSF funded earthquake engineering research centers. This has been accomplished through three annual competitions sponsored by PEER, two annual competitions sponsored by MCEER, and team sponsorship from MAE. An additional phase will involve securing funds to allow the competition to grow to the same competitive level as the concrete canoe and steel bridge competitions.

7. REFERENCES

1. American Society of Civil Engineers (2005a). "ASCE National Concrete Canoe Competition." <http://www.asce.org/inside/nccc2006/index.cfm> (Dec. 7, 2005)
2. American Society of Civil Engineers (2005b). "ASCE/AISC Student Steel Bridge Competition." http://www.aisc.org/Content/NavigationMenu/Learning_Opportunities/University_Programs/AISC_Student_Steel_Bridge_Competition/Default329.htm (Dec. 7, 2005).
3. Pacific Earthquake Engineering Research Center Student Leadership Council (2005). "PEER Student Leadership Council (SLC) and PEER Student Association (PSA)." <http://peer.berkeley.edu/students/> (Dec 7, 2005).
4. Porter, K.A. (2003). "An Overview of PEER's Performance-Based Earthquake Engineering Methodology." *Proc. Ninth International Conference on Applications of Statistics and Probability in Civil Engineering (ICASP9)*. July 6-8, San Francisco, CA.

A PRACTICE OF INTERNATIONAL DISTANCE LECTURE AMONG THREE UNIVERSITIES THROUGH THE INTERNET

H. Morikawa¹⁾, Anat Ruangrassamee²⁾, and H.-T. Chen³⁾

1) Associate Professor, Department of Built Environment, Tokyo Institute of Technology, Japan

2) Assistant Professor, Department of Civil Engineering, Chulalongkorn University, Thailand

3) Associate Professor, Department of Civil Engineering, National Central University, Taiwan

morika@enveng.titech.ac.jp, fcearr@eng.chula.ac.th, chenhtofpadau@seed.net.tw

Abstract: We introduce the distance learning course through the Internet for the lecture entitled “Earthquake and Tsunami Disaster Reduction.” First, we outline the course and the system. Then, on the basis of our experiences, some instructive topics are listed to perform this kind of international distance lecture.

1. INTRODUCTION

The great Sumatra Earthquake ($M_w 9.0$) of December 26th, 2004 brought destructive damage to the countries around the Indian Ocean. After this poignant experience, we realized the importance of the appropriate knowledge on the earthquake and Tsunami disaster again. Thus, in March 2005, a mission team of the Center for Urban Earthquake Engineering (CUEE), Tokyo Institute Technology made a proposal on a distance learning (D-learning) program for graduate students in Asian countries.

For the first year, 2005, we only offered the D-learning course between Chulalongkorn university (CU), Thailand and Tokyo Institute of Technology (Tokyo Tech), Japan. Despite facing many difficulties, we learned many things with respect to the international joint course, enabling us to include the National Central University (NCU), Taiwan, R.O.C. as the new counterpart for the international course for the semester of 2006-2007.

In this short report, we will describe the outline of the course and some typical problems encountered in this kind of international course.

2. OUTLINE OF THE D-LEARNING COURSE

2.1 Contents and Lecture Arrangement

With the above-mentioned aim in mind, the course is entitled “Earthquake and Tsunami Disaster Reduction.” The contents include the following seven topics and 90-minute lectures are carried out every week for seven weeks:

- Earthquake Ground Motion (Dr. Yamanaka)
- Earthquake-induced Disaster (Dr. Seo)
- Tsunami Science (Dr. Ohmachi)
- Risk Management (Dr. Morikawa)
- Real-time Information (Dr. Midorikawa)

- Earthquake Hazard Mitigation (Dr. Kasai)
- Tsunami Hazard Mitigation (Dr. Hiraishi)

For the semester of 2006-2007, three universities were involved, and we encountered difficulty in arranging lecture hour due to the fact that three universities have different starting date of semester and holidays and furthermore we have to consider the time difference among the three countries: +0700 in Thailand, +0800 in Taiwan, and +0900 in Japan. As a result, the class hour was set to be in the Friday afternoon for seven weeks, starting 13:00 in Thailand, 14:00 in Taiwan and 15:00 in Japan, respectively.

Figure 1 shows the lecture rooms for the D-learning system in each university. Regularly, more than 30 students and academic staffs attended the course from the three universities. Since the students are generally shy, they make few questions. The Q&A session can become more active if we contrive a good atmosphere for students to speak something, for example, we implement such a Q&A web-board.

2.2 System

We used the Internet TV conference system, which was produced by Polycom. In the first season, it was not so difficult to connect between CU and Tokyo Tech, because the system can be used under the default configurations.

At the end of December, 2005, a new broad band connection was made available between Thailand and Japan, which is named Japan Gigabit Network 2 (JGN2), and we changed the route for the packets. However, because of the security policy, the network operation center at CU did not agree to change the configuration of route and their firewall in that time. Consequently, the packets from Japan to Thailand went through JGN2, but the packets came back via another way (maybe, USA). Even so, the round trip time (RTT) was reduced to about 100ms from 200ms after the opening of JGN2 and we can obtain enough quality for not only the video image and voice but also the animation on PC.

In the second season, originally we planned to deliver the lectures from Suzukake-dai campus of Tokyo Tech to CU, NCU, and Oo-okayma campus of Tokyo Tech. This means that we have to acquire the multi-site connection. The system at Tokyo Tech cannot complete the multi-site connection if the first connection is not established from the system at Tokyo Tech to the remote system. Unfortunately, since a port is blocked by the firewall at CU, the system of Tokyo Tech cannot be used as the server for the multi-site connection. This was very serious problem for our projects.

However, to avoid this problem, we concentrated the packets for the TV conference to the “gate keeper” at NCU and then, the packets were re-distributed to CU and Tokyo Tech. With this, the packets did not pass through JGN2. Although the connection is not so broad as before, it was much better than no connection. Figure 2 shows a scene of the multi-site connection.

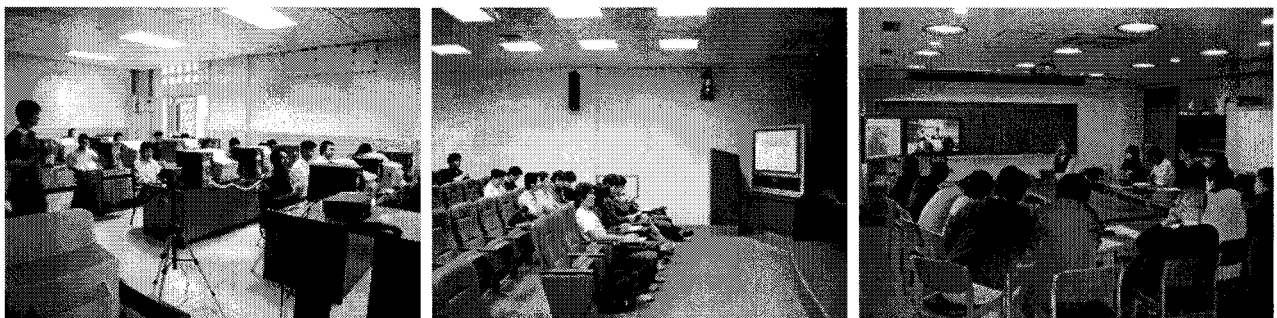


Figure 1 The lecture room for the D-learning system. From left to right, CU, NCU, and Tokyo Tech.



Figure2 A scene of multi-site connection. In this photo, four sites are shown in one screen. From upper left to lower right, NCU, Suzukake-dai campus and Oo-okayama campus of Tokyo Tech, and CU.

In the end of 2006, a slightly big earthquake hit Southern Taiwan, damaging many submarine cables between Taiwan and Thailand or Taiwan and Japan. After that event, JGN2 was down for long time and it was very difficult to keep the broad connection among three universities. At the final lecture on the first week of January, 2007, the quality of the video and voice was very poor; furthermore, the connection was sometimes lost and it was difficult to communicate smoothly.

2.3 Review

After the first season, we sent a questionnaire sheet to the students of CU and asked their comments on the course. The results of the questionnaire survey are shown in Figure 3.

Generally speaking, they are satisfied with the course, deeming that it provided a good opportunity for foreign students to communicate with each other. Usually, they know only their own university, but to catch a glimpse of the atmosphere of foreign university is a good experience.

3. PROBLEMS FOR THE INTERNATIONAL D-LEARNING PROGRAM

Through our experiences, we will list the typical problems to perform this kind of international D-learning program.

- Time difference:

The office hour is different at different countries. We should deliver the lecture during the mutual time in the office hour. Under this situation, to keep the 90-minute time frame is very difficult. We, furthermore, have to consider the time differences. The maximum of the time difference is two hour to find the appropriate time frame for the lecture. This means that this kind of project should be performed among not so distant countries.

- Difference in semester system and vacation season:

These are also very different at different countries. In our case, for example, the first date of the autumn semester is different one month between NCU (September) and Tokyo Tech (October) and further one month between Tokyo Tech and CU (November). Thus, the maximum weeks for the lecture should be less than six or seven. If it is needed more weeks, we may have to consider a kind of the intensive course.

- Difference in the credit and grading system:

To give students an incentive, the credit must be effective. However, the credit and grading system is very different for different countries. It is very difficult for the D-learning class to be a regular course. In our case, the D-learning class is included in a regular course at CU and NCU.

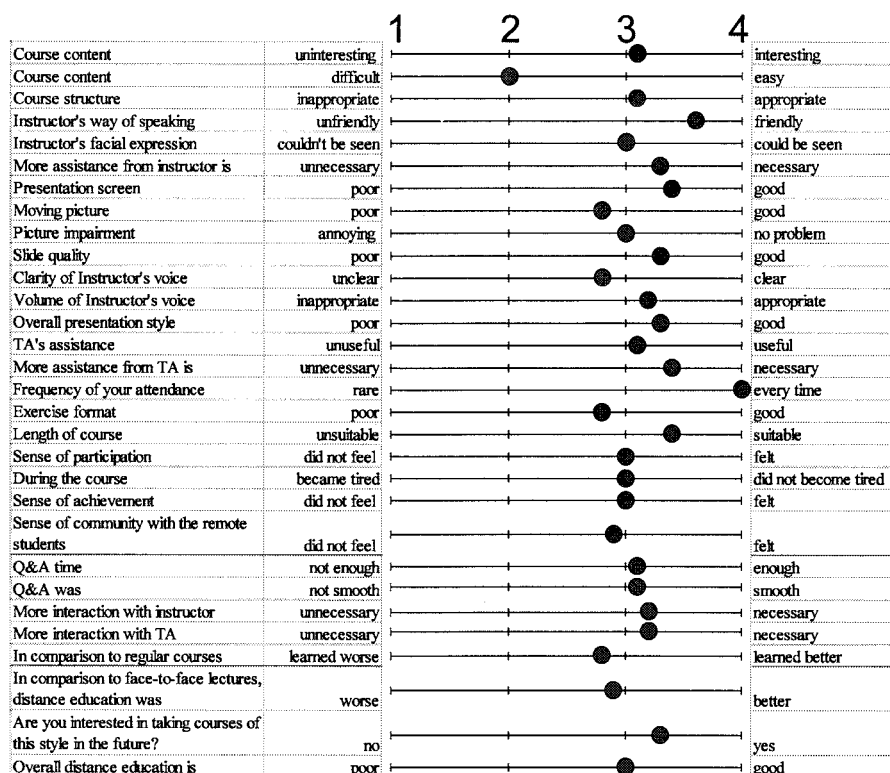


Figure 3 Results of the questionnaire survey for the first-season students of CU. The standard questionnaire sheet for D-learning course is provided from the Center for Research and Development of Educational technology, Tokyo Tech.

- Compatibility of the system:

There is the standard for the video conference, but the compatibility is usually not supported between the systems produced by different companies.

- Difference in the security policy for the network operation:

Usually, the configuration of the firewall is not changed. In a case where the Internet is used for the D-learning class, a firewall system may block the packets. This means that we cannot establish the connection sometimes.

- Operators with enough skill with respect to the network system:

To make the trouble shooting, the person concerned should have enough knowledge about the network system and operation. If the person does not have enough skill, the support by a specialist will play a very important role. Furthermore, if the operation depends on a particular person, the project cannot continue without him.

- Constant co-operation and communication:

To keep and continue this kind of project, the most important thing is the mutual reliance and frequent communications. Of course, people know this, but this is also the most difficult task to execute. After losing the communication, the project will be discontinued easily.

Acknowledgments:

The authors wish to thank Prof. Panitan Lukkumaprasit of Chulalongkorn University and Prof. Tatsuo Ohmachi of Tokyo Institute of Technology for their kindness and leadership to continue this project. Furthermore, we gratefully acknowledge the warmest support for this project with the following people: Prof. A. Nishihara of Center for Research and Development of Educational technology, Tokyo Tech; Dr. M. Kakuta, Dr. K. Iida, and Dr. S. Shinomiya of the Network Operation Center, Tokyo Tech; Mr. Chanin Maharak and Mr. Sanya Vasoppakarn of CU; Mr. Where Paul of Computer Center, NCU.

COMMUNICATION AND ENGINEERING MANAGEMENT FOR THE GLOBAL ENGINEER

K. Shankar¹⁾, and K. Tokimatsu²⁾

1) Lecturer, Center for Urban Earthquake Engineering, Tokyo Institute of Technology, Japan

*2) Professor, Dept. of Architecture and Building Engineering, Tokyo Institute of Technology, Japan
kirthana.s@cuee.titech.ac.jp, kohji@o.cc.titech.ac.jp*

Abstract: This paper presents the integration of a Communication and Engineering Management course into the Engineering curriculum at the Tokyo Institute of Technology under the Center of Urban Earthquake Engineering (CUEE) to meet the needs of Global Engineers. Two innovative courses, Advanced Technical and Communication Skills (ATCS) 61062 & 61063 have been introduced into CUEE curriculum to equip post-graduate engineering students with effective Communication and Engineering Management skills.

1. INTRODUCTION

Success in any field today is linked to *People Management*. The clarion is to develop human capital for extraordinary gains. In such a turbulent, ever-changing global economy, it has become essential for engineers to be effective at understanding the significance of Communication and Engineering Management. In Japan, while Engineering faculties have a fine record of accomplishments and have adapted well to rapid changes in science and technology, increasing pressures and challenges arising from the broadening of roles that engineers fill has brought forth the importance of Engineers in Japan to be equipped with not only traditional technical skills called hard skills but also with non technical skills often called soft skills.

The rapid advancement in globalization requires global awareness and internationalized communication skills for success in the current international business world. It has become a requirement for engineers to have a global perceptive and an understanding of the requirements of being a Global Engineer. In the context of building Global Engineers, we mean educating engineers with a global mindset to improve their Global Competency. This can be done in many ways and a university can play a vital role in creating programs that provide engineers with a good understanding of global engineering management, culture, communication and collaboration.

Globalization directly influences industry needs and global engineers must be able to cross national and cultural boundaries. The focus towards building Global Engineers in an organization has become essential with the expectation and belief that

good communication and management skills will lead to successful International projects. To meet the Communication and Engineering Management needs of the engineering students, The Center for Urban Earthquake Engineering (CUEE) established on September 1, 2003, to carry out the 21st Century Center of Excellence (COE) program, at Tokyo Institute of Technology offers two courses, *Advanced Technical and Communication Skills (ATCS)* 61062 & 61063 for post-doctoral and doctoral Students from the Engineering school with the aim to develop broad based soft-skills.

2. ADVANCED TECHNICAL AND COMMUNICATION SKILLS, 61062 & 61063 - AN OVERVIEW

One of the mission's of the Center of Urban Earthquake Engineering (CUEE) was to foster ability in international communication and management, teaching, research, creativity, and practice for doctoral and post-doctoral fellows. The objective of the two courses, ATCS 61062 & 61063 was to provide engineering students with concepts and theories which will enable them to understand the dynamics of Communication and Engineering Management from a global perspective and to prepare them to effectively use these skills. Since April 2004, The Center for Urban Earthquake Engineering at the Tokyo Institute of Technology has introduced ATCS 61062 & 61063 courses in its curriculum structure. A draw card of the courses is the variety of topics across dynamic fields that are being addressed. The courses provide a forum for interactive learning and demand a high level of person to person communication and interaction. Each course offers 4 units of credits. The grading for the courses is based on group oral presentation, individual essay, business case study and class participation. At present CUEE has the sixth batch of students who have been enrolled into the course. The two courses are taught by Ms. Kirthana Shankar and the course coordinators are Prof Kohji Tokimatsu and Prof Osamu Kusakabe.

There are many topics that are integrated within the two courses which are investigated through critical examination of relevant literature, documented case studies and contemporary business practices. Some of the topics that are covered in the courses are:

ATCS 61062	ATCS 61063
Engineering Communication	Business Skills
Creative and Critical Thinking	Leadership Training
Technical and Business Writing	Personality Profiling
Presentation Skills	Stress Management
Cross Cultural Communication	Team Building

3. VALUE PROPOSITION

For the above courses to appeal to the Engineering students and the Engineering faculty, good comprehension of the real value proposition is required.

Suggested value propositions for students, faculty, and industry are listed below:

Value to Students	Value to Engineering Faculty	Value to Industry
Better Career potential	Help to Remain competitive	Global engineers
Being Globally competitive	Enhance industry connections	Reduce “in-company” training
Creation of new opportunity	Expand Global Network	Enhance company’s competitiveness

4. OUTCOMES AND ASSESSMENT INSTRUMENTS

To make progress in the two courses offered and taught, it is a requirement to benchmark and assess the outcomes for the continuous improvement of the courses. Upon completion of the courses, students attain:

- Improved communication skills
- Global Management and Business Skills
- Ability to function on multi-disciplinary teams
- Ability to adapt to new environments
- Cross-cultural fluency
- Ability to produce professional caliber technical documents
- Increased disposition to work in global economy

The lecturer for the two courses uses formal and informal student feedback in an ongoing basis to help plan instruction and assessment of student learning throughout the semester. The following assessment instruments were used as ways to evaluate the courses outcomes.

- Student reports/presentations and surveys
- Industry feedback
- Student enrollments
- Anecdotes

5. CONCLUSION

Importance of good communication and management skills as vital tools for engineering graduates has become eminent in today’s globally competitive workplace. In order to foster ability in communication and engineering management, for doctoral and post-doctoral fellows, the CUEE education program had found the necessity to design and offer ATCS 61062 & 61063 courses to help the students to meet the global engineering needs. The course has proven to be very successful at generating excitement and enthusiasm and has instilled great self-confidence in students.

6. ACKNOWLEDGEMENTS

The authors would like to express their gratitude to the Center for Urban Earthquake Engineering of the Tokyo Institute of Technology for the encouragement and the support for the new courses.

